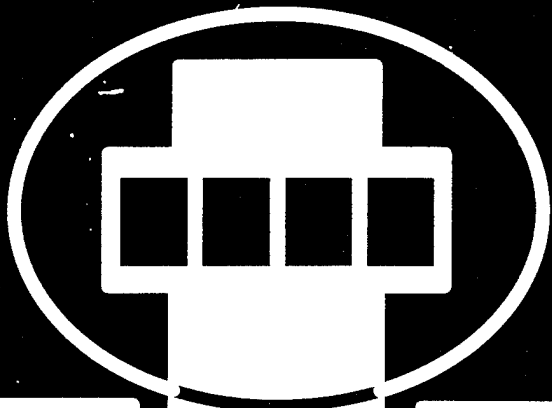


**Proceedings of the 1995
Particle Accelerator Conference
and International Conference
on High-Energy Accelerators**



PROCEEDINGS OF THE 1995
PARTICLE ACCELERATOR CONFERENCE
AND INTERNATIONAL CONFERENCE
ON HIGH-ENERGY ACCELERATORS





The
American
Physical
Society

Proceedings of the 1995 Particle Accelerator Conference

N00014-95-1-0791

Volume 3 of 5

Papers from the sixteenth biennial Particle Accelerator Conference, an international forum on accelerator science and technology held May 1-5, 1995, in Dallas, Texas, organized by Los Alamos National Laboratory (LANL) and Stanford Linear Accelerator Center (SLAC), jointly sponsored by the Institute of Electrical and Electronics Engineers (IEEE) Nuclear and Plasma Sciences Society (NPSS), the American Physical Society (APS) Division of Particles and Beams (DPB), and the International Union of Pure and Applied Physics (IUPAP), and conducted with support from the US Department of Energy, the National Science Foundation, and the Office of Naval Research.

19960705 129

PROCEEDINGS OF THE 1995 PARTICLE ACCELERATOR CONFERENCE

Abstracting is permitted with credit to the source. Libraries are permitted to photocopy beyond the limits of U. S. copyright law for private use of patrons those articles in this volume that carry a code at the bottom of the first page, provided the per-copy fee indicated in the code is paid through the Copyright Clearance Center, 222 Rosewood Drive, Danvers, MA 01923. Instructors are permitted to photocopy isolated articles for noncommercial classroom use without fee. For other copying, reprint, or republication permission, write to the IEEE Copyright Manager, IEEE Operations Center, 445 Hoes Lane, Piscataway, NJ 08855-1331. All rights reserved. Copyright © 1996 by the Institute of Electrical and Electronic Engineers, Inc.

IEEE Catalog Number: 95CH35843 (softbound)
95CB35843 (casebound)

Library of Congress Number: 88-647453

ISBN Softbound: 0-7803-2934-1
ISBN Casebound: 0-7803-2935-X
ISBN Microfiche: 0-7803-2936-8
ISBN CD-ROM: 0-7803-2937-6

Additional copies of this publication are available from

IEEE Operations Center
445 Hoes Lane
P. O. Box 1331
Piscataway, NJ 08855-1331 USA

Phone: 1-800-678-IEEE (1-800-678-4333)
1-908-981-1393
FAX: 1-908-981-9667
Telex: 833-233
e-mail: customer.service@ieee.org

The CD-ROM version is available from

Dan Rusthoy, PAC95 Treasurer
Los Alamos National Laboratory
P. O. Box 1663 - M/S H811
Los Alamos, NM 87545 USA

Phone: 505-667-2796
FAX: 505-667-0919
e-mail: drusthoy@lanl.gov

Volume 1

Plenary and Special Sessions

CEBAF Commissioning and Future Plans (<i>Invited</i>) — Hermann A. Grunder.....	1	MAD01
The Advanced Photon Source (<i>Invited</i>) — John N. Galayda.....	4	MAD02
Commissioning and Performance of the HIMAC Medical Accelerator (<i>Invited</i>) — S. Yamada.....	9	MAD03
Accelerator Field Development at Novosibirsk (History, Status, Prospects) (<i>Invited</i>) — A. Skrinsky.....	14	MAD04
A Personal Perspective of High Energy Accelerators (<i>Invited</i>) — Gustav-Adolf Voss.....	27	FPD01
Photon-Photon Colliders (<i>Invited</i>) — Andrew M. Sessler.....	30	FPD02
Transmutation and Energy Production with High Power Accelerators (<i>Invited</i>) — G.P. Lawrence.....	35	FPD03
The Large Hadron Collider (<i>Invited</i>) — L.R. Evans.....	40	FPD04
Frontiers of Particle Physics (<i>Invited</i>) — L. Okun.....	45	FPD05
R. R. Wilson Prize Lecture: Pretzels (<i>Invited</i>) — R. Littauer.....	manuscript not submitted	MXG01
Experimental Studies of Longitudinal Dynamics of Space-Charge Dominated Electron Beams (<i>Invited</i>) — D.X. Wang.....	48	MXG02
High-Energy High-Luminosity $\mu^+ \mu^-$ Collider Design (<i>Invited</i>) — Robert B. Palmer, Richard Fernow, Juan C. Gallardo, Y.Y. Lee, Yagmur Torun, David Neuffer, David Winn.....	53	MXG03
Cosmic Acceleration Mechanisms (<i>Invited</i>) — J. Arons.....	manuscript not submitted	MXG04

Accelerator Applications

Hadron Particle Therapy (<i>Invited</i>) — Jose R. Alonso.....	58	WPE01
Micromechanics via Synchrotron Radiation (<i>Invited</i>) — H. Guckel.....	63	WPE02
Radionuclide Production for the Biosciences (<i>Invited</i>) — Thomas J. Ruth.....	67	WPE03
X-Ray Lithography - Status and Projected Use (<i>Invited</i>) — W.A. Johnson.....	manuscript not submitted	WPE04
Microelectronic Applications for RF Sources and Accelerators (<i>Invited</i>) — Cha-Mei Tang.....	70	WPE05
A High-Gradient Electron Injector to an X-Ray Lithography Ring (<i>Invited</i>) — D. Yu.....	manuscript not submitted	FAG01
X-Ray Holography (<i>Invited</i>) — I. McNulty.....	manuscript not submitted	FAG02
Medical and Surgical Applications of FELs (<i>Invited</i>) — Benedikt Jean.....	75	FAG03
Medical Uses of Monochromatic X-Rays (<i>Invited</i>) — Frank E. Carroll.....	80	FAG04
Texas Regional Medical Technology Center — R. Sah, T.D. Cain, E.K. Cleveland, K. Saadatmand, M.E. Schulze, R.A. Winje.....	83	FAG05
A Proposed 100-400 MeV Beam Facility at Fermilab — C. Johnstone, C. Ankenbrandt, S. Bjerklie, D. Boehnlein, M. Foley, T. Kroc, J. Lackey, A. Lennox, A. Leveling, E. McCrory, M. Popovic, C. Schmidt, K. Vaziri.....	86	FAG06
Cyclotrons for Isotope Production — B.F. Milton, N.R. Stevenson.....	89	FAG07
European Heavy Ion ICF Driver Development — G. Plass.....	92	FAG08
A 3-Stage Cyclotron Complex for Driving the Energy Amplifier — P. Mandrillon, N. Fietier, C. Rubbia.....	95	FAG09
Accelerator-Based Gamma Neutron Transmutation of Radionuclides as a New Technology for the Nuclear Fuel Cycle — I.P. Ereameev.....	98	FAG10
A High-Average-Power FEL for Industrial Applications — H.F. Dylla, S. Benson, J. Bisognano, C.L. Bohn, L. Cardman, D. Engwall, J. Fugitt, K. Jordan, D. Kehne, Z. Li, H. Liu, L. Merminga, G.R. Neil, D. Neuffer, M. Shinn, C. Sinclair, M. Wiseman, L.J. Brillson, D.P. Henkel, H. Helvajian, M.J. Kelley.....	102	FAG11
X-Ray Radiation by Relativistic Electrons in Condensed Media on Base of MSU Race-Track Microtron — V.K. Grishin, A.S. Chepurinov, K.A. Gudkov, B.S. Ishkhanov, S.A. Kosterin, E.V. Lasutin, S.V. Blazhevich, N.N. Nasonov.....	105	FAG12
Applications of MeV Proton and Deuteron Linear Accelerators — George H. Gillespie, Gerald E. McMichael.....	107	FAG13
Accelerator Requirements for Fast-Neutron Interrogation of Luggage and Cargo — B.J. Micklich, C.L. Fink, T.J. Yule.....	110	FAG14

Energy Varying Resonant Beam Extraction from the Synchrotron — K. Hiramoto, M. Tadokoro, J.I. Hirota, M. Nishi, K. Noda.....	113	TAB03
Radiotherapy Process Integration Using a Compact Photon Source Together with Fluence Control and Patient Imaging — D. Tronc, F. Dugardin, J.P. Georges, R. Letoumelin, J.L. Pourre.....	116	TAB04
A 1.5 GeV Compact Light Source with Superconducting Bending Magnets — A.A. Garren, D.B. Cline, M.A. Green, D.E. Johnson, J.J. Kolonko, E.M. Leung, D.D. Madura, L.C. Schachinger.....	119	TAB06
Applications of Industrial Electron Accelerators at Samsung Heavy Industries — Bumsoo Han, Keeman Kim, Kihun Joh, Sungmyun Kim, Byungmun Kim, Heunggyu Park, Jongpil Park, Jinsoo Kim, Wongu Kang, Kyungwoo Kang, Yuri Kim, Sangil Lee, Younghee Kim	122	TAB09
Application of Accelerated Electron Beams for Rubber and Polymer Modification — A. Shalnov, B.Yu. Bogdanovich, A. Ignatyev, V. Senyukov.....	125	TAB13
Status on Low Energy (10 MeV Range) X-band Linacs Developed Worldwide — A.V. Michine.....	128	TAB15
Linear Accelerator for Radiation Chemistry Research at Notre Dame — K. Whitham, S. Lyons, R. Miller, D. Nett, P. Treas, A. Zante, R.W. Fessenden, M.D. Thomas, Y. Wang.....	131	TAB17
IREN Status: New Electron Linac Driven Intense Resonance Neutron Source — A. Krasnykh.....	134	TAC01
A Cost Estimation Model for High Power FELs — George R. Neil	137	TAC03
Details of the Initial Part of the Tungsten Ion Linac for Particle Track Membranes Production — V. Kushin, T. Kulevoy, N. Nesterov, A. Oreshnikov, S. Plotnikov, D. Seleznev, V. Zubovskiy.....	140	TAC05
A Series of Ion Accelerators for Industry — B.N. Sukhina, N.I. Alinovsky, I.L. Chertok, S.N. Chumakov, N.S. Dikansky, A.D. Goncharov	143	TAC06
A Pulsed Source of Neutron Focus for Fundamental and Applied Research in High-Energy Electron Accelerator Centres — I.P. Ereemeev.....	146	TAC11
Moderator/Collimator for a Proton/Deuteron Linac to Produce a High-Intensity, High- Quality Thermal Neutron Beam for Neutron Radiography — R.C. Singleterry Jr., G.R. Imel, G.E. McMichael	149	TAC12
Experimental Set-up for Multiplication Coefficient Fluctuation Study vs Accelerator Parameter Deviations on the JINR Pulsed Accelerator Driven Neutron Source — V. Belkovets, A. Ivanov, A. Kaminsky, A. Krasnykh, N. Malakhov, L. Menshikov, Yu. Popov, V. Piataev, N. Pilyar, V. Rudenko, L. Somov, A. Sumbaev, V. Tarabrin.....	152	TAC16

Synchrotron Light Sources and Free Electron Lasers

European Synchrotron Radiation Storage Rings (Invited) — H. Zyngier.....	155	TPG01
Development of the JAERI FEL Driven by a Superconducting Accelerator (Invited) — E.J. Minehara, M. Sugimoto, M. Sawamura, R. Nagai, N. Kikuzawa.....	159	TPG02
Status of New Light Sources in Russia (Invited) — G. Kulipanov.....	manuscript not submitted	TPG03
Free Electron Laser Research in China (Invited) — Jialin Xie.....	162	TPG04
Accelerator Physics Trends at the ESRF — A. Ropert, L. Farvacque, J. Jacob, J.L. Laclare, E. Plouviez, J.L. Revol, K. Scheidt	167	TPG05
Commissioning of the PLS 2 GeV Storage Ring — M. Yoon, J.Y. Huang, J.S. Jang, M. Kwon, T. Lee, S.H. Nam.....	171	TPG06
Femtosecond X-Rays from 90° Thomson Scattering — W. Leemans, R. Schoenlein, A. Chin, E. Glover, R. Govil, P. Volfbeyn, S. Chattopadhyay, K.-J. Kim, C.V. Schank.....	174	TPG07
Design of a Diffraction Limited Light Source (DIFL) — D. Einfeld, J. Schaper, M. Plesko	177	TPG08
Updated Plans for DIAMOND, a New X-ray Light Source for the UK — V.P. Suller, J.A. Clarke, J.B. Fitzgerald, H.L. Owen, M.W. Poole, X. Queralt, S.L. Smith.....	180	TPG09
Design Optimization for an X-Ray Free Electron Laser Driven by SLAC Linac — Ming Xie.....	183	TPG10

The FERMI FEL Project at Trieste — <i>D. Bulfone, F. Cargnello, G. D'Auria, F. Daclon, M. Ferianis, M. Giannini, G. Margaritondo, A. Massarotti, A. Rindi, R. Rosei, C. Rubbia, R. Visintini, R.P. Walker, A. Wrulich, D. Zangrando, F. Ciocci, G. Dattoli, A. De Angelis, A. Dipace, A. Doria, G.P. Gallerano, F. Garosi, L. Giannessi, E. Giovenale, L. Mezi, P.L. Ottaviani, A. Renieri, E. Sabia, A. Segreto, A. Torre, M. Castellano, P. Patteri, S. Tazzari, F. Tazzioli, F. Cevenini, A. Cutolo</i>	186	TPG11
Studies on a Free Electron Laser for the TESLA Test Facility — <i>J. Rossbach</i>	189	TPG12
MIT Microwiggler for Free Electron Laser Applications — <i>P. Catravas, R. Stoner, J. Blastos, D. Sisson, I. Mastovsky, G. Bekefi, X.-J. Wang, A. Fisher</i>	192	TPG14
DORIS III as a Dedicated Source for Synchrotron Radiation — <i>H. Neesemann, W. Brefeld, F. Brinker, W. Decking, O. Kaul, B. Sarau</i>	195	FAA02
Beam Lifetime and Beam Brightness in ALS — <i>C. Kim, A. Jackson, A. Warwick</i>	198	FAA03
Asynchronous Energy Ramping at SRRC Storage Ring — <i>Gwo-Huei Luo, L.H. Chang, Y. Cheng, K.T. Hsu, C.C. Kuo, W.C. Lau, Ch. Wang, P.K. Tseng, Y.C. Liu</i>	201	FAA04
Emittance Measurements in the ALS Booster Synchrotron — <i>D. Massoletti, C.H. Kim, A. Jackson</i>	204	FAA05
Compton Scattering in the ALS Booster — <i>D. Robin, C. Kim, A. Sessler</i>	207	FAA06
Beam Stability at SRRC Storage Ring — <i>W.T. Weng, H.P. Chang, J.R. Chen, Y. Cheng, K.T. Hsu, C.C. Kuo, J.C. Lee, K.K. Lin, Y.C. Liu, G.H. Luo, K.L. Tsang</i>	210	FAA07
Commissioning of the Duke Storage Ring — <i>V.N. Litvinenko, Y. Wu, B. Burnham, J.M.J. Madey, F. Carter, C. Dickey, M. Emamian, J. Gustavsson, N. Hower, P. Morcombe, S.H. Park, P. O'Shea, R. Sachtshale, D. Straub, G. Swift, P. Wang, J. Widgren</i>	213	FAA08
Pulsed VUV Synchrotron Radiation Source — <i>S.H. Kim, Y.S. Cho, T.Y. Kim, K.H. Chung</i>	216	FAA10
Merits of a Sub-Harmonic Approach to a Single-Pass, 1.5-Å FEL — <i>W.M. Fawley, H.-D. Nuhn, R. Bonifacio, E.T. Scharlemann</i>	219	FAA12
Operation of the ELETTRA Injection Linac in the FEL Mode — <i>G. D'Auria, C.J. Bocchetta, M. Plesko, C. Rossi, L. Tosi, R.P. Walker, A. Wrulich</i>	222	FAA13
Free Electron Laser - FEL - Study in Institute of Nuclear Physics of MSU — <i>V.K. Grishin, B.S. Ishkhanov, T.A. Novikova, V.I. Shvedunov</i>	225	FAA14
A Chirped-Pulse Regenerative-Amplifier FEL for the Gamma-Gamma Collider — <i>K.C.D. Chan, J.C. Goldstein, D.C. Nguyen, H. Takeda</i>	228	FAA16
Alignment and Magnet Error Tolerances for the LCLS X-Ray FEL — <i>H.-D. Nuhn, E.T. Scharlemann, R. Schlüter</i>	231	FAA17
Electron Transport and Emittance Diagnostics in CIRFEL — <i>J. Krishnaswamy, I.S. Lehrman, R. Hartley, R.H. Austin</i>	234	FAA19
Study on Accelerator Noise Effects on a Far-Infrared FEL Oscillator — <i>Shinian Fu, Yinbao Chen, Zhibin Huang</i>	237	FAA21
Status of the UCLA High-Gain Infrared Free Electron Laser — <i>M. Hogan, C. Pellegrini, J. Rosenzweig, G. Travish, A. Varfolomeev</i>	240	FAA23
Accelerator Design for the High-Power Industrial FEL — <i>D.V. Neuffer, S. Benson, J. Bisognano, D. Douglas, H.F. Dylla, D. Kehne, J. Fugitt, K. Jordan, Z. Li, H.-X. Liu, L. Merminga, G. Neil, M. Shinn, C. Sinclair, M. Wiseman, M. Cornacchia</i>	243	FAA25
Free Electron Laser Amplifier Experiment Based on 3.5 MeV Linear Induction Accelerator — <i>Ding Bainan, Deng Jianjun, Hu Shenzong, Shi Jinsui, Zhu Wenjun, Li Qing, He Yi</i>	246	FAA26
A High Duty Factor Electron Linac for FEL — <i>T.D. Hayward, D.H. Dowell, A.M. Vetter, C. Lancaster, L. Milliman, D. Smith, J. Adamski, C. Parazzoli</i>	248	FAA27
A Kilowatt Class Visible Free Electron Laser Facility — <i>J.L. Adamski, D.H. Dowell, T.D. Hayward, C.G. Parazzoli, A.M. Vetter</i>	251	FAA28
Self-Consistent Analysis of Radiation and Relativistic Electron Beam Dynamics in a Helical Wiggler Using Lienard-Wiechert Fields — <i>M. Tecimer, L.R. Elias</i>	254	FAA29
First Lasings at Visible and IR Range of Linac-Based FELs at the FELI — <i>T. Tomimasu, E. Oshita, S. Okuma, K. Wakita, K. Saeki, A. Zako, T. Suzuki, Y. Miyauchi, A. Koga, S. Nishihara, A. Nagai, E. Tongu, K. Wakisaka, A. Kobayashi, M. Yasumoto</i>	257	FAA30
The Northrop Grumman Compact Infrared FEL (CIRFEL) — <i>I.S. Lehrman, J. Krishnaswamy, R.A. Hartley, R.H. Austin</i>	260	FAA31
A Proposed NSLS X-Ray Ring Upgrade Using B Factory Technology — <i>E.B. Blum</i>	263	FAR01
A Low Emittance Lattice for the NSLS X-Ray Ring — <i>J. Safranek</i>	266	FAR02

Design of a 1.2 GeV Synchrotron Light Source for X-Ray Lithography at Samsung Heavy Industries — Keeman Kim, Bumsoo Han, Kihun Joh, Sungmyun Kim, Byungmun Kim, Heunggyu Park, Jongpil Park, Jinsoo Kim, Wongu Kang, Kyungwoo Kang, Yuri Kim, Sangil Lee, Younghee Kim.....	269	FAR03
ANKA, A Synchrotron Light Source for Microstructure Fabrication and Analysis — H.O. Moser, M. Ballauff, V. Bechtold, H. Bertagnolli, J. Bialy, P. v. Blanckenhagen, C. Bocchetta, W. Bothe, C. Coluzza, A.N. Danilewsky, K.D. Eichhorn, B. Eigenmann, D. Einfeld, L. Friedrich, M. Haller, N. Holtkamp, V. Honecker, K. Hümmer, E. Huttel, J. Jacob, V. Kashikin, J. Kircher, H. Klewe-Nebenius, A. Knöchel, A. Krüssel, G. Kumpe, K.D. Möller, J. Mohr, M. Nagaenko, F.J. Pantenburg, M. Plesko, J. Schaper, K. Schlösser, G. Schulz, S. Schuppler, H. Schweickert, I. Seidel, Y. Severgin, I. Shukeilo, L. Steinbock, R. Steininger, M. Svandrlík, G. Williams, K. Wilson, J. Zegenhagen.....	272	FAR06
An Undulator at PETRA II - A New Synchrotron Radiation Source at DESY — K. Balewski, W. Brefeld, U. Hahn, J. Pflüger, R. Rossmanith.....	275	FAR07
Electron Storage Ring, KSR for Light Source with Synchrotron Radiation — A. Noda, H. Dewa, H. Fujita, M. Ikegami, Y. Iwashita, S. Kakigi, M. Kando, K. Mashiko, H. Okamoto, T. Shirai, M. Inoue.....	278	FAR08
A Lattice for the Future Project of VUV and Soft X-Ray High Brilliant Light Source — H. Takaki, Y. Kobayashi, K. Matsuda, Y. Kamiya.....	281	FAR09
Millimeter Wave Coherent Synchrotron Radiation in a Compact Electron Storage Ring — J.B. Murphy, E. Blum, R. Heese, J. Keane, S. Krinsky.....	284	FAR10
Commissioning of the Argonne Positron Accumulator Ring — M. Borland.....	287	FAR11
APS Storage Ring Commissioning and Early Operational Experience — G. Decker.....	290	FAR13
New Specifications for the SOLEIL Project — M.-P. Level, P. Brunelle, A. Nadjí, M. Sommer, H. Zyngier, J. Faure, P. Nghiem, J. Payet, A. Tkatchenko.....	293	FAR14
A Combined Magnet Lattice of the Synchrotron Light Source ISI-800 — I. Karnaukhov, S. Kononenko, A. Shcherbakov, V. Nemoshkalenko, V. Molodkin, A. Shpak.....	296	FAR16
Progress of the ISI-800 Project — E. Bulyak, S. Efimov, A. Gevchuk, P. Gladkikh, I. Karnaukhov, S. Kononenko, V. Kozin, V. Markov, N. Mocheshnikov, A. Mytsykov, A. Shcherbakov, Yu. Telegin, A. Zelinsky, V. Molodkin, V. Nemoshkalenko, A. Shpak.....	299	FAR17
Reduction of Open-Loop Low Frequency Beam Motion at the APS — G. Decker, Y.G. Kang, S. Kim, D. Mangra, R. Merl, D. McGhee, S. Sharma.....	303	FAR19
Horizontal-Vertical Coupling Correction at Aladdin — R.A. Bosch, W.S. Trzeciak.....	306	FAR20
One and a Half Years of Experience with the Operation of the Synchrotron Light Source ELETTRA — C.J. Bocchetta, D. Bulfone, F. Daclon, G. D'Auria, A. Fabris, R. Fabris, M. Ferianis, M. Giannini, F. Iazzourene, E. Karantzoulis, A. Massarotti, R. Nagaoka, N. Pangos, R. Richter, C. Rossi, M. Svandrlík, L. Tosi, R. Visintini, R.P. Walker, F. Wei, A. Wrulich.....	309	FAR21

Low and Intermediate Energy Accelerators

First Generation ISOL Radioactive Ion Beam Facilities (Invited) — D.K. Olsen.....	312	RPG01
Latest Developments in Superconducting Cyclotrons (Invited) — H.W. Schreuder.....	317	RPG02
Synchrotron-Driven Spallation Sources (Invited) — P.J. Bryant.....	322	RPG03
Heavy Ion Cooling Rings (Invited) — J.S. Hangst.....	manuscript not submitted	RPG04
Commissioning the MIT-Bates South Hall Ring — K. Jacobs, R. Averill, S. Bradley, A. Carter, G. Dodson, K. Dow, M. Farkhondeh, E. Ihloff, S. Kowalski, B. McAllister, W. Sapp, C. Sibley, S. Sobczynski, D. Tieger, C. Tschalaer, E. Tsentalovich, W. Turchinets, A. Zolfaghari, T. Zwart.....	327	RPG05
The AmPS Ring: Actual Performance and Future Plans — G. Luijckx, R. Bakker, H. Boer Rookhuizen, C. de Jager, F. Kroes, J. van der Laan, R. Maas, J. Noomen, Y. Wu.....	330	RPG06
Feasibility Study for Using the FNAL Antiproton Source as a Low Energy Proton-Antiproton Collider — Mike Church, Stephan Maury.....	333	RPG07
CIS, A Low Energy Injector for the IUCF Cooler — D.L. Friesel, S.Y. Lee.....	336	RPG08
The R&D Works on the High Intensity Proton Linear Accelerator for Nuclear Waste Transmutation — N. Ito, M. Mizumoto, K. Hasegawa, H. Oguri, J. Kusano, Y. Okumura, M. Kawai, H. Ino, H. Murata, Y. Touchi.....	339	RPG09
Development of the RFD Linac Structure — D.A. Swenson, K.R. Crandall, F.W. Guy, J.W. Lenz, A.D. Ringwall, L.S. Walling.....	342	RPG10

Proposed Upgrade of the NSCL — R.C. York, H. Blosser, T. Grimm, D. Johnson, D. Lawton, F. Marti, J. Vincent, X. Wu, A.F. Zeller	345	RPG11
ISAC-1: Radioactive Ion Beams Facility at TRIUMF — P.G. Bricault, R. Baartman, J.L. Beveridge, G.S. Clark, J. Doornbos, G. Dutto, T. Hodges, S. Koscielniak, L. Root, P.W. Schmor, H.R. Schneider	348	RPG12
First Beam Tests of the INS Split Coaxial RFQ for Radioactive Nuclei — S. Arai, A. Imanishi, K. Niki, M. Okada, Y. Takeda, E. Tojyo, N. Tokuda	351	RPG13
Accelerator Complex for a Radioactive Ion Beam Facility at ATLAS — J.A. Nolen	354	RPG14
The Lattice Design of Indiana University Cyclotron Facility Cooler Injector Synchrotron — D. Li, X. Kang, D.L. Friesel, S.Y. Lee, J.Y. Liu, A. Pei, A. Riabko, L. Wang	357	TAP03
Design Study of AntiProton Accumulation and Deceleration Ring in the KEK PS Complex — S. Machida, M. Yoshii, Y. Mori, N. Tokuda, Y. Ishi	360	TAP04
Feasibility Study of a 1-MW Pulsed Spallation Source — Y. Cho, Y.-C. Chae, E. Crosbie, M. Fathizadeh, H. Friedsam, K. Harkay, D. Horan, S. Kim, R. Kustom, E. Lessner, W. McDowell, D. McGhee, F. Mills, H. Moe, R. Nielsen, G. Norek, K.J. Peterson, A. Rauchas, K. Symon, K. Thompson, D. Warner, M. White	363	TAP05
ORIC Central Region Calculations — J.D. Bailey, D.T. Dowling, S.N. Lane, S.W. Mosko, D.K. Olsen, B.A. Tatum	366	TAP07
An Internal Timing Probe for Use in the MSU K1200 Cyclotron — J.D. Bailey, J. Kuchar, F. Marti, J. Ottarson	369	TAP08
Axial Injection and Phase Selection Studies of the MSU K1200 Cyclotron — J.D. Bailey	372	TAP09
Study and Redesign of the NSCL K500 Central Region — S.L. Snyder, F. Marti	375	TAP10
Heavy Ion Acceleration Strategies in the AGS Accelerator Complex -- 1994 Status Report — L.A. Ahrens, J. Benjamin, M. Blaskiewicz, J.M. Brennan, C.J. Gardner, H.C. Hseuh, Y.Y. Lee, R.K. Reece, T. Roser, A. Soukas, P. Thieberger	378	TAP11
Observation of Intensity Dependent Losses in Au(15+) Beams — M. Blaskiewicz, L.A. Ahrens, H.C. Hseuh, T. Roser, Y. Shoji, K. Zeno	381	TAP12
High Intensity Proton Operations at the Brookhaven — M. Blaskiewicz, L.A. Ahrens, E.J. Bleser, J.M. Brennan, C.J. Gardner, J.W. Glenn, R.K. Reece, T. Roser, M.J. Syphers, W. VanAsselt, S.Y. Zhang	383	TAP13
Fast Extracted Proton Beams at Low Energies in the CPS East Experimental Area — R. Cappel, L. Durieu, J.-Y. Hémerly, M. Martini, J.-P. Riinaud, Ch. Steinbach	386	TAP14
Ion-Optics Systems Of Multiply Charged High-Energy Ions For High Emittance Beams — V.O. Naidenov, L.A. Baranova, G.M. Gusinskii, A.V. Matyukov, S.Ya. Yavor	389	TAP16

High Energy Hadron Accelerators and Colliders

The Status of the Fermilab Main Injector Project (Invited) — D. Bogert, W. Fowler, S. Holmes, P. Martin, T. Pawlak	391	MPG01
Status and Future of the Tevatron (Invited) — V. Bharadwaj	396	MPG02
The RHIC Project - Status and Plans (Invited) — M. Harrison	401	MPG03
HERA Status and Plans (Invited) — R. Brinkmann	406	MPG04
The CERN Heavy Ion Accelerating Facility (Invited) — H.D. Haseroth	411	MPG05
UNK Status and Plans (Invited) — G. Gurov	416	MPG06
Reduction of Particle Losses in HERA by Generating an Additional Harmonic Tune Modulation — O.S. Brüning, F. Willeke	420	MPG07
Acceleration of Lead Ions in the CERN PS Booster and the CERN PS — F. Blas, P. Bossard, R. Cappel, G. Cyvoct, R. Garoby, G. Gelato, H. Haseroth, E. Jensen, D. Manglunki, K. Metzmacher, F. Pedersen, N. Rasmussen, K. Schindl, G.C. Schneider, H. Schöner, L. Sermeus, M. Thivent, M. van Rooij, F. Völker, E. Wildner	423	MPG09
Highly Efficient Deflection of the Divergent Beam by Bent Single Crystal — V.I. Baranov, V.M. Biryukov, A.P. Bugorsky, Yu.A. Chesnokov, V.I. Kotov, M.V. Tarakanov, V.I. Terekhov, S.V. Tsarik, O.L. Fedin, M.A. Gordeeva, M.P. Gur'yev, Yu.P. Platonov, A.I. Smirnov	426	MPG10
Potential Accelerator Improvements Required for the Tevatron Upgrade at Fermilab — G. Jackson, G.W. Foster	428	MPG11
Beyond the LHC: A Conceptual Approach to a Future High Energy Hadron Collider — M.J. Syphers, M.A. Harrison, S. Peggs	431	MPG12

132 nsec Bunch Spacing in the Tevatron Proton-Antiproton Collider — S.D. Holmes, <i>J.A. Holt, J. Johnstone, J. Marriner, M. Martens, D. McGinnis</i>	434	WAP01
Aluminum Beam Tube for the Super Collider: An Option for No-Coating & No-Liner — <i>W. Chou</i>	437	WAP02
Variable Bunch Spacing in Super Collider — W. Chou	440	WAP03
Fermilab Collider Run 1B Statistics — V. Bharadwaj, J. Crawford, R. Mau	443	WAP04
Optimizing the Luminosity in the Tevatron by Independently Moving the Horizontal and Vertical Beta Stars Longitudinally — M.A. Martens, G.P. Goderre	446	WAP05
A Model of the Fermilab Collider for Optimization of Performance — Elliot S. McCrory, <i>Peter W. Lucas</i>	449	WAP06
Coupling in the Tevatron — Norman M. Gelfand	452	WAP07
Calculating Luminosity for a Coupled Tevatron Lattice — J.A. Holt, M.A. Martens, <i>L. Michelotti, G. Goderre</i>	455	WAP08
Remarks Concerning the γ-Production Probability of High Relativistic Dirac-Electrons in the Positron Bunch — Huschang Heydari	458	WAP09
Field Quality Evaluation of the Superconducting Magnets of the Relativistic Heavy Ion Collider — J. Wei, R.C. Gupta, A. Jain, S.G. Peggs, C.G. Trahern, D. Trbojevic, P. Wanderer	461	WAP10
High Intensity Proton Beams in a Multi-cycled SPS — A. Faugier, X. Altuna, R. Bailey, <i>R. Blanchard, T. Bohl, H. Burkhardt, P. Collier, K. Cornelis, N. Garrel, A. Hilaire, M. Jonker,</i> <i>R. Keizer, M. Lamont, T. Linnecar, G. de Rijk, G. Roy, H. Schmickler, J. Wenninger</i>	464	WAP12
The SPS as Accelerator of Pb^{82+} Ions — A. Faugier, X. Altuna, R. Bailey, R. Blanchard, T. Bohl, <i>E. Brouzet, H. Burkhardt, P. Collier, K. Cornelis, G. de Rijk, F. Ferioli, A. Hilaire, M. Lamont,</i> <i>T. Linnecar, M. Jonker, C. Niquille, G. Roy, H. Schmickler</i>	467	WAP13
Experimental Evidence for Multi-pass Extraction with a Bent Crystal — B. Dehning, <i>K. Elsener, G. Fidecaro, M. Gyr, W. Herr, J. Klem, W. Scandale, G. Vuagnin, E. Weisse,</i> <i>S. Weisz, S.P. Møller, E. Uggerhoj, A. Freund, R. Hustache, G. Carboni, M.P. Bussa, F. Tosello</i>	470	WAP14
Storage Ring for Enhanced Antiproton Production at Fermilab — G. Jackson, G.W. Foster	473	WAP16

Circular Electron Accelerators and Colliders

LEP Status and Plans (Invited) — S. Myers	476	WPG01
CESR Status and Plans (Invited) — David L. Rubin	481	WPG02
PEP II Status and Plans (Invited) — John T. Seeman	486	WPG03
KEKB Status and Plans (Invited) — Shin-ichi Kurokawa	491	WPG04
DAΦNE Status and Plans (Invited) — G. Vignola	495	WPG05
Electron-Positron Colliders at Novosibirsk (Invited) — N. Dikansky	500	WPG06
BEPC Status and Plans (Invited) — Shu-Hong Wang	506	WPG07
The First Attainment and Routine Use of Longitudinal Spin Polarization at a High Energy Electron Storage Ring — D.P. Barber	511	WPG08
Experiments with Bunch Trains in LEP — O. Brunner, W. Herr, G. von Holtey, E. Keil, <i>M. Lamont, M. Meddahi, J. Poole, R. Schmidt, A. Verdier, C. Zhang</i>	514	WPG09
Trapped Macroparticles in Electron Storage Rings — F. Zimmermann, J.T. Seeman, <i>M. Zolotarev, W. Stoeffl</i>	517	WPG10
A Compact-High Performance NLC Damping Ring Using High Magnetic Field Bending Magnets — D.B. Cline, A. Garren, M. Green, J. Kolonko, D. Madura	520	WPG11
Application of Precision Magnetic Measurements for Control of the Duke Storage Ring — <i>B. Burnham, V.N. Litvinenko, Y. Wu</i>	524	RAA01
Wiggler Insertion of the PEP-II B-Factory LER — J. Heim, L. Bertolini, J. Dressler, O. Fackler, <i>B. Hobson, M. Kendall, T. O'Connor, W. Stoeffl, T. Swan, A. Zholents, M.S. Zisman</i>	527	RAA03
Status of the High Energy Ring of the PEP II B-Factory — U. Wienands, E. Reuter, <i>J.T. Seeman, W. Davies-White, A. Fisher, J. Fox, L. Genova, J. Gracia, C. Perkins,</i> <i>M. Pietryka, H. Schwarz, T. Taylor, T. Jackson, C. Belser, D. Shimer</i>	530	RAA04
Design of the PEP-II Low-Energy Ring — M.S. Zisman, R.B. Yourd, H. Hsieh	533	RAA05
Injection Envelope Matching in Storage Rings — M.G. Minty, W.L. Spence	536	RAA06
A Mathematical Model for Investigating Chromatic Electron Beam Extraction from a Pulse Stretcher Ring — Yu.N. Grigorev, A.Yu. Zelinsky	539	RAA07

The Dynamical Aperture of ISI - 800 — S. Efimov, I. Karnaukhov, S. Kononenko, A. Shcherbakov, A. Tarasenko, A. Zelinsky.....	542	RAA08
The Influence of Residual Vertical Dispersion on LEP Performance — P. Collier, H. Schmickler.....	545	RAA10
Operational Procedures to Obtain High Beam-Beam Tune Shifts in LEP Pretzel Operation — R. Bailey, P. Collier, T. Bohl, H. Burkhardt, K. Cornelis, G. De Rijk, A. Faugier, M. Jonker, M. Lamont, G. Roy, H. Schmickler, J. Wenninger.....	548	RAA11
Synchrotron Phase Space Injection into LEP — P. Collier.....	551	RAA12
Systematic Studies of the LEP Working Point — P. Collier, H. Schmickler.....	554	RAA13
Modification of the LEP Electrostatic Separator Systems for Operation with Bunch Trains — B. Balhan, A. Burton, E. Carlier, J.-P. Deluen, J. Dieperink, N. Garrel, B. Goddard, R. Guinand, W. Kalbreier, M. Laffin, M. Lamont, V. Mertens, J. Poole, H. Verhagen.....	557	RAA15
Low Emittance Lattice for LEP — Y. Alexahin, D. Brandt, K. Cornelis, A. Hofmann, J.P. Koutchouk, M. Meddahi, G. Roy, A. Verdier.....	560	RAA17
Radiation Damping Partitions and RF-Fields — M. Cornacchia, A. Hofmann.....	564	RAA18
Experiments on Beam-Beam Depolarization at LEP — R. Assmann, A. Blondel, B. Dehning, A. Drees, P. Grosse-Wiesmann, H. Grote, M. Placidi, R. Schmidt, F. Tecker, J. Wenninger.....	567	RAA19
Measurements of Impedance Distributions and Instability Thresholds in LEP — D. Brandt, P. Castro, K. Cornelis, A. Hofmann, G. Morpurgo, G.L. Sabbi, J. Wenninger, B. Zotter.....	570	RAA20
A Preliminary Lattice Design of a Tau-Charin Factory Storage Ring in Beijing — N. Huang, L. Jin, Y. Wu, G. Xu.....	573	RAA21
Low Energy Ring Lattice of the PEP II Asymmetric B-Factory — Y. Cai, M. Donald, R. Helm, J. Irwin, Y. Nosochkov, D.M. Ritson, Y. Yan, E. Forest, A. Zholents.....	576	RAA22
Damping Rates of the SRRC Storage Ring — K.T. Hsu, C.C. Kuo, W.K. Lau, W.T. Weng.....	579	RAA23
Performance of the SRRC Storage Ring and Wiggler Commissioning — C. Kuo, K.T. Hsu, G.H. Luo, W.K. Lau, Ch. Wang, H.P. Chang, L.H. Chang, M.H. Wang, J.C. Lee, C.S. Hsue, W.T. Weng, Y.C. Liu.....	582	RAA24
Detector Solenoid Compensation in the PEP-II B-Factory — Y. Nosochkov, Y. Cai, J. Irwin, M. Sullivan, E. Forest.....	585	RAA25
Swamp Plots for Dynamic Aperture studies of PEP-II Lattices — Y.T. Yan, J. Irwin, Y. Cai, T. Chen, D. Ritson.....	588	RAA26
Lattice Design for the High Energy Ring of the SLAC B-Factory (PEP-II) — M.H.R. Donald, Y. Cai, J. Irwin, Y. Nosochkov, D.M. Ritson, J. Seeman, H.-U. Wienands, Y.T. Yan.....	591	RAA27
The APS Booster Synchrotron: Commissioning and Operational Experience — S.V. Milton.....	594	RAA28
A Preliminary Design for a Tau-Charin Factory — J. Norem, E. Crosbie, J. Repond, L. Teng.....	597	RAA29
A Spin Control System for the South Hall Ring at the Bates Linear Accelerator Center — T. Zwart, P. Ivanov, Yu. Shatunov, R. Averill, K. Jacobs, S. Kowalski, W. Turchinets.....	600	RAA31
Beam-Based Alignment of Sextupoles with the Modulation Method — M. Kikuchi, K. Egawa, H. Fukuma, M. Tejima.....	603	RAA33

Linear Colliders and Advanced Accelerator Concepts

The Stanford Linear Collider (Invited) — Paul Emma.....	606	WAG01
Options and Trade-Offs in Linear Collider Design (Invited) — J. Rossbach.....	611	WAG02
Test Facilities for Future Linear Colliders — Ronald D. Ruth.....	616	WAG03
Channel Guided Lasers for Plasma Accelerators (Invited) — H.M. Milchberg, C.G. Durfee III, T.M. Antonsen, P. Mora.....	621	WAG04
Inverse Cerenkov Accelerator Results (Invited) — W.D. Kimura.....	626	WAG05
Measurements of Plasma Wake-Fields in the Blow-Out Regime — N. Barov, M. Conde, J.B. Rosenzweig, P. Schoessow, G. Cox, W. Gai, R. Konecny, J. Power, J. Simpson.....	631	WAG06
Experimental Study of Electron Acceleration by Plasma Beat-Waves with Nd Lasers — F. Amiranoff, F. Moulin, J. Fusellier, J.M. Joly, M. Juillard, M. Bercher, D. Bernard, A. Debraine, J.M. Dieulot, F. Jacquet, P. Matricon, Ph. Miné, B. Montès, R. Morano, P. Poilleux, A. Specka, J. Morillo, J. Ardonneau, B. Cros, G. Matthieussent, C. Stenz, P. Mora.....	634	WAG07
A Broadband Electron Spectrometer and Electron Detectors for Laser Accelerator Experiments — C.E. Clayton, K.A. Marsh, C. Joshi, C.B. Darrow, A.E. Dangor, A. Modena, Z. Najmudin, V. Malka.....	637	WAG08

Photon Acceleration from Rest to the Speed of Light — C.H. Lai, T. Katsouleas, R. Liou, W.B. Mori, C. Joshi, P. Muggli, R. Brogle, J. Dawson.....	640	WAG09
A Constant Gradient Planar Accelerating Structure for Linac Use — Y.W. Kang, P.J. Matthews, R.L. Kustom.....	643	WAG10
Pulse to Pulse Stability Issues in the SLC — C. Adolphsen, R. Assmann, F.J. Decker, P. Emma, J. Frisch, L.J. Hendrickson, P. Krejcik, M. Minty, N. Phinney, P. Raimondi, M.C. Ross, T. Slaton, W. Spence, R. Stege, H. Tang, F. Tian, J. Turner, M. Woodley, F. Zimmermann.....	646	WAG11
HOM-Free Linear Accelerating Structure for e+e- Linear Collider at C-Band — T. Shintake, K. Kubo, H. Matsumoto, O. Takeda.....	649	WAG12
SLAC/CERN High Gradient Tests of an X-Band Accelerating Section — J.W. Wang, G.A. Loew, R.J. Loewen, R.D. Ruth, A.E. Vlieks, I. Wilson, W. Wuensch.....	653	WAG13

Linear Colliders

Performance of the 1994/95 SLC Final Focus System — F. Zimmermann, T. Barklow, S. Ecklund, P. Emma, D. McCormick, N. Phinney, P. Raimondi, M. Ross, T. Slaton, F. Tian, J. Turner, M. Woodley, M. Placidi, N. Toge, N. Walker.....	656	RPB01
Direct Measurement of Transverse Wakefields in the SLC Linac — P. Krejcik, R. Assmann, F.-J. Decker, S. Hartman, R. Miller, T. Raubenheimer.....	659	RPB02
Feedback Performance at the Stanford Linear Collider — M.G. Minty, C. Adolphsen, L.J. Hendrickson, R. Sass, T. Slaton, M. Woodley.....	662	RPB03
Vibration Studies of the Stanford Linear Accelerator — J.L. Turner, C. Adolphsen, G.B. Bowden, F.J. Decker, S.C. Hartman, S. Matsumoto, G. Mazaheri, D. McCormick, M. Ross, R. Stege, S. Virostek, M. Woodley.....	665	RPB04
SLAC Modulator Availability and Impact on SLC Operation — A.R. Donaldson, J.R. Ashton.....	668	RPB05
The SLC as a Second Generation Linear Collider — J.E. Spencer.....	671	RPB06
Status of the Design for the TESLA Linear Collider — R. Brinkmann.....	674	RPB07
The TESLA Test Facility (TTF) Linac - A Status Report — H. Weise.....	677	RPB08
The Infrastructure for the TESLA Test Facility (TTF) - A Status Report — S. Wolff.....	680	RPB09
The Status of the S-Band Linear Collider Study — N. Holtkamp.....	683	RPB12
The S-Band Linear Collider Test Facility — N. Holtkamp.....	686	RPB13
Beam Dynamics Studies for the SBLC — M. Drevlak, R. Wanzenberg.....	689	RPB14
S-Band HOM-Damper Calculations and Experiments — M. Dohlus, M. Marx, N. Holtkamp, P. Hülsmann, W.F.O. Müller, M. Kurz, H.-W. Glock, H. Klein.....	692	RPB15
The S-Band 36-Cell Experiment — B. Krietenstein, O. Podebrad, U. v.Rienen, T. Weiland, H.-W. Glock, P. Hülsmann, H. Klein, M. Kurz, C. Peschke, M. Dohlus, N. Holtkamp.....	695	RPB16

Volume 2

Linear Colliders (cont'd)

Parameters for the SLAC Next Linear Collider — T. Raubenheimer, C. Adolphsen, D. Burke, P. Chen, S. Ecklund, J. Irwin, G. Loew, T. Markiewicz, R. Miller, E. Paterson, N. Phinney, M. Ross, R. Ruth, J. Sheppard, H. Tang, K. Thompson, P. Wilson.....	698	RPC01
A Damping Ring Design for the SLAC Next Linear Collider — T.O. Raubenheimer, J. Byrd, J. Corlett, R. Early, M. Furman, A. Jackson, P. Krejcik, K. Kubo, T. Mattison, M. Minty, W. Moshhammer, D. Robin, B. Scott, J. Spencer, K. Thompson, P. Wilson.....	701	RPC02
A Bunch Compressor for the Next Linear Collider — P. Emma, T. Raubenheimer, F. Zimmermann.....	704	RPC03
A Final Focus System for the Next Linear Collider — F. Zimmermann, K. Brown, P. Emma, R. Helm, J. Irwin, P. Tenenbaum, P. Wilson.....	707	RPC06
Optimization of the NLC Final Focus System — F. Zimmermann, R. Helm, J. Irwin.....	710	RPC07
The SLAC NLC Extraction & Diagnostic Line — J. Spencer, J. Irwin, D. Walz, M. Woods.....	713	RPC08

CLIC - A Compact and Efficient High Energy Linear Collider — <i>H. Braun, R. Corsini, J.-P. Delahaye, G. Guignard, C. Johnson, J. Madsen, W. Schnell, L. Thorndahl, I. Wilson, W. Wuensch, B. Zotter</i>	716	RPC09
CLIC Test Facility Developments and Results — <i>R. Bossart, H. Braun, F. Chautard, M. Comunian, J.P. Delahaye, J.C. Godot, I. Kamber, J.H.B. Madsen, L. Rinolfi, S. Schreiber, G. Suberlucq, I. Wilson, W. Wuensch</i>	719	RPC10
Generation of a 30 GHz Train of Bunches Using a Magnetic Switch-Yard — <i>B. Autin, R. Corsini</i>	722	RPC11
A New Family of Isochronous Arcs — <i>G. Guignard, E.T. d'Amico</i>	725	RPC12
Updating of Beam Dynamics in the CLIC Main Linac — <i>G. Guignard</i>	728	RPC13
Improved CLIC Performances Using the Beam Response for Correcting Alignment Errors — <i>C. Fischer</i>	731	RPC14
Experimental Studies of a CERN-CLIC 32.98 GHz High Gradient Accelerating Structure Driven by the MIT Free Electron Laser Amplifier — <i>P. Volfbeyn, I. Mastovsky, G. Bekefi, I. Wilson, W. Wuensch</i>	734	RPC15
Design of a Relativistic Klystron Two-Beam Accelerator Prototype — <i>G. Westenskow, G. Caporaso, Y. Chen, T. Houck, S. Yu, S. Chattopadhyay, E. Henestroza, H. Li, C. Peters, L. Reginato, A. Sessler</i>	737	RPC16
Beam Dynamics Issues in an Extended Relativistic Klystron — <i>G. Giordano, H. Li, N. Goffeney, E. Henestroza, A. Sessler, S. Yu, T. Houck, G. Westenskow</i>	740	RPC17
Engineering Conceptual Design of the Relativistic Klystron Two-Beam Accelerator Based Power Source for 1-TeV Next Linear Collider — <i>L. Reginato, C. Peters, D. Vanecek, S. Yu, F. Deadrick</i>	743	RPC18
Design of Inductively Detuned RF Extraction Cavities for the Relativistic Klystron Two Beam Accelerator — <i>E. Henestroza, S.S. Yu, H. Li</i>	746	RPC19
Beam-Based Optical Tuning of the Final Focus Test Beam — <i>P. Tenenbaum, D. Burke, S. Hartman, R. Helm, J. Irwin, R. Iverson, P. Raimondi, W. Spence, V. Bharadwaj, M. Halling, J. Holt, J. Buon, J. Jeanjean, F. Le Diberder, V. Lepeltier, P. Puzo, K. Oide, T. Shintake, N. Yamamoto</i>	749	RPC20
Fermilab Contributions to the FFTB — <i>V. Bharadwaj, A. Braun, M. Halling, J.A. Holt, D. Still</i>	752	RPC21
HV Injection Phase Orbit Characteristics for Sub-Picosecond Bunch Operation with a High Gradient 17 GHz Linac — <i>J. Haimson, B. Mecklenburg</i>	755	RPC22

New Acceleration Techniques

Electron Acceleration in Relativistic Plasma Waves Generated by a Single Frequency Short-Pulse Laser — <i>C.A. Coverdale, C.B. Darrow, C.D. Decker, W.B. Mori, K.-C. Tzeng, C.E. Clayton, K.A. Marsh, C. Joshi</i>	758	RAB01
Theory and Simulation of Plasma Accelerators — <i>W.B. Mori, K.-C. Tzeng, C.D. Decker, C.E. Clayton, C. Joshi, T. Katsouleas, P. Lai, T.C. Chiou, R. Kinter</i>	761	RAB02
An Injector-prebuncher for a Plasma Electron Accelerator — <i>M. Lampel, C. Pellegrini, R. Zhang, C. Joshi, W.M. Fawley</i>	764	RAB03
Measurements of the Beatwave Dynamics in Time and Space — <i>A. Lal, K. Wharton, D. Gordon, M.J. Everett, C.E. Clayton, C. Joshi</i>	767	RAB04
A Novel Technique for Probing the Transverse Interactions Between an Electron Beam and a Plasma — <i>D. Gordon, A. Lal, C.E. Clayton, M. Everett, C. Joshi</i>	770	RAB05
Studies of Intense Laser Propagation in Channels for Extended Length Plasma Accelerators — <i>T. Katsouleas, T.C. Chiou, W.B. Mori, J.S. Wurtele, G. Shvets</i>	773	RAB08
UV Laser Ionization and Electron Beam Diagnostics for Plasma Lenses — <i>R. Govil, P. Volfbeyn, W. Leemans</i>	776	RAB10
Plasma Wakefield Acceleration Experiments in Overdense Regime Driven by Narrow Bunches — <i>T. Kozawa, T. Ueda, T. Kobayashi, M. Uesaka, K. Miya, A. Ogata, H. Nakanishi, T. Kawakubo, M. Arinaga, K. Nakajima, H. Shibata, N. Yugami, Y. Nishida, D. Whittum, Y. Yoshida</i>	779	RAB13
The Wake-Field Excitation in a Plasma-Dielectric Structure by a Sequence of Short Bunches of Relativistic Electrons — <i>I.N. Onishchenko, V.A. Kiseljov, A.K. Berezin, G.V. Sotnikov, V.V. Uskov, A.F. Linnik, Ya.B. Fainberg</i>	782	RAB15

A Beam Focusing System for a Linac Driven by a Traveling Laser Focus — A.A. Mikhailichenko	784	RAB18
2 x 2 TeV $\mu^+\mu^-$ Collider: Lattice and Accelerator-Detector Interface Study — N.M. Gelfand, N.V. Mokhov	787	RAB19
Muon Cooling and Acceleration Experiment at TRIUMF — S.A. Bogacz, D.B. Cline, P.H. Sandler, D.A. Sanders	790	RAB20
Helical Siberian Snakes — E. Ludmirsky	793	RAB21
Performance of Achromatic Lattice with Combined Function Sextupoles at Duke Storage Ring — V.N. Litvinenko, Y. Wu, B. Burnham, J.M.J. Madey, S.H. Park	796	RAB22

Accelerators and Storage Rings, Misc.

Matreshka High-Intensity Accelerator of Continuous Particle Beams — F.A. Vodopianov	799	TAR02
The Amplitude and Phase Control of the ALS Storage Ring RF System — C.C. Lo, B. Taylor, K. Baptiste	801	TAR03
Integral Dipole Field Calibration of the SRRC Storage Ring Combined Function Bending Magnets — J.C. Lee, Peace Chang, C.S. Hsue	804	TAR04
Improved Mobile 70 MeV Race-Track Microtron Design — V.I. Shvedunov, A.I. Karev, V.N. Melekhin, N.P. Sobenin, W.P. Trower	807	TAR05
The Improvement of Energy Measurement in BTS Transport Line by Using Beam Tracing Method — M.H. Wang, J.C. Lee	810	TAR06
Design Study of PAL-Stretcher Ring — I.S. Ko, G.N. Kim, J. Choi, M.H. Cho, W. Namkung	813	TAR07
Thermomechanical Analysis of a Compact-Design High Heat Load Crotch Absorber — I.C. Sheng, S. Sharma, R. Rotela, J. Howell	816	TAR08
Novosibirsk Tau-Charm Factory Design Study — N. Dikansky, V. Parkhomchuk, A. Skrinsky, V. Yakimenko	819	TAR11
Development of a RAMI Program for LANSCE Upgrade — K.C.D. Chan, A. Browman, R.L. Hutson, R.J. Macek, P.J. Tallerico, C.A. Wilkinson	822	TAR12
Accelerator Waveform Synthesis and Longitudinal Beam Dynamics in a Small Induction Recirculator — T.J. Fessenden, D.P. Grote, W.M. Sharp	825	TAR13
Progress Toward a Prototype Recirculating Induction Accelerator for Heavy-Ion Fusion — A. Friedman, J.J. Barnard, M.D. Cable, D.A. Callahan, F.J. Deadrick, S. Eylon, T.J. Fessenden, D.P. Grote, D.L. Judd, H.C. Kirbie, D.B. Longinotti, S.M. Lund, L.A. Natrass, M.B. Nelson, M.A. Newton, T.C. Sangster, W.M. Sharp, S.S. Yu	828	TAR14
Three Dimensional Simulations of a Small Induction Recirculator Accelerator — D.P. Grote, A. Friedman, I. Haber	831	TAR15
A Dynamic Momentum Compaction Factor Lattice in the FERMILAB DEBUNCHER Ring — D.N. Olivieri, M. Church, J. Morgan	834	TAR16
Mechanical Design of Recirculating Accelerator Experiments for Heavy-Ion Fusion — V. Karpenko, J. Barnard, F. Deadrick, A. Friedman, D. Grote, S. Lund, J. Meredith, L. Natrass, M. Nelson, G. Repose, C. Sangster, W. Sharp, T. Fessenden, D. Longinotti, C. Ward	837	TAR17
The PEP-II Project-Wide Database — A. Chan, S. Calish, G. Crane, I. MacGregor, S. Meyer, J. Wong, A. Weinstein	840	TAR18
Chromaticity Compensation - Booster Sextupoles — S.A. Bogacz, K.-Y. Ng, J.-F. Ostiguy	843	TAR20
Overview of $\mu^+\mu^-$ Collider Options — D.B. Cline	846	TAR21
HIRFL Status and HIRFL-CSR Proposal — Ye Fang, Wang Yifang	850	TAR22

Particle Sources and Injectors

A Review of Polarized Ion Sources (Invited) — P.W. Schmor	853	MPE01
Sources for Production of Radioactive Ion-Beams (Invited) — Helge L. Ravn	858	MPE02
The TRIUMF High-Curent DC Optically -Pumped Polarized H⁺ Ion Source — A.N. Zelenski, C.D.P. Levy, K. Jayamanna, M. McDonald, P.W. Schmor, W.T.H. van Oers, J. Welz, G.W. Wight, G. Dutto, Y. Mori, T. Sakae	864	MPE03

Lifetime Test on a High-Performance DC Microwave Proton Source — J. Sherman, <i>D. Hodgkins, P. Lara, J.D. Schneider, R. Stevens Jr.</i>	867	MPE04
Performance Enhancement of a Compact Radio Frequency Ion Source by the Injection of Supplemental Electrons — R.F. Welton, G.D. Alton, D. Becher, G.D. Mills, J. Dellwo, <i>S.N. Murray</i>	871	MPE05
A High-Current Position Source — V.V. Gorev	874	MPE06
Polarized Electron Sources (Invited) — J.E. Clendenin	877	MPE08
High Brightness Electron Sources (Invited) — Richard L. Sheffield	882	MPE09
Polarization Studies of Strained GaAs Photocathodes at the SLAC Gun Test Laboratory — <i>P. Sáez, R. Alley, J. Clendenin, J. Frisch, R. Kirby, R. Mair, T. Maruyama, R. Miller,</i> <i>G. Mulhollan, C. Prescott, H. Tang, K. Witte</i>	887	MPE10
Experimental Results of the ATF In-line Injection System — X.J. Wang, T. Srinivasan-Rao, <i>K. Batchelor, M. Babzien, I. Ben-Zvi, R. Malone, I. Pogorelsky, X. Qiu, J. Sheehan, J. Skaritka</i>	890	MPE11
High Power Testing of a 17 GHz Photocathode RF Gun — S.C. Chen, B.G. Danly, J. Gonichon, <i>C.L. Lin, R.J. Temkin, S.R. Trotz, J.S. Wurtele</i>	893	MPE12
Analytical Model for Emittance Compensation in RF Photo-Injectors — L. Serafini, <i>J.B. Rosenzweig</i>	896	MPE13
Emission, Plasma Formation, and Brightness of a PZT Ferroelectric Cathode — <i>S. Sampayan, G. Caporaso, D. Trimble, G. Westenskow</i>	899	MPE14

Radio Frequency Guns and Linac Injectors

Design and Testing of the 2 MV Heavy Ion Injector for the Fusion Energy Research Program — W. Abraham, R. Benjegerdes, L. Reginato, J. Stoker, R. Hipple, C. Peters, J. Pruyn, <i>D. Vanecek, S. Yu</i>	902	WPA01
K⁺ Diode for the LLNL Heavy Ion Recirculator Accelerator Experiment — S. Eylon, <i>E. Henestroza, F. Deadrick</i>	905	WPA02
A Single Bunch RFQ System for Heavy Ions — J. Madlung, A. Firjahn-Andersch, A. Schempp	908	WPA03
The Design of Low Frequency Heavy Ion RFQ Resonators — A. Schempp, H. Vormann, <i>U. Beisel, H. Deitinghoff, O. Engels, D. Li</i>	911	WPA04
A VE-RFQ-Injector for a Cyclotron — A. Schempp, O. Engels, F. Marhauser	914	WPA05
Fermilab Linac Injector, Revisited — M. Popovic, L. Allen, C.W. Schmidt	917	WPA06
New RF Structures for the Fermilab Linac Injector — M. Popovic, A. Moretti, R.J. Nobel	920	WPA07
High-Power RF Operations Studies with the CRITS RFQ — G.O. Bolme, D.R. Keffeler, <i>V.W. Brown, D.C. Clark, D. Hodgkins, P.D. Lara, M.L. Milder, D. Rees, P.J. Schafstall,</i> <i>J.D. Schneider, J.D. Sherman, R.R. Stevens, T. Zaugg</i>	923	WPA08
Beam Dynamics Studies of the Heavy Ion Fusion Accelerator Injector — E. Henestroza, <i>S.S. Yu, S. Eylon, D.P. Grote</i>	926	WPA09
First Tests at Injector for the S-Band Test Facility at DESY — M. Schmitz, W. Herold, <i>N. Holtkamp, W. Kriens, R. Walther</i>	929	WPA12
RF Phasing of the Duke Linac — Ping Wang, Nelson Hower, Patrick G. O'Shea	932	WPA13
Simulations and Measurements of the TTF Phase-1 Injector Gun — T. Garvey, M. Omeich, <i>M. Jablonka, J.M. Joly, H. Long</i>	935	WPA14
Experimental Studies on Cold Cathode Magnetron Gun — A.N. Dovbnya, V.V. Zakutin, <i>V.F. Zhiglo, A.N. Opanasenko, V.P. Romasko, S.A. Cherenshchikov</i>	938	WPA15
Secondary Emission in Cold-Cathode Magnetron Injection Gun — S.A. Cherenshchikov, <i>A.N. Dovbnya, A.N. Opanasenko</i>	939	WPA16
Design of a High Charge CW Photocathode Injector Test Stand at CEBAF — H. Liu, <i>D. Kehne, S. Benson, J. Bisognano, L. Cardman, F. Dylla, D. Engwall, J. Fugitt, K. Jordan,</i> <i>G. Neil, D. Neuffer, C. Sinclair, M. Wiseman, B. Yunn</i>	942	WPA17
CANDELA Photo-Injector Experimental Results With a Dispenser Photocathode — <i>C. Travier, B. Leblond, M. Bernard, J.N. Cayla, P. Thomas, P. Georges</i>	945	WPB01
A Multi-Cell RF Photoinjector Design — Sanghyun Park	948	WPB02
On the Frequency Scalings of RF Guns — Leon C.-L. Lin, J.S. Wurtele, S.C. Chen	951	WPB03
Waveguide Broad-Wall Coupling for RF Guns — Leon C.-L. Lin, S.C. Chen, J.S. Wurtele	954	WPB04

Charge and Wavelength Scaling of RF Photoinjectors: A Design Tool — <i>J. Rosenzweig, E. Colby</i>	957	WPB05
A Photocathode RF Gun Design for a mm-Wave Linac-Based FEL — <i>A. Nassiri, T. Berenc, J. Foster, G. Waldschmidt, J. Zhou</i>	961	WPB06
The RF Gun Development at SRRC — <i>C.H. Ho, W.K. Lau, J.I. Hwang, S.Y. Hsu, Y.C. Liu</i>	964	WPB07
Design and Construction of High Brightness RF Photoinjectors for TESLA — <i>E. Colby, V. Bharadwaj, J.F. Ostiguy, T. Nicol, M. Conde, J. Rosenzweig</i>	967	WPB08
Jitter Sensitivity in Photoinjectors — <i>Patrick G. O'Shea</i>	970	WPB09
Asymmetric Emittance Beam Generation Using Round Beam RF Guns and Non-linear Optics — <i>G. Fiorentini, C. Pagani, L. Serafini</i>	973	WPB10
The Argonne Wakefield Accelerator High Current Photocathode Gun and Drive Linac — <i>P. Schoessow, E. Chojnacki, G. Cox, W. Gai, C. Ho, R. Konecny, J. Power, M. Rosing, J. Simpson, N. Barov, M. Conde</i>	976	WPB11
Witness Gun for the Argonne Wakefield Accelerator — <i>J. Power, J. Simpson, E. Chojnacki, R. Konecny</i>	979	WPB12
Microwave Measurements of the BNL/SLAC/UCLA 1.6 Cell Photocathode RF Gun — <i>D.T. Palmer, R.H. Miller, H. Winick, X.J. Wang, K. Batchelor, M. Woodle, I. Ben-Zvi</i>	982	WPB13
Subpicosecond, Ultra-Bright Electron Injector — <i>Bruce E. Carlsten, Martin L. Milder, John M. Kinross-Wright, Donald W. Feldman, Steven Russell, John G. Plato, Alan Shapiro, Boyd Sherwood, Jan Studebaker, Richard Lovato, David Warren, Carl Timmer, Ronald Cooper, Ronald Sturges, Mel Williams</i>	985	WPB15
Energy Spread Compensation in an Electron Linear Accelerator — <i>Yu.D. Tur, A.N. Dovbnaya, V.A. Kushnir, V.V. Mitrochenko, D.L. Stepin</i>	988	WPB16
On Enhancement of Limited Accelerating Charge — <i>Yu. Tur</i>	990	WPB17
Magnetic Pulse Compression Using a Third Harmonic RF Linearizer — <i>D.H. Dowell, T.D. Hayward, A.M. Vetter</i>	992	WPB20
A Comparison of L-Band and C-Band RF Guns as Sources for Inline-Injection Systems — <i>Juan C. Gallardo, Harold G. Kirk, Thomas Meyer</i>	995	WPB21
Progress in the Study and Construction of the TESLA Test Facility Injector — <i>R. Chehab, M. Bernard, J.C. Bourdon, T. Garvey, B. Jacquemard, M. Mencick, B. Mouton, M. Omeich, J. Rodier, P. Roudier, J.L. Saury, M. Taurigna-Quere, Y. Thiery, B. Aune, M. Desmons, J. Fusellier, F. Gougnaud, J.F. Gournay, M. Jablonka, J.M. Joly, M. Juillard, Y. Lussignol, A. Mosnier, B. Phung, S. Buhler, T. Junquera</i>	998	WPB22

Particle Sources

Hollow Beam Profile in the Extraction System of ECR Ion Source — <i>Y. Batygin, A. Goto, Y. Yano</i>	1001	WPC01
Ion Sources for Use in Research and Applied High Voltage Accelerators — <i>S. Nikiforov, V. Golubev, D. Solnyshkov, M. Svinin, G. Voronin</i>	1004	WPC03
Direct Fast Beam Chopping of H⁻ Ion Beam in the Surface-Plasma H⁻ Ion Source — <i>K. Shinto, A. Takagi, Z. Igarashi, K. Ikegami, M. Kinsho, S. Machida, M. Yoshii, Y. Mori</i>	1007	WPC07
Emittance Measurements of the High Intensity Polarized Ion Source at IUCF — <i>V. Derenchuk, R. Brown, H. Petri, E. Stephenson, M. Wedekind</i>	1010	WPC08
Report on EBIS Studies for a RHIC Preinjector — <i>E. Beebe, A. Hershcovitch, A. Kponou, K. Prelec, J. Alessi, R. Schmieder</i>	1013	WPC09
Development of a Volume H⁻ Ion Source for LAMPF — <i>D.R. Swenson, R.L. York, R.R. Stevens Jr., C. Geisik, W. Ingalls, J.E. Stelzer, D. Fitzgerald</i>	1016	WPC10
Generation of High Purity CW Proton Beams from Microwave-Driven Sources — <i>David Spence, Keith R. Lykke</i>	1019	WPC11
Computational Studies for an Advanced Design ECR Ion Source — <i>G.D. Alton, J. Dellwo, R.F. Welton, D.N. Smithe</i>	1022	WPC12
Pulsed Ion Sources of Duoplasmatron Type with Cold and Hot Cathodes — <i>A. Glazov, V. Krasnopolsky, R. Meshcherov, V. Masalov</i>	1025	WPC13
Double Pulse Experiment with a Velvet Cathode on the ATA Injector — <i>G. Westenskow, G. Caporaso, Y. Chen, T. Houck, S. Sampayan</i>	1027	WPC16

Emittance Measurements for the Illinois/CEBAF Polarized Electron Source — <i>B.M. Dunham, L.S. Cardman, C.K. Sinclair.....</i>	1030	WPC17
The NLC Positron Source — H. Tang, A.V. Kulikov, J.E. Clendenin, S.D. Ecklund, R.A. Miller, <i>A.D. Yeremian.....</i>	1033	WPC18
Ferroelectric Cathodes as Electron Beam Sources — D. Flechtner, G.S. Kerslick, J.D. Ivers, <i>J.A. Nation, L. Schächter.....</i>	1036	WPC19
Studies of Linear and Nonlinear Photoelectric Emission for Advanced Accelerator Applications — R. Brogle, P. Muggli, P. Davis, G. Hairapetian, C. Joshi	1039	WPC20
A Derivative Standard for Polarimeter Calibration — G. Mulhollan, J. Clendenin, P. Sáez, <i>D. Schultz, H. Tang, A.W. Pang, H. Hopster, K. Trantham, M. Johnston, T. Gay, B. Johnson,</i> <i>M. Magugumela, F.B. Dunning, G.K. Walters, G.F. Hanne</i>	1043	WPC21
Analysis of Positron Focusing Section for SPring-8 Linac — A. Mizuno, S. Suzuki, <i>H. Yoshikawa, T. Hori, K. Yanagida, H. Sakaki, T. Taniuchi, H. Kotaki, H. Yokomizo</i>	1046	WPC22
R & D Activity on High QE Alkali Photocathodes for RF Guns — P. Michelato, A. Di Bona, <i>C. Pagani, D. Sertore, S. Valeri.....</i>	1049	WPC23
Development of an Accelerator-Ready Photocathode Drive Laser at CEBAF — S. Benson, <i>M. Shinn.....</i>	1052	WPC24

Linear Accelerators

Analytical Formulae for the Loss Factors and Wakefields of a Disk-loaded Accelerating Structure — J. Gao.....	1055	RPA03
Design Parameters for the Damped Detuned Accelerating Structure — K. Ko, K. Bane, <i>R. Gluckstern, H. Hoag, N. Kroll, X.T. Lin, R. Miller, R. Ruth, K. Thompson, J. Wang</i>	1058	RPA04
Operation of PLS 2-GeV Linac — W. Namkung, I.S. Ko, M.H. Cho, J.S. Bak, J. Choi, H.S. Lee	1061	RPA06
Radiation Measurements at the Advanced Photon Source (APS) Linear Accelerator — <i>H.J. Moe, J.H. Vacca, V.R. Veluri, M. White</i>	1064	RPA07
Positron Focusing in the Advanced Photon Source (APS) Linear Accelerator — Y.L. Qian, <i>M. White</i>	1067	RPA08
Bunch Length Measurements at the Advanced Photon Source (APS) Linear Accelerator — <i>N.S. Sereno, R. Fuja, C. Gold, A.E. Grelick, A. Nassiri, J.J. Song, M. White</i>	1070	RPA10
Performance of the Advanced Photon Source (APS) Linear Accelerator — M. White, <i>N. Arnold, W. Berg, A. Cours, R. Fuja, J. Goral, A. Grelick, K. Ko, Y.L. Qian, T. Russell,</i> <i>N.S. Sereno, W. Wesolowski</i>	1073	RPA11
TW Accelerating Structures with Minimal Surface Electric Field — O. Nezhevenko, <i>D. Myakishev, V. Tarnetsky, V. Yakovlev</i>	1076	RPA12
A 100 MeV Injector for the Electron Storage Ring at Kyoto University — T. Shirai, M. Kando, <i>M. Ikegami, Y. Iwashita, H. Okamoto, S. Kakigi, H. Dewa, H. Fujita, A. Noda, M. Inoue,</i> <i>K. Mashiko</i>	1079	RPA13
Phase Control and Intra-Pulse Phase Compensation of the Advanced Photon Source (APS) Linear Accelerator — A.E. Grelick, N. Arnold, K. Ko, N. Sereno, M. White	1082	RPA14
Error Sensitivity Study for Side Coupled Muffin Tin Structures using a Finite Difference Program — Warner Bruns.....	1085	RPA15
Design of Input Couplers and Endcells for Side Coupled Muffin-Tin Structures — <i>Warner Bruns</i>	1088	RPA16
Accelerator Archeology - The Resurrection of the Stanford MARKIII Electron Linac at Duke — P.G. O'Shea, F. Carter, C. Dickey, N. Hower, V.N. Litvinenko, R. Sachtshale, <i>G. Swift, P. Wang, Y. Wu, J.M.J. Madey.....</i>	1090	RPA17
Cold Model Test of Biperiodic L-Support Disk-and-Washer Linac Structure — Y. Iwashita, <i>A. Noda, H. Okamoto, T. Shirai, M. Inoue</i>	1093	RPA18
Compact Low Energy CW Linac with High Beam Current — A. Alimov, A. Chepurnov, <i>O. Chubarov, D. Ermakov, K. Gudkov, B. Ishkhanov, I. Piskarev, V. Shvedunov, A. Shumakov</i>	1096	RPA19
C-Band Linac RF-System for e+e- Linear Collider — T. Shintake, N. Akasaka, K.L.F. Bane, <i>H. Hayano, K. Kubo, H. Matsumoto, S. Matsumoto, K. Oide, K. Yokoya.....</i>	1099	RPA20
Initial Operation of the UCLA Plane Wave Transformer (PWT) Linac — R. Zhang, P. Davis, <i>G. Hairapetian, M. Hogan, C. Joshi, M. Lampel, S. Park, C. Pellegrini, J. Rosenzweig,</i> <i>G. Travish.....</i>	1102	RPA21

The UCLA Compact High Brightness Electron Accelerator — P. Davis, G. Hairapetian, M. Hogan, C. Joshi, M. Lampel, S. Park, C. Pellegrini, J. Rosenzweig, G. Travish, R. Zhang	1105	RPA22
A Semi-Automated System for the Characterization of NLC Accelerating Structures — S.M. Hanna, G.B. Bowden, H.A. Hoag, R. Loewen, A.E. Vlieks, J.W. Wang	1108	RPA23
SLAC Accelerator Operations Report: 1992-1995 — R. Erickson, C.W. Allen, T.K. Inman, W. Linebarger, M. Stanek	1111	RPA24
Beam Current Limitation in Microwave Accelerators — A.V. Mishin, I.S. Shchedrin	1114	RPA25
Installation and Commissioning of the e+/e- Injector for DAΦNE at Frascati — K. Whitham, H. Amankath, J. Edighoffer, K. Fleckner, E. Gower, S. Lyons, D. Nett, D. Palmer, R. Sheppard, S. Sutter, P. Treas, A. Zante, R. Miller, R. Boni, H. Hsieh, F. Sannibale, M. Vescovi, G. Vignola	1116	RPA26
Recent Studies of Linac for Production of Radioactive Beams in the INR — I.N. Birukov, I.V. Gonin, D.V. Gorelov, A.N. Iljinov, V.A. Moiseev, P.N. Ostroumov, A.V. Tiunov	1119	RPR01
RFQ Cold Model Studies — P.G. Bricault, D. Joffe, H.R. Schneider	1122	RPR02
Simulation of the TRIUMF Split-Ring 4-Rod RFQ with MAFIA — P.G. Bricault, H.R. Schneider	1125	RPR03
A Low-charge-state Injector Linac for ATLAS — K.W. Shepard, J.W. Kim	1128	RPR05
Progress of the Heidelberg High Current Injector — C.-M. Kleffner, S. Auch, M. Grieser, D. Habs, V. Kößler, M. Madert, R. Repnow, D. Schwalm, H. Deitinghoff, A. Schempp, E. Jaeschke, R. von Hahn, S. Papureanu	1131	RPR06
The New Concepts in Designing the CW High-current Linacs — B.P. Murin, G.I. Batskikh, V.M. Belugin, B.I. Bondarev, A.A. Vasiljev, A.P. Durkin, Yu.D. Ivanov, V.A. Konovalov, A.P. Fedotov, I.V. Shumakov	1134	RPR07
A Versatile, High-Power Proton Linac for Accelerator Driven Transmutation Technologies — J.H. Billen, S. Nath, J.E. Stovall, H. Takeda, R.L. Wood, L.M. Young	1137	RPR08
A Compact High-Power Proton Linac for Radioisotope Production — H. Takeda, J.H. Billen, S. Nath, J.E. Stovall, R.L. Wood, L.M. Young	1140	RPR09
Potentialities of Electron and Ion Beam Accelerators for Long-Lived Nuclear Waste Transmutation — A. Shalnov, N. Abramenko, B. Bogdanovich, M. Karetnikov, A. Nesterovich, A. Puchkov	1143	RPR10
RFQ Design for High-Intensity Proton Beams — R. Ferdinand, J.-M. Lagniel, P. Mattei	1146	RPR11
Methods for Increasing of Beam Intensity in Undulator Linear Accelerator — E.S. Masunov	1149	RPR12
Linac Integrated Scheme Using RF Energy Storage and Compression — A.V. Smirnov	1152	RPR13
Magnetic Field Influence on RF-Structures Electrodynamical Characteristics and Sparking Limit — A. Shalnov, N. Abramenko, B. Bogdanovich, M. Karetnikov, A. Nesterovich, M. Tubaev	1155	RPR15
Calculations on the Possibility of the Simultaneous Acceleration of Ions with Different Charge States in a RFQ — H. Deitinghoff	1158	RPR18
Phase-Scan Analysis Results for the First Drift Tube Linac Module in the Ground Test Accelerator: Data Reproducibility and Comparison to Simulations — K.F. Johnson, O.R. Sander, G.O. Bolme, S. Bowling, R. Connolly, J.D. Gilpatrick, W.P. Lysenko, J. Power, E.A. Wadlinger, V. Yuan	1161	RPR19
Accelerator Systems Optimizing Code — C.C. Paulson, A.M.M. Todd, M.A. Peacock, M.F. Reusch, D. Bruhwiler, S.L. Mendelsohn, D. Berwald, C. Piaszczyk, T. Meyers, G.H. Gillespie, B.W. Hill, R.A. Jamison	1164	RPR20
Unexpected Matching Insensitivity in DTL of GTA Accelerator — V.W. Yuan, O.R. Sander, R.C. Connolly, J.D. Gilpatrick, K.F. Johnson, W.P. Lysenko, D.P. Rusthoi, M. Smith, R. Weiss	1167	RPR22
Current Losses and Equilibrium in RF Linear Accelerators — Nathan Brown, Martin Reiser	1170	RPR23
MMF Linac Upgrade Possibilities for the Pulsed Neutron Source — S.K. Esin, L.V. Kravchuk, A.I. Kvasha, P.N. Ostroumov, V.L. Serov	1173	RPR24
Moscow Meson Factory DTL RF System Upgrade — S.K. Esin, L.V. Kravchuk, A.I. Kvasha, V.L. Serov	1175	RPR25

Pulsed and High Intensity Beams and Technology

Heavy Ion Fusion 2 MV Injector (Invited) — S. Yu, S. Eylon, E. Henestroza, C. Peters, L. Reginato, D. Vanecek, F. delaRama, R. Hipple, J.D. Stoker, D. Grote, F. Deadrick	1178	TAE01
Linac-Driven Spallation-Neutron Source (Invited) — Andrew J. Jason	1183	TAE02

High Average Power, High Current Pulsed Accelerator Technology (Invited) — <i>Eugene L. Neu</i>	1188	TAE03
Studies of Localized Space-Charge Waves in Space-Charge Dominated Beams (Invited) — <i>J.G. Wang, M. Reiser</i>	1193	TAE04
Design of the Jupiter Accelerator for Large X-ray Yields — J.J. Ramirez	1198	TAE05
Design and Power Flow Studies of a 500-TW Inductive Voltage Adder (IVA) Accelerator — <i>M.G. Mazarakis, J.W. Poukey, J.P. Corley, D.L. Smith, L. Bennett, J.J. Ramirez, P. Pankuch,</i> <i>I. Smith, P. Corcoran, P. Spence</i>	1201	TAE06
COBRA Accelerator for Sandia ICF Diode Research at Cornell University — David L. Smith, <i>Pete Ingwersen, Lawrence F. Bennett, John D. Boyes, David E. Anderson, John B. Greenly,</i> <i>Ravi N. Sudan</i>	1204	TAE07
Beam Injector and Transport Calculations for ITS — Thomas P. Hughes, David C. Moir, <i>Paul W. Allison</i>	1207	TAE08
Status of the AIRIX Induction Accelerator — Ph. Eyharts, Ph. Anthouard, J. Bardy, <i>C. Bonnafond, Ph. Delsart, A. Devin, P. Eyl, J. Labrousche, J. Launspach, J. De Mascureau,</i> <i>E. Merle, A. Roques, P. Le Taillandier, M. Thevenot, D. Villate, L. Voisin</i>	1210	TAE09
Pulse Modulators for Ion Recirculator Cells — T.F. Godlove, L.K. Len, F.M. Mako, <i>W.M. Black, K. Sloth</i>	1213	TAE10
A High Charge State Heavy Ion Beam Source for HIF — S. Eylon, E. Henestroza	1216	TAE11
Design and Operation of a 700kV, 700A Modulator — J.D. Ivers, G.S. Kerslick, J.A. Nation, <i>L. Schächter</i>	1219	TAE12
The 3 MEV, 200 KW High Voltage Electron Accelerator for Industrial Application — <i>N.G. Tolstun, V.S. Kuznetsov, A.S. Ivanov, V.P. Ovchinnikov, M.P. Svinjin</i>	1222	TAE13
Klystron Modulator for Industrial Linac — Yu.D. Tur, V.I. Beloglazov, E.A. Khomyakov, <i>V.P. Krivchikov, V.B. Mufel, V.V. Zakutin</i>	1225	TAE14
Optimization of High-Current Ion Beam Acceleration and Charge Compensation in Two Cusps of Induction Linac — Vyacheslav I. Karas', Nadya G. Belova	1227	WAA01
2,5-Dimensional Numerical Simulation of Propagation of the Finite Sequence of Relativistic Electron Bunches (REB) in Tenuous and Dense Plasmas — V.I. Karas', Ya.B. Fainberg, <i>V.D. Levchenko, Yu.S. Sigov</i>	1230	WAA02
Kinetic Simulation of Fields Excitation and Particle Acceleration by Laser Beat Wave in Non-Homogeneous Plasmas — V.I. Karas', Ya.B. Fainberg, V.D. Levchenko, Yu.S. Sigov	1233	WAA03
An Upgraded Proton Injection Kicker Magnet for the Fermilab MIR — J. Dinkel, R. Reilly	1236	WAA05
Fermilab Main Injector Abort Kicker System — C.C. Jensen, J.A. Dinkel	1239	WAA07
Analysis of the Electrical Noise from the APS Kicker Magnet Power Supplies — <i>J.A. Carwardine, J. Wang</i>	1242	WAA08
Design and Test Results of Kicker Units for the Positron Accumulator Ring at the APS — <i>J. Wang</i>	1245	WAA09
Development of a Modular and Upgradeable Fast Kicker Magnet System for the Duke Storage Ring — R.J. Sachtshale, C. Dickey, P. Morcombe	1248	WAA10
High Current High Accuracy IGBT Pulse Generator — V.V. Nesterov, A.R. Donaldson	1251	WAA11
Analysis and Design Modifications for Upgrade of Storage Ring Bump Pulse System Driving the Injection Bump Magnets at the ALS — G.D. Stover	1254	WAA14
Eddy Currents Induced in a Muon Storage Ring Vacuum Chamber Due to a Fast Kicker — <i>W.Q. Feng, E.B. Forsyth</i>	1257	WAA15
High Pulse Power Modulator for a S-Band Transmitter — J. DeCobert, B. Binns, R. Campbell, <i>A. Hawkins, D. Wang, A. Zolfaghari</i>	1260	WAA16
Modulator for Klystron 5045 — N.S. Dikansky, V. Akimov, B. Estrin, K. Gubin, I. Kazarezov, <i>V. Kokoulin, N. Kot, A. Novokhatsky, Yu. Tokarev, S. Vasserman</i>	1263	WAA17
High Voltage Nanosecond Generators for SIBERIA - 2 — A. Kadnikov, V. Deviatilov, <i>V. Korchuganov, Yu. Matveev, D. Shvedov</i>	1266	WAA18
High Gradient Insulator Technology for the Dielectric Wall Accelerator — S. Sampayan, <i>G. Caporaso, B. Carder, Y. Chen, C. Holmes, E. Lauer, D. Trimble, J. Elizondo, M. Krogh,</i> <i>B. Rosenblum, C. Eichenberger, J. Fockler</i>	1269	WAA19
Status of the First Stage of Linear Induction Accelerator SILUND-21 — A.A. Fateev, <i>G.V. Dolbilov, I.I. Golubev, I.N. Ivanov, V.V. Kosukhin, N.I. Lebedev, V.A. Petrov,</i> <i>V.N. Razuvakin, V.S. Shvetsov, M.V. Yurkov</i>	1272	WAA20

EMIR-M Installation in the Mode of Operation with Plasma Opening Switch — <i>V.P. Kovalev, V.M. Korepanov, B.M. Lavrent'ev, R.N. Munasyrov, B.A. Filatov</i>	1274	WAA21
--	------	-------

Magnet Technology

New Developments in Niobium Titanium Superconductors (Invited) — D.C. Larbalestier, <i>P.J. Lee</i>	1276	TPE01
Superconducting Magnets (Invited) — R. Perin	1282	TPE02
Assembly and Commissioning of the LHC Test String (Invited) — P. Faugeras	1288	TPE03
Construction and Testing of Arc Dipoles and Quadrupoles for the Relativistic Heavy Ion Collider (RHIC) at BNL (Invited) — P. Wanderer, J. Muratore, M. Anerella, G. Ganetis, A. Ghosh, A. Greene, R. Gupta, A. Jain, S. Kahn, E. Kelly, G. Morgan, A. Prodel, M. Rehak, W. Sampson, R. Thomas, P. Thompson, E. Willen	1293	TPE04
Permanent Magnet Design for the Fermilab Main Injector Recycler Ring — G.W. Foster, <i>K. Bertsche, J.-F. Ostiguy, B. Brown, H. Glass, G. Jackson, M. May, D. Orris, Dick Gustafson</i>	1298	TPE05
Recent Advances in Insertion Devices (Invited) — E. Gluskin, E.R. Moog	1301	TPE06
Permanent Magnet Beam Transport (Invited) — R.F. Holsinger	1305	TPE07
Statistical Analyses of the Magnet Data for the Advanced Photon Source Storage Ring Magnets (Invited) — S.H. Kim, D.W. Carnegie, C. Doose, R. Hogrefe, K. Kim, R. Merl	1310	TPE08
The Magnet System for the BESSY II Injector Synchrotron — T. Knuth, D. Krämer, <i>E. Weihrer, I. Chertok, S. Michailov, B. Sukhina</i>	1316	TPE09
Segmented High Quality Undulators — J. Chavanne, P. Elleaume, P. Van Vaerenbergh	1319	TPE10
Design of the PEP-II Low-Energy Ring Arc Magnets — T. Henderson, N. Li, J. Osborn, <i>J. Tanabe, D. Yee, R. Yourd, W. Du, Y. Jiang, Y. Sun</i>	1322	FAP01
Prototype Development of the BESSY II Storage Ring Magnetic Elements — T. Becker, <i>D. Krämer, S. Küchler, U. Strönisch, V. Korchuganov, N. Kuznetsov, E. Levichev</i>	1325	FAP02
Design, Construction, and Procurement Methodology of Magnets for the 7-GeV Advanced Photon Source — A. Gorski, J. Argyrakis, J. Biggs, E. Black, J. Humbert, J. Jagger, <i>K. Thompson</i>	1328	FAP03
The Main Injector Trim Dipole Magnets — R. Baiod, D.J. Harding, D.E. Johnson, P.S. Martin, <i>S. Mishra</i>	1331	FAP04
The Main Injector Chromaticity Correction Sextupole Magnets: Measurements and Operating Schemes — C.M. Bhat, A. Bogacz, B.C. Brown, D.J. Harding, Si J. Fang, <i>P.S. Martin, H.D. Glass, J. Sim</i>	1334	FAP05
Magnetic Field Measurements of the Initial Fermilab Main Injector Production Quadrupoles — D.J. Harding, R. Baiod, B.C. Brown, J.A. Carson, N.S. Chester, E. Desavouret, J. DiMarco, J.D. Garvey, H.D. Glass, P.J. Hall, P.S. Martin, P.O. Mazur, C.S. Mishra, A. Mokhtarani, J.M. Nogiec, D.F. Orris, J.E. Pachnik, A.D. Russell, S.A. Sharonov, J.W. Sim, J.C. Tompkins, K. Trombly-Freytag, D.G.C. Walbridge, V.A. Yarba	1337	FAP06
Magnetic Field Measurements of the Initial Fermilab Main Injector Production Dipoles — D.J. Harding, R. Baiod, B.C. Brown, J.A. Carson, N.S. Chester, E. Desavouret, J. DiMarco, J.D. Garvey, H.D. Glass, P.J. Hall, P.S. Martin, P.O. Mazur, S. Mishra, A. Mokhtarani, J.M. Nogiec, D.F. Orris, J.E. Pachnik, A.D. Russell, S.A. Sharonov, J.W. Sim, J.C. Tompkins, K. Trombly-Freytag, D.G.C. Walbridge, V.A. Yarba	1340	FAP07
The Fermilab Main Injector Dipole and Quadrupole Cooling Design and Bus Connections — J.A. Satti	1343	FAP08
Design of the Fermilab Main Injector Lambertson — D.E. Johnson, R. Baiod, D.J. Harding, <i>P.S. Martin, M. May</i>	1346	FAP09
Three-Dimensional End Effects in Iron Septum Magnets — J.-F. Ostiguy, D.E. Johnson	1349	FAP10
Design and B-field Measurements of a Lambertson Injection Magnet for the RHIC Machine — N. Tsoupas, E. Rodger, J. Claus, H.W. Foelsche, P. Wanderer	1352	FAP11
The APS Direct-Drive Pulsed Septum Magnets — S. Sheynin, F. Lopez, S.V. Milton	1355	FAP12
Development of the Pulse Magnets for the Booster Synchrotron of SPring-8 — H. Yonehara, <i>H. Suzuki, T. Nagafuchi, M. Kodaira, T. Aoki, N. Tani, S. Hayashi, Y. Ueyama, T. Kaneda, Y. Sasaki, H. Abe, H. Yokomizo</i>	1358	FAP13
Magnetic Design of the LNLs Transport Line — R.H.A. Farias, Liu Lin, G. Tosin	1361	FAP14
Construction and Characterization of Combined Function Quadrupoles — G. Tosin	1364	FAP15

Dipole Magnets for the SLAC 50 GeV A-Line Upgrade — R. Erickson, S. DeBarger, C.M. Spencer, Z. Wolf.....	1366	FAP16
Design and Testing of the Magnetic Quadrupole for the Heavy Ion Fusion Program — R. Benjegerdes, A. Faltens, W. Fawley, C. Peters, L. Reginato, M. Stuart	1369	FAP17
Design and Construction of a Large Aperture, Quadrupole Electromagnet Prototype for ILSE — M. Stuart, A. Faltens, W.M. Fawley, C. Peters, M.C. Vella.....	1372	FAP18
A Permanent Race-Track Microtron End Magnet — A.I. Karev, V.N. Melekhin, V.I. Shvedunov, N.P. Sobenin, W.P. Trower.....	1375	FAP19
Planar Permanent Magnet Multipoles: Measurements and Configurations — T. Cremer, R. Tatchyn.....	1378	FAP20
Temperature Considerations in the Design of a Permanent Magnet Storage Ring — K. Bertsche, J.-F. Ostiguy, W.B. Foster.....	1381	FAP21
3D Numerical Analysis of Magnets and the Effect of Eddy Current on Fast Steering — T. Nagatsuka, T. Koseki, Y. Kamiya, Y. Terada	1384	FAP22
MEB Resitive Magnets Prototypes Manufacturing — G. Batskikh, G. Mamaev, T. Latypov, I. Tenyakov, Y. Tereshkin.....	1387	FAP24

Volume 3

Magnet Technology (cont'd)

Quench Antennas for RHIC Quadrupole Magnets — T. Ogitsu, A. Terashima, K. Tsuchiya, G. Ganetis, J. Muratore, P. Wanderer.....	1390	FAQ02
Superconducting 8 cm Corrector Magnets for the Relativistic Heavy Ion Collider (RHIC) — A. Morgillo, J. Escallier, G. Ganetis, A. Greene, A. Ghosh, A. Jain, E. Kelly, A. Marone, G. Morgan, J. Muratore, W. Sampson, P. Thompson, P.J. Wanderer, E. Willen.....	1393	FAQ03
Superconducting Sextupoles and Trim Quadrupoles for RHIC — P. Thompson, M. Anerella, G. Ganetis, A. Ghosh, A. Greene, R. Gupta, A. Jain, E. Kelly, M. Lindner, G. Morgan, J. Muratore, W. Sampson, P. Wanderer, E. Willen.....	1396	FAQ04
Study of UNK Quench Protection System on the String of 4 UNK Superconducting Magnets — A. Andriishchin, O. Afanasiev, V. Gridasov, A. Erochin, E. Kachtanov, K. Myznikov, V. Sytchev, L. Vassiliev, O. Veselov, N. Yarygin.....	1399	FAQ06
Two Alternate High Gradient Quadrupoles; An Upgraded Tevatron IR and a "Pipe" Design — A.D. McInturff, J.M. van Oort, R.M. Scanlan.....	1402	FAQ07
Superconducting Focusing Solenoid for X-band Klystron — T. Ogitsu, T. Higo, H. Mizuno, Y. Imai, T. Inaguchi, T. Minato, T.H. Kim, T. Uemura, S. Yokoyama, Z. Wolf, D. Jensen, P. Radusewicz.....	1405	FAQ08
A High Gradient Superconducting Quadrupole for a Low Charge State Ion Linac — J.W. Kim, K.W. Shepard, J.A. Nolen.....	1408	FAQ09
Status of the High Brilliance Synchrotron Radiation Source BESSY-II — E. Jaeschke, S. Khan, D. Krämer, D. Schirmer	1411	FAQ12
Harmonic Generation FEL Magnets: Measured B-fields Compared to 3D Simulations — W.S. Graves, L. Solomon.....	1414	FAQ13
Measurement of Ramp Rate Sensitivity in Model Dipoles with Ebanol-Coated Cable — C. Haddock, V. Kovachev, D. Capone.....	1417	FAQ14
Combined Element Magnet Production for the Relativistic Heavy Ion Collider (RHIC) at BNL — S. Mulhall, H. Foelsche, G. Ganetis, A. Greene, E. Kelly, S. Plate, E. Willen	1420	FAQ15
Field Quality Control Through the Production Phase of the RHIC Arc Dipoles — R. Gupta, A. Jain, S. Kahn, G. Morgan, P. Thompson, P. Wanderer, E. Willen	1423	FAQ16
The Elliptical Multipole Wiggler Project — E. Gluskin, D. Frachon, P.M. Ivanov, J. Maines, E.A. Medvedko, E. Trakhtenberg, L.R. Turner, I. Vasserman, G.I. Erg, Yu.A. Evtushenko, N.G. Gavrilov, G.N. Kulipanov, A.S. Medvedko, S.P. Petrov, V.M. Popik, N.A. Vinokurov, A. Friedman, S. Krinsky, G. Rakowsky, O. Singh	1426	FAQ17
Results of Magnetic Measurements and Field Integral Compensation for the Elliptical Multipole Wiggler — D. Frachon, P.M. Ivanov, E.A. Medvedko, I. Vasserman, O. Despe, Y.G. Kang	1429	FAQ18

Status of ELETTRA Insertion Devices — <i>R.P. Walker, R. Bracco, A. Codutti, B. Diviacco, D. Millo, D. Zangrando</i>	1432	FAQ19
Expected Radiation Spectra of a 30-m Long Undulator in SPring-8 — <i>M. Takao, Y. Miyahara</i>	1435	FAQ20
Analytical Formulation of a Quasi-periodic Undulator — <i>M. Takao, S. Hashimoto, S. Sasaki, Y. Miyahara</i>	1438	FAQ21
High-Field Strong-Focusing Undulator Designs for X-Ray Linac Coherent Light Source (LCLS) Applications — <i>S. Caspi, R. Schlueter, R. Tatchyn</i>	1441	FAQ23
Wigglers at the Advanced Light Source — <i>E. Hoyer, J. Akre, D. Humphries, T. Jackson, S. Marks, Y. Minamihara, P. Pipersky, D. Plate, G. Portmann, R. Schlueter</i>	1444	FAQ24
Design of End Magnetic Structures for the Advanced Light Source Wigglers — <i>D. Humphries, J. Akre, E. Hoyer, S. Marks, Y. Minamihara, P. Pipersky, D. Plate, R. Schlueter</i>	1447	FAQ25
Passive End Pole Compensation Scheme for a 1.8 Tesla Wiggler — <i>L.H. Chang, Ch. Wang, C.H. Chang, T.C. Fan</i>	1450	FAQ26
Insertion of Helical Siberian Snakes in RHIC — <i>A. Luccio, F. Pilat</i>	1453	FAQ28
Modeling of WLS Field with Piecewisely Constant Magnets — <i>Zuping Liu, Aihua Zhao</i>	1456	FAQ29
A BESSY-1 6 Tesla WLS Effect Compensation Scheme — <i>Zuping Liu, Aihua Zhao</i>	1459	FAQ30
16 Tesla Block-Coil Dipole for Future Hadron Colliders — <i>Peter M. McIntyre, Weijun Shen</i>	1462	FAQ31
Automated Methods of Field Harmonic Signal Extraction and Processing for the Magnets in Superconducting Supercollider — <i>T.S. Jaffery, J. Butteris, M. Wake</i>	1465	FAQ32

Radio Frequency Technology

Review of the Development of RF Cavities for High Currents (Invited) — <i>J. Kirchgessner</i>	1469	F AE01
Performance of Normal Conducting Structures for Linear Colliders (Invited) — <i>Toshiyasu Higo</i>	1474	F AE02
High Gradient Superconducting RF Systems (Invited) — <i>J. Graber</i>	1478	F AE03
Development and Advances in Conventional High Power RF Systems (Invited) — <i>P.B. Wilson</i>	1483	F AE04
The Upgraded RF System for the AGS and High Intensity Proton Beams (Invited) — <i>J.M. Brennan</i>	1489	F AE05
Phase-Stable, Microwave FEL Amplifier — <i>Bruce E. Carlsten, Michael V. Fazio, W. Brian Haynes, Lisa M. May, James M. Potter</i>	1494	F AE06
1.2 MW Klystron for Asymmetric Storage Ring B Factory — <i>W.R. Fowkes, G. Caryotakis, E. Doyle, E. Jongewaard, C. Pearson, R. Phillips, J. Sackett, E. Wright, H. Bohlen, G. Huffman, S. Lenci, E. Lien, E. McCune, G. Miram</i>	1497	F AE07
Analysis of Multipacting in Coaxial Lines — <i>E. Somersalo, P. Ylä-Oijala, D. Proch</i>	1500	F AE08
An Accelerator Resonantly Coupled with an Energy Storage (ARES) for the KEKB — <i>Y. Yamazaki, K. Akai, N. Akasaka, E. Ezura, T. Kageyama, F. Naito, T. Shintake, Y. Takeuchi</i>	1503	F AE09
Non Integer Harmonic Number Acceleration of Lead Ions in the CERN SPS — <i>D. Boussard, T. Bohl, T. Linnecar, U. Wehrle</i>	1506	F AE10
Analysis and Results of the Industrial Production of the Superconducting Nb/Cu Cavities for the LEP2 Project — <i>E. Chiaveri, C. Benvenuti, R. Cosso, D. Lacarrere, K.M. Schirm, M. Taufer, W. Weingarten</i>	1509	F AE11
Performance Experience with the CEBAF SRF Cavities — <i>C. Reece, J. Benesch, M. Drury, C. Hovater, J. Mammoser, T. Powers, J. Preble</i>	1512	F AE12
Beam Test of a Superconducting Cavity for the CESR Luminosity Upgrade — <i>H. Padamsee, P. Barnes, S. Belomestnykh, K. Berkelman, M. Billing, R. Ehrlich, G. Flynn, Z. Greenwald, W. Hartung, T. Hays, S. Henderson, R. Kaplan, J. Kirchgessner, J. Knobloch, D. Moffat, H. Muller, E. Nordberg, S. Peck, M. Pisharody, J. Reilly, J. Rogers, D. Rice, D. Rubin, D. Sagan, J. Sears, M. Tigner, J. Welch</i>	1515	F AE13

Radio Frequency Power Sources

Development of Input & Output Structures for High Power X-Band TWT Amplifiers — <i>S. Naqvi, Cz. Golkowski, G.S. Kerslick, J.A. Nation, L. Schächter</i>	1518	TAQ01
Characterization of a Klystron as a RF Source for High-Average-Power Accelerators — <i>D. Rees, D. Keffeler, W. Roybal, P.J. Tallerico</i>	1521	TAQ02
Choppertron II — <i>T.L. Houck, G.A. Westenskow, J. Haimson, B. Mecklenburg</i>	1524	TAQ03

The Resistive-Wall Klystron as a High-Power Microwave Source — Han S. Uhm.....	1527	TAQ04
Operating Conditions of High-Power Relativistic Klystron — Han S. Uhm	1530	TAQ05
Spurious Oscillations in High Power Klystrons — B. Krietenstein, K. Ko, T. Lee, U. Becker, T. Weiland, M. Dohlus.....	1533	TAQ06
In-House Repair of a 30 Megawatt S Band Klystron — R. Sachtschale, P.G. O'Shea, M. Ponds, G. Swift	1536	TAQ07
Development of a High Power 1.2 MW CW L-Band Klystron — K. Hirano, Y.L. Wang, T. Emoto, A. Enomoto, I. Sato	1539	TAQ08
Ultrarelativistic Klystron - a Future Super Power UHF Generator — F.A. Vodopianov	1542	TAQ10
A 200 KW Power Amplifier and Solid State Driver for the Fermilab Main Injector — J. Reid, H. Miller	1544	TAQ11
A 476 MHz RF System for the Storage Mode of the AmPS Ring — F. Kroes, P. de Groen, E. Heine, B. Heutenik, A. Kruijer, B. Munneke, R. Piovano, T. Sluijk, J. Verkooyen.....	1547	TAQ12
Lifetime Experience with Low Temperature Cathodes Equipped in Super Power Klystrons — Rudolf Backmor.....	1550	TAQ13
Microwave System of PLS 2-GeV Linac — H.S. Lee, O.H. Hwang, S.H. Park, C.M. Ryu, W. Namkung	1553	TAQ14
Klystron-Modulator System Performances for PLS 2-GeV Linac — M.H. Cho, J.S. Oh, S.S. Park, W. Namkung.....	1556	TAQ15
Klystron Modulator Operation and Upgrades for the APS Linac — Thomas J. Russell, Alexander Cours	1559	TAQ16
Prospects for Developing Microwave Amplifiers to Drive Multi-TeV Linear Colliders — V.L. Granatstein, G.S. Nusinovich, J. Calame, W. Lawson, A. Singh, H. Guo, M. Reiser	1561	TAQ17
Design of 100 MW, Two-Cavity Gyroklystrons for Accelerator Applications — J.P. Calame, W. Lawson, J. Cheng, B. Hogan, M. Castle, V.L. Granatstein, M. Reiser.....	1563	TAQ18
Design of Three-Cavity Coaxial Gyroklystron Circuits for Linear Collider Applications — W. Lawson, G. Saraph, J.P. Calame, J. Cheng, M. Castle, B. Hogan, M. Reiser, V.L. Granatstein, H. Metz	1566	TAQ19
Numerical Simulation of Magnicon Amplifier — V. Yakovlev, O. Danilov, O. Nezhevenko, V. Tarnetsky.....	1569	TAQ21
RF-Power Upgrade Systems with Energy Compression for Electron Linacs — A. Shalnov, B.Yu. Bogdanovich, A. Ignatyev, V. Senyukov.....	1572	TAQ23
RF-Power Upgrade System with Resonant Loading — A. Shalnov, B. Bogdanovich, A. Ignatyev, V. Senyukov.....	1575	TAQ24
High-Power Test of Traveling-Wave-Type RF-Pulse Compressor — S. Yamaguchi, A. Enomoto, I. Sato, Y. Igarashi.....	1578	TAQ25
Active Radiofrequency Pulse Compression Using Switched Resonant Delay Lines — Sami G. Tantawi, Ronald D. Ruth, A.E. Vlieks	1581	TAQ26
Design of a Multi-Megawatt X-Band Solid State Microwave Switch — Sami G. Tantawi, Terry G. Lee, Ronald D. Ruth, A.E. Vlieks, Max Zolotarev	1584	TAQ27
Reduced Field TE01 X-Band Traveling Wave Window — W.R. Fowkes, R.S. Callin, S.G. Tantawi, E.L. Wright.....	1587	TAQ28
Design and High-Power Test of a TE11-Mode X-Band RF Window with Taper Transitions — Y. Otake, S. Tokumoto, H. Mizuno.....	1590	TAQ29
Feasibility Study of Optically Coupling RF-Power at mm Waves — B. Littmann, H. Henke.....	1593	TAQ30
A Low-Frequency High-Voltage RF-Barrier Bunching System for High-Intensity Neutron Source Compressor Rings — T.W. Hardek, D. Rees, C. Ziomek.....	1596	TAQ31
Temporal Evolution of Multipactor Discharge — R. Kishek, Y.Y. Lau, R.M. Gilgenbach.....	1599	TAQ32
Stabilizing a Power Amplifier Feeding a High Q Resonant Load — A.K. Mitra, R.L. Poirier, J.J. Lu, R. Hohbach.....	1602	TAQ33
Study of 14 GHz VLEPP Klystron With RF Absorbing Drift Tubes — G.V. Dolbilov, N.I. Azorsky, A.A. Fateev, N.I. Lebedev, V.A. Petrov, V.P. Sarantsev, V.S. Shvetsov, M.V. Yurkov.....	1605	TAQ34
24-MW, 24-μs Pulse RF Power Supply For Linac-Based FELs — E. Ohshita, Y. Morii, S. Abe, S. Okuma, K. Wakita, T. Tomimasu, I. Ito, Y. Miyai, K. Nakata, M. Hakota	1608	TAQ35
Initial Operation of an X-Band Magnicon Amplifier Experiment — S.H. Gold, A.K. Kinkead, A.W. Fliflet, B. Hafizi	1611	TAQ37

Superconducting RF

The Effects of Tuning and Terminating on the Operating Mode of Multi-Cell Coupled Cavity — Zubao Qian.....	1614	TPP01
Response of Superconducting Cavities to High Peak Power — T. Hays, H. Padamsee.....	1617	TPP02
Development of HOM Damper for B-Factor (KEKB) Superconducting Cavities — T. Tajima, K. Asano, T. Furuya, M. Izawa, S. Mitsunobu, T. Takahashi, N. Gamo, S. Iida, Y. Ishi, Y. Kijima, S. Kokura, M. Kudo, K. Sennyu, S. Tachibana, H. Takashina, N. Taniyama.....	1620	TPP03
Microscopic Examination of Defects Located by Thermometry in 1.5 GHz Superconducting Niobium Cavities — J. Knobloch, R. Durand, H. Muller, H. Padamsee.....	1623	TPP04
RF System for the NSLS Coherent Infrared Radiation Source — W. Broome, R. Biscardi, J. Keane, P. Mortazavi, M. Thomas, J.M. Wang.....	1626	TPP06
Development of TESLA-type Cavity at KEK — M. Ono, E. Kako, S. Noguchi, K. Saito, T. Shishido, M. Wake, H. Inoue, T. Fujino, Y. Funahashi, M. Matsuoka, T. Suzuki, T. Higuchi, H. Umezawa.....	1629	TPP07
Study of Luminous Spots Observed on Metallic Surfaces Subjected to High RF Fields — T. Junquera, S. Maïssa, M. Fouaidy, A. Le Goff, B. Bonin, M. Luong, H. Safa, J. Tan.....	1632	TPP09
Test Results for a Heat-Treated 4-Cell 805-MHz Superconducting Cavity — Brian Rusnak, Alan Shapiro.....	1636	TPP10
An Advanced Rotating T-R Mapping & its Diagnoses of TESLA 9-Cell Superconducting Cavity — Q.S. Shu, G. Deppe, W-D. Möller, M. Pekeler, D. Proch, D. Renken, P. Stein, C. Stolzenburg, T. Junquera, A. Caruette, M. Fouaidy.....	1639	TPP11
Improvements to Power Couplers for the LEP2 Superconducting Cavities — J. Tückmantel, C. Benvenuti, D. Bloess, D. Boussard, G. Geschonke, E. Haebel, N. Hilleret, S. Juras, H.P. Kindermann, J. Uythoven, C. Wyss, M. Stirbet.....	1642	TPP12
Arcing Phenomena on CEBAF RF-Windows at Cryogenic Temperatures — Tom Powers, Peter Kneisel, Ray Allen.....	1645	TPP13
Surface Scanning Thermometers for Diagnosing the TESLA SRF Cavities — T. Junquera, A. Caruette, M. Fouaidy, Q.S. Shu.....	1648	TPP14
Microwave Surface Resistance of YBaCuO Superconducting Films Laser-Ablated on Copper Substrates — J. Liu, K. Asano, E. Ezura, M. Fukutomi, S. Inagaki, S. Isagawa, K. Komori, S. Kumagai, H. Nakanishi, M. Tosa, K. Yoshihara.....	1652	TPP16

Room Temperature RF

Transverse Coupling Impedance Measurement Using Image Current — D. Sun, P. Colestock, M. Foley.....	1655	WPP01
Decreasing Transient Beam Loading in RF Cavities of U-70 Accelerator — O.P. Lebedev.....	1658	WPP02
RF System for Bunch Lengthening — R. Biscardi, G. Ramirez.....	1660	WPP03
Electromagnetic Field Vector Components Precise Measurements in Accelerating Structures — M.A. Chernogubovsky, M.F. Vorogushin.....	1663	WPP04
A New Tuning Method for Traveling Wave Structures — T. Khabiboulline, V. Puntus, M. Dohlus, N. Holtkamp, G. Kreps, S. Ivanov, K. Jin.....	1666	WPP05
RF Systems for RHIC — J. Rose, J. Brodowski, R. Connolly, D.P. Deng, S. Kwiatkowski, W. Pirkel, A. Ratti.....	1669	WPP07
A New RF System for Bunch Coalescing in the Fermilab Main Ring — J. Dey, I. Kourbanis, D. Wildman.....	1672	WPP08
Higher Order Modes of the Main Ring Cavity at Fermilab — J. Dey, D. Wildman.....	1675	WPP09
RF Measurements and Control of Higher Order Modes in Accelerating Cavities — V. Veshcherevich, S. Krutikhin, I. Kuptsov, S. Nosyrev, A. Novikov, I. Sedlyarov.....	1678	WPP10
RF System of VEPP-4M Electron-Positron Collider — E. Gorniker, P. Abramsky, V. Arbutov, S. Belomestnykh, A. Bushuyev, M. Fomin, I. Kuptsov, G. Kurkin, S. Nosyrev, V. Petrov, I. Sedlyarov, V. Veshcherevich.....	1681	WPP11
Storage Ring Cavity Higher-Order Mode Dampers for the Advanced Photon Source — Paul Matthews, Yoon Kang, Robert Kustom.....	1684	WPP12

Reduction of Multipactor in RF Ceramic Windows Using a Simple Titanium-Vapor Deposition System — <i>K. Primdahl, R. Kustom, J. Maj</i>	1687	WPP13
Cooling the APS Storage Ring Radio-Frequency Accelerating Cavities Thermal/Stress/Fatigue Analysis and Cavity Cooling Configuration — <i>K. Primdahl, R. Kustom</i>	1690	WPP14
RF Cavities for the Positron Accumulator Ring (PAR) of the Advanced Photon Source (APS) — <i>Y.W. Kang, A. Nassiri, J.F. Bridges, T.L. Smith, J.J. Song</i>	1693	WPP16
The Proposal of Complex Impedance Termination for Versatile HOM Damper Cavity — <i>V.V. Paramonov</i>	1696	WPP17
The Magnetron-Type Varactor for Fast Control in Accelerator RF Systems — <i>M.I. Kuznetsov, V.V. Paramonov, Yu.V. Senichev, I.B. Enchevich, R.L. Poirier</i>	1699	WPP18
The Distortion of the Accelerating Field Distribution in Compensated Structures due to Steady-State Beam Loading — <i>V.G. Andreev, V.V. Paramonov</i>	1702	WPP19
The Indiana University Cooler Injector Synchrotron RF System — <i>A. Pei, M. Ellison, D. Friesel, D. Jenner, X. Kang, S.Y. Lee, D. Li, J. Liu, A. Riabko, L. Wang, K. Hedblom</i>	1705	WPP20
The Indiana University Cooler Injection Synchrotron RF Cavity — <i>A. Pei, M. Ellison, D. Friesel, D. Jenner, X. Kang, S.Y. Lee, D. Li, J. Liu, A. Riabko, L. Wang, K. Hedblom</i>	1708	WPP21
Determination of Resonant Frequency and External Q Values for the Bessy II HOM-Damped Cavity — <i>Frank Schönfeld, Bengt Littmann</i>	1711	WPP22
106 MHz Cavity for Improving Coalescing Efficiency in the Fermilab Main Ring — <i>J. Dey, I. Kourbanis, D. Wildman</i>	1714	WPP23
On the Higher Order Mode Coupler Design for Damped Accelerating Structures — <i>Jie Gao</i>	1717	WPQ01
High Power Window Tests on a 500 MHz Planar Window for the CESR Upgrade — <i>M. Pisharody, P. Barnes, E. Chojnacki, R. Durand, T. Hays, R. Kaplan, J. Kirchgessner, J. Reilly, H. Padamsee, J. Sears</i>	1720	WPQ02
Operational Performances and Future Upgrades for the ELETTRA RF System — <i>A. Fabris, A. Massarotti, C. Pasotti, M. Svandrlík</i>	1723	WPQ04
X-Band High Power Dry Load for NLCTA — <i>K. Ko, H. Hoag, T. Lee, S. Tantawi</i>	1726	WPQ05
Development of a High-Power RF Cavity for the PEP-II B Factory — <i>R.A. Rimmer, M.A. Allen, J. Saba, H. Schwarz, F.C. Belser, D.D. Berger, R.M. Franks</i>	1729	WPQ06
A Design of Input Coupler for RF-Cavity — <i>T. Nagatsuka, T. Koseki, Y. Kamiya, M. Izawa, Y. Terada</i>	1732	WPQ07
Design of the KEKB RF System — <i>K. Akai, E. Ezura, Y. Yamazaki</i>	1735	WPQ08
RF Characteristics of ARES Cold Models — <i>N. Akasaka, K. Akai, T. Kageyama, T. Shintake, Y. Yamazaki</i>	1738	WPQ09
Design of Traveling Wave Windows for the PEP-II RF Coupling Network — <i>N.M. Kroll, C.-K. Ng, J. Judkins, M. Neubauer</i>	1741	WPQ10
Impedance Spectrum for the PEP-II RF Cavity — <i>X.E. Lin, K. Ko, C.-K. Ng</i>	1744	WPQ12
Measurement and Analysis of Higher-Order-Mode (HOM) Damping in B-Factory R-F Cavities — <i>D.A. Goldberg, M. Irwin, R.A. Rimmer</i>	1747	WPQ13
Planar Structures for Electron Acceleration — <i>H. Henke</i>	1750	WPQ14
Precise Fabrication of X-Band Detuned Accelerating Structure for Linear Collider — <i>T. Higo, H. Sakai, Y. Higashi, T. Takatomi, S. Koike</i>	1753	WPQ15
Development of a Beam-Pipe HOM Absorber for the ATF Damping Ring — <i>F. Hinode, S. Sakanaka</i>	1756	WPQ16
Development of a HOM-Damped Cavity for the KEK B-Factory (KEKB) — <i>T. Kageyama, K. Akai, N. Akasaka, E. Ezura, F. Naito, T. Shintake, Y. Takeuchi, Y. Yamazaki, T. Kobayashi</i>	1759	WPQ17
Possible Cavity Construction Techniques for the DIAMOND Storage Ring — <i>D.M. Dykes, D.S.G. Higgins</i>	1762	WPQ18
The Design of the 26.7 MHz RF Cavity for RHIC — <i>J. Rose, J. Brodowski, D.P. Deng, S. Kwiatkowski, W. Pirkel, A. Ratti</i>	1765	WPQ19
A Design Upgrade of the RF Cavity and Its Power Window for High Current Operation of the NSLS X-Ray Storage Ring — <i>P. Mortazavi, M. Thomas</i>	1768	WPQ20
A Ferrite Loaded Untuned Cavity for a Compact Proton Synchrotron — <i>J.I. Hirota, K. Hiramoto, M. Nishi, Y. Iwashita, A. Noda, M. Inoue</i>	1770	WPQ21
On the Theory of Two Coupled Cavities — <i>N.I. Aizatsky</i>	1773	WPQ22

Measurement of Multipacting Currents of Metal Surfaces in RF Fields — D. Proch, <i>D. Einfeld, R. Onken, N. Steinhauser</i>	1776	WPQ24
Optimization of CLIC Transfer Structure (CTS) Design to Meet New Drive Beam Parameters — A. Millich	1779	WPQ25
A High-Power Multiple-Harmonic Acceleration System for Proton- and Heavy-Ion Synchrotrons — P. Ausset, G. Charruau, F.J. Etzkorn, C. Fougeron, H. Meuth, S. Papureanu, <i>A. Schnase</i>	1781	WPQ26
A Bunch Lengthening RF Cavity for Aladdin — K.J. Kleman	1785	WPR01
Design of a High-Power Test Cavity for the ATF Damping Ring — S. Sakanaka, F. Hinode, <i>M. Akemoto, S. Tokumoto, T. Higo, J. Urakawa, T. Miura, Y. Hirata, K. Satoh</i>	1788	WPR02
Design of an RF System for the ATF Damping Ring — S. Sakanaka, F. Hinode, M. Akemoto, <i>H. Hayano, H. Matsumoto, K. Kubo, S. Tokumoto, T. Higo, J. Urakawa</i>	1791	WPR03
Development of a Damped Cavity with SiC Beam-Duct — T. Koseki, M. Izawa, Y. Kamiya	1794	WPR04
HOM Absorber for the KEKB Normal Conducting Cavity — Y. Takeuchi, K. Akai, <i>N. Akasaka, E. Ezura, T. Kageyama, F. Naito, T. Shintake, Y. Yamazaki</i>	1797	WPR05
PEP-II B-Factory Prototype Higher Order Mode Load Design — R. Pendleton, K. Ko, C. Ng, <i>M. Neubauer, H. Schwarz, R. Rimmer</i>	1800	WPR07
High-Power RF Window and Coupler Development for the PEP-II B Factory — M. Neubauer, <i>K. Fant, J. Hodgson, J. Judkins, H. Schwarz, R.A. Rimmer</i>	1803	WPR08
Input Coupler for the KEKB Normal Conducting Cavity — F. Naito, K. Akai, N. Akasaka, <i>E. Ezura, T. Kageyama, T. Shintake, Y. Takeuchi, Y. Yamazaki</i>	1806	WPR09
Minimum Wakefield Achievable by Waveguide Damped Cavity — Xintian E. Lin, <i>Norman M. Kroll</i>	1809	WPR10
PLS RF System Operation During the Commissioning — M. Kwon, I.H. Yu, H.J. Park, <i>D.H. Han, M. Yoon, Y.S. Kim</i>	1812	WPR11
Acoustic Experimental Studies of High Power Modes in Accelerating Structure of Kurchatov SR Source — M. Gangeluk, A. Kadnikov, Yu. Krylov, S. Kuznetsov, V. Moiseev, <i>V. Petrenko, V. Ushkov, Yu. Yupinov</i>	1815	WPR13
Computer Simulations of a Wide-Bandwidth Ferrite-Loaded High-Power Waveguide Termination — J. Johnson, R. Rimmer, J. Corlett	1818	WPR14
Effects of Temperature Variation on the SLC Linac RF System — F.-J. Decker, R. Akre, <i>M. Byrne, Z.D. Farkas, H. Jarvis, K. Jobe, R. Koontz, M. Mitchell, R. Pennacchi, M. Ross,</i> <i>H. Smith</i>	1821	WPR15
Broadband Coax-Waveguide Transitions — T. Rizawa, R. Pendleton	1824	WPR16
Rectangular Microtron Accelerating Structure — N.P. Sobenin, V.N. Kandrunin, <i>V.N. Melekhin, A.I. Karev, V.I. Shvedunov, W.P. Trower</i>	1827	WPR17
Investigation of the Biperiodic Accelerating Structure For The Free Electron Laser Buncher — N.P. Sobenin, S.N. Yarygin, D.V. Kostin, A.A. Zavadtsev	1830	WPR18
Ferromagnetic Cores Made from Amorphous Material for Broad-Band Accelerating System — I. Bolotin, V. Budilin, A. Glazov, V. Krasnopolsky, V. Skuratov	1833	WPR19
A New Structure with Continuous RF Acceleration and Focusing — J.J. Manca, M.C. Fallis, <i>J.P.J. Manca</i>	1835	WPR20
Spark Location in RF Cavities — Q. Kerns, M. Popovic, C. Kerns	1838	WPR21
RF System for the Duke 1 GeV Storage Ring — Ping Wang, Peter Morcombe, Ying Wu, <i>Grigori Kurkin</i>	1841	WPR22

Injection, Extraction and Targetry

Matching Section to the RFQ Using Permanent Magnet Symmetric Lens — M. Kando, <i>M. Ikegami, H. Dewa, H. Fujita, T. Shirai, H. Okamoto, Y. Iwashita, S. Kakigi, A. Noda,</i> <i>M. Inoue</i>	1843	WAQ01
Conceptual Designs of Beam Choppers for RFQ Linacs — Subrata Nath, Ralph R. Stevens Jr, <i>Thomas P. Wangler</i>	1846	WAQ02
The Role of Space Charge in the Performance of the Bunching System for the ATLAS Positive Ion Injector — R.C. Pardo, R. Smith	1849	WAQ03

Experimental Investigations of Plasma Lens Focusing and Plasma Channel Transport of Heavy Ion Beams — A. Tauschwitz, S.S. Yu, S. Eylon, L. Reginato, W. Leemans, J.O. Rasmussen, R.O. Bangerter.....	1852	WAQ04
A Low Energy Ion Beam Transport System with Variable Field Permanent Magnetic Quadrupoles — Y. Mori, A. Takagi, M. Kinsho, T. Baba, K. Shinto.....	1855	WAQ06
A Comparison of Two Injection Line Matching Sections for Compact Cyclotrons — T. Kuo, R. Baartman, L. Root, B. Milton, R. Laxadal, D. Yuan, K. Jayamanna, P. Schmor, G. Dutto, M. Dehnel, K. Erdman.....	1858	WAQ07
Stripping Injection Into the New Booster Ring at IUCF — K. Hedblom, D.L. Friesel.....	1861	WAQ08
Accurate Tuning of 90° Cells in a FODO Lattice — K. Bertsche, N. Mao.....	1864	WAQ09
Design Principles for High Current Beam Injection Lines — H. Liu, D. Neuffer.....	1867	WAQ11
Survey and Analysis of Line-Frequency Interference in the CEBAF Accelerator — M.G. Tiefenback, Rui Li.....	1870	WAQ12
Location and Correction of 60 Hz in the CEBAF Injector — R. Legg, D. Douglas, G.A. Krafft, Q. Saulter.....	1873	WAQ14
PEP-II Injection Transport Construction Status and Commissioning Plans — T. Fieguth, E. Bloom, F. Bulos, T. Donaldson, B. Feerick, G. Godfrey, G. Leyh, D. Nelson, M. Ross, D. Schultz, J. Sheppard, P. Smith, C. Spencer, J. Weinberg.....	1876	WAQ15
Beam Transport Lines at BESSY-II — D. Schirmer, M. v.Hartrott, S. Khan, D. Krämer, E. Weihreter.....	1879	WAQ17
Matching the Emittance of a Linac to the Acceptance of a Racetrack Microtron — R.W. de Leeuw, M.C.J. de Wijs, J.I.M. Botman, G.A. Webers, W.H.C. Theuws, C.J. Timmermans, H.L. Hagedoorn.....	1882	WAQ19
The Extraction Orbit and Extraction Beam Transport Line for a 75 MeV Racetrack Microtron — R.W. de Leeuw, H.R.M. van Greevenbroek, J.I.M. Botman, G.A. Webers, C.J. Timmermans, H.L. Hagedoorn.....	1885	WAQ20
Electromagnetic, Thermal and Structural Analysis of the Fermilab Antiproton Source Lithium Collection Lens — S. O'Day, K. Anderson.....	1888	WAQ22
A New Concept in the Design of the LHC Beam Dump — J.M. Zazula, M. Gyr, G.R. Stevenson, E. Weisse.....	1891	WAQ24
Loss Concentration and Evacuation by Mini-Wire-Septa from Circular Machines for Spallation Neutron Sources — H. Schönauer.....	1894	WAQ25
Status of the Radioactive Ion Beam Injector at the Holifield Radioactive Ion Beam Facility — D.T. Dowling, G.D. Alton, R.L. Auble, M.R. Dinehart, D.L. Haynes, J.W. Johnson, R.C. Juras, Y.S. Kwon, M.J. Meigs, G.D. Mills, S.W. Mosko, D.K. Olsen, B.A. Tatum, C.E. Williams, H. Wollnik.....	1897	WAQ26
A New Fast Rise Time Kicker System For Antiproton Injection Into The Tevatron — B. Hanna, J. Dinkel, C. Jensen, D. Qunell, R. Reilly, D. Tinsley, J. Walton.....	1900	WAR01
Design of the M140 Beam-Abort Dump — C.M. Bhat, P.S. Martin, A.D. Russell.....	1903	WAR02
Study on the Metallic Coating of the Ceramic Chamber for the ATF Damping Ring Kicker Magnets — N. Terunuma, H. Nakayama, J. Urakawa.....	1906	WAR03
Prospect of the Fast Extraction from KEK-PS for the Long Base Line Neutrino Experiment — H. Sato, Y. Shoji, T. Kawakubo.....	1909	WAR04
Helium Beam Acceleration in the KEK Proton Synchrotron with a Newly Developed Injection System for Positive/Negative Ions — I. Sakai, A. Takagi, Y. Mori, S. Machida, M. Yoshii, T. Toyama, M. Shirakata, Y. Shoji, H. Sato.....	1912	WAR05
Fast and Reliable Kicker Magnets for the SLC Damping Rings — T.S. Mattison, R.L. Cassel, A.R. Donaldson, G. Gross.....	1915	WAR06
Status of the Nuclotron Slow Extraction System — V.I. Chernikov, I.B. Issinsky, O.S. Kozlov, V.A. Mikhailov, S.A. Novikov.....	1918	WAR09
The RHIC Injection Fast Kicker — E.B. Forsyth, G.C. Pappas, J.E. Tuozzolo, W. Zhang.....	1921	WAR10
The Active Filter Voltage Ripple Correction System of the Brookhaven AGS Main Magnet Power Supply — I. Marneris, R. Bonati, J. Geller, J.N. Sandberg, A. Soukas.....	1924	WAR11
The Injection Kicker System for the Muon G-2 Experiment — G.C. Pappas, E.B. Forsyth, W. Feng.....	1927	WAR12
The AGS Accelerator Complex with the New Fast Extraction System — M. Tanaka, E.J. Bleser, J.W. Glenn, Y.Y. Lee, A. Soukas.....	1930	WAR13
DESY III - Dump System with One Fast Kicker — J. Ruemmler.....	1933	WAR14

Utilizing a Pulsed Deflector for Extraction of Pulsed Beams from the TRIUMF Cyclotron — <i>R.E. Laxdal</i>	1936	WAR15
Requirements for a Beam Sweeping System for the Fermilab Antiproton Source Target — <i>F.M. Bieniosek, K. Anderson, K. Fullett</i>	1939	WAR17
Measurement and Reduction of Quadrupole Injection Oscillations in the Fermilab Antiproton Accumulator — <i>F.M. Bieniosek, K. Fullett</i>	1942	WAR18
Results from Experiments of Crystal Extraction of 900 GeV Proton Beams from the Tevatron Collider — <i>G. Jackson, D. Carrigan, D. Chen, C.T. Murphy, A. Bogacz, S. Ramachandran, J. Rhoades, A. McManus, S. Baker</i>	1945	WAR19
High Energy Beam Line Based on Bending Crystal — <i>V.M. Biryukov, Yu.A. Chesnokov, V.N. Greth, A.A. Ivanov, V.I. Kotov, V.S. Selesnev, M.V. Tarakanov, V.I. Terekhov, S.V. Tsarik</i>	1948	WAR20
Observation of the Influence of the Crystal Surface Defects on the Characteristics of the High Energy Particle Beam Deflected With a Bent Monocrystal — <i>V.I. Baranov, V.M. Biryukov, Yu.A. Chesnokov, V.I. Kotov, M.V. Tarakanov, S.V. Tsarik</i>	1949	WAR21
Beam Extraction with Using of Volume Reflection Effect in Crystals — <i>I. Yazynin</i>	1952	WAR22
Use of a Bent Crystal for Beam Extraction in a Slow Extraction Mode — <i>A.A. Asseev, M.Yu. Gorin</i>	1955	WAR23
Computer Simulation of the Tevatron Crystal Extraction Experiment — <i>Valery Biryukov</i>	1958	WAR24

Power Supplies

PEP-II Magnet Power Conversion Systems — <i>L.T. Jackson, A.H. Saab, D.W. Shimer</i>	1961	RPP01
The AGS Main Magnet Power Supply Upgrade — <i>J.N. Sandberg, R. Casella, J. Geller, I. Marneris, A. Soukas, N. Schumburg</i>	1964	RPP02
Performance of the Ramping Power Supplies for the APS Booster Synchrotron — <i>J.A. Carwardine, S.V. Milton, D.G. McGhee</i>	1967	RPP03
A Distributed Dipole Power Supply System for the EUTERPE Electron Ring — <i>A.H. Kemper, Boling Xi, R.W. de Leeuw, W.H.C. Theuws, J.I.M. Botman, C.J. Timmermans, H.L. Hagedoorn, R.G.J. Oude Velthuis</i>	1970	RPP04
A 20 Ampere Shunt Regulator for Controlling Individual Magnets in a Seriesed String — <i>E.J. Martin, N. Dobeck, G.S. Jones, M.K. O'Sullivan</i>	1973	RPP06
A Multi-Channel Corrector Magnet Controller — <i>G.E. Leyh, A.R. Donaldson, L.T. Jackson</i>	1976	RPP07
Advances in Power Supply and Control System for Electrostatic Accelerators — <i>S.N. Chumakov, A.D. Goncharov, A.N. Malygin, V.P. Ostanin, B.N. Sukhina, V.S. Tupikov</i>	1979	RPP08
Mode Analysis of Synchrotron Magnet Strings — <i>M. Kumada</i>	1982	RPP09
Autotransformer Configurations to Enhance Utility Power Quality of High Power AC/DC Rectifier Systems — <i>Sewan Choi, Prasad N. Enjeti, Ira J. Pitel</i>	1985	RPP11
Performance of a 2-Megawatt High Voltage Test Load — <i>D. Horan, R. Kustom, M. Ferguson</i>	1988	RPP12
Early Operating and Reliability Experience with the CEBAF DC Magnet Power Supplies — <i>W. Merz, R. Flood, E.J. Martin, M. O'Sullivan</i>	1991	RPP13

Cryogenics, Vacuum, Alignment and Other Technical Systems

CEBAF Cryogenic System (Invited) — <i>Claus H. Rode</i>	1994	RPE01
The Large Hadron Collider Vacuum System (Invited) — <i>B. Angerth, F. Bertinelli, J.-C. Brunet, R. Calder, F. Caspers, P. Cruikshank, J.-M. Dalin, O. Gröbner, N. Kos, A. Mathewson, A. Poncet, C. Reymermier, F. Ruggiero, T. Scholz, S. Sgobba, E. Wallén</i>	1999	RPE02
Large Medical Gantries (Invited) — <i>J.B. Flanz</i>	2004	RPE03
Alignment Considerations for the Next Linear Collider (Invited) — <i>Robert E. Ruland</i>	2009	RPE04
Reliability of the LEP Vacuum System: Experience and Analysis — <i>P.M. Strubin, J.-P. Bojon</i>	2014	RPE06
On the Electron Beam Lifetime Problem in HERA — <i>D.R.C. Kelly, W. Bialowons, R. Brinkmann, H. Ehrlichmann, J. Kouptsidis</i>	2017	RPE08
Design and Testing of a High Power, Ultra-High Vacuum, Dual-Directional Coupler for the Advanced Photon Source (APS) Linear Accelerator — <i>S.O. Brauer, A.E. Grelick, J. Grimmer, R.D. Otocki, Y.W. Kang, J. Noonan, T. Russell</i>	2020	RPE09
A Pulse Septum Magnet with Low Outgassing Rate — <i>Yuan Ji Pei, W.M. Li, D.M. Jiang, X.Q. Wang</i>	2023	RPE10

Surveying the Monument System at Lawrence Berkeley Laboratory's Advanced Light Source Accelerator — W. Thur, T. Lauritzen.....	2026	RPE12
Induced Radioactivity of Thick Copper and Lead Targets Irradiated by Protons, ^4He and ^{12}C Nuclei with Energy 3.65 GeV/Nucleon — A.A. Astapov, V.P. Bamblevski.....	2029	RPE13
The PEP-II High Power Beam Dumping System — A. Kulikov, J. Seeman, M. Zolotarev.....	2032	RPE14
Cryogenic Thermometry in Superconducting Accelerators — V.I. Datskov, J.A. Demko, J.G. Weisend, M. Hentges.....	2034	MPP01
Cryogenic Operation and On-line Measurement of RF Losses in the SC Cavities of LEP2 — G. Winkler, Ph. Gayet, D. Güsewell, Ch. Titcomb.....	2037	MPP02
Pressure Measurement for the UNK-1 Vacuum System — A. Kiver, V. Komarov, K. Mirzoev, V. Terekhov, A. Vasilevsky.....	2040	MPP03
Total Pressure Measurements in the ELETTRA Storage Ring According to the Performance of the Sputter-Ion Pumps — F. Giacuzzo, J. Miertusova.....	2042	MPP04
Insertion Device Vacuum Chamber for the ELETTRA Storage Ring — J. Miertusova, N. Pangos.....	2045	MPP05
Bellows Design for the PEP-II High Energy Ring Arc Chambers — M.E. Nordby, N. Kurita, C.-K. Ng.....	2048	MPP07
A Zero-Length Bellows for the PEP-II High-Energy Ring — M. Nordby, E.F. Daly, N. Kurita, J. Langton.....	2051	MPP08
Processing of O.F.E. Copper Beam Chambers for PEP-II High Energy Ring — E. Hoyt, M. Hoyt, R. Kirby, C. Perkins, D. Wright, A. Farvid.....	2054	MPP09
Stretchforming Vacuum Chambers for the PEP-II B-Factory High Energy Storage Ring — E.F. Daly, D. Bostic, A. Lisin, M. Palrang, C. Perkins, K. Skarpaas.....	2057	MPP10
Beam Vacuum Chambers for Brookhaven's Muon Storage Ring — H.C. Hseuh, L. Snyderstrup, W.S. Jiang, C. Pai, M. Mapes.....	2060	MPP11
Test Results of Pre-Production Prototype Distributed Ion Pump Design for the PEP-II Asymmetric B-Factory Collider — F.R. Holdener, D. Behne, D. Hathaway, K. Kishiyama, M. Mugge, W. Stoeffl, K. van Bibber, C. Perkins, E.F. Daly, E. Hoyt, M. Hoyt, M. Nordby, J. Seeman, D. Wright.....	2064	MPP12
Design of the PEP-II Low Energy Ring Vacuum System — D. Hunt, K. Kennedy, T. Stevens.....	2067	MPP13
The Vacuum Upgrade of the CERN PS and PS Booster — M. van Rooij, J.-P. Bertuzzi, M. Brouet, A. Burlet, C. Burnside, R. Gavaggio, L. Petty, A. Poncet.....	2069	MPP15
The Vacuum System for Insertion Devices at the Advanced Photon Source — E. Trakhtenberg, E. Gluskin, P. Den Hartog, T. Klippert, G. Wiemerslage, S. Xu.....	2072	MPP16
Test Results of a Combined Distributed Ion Pump/Non-Evaporable Getter Pump Design Developed as a Proposed Alternative Pumping System for the PEP-II Asymmetric B-Factory Collider — F.R. Holdener, D. Behne, D. Hathaway, K. Kishiyama, M. Mugge, W. Stoeffl, K. van Bibber, C. Perkins, E.F. Daly, E. Hoyt, M. Hoyt, M. Nordby, J. Seeman, D. Wright.....	2075	MPP20

Volume 4

Cryogenics, Vacuum, Alignment and Other Technical Systems (cont'd)

Ground Motion Measurements in HERA — V. Shiltsev, B. Baklakov, P. Lebedev, C. Montag, J. Rossbach.....	2078	TAA01
Alignment of Duke Free Electron Laser Storage Ring — M. Emamian, N. Hower, Y. Levashov.....	2081	TAA02
Beamline Smoothing of the Advanced Photon Source — H. Friedrich, M. Penicka, S. Zhao.....	2084	TAA03
Improvement of the Alignment System for the KEK 2.5-GeV Electron Linac — Y. Ogawa, A. Enomoto, I. Sato.....	2087	TAA04
A Mechanical Feedback System for Linear Colliders to Compensate Fast Magnet Motion — C. Montag, J. Rossbach.....	2090	TAA06
A Microstrip Based Position System for the Alignment of the TTF Cryostat — D. Giove, A. Bosotti, C. Pagani, G. Varisco.....	2093	TAA07
Beam-Based Magnetic Alignment of the Final Focus Test Beam — P. Tenenbaum, D. Burke, R. Helm, J. Irwin, P. Raimondi, K. Oide, K. Flöttmann.....	2096	TAA08

Alignment and Survey of the Elements in RHIC — <i>D. Trbojevic, P. Cameron, G.L. Ganetis, M.A. Goldman, R. Gupta, M. Harrison, M.F. Hemmer, F.X. Karl, A. Jain, W. Louie, S. Mulhall, S. Peggs, S. Tepikian, R. Thomas, P. Wanderer</i>	2099	TAA09
RF Radiation Measurement for the Advanced Photon Source (APS) Personnel Safety System — <i>J.J. Song, J. Kim, R. Ostocki, J. Zhou</i>	2102	TAA11
Radiation Shielding of the Main Injector — <i>C.M. Bhat, P.S. Martin</i>	2105	TAA12
The Safety Interlock System of Synchrotron Radiation Research Center — <i>T.F. Lin, J.P. Wang</i>	2108	TAA14
Radiological Protection Policy Aspects Concerning the Preliminary Design and Operation Modus of the Athens RT Microtron Facility — <i>B. Spyropoulos</i>	2111	TAA15
SLAC Synchronous Condenser — <i>C. Corvin</i>	2114	TAA16
Printed-Circuit Quadrupole Design — <i>Terry F. Godlove, Santiago Bernal, Martin Reiser</i>	2117	TAA17
Microprocessor Controlled Four-Axis Goniometer — <i>A. Bortnyansky, M. Klopenkov, M. Pavlovets, M. Svinin, P. Kovach, J. Dobrovodsky</i>	2120	TAA18
Optically Induced Surface Flashover Switching for the Dielectric Wall Accelerator — <i>S. Sampayan, G. Caporaso, B. Carder, M. Norton, D. Trimble, J. Elizondo</i>	2123	TAA20
Measurements of Magnet Vibrations at the Advanced Photon Source — <i>V. Shiltsev</i>	2126	TAA21
The Vacuum System for the PEP II High Energy Ring Straight Sections — <i>U. Wienands, E. Daly, S.A. Heifets, A. Kulikov, N. Kurita, M. Nordby, C. Perkins, E. Reuter, J.T. Seeman, F.C. Belser, J. Berg, F.R. Holdener, J.A. Kerns, M.R. McDaniel, W. Stoeffl</i>	2129	TAA22
Compact X-band High Power Load Using Magnetic Stainless Steel — <i>Sami G. Tantawi, A.E. Vlieks</i>	2132	TAA27
Progress on Plasma Lens Experiments at the Final Focus Test Beam — <i>P. Kwok, P. Chen, D. Cline, W. Barletta, S. Berridge, W. Bugg, C. Bula, S. Chattopadhyay, W. Craddock, I. Hsu, R. Iverson, T. Katsouleas, P. Lai, W. Leemans, R. Liou, K.T. McDonald, D.D. Meyerhofer, K. Nakajima, H. Nakanishi, C.K. Ng, Y. Nishida, J. Norem, A. Ogata, J. Rosenzweig, M. Ross, A. Sessler, T. Shintake, J. Spencer, J.J. Su, A.W. Weidemann, G. Westenskow, D. Whittum, R. Williams, J. Wurtele</i>	2135	TAA28
Measurement of the Electric Field Uniformity in an Electrostatic Separator — <i>Weiran Lou, James J. Welch</i>	2138	TAA29
Analysis and Redesign of RF Filter Bar to Relieve Thermal Stresses — <i>E.G. Schmenk, K.W. Kelly, V. Saile, H.P. Bluem</i>	2141	TAA32
Loaded Delay Lines for Future R.F. Pulse Compression Systems — <i>R.M. Jones, P.B. Wilson, N.M. Kroll</i>	2144	TAA33

Controls and Computing

Integrating Industrial and Accelerator Control Systems (Invited) — <i>R. Saban</i>	2147	WAE01
Control System for Fermilab's Low Temperature Upgrade (Invited) — <i>B.L. Norris</i>	2152	WAE02
Databases for Accelerator Control - An Operations Viewpoint (Invited) — <i>J. Poole</i>	2157	WAE03
Taking an Object-Oriented View of Accelerators (Invited) — <i>Hiroshi Nishimura</i>	2162	WAE04
The CEBAF Control System (Invited) — <i>William A. Watson III</i>	2167	WAE05
MECAR (Main Ring Excitation Controller and Regulator): A Real Time Learning Regulator For The Fermilab Main Ring Or The Main Injector Synchrotron — <i>R. Flora, K. Martin, A. Moibenko, H. Pfeffer, D. Wolff, P. Prieto, S. Hays</i>	2172	WAE07
Framework for a General Purpose, Intelligent Control System for Particle Accelerators — <i>R.T. Westervelt, W.B. Klein, G. Luger</i>	2175	WAE08
Automatic Beam Steering in the CERN PS Complex — <i>B. Autin, G.H Hemelsoet, M. Martini, E. Wildner</i>	2178	WAE09
Integrated On-Line Accelerator Modeling at CEBAF — <i>B.A. Bowling, H. Shoaee, J. van Zeijts, S. Witherspoon, W. Watson</i>	2181	WAE10
A Self-Describing File Protocol for Simulation Integration and Shared Post-Processors — <i>M. Borland</i>	2184	WAE11
Analytic Computation of Beam Impedances in Complex Heterogenous Accelerator Geometries — <i>S. Petracca, I.M. Pinto, F. Ruggiero</i>	2187	WAE12
Comparison of CONDOR, FCI and MAFIA Calculations for a 150MW S-Band Klystron with Measurements — <i>U. Becker, T. Weiland, M. Dohlus, S. Lütgert, D. Sprehn</i>	2190	WAE13

Controls

The BEPC Control System Upgraded — J. Zhao, X. Geng, Y. Yu, B. Wang, C. Wang, J. Xu, W. Liu, H. Luo, Y. Wang, M. Zhan.....	2193	MPA01
Control System of PLS 2-GeV Linac — I.S. Ko, W. Namkung.....	2196	MPA02
Control System of the Synchrotron Radiation Source SIBERIA-2 — A. Valentinov, A. Kadnikov, Y. Krylov, S. Kuznetsov, Y. Yupinov.....	2199	MPA04
Control System for the Holifield Radioactive Ion Beam Facility — B.A. Tatum, R.C. Juras, M.J. Meigs.....	2202	MPA05
Control System Design for KEKB Accelerators — S.-I. Kurokawa, T. Katoh, T.T. Nakamura, T. Mimashi, N. Yamamoto.....	2205	MPA06
Design of SPring-8 Linac Control System Using Object Oriented Concept — H. Sakaki, H. Yoshikawa, Y. Itoh, A. Kuba, T. Hori, A. Mizuno, H. Yokomizo.....	2208	MPA07
The Slow Control System of the Muon g-2 Experiment — Arnold Stillman.....	2211	MPA09
The Duke Storage Ring Control System — Y. Wu, B. Burnham, V.N. Litvinenko.....	2214	MPA10
EPICS at Duke University — C. Dickey, B. Burnham, F. Carter, R. Fricks, V. Litvinenko, A. Nagchadhuri, P. Morcombe, R. Pantazis, P. O'Shea, R. Sachschtale, Y. Wu.....	2217	MPA11
The Integration of Two Control Systems — M. Bickley, K. White.....	2220	MPA12
Upgrade of NSLS Timing System — O. Singh, S. Ramamoorthy, J. Sheehan, J. Smith.....	2223	MPA15
Accelerator Timing at Brookhaven National Laboratory — B. Oerter, C.R. Conkling.....	2226	MPA16
The RHIC General Purpose Multiplexed Analog to Digital Converter System — R. Michnoff.....	2229	MPA17
The Datacon Master - Renovation of a Datacon Field Bus Communications System for Accelerator Control — T.M. Kerner, R. Warkentien.....	2232	MPA18
Upgrade of the Controls for the Brookhaven Linac — W.E. Buxton.....	2235	MPA19
Commissioning Software Tools at the Advanced Photon Source — L. Emery.....	2238	MPR01
Rapid Application Development Using the Tcl/Tk Language — Johannes van Zeijts.....	2241	MPR02
Accelerator Operation Management Using Objects — H. Nishimura, C. Timossi, M. Valdez.....	2244	MPR03
Orbit Control at the ALS Based on Sensitivity Matrices — H. Nishimura, L. Schachinger, H. Ohgaki.....	2247	MPR04
Error Handling in the NSLS Control System — Susila Ramamoorthy, Pauline Pearson, John Smith.....	2250	MPR07
History Data Collection, Retriving and Display in the NSLS Control System — Y.N. Tang, J.D. Smith.....	2253	MPR08
Virtual Instrumentation Interface for SRRC Control System — Jenny Chen, C.H. Kuo, Gloria Huang, J.S. Chen, C.J. Wang, K.T. Hsu, G.J. Jan.....	2256	MPR10
User-Friendly Interface for Operator in the Controls of UNK Beam-Transfer Line. — Yu. Karshev, Yu. Fedotov, V. Komarov, I. Lobov.....	2259	MPR11
Macmon: A Monitoring Program for ELETTRA — Emanuel Karantzoulis, Mark Plesko.....	2262	MPR12
Device Control at CEBAF — S. Schaffner, D. Barker, V. Bookwalter, B. Bowling, K. Brown, L. Doolittle, T. Fox, S. Higgins, A. Hoffer, G. Lahti, P. Letta, B. Montjar, N. Patavalis, J. Tang, W. Watson, C. West, D. Wetherholt, K. White, S. Witherspoon, M. Wise.....	2265	MPR13
Automated Frequency Tuning of SRF Cavities at CEBAF — M. Chowdhary, L. Doolittle, G. Lahti, S.N. Simrock, R. Terrell.....	2268	MPR14
Operational Monitoring of the CEBAF RF System — J. Karn, B. Dunham, M. Tiefenback.....	2271	MPR15
Operating Experience with the New TRIUMF RF Control System — K. Fong, M. Laverty, S. Fang.....	2273	MPR16
Managing Control Algorithms with an Object-Oriented Database — M. Bickley, W. Watson.....	2276	MPR19
Design of the Commissioning Software for the AGS to RHIC Transfer Line — C.G. Trahern, C. Saltmarsh, T. Satogata, J. Kewisch, S. Sathe, T. D'Ottavio, S. Tepikian, D. Shea.....	2279	MPR20

Computer Codes

A Relational Database for Magnets and Measurement Systems at the Fermilab Magnet Test Facility — J.W. Sim, B.C. Brown, H.D. Glass, D.J. Harding, C.S. Mishra, A.D. Russell, K. Trombly-Freytag, D.G.C. Walbridge.....	2282	MPB05
---	------	-------

Software for a Database-Controlled Measurement System at the Fermilab Magnet Test Facility — J.W. Sim, R. Baiod, B.C. Brown, E. Desavouret, H.D. Glass, P.J. Hall, D.J. Harding, C.S. Mishra, J.M. Nogiec, J.E. Pachnik, A. Russell, K. Trombly-Freytag, D.G.C. Walbridge	2285	MPB06
BBAT: Bunch and Bucket Analysis Tool — D.-P. Deng.....	2288	MPB08
MASTAC - New Code for Solving Three-Dimensional Non-linear Magnetostatic Problems — M. Rojak, E. Shurina, Yu. Soloveichik, A. Grudiev, M. Tiunov, P. Vobly.....	2291	MPB09
The Computer Code BPERM for Wakepotential & Impedance Calculations — T. Barts, W. Chou.....	2294	MPB10
RESOLVE at CEBAF — Byung C. Yunn, Rui Li, Stefan Simrock.....	2297	MPB11
New Graphic User Interface for the Charged Particle Beam Program PARMILA — George H. Gillespie, Barrey W. Hill.....	2300	MPB14
XWAKE 1.1: A New Impedance and Wake Field Software Package — G.W. Saewert, T.G. Jurgens.....	2303	MPB15
The Los Alamos Accelerator Code Group — Frank L. Krawczyk, James H. Billen, Robert D. Ryne, Harunori Takeda, Lloyd M. Young.....	2306	MPB16
Beam Simulation and Radiation Dose Calculation at the Advanced Photon Source with SHOWER, an Interface Program to the EGS4 Code System — L. Emery.....	2309	MPB17
An Interactive Version of the PBGUNS Program for the Simulation of Axisymmetric and 2-D, Electron and Ion Beams and Guns — Jack E. Boers.....	2312	MPB18
Vector Computer Used for Calculation of 3D Magnetostatic Fields — E.P. Zhidkov, M.B. Yuldasheva, I.P. Yudin, O.I. Yuldashev	2314	MPB19
Impedance Study for the PEP-II B-factory — S. Heifets, A. Chao, E. Daly, K. Ko, N. Kurita, X. Lin, C. Ng, M. Nordby, C. Perkins, J. Seeman, G. Stupakov, U. Wienands, D. Wright, M. Zolotarev, E. Henestroza, G. Lambertson, J. Corlett, J. Byrd, M. Zisman, T. Weiland, W. Stoeffl, C. Bolser	2317	MPC01
Pressure Stability under a Pump Failure — S.A. Heifets, J. Seeman, W. Stoeffl.....	2319	MPC02
Investigation of the Beam Impedance of a Slowly Varying Waveguide — R.M. Jones, S.A. Heifets.....	2321	MPC03
Optimal Transport of Low Energy Particle Beams — Christopher K. Allen, Samar K. Guharay, Martin Reiser.....	2324	MPC04
Simulation of the Space Charge Effect in RHIC — G.F. Dell, S. Peggs	2327	MPC05
Magnetic Shielding for the D0 Detector Solenoid Upgrade — J.-F. Ostiguy, R. Yamada.....	2330	MPC07
Trapped Modes in the PEP-II B-Factory Interaction Region — E. Henestroza, S. Heifets, M. Zolotarev.....	2333	MPC08
A Proof of Principle of a Storage Ring with Fifth-Order Achromatic Bending Arcs — Weishi Wan, Martin Berz.....	2336	MPC09
Analytic Electrostatic Solution of an Axisymmetric Accelerator Gap — John K. Boyd.....	2339	MPC13
3D-Finite Difference Analysis of Planar Loop Couplers as Beam Electrodes in Stochastic Cooling Systems — R. Schultheis, H.L. Hartnagel, B. Franzke.....	2342	MPC15
Some Remarks on the Location of Higher Order Modes in Tapered Accelerating Structures with the Use of a Coupled Oscillator Model — G. Romanov, S. Ivanov, M. Dohlus, N. Holtkamp.....	2345	MPC16
The New Possibilities of SuperLANS Code for Evaluation of Axisymmetric Cavities — D.G. Myakishev, V.P. Yakovlev.....	2348	MPC17
Transverse EM Fields in a Detuned X-band Accelerating Structure — S.A. Heifets, S.A. Kheifets, B. Woo.....	2351	MPC18
RF Cavity Computer Design Codes — P.A. McIntosh.....	2353	MPC19
Arbitrary Order Transfer Maps for RF Cavities — Johannes van Zeijts.....	2356	MPC20
The Computation of the Dynamic Inductance of Magnet Systems and Force Distribution in Ferromagnetic Region on the Basis of 3-D Numerical Simulation of Magnetic Field — N. Doinikov, V. Kukhtin, E. Lamzin, B. Mingalev, Yu. Severgin, S. Sytchevsky.....	2359	MPC21
Advanced Electromagnetic Design of Cavities for High Current Accelerators — Frank L. Krawczyk.....	2361	MPC22
Modified PARMILA Code for New Accelerating Structures — H. Takeda, J.E. Stovall.....	2364	MPC23
Tracking Particles with Wake Fields and Space Charge Effects — A.J. Riche	2367	MPC24
On the Importance of Fourth Order Effects on Wakefield Calculations for Short Bunches — Zenghai Li, Joseph J. Bisognano.....	2370	MPC25

Coupling Impedances of Muffin-Tin Structures with Closed and Open Sides — <i>M. Filtz</i>	2373	MPC28
Explicit Soft Fringe Maps of a Quadrupole — <i>John Irwin, Chun-xi Wang</i>	2376	MPC31

Instrumentation and Feedback

Bunched Beam Cooling for the Fermilab Tevatron (<i>Invited</i>) — <i>Ralph J. Pasquinelli</i>	2379	RAE01
Fast Digital Dampers for the Fermilab Booster (<i>Invited</i>) — <i>James M. Steimel Jr.</i>	2384	RAE02
Fast Feedback for Linear Colliders (<i>Invited</i>) — <i>L. Hendrickson, C. Adolphsen, S. Allison, T. Gromme, P. Grossberg, T. Himel, K. Krauter, R. MacKenzie, M. Minty, R. Sass, H. Shoaee, M. Woodley</i>	2389	RAE03
Instrumentation in Medical Systems (<i>Invited</i>) — <i>W.T. Chu</i>	2394	RAE04
Laser Diagnostics of a One-Dimensional Ordered Ion Beam — <i>R. Calabrese, V. Guidi, P. Lenisa, U. Tambini, E. Mariotti, L. Moi</i>	2399	RAE05
Determining Electron Beam Parameters from Edge Radiation Measurement Results on Siberia-1 Storage Ring — <i>O.V. Chubar</i>	2402	RAE06
Absolute Energy Measurement in e- e+ Linear Colliders — <i>Blaine E. Norum, Robert Rossmanith</i>	2405	RAE07
INR Activity in Development and Production of Bunch Shape Monitors — <i>S.K. Esin, A.V. Feschenko, P.N. Ostroumov</i>	2408	RAE08
Conceptual design of a Charged Particle Beam Energy Spectrometer Utilizing Transition Radiation Grating — <i>X.Z. Qiu, X.J. Wang, K. Batchelor, I. Ben-Zvi</i>	2411	RAE09
An Analysis of the Operational Performance of the Automatic Global Horizontal Beam Position Control System on the SRS at Daresbury — <i>J.B. Fitzgerald, B.G. Martlew, P.D. Quinn, S.L. Smith</i>	2414	RAE10
A Prototype Fast Feedback System for Energy Lock at CEBAF — <i>M. Chowdhary, G.A. Krafft, H. Shoaee, S.N. Simrock, W.A. Watson</i>	2417	RAE11
Operation and Performance of the PEP-II Prototype Longitudinal Damping System at the ALS — <i>D. Teytelman, R. Claus, J. Fox, H. Hindi, J. Hoefflich, I. Linscott, J. Olsen, G. Oxoby, S. Prabhakar, W. Ross, L. Sapozhnikov, A. Drago, M. Serio, J. Byrd, J. Corlett, G. Stover</i>	2420	RAE12
Commissioning of the ALS Transverse Coupled-Bunch Feedback System — <i>W. Barry, J. Byrd, J. Corlett, J. Johnson, G. Lambertson, J. Fox</i>	2423	RAE13
Operation of a Fast Digital Transverse Feedback System in CESR — <i>J.T. Rogers, M.G. Billing, J.A. Dobbins, C.R. Dunnam, D.L. Hartill, T. Holmquist, B.D. McDaniel, T.A. Pelaia, M. Pisharody, J.P. Sikora, C.R. Strohman</i>	2426	RAE14
Measuring and Adjusting the Path Length at CEBAF — <i>G.A. Krafft, M. Crofford, D.R. Douglas, S.L. Harwood, R. Kazimi, R. Legg, W. Oren, K. Tremblay, D. Wang</i>	2429	WXE01
Simulations of the BNL/SLAC/UCLA 1.6 Cell Emittance Compensated Photocathode RF Gun Low Energy Beam Line — <i>D.T. Palmer, R.H. Miller, H. Winick, X.J. Wang, K. Batchelor, M. Woodle, I. Ben-Zvi</i>	2432	WXE03
Small Gap Undulator Experiment on the NSLS X-Ray Ring — <i>P.M. Stefan, S. Krinsky, G. Rakowsky, L. Solomon</i>	2435	WXE04
Measurements of Longitudinal Dynamics in the SLC Damping Rings — <i>R.L. Holtzapple, R.H. Siemann, C. Simopoulos</i>	2438	WXE05
Single Bunch Collective Effects in the ALS — <i>J.M. Byrd, J.N. Corlett, T. Renner</i>	2441	WXE06
Experiments of Nanometer Spot Size Monitor at FFTB Using Laser Interferometry — <i>T. Shintake, K. Oide, N. Yamamoto, A. Hayakawa, Y. Ozaki, D. Burke, R.C. Field, S. Hartman, R. Iverson, P. Tenenbaum, D. Walz</i>	2444	WXE07
Transverse Electron Beam Size Measurements Using the Lloyd's Mirror Scheme of Synchrotron Light Interference — <i>O.V. Chubar</i>	2447	WXE08

Instrumentation

Charge Balancing Fill Rate Monitor — <i>J.L. Rothman, E.B. Blum</i>	2450	MPQ01
Sensitivity and Offset Calibration for the Beam Position Monitors at the Advanced Photon Source — <i>Y. Chung, D. Barr, G. Decker, K. Evans Jr., E. Kahana</i>	2452	MPQ03
An Sampling Detector for the RHIC BPM Electronics — <i>W.A. Ryan, T.J. Shea</i>	2455	MPQ04
RHIC Beam Position Monitor Characterization		

— P.R. Cameron, M.C. Grau, M. Morvillo, T.J. Shea, R.E. Sikora.....	2458	MPQ05
Duke Storage Ring Tune Measurements System using Razor Blade and Photomultiplier —		
V.N. Litvinenko, B. Burnham, N. Hower, P. Morcombe, Y. Wu	2461	MPQ06
The Development of Beam Current Monitors in the APS — X. Wang, F. Lenkszus, E. Rotela.....	2464	MPQ07
Overall Design Concepts for the APS Storage Ring Machine Protection System —		
A. Lumpkin, R. Fuja, A. Votaw, X. Wang, D. Shu, J. Stepp, N. Arnold, G. Nawrocki, G. Decker, Y. Chung	2467	MPQ08
Status of the Synchrotron Radiation Monitors for the APS Facility Rings — A. Lumpkin,		
B. Yang	2470	MPQ09
Initial Diagnostics Commissioning Results for the Advanced Photon Source (APS) —		
A. Lumpkin, D. Patterson, X. Wang, E. Kahana, W. Sellyey, A. Votaw, B. Yang, R. Fuja, W. Berg, M. Borland, L. Emery, G. Decker, S. Milton.....	2473	MPQ10
Initial Tests of the Dual-Sweep Streak Camera System Planned for APS Particle-Beam		
Diagnostics — A. Lumpkin, B. Yang, W. Gai, W. Cieslik.....	2476	MPQ11
A Transverse Tune Monitor for the Fermilab Main Ring — P.J. Chou, B. Fellenz, G. Jackson.....	2479	MPQ13
Recalibration of Position Monitors With Beams — Kotaro Satoh, Masaki Tejima.....	2482	MPQ14
Simulation of PEP-II Beam Position Monitors — C.-K. Ng, T. Weiland, D. Martin, S. Smith,		
N. Kurita.....	2485	MPQ15
Prototype Bunch Killer System At SRRC — G.J. Jan, Jenny Chen, C.H. Kuo, T.F. Lin, K.T. Pan,		
Glory Lin, K.T. Hsu	2488	MPQ16
Beam Diagnostics for the Amsterdam Pulse Stretcher AmPS — J.G. Noomen,		
H. Boer-Rookhuizen, N. Dobbe, J. v.Es, E. Heine, F. Kroes, J. Kuijt, J. v.d.Laan, A. Poelman, H. Nieuwenkamp, T. Sluijk.....	2491	MPQ17
Non-Destructive Beam Profile Measuring System Observing Fluorescence Generated by		
Circulating Beam — T. Kawakubo, E. Kadokura, T. Kubo, T. Ishida, H. Yamaguchi	2494	MPQ18
The Closed Orbit Measurement of SRRC Booster During Ramping — T.S. Ueng, K.T. Hsu,		
K.H. Hwu, K.K. Lin	2497	MPQ19
Lattice Function Measurement with TBT BPM Data — Ming-Jen Yang.....	2500	MPQ20
Optimal Placement of Profile Monitors in a Mismatched FODO Lattice — K. Bertsche	2503	MPQ21
SSRL Beam Position Monitor Detection Electronics — J. Sebek, R. Hettel, R. Matheson,		
R. Ortiz, J. Wachter	2506	MPQ22
Single-Turn Beam Position Monitor for the NSLS VUV Electron Storage Ring —		
R.J. Nawrocky, S.L. Kramer.....	2509	MPQ23
Design of the Button Beam Position Monitor for PEP-II — N. Kurita, D. Martin, S. Smith,		
C. Ng, M. Nordby, C. Perkins.....	2512	MPQ25
Study of Fast Electron Beam Profile Monitor System — Ian Hsu, C.I. Yu, C.C. Chu.....	2515	MPQ26
The Average Orbit System Upgrade for the Brookhaven AGS — D.J. Ciardullo, J.M. Brennan	2518	MPQ30
Feasibility Study of an Orbit Feedback System for the KEKB Facility — Y. Funakoshi,		
M. Tejima, H. Ishii	2521	MPQ31
Turn-by-Turn Beam Position Measurement for 1.3 GeV Booster Synchrotron — T.S. Ueng,		
K.T. Hsu, C.S. Fang, Y.M. Chang, K.K. Lin	2524	MPQ32
Beam Position Monitor for the LNLS UVX Synchrotron Light Source — F.S. Rafael,		
E.K.C.S. Hayashi	2527	MPQ33
Transition Radiation Electron Beam Diagnostic Study at ATF — X.Z. Qiu, X.J. Wang,		
K. Batchelor, I. Ben-Zvi.....	2530	TPB01
Machine Parameter Measurement of the Amsterdam Pulse Stretcher AmPS — Y.Y. Wu,		
R. Maas	2533	TPB03
Wire Setup Calibration of Beam Position Monitors — D. Wang, B. Binns, M. Kogan,		
A. Zolfaghari	2536	TPB04
Beam profile data analysis for the RHIC Injection Line — Ping Zhou.....	2539	TPB05
Energy Spread of Ion Beams Generated in Multicusp Ion Sources — M. Sarstedt, P. Herz,		
W.B. Kunkel, Y. Lee, K.N. Leung, L. Perkins, D. Pickard, M. Weber, M.D. Williams, E. Hammel.....	2542	TPB07
A 2 MHz 3-Port Analog Isolation and Fanout Module — Edward R. Beadle	2545	TPB08
A General Purpose Fiber Optic Link with Radiation Resistance — Edward R. Beadle	2548	TPB09
DSP Based Data Acquisition for RHIC — T.J. Shea, J. Mead, C.M. Degen.....	2551	TPB12

Ion-Chamber Beam-Loss-Monitor System for the Los Alamos Meson Physics Facility — <i>M. Plum, D. Brown, A. Browman, R. Macek</i>	2554	TPB13
Development of Beam Position Monitors for Heavy Ion Recirculators — F.J. Deadrick, <i>J.J. Barnard, T.J. Fessenden, J.W. Meredith, J. Rintamaki</i>	2557	TPB14
Laser Compton Polarimetry of Proton Beams — A. Stillingman	2560	TPB15
Phase and Synchronous Detector Theory as Applied to Beam Position and Intensity Measurements — J.D. Gilpatrick	2563	TPB16
Testing Coaxial Switches of BPM using a High-Resolution RF Detector — Takao Ieiri	2566	TPB17
A Beam Size Monitor Based on Appearance Intensities for Multiple Gas Ionization — <i>T. Katsouleas, J. Yoshii, W.B. Mori, C. Joshi, C. Clayton</i>	2569	TPB18
Beam Profile Measurement in the Presence of Noise — K. Bertsche, J. Palkovic	2572	TPB19
Beam Shaping Using a New Digital Noise Generator — H. Stockhorst, G. Heinrichs, <i>A. Schnase, S. Papureanu, U. Bechstedt, R. Maier, R. Tölle</i>	2574	TPB20
The RHIC Transfer Line Cable Database — E.H. Scholl, T. Satogata	2577	TPB21
Characterization of Beam Position Monitors for Measurement of Second Moment — <i>S.J. Russell, J.D. Gilpatrick, J.F. Power, R.B. Shurter</i>	2580	TPB22
Beam Diagnostic Systems and Their Use in the New IUCF Beam Line — W.P. Jones, M. Ball, <i>J. Collins, T. Ellison, B. Hamilton</i>	2583	TPB24
Tomographic Method of Experimental Research of Particle Distribution in Phase Space — <i>V.V. Kalashnikov, V.I. Moiseev, V.V. Petrenko</i>	2586	TPB25
Design of the Beam Profile Monitor System for the RHIC Injection Line — R.L. Witkover	2589	TPB26
Beam Intensity Observation System at SRRC — C.J. Wang, C.H. Kuo, J.S. Chen, Jenny Chen, <i>K.T. Hsu, G.J. Jan</i>	2592	TPB29
Performance of the Advanced Photon Source (APS) Linac Beam Position Monitors (BPMs) with Logarithmic Amplifier Electronics — R.E. Fuja, M. White	2595	TPC01
Preliminary Calculations on the Determination of APS Particle-Beam Parameters Based on Undulator Radiation — A. Lumpkin, B. Yang, Y. Chung, R. Dejus, G. Voykov, G. Dattoli	2598	TPC03
Coherent Synchrotron Radiation Detector for a Non-Invasive Subpicosecond Bunch Length Monitor — G.A. Krafft, D. Wang, E. Price, E. Feldl, D. Porterfield, P. Wood, T. Crowe	2601	TPC04
A Beam Test of Button-Type Beam Position Monitor for the ATF Damping Ring — <i>F. Hinode, H. Hayano, M. Tejima, N. Terunuma, J. Urakawa</i>	2604	TPC05
Application of a Transverse Phase-Space Measurement Technique for High-Brightness, H- Beams to the GTA H- Beam — K.F. Johnson, R.C. Connolly, R.C. Garcia, D.P. Rusthoi, <i>O.R. Sander, D.P. Sandoval, M.A. Shinas, M. Smith, V.W. Yuan</i>	2607	TPC06
Precision Intercomparison of Beam Current Monitors at CEBAF — R. Kazimi, B. Dunham, <i>G.A. Krafft, R. Legg, C. Liang, C. Sinclair, J. Mammosser</i>	2610	TPC07
Damped Button Electrode for B-Factory BPM System — T. Obina, T. Shintake, Y.H. Chin, <i>N. Akasaka</i>	2613	TPC08
Beam Monitors for the S-Band Test Facility — W. Radloff, M. Wendt	2616	TPC09
Low Energy Regime for Optical Transition Radiation Emission — D. Giove, C. De Martinis, <i>M. Pullia, P. Mangili</i>	2619	TPC10
Recovery of CTF Beam Signals from a Strong Wakefield Background — Yan Yin, <i>Elmar Schulte, Tord Ekelöf</i>	2622	TPC11
A Low-Cost Non-Intercepting Beam Current and Phase Monitor for Heavy Ions — <i>J.M. Bogaty, B.E. Clift</i>	2625	TPC12
Transverse Emittance Systematics Measured for Heavy-Ion Beams at ATLAS — J.A. Nolen, <i>T.A. Barlow, K.A. Beyer, K.A. Woody</i>	2628	TPC13
Beam Position Monitors in the TESLA Test Facility Linac — R. Lorenz	2631	TPC14
Energy Measurement of Relativistic Electrons by Compton Scattering — Ian Hsu, C.-C. Chu, <i>C.-I. Yu, C.-I. Chen, A.-T. Lai, Y.-C. Liu, P.-K. Tseng, G.-Y. Hsiung, R.-C. Hsu, C.-P. Wang, R.-</i> <i>C. Chen</i>	2634	TPC15
Tests of a High Resolution Beam Profile Monitor — J. Norem, J. Dawson, W. Haberichter, <i>R. Lam, L. Reed, X.-F. Yang, J. Spencer</i>	2637	TPC16
Airix Alignment and High Current Beam Diagnostics — D. Villate, Ch. Bonnafond, A. Devin, <i>E. Merle</i>	2640	TPC17
A New Beam Intensity Monitoring System with Wide Dynamic Range for the Holifield Radioactive Ion Beam Facility — M.J. Meigs, D.L. Haynes, C.M. Jones, C.T. LeCroy	2643	TPC18

Diagnostic Beam Pulses for Monitoring the SLC Linac — <i>F.-J. Decker, M. Stanek, H. Smith, F. Tian</i>	2646	TPC20
Observation of Thermal Effects on the LEP Wire Scanners — <i>J. Camas, C. Fischer, J.J. Gras, R. Jung, J. Koopman</i>	2649	TPC21
CEBAF Beam Loss Accounting — <i>R. Ursic, K. Mahoney, C. Hovater, A. Hutton, C. Sinclair</i>	2652	TPC26
Nanometer Resolution BPM Using Damped Slot Resonator — <i>S.C. Hartman, T. Shintake, N. Akasaka</i>	2655	TPC29
An Automatic Tune-Measurement System for the CELSIUS Ring — <i>T. Lofnes</i>	2658	TPC31

Feedback

Software Architecture of the Longitudinal Feedback System for PEP-II, ALS and DAΦNE — <i>R. Claus, J. Fox, I. Linscott, G. Oxoby, W. Ross, L. Sapozhnikov, D. Teytelman, A. Drago, M. Serio</i>	2660	RPQ01
Digital I/Q Demodulator — <i>C. Ziomek, P. Corredoura</i>	2663	RPQ02
RF Feedback Simulation Results for PEP-II — <i>R. Tighe, P. Corredoura</i>	2666	RPQ03
TM0,1,5,0 Mode Cavity for Longitudinal Bunch Feedback Kicker — <i>T. Shintake</i>	2669	RPQ04
Low Level RF System Design for the PEP-II B Factory — <i>P. Corredoura, R. Claus, L. Sapozhnikov, H. Schwarz, R. Tighe, C. Ziomek</i>	2672	RPQ05
Experiment of the RF Feedback using a Parallel Comb Filter — <i>S. Yoshimoto, E. Ezura, K. Akai, T. Takashima</i>	2675	RPQ06
Digital Transverse Beam Dampers for the Brookhaven AGS — <i>G.A. Smith, V. Castillo, T. Roser, W. Van Asselt, R. Witkover, V. Wong</i>	2678	RPQ07
Design of the PEP-II Transverse Coupled-Bunch Feedback System — <i>W. Barry, J. Byrd, J. Corlett, M. Fahmie, J. Johnson, G. Lambertson, M. Nyman, J. Fox, D. Teytelman</i>	2681	RPQ08
Simulations of the PEP-II Transverse Coupled-Bunch Feedback System — <i>J.M. Byrd</i>	2684	RPQ09
Fermilab Booster Low Level RF System Upgrades — <i>Robert C. Webber</i>	2687	RPQ10
Energy Stability in a High Average Power FEL — <i>L. Merminga, J.J. Bisognano</i>	2690	RPQ11
Automated Beam Based Alignment of the ALS Quadrupoles — <i>G. Portmann, D. Robin, L. Schachinger</i>	2693	RPQ13
First Results with a Nonlinear Digital Orbit Feedback System at the NSLS — <i>Eva Bozoki, Aharon Friedman, Susila Ramamoorthy</i>	2696	RPQ14
Local Beam Position Feedback Experiments on the ESRF Storage Ring — <i>Y. Chung, E. Kahana, J. Kirchman, A. Lumpkin, J. Meyer, E. Plouviez, K. Scheidt, E. Taurel, A. Ando, S. Sasaki, A. Taketani</i>	2699	RPQ15
Implementation of the Global and Local Beam Position Feedback Systems for the Advanced Photon Source Storage Ring — <i>Y. Chung, D. Barr, G. Decker, J. Galayda, J. Kirchman, F. Lenkszus, A. Lumpkin, A.J. Votaw</i>	2702	RPQ16
The RHIC Accelerating Cavity Prototype Tuner — <i>A. Ratti, J.M. Brennan, J. Brodowski, E. Onillon, J. Rose</i>	2705	RPQ17
Ramp Tuning of the APS Booster Synchrotron Magnet Power Supplies — <i>S.V. Milton, J.A. Carwardine</i>	2708	RPQ18
Orbit Stability Improvements at the NSLS X-Ray Ring — <i>J. Safranek, O. Singh, L. Solomon</i>	2711	RPQ19
Digital Orbit Feedback Compensation for SPEAR — <i>J. Corbett, R. Hettel, D. Keeley, D. Mostowfi</i>	2714	RPQ21
Digital Orbit Feedback Control for SPEAR — <i>R. Hettel, J. Corbett, D. Keeley, I. Linscott, D. Mostowfi, J. Sebek, C. Wermelskirchen</i>	2717	RPQ22
Beam Position Feedback Systems for the PF Storage Ring — <i>N. Nakamura, K. Haga, T. Honda, T. Kasuga, M. Katoh, Y. Kobayashi, M. Tadano, M. Yokoyama</i>	2720	RPQ23
The New Booster Synchronization Loop — <i>E. Onillon, J.M. Brennan</i>	2723	RPQ25
Recent Progress in the Development of the Bunch Feedback Systems for KEKB — <i>E. Kikutani, T. Kasuga, Y. Minagawa, T. Obina, M. Tobiya</i>	2726	RPQ26
60 Hz Beam Motion Reduction at NSLS UV Storage Ring — <i>Om V. Singh</i>	2729	RPQ27
The CEBAF Fiber Optic Phase Reference System — <i>K. Crawford, S. Simrock, C. Hovater, A. Krycuk</i>	2732	RPQ29
RF System Modeling for the High Average Power FEL at CEBAF — <i>L. Merminga, J. Fugitt, G. Neil, S. Simrock</i>	2735	RPQ30

Beam Positioning and Monitoring in the Racetrack Microtron Eindhoven — W. Theuws, <i>R.W. de Leeuw, G.A. Webers, J.I.M. Botman, C.J. Timmermans, H.L. Hagedoorn</i>	2738	RPQ31
Multi-Bunch Systems at DESY — Rolf-Dieter Kohaupt	2741	RPQ32

High Energy Accelerator Beam Dynamics

Results of Final Focus Test Beam (Invited) — V.A. Alexandrof, V. Balakin, A. Mikhailichenko, <i>K. Flöttmann, F. Peters, G.-A. Voss, V. Bharadwaj, M. Halling, J.A. Holt, J. Buon, J. Jeanjean,</i> <i>F. LeDiberder, V. Lepeltier, P. Puzo, G. Heimlinger, R. Settles, U. Stierlin, N. Akasaka,</i> <i>H. Hayano, N. Ishihara, H. Nakayama, K. Oide, T. Shintake, Y. Takeuchi, N. Yamamoto,</i> <i>F. Bulos, D. Burke, R. Field, S. Hartman, R. Helm, J. Irwin, R. Iverson, P. Raimondi, S. Rokni,</i> <i>G. Roy, W. Spence, P. Tenenbaum, S.R. Wagner, D. Walz, S. Williams</i>	2742	TAG01
Comparison of Measured and Calculated Dynamic Aperture (Invited) — F. Willeke	2747	TAG02
Ion Effects in Future Circular and Linear Accelerators (Invited) — T.O. Raubenheimer	2752	TAG03
Nonlinear Wave Phenomena in Coasting Beams (Invited) — P.L. Colestock, L.K. Spentzouris, <i>F. Ostiguy</i>	2757	TAG04
The Cure of Multibunch Instabilities in ELETTRA — M. Syandrlík, C.J. Bocchetta, A. Fabris, <i>F. Iazzourene, E. Karantzoulis, R. Nagaoka, C. Pasotti, L. Tosi, R.P. Walker, A. Wrulich</i>	2762	TAG05
Nonlinear Analyses of Storage Ring Lattices Using One-Turn Maps — Y.T. Yan, J. Irwin, <i>T. Chen</i>	2765	TAG06
Precise Determination and Comparison of the SPS Dynamic Aperture in Experiment and Simulation — W. Fischer, F. Schmidt	2768	TAG07
Coherency of the Long Range Beam-Beam Interaction in CESR — Alexander B. Temnykh, <i>James J. Welch</i>	2771	TAG08
Effect of Quadrupole Noise on the Emittance Growth of Protons in HERA — T. Sen, <i>O. Brüning, F. Willeke</i>	2774	TAG09
Nonlinear Mode Coupling Analysis in the Tevatron — S. Assadi, C.S. Mishra	2777	TAG10
Lattice Design for KEKB Colliding Rings — H. Koiso, K. Oide	2780	TAG11
Entropy and Emittance Growth — Patrick G. O'Shea	2783	TAG12
Analysis of Optical Stochastic Cooling Including Transverse Effects — K.-J. Kim	2786	TAG13

Volume 5

Linear and Nonlinear Orbit Theory

Reduction of Non Linear Resonance Excitation from Insertion Devices in the ALS — <i>D. Robin, G. Krebs, G. Portmann, A. Zholents, W. Decking</i>	2789	FAB01
Sum Betatron Resonances under Linear Coupling of Oscillations — P.N. Chirkov, <i>I.I. Petrenko</i>	2792	FAB02
Linear Orbit Parameters for the Exact Equations of Motion — G. Parzen	2795	FAB03
Tune Modulation Due to Synchrotron Oscillations and Chromaticity, and the Dynamic Aperture — G. Parzen	2798	FAB04
Normal Mode Tunes for Linear Coupled Motion in Six Dimensional Phase Space — <i>G. Parzen</i>	2801	FAB05
Fast Symplectic Mapping and Quasi-invariants for the Large Hadron Collider — <i>R.L. Warnock, J.S. Berg, E. Forest</i>	2804	FAB06
Nonlinear Dependence of Synchrotron Radiation on Beam Parameters — G.H. Hoffstätter	2807	FAB07
Effects of Imperfections on the Dynamic Aperture and Closed Orbit of the IPNS Upgrade Synchrotron — E. Lessner, Y.-C. Chae, S. Kim	2811	FAB09
Paraxial Expansion of a Static Magnetic Field in a Ring Accelerator — Lee C. Teng	2814	FAB10
Experimental Determination of Linear Optics Including Quadrupole Rotations — <i>J. Safranek</i>	2817	FAB11
Perturbation of Beam Energy Due to Steering and Pretzel Orbit — W. Lou, M. Billing, <i>D. Rice</i>	2820	FAB12
Lattice Studies for a High-Brightness Light Source — D. Kaltchev, R.V. Servranckx, <i>M.K. Craddock, W. Joho</i>	2823	FAB14

Transfer Maps Through Ideal Bends (Again?) — Leo Michelotti	2826	FAB15
Skew Chromaticity in Large Accelerators — S. Peggs, G.F. Dell	2829	FAB20
The Effect and Correction of Coupling Generated by the RHIC Triplet Quadrupoles — <i>F. Pilat, S. Peggs, S. Tepikian, D. Trbojevic, J. Wei</i>	2832	FAB22
The Beam Envelope Equation - Systematic Solution for a FODO Lattice with Space Charge <i>— Edward P. Lee</i>	2835	FAC01
Analytic Second- and Third-Order Achromat Designs — Chunxi Wang, Alex Chao	2838	FAC02
Measurement of Chromatic Effects in LEP — D. Brandt, P. Castro, K. Cornelis, A. Hofmann, <i>G. Morpurgo, G.L. Sabbi, A. Verdier</i>	2841	FAC03
The Lattice of the CERN Large Hadron Collider — W. Scandale, B. Jeanneret, J.- <i>P. Koutchouk, X. Luo, F. Méot, R. Ostojic, T. Risselada, C. Rufer, T. Taylor, T. Trenkler,</i> <i>S. Weisz</i>	2844	FAC04
Sorting Strategies for the LHC Based on Normal Forms — W. Scandale, M. Giovannozzi, <i>R. Grassi, E. Todesco</i>	2847	FAC06
Algorithms to get a Circulating Beam — André Verdier, Frank Richard	2850	FAC07
Non-Linear Chromaticity Correction with Sextupole Families — André Verdier	2853	FAC08
Simulation of Charged Particle Transport in Nonlinear Axisymmetrical Electrostatic Potential — I.P. Yudin, V.V. Andreev	2856	FAC09
Stochastic Effects in Real and Simulated Ion Beams — Jürgen Struckmeier	2860	FAC10
Magnetic Field Correction in Nuclotron — I.B. Issinsky, V.A. Mikhailov, V.A. Shchepunov	2863	FAC12
Effects of the CHESS Wigglers on a Beam with an Angular Offset — James J. Welch	2866	FAC14
Particle Tracking with Generating Functions of Magnetic Fringing Fields — <i>Godehard Wüstefeld</i>	2868	FAC16
Computation of Lattice Maps Using Modular BCH and Similarity Composition Rules — <i>J. Irwin</i>	2871	FAC18
Treatment of Wiggler and Undulator Field Errors in Tracking Codes — W. Decking, <i>O. Kaul, H. Nesemann, J. Roßbach</i>	2874	FAC19
Experimental Study of the Duke Storage Ring Dynamic Aperture — Y. Wu, V.N. Litvinenko, <i>B. Burnham, J.M.J. Madey</i>	2877	FAC20

Beam-Beam Interaction and Beam Cooling

A New Model of the e+e- Beam-Beam Interaction — K.D. Cromer, B.E. Norum	2880	RAP01
A Study of Beam-Beam Interactions at Finite Crossing Angles for a B-Factory — K. Hirata, <i>K. Ohmi, N. Toge</i>	2883	RAP02
Simulation of Beam-Beam Effects in Tevatron — C.S. Mishra, S. Assadi, R. Talman	2886	RAP03
The Dynamic Beta Effect in CESR — David Sagan	2889	RAP04
Lifetime and Tail Simulations for Beam-Beam Effects in PEP-II B Factory — D.N. Shatilov, <i>A.A. Zholents</i>	2892	RAP05
Gamma Ray Sources Based on Resonant Backscattering of Laser Beams With Relativistic Heavy Ion Beams — E.G. Bessonov, Kwang-Je Kim	2895	RAP06
Observations of the Effects of the Beam-Beam Interaction on the Orbits of Stored Beams in CESR — E. Young	2898	RAP07
Calculations on Depolarization in HERA due to Beam-Beam Effects — M. Böge, T. Limberg	2901	RAP08
A Map for the Thick Beam-Beam Interaction — J. Irwin, T. Chen	2904	RAP09
Transient Beam Loading in the SLC Damping Rings — M.G. Minty, R.H. Siemann	2907	RAP10
Studies of Halo Distributions Under Beam-Beam Interaction — T. Chen, J. Irwin, <i>R.H. Siemann</i>	2910	RAP11
The Effect of Phase Advance Errors Between Interaction Points on Beam Halos — T. Chen, <i>J. Irwin, R.H. Siemann</i>	2913	RAP12
Compensation of the "Pacman" Tune Spread by Tailoring the Beam Current — <i>Miguel A. Furman</i>	2916	RAP14
Disruption Effects on the Beam Size Measurement — P. Raimondi, F.-J. Decker, P. Chen	2919	RAP15
Flat Beam Spot Sizes Measurement in the SLC-Final Focus — P. Raimondi, F.-J. Decker	2922	RAP16
Polarization Correlations in the SLC Final Focus — F.-J. Decker	2925	RAP17
Supercooling of Bunched Beams by Coherent Synchrotron Radiation — M. Bergher	2928	RAP19

Analysis of the Tevatron Collider Beam Spectrum for Bunched Beam Stochastic Cooling — <i>G. Jackson</i>	2931	RAP20
Asymmetric Hopf Bifurcation for Proton Beams with Electron Cooling — <i>X. Kang, M. Ball, B. Brabson, J. Budnick, D.D. Caussyn, P. Colestock, G. East, M. Ellison, B. Hamilton, K. Hedblom, S.Y. Lee, D. Li, J.Y. Liu, K.Y. Ng, A. Pei, A. Riabko, M. Syphers, L. Wang, Y. Wang</i>	2934	RAP21
Space Charge Effects and Intensity Limits of Electron-Cooled Bunched Beams — <i>S. Nagaitsev, T. Ellison, M. Ball, V. Derenchuk, G. East, M. Ellison, B. Hamilton, P. Schwandt</i>	2937	RAP22
Stability Conditions for a Neutralised Electron Cooling Beam — <i>J. Bosser, S. Maury, D. Möhl, F. Varenne, I. Meshkov, E. Syresin, E. Mustafin, P. Zenkevich</i>	2940	RAP23
Neutralisation of the LEAR Electron-Cooling Beam: Experimental Results — <i>J. Bosser, F. Caspers, M. Chanel, R. Ley, R. Maccaferri, S. Maury, G. Molinari, G. Tranquille, F. Varenne, I. Meshkov, V. Polyakov, A. Smirnov, O. Stepashkin, E. Syresin</i>	2943	RAP24
Crystalline Beam Properties as Predicted for the Storage Ring ASTRID and TSR — <i>Jie Wei, Xiao-Ping Li, Andrew Sessler</i>	2946	RAP25

Instabilities and Cures

Impedance Matrix - an Unified Approach to Longitudinal Coupled-Bunch Feedbacks in a Synchrotron — <i>S. Ivanov</i>	2949	TPQ01
The Coupling Impedance of Toroidal Beam Pipe with Circular Cross Section — <i>H. Hahn</i>	2952	TPQ02
Bunch Lengthening Study in BEPC — <i>Z. Guo, Q. Qin, G. Xu, C. Zhang</i>	2955	TPQ03
Practical Criterion of Transverse Coupled-Bunch Head-Tail Stability — <i>S. Ivanov, M. Pozdeev</i>	2958	TPQ04
A Code to Compute the Action-Angle Transformation for a Particle in an Arbitrary Potential Well — <i>J. Scott Berg, Robert L. Warnock</i>	2962	TPQ07
Study of Longitudinal Coupled-Bunch Instabilities in the SRRC Storage Ring — <i>W.K. Lau, M.H. Wang, K.T. Hsu, L.H. Chang, Ch. Wang, C.C. Kuo</i>	2965	TPQ08
Suppression of the Transverse Oscillation in the SRRC Storage Ring by RF Knockout Method — <i>J.C. Lee, M.H. Wang, K.T. Hsu, R.J. Sheu, G. Lin, C.S. Hsue</i>	2968	TPQ09
The Observation of Longitudinal Coupled Bunch Motion on Streak Camera at SRRC — <i>M.H. Wang, K.T. Hsu, W.K. Lau, C.S. Hsue, H.J. Tsai, H.P. Chang, J.C. Lee, C.C. Kuo</i>	2971	TPQ10
Resistive-Wall Instability Experiment in Space-Charge Dominated Electron Beams — <i>H. Suk, J.G. Wang, M. Reiser</i>	2974	TPQ11
Mode-Coupling Instability and Bunch Lengthening in Proton Machines — <i>K.Y. Ng</i>	2977	TPQ12
Longitudinal Wakefield for Synchrotron Radiation — <i>J.B. Murphy, S. Krinsky, R.L. Gluckstern</i>	2980	TPQ14
Review of Beam Instability Studies for the SSC — <i>W. Chou</i>	2983	TPQ15
Collective Effects in the NLC Damping Ring Designs — <i>T. Raubenheimer, K.L.F. Bane, J.S. Berg, J. Byrd, J. Corlett, M. Furman, S. Heifets, K. Kubo, M. Minty, B. Scott, K.A. Thompson, P.B. Wilson, F. Zimmermann</i>	2986	TPQ16
Emittance and Energy Control in the NLC Main Linacs — <i>C. Adolphsen, K.L.F. Bane, K. Kubo, T. Raubenheimer, R.D. Ruth, K.A. Thompson, F. Zimmermann</i>	2989	TPQ17
Digital Signal Processing for the APS Transverse and Longitudinal Damping System — <i>D. Barr, W. Sellyey</i>	2992	TPQ19
Longitudinal Coupling Impedance of a Hole in an Infinite Plane Screen — <i>Yong-Chul Chae</i>	2995	TPQ20
Investigation of Resistive Wall Instability in the 7-GeV APS Storage Ring — <i>Yong-Chul Chae</i>	2998	TPQ21
Longitudinal Instability Analysis for the IPNS Upgrade — <i>K. Harkay, Y. Cho, E. Lessner</i>	3001	TPQ22
Transverse Instability Analysis for the IPNS Upgrade — <i>K. Harkay, Y. Cho</i>	3004	TPQ23
Longitudinal Emittance Measurements in the Fermilab Booster — <i>D.A. Herrup</i>	3007	TPQ25
Analog Dampers in the Fermilab Booster — <i>D.A. Herrup, D. McGinnis, J. Steimel, R. Tomlin</i>	3010	TPQ26
A Study of the Longitudinal Coupled Bunch Instability in the Fermilab Main Ring — <i>K. Junck, J. Marriner, D. McGinnis</i>	3013	TPQ28
Inference of Wake Field Structure by Driving Longitudinal Coupled Bunch Modes in Main Ring — <i>S. Assadi, K. Junck, P. Colestock, J. Marriner</i>	3016	WAB01
Simulation of Transverse Coupled Bunch Instabilities — <i>S. Khan</i>	3019	WAB03
The Transition Jump System for the AGS — <i>W.K. van Asselt, L.A. Ahrens, J.M. Brennan, A. Dunbar, E. Keith-Monnia, J.T. Morris, M.J. Syphers</i>	3022	WAB04

Measurements of Longitudinal Phase Space in the SLC Linac — R.L. Holtzapple, F.-J. Decker, R.K. Jobe, C. Simopoulos	3025	WAB05
Observation of Induced Beam Oscillation from Actively Displaced RF Accelerating Structures — John T. Seeman, Henk Fischer, William Roster	3028	WAB06
Measurement of the Effect of Collimator Generated Wakefields on the Beams in the SLC — K.L.F. Bane, C. Adolphsen, F.-J. Decker, P. Emma, P. Krejcik, F. Zimmermann	3031	WAB07
Beam Trajectory Jitter in the SLC Linac — Chris Adolphsen, Tim Slaton	3034	WAB08
Emittance Growth due to Decoherence and Wakefields — M.G. Minty, A.W. Chao, W.L. Spence	3037	WAB09
A Weak Microwave Instability with Potential Well Distortion and Radial Mode Coupling — Alex Chao, Bo Chen, Katsunobu Oide	3040	WAB10
Wake Field and the Diffraction Model Due to a Flat Beam Moving Past a Conducting Wedge — A.W. Chao, H. Henke	3043	WAB11
Operating Experience with High Beam Currents and Transient Beam Loading in the SLC Damping Rings — M.G. Minty, R. Akre, P. Krejcik, R.H. Siemann	3046	WAB12
Deflecting Forces for the Case of Multi Mode Beam - RF Cavity Interaction in Linear Accelerators — V.G. Kurakin	3049	WAB14
Photoelectron Trapping Mechanism for Transverse Coupled Bunch Mode Growth in CESR — J.T. Rogers	3052	WAB15
Electron Cooler Impedances — A. Burov	3055	WAB16
Wall Impedances for Low and Moderate Energies — A. Burov	3058	WAB17
Impedance Analysis of the PEP-II Vacuum Chamber — C.-K. Ng, T. Weiland	3061	WAB18
Microwave Instabilities in Electron Rings with Negative Momentum Compaction Factor — S.X. Fang, K. Oide, K. Yokoya, B. Chen, J.Q. Wang	3064	WAB20
Microwave Stability at Transition — J.A. Holt, P.L. Colestock	3067	WAC01
Experimental Observations of Nonlinear Coupling of Longitudinal Modes in Unbunched Beams — Linda Klamp Spentzouris, Patrick L. Colestock, Francois Ostiguy	3070	WAC02
Damping Rate Measurements in the SLC Damping Rings — C. Simopoulos, R.L. Holtzapple	3073	WAC04
Transverse Multibunch Instabilities for Non-Rigid Bunches — J. Scott Berg, Ronald D. Ruth	3076	WAC05
Simulations of Transition Crossing in the Main Injector — C.M. Bhat, J.A. MacLachlan	3079	WAC06
Impedance Budget for the KEK B-Factory — Y.H. Chin, K. Satoh	3082	WAC07
Single-Beam Collective Effects in the KEK B-Factory — Y.H. Chin, K. Akai, Y. Funakoshi, K. Oide, K. Satoh	3085	WAC08
Beam Transfer Function and Transverse Impedance Measurements in the Fermilab Main Ring — P.J. Chou, G. Jackson	3088	WAC09
Experimental Studies of Transverse Beam Instabilities at Injection in the Fermilab Main Ring — P.J. Chou, G. Jackson	3091	WAC10
Longitudinal Multibunch Feedback Experiment with Switched Filter Bank — A. Pei, M. Ball, M. Ellison, X. Kang, S.Y. Lee, D. Li, J. Liu, A. Riabko, L. Wang	3094	WAC12
Field Propagation Effects and Related Multibunch Instability in Multicell Capture Cavities — M. Ferrario, A. Mosnier, L. Serafini, F. Tazzioli, J.-M. Tessier	3097	WAC13
Cure of Transverse Instabilities by Chromaticity Modulation — T. Nakamura	3100	WAC14
A Fast Beam-Ion Instability — F. Zimmermann, T.O. Raubenheimer, G. Stupakov	3102	WAC15
Simulations of the Longitudinal Instability in the New SLC Damping Rings — K.L.F. Bane, K. Oide	3105	WAC16
High-Intensity Single Bunch Instability Behavior In The New SLC Damping Ring Vacuum Chamber — K. Bane, J. Bowers, A. Chao, T. Chen, F.J. Decker, R.L. Holtzapple, P. Krejcik, T. Limberg, A. Lisin, B. McKee, M.G. Minty, C.-K. Ng, M. Pietryka, B. Podobodov, A. Rackelmann, C. Rago, T. Raubenheimer, M.C. Ross, R.H. Siemann, C. Simopoulos, W. Spence, J. Spencer, R. Stege, F. Tian, J. Turner, J. Weinberg, D. Whittum, D. Wright, F. Zimmermann	3109	WAC17
Alignment Tolerance of Accelerating Structures and Corrections for Future Linear Colliders — K. Kubo, C. Adolphsen, K.L.F. Bane, T.O. Raubenheimer, K.A. Thompson	3112	WAC18
Refinements to Longitudinal, Single Bunch, Coherent Instability Theory — S.R. Koscielniak	3115	WAC19
Simulations of Sawtooth Instability — R. Baartman, M. D'Yachkov	3119	WAC20
Characterisation of a Localised Broad-Band Impedance Phenomenon on the SRS — S.F. Hill	3122	WAC21
Cavity-Beam Instabilities on the SRS at Daresbury — P.A. McIntosh, D.M. Dykes	3125	WAC22

Bunch Lengthening Thresholds on the Daresbury SRS — J.A. Clarke.....	3128	WAC23
Estimation of Collective Instabilities in RHIC — W.W. MacKay, M. Blaskiewicz, D. Deng, V. Mane, S. Peggs, A. Ratti, J. Rose, T.J. Shea, J. Wei.....	3131	WAC24
RHIC Injection Kicker Impedance — V. Mane, S. Peggs, D. Trbojevic, W. Zhang.....	3134	WAC25
KRAKEN, a Numerical Model of RHIC Impedances — S. Peggs, V. Mane.....	3137	WAC26
Lattice Design of Beijing Light Source — N. Huang, L. Jin, D. Wang, L. Wang, A. Xiao, G. Xu.....	3140	WAC27
A Theoretical Study of the Electron-Proton Instability in a Long Proton Pulse — Tai-Sen F. Wang.....	3143	WAC28
Recent Progress on Beam Stability Study in the PSR — T. Wang, P. Channell, R. Cooper, D. Fitzgerald, T. Hardek, R. Hutson, A. Jason, R. Macek, M. Plum, C. Wilkinson, E. Colton.....	3146	WAC29

Low Energy Accelerator Beam Dynamics

Halos of Intense Proton Beams (Invited) — Robert D. Ryne, Salman Habib, Thomas P. Wangler.....	3149	RAG01
Polarized Proton Beams (Invited) — T. Roser.....	3154	RAG02
Beam Dynamics in Heavy Ion Fusion (Invited) — Peter Seidl.....	3159	RAG03
Crystalline Beams (Invited) — John P. Schiffer.....	3164	RAG04
Injecting a Kapchinskij-Vladimirskij Distribution into a Proton Synchrotron — E. Crosbie, K. Symon.....	3167	RAG05
Halo of a High-Brightness Electron Beam — G. Haouat, N. Pichoff, C. Couillaud, J.P. De Brion, J. Di Crescenzo, S. Joly, A. Loulergue, C. Ruiz, S. Seguin, S. Striby.....	3170	RAG06
Studies on Halo Formation in a Long Magnetic Quadrupole FODO Channel First Experimental Results — P.-Y. Beauvais, D. Bogard, P.-A. Chamouard, R. Ferdinand, G. Haouat, J.-M. Lagniel, J.-L. Lemaire, N. Pichoff, C. Ruiz.....	3173	RAG07
Radial Mode Evolution in Longitudinal Bunched Beam Instability — S.Y. Zhang, W.T. Weng.....	3176	RAG08
Stability of a Breathing K-V Beam — Robert L. Gluckstern, Wen-Hao Cheng.....	3179	RAG09
Hamiltonian Formalism for Space Charge Dominated Beams in a Uniform Focusing Channel — A. Riabko, M. Ellison, X. Kang, S.Y. Lee, J.Y. Liu, D. Li, A. Pei, L. Wang.....	3182	RAG10
Simulation Studies of the LAMPF Proton Linac — R.W. Garnett, E.R. Gray, L.J. Rybarczyk, T.P. Wangler.....	3185	RAG11
Functional Dependence of Wakefunctions for $v < c$ — Zenghai Li, Joseph J. Bisognano.....	3188	RAG12
Betatron Transients Caused by Rapid Changes in the Closed Orbit — James J. Welch.....	3191	RAG13
Phenomenology of Crystalline Beams in Smooth Accelerators — A.F. Haffmans, D. Maletic, A.G. Ruggiero.....	3194	RAG14
Beam Dynamics in the 1.3 GeV High Intensity ESS Coupled Cavity Linac — M. Pabst, K. Bongardt.....	3197	TPA01
Final Bunch Rotation and Momentum Spread Limitation for the ESS Facility — K. Bongardt, M. Pabst.....	3200	TPA02
Design Criteria for High Intensity H⁻ Injector Linacs — K. Bongardt, M. Pabst.....	3203	TPA03
Measurements of Vacuum Chamber Impedance Effects on the Stored Beam at CESR — M. Billing, Z. Greenwald, W. Hartung, W.R. Lou, M. Pisharody, J. Rogers, D. Sagan, J. Sikora.....	3206	TPA04
The Study of Nonlinear Effects Influenced by Space Charge in High Intensity Linac — A.A. Kolomiets, S.G. Yaramishev, P.R. Zenkevich, A.P. Korolev.....	3209	TPA05
Beam Size Versus Intensity for Resonant Extracted Beam at the Brookhaven AGS — K.A. Brown, R. Thern, H. Huang.....	3212	TPA06
Review of Longitudinal Perturbation Formalism — S.Y. Zhang.....	3214	TPA08
Klystron Power Specifications Based on Transient Beam Loading Analysis in Damping Rings — M.G. Minty, R.H. Siemann.....	3217	TPA09
Transverse Combining of Four Beams in MBE-4 — C.M. Celata, W. Chupp, A. Faltens, W.M. Fawley, W. Ghiorso, K.D. Hahn, E. Henestroza, C. Peters, P. Seidl.....	3220	TPA10
Ion Core Parameters in the Bending Magnets of Electron Storage Rings — E. Bulyak.....	3223	TPA12
Ion Driven Effects in the Intence Electron Beam Circulating in Storage Rings — E. Bulyak.....	3226	TPA13
Disk-Loaded Waveguides for Accelerating High Intensity Short Pulse Electron Beams — N.I. Aizatsky.....	3229	TPA14
The Description of High Current Beam Dynamics Using Lie Algebraic Methods — A.I. Borodich, A.A. Khrutchinsky, V.I. Stolyarsky.....	3232	TPA15

Chaos, a Source of Charge Redistribution and Halo Formation in Space-Charge Dominated Beams — Jean-Michel Lagniel, David Libault.....	3235	TPA17
Transport of a Partially-Neutralized Ion Beam in a Heavy-Ion Fusion Reactor Chamber — Debra A. Callahan, A. Bruce Langdon	3238	TPR01
Emittance Growth from Rotated Quadrupoles in Heavy Ion Accelerators — John J. Barnard.....	3241	TPR02
Wakefield Effects on the Beam Accelerated in a Photoinjector: Perturbation Due to the Exit Aperture — J.-M. Dolique, W. Salah	3245	TPR04
Influence of the Photoinjector Exit Aperture on the Wakefield Driven by an Intense Electron Beam Pulse: a Theoretical Approach — J.-M. Dolique	3248	TPR05
Invariability of Intense Beam Emittance in Nonlinear Focusing Channel — Y.K. Batygin.....	3251	TPR06
Beam Transport for Uniform Irradiation: Nonlinear Space Charge and the Effect of Boundary Conditions — D. Bruhwiler, Yuri K. Batygin.....	3254	TPR07
Transport of Bunched Beams with Space Charge Through a Periodic Lattice — M.F. Reusch, D.L. Bruhwiler.....	3257	TPR08
Modeling Space Charge in Beams for Heavy-Ion Fusion — W.M. Sharp	3260	TPR09
Impedance of Periodic Irises in a Beam Pipe — Shicheng Jiang, Robert L. Gluckstern, Hiromi Okamoto	3263	TPR11
Frequency Dependence of the Polarizability and Susceptibility of a Circular Hole in a Thick Conducting Wall — Wen-Hao Cheng, Alexei V. Fedotov, Robert L. Gluckstern	3266	TPR12
Spatial-Temporal Hysteresis Effects in an Intense Electron Beam — A.V. Agafonov, A.N. Lebedev, V.S. Voronin	3269	TPR13
General Wave Equation in the Electrostatic Approximation — A.V. Agafonov.....	3272	TPR14
Space Charge Effects at KEK-Booster Synchrotron — Chihiro Ohmori, Toshikazu Adachi, Tadamichi Kawakubo, Motohiro Kihara, Isao Yamane	3275	TPR16
On the Relaxation of Semi-Gaussian and K-V Beams to Thermal Equilibrium — S.M. Lund, J.J. Barnard, J.M. Miller.....	3278	TPR18
Transverse-Longitudinal Energy Equilibration in a Long Uniform Beam — I. Haber, D.A. Callahan, A. Friedman, D.P. Grote, A.B. Langdon	3282	TPR19

Beam Dynamics, Misc.

Variants of Optics Schemes and Accelerator Configurations for Athens Microtron: Preliminary Considerations — A.V. Tiunov, V.I. Shvedunov, I.V. Surma, K. Hizanidis, C. Kalfas, C. Trikalinos, J. Tigelis.....	3285	RAQ01
Study of Beam Decoherence in the Presence of Head-Tail Instability Using a Two-particle Model — G.V. Stupakov, A.W. Chao.....	3288	RAQ02
Beam Distribution Function after Filamentation — T.O. Raubenheimer, F.-J. Decker, J.T. Seeman.....	3291	RAQ03
Measurement of the Interaction Between a Beam and a Beam Line Higher-Order Mode Absorber in a Storage Ring — W. Hartung, P. Barnes, S. Belomestnykh, M. Billing, R. Chiang, E. Chojnacki, J. Kirchgessner, D. Moffat, H. Padamsee, M. Pisharody, D. Rubin, M. Tigner.....	3294	RAQ04
A New Analytical Model for Axi-symmetric Cavities — D. Burrini, C. Pagani, L. Serafini.....	3297	RAQ05
Impurity Growth in Single Bunch Operation of PF — M. Tobiyaama, A. Higuchi, T. Mitsuhashi, T. Kasuga, S. Sakanaka.....	3300	RAQ06
Coupling Impedance of a Periodic Array of Diaphragms — G.V. Stupakov.....	3303	RAQ09
Coupling Impedance of a Long Slot and an Array of Slots in a Circular Vacuum Chamber — G.V. Stupakov.....	3306	RAQ10
Dark Currents for CEBAF Linacs — Byung C. Yunn	3309	RAQ11
Improvements in Bunch Coalescing in the Fermilab Main Ring — J. Dey, I. Kourbanis, D. Wildman	3312	RAQ13
Slow Extraction of Particles Using a Thin Target for Driving for Resonance — Yu. Severgin, W. Belov, A. Makarov, M. Tarovik.....	3315	RAQ14
Properties of a Transverse Damping System, Calculated by a Simple Matrix Formalism — S. Koscielniak, H.J. Tran.....	3317	RAQ15
A Concept for Emittance Reduction of DC Radioactive Heavy-Ion Beams — J.A. Nolen, J.C. Dooling.....	3320	RAQ16

Measurements of the Octupole-Induced Amplitude-Dependent Frequency Shift in SPEAR — P. Tran, C. Pellegrini, J. Yang, M. Cornacchia, J. Corbett.....	3323	RAQ17
Radiation Damping in Focusing-Dominated Systems — Zhirong Huang, Pisin Chen, Ronald D. Ruth.....	3326	RAQ18
Colliding Crystalline Beams — A.F. Haffmans, D. Maletic, A.G. Ruggiero.....	3329	RAQ20
Helical Spin Rotators and Snakes for RHIC — V.I. Ptitsin, Yu.M. Shatunov, S. Peggs.....	3331	RAQ21
Effects of Enhanced Chromatic Nonlinearity during the AGS gt-Jump — J. Wei, J.M. Brennan, L.A. Ahrens, M.M. Blaskiewicz, D.-P. Deng, W.W. MacKay, S. Peggs, T. Satogata, D. Trbojevic, A. Warner, W.K. van Asselt.....	3334	RAQ22
Effect of Parametric Resonances on the Bunched Beam Dilution Mechanism — L. Wang, M. Ball, B. Brabson, J. Budnick, D.D. Caussyn, G. East, M. Ellison, X. Kang, S.Y. Lee, D. Li, J.Y. Liu, K.Y. Ng, A. Pei, A. Riabko, D. Rich, T. Sloan, M. Syphers.....	3337	RAQ23
Parametric Resonances and Stochastic Layer Induced by A Phase Modulation — J.Y. Liu, M. Ball, B. Brabson, J. Budnick, D.D. Caussyn, P. Colestock, V. Derenchuk, G. East, M. Ellison, D. Friesel, B. Hamilton, W.P. Jones, X. Kang, S.Y. Lee, D. Li, K.Y. Ng, A. Pei, A. Riabko, T. Sloan, M. Syphers, L. Wang.....	3340	RAQ24
Nonlinear Space Charge Effect of Gaussian Type Bunched Beam in Linac — Yinbao Chen, Shinian Fu, Zhibin Huang, Zhenhai Zhang.....	3343	RAQ25
Emittance Growth Caused by Bunched Beam with Nonuniform Distributions in Both Longitudinal and Transverse Directions in Linac — Zhibin Huang, Yinbao Chen, Shinian Fu.....	3346	RAQ26
The Envelopes of Beam Motion in the Charged Particle Cyclic Accelerator — Yu.P. Virchenko, Yu.N. Grigor'ev.....	3349	RAQ28
A Semi-analytical Approach to the Design of Low Energy Cylindrically Symmetric Transport Lines — Pedro F. Tavares.....	3352	RAQ29
Stability of Trapped Ions in Electron Storage Rings in View of Parametric Resonance — Y. Miyahara.....	3355	RAQ30
Entropy and Emittance of Particle and Photon Beams — K.-J. Kim, R.G. Littlejohn.....	3358	RAR02
Effect of the Coupling Slots on Beam Dynamics in Accelerator Structure of Moscow CW RTM — V.I. Shvedunov, A.S. Alimov, A.S. Chepurnov, O.V. Chubarov, D.I. Ermakov, A.V. Tiunov, P.L. Tkachev.....	3361	RAR04
The Electron Beam Orbit Sensitivity on the Photon Flux of the Photon Beam Line — Ian Hsu, G.H. Luo, K.L. Tsang, C.C. Chu, C.I. Yu, W.T. Weng, S.C. Chung.....	3364	RAR05
Ground Motion in LEP and LHC — L. Vos.....	3367	RAR07
Cosmic Particle Acceleration at Very High Energies — K.O. Thielheim.....	3370	RAR09
Trapped Modes in the Vacuum Chamber of an Arbitrary Cross Section — Sergey S. Kurennoy, Gennady V. Stupakov.....	3373	RAR11
A General Approach for Calculating Coupling Impedances of Small Discontinuities — Sergey S. Kurennoy, Robert L. Gluckstern, Gennady V. Stupakov.....	3376	RAR12
Polarizabilities of an Annular Cut and Coupling Impedances of Button-Type Beam Position Monitors — Sergey S. Kurennoy.....	3379	RAR13
The Effect of Coupling on Luminosity — D. Sagan.....	3382	RAR15
RFQ-DTL Matching Solutions for Different Requirements — D. Raparia.....	3385	RAR16
Low-Dispersion γ_t Jump for the Main Injector — K.Y. Ng, A. Bogacz.....	3388	RAR17
Wakefields and HOMs Studies of a Superconducting Cavity Module with the CESR Beam — S. Belomestnykh, W. Hartung, G. Flynn, J. Kirchgessner, H. Padamsee, M. Pisharody.....	3391	RAR18
Comparison of the Predicted and Measured Loss Factor of the Superconducting Cavity Assembly for the CESR Upgrade — S. Belomestnykh, W. Hartung, J. Kirchgessner, D. Moffat, H. Muller, H. Padamsee, V. Veshcherevich.....	3394	RAR19
Control of Trapped Ion Instabilities in the Fermilab Antiproton Accumulator — Steven J. Werkema.....	3397	RAR20
Longitudinal Emittance Oscillation in a Superconducting Drift Tube Linac — J.W. Kim, K.W. Shepard.....	3400	RAR21
Electric Fields, Electron Production, and Electron Motion at the Stripper Foil in the Los Alamos Proton Storage Ring — M. Plum.....	3403	RAR22
Electron Clearing in the Los Alamos Proton Storage Ring — M. Plum, J. Allen, M. Borden, D. Fitzgerald, R. Macek, T.S. Wang.....	3406	RAR23

Advanced Photon Source Insertion Device Field Quality and Multipole Error Specification — <i>Yong-Chul Chae, Glenn Decker</i>	3409	RAR24
Study of Field Ionization in the Charge Exchange Injection for the IPNS Upgrade — <i>Yong-Chul Chae, Yanglai Cho</i>	3412	RAR25
Lattice Considerations for a Tau-Charm Factory — <i>L.C. Teng, E.A. Crosbie</i>	3415	RAR26
Effects of Vertical Aperture on Beam Lifetime at the Advanced Photon Source (APS) Storage Ring — <i>Hana M. Bizek</i>	3418	RAR27
Rebucketing After Transition in RHIC — <i>D.-P. Deng, S. Peggs</i>	3421	RAR29
Closed-Orbit Drifts in HERA in Correlation with Ground Motion — <i>V. Shiltsev, B. Baklakov,</i> <i>P. Lebedev, C. Montag, J. Rossbach</i>	3424	RAR30
Simulation of the Acceleration of Polarized Protons in Circular Accelerators — <i>Yu. Shatunov, V. Yakimenko</i>	3427	RAR31

QUENCH ANTENNAS FOR RHIC QUADRUPOLE MAGNETS

T. Ogitsu, A. Terashima, and K. Tsuchiya,
KEK, National Laboratory for High Energy Physics, Tsukuba, Ibaraki, 305, Japan
G. Ganetis, J. Muratore, and P. Wanderer,
BNL, Brookhaven National Laboratory, Upton, Long Island, NY 11973 USA

Quench antennas for RHIC quadrupole magnets are being developed jointly by KEK and BNL. A quench antenna is a device to localize a quench origin using arrays of pick-up coils lined up along the magnet bore. Each array contains four pick-up coils: sensitive to normal sextupole, skew sextupole, normal octupole, and skew octupole field. This array configuration allows an azimuthal localization of a quench front while a series of arrays gives an axial localization and a quench propagation velocity. Several antennas have been developed for RHIC magnets and they are now routinely used for quench tests of production magnets. The paper discusses the description of the method and introduces a measured example using an antenna designed for quadrupole magnets.

I. INTRODUCTION

Although the best method to localize a quench origin is use of voltage taps [1], the method is not desirable for production magnets because of the risks associated with mounting voltage taps. A technique which uses a set of pick-up coils has been developed in order to localize a quench origin without using voltage taps. The technique was originally developed at CERN, and used to localize quench origins of LHC dipole magnets [2,3]. A similar method was then developed at SSCL in order to measure quench locations for SSC dipole magnets. The method developed at SSCL relies on a set of pick-up coils which are sensitive to higher order multipole fields, e.g. quadrupole or sextupole fields, but not sensitive to the main dipole field[4]. Quench antennas relying on the same method were developed for RHIC dipole magnets, and are now being used routinely during the quench tests of the RHIC production dipole magnets. Quench antennas for quadrupole magnets were also developed. The antennas contain pickup coils which are sensitive to sextupole and octupole fields, but not sensitive to the main quadrupole fields. Recently, one of the antennas, being used for 13 cm-aperture interaction region (IR) quadrupole magnets [5], was tested with a magnet which is heavily instrumented with voltage taps. It was confirmed that the quench locations derived from the voltage taps and the quench antenna agreed with each other. This paper briefly describes the antenna system and then presents quench antenna and voltage tap data taken on this magnet.

II. SYSTEM CONFIGURATION

The antenna used for the IR magnets consists of two coil arrays which are lined up along the magnet length. Each coil array contains four pickup coils; the first one is sensitive to normal sextupole, the second to skew sextupole, the third to normal octupole, and the fourth to skew octupole field. Figure 1a presents a cross-sectional view of a coil array. A three dimensional view of a single turn sextupole coil is shown in Figure 1b. It was shown by Morgan [6] that this kind of winding is primarily sensitive to the sextupole field. The octupole coil is similar to the sextupole coil except the wire crosses the coil form every $\pi/4$. The skew coils are rotated from normal coils by $\pi/6$ for sextupole and $\pi/8$ for octupole.

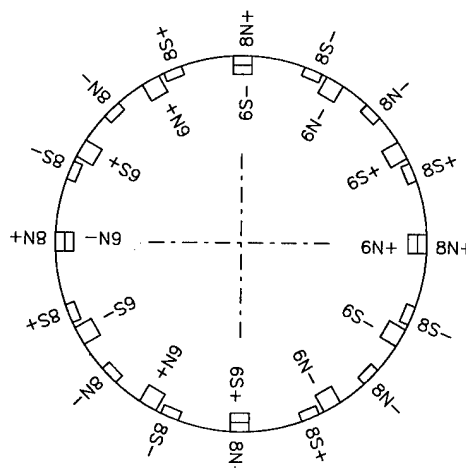


Figure 1a Cross-sectional view of a coil array. 6N, 6S, 8N, and 8S indicate normal sextupole, skew sextupole, normal octupole, and skew octupole coil, respectively.

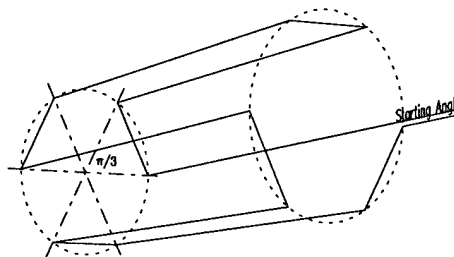


Figure 1b Three dimensional view of a single turn sextupole coil.

The length of each coil is 150 mm, and the diameter is 79 mm. The centers of the two coil arrays are located 155 mm from the center of the magnet toward the ends. The coil array close to the lead end is named C-1 and the other is C-2. The number of turns in each windings in the coil array C-1 is 8, and the number in C-2 is 4.

III. MEASUREMENT RESULTS

The example shown here is the first spontaneous quench taken on magnet QRI998. The quench current is 6745 A, at which the expected gradient is 63.2 T/m. The quench started in the pole turn, where the voltage taps are instrumented such that terminal voltages of the straight section, the lead end, and the return end can be monitored. The length of the straight section of the magnet is 1309 mm. The voltage taps are mounted slightly inwards so that the length between the taps is 966 mm.

A. Axial Quench Localization

Figure 2a presents signals of the normal sextupole coils in both arrays in comparison to voltage tap signals of the straight section and both ends of the quenched turn. The signals of the straight section voltage taps and coil C-1 appear to take off almost simultaneously indicating that the quench started in the region where C-1 is located. Following these, the signals of the lead end voltage taps and the coil C-2 take off almost simultaneously. This indicates that the quench origin is halfway between the lead end tap and coil C-2.

More detailed quench propagation analysis can be performed using the voltage tap signal of the straight section. Figure 2b shows quench front locations as a function of time. The locations of antenna coil arrays and the end taps are also indicated at the time when each signal takes off. The plot is derived from the voltage tap signal of the straight section. The voltage increase due to the temperature rise is compensated using the following equation:

$$V_c(t) = V_{ss}(t) - \int_{t_{q1}}^t \frac{V_{ss}(t_{q3} + t - \tau) - V_{ss}(t_{q3})}{V_{ss}(t_{q3})} \frac{dV_{ss}(\tau)}{d\tau} d\tau \quad (t_{q1} < t < t_{q3}) \quad (1)$$

where V_c is the compensated voltage, V_{ss} is the raw voltage of the straight section, t_{q1} is the time when the voltage of the straight section takes off, and t_{q3} is the time when the return end voltage starts to rise. The size of the normal zone in the straight section is assumed to increase in proportion to V_c toward both ends until the quench front reaches the lead end, and after that only toward the return end. The quench start location is derived so that the plot is

consistent with the times when the voltage tap signals of both ends take off. The plot starts at the lead end edge of C-1, and then passes through the lead end edge of C-2. This indicates that the antenna signals are in good agreement with the axial quench propagation derived from the voltage tap signals.

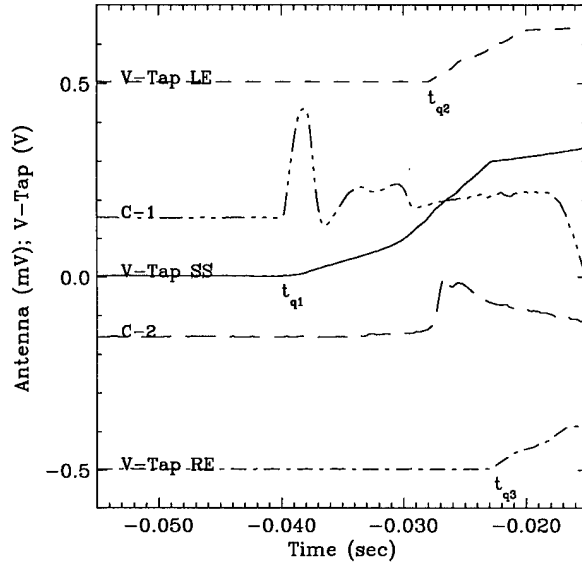


Figure 2a Measured signal of antenna coils and voltage taps. Some of the signals are offset.

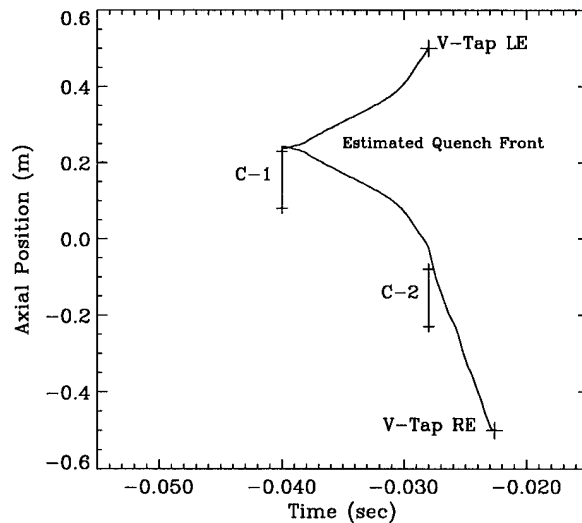


Figure 2b Axial quench localization.

B. Azimuthal Quench Localization

Figure 3a presents signals of the four coils in the coil array C-1. The signal is believed to be caused by a field distortion due to current redistribution in the quenching turns. Following the analysis performed in Reference 4, we assume that the field distortion is produced by a moving current line. Let us define a Cartesian coordinate system

such that the z-axis is parallel to the coil array and the origin is at the center of the coil array. The current I_s parallel to the z-axis positioned at $(x,y)=r_s e^{i\alpha}$, moving with velocity $(v_x,v_y)=v_s e^{i\beta}$, induces voltages approximated as,

$$V_{6n} = N_{6n} \frac{3 r_{6n}^3 \mu_0 L_{6n} I_s v_s}{\pi r_s^4} \cos(-4\alpha+\beta) \quad (2a)$$

$$V_{6s} = N_{6s} \frac{3 r_{6s}^3 \mu_0 L_{6s} I_s v_s}{\pi r_s^4} \sin(-4\alpha+\beta) \quad (2b)$$

$$V_{8n} = N_{8n} \frac{4 r_{8n}^4 \mu_0 L_{8n} I_s v_s}{\pi r_s^5} \cos(-5\alpha+\beta) \quad (2c)$$

$$V_{8s} = N_{8s} \frac{4 r_{8s}^4 \mu_0 L_{8s} I_s v_s}{\pi r_s^5} \sin(-5\alpha+\beta) \quad (2d)$$

where the subscripts 6n, 6s, 8n, and 8s used for the voltage V, the number of turns N, the length L and the radius R, refer to the normal sextupole, skew sextupole, normal octupole, and skew octupole coil, respectively. The system of equations allows us to obtain four unknowns, r_s , α , $I_s v_s$, and β , analytically. Figure 3b summarizes these four values derived for the range indicated by a pair of dotted

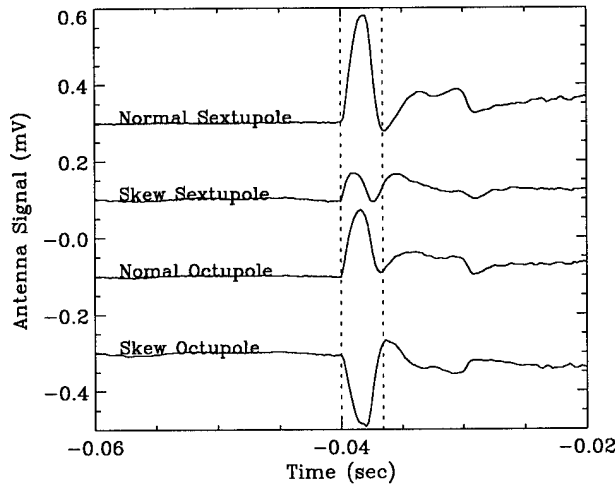


Figure 3a Signals of the coils in C-1. The signals are offset.

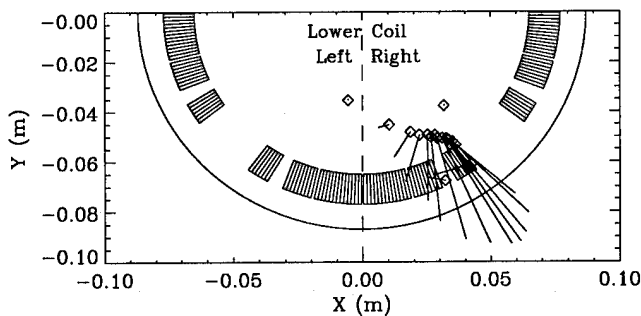


Figure 3b Azimuthal quench localization, as viewed from the lead end.

lines in Figure 3a. The diamonds present the position given by r_s and α and length and direction of the lines indicate $I_s v_s$ and β , respectively. The diamonds are mostly located close to the left pole turn of the lower right coil. The voltage tap signals show that the quench starts in the straight section of the left pole turn in the lower right coil. Although the analysis used here is based on a crude two dimensional model, the azimuthal quench localization result appears to be consistent with the voltage tap result.

This kind of analysis has been performed for most of the quenches of this magnet. In many cases the results are more scattered than the case shown here due to bad signal-to-noise ratios. Averaging the data over a range covering the first peak and using the least squares technique, but relying on a similar two dimensional model, a quench origin was determined within several turns of cable of the actual location in most of the cases. Although the two dimensional model is sufficient for the azimuthal quench localization, three dimensional analyses should be performed in order to determine the causes of the signals.

IV. CONCLUSION

The quench antenna tests made on the RHIC IR quadrupole magnets showed that quench localization based on the quench antenna is consistent with that based on the voltage taps. This proves that the quench antenna introduced here is an adequate device for quench localization in quadrupole magnets.

V. REFERENCES

- [1] A. Devred, *et al.*, "Quench Start Localization in Full-Lenght SSC R&D Dipoles," *Supercollider-1*, M. McAshan ed., Plenum Press, N.Y., 1989, p.73.
- [2] D. Leroy, *et al.*, "Quench Observation in LHC Superconducting One Meter Long Dipole Model by Field Perturbation Measurements," *IEEE Trans. on A.S.C.*, Vol.3 No.1, 1993, p.781.
- [3] A. Siemko, *et al.*, "Quench Localization in the Superconducting Model Magnets for the LHC by Means of Pick-up Coils," presented at A.S.C., Boston, 1994.
- [4] T. Ogitsu, *et al.*, "Quench Antenna for Superconducting Particle Accelerator Magnets," *IEEE Trans. on A.S.C.*, Vol.3 No.1, 1993, p.781.
- [5] G. Gupta, *et al.*, "Large Aperture Quadrupoles for RHIC Interaction Regions" *Proc. 1993 PAC*, p. 2745.
- [6] G. Morgan "Stationary Coil for Measuring the Harmonics in Pulsed Transport Magnets," *Proc. of 4th Int. Conf. on Mag. Tech.*, BNL, Upton NY, USA, Sep. 19-22, 1972, p. 787.

SUPERCONDUCTING 8 CM CORRECTOR MAGNETS FOR THE RELATIVISTIC HEAVY ION COLLIDER (RHIC)*

A. Morgillo, J. Escallier, G. Ganetis, A. Greene, A. Ghosh, A. Jain, E. Kelly, A. Marone,
G. Morgan, J. Muratore, W. Sampson, P. Thompson, P.J. Wanderer, E. Willen
Brookhaven National Laboratory, Upton, New York 11973-5000

RHIC will require 420 80 mm Corrector magnets. The magnets are made up of coils wound on a computer controlled wiring machine using ultrasonic power to bond the wire into an epoxy coated flat substrate. The coils are wrapped onto support tubes and concentrically assembled inside an iron yoke. These magnets are being built at Brookhaven National Laboratory (BNL) with more than 280 constructed by May, 1 1995. Design, construction and test results are presented.

I. DESIGN

A total of 432 80 mm aperture correctors, including 12 spares, is being built for the accelerator. Each is composed of up to four separate multipole elements. This large number of elements was the dominant consideration in the basic design, resulting in the following criteria.

1. Design was to have a minimum number of interchangeable parts. A completed corrector was to be achieved by assembly of concentric cylinders each containing one multipole. With this approach it is possible to build correctors with differing multipole selections and different choices of skew and normal multipoles out of "stock" tubes.
2. Low cryogenic load. Since these magnets are individually powered, the heat load of the current leads is an important consideration. This was reduced by choosing 50A as the nominal operating current. The cost of the numerous power supplies is also dependent upon the choice of operating current.

The nominal magnetic length (0.5m) was determined by the space available in the lattice. The strengths came from computer simulations of the accelerator with some additional margin added. Since the design, the simulations have been refined, and roughly 25% of the main arc dipoles and quadrupoles have been constructed and measured. In most cases the original design strengths are more than adequate for the accelerator as now simulated. The necessary strength and the 50A nominal current determine the number of turns required. A design with a superconductor short sample current limit three times this nominal current was chosen, which then determines the wire size. The multipoles required are a_0/b_0 , a_1/b_1 , b_3 , b_4 . The multipole elements are assembled radially in inverse order of their multipolarity (i.e., b_4 inner most et. seq.).

A. Detailed Design

To control the deflections produced by the Lorentz forces, it was necessary to use thicker walled tubes to support the dipole & quadrupole windings (4.4mm and 3.5mm respectively). The other support tubes are at the minimum economic wall thickness (1.7mm). Because of the large number of turns (as many as 600 in the dipole windings) it was decided to bond the wires onto a flat substrate with a computer-controlled wiring machine. The maximum wire diameter for this technique is 0.33mm which limits the dipole quench margin to 150%; all other windings retain the desired 300% margin. To successfully wrap the winding pattern around the support tube, the OD of the latter must be machined to a precise diameter, with a tolerance of 0.16mm. Experimentation showed that it is possible to wind two layers of wires onto a substrate, the turns of the second layer nesting above the spaces in the first layer. The required field strengths are obtained by one such double layer for all multipoles except the dipole which requires three double layers. To secure the windings against the Lorentz force, a pretensioned Kevlar overwrap is used. An iron yoke is used both as a return path and a mechanical support for the cylinders. This is composed of low carbon steel laminations whose diameter is that of the main quadrupoles. In RHIC, all the 80mm magnets have the same outside dimensions, which simplifies construction, cryogenics and electrical buswork.

B. Field Quality Design

In principle, this winding technique can produce any wiring pattern and hence arbitrarily good field quality. In practice, patterns are limited to coils made up of straight sections and 90° arcs, with the further restriction that each pole consists of a single continuous block of turns with uniform spacing. With these constraints, the coils extend from the midplane to $2B/(3 \cdot 2m)$ angle, where $2m$ is the multipolarity number ($=2$ for dipole). This cancels the first harmonic allowed by symmetry in the straight section. The number of turns and the radius of the curves on the end are adjusted slightly to achieve a field purity of better than 0.4% at the good aperture radius of 25mm. For the dipole windings, the second allowed harmonic does not fall off very rapidly with radius and it is necessary to adjust the three double coils to produce acceptable cancellation in the complete package. In production it has been found that the errors in wrapping the substrate around the tube, and the positioning of the tube within the magnet iron, contribute comparable field errors. Since the dipole correctors have a strength of 0.9% of the main dipoles, and the other correctors have less than 0.14%, a 1% field error in the correctors is less than 1×10^{-4} referenced to the main magnets. Thus 1% errors in the correctors are acceptable.

*Work supported by the U.S. Department of Energy under Contract No. DE-AC02-76CH00016.

II. Construction Details

The coils are wound using a 0.33 mm diameter superconducting wire coated with 50% overlap of 25 μ thick Kapton insulating film and coated with 12 μ thick bondall coating. The wire is wound with a 0.15 mm spacing between wires onto a flat epoxy coated substrate consisting of 0.076 mm thick Kapton base with 0.20 mm thick of a b-staged epoxy filled with glass fibers. A second layer of wire is wound on top of the first nested between wires. The wire is bonded to the substrate or bondall coated first layer using an ultrasonic welding process on a computer-controlled wiring machine. A resonant stylus, with a tip formed to capture the insulated wire is excited at 25 KHz, transferring the ultrasonic power through the wire to the underlying substrate material, causing the wire to bond to the epoxy coated substrate. The wiring machine is computer-controlled in a closed loop allowing flexibility in the selection of the wiring pattern, the number of layers, the wire size, and the speed of the wiring. Five wiring machines are operated simultaneously by two operators. Each machine is connected to a common local area network. Production wiring files are electronically transferred from the magnet design group to the production group. Modifications or design changes to the wiring files can be converted into finished coils quickly.

The earlier coil design consisted of cornered ends with 45 degree angles [1]. These 45 degree bends proved to be a source of wire damage where the stylus would stop and rotate to the next path. This would cut the Kapton insulation and damage the copper coating of the wire with occasional damage to the superconducting strands. Bonding problems were also encountered in the earlier design between the first and second layers because the second layer wires were laid directly on top of the first layer wires. The design was revised to rounded ends and nested wires to alleviate these problems. Nomex coil supports are installed into a wound flat coil to act as a filler where the wires are not located thus making the thickness constant throughout the assembly. The coil assembly is bonded to stainless steel support tube with epoxy supported with fiberglass cloth. The quadrupole, octupole, and decapole tube assemblies are then coated with epoxy and butt wrapped with a single layer fiberglass cloth and a double layer of Kevlar yarn at 32 turns per inch at a tension of 22 lbs. The dipole tube assembly is coated with epoxy and butt wrapped fiberglass cloth and a single layer of Kevlar yarn. Second and third layers of dipole coils are placed onto the assembly in the same fashion. The assembly is coated with epoxy, fiberglass cloth and a double layer of Kevlar (see Fig. 1). The dipole coils are spliced in series as one assembly. The four different coil assemblies are assembled concentrically as shown in Fig. 2. The support tubes are supported by Ryton molded yoke keys inside the iron yoke.

The iron yoke is made up of punched 1.52 mm thick low carbon steel half laminations pinned together into yoke modules with the weight carefully controlled. The yoke modules are keyed and welded together at the 0E and 180E seams.

Table 1 lists the correctors completed to date.

Table 1. Construction Status as of April 25, 1995

Corrector Type	Number Required	Number Produced to Date	Coil Configuration
CRB	100	79	b_0, b_1, b_3, b_4
CRC	136	67	a_0, a_1, b_3, b_4
CRD	78	66	b_0
CRE	78	50	a_0
CRF	40	19	b_0, a_1, b_3, b_4
Total	432	281	

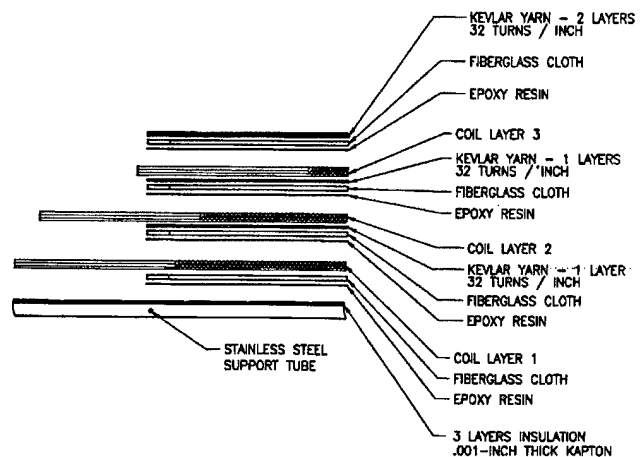


Fig. 1. Dipole concentric assembly section

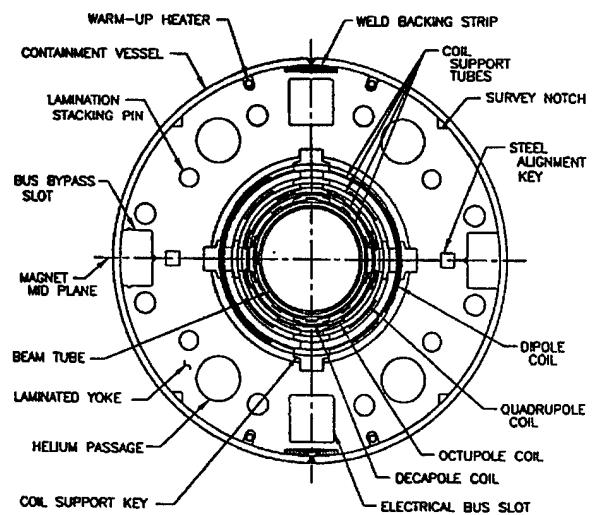


Fig. 2. Magnet cross section

III. HARMONICS TEST RESULTS

Warm measurements of field quality have been performed on all the corrector magnets built so far. The integral transfer function and other harmonic components at a reference radius, R_{ref} , of 25 mm are measured using a rotating coil of radius 35.6 mm ($1.42 R_{ref}$). These measurements are carried out at magnet current of 0.2A. The contribution from remnant fields is subtracted by making measurements at both positive and negative currents. The measuring coil is radially centered in the iron yoke using a well aligned fixture. The magnetic centers of the corrector layers (derived from feed down) are generally within 0.25 mm of the center of the iron yoke.

The results from the warm measurements in the correctors are summarized in Table 2. The integral transfer functions are expressed in T.m/kA at the reference radius of 25mm. The most dominant harmonic terms are typically below 1% of the fundamental field. These harmonic distortions are at an acceptable level for the accelerator.

The correctors are tested at liquid helium temperature for quench performance. Field quality measurements are also carried out on most of the correctors. There is good agreement between the warm and the cold measurements. The transfer functions increase slightly as a result of cool down, as indicated in Table 2.

Table 2. Corrector Field Quality

Layer Type	Transfer Function T.m/kA @25mm (Warm)	Std. Dev. In T.F.	Change in T.F. on Cool-down	Harmonics as fraction of the Fund. Field
b_0 / a_0	5.5514	0.11%	+1.0%	<0.3%
b_1	0.7630	0.07%	+0.7%	<0.5%
a_1	0.7569	0.07%	+0.7%	<0.5%
b_3	0.1920	0.45%	+0.8%	<1.5%
b_4	0.1495	0.30%	+1.2%	<1%

IV. QUENCH PERFORMANCE

As of April 18, 1995, 101 80 mm RHIC production correctors have been cold-tested. The design operating current for all corrector layers is 50A, and all have a conductor limit above 130A for all operating conditions at the RHIC temperature of 4.6K.

Because of the stress imposed on the thin superconducting wires during coil winding, it is considered necessary to cold-test all corrector coils as part of the acceptance process. Cold-testing is performed in vertical dewars filled with liquid helium at 4.4K (nom).

The minimum test procedure for any corrector is:

1. Ramp the dipole layer to +70A, then to -70A, and back to 0;
2. With the dipole at +70A, each of the other three layers is ramped to +100A, then -100A, then again to +100A, then back to 0.

If any layer quenches in the course of these ramp tests, the ramps for that layer are started over again and repeated until the three ramps can be performed without quench. Occasionally, magnets were subjected to more rigorous testing, with more bipolar ramps, one hour tests at maximum test current, and sometimes quench testing. The maximum test current of 100A for ramp tests was selected to provide 100% quench margin. This was reduced to 70A for the dipole layers to avoid quenches that might overheat the conductor wire. This was found necessary because of the high inductance of the dipole layers and the nature of the quench detection system being used.

The results are presented in Table 3 and are grouped according to layer type and performance category. For each type, the first column denotes 1) total layers tested, and the number of layers which 2) did not quench, 3) trained smoothly (monotonically), 4) trained erratically, 5) failed, and 6) had an initial quench below 50A but trained acceptably. A layer is rejected if its current limit is low due to conductor damage or if it does not train to the maximum test current.

As can be seen from the table, approximately half of the dipole layers (44%) and quadrupole layers (53%) did not quench at all during initial ramp testing, while 68% and 77% of octupole and decapoles, respectively, did not quench. All other layers except two dipoles and two quadrupoles trained satisfactorily, though a small number of them were slightly erratic.

Table 3. Quench Performance Results of RHIC Arc Corrector Layers (Multipole layer tested with dipoles @ +70A)

Performance	Dipole	Quad.	Octu.	Deca.
Total Tested	94	53	53	53
No quenches	41	28	36	41
Smooth training	46	19	12	6
Erratic training	5	4	5	6
Failed	2	2	0	0
$I_{init} < 50A$	10	0	2	1

V. Summary

The construction of corrector magnets required for RHIC is well underway. The design of these magnets is versatile and robust, allowing easy assembly into the many configurations required for the machine. Construction techniques have been adopted that ensure reproducible magnets while minimizing construction labor. Test results indicate that the magnets perform well beyond the level required for successful operation of the Collider.

V. REFERENCES

- [1] G.H. Morgan, "Optimization of Multiwire Coil Ends Having 45 Degree Bends," Internal Report AD/RHIC-30, 1987; G.H. Morgan et al, "Geometry of an All-Multiwire RHIC Corrector, Magnet Division Note MDN-256-16 (RHIC-MD-68), 1988.

SUPERCONDUCTING SEXTUPOLES AND TRIM QUADRUPOLES FOR RHIC *

P. Thompson, M. Anerella, G. Ganetis, A. Ghosh, A. Greene, R. Gupta, A. Jain, E. Kelly, M. Lindner, G. Morgan, J. Muratore, W. Sampson, P. Wanderer, E. Willen

RHIC Project, Brookhaven National Laboratory, Upton, NY 11973

Abstract

RHIC requires 288 sextupole and 72 trim quadrupole magnets. These iron poletip superconducting magnets have been constructed by Everson Electric Co. Room temperature field measurements have been completed for 75% of these magnets with acceptable results. Approximately 15% of them have been tested at 4.6 K for maximum (quench) current. The quench performance for the early magnets was good and improved to excellent during the production run. These magnets have more than 100% margin at quench.

I. INTRODUCTION

The Relativistic Heavy Ion Collider (RHIC) will be a colliding beam facility with design energy of 100 X 100 GeV/u for heavy ions. The two accelerator/storage rings are divided into "regular arcs" and intersection regions. A set of 288 sextupole elements are necessary to reduce the natural chromaticity ($\chi \sim -42$) and correct sextupole field imperfections in the dipole magnets.

These are positioned at every quadrupole in the regular arcs, and have a design strength of 588 Tesla/meter with an inner bore of 80 mm and length of 750 mm. The detailed design of these "superferic" magnets has been published previously [1]. In addition, to vary the β^* in the interaction regions 72 trim quadrupoles are required. These are assembled with quadrupoles Q4, Q5, and Q6. Their overall dimensions are identical to the sextupoles and their detailed construction is very similar. This paper will emphasize the test results and design differences of the quadrupoles.

II. DESIGN

Table I lists the basic parameters of these magnets. They consist of racetrack layer wound coils mounted on iron poletips. The method used in the sextupoles for securing the coils proved somewhat cumbersome. For the quadrupoles, a projection was added to the iron yoke so that the coil fits in a slot between this projection and the poletip (see Figure 1). A thin non-ferrous spring is inserted between the poletip and the coil to hold it against the support projection. There is no real "prestress" in this design. A small tab is placed over the ends of the coils so that they can not move radially but the ends are unsupported against the Lorentz forces.

A. Magnetic Design

Since these magnets operate with a pole tip field of ~ 1.1 Tesla, iron poletips were used. At low field, the poletip dominates the field, reducing the sensitivity to coil location errors.

*Work supported by the U.S. Department of Energy under Contract No. DE-AC02-76CH00016

Table I

Parameters of RHIC Sextupoles and Trim Quadrupoles

Parameter	Value	
	Sextupole	Quadrupole
Wire Diameter	0.508mm	0.508mm
Copper/SuperConductor	3:1	3:1
Ic(2.0 T, 4.22 K)	230 A	230 A
Turns per pole	200	200
Clear Bore	80 mm	80 mm
Length	750 mm	750 mm
Design Current	100 A	100 A
Design Strength	588 Tesla/meter	22 Tesla
Quench Current	220 A	205 A
Quench Strength	780 Tesla/meter	37 Tesla
Inductance at 100 A	530 mH	590 mH
Number for RHIC	288	72

For the sextupole, because of mechanical limitations, the actual poletip is narrower than optimum. This results in very noticeable saturation. For the trim quadrupole the poletip was widened to reduce this saturation. The poletip was also shaped and a hole was put in it to further reduce the saturation. The coil support projection of the yoke does not affect the field. For ease in coil manufacture, the ends are semi-circular and generate acceptably small error fields.

III. QUENCH RESULTS

The results of quench testing are summarized in Figure 2. Note that only the last and the worst (usually the first) quenches are plotted. For the initial sextupoles the worst quench was at least 80% of the conductor limit. As production progressed, a problem developed with the coil support hardware. This subset typically displayed a first quench in the range 55 to 75% of I_{cs} and very rapid training to short sample. At about magnet SRE260, a problem developed in the epoxy potting of the coils. This group of magnets trained slowly, and many of them were not trained to short sample. At magnet SRE280 all known problems were fixed and the quench plot looks much better.

For the trim quadrupoles, the support mechanism was much more robust and the problems of quality control in production were understood. Twelve quadrupoles have been tested with only one quench below (92%) the conductor limit. Except for the epoxy problem sextupoles (which are being 100% tested), only 10% of these units are subjected to quench testing.

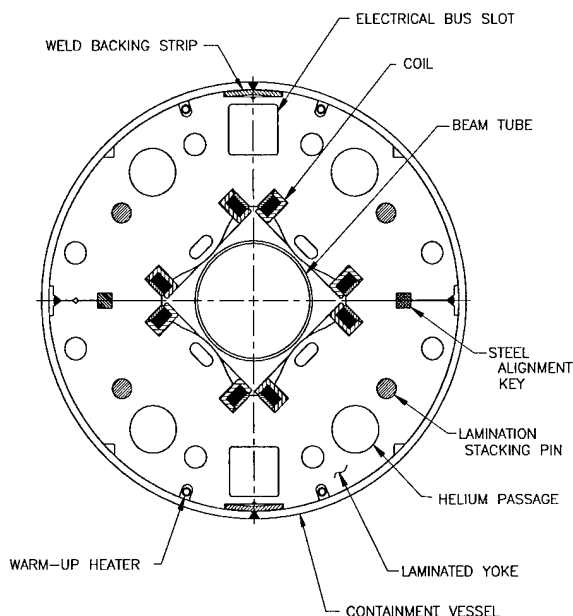


Figure 1. Cross Section of RHIC Trim Quadrupole.

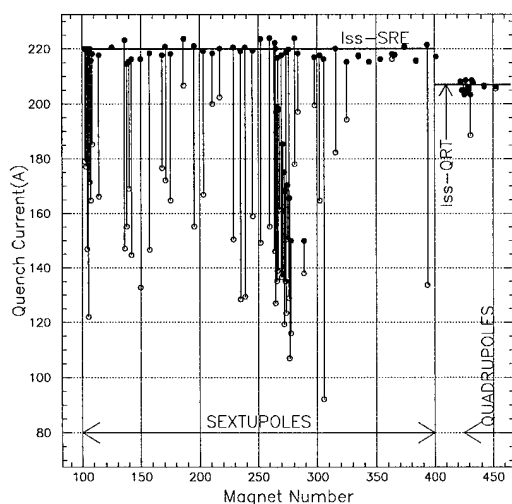


Figure 2. Quench Histories

IV. FIELD QUALITY -SEXTUPOLE

All of these magnets are measured at room temperature at 0.25 A. A small sample is also measured at 4.5 K with currents ranging up to 150 A. There is good agreement between the two measurement techniques. Table II shows the low current integral field measurements. The non-negligible b_0 and b_4 terms are probably due to the dipole symmetry of the yoke assembly. Figure 4 shows a trend plot of the transfer function. There appear to be steps associated with the fixes in the assembly technique. The allowed harmonics measured in 49 magnets at 4.6 K are presented in Figure 5. The strong saturation arises from the "neck" of the poletip which is narrower than optimum. The reproducibility is apparent.

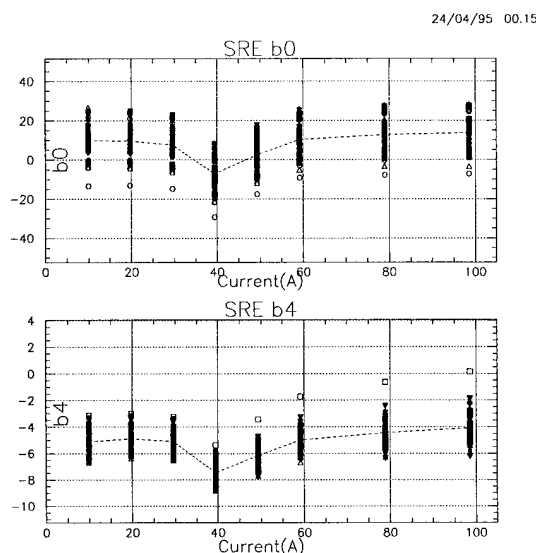


Figure 3. Sextupole Notch Harmonics

Table II
Sextupole Integral Field Harmonics measured at 0.25 A - 300 magnets

Harmonic	Calculated	Measured	
	b_n only ^a	b_n	a_n
$B_2/A(T/m \cdot A)$	8.66	8.69(0.013)	...
b_3	0	-0.27(1.14)	-0.06(2.82)
b_4	0	-4.58(1.37)	-0.14(1.17)
b_5	0	0.24(0.21)	0.15(1.01)
b_6	0	-2.67(0.55)	-0.12(0.54)
b_8	-93.15	-90.3(0.19)	-0.31(0.12)

^a...All skew(a_n) harmonics are calculated to be 0
 b_n is 10^{-4} of the Sextupole field at $R = 25mm$
 The measured values are the mean of 300 magnets.
 The rms spread is given in ()

A. Anomalous Behavior

The b_0 and b_4 data in Figure 3 show a distinct "notch" at 45 A, this may be a manifestation of the dipole symmetry of the assembly. This has persisted through 300 magnets and appears in both up and down ramps. For mechanical compatibility with the rest of the magnets, the sextupole yoke is assembled in two pieces with an overall dipole symmetry. These harmonics are dipole symmetric, but why they should have this reproducible variation with excitation is unknown.

V. FIELD QUALITY -QUADRUPOLE

The low current measurements for the trim quadrupole are presented in Table III. The b_3 term is probably a manifestation of the dipole assembly symmetry. The difference between calculation and measurement for b_5 is unexpectedly large, however this harmonic is well within the accelerator requirements.

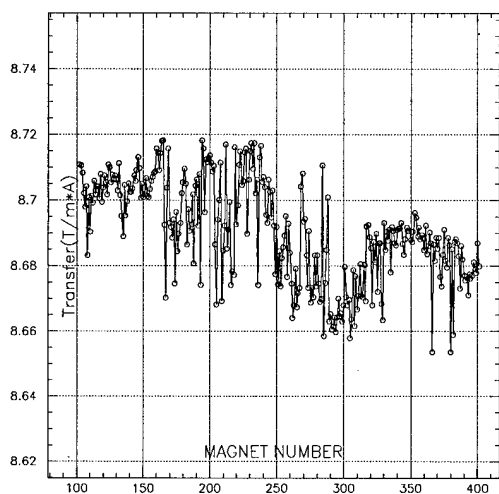


Figure 4. Sextupole Transfer Function History

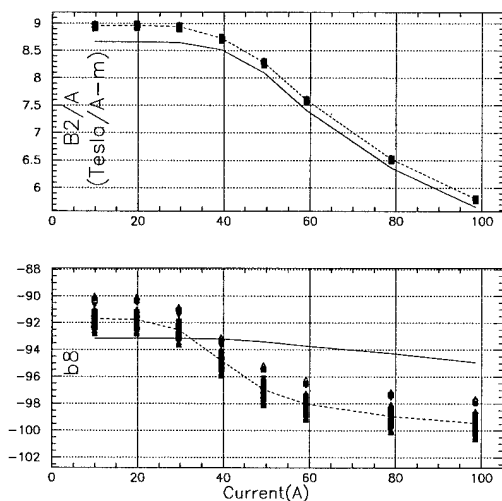


Figure 5. Sextupole Allowed Harmonics.
Total 49 Magnets Measured.
average=dashed curve. calculation=solid curve.

VI. CONCLUSIONS

Almost 400 of these two types of magnets have been built. The racetrack coil mounted on an iron poletip design has proven straightforward for commercial construction. The field quality of all the magnets tested has been acceptable without any iteration. With the final design used for the trim quadrupoles the quench performance is essentially perfect.

Table III
Integral Field Harmonics for Trim Quadrupoles. Total 53 Magnets. 0.25 A measurements.

Harmonic	Calculated	Measured	
		bn	an
B1/A(Tesla/A)	0.2437	.2357(0.0002)	...
b2	0	0.692(0.684)	-0.837(1.510)
b3	0	-3.98(0.581)	-0.038(0.197)
b4	0	-0.031(0.168)	0.063(0.197)
b5	+2.5	-10.22(0.247)	-0.157(0.114)
b9	-0.73	-0.816(0.028)	-0.001(0.06)

^a...All skew(an) harmonics are calculated to be 0
bn is 10^{-4} of the Sextupole field at R= 25mm
The measured values are the mean of 53 magnets.
The rms spread is given in ()

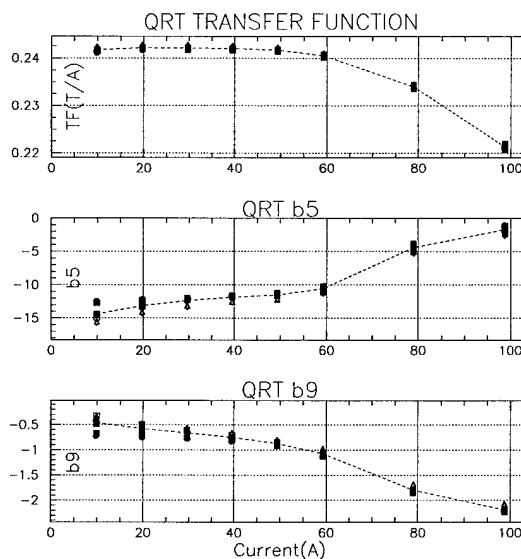


Figure 6. Trim Quadrupole Allowed Harmonics Saturation Behavior. Total 11 magnets measured.

References

- [1] M. Lindner et al., *Construction Details and Test Results from RHIC Sextupoles*, IEEE Trans. on Magnetics, Vol. 30, No. 4, pp. 1730-3 (1994).

STUDY OF UNK QUENCH PROTECTION SYSTEM ON THE STRING OF 4 UNK SUPERCONDUCTING MAGNETS

A.Andriischin, O.Afanasiev, V.Gridasov, A.Erochin, E.Kachtanov,
K.Myznikov, V.Sytchev, L.Vassiliev, O.Veselov, N.Yarygin
Institute for High Energy Physics, Protvino, Russia.

Abstract

The prototypes of the elements of UNK quench protection system — quench detectors on magnetic modulators, quench stopper, safety leads, bypass switches — are studied on the string of 4 UNK superconducting magnets. The string simulates the operation of two quench protection units (QPU). Many quenches at the various parts of SC circuit from 1kA up to UNK nominal current 5kA were induced. No quench propagation from one to another QPU was observed. Parameters of quench protection system elements corresponded to tolerated ones.

I. INTRODUCTION.

The quench protection system (QPS) for the UNK ring electromagnet is based on breaking the whole ring into cells (QPU), shunting them with thyristor switches placed at the exterior of the cryostats at the ambient temperature and energy removal from the remaining part of the ring onto dump resistors [1]. QPUs, each consisting of 12 dipole and 2 quadrupole magnets, are separated by quench stoppers, containing a pair of safety leads. Each QPU is shunted with two quench bypass switches. The status of the SC circuit is monitored by the quench protection monitor system. It consists of 24 quench protection monitors (QPM) placed equidistantly along the ring and connected by one network. Each QPM monitors 8 QPU.

The QPM contains a bridge type quench detector on magnetic modulators (QDMM) [2]. Such system has two advantages: all of the elements have high radiation resistance, and magnetic modulators have the output signal isolated from power circuit of SC magnets, possessing an appreciable amplitude on low output impedance. This allows one to place QDs in the tunnel just near magnets and to transmit noise-immune signals at distances of about 1km to the technological buildings.

The study of QPS components — QPM prototype, quench stoppers (QS), safety leads (SL) and quench bypass switches (QBS) — was carried out on the string of 4 SC magnets [3].

Results of this tests are presented below.

II. DESCRIPTION OF THE EXPERIMENTAL FACILITY.

The string of 4 UNK SC dipoles simulates an action of two QPUs. Each QPU consists of two SC dipoles (Fig.1).

In first QPU the coil of M1 and return bus of M2 are shunted with QBS1 while the coil of M2 and return bus of M1 are shunted with QBS2. In second QPU both dipoles and their return buses are shunted with single QBS3.

Bypass switches with their firing systems were placed inside a steel tube 200mm in diameter for imitation the cooling con-

ditions at the UNK tunnel, where they have to be placed into special holes in the wall of the tunnel to be protected against irradiation.

The QS is two massive copper pieces with a copper radiator, connecting them. The SC cable is soldered to one piece, while the safety lead — to another one. Two such packets are placed inside one jacket and cooled by helium flow.

The SC circuit is monitored with 4-channel quench detector (QD) based on extraction of resistive voltage of the coil by means of compensation technique. The threshold of this QD is 1V. When there is a quench in one of the magnet, e.g. M2, the QD fires the strip heaters in M1 and M2, the coils of these magnets are shunted with QBS1 and QBS2, and power supply is turned out to the reverse mode. As a result the current in the magnets M1 and M2 decays very quickly and dissipates the energy inside coils, whereas the current in M3 and M4 falls down with certain velocity through SL1, SL2, QBS1 and QBS2.

Numerous spot heaters and voltage taps, placed at various parts of SC circuit, are employed to induce the normal phase and observe the quench propagation.

Tests of QPM prototype were made in passive mode, i.e. its output signals were recorded but made no actions. Fig.1 shows the scheme of connecting magnetic modulators (MM) to the magnets. Four MMs (MM1-MM4) are connected to the diagonal of the bridge circuit (BC), two arms of which are combined by two half coils of each dipole. The fifth MM (MMg) is connected to the diagonal of the BC, two arms of which are combined by two coils each. One MM (MMu) is connected directly to power leads and used in the mode of linear amplifier to measure the voltage drop of the string. The BCs with MMs are enclosed into steel boxes which are fixed directly at SC dipole cryostats and connected with QPM by means of cables 700m long.

Fig.2 shows the structure of the QPM prototype. It contains modules needed for registration of signals from one QPU only (instead of 8 for the series QPM [2]): an amplifier-shaper (AMP), module of the cell, module of counters and also some modules common for all cell: timer, 16-bit microprocessor, RAM, interface and input/output module.

AMP supplies all of MMs with ac voltage (meander having a frequency of 1kHz and amplitude of 40V). The cell module is used to convert signals from output coils of all MMs. Each conversion channel contains a scheme to detect breaks of wires in the input circuits of MMs, a differential amplifier, demodulation scheme, filter and voltage-frequency converter (VFC). Signals from outputs of all VFCs are converted into a parallel binary code with the help of 20-channel module of counters, whose measurement time, 20mS, is specified by timer.

All status signals are collected and steering signals are

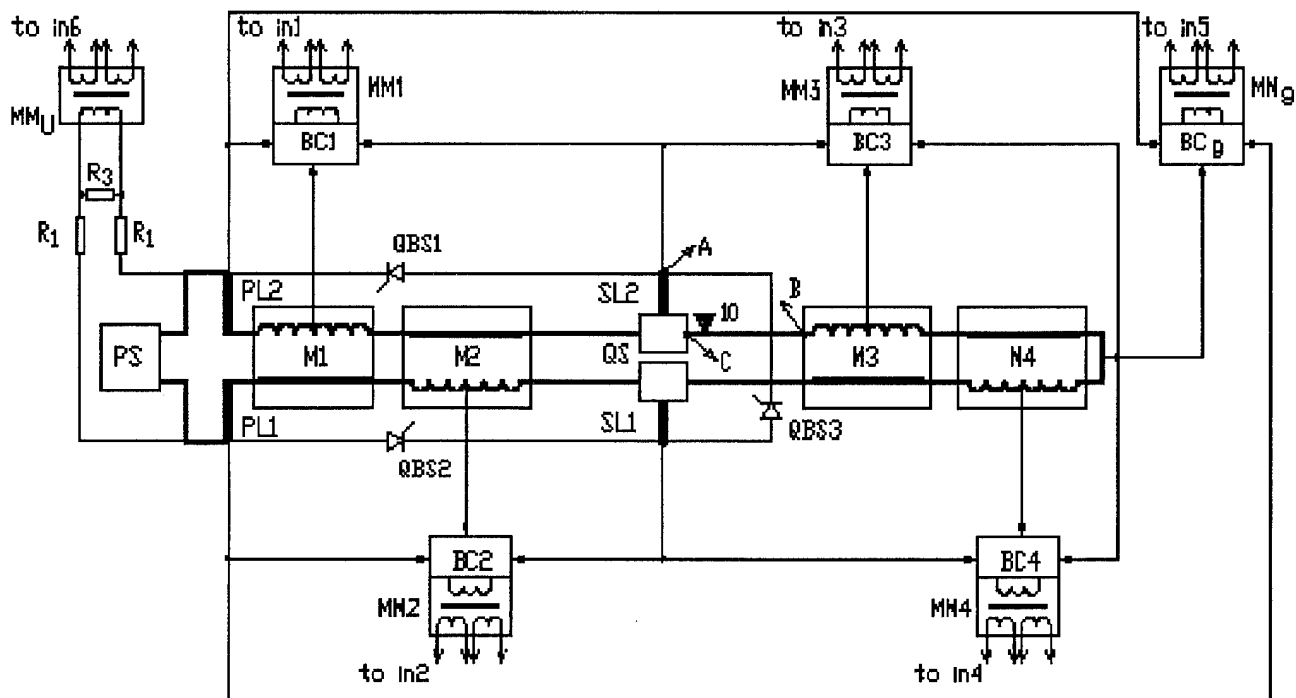


Figure 1. Electrical diagram of 4 magnet string with quench detectors: M1-M4 - SC dipole magnets, PS - power supply, PL - power leads, SL - safety leads, QBS - quench bypass switches, ∇ - spot heater, A,B,C - potential taps, BC - bridge circuits, MM - magnetic modulators.

sent to executive blocks through the input/output module. A K1810BM86 microprocessor monitors the operation of all blocks as well as performs the on-line data acquisition task, so the information before and during quench is recorded. IBM PC-AT serves as an operator's console and allows one to set the QPM operation mode and to stock quench data.

III. TEST RESULTS.

Quenches in some QPU were induced by strip or spot heaters on various currents in the string. The current in magnets, where quench induced, is dumped within ~ 1 s whereas the string current is forced to fall down with constant rate 170A/s through safety leads and bypass switches. This fall down rate was chosen so, that on the UNK operation current, 5250A, the load integral $\int i^2 dt$ at SL and QBS to be slightly above of the UNK operational level (260 MIITs). The maximum energy dissipated in thyristors was 80kJ but their temperature increased for 20-30 C only.

The maximum temperature of cold part of SL attained 10K whereas the temperature of copper piece of QS where the SC cable is soldered did not exceed 6K and caused no quench in the SC cable. In all cases of quenches induced in some QPU, no quench propagation to another QPU was observed at the range of currents from 600 to 5250A.

The balancing of bridge circuits was carried out at ambient temperature by means of powering the string with ac of 50Hz

frequency and 16V voltage. After string cool down the balance was verified on the 500A triangular current pulses with a nominal UNK ramp rate of 120A/s. The string voltage was ~ 20 V. The disbalance of MM1-MM4 did not exceed some millivolts and the MMg disbalance — 40mV. For magnet protection purposes the threshold of quench detection on the single dipole should be ~ 250 mV and on group of dipoles — 0.5–1V. So, the MMs disbalance is ten times less than tolerated threshold levels.

During tests the QPM reliably detected all induced quenches as well as spontaneous ones. For the illustration Fig.3 and 4 show output signals of MM2 and MM3 during the quench induced in dipole M3 at the current 2000A, while there were no quenches in M1 and M2. It is seen that after heater firing the output signal of MM3 (Fig.3) rapidly increased up to threshold level (further behavior of this signal is determined by MM core saturation as well as by quench development in the coil and is not yet essential for quench detection purposes). The MM2 output signal was 20 times less than the threshold level (Fig.4).

In order to investigate the possibility to use the QDMM for quench detection in long SC cables the following test has been done. Instead of voltage tap A (Fig.1) the voltage tap B was connected to the BC1, i.e. a piece of SC cable BC 2.5m long from the half cell M3 was additionally introduced into an arm of BC1. The quench was initiated in SC cable BC by spot heater $\nabla 10$ (Fig.1) at the current 5000A. The normal phase propagated into coil of dipole M3 and was detected by QD as a quench in dipole M3. There was no quench in the half cell M1, but the

MM1 output signal had shown the quench development in the SC cable BC (Fig.5).

The analysis of these results lead to the conclusion, that the reliable detection of normal phase in the long SC cable can be achieved, choosing the proper transfer function of the MM.

For checking the possibility to localize shorts of the power circuit onto ground the string was powered by ac like in the case of MM balancing, and different points of the power circuit connected onto ground through potential taps. Short circuit points were localized by QPM.

IV. CONCLUSION.

The string tests demonstrated good operational performances of quench protection system components — quench stopper, safety leads, quench bypass switches. Their parameters correspond to tolerable ones for the reliable protection of UNK SC magnets during a quench. Simple and nonexpensive quench detectors on magnetic modulators can be used for developing of reliable quench protection system for the high energy accelerators.

References

- [1] O.V. Afanasiev et al., "The Protection System for the Superconducting Electromagnet Ring of the UNK", Supercollider4, Plenum Press, N.Y.,p.867, 1992.
- [2] I.M. Bolotin et al., "The Quench Detector on Magnetic Modulator for the UNK Quench Protection System", Supercollider 4, Plenum Press, N.Y.,p.881, 1992.
- [3] A. Alexandrov et al., "Investigation of the String of 4 UNK Superconducting Magnets", Proceedings of fourth European Particle Accelerator Conference, Vol.3, p.2313, 1994.

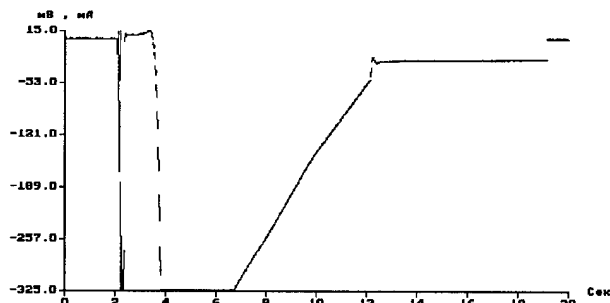


Figure 3. Output signal from MM3 during the quench induced in dipole M3 at the current 2000A.

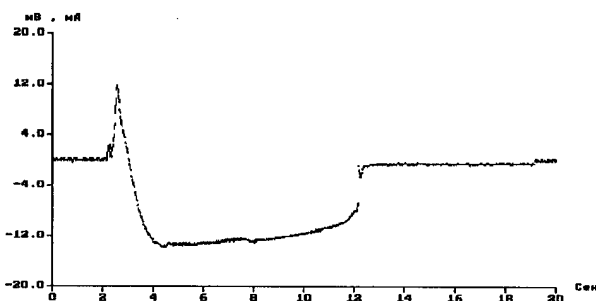


Figure 4. Output signal from MM2 during the quench induced in dipole M3 at the current 2000A.

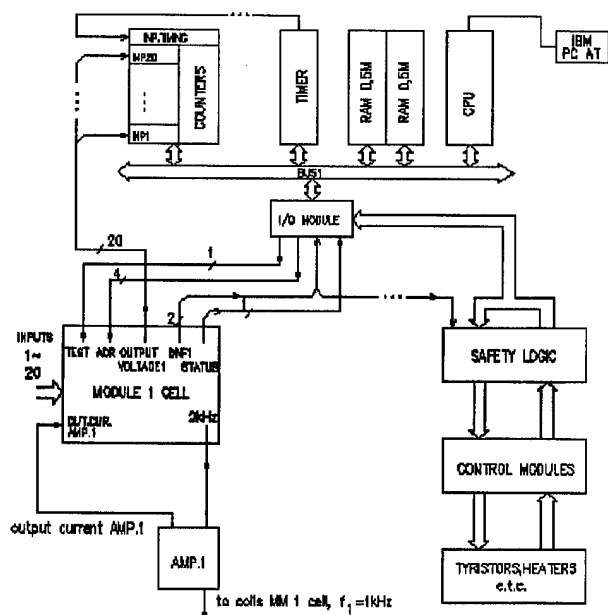


Figure 2. Diagram of QPM prototype.

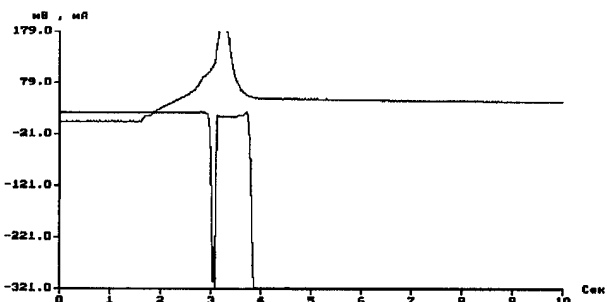


Figure 5. Output signals from MM1 corresponded to normal phase in the connecting cable (up) and from MM3 (down).

TWO ALTERNATE HIGH GRADIENT QUADRUPOLES; AN UPGRADED TEVATRON IR AND A "PIPE" DESIGN , *

A.D. McInturff, J.M. van Oort and R.M. Scanlan, Lawrence Berkeley Laboratory, Berkeley, CA 94720

The present Fermilab IR quadrupole lenses achieve a 50% increase in gradient over their predecessors. This was accomplished by the following developments: a) a more dense winding (Kapton insulation only, eliminating the fiberglass-epoxy), b) an improvement in critical current density to $J_c(5T, 4.2K) = 3 \text{ kA/mm}^2$ and c) a higher aspect ratio cable $>11/1$ and d) finer strand (0.53 mm diameter). The natural evolution of this design to the CERN 70 mm aperture quadrupole results in the following : a) a reduction in operational temperature (4.8K - 1.9K), b) improvement of $J_c(10T, 2.0K) > 2 \text{ kA/mm}^2$ and c) a higher aspect ratio cable $> 13/1$ and d) finer strand (0.48 mm diameter). These two-layer designs should achieve the required operational gradient of 250 T/m with at least a 5% margin on the short-sample load-line intersection. These high current densities also require turn-off times $< 0.2 \text{ s}$ after transition to the normal state. Such a short time requires an advanced protection heater design. The status of the design and the experimental development will be reported. New design concept quadrupole calculations are presented as well. This concept, using an active flux return is being proposed as a possible candidate design for a future higher gradient requirement.

I. INTRODUCTION

With the U.S. cancellation of the SSC project, the only large approved hadron accelerator project is CERN's LHC [1]. One of the more critical elements in the performance of a collider is the quadrupole lens at the beam collision points. These quadrupoles, usually referred to as the "insertion quads" normally form a set of triplets around the interaction region. Their focal power directly affects the luminosity available at the crossing point. In order to achieve as high a gradient as possible, the CERN design team has proposed a very efficient high gradient quadrupole which is based on a graded four-layer winding structure [2]. At Fermilab's Tevatron, an upgraded two layer winding quadrupole has been in operation since 1989, and has provided a 50% higher gradient than it's predecessor. The quadrupole was basically state of the art when it was designed in 1985 [3]. Since then however, improvements have been made in cabling, conductor performance, etc. Naturally, operation of a modernized version of this design can provide higher capabilities. This improved two layer design can serve as an alternative to the more intricate graded four layer design now envisioned for the LHC, provided it can obtain the proposed gradient. An outline for the development program required for the implementation of this option is as follows :

I Raise the coil current density by

- A. Improved conductor performance at high field by
 1. Lowering the temperature to superfluid helium at 1.8 K
 2. New higher j_c ternary material (NbTiTa)
 3. Concentrating artificial pinning center work on high field j_c 's.
- B. Better coil quench protection, thus lowering the copper volume required by
 1. Increasing the quench detection sensitivity
 2. Improving the protection heater design to produce a shorter current decay time (more distributed quench)
- C. Implement a "wind and react Nb₃Sn" technology into the quadrupole program [4].

II Increase the cable aspect ratio (more turns closer to the aperture) to increase magnetic efficiency

- A. Coupling problems need to be addressed
 1. Higher and more consistent strand/strand resistances
 2. Reduction of the filament size ($< 6 \mu\text{m}$) and a better inherent magnetization value.

II. THE ALTERNATE DESIGN PARAMETERS

The proposed conductor parameters are given in Table 1. These parameters have been achieved, however, in some cases it was only on a few laboratory samples. No improvement is necessary however to achieve the operational field plus a five percent margin point for the conductor current density.

Table 1 Conductor parameters

Alloy	NbTiTa
Strand diameter (mm/inch)	0.4775 / 0.0188 ^{+0.0000} _{-0.0002}
Strand twist pitch (twists/cm)	1 (left)
Number of strands	44
Copper to superconductor ratio	1.5/1
Number of filaments, spacing	2450, $< 0.2 \mu\text{m}$
j_c at 1.8 K, 10 T (A/mm ²)	2390 (~1850 ternary[5])
Cable twist length	89.27 mm (right)
Cable dimensions and keystone angle	0.792x10.744 mm 0.940 degrees

Even though the minimum conductor performance numbers have been achieved, the higher design goal values would allow the limitations to be removed.

* This work was supported by the Director, Office of Energy Research, Office of High Energy and Nuclear Physics, High Energy Physics Division, U.S. Department of Energy, under contract No. DE-AC03-76SF00098.

The margins are increased in other critical areas if they are obtained. The higher aspect ratio cable will certainly require strand to strand cross-over resistances which are higher and well controlled to minimize ramp rate effects of quenches, harmonics, their variations in magnitude as well as their change with respect to time. The present Tevatron quadrupole has up to a 20% linear degradation of achievable peak gradient with ramp rates up to 200 A/s [6]. This sensitivity can and should be substantially reduced. The parameters of the cold mass including the winding and iron shield are given in Table 2. The two layer quadrupoles that had been previously constructed for the Tevatron have a history of training. They have on the average required approximately 10 quenches to reach the estimated short sample (or slightly above) critical current [6].

Table 2 Winding and cold mass parameters

	Inner layer	Outer layer
Number of turns per pole	22, 1 wedge	32, 1 wedge
Inner dia. w/o insulation	70.00 mm	92.14 mm
Outer dia. w/o insulation	91.64 mm	113.78 mm
Cable length / mass	231 ft/pole	336 ft/pole
Heater composite Kapton / Cu or w/o Cu steel	12.5 μ m s.s. with 8 μ m	total 17 μ m ground insul.
Coil inductance /unit l.	8.74 mH/m	
Calculated field harmonics $(1/(cm)^{N-1}) \times 10^4$	b(6) = 0.31 b(10) = 0.0057 b(14) = 0.00005	
Transfer function	41.37 T/mkA	
Iron shield diameters	13.6 cm (ID)	30.5 cm (OD)

This problem, though not fatal, should be addressed. The superfluid tests of those quads were not completed to the (estimated) short sample current due to marginal protection heaters.

When measured, the series of thirty plus low-beta Fermilab quads were found to have a few units of harmonics due to construction variations and distortions. The largest was found to be the out of phase sextupole term. The updated version of the two layer coil has the following features which should alleviate or at least reduce the problems previously found in the older series as well as simplifying construction when compared to a four layer graded structure. The outer winding is actually radial. This enables an easier and more symmetric loading of the inner winding. The pole angle is exactly the same for the inner and outer windings. This again facilitates the uniform loading.

A 60 mm quadrupole load line intersects the short sample surface at 310 T/m, whereas a 70 mm aperture would intersect at 265 T/m. This illustrates the effect of the aperture on the maximum gradient, the comparison was made between 60 mm and 70 mm bore size two layer windings. If the two layer structure turns out to be accurate enough and the beam

is collimated well enough, then a reduction in aperture to 60 mm would increase the gradient margin significantly. The single wedge will allow the ends to be integrally corrected for one harmonic.

There are some rather general comments that can be made about coil protection and examples given to illustrate these points. The current decay time constant after a quench for the existing Tevatron quadrupoles is required to be less than 500 ms at 4.8 K, where the old double strip heaters work well. The required time constant reduces to 250 ms at 1.8 K, and the strip heaters are then marginal. The time constant for the LHC four layer quad must also be less than 250 ms, as well as for the alternate two layer design. The two layer design has an inductance on the order of 8.7 mH/m, the four layer has about 24 mH/m, therefore both must have a very effective state of the art quench protection heater and detection system, the more critical obviously being the four layer structure. There have been photo-etched stainless steel heaters that are partially copper plated, sandwiched between Kapton films, which are capable of producing the down ramps needed. The advantages of the high aspect ratio cables and finer strands are shown in Figure 1. These cables result in approximately the same maximum winding temperature versus current decay time after quench for a given initial current.

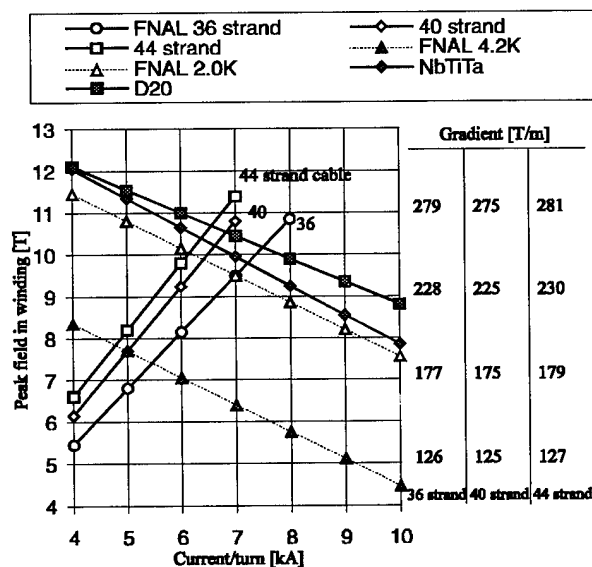


Figure 1 Alternate two layer design LHC IR quadrupoles

III. AN ALTERNATE ACTIVE FLUX RETURN "PIPE-QUADRUPOLE"

Another important issue in the design of an IR quadrupole is the large radiation load in the magnet. This radiation might cause a significant temperature rise in the winding package when it is not adequately cooled. This problem will become especially important for possible future higher luminosity accelerators. A Nb₃Sn quadrupole design that significantly reduces the radiation heating problem at the expense of more superconductor is presented here. The design is an extrapolation of a so-called pipe-dipole [7] to a

quadrupole geometry. The magnet is essentially built with four intersecting elongated toroids, of which the inner coils provide the high gradient and harmonics optimization, and the outer coils an active flux shield. The whole structure is wound on a stainless steel "pipe", and contained in a relatively small iron yoke. The design concept is illustrated in Figure 2. The figure shows a cross-section of one quadrant of the magnet, in which the inner coil at the bottom returns to the right outer coil, and the top outer coil to the left inner coil. The diameter of the entire structure is about 40 cm.

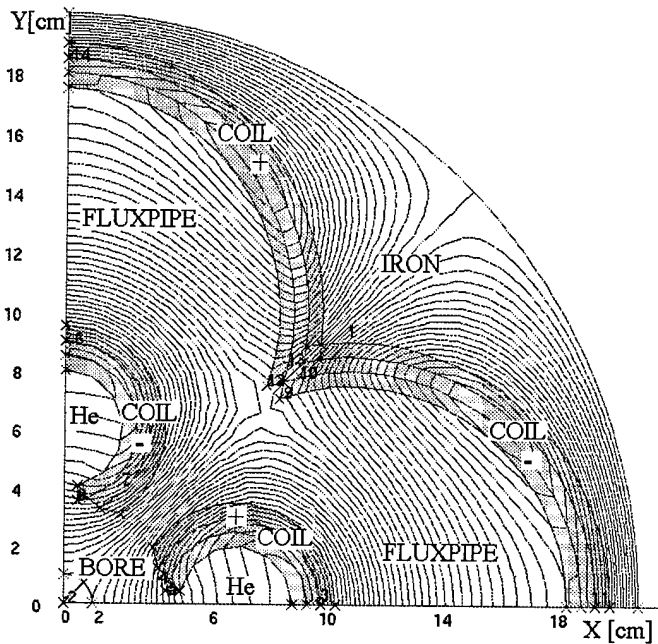


Figure 2 A conceptual Nb₃Sn "pipe-quadrupole"

The major benefit of this coil arrangement is the absence of conductor volume in the horizontal axis close to the beam-pipe, where the radiation load is the highest. The free volume within those coils can be used to cool the coils from the inside with a liquid helium cooling pipe. Due to the fact that the conductor windings are positioned further away from the bore, more conductor is needed than in a conventional quadrupole design.

The current design uses no internal iron within the "flux-pipe" to minimize the non-linearity of the field harmonics. The multipoles are minimized by shaping the area of the coil closest to the beam-pipe, and by grading the coils in three layers with two different conductors. It is possible to change the material in the flux-pipe to iron and shape it to minimize the unwanted field harmonics, however, the multipoles would become non-linear with current.

The gradient of the design can range between 280 T/m up to 350 T/m depending on the material used, and whether aggressive current grading is used. The maximum gradient of 350 T/m is obtained with a Teledyne Wah Chang Albany (TWCA) Modified Jelly Roll material at the short sample limit, however, this conductor has a fairly large effective filament diameter in the order of 50 μ m after reaction. By

using a more conservative conductor, i.e. not optimized for high current density, one can obtain a field gradient of about 280 T/m. This gradient is comparable to the maximum gradient for the LHC design, with the added benefit of a smaller quadrupole magnet and less sensitivity to radiation heating of the windings. With a total cross-section (including the iron yoke) of about half the size of a conventional quadrupole magnet, such a design has the advantages previously mentioned over the cosine- θ geometry.

The construction of a winding like this might look difficult at a first glance, but is actually quite simple. The conductor, which can be a standard Rutherford type cable, or even a tape, would be wound onto the flux-pipe material in segments, just like a toroid winding. The flux-pipe itself can be made out of a large stainless steel or iron rod by machining out the liquid helium conduits and slots for the inner coil. This automatically assures accurate placement of the conductors, which minimizes field harmonic errors due to imprecise winding. After winding the coil would be reacted, and then clamped in the iron outer yoke. The entire structure would then be held together by either an outer cylinder or a wire-wrap technique similar to the "D20" magnet [4].

In summary, a high gradient quadrupole with a "pipe" layout can be considered as a possible candidate for future large collider insertion regions. It is possible to fine-tune the design to obtain a good field-quality, the conductor is well cooled in case of a large radiation heat load, and the overall structure is smaller than a conventional quadrupole with a comparable field gradient.

IV. REFERENCES

- [1] The LHC study group, "Design study of the Large Hadron Collider (LHC)", CERN 91-03, May 1991.
- [2] T. Taylor, R. Ostojic, "Conceptual design of a 70 mm aperture quadrupole for LHC insertions", IEEE Trans. on Appl. Superconductivity, Vol.3, No.1, pp.761-764, March 1993.
- [3] A.D.McInturff et.al., "The Fermilab Collider D0 Low β System", Proc. Europ. Part. Acc. Conf., Ed.S. Tazzari, Rome, Italy, Vol.2., pp.1264-1266, 1988.
- [4] D.Dell'Orco, "Design of the Nb₃Sn dipole D20", IEEE Trans. on Appl. Superconductivity, Vol.3, No.1, pp.82-86, March 1993.
- [5] B.G. Lazarev et.al., "The study of the microstructure and j_c in Nb-37Ti-22Ta superconductor produced with different duration of treatments", Proc. 7th Int. Workshop on Critical Currents in Superconductors, Alpbach, Austria, Ed. H.W. Weber, World Scientific Press, Singapore, 1994.
- [6] S.A.Gourlay, et.al. "Quench performance of superconducting quadrupole magnets for the new Fermilab low beta insertion", Proc. IEEE Part. Acc. Conference, Ed. L. Lizama, L. Chew, New York, Vol.4., pp. 2227-29, 1991.
- [7] E. Badea, P.M. McIntyre and S. Pissanetzky, "The Pipe Magnet - Compact 13 Tesla Dual Dipole for Future Hadron Colliders", presented at the Annual High Field Accelerator Magnet Workshop, Berkeley CA, March 9-11, 1993.

SUPERCONDUCTING FOCUSING SOLENOID FOR X-BAND KLYSTRON

T. Ogitsu, T. Higo and H. Mizuno,

KEK, National Laboratory for High Energy Physics, Tsukuba, Ibaraki, 305 Japan

Y. Imai, T. Inaguchi, T. Minato, T.H. Kim, T. Uemura, and S. Yokoyama,

MELCO, Mitsubishi Electric Corporation, Wadasaki-cho, Hyogo-ku, Kobe, 661 Japan

Z. Wolf, D. Jensen, and P. Radusewicz,

SLAC, Stanford Linear Accelerator Center, Stanford University, Stanford, CA 94309 USA

A superconducting focusing solenoid for X-band klystron has been developed. The system consists of a conduction cooled NbTi solenoid, high T_c superconductor current leads, and a GM refrigerator. The GM refrigerator can cool down the solenoid from the room temperature to below 4 Kelvin by 4 days. This allow us to operate the system without supplying any cryogen such as liquid helium or nitrogen. The solenoid produces a desired field profile whose maximum value is about 7 kGauss. A normal conducting bucking coil is also implemented in order to tune the field at the cathode. Cool down tests performed at MELCO, KEK, and SLAC confirmed that the system can be cooled down by 4 days. Field measurements performed at those places confirmed that the field profile is very stable between thermal cycles.

I. INTRODUCTION

The X-band klystron, now being developed at KEK [1], requires a focusing solenoid whose warm bore aperture is about 180 mm and maximum axial field is 7 kGauss. The normal conducting solenoid used now consume electric power of about 50 kW. Use of superconducting solenoid, therefore, was considered in order to reduce this electric power consumption. A superconducting magnets, in general however, is needed to be cooled down by liquid helium and special skills are required to cool down the magnet. The superconducting solenoid system developed for the X-band klystron contains a conduction cooled superconducting solenoid, cooled by a Gifford-McMahon type refrigerator, which allows us to operate the system without supplying any cryogen [2,3]. The solenoid is cooled down to an operation temperature of about 4 K just by supplying electric power of 6 kW and cooling water. The system is successfully tested at MELCO, KEK, and SLAC. The cool down performance and field measurement results obtained during these tests will be reported.

II. SYSTEM CONFIGURATION

Figure 1 shows a configuration of the superconducting focusing solenoid system for the X-band klystron. The main components of the system are a conduction cooled

superconducting solenoid, a Gifford-McMahon type refrigerator, and high T_c superconductor current leads.

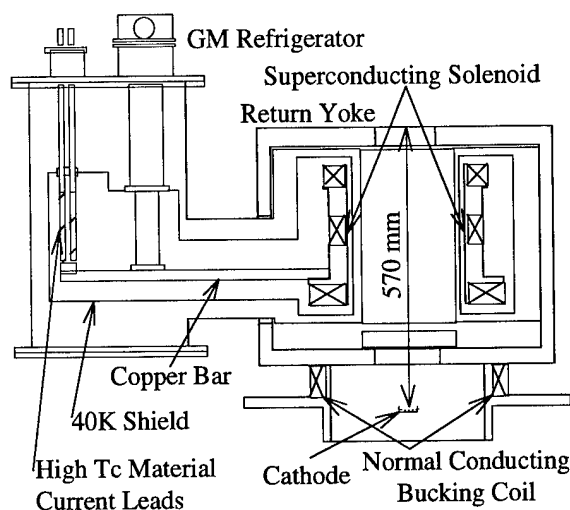


Figure 1 Configuration of the superconducting focusing solenoid system for the X-band klystron

A. Solenoid [2-4]

The solenoid consists of three coils which are wound in series on a stainless steel bobbin which is thermally connected to the cold head of the refrigerator by a copper bar. The coils were cooled by heat conduction through the copper bar and stainless steel bobbin. The solenoid, the inner diameter 250 mm, the outer diameter 400 mm, the overall axial size 280 mm and the overall inductance 36 H, produces a maximum central field of about 0.7 T at the operation current of 17.62 A. The critical temperature at the operation is about 9 K. The solenoid is wound from a wire whose copper to NbTi ratio is 4.5 and diameter is ϕ 0.76 mm. A normal conducting bucking coil is implemented in order to tune the field in the region where a cathode will be placed.

B. GM Refrigerator [2,3]

The system is implemented with a two staged Gifford-McMahon type refrigerator whose refrigeration power is 30 W at 40 K and 1.1 W at 6 K. The fact that the actual heat load to the 6 K head is about 0.2 W allows the system

to cool down the coils to below 4 K which give us a significant amount of operation margin.

C. High T_c Material Current Leads [2,3,5]

High T_c material current leads are used to reduce the heat penetration from the 40 K shield to the 6 K cold head. The leads are constructed from a pair of 200 mm length, 10 mm width, and 1 mm Bi-2223 phase bulk plates reinforced by GFRP. The calculated critical current at 77 K is about 70 A and tested at 25 A under warm and cold head temperatures of about 50 K and 4 K. The heat penetration from the 50 K head from the 4 K head is 46 mW which is significantly smaller than the case using the optimized copper leads which is about 450 mW. Copper leads, 300 mm length and 5 mm² cross section, are used between room temperature and the 40 K shield.

III. CRYOGENIC PERFORMANCE

Temperatures of three coils during a thermal cycle is shown in Figure 2. The data is taken during the first testing cycle at KEK. The figure shows that the solenoid is cooled down from the room temperature to the operation temperature of about 4 K by 4 days. After cold testing, the refrigerator is turned off and the system is warmed up to the room temperature which takes about 10 days. Another thermal cycle has been performed at KEK and three more cycles have been performed at SLAC. In all the cycles the cool down and warm up duration were nearly the same indicating the cryogenic performance is stable over the cycles.

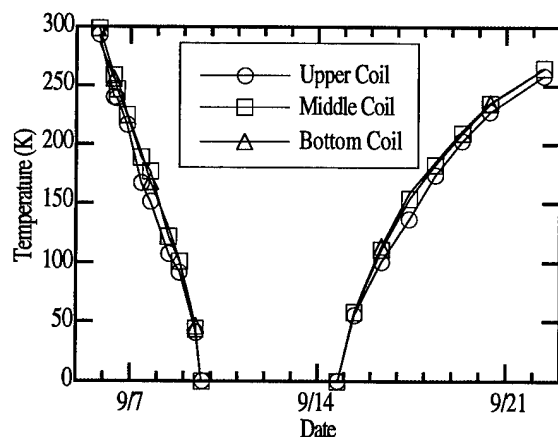


Figure 2 Temperature of the coils during a thermal cycle

A quench test was performed at MELCO [6]. The refrigerator was turned off while the solenoid was excited to 105 percent of the operation current. The solenoid quenched about 1 hour and 20 minutes after the refrigerator was stopped. The solenoid quenched at 9 K and

temperature reached to 20 K after the quench. After the quench, three hours of refrigerator operation was required to recover the system to the operation temperature.

IV. FIELD MEASUREMENTS

Both axial and transverse field measurements were made over several thermal cycles in order to confirm the reproducibility of the field through cycles.

A. Axial Field Measurement

Examples of measured results are shown in Figure 3 in comparison with specification. The measurements shown were taken during the first thermal cycle at KEK and the first thermal cycle at SLAC. The both measurements were made using hall probes which are aligned and moved to measure the axial field along the solenoid center. The measurements are taken under the nominal operation currents for the superconducting solenoid of 17.62 A. No current is fed to the bucking coil. The two measured results overlay each other indicating that field reproducibility over thermal cycles, including the shipping from Japan to USA, is satisfactory. The differences between the specification and the measured results are below 5 percent, the required axial field tolerance, except in the low field region around the cathode position where the field can be tuned by the bucking coil. The current required for bucking coil to tune the field at the cathode position turns out to be about 14 A. The bucking coil is tested and confirmed that it can reach to that current.

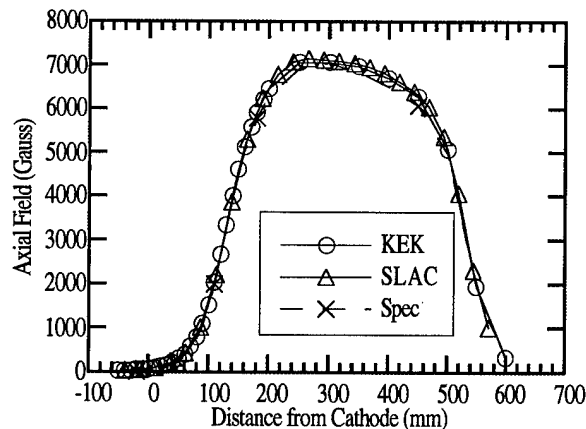


Figure 3 Axial field measurements

B. Transverse Field Measurement

Transverse field measurements are made at SLAC using a rotating coil system. The rotating coil is a radial coil whose radius is about 5 cm and length is about 2.5 cm. The coil was calibrated under an uniform field and it

produces 1 V at 167 Gauss under a rotation speed of 37 Hz. The rotating coil is aligned such that its rotating axis is normal to the top surface of the top pole piece, and it travels along the solenoid center. Measured results taken during the second and third thermal cycle is presented in Figure 4. Figure 4-a shows amplitudes of the transverse fields and Figure 4-b shows phases. The phases are defined counter clockwise looking the solenoid from the top starting from the angle which is rotated 90 degree clockwise from the refrigerator. The measurements were taken under nominal currents of 17.62 A for the solenoid and 0 A for the bucking coil. The measurements were made without changing the alignment of the measuring system from the second thermal cycle to the third one.

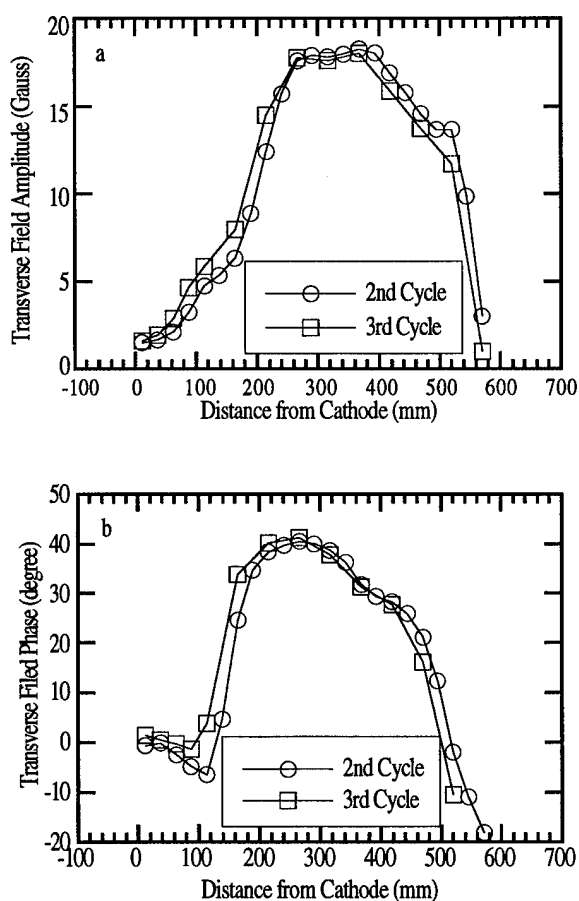


Figure 4 Transverse field measurements a) amplitude b) phase

Two plots overlay each other indicating that the field alignment is not changed from the second to third thermal cycle. The maximum amplitude of the transverse field is about 18 Gauss which is beyond the tolerance required for this solenoid which is 1/500 of the axial field, i.e. about 14 Gauss. Two sources can be considered for this transverse field; 1) misalignment of the solenoid, 2)

misalignment of the rotating coil. In order to examine the source 2, the alignment of the rotating coil is re-checked after measurements. It was confirmed that the rotating coil was aligned correctly with respect to the top surface of the top pole piece. It was found, however, the top surface of the top pole piece is not exactly perpendicular to the solenoid axis, defined by the line connecting the centers of the top and bottom pole pieces. This results in the rotating coil misalignment of about 0.9 mrad towards 56 degree direction with respect to the solenoid axis which can produce about 6 Gauss of transverse field. In fact, the transverse field compensated for this effect reduced its maximum amplitude to 12 Gauss. The value is below the tolerance and that the field quality of the solenoid may sustains actual use of the solenoid on power tests of a klystron.

V. CONCLUSION

A superconducting focusing solenoid system for an X-band klystron has been developed. The system consists of a conduction cooled superconducting solenoid, a GM refrigerator and high T_c material current leads. The system cools down to the operation temperature of about 4 K by 4 days just by turning on the refrigerator. Axial field measurements were performed at KEK and SLAC. It was confirmed that the field is stable over the thermal cycles and the field profile is satisfactory. Transverse field measurements were performed at SLAC. It was also confirmed that the field is unchanged over a thermal cycle. The amplitude of the transverse field appears to be within the tolerance. The system is now shipped backed to KEK and waiting for actual use on power tests of a klystron.

VI. REFERENCES

- [1] H. Mizuno et al., submitted to EPAC94, London, U.K., June 27 - July 1, 1994
- [2] S. Yokoyama et al., to be presented in MT-14 at Tempere Finland 11-16 Jun. 1995.
- [3] S. Yokoyama et al., submitted to Trans., I.E.E., Japan
- [4] R. Imai et al., presented in 52nd Meeting on Cryogenics and Superconductivity 3-5 Nov. 1994.
- [5] S. Yokoyama et al., presented in 52nd Meeting on Cryogenics and Superconductivity 3-5 Nov. 1994.
- [6] R. Imai et al., presented in 52nd Meeting on Cryogenics and Superconductivity 3-5 Nov. 1994.

A HIGH GRADIENT SUPERCONDUCTING QUADRUPOLE FOR A LOW CHARGE STATE ION LINAC

J.W. Kim, K.W. Shepard, and J.A. Nolen, Argonne National Laboratory, Argonne, IL 60439 USA

A superconducting quadrupole magnet has been designed for use as the focusing element in a low charge state linac proposed at Argonne. The expected field gradient is 350 T/m at an operating current of 53 A, and the bore diameter is 3 cm. The use of rare earth material holmium for pole tips provides about 10 % more gradient than iron pole tips. The design and the status of construction of a prototype singlet magnet is described.

I. INTRODUCTION

A radioactive ion beam facility proposed at ANL [1] [2] requires accelerating ions with $q/m \geq 1/66$ and $\beta (=v/c) \geq 0.004$ through a superconducting drift tube linac. In the present ATLAS linac, the transverse focusing elements are 8 tesla superconducting solenoids, which are used for beams with a $q/m \geq 1/10$ and $\beta \geq 0.008$ [3]. However, the low charge state beams contemplated here require much stronger focusing; magnetic solenoid elements would need to produce axial fields higher than 15 tesla for adequate transverse focusing. More effective focusing can be obtained with either magnetic or electric quadrupoles. We ruled out electrostatic quadrupoles because of uncertainty both in holding the required voltage and in operation at 4 K. Considering magnetic elements, permanent magnet quadrupoles have been used for drift-tube linacs, but in the present application would need complete shielding to avoid trapped flux and excessive rf loss in the neighboring superconducting cavities. Also, permanent magnet quadrupoles would not provide an adequate gradient for the required aperture.

A series of beam optics calculations has shown that quadrupole triplets with a gradient of 350 T/m, a bore radius of 3 cm, and an overall length of approximately 20 cm can provide adequate transverse focusing. The design is simplified by the fact that harmonic components in quadrupole field are not so detrimental to beam quality in the present application as in recirculating machines. Beam dynamics calculations indicate that non-quadrupole harmonics with an integrated effect up to 1 % at a radius of 1 cm are tolerable. The design of a prototype magnet which can meet these requirements is discussed below.

II. DESIGN OF A PROTOTYPE QUADRUPOLE

Design options for superconducting quadrupoles include $\cos 2\theta$ or superferric types. Construction methods for forming $\cos 2\theta$ coils with NbTi wires have been established, but such high field quality (and high construction cost) is not needed in this linac application. Also, it is desirable to use a small size of wire to reduce the refrigeration budget, which would make a $\cos 2\theta$ winding even more difficult. For these reasons, we have chosen a magnet design based on simple racetrack coils with pole tips.

A schematic view of the prototype is shown in Fig.1. The configuration of the prototype is similar to a superconducting quadrupole developed at LANL [4], but with a modified winding

to accommodate a substantially increased bore radius. Each of the four coils is composed of three blocks to increase the coil size and to keep the coil configuration simple. In fact, coil currents could be more effectively used if the coil were expanded closer to the field region, maintaining a $\cos 2\theta$ current distribution (e.g. ref.[5]), but then the coil winding becomes more difficult and expensive.

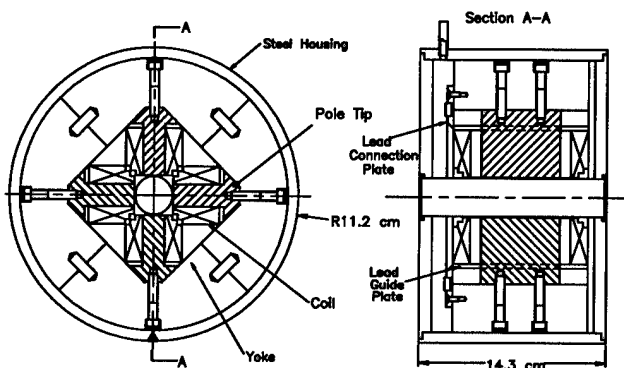


Figure. 1. A schematic view of a prototype quadrupole

The pole tips are made of rare earth material holmium to enhance the magnetic flux concentration. This technique has been utilized for high field solenoids [6] as well as for the LANL prototype quad; the saturation magnetization of holmium at 4.2 K is 3.8 tesla. The pole tip has a simple flat face since it is saturated at the operating field. Flat pole tips have been employed for room temperature quadrupoles in drift tube linacs [7]. The prototype is a quadrupole singlet with a length equal to the longest element of the proposed triplet, since the longer quadrupole magnet could be more subject to wire motion problems. The inner corner of the section of the coil near the pole face has a small notch (1.3×2 mm) removed to reduce the peak field on the conductor.

The magnetic fields were numerically calculated first using the OPERA-2d code [8] to optimize the pole tip width and minimize the higher order harmonics. This was a compromise process, trading-off useful aperture against low harmonic content. At 350 T/m, the 12th pole is about 0.1 % of quadrupole field, and the 20th pole is less than 0.1 %. In Fig.2, the field lines are plotted for a quadrant of the quadrupole. The B-H curve of holmium used in the numerical calculation was taken from ref.[6]. At 350 T/m the gradient gain from using holmium is about 35 T/m higher than for iron pole tips. Major design parameters of the prototype are listed in Table.1.

Since the prototype quadrupole length is short, 3-d effects are important to field quality. A 3-d finite element program TOSCA [8] was used to calculate fringe fields. The field profile of a

Table 1: Design parameters of a prototype quadrupole

Gradient	350 T/m
Operating current	53 A at 350 T/m
Current density in coil	47,000 A/cm ²
Pole tips	holmium (99.6 %)
Inductance	0.55 H
No of turns	3800
Yoke	SAE 1008 steel
Wire	NbTi
Diameter	0.305 mm
Cu/Sc	1.35
Critical current	57 A at 6.3 tesla, 4.2 K
Insulation	Formvar, 0.0127 mm thick

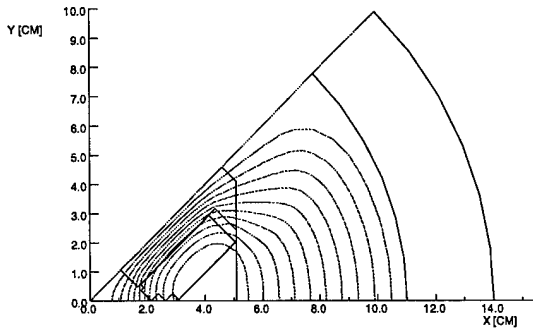


Figure 2. Magnetic field lines for a quadrant of the quadrupole, as calculated with the OPERA-2d code

transverse field component (B_t) is plotted in Fig.3 at a radius of 1 cm and 350 T/m. The effective magnetic length is 7.6 cm.

The effect of harmonic field components on the beam is determined by the integrated gradient along the quadrupole. The integrated gradient error defined in the equation below is used to specify the field quality;

$$\Delta I_G(r, z) = \frac{\int_0^z B_t(r, \theta_{max}) dz - \int_0^z B_t(r, \theta_{min}) dz}{\int_0^z B_t(r, \theta_{min}) dz}, \quad (1)$$

where θ_{max} is an angle which gives a maximum of the integral, and θ_{min} for a minimum at a radius of r . The dashed line in Fig.3 shows $\Delta I_G(r, z)$ as a function of z at $r=1$ cm. Note that the integrated error is reduced as the beam traverses the coil ends: this effect has been used to design high quality $\cos 2\theta$ quadrupoles. The integrated harmonic content increases for lower fields; it rises to 0.6 % at 200 T/m, and further to 2.5 % at 100 T/m when the current density is 6400 A/cm².

The coil end design has two important issues: 1) harmonic errors, 2) enhancement of field on the conductor. To reduce both effects, the coil ends could be spread out using spacers [9]. However, such control of the end effect was not necessary for the present application. The harmonic error is reduced as the beam passes through the quadrupole as shown in Fig.3, although some field enhancement is unavoidable. The highest field on conductor is about 6.3 T at the ends compared to 6.0 T in the straight section, as calculated with TOSCA.

The coil is an orderly winding, with insulation sheets embedded between layers and impregnated with epoxy. The winding

is placed directly on the holmium pole, eliminating several steps needed when a winding form is used. The winding load is about 8 N, producing a winding tension of 9×10^3 N/cm². The coil is continuously wound without splice, and G-10 spacers are used to fill the rectangular gaps during winding.

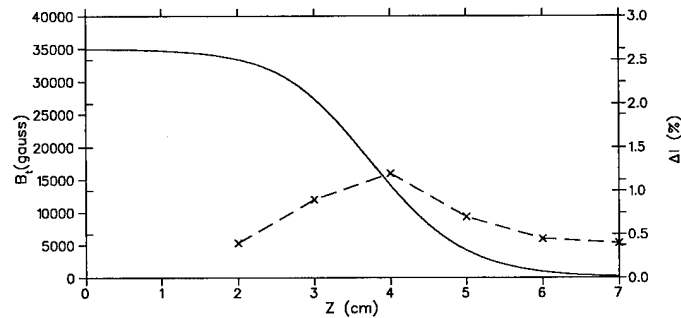


Figure 3. The field profile of B_t at $r=1$ cm (solid line) and the integrated gradient error (dashed line) are shown as a function of axial distance. The axial distance is from the center of the quadrupole.

III. COIL FORCE AND QUENCH CALCULATIONS

The electromagnetic forces on the straight section of the coil are depicted in Fig.3 for an excitation of 350 T/m. Although the winding tension prevents wire motion on the curved coil ends and although the coil is rather short, the straight section still needs a support. Without support the coil may expand as much as 0.3 mm at 350 T/m in the middle of the straight section, as calculated using the deflection formula for the case of supported edges in ref. [10]. The straight section is simply supported by stainless steel spacers. To avoid motion of lead wires from the coils, the leads are fixed onto the lead connection plates made of G-10, as noted in Fig.1.

An estimate of quench voltage at the junction between quenched and normal coils is about 400 volts as calculated with the program QUENCH [11]. Although such a voltage is not difficult to insulate, when 2 or 3 singlets of a given triplet are wired in series quench voltages of 1 kV or more can appear. For triplet elements, a compromise between quench voltage and the number of connecting leads into cryostat will need to be made.

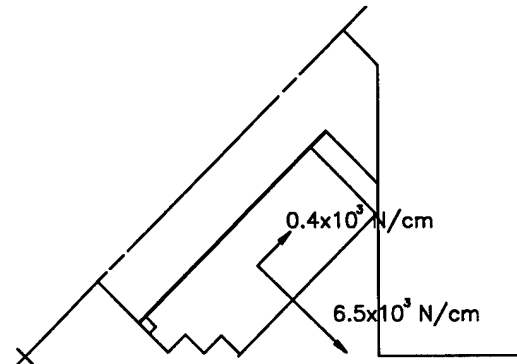


Figure 4. Forces on the straight section of the coil at 350 T/m

IV. STATUS AND CONCLUSIONS

A prototype superconducting quadrupole with a 3 cm aperture has been designed for use in a low charge state injector linac for ATLAS. The design field gradient of 350 T/m can be achieved when the operating current is 91 % of the critical current at 4.2 K. This tight design margin demands a high quality winding. 3-d field calculations showed that the integrated field gradient error is 0.45 % at 350 T/m and less than 1 % in a wide range of coil excitations.

Construction of a prototype singlet is well advanced. The winding is being carried out by Cryomagnetics Inc. The winding and testing of the first coil is expected to be completed in May 1995. Following testing of the first coil, the remaining 3 coils for the prototype singlet will be wound. Final assembly and field measurements will be carried out at Argonne. The prototype is designed to allow testing different coil supporting structures with little modification. The final design will be optimized for economic production of several dozen units.

Acknowledgment

We would like to thank Drs. L. Turner and K. Thompson of the Advanced Photon Source at Argonne National Laboratory for their generous help in using TOSCA, and Dr. A. Zeller at Michigan State University for providing the B-H data.

References

- [1] J.A. Nolen, Accelerator Complex for a Radioactive Ion Beam Facility at ATLAS, in the proceedings of this conference
- [2] K.W. Shepard and J.W. Kim, A Low-Charge-State Injector Linac for ATLAS, in the proceedings of this conference
- [3] A.H. Jaffey et al., *Nucl Instr Meth*, 121 (1974) 413
- [4] D.B. Barlow et al., *Nucl Instr Meth*, A313 (1992) 311
- [5] G. Ambrosio, et al., *Proceedings of 1994 European Particle Accelerator Conference*, (1994) 2268
- [6] W. Schauer and F. Arendt, *Cryogenics*, 23 (1983) 562
- [7] I.M. Kapchinskiy, *Theory of Resonance Linear Accelerators*, 81 (1985) Harwood Academic Publishers
- [8] OPERA-2d and TOSCA are products of Vector Fields, Oxford, England
- [9] S. Caspi, M. Helm, and L.J. Laslett, Magnetic Field in the End Region of the SSC Quadrupole Magnet, LBL-29819, (1991)
- [10] R.D. Cook and W.C. Young, *Advanced Mechanics of Materials*, Macmillan Publishing Co. (1985)
- [11] M.N. Wilson, program QUENCH, Rutherford Laboratory Report, RHEL/M151 (1968)

STATUS OF THE HIGH BRILLIANCE SYNCHROTRON RADIATION SOURCE BESSY-II *

E. Jaeschke, S. Khan, D. Krämer, D. Schirmer for the BESSY II project team,
BESSY II, Rudower Chaussee 5, Geb. 15.1, 12489 Berlin, Germany

Abstract

BESSY II is designed as a high brilliance synchrotron light source in the VUV/XUV region with 1.7 GeV nominal beam energy. Being under construction at Berlin-Adlershof, the machine is expected to start routine operation in 1998. An overview of the status of the project is given.

I. INTRODUCTION

The synchrotron radiation (SR) source BESSY II is based on a 240 m circumference storage ring of 8-fold symmetry. Sixteen DBA cells provide alternating dispersion-free straight sections of high and low horizontal beta function and no dispersion. Thus, high flexibility is achieved to install various types of undulators, wigglers and also superconducting wavelength shifters [1] in max. 14 places. Six undulators and wigglers and two wavelength shifters will be available within the first two years after commissioning of the new SR source.

The injection system consists of a 50 MeV racetrack microtron (RTM), and a 10 Hz booster synchrotron which ramps the electron beam to its final operation energy of max. 1.9 GeV.

Prototypes of the magnets for the synchrotron were built at The Budker Institute for Nuclear Physics, Novosibirsk and a complete unit cell was received and tested recently [2].

Prototypes of the storage ring magnets (32 dipole, 144 quadrupole and 112 combined function sextupole and correction magnets) are expected for mid of 1995. Delivery of all elements is scheduled for the 2nd half of 1996.

Major progress has been made concerning the storage ring vacuum system and a prototype section (1/16 of the whole system) will be available in July this year. The vacuum components for the injector have been ordered. Their installation will start in beginning of 1996 followed by the the storage ring approximately six month later.

II. BUILDINGS

The buildings activities have started in September 1994 and are progressing according to the time schedule. An experimental hall of 1000 m² for assembly and measurements been completed recently. The building is now, for example, used for magnetic measurements, rf tests and commissioning of the 50 MeV RTM. Previously existing buildings have been renovated and are in use since March 1994.

The main experimental hall of 120 m diameter with the storage ring tunnel and experimental area is under construction and casting of concrete is expected to be finished in July 1995. This will allow to start the installation of the machines on a large

scale by the end of this year. Final assembly of the storage ring is schedule for mid of 1997 allowing to start commissioning of the storage ring in late 1997. First light from an undulator is expected at the end of 1997.

III. THE STORAGE RING

A. Magnets

Prototypes of all storage ring magnets (dipoles, quadrupoles, sextupoles) were designed and all major orders were placed. Delivery of the pre-series bending magnets and multipole magnets is scheduled for mid of this year. After careful measurements and optimizations of the chamfers by BESSY, the series production will start in Autumn 1995. The storage ring magnet design and the expected magnetic performance is discussed in [3].

B. Storage Ring Injection System

The injection components, comprising 4 fast kicker magnets and the injection septa are located in one of the high beta sections ($\beta_x \approx 17$ m) of the storage ring. The kickers, driven by sine half wave pulsers, will displace the closed orbit by 17 mm. Two septum magnets will inject the beam coming from the synchrotron ($\epsilon = 1.7 \cdot 10^{-7}$ rad m). In order to increase the injection efficiency, detailed calculations were carried out to optimize the optics of transfer line and the injection parameters [4], [5]. The calculated efficiency for a matched beam is 98%. Table I summarizes the main magnet parameters of the injection elements and Figure 1 shows their geometrical arrangement. Since the injection system of ELETTRA is rather similar, it was agreed that Synchrotrone Trieste will manufacture the complete injection system (septa, kicker, pulser).

The layout of the transfer lines is finalized and the specifications of all components are ready for call for tender. A detailed description is given in [5].

	kicker 1-4	septum 1	septum 2
pulse length	5 μ s	40-50 μ s	40-50 μ s
magnetic field	0.24 T	0.750 T	0.761 T
deflection angle	20.9 mrad	65.8 mrad	66.8 mrad
peak current	8413 A	8962 A	9090 A
capacitor charging			
voltage	9.796 kV	1058 V	1073 V
core length	552 mm	555 mm	555 mm
overall length	595 mm	595 mm	595 mm

Table I

Parameters of the storage ring injection components.

*Funded by the Bundesministerium für Bildung, Wissenschaft, Forschung und Technologie and by the Land Berlin.

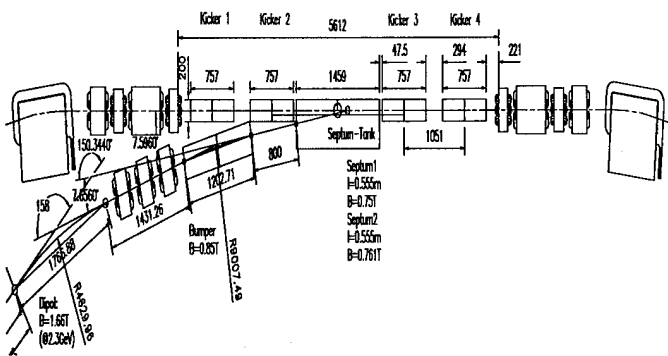


Figure 1. Storage ring injection region.

C. Vacuum Chamber and Girder Layout

Theoretical investigations and computer simulations concerning the beam lifetime and impedance-driven instabilities have helped to finalize the vacuum chamber layout. Being a major threat, transverse coupled bunch instabilities (resistive wall effect) have been investigated analytically and with numerical simulations. The beam lifetime, limited by the Touschek effect as well as residual gas scattering (Coulomb scattering and Bremsstrahlung) is expected to be at least 10h at 1.7 GeV, assuming a mean vacuum pressure of $2 \cdot 10^{-9}$ mbar N_2 equivalent and a momentum acceptance of 3%. As a consequence of these investigations, the beam pipe aperture was chosen to be ± 35 mm horizontally and ± 17.5 mm vertically. The minimum vertical wiggler/undulator gap has been fixed to ± 8 mm which reduces the lifetime due to Coulomb scattering only little. Keeping the resistive wall effect in view [6], the ID chambers will be made of aluminium.

The different vacuum chamber profiles for the dipole, quadrupole and ID region are shown in Figure 2. A prototype vacuum section (1/16 of the whole system) has been ordered and will be available for testing mid of this year.

The proposed BESSY II vacuum chamber is made of stainless steel with a copper absorber all around the circumference

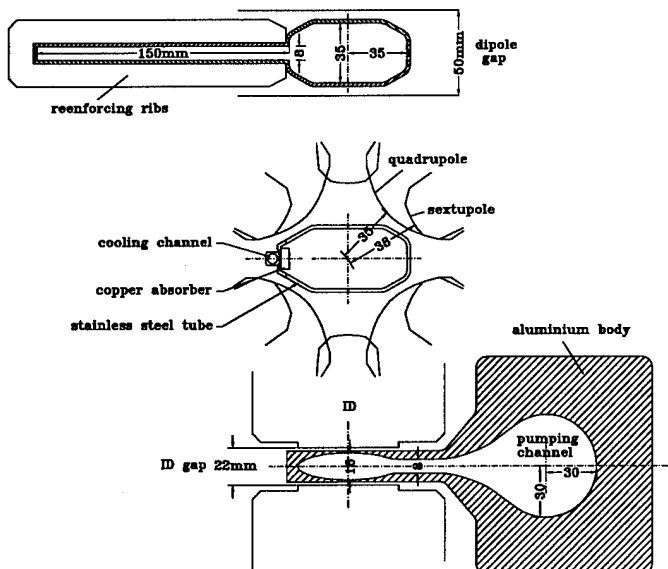


Figure 2. Cross sections of the different vacuum chambers in the dipole, quad and ID region.

to reduce the maximum temperature on the chamber due to SR power. The copper absorber will be brazed or explosively bonded to the chamber and indirectly cooled from the outside. Finite element calculations including the effect of scattered photons show that max. absorber temperature is 10° above the cooling water temperature. There will be no antechamber except in the ID region and in the dipole chamber. The mechanical stability of the dipole chamber has been checked by finite element simulations. With the inclusion of reinforcing ribs, the maximum distortion due to the atmospheric pressure is 0.1 mm for a chamber of 2 mm wall thickness. The pumping concept for BESSY II includes a 400 l/s ion getter pump for each crotch absorber, and three to five ion getter pumps of approximately 75 l/s in the straight sections outside of the IDs. The pumping scheme in the IDs depends on their respective design. NEG-cartridges and Ti sublimator pumps are considered as an option to be installed in the vicinity of the crotch absorbers.

The elements of each storage ring DBA-cell will be mounted on 3 girders made of concrete blocks, which are expected to damp vibrations more effectively than metallic structures. Extensive tolerance studies [7] were performed to optimize the girder scheme with respect to the sensitivity of the installend lattice elements to coherent movements of the assembly. The result is shown in Figure 3.

The magnetic elements will be mounted on the girders and aligned prior to their installation in the tunnel, where the final alignment of the complete girders will be done.

There are 3 SR beam lines emerging from the first dipole chamber, one for the respective ID and two for SR from the dipole, while the second dipole chamber is, for geometrical reasons, equipped with 1 SR outlet only. Seven BPMs per cell form an integral part of the vacuum system. Their positions coincide with the fixed points of the chambers which may undergo deformations due to the received heat load. They are mechanically decoupled from the magnets in order to avoid mechanical stress and displacements of the optical elements which would create closed orbit distortions.

D. RF system

Major progress has been made on the rf sector. It was decided to use four already available DORIS type single cell cavities which will be installed in one of the low beta straight sections. The pill box shaped resonators will be fed by individual 500 MHz generators making use of Thompson TH2123

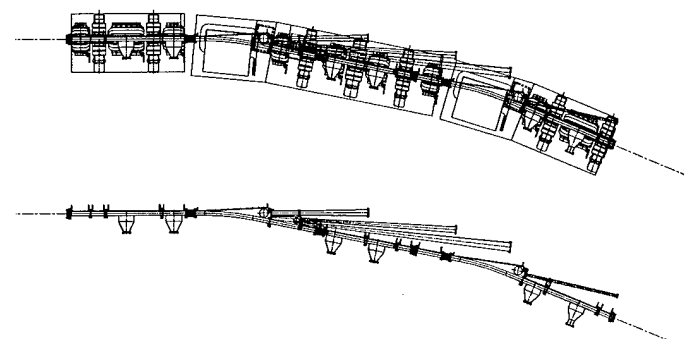


Figure 3. Top view of the girder scheme and the vacuum system.

klystrons with a power of 75 kW each. All rf generators are ordered and the first one is expected to be delivered in June 1995.

E. Diagnostics

The availability of suitable beam diagnostics is a crucial prerequisite for reliable and smooth operation of the machine. The relative accuracy of each of the 112 BMPs is $5 \mu\text{m}$, their absolute position error is 0.1 mm. For the first turn, a fast albeit less accurate mode of measuring is foreseen.

SR light monitors attached to one of the dipole radiation sources will allow to image the beam. For intensity measurement, a Bergoz PCT-175 is already being tested.

Foil monitors, scrapers and various striplines are foreseen in a separate straight section.

IV. MICROTRON AND BOOSTER

A. Booster Prototype Magnets

The dipoles and quadrupoles of the full energy booster are presently manufactured by the Budger Institute for Nuclear Physics (BINP), Novosibirsk. A prototype of a complete booster FODO cell has been delivered in April 1995. First magnetic measurements of the booster prototype magnets (2 quadrupoles and 1 dipole) gave excellent results with respect to mechanical tolerances, field homogeneities and higher order multipoles. A detailed description of the magnetic measurements is given in [2].

B. Microtron Recommissioning

A Scanditronix 50 MeV racetrack microtron will be used as a pre-injector to feed the 10 Hz booster synchrotron. This microtron was recommissioned in March 1995. Already at the first test run produced an electron beam pulse after 9 turns which was detected using a faraday cup (Figure 4). The data correspond to a beam energy of 50 MeV, a current of 9 mA and a pulse length of $1 \mu\text{s}$. Additional diagnostics to simplify its operation will be added to the machine, e.g. an internal video signal monitor and computer control. Work is in progress to upgrade the RTM with a triode gun to produce 1 ns pulses and with a 500 MHz subharmonic buncher to be able to operate the storage ring in single bunch mode. The main design parameters of the microtron are summarized in table II.

References

- [1] G. Wüstefeld, B. Kuske, V. Sajaev, D. Schirmer *Optimization and Tracking Studies for the 1.7 GeV Light Source BESSY II*, EPAC, 1994, London
- [2] I. Chertok, T. Knuth, D. Krämer, E. Weihreter, *The Magnetic Lattice of the BESSY-II Injector Synchrotron*, these proceedings
- [3] T. Becker, V. Korschuganov, D. Krämer, S. Küchler, N. Kuznetsov, E. Levichev, U. Strönisch, *Prototype Development of the BESSY-II Storage Ring Magnets*, these proceedings
- [4] D. Krämer, R. v. Hahn, *Injektion in den Speicherring*, Technical Note, TN9/BESSY II/03/95/RvH

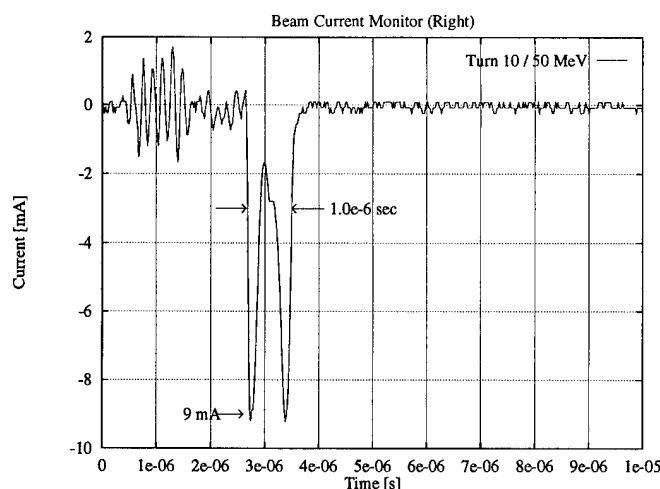


Figure 4. Electron beam pulse at the microtron exit.

Main RTM Parameters		
beam	max. energy	50 MeV
	max. current	28 mA
	energy width	0.5%
	emittance	$< 0.5 \text{ mm} \cdot \text{mrad}$
	pulse	$1 \mu\text{s}$, 10 Hz
system	gun	100 kV, 600 mA
	RF	2998 MHz
	klystron (in/out)	100 kV, 140 A / 6 MW
	dipole	1.0479 T
	energy gain/turn	5 MeV
	no. of turns	10
	tot. orbit length	$26 \text{ m} \pm 72 \text{ ns}$

Table II

Design parameters of the racetrack microtron.

- [5] D. Schirmer, M. v. Hartrott, S. Khan, D. Krämer, E. Weihreter, *Beam Transfer Lines at BESSY-II*, these proceedings
- [6] S. Khan, *Simulation of Transverse Coupled Bunch Instabilities*, these proceedings
- [7] G. Wüstefeld, *Estimate of the Closed Orbit Sensitivity of Different Girdler Schemes for the BESSY II Storage Ring*, Technical Note, BESSY TB Nr.193/95

HARMONIC GENERATION FEL MAGNETS: MEASURED B-FIELDS COMPARED TO 3D SIMULATIONS

W. S. Graves, L. Solomon, Brookhaven National Laboratory, Upton, NY 11973 USA

The Harmonic Generation Free Electron Laser[1] is a short period, high-gain amplifier FEL configured as an optical klystron. It is designed to lase at $3.47\mu\text{m}$ using a 30 MeV electron beam at the Accelerator Test Facility at BNL. Each of the three superconducting wiggler magnet sections (modulator, dispersion, radiator) has been built and the magnetic fields have been measured. This paper compares the measurement results with three-dimensional nonlinear computer models created with the TOSCA code.

I. Introduction

The HGFEL currently under construction at BNL will lase on the 3rd harmonic of a conventional CO_2 seed laser. The wiggler is split into 3 sections. The first section (modulator) energy-modulates the electron beam in resonance with the fundamental wavelength of the seed laser. Following this, the dispersive section causes the energy modulation to become spatial bunching (also at the fundamental). Finally the bunched beam enters the radiator which is tuned to the 3rd harmonic and lases.

HGFEL Wiggler Parameters			
	Modulator	Dispersive	Radiator
Period (cm)	2.6	—	1.8
a_w	1.35	—	0.6
B-field (T)	0.79	0.81	0.51
N poles	24	5	168
Gap (mm)	8.6	8.6	6.0

The computer models were created with the finite-element program TOSCA [2]. The primary goals of the computer simulations of the magnets are to:

1. Predict the current excitation necessary to reach the desired magnetic fields.
2. Design the appropriate magnet end winding configuration so that the electron beam is not steered when the iron is saturated.
3. For the dispersion section, design the yokes and coils to give the full range of dispersion needed without introducing beam steering.

II. Modulator Magnet

The modulator magnet is machined from a single iron yoke. It has 12 2.6 cm periods. The operating current is 80 Amps through 96 turns in each main coil. The peak magnetic field is 7900 gauss. The entrance and exit windings use the lowest order binomial transition [3]. There are $1/4''$ thick field clamps at each end of the yoke to ensure that the magnetic scalar potential is zero there. In addition to the main windings, there are two sets of trims at each end to perform steering correction[4](Fig. 1).

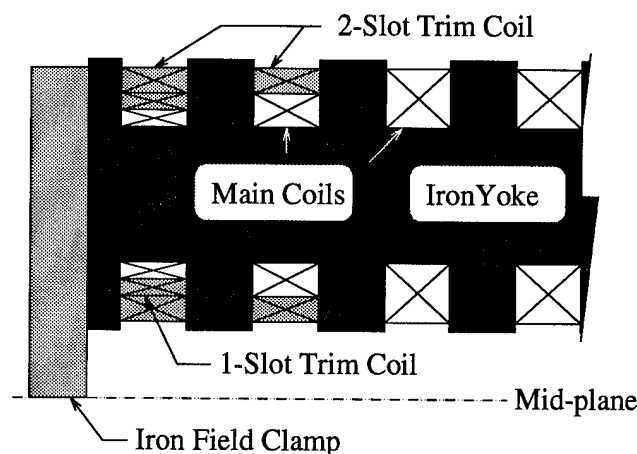


Figure 1. One end of the modulator magnet section, showing the main coil and trim winding configuration.

The trims are necessary because the steel in the nominally $1/2$ -strength pole at each end are less saturated than the full-strength poles, leading to an error in the magnetic scalar potential at that point. The optimum trim configuration has been found to be as shown, where 2 coils in series on either side of the $1/2$ -strength pole buck the main field, and 1 coil in the last slot provides fine adjustment. Typical trim strengths are 530 Amp-turns in the 2-slot trim and the 1-slot trim off when the main coils are at their operating value. Note that when the main coils are set at low enough current, the iron is unsaturated, and the trims are unnecessary. In the future it would be advantageous to design the number of turns in the last slots to account for the saturation at the operating point so that only very small corrections are required.

Using appropriate boundary conditions, the entire magnet may be modelled using just one octant of the 3D space containing the real magnet and surrounding air. Nonlinear saturation is taken into account using a B-H lookup table, and iteratively solving until a predefined maximum change in the solution at any node is achieved. The model contained 55×10^3 nodes, and takes about 8 cpu-hours to execute on an IBM RS6000/370. Figure 2 shows the measured B-fields and its second integral (equivalent to the electron trajectory) for the modulator. The mean peak field is 7787 gauss with RMS variation of just 0.2%. The peak fields in the simulation agree with the measured value to within 0.8%. The simulated fields are not shown in the figures because the differences from the measured values are indistinguishable on this scale. Of particular interest is the behavior near the magnet ends. Figure 3 shows the 2nd integral of the B-field for the modelled and measured fields with trims off. The difference in deflection angles is less than $1.0\mu\text{rad}$. The close agreement indicates that the model accurately predicts the level

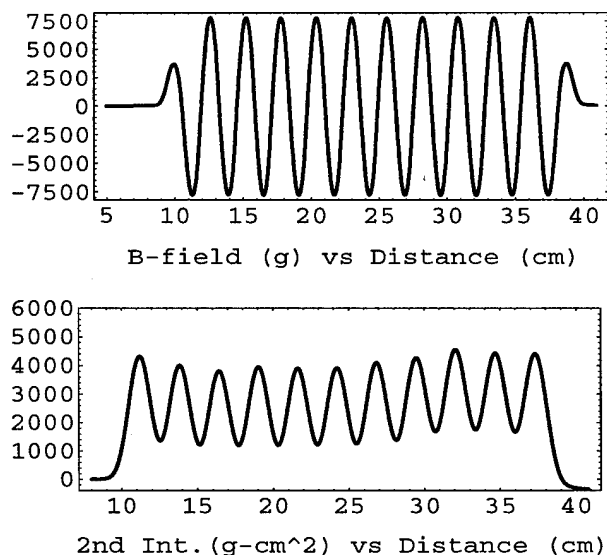


Figure 2. Measured B-fields and second integral for the modulator section. Main coils at 80 Amps, trims at 22 Amps. RMS variation among peaks is 0.2%.

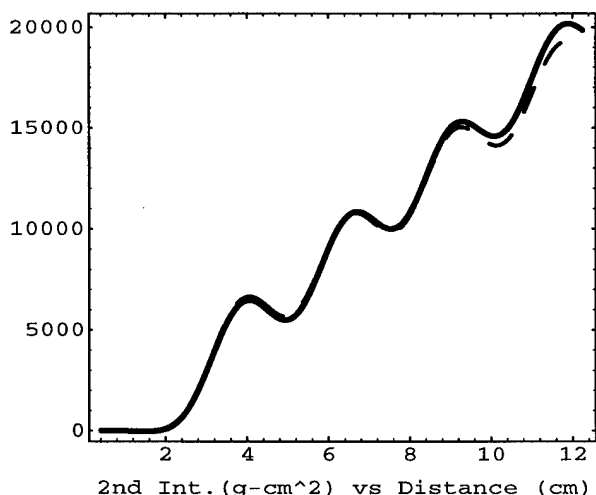


Figure 3. Measured (solid line) and modelled (dashed line) 2nd integrals of the modulator B-field at the entrance of the modulator. Main coils at 80 Amps, trims off.

of saturation and necessary trim correction.

III. Dispersion Magnet

The dispersion magnet (Fig. 4) is spaced 5cm downstream from the modulator. It has just 3 excited poles with a total length of 120 cm. The winding scheme is 23-147-147-23 turns. There is a trim coil to compensate for beam steering. Here, dispersion means change in longitudinal phase ψ with energy γ . The dispersion relation is approximately [5]

$$\frac{d\psi}{d\gamma} = \frac{k_s e^2}{m^2 c^2 \gamma^3} \int_0^L dz \left[\int_0^z dz' B_y(z') \right]^2 \quad (1)$$

where k_s is the radiation wavenumber. It is important that the dispersion be adjustable over as wide a range as possible to

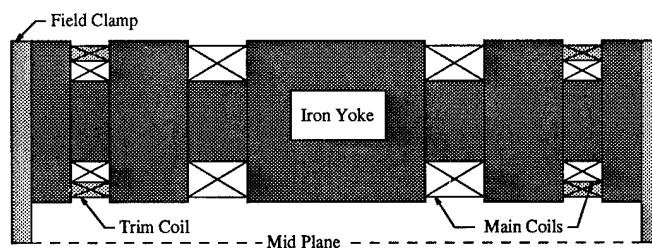


Figure 4. Dispersion magnet showing main and trim coils.

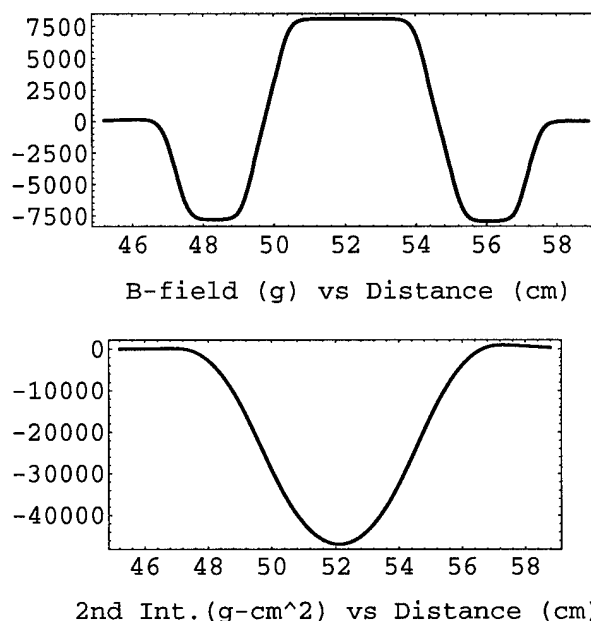


Figure 5. Measured B-field and 2nd integral for the dispersive section. Main coils at 100 Amps, trim coil at 8.5 Amps.

investigate the effect of varying the bunching on the laser performance.

The computer model is again one octant of the three dimensional space containing the iron and surrounding air plus the appropriate boundary conditions. It contains 59×10^3 nodes, and takes about 2.7 cpu-hours to solve. The execution time is reduced substantially from the modulator magnet because there are fewer coils. The time scales linearly with the number of coils.

The magnet was originally designed based on results from POISSON, a 2D magnetostatic solver. The 3D simulation results (obtained after the iron was cut) differed dramatically from the 2D because the finite size in the excluded dimension (transverse horizontal) severely limits the cross-sectional area available for flux transport in the iron. Thus the iron is far more saturated than predicted by the 2D model. The final coil configuration was modified based on the 3D results, and the measurements show very good agreement with this model. The peak field in the simulation differs from the measurement by 0.3%. The peak magnetic field at 100 Amps is 8100 gauss and the maximum dispersion is limited to 34.

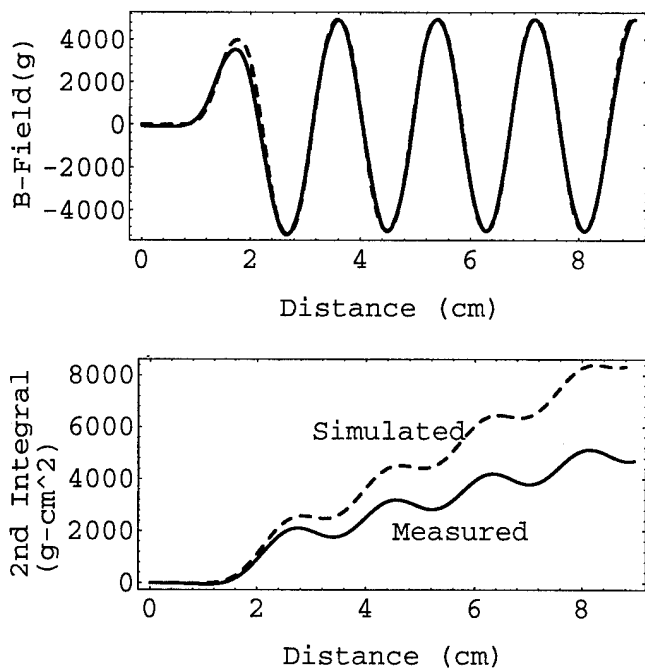


Figure 6. Measured (solid line) and simulated (dashed line) B-field and 2nd integral at the entrance of the radiator section. Main coils at 90 Amps, trim coils off.

IV. Radiator Magnets

The radiator section consists of six separate iron yokes, each with 18mm period, 0.51 Tesla peak magnetic field, and 6.1mm gap. Each yoke is physically very similar to the modulator magnet (Fig. 1) with two exceptions: the period is shorter, and the pole faces have a parabolic cut to provide horizontal electron beam focusing. The results of 3D simulations and measurements of the radiator magnets have been reported previously [4]. The earlier work studied the advantages of various entrance configurations of the coils in an effort to reduce the effects of saturation.

Figure 6 shows both the simulated and measured magnetic field and its 2nd integral at the entrance of the radiator section. The agreement between model and measurement is not as good as for the previous sections. There are several discrepancies between the computer model and the as-built configuration that may account for the disagreement. The model has a 5.6mm gap whereas the real magnet uses a 6mm gap. This changes the saturation in the iron and may account for different beam steering at the magnet entrance. The model also differs from the real magnet in that it has no parabolic pole face. A new simulation model is now being designed that matches the magnet as built. It is expected to perform as well as the modulator and dispersion section models.

V. Conclusions

Three dimensional simulations of each of the three distinct sections of a FEL configured as an optical klystron have been performed, and the results compared to measurements. These simulations include nonlinear saturation. The simulated on-axis magnetic fields for the modulator section agree with the measurements to 0.8%. Beam steering near the magnet entrance

due to iron saturation is also accurately modelled. For the dispersive section, simulation agrees with measurement to 0.3%. These results differ substantially from the 2D models because the limited cross-sectional area of the magnet changes the flux density in the iron. The radiator model does not yet perform as well and efforts are underway to gain better agreement with measurements.

VI. Acknowledgements

The authors would like to thank Bob Harrington and George Stenby for their technical assistance, and Ilan Ben-Zvi, Li-Hua Yu, and Sam Krinsky for their useful advice.

References

- [1] I. Ben-Zvi et al. Design of a harmonic generation fel experiment at bnl. *NIM A*, 318:208-211, 1992.
- [2] Vector Fields Limited, 24 Bankside, Kidlington, Oxford OX5 1JE, England. *OPERA-3d Reference Manual*, 1992.
- [3] K. Halbach. Desirable excitation patterns for tapered wigglers. *NIM A*, 250:95-99, 1986.
- [4] W.S. Graves, L. Solomon. End fields in the harmonic generation superconducting fel at bnl-nsls. *NIM A*, 358:414-417, 1995.
- [5] R. Bonifacio, R. Corsini, P. Pierini. Theory of the high-gain optical klystron. *Physical Review A*, 45(6):4091-4096, 1992.

Measurement of Ramp Rate Sensitivity in Model Dipoles With Ebanol-Coated Cable

C. Haddock*, V. Kovachev*, and D. Capone*

Superconducting Super Collider Laboratory†

2275 North Highway 77, Waxahachie, Texas

Abstract: Ramp rate sensitivity in superconducting dipole magnets has been shown to vary in an unpredictable fashion between magnets constructed using similar fabrication techniques. Test results from a series of model magnets are presented, one of which was constructed using ebanol-coated strands. The ramp rate sensitivity and ac loss observed is described.

I. INTRODUCTION

In order to determine the training, ramp rate and magnetic field performance of prototype dipoles intended for the SSC, a comprehensive program of cold magnet testing was performed at Fermi and Brookhaven National Laboratories [1]. The results showed two distinct families of quench current versus current ramp rate, as shown in figure 1. The first family (known as type "A") showed an initial nearly flat quench current up to about 20 A/s, then an almost linear decrease of quench current with ramp rate. The linear portion of the curve, however, varies significantly amongst members of this family.

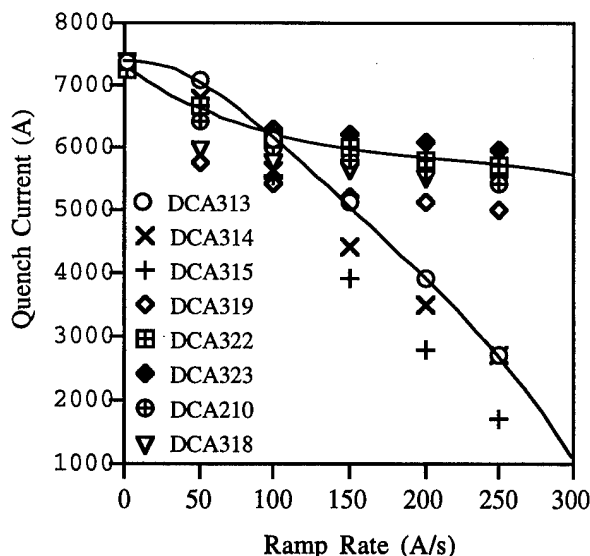


Figure 1: Quench current dependence on ramp rate for 50 mm aperture 15 m length dipole magnets.

*Present address: Texas National Research Laboratory Commission, 2275 North Highway 77, Suite 100, Waxahachie, Texas 75165

†Operated by Universities Research Association under contract with the Department of Energy.

The second family (type "B") showed a rapid initial decrease in quench current at low ramp rates followed by a much slower decrease at high ramp rates. The curves shown in the figure are not intended to fit all data sets, but rather to illustrate the two trends. The 50 mm short model magnets have shown similar behavior but somewhat less pronounced.

The collider ring of the SSC was to have been filled with beam from a smaller synchrotron known as the High Energy Booster (HEB) whose dipole magnets were intended to utilize essentially the same design as those of the collider. The HEB was to accelerate beam up to 2 TeV for injection into the collider, at which point the peak current in the dipole magnets would be 6600 A. In order to achieve this acceleration the ramp rate of current in the dipoles was to be 62 A/s. It can be seen from figure 1 that some dipoles exhibiting type B behavior would quench before reaching the peak current planned for HEB operation, while some of those exhibiting type A behavior would reach the required current with inadequate current margin.

II. RAMP RATE STUDIES

In order to study this problem further, a program was initiated between the SSC and Westinghouse Corporation (WEC), the designated contractor for the HEB dipole manufacture. A considerable enhancement in the understanding of ramp rate behavior has resulted [2,3,4].

The combination of cable twist pitch and interstrand resistance produces trapezoidal loops within the Rutherford Cable [4]; ramping the magnet produces eddy currents within these loops. These currents flow through the interstrand resistance generating heating, and superpose to the transport current of one side of the cable. The eddy current distribution within the cable depends upon both the "crossover" resistance of overlapping strands as well as the parallel resistance of side-by-side strands. Furthermore, these resistance values vary along the magnet length as strand surface conditions and interface pressure values change. The combined effect is to produce eddy current induced heating and local enhancement of the transport current, both of which effectively reduce the margin of the conductor.

For type A ramp rate sensitivity it is believed that the interstrand heating dominates. The resistance between strands can be as low as 1 $\mu\Omega$ or less and interstrand heating is uniformly distributed throughout the cable. Eddy current heating within the cable may therefore be fit to the magnet dependence observed.

Type B behavior is less well understood. It is believed that for this behavior, crossover resistance for most of the coil is

relatively high, resulting in loops of large inductance along the cable, which are finally closed by a less frequent low value of interstrand resistance [5]. The result is a greater sensitivity at lower values of ramp rate.

A. Model Magnet Studies

Short versions of the full-length designs allow cost effective and timely testing of most features of full-length magnets. A short dipole program was begun to assess the performance of the WEC dipole design. The magnet cross section consisted of a two-layer $\cos \theta$ design with inner and outer coil sections connected via a ramp splice internal to the coil. The NbTi cable consisted of 30-strand, 0.81 mm diameter 1.3:1 copper to superconductor ratio for the inner coil and 36-strand, 0.67 mm diameter 1.8:1 copper to superconductor ratio for the outer coil. The cable twist pitch was 88 mm. Single strand crossover resistance for the uncoated cable was expected to be of the order of 1 or 10 $\mu\Omega$ based on studies of sectioning of similar magnets [6], while the interstrand resistance of the ebanol-coated cables was expected to be much larger, of the order of 10 m Ω .

The quench performance of the cross section was quite acceptable, with typically two training quenches to plateau. Ramp rate performance of the first two magnets of the series, which had untreated cable, was type A.

III. EBANOL-COATED CONDUCTOR FABRICATION

The practice of insulating adjacent strands or every other strand for the purposes of reducing ramp rate sensitivity is not new; it was first pursued at Fermi National Laboratory while building the Tevatron. That cable was composed of alternating strands with ebanol and stabrite coatings, respectively. Ebanol is a commercial copper-oxide-based coating material which converts a copper surface to a robust copper-oxide coating. The stabrite coating is a silver-tin solder coating. This cable configuration is commonly referred to as "zebra" because of the alternating black and "white" appearance.

For this study, two cable configurations were prepared in order to determine the resulting effects of the coatings on the ramp-rate-dependent quenching of short SSC dipole magnets. The first is identified as "panther" cable (every strand coated with ebanol) and the second is identified as "tiger" cable (alternate strands were left uncoated). The magnet mechanical design performed sufficiently well so that changes to improve training were unnecessary. Thus, the comparisons in ramp rate performance due to cable coating alone could be evaluated. Unfortunately, funding was terminated for the SSC project during the program and only the results for the panther versus bare cable can be presented here.

Strands of Inner wire, taken from a single production unit, were used for this set of magnets. Sufficient wire for four complete sets of Inner coils was used. Approximately two-thirds of the wire was coated with ebanol using a commercial dipping process. The strands were uniformly coated with

ebanol upon return from the vendor. The wires had a high degree of debris on the strands due to deposition of the ebanol onto the spools during the processing. The wires were thoroughly cleaned with alcohol wipes on the respooling line prior to the fabrication of the cables.

Bare copper strands were spliced onto the front of each of the coated strands as a leader which was used to set up the appropriate cable parameters prior to fabricating the actual cables. This turned out to be ineffective, since the surface friction of the ebanol-coated strands is sufficiently different as to require a new set of cabling machine parameters to produce the cables with the coated strands. The set-up for both the panther and tiger cables was quite similar but were very different from cables made with bare copper strands.

III. TEST RESULTS

The ramp rate sensitivity measured on the ebanol-coated cable magnet, known as DSB703, is shown in figure 2. The first two magnets produced in the series, which have no coating on the cable, are also shown for comparison.

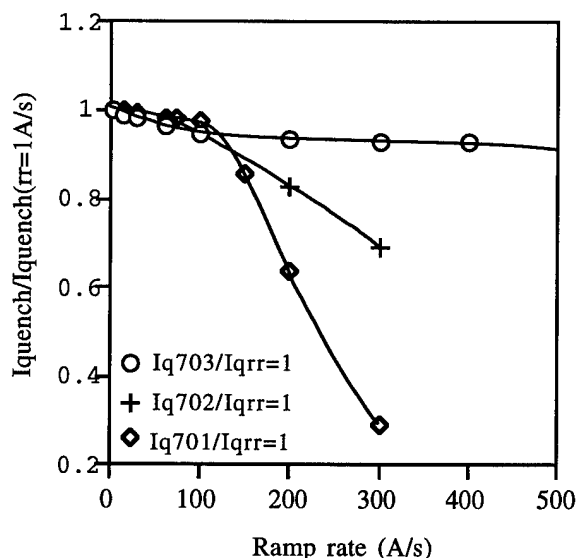


Figure 2: Quench current dependence on ramp rate for ebanol-coated and uncoated cable magnets.

The plateau (field limited) currents for DSB701,2 and 3 are 7758 A, 8058 A and 7914 A, respectively. For comparison of ramp rate performance, figure 2 shows the quench currents as fractions of the plateau current. The plateau currents were measured at low ramp rates ~ 1 A/s where ramp rate induced heating effects can be neglected.

AC losses measured on the uncoated and coated cable magnets are shown in figure 3. Eddy current losses have been reduced from 1.15 J/m/cycle/(A/s) to 0.58 J/m/cycle/(A/s). Bipolar losses are shown, as the magnet was intended for bipolar use.

The hysteresis losses remain the same as expected and provide a convenient verification of the two measurements.

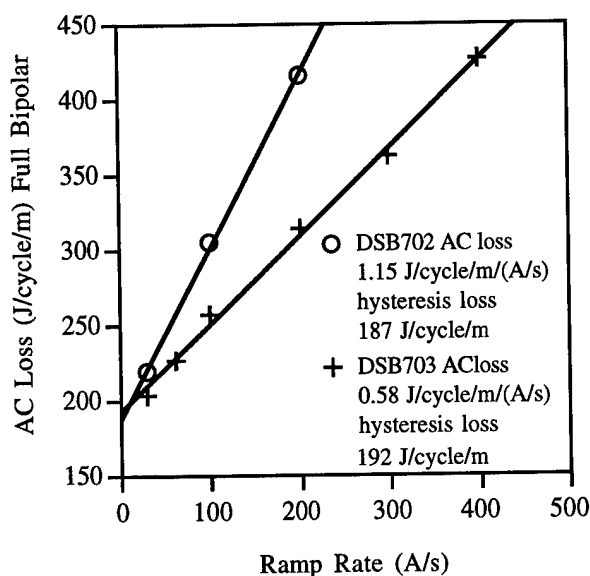


Figure 3: AC loss data for ebanol-coated and uncoated cable magnets.

A. Discussion

It can be seen that the ebanol-coated cable has a type B behavior, which was somewhat unexpected. This may be explained by mechanical instability of the ebanol insulation, which during cable fabrication and coil winding results in small areas of bare cable and low interstrand resistance. Although ramp rate sensitivity at the higher ramp rates has been significantly reduced, at the lower rates one has the situation we wished to avoid. It would appear that the solution is to have a uniformly distributed crossover interstrand resistance in order to induce type A behavior, but to keep the value high enough such that extreme behavior (somewhat shown by DSB701) is avoided. This may be accomplished by coating the cable with a different material which has a relatively high resistivity and yet does not wear off the strand during the cable and magnet fabrication processes, resulting in the type B behavior observed.

IV. CONCLUSIONS

A program of short magnet fabrication has allowed us to compare the ramp rate performance of a magnet design where only the coating on the magnet cable was changed. Coated cables show promise for the control of ramp rate sensitivity and ac losses.

V. REFERENCES

- [1] J. Tompkins et al, "Summaries of Quench vs Ramp Rate Studies on Full length 50 mm Dipole Magnets" SSC Internal Publication MD-TA-241 January 1992.
- [2] V. T. Kovachev, M. J. Neal, D. W. Capone II, and W. J. Carr Jr., "Interstrand Resistance of SSC Magnets" Cryogenics 34 Number 10 1994 pp 813-820.
- [3] G. T. Mallick Jr., W. J. Carr Jr., J. M. Toms, V. T. Kovachev, "Eddy Currents in Superconducting Rutherford Cables" Accepted for publication in Cryogenics.
- [4] W. J. Carr Jr., and V. T. Kovachev, "Interstrand Eddy Current Losses in SSC Magnets". Accepted for publication in Cryogenics.
- [5] W. J. Carr Jr., G. T. Mallick Jr., and V. T. Kovachev, "Theory of the Quench Current of B type SSC Magnets". Westinghouse STC Internal report, Pittsburgh Pennsylvania September 30, 1994.
- [6] V. T. Kovachev, M. J. Neal, J. Seuntjens, J. Madison, S. Graham, P. Cline, D. W. Capone II, and M. Wake, "Interstrand Resistance of Selected Sections of DCA312". SSC Internal Publication SSCL-651 November 1993.

COMBINED ELEMENT MAGNET PRODUCTION FOR THE RELATIVISTIC HEAVY ION COLLIDER (RHIC) AT BNL*

S. Mulhall, H. Foelsche, G. Ganetis, A. Greene, E. Kelly, S. Plate, E. Willen
Brookhaven National Laboratory, Upton, New York 11973-5000

The production of 432 combined element magnets for RHIC is well underway. These magnets consist of a superconducting corrector, a quadrupole, and a sextupole combined into an integrated cold mass which is inserted into a cryostat. Production experiences as well as test results are reported.

DE-AC02-76CH00016.

issues and problems that are common to industry. In addition to technical issues that occur, these include problems of scheduling, manpower, documentation, parts deliveries, and Quality Assurance.

I. INTRODUCTION

A total of (432) 80-mm aperture combined element magnets (CEM) are currently being fabricated at Brookhaven National Laboratory for installation into the RHIC ring. To date, (40) assemblies have been completed, with (60) additional units in various stages of assembly. These CEM's consist of various combinations of corrector, quadrupole, and sextupole elements, assembled together into a common cold mass containment and vacuum vessel. The majority of these magnets (294) are CQS assemblies, containing all three elements (see Fig. 1).

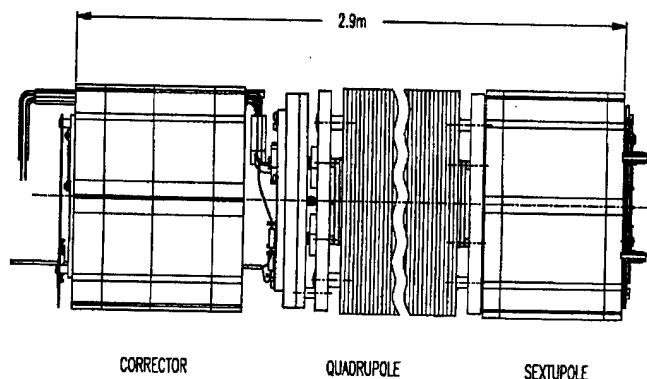


Fig. 1. CQS elements

The quadrupole and sextupole elements are manufactured industrially; the corrector elements are manufactured in-house at Brookhaven. The CEM program takes these three individual elements and assembles them, along with dozens of other components, into a single complete unit, ready for installation into the RHIC ring. Brookhaven elected to build the CEM in-house because of the large variety of types required, and the diverse origin of the many component parts.

Undertaking such a large-scale production program "in-house" at Brookhaven has presented a unique opportunity for the laboratory to experience first-hand many of the production related

II. CONFIGURATIONS

The (432) CEM's consist of eighty separate and distinct "models", varying in required quantity from one to eighteen. In addition to the (294) standard CQS assemblies, there are seven other basic CEM types. These other assemblies do not contain the sextupole element and vary in design by incorporating a trim-quadrupole in its place and/or the use of a different length quadrupole element. These CEM's are designated CQT4, CQT5, CQT6, CQ7, CQ8, CQ9, and CQ9 (Special). The total number of different configurations is brought to eighty by the incorporation of the following additional variables:

- Corrector Type (five options)
- Clockwise/Counterclockwise Ring Orientation
- Quench Protection Diode Polarity (Quadrupole)
- Beam Position Monitor Direction (Horiz/Vert/Both)
- Presence of Cryogenic Recooler

III. PRODUCTION

A. Plan

The overall plan for producing CEM assemblies at Brookhaven, and the required tooling, had been developed during the RHIC magnet R&D program over several years. In late 1993, following a pre-production program that consisted of two complete assemblies (using non-production tooling), the present CEM production schedule was developed. An aggressive schedule was adopted, in which production would run for roughly twenty-six months (ending October, 1996). After an initial ramp-up to full production, a magnet delivery rate of one-per-day was targeted as an achievable goal. The sequence of producing the various models was arranged based upon providing the magnets required for the RHIC sextant test by early 1996 while minimizing perturbations to the production line due to tooling changeovers.

Detailed manpower plans were developed and coordinated with other Brookhaven magnet construction programs. A full-scale Quality Assurance program was implemented, encompassing virtually every aspect of the upcoming production: parts procurement, material control,

*Work supported by U.S. Department of Energy under Contract No.

production travelers, discrepancy reporting system, etc.... Magnet assembly drawings and procedures were developed (and continue in development as production of different models begins).

Production readiness reviews were held in mid-1994 with Brookhaven scientists and engineers. Two independent production reviews were conducted including experts from private industry, and their recommendations incorporated into the program. Production of the first magnet began in June, 1994.

B. Process

The CEM is designed to incorporate many subsystems required in the machine into a single integrated unit that can be assembled and tested in a factory setting. Tooling is set up to provide accurate alignment between components, to minimize manual labor, and to reduce assembly errors. CEM assemblies are built to fit into specific positions in the RHIC lattice.

The CEM production process begins with the initial assembly of the individual elements onto a common fixture and the wiring of the center element (quadrupole) (Fig. 1). A fully automated dual-head MIG machine is used to weld the stainless steel shells around the elements. Subsequent assembly stations align and weld the end plates and support cradles. Electromechanical assembly comes next, including installation of

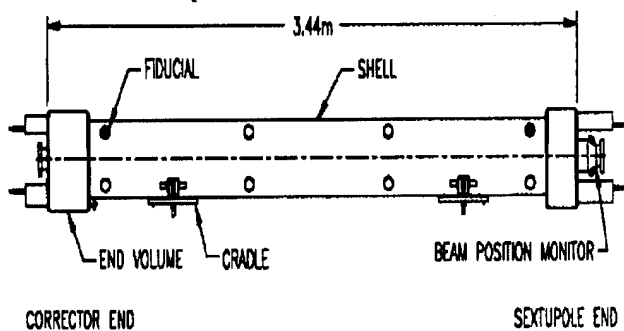


Fig. 2. CQS cold mass assembly

the quench protection diode for the quadrupole. The beam tube/beam position monitor assembly is then installed, and the cold mass end volumes welded in place (Fig. 2).

The next critical step is measurement of the alignment between the individual cold mass elements, followed by fiducial installation. This operation is performed on a granite surface plate using digital-mechanical instruments reading directly into a computerized data-base. The reliability of the measurements taken during this process has improved significantly since the start of the program, and will likely continue to evolve as data accumulates and opportunities for improvement occur. Following these alignment measurements, the completed cold mass is pressurized internally to 345 psig, while simultaneously drawing a vacuum on the outside. Leak tightness down to 2×10^{-10} Std-cc He/sec is thus assured.

Insulation blankets, pipes, heat shield, and support posts are then assembled to the cold mass and the entire sub-assembly is inserted into its vacuum vessel (Fig. 3). Final electrical connections and polarity checking are then completed. The

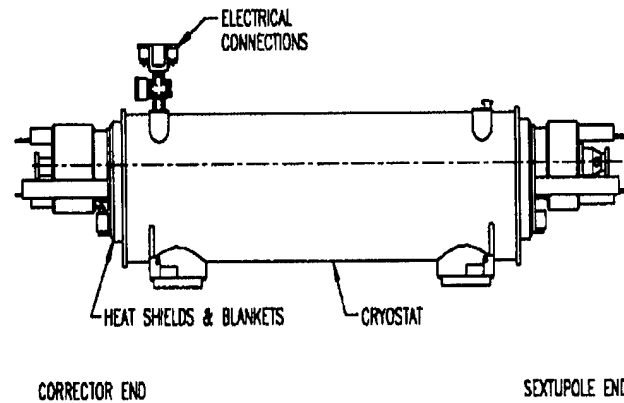


Fig. 3. Completed CQS assembly

finished assembly is vacuum leak tested and, following warm magnetic measurements, ready for delivery to either horizontal cold testing or directly to the RHIC ring.

IV. STATUS & EXPERIENCE

The CEM program is close to schedule with regard to magnets under construction, but has fallen behind in terms of completed units. This shortfall is primarily due to parts delivery problems. These delivery problems have only recently been resolved, and an aggressive effort is being made to clear the backlog of partially assembled magnets.

To date, some twenty-three CQS magnets have been successfully cold tested in the horizontal test facility. Corrector and sextupole elements have been ramped to the limit of their leads (20% above their maximum operating current), with only one quench among all the magnets. Quadrupole elements consistently quench at 7.5 kA with little training, 50% above their nominal operating current. Note that CQS quadrupole quench currents are below those obtained for the individually tested quadrupole elements because of the heat load from the warm finger inserted into the CQS for magnetic measurements [1].

In bringing the CEM production program to this point, the following experiences, in the nature of "lessons learned", are noteworthy:

A. Tooling

he ability to build pre-production magnets using the final production tooling would have resulted in a significantly smoother start-up in the actual construction program. Tooling shake-outs and modifications contributed to delays in program start-up.

B. Parts

The issue of parts availability has proven to be more difficult than anticipated. Some of these issues are attributable to allowing insufficient lead time to the vendors, but most are not. Problems related to the major contracts run the gamut from vendors simply falling behind schedule to their outright inability

to produce parts to specification. These problems represent the primary reason for the program having fallen behind schedule. It is unclear whether these problems could have been mitigated by more diligent up-front efforts (e.g. using Requests for Proposals and technical evaluation boards). Given current government contracting procedures and the fact that private industry is similarly plagued by problems of this nature, it may well be that these situations should be classified as "essentially unavoidable".

In any event, it is apparent that Brookhaven staff was too optimistic in this regard, and in the future should be more cautious.

C. Technical Issues

Relatively few technical issues have arisen during the initial production phase, and these might be classified as "nagging" rather than "critical" in nature.

Perhaps the primary technical issue to-date has been with regard to magnet alignment and distortions caused by welding. One such distortion was noted early-on: the welding of the cold mass support cradles to the shell caused an unacceptable bend in the entire cold mass assembly. It was then necessary to modify the welding procedures so that a roughly equal quantity of weld metal would be added directly opposite to the cradle welding, thus effectively canceling any distortion. Other distortions are caused by the welding of the fiducial discs, and by the welding of the cold mass end volumes.

To help quantify and deal with the welding distortions, it was found necessary to upgrade the alignment measurement data acquisition method. Fiducial measurements, for example, were initially taken mechanically, and recorded by hand; optical surveying was then performed as a check of accuracy. Since performing an optical survey on each cold mass is extremely time consuming, it was decided to upgrade the mechanical system by incorporating digital gauges and a computerized data collection system, generating on-line plots of magnet alignment. Initial results from the new system are very encouraging. It should be noted that the magneto-optical colloidal cell is being utilized on all CEM units as a final check of alignment data [2].

Another technical issue which arose early-on concerned the method of pressure/leak checking the cold mass assembly. A combined test is done, wherein the magnet, suspended in a test dewar, is pressurized internally to 345 psig using helium while simultaneously drawing a vacuum on the outside of the assembly. In this condition, a leak detector monitors the dewar for helium leakage for 15 minutes. A successful test certifies the cold mass assembly to a maximum leak rate of 2×10^{-10} Std cc He/sec. In several instances, leaks have been detected in the cold mass (in the end volumes) that were not previously discovered when the individual component was given only a simple leak check. Under internal pressure, small movements and flexing occurs that reveal leaks that would otherwise go undetected. It is thus concluded that the combination pressure/leak test, replicating the actual in-service condition, is an extremely valuable production step.

V. SUMMARY

Ten months into actual magnet production, the construction of CEM assemblies has reached full-speed, with ongoing deliveries to the RHIC ring. Tooling shake-out is complete and assembly technicians are well trained in their tasks. Some vendor problems remain and are being dealt with appropriately. A way has been found to deal with the technical issue of distortions caused by welding. Though start-up took longer than anticipated, the program appears poised for a successful run, with completion on or near schedule.

VI. ACKNOWLEDGEMENTS

We acknowledge with pleasure the hard work and technical expertise of our industrial partners Northrop Grumman Corporation and Everson Electric.

VII. REFERENCES

- [1] J. Wei et al., "Field Quality Evaluation of the Superconducting Magnets for the Relativistic Heavy Ion Collider," Proc. PAC '95.
- [2] D. Trbojevic et al., "Alignment and Survey of the Elements in RHIC," Proc. PAC '95.

FIELD QUALITY CONTROL THROUGH THE PRODUCTION PHASE OF RHIC ARC DIPOLES

R. Gupta, A. Jain, S. Kahn, G. Morgan, P. Thompson, P. Wanderer, E. Willen
Brookhaven National Laboratory, Upton, NY 11973, USA

Abstract

The field quality in the arc dipoles built thus far for the Relativistic Heavy Ion Collider (RHIC) not only meets machine requirements¹ but is significantly better than that expected from scaling laws based on previous large scale superconducting magnet production for particle accelerators. In this paper we describe the evolution of the present cross section and the design philosophy that has led to these improvements. The techniques described here have been found quite efficient to adopt in the production environment, where schedule and cost considerations become important. Moreover, the techniques developed during the R&D program have resulted in making the saturation induced harmonics negligible, despite the fact that the iron is very close to the coil.

I. INTRODUCTION

The Relativistic Heavy Ion Collider being built at the Brookhaven National Laboratory will require 288 superconducting dipole magnets in the arcs. The cross section of these magnets is shown in Figure 1 and the basic design parameters are given in Table I. About half of them are already built by Northrop-Grumman Corporation and the field harmonics are measured². The field harmonics are defined in the following relation:

$$B_y + iB_x = 10^{-4} B_0 \sum_{n=0}^{\infty} [b_n + ia_n] \left(\frac{x + iy}{R_0} \right)^n,$$

where B_x and B_y are the components of the field at (x, y) and B_0 is the central field. a_n are the skew harmonics and b_n are the normal. R_0 is the normalization radius which is chosen to be 25 mm in these magnets.

Table I
Basic design parameters of RHIC arc dipoles

Coil inner, outer radius	40 mm, 50 mm
Yoke inner, outer radius	59.7 mm, 133.4 mm
Field, current at injection	0.40 T, 0.57 kA
Maximum design field, current	3.46 T, 5.09 kA
Computed quench at 4.5° K	8.25 kA
Magnetic length at 3.46 Tesla	9.44 m

The major sources of harmonic content in superconducting magnets are : (a) *Geometric multipoles* due to a non-ideal magnet geometry, (b) *Persistent current induced multipoles* due to

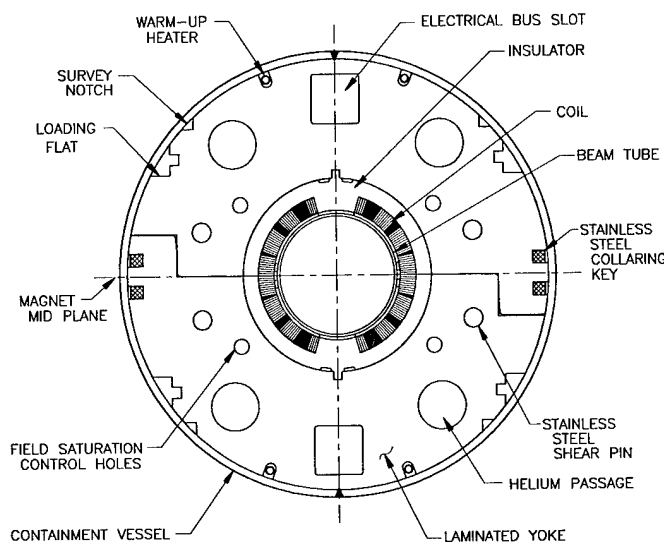


Figure 1. The cross section of the RHIC arc dipoles.

the superconducting properties of the cable, (c) *Saturation induced multipoles* due to non-linear properties of the iron yoke, (d) *Coil deformation multipoles* due to changes in the shape of the collared coil due to Lorentz forces.

II. COIL DESIGN ITERATIONS

To obtain a high field quality such as that measured in RHIC magnets, the conductors must be placed at the appropriate location to an accuracy of $\sim 50 \mu\text{m}$ ($0.002''$). However, after the coils are manufactured, they go through significant deformation during curing, collaring and cool down processes and there is no direct control on where an individual turn will exactly go. The mechanical deformation in the coil and iron shape during manufacturing is not calculable to a combined accuracy of $50 \mu\text{m}$. To overcome this limitation, we empirically remove the influence of these distortions by calculating the offsets in measured field harmonics from the computed values after including all known sources. These offsets are subtracted out during the cross section iterations. In addition, the required changes in the iterated design are specified in terms of relative changes in dimensions as compared to the previous design so that the errors in tooling etc. get subtracted out.

The successful outcome of this approach is clear from Table II where the measured averages for the allowed harmonics are given for the Prototype, Phase 1, Phase 1A and Phase 2 dipoles. The Phase 1 cross section was the initial cross section used in the first 19 industry-built magnets which was based on the cross section used in the last two prototype magnets built at BNL. The coil midplane gap was deliberately made larger by 0.05 mm than the required³ minimum value of 0.10 mm. This

*Work supported by the U.S. Department of Energy under the contract No. DE-AC02-76CH00016.

was to compensate for a potential change in field quality associated with the change in tooling between the prototype and industry built magnets. An adjustment in the midplane gap is much more powerful than an alternate method of adjusting coil pole shim, particularly for the crucial b_4 harmonic. In fact, this adjustment got quickly implemented in the Phase 1A cross section (used in the next 86 magnets), when the coil midplane gap was changed from 0.15 mm to 0.10 mm to reduce b_4 . The change in midplane gap back to 0.15 mm together with a change in one wedge by $63.5\mu\text{m}$ was incorporated in the Phase 2 cross section. The current production is proceeding on this design and 24 dipoles are included in Table II. In all cases good agreement has been found between the calculations and measurements.

Table II

The average and RMS values of field harmonics in various cross section designs for RHIC arc dipoles. The b_2 harmonic is given at the maximum field (3.46 T) and the other harmonics at injection (0.4 Tesla). The measured warm cold correlation of 40 magnets is used to estimate harmonics in 129 magnets measured warm.

Design	b_2	b_4	b_6	b_8
Prototype	1.3 ± 0.8	0.3 ± 0.2	-0.1 ± 0.05	0.40 ± 0.03
Phase 1	0.4 ± 1.6	-1.0 ± 0.4	-0.38 ± 0.09	0.20 ± 0.06
Phase 1A	1.2 ± 1.2	-0.4 ± 0.30	-0.10 ± 0.08	0.24 ± 0.03
Phase 2	-0.3 ± 1.3	0.1 ± 0.32	-0.21 ± 0.09	$0.00 \pm 0.03a$

Table III

The computed changes in the values of harmonics produced by a systematic azimuthal error of $+25\mu\text{m}$ ($0.001''$) in crucial parts in RHIC arc dipoles.

Parameter	δb_2	δb_4	δb_6	δb_8
Wedge 1	-0.98	-0.122	0.061	0.043
Wedge 2	0.69	0.423	0.022	-0.050
Wedge 3	1.42	-0.090	-0.068	0.041
Pole Width	-1.11	0.154	-0.039	0.014
Midplane Gap	-1.68	-0.557	-0.156	-0.050

In RHIC magnets, the specified tolerances in the dimensions of the most crucial parts are typically $\pm 25\mu\text{m}$ ($0.001''$). In Table III we list the harmonics produced by a systematic $+25\mu\text{m}$ azimuthal error in the three wedges, pole width and the coil midplane gap. The coil midplane can not have such a large error and is given for $25\mu\text{m}$ only for consistency. Moreover, field harmonics are also created by other parts used in the magnets, such as the errors in yoke dimensions etc., but they are generally expected to have a smaller impact on harmonics. In a few magnets the spacers used between the coil and iron were just outside the thickness tolerance and caused a noticeable change in the transfer function².

The harmonics in Table II are comparable to those in Table III. This suggests that the harmonics are not limited by the design

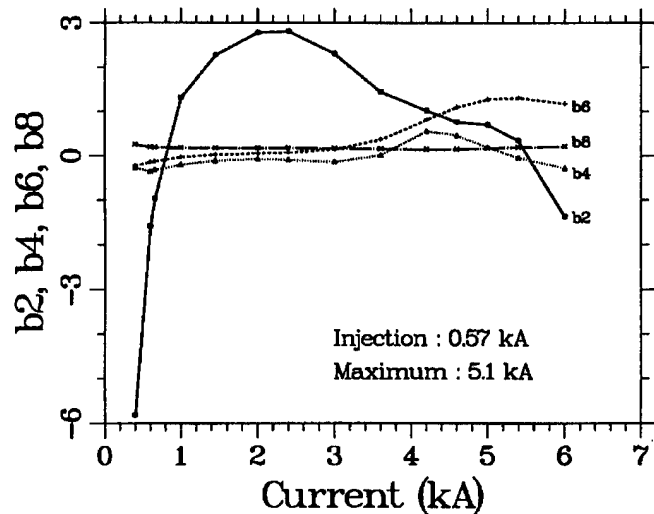


Figure 2. The measured current dependence of harmonics during up ramp (and 20 second wait) in RHIC arc dipoles.

and that these are probably the best harmonics one may hope for with reasonable values of mechanical tolerances and normal variations in the manufacturing process.

III. YOKE DESIGN ITERATIONS

In RHIC magnet designs, the yoke has been brought very close to the coil in an attempt to get the maximum contribution from the iron. The conventional wisdom against such attempts in the past had been that the saturation induced harmonics would become unavoidably large. However, the results from RHIC magnets show that despite a high ($\sim 35\%$) contribution from iron (50% to 100% higher than those used in major accelerator magnets) the saturation induced harmonics can be controlled to a small value. In Figure 2, we have plotted the average values of field harmonics as a function of current during the up ramp in 129 magnets. Only 40 of them are actually measured cold and for others an already well established warm-cold correlation from 40 magnets is used². The dominant source for the current dependence below 2 kA is the persistent current in the superconductors, whereas above 2 kA it is the iron saturation and the change in coil and iron shape when Lorentz forces are unloading the pre-compression on the coil. In the present cross section, the deviation from the average in the design range of operation is ± 2.5 unit in b_2 and ± 0.4 unit in b_4 . These values are comparable to those generated by $\pm 25\mu\text{m}$ error in more than one part (Table III). Except for the b_2 harmonic, all harmonics were optimized at the injection field. The b_2 harmonic was minimized at the maximum field where it is 2.5 units higher than at the injection. In addition, the variation in them is also minimized at the intermediate fields. The saturation induced b_6 harmonic was not optimized, as long as it did not become too large.

In Figure 3, we show the current dependence in the b_2 and b_4 harmonics in various yoke designs. The harmonics are an average of up and down ramps to remove the persistent current induced harmonics to first order. Also, an offset is added in each magnet so that they coincide at 2 kA for easy comparison. One

can see an order of magnitude improvement.

The first yoke design was used in four (DRA series) magnets – the last one (DRA004) had a minor modification at the yoke outer surface. This cross section had a coil locating notch at the pole and a small coil-to-yoke gap of 5mm. Both of these features contributed to a large saturation. In the second design, used in two (DRB series) magnets, the coil-to-yoke gap was increased to 10 mm and the notch was moved to the midplane to reduce saturation. Then in the next two (DRC series) magnets, the material of the yoke-yoke alignment key was changed from non-magnetic stainless steel to magnetic steel. This made b_2 very small and b_4 significantly smaller but still large enough to require the external decapole correctors. Moreover, in order to improve the coil pole definition/location, it was decided to move the coil locating notch back to the pole from the midplane. At this stage, the yoke cross section was completely redesigned for the next two (DRD series) magnets and b_4 saturation was made small enough to consider dropping the decapole correctors from the lattice. However the pole notch, as expected, gave a relatively large b_2 saturation. Finally, a saturation control hole was added at a critical location near the yoke inner radius in the last two prototype magnets (DRE series) to make saturation induced b_2 and b_4 practically zero. However, in the DRG series yoke design, which is used in the industrially built magnets, the material of the yoke-yoke alignment key was changed from the magnetic low carbon steel to non-magnetic stainless steel to match the thermal contraction of the shell during cool down. The location of the saturation control hole was changed to compensate for extra saturation introduced by this change.

In the RHIC arc dipoles, the cold mass is not vertically centered in the cryostat. At high field this creates a skew quadrupole harmonic of ~ 2 units. In the present design, the yoke weight difference between the top and bottom halves is adjusted to compensate for this effect.

IV. CONCLUSIONS

The R&D program carried out at Brookhaven has resulted in a significant improvement in field quality of the critical arc dipole magnets for RHIC. In Figure 4 the net field error on the midplane in these magnets is compared with the similar aperture dipoles for other large accelerators.

References

- [1] J. Wei, et al., "Field Quality Evaluation of the Superconducting Magnets for the Relativistic Heavy Ion Collider", this conference.
- [2] P. Wanderer, et al., "Construction and Testing of Arc Dipoles and Quadrupoles for the Relativistic Heavy Ion Collider (RHIC) at BNL", this conference.
- [3] R. Gupta, et al., "Field Quality Improvements in Superconducting Magnets for RHIC", 1994 European Particle Accelerator Conference.
- [4] S. Peggs, "Private Communication."

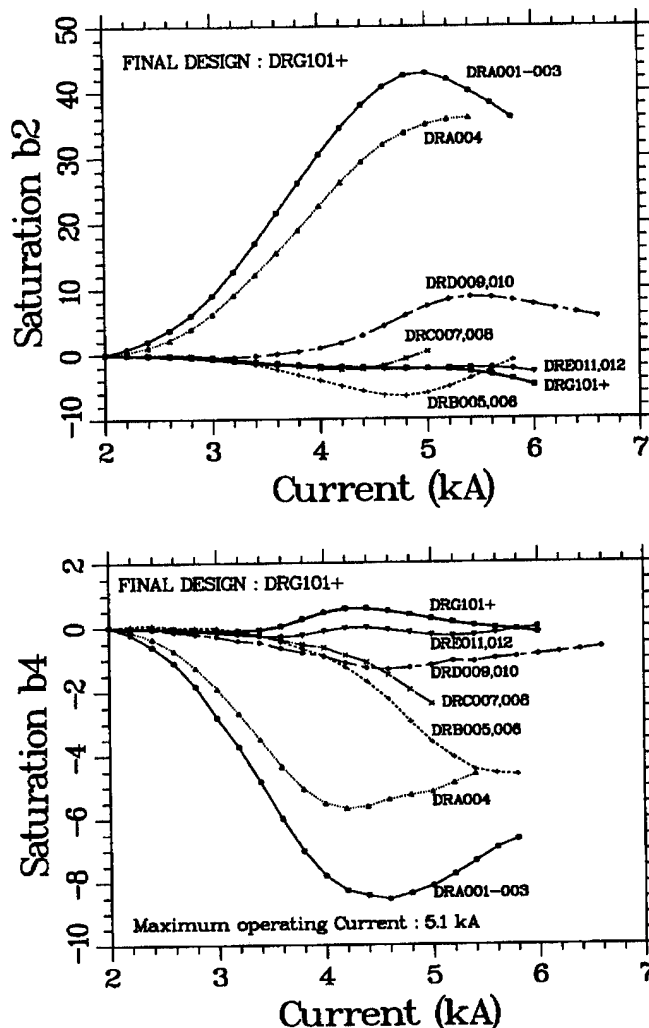


Figure 3. The current dependence of b_2 and b_4 in various designs of RHIC arc dipoles after removing the persistent current effects.

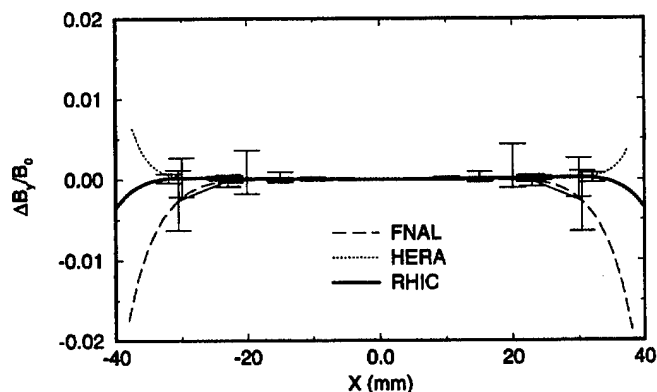


Figure 4. The field error at top operating field on the midplane of the 80 mm aperture RHIC arc dipoles compared with 76 mm aperture HERA and 76.2 mm aperture Tevatron dipoles. The error bars show the RMS variations. (Courtesy S. Peggs⁴ and J. Wei).

THE ELLIPTICAL MULTIPOLE WIGGLER PROJECT

E. Gluskin, D. Frachon, P.M. Ivanov, J. Maines, E.A. Medvedko, E. Trakhtenberg, L.R. Turner,
and I. Vasserman,
APS Division, Argonne National Laboratory, Argonne, IL, 60439

G.I. Erg, Yu.A. Evtushenko, N.G. Gavrilov, G.N. Kulipanov, A.S. Medvedko, S.P. Petrov,
V.M. Popik, and N.A. Vinokurov,
Budker Institute of Nuclear Physics, Novosibirsk, Russia, 630090

A. Friedman, S. Krinsky, G. Rakowsky and O. Singh,
NSLS, Brookhaven National Laboratory, Upton, NY, 11973

ABSTRACT

The elliptical multipole wiggler (EMW) has been designed, constructed, and installed in the X13 straight section of the NSLS X-ray Ring. The EMW generates circularly polarized photons in the energy range of 0.1-10 keV with AC modulation of polarization helicity. The vertical magnetic field of 0.8 T is produced by a hybrid permanent magnet structure with a period of 16 cm. The horizontal magnetic field of 0.22 T is generated by an electromagnet, the core of which is fabricated from laminated iron to operate with a switching frequency up to 100 Hz. There are dynamic compensation trim magnets at the wiggler ends to control the first and second field integrals with very high accuracy throughout the AC cycle. The residual closed orbit motion due to the electromagnet AC operation is discussed.

I. INTRODUCTION

An elliptical multipole wiggler with an AC electromagnet has been selected for the NSLS X-Ray Ring to generate x-ray radiation in the energy range of 0.1-10 keV with time-dependent polarization [1,2]. The AC elliptically polarized wiggler will make it possible to detect the very weak signatures of circular dichroism and other effects associated with right- vs. left-handedness of some physical systems. In order to generate polarized photons near the upper limit of the energy spectrum, the vertical deflection parameter K_y should approach a value of about 12, corresponding to a hybrid wiggler peak field of 0.8 T. Since there is a trade-off between the on-axis photon flux and degree of circular polarization, the horizontal parameter K_x should be optimized for each specific experiment. For this electromagnet, the maximum design value of K_x is about 2.5 at a current of 1 kA.

Originally, the EMW as a source of circularly polarized photons was proposed by Yamamoto and Kitamura [3]. Their device consisted of permanent magnet wigglers with crossed fields capable of generating circularly polarized radiation with higher harmonics on the wiggler axis. The next step in the development of EMW design was made by Walker and Diviacco [4] who suggested replacing the horizontal permanent magnet structure by an AC electromagnetic wiggler to modulate in time the helicity of the on-axis circularly polarized radiation.**

To increase the measurement accuracy of the asymmetry between the effect of left and right circularly polarized radiation, the modulation frequencies should be located in the

** The first proposal to use an electromagnet to vary the helicity of undulator polarized radiation was made by Onuki [5].

ranges with the minimum spectrum power density of closed orbit noise. From this point of view, for the NSLS X-ray Ring, the preferable modulation frequencies are:

$$0 < f_{\text{mod}} < 10 \text{ Hz and } f_{\text{mod}} \sim 100 \text{ Hz.}$$

Great care has been taken in the design of the EMW to minimize the orbit disturbance generated by its operation. The following requirements for field integrals of the electromagnetic structure have been imposed:

$$\int_0^{L_w} B_x(z, t) \cdot dz \leq \pm 1 \text{ Gauss} \cdot \text{cm} \quad (1)$$

$$\int_0^{L_w} d\tilde{z} \int_0^{\tilde{z}} B_x(z, t) \cdot dz \leq \pm 100 \text{ Gauss} \cdot \text{cm}^2 \quad (2)$$

Where $B_x(z, t)$ is the AC horizontal magnetic field, z, \tilde{z} are longitudinal coordinates, and L_w is the wiggler length.

In the X-Ray Ring, these field integral limitations restrict the vertical closed orbit motion to be less than 1.5 micron. These requirements are applied for the modulation frequency range up to 100 Hz and must hold throughout the AC cycle. Both wiggler magnetic structures were optimized in a magnetostatic approximation by means of the 3-D code TOSCA. The computer simulations of power dissipation due to eddy currents induced in the design elements of EMW were carried out with the 3-D code ELECTRA.

II. HYBRID STRUCTURE

The vertical magnetic field is produced by a hybrid wedge-pole configuration consisting of Nd-Fe-B rectangular magnetic blocks and vanadium-permendur wedge poles. One pole and two permanent magnets form a half-period block, each of which is mounted on an iron backing beam between iron "neutral" poles having zero scalar potential (Figure 1.)

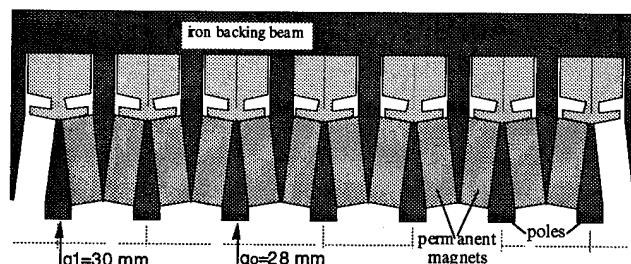


Figure 1. The wedge-pole hybrid configuration

Five full-field and two half-field poles produce a mirror-symmetric magnetic field distribution with a period length of 16.0 cm. A peak field magnitude of 0.8 T at a minimum gap g_0 of 28.0 mm was achieved. The nonsteering termination was realized with the magnetic gap g_1 increasing by 2 mm at the half-field poles. The upper and lower hybrid assemblies are attached to independent drive trains, providing a continuously variable gap motion from a minimum of 28.0 mm to a maximum of 160 mm. At an extreme AC regime, when the electromagnet is energized with 100 Hz alternating current with an amplitude of 550 A, the computed total losses due to eddy currents induced in the vanadium-permendum poles, the permanent magnets, and the iron "neutral" poles can reach about 60 W per wiggler period.

III. ELECTROMAGNETIC STRUCTURE

The electromagnetic structure generates a periodic alternating horizontal magnetic field of antisymmetric configuration in order to provide the periodic vertical beam trajectory deflection along the wiggler. The electromagnet includes six uniform poles with a magnetic gap of 54 mm and end structures consisting of two poles at each side. The current excitation is provided by means of two water-cooled, "snake-type" coils [6] with a copper cross section of about 140 mm². The magnetic gaps of the end structure poles and number of turns around the first and last poles are different from those in the main periodic structure. This end structure performance was designed to attain a nonsteering {first field integral, Eq. (1)} and a displacement-free {second field integral, Eq. (2)} termination provided that the pole strength pattern is close to theoretical 1/4 : 3/4 : 1. The iron cores of the first and last poles are separated from the main yoke and are provided with adjusting systems to vary their magnetic gaps. To reduce the generation of eddy currents, the yoke of the electromagnet was constructed from 0.5-mm-thick laminations of transformer iron with a silicon content of 3.5%. At the extreme regime ($I=0.55$ kA and $f_{\text{mod}}=100$ Hz), the computed power loss does not exceed about 5 W per wiggler period.

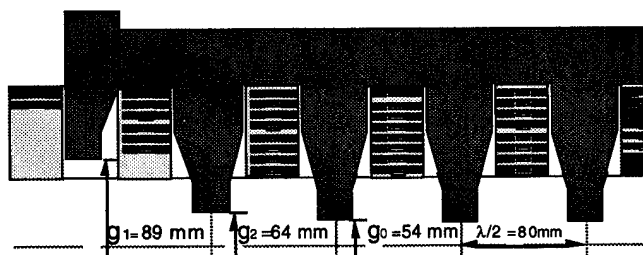


Figure 2. Electromagnetic structure design.

IV. VACUUM CHAMBER

The vacuum chamber of the EMW was manufactured by the deformation of a stainless steel circular pipe to an elliptical cross section of inner dimensions: major axis of 50 mm and minor axis of 25 mm. To decrease the eddy current losses in the vacuum chamber, a wall thickness of 0.6 mm was chosen as the minimum possible from a mechanical collapse point of view. The power dissipation computed by ELECTRA does not exceed 0.8 W per wiggler period at the extreme AC regime.

V. POWER SUPPLY FOR ELECTROMAGNET

The principle of forced DC current commutation is used in the power supply for the electromagnetic structure. It consists of a thyristor-stabilized DC power supply as an initial current source and a commutator based on the fast thyristor bridge-inverter. The bridge-inverter output is connected to the electromagnet coil in parallel with capacitor. This scheme is designed to supply the electromagnet by direct current or by trapezoidal shape alternating current with a switching frequency range from 0 up to 100 Hz. The switching time (current polarity reversing time) does not exceed 2 msec, and it retains the same duration up to the upper limit of switching frequencies. The power supply can provide an output current range of 0.2 - 1.2 kA with the current magnitude difference between both polarities less than 0.5%.

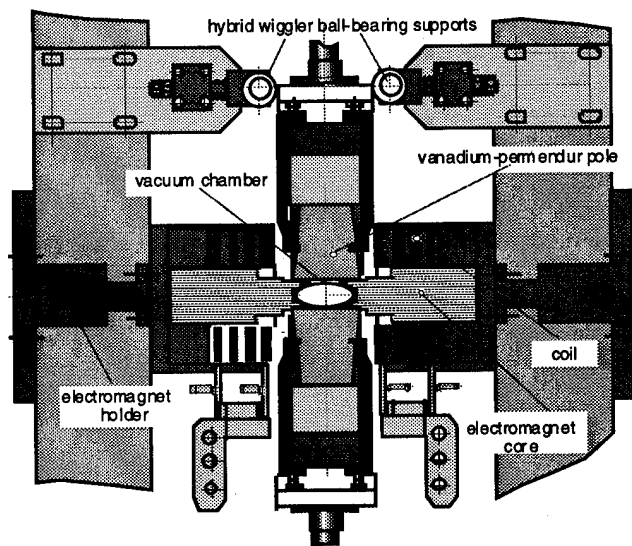


Fig. 2. Side sectional view of the elliptical multipole wiggler.

VI. TIME-DEPENDENT WIGGLER FIELD INTEGRALS

The electromagnet design includes some nonuniformities related mostly to anti-symmetric locations of the coil current leads. In turn, these nonuniformities give rise to a disturbance of the ideal antisymmetric magnetic field configuration at both ends of the electromagnetic structure. This effect has been corrected easily for DC operation by means of the passive gap adjusting systems at the end poles. However, during switching, periodic time-dependent components arise for both the first and second field integrals. Due to the slightly different geometry of the electromagnet ends, the eddy currents induced in the copper turns, the iron elements of hybrid structure, and the vacuum chamber lead to different magnetic field time delays along the wiggler, hence, to different conditions of field integral compensation at each time moment.

On the other hand, the surroundings of the electromagnet include some conductive elements with a thickness a few times the skin depth at frequencies corresponding to the switching time (0.5 kHz). As the switching frequency is increased, the time of magnetic field diffusion through these materials becomes comparable or greater than a half-period of current pulse. It is obvious that the time-dependent

components of integrated fields should have different behaviors and magnitudes for each range of switching frequencies. Besides, there is a relatively weak saturation in periodic structure poles that can cause a nonlinear behavior of the time-dependent field integral components at the higher current amplitudes (above 0.6 kA).

Moreover, a strong magnetic coupling between both magnetic structures leads to time modulation of the field integrals in the hybrid wiggler. This effect was experimentally observed during magnetic field measurements. Because electromagnetic poles are arranged directly opposite to the "neutral" poles of hybrid structure, some part of the magnetic flux shunts into the adjacent iron. The magnetization of the thin "neutral" pole tips alternates periodically with the horizontal field. Consequently, in the areas of the tip that are magnetically saturated, there is a time modulation of the magnetic conductivity in the perpendicular direction. This, in turn, leads to a time variation of the integrated field in the hybrid structure. The magnitude of the vertical field time-dependent component has a complicated nonlinear dependence on the magnetization amplitude but its sign does not depend on the sign of alternating magnetization field. Results of magnetic field measurements for both structures at the DC and AC electromagnet modes are presented in detail in [8]. The above mentioned reasons forced us to develop an active system for dynamic compensation of the time-dependent integrated field components.

VII. DYNAMIC COMPENSATING SYSTEM

The active system consists of two trim magnets mounted at each side of the EMW and separately powered by computer-controlled special bipolar power supplies (BPS). The sum of the electromagnet shunt signal and synchronous arbitrary function generator (AFG) signal is used as a reference voltage for the BPS. As a result, the current of each trim magnet follows the current shape in the electromagnet main coil during the entire AC cycle. Since the time-dependent components of field integrals are periodic in time and rigidly connected to switching frequency, the trim magnet current wave form can be corrected by a synchronous pulse with a programmed shape (AF). The AF technique was originally developed for the APS synchrotron correction magnets [7] and has been incorporated in this active system. The shape of the AF is based on magnetic measurement data but can be programmed using the information from storage ring BPMs. Results of the compensation of the time-dependent integrated field by the active system obtained at the magnetic measurement stage are described in [8].

VIII. BEAM STUDIES AT NSLS X-RAY RING

The first beam studies have been carried out at modulation frequencies of 2 and 100 Hz. The effect of the EMW on the tune shift and beta-function distortion is negligibly small. For the beam orbit distortion studies, a number of tools, such as the NSLS X-ray Ring BPMs, spectrum analyzer, and photon beam monitor, were used. Dynamic compensation of the time-dependent integrated field of electromagnetic structure has been attained within the requirements expressed by Eqs. (1) and (2) at the 2 Hz AC mode and current amplitude of 0.4 kA. With the active system switched off, the initial rms amplitudes of the closed orbit oscillation reached:

$$a_y \approx 13\mu \text{ and } a_x \approx 4.9\mu.$$

Using the compensation current feedback additionally corrected by the AFG, the vertical orbit motion was suppressed down to an rms amplitude of 1.1 micron. After turning on the storage ring global feedback, the residual rms amplitudes of the beam orbit noise corresponding to modulation frequency of 2 Hz were reduced and did not exceed:

$$a_y \leq 0.2\mu \text{ and } a_x \leq 0.5\mu.$$

These spectrum amplitudes correspond to the beam orbit angle rms errors at the straight section within the angles of:

$$\Delta y' \leq \pm 0.75 \cdot 10^{-7} \text{ rad and } \Delta x' \leq \pm 2 \cdot 10^{-7} \text{ rad}.$$

It is necessary to note that the horizontal orbit motion caused by the time-dependent field component of the hybrid wiggler was suppressed only by means of global feedback. At the 100 Hz AC mode, the compensation of the horizontal time-dependent component related to the second field integral is in good agreement with the magnetic measurement data. The corresponding residual spectrum amplitude of beam noise did not exceed 1.1 micron. However, there were some difficulties in compensating the time-dependent first integral component. The beam orbit motion measurement synchronized with the switching frequency showed a phase misalignment between the AF and current pulses. Probably, this effect was due to a lengthening of transmission line between the EMW and power supply that caused changing of the current pulse rise rate. Since the global feedback is not effective at frequencies as high as 100 Hz, a new 2-D compensation active system is being developed to suppress the time-dependent field integral components of both the electromagnetic and hybrid structures. A 2-D Panofsky's-type dipole has been chosen as an optimal trim magnet for the new active system. This system is under construction, and it will be installed in the EMW in the near future. After its adaptation, the beam studies at the frequency of 100 Hz will be continued to attain the restrictions for orbit motion specified by Eqs. (1) and (2) for both the horizontal and vertical betatron plane.

IX. ACKNOWLEDGMENTS

Work performed under contracts W-31-109-ENG-38 and DEAC-02-76-CH-00016 of the US Department of Energy.

X. REFERENCES

- [1] A. Friedman, S. Krinsky, E. Blum, "Polarized Wiggler for NSLS X-ray Ring Design Consideration", BNL-47317 Informal Report, March, 1992
- [2] A. Friedman, X. Zhang, S. Krinsky, E. Blum, and K. Halbach, Proc. of IEEE Part. Acc. Conf., Washington, D.C., May, 1993, p.1599.
- [3] S. Yamamoto and H. Kitamura, Japan. Journal of Applied Phys., Vol.26, October, 1987, pp. L1613-L1615.
- [4] R. Walker and B. Diviacco, Rev. Sci. Instrum., Vol. 63, No.1(Part IIA), January, 1992, pp. 332-335.
- [5] H. Onuki, NIM A246, 1986, pp. 94-98
- [6] N.G. Gavrilov et. al., "Electromagnetic undulators for the VEPP-3 optical klystron", NIM A282, 1989, p. 422.
- [7] O.D. Despe, "Arbitrary Function Generator for APS Injector Synch. Correct. Magnet", ANL, LSN-158, Nov. 1990
- [8] D. Frachon et. al., "Results of Magnetic Measurements and Field Integral Compensation for the Elliptical Multipole Wiggler", APS, ANL., this conference.

Results of Magnetic Measurements and Field Integral Compensation for the Elliptical Multipole Wiggler

D. Frachon, P. M. Ivanov, E. A. Medvedko, I. Vasserman, O. Despe, Y. G. Kang
APS, Argonne National Laboratory, Argonne, IL 60439

I. ABSTRACT

A prototype of the Elliptical Multipole Wiggler (EMW) [1] has been assembled, tested and tuned at the APS. This prototype has a period of 160 mm with 7 poles for the hybrid structure and 10 poles for the electromagnet part of the EMW. The hybrid structure of the EMW produces a vertical magnetic field of 0.83 T with $K_y = 12$ for a gap of 27 mm, and the electromagnetic structure provides a horizontal field change up to 100 Hz with a maximum field of 0.12 T ($I = 0.6$ kA, $K_x = 1.6$). The current pulse has a trapezium-type shape with a switching time to change the current polarity of about 2 ms. The measurements and tuning were done for direct current (DC) mode and alternating current (AC) mode. Fine adjustment during the test at the NSLS X-ray ring using the BPMs and active correction system allowed to achieve about 1 μ m of beam distortion. It corresponds to the peak-to-peak variations during the time less than ± 0.5 G-cm and ± 100 G-cm² of the first and second horizontal field integrals respectively.

II. INTRODUCTION

Two different correction systems were used to adjust the first and the second field integrals dependence on time. A passive correction system includes manually adjustable gaps for the end poles. The adjustment of the first horizontal field integral was performed by moving the gap of each end pole in the opposite direction. The adjustment of the second horizontal field integral was performed by moving the gap of each end pole in the same direction without distortion of the first field integral due to the antisymmetric configuration of the device. The active correction system is based on the use of a set of two trim magnets mounted on each end of the device. The magnet coils are fed by a power supply with an arbitrary function generator [2].

III. MAGNETIC MEASUREMENT TECHNIQUE

The conventional Hall probe technique was used for measurements of the magnetic field distribution in the longitudinal direction. The rotating coil magnetic measurement technique was used for field integral measurements. Actually the rotating mode was necessary only for the DC mode. For the AC mode, the FAST 16-1 ADC board was used with a sampling time of 0.1 ms for a frequency of 100 Hz. The CTM05 board was installed on the PC bus and used to generate pulses to define the frequency of the power supply and to trigger the FAST 16-1 ADC board to synchronize measurements. The integration of the signal from the coil provides the flux dependence on time through the coil. The most important part of the EMW measurements is the

field integral dependence of electromagnetic structure on time for the AC mode. Measurements of the second field integral by the usually applied technique of measuring the field map are very time consuming. The reason is that such measurements are based on the step-by-step motion of magnetic sensors along the main axis of the device and on time-dependent measurements at each point. That is why a novel technique using a twisted long coil was used for fast and precise magnetic measurements of second field integrals [3].

IV MAGNETIC FIELD MEASUREMENTS

The results of Hall probe measurements of the vertical and horizontal field distributions are shown in Fig. 1.

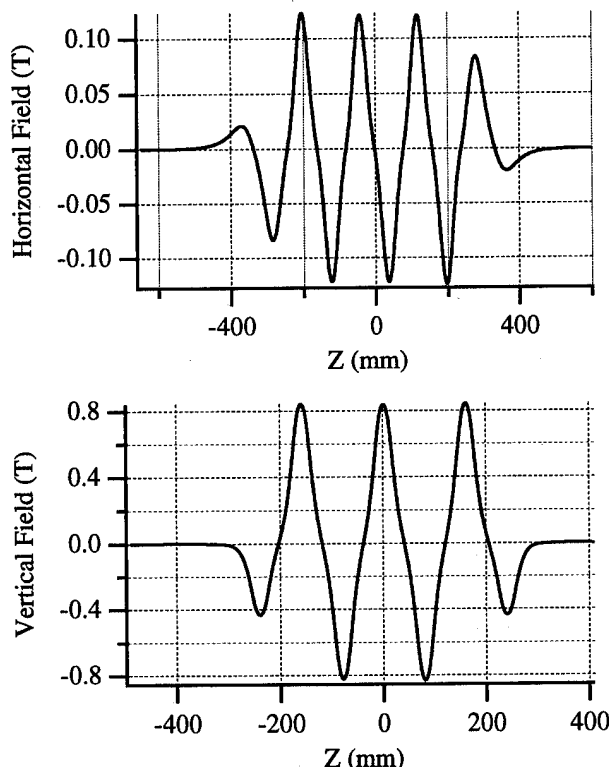


Fig. 1. Horizontal and Vertical Field vs. Z

It is important that we have very tight requirements for the average horizontal first field integral at regular parts of the device, which is usually not important. Due to the AC operational mode, the averaged angle of trajectory changes its sign according to current polarity. This results in the requirement that this angle be much less than the particle angle spread of the beam, that is $2 \cdot 10^{-4}$, in order not to distort the radiation quality of the device. Thus the strength of the field of the last and next-to-last end poles was chosen to make the trajectory as close to ideal as possible. The result of

the calculation of the second horizontal field integral from the Hall probe data is shown in Fig. 2.

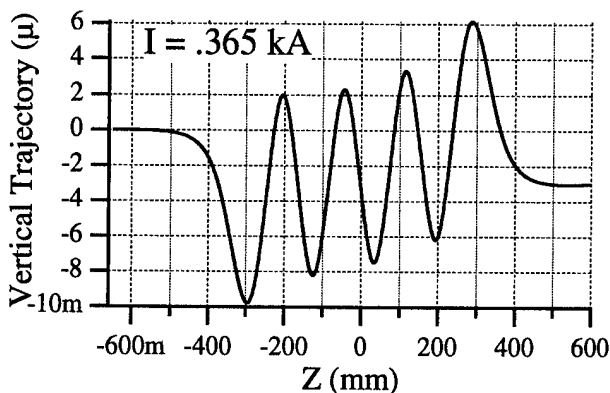


Fig. 2. Vertical Trajectory in the DC mode

V. FIRST FIELD INTEGRAL MEASUREMENTS

A conventional long coil with parallel wires was used for first field integral measurements. For measurements of hybrid structure and of the electromagnet in the DC mode, coil rotating at 360° was used. Actually these measurements were complementary to the main set of measurements that was done in the AC mode without rotating the coil. The results of the AC first horizontal field integral measurements are shown in Fig. 3 with active correction on and off. The first horizontal field integral change during the cycle is less than 10 G-cm without active correction and less than 1 G-cm with active correction switched on.

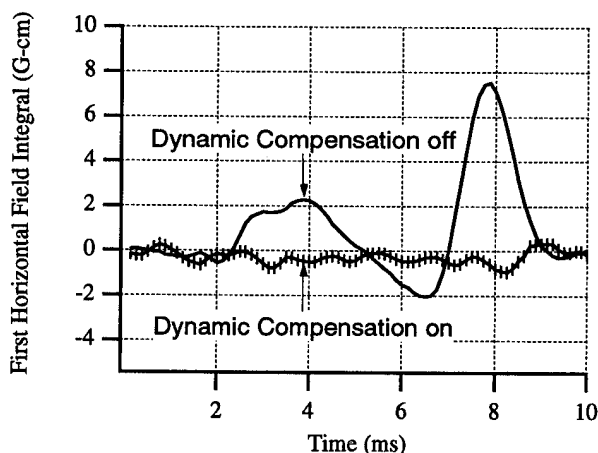


Fig. 3. First Horizontal Field Integral vs. Time. $f = 100$ Hz

The time dependence of the field integrals can be divided into two parts:

1. DC part. This part is a result of different signs of the current and can be easily adjusted by choosing the proper gaps for the end poles. This part manifests mainly for low frequencies (less than 10 Hz).
2. AC part. The length of this part is much longer than the switching time (2 ms) and is about 50 ms. It is due to an eddy-current-produced delay of the field penetrating to the air space. Small differences in the design produce different delay times for different parts of the device and result in field integral dependence on time. The only way to correct for this

is to apply an active system fed by a special power supply with an arbitrary function generator. Both parts of the first field integral time dependence can be easily seen at a frequency of 1 Hz (Fig. 4) without dynamic correction. Only the DC part was adjusted here by means of a passive end-correction system.

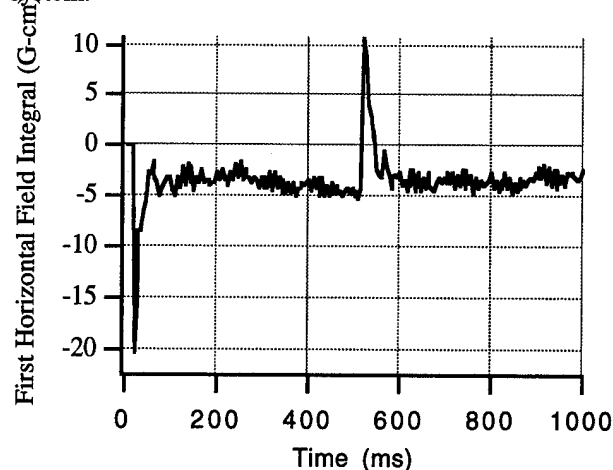


Fig. 4. First Horizontal Field Integral vs. Time. $f = 1$ Hz

The dependence of the first and second vertical field integrals on time exists due to the saturation effect of the electromagnetic field on hybrid structure. There was no active correction system for the vertical direction at the time of the measurements, and the change in the field integral therefore is bigger than that for the horizontal direction. The first vertical field integral change during the cycle is less than 45 G-cm. The results of the measurements of the AC first vertical field integral are shown in Fig. 5

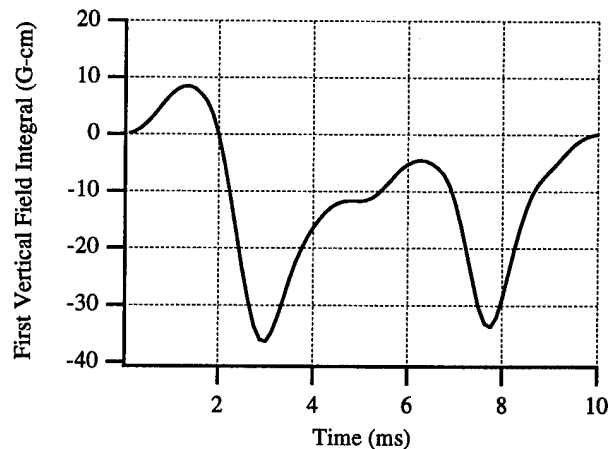


Fig. 5. First Vertical Field Integral vs. Time. $f = 100$ Hz

VI. SECOND FIELD INTEGRAL MEASUREMENTS

Coil twisted by 180° was used to obtain the second field integral from these measurements. At such a configuration, the expression for the second field integral dependence on the measured magnetic flux and the first field integral is [3]:

$$I_2(L) = -\frac{\Phi}{\Theta} + L \cdot I_1(L), \quad \text{where: } I_1(L) \text{ and } I_2(L) \text{ are the}$$

first and second field integrals, respectively; Φ is the magnetic flux through the coil; L is the half length of the coil; and Θ is the crossing angle of the coil. This expression becomes especially simple and allows one to achieve the most reliable and precise results in the case in which the first field integral is equal to zero.

The results of second field integral measurements are shown in Fig. 5 at a frequency of 100 Hz. Change in the second horizontal field integral during the cycle is less than 4000 G-cm² without active correction and about 1000 G-cm² with active correction switched on. Change in the second vertical field integral change during the cycle is less than 3000 G-cm².

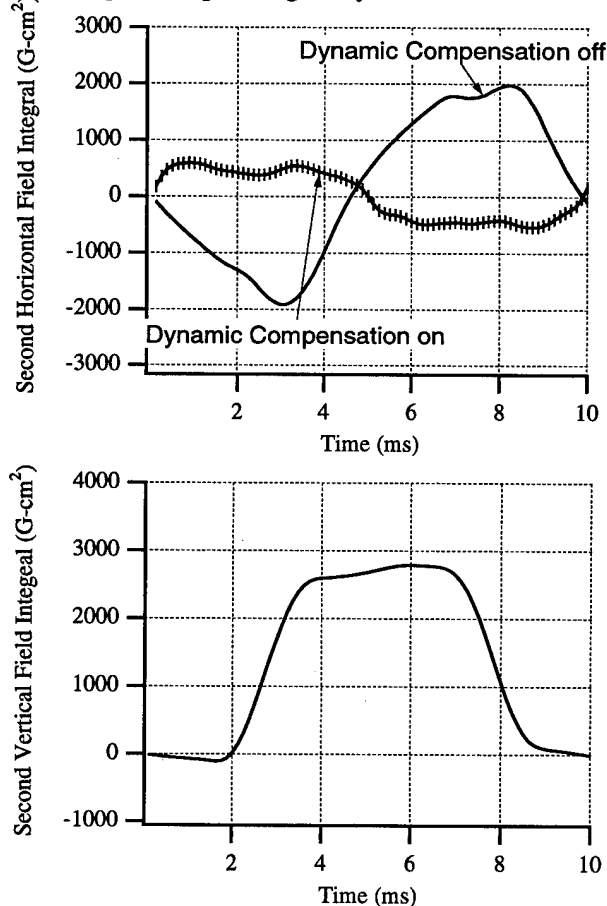


Fig. 6. Second Horizontal and Vertical Field Integral Dependence on Time. $f = 100$ Hz

VII. INTEGRATED MULTIPOLE COMPONENTS

There were no special requirements for multipole components, but this question is rather important from the point of view of beam life time and beam dimensions in the storage ring. So a set of measurements was performed in order to obtain the dependence of the first field integral on the horizontal position (X) for both the AC mode and the DC mode. The DC mode originates mostly from the hybrid structure, and the AC mode originates from the electromagnetic part and time-dependent part of the hybrid structure due to a saturation effect induced by the electromagnet. The results of measurements of the DC

mode obtained from the rotating coil measurements are shown in Table 1.

Table 1. Integrated Multipole Components at DC mode

Skew components

Quadrupole (G)	Sextupole (G/cm)	Octupole (G/cm ²)
183.	29.	29.4

Normal Components

Quadrupole (G)	Sextupole (G/cm)	Octupole (G/cm ²)
48.3	-383.	0.23

The results of the time-dependent part of the multipole components are shown in Table 2. For each X position, the dependence of the first field integral on time was obtained and the RMS value was calculated. The results, shown in Table 2, correspond to dependence of these RMS values on X.

Table 2. Integrated Multipole Components in the AC mode

Skew Components

Quadrupole (G)	Sextupole (G/cm)	Octupole (G/cm ²)
-1.38	11.6	-13.8

Normal Components

Quadrupole (G)	Sextupole (G/cm)	Octupole (G/cm ²)
0.13	4.39	0.91

VIII. CONCLUSION

The first tests of the EMW at the NSLS X-ray ring with frequencies of 2 Hz and 100 Hz were successful and showed rather good performance of the device [1]. Further improvements in vertical magnetic field are possible with the help of an additional set of trim magnets. This system is under construction now and will be incorporated into the EMW later.

IX. ACKNOWLEDGMENTS

Work performed under contracts W-31-109-ENG-38 and DEAC-02-76-CH-00016 of the U.S. Department of Energy.

IX. REFERENCES

1. E. Gluskin et al. "The Elliptical Multipole Wiggler Project," This conference
2. O. D. Despe, "Arbitrary Function Generator for APS Injector Synchrotron Correction Magnets," PAC-1991, San-Francisco
3. D. Frachon, I. Vasserman, P. M. Ivanov, E. A. Medvedko, E. Gluskin, N. A. Vinokurov. "Magnetic Measurements of the Elliptical Multipole Wiggler Prototype," ANL/APS/TB-22, March 1995 (unpublished)

STATUS OF ELETTRA INSERTION DEVICES

R. P. Walker, R. Bracco, A. Codutti, B. Diviacco, D. Millo and D. Zangrando
Sincrotrone Trieste, Padriciano 99, 34012 Trieste, Italy

The design, construction and testing of the fourth ELETTRA insertion device, undulator U8.0, is described and some details are given of recent developments of a "phase shimming" technique and of a new "moving wire" system for insertion device integrated field measurements.

I. INTRODUCTION

The ELETTRA storage ring will shortly contain four insertion devices, three pure permanent magnet undulators (U) and one hybrid multipole wiggler (W). The main parameters of the devices are summarized in Table 1. The first three devices are each composed of 3 separate sections, with a total length of approximately 4.5 m, and the values in the table refer to the present minimum operational gap in the storage ring. The latest device (U8.0) consists of a single section which will be installed at the beginning of May this year.

Table 1. Main parameters of the ELETTRA Insertion Devices; the number following U/W indicates the period length in cm. N = number of periods.

ID	N	Gap (mm)	B_0 (T)	K
U12.5	36	28.0	0.506	5.91
U5.6	81	27.0	0.444	2.34
W14.0	10	26.0	1.30	17.0
U8.0	19	25.0	0.713	5.33

The construction of the first three devices have been reported previously [1,2,3] and the initial operation in ELETTRA has been described in ref. [4].

II. UNDULATOR U8.0

Undulator U8.0 was designed to cover a very wide photon energy range from 250 eV to 8 keV, with operation at 2 GeV. Below about 2 keV the device operates in an undulator mode, (variable gap) and above 2 keV in a wiggler mode (fixed minimum gap). The parameters were optimized for the final vacuum vessel which will permit a minimum gap of 20 mm; in an initial phase the minimum gap will be 25 mm. A period length of 8 cm was selected as a compromise between the conflicting requirements to optimize the undulator (short period length) and wiggler (long period length in order to maximize the field amplitude) modes. A standard pure permanent magnet arrangement of 4 blocks per period with 40 mm block height was used. A block width of 100 mm was chosen to obtain a field roll-off at minimum gap given by $k_x/k < 0.1$, where $B_y = (1 - k_x^2 x^2/2) \cos(kz)$. The mechanical design of the magnetic arrays is the same as used for the U5.6 device [2]: blocks are clamped into individual holders, which are

assembled onto 0.5 m long baseplates, which are then mounted on the 1.5 m I-beams of the standard support structures.

NdFeB permanent magnet blocks were obtained from Outokumpu magnets (NEOREM 450i), with an average measured magnetization of 1.17 T and minimum intrinsic coercive force of 1400 kA/m. The estimated remanent field, taking into account the average working points of the different block types, is 1.19 T. The blocks were passivated and oiled to prevent corrosion. Each block has been measured in detail in the two possible orientations that were allowed for assembly using a small Hall plate bench dedicated to block measurements. Both transverse field components were measured at a grid of points, 81 points in z over ± 2 period lengths and 13 points in x over ± 60 mm; the vertical height (y) corresponded to the future minimum gap of 20 mm. About 15 minutes were required for each block and about 3 weeks to measure all 190 blocks. A reference block was measured each day in order to guarantee that there were no changes in conditions during the measurement period.

Data from the measurements were used in a "simulated annealing" program to optimize the block configuration, based on linear superposition of the fields of different blocks. The cost function to be minimized included the following terms: first and second field integrals of both field components at all x positions within ± 60 mm, r.m.s. phase error and trajectory straightness separately for the top and bottom arrays [5].

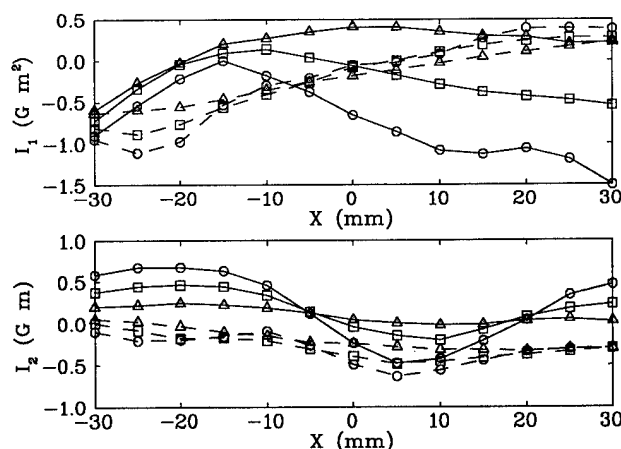


Figure 1. First (I_1) and second (I_2) field integrals for U8.0, at 20 mm (circles), 30 mm (squares) and 50 mm (triangles) gap, horizontal (dashed) and vertical (solid) planes.

Measurements after assembly confirmed the accuracy of the block measurements and sorting procedure: the variation of horizontal (x) and vertical (y) first and second field integrals with transverse position (x) were within the specified ± 1 Gm and ± 2.5 Gm² within ± 25 mm, as shown in fig. 1

The r.m.s. phase error was also acceptable : 2.7° at minimum (20 mm) gap, 3.0° at 30 mm and 3.3° at 50 mm.

III. PHASE SHIMMING

Further significant improvement of the quality of the undulator, and hence of the radiation output, have been made using a new technique of "phase shimming" [6]. Previously shimming has been applied in such a way to optimize simultaneously both field integral and phase error performance [5]. The new method consists of a separate correction of the phase errors, leaving the field integrals unchanged. With this method we have succeeded in reducing the phase error to the level of 1 degree. Such a value leads to essentially ideal performance up to very high harmonic numbers : on average, a rms error of 1° gives an intensity (on-axis angular flux density, for zero emittance and energy spread) of 80% (50%) of the ideal intensity for the 27th (47th) harmonic respectively [7].

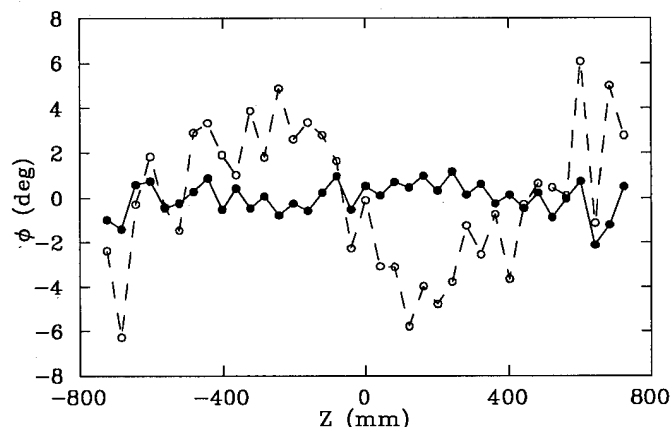


Figure 2. Radiation phase errors at minimum gap, before (dashed) and after (solid) phase shimming for U8.0.

Figure 2 shows the phase errors at each pole of U8.0 before and after shimming and figure 3 shows the corresponding calculated on-axis spectra. The intensities for an ideal undulator (analytic formula) are as indicated. The improvement in phase error and the significant increase in the intensity of the higher harmonics in the radiation spectrum are quite evident.

Table 2. Final magnetic measurement results for U8.0

Gap (mm)	20.0	30.0	50.0
B_ρ (T)	0.895	0.608	0.276
K	6.7	4.5	2.1
σ_B (%)	0.24	0.17	0.19
σ_ϕ (deg.)	0.6	0.9	1.7

Table 2 summarizes the main results of the magnetic measurements obtained after shimming. Some increase in phase error is observed at larger gap, however in this situation high harmonic numbers are unlikely to be used.

Figure 4 shows the calculated electron trajectories, that remain essentially unchanged by the phase shimming.

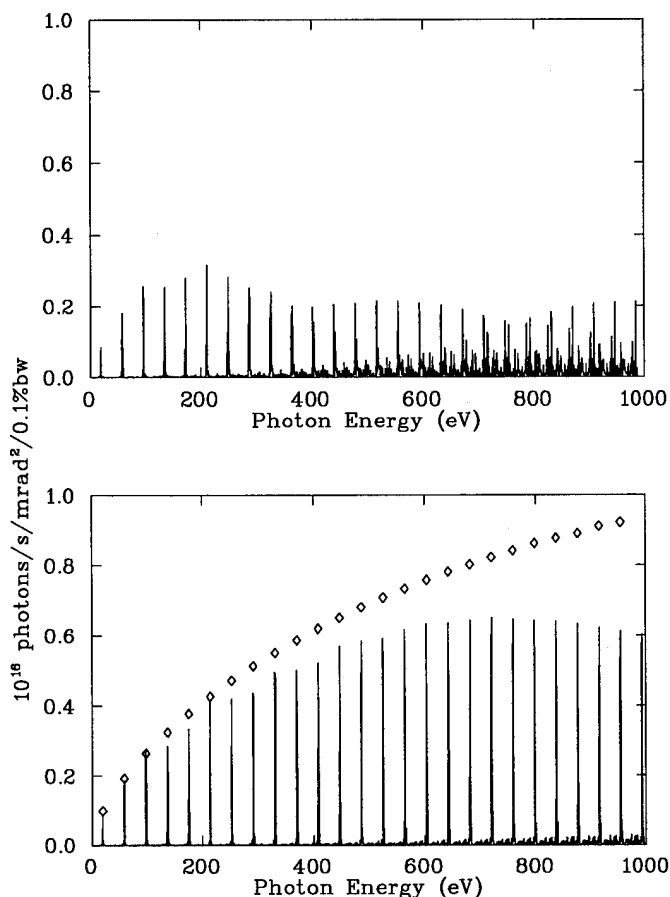


Figure 3. Calculated on-axis spectrum at minimum gap, before (upper) and after (lower) phase shimming for U8.0. The intensities of an ideal undulator are as indicated.

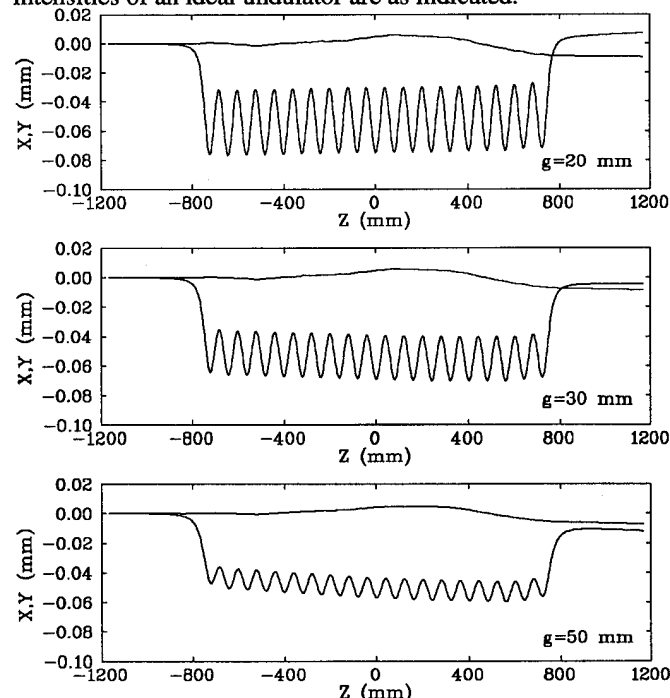


Figure 4. Calculated electron trajectories for U8.0 at various gaps.

To verify the general applicability of the phase shimming technique, further tests have been carried out using the prototype 5.6 cm device constructed in 1992. In this case it proved possible to reduce the rms phase error from an initial 3.7° to 0.8° at minimum gap without affecting significantly the multipole terms, thus giving us confidence that similarly good results can be obtained for future devices. Full details of the technique will be published in a forthcoming report [8].

IV. MOVING-WIRE METHOD FOR INSERTION DEVICE INTEGRATED FIELD MEASUREMENTS

A new method of measuring both first and second field integral distributions and integrated multipole errors has recently been implemented. The previous technique was a flipping coil method, using a coil made from stretched multistrand Litz wire [9,10]. Such a technique yields values of I_x and I_y as a function of transverse position (usually, the horizontal, x). In the new method only a single side of the coil passes inside the magnet, the return being static and outside the magnet. The wire is translated in x or y to yield individual measurements of I_y and I_x respectively at a given point. The advantages of this method for first integral measurements are that it eliminates the sensitivity of the flipping coil output to variations in coil width, and allows a variable integration step (equivalent to the coil width) to be used. It also allows a simple measurement of the second field integrals, by translating the two ends of the wire in opposite directions. Further, by making the wire follow a circular path, the multipole terms can be obtained directly from a Fourier analysis of the integrated voltage as a function of angle. In this way the uncertainties involved in determining the multipole terms from flipping coil data, that result from making a polynomial fit to the $I_x(x)$ and $I_y(x)$ distributions, as well as the smoothing effect of a finite coil width, are eliminated.

In the present case with a 40-turn coil and using a Schlumberger 7061 Voltmeter as an integrator, the reproducibility (rms) of the first and second field integral measurements is 0.02 G m and 0.01 G m² respectively for a wire translation of 10 mm.

For the multipole measurement, a radius of 10 mm is used as standard, reduced to 8 mm at the minimum 20 mm gap, with 16 measurements per 360°. The reproducibility of the single measurement in this case (worst case rms deviation for a series of 10 measurements at various gaps) is 1.8 G cm, 3 G, 4 G/cm, and 6 G/cm² for the dipole, quadrupole, sextupole and octupole terms respectively. An improvement in accuracy can of course be achieved by averaging over a series of measurements. The method is therefore sufficiently accurate to be used as a direct means of determining the multipole terms even in the case of the most stringent tolerance limits.

Table 3 summarizes the results of the multipole measurements of undulator U8.0 made with the new system. The results presented are the maximum absolute values of the normal (B_n) and skew (A_n) multipole coefficients from dipole ($n=1$) to octupole ($n=4$) between 20 mm and 100 mm gap. As

mentioned earlier, the device is within the specified limits as regards the first and second field integral distribution, whereas limits were not set for the individual multipole terms. The normal quadrupole term is the largest error, at minimum gap, however the maximum tune shift introduced (in the horizontal plane) is negligible ($\sim 5 \cdot 10^{-4}$).

Table 3. Maximum multipole coefficients for undulator U8.0.

n	A_n	B_n	units
1	63.	47.	G cm
2	30.	70.	G
3	20.	45.	G/cm
4	< 10	< 10	G/cm ²

V. FUTURE PLANS

The first four insertion devices have been installed with a vacuum chamber that permits a nominal 25 mm magnetic gap (20 mm internal), which is sufficient to give acceptable performance only in the case of U12.5 and possibly also the U5.6 device. A first chamber permitting a reduced gap of 20 mm (15 mm internal) is presently under construction and will be installed this Summer, replacing the existing wiggler vessel, thereby allowing the design field of 1.6 T to be reached. The spare vessel will be used for the 5th device, a second 4.5 m U12.5 undulator that is presently under construction.

It is hoped that the sixth ID to be approved for construction will be an electromagnetic elliptical wiggler. Development of a prototype mini-gap undulator is also being considered.

VI. REFERENCES

- [1] R.P. Walker et. al., Proc. 1993 US Particle Accelerator Conference, p. 1587.
- [2] B. Diviacco et al., Proc. 4th European Particle Accelerator Conference, World Scientific (1994) p. 2250
- [3] A. Codutti et al., *ibid* p. 2253.
- [4] R.P. Walker and B. Diviacco, to be published in Rev. Sci. Instr.
- [5] B. Diviacco, Proc. 1993 US Particle Accelerator Conference, p. 1590.
- [6] B. Diviacco and R.P. Walker, Proc. Second Annual Workshop on Synchrotron Radiation Light Sources, ESRF, Grenoble, Nov. 1994.
- [7] R.P. Walker, Nucl. Instr. Meth. A335 (1993) 328.
- [8] B. Diviacco and R.P. Walker, report in preparation.
- [9] J. Chavanne et al., ESRF-SR/ID-89-27 (Sept. 1989).
- [10] D. Zangrando and R.P. Walker, Proc. 3rd European Particle Accelerator Conference, Editions Frontières (1992) p. 1355.

EXPECTED RADIATION SPECTRA OF A 30-M LONG UNDULATOR IN SPRING-8

M. Takao and Y. Miyahara, SPring-8, Kamigori, Ako-gun, Hyogo 678-12, Japan

I. INTRODUCTION

In addition to 44 straight sections of 5 m long, SPring-8 storage ring comprises four long straight sections of length 30 m. These sections are prepared for insertion devices and highly brilliant quasi-monochromatic photon source is available for experiments in hard X-ray region. In a simple minded expectation, the brilliance of the undulator radiation is proportional to the square of the number of the undulator period. So that we expect a 60 times higher brilliance from a 30 m long undulator compared with a 4 m long undulator. According to a numerical calculation, however, it turn out that the brilliance is not so high as expected. This is because the brilliance is closely related to the emittance of the electron beam.

In this note we study the spectral properties of the synchrotron radiation from a 30 m long undulator. The decreasing rate of the peak intensity of 30 m long undulator in terms of broadening of spectral band width by the electron beam emittance is larger than that of 4 m. To see this fact, we investigate the dependence of radiation intensity on the electron beam emittance. In addition, the dependence on the transverse emittance coupling, i.e. the shape of the electron beam, is also studied.

The spectral formula used in the above investigation is derived by means of the far field approximation. Since in the present case the undulator is relatively long compared to the observing distance, we estimate the near field effect in the radiation intensity.

II. SPECTRAL PROPERTIES OF RADIATION FROM 30 M LONG UNDULATOR

A. Spectrum of 30 m long undulator

In calculating the radiation from 30 m long undulator, electron beam parameters are assumed to be the design values of the storage ring, which are listed Table I.

Table I
Storage ring parameters

Beam energy	8 GeV
Beam current	100 mA
Total emittance	6.89 nm rad
Transverse emittance coupling	10 %
Horizontal beta function β_{x0}	17.5 m
Vertical beta function β_{y0}	19.5 m

We also assume the long planer undulator to be a idealized one with the reasonable parameters given in Table II.

The spectral formula of the radiation from a single electron in a planer undulator is well-known [1], [2], [3]. In order to incorporate the effect of finite size and divergence of electron

Table II
Undulator parameters

Period length	3 cm
Number of periods	1000
K-parameter	1

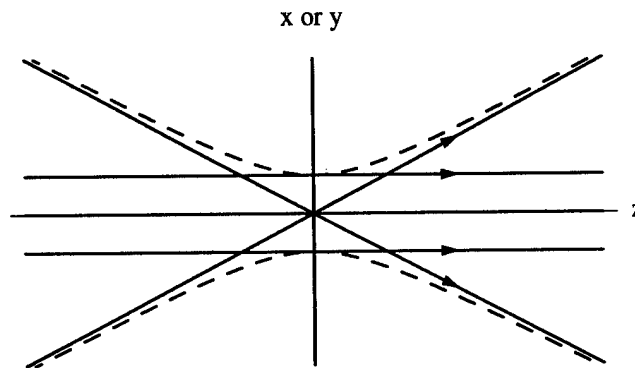


Figure 1. Each straight line corresponds to a mean trajectory of an electron in an undulator. The outer dotted curves indicate the envelope.

beam into the spectral formula, we make convolution of spectral formula with electron distribution [4].

Since a mean trajectory of an electron in an undulator is a straight line, an electron beam is described by a gathering of straight lines (see Fig. 1). Giving a transverse position (x_0, y_0) and a divergence (x'_0, y'_0) of an electron at some location in an undulator, we can designate the mean trajectory. The distributions of electron positions and divergences are determined by the emittance and the Twiss parameters. In usual we place a waist of a beam envelope on the center of an undulator so that the Twiss parameters in the undulator are described by the beta functions at the center of the undulator β_{x0} and β_{y0} . Hence the distributions of electron trajectories in an undulator are given by the transverse emittances and the beta functions β_{x0} and β_{y0} .

Figure 2 shows the angular flux density of the synchrotron radiation from the 30 m long undulator at an observing distance 50 m from the center of the undulator. To compare the spectrum with that of 4 m long undulator, we show its angular flux density in Fig. 3.

The peak value of the fundamental mode of 30 m undulator is only about ten times larger than that of 4 m one, which is expected to be $56.5 (= 1000^2/133^2)$ times larger in case of a single electron. This is supposed to be caused by the broadening effect of spectral band width due to transverse spread of electron beam. To see this fact, we investigate the dependence of the intensity spectrum of the undulator radiations on the transverse emittance.

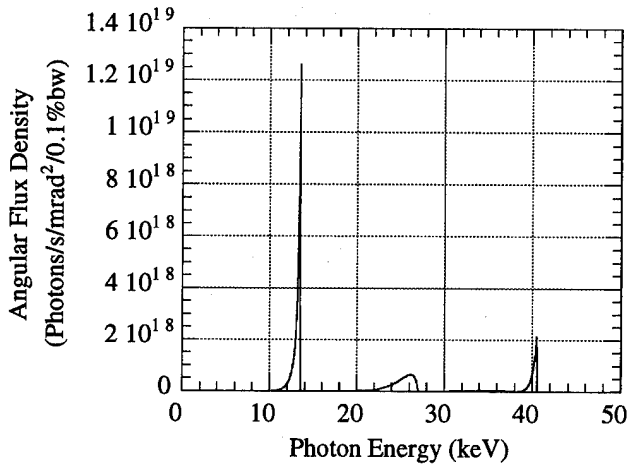


Figure 2. An expected radiation spectrum from the 30 m long undulator up to the third harmonics.

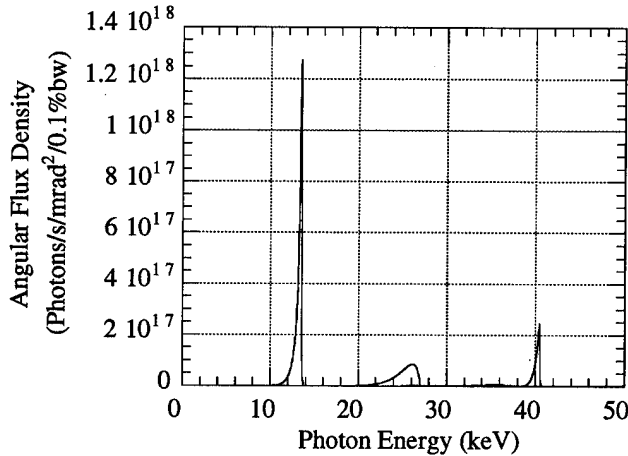


Figure 3. An expected radiation spectrum from the 4 m long undulator up to the third harmonics.

B. Dependence on transverse emittance

Figure 4 shows the emittance dependence of the peak radiation intensities of 4 and 30 m long undulators. We see that at a low emittance the intensity ratio is 56 as expected and that the intensity of the radiation from 30 m long undulator decreases more rapidly than that from 4 m. This is approximately explained as follows.

At a sufficiently low emittance, the broadening effect due to emittance is invisible and then the peak of the radiation intensity scarcely changes. On the other hand, at a large emittance the band width of the radiation spectrum is proportional to the electron emittance. The critical value of the emittance is determined by the band width of radiation spectrum from a single electron. Since the band width of the radiation spectrum of a single electron is inversely proportional to number of undulator periods, the longer the undulator is, the smaller the critical value becomes. Hence, the decreasing rate of the peak intensity is larger for a longer undulator.

For the purpose of utilizing the long straight section efficiently, it is preferable to achieve an electron beam with lower emittance.

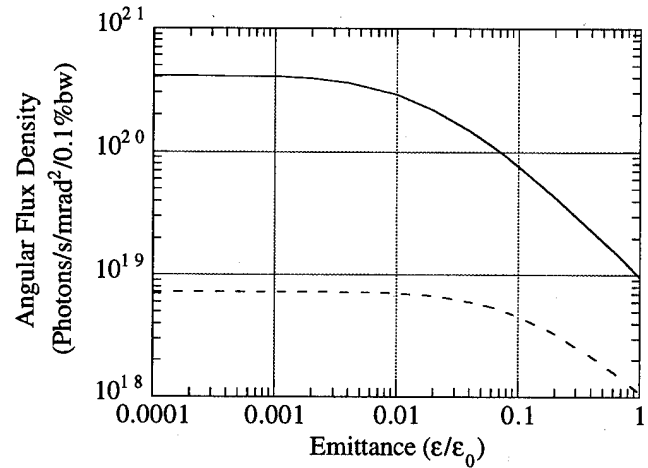


Figure 4. Effect of an electron beam emittance on the peak intensity of fundamental undulator radiation. The emittance is normalized by the design value. The solid line indicates the radiation from 30 m long undulator and the dashed line that from 4 m.

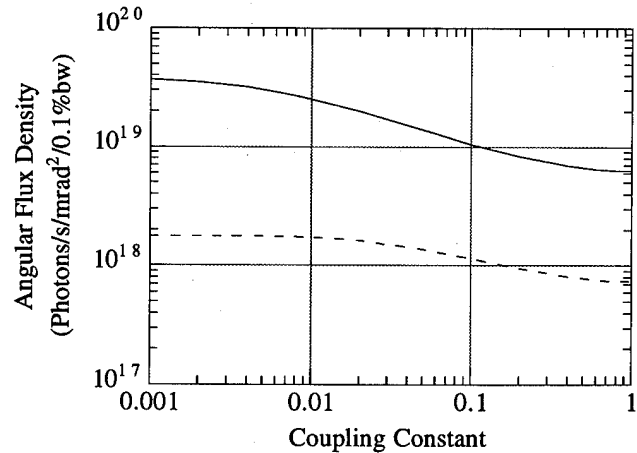


Figure 5. Effect of the transverse emittance coupling on the peak intensity of fundamental undulator radiation. The solid line indicates the radiation from 30 m long undulator and the dashed line that from 4 m.

C. Dependence on the coupling of transverse emittances

In the previous subsection, we saw that the finite emittance significantly reduces the intensity spectrum of undulator radiation. Now we investigate the effect of the electron beam shape, i.e. the transverse emittance coupling, on the spectrum of undulator radiation. In Fig. 5 we plot the peak intensity of the first harmonic radiation versus the coupling constant of horizontal and vertical betatron oscillations. Figure 5 shows that the peak intensity of flat electron beam is larger than that of round electron beam.

As shown in the previous subsection, the smaller the emittance is, the larger the peak value of the intensity spectrum is. If one makes the electron beam flat with keeping the total emittance, the horizontal emittance increases while the vertical one decreases. The increment of the peak intensity due to lowering the vertical emittance overcomes the decrement owing to height-

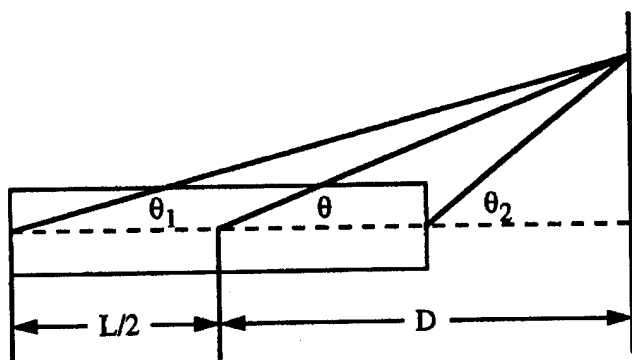


Figure 6. Geometry of near field case.

ening the horizontal emittance. Hence the flatter beam radiates the photon flux with the stronger peak intensity.

D. Near field effect

In the above investigation we used the far field approximation, where we assume the observing distance to be sufficiently large compared to the undulator length. If the observer is located at a finite distance from the center of the undulator, the observation angle varies as the electron travels from the entrance of the undulator to the exit (see Fig. 6). The change of the observation angle gives rise to an additional phase difference to the far field approximation. In the case of the observing distance comparable to the undulator length, the near field effect should be included into the radiation with a large angle between the observation direction and the electron mean trajectory.

Since electron beam has a finite divergence, some electron trajectory possesses a large angle to the observation direction. In the case of 30 m long undulator the length is relatively large compared to the observation distance, so that we investigate the near field effect on the undulator radiation of an electron beam with finite emittance. Fig. 7 shows the angular flux density at an observation distance 50 m, where the solid curve indicates the far field approximation and the circles correspond to the intensity with including near field effect. The spectrum shows that at an observation distance 50 m the near field effect is negligible.

Although the near field effect is remarkable at a neighborhood of the undulator exit, we can ignore the effect at a practical observing distance.

III. CONCLUSIONS

In this note we have studied the spectral properties of 30 m long undulator in SPring-8. The investigation of the dependence of the radiation intensity on the electron beam emittance shows that low emittance is preferable for the long undulator. It is also shown that peak intensity radiated by flat electron beam is stronger than that from round one. Although the length 30 m of the undulator is relatively long, the near field effect can be ignored for our practical observing distance about 50 m.

References

- [1] H. Kitamura, Jpn. J. Appl. Phys. **19** (1980), L185.
- [2] S. Krinsky, Nucl. Instrum. Methods **172** (1980), 73.

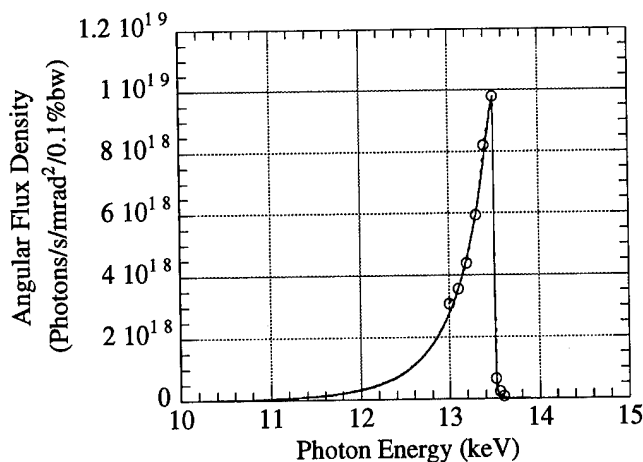


Figure 7. Spectral intensity observed at a distance 50 m. The solid line corresponds to the far field approximation and the circles indicate the intensity including the near field effect.

- [3] S. Krinsky, M.L. Perlman and R.E. Watson, "Characteristics of Synchrotron Radiation and of Its Sources", in "Handbook on Synchrotron Radiation" ed. E.-E. Koch (North-Holland Publishing Company, Amsterdam, 1983), p.65.
- [4] H. Rarback, C. Jacobsen, J. Kirz and I. McNulty, Nucl. Instr. and Meth. **A266** (1988) 96.
- [5] R.P. Walker, Nucl. Instr. and Meth. **A267** (1988) 537.

Analytical Formulation of a Quasi-periodic Undulator

M. Takao, S. Hashimoto, S. Sasaki and Y. Miyahara,
SPRing-8, Kamigori, Ako-gun, Hyogo 678-12, Japan

Abstract

Recently two of the present authors (S. H. and S. S.) introduced the concept of a new class of undulators, a quasi-periodic array of magnet poles, to discriminate the rational higher harmonics of radiation that are harmful in some synchrotron experiments. In this paper the analytical formula of the radiation spectrum from the quasi-periodic undulator is reported.

I. Introduction

Ordinary undulators consist of a periodic array of magnet poles of alternating polarity. The radiation emitted in each magnet pole interferes with each other, producing enhanced emission at a fundamental frequency and its harmonics. Since a mixture of the harmonics degrades the ratio of signal to noise in many experiments, the higher harmonics are required to be eliminated. In the high energy region of x-rays above 30 keV, however, it is practically difficult to exclusively pick up the fundamental radiation. Hashimoto and Sasaki proposed a new undulator, which comprises a quasi-periodic array of magnet poles [1], [2] and will be called "Quasi-periodic undulator" (hereafter, referred to as QPU). No rational higher harmonics of the fundamental frequency are contained in the radiation from the QPU. Here we analytically formulate the QPU radiation spectrum.

In a normal planer periodic undulator (PU) an electron moves sinusoidally in the horizontal plane. It takes the time $\lambda_U/(c\beta_z)$ that the electron traverses one period of the undulator λ_U , where β_z is the average longitudinal velocity. During this time the light travels the distance $L = \lambda_U/\beta_z$ along the undulator axis, so that the light emitted by an electron at a top of the sinusoidal motion precedes the one emitted at the next top by the phase $\Delta\phi = 2\pi\omega/\omega_1$. Here ω is the angular frequency of the light, and ω_1 is the resonant frequency of the undulator radiation given by $\omega_1 = 2\gamma^2\omega_U/(1 + K^2/2)$ with the undulator angular frequency $\omega_U = 2\pi c/\lambda_U$. Gathering the radiations from the individual periods, one finds that the intensity is proportional to [3], [4], [5]

$$\sum_{m=0}^{N-1} \exp\left(2\pi i m \frac{\omega}{\omega_1}\right) = e^{\pi i (N-1) \frac{\omega}{\omega_1}} \frac{\sin\left(N\pi \frac{\omega}{\omega_1}\right)}{\sin\left(\pi \frac{\omega}{\omega_1}\right)}, \quad (1)$$

where N is the number of periods of the undulator. This implies that the intensity of the undulator radiation is strengthened at $\omega = n\omega_1$ with an integer n and that the spectrum has the harmonic structure.

The explicit formula of the radiation spectrum from the PU is well-known and expressed by infinite series of Bessel functions [6], [7], [8]. In the next section we briefly review the irrational harmonic structure of the radiation spectrum from a QPU and give the explicit expression.

II. Radiation Spectrum for a QPU

The m th quasi-periodic lattice point is represented as [1], [2], [9]

$$\hat{z}_m = m - (\tan \alpha - 1) + (\tan \alpha - 1) \left[\frac{\tan \alpha}{1 + \tan \alpha} m + 1 \right], \quad (2)$$

where $\tan \alpha$ is the tangent of the inclination angle of a 1D quasi-lattice against a 2D square lattice. The symbol $[\dots]$ represents the greatest integer operator. The first term on the right hand side in Eq. (2) corresponds to a periodic component of spacing between the lattice points, the second term represents the constant translation of lattice points, which moves the initial lattice point \hat{z}_0 to the origin, and as m is increased the third term quasi-periodically increases by $(\tan \alpha - 1)$ due to the irrational nature of $\tan \alpha$. Hence the distance between any two consecutive positions $(\hat{z}_m - \hat{z}_{m-1})$ takes a value of 1 or $\tan \alpha$, forming a quasi-periodic array.

A basic magnetic structure for the planer QPU can be realized by aligning positive and negative magnet poles alternately at the 1D quasi-lattice points designated by Eq. (2) [1], [2]. From the symmetry of the 2D square lattice, where a 1D quasi-lattice is embedded, we can restrict $0 < \tan \alpha < 1$ without loss of generality. Thus we denote the two distances between the quasi-lattice points as $d, d' (= d/\tan \alpha > d)$. To realize a QPU, the length of the magnet block w should be shorter than the distance d .

As in a regular PU we here assume that the magnetic field $B_y(z)$ of the transverse QPU with N' poles has the sinusoidal dependence

$$B_y(z) = \sum_{m=0}^{N'-1} B_0 (-1)^m \cos \left[\frac{\pi}{w} (z - z_m) \right], \quad (3)$$

where B_0 is the peak magnetic field and $z_m (= d' \hat{z}_m)$ the center of the m th magnet region. The function $\cos(\alpha)$ is here defined to take $\cos(\alpha)$ for $-\pi/2 \leq \alpha < \pi/2$ and 0 otherwise. The magnetic field distribution with $w = d$ is shown in Fig. 1. For the sake of later convenience we here define analogue of the wave number, $k_0 = \pi/w$, and the undulation parameter, $K = (eB_0)/(m_0 c k_0)$, in the QPU.

In estimating the phase interference in the radiation from the QPU, we must sum up the phase differences of the individual magnet poles instead of the periods in the PU. Then the function that contains the phase interference of the QPU with N' magnet poles is

$$Q_\ell(\omega) = \frac{1}{N'} \sum_{m=0}^{N'-1} \exp \left[i\pi \left\{ \frac{\omega}{\omega_2} (\hat{z}_m - \eta m) - \ell m \right\} \right], \quad (4)$$

where

$$\omega_2 = \frac{w}{d'} \frac{2\gamma^2\omega_0}{1 + K^2 + (\gamma\theta_0)^2}, \quad (5)$$

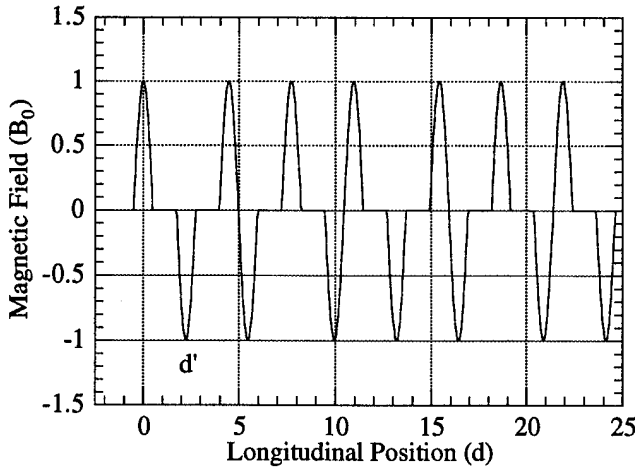


Figure 1. Magnetic field distribution along the axis of the quasi-periodic undulator.

$$\eta = \frac{w}{2d'} \frac{K^2}{1 + K^2 + (\gamma\theta_0)^2}. \quad (6)$$

In the exponent of Eq. (4) the term $i\pi(\omega/\omega_2)\hat{z}_m$ is the counterpart of the phase difference in the PU $2i\pi m(\omega/\omega_2)$. The factor 2 in the phase of the PU reflects the fact that one period of a PU consists of two magnet poles. Since in the free spaces between the magnet regions the electron possesses the transverse velocity, the phase of the electron against the light delays while the electron runs through the free spaces. The second term in the exponent of Eq. (4) containing η corresponds to this phase delay. The index ℓ of Q_ℓ represents the order of the Bessel expansion of the sinusoidal phase motion in the magnet regions.

Since for even ℓ the second term in the exponent in Eq. (4) is an integer multiple of $2\pi i$ and then vanishes in the exponentiation, the summation $Q_\ell(\omega)$ can be simplified as

$$Q_{\ell=\text{even}}(\omega) = \frac{1}{N'} \sum_{m=0}^{N'-1} e^{i\pi \frac{\omega}{\omega_2} (\hat{z}_m - \eta m)}, \quad (7)$$

which represents the Fourier transform of the quasi-periodic lattice except for the additional term ηm . Following the description of the quasi-crystal [9], we can derive the approximated expression of $Q_\ell(\omega)$. For large N' approximation, Eq. (7) can be easily rewritten as [9]

$$Q_{\ell=\text{even}}(\omega) = \sum_{p,q} e^{iX_{pq}/2} \frac{\sin(X_{pq}/2)}{X_{pq}/2} \delta\left(\pi \frac{\omega}{\omega_2} - k_{pq}\right), \quad (8)$$

where

$$k_{pq} = 2\pi \left(p + q \frac{\tan \alpha}{1 + \tan \alpha} \right) / \left(\frac{1 + \tan^2 \alpha}{1 + \tan \alpha} - \eta \right), \quad (9)$$

$$X_{pq} = 2\pi q - (\tan \alpha - 1) k_{pq}. \quad (10)$$

This implies that bright peaks occur at the discrete values of k_{pq} 's where X_{pq} 's are small and that intense peak positions (p, q) should be associated with the Fibonacci sequence [9]. Hence, in general, there appears no rational higher harmonic in the radiation spectrum from the QPU.

In the case of odd ℓ , the summation $Q_\ell(\omega)$ is reduced to

$$Q_{\ell=\text{odd}}(\omega) = \frac{1}{N'} \sum_{m=0}^{N'-1} e^{i\pi \frac{\omega}{\omega_2} (\hat{z}_m - \eta m) - i\pi m}, \quad (11)$$

which implies that it corresponds to the Fourier transform of the quasi-lattice with positive and negative matters, since the additional phase factor $\exp(-i\pi m)$ alternately changes the sign as m increasing. Then the peak position k_{pq} is shifted by the second term of Eq. (11) from the positions of $\ell = \text{even}$, and given by

$$k_{pq} = \left[2\pi \left(p + q \frac{\tan \alpha}{1 + \tan \alpha} \right) - \pi \right] / \left(\frac{1 + \tan^2 \alpha}{1 + \tan \alpha} - \eta \right). \quad (12)$$

In both the cases the resonant frequency of the synchrotron radiation from the QPU ω_{pq} is represented as

$$\omega_{pq} = \frac{k_{pq}}{\pi} \omega_2. \quad (13)$$

It is emphasized that the resonant frequency of the radiation from QPU ω_{pq} has the extra K dependence through η in k_{pq} in addition to through ω_2 while the one from a PU is a simple integer multiple of ω_1 .

Evaluating the radiation intensity from one magnet pole, we can derive the explicit form of the spectrum formula

$$\frac{d^2 I(\omega)}{d\omega d\Omega} = \frac{e^2 N'^2 \gamma^2}{16\pi \epsilon_0 c} \sum_{p,q} \left(\left| \gamma \theta_0 \cos \phi_0 F_{pq} - \frac{K}{2} G_{pq} \right|^2 + \left| \gamma \theta_0 \sin \phi_0 F_{pq} \right|^2 \right) H_{pq}(\omega), \quad (14)$$

where, for an odd mode

$$F_{pq} = \left[\frac{2\tilde{k}_{pq}}{1 + K^2/2 + (\gamma\theta_0)^2} \times \sum_{\ell=\text{odd}} \frac{S_\ell^{(0)}(\tilde{k}_{pq})}{\frac{\pi}{2}(\tilde{k}_{pq} - \ell)} - \frac{4}{\pi} C \right] \cos\left(\frac{\pi}{2} \tilde{k}_{pq}\right), \quad (15)$$

$$G_{pq} = \left[\frac{2\tilde{k}_{pq}}{1 + K^2/2 + (\gamma\theta_0)^2} \times \sum_{\ell=\text{odd}} \frac{S_\ell^{(1)}(\tilde{k}_{pq}) + S_\ell^{(-1)}(\tilde{k}_{pq})}{\frac{\pi}{2}(\tilde{k}_{pq} - \ell)} - \frac{8}{\pi} B \right] \cos\left(\frac{\pi}{2} \tilde{k}_{pq}\right), \quad (16)$$

and for an even mode

$$F_{pq} = \left[\frac{2\tilde{k}_{pq}}{1 + K^2/2 + (\gamma\theta_0)^2} \times \sum_{\ell=\text{even}} \frac{S_\ell^{(0)}(\tilde{k}_{pq})}{\frac{\pi}{2}(\tilde{k}_{pq} - \ell)} - \frac{4}{\pi} B \right] \sin\left(\frac{\pi}{2} \tilde{k}_{pq}\right), \quad (17)$$

$$G_{pq} = \left[\frac{2\tilde{k}_{pq}}{1 + K^2/2 + (\gamma\theta_0)^2} \times \sum_{\ell=\text{even}} \frac{S_\ell^{(1)}(\tilde{k}_{pq}) + S_\ell^{(-1)}(\tilde{k}_{pq})}{\frac{\pi}{2}(\tilde{k}_{pq} - \ell)} - \frac{8}{\pi} C \right] \sin\left(\frac{\pi}{2} \tilde{k}_{pq}\right). \quad (18)$$

In the spectral formula (14) $H_{pq}(\omega/\omega_1)$ is the structural function given by

$$H_{pq}(\omega) = \left[\frac{\sin(X_{pq}/2)}{X_{pq}/2} \right]^2 \delta\left(\omega - \frac{k_{pq}}{\pi} \omega_2\right). \quad (19)$$

In Eqs. (15)-(18)

$$\tilde{k}_{pq} = \frac{d' [1 + K^2/2 + (\gamma\theta_0)^2]}{\pi w [1 + K^2 + (\gamma\theta_0)^2]} k_{pq}, \quad (20)$$

$$S_\ell^{(p)}(x) = \sum_{n=-\infty}^{\infty} J_n(\xi_z x) J_{2n+\ell+p}(\xi_x x) \quad (21)$$

with

$$\xi_x = \frac{2K\gamma\theta_0 \cos \phi_0}{1 + K^2/2 + (\gamma\theta_0)^2}, \quad (22)$$

$$\xi_z = \frac{K^2}{4 [1 + K^2/2 + (\gamma\theta_0)^2]}. \quad (23)$$

In the form factors (15)-(18) the terms B and C , given by

$$B = \frac{1 + K^2 + (\gamma\theta_0)^2}{[1 + K^2 + (\gamma\theta_0)^2]^2 + (2K\gamma\theta_0 \cos \phi_0)^2}, \quad (24)$$

$$C = \frac{2K\gamma\theta_0 \cos \phi_0}{[1 + K^2 + (\gamma\theta_0)^2]^2 + (2K\gamma\theta_0 \cos \phi_0)^2}, \quad (25)$$

are understood as the contributions from the radiation in the free spaces between the magnet poles in the QPU.

III. Concluding Remarks

We derived the analytical formula of the radiation from the QPU (14) under the assumption that the magnetic field is given by Eq. (3).

It is worth emphasizing that the intensity of the even modes vanishes on axis as seen in the case of the PU. This is because G_{pq} , consisting of $S_\ell^{(\pm 1)}$ for even ℓ and C , vanishes on axis ($\theta_0 = 0$). Furthermore, note that, although one infinite Bessel series $S_\ell^{(m)}$ for some ℓ corresponds to one peak in the radiation spectrum of the PU, a peak intensity of the QPU comes from all the even series or the odd series.

To confirm the validity of the analytical formula, we compare it with the numerical computation of the radiation spectrum from a QPU with the magnetic field given by Eq. (3). Figure 2 shows the radiation spectra of the QPU with $K = 1.0$ given by the numerical and the analytical calculations. Here we take $w = d$ and $\tan \alpha = 1/\sqrt{5}$. In the numerical calculation we assume the number of poles to be 100. The full circles in Figure 2 represent the bright peaks of the spectrum designated by the generalized Fibonacci integers. Thus one is convinced that the analytical formula for the radiation from the QPU correctly gives the peak position in the spectrum and the peak intensity.

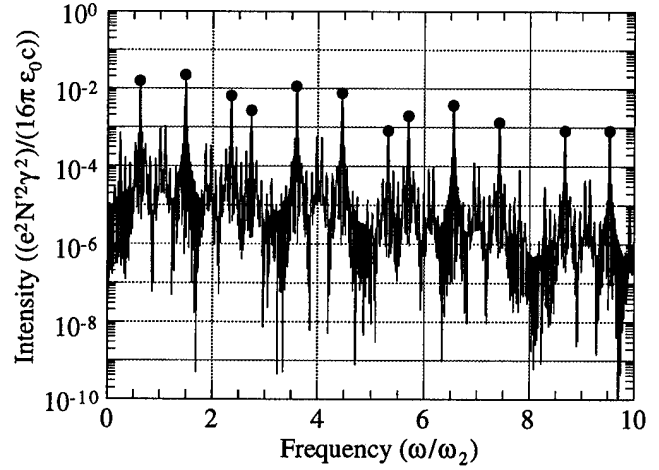


Figure 2. Radiation spectra from the quasi-periodic undulator with $K = 1.0$. The solid curve indicates the numerically computed spectrum and the dots correspond to the peaks given by the analytical formula.

References

- [1] S. Hashimoto and S. Sasaki, *JAERI-M Report 94-055* (1994).
- [2] S. Sasaki, S. Hashimoto, H. Kobayashi, M. Takao and Y. Miyahara, in *Proc. of Inter. Conf. of Synchrotron Radiation Instrumentation '94*, New York, U.S.A., 1994.
- [3] R. Tachyn and I. Lindau, *Nucl. Instrum. Methods* **222** (1984), 14.
- [4] R. Tachyn, A.D. Cox and S. Quadri, in *Proc. of Inter. Conf. of Insertion Devices for Synchrotron Sources SPIE 582* (1986), 47.
- [5] R.P. Walker, *Nucl. Instrum. Methods* **335** (1993), 328.
- [6] H. Kitamura, *Jpn. J. Appl. Phys.* **19** (1980), L185.
- [7] S. Krinsky, *Nucl. Instrum. Methods* **172** (1980), 73.
- [8] S. Krinsky, M.L. Perlman and R.E. Watson, "Characteristics of Synchrotron Radiation and of Its Sources", in "Handbook on Synchrotron Radiation" ed. E.-E. Koch (North-Holland Publishing Company, Amsterdam, 1983), p.65.
- [9] D. Levine and P.J. Steinhardt, *Phys. Rev.* **B34** (1986) 596.

High-Field Strong-Focusing Undulator Designs for X-Ray Linac Coherent Light Source (LCLS) Applications*

S. Caspi[†], R. Schlueter[†], R. Tatchyn

Stanford Linear Accelerator Center, Stanford, CA 94305, USA

[†]Lawrence Berkeley Laboratory, Berkeley, CA 94720, USA

Abstract

Linac-driven X-Ray Free Electron Lasers (e.g., Linac Coherent Light Sources (LCLSs)), operating on the principle of single-pass saturation in the Self-Amplified Spontaneous Emission (SASE) regime typically require multi-GeV beam energies and undulator lengths in excess of tens of meters to attain sufficient gain in the 1Å-0.1Å range. In this parameter regime, the undulator structure must provide: 1) field amplitudes B_0 in excess of 1T within periods of 4cm or less, 2) peak on-axis focusing gradients on the order of 30T/m, and 3) field quality in the 0.1%-0.3% range. In this paper we report on designs under consideration for a 4.5-1.5 Å LCLS based on superconducting (SC), hybrid/PM, and pulsed-Cu technologies.

I. INTRODUCTION

In recent years, a multi-institutional study group has been considering the use of a portion of the 3km S-band linac to drive a 4.5-1.5 Å LCLS at the Stanford Linear Accelerator Center (SLAC) [1]. The idea is to accelerate and compress a low-normalized-emittance beam from a laser-driven photocathode rf gun to peak currents in the 2.5-7.5 kA range and emittances approximating $\epsilon \leq \lambda/4\pi$ (where λ is the output wavelength), and then induce gain saturation by passing the beam through a sufficiently long undulator with superimposed strong focusing. In modeling lasing performance at 4.5-1.5Å, undulator periods in the range $2\text{cm} < \lambda_u < 4\text{cm}$, K parameters ($K = 0.934\lambda_u B_0 [T]$) in the range $2.5 < K < 4$, and quadrupole focusing with gradients ranging from 25-75 T/m, have been studied [2]. In view of the single-pass mode of operation and 120 Hz repetition rate of the linac, a wide range of undulator technologies, a number of which are depicted in Fig. 1, can in principle satisfy the given field and period requirements. In considering these technologies, a number of practical factors must be taken into account. These include: 1) fabrication cost (proportional to length); 2) operating cost; 3) attainable field quality; 4) tunability; 5) means for implementing strong focusing; and 6) stability in the linac environment.

In outlining a research and development program expected to culminate in the construction of a 4.5-1.5 Å LCLS at SLAC, technologies that promise the highest on-axis undulator fields (viz., the shortest structures) and focusing gradients have been emphasized. Thus, despite a strong base of experience in E&M (DC) technology at LLNL [3] and a prior study of pure PM structures for a longer-wavelength LCLS [4], the r&d

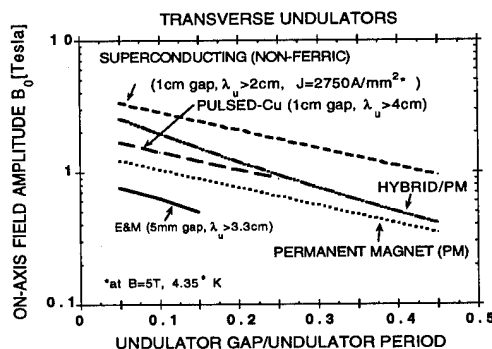


Figure 1. On-axis field performance of selected technologies.

effort at SLAC is currently centered on (non-ferric) SC [5], hybrid/PM [6], and pulsed-Cu [7] technologies, with a practical emphasis on the first two. To date, ferric SC technology [8,9] has not been pursued due to as-yet-unresolved methods for attaining the desired focusing. In this paper we report on the following design studies currently underway in the three cited technologies: 1) a bifilar helical SC undulator [10]; 2) a new hybrid/PM design with monogenic dipole/focusing fields[11]; 3) a weakly-focusing hybrid/PM design with superimposed strong PM focusing [12,13]; and 4) a pulsed-Cu design. For definiteness, we restrict each design to $\lambda = 1.5$ Å and an electron beam energy of 14.3 GeV ($\gamma \approx 28,000$). The (transverse) undulator period is then $\lambda_u [cm] \approx 24/(1 + K^2/2)$, with $K \rightarrow 2^{1/2} K$ for a helical structure.

II. SC BIFILAR HELICAL DESIGN

In the past two decades high-current-density accelerator magnets up to 17 m long have been built, achieving 4-10 Tesla central fields with error levels in the 10^{-4} range. Made of superconducting NbTi and nested in a two-layer "cosine-theta" fashion, these electromagnets employ "Rutherford" cable, include a large return iron yoke, and are restrained with a thick structural shell [14]. Operating at temperatures between 1.8-4.2 K and at currents of several thousand Amperes, these magnets attain a stored energy of several tens of kJ/m and require an insulator that can withstand several kV. With a current-carrying capacity of 3000 A/mm² (at 5 Tesla), these components require special attention to ensure their safety in the event of a quench.

In contrast, a non-ferric SC helical undulator will most likely be: 1) lower-field (viz., 2-3 Tesla), 2) current-dominated, 4) small, and 5) self-protecting. A single wire strand will replace the cable while maintaining the "cosine-theta" configuration. On the other hand, since a SC device can

* Supported in part by DOE Offices of Basic Energy Sciences and High Energy and Nuclear Physics and Department of Energy Contract DE-AC03-76SF0015.

be current and field limited, field non-linearities that are common in helical magnets are likely to cause the field at the conductor to increase at the expense of a reduced central field. Keeping the non-linearities as low as possible will require the use of magnets whose ratio of circumference to period is small (on the order of 1 or less), mitigating parasitic effects that can strongly alter the purity of the dipole field [15]. An undulator with a period of 27 mm would consequently imply the use of a coil with a diameter ≤ 8 mm. In a recent conceptual study a single SSC-type strand [16] has been used to structure a 2-layer helical bifilar magnet in a geometry designed to minimize the sextupole component (see Fig. 2). This (0.72 mm diameter) wire - with a Cu/SC ratio of 1.3:1 - carries about 900 A and generates a central field of 2 Tesla. Replacing it with an Artificial Pinning Center (APC) wire, which has a greater current carrying capacity at low fields (e.g., 5000 A/mm² at 3.5 Tesla), the maximum central field could be made to approach 2.5 Tesla.

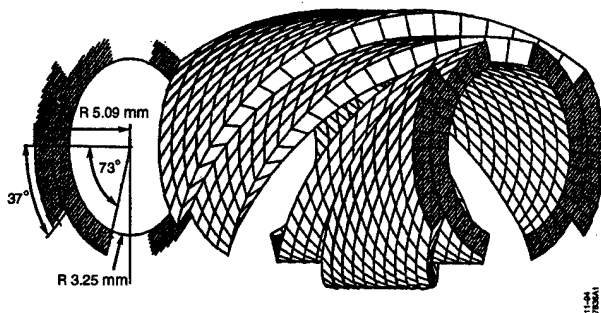


Figure 2. SC bifilar winding design with low field harmonics.

With regard to magnet safety and protection, present estimates are that with a low operating stored energy (on the order of 200 J/m) [17], and with a high current density in the copper (5000 A/mm²), quench propagation may be fast and the magnet may dissipate its energy in about 13 ms while generating only several tens of Volts. To test the self-protection of the windings under these conditions, as well as to investigate issues of field quality, SC focusing, charging time, and specific quenching mechanisms, the construction of a short LCLS prototype is planned within the coming year.

III. HYBRID/PM SINGLE-STRUCTURE DESIGN

One hybrid/PM LCLS design under study is a novel strong-focusing configuration featuring vanadium permendur poles excited by NdFe/B permanent magnets, sections of which have poles that are alternately tilted in the \pm -transverse direction with respect to the midplane and simultaneously wedge-shaped, as viewed from above. For example, such a device with a 4 cm period, a 0.6 cm gap on-center, a $\pm 8.6^\circ$ tilt, and a $\pm 10.7^\circ$ wedge could provide a 45 T/m gradient and an on-axis field strength of 0.97 T; $\Rightarrow K=4$. Minimum/maximum gap at transverse position $x=\pm 0.66$ cm would be 0.4/0.8 cm. Pole thickness at $x=\pm 0.66$ cm is 1.0 ± 0.25 cm. The iron pole pieces shape the field, affording better design quality than is possible with a pure PM device at this small gap.

The choice of simultaneous pole tilt with respect to the

midplane and nonuniform pole thickness follows from a 3-D analysis of the ideal pole shape for the superposition of fields from an undulator and a quadrupole. Let (x,y,Z) be the horizontal, vertical, and axial directions. Define complex variables $w \equiv Z + iy$ and $z = x + iy$. The desired wiggle field and focusing field are, respectively, $B_{wig}(w) = iB_0 \cos kw$ and $B_{foc}(z) = i2az$, where $k \equiv 2\pi/\lambda_u$ and a is a (focusing-strength) constant. The corresponding scalar potential in the gap is given by $V_{SD} = V_{wig} + V_{foc} = (B_0/k) \sinh ky \cos kZ + 2axy$. A contour along which V is constant is an equi-scalar potential surface to which the magnetic field is orthogonal. Choosing the boundary of the vanadium permendur pole, whose permeability is effectively infinite, to lie along a constant- V contour specified by $V = f(B_0, 2a, \lambda_u, h)$, where h is the half-gap, gives rise to the wiggle and focusing fields described above. The equi-scalar potential contour along the ideal pole surface passing through the point $(0, h, 0)$ is $V_{3D}(0, h, 0) = (B_0/k) \sinh kh$. Thus, the ideal pole contour lies along the surface defined by

$$1 = \cos kZ \left(\frac{\sinh ky}{\sinh kh} \right) + \left(\frac{y}{h} \right) \left(\frac{x}{g} \right) \left(\frac{kh}{\sinh kh} \right),$$

where $g \equiv B_0/2a$. The complicated 3-D curved pole shape is approximated by the canted, wedged pole having flat surfaces described at the beginning of this section. This practical design has the desirable feature that the PM material placed between poles remains a simple cuboid. TOSCA [11] modeling of the canted, wedged, flat-surfaced pole achieves very nearly the performance attained in the ideal analytical design.

Hybrid technology is proven, and PM forces for the LCLS design are small. Modular construction of a 55m-long device is convenient, possibly being in-vacuum. The PM cost for 1000 periods, each consisting of four 1cm x 3cm x 3cm blocks at $\sim \$4/\text{cm}^3$ is only \\$144,000. Alternating gradient focusing can be achieved by having a ~ 0.5 m-long focusing section, followed by "drift" and defocusing sections. The wiggle field is matched throughout the sections (see Fig. 3).

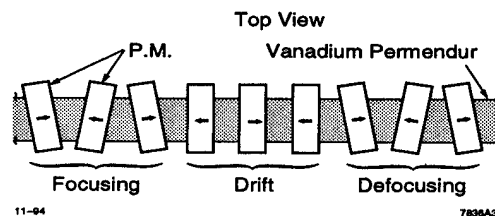


Figure 3. Wedged/canted hybrid/PM undulator section.

IV. HYBRID/PM SEPARATED-FUNCTION DESIGN

A second hybrid/PM LCLS design utilizes a conventional array of simple cuboid poles and NdFe/B magnets to generate a weakly-focusing undulator field, with strong quadrupole focusing provided by superimposed arrays of PM pieces. In one version of this design the PM pieces comprise simple block-pairs inserted into the gap from the sides [13]; in another version the PM pieces are thin strips (1-2 mm) arranged into planar quadrupoles [12] and affixed, along with Beam Position

Monitors (BPMs), to the vacuum duct, which remains mechanically independent of the undulator structure [18]. Potential advantages of this approach include: 1) easier lateral access to the beam, 2) higher attainable undulator fields (1.2-1.4 T), 3) amenability to undulator tuning with shunt plates, and 4) quadrupole field tuning with mechanical actuators.

V. PULSED-Cu DESIGN

Based on prior work on pulsed-Cu undulator prototypes at LANL [7,19], estimates of the operating parameters of a pulsed-Cu LCLS indicate that such a design, in principle, could be realized with existing technology. For example, for a 30m structure operating at 120 Hz, a Pulse Forming Network (PFN) would need to generate 120 μ s current pulses (with tops sufficiently flat over a 0.2 μ s interval) per second. For a total bifilar wire cross section of 0.25 cm² and a resistance of 0.15 Ω , pulsing with a peak current of 50 kA would require peak and average powers of 375 MW and 90 kW, respectively. As suggested by the cited research, prototype r&d for the LCLS would need to focus on field quality issues stemming from: 1) impulsive and oscillatory stresses, 2) longer-term (irreversible) strains, and 3) thermal loading.

VI. SUMMARY

A summation of critical parameters and r&d areas associated with the undulator technologies described above is listed in Table 1. Over the next two years the LCLS program

Table 1	SC	Hybrid/PM	Pulsed-Cu
Minimal Period[cm]	2	3	2
Sat. Length [m]	30	55	30
Minimal Gap [mm]	6	6	6
K at Minimal Period	~3.5	~3.5	~3.5
Focusing Methods	SC, PM	PM,PS ^a	Pulsed, PM
$\Delta B/B$	~0.01% (in dipoles)	~0.2% (at 3rd gn. sources)	>2% (attained at LANL)
Advantages	Shortest	Proven Technology	Short, No Rad. Damage
Potential Problems & Engineering Issues	Tolerances Quenching Rise Time	PM Damage ^b	Field Quality Mech&Thrm. PFN ^c

^aPole Shaping [11]; ^bRef. [20]; ^cPulse Forming Network

plans to address these issues, either at SLAC or in collaboration with laboratories specializing in the individual technologies. Problems common to all technologies, such as, e.g., undulator modularization [21,22], field metrology, and field and e-beam alignment strategies will also be addressed.

VII. ACKNOWLEDGMENTS

The authors would like to thank the members of the LCLS research group, in particular Klaus Halbach, Claudio Pellegrini, Roger Warren, and Herman Winick for their valuable critical and conceptual support.

VI. REFERENCES

- [1] R. Tatchyn, K. Bane, R. Boyce, G. Loew, R. Miller, H.-D. Nuhn, D. Palmer, J. Paterson, T. Raubenheimer, J. Seeman, H. Winick, D. Yermian, C. Pellegrini, J. Rosenzweig, G. Travish, D. Prosnitz, E. T. Scharlemann, S. Caspi, W. Fawley, K. Halbach, K.-J. Kim, R. Schlueter, M. Xie, R. Bonifacio, L. De Salvo, P. Pierini, "Prospects for High Power Linac Coherent Light Source (LCLS) Development in the 100nm-0.1nm Wavelength Range," presented at the 4th International X-Ray Laser Colloquium, Williamsburg, VA, May 16-20, 1994.
- [2] H.-D. Nuhn, E. T. Scharlemann, W. M. Fawley, and R. Schlueter, "Alignment and Magnet Error Tolerances for the LCLS X-Ray FEL," this conference, - FAA17.
- [3] G. A. Deis, M. J. Burns, T. C. Christensen, F. E. Coffield, B. Kulke, D. Prosnitz, E. T. Scharlemann, and K. Halbach, IEEE Trans. Mag. 24(2) 986(1988).
- [4] R. Tatchyn, R. Boyce, K. Halbach, H.-D. Nuhn, J. Seeman, H. Winick, and C. Pellegrini, "Design Considerations for a 60 Meter Pure Permanent Magnet Undulator for the SLAC Linac Coherent Light Source (LCLS)," Proc. IEEE Particle Accelerator Conference, IEEE Cat. No. 93CH3279-7, pp. 1608-1610.
- [5] L. R. Elias and J. M. Madey, Rev. Sci. Instrum. 50(11), 1335(1975).
- [6] K. Halbach, J. Appl. Phys. 57(8), Part IIA, 3605(1985).
- [7] R. W. Warren and C. M. Fortgang, Nucl. Instrum. Meth. A331, 706(1993).
- [8] I. Ben-Zvi, R. Fernow, J. Gallardo, G. Ingold, W. Sampson, and M. Woodle, Nucl. Instrum. Meth. A318, 781(1992).
- [9] S. C. Gottschalk, A. L. Pindroh, D. C. Quimby, K. E. Robinson, and J. M. Slater, Nucl. Instrum. Meth. A304, 732(1991).
- [10] S. Caspi, "A Superconducting Helical Wiggler for Short Wavelength FELs," LBID-2052, SC-MAG-475, September 1994.
- [11] R. D. Schlueter, Nucl. Instrum. Meth. A358, 44(1995).
- [12] R. Tatchyn, Nucl. Instrum. Meth. A341, 449(1994).
- [13] A. A. Varfolomeev, V. V. Gubankov, A. H. Hairtdinov, S. N. Ivanchenkov, A. S. Khlebnikov, N. S. Osmanov, and S. V. Tolmachev, Nucl. Instrum. Meth. A358, 70(1995).
- [14] D. Dell'Orco, S. Caspi, J. O'Neill, A. Lietzke, R. Scanlan, C. E. Taylor, and A. Wandesforde, IEEE Trans. Appl. Superconduct. 3(1), 637(1993).
- [15] S. Caspi, "Magnetic Field Components in a Sinusoidally Varying Helical Wiggler," LBL-35928, SC-MAG-464, July 1994.
- [16] S. Caspi, "Magnetic Field Components in a Helical Dipole Wiggler with Thick Windings," LBID-2048, SC-MAG-472, September 1994.
- [17] S. Caspi, "Stored Energy in a Helical Wiggler," LBID-2051, SC-MAG-474, September 1994.
- [18] D. C. Quimby, S. C. Gottschalk, F. E. James, K. E. Robinson, J. M. Slater, and A. S. Valla, Nucl. Instrum. Meth. A285, 281(1989).
- [19] C. M. Fortgang and R. W. Warren, Nucl. Instrum. Meth. A341, 436(1994); R. Warren, private communication.
- [20] W. V. Hassenzahl, T. M. Jenkins, Y. Namito, W. R. Nelson, and W. P. Swanson, Nucl. Instrum. Meth. A291, 378(1990).
- [21] K. E. Robinson, D. C. Quimby, and J. M. Slater, IEEE Jour. Quant. Electr., QE-23, 9, 1497(1987).
- [22] K.-J. Kim and M. Xie, "Effects of Wiggler Interruption on LCLS Performance, CBP Tech. Note-77, March 1995.

Wigglers at the Advanced Light Source

E. Hoyer, J. Akre, D. Humphries, T. Jackson, S. Marks, Y. Minamihara, P. Pipersky, D. Plate, G. Portmann, R. Schlueter *, Lawrence Berkeley Laboratory, University of California, Berkeley, CA 94720 USA

ABSTRACT

Two 3.4 m long wigglers are being designed and constructed at Lawrence Berkeley Laboratory's (LBL) Advanced Light Source (ALS). A 19 period planar wiggler with 16.0 cm period length is designed to provide photons up to 12.4 keV for protein crystallography. This device features a hybrid permanent magnet structure with tapered poles and designed to achieve 2.0 T at a 1.4 cm magnetic gap. An elliptical wiggler is being designed to provide circularly polarized photons in the energy range of 50 eV to 10 keV for magnetic circular dichroism spectroscopy. This device features vertical and horizontal magnetic structures of 14 and 14 1/2 periods respectively of 20 cm period length. The vertical magnetic structure is a 2.0 T hybrid permanent magnet configuration. The horizontal structure is an iron core electromagnetic design, shifted longitudinally 1/4 period with respect to the vertical magnetic structure. A maximum horizontal peak field of 0.1 T at an oscillating frequency up to 1 Hz will be achieved by excitation of the horizontal poles with a trapezoidal current waveform.

I. INTRODUCTION

The ALS, a third generation synchrotron light source, is now in routine operation with three 4.6 m long undulators. Two of these devices have 5.0 cm period lengths (IDA-U5.0 and IDB-U5.0) and the third device has an 8.0 cm period length (IDC-U8.0), which, at 1.5 GeV ALS operation, produce high brightness in the 50 to 1500 eV and 15 to 1000 eV ranges respectively.[1] A fourth 4.6 m long undulator, with a 10.0 cm period length (IDG-U10.0), is nearing completion and is slated for installation later this year and will produce high brightness radiation, in the 5 to 900 eV range when the ALS operates at 1.5 GeV.[2] Currently, two 3.4 m long wigglers are being designed and constructed. One is a 19 period planar wiggler with 16.0 cm period length (IDD-W16.0) designed to provide photons up to 12.4 keV for protein crystallography.[3] The other is a 14 period, 20 cm period length cross-field elliptical wiggler (IDH-EW20.0) being designed to provide circularly polarized photons in the energy range of 50 eV to 10 keV with chirality switching up to 1 Hz for magnetic circular dichroism spectroscopy.[4] The principal parameters for the wigglers are tabulated in Table I.

II. W16.0 WIGGLER

The planar wiggler, W16.0 Wiggler, includes a mag

netic structure, support/drive system, control system and vacuum system and is shown in Fig.1.

Table I Wiggler Parameters

Parameter (units)	W16.0	EW20.0
Min.Vert. Mag. Gap (cm)	1.4	1.4
Horizontal Magnetic Gap (cm)		7.2
Peak Vertical Field (T)	2.0	2.0
Peak Horizontal Field (T)		0.095
Max. Hor. Field Freq. (Hz)		1.0
Period Length (cm)	16.0	20.0
No. of Periods	19	14 V, 14 1/2 H
Entrance/Exit Sequence	0, -1/4, 3/4, -1, 1..	
Vertical End Cor. Range (G-cm)	4000	5000
MTM Range (G-cm)	+/- 3000	+/- 3000

The variable gap, hybrid-permanent magnet magnetic structure design and construction are different from those of the ALS undulators. To achieve the 2.0 T peak field, the design requires that the vanadium permendur poles be tapered in the poletip region in both the longitudinal and transverse directions to reduce saturation. To null the dipole field integral through the device, water cooled coils in the end structures with bipolar power supplies are used. To meet the higher order field integral requirements, in the 1.0 cm by 6.0 cm aperture, block sorting to minimize the effects of the minor components is planned and multiple trim magnets will be used for final tuning.[5,6] The basic building block of the magnetic structure is the half-period pole assembly. This unit consists of an aluminum keeper, a pole that is pinned in the keeper and 12 Nd-Fe-B blocks, 6 on each side of the pole, that are bonded to both the pole and keeper. The 25 kg half-period pole assemblies, are individually mounted on two backing beams and the pole surfaces are aligned to within 25 microns with respect to each other on each backing beam.

The support/drive system, which provides the framework for holding the magnetic structures and the drive system that opens and closes the vertical magnetic structure gap, is very similar to that of the ALS undulators, but shorter. 3.5 m in length and wider, 1.5 m in width. Gap motion is achieved with a stepper-motor/gear box/roller chain drive with coupled left-hand and right-hand 2 mm pitch Transrol roller screws that are attached to the upper and lower backing beams. The control system, a Compumotor system, is identical to those used on the ALS undulators. The vacuum system is also similar to those of the ALS undulators, but only 3.8 m in length.

* This work was supported by the Director, Office of Energy Research, Office of Basic Energy Sciences, Materials Sciences Division, of the U.S. Department of Energy under Contract No. DE-AC03-76SF00098.

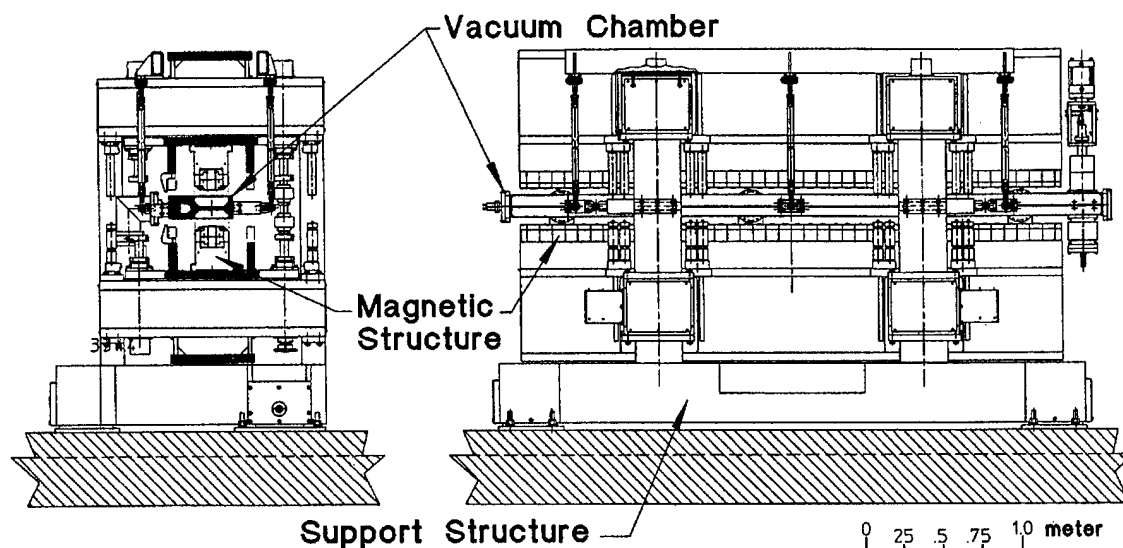


Fig. 1 W16.0 Wiggler end sectional and elevation views

Predicted spectral output of the W16.0 Wiggler, when inserted in the ALS operating at 1.5 and 1.9 GeV - 400 mA, is shown in Figure 2. Design of W16.0 Wiggler is nearly completed and fabrication is well along. Completion is slated for the end of this year.

III. EW20.0 ELLIPTICAL WIGGLER

The mechanical configuration of the Hybrid-Electromagnet Elliptical Wiggler is shown in Fig. 3. The vertical magnetic field is generated with a variable gap hybrid-permanent magnetic structure; the horizontal magnetic field comes from an iron core electromagnetic structure. The support structure/drive and control systems are identical to the W16.0 Wiggler. The vacuum chamber configuration features a beam tube with multiple pumping ports that are connected to a pumping chamber.

The vertical magnetic field structure consists of a periodic structure with 14 periods. To achieve the 2.0 T peak field, the vanadium permendur poles are tapered in both the transverse and longitudinal directions near the pole tip. The design requires that the Nd-Fe-B material be retracted from the midplane to allow the horizontal magnetic field structure to be brought as close to the vacuum chamber as possible. The entrance and exit vertical magnetic structures are configured so that the central electron beam orbit is on-axis for all field values. To achieve this, the normalized pole potential sequence for the entrance/exit is 0 (field clamp), $1/4$, $-3/4$, 1, -1 ... The appropriate pole potentials are achieved by modifying the amount of permanent magnet material and adjusting with electromagnetic coils. Except for period length and pole configuration, design and construction of the EW20.0 vertical magnetic structure is very similar to the W16.0 Wiggler.

The horizontal magnetic structure has the same period length as the vertical magnetic structure but is longitudinally phase shifted $1/4$ period relative to the vertical magnetic structure. The poles and coils of the horizontal magnetic field structure are tucked between the upper and

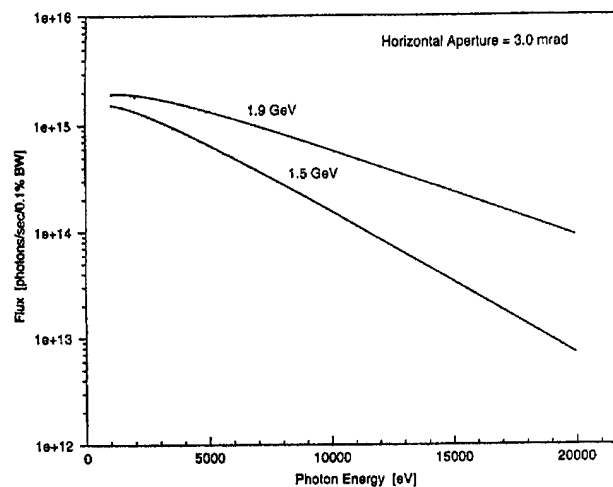


Fig. 2. Estimated flux from W16.0 Wiggler at ALS storage ring energies of 1.5 and 1.9 GeV.

lower vertical magnetic field structures. The magnetic field distribution includes $14 \frac{1}{2}$ periods and the ends are modified to achieve the same normalized potential structure as those for the vertical field. At both wiggler ends, the horizontal structure extends $1/4$ period past the vertical structure so as to avoid linear polarization contamination of the circularly polarized photon beam.

The horizontal structure cores are laminated from 0.64 mm thick M-36 electrical steel. They are powered by water cooled electrical coils. A system of struts are used for support and adjustment of the horizontal magnetic structure. Coil excitation is with a bipolar, regulated power supply that will provide a trapezoidal wave form for frequencies from DC up to 1 Hz.

The elliptical wiggler vacuum chamber is a welded stainless steel assembly that includes a beam chamber, 18 pumpout tubes and a pump tube. The beam chamber aperture, with internal dimensions of 1.0 cm by 6.1 cm, is adequate for dynamic aperture requirements. With this beam aperture, a minimum vertical gap of 1.4 cm and a horizontal magnetic gap of 7.2 cm are achievable. The

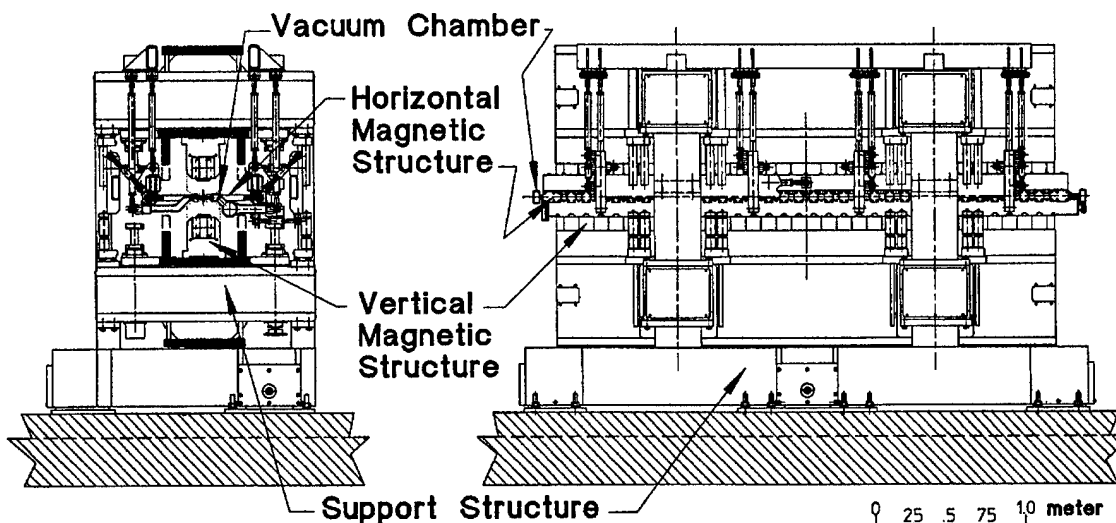


Fig. 3 Side sectional and elevation views of the EW20.0 Elliptical Wiggler

chamber has a rectangular water cooling channel on the side where the synchrotron light from the upstream bend magnet strikes; this reduces thermal distortions. With ALS operation at 1.9 GeV and 400 mA, the maximum chamber temperature rise is 4 °C. To achieve good vacuum, 18 distributed pump-out ports are located along the length of the beam chamber. To further reduce photon induced desorption, a photon stop is located upstream of the chamber to block some of the beam that would otherwise impinge on the chamber. The pump-out ports are connected to the pump tube to which ion pumps and titanium sublimation pumps are attached. The pump-out ports are slotted to provide satisfactory impedance to the electron beam along the length of the beam chamber. The vacuum chamber configuration and planned pumping should provide an average gas pressure of less than 10^{-9} Torr after 40 A hr of beam operation in the ALS.

Supporting and adjusting the vacuum chamber in the elliptical wiggler is accomplished with a system of struts. This arrangement allows the chamber-pumptube assembly to be lowered in the wiggler and then removed from the device for UHV processing after completion of the magnetic measurements.

Spectral calculations, shown in Fig. 4, indicate that the device will produce a figure of merit, defined as flux times degree of circular polarization squared, of greater than 10^{14} photons/sec/0.1% BW at photon energies up to 5 keV and greater than 10^{13} photons/sec/0.1% BW for photon energies between 5-10 keV, for a 5 mrad horizontal fan with the ALS operating at 1.5 GeV and 400 mA.[7] Status of the elliptical wiggler is that the conceptual design is complete and design and fabrication has started. The project is currently on hold.

IV. REFERENCES

- [1] E. Hoyer, et al., "Undulators at the ALS, 5th International Conf. on Syn. Rad. Inst.", [LBL-35844], Rev.Sci. Inst 66 (2), 1898 (February 1995).
- [2] "U10.0 Undulator Conceptual Design Report", LBL PUB-5390 (June 1994).
- [3] "W16.0 Wiggler Conceptual Design Report", LBL PUB-5288 (Feb. 1991).
- [4] "EW20.0 Elliptical Wiggler Conceptual Design Report", LBL-PUB -5400 (March 1995).
- [5] D. Humphries, et. al., "A Multiple Objective Magnet Sorting Algorithm for the ALS Insertion Devices", 5th International Conf. on Syn. Rad. Inst.", [LBL-35535], Rev. Sci. Inst 66 (2), 1904 (February 1995).
- [6] E. Hoyer, et. al., "Multiple Trim Magnet, or "Magic Fingers", for insertion device field integral correction, 5th International Conf. on Syn. Rad. Inst.", [LBL-35865], Rev. Sci. Inst 66 (2), 1901 (February 1995).
- [7] S. Marks, et. al, "Optimization Design Study for an elliptical wiggler at the ALS", 5th International Conf. on Syn. Rad. Inst.", [LBL-35510], Rev. Sci. Inst 66 (2), 1940 (February 1995).

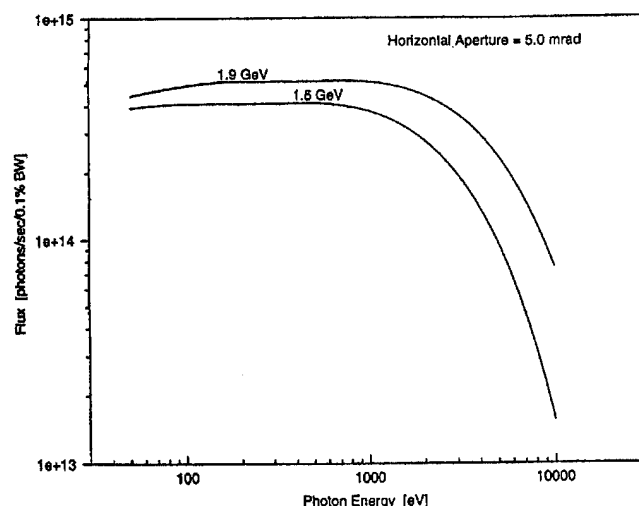


Fig. 4 Polarization figure of merit for the EW20.0 Elliptical Wiggler

Design of End Magnetic Structures for the Advanced Light Source Wigglers*

D. Humphries, J. Akre, E. Hoyer, S. Marks, Y. Minamihara, P. Pipersky, D. Plate, R. Schlueter
Lawrence Berkeley Laboratory, University of California, Berkeley, CA 94720 USA

The vertical magnetic structures for the Advanced Light Source 16 cm planar wiggler and 20 cm period elliptical wiggler are of hybrid permanent magnet design. The ends of these structures are characterized by diminishing scalar potential distributions of the poles which control beam trajectories. They incorporate electromagnetic correction coils to dynamically correct for variations in the first integral of the field as a function of gap. A permanent magnet trim mechanism is incorporated to minimize the transverse integrated error field distribution. The ends were designed using analytic and computer modeling techniques. The design and modeling results are presented.

I. INTRODUCTION

Previous ALS undulators [1] incorporated rotatable permanent magnet tuning elements to adjust the integral of the B_y fields produced by the end magnetic structures. These correctors were adjusted and locked in a fixed setting. Gap dependency of integral B_y for these devices is compensated for by external corrector magnets.

The current ALS wigglers [2] have been designed with electromagnetic end coils which can be dynamically tuned to compensate for gap dependency of integral B_y .

The configuration of the end structure is shown in cross section in Figure 1. The poles, labeled 0, 1, 2, etc. are vanadium permendur and are powered by Nd-Fe-B permanent magnets which can be seen between the poles. The corrector coil can be seen around pole 1. Trim magnets [3] are located between poles 0 and 1. These are used to correct variation in field integrals as a function of the transverse coordinate x .

The truncation field distribution of the ends is a function of the scalar potential distribution of the poles beginning with the end pole (pole 0). The nominal entry scheme is for nominal, normalized scalar potentials of 0, 1/4, -3/4, 1, -1, etc. This distribution is achieved by manipulating the quantities of fixed permanent magnet material in the spaces between poles 0 through 3.

II. CORRECTOR COILS

The corrector coils are powered by a 13 v, 120 A, bi-polar power supply which is controlled by the ALS control system. They consist of ten turns of .250" sq. x .125" i.d. hollow copper conductor potted in glass filled epoxy. They are wired in series to achieve maximum magnetic symmetry with cooling circuits in parallel.

Fluid flow and heat transfer calculations were incorporated in a spread sheet program for rapid optimization of the coil design.

Table I Coil and Power Supply Parameters

Coil Parameters:

Electrical:

Current	100 A
Power	.358 kW
Voltage	3.58 V
Resistance	35.8 m Ω
Inductance	0.5 mH

Cooling:

Velocity	8.79 ft/s
Flow Rate @ 40 psi	.34 GPM
Temperature Rise	4.0° C

Power Supply Requirements:

Output:

Voltage	± 13.0 V
Voltage Ripple (p-p)	<1% V_o
Current	± 120 A
Current Regulation	± 100 ppm
Bipolar Offset	± 25 ppm
Overcurrent	130 A-dc

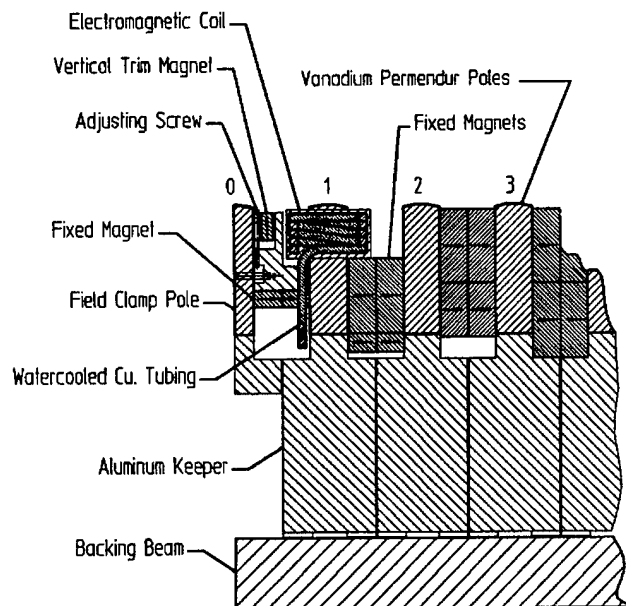


Figure 1: End structure cross section

*This work was supported by the Director, Office of Energy Research, Office of Basic Energy Sciences, Materials Sciences Division, of the U.S. Department of Energy under Contract No. DE-AC03-76SF00098.

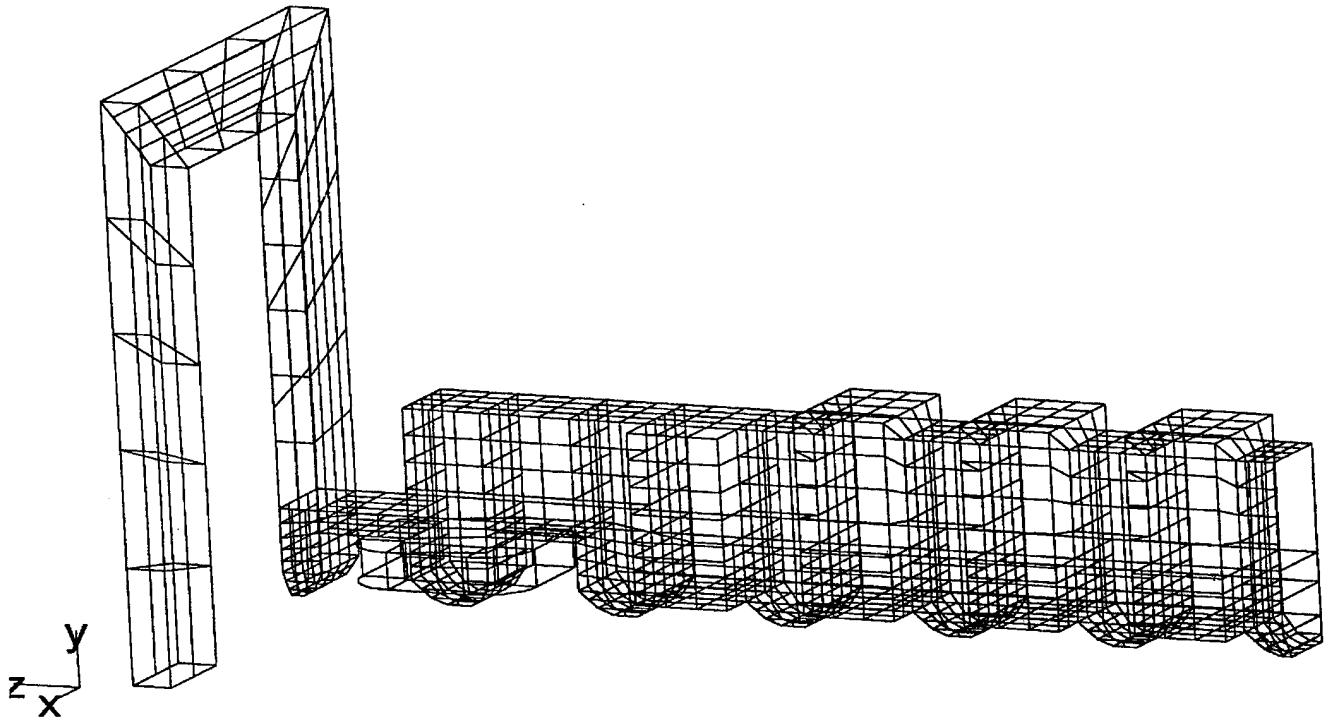


figure 2: 3-D Boundary element model for end field calculations

III. 3-D NUMERICAL MODELING

The end structures are complicated, non-linear structures with significant three dimensional aspects. To perform the magnetic design, the code AMPERES [4] was used. AMPERES is a 3-D code which uses a boundary element method to solve for the fields.

Figure 2 illustrates the 3-D model with boundary elements shown. This represents one fourth of one end of the 20 cm wiggler magnetic structure. Symmetry planes are utilized at the $x=0$, $y=0$ and $z=0$ planes of the geometry. One half of one coil can be seen around pole 1.

The poles are modeled using a non-linear B-H curve for vanadium permendur. The permanent magnets are described by the usual linear B-H representation while the coil in the model consists of current volume elements with total current NI .

At the left end of the model in Figure 2, a magnetic shunt can be seen which connects the last or "field clamp" pole to the corresponding pole below the midplane. The intended purpose of this shunt is to force the fields clamp poles to zero scalar potential.

IV. MODELING RESULTS

A. Fields and Trajectories

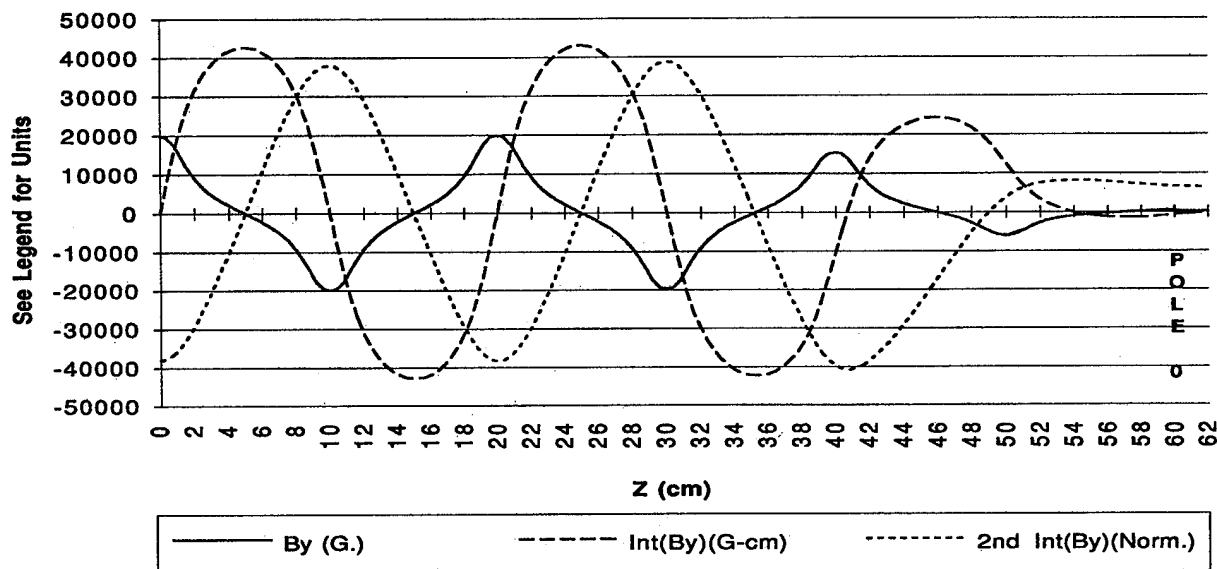
Figure 3 shows a result for the 20 cm wiggler calculated by AMPERES. The B_y field distribution, the first integral of the fields, and the second integral or trajectory are shown.

The high third harmonic content of the wiggler fields can be seen in the shape of the field peaks. Pole 0, the field clamp pole is indicated on the right side of the graph. The first integral of B_y (steering), decays to a small value as desired. The second integral indicates a benign exit trajectory with a final beam offset which is small relative to the wiggle amplitude which can be seen at the left side of the graph.

B. Coil Positioning

3-D calculations were performed with correction coils in various locations in order to determine the optimum arrangement. The results indicate that coils which are positioned further from the end poles have significant diminished capacity. A coil located at pole 2 performed at approximately one tenth the correction capacity of the same coil located at pole 1 for the 20 cm period wiggler ends.

A second result of the modeling is that the vertical position of the correction coil on the pole has a major impact on its capacity. A coil placed on the end of the pole away from the midplane of the device produced only two fifths the correction capacity of the same coil positioned near the midplane as shown in Figure 1.



3: B_y , integral of B_y and trajectory (2nd Integral) from AMPERES calculation

Figure

D. Corrector Coil Capacity

A value of $NI = \pm 1000$ A was set for the correction coils in the models and the differences were calculated for the integrals. The indicated capacity for the 20 cm period wiggler is 5000 G-cm per end and that of the 16 cm wiggler is 4000 G-cm.

V. REFERENCES

- [1] E. Hoyer, et al, "First Undulators for the Advanced Light Source", IEEE PAC (May 1993).
- [2] E. Hoyer, et al, "Wigglers at the Advanced Light Source", IEEE PAC (May 1995).
- [3] E. Hoyer, et al, "Multiple Trim Magnet, or 'Magic Fingers', for insertion device field integral correction", 5th International Conference on Synchrotron Radiation Instrumentation, [LBL-35865], Rev. Sci. Instr. 66 (2), 1901 (February 1995).
- [4] AMPERES Three-Dimensional Magnetic Field Solver, "Users and Technical Manual", Integrated Engineering Software Inc., Winnipeg, Manitoba, Canada (1991).

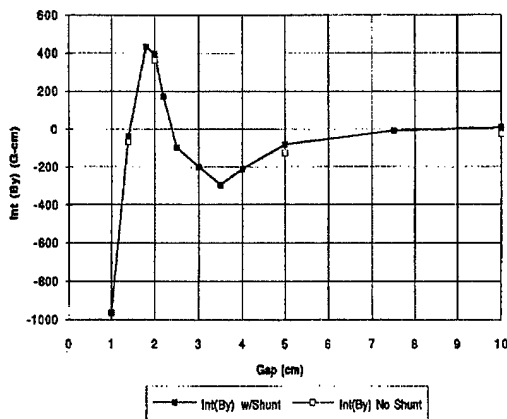


Figure 4: Gap dependency of integral of $B_y dz$

C. Gap Dependency

Extensive modeling was performed to attempt to predict the dependency of the integral of $B_y dz$ on the change in gap of the device. Figure 4 shows the results of a series of 3-D calculations for gap dependency. The indicated range of the integral from the minimum operating gap of 1.4 cm to the largest gap of 22 cm is approximately 800 G-cm.

In the 2-D modeling case the end shunt is required to achieve the necessary integral B_y capacity of correction elements. Conversely, 3-D modeling indicates that the shunt has a minimal effect on both the capacity of correctors and on the gap dependency of the integral of B_y through the ends. This can be seen in the graph of Figure 4.

PASSIVE END POLE COMPENSATION SCHEME FOR A 1.8 TESLA WIGGLER

L.H.Chang, Ch.Wang, C.H.Chang, T.C.Fan
Synchrotron Radiation Research Center, Hsinchu, Taiwan

Abstract

An optimized end pole compensation scheme for the 1.8 Tesla, 25-pole wiggler W20/SRRC was studied by using 2D magnetostatic code OPERA-2d. The maximum deviation of the dipole steering for this wiggler can be minimized either by optimizing the sizes of the bias magnets or by optimizing the easy-axis rotating angles of the permanent rotators. After optimization, the dipole steering is within 100 Gauss-cm in the operating gap range so that a passive compensation scheme is possible even for an insertion device configured with very strong on-axis magnetic field strength.

I. INTRODUCTION

There are usually end correctors located at both ends of the insertion device to compensate the residual dipole steering due to the fringe magnetic field contributions as well as the magnetic field errors, which can be characterized by the first integral of the magnetic field (I_1) through the entire magnetic structure. Basically, the design goal of the end correction scheme could be guided in two directions: passive correction and compact size. A passive end correction scheme means that the maximum deviation of the dipole steering between the minimum and maximum gap range can be within a reasonable small value like 100 Gauss-cm without help of any gap-dependent active compensation mechanism. Recess of the next-to-last pole pieces[1] demonstrates one of the solutions. However, optimization of the size of the permanent bias magnets in the end correction configuration gives another possibility.

The hybrid permanent periodic magnetic structure of the STI delivered 1.8 Tesla, 25-pole wiggler W20/SRRC was used as an example for numerical study of this possibility in this report. The magnetostatic code OPERA-2d[2] was used. A Halbach rotator type end pole compensation scheme[3] composes of two sets of permanent bias magnets (1 and 2) and rotators (α and β) located between pole 0 (field clamp) and pole 2, as shown in Fig. 1.

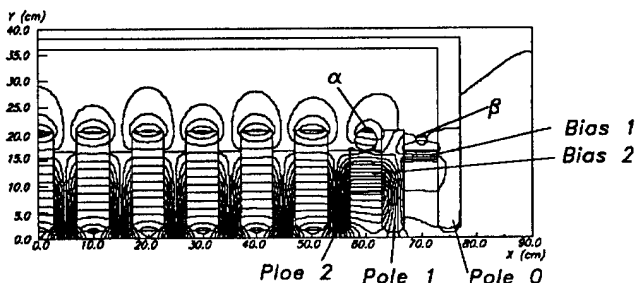


Figure 1. 2D numerical modelling of the new proposed end correctors for the wiggler W20/SRRC

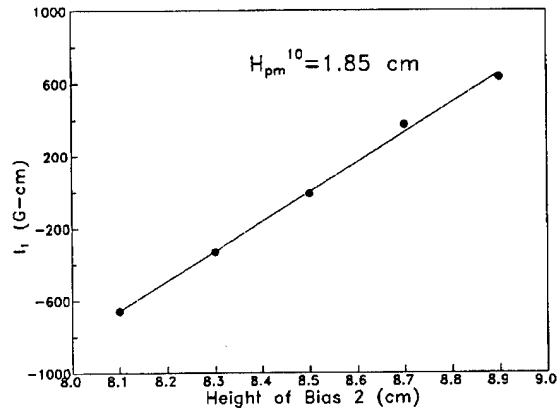


Figure 2. Dipole steering I_1 at 22 mm gap as a function of the height of the bias magnet 2. The height of bias magnet 1 is equal to 1.85 cm.

II. OPTIMIZATION OF BIAS MAGNETS

The maximum deviation of the first integral of the magnetic field (ΔI_1) through the entire insertion device is strongly dependent on the size of the bias magnets. With a fixed size of the bias magnet 1, the calculated dipole steering at a fixed gap (here 22 mm gap) is proportional to the height of the bias magnet 2, as shown in Fig. 2. On the other hand, with a fixed size of the bias magnet 2, the calculated dipole steering at a fixed gap as a function of the height of the bias magnet 1 has a negative slope, as shown in Fig. 3. Fig. 4 shows the maximum deviation of the dipole steering in the gap range from 22 mm to 102 mm as a function of the height of the bias magnet 2. Here the heights of the bias magnet 1 was optimized so that the dipole steering always keeps zero at 22 mm gap.

With fixed heights of the bias magnets, the dipole steering is usually gap-dependent, as shown in Fig. 5. The maximum deviation of the dipole steering could be huge, if the dimension of the bias magnets is not properly optimized. For example, the maximum deviation of the dipole steering is more than 1500 Gauss-cm, if the height of the bias magnet 2 is equal to 9.5 cm. However, the maximum dipole steering deviation is within 100 Gauss-cm, if the height of the bias magnet 2 is equal to 7.95 cm. In Fig. 5, the heights of the bias magnet 1 were optimized to keep zero dipole steering at 22 mm gap, i.e. the heights of the bias magnet 2 are equal to be 7.95 cm and 9.50 cm individually.

After comparison between the results shown in the Fig. 2 and Fig. 4, we found that the maximum deviation of the dipole steering in the gap range from 22 mm to 102 mm can be minimized by reducing the height of the bias magnet 2 to about 7.95 cm.

III. FINE TUNE WITH ROTATORS

A discrepancy between the simulated and measured dipole steering for a given end correction scheme is The unavoidable

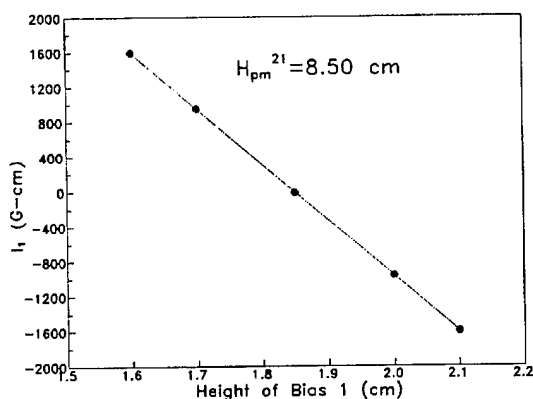


Figure 3. Dipole steering I_1 at 22 mm gap as a function of the height of bias magnet 1 at 22 mm gap. The height of bias magnet 2 is equal to 8.5 cm.

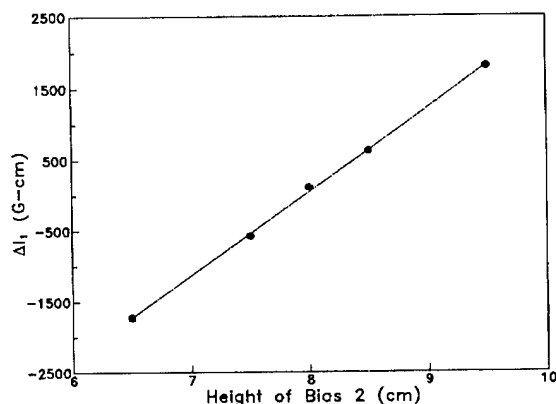


Figure 4. Maximum deviation of the dipole steering ΔI_1 in the gap range from 22 mm to 102 mm as a function of the height of bias magnet 2.

magnetic field errors and 3d effect due to finite width of the magnetic structure are two of the most possible sources for this discrepancy. A mechanism for fine tuning of the dipole steering after assembly of the insertion device magnetic structure is therefore necessary. There are two tunable permanent magnetic rotators equipped in the Halbach rotator type end pole scheme for this purpose (see Fig. 1). However, the rotators could be replaced by electromagnetic coils for some other reasons.

As shown in Fig. 6, a pair of the permanent rotators with steering tuning capability larger than ± 3000 Gauss-cm for the wiggler W20/SRRC at 22 mm gap was used for our preliminary numerical study. Here the radius of the rotators are 2.0 cm and 1.0 cm individually. At a given gap, the dipole steering can be completely compensated by rotating either the rotator α or β . In Fig. 7, the maximum deviation of the dipole steering is shown as a function of the easy-axis rotating angle of the permanent rotator α , with fixed rotating angle of the rotator β such that the dipole steering keeps zero at 22 mm gap. In Fig. 8, the dipole steering as a function of gap is shown. With help of the rotators, the residual dipole steering can be within 100 Gauss-cm without difficulty after optimization of the easy-axis rotating angles of both rotators. On comparison of the results shown in Fig. 7 and 8 with those shown in Fig. 4 and 5, we found that to optimize

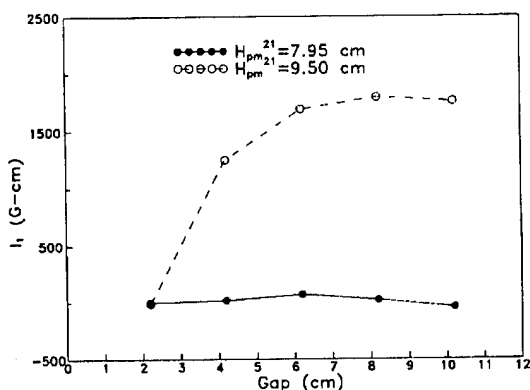


Figure 5. Dipole steering as a function of gap for the heights of the bias magnet 2 equal to 7.95 cm and 9.50 cm.

the size of the bias magnets is similar to optimize the rotating angles of the permanent rotators.

IV. DISCUSSIONS

The maximum deviation of the dipole steering in the operating gap range of an insertion device can be achieved either by optimizing the heights of bias magnets or by optimizing the easy-axis rotating angles of the permanent rotators, if a Halbach rotator type end pole compensation scheme is to be used. Numerically, it is possible to have a maximum deviation of the dipole steering within 100 Gauss-cm with each approaches. Therefore, a passive end compensation scheme can be achieved with help of prior optimization of the heights of bias magnets by using magnetostatic code and with fine tune of the easy-axis rotating angles of the permanent rotators after assembly of the magnetic structure of the insertion device.

References

- [1] I.Vasserman and E.R. Moog, "A Passive Scheme for ID End Correction," presented at the *International Conference on Synchrotron Radiation Instrumentation*, held 18-22, July, 1994 New York, USA; I.Vasserman and E.R. Moog, "A Passive Scheme for Undulator End Correction," Appendix 2 of the Technical Specification for Undulator A, APS Document No. 41010101-00002.
- [2] OPERA-2d is a trade mark of Vector Fields.
- [3] U5.0 Undulator Conceptual Design Report, LBL PUB-5256, November 1989.

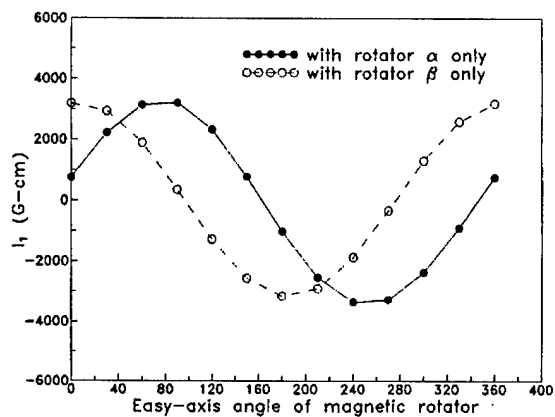


Figure 6. Dipole steering as a function of the easy-axis rotating angle of the permanent magnet.

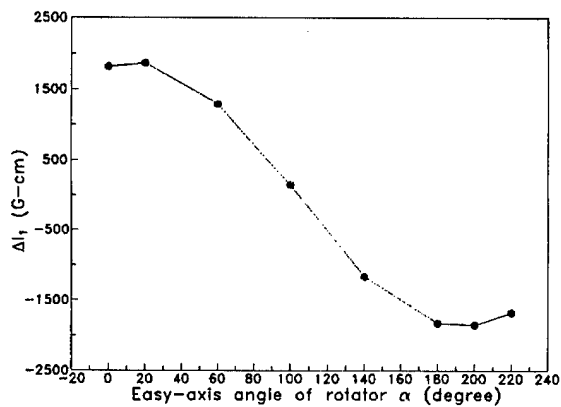


Figure 7. Maximum deviation of the dipole steering ΔI_1 in the gap range from 22 mm to 102 mm as a function of the easy-axis rotating angle of the permanent rotator α .

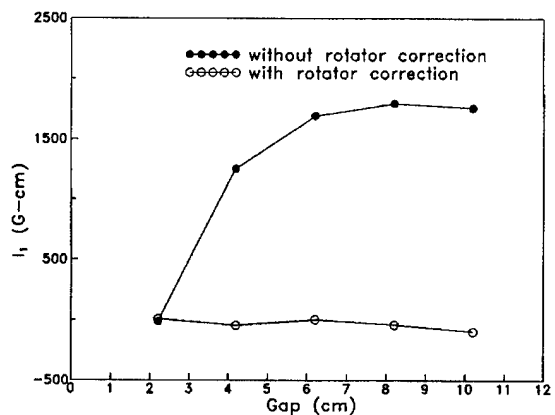


Figure 8. Dipole steering as a function of gap for an end correction scheme with (solid curve) and without (dashed curve) help of the rotators.

INSERTION OF HELICAL SIBERIAN SNAKES IN RHIC*

A.Luccio and F.Pilat, Brookhaven National Laboratory, Upton, NY 11973-5000

I. HELICAL SNAKES AND SPIN ROTATORS

For polarized protons in RHIC, two Siberian snakes and four spin rotators per ring will be used [1]. Snakes, 180° apart, and with their axis of spin precession at 90° to each other, are an effective means to avoid depolarization through resonances. Spin rotators, in pairs, rotate the spin from the vertical to the horizontal and back at an interaction. They are needed to study proton collisions with the spin in the horizontal plane.

We adopted a solution with four identical helical magnets for snakes and rotators [2]. Our choice is dictated by distinctive advantages of helical over transverse magnets. (i) they are modular, (ii) the maximum orbit excursion is smaller, and (iii) independent from the separation of magnets, (iv) they allow an easier control of the angle of the spin precession axis. To use the standard RHIC dipole cryostats, the length of the devices is limited to 12 meters. We have chosen 2.4 m as the length of each module.

An analytical approximate calculation of the properties of a four helical magnet was made [3]. Since we have found that the fringe field is important both for orbits and spin rotation, a systematic study by numerical integration of the equations of motion and of spin through the magnetic field was performed [4], using the field expression first described by Blewett and Chasman [5]

$$\begin{cases} b_x \approx \left[-1 - \frac{1}{4}(3u^2 + v^2) \right] \sin kz + \frac{1}{2}uv \cos kz \\ b_y \approx \left[1 + \frac{1}{4}(u^2 + 3v^2) \right] \cos kz - \frac{1}{2}uv \sin kz \\ b_z \approx -\sqrt{2} \left[v + \frac{1}{4}(u^2v + v^3) \right] \sin kz - \sqrt{2} \left[u + \frac{1}{4}(u^3 + uv^2) \right] \cos kz \end{cases}$$

$$\text{with } b = \frac{B}{B_0} \quad \begin{cases} u = kx/\sqrt{2} \\ v = ky/\sqrt{2} \end{cases} \quad k = \frac{2\pi}{\lambda}$$

For the fringe, we assumed that the field decays as 1/cosh in a distance equal to half the magnet aperture.

In the the program, the equation of motion

$$\frac{d\beta}{dt} = \beta \times \Omega \quad \Omega = \frac{e\mathbf{B}}{m\gamma}$$

and the spin precession equation

$$\frac{ds}{dt} = C_1 s \times \Omega + C_2 (\beta \cdot \Omega) s \times \beta,$$

$$\text{with } C_1 = 1 + G\gamma \quad C_2 = -\frac{G\gamma^2}{1 + \gamma} \quad G = \frac{1}{2}g - 1$$

are integrated. The results described in the following are obtained by numerical calculation,

Rotator parameters are given in Table I. Orbit and spin are shown in Figs. 1A and 1B. To compensate the field integral including fringe, the angle of rotation of the field in each helix is less than 360°. So, a particle entering the magnet on axis will emerge on axis. In RHIC, collisions will be done at energies from $\gamma = 27$ to the maximum $\gamma = 250$. Since the rotator beam line is at an angle $\phi = 3.674$ mrad with the adjacent interaction straight, after the rotator the spin precedes further. To obtain a proper polarization at the interaction, the spin should emerge from the rotator at an angle $G\gamma\phi$ with the rotator axis. The field to provide a longitudinal polarization at the interaction is shown in Fig. 2.

Snake parameters are in Table II. Orbit and spin are shown in Figs. 3A and 3B, for the condition of the axis of spin precession at an angle of 45° with the beam direction. This angle is slightly adjustable by varying B1 and B2 to compensate for effects of solenoidal fields in the detectors.

Table I. Parameters of the helical magnets at injection ($\gamma=27$).

Spin Rotator				
Length [m]	Field ^a [tesla]	Field rotation ^b	Field orientation ^c	Max orbit [mm]
2.40	2.047	+345°	97.5°	24.1(hor) 10.0 (vert)
2.40	2.654	-345°	82.5°	
2.40	2.654	+345°	97.5°	
2.40	2.047	-345°	82.5°	
Siberian Snake				
2.40	1.191	+345°	7.5°	14.7 (hor) 31.5 (vert)
2.40	3.864	+345°	187.5°	
2.40	3.864	+345°	7.5°	
2.40	1.191	+345°	187.5°	

^a For longitudinal polarization (Rotators). For precession axis at 45° (Snakes).

^b "+", right-handed helix. "-", left-handed.

^c Angle of field with the vertical at magnet's entry.

* Work performed under the auspices of the U.S. Department of Energy

II. LINEAR COUPLING EFFECTS

Transfer matrices up to the third order have been numerically calculated by tracking many particles with random initial coordinates and performing a polynomial fit of the final vs. the initial conditions. The dependence of the numerical matrix on input parameters has been systematically checked. The fit results proved insensitive ($< 1\%$) to most of the parameters varied. Only a center offset of 3 cm, unrealistic, produced variations greater than 1%. The values are also in excellent agreement with differential algebra results [6], and in reasonable agreement with the analytical approximation

The linear coupling effect of helical snakes and rotators in RHIC is calculated with a one turn linear map [7]. In the model, Fig. 4, we place snakes and spin rotators in their lattice position, and connect their locations by phase space rotations.

From the one-turn matrix

$$T = R_{61} \times \sigma \times R_{56} \times \pi \times R_{45} \times \pi \times R_{34} \times \pi \times R_{23} \times \pi \times R_{12} \times \sigma$$

with the phase space rotation between points i and j

$$\begin{bmatrix} R_{ij}^x & 0 \\ 0 & R_{ij}^y \end{bmatrix},$$

the linear coupling effect, i.e. the distance of minimum tune separation ΔQ_{\min} is derived. We write the 4x4 one-turn

matrix T as $\begin{bmatrix} M & m \\ n & N \end{bmatrix}$. Then, in the particular case when

$Q_x=Q_y=Q_0$ (fractional tune), obtain

$$\Delta Q_{\min} = \frac{1}{2\pi} \frac{\sqrt{\det H}}{\sin(2\pi Q_0)},$$

where $H = m + n^\dagger$.

With $Q_x=28.185$, $Q_y=29.185$ and only 2 snakes, the results for the linear model are in Table II. The prediction from the analytical and numerical models are within a factor 2, due to different representation of the fringe field. Table II also shows the coupling when we add 4 rotators.

III. CONCLUSIONS

Spin rotators and Siberian snakes for RHIC can be built using 4 helical magnets obtained, by twisting, from the cosine dipoles. We found that the fringe fields are important. In the calculations we have used a plausible model for the fringe. However, only magnetic measurements on the prototypes presently being built will allow a final optimization. The linear coupling at injection, $\Delta Q_{\min} < 10^{-2}$, is well within the range of the RHIC decoupling system. At storage, the coupling introduced by the devices ($\Delta Q_{\min} < 10^{-4}$) is negligible.

IV. ACKNOWLEDGMENTS

We acknowledge constant discussions and criticism by T. Roser, S. Peggs, and E.D. Courant. We are indebted to N. Malitsky for careful reviewing the numerical calculations.

Table II. Linear coupling in RHIC at injection ($\gamma=27$).

2 snakes ΔQ_{\min}	analytical 0.00157	numerical 0.00289
2 snakes + 4 rotators ΔQ_{\min}	no fringe fields 0.00303	with fringe fields 0.00383

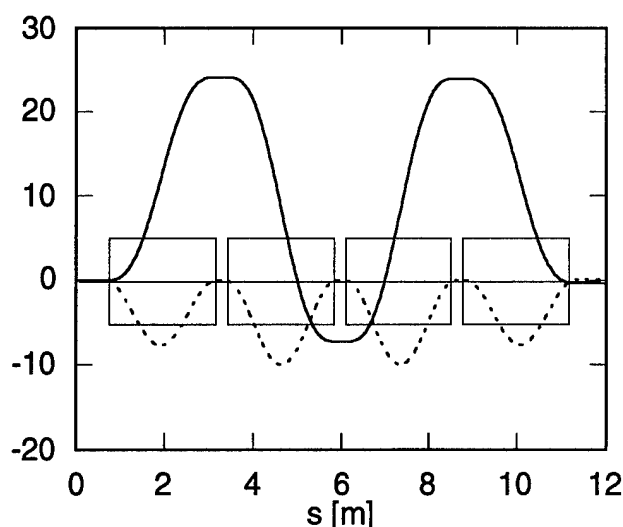


Fig. 1A. Spin rotator. Orbits [mm]. $\gamma=27$.

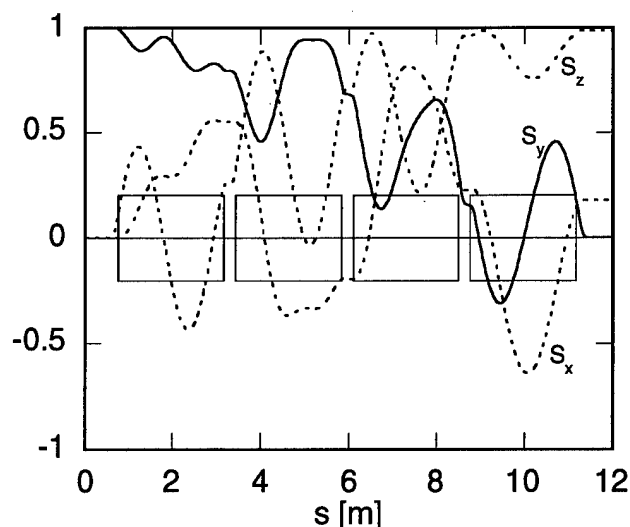


Fig. 1B. Spin rotator. Spin precession ($\gamma=27$).

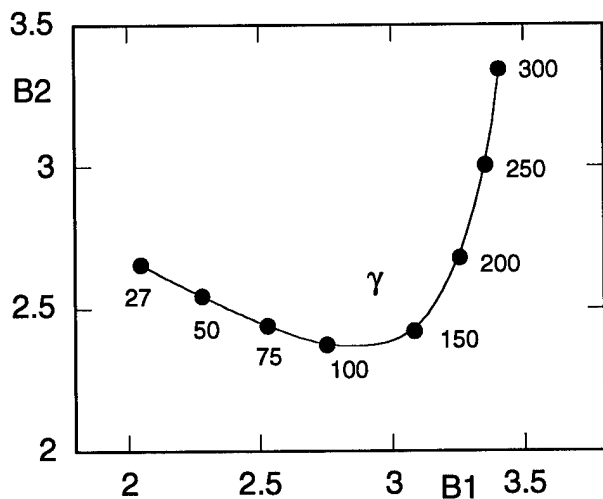


Fig. 2. Spin Rotator. Field [Tesla] to achieve longitudinal polarization in the interaction, vs γ .

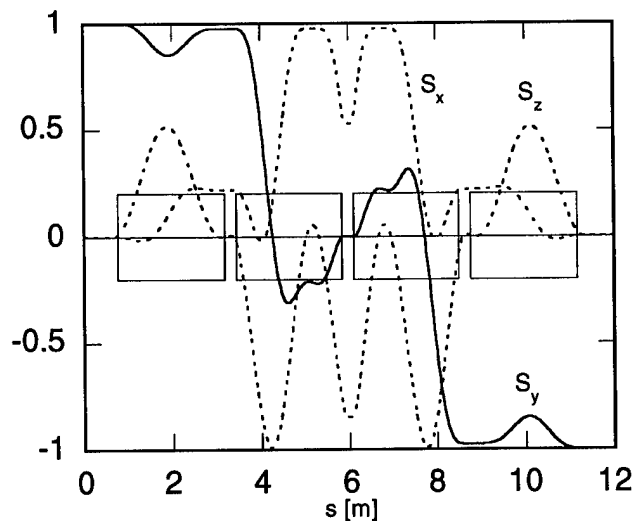


Fig. 3B. Snake. Spin precession. $\gamma = 27$.

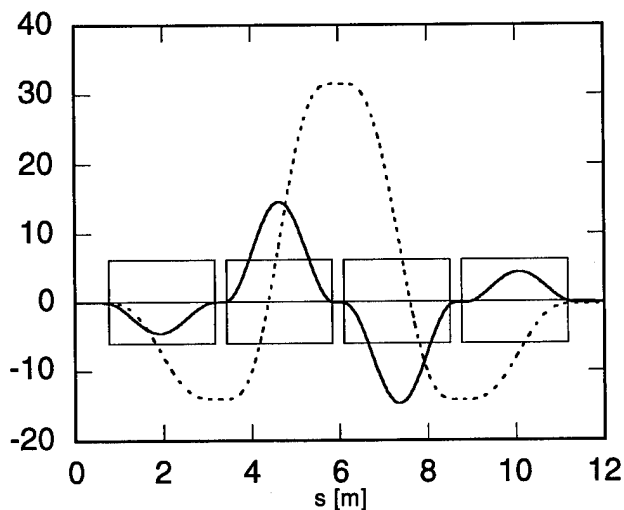


Fig. 3A. Snake orbits [mm]. $\gamma = 27$.

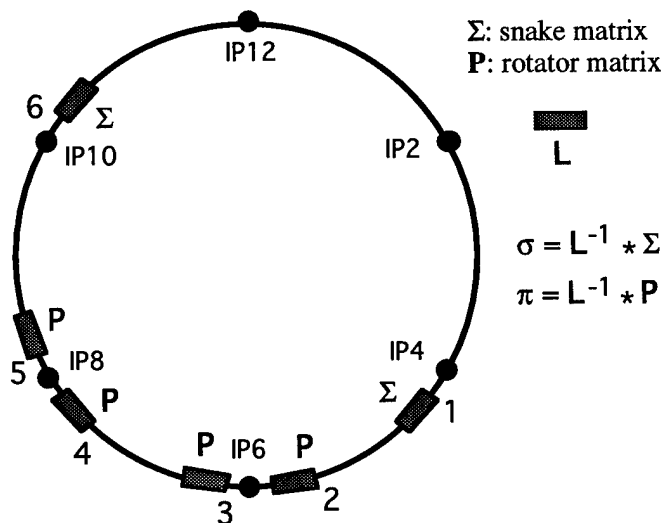


Fig. 4. Model of RHIC for the one-turn matrix.

V. REFERENCES

- [1] Conceptual Design for the Acceleration of Polarized Protons in RHIC (T. Roser, Coordinator). May 24, 1993, revised September 3, 1993.
- [2] V.I. Ptitsin and Yu.M. Shatunov, 3.rd Workshop on Siberian Snakes. Upton, NY, Sept. 12-13, 1994, p.15.
- [3] E.D. Courant, RHIC/AP/47
- [4] J.P. Blewett and R. Chasman, J.Ap.Phys. 48 (1977) 2692
- [5] A. Luccio, 3.rd Workshop on Siberian Snakes, *loc. cit.*, p. 193
- [6] S. Peggs, IEEE PAC Conference 1983, p.2460
- [7] N. Malitsky, RHIC/AP/51

MODELING OF WLS FIELD WITH PIECEWISELY CONSTANT MAGNETS

Zuping Liu and Aihua Zhao
NSRL, USTC, Hefei, Anhui 230029, P.R.China

I. INTRODUCTION

A WLS, or a WaveLength Shifter, indicates in this note a superconducting wiggler which, installed as an ID (Insertion Device) in a storage ring, can provide short wavelength synchrotron light and will usually impose a strong effect upon the stored beam.

The magnetic field in a WLS varies dramatically with longitudinal positions in such a way that differs by far from either approximately piecewisely-constant fields in most ring magnets, or sine-like periodical fields in long multi-period ID's. WLS effect analysis is hence made difficult. To refer to commonly used accelerator physics computer codes, a 3-rectangular-pole modeling method is used most frequently, with the parameters chosen according to the 0th order effect of the WLS in question. Unfortunately, such a modeling often gives a distorted account of its 1st order effect and fails to properly represent the WLS effect on the beam motion.

During a visit to BESSY, Germany, the authors carries out studies on WLS effects, including: theoretical study on the field and beam motion, field analysis, particle tracking, up-to-3rd order transport (Taylor's expansion) coefficients calculation, modeling of the field with 3 edge-angled piecewisely constant magnets, and error analysis for the modeling. Detailed calculation results for BESSY-1 WLS's and discussions are presented in a BESSY technical note[1]. This paper will focus on 2 creative pieces of the work: estimation of the biggest 1st and 3rd order terms with field integrals; linear effect modeling by parameters fitting. Most methods and ideas herein described, such as "higher order edge effect", apply in principle to other ID's.

Discussions with P.Kuske are very helpful to the work.

II. WLS EFFECTS

In the terminology of machine physics, motion of a particle is described by 6 variables: the 2 transverse displacements and 2 slopes (x, y, x' and y'), the orbit length (L) and the momentum deviation (δ). When going through a magnet, the first 5 of them change so that their final values are determined by the initial values of the first 4 variables and δ . By Taylor's expansion of the functions, the effect of the magnet can be resolved into orders. Of the 1st order terms (linear transport matrix elements), 25 are dependent on and descriptive of the magnet field. Similarly, there are 5 terms to account for the 0th order effect, 15×5 terms to indicate the 2nd order, 35×5 to go to the 3rd, and much more for even higher.

The WLS effects are thus itemized as: 1) 0th order effect, the closed orbit distortions, increase of the orbit length, as well as the orbit deflection and displacement within the WLS. 2) 1st order effect, an inevitable vertical focusing and maybe a weak horizontal defocusing, causing tune shifts and beta function beating, breaking the superperiodicity and the symmetry of lattice functions in the machine and changing the phase advances be-

tween ring components; hence often restricting the ring's dynamic aperture. The 1st order effect is always the most important. 3) 2nd and higher order effects, causing chromatic and geometric aberrations, affecting dynamic aperture and energy acceptance, inducing tune spread and maybe high order resonances. 4) Effect due to the radiated energy in the WLS, i.e. changes of the "synchrotron radiation integrals", therefore a bigger energy loss, shorter damping times, a larger energy spread and longer bunch length, some change in the beam emittance and momentum compaction factor, and so on.

In most WLS's, plane $y = 0$ is the magnetic median plane in which the field is purely vertical and the central orbit lies. Then, the field at position (x, y, s) , up to the 3rd order, can be found as

$$\begin{aligned} B_y &= B_y(s) + x \frac{\partial B_y}{\partial x} + \frac{1}{2}(x^2 - y^2) \frac{\partial^2 B_y}{\partial x^2} - \frac{1}{2}y^2 \frac{\partial^2 B_y}{\partial s^2} \\ &\quad + \frac{1}{6}x(x^2 - 3y^2) \frac{\partial^3 B_y}{\partial x^3} - \frac{1}{2}xy^2 \frac{\partial^3 B_y}{\partial x \partial s^2} \dots \\ B_x &= y \frac{\partial B_y}{\partial x} + xy \frac{\partial^2 B_y}{\partial x^2} + \frac{1}{6}y(3x^2 - y^2) \frac{\partial^3 B_y}{\partial x^3} - \frac{1}{6}y^3 \frac{\partial^3 B_y}{\partial x \partial s^2} \dots \\ B_s &= y \frac{\partial B_y}{\partial s} + xy \frac{\partial^2 B_y}{\partial x \partial s} - \frac{1}{6}y^3 \frac{\partial^3 B_y}{\partial s^3} + \frac{1}{6}y(3x^2 - y^2) \frac{\partial^3 B_y}{\partial x^2 \partial s} \dots \end{aligned}$$

where the on-axis field and its on-axis derivatives are s -dependent only, and the 3rd order components in the first 2 equations are much smaller than those in the 3rd.

In the x - y - s Cartesian coordinate system the particle motion equations are ($'$ denotes derivation with respect to s , $B\rho$ is the nominal rigidity of the beam):

$$L' = \sqrt{1 + x'^2 + y'^2}$$

$$x'' = -L'((1 + x'^2)B_y - y'B_s - x'y'B_x)/((1 + \delta)B\rho)$$

$$y'' = L'((1 + y'^2)B_x - x'B_s - x'y'B_y)/((1 + \delta)B\rho)$$

The whole procedure for the authors to deal with WLS effect is summarized as follows. 1) Field mapping. From the WLS field measurement data, it determines the on-axis field components (field itself and its partial derivatives) by a least square fitting, to be used in field reestablishment during tracking. 2) Particle tracking. A lot of particles are tracked through the WLS with Runge-Kutta's method. 3) Taylor's expansion. Another least square fitting, taking the variables' final values of all the particles as functions of their initial values, gives the coefficients up to the wanted order. 4) Modeling. It keeps the above-obtained linear transport matrix of the WLS as intact as possible. 5) Calculation with machine physics codes. The model magnets are put in the place of the WLS for its linear effect and chromatic aberrations. The terms other than 1st order can be used for their corresponding effects.

A few computer codes (in VAX Fortran) are developed by the authors for this purpose. The modeling and tracking/coefficients-fitting codes have been used for BESSY WLS's[1,2].

III. HIGHER ORDER EDGE EFFECTS AND ESTIMATION FORMULAS

Insertion devices always produces vertical focusing because the inside beam orbit does not coincide with the gradient of the field. This is often named as edge effect by analogy to edges in ordinary magnets. The same mechanism gives rise to 3rd and other odd order effects, which the authors refer to as "higher order edge effects".

The WLS field varies slowly in respect to x , but so fast along s -axis that, by Maxwell's law, there must be strong longitudinal field component off the midplane, which gives a vertical focusing to particles on an inclined orbit. This need not be related to x -dependent field component. In general, a beam travelling on a inclined orbit in a varying field will "see" a "one order higher" effect of any transverse field components; here the gradient may translate into a higher order derivation. If the orbit wiggles in a quasi-periodic field, the even orders cancel while the odd ones add up. These edge effects are inevitable in ID's, and often significant, especially when the field is strong, or the ID is of a lot of periods, or there are many ID's in the ring.

The most important edge effects are the 1st and 3rd order ones; of their many terms, the biggest are vertical focusing ones, normal quadrupole-like and octupole-like, respectively. The authors find a way to estimate such biggest terms with on-axis field integrals. The 3rd order field component, which can hardly be extracted convincingly from measurement, need not be explicitly evaluated.

Omit irrelevant terms for simplicity, e.g. suppose the field is not x -dependent. Let $b = B_y(s)/B\rho$. Then the particle motion equations turn into

$$x'' \approx -B_y/B\rho \approx -b + \frac{1}{2}y^2b''$$

$$y'' \approx -x'B_s/B\rho \approx -x'(yb' - \frac{1}{6}y^3b''')$$

Here x is the central orbit. Assume y not to change much on the way though y' changes. The equations are combined to yield

$$\Delta y' = - \int y'' ds \approx -y \int b^2 ds + \frac{2}{3}y^3 \int bb'' ds + \dots$$

with the integrals made over the whole device.

If the field is x -dependent, the linear term has to be revised. More often than not, the strong field in the central pole goes down with x squared where the beam runs off-axis and sees a negative $\partial B_y/\partial x$, giving a horizontal defocusing and an additional vertical focusing. In building a WLS, attention is usually paid to 2nd order field variation with x , but often only to field integrals along straight lines, on which the central pole term and the side pole terms cancel partially. Along the curved orbit, however, the central pole term is the dominant. Since any additional transverse focusing must be of the same strength but of opposite signs on the 2 planes, the revised estimation formulas are

$$(\Delta y'/y_o) + (\Delta x'/x_o) = - \int b^2 ds$$

$$(\Delta y'/y_o^3) = -\frac{2}{3} \int b'^2 ds$$

A few conclusions are drawn from the formulas: Both terms are focusing vertically, with a definite sign and therefore ineradicable, dependent on on-axis field distribution, going up with device length and with maximum field over particle energy squared. For a WLS, the ideal distribution is made of a narrow positive field peak and flat negative fields in side poles.

Calculation results agree well with the estimations. The accuracy is about 1% for the 1st order and 9% for the 3rd. The 1st order revision is necessary, for the discrepancy in vertical focusing alone may be over 20% in BESSY examples, while in general unknowable without tracking.

IV. MODELING OF WLS 1ST ORDER EFFECT

Modeling of WLS field with commonly used magnet types sets a bridge from the tracking and coefficients-fitting results to machine physics tools.

The models of the authors are still 3 separate bending magnets. But their parameters, namely, their lengths, bend angles, edge angles and the drift space lengths in between, all are set as variables and chosen by one more fitting so as to reproduce the linear transport matrix, with its elements set as goal functions and a few more relations (total length, final deflection and displacement) as limiting conditions. The fitting is by "Variable Metric Method for Minimization"[3], which minimizes the gradient of the "function of goodness" in steps of accumulative multi-dimensional space metric variation and has been used successfully in lattice function fitting. The number of variables need not equal to that of goals. The accuracy of fitting is comparable to that in the preceding measurement and matrix calculation. Because of errors in the preceding steps and inner contradictions between a few goals and conditions, the fitting function of goodness cannot and need not be down to zero. One can choose weight factors to make the more significant goals reached sufficiently close.

Modeling calculations are done for the BESSY-1 operational 3.2 T WLS (and a planned 6 T WLS). As sketched in Fig.1, the modeling assumes the bending field is compressed into 3 short magnets, sitting at the turning points of the orbit, with the central field about 10% weaker than the maximum field, and the bend angles about 20% smaller than the maximum deflection angle. The edge angles are so chosen as to produce the focusing strengths more properly. Fig.2 shows the shape of the inclined magnet faces with the angles enlarged 10 times. Because of the horizontal defocusing, the magnet poles are not rectangular, but look like curved edge faces, the "curvatures" of which are convex outward so as to resemble the isomagnetic surfaces of the field. This is in accord with the concept of edge effect, and with existence of 2nd order field variation with x . To follow the tracking results, the parameters of the models are slightly assymetric about the midpoint, and the system is not completely achromatic.

Calculations reveal that the WLS effects on the synchrotron radiation integrals and consequently on the related ring parameters are evaluated in the models in close approximations. The higher order effects are also studied. A key point is to "condense" the matrices into "thin lenses" at the WLS midpoint to get rid of the influence of path length, leaving only a few significant terms outstanding. Of them, the chromatic terms (variance of focusing with energy deviation) of the WLS are well

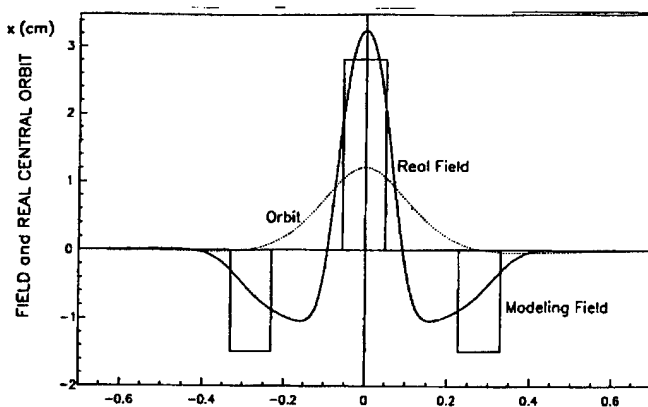


Figure 1. WLS Modeling, Field and Real Orbit

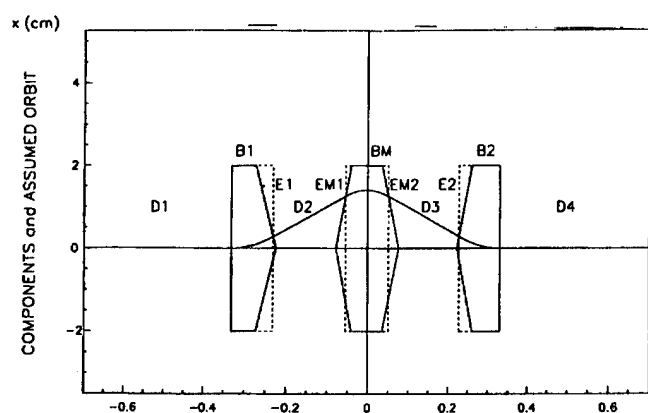


Figure 2. Fig.2 Modeling Magnets and Assumed Orbit

represented by the models; while the geometric aberrations held poorly. The latter may be improved by 2nd order parameter fitting with curved edges, or by inserting a high order thin lens at the WLS midpoint. The coupling terms (skew magnet generated terms) are trivial.

There are other methods formerly used in WLS modeling. 1) One is the 3-rectangular-magnet modeling, usually having the field integral of a pole or the maximum bend angle the same as in the real field. In this way the method has the 0th order effect to some extent reproduced, rather than the 1st order. Selection of the field values is still somehow arbitrary. The WLS effect may easily be either overestimated (if at peak field) or underestimated (if at full length). With only rectangular magnets, no way to take into account the horizontal defocusing, which might disturb the lattice quite seriously. Therefore, such a modeling may have the effect distorted. 2) Some computer codes allow transport matrix directly used as a magnet type. It is fine for the tunes and the lattice functions all over the ring. But the functions and beam parameters inside the WLS are not presented, not even their approximations; neither are the influences on the synchrotron radiation integrals; nor the 2nd order chromatic effect of WLS included without special treatment.

V. CONCLUSION

Starting with the field data (from measurement or prediction), the methods and computer codes mentioned in this note can do calculations for the WLS effect on the beam and for compensation considerations. Either the simple estimations or the complicated calculations agree with the reality satisfactorily. As for the modeling method, so far as the 1st order effect is concerned in the first place, it can gain its user an access to all the existing accelerator physics computer codes without fear of being misled. There is yet much room for further work in WLS higher order effect study.

VI. REFERENCES

- [1] Z.Liu, A.Zhao, Modeling of WLS Field with Piecewisely Constant Magnets, BESSY Technical Note, Nov. 1994.
- [2] Z.Liu, A.Zhao, A BESSY-1 6 Tesla WLS Effect Compensation Scheme, BESSY Technical Note, Nov. 1994, also presented at PAC'95.
- [3] W.C.Davidson, Variable Metric Method for Minimization, ANL-5990, Rev.2. Also see computer code (COMFORT), developed at SLAC.

A BESSY-1 6 TESLA WLS EFFECT COMPENSATION SCHEME

Zuping Liu and Aihua Zhao
NSRL, USTC, Hefei, Anhui 230029, P.R.China

I. INTRODUCTION

A WLS (superconducting wavelength shifter) is now in operation in the BESSY-1 storage ring. The maximum field therein is 3.25 T(esla). To its weak effect on the stored beam, so far no compensation in quadrupole strengths is needed.

It is planned to install a 6 T WLS to replace the present one. A study on its effect and compensation considerations is carried out in 1994 by the authors, then as visitors to BESSY.

The WLS has first to be characterized in terms comprehensible to commonly used machine physics computer codes. The work involves field analysis, particle tracking, transport matrix calculation and modeling of the field with piecewisely constant magnets, and is described in another note[1]. The calculations for the 3.25 T WLS are in good agreement with observations. The work presented in this paper is based on the modeling, that is, the model magnets are put in the place of the WLS for all the relevant calculations. The 6 T WLS field in the modeling is scaled up from the 3.25 T WLS field measurement data; so it may differ from the real field in the future WLS.

According to the study, the 6 T WLS will have quite annoying effects on linear optics and non-linear/chromatic beam behavior, inducing beta function beatings and depressing the dynamic aperture, especially for off-energy or off-x-axis particles.

A compensation scheme with 4 additional independent quadrupole power supplies is hence proposed. The beta function beatings can be fully localized in the WLS seated drift section, while the superperiodicity and symmetry of the lattice functions be saved to a large extent. The tunes are the same as in the currently operational optics. The quadrupole strengths are optimized to assure a sufficiently large dynamic aperture.

The authors are not to declare that such a compensation is absolutely necessary, because of the uncertainty about the real field and about interactions between the WLS's disturbance and existing magnet errors and misalignments. But rather, this paper is to present that, if a compensation is needed, how it should be made and what it can achieve.

II. EFFECT OF THE 6 T WLS IN BESSY-1

The lattice configuration now in operation is named as "WLS" optics. To avoid confusion, we refer to the original WLS optics as "WLS-0", in which the WLS field is zero; the configuration with 6 T WLS on but "No Compensation" (with the same quadrupole settings as in WLS-0) is referred to as "WLS-NC"; and the proposed configuration, with the WLS on and new quadrupole settings for compensation, as "WLS-C".

The main magnet strength settings, ring parameters and lattice functions in all the configurations are given in tables and/or figures in a BESSY technical note[2]. In any case, the sextupoles are set to correct the chromaticities both to plus one.

The linear lattice calculations and function fittings are made with the authors' self-developed codes (LAMP) and (LATGH).

The latter features graphic output based on CERN-developed software package HIGZ and interactive execution mode. Particle tracking and other non-linearity and chromatism studies are fulfilled mainly with (PATRICIA)[3], to which a few additions[4] by an author are found useful in the studies, like harmonics analysis in an asymmetric ring.

In WLS-0, the beta functions are well matched, with the tunes as $\nu_x/\nu_y = 5.619/3.284$, and with maximum $\beta_x/\beta_y = 16.1/14.0$ m.

When the 6 T WLS is turned on, a strong vertical focusing and a relatively weak horizontal defocusing are exerted on the beam. Its most eye-catching effect is that on the two beta functions. The β_y beating amplitude is as high as 1/4 of the β_y peaks, making the original peaks fluctuate a lot. The β_x function is also distorted. The tunes shift to 5.601/3.324, and maximum β 's rise to 18.8/17.4 m.

The DA(dynamic aperture)'s shrink obviously, especially for particles with large energy deviations and hence falling into synchrotron oscillations. On-energy particles with $15\sigma_x \times 15\sigma_y$ betatron oscillation amplitudes can stay in the ring, but those with $20 \times 20 \sigma$'s get lost.

The effect of the 6 T WLS seems more serious than anticipated. The vertical focusing, always the strongest part in the 1st order effect, can be estimated with the integral value of the WLS field ($1/\rho$) squared. A previous technical note[5] estimates the vertical focusing element $M(4,3)$ would be $-0.51(\text{m}^{-1})$. Provided that the 6 T WLS field is in proportion to the 3.25 T WLS field, the integral will be 20% larger, because its on-axis field distribution differs from that anticipated (see [5,6]), in which the positive central field is sharper and the negative side fields flatter. The effect goes further beyond because the beam orbit lies off-axis in the central field where, due to the 2nd order field descending with x, the beam sees a negative $\partial B_y/\partial x$ and is horizontally defocused as well as vertically more focused. As obtained from tracking, the $M(4,3)$ term goes to -0.73 , altogether 43% larger than the anticipation; and the horizontal defocusing term $M(2,1)$ is 0.115, big enough to cause trouble in x-plane oscillation.

There are several factors that also depress the DA. The superperiodicity and symmetry of the lattice functions are seriously broken. This is made worse by the "asymmetric location" of the WLS, whose center is 30 cm away from the straight section center. The phase advances between the sextupoles are changed, not only $\Delta\phi_y$ but $\Delta\phi_x$ as well. For off-energy particles, the big beatings in the β 's are superposed with their chromatic beatings, which are quite big even in WLS-0.

The tunes in WLS-NC can be adjusted back to the old values with the existing quadrupoles. Many options are tried but none is satisfactory, with the β distortions on the same scale, if not larger. This proves that an asymmetric disturbance can hardly be pressed down by symmetrically located means.

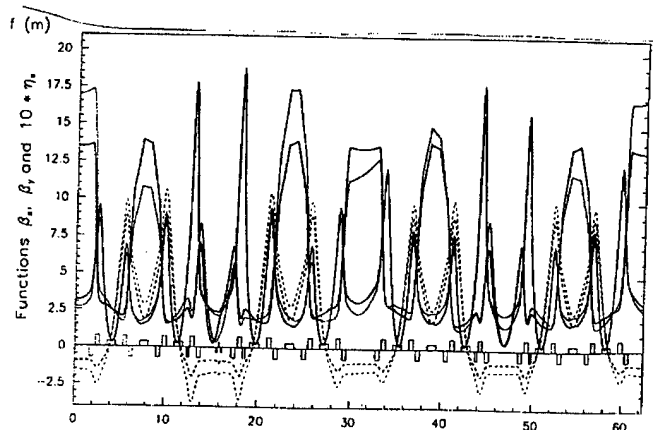


Figure 1. Lattice Functions in WLS-C/WLS-NC

III. THE COMPENSATION SCHEME

To fully correct the β distortions, at least 4 more "variables" are needed and all of them must be "asymmetric", that is, independent of other ring components. The proposed scheme requires 4 quadrupoles to be excited separately. They are the 4 closest to the WLS location, named as Q2A, Q1A, Q1B and Q2B, respectively, in the sequence as in the beam motion. Q2A and Q2B belong currently to the QT2 family, similarly for the Q1's. In WLS-C, their K1 values (normalized field gradient, in m^{-2} , positive if horizontally focusing) are: Q2A, Q2B = 4.7011, 4.4402; Q1A, Q1B = -3.7587, -2.8912. (cf. QT2, QT1 = 4.5423, -3.3352 in WLS-C or 4.5741, -3.3787 in WLS-0.)

The lattice functions (β_x , β_y and $10 \times \eta$) in the whole ring are plotted in Fig.1, which compares the functions with those in WLS-NC by plotting the latter in thinner lines as a background.

The WLS-C returns to the WLS-0 working point, and gets rid of the big beta function beatings, having maximum $\beta_x/\beta_y = 18.0/13.9$ m. The linear disturbance of the WLS effect is fully localized in the WLS seated section, or between Q2A and Q2B. The superperiodicity and symmetry of the lattice functions are saved to a large extent. The β_y peaks, that at the injection point included, are kept roughly the same as in WLS-0. This is good for beam injection performance. And, for all the lattice functions in the bending magnets, WLS-C and WLS-0 make little difference (while WLS-NC makes some). This should be good for the photon beamline users. The new quadrupole power supplies increase the flexibility of the ring lattice, by which other improvements can be made possible. For example, the authors intentionally reduce the η function fluctuation so that the beam emittance in WLS-C is down to 34 nm-rad, about 30% lower than that in WLS-0 to gain a factor of 2 increase in the photon beam brightness, and a little lower than the emittance in Super ACO, which is sometimes taken as a marker of the level of those so-called 3rd generation light sources.

Fig.2 gives tracking results for the configurations. Shown are DA's for particles with energy oscillation at an amplitude of 0.5% dE/E (about $8 \times \sigma_E$), printed at the injection point, roughly of the size of the physical aperture, horizontally ± 10 mm and vertically 20 mm high, filled with characters to mark the starting positions of the particles, "*" for those who survive the 1000 turn tracking in WLS-C or "o" for those who fail to. The DA in

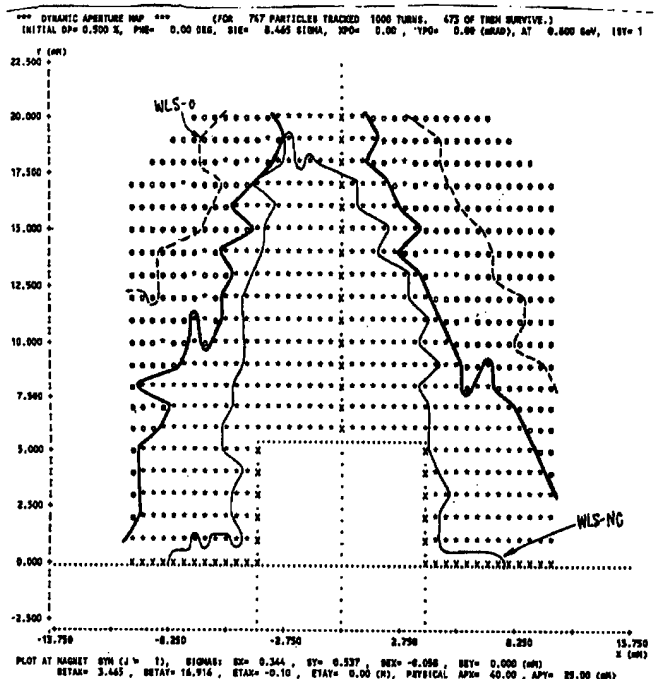


Figure 2. Dynamic Apertures for Off-energy Particles

WLS-C is then drawn to include the survivors, with the DA's in WLS-NC and in WLS-0 drawn with thin lines and broken lines, respectively, for comparison. Also tracked are on-energy particles and a few typical particles, whose betatron oscillations start with 10×10 to 25×25 σ 's, with the σ 's as the standard (r.m.s.) beam sizes, the horizontal one at zero coupling and the vertical at full coupling. Figures of on-energy DA's and phase space plots for the typical particles are omitted.

The DA's in WLS-C are obviously larger than those in WLS-NC, though still smaller than those in WLS-0 to a similar extent. The improvement is more substantial for particles of large amplitudes in energy oscillations or in vertical betatron oscillations. This should turn to longer beam lifetime and faster injection rate. As for the typical particles, a "15 σ " particle may feel somehow the same in the 3 optics; but a "20 σ " or even "25 σ " particle experiences a big difference, finding himself stable in WLS-C but not in WLS-NC.

During the search for an ideal compensation scheme, some attempts to use less independent power supplies were made without success. The WLS is located at a "double-asymmetric" position, breaking the symmetry not only about the injection point but also about the center of the section where it is installed. To correct its influence, only the differences between those quadrupoles which used to belong to one family count as useful variables.

The more tricky part is about the DA or the tracking. We had a few somehow better-looking linear solutions that, unfortunately, turn out to be ugly in tracking calculations. It is not the case when we did similar work at NSRL, where we found a good linear effect compensating scheme and it behaves reasonably well in tracking studies. The NSRL machine, HLS ring, resembles BESSY-1 ring in many respects. But there are at least 3 differences to account for why non-linear effects in BESSY-1 are

relatively difficult to cope with: 1) The WLS optics has a lower beam emittance, which usually means a more restricted DA. 2) There are fewer sextupoles in BESSY-1, so their strengths have to be higher. 3) The sextupoles in BESSY-1 are asymmetrically located, so the ring is, in the sense of higher order effects, an asymmetric ring. The optimization of the quadrupole strengths to assure a sufficiently large DA was time taking, in which main progresses are made with two key steps. First, (PATRICIA) is able to do harmonics analysis for a few sextupole strengths related functions, one of which is responsible for on x-axis particle motion. A component of $\sin(N\phi_x)$ is found too large, with $N = 17$, close to $3 \times \nu_x$. The component should vanish if the ring has a superperiodicity of two (then no odd terms) or the ring is symmetric (then no sin-terms). Efforts are made to lower that component and the on x-axis particles feel better. Second, for off x-axis particles, there must be coupling between the two transverse betatron oscillations. In BESSY-1 it is always the vertical amplitude that rises first, and the horizontal one follows. It is because, among the β 's at all the sextupoles, β_y at the SD's is the highest. The particles get a vertical kick, proportional to its x and y displacements multiplied, at every sextupole. The kick may be thought as a vertical focusing force varying, from one sextupole to another, with the horizontal displacement x. If the horizontal phase advances between the 4 SD's are roughly equal, the additional focusing cancels over one turn. That is how the phase advances are distributed in WLS-0, and may be why the tracking is tough for far off x-axis particles in WLS-NC and in compensation schemes. The horizontal defocusing term, not big though, plays in this sense a bad role. From this understanding, we use fitting calculations to make (it sounds strange) the horizontal phase advances between the SD's as equally paced as possible, even at the cost that β_x is a little mismatched (and worse-looking, as shown in the figures). This step gains a lot in the DA.

IV. CONCLUSION

As described above, the proposed scheme can compensate the effect of the planned 6 T WLS, keep its disturbance under an acceptable level and make the performances of the BESSY-1 light source nearly the same as when the WLS is off.

The required hardware changes are four power supplies and associated wiring. The new power supplies may be of less ability than the currently used ones, or four controllable shunts across the quadrupoles, with the advantage that the configuration can return to normal by simply turning off the shunt currents.

V. ACKNOWLEDGEMENTS

Discussions with P.Kuske and G.Wuestefeld are very helpful and inspiring.

VI. REFERENCES

- [1] Z.Liu, A.Zhao, Modeling of WLS Field with Piecewisely Constant Magnets, BESSY Technical Note, Nov. 1994. Also presented at PAC'95.
- [2] Z.Liu, A.Zhao, A BESSY-1 6 Tesla WLS Effect Compensation Scheme, BESSY Technical Note, Nov. 1994.

- [3] H.Wiedemann, Chromaticity Correction in Large Storage Rings, PEP Note-220, Sep. 1976.
- [4] Z.Liu, Addition to PATRICIA, the Non-linear Effects Treating Program, SSRL ACD-Note 15, 1984.
- [5] G.Wuestefeld, V.Sajaev, WLS - Optic for BESSY-I, BESSY Technical Note, Aug. 1992.
- [6] M.Martin, Supraleitender Wiggler bei BESSY I, BESSY Technical Report, July 1994.

16 Tesla Block-Coil Dipole for Future Hadron Colliders*

Peter M. McIntyre and Weijun Shen

Department of Physics, Texas A&M University, College Station, TX 77843

Ronald M. Scanlan

Lawrence Berkeley Laboratory, Berkeley, CA 94720

Abstract—Several new concepts in magnetic design and coil fabrication are being incorporated into a design for an ultra-high field dipole magnet for future hadron colliders. The 16 Tesla block-coil dual dipole uses Nb₃Sn cable, a simple pancake coil construction, and face-loaded prestress geometry to achieve high magnetic efficiency and stable stress distribution at the limit of Nb₃Sn performance. A reverse-field end coil is used to cancel the concentration of field and stress at the coil ends and thereby eliminate the dipole ends as a limit to performance.

I. INTRODUCTION

The cost and performance of a hadron collider are largely determined by the field strength and field quality of its superconducting magnets. The dipole strength determines the circumference of the collider for a given beam energy; the quadrupole strength determines the low-beta squeeze of the beams at the collision point; the dipole field quality determines the sustainable luminosity and the complexity of correction elements required in the collider lattice. As the high energy physics community assesses its options for future hadron colliders, magnet technology will set the limits for cost, performance, and siting.

In conventional dipole design^[1], a $\cos \theta$ coil configuration is supported within a non-magnetic collar within a steel yoke. In a previous paper^[2], we reported a design for a 16 Tesla block-coil dipole, consisting of a rectangular coil configuration closely coupled to a steel yoke. It offers improved magnetic efficiency, stable confinement of the Lorentz forces, and simple coil fabrication. The block-coil dipole is being developed in a collaboration between Lawrence Berkeley Laboratory and Texas A&M University. In this paper we report progress in the design and preparations for construction of short model magnets.

Figure 1 shows the overall magnet design and coil configuration for a 16 Tesla dual dipole utilizing Nb₃Sn Rutherford cable. Table I presents its main parameters. All coil elements are arranged in flat pancake coils, in which the cable is oriented flat to the direction of Lorentz forces. The coil is divided into three segments to facilitate grading of the conductor with $j_c(B)$ and optimization of field quality. This coil configuration provides a stiff modulus for preload, a simple procedure for coil winding and positioning, and a compact current geometry for minimum amp-turns.

*This work was supported in part by DOE grant DE-FG02-91ER40613.

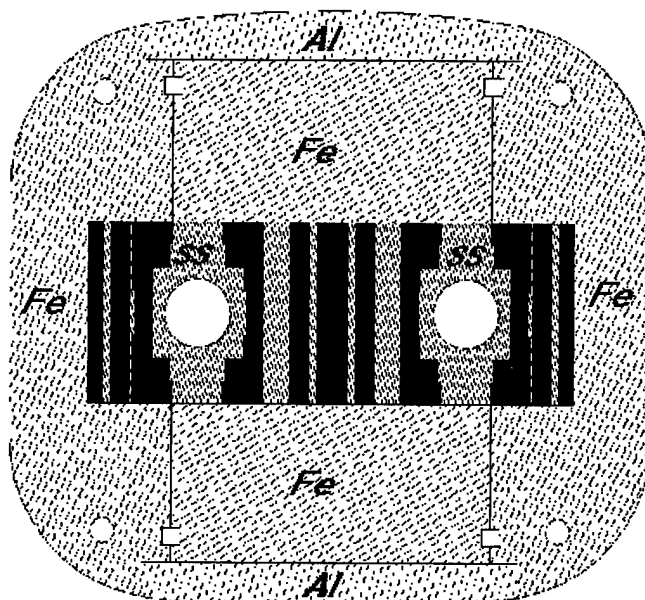


Figure 1. Block-coil dual dipole: coil configuration and preload strategy.

TABLE I
PARAMETERS OF BLOCK-COIL DUAL DIPOLE

Peak Field	16	Tesla
Beam tube aperture radius	2.5	cm
Maximum current	9,300	Amperes
Operating temperature	4.2	°K
Stored energy	4.36	MJ/m
Inductance	101	mH/m
Total turns	580	
Lorentz stress	170	MPa
Maximum j_{Cu} during quench	1,100	A/cm ²
Overall cold mass: radius	25	cm
mass	1,260	kg/m
Fringe field at cryostat surface	.1	Tesla

I. FIELD DESIGN

Figure 2 shows the calculated field distribution in the magnet at 16 Tesla excitation. We have designed the coil geometry to produce collider-quality field uniformity (all multipoles $b_n < 10^{-4} \text{ cm}^{-n}$) at full excitation B_0 , using equal current in all three coils. The innermost coil segment approximates a $\cos \theta$ distribution; the outer two segments are planar current sheets; the gaps between coil segments are made asymmetric to compensate the asymmetry produced by the opposite dipole. We can produce quality field at all in-

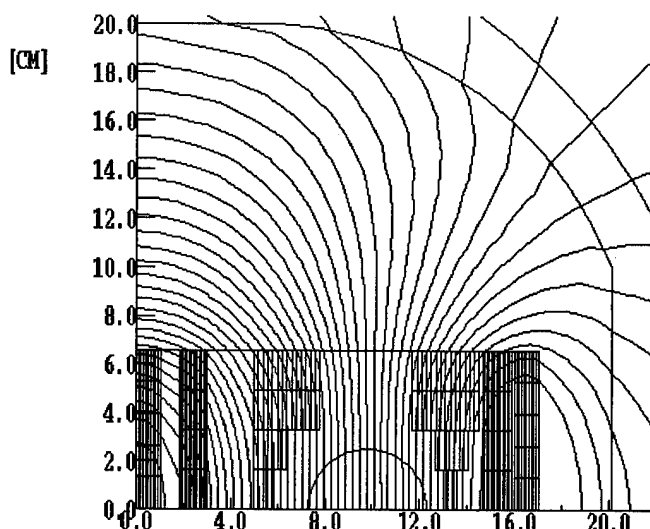


Figure 2. Calculated field distribution in one quadrant of block-coil dipole. intermediate field strengths by current programming the three coil segments. Figure 3 shows the current program as a function of excitation over a 20:1 dynamic range.

Persistent-current multipoles and AC losses.

The planar steel boundary above and below each beam tube serves to suppress the multipole fields induced by magnetization currents in the superconducting strands as the magnet is ramped from injection to full field and back. Figure 4 shows the calculated persistent current sextupole in the block dipole. The hysteresis at injection is ten times smaller than that in a $\cos \theta$ dipole with similar filament size.

Because the cable elements are turned edge-on to the magnetic flux in the coil region, AC losses should also be ~ 10 times smaller than in $\cos \theta$ dipoles.

II. COIL STABILIZATION

Reverse-Field End Stabilization

In any superconducting dipole, the coil ends are one of the most challenging limits for high-field stability. The fields are greatest at the ends; the forces are greatest in the ends and are difficult to preload around there; the conductor is somewhat degraded by bending there so that $j_c(B)$ is less there than in the body of the coil. All three effects make the end the "weak sister" of the dipole - the first location for failure.

We have conceived a means to eliminate this problem, by bracketing the end region with an array of reverse-field coils which cancel $\sim 30\%$ of the field at the location of the end turns of the dipole coil. The reverse-field coil arrangement is shown in Figure 5. The reverse coils are tilted so that their field cancels part of the primary field at the coil ends but does not produce significant field on the body portion of the main coil. The reverse coils of course experience large forces and fields. They are supported within an end steel structure and are designed with ample margin ($j/j_c \sim 0.5$) and stability ($Cu:SC \sim 2$).

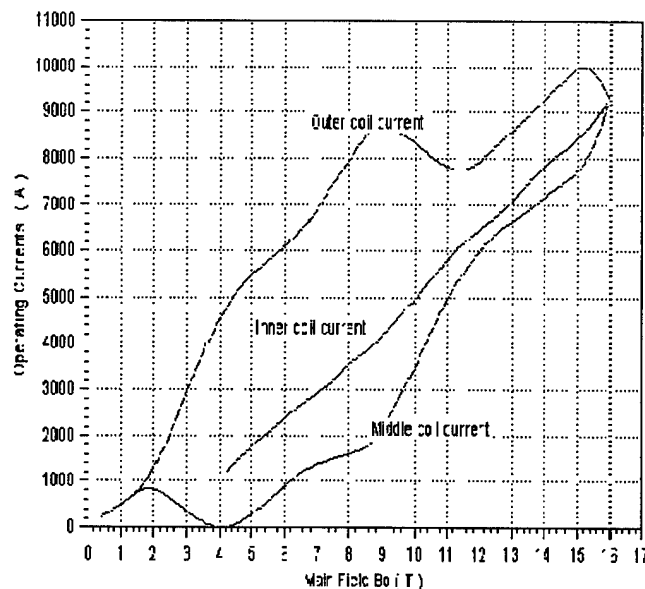


Figure 3. Current programming of the three coil segments.

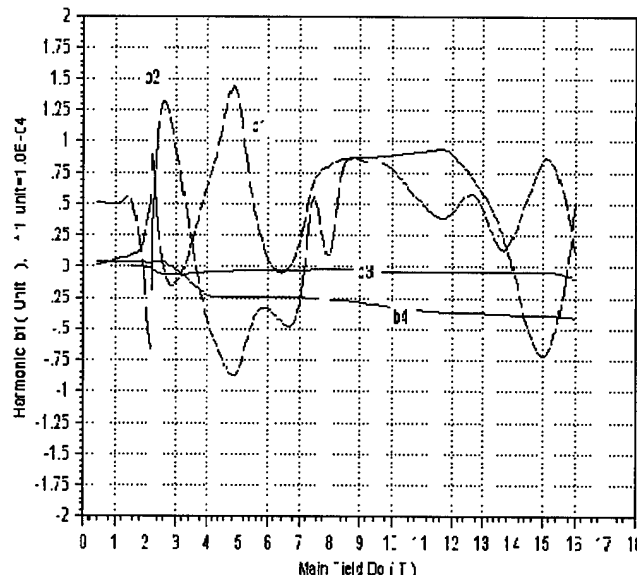


Figure 4. Residual multipoles including magnetization during ramping (PE2D).

The essential novelty of the reverse coil is to displace the problem of end fields and stresses to a compact coil which is only provided at the ends. The body coil must be driven to its practical limit, $j/j_c \rightarrow 90\%$, because most of the collider circumference is filled with dipole body and the conductor dominates the magnet cost. The ends, on the other hand, occupy only a few % of the magnet length, and the additional conductor to provide stable reverse coils is insignificant in the overall conductor budget.

Quench protection.

With a stored energy of 2.2 MJ/m in each dipole, quench protection is a critical consideration for reliable magnet operation. The parameter which is of greatest importance in quench dynamics is the maximum current density j_{Cu} which would appear in the copper stabilizer of the cable

during a quench. If $j_{Cu} < 1,100 \text{ A/cm}^2$, active quench protection using appropriate arrangements of clamp diodes, limiting resistors, and pulsed heaters can typically be used to safely distribute a quench so that a magnet consumes its stored energy without overheating at any location. We have adopted this limit in the block-coil dipole. Preliminary simulations have been made of quench propagation in the block-coil dipole using a heater/diode/resistor protection network. During a quench the current decays with a time constant $\sim 0.2 \text{ s}$, the maximum coil temperature is $\sim 430^\circ\text{K}$, and the maximum voltage is $\sim 1,300 \text{ V}$.

III. FABRICATION ISSUES

Coil preload strategy.

The rectangular coil package and rectangular steel flux return presents a particularly simple means for delivering a uniform preload to the entire coil. The steel flux return is divided along the in/out bifurcation of the return flux. The blocks are assembled with an aluminum bar to provide a gap at room temperature. The gap closes as the magnet is cooled down, and the bar dimensions are chosen so that the gap closes at 4.2°K and compensates the loss of compression which would otherwise occur from the differential contraction of the coil and the steel. The steel assembly is preloaded by wrapping a high-strength steel banding around the overall assembly. Preliminary stress analysis shows that this approach can be used to provide a uniform laminar horizontal prestress of 200 MPa to the coil while containing vertical coil dimensions.

E. Coil fabrication.

The coils of Nb_3Sn Rutherford cable must be fabricated using the wind-and-react method. We are developing a flat/bend winding procedure to simplify and improve coil fabrication. All coil elements are wound as flat racetrack coils. Adjacent pairs of coil elements are wound from the inside out from a single length of cable, so that all leads emerge on the outside ends of the coil package.

The racetrack coil is an ideal geometry in which to eliminate the flexure and handling of the coil and its insulation during fabrication. It presents a problem, however, for the coil elements which flank each beam tube: they must be bent up and over the beam tube at the ends. We have developed a procedure whereby these coils are also wound as flat racetracks, and then bent at the ends in a simple fixture so that each clears the beam tube. The final end configuration can be preloaded using precast spacer/tensor elements.

Inorganic cable insulation matrix.

Even with the elimination of stress concentrations, the Lorentz stress at 16 Tesla is immense - 170 MPa. Impregnation of the cable elements within the coil is essential, both to prevent stress concentrations where strands overlap in the cable and to provide electrical insulation during quench.

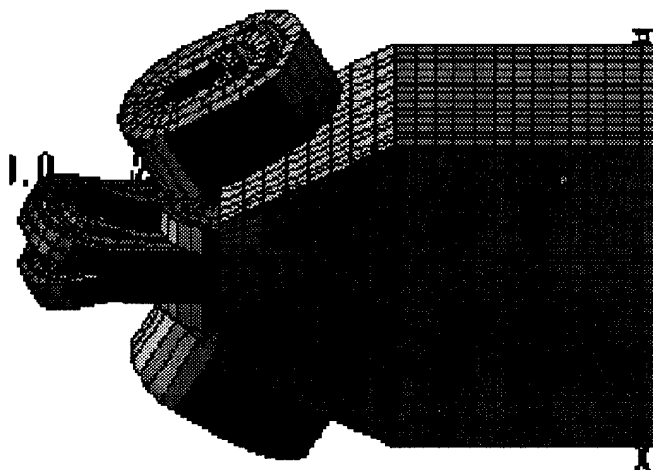


Figure 5. Reverse-field stabilization of the coil ends (TOSCA simulation)

Conventionally Nb_3Sn coils are impregnated with organic polymers after reaction bake. The poor heat conductivity of such materials limits heat transport through the thick coil package required for a 16 Tesla dipole. Both beam losses and synchrotron radiation produce substantial heat loads to the inner coil elements. Poor heat transport also compromises stability against micro-quenches.

We are endeavoring to overcome these problems by using an "inorganic B-stage" process which would provide inter-strand mechanical support and electrical insulation but preserve an open porosity for liquid He to permeate the coil package. The approach is motivated by work at Ceramphysics and Westinghouse^[3], Tanaka *et al.*^[4], and Shultz and Reed^[5]. A glass/ceramic mixture is mixed with a silicone binder to coat the strands of each cable element in the green state (before winding). The treated cable is sheathed in an E-glass wrap to provide inter-cable isolation. The glass component is chosen to have a vitrification temperature near the high end of the reaction bake cycle. It flows to uniformly fill the inter-strand space. The ceramic component provides powder reinforcement of the glass and local heat capacity at 4°K . After the Nb_3Sn reaction bake, the insulation provides mechanical support and electrical insulation to each cable element, but leaves open for helium percolation. Liquid helium can permeate this space, bathe the coil, and provide local enthalpy to stabilize against microquenches.

It is a pleasure to acknowledge the ongoing help of S. Caspi, F. Clark, W. Kroenke, A. McInturff, N. Munshi, H. van Oort, W. Sampson, and C. Taylor.

REFERENCES

- [1] R. Perin, "Status of the LHC programme and magnet development", Proc. Appl. Superconductivity Conf., Boston, MA, October 14-17, 1994.
- [2] D. Dell'Orco *et al.*, "Fabrication and preliminary test results for a Nb_3Sn dipole magnet", *ibid.*
- [3] P. McIntyre, R. Scanlan, and W. Shen, "Ultra-high-field magnets for future hadron colliders", *ibid.*
- [4] W.N. Lawless and C.F. Clark, J. Appl. Phys. **64**, p.2729 (1988).
- [5] K.H. Tanaka *et al.*, IEEE Trans. Magnetics **30**, p.2511 (1994).
- [6] J. Schultz and R.P. Reed, "Inorganic and hybrid insulation materials for ITER", MIT Plasma Fusion Center (1993).

AUTOMATED METHODS OF FIELD HARMONIC SIGNAL EXTRACTION AND PROCESSING FOR THE MAGNETS IN SUPERCONDUCTING SUPERCOLLIDER * †

T.S.Jaffery, J.Butteris[†], and M.Wake^{††}

SSC Laboratory, Dallas, TX 75237 U.S.A

[†]Highland Technology Inc. San Francisco, CA.94122 U.S.A.

^{††} KEK National Laboratory for High Energy Physics, Tsukuba, Japan 305

Abstract

A versatile field measurement system HAL2 was developed and used for SSC magnet measurements. The system based on V/F converter and 32 bit counters are set on a VME /modified VME bus. The system was capable of measuring the high ramp rate harmonics which was a vital issue especially for the construction of SSC High Energy Booster. System description and the implementation techniques for high ramp rate application is presented together with the measurement data in SSC dipole model magnet. The measurement up to 128 A/s was successful. Anomaly in the eddy current quadrupole was clearly observed.

I. INTRODUCTION

Measurement of magnetic fields, generated by high field magnets such as in SSC, with high accuracy is very important to fully understand the design construction, installation and operations issues of machines in which these magnets will be used. Many techniques and instrumentation systems have been developed and are commonly used for magnetic field quality measurements. Measurement systems for SSC superconducting magnets were mostly developed and used by the laboratories involved in R&D efforts of magnet development. The description of the field in particle accelerator is made using a concept of harmonic components. Very accurate measurement of the field is done directly measuring the harmonic components. Such method of direct harmonic field measurement[1] in superconducting dipole magnets was found very efficient during the TEVATRON construction at Fermilab and became a standard method for superconducting accelerator magnets. The requirement and restriction of the measurement are different in every case. SSC dipole magnets are required to be measured in a small space of radius 1.6 cm. First priority of measurement was the precision up to 30 pole with DC field. However, the eddy current effect in the superconducting cable was found to be much larger and complicated than what was estimated in the design phase[4]. The field measurement at high ramp rates became important. Such change in measurement priority happens to superconducting magnet project because state of the art technologies are always under development. The versatility of the measurement system is thus an important feature for the measurement system. The system, named HAL2, described in this paper is the system used for SSC magnet R&D at Fermilab. This system allows to use various kinds of harmonic

probes and measurement modes. Although the versatility of the system is capable of doing many other things, the emphasis is put on the high ramp rate measurement of the harmonic components in this report. We developed a technique of measuring harmonic components under high ramp rates of up to 128 A/s using the HAL2 system as described here.

II. FIELD HARMONIC COMPONENTS

The magnetic field, in the long straight section of the magnet can be considered as two-dimensional and the harmonic coefficients can be defined by following equation:

$$B_y + iB_x = B_0 + \sum_{n=1}^{\infty} (B_n + iA_n) \left(\frac{x + iy}{r_0} \right)^n \quad (1)$$

where B_0 is the dipole field strength, B_x and B_y are the x and y-components of the field, A_n and B_n are the skew and normal $2(n+1)$ -pole field coefficients respectively with r_0 as the reference radius chosen to be 1cm for SSC magnets. The x and y direction is chosen so that the skew dipole term (A_0) is zero for non-zero transport current, and the normal dipole term (B_0) is positive for positive transport current. The coefficients A_n and B_n are in units of Gauss evaluated at the reference radius r_0 . It is customary to normalize A_n and B_n and suppress them by a factor of 10^{-4} . These normalized resulting multipole coefficients a_n and b_n are said to be in units. For a perfectly constructed dipole having both up-down and left-right symmetry, all the terms except b_n with even n are zero. Even b_n are minimized in magnet design but have some finite values. For n =odd, non-zero b_n and a_n are due to left-right and up-down asymmetries respectively. Non-zero a_n , n =even, are caused by rotational asymmetry. The mechanical size differences between the upper and lower coils can be responsible for up-down asymmetry. The manufacturing errors in a magnet can cause the asymmetries which can lead to "non-allowed" multipole coefficients. Similarly for a perfectly constructed quadrupole, the skew terms vanish and only the normal terms with $n = 4m+1$ ($m = 0, 1, 2, 3...$) are the "allowed" components.

III. MEASUREMENT SYSTEM

HAL2 system was used to measure the field quality of SSC R&D dipole magnets in Lab2 of Fermilab[6]. The probe used in the field quality measurement is a rotating coil inside the bore of the magnet. Geometry of the coil is made so that the coil picks up the field deviation from the magnet center. There are several types of measurement coils. Multipole coil is used to pick up

*Work supported by U.S. Department of Energy

†manuscript received May 8, 1994

particular order of multipole. Radial coil is arranged in a radial plane so that it picks up the difference of the azimuthal component of the field at different radii. The one mostly used at LAB2 was a tangential coil. Tangential coil picks up the difference of the radial components of the field at different azimuth. The coil was made from formwared wire that were located onto the grooved surface of G-10 cylinders which has maximum rigidity in torsion and flexion. The induced voltages, due to the field, across the coil terminals are integrated and sampled over equally spaced angular intervals. Signal level from the multipole fields are smaller for slower rotation speed and to increase the signal level the coil has to be rotated faster. The HAL2 rotation speed is limited by the mechanical stability of the probe shaft system otherwise it can accept wide range of rotation speed. the nominal coil rotational speed was set at 6Hz. Commonly used measurement systems without integrators[3] are operated in slower rotation speeds not only to avoid the mechanical vibration but also to average out the noises. Slow rotation speed in such system limits the ability to measure high ramp rate harmonics, because the magnet current changes by many amperes during a rotation.

The coil cylinder is attached to G-10 shafts that are joined together by journals made with delrin . The twisted coil leads pass through this shaft. Bearings placed on the journals snugly fit into the inner wall of the warm bore tube when the assembly is lowered into it for measurements. The other end of the shaft was connected to a gear shaft which could travel vertically through the entire length of the magnet bore. A stepping motor controlled by a PC moved the probe assembly vertically. A rotational encoder module was placed in series with the probe gear shaft. The coil leads coming through the G-10 shaft are attached to slip rings or mercury wetted contacts. The slip rings or contacts transfer the coil signal from the coil wires to the signal processing system. A periodic noise introduced due to vibration across the silver coated graphite slip rings may distort the harmonic signals. However, the use of mercury wetted contacts minimizes these noise. The stepper motor, used for vertical motion of the probe, had to be completely stopped before taking data. This is necessary to avoid the effect of stray field from the motor which can affect the harmonics signal.

HAL2 has modular input channels with a gain/attenuator, a V/F converter and a scaler. Normally the system was operated with 6 channels but it can increase the number of modules easily. Required number of channels depend on the configuration of the pick-up coil and the pole number of the magnet. The gain/attenuator card converts the differential coil signal into a single ended signal with an amplitude gained/attenuated to match the range of the V/F converter. The adjustment of gain/attenuation is controlled on-line. The V/F board has a bipolar AD652 with 1 MHz(+5 volts) full range V/F converter tied to a 2 MHz quartz clock for timing signal. The TTL logic pulses from V/F converter were sent to 32 bit scalars which can integrate the signal without saturation even if the signal has a offset due to thermal emf and base V/F frequency. The scaler counts are stored as the measurement data triggered by the encoder pulses. One of the input channels is used as the dummy to subtract the base signal. External noises are also cut down by the dummy signal subtraction. In standard configuration the rotational encoder with 256 pulses per revolution determined when

the data was to be sampled. Each data point represents an encoder angle of 1.4 degree. Other encoder pulses such as 180/rotation were also used when the availability of the memory size is limited. Modules are installed on a digital/analog bus (L2bus) and interfaced to VME bus through an Force Computer IPIO module based on 68000 CPU. The data acquisition system used a UNIX based real time Concurrent 6400 with a VME bus and a GPIB interface through which a HP3457A DVM read the magnet current. The Concurrent acts as a user interface for the data acquisition hardware. An ethernet link on the Concurrent provided connection to MicroVax for data transfer and off-line analysis. The use of L2bus is considered as a transient to the future entire use of VME bus. The analog lines of L2bus were physically separated from the digital bus and it used its own linear power supply. Presently the VME bus is too noisy for low level analog signals. Although there are noise problems, VME is a widely accepted standard bus and has possibilities to have commercial modules available without using L2-bus in the future. We think VXI is over for low frequency application and yet, not quite feasible to low level signals. The schematic diagram of the system is shown in Fig. 1.

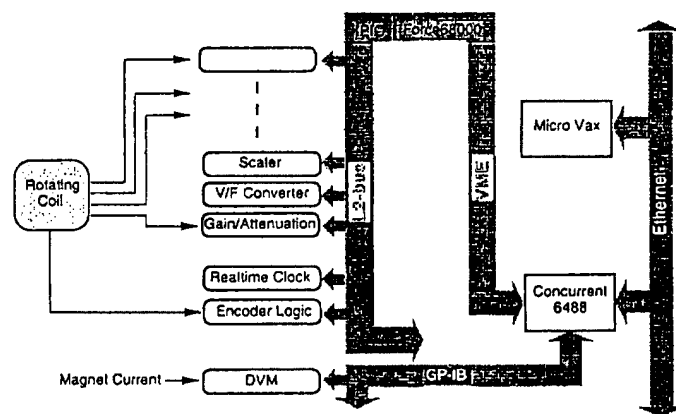


Figure. 1. System Schematic Diagram

IV. DATA PROCESSING

Since the field quality measurement is a relative measurement to the central field. The signal is always processed as the difference between the data at poriferal and the reference data at the center. It is intended to cancel the effects of mechanical noise and slip ring noise at the same time when the reference signal is subtracted. The reading of the scaler count of the V/F converter output as a function of angular encoder pulse gives the magnetic flux as a function of the rotation angle. The integration technique , in general, is immune to the effects of probe speed variations. The signals were normalized for geometric factors and amplifier gains.

Since the radial component of the n-pole field gives a sinusoidal signal of period $2\pi/n$, the Fourier components of the signal give the harmonic components of the field. To get harmonic coefficients a Fast Fourier Transform algorithm was used on the flux data collected. Since the function is periodic and the result is a Fourier series so the encoder having 2^N points per turn

is simpler to use. Any noise, if uncorrelated, reduces with the square root of the number of points. When the encoder is not divided into suitable power of two increments, discrete Fourier transformation is used. Since physical location of the rotating coil can not be exactly at the magnetic center, there is always an off center of Δx and Δy . The measured harmonics have mixing among terms because of the off center. The true harmonics are:

$$b_n + ia_n = \sum_{k=n}^{\infty} \binom{k}{n} (b'_n + ia'_n) (\Delta x + i\Delta y)^{k-n} \text{ where } b'_n$$

and a'_n are the components given by the Fourier analysis. Δx and Δy are determined to make unlikely poles such as 17 or 21 pole to be zero.

V. Fast Ramp Measurement

The HAL2 system with a 3.155 cm diameter tangential coil was successfully used to measure harmonics at high ramp rates. The encoder pulse of 180/rotation are generated to trigger the measurement. In the standard configuration 180 data points are taken every rotation of the coil. The current measurement of the magnet is the average of 10 line cycles readout by HP3457A DVM. The measurement time is limited by the rate of data transfer. The data sampling rate was modified in the acquisition software to acquire faster ramp rate measurement. The data sampling frequency was cut down to 90 sample/rotation so that 57 points of data could be stored and analyzed at every rotation. In this measurement method, 57 data points at the rate of 6Hz were taken for 9.5 second with an interval of 5 seconds to repeat the burst. Simple software modifications allowed us to measure harmonics in the magnet, DSA333, at 8A/s, 16A/s, 32A/s, 64A/s and 128A/s. SSC magnets showed the existence of large skew quadrupole components[2]. This was explained by the size asymmetry of the upper and lower coils. However, some of the magnets showed unexpectedly large quadrupole components sensitive to the ramp rate. By making harmonics measurements at high ramp rates we were able to show the linear dependence of eddy current harmonics on dI/dt . Fig. 2 shows the hysteresis width of skew quadrupole field at various ramp rates. This confirms that the large skew quadrupole comes from eddy current. Skew quadrupole is created by the eddy current distribution difference between upper and lower coil. If such a large effect in skew quadrupole component is left for the accelerator construction, it is influential to the accelerator operation.

The hysteresis width linearly increases with ramp rate indicating that there is a large eddy current in SSC magnets. The origin of the eddy current is due to the contacts between strands. However, the behavior of the eddy current is not as simple as uniform distribution. Fig. 3 shows the ramp dependence of the sextupole components. Sextupole component is supposed to have highest eddy current by symmetry but the observed effect was very small. Eddy current reconstruction from the measured harmonics and the ac loss data shows quite unequal distribution of the eddy current[5]. Contact resistance between strands have to be distributed in a wide variety. Control of the contact resistance will be an important problem to be solved for the construction of large superconducting accelerator. The magnet with larger cable width such as LHC magnets will have more serious problems on this matter.

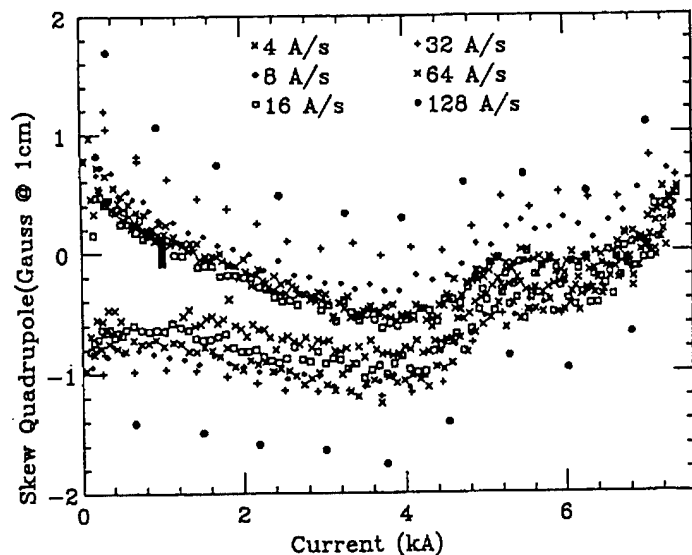


Figure 2. Quadrupole Hysteresis

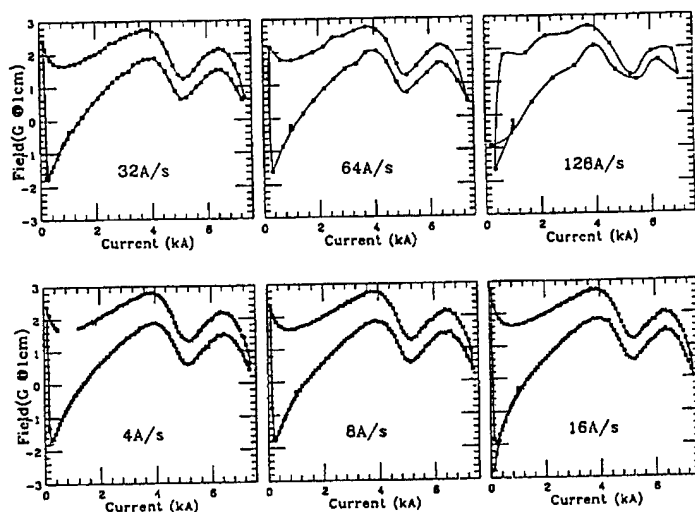


Figure 3. Sextupole at various ramp rate

VI. CONCLUSION

A versatile magnetic field measurement system HAL2 was developed and successfully applied for the high ramp rate measurement of the harmonic components. Data shown above is the only set of 128 A/s data for SSC magnets to be ever recorded, and it was possible due to HAL2. The magnets ramped at 50A/s or higher, such as HEB of SSC, need to be measured at their operation ramp rate. Magnets with wider cable will also have the necessity for the measurement at high ramp rate. HAL2 system, with versatility and flexibility, showed a prototype for the magnetic field measurement system which is suitable for the R&D phase of the superconducting magnet projects.

We would like to acknowledge the work of many engineers and technicians whose efforts made it possible to present these results.

References

- [1] M.Wake, D.A.Gross, R.Yamada, "Harmonic Measurements in Superconducting Magnets for High Energy Accelerator", *cryogenics* 21 341, (1981)
- [2] J.Strait *et al.* "Magnetic Field Measurements of Full Length 50-mm Aperture SSC Dipole Magnets at Fermilab" FERMILAB-CONF-92-240, Presented (HEACC'92), Hamburg,(1992)
- [3] G.Ganetis *et al.* "Field Measuring Probe for SSC Magnets", BNL-39607, (1987)
- [4] M.Wake "Ramp Rate Behavior of SSC Magnets ", MSD Technical Note MD-MKA-93-007, SSC Laboratory, (1993)
- [5] T.Ogitsu *et al.* "Influence of Eddy Currents on Magnetic Field Harmonics", *proc.ICFA workshop on AC Superconductivity*, pp23 (1992)
- [6] M.J.Lamm *et al.*, "A Facility to Test Short Superconducting Accelerator Magnets At Fermilab" *IEEE Trans.Appl.Sup.* 3 740 (1993) Dipole Cross Section",

Review of the Development of RF Cavities for High Currents*

J. KIRCHGESSNER,
Laboratory of Nuclear Studies,
Cornell University,
Ithaca, NY 14853 USA

Abstract

To fulfill the need for ever higher luminosities, the magnitude of the beam currents continues to increase. This is true for the electron-positron rings, the hadron colliders, and the synchrotron light sources. These high currents bring a set of new and difficult challenges. Both normal conducting and superconducting cavity^{1,2,3} structures will be considered. While these two alternatives have significant differences, the challenges addressed are rather similar.

RF cavities present an impedance to the beam by virtue of the wakefields left behind in the cavity cells. This energy extracted from the beam and left behind has an adverse effect on other particles encountering these fields. The broadband impedance presents current stability thresholds for the beam bunches, both due to the longitudinal and transverse impedance of the cavities.

The broad band impedance is characterized in a simple way by the Kloss factor of the cavity. For a given bunch length and cavity shape Kloss tells us the HOM beam power loss and the threshold of single bunch instabilities.

The current threshold for beam instabilities depends on the total Kloss for the whole machine which includes all other components in the machine as well. But the highest Kloss factors are generally in the RF cavities. The total loss factor of the RF system is essentially the Kloss per cavity multiplied by the number of cavities. Therefore there is advantage in having as high a cavity voltage as possible in order to reduce the number of cavities and therefore the total Kloss. SC cavities typically provide 3-5 times higher the voltage than copper cavities used for CW operation, as in high current storage rings

Figure 1 shows the shape of two accelerating cells. The CESR NRF cavity shape is typical of the shape used for copper cavities. The shunt impedance is made as high as is possible in order to maximize the accelerating field, E_{acc} , for a given amount of dissipation in the cell. The two factors leading to this high value of R/Q is the small beam hole size and the reentrant noses on the cell. Both these factors unfortunately lead to high values of Kloss. All of the NRF cavities that are listed in Table 1 have a cavity shape similar to the left hand picture in Figure 1.

*Supported by the National Science Foundation, with supplementary support under the U. S. - Japan Agreement.

At the other extreme, the shape on the right in Figure 1 approximates the shape used for the SRF cavities for KEK-B, CESR-B and the LHC cavity. The shape is similar to that used in LEP II, HERA and TRISTAN, all SRF, but the beam hole is larger still. R/Q of the fundamental and HOMs are substantially lower with great benefits to the multibunch stability of the beam as discussed below. The very large beam hole size is important in damping all of the cavity HOMs in order to avoid resonant buildup of the fields that would cause multibunch instabilities at high currents.

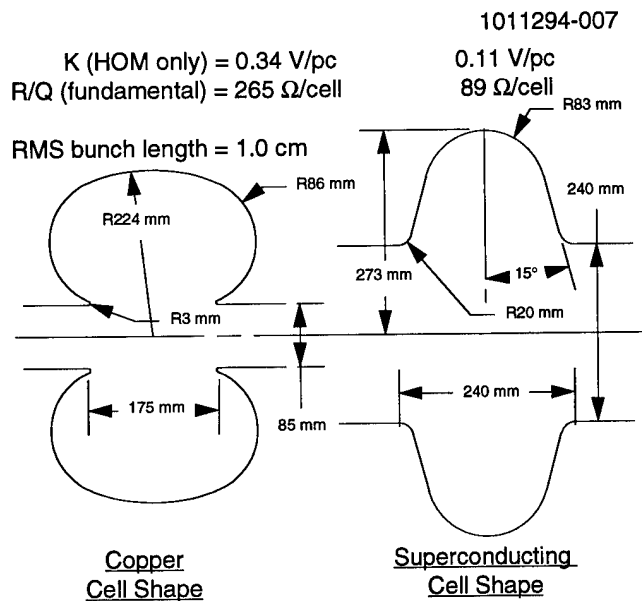


Figure 1: Comparison of Cell Shapes

CONSEQUENCES OF VOLTAGE GRADIENT

In high current systems the multibunch longitudinal instability arising from the fundamental accelerating mode can be very serious. In storage rings, beams are accelerated off the crest for phase stability. This generates reactive power into the cavity. In order to compensate for the imaginary part of the beam loading current and to minimize the required generator power, the RF cavity is operated off resonance. In a high beam current machine, the detuning frequency becomes significant:

$$\Delta f/f_{RF} = I(R/Q) \sin(\phi) / (2V_c)$$

where I is the total beam current, V_c is the cell voltage, and ϕ is the synchronous phase.

For NRF cavities, Δf could approach or even exceed the revolution frequency of the beam. In this case, the dangerous

Location	Type	Freq. MHz	Particles	Current Amperes	# of Cav.	E _{acc} /Cav MV	Wall Diss.	Q _{loaded}	Q ₀	In Pwr/ Coupler	HOM Q
LEP II ⁴	SRF(O)	352	e ⁺ e ⁻	0.01	168 x 4	10.3	.036 kW	2 10 ⁶	2 10 ⁹	60 kW	10 ⁴
TRISTAN	SRF(O)	508	e ⁺ e ⁻	0.01	32 x 5	7.5	.036 kW	10 ⁶	2 10 ⁹	100 kW	10 ⁴
HERA ⁵	SRF(O)	500	e ⁻	0.06	16 x 4	6	.044 kW	2.4 10 ⁵	10 ⁹	100 kW	10 ³
CESR-II ⁶	NRF(O)	500	e ⁺ e ⁻	0.25	4 x 5	1.5	70 kW	8 10 ³	3.2 10 ⁴	280 kW	10 ³
APS ⁷	NRF	352	e ⁺	0.3	16	0.75	90 kW	1.5 10 ⁴	4.8 10 ⁴	248 kW	10 ² -10 ³
PEP II (LER) ⁸	NRF	476	e ⁺	2.25	10	.59	50 kW	6.5 10 ³	3 10 ⁴	393 kW	10 ²
PEP II (HER)	NRF	476	e ⁻	1.03	24	.77	85 kW	6.5 10 ³	3 10 ⁴	245 kW	10 ²
KEK B (LER) ⁹	NRF	508	e ⁺	2.6	20	.6	160 kW	6 10 ³	3.3 10 ⁴	400 kW	10 ²
KEK B (HER) ¹⁰	SRF	508	e ⁻	1.1	13	1.5	.02 kW	2 10 ⁵	2 10 ⁹	400 kW	10 ²
CESR-III ¹¹	SRF(*)	500	e ⁺ e ⁻	1	4	2	.05 kW	2 10 ⁵	10 ⁹	325 kW	10 ²
LHC ¹²	SRF	400	p p	1.6	8	2	.05 kW		10 ⁹	150 kW	

(O) - Operating, the rest are at various stages of design or construction.

(*) - This design is also intended to be used on the Syn. Light Source at Orsay.

Table 1: Comparison of Various Medium and High Current Cavities

multibunch longitudinal instability is excited by the high impedance of the fundamental (accelerating) mode. One solution is to use multiple levels of sophisticated feedback circuits around the klystron-cavity-beam system.

With an SRF cavity the detuning frequency is substantially reduced by virtue of the lower R/Q from the cell shape, and the higher cell voltage made possible by the higher gradient with SRF cavities. Consequently, the values for $\Delta f/f_{rev}$ are low and, therefore, safe.

In the case of p-p colliders such as the LHC, transient beam loading effects are very important. High beam current, high RF frequency and a long revolution period along with the lack of synchrotron radiation damping make the effect of transient beam loading extremely important. The power delivered to the beam is negligible and therefore the beam loading is almost purely reactive. The average effect of this reactive component may be compensated by detuning the cavities by an amount:

$$\delta f = (R/Q) (f_0/2V) I_{av}$$

where R/Q is the characteristic impedance of the cavity, f_0 is the frequency of the cavity, V the cavity voltage and I_{av} the average RF component of the beam current. When the equilibrium of the beam is disturbed as when a new pulse is added during injection, due to the inherent slow response of the cavity tuner, the transmitter must provide the transient reactive power until the tuner settles to its new equilibrium position in order to avoid the excitation of coherent longitudinal oscillations.

Likewise any gaps in the train of bunches, in a manner as above, cause a phase modulation of the beam. The maximum phase excursion is given by: $\Delta\phi = (R/Q) (2\pi f_0/2V) I_b \Delta t$ where I_b is the maximum RF component of the beam current and Δt is the gap in the beam. As we can see both of these transient effects, δf and $\Delta\phi$ depend on the quantity R/QV.

As we have pointed out, the value for R/Q for the superconducting type cells is a factor of several lower, and the quantity V is a factor of several higher than NC cells. The net result is that δf and $\Delta\phi$ are both an order of magnitude lower in a superconducting system as compared to a normal conducting system.

HOM RESONANT BUILDUP

The effects of the cavity impedance on the beam can be drastic even at low currents if there is a resonant buildup of electric field in the cavity. In Figure 2 is shown a plot of R/Q versus frequency for the lower frequency HOMs of typical NRF and SRF cavity shapes.

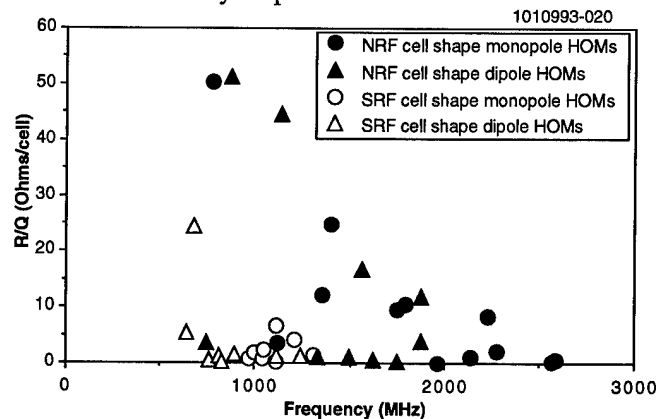


Figure 2: R/Q vs. Frequency for NRF and SRF Cavity Shapes

As can be seen the R/Q values for the NRF shapes are higher in general and therefore, to attain equally low impedances, NRF structures must be damped to correspondingly lower Q values. If any of the Fourier

components of the multibunch beam bunch train coincide with the multitude of higher order resonances of the cavity then the voltage in the cavity continues to build up limited only by the Q of that mode in the cavity. One may be so fortunate as to not have any of the cavity resonances lie directly on one of these beam Fourier frequencies but the only safe solution is to damp all of these cavity resonant modes to a Q value sufficiently low to prevent the exponential growth of the HOM field in the cavity that will destroy the beam.

Even though the bunch lengths in the p-p machines are much longer than in the e-e machines, the lack of synchrotron radiation damping requires that the Q_{ext} values of the HOMs be about the same as in the e-e machines.

Comparison of Various Systems

In Table 1 are listed parameters of some of the systems that are operating or are being constructed. A range of currents is shown but this list does not mention all of the systems that might have been considered. Of the systems listed, the four cavities with the highest planned current, namely PEP II (NRF), KEK B-LER (NRF), KEK B-HER (SRF), and CESR B (SRF) will be examined in greater detail and comparisons will be made.

PEP II

The first system to be considered is the accelerating cavities planned to be used with the PEP II B Factory. This is an NRF cavity that has been specifically designed to encounter the challenges of very high electron currents. As can be seen in Table 1, the gradients are as high as 0.8 MV/cell. This value has required careful engineering of the water cooling of the cavity to prevent overheating of the inside copper surface.

1011294-002

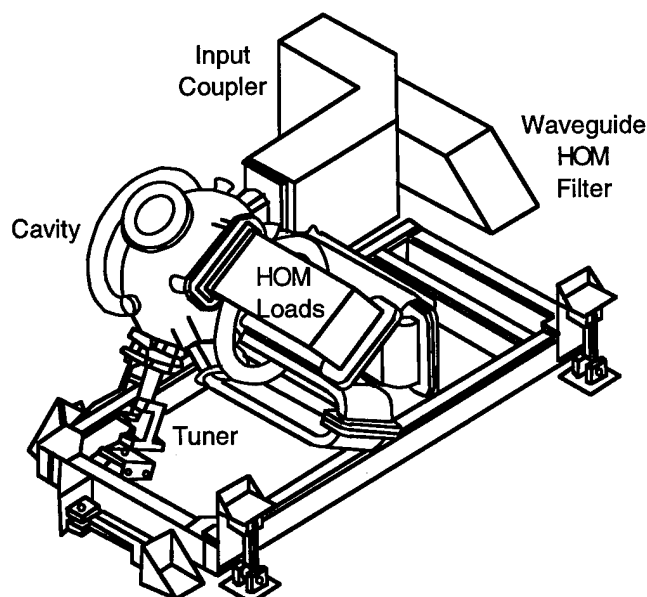


Figure 3: PEP II RF Accelerating Station

The input power per cell, up to 400 kWatts, is coupled in through a planar waveguide window¹³, then into the cell with

either a loop or an iris.¹⁴ Some of the HOM power (TM₀₂₁ mode) will be coupled out through the input coupler. The damping of the rest of the HOMs with significant R/Q is accomplished with three waveguide coupling slots. The insertion of these three slots, unfortunately, further increase the peak dissipation density of the fundamental mode to as high as 70 W/cm².

A drawing of the Accelerating station "Raft" that would be used in both the LER and the HER rings is shown in Figure 3. As can be seen, the damping Waveguides are folded back along the beam line to make as compact a package as possible that could be preassembled and tested and then placed in the rings. It is expected that the overall system, consisting of 34 cavities damped to Q values of 100 or less¹⁵, will require a rather high power longitudinal multibunch feedback system in order to prevent any instabilities.

KEK LER Accelerating Cavity

This cavity (Figure 4) is rather unique in all the high current cavities. It is made of three separate cavities coupled together in a way to give special advantages in the acceleration of high currents. The one cell is for acceleration, the second cell is for coupling and the third cell is for energy storage.

1011294-003

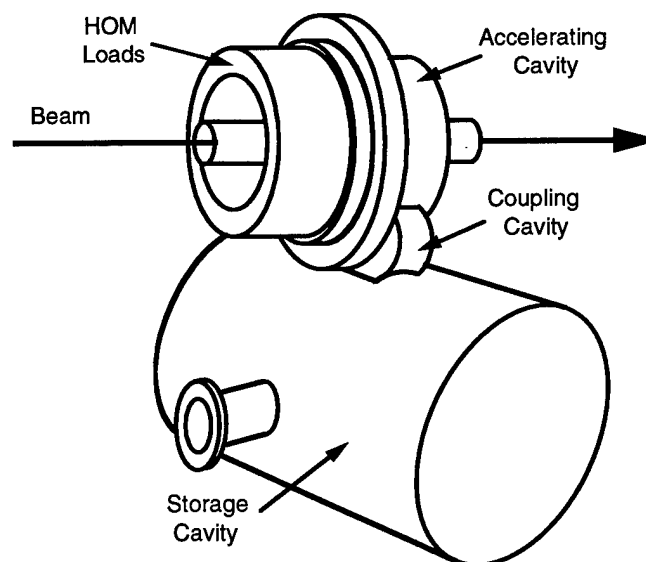


Figure 4: KEK B LER Accelerating Cavity System

Three cells give rise to three resonant frequencies in the TM₀₁₀ accelerating mode. The $\pi/2$ mode is used for acceleration. In this mode there is little energy in the coupling cell so the cell is heavily damped. In the 0 and π modes, the coupling cell has energy and are therefore heavily damped.

The damping of the HOMs is done in the accelerating cell.¹⁶ There is a choke joint at the equator of this cell. The accelerating mode is stopped and little energy is lost. All other modes are transmitted by the choke joint and heavily damped by the load. This arrangement is shown in Figure 5.

These features give the following results. The HOMs are heavily damped in the accelerating cavity and the energy of the system has been increased without adding to cavity dissipation. The effective fundamental mode R/Q of this three cavity system is only 10-15 Ω . The increase in the stored energy has, of course, decreased the negative effects usually encountered in NRF cavities associated with reactive beam detuning without increasing the wall dissipation in the accelerating cell.

The usual challenges associated with the high power input coupler are essentially the same as in the PEP II cavity. The one advantage is that the input coupler can be located on the storage cell.

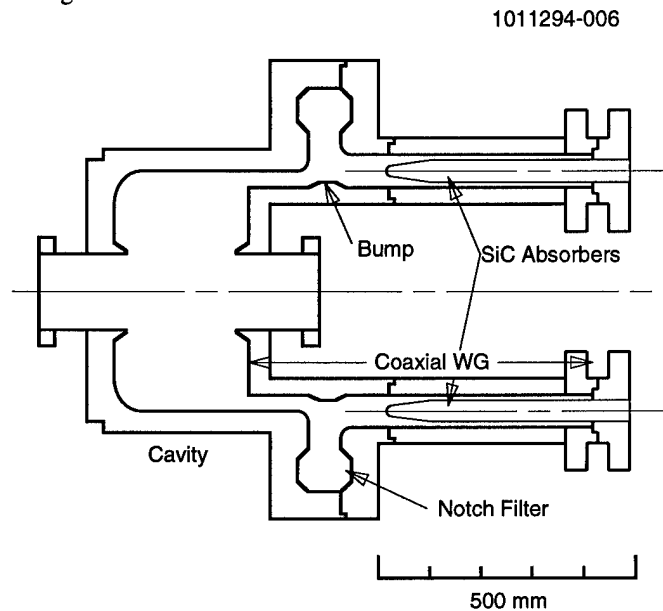


Figure 5: KEK B LER Accelerating Cavity Damping

SRF CAVITIES

There are two cavities that have been manufactured and tested that are of the so called "single mode" type. These cavities are the KEK B SRF cavity and the CESR B cavity.

The basic concept for both of these is to have the beam tube on one or both ends of the cell of adequate diameter such that all cavity modes above the fundamental, both longitudinal and transverse, propagate in a waveguide mode through the beam tube. The only mode trapped in the cell is the TM_{010} accelerating mode. A sketch of these two cavities is shown in Figure 6 and Figure 7.

All of the longitudinal modes except the fundamental mode propagate out both ends of the cavity but this 120 m radius size will not pass the two lowest dipole modes, the TE_{111} and the TM_{110} . The solution adapted by KEK is to make the beam tube large enough on one end to pass these transverse modes. The method used by Cornell is to use a fluted shape¹⁷ which has a lower cutoff frequency for the transverse modes without affecting the decay rate of the trapped TM_{010} mode. This allows the length of the beam tube on both ends to be equal, giving a shorter overall length.

The method employed for damping the HOMs in the KEK¹⁸ and the Cornell B Factory cavity designs¹⁹ are to line

a section of the beam pipe at room temperature at the large diameter with a lossy ferrite. With this damping material the HOM Q values have been measured on the CESR B cell and all fall within the limit of $Q \leq 100$ for all modes.²⁰

A possible problem with this type of HOM damping is that the beam pipe, lined with ferrite or other lossy material, is subject to the fields generated by the beam directly. This will increase the broad band impedance of overall system due to the lossy beam pipe. This effect has been examined and measured and found to cause no difficulty to the beam even though the HOM loads must be able to handle a few extra kWatts of power deposited directly by the beam at beam current levels of 1 Ampere.²¹

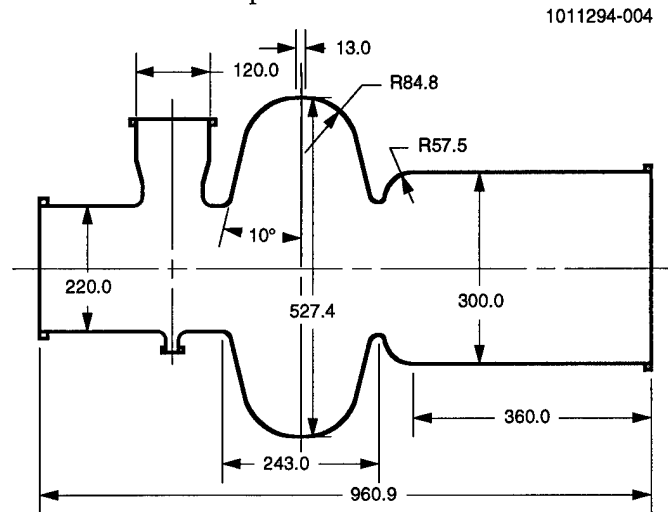


Figure 6: KEK B HER (SRF) Cavity

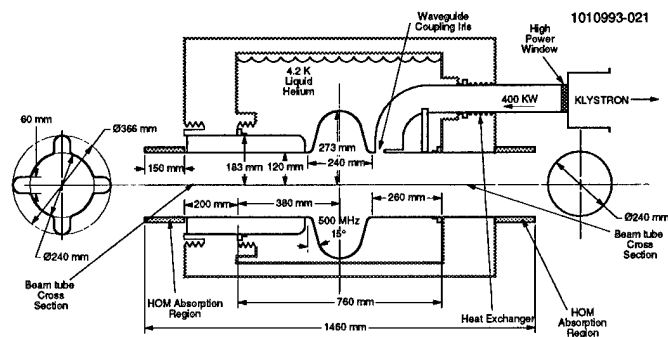


Figure 7: CESR B Cell

RF Power Input Couplers

All of the high current cavities share the challenge of very high input power (300-400 kW/cell). This is true of both NRF and SRF designs. As we have seen, the PEP II design is undecided as to whether they will use an aperture coupler or a loop coupler but they have decided upon a planar waveguide window. The KEK NRF design will use a coaxial window input with antenna into the storage cavity. Likewise with the KEK SRF design they have chosen the type of coupler with which they have experience, a coaxial window with antenna into the beam pipe.

In the CESR B design a planar waveguide window is chosen followed by a resonant aperture between the waveguide and the beam tube. A prototype of such a window has been made and tested. A pair of these windows have been tested to 250 kWatts CW traveling wave and to a power level of 125 kWatts of reflected standing wave, into a short.²² A new window of a different design has been procured and the results of this test will be reported.²³

During the vertical test of this cavity, the input waveguide was resonated with a superconducting short so that the energy and field levels in the coupler and input waveguide were the same in the vertical test as they will be in final operation. A weakly coupled probe was used to drive this waveguide resonator up to full cavity field levels.²⁴

TEST RESULTS

A prototype PEP II cavity at low power has been built and tested. The HOMs have been measured and all modes are damped to the desired amount. High power feedback will however be required. A high power test cavity and high power window are under construction.

The KEK NRF cavity is in the design stage with a low power prototype under construction. The KEK SRF cavity has been built and tested in a vertical dewar. In these tests the cavity achieved the desired field of 10 MV/m at a Q_0 value of $1 \cdot 10^9$. Measurements have been made at low level of all the HOM damping and found to be satisfactory.

The CESR B cavity was tested in a vertical dewar and achieved 10 MV/m at a Q_0 value of $1 \cdot 10^9$.²⁵ A beam test has been made in CESR with the CESR B cell cavity.^{26,27} Beam currents as high as 220 mA with 27 bunches and single bunch currents to 41 mA were accelerated by the cavity with no beam instabilities. This current value was not limited by the cavity but was limited by beam induced heating of other components in CESR. This beam current limit was unaltered by the presence of the SRF cavity. The HOM power extracted from the cavity and absorbed by the HOM loads was as high as 2 kWatts. Experiments were also performed with the TM₀₁₀ cavity mode detuned and with no RF drive to see if a resonant buildup of RF fields could be measured as the cavity frequency was scanned by as much as 100 kHz. The Q of all the modes was low enough to prevent significant field buildup in the cavity or beam instabilities.

Experiments were also made to measure the maximum power that could be transferred to the beam. 155 kW was achieved. This value was limited not by cavity or coupler behavior but by electronic driven vacuum deterioration at the window. As mentioned, a new window design will be tested.²⁸ A second cavity and cryostat will be placed in CESR for a long term beam test.

CONCLUSIONS

The first generation of cavities, both NRF and SRF, operating at currents up to several hundred mA have been successful. They have operated much as predicted and the reliability has been satisfactory. The next step has yet to take

place, namely, the cavities operating at currents of 1-2 amperes.

At ever higher currents the problems associated with RF windows and input couplers become increasingly challenging and the differences between SRF and NRF become less significant as the voltage per cavity is limited by the power input capabilities.

The ultimate test for this next generation of high current superconducting cavities will take place when accelerators are operating with planned higher currents.

REFERENCES

- 1J. Kirchgessner, Particle Accelerators, 46 (1994), pp. 151
- 2H. Padamsee et al., Particle Accelerators, 40 (1992), pp. 17
- 3J. Kirchgessner et al., Proc. of the 1992 Linear Accelerator Conf., (Ottawa, Canada) ACEL Rpt. 10728 (1992), pp. 453
- 4C. Anaud et al., Proc. 4th Workshop on RF Superconductivity, Tsukuba, Japan, (1989), pp. 19
- 5A. Matheisen, et. al., Proc. 5th Workshop on RF Superconductivity, Hamburg, Germany, (1991), V1, pp. 44
- 6S. Greenwald, et. al., Proc. 1989 Particle Accelerator Conf., Chicago, IL, (1989), V1, pp. 226
- 7J. F. Bridges et. al., Proc. 1993 Particle Accelerator Conf., Washington, DC, (1993), V2, pp. 766
- 8R. Rimmer, et. al., Proc. 4th European Particle Accelerator Conf. (EPAC'94), London England, (1994), pp. 2101
- 9T. Shintake, et. al., *ibid.* 7, pp. 1051
- 10T. Takahashi et. al., 9th Symposium on Accelerator Science and Technology, Tsukuba, Japan, (1993) pp. 327
- 11H. Padamsee et. al., Proc. 1991 Particle Accelerator Conf., San Francisco, CA, (1991), V2, pp. 786
- 12Design Study of the Large Hadron Collider, CERN 91-03, (1991), pp.108
- 13M. Neubauer, et. al., *ibid.* 8, pp. 2033
- 14C.-K. Ng, et. al., *ibid.* 8, pp. 2140
- 15R. Pendleton, et. al., *ibid.* 8, pp. 2013
- 16T. Kageyama, et. al., *ibid.* 8, pp. 2098
- 17T. Kageyama, et. al., Proc. KEK B-Factory Workshop, (1990)
- 18T. Tajima et. al., Proc. Workshop on Microwave-Absorbing Materials for Accelerators (MAMAs), CEBAF, (1993)
- 19D. Moffat, et. al., *ibid.* 7, pp. 977
- 20V. Vescherevich et. al., Cornell U. Internal Note, SRF920701-04 (1992)
- 21W. Hartung, et. al., *ibid.* 7, pp. 3450
- 22D. Metzger, et. al., *ibid.* 7, pp. 1399
- 23M. Pisharody, et. al., Proc. 1995 Particle Accelerator Conf., Dallas, TX, (1995)
- 24D. Moffat, et. al., *ibid.* 7, pp. 763
- 25D. Moffat, et. al., *ibid.* 7, pp. 763
- 26H. Padamsee, et. al., *ibid.* 23
- 27S. Belomestnykh, et. al., *ibid.* 23
- 28M. Pisharody, et. al., *ibid.* 23

PERFORMANCE OF NORMAL CONDUCTING STRUCTURES FOR LINEAR COLLIDERS

Toshiyasu Higo, KEK, National Laboratory for High Energy Physics
1-1 Oho, Tsukuba-shi, Ibaraki-ken 305, Japan

In the present paper are described the status of the design, fabrication and various performance studies such as the high-field characteristics and the wake fields on the accelerating structures for the linear collider linacs in such projects as CLIC, VLEPP, NLC, JLC and SBLC[1].

The structure design and the fabrication of the structures for the single-bunch machine has almost finished, while those of the structures for the multi-bunch operation are in progress. For the design of the latter structures, various calculation methods of the long-range wake field are being discussed in addition to the experimental evaluation of the HOM parameters.

A direct measurement of the long-range wake field in a detuned structure was successfully performed and was proved to be a nice tool for the evaluation of design and fabrication of the structure. In addition, the beam induced dipole modes coming out of the coupler into wave guide was measured which makes it possible to use the accelerating structure as the BPM.

A heavily damped choke-mode structure at S-band was tested at high power showing stable operation at more than 50MV/m. Another choke-mode structure with integrated damping loads is in progress.

Stable operations of the disk-loaded structures from S-band to 30GHz were verified at the design fields.

Fabrication studies are proceeded in all projects focusing on various issues such as a good alignment, cheapness and less dark current.

I. INTRODUCTION

A review paper on the linear collider structures was presented by the author at the previous conference[2] and the present paper is focused on the later progress.

Accelerating structures for linear collider main linac are designed as at a high frequency as possible from the structure efficiency point of view. However, higher frequency structures cause larger wake fields which increase the emittance both in single-bunch and multi-bunch machines. Though there are various beam-based correction schemes proposed to suppress these effects, the structure should also be designed to suppress the wake field itself.

The designs of the structures for the single-bunch machines were almost fixed. The fabrication of the prototype structures were finished[3,4] and the high power performance of those structures are in progress.

On the other hand, the design of the structure for the multi-bunch operation should have significant considerations of the higher order modes in the structures and various designs are still discussed. Even in CLIC, the feasibility study on the

multi-bunch operation by re-designing of the structure has been started in order to increase the luminosity[5].

A straightforward way of reducing the long-range wake field, damping HOM field heavily toward outside accelerating cell, was proposed in a choke mode structure. An S-band choke-mode structure was tested in high power and proved the stable operation at 50MV/m[6].

Another idea to reduce the long-range wake field, cancellation among the wake fields of all modes by detuning of HOM frequencies of the cells, has been considered[7]. To accomplish the cancellation, it is necessary to keep the HOM frequency distribution very well or to incorporate a medium damping mechanism. Various approaches are studied and presented in the present paper such as the possibility of pure detuned structure realized with precise fabrication technique[8], medium-damped detuned structure[9] and the detuned structure with some heavily damped cells[10].

Prototype structures have been fabricated in all of the projects. In the process, various important experiences such as the alignment of the cells in a structure are being obtained. Studies on the high field operation of those structures are also performed. It was proved that the stable operation of the structures at the accelerating field of the initial stage of the linear colliders was quite easily obtained. Some of these recent results are reviewed in the present paper.

II. REQUIREMENTS FOR THE STRUCTURE

Typical design parameters related to the accelerating structures are depicted from the parameters in reference [11] and listed in the following table for reminding in mind the rough idea of each approach. In order to preserve the single-bunch emittance, the alignment of the beam hole aperture is essential. The tolerances in the case of multi-bunch operation depend on the details of the HOM characteristics and the alignment of the cells where most of the stored energy exists. Design accelerating field are determined mainly from the available RF power generation scheme aiming at the low and initial version of cm energy of each project.

Table 1. Typical parameters of structures.

	CLIC	VLEP	NLC	JLC	SBLC
Freq [GHz]	30	14	11.4	11.4	3
Bunch Space	10	-	16	16	48
# Bunch	1-10	1	90	85	125
Field [MV/m]	80	100	50	73	21
Length [m]	0.28	1	18.	1.3	6
Filling [ns]	11.6	110	100	110	800
Align [μ m]	5	1	6	1	30

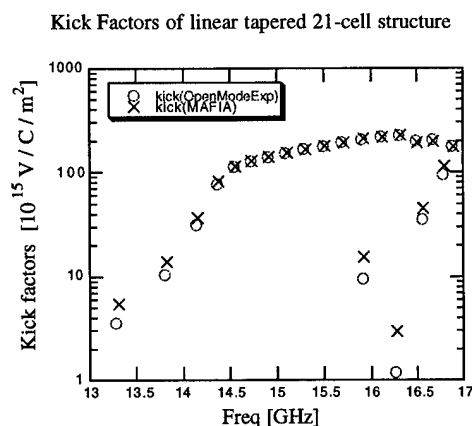


Fig. 1. Kick factors of 21-cell structure.

IV. DAMPED STRUCTURE

The study on heavily damped structures for linear colliders was initiated from the structure with radial slots in the disk. The structure with circumferential slots in a cell was also studied as a candidate for the heavily damped structure. However, the application of these structures for heavily damped scheme was almost closed due to the reduction of the Q value of the accelerating mode in addition to the complicated shape of the cells. However, this heavily damped cell is studied aiming at the damped cells for SABLE, where several cells out of 180 are heavily damped serving as a medium damping for particular modes of the whole structure[9].

An extreme of the above circumferential slot, i.e. opening the slot over 2π while trapping the accelerating mode inside the cell by choke, was proposed[5]. This choke-mode structure damps almost all the relevant modes in the cell with sacrificing the shunt impedance of the accelerating mode by only 25% by mainly establishing the field in the choke. An S-band choke-mode structure with 12 choke-mode cells, though without loads for HOM, and two coupler cells was fabricated for a proof of the high power operation and tested in high power[5]. The structure was conditioned up to 50MV/m and accelerated beam without any problem. A prototype structure with choke-mode cells with HOM loads equipped and collinear loads at the end of the structure, making the vacuum vessel insertion simple, is under design[12].

V. DETUNED STRUCTURE

A. Estimation of wake fields

Various codes to estimate the wake field in the structure with detuning of the HOM frequencies were reviewed in the previous paper[2]. Those estimations should be proved experimentally.

Direct MAFIA calculation[13,14] of 21-cell linear tapered structure was compared with open mode expansion method[15]. The results are plotted in the following figure. The agreement is quite nice at least for the structure with this small number of cells.

The frequencies of another structure, a 28-cell detuned structure was evaluated by using the open mode expansion technique and compared to those measured showing good agreement, while the measurement of the kick factors was too difficult to compare with those calculated[15]. The frequencies agree within 0.1% for almost all high kick factor modes. Similarly, the study on 36-cell structure was started to evaluate the kick factors[16] and compare with those calculated by such as the mode matching technique[17].

B. Damped Detuned Structure

In order to keep the wake field below the tolerable level at longer time range of say 50'th bunch or later, the medium damping mechanism seems hopeful. A simple way to realize this condition is to make the Q values of higher modes in all of the cells less than 2000 at X-band[18]. To reduce the number of loads and make them reside far from the accelerating cells, a manifold damping mechanism was proposed[8]. This structure is called Damped Detuned Structure, DDS, and seriously considered to study in fabrication, high power and wake field point of view.

C. Lossy cells

An old idea of the Kanthal coating on the copper cells near the beam hole was proposed to reduce the Q value of the higher modes while keeping that of the accelerating mode fairly small[19]. The Q values of the dipole modes can be a few thousands at S-band while maintaining the reduction of the accelerating mode less than 10%. This technique will also be applicable to replace the output coupler cell with several lossy cells.

D. Coupler designs

The extensive studies on the coupler for SBLC is continuing[20]. The coupler has symmetrical inputs which makes the transverse kick due to the accelerating mode negligibly small and also absorbs the dipole modes of one of two polarizations. The dipole modes of another polarization are absorbed into the other two ports which are opened at the position perpendicular to the input ports. These ports can be used for the beam position monitoring in the structure.

VI. MEASUREMENT OF LONG RANGE WAKE FIELD

A direct measurement of the wake field of a 1.8m detuned structure was performed at ASSET using SLC beam[21]. The results was shown in the Fig. 2 with those

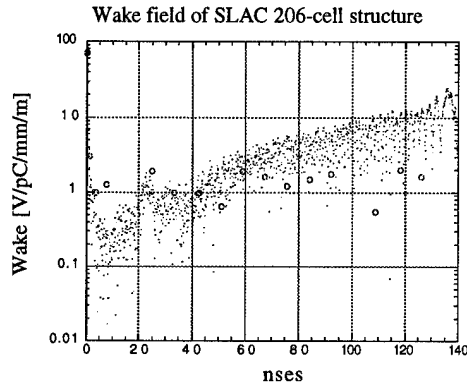


Fig. 2. Envelope of the wake field of SLAC 1.8m structure. Dots are those calculated and open circles are those measured.

estimated by open mode expansion method[15]. The measured wake field is in fairly good agreement with that calculated, showing non-negligible contribution from those of higher modes than second dipole pass bands in the region of up to 30ns. It should be noted that there still remains the disagreement later than 60ns, which should be understood.

This experiment was proved to have the sensitivity of 0.1V/pC/mm/m. Since the rule of thumb of the required damping for X-band structure is 1/100, this sensitivity is large enough to practically judge the wake field of the structure. It also makes the serious checking of the theoretical estimations possible.

The beam induced powers of the dipole modes extracted from both input and output coupler of the SLC accelerating structure were measured. Some modes were linearly correlated to the beam transverse position, indicating the possibility to use this signal for the BMP[22]. A similar experiment will be performed in the ATF for the VLEPP 14GHz structure equipped with the high precision BPMs to detect the power output from the coupler cells[23].

VII. HIGH FIELD CHARACTERISTICS

The 30GHz structure was tested in CTF by feeding the power extracted from the same type of cavity into the test cavity. The accelerating field of 94MV/m in 12nsec duration was obtained without any sign of the breakdown[10]. This field is above the design field of the CLIC.

The X-band short-length structures were proved to be operated at over than 100MV/m. The dark current from 26-cm structure at 125MV/m was 2mA, while that at 50MV/m was a few μ A[10]. The tolerable amount of the dark current and its characteristics should be studied especially in full-size structure. The high power testing of the NLC detuned 1.8m-structure showed the operation at the 50MV/m level is quite feasible and the test with more peak power is in progress.

A 5.2m-structure was fabricated as a test of fabrication and high power operation for the structure of 6m-structure of

SBLC[24]. The required level of accelerating field was easily obtained.

X-band structure showed a stop band, where no field emitted electrons cannot come out of the structure with more than 100 cells even above the critical gradient[26].

VIII. FABRICATION

The cells in any structure for the linear collider should be aligned to make the emittance preservation. The alignment tolerances for the structures above 11GHz are ranging from a micron to ten. The short stack of the cells proved to be made within several microns such as shown in the 30-cm structure[27]. A 1.2m stack of X-band cells was also tried and the alignment of better than 40 μ m was observed[28]. The structures for the multi-bunch operation with keeping the wake field low by detuning need the precise alignment. The R&D's for the better alignment during the fabrication or correction scheme are in progress.

All of the structure except JLC seem to adopt the frequency tuning after joining cells at fairly high temperature. In order to control the higher mode frequencies well and possibly reduce the mass production cost, the JLC X-band activity keeps the R&D on fabrication without tuning. The diffusion bonding seems to be a promising technique to make the bonding of the cells without large deformation of the cells resulting in a good frequency control capability. Several 30-cm structures were fabricated at various diffusion parameters and will be high power tested to examine the feasibility of high field operation. Up to now, no limitation arising from the structure itself was observed. However, the detailed studies on the prototype structures should be performed.

No evidence of breakdown of the 30GHz structure stated above may reflect the fact that the field emitted electrons cannot transmit more than one cell unless the accelerating field exceeds the critical gradient of more than 200MV/m at such a high frequency as 30GHz. The simulation results on X-band structure show the trapping of the field emitted electrons inside structure even above the critical gradient of 60MV/m for the structure with more than 100 cells while the amount of the dark current measured smoothly increases above 50MV/m[10,25].

Table 1 High-Field Experimental Results

Frequency	GHz	3	11.4	11.4	30
Length	m	5.2	0.26	1.8	0.3
Type		CG	CI	Det.	CZ
Input	MW	80	69	105	69
Eav	MV/m	21	125	55	94
Pulse	ns	SLED	150	75	12
Fill Time	ns	750	74	100	11.6

IX. SUMMARY

The design accelerating fields were already verified in the test structures in almost all of the projects. It is to be noted that the test of CLIC 30GHz structure did not show any sign of the break down. The further studies of fabrication of the prototype structures are in progress. One of the main studies being performed is to obtain the required straightness of the structure. In addition, the design studies to suppress the effect of the transverse higher modes in detuned structures are in progress. Theoretical estimations are compared to those calculated by such a code as MAFIA, those measured in cold test stack or those obtained by the actual measurement of the wake field using two beams, drive and test beam. A heavily damped structure of choke-mode type will be fabricated to study the wake field performance in addition to the high field characteristics. The design and fabrication of the prototype structures can be checked on their wake fields experimentally.

X. ACKNOWLEDGMENTS

Numerous colleagues for linear collider studies are cordially acknowledged for providing me various information, though I cannot refer independently. Many of the information comes from the recent workshop LC95[29].

XI. REFERENCES

- [1] R. H. Siemann, "Linear Collider Research and Development", Proceedings of 1994 Int. Linac Conf., p24, Tsukuba, Japan 1994.
- [2] T. Higo, "Linear Collider Structures", Proc. of 1994 Int. Linac Conf., p621, Tsukuba, Japan 1994 and KEK Preprint 94-88, Sep., 1994.
- [3] I. Wilson et al., "The Fabrication of a Prototype 30GHz Accelerating Section for CERN Linear Collider Studies", CERN-SL/90-84(RFL) and CLIC Note 114, 1990.
- [4] M. A. Avdyev et al., "Accelerating Section VLEPP at 14GHz", INP 93-7.
- [5] I. Wilson, presented in LC95, Tsukuba, Japan, 1995.
- [6] T. Shintake et al., "High Power Test of HOM-Free Choke-Mode Damped Accelerating Structure", Proc. of 1994 Int. Linac Conf., p293, Tsukuba, Japan 1994 and KEK-Preprint 93-27.
- [7] H. Deruyter et al., "Damped and Detuned Accelerator Structure", Linear Acc. Conf., Albuquerque, USA 1990 and SLAC-PUB-5322.
- [8] T. Higo et al., "Precise Fabrication of X-band Detuned Accelerating Structure for Linear Collider", in this conference.
- [9] N. Kroll et al., "Higher Order Mode Damping for a Detuned Structure", Proc. of 1994 Int. Linac Conf., p260, Tsukuba, Japan 1994.
- [10] T. Weiland, "A 500GeV S-Band Linear Collider Study Status Report 1992", ECFA Workshop on e+e- Linear Colliders, Garmisch Partenkirchen, Germany, 1992 and MPI-PhE/93-14, ECFA 93-154, p123, 1993.
- [11] G. Loew, Proc. of the 5th Int. Workshop on Next-Generation Linear Colliders, SLAC, USA, 1993 and from a draft by P. Wilson, "Linac Technology" after LC95, Tsukuba, Japan, 1995.
- [12] T. Shintake, Presented in LC95, Tsukuba, Japan, 1995.
- [13] K. Ko, private communication.
- [14] K. Klatt et al., Proc. of the 1986 Linear Accelerator Conf., SLAC-Report-303, 1986, p276-278.
- [15] M. Yamamoto, "Study of Long-Range Wake Field in Accelerating Structure on Linac" in Japanese, Thesis for The Graduate University for Advanced Studies, and KEK Report 94-9, 1995.
- [16] M. Kurz, "Status of the 36-cell Model Measurements", Presented in LC95, Tsukuba, Japan, 1995.
- [17] U. Van Rienen, "Higher Order Mode Analysis of Tapered Disk-Loaded Wave guides Using the Model Matching Technique", Part. Accel., Vol41, p173, 1993.
- [18] T. Higo, Presented in 5th Int. Workshop on Next Generation of Linear Colliders, SLAC, USA, 1993, and SLAC-436, 1993.
- [19] N. Holtkamp, Presented in LC95, Tsukuba, Japan, 1995.
- [20] N. P. Sobenin et al., "DESY Linear Collider Accelerator Section Coupler", Proc. of 1994 Int. Linac Conf., p74, Tsukuba, Japan 1994.
- [21] C. Adolphsen, "Measurement of Wake Field Suppression in a Detuned X-Band Accelerator Structure", Proc. of 1994 Int. Linac Conf., p621, Tsukuba, Japan 1994.
- [22] P. Krejcik, "Observation of Beam-Induced Dipole Modes in the SLC Linac", presented in LC95, Tsukuba, Japan, 1995.
- [23] N. Solyak, private communication.
- [24] G. Beneke et al., "Accelerating Structures Technology for an S-Band Linear Collider", Proc. of 1994 Int. Linac Conf., p53, Tsukuba, Japan 1994.
- [25] T. Higo et al., "High Gradient Performance of X-band Accelerating Sections for Linear Colliders", Particle Accelerators, Vol 48, pp.43-59, 1994.
- [26] S. Sun et al., "Trajectory of Field Emitted Electrons in Disk-Loaded Structure", JLC Note No. 62, 1995.
- [27] T. Higo et al., "Precise Fabrication of X-band Accelerating Structure", Submitted to the 9th Symposium on Accelerator Science and Technology, KEK, Japan, 1993 and KEK-Preprint 93-57, 1993.
- [28] T. Higo, Presented in LC95, KEK, Tsukuba, Japan, 1995.
- [29] LC95, Presentations at the 6th Int. Workshop on Next-Generation Linear Colliders, KEK, Tsukuba, Japan, 1995.

HIGH GRADIENT SUPERCONDUCTING RF SYSTEMS

J. Graber, F.R. Newman Laboratory of Nuclear Studies, Cornell University, Ithaca, NY 14853 USA

Abstract

Superconducting Radio-Frequency (SRF) cavities are a promising technology for the next generation of electron positron colliders. In order to apply SRF technology in such machines, accelerating gradients must be improved, from the 5 to 10 MV/m level achieved in accelerators today, to the range of 20 to 30 MV/m. The state of the art in high gradient SRF technology will be discussed. Topics include achieved cavity performance, fabrication, preparation, handling, and processing techniques. Significant progress, e.g. multi-cell cavities with gradients > 25 MV/m and single-cell cavities with gradients > 40 MV/m, has been achieved over the past several years towards the goal of increased gradients. The major improvements have been in the areas of understanding and reducing cavity loading due to field emission and thermal quenches.

I. INTRODUCTION

Superconducting Radio-Frequency (SRF) technology has been an active field of research for accelerator cavities for the last 25 years. The SRF field has grown from the use of simple single-cell test cavities in a laboratory environment to reliable installation of hundreds of multi-cell structures in an operational accelerator. Hundreds of meters of SRF cavities are now used in accelerators around the world.

The SRF cavities used at such laboratories as KEK,[1] CERN,[2] Darmstadt,[3] Argonne,[4] and DESY[5] have retained their performance over time, showing SRF technology to be a reliable basis for continued construction of accelerators.

SRF cavities are presently being investigated as the basis for future electron positron colliders in the 0.5-2 TeV center of mass energy regime. Under the aegis of the TESLA[6] project, an international collaboration is operating towards this goal. SRF based accelerators present several advantages when compared with their normal conducting (NC) counterparts.[7]

Cryogenic considerations[8] have determined the choice of RF frequency for a high gradient cavity to be in the range of 1-3 GHz. Further consideration of thermal stability, wakefields, and availability of RF power sources has led the TESLA collaboration to the choice of a 9-cell 1.3 GHz cavity.

If SRF technology is to be used for construction of a TESLA machine, the accelerating gradients must be improved from the 5 to 10 MV/m level achieved in presently operated accelerators to 20 to 30 MV/m. In this presentation, I will review the efforts being made towards achieving this goal, showing the "state of the art" in obtaining high gradients, specifically as measured in multi-cell SRF cavities built for electron-positron machines.

It is useful to begin with a brief summary of the salient operational experience with SRF cavities in full accelerators. The observed limitations of these cavities will then be used as a launching point to discuss the current experimental efforts being pursued in order to overcome these limitations.

Finally, I will conclude with a discussion of future directions of SRF high gradient research.

II. OPERATIONAL EXPERIENCE

SRF cavities have proven themselves to be a viable and reliable basis for construction of accelerators. Cavities at DESY[9] and KEK[1] have to date logged many ten thousands of hours of operation with no significant degradation of cavity performance.

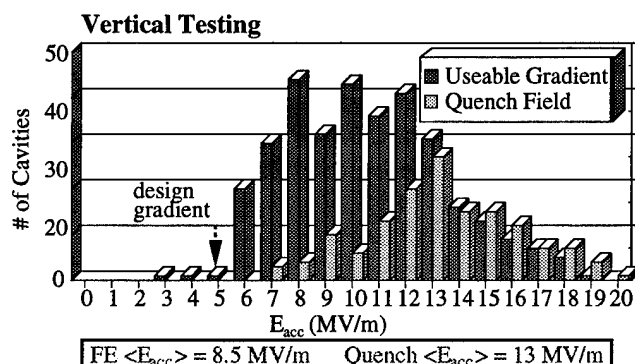
From the point of view of TESLA and other high gradient machines, it is most informative to investigate the experience to date of the SRF cavities of CEBAF. [10]

Figure 1 shows the achieved gradients in the CEBAF cavities, both in vertical testing and in horizontal commissioning in the accelerator. The cavities at CEBAF were constructed from niobium with RRR = 250. RRR (Residual Resistivity Ratio) is the ratio of bulk resistivity at room temperature to the NC resistivity at 4.2 K, and is used as a measure of the purity and thermal conductivity of the niobium.

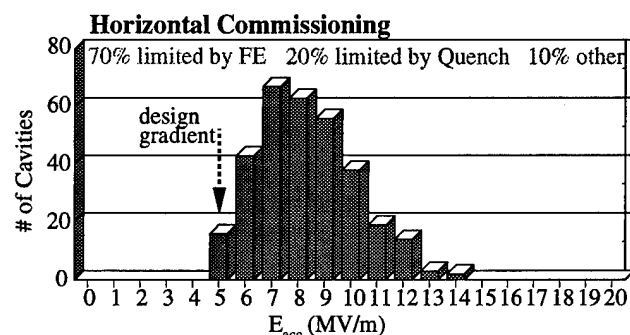
The design parameters of the CEBAF cavities were an accelerating gradient of 5 MV/m, with an unloaded quality factor (Q_0) greater than 2.4×10^9 (operation at 2 K). In all, 338 cavities (in 169 pairs) have been installed in CEBAF, and have exceeded specifications. It is equally impressive that 70% of the cavities passed acceptance tests the first time that they were assembled and tested.

The excellent performance of the CEBAF cavities is

3060594-001



(a) Vertical tests of the cavities.



(b) Horizontal commissioning in the accelerator.

Figure 1. Results from CEBAF on 5-cell 1.5 GHz cavities.

nonetheless not adequate for the proposed TESLA machine. The two primary limiting phenomena for the CEBAF cavities are listed in Figure 1(a), quench (thermal breakdown) and field emission (FE). These are the same phenomena encountered in all other facilities with SRF cavities, and are thus the primary focus of nearly all SRF research groups. As is shown in Figure 1(b), 90% of the cavities installed in CEBAF had their final limitation due to one of these two phenomena.

It is worth noting that the achieved gradient and performance to date in CEBAF are significantly higher than that in previous facilities, largely due to the increased knowledge gained by the SRF research programs over the last 15 years.

III. STATE OF THE ART

For reasons of brevity, this discussion of the present state of the art of high gradients will be largely restricted to results obtained with multi-cell cavities, primarily because it is with multi-cell cavities that a TeV collider must be built. This approach will regrettably neglect excellent results obtained at many laboratories, including 1-cell test cavities,[11-13] and basic FE studies.[14,15] Interested readers are encouraged to consult the references for further information.

A. Quench

Quench, or thermal breakdown, is the phenomenon where as cavity fields are increased, a local heat source (defect) increases its dissipation until the heat dissipation overwhelms the local thermal conductivity, raising the local temperature of the RF surface above the critical temperature. The local hot spot will quickly grow to macroscopic size, eventually driving the entire cavity RF surface normal conducting, which then collapses the cavity fields.

The most natural solution to the problem of quench is increased thermal conductivity, in order that the dissipated heat can be conducted away before the critical temperature is surpassed. The most common method for obtaining higher thermal conductivity has been to improve the purity of the bulk niobium used in cavity fabrication. Figure 2 displays measured quench fields at several different laboratories plotted as a function of cavity RRR. The data from CEBAF in Figure 1(a) is shown in the form of its average and range. The two diagonal lines are meant to show an approximate value of RRR necessary to insure a quench field above a given value. The upper line is for 1-cell cavities, while the lower line bounds the 5-cell and 9-cell cavities.

The purity of bulk niobium as delivered by industry has increased from RRR = 40 in the early 1980s to in excess of 500 today. Through solid state gettering,[16] the RRR can be further increased by up to a factor of 2, making RRR ≥ 1000 now a possibility. Extrapolation of the plots in Figure 2 show that RRR ≥ 500 is necessary for multi-cell cavities with quench fields consistently above $E_{acc} = 25$ MV/m.

One more possibility for increased thermal conductivity is the possibility of niobium-copper sputtered cavities,[17] where the increased thermal conductivity of the copper substrate would be used to conduct the heat. This technology is not yet feasible, however, due to an exponential decrease in Q_0 with increasing fields from granular superconductivity effects.

B. Field Emission

Field emission has been the dominant limitation on SRF cavities for the last ten years (since niobium with RRR greater than 100 became widely available). FE is tunneling of electrons out of the niobium surface in the presence of high surface electric fields. Many comprehensive reviews of the subject and its relationship to SRF cavity behavior are available.[18-21] FE related dissipation grows exponentially with increasing fields, quickly consuming all power available in a low power SRF setup. Furthermore, the impact of emitted electrons on the cavity surface causes heating, further degrading the RF performance of the cavity.

The most important information that has come from field emission studies, in both DC[14,22] and RF[15,23] conditions, is that FE is directly related to micron sized surface contaminations, in particular metallic particles. Table 1 shows a listing of the various contaminants found in emission studies at several different laboratories. Most of the elements detected can be traced to either actions or materials related to the processing or assembly of the cavities and their test apparatus.

Recent results indicate the further possibility that RF surface contamination could lead to a thermal quenches.[26]

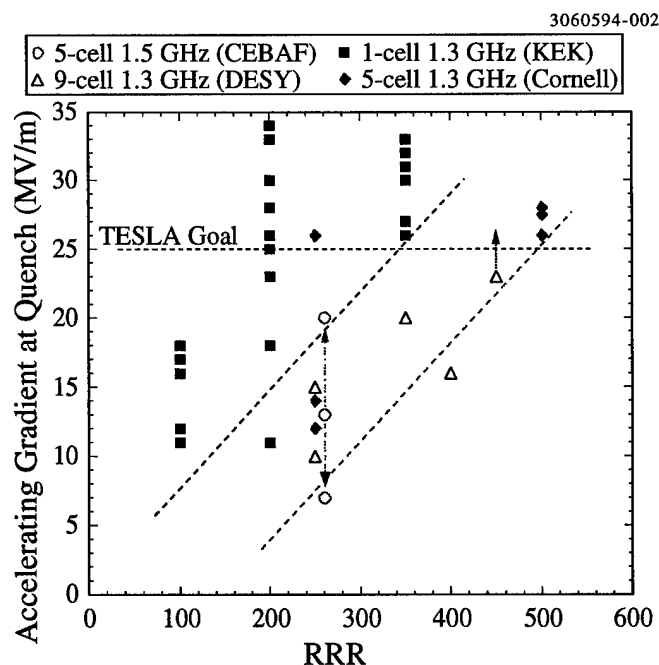


Figure 2. Achieved accelerating gradient plotted as a function of RRR (residual resistivity ratio) of the niobium in the cavities. A more complete description of this plot is provided in the text.

TABLE 1. Contaminants found in FE sites.

Geneva DC	Saclay DC	Wuppertal DC	Cornell RF
Ag,Al,C,Ca, Cr,Cu,Mn,O, S,Si,W	Ag,Al,C,Ca, Ci,Cr,F,Fe, K,Mg,N,Na Ni, O, Si, Ti, Zn	Al,Cs,Ca,Cu, Mn,O,S,Si Ti,W	C,Ca,Cr,Cu F,Fe,In,Mn Ni,O,Si,Ti

Given the effect of surface preparation on FE performance, the thrust of many of the investigations into SRF cavities has been in the area of producing a cleaner RF surface. It is likely that the most important gains in performance have come through use of clean rooms and protocols for assembly of cavity testing systems. Past studies on ultra high vacuum baking of the cavity[24,25] produced the first major breakthroughs to the 20 to 30 MV/m range that we seek. However furnace treatment is an expensive procedure, in time and resources, thus the effort to find alternative methods of obtaining clean, and therefore emission free, surfaces has been continued.

Recent, promising results have been obtained at several laboratories using a high pressure water rinse (HPR) as the final step prior to assembly to the vacuum apparatus. In HPR, a jet of ultra pure water (pressure ≥ 80 bar), is used to dislodge surface contaminants which are believed to be resistant to more conventional rinsing procedures.

An example of an HPR results on a 5-cell cavity at CEBAF is shown in Figure 3. On first measurement, the cavity was limited as shown to $E_{acc} = 9$ MV/m, with severe FE loading. The cavity was disassembled, rinsed with HPR, and then reassembled. Upon re-testing, the open circled curve was measured, limited only by a quench at 14 MV/m.

1-cell cavities have had even more impressive results, with many different labs[11,12,27] reporting multiple measurements of accelerating gradients in excess of 30-35 MV/m following HPR treatment. Indeed, the highest gradient reported to date is $E_{acc} = 43$ MV/m in a 1-cell cavity tested at CEBAF following HPR.[28]

Despite this promising work, however, consistently emission free surfaces continue to elude us, especially in the case of multi-cell cavities, where the larger surface area brings a proportionally larger probability of a contamination. One emitter is sufficient to limit the performance of an SRF cavity to unacceptable levels. This concern is especially daunting when one considers that with the proposed gradient, a 0.5 TeV collider would require 20,000 cavities.

The best results in reducing or eliminating FE after the cavity has been assembled have been obtained through High Power Processing (HPP).[29] HPP is an extension of the successful practice of conditioning an RF cavity, where the

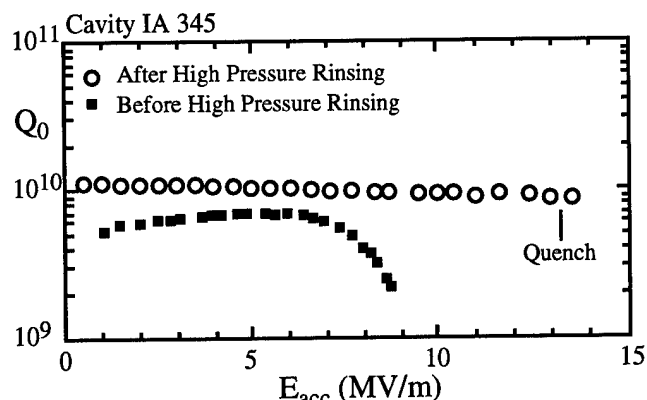


Figure 3. Q_0 vs. E_{acc} plots showing high pressure rinsing results on a 5-cell 1.5 GHz cavity at CEBAF.

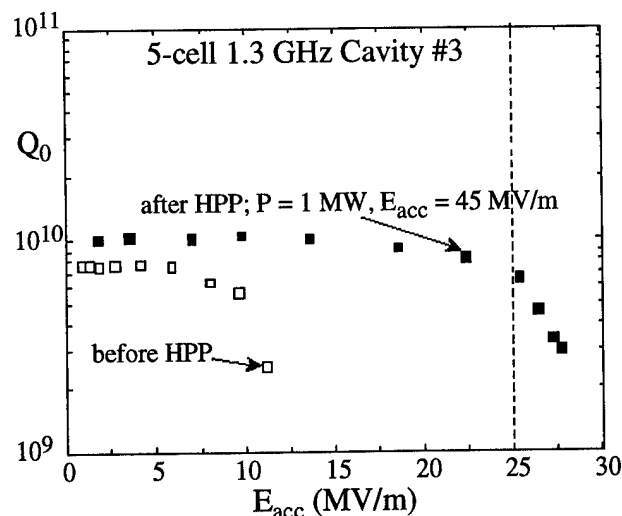


Figure 4. Q_0 vs. E_{acc} plots showing high power processing (HPP) results on a 5-cell 1.3 GHz cavity at Cornell.

emission in a cavity is reduced to acceptable levels through gradual raising of the incident power. Thermometry has shown that processing occurs through a local reduction in FE,[29] as evidenced by reduced electron impact heating. Microscopic investigation of RF surfaces following processing[23,29] has determined that processing occurs when the FE current is raised high enough to cause melting and/or vaporization of micron sized regions of the RF surface, presumably the emitter.

Continuous wave (CW) low power (≤ 100 W) RF processing of SRF cavities is severely limited by the exponential growth of the power dissipation under FE conditions. All available power is consumed before the fields, and therefore the FE current, can be raised high enough to initiate processing. With HPP, the incident power is raised to the order of hundreds of kilowatts to a megawatt, allowing fields to be increased high enough for processing to occur. Figure 4 shows the Q_0 vs. E_{acc} plot of a 5-cell 1.3 GHz cavity tested at Cornell. The pattern of measurement shown is typical: a cavity is severely limited by FE, which is impervious to conventional, low power, RF processing. HPP is applied with high power (in this case up to 1 megawatt), following which the attainable CW fields are greatly improved, sometimes by more than 100%. Three different 5-cell 1.3 GHz cavities reached gradients higher than 25 MV/m with this procedure.[30]

Studies of HPP on multi-cell cavities at both 1.3 GHz and 3 GHz have shown that success in processing is directly related to the magnitude of the fields reached during the HPP procedure. Put more succinctly, as long as the fields continue to increase in HPP, the CW performance will similarly improve. Empirically, it has been found in 5-cell 1.3 GHz that FE loading will be essentially eliminated in fields up to 50 % of the level reached during HPP.[30]

Finally, HPP also provides the possibility for *in situ* treatment of cavities which have been degraded by vacuum accidents. Normally a vacuum accident would require complete disassembly and re-cleaning of an affected cavity. With HPP,

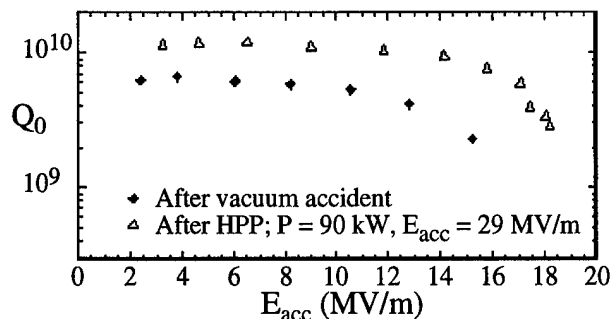


Figure 5. Q_0 vs. E_{acc} plots showing recovery of cavity performance with HPP following a vacuum accident.

the principle has been established that the cavity could regain all or most of its pre-accident performance without disassembly. Three separate 9-cell 3 GHz cavities were tested following vacuum accidents,[29,31] and, in each case, at least 80% of the cavity's previous performance was regained through HPP. The Q_0 vs. E_{acc} plots for one of these accidents are shown in Figure 5.

C. Putting It All to Work: The TESLA Test Facility

In order to further demonstrate the feasibility of the TESLA approach to a TeV collider, the TESLA Collaboration has begun work on the TESLA Test Facility (TTF), a 50 meter, SRF based linac, to be constructed with SRF technology at DESY. Current status of the TTF was discussed in another presentation at this conference.[32,33]

In setting up the TTF, the TESLA Collaboration has taken advantage of the latest information from the SRF community regarding the best methods of preparing cavities for RF performance. The TTF has a state of the art chemical and clean room facility, which includes a high pressure rinse system capable of delivering rinse water at up to 100 Bar, and a UHV furnace for surface preparation and/or RRR improvement. Figure 6 shows the Q_0 vs. E_{acc} plots from measurement of the capture cavity, which was procured by Saclay, then prepared and tested at DESY. As can be seen, the cavity

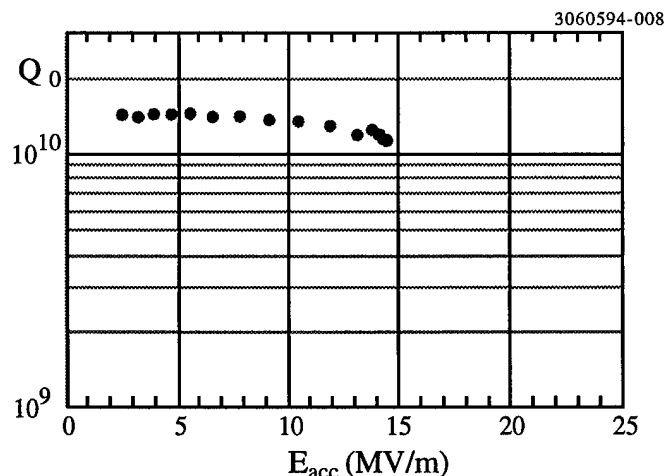


Figure 6. Q_0 vs. E_{acc} plot showing the performance of the TTF capture cavity (9-cell, 1.3 GHz, RRR = 250), tested at DESY.

was essentially emission free up to 14.5 MV/m, where a quench was encountered. This cavity has RRR of only 250, as it is designed for operation at only 12 MV/m.

The TTF also has an HPP setup capable of delivering up to 1 Megawatt pulses of up to 2 msec. The HPP procedure has been successfully used on several cavities to date, the most successful being the vertical test of cavity # 2, a production cavity with HOM couplers.

Figure 7 shows the CW measurements; through HPP processing, the cavity reached a CW accelerating gradient of 22 MV/m. More significantly, during HPP, the cavity was operated in the conditions prescribed for TESLA- input coupling $Q_{ext} = 3 \times 10^6$, RF pulse length = 1.3 msec, incident power of 250 kW. Figure 8 shows oscilloscope traces of the power transmitted to a monitor probe (upper trace), and the incident power delivered to the cavity (lower trace). As can be seen in Figure 8, the cavity reached an accelerating gradient of

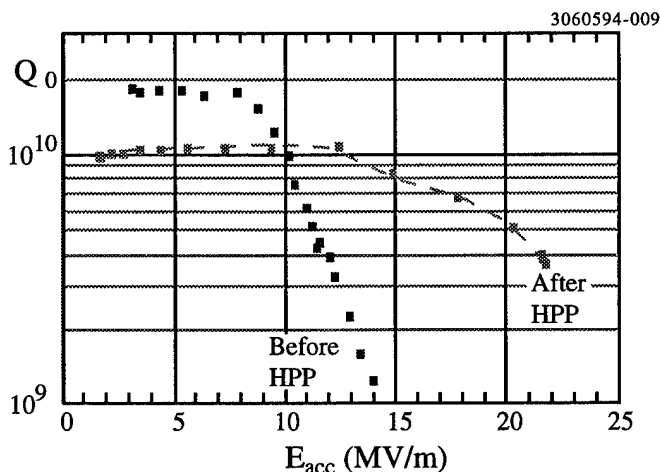


Figure 7. CW Q_0 vs. E_{acc} plots of TTF cavity #2, (9-cell, 1.3 GHz, RRR = 350), before and after HPP ($P \leq 400$ kW, $E \leq 32$ MV/m).

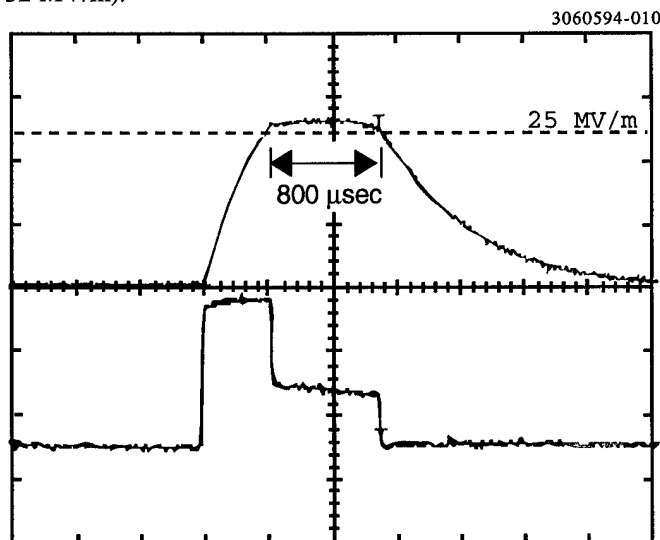


Figure 8. Oscilloscope traces captured during operation of TTF Cavity #2 operated under pulsed conditions at an accelerating gradient of approximately 26 MV/m. A description of this figure be found in the text.

26 MV/m after filling for 500 μ sec. At this point, the forward power was stepped down to 100 kW, in order to simulate the effect of beam load on cavity fields. The cavity maintained $E_{acc} = 26$ MV/m for the entire 800 μ sec designed for TESLA operation, and then decayed away naturally when the incident power was turned off.

Horizontal testing, followed by installation in the TTF, of this and subsequent cavities will proceed beginning this summer.

IV. FUTURE DIRECTIONS AND REMARKS

The prospect for further gains in high gradient superconducting RF accelerators is very bright. The concerted research effort undertaken in the last fifteen years to extend the attainable gradients has paid off with significant gains. The progress in achieved gradients (CW testing) is shown clearly in Figure 9. The maximum achieved gradients at the time of compilations in 1980 and 1989 are included as line plots for reference to show the gains made over time. Nearly all research in extending gradients today is being performed with 1-3 GHz cavities, with surface area between 0.05 and 0.8 square meters, hence the lack of gains in other regions.

The two primary limiting phenomena, field emission and quench are well understood. Improved purity of niobium has increased quench limits significantly. A clean RF surface is the most important determining factor in reducing FE. HPR and clean assembly procedures are helping provide such a surface. HPP is effective in reducing field emission in cavities which exhibit FE in spite of clean assembly procedures.

The design gradient for TESLA has been met in vertical testing of the TTF cavity at DESY. Repetition of this measurement in a horizontal cryostat, followed by installation in the TTF are scheduled for later this summer. By the 1997

3060594-011

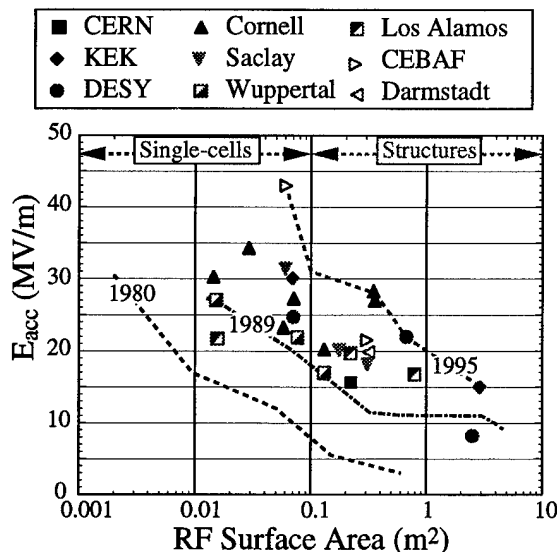


Figure 11. Historical progress in the attainable accelerating gradients, plotted as a function of RF surface area per cavity. High gradient studies are now performed primarily for cavities with area between 0.05 and 0.8 square meters.

PAC, we expect to show how the TTF project has further demonstrated the feasibility of TESLA.

VI. ACKNOWLEDGMENTS

The author would like to thank the following for their assistance and input in preparing this paper: H. Padamsee (Cornell); D. Proch, W.-D. Moeller, and M. Pekeler (DESY); S. Noguchi and E. Kako (KEK); B. Rusnak (LANL); W. Weingarten (CERN); B. Bonin (Saclay); P. Kneisel and C. Reece (CEBAF).

VII. REFERENCES

- [1] K. Akai, *Proc. of the 5th Workshop on RF Superconductivity*, D. Proch ed., DESY, Hamburg, Germany, **DESY M-92-01**, 126 (1992).
- [2] G. Cavallari, et al, *Proc. of the 6th Workshop on RF Superconductivity*, R. Sundelin ed., CEBAF, Newport News, VA USA, 49 (1994).
- [3] H.D. Graef, et al, *ibid* ref. 2, 1203 (1994).
- [4] K. W. Shepard, et al, *ibid* ref. 2, 1 (1994).
- [5] B. Dwersteg, et al, *Proc. of 4th European Particle Accelerator Conference*, London, England, 2039 (1994).
- [6] R. Brinkmann, this conference paper RPC07.
- [7] H. Padamsee, et al, *Ann. Rev. Nucl. Sci.* **43**, 635 (1993).
- [8] D. Proch, *ibid* ref. 2, 382 (1994).
- [9] C. Hovater, *ibid* ref. 2, 198 (1994).
- [10] C. Reece, et al, this conference paper FAE12.
- [11] D. Reschke, et al, *ibid* ref. 2, 1095 (1994).
- [12] B. Bonin and M. Juillard, *ibid* ref. 5, 2045 (1994).
- [13] B. Rusnak, et al, *Proc. of the 1993 IEEE Particle Accelerator Conference*, Washington DC, USA, 1021 (1993).
- [14] J. Tan, et al, *J. Phys D: Appl. Phys.*, **27**, 2654 (1994).
- [15] E. Mahner, *ibid* ref. 2, 252 (1994).
- [16] H. Padamsee, *IEEE Trans. Mag.*, **21**, 1007 (1985).
- [17] D. Bloess, et al, *ibid* ref. 5, 2057 (1994).
- [18] P. Kneisel, *J. Vac. Sci. Technology*, **A11**, 1575 (1993).
- [19] W. Weingarten, *Particle World* **1**, 93 (1990).
- [20] Y. Kojima, *Proc. of the 1991 Particle Accelerator Conference*, San Francisco, CA, USA, 16 (1991).
- [21] D. Proch, *ibid* ref. 13, 758 (1993).
- [22] Ph. Niedermann, Ph.D. Thesis No. 2197, Univ. of Geneva (1986).
- [23] D. Moffat, et al, *ibid* ref. 1, 245 (1992).
- [24] D. Reschke, et al, *ibid* ref. 5, 2063 (1994).
- [25] H. Padamsee, et al, *Proc. of the 4th Workshop on RF Superconductivity*, Y. Kojima ed., KEK, Tsukuba, Japan 207 (1989).
- [26] J. Knobloch, *priv. comm.*
- [27] K. Saito, et al, *ibid* ref. 2, 372 (1994).
- [28] P. Kneisel, *priv. comm.*
- [29] J. Graber, Ph.D. Dissertation, Cornell Univ. (1993).
- [30] C. Crawford, et al, *Particle Accelerators*, **49**, 1 (1995).
- [31] P. Schmueser, et al, Cornell Report **SRF-920925-10** (1992).
- [32] S. Wolff, this conference, paper RPB09.
- [33] H. Weise, this conference, paper RPB08.

Development And Advances In Conventional High Power RF Systems*

P. B. Wilson

Stanford Linear Accelerator Center, Stanford University, Stanford, CA 94309 USA

The development of rf systems capable of producing high peak power (hundreds of megawatts) at relatively short pulse lengths (0.1-5 microseconds) is currently being driven mainly by the requirements of future high energy linear colliders, although there may be applications to industrial, medical and research linacs as well. The production of high peak power rf typically involves four basic elements: a power supply to convert ac from the "wall plug" to dc; a modulator, or some sort of switching element, to produce pulsed dc power; an rf source to convert the pulsed dc to pulsed rf power; and possibly an rf pulse compression system to further enhance the peak rf power. Each element in this rf chain from wall plug to accelerating structure must perform with high efficiency in a linear collider application, such that the overall system efficiency is 30% or more. Basic design concepts are discussed for klystrons, modulators and rf pulse compression systems, and their present design status is summarized for applications to proposed linear colliders.

I. INTRODUCTION

There now exists an *Interlaboratory Collaboration for R&D Toward TeV-Scale Electron-Positron Linear Colliders*. The collaboration consists of some 23 member institutions in Europe, Asia and the United States with an interest in linear collider development. The Council of the Collaboration (consisting of one representative from each member institution) met at EPAC'94, and decided to appoint a Technical Review Committee (TRC). This committee was charged with preparing a report on the present status of linear collider technology, and the further R&D needed over the next few years to reach these design goals: an initial luminosity in excess of $10^{33} \text{cm}^{-2}\text{s}^{-1}$ at a center-of-mass energy of 500 GeV, with the capability of being expanded in energy and luminosity to reach 1 TeV center-of-mass energy with a luminosity of $10^{34} \text{cm}^{-2}\text{s}^{-1}$. A draft of the report will be submitted to the Collaboration Council in June, 1995. This paper is based in large part on material collected for Chapter 3 (Linac Technology) of the TRC report.

The major proposals for future linear colliders have been described in detail elsewhere (see for example the survey talks in [1]). TESLA (TeV Superconducting Linear Accelerator) is a proposal for a linear collider based on the use of superconducting accelerating cavities at 1.3 GHz. The TESLA R&D program is an international collaboration of about a dozen laboratories, coordinated by the DESY laboratory in Hamburg, Germany. Use of a superconducting cavity avoids the need for very high peak rf power. Such a cavity is in essence an rf pulse compressor, storing energy over a relatively long time period (on the order of a millisecond) from an RF pulse with a relatively low peak power. An advantage of the low TESLA rf frequency is a larger beam cross-section and looser tolerances on construction and alignment. The SBLC (S-Band Linear Collider) is a proposal, also based at DESY, for a linear

collider with an rf frequency of 3 GHz. Because of the relatively low rf frequency, the SBLC also has comparatively loose tolerances. A strong point of this proposal is that it is supported by a wide base of existing S-band accelerator technology, in particular the SLC prototype linear collider at SLAC. The NLC (Next Linear Collider) is a proposal by SLAC for a linear collider at 11.4 GHz, exactly four times the SLC frequency. The principal advantage of a higher rf frequency is that a higher accelerating gradient can be obtained for the same ac input power, resulting in a shorter length and possibly lower cost for the main linac. A major disadvantage is that tighter tolerances are required for the construction and alignment of the accelerating sections and focusing magnets. Also, higher peak power is required from the rf sources, with a consequence that some form of rf pulse compression is necessary. The KEK laboratory in Tsukuba, Japan, has proposed the JLC (Japan Linear Collider), also at 11.4 GHz; it is quite similar to the NLC in its main design parameters. VLEPP (standing for "Colliding Linear Electron-Positron Beams" in Russian) is a proposal for a linear collider at 14 GHz, which originated at the Institute of Nuclear Physics (INP) in Novosibirsk, Russia. The R&D for the collider is actually taking place at Protvino, Russia, near Serpukhov (about 100 km south of Moscow). It is being carried out by personnel from a Branch of the above institute (BINP). Unfortunately, the economic situation in present-day Russia is such that a full-scale VLEPP will probably not be funded. However, a strong R&D program is still going forward at Protvino; this work will provide useful results which can expedite the other collider programs. CLIC (CERN Linear Collider) is a proposal for a two-beam linear collider based at CERN in Geneva, Switzerland. In the CLIC design (see paper by K. Hübner in [1]), 350 MHz superconducting cavities are used to accelerate a high-current drive beam to 3 GeV. The drive beam consists of trains of bunches in which the spacing between bunches in each train is the rf wavelength at 30 GHz. These trains pass through a series of low impedance "transfer structures", where they induce about 90 MW of peak rf power for a pulse duration of 12 ns. This power is then transferred through waveguides (two for each transfer structure) to the accelerating sections in the main linac. The TBNLC (Two-Beam NLC), proposed by a group at LBL and LLNL, is also a two-beam accelerator scheme, but in this case the drive beam is powered by induction linac modules. The TBNLC is proposed as an alternative power source for the NLC, in particular as a high-gradient upgrade to 1 TeV. Instead, of a single drive beam per main linac, as in the case of CLIC, the TBNLC would consist of 18 separate drive beam units for each of the two main linacs. There would be 150 transfer structures per drive beam, each supplying 360 MW of power to a single 1.8 m NLC accelerating section.

The various proposed colliders and their operating frequencies are listed in Table I, along with other basic

* Work supported by the Department of Energy, contract DE-AC03-76SF00515.

parameters to be discussed in the following sections. The SLC is listed for comparison.

II. SCALING COLLIDER PARAMETERS WITH FREQUENCY

All of the proposed linear collide designs are based on the production and manipulation of RF power in the frequency range 1.3-30 GHz. The rf system itself must convert power from the ac mains (wall plug) to rf power at the input of the accelerating structure with the greatest possible efficiency. In general, it is easier to attain a high accelerating gradient at a higher rf frequency. Nature has, however, imposed a powerful limitation on the gradient achievable for routine operation of a copper accelerating structure --- the dark current capture threshold. This threshold is given by

$$G_{th}\lambda = 1.605 \text{ MV} \quad (1)$$

where λ is the RF wavelength. The threshold gradients for the various colliders are listed in Table I, together with the design gradients for a 500 GeV machine. It is indeed possible to exceed this threshold gradient by some reasonable factor; for example the SLC routinely operates 30% above it with barely detectable dark current. However, the dark current beam power dissipation, and hence the difficulty in processing a structure to a given gradient level, tends to become worse exponentially as the capture threshold is exceeded by a still larger factor. In the case of a superconducting structure, field emission will necessarily be reduced to a low level by special cleaning and processing techniques to avoid unacceptable power dissipation at low temperature. Perhaps these heroic cleaning and handling procedures can be adapted to copper structures as well. But in any case, if operation is planned at a gradient significantly above the capture threshold, dark current effects must be carefully studied in an appropriate test facility (such as the TESLA Test Facility under construction at DESY).

For a high frequency high gradient linear collider with a copper accelerating structure, nature has unfortunately imposed another limitation on the rf system. The energy stored per unit length on the accelerating structure will scale roughly as $G^2\lambda^2$. If the gradient is set at some factor times the capture threshold gradient, then the stored energy per unit length remains roughly constant, independent of frequency. However, the time allowed for this energy to be collected in the accelerating structure depends on the energy decrement time,

$$\tau_d = Q / \omega \sim \omega^{-3/2} \quad (2)$$

Thus the RF pulse length will also tend to scale as $\omega^{-3/2}$, and since the stored energy per meter is roughly constant under the above scaling assumption, the peak power required per meter will tend to scale as $\omega^{3/2}$. Unfortunately, the maximum output power available from a klystron tends to decrease rather than increase as frequency increase. Therefore high frequency RF systems using klystrons to

generate the RF power (NLC, JLC, VLEPP) require some sort of pulse compression to enhance the peak power output. However, the additional loss associated with the compression process tends to lower the overall efficiency of the RF system. The two-beam accelerator concept (TBNLC, CLIC) bypasses the limitations imposed by conventional klystrons in producing high frequency, high peak power at short pulse lengths. The drive beam in a two-beam accelerator is, in fact, equivalent to the beam in a klystron, and the TBA scheme is also called a "relativistic klystron." A collider using a superconducting accelerating structure (TESLA) increases the Q/ω limitation on energy collection time by a large factor over that of copper, allowing a long pulse, low peak power, efficient RF system. (As will be discussed later, a long pulse modulator tends to be more efficient than one which must produce short, very high peak power pulses). However, this gain in the efficiency of RF power generation is offset to a large extent by the additional power required by the refrigeration system.

Energy decrement times and peak RF power requirements for the collider designs are listed in Table I. For machines with copper structures, the structure filling times (except for CLIC) are quite close to the values given for τ_d ; the RF pulse lengths are typically several times longer to allow for acceleration of a bunch train. The pulse lengths at the accelerating structure (in nanoseconds) are: SBLC (2800); JLC (230); NLC (240); VLEPP (110); CLIC (12). In the case of TESLA, the pulse length (1.3 ms) is reduced below the decrement time approximately by the ratio of the refrigeration power required per Watt of power dissipated at 4.2°K (≈ 300). The peak powers do not scale as $\omega^{3/2}$ as discussed above, because the actual design gradients do not closely follow a G_{th} scaling. However, as seen in Table I, the peak power per meter does increase rapidly with increasing frequency. Likewise, the linac length would be roughly proportional to λ for $G \sim G_{th}$ scaling. The actual design lengths do show a strong correlation with frequency. Since the stored energy per meter remains approximately constant for $G \sim G_{th}$ scaling, the average AC wall-plug power should scale roughly as $\bar{P}_{AC} \sim f_r \lambda / \eta_{rf}$, where f_r is the repetition rate and η_{rf} is the RF system efficiency. As frequency increases, the colliders in Table I trade at least part of their wavelength advantage for a higher repetition rate. These rates are (in Hz): TESLA (10); SBLC (50); JLC (150); NLC (180); VLEPP (300).

III. RF SYSTEM TECHNOLOGY

A. Klystrons

At a constant beam voltage, the RF output of a klystron (or other microwave power source) increases as the beam current increases. However, a higher beam current, I_b , at a given beam voltage, V_b , inevitably lead to a lower efficiency because of the detrimental effects of space charge forces. These forces tend to blow apart the sharply defined bunches needed for high output efficiency. The micropervance (defined by $K_\mu = I_b/V_b^{3/2} \times 10^6$) is commonly taken as a measure of these space charge effects. If klystron efficiencies, obtained from both measured performance and

simulations, are plotted as a function of micropervance, it is found that the collection of points (see for example [2], Fig. 3) is quite sharply bounded by the line

$$\eta_{kly} \approx 0.80 - 0.15K_{\mu} \quad (2)$$

Low frequency, long pulse or CW klystrons tend to fall closer to this performance limit than high frequency, high peak power tubes. The intercept at zero pervance has some theoretical justification. A 100% efficiency implies that all the electrons in the beam are just brought to rest by the RF voltage of the output circuit. This is not possible in a real klystron because there is an energy spread in the beam due to the bunching process, and because the RF voltage varies with radius across the gap. Also, even a single electron cannot be stopped in a gridless gap; an electron on axis can lose at most about 85% of its energy [3].

There is also the perennial question concerning limitations on peak klystron output power as a function of frequency. This can be roughly estimated as follows. First, the beam radius is limited to something like $\lambda/8$ to allow for reasonable gap coupling. Second, the current density per unit area from the cathode (cathode loading, I_A) is limited to about 10 A/cm^2 for good cathode lifetime. Third, the area compression ratio, C_A , of the beam in the gun region is limited by optics and tolerances to perhaps 150. Putting these factors together gives

$$P_{\max} \approx \eta V_b [I_A C_A \pi (\lambda/8)^2] = 74 \eta V_b (\lambda/\text{cm})^2 \quad (3)$$

where η is the electronic efficiency. If the tube is to be efficient, and if we apply Eq. (2) conservatively, then the micropervance for an efficiency of 50-60% is limited to $K_{\mu} \leq 1$. Using Eq. (2) together with $P_K = \eta (K_{\mu} \times 10^6) V_b^{5/2}$, we find that for $V_b = 500 \text{ kV}$ the maximum output power is about 100 MW up to 14 GHz, then falls off as λ^2 above this frequency.

Table II lists klystron parameters for the five collider proposals that use klystrons as an RF source. Both design parameters and values actually achieved to date are shown. The numbers given for "scaled maximum efficiency" are obtained from Eq. (2). Note that the design values for efficiency are all well below these maximum values, except for the low frequency, long pulse TESLA klystron where good efficiency should be relatively easy to achieve. Two of the klystrons have achieved the design peak power. The SBLC S-band klystron, designed in collaboration with SLAC, has reached 150 MW at a $2.8 \mu\text{s}$ pulse length [4]. The NLC X-band klystron has achieved 50 MW at $1.5 \mu\text{s}$ [5]. Both klystrons still fall short in efficiency, and both must eventually replace power-consuming solenoids with PPM (periodic permanent magnet) focusing or superconducting solenoids.

B. Modulators

The rise time of a modulator pulse is an important parameter in determining the modulator efficiency. In a conventional modulator, the pulse forming network (PFN) capacitance is charged by a DC power supply to a voltage

VPFN. This network can be either a length of smooth transmission line, or a series of discrete capacitors and inductors which model such a line. The line is then discharged by a switching device, usually a thyatron, through the primary of a pulse transformer with a turns ratio n . The output of the pulse transformer produces a voltage $nV_{PFN}/2$ (single stage PFN), or nV_{PFN} (two stage, or Blumlein PFN). In the case of the TESLA modulator, an energy storage capacitor is partially discharged through the primary of the pulse transformer. The switching is done by solid state devices (thyristors). A "bouncer" circuit is used to compensate for voltage droop.

The energy efficiency, η_E , of the pulse transformer is defined as the useful energy in the flat-top portion of the pulse divided by the total energy in the pulse. The energy in the fall-time portion of the pulse tends to scale in proportion to the rise time, T_R , so that the energy efficiency can be written as $\eta_E \equiv T_K/T_E = T_K/(T_K + \alpha T_R)$, where T_K is the useful flat-top pulse width, T_E is the energy width, and α is a coefficient between 1.0 and 1.2 which depends on the pulse shape and the definition of rise time. In turn, a simple physical argument [6] leads to the scaling $T_R \sim nT_E^{1/2}$. Combined with the preceding relation, this gives

$$T_E = \frac{1}{4} [\beta n + (\beta^2 n^2 + 4T_K)^{1/2}]^2 \quad (4)$$

where β is a constant that can be obtained by fitting to existing pulse transformer designs. For the pulse transformer driving the 5045 SLAC klystrons, $\beta = 0.033 (\mu\text{s})^{1/2}$. It is found that the above expression then gives a good fit to a number of other pulse transformers measured at SLAC having a variety of turns ratios and pulse lengths. Using Eq. (4), the energy efficiency is plotted in Fig. 1.

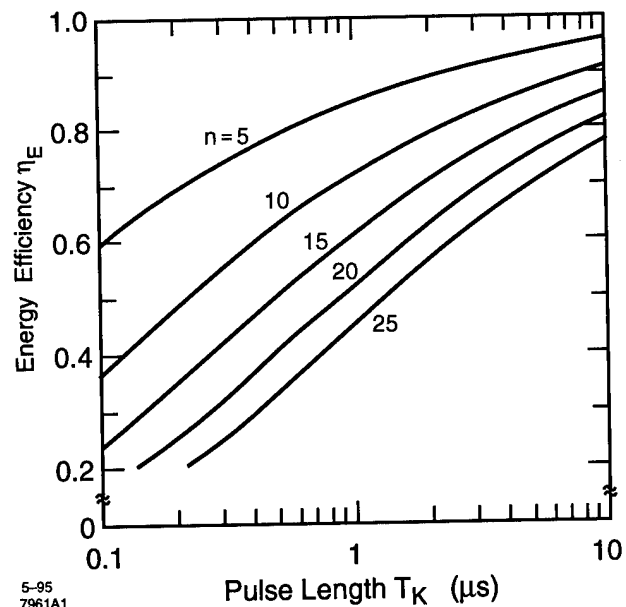


Figure 1 - Energy Efficiency for a typical pulse transformer as a function of pulse length and turns ratio n .

Along with T_K and n , values of η_E from Eq. (4) are listed in Table III (as the scaled energy efficiency) for the

modulator designs for the various collider proposals. An accurate calculation of energy efficiency must also include the effect of the load (klystron) capacitance, the series inductance of the thyatron, transformer core losses, and the inductances of the cables and leads connecting the components. Of course, the best efficiency is obtained by eliminating the modulator entirely by using a klystron with a gridded gun to switch the beam, as proposed for VLEPP.

C. RF Pulse Compression

RF pulse compression is a method of enhancing klystron output power at the expense of pulse width. Although some energy is lost in the compression process, the efficiency can in principle be quite high. High-Q energy storage elements are required to achieve efficient pulse compression; these can be either resonant cavities or lengths of shorted delay line.

RF pulse compression is used in three of the 500 GeV collider designs. VLEPP and NLC use a SLED-type scheme (SBLC plans to use a SLED system in a 1 TeV upgrade). In a SLED pulse compression system [7], energy builds up in a storage element (resonant cavity or resonant delay line) over the major part of the klystron output pulse. During the final part of the pulse, equal to the desired output pulse length, a phase reversal at the klystron input triggers a discharge of this stored energy, which then adds to the energy coming directly from the klystron. During the filling time of the storage device, there is an unavoidable power reflection; in addition, some energy is left behind in the storage element. Together, these factors lead to a maximum intrinsic efficiency for a SLED system on the order of 80%, even assuming lossless components. Taking losses into account reduces the efficiency to approximately 75%. On the other hand, the JLC uses a compression method, the Delay Line Distribution System (DLDS), which is inherently 100% efficient. Although related to Binary Pulse Compression [8], the DLDS system uses less delay line pipe by feeding power in the up-stream beam direction, thus taking advantage of the beam transit time to achieve a factor of two reduction in the required delay line length. Both the DLDS and the SLED-II compression systems have the advantage of producing a flat output pulse. This is a necessity for accelerating long bunch trains (the beam pulse length is about 120 ns for JLC and NLC). The VLEPP compression system is based on the use of a single traveling-wave "open" cavity resonator of unique design [9], and is therefore very compact. Although the output pulse is not inherently flat, this is of no consequence for the acceleration of a single bunch, as is the case for VLEPP. Parameters for the three pulse compression systems are given in Table IV.

IV. RF SYSTEM EFFICIENCY

The overall RF system efficiency is an important parameter for a linear collider. The AC power requirements (see Table I) for the various collider proposals range from 60-150 MW. Thus a 1% improvement in efficiency can reduce the AC power consumption by a megawatt or more. The net system efficiency, shown in the last column in Table I, is the product of the separate efficiencies of the klystron,

modulator, and pulse compression systems. If there is no compression system, the efficiency for transmitting power from the klystron to the accelerating structure must be included instead. The system efficiency can be calculated with and without auxiliary power. This includes power for the klystron cathode heater, klystron focusing solenoid, thyatron cathode and reservoir heaters, and power for the cryogenic systems in TESLA and CLIC (which uses superconducting cavities to accelerate the drive beam). The net RF system efficiency is, on the average, about one-third.

It is obviously highly desirable to increase the net RF system efficiency. For example, one can think of eliminating the pulse compression system and the losses associated with it. However, more dc pulse compression must then be carried out in the modulator (or in the induction linac modules in the case of the TBNLC). As another example, a better klystron efficiency can be obtained by raising the beam voltage and lowering the perveance. Again, this implies a lower modulator efficiency because a pulse transformer with a larger turns ratio will be required (or a higher V_{PFN} could be used, which is more expensive and technically difficult). There are losses and inefficiencies in each stage of the power handling and processing chain between the AC wall plug and RF at the input to the accelerating structure. Care must be taken that an efficiency improvement at one step in this chain is not made at the expense of increases loss at another stage.

A long-range expectation for the efficiency of the RF system for a linear collider might be on the order of 50%. This efficiency could be attained by a low perveance, high efficiency klystron (65%) with grid switching (95% efficient), and a high-gain Binary Pulse Compression system (81% efficient including power transmission). The BPC system would use 10 or so discrete cavities per stage to eliminate long delay lines.

V. ACKNOWLEDGMENT

The principal results on the status and development of high power RF systems, as reported here, are contained in Tables I through IV. These tables are the result of hard work over many months by members of the Linac Technology working group of the Technical Review Committee mentioned in the Introduction. In particular D. Proch (TESLA), N. Holtkamp (SBLC), T. Higo and H. Mizuno (JLC), N. Solyak (VLEPP), G. Westenskow (TBNLC) and I. Wilson (CLIC) were responsible for the major portion of this effort, with substantial input from A. Gamp on the TESLA rf system.

VI. REFERENCES

1. See survey papers on linear colliders by N. Holtkamp (p. 770), G. Loew (p. 777), V. E. Balakin (p. 784), K. Hübner (p. 791), M. Tigner (p. 798) in: HEACC'92, Inst. J. Mod. Phys. A (Proc. Suppl.) 2B (World Scientific, Singapore, 1993).
2. R. B. Palmer, W. B. Herrmannsfeldt and K. R. Eppley, "An Immersed Field Cluster Klystron", SLAC-PUB-5026 (1989).

3. Z. D. Farkas and P. B. Wilson, "Dynamics of an Electron in an RF Gap", SLAC-PUB-4898 Rev. (1989).
4. U. Becker *et al.*, "Comparison of CONDOR, FCI and MAFIA Calculations for a 150 MW S-Band Klystron with Measurements"; paper WAE13, these proceedings.
5. E. Wright *et al.*, "Design of a 50 MW X-Band Klystron", SLAC-PUB-6676 (1995).
6. P. B. Wilson, "Application of High Power Microwave Sources to TeV Linear Colliders", in *Applications of High-Power Microwaves*, A. Gaponov-Grekhov and V. Granatstein, eds. (Artech House, Boston, 1994), Sec. 7.4.2..
7. For a brief description of SLED and SLED-II with additional references, see [6], Sec. 7.4.3.
8. Z. D. Farkas, IEEE Trans. Microwave Theory and Techniques MTT-34, 1036 (1986).
9. V. E. Balakin and I. V. Syrachev, Proc. 3rd European Part. Accel. Conf. (Editions Frontiers, Gif-sur-Yvette, France, 1992), p. 1173.

Table I Basic Parameters for Proposed Linear Colliders Designs at 500 GeV

Collider Proposal	Type ⁽¹⁾	RF Freq (GHz)	G _{th} from Eq. (1) (MV/m)	Gradient ⁽²⁾ (MV/m)	Decrement Time τ_d (ns)	Peak Power per meter (MW/m)	Active Length ⁽³⁾ (km)	AC Power ⁽⁴⁾ (MW)	RF System Efficiency ⁽⁵⁾ (%)
TESLA	SCA	1.3	7	25/25	0.6×10 ⁹	0.21	20	154	35/58
SLC	Cu	2.856	15	20/21	730	12	2.8	24	13.6/14.5
SBLC	Cu	3.0	16	17/21	720	12	30	139	37/38
JLC	Cu	11.4	61	53/73	95	100	10	114	30/34
NLC	Cu	11.4	61	37/50	98	50	14	103	30/31
VLEPP	Cu	14	75	91/100	68	120	6	57	39/40
TBNLC	TBA	11.4	61	74/100	98	200	7	106	39/40
CLIC	TBA	30	160	78/80	22	144	6	100	26/35

(1) SCA = superconducting accelerating structure; Cu = copper accelerating structure; TBA = two-beam accelerator (with copper main linac structure).

(2) Design gradient with/without beam loading (bunch on crest).

(3) Includes overhead for BNS damping and energy management (see text).

(4) AC power required for producing main linac RF; includes cryogenic and auxiliary power (see text).

(5) Efficiencies are given with/without cryogenic and auxiliary power included.

Table II Klystron Parameters: Design Goals and Achieved to Date

	TESLA		SBLC		JLC		NLC		VLEPP	
	Design	Ach.'d	Design	Ach.'d	Design	Ach.'d	Design	Ach.'d	Design	Ach.'d
RF Frequency (GHz)	1.3	1.3	3.0	3.0	11.4	11.4	11.4	11.4	14	14
Peak Output Pwr. (MW)	7.1	5.0	150	150	135	96/50	50	58/52	150	60
Pulse Length (μs)	1314	2010	2.8	3	0.5	0.1/0.2	1.2	0.2/1.5	0.50	0.7
Repetition Rate (Hz)	10	10	50	60	150		180	60	300	2
Ave. Output Pwr. (kW)	93		21	27	10		11	1/5	24	
Microperveance	0.5 ¹⁾	2.0	1.2	1.8	1.2	1.2	0.6	1.2	0.25	0.15
Electronic Effic. (%)	70	45	50	42	45	33	60	43/37	60	40
Scaled Max. Effic. ²⁾ (%)	73	50	62	53	62	62	71	62	76	78
Beam Voltage (kV)	110	130	575	528	600	620	455	400	1000	1000
Beam Energy/Pulse ³⁾ (J)	13,300	10,100	840	1070	150	170	100		125	
Cathode Load(A/cm ²)	3.1		6	6	13.5	13.5	7.4	7.6.	5	5
Cathode Heat Pwr. (kW)	0.5		1	2	0.5	0.5	0.4		1.0	1.0
Focusing Type	Sol.	Sol.	PPM	Sol.	SCM	Sol.	PPM	Sol.	PPM	PPM
Solenoid Power (kW)	4	4	—	15	1	40	—	≈20	—	—
Output Window Type	Coax	Pillbox	Pillbox	Pillbox	TE ₁₁	TE ₁₁	TE ₀₁	TE ₀₁	TE ₁₁	TE ₁₁
					TW	λ/2	TW	TW	TW	
Windows/Klystron	1	1	2	4	2	2	1	1	2	2
Overall Length (m)		2.0	2.5	2.5	1.5	1.5	1.3	1.3	1.46	1.46

(1) Perveance per beam in multibeam klystron. (2) $\eta(\text{Max}) \approx 0.80 - 0.15 \times \text{Microperveance}$. (3) In flat-top portion of pulse.

TableIII. Modulator Parameters: Design Goals and Achieved to Date

	TESLA		SBLC		JLC		NLC		VLEPP	
Modulator Type ¹⁾	Storage cap. with bounce		PFN		Blumlein PFN		Blumlein PFL		Gridded Gun see 6)	
	Design	Ach.'d	Design	Ach.'d	Design	Ach.'d	Design	Ach. ⁵⁾	Design	Ach.'d
Flat Top Pulse Length, Tk (μs)	1314	2010	2.8	3.0	0.5	0.7	1.2	1.5	0.50	0.50
PFN Voltage (kV)	9	10	65	43	120	80	455	400	1000	960
Transformer Ratio n	1:13	1:13	1:18	1:23	1:5	1:7	1:7	1:20	—	—
Rise/Fall Energy Effic (%)			86.5	≈ 65	89	70	80	≈ 60		
Scaled Energy Effic. ²⁾ (%)	99	—	70	65	79	70	81	58	—	—
I ² R/Thy./Core Loss Effic. (%)			97	95	97		97			
Energy Stored on PFN ³⁾ (J)			1000	1650	174		258			
Power Supply Efficiency (%)			95	90	95		93	≈ 90		
Mod. Eff. without Aux. Power (%)			79.5	≈ 60	82		72	≈ 52	95	
Auxiliary Power ⁴⁾ (kW)			1.5	3	1.5		1.5	1.5	0.3	
Net Modulator Efficiency (%)	86	86	77.5	59	80		70		92.5	
Ave. AC Input Power (kW)	155		54.2	88	29		51.5		40.5	
(Including Auxiliary Power)										

(1) PFN = lumped element pulse forming network; PFL = pulse forming line (transmission line).

(2) See text.

(3) Energy switched per pulse from storage element for TESLA and VLEPP.

(4) Includes thyatron cathode heater and reservoir heater power.

(5) With standard (not Blumlein) PFN.

(6) Uses a PFL as energy storage element.

Table IV. RF Pulse Compression and Power Transmission: Design and Achieved to Date

	JLC		NLC		VLEPP	
Type of Pulse Comp. System ¹⁾	DLDS		SLED-II		SLED-I (VPM)	
	Design	Ach.'d	Design	Ach.'d	Design	Ach.'d
Compression Ratio	2		5	6	4.55	4.55
Input/Output Pulse Length (ns)	500/250		1200/240	900/150	500/110	500/110
Compression Efficiency (%)	98		76.5	73	74	72
Power Gain	1.96		3.83	3.7	3.37	3.3
Power Transmission Efficiency (%) ²⁾	95		94	84	95	95
Power Gain Including Transmission Loss	1.86		3.60	3.0	3.20	3.1
Net Efficiency Including Trans. Loss (%)	93		72		70	
Length of Structure per Power Unit (m) ³⁾	5.24		7.20		4.00	
Power at Structure per Power Unit (MW)	524		360	150	480	
Maximum Power in P.C. System (MW)	282		380	205	250	150
Required Klystron Power (MW)	2 × 141		2 × 50		2 × 75	

(1) DLDS = Delay Line Distribution System; VPM = VLEPP Power Multiplier.

(2) The power transmission efficiency in percent for TESLA, SBLC, TBNLC and CLIC are, respectively, 96, 97, 98, and 90.

(3) A power unit is: TESLA, one klystron with modulator feeding thirty-two 1.04 m accelerating sections; SBLC, one klystron with modulator feeding two 6.0 m sections; JLC, two klystrons with two modulators driving one pulse compression unit which feeds four 1.31 m sections; NLC, one modulator driving two klystrons which together drive one pulse compression unit feeding four 1.8 m sections; TBNLC, one transfer structure for each 1.8 m section; VLEPP, one grid-modulated klystron driving two VPM cavities which together feed four 1.0 m sections; CLIC, one transfer structure driving two 0.28 m sections. The total number of power units (2 linacs) are: TESLA, 604; SBLC, 2517; JLC, 1804; NLC, 1968; TBNLC, 3938; VLEPP, 1400; CLIC, 11233.

THE UPGRADED RF SYSTEM FOR THE AGS AND HIGH INTENSITY PROTON BEAMS*

J.M. Brennan

AGS Department, Brookhaven National Laboratory
Upton, New York 11973-5000 USA

Abstract

The AGS has been upgraded over the past three years to produce a record beam intensity of 6×10^{13} protons per pulse for the fixed-target physics program. The major elements of the upgrade are: the new 1.5 GeV Booster synchrotron, the main magnet power supply, a high frequency longitudinal dilution cavity, a feedback damper for transverse instabilities, a fast gamma transition jump system, and a new high-power rf system. The new rf system and its role in achieving the high intensity goal are the subjects of this report.

The rf system is heavily beam loaded, with 7 Amps of rf current in the beam and a peak power of 0.75 MW delivered to the beam by ten cavities. As an example of the scale of beam loading, at one point in the acceleration cycle the cavities are operated at 1.5 kV/gap; whereas, were it not for the new power amplifiers, the beam-induced voltage on the cavities would be over 25 kV/gap. The upgraded rf system, comprising: new power amplifiers, wide band rf feedback, improved cavities, and new low-level beam control electronics, is described. Results of measurements with beam, which characterize the system's performance, are presented. A typical high intensity acceleration cycle is described with emphasis on the key challenges of beam loading.

I. CAVITY

Figure 1 shows a schematic drawing of one of the ten cavity stations, comprising four ferrite-loaded(4L2) push-pull cells connected in parallel. Each cell provides up to 10 kV. The ferrite bias current, 0 to 1500 A, flows in the walls and interconnecting "bus bars". They operate between 1.6 and 4.5 MHz. The range for protons is 2.7 to 3.0 MHz, but the full range is needed for heavy ions. The upgrade program did not need to substantially change the cavities, however, two important improvements were made.

R/Q

With batch filling from the Booster, the AGS must operate with a partially filled ring at high intensity and is subject to transient beam loading. The best cure for transient beam loading is to reduce the R/Q of the cavity. For these cavities

*Work performed under the auspices of the U.S. Department of Energy.

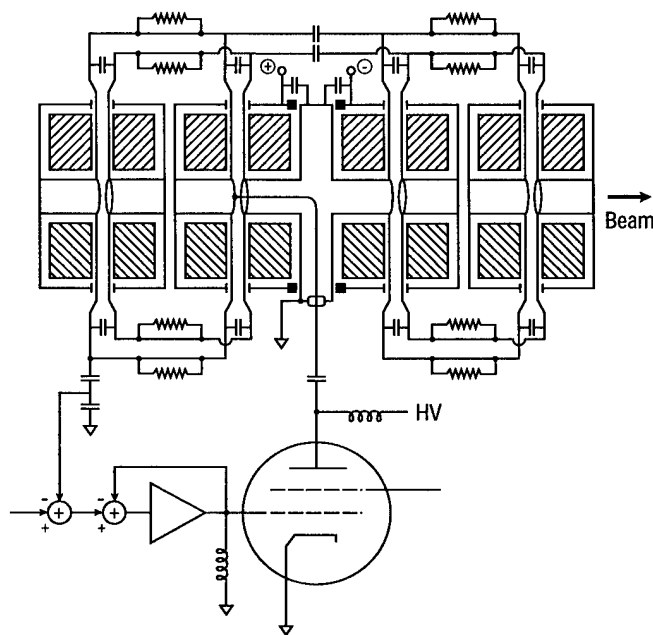


Figure 1. The four-cell cavity with, tetrode power amplifier, feedback amplifier, split loading capacitors at the gaps, and damping on the bus bars.

the R/Q is easily controlled by the external capacitors loading the gaps. For the upgrade the capacitance was increased as much as possible. The limit is given by the ferrites. As the capacitance increases, the biasing of the ferrites must increase. However, the dissipation in the ferrites increases with bias but must be below 300 mW/cm³. In addition, the ferrite exhibits a Q-loss instability at the top frequency which also depends on bias. The capacitors were increased from 275 pF to 600 pF. The intrinsic capacitance of the structure is 130 pF. Therefore, the R/Q was decreased by a factor of 1.8 to a value of 80 Ω at midband.

Higher Order Modes

Larger loading capacitors brought down the frequencies of resonant modes on the "bus bars" connecting the cells. These higher order modes interfere with the rf feedback and cause narrowband impedances capable of driving coupled-bunch longitudinal beam instabilities. Damping of these modes was facilitated by existing extra leadouts from the gaps, on the left side of the beam tube as well as the right. By adding "bus bars"

on the left side, in parallel with those on the right, and splitting the loading capacitors to 300 pF on each side, the frequencies of the higher order modes were increased. Then, the modes were effectively damped by resistors in parallel with all the "bus bars". The resistors are 40 Ω , 25 mm by 600 mm low-inductance power resistors.

II. POWER AMPLIFIER

Power Tetrode

The power amplifier uses a Thomson-CSF TH573 300 kW tetrode in the grounded-cathode configuration. The anode power supply can deliver an input power of 390 kW. The tube must provide 60 kW to drive the four-cell cavity to 40 kV, and provide up to 75 kW of beam power at 6×10^{13} ppp. There are ten amplifier/cavities in the system. The surplus installed power provides the opportunity for future intensity upgrades but also is instrumental for achieving stability under the heavily beam-loaded conditions. The choice of a tetrode is attractive because it leads straightforwardly to a stable amplifier. The high power tetrode has the additional feature of a relatively low anode resistance which significantly loads the cavity, thereby reducing its impedance. This property is an integral part of rf system's design, as it yields a factor of three or more of broadband impedance reduction. A beneficial aspect of this type of impedance reduction is that it can be dynamically controlled by changing the grid bias of the tube. In this way the loading effect can be enhanced at key points in the acceleration cycle and then reduced, to conserve power, when not necessary. Typically the amplifier operates in class AB1, but is put into class A at peak beam loading times and is biased to cut-off when the rf system is off (roughly 60% of the repetition period).

Reactive Power

At times the power amplifier must drive a de-tuned load. Transients occur at injection, transition, and de-bunching (at the unstable fixed point) before the slow extraction. The cavity tuning servos require about 3 ms to settle to the new compensation current. To maintain constant cavity voltage during the settling time, the power amplifiers must deliver reactive current. As much as 50 A average reactive current could be called for at transition. In this case the power tetrode would reach 180 A peak during the rf cycle.

Coupling to the Cavity

To fully exploit the low plate resistance of the power tube, it must couple to the gap without impedance transformation. Further, the line must be short to prevent standing wave modes at low frequency. Also, wideband rf feedback requires a minimum of delay in the feedback path. Figure 1 shows the coupling line between tube and gap, which is 1.5 m long. The line crosses a gap and the current returns to ground by encircling the ferrite of both halves of the cavity cell. The single-ended voltage on the anode appears as an equal magnitude push-pull

voltage on the gap, hence the impedance ratio is 1:1. Referred to a single gap, however, the tube impedance is effectively quadrupled because the four cells are in parallel. The line travels inside the beam tube in the vacuum, eliminating potential high voltage breakdown problems. The beam is shielded from the line by a grounded inner sleeve. To install the coupling line, the cavities were disassembled into individual cells. This provided an opportunity to upgrade all the vacuum seals of the cavities. Fortunately, neither the ceramic insulators at the gaps nor the ferrite stacks had to be disassembled. The coupling line is water cooled with approximately 2 gpm of flow.

III. RF FEEDBACK

At injection the cavities are operated at 1.5 kV/gap, which requires 0.5 A of current from the power amplifier (I_b). At 6×10^{13} ppp the rf beam current, (I_b), is 6.0 A, implying a beam loading parameter, I_b/I_0 , of 12. It has been shown [1,2] that when the beam loading parameter becomes greater than 2 the beam control loops, tuning, AVC, and phase, are cross-coupled and become unstable. RF feedback is needed to reduce the effective beam loading parameter. Feedback reduces the perturbations of the gap voltage by the value of the loop gain, and the beam current, seen from the control loops, is effectively reduced. Loop gains of 17 dB and greater (depending on the operating point of the tetrode) are used to reduce the beam loading parameter to less than 1.7.

Other peripheral benefits follow from rf feedback: 1. cavity control is linearized, the AVC loop does little; 2. phasing of the cavities is essentially independent of tuning servo errors; and 3. the modulation response time of the cavities is reduced by the loop gain. The hardware of the rf feedback is described in some detail elsewhere.[3,4] Some key points deserve emphasis. The feedback amplifier is a closed-loop circuit itself. It must have wide bandwidth to add minimal phase shift in the cavity loop. For phase margins less than 60° the closed loop response will exhibit gain peaking which, increases the cavity impedance at adjacent revolution harmonics. Unstable coupled-bunch modes could be driven by the peaking. Closed loop operation of the feedback amplifier adds negligible delay to the cavity loop, and phase margins greater than 60° are maintained. The key component for achieving the wide bandwidth is the attenuator that senses the grid voltage. The load resistance on the grid is set to 200 Ω . This is a compromise between a low value to keep the Q of the tuned circuit low and a high value to limit the required current from the amplifier. Attempts to transform a standard 50 Ω load to 200 Ω resulted in spurious resonances that destabilized the loop. A better solution was to obtain a special (-Altronics Research Inc.), water-cooled, 200 Ω 10:1 attenuator which gave a clean spectrum to very high frequencies. Finally, the control grid of the tetrode constitutes a significant capacitive load (~ 1 nF) which must be driven to 300 Volts.

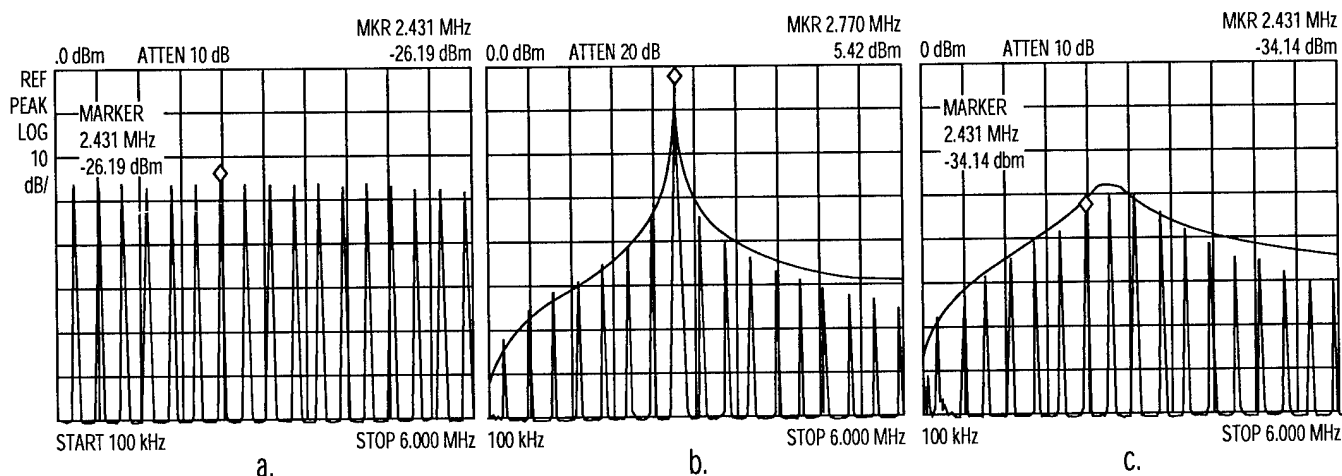


Figure 2. Cavity Impedance measurements; a. Beam current, b. Cavity voltage with amplifier off, c. Cavity voltage with amplifier and rf feedback on.

By resonating the grid capacitance with a variable inductor, the size of the feedback amplifier is kept modest. The inductor is a biased ferrite (4M2). Bias current is derived from a measurement of the operating frequency.

Protection Systems

Six systems prevent damage from over-power situations. 1. A fast crowbar circuit on the tetrode anode voltage protects against arcs within the tube or sudden loss of grid bias. 2. A slow overload circuit shuts down the anode power supply at 35 A average current. 3. If the rf voltage at the control grid exceeds 300 V, the drive signal to the power amplifier is shut down. 4. A window comparator about the reference signal for the AVC loop checks for out-of-range situations, such as, a spark in the cavity. This circuit inhibits the power amplifier drive. 5. The feedback amplifier is equipped with an input voltage limiter made from PIN diodes. The limiter would act in the event that the feedback signal from the cavity failed. 6. The bias current for the ferrites of the cavity and grid resonator are monitored and interlock the rf drive on a fault.

IV. MEASUREMENTS WITH BEAM

The beam provides a pure current source and makes a definitive probe of the cavity impedance. By storing the beam with nine of the cavities, the voltage induced on a test cavity was measured. Three aspects of the cavity impedance have been measured: 1. the transient response to a single bunch yields the R/Q, 2. the impedance at the fundamental rf component yields the cavity and power-tube resistance, 3. the shape of the impedance shows the effect of rf feedback.

R/Q

A single bunch of 2×10^{12} protons, 120 ns wide was injected into the ring and the induced voltage on a cavity was observed. From the response of the cavity to the first bunch passage, an R/Q of 81Ω was obtained. This is consistent with the size of loading capacitors, 600 pF.

RF Feedback

RF feedback does not reduce the impedance of the cavity but it does reduce the impedance that the beam "sees". It also reduces the beam intensity that the beam control loops "see". To measure the effectiveness of the feedback the cavity was stimulated with beam of wide spectral content by using a single bunch, kept short by the other cavities. Figure 2a shows the spectrum of the beam current. The short bunch makes spectral lines of almost constant amplitude over the first 17 revolution harmonics. The cavity is tuned to the eighth resonant with the power amplifier off and shows a characteristic resonance response with a Q of 50 in Figure 2b. In Figure 2c the power amplifier and the rf feedback have reduced the Q to 5, which is consistent with the feedback loop gain. These results agree well with low-level network analyzer measurements but are more rigorous in that they stimulate the cavity directly at the gap with beam and are done at high level. At 25 MHz, the beam signal is down by 20 dB but is still useful in showing that the higher order modes on the busbars have been effectively damped.

Tetrode Output Resistance

The output resistance of the power tube can be varied over a wide range by changing the grid bias of the tube. The output resistance was measured as a function of plate current with a full complement of bunches in the ring. Two spectrum analyzers, triggered simultaneously, measured the beam from a longitudinal pick-up and the cavity voltage. By measuring with the tetrode switched off, the resistance of bare cavity was determined. Three precautions were necessary to insure that only the tube resistance changed as the tube current was varied: 1. the cavity was kept on resonance by locking the tuning servo to the beam, 2. incidental negative feedback around the tube caused by plate-to-grid capacitance was negated by switching the input of the feedback amplifier to ground, 3. the level-dependence of the ferrite loss was avoided by making measurements at constant gap voltage by varying the beam current. Figure 3 shows the results as function of tube current. Measured conductances are plotted, along with values obtained from manufacturer's tube characteristics curves.

The agreement is good. These results demonstrate that the beam loading capability of the rf system can be boosted by a factor of three at key points in the cycle by changing the operating point of the tube.

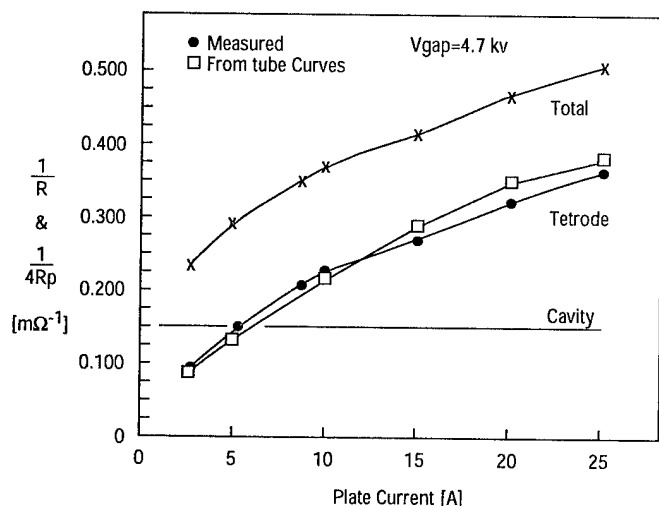


Figure 3. Output conductance of the power tetrode versus average plate current. Squares are from tube characteristics.

V. HIGH INTENSITY OPERATION

A comprehensive discussion of the challenges of high intensity operation is given elsewhere in these proceedings.[5] The discussion here focuses on the issue of beam loading. The critical points in the cycle for beam loading are at: injection and accumulation, gamma transition, and de-bunching before the slow beam extraction. Figure 4 shows some key signals of the high intensity proton operating cycle. One can see that at the critical points the rf voltage is low, aggravating the beam loading effect. At transition and de-bunching the tube current is momentarily bumped up.

Injection and Accumulation

The Booster supplies two bunches of 1.5 GeV (kinetic) protons four times at 133 ms intervals. At high intensity it is essential to keep the bunches as long as possible to minimize space charge tune shifts. This implies that the rf voltage be low, but not zero, so that the beam stays bunched to provide clear space on the ring for the incoming beam. The voltage is limited on the low side by the need for enough bucket height to cover the Booster beam momentum spread. How the bunches become long (roughly double in length) is an important matter. Simple filamentation in a mismatched bucket leads to "hot spots" in the bunch distribution. Furthermore, each batch of bunches has a different history with the first batch waiting 400 ms for the last to arrive. While at transition one wants the eight bunch distributions to be as equal as possible. An additional constraint on the possibilities at injection comes from the fast transition jump system. In perturbing the machine lattice it multiplies the dispersion function by a factor of four and constricts the

momentum aperture of the machine. This constriction limits the maximum longitudinal emittance before transition and implies low rf voltage must be used to make long bunches. In the fixed-target, slowly-extracted-beam mode there is no premium on low emittance. In fact, after transition the emittance is intentionally blown up by a factor of three before extraction.

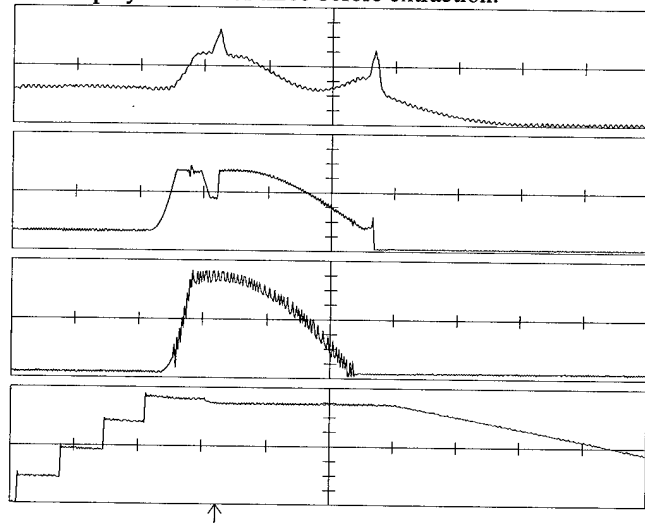


Figure 4. High intensity proton operation. From bottom: beam intensity, main magnet field derivative, net rf voltage, and typical power amplifier average current. Arrow at bottom indicates transition. Time axis is 2 s full scale.

The injection and accumulation phase is the principal challenge of high intensity operation. The following strategy has evolved. The rf is operated at low voltage, 1.5 to 2 kV/gap (x 40 gaps). The bunches are injected off-center in the bucket, causing a dipole synchrotron oscillation, mixed with quadrupole oscillation from the low voltage. A high frequency ($33x f_r$) "dilution" cavity supplies 20 kV for 50 ms after each injection. The local non-linearities from the high frequency smooth out the bunch distribution and eliminate the hot spots[6]. To prevent the dipole oscillation of the new batch from imposing a new dipole oscillation on the old batches via the phase loop (average phase), and driving additional dilution, the new batch is gated out of the phase measurement, turn-by-turn, until the dipole signal has damped to zero from filamentation and dilution.

Transition

Because of the dispersion blow-up caused by the transition jump system the rf voltage is dropped to the point where the bucket area equals the emittance while the jump system operates. This minimizes the beam momentum spread and is essential for controlling losses. From Figure 4 one can see that the beam loss occurs before the actual transition, while the jump quadrupoles are ramping up.

The power amplifier must drive a de-tuned (anti-compensated) cavity for 3 to 5 ms after the transition phase jump until the tuning servo settles to compensate the reactive beam current. For the cavity voltage to remain stable the amplifier must supply $2I_B \cos(\phi_s) \times (4 \text{ gaps})$ of reactive current. At 6×10^{13} ppp, and synchronous phase angle, $\phi_s=63^\circ$, this is 25 A. While the real

part of the current is 35 A. A vector diagram, following the conventions of Pedersen [1], of the currents at transition is shown in Figure 5. As shown in Figure 4 the average tube current has been bumped up to 23 A dc for 20 ms at transition. The benefits of the power boost are, lower plate resistance, as discussed above, and higher transconductance of the tube which increases rf feedback loop gain. The currents at this intensity are well within the capability of the tetrode.

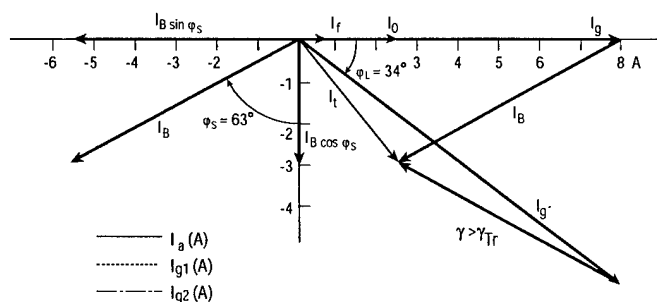


Figure 5. Phasor diagram of currents at transition. The voltage is horizontal to the right. I_0 is current with zero beam. I_B is beam current, which flips at transition. I_g is tube current.

Duck Under Transition

The diagram of Figure 5 illustrates that a larger synchronous phase angle leads to less reactive current. Ultimately, at 90° there is zero reactive current. This fact was actually exploited in the first year's run with the new power amplifier. A problem with the dc power supply for the anode voltage, limited the available voltage and current to the extent that insufficient reactive current was produced[4]. To get smoothly through transition the synchronous phase was raised to 90° at transition by dropping the rf voltage, then returned to the normal value in about 5 ms. The tuning servo can track this rate, so the cavity remains compensated at all times. This is the old scheme of "ducking under transition"[7], which was proposed as a cure for transition problems before the transition jump scheme came into use. The problem with ducking under transition is that at 90° there is zero bucket area and all the beam is unstable. It never really solved the transition problem but it does have this spin-off benefit for the rf system. However, when the transition jump is used one never really gets too close to transition and although distortions may occur as the bucket collapses, they tend to reverse after the jump when the voltage is raised again. Our experience has been that no beam loss is incurred by using the duck-under, but the benefit to the power amplifier can be important. This maneuver could be useful again in the AGS at higher intensities.

De-bunching for Slow Extraction

The most severe moment of beam loading is at de-bunching for slow extraction. The power boost indicated in the top trace of Figure 4 is used here. The rf voltage is low and the beam phase is flipped 180° to the unstable fixed point to drive up the momentum spread and cause de-bunching. The rf voltage is dropped by a factor of three because this produces the flattopped momentum distribution needed for a constant extraction rate over 1.2 s. The combination of low rf voltage and a fast 180° phase jump taxes

the power amplifier/cavity system. All the beam current is reactive so the amplifier must supply over 50 A while the tuning servo changes the impedance angle by 160° .

A much less demanding situation occurs if the net voltage reduction is obtained by counter phasing the cavities in pairs to 144° . The individual cavity voltage is not reduced so I_0 stays high (the ferrite resistance is also lower by a factor of two). Most importantly, there is zero reactive current called for. There is real current of opposite sign and different magnitude between the cavity pairs, but the magnitude is less than the reactive current without counter phasing. Before the phase flip all the cavities are compensated by the tuning servos with the same impedance angle. When the net cavity phase jumps 180° , the counter-phased cavities just change roles. The signs and magnitudes of the real currents interchange but the tuning servo is not perturbed, since it feeds back on the reactive current. See Figure 6.

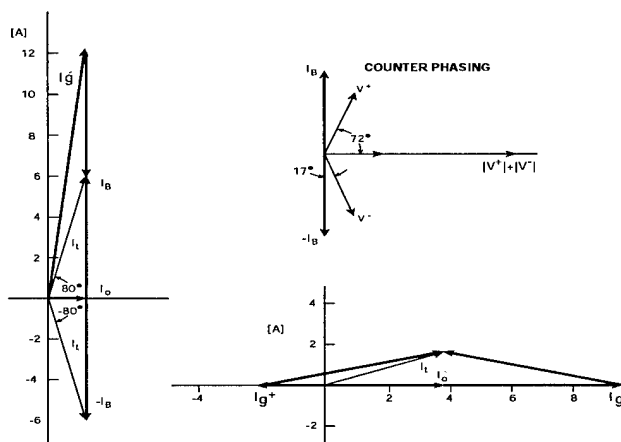


Figure 6. Left, current phasors without counter phase. Right, cavity voltage vectors with counter phase. Bottom, phasors with counter phase.

VI. CONCLUSION

The new high power rf system for the AGS has been completed and accelerates a record intensity of 6×10^{13} protons per pulse. Measurements with beam of the impedance of the cavity-power amplifier system have been carried out. The capability to accommodate heavy beam loading has been demonstrated and indicate that the intensity goal of 7×10^{13} protons per pulse for 1996 is realistic.

REFERENCES

- [1] F. Pedersen, IEEE Trans. Nuc. Sci., NS-22, 1975, p. 1906.
- [2] D. Boussard, Proc. CERN School on RF Engineering, Oxford, England, April 1991.
- [3] J.M. Brennan, et al. Proc. 1993 IEEE PAC, Vol 2, p. 1241.
- [4] J.M. Brennan, et al. EPAC June 1994, Vol. 3, p. 1897, London England.
- [5] M. Blaskiewicz, et al. these proceedings.
- [6] R. Cappi, et al. Proc. 1993 IEEE PAC, Vol 5, p. 3570.
- [7] A. Sorensen, Particle Accelerators, 1975. Vol 6. p. 141.

PHASE-STABLE, MICROWAVE FEL AMPLIFIER*

Bruce E. Carlsten, Michael V. Fazio, W. Brian Haynes, Lisa M. May, and James M. Potter**
Los Alamos National Laboratory
Los Alamos, NM 87545 USA

Free-electron laser (FEL) amplifiers have demonstrated high efficiency and high output power for microwave wavelengths. However, using present technology, microwave FEL amplifiers are not phase stable enough to be suitable for driving linear accelerators, where several such amplifiers need to be phase locked. The growing wave's phase sensitivity to the beam voltage in the small-signal regime is responsible for the largest contribution to this phase instability. We discuss a scheme that reduces the phase sensitivity to the beam voltage by operating off synchronism and matching the phase variation resulting from the desynchronism to the phase variation from the reduced plasma wavenumber as the beam voltage changes.

I. INTRODUCTION

Free-electron lasers (FELs) have demonstrated both high beam-to-rf power extraction efficiencies (~30%) [1] and high output power (on the order of gigawatts) [2], and have been considered as candidates to drive high-frequency advanced accelerators like those proposed for linear colliders [3]. However poor phase stability has been predicted and measured for FELs [4,5]. Typical accelerator applications require rf phase stability on the order of 5° of phase, and advanced accelerator applications such as bunch compression [6] and short-wavelength FELs require stability to 1° or less [7]. Phase noise in microwave FELs arises from fluctuations in tube voltage, current, confining magnetic field strength, and other tube parameters. Typically, the largest effect is from voltage fluctuations. Electron beams for practical FELs used as rf sources will have diode voltages of 1/2 to 1 MV with voltage stabilities on the order of 1/4%. Measured and simulated FEL phase stability to date has been on the order of a 20° to 40° shift per percent voltage fluctuation [5,8,9]. This level of phase stability does not satisfy advanced accelerator requirements.

In a klystron, the phase of a cavity is completely determined by the absolute phase of the harmonic current at that location. If the beam energy is shifted slightly by $\delta\gamma$, we can expect that the output phase will shift by $\delta\Phi = -(\beta_e L / \gamma(\gamma+1))(\delta\gamma / (\gamma-1))$ where L is the total device length and the electron propagation number is $\beta_e = \omega / \beta c$, and where ω is the frequency of operation and β is the beam axial velocity normalized to the speed of light. For a 500 keV beam in a half-meter-long 11.4 GHz klystron, a 1/4% shift in the voltage will lead to about a 3° phase

shift. Note that if the product ωL is kept constant, tubes at other frequencies will have the same phase shift for the same voltage shift. However, since the space-charge bunching length is independent of operating frequency, the product ωL will in general increase as the frequency is increased and we can expect that a 20 GHz tube will have phase variations on the order of 5° , and higher frequency tubes will have even larger phase variations. Lower frequency klystrons typically have phase stability better than 1° [7].

The phase shift in an FEL due to the transit time effect is the same as for a klystron. However, the effect of the space-charge wave and the transit time of the electron beam are not separable in a FEL as they are in a klystron. This will introduce new physical effects, one of which is the possibility of using fluctuations in the space-charge wave to counter fluctuations in the beam's transit time through the device.

In this paper we will explicitly demonstrate that the phase dependency on the space-charge wave can effectively cancel the phase dependency on the beam's transit time factor for the FEL interaction. We will do this by analyzing the dispersion relation for an axial FEL, which is used instead of the conventional transverse FEL for simplicity. We will also present numerical solutions of the dispersion relation exhibiting the phase-stable condition.

II. DISPERSION RELATION FOR AN AXIAL FEL

Recently, an axial FEL interaction was proposed for the generation of gigawatt microwave radiation [10]. In this device, an annular electron beam interacts with the axial electric field of a TM_{0m} mode in a circular waveguide. The radius of this waveguide is periodically rippled which causes the mode to radially expand and contract. The ripple amplitude is only a few percent of the average radius, and the mode is able to adiabatically conform to the gradual change in the waveguide radius. The axial FEL interaction for a synchronous particle is shown in Figure 1. The annulus is located at a radius corresponding to a zero of the axial electric field of that mode in a waveguide with a radius equaling the mean radius of the rippled waveguide. When an electron is at the axial position of the smallest waveguide radius the axial electric field at the location of the electron opposes the electron's motion. As the electron travels to the region of larger radius the rf slips by the electron. When the electron is at the location of the maximum waveguide radius one half of a rf wavelength has slipped by, resulting in a sign change in the mode's fields. Additionally, the electron is experiencing the electric field at a radius larger than the axial field zero instead of a radius smaller. This switch from one side of the null of the axial electric field to the other provides another sign change in the axial field at the location of the electron, and the electric field is again opposing the electron's motion. This interaction is equivalent to the interaction of a

* Work supported by the Los Alamos Laboratory Directed Research and Development program, under the auspices of the US Department of Energy, and by a Department of Energy STTR grant, grant number DE-FG02-94ER86021.

** JP Accelerator Works, Inc., Los Alamos, NM 87544

transverse-coupling FEL except the rf field is wiggled instead of the electrons to provide synchronism.

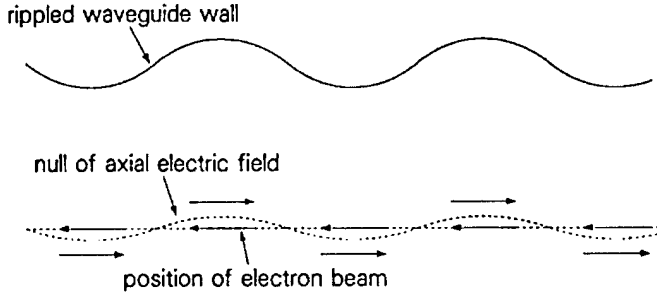


Figure 1: Axial electric field orientations for a synchronous particle when the particle reaches the centers of the ripples in an axial FEL, in r - z geometry

If we assume that the growing rf mode components have an $e^{j\omega t - \Gamma z}$ exponential behavior, this dispersion relation can be derived [11] for the axial FEL:

$$\left((\beta_e + j\Gamma)^2 - (j\Gamma)^2 - k^2 \right) \hat{\beta}_q^2 \left((\Gamma - jk_w)^2 + \beta_1^2 \right) = 2C^3 \beta_1^4 \quad (1)$$

where the cold rf mode propagation constant is $\beta_1 = \omega / v_{\text{phase}}$, the gain parameter C is proportional to the beam current divided by $\gamma \beta^3$, all to the 1/3 power, and the normalized space-charge wavenumber is $\hat{\beta}_q^2 = 4\chi_o \frac{I}{I_A} \ln \frac{r_w}{r_b}$, where now r_w is the wall radius, r_b is the beam annulus radius, I is the beam current, I_A is about 17 kA, and χ_o is a slowly varying term close to unity that depends on r_w and r_b . We can define the normalized gain δ and the detuning Δ by

$$\begin{aligned} \Gamma &= j\beta_1 + jk_w + \delta C \beta_1 \\ \beta_e &= \beta_1 + k_w + \Delta \end{aligned} \quad (2)$$

where k_w is the wiggler wavenumber, given by 2π divided by the wiggler period. Eq. (1) now becomes

$$\begin{aligned} &(\Delta^2 + 2j\Delta\delta C\beta_1 - (\delta C\beta_1)^2) \\ &- \left((\beta_1 + k_w)^2 - k^2 - 2j\delta C\beta_1(\beta_1 + k_w) \right) \hat{\beta}_q^2 (j\delta) = C^2 \beta_1^2 \end{aligned} \quad (3)$$

Now δ and thus the output phase can be made stable if

$$\begin{aligned} &\frac{d}{d\beta_e} \left(\Delta^2 + 2j\Delta\delta C\beta_1 - \left((\beta_1 + k_w)^2 - k^2 \right. \right. \\ &\quad \left. \left. - 2j\delta C\beta_1(\beta_1 + k_w) \right) \hat{\beta}_q^2 \right) = 0 \end{aligned} \quad (4)$$

for the case the derivative of the interaction strength with respect to β_e vanishes. Eq. (4) is satisfied by the conditions (for a constant perveance gun):

$$\begin{aligned} \Delta &= -\beta_e / \gamma \\ \hat{\beta}_q^2 &= \frac{2}{3\gamma(\gamma+1)(1-\Delta/\beta_e)} \end{aligned} \quad (5)$$

This solution only makes sense for γ on the order of 10 or greater because of the typically narrow window of detunings that lead to growing mode solutions. However, we will next show that the first equation in Eq. (5) is required for gain stability, and a minor modification to the second equation will lead to phase stability for small detunings.

Let us assume that $\Gamma = j\beta_1 + jk_w + \delta_o C \beta_1$ is a solution of the dispersion relation, Eq. (1). Now let us consider the solution of the dispersion relation where Δ is slightly shifted (by δ_Δ), $\hat{\beta}_q^2$ is slightly shifted (by $\delta \hat{\beta}_q^2$), and C is

slightly shifted (by δ_C), and where we denote the new solution by $\Gamma = j\beta_1 + jk_w + \delta_o C \beta_1 + \delta_1 C \beta_1$. Since the solution to the growing mode has a negative real component and lags behind the electron's phase velocity, we can write $\delta_o = -a + jb$, where both a and b are positive and typically on the order of unity. After solving for δ_1 by performing a first-order expansion we find

$$\begin{aligned} \hat{\beta}_q^2 &= \frac{2}{3\gamma(\gamma+1)} \\ &\times \left[\frac{1 - \frac{b\Delta}{3(a^2+b^2)C\beta_1} - \frac{dC/d\gamma}{C} \frac{3(a^2-b^2)C\beta_1\beta^2\gamma^3}{2(a^2+b^2)^2\beta_e}}{(1-\Delta/\beta_e) + \frac{b((\beta_1+k_w)^2-k^2)}{2(a^2+b^2)C\beta_1\beta_e}} \right] \end{aligned} \quad (6)$$

as the condition for phase-stable operation.

III. NUMERICAL SOLUTIONS OF THE DISPERSION RELATION SHOWING PHASE STABILITY

We can numerically find the growing root of the dispersion relation, Eq. (1). In this section we will do this for a variety of beam energies, demonstrating the phase-stable conditions found in the last section over a broad operating range.

A. High energy, low gain

For the case of high energy and low gain, the solution specified in Eq. (5) is valid if the interaction strength is independent of beam energy. For the case $\gamma=100$, $\beta_e = 300 \text{ m}^{-1}$, and $C=0.03$, this solution is given by $\Delta = -3 \text{ m}^{-1}$ and $\beta_q^2 = 6.7(10^{-5})$. In Figure 2 we plot the

derivatives of the phase change per unit length and the amplitude growth with respect to beam energy, respectively, as calculated numerically from Eq. (1) for $\Delta = -3 \text{ m}^{-1}$ while varying β_q^2 , and while assuming the interaction strength is independent of beam energy and the beam has constant perveance. As predicted, both derivatives vanish at $\beta_q^2 = 6.7(10^{-5})$, which is an autostable operating point.

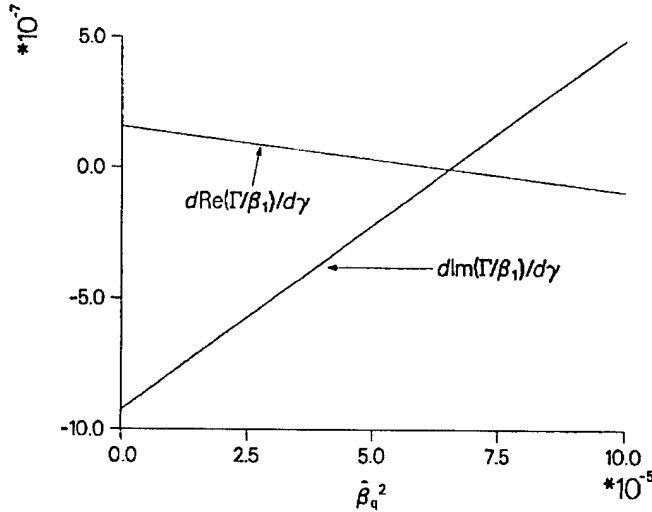


Figure 2: Sensitivity of phase and gain to beam energy for low gain, high energy case satisfying Eq. (5) as a function of space-charge wavenumber.

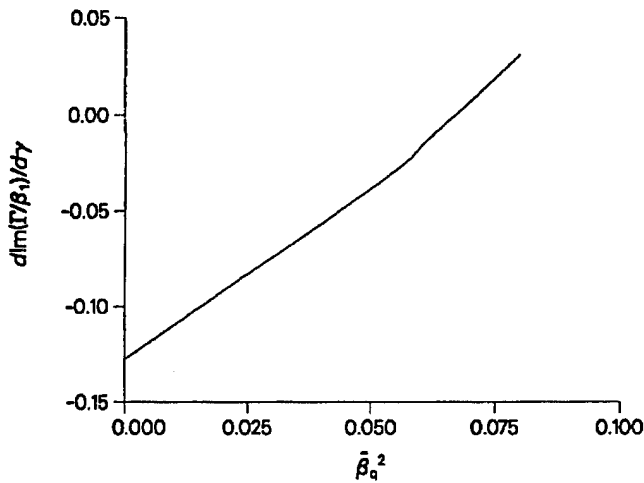


Figure 3: Sensitivity of phase to beam energy for medium gain ($C = 0.1$), low energy ($\gamma = 2$) case as a function of the space-charge wavenumber, for a detuning $\Delta = -50 \text{ m}^{-1}$.

B. Low energy, moderate gain

Now let us consider another constant perveance case with $\gamma = 2$ at 13 GHz (so the beam propagation constant is about 300 m^{-1}), an output power of about 1 GW, and with a device length of about 1 m. For these parameters the gain constant C is on the order of 0.1. For a detuning of $\Delta = -50 \text{ m}^{-1}$, Eq. (6) predicts phase-stable operation at a space-charge wave

number of about 0.08. In Figure 3 we have plotted the derivative of the phase change per unit length with respect to beam energy as a function of the space-charge wave number numerically calculated for this detuning. The calculated growth rate is about 11 m^{-1} , or about a factor of 2 per wiggler period if the wiggler wave number $k_w = 100 \text{ m}^{-1}$ (a 6 cm wiggler period), and phase-stable operation is achieved with a beam current of about 5 kA at nearly the predicted space-charge wave number.

IV. CONCLUSION

We have examined the FEL dispersion relation in the Raman regimes and shown that if the interaction strength is independent of beam energy, there is a stable phase and gain operating point. We have additionally shown that even if the interaction strength depends on the beam energy there is a phase-stable operating point, which we then demonstrated numerically. It should be noted that this technique of reducing the phase stability of an FEL is not possible with a klystron, and that by proper design an FEL can have a phase stability an order of magnitude greater (or more) than a klystron.

V. REFERENCES

- [1] M. E. Conde and G. Bekefi, "Amplification and superradiant emission from a 33.3 GHz free electron laser with a reversed guide magnetic field," *IEEE Trans. Plasma Sci.*, **20**, p. 240, 1992.
- [2] T. J. Orzechowski, B. R. Anderson, J. C. Clark, W. M. Fawley, A. C. Paul, D. Prosnitz, E. T. Scharlemann, S. M. Yarema, D. B. Hopkins, A. M. Sessler, and J. S. Wurtele, "High-efficiency extraction of microwave radiation from a tapered-wiggler free-electron laser," *Phys. Rev. Lett.*, **57**, p. 2172, 1986.
- [3] *Proceedings from the International Workshop on Pulsed RF Power Sources for Linear Colliders (RF'93)*, V. Balakin and N. Solyak, editors, Dubna, Russia, 1993.
- [4] R. Corsini, C. D. Johnson, J. Gardelle, J. Grenier, "CLIC drive beam generation by induction linac and FEL experimental studies for the CERN linear collider," *Proc. 1993 Part. Accel. Conf.*, IEEE Cat. No. 93CH3279-7, p. 626, 1993.
- [5] P. Volfbeyn, K. Ricci, B. Chen, and G. Bekefi, "Measurement of the temporal and spatial phase variations of a pulsed free electron laser amplifier," *IEEE Trans. Plasma Sci.*, **22**, p. 659, 1994.
- [6] B. E. Carlsten, B. D. McVey, E. M. Svaton, G. R. Magelssen, and L. M. Young, "Magnetic bunchers for the generation of high peak current, low emittance electron pulses at medium energy," *Proc. 1990 Linear Acc. Conf.*, Los Alamos National Laboratory report LA-12004-C, Albuquerque, NM, p. 641, 1991.
- [7] W. E. Stein, W. J. D. Johnson, J. F. Power, and T. J. Russel, "Stability requirements of rf-linac-driven free-electron lasers," *Nucl. Instrum. and Meth. Phys. Res.*, **A296**, p. 697, 1990.
- [8] S. Alberti, private communication.
- [9] R. A. Jong, R. D. Ryne, G. A. Westenskow, S. S. Yu, D. B. Hopkins, and A. M. Sessler, *Nucl. Instrum. and Methods Phys. Res.*, **A296**, p. 776, 1990.
- [10] B. E. Carlsten, "Axial free-electron laser interaction between an annular electron beam and an axisymmetric TM mode," submitted to *IEEE Journ. Quant. Elect.*
- [11] B. E. Carlsten, "Enhanced phase stability for a Raman free-electron laser amplifier in the exponential growth regime," submitted to *Physics of Plasmas*.

1.2 MW KLYSTRON FOR ASYMMETRIC STORAGE RING B FACTORY

W. R. Fowkes, G. Caryotakis, E. Doyle, E. Jongewaard, C. Pearson, R. Phillips, J. Sackett, E. Wright
Stanford Linear Accelerator Center, Stanford University, CA 94309 USA

and

H. Bohlen, G. Huffman, S. Lenci, E. Lien, E. McCune and G. Miram
Varian Associates, Palo Alto, CA 94304 USA

Abstract

A cw klystron operating at 476 MHz has been developed jointly by SLAC and Varian Associates. The unique set of characteristics of this tube were strongly guided by requirements of the fast feedback necessary to prevent oscillations of the storage ring beams caused by the detuned accelerating cavity. This requires a combination of bandwidth and short group delay within the klystron. The RF feedback stabilization scheme also requires amplitude modulation making it necessary to operate the klystron about 10% below saturation. Performance specifications and initial operating results are presented.

I. INTRODUCTION

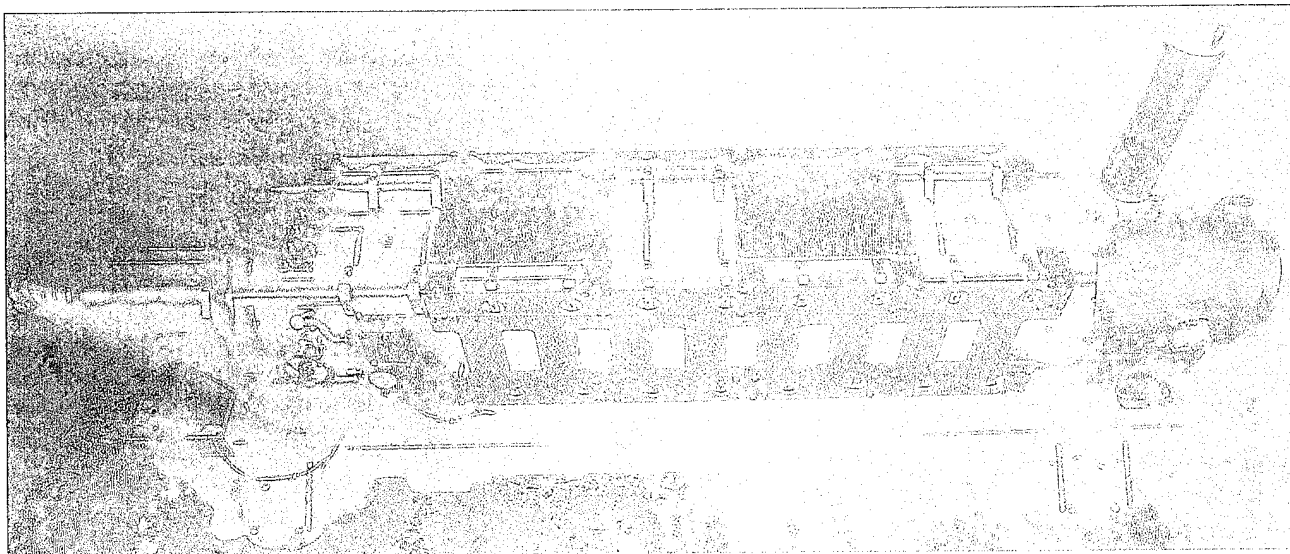
SLAC and Varian have joined efforts under a Cooperative Research and Development Agreement (CRADA) to develop and test a new UHF super power klystron as a prototype 476 MHz RF source for the Asymmetric Storage Ring B Factory under construction at SLAC. This klystron was originally designed to produce 1.6 MW CW saturated to be operated at 90 KV, 27 amperes. After the klystron development was well underway, some of the requirements were relaxed as a result of further study in the accelerator physics aspects of the machine. As a result, the klystron will be operated conservatively at 83.5 KV and would deliver 1.2 MW if saturated. The klystron will be operated 10% below saturation and must be able to respond to fast feedback

correction in both amplitude and phase in order to damp accelerating cavity oscillations induced by high current storage ring beams. This feedback scheme requires the klystron to have very short group delay ($d\phi/d\omega$) and wide bandwidth. When this development effort began neither of these features were available off the shelf in commercial tubes of similar power and frequency such as those used at LEP and TRISTAN storage rings.

A multistage depressed collector, designed by Varian was very seriously pursued because much of the efficiency that is given up running underdriven is recovered. The operating cost savings would have been substantial but the manufacturing risks and additional upfront costs were considered too great to continue along the MSDC path. The "headroom" needed for amplitude modulation was reduced from 25% to 10%. The design parameters for this tube are listed in the table below.

DESIGN PARAMETERS

Operating Frequency (MHz)	476
Output Power at Saturation (KW)	1200
Operating Point Below Saturation (KW)	1100
Beam Voltage (KV)	83.5
Beam Current (A)	24.1
Efficiency (%)	>60
Saturated Gain (dB)	>43
1 dB Bandwidth (MHz)	± 3.0
Group Delay at ± 0.5 MHz (nanosec.)	100



*Work supported by Department of Energy contract
DE-AC03-76SF00515

II. ELECTRICAL DESIGN

The Varian electron gun design has a peak cathode loading of 0.31 A/cm^2 and a maximum surface gradient of 50 KV/cm . Computer simulation predicts a beam diameter of 4.5 cm with a 5.8% scallop in a 7 cm tunnel diameter. The mechanical design was borrowed from the SLAC 5045 gun which allows adjustment of the radial and axial position of the cathode and focus electrode with respect to the anode. The alignment must be preserved while operating horizontally. It is primarily radiatively cooled to the anode housing. An internal copper web conducts heat from the region of the focus electrode adjacent to the cathode out to the large outside diameter where it is radiated away to the anode housing.

The 7 cavity interaction region designed by Varian was optimized for 90 KV to provide the required combination of bandwidth and low group delay without compromising gain or efficiency. As mentioned earlier it will be operated at 83.5 KV corresponding to a 3% lower average beam velocity. The staggered tuning arrangement of the first three cavities is expected to provide about 6 MHz of 1 dB bandwidth and about 150 nanoseconds of group delay across that bandwidth as shown in figures 1 and 2 respectively. A cavity tuned slightly below the second harmonic of the operating frequency followed by two inductively tuned cavities provide a highly optimized bunch passing through the output resonator. The second harmonic cavity plays an important role in achieving a low electron density in the antibunch region as the beam passes through the output gap[1][2].

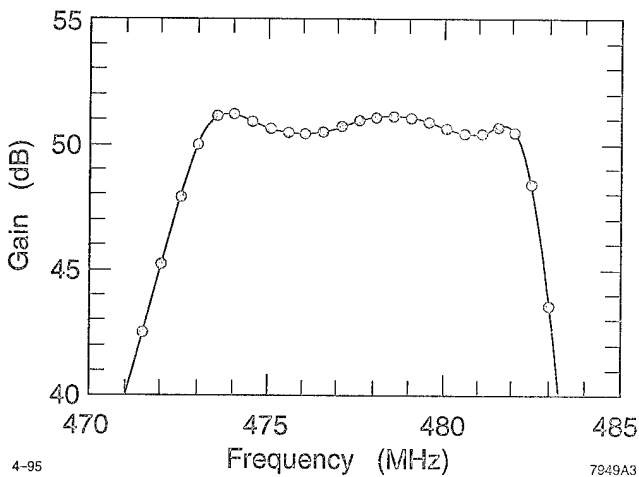


Figure 1. Predicted Small-Signal Gain versus Frequency Response at 90 KV

The output coupling loop is designed to give an external Q of 36 for the output cavity. This value is slightly below that which gives optimum efficiency but assures that the lowest velocity electrons will not cause regeneration. The entire output coupling circuit was modeled using MAFIA. The measured results for both resonant frequency and external Q agreed with the simulation to better than 0.1%

Both 1D and 2D PIC codes developed at Varian were used in the interaction design simulation. Figure 3 shows the predicted saturation curves using each of the simulation codes. Similar results were obtained using JPNDISK and CONDOR. The 2-D simulations have historically shown good agreement with measured results while the 1-D results need to be derated by about 10% .

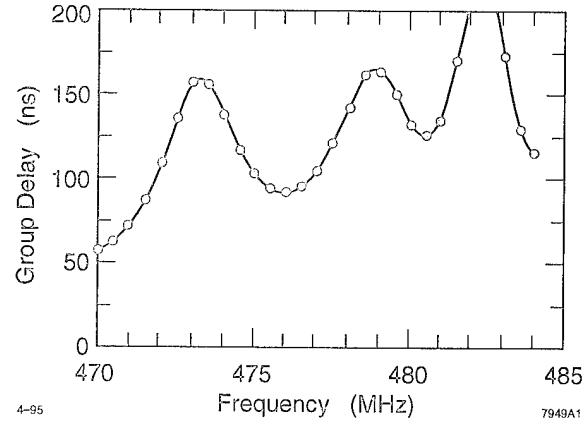


Figure 2. Predicted Group Delay versus Frequency at 90 KV

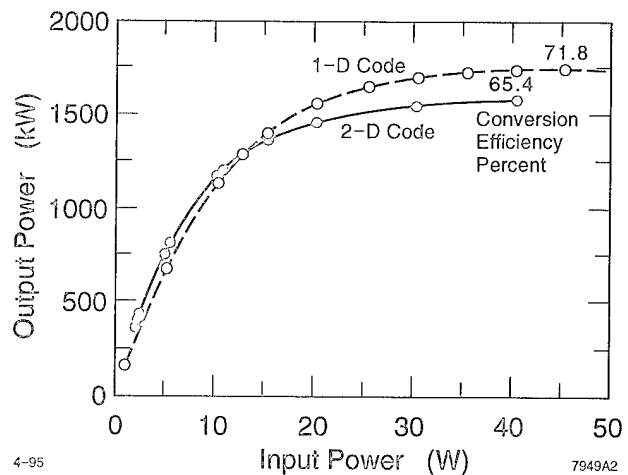


Figure 3. Predicted Output Power versus Drive at 90 KV

III. MECHANICAL DESIGN

All the cavities except the output cavity are made from stainless steel cylinders and end plates which are copper plated for good RF conductivity. The output cavity, owing to its high wall losses, has OFE copper walls with an outer stainless steel reinforcing structure. Each cavity except the output has a tuning mechanism whereby a series of differential screws are driven by chains to move one of the reentrant cavity noses relative to the other. The cavities with this tuning arrangement have a flexible copper end wall to allow the movement of the cavity nose. The tuning rate for the cavities are such that the $\pm 0.025 \text{ inch}$ adjustment range gives a frequency shift of $\pm 1.8 \text{ MHz}$ for the fundamental cavities and approximately twice that for the second harmonic cavity. The tuners may be used while

the tube is operating. Each cavity except the output cavity has its own diagnostic RF monitor loop. The noses of all cavities except the prepenultimate and the second harmonic were coated with TiN to help suppress multipactor. In addition the input cavity drive loop, the output coupling loop and the vacuum side of the output window were also coated for the same reason. The output coupling loop and all cavities are water cooled to stabilize their operating temperature and hence frequency. All drift tubes are also water cooled as protection against electron beam interception.

The limited bakeout station clearance required optimization of the collector design to minimize the tube length. The interior is contoured to have nearly constant flux for highest surface cooling efficiency. The large inside diameter of the collector necessitated a departure from standard collector designs where there is an inner collector with milled cooling channels and an outer, separable water jacket. This is to avoid excessively high stresses in the collector wall due to the pressure of the cooling water. This construction technique allows optimal design of the cooling channels and wall thickness for best cooling performance. In addition, one-piece construction allows the monitoring of beam deposition by measuring temperatures on the outer jacket.

The coaxial output window has matching choke hubs in 50 ohm 6.125 " diameter coax line. Air cooling of the inner conductor and window face is accomplished by ducting air (approximately 50 scfm dry air) through the T-bar coupler into the inner conductor and across the window through jets at the bottom of the inner conductor matching choke. The air exits to the atmosphere via holes at the bottom of the outer conductor choke hub. The inner and outer conductors are water cooled on the vacuum side only.

The T-bar coax to WR2100 waveguide transition was preferred over the doorknob type because of its good bandwidth and the configuration allows access to the inner conductor for blowing air and placing window temperature monitoring thermocouples. It also allows compliant coupling between the inner conductor and the T-bar to prevent excessive mechanical loading on the output window. A compliant membrane is also designed into the vacuum side output coax center conductor.

The magnet consists of twelve individual convection cooled coils that are airspaced with approximately a 45% fill factor to allow access to the tube body for tuning. The magnet return path is formed by four symmetrically placed four inch diameter steel pipes that run the length of the klystron between the gun end and collector end polepieces. The magnet return path also serves to support and space the coils as well as to support the klystron in the horizontal position. Rails attached to the klystron body engage support shoes on each magnet coil support allowing transverse support and longitudinal freedom to allow differential thermal expansion between the klystron body and the magnet support structure.

The support structure under the magnet frame has both heavy duty casters and jack screws so that the entire assembly including gun oil tank can be rolled into place in the final operating position in the B-Factory klystron housing.

IV. TEST RESULTS

The klystron went into test in mid-February and processed cleanly up to 60 KV. At this point the 2.6 MW dc power supply failed, putting an end to publishing any test results in time for this conference. The measured RF output power the lower voltages showed good agreement with simulation predictions where the efficiency is expected to be low. As of this printing the klystron is awaiting the repair of the power supply so that testing may continue. There is every indication that the klystron will meet all of the performance predictions.

V. ACKNOWLEDGMENTS

The authors wish to thank the many members of both Varian and SLAC for their valuable contributions to this development and manufacturing effort. G. Hu, F. Friedlander, L. Ives, R. Vranas of Varian provided much of the computer simulation work on the gun, output window collector and RF interaction region. Many valuable engineering contributions, advice and technical support were provided by several departments and shops at SLAC. These efforts will continue through the testing and installation of this tube.

VI. REFERENCES

- [1] E. L. Lien, "High Efficiency Klystron Amplifier", Publication OF Eight Int-l Conf. on M/W and Optical Generation and Amplification, Sept. 1970
- [2] E. L. Lien, US Patent #3,811,065 May 14, 1974
- [3] W. R. Fowkes et al., "PEP-II Prototype Klystron", Proceedings of the 1993 Particle Accelerator Conference, Wash. D. C. Vol. 2, p. 1259

ANALYSIS OF MULTIPACTING IN COAXIAL LINES

E. Somersalo, P. Ylä-Oijala, Rolf Nevanlinna Institute, University of Helsinki, PO Box 26, 00014

University of Helsinki, Finland

D. Proch, DESY, Notkestrasse 85, 2000 Hamburg 52, Germany

Abstract

Multipacting can cause breakdown in high power rf components like couplers, windows, etc. This phenomenon starts if certain resonant conditions for electron trajectories are fulfilled and if the impacted surface has a secondary yield larger than one. A general cure against multipacting is to avoid the resonant conditions. Therefore we investigated the dynamics of the electron trajectories in order to find rules for these resonances and thus suppress multipacting by appropriate design. We developed a new code which combines standard trajectory calculations with advanced searching and analyzing methods for multipacting resonances. As a first step, coaxial power lines are investigated. We characterize multipacting behavior in straight and tapered lines and give scaling laws with respect to dimension, frequency and impedance. The calculations are compared with experimental observations.

I. INTRODUCTION

This paper gives a brief description of a code developed for analyzing multipacting in rf cavities. The code consists of two main elements: The first step is to recognize those rf power levels in the given geometry that are able to multipact. The second step is to locate and identify the possible multipacting processes. The core of the code consists of standard trajectory calculations. The novel feature is a systematic application of ideas arising from the theory of dynamical systems.

II. THEORETICAL BACKGROUND

Physically, the multipacting process is described as follows. An electron is emitted from the surface of an rf cavity and driven by the field. When it impacts the cavity wall, it may release one or more electrons from the surface layer of the wall, the number of the secondary electrons depending on the impact energy and the wall material characteristics. These secondary electrons are again accelerated by the field, yielding new impacts and possibly new secondary electrons. In appropriate conditions, the number of electrons may increase exponentially, leading to remarkable power losses, gassing of the surface and heating of the walls.

The following is a brief summary of the mathematical description of the process, which constitutes the background of the programs used for analyzing the multipacting processes in rf cavities.

A. Dynamical system

Consider a void cavity Ω with a time harmonic rf field. Denoting by f the rf frequency, the electric and magnetic fields can be written as

$$\vec{E}(x, t) = \vec{E}(x) \sin 2\pi ft, \quad \vec{B}(x, t) = \vec{B}(x) \cos 2\pi ft,$$

where $\vec{E}(x)$ and $\vec{B}(x)$ are the spatial amplitudes of the fields. Let φ denote the phase angle of the field, $0^\circ \leq \varphi < 360^\circ$. Consider an electron being emitted at a point x of the cavity wall $\partial\Omega$, the field phase at the time of emission being φ . Assuming that the rf field map in the cavity is known, it is a straightforward matter to compute the relativistic trajectory of the electron driven by the field. Denote by x' the point where the electron hits the cavity wall for the first time. If the phase of the field at the time of the impact is denoted by φ' , we have a mapping

$$R : (x, \varphi) \mapsto (x', \varphi').$$

Using the notation $X = \partial\Omega \times [0^\circ, 360^\circ]$, the above mapping R defines a dynamical system in the phase space X : Each point $p = (x, \varphi) \in X$ generates a discrete trajectory $\{p, R(p), R^2(p), \dots\}$. For each initial point $p \in X$, there are two possibilities: It may happen that after a finitely many impacts, the field phase is such that the electric field prevents the electron from escaping the wall. In this case, the discrete trajectory remains finite. The other possibility is that the discrete trajectory is infinite. The latter case is the geometric condition for the multipacting to occur.

Besides the geometry of the trajectories, the analysis needs to contain the secondary electron yield characteristic to the surface properties. Given an electron trajectory starting at a point p , the kinetic impact energy $E_{\text{kin}}(p)$ can be computed. If the secondary electron yield of the cavity wall is denoted by δ , the number of secondary electrons due to one single electron starting at p is in the average given by $\alpha(p) = \delta(E_{\text{kin}}(p))$. Considering the full discrete trajectory, the number of secondary electrons due to one single electron starting at p after n impacts is

$$\begin{aligned} \alpha_n(p) &= \alpha(p) + \alpha(p)\alpha(R(p)) + \dots \\ &+ \alpha(p)\alpha(R(p)) \dots \alpha(R^n(p)). \end{aligned}$$

B. Distance function

A special case of the infinite trajectories that leads to resonant multipacting is when periodic trajectories appear. This corresponds to fixed points of the mapping, i.e.,

$$R(p) = p$$

for some $p \in X$, or more generally,

$$R^n(p) = p, \quad n = 1, 2, \dots$$

Physically, this corresponds to a situation where an electron trajectory hits eventually the same wall point in the same field phase where it started. This condition is fulfilled in the earlier described multipacting phenomena, and it seems to be a potentially dangerous resonant condition in general. An effective way

of searching for those points p in the phase space is to consider the distance function

$$d_n(p) = \sqrt{|x - x_n|^2 + \gamma |e^{i\varphi} - e^{i\varphi_n}|^2},$$

where $p = (x, \varphi)$ and $(x_n, \varphi_n) = R^n(p)$. Here, γ is a scaling constant. The distance function d_n tells how far away the trajectory is after n impacts from the initial point. If $d_n(p)$ is small for n large, the point p is likely to be prone to multipacting.

III. COMPUTATIONS

To obtain reliable results, the rf field maps have to be known rather accurately in the cavity. In straight coaxial lines discussed below, the field map is no problem since it is analytically known. In the other cases, one has to use a numerical scheme. We have developed a suitable numerical code for computing the fields in axisymmetric geometries. The code is based on boundary integral equations, with extra care being taken for the accuracy of the computations close to the walls.

The multipacting analysis was implemented along the following lines. Given a cavity Ω and the corresponding rf field map, we picked a large number of initial points p_j in the phase space X associated to the boundary and for each point p_j computed the discrete trajectory $\{p_j, R(p_j), R^2(p_j), \dots\}$. After a fixed number n of iterations of the map R , we counted those electron trajectories that were still able to multipact. This number, denoted by c_n , was computed repeatedly for different incident rf field powers. If at a given incident power no multipacting can occur and the discrete trajectories $\{p_j, R(p_j), R^2(p_j), \dots\}$ are short, the number c_n is very small. The multipacting powers stand out clearly as having an elevated c_n value.

Having the counter function c_n computed, we plotted the distance function $d_n(p_j)$ for those rf power values where c_n was large. The minima of d_n give the initial points of those trajectories that correspond to multipacting. A recomputation of the trajectories starting at the minima of d_n can be used to analyze the nature of the multipacting process. The important questions are the order of the multipacting (number of rf cycles per wall impact), whether it is a one-point or multi-point multipacting and whether it is due mostly to the magnetic or electric field.

Finally, the kinetic energy condition for each multipacting process has to be checked. If the impact energies are too low or too high, no multipacting will occur even if the geometric conditions are satisfied. The kinetic energy check was done by computing the number α_n defined earlier for the potentially multipacting trajectories.

A. Coaxial cable: Scaling laws in SW operation

The multipacting analyzer was first applied to straight coaxial lines in standing wave (SW) operation. The computations were done in a half wavelength long section of the line.

The following is a summary of the results. First, the analysis showed that multipacting in SW coaxial line fields is due to the electric field only. In fact, the powers that yield multipacting can be found by computing the trajectories at the electric field maximum only. Second, both one-point multipacting (from outer conductor to itself) and two-point multipacting (from outer to inner conductor and back) may occur. We analyzed the multipacting in lines with different sizes, different rf frequencies and

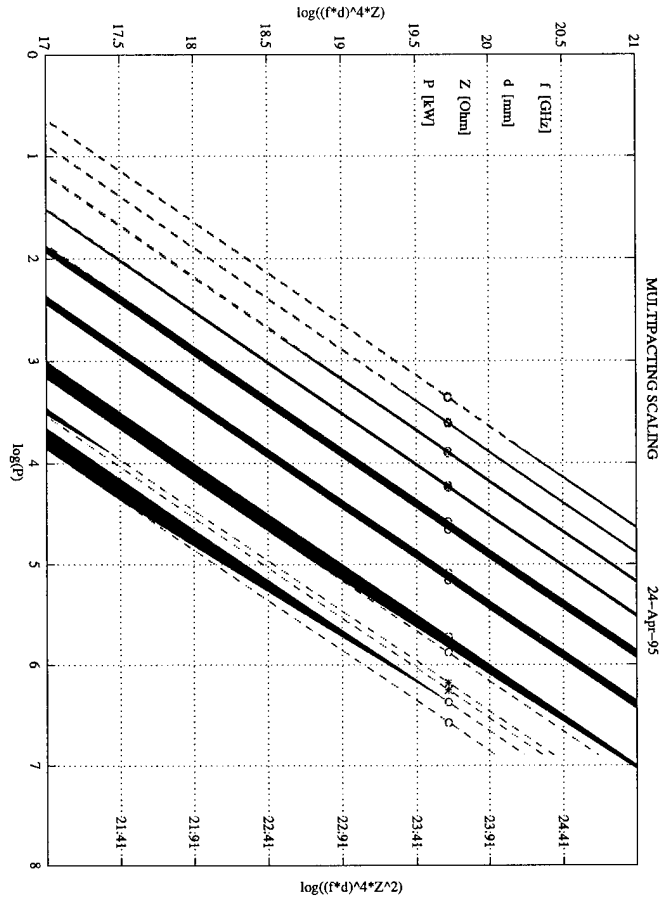


Figure 1. Multipacting bands in coaxial lines

different line impedances. It turned out that the multipacting powers obey quite accurately the following scaling laws:

$$P_{\text{one-point}} \sim (fd)^4 Z, \quad P_{\text{two-point}} \sim (fd)^4 Z^2,$$

where f is the rf frequency, d is a size parameter (in this paper d is the diameter of the outer conductor) and Z is the line impedance.

We computed the average impact energy of the electrons in multipacting trajectories. It was verified numerically that the average impact energy obeys roughly the scaling law

$$E_{\text{kin}} \sim (fd)^2,$$

in accordance to a simple dimension analysis. Typically the secondary electron yield for Niobium has a maximum around 400 eV, and is larger than one in the range $\sim 100 - 1500$ eV.

Figure 1 is a graphical summary of the analysis. The upper horizontal axis is the natural logarithm of the number $(fd)^4 Z$ (in $(\text{GHz} \times \text{mm})^4 \times \text{Ohm}$). The one-point multipacting powers for a given coaxial line can be found by computing this number, drawing a vertical line and reading the powers where this line intersects the bands marked by circles. The lowest band is the first order one-point multipacting band. The next band upwards is a two-point first order band, then follows a set of one-point bands, the order increasing up to 8 when one moves up in the figure to lower powers. The kinetic energy condition $100 \text{ eV} \leq E_{\text{kin}} \leq 1500 \text{ eV}$ when multipacting may occur is marked in

the picture by shading. Similarly, the lower horizontal axis is the logarithm of the number $(df)^4 Z^2$ (in $(\text{GHz} \times \text{mm})^4 \times \text{Ohm}^2$), characteristic for two-point multipacting. By computing this number and reading the intersection with the band marked with asterisks gives the multipacting powers. Note that there is only the first order two-point band in the picture; the higher order bands tend to get mixed with the more prominent two-point bands. Again, shading at the far left of the band indicates where the kinetic energy condition holds. With typical design parameters, the two-point process has a too large kinetic energy for multipacting. The circles and asterisks in the picture correspond to the 50 Ohm 1.3 GHz TESLA line.

B. Transition to TW operation

It is important to understand the behavior of the multipacting levels when the field switches from standing wave to the traveling wave, i.e., the reflected wave vanishes. We repeated the computation with the coaxial line with no reflected wave, and found that the multipacting levels shift according to the simple rule

$$P_{TW} = 4P_{SW},$$

i.e., in the traveling wave operation each multipacting level appears at four times higher one-way rf power. There is a simple physical heuristics behind this phenomenon: The peak voltage in standing wave operation is twice the peak voltage of the traveling wave. The analysis of the trajectories show, however that the situation is a bit more subtle, since the multipacting electrons have to be traveling as the wave form moves.

C. Other coaxial structures

The analysis algorithm has been applied so far to a set of coaxial structures. These include the tapered coaxial line and coaxial lines with an impedance step. Currently, we are running computations with grooved lines and certain ceramic window designs. The results will be reported in a forthcoming article.

D. Test cavity

To test the method, we made computations in a geometry where direct multipacting measurements can be made. A test cavity with a direct access to the multipacting current as well as the experiment are described elsewhere in this proceedings ([2]). The electric field in the gap between the electrodes is fairly homogenous, and two-point multipacting of order n between the electrodes is expected at voltage drop close to

$$V_{(n)} = \frac{m_e}{e} \frac{4\pi f^2 d^2}{2n-1}. \quad (1)$$

This is the field giving resonant trajectories between two infinite parallel plates with time harmonic voltage drop. Figure 2 shows the counter function c_{30} versus the voltage between the electrodes on the symmetry axis. The two prominent bands correspond to the first and second order two-point multipacting between the electrodes. They agree well with the theoretical values (1), marked by an asterisk. The slight shift to the left is due to the positive initial velocity used in the trajectory calculations, not included in (1). This figure corresponds to the measured

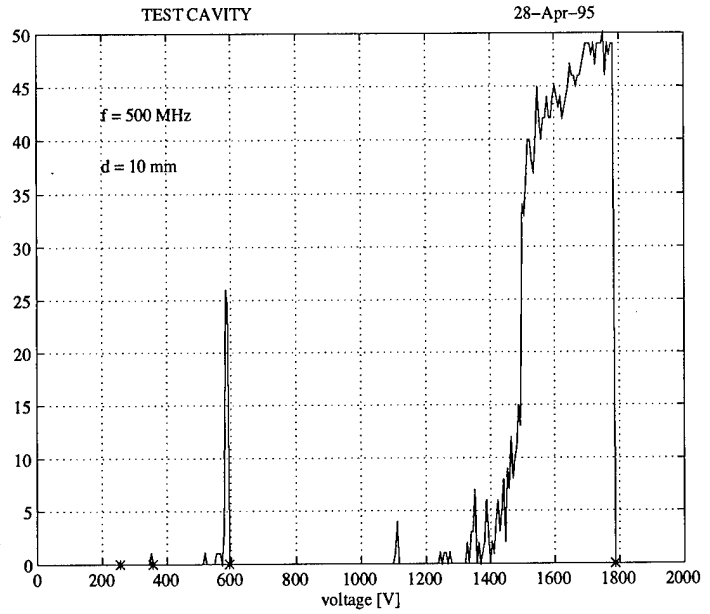


Figure 2. Multipacting counter function for the test cavity

curve in Figure 3 in [2]. Let us mention that the computed kinetic energy for the second order process is typically too low to appear with secondary electron yields characteristic e.g. to Niobium surfaces.

References

- [1] E. Somersalo, P. Ylä-Oijala and D. Proch: Electron multipacting in RF structures. TESLA Reports 14-94.
- [2] D. Proch, D. Einfeld, R. Onken and N. Steinhauser: Measurement of multipacting currents of metal surfaces in RF fields. WPQ24 (This conference).

AN ACCELERATOR RESONANTLY COUPLED WITH AN ENERGY STORAGE (ARES) FOR THE KEKB

Y. Yamazaki, K. Akai, N. Akasaka, E. Ezura, T. Kageyama, F. Naito, T. Shintake, and Y. Takeuchi, KEK, Natinal Laboratory for High Energy Physics, Oho 1-1, Tsukuba-shi, Ibaraki-ken 305, Japan

In a large ring with extremely heavy beam loading, such as a B-factory, it is possible that the accelerating mode, itself, gives rise to a longitudinal coupled-bunch instability. In order to solve this problem, T. Shintake has proposed to attach a TE015-mode storage cavity to an accelerating cavity. It has subsequently been shown that the system can be put into practical use if a coupling cavity is added in between the two cavities. The three-cavity system, which is now referred to as an accelerator resonantly coupled with an energy storage (ARES), is under development for the KEKB.

I. INTRODUCTION

At this conference the development of the KEKB room-temperature (normal-conducting) RF system is being systematically reported in detail. The newly invented accelerating cavity [1-3] will be used for this system. This cavity, referred to as "an accelerator resonantly coupled with an energy storage (ARES)," is actually a coupled-cavity system comprising three cavities: an accelerating cavity (a-cavity) and an energy-storage cavity (s-cavity) with a coupling cavity (c-cavity) in between (see Fig. 1). This report introduces the concept of ARES by presenting the reason why it is necessary.

It has been empirically confirmed by measuring the RF characteristics of ARES cold models (see Ref. [4]) that ARES behaves as theoretically expected in this report. The total consistent set of RF parameters for the KEKB is presented in Ref. [5], showing that ARES can meet the requirements for the KEKB.

The accelerating cavity of the ARES should be a "damped cavity," the higher-order modes of which are sufficiently damped in order to suppress any coupled-bunch instability. Among the various proposed damped cavities, the choke-mode cavity, which was independently devised by T. Shintake [6] and K. Akai [7], has been chosen [8, 9] for the KEKB. The result of the first high-power test of the choke-mode cavity is presented in Ref. [10]. Since the performances of the ceramics parts are critical technical issues for this kind of high-power RF system, the performance of the higher-order mode absorbers made of SiC is reported in Ref. [11], while the design of the input coupler is described in Ref. [12].

II. THE COUPLED-BUNCH INSTABILITY ARISING FROM THE ACCELETATING MODE

In order to store a high-beam current in an electron/positron storage ring, the threshold current of any coupled-bunch instability must be sufficiently high. For this purpose it is essential to sufficiently damp any dangerous higher-order modes in the accelerating cavities. This, however, is not sufficient for a large ring with extremely heavy beam loading, such as a B-factory. The accelerating mode, itself, may give rise to a longitudinal (synchrotron) coupled-bunch instability for the following reason [13].

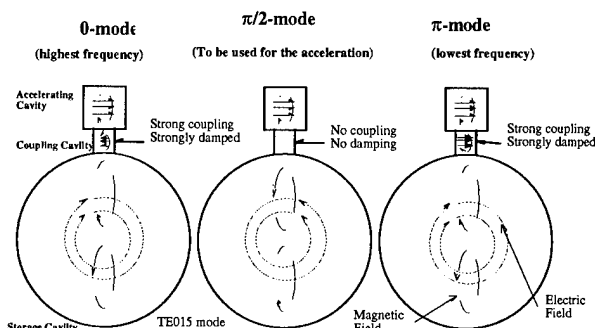


Figure 1: Three-cavity system with a coupling cavity in between the accelerating and storage cavities.

In order to keep the quantum lifetime sufficiently long, the bunch of the beam is accelerated out of phase from the crest of a sinusoidal function of the RF-field oscillation (this phase difference is referred to as a synchronous phase (ϕ_s)). As a result, the beam induces a reactive component in an accelerating cavity. In order to compensate for the reactive component, the cavity is detuned by an amount of Δf , given by [14]

$$\frac{2\Delta f}{f} \equiv \frac{R_{sh}}{Q_L} \frac{I}{V_C} \sin \phi_s, \quad (1)$$

where R_{sh} and Q_L are the shunt impedance and the loaded Q-value of the accelerating mode, respectively. The average beam current (I) is accelerated by the cavity voltage (V_C).

Usually, the detuning contributes to the damping of the $\mu = 0$ mode of longitudinal coupled-bunch oscillations (Robinson damping), where μ designates the mode number in such a way that the phase difference between one bunch and the following one is given by $2\pi\mu/N_b$ (N_b is the number of bunches in a ring). When the beam is executing the longitudinal coupled-bunch oscillation of the μ mode, it has a frequency component given by

$$f_{\mu,n}^{\pm} = nN_b f_r \pm (\mu f_r + f_s), \quad (2)$$

where f_s is the synchrotron oscillation frequency. If the $f_{\mu,n}^-$ component of the impedance of a ring is higher than the $f_{\mu,n}^+$ component, the oscillation is damped, and vice versa. Since the $f_{\mu=0,n}^-$ component of the impedance is increased by the detuning, while the $f_{\mu=0,n}^+$ component is decreased, the $\mu = 0$ mode oscillation is damped.

However, if the beam current is extremely high, the detuning frequency becomes very high, and if, in addition, the circumference of the ring is very large, that is, the revolution frequency is low, we must detune the cavity by two or three times as much as the revolution frequency. During the course of storing the beam the accelerating-mode frequency passes through $f - f_r$, $f - 2f_r$ (see Fig. 2) and so forth, resulting in extremely high growth rates of the $\mu = h - 1$, $h - 2$ modes, respectively.

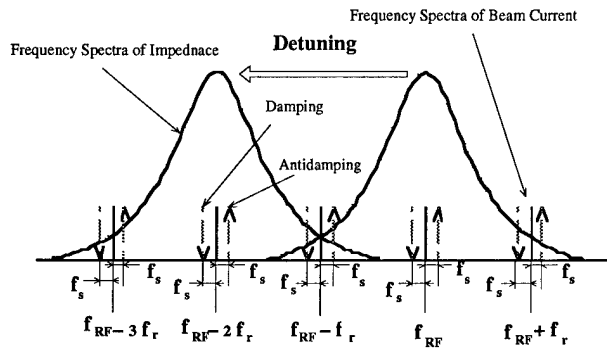


Figure 2: Frequency spectrum of the cavity impedance and beam current. The RF frequency is designated by f_{RF} .

III. ARES

One may argue that the instability can be avoided by giving up the detuning. Although this is theoretically correct, it is practically unrealistic, since an extremely high power must be provided to the cavity in order to maintain the necessary cavity voltage against the high reflected power arising from the large reactive component induced by the beam.

Another way is to decrease the detuning. In order to gain a deeper insight into the detuning, it may be useful to rewrite Eq. (1) as

$$2\Delta f = \frac{P_b \tan \phi_s}{2\pi U} \quad (3)$$

This is nothing but the beam loading (P_b) divided by the stored energy (multiplied by the tangent of ϕ_s). It should be noted that ϕ_s (P_b either) is not an adjustable parameter in a B factory, since the cavity voltage is determined by sufficiently decreasing the bunch length in order to realize an extremely high luminosity (the bunch length should be shorter than the extremely small beta function (β^*) at the colliding point).

Then, we can just increase the stored energy; however, it is necessary to increase it by an order of magnitude. Usually, the high power dissipation (P_c) is induced by increasing the stored energy, since the ratio of the power dissipation to the stored energy is fixed as the inverse of a quality factor multiplied by an angular frequency ($P_c = \omega U / Q_0$, where Q_0 is an intrinsic Q-value). In order to maintain the power dissipation within the practically tolerable limit, although the use of a superconducting cavity is one solution, we cannot increase U as much as we want, since U is related to an unadjustable parameter (V_C).

It was proposed by Shintake [1] to attach an s-cavity operating in a very high-Q TE015 mode to an a-cavity. Such an s-cavity has been successfully used in a SLED system. In order to realize his concept, it is necessary to attach one more cavity, referred to as a coupling cavity (c-cavity), in between the a- and s-cavities, as schematically shown in Fig. 1. The thus-formed three-cavity system is now referred to as ARES.

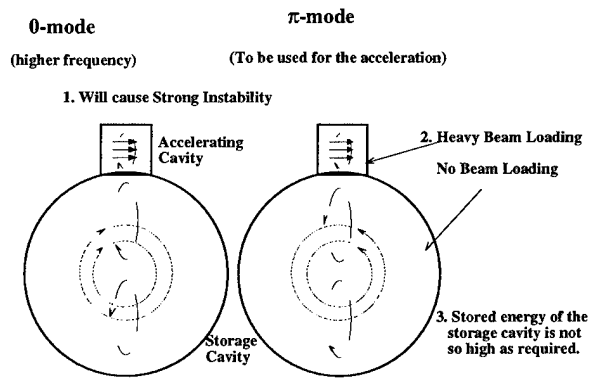


Figure 3: Two-cavity system comprising an accelerating cavity and a storage cavity.

The c-cavity is necessary for the following reason. Suppose that one immediately attaches the s-cavity to the a-cavity as shown in Fig. 3. If one mode is used as an accelerating mode, the other mode as a parasitic mode gives rise to a very strong beam instability. Second, these modes, referred to as the π -mode and the 0-mode, have no group velocity. Since the a-cavity is heavily beam-loaded, while the s-cavity is not, the stored-energy distribution is significantly unstable against the beam loading. Finally, if the resonant frequencies of two cavities are identical, as is usually the case in a coupled-cavity system, the stored energy of the s-cavity becomes the same as that of the a-cavity. In order to increase the stored energy of the s-cavity by an order of magnitude, one must significantly deviate the frequency of the a-cavity from that of the s-cavity. Then, the energy flow from the s-cavity to the a-cavity would be seriously blocked, resulting in a practically isolated cavity system, rather than a closely coupled system.

These three problems can be solved by attaching the c-cavity and operating the three-cavity system in the $\pi/2$ mode. The energy flow between the a-cavity and s-cavity is significantly improved by the famous characteristic of the $\pi/2$ mode operation; that is, the system is stable against the beam loading. The last problem is also solved by adjusting the coupling constant (k_a) between the a-cavity and c-cavity with respect to the coupling (k_s) between the s-cavity and c-cavity, since the ratio of the stored energy (U_s) of the s-cavity to that (U_a) of the a-cavity is given by [15,16]

$$(U_s/U_a) = (k_a/k_s)^2. \quad (4)$$

It may sound paradoxical that we can solve the first problem, (the strong beam instability arising from the parasitic mode) by adding one more cavity (by increasing the number of parasitic modes). Fortunately, no field is excited in the c-cavity operating in the $\pi/2$ mode while very high fields exist in both the 0-mode and π -mode (see Fig. 1). Therefore, if one installs a coupler to extract power from the c-cavity, it is effective on the 0-mode and π -mode, while having no effect on the accelerating $\pi/2$ mode. This was confirmed by a low-power test of a model at one-fifth scale, as can be seen in Ref. [4].

Furthermore, the frequencies of the 0-mode and π -mode are approximately symmetrically distributed with respect to the $\pi/2$ mode. Thus, the antidamping effect of the mode μ beam oscillation due to the $f_{\mu,n}^+$ component of the impedance of one of the two parasitic modes is approximately canceled by the damping effect of the $f_{\mu,n}^-$ component arising from the other parasitic mode.

IV. CONCLUSIONS

The discussion given here was based upon two assumptions. First, the system is made of perfect conductors. Second, the storage cavity has only one mode, or, practically speaking, the TE015 mode is well separated from the other modes. Since neither assumption is correct, we have carefully studied these two effects, using the coupled-resonator model calculation for the first problem [2] and a three-dimensional analysis for the second one [3]. The result was quite promising, although an extensive study was necessary in order to sufficiently separate the TE015 mode from the other modes.

As long as no serious problem is found during the course of development, ARES will be fully used for the KEKB. The RF-related parameters of both the low-energy ring (LER) and high-energy ring (HER) are presented in Ref. [5].

Finally, it should be emphasized that ARES will reveal the full advantage of its extremely high stored energy when

missing-bunch (or partially filled bunch) operation [17] is necessary in order to suppress any ion-trapping effects. The thus-introduced phase modulation will be minimized by increasing the stored energy.

V. REFERENCES

- [1] T. Shintake, Part. Accel. **44**, 131 (1993).
- [2] Y. Yamazaki and T. Kageyama, Part. Accel. **44**, 107 (1994).
- [3] K. Akai and Y. Yamazaki, Part. Accel. **46**, 197 (1994).
- [4] "RF Characteristics of ARES Cold Models," N. Akasaka, K. Akai, T. Kageyama, T. Shintake, and Y. Yamazaki, WPQ09 in this Conference.
- [5] "Design of the KEKB RF System", K. Akai, E. Ezura, and Y. Yamazaki, WPQ08 in this Conference.
- [6] T. Shintake, Jpn. J. Appl. Phys. Lett. **31**, L1567 (1992).
- [7] K. Akai, J. Kirchgessner, D. Moffat, H. Padamsee, J. Sears, T. Stowe and M. Tigner, Proc. 15th Int. Conf. on High Energy Accelerators, 757 (1992).
- [8] T. Kageyama, N. Akasaka, Y. Takeuchi, and Y. Yamazaki, Proc. 4th European Par. Accel. Conf., 2098 (1994).
- [9] N. Akasaka, T. Kageyama, and Y. Yamazaki, Proc. 4th European Par. Accel. Conf., 2137 (1994).
- [10] "Development of a HOM-Damped Cavity for the KEK B-Factory(KEKB)," T. Kageyama, K. Akai, N. Akasaka, E. Ezura, F. Naito, T. Shintake, Y. Takeuchi, and Y. Yamazaki, WPQ17 in this Conference.
- [11] "HOM Absorber for the KEKB Normal Conducting Cavity," Y. Takeuchi, K. Akai, N. Akasaka, E. Ezura, T. Kageyama, F. Naito, T. Shintake, and Y. Yamazaki, WPR05 in this Conference.
- [12] "Input Coupler for the KEKB Normal Conducting Cavity," F. Naito, K. Akai, N. Akasaka, E. Ezura, T. Kageyama, T. Shintake, Y. Takeuchi, and Y. Yamazaki, WPR09 in this Conference.
- [13] An Asymmetric B Factory based on PEP Conceptual Design Report (1991).
- [14] P. B. Wilson, SLAC-PUB-2884 (1982).
- [15] E. A. Knapp, B. C. Knapp, and J. M. Potter, Rev. Sci. Instr. **39**, 979 (1968).
- [16] Y. Morozumi, T. Kageyama, and Y. Yamazaki, Proc. 1990 Linear Accel. Conf., 153 (1990).
- [17] Y. Yamazaki, M. Kihara, and H. Kobayakawa, KEK Report 83-17 (1983).

NON INTEGER HARMONIC NUMBER ACCELERATION OF LEAD IONS IN THE CERN SPS

D. Boussard, T. Bohl, T. Linnecar, U. Wehrle, CERN, 1211 Geneva 23, Switzerland

Abstract

The project to accelerate lead ions in the CERN complex has been successfully completed and physics has begun. In the SPS, the final machine in the chain, the ions are accelerated from an energy of 5.1 GeV/nucleon to 160 GeV/nucleon using the existing 200 MHz travelling-wave cavities. The change in revolution frequency during acceleration is much larger than can be accepted by the untuned cavities when operated at constant harmonic number. A technique has been developed to overcome this limitation which takes advantage of the filling time of this type of cavity which is shorter than one turn. Fast amplitude and frequency modulation of the RF waveform allows the cavities to operate at a constant, optimum frequency during the passage of a batch of particles in the structure. This frequency is not a multiple of the revolution frequency and therefore during the gaps between batches the phase of the composite RF waveform is changed to maintain synchronism from turn to turn as the beam accelerates. The technique and hardware are described in detail together with the first operational experience.

I. THE SPS TRAVELLING-WAVE CAVITIES

The SPS is a high intensity proton synchrotron with an injection energy ranging from 10 GeV to 26 GeV. The RF frequency swing during acceleration up to 400 GeV is therefore fairly small (4.4×10^{-3}). This fact has been exploited in the design of the RF cavities, which are of the travelling wave type, like in an electron linac, for instance [1].

Each cavity is a chain of coupled resonant cells, which behaves like a backward transmission line. The RF power is fed at the downstream end and dumped in a matched load at the upstream end of the structure. The major characteristics of the SPS RF system are given in Table 1.

Table 1

RF frequency at	199.5 MHz (10 GeV)
harmonic number $h = 4620$	200.4 MHz (400 GeV)
Cavity centre freq. ($\omega_0/2\pi$)	200.22 MHz
Operating mode at ω_0	$\pi/2$
Cell length ($\beta\lambda/4$)	374 mm
Group velocity v_g/c	-0.0946 (backward wave)
Cavity length	
two units of ℓ	= 20.2 m (54 cell cavity)
two units of ℓ	= 16 m (42 cell cavity)
Cavity voltage at 500 kW	2.35 MV (54 cell cavity)
transmitted power	1.86 MV (42 cell cavity)

One major advantage of such cavities is their inherent bandwidth, determined by the phase slip θ between particle and wave along the structure. For a cavity of length ℓ , θ is given by:

$$\theta = \underbrace{\frac{\ell}{v_g}(\omega - \omega_0)}_{\text{RF wave}} - \underbrace{\ell\left(\frac{\omega}{v} - \frac{\omega_0}{v_0}\right)}_{\text{particle}} \quad (1)$$

where $\omega_0/2\pi$ and v_0 are the synchronous frequency and the synchronous particle velocity respectively.

In the classical constant harmonic number acceleration, for protons, ω/v is constant and equation 1 reduces to its first term only. The energy gain through a cavity traversal is reduced by the transit time factor:

$$T = \sin(\theta/2) / (\theta/2)$$

with respect to the maximum obtained for the synchronous condition ($\omega = \omega_0$, $v = v_0$).

At the minimum injection energy of 10 GeV, T is reduced by only a factor 0.7 which is perfectly acceptable and shows one of the great advantages of the travelling wave cavities, namely no need for a programmed or a servo tuning system.

The SPS is also used for lead ion acceleration [2], with an injection energy of 5.08 GeV/c/u corresponding to $T = -0.113$ (short cavities) and $T = 0.099$ (long cavities). The standard $h = 4620$ acceleration would not work in this case, as the RF effective voltage would disappear as acceleration proceeds. To avoid building a new, dedicated RF system for ion acceleration, one can look again at eq. 1 and assume that the RF frequency ω is a free parameter. In this case θ can be made to vanish, for the optimum frequency $\omega = \omega_0(\ell - v_g/v_0)/(\ell - v_g/v)$. As $v_g \ll v$, v_0 , this corresponds approximately to $\omega = \omega_0$.

For constant h acceleration, the centre frequency of classical resonant cavities follows the particle velocity. In this case a large fraction of their stored energy is still useful for acceleration after one machine turn. This is not the case for the SPS cavities because of their travelling wave nature: the energy stored in the resonant cells propagates to the matching load in a time ℓ/v_g short compared to the revolution period of 23 μ s. In other words the cavities have no memory after one turn, and therefore *can be powered at their optimum frequency, provided there is a gap in the RF waveform — and in the beam* — to let the structure be emptied (and filled) at every turn. In this way, at each turn, we have a new, independent acceleration event, optimized to obtain the best efficiency of the structure.

II. HOW TO RESYNCHRONIZE WITH THE BEAM AT EVERY TURN

Although it is not a new idea [3] to use an RF burst frequency $\omega \approx \omega_0$ different from $h f_{\text{rev}}$ ("non integer harmonic number acceleration"), the problem of keeping the successive RF bursts in perfect synchronism with the orbiting beam has

to be faced. This is imperative to avoid excessive radial excursions especially close to the transition energy.

The solution is an FM modulated wave, with a rectangular modulation periodic at the revolution frequency f_{rev} (Fig. 1) [4]. The average (carrier) frequency is $h f_{rev}$ but the frequency during the useful RF burst can be made equal (or close to) $\omega_0/2\pi$ to optimize the cavity behaviour. The various revolution frequency clocks (and therefore the modulation waveform) are obtained by divide-by-h counters on the FM modulated signal f_{RF} .

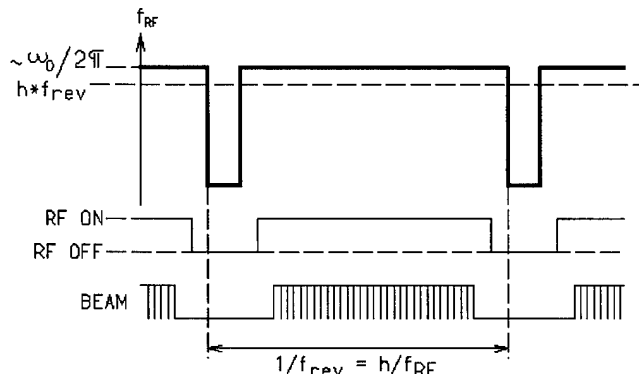


Fig. 1. FM-modulated RF

A fast voltage-controlled oscillator (VCO) is driven by two sources (Fig. 2): a) a slowly varying control voltage which defines $h f_{rev}$, and b) a fast modulation, with zero average (AC coupled) synchronous with f_{rev} , and which keeps the RF burst frequency close to $\omega_0/2\pi$.

The first control voltage is obtained from the classical phase, radial or frequency loops and plays the same role as usual. The modulating amplitude is derived from a frequency programme (the modulating amplitude is proportional to $\omega_0/2\pi - h f_{rev}$). During the off time of the cavities the VCO runs far away from $h f_{rev}$ (especially for short gaps), which imposes severe constraints on the linearity and speed of the oscillator.

Clearly this scheme will also work with more than one batch of ions around the circumference provided the cavity filling times are sufficiently short.

III. THE VOLTAGE-CONTROLLED OSCILLATOR

The main characteristics are given in Table 2. The oscillator is basically simple with an LC tank circuit consisting of a low-loss transmission line for the inductor and a high Q varicap, and two low-loss FETs in the feedback path. The components in the feedback and drive circuits are carefully chosen for their speed, temperature stability and noise properties. The latter is particularly important due to the high sensitivity of the oscillator. Noise measurements show that the static, non-switching, phase noise level is similar to that used for high intensity proton operation. The linearity was improved by external correction to ± 2.5 kHz to limit the correction swing needed from the phase loop amplifier (DC input).

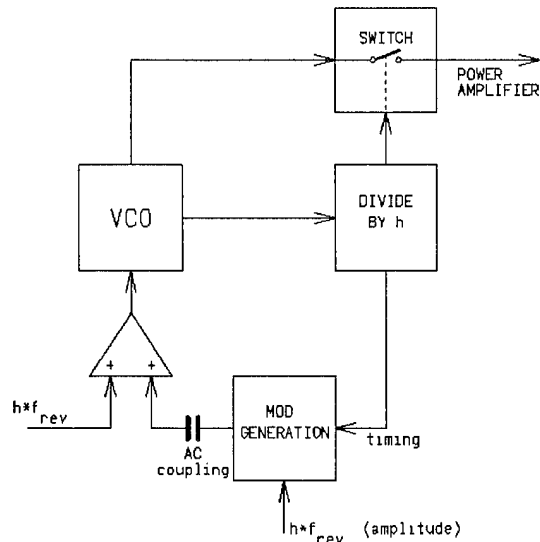


Fig. 2. Principle of the VCO drive

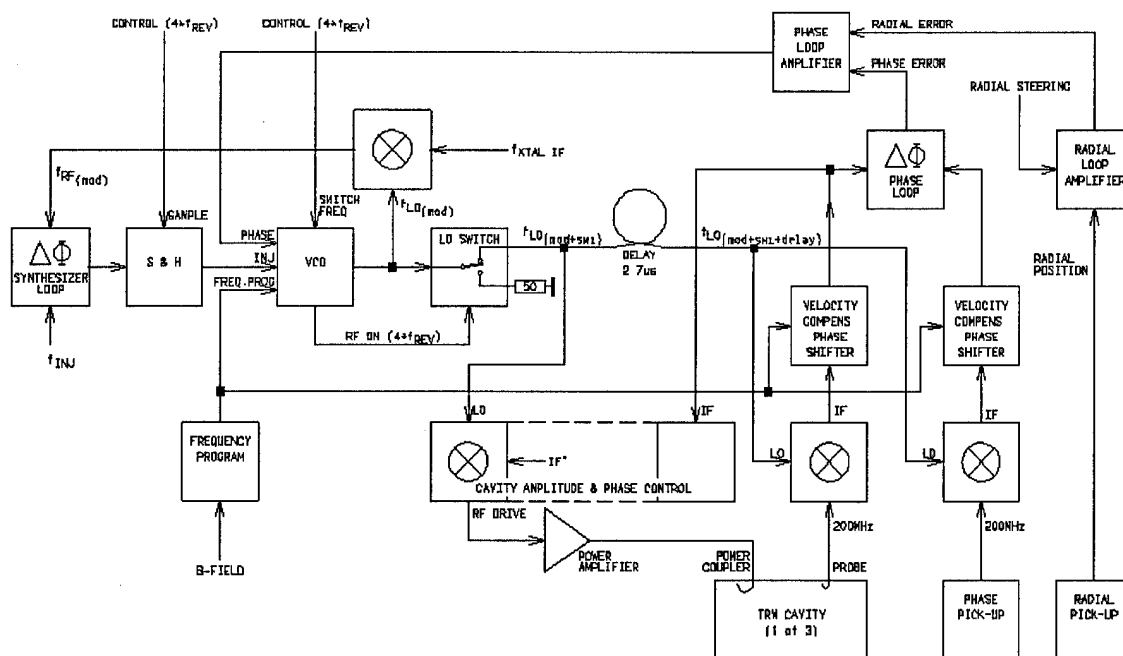
Table 2. VCO Characteristics

Max. freq. range	177.1 - 191.7 MHz
DC/AC Sensitivity	2 MHz/V
Non-linearity	± 2.5 kHz
Output power	0 dBm
Temperature Stability	< 2 kHz / $^{\circ}\text{C}$ at 25°C
AC switching speed	200 ns, full range
DC bandwidth	> 250 kHz
Noise at 1 kHz, 10 kHz	-78dBc, -100dBc

IV. THE RF SYSTEM

Four batches of ions, $2.2 \mu\text{s}$ long, are injected equispaced around the circumference, at 1.2 s intervals. During this process the mean RF frequency is locked using the synthesiser loop to the injection/capture frequency also sent as revolution frequency information to the injector. Each batch partially debunched in the SPS is independently adiabatically captured using fast counterphasing modulation at $4f_{rev}$ on two cavity voltages to produce the required capture function. After the injection process the radial loop is used to accelerate the beam from 5.08 GeV/c/u to 157.8 GeV/c/u.

A simplified block diagram of the RF system is given in Fig. 3. The synthesiser loop compares the injection frequency with the modulated RF, the output of the mixer being sampled at $4f_{rev}$ to provide the correction signal to the VCO. The main cavity phase and amplitude control circuits and the beam/RF phase discriminator work at an intermediate frequency, IF, of 10.7 MHz. The VCO works at $f_{RF} - 10.7$ MHz and input and output mixers are used. The VCO and the RF switch which allows drive to the amplifiers only when the modulated frequency is suitable, are switched at $4f_{rev}$ (173 kHz), with a mark-space ratio of $3.63 \mu\text{s}$ to $2.13 \mu\text{s}$ using external trigger pulses derived by division of the modulated RF. The total oscillator frequency swing is then ≈ 7 MHz compared to the IF of 10.7 MHz. The filters in the output mixer are quite critical with a rejection of the local oscillator signal greater



than 20 dB, 3 MHz from the passband where the phase response is $\pm 10^\circ$.

At constant harmonic number the number of bunches between elements in the machine is fixed during acceleration. This is not so with this scheme; the RF phase varies with velocity and must be compensated by phase shifters programmed according to the revolution frequency. The information is not available from the bunch frequency, (fixed frequency acceleration). The long delays, surface to tunnel, also require compensation so that synchronism between the RF burst on the surface and that generated from the cavities or by the beam is obtained at the measurement points.

The amplitude circuits in the cavities have narrowband filters to eliminate revolution frequency components. This means that they measure mean RF voltage as opposed to peak and must be corrected according to the mark-space ratio. The power measurements used to protect amplifiers and cavities use peak detection and are not affected by this scheme. The amplifiers themselves required considerable modification in the power supply regulation circuits to permit this fast switching at full power, 500 kW/amplifier.

V. RESULTS WITH Pb BEAM

Fixed frequency acceleration worked well from the beginning of the physics run. As optimisation of the various transverse and longitudinal parameters proceeded, the overall transmission in the SPS rose from 50 to 75%. Capture efficiencies were about 80%.

The optimum operational voltage to hold the ions along the injection plateau corresponds to a bucket height comparable to the injected momentum spread. In principle, good adiabatic capture requires a value approximately twice this. However, raising the voltage produces a diffusion loss of particles from the bucket which becomes important during the

3.6 s holding period. The phase noise measured on the beam suggests diffusion rates of the order of seconds and indeed injecting white noise into the RF to double the observed phase noise produces loss rates similar to that with higher voltages. Diffusion rates increase with the square of the synchrotron frequency for a flat noise spectrum. Detailed measurements point to the high frequency noise, at multiples of the revolution frequency, in the VCO as the source. It may therefore be possible to increase the capture efficiency, already good, by using higher voltage if the noise on the VCO can be reduced.

In conclusion, fixed frequency acceleration has proved a powerful method for extending the capabilities of the existing SPS as a particle accelerator.

VI. ACKNOWLEDGEMENTS

Many people in the RF/LS (beam control) and RF/CP (power) sections have contributed to the success of the lead ion acceleration. In particular we thank H-P. Kindermann, W. Sinclair and F. Oude-Moleman for their work on the power amplifiers.

VII. REFERENCES

- [1] G. Dôme, CERN SPS/ARF/77-11.
- [2] A. Faugier *et al.*, this conference.
- [3] C. Zettler, CERN LABII/RF/CZ/Note 75-32.
- [4] D. Boussard, J.M. Brennan, T.P.R. Linnecar, CERN SPS/89-49 (ARF).

ANALYSIS AND RESULTS OF THE INDUSTRIAL PRODUCTION OF THE SUPERCONDUCTING Nb/Cu CAVITIES FOR THE LEP 2 PROJECT

E. Chiaveri, C. Benvenuti, R. Cosso, D. Lacarrere, K.M. Schirm, M. Taufer, W. Weingarten
CERN, 1211 Geneva 23, Switzerland

Abstract

For the energy upgrade of the Large Electron Positron Collider at CERN, 216 RF superconducting cavities were ordered from three European industrial firms (Ansaldo, Cerca, Siemens/Accel) at the beginning of 1991. These cavities are made of copper (Cu), internally coated with niobium (Nb) according to a procedure developed at CERN. Up to now about 147 of these cavities fulfilling the specifications have been produced. The large-scale statistics available and the use of dedicated analytical and optical inspection techniques shed new light on the relationship between production procedures, niobium film properties and cavity performance. An overview of this subject is presented, together with some significant trends and results.

I. INTRODUCTION

Niobium sputter coating of four-cell 350 MHz cavities built from OFE copper sheet material has been chosen at CERN for series production. This technology presents some interesting advantages in terms of thermal stability, costs and future potential [1]. Until now 147 "bare" cavities meeting the technical specification ($Q = 3.4 \times 10^9$ at $E = 6$ MV/m at 4.5 K) have been produced representing 65% of the total present contractual number (216). After a period of about one year for the transfer of technology, the three firms started to produce one cavity per week according to the planning. However, we were faced with a problem of reproducibility of the coating process related to the very delicate procedures which require a high level of quality control.

The cavity performance is sometimes limited by local defects (up to several mm in size) of the Nb layer. Major defects like poor bonding (blister) of small Nb areas (Fig. 1) are usually detected as "hot spots" in the temperature maps [2] of RF tests. Investigations of such defective layers by optical [3] and surface analytical tools [4,5] have been launched in order to clarify the nature and origin of various types of defect and also of other minor irregularities that can occur in considerable numbers without being detected in temperature maps. After inspection, these cavities must have the defective Nb layer chemically removed at CERN and are then returned to the manufacturer for a second or even a third Nb coating.

II. ANALYSIS OF THE CAVITY SURFACE

Cavities that are rejected after the RF measurements are systematically investigated by means of a video camera set-up on a computer controlled optical inspection bench [3]. Pictures of surface defects and irregularities (fig.1 and 2) are taken at different magnification together with the position coordinates.

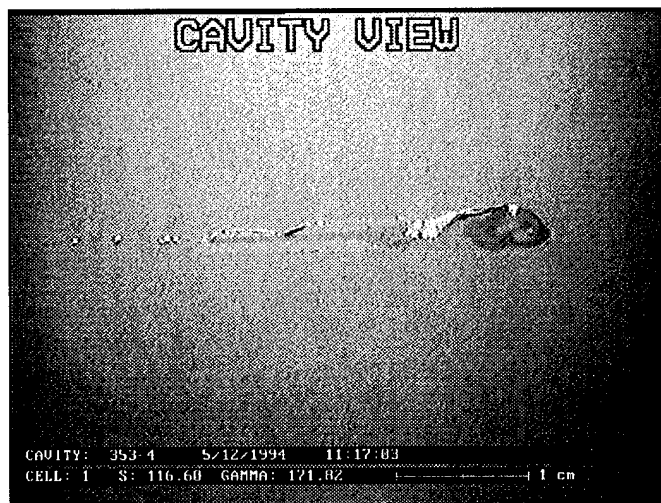


Fig.1: Major defect on the inner cavity surface (~2 cm).

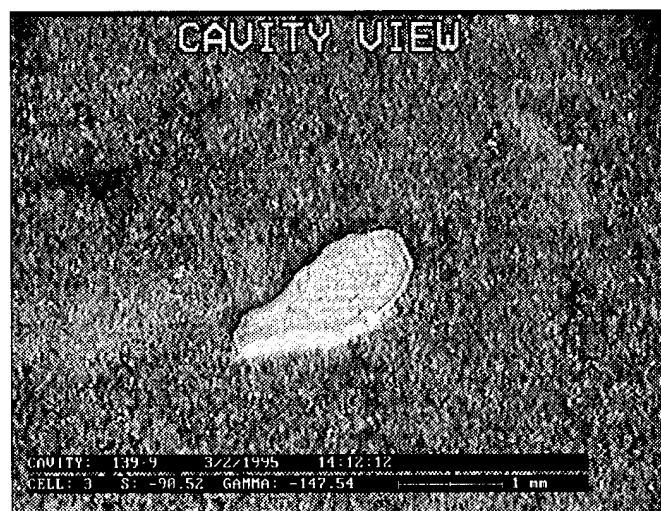


Fig.2: Inner cavity surface with 1.5 mm long irregularity.

The results of the optical inspection and the temperature maps provide in most cases an explanation for the inadequate performance. However further specific surface

analysis is necessary for understanding the nature of these defects. In view of this, a computer controlled surface analysis instrument, incorporating Secondary Electron Microscopy (SEM) imaging, Auger Electron Spectroscopy (AES) and Scanning Auger Mapping (SAM) has been designed and built at CERN [4,5]. This diagnostic tool provides both topographical information and elemental composition of surface defects.

Some characteristic defects of the Nb film were observed during industrial cavities investigation carried out so far. For example, corresponding to defective areas located by SED imaging, the Nb film was often found to be very thin or missing by AES analysis; the Cu substrate was in some cases highly contaminated, mainly with C, and also with S, Cl, N; in other cases, particles containing Fe and Ni were detected, embedded in the Cu substrate.

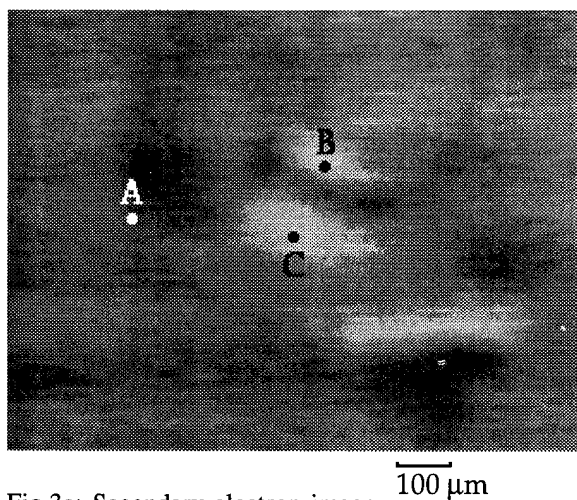


Fig.3a: Secondary electron image

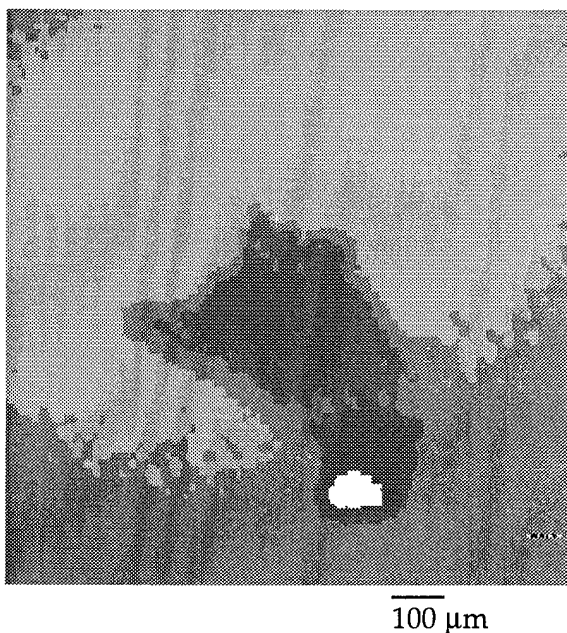


Fig.3b: Scanning Auger O map (darker areas correspond to lower concentration of O)

In figure 3 an example of characterization of a defective area is shown. A Secondary Electron Image of the defective area (3a), its associated O elemental map (3b), and related Auger electron spectra (3c) are presented. Since the surface of the film consists of Nb oxidised mainly in the form Nb_2O_5 [6], corresponding to an atomic concentration of oxygen $X_{\text{O}} \approx 0.7$, it can be concluded that the light area in fig. 3b corresponds to a region where the Nb film is present and the dark area to a region where it is either very thin or missing. The black spot at the bottom of the picture corresponds to the highest concentration observed in this area. This conclusion is supported by the Auger spectra shown in 3c, corresponding to points A, B and C in the SED image (3a). In spectrum A no signal from the substrate is detected, whilst in B the copper 'fingerprint' is clearly visible; in C, copper is still present but the main contribution to the spectrum is given by the carbon line.

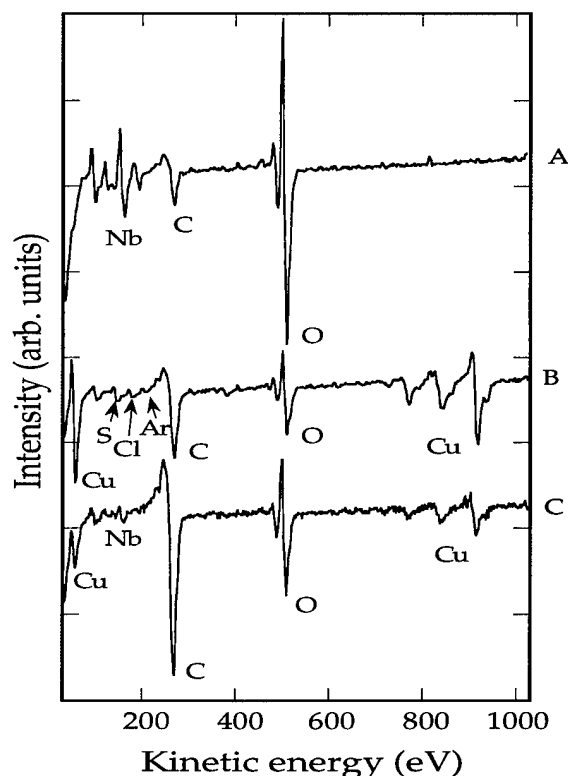


Fig.3c: Auger spectra taken at points A, B and C

III. RESULTS AND DISCUSSION

It seems clear by now that we have to distinguish between defects originating from the production of the raw Cu cavities and accidents happening to them afterwards before coating, e.g. during the chemistry/drying cycles. Some types of defect are company-specific, others have a more general nature, but all of them can lead to noticeable peeling of the active layer. It was recently found that the probability of such defects occurring is reduced by applying additional successive cycles of

electrolytical and chemical polishing to the copper. Removing the copper surface to an increased depth (more than 150 μm total) not only reduces the risk of chemical retention in pits [7] but also eliminates traces of the mechanical polishing done after the electron-beam welding assembly.

For cavities without noticeable defects we have identified two process parameters in the industrial production that could be highly relevant for the RF performance:

- i) The vacuum quality before the Nb coating
- ii) The temperature chosen for baking and sputtering.

These parameters are interconnected since the bake-out protocol also determines the vacuum quality. Various possible incidents in the delicate manufacturing process preceding the coating can change the residual gas composition as indicated by mass spectrometry and the attainable pressure limit in the cavity (usually $< 10^{-9}$ Torr). Consequences range from a decreased Q value at low field by the getter pumping effect of light gases during Nb deposit [1] to an insufficient Nb adhesion in presence of organic residues. The choice of the cavity temperatures for baking and sputtering determines not only the diffusion and outgassing rates but also the growth properties of the Nb layer and structural aspects of the copper substrate and their influence on its mechanical properties. In view of these partly conflicting aspects the best compromise appears to be the following: baking the cavities at 150°C for 24 h and coating them at cell temperatures strictly limited to $\leq 200^\circ\text{C}$ (temperature maxima usually $180^\circ\text{C} \pm 10^\circ\text{C}$). Respecting all the criteria mentioned above has resulted, at all three companies, in cavity performances well above the specification requirements (Fig.4) and considerably increased acceptance rates of cavities with only one Nb coating (Fig.5).

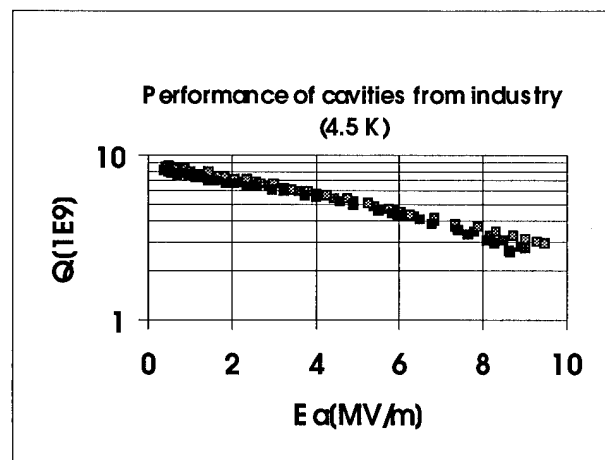


Fig.4: Recently obtained cavity performance for different manufacturers.

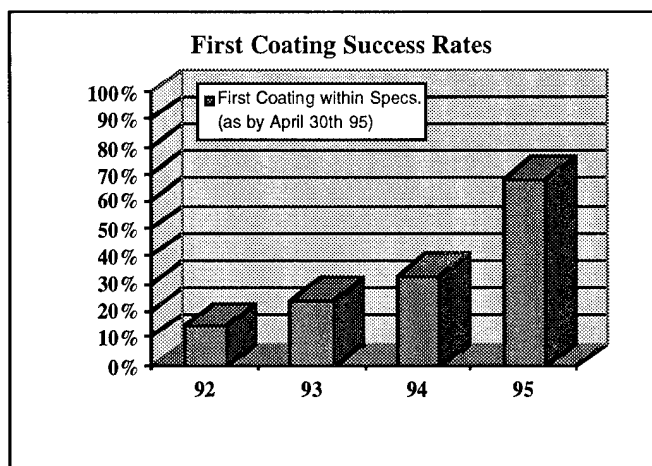


Fig.5: Total first coating success rates in industry

IV. CONCLUSION

Superconducting Nb/Cu cavity production technology has been improved in the course of the large-scale series manufacturing of 350 MHz cavities. Statistical survey of the correlation between key process parameters and performance tests as well as the use of dedicated analysis tools have helped to improve our understanding of the fabrication process and to modify it effectively. Q-factors are now consistently better than specifications (by 25% on average) but the random occurrence of surface defects still limits the coating success rate. A rigorous quality control is mandatory.

V. ACKNOWLEDGEMENTS

The dynamism and the technical competence of R.Hanni, E.Magnani, A.Scharding have been instrumental in the successful advancement of the project. We also would like to thank B.Thony for his useful help on the optical analysis. We appreciate the effort of G.Bressani for the set-up of the optical inspection bench. Many thanks to D.Boussard for his critical remarks.

VI. REFERENCES

- [1] C. Benvenuti et al.; Physica B **197** (1994) 72
- [2] Ph.Bernard et al. Nucl. Instr. and Meth. **190** (1981) 257-282
- [3] G.Bressani et al. paper in preparation
- [4] D. Lacarrere et al., Proceedings of the 6th workshop on RF Superconductivity, Newport News, Virginia USA, 4-8 Oct. 93; p.702/717
- [5] C. Benvenuti et al., submitted to NIM
- [6] J. Halbritter, Appl. Phys. A **43** (1987) 1.
- [7] S. Calatroni et al., Proceedings of the 6th workshop on RF Superconductivity, Newport News, Virginia USA, 4-8 Oct. 93; p.702/

Performance Experience with the CEBAF SRF Cavities*

C. Reece, J. Benesch, M. Drury, C. Hovater, J. Mammoser, T. Powers, and J. Preble
CEBAF, Newport News, VA 23606 USA

Abstract

The full complement of 169 pairs of niobium superconducting cavities has been installed in the CEBAF accelerator. This paper surveys the performance characteristics of these cavities in vertical tests, commissioning in the tunnel, and operational experience to date. Although installed performance exceeds specifications, and 3.2 GeV beam has been delivered on target, present systems do not consistently preserve the high performance obtained in vertical dewar tests as operational capability. The principal sources of these limitations are discussed.

I. INTRODUCTION

The CEBAF recirculating linac uses 338 superconducting rf cavities to accelerate the beam. With four passes through the linacs, 3.2 GeV beam has been delivered onto a target. Operation to date has been limited to low current, pulsed beam. As commissioning continues, the delivery of 200 μ A CW beam at > 4 GeV is anticipated. Installed capacity may support operation above 5 GeV.

This paper reviews the characteristics and performance of the CEBAF SRF cavities. The cavities are but a part of the integrated system which delivers beam for nuclear physics research. At the start of the construction project these cavities together with the attendant 2 K liquid helium system were considered to present considerable technical risk. High-quality performance by our vendor [1] and careful attention to QA procedures, though, have resulted in the cavities performing reliably well above their design specifications of $E_{acc} = 5$ MV/m in qualifying tests.

Performance summaries have been presented previously for subsets of the cavities.[2-6] Process details described there will not be repeated here.

II. CAVITY PERFORMANCE AND LIMITATIONS

A. Cavity Performance Parameters

CEBAF was able to exploit a tested SRF cavity design developed at Cornell University for storage ring applications.[7] With only minor modifications, the cavity design was directly applicable to CEBAF. The nominal values of various parameters of the cavity are collected in Table 1. The principal figures of merit, of course, are the accelerating gradient and the unloaded quality factor (Q_0).

The CEBAF five-cell cavities were assembled and tested as pair units prior to assembly of four pairs into the horizontal cryomodules. In this cryomodule configuration, the cavities were commissioned for operation in the accelerator tunnel. Systematic performance tests in this configuration are difficult, principally because Q_0 must be measured calorimetrically.

SRF cavity performance is the combination of:

(1) physical design factors—these determine the beam-cavity interaction characteristics,

Table 1: CEBAF SRF Cavity Design Parameters

fundamental frequency	1497.0 MHz
accelerating gradient, E_{acc}	> 5 MV/m
active length	0.5 m
cell-to-cell coupling	$(3.09 \pm .02)\%$
geometry factor	275 Ω
R/Q	960 Ω/m
E_{pk}/E_{acc}	2.56
Q_{ext} input coupler	$6.6 \times 10^6 \pm 20\%$
tuner phase error budget	10°
microphonic phase error budget	30°
Lorentz force frequency sensitivity	$-2.2 \text{ Hz}/(E_{acc}[\text{MV/m}])^2$
pressure frequency sensitivity	80–137 Hz/torr
niobium RRR	≥ 250
HOM Q_1 - 1976 MHz mode	4000
HOM Q_1 - 1980 MHz mode	1800
beam pipe ID	70.4 mm
At $E_{acc} = 5$ MV/m:	
Q_0	$\geq 2.4 \times 10^9$
2 K dynamic heat load	< 2 W
x-plane effective dipole steering	$7.5 \times 10^{-3} \text{ MeV}/c$
y-plane effective dipole steering	$-1.7 \times 10^{-3} \text{ MeV}/c$
effective normal quadrupole	$1.2 \times 10^{-3} \text{ MeV}/c/\text{cm}$
effective skew quadrupole	$-1 \times 10^{-3} \text{ MeV}/c/\text{cm}$

(2) material and surface dependent factors—these determine the maximum sustainable stored energy and the 2 K heat load,

(3) extrinsic operability factors—these include availability of rf drive, total 2 K cooling capacity, and reliability concerns such as frequency of interruptions to operations due to interlock trips.

The design factors have been well characterized elsewhere,[4,7,8] and the principal parameters are included in Table 1. The particular limitations of each cavity were established during the vertical cryostat tests, and the integrated system limitations have been determined from cryomodule commissioning and accumulating operating experience.

B. Performance Limitations

Using the hermetic cavity pair configuration and coax-to-waveguide variable couplers,[9] CEBAF characterized the cavity-specific factors of all cavities in a vertical dewar testing arrangement. This test also provided a thorough leak-check of the assemblage. The ceramic rf windows are attached to the cavity prior to this test, and are thus part of the tested system, as are the higher-order-mode loads and beamline gate valves.

*Supported by DOE contract DE-AC05-84ER40150.

Figure 1 illustrates the typical performance limitations encountered during vertical cavity pair testing. Either a thermal-magnetic quench provides a hard limit on the stored energy, or electron loading degrades the cavity Q intolerably.

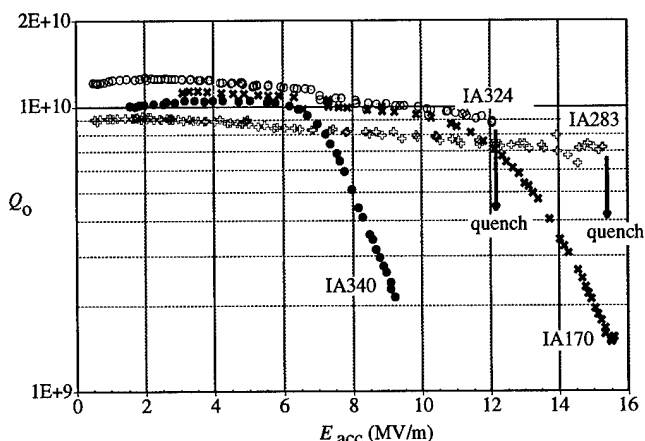


Figure 1. Typical quench and field emission loading seen in vertical tests.

Toward using the cryogenic capacity most efficiently and minimizing steady-state x-radiation fields, the *usable* gradients have been constrained to fields which induce less than 1 Watt of electron loading and, for commissioning tests, less than 1 rad/hr of generated x-rays external to the cryomodule. When cavity quench was encountered within these constraints, the usable gradient was derated 10% from the quench field.

Figure 2 presents the distribution of usable gradients and corresponding Q_0 of the CEBAF cavities as determined by the vertical pair testing. While some cavities performed well above 15 MV/m, there is a wide spread in fields attained even in these isolated tests.

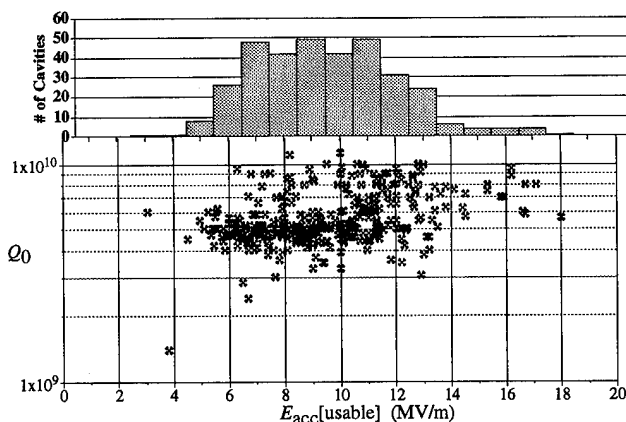


Figure 2. Distribution of usable SRF cavity gradients during vertical pair tests.

The distribution of peak fields reached in cavities which exhibited quenching is presented in Figure 3. In many cases heavy electron loading attended the quench. Again, there is a wide spread in the quench field, suggesting that significant improvements will be needed in the thermal stabilization of such cavities before one may reliably attain fields greater than about 12 MV/m.

The distribution of usable cavity capability observed during the commissioning tests is presented in Figure 4.

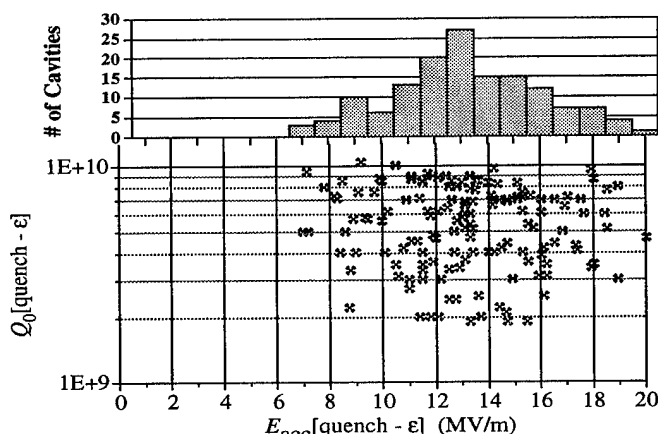


Figure 3. Distribution of quench fields in vertical tests.

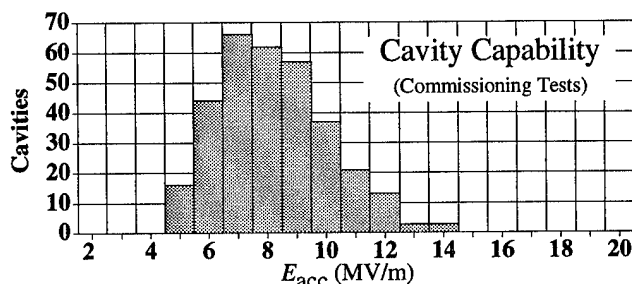


Figure 4. Distribution of usable SRF cavity gradients at commissioning.

C. Cold Ceramic Rf Windows and Arcing

The CEBAF ceramic rf window is mounted directly to the cavity waveguide fundamental power coupler. The alumina ceramic is located 100 mm off of the beamline. In this location, the window is subjected to the expected rf power, but also may be subject to charging via electron and x-ray flux.

Some of the electron loading observed in cavity tests has been attributed to cooperative and perhaps complex interactions between the cavity and windows.

On at least two occasions, particular cavities, with presumably specific field emission characteristics, repeatedly induced damage on windows mounted onto them, suggesting that secondary or photo electron flux on the window induced unsupportable charging. In other cases, it appeared that particular windows induce or significantly enhance electron loading in the cavities.

During sustained operation, quite a few cavities exhibit "arcing" in the region of the cold window at a rate which is otherwise unacceptable for operations—as high as 45 times per day. The additional constraint of < 2 arcs/day has thus been added to the criteria for usable maximum gradient for each cavity. This operational derating of maximum gradients has been necessary for 13% of the cavities.

Arcing in cavities appears to be correlated with the presence of nearby field emission—either in the arcing cavity or its neighbor. When arcing does occur, its frequency is strongly dependent on cavity gradient. Note that other cavities function stably, without arcing, above 9 MV/m. Several studies are exploring different aspects of this arcing phenomenon, including its dependence on the physical position of the window and spectral analysis of the light generated.[10,11]

III. CURRENT OPERATING CONDITIONS

During the installation and commissioning of individual cryomodules, cavity gradient and Q performance were tested, and stable operating bounds were established for short periods of time. The limiting constraint was noted for each cavity. To these limits the operational derating due to arcing has been added. The present distribution of types of cavity gradient limitations is provided in Figure 6. Clearly, the arcing and electron loading limitations, which as mentioned above we believe to be coupled, represent the most significant gradient performance constraints for CEBAF.

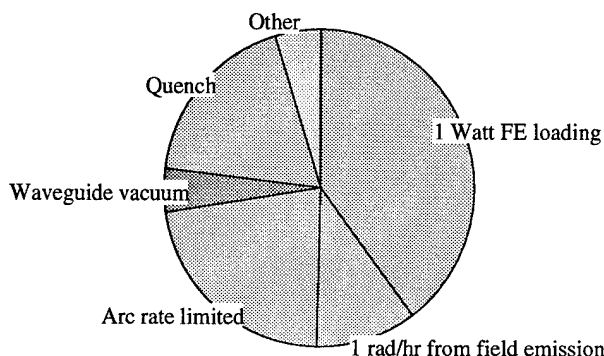


Figure 6. Distribution by type of cavity performance limitation—commissioning and operating experience

The installed cryomodules and rf drive systems are currently set up to support delivery of 15 μ A, 4 GeV beam on Hall C targets. To reduce the consumption of ac line power during low current commissioning, the klystron supplies have been set to a lower tap setting. This has limited the available rf power per klystron to about 1.7 kW, down from their full 5 kW capability. This change has also had the benefit of extending the MTBF of the klystrons.

The present view of CEBAF SRF cavity operating performance is depicted in Figure 7 on a per-cryomodule basis. Five cavities are turned off, three with locked tuners, one with a broken interlock sensor, and one with a defective rf pickup probe. The operational derating of cavities has reduced the net usable voltage by 5% relative to commissioning test data.

In the fall of 1995, we anticipate raising the tap settings to accommodate higher current operation. Under those conditions we expect significantly higher performance from the SRF cavities—supporting up to 200 μ A beam at energies greater than 5 GeV. At that time we plan to examine the arcing behavior of cavities that otherwise function well at high gradients. The CEBAF acceleration system now appears capable of supporting operation at least 25% above initial design requirements. We envision opportunities for further improvements toward yet higher energies.

IV. ACKNOWLEDGEMENTS

The staff of the SRF and RF groups are pleased to have provided and commissioned the acceleration system for CEBAF. Particular credit goes to R. Sundelin and P. Kneisel for their work designing and refining the core building blocks of the accelerator. Production assembly and commissioning of cryomodules were coordinated by H. F. Dylla and W. Schneider.

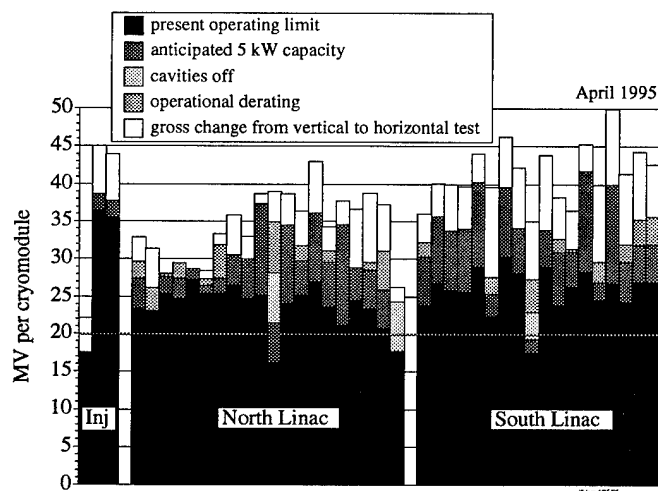


Figure 7. Capability of installed CEBAF cryomodules.

V. REFERENCES

- [1] M. Dzenus *et al.*, "Production of Superconducting Niobium Cavities for CEBAF," *Conference Record of the 1991 IEEE Particle Accelerator Conference*, Vol. 4, pp. 2390–92.
- [2] J. Mammoser, "Status Report: SRF Activities at CEBAF," *Proceedings of the 6th Workshop on RF Superconductivity*, October 4–8, 1993, Newport News, VA, Vol. 1, pp. 33–48.
- [3] M. Drury *et al.*, "CEBAF Cryomodule Commissioning in the South Linac," *ibid.*, pp. 610–616.
- [4] J. Mammoser, "Analysis of Mechanical Fabrication Experience with CEBAF's Production SRF Cavities," *Proceedings of the 1993 Particle Accelerator Conference*, Vol. 2, pp. 947–949.
- [5] H. F. Dylla *et al.*, "Operating Experience with High Beta Superconducting RF Cavities," *ibid.*, pp. 748–752.
- [6] C. Reece *et al.*, "Performance of Production SRF Cavities for CEBAF," *ibid.*, pp. 1016–1018.
- [7] R. M. Sundelin, "High Gradient Superconducting Cavities for Storage Rings," *IEEE Trans. Nucl. Sci.*, NS-32, 3570 (1985).
- [8] Z. Li, *Beam Dynamics in the CEBAF Superconducting Cavities*, Ph.D. dissertation, College of William and Mary (1995).
- [9] P. Kneisel, "Test of Superconducting Accelerator Structures in a Closed Vacuum System," *Proceedings of the 1987 IEEE Particle Accelerator Conference*, Vol. 3, pp. 1893–95.
- [10] T. Powers and P. Kneisel, "Arcing Phenomena at CEBAF RF-Windows at Cryogenic Temperatures," these proceedings.
- [11] V. Nguyen-Tuong *et al.*, "Electronic Activity at CEBAF Cold RF Window Induced by Cavity Operation," *Proceedings of the Fourth European Particle Accelerator Conference*, 27 June–1 July 1994, London, Vol. 3, pp. 2200–2202.

Beam Test of a Superconducting Cavity for the CESR Luminosity Upgrade*

H. Padamsee, P. Barnes, S. Belomestnykh, K. Berkelman, M. Billing, R. Ehrlich, G. Flynn, Z. Greenwald, W. Hartung, T. Hays, S. Henderson, R. Kaplan, J. Kirchgessner, J. Knobloch, D. Moffat, H. Muller, E. Nordberg, S. Peck, M. Pisharody, J. Reilly, J. Rogers, D. Rice, D. Rubin, D. Sagan, J. Sears, M. Tigner and J. Welch

Laboratory of Nuclear Studies, Cornell University, Ithaca, NY 14853

ABSTRACT

The prototype superconducting cavity system for CESR-Phase III was tested in CESR in August 1994. The performance of the system was very gratifying. The cavity operated gradients of 4.5-6 MV/m and accelerated beam currents up to 220 mA. This current is a factor of 3 above the world record 67 mA for SRF[1]. The high circulating beam current did not increase the heat load or present any danger to the cavity. No instability attributable to the SRF cavity was encountered. A maximum of 155 kW of rf power was transferred to a 120 mA beam. The window was subjected to 125 kW reflected power and processed easily. In the travelling wave mode, vacuum bursts and arc trips prevented us from going above 165 kW. The maximum HOM power extracted was 2 kW. Beam stability studies were conducted for a variety of bunch configurations. In other tests a 120 mA beam was bumped horizontally and vertically by ± 10 mm. While supporting a 100 mA beam, the cavity was axially deformed with the tuner by 0.4 mm to sweep the HOM frequencies across dangerous revolution harmonics. In all such tests, no resonant excitation of HOMs or beam instabilities were observed, which confirms that the potentially dangerous modes were damped strongly enough to be rendered harmless.

INTRODUCTION

The rationale for using superconducting cavities in high current storage rings is discussed in [2]. To increase the luminosity of CESR with currents of the order of 1 amp, a superconducting cavity is the ideal way to lower cavity impedances that cause multibunch instabilities. The impedance for CESR-III will be reduced by using a small number of high gradient (6 MV/m) superconducting cavities which have a low impedance cell shape.

Before the beam test, the niobium cavity was tested in the vertical cryostat to 3 MV (gradient = 10 MV/m) [3], the window was tested off-line to 250 kwatt travelling wave and 125 kwatt standing wave[4], the ferrite lined beam pipe HOM loads were tested to withstand a power density of 20 watt/cm²[5].

Fig. 1 shows the cavity, cryostat, input coupler, planar window, ferrite beam pipe HOM couplers, tuner, gate valves, sliding joints, tapers to the CESR beam pipe, vacuum pumps, refrigerator interface box (cold box), and other

components needed for the CESR beam test. The cavity was first tested in the processing area with high power without beam. Once it operated CW at 6 MV/m it was installed in the CESR beam line, in the high bay area, west of the CLEO detector. The refrigeration system consisted of two units, nominally rated at 100 watt, feeding into a 1000 litre dewar. The cold gas from the cryostat was returned to the refrigerator. On one side, CESR dipole magnets were located < 1 m away from the SRF cavity; but on the detector side, the closest magnet was > 15 m away. Therefore most of the high current tests were carried out with a positron beam, so as not to irradiate the cavity region with too high a synchrotron radiation (SR) dose from the nearby magnet. Near the end of the test, however, a 57 mA electron beam was also run through the cavity, to evaluate how the cavity would perform in the presence of a severe SR dose. Most of the beam tests were conducted at 5.3 GeV, for which the total voltage required was 7-7.5 MV. Through most of the tests, the CESR NRF system of four 5-cell copper cavities provided 6 MV (gradient = 1 MV/m) and the SRF cavity provided about 1.5 MV.

HIGH CURRENT OPERATION

The maximum current for the test was 220 mA (in 27 bunches) which is 1 mA less than the maximum total current ever run in CESR up to the time of the SRF beam test. The current limit was set not by the performance of the cavity but by the heating (80-100C) of CESR components, in particular the sliding joint of the CLEO beam pipe. Immediately following the multibunch 220 mA run, we stored a maximum of 44 mA in a single bunch. Again, the heating of CESR components was the limit. Note that the quantity: (number of bunches) x (single bunch current)² was nearly the same (actually 8% higher) as the 220 mA, 27 bunch run.

The cavity was kept in CESR for 7 days, during which beam was run through the cavity for a total period of approximately 65 hours. For most of this time the operating conditions were at a beam energy of 5.3 GeV and a beam current of 100 mA.

Fig. 2 shows the response of the total cryogenic losses to the injection of high beam current. Starting at 5:30 am, as the beam was increased from 0 to 220 mA, there was no observable increase in total cryogenic loss (80 watt). Note however, the increase in heat load, from 50 to 80 watt, when the rf was turned on (before the beam) at 5:24 to establish a gradient of 4.7 MV/m (1.4 MV for the cell). The ambient losses due to the static cryostat heat leak (25 watt) and the transfer lines was (25 watt) were measured independently to give a total of 50 watt.

*Supported by the National Science Foundation, with supplementary support from the US-Japan Collaboration.

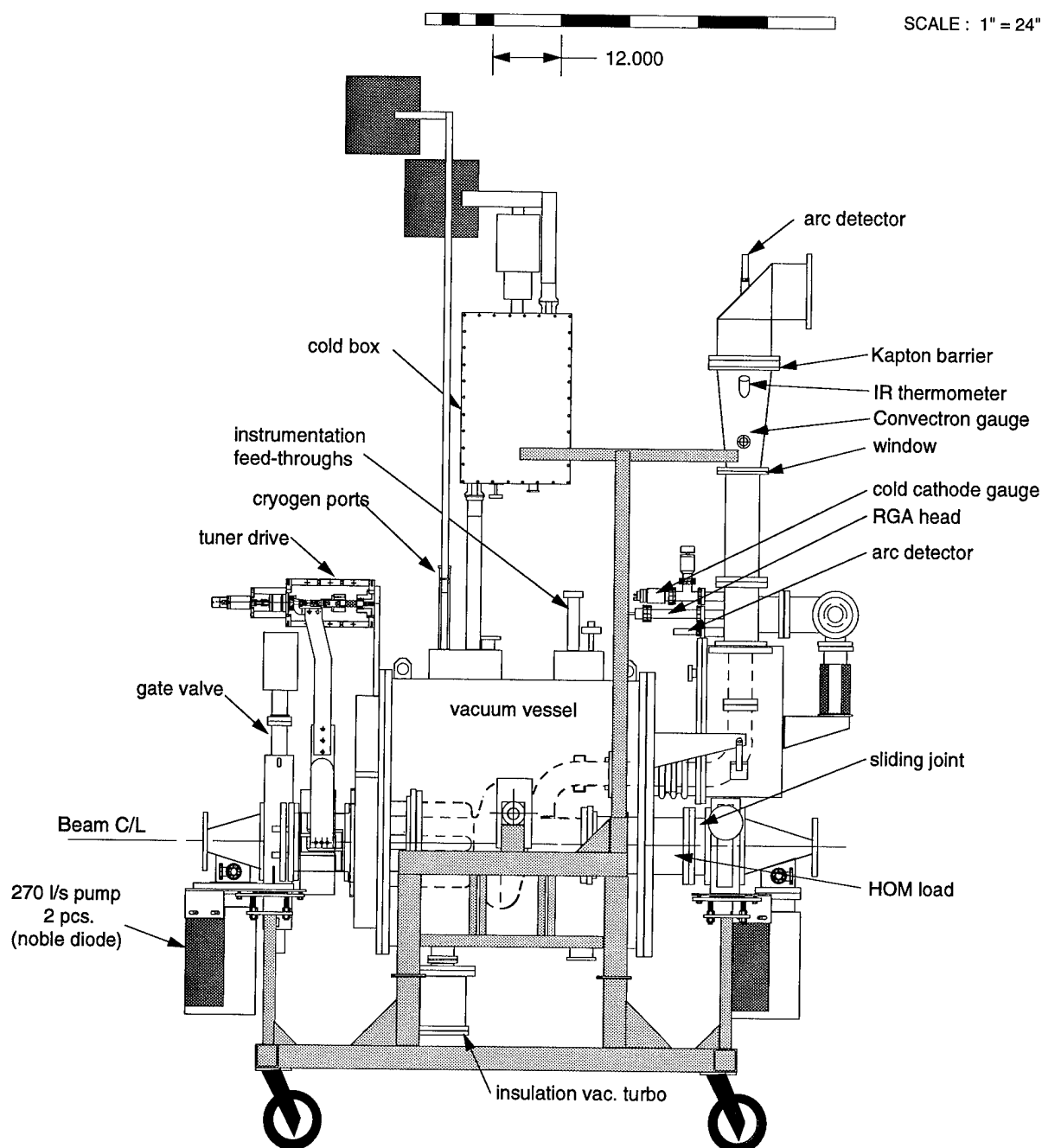


Fig. 1: Layout of all components the CESR high current beam test of the superconducting cavity.

HIGHER GRADIENT OPERATION

Fig. 3 shows the Q_0 vs. E_{acc} of the cavity as measured on-line, but without beam. We used a cold gas flow meter to continuously monitor the He mass flow, and cross calibrated the flow meter with a bath heater.

At 5.0 MV/m ($Q_0 = 10^9$) the cavity was run stably for 1/2 hour at 100 - 110 mA beam current. Between 5 and 6 MV/m the total heat load increased because of field emission to 150 watt at 6 MV/m, the highest load that the refrigeration system could handle. Our ability to process away field emission to reach gradients higher than 6 MV/m was limited by the performance of the high power window (as discussed below).

Due to higher heat loads above 5 MV/m, it was only possible to run the cavity for short periods as the cryostat pressure would rise steadily, requiring the tuner to keep moving to maintain the cavity at the right frequency. Eventually the tuner ran into its safety stop. Nevertheless we ran the cavity for short periods (few minutes) with beam currents between 95 and 120 mA and cavity gradient up to 6 MV/m.

DELIVERING BEAM POWER

As shown in Fig. 4, the maximum power delivered to the beam was 155 kW, a factor of 2 above the world record of the SRF cavity tested in TAR at 2 MV/m[1]. For the

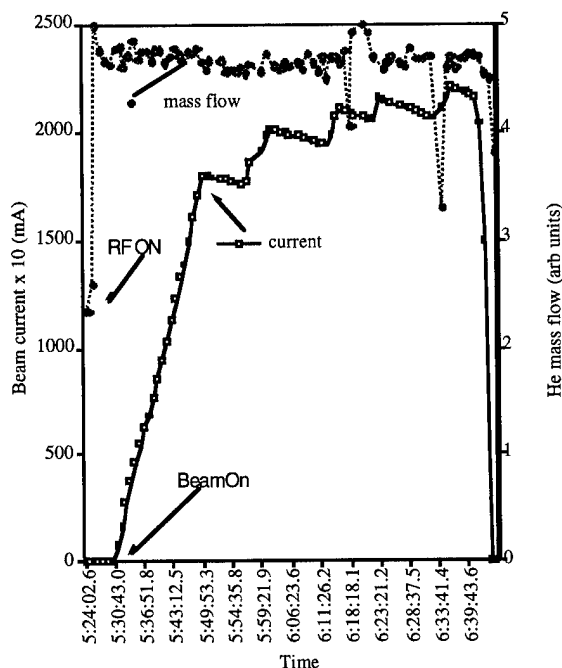


Fig. 2: Total cryogenic loss and beam current as a function of time. The cavity gradient for the record beam current run was 4.7 MV/m.

CESR/SRF high beam power test, the relative phasing between the NRF and SRF was adjusted so that the bunches went through the SRF cavity at the peak of the RF voltage. The NRF cavities were run at the synchronous phase, provided beam stability and extracted the excess power delivered to the beam.

With no beam, and with the SRF cavity off resonance, the window processed in less than one hour to 125 kW full reflected power. With beam and the cavity on resonance, processing took much longer (30 hours) and 42 trip events. Most of the trips were triggered by a vacuum degradation in the window region. Six trips were accompanied by light emission. (Note that between the high power, off line window test and the beam test, the window was let up to clean air for several days during assembly.)

OTHER TESTS

The performance of the HOM loads, the interaction of ferrite HOM loads with the beam, and beam stability studies are discussed in other papers at this conference[5,6]. Briefly, we confirmed that the loads will tolerate the power expected for a one amp in CESR-III and that there would be no instabilities due to the narrow band and broad band impedances of the SRF cavity system with ferrite HOM loads.

After choosing a new optics at 4.3 GeV, the SRF cavity was operated without NRF. The maximum beam current stored was 29 mA in 9 bunches, limited by injection into the unconventional optics. There was no evidence of instability and all regulation systems (tuner, rf amplitude, phase, bath pressure etc.) worked well. A maximum 57 mA, 9 bunch electron beam was stored at 5.3 GeV. 100 watt of synchrotron

radiation power incident on the stainless steel taper increased the temperature to 100 C and degraded the vacuum in this region from 6×10^{-9} to 6×10^{-8} torr. The cavity operated stably in the presence of this large SR dose and there was no increase in cryogenic losses.

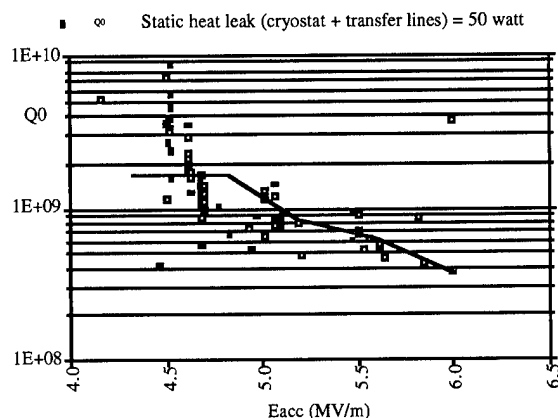


Fig. 3: Q_0 vs. E_{acc} measured on line without beam

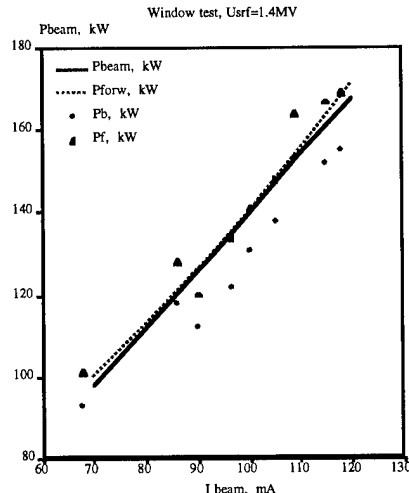


Fig. 4: Power delivered to the beam vs beam current. The operating gradient during these tests was 4.7 MV/m

CONCLUSIONS AND FUTURE

The SRF cavity stored the limit of current that CESR could deliver. For most of the test the cavity was run near 5 MV/m. A 100 mA beam was stored for a short time at 6 MV/m gradient. The input coupler and window delivered 155 kW to a 100 mA beam. A new window was received from Thomson and tested to 300 kW CW and 400 kW at 33-50% duty cycle[7]. A new cavity and a new compact cryostat are on order in preparation for a long term test in CESR in 1996. Four cavities will be installed in 1998-1999 for CESR-III.

REFERENCES

- [1] K. Akai et al, Proc. of the KEK SRF Workshop, p. 189
- [2] J. Kirchgessner, this conference.
- [3] D. Moffat et al, 1993 Part. Acc. Conf. p. 763.
- [4] D. Metzger et al, ibid [2], p. 1399.
- [5] S. Belomestnykh et al, this conference.
- [6] W. Hartung et al, this conference.
- [7] M. Pisharody et al, this conference.

DEVELOPMENT OF INPUT & OUTPUT STRUCTURES FOR HIGH POWER X-BAND TWT AMPLIFIERS *

S. Naqvi, Cz. Golkowski, G. S. Kerslick, J. A. Nation and L. Schächter, Laboratory of Plasma Studies & School of Electrical Engineering, Cornell University, Ithaca, NY 14853, USA

Abstract

Our recent research into multi-stage X-Band TWT amplifiers producing output powers of 100 – 200 MW has shown that it is essential to minimize the reflections in each stage of the amplifier in order to avoid sideband development. These reflections also cause fluctuations in the RF output power envelope. One solution to this problem is to isolate the two stages of the amplifier. Following extensive PIC code simulations and analytical work we have designed the first amplifier stage to provide beam modulation over a range ($\sim 200\text{MHz}$) of input frequencies. The second stage is a quasi-periodic structure designed to minimize reflections, and allow the radial or longitudinal RF power extraction to be distributed over an extended region. A second approach uses tapers that adiabatically reduce the loading in the output sections of the amplifier to provide a smooth, broad-band transition from the slow-wave structure to cylindrical waveguide. We are also developing mode converters that will allow extraction in TEM and subsequently in a TE mode of rectangular waveguide.

I. INTRODUCTION

Recent experiments, seeking to optimize the RF input sections of high power TWT amplifiers, have shown significant reductions in efficiency due to beam loading and reflections at impedance mismatches. As a result of these observations we are developing an two-stage amplifier in which the first stage is independently tuneable under vacuum conditions. The input section consists of two waveguide feeds separated by a short section of slow wave structure. RF power is fed into one arm, beam modulation is produced in the structure and the reflections minimized by coupling RF from the system via the output arm. The degree of beam modulation can be increased by passing the beam through additional, passive structures, separated from the input stage by a drift region which is beyond cutoff. Once tuned, the input structure bandwidth is sufficient to accommodate beam detuning, and any reflections at adjacent frequencies are not significant to the interaction.

A second method of reducing reflections in TWT amplifiers uses coupled cells that are tapered to provide a broad-band transition from the slow wave structure to a cylindrical waveguide. MAGIC simulations show that such transitions, if properly designed, can provide efficient power coupling in a coaxial extraction geometry.

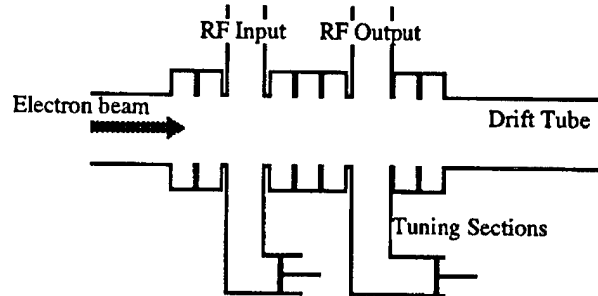


Figure. 1. Tuneable first stage of TWT amplifier.

II. TWT AMPLIFIER INPUT STRUCTURE DESIGN

The input structure has been designed, using an analytical code written at our laboratory, to maximize the input bandwidth while maintaining a useful gain to produce the desired beam modulation. This should significantly reduce problems due to electromagnetic feedback at frequencies close to the design frequency. The structure has a phase advance per cell of $\pi/2$ at an operating frequency of 9GHz for an 850kV beam. With these parameters each cell has a period, $L = 7.7\text{mm}$ a coupling iris length, $d = 1.0\text{mm}$ an outer radius, $R_{ext} = 15.3\text{mm}$ and an inner radius $R_{int} = 9.0\text{mm}$. Note that the output tube connected to the structure also has $R_{int} = 9.0\text{mm}$ which has a cutoff frequency of 12.7GHz for the TM_{01} mode. The calculated gain is 2.6dB/cm or approximately 2dB per cell, with a transmission bandwidth of $\sim 200\text{MHz}$. This is in contrast to our previous input stages, where the transmission characteristics were limited, by reflections, to a series of narrow transmission peaks, typically separated by tens of MHz , that allowed the development of unwanted sidebands. A schematic of the vacuum tuneable structure is shown in fig. 1

The input structure operation has been simulated using the MAGIC code and while the full 3-D nature of the problem can not be modeled some characteristics can be determined. Based on output from the analytical code many configurations were simulated, until the setup shown in fig. 1 was found to show the most promise. The modulation produced on an 850kV , 500A beam was examined for a range of input frequencies. This short structure is capable of producing a 7% modulation on the beam for 100kW input power. We are currently running simulations on longer structures with the aim of increasing this. The transmission is essentially 100% at 9.08GHz , and for an input power of 100kW the E_z field on axis is $\approx 1.75\text{MV/m}$. In numerous simulations the transmission efficiency remains good on both sides of this frequency but the net power injected drops, giving a 3dB transmission bandwidth of $\approx 200\text{MHz}$.

*Work supported by US Dept. of Energy

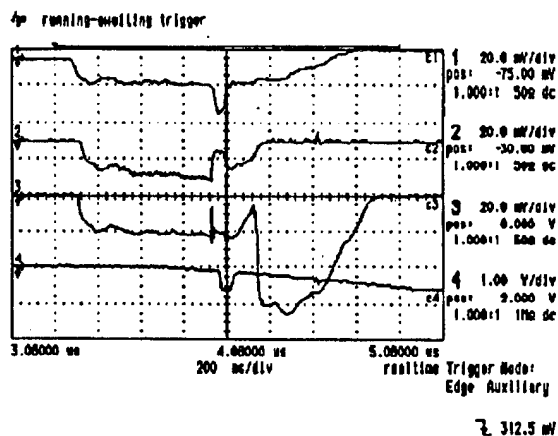


Figure 2. Microwave waveforms

III. INPUT STRUCTURE RESULTS

The cold passband and tuning characteristics have been measured using a network analyzer for a number of cell configurations. The best tuning characteristic, with the maximum transmission bandwidth is obtained with an odd number of cells between the input arm and the output arm.

The transmission and return loss for the 2-3-2 configuration have been measured using an X-Band magnetron. At the tuned frequency the peak transmission is -0.86 dB , i.e. 82% of the input power is coupled through the output arm, with a 3 dB width of $\approx 100\text{ MHz}$. The return loss at this frequency is -23.4 dB , i.e. less than 1% of the input power is reflected.

The input structure has been operated using a 850 kV , 500 A , 50 ns electron beam and initial results are encouraging. Figure 2 shows the input signal combined with the 50 ns diode voltage pulse (top trace). Trace 2 is the signal transmitted along the output waveguide, showing the power absorbed during beam passage through the slow wave structure. Trace 3 shows the signal reflected from the structure. The level of this signal does not change significantly until 100 ns after the beam pulse. Trace 4 shows the beam current measured by a Rogowski coil located in the drift tube 25 cm beyond the slow wave structure.

The signal from an output horn attached to the structure by a 25 cm length of drift tube, which is cutoff at this frequency, shows that beam modulation has been achieved. As the modulated beam propagates through the non-adiabatic tube-horn transition the RF signal is reconstructed from the space charge modulated beam. The measured signal is heterodyned with a fixed frequency local oscillator. The FFT of this mixed signal shows that the output is single frequency and follows the input magnetron frequency over the full $8.9 - 9.1\text{ GHz}$ bandwidth of the input structure.

IV. TAPERED SLOW-WAVE STRUCTURES

An extensive study using the MAGIC simulation code has shown that reflections in all stages of an amplifier can be minimized by using correctly designed tapered transition sections. These tapers provide broad-band transitions to a circular TM_{01} mode, and the reduction in reflections also minimizes fluctua-

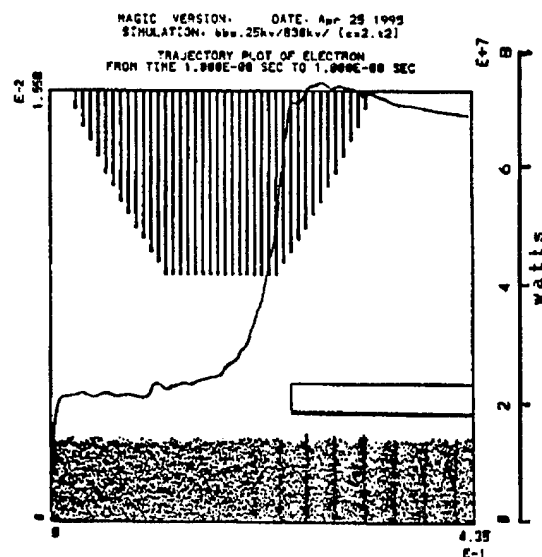


Figure 3. MAGIC simulation of tapered TWT with coaxial power extraction

tions in the output power level. The phase velocity increases from less than c in the slow-wave structure to greater than c in the uniform circular guide. At some point within the tapered region, the phase velocity equals c and close to that point, a coaxial inner conductor can be placed to extract the RF power. Once the beam is within this conductor, it does not interact with the RF flowing in the TEM mode of the coaxial line and can be safely dumped anywhere within the inner conductor. The results of one MAGIC simulation using a 830 kV , 550 A beam are presented in fig. 3. Electron trajectories are shown as the pencil beam propagates through the tapered slow wave structure and into a cylindrical beam dump that is cutoff to the RF signal. The beam enters the left boundary with a 25 kV voltage modulation. Following the interaction region the axial Poynting flux (time-averaged over one RF period, and shown as the solid line) shows a power flow of $\sim 50\text{ MW}$ in a TEM mode in the coaxial extraction section. The peak power can be increased to about $\sim 100\text{ MW}$ if the input modulation is increased or more cells are added to the structure.

V. HIGH EFFICIENCY OUTPUT STRUCTURES

We have investigated the interaction in traveling wave output structures which are expected to generate radiation at an efficiency of 50% and higher. Two different configurations, as described above, are under consideration: (i) Transverse extraction, where the electromagnetic power is extracted perpendicular to the beam flow and therefore an abrupt change in the direction of the power flow is required. Since successful operation requires tuning, the abrupt change in geometry makes this system sensitive to any change in the operation parameters. (ii) Longitudinal extraction, in which case the radiation power is extracted parallel to the beam and the electromagnetic field is gradually decoupled from the beam. This extraction results in the conversion of the TM mode into a TEM mode; at a later stage the TEM can be converted into the TE mode.

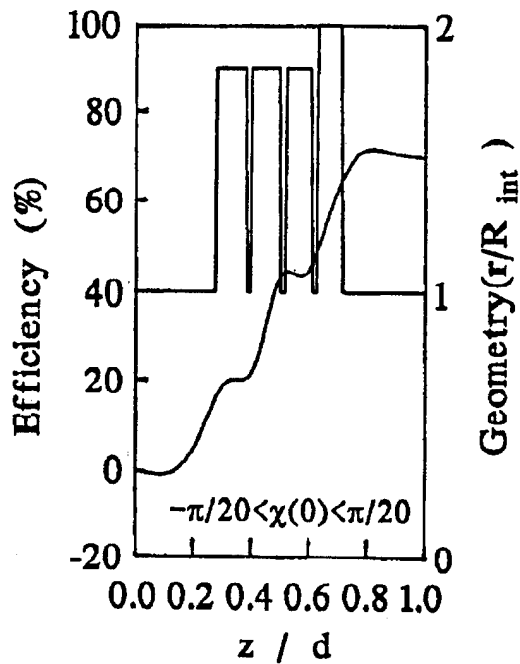


Figure. 4. The variation of the *RF* conversion efficiency in space for a narrow ($-9^\circ < \chi(0) < 9^\circ$) initial phase distribution.

In both configurations we use the formulation of beam-wave interaction in quasi-periodic structures which was developed recently [1], [2]. This is a method which permits analytic calculation of the characteristics of a disk loaded structure with significant variations in the geometry. In principle, once the structure is no longer periodic, the field can not be represented by a single wavenumber. However, in case of adiabatic variations the characteristics of the structure (phase velocity, group velocity and interaction impedance) are assumed to be determined entirely by the geometry of the local cell. This is not the case when significant changes in geometry are required to achieve efficient radiation extraction. This is to say that a non-adiabatic local perturbation of geometry affects *global* electromagnetic characteristics, and a change in a given cell affects the interaction impedance or the group velocity several cells before and after the point where the geometry was altered.

The model consists of a cylindrical waveguide to which a set of pill-box cavities and a radial arm are attached. In principle the number of cavities and arms is arbitrary. The boundary condition problem is formulated in terms of the amplitudes of the electromagnetic field in the cavities and arms. The elements of the matrix which relates these amplitudes with the source term are analytic functions - thus no a-priori knowledge of the functional behavior of the electromagnetic field is necessary. We examined [1] the homogeneous electromagnetic characteristic of quasi-periodic structures; the technique was further developed to include Green's function and the beam-wave interaction within the framework of the linear hydrodynamic approximation for the beam dynamics. It was shown that the method [2] combines the features of the beam-gap (local) interaction, as in a klystron, with those of the beam-wave (distributed) interaction in a traveling wave structure. The linearity of the model above is a serious limitation for a high efficiency interaction, since it is valid only for

small variations from the initial average velocity. For this reason, the tools developed previously were used to formulate the beam-wave interaction within the framework of macro-particle dynamics, which permits description of large deviation from average velocity. It was shown that the interaction is controlled by the *matrix interaction impedance*, which can be conceived as a generalization of the scalar interaction impedance concept, used for uniform structures. The design and analysis of a high efficiency (70%) traveling wave section is described in detail elsewhere [3]. Figure 4 shows the *RF* conversion efficiency in a quasi-periodic output structure, where the cell length decreases from 6.5mm in the first cavity to 5.4mm in the radial output arm. Results from the formulation of the interaction in the case of longitudinal extraction will be presented elsewhere.

References

- [1] L. Schächter and J. A. Nation, *Appl. Phys. Lett.* **63**, 2441 (1993).
- [2] L. Schächter and J. A. Nation, *Phys. Plasmas* **2**, 889 (1995).
- [3] L. Schächter, submitted for publication in *Phys. Rev. E*.

CHARACTERIZATION OF A KLYSTRODE AS A RF SOURCE FOR HIGH-AVERAGE-POWER ACCELERATORS*

D. Rees, D. Keffeler, W. Roybal, and P. J. Tallerico
Los Alamos National Laboratory, Los Alamos, NM 87545 USA

Abstract

The klystrode is a relatively new type [1]–[4] of RF source that has demonstrated dc-to-RF conversion efficiencies in excess of 70% and a control characteristic uniquely different from those for klystron amplifiers. The different control characteristic allows the klystrode to achieve this high conversion efficiency while still providing a control margin for regulation of the accelerator cavity fields. We present test data from a 267-MHz, 250-kW, continuous-wave (CW) klystrode amplifier and contrast this data with conventional klystron performance, emphasizing the strengths and weaknesses of the klystrode technology for accelerator applications. We present test results describing that limitation for the 250-kW, CW klystrode and extrapolate the data to other frequencies. A summary of the operating regime explains the clear advantages of the klystrode technology over the klystron technology.

I. INTRODUCTION

The klystrode combines attributes from both the gridded-tube and klystron technologies, with an input structure borrowed from gridded-tube technology and a klystron-like output cavity. It is a density-modulated amplifier. Figure 1 is a schematic of the klystrode.

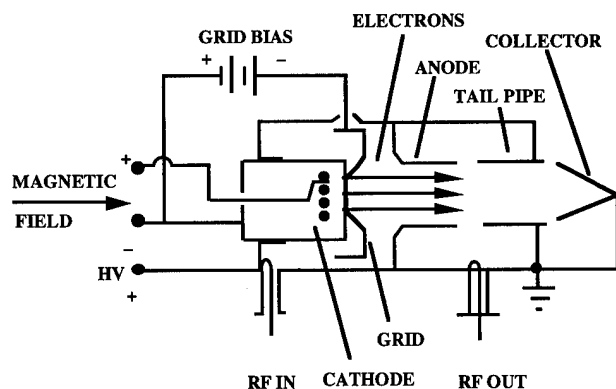


Figure 1: Schematic of the klystrode amplifier tube.

Since the dc acceleration region is separate from the power extraction region in the klystrode, it has transit-time advantages over conventional gridded tubes. Because it is a current-modulated device, the current bunch is more nearly monoenergetic and high efficiencies can be achieved without the stability issues surrounding high-efficiency klystrons. The primary klystrode market is UHF television transmission,

where the klystrode provides up to 60 kW of peak power. Two high-power klystrode developments promise the extension of TV technology to power levels that are of interest to the particle accelerator community. The first development produced a pulsed klystrode at 425 MHz, which achieved in excess of 750 kW peak at a 10% duty factor [1]. The klystrode gain was in excess of 20 dB, and an efficiency greater than 70% was demonstrated. The second high-power klystrode development provided a 250-kW continuous-wave (CW) klystrode at 267 MHz and is the basis for the information presented in this paper [4]. This klystrode was originally developed by Varian for the Chalk River Nuclear Laboratories of Atomic Energy of Canada Limited as a power source for a radio frequency quadrupole accelerating cavity [5]. The program has since moved to Los Alamos National Laboratory, where the system is being used as a test stand for advanced accelerator applications [6]. Our interest in high-power klystrons is motivated by their high efficiency and their control characteristic. All high-power klystrode developments have achieved an efficiency in excess of 70%, which is better than that for klystrons currently in accelerator service; and unlike the klystron, it is possible to modulate the input signal to the klystrode and vary the output while still achieving high efficiency.

In accelerator service, the high-power amplifier is part of a fast control loop, which maintains the accelerating cavity field amplitude and phase at a desired set point. The klystron provides its maximum efficiency only at saturation, where the power transfer curve is essentially flat, making control by amplitude modulation of the drive signal impossible. In order to exercise control over the cavity field, we must typically operate the klystron with a control margin (the amount of operation below saturation) of 10% to 20%. A 20% control margin decreases the efficiency of a klystron operating at 70% efficiency at saturation to 56% at the nominal operating point. In contrast, we demonstrate that the klystrode can provide a relatively constant, high efficiency over the last 30% of its power capability.

One advantage of the klystron over the klystrode is its high gain. In many klystron-based accelerator RF systems a small solid-state amplifier drives a klystron with 45–55 dB of gain. The klystrode gain of 20–22 dB increases transmitter complexity and requires an intermediate amplification stage for high-power applications; however, the klystrode does not require a modulator, as does a klystron, for pulsed service because it is configured as a class B amplifier. When large CW accelerators lose their vacuum, they are often pulse-conditioned, and with klystrons expensive modulators are sometimes built solely for conditioning. Such modulators are not required for the klystrode. Klystrons also have demonstrated much higher peak and average power capabilities than have klystrons.

As an additional advantage of klystron technology, the drive signal is applied to a modulating gap that is not collocated with the cathode surface as is true with the

*Work supported by the United States DOE, contract W-7405-Eng-36.

klystron. A portion of the klystron drive power is dissipated on the cathode surface, providing an additional source of cathode heating. Because of the relatively low gain, this characteristic may ultimately limit the average power capability of the klystron without additional technology advances in the input structure or cathode material.

II. EXPERIMENTAL RESULTS

Data representing the klystron's linearity, phase variation with output power, efficiency variation with output power, and bandwidth is presented in Figures 2-5. The data was taken at 267 MHz. We integrated power meters, a swept-frequency source, and sampled values of beam current and voltage into a LabVIEW-controlled automated test to generate the power transfer, bandwidth, and efficiency plots. We used a network analyzer to measure the phase variation with input power, which we then converted to a plot of phase variation with output power by using the power transfer characteristic. The klystron transmitter is a three-stage transmitter with the 250-kW klystron as the final stage. The data presented here are only for the final klystron stage. The curves in Figures 2 and 3 illustrate the klystron power-transfer curve and phase response. Figure 4 shows the klystron efficiency as a function of output power. Figure 5 illustrates the klystron bandwidth. Inspection of Figure 4 shows that the klystron provides almost constant efficiency from 180 to 250 kW. Inspection of Figure 2 shows that the power-transfer characteristic is relatively linear in this region. Taken together, Figures 2 and 4 support the earlier assertion that the strength of the klystron for accelerator service is its capability to provide simultaneously high efficiency and a control margin for regulating accelerator cavity fields.

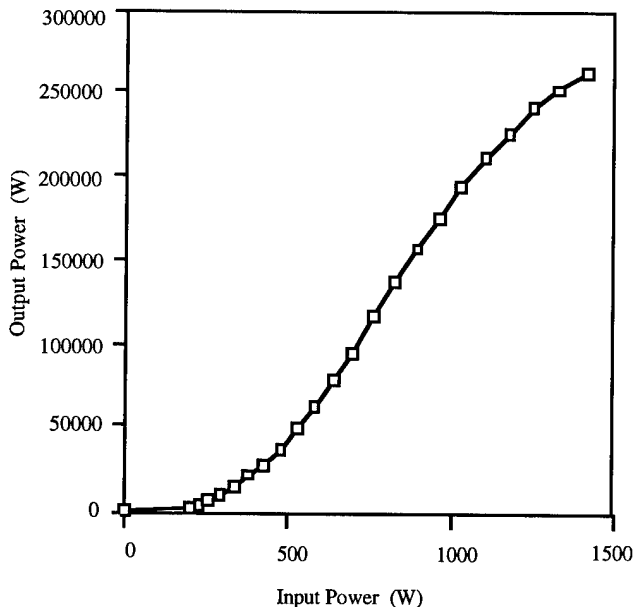


Figure 2: Klystron power transfer characteristic.

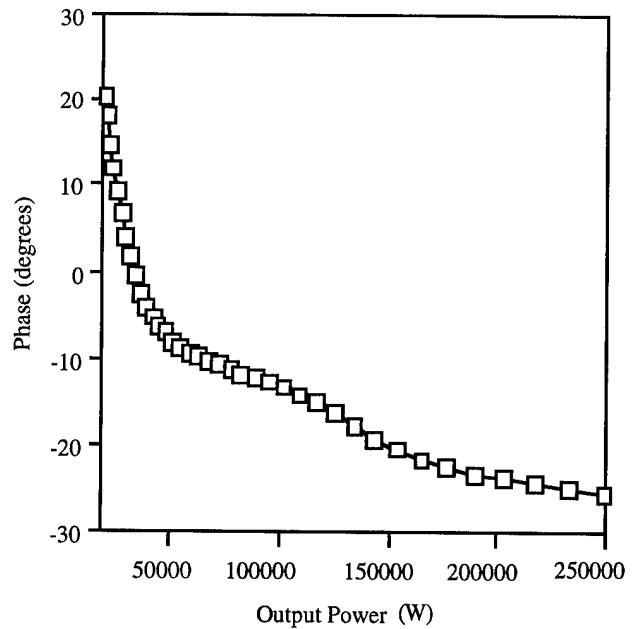


Figure 3: Klystron phase response.

Figure 6 illustrates the output power versus filament power for the 250-kW klystron at three nominal output power levels. Tests were performed at nominal output powers of 60 kW, 180 kW, and 234 kW over the filament power range of 175 to 300 W. The filament power was controlled by varying the filament current. The klystron operates at a nominal value of filament power slightly larger than 250 W (the third data point on each curve).

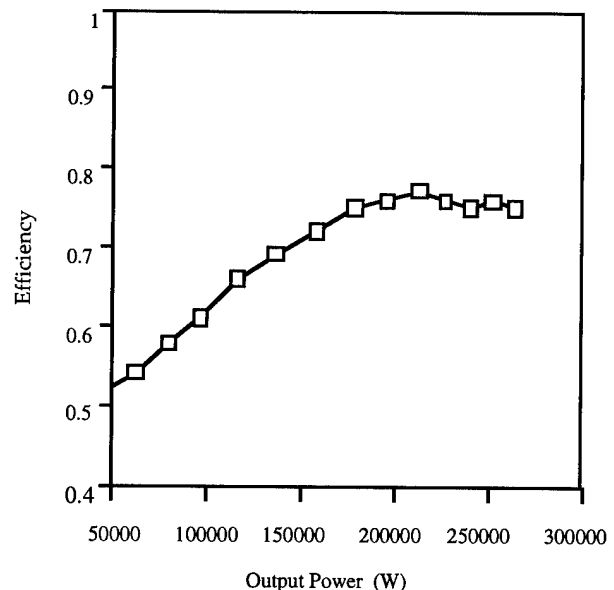


Figure 4: Klystron efficiency as a function of output power level.

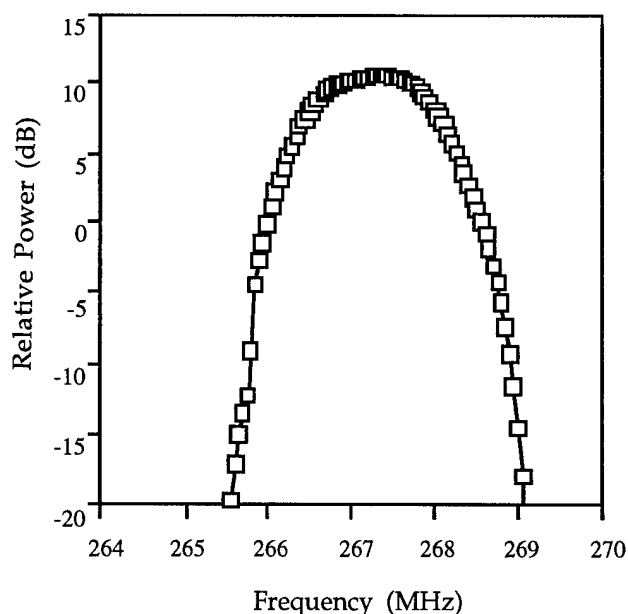


Figure 5: Klystrode bandwidth.

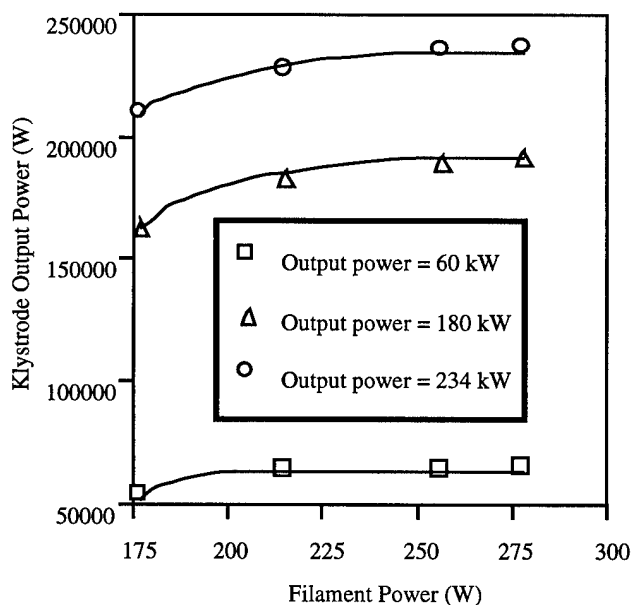


Figure 6: Klystrode output power vs. filament power for three output power levels.

The test results in Figure 6 were intended to quantify the level of filament heating. Inspection of the 180-kW and 234-kW curves shows that the knee is at approximately the same filament power level even though the beam current is different by 30%. This could lead to the conclusion that an appreciable amount of cathode heating is taking place, but more tests are necessary to further quantify this effect.

III. CONCLUSION

Because of its high efficiency, the variation of its efficiency with output power, and its linearity, we have demonstrated the klystrode to have performance

characteristics that are very appealing for accelerator RF systems. The relatively constant efficiency over a broad range of output power provides a control margin for accelerating cavity fields without the efficiency penalty that must be suffered with klystron amplifiers. The smoothly varying, monotonic phase characteristic of the klystrode is easily controllable, and the magnitude of the phase variation provides abundant phase margin for the other components of the system that contribute to phase variation (capacitor bank droop, beam effects, etc.). We believe that the klystrode has proved its viability as a high-power source at frequencies less than 300 MHz for output powers up to 250 kW CW. It is extremely attractive for CW service because of its high operating efficiency. The klystrode also appears to be a very attractive candidate for low-frequency superconducting accelerator applications that require reduced power levels.

At frequencies in excess of 1 GHz or for high-power, short-pulse service (>500 kW, $<10\%$ duty factor) where efficiency is not an issue, we believe the klystron to be the RF tube of choice. Its high gain and proven reliability will reduce total costs. It also tends to be higher perveance than the klystrode, decreasing high-voltage power supply cost.

We are concerned that at higher average power levels, the klystrode technology does not have an appreciable operating history on which to base reliability estimates. We have approximately 664 high-voltage hours on the 250-kW CW klystrode at Los Alamos, and we have had to process the grid at least three times to remove material deposited on the grid by the cathode. We are afraid that the cathode is being overheated by the RF drive power and that the result will be a reduced tube life.

IV. REFERENCES

- [1] Donald H. Preist and Merrald B. Shrader, "A high-power klystrode with potential for space applications," *IEEE Trans. Electron Devices*, vol. 38, no. 10, October 1991.
- [2] Donald H. Preist and Merrald B. Shrader, "The klystrode - an unusual transmitting tube with potential for UHF-TV," *Proc. IEEE*, vol. 70, no. 11, November 1982.
- [3] C. Loring, Jr. and M. Shrader, "The klystrode, a new high efficiency, high-power electron tube for UHF industrial applications," *J. Microw. Power Electromagn. Energy*, vol. 28, no. 3, 1993.
- [4] M. B. Shrader, D. H. Preist, and R. N. Tornoe, "The 267 MHz high-power CW klystrode amplifier," *Int. J. High Speed Electron. Syst.*, vol. 4, no. 4, 1993.
- [5] J. Y. Sheikh et al., "Operation of a high-power CW klystrode with the RFQ1 facility," *Proceedings of the 1993 IEEE Particle Accelerator Conference*, vol. 2, p. 1175.
- [6] M. Lynch, D. Keffeler, D. Rees, W. Roybal, "Installation and test results of a high-power, CW klystrode amplifier at Los Alamos National Laboratory," *Proceedings of the 1994 International Linac Conference*, vol. 1, p. 451.

CHOPPERTRON II

T.L. Houck, G.A. Westenskow, Lawrence Livermore National Laboratory, Livermore, CA 94550,*
J. Haimson and B. Mecklenburg, Haimson Research Corporation, Santa Clara, CA 95054 USA†

We present experimental results of a version of the Choppertron microwave generator designed to work with the high emittance beam of the Advanced Test Accelerator (ATA). Simulations showed that a 800-A, 120π cm-mrad beam (typical of ATA), could produce 800 MW of rf (11.4 GHz) power using two 12-cell, traveling-wave output structures. Funding constraints prevented final tuning of the modulator system and limited the experiment to 530 MW in narrow pulses. Over 400 MW were extracted from a single output structure through fundamental waveguide. Beam breakup was successfully suppressed with >800 amperes of current transported through the extraction section.

1. INTRODUCTION

We have performed a series of experiments over the past several years to study the application of induction accelerator technology to rf power production for a linear collider in the Two-Beam Accelerator concept. [1,2] Areas of study included high-power (several hundred megawatts at 11.4 GHz) output structures, multiple output structures, transverse beam instabilities caused by excitation of higher order modes (HOM), phase coherency, amplitude stability, and the acceleration of a modulated beam. The Choppertron II completed our microwave experiments at the ATA facility and was designed primarily to expand the limits of peak power extraction and suppression of HOMs.

Figure 1 is a schematic of the Choppertron II. The modulator section has a multi-cavity deflection structure and two off-axis apertures. A schematic of the deflection structure is shown in Fig. 2. The modulator operates by deflecting the beam in the horizontal plane with the 5.7 GHz deflection structure. This causes the B_z -field-immersed beam to describe semi-helical trajectories that scan across a pair of off-axis apertures in a collimator located between the drive cavity and the rf output structures. The 5.7 GHz spatially modulated dc beam incident on the collimator is transformed into a phase coherent, amplitude modulated beam at 11.4 GHz. The axial magnetic field is matched to the beam's energy and emittance to keep the desired beam radius and betatron wavelength for efficient operation. The output section has two 12-cell traveling-wave structures. Each has de-Qing circuits built into the first two cells to extract power from the HOMs, and a damping cavity after the output coupler.

*The work was performed under the auspices of the U.S. Department of Energy by Lawrence Livermore National Laboratory under contract W-7405-ENG-48.

†Work supported by U.S. Department of Energy SBIR Grant No.DE-FG03-92ER81285.

II. EXPERIMENTAL LAYOUT

A schematic of the experiment is shown in Fig. 3. The injector is operated at ~ 2.1 MV producing a 6-kA, 80-ns fwhm, current pulse. A 2-cm aperture, 1-m long collimator immersed in a solenoidal field reduces the current to 1-kA and removes low energy electrons from the front/back of the pulse (effective fwhm < 50 ns). The beam energy is increased to 4.6 MeV with 10 ATA induction cells. The beam is deflected upon entering the Choppertron modulator section and swept back and forth across the two apertures. This reduces the dc current by about half, but produces a well modulated beam. A dc deflection magnet located around the deflection structure is used to assist with initial magnet settings. The solenoidal field is increased at the entrance of the rf output section to limit the beam motion to within the 16-mm aperture of the output structures.

The dc current component is measured with resistive wall current monitors before and after the Choppertron. RF loops inserted in a safety collimator in front of the deflection structure measures the current entering the structure. Resistive dividers on the induction modules are used to determine gap voltage and infer beam energy. The dc deflection magnet also functions as an energy spectrometer. The amplitude and frequency of the rf power entering and exiting the deflection structure is monitored. The output power pulses are sampled with 56 db directional couplers and measured using Schottky diode detectors. Phase coherency and power spectra of the pulses is also measured.

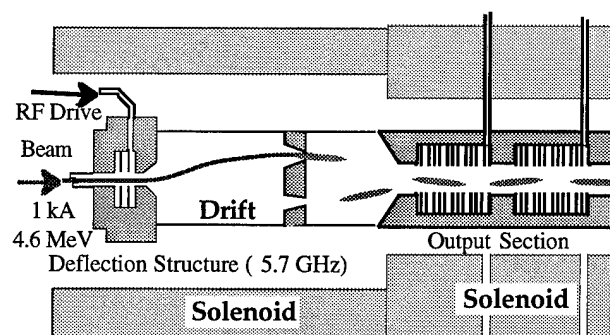


Figure 1. Schematic of Choppertron II.

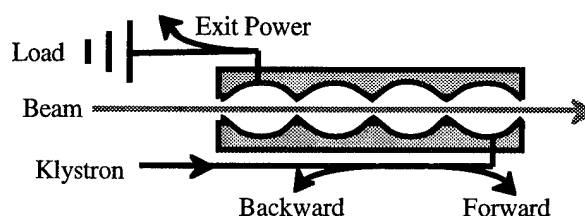


Figure 2. Schematic of the deflection structure.

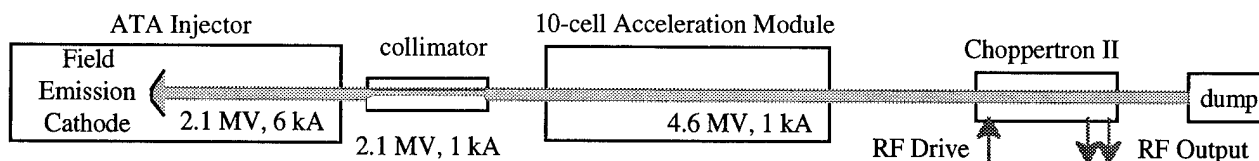


Figure 3. Schematic of the experimental layout.

III. EXPERIMENTAL RESULTS

A. Deflection Cavity Measurements

The original Choppertron [3] had been designed for a 30π cm-mrad beam that could have been produced with an induction accelerator using a dispenser cathode. To accommodate the ATA beam, modifications were made to the modulator that required increasing the solenoidal field and shortening of the drift distance. A significant increase of the rf deflection fields was also needed. The new deflection structure requires about 2 MW of forward rf power at 5.7 GHz. The rf energy stored in a TM_{110} -like resonant mode deflects the beam as it passes through the structure. The beam then drives the resonant mode increasing the deflecting fields to the desired level.

A bi-directional coupler was used to measure forward and backward propagating power with respect to the deflection structure input port. The observed backward propagating power from the input port, with and without beam, is shown in Fig. 4. The drive power pulse started about 200 ns prior to the ≈ 50 ns beam pulse to allow for transients. The effect of beam loading is obvious.

A desired characteristic of the deflection system is that the beam-generated power be proportional to the drive power. The peak reflected power from the input port for two different beam loadings as a function of drive power is shown in Fig. 5. A major difficulty is avoiding other resonance's and adjusting the beam loaded frequency of the desired resonance. The spectrum analysis of the power generated in the deflection structure by the beam indicated

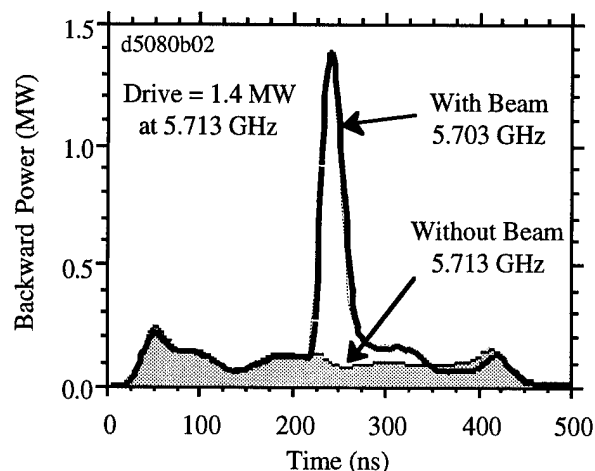


Figure 4. Backward power from the deflection structure indicated substantial power was generated by beam loading.

a resonant frequency of 5.703 GHz. This is the cutoff frequency for the coupling port.

B. Output Power Pulses

Low power conditioning of the Choppertron, at output power levels of 10 to 20 MW, was accomplished using beam currents below 200 A. As the current is increased, the shape of the output power pulses, and transmitted current pulse measured at the beam dump, changed. Figure 6 shows typical pulses from the first output structure for several different currents. The second output and transmitted current pulses had similar shapes. No evidence of electrical breakdown or transverse instability was noted in the output structures to explain the shortening of the pulses.

At higher currents (> 300 A), the driving frequency of the deflection structure effected the output pulse shape. Figure 7 shows typical pulses from the second output structure at different drive frequencies. Maximum power levels occurred at a drive frequency of 5.709 GHz, dropping rapidly with lower, and gradually with higher, frequencies. Pulse shape variation occurred for different currents and magnetic transport, but the trend is consistent with Fig. 7, i.e. the peak power would occur later with respect to the current pulse with increased frequency. The pulse from the first output did not display the notch shown for the 5.709 GHz pulse in Fig. 7.

Below drive frequencies of 5.718 GHz, up to twice the power could be extracted from the first structure than from the second. Above 5.720 GHz, about equal powers were extracted. Maximum powers measured were 426 MW for

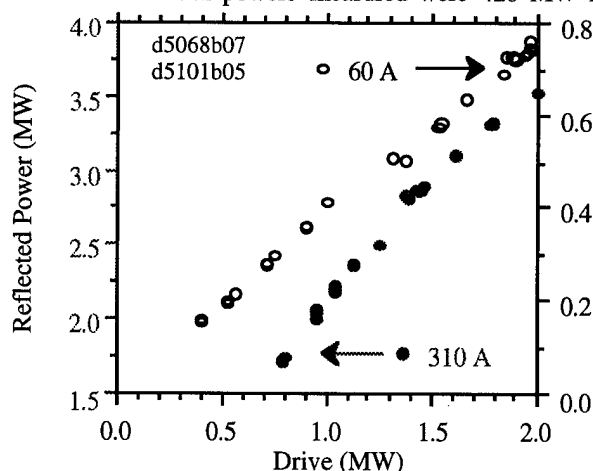


Figure 5. Power generated by beam loading in the deflection structure varied linearly with drive power.

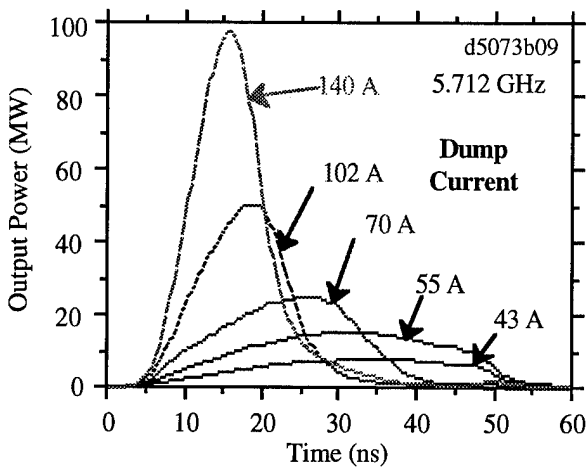


Figure 6. Power pulses from the first output structure.

the first and 260 MW for the second. Combined totals of over 500 MW, e.g. $379 + 151 = 530$ and $285 + 231 = 516$, were obtained. These powers were associated with pulse shapes similar to the narrower pulses shown in Fig. 6 and 7.

C. Frequency Analysis

Power spectra were made of rf pulses related to the deflection structure and output power structures. Initial measurements on the deflection structure indicated resonant peaks during beam loading at 5.689 and 5.722 GHz (drive frequency = 5.714 GHz). After tuning, resonant peaks were measured with beam at 5.703 and 5.713 GHz (drive frequency = 5.713 GHz). Typical spectra for pulses from each of the output structures are shown in Fig. 8. At lower drive frequencies, the output power is primarily at 11.393 GHz. Increasing the drive frequency leads to the power being split in two frequency components.

D. Comments on Transverse Instabilities

Over 800 A was transported through Choppertron II using the dc deflector magnet with no indication of beam disruption due to transverse instabilities. This is an important accomplishment due to the number of cells involved

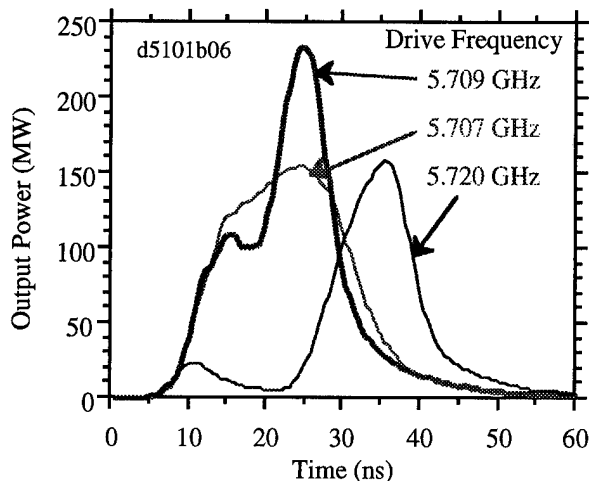


Figure 7. Power pulses from the second output structure.

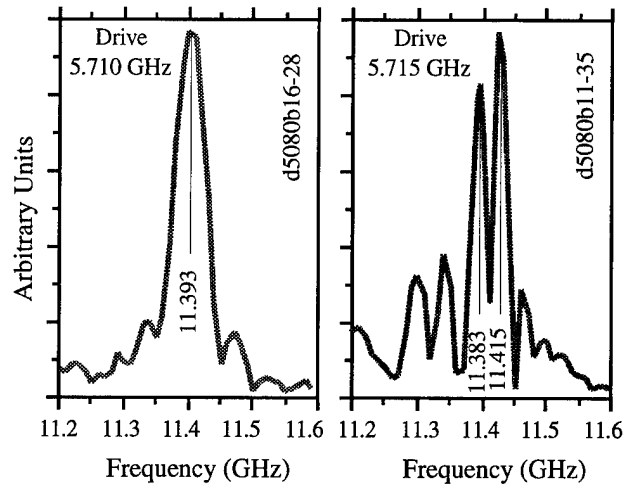


Figure 8. Power spectra of rf output pulses.

the fact that the two output structures are identical, and that the beam is deflected off-axis prior to the output section.

IV. CONCLUSIONS

Extracting 426 MW from a single output structure into fundamental waveguide nearly doubled the power level achieved with the original Choppertron using the same output structure [2]. This peak power increase is attributed to improved vacuum conditions and increased rf current from the new modulator. While high peak powers were attained, the pulses were narrow and we had difficulties with mode purity at higher drive frequencies. Several corrective actions are possible, e.g. decreasing the separation of the off-axis apertures to reduce the necessary beam deflection and lessen excitation of unwanted resonances, and additional tuning of the deflection structure to reduce the strength of these resonances. Tuning of the deflection structure after initial testing substantially reduced the effect of these resonances in the final experiment. Unfortunately, we are unable to perform further experiments due to funding constraints. The output structures may be used in future experiments on relativistic klystrons. [4]

V. ACKNOWLEDGMENTS

We thank A. Sessler and S. Yu for their insights and assistance. A. Meyers and S. Petz provided technical support for the experiment.

VI. REFERENCES

- [1] A. Sessler and S. Yu, *Phys. Rev. Lett.* **54**, 889 (1985).
- [2] G. Westenskow and T. Houck, *IEEE Trans. on Plasma Sci.*, **22**, 750 (1994).
- [3] J. Haimson and B. Mecklenburg, 1989 PAC IEEE Conf. 89CH2669-0, p. 243.
- [4] Westenskow, et al., "Design of a Relativistic Klystron Two-Beam Accelerator Prototype," this conference.

THE RESISTIVE-WALL KLYSTRON AS A HIGH-POWER MICROWAVE SOURCE

Han S. Uhm, Naval Surface Warfare Center, Silver Spring, MD 20903-5640

A novel high-power high-frequency klystron is presented in which a relativistic electron beam is modulated at the first cavity and propagates downstream through a resistive wall. Because of the self-excitation of the space charge waves by the resistive-wall instability, a highly nonlinear current modulation is accomplished. Due to the relatively large growth rate of the instability, the required tube length of the klystron is short for most applications.

I. INTRODUCTION

Recent experiments with the relativistic klystron amplifier (RKA) indicate that the frequency and efficiency of current modulation are monochromatic and almost 100 percent in appropriate system parameters¹. One of the main issues in the RKA is enhancement of power at high frequency. The size and opening of cavities in the RKA should be reduced, to increase the excitation frequency. Therefore, a high-power high-frequency klystron amplifier has inherent problems due to reduced cavity size, including electron emission and ac beam loading at the gap opening of cavities. To minimize these problems, we propose to eliminate the intermediate cavities and to modulate beam current by means of the resistive-wall instability. In the conventional klystron, the beam energy is modulated at the first cavity and this modulation is reinforced in the intermediate cavities before the beam segments arrive in the extraction cavity.¹ In the resistive-wall klystron, the energy modulation at the first cavity initiates self-excitation of the space charge waves in the resistive medium of the wall. Because of the self-excitation of these waves, a relatively low-level modulation is needed at the first cavity. A highly nonlinear current modulation of the electron beam is accomplished as the beam propagates through the resistive tube. The frequency of the resistive-wall instability is lower than the cut-off frequency in the waveguide and the microwaves cannot propagate through the drift section by themselves. Thus, these self-excited space charge waves move together with beam segments, further modulating their current. The resistive-wall instability has been interesting subject to other areas, including circular high energy particle accelerators and heavy ion inertial fusion.

II. RESISTIVE-WALL INSTABILITY

The system configuration of the resistive-wall klystron consists of a relativistic electron beam with radius R_b propagating through a resistive tube. A strong, externally applied magnetic field is needed to confine the beam electrons radially.

The radius of the grounded resistive tube in the klystron is denoted by R_w . This drift tube is wrapped by a cylindrical conductor with radius R_c . The conductivity of the resistive medium in the range of $R_w < r < R_c$ is denoted by σ . The skin depth δ of the resistive medium is assumed to be much less than its thickness ΔR , i.e., $\delta = c/(2\pi\mu\sigma\omega)^{1/2} \ll \Delta R = R_c - R_w$, where μ is the permeability of the resistive medium, ω is the oscillation frequency of the electric field, and c is the speed of light in vacuum. The first cavity in the klystron is excited by input microwaves with frequency ω . We also assume the initial condition that the beam segment labeled by $\theta = \omega t_0$ passes through the opening of the first cavity at time $t = t_0$. Note that the first cavity is located at $z = 0$. Then the energy gain $\Delta\gamma mc^2$ of the segment θ is expressed as

$$\Delta\gamma = -e(\Delta\phi/mc^2) \sin \theta, \quad (1)$$

where $\Delta\theta$ is the maximum voltage at the cavity, and $-e$ and m are the charge and rest mass of electrons, respectively. The energy gain or loss at the first cavity introduces the initial perturbation needed in the resistive-wall instability.

Any charge and current deviations from their equilibrium values will generate the axial component $E_z(r, z, t)$ of the perturbed electric field downstream. This perturbed electric field is obtained from the Maxwell equations. After a straightforward algebraic manipulation, we obtain

$$\begin{aligned} \frac{1}{r} \frac{\partial}{\partial r} \left(\frac{r}{\mu} \frac{\partial}{\partial r} E_z \right) + \frac{1}{\mu} \frac{\partial^2}{\partial z^2} E_z - \frac{\epsilon}{c^2} \frac{\partial^2}{\partial t^2} E_z \\ - \frac{4\pi\sigma}{c^2} \frac{\partial}{\partial t} E_z = 4\pi \left(\frac{1}{c^2} \frac{\partial}{\partial t} J_z + \frac{1}{\mu} \frac{\partial}{\partial z} \rho \right), \end{aligned} \quad (2)$$

where J_z is the axial component of the beam current density.

In order to make the subsequent calculation analytically simple, we assume that $\mu\epsilon\beta^2 \gg 1$, where μ and ϵ are the permeability and dielectric constant, respectively, of the resistive medium, and βc is the instantaneous beam velocity. This inequality can easily be satisfied for a broad range of system parameters. In addition, the resistive medium is conductive rather than dielectric, satisfying $c/R_w\omega \gg (\delta/R_w)^2(\mu\epsilon)^{1/2}$. Thus, the term proportional to $\epsilon(\partial^2/\partial t^2)$ in Eq. (2) is negligibly small in comparison with the term proportional to $4\pi\sigma$. The charge and current densities in the right-hand side of Eq. (3) are approximated by

$$\frac{\partial J_z}{\partial t} = \omega \left(\frac{\partial J_z}{\partial \theta} \right), \quad \frac{\partial \rho}{\partial z} = -\frac{\omega}{\beta c} \left(\frac{\partial \rho}{\partial \theta} \right), \quad (3)$$

where use has been made of the definition $\theta = \omega t_0$. Because the phase velocity of the perturbations in a specified beam

¹ This work was supported by IR Fund at NSWC.

segment is very close to the beam velocity, the charge density is approximately related to the current density by $J_z = \beta c \rho$. Assuming that the radial variation of the axial electric field dominates its axial variation, which is common in the relativistic klystron application, we can neglect the terms proportional to $(\partial^2 / \partial z^2)$ in Eq. (2).

Making use of all these assumptions, Eq. (2) is simplified to

$$\frac{1}{r} \frac{\partial}{\partial r} \left(r \frac{\partial E_z}{\partial r} \right) - \frac{4\pi\sigma\mu}{c^2} \frac{\partial}{\partial t} E_z = \frac{4\pi\mu}{c^2} \frac{\partial}{\partial t} J_z, \quad (4)$$

for the electric field in the range of $R_w < r < R_c$ and

$$\frac{1}{r} \frac{\partial}{\partial r} \left(r \frac{\partial E_z}{\partial r} \right) = -\frac{4\pi}{\gamma^2 \beta^2 c^2} \frac{\partial}{\partial t} J_z, \quad (5)$$

for the electric field in the range of $r < R_w$. In Eq. (5), the relativistic mass factor γ is defined by $\gamma^2 = (1 - \beta^2)^{-1}$.

Whenever the beam current changes, the induced electric field $E_z(r, z, t)$ calculated from Eqs. (4) and (5) appears in the system. In terms of the Maxwell equation, the induced electric field is contributed by the change of the radial electric field E_r and the azimuthal magnetic field B_θ . However, we note in the resistive medium that the induced electric field due to the radial electric field is negligible in comparison with that due to the azimuthal magnetic field. In this context, the axial electric field E_z in the resistive medium is related to the azimuthal magnetic field B_θ by $(\partial / \partial r) E_z = (1/c)(\partial / \partial t) B_\theta$. Differentiating both sides of Eq. (4) by r , we obtain

$$\frac{\partial}{\partial r} \left[\frac{1}{r} \frac{\partial}{\partial r} (r B_\theta) \right] - \frac{4\pi\sigma\mu}{c^2} \frac{\partial}{\partial t} B_\theta = \frac{4\pi\mu}{c} \frac{\partial}{\partial r} J_z, \quad (6)$$

for the azimuthal magnetic field B_θ inside the resistive medium ($R_w < r < R_c$). The electric field penetrates a few skin depths into the resistive medium. The electric field E_z in the resistive medium is proportional to $\exp[-(r - R_w)/\delta]$. From a practical point of view, the radius ratio R_c/R_w is infinite if the thickness ΔR of the resistive medium is more than a few times the skin depth. The error associated with a finite value of R_c is on the order of $\exp(-\Delta R/\delta)$ or less. In the evaluation of the axial electric field at the inner surface of the drift tube ($r = R_w$), we thus assume that the radius R_c of the wrapping conductor is much larger than the inner radius R_w , i.e., $R_c/R_w \rightarrow \infty$.

One of the most important issues in the resistive-wall instability is the evaluation of the axial electric field at the inner surface ($r = R_w$) of the resistive medium. In the case when the skin depth of the resistive medium is much less than the wall radius R_w ($\sigma \ll R_w$), Eq. (6) is represented by a planar approximation and the axial electric field at the inner surface of the resistive medium is given by⁷

$$E_z(R_w, z, t) = -\sqrt{\frac{2}{\pi}} \frac{\mu\omega}{c^2} \frac{\delta}{R_w} \int_{\theta_h}^{\theta} \frac{d\theta'}{\sqrt{\theta - \theta'}} \frac{\partial}{\partial \theta'} I(z, \theta'), \quad (7)$$

which is employed for the subsequent analysis of the resistive-wall instability. Here $I(z, \theta)$ is the instantaneous beam current. In Eq. (7), the normalized time $\theta_h = \omega t_h$ represents the time $t = t_h$ at which the head of the electron beam passes through the first cavity.

In order to find the axial electric field $E_z(r, z, \theta)$ in the range of r satisfying $r < R_w$, we solve Eq. (5) and make use of the boundary value $E_z(R_w, z, \theta)$ in Eq. (7). After carrying out straightforward algebra, we find the average axial electric field

$$E(z, \theta) = 2G(R_b) \frac{\omega}{\beta^2 \gamma^2 c^2} \left(\frac{\partial I}{\partial \theta} \right)_z + E_z(R_w, z, \theta), \quad (8)$$

which acts on the beam electrons in the segment labeled by θ . In Eq. (8), $G(R_b)$ is the geometric factor of the configuration, i.e.,

$$G(R_b) = \begin{cases} \ln(R_w/R_b) + 0.25, & \text{solid beam,} \\ \ln(R_w/R_b), & \text{hollow beam.} \end{cases} \quad (9)$$

Velocity modulation of the beam segment labeled by t_0 is obtained from

$$mc^2 \frac{d}{dz} \gamma = -eE, \quad (10)$$

with the boundary condition

$$\gamma_0(\theta) = \gamma_b - (e\Delta\phi/mc^2) f(\theta), \quad (11)$$

where E is the average axial electric field in Eq. (8) and γ_b is the initial relativistic mass factor of electrons before they pass through the cavity opening. For convenience in the subsequent analysis, we define the normalized current $F(\zeta, \theta)$ by

$$F(\zeta, \theta) = I(\zeta, \theta) / I_b, \quad (12)$$

where the normalized propagation distance $\zeta = \alpha z / \beta_b c$ and I_b is the injection current of the beam before it passes through the first cavity. It is also useful in the subsequent analysis to introduce the Budker's parameter ν of the beam defined by $\nu = -eI_b / m\beta_b c^3$.

Substituting Eqs. (8) and (9) into Eq. (11), we obtain the relativistic mass factor $\gamma(\zeta, \theta)$,

$$\begin{aligned} \frac{\gamma}{\gamma_b} = 1 - \frac{e\Delta\phi}{\gamma_b mc^2} \sin \theta + \int_0^\zeta d\zeta' \left[\frac{2G\nu}{\gamma_b^3} \left(\frac{\partial F}{\partial \theta} \right)_{\zeta'} \right. \\ \left. - \sqrt{\frac{2}{\pi}} \frac{\nu\beta_b^2}{\gamma_b} \frac{\delta}{R_w} \int_{\theta_h}^{\theta} \frac{d\theta'}{\sqrt{\theta - \theta'}} \left(\frac{\partial F}{\partial \theta'} \right)_{\zeta'} \right], \end{aligned} \quad (13)$$

where use has been made of the assumption that the instantaneous velocity βc of the beam segment θ is close to the beam injection velocity $\beta_b c$. The instantaneous velocity $\beta(\zeta, \theta)c$ of the beam segment θ is expressed as

$$\beta_b / \beta = 1 + (\gamma_b - \gamma) / \gamma_b (\gamma_b^2 - 1). \quad (14)$$

Making use of the velocity definition $dz/dt = \beta c$ and the definition $\varphi = \omega t$, we obtain the relation

$$\varphi - \theta = \int_0^\zeta \frac{\beta_b}{\beta} d\zeta, \quad (15)$$

where the normalized propagation distance $\zeta = \omega z / \beta_b c$.

The beam current at the injection point is a constant value of I_b . The beam segment t_0 passes the injection point at time $t = t_0$. When this segment arrives at z in time t , it is stretched by a factor of dt/dt_0 . Thus, the beam current of the segment t_0 at z is proportional to $d\theta/d\varphi$. In this regard, the normalized current ratio $F(\zeta, \theta)$ in Eq. (12) is expressed as

$$F(\zeta, \theta) = \frac{N(\zeta)}{d\varphi/d\theta}, \quad (16)$$

where the normalization constant $N(\zeta)$ is defined by

$$\frac{2\pi}{N(\zeta)} = \int_0^{2\pi} d\theta |d\theta/d\varphi|. \quad (17)$$

The normalization constant $N(\zeta)$ ensures the charge conservation. Substituting Eq. (15) into Eq. (16) gives⁴

$$\begin{aligned} \frac{N(\zeta)}{F(\zeta, \theta)} = & 1 + \zeta \frac{df}{d\theta} - \int_0^\zeta d\zeta' \int_0^{\zeta'} d\zeta'' [h \frac{\partial^2}{\partial \theta^2} F(\zeta'', \theta) \\ & - K \frac{\partial}{\partial \theta} W(\zeta'', \theta)], \end{aligned} \quad (18)$$

where the phase delay function $W(\zeta, \theta)$ is defined by

$$W(\zeta, \theta) = \sqrt{\frac{2}{\pi}} \int_{\theta_h}^\theta \frac{d\theta'}{\sqrt{\theta - \theta'}} \left(\frac{\partial F}{\partial \theta'} \right) \zeta, \quad (19)$$

and the initial energy gain ϵ , the self-field effects h , and the resistive-wall effects κ are defined by

$$\begin{aligned} \epsilon = & \frac{1}{\gamma_b (\lambda_b^2 - 1)} \frac{e \Delta \phi}{mc^2}, \quad h = \frac{2Gv}{\gamma_b^3 (\gamma_b^2 - 1)}, \\ K = & \frac{v\mu}{\gamma_b^3} \frac{\delta}{R_w}. \end{aligned} \quad (20)$$

The initial condition of Eq. (18) is $F(\zeta, \theta) = 1$ at $\zeta = 0$. For specified values of the physical parameters ϵ , h and κ , this integrodifferential equation can be solved by a numerical method. Once the normalized current $F(\zeta, \theta)$ in Eq. (18) is determined in terms of the time θ and the propagation distance ζ , the energy modulation in Eq. (13) is calculated from the current modulation for a specified injection energy γ_b .

Numerical calculation of Eq. (18) has been carried out, neglecting the transient behavior of the current modulation caused by the beam head ($\theta_h = -\infty$). A typical example of the current modulation calculated from Eqs. (18) and (19) for $\epsilon = 0.02$, $h = 0.02$, $\kappa = 0.02$, the injection energy $\gamma_b =$

1.5 and the propagation distance $\zeta = 21$. These physical parameters are easily attainable under the present experimental conditions. The current profile is very different from a sinusoidal wave form although the initial energy modulation at the first cavity is a sine function. The current peak occurs near the time at which d/d has a local maximum. The later segment with more energy speeds up and the previous segment with less energy slows down, piling up the beam current at this point. In order to investigate nonlinear mode evolution in the current profile systematically, we Fourier-decompose the current modulation in Eq. (19) with harmonic mode number ℓ . The mode strengths grow exponentially with respect to the propagation distance ζ except at the beginning and near to the location, where the peak modulation occurs. The strength c_1 of the fundamental mode is proportional to $\exp(0.102\zeta)$ in the propagation range of the exponential growth, which agrees with its analytical estimation of $\exp(0.1\zeta)$ from the linear theory of the resistive-wall instability. The peak modulation occurs at $\zeta = \zeta_m = 22$ for the parameters mentioned above. The normalized mode strength c_ℓ of order unity can easily be attainable in the resistive-wall klystron. We also note from numerical calculation that the mode structure at the peak modulation exhibits a broad spectrum.

The propagation distance $\zeta = \zeta_m$ of the peak current modulation determines the length of the resistive-wall klystron. The oscillatory wave of the current modulation beyond the propagation distance of $\zeta = \zeta_m$ breaks down to many wavelets. We thus call the propagation distance $\zeta = \zeta_m$ the wave breaking point. The main nonlinear saturation mechanism for the resistive-wall instability is the wave breaking phenomenon and multi-mode coupling. The tube length longer than ζ_m may not be advantageous for the fundamental mode ($\ell = 1$) klystron. However, a long tube may be useful for the high-harmonic klystron. As an example, we consider the parameters mentioned above. The resistive-wall effect of $\kappa = 0.02$ corresponds to the beam current of $I_b = 4$ kA for $\gamma_b = 1.5$, $\mu = 2.5$ and the ratio $\delta/R_w = 0.1$. For the microwave frequency of 10 GHz, the conductivity of the resistive medium is given by 100 siemens/m, which is the conductivity of typical ferrite. The propagation distance $\zeta_m = 22$ of the peak current modulation corresponds to the tube length of $z_m = 10$ cm for $\omega = 10$ GHz. These parameters are easily attainable in the present experimental conditions. There is a broad range of system parameters which the present technology allows. Obviously, the resistive-wall klystron has great potential for a high-power high-frequency microwave device.

III. REFERENCES

1. M. Friedman, J. Krall, Y. Y. Lau, and V. Serlin, J. Appl. Phys. **64**, 3353, (1988) and the references therein.

Operating Conditions of High-Power Relativistic Klystron

Han S. Uhm, Naval Surface Warfare Center, Silver Spring, MD 20903-5640

An electron beam pre-modulated at the first cavity in a klystron enters the second cavity opening, exciting it. Induced voltage at the second cavity in a high-power klystron forms a virtual cathode momentarily, sending back a part of the beam toward the first cavity. The relationship between the induced voltage and the return current at the first cavity is investigated. The boundary between the amplifier and oscillator operation regions is described in the parameter space defined by the return current strength and inter-cavity distance.

I. INTRODUCTION

There is a growing body of literature on theoretical and experimental studies of relativistic klystron amplifiers driven by modulated intense relativistic electron beams. The relativistic klystron amplifier (RKA) exploits the strong self-electric field, which effectively modulates the beam current, thereby enhancing electron bunching and amplifier efficiency. The frequency and efficiency of the current modulation in a RKA are monochromatic and almost 100 percent in appropriate system parameters. One of the main issues in present RKA development is the enhancement of power and frequency simultaneously. The size and opening of the cavities in RKA should be reduced, to increase the excitation frequency. Therefore, a high-power high-frequency klystron amplifier has inherent problems due to reduced cavity size, including electron emission and ac beam loading at cavity gap opening. However, if the induced voltage at the second cavity is high enough, it forms a virtual cathode and reflects part of the electron beam back to the first cavity. The return beam from the second cavity enters the first cavity opening and excites it further if the return current modulation is in phase with first cavity excitation. The in-phase return-current modulation may reduce the ac beam loading at the first cavity, significantly improving the klystron performance. As a proof-of-principle experiment, Serlin and Friedman¹ built the two-beam klystron, where two annular electron beams propagate through a grounded tube. These beams are pre-modulated at the first cavity by input microwaves. Because the inner beam energy is considerably less than the outer beam energy, part of the inner beam is reflected by the virtual cathode formed at the second cavity and further excites the first cavity. Significant improvement of the current modulation has been reported from this experiment.¹ A theory describing the relationship between the induced voltage and the modulated return current at the first cavity opening is developed. Boundaries defining the amplifier and oscillator operation regions are also described in terms of the normalized return-current strength h and the inter-cavity distance represented by the phase angle α .

II. TWO BEAM KLYSTRON

High-level stable excitation of the first cavity is very important for current modulation in a high-performance klystron. The first cavity is excited first by external input microwaves, which have enough pulse length, saturating the induced voltage to the steady-state value ϕ_w . Sometime during this microwave pulse, the electron beam is allowed to enter the klystron. The relationship between the induced voltage and the ac return current in the first cavity opening can be found from an equivalent circuit representation of the cavity impedance L_1 , C_1 and R_1 . The inductance L_1 and capacitance C_1 are related to the resonance frequency ω_1 of the cavity by $\omega_1 = (L_1 C_1)^{-1/2}$ and the cavity Q-value is related to the resistance R_1 of the equivalent circuit by $Q = \omega R_1 C_1$ (Ref.2). The resonance frequency ω_1 of the first cavity is assumed to be in resonance with the input microwave frequency ω , i.e., $\omega_1 = \omega$. The intensity of the return current is unknown. However, the level of the return current modulation increases as amplitude ϕ_2 of the induced gap voltage at the second cavity increases. Note that the amplitude ϕ_2 is proportional to the amplitude ϕ of the induced voltage at the first cavity.³ In this regard, we assume that the return current modulation is proportional to the amplitude ϕ of the induced voltage at the first cavity.

Collecting all terms together, the induced gap voltage $V_1(t)$ at the first cavity can be calculated from²

$$\frac{d^2 V_1}{dx^2} + \frac{1}{Q_1} \frac{dV_1}{dx} + V_1 = \frac{1}{Q_1} \phi_w \sin \left[\frac{\omega x}{c} + \alpha \right] + f_s \phi(x) \sin [x - \Psi(x) + \alpha], \quad (1)$$

where f_s represents the intensity of the return current and other coupling mechanisms, the variable x is the normalized time defined by $x = \omega t$, and the phase angle α is related to the inter-cavity distance L by

$$\alpha = \Psi_3 - \frac{\omega L}{c} \left(\frac{1}{\beta_1} + \frac{1}{\beta_2} \right) - \Psi_2. \quad (2)$$

In Eq. (2), $\beta_1 c$ and $\beta_2 c$ represent velocities of the forward and backward beams, Ψ_2 is the phase shift of the induced voltage at the second cavity relative to the forward current modulation, and Ψ_3 is the phase shift of the return current due to reflection at the virtual cathode. In Eq. (2), the term proportional to ϕ_w represents the contribution from the input microwaves and the term proportional to f_s originates from the incoming return current. In obtaining Eq. (2), we have assumed that the induced gap voltage $V_1(t)$ is expressed as

$$V_1(t) = \phi(x) \sin [x - \Psi(x)], \quad (3)$$

This work was supported by IR Fund at NSWC

where $\phi(x)$ and $\Psi(x)$ are amplitude and phase shift, respectively, of the induced voltage at the first cavity. They are slowly varying functions of time x . We assume that the input microwaves and modulated return current drive the excitation of the first cavity, which accommodates the driving signals by changing its amplitude and phase. Thus, selecting the time frame in which the phase is a non-zero value of $\Psi(x)$ as shown in Eq. (3) is quite appropriate in the subsequent theoretical analysis.

Substituting Eq. (3) into Eq. (1), and defining the normalized amplitude Y and normalized time y by

$$= \phi(y) / \phi_w, \quad y = x / 2Q_1 = \omega t, \quad (4)$$

we find the equations which govern the phase Ψ and amplitude Y . They are

$$\frac{d\Psi}{dy} = \frac{\cos\Psi}{Y} + h\cos\alpha \quad (5)$$

and

$$\frac{dY}{dy} + (1 - h\sin\alpha) Y = \sin\Psi, \quad (6)$$

where the normalized return-current strength h is defined by $h = f_s Q_1$. Although the parameter f_s is a small number, the normalized return-current strength h can easily be on the order of unity because of a large cavity- Q value. Before solving Eqs. (5) and (6), we assume the initial condition that at time $y = 0$, the electron beams enter the system, thereby turning on the terms proportional to h in Eqs. (5) and (6). Otherwise, the cavity is saturated by the microwave input at $y < 0$ and the initial conditions for the phase and amplitude are given by $\cos[\Psi(0)] = 0$ and $Y(0) = \sin[\Psi(0)]$ at $y = 0$. These conditions are equivalently expressed as $\Psi = \pi/2$ and $Y = 1$ at $y = 0$. After a careful examination of Eqs. (5) and (6), we note the functional properties of $Y(\pi - \alpha) = Y(\alpha)$ and $\Psi(\pi - \alpha) = \pi - \Psi(\alpha)$. Therefore, the amplitude Y and phase shift Ψ for $\alpha = \pi - \alpha_1$ can be expressed by those for $\alpha = \alpha_1$.

The homogeneous solution Y_h to Eq. (6) increases exponentially, provided $h\sin\alpha > 1$, which is called the self-excitation. On the other hand, when the phase angle α satisfies $h\sin\alpha < 1$, the solution Y to Eq. (6) is bounded and the klystron is the amplifier operation region. The boundary between the amplifier and oscillator regions in the (α, h) parameter space can be illustrated and the border line is obtained from $h\sin\alpha = 1$.

Amplifier Operation: In the amplifier operation region characterized by $h\sin\alpha < 1$, the solution Y to Eq. (6) is bounded, and the steady-state values of the amplitude Y and phase Ψ induced at the first cavity opening are determined by $d\Psi/dy = dY/dy = 0$ at the time $y = \infty$. Thus, after a straightforward calculation, we obtain

$$\begin{aligned} \cos\Psi_1 + \chi h\cos\alpha &= 0, \\ \sin\Psi_1 + \chi h\sin\alpha &= \chi, \end{aligned} \quad (7)$$

for amplifier operation from Eqs. (5) and (6). In Eq. (7), $\chi = \phi_1/\phi_w$ and Ψ_1 are steady-state values of the amplitude and phase

shift. It is important to find in what parameter regime the steady-state value χ is larger than unity. The modulated return current amplifies the induced voltage only in this parameter regime. Otherwise, the return current dampens the induced voltage. To find boundary of the amplifying region, we substitute $\chi = 1$ into Eq. (7) and obtain

$$\begin{aligned} \cos\Psi_1 + h\cos\alpha &= 0, \\ \sin\Psi_1 + h\sin\alpha &= 1. \end{aligned} \quad (8)$$

We remind the reader that the phase shift Ψ_1 satisfies $\sin\Psi_1 > 0$ for $\chi > 0$. After a straightforward algebraic manipulation, Eq. (8) is expressed as $h = 2\sin\alpha$ for $0 < \alpha < \pi$. Note that the value of the parameter h in Eq. (8) at $\alpha = \pi/4$ or at $\alpha = 3\pi/4$ is $2^{1/2}$. The curves obtained from $h = 2\sin\alpha$ represent the boundary of the amplifying region in the (α, h) parameter space. For a specified value of the normalized return-current strength h , the amplifying region is defined by

$$\sin^{-1}\left(\frac{h}{2}\right) < \alpha < \pi - \sin^{-1}\left(\frac{h}{2}\right), \quad (9)$$

where h is less than $2^{1/2}$. To investigate transient behavior of the induced voltage $V_1(t)$, we solve the coupled differential equations (5) and (6) numerically. As expected, we find from the numerical calculation that the amplitude Y and phase shift Ψ approach their steady-state values as time goes by. The closer the steady-state amplitude to unity, the quicker the transient behavior dies out. In the limit of the angle $\alpha = \pi/2$, we note $d\Psi/dy = 0$ from Eq. (5), and Eq. (6) is simplified to

$$\frac{dY}{dy} + (1 - h) Y = 1, \quad \alpha = \frac{\pi}{2}. \quad (10)$$

Solution to Eq. (10) is given by

$$Y = \frac{1}{1-h} \{1 - h \exp[-(1-h) y]\}, \quad (11)$$

which eventually saturates to $Y = \chi = 1/(1-h)$. The maximum amplification of $1/(1-h)$ occurs at $\alpha = \pi/2$, which is called the in-phase condition. The steady-state amplitude at $\alpha = \pi/2$ increases to infinity as the strength h approaches unity. This observation may mislead the outcome of practical present experiments. When $h \rightarrow 1$, Eq. (11) is further simplified to $Y = 1 + y$, which increases linearly in time. Therefore, amplification for $\alpha = \pi/2$ and $h = 1$ is limited by the electron beam pulse. In the out-of-phase case characterized by $\alpha = -\pi/2$, the solution to Eq. (6) is given by

$$Y = \frac{1}{1+h} \{1 + h \exp[-(1+h) y]\}, \quad (12)$$

where the return current dampens significantly the gap voltage induced by the microwaves.

Oscillator Operation: It is pointed out that Eq. (1) for the induced gap voltage at the first cavity is a linear equation, which is an excellent representation for an amplifier operation. However,

mentioned earlier, the amplitude Y in Eq. (6) increases exponentially in the oscillator operation region satisfying $h \sin \alpha > 1$. In reality, the term proportional to the parameter f_s in Eq. (1), which represents the modulated return current, may stop to grow as the amplitude ϕ approaches saturation. For example, the location at which the maximum current modulation of the forward beam occurs, starts to shift toward the first cavity from the second cavity location, if the amplitude ϕ increases significantly.³ Remember that the second cavity location was initially selected for a maximum forward current modulation of moderate amplitude ϕ . Once the maximum modulation location starts to shift, the term proportional to f_s in Eq. (1) does not increase linearly with ϕ ; instead, it may start to saturate. We also observe that the modulated return current originates from reflection at the second cavity. As long as the return current is much less than the forward beam current, it may be proportional to the excitation level of the second cavity, which is also proportional to the first cavity excitation. This assures linearity in Eq. (1). If the return current is a substantial fraction of the forward current, due to lack of a sufficient amount of the forward current, it may start to saturate as the cavity excitation increases. There may be other saturation mechanisms for the modulated return current as the amplitude ϕ of the induced voltage grows. In this regard, Eqs. (5) and (6) for the oscillator operation are modified to

$$\frac{d\Psi}{dY} = \frac{\cos \Psi}{Y} + h(1 - eY^2) \cos \alpha, \quad (13)$$

$$\frac{Y}{Y_s} - [h(1 - eY^2) \sin \alpha - 1] Y = \sin$$

where the nonlinear saturation coefficient e is much less than unity in a typical klystron. Equation (13) is a typical van der Pol equation for a forced oscillator. Obviously, the terms proportional to eY^2 in Eq. (13) provide a saturation of the amplitude. The normalized saturation amplitude Y_s is obtained from Eq. (13) and is given by

$$Y_s = \sqrt{\frac{h \sin \alpha - 1}{e h \sin \alpha}}, \quad (14)$$

which is typically much larger than unity, i.e., $Y_s \gg 1$. As expected from Eq. (11), the maximum amplitude of the induced voltage appearing on the first cavity occurs at the in-phase angle $\alpha = \pi/2$ for either the amplifier or the oscillator operation.

From a numerical calculation of Eq. (13), we find that the amplitude Y for an oscillator grows exponentially at the beginning and then executes a small oscillation about the saturation value Y_s . Meanwhile, the phase shift Ψ increases almost linearly in time. For a large-amplitude operation typical of the klystron oscillator, the phase shift equation is approximated by $d\Psi/dy = \cot \alpha$ from Eq. (13) and the frequency shift at the saturation is expressed as

$$\delta\omega = \omega \cot \alpha / 2Q_1. \quad (15)$$

The frequency shift $\delta\omega$ of the oscillator in Eq. (15) is determined

in terms of the phase angle α and the cavity Q-value. The in-phase condition of $\alpha = (0.5 - 2n)\pi$, at which the modulated return current is in phase with the first cavity excitation, can be expressed in terms of the inter-cavity distance L , once the phase shifts Ψ_2 and Ψ_3 are known. Here, n is an integer. When segments of the forward beam arrive on the second cavity, a certain limited portion of the beam will be reflected at the cavity. The phase of the return current may be very close to the phase of the induced voltage at the second cavity. We thus approximate $\Psi_3 = \pi/2$. According to a previous study,² the optimum current modulation occurs at the phase shift satisfying $0 < \Psi_2 < \pi/2$. We assume $\Psi_2 = \pi/4$, which is the value corresponding to the middle in the allowable range of the phase Ψ_2 . The error associated with this assumption is one-sixteenth of the wavelength or less in the klystron. Substituting these phase shifts into Eq. (2), the in-phase condition is simplified to

$$\frac{L\omega}{c} \left(\frac{1}{\beta_1} + \frac{1}{\beta_2} \right) = \left(2n - \frac{1}{4} \right) \pi. \quad (16)$$

The second cavity should be located where the forward current has a maximum modulation. The second cavity location is therefore determined in terms of the beam parameters and geometrical factor G . Maximum modulation location is given by³

$$z_o = \beta_1^2 \gamma_1^2 \frac{\pi c}{2\omega} \sqrt{\frac{\gamma_1}{2vG}}, \quad (17)$$

where $\gamma_1^2 = (1 - \beta_1^2)^{-1}$ and v is Budker's parameter of the forward beam. As a numerical example, we consider the physical parameters of the two-beam klystron experiment¹ at the Naval Research Laboratory. The theoretical result from Eqs. (16) and (17) predicts the optimum inter-cavity distance $L = 14$ cm, which is close enough to the experimental observation of $L = 14.1$ cm. We also observe from this numerical example that a deviation of about 13 percent ($\Delta L = 2$ cm) from 14 cm results in a significant reduction of the current modulation, which also agrees with the experimental observation.

REFERENCES

1. V. Serlin and M. Friedman, *Appl. Phys. Lett.* **62**, 2772 (1993).
2. H. S. Uhm, G. S. Park, and C. M. Armstrong, *Phys. Fluids B* **5**, 1349 (1993).
3. H. S. Uhm, *Phys. Fluids B: Plasma Physics*, **5**, 190 (1993).

SPURIOUS OSCILLATIONS IN HIGH POWER KLYSTRONS*

B. Krietenstein, THD, Darmstadt, Germany, K. Ko, and T. Lee,
Stanford Linear Accelerator Center, Stanford University, Stanford, CA 94309
U. Becker and T. Weiland, THD, Darmstadt, Germany
M. Dohlus, DESY, Hamburg, Germany

Abstract

Spurious oscillations in high power klystrons are found to occur in the gun region, in the cavities in the main body of the tube, or in the drift tunnel. The criteria that determine whether a mode will oscillate is that its beam loading be negative, and that the power it extracts from the beam exceeds its losses to external loading and wall dissipation. Using the electromagnetic and particle-in-cell modules of MAFIA, we have devised numerical techniques with which the quality factors Q_b , Q_e and Q_o can be evaluated and compared. Simulations involving a gun oscillation observed in the SLAC/DESY S-Band klystron will be reported.

I. INTRODUCTION

Oscillations at frequencies other than the operating frequency are not uncommon in high power klystrons. The unwanted signals have been detected in the pulse transformer tank in the gun region, and also in the input and output RF couplers. They occur without the RF drive signal, and have the signature of high- Q resonances in that their frequencies are not affected by variation in operating parameters, such as the focussing magnetic field. S-Band klystrons built at SLAC have experienced oscillations in the gun diode [1]), in the drift tunnel [2], and also in an output circuit of the double-gap type [3].

Spurious oscillations are undesirable since the electron beam couples to these modes as well as the desired signal frequency. If the amplitude of the spurious oscillation becomes very large the performance of the tube can be compromised. The main output signal may suffer from amplitude and phase instability which results in pulse shortening or decrease in efficiency. Thus, spurious oscillations can be a serious factor in limiting a klystron from reaching its designed performance if left unsuppressed. The identification and analysis of spurious modes are not easy to accomplish experimentally because the diagnostics are not set up to monitor such signals. Numerical modeling has proved to be valuable in microwave design and this paper describes the analytical efforts to address the spurious mode issue by computer simulation.

II. COMPUTER ANALYSIS

The ability of modern electromagnetic codes to study RF modes in complex geometries, both in 2 and 3D, has enabled the klystron designer to identify spurious modes once their frequencies are known from measurements. Guided by the numerical solutions, he can then devise a method of suppression to be

incorporated into the next prototype. Ideally, it would be more cost-effective to catch potentially unstable modes in the design stage before fabrication and testing take place, thereby reducing the number of prototypes to be built. But this would require a complete analysis of the numerous modes that a klystron circuit can support, which is a nontrivial task. The analysis would have to include not only the vacuum RF properties, but also the mode interaction with the electron beam under a range of operating conditions, in order to determine if any of them is unstable or not.

Beam-field interaction can be modeled by the Particle-In-Cell (PIC) method, and 2D PIC codes such as CONDOR have been used quite routinely in klystron tube design to optimize the extraction of power from the beam [4]. In this application, one is concerned only with the main signal which is an axisymmetric mode so that, except for the input and output RF couplers, a 2D(r, z) geometry suffices. Spurious oscillations, on the other hand, are not limited to monopole modes, but have been observed to be dipole modes as well. Furthermore, external loading by coupling waveguides now plays an important role. PIC modules are available in 3D codes such as MAFIA, but their usage in klystron design has been restricted, largely because of the substantial computer resources such simulations demand. In this work, we will deal with a spurious mode that is axisymmetric so that only 2D calculations are required. We first formulate the criteria that determine oscillation in a way that is computationally efficient. Instead of treating the problem in one simulation, we consider separately three competing effects: beam-field interaction, external loading and wall dissipation. We use the electromagnetic/PIC modules of MAFIA [5] to analyse a gun oscillation problem and demonstrate the method with which to evaluate each effect. We next present the numerical results and discuss the efficacy of the approach.

III. CRITERIA FOR OSCILLATION

There are two criteria that determine whether a mode can be driven to oscillate by a beam. The first and necessary condition is that the beam transfers power to the mode. The second condition is that the power lost by the mode to external loading and wall dissipation is less than the power obtained from the beam. As a result, there is a net gain in mode energy and the oscillation grows. Computationally, it is prohibitively expensive to model this power balance process. To begin with, one needs a disproportionately small grid step to resolve the skin depth due to finite wall conductivity. It also takes an unrealistic number of particles to maintain an electron beam flow over the long growth time of the instability.

Alternatively, one argues that up to the instability threshold each power transfer acts independently, so therefore they can be

*Work supported by the Department of Energy, contract DE-AC03-76SF00515.

treated separately. We define the total quality factor Q_{tot} of a mode as:

$$1/Q_{tot} = 1/Q_o + 1/Q_e + 1/Q_b, \quad (1)$$

where Q_o , Q_e and Q_b are the *wall loss* Q , the *external* Q and the *beam - loaded* Q respectively. If we express Q as

$$Q = \omega U / P, \quad (2)$$

where ω is the angular frequency of the mode, U is the time-averaged stored energy and P is the power transferred, then Eq. (1) describes the power exchange between the mode and the beam, and the power loss by the mode to the circuit environment. If we take power gain as negative, it follows from Eq. (1) that the oscillation criterion is

$$Q_{tot} < 0. \quad (3)$$

Since Q_o and Q_e are always positive, then the sign and value of Q_b will determine unstable resonant modes. A necessary step before one can calculate the quality factors is the identification of the spurious mode, and this we will take up next.

IV. MODE IDENTIFICATION

One outstanding feature of spurious modes is their localization within some region of the klystron to form a resonant circuit. The most efficient way to search for resonances is with eigenmode solvers. Among the many solutions such solvers generate, one looks for modes in the proper frequency range that have diminishing fields towards the enclosing boundaries. Non-localized modes will form standing waves between opposing boundaries while localized modes will have exponentially decaying fields. A direct consequence is that localized modes will experience relatively small frequency shifts when different field conditions (*electric wall* : $E_{tangential} = 0$ or *magnetic wall* : $B_{tangential} = 0$) are imposed at the boundaries.

During the testing of the 150 MW S-band klystron that SLAC is building for DESY, a gun oscillation was discovered when a stable 1.365 GHz signal was detected at the sight window of the pulse transformer tank [1] (with no RF signal applied). Fig. 1 shows a MAFIA calculation of a mode at the same frequency that is localized inside the focus electrode. A small gap connects this small cavity to the main body of the gun diode. By comparison, Fig. 2 shows a nearby mode at 1.277 GHz that occupies the entire diode. Changing the top boundary from an electric to a magnetic wall results in a frequency shift and a different mode pattern for this mode. In contrast, the localized mode is relatively unchanged, indicating the presence of a high- Q resonant structure. We conclude that it is a likely candidate responsible for the spurious oscillation and proceed to determine its Q factors.

V. Q DETERMINATION

Wall Loss- Q_o

Once a likely resonant mode is identified from the eigenmode spectrum, it is straightforward to calculate its Q_o by

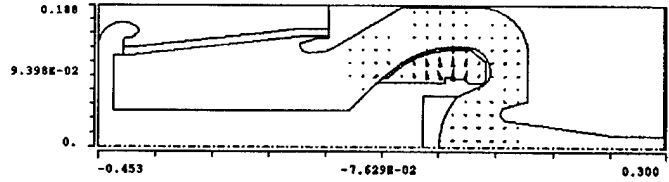


Figure 1. 1.365 GHz mode in the SLAC/DESY gun diode.

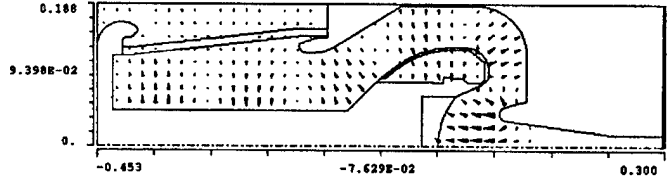


Figure 2. 1.277 GHz mode in the same geometry.

standard perturbation method. Most field solvers, including MAFIA, provide this result automatically via postprocessing. The time-average power absorbed per unit area at the wall is given by

$$\mu\omega\delta|H_{tangential}|^2/4, \quad (4)$$

where δ is the skin depth $(2/\mu\omega\kappa)^{1/2}$ and κ the finite conductivity of the wall material. From Eq. (2), then

$$Q_o = \omega U / P_w, \quad (5)$$

where P_w is the integral of Eq. (4) over the wall surface. Q_o due to copper loss typically ranges from several to tens of thousands at RF frequencies, and is not a major factor in determining Q_T . However, in situations where external loading is ineffective or not applicable, lossy wall material (e.g. stainless steel) is sometimes introduced in areas of high surface currents to provide additional Ohmic loss for mode suppression.

External Loading- Q_e

Of the various methods to determine the external Q of a mode, we will choose the one which is the most direct. We load the eigenmode from the previous calculation as the initial conditions to a time-domain simulation. As opposed to the eigenmode analysis which assumes a closed cavity, power flow across the boundaries are now permissible via ports that are terminated in matched loads. In the gun-diode of Fig. 1, one port is the outer boundary of the pulse transformer tank at top left, while the other is at the entry into the drift tunnel to the bottom right. With the ports open, the initially confined electromagnetic fields can radiate through these apertures and decay. After the initial transient has subsided, one can calculate the decay time constant τ_e from the field values at successive time intervals. The external loading effect is then determined directly from the relation

$$Q_e = \omega\tau_e/2. \quad (6)$$

Beam Loading- Q_b

The beam loading of a mode comes about because the mode induces bunching in the beam which then interacts with the mode field to produce energy exchange. In the absence of losses,

we can use energy conservation and equate the rate of change of stored energy to the power transfer between the mode and the beam. We arrive at an expression for Q_b similar to Eq. (2), namely,

$$Q_b = \omega U / P_b. \quad (7)$$

The time-average power flow P_b is given by the integral over the beam volume

$$P_b = \frac{1}{T} \int_t^{t+T} \int_V \vec{J}_m \cdot \vec{E}_m dV dt \quad (8)$$

where J_m is the induced current density, E_m is the electric field of the mode, and T its period. The facility to evaluate P_b is currently under construction in MAFIA, but we can alternatively find Q_b from the time constant the same way it is done in determining Q_e .

VI. GUN OSCILLATION SIMULATION

As noted before, the computation of Q_b requires a full PIC simulation that includes relativistic and space charge effects [6]. The MAFIA PIC module has this capability so we use it to model the gun oscillation problem. The MAFIA simulation consists of a dc beam, a static field between cathode and anode, a focussing magnetic field and the RF mode under consideration. The injection parameters for the beam at the cathode are taken from previous EGUN [7] results, while the MAFIA static module provides the gradient E_s and the magnetic field B_o . The RF mode E_m is taken from the eigenmode calculation as before.

Without the RF mode, the PIC module essentially reproduces the beam optics results from EGUN. The RF mode is then added with its amplitude scaled to a small fraction of the static field amplitude. This way the RF mode serves as a test field that modulates the lowest order beam equilibrium. Fig. 3 shows a time snapshot of the simulation. The beam is constituted of fifteen rays and the field ratio used is $E_m/E_s = 0.1$. Note that the gun diode is much smaller than previously considered. We provide the justification for the reduced geometry below.

In the absence of external loading and wall loss, the RF mode is basically a standing wave resonance. A resonant circuit is essentially unchanged if shorted properly at one of its node points. The region from the focus electrode to the pulse transformer tank does not play a part in beam-loading except for the energy stored there. Fig. 3 shows the placement of a shorting plane which removes this part of the circuit but leaves the frequency and field pattern of the RF mode unchanged. The geometry is now smaller, and because the total stored energy is less, any time constant related to it also is faster, both of which is good for simulation. However, one needs to scale by the proper ratio of the stored energy in the full geometry to that in the reduced one to obtain the physically correct values.

VII. NUMERICAL RESULTS

The calculations from the previous sections on the localised 1.365 GHz mode are summarized in Table 1. For comparison, the results on the 1.277 GHz mode are also given. As expected, the Q_o 's do not play a role. The 1.277 GHz signal has negative

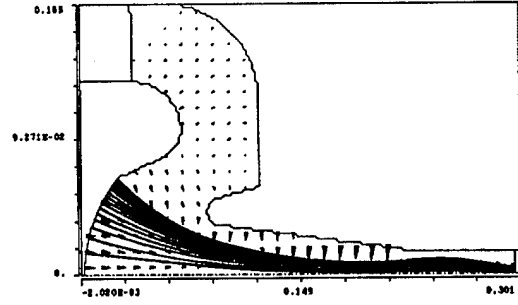


Figure 3. Reduced geometry for the PIC simulation.

beam loading, but is negligible when compared with the heavy external loading, so the net result for Q_{tot} is positive. On the other hand, the 1.365 GHz signal couples so weakly to external loads that the stronger negative beam loading leads to a negative Q_{tot} , and results in oscillation. After the gap at the focus electrode in the SLAC/DESY klystron gun was shorted to eliminate the 1.365 GHz unstable mode, the klystron was processed up to full power without experiencing the previously observed gun oscillation.

Frequency [GHz]	Q_o	Q_e	Q_b	Q_{tot}
1.277	25500	45	-1340	46
1.365	13300	5000	-728	-910

Table 1. Calculated Q 's for the 1.365 and 1.277 GHz signal.

VIII. SUMMARY

We have presented an analytical method to study spurious oscillation by computer simulation, and have applied it to a gun oscillation problem with encouraging results. Further generalization of this approach to other klystron oscillations, including those in which 3D effects can be important, is being considered.

Acknowledgements

We thank D. Sprehn for useful discussions. One of the authors (B. Krietenstein) also acknowledges R. Ruth for his generous hospitality and support during his stay with the ATSP Dept. at SLAC.

References

- [1] D. Sprehn, R.M. Philips, and G. Caryotakis, The Design and Performance of 150-MW S-Band Klystrons, SLAC PUB 6677, Stanford Linear Accelerator Center, Sep. 1994.
- [2] K. Ko, Private communication.
- [3] K. Ko et. al., Linear Collider RF Structure Design Using ARGUS, Proceedings of the First Energy Research Power Supercomputers Users Symposium, Gaithersburg, MD 1991.
- [4] K.R. Eppley, Modelling RF Sources Using 2-D PIC CODES, AIP Conference Proceedings on Computational Accelerator Physics, Los Alamos, NM 1993.
- [5] The MAFIA collaboration, *User's Guide MAFIA Version 3.2*, CST GmbH, Lauteschlagerstr.38, D6100 Darmstadt.
- [6] B. Krietenstein, Simulation of Oscillations in High Voltage Klystrons with MAFIA, Institut f'ur Hochfrequenztechnik, Technische Hochschule Darmstadt, Juli 1994.
- [7] W.B. Herrmannsfeldt, Electron trajectory program, SLAC PUB 226, Stanford Linear Accelerator Center, Nov. 1979.

In-House Repair of a 30 Megawatt, S Band Klystron*

R. Sachtschale, P.G. O'Shea, M. Ponds, G. Swift
Duke University, Free Electron Laser Laboratory
Box 90319 Durham, NC 27708-0319

Abstract

This paper documents the repair and reconditioning of an ITT 2960 klystron that had been at atmospheric pressure for eight months due to a leak in the compression seal for the waveguide window. All work was done in the Duke FEL Vacuum Shop by laboratory staff without any external purchases. The reconditioned klystron is currently being operated at full power on the injection linac for the electron storage ring at Duke.

1 Introduction

With the passage of time since this abstract was first submitted, the Duke FEL Lab has refurbished and put into service a second 30 Megawatt ITT 2960 klystron. These tubes had never been operated and developed vacuum leaks. The leaks occurred during shipping from Stanford to Duke or during storage at Duke while facilities were being constructed. The tubes were sent back to ITT for repair evaluation. The total repair cost being \$37,000. Since the tubes have barium dispenser cathodes, rather than coated oxide cathodes, it was felt that the cathodes could be successfully reactivated once the vacuum problems were solved. See [1] for a thorough description of microwave tubes and their cathodes.

The repair process can be summarized as follows:

- Build the necessary support stands and fixtures.
- Connect vacuum hardware to support leak detection and bake-out.
- Leak detection.
- Repair or isolation of leak.
- Bake-out.
- Reactivation of cathode.
- Low-level perveance test.
- High-power testing.

The repair of the first tube (ITT serial number 4016) was started on 14 April 1994, with completion of high-power testing on 14 July 1994. Repair of the second tube (ITT serial number 4011) was begun in September 1994, with high-power testing completed on 28 February 1995. Both tubes are currently being

operated in excess of 30 Megawatts on the injection linac for the storage ring [2, 3].

2 Construction of Mechanical Support Fixtures

The first task was to build a mobile stand (similar to an engine stand) to support the tube while it was being repaired. Upon return from ITT, the pinch off port on the output waveguide of the klystron had been ground off. A convoluted bellows with a 2.75" con-flat flange was welded to the ground off port. Brackets were made from 1/8" aluminum plate to support a 20 l/s ion pump, bakeable valve and bellows. The brackets were fastened to a protrusion on the side of the klystron collector. This protrusion was originally used for mounting a bracket to support a C-magnet for the OEM 8 l/s ion pump. These components are displayed in figure 1.

3 Pump-Down, Leak-Check and Bake-out Preparation

Leak-checks were performed with helium and a mass spectrometer leak detector. The first tube worked on had a leak around the compression seal for the output waveguide window. Our lab doesn't have the necessary rf-induction hydrogen furnace for such a repair. It was decided to leave the window in place and add a waveguide elbow, with a factory installed window, from our inventory. This also required a transition piece to which a 10 l/s ion pump was attached.

The second tube had a leak in a braze joint between the vacuum side of the waveguide and the OEM 8 l/s ion pump. The ion pump and the leaky braze joint were removed using a tubing cutter. A 2-1/8" con-flat flange was welded to the remaining stub and sealed with a blank flange. The second tube did not require the addition of a second waveguide window.

Once the leaks were repaired, the tubes were stripped of all ancillary components in preparation for a vacuum bake-out. The output waveguide above the rf window was evacuated and pumped continuously by a sieve trapped roughing pump. The collector cooling jacket was purged with N_2 at very low flow. The klystron was wrapped with heater tapes and covered with foil. An auxiliary roughing cart was attached to the bakeable valve. The base pressure prior to bake-out was 3×10^{-8} torr at the 20 l/s pump with the auxiliary pump cart also pumping.

*Supported by the U.S. Air Force Office of Scientific Research, contract F49620-93-1-0590 and the U.S. Army Space & Strategic Defense Command, contract DASG60-89-C-0028.

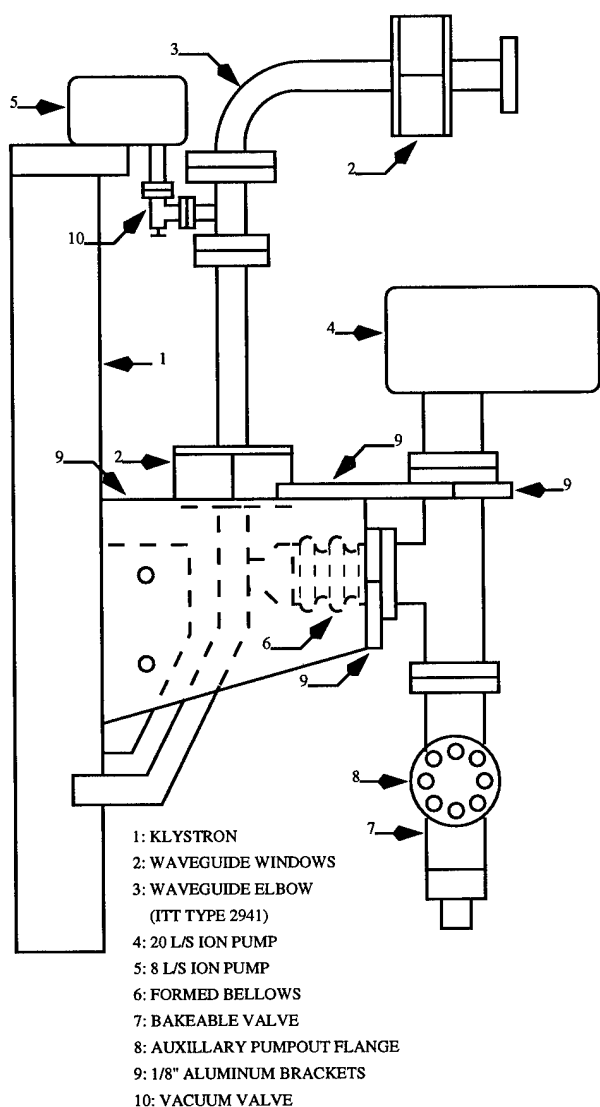


Figure 1: Mounting of Hardware for Klystron Repair

4 Bake-Out

The first klystron was slowly heated over a period of 10 days, reaching a peak of 400°C for 72 hours. The vacuum was kept below 10^{-6} torr during bake-out. The temperature was lowered at a maximum rate of 1°C/min. Two days after bake-out the pressure was 2×10^{-10} torr at room temperature.

Due to faulty heater tapes, the second tube was heated for 21 days and reached a peak temperature of 380°C for 6 days. Following bake-out the pressure at the 20 l/s ion pump was too high (5×10^{-6} torr) with the auxiliary pump cart valve closed. The auxiliary pump cart contains a residual gas analyzer (RGA). The pump cart was valved in and the klystron was helium leak checked using the RGA as a detector. A leak was found in the ceramic to metal braise of the 20 l/s ion pump high voltage feed-through. The leak was sealed with Vac Seal (a silicone resin).

5 Reactivation of the Cathode

Following bake-out the cathode filament was slowly powered up while monitoring vacuum pressure. Pressure was maintained in the 10^{-7} torr range. RGA spectra showed H_2 to be the major gas component. To assist in the pumping of the H_2 a Titanium Sublimation Pump on the pump cart was activated daily for 1 minute. At 450W of cathode filament power, it has taken several months for the pressure to come down into the 10^{-9} torr range. The tube was operated at full power in this condition while keeping a daily record of the ion pump current.

Once the cathode filament was at full power, a low level perveance test was done at -500 volts. The μ perveance was found to roll off at 2.0 for a filament power of 200W.

At this point the tube is ready for reassembly and high-power testing.

6 High-Power Testing

For high-power testing the tubes were installed in 300kV, 2 μ sec. modulators. First the ion pumps and cathode filaments were restarted. The μ perveance was checked and plotted against filament power. The results of both tubes are shown in figure 2. #4016 is the first tube we reconditioned and #4011 was done second. We believe that much of the offset results from differences in measuring devices between the two modulators. Principally the high voltage capacitive dividers and the calibration of the filament power supplies.

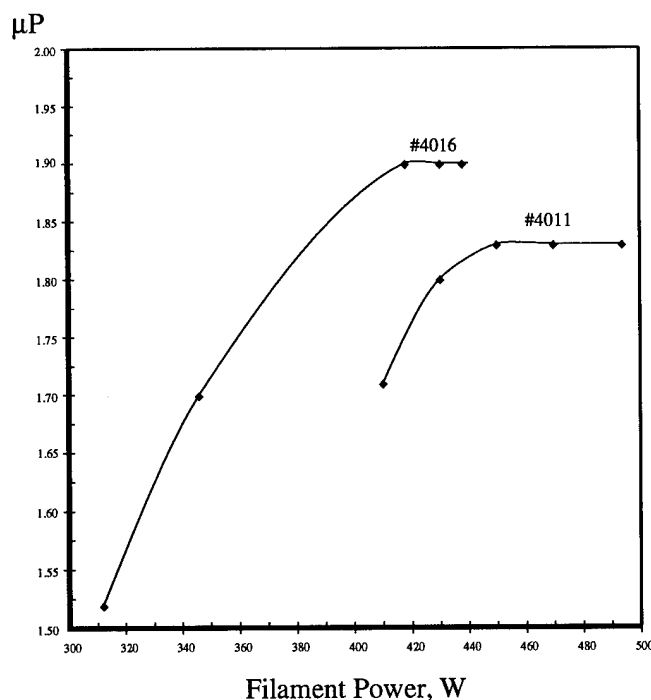


Figure 2: Micro-Perveance vs. Filament Power

It took the better part of a day to get the tubes up to 300kV. The tubes were operated at various drive voltages and the input

power was increased until the output began to saturate. Plots of this data for tube #4011 are shown in figure 3.

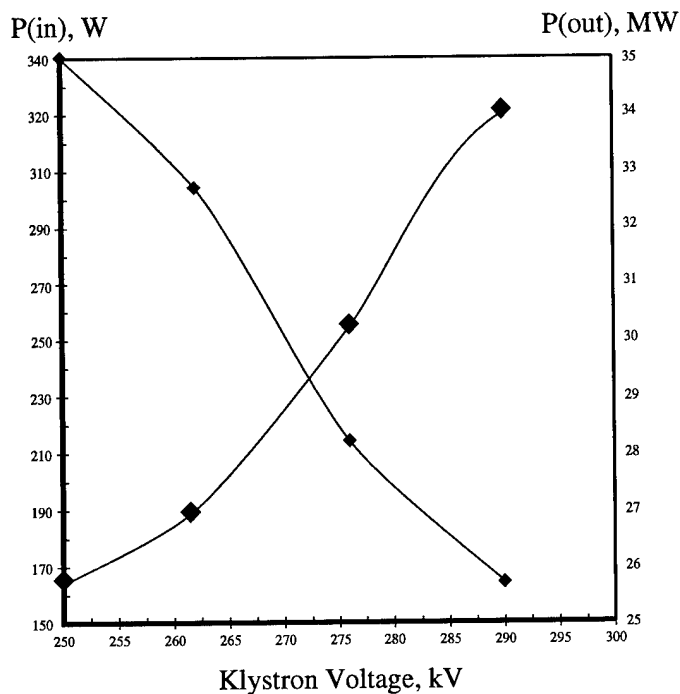


Figure 3: Saturated Input and Output RF Power vs. Klystron Beam Voltage

Finally klystron output power is plotted against rf input power for a fixed beam voltage. A plot from the data for tube #4011 is shown in figure 4.

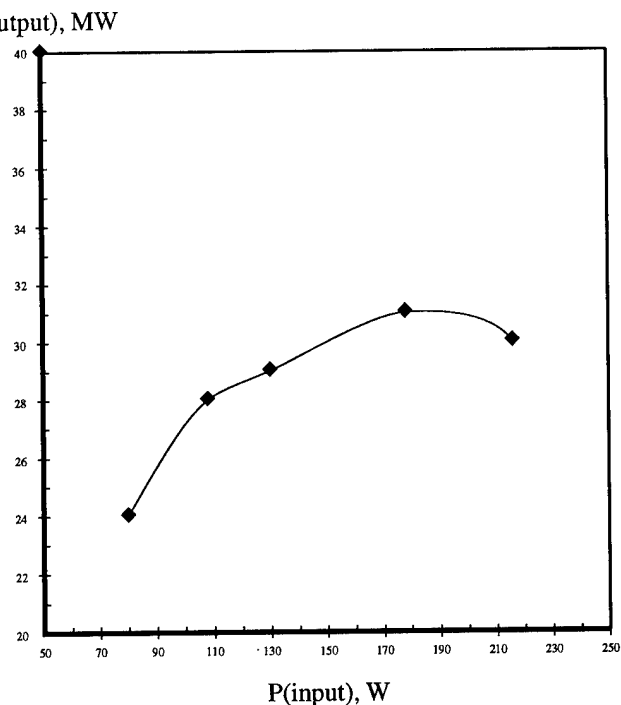


Figure 4: Klystron Output Power vs. RF Input Power at 290kV

References

- [1] A.S. Gilmour, Jr. *Microwave Tubes*. Copyright 1986, Artech House, Inc. Dedham, MA 02026 ISBN: 0-89006-181-5.
- [2] P.G. O'Shea et al. *Accelerator Archeology - The Resurrection of the Stanford Mark III Electron Linac at Duke*. In these proceedings.
- [3] V.N. Litvinenko et al. *Commissioning of the Duke Storage Ring*. In these proceedings.

7 Conclusion

The repair of our ITT 2960 klystrons has been a great success. The skills that were gained will enhance our abilities to resurrect klystrons used in old accelerators or obtained from government surplus lists. Future plans include the repair of an inoperable RCA klystron. The plan is to remove the oxide cathode and replace it with a new dispenser cathode. If successful, we should be able to upgrade the cathodes in all of our old RCA klystrons. These tubes can't provide more than 20 megawatts of power with their vintage oxide cathodes. The installation of dispenser cathodes should yield 30 megawatts of rf power.

8 Acknowledgements

We would like to acknowledge the dedication of the entire team of people at the Duke FEL Lab. Their dedication, to the many requests in attempting the impossible, has resulted in an astonishing and ongoing string of success.

Development of a High Power 1.2MW CW L-band Klystron

K. Hirano, Y. L. Wang, T. Emoto, A. Enomoto[†], I. Sato[†]

Power Reactor and Nuclear Fuel Development Corporation (PNC)

4002 Narita, Oarai-machi, Ibaraki, 311-13 Japan

ABSTRACT

The high power CW L-band klystron has been developed as the RF source of the PNC high power CW electron linac (10MeV, 100mA). CW power of 1.2 MW at 1.249135GHz and efficiencies over 65% were the design goals. RF analysis of the windows using high-frequency simulation codes provided information about power loss distribution in the ceramic and optimizing properties of the RF structure. The prototype klystron window was replaced with a long pill-box type beryllia window as a result of the simulation and hardware tests. The klystron has reached CW power of 885kW with efficiency above 45%. This paper describes key points of the designs and results of the high power RF tests.

I. INTRODUCTION

The development of a high power CW electron linac was started in 1989 to study the feasibility of nuclear waste transmutation [1]. Figure 1(a) shows the prototype klystron with the original pill-box type beryllia window (standard window). The maximum power of the prototype klystron was limited to 330 kW with CW operation because the temperature of the window increased by 53 degrees, reaching near the critical point of destruction by thermal stress. The results of high power tests of the prototype klystron indicated that the maximum RF output power was limited by the heating of the klystron RF window. A long pill-box type beryllia window (long window) was designed and measured using an L-band resonant ring in KEK (National Laboratory for High Energy Physics) [2]. The transmission RF power through the test window in the resonant ring is thirty-six times the RF input power. Surface temperature changes were observed in the beryllia disk with the RF window. The temperature of the window increased by 51 degrees at 1.7 MW CW RF power.

The standard window of the prototype klystron was replaced with the long window. High power tests were carried out for the klystron with the long window (shown in Figure 1(b)) in a factory of the klystron's manufacturer.

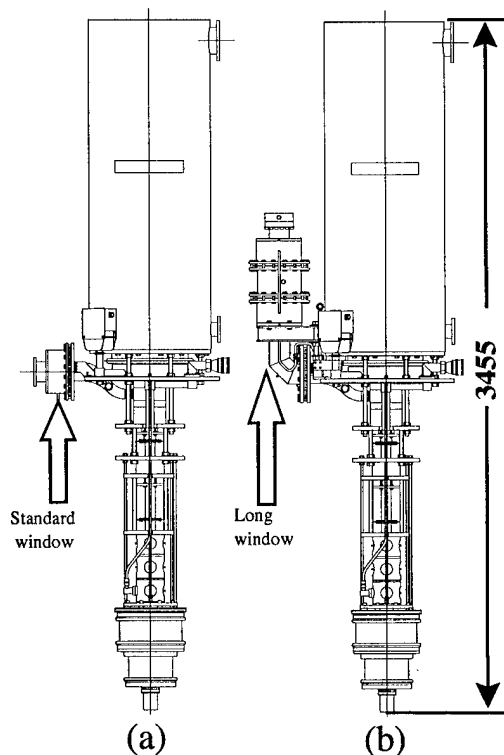


Figure 1. (a) Prototype klystron with the standard window. (b) Klystron with the long window

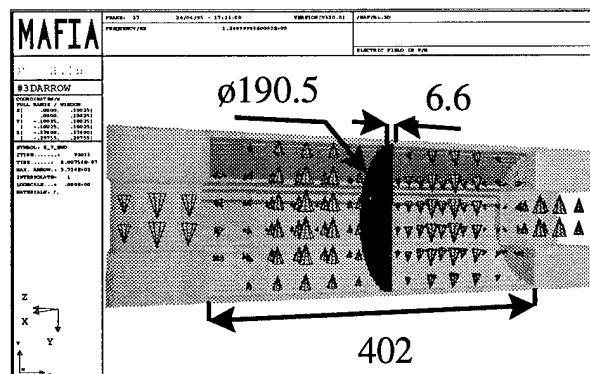


Figure 2. Dimension and electric field of the long window.

[†] Guest Scientist from National Laboratory for High Energy Physics (KEK)

II. DEVELOPMENT OF AN RF WINDOW

The long window was designed for decreasing the electric field along the ceramic disk. Figure 2 shows a dimension of the long window and electric field calculated by MAFIA. The maximum electric field in the standard and long window is shown in Figure 3. The dielectric loss of long window is approximately half of standard one from the result of the maximum electric field on the ceramic surface.

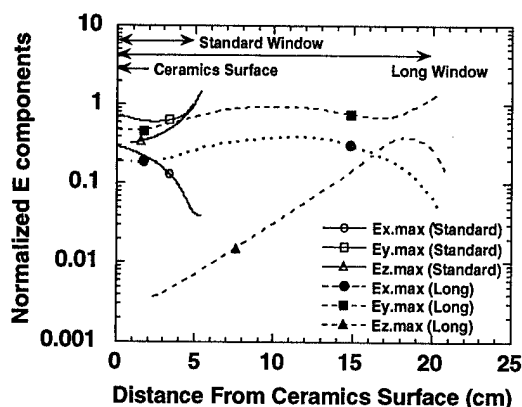


Figure 3. Maximum electric field in the long and standard window.

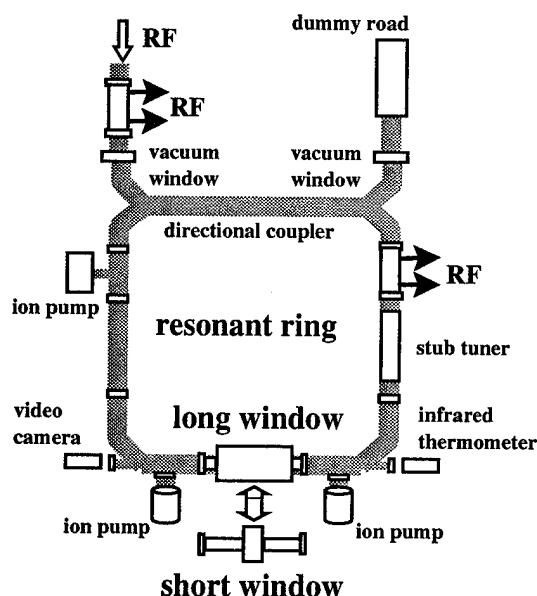


Figure 4. Resonant ring experiment of the long window and the standard window.

The electric field perpendicular to the surface of the disk is lower in the long window, which prevents multipactor more than the standard one.

The standard and long window were evaluated in the resonant ring (shown in Figure 4). Figure 5 shows the dimension of the tested pill-box windows. The light emission from the ceramic surface was observed by a video camera and the surface temperature measured by a infrared-thermometer. Figure 6 shows the window temperature vs. RF power of the two type windows tested in the resonant ring and of the standard window of the prototype klystron and the long window of the klystron tested in a factory of the klystron's manufacturer.

Test window		Standard Window	Long Window
Ceramics		beryllia	
Total length of pill-box L(mm)		293.0	595.0
Length of the cylinder A(mm)		106	402
Inside diameter of the cylinder ϕ (mm)		190.5	
Thickness of the RF window disk D(mm)		6.6	
VSWR	MAFIA calculation	1.039	1.001
	Measurement	1.04	1.03
Phase length	MAFIA calculation	$2\pi+8.8$	$2\pi+297.3$
	Measurement	$2\pi+9.7$	$2\pi+298.9$

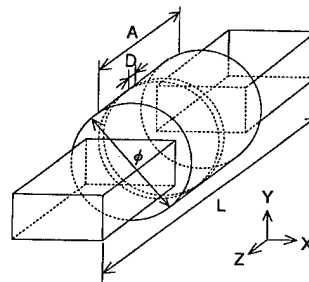


Figure 5. Dimension of the tested pill-box windows.

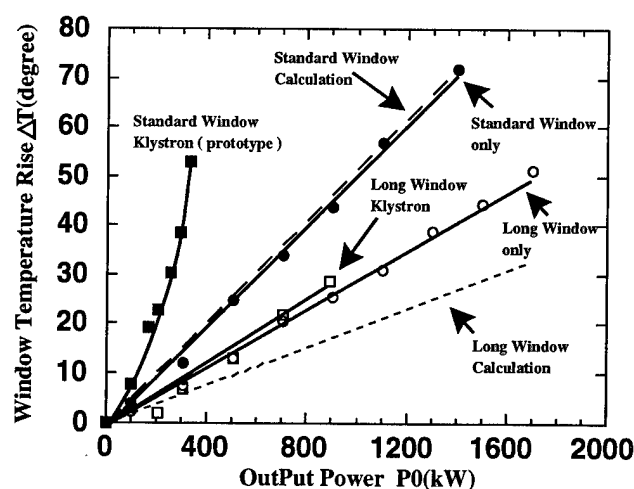


Figure 6. Window temperature rise vs. RF power.

The standard window endured 1.4 MW CW RF power. The long window endured the 1.7 MW CW RF power. Both sides of the window were coated with 60 Å thick Titanium Nitride (TiN) to prevent multipactor. No multipactor was observed on the window during the RF test. MAFIA was used to calculate the power dissipation of the ceramic window (shown in Figure 6) and model RF fields.

The perimeter of the ceramic is brazed into the thin copper cylinder cooled by water. The finite element nonlinear structural analysis system (FINAS) was used for thermal and stress analysis of the window. The variance of dielectric loss ($\tan\delta$) of ceramic disks showed that measurement in the long type window is 1.5 times larger than calculation and showed good agreement in the standard one.

The window of the prototype klystron was replaced with the long pill-box type window. A change in the color from white to yellow of the ceramic surface on the vacuum side was found when the standard pill-box was removed from the prototype klystron. The prototype klystron window faced to the output cavity. The impact of drifting electrons from output cavity caused to make color change.

III. KLYSTRON WITH THE LONG WINDOW

The long window was attached to the klystron with E-corner, by which electrons could not travel directly from output cavity to the ceramic. The observed temperature increase in the window of the klystron with the long window agreed approximately with the results of the resonant ring measurement. The klystron with the long window was tested with the CW operation and the pulse operation of 50msec long at a repetition of 1 pps. Figure 7 shows RF peak power vs. beam voltage.

The window temperature increase was 29 degrees when the klystron with the long window had achieved CW RF output power of 885kW, efficiency of 45%, and beam voltage of 85kV in the present measurement. The pulse operation at 85kV produced 1MW with this measurement. 1.2MW will be expected of the nominal beam voltage of 90kV for the pulse operation and 1MW for CW. RF power difference above beam voltage 75kV is the dimension changes of cavities due to thermal expansion. High power RF tests up to 1MW will be conducted upon the completion of the PNC linac power facility in mid-1995.

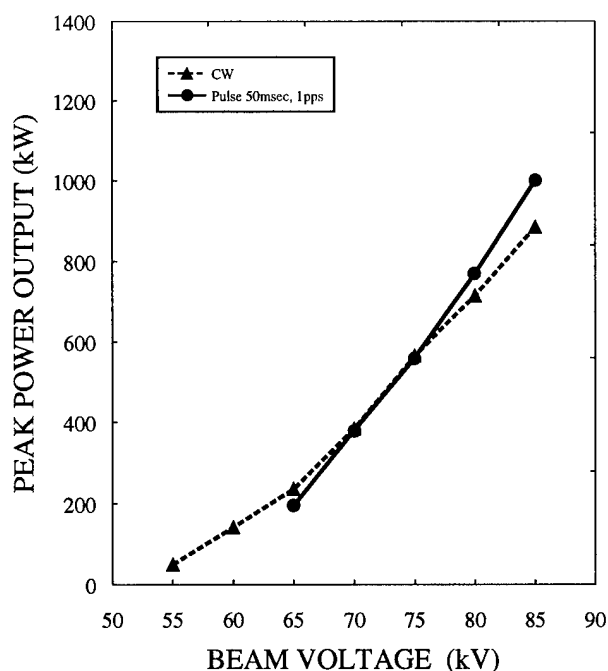


Figure 7. RF peak power vs. beam voltage of the klystron with the long window, provides that the beam perveance is constant at 9×10^{-7} .

IV. SUMMARY

Considerable progress has been made towards the realization of a high power 1.2MW L-band CW klystron. Simple approach using a pill-box type RF window has been shown to handle 1.7 MW CW, which is optimized by simulation codes. The klystron with the long window has achieved output power of 885kW CW and efficiency of 45% in the present measurement. High power RF tests up to 1MW will be carried out at the PNC linac facility in mid-1995.

V. ACKNOWLEDGEMENT

The authors wish to thank the KEK colleagues, especially Dr. S. Fukuda for his invaluable guidance in designing the klystron window.

VI. REFERENCES

- [1] S. Toyama et al, "High Power CW Linac in PNC", **Proc. PAC 93** 546 (1993)
- [2] M. Nomura et. al, "Status of High Power CW Linac at PNC", **Proc. EPAC 94** 745 (1994)

ULTRARELATIVISTIC KLYSTRON-A FUTURE SUPER POWER UHF GENERATOR

F.A. Vodopianov // Moscow Radiotechnical Institute RAN, Moscow, Russia

I. INTRODUCTION

At the beginning of work on the 76 GeV Serpuchov accelerator (after 14 October 1967 y.), a presence of HF voltage on accelerating resonators without power tube exiting was marked. This voltage was excited by rotating proton bunches. With proton current about 0.1 A and energy 76 GeV, the beam power had gigantis value 7.6 GWt. After an invention of magnetic energy analyser type grouping device, the theoretical and experimental investigations were begun. The initial structural scheme is presented in Figure 1. In 1975 the preliminary understanding have been published [1]. Here at the first time was discussed the problem of gigawatt power consumption by means of many resonators for a feeding resonators of very long linac, the problem of a o- pulse grouping of superrelativistic particle bunches, a problem of high efficiency accelerating such bunches to superrelativistic energy (energy $1; W_i$ 10 MeV). Many model elements of superrelativistic generator were constructed and made in the decade of 1975–1985—electronic guns, grouping devices, electronoguides with magnetic focusing. During the last decade, due to financial limitations work was narrowed, but namely in this time some important conceptions were suggested.

II.

Maximal electron energy must be lowered to 5-7 MeV, as at higher energy the residual radioactivity will appear. At 5 MeV the current must be about 200 A for the power 1 GWt to be conserved. The caculation shows a grouping length about 30m at energy 5 MeV and only 3.4 m at energy 1 MeV. Therefore the particle breaking can be only to energy 1 MeV and an energy using coefficient is only 83% at initial energy MeV. A consumed by one resonator power must be as high as possible. At the frequency wave length 10 cm a consumed by two outputted resonator power about $P_{ir}=20$ MWt and a whole power of 34 resonators can be about 680 MWt.

The value P_{ir} at first harmonic current amplitude $I_1=320$ A (due to real grouping coefficient $n=0,8$) depends on shunt impedance, with equal in this case 400 Ohm. Consequently the amplitude voltage drop will be 130 kV at one resonator and 440 kV at 34 resonators. The efficiency of a voltage using

$$\eta_g = 1 - W_e/W_{in} \quad (1)$$

will be about 88% at $W_{in}=5$ MeV and $W_e=0.6$ MeV. but the power efficiency of generator is of course only 68% due to $I_1=0.8I_0$. For a UHF power GWt the W_{in} must be 7 MeV.

III.

the bunch parameters 5 MeV and 200 A can easily be provided by means of the Kokroft-Wolton accelerator. The involved improvements—screening every accelerating steps [2], and using an energy feedback [3], give the possibility of having a high

efficiency ultrarelativistic bunch source (to 95%). I at the bunch power 1 GWt the 50 MWt consumption from the electrical net will be real than the efficiency coefficient of ultrarelativistic generation with 680 MWt UHF power will be $680/(680+50)=93\%$.

IV. CONCLUSION

The concentration of 34 resonators with summ UHF power 680 MWt at 3.4 m length will lead to the inadmissible power dissipation in waveguides in case a feeding the long (1 km) linac resonators. In this case the number generator resonators can be more than 34 (for example 100) and install with distance about 10 m between them with high number passive (untuned) resonators, serving for additional bunches grouping. At the 100 working resonators the power losses at 5.m length guides $0.02 \times 5 = 0.1$ dB (about 1%) will be quite admissible.

References

- [1] F.A. Vodopianov, B.P. Murin, Proceedings of Radiotechnical Institute, USSR Academy of Sciences, Accelerators teckhnics, Moscow, 1975, p. 20.
- [2] F.A. Vodopianov, SC-techn. Reports of Moscow Radiotechnical Institute, USSR Academy of Sciences, Moscow, USSR, 1990, p. 105.
- [3] F.A. Vodopianov, "MATRESHKA—High Intensity Accelerator of Continuous Particle Beams". Report PAC-95, TAR02.

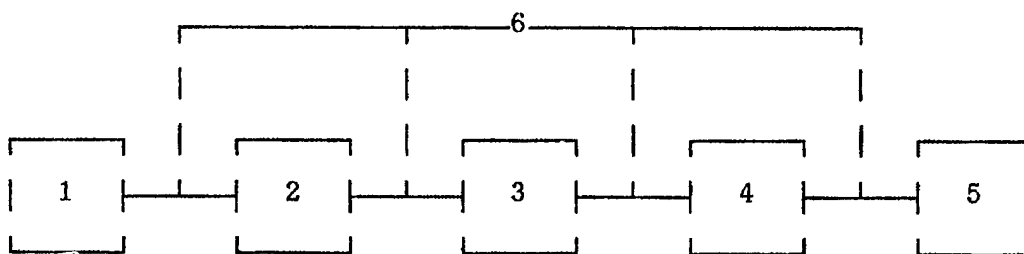


Figure 1. Structural scheme: 1 – electron gun; 2 – accelerator; 3 – grouping device; 4 – resonator system; 5 – collector; 6 – electron guide.

A 200 KW POWER AMPLIFIER AND SOLID STATE DRIVER FOR THE FERMILAB MAIN INJECTOR

J. Reid and H. Miller, Fermi National Accelerator Laboratory*, P.O. Box 500 MS-306, Batavia, IL 60510 USA

Abstract

A limitation of the existing Main Ring rf system is the power that it can deliver. The Fermilab Main Injector will require 112 KW for accelerating the full intensity at 240 GeV per second, which is pushing the upper limits for the present rf power amplifiers used in the Main Ring. New 200 KW power amplifiers will be placed on the cavities in the tunnel with 4 KW solid state drivers and 30 KV series tube modulators in the equipment gallery. Design, reliability, and solid state driver operating in a Main Ring rf station will be presented.

I. INTRODUCTION

Reliability testing of the newly designed equipment built under an R&D program by the rf department was made by installing it in the present Fermilab Main Ring accelerator. This gave real time operating experience under beam loading conditions before the equipment went into full production for the Main Injector. The 200 KW power amplifier and a 4 KW solid state driver were installed in May of 1994 on RF-RF station 7. For over 11 months they have operated flawlessly.

II. 200 KW POWER AMPLIFIER

The new amplifier design is based on the following:

1. Reliability. Since this component is located in the tunnel and mounted on top the MR cavities, a failure requires downtime. Only the power module housing the Y-567B tetrode and the cathode resonator would now be in the tunnel. Previous designs have a 14 tube cascode and a 6 tube distributed amplifier attached to the power module in the tunnel.
2. Geometry of the mounting flange and anode circuit had to be compatible with the present MR-RF cavity.
3. We will use the Y-567B power tetrode along with Fermilab's existing tube socket parts (fingers and collets). We have used the Y-567B in our existing amplifiers for many years and the power stage has proven to have excellent reliability.
4. Provide improved water cooling on and around the tube socket and bypass capacitors to remove heat.
5. Provide peak rf current of approximately 21 amps.

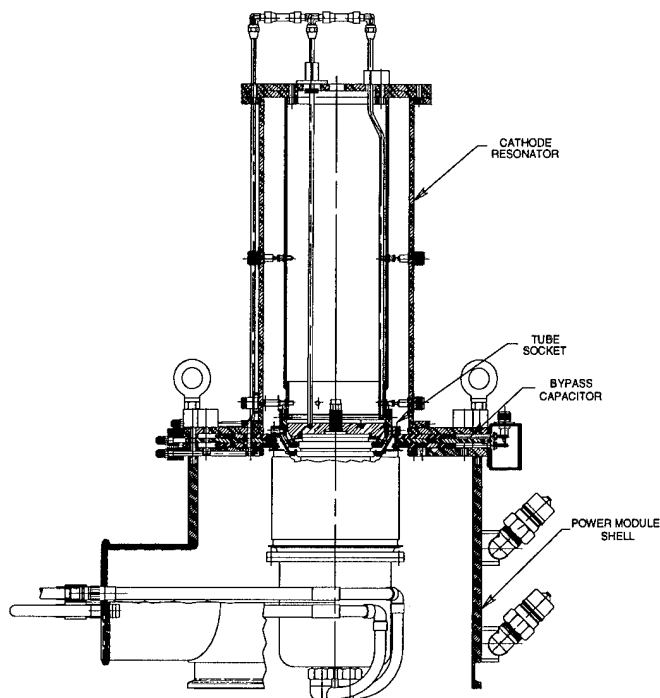


Figure 1. Cross section of the 200 KW power amplifier.

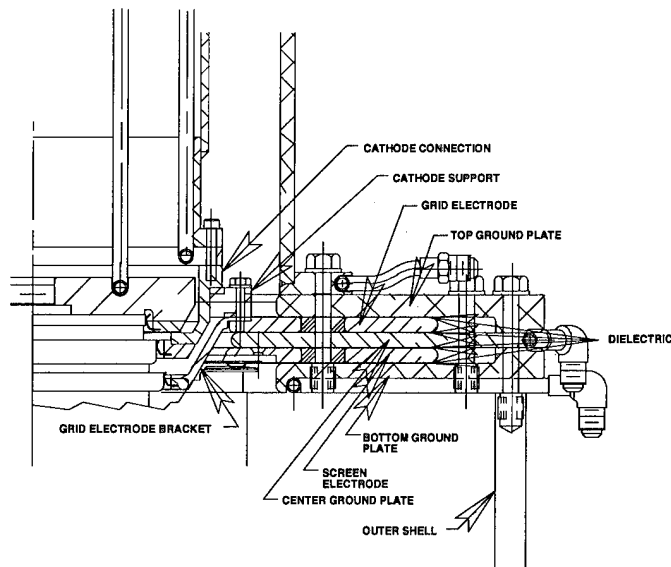


Figure 2. Detailed cross section of tube socket.

* Operated by Universities Research Association, Inc. under contract with U.S. Department of Energy.

Figure 1 is a detailed cross section of the complete amplifier. The grid and screen electrodes, grid bracket, cathode collet, filament block, center ground plane, and cooling rings are made of OFHC copper. The top and bottom ground plates are fabricated using aluminum tooling plate. Most of the other major parts are made from aluminum alloy 6061 T6.

Figure 2 shows the tube socket assembly with bypass capacitors. The screen and grid bypass capacitors are made of copper clad Kapton that is photo etched for the desired copper outline. The use of copper clad Kapton is preferred over plain Kapton. Copper clad provides a more uniform surface area for the electrodes, thus eliminating localized heating due to imperfections in electrodes or ground plates. It also provides consistent capacitance from unit to unit. The grid bypass capacitance is 12.9 nF and the screen bypass capacitance is 12.4 nF.

A filament lead bypass capacitor is located at the top of the cathode resonator. It is constructed using a copper electrode connected to the filament lead. Plain .005" Kapton sheet is sandwiched on either side of the electrode. Capacitance is 14.9 nF. The filament is powered by a commercial DC high efficiency switching supply (15.5 volts at 225 amps) located in the series to modulator.

The cathode resonator is tuned to 53.1 MHz. and has a Q of 10. The low Q and hence wide bandwidth is accomplished by tapping the cathode resonant structure with two 50 ohm terminations tapped for a 4:1 impedance transformation at the cathode (100 ohms). The terminations are physically located upstairs in the equipment gallery and connected to the amplifier's cathode circuit by two 1/2 inch Heliac cables. Over the full dynamic swing of cathode impedance the rf power loss in the cathode circuit is minimal and the impedance range is limited for the solid state amplifier load.

The cathode is driven directly at the base of the tube socket with four phase matched 50 ohm 1/2 inch Heliac cables in parallel (for 12.5 ohms) from the output combiner of the solid state amplifier. The combiner's output impedance is 12.5 ohms, but due to the dynamic impedance swing of the cathode, we only approach a matched 12.5 ohm cathode impedance at full output. Therefore, these cables are not always run as a flat line so lengths are kept near $1/2 \lambda$ multiples of 53.1 MHz. This provides tight coupling between driver and cathode.

The grid bias supply is a fast 100 KHz (bandwidth) programmable type with compliance of -500 volts to 0 volts for 0 to 10 volt program. The screen supply is a 3 phase bridge type rated at 1050 volts at 2 amps. Both of these supplies are identical to the ones used in the Tevatron rf system (Fermilab design).

A cathode monitor is installed at the same point as the rf drive. This serves as a voltage monitor and phase reference for system tuning. A second monitor (anode monitor) is placed in the outer shell's side wall in the anode circuit and is used for voltage monitoring. The cathode and

anode signals are monitored by a phase detector which controls cavity tuning.

III. 4 KW SOLID STATE DRIVER AMPLIFIER

When we first started our R&D program for the new power amplifier, we made the decision it would be driven by a solid state amplifier located in the equipment gallery. With 20 years' experience maintaining our existing power amplifiers which have tube drivers built on top of the power module we learned that a lot of our failures, while acceptable, were related to the driver components. Our existing 2 KW drivers are made up of 14 parallel 4CW-800F tetrodes (cascode amplifiers) driven by a 6 tube 100 watt distributed amplifier mounted on top of the 2 KW driver. The complexity of small tubes in the tunnel along with their associated power supplies in the equipment gallery led to a higher mean time to failure than we liked.

Initially we could find no commercial solid state amplifier that met our specification (insisting on water cooled units). This led to an in-house design using the MRF-151G Mosfet for the output stage mounted to a copper water cooled heatsink which provided 250 watts of rf power per device. We assembled 16 of these devices (mounted two devices per copper heatsink) and combined them for 4 Kwatts to drive the cathode of the power amplifier. All our initial testing of the 200 KW amplifier was done using this solid state driver.

Later a commercial solid state amplifier was uncovered which, with the exception of narrower bandwidth, could nearly meet our requirements. This amplifier with a few modifications was adapted to meet our water cooling specification and bandwidth requirements.

Past experience with air cooled heatsinks in solid state drivers have led to poor long term reliability because of excessive junction temperatures. It has been our experience that water cooling has proven to increase mean time to failure by more than an order of magnitude. Requiring copper tubing for water paths rather than organic hose greatly reduces the chances of water leaks.

Two of the commercial 1 KW amplifier chassis were modified to give the desired results:

1. Wider bandwidth.
2. Faster gated pulse response without ringing.
3. Improved chassis shielding.
4. Added 37.5 degree flare fittings for water connections.
5. Eliminated all rubber hose inside the 1 KW chassis and replaced them with copper refrigeration tubing.

One of the modified chassis was sent back to the vendor to see if they would modify their design to incorporate our changes. Since they agreed to do this, we ordered 12 additional amplifier chassis for the completion of the three R&D amplifiers.

Table 1 is an abbreviated list of specifications for the 1 KW solid state amplifier chassis.

Frequency:	30 MHz - 80 MHz
Gain:	50 dB
Gain Flatness:	+/- 1.0 dB
Phase Delay:	Less than 24 nSec
Phase:	All amps matched to +/-5 degree
Rf Power Out:	1000 watts
Cooling:	Demineralized LCW

Table 1. Abbreviated Solid State Amplifier Specification.

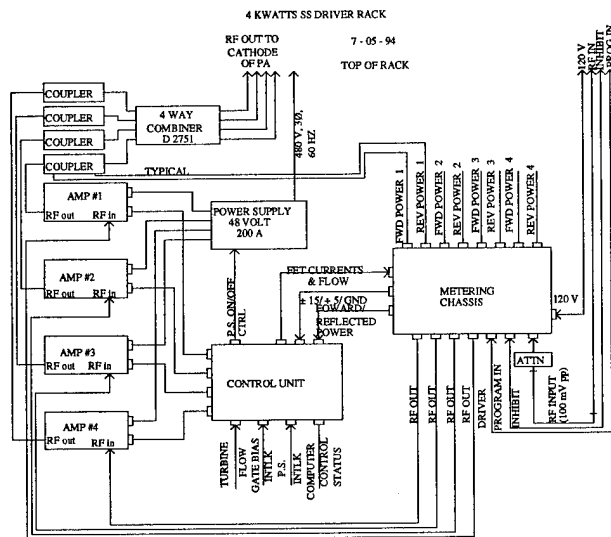


Figure 3. Diagram of the 4 KW solid state amplifier rack.

The control unit and metering chassis are Fermilab designed and fabricated. The final output combiner, dual directional couplers, and 48 volt 200 amp power supply were purchased commercially.

The metering chassis performs the following functions:

1. Measures and displays Mosfet current in each output stage.
2. Diode detectors for processing forward and reflected power of each amplifier for local and remote readout along with protection circuitry for each.
3. Variable gain rf amplifier for programming rf level to 1 KW amplifier modules in response to an input program of 0 to 10 volts (constant phase).
4. Program inhibit (TTL line).
5. Four - way rf splitter.

The control unit provides the protection, local control, and remote interface for the solid state amplifier. It utilizes a Europac HF 3U chassis with 9 plug-in modules. The modules include a water flow processor for the turbine flow meter, forward power, reflected power, amplifier monitor module for each 1 KW amplifier (4 total), power supply controller, and on/off master controller with remote status and control.

IV. INSTALLATION AT MR-RF STATION 7

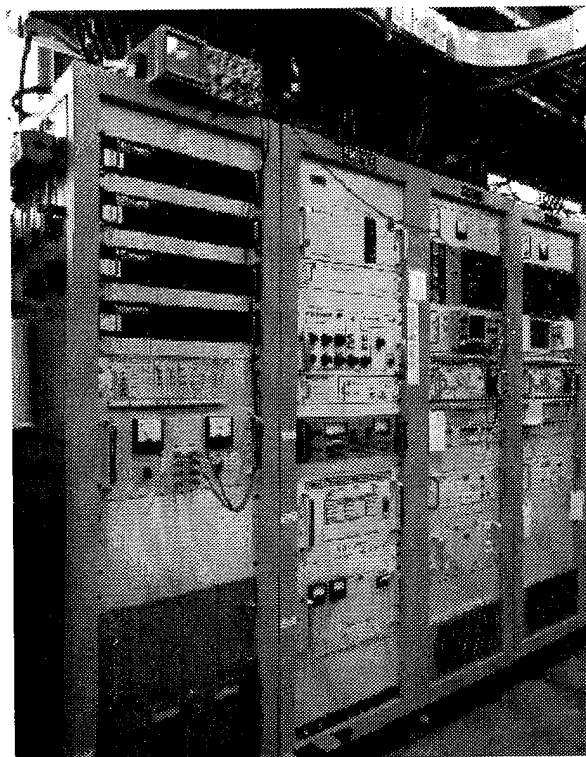


Figure 4. Installed Solid State Driver at MR-RF St. # 7.

In the foreground of Figure 4, is the 4 KW solid state driver rack positioned next to the station 7's control racks. From top to bottom are the four - 1 KW solid state rf amplifier modules, control unit, metering chassis, four - way output combiner, and power supply.

A condition for installing and running a long term test was the station had to be controlled in the normal fashion from the control room by the operations' group. The solid state driver's control unit was interfaced to the station's existing control system. With minor software programming modifications, new parameters for the solid state driver could be displayed on the usual parameter pages. This provided the operations' group full remote control, read-backs, and alarms to the control room as with a normal station.

In May of 1994 the station was made operational with the new 200 KW power amplifier and solid state driver. The 200 KW power amplifier typically runs with a peak anode voltage of 18 KV from the series tube modulator, a peak negative grid bias of -300 volts, and a peak forward power of 1700 watts from the solid state driver with beam intensities of 3.1 E12 on pbar production cycles (beam loading compensation active).

To date we have had no failures or downtime associated with the new 200 KW amplifier and solid state driver. Even though this is the only station operating this way, it is a good indication that the designs are sound.

A 476 MHZ RF SYSTEM FOR THE STORAGE MODE OF THE AmPS RING

F. Kroes, P. de Groen, E. Heine, B. Heutenik, A. Kruijer, B. Munneke, R. Pirovano, T. Sluijk, J. Verkooyen, NIKHEF-K, P.B. 41882, 1009DB Amsterdam, the Netherlands

Abstract

The Amsterdam Pulse Stretcher (AmPS) is an electron storage and pulse stretcher ring. The ring operates at energies between 300 and 900 MeV at circulating currents up to 200 mA. A 50 kW RF source with fast amplitude- and phase modulation drives a 2856 MHz accelerator section in the stretcher mode of operation. This RF source doesn't provide enough power to ensure acceptable beam lifetime for storage mode operation at energies above 550 MeV. Therefore a 476 MHz CW RF system has been implemented. Its cavity is a modified, former DORIS (DESY), 500 MHz single cell pillbox cavity. In the cavity a gap voltage of over 400 kV is generated at the maximum 30 kW CW power from a YK1233 Philips klystron. Three RF feedback control circuits are incorporated to stabilize the cavity parameters; one for frequency, the second for the phase and the third for the amplitude. Design, realization and operation of this RF system is described.

I. INTRODUCTION

For the stretcher mode of AmPS a 2856 MHz RF source has been built[1,2]. To obtain reasonable lifetimes in the Storage Mode of operation, a rather high rf voltage will be required at this frequency. At 900 MeV a rf voltage of 700 kV is needed to create a bucket size of $7\sigma_E$ (σ_E being the equilibrium energy spread). The amount of rf power which is needed to generate this voltage in the 12 cavities long travelling wave structure is 1.5 MW CW and not realistic.

At 476 MHz, the sixth subharmonic of the accelerator frequency, only 150 kV is needed to create the same bucket size. For a bucket size of $10\sigma_E$, the rf voltage is 270 kV at 476 MHz

For future operation, after 1998, AmPs can be used as a driver for FELINA (Free-Electron Laser in Amsterdam) for the generation of narrow bandwidth radiation in the ultra-violet spectral range ($\lambda \geq 200$ nm). The rf voltage needed for this application at 476 MHz is 350 kV [3].

To fulfill these requirements at a frequency of 476 MHz a new source which have to be realized. The rf related specifications for the present storage mode of operation are:

Energy range	E	[MeV]	300-900
Circulating current	I_b	[mA]	200
Energy spread bucket	δ	[%]	± 0.1
Frequency	f	[MHz]	476
Harmonic number	h		336
Compaction factor			0.027
Bending radius magn.	ρ	[m]	3.3
Ring circumference	L	[m]	211.618
Circumference period	T	[μ s]	0.7

The rf power requirement is calculated for a bucket size of $10\sigma_E$. Table1 shows for the energy range of 500 to 900 MeV and a beam current of 200 mA the effective cavity gap voltage

and corresponding rf powerlevels for a single cell reentrant cavity with transit time corrected $R_{sh}=4M\Omega$ ($V^2/2P$) and coupling factor of $\beta=1.6$. U_s is the synchrotron radiation loss per turn. U_t is total loss including the parasitic loss. The cavity wall losses for an effective gap voltage of 400 kV are 21 kW.

Table 1

Beam Energy (MeV)	U_s (keV)	U_t (keV)	V_{rf} (kV)	P_{rf} (kW)
500	1.7	2.7	45	0.8
600	3.5	4.5	80	1.8
700	6.5	7.5	125	3.6
800	11.0	12.0	190	7.2
900	17.6	18.6	270	13.4

II. CAVITY MODIFICATION

Modification of the cavity to 476MHz (Fig. 1)

The University of Bonn[5] provided us with a former DORIS (DESY) 500 MHz copper pillbox cavity[4] together with a rf input loop coupler and plunger system from a 5-cell PETRA (DESY) cavity. The cavity modification steps were as follows,

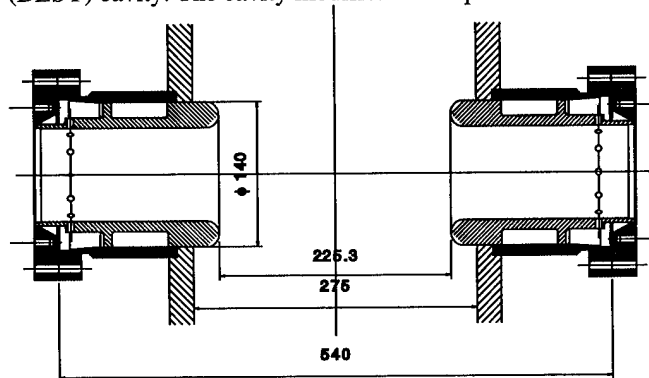


Fig.1 Nose cone inserts

-Calculation by Urmel-T of the cavity RF parameters when it is modified to the operation frequency of 476MHz by the insertion of nose cones. The results are a transit time($T=0.73$) corrected R_{sh} of $4.5M\Omega$ ($V^2/2P$) with a $Q_{unl.}$ of 40000 and R/Q of 112Ω . In the real cavity this impedance is degraded by about 10% due to the addition of ports and the condition of the copper inside surface. The frequency dependency of the nose-cone distance is .62 MHz/mm

-The beamports of the cavity were slightly tapered, they are machined to a final fixed diameter.

-The plunger diameter is machined to a 4 mm smaller diameter to fit the plunger port of the cavity with a 4mm circular spacing. The plunger is water cooled and is tested at 10 Bar waterpressure in vacuum because of the remaining 2mm copper wall thickness with braze joint. The rf input loop coup-

ler was original coupled to a waveguide. In this design it is coupled to a coaxial guide. The diameter of the coaxial window has the EIA 6 1/4" dimensions. To get the cooling pipes of the rf input loop coupler to ground level it was needed to insert a $1/4\lambda$ shorting stub of the same dimension coaxial guide into the loop coupler connection with the cooling pipes into the center conductor as shown in fig.2. For the exact coupling range a 4 cm thick adapter is inserted between the cavity and the input loop coupler [6].

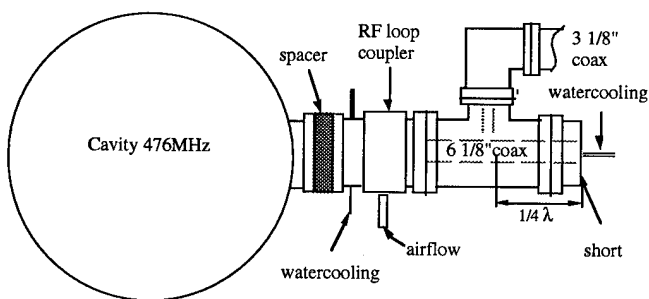


Fig.2 RF input loop coupler

-For the preliminary measurements alumina nose cones are made. In the nose cones there is a groove in which a silver spring is mounted to get good electrical contact for the rf currents.

-Measurement of the actual specs of the cavity while all the components are tuned to the desired specification. Plunger at +7.5 mm depth, angle of rotation of the rf input loop with respect to the beam direction of about 30° at an overcoupled β of 1.6. Nosecone distance tuned to a resonant frequency of 476 MHz taken into account the temperature of the cavity. Frequency dependency of temperature is $8 \text{ kHz}/^\circ\text{C}$. The measured $Q_{unl.} = 36000$ and $Q_l = 13800$. The tuning range of the plunger is from 475.4 to 477 MHz for depth of -15 to +25 mm. -Low temperature braze of the final copper nosecones into the beamports of the cavity with all the other elements removed.

Vacuum and RF conditioning

The copper cavity had been stored in open air for many years. The inside surface was totally black. The first action was cleaning of the inside surface by polishing and not etching solvents. The low temperature silver-tin braze of the copper nosecones is done under vacuum at 220°C . After assembling of the cavity with all its accessories it is baked to 100°C for two weeks connected to a 180l turbopump set with mass-spectrometer. The end pressure was $3.1 \cdot 10^{-9}$ Torr and the partial pressure content of the carbon-hydrogens was .35% and the cavity ready for installation in the Ring. The rf power test of the cavity is combined with the rf- and vacuum conditioning. For this activity the cavity was still on its position in the ring but isolated from the ring vacuum with a separate turbo molecular pump and mass-spectrometer. It take two weeks till it was possible to handle 25 kW of CW rf power in the cavity without the appearance of incidental gas bursts. Multipactoring was observed in the peakpower range of .5 to 1 kWatt especially during the very beginning of the rf conditioning.

III. RF SOURCE DETAILS (fig. 3)

Synchronozation

The 476 MHz signal is delivered either by a local synthesizer or by the 6th subharmonic masteroscillator of the MEA accelerator and can be chosen by remote control. When synchronization to the accelerator bunch structure is important for injection purposes the exact phase for optimum capture can be set with phase shifter ps-1.

RF drive details

-PIN switch which is used for protection purposes. If there is an arc in the klystron cavities or in the circulator or the rf power reflection from the circulator exceeds 4% (VSWR=1.5) the rf power will be switched off to protect the klystron.

-Electronic variable attenuator att-2 of 20 dB as the control device for the cavity voltage level control. Att-1 is used for the adjustment of this control loop.

-Electronic variable phaseshifter ps-3 of $0-360^\circ$ as the control device for the cavity voltage phase control.. Ps-2 is used for the adjustment of this phase control loop.

-Solid state power amplifier of 50dB to deliver the 50W maximum drive power for the klystron power amplifier.

30 kW power amplifier

The klystron is a Philips YK 1233A normally used for a TV transmitter in the range of 470 to 860 MHz. Philips has tested this klystron at 476 MHz CW operation condition of 29.3 kW. In table 3 the typical specs are given for two levels of operation. Recommended CW operation is at max. 90% of the saturated output power. This tube has two control electrodes.

-Modulation anode which is powered to 75% of the DC beam voltage to give the desired perveance.

- U_{abc} which is close to the cathode and can be varied from 0 to -1000V to change the gain of the tube by means of DC beam current variation.

Table 3. YK 1233A specifications (typical)

Pout 90% sat.	kW	15	25
Beam voltage	kV	17	20.5
Beam current	A	2.2	2.9
Pdrive sat.	W	6.5	6.5
Bandwidth(-3dB)	MHz	5	5
efficiency	%	45	42

High power coaxial transmission line

The coaxial line close to the cavity and the klystron which contains the directional couplers are of the standard 3 1/8" EIA. For the coaxial waveguide connections between the klystron, circulator and cavity the 100mm diam. fast mounting system(SMS) coaxial guide of Spinner is used because it is easy to install. The circulator is a commercial type from ANT Bosch and can handle the full reflection of 30 kW. The isolation is more than 40 dB and it is stabilized for the change in power level and temperature of the cooling water.

RF control loops

The rf source has three control loops. The electronics of all three systems are in the transmitter area. For this reason two 15m long phase stable 7/8" Flexwell cables are used for the transmission of the the cavity- input and measurement loop signal from the ring vault to the transmitter room.

-The first loop controls the frequency of the cavity under the change of temperature and beamloading. A phase change will be compensated by adjusting the tuning plunger by means of a stepper motor. The response time is in the 0.1sec. order.

-The second loop controls the phase of the cavity voltage. The phase reference is the master oscillator. Any phase change introduced by a temperature change of the coaxial network or a change of the klystron's electrical length or beamloading will be corrected for by the electronic phase shifter.

-The third loop stabilizes the cavity voltage. The rectified output signal from the cavity measurement loop is compared with an adjustable reference level. Any change introduced by the amplifiers or beam will be adjusted for. By changing the reference level the operational cavity voltage can be set. The response time for the last two controls is in the 0.1 msec order.

Higher order modes (HOM)

No effort has been put into the damping of the higher order modes. The maximum beam current level in the ring is 200mA and seems to be just below the level where problems with bunch instabilities will occur. During the operation of the ring in stretcher mode at 2856 MHz problems are observed during the optimization of the extracted current influenced by the 476 MHz cavity in the ring. This effect totally disappeared by detuning the cavity about 0.5 MHz with the plunger..

Operation results

The first experiments in the internal target hall with the ring in storage mode at 476 MHz were during Dec/Jan '94/95. The lifetime T of the beam was in the order of 1/2 hour. The max. injected peak current was 50 mA for 3-turn injection which means a circulating current of 150mA. During this period the 476MHz station was started up and operates for 2 month without interruption. The accelerator was in operation at its lowest repetition rate of 10pps. Storage mode experiments are preferently planned in winter time to reduce the electricity costs.

IV. ACKNOWLEDGEMENTS

The work described in this paper is part of the research program of the Nuclear Physics section of the National Institute for Nuclear Physics and High Energy Physics (NIKHEF-K), made possible by financial support from the foundation for Fundamental Research on Matter (FOM) and the Netherlands Organization for Scientific Research (NWO)

V. REFERENCES

- [1] F.B. Kroes e.a., A fast Amplitude and Phase modulated RF source for AmPS, "proc. of the IEEE PAC, San Francisco 1991, pp. 684-686.
- [2] R. Maas e.a., "Commissioning results of the Amsterdam Pulse Stretcher/Storage Ring", Proc. of the IEEE PAC, Washington 1993, pp. 1998-2000.
- [3] R.J. Bakker e.a., "Expected performance of FELINA, the Dutch VUV-FEL in Amsterdam", Nucl. Instr. & Meth. april 11, 1995, Vol.358 nos 1-3, pp. 358-361
- [4] H. Gerke, W. Quarz, "Cavity resonators for a 3 GeV double ring storage facility", Kerntechnik 16, Jahrgang 1974 No. 6
- [5] W. von Drachenfels, UNI Bonn, Private communication.
- [6] M. Sommerfeldt, DESY, Private communication

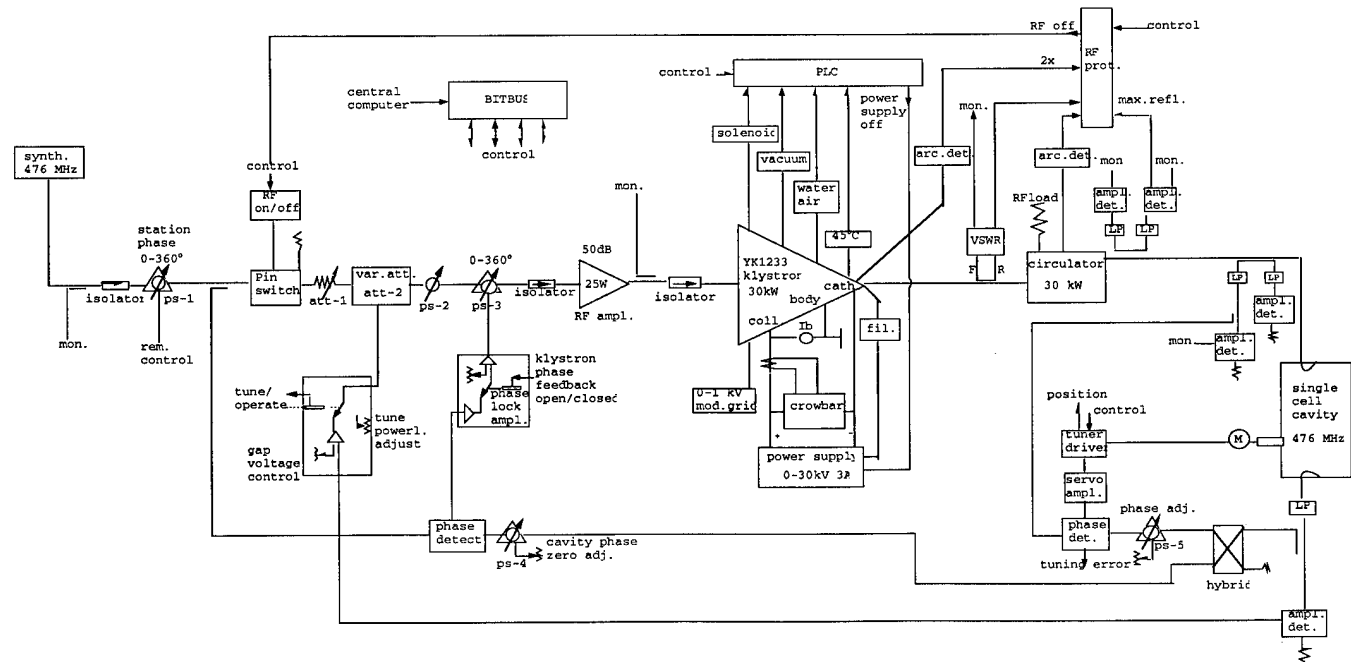


Fig.3 476 MHz RF source

Lifetime Experience with low Temperature Cathodes equipped in Super Power Klystrons.

Rudolf Bachmor, Philips GmbH, RHW Hamburg, Germany

0. ABSTRACT

When Philips started the production of super power klystrons in 1976 the electron emitter was a tungsten dispenser cathode of the well-known Philips "B" type. One disadvantage of this cathode type is the relative high cathode temperature. Many efforts have been spent from researchers world-wide to decrease the operating temperature of the dispenser cathode.

Since 1990 we have tested several sputter coated Os/Ru cathodes in cw super power klystrons. The expected decrease of the temperature has been entirely confirmed. Measured emission data compared to "B" cathodes during factory acceptance test are presented. Positive experience concerning lifetime under real operation conditions has been gained at different international accelerator centers and will be reported.

1. INTRODUCTION

The Philips Röhren- und Halbleiterwerke in Hamburg, Germany, is a manufacturer of high power microwave tubes. In the scope of current production are klystrons and inductive output amplifiers (IOA) for the UHF-TV market and high power continuous wave klystrons for high energy research and pulsed klystrons for radar application.

Most of the cathodes equipped in tubes are tungsten dispenser cathodes of the well-known "B" type developed in the Philips research laboratories in the Netherlands and the United States of America [1]. The cathode consists of a porous tungsten body with roughly 80% density. The pores are filled with a mixture of bariumoxid, calciumoxid and alumina with a molar ratio of 5:3:2.

In 1976 Philips started the production of super power cw klystrons with 600kW RF output power installed in high energy research laboratories. For this application the proven technology of the Philips "B" cathode was chosen too.

A typical operating temperature of the "B" type cathode is about 1040°C_b . This relative high temperature creates a number of problems related to the evaporation of barium from the cathode:

- Electrical breakdown strength across ceramic insulators.
- Primary electron emission from the focus electrode.
- Flaking of condensated barium from the anode under electrical forces.

Due to this disadvantages it is one main goal of thermionic cathode improvement to increase the electron emission density

at a given operation temperature permitting the same current at reduced temperature.

2. LOW TEMPERATURE CATHODES

2.1 The "M" type Cathode

A significant improvement in dispenser cathode technology was made in the 1969's at the Philips research laboratories in Eindhoven [2]. Zalm and van Stratum found that a coating of the cathode emission surface with a metal of the platinum group (osmium, iridium, ruthenium or rhenium) gives a reduction in work function of about 0.2eV. This means in practice that the cathode can deliver the same current density as the "B" cathode at 60°C to 100°C lower temperature. The "M" type cathode was born.

2.2 The Philips "M" type Cathode

In the present state the Philips "M" type cathode is a conventional "B" type cathode with a osmium-ruthenium coating of about $1\mu\text{m}$ thickness.

3. CATHODE PREPARATION

Deposition of Os/Ru films on porous tungsten with modern sputtering facilities is an usual process in Philips cathode ray tube production.

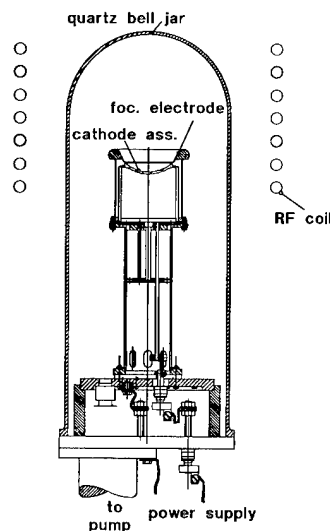


Fig.1 Gun Pretreatment Station

The emitting surface has a diameter of 1mm. Five thousand cathodes are sputter coated in one procedure. These cathodes give good results in Philips TV colour tubes with respect to grid emission and lifetime.

In recent years this technique was also been used for the large cathodes (up to 80mm in diameter) of super power conotinous wave klystrons. There is only one additional step in the cathode production line:

After impregnation the pellet is sputter etched and than coated with Os/Ru.

Before installation into the gun structure each cathode assembly will be vacuum fired in a quartz bell jar (Fig.1) for several days. The reason is to degas the cathode assembly and to evaporate residual impregnant from the cathode surface. During pre-firing the pressure is be maintained at less than 5×10^{-6} torr while the cathode temperature is slowly increased up to the operating value.

The relationship between heater power and cathode brightness temperature ($^{\circ}\text{C}_B$) was measured by an optical pyrometer through a $0.650 \mu\text{m}$ filter.

4. RESULTS

4.1 Factory Test

After tube bake-out and burn-in a detailed underheating characteristic was measured at constant gun voltage. Fig.2 shows the measured normalized cathode emission curve (Miram plot) of three Os/Ru coated cathodes compared to a standard "B" cathode.

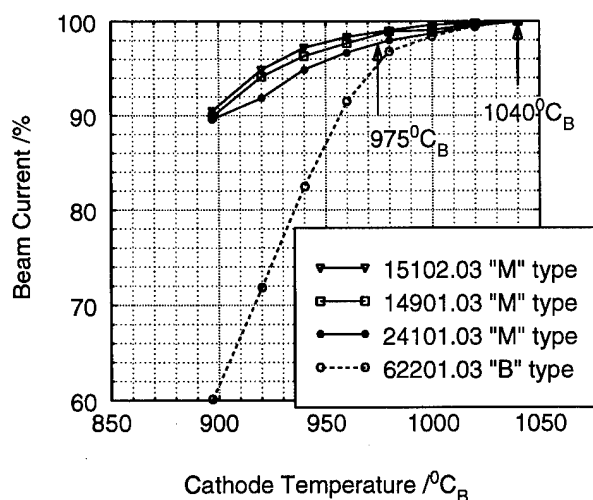


Fig. 2 Underheating characteristic plot measured during factory test. Comparison between "B" cathode and "M" cathode

The transition point between the temperature limited zone and the space charge limited region was shifted to lower temperatures. A decrease of about 65K in cathode operating temperature can be allowed to guarantee stable emission conditions. The temperature was fixed at 975°C_B instead 1040°C_B for standard "B" cathodes. This reduction gives a decrease in barium evaporation down to about 25%.

4.2 Emission Tests during Life

Since 1990 more than twenty five super power klystrons of various types were equipped with Os/Ru coated "M" type cathodes.

Some tubes are under special lifetime observation at the customer.

Cathode current measurements are carried out periodically and with the known relationship between heater power and cathode temperature beamcurrent-temperature plots can be made.

The behaviour of one tube during life is shown in Fig. 3.

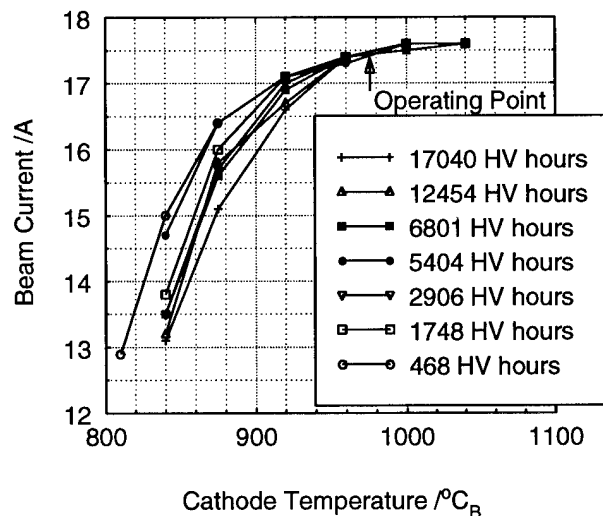


Fig. 3 YK1304 Underheating characteristic during life. The operating temperature is fixed at 975°C_B .

Another indicator of cathode emission condition is the tube perveance. The operating time dependence of perveance shows Fig. 4. In the beginning a little fluctuation can be observed. After about 5.000 hours the perveance increases slowly. A reduced anode voltage can be applied to achieve the same beam current.

From [3] it is known that at normal cathode operating temperatures interdiffusion of tungsten substrat and the osmium-ruthenium layer occurs. The cathode performance first improves with life because the work function will go through a minimum (that means a maximum in emission) at 80% W concentration in surface. When the surface became more rich in tungsten the emission decreases.

The time for degradation is temperature dependent. The expected time to reach the minimum in work function at $975^{\circ}\text{C}_\text{B}$ is more than 100.000 hours.

6. REFERENCES

- [1] R. Levi: Improved impregnated cathode
J. Appl. Phys., 1955, 26, p. 639
- [2] P. Zalm, A. van Stratum:
Osmium dispenser cathodes
Philips Techn. Rev., 1966, 27, p. 36
- [3] L. Falce: Dispenser cathodes: The current state of the
technology
IEDM Techn. Digest 1983 p. 448

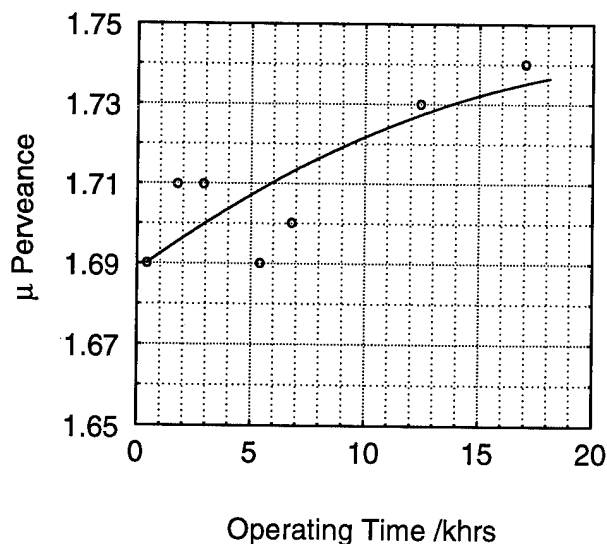


Fig. 4 Perveance during life

5. CONCLUSION

In total more than twenty five Philips super power klystrons equipped with Os/Ru coated "M" type cathodes are working trouble-free in different accelerator centers world-wide. The RF output power is between 800kW and 1.3MW. Some tubes have exceed 18.000 high voltage operating hours.

The Philips low temperature "M" coated cathode accomplishes the strong demands in super power klystrons.

The advantages for running tubes in transmitters are:

- Low evaporating rates of the impregnants.
- Low operating temperature.
- Temperature decrease of focusing electrode leads to depression of unwanted primary emission
- Long-term stability of emission.
- Long service life of klystron.

The emission behaviour of the Philips "M" type cathode also has been tested with success in several TV klystrons and inductive output amplifiers. A lifetime testprogramme is started in cooperation with the German Telecom.

MICROWAVE SYSTEM OF PLS 2-GeV LINAC*

H. S. Lee, O. H. Hwang, S. H. Park, C. M. Ryu, and W. Namkung
Pohang Accelerator Laboratory, POSTECH
Pohang 790-784, Korea

The microwave system of the PLS 2-GeV linac is systematically divided into two parts. One is a drive system, the other is a waveguide system. The drive system consists of an RF signal source (2,856 MHz), a solid state amplifier (SSA), a phase shift key (PSK), a main drive line (MDL), and IPA units. There are 11 high power klystrons, 10 SLED-type pulse compressors, and 42 constant gradient accelerating sections in the waveguide network. One module of the waveguide network consists of 63 pieces of waveguide components and four accelerating sections. After installation of the waveguide system, phases for each branch of the system are measured, and phase differences between branches are adjusted within 1 degree. The attenuation of the waveguide system from the klystron output to the input port of each accelerating section is about 0.8 dB. This paper presents the design of the microwave system and its performance.

I. INTRODUCTION

The PLS 2-GeV linac is completed by the end of June 1994 as a full energy injector to the storage ring, a third generation synchrotron light source. There are 11 klystrons and modulators, 10 SLED-type pulse compressors, and 42 accelerating sections [1,2]. The electron beam is accelerated with a pulsed RF of 2,856 MHz. The RF frequency, phase, and power are very important factors in linac operations. The change of these factors gives influences on the energy and the energy spread of accelerated beams. The magnitude of the change of these factors depends on various reasons such as the drive signal of klystrons, modulator beam voltages, and even environmental conditions. The beam voltage of the modulator is stabilized within the design specification of $\pm 0.5\%$ in two stages [3]. The temperature of accelerating sections is routinely controlled within $45 \pm 0.2^\circ \text{C}$. For the drive system, the design tolerance of phase stability is less than $\pm 3.5^\circ$ during 72 hours for the entire 145-m long drive line.

The drive system was completely installed by the end of August 1993, and the waveguide system was completed in December, 1993. The RF conditioning for the whole waveguide system and the beam commissioning have been continued since then. Until now, the whole microwave system is being operated without a serious problem.

II. DRIVE SYSTEM

There are three parts in the drive system; the signal source to drive the preinjector klystron, the main drive line to supply the drive power to 10 klystrons out from the preinjector klystron, and IPA units to adjust the power level and the phase angle of the drive

power. The schematic diagram of the PLS linac drive system is shown in Fig. 1.

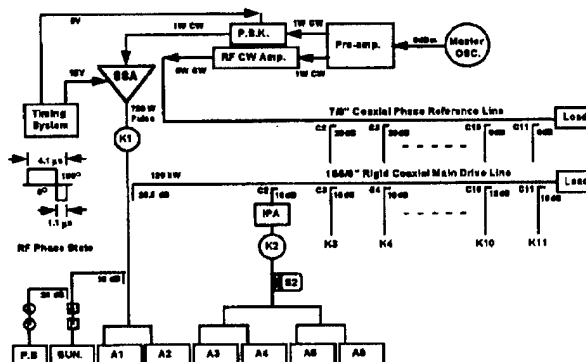


Fig. 1: Schematic diagram of PLS microwave system.

A. Signal Source

The signal source consists of a master oscillator, a low-level signal conditioning unit, and a solid-state amplifier. The high precision synthesized signal generator is used as a master oscillator. The frequency stability of the master oscillator is 5×10^{-10} /day, and the phase noise is -137 dBc/Hz at 10 kHz offset. The low-level signal conditioning unit consists of a pre-amplifier, a CW RF amplifier, an isolator, and a PSK. The PSK unit can be operated up to 2-W CW power and its switching time is shorter than 50-ns. The solid-state amplifier is a C-class pulse amplifier. The PSK output of 1-W CW is amplified by the SSA to 720-W pulse power by using the multi-cascade method and the power combination method. The SSA provides the drive power to the preinjector klystron. The output of the solid-state amplifier is adjustable from 400-W to 720-W, and the pulse width adjustable from 2 μ s to 7 μ s. Its rise and fall times are about 0.2 μ s and 0.1 μ s, respectively.

B. Main Drive Line

The main drive line of 1-5/8" air-dielectric rigid coaxial line transmits the 2,856 MHz RF power from a cross coupler waveguide located in the preinjector waveguide system to the end of the accelerator. It consists of 45 straight pieces, 2 right angle elbows, 2 expansion sections, 11 couplers, and a load. The total length of the main drive line is 145 m. The expansion sections are for compensations of the longitudinal thermal expansion due to the temperature variation in the drive line. There are 4 kinds of coupling coefficients in 10 couplers to extract proper drive power to the klystron from the main drive line. Approximately 120-kW

* Work supported by Pohang Iron & Steel Co. and Ministry of Science and Technology, Korea

power is supplied to the main drive line. The output power at each directional coupler is 2~3 kW ranges.

C. Isolator-Phase Shifter-Attenuator (IPA)

The IPA system provides the isolation of the main drive signal from the reflected drive signal at each klystron as well as the control of the phase and the amplitude of the drive power for each klystron. An IPA system consists of two units. One is an RF unit and the other is an electronic control unit. There are two controllable components in the RF unit; a phase shifter and an attenuator. The phase shifter is a rotary-field type and is digitally controlled from 0° to 360° by a current drive. The attenuator is a strip-line variable type and its attenuation is varied from 0 to 20 dB by a DC motor. An Intel 8751 microprocessor is used in the electronic control unit which is connected to the main control system via a special VME I/O port. The main parameters of the IPA system are shown in Table 1.

Table 1: Main parameters for the IPA unit.

Frequency Range	2,856 +/- 0.1 MHz
Total Insertion Loss	< 3.0 dB
VSWR	< 1.2
Max. In/Out RF Power	3/1.5 kW peak, 4 μ s, 60 Hz
Phase Shift Range	Modulo 360°
Phase Error	< +/- 3.0°
Variable Attenuation Range	20 dB max.
Isolation	> 30 dB

III. WAVEGUIDE SYSTEM

The waveguide system consists of the waveguide network, pulse compressors (SLEDs), and accelerating sections. The waveguide network transfers the microwave power from the klystron to the accelerating sections. The pulse compressor is for increasing the peak power of microwaves instead of reducing the pulse width. The electron beam is accelerated in the accelerating section with microwaves as shown in Fig. 1.

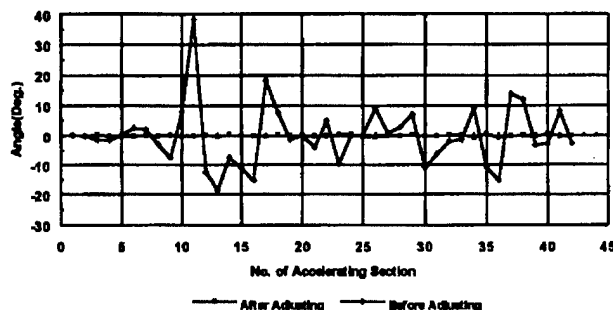


Fig. 2: Phase adjustment result of the waveguide system.

A. Waveguide Network

This system consists of 63 pieces of S-band standard waveguide components. The thickness of each component is 5 mm. The length of one branch from the klystron output to the input port of an accelerating section is about 16 m. One klystron feeds the microwave power to four accelerating sections. Each klystron is individually phased by an IPA system to obtain the correct phase relationship between bunched beams and the microwaves. In the PLS linac, the distance between the input couplers of accelerating sections in one module is 31 wavelengths. The high power waveguide network must be adjusted to be equal in phase length, or to differ by only integral numbers of wavelengths. The waveguide branches from a klystron output to the output ports of the four accelerating sections were adjusted to be equal in phase length within tolerance of +/- 1° by using a network analyzer (HP 8510C). The results of the phase adjustment is shown in Fig. 2. During the phase adjustments, the vacuum pressure of the waveguide system was kept in order of 10⁻⁵ torr to reduce the error occurred by distortion of the waveguide due to the atmospheric pressure. And the temperature of adjusted waveguide branch was maintained within 45 +/- 0.1°C. The pulse compressor was detuned during the adjustment. The average loss of the waveguide network between the klystron output and the input ports of accelerating sections was 0.8 dB.

B. Pulse Compressor

We use 10 pulse compressors to get a high energy gain in the accelerating sections. Several RF tests are conducted before being installed. The measured unloaded Q-value is about 100,000 and coupling coefficient is about 4.8. Also the measured power gain is about 7.5 dB. We have two kinds of pulse compressors which is different in detuning needles. One half of them are old type which is the same as the SLAC type. The others are a new type in which the position of the detuning needle is changed. Currently, all pulse compressors are operated at about 60-MW RF power. When the RF phase is reversed at 3 μ s after the RF pulse turn-on, the measured power gain is higher than 7.4 dB.

C. Accelerating Section

There are 42 accelerating sections in the PLS linac. They are all SLAC-type constant gradient structures. Three kinds of accelerating sections are periodically arranged in order to compress higher order modes. To compensate disturbances on electron beams due to the coupler asymmetry, all accelerating sections are installed with BA-ABBA-AB-BABA etc. configuration. Each accelerating section operated with $3\pi/2$ mode is 3.072 m long and has conflat flanges for easy installation and maintenances. The attenuation of an accelerating section is less than 4.9 dB. Presently, about 70-MW of RF power (peak) is fed into each accelerating section.

IV. PERFORMANCE OF M/W SYSTEM

The slippage between RF wave crests and electron bunches may take place in accelerating sections. When the operation

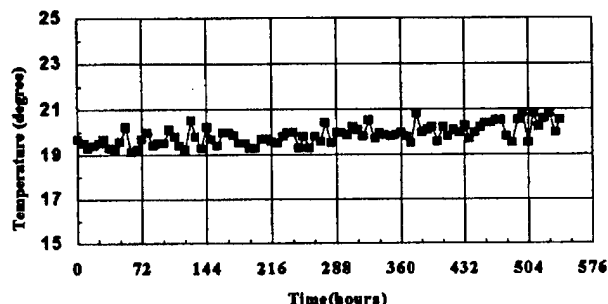


Fig. 3: Temperature variation of the main drive line.

frequency is drifted or the temperature of accelerating sections is shifted from the desired value, the derivation of the phase velocity from the speed of light occurs. The variation of the operating frequency is most influential to the beam quality than other reasons such as the phase shift in the main drive line. We observe that the operating frequency of the master oscillator varies within several Hz per day.

There are three relevant factors which affect the phase stability of the main drive line; the length, the dielectric constant of the gas inside the line, and the dielectric constant of the Teflon for supporting the center conductor. These factors vary as the temperature of the environment changes. The length variation causes the greatest phase errors compared to the phase errors raised by other two factors. The length variation of 145-m long main drive line is about 2.44-mm per 1°C change. This value causes a phase error of about 8.8° at the end of the main drive line. The temperature of main drive line is measured as shown in Fig. 3.

The phase variation of the drive signal of each klystron is measured at the RF input and output monitoring ports in IPA units with a double-balanced mixer. The measured result shows that the maximum phase variation of the drive signal in each klystron is less than $\pm 3^\circ$.

There is usually a time delay between the microwave and the electron beam due to the propagation speed of the microwave in the main drive line and the drop-out cable. The length of the drop-out cable of each module is nearly the same to avoid the irregular delay time. The delay time of the RF signals between nearby modules is measured as shown in Fig. 4. In the PLS linac, the largest delay time between adjacent module is occurred at the preinjector and the #2 klystron. This raised from the PSK trigger time in SLED operations.

The energy multiplication factor is measured at #10 module by comparing the beam energy with the tuned and detuned pulse compressor. The energy multiplication factor shows 1.56 with PSK trigger at 3 μ s.

V. SUMMARY

The microwave system is in a good working condition without any serious problem during the commissioning period and the normal operation at present. As a result, the measured energy spread is 0.3% with 2-GeV beams. The beam energy is very stable even in 24-hour continuous beam operation. The preinjector

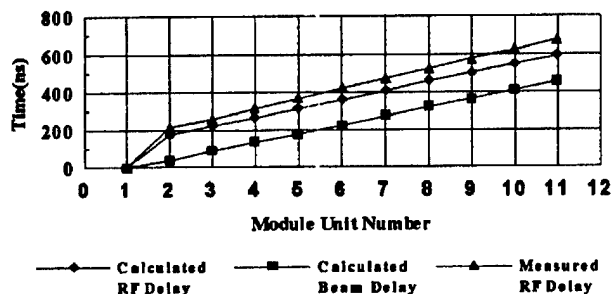


Fig. 4: Delay time of RF and electron beam.

klystron is SLAC-5045 type. The drive power of this unit is about 500-W. Currently, this klystron is operated at 50-MW output power. The drive power to operate a klystron at its saturation is usually increased as the output power of the klystron is decreased. The present system which is a little lower than to the saturation level can provide the maximum power of 500-W to the preinjector klystron.

The solid-state amplifier developed in the PLS whose maximum output power is about 800-W will be installed and tested in the near future. We will also test the TWT (travelling wave tube) system instead of the solid state amplifier for future improvement of the stability of the drive signal of the klystron.

VI. ACKNOWLEDGMENTS

We are grateful to thank J. T. Noh, K. T. Kim, W. W. Lee, and M. K. Lee for their enormous efforts for installing the drive system and measuring the RF characteristics of this system, and to POSCO and MOST for their commitment and endorsement to the PLS project.

VII. REFERENCES

- [1]. Design Report of Pohang Light Source (revised ed.), Pohang Accelerator Laboratory, 1992.
- [2]. W. Namkung, "PLS 2-GeV Linac," Proc. 1994 International Linac Conf., Tsukuba, Japan, August 1994, pp. 14-18.
- [3]. M. H. Cho, et. al, "High Power Microwave System for PLS 2-GeV Linac," Proc. 1994 International Linac Conf., Tsukuba, Japan, August 1994, pp. 418-420.

KLYSTRON-MODULATOR SYSTEM PERFORMANCES FOR PLS 2-GeV LINAC*

M. H. Cho, J. S. Oh, S. S. Park, and W. Namkung
Pohang Accelerator Laboratory, POSTECH
Pohang 790-784, Korea

The PLS 2-GeV linac employs 11 units of high-power pulsed klystrons (80-MW) as the main RF sources. The matching modulators of 200-MW (400-kV, 500-A) can provide a flat-top pulse width of 4.4 μ s with a maximum pulse repetition rate of 120-Hz at the full power level. For a good stability of electron beams, the pulse-to-pulse flat-top voltage variation of a modulator requires less than 0.5%. In order to achieve this goal, we stabilized high-voltage charging power supplies within 1% by a phase controlled SCR voltage regulator. In addition, we employed ac/dc feedback together with a resistive De-Q'ing system to achieve far less than 0.5% variation of the PFN charging voltage. This paper presents the main features of the klystron-modulator system and the characteristics of the pulsed high-power RF system performance during the beam injection operation for the Pohang Light Source commissioning.

I. INTRODUCTION

PLS linac has been injecting 2-GeV electron beams to the Pohang Light Source (PLS) storage ring as a part of the ring commissioning operation since September, 1994 [1]. The linac klystron-modulator (K&M) system has been in operation well before the ring commissioning, and the total accumulated high voltage run time of the oldest unit has reached beyond 14,000 hours [2]. The K&M systems are normally operating in 70 to 80% of the rated peak-power level to avoid the multipactoring phenomena occasionally occurred in a random fashion for the waveguide networks and accelerating structures of the linac system. Considering total 11 K&M systems installed in the PLS linac, the sum of all the high voltage run time is approximately 120,000 hours.

In this paper, we review overall system performance of the high-power K&M system. A special attention is paid on the analysis of all failures and troubles of the K&M system which affected the linac RF operations as well as beam injection operations for the period of September 1994 to March 1995. During this period, the machine has been in the operational mode for total 198 days. Summer shut-down (1.5 month) and the scheduled maintenance shut-down time are excluded in the analysis.

II. K&M SYSTEM OVERVIEW AND PERFORMANCE

The key features of the K&M system design include the 3-

phase SCR controlled AC-line power control, resonant charging of the PFN, resistive De-Q'ing, end-of-line clipper with thyrite disks, pulse transformer with 1:17 step-up turn ratio, and high power thyatron tube switching. The major operational parameters of the PLS-200-MW klystron-modulator system are listed in Table 1. The details of the system design and performance characteristics are described elsewhere [2].

Table 1. Operation parameter summary for klystron-modulator.

Peak beam power	200-MW max. (400 kV @ 500A)
Beam vol. pulse width	ESW 7.5 μ s, 4.4 μ s flat-top
Pulse rep. rate	120 pps max. (currently 30 pps)
PFN impedance	2.64 Ω (5% positive mismatch)
Voltage stabilization	SCR, DC feedback & 5% De-Q'ing
Pulse transformer	1:17(turn ratio), L_k :1.3 μ H, C_{st} :69nF
Thyratron switch	Heating factor: 46.8x10 ⁹ , 8.5 kA peak anode current
Klystron tube	Drive power:~300 W, efficiency:40%, gain:~53dB, peak power:80/65 MW (currently running at 50 to 65MW)

The shot-to-shot beam voltage stability is controlled by (1)the feedback of the DC high voltage from PFN to SCR primary input voltage control and (2)the resistive De-Q'ing. SCR DC feedback provides less than $\pm 0.5\%$ fluctuation, and additional De-Q'ing stabilizes the beam voltage better than $\pm 0.1\%$ fluctuation level. Fig. 1 shows the sample traces of the beam voltage accumulated more than an hour which exhibits less than $\pm 0.1\%$ fluctuation.

For the fault free stable operation of the system, the thyatron tube is one of the most important active components which require continuous maintenances and adjustments. The thyatron tubes which meet the PLS-200-MW system specifications are listed in Table 2 together with their specifications. IIT/F-303 and Litton/L-4888 are installed in our system, and the performance evaluations are underway. EEV/CX-1836A will be installed also for the comparison. This effort is initiated to improve the system from the frequent occurring faults (see Fig. 2) caused by the irregular recovery action of the thyatrons, which strongly depends upon the reservoir control.

There are three types of system interlocks, namely dynamic, static, and personal protection interlocks. All the static fault activation is initiated by the relay logic circuit, and the dynamic faults which require a fast action response are activated using the electronic comparator circuit. When the system operation is interrupted by the static fault, it can be recovered either by the

* Work supported by Pohang Iron & Steel Co. and Ministry of Science and Technology, Korea

remote control computer or manual reset. However, we have been performing all manual resets for the purpose of the experience accumulation, such as to find the type of troubles and system bugs which can provide the idea of the system improvement. The statistical analysis of the machine availability presented in this paper is based on the operation method of the manual reset by the maintenance crew only, without using the remote computer control. On the other hand, in the case of dynamic faults, the system recovers automatically without the help of the control computer when the condition returns to a normal state.

Table 2. Comparison of the thyatron tubes.

ITEM	ITT F-303	Litton L-4888	EEV CX- 1836A
Heater (Vac/A) <i>max</i>	6.6 / 80	6.7 / 90	6.6 / 90
Reservoir (Vdc/A) <i>max</i>	6.0 / 20	5.5 / 40	6.6 / 7
Peak anode (kV/kA) <i>for</i>	50 / 15	50 / 10	50 / 10
Peak anode vol.(kV) <i>inv</i>	50	<i>n/c</i>	50
Avg. anode cur.(A) <i>max</i>	8	8	10
<i>min</i> DC anode vol.(kV)	2	10	5
Heating factor ($\times 10^9$) <i>max</i>	300	400	<i>n/c</i>
dI/dt (kA/ μ s) <i>max</i>	50	16	10
Anode delay (μ s) <i>max</i>	0.3	0.4	0.35
Trigger jitter (ns) <i>max</i>	2	10	10

III. SYSTEM AVAILABILITY STATISTICS

Since the completion of the PLS 2-GeV linac installation in December 1993, all the K&M systems have been operating continuously except scheduled short terms and a long term summer shut down. Table 3 shows the total accumulated times of klystron's and thyatron's heater operation, and the high voltage run. Sum of the high voltage run time of each modulator has reached over 120,000 hours, and the experience accumulated so far provides the

valuable information for the system's stable operation. Fig. 2 is the Pareto chart of the total system's static fault count data collected for the period of September 1994 to March 1995. Net operation days during this period is 198. As mentioned in the previous section, the reset has been done by the maintenance crew only, and the most of nights and weekends during the 198-days, no extra maintenance work has been performed. Therefore the down time for the circuit breaker (①CB) trip which occurred the most frequently is unusually high among others. Other faults, such as fan(③) and key switch(④) are due mainly to faulty components, which no longer occur in any appreciable numbers after the replacement.

Table 3. Accumulated run times (in hours) of the PLS 2-GeV Linac's K&M systems (total 11 sets); on April 21, 1995.

Unit No.	H.V. run time	Kly. heater	Thyatron
MK-01	11,498	13,435	13,639
MK-02	14,025	13,111	13,252
MK-03	12,710	13,376	15,464
MK-04	11,784	13,326	13,541
MK-05	11,137	12,719	13,215
MK-06	11,135	12,284	3,135 (*1)
MK-07	10,040	11,456	12,246
MK-08	10,966	12,276	12,189
MK-09	9,879	11,320	11,730
MK-10	9,784	11,138	7,758 (*2)
MK-11	9,848	11,251	4,908 (*1)

*1) Thyatrons replaced with L-4888 due to the failure of F-303.

*2) Thyatrons replaced with F-241 due to infant failure of F-303.

Machine availability analysis has been performed based on the data using the techniques described in detail in reference [4]. The results are summarized and compared with the SLAC's in Table 4. The MTBF stands for the mean time between failures, and it is calculated by dividing the sum of the accumulated modulator run time with the total fault count ($MTBF = N \cdot TO / FC$). The MTTR (mean time to repair, which is equal to the total down time divided by total fault counts, $MTTR = TD / FC$) is rather longer than the SLAC's. This excellent performance is due to the extensive inspection work of the entire system for the trouble shooting as well as crew training for the system maintenance. Especially, the lack of the experience on the thyatron operations and severe EMI environment have contributed a lot for the longer MTTR.

Only 71% of the machine availability ($A = 1 - MTTR \cdot FC / TO$) has been obtained with the regular type maintenance of 44-hr-work-per-week. However, during the beam operation mode when the maintenance crews are standby, approximately 91% of availability has been reached. It indicates most of the system troubles are not so serious, and in many cases they are easily recoverable.

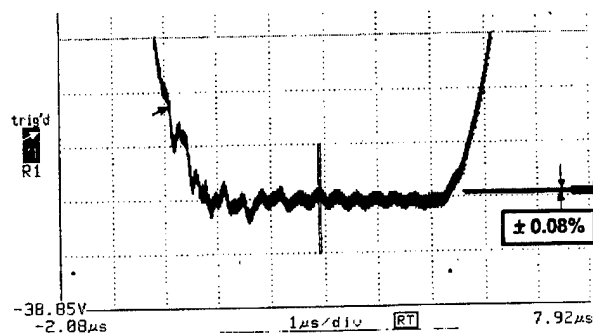


Fig. 1. The flat-top ripple and the cumulative (>1 hr) stability measurement of the klystron beam voltage (Tektronix DSA-602 signal analyzer is used) with DCHV feedback & De-Q'ing.

Table 4. Comparison of the K&M system fault analysis based on the data for the period of September 1994 ~ March 1995.

ITEM	PLS ^{*2}	SLAC ⁽⁴⁾
Number of modulators, <i>N</i>	11	243
Spare no. of modulators	0	14
Operation time (hr) ^{*1} , <i>TO</i>	4752	4000
Total failure counts, <i>FC</i>	168	997
Total down time (hr), <i>TD</i>	493 (1150)	401
MTBF (hr)	311	975
MTTR (hr/failure count)	2.6 (6.8)	0.4
System Availability, <i>A</i>	0.91 (0.71)	0.94 ^{*3}

*1) Operation time for the statistical analysis.

*2) Numbers in () indicates the standby RF operation mode without extended hour maintenance work (only 44 hr/week).

*3) Standby spare unit included

IV. COMMENTS ON SYSTEM TROUBLES

The most frequent system fault is the circuit breaker (CB) trip as shown in Pareto chart. This is due mainly to the problems in thyatron recovery actions which require elaborate reservoir rangings. Thyatron tubes of F-303 and L-4888 require ranging adjustment (see Table 2). According to our experience, they are changing in irregular patterns such that there exist no normal patterns or pre-symptoms which can be used for the preventive maintenance. Once it is out of normal operating point, there occur self-fire, firing miss, or slow recovery. The CX-1836A thyatron tubes require not so delicate ranging according to the manufacturer's

specifications, and we are planning to test them in the near future.

Klystron tubes also showed an internal arcing causing the vacuum pressure trip in a random fashion (see ② in Fig. 2). When this occurs in a row, we could recover to the normal operation after performing the short pulse processing (with approximately 1 μ s pulse width) for more than one day.

Other frequently occurred troubles are caused by the corona discharges. They occur when bad contacts exist in high voltage components, especially for the components which are connected by the spring action sockets. It has been found also that even a small corona discharge disturbs the ground potential, which are configured to have a single point ground connection inside the modulator, causing noise interferences in digital displays as well as SCR phase controls. Occasionally, this kind of EMI also affects LCD type displays of the nearby electronic equipment without affecting the performance, which became one of the normal check points for the systems.

V. SUMMARY

It is approximately 10 months since the PLS 2-GeV Linac has started its normal operation. We have analyzed the klystron modulator system's performance record for the period of the recent six months. It is observed that the reliability of klystrons is well over our expectations compared with other components in the modulators. The life time of thyatron tubes appears to be reasonable except the occurrence of infant failures. However, the major improvement is necessary for the reservoir control which is the main source of system troubles. The machine availability statistics of the K&M system for the beam operation mode (typically 2 operators are on-duty) is calculated to be over 90%. It appears to us that there are still lots of rooms for the improvement toward the availability more than 95% with proper choices of the protection circuits and control logic.

VI. REFERENCES

- [1] W. Namkung, "PLS 2-GeV Linac," Proc. 1994 International Linac Conf., Tsukuba, Japan, Aug. 21-26, pp.14-18 (1994).
- [2] M. H. Cho *et. al*, "High Power Microwave System for PLS-2-GeV Linac," Proc. 1994 International Linac Conf., Tsukuba, Japan, Aug. 21-26, pp. 418-420 (1994), M. H. Cho *et. al*, "Design of 200-MW Pulse Modulator for PLS 2-GeV Electron Linac," Proc. 3rd European Particle Accelerator Conf., Berlin, Germany, Vol.2, pp. 1591-1593 (1992).
- [3] I. S. Ko *et. al*, "Control of PLS 2-GeV Linac," Proc. 1994 International Linac Conf., Tsukuba, Japan, Aug. 21-26, pp. 825-827 (1994).
- [4] A. R. Donaldson and J. R. Ashton, "SLAC Modulator Operation and Reliability in the SLAC Era," IEEE Conf. Proc. 20th Power Modulator Symposium, pp.152-156 (1992).

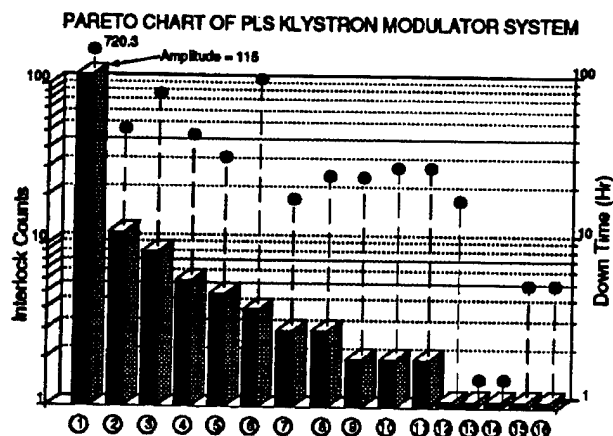


Fig. 2. Pareto chart of the system fault statistics. Numbers in the x-axis indicate type of faults; 1) CB trip, 2) klystron vacuum, 3) cooling Fan, 4) thyatron grid circuit, 5) core bias current low, 6) key switch, 7) DCPS overvoltage, 8) magnet current low, 9) core bias current high, 10) SCR gate hold, 11) ground hook, 12) magnet temperature high, 13) thyatron heater, 14) PFN RC-snubber, 15) SCR control board replace, 16) De-Q current high. Solid circle indicates down times, and the bar indicates interlock counts.

Klystron Modulator Operation and Upgrades for the APS Linac*

Thomas J. Russell and Alexander Cours

Advanced Photon Source, Argonne National Laboratory
9700 South Cass Avenue, Argonne, Illinois 60439 USA

Abstract

The Advanced Photon Source (APS) linac requires five 100-MW modulators to achieve its required energy. In-house construction of these modulators was under an extremely compressed time schedule and, while the original design was successful, it had a few shortcomings. The operation of the modulators was hindered by excessively sensitive controls and overheating during the hot summer months. The system underwent minor changes that resulted in major improvements. Additionally, improvements have been made to the high voltage circuits to improve the rise time of the output pulse shape, reduce the initial ringing of the pulse, and enhance the reliability of the system. This paper will outline the changes and explain the results of the improvements.

I. SYSTEM UPGRADES

There were three primary changes made: repackaging of components, changes to the control electronics, and elimination of cabling connecting the thyatron switch to the pulse forming network (PFN). All these changes have been executed on the five modulator systems used for the APS linac.

A. Repackaging of Components

The system was repackaged to improve cooling of the components, high voltage performance, and maintainability of the modulator. Seven control chassis were removed from the cabinet that housed the main power supply for the modulator. These chassis generated a constant 4-5 KW of waste heat within the cabinet, occupied a large amount of space, and restricted the airflow through the cabinet. By removing several substantial heat sources and improving the airflow within the modulator, the air temperature was reduced by approximately 25-40° C. The amount of actual temperature reduction depends primarily upon weather-related factors.

The removal of these heat sources also allowed more room for the remaining components. With the additional space it was possible to increase cooling of critical components by increasing airflow. This, in turn, allowed removal of insulation sheets which collected dust, required downtime to clean, and represented a source of fuel in the case of fire. As an added benefit, several system control chassis were now more accessible since they were outside the high voltage cabinet.

B. Changes to the Control Electronics

The second purpose for the upgrade was to eliminate many of the unnecessary modulator controls. The first change

made during the upgrade was to replace the existing interface with a more robust interface. In the initial design there was insufficient filtering and clamping of the input signals to the control system. During the upgrade, additional filtering and clamping were added to the input circuits. This simple change decreased failure and false alarms by 15-20%.

The original philosophy of the system was reevaluated. Initially the response of almost any slight irregularity was to trip the modulator to a state where operator intervention was required. Presently the system shuts off only if the system that is out of tolerance would cause damage to equipment or would present an operation that is unsafe for personnel. In many cases all that is issued is an alert message for the operator to notify the engineering staff.

The klystron focus current and heater power are both excellent examples of this change. The focus current was required to be above a set minimum to prevent damage to the klystron and below a maximum value to protect the current capacity of the focus magnet. Initially, the focus supply was controlled to within $\pm 5\%$. The system was changed to only trip when the current went too low, and the focus magnet was protected by a set of fuses. Since this change was implemented, there has not been a single failure or trip. The same rethinking process resulted in a different result in the filament supplies. In that case very little damage can occur if the filament is slightly low but the life of the various tubes are severely reduced by exceeding the rated power of the heaters. Therefore, if heater power is low, the system only generates an alert to the operators who log the alert. Engineers can then assess the problem without bringing down the modulator. If the heater power is too high, a fault is generated and an immediate response is required.

The first two categories of upgrades resulted in improvements in operational reliability. Previously, operation was dominated by the false alarms or noise generated by the control system. Currently, the false alarms from the control system have been nearly eliminated and the system is exceeding the reliability requirements of the project more than 99% of the time. This is up from previous statistics of about 90% reliability, which was unacceptable.

C. Elimination of Cabling

The final issue that was dealt with was the output pulse. In three of the five modulators, the output of the klystron feeds a pulse compression device. The gain of the pulse compression device is partially determined by pulse width of the signal feeding the unit. Any pulse width that is wasted by a poor rise time will reduce the gain of the compression unit. The rise time of the output pulse is greatly affected by three parameters. The first two are the inductance and stray capacitance of the

* Work supported by the U.S. Department of Energy, Office of Basic Energy Sciences, under Contract No. W-31-109-ENG-38.

interconnecting cables and the system, and the third is the leakage inductance of the main pulse transformer. There is very little that can be done to eliminate the leakage inductance of a transformer. Neither is stray capacitance within the cabinet easily changed since the cabinets already exist and presently fill the available space. Therefore, the only practical solution was to eliminate some cables.

In the original configuration, coaxial cables (RG-220) were used to connect the main switch tube to the PFN. These cables were eliminated by mounting the thyatron within the PFN cabinet. This change resulted in an improved rise time from more than $1.2\mu\text{s}$ prior to the upgrade to about $0.8\mu\text{s}$ after the upgrade. This is a widening of the pulse of more than 10%. As an added benefit, there are now two fewer cables that might fail. In the past, these cables contributed substantially to the failure rate. Figures 1 and 2 compare the output pulse before and after the upgrade.

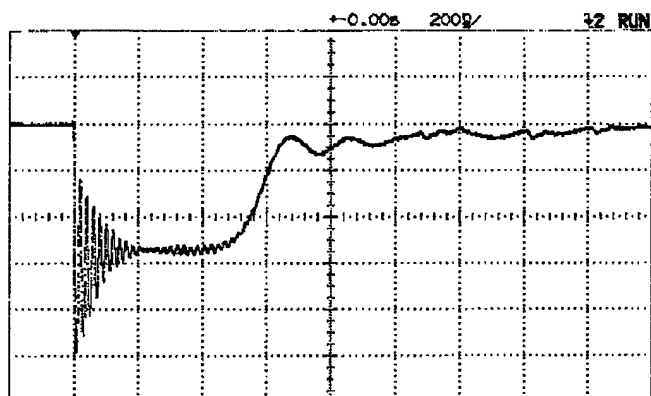


Figure 1: Original PFN Pulse

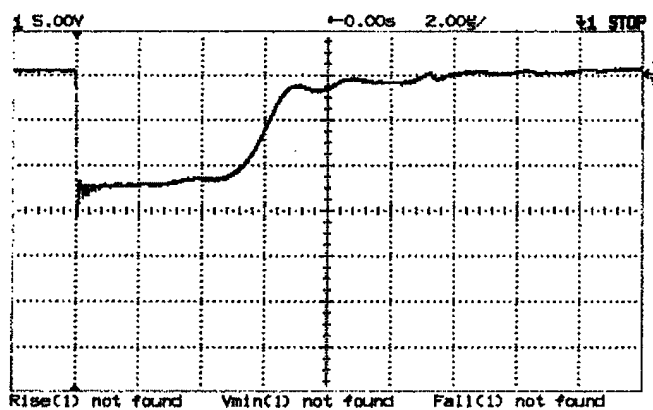


Figure 2: Improved PFN Pulse

The pulse width was also increased by simply changing the configuration of the inductors in the PFN. The PFN was rewired so that the magnetic field of the coils aided the next coil to increase the inductance within the PFN. This resulted in an increased pulse width of about $0.5\mu\text{s}$ to $0.7\mu\text{s}$.

As noted in Fig. 3, the initial overshoot of the pulse is 100%. A simple RC filter network was designed and installed directly across the primary of the output transformer. The ring-

ing of the output pulse of about 20% as configured is shown in Fig. 4. This additional circuit was modeled with great detail using SPICE and the model results matched nearly exactly to the implemented results. It should be noted that there are very few detrimental effects on the rise time of the output pulse.

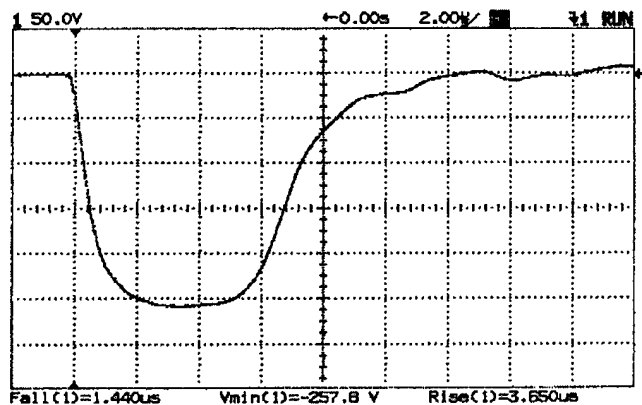


Figure 3: Original Klystron Pulse

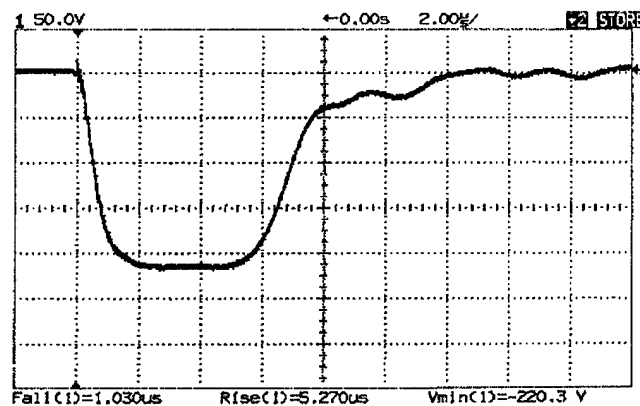


Figure 4: Improved Klystron Pulse

II. CONCLUSIONS

Great improvements have been made to the klystron modulators in the APS linac. Reliability of the system has improved from an initial availability of 90% to better than 99%. The pulse rise time has improved while at the same time the overshoot has been reduced. In addition, maintainability has improved with the increased accessibility of the system.

III. ACKNOWLEDGEMENTS

The authors would like to thank David Meyer and Tim Jonasson, RF Group, who did most of the construction of the assemblies in the system. The author would also like to thank Bryan Taylor, ASD, Ron Koontz and Dick Cassel, SLAC, and Howard Pfeffer and Ralph Pasquinelli, FNAL, for their contributions as a review committee.

PROSPECTS FOR DEVELOPING MICROWAVE AMPLIFIERS TO DRIVE MULTI-TeV COLLIDERS

V. L. Granatstein, G. S. Nusinovich, J. Calame, W. Lawson, A. Singh, H. Guo, and M. Reiser
Institute for Plasma Research, University of Maryland, College Park, MD 20742

Abstract

In multi-TeV linear colliders, overall accelerator length can be kept reasonable only if a high value of accelerating field is chosen, and this implies a relatively high value of rf frequency in order to avoid excessive dark current. We consider the feasibility of developing 30 GHz gyrokystron amplifiers. Amplifier output would be at the fourth harmonic of the electron cyclotron frequency to keep the magnetic field small ($B_0 = 4.3$ kG). Efficiency would be maximized both by a scheme of doubling the amplifier input frequency in two stages and by using depressed collectors. We estimate that output power in a single amplifier would be >80 MW with overall electronic efficiency $\sim 66\%$. With a high degree of pulse compression (32X), 1800 such amplifiers would drive a 3 TeV collider.

I. INTRODUCTION

The design study of future linear colliders which was carried out at the Snowmass Workshop in 1990 included consideration of a collider with final energy $U_f = 3.0$ TeV, and accelerating gradient $E_a = 100$ MV/m [1]. To avoid excessive dark current emission in the accelerator at this value of E_a , a relatively high value of rf frequency was chosen; i.e., 30 GHz. We note that a similar frequency has been chosen for the two-beam, CLIC accelerator design at CERN [2]. In this paper, we consider the alternative of developing individual 30 GHz amplifier tubes; larger efficiency may be realizable in individual microwave tubes than with a two-beam arrangement.

The advantage of using a high rf frequency is clear if the pulsed microwave energy from each amplifier can be made comparable to pulsed energy obtainable from lower frequency amplifiers. In Eq. (1), an expression is given for N_t , the number of microwave amplifiers required to drive a collider with given final energy U_f and accelerating gradient E_a ; viz. [3]

$$N_t \approx 1.7 \times 10^7 \frac{U_f E_a \lambda^2}{P_p \tau_p \eta_c} \quad (1)$$

where mks units are used, and λ , p_p , and τ_p are, respectively, the operating wavelength, the peak output power and the output pulse duration of a single microwave amplifier; η_c is the efficiency of any pulse comparison circuit that is used.

It should be noted that a new pulse compression scheme is being studied at SLAC [4] which, if successful, would keep η_c large even when there is a high degree of pulse compression. In line with the most optimistic projections of the SLAC study, we consider pulse compression by a factor $C_r = 32$ and a corresponding compression efficiency of $\eta_c = 80\%$; at 30 GHz, $C_r = 32$ implies that the amplifier output would have a pulse duration of $\tau_p = 0.7$ μ s. Then if one could achieve an amplifier

output power of 80 MW, the number of amplifiers required to drive a 3 TeV collider with $E_a = 100$ MV/m, can be calculated from Eq. (1) as $N_t = 1800$.

In contrast, one can consider the case of a 3 GeV collider driven by 11.4 GHz klystrons with output power 50 MW and pulse duration 1.5 μ s. The acceptable value of E_a would then be limited to ~ 50 MV/m, making the collider twice as long. Moreover, the number of amplifiers required would be $N_t = 3600$.

II. A PROPOSED 30 GHz, FOURTH-HARMONIC GYROKLYSTRON

When considering what type of amplifier to choose at 30 GHz, the gyrokystron stands out as a preferred choice. Gyrokystrons have been successfully operated with cavities resonant in high order modes, and with drift spaces which are not cut-off. In general, as gyrokystrons are scaled to higher frequency, their transverse dimensions can remain large by choosing resonant modes of higher order in the cavities, and by taking measures to stabilize the drift spaces against a larger number of potential instabilities. Thus, the power rating of gyrokystrons does not need to decrease as frequency is raised.

A 20 GHz gyrokystron has already been demonstrated with output power $P_p = 32$ MW, and $\tau_p = 0.8$ μ s [5]. The output cavity was driven at 10 GHz near the electron cyclotron frequency, ω_{ce} , and the output cavity operated at the second harmonic; efficiency was 28%. A more powerful gyrokystron with second harmonic output cavity and design values of $P_p \gtrsim 100$ MW at 17.4 GHz is under construction; a co-axial circuit is being used to increase stability against spurious oscillations [6]. Efficiency as high as 42% has been calculated [7].

We now consider the feasibility of a 30 GHz gyrokystron with desirable parameters for application to driving a 3 TeV collider. It would be advantageous to operate the output cavity at the fourth harmonic of ω_{ce} so as to minimize the solenoidal magnetic field requirement. In its simplest embodiment, the gyrokystron circuit would be made up of three cavities, the input cavity operating at $\omega \approx \omega_{ce}$, the center cavity at $\omega \approx 2\omega_{ce}$, and the output cavity at $\omega \approx 4\omega_{ce}$; modes in the three cavities might be TE₀₁₁, TE₀₂₁, and TE₀₄₁. Efficiency which can be achieved with such a two-stage multiplication of frequency is much larger than efficiency in an amplifier which transitions from the fundamental frequency to the fourth harmonic in a single stage [8].

A recent calculation [8] of the maximum electronic efficiency which can be achieved in such a staged frequency quadrupling gyrokystron indicates that an electronic efficiency $\eta_e \approx 30\%$, is achievable for a gyrokystron electron beam with aspect ratio $v_\perp/v_\parallel = 1.5$ and parallel velocity spread $\Delta v_\parallel/v_\parallel < 6\%$. In the 500 kV electron gun built for the 17.1 GHz gyrokystron [6],

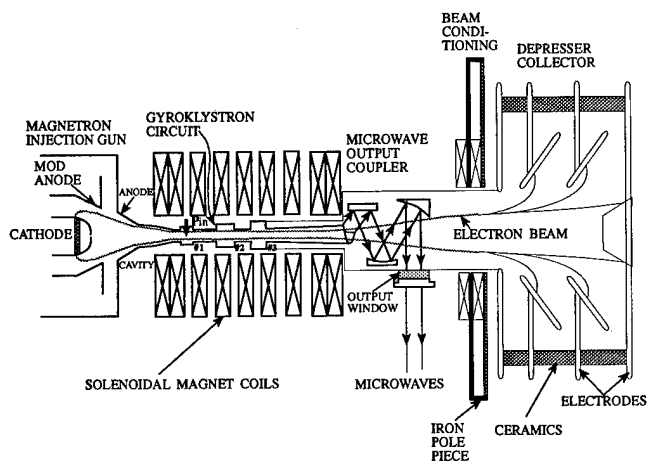


Figure 1. Schematic of a fourth-harmonic gyrokyklystron including depressed collector.

$\Delta v_{\parallel}/v_{\parallel} \lesssim 6\%$ is achievable for beam current $I_b \lesssim 600$ A. Very preliminary attempts [7] to design a specific fourth harmonic gyrokyklystron circuit have produced calculated values of $\eta_e = 13\%$.

III. EFFICIENCY ENHANCEMENT BY USING A DEPRESSED COLLECTOR

To enhance efficiency over the single-pass values of η_e cited above, one can employ depressed collectors. A numerical study of depressed collectors for a gyrokyklystron with 30 MW output power has been carried out [9] with results summarized in Table I where η_c is the collective efficiency and $\eta_t = \eta_e / (1 - \eta_c(1 - \eta_e))$ is the total electronic efficiency. Note that even with only two electrodes in the depressed collector a single pass efficiency η_e near 30% results in a total electronic efficiency $\eta_t \sim 60\%$.

Figure 1 is a schematic of a three-cavity gyrokyklystron with a multi-electrode depressed collector. A three electrode magnetron injection gun is used so that dc power supplies can be employed in the collector circuits with the beam current controlled by applying voltage pulses to the mod anode. Also shown is a microwave output coupler of the Vlasov type which couples microwave energy out through a window mounted on the sidewall of the gyrokyklystron [10]; thus, the microwave energy does not enter the collector structure where it would constrain collector design. Finally, it will be noted that a beam conditioning section precedes the depressed collector; such a section provides magnetic fields which convert transverse energy to axial energy, and has been used to advantage in combination with gyrotron depressed collectors [11].

The operating parameters of a 30 GHz gyrokyklystron which might be achieved in the future are estimated to be those displayed in Table 2. Such performance would merit consideration in planning a 3 TeV collider.

References

[1] D. L. Burke, et al, "Linear Colliders" in *Research Directions for the Decade, Snowmass 1990*, ed. E.L. Berger, World Scientific Publishing Co., Singapore, 1992.

[2] H. Braun, et al., "CLIC – a compact and efficient high energy e^+e^- linear collider," these proceedings.
 [3] V.L. Granatstein and G. S. Nusinovich, Proceedings of the IEEE Particle Accelerator Conference, Washington DC, May 17-20, 1993, pp. 2572-2575.
 [4] S.G. Tantawi et al., "Active radio frequency compression using switched delay lines," these proceedings.
 [5] H.W. Mathews et al., IEEE Trans. Plasma Sci. **22**, 825 (1994).
 [6] J. Calame et al., "Design of 100 MW, two-cavity gyrokyklystrons for accelerator applications," these proceedings.
 [7] W. Lawson et al., "Design of three-cavity, co-axial, gyrokyklystron circuits for linear collider applications," these proceedings.
 [8] G.S. Nusinovich and O. Dumbrajs, Phys. Plasmas **2**, 568 (1995).
 [9] M. Read et al., IEEE Trans. Electron. Dev. **37**, 1579 (1990).
 [10] G.G. Denisov et al., Int. J. Electron. **72**, 1079 (1992).
 [11] A. Singh et al., Int. J. Electron. **72**, 827 (1992).

Table I. Efficiency of gyrokyklystrons with multiple stage depressed collectors.

Single-pass electronic efficiency	No. of collector electrodes					
	2		3		4	
	η_c	η_t	η_c	η_t	η_c	η_t
10%	79%	35%	85%	43%	86%	44%
20%	76%	51%	82%	58%	84%	61%
30%	74%	62%	81%	69%	83%	72%

Table II. Estimated operating parameters that might be achieved in a 30 GHz gyrokyklystron.

e-beam energy	500 keV
e-beam current	600 A
η_e , single pass electronic efficiency	28%
P_p , microwave output power	84 MW
η_c , depressed collector efficiency	80% (3 electrodes)
η_t , total electronic efficiency	66%
τ_p , microwave pulse duration	0.7 μ s
f_{in} , input frequency	7.5 GHz
B_0 , solenoidal magnetic field	4.3 kG
f_{out} , output frequency	30 GHz

Design of 100 MW, Two-Cavity Gyroklystrons for Accelerator Applications*

J.P. Calame, W. Lawson, J. Cheng, B. Hogan, M. Castle, V.L. Granatstein, and M. Reiser,
Institute for Plasma Research, University of Maryland, College Park, MD 20742 USA

Abstract

We present designs for gyrokylystron amplifiers capable of producing 100-150 MW of output power in 1-2 μ s pulses.* For accelerator applications we plan to employ a second harmonic output cavity operating at 17.136 GHz. Initial experiments to test our new beam production and transport facilities will involve energy extraction from the fundamental cyclotron harmonic at 8.568 GHz. In both cases the microwave circuits employ coaxial cavities and drift tubes to limit spurious oscillations and cavity cross-talk.

I. INTRODUCTION

Our group at the University of Maryland has been examining the possibility of using gyrokylystrons to energize future linear electron-positron colliders for the past several years. Previously we have produced approximately 30 MW of output power in 1 μ s pulses at both 9.85 and 19.7 GHz, using fundamental and second harmonic output cavities, respectively [1,2]. All these experiments employed a beam power near 100 MW and efficiencies ranged from 28-35 %. In order to meet the projected 100-150 MW power level requirements needed for collider applications, we are upgrading our experimental facilities to produce a 400 MW electron beam. New coaxial microwave circuits with 17.136 GHz second harmonic output cavities will be described below, along with plans for an initial 8.568 GHz fundamental experiment.

II. EXPERIMENT DESCRIPTION

The electron beam for the experiments is produced by a single anode magnetron injection gun, powered to 500 kV at up to 800 A by a line type modulator. This modulator is a reconstructed version of our existing 400 A device; the extra current is produced by an increase in the number of pulse forming networks from 4 to 8. Additionally, in the older system only 250 A was available for the electron beam since the remainder of the current powered a modulation anode via a resistive divider. In the new configuration the entire modulator output is available to the gun. The new modulator has been completely constructed and tested. A representative voltage vs. time pulse for a resistive load is shown in Fig. 1. It is characterized by a 1.5 μ s rise time and 1.5 μ s flat-top time. We expect the pulse to be considerably smoother when the gun is connected to the system, due to the filtering action of the gun capacitance.

The electron gun was constructed at Varian Associates and is now in our possession, awaiting final installation and testing. Simulations indicate that the new gun can produce a beam with an average alpha of 1.5 and a velocity spread below 10% over the full range of currents. Over the lower current range of 0-500 A, the spread remains below 6%. The final beam has an average guiding center radius of 2.56 cm and a total beam thickness of 1.26 cm. A diagram of the electrode geometry and representative orbits is displayed in Fig. 2. Filament power for the gun is expected to be 1200 W or less.

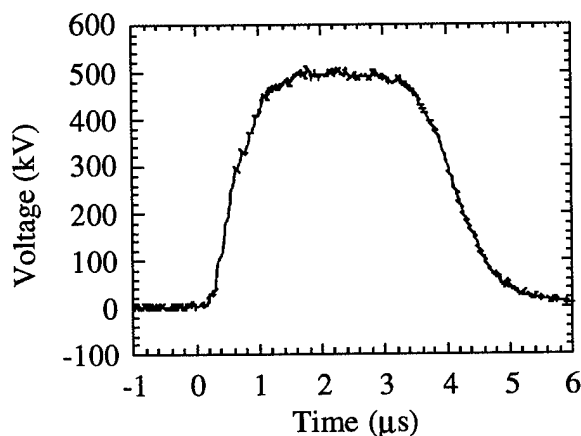


Figure 1. Modulator output pulse

The microwave circuit under test is located within an existing set of seven water cool pancake coils. These coils, plus an additional large coil located around the gun at the axial position of the cathode, create a central field near 5.1 kG and a circuit to cathode magnetic compression ratio of 8.8. Considerable tapering of the magnetic field profile is also possible in this configuration. We are currently performing measurements of magnetic field as a function of position prior to installation of the gun; this should allow more accurate modeling of the electron trajectories than simply using theoretical magnet coil profiles. Located between the electron gun and the microwave circuit is the gun downtaper, a conical vacuum vessel lined with lossy dielectrics of various compositions and thicknesses to suppress spurious (mainly TE_{1m} and TE_{2m}) oscillations. A close-up of a typical microwave circuit is shown in Fig. 3. In this diagram the beam flows into the TE_{011} input cavity, which has a pair of input windows and coupling slots located on opposite sides of the cavity and driven in phase. This arrangement helps produce good coupling to the low-Q (about 50) cavity and provides considerable immunity to the excitation of unwanted modes. The cavity itself is formed by

* Work supported by the U.S. Department of Energy.

a decrease in the inner conductor radius from the normal 1.83 cm to 1.1 cm, over a length of 2.29 cm. Lossy dielectrics line on the cavity endwalls. We will drive the input cavity with a 150 kW, 3 μ s microwave pulse from a magnetron. The input waveguide system will be filled with SF₆ to discourage breakdown at the waveguide to window interface.

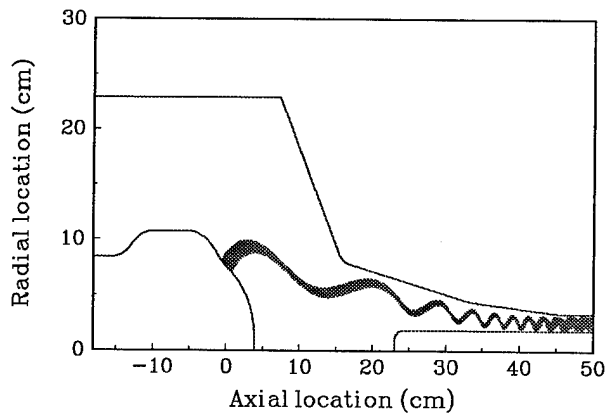


Figure 2. Diagram of the gun electrodes and electron trajectories

The drift tube is lined with lossy dielectrics on both the inner and outer conductors. The inner and outer beam tunnel radii are 1.83 and 3.33 cm, respectively. On the outer conductor there are two concentric layers of material, with the inner layer consisting of carbon impregnated aluminum silicate (CIAS) and the outer layer made from 80% BeO-20% SiC. The inner conductor is lined by alternating regions of CIAS and the BeO-SiC material. Calculated values of attenuation per unit length associated with a variety of hybrid $n=1$ modes in this structure are shown in Fig. 4. Further theoretical analysis based on these results indicates that this 9 cm long configuration should reduce the quality factors of all spurious drift tube modes to below 15 over the 0-25 GHz range. More importantly, the quality factors are below 5 at those frequencies where the fundamental or second-harmonic beam lines intersect with the dispersion curves associated with electromagnetic modes.

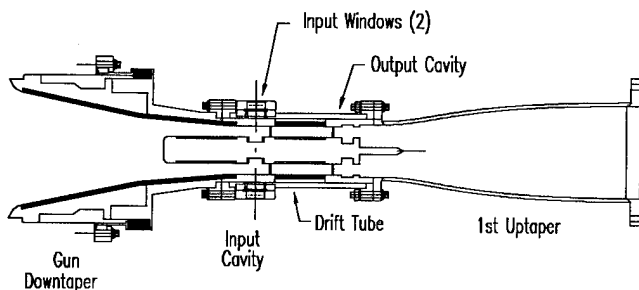


Figure 3. Diagram of the microwave circuit, shown here with the gun downtaper, first uptaper, and the fundamental output cavity.

Because we are retrofitting these tubes into an existing horizontal system, the inner conductor is supported by pins located on each side of the dielectrically lined region (after the input cavity and before the output cavity). The pins will intercept no more than 3% of the electron beam. Ultimately we will use diamond pins (with tantalum cores for charge removal), but initially we will use 2 mm diameter tungsten pins. Calculations indicate that the tungsten will withstand the beam heating at 0.5 Hz. Higher repetition rates will require the use of the diamond. Of course, in a production tube for linear collider applications, one would employ a vertical arrangement in which the inner conductor hangs down from radial vane supports located beyond the beam dump. This arrangement may also be combined with an inverted magnetron injection gun geometry for added inner conductor support.

Initial designs for a TE₀₂ second harmonic output cavity operating at 17.136 GHz have been completed. A diagram of the cavity appears in Fig. 5. It is formed by increasing the outer drift tube radius to 3.65 cm over a 3 cm transition length, followed by a 0.64 cm long flat section. The energy is extracted through an axial output lip of 0.1 cm length and 3.58 cm radius, with a 1 cm long transition region between the lip and the cavity body. All of the transitions are smooth to minimize mode conversion. This geometry exhibits a Q of 530 and a forward to reverse power ratio of 24 dB. Theoretical modeling predicts an efficiency of 35% with the expected beam velocity spread of 6%. Higher efficiencies should be achievable with the use of a buncher cavity. Start oscillation studies predict that this design is marginally stable to TE_{1m} modes at 500 A; we plan to further explore mode competition in this geometry with a multi-mode code. We are also currently investigating the tradeoffs between stability and efficiency in this style of cavity.

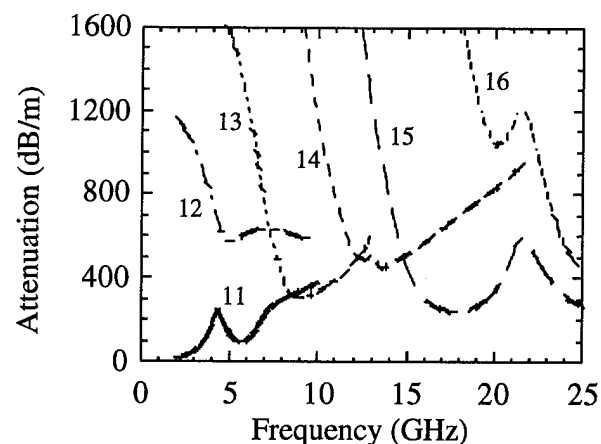


Figure 4. Attenuation per unit length of the drift tube to various $n=1$ hybrid modes.

We are also considering a complex TE₀₂/TE₀₃ second harmonic cavity with an overall physical length of 10.6 cm, a Q of 295, a forward to reverse power ratio of 36.5 dB, and an output radiation purity of 96% TE₀₃. It is formed by a variety

of smooth and abrupt transitions on both the inner and outer conductors. This design is considerably more stable than the cavity described above. However, at present the efficiency is only 20%, which is far too low for practical applications. Further analysis has indicated that the low efficiency is caused by competition with third harmonic operation, and that this can be minimized by careful selection of the cavity radii relative to the beam guiding center radius. Further work to understand this phenomenon and improve efficiency is under way.

The first tube to be studied on our new test bed will actually employ a fundamental 8.568 GHz TE_{01} output cavity (pictured in Fig. 3). This initial step is required to simplify the study and suppression of any instabilities which may occur in the drift tube and gun downtaper regions. The cavity employs abrupt transitions, and is realized by decreasing the inner radius to 1.01 cm and increasing the outer radius to 3.59 cm. This main section is 1.7 cm long, and it is followed by an axial energy extraction lip 0.9 cm in length with the same radii as in the main drift tube. Simulations indicate that this cavity will operate with nearly 40% efficiency at 6% velocity spread and 600 A beam current.

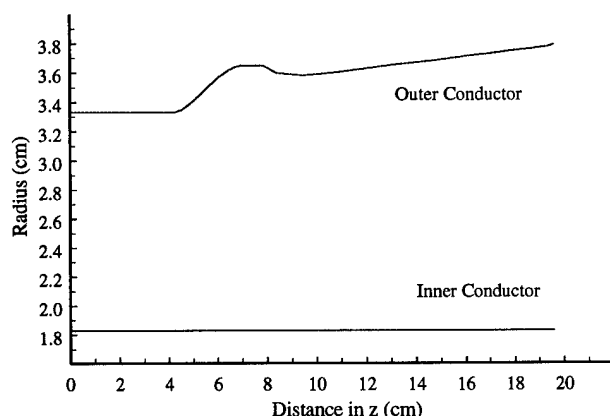


Figure 5. Radial profile of the TE_{02} second harmonic coaxial output cavity.

The post-output cavity system is being completely rebuilt to accommodate the different operating frequencies and higher power levels present in the new experiments. Following the output cavity will be a 40 cm long nonlinear taper which will raise the beam tunnel diameter to 12.7 cm, at which point the electron beam will land in a water cooled copper beam dump. An iron-cored electromagnet, located at the end of the beam dump, produces a transverse magnetic field at up to 800 G to ensure that all electrons are collected. This magnet has been constructed and tested. The output radiation will pass through a perforated pumping manifold and arrive at a 12.7 cm diameter aluminum oxide output window which will be a half wavelength long at the fundamental and a whole wavelength long at the second harmonic. These windows have been procured and are

currently being brazed into vacuum flanges. The custom-built pumping manifold has been completed. We will employ two 60 l/s ion pumps to maintain the downstream vacuum during operation; two additional 60 l/s pumps will be located near the electron gun. We expect base pressures in the low 10^{-9} torr range, and operating pressures near 10^{-8} torr.

A number of microwave diagnostics will be used to study the output radiation. Initially a second nonlinear uptaper will be placed between the window and an anechoic chamber. This uptaper will be about 1m long and will raise the diameter to 25.4 cm, at which point the radiation electric field will be below the breakdown limit of air. The taper itself will be filled with SF_6 and will employ a thin Mylar window on the anechoic chamber side. A movable antenna located within the far field region inside the anechoic chamber will allow measurement of output power and radiation patterns. We are also designing a 12.7 cm diameter, SF_6 filled, mode selective directional coupler with side arms optimized for the TE_{01} mode at 8.568 GHz and the TE_{02} and TE_{03} modes at 17.136 GHz. It will be used in conjunction with a new liquid calorimeter for peak power and pulse energy measurements.

III. SUMMARY

The modulator upgrade and electron gun construction for this new experiment have been completed, and we are currently constructing and procuring the remaining beam transport hardware. Following a period of cold tests, we will arrive at a final design for a vacuum-compatible version of the fundamental tube. Construction will follow immediately afterward. Efficiencies of 35-40% appear likely in both fundamental and second harmonic devices, with the possibility of higher efficiency with the addition of a buncher cavity. We anticipate the production of output power levels in the 100-150 MW range at frequencies suitable for collider applications in the near future.

IV. REFERENCES

- [1] W. Lawson *et. al.*, "Performance characteristics of a high power X-Band two cavity gyrokystron," *IEEE Trans. Plasma Sci.*, **20**, 216 (1992).
- [2] H.M. Matthews, *et. al.*, "Experimental studies of stability and amplification in a two cavity second harmonic gyrokystron," *IEEE Trans. Plasma Sci.*, **22**, 825 (1994).

DESIGN OF THREE-CAVITY COAXIAL GYROKLYSTRON CIRCUITS FOR LINEAR COLLIDER APPLICATIONS*

W. Lawson, G. Saraph, J. P. Calame, J. Cheng, M. Castle, B. Hogan, M. Reiser, V. L. Granatstein, and H. Metz, Institute for Plasma Research, University of Maryland, College Park, MD, 20742 USA

In this paper we consider the preliminary designs of three-cavity microwave circuits for coaxial gyroklystrons. These tubes are predicted to produce over 100 MW of power in 1 μ s pulses in X- and Ku-Band for linear collider applications with efficiencies exceeding 40% and gains above 50 dB. In particular, we examine the effect of first and second harmonic buncher cavities on the efficiency and gain of both first and second harmonic microwave circuits. We also examine the necessary conditions to contain the axial field profile of overmoded buncher and output cavities. Performance is contrasted with current two-cavity designs. [1]

I. INTRODUCTION

At the University of Maryland, we have been exploring the suitability of gyroklystrons as drivers for the next generation of linear colliders. When our investigation began, the state-of-the-art was represented by a 52 kW, 4.5 GHz 3 cavity gyroklystron at NRL [2]. As an intermediate step to the 100+ MW microwave power levels anticipated to be necessary for a 1 TeV collider, we designed 30 MW, 10 and 20 GHz, first and second harmonic gyroklystrons, respectively. These tubes utilized the interaction of a 450 kV, 160-260 A, 1 μ s (flat top) beam with a series of circular electric mode cavities separated by heavily loaded drift regions. The ratio of the velocities perpendicular and parallel to the axial magnetic field hovered near one in all experiments. Likewise, all tubes utilized a simple TE_{011} input cavity with radial wall input coupling and a lossy ring to lower the quality factor. [3,4]

We have just completed modifications to the gyroklystron test bed that should enable us to exceed the 100 MW level for output power. The modulator voltage was upgraded to 500 kV and the current capability was increased to 800 A by adding additional pulse-forming networks in parallel with the existing hardware. A new single-anode magnetron injection gun that can take advantage of the new modulator capabilities has been designed, constructed, and delivered. The minor modifications to the magnet system that are required by the new gun have been completed.

To increase the flexibility of the magnet system and to enhance the compatibility of our system to other current experimental investigations, we have decreased the drive frequency to three times the current SLAC frequency. Our magnetron drive hardware has been modified to accommodate this change. Detailed designs of two-cavity systems employing first and second-harmonic output cavities have been de-

signed, are currently under construction, and have been described in a companion paper in these proceedings. [1]

A recent theoretical effort [5] has indicated that, in addition to improved gain, a buncher cavity can also enhance the maximum gyroklystron efficiency of several configurations. In this paper we use our partially self-consistent, large-signal code [6] to investigate the effects of a buncher cavity on the performance of coaxial gyroklystrons (which are always driven by first-harmonic input cavities). First, we present the design of abrupt-transition TE_{02} second harmonic cavities that minimize TE_{01} mode conversion. Then the large signal performances of fundamental output circuits with fundamental and second harmonic buncher cavities are described. The results of a second harmonic buncher/output gyroklystron are then analyzed. We close with a preliminary discussion of a three cavity design which has a second-harmonic buncher cavity and a fourth harmonic output cavity.

II. ABRUPT-TRANSITION OVERMODED CAVITIES

A schematic of the three cavity design with second-harmonic buncher and output cavities is given in Fig. 1. The length and the inner and outer radii of the TE_{021} buncher cavity have been selected to minimize mode conversion to the TE_{01} mode and subsequent leakage of fields into the drift regions. This is typically achieved by forming the cavity with equal radial transitions from the drift tube radii. The diffractive quality factor of this cavity, according to our scattering matrix code is over 750,000. The required quality factor for optimal efficiency will be achieved by the insertion of lossy ceramics into the cavity. Similar criteria are used to design the output cavity, though the quality factor is achieved solely through diffractive coupling at the output end. The cavity parameters are given in Table I. The drift radii given correspond to the regions downstream from the respective cavities.

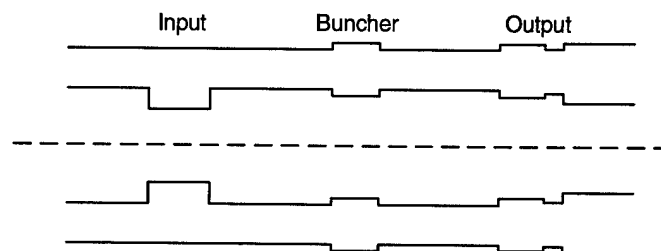


Figure 1. The second-harmonic output three cavity design.

* Work supported by the US Department of Energy.

The buncher cavity's azimuthal electric field profile (in arbitrary units) at the first radial maxima in the cavity is given in Fig. 2 as a function of axial location. The tails of the field are negligible after about 2 cm. The start oscillation curves in the magnetic field range of interest for relevant circular electric modes is given in Fig. 3. This figure assumes that the lossy dielectrics load all modes equally. The operating mode is completely stable for currents below 780 A but the TE_{01} mode is highly unstable at the upper range of the magnetic field. Consequently, if the method for loading the cavity cannot preferentially load the lower radial mode, the cavity length will have to be shortened to push the unstable range to higher magnetic fields. The start currents for modes with azimuthal indices between 1 and 3 were also evaluated, but they were all at least as stable as the TE_{02} mode.

Table I. Abrupt transition harmonic cavity dimensions.

Parameter	length (cm)	
	buncher	output
Inner drift/lip radius	1.83/-	1.40/1.75
Inner cavity radius	1.62	1.61
Outer drift/lip radius	3.33/-	3.55/3.35
Outer cavity radius	3.54	3.50
cavity axial/lip length	1.63/-	1.7/0.7

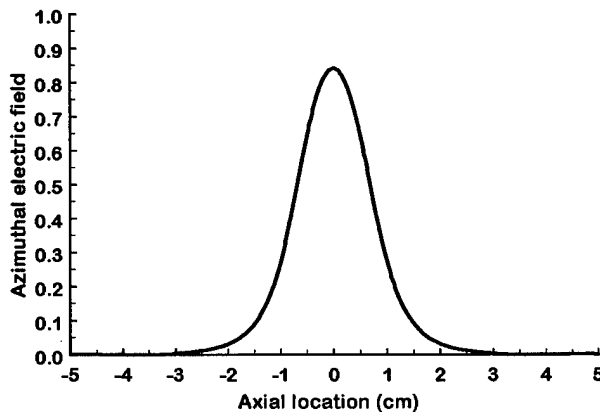


Figure 2. Field profile of the second harmonic buncher cavity.

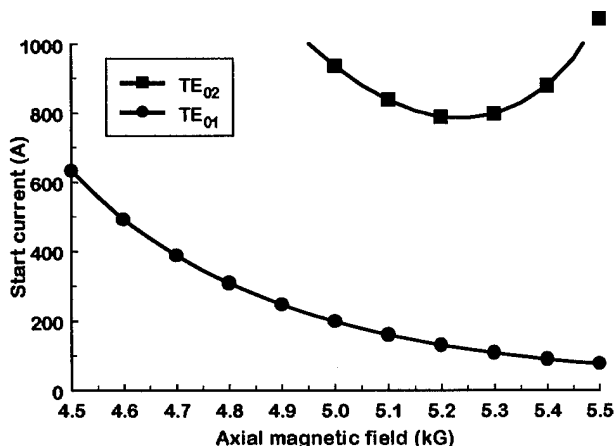


Figure 3. Start oscillation curve for the second harmonic buncher cavity.

III. LARGE-SIGNAL OPERATION

The single anode Magnetron Injection Gun is designed to produce a 500 kV, 500 A beam with an average perpendicular-to-parallel velocity ratio of 1.5 and an axial velocity spread of 6.4%. [1] The velocity spread remains below 10% for currents up to about 800 A. Optimizations of the three-cavity designs were carried out at the nominal beam parameters and efficiency was subsequently characterized as a function of velocity spread.

The drift tube lengths and the cavity quality factors for the three basic designs are indicated in Table II. The three digit sequence that identifies the particular design indicates the expected amplified harmonic in each of the cavities. The same basic TE_{011} input cavity is assumed for all designs, though the required Q varies somewhat. The cavity is formed by decreasing the inner radius of the drift tube to 1.1 cm for a distance of about 2.29 cm and is stable to all modes at the nominal operating parameters. The length is chosen to correspond to the broadwall length of the X-band waveguide that will couple the input power to the cavity via two radial wall slots that are 180° apart. All first harmonic cavities resonate at 8.568 GHz in the TE_{011} mode and all second-harmonic cavities resonate at 17.136 GHz in the TE_{021} mode. For simplicity, the fundamental buncher cavity in the 1-1-1 design has the same dimensions as the input cavity. The fundamental output cavity in the first two designs was taken from the planned two-cavity experiment. [1] The dimensions of the buncher and output cavities of the 1-2-2 design are given in Table I.

Table II. The three-cavity design parameters and performance characteristics.

Parameter	Design		
	1-1-1	1-2-1	1-2-2
Input cavity Q	80	119	70
Drift 1 length (cm)	4.5	5.5	4.5
Buncher cavity Q	65	727	389
Drift 2 length (cm)	6.5	5.0	4.5
Output cavity Q	124	124	322
Efficiency (%)	41.7	38.8	41.1
Large signal gain (dB)	51	31	50

The optimal efficiencies and gains at the nominal operating parameters are also given in Table II for the three designs. Both designs for which the buncher and output cavity harmonics are the same achieve efficiencies above 41%, which corresponds to an output power exceeding 100 MW. The large signal gain in both cases is about 50 dB. The first harmonic output cavity is quite stable at the design parameters, but the second harmonic output cavity is only marginally stable and requires further work. The fundamental output design with a second harmonic buncher has considerably lower gain and somewhat lower efficiency than the other designs. Furthermore, the required buncher cavity quality factor is unrealistically high.

In spite of its potential drawbacks, the 1-2-1 design is still of interest because of the dependence of efficiency on velocity spread. This dependence is indicated in Fig. 4 for both first harmonic output designs. The 1-2-1 design has a strong dependence on velocity spread but achieves a theoretical efficiency of nearly 50% with zero spread. The 1-1-1 design has a weak dependence on velocity spread and achieves a maximum value above 45% with zero spread. This performance is consistently about 2% higher than the simulated two-cavity first harmonic design. [1]

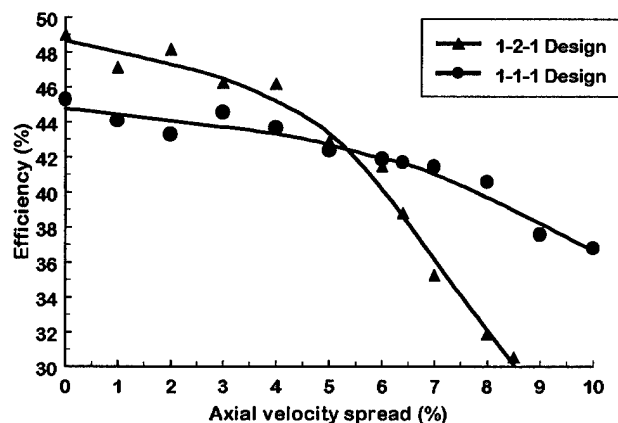


Figure 4. Simulated efficiencies of the first-harmonic output circuits.

The dependence of efficiency on velocity spread for the 1-2-2 design is indicated in Fig. 5. The decrease in efficiency with spread is fairly weak up until about 6%. From zero velocity spread up until this point, the second harmonic efficiencies are only about 1% lower than the corresponding first harmonic efficiencies. The three-cavity second harmonic efficiency is over 6% higher than the corresponding two-cavity design. [1] This represents a significant improvement. A 1-1-2 design was attempted during this investigation, but zero spread efficiencies were limited to about 30%.

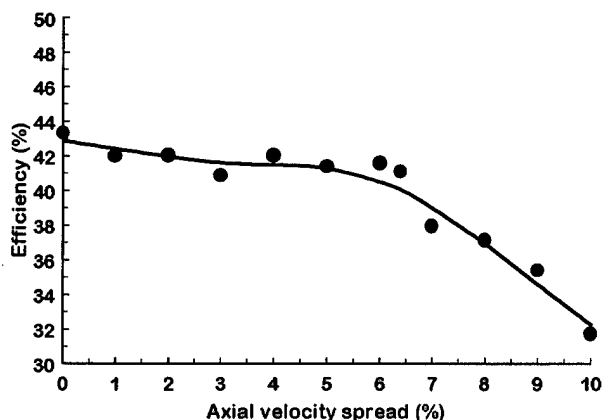


Figure 5. Efficiency of the second-harmonic output circuit.

A 1-2-4 design has also been attempted for which the abrupt transition output cavity would operate at 34.272 GHz in the TE_{041} mode. This design was again motivated by ear-

lier work [5] and would represent a device with extremely attractive properties for a variety of applications. The output cavity designed for this simulation has a quality factor of 625, an axial length of 1.3 cm and a lip length of 0.3 cm. The wall radii were again selected to minimize mode conversion to lower radial modes. The output power is predicted to be 94.5% in the TE_{04} mode. The amount of power flowing back into the drift tube is about 0.2% of the total output power. Unfortunately, our best results to date have produced efficiencies of only about 13%.

V. SUMMARY

This theoretical investigation represents a first look at the design of three-cavity coaxial gyrokystrons and the results are somewhat preliminary. Nonetheless, these results appear to be quite promising for first and second harmonic designs. Efficiencies of 40% and gains of 50 dB appear to be achievable with realistic beam parameters. The abrupt transitions of the second harmonic TE_{021} cavities enable quite compact drift regions to be utilized. This is a distinct advantage over previous circular waveguide tubes which required smooth radial wall transitions to minimize mode conversion. The large-signal gains of the three-cavity systems are significantly better than the corresponding two-cavity designs. The improvement in efficiency is moderate for first harmonic tubes but dramatic for second harmonic design.

Additional work needs to be done to determine and improve the stability of the second harmonic cavities to first harmonic modes. Also, the effect of lossy ceramics on the harmonic buncher cavities needs to be examined. Finally, the performance limits of 1-2-4 designs need to be understood to determine if high efficiency circuits are possible.

V. REFERENCES

- [1] J. P. Calame, *et al.*, "Design of 100 MW, two-cavity gyrokystrons for accelerator applications," in these proceedings.
- [2] W. M. Bollen, *et al.*, "Design and performance of a three-cavity gyrokystron amplifier," IEEE Trans. Plasma Sci., PS-13, 424 (1985).
- [3] W. Lawson, *et al.*, "Performance characteristics of a high power X-Band two cavity gyrokystron," IEEE Trans. Plasma Sci., 20, 216 (1992).
- [4] H. W. Matthews, *et al.*, "Experimental studies of stability and amplification in a two cavity second harmonic gyrokystron," IEEE Trans. Plasma Sci., 22, 825 (1994).
- [5] G. S. Nusinovich and O. Dumbrajs, "Two-harmonic pre-bunching of electrons in multicavity gyrodevices," Phys. Plasmas, 2, 568 (1995).
- [6] P. E. Latham, W. Lawson, and V. Irwin, "The design of a 100 MW, Ku-Band second harmonic gyrokystron experiment," IEEE Trans. Plasma Sci., 22, 804 (1994).

NUMERICAL SIMULATION OF MAGNICON AMPLIFIER

V.Yakovlev, O.Danilov, O.Nezhevenko, V.Tarnetsky, Budker INP, Russia

I. INTRODUCTION

Magnicon is a new RF source with the round beam deflection [1,2]. The main features of this device are high efficiency and reduced sensitivity to variations in load impedance. Those features make magnicon to be attractive for accelerator applications. Magnicon may be designed as an amplifier and as a frequency multiplier. Magnicon with the frequency multiplication in centimeter wave range may turn into one of main RF sources for future linear colliders.

Magnicon theory is developed for ideal RF field and for small deflecting angles of infinitely thin electron beam [3]. But large deflecting angle and, thus, large beam tunnel apertures are necessary for power generating of tens and hundreds of MW. Fringing fields of the beam tunnels, RF-field non-linearity far from the cavity axis and finite beam diameter lead not only to quantitative perturbations of device parameters, but change the process of beam-cavity interaction in principle [4,5]. It is necessary to take into account all mentioned phenomena to build a working device.

We have developed methods and computer codes for particle simulations of the beam-cavity interaction in magnicon employing the realistic DC magnetic and RF fields and finite beam diameter. Computer simulation codes presented in this report does not treat electron gun problems, which are described in details in [6].

II. PHYSICAL MODEL

We developed the two models for magnicon analysis to find a working version providing optimal efficiency:

- a. the steady-state model;
- b. the time-dependent one.

The steady-state model employs fixed amplitudes and phases of RF-fields in magnicon cavities. Self-consistency is achieved by iteration until power balance takes place in each cavity (i.e. until the beam energy loss equals to energy dissipation in the cavity wall or in the load). Dominance of the beam energy loss in the cavity in the absence of preliminary beam deflecting indicates the self-excitation on the working frequency [4]. Longitudinal DC magnetic field is formed by the magnetic system, which includes not only separate coils with independent current supplies, but magnetic shields having relevant configuration [3]. In our model we use the field calculated for real magnetic system without taking into account iron saturation, which are negligible in our case because of small field value [6]. We use for calculations the realistic rotating RF-fields of the cavities connected by beam tunnels to take into account influence of the fringing field. The resonance frequency of a cavity may be multiple of the drive frequency with corresponding azimuthal number. The simulations propagate an electron beam through a sequence of deflection cavities and an output cavity. We use $2\frac{1}{2}D$

macroparticle model of the beam without space charge. To estimate influence of the space charge scalloped beam is considered with arbitrary value of the cathode magnetic field. The simulation may be carried out by following a single temporal slice because of phase synchronism. During calculations of the beam dynamics in the fixed fields the beam power losses and the cavities detuning caused by the beam are calculated. When the self-consistent solution is found, it is necessary to produce its stability test, because the regime obtained as a result of optimizing may be unstable both in the deflecting system and in the output cavity. In the deflecting system this instability may have a view of RF field amplitude jump lead to the cavity breakdown [10]. In the case of instability in the output cavity the regime of small efficiency may be realized. For stability analysis Lyapunov's method is used: differential equations for RF field amplitude growth in the cavity are linearized near the working point in amplitude-phase coordinates. The resulting system of the linear equations is used for determination of the instability growth rate.

After magnicon optimizing by the steady-state code and stability test, we use the time dependent model to calculate duration and type of a transient process of magnicon excitation. Time dependent simulation is fulfilled based on slow amplitude approximation of the differential equations for RF field complex amplitudes. During each step of numerical integration of those equations it is necessary to calculate complex power of the beam losses, and thus, to solve the steady-state problem.

III. COMPUTER MODELS

a. Axial DC magnetic field is calculated using SAM code [7] for a real geometry of the magnetic system in linear approximation. In this case we solve N magnetostatic problems (N is the number of coils in the magnetic system). When we solve the i -th problem, we assume the current in the i -th coil to be unit, and in another coils to be zero. The total field is calculated as a superposition when all the coil currents are distributed previously. It gives the possibility of operative changes of the coil currents during the beam dynamics calculations.

b. The cavity RF-field is calculated by the next way [8]: the resonance frequency and H_r and H_z components are calculated by SUPERLANS2 code [9] for arbitrary azimuthal wave number m . The azimuthal component H_φ is determined using the next equation:

$$\Delta H_\varphi - \frac{H_\varphi}{r^2} + \left(\frac{\omega}{c}\right)^2 H_\varphi = \frac{2m}{r^2} H_r, \quad (1)$$

where ω is the resonance frequency, c is speed of light. The calculating error does not increase because of smoothing properties of Laplace operator. But it is not possible to use the electric field calculated by numerical derivation because of unacceptably large errors. We calculate the current surface distribution using the magnetic field calculated by

SUPERLANS2 and then find the RF-field in arbitrary point integrating the surface source field over the cavity boundary [8]. For the approximation of the surface current distribution, we use a third-order spline fit. In this case, all six field components will satisfy Maxwell equations and we have the same precision of calculations. To reduce the RF field calculation time inside the cavity, we use paraxial field expansion. We have found an analytical formula for arbitrary-order paraxial expansion of the surface source fields of arbitrary azimuthal dependence. The longitudinal dependences of paraxial expansion coefficients are approximated by a third-order spline. It is possible to calculate the excitation of several modes in the same cavity. The maximal surface electric field is calculated and displayed for electric strength analysis of the cavity working in investigating regime.

c. For integration of macroparticle equations of motions a third-order Runge-Kutta method is used. Simultaneously we integrate the complex electric field along the trajectory to find the complex power loss of macroparticle. The total beam power loss P is determined by sum of the power losses over all macroparticles. Imaginary part of the beam power loss determines the cavity detuning caused by the beam:

$$\Delta\omega = \frac{\text{Im}(P)}{w} \quad (2)$$

where w is the energy stored in the cavity. The beam kinetic energy changes in process of deflection and deceleration in the output cavity and real part of the total beam power loss are used to check the calculation precision. Thirty-seven macroparticles are typically employed, but up to 177 macroparticles are used to verify the accuracy of the final simulations.

d. For stability analysis we use the next equations for the RF-field amplitude u_i and phase ϕ_i in i -th cavity:

$$\begin{aligned} \frac{du_i}{dt} &= -\frac{u_i}{\tau_i} \left(1 - \frac{\text{Re}(P_i)}{P_{id}} \right) \\ \frac{d\phi_i}{dt} &= \delta\omega_i + \frac{\text{Im}(P_i)}{w_i} \end{aligned} \quad (3)$$

where P_{id} is power dissipation in the cavity wall (or in the load), τ_i is the time constant, $\delta\omega_i$ is the difference between the cavity resonance frequency and the working frequency. Then we produce linearizing of (3) near the stationary point, the derivatives of right-hand side of (3) we find numerically, solving the steady-state problems with perturbed amplitude and phase. Eigen values of the matrix of the linear system are equal to the instability growth rates.

e. For time-dependent simulations we use the same system of equations (3) for all cavities excluding the first one, where the field is determined by the drive power. This system is integrated using the third-order Runge-Kutta method. One should notice that the system (3) is stiff because the time constant of the output cavity is much less than the time constants for deflecting cavities. Thus, we plan to use an implicit method to solve (3) to decrease the calculation time.

IV. THE COMPUTER CODES

We have designed the computer codes for magnicon simulations for PC and VAX based on the methods described above. Because it is necessary to make calculation of

considerably large number of variants during magnicon optimizing, and the number of input parameters is large too, friendly user's interface with graphics is needed for effective work with the codes. The dialogue used in those codes is based on menu system and table input/output of symbol information. Mouse is used for an output data processing in the graphic window directly. The final document containing the total input and output information with graphics is prepared automatically as a result of the code run.

V. EXAMPLES

In the Fig.1 there are the results of calculation of the 7 GHz frequency doubling magnicon having the beam power of 100 MW [4,6]. The beam voltage is 430 kV, the beam current is 230 A. Calculated efficiency for this version is 54%. The trajectories of 37 macroparticles in (r,z) coordinates are shown as well as longitudinal dependence of the energy of each macroparticle. The longitudinal distribution of axial DC magnetic field is shown in the Fig. 2. Fig. 3 shows the field map of the operating mode of the penultimate cavity. The transient processes of amplitude growth in all cavities are shown in Fig. 4. The bold curve corresponds to the process in the output cavity. Fig. 5 illustrates an unstable (for the output cavity) transient process in the output cavity for one of the regimes with small efficiency.

VI. SUMMARY

Simulation model and computer codes are developed for calculation of the fields and the beam dynamics in magnicon taking into account beam tunnel fringing field and finite beam diameter. Those codes were used in investigations of physical processes in magnicon and helped to develop the first operating magnicon design [10] and its improved version, which is under fabrication.

VII. REFERENCES

- [1] M.M.Karliner, *et al.*, "The magnicon- An advanced version of the gyrocon", Nucl. Instrum. Methods Phys. Res., vol. A269, pp. 459-473, 1988.
- [2] O.A.Nezhevenko, "The magnicon: A new RF power source for accelerators", in IEEE Particle Accelerator Conf. Rec., 1991, vol.5, pp. 2933-2942..
- [3] M.M.Karliner, E.V.Kozyrev, A.Yu.Maximov, O.A.Nezhevenko, "An approximate theory of the magnicon", Preprint INP 88-64, Novosibirsk, 1988 (in Russian).
- [4] O.Nezhevenko, "Gyrocons and magnicons: microwave generators with circular deflection of the electron beam", IEEE Trans. on Plasma Science, vol. 22, pp. 756-772, 1994.
- [5] O.Nezhevenko, *et al.*, "First test of the X-band pulsed magnicon", in Proc. IEEE Particle Accelerator Conf., 1993, vol.4, pp. 2650-2652.
- [6] Y.V.Baryshev, *et al.*, "Electron optic system for forming 100 MW beam with high current density and microsecond pulse duration for X-band magnicon", in Proc. 8th Int. Conf. High power Particle Beams, Novosibirsk, Russia, vol. 1, pp. 598-603, 1990.

[7] B.M.Fomel, M.A.Tiunov, and V.P.Yakovlev, "Computer-Aided Electron Gun Design", in Proc. XIII International Conference on High Energy Accelerators, 1987, vol. 1, pp.353-355.

[8] O.A.Nezhevenko, V.P.Yakovlev, S.H.Gold, and B.Hafizi, "Design of a High Power X-Band Magnicon Amplifier", IEEE Trans. on Plasma Science, vol.22, pp. 785-795, 1994.

[9] D.G.Myakishev, and V.P.Yakovlev, "The new possibilities of SUPERLANS2 code", these Proceedings.

[10] I.Zapryagaev *et al.*, "Status of X-Band Pulsed Magnicon", in Proc. Eur. Particle Accelerator Conf., 1994, vol. 3, pp. 1927.

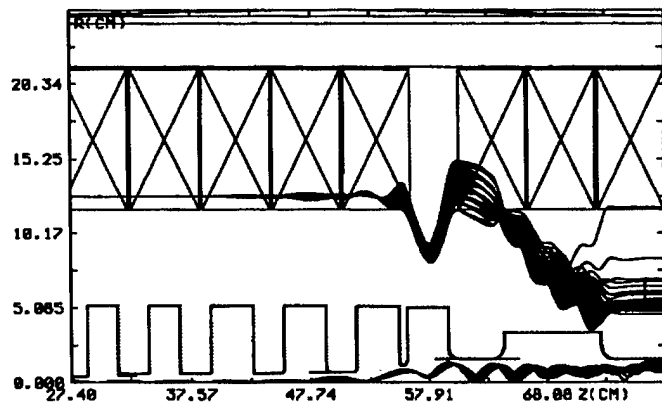


Fig. 1. Steady-state simulation of the magnicon design with the efficiency of 54%.

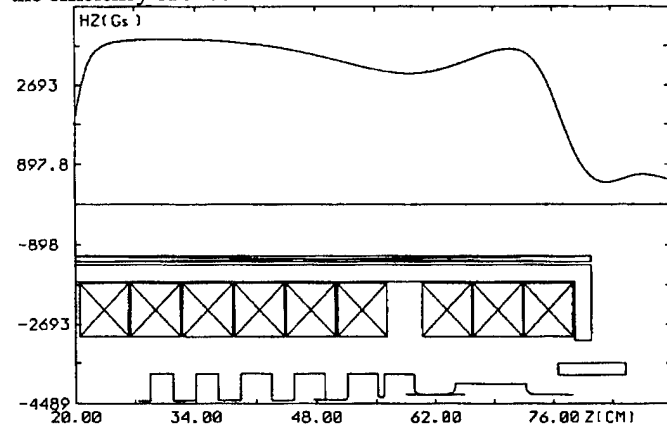


Fig.2. The Axial DC magnetic field profile used in the simulations.

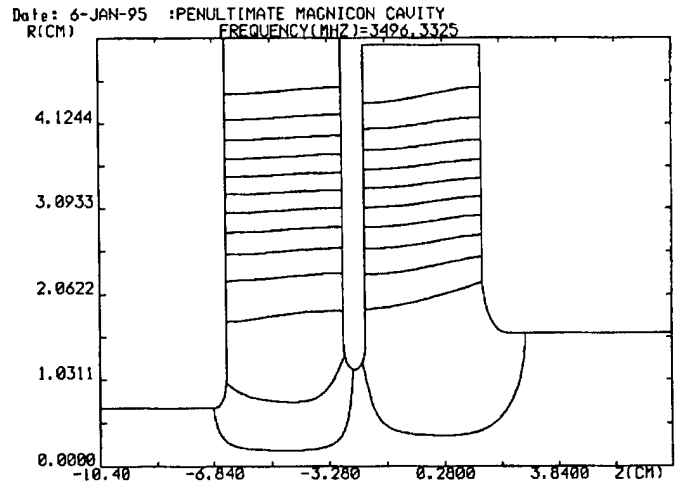


Fig. 3. The field map of the operating mode in the penultimate cavity.

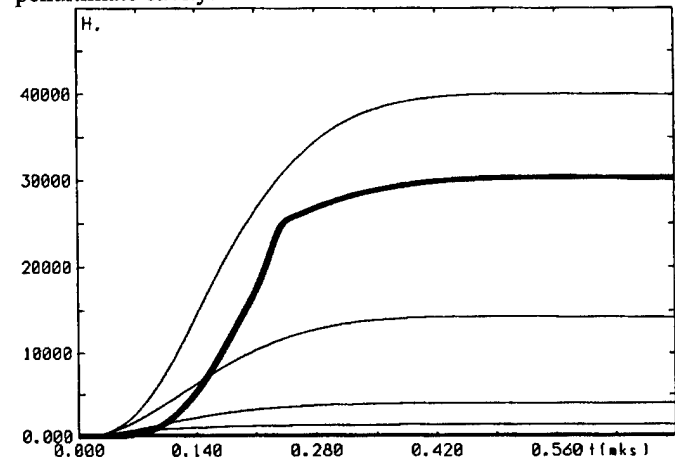


Fig. 4. The transient process in the magnicon.

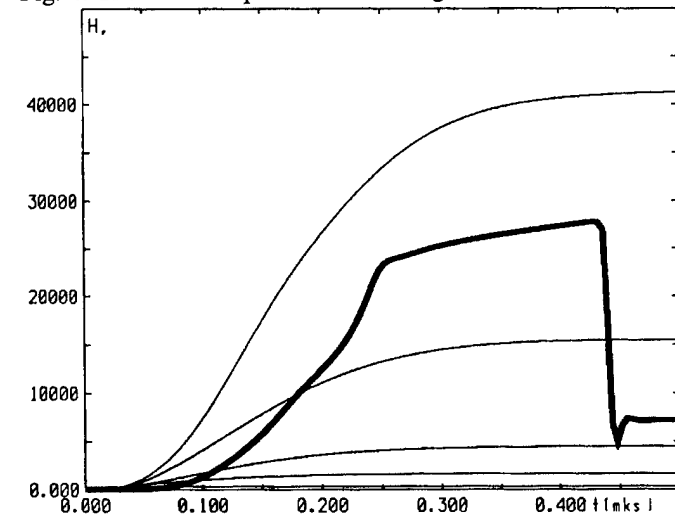


Fig.5. The unstable regime of the output cavity excitation.

RF-POWER UPGRADE SYSTEMS WITH ENERGY COMPRESSION FOR ELECTRON LINACS

A. Shalnov, B. Yu. Bogdanovich, A. Ignatyev, V. Senyukov

Moscow State Engineering-Physics Institute,
MEPhI, Moscow, 115409, Russia.

Application of the RF-energy compression systems as an RF-source for linear charged particles accelerators is represented to be rather perspective, as far as they permit to increase pulsed power of accelerating wave without application of any additional or more powerful RF-generators and, hence, to increase an output beam energy of an accelerator. More over, application of such systems enables an essential expand of a beam energy adjustment range, that in some cases permits to use only one unit instead of a number.

The systems can be used for existing units modernization, as well as for development the new ones. The theoretical questions of the energy compression systems using as an RF-power source for linacs were already considered in details a long time ago [1, 2]. But this considerations deals only with a possibility of use of a unique energy compression system with an RF-energy storage in a high-quality-factor cavity with a variable connection factor. Practically, however, for particle acceleration such systems was not used.

The only type of the RF-energy compression systems, that was practically used for particle acceleration, is the SLED system, which was offered in 1974 at SLAC for 20 GeV accelerator energy increase [3]. In a consequence the similar systems were realized on acting accelerators in China (1986) [4] and USSR (MEPhI, 1987) [5]. In 1985 P. Wilson offered an RF-energy compression system with the time delay lines (DL) used for an energy storage [6]. Actually, a modernized variant of a SLED system, offered by V. Balakin in 1990 as an RF-source for a linear collider VLEPP [7], also may be considered as a DL application for RF-energy storage.

The new types of energy compression systems recently suggested delivered a question on necessity of these systems classification and researching the questions on perspective and expediency of their use as the RF-feed sources for electron linacs (and, in general case, not only for electron).

The present report is devoted to classification of the RF-energy compression systems (ECS), that may be used as the RF-feed sources for electron linacs.

The classification scheme of ECS is shown on fig. 1. As far as the working principle of each particular system is basically determined by an energy storage element used, from this point if view all systems can be divided into three groups: a) the systems with energy storage in cavities; b) the systems with energy storage in DL; c) the systems with energy storage in combined storing elements.

The first group concern ECS, in which the RF-field energy is accumulated in a high-quality-factor cavity and the output pulse is formed at the expense of a wave, emitted from a cavity. In systems of the second group the RF-energy is accumulated in DL, and the output pulse is formed by the initial RF-pulse separate parts detained in time with the

subsequent addition in a load. The third group concerned with systems that used for energy storage cavities and DL both.

The first group systems can be divided with respect to load used: a) with an active load; b) with a resonant load (in these systems the reflected wave affected essentially on a system operation). The systems with an active load can be divided in conformity on a way of a system operation mode (energy storage or use) transfer into following types: a) systems with variable cavity parameters (any of cavity parameters is changed for stored energy using); b) system with constant cavity parameters (operation mode changes only by a generator wave phase and/or amplitude modulation).

The systems with an energy storing in DL can be divided by a principle of DL use: a) with DL use for time detained of RF-pulses; a) with DL use as a resonator elements (such resonators using enables to form the flat top output pulses). The first group of ECS can be divided for switching elements used: a) high power switching; b) low power switching; c) without any switching elements (such systems can be related to ECS conditionally). This division matters for practical application of ECS.

Certainly, a further division on the various attributes can be carried out, however at present it seems to be inexpedient, since will cause an unjustified complication of the classification scheme. It is necessary also to note, that the indicated scheme is conditional up to a certain degree, as far as some systems can be simultaneously referred to different types.

The systems with constant parameters of storage cavities (SC) can be divided on the output pulse top form (system with variable SC parameters practically always form pulses with exponentially dropping top, and system with DL - the flat top pulses): a) systems without pulse top correction; b) systems with pulse top correction. Such division is connected to the possible areas of system practical use.

The ECS are characterized by the following main parameters:

- factor of a wave power increase - K_p - relation of a system output wave pulsed power to a feeding generator power;
- energy transfer efficiency η_e , which is defined as a relation of energy, transferred by system into a load, to energy "received" by system from generator;
- duration of an output RF-pulse - t_p . Parameter is important for ECS practical use. The real values of the various types ECS main characteristics are listed in table.

System type		Output pulse top form	Power increase factor, K_p	Efficiency, η_e	Output pulse duration, t_p
with storage cavities	variable parameters	dropping	30 - 50 (dB)	0,4 - 0,6	1 - 100 ns
	constant parameters	arbitrary, dropping	6 - 7	0,6 - 0,7	0,1 - 1 μ s
	with resonant loading	bell waveform	10 - 30 (dB)	0,6 - 0,7	0,1 - 1 μ s
with time delay lines	high power switching	flat	2 - 8	0,8 - 1,0	10 - 100 ns
	low power switching	flat	2 - 8	0,8 - 1,0	
	without switching	flat	2 - 5	0,8 - 1,0	
	DL - elements of resonators	flat, dropping	2 - 10	0,6 - 0,7	

The main work principle of the ECS with SC variable parameters based on a fact that at a sharp increase of the SC connection factor after the energy storage process completed results in stored energy fast outcome thus forming a high-power RF-pulse. The running or standing waves resonators can be used here for energy storage. Such systems were well enough investigated theoretically and experimentally. The maximum efficiency of energy transforming for such systems does not exceed 0,815, that is due to features of energy storing processes in cavities (though there are the methods of an energy transfer efficiency increase practically up to 1,0 [8]). The main disadvantages of ECS with SC variable parameters are: a) necessity of high-power RF-switches use (at the power levels of hundreds megawatts such switch represents rather complicated and power-intensive device), and b) significant output power variations within RF-pulse.

Typical representative of ECS with SC constant parameters is the system SLED. Such systems are largely free from defects, inherent to systems with variable SC parameters. They don't need to use high-power switches, and the output pulse top has less abrupt recession (besides, there exist some ways to change the top form). However, the maximum value of factor K_p for such systems is not more than 9 (real value do not exceed 6...7, due to the finite value of a SC connection factor). This is their main disadvantage (though, there are ways for the K_p value increase to some extend).

In the ECS with combined methods of operation mode transfer (storing or using energy) a SC parameters variation and a generator wave modulations are used both.

The main difference of the ECS with a resonant loading from the other types is that here the load is an essential element, that appreciably influence on a system characteristics. Also they can be named as systems with connected resonators. The principle of these systems work is based on following: at certain parameters of a stored in one of them completely passes serially from one resonator into another. The relation of maximum equivalent RF-power in these resonators is reverse proportional to the relation of their unloaded quality factors. For resonators with running waves the equivalent power

represents quite certain RF-power, circulating in a resonator ring. The practically achievable values of K_p in such systems are about 150 ...200 (for SC with $Q_0 = 10^5$) and more (for superconducting resonators). The wave with such power "existence" time in a ring is about an order higher, than for case with pulse outcoming into an active load.

The DL application as an energy storing elements in ECS, used for linacs feed, has a number of advantages in comparison with SC. The main advantages of such systems are the following: 1) they always formed a flat top output pulse, and 2) the energy transfer factor can come nearer to 1.0 when using a small loss DL, because the basic energy losses inherent to systems with SC are here away.

The main work principle of the ECS in which DL are used for RF-pulse separate parts time delay consists in dividing the initial pulse by a switching device in a number of equal duration parts, which with the help of DL are displaced in time so, that to a target summing device (to a load) they would come simultaneously. Thus the power of a wave in this summing device will increase in so much time, in how many parts an initial pulse was divided. Such pulse division can be executed with the help of amplitude (switching at a high power level) or phase (switching at a low level) modulation.

When using DL as a storing elements a creation of ECS without any switching elements is possible. In this case the useful load - accelerating structure - is an integral part of a system. The accelerating structure actually appears included in a resonator with running waves. The application of DL permits to reduce the transient process time in such a resonator up to a minimum. The systems with DL as elements of resonators unite the properties of systems with SC and DL. The positive properties of such systems are the flat top output pulse forming and a relatively simplicity of construction. On the other hand, they have relatively low efficiency as the systems with SC.

The considered classification scheme of the energy compression systems that can be used as RF-sources for linacs feed permits to evaluate the main properties of such systems and also an expediency of its use for achieving of required

parameters of accelerated beam. Besides this it enables to determine the main ways of developing of the energy compression systems with required characteristics.

REFERENCES

- [1] Alvarez R.A., Birx D.L., Byrne D.P. Et.al. Application of Microwave Energy Compression to Particle Accelerators. Particle Accelerators, 1981, v.11, p. 125-130.
- [2] Didenko A.N., Dzerliczin A.G., Sulakshin I.S. et.al. Formirovanie moshnich impulsiv pri nakoplenii SVCh-energii v rezonatore. Radiotekhnika i elektronika, 1980, v.25, No 6, p.1227.
- [3] Farkas Z.D., Hogg H.A., Loew G.A., Wilson P.B. SLED: A Method of Doubling SLAC's Energy, - Proc. Of the 9 th Int. Conf. On High Energy Accelerators, 1974, SLAC, p.576-583.

[4] A 90 MeV Electron Linac of IHEP / Electron Linac Group. SLAC-Report-303, September 1986, p.505-507.

[5] Bogdanovich B.Yu., Sunyukov V.A., Shalnov A.V. Lineinyy uskoritel elektronov s nakopleniem energii v sisteme VCh-pitaniya. M: Preprint / MEPhI. 039-88, 1988.

[6] Wilson P.B. Linear Accelerators for TeV Colliders. SLAC-PUB3674, May 1985.

[7] Balakin V.E., Syrachev I.V. A New Approach in RF Multiplication. - 2-nd Int. Workshop on Next Generation Linear Collider, LC-90, March 28 - April 5, 1990, KEK, Tsukuba, Japan, p.643-654.

[8] Baraev S.V., Korovin O.P. Conditions of effective input of energy in an accelerating resonator. JTF, 1985, v.55, No 4, p.723-725

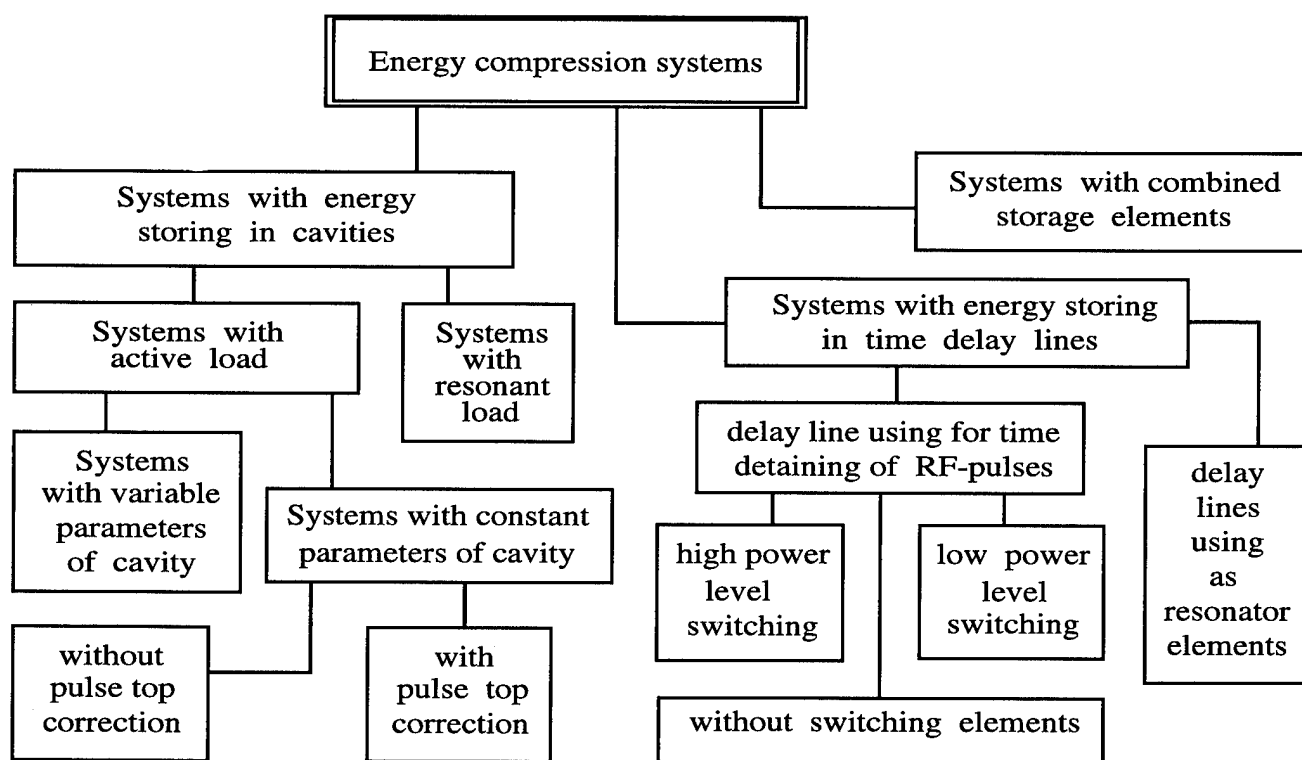


Fig. 1. Energy compression systems (ECS) classification scheme.

RF-POWER UPGRADE SYSTEM WITH RESONANT LOADING

A. Shalnov, B. Bogdanovich, A. Ignatyev, V. Senyukov

Moscow State Engineering-Physics Institute, MEPhI, Moscow, 115409, Russia.

The RF-power upgrade systems with RF-field energy compression are intended for accelerating wave power increase in order to increase an accelerated beam energy or decrease the feeding RF-generators power. At present a number of energy compression system (ECS) types and designs with various properties are known [1]. Among these a system with a resonant load presents the certain interest for practical use. The main difference of such ECS from the other types is that here a resonant load is an essential part of the system that influence significantly on its parameters. They can be named as systems with connected resonators also.

I. THEORY

A. The main principles of work and a system characteristics

The main principle of the system with resonant loading operation is based on the following: for certain parameters of a system formed by two connected resonators all energy primarily stored in one resonator passes by turns from one resonator to another. For the first approximation it may be considered that a maximum value of equivalent RF-power in each resonator is determined by expression:

$$P_1 / P_2 = Q_2 / Q_1 \quad (1)$$

where P_1 and P_2 - equivalent RF-wave power in the first and second resonators; Q_1 and Q_2 - the first and second resonator quality factors. From expression (1) it follows that the higher resonators q-factor relation the more equivalent power increase can be achieved. The resonators can be with standing or travelling waves. In case of resonators with travelling waves (TWR) the equivalent power is the quite certain power of RF-wave circulating in resonator ring.

The variant of ECS with a resonant load is submitted on fig.1 [2]. Here accelerating structure 4 is a part of a TWR. The switched coupler 2 transfers the system operation mode from storing energy to its use. During the energy storing period (state A) the coupler 2 connects generator 1 output to storing resonators 3 and the acceleration structure 4 output - to an absorbing load 5. To use the stored energy (state B) the coupler 2 is switched in such way that the acceleration structure output becomes connected to storing resonators, forming TWR.

The system works as following. In state (A), an energy storing in resonators 3 occurs. The wave, reflected from storing resonators (SR), passes through a TWR and arrives in a load 5. When the energy storing process ends the coupler

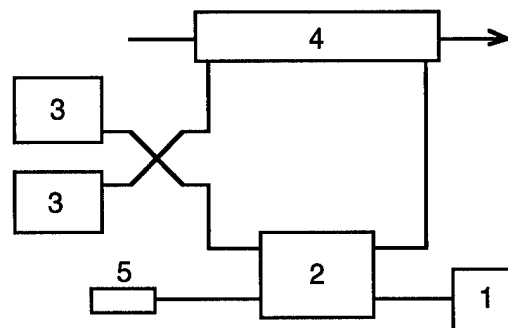


Fig. 1. An RF-energy compression system with a resonant load (1 - RF-generator; 2 - switched coupler; 3 - storing resonators; 4 - accelerating structure; 5 - absorbing load).

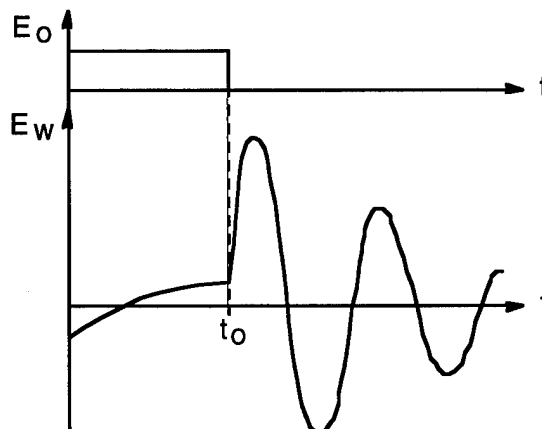


Fig. 2. The RF-wave average amplitude variations in a system with a resonant load (E_o - generator wave amplitude; E_w - wave in TWR ring).

transformed in state B. So the wave coming to SR is a wave leaving from accelerating structure. A wave phase shift in a TWR is chosen so that the wave coming on SR has the same phase as the wave irradiated from them. Then after each turn-over the amplitude of a wave circulating in TWR ring will grow so long as all accumulated in SR energy will not pass completely in TWR. And after this the return swapping of energy from TWR to SR will begin. The qualitative graph of the circulating in TWR wave average amplitude variations are shown on fig.2. If the energy losses in TWR are insignificant, the factor of wave power increase K_p in such system can be evaluated on following expression:

$$K_p = P_w / P_o = W_s / (T \cdot P_o) \quad (2)$$

where P_w and P_o - the power of RF-waves in TWR and on a generator output, accordingly; W_s - energy stored in resonators; T - time (duration) of one turn-over of a wave in a TWR. Practically the achievable values of factor K_p in such system can make 150 ...200 (for SR with self q-factor $Q_o = 10^5$ and more (for superconductor resonators). The time of the high power wave existence in TWR appears to be about an order higher, than for the case when RF-pulse is formed on active load.

B. Field calculation equations

Let's consider a system shown in fig.1. After a generator switching-off and TWR forming the wave, emitted from the SR is added to a wave circling in the TWR. In this case the amplitude of a summarised wave at the acceleration structure entrance during the energy use period is described by a following expression:

$$E_w(t) = \begin{cases} \left(-\frac{2\beta}{1-\beta} (1 - e^{-t/\tau}) + 1 \right) \cdot E_o, & \text{for } 0 \leq t < t_0 \\ \sum_{n=0}^N E_{wn}(t), & \text{for } t \geq t_0 \end{cases} \quad (3)$$

where :

$$E_{wn}(t) = -\frac{2\beta}{1+\beta} \cdot E_o \left(1 - e^{-\frac{t_0}{\tau}} \right) \cdot e^{-n\alpha} \cdot e^{-\frac{t-t_0-T}{\tau}} \cdot F(-n, 1, A)$$

$$F(-n, 1, A) = \sum_{k=0}^n \frac{C_n^k}{k!} (-1)^k A^k$$

$$A = \frac{2\beta}{1+\beta} \cdot \frac{t-t_0-nT}{\tau}$$

$N = [(t-t_0)/T]$ - number of wave revolutions in TWR.

C. Calculation results

The graph of dependence of wave amplitude at an accelerating structure entrance on time t for $t > t_0$ is indicated in fig.3. Calculations were made for a system with following parameters: $Q_o = 100 \cdot 10^3$; $\beta = 5$; $t_0 = 2,5 \mu s$; $T = 40 ns$; $\alpha = 0,01$. One can see, that the wave amplitude changes are executed by inherent steps, the duration of which is equal for a wave turn-over time in a TWR (it is supposed, that changing of the system operation mode is executed instantly).

On fig.4 the graphs of a maximum normalized wave amplitude at an acceleration section entrance averaged for a time of one turn-over in a ring dependence on a duration of turn-over period T for various values of attenuation in a ring are given for the same system parameters.

The results presented show, that the attenuation in a TWR appreciably influences on the wave amplitude E_w (and, hence, and on K_p value) only for small magnitudes of the turn-over time ($T < 50 ns$). Also researches have shown, that the optimum value of a coupling factor β (for a maximum

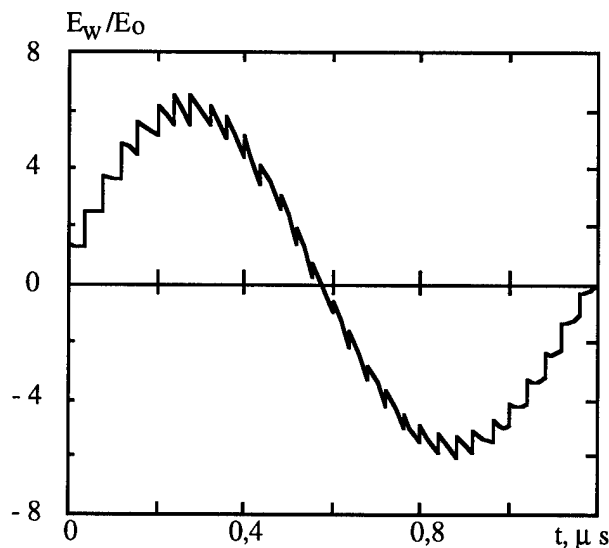


Fig.3. Changes of normalized amplitude of a wave at an accelerating structure entrance E_w/E_o from the time t for $t > t_0$.

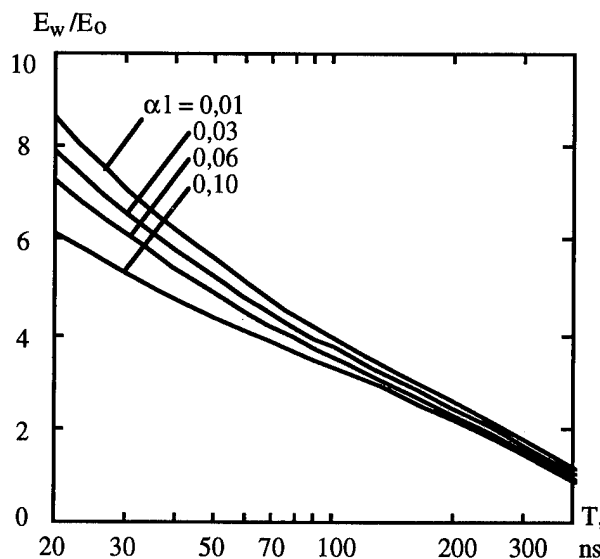


Fig.4. Dependence of maximum averaged for a one turn-over time wave amplitude at an accelerating structure entrance E_w/E_o on a duration of one turn-over period T .

wave amplitude E_w) is determined only by a duration of an energy storing period t_0 .

Theoretical researches of an accelerated beam energy changes within a stored energy using period have shown, that in difference from time dependence of wave amplitude in TWR (see fig.2) the time dependence of beam energy is smooth and has no any steps.

II. EXPERIMENTAL RESULTS

The experimental researches of a ECS with resonant load were conducted at RF-generator pulsed power up to 100

kW in S-band. For energy storing there were used a copper cylindrical cavities with H_{015} mode. This cavities had an unloaded q -factor $Q_0 = 90 \cdot 10^3$ and coupling factor $\beta=6$. For changing the system operation mode a waveguide discharge switches were used. The experiments were conducted at two values of a wave turn-over duration in a ring: 40 ns and 24 ns. The summary energy losses in a ring in both cases were about 0,05.

The typical RF-wave normalized power variations in a TWR within the energy using period is shown in fig.5.

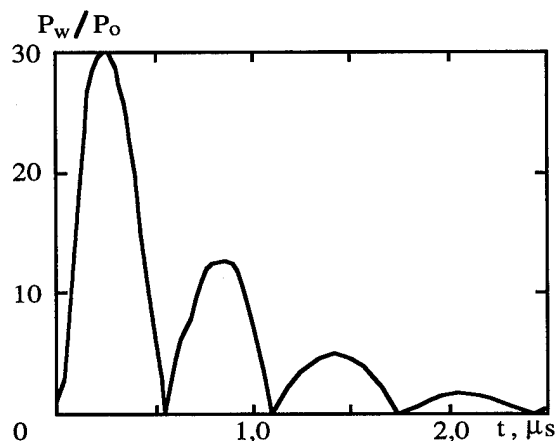


Fig. 5. The RF-wave normalized power variations in a TWR within the energy using period P_w/P_0 .

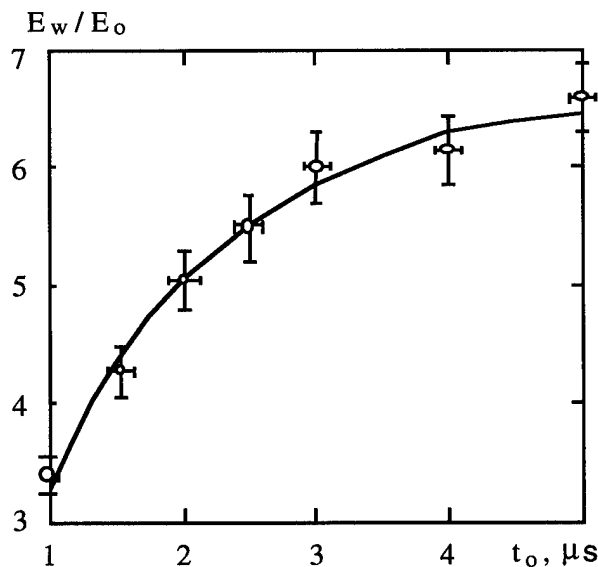


Fig. 6. A maximum normalized wave amplitude in TWR E_w/E_0 dependence on an energy storing period duration t_0 .

The results of measurements and calculations (on expression (3)) of a maximum wave amplitude E_{wm} in TWR dependence for considered parameters of a system on an energy storing period duration are shown in fig.6. The measurements and accounts were made for a ring with a one turn-over duration $T = 40$ ns and RF-generator output pulsed

power up to 10 kW. A measured values of a maximum power increasing factor K_p for $t_0 = 2,5$ μ s are the following: for a ring with $T = 40$ ns $K_p = 15,0 \pm 0,5$ dB (~ 32 times); for a ring with $T = 24$ ns $K_p = 17,0 \pm 0,5$ dB (~ 50 times). The calculated values are 14,9 dB and 16,8 dB, accordingly. A number of experiments on a system work research was also conducted at an RF-generator power up to 100 kW in a pulse. In these experiments the high-voltage switch modulator was used only for initialization of discharge, and the formation of a plasma in a switch was executed at the expense of a dropping RF-wave power. In this case a system was capable to work also. As it was expected, there occur a little decrease of a power increasing factor K_p (at the expense of losses in the switches while plasma formation). At source power about 100 kW the measured value of K_p was about $14 \pm 0,5$ dB (~ 25 times). Further increase of source power resulted in appearing of RF-discharges in a TWR waveguides, since the path was under atmospheric pressure, and the maximum wave power in a waveguide for this conditions is about the permissible one (corresponded to electrical strength for used waveguide: 72×34 mm²), i.e. about 2 - 2,5 MW.

As far as in a given system a mode transfer switching is executed at a high power level there is a necessity to use the discharge switches, that limits to some extend an opportunities of such systems application. However, as a positive fact it should be noted, that here the switches in an opened state (i.e. in absence of discharge) operates only at a feeding generator power level. In the other type systems with storing resonators (for example, the system with variable resonator parameters [1]) a switch in opened state should maintain the power levels equal to those of an output RF-wave. This permits a considerable simplifying of constructions of a switch and a managing high-voltage modulator, and in a number of cases (at not so large power levels) to use for switching a solid-state devices.

III. REFERENCES

- [1] Shalnov A., Bogdanovich B., Ignatyev A., Senyukov V. RF-power Upgrade Systems with Energy Compression for Electron Linacs. (1995 Particle Accelerator Conference). 1995.
- [2] Ignatyev A.P., Senyukov V.A. Sistema vysokochastotnogo pitaniya uskoritelya zaryajennich chasticz. Pat. 1832406, Russia, 5 H05 H7 / 02, Priority from 25.12.1990.

High-Power Test of a Traveling-Wave-Type RF-Pulse Compressor

S. YAMAGUCHI, A. ENOMOTO and I. SATO, KEK, National Laboratory for High Energy Physics
1-1, Oho, Tsukuba, Ibaraki, 305 Japan

Y. IGARASHI, Mitsubishi Heavy Industries, Ltd., 10, Oye, Minato, Nagoya, Aichi, 455 Japan

A high-power model of an *S*-band rf-pulse compressor utilizing a coaxial traveling-wave resonator has been designed, manufactured and tested regarding the energy upgrade of the PF 2.5-GeV linac for the KEKB project. An output peak power of 201 MW was obtained at an input RF power of 45 MW with no serious rf breakdown. The average energy gain was estimated to be 1.75.

I. INTRODUCTION

An energy upgrade of the PF 2.5-GeV linac up to 8 GeV is underway for the KEK B-factory project with an extension of the linac and a reinforcement of the rf power [1]. For the rf power reinforcement, a new-type rf-pulse compressor utilizing a TE₆₂₀-mode coaxial traveling-wave resonator has been developed in parallel with the SLED [2] application. The advantages of the new-type pulse compressor are simple structure and low cost.

A cold test using a low-power model was completed in 1994, and the expected pulse-compression ability has been demonstrated [3]. However, since the electric-field lines are perpendicular to the metal surface and the electric field gradient is extremely high (~ 100 MV/m for 45 MW input power), high-voltage breakdown may well occur. To test the breakdown and related problems, such as the radiation of X-rays and temperature rise, a high-power test has been carried out. The design and fabrication of a high-power model and the high-power test results are described in this paper.

II. DESIGN AND FABRICATION

The cavity comprises four parts: an inner cylinder, an outer cylinder, a bottom board and a ceiling board. These four parts and waveguide were assembled by silver and gold brazing. The material of the cavity is oxygen-free copper. The cavity dimensions were just the same as those of the cold model. Because the direction of the real current on the metal surface is normal to that of the lathe's blades, the surface flatness should be sufficiently smaller than the skin depth to obtain a high Q -value. The inner wall of the cavity was planed to less than $0.1 \mu\text{m}$ and finished by electrolytic polishing. A photograph of the high-power model of the pulse compressor is shown in Figure 1.

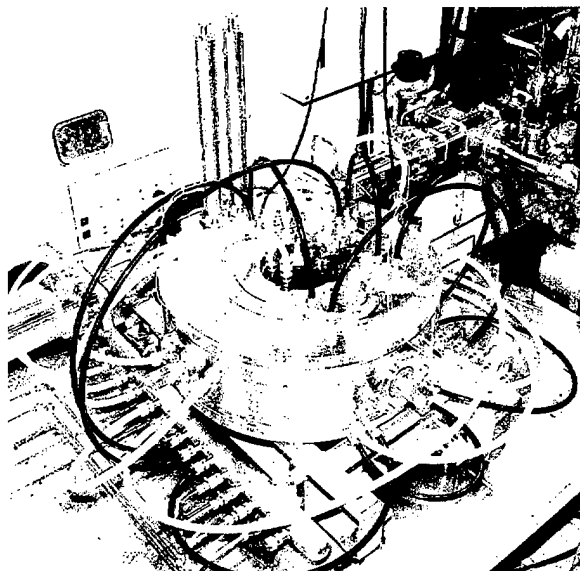


Figure 1: Photograph of the high-power model set at the test bench.

The measured rf characteristics of the cavity are summarized in Table 1 along with the design values. The decrease in Q_0 (unloaded Q -value) is attributed to insufficient electrical contact between the inner, outer cylinders and the bottom, ceiling boards. The total weight of the cavity, including support structure, is 179 kg.

Table 1

Electrical characteristics of the pulse compressor.

	designed	measured
f_0 [MHz]	2.856	2.858
Q_0	59000	48000
β	3.8	2.7
VSWR (tuned)	1.00	1.03
VSWR (detuned)	1.00	1.01
M	1.89	1.75

M : energy multiplication factor

Fine tuning of the resonant frequency was performed by adjusting the rf frequency during this work. The reflection from the cavity to the klystron was minimized by adjusting the stubs set at the ceiling board of the cavity.

III. PERFORMANCE TEST

A. SETUP

A test bench was constructed in order to perform a high- power test of the pulse compressor. The layout of the test bench is shown in Figure 2. The output power from the pulsed high- power klystron (45 MW, 2856 MHz, 3.8 μ s,

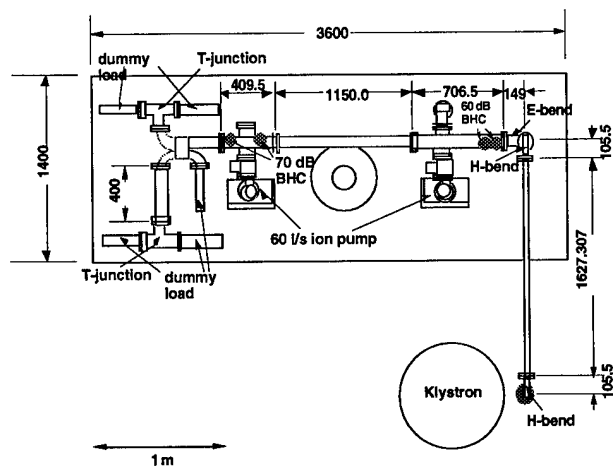


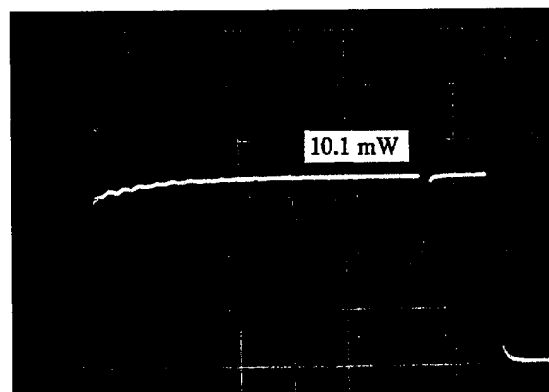
Figure 2: Layout of the test bench.

50 pps) was fed into the cavity, and the output power from the cavity was divided between a 3-dB hybrid and two T-junctions, and absorbed by four high-power water loads (1 μ s, 50 pps, 100 MW) developed by Nihon Koshuha Co. The rf power was monitored for forward and backward waves before and after the cavity. The vacuum was evacuated by two ion pumps (60 l/min) and the pressure was monitored by cold cathode gauges. The cavity temperature was monitored using a thermistor thermometer. For the interlock to stop the klystron, vacuum pressures were used as well as the cooling water for the klystron and modulator. The flow rate of the cavity cooling water was 80 l/min (30 \pm 0.2 $^{\circ}$ C).

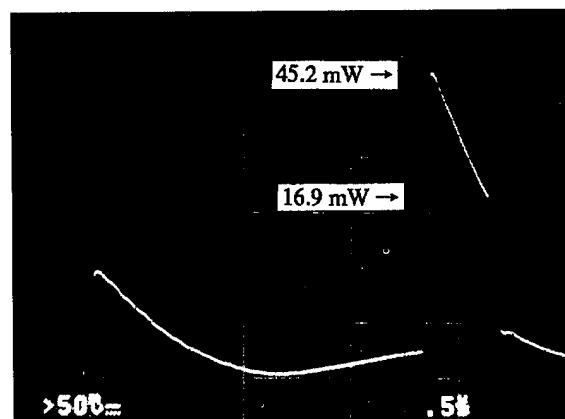
B. RESULTS

The rf conditioning was carried out while monitoring the vacuum pressure and rf power. The base pressure was $\sim 10^{-6}$ Pa after a bakeout at 100 $^{\circ}$ C for 4 hours; the pressure was kept below 2×10^{-4} Pa during rf operation.

After 250 hours rf conditioning, an output peak power of 201 MW was obtained for an input RF power of 45 MW with a pulse width of 3.8 μ s. An example of the output wave form from the pulse compressor is shown in Figure 3. The



(a)



(b)

Figure 3 : Output wave form, (a) detuned, (b) tuned.

average energy multiplication factor (M) was estimated to be 1.75 from the pulse shapes for the tuned and detuned conditions, assuming that the output power decreases linearly with time :

$$M = \sqrt{\frac{(45.2 + 16.9)/2}{10.1}} = 1.75.$$

The temperature rise of the cavity was 1.0 $^{\circ}$ C for an input power of 45 MW, 25 pps.

Figure 4 shows the dose-equivalent rate of bremsstrahlung X-rays as a function of the input rf power measured by ionization chamber at a point 2 m away from the cavity center without shielding. The extrapolated value of the dose rate for an input power of 45 MW, 50 pps is about 100 μ Sv/h. The measured maximum energy of the X-ray was 1.8 MeV for a 40 MW input.

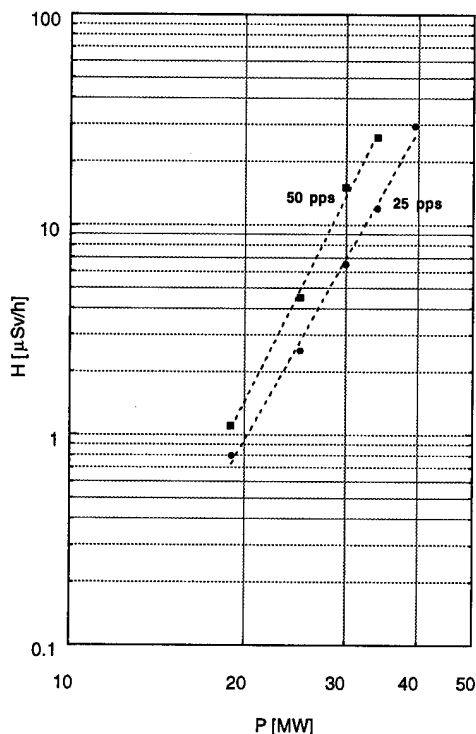


Figure 4: Dose-equivalent rate vs. input rf power. The pulse repetition rates are 25 and 50 pps.

IV. DISCUSSIONS

The high-power capability of the new-type rf pulse compressor was demonstrated experimentally in this work. To apply this pulse compressor to the PF-linac, however, there are two problems. One is that the energy multiplication factor (M) is slightly smaller than that required for the KEKB injector linac. The other is that the radiation-dose rate is too high to use this device in the klystron gallery from a radiation protection point of view (the maximum permissible dose rate is $20 \mu\text{Sv/h}$). Figure 5 shows the simulated trajectories of field-emitted electrons in a simple model using a tracking code for electrons in a traveling-wave field [4]. It is shown that some electrons are incident on the metal surface with very high kinetic energy, and that multipactoring-like motion is not observed. If we use a quite "clean" and flat surface metal, the amount of the radiation, which is caused by the bombardment of field-emitted electrons, will be reduced. It is not so easy, however, to obtain such a high-quality surface, especially at the mass production base.

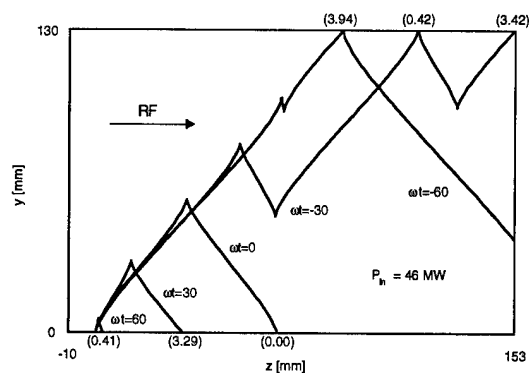


Figure 5: Typical trajectories of field-emitted electrons in a waveguide; field gradient is 130 MV/m and the phase velocity is $1.46c$. The numbers in parenthesis are the kinetic energy of the incident electrons.

To overcome these problems, such an electromagnetic mode with a much higher Q -value (unloaded) than this cavity and with no component of electric field perpendicular to the metal surface should be selected. Design work for the cavity that satisfies these criteria is now in progress.

V. ACKNOWLEDGEMENTS

The authors would like to express thanks to the RF group of the PF-Linac for preparing the rf source (klystron, modulator and rf driver) and Mr. K. Kakiyama for setting up the vacuum system. We also acknowledge to Dr. S. Ban and Mr. H. Nakamura of the Radiation Safety Center for measuring the X-ray energy spectrum.

VI. REFERENCES

- [1] A. Enomoto, *et al.*, "RE-FORMATION OF THE PF 2.5- GeV LINAC TO 8 GeV", Proc. of 1994 Linac Conference, Aug. 21-26, Tsukuba, Japan pp. 184-186.
- [2] Z. D. Farkas, *et al.*, "SLED: A Method of Doubling SLAC's Energy", Proc. 9th Int'l Conf. on High Energy Accelerators, SLAC pp. 576-583 (1974).
- [3] S. Yamaguchi, *et al.*, "DEVELOPMENT OF AN RF PULSE COMPRESSOR USING A TRAVELING-WAVE RESONATOR", Proc. of 1994 Linac Conference, Aug. 21-26, Tsukuba, Japan, pp. 478-480.
- [4] S. Yamaguchi : "Simulation Studies on High-Gradient Experiments," LAL/RT 92-18 (1992).

Active radio frequency pulse compression using switched resonant delay lines

Sami G. Tantawi[†], Ronald D. Ruth, and A. E. Vlieks
Stanford Linear Accelerator Center Stanford University, Stanford, CA 94309

Abstract :

This paper presents a study and design methodology for enhancing the efficiency of the SLED II rf pulse-compression system [1]. This system employs resonant delay lines as a means of storing rf energy. By making the external quality factor of these lines vary as a function of time, the intrinsic efficiency of the system can reach 100%. However, we demonstrate a considerable increase in efficiency even if the change of the quality factor is limited to a single event in time. During this event, the quality factor of the lines changes from one value to another. The difference between these two values is minimized to simplify the realization of the quality factor switch. We present the system optimum parameters for this case. We also show the extension of this system to two events in time, during which the quality factor of the line changes between three predetermined states. The effects of the losses due to the delay lines and the switch used to change the quality factor are also studied.

I. INTRODUCTION

The SLED II pulse compression system employs high-Q resonant delay lines to store the energy during most of the duration of the incoming pulse. The round trip time of an rf signal through one of the lines determines the length of the compressed pulse. To discharge the lines, the phase of the incoming pulse is reversed 180°, so that the reflected signal from the inputs of the lines and the emitted field from the lines add constructively, thus forming the compressed high-power pulse.

The SLED II system suffers from two types of losses that reduce its intrinsic efficiency. During the charging phase, some of the energy is reflected and never gets inside the line. Also, after the phase is reversed, the energy inside the line is not discharged completely during the compressed pulse time period. These two effects make the intrinsic efficiency of SLED II deteriorate very rapidly as the compression ratios increases [1]. Increasing the coupling of the line just before the start of the output pulse will reduce the amount of energy left over after the output pulse is finished. This allows more energy to get out of the storage line during the compressed pulse. Losses due to reflection are reduced by keeping the line coupling as a constant value that is optimized for maximum energy storage during the charging phase. If the coupling during the charging phase is a function of time, then all the energy during the charging phase can be stored in the line. However, it will be shown in Sec. II that if the line coupling changes only once during the charging phase, a charging efficiency close to 100% can be achieved. Indeed, with two changes in the line coupling, the first during the charging phase and the other just before the discharging phase, intrinsic

efficiencies greater than 90% can be achieved for reasonably high compression ratios.

We first introduce a theory for optimizing the efficiency of the pulse compression system using a single change in line coupling. We then study the situation of two changes.

II. THEORY OF SINGLE-TIME-SWITCHED RESONANT DELAY LINE

A. SLED II

Consider the waveguide delay line with a coupling iris shown in Fig. 1.

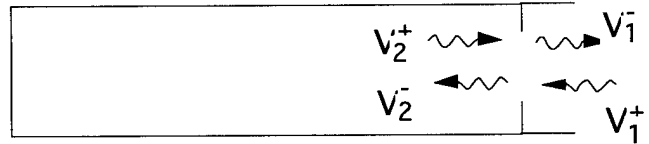


Figure 1. Resonant delay line.

The *lossless* scattering matrix representing the iris is unitary. At certain reference planes, it takes the following form:

$$\underline{S} = \begin{pmatrix} -R_0 & -j(1-R_0^2)^{1/2} \\ -j(1-R_0^2)^{1/2} & -R_0 \end{pmatrix} \quad (1)$$

In writing Eq. (1) we assumed a symmetrical structure for the iris two-port network. With the exception of some phase change, the incoming signal V_2^+ at time instant t is the same as the outgoing signal V_2^- at time instant $t - \tau$, where τ is obviously the round trip delay through the line; i.e.,

$$V_2^+(t) = V_2^-(t - \tau)e^{-j2\beta l} \quad (2)$$

where β is the wave propagation constant within the delay line, and l is the length of the line. During the charging phase we assume a constant input, i.e., $V_1^+(t) = V_{in}$ which equals a constant value; If the delay line has small losses, where β has a small imaginary part, then at resonance the term

$$e^{-j2\beta l} = -p \quad (3)$$

where p is a positive real number close to 1. Hence, we have

$$V_1^-(i) = -V_{in} \left[R_0 - (1-R_0^2) \frac{1-(R_0 p)^i}{1-R_0 p} p \right] \quad (4)$$

In Eq. (4), $V_1^-(i)$ means the ingoing wave in the time interval $i\tau \leq t < (i+1)\tau$ and $i = 0, 1, 2, \dots$. After the energy has been stored in the line it is possible to dump part of the energy in a time interval τ by flipping the phase of the incoming signal just after a time interval $(n-1)\tau$; i.e.,

$$V_1^+(t) = \begin{cases} V_{in} & 0 \leq t < (n-1)\tau \\ -V_{in} & (n-1)\tau \leq t < n\tau \\ 0 & \text{otherwise.} \end{cases} \quad (5)$$

[†]Also with the Electrical Communications and Electronics Department, Cairo University, Giza, Egypt.

The output pulse level during the time interval $(n-1)\tau \leq t < n\tau$ is then

$$V_{\text{out}} = V_1^-(n-1) = V_{\text{in}} \left[R_0 + (1-R_0^2) \frac{1-(R_0 p)^{n-1}}{1-R_0 p} p \right]. \quad (6)$$

This is the essence of the SLED II pulse compression system. The optimum values of the iris reflection coefficient such that V_{out} is maximized for a given value of n are given in Ref. [1].

If a high-power rf switch existed, it would be possible to have 100% efficiency. This switch would have to change the iris reflection coefficient in a time δt such that $\delta t \ll \tau$. Most applications that utilize such pulse compression techniques employ very high-power rf fields; but high-power switches are not readily available and are still a subject of extensive research. It is foreseen that an optical high-power rf switch can be developed to switch at least once every few milliseconds [2].

Switching the system *once* can definitely improve its efficiency. There are two possibilities. First, the iris reflection coefficient can be changed during the charging time to put more energy in the line. Second, the system can be switched just before discharging it to get all the energy out of the line during the compressed pulse.

B. Switching during charging time

During the charging period the power reflected from the line reaches a peak during the first time interval τ . We therefore make the iris reflection coefficient equal zero at the beginning. After the first time interval τ we switch the iris so that the reflection coefficient has a value R_0 . Assuming a resonant line and flipping the phase according to Eq. (5), the output pulse expression takes the form

$$V_{\text{out}} = \left\{ \frac{1-(R_0 p)^{n-2}}{1-R_0 p} (1-R_0^2) p + (1-R_0^2)^{1/2} p (R_0 p)^{n-2} + R_0 \right\} V_{\text{in}}. \quad (7)$$

The choice of the value of R_0 is such that V_{out} is maximized.

C. Discharging By Active Switching

CASE1: Discharging After The Last Time Bin

To discharge the line, the input signal can be kept at a constant level during the time interval $0 \leq t < n\tau$ but switching the iris reflection coefficient to zero so that all the energy stored in the line is dumped out. In this case

$$V_{\text{out}} = \frac{1-(R_0 p)^n}{1-R_0 p} (1-R_0^2)^{1/2} p V_{\text{in}}. \quad (8)$$

CASE2: Switching Just Before The Last Time Bin

The ingenious idea of reversing the phase, together with changing the iris reflection coefficient, can be utilized to reduce the burden on the switch. In this case, all the energy can still be dumped out of the line, but the iris reflection coefficient need not be reduced completely to zero. During the discharge interval, the new iris reflection coefficient can be shown to be

$$R_d = \cos \left[\tan^{-1} \left(\frac{1-(R_0 p)^{n-1}}{1-R_0 p} (1-R_0^2)^{1/2} p \right) \right]. \quad (9)$$

This new reflection coefficient is greater than zero, so the switch need only change the iris between R_0 and R_d . The output reduces to

$$V_{\text{out}} = R_d \left[1 + \left(\frac{1-(R_0 p)^{n-1}}{1-R_0 p} \right)^2 (1-R_0^2) p^2 \right] V_{\text{in}}. \quad (10)$$

The compressed pulse takes place in the interval $(n-1)\tau \leq t < n\tau$. The optimum value of R_0 is such that it fills the system with maximum possible amount of energy in the time interval $(n-1)\tau$ instead of $n\tau$ as in CASE 1. Also, unlike CASE 1, the incident power during this interval will not be coupled to the line nor suffer from a round trip loss; therefore, in CASE 2, the system has a higher efficiency.

D. Comparison

Table 1 compares the different types of pulse compression systems. It also gives the optimum system parameters for each compression ratio C_r defined here as the total time interval divided by the duration of the compressed pulse, n . The efficiency of the system η is defined as the energy in the compressed pulse divided by the total incident energy; namely,

$$\eta = \frac{1}{C_r} \left(\frac{V_{\text{out}}}{V_{\text{in}}} \right)^2. \quad (11)$$

In these calculations we assume a lossless system, $p = 1$.

At small values of C_r , switching the iris just after the first time bin is the most efficient solution. When $C_r \geq 5$, switching the iris just before the last time bin, while reversing the phase by 180° , is more efficient. At high compression ratios, the last time bin does not contribute much; hence, switching the iris after the last time bin is almost equivalent to switching it just before the last time bin. For applications that require one pulse compression system or several pulse compression systems with no phase synchronization, switching after the last time bin may be advantageous because it can use an oscillator as the primary rf source instead of an amplifier or a phase locked oscillator.

	SLED II		Switching during charging time		Discharging just before the last timebin		
C_r	η (%)	R_0	η (%)	R_0	η (%)	R_0	R_d
2	78.1	0.5	100	0.707	100	0.0	0.707
4	86.0	0.607	92.6	0.658	87.0	0.646	0.536
6	74.6	0.685	78.1	0.714	84.9	0.775	0.443
8	64.4	0.733	66.5	0.754	84.0	0.835	0.386
10	56.2	0.767	57.7	0.783	83.4	0.869	0.346
16	40.6	0.828	41.2	0.837	82.7	0.920	0.275
32	23.3	0.893	23.4	0.897	82.0	0.960	0.195
64	12.6	0.936	12.7	0.938	81.7	0.980	0.138
128	6.6	0.962	6.6	0.963	81.6	0.990	0.099

Table 1. Comparison between different methods of single event switching pulse compression systems.

E. Effect of losses

As the compression ratio increases, the stored energy spends more time in the storage line and the finite quality factor of the line affects the efficiency. Figure 2 shows the effect of losses for different compression ratios. The round-trip line losses, plus reflection losses at the end of the line and reflection losses at the active iris, is defined as

$$\text{Round Trip Power Losses} = 1 - p^2. \quad (12)$$

In Fig. 2, for a given C_r , the method used to switch the iris is the optimum one for that particular C_r .

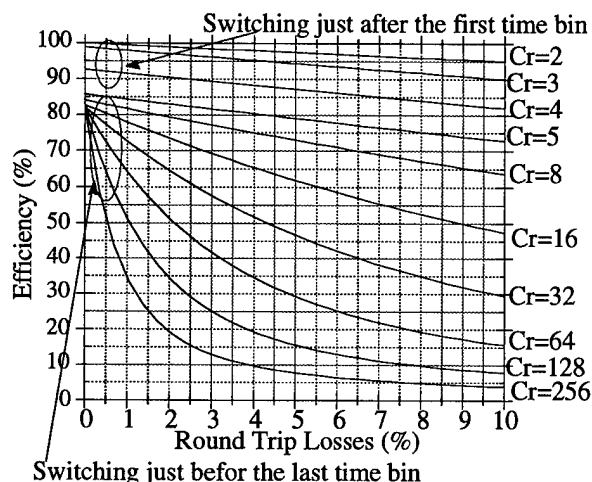


Figure 2. Effect of line and switching iris losses on compression efficiency for a one-time-switched, resonant delay line

III. THEORY OF TWICE-SWITCHED RESONANT DELAY LINE

If an iris changing its S-matrix parameters can be realized twice during the time period of charging and discharging the resonant line, a near perfect pulse compression system can be achieved. To see this, the system starts with an iris that has a zero reflection coefficient. After the first time bin, the iris reflection coefficient changes to R_0 ; To discharge the line, the iris reflection coefficient is changed from R_0 to R_d just before the final time bin, while reversing the phase according to Eq.(5); optimum R_d takes the form

$$R_d = \cos \left[\tan^{-1} \left(\frac{1 - (R_0 p)^{n-2}}{1 - R_0 p} (1 - R_0^2)^{1/2} p + p(R_0 p)^{n-2} \right) \right] \quad (13)$$

The output now has the following form

$$\frac{V_{\text{out}}}{V_{\text{in}}} = R_d \left[1 + \left(\frac{1 - (R_0 p)^{n-2}}{1 - R_0 p} (1 - R_0^2)^{1/2} p + p(R_0 p)^{n-2} \right)^2 \right]. \quad (14)$$

Table 2 shows the optimum system parameters and the efficiency for different compression ratios. The system is assumed lossless in these calculations.

C_r	R_0	R_d	η (%)
4	0.776	0.502	99.2
8	0.881	0.361	96
16	0.937	0.26	92.6
32	0.967	0.187	89.7
64	0.983	0.134	87.5
128	0.991	0.095	85.8
256	0.995	0.068	84.6

Table 2. Efficiency and optimum parameters for a twice-switched resonant delay line

IV. CONCLUSION.

We have developed the theory for a single-time-switched and a twice-switched resonant delay line pulse-compression system. Comparison between different methods of switching and the original passive SLED II pulse-compression system shows that a significant improvement in efficiency can be obtained with a single-time-switched line. Furthermore, a twice-switched line can achieve efficiencies near 100% for a relatively large compression ratio. We basically have three methodologies for switching a single-time switched resonant delay line. First, we can switch the iris that governs the quality factor of the line after the first time bin; this is suitable for compression ratios less than 5. For compression ratios greater than 5, the iris should be switched just before the last time bin. At the same time, the phase of the input during the last time bin should change by 180° . For compression ratios greater than 16, switching the line after the last time bin is almost equivalent to switching the line just before the last time bin. If the application does not require control over the phase of the output, an oscillator can be used (instead of an amplifier or a phase locked oscillator) while switching after the last time bin. In all cases, losses will reduce the system efficiency greatly, especially at high compression ratios. Unlike SLED II, the gain is not limited to 9. At high compression ratios, in order to make use of the high gain provided by switching the line, a superconducting structure may be required.

V. ACKNOWLEDGMENT

The Authors wish to thank Prof. P. Wilson, and Dr. Z. D. Farkas for many useful discussions. This work is supported by the U.S. Department of Energy under contract DE-AC03-76SF00515.

VI. REFERENCES

- [1] P. B. Wilson, Z. D. Farkas, and R. D. Ruth, "SLED II: A New Method of RF Pulse Compression," Linear Accel. Conf., Albuquerque, NM, September 1990; SLAC-PUB-5330 (1990).
- [2] Sami G. Tantawi et al., "Design of a Multi-Mega Watt X-Band Solid State Microwave Switch," This proceedings.

Design of a Multi-Megawatt X-Band Solid State Microwave Switch*

Sami G. Tantawi†, Terry G. Lee, Ronald D. Ruth, A. E. Vliks and Max Zolotarev
Stanford Linear Accelerator Center Stanford, CA 94309

Abstract:

We present design methodology for high power microwave switches. Among all possible applications for such a switch we emphasize the design parameters for application to the pulse compression system associated with the Next Linear Collider. (NLC)[1]. The switch is based on the excitation of a plasma layer within a silicon wafer by either a laser or an electron beam. We investigate problems associated with high power operation of such a switch. Mainly, we explore solutions to the problems of thermal runaway, avalanche breakdown, photo-emission, and secondary emission. Different design methodologies are presented.

I. INTRODUCTION

Optical control of microwave components have been under investigation for over two decades. A review of the basic ideas and device physics may be found in [2]. Most of the work in that field was done at milli-meter wavelengths around 94 GHz for application with phased array antennas. For this type of applications the devices need not handle large amounts of power. Also, there is not big constraints on the amount of losses that these devices may exhibit. However, the main emphasis in designing these devices was speed. Pico-second switches and phase shifters is reported on the literature [2]. On the other hand, development of optical control of high power DC. switches required a low loss devices and an appropriate design to deal with thermal runaway problems [2]. Activation with electron beam for these DC switches was also considered[3].

To date, there is no active devices that can control and manipulate multi-megawatt microwave signals. Applications that can make use of such a device include, but not limited to, pulse compression systems required to drive linear accelerators (for scientific research such as NLC, for medical applications and for remote sensing) and , broadening the band width of high power sources such as klystrons and magnetrons by actively detuning there cavities (for radar applications). Bulk effects in semiconductors have the potential of producing a working device in that regime. Of course, the design parameters will depend on the application. In the following presentation we will emphasize on the design parameters required for the NLC. Although the ideas presented may be extended to any of these other applications.

We start by the analysis of a symmetric 3-port device. We explore the ability of controlling the coupling between two of the ports by actively changing the termination of the third port. We derive general expression for, power, losses, and peak electric field in that third arm, which we shall call the active arm. In section III. we explore silicon as an active material for

our device. In section IV we explore different operating modes of the device.

II. MICROWAVE CONTROL WITH A THREE PORT DEVICE.

Consider the three port device shown in Figure 1. The device is composed from a basic *lossless* three port device with two similar ports namely, port 1 and port 2 followed by a two port junction cascaded after port 2. Since the scattering matrix \underline{S} of the symmetric 3-port junction is unitary, at certain reference planes we have

$$\underline{S} = \begin{pmatrix} \sin^2(\frac{\theta}{2}) & -\cos^2(\frac{\theta}{2}) & \frac{\sin \theta}{\sqrt{2}} \\ -\cos^2(\frac{\theta}{2}) & \sin^2(\frac{\theta}{2}) & \frac{\sin \theta}{\sqrt{2}} \\ \frac{\sin \theta}{\sqrt{2}} & \frac{\sin \theta}{\sqrt{2}} & \cos \theta \end{pmatrix}; \quad (1)$$

where θ is a parameter that completely define the scattering matrix. The scattered rf signals \underline{V}^- is related to the incident rf signals \underline{V}^+ by

$$\underline{V}^- = \underline{S}\underline{V}^+; \quad (2)$$

where V_i^\pm represents incident/reflected rf signal from the i .th port. We terminate the third port so that all the scattered power off that port is completely reflected; i.e.,

$$V_3^+ = V_3^- e^{i\psi} \quad (3)$$

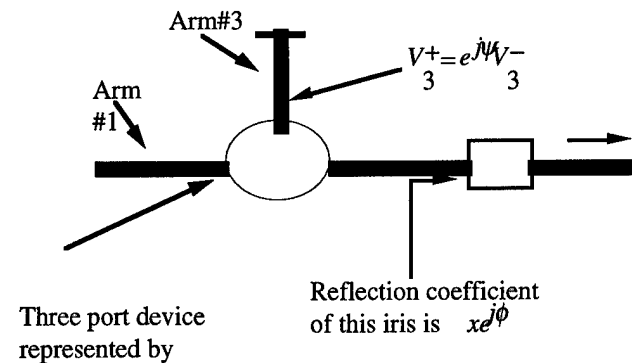


Figure 1 Schematic diagram of the active switch.

By changing the angle ψ of the third port terminator, the coupling between the first and the second ports can vary from 0 to 1.

Let the reflection coefficient from the cascading two port junction equals to $xe^{j\psi}$. After some algebra one can show that the total reflection coefficient of the two cascaded junctions is

$$|R_{total}(\psi)| = \left| \frac{V_1^-}{V_1^+} \right| = \left(\frac{N_1}{D} \right)^{1/2}; \quad (4)$$

*This work is supported by the U.S. Department of Energy under contract DE-AC03-76SF00515

†Also with Electrical Communications and Electronics Dept. Cairo University, Giza, Egypt.

where

$$D = 2 \left\{ 1 + r_3^2 - 2r_3 \cos \psi + 2(1 - r_3)x \cos\left(\frac{\psi}{2}\right) \left[r_3 \cos\left(\phi - \frac{\psi}{2}\right) - \cos\left(\phi + \frac{\psi}{2}\right) \right] + (1 - r_3)^2 x^2 \cos^2\left(\frac{\psi}{2}\right) \right\}, \quad (5)$$

and

$$N_1 = 2 \left\{ (1 - r_3)^2 \cos^2\left(\frac{\psi}{2}\right) + 2(1 - r_3)x \cos\left(\frac{\psi}{2}\right) \left[r_3 \cos\left(\phi - \frac{\psi}{2}\right) - \cos\left(\phi + \frac{\psi}{2}\right) \right] + x^2 [1 + r_3^2 - 2r_3 \cos \psi] \right\}. \quad (6)$$

and $r_3 \equiv \cos \theta$ is the reflection coefficient from the third port when the other two ports are matched.

The outgoing wave in the third arm has an amplitude

$$|V_3| = \left(\frac{N_3}{D} \right)^{1/2} |V_1^+|; \quad (7)$$

where

$$N_3 = (1 - r_3)^2 [2x \cos \phi - x^2 - 1], \quad (8)$$

III. THE SILICON SWITCH

To actively change the angle of the reflection coefficient at the third port we place a piece of semiconductor material in the third arm. An external stimulus such as an electron beam or a laser light can induce an electron-hole plasma layer at the surface of the semiconductor, thus changing its dielectric constant. Therefore, the propagation constant of rf signals through the active arm changes; and consequently the coupling between the other two ports also changes.

For the pulse compression system application associated with the NLC, it is required to change the reflection coefficient at the first arm between two fixed values[4]. The device should remain in one state for approximately 2μsec, and in the other state for 250 nsec. Since silicon has a carrier life time that can extend from 1 μsec to 1 msec it seems like a natural choice for this application. One can excite the plasma layer with a very short pulse from the external stimulus (~5nsec) and the device will stay in its new status long enough till all the rf signal is terminated. The repetition rate for this pulse compression system is 180 pulse/sec. This will give enough time between pulses for the switch to completely recover.

Indeed, this switch need to have a very small amount of losses. Following classical arguments[5], one can show that the dielectric of constant of a semiconductor material is

$$\epsilon = \epsilon_0 \epsilon_r \left(1 - \sum_i \frac{X_i}{1 - jZ_i} \right); \quad (9)$$

where

$$X_i = \frac{N_i e^2}{\epsilon_0 \epsilon_r m_i^* \omega^2}, \quad (10)$$

$$Z_i = \frac{v_i}{\omega}, \quad (11)$$

ω is the radial frequency of the rf signal, m_i^* is the effective mass of carrier i (electron, light hole and heavy hole), N_i is carrier density, e is the electron charge, and v_i is the collision frequency. This later quantity is related to the measured values of the dc. mobility μ_i [6] as follows:

$$\frac{1}{v_i} = \frac{\mu_i m_i^*}{e}. \quad (12)$$

Comparison between estimates of v_i for silicon to 11.424 GHz, the operating frequency of the NLC, shows that $Z_i \gg 1$. Hence, one can show that the dielectric constant is given by the classical relation

$$\epsilon = \epsilon_0 \epsilon_r \left(1 - j \frac{\sigma}{\omega \epsilon_0 \epsilon_r} \right); \quad (13)$$

where

$$\sigma = e \sum_i \mu_i N_i, \quad (14)$$

which is the conductivity of the semiconductor.

To minimize the losses in the *off* state, i.e., when there is no plasma excited, we need to have a very pure semiconductor material such that the intrinsic carrier density is very small. In the *On* state, i.e., when the plasma layer is excited, the carrier density should be large enough so that the semiconductor acts like a good conductor and thus minimizing the losses.

At a carrier density $10^{19}/\text{cm}^3$ silicon would have a conductivity of $\sim 3.3 \times 10^3$ mho/cm. This is two orders of magnitude smaller than that of copper. However, it is high enough to make an effective reflector. The skin depth of rf signal at the NLC frequency at this conductivity level is $\sim 8\mu\text{m}$. In choosing the laser wavelength to produce the photo-induced carriers, light penetration depth should be comparable to this skin depth.

IV. HIGH POWER SWITCH FOR NLC

To compress the rf signal efficiently by a factor of 8 the magnitude of the reflection coefficient of an iris need to change between 0.84 and 0.39[4]. This change should take place in less than 5 nsec. This iris should be able to handle 300 MW when it has a reflection coefficient of 0.84 for a period of 1.75 μsec, and 1.9GW for a period of 250 nsec when it has a reflection coefficient of 0.39. The repetition rate for the whole process is 180 Hz.

Consider making the active arm, in the device discussed in section III, from a circular waveguide operating at the fundamental mode (TE_{11}). By placing a silicon wafer that has the same cross sectional area as the waveguide we can change the reflection coefficient angle ψ between two values. At the *off* state the rf signal will be reflected from a short circuit that terminate the active arm. At the *on* state the signal will be reflected from the silicon wafer that acts like a good conductor because of the induced plasma layer.

The high power constrains on the switch discussed above now translates to the following two conditions:

1. in the off state the silicon wafer should not be subjected to an electric field that exceed 150 kV/cm which is the estimated limit for the avalanche break down of a piece of silicon that has dimensions of few cm.
2. At the on state, the amount of power dissipated in the silicon wafer should not raise its temperature so that it exceeds 70C when switch is to be operated at the off state once more.

Making the switch operate at the off state during 1.75μsec when the power levels are relatively low seems a natural choice. One can show that peak electric field in this arm in terms of the incident power, P_{inc} , to the first port is

$$E_{max} = 2.31 \left[\epsilon_r - 0.0859 \left(\frac{\lambda}{a} \right)^2 \right]^{-1/4} \left(\frac{N_3}{D} \right)^{1/2} \frac{(Z_0 P_{inc})^{1/2}}{a}; \quad (15)$$

where λ is the free space wavelength, Z_0 is the free space wave impedance, a is the circular waveguide radius, and ϵ_r is the dielectric constant of the material filling it.

By making the coupling to the third port as small as necessary one can reduce the peak field for any given amount of incident power. Also, increasing the diameter of the waveguide will reduce the field.

On the other hand, the power dissipated at the silicon wafer during the on state is

$$P_{losses} / P_{inc} = 4\pi \frac{\delta}{\lambda} \left[\epsilon_r - 0.0859 \left(\frac{\lambda}{a} \right)^2 \right]^{1/2} \left(\frac{N_3}{D} \right); \quad (16)$$

where

$$\delta = (\omega \mu_0 \sigma / 2)^{-1/2}, \quad (17)$$

which is the skin depth of the rf signal inside the silicon wafer. Reducing the coupling to the third port increases the losses. Further, increasing the diameter also increase the losses.

Hence, the conditions for minimum peak field and small losses contradict each other. However, a reasonable compromise can be reached. For example, we choose the value of $r_3 = 0.866$, the value of $x = 0.84$, the angle $\phi = 23^\circ$, and the waveguide radius $a = 0.35$ ", we would have an active iris that have a peak electric field of less than 150kV/cm in the active arm for an incident power of 500 MW, while maintaining a reflection coefficient of 0.84. This is illustrated in Fig 2. At the on state, the losses in the third arm is less than 2%, while maintaining a reflection coefficient of 0.39. This is illustrated in Fig. 3.

To cool the silicon during the on state, we are currently investigating the possibility of using a diamond substrate.

V CONCLUSION

We reported a three port device that can serve as an active iris for the NLC pulse compression system. We presented the design equations and design methodology for such an iris. We finally gave a design example for such an iris. We demonstrated the possibility of such a device to work at the high power levels required by the NLC rf pulse compression system.

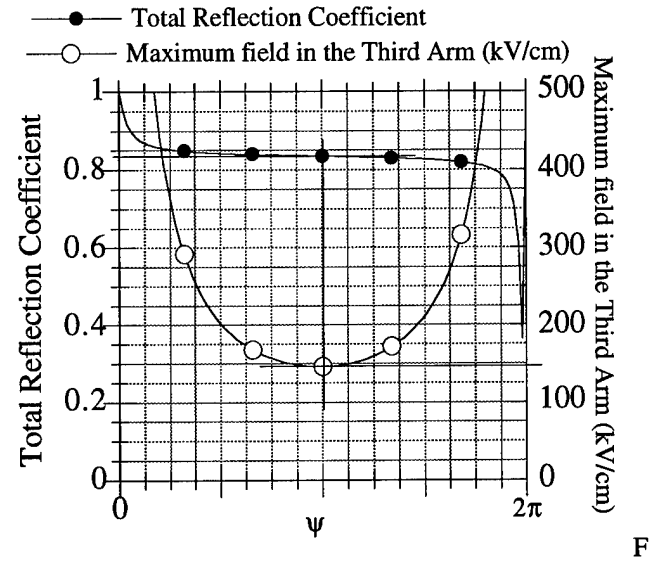


Figure 2. Reflection coefficient and peak electric field versus the phase angle of the active port

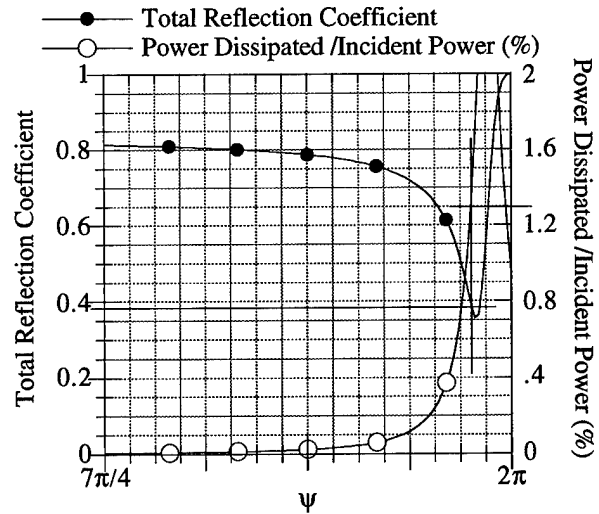


Figure 3. Reflection coefficient and power dissipated in the silicon wafer during the on state versus the phase of the active port.

VI. REFERENCES

- [1] R. D. Ruth et. al., "The Next Linear Collider Test Accelerator," Proc. of the IEEE Particle Accelerator Conference, Washington DC, May 1993, p. 543.
- [2] Lee, H. Chi, Editor, "Picosecond optoelectronic devices," Academic Press Inc., Orlando, 1984.
- [3] Nunnally, W. C., and Hammond R. B., "Optoelectronic switch for pulsed power," Ch. 12 in Ref[2]
- [4] Tantawi, S. G., Ruth, R. D., Vlieks A. E., "Active pulse compression using resonant delay lines," This proceedings, also in SLAC-PUB 6748
- [5] Wait, J. R. "Electromagnetics and plasmas," Holt, Rinehart and Winston, Inc. New York, 1968
- [6] SZE S. M. "Physics of semiconductor devices," John Wiley & Sons, Inc., New York, 1969.

REDUCED FIELD TE₀₁ X-BAND TRAVELING WAVE WINDOW

W. R. Fowkes, R. S. Callin, S. G. Tantawi and E. L. Wright

Stanford Linear Accelerator Center, Stanford University, Stanford, CA 94309 USA

Abstract

The RF electric field is reduced by more than a factor of two using a pair of symmetrically located irises in a new type of klystron window operating in the TE₀₁ mode at X-Band. The advantages of this window over the usual TE₀₁ half-wave resonant window are discussed as well as theory and operating results. Ultra high purity alumina formed by the HIP process is used. This window has been successfully tested at 100 MW with a 1.5 microsecond RF pulse width and is being used on the XL series klystrons.

I. INTRODUCTION

RF electric field breakdown in the output window is one of the mechanisms that frequently limits the peak power that can be produced by klystrons at X-band. Conventional pillbox windows operating in the TE₁₁ mode in single-mode sized circular waveguide are at risk when operated above about 10 MW depending on pulse width. Thicker, sometimes larger diameter, windows have been successfully tested at SLAC to 85 MW in a resonant ring but have a history of failing in the 25 to 60 MW range when operating at pulse widths in the 1 microsecond range [1]

Windows operating in the TE₀₁ circular mode have the advantage of having no electric field lines terminating in the braze fillet area at the edge of the ceramic disk thereby reducing the likelihood of RF breakdown originating at this vulnerable location. The very compact flower petal rectangular TE₁₀ to circular TE₀₁ high power mode transducer [2][3] has recently been incorporated into the

vacuum envelope of the XL series klystrons at SLAC.

Historically, TE₀₁ windows are usually half-wave resonant in thickness and therefore self-matched. There are still several drawbacks that should be mentioned regarding operation in the TE₀₁ mode with a half-wave resonant window. Thick ceramic always have trapped resonances (ghost modes) that may be close to the operating frequency. The bandwidth is narrow (typically 3% where the VSWR is <1.20) unless broadbanding elements are used.

A new type of window, operating also in the TE₀₁ mode, but with the RF electric field in the ceramic reduced by more than a factor of two for a given power has been built and tested in a traveling wave resonant ring to 100 MW with a 1.5 microsecond pulse. Furthermore the field within the ceramic exists in a pure traveling wave.

The field reduction is accomplished by symmetrically locating two circular inductive irises on each side of the window. The resulting RF electric field variation as a function of axial position for a given r and ϕ is shown in figure 1. The field reduction is accompanied by a reciprocal field enhancement further away from the window if the iris is inductive. A conjugate capacitive element would, in theory, produce the same field reduction at the window surface without the accompanying field enhancement. Capacitive irises however are impractical and susceptible to breakdown themselves in TE mode transmission.

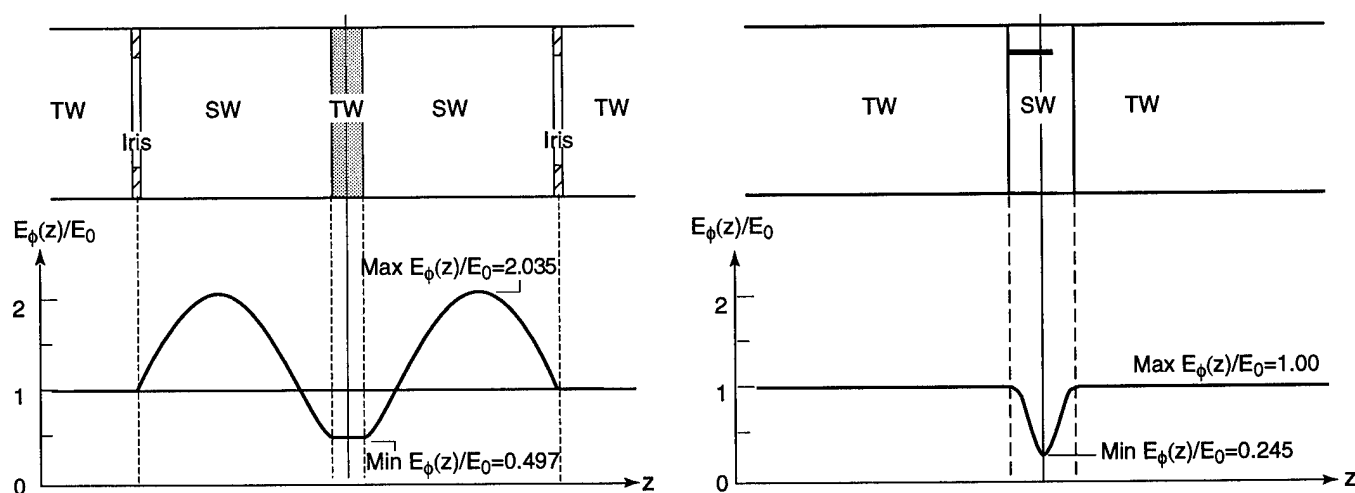


Figure 1. Comparison of the reduced field TW window (left) with a half-wave resonant window (right), both operating in the TE₀₁ circular mode. In addition to the TW version having substantially lower RF electric field at the window surface, the integrated dielectric power losses are only 23% that of the half-wave resonant window. The axial coordinate is expanded for clarity.

Work supported by Department of Energy contract
DE-AC03-76SF00515

Reduced field pure TW windows have been used previously but these were operating in the TE_{11} mode. Sergi Yu. Kazakov described a successful X-Band version of the above at the LC93 Workshop [4]. An S band version was used at SLAC in the early 1980's but was abandoned because it was very narrow band and therefore sensitive to dimensional tolerances and also field emission occurred at the enhanced field location. The field enhancement does not appear to be a problem in the TE_{01} mode because the field is zero at all the metal surfaces.

Among the advantages of the reduced field TW over the half-wave resonant window, both in the TE_{01} mode, are:

- 1) Lower surface electric field ($>2\times$)
- 2) Lower dielectric loss (23% that of $\lambda'/2$)
- 3) Better bandwidth
- 4) Uniform loss in axial direction
- 5) Fairly insensitive to ϵ'
- 6) TW at any thickness but $\lambda'_g/4$ is optimum for BW

II. THEORY

The normalized susceptance of each iris required to produce the field reduction and at the same time produce the pure TW condition within the ceramic is given by

$$\left| \frac{B}{Y_0} \right| = \frac{\lambda_g - \lambda'_g}{\sqrt{\lambda_g \lambda'_g}} \quad (1)$$

where λ_g and λ'_g are the guide wavelengths at the design frequency for the TE_{01} modes in the circular waveguide outside and inside the ceramic window respectively.

The distance from the face of the ceramic to the equivalent plane of a thin inductive iris with the above susceptance is given by

$$\ell = \lambda_g \left[\frac{1}{2} - \frac{1}{4\pi} \tan^{-1} \left[\frac{2}{\left| \frac{B}{Y_0} \right|} \right] \right] \quad (2)$$

The resulting symmetrical wave configuration at the given frequency is a partial standing wave between the iris and the window and a pure traveling wave both inside the ceramic and outside the irises.

The RF electric field is reduced at the surface of the ceramic window by

$$\text{RF Field Reduction Ratio} = \frac{\lambda_g}{\lambda'_g} \quad (3)$$

compared with the RF electric field in a TE_{01} traveling wave and that which exists at the surface in a TE_{01} half-wave resonant window. A pure traveling wave exists within the ceramic at only a single frequency. At this frequency the match is independent of the window thickness. The bandwidth characteristics however vary widely with window thickness and it turns out that the optimum passband response is obtained when the dielectric window thickness is approximately one-quarter of a guided wavelength in the dielectric as shown in Figure 2.

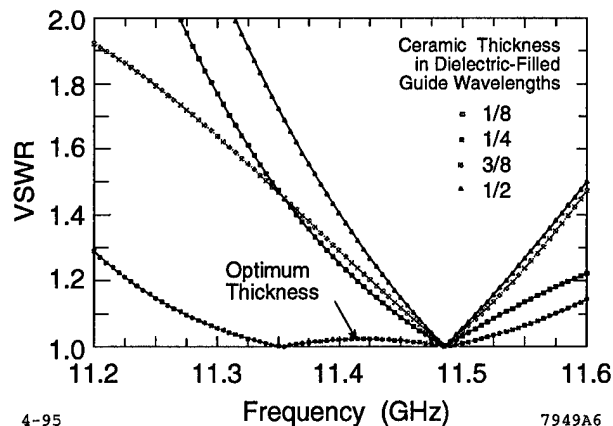


Figure 2. A pure TW condition and a perfect match at 11.486 MHz exists for all thicknesses but BW is optimum for $\lambda'_g/4$.

A program has been written using cascaded equivalent circuit elements to model this window/iris assembly taking into account the behavior with frequency of each element and connecting waveguide electrical lengths.

The response resembles a second order Tchebycheff matching transformer where there are two frequencies where a perfect match exists. The upper frequency match is the pure TW condition just described where the admittance throughout the dielectric is constant and real. The lower frequency match is the condition where the admittance varies throughout the dielectric but is purely real at the ceramic midplane. (A symmetrical structure is matched if the admittance at the plane of symmetry is real.) Since it is usually desirable to operate in the center of the passband it is reasonable to modify the design so that the operating frequency is midway between the upper and lower match frequencies. The field variation within the ceramic at the center frequency is still nearly a pure traveling wave.

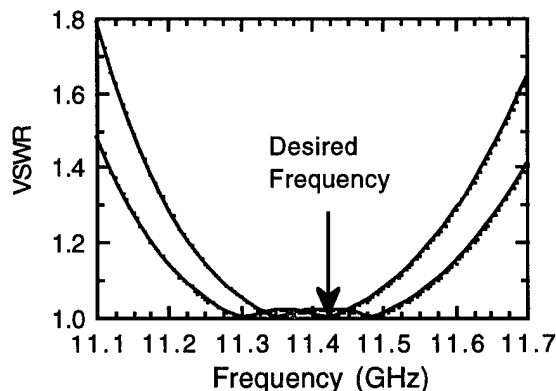


Fig 2 (left) Pure TW at 11.424 GHz but not centered and (right) Pure TW at 11.486 GHz but centered at 11.424 GHz

The theoretical passband responses shown in Figure 2 were calculated for an operating frequency of 11.424 MHz. The curve on the left corresponds to a pure traveling wave at the design frequency but the passband is not centered. By redesigning the window circuit for approximately 11.486 MHz, the passband is centered at the design frequency, midway between the two match frequencies.

The exact size of the TE_{01} iris aperture to obtain the required inductive susceptance in Eq. (1) and its variation with frequency was calculated using mode matching methods.

III. MECHANICAL DESIGN

The mechanical properties of the TW TE_{01} window are similar to the X-band window described in earlier papers [1]. The window surface must be titanium nitride coated to suppress multipactor as described in earlier papers. This requires that the irises be separate from the window cylinder so as not to mask the window surface during the coating process. The exact iris positions relative to the window surface are therefore subject to the amount of torque applied to the bolts on the crush seal flanges. Test were done to determine this effect and the flange dimension adjusted accordingly.

IV. TEST RESULTS

Ceramics formed by the Hot Isostatic Press (HIP) process have been successfully used for two of the six windows of this type that have been built. These two were super high purity alumina that is magnesium free. Both of these were metallized and brazed but one braze developed a very small leak during testing. There has not been enough confidence to date to risk using the super high purity material on a window destined for installation on a klystron because of brazing experience at SLAC and elsewhere.

Four windows were tested on the Traveling Wave Resonant ring to power levels between 75 and 100 MW with a 1.5 microsecond pulse. One of the AL-995 windows failed at 100 MW while the others survived. The two

windows that were installed on 50 MW klystrons are still in operation.

V. SUMMARY

It is believed that past X-Band high peak power window failures at SLAC can be attributed to breakdown originating at the braze fillet at the edge of the ceramic and also to multipactor. The TE_{01} TW window has been shown to be very resistant to both of those failure mechanisms and has enabled us to push RF breakdown thresholds to higher peak power levels and longer pulse widths.

VI. ACKNOWLEDGEMENTS

The authors would like to express their appreciation to many people in the Klystron Department whose varied and considerable skills made this effort a success. Special thanks to Norman Kroll for several valuable discussions on reduced field windows.

REFERENCES

- [1] W. R. Fowkes, R. S. Callin and A. E. Vliks, "High Power RF Window and Waveguide Component Development and Testing Above 100 MW at X-Band", Proceedings of the 1992 Linac Conference, Ottawa, August 1992.
- [2] S. Tantawi et al., "Flower-Petal Mode Converter for NLC", Proceedings of the 1993 Particle Accelerator Conference, Wash. D. C., May 1993 p. 1121.
- [3] S. G. Tantawi et. al., "Numerical Design and Analysis of a Compact TE_{10} to TE_{01} Mode Transducer, " Conf. on Computational Accelerator Physics, Los Alamos, NM 1993, AIP Conference Proceedings 297, pp 99-106.
- [4] Sergi Yu. Kazakov, Presentation at LC93 Workshop, SLAC, Stanford University, Oct. 1993.

DESIGN AND HIGH-POWER TEST OF A TE11-MODE X-BAND RF WINDOW WITH TAPER TRANSITIONS

Y. Otake, S. Tokumoto and H. Mizuno, KEK, National Laboratory for High Energy Physics, 1-1 Oho, Tukuba-shi, Ibaraki-ken, 305, JAPAN

A TE11-mode X-band RF window capable of passing RF power above 70 MW with 500 ns duration has been developed for installation to a pulse high-power klystron. The window comprises: a) TE10(WRJ-10) - TE11-mode (WC-5) converters, b) circular-waveguide tapers and c) an alumina ceramic with a circular-waveguide frame. This paper describes its design and high-power performance. The basic design concept is to reduce the RF field strength on the ceramic surface by increasing the diameter of its ceramic part compared to an ordinary pill-box-type window. The design of its RF structure was achieved by using a circuit model, and was confirmed by numerical simulations. The dimensions of the window necessary to obtain good RF transmission were found by changing the length of the circular-waveguide frame. A high-power test using a traveling-wave resonator has been successfully carried out up to a circulating power of 100 MW with a 300ns pulse width. The tests showed that the break-down limit of the electric-field strength on the ceramic surface was about 8 kV/mm. This limit was the same as in the case of S-band pill-box window experiments.

I. INTRODUCTION

In high-energy physics institutes, such as KEK, SLAC and BNIP, the development of 100MW-class X-band klystrons is underway for future linear colliders. For realizing klystrons, the alumina-ceramic RF window is one of the key-technologies. Therefore, the development of a window capable of passing RF power above 100 MW is necessary.

Ordinary pill-box type windows have been evaluated in high-power tests of the XB50K(30MW class output) and 72K(100MW class output) series in accordance with an X-band klystron R&D program.¹⁾ These tests have shown that the limitation of its peak RF-power is around 20 - 30 MW with a 200 ns pulse width.

Generally, the electrical-breakdown phenomena of an alumina ceramic depends on its surface electric-field strength. In a series of experiments concerning S-band ceramic windows by Y. Saito of KEK,²⁾ the maximum field strength on the ceramic surface was found to be 8 kV/mm(Peak value). Above this field strength, ceramic showed fatal destruction, such as blow holes, cracks and

vacuum leaks. In order to reduce the ceramic surface-field strength, an over-size TE11-mode ceramic window with tapered transitions was designed and tested. The window is shown in Fig. 1.

II. DESIGN AND LOW-POWER MEASUREMENTS

The basic criteria for designing the TE11 window are as follows: a circular ceramic-disk was chosen for easy machining and brazing; furthermore, a large-diameter ceramic-disk, compared with the wavelength of the window operation frequency(11.424 GHz), was adopted. The cut-off frequency(1.125GHz) of the ceramic part is far lower than the operation frequency. In some cases, higher-order mode RF-signals generated by the ceramic surfaces, the mode-converters and the taper transitions could be trapped in the ceramic and between the tapers(so-called trapped-mode resonance); this may cause a local higher field or heat up of the ceramic. Therefore, the mode selection of the window becomes important and the trapped-mode resonances must be separated from the operating frequency. The TE11-mode was chosen for simplicity of mode-conversion from the TE01-mode.

The TE11-mode circular-ceramic window with taper transitions is divided in to 3-parts: a) mode-converters from a rectangular-waveguide mode(TE01) to a circular-waveguide mode(TE11); b) two circular-waveguide tapers and c) a 51φ circular-waveguide frame(WC-5) installing an about 0.8nm TiN coated ceramic-disk(NITOKU, UHA-99 & HA-997, 4.1 mm thickness).

In the design stage of the window, the RF characteristics, such as the frequency responses, of this type over-size window were not clear. The dimensions of the window must be chosen in order to avoid any trapped-mode resonance. For this reason, the following 4 design steps were carried out: a) impedance matching using a circuit-model method³⁾ was used and determines roughly the S-parameter behavior; b) the trapped-modes of the ceramics and the susceptance components of the taper transitions were analyzed by a field-matching method;^{4),5)} c) numerical simulations using RF-structure analysis codes, such as "MAFIA" and "HFSS", were carried out in order to confirm the results of the analysis above mentioned and d)

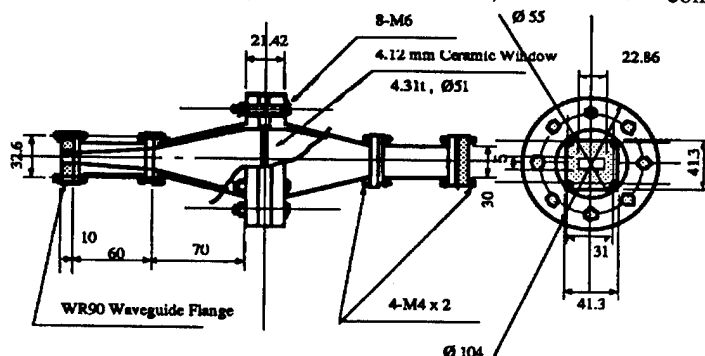


Fig. 1: Schematic diagram of the TE11 window

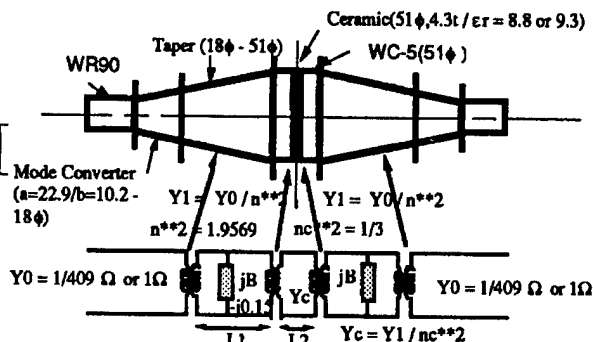


Fig. 2: Circuit model of the window

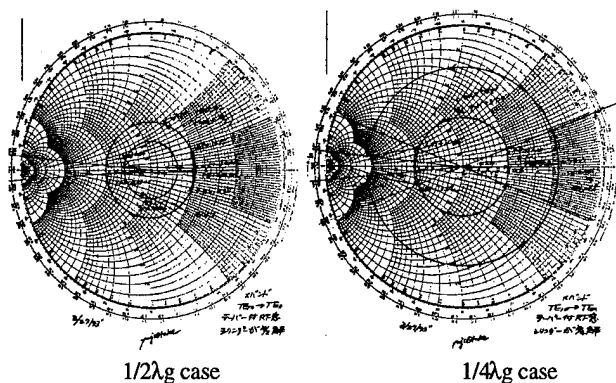


Fig. 3 Admittance transformation of the window

to also confirm the results obtained above and to determine the final dimensions of the window, several cold models were tested.

A. Circuit model and electromagnetic field analysis

The circuit model of the window was constructed as shown in Fig. 2, and used for the analysis. The definition of a waveguide characteristic-admittance is " $Y_0 = P/V^2$ ", which Schelkunoff defined,⁶⁾ where the Vs are the values integrated along the maximum electric-field lines of the circular and rectangular waveguide cross sections; P is their transmitting power. The frequency response of the window using the circuit model and the characteristic admittance(Y_0) defined above was solved using the equation

$$\frac{Y_{in}}{Y_0} = \frac{Y(L) + jY_0 \tan \beta L}{Y_0 + jY(L) \tan \beta L},$$

where Y_{in} is the input admittance of the window and β is the propagation constants of the waveguides; L is the length measured along their RF propagation direction. The susceptance components of the taper transitions to be used in the circuit model were calculated by field-matching⁵⁾ and "HFSS" and, measured by the cold model. Electromagnetic-field analyses were also performed by "HFSS" and "MAFIA".

The next RF characteristics of the window became clear through the studies mentioned above: a) The ceramic thickness which produces a good RF transmission is slightly less than $1/2\lambda_g$ for compensating the susceptance components. b) There are three optimum solutions for the cylinder length from the ceramic surface to the taper. The Smith-chart in Fig. 3 shows these solutions, which are for cylinder lengths of $1/4\lambda_g$ (8.625mm) and $1/2\lambda_g$; the $1/2\lambda_g$ solutions have two slightly different cylinder lengths (11.7mm, 13.845mm). The example of the window frequency response simulated by the circuit model is shown in Fig. 4. c) Where the admittance of the ceramic part transforms to the near center on the Smith-chart as in the $1/2\lambda_g$ case, the solution has a wider frequency band-width in order to obtain a good transmission and a lower ceramic surface-field than in the $1/4\lambda_g$ case. d) The solutions for the TE11 window are periodic with every $1/2\lambda_g$ wavelength step. e) By using "HFSS" the field distributions for the 6-types of RF-windows were determined. The relative field strength of the ceramic surface and their band-width are summarized in Table 1. The results show that one of the $1/2\lambda_g$ solutions of the TE11 window has almost the same performance as the "KAZAKOV" type, and can reduce the

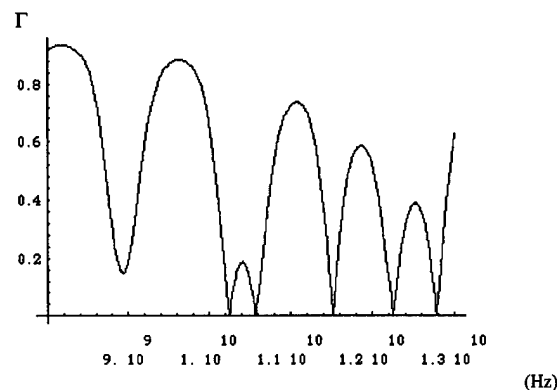


Fig. 4: Frequency response of the window using the circuit model($1/4\lambda_g$ solution)

Table 1: Comparison of the electric-field strengths on the ceramic surfaces and the band widths among the windows.

Type	Field strength*	Band width
Pill-box	0.868	500 MHz
Long pill-box	0.414	300 MHz
TE11 $1/4\lambda_g$	0.424	250 MHz
TE11 $1/2\lambda_g$ -1	0.400	300 MHz
TE11 $1/2\lambda_g$ -2	0.369	700 MHz
KAZAKOV	0.362	300 MHz

Normalized to the TE10 rectangular-waveguide. $E = \sqrt{E_x E^}$ maximum surface electric-field to about 37% of the rectangular-waveguide field.

B. Trapped-mode resonance

In the design stage trapped-mode resonances were expected at the ceramic part (generally called the ghost-mode in the case of a ceramic) and between both tapers. They were calculated in order to obtain the frequencies and modes by "MAFIA". However, the electromagnetic field strengths of the ghost-modes which were found by low-power measurements were at a very low-level. In this case the "MAFIA" calculations did not have sufficient accuracy. For this reason, another calculation method, such as field-matching, was employed in order to obtain more accuracy. The method was used in order to find mode transmitting only in the ceramic while maintaining continuity of the electromagnetic fields of the circular-waveguide part and the ceramic part at the ceramic surface. The ghost-mode observed in the low-power measurements were all confirmed in the MAFIA and the field-matching calculations. Experiments to pick up the ghost-modes were carried out by setting the ceramics in to the circular-waveguide frame with antennas.⁴⁾ To find the trapped-mode between the tapers, "MAFIA" was used; the results coincide with the low-power measurements shown in Fig. 5. The trapped and the ghost modes are tabulated in Table 2.

Table 2: Trapped modes around 11.424GHz

	Calculated	Measured
Between tapers	$\approx 10.5\text{GHz}$ $\approx 11.3\text{GHz}$ $\approx 11.7\text{GHz}$	$\approx 10.9\text{GHz}$ $\approx 11.23\text{GHz}$ $\approx 10.65\text{GHz}$
In Ceramic	$\approx 10.1\text{GHz}$ (TE221 like) $\approx 11.5\text{GHz}$ (TE131 like)	$\approx 10.8\text{GHz}$ $\approx 11.3\text{GHz}$

C, Low-power measurements of the cold

In a previous step for the high-power model, a cold model window of brass was produced according to the dimensions determined from the design. However, a calculation of the TE11 window was not sufficiently accurate because of its over-size. Therefore, the center frequency of the pass-band was adjusted by changing the length of the circular-waveguide frame. The frequency shift of the length was measured as being 50MHz/mm; this value was in good agreement with the circuit models and MAFA calculations. Fig. 5 shows the measurement results of the cold model having the $1/2\lambda_g$ -2 solution. As the 1st stage of a comparison among the three solutions of the TE11 window in a high-power RF, a high-power model with the $1/4\lambda_g$ cylinder and the UHA-99 ceramic has been made of oxygen-free copper (OFC, Class 1, HITACHI).

III. HIGH-POWER TEST

A high-power test of the window was carried out using a traveling-wave resonator(TWR).⁸⁾ At first, the input RF pulse width of TWR and its pulse repetition-rate were adjusted to 300ns and 25pps. The conditioning of TWR and the window proceeded below a circulating power of 10MW for a net time of 5 hours. After conditioning, the power was increased up to 100MW with an input RF power of 15MW; this process was continued for 15 hours(net). Then, a discharge on the ceramic surface was ordinary uniform blue-light; no significant RF reflection or bright-spot due to the discharge was observed. After this operation, the leakage of the window was checked using a He leak detector; it did not show any problem, such as cracks of the ceramic. Next, the circulating power was set to 70MW and the RF pulse width was gradually expanded from 300ns to 700ns. The repetition-rate was also changed to 50pps. Then, steady blight-spots appeared on the ceramic surface, and the window became broken due to a flash-over. Fig. 6 shows a picture of the RF power in TWR with 100MW, 300ns.

IV. CONCLUSIONS

The design has almost been successfully completed. The electric field in the ceramic of the $1/2\lambda_g$ -2 solution is quiet low (about 37% of the rectangular-waveguide field), the same as the "KAZAKOV" type. Furthermore, the electromagnetic field adjacent to the ceramic is also low compared with that of the "KAZAKOV" type. We think that it has some advantage. The power capability shown in the high-power test is sufficient for our requirements. It is a great step for the 100MW X-band klystron development. However, the surface field of the ceramic surface was around 7kV/mm when the ceramic was broken in the 70MW case. This fact is similar to the situation in the S-band window experiments. The power could be thought of as the limit of this type of ceramic. For the next step of the high-power test, we will employ a finer ceramic, like HA-997(NITOKU), and the $1/2\lambda_g$ -2 solution.

Acknowledgments

The authors wish to thank Drs. T. Higo and H. Sakai, Y. Sito, S. Mitazono for their help and discussions.

V. REFERENCES

- 1)J. Odagiri et al., "Development of X-Band High Power Klystrons", Proc. of 18th Linear Accelerator Meeting in Japan, Tsukuba, 21-23 July 1993.
- 2)Y. Saito et al., "Surface Flashover on Alumina rf Window for High-power Use", IEEE Transaction on Electrical Insulation, Vol. 28 No. 4, August 1993.
- 3)W. R. Fowkes, SLAC, (private communication).
- 4) M. P. Forrer and E. T. Jaynes, "Resonant Mode in Waveguide Windows", IRE Trans. of Microwave Theory and Techniques, Vol. MTT-8, Number 2, March 1960.
- 5)C. H. Tang, "Optimization of Waveguide Tapers Capable of Multimode Propagation", IRE Trans. of Microwave Theory and Techniques, P 442-452, September 1961.
- 6)S. A. Schelkunoff, "Impedance Concept in Waveguides", Quarterly of Applied Mathematics, Vol. II, April 1944.
- 7)S. Yu. Kazakov, "Increased Power RF-Window", BNIP Preprint 92-2, Protvino 1992.
- 8)H. Mizuno et al., "RF High-Power Test of the X-Band Windows in the TWR", Proc. of the International Linac Conference, Tukuba, Aug. 1994.

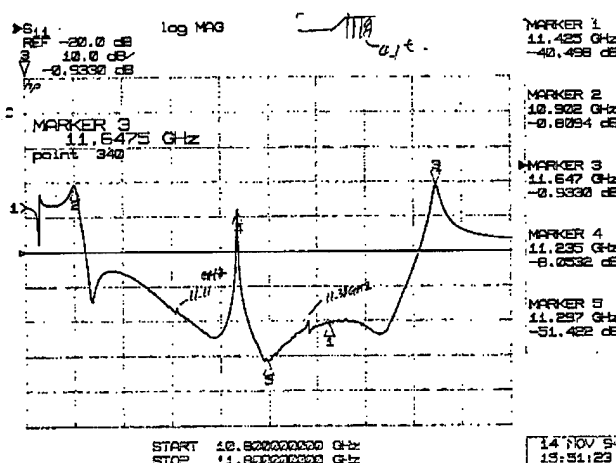


Fig. 5: Frequency response of the TE11 window ($1/2\lambda_g$ -2 case)

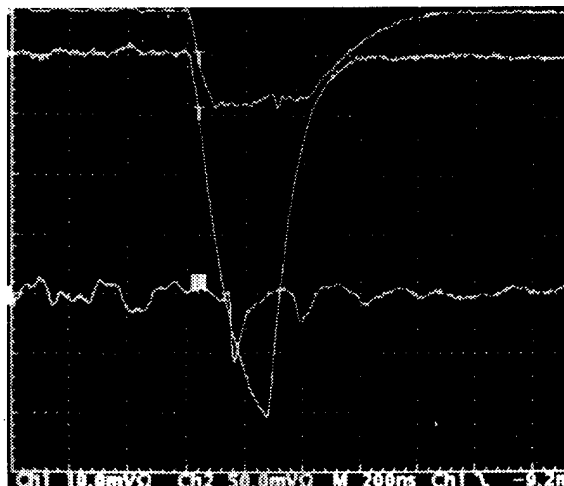


Fig. 6: RF power picture of the window high-power test in TRW(100MW peak-power, 15MW with 300ns input)

Feasability Study of Optically Coupling RF-Power at mm Waves

Bengt Littmann and Heino Henke, TU Berlin, EN2, Einsteinufer 17, 10587 Berlin

Abstract

At mm-wavelengths, ordinary waveguides show considerable attenuation. Corrugated overmoded waveguides have strongly reduced attenuation, while maintaining stability by introducing the well known pattern of passbands and stopbands. Fields either transform to surface waves with very high losses, or concentrate at the center of the waveguide and propagate with very low loss. The latter, are employed to transport RF-power. Considering the field pattern, optical free space coupling to an accelerator structure, is thinkable. We have investigated the coupling mechanism itself, e.g. field leakage and power losses to the outside and designed a device for optical coupling from a corrugated waveguide into a planar muffin-tin structure.

I. INTRODUCTION

Since the original idea came up to build particle accelerators at mm-waves, [1] intense research has been going on at Argonne and the universities of Madison, Chicago and Berlin. For an overview, the reader is referred to [2] and to numerous publications at this conference e.g. [3]. Early in the investigations, we decided to look at more detailed problems, like an rf-coupler, since the frequency band above 100 GHz leads to very different requirements and to surprisingly different designs. This fact is well demonstrated by the design process of an rf-coupler which we present below. This process starts with the choice of a corrugated and overmoded waveguide to keep losses low, and to reach the intended levels of power transport (for a rectangular waveguide typical values of attenuation would be 1 db/ft with a maximum CW-power of few kW!). Since this waveguide aperture is an order of magnitude bigger than all sizes within the structure itself, a taper is needed. Such huge geometric differences make the design difficult (how to model a periodic structure feeding another, but different periodic structure). We opted to model the structure itself with MAFIA [6] and used a mode matching technique to model the corrugated waveguide and the taper.

II. CHOICE OF THE CORRUGATED OVERMODED WAVEGUIDE

Industry [5] offers a variety of oversized low-loss components for use at high frequencies. We found the waveguides to be optimized for power transport over longer distances with extremely wide apertures. Since this does not exactly meet our situation, we decided to design our own waveguide. The following describes the procedure we carried out. We relaxed on the attenuation to reduce aperture (circular symmetry assumed), which benefited our taper design later on. We chose an aperture diameter of 0.75" rather than 1.25". We inserted corrugations and increased their depth until we encountered a clean separation of

modes with $\varphi=1$ dependence.

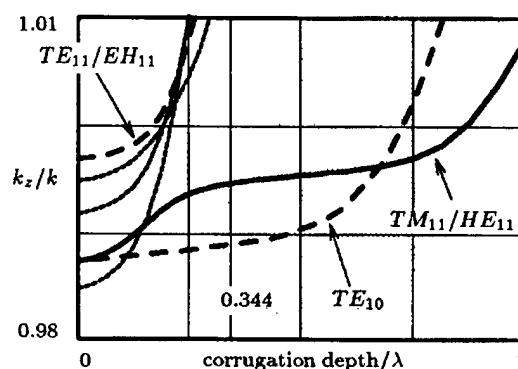


Figure 1. Normalized propagation constant versus normalized corrugation depth ($f_0=120\text{GHz}$, phase advance= 0.73π , tolerance $\leq 10^{-4}$).

We also observed the slope of the propagation constant versus corrugation depth, which should be as low as possible, since then little field is present in the corrugations. The field is rather concentrated around the waveguide center. We obtained a whole band of possible corrugation depths at $0.3\lambda - 0.75\lambda$ (shaded region in Fig. 1). Our design tends towards the lower end at 0.344λ . Consult Table 1 for the exact dimensions.

geometry	size/mm
inner radius	9.5250
outer radius	10.3840
period	0.9144
iris thickness	0.2540

Table 1. HE_{11} -mode waveguide dimensions.

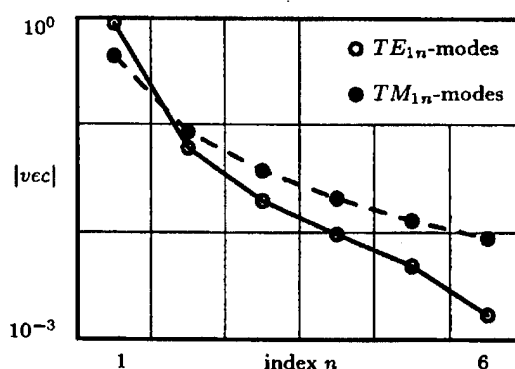


Figure 2. Absolute value of eigenvector versus index n (φ -dependence, $\varphi = 1$ -dependence).

Calculations were done using the mode matching technique. Periodic boundaries were applied and eigenvalues and eigenvectors found after decomposing the scattering matrix into singular

values (SVD). The main advantage of Singular Value Decomposition is that, it returns the eigenvectors without further computational effort. It also neatly finds all eigenvalues of multiple order. To check convergence we observed the eigenvector amplitudes decline with increasing mode order (Fig. 2). We found convergence generally to be good with few modes. Note that convergence for TM -modes is slower than that for TE -modes.

III. DESIGN OF THE OPTICAL COUPLING DEVICE

Before we design the optical coupling device we investigate the optical coupling itself. Three questions come to mind:

Which gap widths are tolerable?

What taper apertures are needed to catch the wave?

What losses, due to reflection, mode conversions and radiation, does the gap inflict?

Where the gap width is the distance to be crossed by optical coupling. The receiving or taper aperture is the aperture of the waveguide facing the corrugated guide. To answer these questions, we investigate the transmission from the corrugated waveguide to a regular (cylindrical) waveguide, and sum the transmitted power of all modes. We assume we can obtain a device that will, without further losses, combine all transmitted modes to the desired one (rectangular TE_{10}). Fig. 3 shows the sum of the amplitudes of the transmitted waves versus gap width. A gap of the order of μm will hardly inflict any losses, in the mm-range we find a minimum transmission of around 92 % and only when the gap width is comparable to the waveguide aperture, do we see serious losses (cm-range).

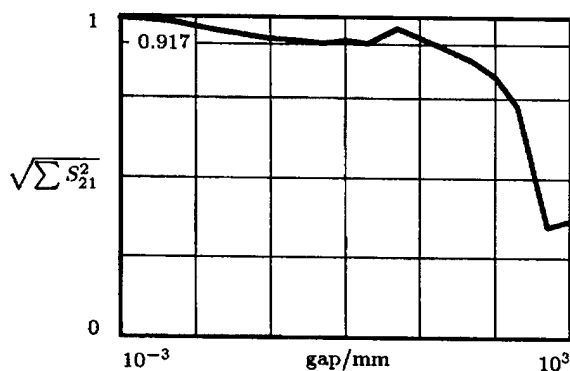


Figure 3. Sum of amplitudes (rms) of transmitted waves versus gap width (phase advance= 0.73π).

Fig. 4 shows the sum of the amplitudes of the transmitted waves versus aperture of the regular waveguide. As expected, we find that, the receiving waveguide should have an aperture size close to the aperture of the corrugated one. Gap losses then converge to about 94 % with a gap width of 1 mm. Both, rather quickly obtained results lead us to think that optical coupling to

a mm-wave structure is possible with a transmission of $\geq 90\%$.

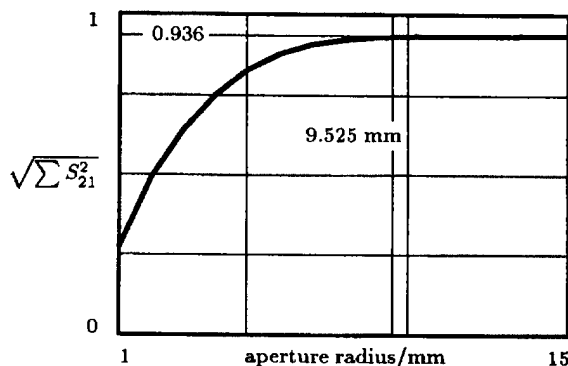


Figure 4. Sum of amplitudes (rms) of transmitted waves versus receiving waveguide aperture (phase advance= 0.73π , gap=1 mm).

Carrying on, with the design of the optical coupling device we arrive at the taper section. Fig. 5 shows a scale drawing of the actual design and gives a good impression on the geometrical differences (the actual size is three times smaller!). Note that up to the last taper step we have circular symmetry, whereas the accelerating structure below is a rectangular one. From the above results (Fig. 4) we set the first taper step aperture to $0.75'' = 19.05\text{ mm}$. After many optimization cycles, we reached a transmission of 90 % with a gap width of 0.5 mm.

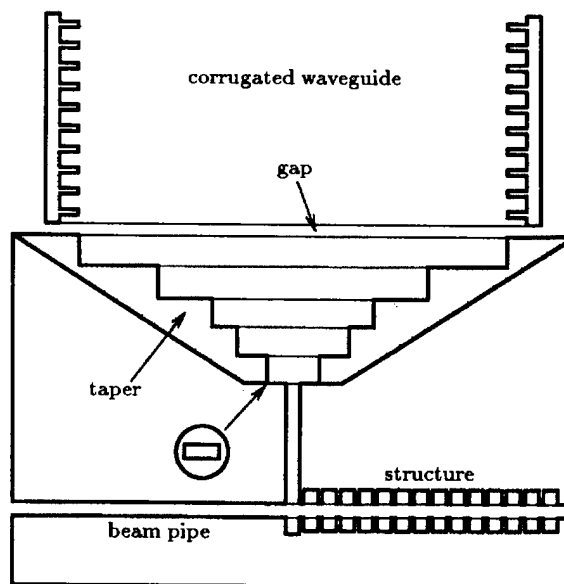


Figure 5. yz-cut of the mm-wave structure with optical coupling and taper section (scale 3:1).

According to Fig. 3, we could improve the transmission by narrowing the gap to 0.2 mm or less. We could also allow more taper steps, which certainly would enhance bandwidth. Altogether, we hope to reach a 95 % transmission, with a more careful design. Fig. 6 shows the field pattern of the electric field inside the accelerating structure, with a matched coupler. There

are two coupler cells and two regular cells. The phase advance is $2\pi/3$, as it should be. Fig. 7 zooms in on the coupler cell again displaying the electric field.

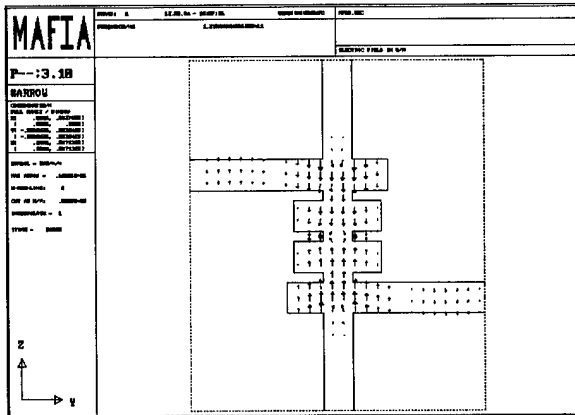


Figure 6. yz-cut of the mm-wave accelerating structure. Arrows display the electric field.

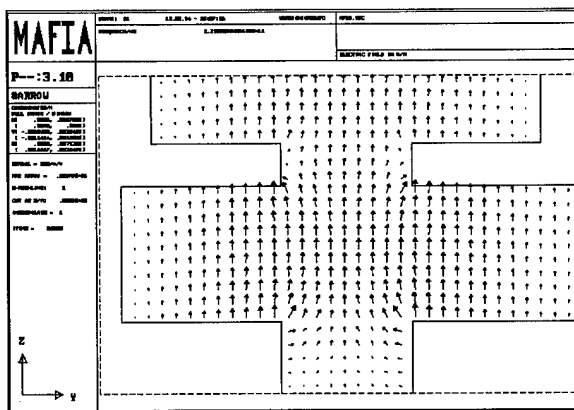


Figure 7. Zoom of coupler cell. Arrows display the electric field.

To be able to simulate the complete structure, a program (Fortran) was written that computes the scattering matrix of various waveguide cross-section jumps (rectangular, circular and mixed). This program is also able to import the scattering matrix of the accelerating structure which was computed with MAFIA. The structure was fed with the eigenvector of the HE_{11} -mode obtained while designing the corrugated waveguide. 1024 corrugations were used to approximate the infinite periodic structure. The accelerating structure, which is infinitely periodical in nature, was terminated by the coupler cell designed earlier [4]. A matched end cell indeed mimicks an infinite continuation of the preceeding structure. The design was automated by minimizing $-\log_{10}(S_{21})$ with Simulated Annealing [7] in 10 dimensions. Simulated Annealing is advantageous, since, unlike Conjugate Gradients, it will not converge into the first minimum it encounters. Instead, it will search and find the global minimum. In waveguide design, especially when geometry steps are located close to one another, there are a countless number of different (and unsatisfactory) minima.

IV. CONCLUSION

At frequencies above 100 GHz power transport is done with overmoded and, often, corrugated waveguides. This power transport system leads to the need of taper sections, but it also gives the opportunity to relax tolerances by adopting optical coupling. In an earlier publication [4] an rf-coupler was designed, which was fed from a mono-mode rectangular waveguide. The transmission thereby was as high as 98 %, but power sources should be located in immediate neighborhood to the accelerating structure, and even then, losses would be considerable, and arcing within the power transport system would be an immediate threat. The optical coupling device designed here reduces transmission to 90 %, but allows more flexibility in the positioning of components all the same. We have reason to believe that we can reach a transmission of 95 % by relatively simple measures like narrowing the gap and including more taper steps. We are confident that our design will hold to scrutiny of measurements, which we plan to engage in.

V. ACKNOWLEDGEMENT

The support of Argonne Natl. Lab. is much appreciated.

References

- [1] H. Henke, Y.W. Kang and R. Kustom, "A mm-wave RF structure for relativistic electron acceleration", Argonne Natl. Lab., ANL/APS/MMW-1, 1993
- [2] H. Henke, "MM-Wave Linac and Wiggler Structures", Proc. European Particle Accelerator Conf., London, 1994, vol. 1, pp. 322
- [3] H. Henke, "Planar Structures for Electron Acceleration", Proc. Particle Accelerator Conf., Dallas, 1995
- [4] B.W. Littmann, M.H. Bairu and H. Henke, "A mm-Wave Coupler Design", Proc. European Particle Accelerator Conf., London, 1994, vol. 3, pp. 2019
- [5] J. Doane, "High Power Microwave Components in Oversized Waveguides", Specifications by General Atomics, P.O. Box 85608, San Diego, CA-92186-9784
- [6] The MAFIA Collaboration, F. Ebeling et al., MAFIA User Guide, 1992
- [7] W.H. Press, S.A. Teukolsky, W.T. Vetterling and B.P. Flannery, "Numerical Recipes in FORTRAN", sec. edition, Cambridge University Press, 1992, pp. 387-448

A LOW-FREQUENCY HIGH-VOLTAGE RF-BARRIER BUNCHING SYSTEM FOR HIGH-INTENSITY NEUTRON SOURCE COMPRESSOR RINGS*

T. W. Hardek, D. Rees, C. Ziomek
Los Alamos National Laboratory
P.O. Box 1663
Los Alamos, NM 87545

Abstract

A Los Alamos design for a 1-MW pulsed neutron source incorporates a ring utilizing an rf-barrier bunching system. This bunching concept allows uniform longitudinal beam distributions with low momentum spread. Bunching cavities are operated at the revolution frequency (1.5 MHz in our case) and each of the 2nd, 3rd, 4th, and 5th revolution frequency harmonics. Their effects combine to maintain a beam free gap in the longitudinal distribution of the accumulated beam. The cavities are driven by low-plate-resistance common-cathode configured tetrode amplifiers incorporating local rf feedback. Additional adaptive feed-forward hardware is included to reduce the beam-induced bunching-gap voltages well below that achievable solely with rf feedback. Details of this system are presented along with a discussion of the various feed-back and feed-forward techniques incorporated.

1. INTRODUCTION

A 1 MW pulsed neutron source ring design developed by a Los Alamos team incorporates an rf longitudinal-barrier [1] to maintain a beam free gap in the circulating beam. An rf Barrier consists of a series of high-voltage bipolar pulses applied across a gap in the beam pipe timed to occur just before and after the beam passes this barrier gap. Beam is forced out of the beam gap by these pulses. Longitudinal beam distribution within the bunch remains essentially uniform and the beam does not suffer the increased momentum spread imposed by a conventional bunching scheme. With a Longitudinal barrier scheme, if some increase in momentum-spread is desired, the energy of the injected beam may be swept. Figure 1 shows a preferred RF barrier pulse train tailored to one particular Los Alamos ring design and gives idealized beam distribution and timing.

Pulse waveforms may be generated by adding several harmonically related sinusoidal waves of appropriate

magnitude. We have chosen this approach to provide the longitudinal RF barrier pulses for this bunching system design. A series of harmonically related frequencies are added to produce the equivalent barrier pulse of Figure 2. Table 1 lists the harmonic amplitudes and frequencies needed to produce this equivalent pulse.

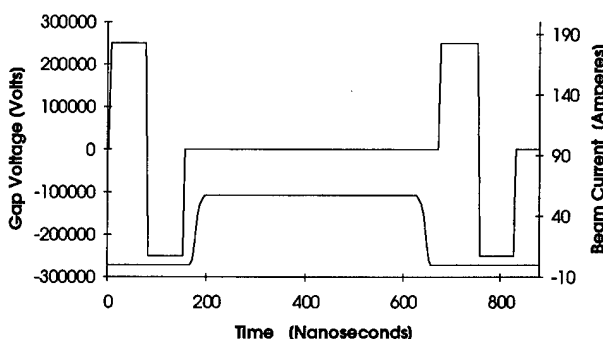


Figure 1: RF Barrier Pulses and Beam Current

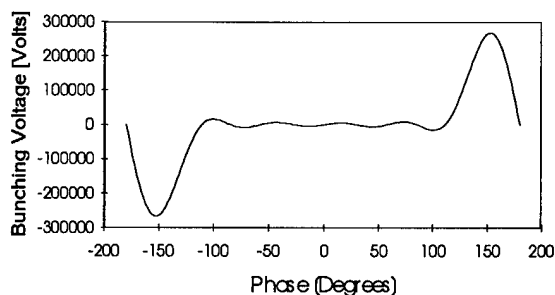


Figure 2: Composite RF Barrier Waveform

Table 1: Longitudinal RF Barrier Harmonic Voltages

Fundamental	1.49 MHz	61.38 kV
Second Harmonic ...	2.98 MHz ...	-98.45 kV
Third Harmonic	4.47 MHz	99.00 kV
Fourth Harmonic	5.96 MHz	-70.30 kV
Fifth Harmonic	7.45 MHz	29.58 kV

Harmonics are all in phase with respect to the fundamental.

*Work performed under the auspices of the U.S. Department of Energy.

It is not necessary to actually add the frequency components within one cavity structure. Separate single-resonant-frequency cavity structures may be installed with an accumulated effect on the beam equivalent to that of the composite waveform.

The waveform of Figure 2 is a worst-case-design RF barrier waveform resulting from a particular set of ring parameters. By relaxing some of the requirements for beam loss and selecting different ring operating parameters major reductions in the peak required voltage can be achieved. Lower peak voltages would allow simplification of the system by reducing the number of rf stations operating at each harmonic and in the total power required to operate the system..

II. GENERAL PARAMETERS

To provide a 250 kV peak barrier waveform this design uses a total of 13 active RF cavities and 1 spare cavity. The cavities are dual-gap single-ended structures with each of the sections driven by its own power amplifier. Cavities that operate on the two lowest frequencies, 1.5 MHz and 3 MHz, are 2.4 meters long while the higher frequency cavities are 1.8 meters in length. The cavities are installed with their ferrite sections downstream of the gaps allowing beam current to add to the forward current of the power amplifier tube. Bias conductors are included in the cavities to provide electronic fine tuning. Gap shorting switches are included in each cavity so any cavity may be removed from service without adverse effects on the circulating beam. The spare cavity can operate on any of the normal cavity frequencies to replace a failed cavity.

Amplifiers consist of a pulsed, class A biased, grounded-cathode super-power tetrode and two driver stages all physically located at the cavities in the beam channel. Bunching gap impedance is kept at a low impedance by the low plate resistance of the output tube, active RF feedback around the three power amplifier stages and feed-forward beam compensation. Each of the two cavity gaps is driven by an independent amplifier, but each amplifier can drive both cavity gaps allowing continued operation in the case where one amplifier fails.

Table 2 gives the main system parameters for a 250 kV peak barrier.

Table 2: System Parameters

Revolution Period.....	671 nsec
Number of Bunches	1
Fundamental Bunching Frequency	1.4901 MHz
RF Cavities	
Total Number	14
Gaps per Cavity	2
Maximum Voltage per Cavity	35kV

Maximum Voltage per Gap17.5kV

Fundamental 3 each....20.6kV/Cavity
 Second Harmonic 3 each....32.8kV/Cavity
 Third Harmonic 3 each....33.0kV/Cavity
 Fourth Harmonic..... 3 each....23.4kV/Cavity
 Fifth Harmonic..... 1 each....29.9kV/Cavity
 Spare (any harmonic) .. 1 each

Ferrite TypePhillips 4M2
 Core Size
 Inner Diameter 30 cm
 Outer Diameter 60 cm
 Thickness 2.71 cm

Final Amplifier

Total Number28 (2 per cavity/ 1 per gap)

Configuration Common Cathode,
 Low Rp Tetrode,
 Class A Pulsed

Tube Type Eimac X2242

Active Rp450 ohms (dependent on bias choices)

Maximum DC Dissipation 100 kW/Amplifier
 2.6 MW Total

Nominal Operating DC Dissipation ... 48 kW/Amplifier
 1.25 kW Total

Duty Factor 8 %

III. RF CAVITY

A conventional ferrite loaded structure employing parallel DC bias has been chosen. Separate cavities will operate at each of the first five harmonics of the 1.5 MHz revolution frequency (1.5 MHz to 7 MHz). Setting a peak voltage-per-cavity of 35 kV will allow a 250 kV peak waveform to be generated with 12 cavities. An additional 1.5 MHz cavity is desirable and increases the total operational complement to 13. A Spare cavity has also been provided for bringing the total installed cavities to 14.

The cavities are configured as single-ended structures. Configuring the cavities this way allows a single, class-A biased, power amplifier tube to be placed directly across the gap. The amplifier provides the required RF bunching voltage and also acts as a resistor connected across the bunching gap to maintain a low gap impedance.

A pair of single ended cavities are combined within one housing with a common bias winding. The bias winding forms a single turn around each ferrite core stack. The complete winding is routed such that the RF voltage induced by one core stack bucks that induced by the second core

stack. As long as both core stacks are operated at the same RF voltage level the induced voltages on the bias windings will cancel.

A single design that can be used for all five frequencies is desirable. Bias windings that are included for fine control of cavity resonance can also provide this feature. To reduce the total permeability swing needed we would remove some of the ferrite for the higher frequency cavities. This also saves some ring space. Assuming type 4M2 ferrite [2,3,4] with 60 cm OD and 30 cm ID rings we would fill the two lowest frequency cavities with 1.26 meters of ferrite, the amount needed to keep the B field below 200 gauss at 1.5 MHz. The remaining higher harmonic cavities would be filled with 0.87 meters of ferrite. The spare cavity would be filled with the full ferrite load and include shorting pins to effectively remove the excess ferrite when operated at the higher frequencies.

IV. AMPLIFIER

The high circulating beam currents of our reference design impose a severe beam loading requirement on the final amplifier design. For the fundamental component of beam current we must provide control for currents in the 30 ampere range. Our reference design places a low-output-impedance-amplifier directly across the cavity bunching gap providing a low-impedance shunting path for the beam current and keeping the beam induced voltage within reasonable limits. The amplifier is effectively acting as a water-cooled resistor connected across the bunching gap. Assuming an amplifier output impedance of 450 ohms the beam induced voltage would be limited to 13.5 kV. Utilization of RF feedback techniques [5,6,7] would further reduce the effective output impedance. We have estimated a reduction factor of 7 for our lowest frequency so we believe we can achieve effective cavity gap impedances in the 35 to 55 ohm range.

An adaptive feed forward technique developed for our Ground Test Accelerator project (GTA) has demonstrated effective impedance reduction factors better than 40 times [8,9]. The technique uses stored error data from previous beam pulses to predict and correct-for beam induced signals on the present beam cycle. The technique is self adjusting to accommodate slowly changing beam conditions and has the potential of reducing the effective impedance well below the 10 ohm range anticipated with a beam-feed-forward approach.

V. ADAPTIVE FEED-FORWARD

A conventional feed-forward technique involves using a direct measurement of the beam current to perform a correction. This technique requires that a correction based upon the measured beam current signal be applied before the beam arrives to compensate for the delays in the amplifier chain. This requires the measured beam current signal to be

transmitted over a shorter distance with a faster propagation velocity than the beam itself. If the beam current is measured just after its corresponding cavity, there is sufficient time to apply the correction because one full revolution occurs before the beam returns to that cavity.

The adaptive feedforward device observes errors in the gap voltage and phase for each bunch revolution, and over time, adaptively determines a correction function that is applied at the RF driver to oppose those effects. In essence the past fluctuations in gap voltage and phase are used to predict the current fluctuation and a corresponding correction function to negate any deviations from the desired operating point. Because this is a feed-forward technique, the apparent longitudinal coupling impedance is reduced over the entire band of interest including all five harmonics and the synchrotron sidebands. Modeling simulations and experimental data are necessary to determine the exact reduction in longitudinal coupling impedance.

VI. REFERENCES

- [1] J.E. Griffin et al., "Isolated Bucket RF Systems in the Fermilab Antiproton Facility", IEEE Transactions on Nuclear Science, Vol. NS-30, 1983, P 3502-3504.
- [2] M.A. Goldman et al., "Studies of Ferrite Materials For The AGS Booster Synchrotron", 1989 IEEE Particle Accelerator Conference Proceedings, P 165-167.
- [3] R.T. Sanders et al., "The AGS Booster Low Frequency RF System", 1991 IEEE Particle Accelerator Conference, P 739- 741.
- [4] R. T. Sanders et al., "The AGS Booster High Frequency RF System", 1991 IEEE Particle Accelerator Conference, P 681-683.
- [5] G. Rakowsky, "RF Accelerating Cavities for the AGS Conversion", IEEE Transactions on Nuclear Science, June 1967, P 315-319.
- [6] J.M. Brennan et al., "The Upgrade Project for the RF System for the Brookhaven AGS", 1993 IEEE Particle Accelerator Conference, P 1241-1243.
- [7] D. Boussard, "Control of Cavities With High Beam Loading", IEEE Transactions on Nuclear Science, Vol. NS-32, No. 5, October 1985, p 1852-1856.
- [8] C.D. Ziomek et al., "Results of Adaptive Feedforward on GTA", 1993 IEEE Particle Accelerator Conference, P 2391-2393.
- [9] S.P. Jachim et al., "The Los Alamos VXI-Based Modular RF Control System", 1993 IEEE Particle Accelerator Conference, P 1154-1156.

Temporal Evolution of Multipactor Discharge

R. Kishek, Y. Y. Lau, and R. M. Gilgenbach
Department of Nuclear Engineering
University of Michigan
Ann Arbor, MI 48109-2104

Abstract: Multipactor is an important resonant discharge phenomenon on which there have been surprisingly few publications in the open literature. Here, we extend the theoretical analysis of an idealized model. Emphases have been placed on the mutual interactions between the multipactor discharge and the rf. We show that the multipactor current may reach a very high level, transiently, before it settles to a steady state. The multipactor current saturates primarily by its loading of the cavity; the image space charge force associated with the multipactor electrons plays a relatively minor role. When saturation occurs, the secondary emission coefficient is unity, corresponding to the "first cross-over point" in the secondary electron yield curve. The parameters attained in the steady state agree with the predicted values from an analytic theory. The analysis is extended to include the effects of an external magnetic field.

Multipactor is a well known phenomenon of rf breakdown in microwave cavities, windows, satellite rf payloads, and accelerator structures [1-3]. When an AC electric field exists across a gap, an electron from one surface is accelerated toward the other surface, the impact upon which may release more than one electron by secondary emission. It is easy to see that if the electron transit time across the gap equals to half of the rf period, a resonant discharge could result.

There exist few theoretical analyses of multipactor, most of which are concentrated on the response of a single electron to an imposed rf electric field. Analytic expressions have been derived for the phase of the emitted electron, and the range of the rf electric field in which a stable, steady state multipactor may exist [1,4]. While some calculations have included the space charge effects associated with the multipactor electrons [4,5], most of these calculations omit the important processes of loading and detuning of the rf cavities as the multipactor current grows [2]. In this paper, we use a simple model to address these issues, the analysis of which yields interesting information on the multipactor saturation level, the saturation mechanism, the time scale over which

multipactor evolves, and possibly the drastic transient growth of multipactor current before the steady state solution is reached.

For simplicity, we shall use a one dimensional model where the multipactor occurs inside a planar gap [Fig. 1]. The gap separation is D and the gap voltage is $V_g(t)$. The multipactor discharge is modeled by a single electron sheet of surface density σ that moves across this gap. Upon impact on a gap surface, a new electron sheet is generated by secondary emission. We assume that the voltage V_g that drives the multipactor is provided by an rf cavity, of characteristic frequency ω_0 and quality factor Q [Fig. 1]. As the multipactor electron sheet moves inside the gap, it induces a wall current, $I_m(t)$, which loads the cavity. Thus, the present model allows for the progressive loading and detuning of the cavity as the multipactor current builds up. This loading, in turn, modifies the electron's energy and phase at impact.

Hereafter, we shall use dimensionless quantities with the following normalization scales: D for distance, ω_0 for frequency, $1/\omega_0$ for time, $v = \omega_0 D$ for velocity, $U = mv^2$ for energy, U/e for voltage, $E = U/eD$ for electric field, $\Sigma = \epsilon_0 E$ for surface charge density, $A\Sigma v/D$ for current. Here, m is the electron mass, $e = 1.602 \times 10^{-19}$ Coulomb, A is the surface area of the gap, and ϵ_0 is the free space permittivity. The cavity is driven by the normalized ideal current source I_d , and by the multipactor current I_m , according to the circuit equation [Fig. 1]:

$$\left(\frac{d^2}{dt^2} + \frac{1}{Q} \frac{d}{dt} + 1 \right) V_g(t) = \frac{d}{dt} [I_{d0} \sin(\omega t + \phi) + I_m(t)] \quad (1)$$

Here I_{d0} is the amplitude of the driver current of normalized frequency ω , and ϕ is the phase at time $t = 0$. We set $\omega = 1$ in this paper (i.e., resonantly driven). The normalized multipactor current I_m is induced by the electron sheet motion:

$$I_m(t) = -\sigma(t) \cdot \frac{d}{dt} x(t), \quad (2)$$

where σ is always positive, by convention. It is this term that is solely responsible for the non-linear beam loading and frequency detuning of the cavity by the multipactor, as readily seen from Eq. (1) and Fig. 1.

The force law for the electron sheet is

$$\frac{d^2 x}{dt^2} + \omega_c^2 (x - x_0) = V_g + \sigma \cdot (x - \frac{1}{2}), \quad (3)$$

where the initial plate of origin is denoted by $x_0 = 0$ or 1. The first term on the right hand side represents the force due to the gap voltage and the second term the force due to the image charge (of the multipacting electron sheet) on the plates. We

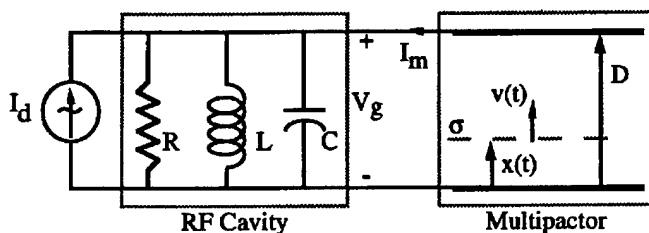


Fig. 1: Model of interaction between rf cavity and multipactor discharge.

have included a general transverse magnetic field with a cyclotron frequency ω_c , normalized to the driver frequency ω .

On impact with a plate at time t_i , the incident electron sheet is removed and a new sheet of surface charge is released by secondary emission. The post-impact surface charge density $\sigma(t_i^+)$ is related to the pre-impact charge density $\sigma(t_i^-)$ by

$$\sigma(t_i^+) = \delta \cdot \sigma(t_i^-), \quad (4)$$

where δ is the coefficient of secondary emission [6] which depends on the electron impact energy, E_i [7]. Here, $E_i = (dx/dt)^2/2$, evaluated at $t = t_i^-$. In addition, we adopt Vaughan's empirical formula [6] for δ . This function is shown in Fig. 2, where δ_{\max} is the maximum value of δ , occurring at an impact energy, E_{\max} . Fig. 2 shows that $\delta = 1$ at two values of impact energies, E_1 and E_2 . The lower energy E_1 is designated as the "first cross-over point".

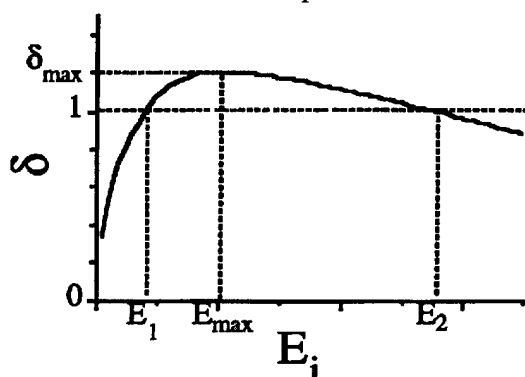


Fig. 2: Secondary electron yield, δ , as a function of impact energy E_i .

In the present formulation, multipactor affects its own evolution in two ways. First, it loads the cavity and changes the gap voltage; this process is entirely accounted for by the term I_m in the circuit equation (1). We may designate this effect as the "beam-loading effect". Second, as the multipactor current builds up, the space charge force may become appreciable, and may influence the arrival phase of the impacting electron relative to the rf phase. This second effect is modeled by the last term in the force law, Eq. (3), and may be called the "space charge effect".

We have established analytically the necessary conditions for the existence of steady state solutions according to Eqs. (1) - (5). One condition for a steady state is that, every cycle, the sheet has to arrive at the same plate when the phase of the voltage is the same (a "fixed-phase" [4]). Otherwise, the sheet will keep drifting in phase, and may eventually hit one of the plates in the wrong phase of the rf cycle, quenching the multipactor. This phase stability is discussed elsewhere [1, 4]. The second condition is that steady-state has to occur when $\delta=1$, resulting in a constant σ in Eqs. (2) and (3) above. This occurs for two impact energies, but a simple physical argument shows that only the first cross-over point E_1 in Fig. 2 gives the stable steady state solution [8]. Hence this condition also fixes the impact energy to E_1 in the steady state.

To obtain the steady state solution, we solved Eqs. (1), (2), and (3) with a constant σ . Then, we used the fixed phase condition and an impact energy of E_1 to relate the initial values of V_g and its derivative in Eq. (1) to their final values. This results in the steady state values of the charge density, the gap voltage amplitude, and its value at impact. The numerical results, to be discussed below, agree quite well with the steady state predictions of the analytic theory.

To study transient evolution, we assume that the driver current I_d has been turned on for all time so that the cavity is already filled with rf for $t < 0$. The multipactor current is "turned on" at $t = 0$, in the form of an electron sheet with initial surface charge density σ_0 that is released from the plate $x = 0$, with zero velocity [9]. The initial phase ϕ [Eq. (1)] at which σ_0 is launched is chosen so that this initial electron sheet strikes the other plate in about half an rf cycle. In most cases we run, the precise values of these initial data are not critical. Our simulations thus far have been restricted to two-surface, first-order multipactor [1], i.e., an electron released from one surface always strikes the other surface without momentarily stopping within the gap. The major free parameters are: Q and I_{d0} , after having fixed $\delta_{\max} = 1.2$, $E_{\max} = 0.36$, and $\omega = 1$. [In dimensional units, if the rf cavity has a natural frequency of 1 GHz, and a gap separation of 0.22 cm, over which multipactor occurs, these parameters correspond to an ideal rf driver current exactly at 1 GHz, and δ reaches a maximum value of 1.2 when the impact energy is 400 eV.]

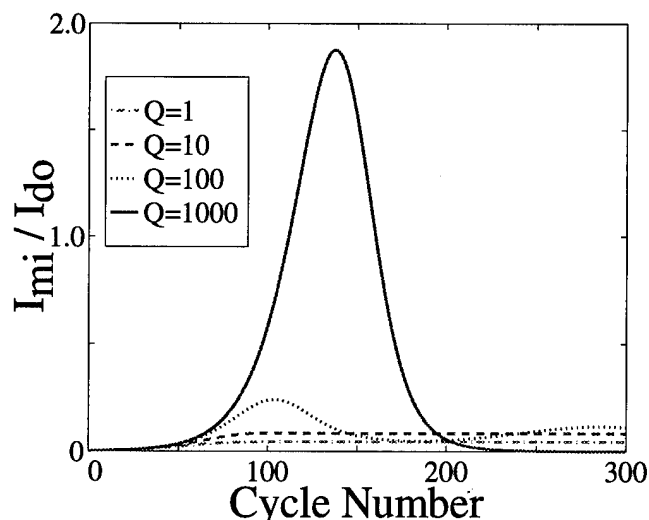


Fig. 3: Transient evolution of multipactor current at impact, in units of the drive current amplitude I_{d0} , for various values of quality factor, Q .

Shown in Fig. 3 is the multipactor current, monitored at impact, in units of the driver current amplitude I_{d0} , for $Q = 1, 10, 100, 1000$. The very low value of Q , e.g., $Q = 1$, is included in our study to show the trend of multipactor in a non-resonant structure -- one that is relatively immune to beam loading, such as a window. It is seen from Fig. 3 that in a high Q cavity, the multipactor current may reach a very high level in a transient manner before it settles down to steady state. Throughout the transient development of the

multipactor, the peak rf gap voltage in each cycle changes relatively little, for either the $Q = 1$ case or the $Q = 1000$ case [Fig. 4]. The secondary emission coefficient δ also stays around unity, specifically in the vicinity of the first cross-over point (E_1) in Fig. 2, as discussed earlier. Our numerical results show that the impact energy indeed approaches E_1 asymptotically in time. When the steady state is reached, the gap voltage at impact, therefore, is insensitive to Q , as shown in Fig. 4. We have spot-checked that the steady state values of the gap voltage, of the electron impact phase in the rf cycle, and of the surface charge density, are all in good agreement with those obtained from our analytic formulation.

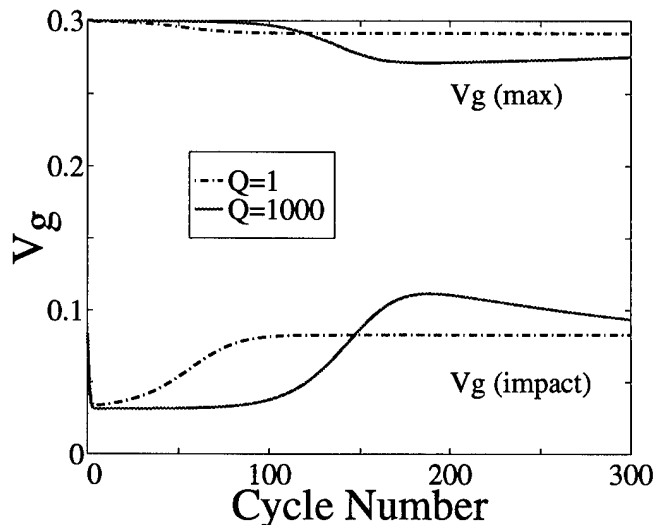


Fig. 4: Evolution of the peak gap voltage, $V_g(\max)$, and of the gap voltage at the instant of electron impact, $V_g(\text{impact})$, for $Q = 1$ and $Q = 1000$.

The numerical results show that, as long as $Q \gtrsim 10$, the beam loading effect is far more important than the space charge effect in determining the saturation level of the multipactor current. The disparity of their relative importance becomes increasingly more pronounced as Q increases, as high Q cavities can be more readily detuned by a multipactor current. This also explains the sensitivity in the high Q cavities. The fraction of rf power dissipated in the RLC circuit,

$\langle -V_g(I_d + I_m) \rangle / \langle V_g I_d \rangle$, is shown in Fig. 5. Here $\langle \rangle$ denotes the average over the transit time of an electron. The rf energy stored in a high Q cavity is capable of driving the multipactor current to a large amplitude when the condition becomes favorable. This gives the tantalizing clue that, in reality, the large amount of energy stored in high Q cavities may relax via a multipactor discharge, albeit transiently in time, and locally in space. In an example, we show that as much as 20% of the energy stored in a high Q cavity may be discharged in a single overshoot of the multipactor!

We have included the effect of a non-zero transverse magnetic field for the $Q = 1000$ case [7]. The presence of the magnetic field is found to reduce the strength of multipactor, according to this (much) simplified model. Specifically, when the transverse magnetic field yields a cyclotron frequency

equal to 0.3 times the drive frequency, the peak multipactor current in the transient evolution is approximately 1/8 of that in the case of zero magnetic field.

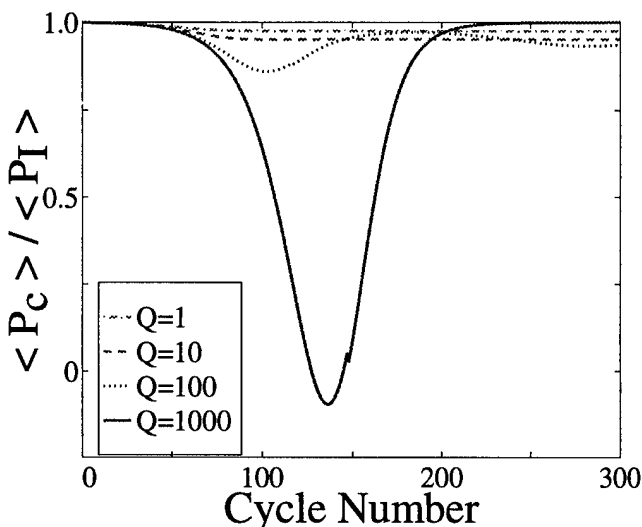


Fig. 5: Time history of the power consumed by RLC circuit, in units of the input power, at various values of Q .

We have benefited from many useful conversations with David Chernin, Spilios Riyopoulos, Perry Wilson, Jake Haimson, and Richard Briggs. This work was supported by NRL/ONR.

References

- [1] J. R. M. Vaughan, IEEE Trans. ED-35, 1172 (1988).
- [2] A. S. Gilmore, *Microwave Tubes*, (Artech House, Norwood, MA), p. 474 (1986).
- [3] G. A. Loew and J. W. Wang, SLAC Pub. No. 4647 (1988); A. D. Woode and J. Petit, *Microwave Journal*, (January, 1992), p. 142.
- [4] S. Riyopoulos, D. Chernin, and D. Dialetis, to be published.
- [5] F. M. Mako and W. Peter, Proc. 1993 IEEE Part. Acc. Conf., p. 2702 (1993).
- [6] J. R. M. Vaughan, IEEE Trans. ED-36, 1963 (1989); A. Shih and C. Hor, IEEE Trans. ED-40, 824 (1993).
- [7] In this paper, we ignore the dependence of δ on the angle of impact, even when an external magnetic field is present. We assume that δ depends only on the total impact energy.
- [8] If the impact energy E_i is greater (less) than the first cross-over point E_1 , more (fewer) electrons will be released by secondary emission. As a result, more (less) energy will be drained from the cavity as it accelerates more (fewer) secondary electrons. This leads to a lower (higher) gap voltage which makes E_i closer to E_1 in subsequent cycles. Thus E_1 is a stable steady state solution. A similar argument shows that the second cross-over point, E_2 in Fig. 2, is unstable.
- [9] It is shown by Riyopoulos et al [Ref. 4] that the inclusion of the initial velocity of the secondary electrons does not qualitatively change their steady state solutions.

Stabilizing a Power Amplifier Feeding a High Q Resonant Load

A. K. Mitra, R. L. Poirier, J. J. Lu and R. Hohbach, TRIUMF, Vancouver, Canada

A grounded grid power amplifier for the booster cavity of the TRIUMF cyclotron, operating at 92 MHz is found to be very stable when operating into a 50Ω load. However, when connected to a high Q cavity via a long transmission line it can become very unstable. Even though a phase shifter (trombone) enables one to adjust the resonant frequency of the cavity to be centered between two transmission line resonances, the amplifier tends to oscillate near the operating frequency due to insufficient isolation between input and output circuits. An expensive but easy solution to such a problem is to decouple the amplifier from the cavity and transmission line by employing a circulator. However, the solution that is presented in this paper uses external feedback from anode to cathode to neutralize the internal feedback inherently present in the tube. The neutralization is adjusted such that the isolation over the amplifier's bandwidth is increased by at least 15 dB. This along with input and output resistive damping has further stabilized the amplifier, which now operates routinely with no parasitic oscillation. Results of computer simulation of the amplifier response are reported.

I. INTRODUCTION

The 92 MHz, 150 kW power amplifier employs a grounded grid EIMAC 4CW150000E tetrode and is driven at the cathode by a 10 kW broad band FM transmitter. The output circuit consists of a $\lambda/4$ cavity (Q of 10000) inductively coupled via a 65 m long transmission line. A variable length section (trombone) is interposed between the output loop of the amplifier and the transmission line to position the operating resonant frequency between the transmission line resonances. The anode loop is set to transform $1 \text{ k}\Omega$ to the anode circuit such that output power of 50 kW can be obtained with rf voltage swing of 10 kV peak. The tube operates in class AB. Figure 1 shows the schematic of the system.

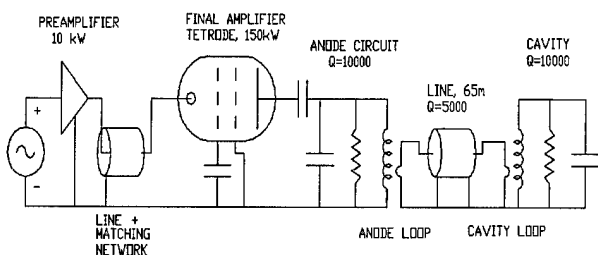


Figure 1: The booster rf system.

The amplifier produces an accelerating voltage at the cavity gap in excess of 120 kV. The amplifier is found to be very stable when tested into a 50Ω load at full power. However, when the amplifier is connected to the booster cavity by a 65 m long rigid transmission line, it tends to oscillate with the slightest detuning in the input and output circuits. This led to the investigation of oscillations in the amplifier to find solutions to stabilize the unit for full power operation into the booster cavity[1].

II. THEORY

A. Stability margin.

A measure of stability margin can be expressed as a ratio of the magnitude of the reverse attenuation (S_{12}) to the magnitude of the forward amplification (S_{21}).

Forward amplification ($|S_{21}|$) $A_f = g_m R_a$

Reverse attenuation ($|S_{12}|$) $A_r = |X|/R_i$

where g_m is the transconductance of the tube, $R_i = 1/g_m$, X is the reactance of the anode to grid capacitance C_{ag} and R_a is the effective anode impedance.

The stability margin $M = A_f/A_r = |X|/R_a$.

B. Transmission line modes.

The input impedance of a short circuited length of lossless transmission line exhibits minima at frequencies where the length of line is $n\lambda/2$. For $l = 65\text{m}$ and $n = 1$ that frequency is 2.3 MHz and therefore the transmission line series resonances (minima) will be 2.3 MHz apart and the parallel resonances (maxima) will also be 2.3 MHz apart. The electrical length of the line in figure 1 was adjusted by a trombone to place the cavity resonance f_0 at the transmission line minima making the difference from f_0 to the first transmission line parallel resonance 1.15 MHz. A microcap simulation [2] of the input impedance at the input of the transmission line is shown in figure 2.

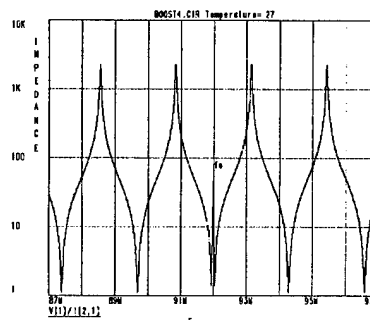


Figure 2: Simulated input impedance for a 20λ length of transmission line connected to the booster cavity.

If we now look at the simulated impedance at the anode in figure 3, the two line resonances which were closest to f_0 in figure 2 are shifted even closer to f_0 , and are now characterized by the parameters of the anode circuit and load cavity rather than the transmission line. They are designated as side resonances (f_{s1} & f_{s2}) in figure 3, where the difference from f_0 to the side resonance is only 0.65 MHz. Further simulations indicate that the resonances will get even closer if the coupling between the output loop and the anode circuit is decreased.

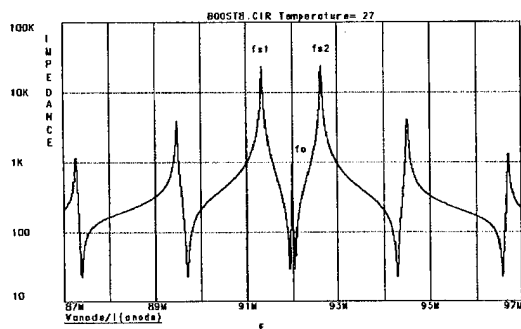


Figure 3: Simulated impedance at the anode coupled to a 20 λ long transmission line and booster cavity.

C. Neutralization

The purpose of neutralization is to make the input and output circuits independent of each other with respect to reactive currents. A completely neutralized amplifier requires that the inter electrode capacitances between the input and the output circuits be canceled. In the grounded grid amplifier, the control grid is at rf ground and serves as a shield to capacitive currents from the output to the input circuit. If the grid, screen and cathode lead inductances are insignificantly small, then neutralization can be achieved by employing a neutralizing capacitor approximately equal to the plate-grid capacitance of the tube, and a $\lambda/2$ transmission line which brings a voltage opposite in phase from the output circuit to the cathode circuit.

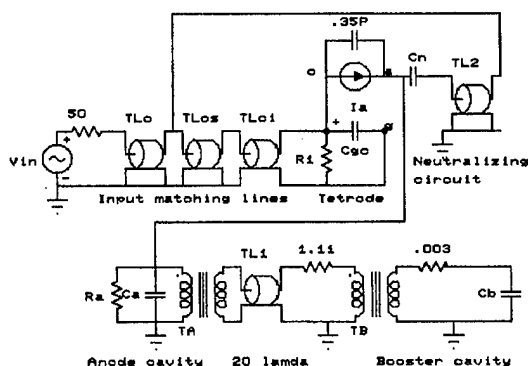


Figure 4: Micro-cap circuit model of the tetrode amplifier with neutralization.

The results of the analysis of the circuit modeled in figure 4 is shown in figure 5. It shows that the voltage gain at the side resonance is reduced by 11.0 dB and 15.7 dB whereas the gain at the operating frequency is reduced by 0.85 dB (although not evident from the graph) when a 0.7 pf neutralizing capacitor is used in conjunction with a $\lambda/2$ line. With neutralization the side resonances shift by 164 kHz and 118 kHz respectively.

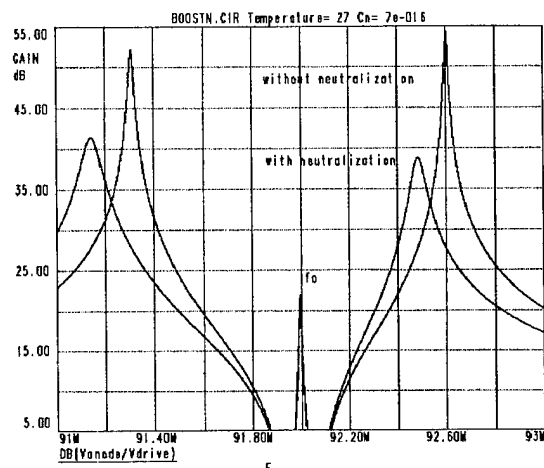


Figure 5: Voltage gain with and without neutralization.

III. MEASUREMENTS AND IMPROVEMENTS

Tests have been carried out at different power levels and operating conditions. The stability margin with and without neutralization was measured at signal level with a 50 Ω load connected to the amplifier (no transmission line) and all voltages applied to the tube. The same signal level measurements were carried out with the cold tube and the resonant load connected via a 65m of transmission line. The above tests helped to identify the parasitic modes, their impedances and proper value of the neutralizing capacitance to provide the largest stability margin. The signal level measurements also showed that a resistance in series with the neutralizing capacitor and the $\lambda/2$ line will increase the stability margin further (this has not been tried at full power).

The following improvements could be implemented without any major modifications to the power amplifier.

A. Additional Anode Loading

Fig 6 shows the effect of a 10% power damping (reduction of Q) in the anode circuit. This is achieved by capacitively coupling a 50 Ω load to the anode cavity. A 2.3 dB improvement in isolation is achieved at the fundamental frequency and 8.3 dB and 11.2 dB improvements at the more dangerous side resonances. The computed values are 1 dB for the fundamental and 12 dB for the side frequencies. Since this wastes 10% of the output power it puts an additional demand on the drive power to produce the same voltage at the cavity gap.

B. Neutralization

Neutralization was accomplished via a neutralization capacitor and a $\lambda/2$ line to bring a voltage opposite in phase from the output circuit to the input circuit. Although the voltage gain was not measured, figure 7 shows an improvement in isolation of 15 dB at f_0 and 15 dB and 26 dB improvements for the respective side frequencies.

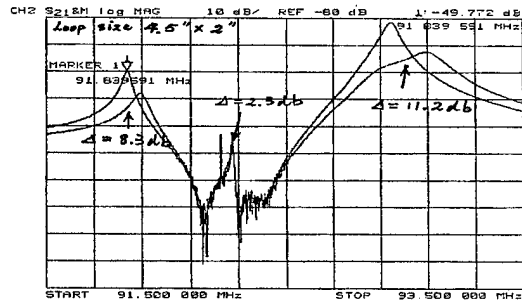


Figure 6: Resonance at the anode with and without loading of the anode circuit.

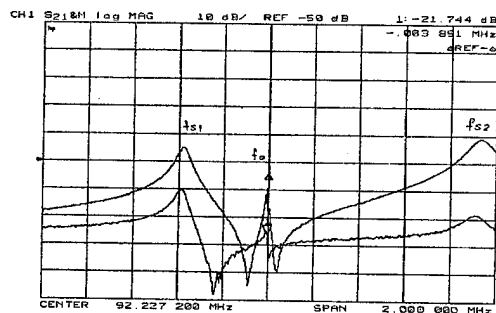


Figure 7: Resonance at the anode with and without neutralization.

C. Additional Input Loading

Although there was no quantitative measurement made of the effect of input loading, an improvement in stability was observed by connecting a 50 Ω load (via a capacitor for dc blocking) to the input cathode circuit where the impedance is approximately 10 Ω . This should give an improvement in stability margin of 2 dB at the fundamental frequency but at the expense of a further increase drive requirement of 2 dB.

Summing up the results of the above three improvements, the stability margin should improve by at least 19.3 dB at f_0 , 23.3 dB at the lower side frequency and 37.2 dB at the higher side frequency. The realistic test of course is the response at high power. One cannot make S_{21} measurements at high power without the risk of damaging the network analyzer. A spectrum analyzer was used to record a spectrum at the anode at an output power of 38 kW (figure 8). The upper plot shows more than 40 dB rejection of sideband signals. The lower plot shows the spectrum

when the amplifier is intentionally detuned to produce all the sidebands and resonances. Before the improvements were implemented it would have been impossible to adjust any tuning without the amplifier becoming unstable.

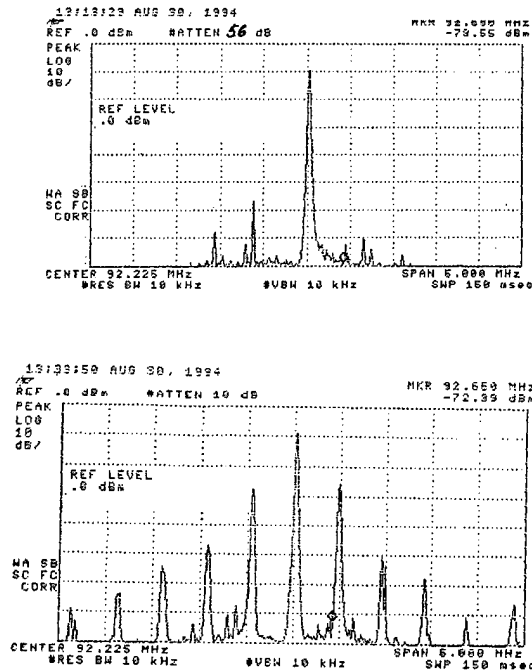


Figure 8: Spectrum of the output wave form at the anode.

IV. CONCLUSION

Although neutralization was not required when the amplifier was connected to a resistive load, it became necessary when connected to the resonant load via a long line in order to reduce the high impedance which were created at the side frequencies f_s near the operating frequency. These impedances were further reduced by anode damping and the overall stability further improved by damping the input circuit. To achieve this, only 10 % of the output rf power and 20 % of the input rf power is wasted in the terminating loads. This has enabled the amplifier to operate reliably on a regular basis without any parasitic oscillations.

V. REFERENCES

- [1] R. Hohbach, "Investigation on Stabilizing the 92 MHz, 150 kW Booster Amplifier", TRIUMF Design Note TRI-DN-95-03-07, Sept. 94.
- [2] Micro-Cap IV, Electronic Circuit Analysis Program, Spectrum Software 1992.

STUDY OF 14 GHZ VLEPP KLYSTRON WITH RF ABSORBING DRIFT TUBES

G.V. Dolbilov, N.I. Azorsky, A.A. Fateev, N.I. Lebedev, V.A. Petrov, V.P. Sarantsev,
V.S. Shvetsov, M.V. Yurkov

Joint Institute for Nuclear Research, 141980 Dubna, Moscow Region, Russia
V.E. Balakin, P.V. Avrakhov, V.I. Chashurin, S.Yu. Kazakov, N.A. Solyak, V.E. Teryaev
Branch of Budker Institute of Nuclear Physics, 142284 Protvino, Moscow Region, Russia

Results of experimental study of a wide-aperture relativistic klystron for VLEPP are presented. Investigations have been performed using the driving beam of the JINR LIA-3000 induction accelerator. To suppress self-excitation parasitic modes we have used technique of RF absorbing drift tubes. We have obtained 75 MW of output power in a long pulse (250 ns) and 100 MW – in a short pulse (50 ns).

I. Introduction

To achieve a high output power of X-band klystron (~ 100 MW) at a moderate value of the emittance of the driving beam, the aperture of the klystron should be done as large as possible. On the other hand, at increasing the aperture, the frequencies of the parasitic modes become quite close to the operating frequency and their increments grow with the beam current which makes the problem of the parasitic oscillation suppression more complicated. Our experience have shown that standard techniques to suppress parasitic oscillations (the use of the wave chokes and the technique of permanent change of the phase velocity of the parasitic modes to decrease the interaction region of the beam with parasitic modes) do not provide the desired results, especially, in the case of a high gain ($\sim 70 - 80$ dB) [2], [3].

In papers [2], [3] we have proposed another idea to suppress parasitic oscillations which consists the use of RF absorbing drift tubes for distributed suppression of parasitic oscillations. We have upgraded the 11 mm aperture klystron with RF absorbing insertions and obtained encouraging results: the self-excitation modes have been suppressed and we have achieved the value of the output RF power about of 45 MW at the beam current $I \sim 150$ A which corresponds to the designed value of the klystron efficiency $\sim 30\%$. A damage of output structure and wave transformer due to high RF power forced us to stop experiments with this klystron [3].

In this paper we present the results of amplification experiments with wide-aperture (15 mm) VLEPP klystron upgraded with absorbing drift tubes.

II. Experimental setup

Parameters of the klystron are presented in Table 1. Peculiar feature of this klystron is that it has large aperture of drift tubes (15 mm). This helps to increase acceptance of the klystron. Nevertheless, there is one harmful consequence of a large aperture – the ground H_{11} waveguide mode is not cut-off one for this klystron. As there are always misalignments of the elements of the klystron, this results in self-excitation of the klystron on the

ground H_{11} mode at 14 GHz.

Investigations have been performed at JINR using the driving beam of LIA-3000 induction accelerator (energy 1 MeV, beam current up to 300 A, beam emittance 0.05π cm-rad, pulse duration 250 ns). We have the possibility to measure the beam current at the accelerator exit, entrance and exit of the klystron and the beam current losses inside the klystron. To obtain a more detailed information about the RF radiation, we have used beam collector in a form of circular waveguide [4].

To study the beam dynamics in the focusing system we have screened the beam from the electromagnetic structure of the klystron by a thin-wall Ti tube. Measurements have shown that there were no losses of the current in the buncher and the output structure. The value of the beam current in the collector was 300 A.

Investigations of the self-excitation regime have shown that

Table I
Parameters of wide-aperture VLEPP klystron

General parameters	
Beam voltage	1 MeV
Beam current	250 A
RF frequency	14.0 GHz
Power gain	80 dB
RF peak output power	100 MW
Efficiency	40 %
Focusing system	
Type of magnets	Permanent magnet
Max. Magnetic field	4.5 kGs
Period	64 mm
Number of periods	14.5
Acceptance	0.1π cm-rad
Buncher	
Drift tube diameter	15 mm
Length of drift section	52 mm
Number of drift sections	10
Length of cavity	12 mm
Number of cavities	11
Mode of operation	π
Output structure	
Mode of operation	$\pi/2$
Number of cells	22
Length	110 mm
Aperture	20 mm

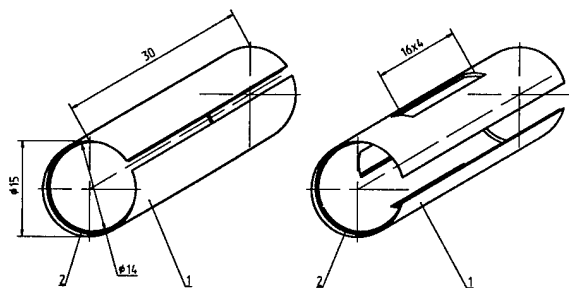


Figure 1. Scheme of RF absorbing insertions. Here (1) – metal foil, (2) – RF absorbing layer. Insertion in the right-hand side is placed together with RF filter 6 (see Fig.2).

there exists strong self-excitation of parasitic oscillations in the klystron at frequency bands:

$$13.9 \text{ GHz} \lesssim f \lesssim 14.15 \text{ GHz}, \quad f_1 = 14.04 \text{ GHz}$$

$$16.3 \text{ GHz} \lesssim f \lesssim 16.50 \text{ GHz}, \quad f_2 = 16.40 \text{ GHz}$$

and their harmonics [4]. Application of standard techniques to suppress the self-excitation was ineffective due to a high gain and a wide aperture of the klystron [4]. The presence of the signal from master oscillator (TWT) does not change the situation.

III. Upgrading of the klystron with RF absorbing drift tubes

In papers [2], [3], [4] we have developed an idea to suppress parasitic oscillations which consists the use of RF absorbing drift tubes for distributed suppression of parasitic oscillations. The main idea of this approach is to find such a klystron design where the increments of parasitic modes are less than their attenuation in the klystron. We have realized this concept in the following way. We have developed technology of RF attenuating insertions and placed them inside the drift tubes of the klystron (see Figs.1 and 2). We have studied several methods to obtain absorbing materials. Investigations have shown that glass-carbon materials are more simple for manufacturing and use in our equipment.

Such a distributed suppression filter provides significant attenuation of the parasitic modes and does not perturb the klystron operating mode [4]. Operating experience has shown that insertions do not affect vacuum conditions and are stable to the heat and radiation load.

We have expected also that the insertions may cause resistive instabilities of the beam. Nevertheless, thorough investigations of the beam dynamics have not shown any evidence of such instabilities.

In the same way as it has been described in the previous section, we have performed the study of the self-excitation mode of operation. It was found that all parasitic modes of the self-excitation have been totally suppressed.

IV. Study of amplification regime

After upgrading of the klystron with RF absorbing insertions, we have performed the study of amplification regime. The master signal was generated by the travelling wave tube. Typical

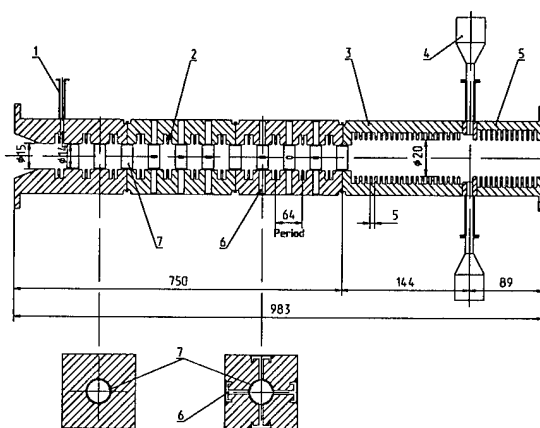


Figure 2. Layout of the klystron with RF absorbing insertions. Here (1) – input waveguide, (2) – resonators of buncher, (3) – output structure, (4) – RF load, (5) – RF filter for E_{01} mode, (6) – RF filters for H_{11} modes (14 GHz and 16.4 GHz), (7) – RF absorbing insertions (placed inside drift tubes).

oscillograms of amplification mode of operation are presented in Fig.3. It is seen from Fig.3a that there are no fluctuations of the beam current in the collector which indicates on the absence of the transverse beam instabilities. We have measured the frequency spectrum of the output radiation and have not observed any frequencies except of operating frequency 14 GHz.

At the beginning of operation at the level of output power of about 10 MW we have obtained that there are temporal instabilities in the form of output signal. At further increasing of the output power we have obtained shortening of the RF pulse with respect to the beam current pulse. This is connected with the RF discharges in the output structure. During RF training procedure [3], [4] we have gradually increased the value of the output power and after 3×10^5 pulses we have reached 75 MW output power within the pulse length of 250 ns. In Fig.4 we present amplitude characteristic of the klystron. It is seen that there is good agreement between theoretical and experimental results.

Upon achieving the level of output power of 75 MW the efficiency of training diminished significantly. short pulse (50 ns) we have achieved the value of the output RF power about of 100 MW at the beam current $I \sim 290$ A.

V. Conclusion

In this paper we developed the concept of the klystron with distributed suppression of parasitic modes. Peculiar feature of the present experiment is that we proved experimentally a possibility to construct wide-aperture klystrons with aperture comparable with the RF wavelength. Such a klystron design possesses significant advantages with respect to standard design revealing perspective of increasing operating current and, as a result, peak output power. We believe that wide-aperture klystrons with RF absorbing drift tubes can form a novel direction in the design of short RF wavelength klystrons.

Acknowledgments

We wish to thank A.M. Biryukov, V.I. Klementyev, V.V. Kosukhin, A.F. Kratko, N.A. Leonov and V.I. Skorpukhin for tech-

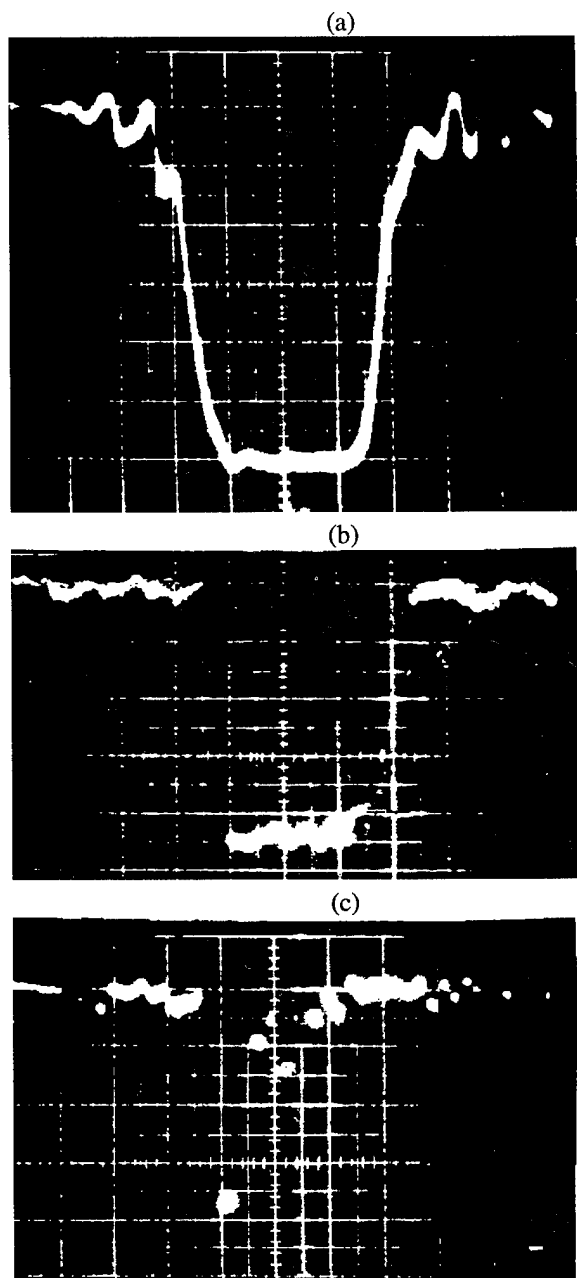


Figure 3. Oscillogram of the amplification regime. Here (a) - the beam current in collector, (b) - RF signal after RF training cycle ($P = 75$ MW), (c) - RF signal at the beginning of the next RF training cycle (maximum corresponds peak power of 100 MW)

nical assistance in preparing and performing experiment.

References

- [1] N.I. Azorskiy et al., "VLEPP Klystron Activity at Dubna", Proc. of the International Workshop on Pulsed RF Power Sources for Linear Colliders (July 5-9, 1993, Dubna, Russia), p.143
- [2] N.I. Azorskiy et al., "Study of the 14 GHz relativistic klystron for VLEPP", presented at 17th International Linac Conference (Tsukuba, Japan, 1994).
- [3] G.V. Dolbilov et al., "Study of 14 GHz VLEPP Klystrons with 11 and 15 mm Aperture", presented at the Workshop

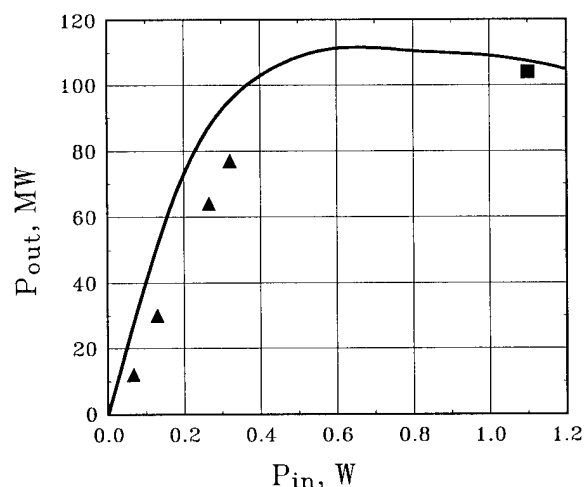


Figure 4. Amplitude characteristic of the klystron. Here solid curve - theoretical calculations at $I = 250$ A, \blacktriangle - output power in a long pulse (250 ns) and \blacksquare - output power in a short pulse (50 ns).

on Pulsed RF Sources for Linear Colliders (Montauk, Long Island, New York, 1994)

- [4] G.V. Dolbilov et al., "Wide aperture VLEPP klystron with absorbing drift tubes" presented at the 6th International Workshop on Linear Colliders (Tsukuba, Japan, 1995)

24-MW, 24- μ s PULSE RF POWER SUPPLY FOR LINAC-BASED FELs

E. Oshita, Y. Morii, S. Abe, S. Okuma, K. Wakita and T. Tomimasu

Free Electron Laser Research Institute, Inc.(FELI): 4547-44, Tsuda, Hirakata, Osaka 573-01, Japan

I. Ito, Y. Miyai, K. Nakata and M. Hakota

Nissin Electric, Co., Ltd.: 47, Umezu-Takase-cho, Ukyo-ku, Kyoto 615, Japan

SUMMARY

Two infrared free electron lasers (FELs) of the FELI are operating using S-band 80-MeV linac with a thermionic gun and a 165-MeV linac and UV-FEL facility are under construction. Since an RF system for linac-based FELs is required of long pulse duration and high quality, a improved pulse klystrons (Toshiba E3729) has been operated in 24-MW, 24- μ s pulse mode for the FELI linac. Our klystron modulator developed by the FELI and NISSIN Electric Corp. has a PFN consisted of 4 parallel networks of 24 capacitors and 24 variable reactors. The line switch is consisted of 30 light triggered thyristors (Toshiba SL1500GX22). A saturable reactor is used in series to protect 30 thyristors from overvoltage caused by a delay of thyristor's turn-on time. The flatness of modulator pulses is 0.08%_{p-p} at 20-MW, 24- μ s pulse operation. The 24- μ s stable RF pulses can increase a conversion efficiency from electron beam power to FEL power at short wavelength FELs. Saturated FEL outputs have been observed for 18- μ s at 5.5- μ m FEL oscillation and for 12- μ s at 1.88- μ m FEL oscillation, respectively.

INTRODUCTION

The FELI is now operating two IR-FELs using an 80-MeV linac with a thermionic gun and is constructing a 165-MeV linac and a UV-FEL facility. It is essentially necessary for linac-based FELs using pulsed rf sources to get a stable and long rf pulse from a klystron. A stable and long rf pulse sources enables to yield a stable and saturated FEL pulse source. The FELIX group has succeeded in keeping a pulsed rf source stable to accelerate a 22.5-MeV, 10- μ s beam with an

energy spread of 0.5%[1]. For this purpose, we have developed a 24-MW, 24- μ s pulse power modulator for an S-band klystron (Toshiba E3729) at three operation modes shown in Tab. 1. Mode 1 and Mode 2 are for FEL generation and Mode 3 is for injection to a storage ring.

Table 1 Parameters of Klystron Modulator

Mode	Mode 1	Mode 2	Mode 3
Output voltage(kV)	285	304	390
Output current(A)	280	305	477
Pulse width(μ s)	24	12.5	0.5
Flat-top(_{p-p})(%)	0.08	0.08	1.5
Stability(%)	0.08	0.08	1.5
Repetition(pps)	10	10	10
Rise time(μ s)	2	2	2
Fall time(μ s)	3	3	3.5

*Rise and fall time is measured from 10-90% of the output pulse.

KLYSTRON MODULATOR

Fig. 1 shows the circuit diagram of the klystron modulator. This modulator is consisted of the charging section using converter-inverter, the pulse forming network(PFN) section with 4 parallel L-C circuit, the main switch section using light triggered thyristors, and the mounting tank for the klystron to supply high voltage by a pulse transformer. The output voltage is measured at the secondary side of the pulse transformer by a capacitive divider. Details of these sections are as follows.

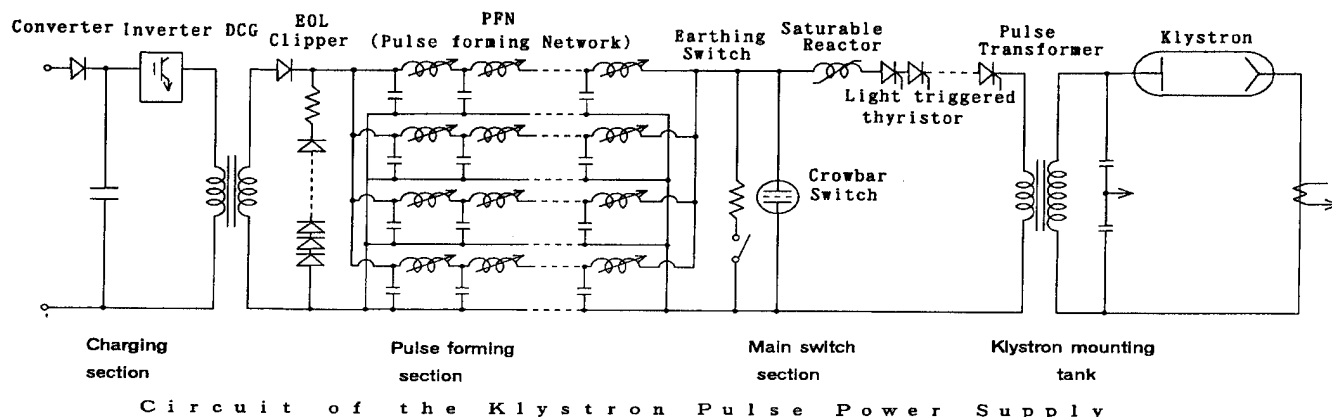


Fig. 1 Circuit Diagram of Klystron Modulator

(1) Charging Section

We use a converter-inverter charging circuit instead of IVR~De-Qing one, because De-Qing one has the following problems.

i) A charging voltage of the PFN involves about 0.2% fluctuation due to an input voltage.

ii) Pulse repetition rate is low (10pps). Therefore, the scale of charging section becomes bigger due to a large time constant at resonant charging.

Therefore, our inverter is consisted of 5 cascades at 15kHz and we have achieved a high stability within $\pm 1 \times 10^{-4}$ of charging voltage.

(2) Pulse Forming Section

The PFN is consisted of 4 parallel networks and the output pulse width are 24 μ s, 12.5 μ s and 0.5 μ s at mode 1, 2 and 3, respectively. Because of the 4 parallel PFNs, an inductance of each variable reactors can be designed to be larger than that of the single PFN. Therefore, effects of the wiring inductance to the modulator pulse waveform is small. Each reactor of the PFN is adjustable by means of a remote control system using a motor driving plunger. The minimum adjustable amount of the PFN reactor is 0.005% and the maximum adjustable span is 45%. Therefore, the adjustment of output waveform has been easily performed, and a 0.08% flat-top of output pulse waveform has been achieved. If the klystron has break down during a high voltage is applied, the PFN capacitors suffer from large reverse voltage. To reduce this damage, an EOL (End of line) clipper circuit is set and the reliability of the modulator becomes high.

(3) Main Switch Section

We have used the light triggered thyristor (Toshiba SL1500GX22, 30series) stack as the main switch for keeping the output voltage stable. Generally speaking, a thyatron is suitable for switching of high voltage and large current. But in this case, the thyatron is not suitable because a change of its resistance is large ($\geq 0.1\%$) during the conduction time.

However, in order to use the light triggered thyristors, we have solved the following problems.

i) The value of dI/dt is more ten times ($\sim 3000A/\mu s$) than the thyristor's specification.

ii) It is necessary to trigger 30 thyristors simultaneously as a switch.

Before adopting light triggered thyristor, we have tested dI/dt of the same device. The result was that the thyristor was broken down at about 1700A/ μ s. Therefore, we have set a saturable reactor in series with the light triggered thyristors to keep a counter-measure to a delay of each thyristor's turn-on and a suitable conduction space at the switching time. The use of the saturable reactor enables us its running under a hard condition of $dI/dt \sim 3000A/\mu s$. On the other hand, the use of the light triggered thyristors makes it easy to insulate the gate drive circuit and to withstand to a high reverse voltage.

PERFORMANCE

1. Light Triggered Thyristors

Fig. 2 shows the time response of the resistance of light triggered thyristors at the mode 1. After the main current reaches the peak, the resistance is about 0.6-0.3 Ω /30devices, that is, 20m Ω -10m Ω /1 device. The resistance at the whole conduction is about 0.5m Ω (at current is 4kA). Therefore, the conduction space of this thyristor is about 1/40-1/20 of the whole conduction at the mode 1. Though we have already tried 3×10^7 shots under this condition, there are no any troubles at all.

It is easily understood from Fig. 2 that the resistance of the light triggered thyristor decreases in micro-second order, so we can adjust the waveform so as to cancel this effect.

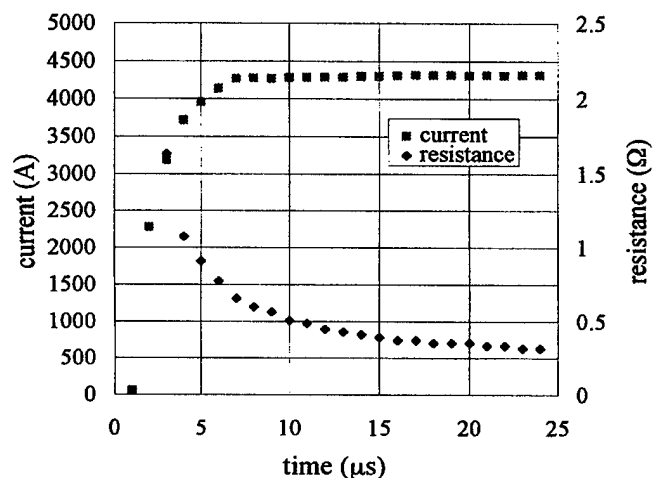


Fig. 2 Time Dependence of the Resistance of Light Triggered Thyristor

2. Klystron Modulator and Klystron

Table 2 shows the characteristics of the output at three modes and Figs. 3 and 4 show the waveforms of the output voltage at the mode 1.

Table 2 Performance of Klystron Modulator and Klystron E3729

Mode	Mode 1	Mode 2	Mode 3
Output voltage(kV)	285	304	390
Output current(A)	280	305	477
Pulse width(μ s)	23.2	12.0	0.5
Flat-top _(p-p) (%)	0.08	0.08	0.3
Stability(%)	0.07	0.06	0.15
Repetition(pps)	10	10	10
Rise time(μ s)	2.0	2.5	2.0
Fall time(μ s)	4.5	6.5	6.4
RF output(MW)	24	34	70

from E3729

*Rise and fall time is measured from 10-90% of the output pulse.

The rise time of the output is about 2-3 μ s. This shows that the light triggered thyristors can withstand for the rise

time of micro-second order due to the effect of the saturable reactor. Fig. 4 shows the flatness of the modulator pulses is kept within 0.08%_{p-p} at 24-MW, 24-μs pulse operation.

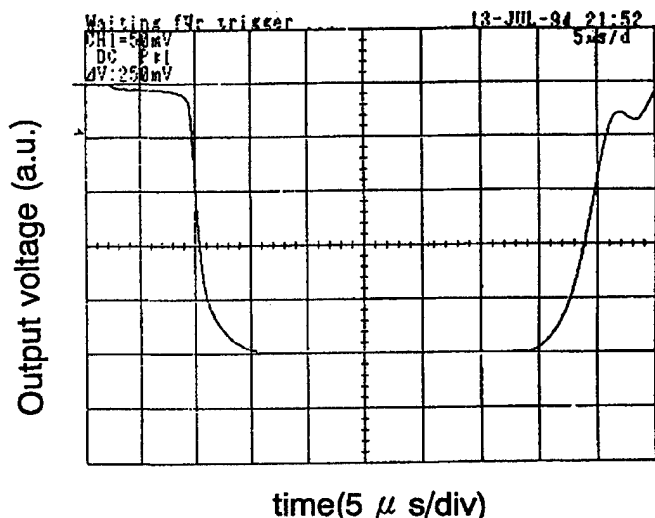


Fig. 3 Waveform of Output Voltage at the Mode 1

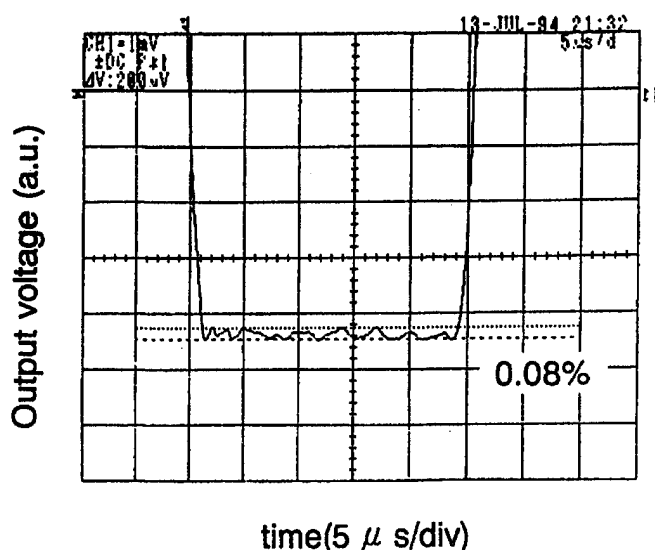


Fig. 4 Expanded View of Top Part of the Waveform shown in Fig. 3

3. Modulator Pulse and 24-μs rf Pulse

Fig. 5 shows the waveforms of the modulator current pulse and 24-μs rf pulse. Tiny ripples seen on the waveforms are due to white noise of the sampling oscilloscope (TDS460-Tecktronics).

4. 24-μs rf Pulse and 5.5-μs FEL Macropulse

Fig. 6 well demonstrates a saturated 5.5-μs FEL macropulse continues for a duration of 18-μs at the 24-μs rf pulse operation[2]. This is a good example to show that a stable and long rf pulses can improve a conversion efficiency from electron beam power to FEL power.

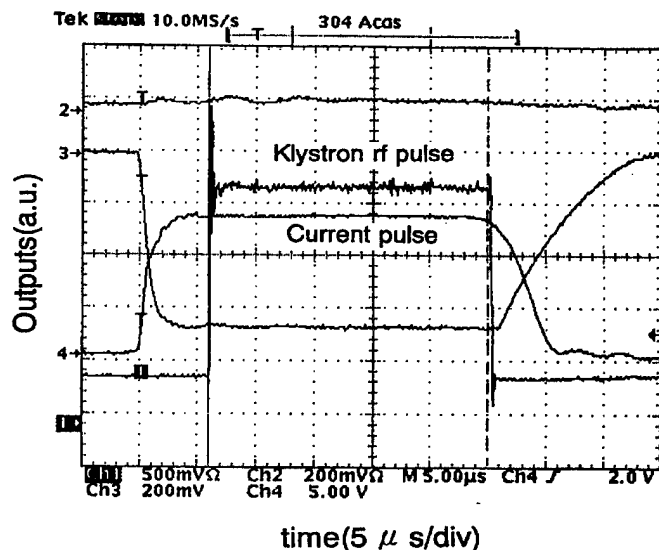


Fig. 5 Modulator Pulse and 24-μs rf Pulse

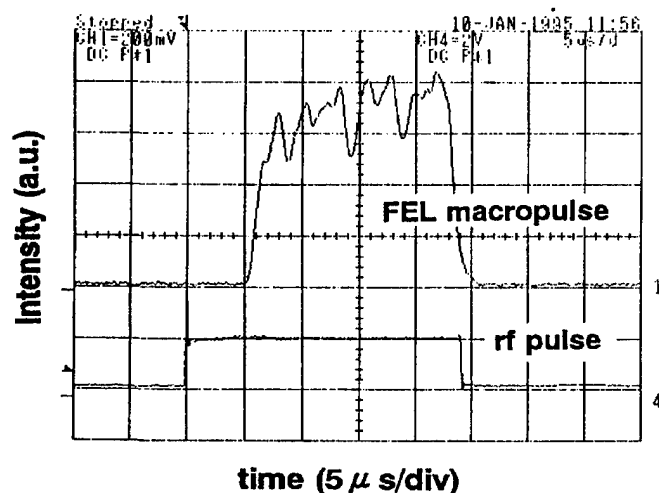


Fig. 6 24-μs rf Pulse and 5.5-μs FEL Macropulse

CONCLUSION

A 24-MW, 24-μs pulse rf power supply has been developed for linac-based FELs. The flatness of the klystron modulator pulses is kept within 0.08% at 24-MW, 24-μs pulse operation by using the light triggered thyristors and remote control systems for variable reactors of the PFNs. Experimental data on FEL oscillations at 5.5μm have demonstrated that stable and long rf pulses can yield saturated and long FEL macropulses can improve a conversion efficiency from electron beam power to FEL power at short wavelength FELs.

REFERENCES

- [1] D. A. Jaroszynski, et al., Nucl. Instr. Meth., A331, 52 (1993)
- [2] T. Tomimasu, et al., in this Proceedings

INITIAL OPERATION OF AN X-BAND MAGNICON AMPLIFIER EXPERIMENT

S. H. Gold, A. K. Kinhead,* A. W. Fliflet, and B. Hafizi,† Beam Physics Branch, Plasma Physics Division, Naval Research Laboratory, Washington, DC 20375 USA

We present a progress report on a program to develop a high-power second harmonic magnicon amplifier at 11.4 GHz for linear accelerator applications. The experiments are being carried out on the NRL Long-Pulse Accelerator Facility using a plasma cathode to create the electron beam. Typical beam parameters are 500–700 kV, 170–250 A, 5.5 mm diameter, with a ~300 nsec voltage flat-top. The accelerator operates single pulse with a $\sim 10^{-2}$ Hz repetition rate. A complete five cavity magnicon circuit was designed via computer simulation, fabricated, and cold tested. In early tests, a low power saturation effect was observed in the deflection cavities, apparently due to plasma formation caused by the diode x-ray flux and by inadequate vacuum conditions. Following a major effort to improve the vacuum and surface conditions, recent experiments have shown that it is possible to “burn through” this low power saturation effect, and achieve high fields in the 5.56 GHz penultimate cavity when the drive cavity is excited by a 10 kW input signal. Synchronous with the penultimate cavity signal, a 100–200 nsec multi-MW frequency-doubled output pulse is observed at 11.12 GHz.

I. INTRODUCTION

The magnicon [1,2] is a scanning-beam microwave amplifier that is under consideration as an alternative to klystrons in powering future high-gradient linear electron accelerators. Scanning-beam amplifiers modulate the insertion point of the electron beam into the output cavity in synchronism with the phase of a rotating rf wave. This synchronism creates the potential for an extremely efficient interaction in the output cavity, since every electron will in principle experience identical decelerating rf fields. In the magnicon, the output interaction is gyrotron-like, and requires a beam with substantial transverse momentum. The transverse momentum is produced by spinning up the electron beam in a sequence of TM_{110} deflection cavities, the first driven by an external rf source. The output cavity employs an rf mode that rotates in synchronism with the deflection cavity modes. As a result, the beam entering the output cavity is fully phase modulated with respect to the output cavity mode. The optimum magnetic field in the deflection cavities is approximately twice the cyclotron resonant value at the drive frequency, while the output cav-

ity operates as a first harmonic cyclotron device. These two constraints lead naturally to the design of a second-harmonic amplifier, in which the output cavity operates at twice the frequency of the deflection cavities and employs a TM_{210} mode (see Fig. 1). This is the configuration that is under investigation at NRL, as well as at the Budker Institute of Nuclear Physics (INP).

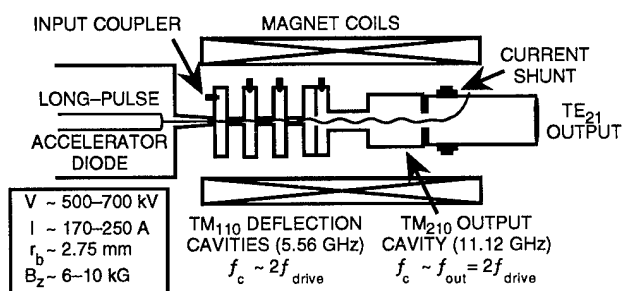


Fig. 1. NRL X-band magnicon schematic.

II. MAGNICON DESIGN

Following a two-deflection cavity gain experiment that demonstrated ~15 dB of gain and good agreement with theoretical predictions [3], a complete 11.4 GHz frequency-doubling magnicon amplifier circuit as illustrated in Fig. 1 was designed via computer simulation [4]. These simulations were designed to produce a pitch angle of $\sim 45^\circ$ at the end of the penultimate cavity, i.e., $\alpha = v_\perp/v_\parallel \sim 1$, where v_\perp and v_\parallel are the electron velocity components perpendicular and parallel to the applied magnetic field. Both single particle and 2-mm-diam. simulations achieved efficiencies of ~56%. (The 2-mm beam corresponds to the predicted performance of the INP thermionic magnicon electron gun for a 6.5 kG magnetic field.) However, the 5.5-mm-diam. simulation, corresponding to the present diameter of the NRL beam, achieved an efficiency of only ~23% due to the substantial energy spread and phase-mixing of the beam entering the output cavity.

III. EXPERIMENTAL RESULTS

The complete five-cavity circuit, including a drive cavity, two gain cavities, and a two-section π -mode penultimate cavity, all operating at 5.56 GHz in the TM_{110} mode, followed by an 11.12 GHz TM_{210} -mode output cavity, was fabricated, cold tested, calibrated, and placed under

* SFA, 1401 McCormick Dr., Landover, MD 20785

† Icarus Research, P.O. Box 30780, Bethesda, MD 20824

vacuum on the NRL Long-Pulse Accelerator (LPA) Facility. Each of the cavities has a calibrated rf pickup, and the output from the last cavity can also be monitored at the end of the experiment using microwave pickups. The power is coupled out of the output cavity through an iris, and simultaneously converted to the TE_{21} mode which is then radiated through a 3.5-cm lucite window. The various rf signals are measured using calibrated attenuators and crystal detectors. The first cavity is driven by rf from a tunable C-band magnetron.

Initial tests were carried out at the design voltage and current (500 kV, ~170 A), and at magnetic fields ranging from 6.5–10 kG. The beam is produced from a velvet cathode by plasma-induced field emission. The voltage pulse consists of a 100 nsec risetime, a ~300 nsec flattop, and a 500 nsec falltime. During the voltage falltime, the diode impedance collapses, often resulting in substantially larger currents than during the voltage flattop. In addition, the deflection cavity gain increases at lower voltage. As a result, oscillation often occurs during the trailing voltage pulse. However, the signal at the voltage flattop seems to correspond to stable amplification. The initial tests of the complete magnicon circuit demonstrated high gain (~40 dB) in the deflection cavities at low values of the drive signal, but showed a nonlinear saturation effect in the deflection cavities at higher drive signals. As the drive power was increased, the signals in each of the deflection cavities appeared to saturate at ~1–10 kW. This saturation effect appears to be due to plasma formation in the cavities, initiated by the diode x-ray pulse, generated due to inadequate vacuum and surface conditions, and sustained by the microwaves. This plasma constitutes a nonlinear load on the cavities, clamping the microwave signal without completely shorting out the cavities. As a result, only small signals (<100 kW) were seen from the output cavity.

A major effort was made to improve the vacuum, including a redesigned vacuum manifold that improved the pumping of the deflection cavities by an order of magnitude. In addition, the cavities were disassembled, thoroughly cleaned with detergents and solvents, reassembled, and put through a low-temperature (~120° C) bakeout. Following this, a new set of measurements were begun. The low power saturation effect was still seen. However, at higher currents, voltages, and magnetic fields (e.g., 650 kV, 300 A, 11 kG), a new regime of behavior was observed in the deflection cavities. Greatly increased signal levels were seen in the second and third deflection cavities (with a nominal 1 kW signal in the first cavity), with the third cavity signal rising rapidly (~30 nsec) to approximately 1 MW, before suffering an rf breakdown. The penultimate cavity also reached high power (~100 kW) in a short pulse, before breaking down.

The next step was to assemble a heterodyne frequency diagnostic to measure the spectrum of the output radiation. This diagnostic combined the output signal with a local oscillator in a double-balanced mixer, and then acquired the difference signal using a Tektronix DSA602 digital oscilloscope with an analog bandwidth of ~1 GHz, a 2 GS/s digitizing rate, and an FFT (fast fourier transform) capability. By varying the local oscillator frequency, spectral components can be determined to a precision of a few MHz.

Using this diagnostic, a search was made for the predicted magnicon output frequency of 11.12 GHz. At the higher magnetic fields (~11 kG) that maximized the deflection cavity gain, only low frequency signals (<9.5 GHz) were observed. However, as the magnetic field was reduced, the predicted magnicon line appeared in the emission spectrum. Under a variety of conditions, the only spectral peak at frequencies greater than 9.5 GHz was a strong feature at 11.12 GHz. In order to assure that only this frequency component would be measured, K_u -band waveguide-to-coax adapters, with a 9.5 GHz cutoff frequency, were used as microwave pickups. Two pickups, one stationary, and one that swept on an 81-cm-radius arc about the output window, were used to measure the radiation antenna pattern. An anechoic enclosure was built around the pickups and the output window. The results for the E_θ scan are shown in Fig. 2. Each point is the average of three experimental shots, and the value from each shot is normalized by the power at the stationary pickup. A similar pattern was measured in E_r . Fig. 2 is in good agreement with the calculated far-field pattern of the TE_{21} mode. Using this data, one can relate the power received by a K_u -band pickup at the angular peak of the pattern to the total power radiated into 2π . The total power received by the pickup is calculated from the signals received by calibrated crystal detectors by determining (in a one-step transmission measurement) the total attenuation due to coaxial cable loss and fixed and variable attenuators.

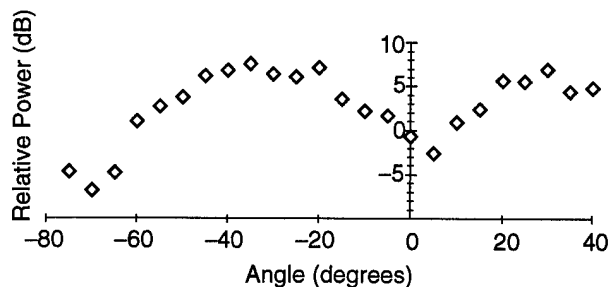


Fig. 2. Angular scan of E_θ component of antenna pattern.

Next, a scan of output power versus magnetic field was made with one pickup at the angular maximum of the antenna pattern. The results are shown in Fig. 3. The

power is seen to peak in the vicinity of 7.3 kG. Using the procedure outlined above, the largest signals correspond to a total radiated power of 99 dBm, or 8 MW. The overall uncertainty in this number is still under investigation, but is estimated as ± 3 dB. At 7.3 kG, the typical beam current is 225 A at 650 kV. Accordingly, the best estimate of the magnicon efficiency is 5.5%. Figure 3 also shows the results from time-dependent simulations of the output cavity, assuming $\alpha=0.3$ [5]. This α was chosen to yield approximately the same peak power as the experimental value. It is noteworthy that the simulations predict high power output over a much broader range of magnetic fields ($P > 2$ MW for $6.5 < B < 11$ kG) than is observed in the experiment.

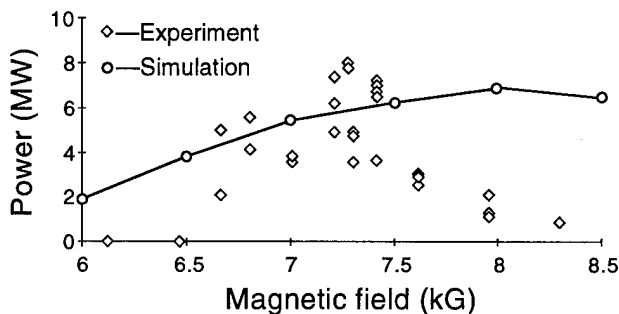


Fig. 3. Output power vs magnetic field.

The microwave measurements are still in progress. At this point, it is known that the signal in the output cavity is precisely $2\times$ the frequency of the penultimate cavity signal. Also, at 7.5 kG, the shot-to-shot variation in the timing of the penultimate cavity signal is tracked by the timing of the output cavity signal. Furthermore, the penultimate cavity signal is only present (during the voltage maximum) if the 5.56 GHz drive signal is present in the first deflection cavity. However, we have not yet determined the gain in each of the cavities, the bandwidth of the interaction, or the degree to which the output signal is frequency or phase locked to the drive signal. We have also not determined the reason for the rapid decrease in output power as the magnetic field is increased (far more rapid than predicted by simulations) or the significance of the low frequency signals observed at higher magnetic fields.

IV. CONCLUSIONS

The NRL magnicon experiment previously demonstrated the basic magnicon gain mechanism in two-deflection-cavity experiments. However, those experiments were forced to operate at very modest power levels to avoid an unanticipated gain saturation effect, that occurred as intracavity powers approached the kilowatt level. In the test of the full five-cavity magnicon circuit, the same gain satu-

ration effects were observed despite substantial improvements in the overall vacuum system. Experimental tests demonstrated that the saturation was due to plasma formation, caused by inadequate vacuum and surface conditions, and initiated by the large x-ray flux from the accelerator diode region. A program of progressively improving the vacuum conditions, while at the same time pushing the envelope of magnicon parameters by operating at higher current, voltage, and magnetic field, has demonstrated that this low power saturation effect can be "burned through" in short (~ 50 – 200 nsec) high power pulses in the deflection cavities, generally followed by rapid rf breakdown. Under the right combination of experimental parameters (650 kV, 225 A, 7.3 kG magnetic field), a large amplified signal is observed in the penultimate cavity at 5.56 GHz, and synchronous with it, a ~ 100 nsec FWHM frequency-doubled output pulse at 11.12 GHz. Based on a scan of the far-field antenna pattern and absolute calibration of the detected microwave signals, the best shots correspond to $8 \text{ MW} \pm 3 \text{ dB}$ at an efficiency of $\sim 5\%$.

Work is in progress to further characterize and optimize the operation of the present magnicon experiment. However, it is evident that the NRL program must transition to a thermionic diode, a cw magnet, and a rep-rated modulator in order to demonstrate the feasibility of efficient, long-pulse, high-duty-factor magnicon amplifiers at 11.4 GHz for linear accelerator applications.

V. ACKNOWLEDGMENTS

The authors are grateful for many useful discussions with W. M. Manheimer, A. Fisher, and R. Fischer, for the expert technical assistance of C. A. Sullivan in earlier phases of this program, and for the design collaboration with O. A. Nezhevenko and V. P. Yakovlev of the INP. This work was supported by the U.S. Department of Energy under Interagency Agreement DE-AI02-94ER40861.A000, and by the Office of Naval Research.

VI. REFERENCES

- [1] M.M. Karliner, *et al.*, *Nucl. Instrum. Methods Phys. Res.* **A269**, 459–473 (1988).
- [2] O.A. Nezhevenko, *IEEE Trans. Plasma Sci.* **22**, 756–772 (1994).
- [3] S.H. Gold, *et al.*, *IEEE Trans. Plasma Sci.* **21**, 383–387 (1993).
- [4] O.A. Nezhevenko, V.P. Yakovlev, S.H. Gold, and B. Hafizi, *IEEE Trans. Plasma Sci.* **22**, 785–795 (1994).
- [5] A.W. Fliflet and S.H. Gold, *Phys. Plasmas*, in press.

THE EFFECTS OF TUNING AND TERMINATING ON THE OPERATING MODE OF MULTI-CELL COUPLED CAVITY*

Zubao Qian, Fermi National Accelerator Lab, Box 500, Batavia, IL 60510 USA

I. INTRODUCTION

The coupled resonator chain is widely used as an accelerating unit. Many people have successfully treated this kind structure with different ways in lossless case to understand the steady state behavior of the chain. A chain of N coupled resonators has N dispersion resonant modes which has different properties. In general, when losses and frequency error are present in cavity the solution are no longer the simple eigenfunction of the homogeneous equations, but are superpositions of all the eigenfunctions. Many such structures, especially superconducting coupled cavity, have been operated in the " π mode" as accelerator elements. According to the theoretical analyze in lossless case, pair-mode operating means group velocity, which is relative to the power flowing in the structure and the energy stored per unit length of the structure, is zero and in steady state no power of this mode can flow in the cavity. Strictly speaking, operation in the π mode is not possible. In practical case any cavity has losses, the energy must be supplied through excitation of adjacent modes to compensate for losses and there are resultant phase changes in the cavity. The phase deviation from π radians per cell is given by [Nagle (1964), Knapp (1964), and Smith (1964)].^[1]

$$\Delta\phi_{(n,n-1)} = [2(1-k)^{\frac{1}{2}} / Q_k](N-n+\frac{1}{2})$$

Any machining error also will produce frequency and phase deviation from theoretical modes. As many papers described what was so called " π mode" only means the field in the cavity has been flattened by tuning individual cell frequency.^[2,3,4,5] It is true the π mode has flat field distribution, but the cavity with flat field may not exactly operate at π mode. This paper discusses the affection of the terminated cell and tuning on operating mode of coupled cavity at an ideal steady state by using eigenequations and perturbation theory.

II. THE SOLUTION OF THE EIGENEQUATION FOR TWO KIND TERMINALS

For the coupled resonator chain there are two different kind terminals, two half end cell terminal which put the shorted plate at a symmetric plan and two full end cell terminal. Many of the electrical properties of a chain with $N+1$ coupled resonators have been investigated by considering the properties of $N+1$ coupled circuits. For $N+1$ cell cavity the circuit equations are

$$X_0(1 + \frac{\omega_0}{jQ\omega} - \frac{\omega_0^2}{\omega^2}) + mX_{N-1} = I_N$$

$$X_N(1 + \frac{\omega_0}{jQ\omega} - \frac{\omega_0^2}{\omega^2}) + mX_{N-1} = I_N$$

$$X_n(1 + \frac{\omega_0}{jQ\omega} - \frac{\omega_0^2}{\omega^2}) + \frac{k}{2}(X_{n-1} + X_{n+1}) = I_n \quad (n=1, 2, \dots, N-1)$$

Here $\omega_0^{-2} = 2LC$; $X_n = I_n(2L_n)^{\frac{1}{2}}$; $QR = 2\omega_0 L$, In the lossless and no generator included case $Q \Rightarrow \infty$ and $I_n = 0$. There are $N+1$ solutions to the homogeneous equation of the form. For half end cell terminated, $m=K$, the solutions are

$$X_n^{(q)} = (const) \cos \frac{qn\pi}{N} e^{j\omega_q t}; \quad \omega_q^2 = \omega_0^2 / (1 + k \cos \frac{q\pi}{N});$$

$$\omega_q = \omega_0(1 + k \cos \varphi)^{-\frac{1}{2}}; \quad \varphi = q\pi/N \quad (q=0, 1, 2, \dots, N)$$

The lowest mode is $q=0$, $\omega_{q=0}^2 = \frac{\omega_0^2}{1+k}$; the highest mode is $q=\pi$, $\omega_{q=\pi}^2 = \frac{\omega_0^2}{1-k}$ ($0, \pi$ mode). The group velocity is

$$v_g = L \frac{d\omega}{d\varphi} = \frac{1}{2} Lk \omega_0(1 + k \cos \varphi)^{-\frac{3}{2}} \sin \varphi$$

(L the length of single cell)

It indicated that for half end cell terminated without loss or other adjustment the chain does have zero and π mode, but for both zero and π modes ($\varphi=0, \pi$) the group velocity $v_g=0$.

As above, for full end cell terminated, $m=k/2$ the solutions are

$$X_n^q = (const) \sin \frac{qn\pi}{(N+2)} e^{j\omega_q t};$$

$$\omega_q^2 = \omega_0^2 / (1 + k \cos \frac{q\pi}{(N+2)}); \quad \omega_q = \omega_0(1 + k \cos \varphi)^{-\frac{1}{2}};$$

$$\varphi = \frac{q\pi}{(N+2)} \quad (q=1, 2, 3, \dots, N+1).$$

The lowest mode $q=1$, $\omega_{q=1}^2 = \omega_0^2 / (1 + k \cos \frac{\pi}{(N+2)})$; and the highest mode $q=N+1$, $\omega_{q=N+1}^2 = \omega_0^2 / (1 + k \cos \frac{(N+1)\pi}{(N+2)})$. There is no zero and π mode, and the field amplitude along axis of the cavity operating in the highest mode is no longer uniform and tilts from the center of the cavity to ends, but if the single cell is the same, both with full and half end cell terminal the dispersion functions have same form. At an unperturbed case the field along axis of the cavity is flatness only when exactly operating at zero or π mode, this is why after the field was tuned flatness, one thinks cavity operating in the " π mode", as mentioned above it may be not right, because of perturbation.

III. PERTURBATION EQUATIONS AND FIRST ORDER SOLUTIONS OF COUPLED CIRCUITS

Since the π mode has a higher effective shunt impedance, most superconducting multi-cell cavities were demanded operating at " π mode". For full end cell terminated cavity there is no π mode, introducing some frequency error in single cell is needed to move the highest mode to " π mode". If the frequency ω_i error is small, it can be considered

*Work Supported By The U. S. Department of Energy under contract No. DE-AC02-76CH03000.

perturbation, the perturbation theory can be used to treat this kind problem.^[6] For simple, five full cell cavity has been treated. In ideal case and steady state, the circuit eigenfuctions of the cavity can be expressed as a matrix form as follow:

$$L = \begin{bmatrix} \lambda_1 & \frac{k}{2}\lambda_1 & 0 & 0 & 0 \\ \frac{k}{2}\lambda_2 & \lambda_2 & \frac{k}{2}\lambda_2 & 0 & 0 \\ 0 & \frac{k}{2}\lambda_3 & \lambda_3 & \frac{k}{2}\lambda_3 & 0 \\ 0 & 0 & \frac{k}{2}\lambda_4 & \lambda_4 & \frac{k}{2}\lambda_4 \\ 0 & 0 & 0 & \frac{k}{2}\lambda_5 & \lambda_5 \end{bmatrix}; X_n = \begin{bmatrix} X_{n1} \\ X_{n2} \\ X_{n3} \\ X_{n4} \\ X_{n5} \end{bmatrix}; LX=AX;$$

Here $\lambda_i = \omega_i^{-2}$; $A = \omega^{-2}$; L is an operator, A_n is the eigenvalues and X_n is the eigenvectors. In unperturbed case $\lambda_i = \lambda$ ($i=1, \dots, 5$), the solutions are ${}^0A_1 = \lambda(1 + \frac{\sqrt{3}}{2}k)$; ${}^0A_2 = \lambda(1 + \frac{1}{2}k)$; ${}^0A_3 = \lambda$; ${}^0A_4 = \lambda(1 - \frac{1}{2}k)$; ${}^0A_5 = \lambda(1 - \frac{\sqrt{3}}{2}k)$

$${}^0X_n = \begin{bmatrix} (\lambda - A_n)^4 - 3(\lambda - A_n)^2(\frac{k}{2}\lambda)^2 + (\frac{k}{2}\lambda)^4 \\ -(\lambda - A_n)^3(\frac{k}{2}\lambda) + 2(\lambda - A_n)(\frac{k}{2}\lambda)^3 \\ (\lambda - A_n)^2(\frac{k}{2}\lambda)^2 - (\frac{k}{2}\lambda)^4 \\ -(\lambda - A_n)(\frac{k}{2}\lambda)^3 \\ (\frac{k}{2}\lambda)^4 \end{bmatrix}$$

$${}^0X_1 = \begin{bmatrix} \frac{1}{2} \\ \frac{\sqrt{3}}{2} \\ 1 \\ \frac{\sqrt{3}}{2} \\ \frac{1}{2} \end{bmatrix}; {}^0X_2 = \begin{bmatrix} -\frac{1}{2} \\ -\frac{1}{2} \\ 0 \\ \frac{1}{2} \\ \frac{1}{2} \end{bmatrix}; {}^0X_3 = \begin{bmatrix} \frac{1}{2} \\ 0 \\ -\frac{1}{2} \\ 0 \\ \frac{1}{2} \end{bmatrix}; {}^0X_4 = \begin{bmatrix} -\frac{1}{2} \\ \frac{1}{2} \\ 0 \\ -\frac{1}{2} \\ \frac{1}{2} \end{bmatrix}; {}^0X_5 = \begin{bmatrix} \frac{1}{2} \\ -\frac{\sqrt{3}}{2} \\ 1 \\ -\frac{\sqrt{3}}{2} \\ \frac{1}{2} \end{bmatrix}$$

All eigenvectors are orthogonal each other, $X_i X_j = 0$ ($i \neq j$) and $X_i X_j = \text{const}$ ($i=j$) ($i, j=1, 2, \dots, 5$), the solutions of 5-cell cavity are the same as results calculated by SUPERFISH shown in Fig.1.

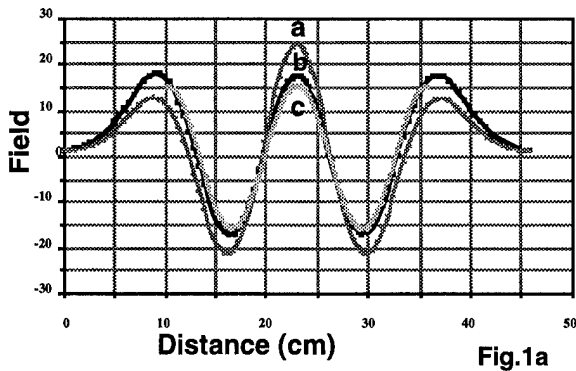


Fig.1a

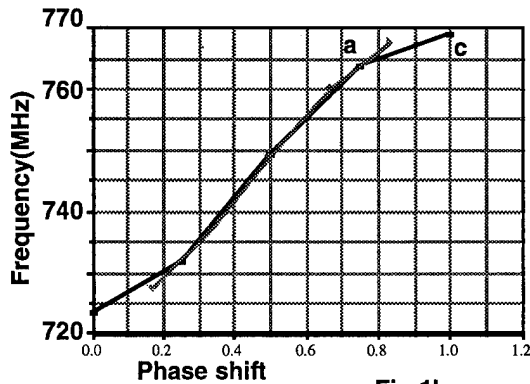


Fig.1b

Fig. 1: The field distribution and dispersion curve of a five-cell cavity calculated by SUPERFISH a) full end cell terminated without tuning b) full end cell terminated with tuning axial field flatness. c) half end cell terminated.

When the individual cell frequencies are not equal to each other but the deviation $\epsilon_i = \lambda_i - \lambda$ is small, $|\epsilon_i|/\lambda \ll 1$, (such as a full end cell cavity after tuning field flatness. If the central cell frequencies are equal, only needed to tuning full end cells) the operator L can be written as $L = L_0 + P$, L_0 is the unperturbed part of the matrix operator, P is the perturbed part, and the matrix elements of perturbation matrix

$Q_{ij} = {}^0X_i^+ P {}^0X_j$; and ${}^0X_i^+$, 0X_j are unperturbed eigenvectors.

$$L_0 = \lambda \begin{bmatrix} 1 & \frac{1}{2} & 0 & 0 & 0 \\ \frac{1}{2} & 1 & \frac{1}{2} & 0 & 0 \\ 0 & \frac{1}{2} & 1 & \frac{1}{2} & 0 \\ 0 & 0 & \frac{1}{2} & 1 & \frac{1}{2} \\ 0 & 0 & 0 & \frac{1}{2} & 1 \end{bmatrix}; P = \begin{bmatrix} \epsilon_1 & \frac{k}{2}\epsilon_1 & 0 & 0 & 0 \\ \frac{k}{2}\epsilon_2 & \epsilon_2 & \frac{k}{2}\epsilon_2 & 0 & 0 \\ 0 & \frac{k}{2}\epsilon_3 & \epsilon_3 & \frac{k}{2}\epsilon_3 & 0 \\ 0 & 0 & \frac{k}{2}\epsilon_4 & \epsilon_4 & \frac{k}{2}\epsilon_4 \\ 0 & 0 & 0 & \frac{k}{2}\epsilon_5 & \epsilon_5 \end{bmatrix}$$

Since most single periodic couple cavities operate in the highest mode, here i.e. mode 5 which so-called " π mode", only this mode has been calculated with first order approximation.

$$Q_{15} = (\frac{1}{4} - \frac{\sqrt{3}}{8}k)(\epsilon_1 - 3\epsilon_2 + 4\epsilon_3 - 3\epsilon_4 + \epsilon_5)$$

$$Q_{25} = (\frac{1}{4} - \frac{\sqrt{3}}{8}k)(-\epsilon_1 + \sqrt{3}\epsilon_2 - \sqrt{3}\epsilon_4 + \epsilon_5)$$

$$Q_{35} = (\frac{1}{4} - \frac{\sqrt{3}}{8}k)(\epsilon_1 - 2\epsilon_3 + \epsilon_5)$$

$$Q_{45} = (\frac{1}{4} - \frac{\sqrt{3}}{8}k)(-\epsilon_1 - \sqrt{3}\epsilon_2 + \sqrt{3}\epsilon_4 + \epsilon_5)$$

$$Q_{55} = (\frac{1}{4} - \frac{\sqrt{3}}{8}k)(\epsilon_1 + 3\epsilon_2 + 4\epsilon_3 + 3\epsilon_4 + \epsilon_5)$$

The first order correction is obtained using

$${}^1A_n = Q_{nn}; {}^1X_n = \sum_{j \neq n} \frac{Q_{jn} {}^0X_j}{({}^0A_n - {}^0A_j)}$$

$${}^1A_5 = Q_{55} = (\frac{1}{4} - \frac{\sqrt{3}}{8}k)(\epsilon_1 + 3\epsilon_2 + 4\epsilon_3 + 3\epsilon_4 + \epsilon_5)$$

$${}^1X_5 = \frac{Q_{15} {}^0X_1}{{}^0A_5 - {}^0A_1} + \frac{Q_{25} {}^0X_2}{{}^0A_5 - {}^0A_2} + \frac{Q_{35} {}^0X_3}{{}^0A_5 - {}^0A_3} + \frac{Q_{45} {}^0X_4}{{}^0A_5 - {}^0A_4}$$

$$= \frac{(1 - \frac{\sqrt{3}}{2}k)}{8k\lambda} \begin{bmatrix} \sqrt{3}(-3\epsilon_1 - \epsilon_2 + 3\epsilon_4 + \epsilon_5) \\ \epsilon_1 + 9\epsilon_2 - 4\epsilon_3 - 3\epsilon_4 - 3\epsilon_5 \\ 2\sqrt{3}(\epsilon_1 - 2\epsilon_3 + \epsilon_5) \\ -3\epsilon_1 - 3\epsilon_2 - 4\epsilon_3 + 9\epsilon_4 + \epsilon_5 \\ \sqrt{3}(\epsilon_1 + 3\epsilon_2 - \epsilon_4 - 3\epsilon_5) \end{bmatrix}$$

First order approximation

$$A_n = {}^0A_n + {}^1A_n; X_n = {}^0X_n + {}^1X_n$$

Here $\frac{\epsilon_i}{\lambda} \cong \frac{-2\delta\omega_i}{\omega}$, $\delta\omega_i$ is the frequency error of the individual cell (normally $\sum \delta\omega_i \neq 0$). Substitute $\delta\omega_i$ to the equation one can get new operating mode ω' and relevant phase φ' . If the perturbation $\delta\omega_i$ is very small, and $\sum \delta\omega_i = 0$ one still can use unperturbed dispersion curve to approximately calculate the group velocity v_g'

$$v_g' = L \frac{d\omega}{d\varphi} = \frac{1}{2} L k \omega_0 (1 + k \cos \varphi')^{-\frac{3}{2}} \sin \varphi'.$$

When tuning, in order to tune cavity field flatness, one can let all parts of the eigenvector are equal and using symmetry, and then calculate the needed ϵ_i . Practically it is opposite, after tuning $\epsilon_i \approx 0$ ($i=1,2,\dots,N-1$) (middle cells) and $\epsilon_0 = \epsilon_N = \epsilon_e$ (end cells); i.e. only two end cells have frequency error, in the case the perturbed operator is simple, one can directly solve the eigenequation to get eigenvalues and eigenvectors.

IV. DISCUSSION

In fact almost all superconducting multi-cell cavities are terminated by full end cell, when the half end cell terminated replaced by full end cell, the full end cell only had one side coupled, the change of the boundary condition broke the symmetry, and the field penetrated into two end beam pipes to extend field area, sequentially, the field amplitude tilted from center of the cavity to the ends, relevant phase shift between cells decreased and the π mode vanished, the highest mode was $(N+1)\pi/(N+2)$ (here $N+1$ are total cell numbers of the cavity). From perturbation theory the individual cell frequency error will cause the operating mode and its properties change, such as phase shift and field distribution, it was used for tuning cavity.

The cavity tuning includes tuning middle individual cell (reduce frequency error ϵ_i) to eliminate field non-uniform caused by mechanical tolerance and tuning end cells (add suitable frequency error $\epsilon_0 = \epsilon_N = \epsilon_e$) to compensate the field tilt caused by full end cell terminated and move the operating mode to close " π mode" in which the field along the axis of cavity is flatness. Fig.2 is the field distribution of the 5-cell cavity calculated by P. Fernandes and R.Parodi using OSCAR2D code.

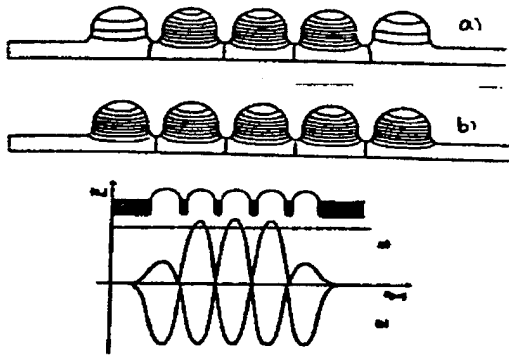


Fig.2 Inner field and axial field distribution of a five cells accelerating structure calculated using OSCAR2D code a)uncompensated, b) compensates.

From Fig 1 and Fig 2 one can see the effects of tuning and terminating on the field distribution and phase shift (modes). In this way after tuning $\sum \delta\omega_i = 2\epsilon_e \neq 0$, the average individual cell frequency ω_0' was changed $\omega_0' = \omega_0 + \delta\omega = \omega_{\pi/2}$ and $\delta\omega = \sum \delta\omega_i / (N+1)$, it means the dispersion curve should parallel move up $\delta\omega$, which also can

directly be got by measuring the $\pi/2$ mode frequency $\omega_{\pi/2}$. The dispersion function and the group velocity still can be described as

$$\omega_q^2 = \omega_0'^2 / (1 + k \cos \varphi')$$

$$v_g' = L \frac{d\omega}{d\varphi} = \frac{1}{2} L k \omega_0' (1 + k \cos \varphi')^{-3/2} \sin \varphi'$$

In theoretical one can tune cavity with $\sum \delta\omega_i = 0$ by lower middle cell and higher end cell frequencies or reverse, it also can be checked by measuring $\omega_{\pi/2}$. In practical tuning case the beadpull was used to check the field amplitude, when the field amplitude along the axis of the cavity is flat, the tuning is done. After tuning with the average single cell frequency ω_0 , which equals new $\pi/2$ mode $\omega_{\pi/2}$ of the tuned cavity (for $\sum \delta\omega_i = 0$), and coupling constant k which is same as unperturbed k , one can calculate the dispersion curve and then substitute the operating mode frequency measured (the highest mode) into the dispersion function to calculate mode properties, such as phase shift between cells and group velocity.

REFERENCE

- 1, Pierre M. Lapostolle and Albert L. Septier "Linear Accelerators" P71, 1970
- 2, A. Marziali and H. A. Schwethman " Structure tuning and its effect on high order modes". P707 1992 Linac conference.
- 3, B. D. Wersteg et.al. "Structure Studies for an S- Band linear Collider" P516 1992 Linac Conference.
- 4, D.J. Laska "Design Features of a Seven-Cell High gradient Superconducting cavity" 1992 Linac Conference.
- 5, P. Terwandes "OSCAR2D A computer code for the design of RF cavities and structures" P 330 1990 Linac Conference.
- 6, T.P Wangler "Calculations for three coupled oscillators- Including eigenvalue problem, perturbation theory and losses" AT-1:84-299 LANL

Response of Superconducting Cavities to High Peak Power*

T. Hays, H. Padamsee, Laboratory of Nuclear Studies, Cornell University, Ithaca, NY 14853 USA

Abstract

A technique to find the transient cavity Q from transmitted power is presented. This technique can facilitate finding the Q as a function of accelerating electric field for low power pulsed measurements, but it has a special application to analyze the thermal breakdown behavior during high peak power pulsing. With high power, in short time scales, the fields in a superconducting cavity can be driven well past the CW breakdown limit. With knowledge of the Q during breakdown, one can show that a large fraction of the surface was still superconducting as the cavity reached high fields. A lower bound to the critical RF magnetic field can then be determined.

Results of pulsing a 1.3 GHz Nb cavity with 340 kW for 150 μ s are presented. The Q extraction technique is used to measure a lower limit of H_c^{RF} over the range of 2 K to 8.3 K despite the presence of a thermal defect.

I. INTRODUCTION

As we continue to push the achievable accelerating gradients in Nb cavities, the critical RF magnetic field, H_c^{RF} , will eventually show up as a hard limit. Improvements in Nb purity and processing of field emission have already advanced practical accelerating gradients above the 25 MV/m level.[1] How much farther can Nb be pushed? When is it time to abandon Nb in favor of other superconductors such as Nb₃Sn that have higher DC critical fields? Is the H_c^{RF} of Nb₃Sn films significantly higher than bulk Nb?

The difficulty in answering these questions is largely due to the presence thermal defects that quench the superconductivity and prematurely limit the sustainable surface magnetic field. In CW operation, in addition to the defect's particular characteristics, the quench field is dependent upon the specifics of the steady state heat transfer. Thus improving the thermal conductivity of Nb serves to raise the quench field. A small normal conducting "hot spot" can be sufficiently cooled and contained to avoid thermal runaway. If the cavity fields are raised above this CW quench field, the normal region grows to eventually encompass the cavity, but this growth takes a finite amount of time.

With high peak power pulsing, the cavity fields can be quickly raised well above the CW quench field while the normal region is growing. To determine H_c^{RF} from this, one must be sure that the cavity is still superconducting at the relevant high field region. A new technique is presented that allows calculation of the instantaneous cavity Q any time during the filling or decay. By knowing Q , one can estimate the size of the normal region and ensure that H_c^{RF} is measured at a superconducting surface. In the present work, we use this technique to measure H_c^{RF} of a 1.3 GHz Nb cavity for temperatures from 2.1 K up to 8.3K.

In addition, since the accelerating field is known at every instant, this Q extraction technique can be used to quickly deter-

mine Q vs E_{acc} . Application in this manner is the subject for further work.

II. FINDING INSTANTANEOUS CAVITY Q

In what follows, the differential equation of the cavity state is derived and solved for Q_0 . Consider a cavity driven on resonance with one coupler. By conservation of energy we can write

$$P_f = P_{diss} + P_r + \frac{dU}{dt} \quad (1)$$

where

$$\begin{aligned} P_f &= \text{forward power (toward the input coupler)} \\ P_{diss} &= \text{cavity dissipated power} \\ P_r &= \text{reverse power} \\ U &= \text{stored energy (inside the cavity)} \\ t &= \text{time.} \end{aligned}$$

The only tricky part about this expression is the reverse power which satisfies

$$P_r = (\sqrt{P_f} - \sqrt{P_e})^2 \quad (2)$$

where

$$P_e = \omega U / Q_{ext} \quad (3)$$

Q_{ext} is the "external" Q of the coupler.

Equation (2) indicates that the net reverse wave results from a superposition of a wave reflected off the input coupler and a wave being emitted from the cavity. Substituting (2) into (1) and using

$$P_{diss} = \frac{\omega U}{Q_0} \quad (4)$$

for the cavity losses and

$$\frac{1}{Q_L} = \frac{1}{Q_0} + \frac{1}{Q_{ext}} \quad (5)$$

for the "loaded Q " as well as (3) we arrive at a differential equation for stored energy:

$$\frac{dU}{dt} = 2\sqrt{\frac{P_f \omega U}{Q_{ext}}} - \frac{\omega U}{Q_L} \quad (6)$$

A clearer form results when written in terms of the fields ($\propto \sqrt{U}$).

$$\frac{d\sqrt{U}}{dt} = \frac{1}{2\tau_L} (\sqrt{U_0} - \sqrt{U}) \quad (7)$$

where

$$U_0 \equiv \frac{4\tau_L^2 \omega P_f}{Q_{ext}} \quad (8)$$

is the steady state stored energy.

Equation (7) shows that the cavity has a natural time constant τ_L for response and that the field changes at a rate proportional to the displacement from its equilibrium value.

*Work supported by the NSF with supplementary support from the U.S.-Japan Cooperative Agreement

If the cavity-coupler system had more than one coupler, (1) would have an additional term with the form of (3) for the emitted power of each coupler. The only effect this has on the subsequent equations is to require that the definition of "loaded Q " in (5) have an additional $1/Q_{ext,k}$ term for each of the k new couplers.

From (7) and (2) the time dependent cavity behavior can be determined analytically or numerically.

The above treatment gives $U(t)$ from Q_0 (and other variables) but to go the other way, one has only to solve for Q_0 in (7) to get

$$\frac{1}{Q_0} = \frac{2 \left(\sqrt{\frac{P_f \omega}{Q_{ext}}} - \frac{d\sqrt{U}}{dt} \right)}{\omega \sqrt{U}} - \frac{1}{Q_{ext}}. \quad (9)$$

Again, if there are k additional couplers, they would show up as further $1/Q_{ext,k}$ terms subtracted from the right side of (9).

Equation (9) is useful for extracting the $Q(t)$ or the $Q(E)$ behavior of a cavity during pulsed operation. And unlike previous methods of getting $Q_0(E)$ from a pulse that examined only the cavity decay[2], this technique can be used any time the cavity has energy. This method also improves over past methods in that it requires only the instantaneous values of U , $d\sqrt{U}/dt$, and P_f . The cavity's history (or future) need not be considered, and no functional fits are needed.

If the cavity is grossly overcoupled ($Q_{ext} \ll Q_0$) then Q_0 plays little role in determining the shape of $U(t)$. For the overcoupled case, in order to extract Q_0 , $U(t)$ must be known to first order within a fractional error of Q_{ext}/Q_0 . When Q_0 does have a negligible contribution, one can take advantage of this to extract Q_{ext} . When ($Q_{ext} \ll Q_0$), Q_{ext} can be found by

$$\frac{1}{\sqrt{Q_{ext}}} = \frac{\sqrt{P_f} \mp \sqrt{P_f - \frac{dU}{dt}}}{\sqrt{\omega U}} \quad (10)$$

where the negative sign is used when d^2U/dt^2 is positive and vice versa.

III. EXPERIMENTAL APPARATUS

Cavities of the DESY shape (1.3 GHz) are tested using a high power klystron and modulator system[3] capable of providing 1.5 MW for 270 μ sec. Currently input coupler limitations allow the full 1.5 MW to be used only when the pulse length is reduced to ~ 150 μ sec.

Results presented here are for a single cell cavity made from Russian Nb sheets with a starting RRR of 460 ± 150 . Subsequent solid state gettering with Ti resulted in a RRR of 1825 ± 700 ¹. Because the cavity's resonance was not at the center frequency of the klystron, the experimental results presented here were limited to a peak power of 1 MW.

Germanium thermometers were mounted on each beam tube to monitor the cavity temperature and any thermal gradient. Three Allen-Bradley resistor thermometers were mounted on the cavity equator to observe fast temperature changes as a result of pulsing. Measurements of incident and transmitted power during pulsing are made by crystal detectors monitored by an 8-bit digital storage oscilloscope (Tektronix 2212). The oscilloscope traces are acquired and processed by a Macintosh computer running LabVIEW software.

¹The RRR measurements were done on small witness samples.

IV. PULSING TO REACH H_c^{RF}

It is thought that H_c^{RF} is equal to the superheating critical field, H_{sh} , a metastable state above the thermodynamic critical field, H_c . [4] H_{sh} can be achieved in RF because the nucleation time for flux penetration is much longer than an RF period. [5] The race to beat the growth of the normal conducting region requires that the cavity fields be ramped up to H_c^{RF} in less than 100 μ s, the faster the better. To do this a very strong input coupling ($Q_{ext} \simeq 10^6$) is used. Higher couplings could ramp the fields faster but that would result in too much of a sacrifice in the measurable range Q_0 .

Oscilloscope traces of up to 1 MW peak power pulses to the liquid helium cooled Nb cavity were acquired at 2.1 K and 4.2 K. By warming the cavity we hoped to be able to lower H_c^{RF} enough to come close to it even with the thermal breakdown. To prepare for warmer measurements, the cavity was cooled with flowing gaseous helium at 4.2 K and the fast pulsed breakdown behavior was found to be similar to that of liquid cooling. There was the worry that the cavity would have a different thermal breakdown behavior due to the inferior cooling power of the gas, but the time scales are so short that the cold reservoir outside the cavity doesn't have time to play a large role in the heat transfer.

Bathed by flowing helium gas, the cavity was slowly warmed up to its transition temperature 9.25 K while high peak power pulsed measurements were made (with $Q_{ext} = 9 \times 10^6$ and $P_f = 340$ kW). Two such pulses and the extracted Q_0 are presented in Figure 1. At the beginning of the pulse, Q_0 is too high to measure, but as the normal region grows, Q_0 plummets until it reaches the value of a completely normal cavity. As the temperature is raised from Figure 1 a) to 1 b), the breakdown field is lower, and Q_0 drops earlier. Note that because of the strong coupling and high incident power, the cavity fields continue to rise despite the plummeting Q_0 . Since the cavity is almost completely normal conducting at its peak field, it is vital to extract Q_0 while the fields are rising to be able to measure a lower bound to H_c^{RF} with confidence.

At the beginning of the pulses in Figure 1, Q_{ext} was successfully extracted using Equation (10). The value thus obtained agreed well with independent measurements of Q_{ext} .

The 8-bit amplitude resolution on the oscilloscope was the most serious limitation to the data. Averaging was required get rid of a little noise and to remove the "steps" caused by this resolution limit.

To be positive that there is a superconducting surface reaching the peak field, we claim the cavity must be at least 90% superconducting. Since the 10% normal region occupies the area around the local defect, it is assured some part of the high field equatorial region of the cavity is superconducting.

A conservative calculation then dictates that Q_0 must be at least 2×10^6 . Applying this criterion to the pulses measured yields the data in Figure 2. The two lowest temperature data points were acquired using liquid helium cooling at 2.1 K and 4.2 K with higher peak power and greater input coupling. Because the breakdown occurred so early in the pulse, testing the cavity much above 8.3 K gave inconclusive results.

For comparison, critical magnetic field curves for Nb are also shown in Figure 2. The curve for H_{sh} is obtained from the simplistic assumption that $H_{sh}(0) = c_{sh} H_c$ with $c_{sh} = 1.2$

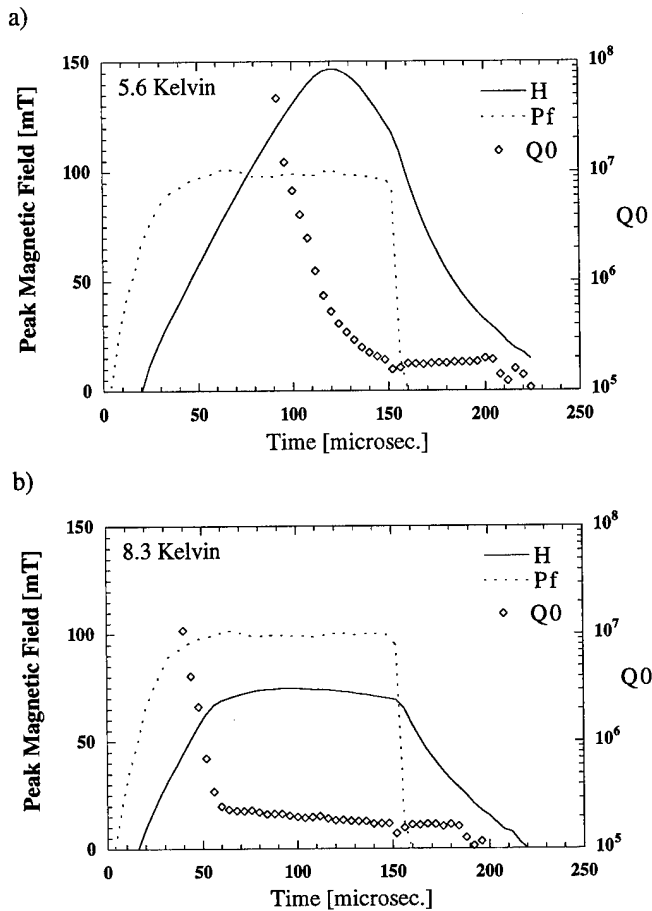


Figure 1. Pulses to the cavity causing thermal breakdown at a) 5.6 K and b) 8.3 K. Peak forward power was 340 kW for both pulses. Forward power is shown with arbitrary units.

throughout the temperature range. The exact values are not easily predicted, but because of the temperature dependence of the Ginsburg-Landau parameter it is expected that c_{sh} is lower for lower temperatures and higher closer to T_c . One might think that it is suggestive that the experimental data in Figure 2 also follows this trend, but the stronger influence of the thermal defect on the lower temperature points is probably dominating the shape.

Note that these first experimental measurements are tentative. Improvements in the reliability of power measurements and better data resolution are in progress.

V. CONCLUSIONS

The new Q_0 extraction technique was successful in exploring high magnetic fields in a superconducting cavity despite the presence of a thermal defect. Measurements on Nb up to 8.3 K are consistent with the idea that H_c^{RF} is the superheating critical field. These measurements suggest that high magnetic field studies of Nb₃Sn are feasible using this Q_0 extraction tool.

VI. ACKNOWLEDGMENTS

We wish to thank our colleagues W. Hartung for helpful criticism on the theory, J. Sears for assistance in cavity purification, and E. Chojnacki for help with the klystron. Thanks go to K. Hosoyama from KEK for assistance with the helium gas cooling. We are also grateful to the many members of the international TESLA Collaboration that aided in setting up the 1.3 GHz cavity test facility at Cornell.

References

- [1] C. Crawford et al. *Particle Accelerators*. Vol. 49, pp. 1-13 (1995).
- [2] D. W. Reschke and R. W. Roth *Fundamentally Fastest Method Measuring $Q_a(E_{acc})$ - Performance of S.C. Cavities* Fachbereich Physik, Bergische Universitat Wuppertal, Germany. Presented at the 6th Workshop on RF Superconductivity at CEBAF in Newport News, VA, USA.
- [3] *ibid.* Ref. [1].
- [4] J. Matricon and d. Saint-James *Phys. Lett.* **24A**, 241 (1967).
- [5] R. B. Flippen *Phys. Lett.* **17**, 193 (1965).
- [6] D. K. Finnemore, et. al. *Phys. Rev.* **149**, 231 (1966).

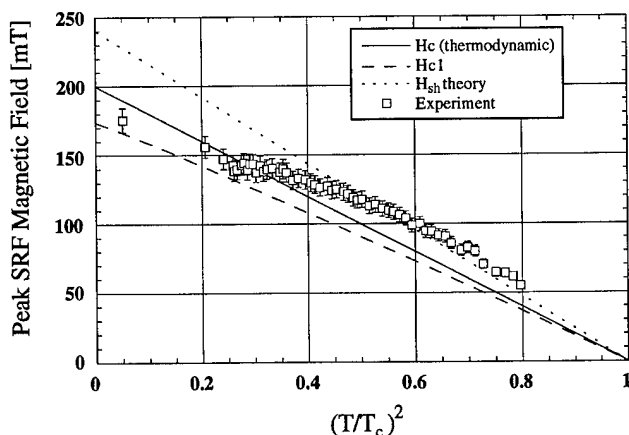


Figure 2. Measured surface magnetic fields on the superconducting Nb surface compared with DC critical fields[6] and a reasonable guess at H_{sh} .

DEVELOPMENT OF HOM DAMPER FOR B-FACTORY (KEKB) SUPERCONDUCTING CAVITIES

T. Tajima, K. Asano, T. Furuya, M. Izawa, S. Mitsunobu and T. Takahashi
National Laboratory for High Energy Physics (KEK), 1-1, Oho, Tsukuba, 305 Japan

N. Gamo¹⁾, S. Iida¹⁾, Y. Ishi²⁾, Y. Kijima²⁾, S. Kokura³⁾, M. Kudo⁴⁾, K. Sennyu⁵⁾,
S. Tachibana¹⁾, H. Takashina⁶⁾ and N. Taniyama⁴⁾,
¹⁾Kinzoku-Giken, Co., Ltd., ²⁾Mitsubishi Electric, Co., Ltd., ³⁾Hitachi Material, Co., Ltd.,
⁴⁾Micro-denshi, Co., Ltd., ⁵⁾Mitsubishi Heavy Industry, Co., Ltd and ⁶⁾TDK, Co., Ltd.

I. INTRODUCTION

Higher Order Mode (HOM) power excited in Superconducting Cavities (SCC) can be on the order of kW in the B-factory due to high current. To extract this power, cavities are designed so that HOM can travel out through beam pipes and be absorbed in a lossy material [1]. Ferrite has been investigated as a candidate material for the absorber [2,3]. Due to its low tensile strength, bonding of tiles has been a problem. To solve this problem, we started R&D on the sinter-bonding of ferrite powder directly on the inner surface of a copper pipe using Hot Isostatic Press (HIP). In this paper, we describe the manufacturing process, low power test, high power test and outgassing rate measurement of the manufactured dampers.

II. MANUFACTURING [4]

In the design of the SCC for KEBK, there are two dampers on up stream and down stream side of the cavity. Their sizes of ferrite layer are 220 mm and 300 mm in outer diameter, 120 mm and 150 mm in length, respectively. The thickness of both dampers is 4 mm. The latest design has 25 mm tapers at the front and rear end, starting with 1 mm-thick ferrite, to lower the surface temperature as will be shown later. Figure 1 shows the process of manufacturing of full size HOM damper. The process is as follows : 1) pack ferrite powder between inner can and outer copper pipe using mechanical press, 2) TIG weld cans and lid, evacuate and degas ferrite at 300 °C for 24 h, 3) chip off and HIP with Ar at 1500 atm x 900 °C for 5 h, 4) remove inner can with lathe, 5) machine ferrite with diamond grinder, 6) electron-beam weld end flanges and 7) machine a cooling channel on the outer surface of copper, then press-insert the copper pipe in the channel. Figure 2 shows the finished damper. The problems we have faced so far are 1) crack of ferrite when stainless steel ring was HIPped together, 2) voids that appear after ferrite machining and 3) delamination of ferrite. Elimination of stainless steel solved the first problem. The second problem was solved by raising HIP pressure from 1000 to 1500 atm, together with lengthening of the degassing time. The third problem, delamination, has become less by elimination of stainless steel and raising HIP pressure, but, still occurs sometimes. We are planning to lower the ramping

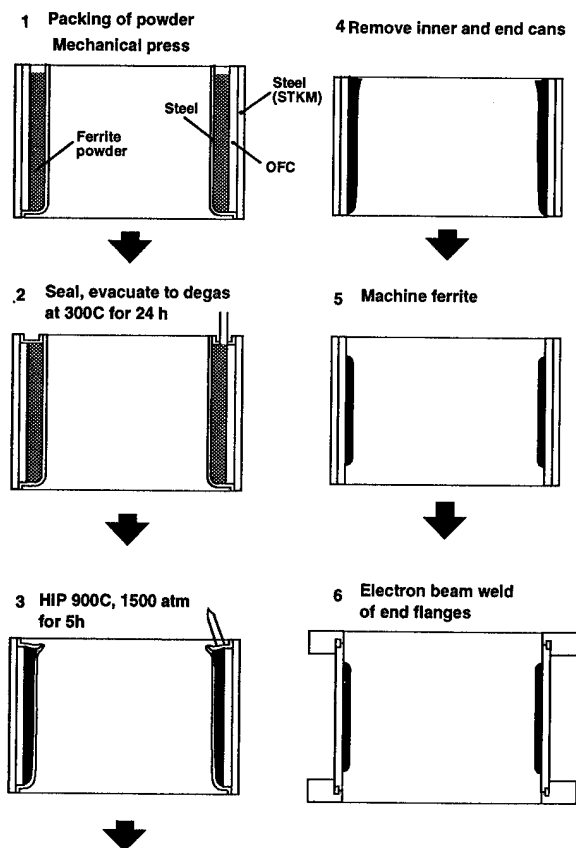


Figure 1: Manufacture process of full size damper.

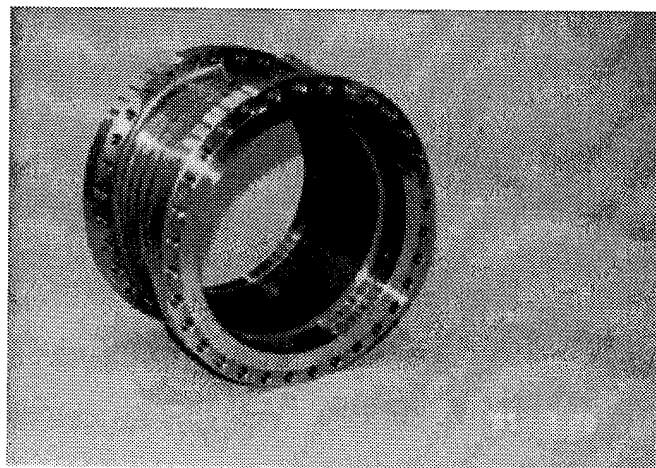


Figure 2: HOM damper . Ferrite size : 220 mm o.d. x 120 mm long x 4 mm thick. Cooling pipe is 3/8" copper pipe pressed in the channel.

rate so that the thermal stress in the ferrite upon cooling down can be less.

III. LOW POWER TEST

A. Mode damping

Damping of each mode has been measured using an aluminum model cavity with a network analyzer [5]. Figure 3 shows the comparison between the cavities with HOM damper and without it. As shown in the figure, most modes were successfully damped. Detailed check of each mode is under way.

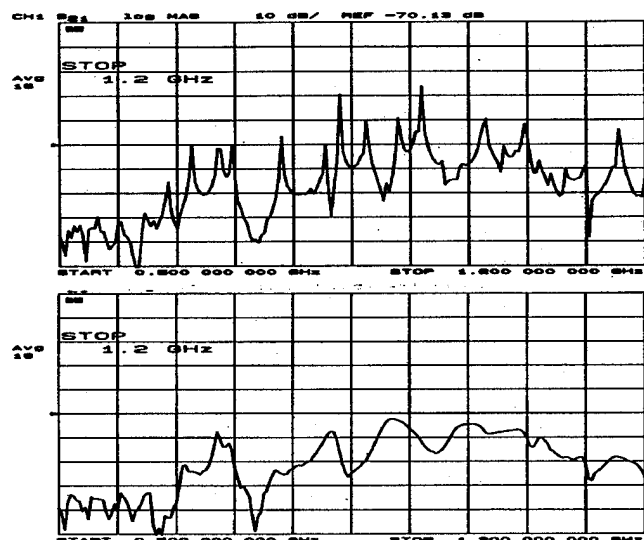


Figure 3: Mode damping with ferrite (lower). 0.5 - 1.2 GHz.

B. Loss factor of ferrite pipe

Loss factor of ferrite pipe alone has been measured by a wire method, so-called synthetic pulse method [6]. 3 mm-diam. inner conductor was set on the central axis, then loss factor was calculated by comparing the inversely Fourier transformed S21 data of the pipes with and without damper. Figure 4 shows the measured loss factor of small damper (220 mm o.d. x 120 mm long) as a function of bunch length. The data for the bunch length shorter than 11 mm is not accurate due to strong reflection for the frequencies corresponding to these data.

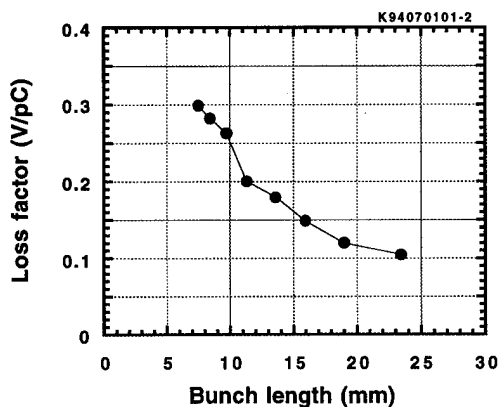


Figure 4: Loss factor of small damper (220 mm o.d. x 120 mm long x 4 mm thick ferrite).

IV. HIGH POWER TEST

We have performed 2 types of high power test as shown below. In both types, tests were performed in air.

A. TM01 mode at 2.45 GHz

Using the smaller diameter model, TM01 mode high power test was performed. The ferrite size was 109 mm o.d. x 150 mm long x 4 mm thick. A 2.45 GHz c.w. magnetron power source (5 kW) was used. The inner surface temperature distribution of ferrite was measured with thermo-labels, i.e., whose white spots change into black at specified temperatures. We tried 3 shapes, without taper and 2 types of tapers as shown in Fig. 5. The max. absorbed power was 3.95 kW and average power density was 8.3 W/cm². Assuming the exponential decay of power, the estimated max power density was about 29 W/cm² at the leading edge of the ferrite. Figure 5 also shows the temperature distribution. As shown in the figure, introducing a taper was proved to be effective to reduce the surface temperature, which is important to reduce outgas from ferrite. Cooling water flow rate was 3 l/min.

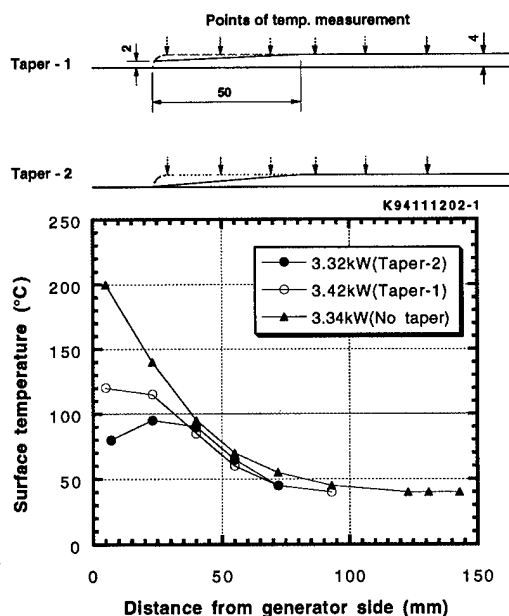


Figure 5: Tapers used in the test (above) and ferrite surface temperature distribution.

B. Coaxial line at 508 MHz

To test power handling capability of full size damper, we started using coaxial line with 508 MHz Klystron. We have tested 2 dampers, both small and large, so far. Small one was tested up to an absorbed power of 11.7 kW and the average power density was 14.6 W/cm². Temperature distribution along the pipe axis was rather flat and the max. temperature was 140 - 149 °C at 10.4 l/min of cooling water flow.

Large damper was tested up to 14.8 kW and the average power density was 10.8 W/cm². The surface temperature was lowered with the power density.

In both tests, there was no damage on the ferrite. In the next tests, higher power will be fed to know the limit power if possible.

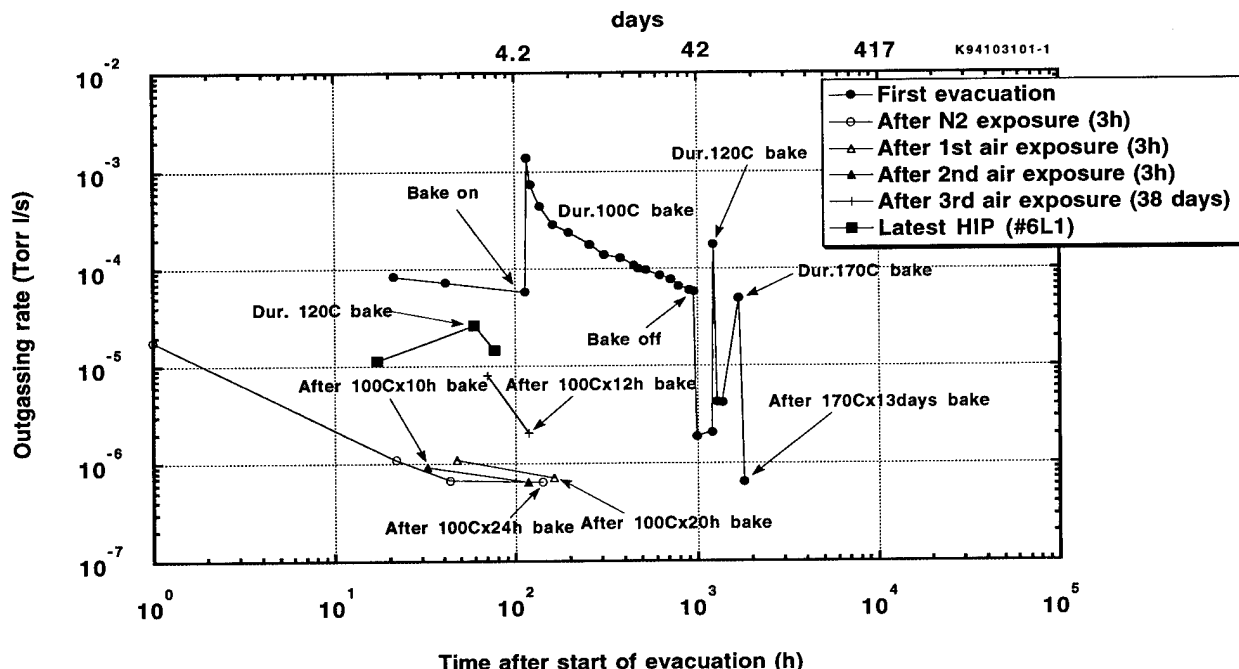


Figure 6: Outgassing rate of large damper. The data except for solid squares were taken from the same damper. #6L1 is the damper that was recently HIPped after improvement of powder degassing. The effects of exposure to N_2 and air are also shown.

V. OUTGAS RATE

Vacuum in the KEKB should be lower than 1×10^9 Torr to get sufficient beam life time. Also, for SCC, since the condensed gas on the Nb surface seems to play a significant role on the trips, the outgassing rate from HOM dampers should be low enough not to cause any problem. The vacuum before cooling down should be at least 1×10^{-8} Torr.

A. Sample test

Outgas rate of commercial ferrite tile (80 mm x 80 mm x 4 mm), TDK IB-004, was measured to be about 5×10^{11} Torr l/s cm^2 at room temperature after $140^\circ C \times 25$ h bake [5].

B. Full size damper

Full size dampers have been measured with through-put method, i.e. the pressure difference between the ferrite chamber and the pump chamber was multiplied with the given conductance to obtain the outgassing rate [4,5]. Figure 6 shows the results of large damper. The ferrite area of large damper is about 1380 cm^2 . As shown with solid circles, the outgassing rate was more than an order of magnitude higher than the sample result even after more than one month of baking. However, once it is baked, it can reach the final rate in a few days after 3 h of air exposure. From the fact that the major gas species was water and that the adsorbed gas on the surface can be easily removed, it was concluded that the gas source was the trapped water vapor in the ferrite. Recently, we tried to degas the powder at about $300^\circ C$ in dry nitrogen gas before packing. The solid square in Fig. 6 shows the result of the powder-degassed damper. As one can see, the outgassing rate before baking was lowered about an order of magnitude. With this outgassing rate, we can probably reach a vacuum lower than 1×10^{-8} Torr before cool down with a pump having effective pumping speed of 100 l/s.

VI. CONCLUSIONS

HOM damper has been manufactured by HIPping of ferrite powder on copper. The small and large dampers were high power tested with 508 MHz coaxial line up to 11.7 kW and 14.8 kW, respectively. There was no damage on the ferrite. The outgassing rate can be sufficiently low to obtain a pressure lower than 1×10^{-8} Torr before cooling down of SCC.

A beam test of large damper as well as 1.3 GHz TM01 mode high power test in vacuum will be performed soon.

ACKNOWLEDGMENTS

We would like to thank Y. Funahashi for EB welding the flanges of dampers. Continuous encouragements of E. Ezura, Y. Kimura, Y. Kojima and S. Kurokawa are greatly appreciated.

REFERENCES

- [1] J. Kirchgessner ; Proc. 6th Workshop on RF Superconductivity, p. 331 (1993).
- [2] T. Tajima et al. ; *ibid.* [1], p. 962, 1160
- [3] D. Moffat et al. ; Workshop on Microwave-Absorbing Materials for Accelerators, Feb. 22-24, 1993.
- [4] T. Tajima et al. ; to be published.
- [5] T. Tajima et al. ; *ibid.* [3]. KEK Preprint 93 - 6.
- [6] M. Izawa et al. ; Rev. Sci. Instrum. **63**, 363 (1992).

Microscopic examination of defects located by thermometry in 1.5 GHz superconducting niobium cavities*

J. Knobloch, R. Durand, H. Muller and H. Padamsee

F.R. Newman Laboratory of Nuclear Studies, Cornell University, Ithaca NY 14853

Abstract

A new high resolution, high speed thermometry system has been built at Cornell to permit the study of anomalous loss regions in 1.5 GHz superconducting Nb cavities in superfluid He. Following a cavity test, the cavity is dissected for examination of these regions in an electron microscope. Presented is a survey of the topographical and elemental characteristics of various defects found so far. Included are field emitters which were known to be active at the end of a cavity test, as well as those which processed.

I. INTRODUCTION

In present day Nb cavities the surface magnetic fields achieved still fall far short of those theoretically attainable. The maximum field possible is believed to be the superheating rf field (2300 Oe @ 1.6 K) [1]. In practice, though, one finds that the cavity Quality (Q) already begins to drop between 300 and 1000 Oe.

Several mechanisms responsible for anomalous power dissipation at these fields have been identified. Presently, the most common ones are dielectric/magnetic losses (thermal defects) [2] and field emission (FE) [3]. Both mechanisms can be attributed to microscopic defects present on the inner cavity wall.

To better understand the nature of the defects we have begun to search for these, using thermometry [2] as a guide. We catalogue their heating characteristics and after cavity tests dissect the cavities to undertake a microscopic and elemental examination of the defects.

II. EXPERIMENTAL SETUP

To facilitate the search a new thermometry system was developed, whose details have been discussed elsewhere [4]. It is designed for L-Band cavities operating in superfluid He at 1.6 K. Its essence is an array of 756 specially prepared carbon thermometers pressed against the outer cavity wall. A map at a resolution of 0.25 mK takes about 1/10 s to acquire. Increasing the acquisition time to 2.5 s permits us to resolve 30 μ K signals. This is a marked improvement over previous systems which either were very slow, requiring several tens of minutes for an acquisition, or were unable to detect signals below 5 mK.

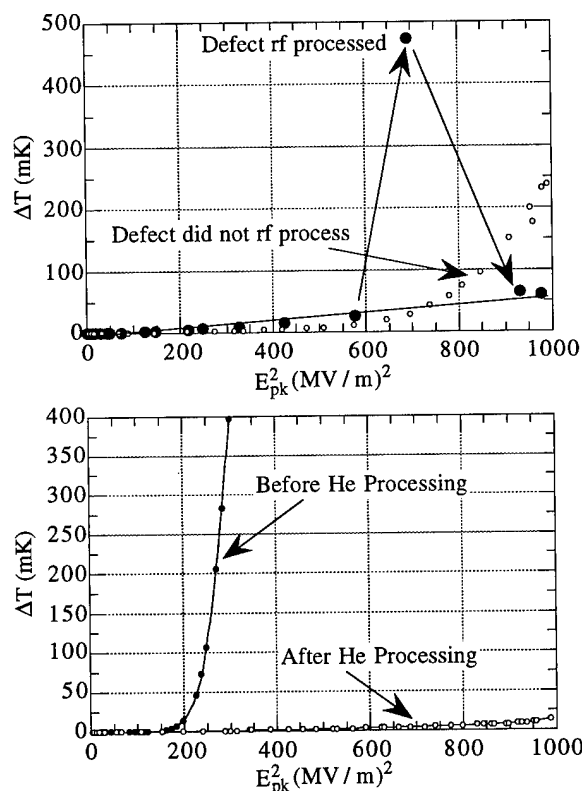
After the tests, cavities that have interesting sites are cut apart. During the cutting process the interior of the cavity is pressurized with filtered N_2 gas, thereby minimizing dust contamination. Cuts are made along the beam tubes (~ 2.5 cm

from the iris) and along the equator using two sizes of conventional pipe cutters. The entire cutting process is carried out in a class 100 clean room.

The chamber of an electron microscope (SEM) has been enlarged to permit the examination of the half cells. We have been able to show that thermometry data is a useful guide to locating defects in the SEM. The defects' elemental composition is also studied by energy dispersive x-ray analysis.

The heating due to thermal defects occurs directly at the defect site. On the other hand, field emitters are more difficult to pinpoint. Generally one detects the power deposited by accelerated FE electrons impacting with other parts of the cavity wall. In that case we revert to trajectory calculations using the program "MULTIP" to determine the emitter location [5].

III. MEASUREMENTS



Figures 1a & 1b: FE heating measured for sites which a) didn't process (shown in fig. 2b), b) processed in the rf field (shown in fig. 2c) and c) He processed (shown in fig. 2d). The heating is plotted vs. the electric field squared so that background heating in the absence of FE is linear.

*Work supported by the NSF with supplementary support from the US - Japan collaboration.

chemically etched with BCP 1:1:2 for 3 minutes. This was followed by rinsing the cavity with continuous flow deionized water for at least 2 hours prior to drying with warm filtered N₂ gas. LE1-Hereaus was only cleaned with DI water in conjunction with ultrasonic agitation.

During the tests the cavity fields were increased while measuring the cavity Q and temperature distributions at regular intervals. In one case an emitter *rf processed* [6], that is, upon raising the field beyond a threshold, the emitter's heating was permanently extinguished. (see fig. 1a).

In another case, the maximum power dissipated in the cavity was 8 W, most of which was absorbed by a single emitter. Subsequently *He processing* [7] was successfully performed on the cavity resulting in the elimination of the emitter (fig. 1b).

IV. RESULTS & DISCUSSION

On average we found the temperature signals of two or three FE sites in each cavity. LE1-Hereaus, which had far more, was the exception. This was not surprising, considering this cavity had not been etched prior to the test.

Of the nine FE sites studied in greater detail, six were located in the bottom halves of the cavities. This observation supports the notion that emitters are primarily caused by foreign particles, accumulating at the bottom due to gravity.

In two cases a microscopic search of an area ± 1 cm and $\pm 10^\circ$ centered on the predicted emitter location failed to turn up any defects that were indicative of FE (discussed later).

In the remaining seven cases we found defects displaying definite signs of FE within at most a 2-3 mm radius of the predicted emitter location. Table 1 summarizes these. Frequently we also searched the surrounding area. Although occasionally we did find micron sized particles, these did not show any signs that FE had occurred and could easily be removed by high pressure N₂ gas, whereas the FE sites remained anchored to the cavity surface.

Table 1: Summary of the emission sites for which microscopic defects could be correlated with the thermometry signals.

#	Melting/Craters Present ?	Starburst?	Pro-cessed?	Contami-nants	Fig.
1	Minimal Melt.	No	No	Fe, Cr	2a
2	Melting	No	No	In, Al	None
3	Minimal Cratering	No	No	C,O,Fe,Ni, Cr,Ti,Ca,Br	None
4	Min. Cratering	Yes	No	None	None
5	Severe Melting	Yes	No	C,O,Cl, Ti	2b
6	Significant	Yes	Yes	C	2c
7	Very Severe	Yes	w/ He	None	2d

Cataloging field emitters

The defects listed above can be categorized as follows:

A) Three unprocessed FE sites (entries 1-3) consisted of foreign particles a few 10's of μm in size which had been partially melted. Fig. 2a shows an example of such a defect. Note the molten region which is magnified in the inset.

B) In two unprocessed cases (entries 4 & 5) we found regions of limited cratering surrounded by a large area (diameter = 500 μm) of reduced secondary electron emission coefficient. This feature has been observed in the past [3],[8] and is known as a starburst because of its dark star shaped appearance in the SEM. In the case of entry 5, we also found a large (70 μm) foreign particle which had melted to a large extent (see fig. 2b)

C) At the location of the rf processed emitter (entry 6) we found an irregularly shaped starburst surrounding a region of significant cratering and melting (see fig. 2c). Some remnants of a foreign particle (carbon) existed as well.

D) The helium processed emitter (entry 7) had a very regularly shaped starburst (see fig. 2d). No foreign elements were detected at the center which consisted entirely of severely molten Nb surrounded by some cratering.

Progression of field emission:

These results suggest the following scenario for the progression of FE:

1. At sufficiently low current densities the FE process is insufficient to alter the appearance of the emitter. This explains why we were unable to find some field emitters in the microscope.

2. As the electric field is increased, the FE current density rises locally to values sufficient to melt parts of the site (fig. 2a). FE may perhaps occur at several points on the defect simultaneously, so that the melting process doesn't noticeably affect the defect's collective FE characteristics.

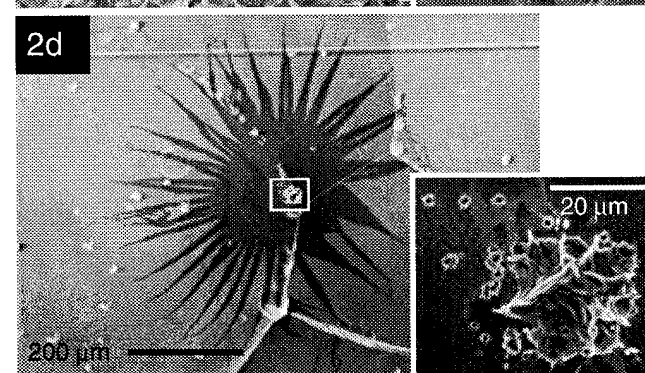
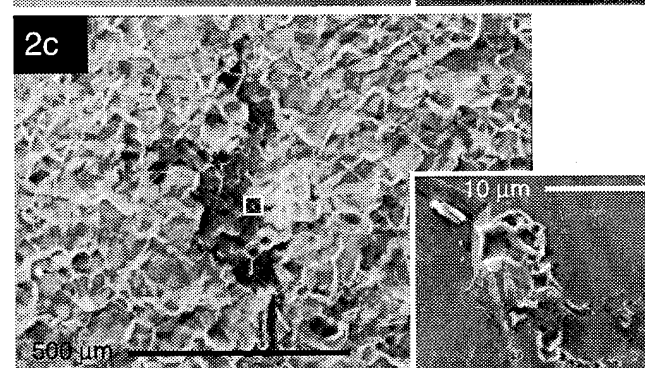
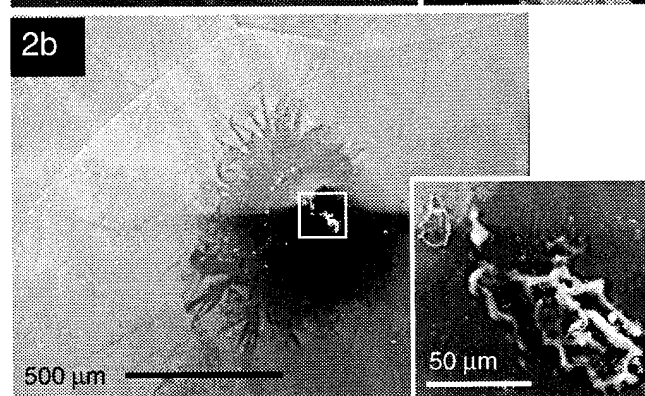
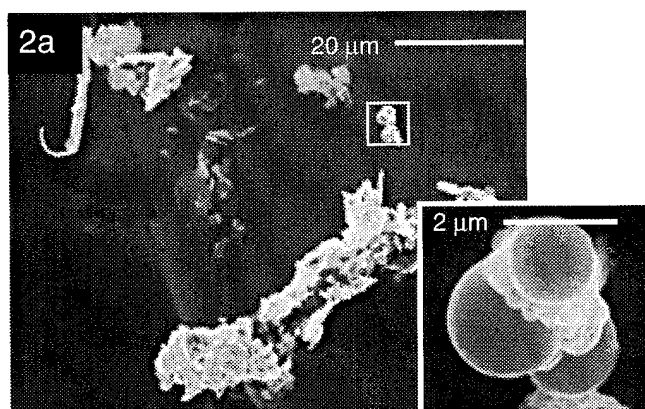
3. Further field increases result in extreme heating (ultimately leading to a local explosive event). A plasma builds up, which is fueled by desorption/evaporation of one or more of the local emitters. Through a cleaning action of the plasma, a starburst is produced [8] (fig. 2b). Neighboring emitters may still be in the first two stages, so that again the overall FE characteristics of the defect are only little changed.

4. Finally, the plasma itself results in significant heating over a region encompassing a large portion of the defect. Once a critical temperature is exceeded the entire defect processes (fig. 2c). The emitter in fig. 2b was perhaps just before this stage. Of particular note is the fact that almost the entire defect seems to have melted.

The new evidence presented here supports that the plasma production is not simply the result of a defect's processing event. Rather it is the heating by the plasma that is essential to its extinction. The heating by the FE current alone may not be sufficient.

The He processed emitter evidence tends to support this notion. The He provides the 'fuel' to enhance the plasma, thereby permitting the defect to process at lower field levels than would ordinarily be possible.

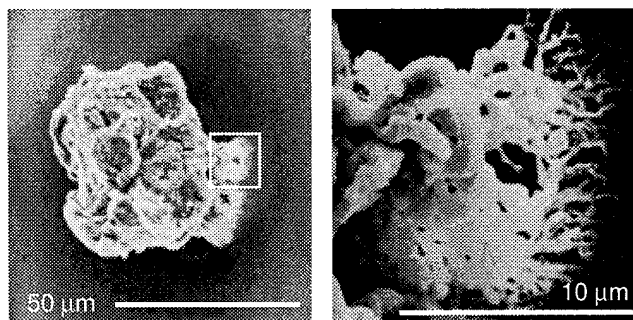
This scenario, of course, is speculative and we are currently running simulations to test our hypothesis. Further cavity tests will be carried out to yield more statistics.



Figures 2a - 2d: Examples of FE defects found for the four cases A - D discussed in the text. It is speculated that these figures represent a natural progression in FE, ultimately leading to the processing of a defect. The insets are magnifications of the areas in the rectangles.

Other Observations:

1. We found a thermal defect (fig. 3), which at higher field levels could have lead to thermal breakdown. The copper particle at that location could not be removed by high pressure solid CO₂ cleaning. Parts of it seem to have melted, which may explain why the particle was so firmly attached. Calculations [9] indicate that melting was possible at the fields attained, provided the particle was thermally isolated.



Figures 3a & 3b: A thermal defect (copper)

2. Comparison with other experiments show that the average starburst size scales inversely with frequency between 1.5 and 5.8 GHz. If starbursts are produced during half an rf cycle, while FE is active, we find that an expansion velocity of $\sim 10^6$ m/s is required. This is consistent with the expansion of electrons thermally emitted from plasmas observed during explosive DC FE [10]. Perhaps such electrons are responsible for the starburst production.

3. Generally, cavities were FE free until a threshold field was exceeded, resulting in the irreversible activation of at least one field emitter. Room temperature cycling of the cavity did not deactivate these. This observation seems to be at odds with the use of the "tip-on-tip" model [11] to explain FE.

4. The main contaminants in emitters were C, Fe, Cr and Ti, which probably came from assembly tools and the ion pump. Steps are being taken to modify the pump system.

V. REFERENCES

- [1] H. Piel, CERN Acc. School (1988) page 149
- [2] H. Piel, Proc. of the Workshop on RF Superconductivity, Karlsruhe (1980), page 85
- [3] D. Moffat et al., Particle Accelerators 40, (1992), page 85
- [4] J. Knobloch et al., Rev. Sci. Instrum., 65 (11), (1994) page 3521
- [5] J. Graber et al., Nucl. Instr. and Meth. in Phys. A 350, (1994) page 582
- [6] J. Graber, Ph.D. Thesis, Cornell University
- [7] H. Schwettmann et al., J. Appl. Phys. 45, (1974) page 914
- [8] T. Hays et al., Proc. of the 6th Workshop on RF Superconductivity, CEBAF (1993) page 750
- [9] J. Graber, Cornell University, private communication
- [10] E. Litvinov, IEEE Transactions on Electrical Insulation, EI-20 (4), (1985) page 659
- [11] M. Jimenez et al., J. Phys. D. 27, (1994) page 1038

RF System for the NSLS Coherent Infrared Radiation Source *

W. Broome, R. Biscardi, J. Keane, P. Mortazavi, M. Thomas, J.M. Wang
Brookhaven National Laboratory, Upton, NY 11973

I. ABSTRACT

The existing NSLS X-ray Lithography Source (XLS Phase I) is being considered for a coherent synchrotron radiation source. The existing 211 MHz warm cavity will be replaced with a 5-cell 2856 MHz superconducting RF cavity, driven by a series of 2 kW klystrons. The RF system will provide a total V_{RF} of 1.5 MV to produce $\sigma_L = 0.3$ mm electron bunches at an energy of 150 MeV. Superconducting technology significantly reduces the required space and power needed to achieve the higher voltage. It is the purpose of this paper to describe the superconducting RF system and cavity, power requirements, and cavity design parameters such as input coupling, Quality Factor, and Higher Order Modes.

II. INTRODUCTION

The XLS Phase I storage ring is a compact racetrack-shaped ring at the National Synchrotron Light Source of Brookhaven National Laboratory. Using a warm 211 MHz RF cavity, currents of up to 0.75 A in 6 bunches have previously been stored at energies ranging from 120 to 200 MeV. Installation of a 5-cell 2856 MHz superconducting cavity will provide an accelerating voltage of 1.5 MV for an average current of up to 5 mA, and create a source of coherent synchrotron radiation with 0.3 mm bunches at an energy of 150 MeV [1]. In order to accommodate the cavity, cryostat and helium vessel, and other associated hardware, the circumference of the ring can be increased to ~ 9.66 from the present 8.5 m by adding a short straight section on both sides, keeping modification costs to a minimum. A partial list of the ring and RF parameters is presented in Table 1.

Table 1. Proposed Ring and RF Parameters

Energy, E	150	MeV
Circumference	9.66	m
Momentum Compaction, α	0.322	
Energy Loss per Turn, U_0	74	eV
Beam Current, I_{AV}	5	mA
RF Frequency	2856	MHz
Peak Cavity Voltage, V_{CAV}	1.5	MV
R_{SH}/Q	240	Ω
Unloaded Quality Factor, Q_0	10^9	
Synchronous phase, Ψ_v	89.997	degrees
$P_{RAD} \equiv I_{AV} U_0$	370	mW
$P_{CAV} \equiv V^2 / 2R_{SH0}$	4.69	Watts
$\rho \equiv P_{RAD} / P_{CAV}$	0.2	

III. CRYOGENICS

The system will use a helium reservoir, operating at 2° K, rather than circulating refrigeration because of the high initial

capital cost of a closed cycle system [Figure 1]. Initially, the cryostat will be filled with normal helium; the 2° K operating temperature will be achieved through cryo-pumping. Although it is rather large, the "top-filled" cryostat is relatively easy to operate and is capable of supplying enough helium for 8 continuous hours of operation. The main difficulties foreseen are with the assembly sequences. The RF cavity will have protective windows and valves as safeguards after cleaning.

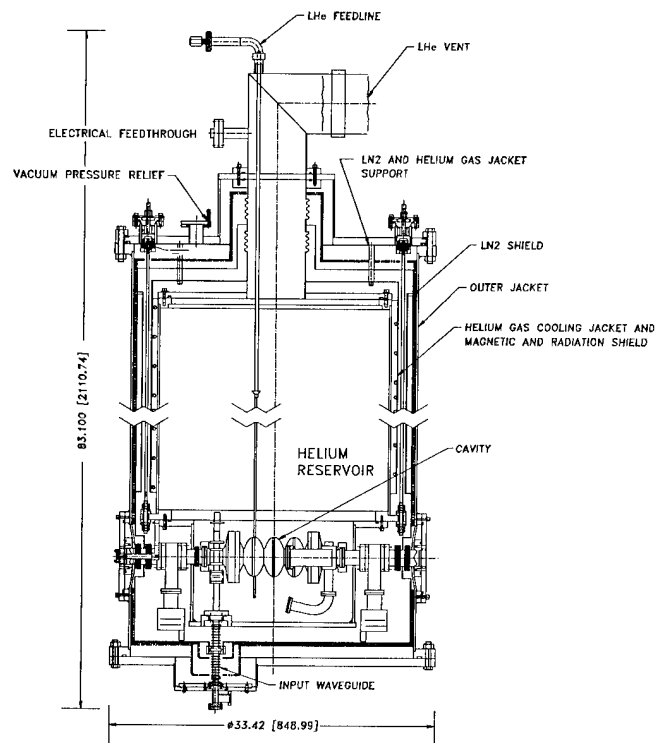


Figure 1. Superconducting Cavity and Helium Reservoir

IV. CAVITY DESIGN

The cavity design [Figure 2] is being adapted and scaled from that currently in use at Cornell and CEBAF [2,3,4], including the input waveguide and the HOM couplers. There are 5 elliptical cells operating in the π mode. Scaling of CEBAF results to a 2856 MHz cavity indicates that a gradient of 8.9 MV/m is achievable. With an active length of 0.262 m, a peak cavity voltage, V_{CAV} of 2.3 MV can be reached, which is 50% greater than specified. The order of magnitude of the unloaded quality factor Q_0 , is approximately 10^9 .

A. Input Coupling

As in the CEBAF design, RF power is propagated in the TE_{10} mode through a rectangular waveguide. A hole in the broad wall of the waveguide that is aligned with the beam tube,

* Work performed under the auspices of the US Department of Energy

provides coupling to the accelerating cavity. The waveguide continues past the coupling hole, into a shorted stub whose length can be varied to change the standing wave pattern at the coupling aperture and whose width is reduced to aid in damping of certain HOMs [2]. This method of coupling will provide a Q_{EXT} in the range of 10^4 to 10^8 .

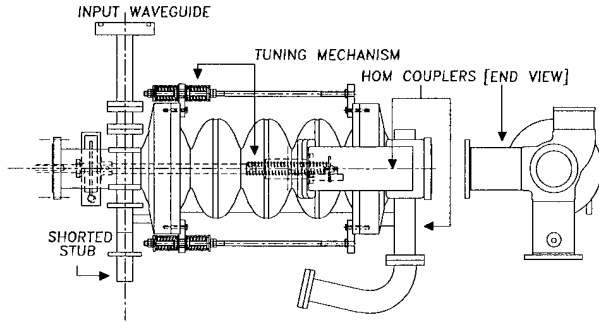


Figure 2. 2856 MHz niobium cavity indicating input waveguide, HOM couplers, and tuning mechanism.

B. Tuning

The cells will be tuned at room temperature by inelastically stretching or compressing the cells axially with plates that grip the equatorial region as illustrated in Figure 2. Compensation will be made for frequency shift due to thermal contraction, chemical treatment, pressure differential, and dielectric constant differential.

V. HIGHER ORDER MODES

A. Mode Damping

In such high Q factor structures as superconducting cavities which store energy so effectively, it is particularly important to damp beam-induced HOMs. A summary of monopole TM modes below the URMEL-calculated cutoff of 6245 MHz, and dipole modes below the URMEL-calculated TE cutoff of 4628 MHz is presented in Table 2.

Table 2. HOMs as calculated by URMEL

Monopoles [MHz]	R/Q (Ω)	Dipoles [MHz]	R/Q (Ω at R_0)
2834.54	243.26	3320.47	0.32
5201.39	0.01	3392.72	0.96
5239.93	1.89	3501.47	19.82
5300.34	0.10	3629.86	73.31
5381.47	13.59	3787.95	39.96
5474.68	54.88	3819.17	0.26
5587.89	0.06	3972.62	18.70
5680.19	7.56	4006.32	28.80
5764.53	0.12	4024.02	4.38
5818.99	0.92	4025.61	4.16
5852.78	0.07		

The limited diameter of the beam pipe aperture at the cavity and space constraints for heat removal, will not allow placement of RF absorbing ferrite material inside the pipe as is used at MIT-Bates [5]. Therefore, as in CEBAF, rectangular waveguide ports at the opposite end from the input port serve as two right angle HOM couplers. The HOM coupler includes a shorted stub that assists in the control of mode polarization.

B. HOM Power

The typical Q_{EXT} obtained by HOM couplers is in the 10^4 range [6]. These findings are corroborated by the HOM measurements made by CEBAF. In order to reduce the consumption of liquid helium and to keep the time between fills at a maximum, plans call for the HOM couplers to be terminated in helium gas - within the reservoir but above the level of the liquid.

HOM power calculations were made by placing each of the modes on the nearest unstable sideband of a rotation line. Using the relationship

$$P_{HOM} = \left[2 \frac{I_{AV}}{\sqrt{2}} e^{-\frac{(\omega\sigma_t)^2}{2}} \right]^2 R_T$$

with a bunch length, σ_t , of $1.6e-12$ s, and an average beam current of 5 mA, the sum of the maximum power deposited by monopoles is < 4 W, and by dipoles < 5 W (0.25 cm off-axis). Based on CEBAF's experience, the actual power coupled from the HOMs is expected to be much less than maximum.

VI. RF POWER SOURCE REQUIREMENTS

Sizing of the RF power source for the superconducting cavity is not an obvious choice. From Table 1, $R_{SH0} = R/Q \times Q = 2.4 \times 10^{11} \Omega$, $P_{RAD} + P_{CAV} = 5.8$ W, and $P_{REACTIVE} = V_{CAV} \times I_{AV} = 7.5$ kW.

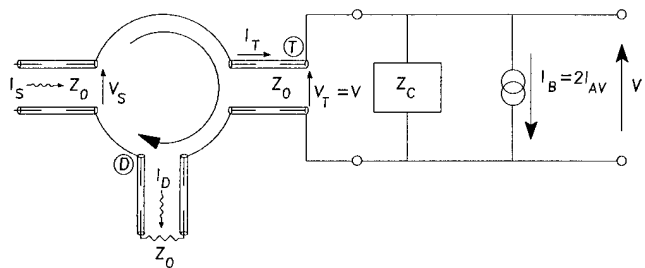


Figure 3. Equivalent Circuit Model of the RF System

The equivalent circuit of the RF system [7] is illustrated in Figure 3, where I_S is the forward source current from the klystron, and I_D is the reflected current which is dissipated through Port D into a dummy load.

The size of the power source assumes that no fast tuner is required and that klystron power and phase are adjusted to compensate for beam loading. Obviously, the majority of the forward power is reflected and absorbed by the waster load of the circulator that has the added advantage of reducing Q_L , thereby increasing the loaded bandwidth, B_L . The amount of "de-Q-ing" is dependent on the transformer ratio N , the coupling transmission ratio between the waveguide and the cavity. From [7] and [8], if the cavity structure is left on resonance, P_S can be expressed as

$$P_S = \frac{I_S^2}{2} Z_0 = \left[\left(\frac{V_{CAV}}{2 Z_0 N} \right)^2 + \left(\frac{I_B N}{2} \right)^2 \right] \frac{Z_0}{2},$$

where I_B is $2 I_{AV}$ and N is the coupling transformer ratio. It is assumed that the coupling factor, $\beta = R_{SH} / (N^2 Z_0) \gg 10$. From this equation, an optimum value of N for a minimum P_S can be calculated. Once N is selected, the following observations can be made:

- The reactive component of the generated voltage to compensate for beam is equal to but in quadrature with the accelerating voltage.
- The power variation from zero to full beam is 2:1, while the incident voltage phase shift is 45° .
- The maximum P_S required is half the reactive beam power loading.

If $N \gg N_{critical}$, the beam induced reactive component requires excessive compensating generator power. If $N \ll N_{critical}$, the generator power required to establish the accelerating field is excessive.

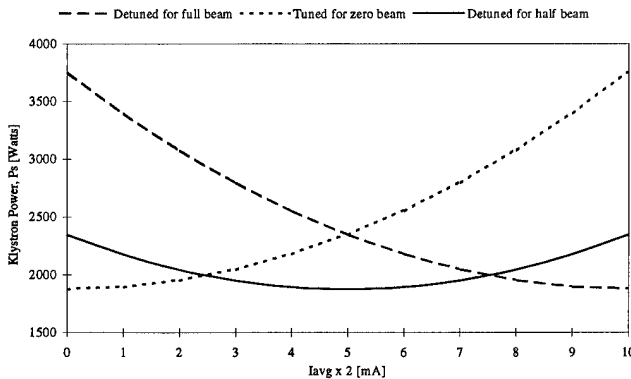


Figure 4. Klystron power required vs beam current

For $V_{CAV} = 1.5$ MV and $I_{AV} = 5$ mA, $N_{CRITICAL} = 6.9 \times 10^4$ and $N = 1.7 \times 10^3$ at $P_{S[minimum]}$. Under these conditions, the required $P_S = 1.875$ kW at $I_B = 0$, and increases to 3.75 kW at $I_B = 10$ mA. The corresponding $Q_L = 6.25 \times 10^5$, and $B_L = 4.57$ kHz. P_S vs I_B is illustrated in Figure 4.

If the cavity is detuned for the full beam reactive power prior to injection with the same coupling factor, $P_S = 1.875$ kW at $I_B = 10$ mA. However, at $I_B = 0$, $P_S = 3.75$ kW if $V_{CAV} = 1.5$ MV is to remain constant. Furthermore, if the cavity detune is preset to compensate for HALF of the full beam reactive power, the generator would be required to deliver 2.34 kW at

$I_B = 0$ and $I_B = 10$ mA, with a minimum of 1.875 kW at $I_B = 5$ mA. These 3 detuning scenarios are illustrated in Figure 4. Further reduction of P_S is possible if the requirement of $V_{CAV} = 1.5$ MV is relaxed at $I_B = 0$. In that case, detuning could be set to compensate for a value $> 0.5 P_{REACTIVE}$.

The most convenient klystron package available is 2 kW. Although easily obtainable, these units have a long lead time and it seems appropriate to buy 2 units for a total combined power source of 4 kW. This will provide adequate power and at the same time build flexibility into the system. If higher currents are required, the system could be easily expanded. Also, if one unit should fail, the other could supply enough power for nearly full current. This could be accomplished with a combination of coupling modification, presetting the cavity tune [Figure 4], or relaxation of the gap voltage at injection. Suitable modifications must be made to the klystron power and phase during injection.

VII. CONCLUSION

The design parameters and behavior of a 2856 MHz superconducting cavity and the corresponding RF power requirements for the NSLS Coherent Radiation Source have been discussed. Results indicate that with relatively minor changes to the XLS Phase I ring, the addition of the superconducting system can provide the large RF voltage necessary for the generation of sub-millimeter wave coherent synchrotron radiation.

VIII. ACKNOWLEDGMENTS

We would like to thank Ron Sundelin, Julie Oyer and the staff of CEBAF as well as James Murphy of NSLS for their valuable insights, contributions, and patience.

IX. REFERENCES

- [1] J.B. Murphy, S. Krinsky, Nucl. Instr. and Meth. in Phys. Res. A 346 (1994) 571-577.
- [2] R. Sundelin, "Application of a 2856 MHz Superconducting Cavity at BNL", NSLS presentation and private communications (1994).
- [3] M. Dzenus et al., Proc. IEEE Part. Acc. Conf. (1991), 2390-2392.
- [4] P. Kneisel et al., Proc. IEEE Part. Acc. Conf. (1991), 2384-2386.
- [5] M.S. de Jong et al., Proc. IEEE Part. Acc. Conf. (1993), 832-834.
- [6] H. Padamsee, "Superconducting RF", AIP Conf. Proc. Vol. 2, The Physics of Part. Accelerators (1992) 1402-1482.
- [7] W. Broome and J.M. Wang, "RF Power Considerations for XLS Coherent Light Source," NSLS Tech Note 491 (1994).
- [8] J. Keane, "RF Power Requirements for Highly Reactive Beam Loaded 2856 MHz Superconducting Cavity," NSLS Tech Note 494 (1995).

DEVELOPMENT OF TESLA-TYPE CAVITY AT KEK

M. Ono, E. Kako, S. Noguchi, K. Saito, T. Shishido, M. Wake, H. Inoue, T. Fujino, Y. Funahashi, M. Matsuoka⁽¹⁾, T. Suzuki, T. Higuchi⁽²⁾, and H. Umezawa⁽³⁾, KEK, National Laboratory for High Energy Physics, Oho, Tsukuba, Ibaraki, 305, Japan, (1)MHI, Mitsubishi Heavy Industries Ltd., Wadasaki, Hyougo-ku, Kobe, Hyogo, 652, Japan, (2)Nomura Plating Co., Ltd., Satuki-cho, Kanuma, Tochigi, 322, Japan, (3)Tokyo Denkai Co.,Ltd., Higashisuna, Koto-ku, Tokyo, 136, Japan

The development of superconducting cavity for high accelerating fields has been continued at KEK on the basis developed for TRISTAN superconducting cavity. Many attempts have been pursued to achieve high field and to understand the phenomena that limit the cavity performance at high field; investigations of how depend on niobium material, surface treatment, heat treatment, surface condition, cavity-shape and cavity-forming. The accelerating fields of more than 25 MV/m have been achieved repeatedly in the several single-cell cavities, even though we did not yet fully understand what had been happened at high field. The present status of those attempts will be reported.

I. INTRODUCTION

The high gradient superconducting cavity is key issue for TESLA (TeV Energy Superconducting Linear Accelerator) project that requires the accelerating field at least 25 MV/m with a Q_0 value of more than 5×10^9 at 1.3 GHz frequency[1]. The cavity performance to fulfill such high field and high Q_0 may be realized by the good surface condition; less dust and less defect, as well as by the properly designed cavity shape to suppress the multi-pacting. The feasibility of mass production of the multi-cell cavity is also kept in mind when the fabrication method is considered. To investigate possible ways of cavity construction, several materials, cavity-shape and methods such as surface-treatment, heat-treatment and cavity-fabrication, have been tried.

A. Surface property

The surface condition or property might depend on the niobium-material itself and the process of cavity construction and preparation:

1. Three RRR materials are used; 100, 200 and 350.
2. Surface treatments such as chemical- (CP) and electro- (EP) polishing were employed as a well-established surface preparation[2]. Tumbling (Tum) was also tried and got promising results. It takes one week for $\sim 50\mu\text{m}$ polishing. Employ the Tum can omit thick CP/EP, then it may lead to less fabrication cost. Final CP ($\sim 20\mu\text{m}$) was still employed, then the degassing was the necessary process.

3. Two types of heat treatment were employed. The treatment at 760 - 800 °C was for degassing of hydrogen that might be absorbed at CP or EP. Whereas, 1400 °C treatments were tried to improve the niobium property; improving RRR.
4. High pressure water rinsing (HPR) of 85 kg/cm² pressure with 13 l/min flow rate are now standard process in addition to the overflow rinsing with ultrasonic agitation (28 kHz) in the hot bath. Megasonic (950kHz) rinsing (MSR) with reflector setting inside the cavity is occasionally used. More effective way such as the agitator itself is setting inside the cavity will be soon ready. Test of megasonic with silicon wafers showed promising result[3].

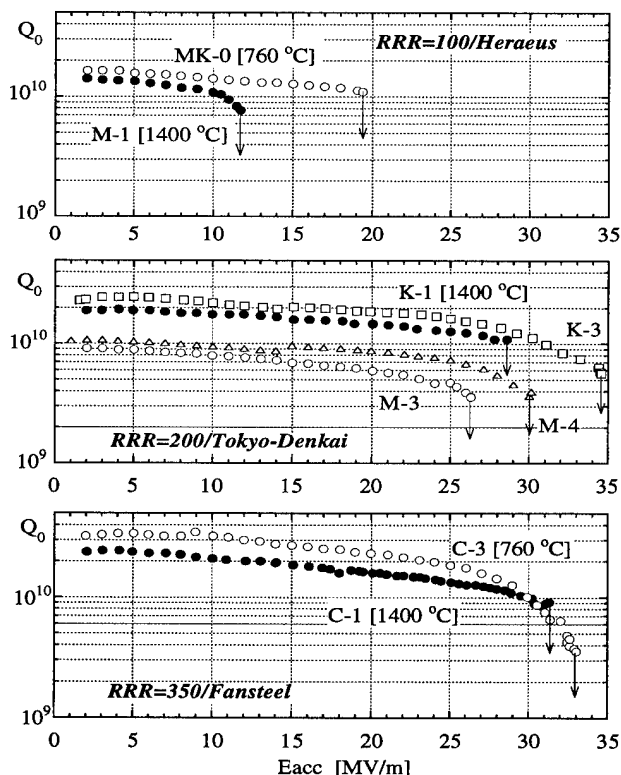


Figure 1. Q_0 vs. E_{acc} of three RRR cavities.

B. Cavity type

Thirteen single-cell cavities have been fabricated and tested since 1991. Two cavities had been already out of order because of too much polishing but these showed good results; $E_{acc} > 20\text{MV/m}$. One of the alive 11 cavities was

fabricated with wave-guide input coupler. The cold test of this cavity has been done once, but the result was not so good; $E_{acc} < 11$ MV/m and limited by quench with self-pulsing. It is too early to discuss about this. The results of our test mainly come from these remaining 10 single-cell cavities.

1. Several cavity shapes called spherical type with 4mm and 1mm flat part at equator and elliptic type were fabricated as discussed in ref.[2]. Also asymmetric type has been tried where "asymmetry" means that the spherical and elliptical half cells were welded to make one single cell cavity.
2. Half cells of both of the spherical cavities and elliptical cavities were made by deep drawing method. Spherical half cells of asymmetric cavities were made by spinning. Electron beam weldings (EBW) were employed for half cell and beam tube welding.

No clear dependence of the cavity performances on these shapes was indicated, even though trying several shapes were motivated to see how the cavity shape affect on the multi-pacting. It seems that the present maximum E_{acc} were mainly governed by the surface property.

C. Experimental apparatus

The cold tests of the cavity have been carried out in the vertical cryostat[2] with movable coaxial input coupler that can be matched to the range of Q_0 from 1×10^8 (4.2°K) to 5×10^{10} (1.8°K). The cavity vacuum is $5-9 \times 10^{-10}$ at cold.

1. Diagnostic; Occasionally the temperature mapping(684 carbon resistors) and X-ray (8 PIN diode) monitor were equipped. With these signals and the electron yield measured at a monitor port can provide convinced field-emission signal at the steady state. While the transient phenomena such as quench can be observed by rf-signals; transmitted and reflected signals.
2. Residual magnetic field; The measured field at room temperature in the cryostat is ~ 15 mG. However, if the T-mapping is equipped, extra field might be introduced as indicated in the Q_0 degradation of factor 2-3; shown in figure 1(M3 and M4).
3. Removing the ceramic at input coupler; The fatal Q-degradation previously reported as Japanese Q-disease was completely disappeared. This phenomenon didn't relate to the surface properties, even though it might be triggered by the break down at the cavity. The data taken after this will be used for discussion.

II. RESULT AND DISCUSSION

The well prepared cavities of several types show the good performances as shown in fig.1 as irrelevant to the shapes and the fabrication methods. It seems that the sur-

face properties are the main issues to determine the performance at least at presently attained E_{acc} region; $25 < E_{acc} < 35$ MV/m.

A. Dependence on the RRR and on Heat treatment

The results of the 200 and 350 RRR attained the E_{acc} more than 25 MV/m with high Q_0 . In the fig.1, the black circles show 1400 °C annealed cavities. The RRR indicated are the initial value of each cavity. The degassing heat treatments taken after CP or EP were enough to attain the high E_{acc} as indicated by the white data points. All 1400 °C annealed cavities show relatively low Q_0 which means the higher residual resistance (R_{res}) compared to non annealed cavities, even though the sample test of the annealing showed the RRR improving. The two non annealing data of the 200 RRR as indicated by M3 and M4 show also relatively low Q_0 , because of extra B-field induced by the T-mapping and not because of less poor surface properties. The two sets of R_{res} of annealing and non annealing show the RRR dependence consistent with the empirical theory; R_{res} is proportional to $1/\sqrt{RRR}$ with 20% larger coefficient for annealing set. If we simply suppose that the 1400 °C annealings improve the RRR, our results are contradicted with this picture. We didn't fully understand these situations, but it can be said that 1400 °C annealing is not necessarily treatment for attaining the present E_{acc} range.

The cavities of 100 RRR didn't reach 25 MV/m yet. However one of these (M1) cavity was the first cavity fabricated at MHI and we recognized some imperfect welding part. The other (MK0) is almost attain 20 MV/m. It is not conclusive whether the RRR of 100 is insufficient for attaining 25 MV/m or not.

There would be another question whether the RRR value is good measure for expecting good cavity performance. If we consider the facts that the three RRR niobium-sheet were supplied from three different companies and the 20% deterioration of R_{res} of the annealed cavities, we can't deny other properties that decide the cavity performance beside the RRR.

B. Dependence on the polishing thickness

Figure 2 shows the correlation between the accumulated polishing thickness and maximum E_{acc} for several cavity tests. We should point out that three data points that exhibit high E_{acc} (K2:elp, K4:asy) though the polishing thicknesses are less than 60 μm . These cavities were treated with Tum ($\sim 50\mu\text{m}$), CP/EP(10 μm), 800 °C degassing, MSR and HPR. Before the degassing both cavities showed Q-disease where only MSR and HPR were applied after CP/EP. If we simply observe the figure 2, the peak is around 300 μm ; if we trace one particular cavity, at more

than 300 μm polishing no improvement or rather degrade the cavity performance can be observed. It should be pointed out here that the horizontal axis represents also different time for different cavities and several efforts intending to improve the cavity performance have been done in these periods; figure 2 shows the history of our tests after removing the ceramic. The cavities attained Eacc below 20 MV/m are already discussed before; expressed as Q-disease, RRR=100 and with W.G. coupler.

Figure 2 may indicate the possibility that the smaller polishing ($\sim 100\mu\text{m}$) will be enough for attaining high field; Eacc>25MV/m.

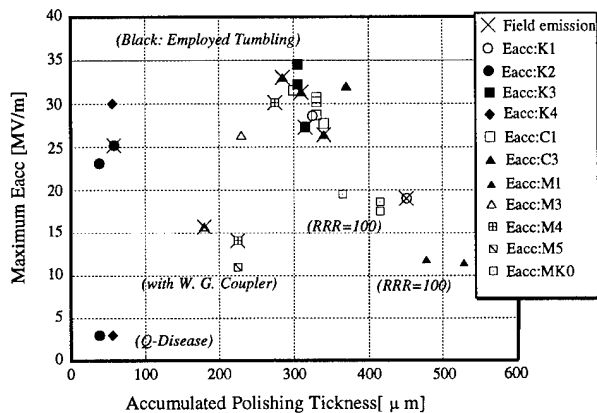


Figure 2. Polishing thickness vs. Eacc. Summary of our cavity cold tests.

C. Decay at maximum Eacc

The observed decay times (τ) of the cavity field at maximum Eacc are $\sim 200 \mu\text{sec}$ where τ is defined by $\tau_{1/2} / \ln 2$. At a glance the decays were almost exponential though we didn't check it precisely. Figure 3 shows the field dependence of τ of several cavities; 16 cold tests of 8 cavities. At high field ($>20\text{MV/m}$) it seems that τ depends on Eacc in a simple way. This behavior may indicate the fact that the quench at maximum Eacc have happened at some limited region of the cavity as explained below. The energy deposit (q) at the surface induce the temperature rise (ΔT) and the quench will be initiated. Two type sources of the q can be considered. The first is ohmic loss given as the product of the defect/dust area (S), current (i) and the extra resistance (ΔR); $q = S i^2 \Delta R$. The second is the deposit by electron irradiation. In this case q , irradiated position and size(S) may be function of Eacc. Assume that whatever the types of q , the τ is mainly determined by the energy deposit at quench-area as given by $q_n = S_n i^2 R_n$ where S_n is area and R_n is resistance of normal state. The S_n may be function of q , S and the thermal quantities of the cavity such as specific heat and thermal conductivity. In the 1st case the q_n is the function of i , R_n and thermal quantities. The position of ohmic loss must be limited to some region to repro-

duce simple Eacc dependence; possibly at equator. In the 2nd case simple Eacc dependence may be natural consequence once the emitter position is limited to some region; possibly at iris. The data are classified to four categories as strong-, weak-, no X-ray detected at quench and not clear data due to lack of monitor (+). The reasons of these are not understand yet. Same cavity showed different X-ray behavior even though same treatments have been applied. Two types possibilities can show similar Eacc dependence if the position of S_n is near the equator and if they have similar q . Recall that the q/S almost define ΔT , then S is determined if q is given. The nature of quench may indicate that the equator and iris are suspicious place for limiting our maximum Eacc; welding part or dust.

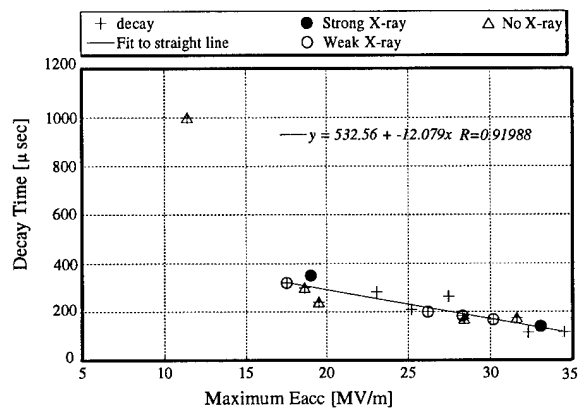


Figure 3. Field dependence of decay time.

III. CONCLUSION

To attain the high field the RRR of 200 is enough. Not so much polishing may be required with our recent treatment. The cavities seem to be limited by thermal quench caused by the defect/dust at equator or iris. The effort to make seamless cavity by explosion is just started for intending to reduce the cost. Eliminating the suspicious welding part may also break through the present limit. The investigations of niobium properties by the magnetization method are now progressing and may reveal important aspects of the surface properties including the welding part.

IV. REFERENCES

- [1] M. Tigner, "Superconducting Linear Collider", Proc. of the LC92, Garmish-Partenkirchen, Germany, July, 1992.
- [2] E. Kako et al., "Test Results on High Gradient...", 6th Workshop on RF superconductivity, CEBAF, USA, 1993.
- [3] K. Saito et al., "Study of Ultra-clean Surface...", ibid. [2]
- [4] E. Kako, et al., and K. Saito, et al., XVth Int. Conf. on High Energy Acc., Hamburg, Germany, 1992, p966-971.

STUDY OF LUMINOUS SPOTS OBSERVED ON METALLIC SURFACES SUBJECTED TO HIGH RF FIELDS

T. Junquera, S. Maïssa, M. Fouaidy, A. Le Goff, IPN (CNRS - IN2P3) 91406 ORSAY cedex, France
B. Bonin, M. Luong, H. Safa, J. Tan, CEA - DAPNIA - SEA, 91191 GIF-SUR-YVETTE cedex, France

Abstract

The performance of high gradient superconducting RF cavities for electron accelerators is mainly limited by field emission. Major improvements have been recently obtained using different surface conditioning techniques confirming the involvement of metallic particles in field emission enhancement. In this paper we present the results obtained with an optical apparatus attached to an RF copper cavity equipped with a removable sample which is subjected to high RF fields ($E_{pk} > 40$ MV/m). Stable light spots are observed on the sample surface and their intensities and optical spectra are measured as a function of the surface electric field. The total emitted current is simultaneously measured by an isolated hollow electrode facing the sample. Particles of different types were deliberately sprinkled over the sample surface and the luminous features are studied. Light intensity, spectral power density and evolution of the luminous sites provide useful information for understanding the field emission phenomena and the conditioning effects.

I. INTRODUCTION

In this paper we report on the development and experimental work performed with an optical apparatus attached to an RF cavity. A detailed description of this device and some preliminary results were presented in previous papers [1] [2]. The initial goal was to develop a diagnostic tool able to localize and characterize the light spots which are observed on the surface of cavities submitted to high electric fields. This effect has been observed in DC experiments [3] and sometimes an intense luminous activity has been reported in RF cavities with heavy field emission.

II. EXPERIMENTAL SET UP

a) Cavity

A simple copper cavity has been proposed by the Saclay Group [4] [5] for studying the RF field emission on removable samples. Field emission from metallic surfaces at room temperature is practically the same as from those at liquid helium temperatures. A simple cavity with a removable sample, operating at room temperature offers fast turn around and low operating costs. The work concerning deliberately contamination with metallic particles was presented in references [4] [5] [6]. An identical cavity was slightly modified to simultaneously observe the top of the sample through an optical window and collect the electron current with a hollow electrode was developed [1] [2]. Two types of samples were used in

the present study [Fig.1]: #1 giving $E_{max} = 60$ MV/m and #2 giving $E_{max} = 100$ MV/m (for 5 kW peak input power). These are the electric fields on the top of the samples which can be maintained for pulse lengths in the range of $10 \mu s$ to 5 ms with a duty cycle of 1 %. The field obtained with #1 samples was calibrated using a X-ray detector and the field with #2 samples was calculated with means of a computational code.

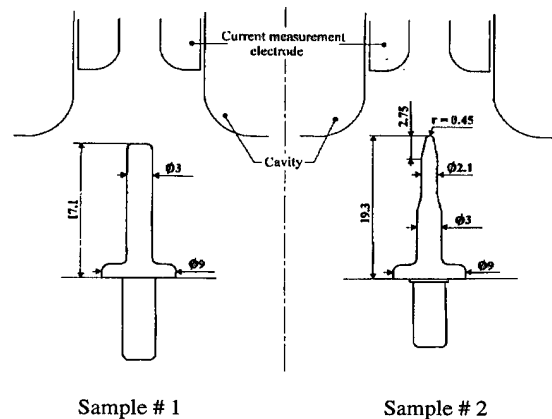


Fig. 1 : Sample geometry (all dimensions in mm)

b) Optical detectors

A simplified scheme is given in Figure 2. The intensified camera has a sensitivity of 5×10^{-4} lux in the wavelength range of 400 - 650 nm (at 40 % of maximum relative response). A detailed description is given in Ref. [2]. During the first tests a series of high-pass filters was used for a rough evaluation of the spectral power density with a resolution of 50 nm. The spectral analysis system was recently improved. A pair of crossed slits (50 μm) was inserted in the optical path. While the slits are moved to select the light emanating from just one spot. A prism is then positioned on the optical path and the dispersed light analysed by a cooled CCD multichannel sensor (Hamamatsu C5809 model).

This two dimensional CCD array (64 vertical x 512 horizontal) integrates the incoming light during the exposure phase. At the end of this time, the photocharges of individual pixels are accumulated, first along the vertical axis (binning phase) and then sequentially transferred to a readout stage. A sample and hold circuit delivers a low impedance video signal which is digitized by an oscilloscope. This signal is processed by a PC computer program which displays the power density spectrum for each exposure phase.

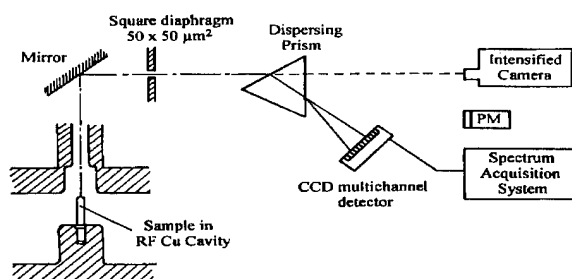


Fig 2 : Optical detectors

Due to the wavelength dependence of the refractive index of the prism, the wavelength range covered by each CCD channel varies from channel to channel : 1nm/channel at 400 nm, 10 nm/channel at 1100 nm (1 channel corresponds to 64 vertical pixels). The CCD sensitivity and channel calibration were performed with different near-monochromatic light sources (laser diode, LED, narrow band filters) [Fig. 3].

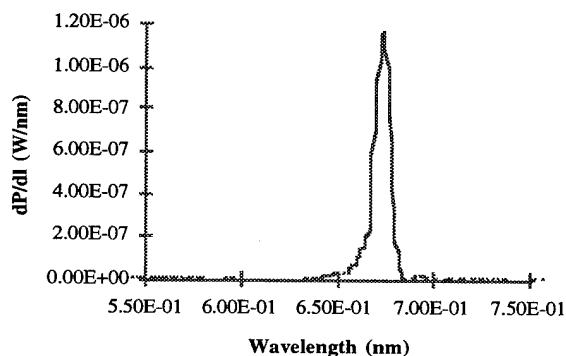


Fig. 3: Calibration spectrum obtained with a 670 nm laser diode

Our calibration of power sensitivity was within $\sim 7\%$ of the manufacturer's values : a spot with luminous intensity of 10^{-14} W is detectable by this means. The correspondance between wavelength and channel numbers was accomplished with ± 1 channel error by using an interpolation method between the monochromatic wavelength values.

III. RESULTS

Samples were prepared using a technique which is now established [4]. Particles are sprinkled on the top of a clean sample placed over the cold vapors of an LN_2 bath. The particles stick to the moistened surface and after drying remain well adhered (for samples prepared in this manner, the particles remain attached during sample mounting in the cavity and the majority remain attached even with the application of electrostatic fields). The samples are mounted in the cavity on a laminar flow bench. The prepared cavity is then evacuated and the experiment starts when the pressure reaches the range of 10^{-7} mbar. The past efforts of the GECS group were concentrated on

field emission from metallic particles and surface scratches [4, 5, 6]. In this paper we focus on observations made on samples contaminated with dielectric (Al_2O_3) particles.

Two sizes of alumina particles have been studied : large particles (50 - μm) and small particles ($\sim 1\mu\text{m}$). On examination of the samples in the SEM, it was found that the smaller particles tended to agglomerate into larger clusters, but there were many individual particles as well.

Large particles

A copper sample (type # 1) contaminated with alumina particles was submitted to RF pulses of 4 ms (1 Hz repetition rate). Luminescent spots were clearly observed starting at a field of 5 MV/m. Increasing the field up to 30 MV/m leads to a higher density of spots on the top of the sample and a higher luminous power [Fig. 4]. The electron current was very unstable (500 μA at 10 MV/m).

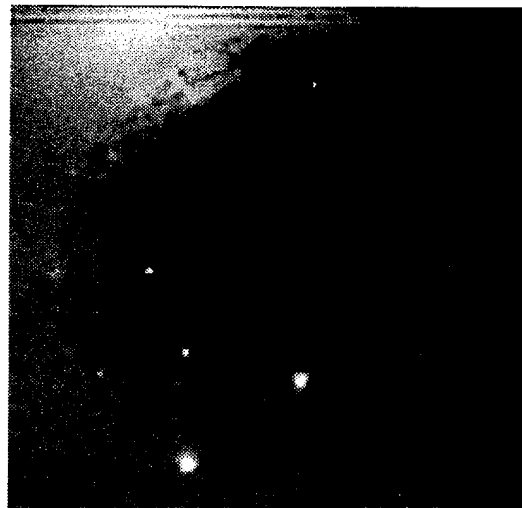


Fig. 4: large alumina particles at $E = 8$ MV/m

Above this field level luminous tracks were observed, sometimes following straight trajectories, other times curved [Fig. 5].

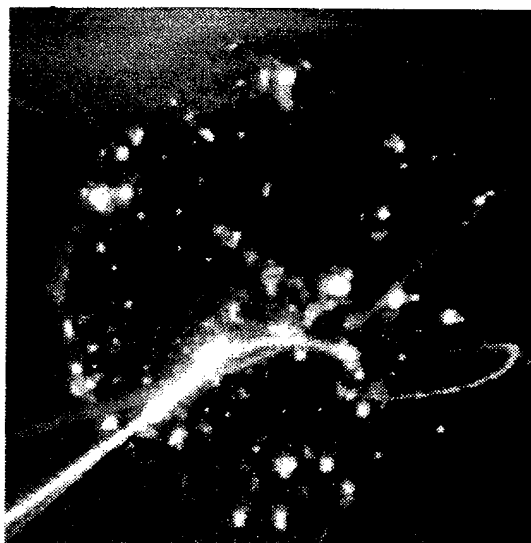


Fig. 5: large alumina particles at $E = 20$ MV/m

These tracks appear to be originated from the light spots and are accompanied with an increase of the vacuum pressure, higher electron current and important disturbances in the frequency tuning of the cavity. After several RF pulses the electron current and luminous effects stabilize, but each time the RF power level is increased it triggers a new spectacular pattern of light tracks and sometimes "explosion-like" luminous effects. Eventually a field level of 40 MV/m was reached and a more stable emission phase was obtained. At this point the RF power was turned off and the cavity vacuum allowed to recover. The cavity behaved very differently during the next experiment. The current was quite stable and found to be roughly Fowler-Nordheim in nature. Luminous activity did not start until 20 MV/m. Several individual spots were measured with the spectral analysis system. Each spot showed a spectrum [Fig. 6] with same shape but with a different spectral density peak value and wavelength (ranging from 600 nm to 800 nm). One spot was studied between 30 - 40 MV/m; it was found that the peak wavelength did not change as the field level was increased. This study took several hours and during this time some of the light spots remained quite stable

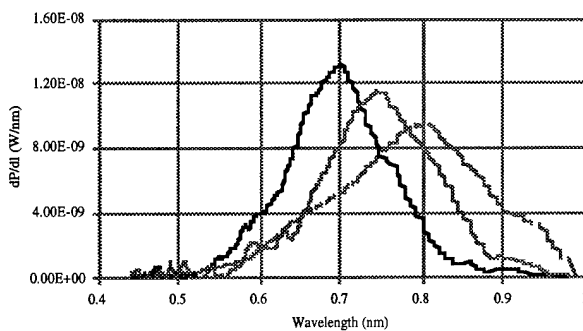


Fig. 6 : Three different light spots

Afterwards, the sample was examined in a SEM. Melted features were found on alumina particles with diameters on the order of 10 μm . Small clusters of smaller particles ($\sim 5\mu\text{m}$ in diameter) coated the sample surface and some craters were also identified in their vicinity.

Small particles

In this experiment a niobium sample of type #2 was used which gave more stable operating conditions. The electron current was quite low (15 μA at 80 MV/m) and unstable during the first few minutes. Small luminous spots [Fig. 7] were observed which remain visible just for 1 or 2 RF pulses (100 μs long, 5 Hz repetition rate, estimated field 80 MV/m). After this conditioning period the pulse length was increased to 2 ms (1.2 Hz repetition rate). This time, no light spots were visible on the top of the sample and the electron current stayed stable ($I_e \approx 2 \mu\text{A}$ at 80 MV/m). Examination in the SEM showed a large number of small craters (1 or 2 μm) in the area where the light spots had been visible. No trace of initial particles was founded over the surface. The short life and instability of the light

spots made the spectral measurement very difficult in this experiment.

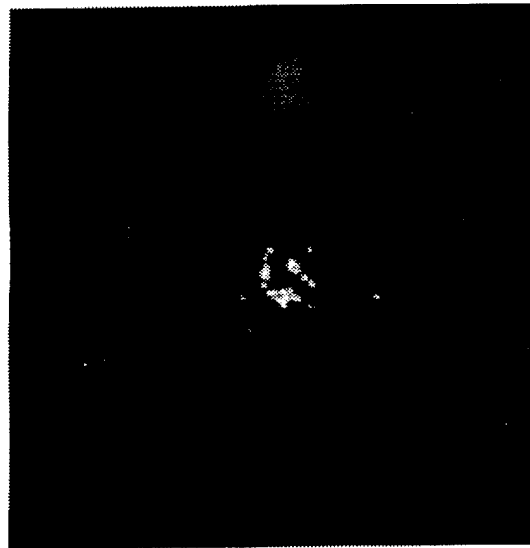


Fig. 7 : Small alumina particles at $E = 80 \text{ MV/m}$

IV. DISCUSSION

These experiments show that dielectric particles interact strongly with the RF fields in the cavity. They emit light and may be responsible for the observed electron current. There is also a clear dependence on the particle size.

The unstable behavior during the conditioning phase is accentuated for the larger particles which produce higher currents and more intense light spots. The light spectra show some similarity to those observed in alumina waveguide windows [7]. Some luminous features observed in the experiment with large particles have been also observed in DC experiments [3] : same order of magnitude of the luminous power in a light spot (10^{-12}W), spectral power density in the range 600 nm - 800 nm and peak wavelength not dependent on the electric field.

Let us consider the RF heating of these particles. The power density absorbed by a dielectric is given by $P(\text{W/m}^3) = 1/2 \epsilon_0 \epsilon_r \omega E^2 \tan\delta/2$. For alumina ($\epsilon_r = 10$, $\tan\delta = 10^{-3}$) in a field of 50 MV/M at 1.5 GHz, we find $P \sim 10^{12}\text{W/m}^3$. The temperature increase of a particle of any size can be calculated using the specific heat ($C_p \approx 756 \text{ J/kg.K}$) and density 3970 kg/m^3) of alumina. The time constant τ , to reach this temperature is proportional to the contact thermal resistance, R_{th} and to the total heat capacity C of the particle. From SEM measurements, a value of $R_{th} \geq 10^7 \text{ K/W}$ has been determined giving time constants in the range 10 μsec - 100 msec.

V. REFERENCES

- [1] T. Junquera, A. Le Goff, B. Bonin, H. Safa, J. Tan : "6th Workshop on RF Superconductivity" (Newport News, Oct. 1993) CEBAF report, p. 1014,
- [2] T. Junquera, S. Maïssa, M. Fouaidy, A. Le Goff, B. Bonin, H. Safa, J. Tan : Proc. EPAC 94 (London 1994), p. 2203,
- [3] R. Hurley, P. Dooley, J. Phys. D : Appl. Phys. 10 (1977) L 195,
- [4] J. Tan, H. Safa, B. Bonin, J.M. Tessier : J. Phys. D : Appl. Phys. 27 (1994) 2644,
- [5] J. Tan, H. Safa, B. Bonin, M. Jimenez : J. Phys. D : Appl. Phys. 27 (1994) 2654,
- [6] J. Tan, H. Safa, B. Bonin, J. Jodet : Proc. EPAC 94 (London 1994), [7] S. Michizono, Y. Saito, S. Yamaguchi, S. Anami, N. Matuda, A. Kinbara, Proc. XVth ISDEIV, Darmstadt (1992), p. 614.
- [7] S. Michizono, Y. Saito, S. Yamaguchi, S. Anami, N. Matuda, A. Kinbara. Proc. XVth ISDEIV, Darmstadt (1992), p. 614.

TEST RESULTS FOR A HEAT-TREATED 4-CELL 805-MHZ SUPERCONDUCTING CAVITY*

Brian Rusnak, Alan Shapiro
Los Alamos National Laboratory, Los Alamos, NM 87545

Abstract

Assessing superconducting technology for potential upgrades to existing proton accelerators as well as applications to future high-current machines necessitates developing expertise in the processing and handling of multicell cavities at useful frequencies. In order to address some of these technological issues, Los Alamos has purchased a 4-cell 805-MHz superconducting cavity from Siemens AG. The individual cavity cells were double-sided titanium heat-treated after equatorial welding, then the irises were welded to complete the cavity assembly. The resulting high RRR (550-730) in the cells enables stable operation at higher cavity field levels than are possible with lower RRR material. Additionally, the high thermal conductivity of the material is conducive to rf and high peak power processing. The cavity was also cleaned at Los Alamos with high-pressure water rinsing. Results from the initial cavity tests, utilizing various processing techniques, are presented.

Introduction

The 4-cell 805-MHz niobium cavity was originally purchased from Siemens AG as a prototype test piece for a proposed pion accelerator [1]. As such, it was fabricated using state-of-the-art techniques for maximum accelerating fields. Most notable was the double-sided titanification and preliminary etching of the niobium cells (with equator welds) before the irises were welded. This gave a residual resistance ratio (RRR) of greater than 550 in the cavity-equator welds, and bulk-material RRR values around 730. These values were obtained by parallel-fired samples. The cavity was designed for a $\beta=0.92$, with a beam-pipe radius of 2.6 inches.

* Work supported by Los Alamos National Laboratory Directed Research and Development, under the auspices of the United States Department of Energy.

In the interest of obtaining high accelerating fields, the cavity manufacturing processes of inspection, forming, machining, welding, firing, and etching were stringently specified [2]. Additional processing refinements were also added, based on LANL research in field emission in single cell cavities. Augmentations to the standard cavity processing used by the manufacturer included a 0.5- μm filter and heat exchanger for the recirculating etch chemistry, a long (90 hours) spray rinse with ultrapure water, and High Purity Liquid Chromatography grade (HPLC) methanol rinsing.

The original manufacturer cleaning was supplemented by additional cleaning at Los Alamos that included high-pressure ultrapure-water cleaning of the cavity and components and microscopic inspection of ancillary components and flanges.

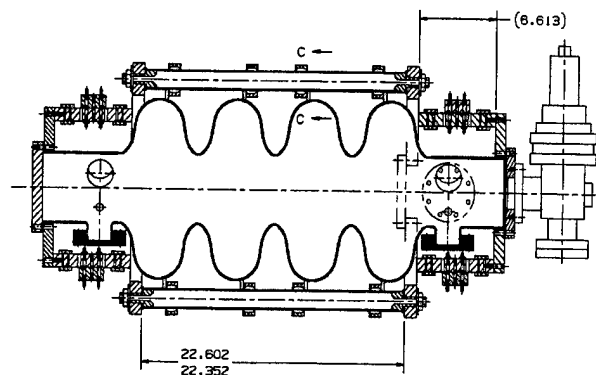


Figure 1. Sectional engineering drawing of the 4-cell 805-MHz cavity.

Mechanically, the cavity was stiffened with 6 titanium tubes connected to the cavity with welded tabs and anchored to two titanium bulkhead rings on each end, as shown in figure 1. The end half-cells are deformed using a titanium tuner that has no backlash. The cavity was designed to be sealed with silver plated Helicoflex Delta seals on niobium-hafnium alloy flanges. The Helicoflex seals remained

leak-tight throughout the test and the stiffening scheme produced no adverse effect. Overall, the mechanical aspects of the cavity performed as expected.

Analysis was done in the cavity design to specify the room-temperature frequency value such that 805-MHz was obtained upon cooldown to 4 K. The targeted room-temperature π -mode resonant value of 803.450-MHz gave a 4 K value of 805.077-MHz, in close agreement with calculations [3]. The ability to reliably predict the final frequency from room temperature values is useful for manufacturing purposes.

RF system

As this was a vertical cavity test in the lab and extensive conditioning was envisioned, an adjustable coupler was designed for delivering power to the cavity. The coupler was based on 3-1/8" coax, and used a choke joint to reduce the current on the rf seals [4,5]. In measurements, the coupler covered an external Q range of 2×10^6 to 1×10^{11} , as designed [6]. Cold and warm windows were used to isolate the cavity vacuum near the cavity, so a long section of the coax line was under vacuum. Quarter-wave stubs were used to support the center conductor without unduly stressing the coaxial windows.

RF power for high-power conditioning was supplied by two klystrons that, combined, provided CW power up to 18-kW and pulsed power up to 180-kW at 10-Hz and with 10-msec pulse lengths.

Test results

Two tests were carried out on the cavity, both at 2 and 4 K. In the first test, cavity characterization and performance evaluation tests were done, which provided initial Q values, coupler range, and the π -mode frequency. RF conditioning with up to 1-kW forward power was also done, usually in conjunction with the performance testing. The cavity responded very well to this rf conditioning, and it took approximately an hour to realize the gains shown in figure 2. Field emission was observed as the limiting mechanism of the cavity at 2 K. The amount of field emission decreased with increased conditioning time, as noted by x-ray levels. At 4 K, the field level was limited by the rf power available.

Higher power processing was attempted using the klystrons, but the test was limited by an arcing problem in the coaxial high-power switch. The arcing required keeping the power level below 100-kW with a pulse length less than 0.5-msec. With this pulse profile, and an external Q of 2×10^6 , the cavity fields only achieved the values obtained during CW conditioning, and thus, further conditioning was not realized.

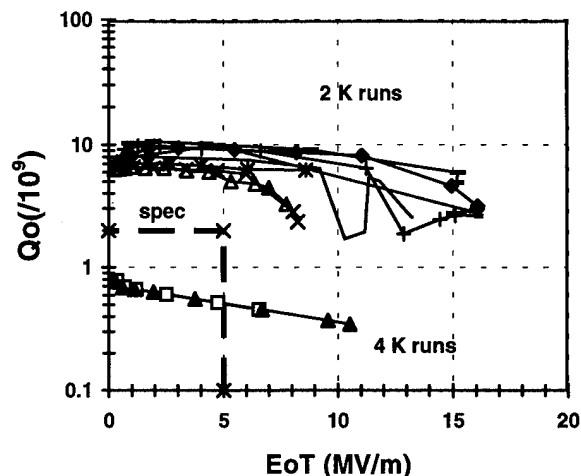


Figure 2. Unloaded Q related to accelerating field in the cavity. The original specification at 2 K is shown as a dashed box in the left corner. The maximum field obtained was field emission limited. The different lines represent different power sweeps.

Conditioning with CW power up to 1.5-kW was also tried, but was limited by center conductor heating leading to breakdown in the driveline.

Conclusion

The cavity performed very well. The fabrication and cleaning techniques used yielded a cavity with high RRR that sustained high field levels. At 2 K, the cavity obtained a maximum E_oT of 16.3 MV/m with field emission at a Q_o of 3×10^9 , and ran at 8-10 MV/m with minimal field emission.

Acknowledgments

As with any experimental endeavor, the test is the final culmination of a great deal of work by many people. The authors would like to acknowledge the work of J.N. DiMarco, E. Gray, and G. Spalek in the design and specification of the cavity tested, and the fabrication efforts of the personnel of Siemens AG.

References

- [1] D. J. Liska, et.al., 1992 Linear Accelerator Conference Proceedings, Ottawa, Ontario, Canada, August, 1992, AECL-10728, vol. 1, pp 163-165.
- [2] J. N. DiMarco, Statement of Work, LANL Purchase Request Z-2876, Specification # 10253, 1992.
- [3] G. Spalek, LANL report, LA-UR 92-1246, April, 1992.
- [4] E. R. Gray, et. al., 1992 Linear Accelerator Conference Proceedings, Ottawa, Ontario, Canada, August, 1992, AECL-10728, vol. 2, pp 450-452.
- [5] G. Spalek, LANL report, LA-UR 92-1344, April, 1992.
- [6] G. Spalek, LANL report, LA-UR 92-1349, April, 1992.

AN ADVANCED ROTATING T-R MAPPING & ITS DIAGNOSES OF TESLA 9-CELL SUPERCONDUCTING CAVITY

Q. S. Shu, G. Deppe, W-D. Moeller, M. Pekeler, D. Proch, D. Renken
P. Stein, C. Stolzenburg, DESY, Hamburg 22603, Germany
T. Junquera, A. Caruette, M. Fouaidy, IPN (CNRS - IN2P3) Orsay, France

Abstract

An advanced rotating temperature and radiation mapping has been developed for investigation of field emission & thermal breakdown of TESLA 9-cell superconducting cavities in superfluid He. More than 10,000 spots on cavity surfaces can be investigated in one turn with 5° angular stepping. We locate a heated area with maximum $\Delta T=3.3\text{K}$ around the 5th cell's equator. A heat flux density of 5 W/cm^2 in the region $\Delta T=3\text{K}$ and total heat power $Q\sim 100\text{W}$ going to LHe from the area were calculated. An emitter responsible for the heating was identified at the iris area ($S_0=8\text{cm}$) of the same cell according to T-maps associated with a simulation of impacting electron trajectories. The cavity reached $E_{acc}=20\text{ MV/m}$. We briefly introduce the technical layout, experimental data and analysis results. The surface scanning thermometers, mechanical structure, moving adapting device and a fast data acquisition are discussed in detail in [1], [2].

I. INTRODUCTION

A. Field Emission and Thermal Breakdown

Great progresses have been achieved in pursuing high accelerating gradients of superconducting cavities due to the world-wide efforts [3]. However, the field emission (FE) and thermal breakdown (TB) are still the main obstacles preventing SRF cavities from confidently reaching $E_{acc} = 25\text{ MV/m}$, the TESLA's goal (TESLA is an international effort for the TeV Energy Superconducting Linear Accelerator).

B. T-R Mapping

Most of the FE sources and TB defects on the inner RF surfaces of cavities are submicro-sizes [4] and activated only at high RF fields while cavities in a superconducting state. The main approaches to understand the FE and TB are to study the hot spots and radiation (X-rays induced by impacting FE electrons) on the cavity surfaces during RF operation. Various advanced T and/or R mapping have been developed and comprehensively used at CERN[5], Cornell [6], DESY, Saclay [7] and Wuppertal [8]. T-R mappings can be classified into two categories:

(1) Fixed Mapping: Thermometers (and/or photodiodes) are fixed on the surfaces of cavity. They have higher thermometer efficiency (using grease as bounding agent) in HeII and simpler mechanical structures than rotating one. However, some 700 of thermometers are needed for an one-cell 1.5 GHz cavity [6].

(2) Rotating Mapping: For a 9-cell 1.3 GHz cavity, a rotating T-R mapping uses about 100-150 of thermometers instead of $\sim 6,000$ (9×700). The thermometer efficiency,

accuracy and reproducibility are highly depending on the heat transfer condition at the sensor location on the cavity wall

The rotating mapping recently developed at DESY combines measurements of T & R for TESLA 9-cell cavities (a complicated geometric structure). Therefore, rather sophisticated mechanical design and surface scanning thermometers is needed to meet all the performance requirements in superfluid He.

II. TECHNICAL LAYOUT

Total 116 specially developed surface scanning thermometers [2] and 32 photodiodes (PIN Silicon/S 1223-01) are assembled into 9-rotating arms as shown in Figure 1 A, B. The thermometer enhance the thermal contact with cavity by a silver tip while isolated from HII with an epoxy housing. Due to a reinforced structure of TESLA cavity, the thermometers can not directly touch the surfaces of cavity iris. Considering the electrical fields reach maximum at iris, 4 photodiodes are mounted in the end of each arm to monitor FE induced X-rays while 14 thermometers are used to monitor the temperatures in the entire region between irises of each cell. Only 9 thermometers are at the first and last arms.

A driving and suspending structure in superfluid He is

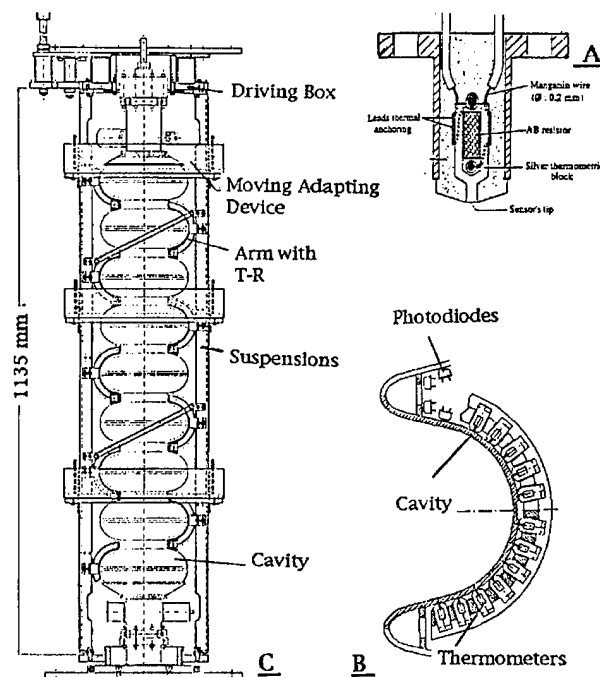


Figure 1: (A) A superfluid He scanning thermometer. (B) A rotating arm. (C) The DESY rotating T-R mapping without rotating measuring cables.

designed to gently turn the arms around and uniformly press the thermometers (through a spring-holder structure, $P=100\text{ g}$

per thermometer) onto the cavity surfaces. A large number of electronic measuring cables have to move with the rotating arms when the T-R mapping rotates. These cable become very rigid in LHe. A moving adapting device is successfully designed to overcome the problem. The space in the TTF vertical cryostat is very constrained that makes the mapping design even more difficult.

Driven by a computer-controlled stepping motor, the T-R arms can be automatically turned to any expected position on the cavity with a accuracy of 1 degree. More than 10,000 spots on cavity surfaces can be investigated in one turn with 5° angular stepping. Two Ge-thermometer and three additional scanning thermometers are used to monitor the change of bath temperature during measurement. Maps can be taken with auto-scanning of entire cavity surface or scanning with time in a fixed position. The effective resolution of temperature measurement is less than 5 mK. One longitudinal measurement in a fixed angular position can be completed in less than 10 ms. All data taken, control and display are performed by a Sun-station computer with a LabViewTM language program. Figure 1 C shows the assembly of TESLA T-R mapping without cabling system. The technical aspects will be presented in detail at [1].

III. TEST AND DIAGNOSES

A TESLA prototype cavity -1 has reached 20 MV/m as shown in figure 2. Previously, cavity -1 had been limited by thermal breakdown at about $E_{acc} = 10$ MV/m. Afterwards, the cavity -1 was heat treated at 1400°C in a vacuum oven [9] for one hour with Titanium purification. The cavity was removed 80 μm of material from the inner RF surface and 30 μm from outer side by chemistry, followed by high pressure rinsing with ultra-pure water [9]. Then, the cavity was equipped with the rotating T-R mapping and tested in a vertical cryostat of $T < 2.1$ K.

A. Locating of Heated Areas and Intensity

We successfully locate the heated areas and their intensities associated with processing of cavity RF test. In the test the cavity -1 was initially stopped by heavy field emission at point A of 11.2 MV/m with a Q , 8.5×10^8 . The T-map

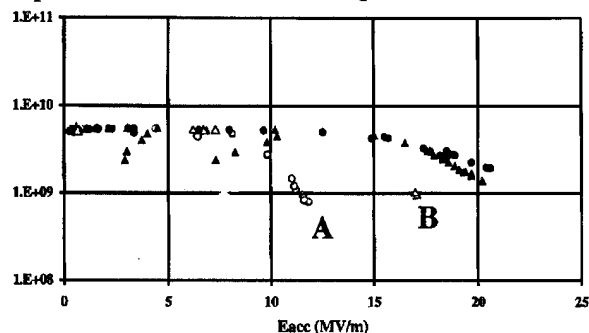


Figure 2: Overall RF performance of the TESLA cavity -1. Dots present first test, triangles present second test. (notice: the low power Q was corrected to about 1×10^{10} by later data)

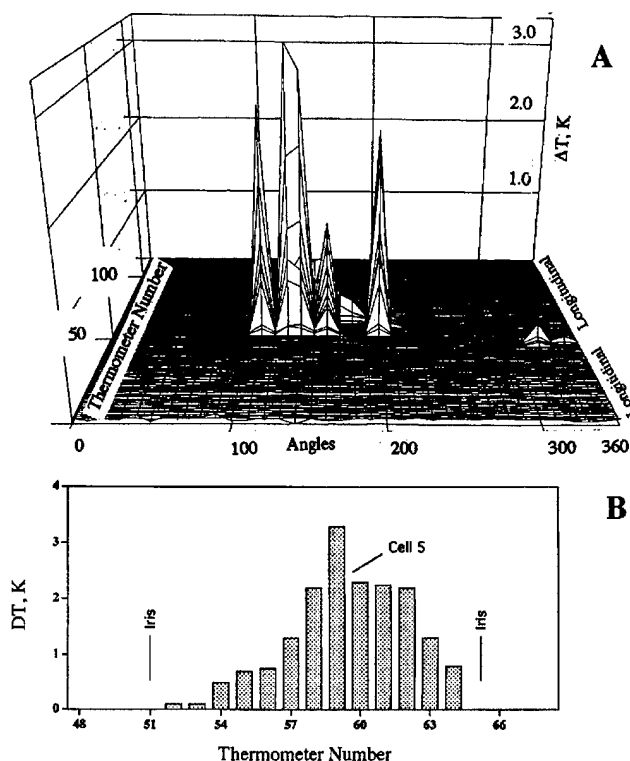


Figure 3: A, A temperature map taken at 11.2 MV/m for TESLA cavity -1. B., Longitudinal ΔT plots, fixed at 140° .

(Figure 3A-3B) indicate an important heated region delimited by 12 thermometers (#53 to #64) centred close to the equator of the 5th cell, between the 110° to 200° angles. out of this region the heating is very low. The ΔT value in this region is 100mK - 3.3K. The x-axial of figure 3 is the thermometer number from 0, close to the top iris of cell-1, to 116, close to the bottom iris of cell-9. The y-axial represents the angular location on the cavity surface. The high pulse RF power processing (HPP, up to $E_{acc}=30$ MV/m) [10] was introduced to the cavity and successfully eliminated the field emitters. Another T-map also witnessed the FE elimination. The shape of Q vs. E plots, map after HPP and FE electron trajectories indicate that a serious defect heating in the area is excluded. After HPP, the cavity finally reached 20 MV/m in cw mode.

The cavity was stayed in the cryostat and naturally warmed up to about 200 K during the New-Year-Eve/95, and then cooled down and tested again. Strong field emission in the cavity was activated about 17 MV/m (point B). The hot spots are located in different angular position from the previous one in figure 3. The cavity reached 20 MV/m again (Q recovered also) only with a low RF power process. Similar phenomena was observed and explained in [11].

B. Analysis of Thermal Performance

The experimental data obtained with the T-R mapping is consistent with the thermal analysis if we consider the following assumptions: high efficiency of thermometer at high heat flux, heat transfer governed by Kapitza regime, and electron trajectories impacts over a large area.

The magnetic field heating at equators of the 5th cell, for $E_{acc}=11.2$ MV/m and $R_s=30$ n Ω , gives only $\Delta T=5$ mK. From the RF measurement, we can estimate the total dissipated power in the cavity and distinguish the two main contributions: (1) dissipated power in the cavity wall due to magnetic losses: $P_{rf}=13$ W, covering entire 9 cells, and (2) the power related to the electron FE: $P_{elec}=173$ W, focusing on local region.

The very high value ΔT measured in this region (100mK-3.3K) can only be explained by assuming that the efficiency of a scanning thermometer increases strongly with the heat flux density at the interface of cavity wall and HeII. This tendency has been observed in several thermometer calibration. We can estimate a heat flux density of 5 W/cm² in the region $\Delta T=3$ K based on experimental values of Kapitza conductance for Nb. Such a high heat flux density is slightly less than the critical heat flux densities reported in experiments with metallic flat heaters in HeII [12], so it is believed that the heat transfer is in the regime governed by Kapitza conductance. The integration of the product of Kapitza conductance and ΔT over the heated region leads to a total heat power going to He bath: $Q \sim 100$ W. This value is consistent with the RF measurements of the experiment.

C. Identifying of FE Origins

Locating origins of FE and TB is very important to understand the influence of various cavity processing and also to a guided reparation of defected cavities. The measured hot spots directly indicate the location of a defect in case of TB. However, the measured hot spots only indicate the landing of impacting FE electrons, but not the emitter.

The simulation of FE electron trajectories demonstrate the following interesting results: FE electrons from an emitter can impact over a very large area, the shape of trajectories are sensitive to emitter location (S_o), and an emitter responsible

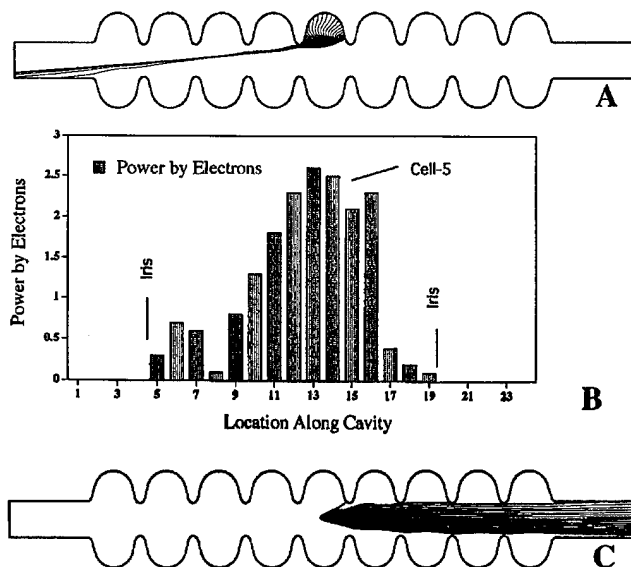


Figure 4: (A) FE electron trajectories of an emitter located at $S_o=8$ cm. (B) Power distribution contributed by impacting FE electrons from $S_o=8$ cm. (C) Electron trajectories, $S_o=9$ cm. for the heating shown in figure 3 is successfully identified.

Since electron trajectories, impacting electron energy and power deposition distribution (dP/ds vs. s) are controlled by the E_{acc} and S_o , a series of simulations are performed by changing S_o at $E_{acc}=11.2$ MV/m, assume $\beta=200$, S_e (emitter area) = 1×10^{-13} m². It is found that an emitter located at $S_o=8$ cm (at the iris area in a curvilinear co-ordination) has electron trajectories shown in figure 4A. Its power distribution (dP/ds vs. S) in figure 4B seems to be closed to the shape of the measured temperature distribution. It is indicated that heated area at equator (usually by defects) can also be caused by FE. The β and S_e (emitter area) of the candidate emitter were adjusted to fit with the thermal analysis and RF experimental data. For instance, at $E_{acc}=11.2$ MV/m, if $S_e=1 \times 10^{-13}$ m², $\beta=400$, the total mean power landed over RF period is 10W.

The FE electron trajectories are very sensitive to the emitter location in the cavity. For example, if an emitter locates at $S_o=9$ cm, FE electrons are driven out of the initial cell and rush to the cut-off tube of the cavity (Figure 4C).

IV. FUTURE DEVELOPMENT

The improvement of the mechanical system and cabling of the mapping is scheduled in the May of 95. The computer data acquisition for photodiodes will also be commissioned at next test.

V. ACKNOWLEDGEMENT

We sincerely thank P. Kneisel (CEBAF), W. Weingarten (CERN), H. Padamsee, J. Graber, W. Hartung (Cornell), M. Champion (Fermilab), C. Pagani (INFN), B. Bonin (Saclay) and G. Wueller, R. Roeth (Wuppertal) for many fresh discussions and hints. Sincere thanks are also presented to our DESY colleagues in the cryogenic group, vacuum group, mechanical group, MHF group for their support.

VI. REFERENCES

1. Q. S. Shu et.al., TU-A3-6, CEC/ICMC Conf., Ohio, 1995.
2. T. Junquera et. al. TTP 14, this Conf., PAC/95.
3. D. Proch: Proc. - 5th workshop on RFS, DESY, 1991.
4. R. Sundelin: Proc. - 6th workshop on RFS, CEBAF, 1993.
5. H. Padamsee, Applied Supercond. Conf., Boston, 1994.
6. Ph. Bernard et. al, Nucl Inst & Met in Phys Res vol 190
7. Ph. Bernard et. al. & S. Buhler et. al, the 5th (and 6th) workshop on RFS, DESY 1991 (and CEBAF, 1993).
8. Q.S. Shu et.al., IEEE transaction, Vol. 27, No. 2, 1991.
9. Q.S. Shu et.al., Nucl Inst & Met in Phys Res A278. 1989.
10. J. Knobloch, et. al., SRF 94-0419-03, Cornell Univ., 1994
11. B. Bonin et. al., Proc. of 6th workshop on RFS, 1993.
12. M. Fouaidy et al Proc 5th workshop on RFS, DESY, 1991.
13. R. Roth and G. Muller et. al., Proc. of the 5th (and 6th) workshop on RFS, DESY 1991 (and CEBAF, 1993).
14. A. Matheisen, D. Trines, TESLA Meeting, 1994.
15. J. Graber et. al., Nucl Inst & Met in Phy Res A278. 1989.
16. Q. S. Shu et. al., IEEE transaction, Vol. 25, No. 2, 1989.
17. A. Kashani, S. W. Van Sciver, Cryogenics 25, 1985.

IMPROVEMENTS TO POWER COUPLERS FOR THE LEP2 SUPERCONDUCTING CAVITIES

J. Tückmantel, C. Benvenuti, D. Bloess, D. Boussard, G. Geschonke, E. Haebel, N. Hilleret, S. Juras, H.P. Kindermann, J. Uythoven, C. Wyss, CERN, Geneva, Switzerland

M. Stirbet, Institute of Atomic Physics Bucharest, Romania

Abstract Power couplers for the 352 MHz LEP2 superconducting RF cavities have been plagued by vacuum and electron outbursts which are attributed to multipacting. Processing of these couplers has been a lengthy operation which was often needed again after high power running even if only for a relatively short time. We report here on recent progress made in improved production methods of coupler parts and special treatment of surfaces, as well as practical tests and simulations of geometrical coupler modifications.

I. INTRODUCTION

All couplers of the LEP 352 MHz superconducting cavities are located on the cut-off tubes to avoid ports on the cavity cells themselves. The first power coupler design used a homogeneous 50 Ω antenna line [1]. Based on this coupler an adjustable version was designed containing a $\lambda/4$ section of 25 Ω impedance which houses a choke construction [2].

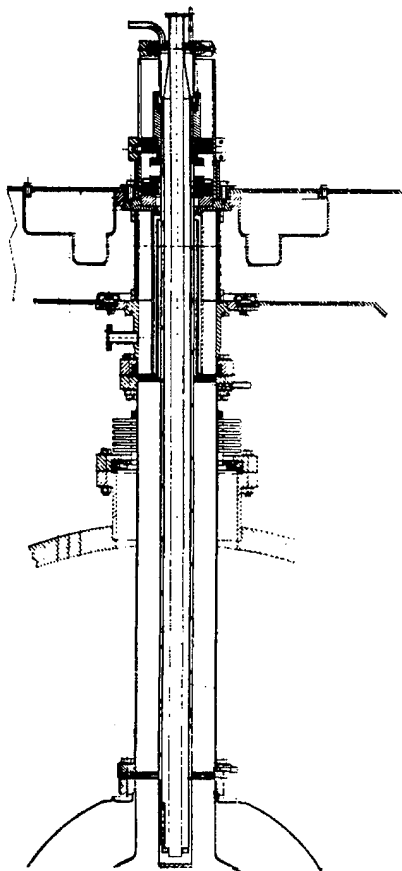


Fig.1 : The adjustable coupler

Keeping the RF-line outer diameter of 103 mm with the proven cylindrical window design as used for the LEP copper cavities (operated at up to 120 kW and being tested up to 180 kW [3]) allowed a sufficient safety margin at the original design value of 60 kW. However, specifications for field level and beam current were increased, swallowing all of this safety margin. It also has to be considered that due to the RF transformation via the 25 Ω choke the RF currents near the ceramic window are strongly increased.

During a surface test of a cavity (standing wave case) a leak developed linked with a burn-mark on the outer coaxial line. Subsequent tests with improved instrumentation (local vacuum gauges on the couplers, electron pick-ups, infrared camera) showed that in fact levels with vacuum and electron bursts could be observed when ramping the power. Static magnetic fields could influence the levels — but not suppress them — thus confirming that multipacting (MP) was the culprit.

One-side MP trajectories in coaxial lines had already been simulated [4], neglecting the magnetic field. In the power range used by us the influence of the magnetic field is small and with a simple BASIC program similar tracks with impacts only on the *outer* coaxial conductor in the 50 Ω part of the line were found at the E-field maxima of a standing wave where the magnetic field is exactly zero [5]. Note the scaling law: the RF power where the MP occurs is proportional to f^4 . Furthermore two-side MP was detected on the 25 Ω line section of the adjustable coupler. Table 1 shows, in the range used, the most dangerous predicted and measured levels for the 50 Ω couplers. P_{sw} is the necessary incident power on the coupler in full reflection (sc. cavity without beam) producing the peak voltage V_{RF} in a 50 Ω line section. Use of a systematic scan procedure including the magnetic field [6] identified the same levels.

order	V_{RF} [kV]	$P_{sw(th)}$ [kW]	$P_{sw(ex)}$ [kW]
3	4.1	42	38-43
4	3.2	26	26-28
5	2.6	17	15-18

Table 1. One-side MP levels theoretical (th) [5] and experimental [ex] in 50 Ω line

II. COUPLER PROCESSING AND DECONDITIONING

Processing of the couplers (with the local coupler vacuum used to control the input power) proceeds in two stages. In the first stage a pair of couplers is mounted on

a resonant copper cavity with strong over-coupling. One coupler is used as input coupler. The second one as output coupler can be connected either to a matched load or an adjustable short circuit. Conditioning takes in general 4-5 days, starting manually to process the low levels, then using pulsed mode with pulse lengths between 10 μ s and 50 ms and a duty cycle around 20 %. Finally ramping up and down under computer control in cycles of 2-5 minutes processes up to 200 kW.

A second processing is necessary on the cold cavities and generally done in parallel on the couplers of a whole module (four cavities in a common cryostat). Initial conditioning has to be repeated and again takes several days including pulsed power processing with peak fields in the cavities reaching 8 MV/m.

For couplers from the first production lot, running at nominal power on the cavities often for only a few minutes was sufficient, to erase the conditioning done before. A reconditioning period of typically several minutes was necessary to regain nominal field. Also, for a perfectly processed coupler, the well known levels reappeared after switching off the RF for several hours. These effects, called deconditioning, were attributed to gas getting trapped on the cold outer conductor.

III. CERAMIC WINDOW IMPROVEMENT

On some of the damaged couplers traces of arcing have been found on the brazing between ceramic cylinder and Kovar ferrule, on the RF contact between Kovar ferrule and copper part, or on the relatively thick titanium coating of the ceramic near to the RF contact (compared to the thin coating on the cylindrical part). It was also observed that during high power operation the windows were strongly heated near the Kovar ferrules.

To avoid these problems the following modifications have been made: i) brazing completely penetrating through the Kovar-ceramic connection, ii) Kovar ferrules machined at the contact surface after brazing and welded to the coupler under pressure to improve the RF contact, iii) more homogeneous titanium coating of the whole ceramic cylinder with a DC resistance decreased from 500 M Ω to 10-20 M Ω , iv) copper plating of the Kovar ferrules to reduce RF losses, v) Improved air cooling around the ceramic cylinder and the ferrule. In fact, couplers equipped with the new windows no longer showed sensitive heating up to 200 kW travelling wave.

In order to permit even higher RF currents the simple pressed contact has been replaced by a spiral contact and tested successfully. But the assembly of this version is much more complicated and delicate.

However, even though the improved windows operated safely under these increased power levels, their use did not eliminate the deconditioning phenomenon and further steps to fight MP itself had to be undertaken.

IV. MEASURES AGAINST MULTIPACTING

Work was done in parallel in several areas and although tests have been done in the warm and cold state of the coupler, a full beam test is still pending.

A Choice of fixed coupler version

Movable couplers are attractive because i) they allow a measurement of the Q versus E curve of a cavity without having to break the cavity vacuum and ii) they can precisely match to a wide range of cavity voltages, beam intensities and stable phases. Unfortunately, due to the restricted space in the LEP tunnel, the choke necessary in the movable coupler had to be folded back into the coupler (25 Ω line). With this geometry two additional MP levels appear. The extra risk associated with these levels was felt to be unacceptable and the movable coupler version was abandoned for the series production. Note that coarse estimates of the cavity Q can be obtained by cryogenic methods and that imperfect matching essentially results in higher fields in the coupler. But even at 200 kW both types of couplers are operated far below any electric field breakdown limit [7].

B Improvement of the surface

As shown by the simulations, the MP takes place on the outer conductor. The corresponding line piece is double walled to allow He-gas cooling. The original work-piece, called 'extension', was produced from rolled and welded sheet-metal, the welding making it difficult to obtain a smooth surface. Therefore the new extensions are now produced — including vacuum flanges — from a single stainless steel forging thus avoiding welding or brazing in critical areas.

The inner surface of the extension has to be copper plated to reduce RF heating. The original fabrication used 'standard' galvanic deposition. To improve the quality of the surface avoiding possible traps for gas, two methods were tried in parallel. One uses a galvanic deposition with pulsed current showing a smoother surface; tests allowed faster MP processing in the warm state. The second deposits copper by sputtering [8]; test showed faster MP processing in the warm but a tedious one on the cold cavities. A version with improved gas cooling also showed good results on a cold cavity. Tests of a sputtered extension submitted to water rinsing are under way. Titanium coating of the extensions has also been tried, but was not successful.

Furthermore, an apparatus to measure the secondary emission coefficient between 1/10 and 2000 eV was constructed and used for measurements on copper and titanium layer specimen.

C. Change of antenna diameter

A geometrical modification [7] was done in changing the antenna line impedance. For impedances of 50 Ω and higher, the multipacting is 'running' only on the outer conductor. By reducing the inner conductor diameter and

scaling the RF voltage proportionally to the line impedance one leaves the fieldmap in the outer coaxial region unchanged. This fact was used to transfer the MP levels to higher powers by reducing the standard antenna diameter of 44.8 mm ($50\ \Omega$) to 30 mm ($75\ \Omega$), thus shifting the levels up by 50% in power [7]. A further decrease of the diameter is not considered due to increased mechanical and thermal problems.

Measurements confirmed this approach: the same MP levels appeared, but at correspondingly higher power, thus giving more margin for operation. The RF currents near the ceramic window are also reduced, compared to the $50\ \Omega$ case, thus permitting the use of the simple pressed contact. All future couplers will be of the $75\ \Omega$ type.

D. Eccentric Coupler

Simulations [9] showed that with an eccentric antenna the MP tracks run around the outer conductor towards the wider gap. Tracks coming from the smaller gap are stopped after only a few impacts due to the changing conditions. It was hoped that tracks starting close to the wide gap would be concentrated on a small strip which would clean more easily.

A pair of such $75\ \Omega$ couplers with 4 mm eccentricity were built and tested on the warm stand. Their behaviour was not better than the average standard coupler. Due to the more complicated fabrication, the idea was abandoned.

E. Injection of Perturbing RF

To break the resonant kinematic conditions of MP, a perturbing RF voltage can be used. This was realised by adding power at an uncorrelated frequency (noise band or single frequency). Since MP can rise in a short lap of time, the injected frequency has to be 'far' away from the fundamental one. An injection of about 2% RF power on a sideband at 200 kHz to 1 MHz frequency distance (klystron bandwidth limitation) was a sufficient perturbation to make (on the warm test stand) MP disappear and significantly reduce it on the cold cavities. Since the cavity bandwidth is below 200 Hz, the second signal does not perturb the cavity voltage

F. Electric DC bias

Perturbation with static magnetic fields had already been tested at an early stage. Influence on the levels had been observed but suppression could not be achieved.

The coaxial antenna geometry offers a relatively simple possibility to apply a DC bias voltage. It is trivial that a DC bias higher than the RF voltage will inhibit all return paths for electrons. Simulations [10] showed that depending on polarity about -1.5 kV or +2.5 kV with respect to ground would already be sufficient to obtain complete suppression up to 200 kW of travelling wave power (5.5 kV RF voltage). Experimentally it was found that with +2.5 kV MP is completely suppressed.

The main problem of this approach has been the capacitors which are needed to separate RF and DC paths. For a first proof of principle with a minimum of

modifications, Mylar or Kapton foils were inserted between the doorknob and the waveguide. During the practical tests on the cold cavities these capacitors showed breakdowns with a rate unacceptable for machine operation. The suspicion is that the breakdowns are caused by sharp edges in the waveguide or by particles introduced in the capacitor during mounting in the open air as it is actually done. As an intermediate solution copper plated Kapton foils will be used. A better version is under development using a coaxial capacitor similar to those of the SPS tetrode amplifiers [11] and mounted in a clean room.

To permit DC bias the He gas cooling of the antenna has been replaced by forced air cooling.

V. CONCLUSION

The RF window has been improved to decrease the window temperature and to reduce the risk of breakdowns. Several approaches to suppress or reduce MP in the LEP2 power coupler have been examined. The choice of a higher antenna line impedance shifted MP levels up by 50% in power. Two perturbation methods have been worked out: Injection of about 2% power on a sideband several 100 kHz above the normal RF frequency and application of a DC bias voltage, achieving complete suppression. For the proof of principle a simplified construction has been used, the safe design for machine application is under way, to be followed by a large scale beam line test.

VI. REFERENCES

- [1] E. Haebel et al., Proc. 3rd Workshop on RF Superconductivity, Ed. K. Sheppard, ANL-PHY-88-1.
- [2] E. Haebel, Part. Accel., Vol. 40, P 155
- [3] J.P. Boiteux, G. Geschonke, LEP note 570
- [4] J.P. Budlinger et A. Laisne, NIM 61 (1968), 253-259 (in French).
- [5] J. Tückmantel, Proc. CERN Main Coupler Workshop, Oct 1992, Editor C. Wyss.
- [6] E. Somersalo et al, TESLA report 94-14.
- [7] E. Haebel, S. Juras, CERN LEP2 Note 95-31
- [8] C. Benvenuti et al, CERN LEP2 Note 94-21.
- [9] J. Tückmantel, CERN LEP2 Note 94-25.
- [10] idem, Note 94-26.
- [11] H.P. Kindermann, R. Maleyran, CERN SPS/88-1 (ARF).

ACKNOWLEDGEMENTS

We would like to thank all technicians for their enthusiastic help, especially J-P. Boiteux and G. Rochepeau, as well as the workshops MT-MF and MT-SM. We also thank M. Karliner, V. Petrov, V. Veshcherevich and V. Yaklev from INP, Novosibirsk, for suggesting the DC bias of the antenna and G. Bachy for proposing the monolithic extension.

Arcing Phenomena on CEBAF RF-Windows at Cryogenic Temperatures*

Tom Powers, Peter Kneisel, CEBAF Newport News, VA and
Ray Allen, Old Dominion University, Norfolk VA

Abstract

During the CEBAF commissioning tests some of the superconducting cavities had light emitting discharges (arcing) which were observed in the guard vacuum space between a warm polymeric rf window and the cold ceramic rf window. A dedicated off-line test system was implemented to investigate the conditions under which arcing may occur and to gain some understanding of the mechanisms leading to this phenomenon through optical spectral analysis. This paper reports on the photoemission spectra observed during the dedicated tests on a single cell 1500MHz niobium cavity with a ceramic window operated at 10MV/m and 2 K. The light emission was detected using a spectrometer with an intensified photodiode array. The effect of moving the window away from the beam line using a waveguide elbow is reported.

I. INTRODUCTION

The CEBAF accelerator system uses 338 superconducting niobium cavity assemblies at 2 K to provide a continuous electron beam of 200 μ A and 4 GeV after 5 recirculations through 2 anti-parallel linear accelerators. Each cavity is equipped with a ceramic rf window located in the input coupler waveguide 7.6 cm away from the beam axis. This window hermetically seals the sensitive superconducting surfaces against the waveguide guard vacuum in line with the 5 kW klystrons. The CEBAF rf windows are presently made from a high-purity (99.9%) polycrystal-line aluminum oxide (Al_2O_3) sheet of dimensions 13.3 cm x 2.5 cm x 0.4 cm thick, which is brazed to a thin niobium foil frame that is in turn electron beam welded to a solid niobium frame for connection to the waveguide system in a bolted flange joint. This window separates the cavity vacuum space from the guard vacuum space which is separated from the pressurized waveguide by a room temperature polyethylene window. During the commissioning of the accelerator many of the cavities were limited by frequent (more than once per day) waveguide vacuum discharge trips which were detected by a photomultiplier tube and caused operation of the machine to be interrupted. In most instances the operating field levels at which this occurred was in excess of the specified operating level of 5 MV/m. To reliably obtain the design value of 400 MeV linacs, the maximum field obtained in 46 of the cavities were limited by arcing. Furthermore, 17 cavities were reduced below 5MV/m because of arcing. Increasing the machine energy above the design value of 4GeV will require that more cavities be operated at levels at which arcing may become a problem. Because of the desire for a 6 GeV to 10 GeV upgrade in the future, a better understanding of the phenomena is required.

* Supported by U.S.DOE Contract DE-AC05-84-ER40150

II. BACKGROUND

These arcing phenomena have been investigated during the past three years and several reports have been published describing the results [1-7]. Two basic phenomena have been observed which are interpreted to be vacuum discharge phenomena [1-4]. In one type of event, the stored energy, as measured by the transmitted power signal, is fully dissipated in less than 5 μ s. This is accompanied by a large, short duration X-ray pulse of approximately 500kRad/hr for less than 5 μ s and a short intense light pulse which is detected at the beam pipe and on both the cavity and waveguide side of the ceramic window. This class of phenomena, which we call "electronic quenches," are interpreted as the effects produced by the sudden injection or liberation of a large number of electrons into the cavity. The electrons and their secondaries quickly absorb the rf energy stored in the cavity and produce an intense bremsstrahlung pulse as they strike the cavity wall, beam pipe, or endplate.

In the second type of event, the cavity stored energy is dissipated in several hundred microseconds (typically 500 μ s) and there is a substantial rise in the pressure of the guard vacuum. During this time light is observed in the waveguide vacuum space. When the cavity energy reaches a minimal level the discharge is extinguished. This type of event is interpreted as a discharge occurring in the window/rf-coupler region which is sustained by the stored energy in the cavity. It has been observed that the discharge may be sustained indefinitely by rf energy supplied by a 2 kW klystron [2]. The light emission during this type of discharge has three different temporal phases. During the first 5 μ s a relatively large light pulse, which has the same temporal and spectral characteristics as that of an electronic quench, is observed. For the next 500 μ s an emission, which has distinctly different spectral characteristics from an electronic quench, is observed. This is followed by a long tail, which has similarities to the long decay tail of the electronic quench. [3]

III. EXPERIMENTAL STUDIES

In an effort to better understand the arcing phenomena, off-line spectroscopic studies of the light emitted by the discharge have been performed. The basic experimental setup which used a single cell cavity is shown in Figure 1. The light produced in the waveguide vacuum space was monitored through a sapphire viewport mounted on the coax-to-waveguide adapter. This light was transmitted from the viewport to a PMT and, through a 300ns optical delay line, to a 0.275m spectrometer. Commercial grade acrylic fibers which provide reasonable transmission from 350nm to 720nm [1] were used as an optical media. The spectrometer configured with a 990

element intensified photodiode array which allowed the available spectrum to be recorded with 0.6 nm resolution. Absolute precision was verified using a mercury vapor source. Through the use of gating and delays different temporal regions of the discharge were examined.

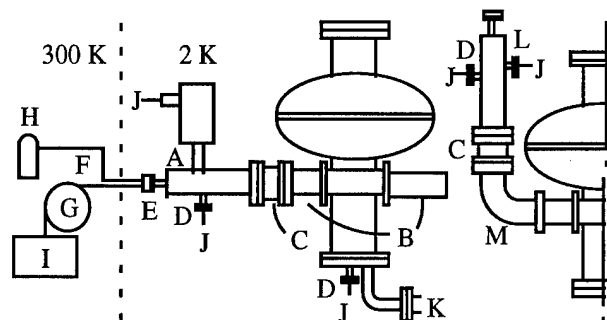


Figure 1. Single-cell cavity configurations showing (A) variable coax-to-waveguide adapter, (B) fundamental power coupler, (C) cold window assembly, (D) field probe adapters, (E) sapphire view port, (F) optical fibers, (G) optical delay line, (H) PMT, (I) spectrometer with intensified detector array, (J) rf cables, (K) vacuum pumpout port, (L) fixed coax-to-waveguide adapter, (M) waveguide elbow.

A series of three experiments were performed. In the first experiment, a standard ceramic window configuration was used. In the second, a right angle elbow of about one-half of a wavelength was placed between the fundamental power coupler (FPC) and the same window top hat configuration, see Figure 1. In the third experiment, the window frame assembly was removed and a 127 μm sheet of kapton was placed between the FPC and the tophat using indium seals. The spectroscopic data taken for each of the experiments is presented as Figure 2. Each spectral plot represents the average of several (11 to 27) individual spectra. For the purpose of identifying observed spectral lines, electroluminescence measurements were made on the ceramic material. For this experiment, a sample of the ceramic material was placed in an electron microscope and irradiated with a 100 pA 30 keV beam. The emitted light was collected and transmitted using UV grade fused silica optics and fibers. The results of this data is presented as Figure 3. Arc rate measurements, presented as Figure 4, were taken for the two ceramic window configurations. The standard position test was performed both before and after the elbow experiment to insure that the cavity arcing characteristics were not effected by the experiment.

Discussion

The irradiated alumina samples, Figure 3, show the commonly present electroluminescence spectra of alumina [9, 10, 11]: a Cr⁺ impurity line located at 694.1nm and a broad spectra centered at 340nm caused by F-centers. The Cr⁺ line was again observed in the spectra of Figure 2a, but, in addition a line at 396.1nm appeared. All of the other lines observed in the ceramic widow discharges were also present in the kapton window discharge. The

hydrogen lines and the line located at 589.9nm seem to be present independent of the window material. These lines are probably due to desorbed gasses which contribute to sustaining the discharge. The group of unidentified spectral lines between 375nm and 500nm on the kapton window are assumed to be generated by the kapton. Further, occurrence of the aluminum line in the data taken

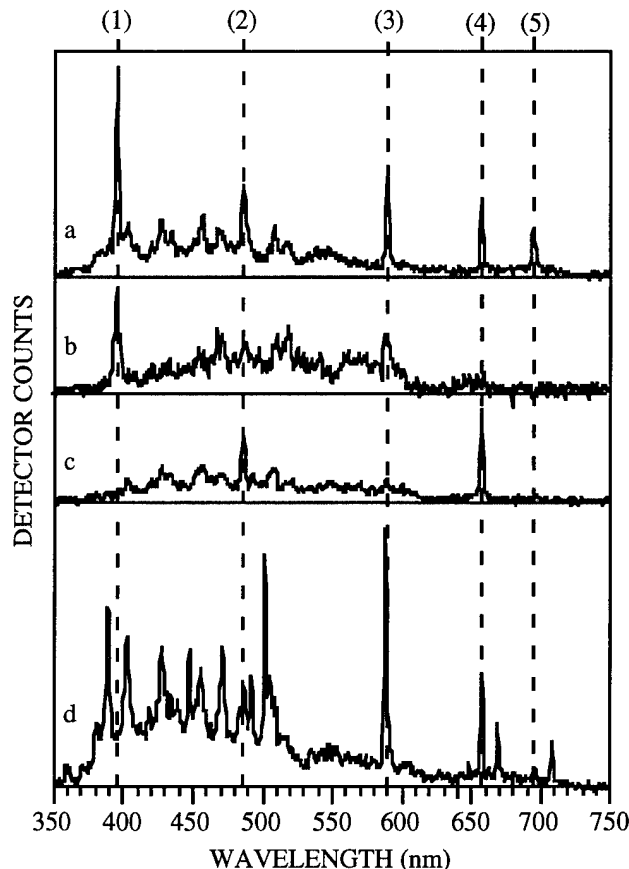


Figure 2. Optical spectra of waveguide vacuum discharges for a) Alumina window, 800us gate b) Alumina window, 1 us gate, c) Alumina window with elbow, 300us gate, d) kapton window, 800 us gate. Marked spectral lines indicate (1) 396.1nm (Aluminum [8]), (2) 486.4nm (Hydrogen [8]), (3) 589.9nm (unknown), (4) 656.3nm (Hydrogen [8]), (5) 694.1(chromium [9]).

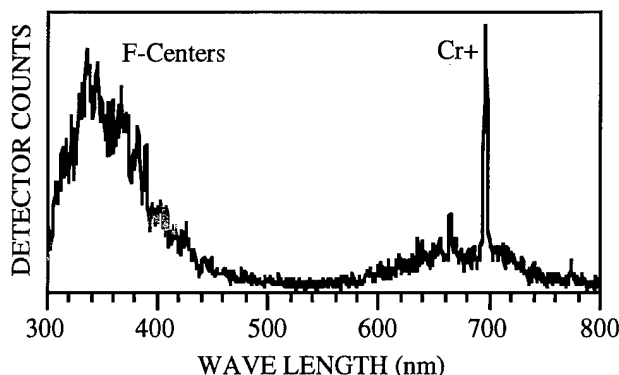


Figure 3. Optical emission spectra from an alumina sample irradiated with a 100pA, 30 keV electron source. The Cr⁺ line is located at 694.1 nm.

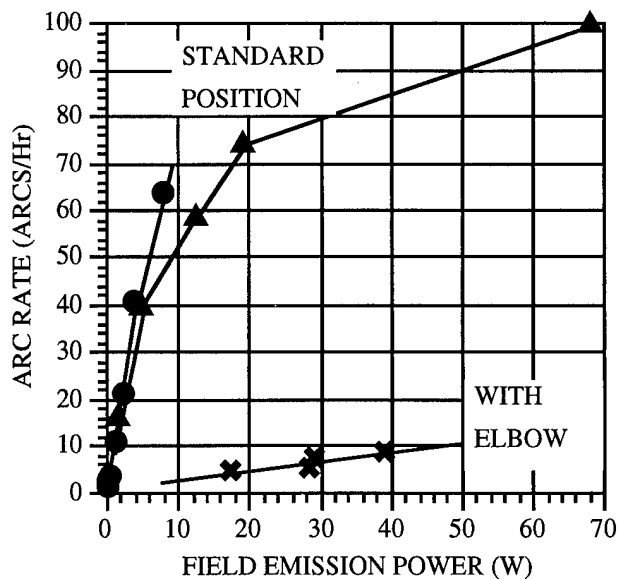


Figure 4. Arc rate as a function of additional power dissipated due to field emission for the same ceramic window with and without a waveguide elbow.

during the first 1 μ s of the discharge indicates that the process which generates it may have a significant roll in the initiation of the discharge. As can be clearly seen in Figure 4, the displacement of the window further away from the beam axis significantly reduces the arcing rate. The absence of the aluminum line in the spectra of these discharges seems to indicate that the arcing phenomenon might be different in nature than in the standard configuration where direct electron impact might be involved in the process. The spectral data taken during this experiment show only the hydrogen lines. This further indicates that the discharge process in this configuration is different than the configuration in which the window has a direct line of sight to the cavity vacuum.

While the exact mechanisms which initiate these discharges are not well understood, two mechanisms which contribute are x-radiation and electron bombardment of the ceramic material. Theoretical studies indicate that secondary electrons, created when field emitted electrons from within the cavities strike the irises adjacent to the fundamental power coupler, have trajectories which would allow them to strike the ceramic window [12]. An additional source of electrons is x-radiation induced photoemission. Electron currents on the order of 10 nA on have been measured on an isolated window frame assembly with a correlation to field emission in the cavity. Some current flow does occur when there is direct radiation through the walls of the cavity. The introduction of a waveguide elbow between the cavity and the window reduces the measured currents [7].

IV CONCLUSIONS

The spectra measured during a waveguide vacuum arc for three different window configurations has been presented. Several spectral lines have been identified. Lines for aluminum (396.1 nm) and Cr+ (694.1 nm) have

been identified as indicators of a possible arc initiation mechanism when the ceramic window is located in the standard position. Other observed spectral lines were also present in the discharges involving kapton window material and a ceramic window in an alternate location. Electroluminescence measurements were performed which confirm the presence of a Cr+ line at 694.1 nm and a broad F-center emission located at 340 nm consistent with previously seen emission from warm resonant ring studies [11]. The location of the window was shown to have a major impact on arcing rate. A reduction of arcing rate by an order of magnitude was seen when a window was separated from the cavity by a half-wave right angle waveguide elbow. More detailed work is required to understand the complex interdependencies involved in the arcing process.

V REFERENCES

- [1] Tom Powers, et al., "Investigation of Arcing Phenomena in the Region Near CEBAF RF Windows at 2K," *Proceedings of the 6th Workshop on RF Superconductivity*, Oct. 1993.
- [2] Tom Powers, et al., "Studies of Arcing Phenomena in the Region of the Cold Ceramic RF Window," CEBAF Technote TN93-030.
- [3] Tom Powers, et al., "Photoemission Phenomena on CEBAF RF Windows at Cryogenic Temperatures," *Proceedings of the 1993 PAC conference*, May 1993.
- [4] L. Phillips, et al., "Some Operational Characteristics of CEBAF RF Windows at 2 K," *Proceedings of the 1993 PAC conference*, May 1993.
- [6] P. Kneisel, et al., "Response of CEBAF's cold RF-Window to Operation in FE-Regime of a Cavity," CEBAF Technote TN94-029.
- [7] V. Nguyen-Tuong, "Electronic Activity at CEBAF Cold RF Window Induced by Cavity Operation," *Proceedings of the fourth EPAC Conference*, June 1994.
- [8] R. W. B. Pearse, et al., *The Identification of Molecular Spectra*, John Wiley & Sons, New York, 1963.
- [9] K. Lee, et al., "Luminescence of the F Center in Sapphire," *Phys. Rev.* 19 (6), 3217-3221 (March 1979).
- [10] B. M. Coaker, et al., "Photon Emission from an Aluminum Insulator in Vacuum Subjected to DC Electrical Fields," *J. Phys. D*, 27, 1994, pp. 1448-1456.
- [11] Y. Saito, et al., "Breakdown of Alumina RF Windows," *IEEE Trans. on Electrical Insulation*, 24 (6), 1029-1032 (1989).
- [12] B. Yunn, et al., "Field-Emitted Electron Trajectories for the CEBAF Cavity," *Proceedings of the 1993 PAC conference*, May 1993.

VI ACKNOWLEDGMENTS

We would like to thank Bret Lewis, Pete Kushnick and Larry Doolittle for their effort in the work described in this paper. We would like to thank Larry Philips and Charlie Reece for their participation in useful discussions.

SURFACE SCANNING THERMOMETERS FOR DIAGNOSING THE TESLA SRF CAVITIES

T. Junquera, A. Caruette, M. Fouaidy, IPN (CNRS - IN2P3) 91406 ORSAY cedex, France
Q.S. Shu, DESY, 2000 HAMBURG 52, Germany

ABSTRACT

In order to investigate the field emission and the thermal breakdown of 9-cell TESLA SRF cavities, 150 specially developed surface scanning thermometers have been built. The description of the thermometers and their calibration in superfluid helium are presented. A special test chamber equipped with a heated niobium plate is used to study the thermometer thermal response versus the heater power at different bath temperature. The comparison of thermometer response with numerical simulations results and experimental data obtained with reference thermometers mounted on the Nb plate using a thermal bonding agent, allows to get an estimation of the measurement efficiency of scanning thermometers. Experimental data obtained with cavities are analysed with the help of the calibration results and numerical simulations.

INTRODUCTION

The development of He II surface thermometers for diagnosing and studying the thermal effects in superconducting RF cavities has been a major activity of the Orsay Group during the recent past years. Several papers describe the different types of thermometers and the main experimental features : fixed thermometers for studies of the anomalous heating of samples mounted on special cavities [1], scanning thermometers for monocell cavities [2] and special vacuum thermometers for Kapitza conductance measurements [3].

In this paper we present the first results of a new development in collaboration with the DESY laboratory, for constructing a diagnostic system for the 9-cell TESLA cavities. As compared to the older devices, a large number of thermometers (> 100) are mounted around the cavity which raises different mechanical and cabling problems. The complete description and the first results are given in an another paper at this conference [5]. In this paper we focus on the calibration of the thermometers and the thermal analysis of the first temperature mapping results obtained.

DESCRIPTION

The surface thermometer design [Fig. 1] is very close to the model developed earlier for the CERN group [2]. The sensitive part is an Allen-Bradley carbon resistor (100 Ohm, 1/8 W) housed in a silver block with a sensor tip of 1 mm diameter for the thermal contact to the external surface of the cavity. This housing is thermally insulated against the surrounding He II by an epoxy envelope (Stycast) moulded around the silver block and into a bronze piece which allows the sensor mounting on the rotating thermometric arm. The thermometers tip must

present a good contact with the cavity wall when scanning: two springs located inside two holes in the body of the rotating arm are used for this purpose, the contact pressure control and adjustment is allowed by means of two screws. Each thermometer has two independent manganin wires thermally anchored to the silver block with ~ 15 cm free length for connecting to each cell board (14 thermometers). At the level of the boards the connectors ensure the cabling dispatching inside the cryostat allowing the motion of the rotating arm.

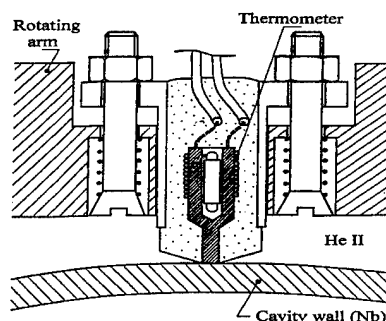


Fig. 1 : Cross section of a HeII surface thermometer

CALIBRATION

Superfluid helium

A representative batch (32) of the 150 thermometers fabricated for this device were tested using a special calibration chamber [1] allowing the mounting of 16 thermometers at every test. In principle all thermometers are located in a region subjected to the same heat flux density. In this experiment the thermometers tip were glued to the Nb heated plate by means of a good thermal bonding agent (Apiezon N Grease) in order to verify the fabrication process. The two thermometers batches (2×16) give a mean thermal response $\langle \Delta T \rangle_1 = 8.0$ mK and $\langle \Delta T \rangle_2 = 8.8$ mK respectively for a total heater power of 195 mW at $T_{bath} = 1.8$ K. Numerical simulation of the plate heater assembly for the same experimental conditions gives $\Delta T = 56$ mK. This calculation was performed in order to evaluate the thermometer efficiency η defined as the ratio of the experimental thermal response ΔT_{exp} to the simulated temperature jump ΔT_{sim} at the Nb - He II interface. In this case we obtained $\eta = 0.14$.

A complementary test was performed by mounting the thermometers in the real operating conditions of the scanning device, (e.g. without any bonding agent between

the thermometer tip and the Nb wall). The results for a batch of 13 thermometers is presented in Fig. 2 at two different heater powers of 1.86 W and 2.8 W. A first group of thermometers was mounted with a contact pressure of ~ 10 bars (spring load of 80 gr) giving $\langle \Delta T \rangle_{1.86} = 2.1$ mK, a second group was mounted with a pressure of ~ 62 bars (spring load of 500 gr) giving $\langle \Delta T \rangle_{1.86} = 6.4$ mK. A third group of fixed thermometers (e.g. glued with grease, not displayed) gives $\langle \Delta T \rangle_{1.86} = 92$ mK. At a higher power (2.8 W) the measurements were $\langle \Delta T \rangle_{2.8} = 6.3$ mK (at a pressure of 10 bars) and $\langle \Delta T \rangle_{2.8} = 16$ mK (at a pressure of 62 bars). All these results clearly show an important decrease of the measurement efficiency when no bonding agent is used : η is now close to 0.01. Notice that in this case, the efficiency is heater power dependant.

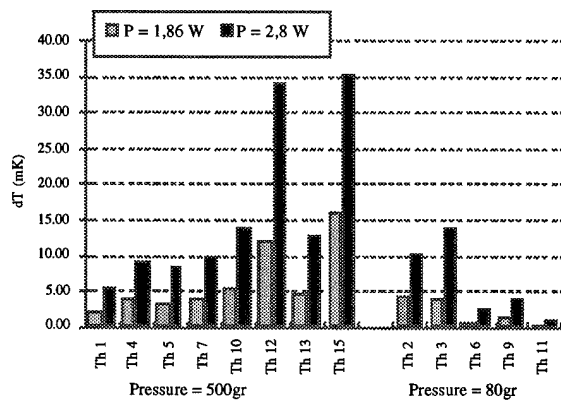


Fig. 2 : Thermal response at $T_{bath} = 1.8$ K (without contact grease)

Subcooled helium I

The subcooled helium bath obtained for temperature over the λ point ($T > 2.2$ K) and a pressure of 1 bar gives the possibility to study heat losses in the cavity wall in a far less constrained mode than in HeII. In this case the heat transfer mechanism is dominated by free convection cooling (laminar or turbulent) which induces the formation of a thick superheated helium boundary layer, the temperature is now quite easy to measure without taking many precautions in the mounting conditions of the thermometers. The calibration was made with the same thermometer batch and the same chamber. The results are displayed in Fig. 3. The same three groups of thermometers were tested giving respectively $\langle \Delta T \rangle_{80g} = 572$ mK, $\langle \Delta T \rangle_{500g} = 651$ mK and $\langle \Delta T \rangle_{fixed} = 537$ mK for a total power of 146 mW at 2.5 K. These values show clearly a rather insensitivity to the mounting conditions and a much reduced dispersion in each group as compared to superfluid helium results. The agreement with a previous published equivalent thermal resistance [4] in subcooled helium at 2.5 K is quite good : the mean measured value is $R_{th} \sim 30$ K/W/cm² which is consistent with the calculated value of 65 K/W/cm² for the same heater [4] power. This agreement

seems to be quite good considering all the hypothesis and simplifications adopted to calculate this thermal resistance in a free convection bath with turbulent flow using dimensional analysis. Anyway and as expected, the comparison with superfluid helium results in terms of thermal boundary resistance (e.g. $R_{th} \sim 2$ K/W/cm², Kapitza resistance at 1.8 K) shows up the benefit of operating in subcooled normal helium. However, the price to be paid is a reduced spatial resolution and a reduced operating accelerating field due to the global cavity heating.

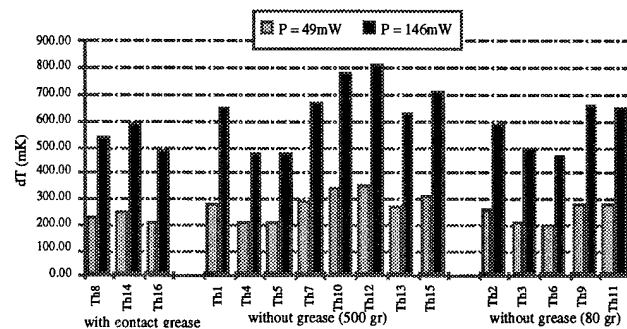


Fig. 3 : Subcooled normal helium test
2.5 K < T_{bath} < 3 K

EXPERIMENTAL RESULTS

The first experimental results using a completely equipped rotating arm (116 thermometers) have been obtained with a prototype TESLA cavity (1.3 GHz, 9 cells) [5]. This cavity, after a heat treatment at 1400 °C in a vacuum furnace, was tested in a vertical cryostat at the DESY TTF facility. During the experiment, high power processing (HPP) was performed which leads to an important improvement of the cavity performances : $E_{acc} = 20$ MV/m at $Q_0 = 2 \times 10^9$ (Q_0 at low field $\geq 10^{10}$). Several T-maps were recorded during the test in superfluid helium bath (before and after HPP) and in a subcooled helium bath (after HPP).

a) Superfluid He II bath

During the first run, the cavity reach a maximum accelerating field (E_{acc}) of 11.2 MV/m limited by a very heavy field emission. The Q_0 decreased from $\geq 10^{10}$ at low field to 8×10^8 at the maximum field. A first T-map was recorded at this value exhibiting very high ΔT in the 5th cell. The heated region was very extended : it concerns 12 thermometers of the 5th cell (Fig. 4) and presents several maximums at different angles between 100 ° and 200 ° (Fig. 5). Very high ΔT were measured (1 K - 3.3 K) in this cell.

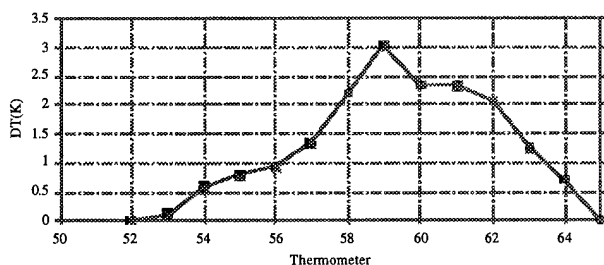


Fig. 4 : ΔT (5th cell thermometers) at 130° azimuthal angle

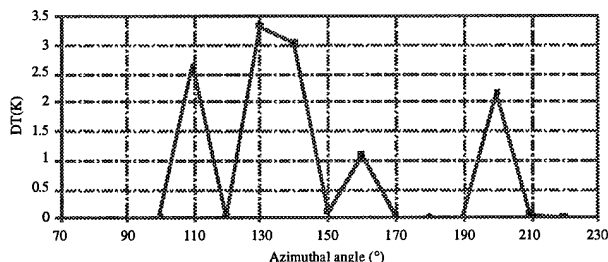


Fig.5 : ΔT (thermometer #59) vs. azimuthal angle

The first question raised by these results is if we may trust the measurements. In order to explain that a very high measurement efficiency of the thermometers must be considered. During the thermometer calibration the measurement efficiency has exhibited a strong dependance on the heat power level : the efficiency is multiplied by 2 when the power is increased from 1 to 3 W. This is completely different from the behaviour of fixed thermometer using a thermal bonding agent (Apiezon grease) which exhibits a ΔT linearly proportional to the heater power. Evidence of high ΔT measured in monocell cavities with scanning thermometers has been observed many times. Values of ΔT in the range of 100 mK to 200 mK have been measured in Nb/copper cavities at CERN [2] with largely lower RF power levels (~ 2 to 10 W).

If we admit a very good efficiency at the high heat flux density encountered in this cavity, another questionable point remains : are such high heat flux density levels compatible with the critical heat flux in He II ? Some references on this subject confirms that metallic heated plates in He II exhibit very high ΔT (5 to 6 K) in the Kapitza regime before reaching the critical flux inducing the transition to film boiling [6].

Extensive calculations of electrons trajectories at 11.2 MV/m shows that emission sites located in the proximity of the iris of the 5th cell could explain such impacts in the equator region of this cell. The azimuthal spreading of the heated area is more difficult to understand. Model calculations simulating a unique emitter site provoking a rather thin electron impact along the azimuthal can explain a smaller angular spreading in the cold face of the cavity. To explain the ΔT shapes observed, a first hypothesis of separated sites located in the same cell at different angles along the iris must be admitted. From the point of view of

the total power involved in this experiment we have performed the integration of the heat power density over the heated region :

$$Q = \int_s q ds \approx S_{th} \sum_n h_k \Delta T_n$$

where S_{th} is an estimation of the equivalent heated surface measured by one thermometer which has been arbitrarily taken equal to the product of the distance between two thermometers and length corresponding to a scanning angle of 10°. h_k is the Kapitza conductance at the measured point

$$h_k = H_k \cdot f(\Delta T) = h_0 T_{bath}^n \cdot f(\Delta T/T_{bath})$$

$$H_k = 0.017 T^{3.62} \text{ W/cm}^2\text{K} [7].$$

This integration gives $Q \sim 100$ W which seems to agree quite well with the RF power measurements. The power attributed to the electrons is easily deducted from the ΔQ_0 at $E_{acc} = 11.2$ MV/m ($\Delta Q_0 = 10^{10} - 8 \times 10^8$). A simple calculation gives $P_{electron} \sim 170$ W. So, we obtain values which are of the same order of magnitude : the discrepancy could be attributed to H_k variations from Nb sample to another and to η which is not exactly 1. This good agreement could add some confidence to the recorded ΔT . This strong field emission was efficiently treated by HPP technique in the same experiment and a very good E_{acc} value was reached (20 V/m). A T-map taken at 17.7 MV/m shows that the heating observed in the 5th cell has disappeared and that some lower heating is now measured in the cells #5 and #7 reaching some peaks of $\Delta T \sim 50$ mK at angles of 100° and 280°.

b) Subcooled helium bath

Several T-maps were performed in a subcooled HeI bath at bath temperature in the range 2.3 - 2.5 K with $E_{acc} \sim 18$ MV/m. All the maps shows a global heating (ΔT) ~ 400 mK of all the cells and some scattered hot points in cells # 5 and # 7. It is interesting to compare this measured values with the results obtained during the calibration : the surface resistance ($R_{BCS} + R_{residual}$) at a wall temperature of 3 K is estimated to be $R_S = 150$ nΩ. In the equator region of the cells the surface magnetic field corresponding to $E_{acc} = 18$ MV/m can be computed : $H_s \cong 6.10^4$ A/m. Then the heat flux density in this area is calculated : $q_s = \frac{1}{2} R_S H_s^2 \approx 27 \text{ mW/cm}^2$. Considering the equivalent thermal resistance measured during the calibration tests in subcooled helium ($R_{th} \sim 30 \text{ K/W/cm}^2$) we can estimate the resulting heating : $\Delta T \sim 800$ mK. This is a good agreement with the measured values when we take into account all the simplifications adopted to perform this estimation the thermal resistance depends on the heated surface orientation with respect to the vertical (buoyancy force).

REFERENCES

- [1] M. Fouaidy, T. Junquera, A. Caruette, Proc. 5th Workshop on RF Superconductivity Hamburg (1991) p. 547,

- [2] Ph. Bernard, D. Bloess, E. Chiaveri, C. Hauviller, T. Schiller, M. Tauffer, W. Weingarten, P. Bosland, A. Caruette, M. Fouaidy; T. Junquera, Proc. 6th Workshop on RF Superconductivity (Newport News, Oct. 1993) CEBAF report, p. 739,
- [3] S. Bühler, A. Caruette, M. Fouaidy, T. Junquera, Proc. 6th Workshop on RF Superconductivity (Newport News, Oct. 1993) CEBAF report, p. 1002,
- [4] R. Romijn, W. Weingarten, IEEE Trans. on Magnetics, Mag 19 (1983), p. 1318,
- [5] Q.S. Shu, G. Deppe, W. Moller, M. Pekeler, D. Proch, D. Renken, P. Stein, C. Stolzenburg, T. Junquera, M. Fouaidy, A. Caruette, (this conference),
- [6] A.Kashani, SW. Van Sciver, Cryogenics 25 (1985) p.238
- [7] K. Mittag, Cryogenics 13 (1973), p. 94.

MICROWAVE SURFACE RESISTANCE OF YBaCuO SUPERCONDUCTING FILMS LASER-ABLATED ON COPPER SUBSTRATES

J. Liu, K. Asano, E. Ezura, M. Fukutomi¹, S. Inagaki, S. Isagawa, K. Komori¹, S. Kumagai², H. Nakanishi, M. Tosa¹ and K. Yoshihara¹

KEK, National Laboratory for High Energy Physics, 1-1 Oho, Tsukuba, Ibaraki 305 Japan

¹National Research Institute for Metals, 1-2-1 Sengen, Tsukuba, Ibaraki 305 Japan

²Mitsuba Electric Mfg. Co., Ltd. Kiryu-shi, Gumma Japan

Abstract

In order to apply high- T_c material to a real accelerator cavity, it may be indispensable that the material is deposited on metal substrate. It is now possible to align the c axis of YBa₂Cu₃O_y (YBCO) film perpendicular to a metal surface. Furthermore, the constituent crystals can be in-plane aligned with a laser ablation technique following the formation of yttria-stabilized-zirconia (YSZ) buffer layer of controlled grain orientation. Using a demountable copper cavity operated at 13 GHz in the TE₀₁₁ mode, the microwave surface resistance was measured over a temperature range from 11 K to 300 K.

I. INTRODUCTION

Since the discovery of a high- T_c superconductivity, the possibility to use a high- T_c material to an accelerator cavity has been discussed. For high-power accelerator cavities, not only must high- T_c films be deposited onto large-area substrates of complex shape, but the use of metallic substrates of high thermal conductivity is also essential. As the thermal conductivity of high- T_c materials is rather low[1], heat must be released to keep the film in a superconducting state even under a high field.

In KEK we have been involved[2] in developing thick high- T_c films of YBCO or Bi₂Sr₂CaCu₂O_y. The YBCO films were prepared through a low-pressure plasma-spraying technique and melt-reaction process either on silver substrate or nickel-plated copper substrate. The Bi₂Sr₂CaCu₂O_y films were prepared either by a screen-printing or spraying method either on silver substrate or silver-plated copper substrate. The microwave surface resistances were measured using a demountable cylindrical cavity made of copper at 3 GHz in the TE₀₁₁ mode. The surface resistance of YBCO film on a silver end plate was 0.2 mΩ at 20 K. However, the preparation of well-controlled surface of this size (the diameter and length is 150mm and 84mm, respectively) is expensive, time-consuming and not necessarily successful.

Therefore we made another demountable cavity operated at 13 GHz of the same mode. It was cooled by a compact refrigerator and temperature-controlled from 11 K up to the room-temperature. The high- T_c films were formed by a laser-ablation method on well-controlled YSZ layer. The surface resistances of the samples were found from the measured quality factors following the same procedure as before[2]. However, as the reflection at 13 GHz was more severe and temperature-dependent than that at 3 GHz, we were required to be more cautious in measuring the rf parameters.

II. FABRICATION OF FILMS

An YSZ/Cr film was used as buffer layer for the deposition of YBCO on copper substrates. The Cr underlayer was found to be essential to protect copper against oxidation, resulting in good adhesion of the YSZ layer on copper. Copper substrates, 36-mm dia. disk with a thickness of 3 mm, were polished to a mirror finish. They were then ion-plated with the Cr layer of about 0.5 μm, subsequently sputter-deposited with the YSZ buffer layer of as thick as 0.8 μm.

The grain orientation of YSZ layer was controlled using a modified bias sputtering technique. The technological fundamentals of this method were reported elsewhere [3], [4], [5].

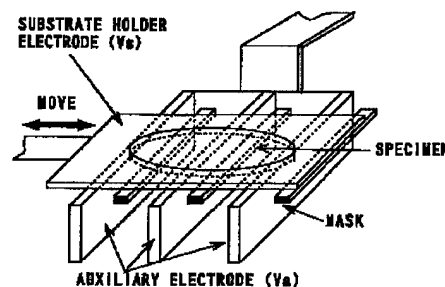


Figure 1. The configuration of electrodes.

Figure 1 shows a pair of specially devised electrodes installed in the sputtering system. Using this equipment, we made an attempt to obtain YSZ films with in-plane texturing over the whole surface of the sample. In brief, the films grown without the biased electrodes showed a poor crystallinity and random orientation. In contrast, when a negative d.c. bias of 200 V was applied both to the substrate holder and auxiliary electrodes, an apparent in-plane texture occurred in the films. However, the degree of in-plane texturing varied depending upon the sample position; films grown on the part of the substrate located directly above the center between the two auxiliary electrode plates, showed comparatively poor texture. This is because glancing angle ion bombardment during deposition is one of the requirements for the achievement of in-plane texturing. However, at this area, Ar⁺ ions impinge on a film not obliquely but at almost right angles. In order to avoid the growth of this poorly-oriented film, masks made of zirconium tape were placed at these positions, as illustrated in Fig.1. In addition, we incorporated a movable substrate holder electrode which enabled us to slide the substrate

horizontally during deposition. After a definite time of deposition, the substrate was moved horizontally so that a film with in-plane texturing could grow on the masked area. Consequently the whole area of the substrate was successfully covered with in-plane textured YSZ thin films. We call this method "masked and moved" deposition mode. In contrast to this, the films grown under "maskless and fixed" mode exhibited poor texturing from place to place. In the present paper, we characterize YSZ buffer layers as "untextured", "partially in-plane textured", and "in-plane textured", each corresponding to the films grown under (1) unbiased-sputtering mode, (2) "maskless and fixed" deposition mode, and (3) "masked and moved" deposition mode, respectively.

The copper substrates thus precoated with YSZ/Cr buffer layer were used for deposition of YBCO films using the laser ablation technique[5]. In order to obtain uniform large area YBCO films, the mirror was oscillated so that an excimer laser beam reflected from the mirror could be scanned on the rotating target surface. However, the film thickness was distributed on the entire substrate between 1.5 and 2 μm . Figure 2(a) shows the pole

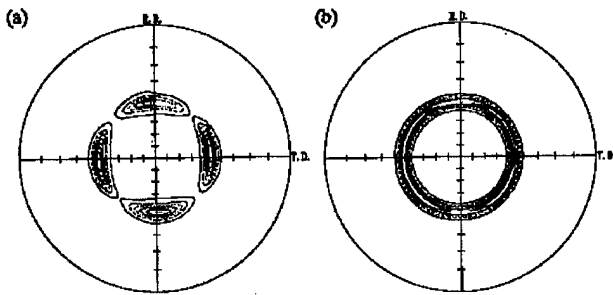


Figure 2. Pole figure for (a) in-plane aligned YBCO, (b) in-plane non-aligned YBCO films.

figure for (103) peaks of the YBCO films deposited on the in-plane textured YSZ buffer layer. From this figure, we can see that the c axis of the YBCO films was oriented normal to the substrate, and the a and b axes were aligned to the YSZ [110] axis at the interface of the films (designated as in-plane aligned YBCO). Figure 2(b) shows the pole figure for the YBCO film grown on untextured YSZ buffer layer. The c axis of the YBCO film was aligned perpendicular to the surface, but the others were distributed randomly (designated as in-plane non-aligned YBCO). Figure 3 shows resistance-vs-temperature

curves of YBCO films deposited on (a) untextured- and (b) textured-YSZ buffer layers, together with that (c) of YBCO film grown on (100)MgO for comparison. This figure reveals that both YBCO films on the YSZ buffer layers have zero-resistance temperature T_{c0} of about 86 K. On the other hand, YBCO film on (100)MgO exhibited the T_{c0} of 88.5 K and the resistance curve can be extrapolated to the origin. These results indicate that the formation of the proper buffer layer can further improve the superconducting properties of polycrystalline YBCO films on copper substrates. Transport J_c was measured using a four-point probe technique. The film grown on in-plane textured YSZ buffer layer gave J_c of $1.0 \times 10^5 \text{ A/cm}^2$, whereas a comparable

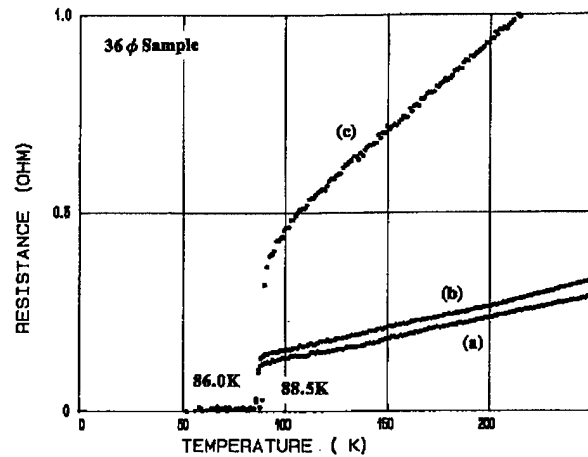


Figure 3. Resistance R vs T of YBCO films grown on (a) in-plane textured, (b) untextured, YSZ buffer layers and (c) (100)MgO.

film on a partially in-plane textured YSZ buffer layer had a J_c of $5.2 \times 10^4 \text{ A/cm}^2$ at zero field and 77 K. This result indicated that the growth quality of YSZ buffer layers was found to determine the texture of subsequently grown YBCO films.

III. MEASUREMENT OF THE SURFACE RESISTANCE

Figure 4 shows the experimental set-up for microwave surface impedance measurements using a 13 GHz cavity. The diameter $2a$ is 30 mm and the length l is also 30 mm. It consists of a copper host cavity and a copper end-plate. The end-plate is a disk with 36 mm diameter and 3 mm thickness and is substituted with one covered with high- T_c film. The temperature of the cavity is controlled from 11 K to 300 K with a closed-cycle refrigerator and a 50 W heater. As the coupling constants change dramatically during temperature rise, we can adjust them from outside the vacuum chamber. With a constant temperature step, we measure the resonant frequency, quality factor Q_L and coupling constant β_1 and β_2 of the two coupling ports. As the reflections from components change during the temperature increase, the reflection coefficients are calculated by fitting their background with an order-two polynomial.

Initially the unloaded quality factor $Q_{0,c}(T)$ of the copper cavity is measured as a function of temperature T , and the surface resistance of copper $R_{s,c}(T)$ is calculated. Then the end-plate is replaced by one covered with a YBCO film, and the unloaded quality factor $Q_{0,s}(T)$ is measured. Using these quality factors and two geometrical factors k and c , the surface resistance $R_s(T)$ of the film at temperature T is given by

$$R_s(T)/R_{s,c}(T) = k(Q_{0,c}(T)/Q_{0,s}(T) - c). \quad (1)$$

For $a = 15\text{mm}$ and $l = 30\text{mm}$, we have $k = 13.903$ and $c = 0.92808$.

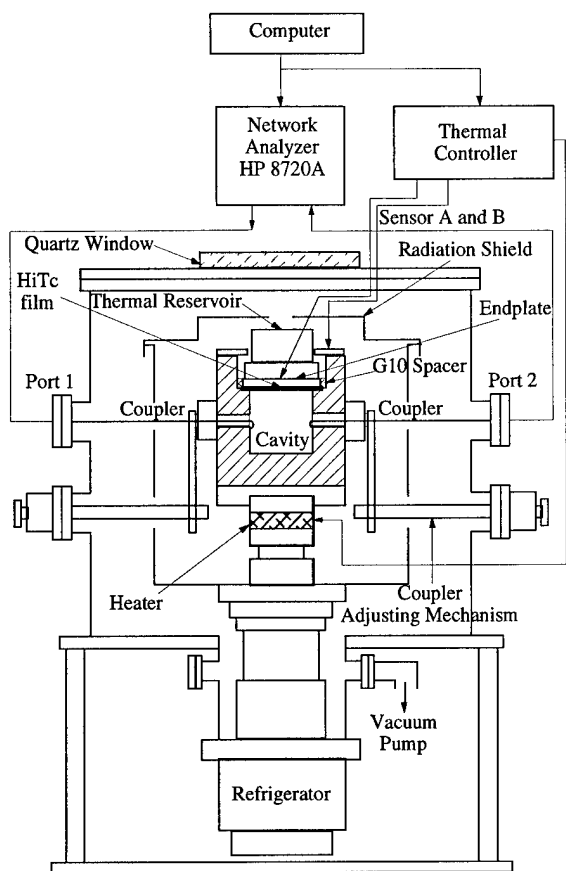


Figure 4. Experimental set-up for microwave surface resistance.

IV. EXPERIMENTAL RESULTS AND DISCUSSION

Fig.5 shows the surface resistance of the copper $R_{s,c}(T)$ composing the host cavity. The value below 32.7 K falls less than 10 mΩ and remains almost constant. The value measured for the 3 GHz cavity is also shown.

As the input power to the cavity is small, the rf losses observed in high- T_c materials are explained by a model of Josephson coupling between the superconducting grains. The thick solid line in Fig.6 shows the surface resistance of the in-plane aligned YBCO film and the thick dotted line shows that of the copper. The surface resistance of the sample below 71.5 K is lower than that of copper and around 1 mΩ below 45 K. As the surface resistance of the material decreases below than that of the copper, the relative error increases as described in Ref.2. Thus with a copper host cavity, the absolute measurement of a low surface resistance is substantially inappropriate. Meanwhile it has an advantage in measuring a surface resistance with the same order of copper and for a wide temperature range. Note that the situation can be improved to some extent, if we change the geometrical factors.

Before long the properties of the samples would be clarified through the analysis of the data and will be reported elsewhere. We can also obtain the complex impedance through the data analysis.

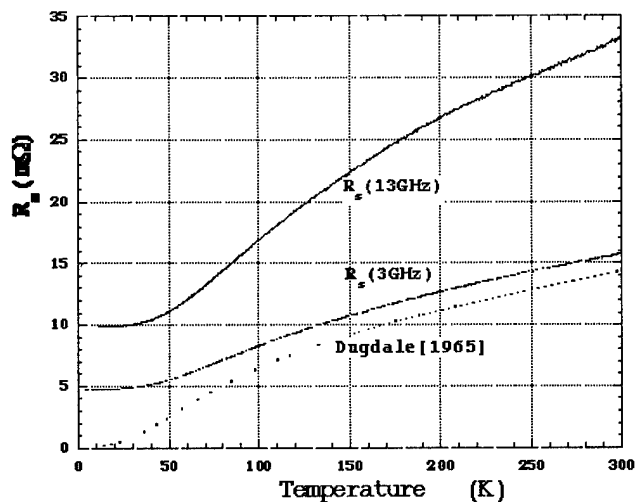


Figure 5. Microwave surface resistance of copper at 3 and 13 GHz.

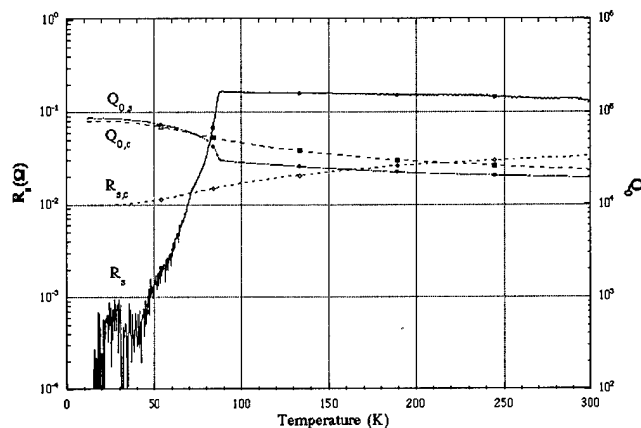


Figure 6. Microwave surface resistance and quality factor of the in-plane aligned YBCO film as well as those of the copper.

References

- [1] C. Uher: J. Supercond. **3** (1990) 337.
- [2] E. Ezura *et al.*: Jpn. J. Appl. Phys. **32** (1993) 3435.
- [3] M. Fukutomi *et al.*: Thin Solid Films **239** (1994) 123.
- [4] S. Aoki *et al.*: J. Vac. Sci. Technol. **A12**(2) (1994) 501.
- [5] M. Fukutomi *et al.*: Physica C **219** (1994) 333.

Transverse Coupling Impedance Measurement Using Image Current *

D. Sun, P. Colestock and M. Foley
Fermi National Accelerator Laboratory
P.O.Box 500, Batavia, IL 60510

Abstract

Results of transverse impedance measurement using image current are reported. The results show that this technique can be used up to frequency of 3.9 GHz and high Q of 3300.

I. Introduction

The transverse coupling impedance is a measure of the interaction between the beam and deflecting modes (TM_{1n0}) in accelerator cavities. Two-wire and bead-pull techniques are usually employed for the measurement of transverse coupling impedance. The principle of the wire technique is to insert wires into cavities and beam line components to transform them into transmission lines and measure the scattering parameters. Coupling impedances (longitudinal or transverse) are extracted from S parameters [1]. For longitudinal coupling impedance measurement, a single wire is inserted in the center of cavities and beam components to form a coaxial transmission line. For transverse coupling impedance, two off-center wires are inserted to form a balanced-two-wire transmission line and a 180 degree, 3 db power splitter (hybrid) is used to excite TM_{1n0} modes. In addition to error sources in the one-wire (center wire) technique, the two-wire technique has more error sources. First, the power splitter causes phase and amplitude errors. Although amplitude differences from two output ports of power splitters are usually small, phase differences of 0-12 degrees over 0-2 GHz range are common among commercial power splitters. Second, phase and amplitude errors are introduced by geometric factors of the two wires. In practice the two wires may not be perfectly parallel to each other and the distances between the symmetric plane and the two wires may not be the same along the wires. These geometric factors can easily introduce about 5% amplitude and phase distortions. Third, unavoidable differences of electrical lengths between two wires due to non-identical connections and matching components etc. produce phase differences between the two wires. In order to avoid the aforementioned error sources and improve the two-wire technique, measurements using image current have been done. This technique uses an off-center wire and half-cylindrical structure covered with a conductive plate which serves as a mirror plane (Fig. 1.) Since the image current plays the role of the second wire, the error sources due to the differences between two wires are minimized. The error sources from the power splitter are eliminated since a power splitter is no longer needed.

*Work supported in part by DOE

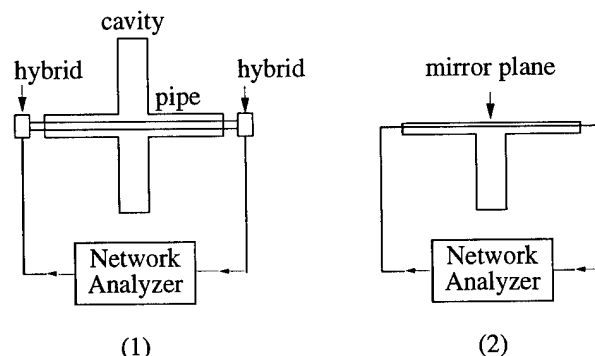


Figure 1: (1) Whole cavity with two wires and hybrids, (2) Half of (1) without hybrids.

II. Measurement Procedure

II.1. Test Apparatus

To use the image current method, an half cylindrical (pill-box) aluminum cavity with beam pipe was built. The length of the cavity was 1.575 cm. The radius of the cavity was 12.057 cm. The radius of the beam pipe was 1.740 cm. The beam pipe and other required components such as reference lines and calibration standards (will be discussed later) were made in a half-cylindrical configuration. A copper plate was mounted on the half cylindrical structure at the cut plane and covered the total length of the structure. A single wire was inserted into the pipe and cavity. The space between the wire and the copper plate could be adjusted. The radius of the wire was 0.0114 cm. To stretch the wire and connect this type of transmission line to the ordinary coaxial cables which are connected to the network analyzer, a pair of half cylindrical matching sections were made. The end of each matching section was sealed by a detachable aluminum block (end block). A pair of semi-rigid coaxial cables were inserted through the end blocks. The wire was soldered onto the inner conductors of these cables. Resistive matching was used to reduce the reflection from the mismatch between matching sections and semi-rigid coaxial cables. The drawback of resistive matching is that magnitudes of signals become much smaller. Also at high frequencies, resistive matching is not effective. In order to get reliable results, it is critical that all parts which have to be disconnected and re-connected during the process of calibration or measurement must have high repeatability. To ensure good repeatability, special measures have been taken. First, the design of detachable end blocks of the matching sections allows the wire, the resistive matching parts, the end blocks and the

coaxial cables to be moved together from the DUT (device under test) to reference lines. This feature reduces the number of times necessary to disconnect wires, resistors and connectors between matching sections and measurement cables. Second, the cavity and its attached beam pipe, the reference and calibration transmission lines can be opened by detaching the copper plate. As a result of this feature, the process of stretching wires and soldering resistors for resistive matching can be controlled more precisely than in a closed structure.

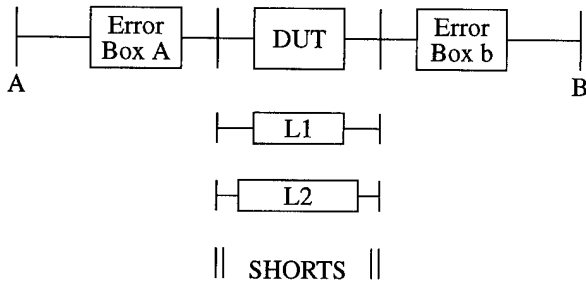
II.2. Calculation of impedance

The calculation of impedance from S parameters of a transmission line (reference line) and a cavity inserted with a wire has been discussed in several publications [1] which is outlined as follows. Since our cavity is short, a lumped impedance approximation may be used. The shunt impedance of the cavity is calculated as:

$$Z = 2Z_0 \left(\frac{S_{21\text{ref}}}{S_{21\text{cav}}} - 1 \right) \quad (1)$$

where $S_{21\text{cav}}$ and $S_{21\text{ref}}$ are the S_{21} parameters of a transmission line with and without cavity respectively while keeping the same total length. Z_0 is the characteristic impedance of the transmission line. The transverse impedance of dipole modes can be deduced from the shunt impedance as:

$$Z_{\perp} = \left(\frac{c}{\omega d} \right)^2 Z \quad (2)$$



A,B: reference planes of network analyzer

Figure 2. Measurement and calibration models.

II.3. De-embedding procedure

The S parameters of a device under test (DUT) are de-embedded from the S parameters measured at the reference planes of the network analyzer as follows. Shown in Figure 2 are the models of what is measured by a network analyzer at its reference planes. The wave cascade matrix R of a two port network is defined as:

$$\begin{bmatrix} b_1 \\ a_1 \end{bmatrix} = [R] \begin{bmatrix} a_2 \\ b_2 \end{bmatrix} \quad (3)$$

where a_1 and a_2 are incident waves at ports 1 and 2, b_1 and b_2 are emergent waves at ports 1 and 2 respectively. The S parameter matrix S of a two port network is defined as:

$$\begin{bmatrix} b_1 \\ b_2 \end{bmatrix} = [S] \begin{bmatrix} a_1 \\ a_2 \end{bmatrix} \quad (4)$$

The R matrix and S matrix are related by:

$$[R] = \frac{1}{S_{21}} \begin{bmatrix} -\Delta & S_{11} \\ -S_{22} & 1 \end{bmatrix} \quad (5)$$

From the definition of R matrix, the R matrix measured at network analyzer reference planes, $[R_m]$, can be expressed as:

$$[R_m] = [R_a] [R_{\text{dut}}] [R_b] \quad (6)$$

where the $[R_a]$, $[R_b]$ and $[R_{\text{dut}}]$ are the wave cascade matrices of error boxes A, B and DUT respectively.

If $[R_a]$ and $[R_b]$ are known, $[R_{\text{dut}}]$ can be obtained through (6) and the S parameters of DUT can be calculated through (5).

II.4. Calibration Procedure

To obtain $[R_a]$ and $[R_b]$, the "generalized through-reflect-line" calibration procedure is used [2][3]. This calibration algorithm requires two lengths of transmission lines and two equal reflects (shorts) of unknown reflection coefficients. In order to ensure the accuracy of the calibration, the phase difference between these two transmission lines (standards) should not be too close to 0 or 180 degrees. The procedure developed in [3] is outlined as follows. Successive measurement of line 1 and line 2 yields:

$$[R_m(L1)] = [R_a] [R_{L1}] [R_b] \quad (7)$$

$$[R_m(L2)] = [R_a] [R_{L2}] [R_b] \quad (8)$$

Measurement of two shorts yields:

$$\Gamma_1 = S_{11A} + \frac{S_{12A} S_{21A}}{\frac{1}{\Gamma_R} - S_{22B}} \quad (9)$$

$$\Gamma_2 = S_{22B} + \frac{S_{12B} S_{21B}}{\frac{1}{\Gamma_R} - S_{11B}} \quad (10)$$

Thus, S parameters of error box A and B and the propagation parameter (γ) of a transmission line with length of (L2-L1) can be obtained by solving equations (7),(8),(9) and (10). In the process of solving equations (7),(8),(9) and (10), however, two complex quadratic equations have to be solved. Each time, only one of the two conjugate roots of the quadratic equation is the right choice. If the correct roots are chosen, the following three conditions should be met [2]: (1) $|R_{a21}/R_{a22}| < |R_{a11}/R_{a12}|$, (2) $|e^{2\gamma(L2-L1)}| < 1$, and (3) the difference between the argument of deduced $e^{2\gamma(L2-L1)}$ and the estimated phase difference $\gamma(L2 - L1)$ from the real length of L2 and L1 should not exceed 90 degrees. Therefore, theoretically any one of these three conditions can be used as a criterion to determine the correct root. In our computer code implementing the calibration and de-embedding procedure, all of these three conditions are checked simultaneously at each data point. The conditions (1) and (3) are used as criteria to choose roots and to check each other. This approach is effective to ensure the reliability of the calibration.

The condition (2), however, can not be used practically as a reliable criterion from our observation which is in agreement with the statement in [2]

To check the generalized TRL algorithm and our computer code, three sections of semi-rigid coaxial lines with SMA connectors were carefully made. Two of them and an SMA short are used as calibration standards. The third section is used as DUT. The results are very close to theoretical values.

III. Measurement and Results

III.1. Repeatability

The repeatability is mainly affected by changing/stretching of wires, and opening/closing of the mirror plane (copper plate) during calibration and measurement. The repeatability was checked at the resonant frequency of the first dipole mode (1489 MHz). The mirror plane was opened and re-connected. The results show that the relative errors of magnitudes of S parameters between these procedures were less than 1%, and the phase errors were less than 0.5 degree. Also wires with a difference of 1 mm in length were used which affected the position of the matching resistors and the penetration of the movable coaxial cables in the matching section. The relative errors of magnitudes of S parameters between the two measurements is also less than 1%, and the phase errors are less than 0.5 degree. These results are in agreement with the repeatability of the final results (Z/Q) of this mode.

III.2. Results

The measurement results for the first three dipole modes are shown in Tables 1 and 2. Theoretically, Z/Q of a cavity is determined only by the geometry of the cavity. However, due to the high Q value of the cavity the magnitude of |S₂₁| was very small (-50~-60 db) which may affect accuracy of the measurement. To check such a possible problem, the Q of the cavity was lowered by inserting a metal wire into the cavity or magnetically coupling resistors through a hole which is 4 cm from the mirror plane. The results show that there is no systematic change of Z/Q when Q and the magnitude of |S₂₁| vary.

As a comparison, the results from measurements using bead pull technique and the calculated results from computer code URMEL-T are also listed.

Table 1. Results of Z/Q (wire spacing: 0.5 inch)

Mode	f ₀	Q	Z/Q	Z/Q	Z/Q
	MHz		Wire	Bead pull	Urmel-T
TM110	1482	9188			2.97
	1487	1319		2.65	
	1489	2539	3.15		
	1487	1890	3.20		
	1486	1524	3.15		
	1488	1111	3.15		
	1487	956	2.90		
	1492	639	2.70		
TM120	2689	11685			7.28
	2703	2800		7.29	
	2723	3019	5.60		
	2736	2461	5.80		
	2725	1826	5.05		
	2736	502	5.55		
TM130	3898	13525			8.79
	3923	3230		13.10	
	3979	3248	15.65		
	3977	2015	15.50		

Table 2. Results of Z/Q (wire spacing: 0.3 inch)

Mode	f ₀	Q	Z/Q	Z/Q	Z/Q
	MHz		Wire	Bead pull	Urmel-T
TM110	1482	9184			1.07
	1487	1867		1.17	
	1488	2127	1.15		
	1485	1753	1.15		
	1480	879	1.15		
	1480	331	1.20		
TM120	2690	11677			2.63
	2706	2612		4.31	
	2712	2641	3.00		
	2711	2540	3.00		
	2712	2364	3.00		
	2724	2234	3.15		
	2714	1471	2.75		
	2724	612	3.20		

References

1. H. Hahn and F. Pedersen, "On coaxial wire measurement of the longitudinal coupling impedance," Brookhaven National Laboratory Report BNL-50870, April, 1978.
2. G. Engen and C. Hoer, "Thru-reflect-line: an improved technique for calibrating the dual six-port automatic network analyzer" IEEE Trans. on Microwave Theory and Techniques, MTT-27, pp. 987-993, December, 1979.
3. R. Pantoja *et al.*, Improved calibration and measurement of the scattering parameters of microwave integrated Circuits," IEEE Trans. on Microwave Theory and Techniques, Vol. 37, pp. 1675-1680, November, 1989.

DECREASING TRANSIENT BEAM LOADING IN RF CAVITIES OF U-70 ACCELERATOR

O. P. Lebedev, IHEP, Protvino, Moscow Region, 142284, Russia

Abstract

The U-70 RF system was worked out to operate with the injector - linac at 100 MeV energy. A wide RF range was (2.6-6.1) MHz. For the U-70 injector Booster the wide RF range decreased and now it is (5.5-6.1) MHz. This fact and simplest method of changing the parameters in RF ferrite dominated cavities allow one to increase of the equivalent value of the cavity capacitance for the main frequency by about a factor of 2.7 and increase of the value of the cavity gap capacitance by about a factor of 5 [1]. The experimental investigation of the U-70 RF cavities due to the injection of bunches from the Booster into the U-70 orbit, near transition and on main flat-top is presented.

I. EXPERIMENTAL RESULTS

When a bunch charge crosses the cavity, it leaves behind a voltage. This voltage will decrease with an increase of an accelerating gap capacity (fundamental theorem of beam loading [2]). The equivalent circuit of a resonator is shown in Fig.1.

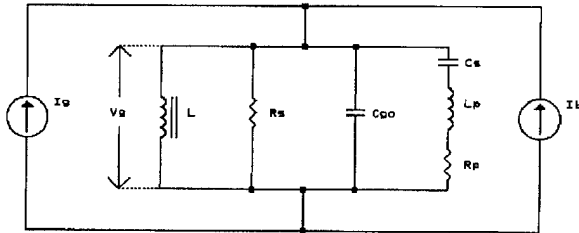


Figure. 1. The equivalent circuit of a resonator.

Here L - inductance of the cavity, C_{g0} - capacity of the accelerating gap, R_s - shunt impedance of the cavity on main working frequency in which the exciting amplifier output impedance, transformed to the cavity gap, is included in R_s as well as the cavity loss. I_a, I_b - current RF generators of the exciting amplifier and bunch accordingly, C_s - capacity of tube, L_p - inductance of a connecting plug-in, it connect the gap to the anode of the final tube, V_g - voltage on the accelerating gap.

Below in the article the experimental characteristics for two cavities will be resulted:

- A - old design,
- B - new design.

In table 1 control parameters of cavities for initial frequency of accelerating field $f_0 = 5,500 \text{ MHz}$, measured in the test cavity without a beam on method [3] are shown.

Table 1.

cavity	$C_g(pF)$	$C_{g0}(pF)$	$L(\mu H)$	$R_s(k\Omega)$	Q_0
A-old	253	89	3,31	7,4	65
B-new	672	480	1.25	6,4	148

C_g - total capacity, indicated to an accelerating gap on main working frequency of a resonator. Q_0 - quality of resonator non-loaded by beam.

On Booster flat-top of U-70, ξ -value of the ratio for beam induced voltage in an idle cavities A, B and a quality Q were measured. The accelerating cavities in test were used resonant of a wall-current monitors. The resonant frequency of cavities was established by change of a bias field current and corresponded to frequency of a accelerating field.

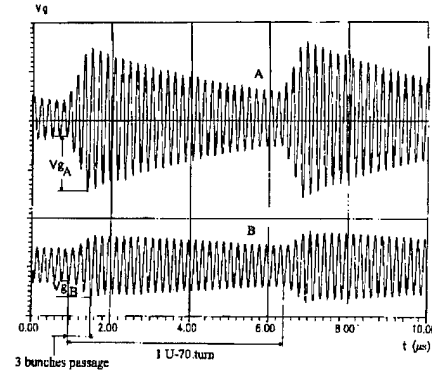


Figure. 2. Beam induced voltage in cavities.

On Fig.2 are shown the voltages in gap of cavities, developed at the passage of three circulating bunches following in succession. The value ξ is equal

$$\xi = \frac{V_{gA}}{V_{gB}} = \frac{C_{gB}}{C_{gA}}, \quad (1)$$

where V_{gA}, V_{gB} - induced voltage of bunches at the passage old and new of cavities accordingly. The measured value was $\xi = V_{gA}/V_{gB} \simeq 2,7$. The ratio C_{gB}/C_{gA} is 2,66 (see table 1).

After passage bunches in cavities free oscillations with frequency of set-up f are made. The constant time of cavity τ_f is connected with a quality Q by a ratio

$$\tau_f = \frac{2Q}{\omega}, \quad (2)$$

where $\omega = 2\pi f$. If a constant time of the cavity to express through number of RF periods during which the amplitude of

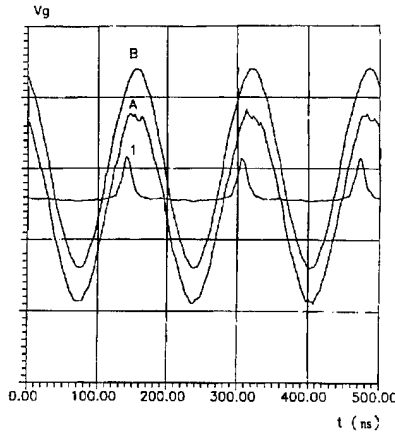


Figure 3. Accelerating voltage in cavities near transition.

free oscillations will decrease in e time, then a quality can be determined as

$$Q = \pi m, \quad (3)$$

where m - number of RF periods f . The measured values were $m_A=21$, $m_B=44$ and then $Q_A=66$, $Q_B=138$. The results of control measurements a quality listed in table by 1 well coincide with experimental made on a beam.

A study of transient beam loading of the U-70 accelerating cavities due to the injection of bunches from the Booster into the U-70 orbit. The theoretical aspects of a problem are described in work [4]. For new U-70 cavities the measurement value of phase shift of a accelerating wave of a electrical field after injection bunch is in free bucket makes about 3 degrees at bunch intensity $N_b = 10^{12}$ protons. This value is by a factor 3 less than in case of old cavities because of a increase cavity capacity of a on such value. It should remind, that in U-70 can be injected 30 bunches.

The transients in the cavity U-70 about transition called by passage the bunches high density are displayed maximally. Excitation of a harmful resonance in old cavity at 42MHz from a circuit plug-in of inductance L_p and output final tube of capacity C_p of a connecting tube with the cavity gap is observed. The similar problem was resolved in PS CERN by installation special a high pass damper connected to the anode of the final tube [5]. In modernized variant of a cavity the suppression of the harmful resonance occurs on self.

On a Fig.3 are shown: 1 - bunches (5×10^{11} protons/bunch), A- accelerating voltage on the gap of the old cavity, B- accelerating voltage on the gap of the new cavity. Peak amplitude of a voltage on gap was equally $V_g = 10\text{kV}$. The appreciable distortion of a accelerating wave for the cavity A is stipulated by L_p, C_{g0}, C_s of a circuit with the resonant frequency $f_{pA} \approx 42\text{MHz}$ and a quality $Q_{pA} \approx 6$. A impedance on this frequency made $Z_{sA} \approx 400\text{Ohm}$. In the cavity B after a increase of capacity C_{g0} the frequency of the harmful cavity resonance has made $f_{pB} \approx 27\text{MHz}$, the impedance was $Z_{sB} \approx 25\text{Ohm}$. The reduction of the impedance was stipulated almost by equal frequencies of parallel and serial resonances. In serial circuit

L_p, C_s the resonant frequency was $f_{sB} \approx 24\text{MHz}$.

In summary some words about stationary interaction of the beam with cavities on main flat-top of U-70. The most of physical experiments on main flat-top are carried out with a coasting beam. By virtue of technical difficulties the gaps of cavities can not be short connected on a time of the beam circulation. Interaction of cavities with a circulating beam is observed. It is expressed in a grouping of beam on the tune frequency of cavities. The reduction an absolute value for the impedance of RF system divided by harmonic number Z_k/k causes a increase of threshold a coasting beam instability in U-70 accelerator (Keil-Schnell criterion [6]).

In our case change of initial frequency of tune RF system with 2.6MHz to 5.35MHz (at absence of a bias field current in cavities) results in the reduction Z_k/k . The value frequency $f = 5.35\text{MHz}$ corresponds to a condition of a finding precisely between $k=26$ and $k=27$ by harmonics of revolution frequency on flat-top. The revolution frequency is $F_0 = 202\text{kHz}$. The reduction of impedance Z_k occurs because of a increase of ferrite losses in cavities on higher frequency. So now we have the reduction Z_k/k on main flat-top of U-70 more than by a factor 5.

References

- [1] O.P. Lebedev, IHEP Preprint 93-142, Protvino, 1993 (in Russian).
- [2] P.B. Wilson, CERN ISR-TH/78-23 (1978).
- [3] O.P. Lebedev, V.A. Chubrik, IHEP Preprint 93-143, Protvino, 1993 (in Russian).
- [4] M. Meth, A. Ratti, in *Proc. of the 1989 IEEE Part. Acc. Conf.*, Chicago, March 20-23, p.168.
- [5] R. Garoby, et. al., CERN/PS 89-28 (RF).
- [6] E. Keil, W. Schnell, CERN-ISR-TH-RF/69-48 (1969).

RF System for Bunch Lengthening*

R. Biscardi, G. Ramirez, Brookhaven National Laboratory, Upton NY 11973

I. ABSTRACT

A harmonic cavity is used in the VUV ring to increase the Touschek lifetime and to help reduce peak current related instabilities. Phase locking servos for such a system normally require comparison of a Fourier component of the beam to a reference or information about the symmetry of the bunch. We have found it simpler to initially set the phase of the drive so that the center of the bunch is positioned at the zero crossing of the harmonic cavity voltage waveform. This phase relationship is then maintained by comparing the amplitude of the harmonic cavity field to the forward power, and adjusting the phase of the drive to keep the two powers equal. A system of this type has been operating in the VUV ring since October, 1993. It consists of a 52.88 MHz accelerating cavity and a 211.54 MHz bunch lengthening cavity providing increased lifetime over all operating currents.

II. INTRODUCTION

Bunch lengthening is achieved by reducing the slope of the accelerating voltage in the vicinity of the electron bunch. Operating with a lengthened bunch increases the Touschek lifetime by decreasing the density of the bunch. In addition to this increased lifetime, peak current effects such as the microwave instability and the head-tail instability can be reduced. Also, a spreading of synchrotron oscillation frequencies can provide Landau damping against coupled bunch instabilities. A. Hofmann[1] has described the RF conditions for a double RF system that yields optimum bunch lengthening. These conditions are given by:

$$V_T = V_1 \cos \phi_1 + kV_1 \cos(n\phi_n) = U_0 \quad (1a)$$

$$\frac{\partial}{\partial \phi} V_T = -V_1 \sin \phi_1 - knV_1 \sin(n\phi_n) = 0 \quad (1b)$$

$$\frac{\partial^2}{\partial \phi^2} V_T = -V_1 \cos \phi_1 - kn^2 V_1 \cos(n\phi_n) = 0 \quad (1c)$$

Where V_1 , ϕ_1 are the peak voltage and synchronous phase for the main RF system and $V_n = kV_1$, $n\phi_n$ are the peak voltage and synchronous phase for the harmonic RF system. All phases are measured from the peak of the waveform. For the VUV ring, the main RF system operates at 52.885 MHz with a peak voltage of 80 kV and the harmonic RF system

operates at 211.54 MHz ($n = 4$). For this n and V_1 the above equations yield the optimum bunch lengthening parameters for the VUV ring:

$$\phi_1 = 78.7^\circ, \quad 4\phi_4 = -92.9^\circ$$

$$\text{and } k = 0.246 \quad \text{or} \quad V_4 = kV_1 = 19.68 \text{ kV}$$

where ϕ_1 , and ϕ_4 are measured in the 52 MHz frame.

III. PASSIVE SYSTEM

Initially, the harmonic cavity system was operated in a "passive" mode[2]. The transmission line to the cavity was shorted at a quarter wavelength from the base of the input loop and the voltage developed in the harmonic cavity was induced entirely by the beam.

The passive system provides added lifetime at high average currents where it is needed the most. But, as the current decreases, the voltage in the harmonic cavity also decreases causing the bunch to return to its normal length at low currents. This bunch length change creates a problem for those experimenters doing fluorescent lifetime experiments[3], since they have to measure and deconvolve the source shape as it changes. To reduce this bunch length change with current, a system which makes the cavity Q , R_{SH} , and δ functions of beam current could be implemented. This requires a variable coupling system which lowers the Q and thereby the shunt impedance of the cavity as stored current is increased. This was considered too costly and complex and for the VUV ring and R_{SH} was left as a constant.

A feedforward system was implemented which attempts to keep the magnitude of the harmonic cavity voltage constant as current changes. A signal proportional to the average beam current was conditioned and used to vary the cavity temperature. This changes the resonant frequency of the cavity and increases the magnitude of the cavity impedance at 211.54 MHz as I_b decreases. Therefore, the cavity voltage remains more constant as I_b changes. Unfortunately this also changes the phase of the impedance of the harmonic cavity as a function of beam current. Although this phase change is not desirable, the overall effect provided added lifetime at lower currents. The improvement in lifetime over a single cavity system is shown in figure 1.

*Work performed under the auspices of the U.S. Dept. of Energy

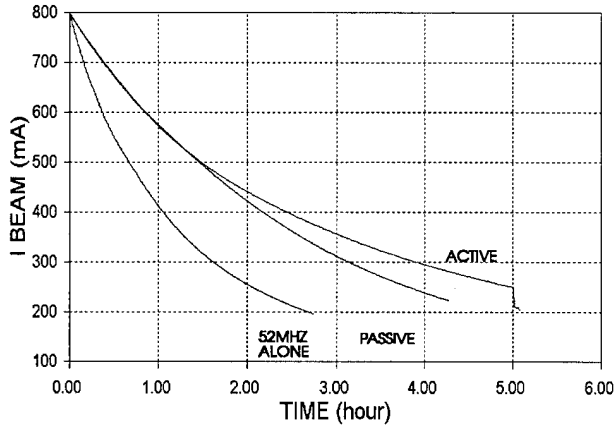


Figure 1 - Lifetime comparisons without the harmonic cavity with the harmonic cavity passive and with the harmonic cavity active.

IV. ACTIVE SYSTEM

The field in the harmonic cavity must be held constant in amplitude and phase to maintain the optimum bunch lengthening conditions. This requires tight phase and amplitude servo systems around both RF cavities to hold these conditions over an entire fill. A simple servo may be implemented if a conservative operating point is chosen. The system can still provide significant lifetime improvement without the need for a phase detection servo.

The operating point of the 211 MHz system is chosen so that the beam crosses the cavity gap on the rising slope of the RF waveform and that the net power given to the beam equals zero ($4\phi_4 = -\pi/2$). All other conditions remain the same as in the optimum case. The result of not operating at the optimum phase results in a bunch length for the VUV ring which is 80% of the optimum condition.

Such a system is shown in figure 3. The RF drive from a synthesizer serves as the reference for both systems. The 52 MHz system has standard NSLS detected amplitude and cavity tuning servo systems to compensate for beam loading. The 211 MHz system is set up with a detected amplitude loop keeping the forward power constant. With no beam, the transmitter drives the cavity at resonance through a near matched input loop. Therefore, there is little reverse power returning to the circulator which isolates the transmitter from the accelerating cavity. As beam is injected, the tuning loop compensates for the reactive beam load. Under ideal conditions the beam is maintained at the zero crossing of the RF waveform and the cavity power will always equal to the forward power from the transmitter.

Under actual conditions, the beam drifts from the zero crossing and the cavity power responds accordingly. The

cavity power rises as $4\phi_4$ becomes more negative and drops as $4\phi_4$ becomes more positive. The difference signal between the forward and cavity power is used to create a slow servo loop which adjusts the harmonic cavity drive phase to keep the beam at $4\phi_4 = -\pi/2$. This keeps the two powers equal. The active bunch lengthening system provides added lifetime over the entire fill (figure 1) with minimal bunch length changes as a function of bunch current (figure 2) as measured using a stripline monitor[4].

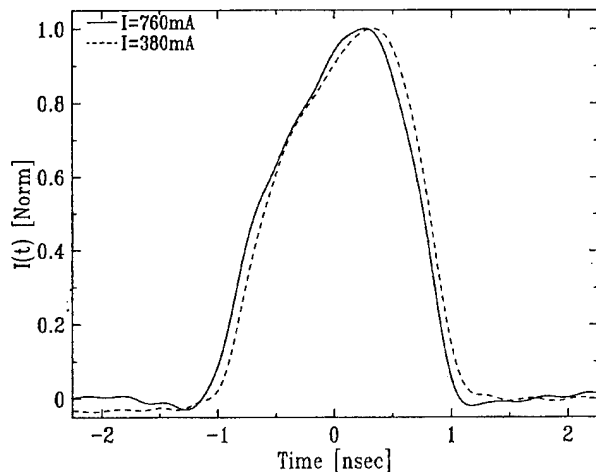
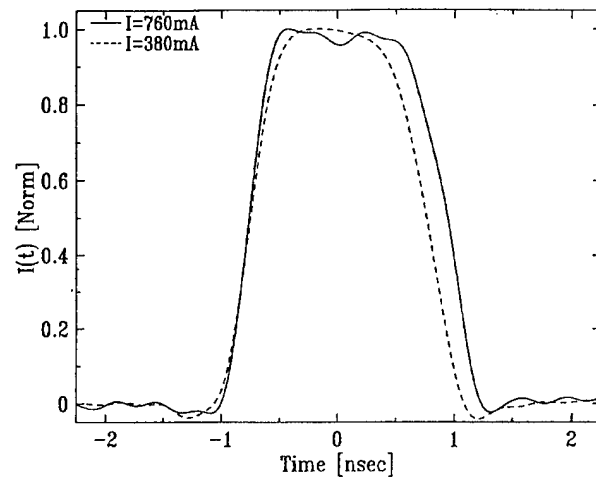


Figure 2 - Comparison of bunch shapes at 760 mA and 380 mA average current. Two different bunches are shown.

V. POWERED SYSTEM EXPERIENCE

The powered harmonic system has been operating reliably in a bunch lengthening mode for one year. The system has provided extended lifetime, and a stable longitudinal current distribution for the bunches in the VUV ring over the operating current range.

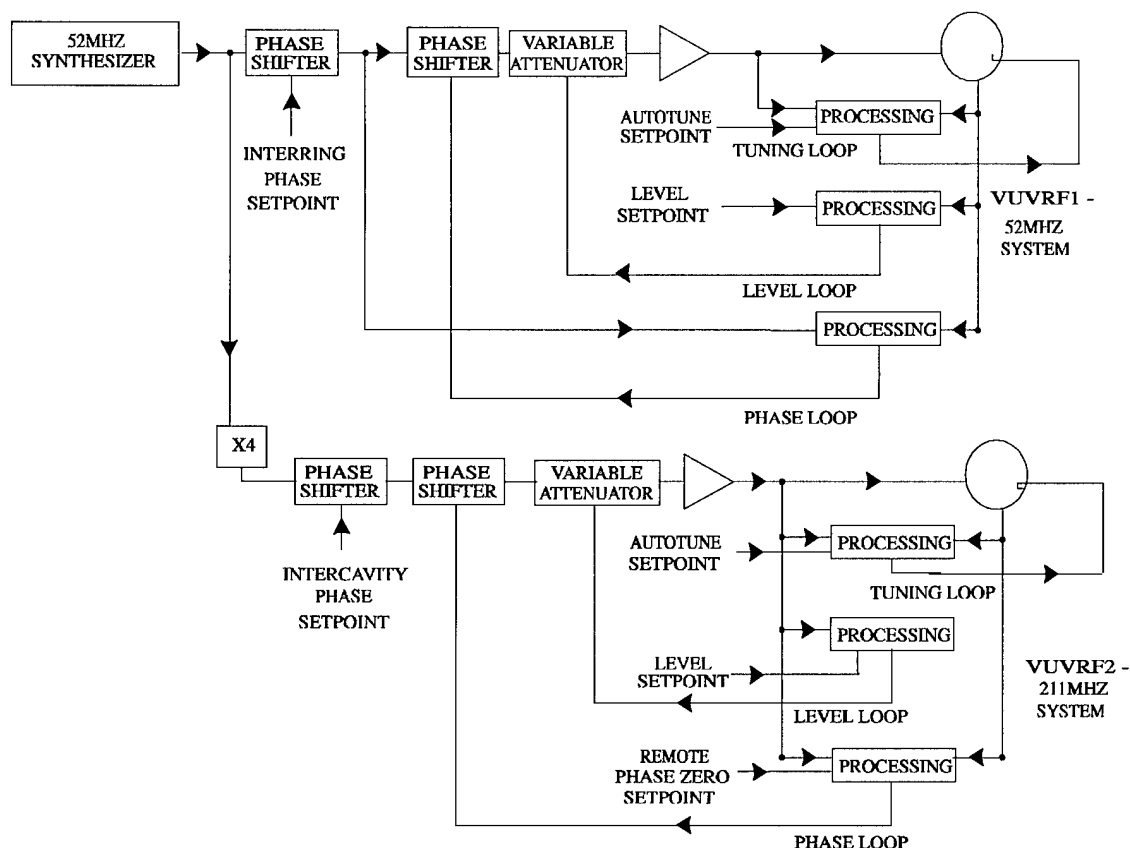


Figure 3 - Block diagram of the system.

During system commissioning it was noticed that the beam was more susceptible to audio frequency phase noise as the optimum bunch conditions were approached. A possible explanation for this is that the coherent synchrotron frequency is lowered and spread as the slope of the accelerating waveform is lessened causing increased coupling of power supply harmonics to the beam. Also, with the flat potential well created by the system, all potential well perturbations will be more noticeable.

Such is the case of a higher order mode (HOM) in the main cavity at 270 MHz. This HOM is at a rotation harmonic which is not an RF harmonic so it distorts the potential well differently for each bunch. This leads to a different shape for each bunch. Without the harmonic cavity, the differences in bunch shape due to this potential well distortion are barely noticeable. With the harmonic cavity in operation the distortion is clearly seen (fig 2). Due to both of these problems the harmonic cavity is currently operated at a lower voltage than the planned 19.68 kV. Priority will be given to removing the sources of power supply harmonic noise and to damp the mode at 270 MHz. Work will then proceed to obtain the necessary conditions for optimum bunch lengthening.

VI. ACKNOWLEDGEMENTS

We thank S. Krinsky, J. Keane and the NSLS RF group for their guidance and support on this project. Conversations with J.B. Murphy and J. M. Wang concerning accelerator theoretical issues are appreciated.

VII. REFERENCES

- [1] A. Hofmann and S. Meyers, *11th Int. Conf. on High Energy Accelerators, 1980, Geneva*, pg 610
- [2] R. Biscardi et al, "Progress on Bunch Lengthening at the NSLS VUV Ring", *1991 IEEE Particle Accelerator Conference*, pg 1326
- [3] K. Polewski et al, "Time Resolved Fluorescence Using Synchrotron Radiation Excitation: A Powered Fourth Harmonic Cavity Improves Pulse Stability", *Rev. Sci. Instrum.*, No. 65, Aug. 1994
- [4] S. Kramer et al, "Bunch Current Density Measurements in the VUV Light Source", *1994 European Particle Accelerator Conference*, pg 1874

Electromagnetic Field Vector Components Precise Measurements in Accelerating Structures

M. A. Chernogubovsky, M. F. Vorogushin

D.V. Efremov Research Institute of Electrophysical Apparatus, 189631 St Petersburg, Russia

Abstract

Precise method for resonator electric or magnetic vector components values and their space positions measurements, based on application of photosemiconductor plate with different configuration lighted images, formed by projections forming and measuring optical system of amplitude modulated light radiation, is presented. The optical system for 433 MHz RFQ accelerating structure is realized by means of serial produced micro-alignment telescopes; the method allows to discriminate the field axis fluctuations on micron level and provides several percents and tenths of percents precision for accelerating efficiency and modulation period measurements respectively.

I. INTRODUCTION

An electromagnetic field distribution measurements in accelerator resonant structures are usually carried out by perturbation method, the data processing gives the field vector modulus as averaged volumetric value on the perturbation object. The measurements accuracy is limited in principle by the object carrying system distortions and unperturbed resonant frequency reading inadequacy. Operative frequency rise as well as applied fields complication will cause inadmissible growth of these inaccuracies. Electro-optical principle is proposed to exclude these errors and to realize different vector components measurements of electric or magnetic fields distributions, the method and system development for RFQ structure is considered.

II. ELECTRO-OPTICAL PRINCIPLE

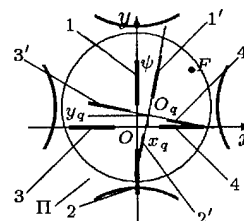
Perturbation object for the method is designed as a high resistivity photosemiconductor flat plate, that can be installed inside the resonator on a thin filament as before. Light radiation of amplitude modulated source passes through a controller of the light beam spatial position and lights up desired configuration region on the plate surface in required position. The resonant frequency difference between the readings in unlighting amplitude modulation half-cycle and in the next lighting one will determine the field in perturbed region. Electric field vector components measurements can be carried out by thin strip light configurations, oriented along the components; for the plate normal magnetic field component a closed-loop configuration is suitable; average properties can be determined by a spot of accordent space. A normal to electric field lighting minimizes the dark and light readings difference (that vanish for infinitesimal thickness of the normal), in quasistatic field it is equipotentials detection without quantity measurements.

Carrying system distortions are entirely excluded, because the perturbation is formed by exact straightforward light beam. The second mentioned error is excluded almost completely by

the dark reading in any measurement point, because high-speed (acusto-optical, e.g.) devices allow to decrease amplitude modulation cycle up to the doubled transient duration. For all this, the precise measurement problem is reduced to implementation of correlated with the resonant mode light configurations.

III. RFQ MEASUREMENTS

The field symmetry axis can be detected by equal thin strips lighting on the round plate (Π), fig.1. By (1) and (2) couple removing in OY direction the equal dark-light frequency differences for each strip can be achieved, i.e. E_y components in (1) and (2) regions are equal, the axis coordinate y_q is geometrical center of the couple; similar OX removing of (3),(4) gives x_q coordinate. Vanes curvature is determined by the strips turn refer $O_q x$ and $O_q y$ untill maximum (but a.m. equal) dark-light differences for (1'), (2'); (3'), (4') will be obtained – fig.1 presents symmetrical ψ bend; for a single element distortion the geometrical centers will not form straight lines under OX displacing of (1),(2) couple, (3),(4) – in OY direction. So, that kind positions research yields the field axis coordinates and symmetry distortions causes all information.



α

Figure 1: Lightings for RFQ measurements.

Obtainable precision analysis is conducted at known [1] electric field in the bore with modulation period l_m , accelerating efficiency θ , inner radius mean r_0 :

$$\begin{aligned} E_x &= Ux(\Lambda - 1/r_0^2), & \Lambda &= 2\theta\kappa \sin \kappa z I_1(\kappa r)/\kappa r, \\ E_y &= Uy(\Lambda + 1/r_0^2), & r &= \sqrt{x^2 + y^2}, \\ E_z &= (U/\pi)2\theta\kappa \cos \kappa z \cdot I_0(\kappa r); & \kappa &= \pi/l_m. \end{aligned} \quad (1)$$

Spatial selectivity is defined by frequency deviations ratio of interfluent and separated components, e.g. l length, $a_s \times a_s$ cross-section strip (4) E_x selectivity in (1) field according

to [App.] is $\Pi_{\perp} = (\delta f_{Ez} / \delta f_{Ex}) \leq 4 \cdot 48 (a_s / 2l)^2 (\ln 2l / a_s - 1) (r_0 \theta / l_m)^2$ - the cylinder circle perimeter is equal to square one. In the structure with $\theta \in [0.003; 0.5]$, $l_m \in [4; 20]$ mm, $r_0 = 3.5$ mm and operating frequency $f_n = (k_n / 2\pi \sqrt{\epsilon_0 \mu_0}) = 433$ MHz for $0.1 \times 0.1 \times 2.5$ mm strip the averaged selectivity is $\Pi_{\perp} < 2 \cdot 10^{-4}$, that is greatly less than instrumental resolution. The cavity analysis in the form of coupled shortcircuited sector radial waveguide sections, loaded by end capacitances, gives according to [App. (11)] the deviation

$$\left| \frac{\delta f_{Ex}}{f_n} \right| = M \left(\left(\frac{x_0}{r_0} \right)^2 + \left(s_1 - \frac{1}{4} \right) \left(\frac{l}{r_0} \right)^2 \right), \quad (2)$$

$M \cong 5.52 \cdot 10^{-6}$. An error in desired equality of deviations at RF phase measurements is determined by minimal phase count discrete $d\varphi_m$, and (2) result yields the strip displacement resolution $dx_0 \cong 2r_0(\pi M Q)^{-1} d\varphi_m$, Q - quality factor. For $d\varphi_m = 2 \cdot 10^{-5}$, $Q = 5 \cdot 10^3$ it is $dx_0 \cong 1.6$ mkm, that cause the development of precise optical system for the images forming inside small aperture, lengthy ($L = 1445$ mm) bore without vanes lighting - the plate excitation by reflection phone is inadmissible. Autoreflective image forming in convergent rays of telescopic objective can be effected by micro-alignment telescope only by placing the light source beyond the graticule on the eye-piece side.

The system fig.2 comprises (4) and (5) micro-alignment telescopes [2]. Collimated image former (1) contains transparency (2) with adjustable in independent square directions transparent region; projective telescope (4) forms the image along its datum optical axis with displacements possibility by optical micrometers.

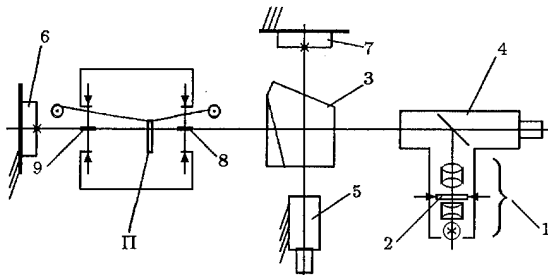


Figure 2: Images forming and measuring system.

Another telescope (5) is interconnected by pentaprism with wedge (3) for the image dimensions measurements on the plate (II). Alignment on the base datum targets (6),(7) sets optical axes of the former and both telescopes in coincidence; the resonator is fixed on the datum axis by (4) viewfinding on removable transparent targets (8),(9); and datum line of sight can be ascertained always by (5) viewfinding on (7) target after (3) removing. Transparency (2) is equipped by rotary device with $30''$ count accuracy. The system allows to form rectangular images with variable $0.05 \dots 3$ mm sides, total error of the image coordinates is $\pm(3 + 2D)$ mkm, D - image distance, M , but the systematic error can be excluded, [2]. So, the strip position inaccuracy is 3.5 mkm and the field axis coordinates real error ≈ 4 mkm. The structure fine tuning properties θ, l_m are defined by the minimum dark-light deviation position detection under radial strip lighting refer to determined axis. According to [App.], this position corresponds to minimal integral value in (6) equation at the current

distribution (7) for (1) field. Direct variation yields the minimum deviation angle α between Ox and the strip

$$\alpha = \frac{\arccos(G\theta \sin \kappa z)}{2}; \quad G = \frac{2(\kappa r_0)^2 \int_0^l I_1(\kappa x) F(x) dx}{\pi \int_0^l \kappa x F(x) dx},$$

$F(x) = kx - kl \sin kx \csc kl$, and it is enough to measure α under the plate removing along the structure for α^{max} , α^{min} values and $\alpha = \frac{\pi}{4}$ positions determination, because

$$\theta = (\cos 2\alpha^{min} - \cos 2\alpha^{max})(2G)^{-1}. \quad (3)$$

Two counts phase method of α mesurment with rms error $(\delta \tilde{\varphi} / \varphi) = 2 \cdot 10^{-4}$ in (1) field gives inaccuracy $(\delta \alpha_m / \alpha) \leq 1.7 \cdot 10^{-6}$, but the phase dependence is not symmetric refer α (except $\alpha = \pi/4$), and systematic innaccuracy $(\delta \alpha_s / \alpha) \leq 4.4 \cdot 10^{-5}$. Spatial selectivity is ample as before, sensitivity decrease is $2.5 \cdot 10^{-3}$ only. The angle reading rms error of the optical system is $1.4 \cdot 10^{-4}$, that determines real precision: for longitudinal coordinate count error $\cong 5 \cdot 10^{-3}$ the modulation period innaccuracy is $(\delta l_m / l_m) \leq 7.1 \cdot 10^{-3}$, and (3) result gives accelerating efficiency with $(\delta \theta / \theta) \leq 1.3 \cdot 10^{-2}$ error.

Asymmetric positioning of R_d radius, T thickness, ϵ dielectric constant plate will distort investigating field (on fig.1: F is fastening point, $\sqrt{2}b$ - sag to 3 quadrant). But only transverse field components inside the plate are used, l_m accuracy under $\alpha = \pi/4$ position determination in 1 and 3 quadrants is not changed, because $\delta \alpha_m$ rise even to two orders due to sensitivity lowering will not exceed determinative value. The θ error electrostatic estimating for $R_d = l$, $\epsilon = 10$, $T = 0.1$ mm, $b = 0.05$ mm gives $(\delta \theta_e / \theta) \leq 6 \cdot 10^{-3}$, the efficiency error grow up to $1.5 \cdot 10^{-2}$.

Photosemiconductor characteristics analysis by [App.] method yields optimized ratio of the active light-dark conductivity: for $\epsilon \leq 10$ the ratio is $125 \dots 130$, and CdS or CdSe materials suit perfectly well.

IV. CONCLUSION

Electro-optical principle and its application for RFQ structures precise measurements method have been developed. Designed optical system provides several micrometers accuracy not only for the field axis coordinates, but for geometrical shapes of the accelerating bore forming elements also - autoreflection method is effected by contact bore targets or master gauges fastening on the same filament. Developed balance technique (that excludes a field quantity measurements) for the structure fine tuning could be used for precise measurements in other types cavity resonators.

APPENDIX. Thin cylinder formfactor for RF nonhomogeneous fields

Use of retarded potential \vec{A} field operator singularity for axially symmetric l length a radius longitudinal current $\vec{I}(x)$ yields on its circumference in ρ, ϕ, x local coordinates

$$\vec{A} = N(\rho) \cdot \vec{I}(x) |_{\rho \approx a}, \quad (4)$$

where $N(\rho) = (1/2\pi)[\ln(2/k\rho\gamma) + Ci(kl) - (\sin kl/kl)]$, $\gamma = 0, 577 \dots$ - Euler's constant, $Ci(kl)$ - integral cosine. In two-component case (4) result inaccuracy will not exceed $(a/2l)^2$

even for equal longitudinal and transverse field components, that follows, e.g., from ellipsoid depolarization tensor principal values [3]; however, the practically used disposing along the supposed field vector will supplement decrease of inaccuracy to 3...4 orders. Boundary conditions in external E_x^e field lead to

$$\frac{\partial I}{\partial x} = -\frac{i\omega\epsilon_0\varphi(x)}{N(a)}; \quad \frac{\partial \varphi}{\partial x} = E_x^e - I(x)(i\omega\mu_0 N(a) + z_l), \quad (5)$$

where z_l - line active resistance of the cylinder material, φ - scalar potential of (4) field. Now a resonator ν -mode $\{\vec{E}_\nu, \vec{H}_\nu\}$ with ω_ν resonant frequency, Q_ν quality factor is excited by some source S together with the cylinder \vec{j} current density, and magnetic h_ν , electric e_ν fields amplitudes equations are

$$h_\nu(\omega_\nu^2 - \omega^2) + \frac{i\omega\omega_\nu h_\nu}{Q_\nu} = S - \frac{\omega_\nu}{W_\nu} \int_v (\vec{j}, \vec{E}_\nu) dv, \quad (6)$$

$e_\nu = i\omega h_\nu / \omega_\nu$; where $W_\nu = \epsilon_0 \int_{v_{re}} |\vec{E}_\nu|^2 dv$; v_{re}, v - resonator and cylinder volumes. Thus, for any $E_{\nu x}(x)$ function the $I(x)$ distribution is defined at $E_x^e = e_\nu E_{\nu x}(x)$ substituting in (5) equations:

$$\frac{\partial^2 I(x)}{\partial x^2} + k^2 \left(1 - \frac{i\omega\epsilon_0 z_l}{k^2 N(a)}\right) I(x) = \frac{\omega^2 \epsilon_0}{N(a) \omega_\nu} E_{\nu x}(x) h_\nu, \quad (7)$$

boundary values are $I(0) = I(l) = 0$ for distant from the cavity walls cylinder. So defined $I(x)$ determines integral value in equation (6), forming the amplitude equation for only S excitation of the resonator with new resonant frequency ω_n and new quality factor Q_n , i.e. the formfactor is defined. Eigenfunctions means substantiate that the summary field of all other modes with gradient summand is described by cylinder own field (4), and only condition for exact measurements is excluding of other modes excitation by S source in the cylinder region.

Simplest homogeneous field analysis for $kl \leq 0.1$ gives

$$Q_n \cong Q_\nu \frac{\omega_\nu}{\omega_n} \left(1 + \frac{\omega_\nu^2 - \omega_n^2}{\omega_\nu \omega_n} Q_\nu \frac{z_l l}{\sqrt{\frac{\mu_0}{\epsilon_0}} N(a)} \frac{k_n l}{(k_n l)^2 + 10}\right)^{-1};$$

quality factor decrease due to finite conductivity of a thin ($N(a) > 1$) cylinder even with $z_l l = 10$ Ohm will be in 4 order only. Therefore, $z_l = 0$ value can be used indeed, and for any kl the method yields (in conventional Slater's form writing):

$$\frac{\omega_n^2 - \omega_\nu^2}{\omega_n^2} = -\frac{[E_{\nu x}(x_0)]^2 \epsilon_0 v}{W_\nu} K, \quad (8)$$

where x_0 - coordinate of the field reading, $K = K_0$ -formfactor:

$$K_0 = \frac{\left(\frac{l}{a}\right)^2 2 \tan \frac{k_n l}{2} - k_n l}{\pi N(a) (k_n l)^3}. \quad (9)$$

Product vK_0 for $(a/l) \ll 1, k \rightarrow 0$ coincides with the result of electrostatic analysis [3]. However, if the cylinder approaches the cavity walls (e.g. $x = 0$ endpoint is near the wall), $I(0) = 0$ value must be interchanged by $\varphi(0) = -I(0)/i\omega C_e$, or $I(0) = \beta(\partial I/\partial x)|_0$, C_e - the cylinder end-wall and the cavity wall capacitance, $\beta = C_e N(a)/\epsilon_0$:

$$K_w = K_0 \left(1 + \beta k_n \frac{1 - 2 \tan \frac{\tau}{2} \cot \tau}{(2 \tan \frac{\tau}{2} - \tau)(1 + \beta k_n \cot \tau)}\right), \quad (10)$$

where $\tau = k_n l$. The end contiguity ($\beta \rightarrow \infty$) yields $K_w \cong 4K_0$ for $kl \leq 0.1$ and than K_w decreases up to K_0 for $\beta \rightarrow 0$ with the cylinder moving off, (10) general relation corresponds to electrostatic model [4].

Practically interesting results of nonhomogeneous field analysis are obtained at polinomial representation, e.g. for $E_{\nu x} = A_2 x^2 + A_1 x + A_0$ the method gives

$$K_p = K_0 \left(\Upsilon + \eta \frac{4(4\eta s_2 + \frac{2\xi s_3 + s_4}{1+\xi}) - \Upsilon(\eta + 2)}{(1+\eta)^2} \right), \quad (11)$$

where $\Upsilon = 1 + (4s_1 - 1)(\frac{\xi}{1+\xi})^2$; $\xi = \frac{A_1 l}{2A_0}$, $\eta = \frac{A_2 l^2}{4A_0(1+\xi)}$ - normalised variability,

$$s_1 = \frac{\frac{\tau^2}{3} + \tau \cot \tau - 1}{\tau(\tau - 2 \tan \frac{\tau}{2})}, \quad s_2 = \frac{\frac{\tau^2}{5} + \tau \cot \tau - \frac{2}{3}}{\tau(\tau - 2 \tan \frac{\tau}{2})} + \frac{2}{\tau^2} \left(\frac{2}{\tau^2} - 1\right),$$

$$s_3 = \frac{1}{2} - \frac{2}{\tau^2} + \frac{\cot \frac{\tau}{2}}{\tau}, \quad s_4 = 1 - \frac{4}{\tau^2} - \frac{\frac{\tau}{3}}{\tau - 2 \tan \frac{\tau}{2}};$$

and $K = K_p$, $x_0 = \frac{l}{2}$ in form (8).

References

- [1] I.M. Kapchinsky, Theory of Linear Resonant Accelerators, Moscow, Energoisdat, 1982, pp. 130-143.
- [2] Micro-Alignment Telescope IIIIC-11: Engineering Description, Optical Mechanical Enterprise LOMO, St Petersburg, 1994.
- [3] L.D. Landau, E.M. Lifshitz, Electrodynamics of Continuous Media, Moscow, Nauka, 1992, pp. 38-46.
- [4] J. Gao "The Precise Measurement of Electric and Magnetic Fields in a Resonant Cavity," Proceedings of the Linear Acc. Conf., Albuquerque, USA, September 1990, pp. 247-249.

A NEW TUNING METHOD FOR TRAVELING WAVE STRUCTURES

T.Khabiboulline, V.Puntus, Institute for Nuclear Research, INR, Profsojuznaja 7a, 117312 Moscow, Russia. M.Dohlus, N.Holtkamp, G. Kreps, Deutsches Elektronen-Synchrotron, DESY, Notkestr. 85, 22603 Hamburg, Germany. S.Ivanov, Moscow Engineering Physics Institute, MEPI, Kashirskoe shosse, 31, 115409 Moscow, Russia. K.Jin, National Synchrotron Radiation Laboratory, USTC, Heifei, Anhui 230029, P. R. China.

At DESY S-Band accelerating structures are under development since 1993. Fourteen 5.2 meter long sections have to be replaced in the injector linac (LINAC II)[1] and overall four 6 meter long sections have to be build for the S-Band test facility at DESY[2]. A new tuning procedure for the accelerating structure after brazing has been developed which uses bead-pull field distribution measurements instead of a detuning plunger. Amplitude and phase of the field are measured simultaneously along the structure without touching the surface on a 13 meter long horizontal bench.

I. INTRODUCTION

To decrease the cost for cavity production the dimensional tolerances are relaxed by oversizing the resonators and tuning after brazing. The resonance frequencies of the cells after brazing of the section are lower by 200-1500 kHz compared to the operating frequency. Four tuning holes are machined with 10mm diameter and 1mm thickness in the wall of each cup (fig. 1.1).

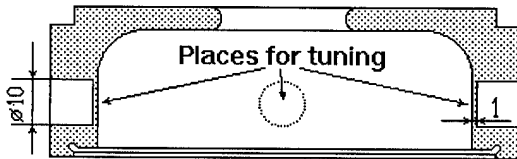


Figure 1.1. One of the cups.

For the measurement of the traveling wave field distribution (amplitudes and phases in the center of the cells) a bead-pull method is used in the section. The tuning method is based on the calculation of the field distribution of the scattered wave from each cell of the structure. During the tuning procedure the amplitudes of the scattered waves are minimized.

II. BEAD-PULL FIELD DISTRIBUTION MEASUREMENTS

The traveling wave field distribution measurement is based on a non-resonant perturbation theory [3]. In this technique the measurements of the reflection coefficient S_{11} are measured at the same frequency with and without a perturbing object placed at the point at which the field parameters have to be determined. On the axes of the section the magnetic component of the field is zero and the dependence of the reflection coefficient from the electric component of the field is expressed by the following formula:

$$2P_i (S_{11p} - S_{11a}) = -j\omega k E_a^2 \quad 2.1$$

with P_i - the input power, S_{11p} - the reflection coefficient in the presence of a perturbing object, S_{11a} - the reflection coefficient in the absence of the perturbing object, k depends on the electric parameters and the geometry of the object and $E_a = A e^{j\phi}$ - the electric component of the field. The perturbing object being used was a metallic needle with a diameter 0.4mm and a length 5mm (fig. 2.1), oriented parallel to the axis of the section. The needle can be moved along the axis of the section using a step motor with a step size about $\Delta L = 0.14$ mm.

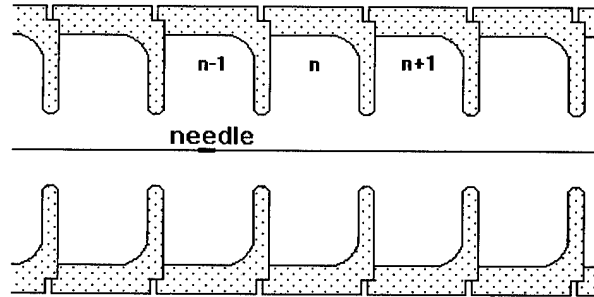


Figure 2.1. Bead-pull measurement.

In the centers of the cells the longitudinal gradient of the phase is smallest with $|\Delta\phi/\Delta z| < 0.9^\circ/\text{mm}$. The transverse gradients, for deviations not larger than $|\Delta x| < 2$ mm and $|\Delta y| < 2$ mm from the axis of the section, are of the order of $|\Delta\phi/\Delta x| < 0.03^\circ/\text{mm}$ and $|\Delta\phi/\Delta y| < 0.03^\circ/\text{mm}$ for the phase, $|\Delta A/A/\Delta x| < 0.05\%/\text{mm}$ and $|\Delta A/A/\Delta y| < 0.05\%/\text{mm}$ for amplitude.

To decrease the required time for one measurement of the 150-180 cell section the field distribution is measured only in the center of the cells. For precise determination of the position Z_1 of the first cell center and distance ΔZ between the centers the complete field profile is measured in the 3 first and 3 last cells of the section (with the exception of coupler and load cells). After data processing the accuracy for positioning in the first cell center is approximately 0.1 mm and for cell to cell length ≈ 0.002 mm for the 5 m section. The minimal step ΔL given by the step motor for bead positioning is not small enough (≈ 0.14 mm) and therefore the field is measured in 2 positions ($Z_{n1} = \text{int}(Z_n / \Delta L) \cdot \Delta L$ and $Z_{n2} = Z_n + \Delta L$), close to the optimum position $Z_n = Z_1 + (n-1) \Delta Z$. The amplitude and the phase in the center of n-th cell are approximated with the formula:

$$A_n = (A(Z_{n1})(Z_{n2} - Z_n) + (A(Z_{n2})(Z_n - Z_{n1})) / \Delta L, \quad 2.2$$

$$\phi_n = (\phi(Z_{n1})(Z_{n2} - Z_n) + (\phi(Z_{n2})(Z_n - Z_{n1})) / \Delta L. \quad 2.3$$

III. A LINEAR MODEL OF THE FIELD DISTRIBUTION IN THE SECTION

With the bead-pull method we can measure and calculate amplitudes and phases of the field in the centers of the cells: $A_1 e^{j\phi_1}$, $A_2 e^{j\phi_2}$, $A_3 e^{j\phi_3}$, For two neighboring cells with number $n-1$ and n , let us consider this values as a superposition of forward and backward waves: $a_n e^{j(2\pi/3(i-n)+\psi_n)}$ and $b_n e^{j(2\pi/3(i-n)+\phi_n)}$, which has passed through n -th disc (between cells $n-1$ and n).

$$A_{n-1} e^{j\phi_{n-1}} = a_n e^{j(2\pi/3+\psi_n)} + b_n e^{j(-2\pi/3+\phi_n)} \quad 3.1$$

$$A_n e^{j\phi_n} = a_n e^{j\psi_n} + b_n e^{j\phi_n} \quad 3.2$$

The solutions of these two complex equations are:

$$a_n e^{j\psi_n} = (A_{n-1} e^{j(\phi_{n-1}-\pi/2)} + A_n e^{j(\phi_n-\pi/6)}) / \sqrt{3} \quad 3.3$$

$$b_n e^{j\phi_n} = (A_{n-1} e^{j(\phi_{n-1}+\pi/2)} + A_n e^{j(\phi_n+\pi/6)}) / \sqrt{3} \quad 3.4$$

From formula (3.4) we can find the amplitude b_n and phase ϕ_n of the backward wave which passed the n -th disc (between cells $n-1$ and n). For the next $(n+1)$ disc we can use the formula (3.4) to calculate the backward wave:

$$c_n e^{j\eta_n} = (A_n e^{j(\phi_n+\pi/2)} + A_{n+1} e^{j(\phi_{n+1}+\pi/6)}) / \sqrt{3} \quad 3.5$$

Let us calculate the difference of these two backward waves in the plane of the n -th diaphragm. The phase shift per cell is about $2\pi/3$ and if attenuation can be neglected we can write:

$$S_n e^{j\theta_n} = b_n e^{j\phi_n} - c_n e^{j(\eta_n-2\pi/3)} \quad 3.6$$

This value is used to characterize the performance of the n -th cell. S_n and θ_n are the amplitude and phase of the wave scattered from n -th cell. In the process of tuning the amplitudes S_n should be decreased. This procedure was tested on a 50-cell constant gradient test section [4]. Figure 3.1 shows the values $S_n e^{j(\theta_n+\pi/2)}$ before and after tuning.

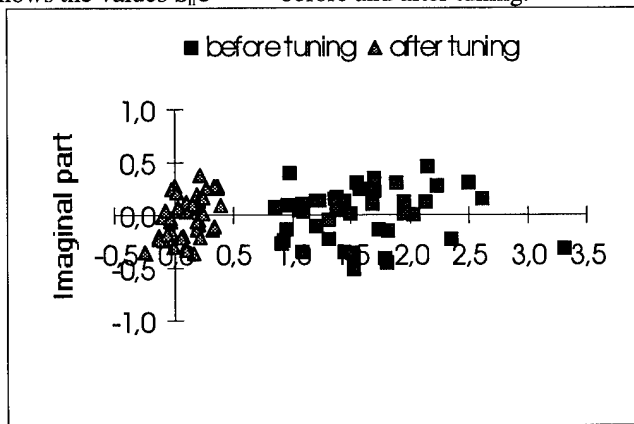


Figure 3.1. $S_n e^{j(\theta_n+\pi/2)}$ before and after tuning of 50-cell constant gradient section.

By definition, pressing the tuning holes of the cell, the frequency of this cell is increased, the real part of $S_n e^{j(\theta_n+\pi/2)}$ is decreased and the reflection coefficient $S11$ in the input of the

section is changed. This effect is used for the automatization of the tuning process.

The process of the tuning is controlled in real time by a computer code. Before tuning of each cell, a computer receives from the Network Analyzer (NWA) the reflected wave value $S11^0$. While tuning the reflected wave value $S11$ is analyzed, so that the calculated value of $|S11 - S11^0|$ should be achieved:

$$U_n = |S11 - S11^0| = \text{Re}(S_n e^{j(\theta_n+\pi/2)}) * K_n \quad 3.7$$

where K_n - is a coefficient to correlate the calculated and measured values for the cell number n :

$$K_n = |S11^*| / a_2 * C_n \quad 3.8$$

The $|S11^*|$ - amplitude of the reflected wave from the structure measured after detuning of the input coupler cavity, characterizes the amplitude of the input power from the NWA. C_n - is the loss factor or attenuation coefficient of the wave, which traveled from n -th cell to the beginning of the structure.

If we take into account the nonuniformity of the amplitude distribution in the structure the expression (3.8) can be rewritten for a constant impedance structure:

$$K_n = (|S11^*| / a_n) * (A_n / a_3)^2 \quad 3.9$$

For the constant gradient structure:

$$K_n = (|S11^*| / a_3) * (A_n / a_n)^2 * \Gamma_n \quad 3.10$$

where Γ_n ($\sim V_{gr}^n$ - group velocity for the n -th cell) is the reflection coefficient measured at the input of the structure for the wave reflected (for full reflection) from the n -th cell.

The results of the test tuning of a 50-cell section was sufficient ($\sigma_{ph} = 0.17^\circ$ for the phase distribution along the section) and we decided to use this method for the tuning of the first 156 cell constant gradient accelerating structure of the LINAC II at DESY.

IV. TUNING OF THE LINAC II SECTION

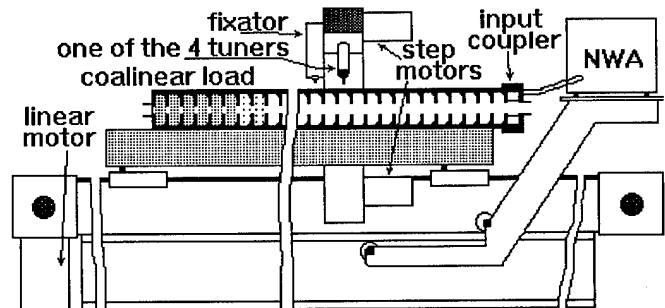


Figure 4.1. Tuning bench.

The structure was installed on a horizontal 13 meter long tuning bench (fig. 4.1) and connected to a water thermostabilization system. To be careful, the tuning of the structure was carried out in 3 steps: a) tuning to the frequency $F = F_{oper} - 900\text{kHz}$; b) tuning to the frequency $F = F_{oper} - 400\text{kHz}$; c)

tuning to the frequency $F=F_{oper}$. For the calculation of the operating frequency F_{oper} ($F_{vac}= 2998$ MHz in the vacuum and 40°C temperature of the structure), T_{str} - the temperature of the structure, T_{air} - the air temperature, H_{air} - the air humidity and P_{air} - the air pressure was taken into account[5]:

$$F_{oper}=F_{vac}/(1+1.7\cdot 10^{-5}(T_{str}-40))/\epsilon^{1/2}$$

$$\epsilon=1+P_{air}/T_{str}\cdot(211+P_0\cdot H_{air}/P_{air}\cdot(10160/T_{str}-0.294))\cdot 10^{-6}$$

$$P_0=10^{(7.45\cdot(T_{str}-273)/(T_{str}-38.3)+0.656)}$$

One step of tuning includes the field distribution measurement, the calculation of the parameters U_n , tuning of the integrated load (last eight cells, nr.: 149-156) and automatic tuning of cell 4-148 in the tuning machine. If the reflection from the load is very large for some reason, the load cells have to be tuned first. In figure 4.1 the field distribution in the section before tuning is shown. There are a lot of reflections from different parts of the section and in addition a large reflection from the load. The graph corresponds to a SWR in the structure of 1.5-1.8 after brazing.

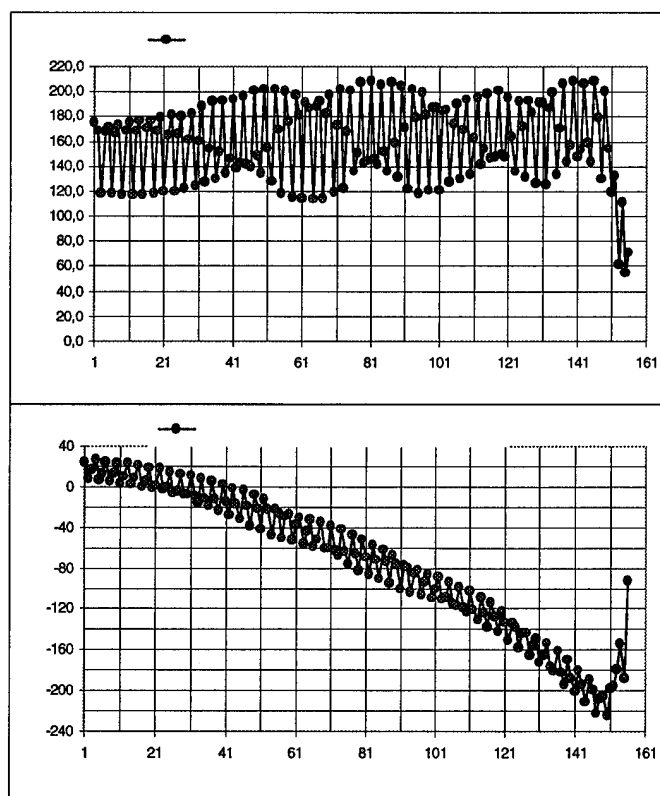


Figure 4.1. Field distribution in the section before tuning.

Figure 4.2 shows the field distribution in the section after three steps of tuning as described before. The field distribution in front of the integrated load is sufficient with a SWR smaller than 1.02. For the phase distribution a σ of 0.3° has been achieved. A small phase error in the load could not be tuned due to a dimensional error in the resonator diameter.

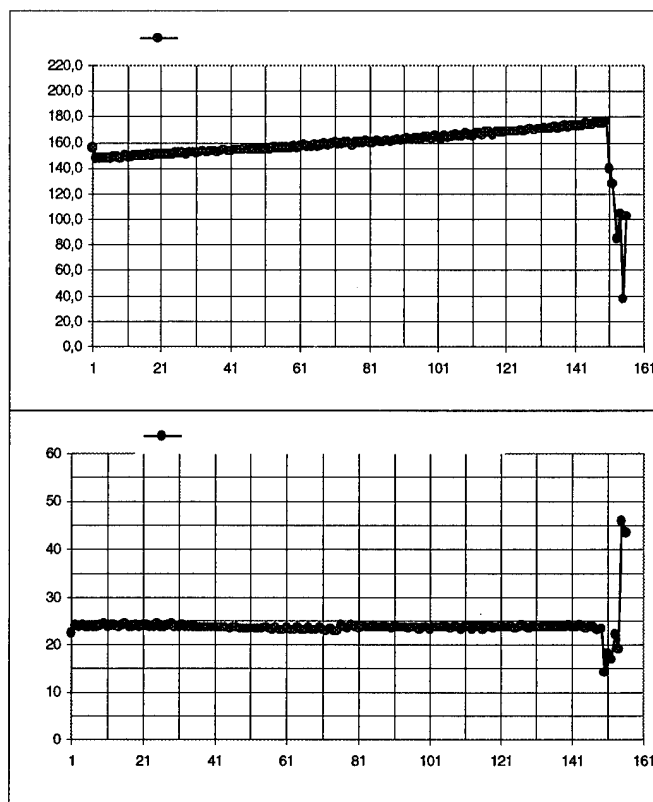


Figure 4.2. Field distribution in the section after tuning.

SUMMARY

It has been proven, that the bead pull measurement being presented in this paper is well suited for the tuning of long (many cell) traveling wave accelerating structures. The results for the tuning of a 156-cell traveling wave constant gradient accelerating structure ($\sigma=0.3^{\circ}$ for the phase) has been presented.

ACKNOWLEDGMENT

The authors would like to express their thanks to the Mr. G.Nawrath and Mr. H.Muench for construction of the effective tuning bench, Mr. P.Schmidt for electronics.

REFERENCES

- [1] A. Febel, G. Stange "New injection system for LINAC II" (in German). Internal report DESY S1-76-02, 1976.
- [2] N. Holtkamp, "The S-Band Linear Collider Test Facility", this conference.
- [3]. Charles W. Steele, "A nonresonant perturbation theory" IEEE Trans. on microwave theory and techniques, Vol. TT 14, No.2 (February, 1966).
- [4]. M. Dohlus, N. Holtkamp, T. Khabiboulline, "Tuning of a 50-cell constant gradient S-band traveling wave structure by using ". Internal Report DESY M-95-02, 1995.
- [5]. K. Andrianov i drugie, "Sprawochnik po elektrotehnicheskim materialam", t 1, M.-L. GEI, 1958.

RF SYSTEMS FOR RHIC*

J.Rose, J.Brodowski, R.Connolly, D.P.Deng, S.Kwiatkowski, W.Pirkel, A.Ratti
Brookhaven National Laboratory, Upton, N.Y. 11973

Abstract

The RHIC rf systems must capture the injected beam, accelerate it through transition to top energy, shorten the bunches prior to rebucketing, and store the beam for 10 hours in the presence of strong intra-beam scattering. These different functions are met by three independent systems. An accelerating system at 26.7 Mhz ($h=342$), a storage system at 196.1 MHz ($h=2508$), and a wideband system for the damping of injection errors.

I. RING PARAMETERS

The Relativistic Heavy Ion Collider (RHIC) under construction at Brookhaven National Laboratories consists of two rings with a 3833.852 meter circumference, with six intersection points for colliding beam experiments. The collider is required to accelerate any ion species from protons to gold. With the exception of protons, all ions must cross transition.

The baseline design calls for 57 bunches to be injected from the Alternating Gradient Synchrotron (AGS) with an upgrade capability to 114. Because of the variety of ions the collider must accelerate the beam parameters are best described in terms of protons and gold, which are listed in table I,

	P (inj)	P (top)	Au (inj)	Au (top)
Energy (γ)	31.2	268.4	12.6	108.4
Bunch length (ns)	6.5	4	13.5	7.5
Synch. freq. (Hz)	45	25	90	27
Bunch area (eV/u)	0.3	0.3	0.2	0.4
Emittance norm, 95% (π mm-mrad)	20	20	10	15
Number ions/bunch	10^{11}	10^{11}	10^9	10^9

Table I RHIC beam parameters

*Work performed under the auspices of the Department of Energy

with other ions falling between these extremes.

II. RF CYCLE

A. Injection

Individual bunches from AGS are injected into any preselected matched bucket in RHIC, to allow complete freedom in how the ring is filled. Issues at injection include emittance growth due to intrabeam scattering for gold (growth rate of 6 min.). Since protons are injected above, but close to transition the nominal matching voltage is 19 kV, whereas the beam induced voltage is 12 kV. In order to avoid beam control problems associated with the large transients a bunch rotation in AGS is proposed to increase the momentum spread, and hence the matching voltage. A decrease in bunch length of 1.8 would lead to a factor of 10 increase in rf voltage, thus relieving the beam loading. Momentum errors of the order 10^{-4} are expected and if not corrected would lead to emittance growth of 30%. A wideband damping system with a kick voltage of 1000 V/turn will reduce emittance growth to 10%.

B. Acceleration

Gold ions are accelerated from $\gamma=12.6$ to $\gamma=108.4$, requiring a 0.5% tuning range of the accelerating system. The superconducting magnets take about 74 s to ramp up to top energy, which relates to a maximum tuning rate of 18 kHz/s. The rf voltage ramp will be varied to prevent the synchrotron frequency from dwelling near power line harmonics. Especially dangerous is the region of $30\text{Hz} < f_s < 40\text{Hz}$, which must be passed through in less than 4 seconds.

C. Transition

The slow acceleration rate of a superconducting machine produces a long (100 ms) non-adiabatic time which can result in both emittance growth and beam loss. Beam is lost from chromatic non-linear effects and microwave instabilities due to bunch shape mis-match during transition crossing. A γ_T jump of 0.8 units in 60 ms is proposed to minimize these effects. The accelerating rf system must be able to switch phase ($\pi-\phi_s$) in this time and the beam induced voltage in the storage system kept below 10kV/turn to minimize emittance blowup.

D. Rebucketing

Rebucketing is the process of moving the bunch from the 26.7 MHz system to the 196.1 MHz system. Because the bucket length in the 196.1 MHz system is 5 ns, in order to have a 20% safety margin the incoming bunches must be 4 ns long. The bunches are nominally 6 ns long in the 300 kV bucket, to adiabatically shorten them with the accelerating cavities would require a prohibitive 1.5 MV. A bunch rotation at top energy is therefore proposed. At top energy the bunch will be shifted to the unstable fixed point where it debunches in a fraction of a synchrotron period, and the bunch shifted back to the stable fixed point. The bunch, now being mismatched, starts to rotate in phase space. In 3/8 of a synchrotron period has reached its minimum length position and the storage system is turned on. The details of this process are described in these proceedings¹.

E. Storage

The storage rf system provides longitudinal focusing to maintain short bunches for the physics program in the presence of large intra-beam scattering forces.

III. ACCELERATING SYSTEM

The accelerating system consists of two 26.7 MHz cavities per ring to provide the necessary 600 kV per turn. The accelerating cavity is a capacitively loaded coaxial quarter wave structure roughly 2 m long and 0.84 m in diameter. It is fabricated from copper plated carbon steel with all metal seals throughout. A complete description of the cavity is given in these proceedings². It is driven by an EIMAC 4CW150000 tetrode which is mounted directly to the cavity and loop-coupled. The configuration is shown in figure 1.

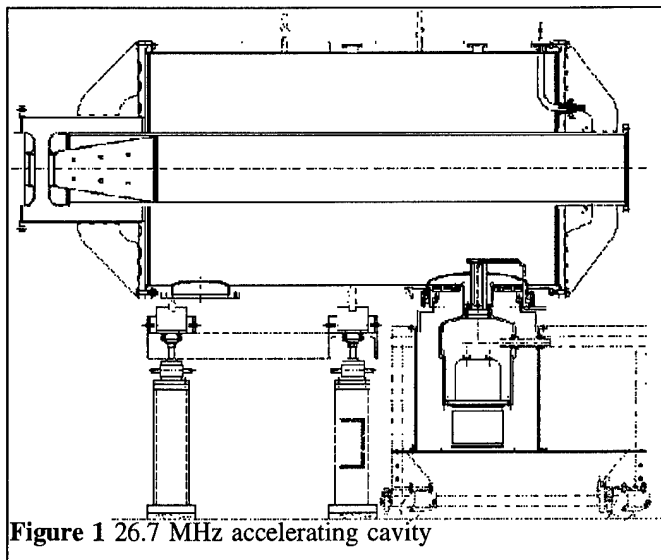


Figure 1 26.7 MHz accelerating cavity

A 1 kW solid state driver amplifier has been developed which will be located within the tunnel to minimize delay. This configuration allows greater than 45 dB of fast rf feedback to be closed around the cavity for impedance reduction. Since this loop is closed around the AVC and tuning loops the tolerances on these loops can be relaxed by either the feedback gain or the limits of the power amplifier, whichever is reached first. A mechanical tuner³ operates by moving one of the gap electrodes to change the capacitance and achieves a range of 300 kHz. The 18 kHz/s tuning rate dictated by the superconducting magnet ramp translates into a bandwidth requirement of less than 20 Hz.

IV. STORAGE SYSTEM

The storage system consists of ten 196.1 MHz ten re-entrant cavities operating in the TM_{010} mode. These are arranged with four cavities common to both beams in an interaction region, and three additional cavities per ring in the separated arc region to maintain control of the individual beams. This gives seven cavities per beam, each capable of 1 MV. The requirement of 6 MV per ring can be met with any single cavity disabled. Originally a 160 MHz system was planned but it happened that CERN was introducing superconducting cavities in the SPS ring and was decommissioning part of the 200 MHz "SWC" system. A feasibility study determined that these cavities could be tuned to 196.1 MHz and adapted for use in RHIC. Each CERN cavity is equipped with a close-coupled power tetrode, two HOM suppressors, a pneumatically controlled damping loop to reduce the impedance of the fundamental and a DC servo driven tuner, with 400 kHz operating range. A complete system description may be found in the reference⁴. The cavity with the power amplifier, damping loop, HOM suppressors and tuner is shown in figure 2.

In the installation at CERN groups of eight cavities share a common driver and power supply. For operation at RHIC individual power supplies are required to allow operations in the event of a power supply crowbar or failure. Individual driver amplifiers are necessary to be able to implement fast rf feedback around the cavities to reduce the impedance of the fundamental and hence the transient beam loading effects. A solid state 4 kW commercial fm broadcast amplifier is being purchased for testing. These drivers must be located in the ring to minimize the delay in the feedback loop, and must be shielded from the radiation environment. The cavities are tuned by squeezing the cavities with a large lead-screw crusher and increasing the capacitance of the gap to lower the frequency. The HOM suppressors are folded coaxial quarter wave notch filters which likewise have to be tuned to the new frequency. The power tetrode is matched to the 16 ohms of the coupling loop through a series of quarter wave transmission lines which again have to be re-tuned to 196.1 MHz. The damping loop is

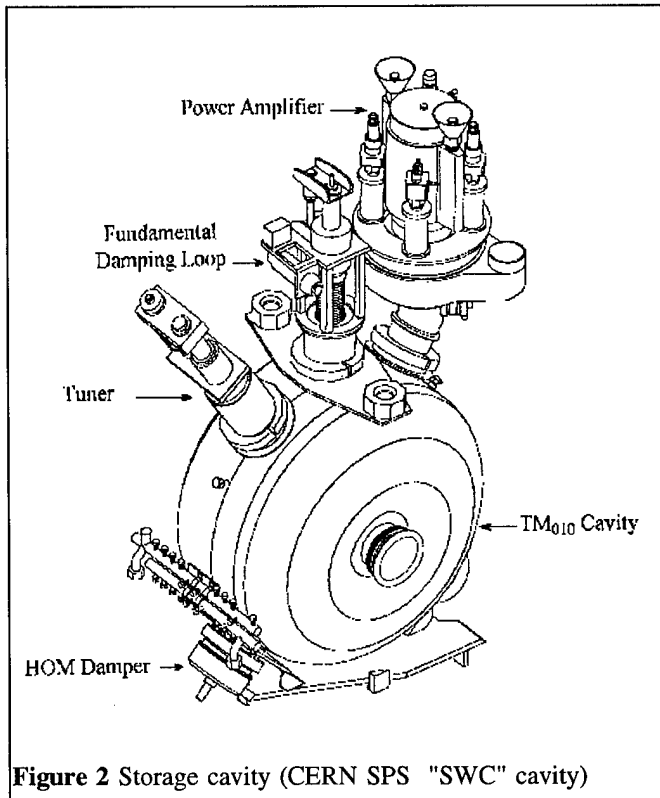


Figure 2 Storage cavity (CERN SPS "SWC" cavity)

still required for RHIC to de-Q the fundamental $8.9 \text{ M}\Omega$ impedance to reduce the beam induced voltage at transition crossing. These also require tuning to operate at 196.1 MHz .

V. WIDEBAND SYSTEM

There is one wideband system per ring to act as a longitudinal damper to damp out momentum errors at injection. Because RHIC operates with bunch to bucket injection this system must act on individual bunches. This requires a bandwidth of at least $\pm 57f_0$ for the case of 114 bunches, where f_0 is the bunch rotation frequency.

Acknowledgements

The authors wish to thank J.M.Brennan for many helpful discussions of the system requirements. M. Harrison, S.Peggs and the RHIC accelerator physics group made significant contributions to Reference (1) which served as the basis of this paper.

References

- 1) RHIC RF and AP groups, "Conceptual Design of the RHIC rf System" RHIC RF-22 technote.
- 2) J.Rose et al "Design of the 26.7 MHz RHIC Cavity" these proceedings

- 3) J.Rose et al "Design and Performance of a Prototype Tuner for RHIC" these proceedings
- 4) P.E.Faugeras "The New rf System for Lepton Acceleration in the CERN SPS" Particle Accelerator Proceedings, 1987

A NEW RF SYSTEM FOR BUNCH COALESCING IN THE FERMILAB MAIN RING

J. Dey, I. Kourbanis, and D. Wildman, Fermi National Accelerator Laboratory*, Batavia, IL 60510 USA

Abstract

A new RF system for improving both the proton and antiproton bunch coalescing efficiencies has been installed in the Fermilab Main Ring. The system consists of five, ferrite-loaded RF cavities operating at a fixed frequency of 2.5 MHz and a second harmonic cavity at 5.0 MHz. Each cavity is driven by a 5 kW solid-state power amplifier and can produce a peak accelerating gap voltage greater than 15kV. An overview of the entire system will be presented along with a detailed description of the RF cavity design including ferrite selection and testing procedures.

I. INTRODUCTION

One of the present functions of the Fermilab Main Ring is to act as a 150 GeV injector for the Tevatron Collider. In this mode of operation, 9 to 13 bunches of protons or antiprotons are combined into a single high intensity bunch before being injected into the Tevatron. This process, known as bunch coalescing [1], is accomplished using two RF bunch rotations. The first rotation, to lower the beam energy spread, takes place in the normal Main Ring RF $h=1113$ (53 MHz) bucket with some additional linearizing $h=2226$ (106 MHz). In the second RF rotation, the low energy spread beam is rotated for a quarter of a synchrotron period in an $h=53$ (2.5 MHz) bucket linearized with some additional $h=106$ (5 MHz) voltage. This rotated ensemble of bunches is then recaptured into a single $h=1113$ bucket and injected into the Tevatron. The efficiency of this coalescing process is a function of both the initial longitudinal emittances of the individual bunches and the RF voltage available for the $h=53$ bunch rotation.

To achieve higher initial luminosity in the Tevatron Collider, the Main Ring has been operating at higher beam intensities and larger longitudinal emittances. To coalesce these higher intensity bunches efficiently, it has become necessary to raise the $h=53$ and $h=106$ RF voltages by a factor of 2.5 from 24kV(6kV) to 60kV(15kV). Simulations of beam dynamics and the results of this upgrade are presented in another paper presented at this conference [2].

The previous coalescing RF system consisted of six modified PPA (Penn-Princeton Accelerator) cavities [3] driven by 25 kW power tetrode amplifiers mounted on top of the cavities in the Main Ring tunnel. The accelerating voltage available from these cavities was limited by the high field losses encountered in the PPA cavities' 4C4 NiZn ferrite cores.

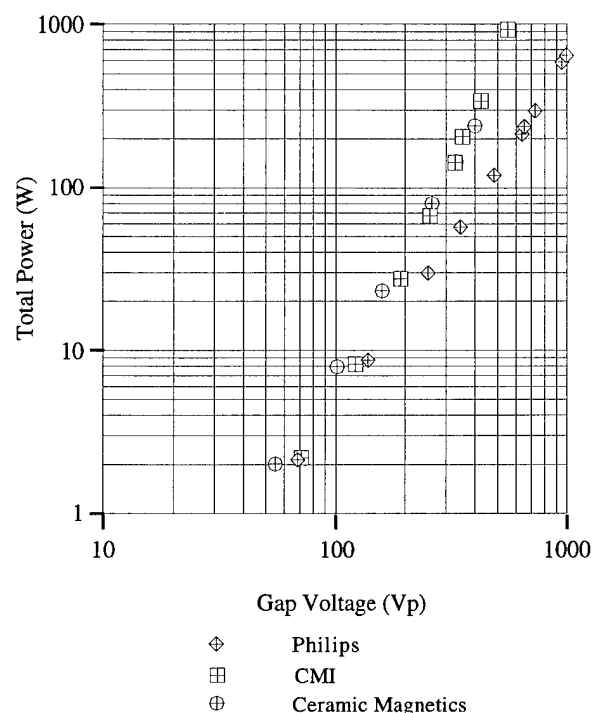


Figure 1: Power Dissipated in Ferrite Cores

II. FERRITE SELECTION AND TESTING

During the initial stages of this coalescing upgrade, a literature search revealed that newer types of NiZn ferrites were commercially available with significantly lower high field losses [4]. A decision was made to test several of these new ferrites to determine their properties and high field losses at 2.5 and 5 MHz. Three different vendors each supplied three full size NiZn rings for our tests. Philips supplied three one-piece type 4M2 rings in their standard size of 500mm OD X 200mm ID X 25.4 mm thick. Ceramic Magnetics delivered three C2025 cores 20"OD X 7.5"ID X 1" thick. Each toroid was assembled from six wedges bonded together. CMI Technology supplied three type N125 cores in sixteen wedges that formed a 20"OD X 7.5"ID X 1" thick toroid.

To accurately measure the RF losses in the ferrites at high magnetic-flux density, Brf, a single ferrite core was inserted into a coaxial aluminum resonator test fixture. The test fixture was tuned to 2.5 MHz using several high Q ceramic transmitting capacitors. Energy was magnetically coupled into the resonator with a thin loop made from .003" thick copper foil. To obtain a 50 ohm input impedance at the coupling loop, each of the test ferrites was sliced in half and the coupling loop area was adjusted between the two halves of the cores. The

* Operated by Universities Research Association, Inc. under contract with the U.S. Department of Energy.

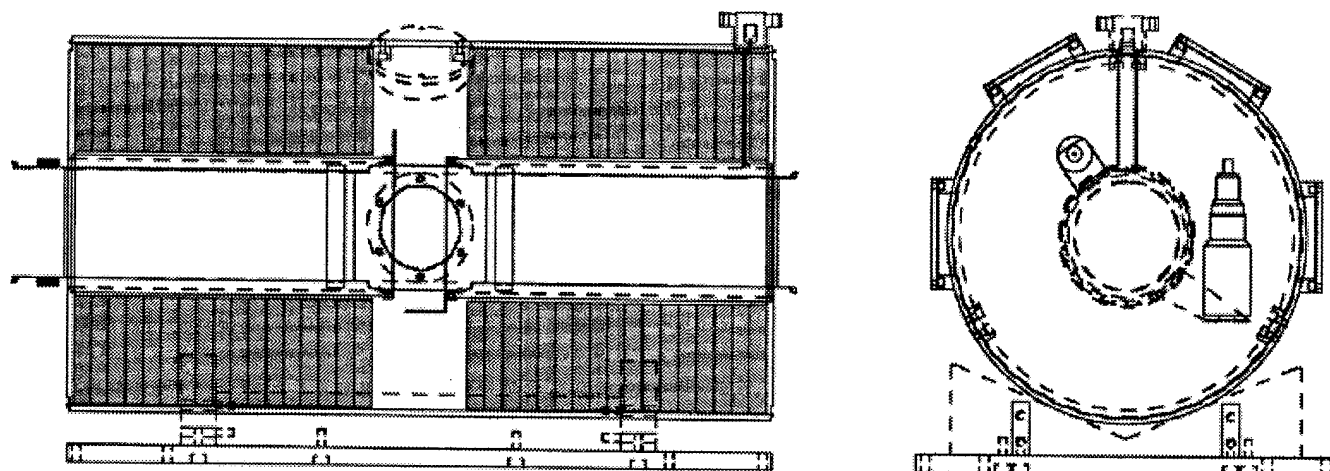


Figure 2: 2.5 Mhz Coalescing Cavity

test fixture was excited using either a 250 watt or 1 kW power amplifier. The power deposited in the ferrite core was measured as the excitation frequency was swept through resonance at 2.5 MHz. The power loss in the ferrite was calculated from the measured forward and reflected power from a calibrated high power directional coupler (Werlatone model C2784) inserted into the drive line. All power measurements were made using an HP 8753C network analyzer. The voltage developed across the test fixture gap was measured using a specially designed capacitively coupled monitor and several different commercially available voltage probes (Tektronix 6015A, HP 85024A, or HP 1124A.) A plot of power lost vs. gap voltage is shown in Fig. 1. for each of the three different cores (Note: the three CMI cores showed significant differences between cores.) A test fixture gap voltage of 600 volts corresponds to an average $\langle B_{rf} \rangle$ of 100 gauss and a maximum Brf of approximately 164 gauss in the ferrite core. All of the manufacturers cores exhibited similar losses at low $\langle B_{rf} \rangle$. However; the Philips 4M2 clearly showed significantly lower losses at the highest Brf and was our choice for the new cavities. In fact, the losses were low enough to allow us to consider driving the new cavities with all solid-state amplifiers. An additional advantage of choosing solid-state power amplifiers is that they could be easily located in an above ground service building; providing easy access for maintenance and repair during a colliding beams store.

III. CAVITY DESIGN

A diagram of the final cavity design is shown in Fig.2. Each cavity consists of two fore-shortened, coaxial, quarter-wave resonators with a single accelerating gap at the center of the cavity. The entire resonator is made from 6061T-6 aluminum components which are TIG welded together. The outer shell is a piece of 5/16" thick aluminum stock, rolled and welded into a 40" long cylinder with an inner diameter of $19.9" \pm 0.1"$. The inner conductors consist of 7.5"OD X 7"ID X 18" long tubes

which are joined at the shorted ends of the cavity by 3/8" thick flanges. The cavity has a separate 6" diameter stainless steel vacuum beam pipe with a 6" ID cylindrical ceramic window (Ceramaseal # 13652-03-W) which slides inside the resonator's inner conductors. Two strips of beryllium copper finger stock, mounted around the outside of the vacuum beam pipe, center the beam pipe inside the inner conductors and prevent any RF leakage out of the cavity. Four 4.5" dia. ports are located around the center of the outer cavity shell to allow access to the gap tuning capacitors. The cavity is supported by two V-blocks mounted on a 1" thick aluminum plate.

The 2.5 MHz and 5 MHz cavities are identical except for the number of ferrite rings and the gap capacitance. The 2.5 MHz cavity has a total of 34 ferrite rings, 17 in each half. The 5 MHz version has 24 ferrites, 12 in each half. Due to the extremely low average power dissipated in the cavities (< 6 watts), direct cooling of the ferrites was unnecessary. The ferrites were placed adjacent to one another (with the exception of the ferrite located at the 50 ohm tap position which has a 1/8" polyethylene spacer ring.) To help cushion the ferrites during transport and installation, the interior of the outer shell was lined with a sheet of 1/8" HDPE and the ferrites were secured at the gap region by six UHMW polyethylene blocks. This polyethylene liner along with the ferrites and a small air gap surrounding the inner conductor forms a coaxial transmission line with a characteristic impedance of 260 ohms. The ferrite rings are maintained at a constant temperature by 95°F water circulating through 0.5" square aluminum tubing (0.25" dia. inner water channel) welded directly to the outer shell.

The cavities are driven by a single 1" wide aluminum coupling loop at one end of the cavity which enters through a standard 1-5/8" EIA flanged port and is welded to the inner conductor. For the 2.5 MHz cavities, the correct 50 ohm tap point was achieved by machining a 1" wide slot, approximately .75" deep, in the second ferrite from the shorted end. A 1/8" thick

HDPE ring was also inserted in these cavities between the second and third rings to reduce the imaginary component of the cavity input impedance. In the 5 MHz cavity the input loops a single ferrite which is spaced from the other ferrites by a 1" thick HDPE ring.

The 2.5 MHz cavities were tuned to resonance with a gap capacitance of approximately 110pf. Two 100pf ceramic transmitting capacitors (Philips 859S-100Z) in series, combined in parallel with a 7-75 pf variable vacuum capacitor (Jennings CVFA-75-0030), provided a simple method of tuning the cavity. In the final cavity tuning process, the cavity was deliberately tuned 10 kHz higher in frequency at low power to compensate for the small frequency shift observed with the cavity RF power level. The cavity gap voltage is monitored by two capacitively-coupled probes symmetrically placed 2-1/4" on either side of the gap. The monitors are made from 3/32" diameter machined brass rods, 3" long, soldered to N-type coaxial feedthroughs extending through the outer cavity shell wall. The monitors were calibrated using two HP 85024A high frequency probes connected to an HP 8753C network analyzer. One high frequency probe was placed directly across the accelerating gap, while the other probe was attached to the gap monitor. The nominal ratio of gap voltage to monitor voltage for the cavities is 15,000/1. This calibration was verified after installation in the Main Ring by observing the synchrotron period of the proton beam rotating in the 2.5 MHz bucket.

The unloaded Q of the 2.5 MHz cavities was 125 ± 5 . The 5 MHz cavity had a slightly lower Q of 95. Using low level RF signals, the cavities' shunt impedances were found to be in the range of 48-52 K Ω using an HP 4193A vector impedance meter probe placed across the accelerating gap. These values agree with the shunt impedances calculated from the measured gap voltage and the power deposited in the cavity from directional coupler measurement in the input transmission line. At cavity gap voltages in the range of 12kV to 17kV, the shunt impedance slowly declined by approximately 10%.

IV. THE AMPLIFIER

Each cavity is powered by a Lambda RF Systems model PA5K-30LC, water cooled, solid-state linear MOS FET amplifier which was specifically designed for Fermilab. Each amplifier consists of 6 power amplifier modules, three 48 volt dc power supplies, one RF combiner, and a system control unit. The amplifier, shown in Fig. 3, has a nominal gain of 60 dB. The total output power is greater than 5 kW into a 50 ohm load over a frequency range of 2.5 to 5 MHz. The amplifier modules can be easily modified for operation at 7.5 and 15 MHz to accommodate future changes in Colliding Beams bunch spacing.

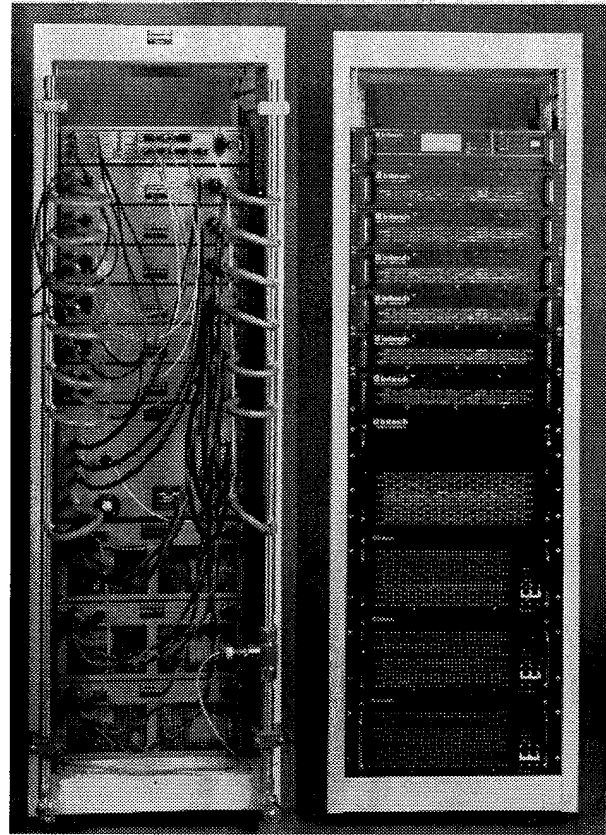


Figure 3: Front and rear views of the 5 kW solid-state power amplifier.

The amplifiers are connected to the cavities in the Main Ring tunnel by approximately 200 ft of 7/8" coaxial transmission line (Andrew LDF5-50A). To obtain the best possible 50 ohm matching conditions, open and shorted tuning stubs, made from lengths of 7/8" coaxial cable, have been added at the 5 kW amplifier outputs.

V. REFERENCES

- [1] "Performance and Comparison of Different Coalescing Schemes Used in the Fermilab Main Ring," I. Kourbanis, G.P. Jackson, and X. Lu. Proc. of the 1993 Particle Accelerator Conf. 3799 (1993).
- [2] "Improvements in Bunch Coalescing in the Fermilab Main Ring," J. Dey, I. Kourbanis, and D. Wildman. these proceedings.
- [3] "The RF System for the Princeton-Pennsylvania Accelerator," J.L. Kirchgessner, D. Barge, G.K. O'Neill, G. Rees and J. Riedel. IRE Trans. Nucl. Sci. NS-9 , 11 (1962).
- [4] "Studies of Ferrite Materials for the AGS Booster Synchrotron," M.A. Goldman, P. Cameron, R.T. Sanders and J. Tuozzolo. Proc. of the 1989 Particle Accelerator Conf. 165 (1989).

HIGHER ORDER MODES OF THE MAIN RING CAVITY AT FERMILAB

J. Dey, and D. Wildman, Fermi National Accelerator Laboratory*, P.O. Box 500 MS-306, Batavia, IL 60510 USA

Abstract

The shunt impedance and frequency of the higher order modes [HOM] of the Main Ring Cavity ($h = 1113$) at Fermilab were measured using the stretched wire method. The results of the stretched wire measurements and a cavity transmission line model of the modes will be given.

I. SHUNT IMPEDANCE MEASUREMENT

Shunt impedance measurements have been made on a Main Ring Cavity [1], shown in Figure 1, that tunes between 52.812 and 53.104 Mhz with two ferrite tuners. The cavity has a typical gap voltage of 250 kV per cavity at the gap. The stretched wire method is essentially a voltage divider circuit where one part of the divider is a 50 Ω

resistor and the other is a fixture (Figure 2) with a wire across the gap of the cavity. The 50 Ω resistor and stretched wire fixture are in series with each other. The frequency drive to the fixture was supplied by an HP 8753C network analyzer. The first voltage measured by the analyzer was across both the fixture and the 50 Ω resistor. The second voltage was measured across just the 50 Ω resistor by a HP 85024A high-frequency probe to the analyzer. The frequency and voltages at each of the resonant modes of the cavity were then recorded. To remove the impedance of the stretched wire fixture, the fixture was placed across only the beam pipe (Figure 2) and the fixture impedance was measured at each frequency of the resonant modes of the cavity. The corresponding impedances of the fixture were then subtracted from each of the cavity modes to give the final shunt impedance.

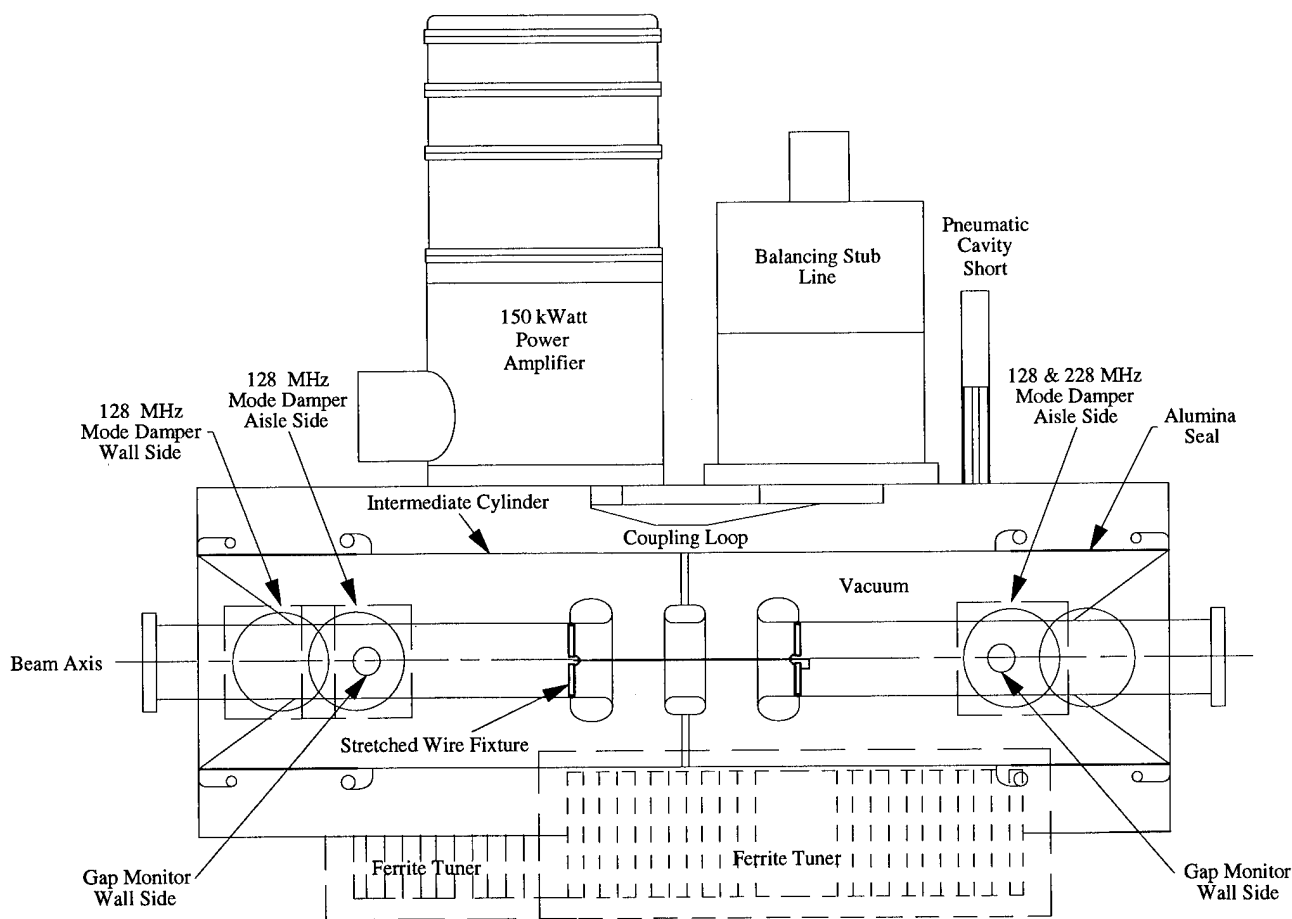


Figure 1: Diagram of Main Ring Cavity ($h = 1113$).

*Operated by Universities Research Association, Inc. under contract with the U.S. Department of Energy.

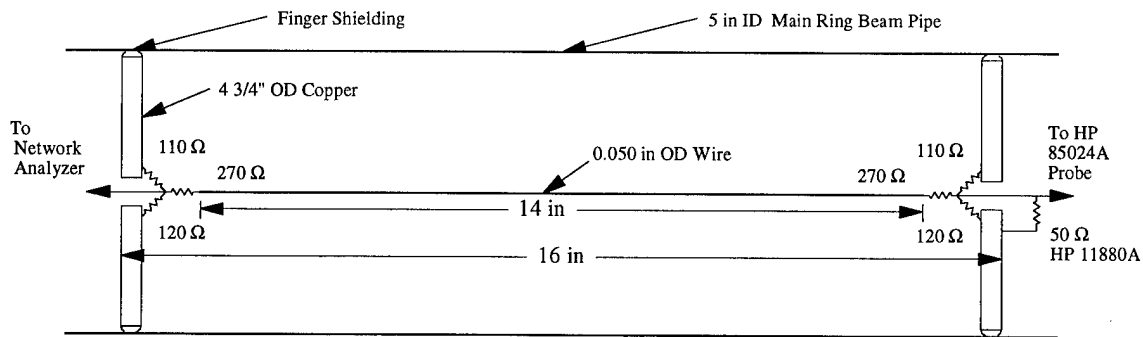


Figure 2: Stretched Wire Fixture.

II. TRANSMISSION LINE MODEL

The circuit in Figure 3 was simulated on RFLab™. The capacitors 1 and 2 represent the gap capacitance of each of the respective cavity gaps. Transmission lines 1 and 2 represent the beam pipe as the inner conductor and the intermediate cylinder as the outer conductor of the line. Transmission lines 3 and 4 represent the folded portion of the cavity. Transmission lines 5 and 6 represent the intermediate cylinder as the inner conductor and the outer shell of the cavity as the outer conductor of the line. Inductor 1 is the inductance of the 1 kV dc bias circuit to the intermediate cylinder. The model predicts (measured) odd modes at 52 (53.191), 131 (127.25), 225 (227.549), and 328 (336.876) Mhz, and even modes at 80 (82.253), 200 (197.776), and 264 (261.996) Mhz when looked at from port 1.

II. HOM OF THE MAIN RING CAVITY

The data presented in Figures 4 and 5 are for the cases where the dc bias current to the ferrite tuners was zero and full bias (2000 A). The data was taken with the cavity mode dampers in place as shown in Figure 1. This is the present state of all the dampers on the eighteen cavities in

the Main Ring tunnel.

IV. REFERENCES

- [1] "Mode Damping in NAL Main Ring Accelerating Cavities," R.A. Dehn, Q. A. Kerns, and J. E. Griffin, IEEE Trans. on Nucl. Sci., Vol. NS-18, No. 3, June 1971

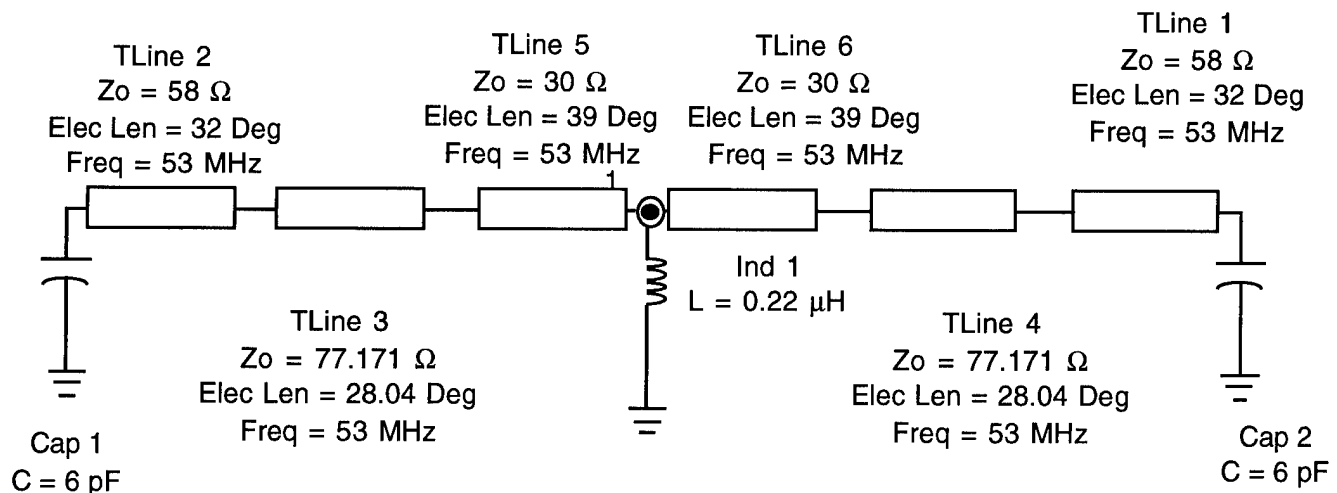


Figure 3: Transmission line model of Main Ring Cavity.

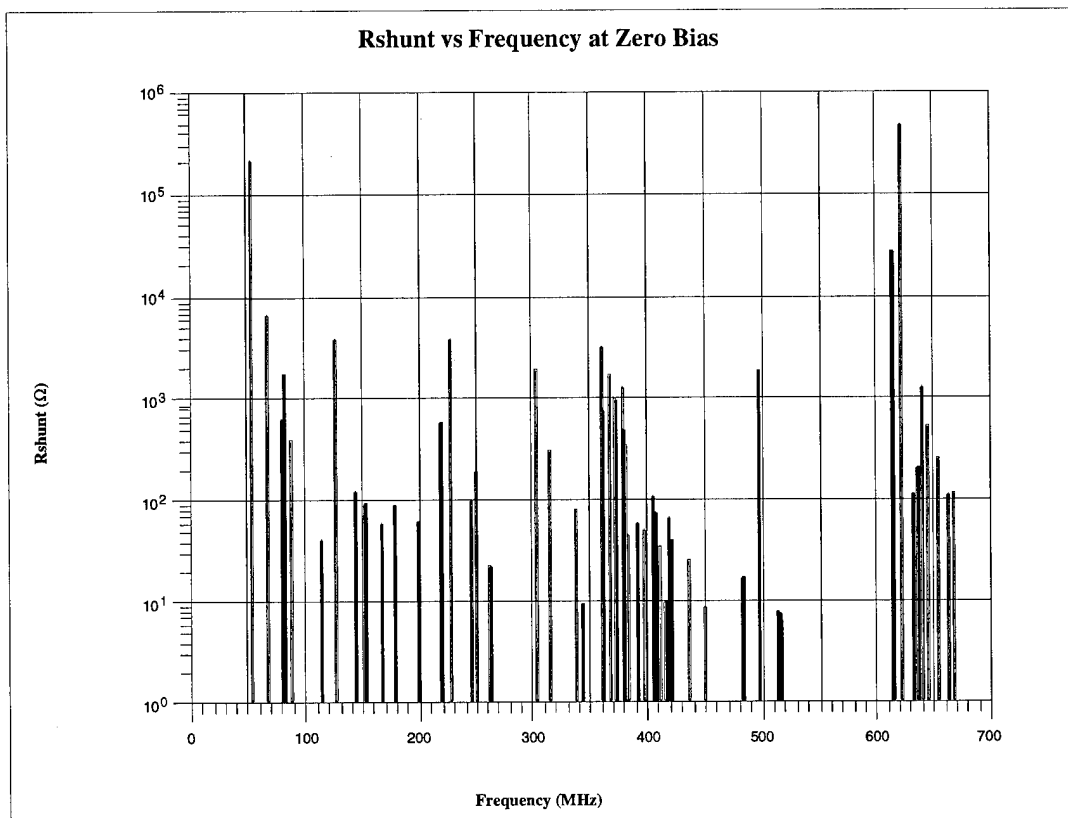


Figure 4: Shunt Impedance at Zero Bias of Main Ring Cavity.

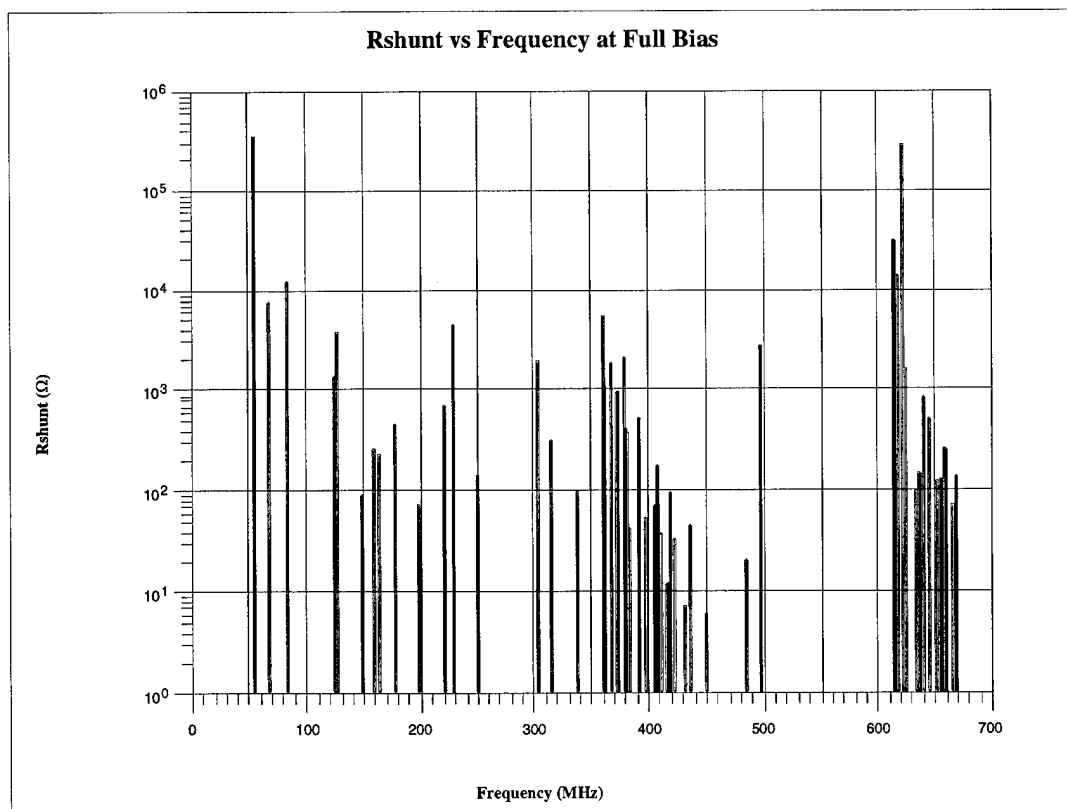


Figure 5: Shunt Impedance at Full Bias of Main Ring Cavity.

RF Measurements and Control of Higher Order Modes in Accelerating Cavities

V. Veshcherevich, S. Krutikhin, I. Kuptsov, S. Nosyrev, A. Novikov, I. Sedlyarov

Budker Institute of Nuclear Physics, 630090 Novosibirsk, Russia

Abstract

In RF cavities, built at BINP for electron-positron storage rings, special tuners are provided for higher order modes (HOMs). The HOM tuners effect on different modes in different ways. Electrical characteristics and tuning curves of cavity modes are measured. Using these experimental data, the beam-cavity interaction at higher order modes is analyzed for different HOM tuner positions. There are combinations of HOM tuner positions, at which the cavity caused beam instabilities may occur, and there are combinations, at which they may not. The last ones are recommended for routine cavity operation.

INTRODUCTION

Beam-cavity interaction on higher order modes may cause beam instabilities, coherent energy losses and other phenomena. Different ways are possible for minimizing negative effects of that interaction for the beam.

In one way the cavity geometry may be chosen so that the frequencies of higher order modes are far from harmonics of beam revolution frequency and beam-cavity interaction is rather weak. This way is especially good when the accelerator or the storage ring is small and therefore, the beam revolution frequency is high, i. e. the distance between harmonics is large.

The other approach is the damping of the Q of higher order modes. If the HOM bandwidths become greater than the repetition rate of the particle bunches, coherent beam instabilities cannot be excited by cavity HOMs. This approach is good for large machines for the necessary Q damping is not strong in that case.

The third way is the evolution of the first one. It is the correction of HOM frequencies of the cavity by special tuners in order to avoid beam instabilities. The smaller the machine is, the easier it is to solve the problem.

At Novosibirsk we have used the last approach to different RF cavities for years [1]. We can do that because our machines are not very large. The largest machine is VEPP-4 electron-positron collider with its revolution frequency of 0.82 MHz. An accelerator of that size is probably the largest machine for which the HOM frequency correction approach can be applied.

HOM TUNERS

We use HOM tuners of different types. In one case it is a barrel that can be plunged into the cavity. In other case it is a

plate of an ∞ -like shape the bigger axis of which is parallel to the beam axis. It may also have a shape of a fork or a rod. If the beam revolution frequency is high, only one HOM tuner can be used. Its position is chosen so that it affects the most dangerous higher order mode. So, the RF cavity of VEPP-3 storage ring (beam revolution frequency is 4 MHz, RF frequency is 72 MHz) has one HOM tuner.

If the beam revolution frequency is low or the bunch size is very small, several HOM tuners are needed for proper correction of the HOM frequencies. Each tuner acts on different modes in different ways. E. g., there are three HOM tuners in each of six cavities of VEPP-4 collider (revolution frequency 0.82 MHz, RF frequency 181 MHz) [2]. Two of them are shown in Figure 1.

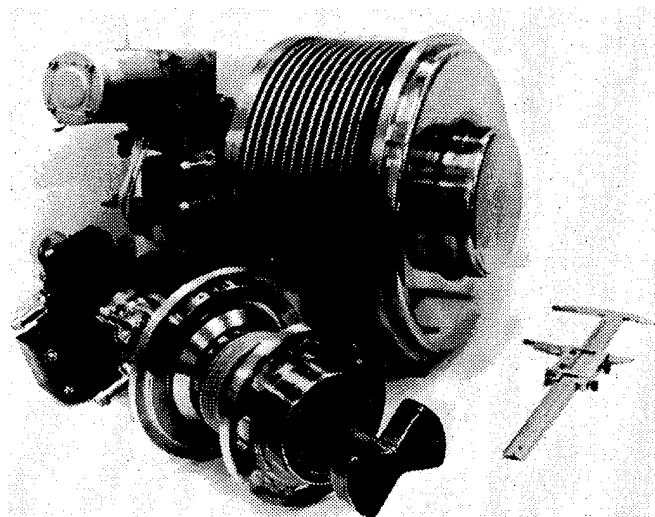


Figure 1: HOM tuners of VEPP-4 cavities.

RF MEASUREMENTS OF HIGHER ORDER MODES IN RF CAVITIES

We have built a specialised automated setup for study of the higher order modes in RF cavities. At the setup characteristics of the fundamental and higher order modes can be measured including Q and R/Q values, shunt impedances, resonance frequencies of the modes, and the effects of tuners on them.

Figure 2 presents experimental frequencies and impedances of the fundamental mode and the higher order

APPLICATION TO BEAM DYNAMICS

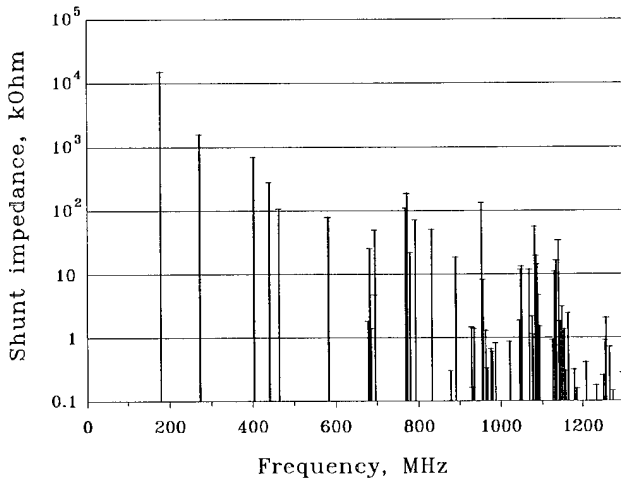


Figure 2: Modes of a VEPP-4 cavity.

modes of a VEPP-4 cavity that have longitudinal electrical field on the beam axis.

The dependence of the frequencies of some higher order modes on HOM tuner positions is shown in Figure 3. The numbers of curves correspond to the numbers of HOM tuners. Thin solid horizontal lines at the plots correspond to harmonics of the beam revolution frequency of the VEPP-4.

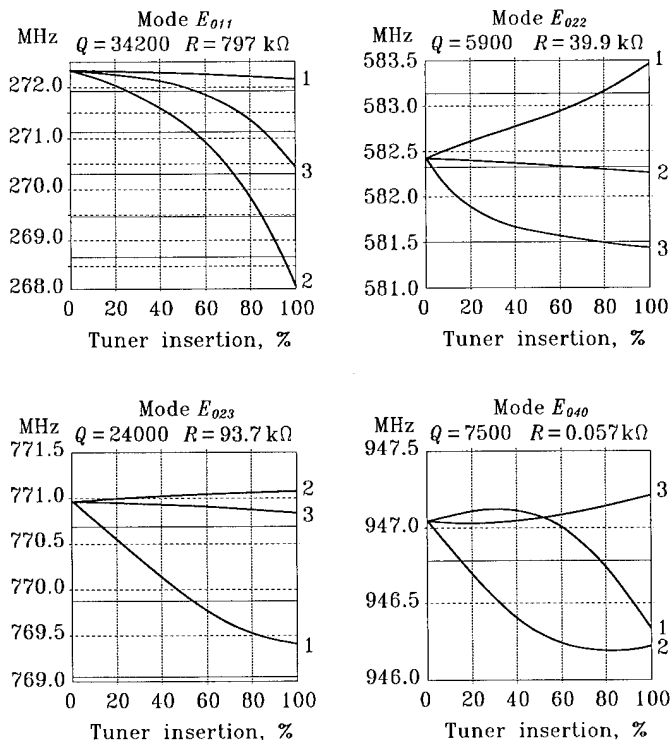


Figure 3: Tuning curves of some higher order modes.

Experimental data allow to compute the integral influence of the higher order modes of the cavity on longitudinal beam dynamics. The results of the analysis for the single bunch mode of operation of the VEPP-4 are presented in Figure 4. 25 higher order modes of one cavity with greater impedances in the frequency range up to 1200 MHz were taken into account. The coordinates X_n at the diagrams are the positions of the cavity tuners of number n .

For each point of the diagram, the value of

$$S = \sum_{n=1}^N \sum_{k=M_n-2}^{M_n+2} R_n(kf_o + f_s) - R_n(kf_o - f_s)$$

is computed. Here $R_n(f)$ is the value of the real part of the impedance of the n -th higher order mode at the frequency f , f_o is the revolution frequency of the beam in the storage ring, $M_n f_o$ (M_n is an integer) is the harmonic of the revolution frequency which is the nearest to the n -th mode, f_s is the frequency of synchrotron oscillations. N is the number of the higher order modes taken into account.

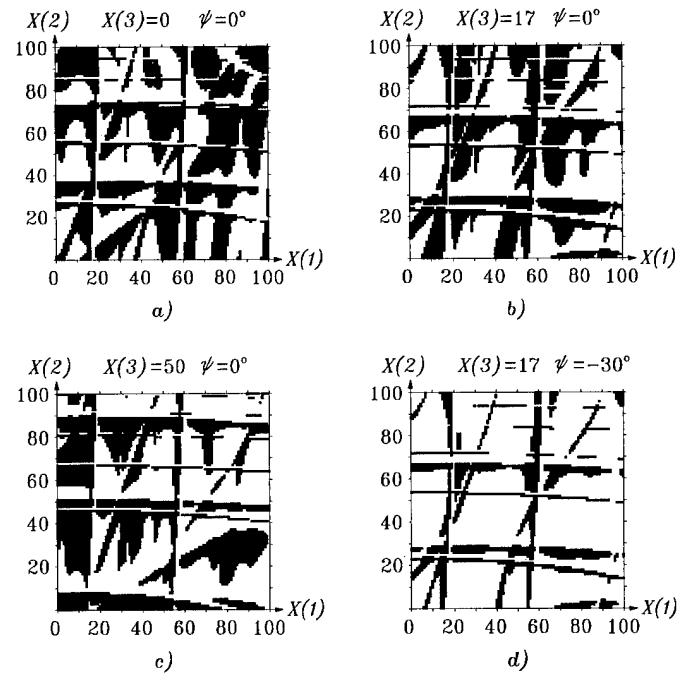


Figure 4: Areas of longitudinal instability as functions of HOM tuner positions and tune ψ of the fundamental mode.

As it is known [3], if the sum $S > 0$ then beam-cavity interaction at the higher order modes may produce a positive increment of the phase oscillations of the bunch that will cause longitudinal beam instability. If $S < 0$, then beam-cavity interaction at the higher order modes produces a

negative increment (i. e. a positive decrement) of the phase oscillations of the bunch and the longitudinal bunch motion would be stable. The black areas at the diagrams correspond to conditions when the increment of the phase oscillations of the bunch due to beam-cavity interaction may be positive. Therefore, one should set tuners at positions corresponding to white areas.

For three HOM tuners the whole diagram is three-dimensional. The diagrams in the Fig. 4 are two-dimensional sections of this three-dimensional picture. They are plotted in coordinates of HOM tuners #1 and #2, for fixed positions of the tuner #3.

The fundamental mode of the cavity plays an important role in the longitudinal beam dynamics due to its great impedance. The effect depends on the tune of the fundamental mode. Figure 4 illustrates it. The first three diagrams are plotted for zero tune of the fundamental mode (i. e. it is tuned exactly to the resonance). The fourth diagram is plotted for the fundamental mode tuned 30° off the resonance to the lower frequency. The positions of the tuner #3 are equal for plots *b*) and *d*). One can see that the forbidden areas become much more narrow with the fundamental mode detuned.

The recommendations obtained in this analysis are to be considered as preliminary ones. During operation of the cavity in the machine the actual frequencies of the higher order modes differ from the values measured at low level. A reason is the deformation of the cavity due to RF heating. This deformation is complex and differs from an ideal model taken into account in our analysis. Another source of error is the impedance of the RF power amplifier connected to the main cavity coupler through the transmission line. Both of these factors cause perturbations of frequencies of the higher order modes. Therefore, the right positions of the HOM tuners are elucidated by beam tests in the machine.

For the multibunch mode of operation of the storage ring a new analysis [4] of HOM tuner positions is required. This analysis should take into account the number of bunches, the distance between them, the numbers of particles in each bunch, and the positions of RF cavities in the storage ring.

A single bunch approach to the beam-cavity interaction can be applied to the multibunch mode of operation, if the frequencies of synchrotron oscillations of the bunches are different enough and they may be considered independent from each other.

CONCLUSION

Right tuning of high order modes of RF cavities is an effective way to avoid beam phase instability for small and medium electron-positron storage rings operating in a single bunch mode. This way is applied to RF cavities of different storage rings built at Novosibirsk. This technique can be applied to the multibunch mode of operation as well. To this end splitting of synchrotron frequencies of bunches is to be done. It can be achieved by an additional RF system which frequency is not multiple of the main RF.

REFERENCES

- [1] V. G. Veshcherevich et al. "Longitudinal Effects during Storing Process of Electrons in VEPP-3", *Proc. of the Third All-Union Particle Accelerator Conf.*, Vol. 1, p. 397. Moscow, 1973 (in Russian).
- [2] E. Gorniker et al. "RF System of VEPP-4M Electron-Positron Collider", *This Proceedings*.
- [3] M. M. Karliner et al. "Stability for the Phase Motion of a Relativistic Bunch in a Storage Ring", *J. of Technical Physics*, **58**, No. 11, p. 1945 (1968) (in Russian). See English translation in *Sov. Phys. Tech. Phys.*, **13**, No. 11, p. 1560 (1969).
- [4] M. M. Karliner et al. "Longitudinal Stability of Colliding Beams in e^+e^- Storage Rings with the Account of Beam Coupling with the Environment", *Proc. of the Third Advanced ICFA Workshop on Beam-Beam Effects in Circular Colliders*, p. 131. Novosibirsk, 1989.

RF System of VEPP-4M Electron-Positron Collider

E. Gorniker, P. Abramsky, V. Arbuzov, S. Belomestnykh, A. Bushuyev, M. Fomin,
I. Kuptsov, G. Kurkin, S. Nosyrev, V. Petrov, I. Sedlyarov, V. Veshcherevich
Budker Institute of Nuclear Physics, 630090 Novosibirsk, Russia

Abstract

RF system of the VEPP-4M collider consists of six 181 MHz copper cavities fed from a single RF power source. The cavity has a Q of 50,000 and a shunt impedance of 15 MOhm. The cavities are connected to a waveguide distributing system with the aid of coaxial lines. The distance between cavity connections is equal to one wave length. Dimensions of the rectangular waveguide are chosen in such a way that the guide wave length is equal to two free-space wave length. Power distribution along the cavity chain is proportional to the distribution of cavity shunt impedances due to a proper design of the coax-to-waveguide transitions. The two-tube tetrode amplifier presently has an output RF power of 300 kW. After upgrading of the RF system its power will increase to 1.2 MW.

INTRODUCTION

VEPP-4M electron-positron collider is the modified VEPP-4 storage ring designed for operation with two electron and two positron bunches at the energy up to 6 GeV for each bunch. The storage ring has the circumference of 366 m and the beam revolution frequency of 819 kHz.

Main RF system of the VEPP-4M consists of the control electronics, RF grid tube power amplifiers, RF power transport and distribution system and six RF accelerating cavities (presently only five RF cavities are installed into the storage ring). The frequency of the main RF system is 181 MHz that corresponds to 222nd harmonic of the beam revolution frequency. Table 1 presents some design parameters of the RF system.

Table 1: Main Parameters of RF System

Energy of particles, GeV -	5.3	6.0
Total electron and positron current, mA -	200	80
Radiation energy loss, MeV -	2.7	4.4
Accelerating voltage, MV -	5.5	8.5
Power loss in RF cavities, kW -	250	600
Power transferred to beam, kW -	550	400
Total RF power, kW -	800	1000

RF CAVITIES

The geometry of the cavity and its design are shown in Figure 1. Cavity characteristics are summarized in Table 2.

Cavity walls and other internal parts are made of copper. They are cooled by demineralized water. The cavity is placed

in a stainless steel tank. A very high vacuum in the cavity (10^{-7} – 10^{-8} Pa) is obtained by a sputter ion pump and a gettering pump. The stainless steel tank is evacuated separately by a sputter ion pump to about 10^{-5} Pa. The cavity can be baked out to a temperature of 300–400°C using tape heaters mounted on the cavity wall inside the vacuum tank. Thermal shields are used for reduction of the heat losses.

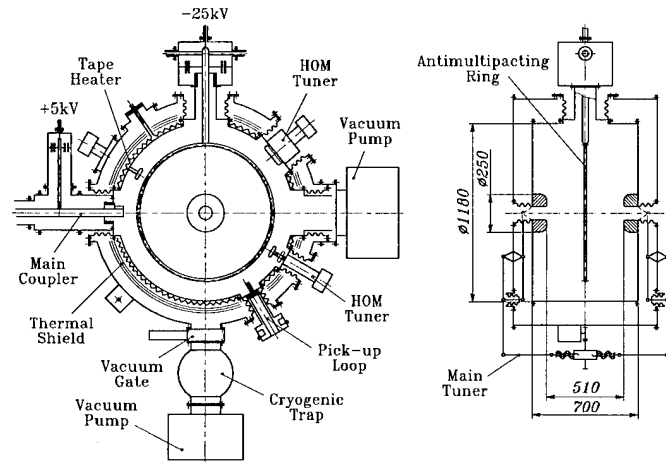


Figure 1: Schematic view of RF cavity

Table 2: Parameters of the cavity

Resonance frequency -	180.9 MHz
Tuning range of cavity frequency -	200 kHz
Tuning rate -	4 kHz/s
Accelerating voltage (V) -	0–1500 kV
Q value -	50,000
R/Q value (*) -	292 Ohm
Shunt impedance (*) -	15 MOhm
Wall loss at $V = 1000$ kV -	150 kW
Maximal power flux at $V = 1500$ kV -	4.8 W/cm ²

(*) Shunt impedance R is defined as $R = V^2/P$,

$$V^2 = (\int E_z \cos(kz) dz)^2 + (\int E_z \sin(kz) dz)^2$$

The tuning of the cavity is performed by squeezing the side walls using a d.c. motor drive with a gear box and levers. There are no sliding joints at this way of cavity tuning.

Three special HOM tuners are provided for tuning the higher order modes of the cavity in order to avoid beam instabilities. This technique is described separately [1].

A ring-shape d.c. biased electrode is placed in the cavity in order to suppress multipacting. For the same purpose the main loop is isolated from the cavity and also d.c. biased.

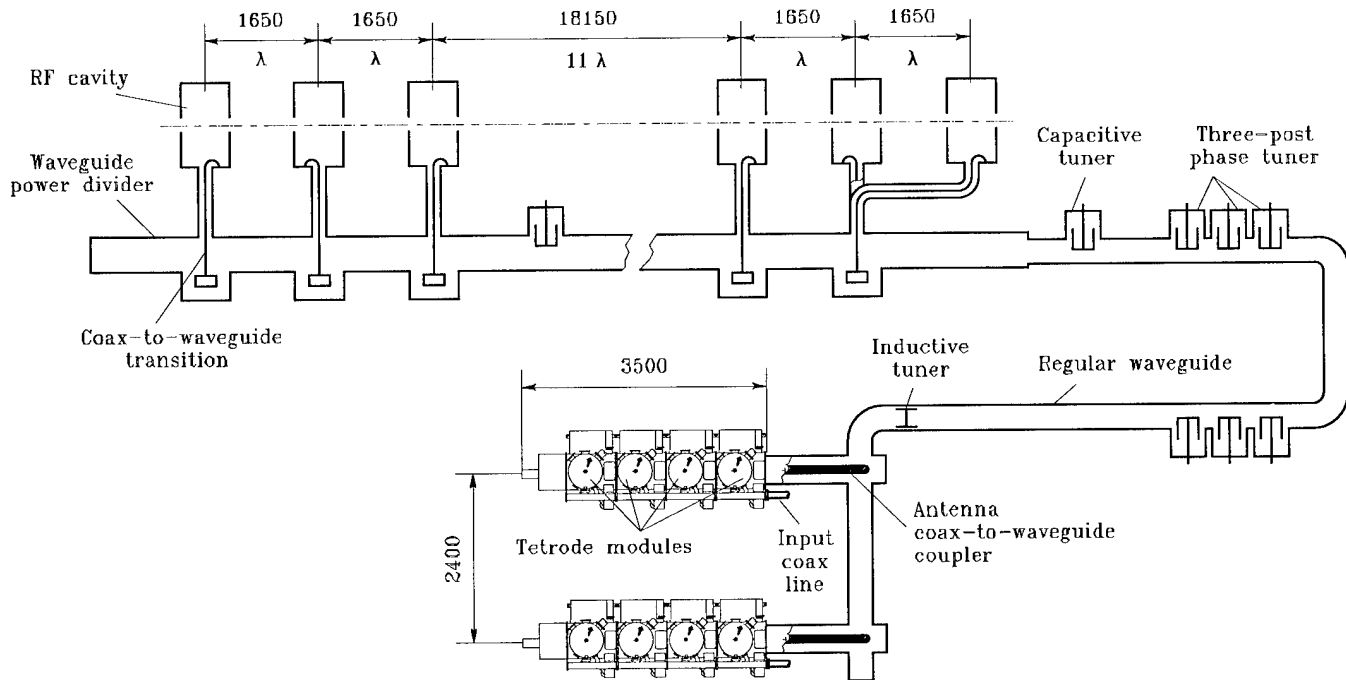


Figure 2: Scheme of RF system

RF POWER TRANSPORT AND DISTRIBUTION SYSTEM

The general scheme of the power part of the RF system is shown in Figure 2. As one can see, there are no magic tees or directional power dividers, no ferrite circulators in the RF system. The cavities in the storage ring are grouped by three. The distance between two cavities in a group is equal to the free-space wave length λ (165 cm). The distance between cavity groups is equal to a multiple of λ . Therefore, the fields in the cavities must be in phase. All cavities are driven by a single RF power source.

RF power is transmitted over a rectangular waveguide. The waveguide has different cross-sections in different parts: between cavities in a group (waveguide power divider), between cavity groups, and between cavities and power amplifier (regular waveguide).

Each cavity has a main coupler of a loop type. It is connected to the waveguide with a short coaxial line using a coax-to-waveguide transition which is placed near a small side wall of the waveguide. The waveguide between RF cavities has cross-section of $95.6 \times 50 \text{ cm}^2$. The guide wave length Λ is equal to two free-space wave length λ . So the distance between coax-to-waveguide transitions in a group is equal to $\Lambda/2$ and the distance between cavity groups is equal to a multiple of Λ .

For obtaining the right phasing of cavity fields, the main coupling loop in the middle cavity of a group is rotated on 180° to the loops of other cavities.

There is a special feature of connection of the cavity #1 to the waveguide divider. Due to a lack of free space the cavity is connected to the waveguide in the cross-section of the cavity #2 but near the other side wall. For the right phasing of the cavity #1, the length of coaxial line is at $3/2$ more than for the cavity #2.

The design of the coax-to-waveguide transition and the length of coaxial line to a cavity are chosen so that the matrix of transmission from the waveguide to a cavity has a form:

$$\begin{bmatrix} 0 & i/G \\ iG & 0 \end{bmatrix},$$

where $G = I_c/V_w$ is a transconductance (I_c is a current, driving a cavity, and V_w is a voltage in the middle point of the waveguide). The G value is adjusted to provide the matched conditions in the waveguide at the highest design level of RF power transferred to cavities loaded by the beam.

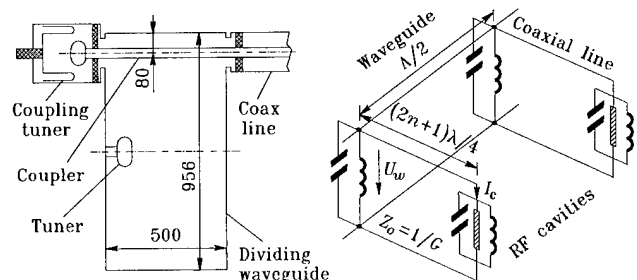


Figure 3: Schematic view and equivalent circuit of coax-to-waveguide transition of RF power dividing system.

The schematic view of the coax-to-waveguide transition and its equivalent circuit is shown in Figure 3. The antenna inductance is compensated by a capacitor tuner placed in the middle point of the waveguide.

With this scheme of driving RF cavities, the driving currents I_c are always equal irrespective of actual values of total cavity impedances Z_c (with due account of beam loading) and are determined only by the waveguide voltage. Therefore, power distribution along the cavity chain is proportional to the distribution of real parts of cavity impedances, $R_c = \Re\{Z_c\}$. If the shunt impedances and tunes of the cavities are equal, the driving powers are also equal. Emergency overload of a cavity main coupler is excluded in this scheme if the waveguide voltage does not go over the value set at the transmission of the maximal RF power. To this end the equivalent length of the transmission line between the anode of the tetrode amplifier and the reference plane of the cavities is adjusted to $(2n+1)\lambda/4$ with a three-post tuner. In this case the driving current I_c is limited by the maximum voltage in the anode resonator of the tetrode amplifier which is, in its turn, limited by the d.c. anode voltage.

Regular waveguide has cross-section of $115 \times 37 \text{ cm}^2$. Matching of the dividing waveguide is performed with two stubs. One of them is a capacitive stub (a plunger), the other is an inductive stub (a rod).

RF POWER AMPLIFIER

The RF power amplifier is built from universal multipurpose units. Figure 4 presents a schematic view of a 4-tube output stage. It is similar to a 2-tube module described in [2]. GU-101A CW tetrodes [3] are used in the amplifier. Parameters of the tube are listed in Table 3, parameters of the 4-tube power stage – in Table 4.

Table 3: Limiting values of the GU-101A RF power tetrode:

D.C. anode voltage –	14 kV
Screen grid d.c. voltage –	1.2 kV
Filament voltage –	15 V
Filament current –	730 A
Anode dissipation –	250 kW
Screen grid dissipation –	3 kW
Frequency (max.) –	200 MHz
Maximum envelope temperature –	200°C
Diameter (max.) –	295 mm
Height (max.) –	600 mm
Weight (max.) –	50 kg

Table 4: Operating conditions for a 4-tube RF power stage (grounded-grid circuit):

Frequency –	181 MHz
Output RF power –	600 kW
Input RF power –	<100 kW
D.C. anode voltage –	8 kV
Screen grid d.c. voltage –	1 kV
Filament voltage –	12.6 V
Filament current –	730 A
Anode dissipation of one tube –	100 kW
Screen grid dissipation of one tube from electron current –	1 kW
Cooling water flow –	300 l/min
Forced air flow –	20 m ³ /min
Efficiency –	56 %

The power amplifier has a coaxial output. The extension of the central conductor of the coaxial line stands duty of the antenna of the coax-to-waveguide transition.

Full RF power is obtained by power combining of two 4-tube amplifiers in a waveguide combiner.

CONCLUSION

Presently the RF system of VEPP-4M collider operates at the power level of 300 kW using a 2-tube power amplifier. It affords operation of VEPP-4M up to 5 GeV. Two 4-tube amplifiers have been built and are being adjusted. Tests and commissioning of the full scale RF system will be done this year.

REFERENCES

- [1] V. Veshcherevich et al., "RF Measurements and Control of Higher Order Modes in Accelerating Cavities", *This Proceedings*.
- [2] V. Arbuzov et al., "RF System of the CW Race-Track Microtron-Recuperator for FELs", *Proc. of the 1993 Particle Accelerator Conf. PAC-93*, Vol. 2, p. 1226.
- [3] Svetlana Corp., 194156 St. Petersburg, Russia.

Storage Ring Cavity Higher-Order Mode Dampers for the Advanced Photon Source*

Paul Matthews, Yoon Kang and Robert Kustom
Argonne National Laboratory
9700 South Cass Avenue
Argonne, IL 60439 USA

Abstract

Coaxial, mode selective higher-order mode (HOM) dampers for the Advanced Photon Source (APS) storage ring cavities have been fabricated and tested. Two types of dampers will be employed. Electric field probe dampers are positioned in the equatorial plane of the cavity so as to not couple to the fundamental TM_{01} accelerating mode. Additionally, two magnetic field probe dampers with quarter-wavelength stub rejection filters are positioned in the cavity equatorial plane 90 degrees apart to facilitate dipole mode damping. Both damper types use a vacuum compatible, aluminum nitride (AlN) ceramic rf absorber as the matched load. Measurements were made to optimize the frequency response of the tapered absorber. The design eliminates the need for a ceramic vacuum window.

I. INTRODUCTION

Higher-order mode (HOM) dampers are routinely used in particle accelerators to maintain beam stability at high currents. The two most important features of any HOM damping approach are the ability to damp higher-order modes over a broad frequency range and the suppression of coupling to the fundamental accelerating mode. Typically, either coaxial electric and magnetic field probe dampers [1], [2], [3], [4] or aperture-coupled, hollow waveguide dampers [5], [6] are used.

Both approaches involve trade-offs in performance. Coaxial probe dampers are broadband in nature which can make fundamental mode rejection difficult. Usually the probe position and orientation is used to minimize fundamental mode coupling. Aperture-coupled, hollow waveguide dampers are also inherently broadband. Rejection of the fundamental mode is achieved by using the cutoff frequency of the waveguide. This can be effective but typically involves a degradation of the Q-factor at the fundamental frequency, f_0 .

Coaxial HOM dampers have been extensively investigated for use on the storage ring cavities of the Advanced Photon Source (APS) [7], [8]. The coaxial probe type dampers were chosen in order to make the dampers compact, lightweight, and inexpensive. Also, A coaxial design allows for convenient cooling and does not disturb the cavity heat distribution. Additionally, fundamental mode power loss may be minimized through the use of a proper rejection scheme. The APS storage ring cavity fundamental frequency is 351.93 MHz. The storage ring parameters are listed in Table I. The instability growth rates and the Q requirements for the higher-order modes are given in [9].

*Work supported by U.S. Department of Energy, Office of Basic Energy Sciences under Contract No. W-31-109-ENG-38.

Table I
APS storage ring parameters.

Beam energy	7 GeV
Beam current	300 mA
Number of bunches	54
Current per bunch	5.6 mA
Revolution frequency	271.55 kHz
Synchrotron frequency	1.5 kHz
Number of cavities	16

Two types of dampers will be employed. Two electric field probe dampers will be positioned in the equatorial plane. Since the radial component of the electric field of the fundamental TM_{01} mode is zero in the midplane, the electric field probes may be used without coupling to the fundamental mode. In the APS storage ring cavities, the TM_{01} mode cutoff frequency for the 5.5-inch beam pipe is approximately 1.6 GHz. The dampers have been designed to damp the higher-order modes below cutoff. Additionally, to facilitate higher-order TM mode damping, two magnetic field probe dampers are situated 90 degrees apart in the equatorial plane with the loop planes perpendicular to the magnetic fields of the TM_{01} mode. In order to reject the fundamental frequency, the dampers were designed with quarter-wavelength stub rejection filters in series. Both damper types will use a tapered, vacuum compatible, AlN ceramic rf absorber as the matched load. The dampers were designed with this absorber in such a way as to allow water cooling of the center conductor and to eliminate the need for a ceramic vacuum window.

II. Absorber Design and Measurements

For efficient HOM damping, a broadband matched load termination must be designed. The load must have good thermal properties to dissipate the power in the damped modes and must also possess good vacuum properties to avoid the use of a ceramic vacuum window. The first two designs tried used an AlN ceramic with 7% glassy carbon content as the absorber. It was decided later to use an AlN ceramic with a 40% SiC content due to its superior properties. The properties of both absorbers are shown in Table II.

Investigations on the absorber shape were carried out to optimize the broadband matching properties of the taper. Numerical simulations of the reflection coefficient can be used for this purpose but were unavailable at the time of this study. In lieu of this approach, a rough taper was designed by making the length of the

Table II
Ceramic properties.

	AlN (7% C)	AlN (40% SiC)
Density (g/cm ³)	2.95	3.19
Thermal exp. (1/°C)	4.7	5.1×10^{-6}
Thermal cond. (W/cm-K)	0.55	0.43
Vacuum levels (torr)	< 10 ⁻¹⁰	< 10 ⁻¹⁰
ϵ_R @ 500 MHz	29-j4	47-j4
ϵ_R @ 1 GHz	23-j5	44-j6
ϵ_R @ 2 GHz	22-j5	40-j9

taper equal to approximately one-quarter of the effective wavelength of the fundamental mode in the ceramic (AlN with 7% C). This gives a taper length of 1.5 inches. The coaxial structure was designed to present a 50- Ω characteristic impedance to the cavity with a 0.5-inch inner conductor diameter. The total absorber length was 4.5 inches.

The design was tested by measuring the reflection coefficient on a network analyzer. Time domain gating techniques were used to eliminate unwanted reflections due to the connecting hardware. These measurements showed that this first design was not very desirable below frequencies of about 1.1 GHz. Increasing the overall absorber length did not significantly improve the performance.

Analysis of the network analyzer data showed that the reflection coefficient was high due to the rather abrupt taper. The taper was then lengthened to 3.143 inches, keeping an overall length of 4.5 inches. This design exhibited acceptable behavior above 800 MHz. By increasing the total length to 9 inches, the absorber showed well-matched performance over all frequencies of interest (above 500 MHz). A typical measurement with this design is shown in Figure 1. The associated time domain measurements showed that the dips in $S_{11}(\omega)$ were due to resonances within the ceramic test structure resulting from a two-piece ceramic absorber. These resonances are not expected to be present in the final one-piece damper structure.

A final design was tried using the AlN with 40% SiC. The taper was 5.5 inches long with an overall length of 7 inches. Ad-

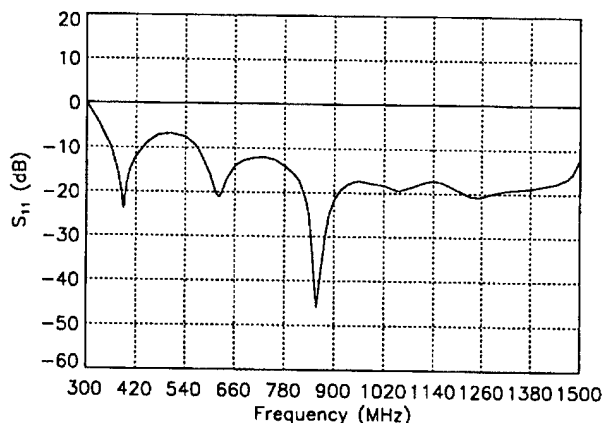


Figure 1. Absorber (AlN with 7% C) reflection with a 3.143" taper and a 9" overall length.

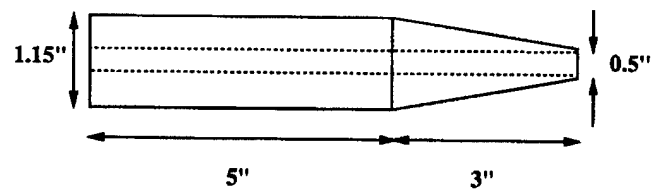


Figure 2. The final absorber design.

ditionally, the outer radius of the coaxial line was slightly increased to give a 55- Ω characteristic impedance. Although the taper is much more gradual, performance was only slightly better than the previous design. Performance was improved by increasing the overall length to 11 inches which results in a rather long structure. However, financial as well as spatial constraints led us to decide on the absorber shape shown in Figure 2 using AlN with 40% SiC. This design is similar to the second design described above. This absorber design will be used in both the electric field probes and the magnetic field probes with the quarter-wavelength rejection stub.

III. Quarter-Wavelength Stub Design

The design of the quarter-wavelength stub magnetic field damper has been previously described [8]. The length of the stub was calculated from the free space wavelength of the fundamental mode, giving a value of 21.31 cm. Measurements showed that the damper still coupled to the fundamental mode and significantly decreased the Q . This was attributed to an effective increase of the stub length from the presence of the loop which acts as a parallel wire waveguide. In order to find the proper length for the stub, the ratio of Q_L/Q_0 was plotted as a function of frequency. A plunger tuner was used to change the cavity fundamental frequency. Results are shown in Figure 3 for a 1-inch coupling loop. An extrapolation from a linear least-squares fit to the data showed that the stub length was optimized for a frequency of 336 MHz. Taking the ratio of the fundamental frequency to this frequency gives the adjustment factor for the stub length. The stub was shortened to 20.96 cm and re-measured. Again the results are shown in Figure 3. Coupling to the fundamental mode was significantly reduced and the damper-loaded Q was approximately 85% of the unloaded Q .

The loop size was then increased to 2" to try to more effectively damp the higher-order modes. Since this changes the geometry of the loop, the effective length of the stub filter will also change. Because of this effect, the design length for any given loop size or geometry should be experimentally determined before manufacturing. Using the modified stub length of 20.96 cm with the 2" loop, the fundamental mode Q factor was decreased to approximately 45% of the unloaded Q factor. By again decreasing the stub length to 20.65 cm, the Q factor could be increased to approximately 73% of the unloaded Q factor. This can be further improved by slightly decreasing the stub length.

IV. Discussion

Measurements have been made on the HOM damping with the prototype dampers in a storage ring cavity. Using the two

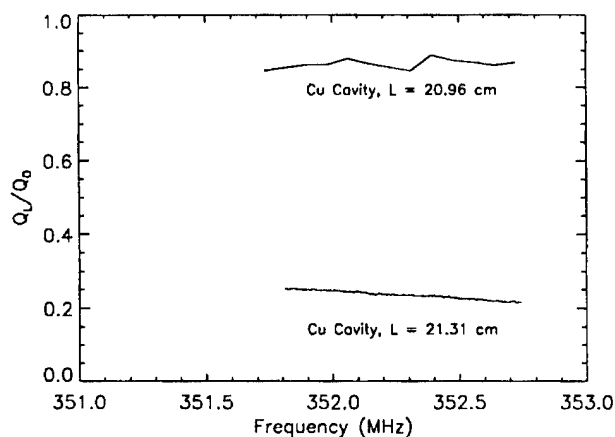


Figure 3. Q_L/Q_0 as a function of frequency for the magnetic field damper.

types of dampers, two of each design, most higher-order modes were sufficiently damped according to the requirements in [9]. The monopole mode at 536 MHz and the dipole mode at 588 MHz were both damped by a factor of approximately 10 [8]. In order to reduce the required damping factor, the storage ring cavity HOM frequencies were staggered by increasing the cavity lengths by 0.3 mm. Assuming that the frequency staggering is not effective for the lowest frequency higher-order modes, the level of damping for the above two modes may not be sufficient [9].

Simulations indicate that the APS multi-bunch beam can be stable for beam currents up to approximately 100 mA without dampers [10]. Further studies of the physics of the machine are needed to determine whether the present level of damping is adequate for a 300 mA beam with cavity frequency staggering.

V. Conclusions

The use of coaxial HOM dampers for the APS storage ring cavities was discussed. Two damper types have been proposed and studied. The coaxial designs for these dampers result in a compact, simple, inexpensive, and effective damping scheme.

The tapered absorber reflection characteristics were measured to ascertain the broadband matching characteristics. Time domain gating techniques on a vector network analyzer were used for these measurements. The results were used to arrive at an optimized absorber design.

The effect of the magnetic field dampers with the quarter-wavelength stub rejection filter on the fundamental accelerating mode was investigated. Measurements showed a significant lowering of the Q factor. Changing the stub length to tune the rejection filter to the proper frequency resulted in improved performance. The length must be experimentally determined for each given loop geometry.

References

- [1] Y. Yamazaki, K. Takata and S. Tokumoto, "Damping Test of the Higher-Order Modes of the Re-entrant Accelerating Cavity," *IEEE Trans. on Nuclear Science*, **NS-28**, pp. 2915-2917, June, 1981.
- [2] B. Dwersteg, E. Seesselberg and A. Zolfaghari, "Higher Order Mode Couplers for Normal Conducting DORIS 5-cell Cavities," *IEEE Trans. on Nuclear Science*, **NS-32**, pp. 2797-2799, Oct., 1985.
- [3] E. Haezel and J. Sekutowicz, "Higher Order Mode Coupler Studies at DESY," DESY M-86-06.
- [4] A. Mosnier, "Developments of HOM Couplers for Superconducting Cavities," *Proc. 4th Workshop on RF Superconductivity*, August 1989.
- [5] G. Conciauro and P. Arcioni, "A New HOM-free Accelerating Resonator," *Proc. 2nd Euro. Particle Accel. Conf.*, Nice, France, June 12-16, 1990, pp. 149-151.
- [6] R. Rimmer, D. Goldberg, G. Lambertson, F. Voelker, K. Ko, N. Knoll, R. Pendleton, H. Schwarz, F. Adams and M. De-Jong, "Higher-order Mode Damping Studies on the PEP-II B-Factory rf Cavity," *Proc. 3rd Euro. Particle Accel. Conf.*, Berlin, Germany, March 24-28, 1992.
- [7] Y.W. Kang, R.L. Kustom and J.F. Bridges, "HOM Damping with Coaxial Dampers in a Pillbox Cavity without Fundamental Mode Frequency Rejection Filter," *Proc. 1993 Int. Particle Accel. Conf.*, Washington, D.C., May 17-20, 1993.
- [8] Y.W. Kang and R.L. Kustom, "HOM Damping with Coaxial Dampers in the Storage Ring Cavities of the Advanced Photon Source," *Proc. 4th Euro. Particle Accel. Conf.*, London, U.K., June 27 - July 1, 1994.
- [9] L. Emery, "Required Cavity HOM deQing Calculated from Probability Estimates of Coupled-bunch Instabilities in the APS Ring," *Proc. 1993 Int. Particle Accel. Conf.*, Washington, D.C., May 17-20, 1993.
- [10] L. Emery, private communication.

Reduction of Multipactor in RF Ceramic Windows Using a Simple Titanium-Vapor Deposition System.¹

K. Primdahl, R. Kustom, J. Maj

Argonne National Laboratory, 9700 S. Cass Avenue, Argonne, IL 60439

Abstract

A brief description of multipactor is followed by a discussion of design parameters for a titanium sublimation system. Efforts to correlate operating parameters (time, temperature, etc.) with thickness of coated titanium are reported. Rutherford backscattering thickness measurements are described and reported.

I. INTRODUCTION

The term "multipactor" is commonly used to describe a phenomena which occurs in vacuum, with a radio frequency field and suitable configurations and types of surfaces. If the surfaces have high secondary emission coefficient (especially if > 1), secondary electrons can move synchronously with the rf, typically arriving at a surface one-half a period after leaving a surface, releasing increasing numbers of secondaries which repeat the process. The secondary electron yield is a function of the primary electron energy and incidence angle and varies with the surface material; moreover, is sensitive to temperature and surface contamination [1]. The CRC Press publishes secondary electron emission properties for many elements and compounds, including "crossover" points. At extremely low or extremely high energies, secondary emission coefficients fall below unity; hence, crossover points exist where the secondary emission function (σ) crosses unity. Of particular interest to coupler windows for the Advanced Photon Source (APS) are secondary emission coefficients of alumina and copper, which are listed at $\sigma_{\max} = 2$ to 9 and 1.3, respectively [2].

Since it is possible to dissipate large amounts of power at microwave frequencies and thereby generate destructive thermal-stress gradients, multipactor is clearly undesirable. Furthermore, this power may be deposited in localized regions, leading to increased outgassing or evaporation (and subsequent sputter deposition) of the material. Ultimately, the multipactor loading may become so great that the desired rf voltage cannot be reached or may cause significant reflection. Unfortunately, few elements have low secondary emission characteristics; moreover, many of these are unsuitable for vacuum and/or rf applications. Titanium, with $\sigma_{\max} = 0.9$, and familiarity from its use in sublimation pumps, has become the multipactor-reduction material of choice.

II. SYSTEM DESIGN

Generally, vacuum evaporation is accomplished by heating a small amount of material under vacuum. With

sufficient heating (e.g., using an electron beam), source material will melt, evaporate, then immediately condense on any cool (i.e., room temperature) surface. Elements, such as titanium, that sublime constitute a special case of vacuum evaporation for thin-film production. Materials that sublime have a vapor pressure sufficiently high that deposition can be achieved without melting. Titanium sublimation lends itself to the simple approach of resistance heating a wire centered in, and coaxial with, our cylindrical alumina window. Accordingly, we chose sublimation over (potentially more complex) sputtering system designs.

Early difficulties with borrowed filaments, reported to be pure titanium, lead us to conclude that a small amount of molybdenum ($< 1\%$) alloyed with titanium would allow the filament to support its own weight while in the sublimation-temperature range. Molybdenum's vapor pressure is sufficiently low that only titanium will evaporate in our system. Interestingly, lowering the pressure decreases the spread between the titanium and molybdenum sublimation temperatures. Increasing the pressure increases the spread, but at the expense of approaching the melting point for titanium. We targeted our operating pressure at 1×10^{-7} Torr, meant to be an optimum in the sense that the sublimation temperature of molybdenum is approximately equal to the melting point of titanium. Hence, our sublimation temperature spread is as large as possible while we are assured that titanium will melt before molybdenum sublimates [3].

Titanium's melting point is 1941 K. At 10^{-7} Torr, its sublimation temperature is approximately 1400 K. Hence, by passing a current through the titanium-molybdenum alloy filament itself, we must heat to at least 1400 K, but no more than 1941 K. The sublimation rate is strongly affected by the operating temperature of the filament. For the purposes of system design, we based subsequent calculations on a filament temperature of 1700 K.

In order to estimate the power supply requirements, an energy balance was performed. Combining equations for resistance as a function of temperature and radiative heat transfer, while ignoring end effects (esp. conduction to filament holders—which will lead to a slightly parabolic temperature profile over the length of the filament) and latent heat of sublimation, the required current is given by:

$$I = \left[\frac{\pi r L \epsilon \sigma (T_2^4 - T_1^4)}{R_{T_1} \{1 + \alpha(T_2 - T_1)\}} \right]^{1/2}$$

I = Required filament current

r = Filament radius

L = Filament length

¹ Supported by U.S. Department of Energy, Office of Basic Energy Sciences, under Contract W-31-109-ENG-38.

- α = Temperature coefficient of electrical resistance
 ϵ = Emissivity
 σ = Stefan-Boltzmann constant
 T_1 = Temperature of surroundings
 T_2 = Filament temperature
 R_{T_1} = Resistance temperature of surroundings

For a 21.6-cm-long x 0.193-cm-diameter titanium-wire filament at a uniform temperature of 1700 K, the required current is calculated to be 34.6 amps. Of course, this is a lower bound; nevertheless, is useful in selection of a constant-current power supply.

Determining the desired titanium thickness involves a trade-off: more titanium is better to suppress multipactor, while too much titanium will result in excessive resistance heating. Saito reports that the effective loss tangent (serving as a metric for excessive heating) of the coating increases "almost exponentially" with the coating thickness [4]. Prest looked at the penetration depth of electrons in the multipactor discharge and found the depth (with electron energy in the range required for $\sigma > 1$) is "of the order of 100 Å" [1]. Elsewhere, the literature reports desired thickness in the range of 15 to 150 Å [4,5,6,7]. We targeted a thickness of 30 Å.

Combining the Langmuir equation for the rate of evaporation [8] with the authors' derivation of required deposition mass, leads to an estimate of coating time as a function of filament temperature:

$$\tau = \frac{m^*}{G^*} = \frac{\frac{\pi D_c M}{d^3 f_{Nest} f_{Stack} N_A}}{\left[\frac{0.0583 (\text{gram} \cdot \text{Kelvin})^{1/2}}{\text{cm}^2 \cdot \text{sec} \cdot \text{torr}} \right] \gamma \pi 2r \left(\frac{M}{T} \right)^{1/2}}$$

- τ = Time required for coating
 m^* = Mass required per unit length
 G^* = Evaporation rate per unit length
 t = Coating thickness
 M = Molecular weight of filament material
 D_c = Diameter of surface to be coated (I.D. of window)
 d = Covalent diameter of titanium atom
 f_{Nest} = Nesting factor for rows of spheres
 $f_{Stacking}$ = Stacking factor for layers of spheres
 N_A = Avogadro's constant
 T = Filament temperature
 P = Vapor pressure (at filament temperature)
 γ = Sticking coefficient (=1 for most metals)

For a 30-Å titanium coating on a 10.16-cm diameter surface with the filament at a uniform 1700 K, coating time is estimated to be 99 seconds (neglecting warm-up and cool-down of filament). We considered this to be in an ideal range; that is, is slow enough for control of thickness by adjusting the coating time (without an investment in a sophisticated control system), yet fast enough that contamination will be insignificant. The result is a function of filament temperature not only by way of the temperature term itself, but also due to the associated vapor pressure term. Relatively small changes in temperature of the titanium-molybdenum filament lead to orders of magnitude changes in

the associated vapor pressure. Increasing the filament temperature has an extraordinary impact on coating time; for example, filament temperatures of 1400 or 1800 K lead to calculated coating times of 25 hours or 17 seconds, respectively.

Finally, we planned a bakeable, all-metal system where we could pumpdown to well below 10^{-7} Torr, then bleed in pure nitrogen purge gas. Following a pumpdown to the 10^{-9} -Torr range, the purge gas at 10^{-7} Torr overwhelms any other remaining vapors; hence, we coat in a nearly pure nitrogen environment. Initially, we believed it was important to produce a nearly pure TiN coating. However, the literature indicates that oxygen may be not only unavoidable, but desirable as well. Isagawa reports that such coatings are more precisely described as TiN_xO_y ; furthermore, TiN_xO_y is a "best possible" coating material. Very high resistivity is ensured by the oxygen-rich grain boundary layers of TiN_xO_y [5]. Discussion with colleagues confirms that resistivity increases upon removal of a coated component from its coating system; presumably as atmospheric oxygen combines with the TiN. Nyaiesh describes how, upon exposure to air, the TiN oxidizes 2 to 3 to monolayers of TiO_2 . This TiO_2 layer is subject to decomposition on heating and, since the secondary electron emission coefficient is very different than for TiN, results in a widely varying σ during klystron processing [6].

Our system, shown in Figure 1, was assembled from (primarily) on-hand equipment: knife-edge-flanged vacuum fittings, flange-mounted electrical feed-through, quartz viewport, variable leak valve, magnetic-bearing turbo (without isolation valve), an oil-free roughing system, and borrowed power supply.

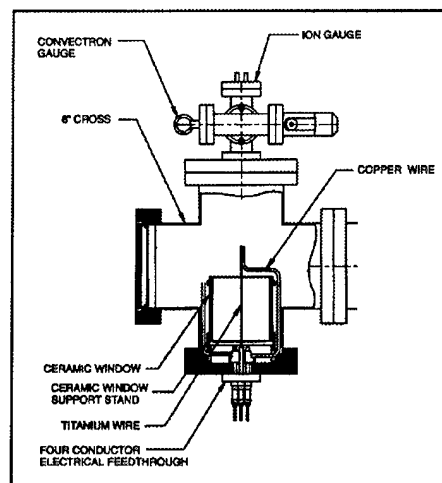


Figure 1: Titanium Sublimation Coating System

III. THICKNESS MEASUREMENT

During early use of the system, a 1-cm-square sample accompanied each window to be coated. These samples were then subjected to a Rutherford backscattering (RBS) analysis for determination of titanium thickness. Using results from

the RBS, current and time were adjusted in a trial and error process.

RBS involves bombarding a sample with high-energy particles (typically ^4He) and measuring the energy of the resulting backscattered particles. Only a small fraction of the incident particles actually have a "collision" with nuclei of the sample; the remainder end up "implanted" in the sample's space between nuclei. The energy of a backscattered particle, at a given angle, depends on both the loss of energy due to transfer of momentum to the target atom, and losses during transmission through the material before and after "collision." Because there is a greater change in energy when transferring momentum to a lighter particle, RBS offers greater resolution (spread between energies) for light elements, but gives a stronger signal (higher energy) for heavy elements [9].

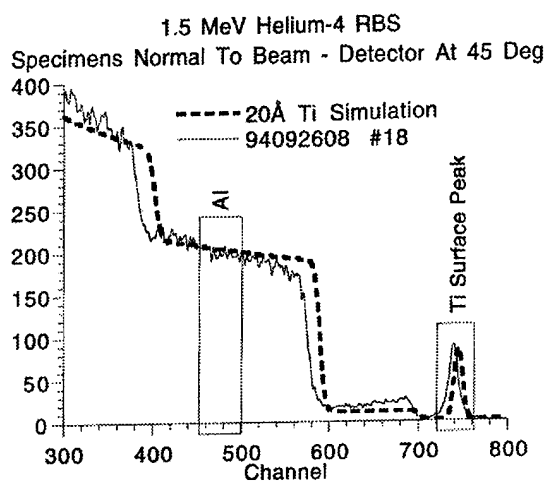


Figure 2: Rutherford Backscattering Plot with Simulation Fit for 20-Å-thick Titanium on Alumina. Vertical axis is number of detected, backscattered particles; hence, is proportional to each elements' concentration.

For our situation, where a heavier element (Ti) is coated over a lighter one (Al), an RBS plot can be "read" from right to left with a correspondence to the sample surface (however, this is not always the case with RBS). In Figure 2, the peak near 750 keV corresponds to titanium at the surface, while its width corresponds to 20 Å (this is said to be accurate within ± 5 Å and is determined from simulation and/or experience of the RBS scientist). The larger rise, centered about 500 keV, corresponds to the aluminum in the ceramic, with a larger energy spread due to varying losses of energy during transmission to/from random depths.

Additionally, we monitored resistance during coating, with the idea that it might be possible to use a determined value of resistance as the cut-off point where a desired thickness had been reached. Whereas starting resistance was a constant $3 \times 10^{14} \Omega$, measured resistance after coating, but still under vacuum with nitrogen purge, varied from 1.5×10^{11} to $2 \times 10^{12} \Omega$. Accordingly, we concluded that feedback from the RBS measurements, though requiring a longer loop time, was more meaningful.

IV. RESULTS

For coating our coupler windows, we are using a 21.6-cm-long x 0.193-cm-diameter titanium-molybdenum wire with 44.5 amps for 65 seconds. Voltage is nearly constant (despite consuming a small amount of the filament) at 5.1 volts. Measured thickness varies from 20 to 28 Å. To date, we have coated 34 coupler windows. Seventeen couplers have been conditioned up to 100 kW; twelve of those have been subjected to rf power with beamloading; all without difficulty. Each pumpdown requires approximately 20 hours; hence, the system can be operated on a daily cycle—sufficient for our demand. We bake the system only occasionally; specifically, when the ultimate pumpdown pressure begins to degrade.

The system has been in operation for sixteen months, coating (along with coupler windows) rf cavity ceramics for the APS positron accumulator ring, rf field probe cups, beam current monitors, and [chromox ceramic] fluorescent screens with thickness requirements over the range of 10 to 300 Å. In many cases, coating has been requested for prevention of static charge build-up (and possible arcing); rather than protection against multipactor.

V. ACKNOWLEDGMENTS & REFERENCES

The authors wish to express their gratitude to R. Callen & E. Hoyt (SLAC), A. Feinerman (UofIC), H. Frischholz & G. Geschonke (CERN), C. Krieger, A. Nassiri & R. Rosenberg (ANL), and E. Roe (SRC) for their contributions via valuable discussions. Also to P. Baldo (ANL-MSD) for his assistance with RBS thickness measurement of our many samples.

- [1] D. Preist, "Multipactor Effects and Their Prevention in High-Power Microwave Tubes." *The Microwave Journal* (Oct 1963).
- [2] *Chemical Rubber Company (CRC) Handbook of Chemistry and Physics*, 64th Ed. Ed. R. Weast. Boca Raton: CRC Press (1983).
- [3] R. Hill, *Physical Vapor Deposition*. Berkeley: The BOC Group (1986).
- [4] Y. Saito, "Breakdown Phenomena in Vacuum." *1992 Linear Accelerator Conference Proceedings* (1992).
- [5] S. Isagawa, et al., "Coating Techniques and Improvement of High Power CW Klystrons for TRISTAN." *European Particle Accelerator Conference Proceedings* (1994).
- [6] A. Nyaiesh, et al. "Properties of Thin Antimultipactor Tin and Cr_2O_3 Coatings for Klystron Windows." *Journal of Vacuum Science and Technology* (Sep/Oct 1986).
- [7] F. Thizy and M. Wurgel, "Cathodic Sputtering of Titanium on Alumina Components Used in Particle Accelerators." CERN Publication ST/TE/FT118gp (1987).
- [8] *Vacuum Physics and Technology*. Ed. G. Weissler and R. Carlson. London: Academic Press (1979).
- [9] *Encyclopedia of Materials Characterization*. Ed. C. Brundle, C. Evans Jr., and S. Wilson, Stoneham: Butterworth-Heinemann (1992).

Cooling the APS Storage Ring Radio-Frequency Accelerating Cavities: Thermal/Stress/Fatigue Analysis and Cavity Cooling Configuration*

K. Primdahl, R. Kustom

Argonne National Laboratory, 9700 S. Cass Avenue, Argonne, IL 60439

Abstract

Heat transfer studies, including finite-element analysis and test results, of the Advanced Photon Source (APS) storage ring 352-MHz radio-frequency (rf) accelerating cavities are described. Stress and fatigue life of the copper are discussed. Configuration of water cooling is presented.

I. BACKGROUND

The 7-GeV Advanced Photon Source positron storage ring requires sixteen separate 352-MHz rf accelerating cavities. Cavities are installed as groups of four, in straight sections used elsewhere for insertion devices. They occupy the first such straight section after injection, along with the last three just before injection. Cooling is provided by a subsystem of the site-wide deionized water system. Pumping equipment is located in a building directly adjacent to the accelerator enclosure.

A prototype cavity was fabricated and tested where cooling was via twelve 19-mm-diameter [3/4 in] brazed-on tubes in a series-parallel flow configuration. Unfortunately, the thermal contact to some tubes was poor due to inadequate braze filler.

II. INTRODUCTION

Concerns include thermal gradient/stress/distortion within the copper, thermal stresses (a function of thermal gradients), hot spots, elastic/plastic deformation, cyclical deformation of copper, and pressure drop of water flow through the cavity. Distortion of the cavity due to thermal stresses affects the resonant frequency, a characteristic which may be used to tune the cavity, provided copper fatigue does not become critical. Keeping all the above in mind, the engineer must arrange for suitable values of the following variable parameters while incorporating the fixed parameters into the analysis and design.

Fixed parameters:

- Heat load per cavity:
 - 7.0-GeV beam, with 16 cavities on-line 35 kW
 - 7.5-GeV beam, with 16 cavities on-line 50 kW
 - 7.5-GeV beam, with 12 cavities on-line 67 kW
 - During cavity conditioning 100 kW
- Minimum supply water temperature of 24° C.

Variable parameters (not all independent):

- Temperature of cavity copper.
- Temperature rise of the water through the cavity.
- Total flow rate of water through the cavity.
- Header size, for each section of four cavities; a practical limit of 4-inch IPS, possibly 6-inch IPS.

- Velocity of water in copper tubes. No more than 227 cm/sec [7.5 ft/sec] to avoid erosion corrosion.
- Size of cooling tubes. Surface area (heat-transfer area) scales with diameter, cross-section (inverse water velocity) with diameter squared.
- Location of cooling tubes.
- Number of cooling tubes.
- Flow configuration (i.e., series-parallel or all-parallel).
- Water supply [to cavity] temperature. Condensation is to be avoided while recirculating some return water puts less demand on site-wide deionized system.
- Heat exchanger area and temperature difference(s).

III. TUBE SIZE

Copper cooling tubes are brazed into machined channels, slightly more than half the tube diameter deep, on the cavity surface. Spreadsheet calculations determined the optimum tube size. The first two cases presented below assume effective tube area (heat transfer area) equal to 60% of the interior surface, while the second set of data employs a sliding scale that favors smaller diameter tubes (nesting the tube into a milled channel, slightly deeper than half the diameter, with a braze fillet along each side serves to "enclose" more of a smaller tube). Heat load and temperature rise of the water fix the required volume flow rate of water—resulting velocity varies with tube cross-section.

Independent Variables		Dependent Variables		
Heat Load (kW)	Temp Rise (°C)	Optimum Tube ϕ (")	Water Velocity (feet/sec)	Cu-Water ΔT (°C)
75	2.0	3/8	18.3	11.2
75	3.0	3/8	12.2	15.4
75	2.0	5/16	21.2	8.6
75	3.0	5/16	14.2	11.8
100	2.0	5/16	21.2	9.1
100	3.0	5/16	14.2	12.4

Each case shows an optimum diameter at which the copper-to-water temperature difference is a minimum. For larger diameters, surface area is not increasing fast enough to compensate for the reduction in water velocity. For smaller diameters, water velocity is not increasing enough to make up for the reduction of surface area. Moreover, enhanced heat transfer with increasing water velocity must be checked against possible erosion corrosion; where the protective layer of copper oxide on the inside wall of copper tubes is stripped away, leaving the soft copper subject to erosion by flowing water (especially at the outer edge of a formed elbow, where the wall has already been thinned by

* Work supported by U.S. Department of Energy, Office of Basic Energy Sciences, under Contract No. W-31-109-ENG-38.

forming). Acceptable maximums are quoted, by experienced engineers, as anywhere from 227 to 364 cm/sec [7.5 to 12 ft/sec]. Our case of all parallel flow is further complicated by the fact that actual water velocity varies among the cooling tubes (the spreadsheet calculations assume uniform velocity); that is, higher velocity in the shorter tubes.

Since the velocities associated with optimum tube sizes could lead to erosion corrosion, a "practical optimum" of 12.7 mm [1/2 in] diameter was selected. Temperature rise of the water can be traded off against water velocity, but both have a wide range of acceptable values. The copper-to-water temperature difference required further study; specifically, to ensure it is within the bounds set by cavity operating temperature and cooling water supply temperature.

IV. THERMAL ANALYSIS

Using spreadsheet-calculated convection coefficients from the analysis described above, and varying the location and number of tubes on each end section, several two-dimensional, axisymmetric ANSYS¹ models were generated for comparison. A two-dimensional, axisymmetric URMEL² model generated the distribution of rf heating on the cavity's inside surface and was used as input to the ANSYS[®] thermal/stress analysis. Large ports of the center section are a non-axisymmetric feature; however, including them in an axisymmetric model is conservative since the heat that would go into solid copper if no port were present concentrates about the inside perimeter of the port. Several variations of the heat distribution about the port were evaluated; the most severe was subsequently used for the results reported here. A less severe heat redistribution is expected where a tuner or coupler, both with integral cooling, is installed.

Case	Tube-to-Water ΔT (°C)	Copper (MPa)	Max Stress (psi)
Four 3/4-in tubes	17.4	36.4	5283
Four 1/2-in tubes	18.1	33.1	4802
Four 1/2-in tubes, shifted towards "hot spots"	14.2	32.4	4699
Six 1/2-in tubes	10.7	27.8	4031

The copper-to-water temperature difference is important as the sum of all temperature rises in the water system (including across the heat exchanger), added to the water temperature, must be lower than the planned operating temperature of the cavities. Increasing the number of tubes increases the copper-to-water surface area and hence, decreases the copper-to-water temperature difference.

¹ ANSYS is a registered trademark of Swanson Analysis Systems, Inc., Houston, PA.

² URMEL was developed by U. Laustroer, et al., DESY, Hamburg, Germany.

The ANSYS[®] thermal analysis shows maximum copper temperature to be 16.9° C above the water temperature. The highest copper temperature was consistently at the port radius; however, the wall thickness there serves to keep stress low. Highest stress was observed at the tip of the nose cone cooling channel where the temperature difference between the inner wall and the 7.8-mm-thick [0.31 in] outer wall is approximately 10° C. This area could be subjected to reverse yielding. Although the change in maximum stress is small for each new model, the overall reduction is meaningful.

V. THERMAL TESTING

Measurements taken on the prototype cavity showed that tubes with only half their diameter embedded in the bulk copper are capable of approximately 93% the heat transfer of fully embedded tubes as predicted by Dittus-Boelter [1]. The Dittus-Boelter formulation is intended for internal flow in round tubes; hence, it was adapted for use on the nose-cone cooling channel's approximately rectangular 12.7 x 76.2 mm [0.5 x 3.0 in] shape. The ANSYS[®] heat transfer coefficients differ from theoretical values in order to be conservative (while we awaited prototype test results).

Cooling Geometry	Tube Diameter (cm [in])	Theory (W/cm ²)	Used for ANSYS [®] (W/cm ²)	Prototype Tests (W/cm ²)
Nose-cone		0.600	0.600	0.837
End	1.90 [3/4]	0.604	0.511	0.600
Center	1.90 [3/4]	0.604	0.511	0.566
End	12.7 [1/2]	0.915	0.604	
Center	12.7 [1/2]	0.915	0.604	

The 1.90-cm-diameter [3/4 in] tube results are based on a water velocity of 182.9 cm/sec [6.0 ft/sec], while the 12.7-cm-diameter [1/2 in] numbers are based on a water velocity of 268.2 cm/sec [8.8 ft/sec]. The ratio of these velocities corresponds to the ratio of cross-sectional areas of six 12.7-cm-diameter [1/2 in] tubes to four 1.90-cm-diameter [3/4 in] tubes; that is, the same total flow.

Meanwhile, the prototype cavity had unexpectedly high temperatures around the ports, especially in the stainless steel where electrical and thermal conductivity are lower than for copper.

VI. STRESS/STRAIN-LIFE

Our ANSYS[®] stress analysis shows a peak stress (total stress, reflecting nonlinear variation between endpoints) intensity of 27.8 MPa [4031 psi] with non-peak stress (membrane plus bending, varying linearly between endpoints) intensity up to about half that value, in the same range as is reported for 0.2% yield strength of fully annealed copper [2]. With such a low yield strength, cycling into the plastic range seems unavoidable; accordingly, a fatigue analysis was performed. Fatigue studies of oxygen-free copper show that the hysteresis loop for fully annealed copper increases in amplitude (constant strain) as the

number of cycles increases. Conversely, the hysteresis loop of cold-worked copper falls off with increasing cycles. Hence, fully-annealed copper cyclically hardens, while cold-worked copper cyclically softens.

The more traditional stress-life fatigue analysis method does not account for plastic strain; therefore, it is inappropriate. However, the strain-life approach, where the allowable strain amplitude is calculated as an exponentially-weighted (exponents are determined empirically) sum of the elastic and plastic cyclic loading, is ideal for the cavity analysis, where knowledge of extreme temperatures leads directly to expected strain amplitude. Application of the strain-life approach [3] shows fully annealed copper to be very accommodating; using conservative boundary conditions, a fatigue life of over 10^{24} thermal cycles is estimated.

VII. FINAL DESIGN

The complete cavities are fabricated as three subassemblies, two ends and a center, which are joined by electron beam welds about the perimeter. A nose-cone cooling channel is milled into each end piece from the outside (sealed with a brazed-on cover), while twenty 12.7-mm-diameter [0.5 in] copper tubes are brazed into milled channels (slightly deeper than half the tube diameter). The final design is optimum in that: (1) temperature differences are within the range of a conventional water cooling system; (2) water velocity can be held to a range where erosion corrosion of the copper tubes is not a concern; (3) thermal gradient/distortion within the copper is not severe; and (4) fabrication/attachment of cooling tubes is straightforward. Additionally, we specified copper tube extruded with rifling on its inside surface to increase turbulence and surface area.

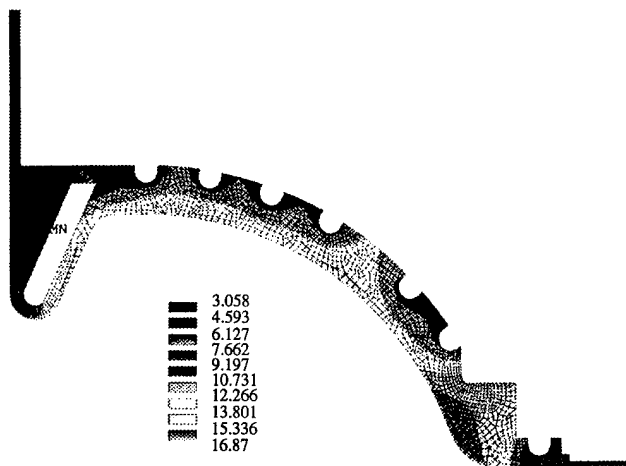


Figure 1: ANSYS® Thermal Analysis Results. Model is axisymmetric about the beamline—a vertical line to the left of the figure. (Degrees Centigrade above Water Temperature)

In order to minimize the flange heating found on the prototype cavity, the amount of stainless steel exposed to rf was reduced. The remaining stainless steel, including vacuum surfaces of blank-off flanges, is copper plated (pure copper). Additionally, we have provided flange cooling via 6-mm-diameter

[0.236 in] copper tubes brazed into the perimeter of each flange. Furthermore, an additional tube was added to each quadrant of the center section, providing twice the cooling used in the ANSYS analysis for that area. This additional tube also provides cooling over the entire port perimeter (the prototype cavity had only 300° cooling tube coverage at each large center-section port). Accordingly, the ANSYS® results most closely resembling the final design are those of the 27.8-MPa [4031 psi] case. Figure 1 presents the temperature distribution in the cavity copper, showing a maximum copper temperature 16.9° C above the water supply temperature.

An innovative manifold arrangement allows balancing of the flows among the two ends and center, yet requires only two supply and two return manifolds. Total flow of 4736 cm³/sec [75 gpm] is supplied in an all parallel arrangement, divided into three groups: center section, end sections, and nose-cones. Orifice plates balance flows among the groups for uniform temperature rise. Within each group are several parallel flows balanced only by uniform pressure drop. Average velocity is 111 cm/sec [3.7 ft/sec]. Since tube lengths are not identical, while pressure drop across the cavity is essentially uniform, actual velocities vary. Calculations for the six end-section tubes show that relative velocities are expected to range up to $\pm 32\%$ of average velocity.

For the case of 75 kW and 75 gpm, a 3.7° C water temperature rise and a copper-to-water temperature difference of 9° C are expected. A minimum copper temperature occurs on the back side of the nose-cone cooling channel where the heat load is nearly zero; hence, the copper temperature closely matches the water temperature. For these conditions, temperatures throughout the system are expected to be:

Planned water supply temperature	32° C
Copper tube temperature	41° C
Average copper temperature	43° C
Maximum copper temperature	49° C
Water return temperature	36° C

Cavities were required to meet resonant frequency specifications when tested at the planned operating temperature; actually, we adjusted for testing at a lower, uniform copper temperature. Final measurements show a variation of -21 kHz to +43 kHz in cavity resonant frequencies. Measurements show a temperature dependence of -3.6 kHz/° C. In light of the fact that piston tuners fabricated for the cavities have a tuner range of approximately 2 MHz, one concludes that actual water supply temperature is not critical. The thermal time constant for the cavity alone, with 75 gpm flow of cooling water, is 30 seconds.

VIII. REFERENCES

- [1] F. Incropera, and D. DeWitt, *Fundamentals of Heat and Mass Transfer, 2nd Ed.*, (John Wiley & Sons, New York, 1985).
- [2] Hitachi Cable, Ltd., Tsuchiura-shi, Ibaraki-ken, Japan; personal communication with the author.
- [3] J. Bannantine, J. Comer, and J. Handrock, *Fundamentals of Metal Fatigue Analysis*, (Prentice Hall, Englewood Cliffs, New Jersey, 1990).

*RF Cavities for the Positron Accumulator Ring (PAR) of the Advanced Photon Source (APS)**

Y. W. Kang, A. Nassiri, J. F. Bridges, T. L. Smith, and J. J. Song
Advanced Photon Source, Argonne National Laboratory
9700 South Cass Avenue, Argonne, Illinois 60439 USA

Abstract

The cavities for the dual frequency system of the APS PAR [1] are described. The system uses two frequencies: a 9.78MHz fundamental system for the particle accumulation and a 117.3MHz twelfth harmonic system for the bunch compression. The cavities have been built, installed, tested, and used for storing the beam in the PAR for about a year. The fundamental cavity is a reentrant coaxial type with a capacitive loading plunger and has 1.6m length. The harmonic cavity is a symmetrical reentrant coaxial type and is 0.8m long. Ferrite tuners are used for frequency tuning. During the accumulation period, the ferrite tuner of the harmonic cavity works as a damper to disable the cavity. During an injection cycle the 9.78MHz system accumulates 24 positron bunches in a bucket and the 117.3MHz system compresses the bunch into a shorter bunch. Measurements were made on the rf properties of the cavities.

I. INTRODUCTION

Previously, the two cavities in the PAR of the APS were designed by computer simulation using URMEL codes [2][3]. The 9.78MHz first harmonic cavity employed a capacitive loading plunger for compactness and the 117.3MHz twelfth harmonic cavity employed a reentrant coaxial structure. The PAR of the APS has been operational for about a year and the rf cavities performed as expected to store the beam. The accumulation and compression functions at both frequencies have been performing adequately. Both the fundamental and the harmonic cavities use ferrite tuners for tuning the resonance frequencies. The fundamental system operates in continuous wave (CW) mode with a continuously varying tuner control current. The harmonic system operates with a pulsed rf and tuner control current at about 20% duty cycle. For fast tuning while pulsing the harmonic cavity tuner, the tuner coupling loop has bypass capacitors in the current path. This prevents limiting the tuner frequency response and unnecessary heating of the tuner housing.

Solid-state MOSFET rf amplifiers have been used to power the cavities. In the 9.78MHz system, rf power from four 1kW solid state amplifiers is combined inside the cavity with four couplers; each amplifier feeds a loop coupler. The couplers are mounted in the cavity outer cylinder and separated by 90 degrees circumferentially. In the harmonic system, the outputs of the four 500W solid-state amplifiers are combined through a 2kW 4-way splitter/combiner to use a single cavity input coupler.

Each cavity uses a ceramic window at the accelerating gap to save the vacuum pumping; only the inside of the beam pipe is evacuated and the outside of the beam pipe is filled with air. The ceramic windows are identical for both cavities; they have 6" diameter and are directly attached to the circular beam pipe.

Next, experience with the measurement and operation of the cavities will be discussed, and the tuner characteristic in each cavity will be shown. The higher-order mode characteristics of the cavities have been measured: measurements of the higher-order modes of the cavities with the beam-induced frequency spectrums will be shown.

II. 9.78MHz FUNDAMENTAL FREQUENCY CAVITY

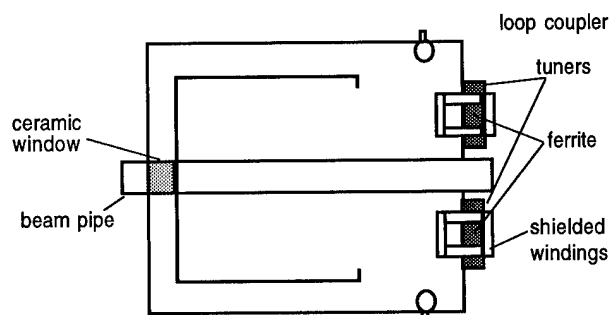


Figure 1: Fundamental frequency cavity construction

The first harmonic cavity was designed with a compact size in mind. A ceramic window is used at the accelerating gap in the beam pipe. Four input loop couplers are used on the outer cylinder and four tuners are used on the end wall. Figure 1 shows the plunger-loaded cavity with the input couplers and the ferrite tuners. A small loop type field probe is used to monitor the amplitude and the phase of the cavity field signal. The outside shell is made of aluminum and the inner conductor is made of copper. The inner conductor is a water-cooled copper cylinder surrounding the stainless steel beam pipe of the ring. Along the end rim of the inner plunger cylinder, a 1" diameter cylindrical corona ring is attached to reduce the chance of arcing inside the cavity. The maximum gap voltage required by the system is 40kV.

Tuner

The fundamental frequency cavity operates in CW mode. The cavity has four ferrite tuners which can tune the cavity resonant frequency up to ± 10 kHz. Each tuner has six ferrite toroids in a copper housing and a coupling loop. The fundamental cavity employs four tuners separated by 90 degrees in a circular wall of the cavity. The ferrite material used in the tuner has fairly low loss at the operating

* Work supported by the U. S. Department of Energy, Office of Basic Energy Sciences, under Contract No. W-31-109-ENG-38

frequency range so that the damping due to the tuner is almost negligible. Table 1 shows the specifications of the ferrite material used in the tuners.

Table 1: Ferrite toroid specifications

Material	Toshiba M4C21A
Outer Diameter	8.0"
Inner Diameter	5.0"
Thickness	1.0"
Resistivity	$3 \sim 10 \times 10^9 \Omega\text{-cm}$
Relative Permittivity	13.0 @40MHz
Electric Loss Tangent	0.00030 @40MHz
Initial Permeability	40 ~ 47
Magnetic Loss Tangent	0.008 ~ 0.009
Curie Temperature	340°C

The rf coupling is made with a single-turn rectangular hollow copper loop which has control windings inside. Forty turns of #12 high-temperature wire were used and the current was limited to 25A for safe operation of the tuners without damaging the insulation. The frequency drift of the cavity due to the rf heating is about 15°F and can be covered by the tuning range of the tuners.

III. 117.3MHz HARMONIC FREQUENCY CAVITY

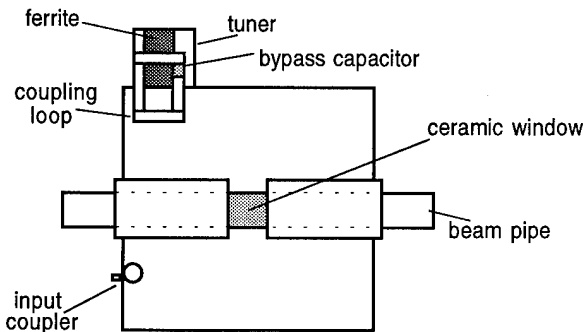


Figure 2: Harmonic cavity construction

Figure 2 shows the 117.3MHz harmonic frequency cavity. The cavity was built using stainless steel for the outer shell and aluminum for the center conductors. Like the fundamental cavity, the accelerating gap has a cylindrical ceramic window. Since the harmonic system operates in pulsed mode, the multipactor on the ceramic at a certain rf power level caused the nonlinear rf reflection at the input coupler and difficulty in normal operation of the automatic gain control (AGC) feedback control loop. The ceramic was replaced with a titanium-coated one to eliminate the problem. The system requires a 30kV maximum gap voltage.

Tuner

The ferrite toroids used in the harmonic cavity tuner are identical to the ones used in the 9.78MHz tuners. Three toroids are stacked inside a copper cylinder to construct a tuner. An rf coupling loop is used to couple rf to the tuner housing. The rf coupling loop also has control current

windings inside. In the rf coupling loop, a bypass capacitor was used to maintain fast response with the pulsed tuning current. The harmonic cavity employs one tuner on the cavity outer shell. The tuner has 80 turns of control winding. For safe operation of the tuners without overheating, the tuner control current was limited to 35A. The system requires damping by ~ 5 and detuning by -180kHz for the off state compared to the on state.

IV. MEASUREMENTS

9.78MHz Cavity

The cavity fundamental resonant frequency vs. the tuner current is shown in Figure 3. The cavity Q vs. the tuner current at the resonance is found to be almost constant. This shows that the ferrite material has low loss at the frequency. Measured Q is about 4,800. The cavity was tested to 36kV and the tuning range was measured as $\pm 10\text{kHz}$.

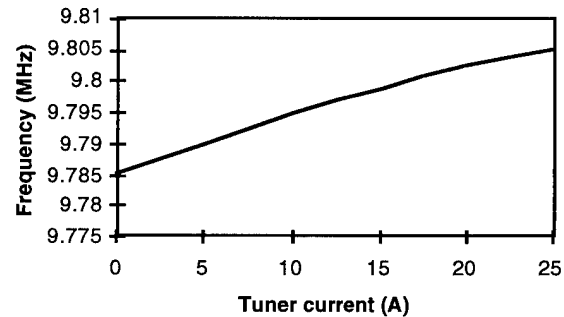


Figure 3: Fundamental cavity frequency vs. tuner current

117.3MHz Cavity

Detuning and damping the cavity are done with a single ferrite tuner at the same time. This can be achieved with the loss characteristic of the ferrite toroid at this frequency; the ferrite is lossy with no bias but lower loss when saturated. The cavity fundamental resonant frequency vs. the tuner current is shown in Figure 4. The cavity Q vs. the tuner current at the resonance is shown in Figure 5. Measured Q at full design current is about 2,400 with maximum control current. Since the ferrite is much lossier at this higher frequency with no bias current, the ferrite tuner works as a damper. The cavity was tested to 30kV gap voltage. The damping factor was 4 and detuning range was -170kHz .

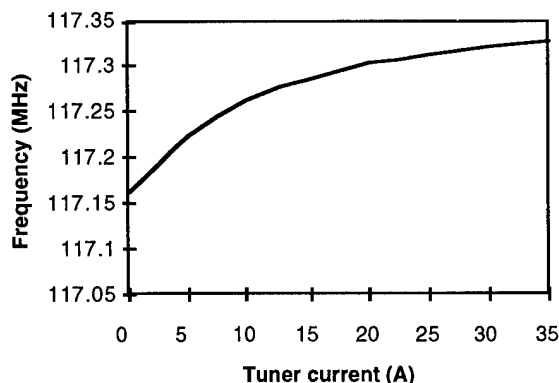


Figure 4: Harmonic cavity frequency vs. tuner current

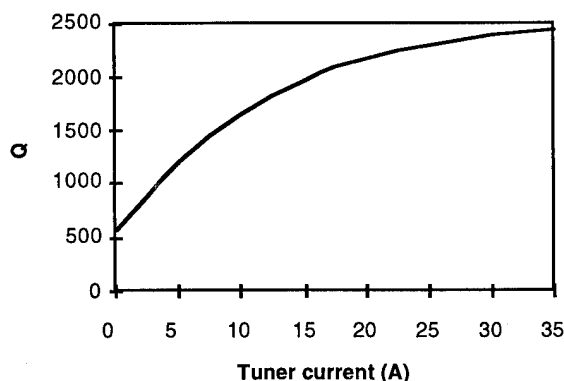


Figure 5: Harmonic cavity Q vs. tuner current

V. HIGHER-ORDER MODES

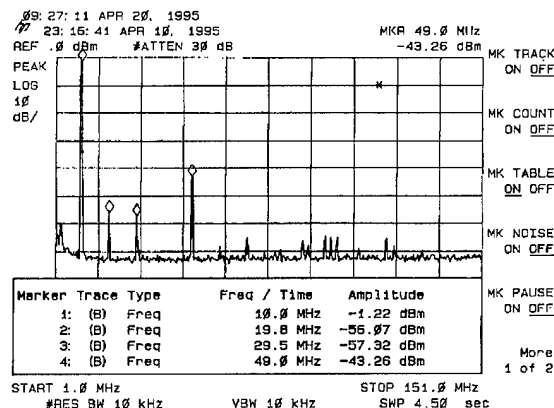


Figure 6: Beam-induced field spectrum of 9.78MHz cavity

Frequency, Q-factor, and shunt impedances of the cavity higher-order modes were found by computer simulation for the cavities[2][3]. Computer simulations were possible for the cavities without accessories such as the tuners and input couplers. The spectrum of the beam-induced higher-order modes of the fundamental cavity and the harmonic cavity have been measured with the field probes and are shown in Figures 6 and 7, respectively. Figure 7 also shows that the revolution harmonics of the fundamental frequency and most higher frequency

components are damped. The bunch current was $\sim 2nc$ and the bunch length was $\sim 0.6ns$.

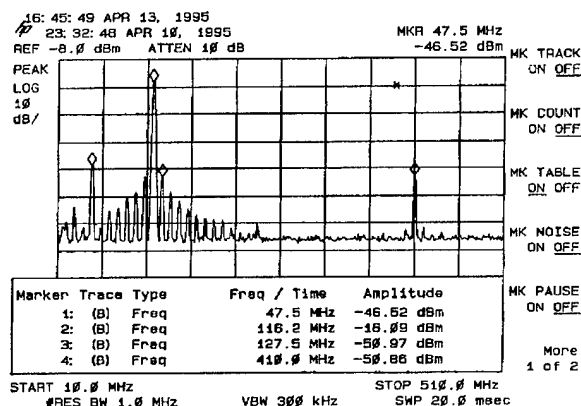


Figure 7: Beam-induced field spectrum of the 117.3MHz cavity

VI. CONCLUSION

The fundamental cavity operates in CW mode while the harmonic cavity works in pulsed mode. During the 'off' state, the tuner detunes and damps the cavity. By adjusting the coupling between the tuner and the coupler, the required damping and detuning could be obtained. The fundamental and the harmonic cavities have been working well so far, but some improvement is required in the fundamental cavity: a higher gap voltage and a greater tuning range. The accelerating gap voltage can be increased if the distance between the two concentric cylinders for capacitive loading is increased. The position of the rf coupling loop of the tuners affects the tuning range of the tuners. For more tuning range the position of the loops must move closer to the center conductor of the cavity.

VII. ACKNOWLEDGMENT

The authors express thanks to E. Wallace, D. Bromberek, J. Maj, G. Waldschmidt, and J. Cho for their efforts in installation and measurement of the cavity systems.

VIII. REFERENCES

- [1] M. Borland, "Commissioning of the Argonne Positron Accumulator Ring," these proceedings.
- [2] Y. W. Kang, R. L. Kustom and J. F. Bridges, "Twelfth Harmonic Cavity of the Positron Accumulator Ring of the Advanced Photon Source," Light Source Note, ANL/LS- 211 (1992).
- [3] Y. W. Kang, J. F. Bridges, and R. L. Kustom, "Reduced Length Design of 9.8MHz RF Accelerating Cavity for the Positron Accumulator Ring of the Advanced Photon Source," *Proc. of the IEEE Particle Accelerator Conference*, pp. 1054-1058, 1993.

THE PROPOSAL OF COMPLEX IMPEDANCE TERMINATION FOR VERSATILE HOM DAMPER CAVITY

V.V. Paramonov

Institute for Nuclear Research of the RAS, 117312, Moscow, Russia

Abstract

The proposal of high order mode (HOM) damping using heavily loaded annular-slot resonant cavity has been described in details and some results have been presented [1]. Investigation has shown, that damper absorbs enough large RF power from fundamental mode, leading to reduction in Q factor. Short physical consideration and results of calculations have shown, that introducing of complex impedance termination (RC chain in series) with simple realization evolves lower power absorption at the fundamental frequency. Reduction in absorbed RF power at low frequencies in 8 ÷ 9 times is due increasing in absolute value of the loading impedance and introducing of the phase shift between RF current and voltage.

I. INTRODUCTION

The proposal of HOM damping using heavily loaded annular-slot resonant cavity has been described in details and some results have been presented in [1], [2]. A prototype HOM damper [3] for the ferrite tuned KAON TRIUMF booster cavity has been constructed to measure damping of all modes up to 1 GHz. The mode damper has a broad range and damps effectively up to 1 GHz, but absorbs power at the fundamental mode. In this paper we consider some recommendation for optimization of the damper cavity and the proposal [4] of complex impedance termination (CIT) to decrease power absorption at fundamental mode.

II. LUMPED CIRCUIT ANALYSIS

Analysis of the dumping effect for the system main cavity - damper cavity with dumping resistor we will provide using lumped circuit method. This case we shall limit consideration with modes of coaxial type field distribution in the vicinity of the accelerating gap. Most of HOM's (except, probably, some modes at high frequency near 1 GHz) fulfill this condition.

Following [1], equivalent circuit for the system is shown in Fig.1, where $Z_c(\omega)$ is the output impedance of the main cavity to accelerating gap, C_g - equivalent capacitance of the accelerating gap, R_c - equivalent resistance of the RF losses in the main cavity, Z_d is the impedance of the damper cavity and Z_l is its loading (in general form complex) impedance.

Let consider, at first, the main cavity (assuming shortening between points A and B at the circuit Fig.1) parameters. The values of Z_c , C_g , R_c have to be adjusted to simulate cavity with the same frequency, impedance to the beam Z_b and Z_b/Q value as for accelerating cavity. Condition for resonant frequencies of the main cavity ω_n is follows:

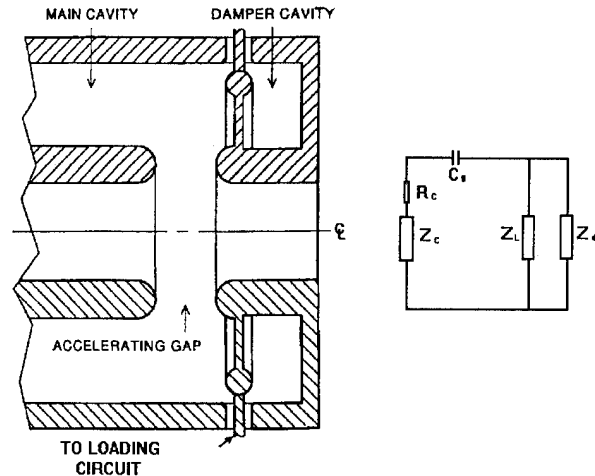


Figure 1. The schematic sketch of the damper cavity and the equivalent scheme of the circuit.

$$Z_c(\omega_n) + \frac{1}{i\omega_n C_g} = 0. \quad (1)$$

Defining the complex impedance presented to the beam at the gap as [1]:

$$Z_b = \frac{(Z_c + R_c)Z_g}{Z_c + R_c + Z_g}, \quad (2)$$

where $Z_g = 1/i\omega C_g$ is the complex impedance of the gap capacitance, and taking into account (1), one can derive for impedance $Z_{bn} = Z_b(\omega_n)$ at the resonant frequencies ω_n of the system:

$$Z_{bn} = \frac{1}{\omega_n^2 C_g^2 R_c} - \frac{1}{i\omega_n C_g} \approx \frac{1}{\omega_n^2 C_g^2 R_c}. \quad (3)$$

It is natural to consider the main cavity as the short-circuited copper coaxial line, because original ferrite tuned accelerating cavity is coaxial type one. But for the short-circuited coaxial line $\omega_n \approx (2m + 1)\omega_1$, where ω_1 is the frequency of the fundamental mode and m is integer, $2m + 1 = n$. For the impedance of the HOM, if $R_c = \text{const}$, one will have (3) $Z_{bn} \sim n^{-2}$. Direct calculations shows for the impedance Z_{bn} the dependence $Z_{bn} \sim n^{-1/2}$. To simulate more realistic case, we will assume $R_c = R_{c0}\omega^{-3/2}$. This case the impedances of the HOM's decrease slightly with frequency increasing and dumping problem

becomes more severe. The values for $Z_c(\omega_1)$, C_g , R_{c0} were fitted to have $Z_{b1} = 210 \text{ kOhm}$, $Z_{b1}/Q_1 = 40 \text{ Ohm}$ at the frequency $\omega_1/2\pi = 62 \text{ MHz}$.

At the second step of the analysis let's consider the main cavity together with the damper one, supposing loading impedance $Z_l = \infty$. This case pure imaginary (inductive type) impedance of the damper cavity $Z_d = \iota|Z_d|$ at the frequency of the fundamental mode is small addition to Z_c , leading to the small shift in the resonant frequency (1). There are no increasing in real part of resistance, and, hence, there are no dumping of the impedance Z_b . Without the loading resistance the damper cavity is insufficiently small addition to the total surface of the main cavity in the region with low magnetic field and don't lead to the increasing of the RF power dissipation.

Then consider the case, when the loading impedance Z_l is active resistance $Z_l = R_l$. We can transform parallel chain 'damper cavity - loading resistance' in series one with the same impedance Z_{d1} :

$$Z_{d1} = \frac{Z_d Z_l}{Z_l + Z_d} = \frac{|Z_d|^2 R_l}{R_l^2 + |Z_d|^2} + \iota \frac{|Z_d| R_l^2}{R_l^2 + |Z_d|^2}. \quad (4)$$

At the frequency of the fundamental mode $|Z_d(\omega_1)| \sim 2 \div 4 \text{ Ohm} \ll R_l$ and for Z_{d1} good estimation will be:

$$Z_{d1} \sim \frac{|Z_d|^2}{R_l} + \iota |Z_d|. \quad (5)$$

One can consider the real part of Z_{d1} as the addition to the equivalent resistance R_c . This addition will lead to increasing in the RF power dissipation at the fundamental mode.

Let's consider more complicated loading circuit - resistance R_l in series with capacitance C_l . We transform total circuit 'damper cavity - loading chain' to the equivalent chain in series with the loading impedance Z_{d2} :

$$Z_{d2} = \frac{|Z_d|^2 R_l + \iota(|Z_d| R_l^2 - \frac{|Z_d|^2}{\omega C_l} + \frac{|Z_d|}{(\omega C_l)^2})}{R_l^2 + (|Z_d| - \frac{1}{\omega C_l})^2} \quad (6)$$

If we choose the loading capacitance C_l to fulfill the condition $\frac{1}{\omega_1 C_l} \gg R_l \sim |Z_d|$ (it is not difficult, for $C_l = 20 \text{ pF}$, $\frac{1}{\omega_1 C_l} \approx 120 \text{ Ohm}$), for the loading impedance Z_{d2} one get:

$$Z_{d2} \sim |Z_d|^2 R_l (\omega C_l)^2 + \iota |Z_d| R_l^2 (\omega C_l)^2. \quad (7)$$

Comparing (5) and (7), we see reduction of the loading impedance at the fundamental frequency in $(R_l \omega_1 C_l)^2$ times. Following [1], the damping resistance R_d is:

$$R_d = 1/\text{real}(1/Z_g, Z_g = Z_c + Z_{dt}, \quad (8)$$

where $Z_{dt} = Z_{d1}$ or $Z_{dt} = Z_{d2}$ - total impedance of the damping chain. After simplification one can get for R_d at the fundamental frequency:

$$R_d \approx \frac{R_l}{\omega_1^2 C_g^2 |Z_d|^2}, \quad (9)$$

if loading circuit is resistance and:

$$R_d \approx \frac{1}{R_l \omega_1^4 C_g^2 C_l^2 |Z_d|^2}, \quad (10)$$

if loading circuit is RC chain. Comparing (9) and (10), one see increasing of the dumping resistance at the fundamental frequency in $(R_l \omega_1 C_l)^2$ times.

III. OPTIMIZATION OF THE DAMPING RESISTANCE

For good damper we need in high value of the damping resistance R_d at the fundamental frequency and low value at frequencies of HOM's. Consideration shows, that introduction of loading capacitance C_l improves the total selectivity of damping circuit in low frequency range. Taking into account $|Z_d| \sim \omega$, one see $R_d \sim \omega^{-4}$ (9) for original proposal and $R_d \sim \omega^{-6}$ (10) for CIT. It allows us have larger difference in damping effect between fundamental mode and HOM's. In comparison with active resistance, CIT allows obtain this difference in one order more. With introducing of additional parameter we obtain more flexibility in optimization of the damping circuit.

Let provide simple qualitative analysis to obtain guidance line in choosing of parameters for the damping circuit. Comparing (9) and (10), one see, that loading capacitance reverse effect from loading resistance at low frequencies. It is clear, because for $\frac{1}{\omega_1 C_l} \gg R_l$ the absolute value of loading impedance is determined by capacitive part and RF current in RC chain is shifted in phase with respect to RF voltage. To have at the fundamental frequency high value of damping resistance, we need in small values of R_d , C_d and Z_d (10). But at high frequency $R_d \sim 1/(Z_d^2 R_d)$ and we can't take R_d too small. To prevent increasing of R_d due to serious resonance of the damper cavity ($Z_d = 0$), this resonance must be higher than range of damping (so, as in original proposal). The dependence $R_d(\omega)$ exhibits the minimum near frequency $Z_d - 1/(\omega C_l)$. The capacitance C_l loads the damper cavity at the frequency of first resonance, shifting it down, and don't effect on frequency of the second resonance. It is additional performance, because damper cavity have to be shorter and mode separation additionally improves. With small values of C_l and R_l the minimum of the dependence $R_d(\omega)$ is enough narrow and deep. To damp successfully the first HOM, the damping circuit have to be tuned to have minimum R_d in the range of the frequency changing for this HOM, closer to the low limit of this range. If we will increase $|Z_d|$ at the fundamental frequency, R_d at high frequency will decrease. One can do it by increasing of the slot width in the damper cavity, provoking so more strong coupling with HOM's of the main cavity. But at the fundamental frequency R_d will decrease too.

These reasons may be considered as recommendations in choosing of the damper cavity option for realization. Another reasons, including technological, have to be taken into account. Because there are analytical expressions for the damping circuit

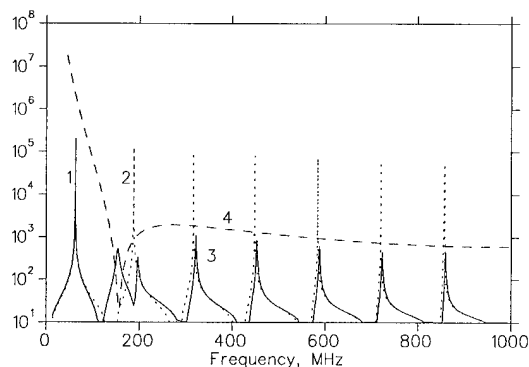


Figure 2. The dependencies as a functions of frequency. 1 - fundamental mode, 2 - undamped HOM's, 3 - damped HOM's, 4 - damping resistance.

parameters, optimization of the damping circuit may be passed to computer.

As the example, for one option the effect of the damping circuit is shown at Fig. 2. Parameters of the damping circuit are $C_d = 1.5C_g$, $R_l = 60\Omega$. At the fundamental frequency reduction in the impedance is $\Delta Z_b/Z_b \approx 0.07$ for $\frac{\omega_1}{2\pi} = 62\text{MHz}$. At the low limit of the fundamental frequency range $\frac{\omega_1}{2\pi} = 46\text{MHz}$ reduction in the impedance is one order less. With decreasing of the fundamental frequency the damping impedance rises fact. Moreover, at low frequency own RF losses in the main cavity increases due to higher losses in ferrite. The RF power, dissipated in the damping circuit depends on RF voltage, induced on damper cavity and don't depends on quality factor Q_0 of the main cavity. So, with high Q_0 relative value in increasing of RF power dissipation will be higher. It is valid for all types of dampers and have to be taken into account under comparison of different types of dampers.

Direct calculation (using codes like SUPERFISH) of the RF voltage induced on damper shows lower RF losses in comparison with lumped circuit results.

Results of this consideration show, that with introducing of CIT RF power dissipation at the fundamental frequency may be decreased significantly and be close to very good results, obtained in [5] (experimentally).

Technical realization of CIT seems not so difficult, because value of the capacitance C_l needed is not so large. At fundamental mode in the gap of the damper cavity there are no large voltages and different design may be realized.

IV. CONCLUSION

Short physical consideration and results of calculations have shown, that introducing of complex impedance termination evolves lower power absorption at the fundamental frequency without deterioration of HOM's damping.

The author thanks R.L. Poirier and A.K. Mitra for discussion and interest in this work.

References

- [1] W.R.Smythe, T.A.Energen and R.L.Poirier. A Versatile RF Cavity Mode Damper. Proc. of the 2nd EPAC, France, 1990, p.976-978
- [2] W.R.Smythe, C.Friedrichs and L.S.Walling, Proton Synchrotron RF Cavity Model Damper Tests, 1991 IEEE Particle Accelerator Conference, May 6-8, 1991, San Francisco, p. 643-645
- [3] A.K. Mitra. Measurements on a prototype HOM damper cavity at TRIUMF. RF Workshop, SSCL, Texas, USA, June 25-26, 1992
- [4] V.V. Paramonov. Possible improvement of the HOM damper cavity using frequency dependent load. RF Workshop, SSCL, Texas, USA, June 25-26, 1992
- [5] A.K. Mitra. A new concept of a higher-order-mode damper for the KAON booster cavity. Proc. of the 4-th EPAC, 1995, p.2158

THE MAGNETRON-TYPE VARACTOR FOR FAST CONTROL IN ACCELERATOR RF SYSTEMS

M.I. Kuznetsov, V.V. Paramonov, Yu.V. Senichev
Institute for Nuclear Research of the RAS, 117312, Moscow, Russia
I.B. Enchevich, R.L. Poirier
TRIUMF, Vancouver, B.C., V6T 2A3, Canada

ABSTRACT

The RF test of the magnetron-type varactors have shown [1] the proof of principle of this device. A comparison with the other power rf tunable devices, such as ferrite tuners, shows, that the varactor has a response time a few orders of magnitude shorter. In the experiments this time was estimated to be in the order of 10^{-6} sec for operating frequency $\approx 66 \text{ MHz}$. This feature of the varactor opens new applications of the varactor for a fast modulation (in order of few tens of the working rf period) of the amplitude and the phase of the accelerating voltage in the rf cavities. Basing on results of numerical simulation, different applications of the device for fast control and improvements in the design to reduce response time are considered.

I. INTRODUCTION

During the development of rf systems for kaon factories a magnetron type varactor was proposed [4] as a tuner for accelerating cavities in synchrotron rings. The Test&Development program was carried out as a collaboration between TRIUMF and INR resulting in the proof of principle of this device.

Varactor may be used as the narrow range tuner for accelerating cavities with moderate or high accelerating voltage [1], but main advantage of the magnetron type varactor is its short time of reaction. It stimulates us in consideration of this device as the instrument of fast control in RF systems.

II. VARACTOR. DESIGN, OPTION OF OPERATION, LIMITATIONS

A schematic sketch of the varactor is presented in Fig. 1. The varactor is a coaxial system consisting of outer conductor (1), inner conductor (2), cathode (3) and reflector (4). The ceramic insulator (5) mechanically supports the construction and provides a dc isolation. The magnetic field B is directed along the z axis, the dc control voltage U_{cc} (with respect to outer conductor) and the rf voltage U_{rf} are applied between the conductors, providing electric fields E_{cc} and E_{rf} in a radial direction. The outer conductor with radius r_a is fixed at ground potential.

The simple theory of the device is described in [2]. Under conditions above the motion of electrons in interaction space between inner and outer conductors may be subdivided in three parts:

- fast cyclotron rotation with the frequency $\omega_h = \left| \frac{eB}{m} \right|$;
- drift of the center of Larmor orbit in azimuth direction with velocity $V \sim (E_{cc} + E_{rf} + E_o)/B$, where E_o is the own electric field of the electron cloud;
- motion along z axis.

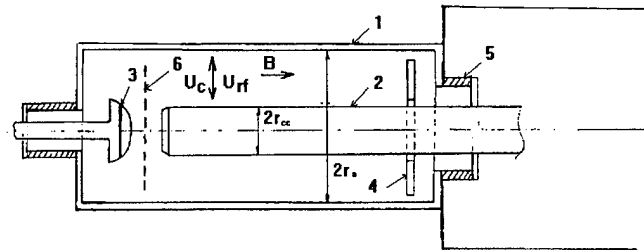


Figure 1. Schematic sketch of the varactor. 1 - outer conductor, 2 - inner conductor, 3 - cathode, 4 - reflector, 5 - insulator, 6 - control grid

It may be shown [2], that presence of the electron cloud or electron beam in the interaction space results in an increase of the effective permittivity:

$$\epsilon = 1 + \frac{ne^2}{m(\omega_h^2 - \omega^2)} \approx 1 + \frac{ne^2}{m\omega_h^2} \quad (1)$$

where n is density of electrons, $\omega = 2\pi f$, f is the self rf frequency of the system. This effect depends on both the charge density and the position of the electron cloud. Treatment of results obtained in experiments [2] have confirmed, that the influence of the charge density is much more stronger, especially if ratio r_a/r_{cc} is not large.

Several reasons:

- a - to have the controllable motion of electrons;
- b - to reduce a absorption of the RF energy;
- c - to reduce radius of cyclotron rotation, and, hence, radial dimension of the beam - lead to the condition $\omega \ll \omega_h$.

Two different options may be realized in the operation of the varactor.

The simplest case is a beam regime, when electron pass varactor one time from the cathode to the reflector (this case reflector really is an absorber). Only heat loading to the reflector limits the range of tuning. Both estimations and the results of numerical simulation shows for the reasonable heat deposition (less than 1 kWt, cooling is necessary) the range $\Delta\epsilon \sim 5\%$ as achievable. A transit time for electron from the cathode to the absorber may be one order less than RF period. Experiments performed

in 1992 have shown this option as realistic [3], but reflector must be specially adapted.

Second option of operation - an accumulation of electron cloud, was investigated in more details [2] in 1993. Providing magnetic mirrors near the cathode and the reflector and probably adding it with reflective potentials at these electrodes we establish a trap for electrons in interaction space. Electron will pass interaction space several times. It leads to sufficient reduction in the emission current and more uniform distribution of losses in the surface of the device. By providing a good magnetic trap one can get narrow band tuning ($\Delta\epsilon = 0 \div 5\%$ for $U_{cc} = 0 \div -20$ kV,) at low RF level practically without any drop in Q - factor of the system with very small value of emission current ($I_{hc} = 18$ mA) [2], [1]. Critical points in this option of operation are regions near reflector and near cathode. In these regions density of electrons is much more higher than average density in interaction space (here electrons change sign of axial velocity). If any instabilities take place in the cloud, they arise in these return points. Moreover, main part of an energy extraction from RF field takes place under injection and near reflector. After investigation the results of experiments we have developed the proposals for improvements in injection and the reflector design to reduce RF energy absorption and for damping instabilities. Specific time for this mode of operation is life-time of electron in the cloud. From a treatment of experimental data we estimate this time in range $1 \div 10$ RF periods, depending on the regime of the varactor (see [2]).

For both options of the varactor operations the response time of the varactor as the controllable device will strongly depend on delay time in a control circuit. Differing from previous versions [4], [3], [1], we consider a new device with constant high DC voltage at the central conductor. Changing of the cloud density will be by modulation of the injection current with low control voltage applied between the cathode and the control grid (Fig.1). All problems, connected with the forming of current pulses in such injection system are good investigated in the development and design of high frequency powerful electron tubes.

The results of numerical simulation have confirmed previous estimations [1] for reasonable parameters of the device at different levels of the rf voltage and have clarified reasons of disadvantages.

The reason of nonlinearity in the varactor is the coaxial design. It leads to the nonuniformity of the electric fields E_{cc} and E_{rf} (the r^{-1} dependence). At low rf voltage level $U_{rf} \approx 500$ V $\ll U_{cc}$ the displacement of electrons under rf field action is small and the nonlinearity mainly depends on ratio r_a/r_{cc} . At moderate rf voltage level (1 kV $\leq U_{rf} < U_{cc}$) additional factor arises. If the density of the cloud is comparable with the Brillouin density $n_b = \frac{m\epsilon_0\omega^2}{e^2}$ (it is needed for $\Delta\epsilon/\epsilon_{min} \approx 30\%$ or more), own electric field of the cloud E_o is comparable with E_{cc} and E_{rf} . The displacement of electrons under rf field action is not small and together with high density leads to significant redistribution of electrons in the cloud. This effect grows fast with the increasing of the cloud density ($\sim n^2$) and very fast with r_a/r_{cc} increasing. To keep nonlinearity in reasonable limits at moderate rf voltage level we need in restriction $r_a/r_{cc} < 1.5$.

It is known, that all controllable reactive devices are nonlinear. The smallest value of nonlinearity was observed for perpen-

dicular biased ferrite-tuned cavities [5]. But in these cavities rf magnetic field is two order less than external control one. For the varactor we are interesting in $U_{rf} \sim U_{cc}$ and a nonlinearity don't looks as the especial problem of this device.

For high rf voltage level $U_{rf} \geq U_{cc}$ direct numerical simulation of electron motion in the interaction space shows interesting but very complicated picture, especially for high density of the cloud. The dependence of the E_o on radius differs from E_{cc} and E_{rf} dependencies - E_o grows in absolute value with a radius increasing. The total electric field inside the cloud changes with time during rf period $E_t = E_{cc} + E_{rf}\sin(\omega t) + E_o$. The cloud becomes subdivided with cylindrical surface $r = const$ in two parts, differing in a direction of the azimuthal rotation. As it is known well, such configuration is unstable. But a boundary between parts moves enough fast in radius due to $E_{rf}\sin(\omega t)$ changing. It provides a very complicated mixture in motion of electron. As it also known well, such effects are very efficient in instabilities damping. The ability of stable operation for varactor at high rf voltage level $U_{rf} \geq U_{cc}$ have to be proved in experiments.

An application of the varactor looks more comfortable at low frequencies. The scaling relationship for the varactor regimes ($U_{rf} \sim U_{cc} \sim B^2 \sim \omega_b^2$) is valid. To meet requirement $\omega_b^2 \gg \omega^2$, with increasing of operating frequency one have to increase magnetic field and control voltage (but will have increase in rf voltage). Another problem is the forming of control pulse at the control grid at high frequency.

III. POSSIBLE APPLICATIONS OF THE VARACTOR FOR FAST CONTROL

Experimentally it was shown that the varactor may be used as a controllable reactive device with an rf voltage amplitude at least close to the control voltage value U_{cc} . Taking into account all improvements proposed, we consider now the tuning range $\Delta C/C_{min} \approx 30\%$ with high Q factor as a reasonable limit at moderate rf voltage level.

With partial connection (through a small dividing capacitor), one may use the varactor for higher values of rf voltage, but with respective reduction in the tuning range.

One can consider the varactor as a part of transmission line with controllable wave-resistance or as a capacitor with controllable capacitance. A lot of applications in rf systems are possible, for example phase regulator and so on. Let consider possible applications for fast control of the frequency, and the phase of the accelerating voltage in the rf cavities.

1. Suppose the varactor is included into a transmission line between an rf amplifier and a cavity. If one will change the capacitance of the varactor as $C = C_0 + C_1\sin(\omega_1 t)$, it will results in amplitude modulation with frequency ω_1 for transmission coefficient of the line. A rf spectrum for a signal after the varactor will contain frequency components $\omega - \omega_1$, ω and $\omega + \omega_1$. It will be the spectrum of amplitude modulated signal. The cavity will accept this signal if a bandwidth $2\omega_1$ is less than a width of a resonant curve of the cavity $\Delta\omega = \omega/Q_l$ and rf voltage in the cavity will be modulated in amplitude. Continuing this proposal, one can change the capacitance in more complicated law $C = C_0 + C_1\sin(\omega_1 t) + \dots + C_m\sin(\omega_1 m t)$. Combin-

ing $C_1 \dots C_m$ in a relation defined one can provide for the cavity rf spectrum for modulation in frequency (but with a reduction in band, because for modulation in frequency $\omega/Q_l \geq 2m\omega_1$). So, using the varactor inserted into transmission line, one can get in the cavity signal with modulation in amplitude or in frequency, or more complicated signal. The bandwidth of the modulation will be defined by passband of the cavity. The depth of the modulation depends on the range of capacitance change and can not exceed it. This case seems not a difficult problem. The length of the interaction space of the varactor is related with a wavelength at an operating frequency (it is nonefficient take length $\geq \lambda/4$). Specific time for the cloud is also related with operating frequency. For the cavity with reasonable high Q_l factor frequency of the modulation is low enough. There will be no difficulties in forming of a pulse on control grid of the varactor.

2. Suppose the varactor is coupled to the cavity by a loop or a probe. One can use the varactor as a delicate fast additional instrument in frequency control system. It may be interesting for accelerating systems with heavy heat loading, for example, linear accelerators in cw mode of operation. A traditional frequency control by cooling liquid may be enough inertial. If a traditional system will eliminate slow main part of the detuning, the varactor can eliminate a small residual detuning in Q_l rf periods. Our calculations, using the coupled circuit method, shows the varactor be able to detune in narrow band tuning range $\Delta\omega/\omega \approx 5 \cdot 10^{-5}$ enough big cavities, like RFQ or short IH and DTL tanks.

In both cases considered above typical frequency of the modulation is determined by cavity Q_l factor. It is more or less evident result, because cavity is mostly inertial chain in the circuit. To provide more fast modulation, one need actively modify parameters of the cavity.

3. Much more interesting results may be obtained when the varactor is directly included in the cavity. Suppose the cavity is good described with lumped parameters, an equivalent capacitance is concentrated near accelerating gap, the varactor is connected in parallel to accelerating gap. If one will change the capacitance of the varactor as $C = C_0 + C_1 \sin(\omega_1 t)$, it will results in changing of total capacitance of the cavity. Using analogy with LRC-circuits, we have LRC chain with floating parameters. Theoretical analysis of such circuit is very complicated and may be done using methods of a theory of nonlinear oscillations. Numerical simulations shows additional peaks at the resonant curve of such system. The position of peaks at a frequency scale depends on the modulation depth of total capacitance, ratio ω_1/ω and may be far from the main resonant peak. It means, that the cavity can accept broadband signal and modulation will be faster (really in order of several tens of the working rf period for high Q_l cavity). But we consider this conclusion as preliminary. Very careful analysis have to be continued, because such systems (as it is known from theory of oscillations) may exhibit undesirable effects (instability, parasitic oscillations, jumps in phase and amplitude...).

IV. CONCLUSION

The magnetron-type varactor now is not the device with specified parameters. It looks now more like principle of operation for new type of controllable reactive RF devices. Our experiments

have shown proof of this principle. It is impossible in one paper describe all possible versions and applications. Different particular requirements will lead to different realizations, will need in detailed development and experimental verification. Varactor will not replace ferrite-based devices for broad-band applications, but as the instrument for the fast control it has promising perspectives.

References

- [1] I.B. Enchevich *et al.* RF Test of the Magnetron-Type Varactors, Proc. of 1994 EPAC, v. 3, p. 1980.
- [2] I.B. Enchevich *et al.*, RF experiments with the magnetron-type varactors. TRIUMF Design Note TRI-DN-94-16, TRIUMF, Vancouver, 1994.
- [3] I.B. Enchevich *et al.*, Experiments with the magnetron-type varactor. TRIUMF Design Note TRI-DN-94-15, TRIUMF, Vancouver, 1994.
- [4] V.A. Konovalov, *et al.*, The Perspectives of Application of the Fast-Acting Varactor with Low Losses in High-Current Cyclic and Linear Accelerators. Proc. of the 1992 EPAC Conference, Berlin, v.2, p. 1242, 1990
- [5] R.L. Poirier, Perpendicular Biased Ferrite-Tuned Cavities, Proc. of the 1993 IEEE PAC, v.2, p. 753-757, 1994

THE DISTORTION OF THE ACCELERATING FIELD DISTRIBUTION IN COMPENSATED STRUCTURES DUE TO STEADY-STATE BEAM LOADING

V.G. Andreev †, V.V. Paramonov

Institute for Nuclear Research of the RAS, 117312, Moscow, Russia

† - Moscow Radiotechnical Institute, Moscow

Abstract

Using general electrodynamic approach and particular properties of compensated accelerating structures the effect of distortions in accelerating field distribution due to RF power losses in surface and for beam acceleration is considered. Consideration shows, that for proton linacs of 'meson facility' type (impulsive beam current $I_b \simeq 50 \text{ mA}$, acceleration rate $U_a \sim 2 \div 6 \text{ MV/m}$) this effect is not important for all accelerating structures known. When beam current $I_b \sim 100 \div 300 \text{ mA}$ and $U_a \sim 1 \text{ MV/m}$ (like linacs for accelerator-driven transmutation technologies), in the structures with small group velocity ($\beta_g \approx 0.04$) significant distortions will arise and efficiency of the structure for beam acceleration will drop. For structures with large group velocity ($\beta_g \approx 0.4$) such effects will arise at beam current in several amperes.

I. INTRODUCTION

The compensated accelerating structures are now widely used for acceleration of charged particles for high energies (relative velocities $\beta_p > 0.4$). Remember, that the 'compensated' is named structure in which at operating frequency coincide frequencies of two modes with differing parity of field distribution with respect to symmetry plane (accelerating and coupling modes) [1]. Examples of compensated structures are well known Side-Coupled Structure (SCS), Annular-Coupled Structure (ACS), On-axis Coupled Structure (OCS), Disk And Washer structure (DAW) and so on. Particularity of compensated structures is ability of propagation of traveling wave 0 or π type with group velocity differing from zero. These structures are used in proton linear accelerators of 'meson facility' type. Under consideration now are projects of accelerators with beam current in several hundreds mA. In this case RF power needed for beam acceleration in several times exceeds RF losses in the structure. It leads to the additional distortion of accelerating field distribution along the structure in steady-state regime.

II. THE FIELD DISTRIBUTION

Below we shall consider (without loss of generality) the accelerating structures with operating π mode. The electromagnetic field in the cavity is a result of adding of two traveling waves - forward wave, from RF source, and backward wave, reflected from the end of the accelerating cavity. The losses of the RF power in really conductive surface and for beam acceleration lead to the attenuation of propagating waves. Suppose that beam bunches are in all accelerating gaps, each bunch we consider as a solid and process is steady-state. Under these assumptions all periods of the structure are equivalent and the field distribution

in the structure must satisfy to the Floquet theorem. Suppose, the accelerating mode and the coupling one have the field distributions, described by:

$$\begin{aligned} H_a &= H_a(\varphi, r, z), \quad 0 \leq z \leq d, \\ H_c &= H_c(\varphi, r, z), \quad 0 \leq z \leq d, \end{aligned} \quad (1)$$

where d - is the length of the period of the structure.

Traveling waves of 0 or π type can propagate if there is no stop-band at the dispersion diagram. In practice it is sufficient to have overlapped resonant curves of accelerating and coupling modes. In this case in positive direction along z axis propagates forward wave with the field distribution in n -th period $nd \leq z' \leq d + nd$:

$$H_+''(\varphi, r, z') = [H_a(\varphi, r, z) - \iota H_c(\varphi, r, z)]e^{\iota n\theta}, \quad (2)$$

with normalization [1,2]:

$$\int_v H_a^2 dV = \int_v H_c^2 dV, \quad (3)$$

where θ - is phase shift per period, v is the volume of the one period of the structure. Propagating in negative direction backward wave have to be described with complex conjugated to (2) expression. With all RF losses θ must be complex value $\theta = \pi - \iota\alpha$, where α have to be founded as the solution of our problem. For the field distributions of forward H_+ and backward H_- waves, we can write:

$$H_+ = A_+ e^{-\alpha z'} H_+''(\varphi, r, z), \quad H_- = A_- e^{\alpha z'} H_+''(\varphi, r, z)^*, \quad (4)$$

where A_+ and A_- - amplitudes. The reflection of the forward wave at the end plate of the cavity ($z = Nd$) provides the relationship for amplitudes: $A_- = A_+ e^{-2N\alpha d}$. For the magnetic field of the standing wave in the n -th period, taking into account (2) - (4), we get:

$$\begin{aligned} H_\tau &= A_+ e^{-\alpha z'} \cos(n\pi) (H_a(1 + e^u) - \iota H_c(1 - e^u)), \\ u &= 2\alpha(z' - Nd). \end{aligned} \quad (5)$$

III. THE RF POWER BALANCE

We can write the RF power balance in the plane $z = 0$: difference in the RF powers, carried by forward P_+ and backward P_- waves is equal to the RF power losses in surface P_s and the RF

power for beam acceleration P_b , and using well known relations for traveling wave power flux transform it to:

$$P_s + P_b = \frac{c\beta_g(W_+ - W_-)}{d} = \frac{c\beta_g W_a(1 - e^{-4N\alpha d})}{2d}. \quad (6)$$

where W_+ and W_- are energies, stored by forward and backward waves in the period, β_g - relative group velocity of waves, N - number of the structure period from the RF input point to the end of the cavity, W_a - energy, stored by standing wave accelerating mode in the period. This paper we shall use set of 'ideal' notions. For example, W_a is the energy, stored by operating - accelerating mode in the period of the structure if forward wave has the amplitude A_+ .

In calculations of RF losses in the surface $P_s = \frac{R_s}{2} \int H_r^2 dS$ we have to know the field distribution including changing due to attenuation. In general form it is impossible, because in cavity with complex real form, field distributions $H_a(\varphi, r, z)$ and $H_c(\varphi, r, z)$ are not described analytically. To calculate P_s , we represent the integral over all surface as a sum of integrals over all periods, and each integral over period represent as a product of integrals from 'ideal' field distribution $H_a(\varphi, r, z)$ and from attenuation.

$$P_s = \frac{N}{8} (P_a (\frac{1 - e^{-4N\alpha d}}{N\alpha d} + 4e^{-4N\alpha d}) + P_c (\frac{1 - e^{-4N\alpha d}}{N\alpha d} - 4e^{-4N\alpha d})), \quad (7)$$

where P_a and P_c are RF power losses in surface for accelerating mode and coupling one (like W_a). The RF power for beam acceleration P_b , taking into account E_z distribution like H_r (3), is:

$$P_b = I_b \int E_z e^{\frac{ikz'}{\beta_p}} dz' \approx \frac{I_b U_a N (1 - e^{-2N\alpha d})}{2N\alpha d}, \quad (8)$$

where k is wave value, I_b - beam current, E_a and T_a are tension and transit time factor for accelerating mode, $U_a = E_a T_a$ - designed energy gain per period (like W_a). One can neglect contribution of the coupling mode to beam acceleration, because its field tension E_c is several orders less in comparison with E_a for accelerating mode.

Introducing (8) and (8) into (6), with simple transformation, one get for α determination:

$$\frac{\beta_g Q_a (1 - e^{-4N\alpha d})}{2\pi\beta_p} = \frac{I_b U_a N (1 + e^{-2N\alpha d})}{2N\alpha d P_a} + \frac{N}{8} \left(\frac{(1 - e^{-4N\alpha d})(Q_a + Q_c)}{N\alpha d Q_c} + 4 \frac{(Q_c - Q_a)e^{-2N\alpha d}}{Q_c} \right), \quad (9)$$

where Q_a and Q_c - are quality factors of the accelerating mode and the coupling one.

IV. DISCUSSION

In the case of small total attenuation ($N\alpha d \ll 1$), transforming (10) in series with $N\alpha d$ power, one find:

$$N\alpha d \approx \frac{1 + \frac{I_b U_a}{P_a}}{\frac{2\beta_g Q_a}{N\pi\beta_p} + 2 + \frac{I_b U_a}{P_a}} \approx (1 + \frac{I_b U_a}{P_a}) \frac{N\pi\beta_p}{2\beta_g Q_a}. \quad (10)$$

In the case $N\alpha d \ll 1$ attenuation coefficient α don't depends on number of periods in the cavity and its increasing due to beam loading is proportional to the ratio of RF power for beam acceleration to RF losses in the surface, or, to the effective increasing of total RF losses in the period. The coupling mode excites in first order of αd (4) and increasing in total RF losses due to this mode excitation is in second order. In this case the radiotechnical parameters of the structure for acceleration are practically the same, as designed. Quality factor don't changes and there is no decreasing in efficiency of acceleration.

Let's define accelerating field tilt as:

$$\frac{\Delta E}{E} = \frac{E_0 - E_N}{E_0} = \frac{(1 - e^{-N\alpha d})^2}{1 + e^{-2N\alpha d}} \approx (N\alpha d)^2 \quad (11)$$

Operating regimes of proton linacs of 'meson facility' type satisfy to the condition:

$$\frac{I_b U_a}{P_a} = \frac{I_b Z_a \cos^2 \Phi}{U_a} < 1. \quad (12)$$

where Φ is synchronous phase. Comparing two accelerating structures - SCS ($\beta_g/\beta_p \approx 0.04$) and DAW structure ($\beta_g/\beta_p \approx 0.4$), assuming these structures to be equivalent with shunt impedance and quality factor ($Z_a = 29 \text{ MOhm/m}$, $Q_a = 1.8 \cdot 10^4$), with 40 periods from RF input to the end of the cavity, $U_a = 2 \text{ MV/m}$, $I_b = 50 \text{ mA}$, one will have tilt 0.58% for SCS structure and 0.0054% for DAW one. The RF power flux, carried through the structure by forward wave at accelerating rate given U_a , is:

$$P_+ = \frac{c\beta_g U_a^2 Q_a}{2\pi\beta_p Z_a \cos^2 \Phi}, \quad (13)$$

and for typical regime of the 'meson facility' linacs P_+ is several hundreds MWt, exceeding in several orders the RF losses in surface P_s and for beam acceleration P_b . This case all RF losses are small perturbation with respect to the RF power flux, carrying through the structure.

Now under consideration are projects of continuous mode linear accelerators with beam current several hundreds of mA - [3,4]. Beam loading in such accelerators in orders exceeds one for 'meson facility' linacs. Attenuation αd becomes larger then 10^{-2} . All assumptions, made in derivation (10) remain valid, but, to find attenuation one must solve equation (10), because estimation (10) gives lowered value for αd . This case αd depends on both beam loading and number of periods in the cavity.

Suppose in the cavity, containing $2N$ periods (RF input is placed in the middle), designed energy gain per period is U_a . From calculations or signal RF level measurements we know quality factor Q_a and effective Z_a . Using this data, we can estimate RF power needed to have designed total energy gain with acceleration of large current. For the structure with ($\beta_g/\beta_p \approx$

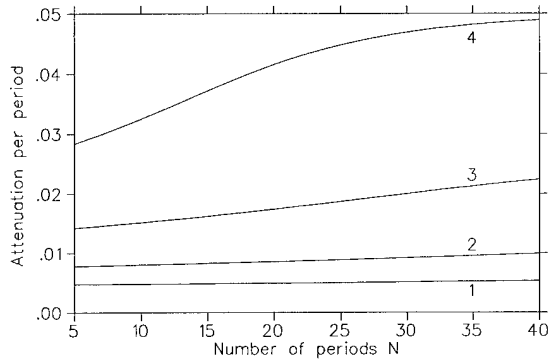


Figure 1. Dependencies of the total attenuation $N\alpha d$ vs number of periods in the cavity N with different beam current I_b , 1 – 125 mA, 2 – 250 mA, 3 – 500 mA, 4 – 1.0 A.

0.04) and parameters, mentioned above, $Q_c = Q_a/3$, and middle accelerating rate 1.5 MV/m plots of the dependencies of the total attenuation along the cavity are shown at Fig.1 for different beam currents.

If the total attenuation becomes enough large, $N\alpha d \geq 0.2$, the dependence of the field tilt differs from square and the value of the tilt $\frac{\Delta E}{E}$ reaches significant value. At least, phase oscillation of particles inside separatrix will occur. To provide RF power flux needed along the cavity, coupling mode in periods near RF input point must be strongly excited (6). For all structures known the quality factor for coupling mode is in several times less than for accelerating one and the excitation of coupling mode leads to significant additional losses near RF input point. Total RF power dissipated increases not so fast, but this increasing presents. It means, that effective shunt impedance of the structure decreases. Relation of the total RF power $P_{a'}$, dissipated in the cavity by accelerating mode and $P_{c'}$ for coupling one to have the designed value of total acceleration $2NU_a$ depends on total attenuation $N\alpha d$ along the cavity, which is proportional to the number of periods:

$$P_{a'} = P_a N \alpha d \frac{1 - e^{-4N\alpha d} + 4N\alpha d e^{-2N\alpha d}}{2(1 - e^{-2N\alpha d})^2}, \quad (14)$$

$$P_{c'} = P_a Q_a N \alpha d \frac{1 - e^{-4N\alpha d} - 4N\alpha d e^{-2N\alpha d}}{Q_c 2(1 - e^{-2N\alpha d})^2}.$$

Fast rise $P_{c'}$ with $N\alpha d$ explains dependence of αd vs number of periods in the cavity.

Analyzing relationships given and plots presented one see, that for beam current 500 mA and more in structures with small group velocities arise unacceptable effects. Practically the structure closes. Acceleration take place in several periods near RF input points and another parts are not used effectively. The ratio of RF losses between the first (near input point) and the last periods rises very fast with the beam current increasing. For acceleration of beam with current in several hundred mA, structures with small β_g have to be tuned specially. Using analogy with disk-loaded waveguide for electron linac, it is preferable to have

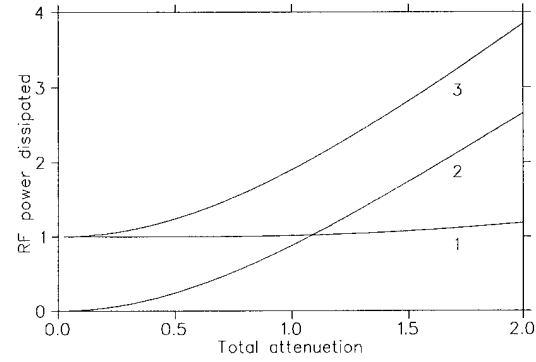


Figure 2. Dependencies of normalized RF power losses for operating mode $P_{a'} = \frac{P_{a'}}{P_a}$ and for coupling one $P_{c'} = \frac{P_{c'}}{P_a}$ vs total attenuation $N\alpha d$. $P_{o'} = P_{a'} + P_{c'}$.

constant gradient along the cavity with current, differing from constant impedance sections of cavities, which are now used in 'meson facility' type linacs. Moreover, number of periods of the structure between RF input points have to be not large. For structures with high group velocity this problems are absent.

V. SUMMARY

In this paper, using electrodynamic approach and general properties of compensated accelerating structures, the effect of distortions in accelerating field distribution due to RF losses in surface and for beam acceleration is considered. Basing on the RF power balance, simple analytical expressions for evaluation of attenuation constant and estimation of RF parameters of the structure are obtained.

Consideration shows, that for proton linacs of 'meson facility' type this effect is not important for all accelerating structures known. When beam current is several hundred mA, in the structure with small group velocity ($\beta_g/\beta_p \approx 0.04$) significant distortions will arise and efficiency of the structure for beam acceleration will drop. It will need special care in the design of the structure.

REFERENCES

1. Linear accelerators /Ed. P.M.Lapostolle and A.L. Septier.- Ams.: North-Holland Publ. Co., 1970.
2. M. Bell, Particle Accelerators, v.8, n. 2, p. 71, 1978
3. G.P. Lawrence, Proc. of the 1994 EPAC, v.1, p.236, 1995
4. I.M. Kapchinskiy et al. Proc. of the 1993 IEEE PAC, v.3, p.1675, 1994

The Indiana University Cooler Injector Synchrotron Rf System*

A. Pei, M. Ellison, D. Friesel, D. Jenner, X. Kang, S.Y. Lee, D. Li, J. Liu, A. Riabko, L. Wang
Indiana University Cyclotron Facility, Indiana University, Bloomington, IN 47405 USA
K. Hedblom, Department of Radiation Sciences, Box 535, S-75121 Uppsala

Abstract

A 2.2 Tesla-meter synchrotron with 17.4 m circumference is being built at the Indiana University Cyclotron Facility (IUCF). The purpose of the project is to achieve higher luminosity for nuclear physics experiments using electron cooled polarized light ion beams in the IUCF Cooler synchrotron. The injection line for the booster synchrotron consists of an RFQ/DTL linear accelerator delivering a 7 MeV proton beam and a 6 MeV deuteron beam for the booster injection. A debunching system will be installed in the injection beamline to reduce the energy spread of beams out of the linear accelerators. Charge-exchange injection is used for high intensity multiturn beam accumulation. The booster output beams, 200 MeV for protons and 105 MeV for deuterons, will be transferred bucket to bucket to the IUCF Cooler synchrotron. The rf system design for the booster synchrotron is presented in this paper.

I. INTRODUCTION

The design of the rf system needs to support the spin-transparent booster synchrotron operation which is described as follows.

The beams from a high intensity polarized ion source are preaccelerated by an industrial RFQ/DTL system to a proton energy of 7 MeV or a deuteron energy of 6 MeV. The beam from the preaccelerator is then debunched to reduce the energy spread. Once the stripping injection beam accumulation is finished, the booster rf system will adiabatically capture the beam in the $h=1$ bucket. Acceleration follows and lasts about 0.6 sec. Higher cycling rates up to 5 Hz are included in the rf system design for possible future upgrades. At the top energy of the booster synchrotron, the beam phase is aligned with the rf phase of the IUCF Cooler Synchrotron. A fast kicker extracts the beam from the booster for bucket-to-bucket transfer into the Cooler.

*Work supported in part by NSF Grant No. PHY-92-21402, PHY-93-14783 and PHY-23-42310.

The booster is designed to achieve an intensity of 2.5×10^{10} particles. The γ_r of the ring is 1.271 and the synchrotron will operate below γ_r .

II. DEBUNCHING SYSTEM

The beam out of the RFQ/DTL system has a tight time structure with a width < 0.2 ns. The energy spread is significant at $\Delta E/E = \pm 1\%$. Such an energy spread would dilute the longitudinal phase space and exceed the energy acceptance of the IUCF Cooler [1]. A debuncher is therefore designed for the injection beamline to reduce the energy spread.

The debuncher operates at a frequency of 425 MHz, the same frequency of the beam bunches delivered by the RFQ/DTL preaccelerator.

A drift distance of 2 meters is chosen to tilt the beam in the longitudinal phase space --- with the higher momentum particles leading the lower momentum particles linearly in time. With such a short drifting, the beam time spread will be within the linear region of the 425 MHz debunching rf sinusoidal wave and debunching can be highly efficient. However, to match the energy versus time slope of the drifted beam, the debunching cavity must operate at 80 to 100 kV.

Because of the beam velocity and the high rf frequency, the transit factor can drastically lower the voltage the beam sees when crossing the cavity. Two measures are taken to bring the transient factor as close to unity as possible: the debunching cavity rf gap distance is designed at 1 centimeter; the diameter of the beam pipe leading to the gap is also limited to 1 centimeter to concentrate the longitudinal component of the rf field near the rf gap. At 425 MHz, the field strength of such an rf cavity is approximately half the classical Kilpatrick limit. Proper surface processing and good vacuum pumping is important to prevent sparking.

The debunching cavity will be driven by a planar triode amplifier manufactured by the AccSys Technology Inc. About 20 kW of rf power will be delivered to the cavity in 300 μ s pulses.

To achieve efficient debunching, it is essential that the debunching cavity rf be precisely phase-locked to the beam.

This will be accomplished by a phase feedback loop controlled by the debunching system's low level rf electronics. Because the cavity time constant is significant compared with the rf pulse width, as indicated by the cavity induced pole in the system transfer function:

$$\frac{1}{s \frac{2Q}{\omega} + 1} \quad (1)$$

an appropriate zero will be introduced in the system transfer function to offset the cavity effect.

The debunching cavity rf amplitude is also regulated by a fast feedback loop. A slower, discrete loop will adjust a mechanical plunger inserted in the cavity to correct drift of the cavity resonating frequency.

III. BOOSTER RING RF SYSTEM

During injection, the rf cavity in the booster synchrotron is turned off. The debunched beam, with an energy spread less than $\pm 0.2\%$, will coast and increase in intensity due to stripping injection accumulation. When stripping accumulation reaches an equilibrium due to emittance growth, the beam is bumped off the stripping foil and the injection stops. The rf cavity is then turned on, capturing the beam adiabatically with an $h=1$ bucket at the center of beam energy distribution. Computer simulations showed that a linear rf turn-on longer than a couple of synchrotron oscillation periods of the final rf bucket is adiabatic enough to capture almost all the beam [2].

The beam motion inside an rf bucket is inherently undamped, given by the following differential equation for small amplitudes:

$$\ddot{x} + \omega_s^2 x = f(t) \quad (2)$$

where x can be either time or energy error with respect to that of the synchronous particle and $f(t)$ the external driving force.

The driving term on the right hand side of the equation consists of rf parameter and guiding magnetic field fluctuations and causes undamped synchrotron oscillation. The oscillation in the longitudinal phase space is also coupled to the transverse phase space, affecting the radial position of the beam. To provide damping of synchrotron oscillations, the driving term in Eq.2 needs to contain a term proportional to the first time derivative of x .

In practice, the above damping concept is realized by beam feedback control. The error signal caused by synchrotron motion is detected and phase-shifted 90 degrees. The processed

error signal is then fed back to the rf cavity with a net differential operation as a part of the rf drive.

Several different approaches are used in modern hadron machines. DC-coupled VCO beam phase feedback with radial compensation [3] is chosen for our system.

In this scheme beam phase is compared with the rf cavity phase. The resulting error is used to drive a VCO that generates the rf cavity signal. Because of the derivative relation between phase and frequency modulations, the VCO introduces a 90 degree phase shift that corresponds to a damping first derivative term of the phase error. Transfer functions of other electronic devices in the feedback path, such as that of the rf cavity, are compensated by introducing classical feedback algorithms at various points of the loop to achieve the necessary overall transfer function.

Such a DC-coupled VCO controlled phase loop is not stable by itself. Because the rf frequency is beam controlled, the beam can accelerate or decelerate itself out of the aperture. An additional radial loop is used to center the beam radially.

It can be shown that for sufficiently large phase loop gain, the response of the phase loop is that of an integrator [3]:

$$\frac{\delta f_b}{\delta f_r} \approx -\frac{\omega_s^2}{G_p s} \quad (3)$$

where δf_b is the beam frequency change, δf_r the rf frequency change and G_p the total phase loop gain.

The radial loop is realized by measuring the deviation of particles from the ideal closed orbit and using the error to control the VCO frequency. It is equivalent to measuring δf_b since the orbit deviation is caused by beam energy error.

Since the phase loop transfer function is treated as a gain block in the forward path of the radial loop, the overall response is:

$$\frac{\delta f_b}{\delta f_r} = \frac{1}{G_r} \frac{1}{1 - \frac{G_p}{G_r \omega_s^2} s} \quad (4)$$

where G_r is the gain of the radial loop with frequency to radial error conversion factor taken into account. The overall transfer function is thus that of a first order low pass response, with a time constant of:

$$\tau_r = \frac{G_p}{G_r \omega_s^2} \quad (5)$$

This time constant can be set much lower than the

synchrotron oscillation frequency ω_s . Rf and guiding magnetic field noise will be heavily filtered. The beam will only move adiabatically at frequencies much slower than ω_s [3].

Eq.5 also shows that with judicious selection of phase and radial loop gains, the beam is essentially self centering in the closed orbit with little error.

Although the cavity impedance is relatively low at the order of 1 k Ω , the overall cavity voltage is also low and the beam intensity induced voltage will significantly affect the rf phase. Fast local feedback around the rf amplifier will be used to compensate the beam loading effect.

IV. SYSTEM IMPLEMENTATION

The rf system will consist of a single ferrite-bias-tuned cavity capable of a wide tuning range, driven by a 300 Watt solid state amplifier and tuned by a 20 Ampere bias supply [4] [5].

The low level signal processing will use an upconverting superheterodyne scheme, with the intermediate frequency (IF) chosen at 10.7 MHz to take advantage of inexpensive consumer FM receiver filters. Preprogrammed local oscillator sweep is chosen for acceleration. A nominal 10.7 MHz VCO will operate within the bandwidth of IF filters to provide precise frequency and phase control.

The beam phase signal will be picked up by the sum signal of a beam position monitor of sufficient bandwidth. The radial error of the beam will be obtained from the averaged difference signals of two beam position monitors half a betatron period apart to compensate closed orbit errors.

Standard analog PID processing techniques will be employed to control rf cavity amplitude and rf tuning. The rf voltage during acceleration will be programmed to provide the correct phase space area for varying synchronous phase angles. The change of synchronous phase angle during acceleration will be adiabatic. This approach makes the control of acceleration synchronous angles extremely simple [6].

Although the rf system frequency and phase controls are beam feedback based, the rf system must also be able to provide precise phase and frequency control with other reference sources. During injection and extraction, the beam phase control must be relinquished to the RFQ/DTL accelerator and the Cooler synchrotron rf. The transition between the reference sources needs to be adiabatic with respect to the beam longitudinal motions.

Fig.1 is a simplified block diagram of the booster synchrotron rf system.

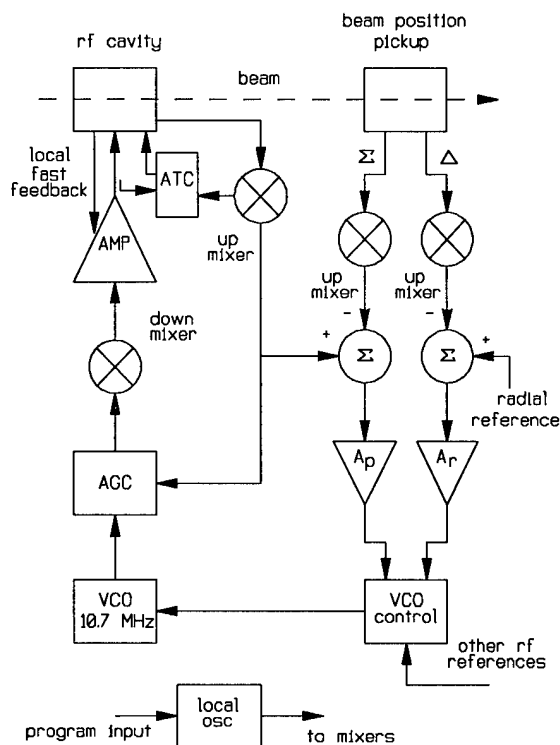


Figure 1. Principle block diagram of the IUCF CIS rf system.

V. ACKNOWLEDGEMENT

The authors wish to thank the members of the Cooler Injection Synchrotron Design Review Committee for many valuable suggestions.

We would also like to thank Dr. J. Griffin who carried out many detailed rf calculations in his personal time after serving the review committee.

VI. REFERENCES

- [1] K. Hedblom and D. Friesel, "Stripping Injection into the New Booster Ring at IUCF", this proceedings.
- [2] A. Pei, "Cooled Rf Stacking Injection in the IUCF Cooler", Ph.D. dissertation, Indiana University, 1991.
- [3] D. Boussard, "Design of a Ring Rf System", CERN 91-04, Julich, 1990.
- [4] A. Pei et al., "The Indiana University Cooler Injection Synchrotron Rf Cavity", this proceedings.
- [5] R. Pollock, "Indiana University Cooler Design Notes", IUCF, 1990.
- [6] J. Griffin, Private communications on CIS rf design, 1995.

The Indiana University Cooler Injection Synchrotron Rf Cavity*

A. Pei, M. Ellison, D. Friesel, D. Jenner, X. Kang, S.Y. Lee, D. Li, J. Liu, A. Riabko, L. Wang
Indiana University Cyclotron Facility, Indiana University, Bloomington, IN 47405 USA
K. Hedblom, Department of Radiation Sciences, Box 535, S-75121 Uppsala

Abstract

A small 2.2 Tesla-meter booster synchrotron is under construction at the Indiana University Cyclotron Facility to boost polarized beam performance in the electron cooled Indiana University Cooler Synchrotron. Polarized light proton or deuteron beam from a high intensity polarized ion source will be preaccelerated to 7 and 6 MeV respectively by an RFQ/DTL accelerator. The beams are then debunched to reduce the energy spread and strip-injected into the booster synchrotron. The booster rf system must accomplish the tasks of beam capture and acceleration. At the end of the acceleration cycle, the beam phase needs to be aligned to the Cooler synchrotron rf for bucket-to-bucket beam transfer. A single rf cavity in the ring will provide the necessary rf field to accomplish the above tasks.

I. INTRODUCTION

A ferrite-bias-tuned cavity is designed to provide the rf field of the room sized synchrotron. The cavity needs to be compact and capable of operating in a very wide frequency range to accelerate the low energy ion beams. The biasing scheme produces sufficient bias field with a compact power supply and is capable of compensating driving port impedance variations over a wide frequency range.

II. CAVITY DESIGN

The rf system will be operating at the $h=1$ harmonic number, which corresponds to a frequency range of 1.2 to 10 MHz in the 17.4 m circumference ring with the required beam types and energies.

While the energy spread of the beam out of the RFQ/DTL is $\pm 1\%$, a debunching rf cavity in the injection beamline will reduce the beam energy spread to less than $\pm 0.2\%$. The stripping injection will let the beam coast and fill

the entire ring. The longitudinal beam emittance will be about 0.014 eV upon the end of stripping injection and start of rf capture. While such a phase space area can be provided by less than 100 V of cavity voltage, the cavity needs to be able to run at higher voltages to keep the beam inside the reduced moving bucket during acceleration.

During the initial design reviews when the booster output energy for protons was set at 80 MeV, a wide band cavity with 50 Ω resistive gap termination was considered. Such a structure has the obvious advantage of construction and operation simplicity. A tuned cavity, however, has a much higher gap impedance and lowers the rf drive power requirement substantially. At the respecified proton output energy of 200 MeV, the voltage requirement can be more easily attained by a tuned cavity. In addition, in the event of temporary outage of the debunching rf system, the booster can still be kept operational by increasing cavity rf voltage. A tuned cavity design is thus chosen and specified for 500 V operation. A 300 Watt solid state amplifier will be used to drive the cavity with sufficient reserve power.

The tuning of the cavity uses an external quadrupole magnet biasing scheme originated in the Max Planck Institute [1]. A cavity of this type has been in use in the IUCF Cooler synchrotron for the past few years [2] [3].

In this biasing method, a quadrupole biasing magnet and its coils are built completely outside a coaxial cavity and do not see the rf fields. The rf cavity can be built in a straightforward fashion without concerns of disturbances caused by biasing elements. The quadrupole DC magnetic fluxes, on the other hand, penetrate the copper outer conductor of the cavity, providing biasing field to the ferrite rings inside. The symmetry of the quadrupole field provides cancellation of biasing field at the cavity axis, minimizing magnetic disturbance to the beam. In addition, any remnant biasing field slightly off the center are shunted by the ferrite rings which have a relatively high permeability.

Fig.1 is an illustration of the ferrite biasing technique.

The biasing field is predominantly parallel with the rf field in the coaxial structure so the effective rf permeability is determined by $\partial B/\partial H$ [4], with minimum permeability achieved

*Work supported in part by NSF Grant No. PHY-92-21402, PHY-93-14783 and PHY-23-42310.

near the saturation field of the ferrite.

The ferrite rings used saturate at about 2700 gauss. Assuming an overall air gap of 0.4 cm between the ferrite

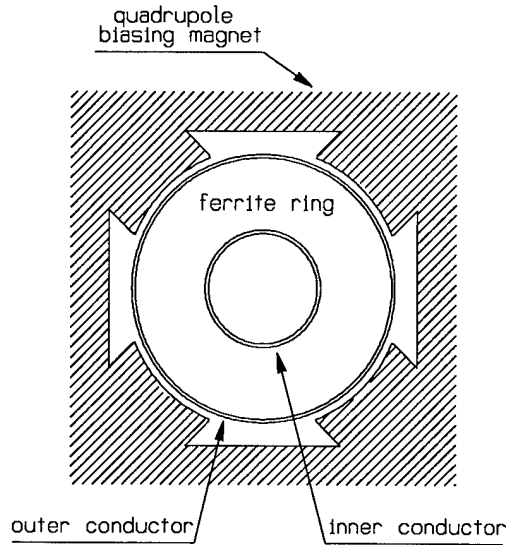


Figure 1. Ferrite ring biasing by external quadrupole magnet.

rings and biasing quadrupole magnet tips, the magnetomotive force (mmf) to drive the ferrite near saturation can be estimated by:

$$\begin{aligned}
 NI &= \frac{B_s l}{\mu_o} \\
 &= \frac{0.27 \text{ T} \times 0.004 \text{ m}}{4\pi \times 10^{-7} \text{ H/m}} \\
 &\approx 860 \text{ amp-turns}
 \end{aligned} \quad (1)$$

In practice, the mmf will be achieved by 50 turns of windings on each quadrupole magnet tip driven at 20 A. This current is modest and a small commercial variable power supply can be used.

In this type of cavities, ferrite loss is by far dominant and determines the gap resonant resistance. The ferrite loss, represented by the imaginary part of ferrite permeability, is heavily frequency dependent and also varies with biasing. Fig.2 is a plot of the gap resonant resistance of an IUCF Cooler rf cavity built with the same ferrite materials to be used.

To transfer power efficiently from the amplifier to the cavity, it is important that the driving port of the cavity presents a fixed impedance matching that of the feed transmission line at all frequencies.

The driving port is directly tapped to the center conductor of the cavity, forming a loop enclosing the rf magnetic fluxes at the bottom of the coaxial cavity. Its

impedance will normally vary widely with the cavity gap impedance.

For a cavity with heavy capacitive loading, the electrical length of the cavity is much shorter than a quarter wave length. Because the standing wave amplitude along a coaxial cavity axis is sine like and the current amplitude is

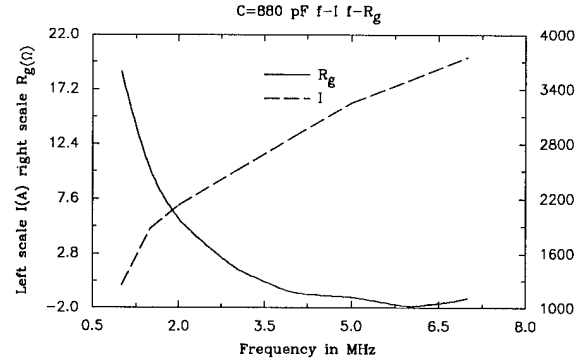


Figure 2. Frequency dependence of IUCF Cooler MPI cavity resonant gap resistance R_g . I is the bias supply current.

cosine like, the voltage distribution is almost linear and the magnetic field is approximately uniform along the axis. Since the power delivered to the driving port equals to the power dissipated on the gap resistance at resonance, the driving loop will see a transformed resistance of :

$$R = R_o \left(\frac{V}{V_o} \right)^2 \quad (2)$$

where R_o and V_o are gap resistance and voltage, R and V are resistance and voltage at the driving port.

Because of the approximate linear voltage distribution along the cavity axis, a tap to the center conductor has a fixed V/V_o ratio. The driving port impedance therefore is equal to the gap impedance multiplied by a constant fraction. When the resonant gap resistance changes due to frequency dependent ferrite losses, the driving port resistance changes accordingly.

Since the cavity sweeps across the whole operating range in a fraction of a second, it is impractical to mechanically adjust the tap position.

We therefore attempt to change the V/V_o ratio electronically. The voltage at the driving port and at the gap can be expressed by:

$$V = \oint_s \frac{\partial \vec{B}}{\partial t} \cdot d\vec{s}, \quad V_o = \oint_{s_o} \frac{\partial \vec{B}}{\partial t} \cdot d\vec{s} \quad (3)$$

where s and s_o are the rf magnetic field areas enclosed by the

driving loop and the entire cavity respectively.

Because the axial current distribution is approximately uniform, we have an approximately uniform H field axially. It is only a function of radius, decreasing with the inverse of radius according to Ampere's Law. If the ferrite permeability does not change axially, integration of Eq.3 yields a driving port resonant resistance of:

$$R = R_o \left(\frac{S}{S_o} \right)^2 \quad (4)$$

which changes with the gap resonant resistance R_o .

If we manage to make the permeability of ferrite rings enclosed by the driving loop different from those in the rest of the cavity, V/V_o no longer depends on s/s_o only. Instead, the integration of Eq.3 yields:

$$R = R_o \left(\frac{\mu_d}{\langle \mu \rangle} \right)^2 \left(\frac{S}{S_o} \right)^2 \quad (5)$$

where $\langle \mu \rangle$ is the average permeability of ferrite rings of the entire cavity and μ_d the average permeability of ferrite rings enclosed by the driving loop.

The V/V_o ratio can therefore be changed by non-uniform axial biasing. The ferrite rings enclosed by the driving loop have adjustable bias strength independent of that for the rest of the cavity. This can be realized by adding trim coils to the quadrupole magnet section that biases the ferrite rings enclosed by the driving loop. The current flowing through the trim coils will have a large effect on the driving port impedance but a small effect on the overall cavity tuning. The trim coil current is pre-programmed as a function of frequency while the main coil current is controlled by the automatic tuning servo loop.

III. CONSTRUCTION

Fig.3 is a sketch of the cavity to be constructed. The ferrite rings are made of Phillips 8C12 material. It has an initial relative permeability of about 800 and saturates at a field of 2700 gauss. The ferrite rings have an inner diameter of 270 mm and outer diameter of 498 mm, with a thickness of 25 mm. The cross section of the cavity will be filled with ferrite, therefore the inner conductor and outer conductor of the coaxial cavity dimensions are about the same as those of the ferrite rings.

Five ferrite rings will be used. Between the ferrite rings, 20 mm spacings provide passage for forced air cooling. Both the inner and outer conductors of the coaxial cavity will

have longitudinal slots for air passage.

A 2000 pf variable vacuum capacitor is loaded across the cavity gap to achieve resonance and provide flexibility of variable frequency bands.

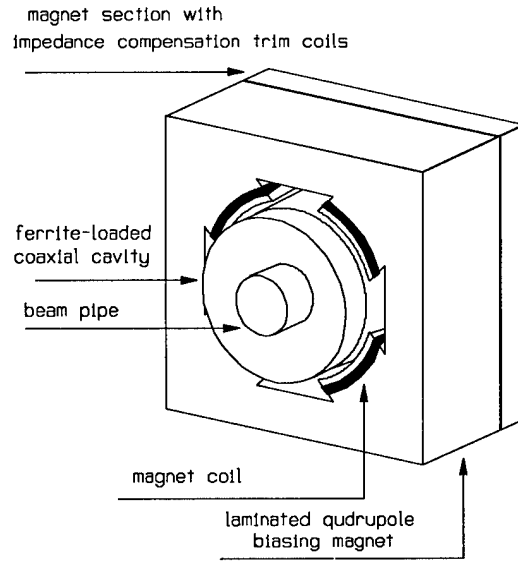


Figure 3. IUCF Cooler Booster Synchrotron rf cavity.

IV. REFERENCES

- [1] S. Papureanu, MPI internal publications, MPI, 1989.
- [2] R. Pollock, "IUCF Cooler Design Notes", IUCF, 1990.
- [3] A. Pei, "A Wide Tuning Range Rf Cavity with External Ferrite Biasing", Proc. PAC 93, p.1421, 1993.
- [4] W. Smythe, "Reducing Ferrite Tuner Power Loss by Bias Field Rotation", IEEE Trans. on Nucl. Sci., Vol. NS-30, No.4, p.2173, 1983.

Determination of Resonant Frequency and External Q Values for the BESSY II HOM-Damped Cavity

Frank Schönfeld* and Bengt Littmann, TU Berlin, EN2, Einsteinufer 17, 10587 Berlin

Abstract

Damping of higher order cavity modes (HOM's) is one way to increase the intensity thresholds for multibunch instabilities in B-factories and state of the art synchrotron radiator sources. Following the idea of Conciauro-Arcioni [1] one of the simplest geometries is the threefold-symmetry cavity-waveguide structure with a broadband absorber terminating the end of every guide. The iris coupling between the cavity and the waveguide has to be designed so that the fundamental cavity-mode remains nearly unperturbed. The values of the external Q and the shift resonant frequencies due to the waveguide loads is determined and tested by known methods with MAFIA.

I. INTRODUCTION

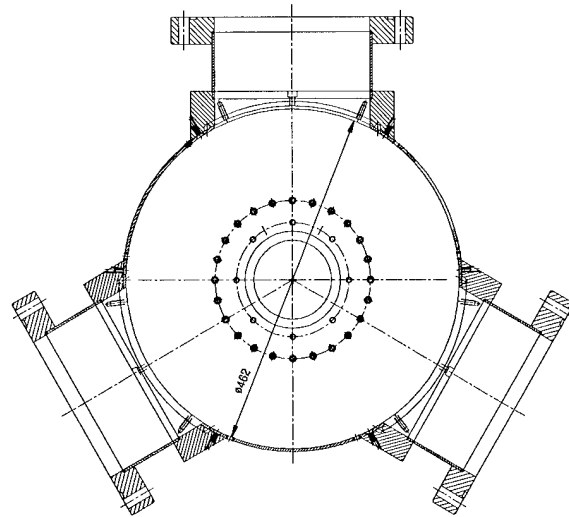
BESSY II is a 1.7 GeV third generation electron storage ring with 16 straight sections to produce highly brilliant synchrotron radiation beams in the spectral range of soft x-ray and vacuum ultraviolet. One of the design goals is a low emittance of 6 nm-rad and a maximum beam current of 200 mA [2], [3]. Therefore it is necessary to reduce all effects which potentially spoil the brilliance of the radiation beam. Especially in RF accelerating cavities, the beam induces parasitic resonant fields which can lead to coherent multibunch oscillation which results in less brilliance. A possible way to suppress the cavity higher order modes (HOM's), is to mount external waveguides on the cavities, and couple strongly to the most dangerous modes. By terminating the end of each waveguide with broadband absorbers the HOM's are damped at a rate depending on the coupling. The accelerating mode is rejected and remains undamped (if the bigger surface is not accounted for). A low power prototype cavity has been built at BESSY II (threefold-symmetry cavity waveguide structure, Fig. 1). For this preliminary investigation the cavity has a pill-box shape with three circular waveguides, distributed on the cavity coat, 120 degrees apart. In order to optimize the design of the waveguide loaded cavity, one has to know the values of the external Q and the shift resonant frequency due to the waveguide loads. These are readily determined by the method of Kroll-Yu [4], with frequencies computed by the MAFIA code [5].

II. NUMERICAL COMPUTATIONS OF Q-VALUES

For the numerical calculation of the BESSY II HOM-Damped Cavity resonance frequency and external Q, we have employed the method developed by Kroll and Yu. We will not elaborate on the method itself, rather share some general views on the method. For further details, consult [4].

Computing Q_{ext} by numerical means is indeed no trivial task, since an infinitely long waveguide would result in an infinite

*BESSY GmbH, 12489 Berlin



Prototyp Cavity ø462

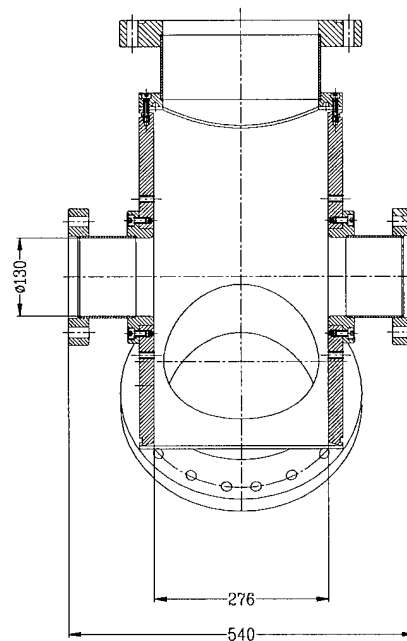


Figure 1. Prototype BESSY II cavity

mesh. Note: waveguide boundaries are unknown in frequency domain. With the Kroll-Yu method, a short is inserted into the waveguide, which first of all makes the mesh size finite. Then, resonance frequency shifts are utilized, that occur as the short position is varied. More volume always decreases resonant frequency, but the slope varies, depending on field strength at the

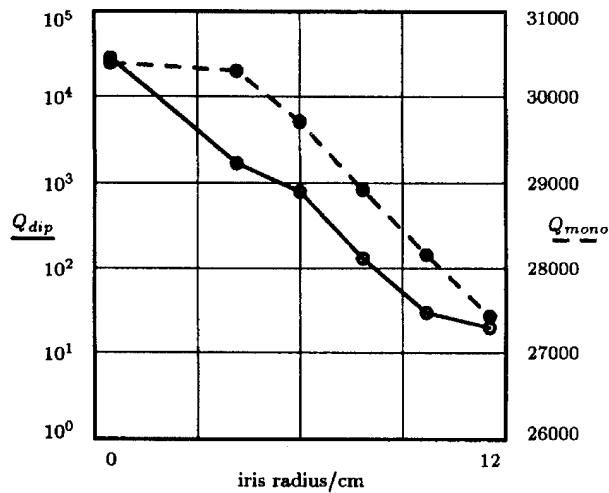


Figure 2. Q_{ext} of the dipole mode and Q_{cond} of the monopole mode versus iris radius. Conductivity is $58 \cdot 10^6 \text{ 1}/(\Omega\text{m})$.

location of change in geometry. Thus, the magnitude of the shift in resonance frequency can be related to the field strength in the waveguide, which again can be related to the external Q of the cavity. We have found the method to be easy to apply.

However, to calculate Q_{ext} , frequency differences are used, which leads to the following considerations. Significant digits are lost when both frequencies are close to one another. By increasing the distance between short positions we may enlarge the frequency shift. However, the wave nature of the waveguide field maps frequencies onto one another, which stem from short positions separated by $n\lambda_g$. Thus, short positions separated by more than λ_g will not improve the situation. Indeed, for each required additional significant Q_{ext} -digit roughly one significant digit in the frequency difference is lost. We employed MAFIA to model our cavity (Fig. 4 and 5). We recognize, that a frequency solution from MAFIA is typically accurate to about three digits and relative frequency to four digits. Thus Q_{ext} -values of up to 1000-2000 can be computed with an accuracy of at least one significant digit. Attempts to compute a $Q_{ext} > 2000$ will fail. Fortunately, one is mostly interested in Q 's in the range of tens to some few hundreds.

Fig. 2 summarizes our results, with both Q_{ext} of the first dipole mode and Q_{cond} for the trapped accelerating mode shown. Q_{cond} of the monopole mode was computed assuming the metal to be copper. Fig. 2 provides the design arguments, where a certain Q_{ext} for the dipole mode has to be reached to achieve the design emittance of 6 nm-rad at 200 mA current. At the same time the effects on the accelerating mode Q_{cond} may be observed. An iris radius of 8 cm would certainly satisfy our needs ($Q_{dip} = 130$ and losses in Q_{mono} below 5 %). However, we will investigate further HOM's before we make a decision.

Fig. 3 shows frequency shifts due to the iris coupling. As soon as some iris radius is chosen on the above mentioned grounds, the cavity radius has to be adapted, to keep the accelerating mode resonance frequency at its design value.

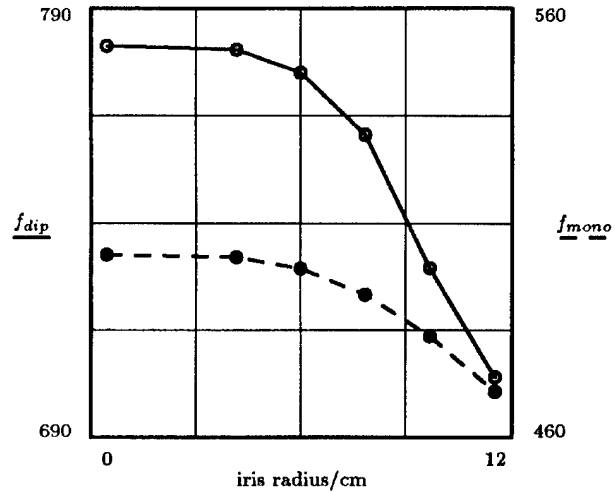


Figure 3. Frequency of the dipole mode and the monopole mode versus iris radius. Conductivity is $58 \cdot 10^6 \text{ 1}/(\Omega\text{m})$.

III. OUTLOOK

We will engage in investigations on further HOM's in due course, employing the Kroll-Yu method. Decision on the final iris size will be based on results from these investigations. A test model will be installed and measured to verify theoretical results.

References

- [1] G. Conciauro, P. Arcioni, "A New HOM-Free Accelerating Resonator", Proc. European Particle Accelerator Conf., Nice, 1990
- [2] E. Jaeschke, et Al., "Lattice Design of 1.7 GeV Light Source BESSY II", Proc. Particle Accelerator Conf., Washington, 1993
- [3] D. Kraemer, et Al., "Status of New High Brilliance Synchrotron Light Source BESSY II", Proc. European Particle Accelerator Conf., London, 1994
- [4] N.M. Kroll and D.U.L. Yu, "Computer Determination of the External Q and Resonant Frequency of Waveguide Loaded Cavities", Particle Accelerators, vol. 34, 1990, pp.231-250
- [5] The MAFIA Collaboration, F. Ebeling, et Al., MAFIA User Guide, 1992

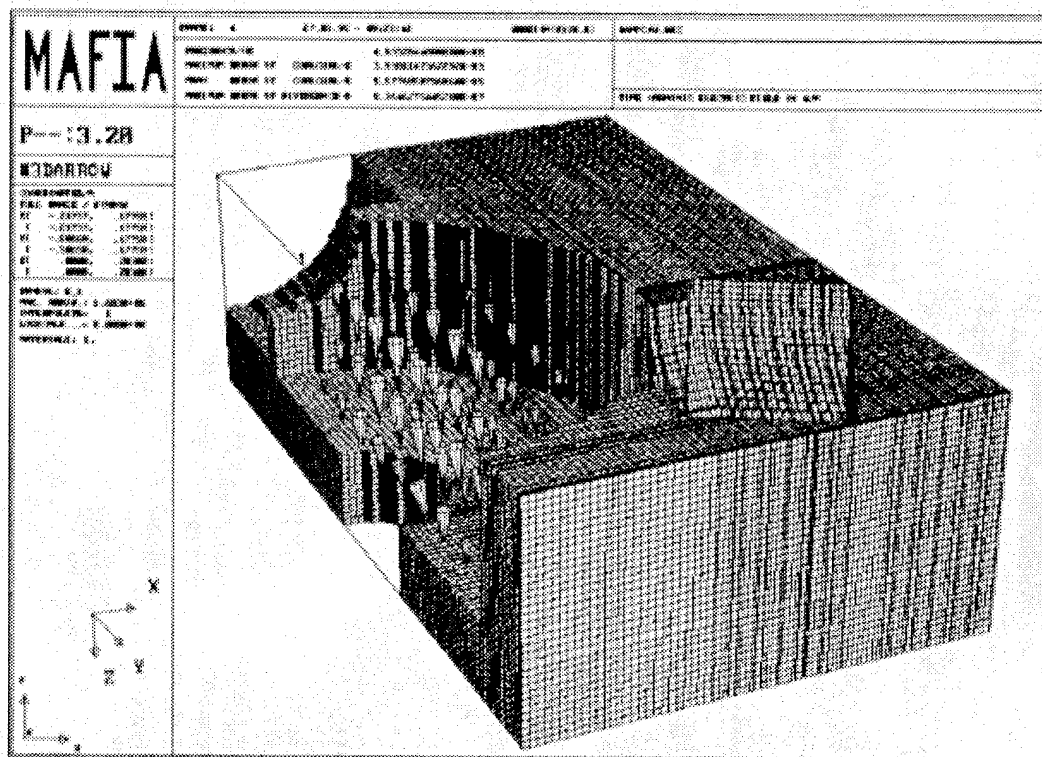


Figure 4. MAFIA mesh (500 000 mesh points) and electric field of the BESSY II cavity and the accelerating (monopole) mode.

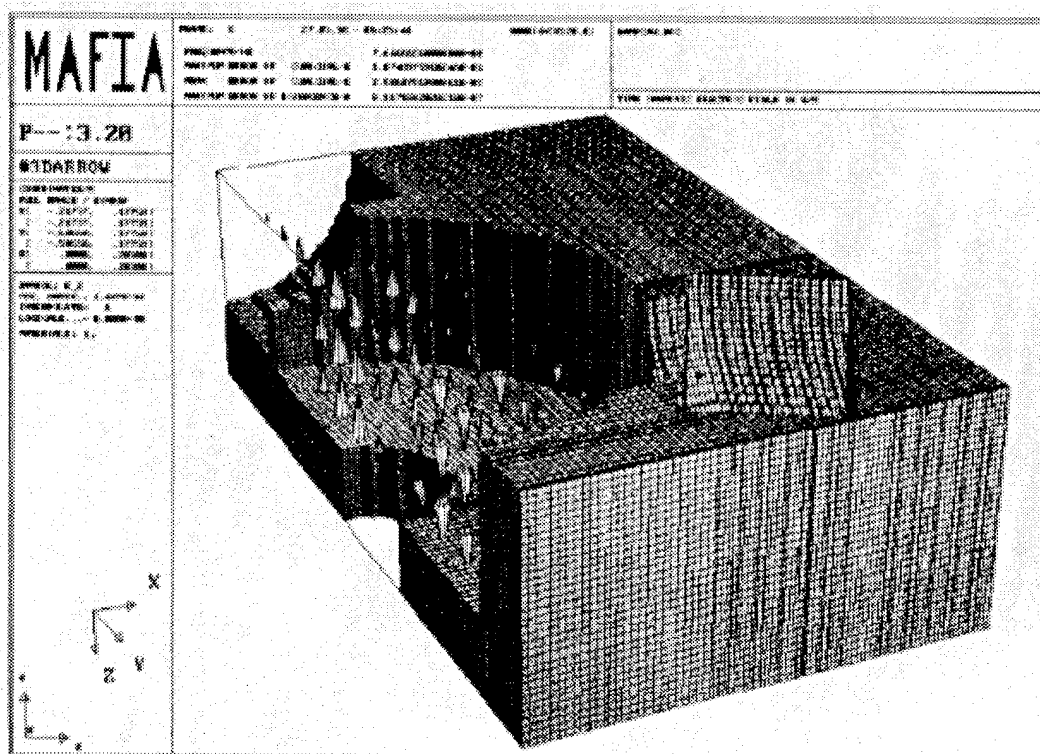


Figure 5. MAFIA mesh (500 000 mesh points) and electric field of the BESSY II cavity and the first dipole mode.

106 MHZ CAVITY FOR IMPROVING COALESCING EFFICIENCY IN THE FERMILAB MAIN RING

J. Dey, I. Kourbanis, D. Wildman, Fermi National Accelerator Laboratory*, P.O Box 500, Batavia, IL. 60510, USA

Abstract

In Fermilab's Main Ring a fast coalescing scheme called "Snap" coalescing[1] has replaced the slower adiabatic coalescing. In Snap coalescing the adiabatic voltage reduction to reduce the dp/p of the bunch has been replaced with a quarter of a synchrotron period rotation in a 53-MHz bucket. A 106 MHz second harmonic cavity has been constructed to help linearize the 53 MHz rotation and reduced the minimum achievable dp/p . The effect of the second harmonic cavity on the 53 MHz rotation and the coalescing efficiency will be described.

I. ESME[2] SIMULATIONS

A series of ESME simulations were done to determine the effect of a second harmonic voltage during the 53 MHz rotation in Snap coalescing. We started with a 0.25 eV-sec bunch matched to a 1 MV, 53 MHz bucket. Then we snapped the voltage down to 60 KV (such that the bucket height equaled the bunch height). Then the bunch was left to rotate for a quarter of a synchrotron period first without a second harmonic and second with different percentages of a second harmonic.

From the simulations we found that a small percentage (20-25%) of a second harmonic was clearly beneficial in reducing the minimum dp/p achieved in the rotation, not only because the second harmonic helped linearize the voltage waveform and eliminated most of the tails, but mainly because the addition of the second harmonic reduced the slope of the voltage i.e. the effective synchrotron period of the small amplitude particles.

In Fig. 1 ESME phase space and θ projection pictures of the 0.25 eV-sec bunch at the end of the 53 MHz rotation without any second harmonic are shown. In Fig. 2 the same ESME pictures are shown but now a 20% second harmonic has been added. The effect of the second harmonic is to more evenly distribute particles towards the edges of the bucket, reducing the tails and the dp/p at the center of the distribution.

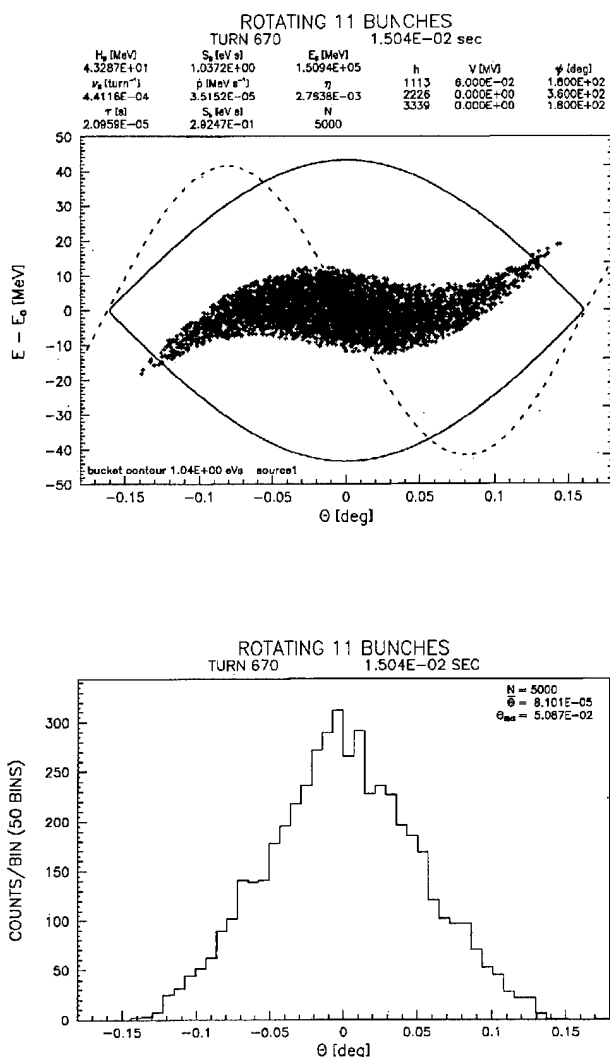


Figure 1: ESME pictures of a 0.25 eV-sec bunch rotated for a quarter of a period in a 53 MHz bucket without second harmonic. Top: Phase space picture. Bottom: θ projection

*Operated by Universities Research Association, Inc. under contract with the U.S. Department of Energy.

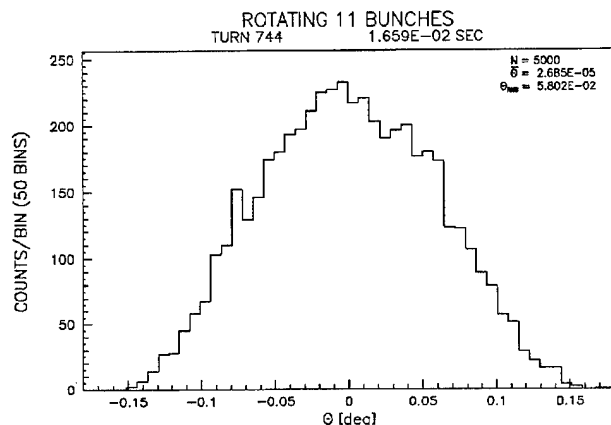
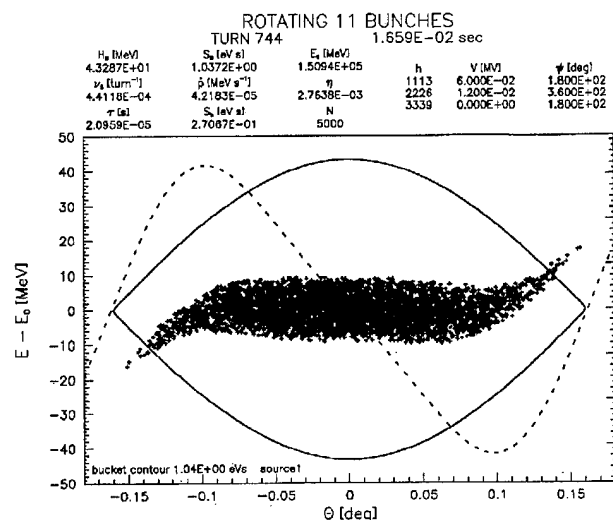


Figure 2: ESME pictures of a 0.25 eV-sec bunch rotated for a quarter of a period in a 53 MHz bucket with 20% second harmonic. Top: Phase space picture. Bottom: θ projection.

II. THE 106 MHZ CAVITY

The second harmonic cavity is a quarter of a wavelength type with a fixed frequency of 106.2 MHz made out of OFHC copper. The physical dimensions of the cavity are shown in Fig. 3.

The design of the cavity minimizes the transient beam loading by having an $R/Q=9$, ten times smaller than the R/Q of the regular 53 MHz cavities. The shunt impedance of the cavity is $R_s = 45k\Omega$, and it is powered by a 5 KW solid state amplifier for a variable voltage of 0-15 KV. The cavity has a Q of 5100, corresponding to a bandwidth

Δf of 21 KHz. To keep the temperature of the cavity constant the cavity is water cooled with 95° water.

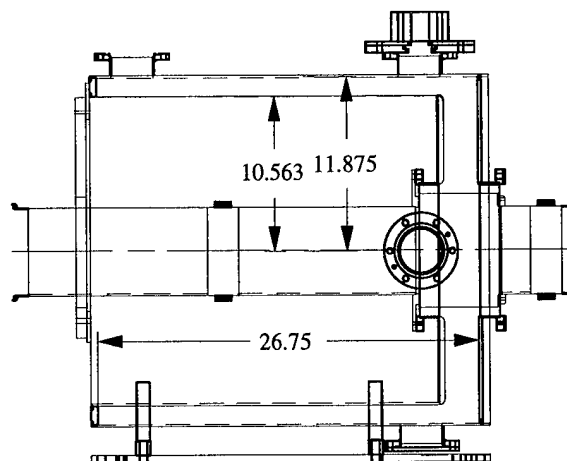


Figure 3: Schematic of the second harmonic cavity.

III. EXPERIMENTAL RESULTS

A picture of a bunch obtained with an HP-54720A 8 Gs/sec scope at the end of the 53 MHz rotation with the 106 MHz cavity off and with 20% second harmonic is shown in Fig. 4. The beam profiles agree with the simulations. The rms. spread of the beam profile with 20% second harmonic is 15% larger than the rms. spread of the beam profile without second harmonic.

Since in coalescing the phase spread is turned into momentum spread and vice versa, the bunches rotated first with 20% second harmonic had a narrower phase spread at the end of coalescing by 25%, indicating that the dp/p at the rotation with a second harmonic was 25% smaller than the dp/p achieved without a second harmonic.

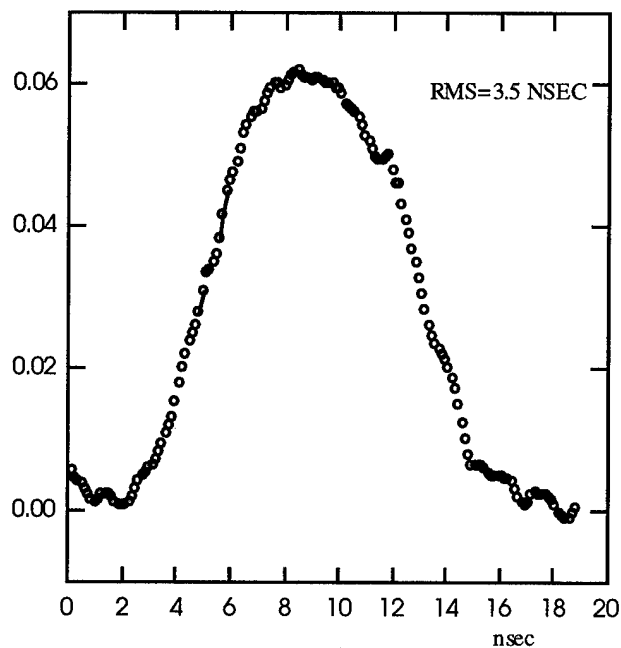
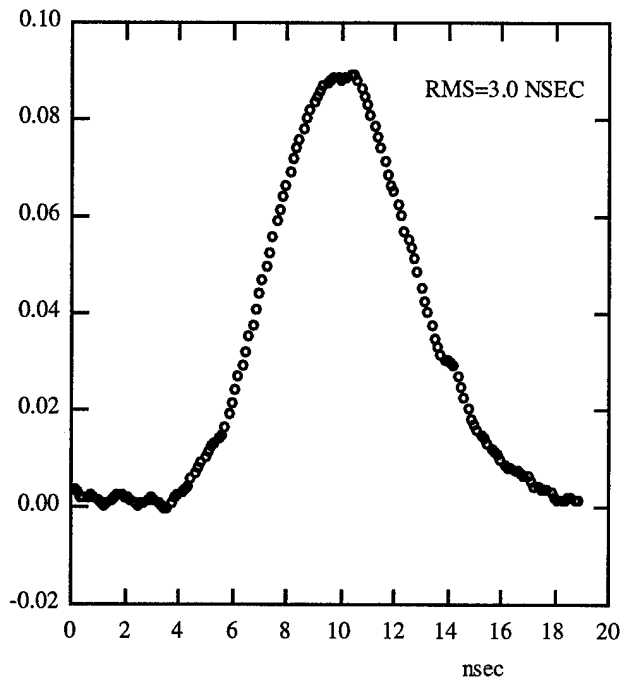


Figure 4: Beam profiles at the end of the 53 MHz rotation. Top: No second harmonic. Bottom: With 20% second harmonic.

IV. CONCLUSION

A second harmonic (106 MHz) cavity has helped us to reduce the minimum dp/p achieved during the 53 MHz rotation in Snap coalescing by 25% and increase the Snap coalescing efficiency by 10%.

VI. REFERENCES

- [1] "Performance and Comparison of Different Coalescing Schemes Used in the Fermilab Main Ring", I. Kourbanis, G.P. Jackson, and X. Lu. Proc. of the 1993 Particle Accelerator Conf. 3799 (1993).
- [2] "Users Guide to ESME v. 7.1", S. Stahl and J. MacLachlan, Fermilab internal note TM-1650 (2/90).

On the Higher Order Mode Coupler Design for Damped Accelerating Structures

Jie Gao

Laboratoire de L'Accélérateur Linéaire
IN2P3-CNRS et Université de Paris-Sud
91405 Orsay cedex, France

Abstract

In this paper we will discuss mainly damped structures and class them into three types. The procedures to make a higher order mode (HOM) coupler design have been given, and some useful analytical formulae, which can be used to determine the coupling apertures' dimensions and the equivalent loaded quality factors, have been derived. It is shown that few couplers to damp a detuned structure is not at all efficient.

I. Introduction

For the linear colliders working in the multibunch mode the long range wakefields have to be properly controlled by using detuned, damped or damped detuned structures depending on the concrete machine design parameters. In this paper we try to class damped structures into three types and to make a detail discussion about how to determine the coupling aperture dimension of a HOM coupler and how to estimate its effect on the damped HOM. In section 2, the first type damped structure is discussed, where each cavity is damped by HOM couplers. In section 3, the second type damped structure is defined as a section of constant impedance structure is damped by a HOM coupler. The essential difference between the first and the second type damped structures is demonstrated. To estimate the effect of this HOM coupler an equivalent quality factor has been introduced and formularized. Finally, in section 4, damped detuned structures are discussed and it is shown that few couplers to damp a detuned structure is not at all efficient.

II. The First Type of Damped Structure

We consider a single pill-box resonant rf cavity resonating at a resonant mode, for example the TM_{110} mode. The quality factor corresponding to this mode is Q_{110} . If this cavity is loaded with some waveguides, the loaded quality factor $Q_{L,110}$ is defined as

$$Q_{L,110} = \frac{Q_{0,110}}{1 + \beta_{N,110}} \quad (1)$$

where $\beta_{N,110}$ is called the coupling coefficient between waveguides and the resonant cavity corresponding to the TM_{110} mode. Where the subscript N denotes the number of the waveguides. If the cavity is loaded with four waveguides distributed uniformly around the cavity's cylindrical surface, from the general expression derived in refs. [1] and [2] one finds that $\beta_{4,110}$ is TM_{110} mode polarization independent and can be expressed analytically

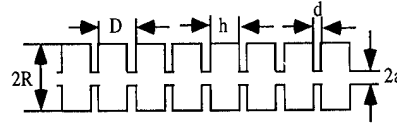


Figure. 1. Constant impedance accelerating structure

as

$$\beta_{4,110}(l) = \frac{\pi Z_0 k k_{10} l^6 e^{-2\alpha_c t} J_1'(u_{11})^2}{144 (\ln(\frac{4l}{w}) - 1)^2 A B R R_{s,110} (R + h) J_2^2(u_{11})} \quad (2)$$

where $k = 2\pi/\lambda_{110}$, $k_{10} = k(1 - (\lambda_{110}/2A)^2)^{1/2}$, $\alpha_c = (2\pi/\lambda_{110})((\lambda_{110}/2l)^2 - 1)^{1/2}$, $R_{s,110} = (\pi c \mu_0 / \sigma \lambda_{110})^{1/2}$, μ_0 is the magnetic permeability and σ is the electric conductivity, A and B are the width and the height of HOM waveguides, l and w are the width and the height of the four rectangular coupling slots with l parallel to the magnetic field, and t is the wall thickness between cavity inner surface and waveguide. Now, if many of this kind of waveguide loaded cavities are coupled together, one obtains the first kind of damped accelerating structure under the condition that the fundamental mode is not damped. For the TM_{11} mode passband one can say that the loaded Q is almost $Q_{L,110}$. If $K_h Q_{L,110} < 2$ there will be no coupling between cavities for the TM_{11} mode [3], where K_h is the coupling coefficient for the TM_{11} mode passband.

III. The Second Type of Damped Structure

Now we consider the second kind of damped structure which is essentially different from the first. Given a constant impedance disk-loaded structure of length L as shown in Fig. 1, one can calculate the passband of the TM_{11} mode (which is the most dangerous mode for multibunch operation). We define $\theta_{1,s}$ as the phase shift of the TM_{11} mode passband at which the phase velocity equals to the velocity of light. Assuming now a charged particle is injected into the structure off axis at a velocity close to that of light, one knows that this particle will loss its energy to the TM_{11} mode mainly at synchronous phase shift $\theta_{1,s}$ and generates behind it so-called wakefield $W_{\perp,11}(s)$, where s is the distance between this exciting particle and a following test particle (of course it will generate wakefields oscillating at other

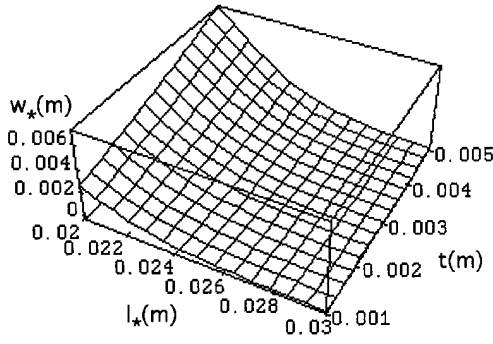


Figure 2. $\beta_{4,11} = 1$ surface with $v_g(\theta_{1,s})/c = 0.001$

frequencies also). If $0 < \theta_{1,s} < \pi$ the energy of the wakefield $W_{\perp,11}$, which is distributed uniformly along the structure length L just after the passage of the exciting electron, will tend to move upstream with the group velocity of $v_g(\theta_{1,s})$. Assuming that four distributed waveguides, for example, are connected to the first cavity at the beginning of the structure, in order to absorb the energy of $W_{\perp,11}$ from the structure via the HOM waveguides without any reflection, one has to match this HOM coupler to the TM_{11} travelling wave mode working at $\theta_{1,s}$ by carefully choosing the slot dimensions on the coupler wall (just like matching the fundamental mode input and output couplers of a constant impedance travelling wave accelerating structure). The coupling slots' width l_* and height w_* have to satisfy the following relation [2][4]:

$$\beta_{4,11}(l_*) = \frac{\pi Z_0 k k_{10} l_*^6 \exp(-2\alpha_c^* t) J_1'(u_{11})^2}{144(\ln(\frac{4l_*}{w_*}) - 1)^2 A B R R_{s,110}(R+h) J_2^2(u_{11})} \times \frac{1}{(1 + \frac{Z_0 R}{2R_{s,110}(R+h)} (\frac{v_g(\theta_{1,s})}{c}))} = 1 \quad (3)$$

where $\alpha_c^* = (2\pi/\lambda_{110})((\lambda_{110}/2l_*)^2 - 1)^{1/2}$ and c is the velocity of light. Comparing eq. 2 with eq. 3, one finds out the fundamental difference between the two kinds of damped structure, that is, the coupling slots of the HOM coupler of the second type damped structure should not be too large or too small but satisfy matching condition shown in eq. 3, however, for the first type damped structure this limitation doesn't exist. Here we will use eq. 3 to find the dimensions of HOM coupling apertures of a 3GHz accelerating structure with $a = 1.5\text{cm}$, $D = 3.33\text{cm}$, $R = 4.1\text{cm}$, $h = 2.83\text{cm}$, $A = 4.4\text{cm}$ and $B = 2\text{cm}$. Fig. 2 shows the relation between w_* and l_* for different wall thickness at $v_g(\theta_{1,s})/c = 0.001$.

Once the HOM coupler is matched one knows the deflecting force of the transverse wakefield $W_{\perp,11}$ on the test particle of charge q which is behind the exciting particle by a distance of s :

$$F_{\perp,11} = q W_{\perp,11} e^{-\frac{\omega(\theta_{1,s})}{2Q_{0,11}}(\frac{s}{c})} D(s) \quad (4)$$

where

$$D(s) = L - v_g(\theta_{1,s})\frac{s}{c}, (s \leq cL/V_g(\theta_{1,s}))$$

$$D(s) = 0, (s > cL/V_g(\theta_{1,s})) \quad (5)$$

where $\omega(\theta_{1,s})$ is the angular frequency of the travelling TM_{11} mode at the phase shift of $\theta_{1,s}$, $Q_{0,11}$ is the quality factor of the structure working at the angular frequency $\omega(\theta_{1,s})$. It is obvious that when $v_g(\theta_{1,s}) = 0$ there is no damping effect (only the coupler cavity is damped). For those who are used to think in terms of loaded quality factor to judge the damping effect of this

HOM coupler, we will use an exponential function $Le^{-\frac{\omega(\theta_{1,s})}{2Q_{e,11}}(\frac{s}{c})}$ to simulate function $D(s)$ in eq. 5 by choosing $Q_{e,11}$ as

$$Q_{e,11} = \frac{\omega(\theta_{1,s})L(1 - e^{-1})}{2v_g(\theta_{1,s})} \quad (6)$$

in the way that both functions drop to the the same value Le^{-1} at the same s . Eq. 4 can be expressed as

$$F_{\perp,11} = q W_{\perp,11} Le^{-\frac{\omega(\theta_{1,s})}{2Q_{L,11}}(\frac{s}{c})} \quad (7)$$

where $Q_{L,11}$ is called the equivalent loaded quality factor which is

$$Q_{L,11} = \frac{Q_{0,11}}{1 + \frac{Q_{0,11}}{Q_{e,11}}} = \frac{Q_{0,11}}{1 + \beta_{eq}} \quad (8)$$

where β_{eq} is called equivalent coupling coefficient which has nothing to do with the coupling coefficients expressed in eq. 2 and eq. 3. If $Q_{0,11} \gg Q_{e,11}$, $Q_{L,11} \approx Q_{e,11}$. From eq. 6 it is very important to note that there are two ways to decrease $Q_{L,11}$, either to reduce L or to increase $v_g(\theta_{1,s})$. The total number N_c of the HOM couplers which should be used to reach a desired $Q_{L,11}^*$ for a constant impedance structure of length L can be calculated from the following expression:

$$N_c = \frac{L\omega(\theta_{1,s})(1 - e^{-1})(Q_{0,11} - Q_{L,11}^*)}{2cQ_{0,11}Q_{L,11}^*(\frac{v_g(\theta_{1,s})}{c})} \quad (9)$$

The second kind damped structure is used, for example, in TESLA linear collider project.

IV. The Third Type of Damped Structure

The third type of damped structure is to damp a detuned structure by few HOM waveguides. We will first discuss it without adding HOM coupler and assuming that cavities' dimensions are different from each other adiabatically. The TM_{11} modes dispersion curves of this detuned structure are shown in Fig. 3. When a particle traverse the structure off axis it will deposit part of its energy on TM_{11} mode oscillating at the frequencies mainly from f_1 to f_n as shown in Fig. 3, where the subscript n is the total number of different cavities in this detuned structure of length L . The deflecting force felt by a test particle can be expressed as

$$F_{\perp,11} = \sum_{i=1}^n 2q K_{\perp,11} \frac{L}{n} \sin(\omega(\theta_{1,s,i})\frac{s}{c}) \exp(-\frac{\omega(\theta_{1,s,i})}{2Q_{0,11,i}}(\frac{s}{c})) \quad (10)$$

with

$$K_{\perp,11} = \left(\frac{k_{1,i}c}{a_i^2 \omega(\theta_{1,s,i})} \right) \quad (11)$$

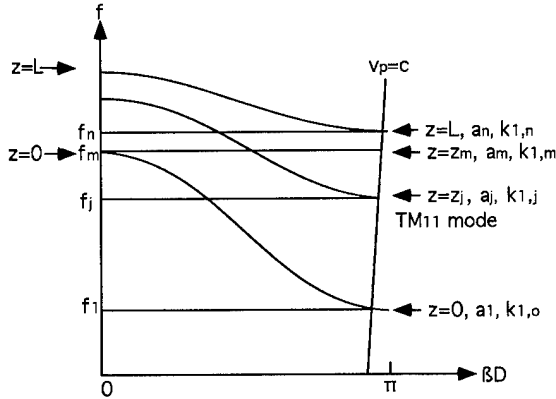


Figure 3. Dispersion curve of a detuned structure

where $k_{1,i}$ is the TM_{11} mode loss factor corresponding to the i th cavity, and it can be calculated analytically [2]

$$k_{1,i} = \frac{a_i^2 u_{11}^2 D \eta_{\theta_{1,s,i}}^2}{4\pi\epsilon_0 h R_i^4 J_2^2(u_{11})} \left(\frac{2R_i}{a_i u_{11}} J_1\left(\frac{u_{11}}{R_i} a_i\right) \right)^2 \quad (12)$$

$$\eta_{\theta_{1,s,i}} = \frac{2}{\theta_{1,s,i}} \sin\left(\frac{\theta_{1,s,i} h}{2D}\right) \quad (13)$$

If we consider an uniformly detuned structure with its iris radius adiabatically decreasing from a_1 at the beginning to a_n at the end, the deposited energies can move inside the structure instead of oscillating locally. The motions of the TM_{11} modes' energies inside the structure can be classified into three different ways. For the modes deposited at the beginning of the structure they will oscillate locally since they could not propagate downstream. For the modes generated at the end of the structure (from f_m to f_n , $v_g(\theta_{1,s,i}) < 0$, $i = m, \dots, n$), however, the energies will propagate upstream and be trapped finally somewhere in the downstream cavities where the group velocities corresponding to these frequencies are equal to zero. Finally, the energies of the modes between f_1 and f_m will propagate upstream until they are reflected by the first cavity. The reflected energies will move downstream and finally be trapped in the cavities where the group velocities are zero.

To damp the TM_{11} modes in a detuned structure via a few HOM couplers is the main idea of the so-called damped detuned structure currently adopted in the S-Band linear collider main linac design [5]. To demonstrate the behaviour of a HOM coupler let's assume that at the beginning of a detuned structure a HOM coupler (four waveguides) is installed and is matched to the i th TM_{11} mode. The equivalent loaded quality factor corresponding to the i th mode can be expressed as

$$Q_{L,11,i} = \frac{Q_{0,11,i}}{1 + \frac{Q_{0,11,i}^2 \langle v_g(\theta_{1,s,i}) \rangle}{\omega(\theta_{1,s,i}) z_i (1-e^{-1})}} \quad (14)$$

where $\langle v_g(\theta_{1,s,i}) \rangle$ is the average group velocity of the i th mode travelling from $z = z_i$ to $z \approx 0$ where the HOM coupler is located. The damping effects of this HOM coupler on the

other modes, however, are less efficient and different from one to another due to mismatching. The reflected HOM energies by this mismatched HOM coupler will be trapped somewhere in the structure. It seems that the first type damping scheme is the most suitable choice for a damped detuned structure (SLAC damped detuned structure is a good example [6]).

V. Acknowledgements

He appreciates the discussions with J. Le Duff and H. Braun.

References

- [1] J. Gao, "Analytical formula for the coupling coefficient β of a cavity-waveguide coupling system", *Nucl. Instr. and Meth.*, **A309** (1991) p. 5.
- [2] J. Gao, "Analytical approach and scaling laws in the design of disk-loaded travelling wave accelerating structures", *Particle Accelerators*, **Vol. 43(4)** (1994) pp. 235-257.
- [3] J. Gao, "The criterion for the coupling states between cavities with losses", *Nucl. Instr. and Meth.*, **A352** (1995) pp. 661-662.
- [4] J. Gao, "Analytical formulae for the coupling coefficient β between a waveguide and a travelling wave structure", *Nucl. Instr. and Meth.*, **A330** (1993) p. 306.
- [5] N. Holtkamp, "S-band test accelerator", Proceedings of the LC93, Oct. 13-21 (1993) Stanford, SLAC-436, 1994.
- [6] N. Kroll, K. Thompson, K. Bane, R. Gluckstern, K. Ko, R. Miller, and R. Ruth, "Higher order mode damping for a detuned structure", SLAC-PUB-6624, Aug. 1994.

High Power Window Tests on a 500 MHz

Planar Waveguide Window for the CESR Upgrade*

M. Pisharody, P. Barnes, E. Chojnacki, R. Durand, T. Hays, R. Kaplan, J. Kirchgessner, J. Reilly, H. Padamsee, and J. Sears

Laboratory of Nuclear Studies, Cornell University, Ithaca, NY 14853.

ABSTRACT

We describe the low power and high power performance of planar waveguide windows designed and fabricated by Thomson Tubes and tested at LNS. These windows are intended for use in the phase III upgrade of CESR.

INTRODUCTION

In the recent CESR beam test of the SRF cavity we used a planar waveguide window designed and built by Premier Microwave, shown in Fig. 1. As reported in [1], this window was tested off-line at 500 MHz with 250 kW traveling wave power and 125 kW reflected power. The conditioning time to reach 250 kW was about 200 hours, with vacuum bursts as the most frequent trip event. When the SRF cavity was installed in CESR[2], the maximum beam power supplied to a 120 mA beam through the window and SRF cavity was 155 kW, again limited by vacuum bursts during window conditioning in the presence of beam and with the cavity on resonance. For the phase III upgrade of CESR, we need to supply 325 kW to the beam. We plan to continue high power off-line tests on the Premier window.

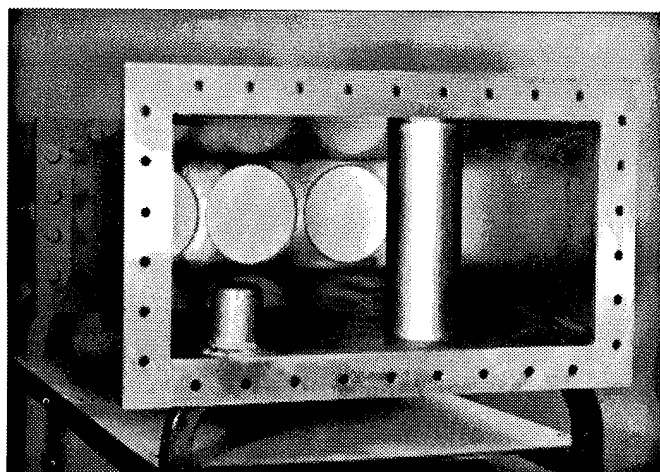


Fig. 1: Premier Microwave window with three BeO disks. Full height WR 1800 waveguide, air side is shown.

*Supported by the National Science Foundation, with supplementary support from the US-Japan Collaboration.

THOMSON WINDOW

We also started to evaluate a 500 MHz planar window design from Thomson. The design is as shown in Fig. 2 and Fig. 3. The disk is alumina ceramic and coated on the vacuum side with TiN.

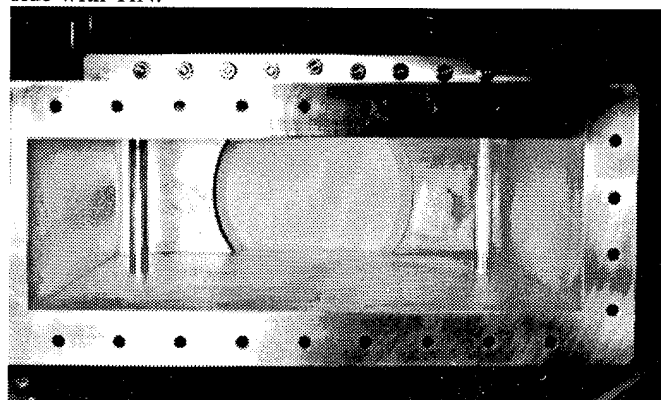


Fig. 2 Thomson Window with one alumina disk. Half-height WR 1800 waveguide, vacuum side is shown.

Thomson Tubes Electroniques High Power RF Waveguide Window

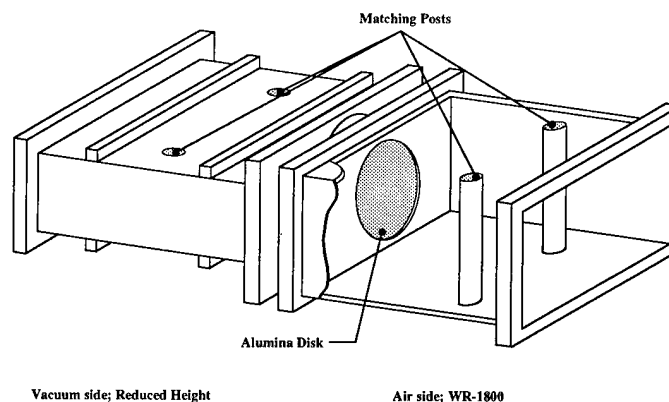


Fig. 3: Schematic layout of Thomson window showing ceramic disk and matching posts.

The VSWR of each window was measured at low power using the TRL method with an HP network analyzer. The geometry of the window was also studied using the MAFIA program. Fig. 4 compares the measured and calculated VSWR, about 1.04 at 500 MHz.

MAFIA calculations also give the electric fields in the window assembly region, and these are shown in Fig. 5. We

note that similar MAFIA studies on the Premier window revealed that the maximum electric field between the posts and the window region was nearly a factor of 5.0 over that of WR 1800 as compared to a factor of 2.0 for the Thomson window, as shown in Fig. 6.

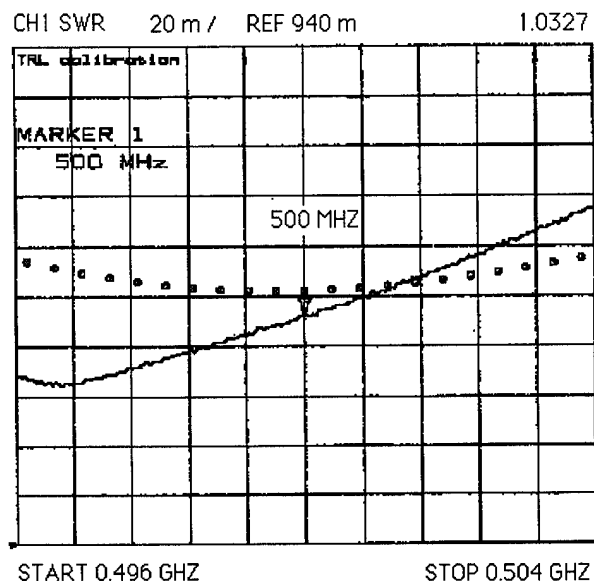


Fig. 4: Measured (line) and calculated (circles) VSWR for the Thomson window.

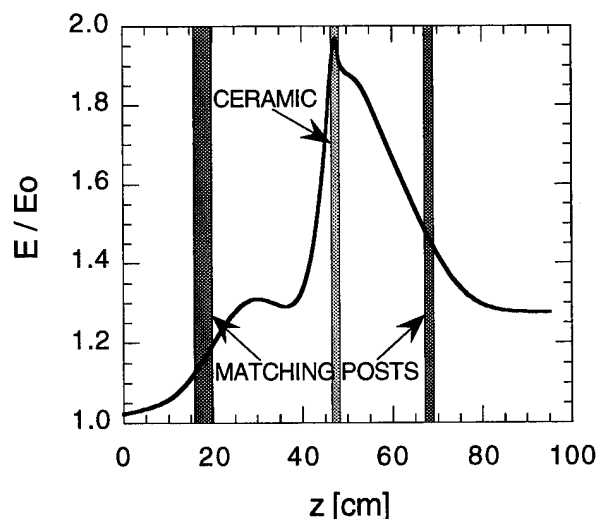


Fig. 5: Enhancement of electric field on axis over that of WR 1800 waveguide due to ceramic and matching posts in the Thomson window.

HIGH POWER TESTS ON THE THOMSON WINDOW

After cleaning, two of the Thomson windows were assembled in a clean room using Helicoflex seals to a copper vacuum pump-out waveguide box which had stainless steel end flanges. The pump-out box had ports with ZnSe windows to view the temperature of the ceramic disks with an infra red camera. (See Fig. 7) Three light detectors were used to

monitor arcing, one on the air side of each window and one in the common vacuum region. An electron pick-up probe was also installed in the vacuum box. The entire assembly was baked at 225 C for 2 days, and the final vacuum was 3×10^{-9} torr at room temperature.

In the traveling wave mode at 500 MHz, we were able to reach 100 kW CW without any significant processing events. Above 100 kW, vacuum bursts started to trip the rf when the vacuum exceeded 10^{-7} torr. These bursts degraded the vacuum quite substantially and it took several minutes to recover.

At this stage we switched to an automated pulsed processing routine. Each time the rf level was raised by 1 kW, the duty cycle of the rf pulses was reduced to a few %, then progressively increased back to 100%. Once the CW conditions were stable at the new power level, the command power was increased by 1 kW and the pulsed procedure repeated. When there was an rf trip in the pulsed mode, we noticed that the electron pick-up current would rise for that pulse. There was no electron current for rf pulses which had no trip. This observation points to multipacting as the cause of the vacuum bursts. Pulsed power processing was also very slow, with substantial off time due to vacuum recovery.

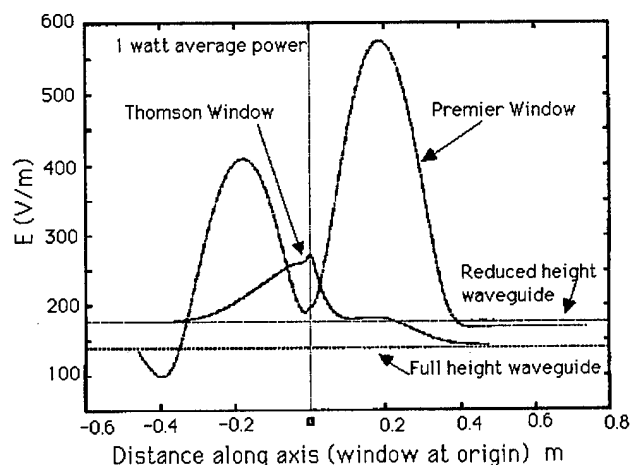


Fig. 6: Comparison of the electric fields for two types of window assemblies.

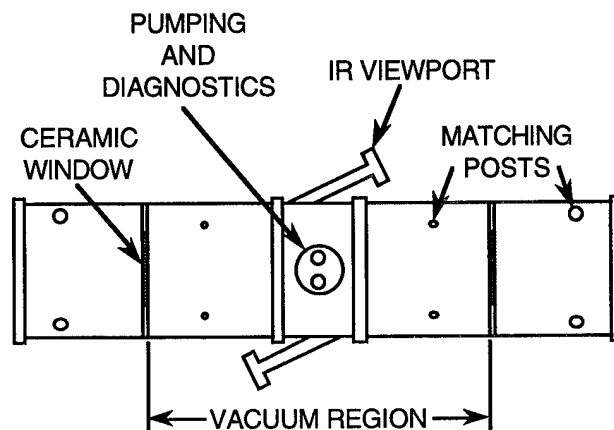


Fig. 7: High power test set up schematic.

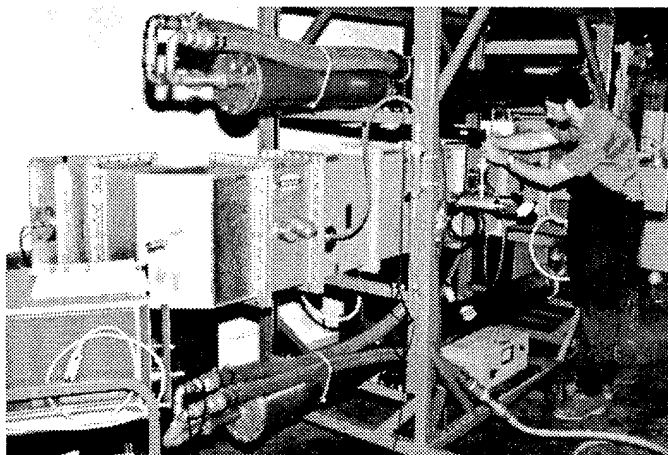


Fig. 8: Typical high power processing set up showing two windows and two 300 kW water loads.

TICKLE PROCESSING

To limit the severity of the vacuum surges, a new method of pulsed processing was applied. We call it "tickle processing". As we continued to use the pulsed processing program, we superposed 20 - 50 kW, 100 μ sec wide pulses on top of the primary rf pulses as shown in Fig. 8. In this way we limited the magnitude of the vacuum bursts and improved the efficiency of the processing achieving much swifter progress. Fig.9 shows that the rate of processing to 300 kW CW was 20 hours. The highest power achieved was 430 kW at 33% duty cycle.

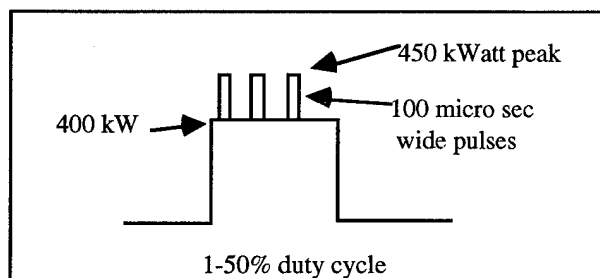


Fig. 9: Tickle processing with primary power 400 kW.

Periodically through the processing stage, we measured the temperature of the ceramic disks with the IR camera. At 250 kW CW, one disk reached $\Delta T = 37$ C and the other 56 C. The temperature profiles across the disks were cylindrically symmetric. Calorimetric measurements show that the window was absorbing 80 watt at 250 kW travelling wave. MAFIA calculations confirm this absorption level assuming a loss tangent of 10^{-4} . At 300 kW CW, the hotter disk reached 66 C, near the maximum temperature recommended by the supplier. Running CW above 300 kW was also troublesome for our aged klystron. Therefore we continued at 50% duty cycle to 350 kW and at 33% duty cycle to 430 kW. We believe that at these duty cycles, we have already carried out the needed conditioning.

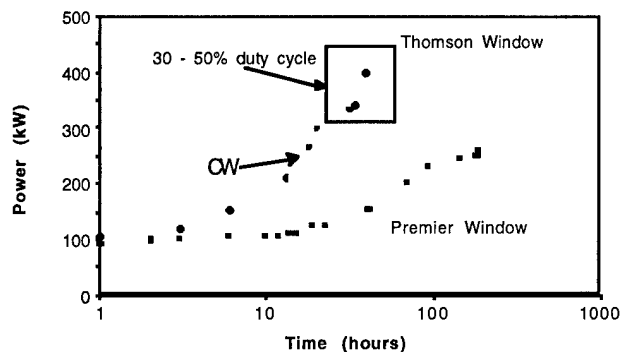


Fig. 10: Conditioning time for two Thomson and two Premier windows.

REFLECTED POWER TESTS

At a duty cycle of 50%, the input power was set constant at 125 kW and the terminating load was replaced by a short. The location of the short was changed in 5 cm steps for a total of 5 measurement positions. The maximum temperature recorded for window #1 was $\Delta T = 40$ C and for window #2 was $\Delta T = 63$ C.

FUTURE PLANS

We plan to replace our old klystron with a 600 kW unit in the near future and to continue high power tests. Meanwhile, stress calculations are in progress to determine the maximum tolerable ΔT . We also plan to provide for air flow cooling on the air side of the ceramic to proceed to 400 kW CW. For final use in CESR, we anticipate placing the window at an electric field minimum position for no beam present. This will allow us to tolerate the maximum possible power in full reflection, which is desirable for high power processing of field emission in the SRF cavity.

REFERENCES

- [1] D. Metzger et al, 1993 Particle Accelerator Conference, p. 1399.
- [2] H. Padamsee et al, this conference.

OPERATIONAL PERFORMANCES AND FUTURE UPGRADES FOR THE ELETTRA RF SYSTEM

A. Fabris, A. Massarotti, C. Pasotti, M. Svandrlik, Sincrotrone Trieste, Padriciano 99, 34012 Trieste, Italy

The ELETTRA RF system is now in operation since 18 months and has demonstrated to be very reliable and flexible. Due to the independence of the four plants, the low failure rate did usually not cause interruption of machine operation. The low level control system has been completed in the last year with the installation of the phase loops. For the present operating conditions, i.e. maximum 250 mA at 2 GeV, no need for HOM dampers became evident, since, by accurate temperature tuning of the cavities, dangerous frequencies can be easily avoided. With the present scenario of insertion devices, a current of 400 mA with sufficiently good lifetime may be stored at 2 GeV in the multibunch mode. New upgrades of the system, like a slow phasing loop among the cavities are also discussed.

I. INTRODUCTION

The ELETTRA RF system is composed of four 500 MHz cavities distributed along the ring [1]. Each cavity is fed by an independent 60 kW RF plant. The RF system has been now operating for more than one and a half years. The operating hours vary from 4070 to 6560 depending on the plant. In routine operation the gap voltage of each cavity is set to 600 kV peak [2]. Injection is performed at 1 GeV at the nominal frequency (499.654 MHz). Beam energy is ramped to 2 GeV without acting on the RF parameters. At 2 GeV the RF frequency is shifted to 499.652 MHz for orbit and beam quality optimisation. RF system parameters for routine operation at 1 and 2 GeV are listed in tab. 1.

Energy (GeV)		1	2
Power loss (keV/turn)		16	255.75
Power to the beam at 200 mA (kW)		3.2	51.15
Number of cavities	4		
Total available RF power (kW)	240		
Power wasted per cavity (kW)		25.7	25.7
Peak cavity voltage (kV)		600	600
Total peak eff. voltage (MV)		1.68	1.68
Synch. phase angle (deg)		0.5	8.7
Syn. frequency (kHz)		15.7	11.0
Overvoltage factor		105.1	6.57
RF Energy acceptance		0.039	0.024

Tab. 1. RF Parameters in routine operation

II. PERFORMANCE OF THE RF SYSTEM

The general performance of the system since start of the commissioning up to now has been very satisfactory. The flexibility created by choosing independent plant has been very useful both in optimising the system itself and to guarantee a low failure rate. All the parameters of the plants

are controlled to verify their operation. The gap voltage in each cavity is always monitored. The measured variation of the gap voltage is always well within the required 1 % stability range. The temperature of the cavities is optimised in order to lower interaction of the beam with HOM so to avoid multibunch instabilities [3]. The relative phasing of the cavities is obtained by equalising the input power to each cavity by means of a 360 degrees phase shifter which is placed on top of each RF plant. Slight modifications of the relative phases of the cavities are required from time to time during operation. These optimisations are in any case in the ± 1 degree electric phase range. The reason for these variations is due to changes in the ambient temperature in the service area.

The option of phase locking the signal generator, which was formerly used only to operate the RF system asynchronously to the linac, has been implemented. So now the RF driving signal can be either phase locked or free with respect to the linac signal generator which provides the machine main clock. In this way the storage ring RF frequency can be varied, once filled the ring with the required filling pattern, without altering the linac working frequency. A phase shifter is placed after the RF generator to optimise the phase of the RF bucket respect to the linac timing. The injection rate is strongly dependent on the relative phase of the storage ring RF and linac. It has been observed that the injection rate can be increased up to ten times by a proper choice of the relative phase.

Very few failures happened in the power plant (actually only five in eighteen months). The amplifiers' faults were mainly due to what can be considered mechanical reasons, however none of them regarded the RF chain. During the time needed to recover from these faults, the machine could be operated with the remaining three cavities with increased gap voltage to 650 kV, i.e. 1.37 MV total peak effective voltage. The only noticeable effect was a slight decrease in lifetime. Hence the choice of having four independent RF plants has proved to be very effective in minimising machine operation time lost due to failures in the RF system. Some circulators arcs have happened randomly. These are generally related to beam dumps at high currents. In fact in this case the tuning system needs some seconds to retune the cavity, while the amplitude control loop is keeping the gap voltage at the required level. This provokes an increase of the direct and reflected power that, depending on the phase relation between incident and reflected wave, could cause either an arc or most probably merely a disturbing signal in the arc detecting electronics. Vacuum trips have become very rare: as expected the number of faults has been vanishing with operating time. Random beam dumps caused by the ion pump interlocks have occurred for certain temperature settings of one cavity when

ramping more than 200 mA at 2 GeV. These requests of beam dump are likely to be caused by an excited cavity mode which propagates through the tube where the ion pump is mounted. The mode which is suspected to be the cause of this effect is the tenth longitudinal mode whose frequency is close to 2.1 GHz. However this is not fully confirmed, but the flexibility of the temperature setting of the cavity has helped to avoid the repetition of the problem. Finally no faults have occurred in the low level system.

III. PHASE LOOPS OPERATION

The original design of the phase loops has been revised. With the former concept in fact, the closure of the loops on all the four plants generally provoked a reduction in lifetime or even beam losses. Furthermore injection seemed to saturate with all the loops in operation and problems with the ramping occurred as well. First of all the speed of the loop has been decreased to 1 msec, so to avoid perturbing interaction with the synchrotron oscillation period. The insertion of the loops has been modified so that now it is performed smoothly instead of abruptly. Finally the return signal of the loop is sampled at the directional coupler just before the cavity input coupler, since the main contribution to the phase variations comes from the klystron. With these modifications the phase loop system works satisfactory, not presenting any of the above mentioned problems. The possibility of implementing a fast RF feedback loop using the cavity voltage sample is under consideration even if at the moment it does not seem necessary being the phase stability of the cavity voltage already in the required range (± 0.5 deg.).

IV. CAVITIES' TEMPERATURE AND HOM SPECTRUM

Excitation of longitudinal multibunch instabilities by the cavity HOMs has been cured by shifting the HOMs' frequency away from overlaps with Coupled Bunch Mode (CBM) frequencies. This shift is obtained by a proper setting of the cavity temperature. This temperature can be regulated in a wide range ($\sim 30^\circ\text{C}$), at a constant cooling water flow.

The first nine monopole HOMs of the smooth shape ELETTRA cavities have been taken into account. For each mode only one resonance is present, since the cavities are single cell. Since no damping device is present, they are high Q resonances and their bandwidth is small compared to the interval between two subsequent CBM frequencies. Along with the wide tuning range this allows to select cavity temperatures at which harmful HOMs are sufficiently far away from CBM frequencies. The cavity temperature setting happens interactively from the general control system.

For an analytical approach to this technique the HOMs' frequencies should be known for the different operating conditions of the cavities and of the machine. Therefore the HOMs' frequencies are measured on the "cold cavity" (i.e. without RF power) at a given cavity temperature T_0 and

accelerating mode (L_0) frequency. The HOM spectra characterisation is completed by measuring the coefficient τ , which gives the HOM frequency shift for a unitary change in cavity temperature at fixed L_0 frequency, and ϕ , which gives the HOM frequency shift induced by a unitary L_0 frequency change. The HOM spectrum characterisation is accurate and reliable. In fact the temperature stability of the cavity is within $\pm 0.05^\circ\text{C}$ and the accelerating mode frequency loop doesn't operate via an internal plunger but via an external tuning cage. Finally the temperature regulation loop operates in such a way that the fundamental mode frequency change from 0 to full RF power is little and can be measured. The corresponding little change on the HOMs' frequency measured without RF power, can be computed. It is equivalent to a shift in the temperature of the measurement, $T_0 + \epsilon_w$. Typical value for ϵ_w is -0.5°C .

On the base of these data a "critical temperature" can be defined for each HOM and the corresponding Coupled Bunch Mode (CBM) [3]. Setting the cavity to this temperature maximises the coupling between that HOM-CBM pair. Computing the critical temperature for all harmful pairs, temperature settings can be sorted out where the coupling is minimised. Dependence on RF frequency, beam current, energy as well as RF voltage can be evaluated [3].

mode	fr (MHz)	Q	R/Q	R//	τ	ϕ
	$T_0 = 43^\circ\text{C}$		Ohm	kOhm	kHz/C	
L0	499.654				0.0	1.0
L1	949.754	24562	34.7	851	-11.5	0.6
L2	1055.533	41265	0.5	20	-19.3	-0.3
L3	1421.287	40781	7.4	302	-43.0	-2.2
L4	1513.606	27953	6.3	176	-28.2	-0.3
L5	1600.458	13169	21.6	284	-41.6	-2.3
L6	1877.557	26911	7.2	194	-33.3	-0.1
L7	1948.013	40963	2.4	99	-52.6	-2.2
L8	2030.998	56767	0.7	37	-34.9	0.1
L9	2072.590	32956	24.7	813	-108.0	-8.3

Tab. 2: Longitudinal HOM characterisation for cavity S3.

As an example tab. 2 shows the characterisation of the longitudinal HOM spectrum for cavity S3. The HOMs' frequency and Q are measured as they would be seen by the beam. The computed value (OSCAR2D) for R/Q is quoted. The values in this table are used for the computation of the critical temperatures as it is discussed in [3].

V. NEW PARAMETERS FOR THE OPERATION WITH 400 mA AT 2 GeV

An effective peak voltage of 1.8 MV at 2 GeV was considered to be necessary in order to reach a reasonable lifetime. This estimate was based on certain assumptions about bunch lengthening (which means broadband impedance) and vertical emittance coupling [4]. This lead to the conclusion that with the foreseen layout, two more plants were needed for a 400 mA beam current at 2 GeV. From the experience with the machine, it became clear that these

requirements could be slightly relaxed for the multibunch case. In fact in routine operation with 4 cavities at 600 kV peak gap voltage, i.e. 1.68 MV total effective voltage, the lifetime at 200 mA, 2 GeV is from 30 to 14 hours depending on machine optics. For this reason the parameters of the existing RF system are already sufficient to store 400 mA at 2 GeV with four plants (see tab. 3). Being limited by the total available RF power, the total voltage has to be obviously decreased so to allow sufficient power to the beam. However the slight decrease in RF voltage does not dramatically lower the lifetime. Up to now operation of the machine at 2 GeV is limited to 250 mA due to overheating problems of BPMs at higher current. These problems are now on the way to be solved, hence high current tests are foreseen to confirm if satisfying operation of the machine can be achieved without increasing the number of cavities.

		A	B	C
Power loss (keV/turn)		255.75	286.15	316.55
Total power to the beam (kW)		102.30	114.46	126.62
Number of cavities	4			
Total available RF power (kW)	240			
Power wasted per cavity (kW)		28	25	22
Peak cavity voltage (kV)		610	570	540
Total peak eff. voltage (MV)		1.70	1.59	1.51
Synch. phase angle (deg)		8.6	10.4	12.1
Synchrotron frequency (kHz)		11.1	10.7	10.4
Overvoltage factor		6.65	5.56	4.77
RF Energy acceptance		0.025	0.023	0.022

Tab. 3. RF Parameters at 2.0 GeV, 400 mA.

Notes: A. Bare machine.
B. Values calculated for presently planned ID.
C. Values calculated for two times the ID in B.

VI. FUTURE IMPROVEMENTS TO THE RF SYSTEM

The improvements which are under study are performed to further reduce the checks and actions by the operator.

It has already been mentioned above that the relative phases of the cavities need to be re-optimised from time to time. Normally this is done once a day and, if required, the correction is generally about 1 degree. The reason is thought to be due to variations in ambient conditions. In fact two cavities are placed in two different nearby sections of the ring and the other two are placed in the diametrically opposite position. RF plant driving signals are distributed via 7/8" flexwell cables running in the service area. These cables are for the moment not pressurised and are longer than 50 metres for two cavities. Their electrical length is obviously dependent on

ambient temperature, pressure and relative humidity. Variations of these parameters have been observed in the service area. Another important parameter is also the ageing of the cables, but after eighteen months of operation this factor causes a minor effect. In order to avoid the action of the machine operator, a slow rephasing system is under study. This could be based either on the measurement of the input power to each cavity or on the measurement of the synchrotron frequency. The first method is actually more straightforward to implement. The measurement of the input power to the cavity is already acquired by the control system of the machine. The drawback of this solution is that it can be influenced by the slightly different input powers at the same gap voltage due to differences in the cavities and their matching to the line. However the error generated with this method is very low. A more precise system could be obtained combining the input power measurement with the measurement of the synchrotron frequency. The maximisation of the synchrotron frequency by phasing the cavities would assure that the gap voltages of the cavities are correctly phased with respect to the beam. A further improvement can be obtained by operating the distribution cables at a slight overpressure. Being the cables air filled, with the dielectric limited to an helical support, this should practically eliminate the effect of variation in ambient pressure and relative humidity. However the temperature dependence remains.

A phase discriminator will be added to measure the relative phase of the RF system driving signal to the Linac injector. This will allow to fix the phase between Linac and RF system to optimise the injection efficiency. The "good" phase will be then restored before injecting by means of a software command acting on the general phase shifter.

The vacuum interlock of the cavities is now based on a Penning gauge fitted in a tube brazed to the cavity. The possibility of adding a further interlock based on the derivative of the vacuum pressure is under study. In fact before a cavity trips, the increase in vacuum pressure in the cavity is very rapid. Therefore a system based on the derivative of the vacuum pressure would be more efficient to protect the system from eventual damages in the cavity or input coupler. This solution has been already adopted in other machines (e.g., ESRF). Of course the interlock based on the pressure measurement has to be maintained as well.

VII. REFERENCES

- [1] A. Massarotti et al., "The R.F. System of ELETTRA", in *Proceedings of the Fourth European Particle Accelerator Conference*, London, U.K., June 1994, pp. 1853-1855.
- [2] C. J. Bocchetta et al., "One and a Half Years of Experience with the Operation of the Synchrotron Light Source ELETTRA", this Conference.
- [3] M. Svandrlik et al., "The Cure of Multibunch Instabilities in ELETTRA", this Conference.
- [4] Sincrotrone Trieste, "ELETTRA Conceptual Design Report", 1989, ch. II-6, pp. II-80-99

X-BAND HIGH POWER DRY LOAD FOR NLCTA *

K. Ko, H. Hoag, T. Lee and S. Tantawi

Stanford Linear Accelerator Center, Stanford University, Stanford, CA 94309

Abstract

The specifications for the RF load to be used for absorbing the traveling wave at the end of an NLCTA accelerator section are that it be well matched over a broad band of frequencies (10% minimum), centered at 11.424 GHz, and capable of handling up to 63 MW peak and 3 kW average power. We present a ceramic (Aluminum Nitride + 7% glassy carbon) load design which satisfies these requirements. It consists of a thin strip of dielectric material with a tapered surface placed inside each narrow wall of the waveguide. The complex dielectric constant of the ceramic at X-Band frequencies was first determined by measurement. Based on the measured values, a MAFIA model is used to evaluate the matching and the power dissipation. Results of the simulations indicate an optimal thickness of 0.045 in and overall length of 10in.

I. INTRODUCTION

The NLCTA requires RF loads to absorb the considerable amount of residual traveling wave power exiting each accelerator section. Very compact, high-power water loads have been developed at X-Band frequencies [1]. These are pill-box windows with water circulating on the air side of the ceramic disk to dissipate the power absorbed. They would be suitable for the present application except that there is a potential danger of water leaking into the accelerator section. That occurs when the braze joint between the ceramic disk and the sleeve fails, or if the ceramic disk cracks under high power due to excessive stress. Therefore it is much preferable to have a dry load in which there is no circulating water in direct contact with critical vacuum joints so that this failure mode is eliminated.

We present here one such dry load design. Fig. 1 shows the right top quarter of the geometry looking into the load. It consists of a short section of WR90 rectangular waveguide into which we braze a wedge of lossy ceramic alongside each narrow wall, and on the outside of which we put water cooling channels. The ceramic material is aluminum nitride AlN loaded with 7% glassy carbon which has been used in HOM loads at CEBAF [2] in a lower frequency range, and at much more moderate power levels.

II. LOAD SPECIFICATIONS

The proposed peak RF input power into each 1.8 m section of the NLCTA is 360 MW. The power exiting the end of the section is estimated to be 35% of the input value, or 126 MW. This exiting power is split into two output waveguides and absorbed by the RF loads. The specifications for each of the loads are given in Table 1. Because of the high average power, the



Figure 1. MAFIA 1/4 model of the high-power load.

important issue in the load design is its power-handling capability. It is necessary for the peak dissipated power density in the ceramic to be reasonably low so as not to cause excessive temperature rise and outgassing. This requires the load to be able to spread the power dissipation over a sufficient length. The electric field associated with 63 MW of peak power is not a concern for such a device because the ceramic wedges, being relatively thin and close to the guide sidewalls, are not in a region of high field strength. Since there are no resonant elements, the bandwidth requirement for matching does not pose a problem either. The ceramic properties at X-Band frequencies, however, need to be characterized before any serious design effort can proceed.

Table I
Specifications for NLCTA high-power load.

Peak power	63 MW
Average power	2.84 kW
Center frequency	11.424 GHz
Bandwidth	10 % min.

III. CERAMIC PROPERTIES AT X-BAND

We have determined the complex dielectric constant (ϵ_r, ϵ_i) of the AlN ceramic by measurements and analytical calculations. The experimental setup consists of a .38 in section of WR90 waveguide connected to a network analyzer by a coax-to-waveguide transition. The waveguide was first shorted at the end and the S_{11} in amplitude and phase was measured from 11 to 11.9 GHz. Then a .0615 in thick layer of AlN was fitted over the short and the measurement was repeated over the same frequency range. Since the ceramic comes in batches and its properties may vary from batch to batch, we performed measurements on samples from three different batches. Knowing the level of variability allows for a margin of safety to be incorporated into the design.

From the measured data, we can find the change in the propagation constant β due to the ceramic and with the known geometry, we can calculate the complex ϵ that corresponds to that

*Work supported by the Department of Energy, contract DE-AC03-76SF00515.

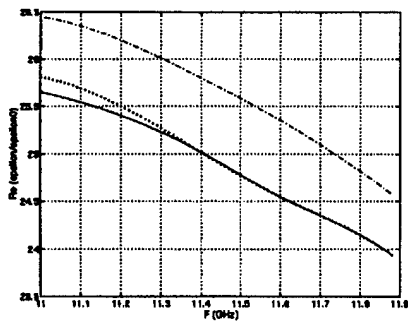


Figure 2. Real part ϵ_r of AlN versus frequency.

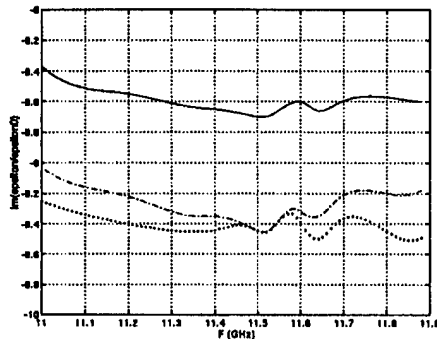


Figure 3. Imaginary part ϵ_i of AlN versus frequency.

change. The results for the three samples are shown in Fig. 2 which refers to the real part ϵ_r , while Fig. 3 is for the imaginary part ϵ_i . The curves are designated as follows: solid line for sample S_1 , dot-dashed for sample S_2 and dotted for sample S_3 . In Table 2 we give their values at 11.424 GHz to indicate the deviation is about a few percent for ϵ_r , whereas the fluctuation can be several times larger for ϵ_i . These measured data will be used in subsequent 3D calculations.

Table II
Complex dielectric constants of three ceramic samples at 11.424 GHz.

Sample	ϵ_r	ϵ_i
S_1	25.0	8.62
S_2	25.8	9.35
S_3	25.0	9.40

IV. LOAD DESIGN

In the load geometry depicted in Fig. 1, the ceramic wedge consists of a front taper transitioning to a constant thickness for the rest of its length. Hence, there are three dimensions to be determined: the total length L , the thickness h , and the taper length s . The last two control the angle of the taper. We will use a 2D analysis to determine L and h approximately.

In the uniform portion of the load, the cross section is that of a rectangular guide filled at each narrow wall with a dielectric of thickness h . If one assumes the end wall of the load is far away, then this simple geometry can be solved readily by mode-matching techniques to give the complex propagation constant

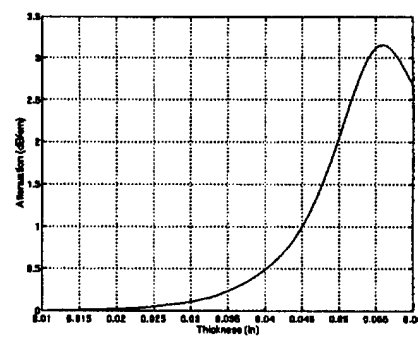


Figure 4. Attenuation rate in dB/cm versus ceramic thickness in inches.

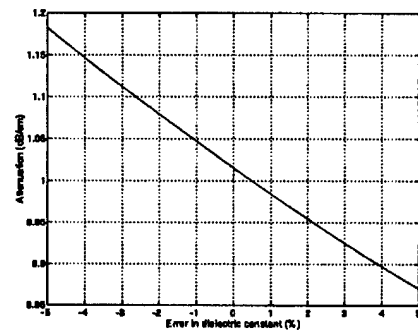


Figure 5. Sensitivity of attenuation rate in dB/cm to fluctuation in ϵ_i in %.

β for a wave traveling down the load. The attenuation rate in dB per centimeter is obtained from the imaginary part of β , and Fig. 4 shows how it depends on h for the mean value of ϵ taken from the three samples in Table 2. It rises slowly at small h , then increases rapidly starting around .045 in to reach a peak near .055 in, and falls off beyond. In Fig. 5 we show the sensitivity of the attenuation rate to variation in ϵ_i in percent assuming $h = .045$ in. A fluctuation of 5% in ϵ_i results in a 15% change in attenuation per centimeter.

In order to dissipate the power gradually to avoid excessively high temperature rise, we opted for 1 dB attenuation per centimeter and fixed h to be .045 in. Then L is chosen to be 10 in for a reasonable length and adequate attenuation, greater than 40 dB. The actual performance of the load has to include the taper whose length s we have yet to determine; this requires modeling the real geometry with the 3D MAFIA code [3].

V. MAFIA SIMULATION

Time-domain S-parameter simulations have been carried out for the load geometry of Fig. 1. An incident TE_{10} mode at a specified frequency propagates down a short section of empty guide towards the load and from its reflection at steady-state, the VSWR can be calculated. At the same time, the electric fields at time intervals a quarter period apart are used to find the power dissipation in the lossy ceramic. Then the peak power density is located and is normalized to 3 kW input power to obtain the correct value. The dielectric properties of the ceramic at the simulated frequency is read off the data shown in Figs. 2 and 3 for the appropriate sample used.

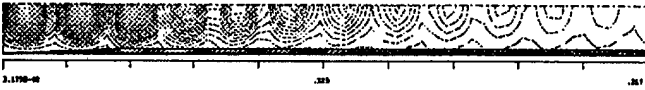


Figure 6. Time-average energy density in the load.

Fig. 6 shows the top view of one half of the load looking down on the broad side of the guide, and the thin ceramic wedge can be seen at the bottom along the narrow wall. The time-average energy density contours are displayed, showing the RF power incident from the left and diminishing in intensity as it propagates to the right into the load. This picture demonstrates vividly how the load works. The incident TE_{10} wave undergoes mode conversion as it encounters the dielectric in the load. The new mode splits its field between the empty guide and the dielectric. The portion inside the dielectric is attenuated (at a rate close to that predicted by the 2D analysis), and is responsible for the power absorption.

The effectiveness of the load depends on how well the incoming power is channeled into the dielectric and how gradually this power transfer can be achieved. It is evident that the optimum is when the power is incident near the grazing angle because this offers the largest surface. Below the grazing angle, the power glances off the dielectric and reflects back from the end wall. Above it, the power penetrates the dielectric over a small area, leading to high dissipation density. Fig. 7 shows a region of power dissipation near the end of the taper. This is the optimal case where the power is spread out over several wavelengths.

VI. LOAD PERFORMANCE

We have evaluated different designs and the results for the final design are summarized in Table 3. It has a taper angle of 1.7 degrees that corresponds to a taper length s of 1.5 in. All three samples were simulated at 11.424 GHz. Sample S_3 was also studied at two other frequencies to determine if the load meets the bandwidth requirement. The peak temperature T_{max} in $^{\circ}C$ is calculated from

$$T_{max} = \frac{Qh^2}{2k_{AIN}} \left\{ 1 + \frac{2dk_{AIN}}{hk_{Cu}} \right\} \quad (1)$$

where Q is the peak power density from MAFIA in W/cm^2 , h is the ceramic thickness as before, d is the distance from the ceramic to the cooling water, and k_{AIN} , k_{Cu} are the thermal conductivity of the ceramic and copper respectively. This 1D model is valid because the variation in the third dimension in Fig. 7 is negligible since the TE_{10} mode is uniform in this direction. It is apparent from Eq. (1) that T_{max} can be kept low by having the peak power density not be excessively high, by making the ceramic as thin as possible, and by moving the cooling water as close to the ceramic as practically possible.

The load performance given in Table 3 indicates that the design has a good match and reasonable temperature rise in the frequency range of interest. We note that the performance may be slightly worse when the ceramic strip is brazed on in the form of buttons.

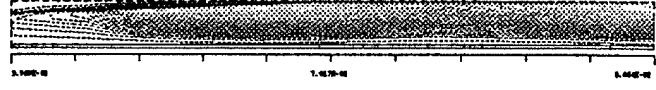


Figure 7. Power dissipation density in the load.

Table III
Load performance using different ceramic samples.

Sample	Frequency (GHz)	VSWR	T_{max} ($^{\circ}C$)
S_3	11.000	1.094	146
	11.424	1.056	132
	11.800	1.038	115
S_1	11.424	1.070	147
S_2	11.424	1.042	156

VII. CONCLUSION

We have presented a dry load design whose performance satisfies the requirements for the NLCTA application. It comprises two tapered strips of $AlN + 7\%$ glassy carbon ceramic, 0.045 in thick and 10 in long. To avoid differential expansion problems between the copper waveguide walls and the ceramic, the strips are broken up into 0.35 in square buttons, which are brazed onto the narrow side walls of WR90 waveguide. Such a load is presently being fabricated for high power test.

References

- [1] W.R. Fowkes *et al.*, High Power RF Window and Waveguide Component Development and Testing Above 100 MW at X-Band, SLAC PUB 5877, Stanford Linear Accelerator Center, Aug. 1992.
- [2] I.E. Campisi *et al.*, The Design and Production of the High-Order-Mode Loads for CEBAF, Proceedings of the 1993 Particle Accelerator Conference, p.1220-1222.
- [3] The MAFIA collaboration, *User's Guide MAFIA Version 3.2*, CST GmbH, Lauteschlägerstr.38, D6100 Darmstadt.

DEVELOPMENT OF A HIGH-POWER RF CAVITY FOR THE PEP-II B FACTORY*

R. A. Rimmer,
Lawrence Berkeley Laboratory,
1 Cyclotron Road, Berkeley, CA 94720, USA

M. A. Allen, J. Saba, H. Schwarz,
Stanford Linear Accelerator Center,
Stanford University, Stanford, CA 94309 USA

F.C. Belser, D.D. Berger, R.M. Franks
Lawrence Livermore National Laboratory,
P. O. Box 808, Livermore CA 94551 USA

We describe the development and fabrication of the first high-power RF cavity for PEP-II. Design choices and fabrication technologies for the first cavity and subsequent production cavities are described. Conditioning and high-power testing of the first and subsequent cavities are discussed, as well as integration of the cavity into modular RF systems for both high-energy and low-energy rings. Plans for installation of the cavity raft assemblies in the RF sections of the PEP tunnel are also considered.

I. INTRODUCTION

The RF system for the PEP-II asymmetric B factory [1] requires a number of accelerating cavities to replenish the energy lost by the beams as they circulate in the high- and low-energy storage rings. We chose to use single-cell normal conducting cavities, see figure 1, designed to operate up to a maximum wall dissipation of 150 kW, which corresponds to a gap voltage of about 1 MV. The cavities are designed to have maximum shunt impedance for the accelerating mode, while the higher-order modes (HOMs) are strongly damped to minimize the overall machine impedance.

We are close to completion of the first high-power RF cavity for PEP-II and the lessons learned in its manufacture have been incorporated into the plans for the production run of cavities.

II. DESIGN

The RF design of the cavity and the thermal analysis have been described previously [2,3,4]. Implementation of the cooling scheme requires the complex pattern of water channels to be constructed in close proximity to the RF surface, while avoiding any potential leak paths between water and vacuum. This is achieved by cutting the channels into the outside of the shell that forms the cavity body and the outside of the various port subassemblies, while not crossing any brazed or welded joints. The individual channels are then covered, on the body by electroforming and on the ports by brazing, and individual inlets and outlets are connected in series or parallel as appropriate.

The finished, interior surface must be suitable for future cleaning and/or surface treatments. Therefore, the design

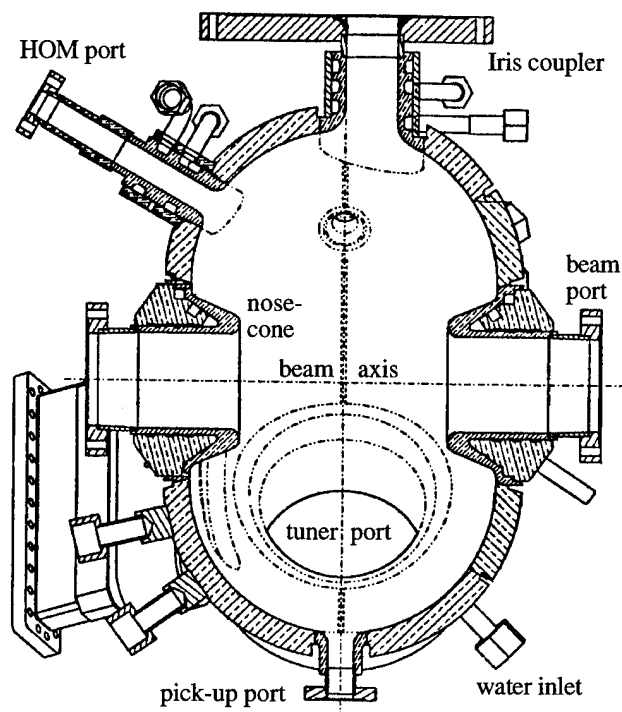


Figure 1: Horizontal cross section through the PEP-II high-power cavity showing the coupler, HOM port, beam ports and small pick-up port.

must avoid leaving any cracks, voids or crevices on the inside surfaces that could trap cleaning solvents and produce virtual leaks. For this reason the major structural joints of the cavity are made by deep penetration electron-beam welding, with the arrangement that the final machined RF surface is sufficiently far from any regions of porosity associated with the root of the weld. Where this is not possible, for example final joints made after the RF surface is finished, the surface region is re-melted with a cosmetic weld to leave a smooth and void-free surface.

Flanges are added by TIG welding to stainless steel inserts brazed into the port subassemblies.

III. FABRICATION

The basic cavity body is made from two bowls, cold-formed from OFE copper plate, which are electron-beam

*This work was supported by the U.S. Department of Energy under contracts DE-AC03-76SF00098 (LBL), DE-AC03-76SF00515 (SLAC), and W-7405-Eng-48 (LLNL).

welded together at the equator. The body cooling channels are cut into the outside of this shell by CNC multi-axis milling and then filled with wax, activated, and covered with electroformed copper, figure 2. The bowl is then turned to the nominal outside dimension and re-installed in the milling machine where the water fitting holes are prepared. The cooling channels are flushed of the wax and then pressure tested. The openings for the HOM and equatorial ports are then machined into the cavity body and the assembly is leak checked.

The ports are machined from OFE copper billet, with cooling channels cut in the outside. The port parts, flange extensions and cooling channel covers are brazed together and leak checked prior to machining the joint which mates with the cavity body.

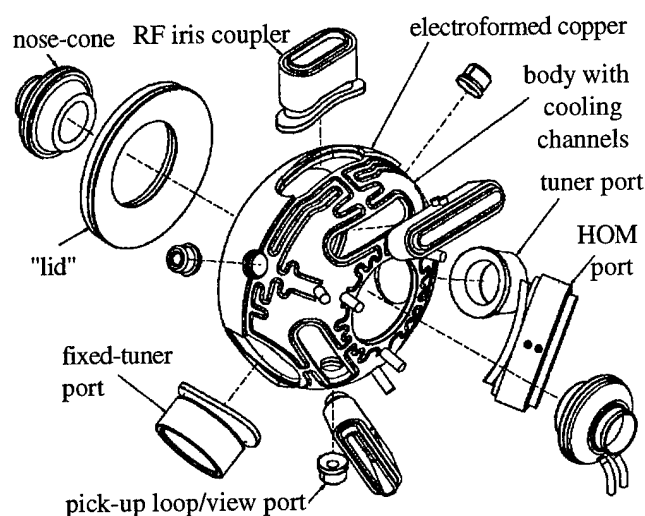


Figure 2: Assembly of high-power cavity showing body cooling channels on one half (exposed), equatorial and HOM port inserts, nose-cones and "lid" section.

The equatorial and HOM ports are clamped in place, tack welded and then joined to the body by electron-beam welding. The HOM port joints, which are accessible through the large "lid" opening on one side of the cavity, are welded from the inside, figure 3, while the equatorial ports are welded from the outside, figure 4.

Once the ports are welded in place, the interior is machined to achieve the finished RF surface, which is also facilitated by the large lid opening. This is an interrupted cut in places where the tool passes over the port openings. With care a surface finish better than 24 micro-inches is attainable with conventional turning using tungsten carbide cutting tools. After surface finishing of the body, the cavity is tuned by machining the nose-cone sections. These are clamped in place while the frequency is measured and then removed for machining. Dummy tuner plungers are inserted during tuning and the temperature and dielectric constant of the purging gas are taken into account. Frequency changes due to vacuum forces and weld shrinkage will also be accounted for in production versions. These effects will be measured in the first cavity and corrected for when machining the real fixed tuner.

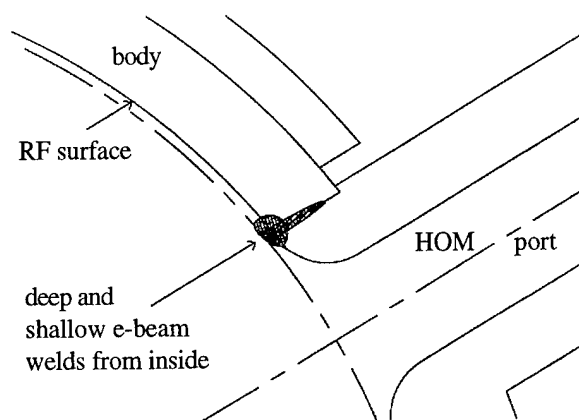


Figure 3: HOM port electron beam welds. Deep weld and shallow re-melt are both made from the inside; the RF surface is cut afterwards.

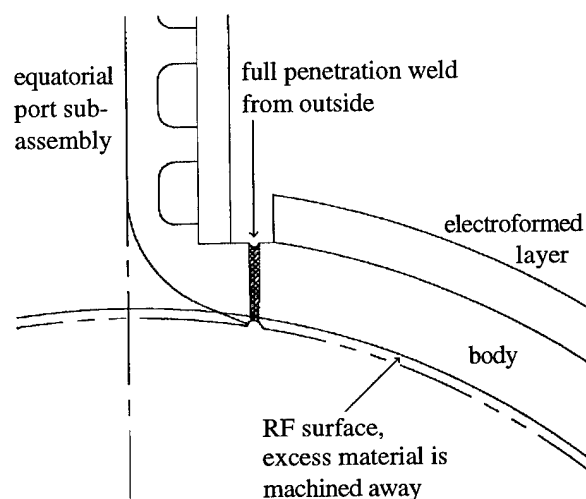


Figure 4: Equatorial port electron beam weld joint. Weld is full penetration from the outside, about 2 mm is removed from the inside during final machining.

The HOM-side nose cone and a larger "lid" containing the other nose cone are then electron-beam welded in place, the main structural welds being done from the outside with cosmetic welds done on the inside through the beam-port openings, figure 5.

After inspection and final cleaning the flanges are TIG welded in place and the cavities are mounted in a support raft, figure 6, plumbed and prepared for high-power testing.

IV. TESTING

It is intended to test all cavities as complete assemblies, with windows, couplers and HOM loads attached, before installation in the tunnel. The cavities will be fitted with fixed and movable tuners, pick-up loops etc., and placed in the test bunker. The cavities will be RF conditioned starting with a low-power, low-duty cycle pulsed mode and working up to full power and CW operation, while monitoring cavity vacuum and window performance. The first cavity will be tested this summer using the existing 500 kW test stand.

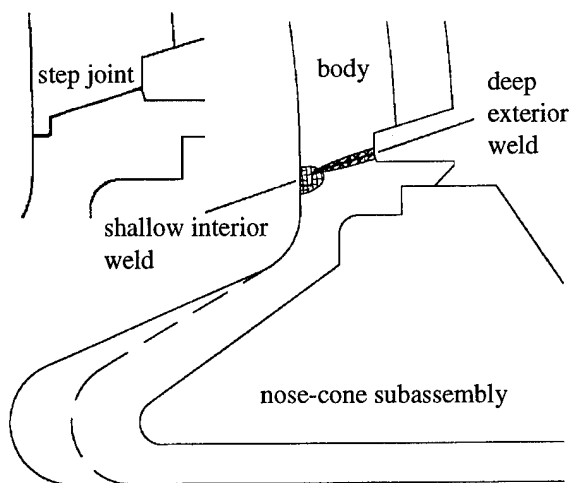


Figure 5: Electron-beam weld joint between cavity body and nose-cone subassembly. Main weld is done from the outside and crack is sealed by shallow interior weld. The step in the joint makes for positive alignment.

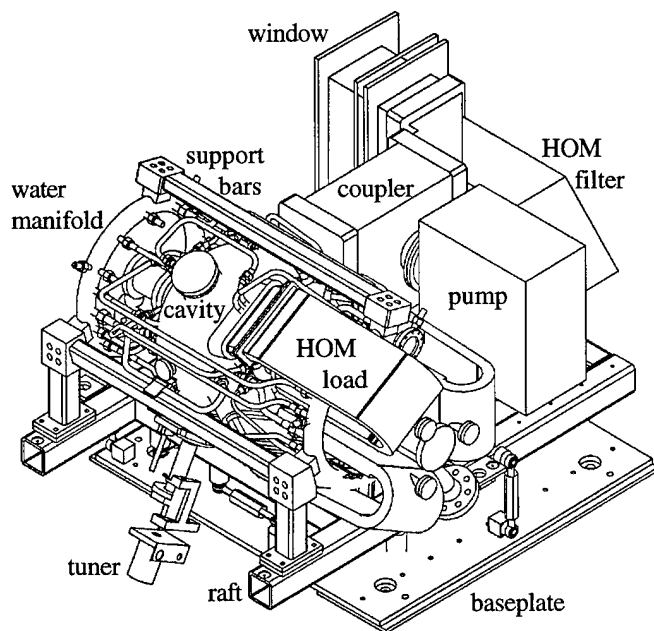


Figure 6: Cavity, coupler, window, tuner, pump and HOM loads mounted on raft for installation

V. INSTALLATION

The tested RF cavity raft assemblies will be delivered to the tunnel in a clean condition and installed in the straight-section vacuum beam-line. The waveguide will be connected to the klystron gallery and the water manifolds on the raft will be joined to the supply and return lines by flexible hoses. All electrical and control cables to the raft will be joined locally to simplify installation and maintenance. In the high-energy ring each klystron will power four cavities while in the low-energy ring, which has higher current, each station will power only two cavities [5]. Cavities will be pre-surveyed to datum points on the raft superstructure so that

alignment in the tunnel, using adjustable struts under each raft, can be accomplished with the more easily accessible raft datum points.

VI. PRODUCTION

Cold-forming of the bowls from plate minimizes material waste while the cost of the dies can be amortized over the production run. Lack of heat in the process minimizes migration of oxygen through the copper, while work hardening improves the machinability of the material. The CNC machining is cost-effective for large-scale production because the investment in tooling and programming is similarly amortized over a large number of cavities. In production, the parts will be processed in batches to make the most efficient use of the machine set-up for each manufacturing step. Alternative means of covering the port cooling channels may be entertained for the production run of cavities because of the relatively high cost of machining the components to the tolerances required for reliable brazing.

VII. CONCLUSIONS

Fabrication of the first high-power cavity has provided many lessons which have been incorporated in the plans for the production cavities. Process development, particularly in the areas of electroforming and deep-penetration electron-beam welding of copper have given us confidence that we have a reliable and repeatable fabrication method.

VIII. ACKNOWLEDGMENTS

This paper describes the work of a large group of people, too numerous to credit individually, who have contributed to the design, fabrication and testing phases of the cavity project.

IX. REFERENCES

- [1] "PEP-II, An Asymmetric B Factory", Conceptual Design Report, June 1993, LBL-PUB-5379, SLAC-418, CALT-68-1869, UCRL-ID-114055, UC-IIRPA-93-01.
- [2] R. A. Rimmer, "RF Cavity Development for the PEP-II B Factory", Proc. Int. Workshop on B-Factories, BFWS92, KEK, Japan, Nov. 17-20, 1992, (PEP-II ME note 2-93, LBL-33360, ESG-242).
- [3] H. Schwarz et. al., "Design of a High-Power Test Model of the PEP-II RF Cavity", Proc US PAC, Washington DC, May 17-20th 1993.
- [4] R. A. Rimmer, "High-Power RF Cavity R&D for the PEP-II B Factory", Proc EPAC 94, June 27-July 1 1994, London, pp 2101-3.
- [5] H. Schwarz, R. Rimmer, "RF System Design for the PEP-II B Factory", Proc EPAC 94, June 27-July 1 1994, London, pp 1882-4.

A DESIGN OF INPUT COUPLER FOR RF-CAVITY

T. Nagatsuka, T. Koseki, Y. Kamiya, M. Izawa^a and Y. Terada^b

Institute for Solid State Physics (ISSP), The University of Tokyo
3-2-1, Midori-cho, Tanashi, Tokyo 188, Japan

^aPhoton Factory, National Laboratory for High Energy Physics (KEK)
1-1 Oho, Tsukuba, Ibaraki 305, Japan

Technical Research Institute, Hitachi-Zosen Corporation
2-2-11, Funa-machi, Taisho, Osaka 551, Japan

I. INTRODUCTION

Characteristics of a newly designed input coupler are presented. The coupler was designed for a 500 Mhz damped cavity [1] to be installed in the high-brilliant VUV and soft X-ray synchrotron radiation ring planned at ISSP [2] and in the Photon Factory (PF) storage ring with a high brilliant configuration [3]. The design study of the coupler has been done mainly using the computer code, High Frequency Structure Simulator (HFSS, HP85180A), which can calculate the S-parameters of high frequency structures.

II. CHECK OF APPLICABILITY OF HFSS

At first, we compared the results of HFSS with experimental results in order to examine how HFSS realizes the rf characteristics of the structure such as input coupler. We simulated the microwave transmission in a cold model of coupler for 714 Mhz cavity to be installed in ATF (Accelerator Test Facility) at KEK [4]. The model coupler was fabricated by TOSHIBA Corp. Figure 1 shows the frequency dependence of VSWR of the coupler. Both results of calculation by HFSS and measurement by TOSHIBA are plotted in the figure. Though a small difference between them is seen, it can be interpreted as due to the reflection at the transformers; a coaxial-rectangle transformer and D - N transformer were used in the measurement and both of them had VSWR of about 1.05. We may conclude from the above that HFSS is well suited to a design of an input coupler.

III. CALCULATION OF VSWR OF APS COUPLER

Figure 2 shows a schematic view of the input coupler which is used for the 508 Mhz alternating periodic structure (APS) cavity of the TRISTAN ring at KEK [5]. We chose the APS coupler as a starting point of our design study. The APS coupler consists of a coaxial line with a loop antenna, a cylindrical ceramic window and a rectangular waveguide. We calculated the transmission response of APS coupler without the loop antenna.

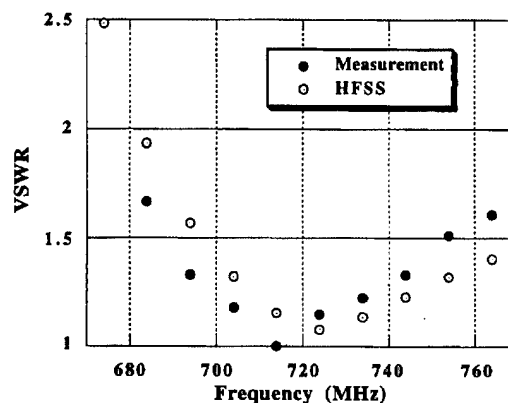


Figure 1: VSWR of the cold model of ATF input coupler.

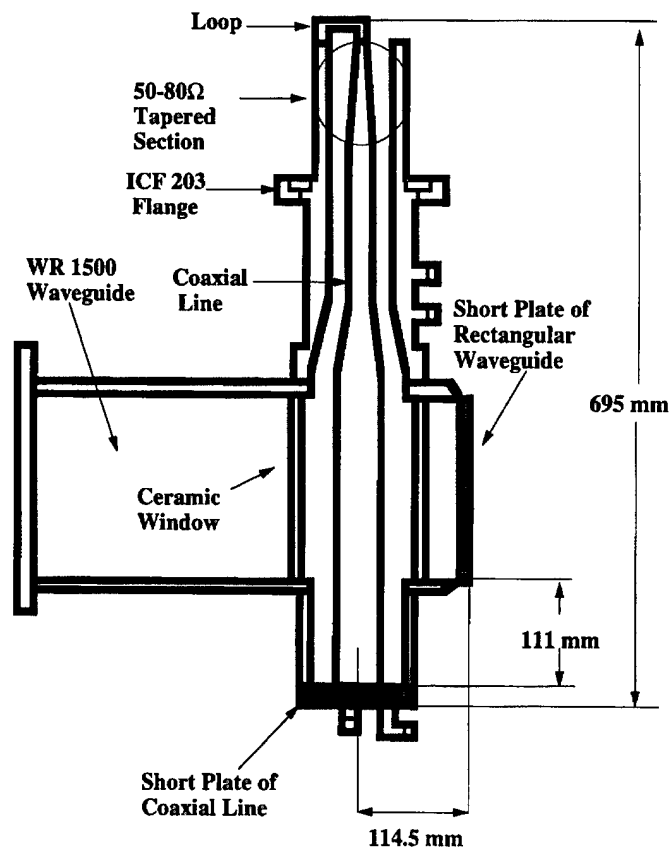


Figure 2: APS input coupler

The closed circles in Fig. 3 show the calculated values of VSWR. As shown in the figure, the VSWR at the operating frequency of 508 Mhz is not close to unity but rather large. This coupler has a tapered section at the end of coaxial line (see Fig. 2), which transforms the characteristic impedance Z from 50 to 80Ω. This impedance transformation thus causes reflection: an approximation of discontinuous change in impedance gives $VSWR \cong 1.6$, while another approximation of smooth change gives $VSWR \cong 1.48$ very close to the calculated value at 515 Mhz, where without tapered section there is almost no reflection (see the open circles in Fig. 3). In the latter approximation, the reflection coefficient is expressed as,

$$\Gamma = \frac{1}{2} \int e^{-2j\beta z} \frac{d}{dz} \log Z(z) dz$$

which gives $|\Gamma| \cong 0.194$.

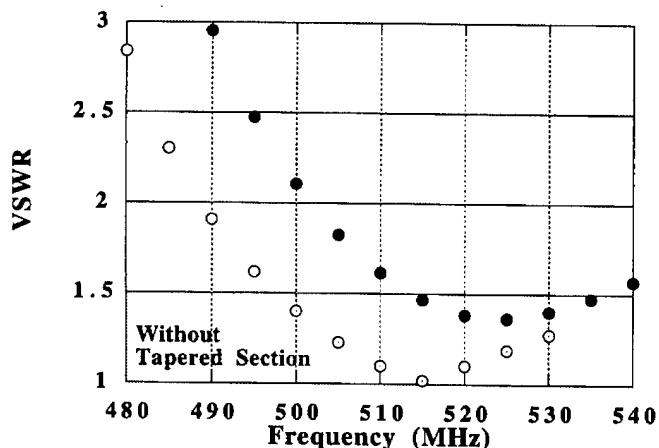


Figure 3: VSWR of APS coupler with and without tapered section.

IV. MEASUREMENT OF COUPLING COEFFICIENT FOR TWO TYPES OF LOOP USING A PROTOTYPE CAVITY

In order to experimentally examine the effect of the tapered part on coupling coefficient, we made two types of coupling loop model. Figure 4 schematically shows the loop models; (a) has a straight coaxial wave guide and (b) has a tapered coaxial wave guide. We attached each type of model to the coupler port of a prototype cavity as described in Ref. [1] and measured the coupling coefficient β with a Network analyzer (HP8510C). Figure 5 shows the dependence of loop position on β . The tapered type has a smaller value of β than the straight type, though the former has apparently a larger cross-section for coupling to the magnetic field in the cavity, therefore we may conclude that the straight type (Fig. 4(a)) is better suited to an input coupler than the tapered one.

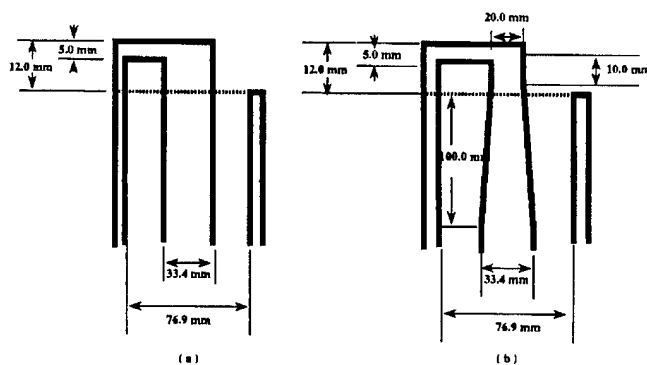


Figure 4: the model loops.

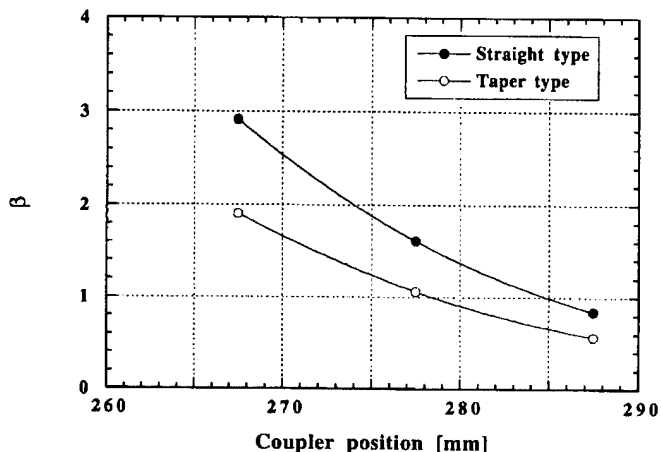


Figure 5: The dependence of loop position on β . the abscissa is the distance between the center of cavity and the broken lines indicated in Fig. 4.

V. FINAL DESIGN OF THE INPUT COUPLER

In order to obtain low-loss transmission of 500 Mhz microwave through the input coupler, we adjusted the positions of the short plates of rectangular waveguide and coaxial line by using HFSS (see fig. 2). The frequency at a minimum value of VSWR tends to change with the position of the short plate of coaxial line (Fig. 6), while the minimum value itself does with the position of the short plate of rectangular waveguide (Fig. 7). the lowest value of VSWR at the frequency of 500 Mhz was obtained with both short plates located at 4.5 mm outside their original position of the APS coupler. The VSWR at the operating frequency of 500 Mhz is almost unity (Fig. 8).

A cold model of our new coupler has been fabricated and attached to a prototype cavity made of aluminum. the coupling loop was mounted at the position of 280 mm away from the center of cavity. The low power test showed that β is 1.35. it is equivalent to 2.27 for the cavity made of Cu. Recently, we fabricated the high power models of cavity and coupler (Fig. 9). the value of β was measured to 2.35 for the set of high power models.

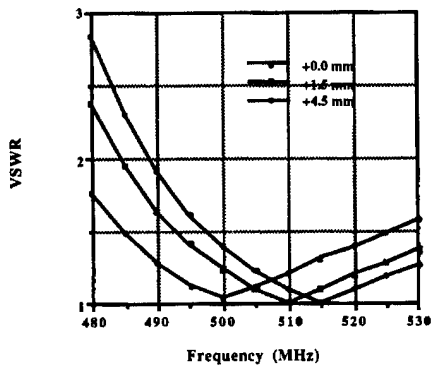


Figure 6: VSWR versus the position of short plate of coaxial line.

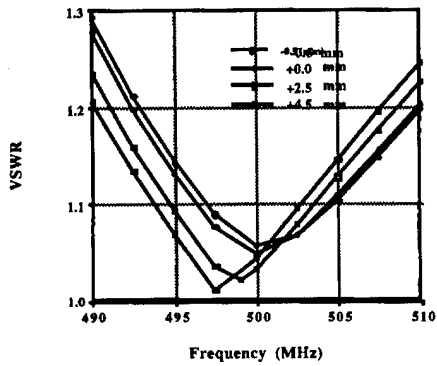


Figure 7: VSWR versus the position of short plate of rectangular waveguide. The position of short plate of coaxial line is fixed at 5.25 mm outside the position of APS coupler.

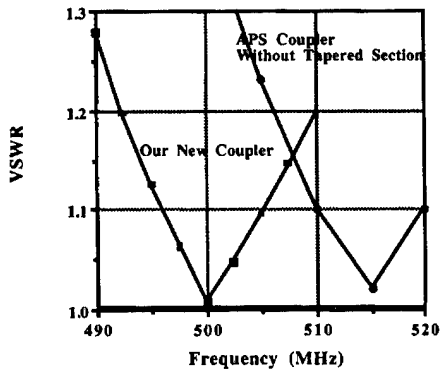


Figure 8: VSWR of our new coupler and that of APS coupler without its tapered section.

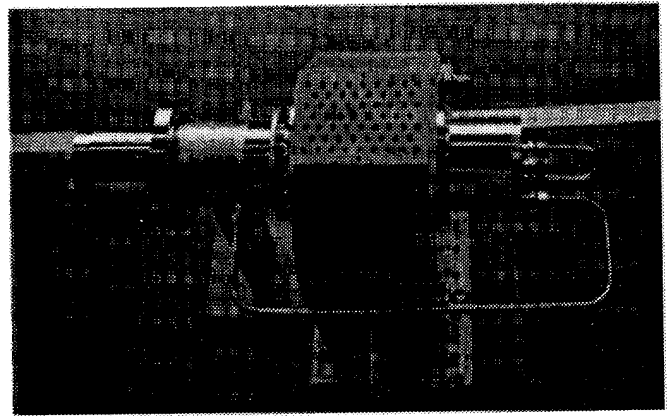


Figure 9: Our new coupler.

VII. REFERENCES

- [1] T. Koseki, M. Izawa and Y. Kamiya, "Development of a Damped Cavity with SiC Beam-Duct" in these proceedings.
- [2] Y. Kamiya *et al.*, Proc. of the 4th European Particle Accelerator conference, London, 1994, p. 639.
- [3] M. Katoh, Y. Hori, N. Nakamura, and H. Kobayakawa, Rev. Sci Instrum., 66 (1995) 1982.
- [4] S. Sakanaka, K. Kubo and T. Higo, Proc. of the 1993 Particle Accelerator Conference, p. 1027.
- [5] M. Akemoto and Y. Yamazaki, Proc. of the 7th Symposium of Accelerator and Technology, Osaka, Japan, 1984, p. 106.

DESIGN OF THE KEKB RF SYSTEM

K. Akai, E. Ezura, and Y. Yamazaki

KEK, National Laboratory for High Energy Physics, 1-1, Oho, Tsukuba, Ibaraki-ken, 305 Japan

Abstract

An RF system for KEKB to be commissioned in FY1998 has been designed. The key issue in the KEKB RF system is to solve problems arising from an extremely heavy beam loading, since the stored current is much higher than that of any existing storage rings. This paper describes an overall view of the requirements and the design of KEKB RF system.

I. INTRODUCTION

An asymmetric two-ring electron-positron collider for B-physics (KEKB) will be commissioned in FY1998. The RF-related machine parameters are listed in Table I [1]. The total RF voltage is required to provide the short bunch length ($\sigma_z=4\text{mm}$) and the desired synchrotron tune (ν_s). From a beam dynamics requirement the synchrotron tune should be variable in a range from 0.01 to 0.02 in order to find the best operation point avoiding synchrotron-betatron coupling resonances. Then the RF voltage should be variable in a range of 5~10 MV (LER) and 10~20 MV (HER). Wiggler magnets are probably installed in LER in order to reduce the damping time from 43ms to 23ms, and to control the emittance. The beam power in LER is then increased from 2.7 MW to 4.5 MW.

We must overcome several problems arising from an extremely heavy beam loading on RF cavities. A high stored current with many bunches causes strong coupled-bunch instabilities. A coupled-bunch instability due to the accelerating mode occurs, because of a large detuning frequency caused by the heavy beam loading, compared with a small revolution frequency (large circumference ring). If we use conventional normal-conducting damped cavities, the growth rate is extremely high. Thus one of the key issues for the KEKB RF system is how to avoid this instability.

Other requirements for the cavity related with the heavy beam loading are: the higher order modes (HOM's) should be sufficiently damped to avoid coupled-bunch instabilities, an input coupler should be able to handle 500 kW, and HOM absorbers attached to the cavity should work normally with 10 kW of HOM power. In addition, the heavy beam loading needs to be taken into account when we design the low level RF control system.

II. RF SYSTEM

A. Accelerating cavity

In order to avoid the coupled-bunch instability caused by the accelerating mode, a new normal-conducting cavity scheme referred to as accelerator resonantly coupled with an energy storage (ARES) was proposed at KEK [2] [3] [4]. It employs an energy storage cavity which couples to an accelerating cavity via a coupling cavity in between. A large stored energy in the storage cavity reduces the detuning frequency by an order of magnitude.

Table I
RF-related machine parameters

Ring	LER	HER	
Particle	positron	electron	
Energy	3.5	8.0	GeV
Beam current	2.6	1.1	A
Bunch length		0.4	cm
Energy spread	7.4×10^{-4}	6.7×10^{-4}	
Bunch spacing		0.59	m
Synchrotron tune	0.01~0.02	0.01~0.02	
Mom. compaction	$1 \sim 2 \times 10^{-4}$	$1 \sim 2 \times 10^{-4}$	
Energy loss/turn	$0.81^\dagger/1.5^{\dagger\dagger}$	3.5	MeV
RF voltage	5~10	10~20	MV
RF frequency		508.887	MHz
Harmonic number		5120	
Damping time	$43^\dagger/23^{\dagger\dagger}$	23	msec
Radiation Power	$2.1^\dagger/4.0^{\dagger\dagger}$	3.8	MW
HOM Power	0.57	0.14	MW
Total Beam power	$2.7^\dagger/4.5^{\dagger\dagger}$	4.0	MW

† — without wiggler

†† — with wiggler

The instability is sufficiently suppressed with this scheme. A 1/5 scale cold model of ARES was tested and the design principle was proved [5].

The accelerating cavity of ARES must be a damped structure. We adopted a HOM-damping scheme with a coaxial waveguide equipped with a notch filter to block the accelerating mode [6] [7]. Based on the calculated R/Q values and the Q values of HOM's, the growth time of the fastest growing mode is about 60 msec in the longitudinal case and 30 msec in the transverse case [1]. A prototype cavity was fabricated and tested in a high power operation. It was successfully tested up to 110 kW of wall dissipation which corresponds to a gap voltage of 0.73 MV, that is beyond the design value [8].

Superconducting cavity is fairly immune against the instability caused by the accelerating mode. Although the growth time is still faster than the radiation damping time in the case of LER, we obtained a reasonable parameter set in the case of HER, where it is sufficiently slow. The growth time of the instability due to the HOM's is also slower than the radiation damping time in HER. Thus the superconducting cavity is considered another candidate in HER. Prototype cavities were tested in liquid helium. The design values of the gap voltage and the Q-value were achieved [9].

A beam test of ARES and a superconducting cavity in TRISTAN-AR is scheduled in 1996. The cavities will be tested with a stored beam of up to 500 mA.

controlled with an accuracy of less than 1 degree to maintain the colliding point at the minimum β^* and to avoid excess generator power into the cavity. We will improve the accuracy of existing RF reference system and phase control modules having been used for TRISTAN. In addition, we will use a computer-aided phase correction scheme, where the input power, reflection power, and cavity voltage of every cavity are measured and then the phase error of each cavity is calculated and corrected. This correction scheme takes advantage of the high beam-induced voltage.

The ARES requires two tuner control loops, as seen in Figure 1; one is for the accelerating cavity and the other for the storage cavity. The accelerating cavity tuner is controlled by its phase with respect to the input phase, which is the usual way to compensate for the reactive component of the beam loading. The storage cavity tuner is controlled not by its own phase but by the phase of coupling cavity; otherwise the tolerance would be extremely severe [10].

The R&D work is in progress for an RF feedback system using a parallel comb filter [11]. It reduces the coupling impedance at the upper synchrotron sidebands of revolution harmonic frequencies. It will be applied to provide additional damping for the accelerating mode instability, when necessary.

D. Bunch gap transient

The effect of a bunch gap was evaluated [12]. In order to prevent an ion trapping, a 5% ~ 10% bunch gap will be introduced in HER. The bunch gap, however, modulates the accelerating field and the synchronous phase. The luminosity can be reduced by the displacement of the collision point from the optimum point with the minimum β^* . The calculated bunch phase modulation is summarized in Table III. Note that the phase modulation is much smaller owing to the large stored energy, compared with the case of conventional normal-conducting damped cavities where it amounts to 20 ~ 30 degrees. The displacement of the colliding point can be further reduced by introducing a corresponding gap in LER, which makes a similar gap transient response in LER to that in HER. Figure 2 shows the relative bunch phase without and with the compensation gap. The displacement is reduced to less than 0.5 degree ($=0.2\sigma_z$), which is acceptable.

Table III
Bunch phase modulation due to a bunch gap

cavity in HER	gap length (%)	bunch phase modulation (p-p, degree)	
		with compensation gap?	
		no	yes
ARES	10	2.7	~ 0.3
	5	1.3	~ 0.1
SCC	10	4.9	~ 0.5
	5	2.4	~ 0.3

III. CRAB SYSTEM

The crab crossing is considered a viable fall-back solution to the problems encountered with the finite angle (± 11 mrad) crossing scheme. As a crab cavity we adopted the design of

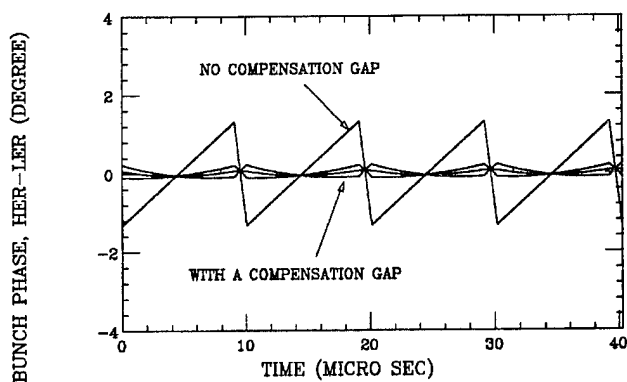


Figure 2. Bunch phase modulation due to a bunch gap and the effect of a compensation gap. The bunch current in the compensation gap is set 50, 55, 60% of that of other bunches.

superconducting squashed crab cavity developed under KEK-Cornell collaboration [7]. The R&D is in progress aiming at fabricating full scale niobium cavities in three years [13].

References

- [1] "KEKB Accelerator Design Report" to be published as a KEK-Report.
- [2] T. Shintake, Part. Accel. **44** 131 (1994).
- [3] Y. Yamazaki and T. Kageyama, Part. Accel. **44** 107 (1994).
- [4] K. Akai and Y. Yamazaki, Part. Accel. **46** 197 (1994).
- [5] N. Akasaka, K. Akai, T. Kageyama, T. Shintake, and Y. Yamazaki, WPQ09 in this conference.
- [6] T. Shintake, Jpn. J. Appl. Phys. Lett. **31** L1567 (1992).
- [7] K. Akai, J. Kirchgessner, D. Moffat, H. Padamsee, J. Sears, T. Stowe and M. Tigner, Proc. 15th Int. Conf. on High Energy Accelerators, 757 (1992).
- [8] T. Kageyama, K. Akai, N. Akasaka, E. Ezura, F. Naito, T. Shintake, Y. Takeuchi, Y. Yamazaki, and T. Kobayashi, WPQ17 in this conference.
- [9] S. Mitsunobu, K. Asano, T. Furuya, Y. Ishi, Y. Kijima, K. Sennyu, T. Tajima, and T. Takahashi, TPP08 in this conference.
- [10] K. Akai, to be submitted.
- [11] S. Yoshimoto, E. Ezura, K. Akai, and T. Takashima, RPQ06 in this conference.
- [12] K. Akai and E. Ezura, Proc. 4th European Part. Accel. Conf. 1141 (1994).
- [13] K. Hosoyama, et. al.

RF CHARACTERISTICS OF ARES COLD MODELS

N. Akasaka, K. Akai, T. Kageyama, T. Shintake, and Y. Yamazaki,
KEK, National Laboratory for High Energy Physics, Oho 1-1, Tsukuba, Ibaraki 305, Japan

RF characteristics were measured for aluminum 1/5 scale cold models of accelerator resonantly-coupled with an energy storage (ARES) for KEKB. The main purpose of ARES is to reduce the frequency shift due to the detuning of the accelerating cavity. Measurement has shown that the frequency shift of the accelerating ($\pi/2$) mode was substantially reduced compared to that of the accelerating cavity itself. Two parasitic modes (0 and π) of ARES have to be damped so that they should not cause longitudinal coupled bunch instability. The coupling waveguides attached at the coupling cavity sufficiently damped these parasitic modes, while having negligible effect on the Q value of the $\pi/2$ -mode.

I. INTRODUCTION

The coupled bunch instability associated with the accelerating mode is a serious problem for successful operation of large ring accelerators with a high current. Its growth rate can be reduced by keeping the detuning frequency sufficiently smaller than the revolution frequency at the maximum current. The original idea of a storage cavity (s-cavity), which was directly coupled to an accelerating cavity (a-cavity), was proposed to reduce the detuning frequency by reducing R/Q of the accelerating mode [1]. Accelerator resonantly-coupled with an energy storage (ARES) was devised to refine the original idea to a practical level, where the two cavities are coupled through another cavity called "coupling cavity" (c-cavity) [2-4]. Three coupled modes are generated according to a coupled-resonator model of ARES. They are designated as 0-, $\pi/2$ - and π -mode in order of increasing frequency, respectively. The $\pi/2$ -mode is used as the accelerating mode. This three-cavity system has several advantages compared with the original two-cavity scheme: (i) the accelerating mode is stable against a heavy beam loading, (ii) the coupled bunch effects due to the parasitic 0- and π -modes almost cancel each other since their frequencies can be adjusted to be equally separated from the RF frequency, (iii) furthermore, the two parasitic modes can be damped without damping the $\pi/2$ -mode by a damping device coupled to the c-cavity, since there are no fields at the center of the c-cavity for the $\pi/2$ -mode. Choke-mode cavity [5] will be used as the a-cavity. An separate test of a choke-mode cavity power test model was very successful [6,7].

Two aluminum 1/5 scale cold models were fabricated to confirm the design described above. As the s-cavity mode, the TE015 mode of a cylindrical cavity is used. Their a-cavity is a simple pillbox cavity since a choke-mode cavity introduces undesirable complexities in the present measurement. No

coupler for damping of the 0- and π -modes are installed on the model fabricated first, which is used for studying the basic characteristics of ARES without damping, while the c-cavity of the other model is damped. The results of the RF measurement of the two cold models are presented in this paper.

II. MEASUREMENT

A. First Model without Damping

The first cold model without a damper is shown in Fig. 1. In order to realize the above mentioned advantages, the individual frequencies of the three cavities must be tuned properly. The cold models are equipped with two tuners for each of the a-, c- and s-cavities driven by micrometers, by which the resonant frequencies of the three cavities were adjusted to coincide with each other. First, the frequencies of the a- and s-cavities were tuned independently to the aimed frequency of the accelerating mode while the c-cavity was detuned by a metallic bar in it to decouple the a- and s-cavities. Then the frequency of the c-cavity was tuned using Slater's tuning curve method with the a-cavity detuned. In Fig. 2, the frequencies of the two coupled modes between the c- and s-cavity are plotted as a function of the tuner position of

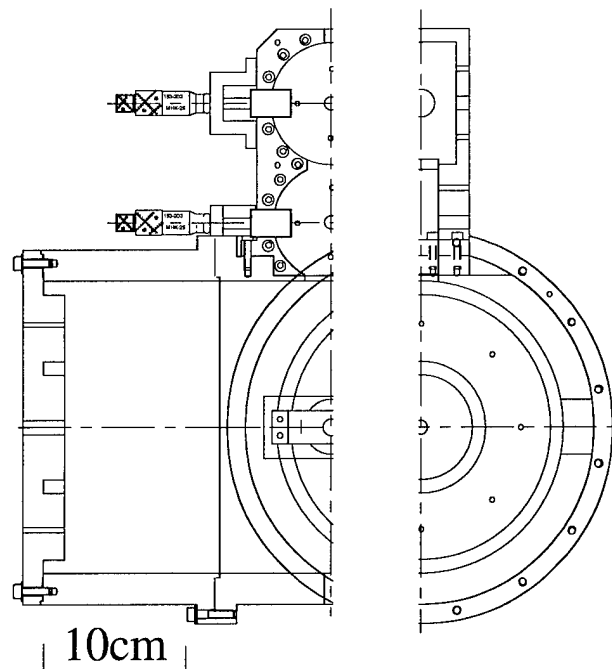


Figure 1: First cold model of ARES without a damper at the c-cavity.

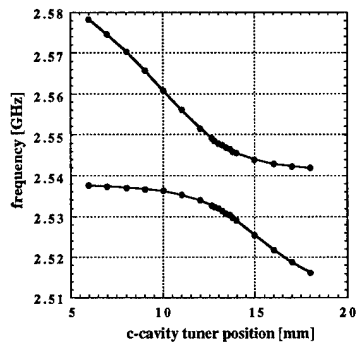


Figure 2: Tuning curve of the c-cavity to the frequency of the s-cavity.

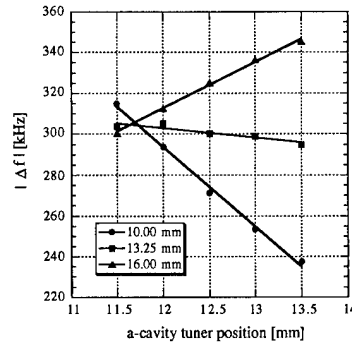


Figure 3: Frequency shift by a metallic bead in the a-cavity as a function of the tuner position of the a-cavity.

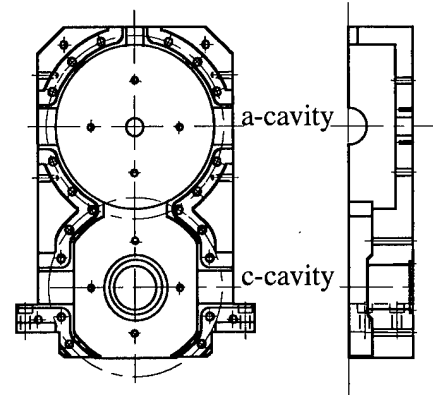


Figure 4: Modified c-cavity for coaxial couplers.

the c-cavity. The tuner of the c-cavity was set to 13.25 mm where the frequency separation between the two coupled modes is minimum.

One of the most prominent features of the $\pi/2$ -mode operation is the mode stability against the frequency change of an a-cavity. Figure 3 shows the frequency shift by a $\phi 6$ metallic bead in the a-cavity as a function of the a-cavity tuner position for three different c-cavity tuner positions. The plot is an almost horizontal line with the c-cavity tuner position of 13.25 mm, which is the "tuned" position from Fig. 2. This indicates that the ratio of the stored energy in the a- and s-cavity is almost unchanged by a perturbation to the a-cavity.

The measured Q value of the $\pi/2$ -mode is 3.3×10^4 , which corresponds to 1.4×10^5 for a full scale copper cavity. The effect of surface finish on the Q value was estimated by measuring the Q value of a pillbox cavity with the same

material, surface finish and inner shape as the a-cavity of the cold model, which we call "reference pillbox" here. Taking this effect into account, the measured Q value of the $\pi/2$ -mode is 0.85 times the value calculated by MAFIA.

The shift in the resonant frequency of the $\pi/2$ -mode was measured by placing a small metallic bead in the a-cavity to simulate the effect of detuning. The ratio of this frequency shift to the shift obtained by the same measurement for the reference pillbox was 0.069, which is in good agreement with the expected value 0.065. This means that R/Q of the accelerating mode is reduced by a factor of about 1/14. This clearly shows that the detuning of the ARES $\pi/2$ -mode due to the beam loading is largely reduced.

B. Second Model with Damping

The next cold model has two ports for coaxial lines at the center of the end plates of the c-cavity as shown in Fig. 2. The

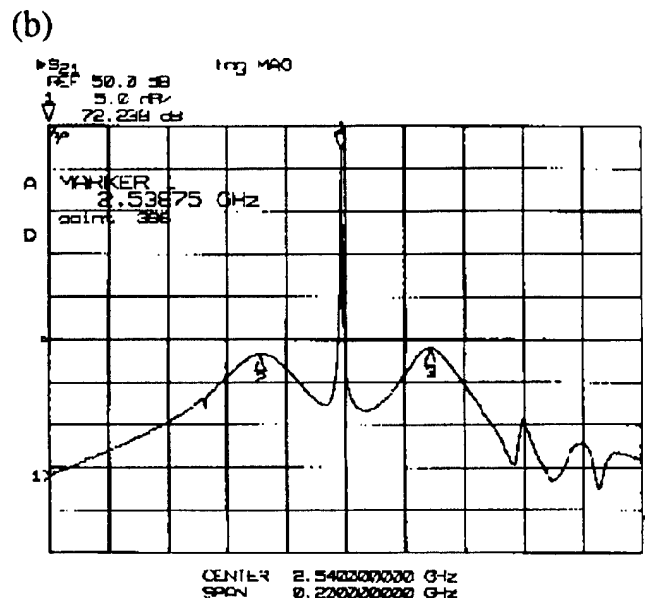
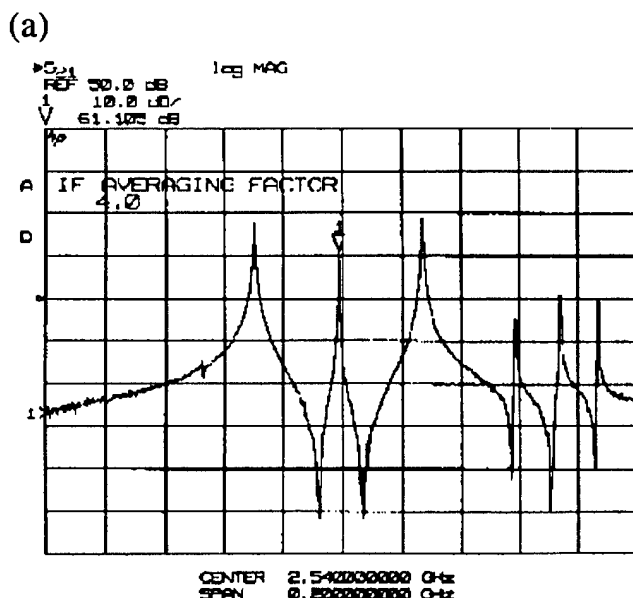


Figure 5: Measured transmission between beam ports at a-cavity: (a) coupling cavity is not damped and (b) is damped.

Table 1: Measured parameters of the 0- and π -modes.

	f [MHz]	Q	R/Q [Ω]*
0-mode	503.4	110	103
π -mode	514.9	150	72

$$* R = V^2/P$$

coupling cavity was damped by connecting loads to these ports. The cavity surface around the inner conductor of a coaxial line protrudes into the cavity like a nose cone for concentration of the electric field. In order to compensate for the frequency drop, part of the cavity was filled to form a racetrack-shaped cylinder. The measured transmission between a beam port and an end plate of the storage cavity is shown in Fig. 5: (a) the coupling cavity is not damped and (b) is damped.

The measured frequency, Q and R/Q are listed in Table 1. With the parameters in Table 1, the growth time of the longitudinal coupled bunch instability is calculated to be 17 ms for 20 ARESs in LER. We have also investigated the response of the growth time to the skewness of the passband, which is defined as

$$\frac{|(f_{\pi} - f_{\pi/2}) - (f_{\pi/2} - f_0)|}{|f_{\pi} - f_0|}$$

It was found that the growth time decreases from 35 ms to 10 ms as the skewness increases from 0 to ~10 %.

III. ARES for KEKB

The use of the TE013 mode as an operating s-cavity mode is now under serious consideration. An smaller TE013 s-cavity has practical advantages regarding low cost, easy optimization

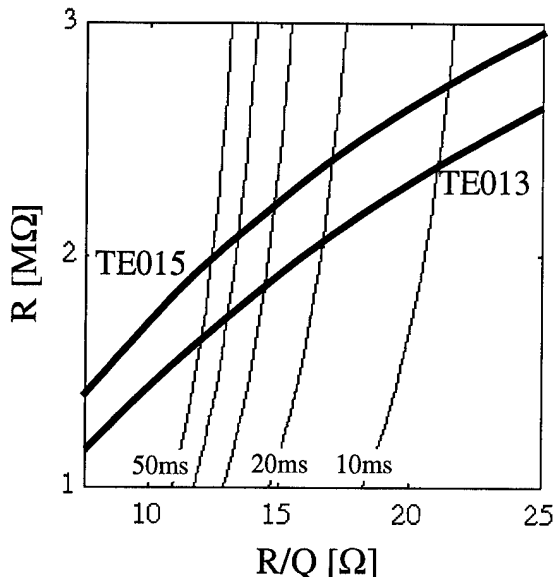


Figure 6: Chart used for comparison between the TE013 and TE015 s-cavity.

and easy installation. Recent study on the coupled bunch instability due to the accelerating mode and expected available power in KEKB suggests that the TE013 s-cavity allows a stable operation even in LER of KEKB. The two thick solid lines in Fig. 6 show the relation between R and R/Q with the ratio of stored energy in the a- and s-cavity as an implicit variable. Thin solid lines are contour lines of the growth time of the longitudinal coupled bunch instability only due to the accelerating mode assuming 20 ARESs in LER. From Fig. 6, R of TE013 is roughly 20 % less than that of TE015 if the growth rate is the same.

A separate TE013 storage cavity is now under construction to test the quality of Cu electroplating on its inner surface. A full-size ARES will be fabricated by late 1996 and installed in AR to be tested under the beam of 500 mA. The coupler for ARES is being designed [8].

IV. CONCLUSION

Basic RF characteristics of the ARES structure, which was proposed for use in high-current and low-emittance rings, was measured. The results demonstrated that it is consistent with theoretical predictions. In addition to that, the two parasitic modes were sufficiently damped for use in KEKB.

V. REFERENCES

- [1] T. Shintake, Part. Accel. **44**, 131 (1993).
- [2] Y. Yamazaki and T. Kageyama, Part. Accel. **44**, 107 (1994).
- [3] K. Akai and Y. Yamazaki, Part. Accel. **46**, 197 (1994).
- [4] "An Accelerator Resonantly Coupled with an Energy Storage (ARES) for KEKB", Y. Yamazaki, K. Akai, N. Akasaka, E. Ezura, T. Kageyama, F. Naito, T. Shintake, and Y. Takeuchi, FAE09 in this Conference.
- [5] T. Shintake, Jpn. J. Appl. Phys. Lett. **31**, L1567 (1992).
- [6] "Development of a HOM-Damped Cavity for the KEK B-Factor (KEKB)", T. Kageyama, K. Akai, N. Akasaka, E. Ezura, F. Naito, T. Shintake, Y. Takeuchi, and Y. Yamazaki, WPQ17 in this Conference.
- [7] "HOM Absorber for the KEKB Normal Conducting Cavity", Y. Takeuchi, K. Akai, N. Akasaka, E. Ezura, T. Kageyama, F. Naito, T. Shintake, and Y. Yamazaki, WPR05 in this Conference.
- [8] "Input Coupler for the KEKB Normal Conducting Cavity", F. Naito, K. Akai, N. Akasaka, E. Ezura, T. Kageyama, T. Shintake, Y. Takeuchi, and Y. Yamazaki, WPR09 in this Conference.

DESIGN OF TRAVELING WAVE WINDOWS FOR THE PEP-II RF COUPLING NETWORK*

N.M. Kroll[†], C.-K. Ng, J. Judkins and M. Neubauer

Stanford Linear Accelerator Center, Stanford University, Stanford, CA 94309

Abstract

The waveguide windows in the PEP-II RF coupling network have to withstand high power of 500 kW. Traveling wave windows have lower power dissipation than conventional self-matched windows, thus rendering the possibility of less stringent mechanical design. The traveling wave behavior is achieved by providing a reflecting iris on each side of the window, and depending on the configuration of the irises, traveling wave windows are characterized as inductive or capacitive types. A numerical design procedure using MAFIA has been developed for traveling wave windows. The relative advantages of inductive and capacitive windows are discussed. Furthermore, the issues of bandwidth and multipactoring are also addressed.

I. INTRODUCTION

The window in the coupling network of the PEP-II RF cavity must transmit up to 500 kW of CW RF power at 476 MHz to the cavity and must also handle considerable reflected power due to sudden beam-loss conditions [1]. The waveguide window used in PEP-II is a ceramic disk mounted on an iris connected to rectangular waveguides [2]. The conventional design of self-matched windows inherently sets up a large standing wave with electric field maximum within the window. Because of the large power requirements of PEP-II, this leads to a large heating load and a requirement for a prestressed mechanical mounting to deal with the resultant thermal stress. Traveling wave (TW) windows, on the other hand, can reduce the heat deposition sufficiently to allow conventional mounting. This is achieved by introducing a reflecting iris at each side of the window in such a way that the reflection at the reflecting iris cancels that at the window-waveguide interface. TW windows can be divided into inductive and capacitive types, depending on the structure of the irises, and the choice affects their positioning in the waveguides. A capacitive TW window, due to its compactness, has been incorporated into the layout of the coupling network of the PEP-II RF cavity as an alternative to the self-matched window.

II. GENERAL CONSIDERATIONS

For qualitative insight, we assume only one mode (circular TE₁₁, for our case) propagating in the window with power flowing to the right. The electric field can be written as:

$$\vec{E} = \vec{e} \sqrt{\frac{2ZP}{1-R^2}} \{ \cos(\omega t - k_z z) + R \cos(\omega t + k_z z) \}, \quad (1)$$

where $\int e^2 da = 1$ (a is the cross sectional area of the window), Z is the impedance of the waveguide with the window cross section, and P is the average transmitted power. R is the ratio of the wave amplitudes (left going/right going) within the window and is equal to the magnitude of S_{11} looking to the right. For a matched window it is also equal to the same quantity looking to the left. We have taken the origin of the z coordinate in Eq. 1 to lie at the maximum of the standing wave pattern and note that for typical self-matched windows (certainly ours) it lies within the window. In general $0 \leq R \leq 1$, and $R = 0$ for the pure traveling wave case. By averaging E^2 over the window cross section, it can be shown that the enhancement factor P_r in power deposition of a symmetric self-matched window to that of a pure TW window is given by:

$$P_r = \frac{1+R}{1-R}. \quad (2)$$

III. DESIGN PROCEDURE

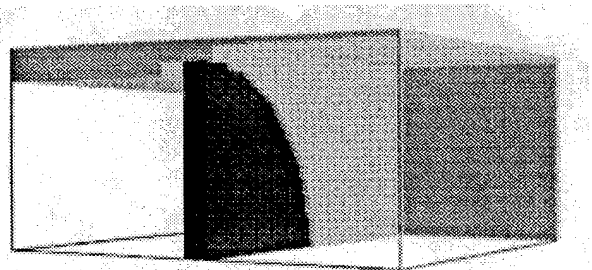


Figure 1. 1/4 MAFIA model of the self-matched window.

For a specified configuration of a mounting iris and waveguides, the matching of a self-matched window is achieved by adjusting its thickness and its position at the mounting iris. For TW windows, we have used MAFIA as a calculation tool for developing a systematic design procedure. To simplify the window development program, our designs have been based upon the self-matched configuration adopted for PEP-II. The self-matched window shown in Fig. 1 is mounted on a frame with a thickness of 1.5" for the purpose of accommodating cooling channels. The air side waveguide is a WR2100, and on the vacuum side a 16"x9" waveguide is connected to the aperture coupler of the RF cavity. The window, a ceramic disk with dielectric constant 9.5 and loss tangent 0.00015, has a diameter of 9.75" and a thickness of 0.7". The procedure for designing a TW window is described as follows.

(1) Determine the S-matrix of the window-waveguide junction.

This is determined by the geometry shown in Fig. 2, in which the window is represented by a circular waveguide filled

*Work supported by the Department of Energy, contract DE-AC03-76SF00515.

[†]Also UCSD, DOE Grant DE-FG03-93ER40759.

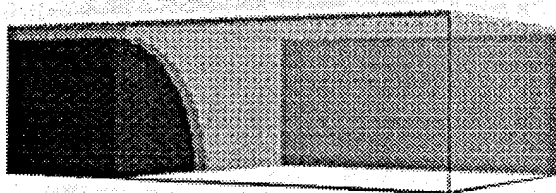


Figure 2. 1/4 MAFIA model of a ceramic-waveguide junction.

with ceramic. The S-parameters are determined by driving the TE_{11} mode at the input end of the circular waveguide.

(2) *Determine the size and position of the matching element.*

The condition which must be satisfied by the matching element (ME) on the RHS of the window is

$$S_{11}(\text{ME}) = S_{22}^*, \quad (3)$$

where S_{22} refers to the configuration of Fig. 2, and the reference plane on the LHS of the ME is taken to coincide with that on the RHS of the Fig. 2 configuration. An analogous condition applies to the ME on the LHS of the window. Trial dimensions for the ME's were obtained from analytic formulas, and MAFIA was used to trim the dimensions so that Eq. 3 holds for the absolute values. From the phases of the MAFIA computed elements of $S(\text{ME})$ one can use standard formulas to determine the position required to satisfy Eq. 3 with respect to phase. The procedure is checked by appending the ME on the RHS of the Fig. 2 configuration and confirming the absence of reflection of the right going wave in the window. If evanescent waves generated near the ceramic overlap the ME or vice versa (as is the case for the capacitive ME), some additional trimming may be required. The analogous procedure is followed for the ME on the LHS of the window. Finally the entire assembly is checked for match using MAFIA. Because the window is thin, some overlap of higher order modes generated on the two sides of the window is expected and further trimming is required to secure a match. The field distribution in the entire assembly is then checked to, for example, compute the power dissipation ratio. In practice some of the steps described above are skipped as the "bottom line" is simply to obtain a matched window assembly with an improvement in power dissipation of the order of that obtained from Eq. 2.

IV. SIMULATION RESULTS

(a) Inductive traveling wave windows

The inductive TW window is made by providing vertical bars along the heights of the waveguides as shown in Fig. 3. The thickness of the matching irises is chosen to be 0.25". The distances of the irises from the window in the WR2100 and 16"x9" waveguides are found to be 13.3" and 18.9" respectively. This additional space poses stringent conditions for the coupler network layout, in particular when the detuned-short position is preferably within the window. The required iris gaps are 8.4" and 8.8" for the two waveguides.

The electric field pattern in the structure is shown in Fig. 4. The minimum of the field is at the window, while field maxima are located in the waveguides between the matching irises and the window, indicating the set-up of standing waves in these regions. The power distribution in the window is shown in Fig. 5. The power dissipation is large in the center and is reminiscent of

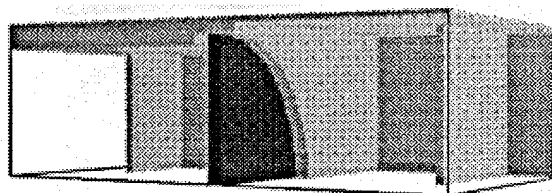


Figure 3. 1/4 MAFIA model of an inductive TW window.

the TE_{11} mode distribution. Thus higher-order mode effects in the window are small. The power is about 7.6 times smaller than that of the self-matched window, where field maximum is found at the window. The self-matched window has a $S_{11} \sim 0.77$ at the window-waveguide junction, and from Eq. 2, $P_r = 7.7$ which is in very good agreement with MAFIA calculation. The dielectric loss in the self-matched window is 157 W, and hence the loss is 20 W for the TW window.

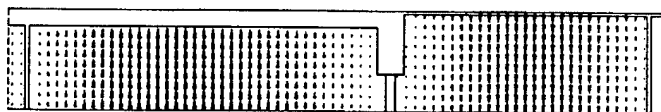


Figure 4. Electric field pattern in the inductive TW window. The plane is chosen such that the matching irises are shown.

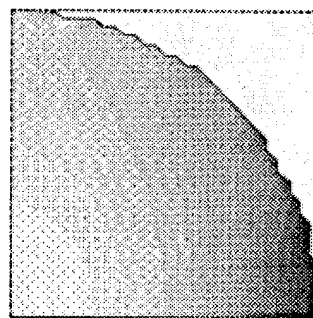


Figure 5. Power distribution in the inductive TW window.

The PEP-II RF feedback system requires a bandwidth of 5 MHz for 3 db transmission and a group delay of ≤ 350 ns. In Fig. 6, we show the variation of S_{11} of the window assembly as a function of frequency. The bandwidth satisfies our requirement. In Fig. 7, we show ϕ_{21} as a function of frequency. Within the relevant bandwidth, the phase variation is linear. Subtracting the group delays of the waveguides in the window assembly from the slope calculated from Fig. 7, the additional time delay due to the window assembly is 14.3 ns, which is relatively small compared with the total allowed group delay.

(b) Capacitive Traveling Wave Windows

The capacitive TW window is made by providing horizontal bars along the widths of the waveguides. Since the waveguide TE_{10} mode has its electric field in the vertical direction, the small gap width between the bars introduces high field gradient. The gap width can be increased by using thicker matching irises. Furthermore, the irises are found very close to the window. For a single gap design, the power distribution highly peaks around the center of the window, making cooling difficult. Thus we introduce a double gap configuration as shown in Fig. 8. In the

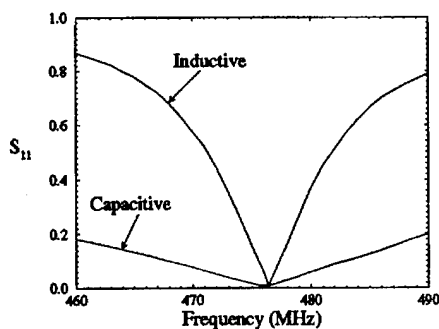


Figure 6. S_{11} as a function of frequency for the inductive and capacitive TW windows.

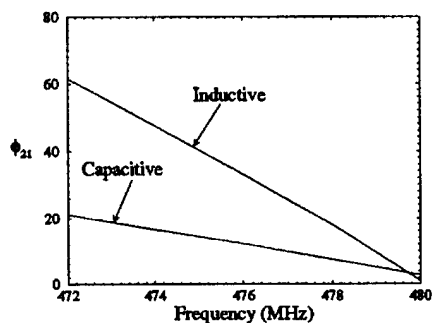


Figure 7. ϕ_{21} as a function of frequency for the inductive and capacitive TW windows.

WR2100, the iris thickness is 3'', the gap width is 1.6'', and the distance of the irises from the window is 0.94''. In the 16''x9'' waveguide, the iris thickness is 4'', the gap width is 1.3'', and the distance of the irises from the window is 0.91''.

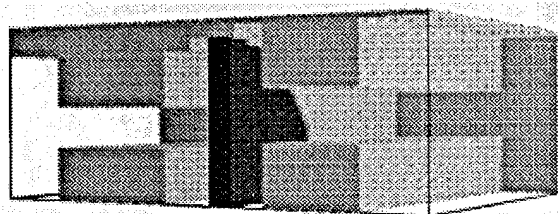


Figure 8. 1/4 MAFIA model of a capacitive TW window.

The electric field pattern in the structure is shown in Fig. 9. The field is small at the window, while field maxima appear in the gaps of the matching irises. For 500 kW average power, the peak fields are 0.54 kV/cm and 0.35 kV/cm in the 16''x9'' and WR2100 waveguides, respectively. It is anticipated that rounding and coating of the irises will be required to avoid multipactoring at the vacuum side and arcing at the air side. The power distribution in the window is shown in Fig. 10. The distribution is more uniform than that of the inductive case, peaks at a distance away from the center, and is not purely TE_{11} -like, presumably because of the closeness of the matching irises to the window. The total dielectric loss is about 6.6 times smaller than that of the self-matched window. This corresponds to 24 W loss for 500 kW average power from the klystron.

From Figs. 6 and 7, the bandwidth is broader than that of the inductive TW window and the additional group delay of the win-

dow assembly is 3.3 ns, which are within the PEP-II requirements.

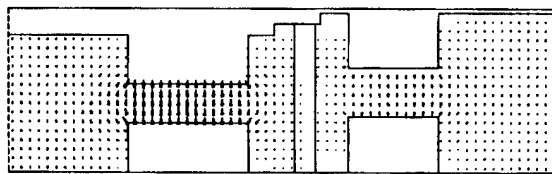


Figure 9. Electric field pattern in the capacitive TW window.

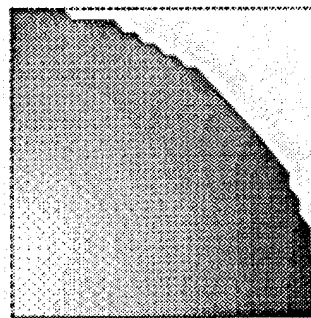


Figure 10. Power distribution in the capacitive TW window.

V. SUMMARY

The relative advantages of the TW windows compared with the self-matched window are summarized in Table 1. The capacitive TW window is a superior design in terms of its compactness, broad bandwidth, small group delay and almost 7 times less dielectric loss than the self-matched window. Despite its complexity compared with the self-matched window, it is an attractive alternative for handling high power throughput of the PEP-II B-Factory.

Window type	Relative power loss	Bandwidth (MHz)	Group delay (ns)
Self-matched	1	acceptable	small
Inductive TW	0.13	acceptable	14.3
Capacitive TW	0.15	acceptable	3.3

Table 1. Comparison of the self-matched, inductive TW and capacitive TW windows.

Acknowledgements

We would like to thank P. Corredoura, K. Ko, R. Rimmer and H. Schwarz for useful discussions.

References

- [1] An Asymmetric B Factory, Conceptual Design Report, LBL-PUB-5379, SLAC-418, CALT-68-1896, UCRL-ID-114055 or UC-IIRPA-93-01, June 1993.
- [2] M. Neubauer et. al., High-Power RF Window and Coupler Development for the PEP-II B Factory, these proceedings.

IMPEDANCE SPECTRUM FOR THE PEP-II RF CAVITY*

X. E. Lin, K. Ko and C.-K. Ng

Stanford Linear Accelerator Center, Stanford University, Stanford, CA 94309

Abstract

The impedance spectrum presented by the PEP-II RF cavity to the beam is calculated using a 3D MAFIA model which includes the damping waveguides and the input coupler. The simulation assumes that all the ports leading out of the cavity, including the beam pipes, are terminated in matched loads. The effect of the external loading on the longitudinal impedances will be examined. This study takes into account the input coupler damping which has not been considered in previous calculations [1].

I. INTRODUCTION

There is an ongoing program at SLAC to minimize the ring impedances in the PEP-II B Factory [2]. PEP-II is a high-current storage ring in which both longitudinal and transverse coupled modes will be excited. These are wakefields generated by the narrow-band (high- Q) impedance in the ring that can cause different beam bunches to interact. The coupled-bunch motion if left uncontrolled, can drive the beam unstable at high beam currents. Most of the high- Q resonances in the ring are attributed to the Higher-Order-Modes (HOMs) of the RF cavities. A distinct feature in the PEP-II cavity design is a set of damping waveguides to couple the HOMs out to external loads. By heavily loading these modes, their contributions to the ring impedance budget can be greatly reduced.

II. PEP-II RF CAVITY

The HOM damping scheme for the PEP-II RF cavity consists of three symmetrically placed waveguides around the cavity wall and connected with the cavity volume through iris apertures (Fig. 1). The positioning of the apertures are such that they interrupt the current flow of the most harmful HOMs. The waveguides are dimensioned to allow the HOMs to propagate while cutting off the fundamental mode so that it is minimally perturbed. This design was tested on a low-power prototype cavity. In Fig. 2, we show the transmission (S_{21}) data between probes on opposing beam pipes up to 1.4 GHz (reproduced from Ref. [1]). When compared with the undamped response, the fundamental mode at around 480 MHz is relatively unchanged (waveguide cutoff is at 600 MHz). The HOM Q 's, however, are significantly lowered; for example, the TM_{011} mode at around 750 MHz is loaded to a Q of 28, down from a calculated unloaded Q_o of around 40000. Because the probes couple differently to different modes, one cannot take the relative amplitudes of the peaks of the modes as a good measure of their relative impedances. An impedance spectrum, however, is essential for detail studies of the collective effects to determine beam instabilities.

*Work supported by the Department of Energy, contract DE-AC03-76SF00515.

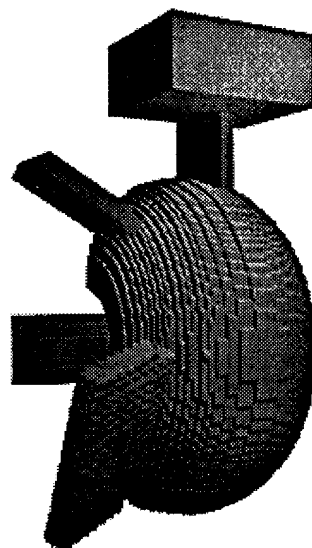


Figure 1. MAFIA model of the PEP-II RF cavity.

III. PREVIOUS IMPEDANCE ANALYSIS

The impedances of the longitudinal and transverse HOMs in the undamped (axisymmetric) PEP-II cavity have been calculated with the 2D URMEL code. HOMs with high impedances were targeted by the damping waveguides. The damping effect in the prototype cavity was studied with the Kroll-Yu method [3] which calculates the frequencies and Q 's of the cavity modes by assuming the waveguides are terminated in matched loads. It made use of the eigenmodes provided by fully 3D codes such as MAFIA, but with the waveguides shorted at various lengths. This indirect method is necessary because the eigenmode solver cannot easily handle complex frequencies when loss is included.

There is generally good agreement between the analytical results and measured data up to 1.2 GHz. Above that frequency, the second waveguide mode is not cut off and the Kroll-Yu method, which assumes a single waveguide mode, may not give reliable results. The POPBCI [4] code does not have this limitation and uses similar numerical input to generate an impedance spectrum. It modeled the PEP-II cavity with some success but no further work with it was carried out.

A good estimate of the effective impedance can be obtained from the R/Q calculated with URMEL and from the Q measured in the damped cavity. The results indicate that the damped modes are reduced to a level that is within the capability of the broad-band feedback system. The possibility of further damping these modes through the drive port for example, is being considered. We point out that the fundamental shunt impedance loss due to the HOM damping scheme is 10% from the MAFIA analysis.

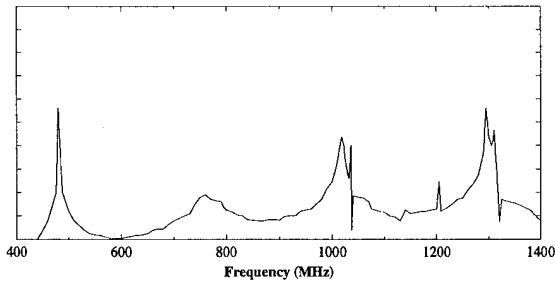


Figure 2. Mode spectrum of low-power test cavity with damped waveguides.

IV. THE MAFIA TIME-DOMAIN MODEL

A straightforward way to calculate the impedance is through the Fourier transform of the wake potential. One moves a bunch charge along the beam axis of the cavity and from the wakefields it generates, it is possible to obtain the wake potential by numerical integration. For cavities of arbitrary shape, codes like TBCI in 2D and MAFIA in 3D are commonly used for such calculations. Normally in an accelerator cavity, the impedance spectrum consists of narrow-band contributions below the beam-pipe cutoff and a broad-band portion that extends above it. The narrow-band impedance comes from cavity resonances which contribute to the long-range wake potential. Without loss, they are delta functions which are best evaluated in the frequency domain using eigenmode solvers. The spectrum above cutoff is due to a continuum of beam-pipe modes, and contributes to the short-range wakes that time-domain calculations can treat more effectively.

In this paper, we describe a time-domain approach to calculate the impedance spectrum for the PEP-II damped cavity, including the narrow-band contributions, with the following justifications. First, the frequency domain methods have been successful in analyzing only a small number of modes. Second, as seen in Fig. 2, most of the HOMs no longer have sharp peaks but are broadened by damping. Since the frequency spacing in the spectrum varies as the inverse of the total wake distance, it is possible to resolve many of the reasonably low Q modes if we calculate the wakefield out to large enough distance. Third, broad-band waveguide boundary conditions are now available in the MAFIA time-domain module, so that not only the standard beam pipes can be modeled. The damping waveguides as well as other 3D insertions such as the input coupler can also be properly treated with matched terminations at their end planes. A passing bunch charge then comes very close to interacting with the realistic cavity, and one can calculate the impedance spectrum from the wakefields it generates in a direct and straightforward manner.

V. WAKEFIELD CALCULATION

We model one half of the geometry to take advantage of symmetry. The symmetry plane splits the cavity, the top waveguide and the iris coupler but leaves the side waveguide intact (hence also the one on the opposite half). The wakefield calculation requires driving a bunch charge along the beam axis. The PEP-II nominal bunch length σ_z is 1 cm and numerically it is preferable to have at least 5 mesh points per bunch length or a .2 cm mesh size. For the half cavity dimen-

sions of 30cmx15cmx50cm, this translates to many millions of mesh points, even without the waveguide and coupler attachments. Furthermore, the time step would accordingly be small (the Courant condition) so simulation time would be very long, especially when we calculate wakes out to large distances.

In the simulation, we used about six mesh points per bunch length and a σ_z of 2 cm (the narrow-band impedance does not depend on the bunch length). The mesh constructed on this grid scale contains close to three million mesh points. The wakefield calculation was carried out to $s=40$ m, where s is the bunch coordinate. Two separate runs were made; one with and one without the iris coupler to distinguish any additional damping effect.

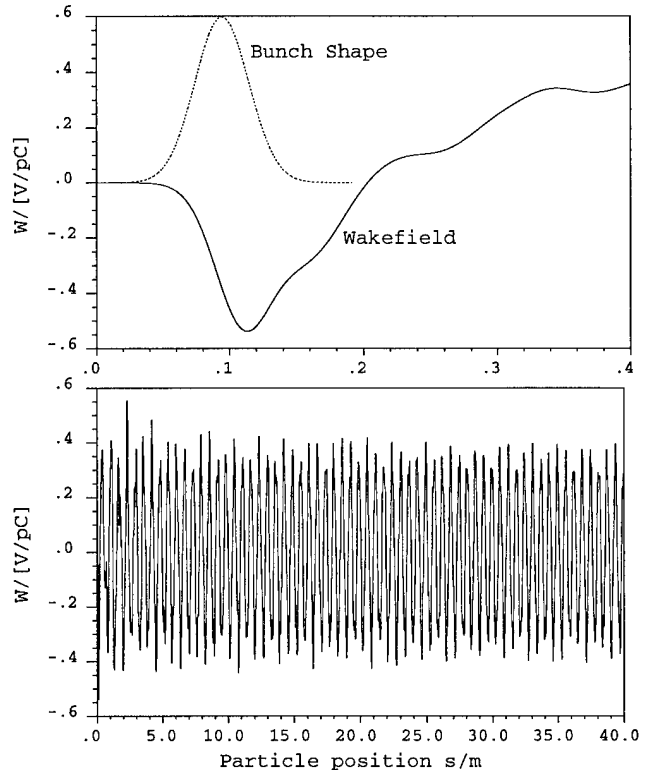


Figure 3. Short-range and long-range wakefields in the PEP-II RF cavity.

The top plot in Fig. 3 shows the short-range longitudinal wakefield up to $s = .4$ m, while the bottom plot shows the wake over the full range (40 m). The short-range wakefield is not affected by the damping waveguides and agrees with previous TBCI results on the undamped cavity. The long-range wakefield exhibits persistent oscillations, indicating the presence of high- Q resonances in the cavity. A snapshot of the electric field distribution in the symmetry plane of the cavity at large time is given in Fig. 4. It shows predominantly the fundamental mode which is undamped and is responsible for the large persistent oscillation in Fig. 3. We also see fields in the beam pipes, the damping waveguide and the iris coupler as well. A series of similar snapshots will verify that these are outgoing waves leaving the cavity. In MAFIA, one can monitor the fields crossing the waveguide boundaries so that the power spectrum can be found at each of the ports also.

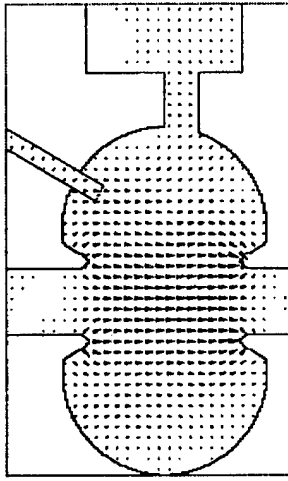


Figure 4. Electric field distribution at large time.

VI. IMPEDANCE SPECTRUM

From the wakefield of Fig. 3, one obtains the impedance spectrum by Fourier transform and then divides by the bunch spectrum. The top plot in Fig. 5 shows the result for the no coupler case whereas the bottom plot is with coupler included. In both spectra, we easily identify three familiar peaks in the frequency range up to 1.5 GHz. These are the modes with the three highest effective impedances, and correspond to the fundamental mode near 480 MHz, the TM_{011} at 760 MHz and the TM_{021} near 1.3 GHz respectively. Note that the TM_{020} peak that was visible around 1 GHz in Fig. 2 is not present because it has negligible residual impedance. The primary interest here is not in the fundamental mode although it constitutes the main contribution to the long range wakefield. Since it is not damped, the resonance broadening of the peak is due to artificial damping introduced by applying the Fourier transform.

To calculate the impedance and the Q of the HOMs, several factors have to be taken into consideration. First and foremost is the graininess of the frequency data which determines how well one can resolve a resonance peak. We will fit each peak with a Breit-Wigner resonant form to get improved accuracy. The other factor is the artificial damping we alluded to earlier and this has to be subtracted out from the Breit-Wigner solution. Yet another factor is the error incurred from mesh discretization, and this effect is especially pronounced in approximating the side waveguide and the iris opening into the cavity. As a result, the waveguide-cavity coupling is different from that in the physical cavity. However, one can correct for it from knowing the power ratio between the top and side waveguides.

The results on the TM_{011} mode after these factors are included agree very well with previous analysis. We found a Q of 28.6 versus 28 from measurement and 26 from the Kroll-Yu method. The impedance is 1.3 k Ω versus 1.26 from the estimate. For the TM_{021} mode near 1.3 GHz, the error due to limited data points is large. The frequency spacing for a wake distance of 40 m is 7.5 MHz, so at 1.3 GHz this resolution limits to a Q of several hundred. The measured Q is 900 which means a smaller frequency spacing, and correspondingly a larger wake distance, is needed. MAFIA has a restart option so one can in principle extend the simulation indefinitely to get finer resolution provided that numerical errors are not a factor. Nevertheless with

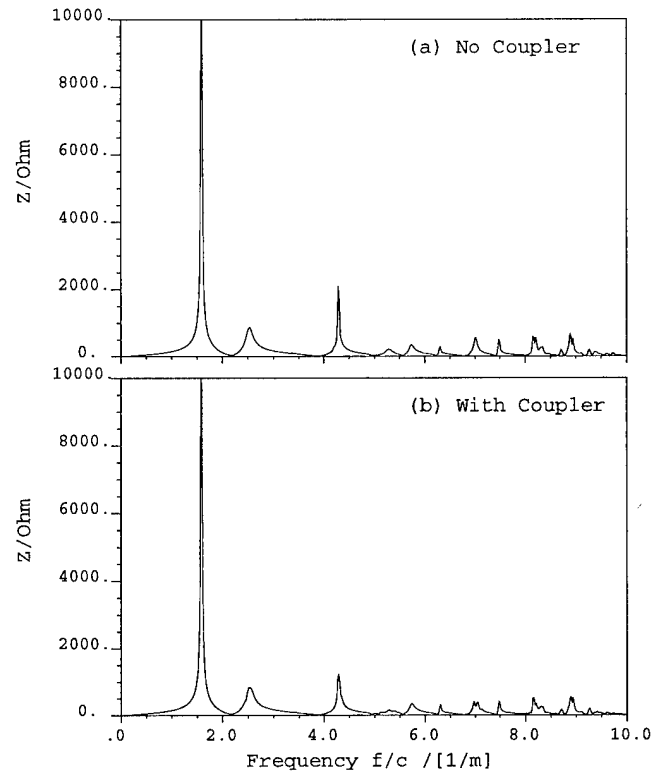


Figure 5. Longitudinal impedance spectrum as a function of frequency for the cavity with and without coupler.

the present data, we extracted a Q of 370 without coupler and 160 with coupler, which is a factor of two reduction. A separate analysis without the beam gives a reduction factor of three [5].

VII. DISCUSSION

We have presented a time-domain wakefield analysis of the PEP-II RF cavity which includes the effect of external loading directly. The longitudinal impedance spectrum for the waveguide-damped cavity is calculated with and without the input coupler. The agreement with previous results is good for low Q modes because of better resolution. We believe that by using a longer bunch to save in total mesh size, and calculating to larger wake distance, even higher Q modes can be adequately resolved. This approach has the potential of providing a more complete model for the narrow-band impedance than was done previously.

References

- [1] An Asymmetric B Factory, Conceptual Design Report, LBL-PUB-5379 or SLAC-418, June 1993.
- [2] S. Heifets et. al., Impedance Budget of the PEP-II B-Factory, these proceedings.
- [3] N. M. Kroll and D. U. L. Yu, Part. Accel. 34, 231 (1990).
- [4] P. Arcioni, POPBCI-A Post-Processor for Calculating Beam Coupling Impedances in Heavily Damped Accelerator Cavities, SLAC-PUB-5444, 1991.
- [5] C.-K. Ng, K. Ko, N. Kroll and R. Rimmer, Coupling Network Simulation for the PEP-II RF Cavity, EPAC94, p2140.

Measurement and Analysis of Higher-Order-Mode (HOM) Damping in B-Factory R-F Cavities

D.A. Goldberg, M. Irwin, and R.A. Rimmer, Lawrence Berkeley Laboratory, *
Berkeley, CA 94720 U.S.A.

We have previously described [1] a fully automated "bead" puller system which can be used to measure both longitudinal and transverse field profiles. Converting bead-puller data to impedances requires knowledge of the Q -values of the individual modes. A second system enables us to acquire cavity spectra and then simultaneously fit up to three resonances plus a uniform background. R/Q measurements on the "bare" cavity (i.e., with only the beam ports open) have been consistent with predictions by URMEL. Due to overlapping resonances, we have not been able to measure R/Q for many of the damped modes, but for those for which we have, there is generally good agreement with the undamped cases. Assuming this to be true in general, we use the measured Q -values for the damped modes in conjunction with the "best available" measured R/Q , and conclude that with a few possible exceptions (which if need be can be dealt with by additional dedicated dampers), the damping for the higher order modes is adequate for the operation of the machine.

I. INTRODUCTION

The main purpose of this investigation was to see whether the higher-order-mode (HOM) dampers which are to be installed on the PEP-II B-Factory RF cavities[2] reduce the impedances of these modes sufficiently that any coupled-bunch oscillations which they caused could be coped with by the proposed feedback systems. Ideally, one need only measure the R/Q 's and corresponding Q 's of the various HOM's for the damped cavity (we use " R " to denote the [transit-time-corrected] shunt impedance [3]).

To determine the R/Q of the various cavity modes, we used the well-established "bead-pulling" technique (see, e.g., Ref. 1, which also describes the automated system which we developed for making such measurements.) To convert from R/Q to R , it is necessary to know Q . Even for the undamped-cavity spectra, adjacent peaks not infrequently interfere with one another; for the damped case, the situation is both more frequent and more severe. In the latter cases, not only is it generally not possible to do bead-pull measurements, but it is difficult even to extract Q values. We have been able in most instances to deal with the latter problem by developing a multiple-peak fitting routine, which can simultaneously fit three peaks (plus a

background). If one can then assume that the R/Q 's for the damped cavity modes are the same as those for the undamped cavity, the impedances for the damped cavity will simply scale with Q .

Because R/Q depends only on geometry, normally one can assume that it is independent of damping. However, for the B-Factory cavity, the dampers take the form of three identical absorber-containing waveguides (whose cutoff frequency is greater than the frequency of the fundamental mode) [2]. If one tries to produce an undamped cavity simply by removing the absorber, the waveguides themselves become resonant cavities, and for much of the frequency range, the resulting structure behaves like a system of coupled resonators whose field shapes differs considerably from those of the damped cavity. As a result it was necessary to remove the waveguides when measuring the undamped system. This removal was done in two different ways: physically removing them, (and covering the blank flanges with copper tape), and taping over the apertures on the inside of the cavity.

The present paper describes the various approaches we used to obtain the impedances of the various HOM's of the cavity. Included are brief descriptions of some of the problems encountered, and techniques used to overcome them. We also describe briefly the multiple-peak fitting routine, along with examples of its effectiveness. To evaluate the validity of using calculated or undamped R/Q 's in situations in which the damped R/Q 's cannot be measured, we present comparisons between URMEL calculations and measurements, and between measurements on the damped and undamped cavity. Finally, we present our current "best estimates" of the impedances for the various modes.

II: DATA ACQUISITION AND ANALYSIS

Without doubt, the greatest source of difficulty in the present series of measurements was the profusion of overlapping modes. This causes a problem not only with resolving the peaks, but more basically, with identifying them. A variety of techniques were used in dealing with these problems. Before discussing them, a brief discussion of the measurement method may be useful.

Both the cavity spectra and the R/Q frequency-shift measurements were obtained in the same fashion. An axial probe was inserted at either end of the cavity, at a radial position a few millimeters inside the nose cone, and axially flush with it. The probes were mounted on copper sleeves that were inserted in the beam tubes at either end of the cavity, and could be rotated about the beam tube axis to

* Work supported by Director of Office of Energy Research, U.S.D.O.E, under Contract DE-AC03-76SF00098

vary the azimuthal position of the probes. A network analyzer was connected to the probes, and the cavity's S21 response was measured.

Basically we had three tools at our disposal in dealing with problems of peak identification and resolution. The first of these, probe orientation, was applicable to both problems. For determining Q values, the multiple peak-fitting program was an extremely effective way of dealing with the resolution problem; however, other than as a diagnostic tool, it was of little help in the R/Q measurements. Oddly enough, a third tool in the identification process was the bead-puller itself, particularly when used in conjunction with the URMEL field calculations. We discuss each of these briefly.

Probe orientation. This tool is particularly useful in cases where the azimuthal symmetry of the cavity is strongly broken, for example by the presence of a coupler, but is still of some use in other cases, because of the small, imperfection-induced asymmetries which are inevitably present. The asymmetry removes the degeneracy between the two components of most of the multipoles. This not only causes the two components to have different frequencies, but also tends to "anchor" their orientation in the cavity: For dipole modes, for example, one component gets oriented in the direction of the couple (in our case, the vertical), and one, perpendicular to it. Setting both probes so that they are horizontally displaced from the center (0°), one will excite only the horizontal component of the dipole; setting them both at 90° , only the vertical.

This enables us to distinguish dipoles from monopoles (whose peaks are unaffected by probe rotation), as well as from higher n -poles (whose intensity exhibits the same behavior at probe rotations of $90/n^\circ$). It can also be used to enhance a given dipole component relative to a nearby monopole, as one would want to do when doing a bead-pull on the dipole. Even more useful, if one orients one probe at 0° and the other at 90° , one can suppress *both* dipole components in the measured spectrum, something one would need to do when measuring a monopole in the presence of a dipole contaminant. In the absence of a strong asymmetry to anchor the modes, this "tool" is less useful because the dominant asymmetry in such cases is due to the probes themselves. Even then, a non co-linear probe orientation can sometimes reduce dipole contaminants.

Multiple-Peak-Fitting Routine. We have used the code IGORTM[4], with its extraordinarily powerful data acquisition and scripting capabilities, as well as its analytical tools, to create a computer program which is capable of acquiring data using a network analyzer, and then performing a least-squares fit to the data. A representative fit for a pair of adjacent peaks, the 0M1 monopole and the 1E1 dipole, from the damped-cavity spectrum is shown in Fig. 1. Absent such a fitting routine it is doubtful that a meaningful Q-value could have been obtained for the left-hand peak.

The functional form chosen for the individual peaks was a Lorentzian. Because the probes are located at opposite ends of the cavity, it is necessary, when combin-

ing the amplitudes of adjacent peaks, to take into account the relative longitudinal reflection symmetry (parity) of their electric fields. This actually proves to be an advantage in identifying the various peaks. In the example shown, because the 0M1 and 1E1 have opposite parities, there is a smooth smooth valley between them. If they had had the same parity, that region would have been characterized by a notch.

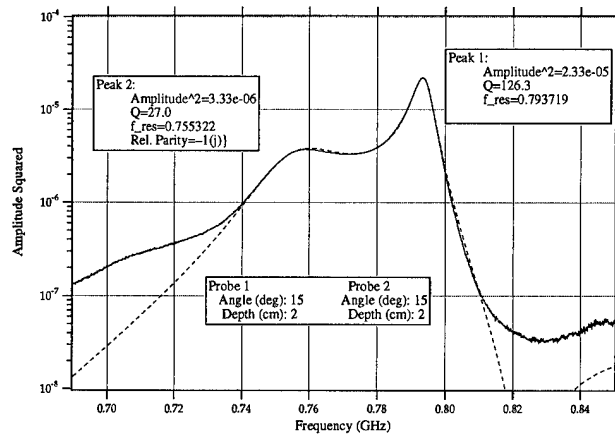


Fig. 1. Simultaneous fit of the 0M1 monopole and 1E1 dipole modes of the fully damped cavity.

An additional feature which we added was in treating the background as a purely imaginary amplitude. This was done because, except for the rare case where the background level is actually determined by the noise floor, it is in fact the sum of the residual amplitudes of all the other peaks (in the entire spectrum); because they represent responses far from resonance, they are essentially purely imaginary.

The Bead Puller as a Diagnostic Tool. Because of its ability to do both azimuthal and transverse scans, the bead puller proved very useful in mode identification, particularly when used in conjunction with the probe orientation technique.

III. EXPERIMENTAL RESULTS

Our original intent was to study the behavior, first of the "bare" cavity, with all ports covered from the inside of the cavity, as a way of facilitating mode identification, and also permitting a comparison of our results on the azimuthally symmetric structure with those calculated in URMEL. For the most part, the frequencies of the various modes were within a few MHz of those predicted by URMEL. However, in some cases, as with the cluster of modes in the neighborhood of 1700 MHz, this did not suffice to confirm identification.

For the most part, these difficulties were more pronounced with the dipoles (also the two highest-frequency monopoles), and so we initially elected to restrict our measurements to monopoles until such time as the pro-

posed new RF coupler became available. As can be seen from table 1, the measured R/Q values for the various monopole modes in the bare cavity are in excellent agreement with the URMEL calculations.

Table 1: Comparison of R/Q for monopole modes as calculated (URMEL) and measured under the conditions shown.

Mode	URMEL	Bare	Blank	Damped
0E1	108.8	106	110	105
0M1	45.0	44	40	33
0E3	7.6	NV	6.6	NM
0M2	6.6	6.6	5.7	5.2
0E4	5.1	5.7	5.2	NM
0M3	4.8	4.8	3.6	NM
0M4	1.7	1.8	1.7	NM
0E6	3.5	NM	NM	NM
0E7	1.2	NM	NM	NM

Note: NM means R/Q not measurable; NV means the peak was not visible in the observed spectrum.

The next column in the table shows the results obtained for the second "undamped" geometry, namely the dampers removed and their flanges taped over, defined as "blank". As discussed earlier, this step might reveal any anomalies caused by the damper apertures, and serve as an indicator that the introduction of the dampers caused significant changes in R/Q. The table does show some changes from the "bare" cavity, but nothing that would cast serious doubt on using the undamped R/Q's for modes where damped R/Q's could not be measured. Most of the discrepancies are on the order of 5-10%; the largest is on the order of 25%, but in a favorable direction.

We then undertook measurements of the damped cavity. The damped Q-values are shown in Table 2a. In several cases, the damped peaks could not be identified unambiguously, and we have entered an upper limit based on the Q of the narrowest of the candidate peaks. Table 2a also shows the R values obtained using the damped Q's and calculated R/Q along with a set of "target" values from Ref. 2.

Table 2a: Comparison of R for damped-cavity monopole HOM's with target values (see Ref. 2)

Mode	R/Q (Ω)	Q _L	R (k Ω)	target (k Ω)	fract. target
0M1	45	27	1.21	3.2	.38
0E3	7.7	NV	6.6	1.9	
0M2	6.6	750	4.9	1.9	2.6
0E4	5.7	<200	<1.1	1.5	<0.7
0M3	4.8	4.8	NM	1.4	
0M4	1.8	1000- 2400	1.8-4.5	1.2	1.1-2.5
0E6	3.5	<450	<1.6	1.1	<1.4
0E7	1.2	NM	NM	1.1	

When it became apparent that the new coupler would not be available in time for use in these measurements, we elected to obtain the best estimates we could of the damped

Q's of the dipole modes with the symmetric cavity, to see whether there might be any unpleasant "surprises." We were able to obtain at least crude upper limits for most of the modes, and the results are shown in table 2b, along with comparisons similar to those in table 2a.

Table 2b: Comparison of R/kr² for damped-cavity dipole HOM's with target values (see Ref. 2)

Mode	R/Q/kr ² (Ω /m)	Q _L	R/kr ² (k Ω /m)	target (k Ω /m)	fract. target
1E1	15.3	125	32	117	.27
1M2	27.6	<10	6.2	117	.05
1M3	.26	1300	8.5	117	.07
1E3	5.86	500	80.6	117	.69
1M4	2.87	1400- 3600	120- 310	117	1.0-2.6
1E5	2.04	NM		117	
1E6	5.14	340-630	61-113	117	.52-97
1M6	.10	NM			

In general we find that the R/Q values in the presence of the damper apertures do not change significantly from those of the bare cavity, and the improved Q measurements are not significantly different from those of Ref. 2. There remain a few modes whose damped impedance remains relatively high. These are modes which, because that high impedance reflects marginal coupling to the dampers, are sensitive to the details of the cavity shape (in the case of the 1M4 and 1E6, the range of Q_L in the table reflects sensitivity to variation with the measurement conditions), and therefore need to be re-measured for the final high-power cavity. Should they then not prove tractable to the present damping scheme, they can be dealt with individually by dedicated dampers, provisions for which have been included in the design of the cavity.

REFERENCES

- [1] D.A. Goldberg and R.A. Rimmer, "Automated Bead-Positioning System For Measuring Impedances of R-F Cavity Modes," Proc. 1993 Part. Accel. Conf.
- [2] R.A. Rimmer, "RF Cavity Development for the PEP-II B-Factory," Proc. Int'l Workshop on B-Factories, KEK, (1993).
- [3] See, e.g., D.A. Goldberg and G.R. Lambertson, "Dynamics Devices: A Primer on Pickups and Kickers," in *Physics of Particle Accelerators*, A.I.P. Conf. Proc., **249**, p.254 et seq., (1992), for the definitions of longitudinal and transverse shunt impedances and their relation to beam impedance.
- [4] © Wavemetrics, Inc.

PLANAR STRUCTURES FOR ELECTRON ACCELERATION

H Henke, Technische Universitaet Berlin, EN-2, 10587 Berlin, Germany

Recently planar RF structures have gained appreciable interest due to their unique features. They have been proposed for very high frequency applications, where they are ideally suited for fabrication by deep X-ray lithography, for linear colliders and for sheet-beam klystrons. The paper presents structures for the different possible applications: Travelling and standing wave structures, side-coupled structures, structures with a position independent accelerating field and cavities for accelerating wide sheet-beams.

I. INTRODUCTION

Planar RF-structures consist of two or more metallic or dielectric slab materials supporting "match-box" like cavity resonators. The slabs can be in direct contact, thus forming closed rectangular structures (Fig. 1 a), or electrically separated forming an open structure where the fields, however, decay exponentially in the gap (Fig. 1 b).

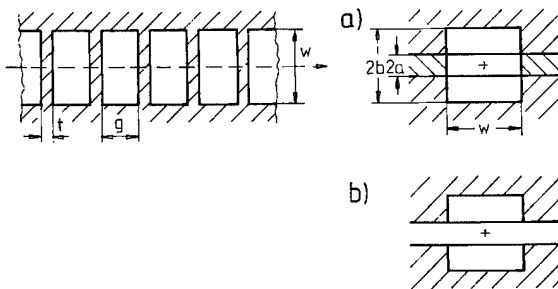


Figure 1. Examples for planar structures; a) closed structure; b) open Muffin-Tin structure.

Recently, these planar structures have gained more and more interest due to some unique features which may be important for special applications. The most important reason is for high frequency applications. It is obvious that above frequencies of 30 - 50 GHz it will be very hard to realize axis-symmetric structures. On the other hand, modern microfabrication techniques like stamping, microvibration or deep X-ray lithography with subsequent electrodeposition (LIGA [1]) offer the possibility to produce planar structures with sufficient precision. Especially LIGA seems to be perfectly suited for very high frequencies, let us say around 100 GHz. It has fabrication tolerances in the micrometer regime and allows for adding complexity to the geometry nearly free of costs. Thus, side-coupled structures, multi-periodic structures, low energy structures with inherent alternating-phase (AP) focusing and many others are possible. This technology is currently explored in a study of a 50 MeV electron linac powering a micro wiggler [2].

Other applications may be for future linear colliders because of several unique system requirements [3]. First, in order to keep the power consumption within reasonable

limits, the linacs must operate at high frequencies, higher than 30 GHz. Secondly, a multibunch operation is necessary and therefore it is vital to reduce the wakefield effects. Planar structures have more geometric degrees of freedom than axis-symmetric structures and this can be used to reduce wakefields. Thirdly, flat beams with a large aspect ratio and an extremely low emittance in one plane are required. Wide rectangular apertures, or even better, open muffin-tins, are ideally suited for such beams because wakefields can be dramatically reduced in the direction of the slit.

Finally, another important application may be for high frequency and/or high power klystrons. The current transport capability of klystrons decays with the square of the RF wavelength because the RF cavities and therefore the beam-pipe scale correspondingly. The only way out of the unfavourable frequency scaling is to use multi-beam or sheet-beam devices. Sheet-beams [8] together with planar RF structures allow for a more favourable frequency scaling because one dimension is independent of the frequency and can thus be increased.

Due to the rectangular geometry with plane interfaces between different subregions, planar structures are well suited for an analysis with the mode matching technique. In case of closed subregions the fields are expanded in series of eigenmodes, whereas in open subregions Fourier integral representations are used [5]. For numerical analysis a finite difference calculus in frequency as well as time domain is the obvious choice. In fact, many geometries were calculated with MAFIA [6]. Recently, we have developed a finite difference code GdfidL [7] which takes advantage of the special geometry in order to increase the speed and to allow for different mesh sizes in subregions.

II. TRAVELLING WAVE STRUCTURES WITH NON-FLAT FIELDS

The simplest planar structure is a chain of rectangular cavities, Fig. 1 a. It might be suited for special applications in the lower part of the frequency range we are considering here, i.e. somewhere between 30 and 60 GHz. The main RF parameters are close to the ones for an open muffin-tin structure, Fig. 1 b.

Open muffin-tin structures are the ideal candidate for very high frequency application, around 100 GHz, and for fabrication with LIGA. They are double-sided and do not need brazing in the region of RF-fields, they are easy to cool from top and bottom and the side openings provide vacuum pumping slots. At $2\pi/3$ travelling wave mode structure at 120 GHz was first studied in ref. [4]. The main parameters are repeated in table 1.

Table 1. Geometrical and RF parameters for a $\pi/3$ travelling wave mode in an open muffin-tin.

$a = 0.3 \text{ mm}$	$b = 0.9 \text{ mm}$	$w = 1.8 \text{ mm}$
$g = 0.633 \text{ mm}$	$t = 0.2 \text{ mm}$	$d = 0.8 \text{ mm}$
$Q_0 = 2160 \text{ for Cu}$	$r_0/Q = 144.6 \text{ k}\Omega/\text{m}$	
$r_0 = 312 \text{ M}\Omega/\text{m}$	$k = 0.0475$	
$v_g = 0.043 c_0$	$\alpha = 13.5 \text{ m}^{-1}$	

The optimum structure length l_{opt} for the highest energy gain ($\alpha l_{\text{opt}} = 1.26$) is $l_{\text{opt}} = 9.3 \text{ cm}$. However, there are many reasons to make l shorter and it was chosen to 7 cm corresponding to 84 cells. Then, the required input power per structure is 29 kW in order to get 10 MV/m average gradient. The ratio of power dissipation at structure input to structure output is 6.6 to 1. This large ratio leads to an appreciable temperature rise in the irises at the input end and will require a powerful cooling system in order to control the heat gradient.

Certainly, the better solution would be a constant gradient (CG) structure which has a constant power dissipation and is less sensitive to frequency errors and to beam break-up. At high frequencies, however, where we would like to use lithography for fabrication, a varying aperture and therefore a varying structure depth would complicate the process enormously. Then, it might be preferable to use standing wave (SW) structures (chapter IV).

Contrary to axis-symmetric structures, the accelerating fields in planar structures depend normally on the transverse position. The synchronous space harmonic of the accelerating field component can be written as

$$E_z = E_0 \cos k_x x \cdot \cos k_y y \cdot e^{j\varphi}, \quad \varphi = \omega t - k_z z \quad (1)$$

where

$$k_z = k/\beta, \quad k_y^2 = -k_x^2 - (k/\beta\gamma)^2, \quad k_x \approx \pi/w.$$

For relativistic particles we have $k_y^2 = -k_x^2$ and the field varies with $\cos k_x x$ in x-direction and with $\cosh k_x y$ in y-direction, that means the acceleration depends on the position which may be tolerable only for very small excursions x and y . By the way, the transverse forces have quadrupole character.

$$F_x = -eE_0 \frac{k_x^2}{k} \sin \varphi \cdot x, \quad F_y = eE_0 \frac{k_x^2}{k} \sin \varphi \cdot y \quad (2)$$

and could be used for focusing.

III. TRAVELLING WAVE STRUCTURES WITH FLAT FIELDS

Some applications require an accelerating field which is independent of the transverse positions, at least over a certain fraction of the aperture area. Planar structures can be modified to meet this requirement. For that purpose we increase either the capacitive load, Fig. 2a, or the inductive load, Fig. 2b, at the cavity sides. As a result, the space harmonic with $k_x = 0$ becomes the dominant space harmonic and the field is independent of x and y over a large fraction of the aperture.

As an example we give a muffin-tin cavity with increased inductive load at the sides which could be used

for a high power sheet-beam klystron at 11.4 GHz similar to the cavity

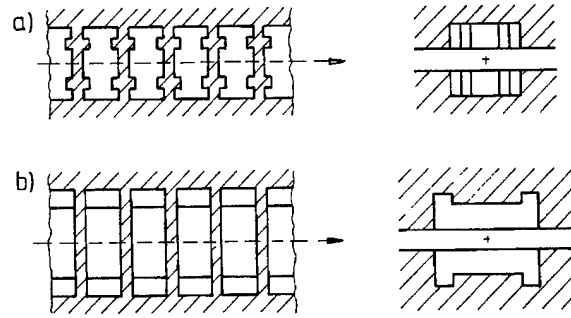


Figure 2. Muffin-tin structures with flat accelerating fields near the beam axis; a) increased capacitive and b) increased inductive load at the sides.

proposed in ref. [8]. Fig. 3a shows the lower half of the cavity with the electric field of the fundamental mode. The beautifully flat distribution of the field over three quarters of the cavity is depicted in Fig. 3b. Clearly, the cavity is well suited for acceleration of a 10 cm wide beam. By the proper choice of the dimensions it was possible to shift the closest higher mode (in horizontal direction) more than 1 GHz up in frequency and it is therefore conceivable to couple it out by means of a high-pass filter structure at the cavity sides.

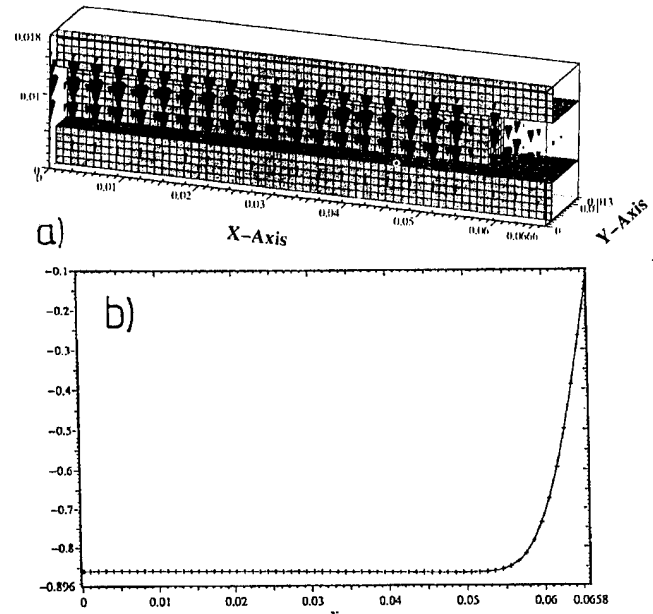


Figure 3. Flat-field muffin-tin structure; a) field plot and b) field distribution along the x-axis.

IV. STANDING WAVE SIDE-COUPLED STRUCTURES

As mentioned above, the TW-CG structure is in many respects the ideal structure for electron acceleration. However, the fabrication by lithography of a structure with varying aperture will be very difficult although in principle possible. Therefore, SW-structures were considered in ref. [9]. They have a constant power dissipation but a shunt impedance which is only half that of a TW-structure,

except for the π -mode. On the other hand, the group velocity and the mode spacing is very small around the π -mode. As a consequence, the structure is sensitive against fabrication and frequency errors, it has a cell-to-cell phase error and only a small number of cells can be coupled.

A way out of these problems is often used in proton machines. The accelerating cells are not coupled directly but via off-axis coupling cells, in such a way that the structure is operated in the $\pi/2$ -mode but the effective phase advance from main-to-main cell is π . Although in our case the direct coupling cannot be lowered we still can get the same behaviour. By making the passbands of two structures, the chain of accelerating cells and the chain of coupling cells, coalesce at the 2π phase shift per period we obtain an effective π -phase advance for the accelerating cells with a high group velocity while the coupling cells remain unexcited. The additional complication due to the coupling cells is only a complication in the design process but is more or less free of extra fabrication costs.

In Fig. 4, geometry (1) the standard arrangement of a side-coupled muffin-tin structure is shown. Because of the large off-axis cells, the accelerating field wiggles slightly around the beam axis. Therefore, we analysed geometry (2) next. This geometry has the largest bandwidth and is expected to be the less sensitive against errors due to the multiple coupling. Unfortunately, it carries a horizontally polarized dipole mode which is synchronous with the beam. Nevertheless, for many applications this may be tolerable because the shunt impedance of the dipole mode is very small. In the third geometry of Fig. 4, the symmetry with respect to the z-axis is broken. In that way the dipole mode is shifted to lower frequencies while the accelerating field remains parallel to the z-axis. All three geometries have a high group velocity, around 5 % of the velocity of light and a π phase shift from main-to-main cell. The shunt impedance is only reduced by typically 15 % as compared to a single-periodic $2\pi/3$ mode TW-structure.

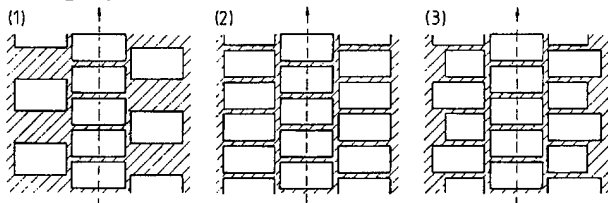


Figure 4. Side-coupled muffin-tin structures with (1) alternating, (2) symmetrically arranged coupling cells and (3) with broken symmetry.

V. CONCLUSIONS

Planar structures have one geometric degree of freedom more than axis-symmetric structures. This freedom in choice can be used in different ways: To adjust the structure geometry to the beam geometry, to modify the transverse dependence of the accelerating field or to reduce wakefields. Every choice has its particular application like for sheet-beam klystrons, linear colliders or for very high frequency structures around 100 GHz.

Although planar structures may stay an exception for applications with frequencies below 30 to 50 GHz, they certainly will be the top choice for higher frequencies. Especially if they can be made with modern microfabrication techniques, such as high-precision stamping or LIGA, they offer unprecedented advantages. Nearly any complex structure, as long as it is planar, can be fabricated with no extra costs. Only the designer's skill limits the possibilities. Thus, input couplers, extraction circuits, filter devices, single- and multiperiodic structures, alternating phase focusing structures and others, they all can be integrated on a slab support.

VI. ACKNOWLEDGEMENT

The author would like to thank the APS project at Argonne National Laboratory for supporting these studies.

VII. REFERENCES

- [1] E.W. Becker, W. Ehrfeld, P. Hagmann, A. Maurer and D. Münchmeyer: *Microelectronic Engineering*, No. 4, 1086, pp. 35-56.
- [2] A. Nassiri et al., "A 50-MeV mm-wave electron linear accelerator system for production of tunable short wavelength synchrotron radiation", *IEEE, International Electron Device Conference*, Washington D.C., December 1993, pp. 169-172.
- [3] D. Yu et al., "High frequency planar accelerating structures for future linear colliders", *AIP Proceedings of the 6th Workshop on Advanced Accelerator Concepts*, Lake Geneva, June 1994.
- [4] H. Henke, Y.W. Kang and R.L. Kustom, "A mm-wave RF structure for relativistic electron acceleration", *Argonne National Laboratory, internal report ANL/APS/MMW-1*, 1993.
- [5] M. Filtz, "Analytical calculation of waves in a muffin-tin structure", *Proceedings of the 4th European Particle Accelerator Conference*, London 1994, pp. 1271 - 1273 and "Coupling impedances of muffin-tin structures with closed and open sides", these proceedings.
- [6] R. Klatt et al., *Proceedings of the 1986 Linear Accelerator Conference*, Stanford internal report SLAC-Report 303, Sept. 1986.
- [7] W. Bruns, "Error sensitivity for side-coupled muffin-tin structures using a finite difference program", these proceedings.
- [8] D. Yu and P. Wilson, "Sheet-beam klystron RF cavities", *IEEE Proceedings of the 1993 Particle Accelerator Conference*, Washington, pp. 2681-2683.
- [9] H. Henke and W. Bruns, "A broad-band side-coupled mm-wave accelerating structure for electrons", *Proceedings of the 1993 IEEE Particle Accelerator Conference*, Washington D.C., May 1993, vol. 2, pp. 94-906.

PRECISE FABRICATION OF X-BAND DETUNED ACCELERATING STRUCTURE FOR LINEAR COLLIDER

T. Higo, H. Sakai, Y. Higashi, T. Takatomi and S. Koike
KEK, National Laboratory for High Energy Physics
1-1 Oho, Tsukuba-shi, Ibaraki-ken 305, Japan

The precise frequency control of the dipole modes in all of the cells in a structure in addition to the control of the accelerating mode is one of the key issue to realize a detuned structure for the main linac of the linear collider. The present approach is to machine the accelerating cell precisely with the use of the ultra-precision machines and keep the precision through the following fabrication processes such as the diffusion bonding aiming at the precision of the dipole-mode frequency better than 0.01%. In addition to this frequency control, the cell alignment should be a few micro meters and this criteria will be accomplished by the precise machining of the outer surfaces of the cells followed by the alignment along a good vee block.

In the present paper are presented some of experimental results on the fabrication of 30cm-long structures. The bonding at the temperature above 800°C was found reliable to obtain the vacuum tight junction. The change of the accelerating mode frequency was found to be less than 1MHz out of 11.4GHz but it seems to have a pressure dependence. The study of 132-cell bonding test was also performed and the alignment of 40 microns along 1.2m stacking was obtained though a severe trouble happened to the jiggings.

Based on these experiences, the possibility of a precise fabrication method for the detuned structure in full size is discussed.

I. INTRODUCTION

Two most important issues to keep the long-range wake field in the accelerating structures of the linear colliders operated in a multi-bunch scheme are (1) frequency control of the dipole mode and (2) alignment of the cells in the structure. In the design of JLC[1], the relative tolerance of the frequency is 10^{-4} and the alignment of the order of a few micrometers. In addition to these characteristics, the structure should be operated in fairly high accelerating field with less dark current and they should be made in mass production of several thousands of them.

Keeping these in mind, the study on a precise fabrication has been started[2]. Even if the cells are machined in very good precision, the brazing process introduced large frequency shift due to the process. Therefore, we decided to study the possibility to apply a diffusion bonding technique between flat surfaces at a lower temperature and with a low pressure[3].

In the present paper are described some of the performances and characteristics relevant to the diffusion

bonding for the cells which are fabricated in ultra-precision lathes and discuss the feasibility of this methods to the fabrication of the structure of linear collider main linacs.

II. MACHINING CELLS

As a first step of the study, some 30-cm long constant-impedance structures were fabricated. The dimensions of the cells was described elsewhere[3].

The positioning of the bite is controlled by comparing the outer diameter of the machined cell to the reference periodically. The most important parameters of the cells, the frequencies and the outer diameters of the machined cells were checked from cell to cell. Typical results are shown in the Fig. 1. The frequencies of the cells are measured using dummy flat surface with choke to trap the mode with a similar field pattern to that of the accelrating mode. The standard deviation of the measured frequencies is 0.1MHz/11.4GHz which is small enough for the detuned structure. The deviation of outer diameters from the reference value is $\pm 0.5\mu\text{m}$, which should be kept to realize the alignment of the cells along the structure better than one micrometer.

III. DIFFUSION BONDING

In order to make several thousands of structures, it is necessary to join nearly one million cells. Therefore, it is important to apply a method with good reliability and

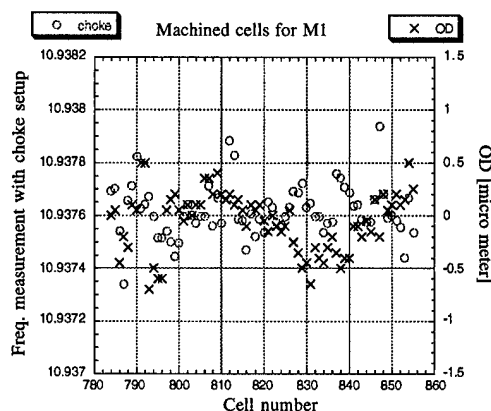


Fig. 1 Measured frequencies (solid circle) and outer diameters (crosses) of the cells for 30cm structures.

Table 1. Typical parameters of three 30cm-long structures.

Type	units	1	2	3
Insert		Au	Non	Au
Thick	μm	2	-	1
Temp	$^{\circ}\text{C}$	890	800	800
Period	min	10	60	10
Pressure	g/mm^2	10	3	5
Vacuum		OK	OK	OK
Δf	MHz	~ -1.0	~ 0	
$\delta F_{\pi/2}$	$\pm\text{MHz}$	0.5	0.7	0.5
$\delta\phi$	degree		$\pm 1^{\circ}$	$\pm 1.2^{\circ}$
$\text{Exp}(-\tau)$	dB	-1.494	-1.273	-1.31
$Q/Q_{\text{cal}}^{\dagger}$	%	81	95	93

\dagger Calculated from the attenuation along the structure, $\text{Exp}(-\tau)$.

cheapness for the mass production. The frequency change due to the brazing sometimes become several MHz, which is not allowed for frequency control point of view. Therefore, the extensive studies on the joining methods without liquidizing the materials for joining have been performed[3].

A. 30cm structures

Typical parameters which were applied to make 30cm-long structures are listed in Table 1. In addition to those parameters of the bonding process, the reliability of vacuum tightness largely depends on the quality of the bonding surface. The flatness of the present machining is better than $0.3\mu\text{m}$ over full 80mm in diameter and the surface roughness is set to 50nm.

As shown in the table, the control of the accelerating mode frequency was kept less than 1MHz. One of the measurement of the frequencies of the pseudo $\pi/2$ mode in the cells of a structure before and after the bonding are shown in Fig. 2 for the case of type 2. The measurement was performed by detuning the adjacent cells using two plungers equipped with

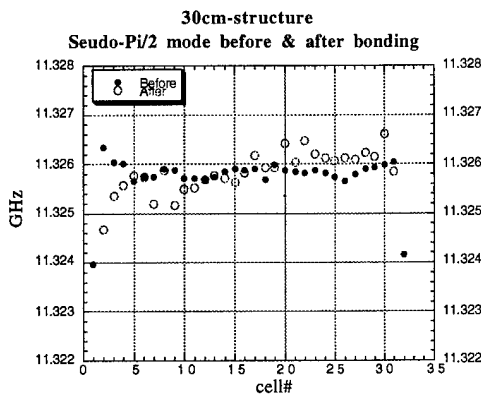


Fig. 2. Frequencies of pseudo $\pi/2$ mode in a 30cm-long structure. Solid circles are those before bonding and open circles are those after.

antenna and measuring transmission between those antennas. The frequency shift due to this type of bonding is quite small, though there was a slight dependence on z-position along the structure, which may reflect the dependence of the pressure applied to the junction.

B. Frequency shift dependence on pressure

All the bondings are performed in vertical furnaces at present. Therefore, for the case of full-size structure, the extra weight of more than 50kg due to the self weight above the relevant cell is added and the contact pressure at bottom is 3 to 4 times larger than that of the top. In Fig. 3 are shown the dependence of the frequency shifts due to the bonding of type 2 on the pressures applied to the bonding surface. The frequency shift of the mode with high phase advance per cell is large, reflecting the dimensional change of z-direction. This may also introduce big changes in frequencies of the higher modes with nodes in a cell such as those of TE111 and TM111. This effect on the accelerating modes can be canceled by applying dimensional offsets for the cells to maintain the frequencies along the structure. In addition, this kind of changes should be smooth function along the structure and therefore it does not perturb the HOM frequency distribution much. The detailed dependence along the full-size structure will be tested soon.

C. Search of other parameter regions

One of the way to reduce this frequency change is to lower the bonding temperature. An example of five-cell stack at 750°C for one hour at $2\text{g}/\text{mm}^2$ was also came out in vacuum leak tight. As shown in Fig. 4, the frequency change due to the bonding is less than $0.2\text{MHz}/11.4\text{GHz}$ for all of the modes in the TM010 pass bands and less than 0.6MHz for those of the HEM11-like modes.

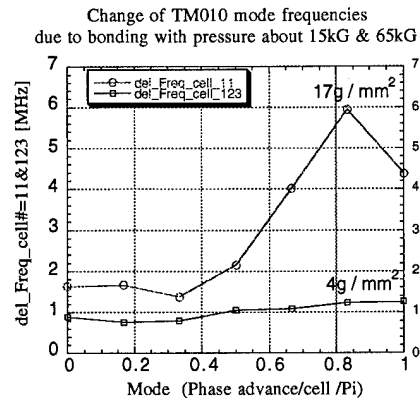


Fig. 3. Frequency differences of the TM010 modes due to the bonding of type 2 with two different pressures applied. The lower pressure corresponds to that at top and the heavier to that at bottom.

V. SUMMARY

Several 30cm-long structures were fabricated using diffusion bonding technique. The frequency change due to this bonding above 800°C was about 1MHz or less though there might be a dependence on the pressure between bonding surface. The alignment of the cells in short structure was better than 4 μ m, while that of the test of 132-cell bonding was 40 μ m. The revision to obtain better alignment will be performed soon. Other parameter regions are being studied to find the optimum on frequency control and good alignment in addition to the reliable vacuum sealing.

VI. ACKNOWLEDGMENT

Many experimental studies were performed with the collaboration with Ishikawajima-Harima Heavy Industry, Mitsubishi Heavy Industry and Nippon Koshuha Corporation and they are greatly acknowledged.

VII. REFERENCES

- [1] JLC-I, KEK Report 92-16, Dec. 1992.
- [2] H. Sakai et al., Proc. 16th. Linear Accelerator Meeting in Japan, 1991, p175.
- [3] T. Higo et al., "Precise Fabrication of X-band Accelerating Structure", Submitted to the 9th Symposium on Accelerator Science and Technology, KEK, Japan, 1993 and KEK-Preprint 93-57, 1993.
- [4] A. Yamamoto et al., "Fabrication of an X-band 30cm Accelerating Structure by Diffusion Brazing", Proc. Fourth European Particle Accelerator Conference, London, July, 1994.

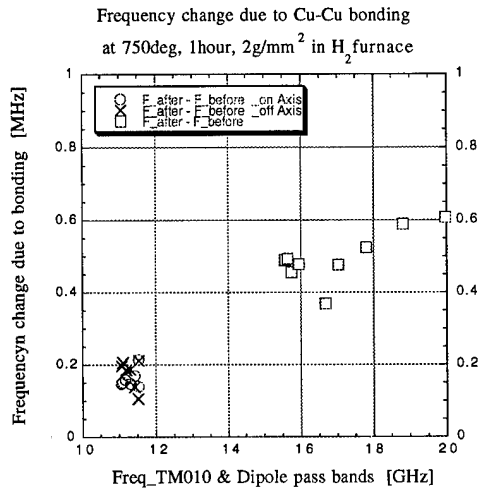


Fig. 4 Frequency shift due to diffusion bonding at lower temperature. Data sitting neat 11.4GHz are those of TM010-like mode while those at 15 to 19GHz dipole modes.

Another test diffusion bonding even at 500°C came out to be also leak tight where the pressure of 5g/mm² was applied between the surfaces with the roughness of 20nm.

From these examples, we hope that there will be a better parameters for the bonding possible at lower temperature than 800°C.

IV. ALIGNMENT

The outer diameter of all the cells are machined to be better than 0.5 μ m as in Fig. 1 or better. The concentricity among the outer wall, beam hole and the cell wall is better than 0.2 μ m, which is automatically fulfilled because the machining is performed without re-setting of the cell. Therefore, the cells can be aligned by putting each of them on a precise vee block. If the alignment is preserved during the following processes, especially the bonding process, we can expect the alignment better than a few microns.

One of the 30cm structures was fabricated followed this idea. The alignment before the bonding was 1 μ m and that after bonding about 4 μ m[4].

The same method was applied to a 1.2m, 132-cell bonding test with the parameter the same as type 2. The alignment before bonding was better than 10 μ m but that obtained after bonding was 40 μ m. The global characteristics of the alignment after bonding was a simple bending of a half wave length in one direction. We hope to obtain much better alignment by modifying some of the jiggings. The total length was shrunk by about 0.5mm, which correspond to about 4 μ m per junction. This is comparable to the value, 3 μ m shrinkage per junction, for the case of diffusion brazing at 890°C for 10 minutes. This characteristics may have to be considered seriously especially in the bonding of a long structure in vertical furnace.

DEVELOPMENT OF A BEAM-PIPE HOM ABSORBER FOR THE ATF DAMPING RING

F. Hinode and S. Sakanaka

KEK, National Laboratory for High Energy Physics, 1-1 Oho, Tsukuba-shi, Ibaraki-ken, 305 Japan

This paper describes the development of a beam-pipe HOM absorber, which is used to damp higher order modes (HOMs) of accelerating cavities for the ATF damping ring (DR). This device is a short beam pipe equipped with a microwave absorber. The requirement for the absorber, to search for an absorbing material, and the design of a prototype absorber-pipe are presented.

I. INTRODUCTION

A HOM damped cavity is under development at KEK [1-3], which is to be used for the ATF damping ring. This cavity has been designed to provide an accelerating voltage of 0.25 MV/cavity with a frequency of 714 MHz, while avoiding coupled-bunch instabilities arising from cavity HOM impedances. In order to damp the HOMs the cavity is equipped with waveguide ports dedicated to HOM damping. Because of the very high cutoff-frequencies of the DR beam pipe (typically, 9.6 and 7.3 GHz for the monopole and dipole modes, respectively), there exist many cavity HOMs ranging from the accelerating frequency to the above-mentioned cutoff frequencies. Even by equipping the HOM damping ports, it is difficult to effectively damp some of the harmful HOMs which have only weak fields near to the waveguide ports. For this reason we have adopted additional HOM damping using a beam-pipe absorber.

In this scheme the RF power of the high-frequency HOMs (> 2.30 GHz for the monopole modes and >1.76 GHz for the dipole modes, respectively) is extracted from beam ports of $\phi 100$ mm (inner diameter). The power is then absorbed in microwave absorbers in the beam pipe, which are located next to the cavity. For the absorbing material, some kind of silicon carbide (SiC) is most promising, since it has good thermal conductivity (~ 100 W/m/K) and a low outgassing rate.

II. REQUIREMENTS FOR THE MICROWAVE ABSORBERS

The microwave dissipative property in lossy dielectrics, such as in the SiC, is characterized by the effective conductivity (σ_{eff}), which is equal to $\omega\epsilon'' + \sigma$, where ϵ'' is the imaginary part of the permittivity, σ the conductivity and ω the angular frequency [4]. In order to effectively damp the HOMs, the loss in the absorber should be as high as possible. On the other hand, an absorber that has too much loss is not acceptable, because it would have a large resistive-wall impedance, which may cause turbulent bunch-lengthening. According to the following considerations, we have concluded that an effective conductivity of ~ 100 siemens/m is a good compromise between these conflicting requirements.

In the ATF DR the major contribution to the broadband impedance comes from the RF section, which comprises four cavity units. Figure 1 shows one cavity unit, where two beam-pipe absorbers are installed next to the cavity. We have considered that the total ring impedance would stay modest if we limit the loss parameter of one absorber to be less than $\sim 10\%$ of that of one cavity unit. The loss parameter of the cavity unit is estimated to be ~ 1.0 V/pC (without absorbers) for an rms bunch length of 5 mm. On the other hand, if we assume the absorber to be a simple resistive wall, having a constant conductivity of σ_{eff} , the loss parameter of the absorber would be given by

$$k_{rw} = \frac{\Gamma(3/4)\ell}{4\pi^2 r \sigma_i^{3/2}} \sqrt{\frac{\mu}{2\sigma_{eff}}},$$

where r is the inner radius of the absorber, σ_i the rms bunch length in time, $\Gamma(x)$ the gamma function, ℓ the absorber length, and μ the permeability. Then, an effective conductivity of higher than 100 siemens/m is required, using the following parameters: $\ell=150$ mm, $r=50$ mm, and $\sigma_i=16.7$ psec. It has been confirmed from a simulation of the longitudinal collective effects that the above-mentioned effective conductivity is acceptable [5].

The performance of HOM damping by the beam-pipe absorbers has been evaluated by two-dimensional calculations based on the cavity shape without waveguide ports. The Q-values were calculated using a perturbation

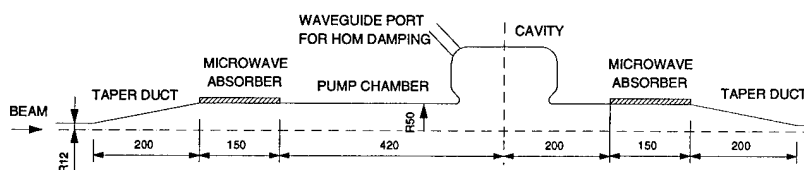
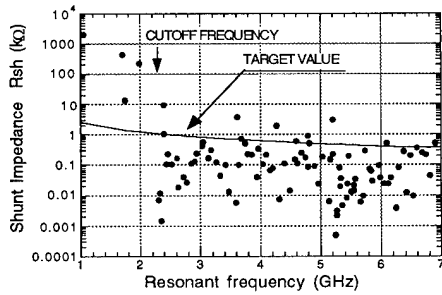
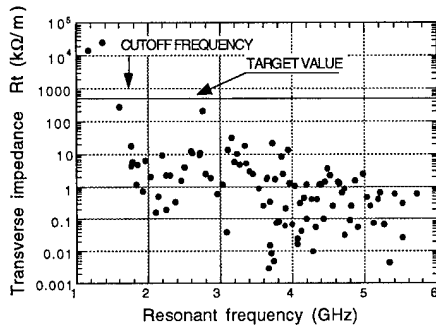


Fig. 1. Inner shape of one cavity unit. The unit for dimensions is mm.



(a) Shunt impedances of the monopole modes.



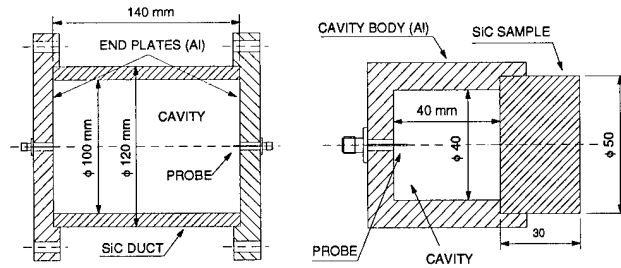
(b) Transverse impedances of the dipole modes.

Fig. 2. Calculated HOM impedances. We assumed an effective conductivity of 100 S/m for the absorbers.

method; the loss due to the finite conductivity was evaluated after the eigenmodes were solved for perfect conducting walls. Note that Koseki et al. found good agreement between the calculated Q-values (by the perturbation method) and the measured ones for their 500-MHz cavity, which was equipped with similar SiC absorbers [6]. Figure 2 shows the results of calculations in which an effective conductivity of 100 siemens/m was assumed for the absorbers. Regarding the monopole modes above the cutoff frequency, except for several modes, the shunt impedances could be reduced below the target value ($R_{sh}[\text{k}\Omega] < 2.5/f[\text{GHz}]$). For several modes that could not be sufficiently damped by the absorbers, we can expect further damping by the waveguide ports, because such modes tend to have strong fields in the cavity. The reduction of the transverse impedances for the dipole modes (above the cutoff frequency) is sufficient.

The maximum power dissipated in the absorber has been estimated to be ~1 kW/absorber under the most severe operation, which includes a resistive wall loss of about 20%.

III. SEARCH FOR AN ABSORBING MATERIAL



(a) Type A.

(b) Type B.

Fig. 3. Cavity resonators used for the measurement.

Table 1. Measured effective conductivity (at 3 GHz) of three samples. The type A cavity was used.

Material	Product name	σ_{eff} (S/m)
Sintered SiC	CERASIC-B ^{*)}	~ 5 ^{***)}
Reaction bonded SiC	TPSS ^{*)}	800
TiC-contained ceramics	HC2 ^{**)}	4.6×10^4

^{*)} Toshiba Ceramics Corp. ^{**)} Nihon-tokusyu-tougyo Corp.

^{***)} Not accurate due to the low Q-value of ~12.

A search for an absorbing material having an appropriate effective conductivity of ~100 siemens/m is under way. The dissipative property of the samples was measured using a dielectric probe or cavity resonators. In the former, the real and imaginary parts of the complex dielectric constant are directly measured by a dielectric probe (HP85070A) attached to an HP8510C network analyzer. However, it was found that the samples having a conductivity higher than several hundreds siemens/m could not be measured by this method. Therefore, we mainly applied the latter method, in which the effective conductivity was estimated based on the Q-values of a pillbox cavity resonator, a part of which is made of SiC (other parts are made of aluminum alloy), using the perturbation method. We used two types of cavities (see Fig. 3). The effective conductivity of the SiC is estimated by:

$$\sigma_{eff} \approx \frac{2}{\omega\mu_0} \left(\frac{Q_0}{R} \right)^2 \quad \text{for cavity A}$$

and

$$\sigma_{eff} \approx \frac{1}{2\omega\mu_0} \left(\frac{Q_0}{\ell} \frac{2}{1 + \delta_{p0}} \right)^2 \quad \text{for cavity B.}$$

Here Q_0 is the unloaded-Q of the TM_{mnp} mode, ω the angular resonant frequency, R the inner radius of the cavity, ℓ the cavity length, and δ the Kronecker delta.

We first investigated several samples which are commercially available from industry. Two samples of SiC which have been investigated by Koseki et al. [6], and a sample of titanium-carbide(TiC)-contained alumina ceramics, were measured. The results are given in Table 1; they showed a wide-ranging effective conductivity.

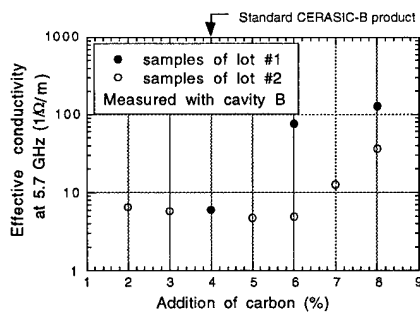


Fig. 4. Measured effective conductivity of the sintered SiC samples as a function of the addition of carbon.

Although the use of a reaction-bonded SiC (TPSS) would be acceptable for HOM damping [2], a search for a more appropriate material is under way.

One such R&D effort is to control the effective conductivity of the sintered SiC during the production process. Because some of the conductive property in the SiC is considered to be due to contaminated free carbon, we tried to control the effective conductivity by changing the addition of carbon to the raw material before sintering. The result is shown in Fig. 4, which is very promising. We could obtain an effective conductivity of ~80 siemens/m with a 6% addition of carbon in the first case (lot #1). However, it could not be reproduced for the second samples (lot #2). In order to obtain reproducible products, we are searching for unknown parameters which also affect the conductivity.

IV. DESIGN AND FABRICATION OF THE BEAM-PIPE ABSORBER

In order to demonstrate the capability of high-power (> 1 kW) absorption, a prototype beam-pipe absorber was designed and fabricated. For fitting the SiC to the inside of the beam-pipe, a shrinking technique was applied, which has been successfully used by Izawa et al. for constructing a similar-type absorber [7]. This method has the clear advantage that it provides good thermal contact between

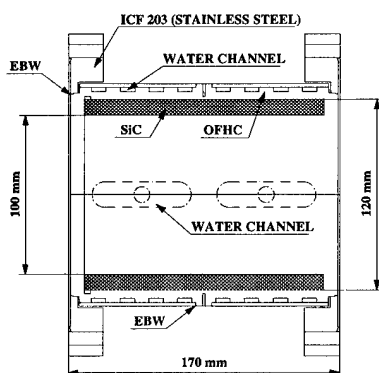


Fig. 5. Cross-sectional view of the beam-pipe absorber.

the SiC and the beam pipe without having to use any difficult joining techniques, such as brazing a large SiC to the metal.

A prototype beam-pipe absorber is shown in Fig. 5. The main body of the beam-pipe is made of OFHC copper. The cooling channels were milled from the outside. UHV flanges, made of stainless steel, were electron-beam welded (EBW) to the pipe. The SiC duct was fit into the copper pipe by shrinking.

The prototype absorber-pipe is ready for a heat-load test, which is to be carried out using a 2.45-GHz microwave source.

V. CONCLUSIONS

Some SiC materials having an effective conductivity of ~100 siemens/m, are suitable for the beam-pipe absorber. A sample of SiC (TPSS) which could be used for the beam-pipe absorber was found, and an R&D effort to produce an SiC having more appropriate properties is under way. The fabrication of a prototype beam-pipe absorber has been completed, and will be tested under heat loads.

A measurement of the wideband characteristics of the SiC and an accurate estimation of the broadband impedance of the absorber using the measured properties are the next subjects to be studied.

VI. ACKNOWLEDGMENTS

We wish to thank Y. Sakai of Toshiba Ceramics Corp. and M. Izawa of KEK for valuable discussions and suggestions concerning the investigation of SiC materials. We also thank N. Terunuma and Y. Funahashi for useful discussions concerning the design of the absorber-pipe.

VII. REFERENCES

- [1] S. Sakanaka et al., *Proceedings of the 1993 Particle Accelerator Conference*, Vol. 2, pp. 1027-1029.
- [2] S. Sakanaka et al., *Proceedings of the 1994 International Linac Conference*, Vol. 1, pp. 281-283.
- [3] S. Sakanaka et al., in these proceedings.
- [4] See for example, R.E. Collin, "Foundations for Microwave Engineering", McGraw-Hill.
- [5] ATF Design and Study Report, pp. 64-67, to be published as a KEK Internal Report.
- [6] T. Koseki et al., *Proceedings of the 9th Symposium on Accelerator Science and Technology*, August 1993, Tsukuba, Japan, pp. 246 - 248.
- [7] M. Izawa et al., *Rev. Sci. Instrum.* **66**, pp. 1910-1912.

DEVELOPMENT OF A HOM-DAMPED CAVITY FOR THE KEK B-FACTORY (KEKB)

T. Kageyama, K. Akai, N. Akasaka, E. Ezura, F. Naito, T. Shintake, Y. Takeuchi,
and Y. Yamazaki

KEK, National Laboratory for High Energy Physics, 1-1 Oho, Tsukuba, Ibaraki, 305 JAPAN

T. Kobayashi

Institute of Applied Physics, Tsukuba University, 1-1 Ten-nodai, Tsukuba, Ibaraki, 305 JAPAN

This paper describes a high-power test model of the normal conducting RF cavity for the KEK B Factory, KEBB. This cavity is loaded with a large coaxial waveguide for higher order mode (HOM) damping. The waveguide is equipped with a notch filter designed to block the TEM wave at the accelerating frequency of 509 MHz. Other waves coupled with the cavity HOMs are guided through the filter and absorbed by bullet-shape sintered SiC ceramics. This prototype model has been designed and built to demonstrate the performance in high power operation and the fabrication technologies involved. The results of the high-power test is reported together with the cavity structure and its RF properties.

I. INTRODUCTION

The KEK B-Factory (KEKB) is a two-ring asymmetric e^+e^- collider capable of producing B meson pairs at a luminosity of $10^{33-34} \text{ cm}^{-2}\text{s}^{-1}$. The collider consists of a 3.5-GeV positron ring and an 8-GeV electron ring. Both rings are required to store high-current beams with low emittances to achieve the design luminosity.

The key issue in the RF cavity design for KEBB is how to reduce the HOM impedances which will drive coupled-bunch instabilities limiting the stored beam current. A straightforward way to reduce the HOM impedances is to damp the HOMs in the cavity by guiding them out through dedicated waveguides. A number of HOM-damped cavity structures have been proposed and studied at accelerator laboratories around the world.

In addition, the operation of the RF cavities under the heavy beam loading in KEBB will give rise to another more serious problem. That is the longitudinal coupled bunch instability driven by the accelerating mode itself. The resonant frequency of the accelerating mode should be detuned from the RF frequency toward the lower side so as to compensate for the reactive component of the cavity voltage induced by the beam. In KEBB, the required detuning frequency for a conventional copper cavity will exceed the revolution frequency, leading to the large excitation of a coupled-bunch synchrotron oscillation.

A new RF structure named accelerator resonantly coupled with an energy storage (ARES) [1] is being expected

as a breakthrough in the development of the KEBB normal conducting RF cavity system. In the ARES scheme, a HOM-damped accelerating cavity and a large energy storage cavity operated in a high-Q mode are coupled via a resonant coupling cavity, where these three coupled cavities are operated in the $\pi/2$ mode. The storage cavity is employed to reduce the required detuning frequency, which is inversely proportional to the amount of the electromagnetic stored energy with respect to the reactive part of the beam-field interaction energy.

A high-power test model of a HOM-damped structure for KEBB, which would be employed in the ARES scheme, has been designed and built [2], [3]. The high-power test was carried out in February, 1995.

II. CAVITY DESIGN

The prototype cavity is designed on the basis of the following HOM-damping scheme: the cavity is loaded with a large coaxial waveguide equipped with a notch filter. The filter blocks the TEM wave coupled with the accelerating mode while passing other waves coupled with the cavity HOMs. Damped structures with this scheme were devised by Shintake [4] and by Akai [5], independently of each other.

A. RF Design

A schematic drawing of the prototype cavity is shown in Fig. 1. RF parameters of the accelerating mode are listed in Table 1. The coaxial waveguide is equipped with a notch filter of a quarter-wavelength radial line. The gap dimensions of the waveguide and filter structures were carefully determined in order to avoid multipactoring discharge at the RF frequency of 509 MHz.

The cavity monopole and dipole modes are coupled with the TEM and TE₁₁ waveguide modes, respectively. The first TEM stop frequency of the filter must be exactly tuned to the RF frequency. The bump structure in Fig. 1 can be lathe-machined for this purpose. The filter structure is deformed in order to raise the second TEM stop frequency from 1390 MHz to 1670 MHz. For the TE₁₁ waveguide mode, the first and second stop frequencies are 530 MHz and 1680 MHz, respectively.

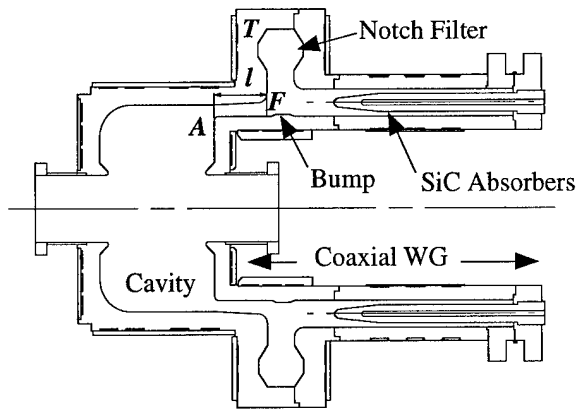


Figure 1: A schematic drawing of the test cavity

Table 1: RF parameters of the accelerating mode

f_{RF} (MHz)	508.6	
V_c (MV)	0.6	
P_c (kW)	75 (*)	
R (M Ω)	5.3	4.8 (*)
R/Q (Ω)	150	
Q	3.5×10^4	3.2×10^4 (*)

(*) A degradation of ~10% due to copper surface imperfection and ports is taken into account.

Around the second TEM and TE₁₁ stop frequencies, some cavity HOMs could be trapped. The beam bore diameter is enlarged to 145 mm in order to lower the cutoff frequencies of the beam pipe for the TM₀₁ and TE₁₁ circular waveguide modes below the second stop frequencies of the filter.

The filter position along the waveguide not only affects the accelerating mode Q value but also the HOM-damping properties. Waves propagating at HOM frequencies are partially reflected at the gap transition denoted by *F* in Fig. 1. Therefore, the distance from the waveguide aperture denoted by *A* to the gap transition should be carefully determined. This issue and the HOM characteristics are discussed in references [2] and [3].

Waves passing through the filter are guided toward sixteen SiC absorbers inserted from the waveguide end. Each absorber is a bullet-shape sintered SiC ceramics with dimensions of 40 mm in diameter and 400 mm in total effective length including a 100-mm nosecone section and directly cooled by water flowing in a circular channel inside. The high-power test of a bullet-shape prototype absorber was carried out using an L-band pulsed klystron. The prototype functioned without any vacuum, thermal, or discharge trouble up to an average RF power of ~2.5 kW. The R&D of the SiC absorber is reported in Ref. [6] at this conference.

B. Mechanical Structure and Assembly

The cavity parts with heat generation inside are made of oxygen-free copper (OFC). Stainless steel is used for the

inner and outer cylindrical parts for the HOM damping coaxial waveguide to mechanically reinforce the whole cavity structure. Vacuum furnace brazing and electron-beam welding techniques are employed to assemble the cavity parts. Finally, the flanges (shown at the right end in Fig. 1) of the outer and inner cavity parts are tightly connected and vacuum-sealed by TIG welding. Both beam bores are aligned by using an optical alignment telescope. The alignment error for the test cavity was within 100 μ m.

III. HIGH-POWER TEST

A. Setup

Figure 2 shows a photograph of the test cavity with an input coupler and a tuner installed. A TRISTAN-APS input coupler [7] capable of 300 kW transmission power was used for RF power feed. This coupler uses a loop coupling and has a cylindrical ceramic window at the rectangular-to-coaxial transition. The coupling factor to the test cavity was adjusted to 1.25 by rotating the loop.

A TRISTAN-APS tuner was used for tuning the cavity in high power operation. The tuner has a 7-cm-diameter plunger with about 6 cm of travel. This gives a tuning range of about 1.8 MHz.

The measured loaded Q value of the accelerating mode was 14000. With the coupling factor of 1.25, the unloaded Q

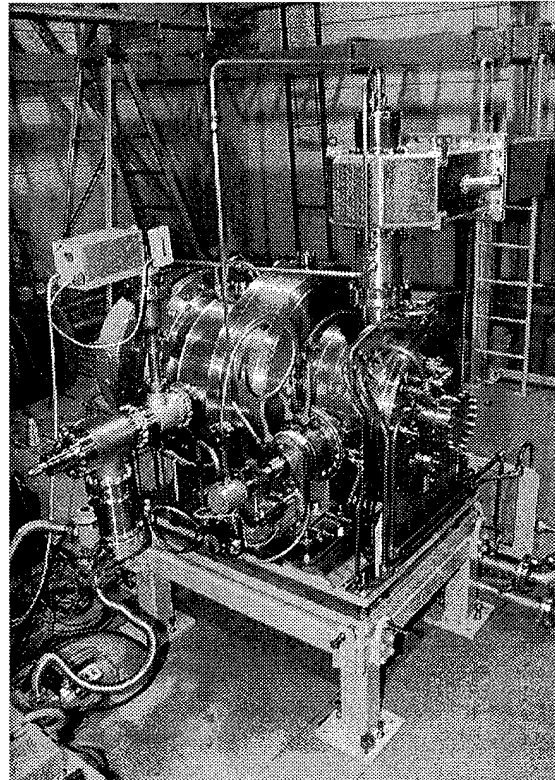


Figure 2: The test cavity with an input coupler and a tuner installed.

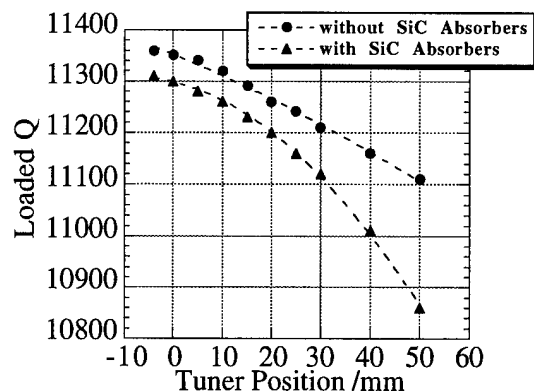


Figure 3: The loaded-Q responses to the tuner position for the cavity with/without the absorbers.

value was 31500, which is 90 % of the theoretical value (see Table 1) by SUPERFISH. The degradation of 10 % is probably due to the wall surface imperfection and the coupler and tuner ports.

Figure 3 shows the loaded-Q responses to the tuner position for the cavity with/without the SiC absorbers installed. The coupling factor is different from 1.25 for high-power test. The response for the cavity with the absorbers shows a more rapid decrease compared with that when no absorber is installed. This is due to distortion of the accelerating field by the tuning plunger. The distorted field will excite higher coaxial-waveguide modes even at the RF frequency. The higher-mode waves are not blocked by the notch filter and thus guided to the absorbers. Analysis of the field distortion using the numerical simulation code HFSS showed that the deformed accelerating mode leaks from the notch filter in the TE₂₁ coaxial-waveguide mode. Further investigation is in progress in order to overcome the field deformation arising from the large coupling to a storage cavity in the ARES scheme.

B. RF Conditioning

RF power was supplied by a CW klystron Toshiba E3786. The whole cavity system was cooled by 100 l/min of water: 70 l/min for the cavity cooling circuits, 10 l/min for the input coupler and tuner, and 20 l/min for the SiC absorbers. The cavity was evacuated from two pumping ports at the HOM damping coaxial waveguide. The base pressure was 3×10^{-8} Torr before the high-power test.

RF conditioning of the cavity was continuously carried out keeping the vacuum pressure below $\sim 5 \times 10^{-7}$ Torr. Figure 4 shows the conditioning history. It took about four hours to go above 0.5 kW of RF input power after the conditioning was started. That was probably due to multipactoring discharge in the coaxial waveguide aperture or in the notch filter although no light emission of discharge was observed. The cavity was conditioned up to 90 kW in about 33 hours and then the first high-power test was ended.

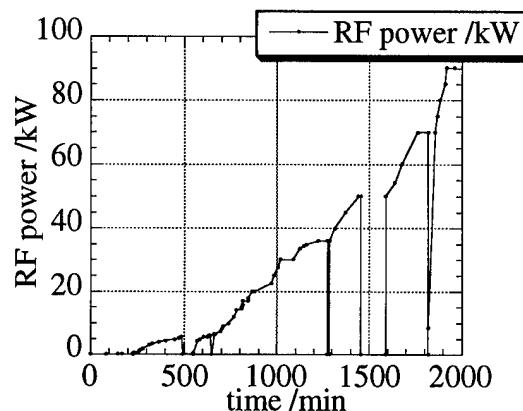


Figure 4: The history curve of the first RF conditioning.

Finally, the cavity was conditioned up to a peak RF input power of 110 kW. Subsequent high-power tests showed that the cavity was stably operated for long time up to 70 kW and the vacuum pressure was below 5×10^{-8} Torr. Small pressure rises due to gas bursts were frequently observed above 80 kW and similar events were sometimes observed at 40 kW. Further RF conditioning is planned for more stable high-power operation.

IV. SUMMARY

We have demonstrated the high-power performance of the HOM-damped accelerating structure for KEKB. However, further R&D work is required for more stable high-power operation and for an ARES scheme employing this damped structure.

V. REFERENCES

- [1] Y. Yamazaki and T. Kageyama, "A Three-Cavity System Which Suppresses the Coupled-Bunch Instability Associated with the Accelerating Mode", Part. Accel., Vol. 44, 1994, pp. 107-127.
- [2] T. Kageyama et al., Proc. 4th European Par. Accel. Conf., 2098 (1994).
- [3] N. Akasaka et al., Proc. 4th European Par. Accel. Conf., 2137 (1994).
- [4] T. Shintake, Jpn. J. Appl. Phys. Vol. 31, Part 2, No. 11A, Nov. 1992, pp. L1567-L1570.
- [5] K. Akai et al., Proc. 15th Int. Conf. on High Energy Accelerators, 757 (1992).
- [6] "HOM Absorber for the KEKB Normal Conducting Cavity", Y. Takeuchi et al., WPR05 in this Conference.
- [7] M. Akemoto, Proc. 1991 Particle Acc. Conf., 1037 (1991).

POSSIBLE CAVITY CONSTRUCTION TECHNIQUES FOR THE DIAMOND STORAGE RING

D.M.Dykes and D.S.G.Higgins, Daresbury Laboratory, Warrington WA4 4AD, U.K.

Various cavity construction techniques are being investigated for the future UK light Source DIAMOND. As well as the usual techniques involving machining, brazing and/or e-b welding, sputtering onto an aluminium former and joining electroformed sections by electroplating are being considered. The results of preliminary test samples will be given.

I. INTRODUCTION

The construction technique used to manufacture an RF cavity is critical in terms of cost, construction time, ease of construction and reliability in the design of a synchrotron radiation source. Three techniques have previously been used by Daresbury. The SRS storage ring cavities used forged components, fitted on a mandrel and electroformed together]. The present booster synchrotron cavity components were e-b welded while the spare was vacuum brazed [1]. Before deciding on any construction technique for the future UK Light Source DIAMOND, complete construction by an electroforming process, and sputtering copper onto an aluminium former are being assessed.

II. DIAMOND Cavity

The preliminary design for the future 3rd generation light source DIAMOND has a 500 MHz cavity without nose cones to give good HOM characteristics [2] [4] [5]. Multipoint temperature sensors will help to control the temperature of the cavity body to better than 0.05°C. Tuning is likely to be of the plunger type, but the method of coupling to the waveguide is undecided.

III. ELECTROFORMED DESIGN

A. SRS Cavity

The Present SRS Storage Ring cavity is a 500 Mhz reentrant solid copper cavity, it has plunger type tuning and is aperture window coupled to the waveguide. The cavity is water cooled, with the temperature controlled to 0.1°C to shift any potentially dangerous higher order modes (HOM's) outside the critical operating region. [10] It was constructed using a combination of electroforming, machining, brazing and E beam welding.

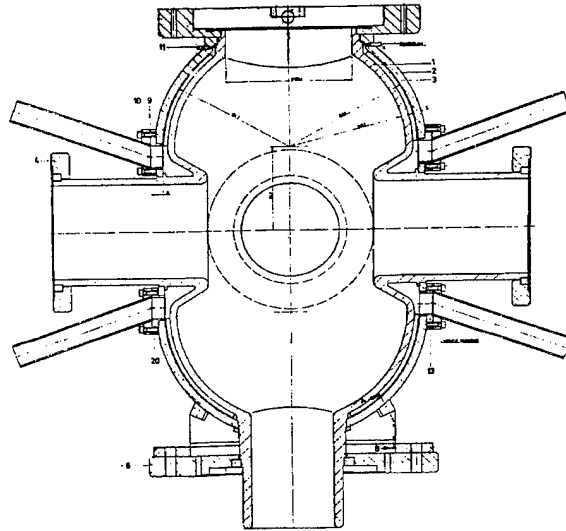


Figure 1. Daresbury SRS cavity

B. Construction method

The objective is to maximise the proportion of the structure electroformed and minimise the proportion that requires machining and other techniques such as welding.

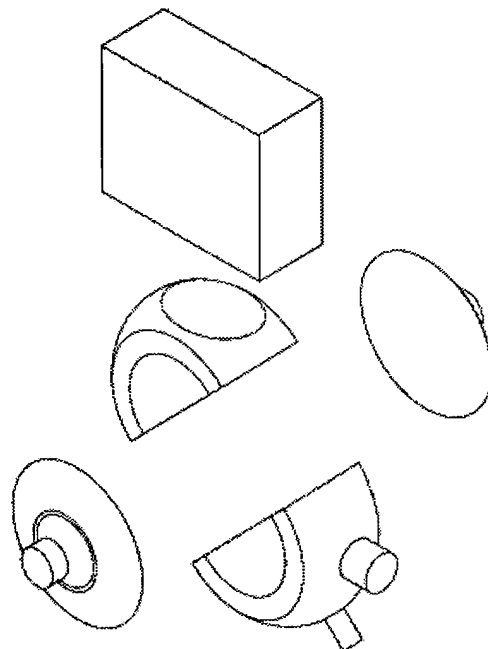


Figure 2. Electroformed Sections before joining

- 1) A stainless steel master of the cavity is produced and split into logical sections by wire EDM.
- 2) Electroforming tools are prepared which also include features to locate flanges and other components which will be grown into the structure to avoid the need for other forms of joining.
- 3) The components are electroformed onto the tools and when the required thickness is reached, the component is removed by pressing and/or heating.
- 4) The completed components are machined to ensure a sound joint when they are grown together.
- 5) The components are then assembled onto a jib and grown together (see fig 2).
- 6) The central supporting spindle is removed and the sacrificial aluminium mandrel is etched out.
- 7) The cavities are then assembled onto the perturbation test rig where the primary frequency is measured and corrected, if necessary, by axial deformation of the cavity.
- 8) Copper baffles are attached to the cavities, wax is placed between the baffles and silver conducting paint is used to coat the wax. Copper is grown over the baffles and wax, which is removed through heating thereby creating cooling channels [7].
- 9) The mechanically complete cavity is assembled onto its support stand and sent for testing under power.

III SPUTTERING

Aluminium cavities although commonly used to evaluate new designs, are rarely used in accelerators because of their inferior performance, they suffer from multipacting and have poorer electrical properties than copper cavities [8]. However aluminium is less expensive and easier to form into a cavity than copper, and by coating with copper will have the same operating performance as a solid copper cavity [11].

Unfortunately aluminium cannot be electroplated directly with copper but requires a precoat with zinc, and this is incompatible with UHV.

Fortunately the development of superconducting cavities has provided the impetus to develop sputtering techniques using cylindrical magnetrons (see Figure 3) which can be used to sputter copper as well as niobium [9] [3] [6].

An aluminium cavity will be constructed by spinning two halves, after machining they will be joined and the ports added by welding or diffusion bonding. Work is continuing on the mechanical design of such a cavity.

After pre-tuning, copper to a thickness of several skin depths will be sputtered on to the inner surface of the cavity.

At present there are no results to report but work is in progress.

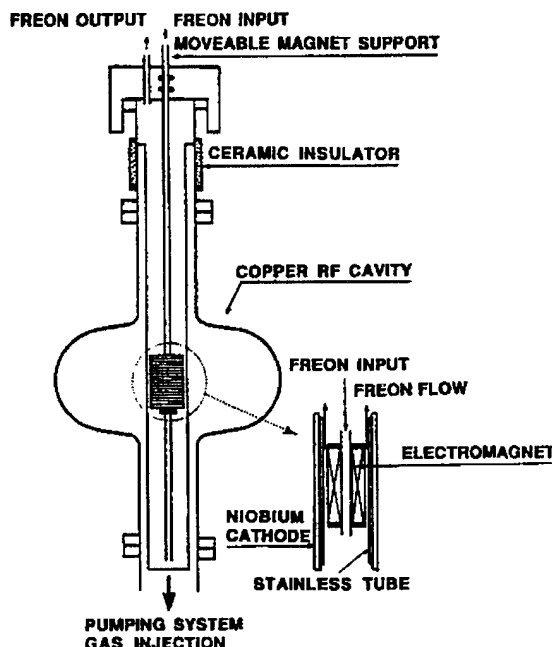


Figure 3. Sputtering Rig (copied from CERN RF School Proceedings 'Cavity Construction Techniques' by I. Wilson)

IV EVALUATION OF MATERIALS AND TECHNIQUES

In order to gain confidence in the manufacturing techniques that we intend to use, the following samples are being prepared and evaluated.

1. electroformed copper sheet (outgassing and microstructural assessments).
2. Electroformed copper to copper vacuum joint (to assess strength, vacuum leak rate and effect of baking).
3. Electroformed copper to stainless steel joint (as for 2).
4. Electroformed copper-gold-stainless steel joint (as for 2 and 3 above).

Outgassing Results of Test Sample

Sample :	Grown Copper Plate.
Sample Form :	Thin copper sheet 14 cm by 14.7 cm.

	Blank Run	Copper Sample
Conductance (l/s)	2.34	2.34
Surface Area Copper (cm ²)	0	412
Q (mbar l/s)	2.6×10^{-09}	4.6×10^{-09}
QT (mbar l/s /cm ²)	-	4.9×10^{-12}
Principle Outgassing Species	CO,H ₂ ,CO ₂ , H ₂ O	CO,H ₂ ,CO ₂ , H ₂ O

Table 1 Outgassing Rates (Copper Plate)

The outgassing rate Q is the total outgassing rate of the sample chamber and sample. The outgassing rate QT is the net outgassing rate of the copper sample. Both outgassing rates are determined after a 24 hour bake at 250 °C.

Gas Species	Partial Outgassing (mbar l/s) Blank Run	Partial Outgassing (mbar l/s) Copper Sample
CO	5.1×10^{-10}	7.5×10^{-10}
H ₂	2.3×10^{-10}	2.8×10^{-10}
CO ₂	7.5×10^{-11}	1.3×10^{-10}
H ₂ O	2.3×10^{-11}	4.7×10^{-11}
CH ₄ ,O	1.4×10^{-11}	2.3×10^{-11}
C	1.4×10^{-11}	1.9×10^{-11}

Table 2 Outgassing Rates (Copper Plate)

These partial outgassing rates are total rates for the system, again after a bake cycle, and taken about 10 hours after the system temperature reached ambient.

Leak Chase of a cylindrical sample of the same material with two joints grown together was satisfactory, with a leak rate better than 1×10^{-9} .

V.CONCLUSIONS AND FUTURE WORK

So far both the electroforming and the sputtering techniques appear promising although the sputtering technique is more expensive.

Work is about to start on testing outgassing rates of joined electroformed copper after the sample has been baked to 250 °C.

Sputtered samples are being prepared for outgassing rate tests.

After evaluation, model cavities, probably at frequency of 1GHz., will be constructed for full evaluation.

VI. REFERENCES

- [1] D.M.Dykes et al An Economical Solution for a High Quality 500 Mhz. RF Cavity for the SRS Booster Synchrotron, Proc EPAC 94 London 27 June- 1 July 1994
- [2] B. Rimmer et al. High-power RF cavity R&D for the PEP-II B Factory, Proc. EPAC 94 London 27 June-1 July 1994.
- [3] A. Bixio et al. Large scale production at Ansaldo of 352MHZ niobium coated LEP-CERN cavities: development activities and first results, Proc. of PAC 1993, U.S.A.
- [4] D. Wisnivesky et al. Construction of an RF cavity for the LNLS synchrotron, Proc. of PAC 1993, U.S.A.
- [5] A.V. Timov et al. Accelerating frequency shift minimisation, Proc. of PAC 1993, U.S.A.
- [6] M. Minestrini et al. Magnetron sputtering for coating 1.3 GHz cavities with a Nb film, Proc. of PAC 1993, U.S.A.
- [7] K. Primdahl et al. Fabrication of the APS storage ring radio frequency accelerating cavities, Proc. of PAC 1993, U.S.A.
- [8] K.J. Keman et al. A new 50 MHz RF cavity for Aladdin, Proc. of PAC 1993, U.S.A.
- [9] G. Cavallari et al. Superconducting cavities for the LEP energy upgrade, Proc. of PAC 1995, U.S.A.
- [10] M. Svandrlik et al. Investigation of Higher Order Modes in the ELECTRA Cavities, Proc. of EPAC 1994, London, U.K.
- [11] Spring-8 Project Facility Design 1991 (revised). JAERI-RIKEN Spring-8 Project Team.

DESIGN OF THE 26.7 MHz RF CAVITY FOR RHIC*

J.Rose, J.Brodowski, D.P.Deng, S.Kwiatkowski, W.Pirkl, A.Ratti
Brookhaven National Laboratory, Upton, N.Y. 11973

Abstract

The accelerating system for RHIC operates at 26.7 MHz ($h=342$) and must capture the injected beam, accelerate it to top energy, and shorten the bunches prior to rebucketing into the storage ($h=2508$) system. These different functions set the design parameters of the cavity. The frequency of 26.7 MHz has been chosen in order to provide large enough buckets to capture the injected beam from the AGS and a large linear region for debunching during a bunch rotation at top energy. Provision of the large linear region also dictates the voltage requirement of 400 kV per cavity. The cavity must be tuned ~ 90 kHz to compensate for the change in speed of the gold beam.

I. ELECTRICAL DESIGN

A. Constraints

The maximum radius of the cavity must be kept under 450 mm so that the cavities in one ring do not encroach upon the beampipe of the adjacent ring. An effort was also made to try and limit the overall length to about 2 meters for ease of fabrication and plating. The 400 kV gap voltage dictated minimum gap dimensions of 53 mm, extrapolated from test data on an existing proof of principle cavity. An EIMAC 4CW150000 tetrode tube was chosen to drive the cavity. The requirement of a feedback gain of 100 predicated a direct coupling of the amplifier to the cavity to minimize the delay in the feedback loop.

B. Final cavity design

The final cavity design has had the benefit of a high power Proof of Principle cavity¹ originally designed to withstand 200 kV across a 40 mm gap. A successful test program has reached 350 kV with 5ms pulses, and 310 kV for 10 s pulses, limited by the present cooling system. For the final design value of 400 kV in the gap, the accelerating and capacitor gaps were scaled to 53.3 mm, while maintaining the peak to average field ratio at 1.6:1. The resulting final cavity design is a capacitively loaded quarter wavelength coaxial

geometry. The major electrical parameters are given in table I.

$R_{\text{shunt}}=0.95\Omega$	$Q=15750$	$R/Q=60.3$
Power Diss. @400kV (Cu, Theor) 84.2kW	Beam Power (X6 upgrade) 16 kW	Maximum Power density $5.2\text{W}/\text{cm}^2$
Maximum E-Field 11.9 MV/m	Maximum H-field 8930 A/m	Stored Energy 8 J
First Higher Monopole 103 MHz	First Higher Dipole 200 MHz	Beampipe cutoff TM_{01} 945

Table I Accelerating cavity electrical parameters

With relatively mild beam loading, and the decision to use a tetrode with a 50% power margin, the cavity geometry was determined largely by thermo-mechanical considerations. The inner conductor has a radius of 134.9 mm, which provides adequate stiffness for its length of 1894.8mm. This also provides sufficient gap capacitance for the design of the mechanical tuner which has a sensitivity of 14 kHz/mm at its null position. The maximum electric field of 11.9 MV/m is on the 40 mm radius of the tip. With the outer radius of the tank fixed by the beamline separation of the collider the last free parameter is the capacitive loading and inner conductor length. A coaxial capacitive loading was used to keep the inner conductor simple. The outer conductor of the capacitor was incorporated with the vacuum tank, allowing cooling channels to be welded to the exterior wall. The amount of loading was influenced by keeping the peak power density at the root of the inner conductor, which increases with increasing capacitance, to $\sim 5\text{W}/\text{cm}^2$. This very conservative value allowed the use of an all steel construction. Rough tuning is to be accomplished by designing the cavity low in frequency, and taking successive machining cuts on the inner diameter of the capacitor assembly to reach the design frequency, taking into account the .005 mm of copper plating to be deposited on both inner and outer capacitor surfaces.

C: Tuner design

The cavity requires a ~ 90 kHz dynamic tuning range to compensate for the increase in ion speed during acceleration,

* Work performed under the auspices of the Department of Energy

from 26.65 to 26.74 MHz. The detuning for beam loading compensation falls within this range. Maximum tuning rate is 18 kHz/s to keep up with the superconducting magnet ramp, and a tuning bandwidth of >15 Hz is required to meet the maximum allowable phase error at the start of the ramp.

Both ferrite and mechanical tuning options were investigated in detail. The mechanical tuner was chosen by virtue of its significantly lower cost, while still meeting the requirements. The mechanical tuner uses a DC servo to drive the gap electrode and vary the gap capacitance. A prototype tuner is described in detail in these proceedings².

C: HOM Analysis and passive damper design

The cavity was designed to incorporate broadband HOM suppressors to de-Q the HOM's which may lead to coupled bunch instabilities. The higher order modes were calculated with the 2½-D code URMEL³ and later expanded to include the amplifier and HOM suppressors which broke the azimuthal symmetry using the 3-D MAFIA code. The resulting HOM impedances and resonant frequencies were incorporated into coupled bunch growth rate calculations using the expression⁴

$$\tau^{-1} = \frac{\omega_{\phi}}{r_{\phi}} \frac{I_0 R}{V_T \cos \phi_T} F_m$$

where ω_{ϕ} is the angular synchrotron frequency, r_{ϕ} is the bunch half length in radians, I_0 is the beam current, R is the shunt impedance and V_T is the total rf voltage. F_m is a form factor⁵ which is a function of bunch length and frequency and is between 0.6 and zero for RHIC parameters. The impedance limits for the HOM's were obtained by setting the growth rate to 2^{-1} , a factor of 5 below the damping rate of the injection error damper, and solving the above equation for the shunt impedance R . The impedance limits for the dipole (dashed) and quadrupole (dotted) instabilities are shown in figure 1, with the undamped higher order monopole modes superimposed.

A loop coupled HOM suppressor reduces these impedances below the imposed limit. It is placed at the shorted wall to get the most coupling with a minimum of self inductance, which limits the high frequency performance. An optimized loop which entered the shorting flange and terminated on the inner conductor was abandoned despite superior performance because of the increased mechanical complexity. The loop is coupled through a folded, coaxial quarter wave notch filter to reject the fundamental and is terminated in a 50 Ω load. An alternate filter approach using a fifth order high pass has been designed and will be prototyped prior to the final design. It has the advantage of a lower fundamental power dissipation (40W versus 1000W for the notch) but presents a low impedance circuit to the coupling loop as opposed to the high shunt resistance for the notch filter. The circulating current in the HOM coupling loop

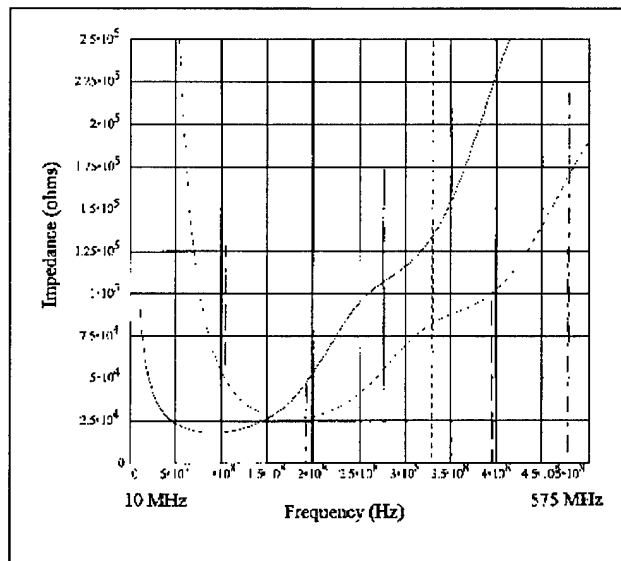


Figure 1 Impedance limits with undamped HOM's superimposed

reaches in this case the value of 85 A rms (less than 0.2 A for the notch), and the current density in the finger stock contacts between the HOM loop and the vacuum feedthrough will be as high as 15 A/cm. The final choice will be made after a high power test program on the existing prototype cavity.

D: Drive loop and window design

Both inductive (loop) and capacitive coupling were investigated, and implemented on the prototype cavity. Loop coupling was chosen for the final design primarily for the ease of introducing a variable coupling, which is advantageous for a combined function system whose maximum voltage and power is likely to be changed in different operating scenarios, as well as being mechanically simpler and easier to cool. A prototype loop has been operating with flat rexolite window for the past year. After analysis of both flat and cylindrical alumina window designs a cylindrical window of 120 mm diameter and 70 mm height has been selected. The power dissipation in the cylindrical window is an order of magnitude less and can be designed to be very uniform, whereas the power density in the flat window varied by a factor of four from the inner diameter of the side closest the cavity short to the outer diameter on the side facing the gap. The cylindrical window can be made thinner while still withstanding the vacuum loading, and can be shielded from the direct cavity environment and so be less likely to be effected by multipacting and contamination.

II. MECHANICAL DESIGN

Although the cavity must provide 400kV and dissipate 85 kW, with 55 kW in the inner conductor alone, a very simple mechanical design allows an all carbon steel

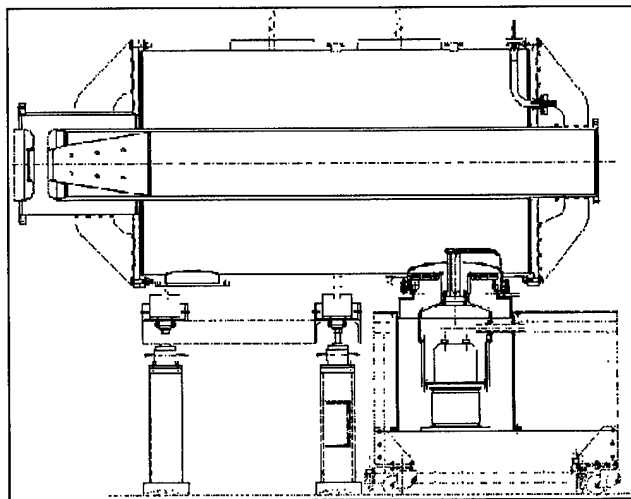


Figure 2 Accelerating cavity with power amplifier, drive loop and HOM coupling loop

construction which is subsequently copper plated. The cavity is composed of three main assemblies, an inner conductor/shorting flange assembly, tank assembly and capacitive spool assembly. The cavity with power amplifier, drive loop and HOM coupling loop is shown in figure 2.

The inner conductor assembly is fabricated from standard steel tubes. The inner part is machined to size and 16 cooling channels are machined into the surface. The outer steel shell is expanded with heating tape and heat shrunk over the inner piece. The two are mig welded together and the part leak checked. After the step which seats the shorting flange is machined into the inner conductor it is installed into the flange and the assembly welded. After all welding of the inner conductor/ end flange assembly the final machining is performed. All distortions caused by the welding are removed in this process, and perpendicularity between the inner conductor and flange assured. The maximum distance from the rf heating to a water channel is 5 mm. This results in a maximum temperature rise of 15 °C. with a local variation over the surface of 5 °C.

The capacitive spool piece is a cylinder made from rolled plate, mated to a flange made from steel plate. Additional stiffness is provided by welding gussets between the flange and the cylinder. Cooling channels are machined into the end flange with cover plates welded over them, while the cylinder has steel channels welded to the exterior for cooling.

The tank is again a cylinder made from rolled plate mated to flanges of plate steel. All cooling channels are welded to the outside skin of the tank. The rf power coupling port and vacuum port are located on the bottom of the tank. A separate water cooling channel encircles the power coupling

port. The vacuum grill is a separate plate sandwiched between the flange on the tank and the vacuum pump. It is a 6.5 mm copper plate with slots machined parallel to the current flow in the tank. Cooling is provided by brazing a cooling tube to its circumference.

All metal seals are used throughout, shielded by beryllium-copper rf spring seals in the high current regions.

Acknowledgements

We would like to acknowledge the technical excellence of Stephen Ellerd, Jeffery Aspenleiter and Joseph Greco in the fabrication and test of the prototypes and to Lou Russo in his execution of the final drawings.

References

- 1) J.Rose et al, "Conceptual Design of the 26 MHz RF System for RHIC" PAC 1993
- 2) A. Ratti et al, "Design and Performance of the RHIC Accelerating Cavity Prototype Mechanical Tuner", these proceedings
- 3) J.Tuckmantel, "Application of SAP in URMEL" CERN-EF/RF 83-5, 83-4
- 4) R.Baartman "Effect of the Beam on RF" US Particle Accelerator School, Florida State Univ. January 1992
- 5) K.Satoh SLAC PEP#357

A Design Upgrade of the RF Cavity and Its Power Window For High Current Operation of the NSLS X-Ray Storage Ring

P. Mortazavi, M. Thomas
National Synchrotron Light Source
Brookhaven National Laboratory
Upton, NY 11973

I. ABSTRACT

The existing rf cavities and their auxiliary equipment have been operating since the onset of the National Synchrotron Light Source project. Although most power supply components have since been upgraded, the rf cavities have remained unchanged. The continuous improvements of the two storage rings, notably the combined increase in energy and current level as well as their reliability, necessitated a new design. A complete description of the newly designed cavity and its input power window will be described in this paper. Selection of material, vacuum seal mechanism and thermal conductive ceramics are discussed. A comparison between the two designs and expected improvements will also be presented.

II. INTRODUCTION

The National Synchrotron Light Source (NSLS) is a dedicated user facility operating since early 1980. Its two electron storage rings provide synchrotron radiation with spectrums ranging from Infra-red to X-Ray. The booster and the two storage rings are powered with rf systems operating at 52.88 MHz.

The two storage rings' rf cavities have almost identical geometry but different output power requirements. Four cavities are currently providing rf power to the x-ray ring under operating conditions of 2.58 GeV at 250 mA. The design current of 500 mA will require an additional 75% power. The corresponding I^2R losses will also increase nearly 50% [1]. Should a fault in one system put demands on the remaining cavities, the cavity losses will be increased significantly.

The present rf cavities were constructed from copper clad steel. Economic restrictions at the time dictated the choice of this material and created both mechanical and electrical deficiencies. These included poor heat transfer, joints vulnerable to vacuum leaks, poor interior surfaces and water to vacuum joints. The performance of these cavities has necessitated the replacement of them with a new design.

III. NEW DESIGN CRITERIA

Most conventional rf cavities are fabricated from copper or aluminum material. The choice of aluminum presents some difficulties due to poor vacuum characteristics. Aluminum tends to adsorb water leading to oxidation. This increases the coefficient of secondary electron emission, a phenomena that is unacceptable for storage rings. Extensive conditioning, as well as employing various suppression techniques, may be needed for reaching an acceptable vacuum level. This characteristic is undesirable for storage rings.

The combined electrical, mechanical and vacuum characteristics of copper make it the better choice for this design. Disadvantages were the physical size and difficulties in joining the flanges to the main body. Therefore, the design philosophy was focused on minimizing the number of joints. This approach, although more expensive, considerably increases the reliability, which was a main criteria.

IV. DESIGN FEATURES

The basic cavity design consists of a center cylindrical piece, two end covers and a mushroom-shaped center electrode. In addition, the number of manufacturing operations were kept to a minimum with emphasis on no water-to-vacuum joints. To accomplish this, use of traditional Conflat flanges were eliminated by machining MARMON type directly onto the main forging. The use of a commercial spring loaded seal/clamp mechanism, such as Helicoflex, required that the sealing surfaces have a hardness of 40 on Rockwell "B" Scale. Several tests under various conditions (i.e. Rb>32, baked at 150°C for 24 hours), were performed to prove the repeatability and reliability of this design. A Rockwell "B" hardness of 30 proved to be a minimum for this type seal.

The center electrode accounts for 80% of thermal power, of which 58% is deposited in the stem section. A series of blind circular holes are to be gun drilled right beneath the rf surface. These holes serve to supply and return cooling water, and are linked to matching cooling channels machined on the center electrode's rear disk.

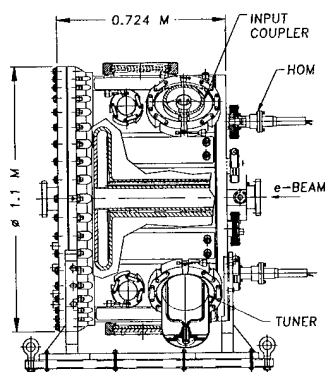


Figure 1. RF Cavity

The equivalent thermal loads were extracted from the output of the SUPERFISH computer code program. These values were used as boundary conditions on structural models using the finite element code ANSYS. A series of rectangular cooling channels are machined at optimum locations to maintain low temperature gradients. These channels will be covered with copper plates sealed by EB welds along all edges [Figure 1].

A detachable front cover provides both access to the interior as well as considerable latitude for coarse tuning. The use of Helicoflex seals is to serve both as a vacuum seal and an RF seal. This feature will provide the opportunity for future consideration of an adjustable gap tuning mechanism similar to that described in reference [2].

V. POWER WINDOW

The present power window utilizes alumina as a barrier between the air and vacuum. It is a six inch diameter, 50 ohm coaxial structure with a water-cooled coupling loop. The assembly is relatively heavy and cumbersome to install. A disadvantage of this design is the low thermal conductivity of the ceramic. This property, when coupled with localized multipactor electron bombardment, leads to vacuum breakdown. Both deficiencies have occurred during the course of NSLS operation. Future increased power requirements have also made it necessary to upgrade this design.

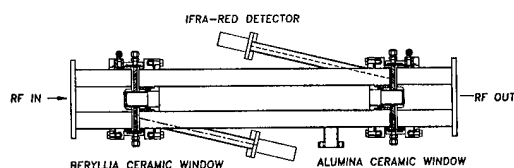


Figure 2. High power window test fixture

It is currently planned to change the alumina (Al_2O_3) to beryllia (BeO), whose electrical and mechanical properties are comparable. Each has a low dielectric constant, low loss tangent, and high electrical resistivity, but the thermal

conductivity of BeO approaches that of aluminum metal. A test set-up consisting of two identical fixtures, but with two different ceramics (Al_2O_3 & BeO) is currently being assembled for comparison [Figure 2].

The temperature gradients of both ceramics will be simultaneously measured while under power with direct Infra-red recording. In addition, multipactoring activity can also be observed from windows on the vacuum side. The secondary electron emission coefficient can be lowered by coating the ceramic surface with metal compounds such as TiN . This technique is well documented and will be applied, if necessary. Although the thermal performance is expected to be proportional to the thermal conductivities, the overall results will be published at a later date. The proposed mechanical design of the coupling loop will be simpler than the existing one.

VI. CONCLUSION

The newly designed rf cavities for the x-ray storage ring are based on all OFHC copper material. This design incorporates use of spring loaded seals for both rf and vacuum, clearly a departure from the present norm of using Conflat flanges. Troublesome transitions between stainless steel and copper are eliminated, and the hardness requirements will be preserved by using EB welding (i.e. localized heating) as the joining technique. While a hardness of 32 on the Rockwell "B" scale on a test piece was found to be acceptable, the cavity's flange will have a requirement for a hardness of 40 or better on the same scale. All peripherals will stay the same, including a series of water cooled antenna type dampers shorted by BeO resistor ceramics. The temperature control system is expected to be more responsive than before. The same feedback technique[3], using infra-red detection will be used. The means of detuning will also be the same as present, which is by insertion of a variable shorting loop in the cavity[3].

VII. REFERENCES

- [1] Thomas, R. Biscardi, W. Broome, S. Buda, R. D'Alsace, S. Hanna, J. Keane, P. Mortazavi, G. Ramirez, J. M. Wang, "NSLS X-RAY SYSTEM UPGRADE", Proc 1993 Part. Acc. Conf. Vol. 2, pp. 1419-1420.
- [2] K. J. Kleman, "A NEW 50 MHZ RF CAVITY FOR ALADDIN", Proc. 1993 Part. Accel. Conf., Vol. 2, pp. 924-926.
- [3] J. Keane, P. Mortazavi, M. Thomas R. D'Alsace, H. Ackerman, J. Aspenleiter, W. Broome, S. Buda, G. Ramirez, "X-RAY RF SYSTEM UPGRADE AT THE NSLS", Proc. 1993 Part. Accel. Conf. Vol. 2, pp. 1419-1420.

A Ferrite Loaded Untuned Cavity for a Compact Proton Synchrotron

J.I. Hirota, K. Hiramoto, M. Nishi,
Hitachi Research Lab., Hitachi Ltd., Hitachi, Ibaraki 319-12, Japan

Y. Iwashita, A. Noda and M. Inoue,
Accelerator Lab., Nuclear Science Research Facility, Institute for Chemical Research,
Kyoto Univ., Uji, Kyoto 611, Japan

Abstract

A small untuned RF cavity using a doubly re-entrant resonator and Ni-Zn ferrite cores with highly complex permeability has been designed for a compact proton synchrotron. A new method for power feeding named as multiple power feeding (multi-feed coupling) as against to direct coupling was developed to increase the accelerating voltage. The RF power is fed into the cavity through a set of couplers with the same number as the ferrites. The coupler consists of one-turn loop which is wound on to each ferrite core. The effect of multi-feed coupling was verified by measurements of the VSWR and electric field in the accelerating gap using the low and the high power model cavities.

1. INTRODUCTION

Recently, proton therapy has been confirmed to have significant advantages for treatment of tumors. A compact proton synchrotron dedicated for medical use which consists of combined type magnets with circumference of about 23m has been proposed[1]. In clinical use, the proton beam energy must be varied from 70 to 230MeV to irradiate various depths of tumors. In the compact ion synchrotron, a required accelerating voltage becomes relatively lower than that for a large ion synchrotron due to its short circumference. Furthermore, the medical accelerator system should be easily operated by non-professionals, for example, a medical doctor, a nurse or a technician, and it should be acceptable in public hospitals. Based on these conditions, an untuned type RF cavity in which resonant frequency tuning procedure is not necessary can be adopted as an accelerating system for the synchrotron.

Untuned type RF cavities have been already constructed in several laboratories[2]-[7]. These cavities consist of a quarter or a half wavelength coaxial resonator and magnetic materials with large permeability. Power loss in the magnetic materials caused by the imaginary part of the complex permeability plays an important role in obtaining a wide operating frequency range. However, in general, this power loss makes it difficult to get a high accelerating voltage in the untuned cavity. We have developed a small ferrite loaded untuned cavity and a new method of power feeding so as to increase accelerating voltage over a wide frequency range for the proton synchrotron. In section 2, the principle of the new power feed method is described. The cavity construction and experimental verifications of the new power feed method are depicted in section 3.

2. METHOD OF POWER FEEDING

2.1 Direct Coupling

At first, the usual method of power feeding, known as direct coupling is considered. The untuned cavity is given as a simple RLC resonant circuit, in which R, L and C correspond to resistance of the cavity, inductance of ferrite cores, and capacitance of the accelerating gap, respectively. Then RF power is fed into the inner conductor directly and returned to the source through the outer conductor. The cavity voltage V_d is given as

$$V_d = \sqrt{2P|Z_d|}, \quad (1)$$

where P and Z_d are net power and the shunt impedance of the cavity, respectively. Thus, the following equation is obtained,

$$V_d = \sqrt{2 \frac{4S}{(1+S)^2} P_g |Z_d|}, \quad (2)$$

where P_g is the generator power and S is the value of the voltage standing wave ratio(VSWR). The Z_d depends only on the inductance L of the ferrite cores because their permeability is large enough to get sufficiently lower operating frequency range, 1 to 10MHz typically, in an ion synchrotron. As Z_d increases, a large impedance mismatching between the cavity and the power source occurs and almost all the generator power is reflected back to the power source. Then the reflection power becomes too large to operate the power source normally under this condition. The V_d can not be increased because of the decrease in the net power fed into the cavity. This impedance mismatching between the cavity and the power source is the main cause of lowering accelerating voltage in the untuned type RF cavity.

2.2 Multiple Power Feeding

In order to reduce the reflection and increase the cavity voltage, the impedance matching must be improved keeping the cavity impedance higher. To solve this problem, a new power feed method, here after we call multiple power feeding (multi-feed coupling), was developed. In this method, the cavity and the generator power are divided into the same number of loaded ferrite cores. Figure 1 shows the equivalent circuit in multi-feed coupling. Assuming n the loaded number of ferrite cores, the cavity is constructed by a series connection of n sub-circuits whose impedance is one-nth of that of direct coupling. So the coupling impedance between the cavity and the power source can be decreased to one-nth while the total cavity impedance is equal to that of direct coupling. In this scheme, it

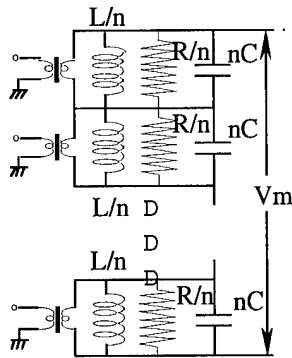


Figure 1. Equivalent circuit in multi-feed coupling.

is expected that the reflection power is much reduced by using the sub-circuits and the cavity voltage is increased by the series connection of sub-circuits. The cavity voltage V_m is given by

$$\begin{aligned}
 V_m &= \sqrt{2P|Z_m|} \\
 &= n \sqrt{2 \frac{4S/n}{(1+S/n)^2} \frac{P_g}{n} \frac{|Z_d|}{n}} \\
 &= \sqrt{n} \frac{1+S}{n+S} V_d \\
 &\sim \sqrt{n} V_d \quad (S \gg n > 1) \quad (3)
 \end{aligned}$$

where Z_m is the cavity impedance in multi-feed coupling. The Z_d/n corresponds to the impedance of the sub-circuit. If the value of VSWR is large enough ($S \gg n > 1$), V_m can be \sqrt{n} times larger than V_d . In this analysis, mutual inductance of each ferrite core is ignored.

3. EXPERIMENTS WITH MODEL CAVITIES

3.1 Cavity Construction

In order to verify the effectiveness of multi-feed coupling, a low power model cavity was made and tested at first. RF characteristics were measured by the VSWR method[8] using a

Table. 1 @Parameters of RF acceleration system

Machine Parameters	
Lattice Composition	Combined Function
Circumference	23m
Injection Energy	7MeV
Extraction Energy	70-230MeV
Proton Velocity (β)	0.12-0.60
Strength of Bending Magnet	0.23-1.43T
Momentum Spread ($\Delta p/p$)	0.3%
Transition Gamma (γ_t)	1.547
Harmonic Number (h)	1
Repetition Rate	0.5Hz
Acceleration Pattern	dB/dt=0 smooth pattern at acceleration start and stop
RF Acceleration Parameters	
RF Cavity	Ferrite Loaded Untuned
Acceleration Method	Constant Area of RF Bucket
Revolution Frequency	1.564-7.769MHz
Energy Gain (V_{rf})	0-100eV
Cavity Voltage (V_c)	150-450V
Synchronous Phase (ϕ_s)	0-22deg
Acceleration Period	0.7sec
Cavity Length (includes monitor)	<1m

network analyzer. The specifications of the proposed compact proton synchrotron and the accelerating system are shown in Table 1. The model cavity was constructed with a double re-entrant coaxial resonator and Ni-Zn ferrite cores manufactured by Hitachi Metals Ltd. The outer and inner diameters of the cavity were 550 and 160mm, respectively. The lengths of the cavity and the accelerating gap were 400 and 50mm, respectively. In results, the cavity impedance is independent of these lengths. The cavity impedance depends only on the number of ferrite cores in the frequency range between 1.5 and 7.8MHz. The dimensions of ferrite cores installed in the cavity were 500 and 280mm in outer and inner diameters, respectively and 25.4mm in thickness with the complex permeability of about (1000,100) at 5MHz. In multi-feed coupling, the RF power was first split into the same number of loaded ferrite cores by the power splitter and then each of them was fed into the cavity through the one-turn coil which was wound on each ferrite core. The winding direction of the one-turn coil must be chosen in order to generate the magnetic field on the same direction in each ferrite core even if the phase of the RF power is

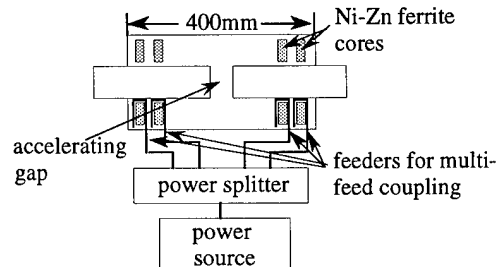
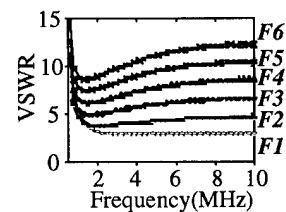


Figure 2. Block diagram for low power measurements

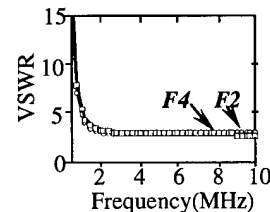
different between each other.

3.2 Measurements of VSWR

In multi-feed coupling, the VSWR or the impedance of the cavity must be decreased to an nth part of the VSWR in direct



(a) direct coupling.



(b) multi-feed coupling.

Figure. 3 The frequency dependence of the VSWR as a function of the loaded number of ferrite cores. F indicates the loaded number of ferrite cores.

coupling. Figure 2 shows the block diagram of the low power measurements in the multi-feed coupling. The frequency dependence of the VSWR was measured by changing the number of ferrite cores in each coupling. Experimental results are shown in Figure 3. The VSWR in direct coupling increases in proportion to the number of ferrite cores. But in multi-feed coupling, the VSWR is nearly constant for any number of ferrite cores in the range from 2 to 10MHz, though the total impedance of the cavity becomes large in proportion to the number of ferrite cores. So the VSWR in multi-feed coupling is equal to that with one ferrite core in direct coupling, and the decrease of the VSWR is confirmed. From these results, it is evident that the mutual inductance of each ferrite core can be neglected and the equivalent circuit analysis is valid.

3.3 Measurements of Electric Field

Direct measurements of electric field in the accelerating gap were performed using the low and the high power model cavities. The high power model cavity is the same as the low power model cavity except for the gap and cooling structures. The accelerating gap was vacuum sealed by a ceramic duct. The electric field was measured by a pick-up antenna consisting of a semi-rigid coaxial cable whose tip was exposed to the gap field. The number of the ferrite cores was fixed at 4 in the low power model and at 8 in the high power model cavity. Figure 4

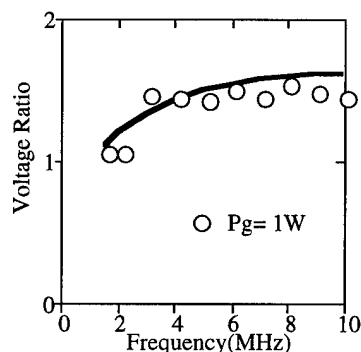


Figure 4. The voltage ratio normalized by the voltage of direct coupling in the low power model cavity.

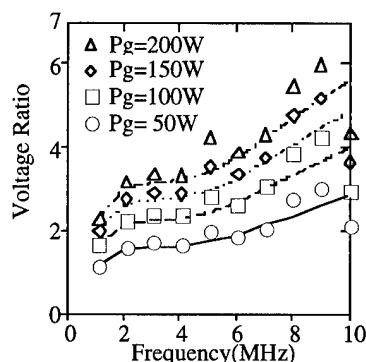


Figure 5. The voltage ratio normalized by the voltage of direct coupling in the high power model cavity. P_g indicates generator power.

4. CONCLUSION

A new method of power feeding named multiple power feeding (multi-feed coupling) has been developed in order to increase the accelerating voltage and reduce the reflection power from the cavity. The RF power is fed into the cavity through one-turn coil which is wound on to each ferrite core. The low and high power model cavities which consisted of the doubly re-entrant coaxial resonator and Ni-Zn ferrite cores have been made and tested. The effects of multi-feed coupling are verified by measurements of the VSWR and electric field of the gap. In multi-feed coupling, for the case with 8 ferrite cores in the cavity, it is possible to get the accelerating voltage about 2.0 times as large as that of direct coupling.

ACKNOWLEDGMENT

The present work is supported by Grant-in Aid for Scientific Research from Ministry of Education Science and Culture of Japan.

REFERENCES

- [1] K. Hiramoto et. al., "A Compact Proton Synchrotron with a Combined Function Lattice for Medical Use", Proc. of PTCOG XXI to be published.
- [2] J.P. Blewett et. al., "Radio-Frequency System. Part IV-Accelerating Unit", Phys. Rev., Vol. 24, pp.795-800, September 1953.
- [3] J.E. Griffin et. al., "Isolated Bucket RF System in Fermilab Antiproton Facility", IEEE Trans. Vol. NS-30, No. 4, August 1983.
- [4] K.Muto et. al., "Ferrite Loaded Untuned RF Cavity for Synchrotron", Proc. of the 1989 Particle Accelerator Conference
- [5] S. Ninomiya, "Conceptual Design of a Non-Resonant Accelerating System for Low-Energy Proton and Heavy-Ion Accelerators", KEK Report 92-2 April 1992 A.
- [6] "Conceptual Design of a Proton Therapy Synchrotron For Loma Linda University Medical Center", Fermilab., June 1986.
- [7] "Loma Linda University Medical Center Proton Therapy Facility Engineering Design Report", Fermilab., Feb. 1987
- [8] E.L. Ginzton, "Micro Wave Measurement", pp.375 1960

shows the voltage ratio normalized by direct coupling in each model cavity. Figure 5 also shows the generator power dependence of the voltage ratios. In the figures, solid and dotted lines are the calculated voltage ratios obtained from equation (3) using the VSWR measured by the low power experiments. Measured and calculated voltage ratios are in good agreement in each model cavities. In figure 5, the accelerating voltage increases as a function of $\sqrt{P_g}$. The mean values of the voltage ratio are 1.5 and 2.0 for the cases in which the loaded number of ferrite cores are 4 and 8, respectively. These values can be obtained from equation (3) substituting $n=4$, $S=10$ for the low power and $n=8$, $S=12$ for the high power model cavity. So it is confirmed that the cavity voltage can be increased and the generator power also can be reduced.

ON THE THEORY OF TWO COUPLED CAVITIES

N.I.Aizatsky, National Science Centre, Kharkov Institute of Physics & Technology (KFTI),

310108, Kharkov, Ukraine.

This work presents research results on a novel analytical model of electromagnetic systems coupling through small size holes. The key problem regarding interactions of two cavities through an aperture in separating screen of finite thickness without making assumption on smallness of any parameters is considered. We are the first to calculate on the base of rigorous electromagnetic approach the coupling coefficients of the cylindrical cavities within the limit of small aperture and infinitely thin separating screen. The numeric results of electromagnetic characteristic dependencies that have been impossible to perform on the base of previous models are given.

INTRODUCTION

The problem of electromagnetic systems coupling has been in the focus of scientific attention for over 40 years. The approach of tackling this problem with the use of the concepts of equivalent electric and magnetic dipole moments, suggested in [1,2], proved to be fruitful. On its base various electromagnetic characteristics of interacting objects have been studied (see [3-10] and literature cited therein). The key element this approach is employment of the "static" analysis used for determination the fields in the immediate vicinity of the hole. Clearly, this procedure is valid only if the hole dimensions are small compared to the wave length. Besides, the apertures have to be placed at a remote distance from the borders of the electromagnetic systems being considered. This notwithstanding, the developed methods allowed not only to calculate the number of important characteristics, but formulate (or lay the basis) for entirely new approaches for consideration of different RF-devices. This approach exerted considerable influence on the

theory of slow-wave structures based on utilization of resonant properties of electromagnetic systems (disk-loaded waveguides, coupled-cavity chains, etc.)

However, even to this day, there have not been developed general methods of calculations of small aperture coupling coefficients from which the "static" results could be obtained by means of the limit transition $\omega a/c \rightarrow 0$. Development of such methods would permit not only to assess the region of applicability of "static" results, but also to expand the frontiers of problems regarding RF-interactions that can be rigorously solve (correct evaluation of the separating screen thickness, the vicinity of walls, etc.) It must be noted that several efforts were made to push forward the frontier of applicability of the "static" approach [4,10]. However, the accurateness of the proposed techniques cannot be proven within the framework of the models considered.

Development of novel analytical method for investigation of electromagnetic systems coupling through small-size apertures is also important considering the fact that there are difficulties of utilization the widely developed electromagnetic simulations techniques in this particular area. These difficulties are associated with the requirements of very high precision mathematical models to be used for small coupling holes, since the relative correctness of a model has to be smaller than the coupling coefficients.

BASIC EQUATIONS AND RESULTS

Let us consider two ideal conducting co-axial cylindrical cavities coupled through a cylindrical aperture of the radius a in the separating planar screen of the thickness t . The radii and lengths of the first and second cavities will be designated b_1, d_1 and b_2, d_2 , respectively. To construct a

mathematical model of the electromagnetic system under consideration, we will use a relatively novel method of partially crossed regions (see, for instance [11,12]. As the first and second regions, we will take the cylindrical cavity volumes; for the third, a cylinder that is co-axial with the coupling hole, its radius being equal $b_3 = a$. This cylinder projects into the area of the first cavity for the length d_{1*} and into the second one for the length d_{2*} , the cylinder length being $\ell_* = d_{1*} + d_{2*} + t$.

In each region, we expand the electromagnetic fields in terms of the orthonormal complete set of field functions without the hole. We can get a set of equations for field amplitudes only in the 1-st and 2-nd regions:

$$a_{k,l}^{(i)} = \sum_{n',s'} (a_{n',s'}^{(1)} V_{n',s',k,l}^{(i,1)} + a_{n',s'}^{(2)} V_{n',s',k,l}^{(i,2)}) , \quad i=1,2 \quad (1)$$

This uniform set of equations describes the interaction of two infinite sets of oscillators, which are eigenmodes of closed cavities (without the coupling hole in the separating screen), being, in principle, fit to be used for calculations of necessary electromagnetic characteristics of coupled cavities. However, this set of equations has three drawbacks that make it difficult to carry out both analytical investigations and numerical calculations. Firstly, the structure of this set of equations does not yield a possibility to obtain analytical results, in particular, in the well studied limit $t=0$ and $a \rightarrow 0$. Secondly, this set is two-dimensional, and it is necessary to have great calculative resources to solve it. Thirdly, owing to the presence of field peculiarities at acute angles of the hole in the screen the coefficients $V_{n',s',k,l}^{(i,j)}$ decrease slowly with increasing indices. Our studies show that this set of equations can be reduced to such a form that has no first or second drawbacks:

$$(\omega_{0,1}^{(1)2} - \omega^2) a_{0,1}^{(1)} = -\omega_{0,1}^{(1)2} \frac{2a^3}{3\pi b_1^2 d_1 J_1^2(\lambda_1)} \times \left[\Lambda_{1,1} a_{0,1}^{(1)} - \frac{b_1^2 \sqrt{d_1}}{b_2^2 \sqrt{d_2}} \Lambda_{1,2} a_{0,1}^{(2)} \right], \quad (2.1)$$

$$(\omega_{0,1}^{(2)2} - \omega^2) a_{0,1}^{(2)} = -\omega_{0,1}^{(2)2} \frac{2a^3}{3\pi b_2^2 d_2 J_1^2(\lambda_1)} \times \left[\Lambda_{2,2} a_{0,1}^{(2)} - \frac{b_2^2 \sqrt{d_2}}{b_1^2 \sqrt{d_1}} \Lambda_{2,1} a_{0,1}^{(1)} \right]. \quad (2.2)$$

where the coefficients $\Lambda_{i,k}$, which determine the frequency shifts and cavities coupling, are defined by the expression

$$\Lambda_{i,k} = J_0^2(\lambda_1 \frac{a}{b_i}) \sum_{s=1}^{\infty} \sigma_{s,1,i} w_s^{(i,k)} \quad (3)$$

and $w_s^{(i,k)}$ are the solutions of some sets of linear algebraic equations.

First of all, let us become clear on the influence of electromagnetic field non-potentiality in the interaction region on $\Lambda_{i,k}$ -values, since in all previous research studies [1-4,7] on coupling through small-size holes the assumption about field potentiality in the vicinity of the hole were made. In our model investigation of this problem is reduced to studying the dependence of the coefficients $\Lambda_{i,k}$ on the frequency f ; the case $f=0$ corresponds to the assumption of field potentiality in the interaction region. Since frequency comes into the appropriate coefficients only in the form of expression $\Omega = \omega a/c$, then it follows that Λ -variation with increasing frequencies from 0 to f_{010} must be dependent on coupling aperture size - the smaller a the weaker dependence of Λ on frequency. This is confirmed by the calculations results (Tab.1.).

Table 1. Dependence of $\Lambda_{i,k} = \Lambda$ coefficients and coupling coefficients $\tilde{\Lambda}$ on frequency f ($d_1 = d_2 = 3.5$ cm, $b_1 = b_2 = 4$ cm, $t = 0.0$ cm, $f_{010} = 2.868563$ GHz)

	(a=1 cm)		(a=1.5 cm)	
f(GHz)	Λ	$\tilde{\Lambda}$	Λ	$\tilde{\Lambda}$
0	0.896590	0.012606	0.788984	0.037440
1	0.897783	0.012623	0.793784	0.037667
2	0.900862	0.012666	0.808207	0.038352
3	0.903614	0.012705	0.831250	0.039445

From Tab.1 it follows that an error in calculations of the coupling coefficients $\tilde{\Lambda}$ ($\tilde{\Lambda} = 2a^3 \Lambda / 3\pi b_1^2 d_1 J_1^2(\lambda_1)$) at

$a=1$ cm is on the order of 10^{-4} (the equivalent frequency shift being ≈ 300 kHz) and, consequently, all calculations can be made in static approximation. Yet, already for $a=1.5$ cm the error is of the order of 2×10^{-3} (the equivalent frequency shift being ≈ 6 MHz), which is inadmissible for precise calculations.

Of importance for applied use is the dependence of the coupled coefficients on the coupling aperture radius a . Analysis indicates that $\Lambda_{i,k}$ depends both on the above parameter $\Omega = \omega a/c$ and on relation of a to all cavity geometrical parameters and screen thickness (a/d_j , a/b_j , a/t , $j=1,2$). Results of the calculations of the relationship of interest on basis of our model in the static approach ($f=0$) are given in Fig.1. Fig.1 also shows the results of calculations for various values of the parameter a/t at $a/d_j \rightarrow 0$, $a/b_j \rightarrow 0$ [9].

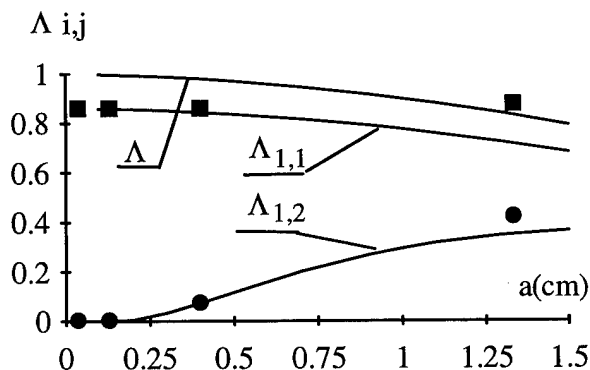


Fig.1. Dependence of coefficients $\Lambda_{i,k}$ on the coupling aperture radius a ($\Lambda_{i,k} = \Lambda$ - $t=0$, $\Lambda_{1,1}$, $\Lambda_{1,2}$ - $t=0.4$ cm, $d_1 = d_2 = 3.5$ cm, $b_1 = b_2 = 4$ cm, $f=0$, marks show the results of calculations from [9]).

It follows from Fig.1 that taking into account the finiteness of parameters a/d and a/b lead not only to a drastic change of the numerical values of the coupling coefficients, but to change the functional dependence of $\Lambda_{i,k}$ on a . For instance, at a finite thickness of the screen the coefficient $\Lambda_{1,1}$ which determines the cavity eigenfrequency shift decreases with increasing a , contrary to what one can obtain from the results of the paper [9].

On this way, we put forward a novel analytical model for studying the coupling of two cavities through an aperture in separating screen of finite thickness without making assumption on smallness of any parameters.

REFERENCES

1. H.A. Bathe. Phys. Rev., 1944, Vol.66, No.7, p.163-182.
2. V.V. Vladimirsky. ZhTF, 1947, Vol.17, No.11, p.1277-1282.
3. A.I. Akhiezer, Ya.B. Fainberg. UFN, 1951, Vol.44, No.3, p.321-368.
4. R.M. Bevensee. Electromagnetic Slow Wave Systems. John Wiley & Sons, Inc., New York-London-Sydney, 1964.
5. H.A. Wheeler. IEEE Trans. Microwave Theory and Techniques, 1964, MTT-12, p.231-244.
6. R.L. Gluckstern, R. Li, R.K. Copper. IEEE Trans. Microwave Theory and Techniques, 1990, MTT-38, No.2, p.186-192.
7. R.L. Gluckstern. AIP Conference Proceedings 249, Vol.1, The Physics of Particle Accelerators, AIP, New York, 1992, p.236-276.
8. N.A. McDonald. IEEE Trans. Microwave Theory and Techniques, 1972, MTT-20, No.10, p.689-695.
9. R.L. Gluckstern, J.A. Diamond. IEEE Trans. Microwave Theory and Techniques, 1991, MTT-39, No.2, p.274-279.
10. N.P. Sobenin, E.Ya. Shkol'nicov. Collected Series: Accelerators, Moscow, Atomizdat, 1970, No.12, p.96-101.
11. I.G. Prohoda, V.I. Lozyanoi, V.M. Onufrienko et al. Electromagnetic wave propagation in inhomogeneous waveguide systems. Dnepropetrovsk, Dnepropetrovsk State University Publishing House, 1977.
12. I.G. Prohoda, V.P. Chumachenko. Izvestia VUZov, Radiophysics, 1993, v.16, No.10, p.1558.

MEASUREMENT OF MULTIPACTING CURRENTS OF METAL SURFACES IN RF FIELDS

D. Proch, Deutsches Elektronen-Synchrotron DESY, Hamburg, Germany and
D. Einfeld, R. Onken, N. Steinhauser, Fachhochschule Ostfriesland, Emden, Germany

Abstract

Multipacting currents can absorb RF energy and produce breakdown in high power components such as couplers, windows, higher order mode absorbers, etc.. This phenomenon starts if certain resonant conditions for electron trajectories are fulfilled and if the impacted surface has a secondary yield larger than 1. There are known recipes to reduce the secondary yield by coating techniques but the success rate is often unsatisfactory. Therefore we have started systematic measurements of the RF multipacting current. We measure the multipacting current between two electrodes of a specially designed coaxial resonator. Technical surfaces (Cu, plated Cu on stainless steel, Al, stainless steel) have been investigated before and after surface treatments such as chemical cleaning, baking and Ti coating. We present data for the strength of multipacting, start current, processing time and possible reconditioning.

I. INTRODUCTION

Multipacting is a phenomenon of resonant electron multiplication:

- one electron is accelerated by the electric RF field and hits the target surface after one even (odd) number of RF half cycles as resonant condition for one (two) surface multipacting,
- the impacting electron produces more than one secondary electron.

These two conditions have to be fulfilled in order to start an electron avalanche. This electron current might result in severe limitations of the stored energy in microwave components or finally ignite a breakdown. To suppress these limitations, the resonant condition can be avoided by proper choice of geometry. Resonant conditions for a parallel plate geometry in pure electric fields can be easily predicted and thus be avoided by the right gap distance. In the case of electromagnetic fields, however, multipacting is simulated by tracking programs. In the case of complicated three dimensional RF components a simulation of electron trajectories becomes very demanding. Furthermore the RF design might not allow to change the geometry by the needed amount.

Therefore attempts are undertaken to suppress multipacting by proper coating of critical surfaces. A material for coating is chosen which has a secondary yield of smaller than or at least near by one. Different coating materials are known, for example Ti, TiN, CrO₂, etc. [1]. Those materials have been investigated by measuring the secondary yield in DC experiments on sample surfaces. RF components might have

complicated geometry to be coated. The improvement also depends on coating conditions of large technical surfaces. Therefore a test resonator was developed to measure the RF multipacting current directly under various coating conditions. For fast turn around this resonator should allow a fast exchange of the multipacting electrodes and should operate at low power. In this paper the design of such a test resonator is given and first measurements on different coatings are presented.

II. DESIGN OF THE TEST RESONATOR

The resonant condition for two side multipacting in an electric field is given by:

$$E_{(n)} = \frac{4m\pi}{e} \cdot \frac{f^2 l}{(2n-1)} \quad (1)$$

n: order of multipacting (n:1,2,3,...)

f [Hz]: frequency

l [m]: gap distance

m [kg]: mass of electron

e [C]: charge of electron

E_(n) [V/m]: resonant electric field gradient

The magnetic RF field in the center gap of a reentrant resonator is small as compared to the electric RF field.

Therefore two side multipacting according to equation (1) is expected in such a resonator. The experiment proved that multipacting actually occurs at the predicted field levels. This

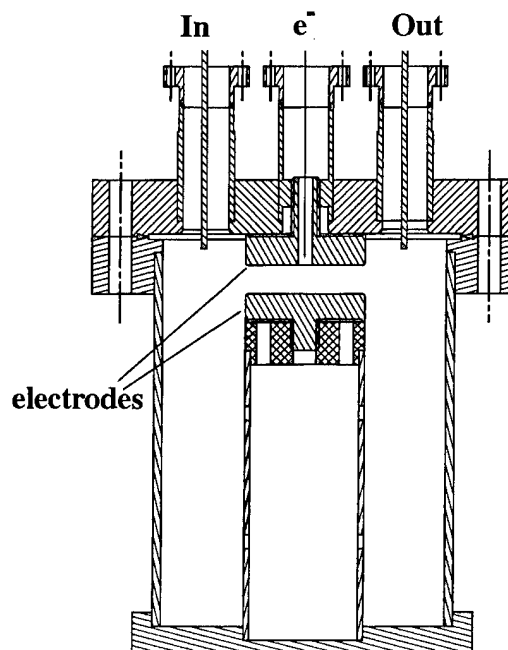


Figure 1: Test resonator

resonator has been also analysed by trajectory calculations and is discussed in [2].

A resonant frequency of 500 MHz has been chosen because of available laboratory equipment. The gap distance of 10 mm is rather large but hereby dimension tolerances by many assemblies can be neglected. Typically 10 watts of RF power is needed to reach first order multipacting. The diameter of the resonator is uncritical and was chosen according to available material.

The resonator is fabricated from copper (resonator) and stainless steel (flange) plated with copper. The two ports on the top cover are used for pumping and RF coupling. Both RF antennas have the same coupling in order to maintain the symmetry of the central electric field. A small coaxial line penetrates the upper center electrode to give a direct measure of the multipacting current.

length	mm	113
outer diam.	mm	100
inner diam.	mm	42
gap distance	mm	10
resonance frequ.	MHz	500
watts/1 kV gap		5.88×10^{-3}
typ. unloaded Q		5×10^3

Table 1: Data of the multipacting resonator

III. MEASUREMENT PROCEDURE

After assembly of a pair of electrodes the upper Conflat flange is closed and the resonator is pumped to better 10^{-6} mbar. The generator is locked to the cavity resonance and the antennas are calibrated at low RF field level. Then the RF power is modulated up to 20 watts with a saw-tooth generator of 0.1 Hz. The onset of multipacting current is measured and the order of multipacting is determined from the calibrated gap electric field gradient. The magnitude and the processing behavior of the multipacting current are measured the following way:

- the RF cavity power is set to 5 watts above the onset of multipacting,
- the cavity is operated under these conditions with the generator frequency locked to the cavity,
- the multipacting current will decrease and the cavity field will increase until the electron current completely disappears. At this moment the cavity field will jump up to the undisturbed value,
- the cavity is operated for about 2 h after the first processing because sometimes multipacting will reappear.

From the above given procedure the following characteristic data are extracted:

- order of observed multipacting,
- typical decay time of multipacting current during processing,
- time needed to overcome multipacting,
- tendency of deconditioning.

IV. MEASURED RESULTS

For each measurement one pair of electrodes (= one sample) is prepared and installed. Most work has been done with Cu and stainless steel samples to calibrate the measurement equipment and to test the reproducibility of the multipacting behavior. 6 Cu samples (3 from OFHC copper, 3 from standard copper) and 4 stainless steel samples have been fabricated. After each measurement the samples were slightly chemically polished so that a new surface was prepared for the next measurement. Some Cu samples were coated with Ti (sputter technique), one sample was coated with TiN (thermal evaporation) [3]. Four stainless steel samples have been electroplated with 20 μm of Cu. Four samples (2 Cu, 2 Ti on Cu) have been stored in a plastic (PE) bag (filled with dry N_2) for one week. Table 2 summarizes the measured results. The numbers of the multipacting current and of the processing time are mean values of the individual measurements. They differ typically from measurement to measurement by 12 % (current) and 40 % (time). The value of the electric field at the onset of multipacting varies only by 7

MATERIAL	N	I [mA]	E1 [kV/m]	E2 [kV/m]	n	t [s]
Copper	18	2.92	132.1	188.4	1	2080
Copper (heated at 400°C)	2	3.52	145.8	231.4	1	1223
Cu, stored one week in PE bag	2	3.30	82.5; 139.0	108.9; 192.8	2 ; 1	>6500
Titanium on Copper	5	3.03	139.9	184.5	1	933,1
TiN on Copper	1	3.00	129.3	170.7	1	552
Titanium on Aluminum	2	2.88	141.8	183.4	1	885,5
Cu Ti, stored one week in PE bag	2	3.21	51.1; 123.6	68.1; 190.0	3 ; 1	>6500
Aluminium	7	4.30	54.7	69.4	3	>6500
Stainless Steel	18	3.37	69.3; 128.8	87.7; 147.6	2 ; 1	2781
Copper electrochemically plated on S.S.	7	3.33	132.7	183.8	1	2571

Table 2: Results of the multipacting measurements (N: number of measurements; I: multipacting current; E1, E2: electric field gradient at onset, stop of multipacting current; n: order of multipacting; t: processing time)

%. The order of multipacting is deduced from equation (1).

Figure 2 shows the typical processing behavior of Al, Cu and stainless steel samples. The multipacting current is plotted versus time under the condition of additional 5 watts RF power above the first onset of multipacting.

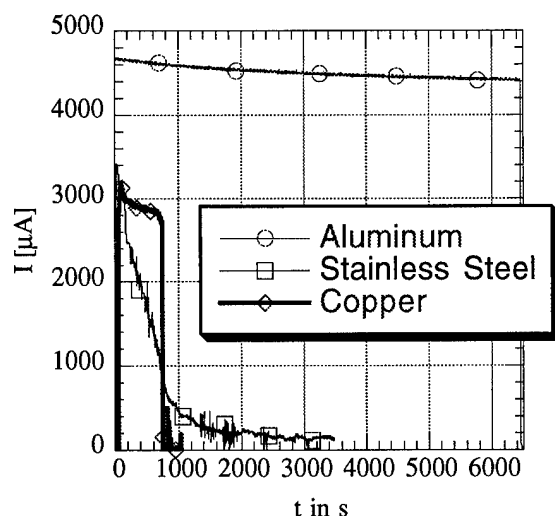


Figure 2: Multipacting current vs. time for 3 different metals

Figure 3 displays the multipacting current versus the gap voltage during processing. The multipacting current drops down so that the power being absorbed from the multipacting process decreases, too. Therefore the stored energy in the resonator and thus the electric field in the gap increase. The condition of equation (1) predicts a resonant voltage of 176 kV/m ($n=1$) for our geometry. The experiment shows multipacting between 150 and 210 kV/m. The width of the multipacting region is larger at lower multipacting orders. This is due to a spread of starting velocity and starting angle of the secondary electrons.

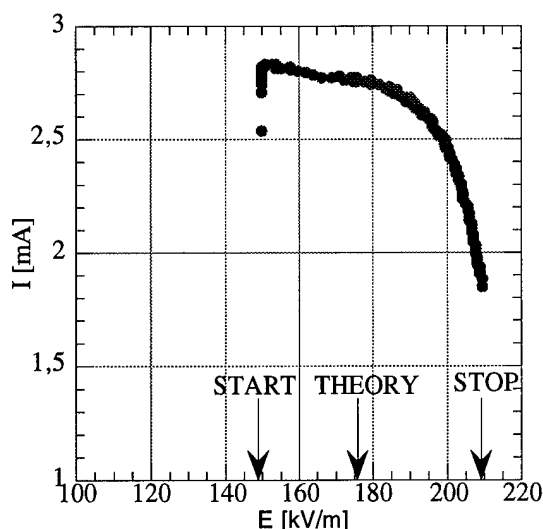


Figure 3: Multipacting current vs. electric field gradient for Titanium on Copper

V. DISCUSSION

All samples show multipacting of at least first order. They differ in magnitude of multipacting current and in processing time. Al samples show the worst behavior, as expected. They do not process within the measurement time of 6500 sec..The multipacting behavior of standard copper and OFHC copper does not differ at all. Heat treatment of 400°C, 6 hours, reduces the processing time to 60 %. Coating of Cu with Ti reduces the processing time to about 45%. A Ti coating of Al has a substantial improvement because of the strong multipacting behavior of the bare Al. After coating with Ti, samples from Cu and Al behave the same. Electroplated Cu on stainless steel is somewhat worse than pure copper before heat treatment.

One interesting result is the dramatic deterioration of Cu and Ti coated Cu samples after storage in a plastic (PE) bag. Both types of samples do not process within 6500 sec. after storage in the bag. This deterioration was also reported by another experiment [4]. The mechanism is not understood. One speculation is, that some lubricant in the PE foil penetrates to the metal surface of the sample. Nevertheless, the common practice to store or transport RF components in plastic bags should be avoided, if multipacting is of concern.

VI. ACKNOWLEDGEMENT

One pair of Cu samples was coated with TiN by M. Kuchnir, FNAL. We gratefully acknowledge this preparation.

VII. REFERENCES

- [1] A. R. NYAIESH, E. L. GARWIN, F. K. KING and R. E. KIRBY; "Properties of Thin Anti-Multipactor Coatings for Klystron Windows"; SLAC-PUB-3760; August 1985
- [2] E. SOMERSALO, P. YLA-OIJALA AND D. PROCH; "Analysis of Multipacting in Coaxial Lines"; FAE08; this conference
- [3] M. KUCHNIR AND E. HAHN; "Coating Power RF Components with TiN"; Fermilab TM-1928; March 1995
- [4] A. WOODE AND J. PETIT; "Investigations into Multipactor Breakdown in Satellite Microwave Payloads"; ESA Journal 1990; Vol. 14; p. 467-478

OPTIMIZATION OF CLIC TRANSFER STRUCTURE (CTS) DESIGN TO MEET NEW DRIVE BEAM PARAMETERS

A. Millich, CERN-SL, CH-1211 Geneva 23

I. INTRODUCTION

In the original CTS design [1] the 2.8 mm-wide slit, joining the cylindrical beam chamber to the teeth-loaded rectangular waveguides provided a sufficient coupling for the 160 nC drive-beam bunches to deposit 40 MW of 30 GHz power in the waveguides. The drive-beam generation studies have recently evolved towards schemes which envisage an increased number of bunches at reduced charge per bunch [2]. In order to cope with the reduced beam intensity while maintaining the correct power output level, the CTS design has been modified to increase the beam coupling parameter. Moreover, the new CLIC Test Facility (CTF2) requires transfer structures with even higher beam coupling because of the reduced bunch frequency (3 GHz) [3]. Additional modifications to the original design were required by manufacturing, which imposed the presence of round lips at the slit edges [4]. We have simulated the new CTS by means of MAFIA in order to explore the range of variation of the coupling parameter with slit aperture, and optimized the design to meet the requirements of both the new drive beam and the CTF2. We report here the results of the simulation studies.

II. CTS COUPLING FACTORS FOR CLIC AND CTF2

In the reference scheme for CLIC, the drive beam is formed by four trains of 22 bunchlets each, separated in time by 2.84 ns. The Gaussian bunchlets have $\sigma = 1$ mm, a 30 nC charge, and a spacing of one 30 GHz period. After the traversal of one bunchlet train, the CTS received the energy

$$U = (R/Q) q^2 F^2(\sigma) \omega / 2 \quad (\text{VAs}) \quad (1)$$

where R/Q is the mode coupling factor, $q = 660$ nC is the charge in one train, $F(\sigma) = 0.82$ is a function of the bunch length, and $\omega = 2\pi f$ is the angular frequency of the coupled mode. The energy U is induced in one burst during the traversal of the bunchlet train and discharges uniformly during 2.84 ns at the rate imposed by the mode group velocity of $0.3c$. Just before the CTS discharges completely, the next bunchlet train traverses the structure and again fills it with energy. The CTS thus acts as a pulse stretcher and delivers a uniform power pulse 11.4 ns long to fill two CLIC Accelerating Structures (CASs), one from each waveguide. The power needed to fill the two CASs is 90 MW, which requires $4U = 1.02$ VAs, and $R/Q = 9.4 \Omega/\text{structure}$ or $R'/Q = 23.0 \Omega/\text{m}$, as the CTS is 41 cm long.

The main goal of the CTF2 experiment is to use one CTS to provide 50 MW power pulses to one CAS by combining the two waveguide outputs. In this case the drive beam will be formed by a continuous train of bunchlets separated by a 3 GHz period or 333.3 ps. The charge which traverses one CTS

during 2.84 ns will initially be limited in CTF2 to 200 nC, so that solving Eq. (1) for R/Q and substituting $U = dP$ with $P = 50$ MW and $d = 2.84$ ns we get for the CTS coupling parameter the value

$$R/Q = 56.7 \Omega/\text{structure} \text{ or } R'/Q = 138.0 \Omega/\text{m}.$$

III. THE NEW CTS GEOMETRY

Figure 1 shows a six-cell section of the CTS as simulated by MAFIA [5].

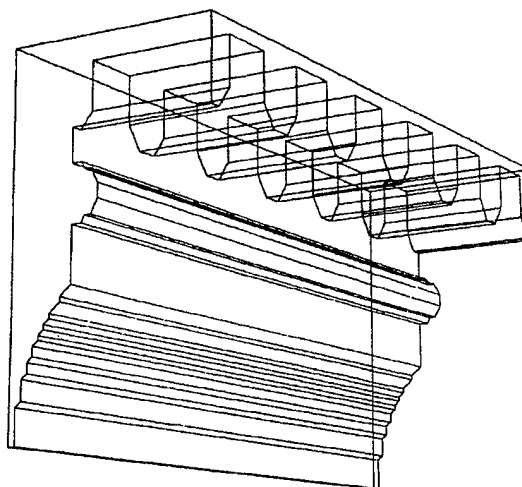


Figure 1: Six cells of CTS as simulated by MAFIA (upper left corner shown).

We notice the presence of the rounded lips, which mark the separation of the beam chamber from the teeth-loaded waveguides. The main geometrical parameters of the CTS are:

Beam chamber radius	6.000 mm
Waveguide width	8.600 mm
Slit aperture*	3.0 to 7.000 mm
Lip radius	0.800 mm
Waveguide height	3.000 mm
Teeth spacing	3.332 mm
Teeth height	2.000 mm
Teeth thickness	1.667 mm
CTS length	410.0 mm

*may vary to change the coupling

The maximum aperture between the lips' edges is given by the waveguide width minus twice the lip radius, or $8.6 - 1.6 = 7.0$ mm. We have explored the variation of the main RF parameters with slit aperture increasing from 3.0 to 7.0 mm while keeping all other parameters constant. Table 1 summarizes the results obtained.

Table 1

Slit (mm)	f (GHz)	Q	R'/Q (Ω/m)	E_w/E_t (%)	\hat{W}'_z (V/pC/m)
3.0	28.85	2651	2.40	99.70	0.95
4.0	29.95	3143	14.42	98.60	2.65
5.0	30.94	3538	89.61	94.67	7.25
6.0	30.88	3832	149.75	92.44	12.34
7.0	30.35	4025	178.20	88.95	19.10

The fifth column in the table gives the ratio of the energy of the mode in the waveguides over the total mode energy. This is an important parameter as it determines the efficiency of the power extraction from the beam. The sixth column shows the peak value of the longitudinal wake potential for a Gaussian bunch with $\sigma = 1$ mm traversing 1 m of structure, computed using the time domain module T3320 of MAFIA.

IV. OPTIMIZATION OF THE CTS FOR THE CLIC REFERENCE SCHEME

From the results shown in Table 1 it appears that a slit aperture of about 4.2 mm would provide the required CTS coupling of 23 Ω/m for the reference scheme, albeit at the expense of relatively high losses, as shown by the low Q value. We have preferred to keep a wider slit aperture and to search for the required coupling parameter value by increasing the waveguide height. The search has been successful and the results are:

Slit aperture:	5.8 mm
Waveguide height:	4.0 mm
Mode frequency:	29.993 GHz
Q factor:	3942
R'/Q:	25.1 Ω/m
E_w/E_t :	97.6%
W'_z :	4.6 V/pC/m
v_g/c :	0.29

The frequency is not exactly at the nominal value but is well within the tolerance imposed by our mesh resolution.

V. OPTIMIZATION OF THE CTS FOR CTF2

The solution to the CTF2 requirement ($R'/Q=138 \Omega/m$) was found by lowering the waveguide height (to increase the coupling parameter) and by increasing the teeth height (to lower the coupled mode frequency). The results were:

Slit aperture:	7.0 mm
Waveguide height:	2.6 mm
Teeth height:	2.11 mm
Mode frequency:	30.016 GHz
Q factor:	3786.0
R'/Q:	146.0 Ω/m
E_w/E_t :	90.2%
W'_z :	28.1 V/pC/m
v_g/c :	0.27

The shape of the longitudinal wake excited by one bunch traversal of a 12-cell section of CTS shows that the bunch interacts mainly with a single mode (Fig. 2).

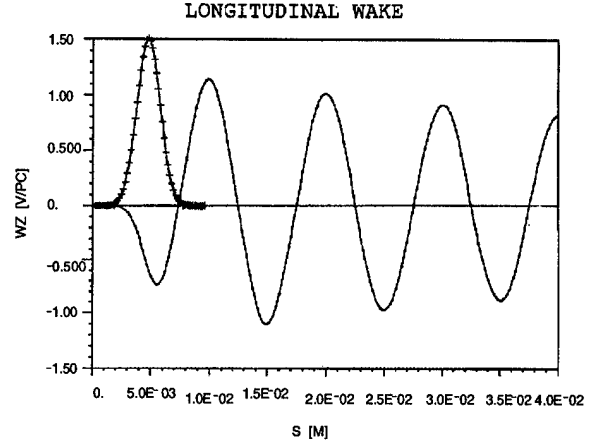


Figure 2: Longitudinal wake.

It is therefore possible to compare the peak value of the longitudinal wake with the coupling factor of the synchronous $2\pi/3$ mode by means of the relation

$$(R'/Q)\omega e^{-1/2(\omega\sigma/c)^2} = \hat{W}'_z.$$

The result for the left-hand side is 22.60 V/pC/m, which compares fairly well with the value of 28.1 V/pC/m for the peak of the longitudinal wake.

VI. CONCLUSION

With our simulation study we have shown that it is possible to increase the CTS beam coupling over a wide range without destroying the chosen mode for power transfer. We have found the frequency and coupling factor characteristics as a function of the slit aperture and have optimized the geometry to meet the requirements imposed by the drive beam properties in both the reference CLIC scheme and the CTF2 experiment. We have shown that a higher beam coupling brings stronger wakefields and a less favourable mode energy distribution between the wave-guides and the beam chamber. This last drawback may, however, be overcome by means of an optimal design of the output waveguide couplers, which recuperate part of the energy in the beam chamber.

VII. REFERENCES

- [1] G. Carron, L. Thorndahl, Progress with the CLIC Transfer Structure (CTS), Proceedings of EPAC 94, London, UK.
- [2] B. Autin et al., CLIC Drive Beam Generation, a feasibility study, Proceedings of EPAC 94, London, UK.
- [3] R. Bossart et al., CTF Developments and Results, these proceedings.
- [4] G. Carron, L. Thorndahl, private communications.
- [5] MAFIA 3.2 Reference Manual, the MAFIA Collaboration, 1994.

A High-Power Multiple-Harmonic Acceleration System for Proton- and Heavy-Ion Synchrotrons

P.Ausset^(a), G.Charruau^(a), F.J.Etzkorn^(b), C.Fougeron^(a), H.Meuth^(c), S.Papureanu^(b), and A.Schnase^(b)

^(a)Laboratoire National Saturne, CEA.CE Saclay, F-91191 Gif-sur-Yvette Cedex

^(b)Forschungszentrum Jülich GmbH, Postfach 1913, D-52425 Jülich

^(c)Fachhochschule Darmstadt, Schöfferstr. 3, D-64295 Darmstadt

Abstract

A novel acceleration system for the (simultaneous) application of higher or multiple-harmonics in proton or heavy-ion synchrotrons has been developed for various uses, e.g. the passage of the transition point, applying stochastic cooling on a bunched beam, or for other longitudinal beam manipulations as bunch stretching or compression. The system consists of a coaxial cavity filled with the ferritic amorphous metal VITROVAC[®] of VAC, Hanau, in lieu of the conventional ceramic materials. In its current configuration, it can support a frequency range of 0.2-8MHz. Amplifier modules for both 10 and 50kW are available to produce gap voltages in the kV-range. By means of digital synthesis techniques, virtually arbitrary voltage waveforms with harmonic admixtures up to fourth order can routinely be generated at the cavity gap. As illuminating examples we achieved at high precision a flat-top wave form suitable, e.g. for the transition crossing, a linearized force law at the center of the bucket, and a fourth-order flattened bucket for bunched-beam cooling. The compact cavity system should be well suited for any synchrotron operating in this frequency range. Actual installation of such a system is projected for the medium energy device COSY Jülich, and the therapy-oriented ring TERA.

1. INTRODUCTION

Traditionally, acceleration systems in proton and heavy ion synchrotrons employ coaxial re-entrant cavity configurations with ceramic ferrite filling with figure-eight,[1],[2] dipole or quadrupole ferrite polarisation.[3] Such systems are frequency tuneable, while narrow-band, and may be phase-locked to the beam, producing a single harmonic of the particle revolution frequency in the ring. In contrast, the admixture of more than one rf harmonic with stationary phase relation opens up considerable flexibility and attractive advantages in manipulating beam dynamics, and has, therefore, been of long-standing interest with rf acceleration in synchrotrons.[4] A variety of technical schemes have been employed for such "non-harmonic" approaches. Due to the narrow-band cavity characteristics, they commonly require a number of separate rf-cavities producing the various harmonics. Such cavities have to be precisely frequency and phase aligned in order to obtain a stationary acceleration voltage pattern in the time domain, a technical complication restricting the use of more than

two harmonics and usually ruling out the wider use of non-sinusoidal acceleration waveforms. We combined a specific ferro-magnetic cavity filling, VITROVAC[®], [5] with novel digital signal processing (DSP) techniques [6] to tackle, and, by-and-large, overcome many of these technical issues for frequencies below about 10 MHz.

While not required by the high-power and cavity part, we restricted ourselves at present to generate gap-voltage waveforms using the fundamental, the second, and the fourth harmonic. This approach simplifies the signal generation techniques, resulting in exact phase fidelity between these three harmonics under any condition including frequency ramping. Thus, we may generate voltage waveforms at the gap of the general form

$$V(t) = V_1 \sin(\omega_0 t + \phi_1) + V_2 \sin 2(\omega_0 t + \phi_2) + V_4 \sin 4(\omega_0 t + \phi_4) \quad (1)$$

Correcting schemes for beam loading effects have not yet been considered in detail, but appear to be feasible. Due to the overall broad-band design, their remedy should be possible by DSP procedures alone, *without* the need of further fast-reacting high-power amplifier stages. [2]

2. BEAM DYNAMICS FOR SPECIFIC WAVEFORMS

Beam gymnastics with anharmonic rf potentials permit adiabatic beam pulse shaping,[4] bunched beam stochastic cooling,[7] or tackling the passage of transition in circulating accelerators by longitudinal dynamics alone.[8] An idealised linear force law may also be of interest for beam studies. Finally, the broad-band characteristics allow, as well, much more rapid rf changes in time, as, e.g., a phase jump for conventional gamma-transition techniques.[9]

Our system is not restricted to the common choice in Equ. (1), $\phi_1 = \phi_2 = \phi_4 = \phi$. With this choice, however, we get a potential function in longitudinal phase space of the form

$$V(\phi) = V_1 \sin \phi + V_2 \sin 2\phi + V_4 \sin 4\phi \quad (2)$$

2.1. linear force law

By imposing a linear force law, e.g. a rigid rotation in phase space can be achieved, leading to one single synchrotron frequency (although at random phase) of all beam bunch particles. We can obtain a force law linear between $\pm 90^\circ$, with an asymptote $45/64\phi V_0$ at the phase

space center when choosing in Equ. (2) $V_2/V_1 = -5/32$, and $V_4/V_1 = 1/256$.

2.2. stochastic cooling force law

A "lawn-chair" shaped accelerating waveform with a flattened (zero-slope) portion at the phase-space center increases the spread in synchrotron frequency. This can overcome cooling force quenching for particles concentrating at the center of the bucket, where rigid phase rotation is prevalent and mixing ceases to be effective.[7] For the lawn-chair voltage law, we may put in Equ. (2) $V_2/V_1 = -5/8$, and $V_4/V_1 = 1/16$.

2.3. beam pulse shaping

More generally, on an adiabatic time scale, i.e. during a time of many synchrotron oscillation periods, the particle beam pulse assumes a shape imposed by the bunching or accelerating potential. Beam bunch shaping with two harmonics has been employed at various accelerators, e.g. the CERN PS Booster.

2.4. transition energy passage

Tackling the transition crossing directly in longitudinal phase space was proposed by J. Griffin at Fermilab.[8] For instance, the minimum flat-voltage portion for the transition passage of COSY, Jülich, must span over a phase width of at least $\Delta\phi \sim \pm 30^\circ$. [8] Choosing $V_2/V_1 = -5/16$, and $V_4/V_1 = 1/64$ in Equ. (2) results in a deviation (from absolute flat) of less than 0.2%.

3. ACCELERATING SYSTEM

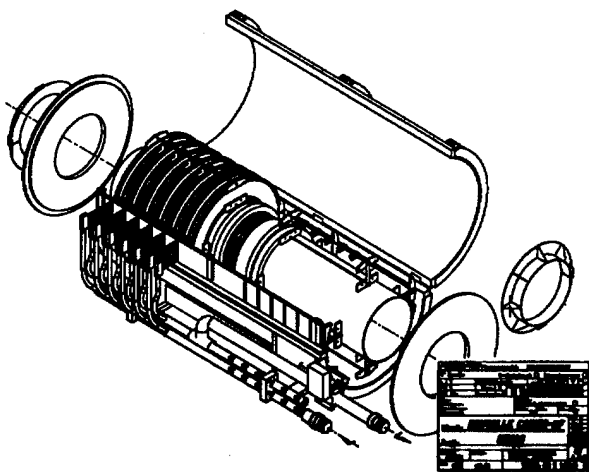


Fig. 1: cut-away drawing of cavity, showing inner and outer conductor, toroids, cooling ducts and polarisation bars

3.1. accelerating cavity

The cavity is of the coaxial, re-entrant symmetric (push-pull) single-gap type, see Fig. 1. In dimensions and design, it is roughly similar to the LNS-developed systems used at SATURNE and COSY.[1] It is, however, loaded with 24 toroids of the material VITROVAC® 6025F of VAC,

with an eight-turn "figure-eight" polarisation winding. Depending on the capacitive gap load, the system has a natural (zero-bias current) resonant frequency of about 500 kHz, and may be tuned with a bias current of only some 5 Amperes to 3 MHz.

In Fig. 2, the (low-level) gap impedance of the-filled cavity is plotted vs. frequency for various bias currents. The actual total gap impedance is twice that of Fig. 2. It shows a marked broad-band characteristic at fixed bias current without major loss of peak impedance. The cavity characteristics are compared in Table I to the LNS and COSY system with conventional ceramic ferrite loading.

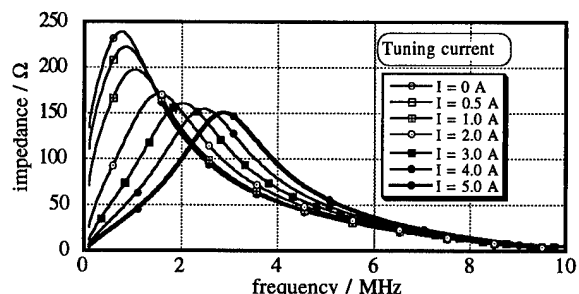


Fig. 2: gap impedance of the VITROVAC®-filled cavity (one-half cavity) vs. frequency for various bias currents.

	LNS and COSY cavity	VITROVAC-cavity
filling material	ferrite 8C12	VITROVAC 6025F
manufacturer	Philips, NL	VAC, Germany
number of rings	46	24
tuning current	- 20 to 70 A	0 to 10 A
frequency range	0.3 - 2 MHz	0.2 - 8 MHz
resonance width	< 50 kHz	~ 2 MHz
total gap impedance		~ 2 kΩ ~ 500 Ω
180°-jump within	10 to 50 rf periods	2 rf periods

Table I: comparison of characteristics of VITROVAC®-filled cavity with standard, ferrite-loaded cavity.

3.2. two alternative power amplifier modules

Two separate drawer-type amplifier modules, both in push-pull configuration, have been developed to fit directly underneath the cavity for closest possible coupling. The two cavity halves are fed completely independently. For both modules, the same driver/preamplifier configuration, again separately for both cavity halves, may be used. A π -type 50Ω driver coupling network into the main amplifier modules ensures broad-band behaviour at constant group delay. The lower-power system with a total of 10kW rf power employs two tetrodes TH541 of Thomson Tubes Electroniques. Peak amplitudes in excess of 2kV may routinely be generated at the accelerating gap. The system has been described in detail in [5]. For higher gap voltage, a second, high-power alternative has recently been developed, which uses two TH120 tubes featuring a total of 50kW rf power, similar to the LNS and COSY power

amplifier systems.[1] Operating tests of this system are presently underway.

3.3. digital low-level signal synthesis and control

The low-level signal synthesis generates the composite waveform by suitably superposing fundamental and higher harmonic components, see Fig. 3. At its heart, a set of custom numerical controlled oscillators (NCO) are used, however with the provision of a variable-frequency common clock, rather than a large phase accumulator used in commercial NCOs. This leads to rigid frequency relations at any time in order to generate the harmonics. An arbitrary real-time digital phase correction via multipliers produces a phase fidelity to within 0.02° , while, similarly, an arbitrary real-time digital amplitude correction of 16 bit resolution is possible. Finally, fixed separate analog attenuation of the various harmonic components set the range of the desired admixtures. Our approach permits preserving the waveform shape in the time domain also under frequency ramping. Further, it also opens up the possibility of a real-time digital signal control, similar to the method as was demonstrated for the single-frequency component system at COSY.[10]

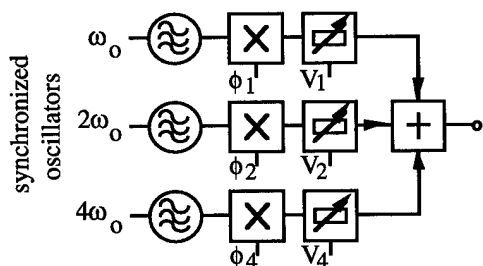


Fig. 3: signal synthesis scheme of harmonic composite

4. TEST PERFORMANCE AND RESULTS

The present test results were obtained with this cavity system without beam, operating at max. 10kW rf power. The gap voltage was monitored directly with a voltage divider.

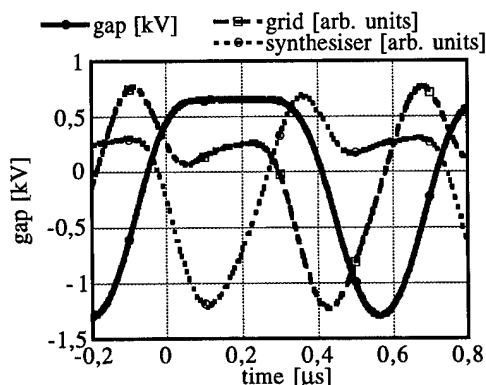


Fig. 4: digitally synthesized waveform, and actual waveform at tube grid and cavity gap

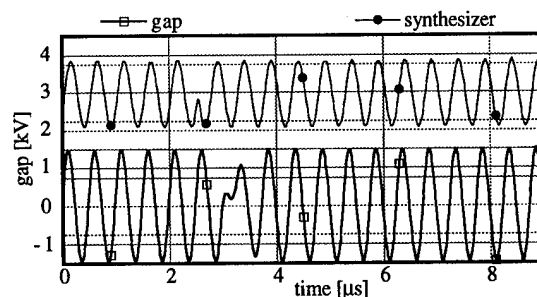


Fig. 5: rapid phase jump actually realised at the gap

Suitable transition waveforms (See 2.4) are shown in Fig. 4. To exemplify the digital signal synthesis performance, Fig. 4 shows also the low-level signal as originally synthesized, and the signal after passing through the driver and amplifier chain. The phase delays are adjusted such, that they compensate the delays incurred by the entire analog chain, including the cavity itself, to result in the desired waveform at the gap.

Figure 5 shows a rapid phase jump of 180° in time, completed in a few rf cycles. This is to be compared with the at least ten cycles needed for sign reversal with a conventional cavity (Table I). [9]

5. CONCLUSIONS AND OUTLOOK

The combination of a broad-band high-power acceleration structure and a digital synthesizer capable of producing precisely composed real-time voltage waveforms with higher harmonic content promises interesting acceleration experiments and performance enhancement in proton and heavy-ion synchrotrons.

Installation of the rf structure presented here, or of a similar system, is intended for both the medium-energy synchrotron COSY-Jülich, and for TERA in Italy, the proposed ring for cancer therapy,[11] for which a collaboration has been set up between LNS and the TERA project with validation tests about to make place at Saclay.

Some issues remain yet to be solved. To increase maximum gap voltage, as needed for COSY, a higher-power amplifier module is put into operation, with which first results were obtained with sinusoidal waveforms. This is to be followed by tests with added higher harmonics.

The signal processing system is presently being upgraded to actually allow for real-time control, or feedback, of phase and amplitude, probably also for the higher harmonics.

6. ACKNOWLEDGEMENTS

We are indebted to D. DeMenezes, J. Peyromaure and H. Stockhorst for helpful comments. The travel support by the Franco-German exchange program PROCOPE is gratefully acknowledged.

7. REFERENCES

- [1] C. Fougeron *et al.*, PAC 79; P. Ausset *et al.*, EPAC 88.

- [2] A. Susini *et al.*, EPAC 90.
- [3] S. Papureanu, private communication.
- [4] A. Hofmann *et al.*, CERN
- [5] C. Fougeron *et al.*, EPAC 90; and PAC 93; P. Ausset *et al.*, EPAC 94.
- [6] H. Meuth, *et al.*, PAC 1993; A. Schnase *et al.*, EPAC 1994; F.J. Etzkorn *et al.*, IKP Annual Report Jül-3035.
- [7] J. Wei, Report BNL-46792, 1991; and EPAC 92.
- [8] J. Griffin, Fermilab Report TM 1734, 1991; H. Stockhorst *et al.*, EPAC 94.
- [9] S. Papureanu *et al.*, PAC 1993.
- [10] A. Schnase *et al.*, EPAC 92; A. Schnase, Dissert. RWTH Aachen 94, Report Jül-2878 Forschungsz. Jülich.
- [11] U. Amaldi and M. Silari, *editors*, *The TERA Project and the Centre for Oncological Hadrontherapy*, 1994.

A Bunch Lengthening RF Cavity for Aladdin

K. J. Kleman

Synchrotron Radiation Center, University of Wisconsin – Madison
3731 Schneider Drive, Stoughton WI 53589 USA

Abstract

A 202 MHz aluminum rf cavity has been constructed for the Aladdin synchrotron light source* at the University of Wisconsin – Madison. The cavity operates on the fourth harmonic of the ring rf frequency and will be used to lengthen the electron bunches in order to increase beam lifetime. The cavity body is machined from a thick aluminum plate with a single penetration for the coupling loop which operates in vacuum. A cover plate at the gap end contains an annular tuner that is moved concentric with the beam axis. The entire inner surface of the cavity is copper plated to increase shunt impedance. The cavity will be initially operated in the beam driven mode with the tuner adjusted by computer to provide optimum bunch lengthening as the beam decays. In the future, active rf drive may be employed to allow a constant bunch length to be maintained at all times. A beam derived rf reference is proposed along with use of rf feedback to avoid instabilities. Results of the first storage ring operation using the new cavity are presented.

I. INTRODUCTION

The Aladdin synchrotron light source is a 0.8 - 1 GeV electron storage ring with four 4 meter straight sections for insertion devices. It is desired to increase beam lifetime when operating at 0.8 GeV to improve the integrated flux delivered to the experiments. This can be accomplished by diluting the longitudinal phase space in order to reduce intrabeam scattering. A higher harmonic RF cavity can be used to flatten the potential in the main RF bucket causing an increase in the bunch length. This occurs without an increase in the transverse emittances. For the present the cavity will be operated in the beam driven mode, with the cavity detuned to make its voltage appear approximately 90 degrees out of phase with the bunch passage.

A. Choice of Frequency

Several considerations are important when choosing the desired harmonic for the cavity. First, the cavity must fit into the available space in the ring. Also its shunt impedance must be high enough to allow the beam to develop the necessary rf voltage. The lower limit on the shunt impedance is determined by the minimum beam current at which the cavity is expected to operate with optimum results. If the cavity impedance is not high enough the cavity will have to be tuned closer to resonance in order to develop the proper voltage. As the cavity is brought closer to resonance the beam will become unstable, thus limiting the available range of tuning angle.

The choice of harmonic also affects the voltage required to achieve a flat potential well. The relationship between the

two cavity voltages required to flatten the potential well for a particular harmonic number n is

where V_H and f_H are the harmonic cavity voltage and frequency, and V_F and f_F are the fundamental cavity voltage

$$\frac{1}{n} = \frac{V_H}{V_F} = \frac{f_F}{f_H},$$

and frequency. The required voltage is lower for a higher harmonic, but the width of the flat portion of the potential is narrower. A low harmonic is therefore desirable for optimal bunch lengthening.

Calculations indicated that the cavity should perform properly if the tuning angle is greater than 85 degrees [1,2]. The minimum beam current the cavity is expected to operate at is 100 mA. The fundamental rf system of Aladdin operates at 50.582 MHz with a nominal cavity voltage of 80 kV. The minimum shunt impedance is given by

$$R_{\min} = \frac{V_F \tan(\psi_{\min})}{2\pi I_0}$$

Operating the cavity at the third harmonic would have been our preferred choice but the cavity would then not fit in the space available in the ring if designed to have the required shunt impedance. This led us to choose the fourth harmonic (202.4 MHz) as an acceptable compromise between high shunt impedance, low field and good bunch lengthening. The minimum shunt impedance for $n=4$ and $I_b=100$ mA is 1.2 MΩ.

The low energy (108 MeV) injection mode of Aladdin imposes additional requirements on the tuning range of the cavity. The main rf cavity voltage at injection is quite low (~9 kV). This means that the fourth harmonic cavity must be detuned enough to keep its voltage lower than 2 kV. The tuner was designed for a tuning range of 2.5 MHz to satisfy this requirement.

II. CAVITY DESIGN

A. General

The cavity (Fig. 1) is a single ended design with an annular tuner in the cover plate that is concentric with the beam axis. It is constructed entirely from 6061 aluminum alloy. The body of the cavity was machined from a single piece of 25 cm thick plate. The cover was machined from 5 cm plate. The vacuum seal for the end cover is a 0.75 mm aluminum wire. The cover also contains the penetrations for pump ports and sampling loops. The pump ports are covered by grids machined into the inner surface of the cover plate. Pumping is provided by two miniature 60 l/s ion pumps. A single penetration is located in the rear wall of the cavity body to accommodate a coupling loop for use when the cavity is actively driven.

* Work supported by the NSF under contract DMR-92-12658

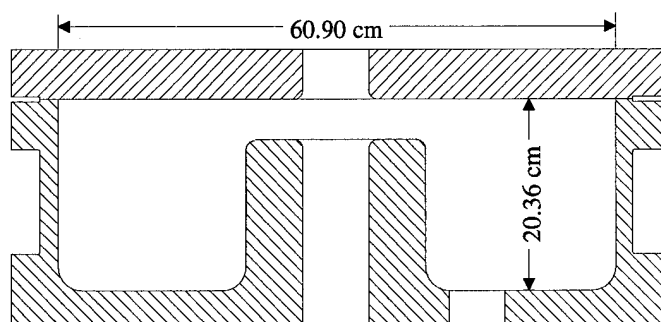


Fig. 1. 202 MHz Cavity Outline

Since the conductivity of 6061 alloy is only 40-45% that of copper, it was necessary to plate the entire inner surface of the cavity with copper to obtain sufficient shunt impedance. The plating was done by Industrial Plating Co. of Seattle, WA. The plating process used has been previously employed on accelerating cavities with excellent results [3,4].

Resonant Frequency	202 - 204.5 MHz
Q_u (calculated)	22000
Q_u (measured)	20250
R/Q	61.1
Shunt Impedance	1.24 M Ω as constructed

Table 1. Harmonic Cavity Parameters

B. Tuner

The tuner (Fig. 2) is a cylindrical copper slug centered on the beam axis through which the beam passes. The end of the tube is threaded onto the moving part of an actuating section of 304SS pipe that is part of the ring vacuum chamber. The pipe is allowed to move through the use of differential bellows. The return for tuner currents is via a ring of 18 flat U-shaped straps fabricated from silver plated 100 μ m thick beryllium copper. The mechanical range of the tuner is about 2 cm with a sensitivity of about 1 MHz/cm.

The original design of the tuner used a spring ring as a sliding contact for the tuner return current. This approach was abandoned after it was found that the lifetime of the contact surfaces was very short, resulting in increased friction. The new design requires no maintenance and is much easier to align in the bore of the cover plate.

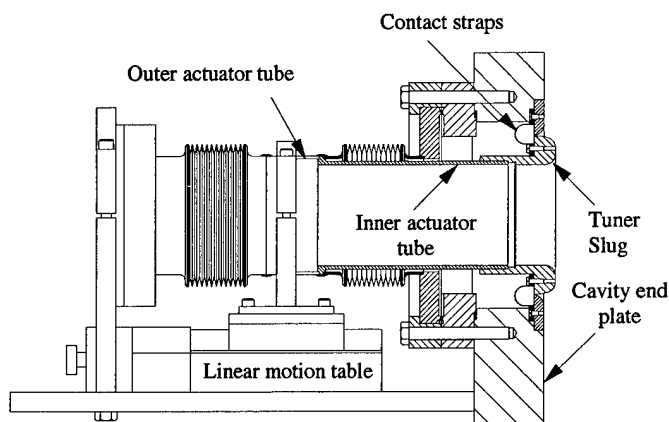


Fig. 2. Tuner Assembly

The cavity is tuned by moving the tuning slug in and out via a stepper motor driven table containing a fine pitch lead screw. The motor is controlled via an analog feedback loop. A conductive plastic linear potentiometer is used for the feedback element. The stepping motor drive contains a voltage controlled oscillator that allows the motor to be driven accurately at low speeds. The resolution of the feedback loop is limited only by the noise on the feedback voltage.

C. Anti-Multipactor Coating

The delicate nature of the stored beam at the injection energy caused some concern about multipacting at low cavity voltage. Since the cavity is passive we are unable to control the drive to the harmonic cavity to permit jumping through the first order multipactor level. In order to reduce any problems to manageable levels we coated the accelerating gap area with a layer of titanium. This was applied via sublimation from a pair of wires held in a fixture that was rotated about the beam axis. The pressure during sublimation was between 10^{-4} to 10^{-5} torr. The cavity was backfilled with nitrogen after sublimation to promote the formation of titanium nitride on the surface. Admittedly this is not an efficient process as the chamber contaminants will certainly form other titanium compounds before backfilling, but the coating formed performs its intended function quite well. The coated cavity was conditioned for about 12 hours. After conditioning, passing through the first order multipactor level during a slow power sweep caused only a small pressure rise without hysteresis effects.

III. OPERATION

A. Procedure

The cavity is set to a detuned condition at injection. After the beam has been stacked and ramped to the operating energy, the cavity is tuned to an approximate starting position and then stepped slowly toward resonance via computer control. The computer monitors the cavity voltage and adjusts the tuner in small steps as required to bring the voltage up to the operating value. The tuning process is stopped when the beam has decayed to the point where additional tuning would cause beam instability.

B. Operational Results

The cavity was installed in the storage ring for a brief period before being removed for the tuner modification mentioned above. The storage ring vacuum did not have much opportunity to recover during the test period. Beam lifetime with the cavity detuned had recovered to about 75% of its nominal value at the time of the test.

Injection proceeded well with the cavity detuned about one half of a revolution frequency (~ 1.6 MHz). Numerous higher order modes, resulting in both bunch lengthening and transverse emittance growth were observed as the cavity was tuned toward resonance, especially while operating at high energy. HOM induced disturbances were smaller at injection because the naturally long bunch (~ 2 ns) at injection does not excite the higher frequency modes effectively.

As the cavity was brought close to resonance the bunch began to lengthen smoothly. At the optimum tuning angle the bunch assumed a pseudo-trapezoidal shape (Fig. 3). Further tuning produced a bunch with a double peak, as expected. Shortly after this point the Robinson instability would set in, with further tuning resulting in beam loss.

The effectiveness of the cavity was impressive, considering the poor state of the storage ring vacuum. When the cavity was optimally tuned the 0.8 GeV lifetime was increased by 70% at 150 mA of beam current. The cavity was able to optimally lengthen the bunch down to currents of approximately 120 mA without instability. The lifetime at 100 mA was 90% of the value obtained at 120 mA when tuning was ceased at that current. These numbers agree well with the computed predictions.

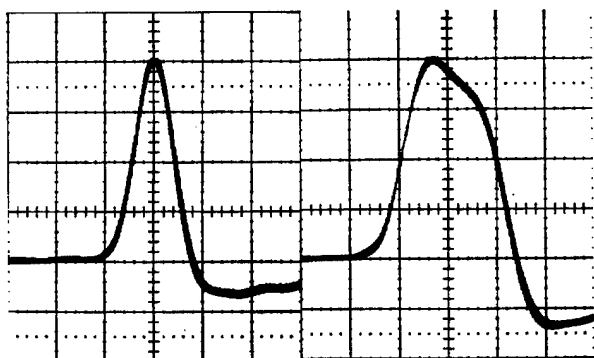


Fig. 3. Longitudinal bunch profiles (1 ns/div) with harmonic cavity detuned (left), and tune for optimal bunch lengthening (right). Droop is due to a capacitive pickup.

IV. ACTIVE OPERATION

It is envisioned that active operation of the cavity may be desirable at some time in the future. Problems caused by the equilibrium phase instability in actively driven bunch lengthening cavities are well documented [5,6]. When operating at lower currents the Robinson instability must also be avoided. To address these difficulties the proposed system will use two techniques to enhance stable operation.

The rf drive signal for the cavity will be obtained from a beam pickup. The pickup signal will be limited to eliminate amplitude variations. The limited signal contains beam phase information and therefore will act to make the harmonic cavity phase follow the beam phase, reducing the coupling between the beam and harmonic cavity. This can also be accomplished by phase locking the RF drive from a generator to a beam derived signal, although with more difficulty.

The phase tracking can be improved by the use of proportional rf feedback around the amplifier/cavity system. This will have the effect of lowering the apparent cavity Q and shunt impedance by a factor of $(1+Gain)$. This technique reduces beam coupling at frequencies up to the bandwidth of the feedback loop.

Steady state control of the harmonic cavity field will be provided by a conventional amplitude and phase control loops

operating off a cavity pickup signal. These loops do not have to be very fast because the rf feedback stabilizes the cavity fields at high frequencies.

Since a pure bunch lengthening cavity does not provide any net energy to the beam, the beam loading in the active case should be entirely reactive. It is easy to show this implies that the generator current vector will be perpendicular to the beam current vector and that the cavity appears as a constant resistive load when it is tuned correctly. The situation is similar to the that of an accelerating cavity in the reactively compensated condition at zero energy gain. The only differences are a 180 degree phase shift of the cavity voltage and a sign change in the tuning angle. Operating the cavity in this way also eliminates the equilibrium phase instability at high current because it approximates the passive case which is unconditionally stable in the high current limit.

To accomplish this a standard tuner control loop will be used with feedback being taken from a directional coupler in the cavity drive line. The forward signal from the coupler is phase compared with the signal from a cavity pickup and used to control the tuner drive. The tuner loop automatically compensates for the changing reactive load as beam current varies.

V. SUMMARY

A copper plated aluminum fourth harmonic cavity has been installed in the Aladdin light source. The cavity approximately doubles the bunch length and provides a greater than 70% increase in the 0.8 GeV beam lifetime. Passive operation of the cavity has begun and is effective for currents greater than 100 mA. Active operation of the cavity has been planned for in the future if necessary. The cavity has fulfilled all of our expectations in tests and should be a very useful addition to the Aladdin facility.

VI. REFERENCES

- [1] R. A. Bosch, "Modeling a Landau Cavity at the Synchrotron Radiation Center", Synchrotron Radiation Center Technical Note, SRC-118 (1993).
- [2] R. A. Bosch, "Modeling a Landau Cavity at the Synchrotron Radiation Center, Part II", Synchrotron Radiation Center Technical Note, SRC-137 (1994).
- [3] H. Mignardot and J. Uher, *Proc. of the 1991 IEEE Particle Accelerator Conf.*, (1991) 777-779.
- [4] A. M. Vetter et al., *Proc. of the 1993 Particle Accelerator Conf.*, (1993) 1075-1077.
- [5] Y. Miyahara et al., *Nucl. Instr. and Meth.*, A260 (1987) 518-528.
- [6] J. Keane et al., *Proc. of the 1989 IEEE Particle Accelerator Conf.*, (1989) 138-140.

DESIGN OF A HIGH-POWER TEST CAVITY FOR THE ATF DAMPING RING

S. Sakanaka, F. Hinode, M. Akemoto, S. Tokumoto, T. Higo, J. Urakawa

KEK, National Laboratory for High Energy Physics, 1-1 Oho, Tsukuba-shi, Ibaraki-ken, 305 Japan

T. Miura, Y. Hirata, K. Satoh

Toshiba Corporation, 2-4 Suehiro-cho, Tsurumi-ku, Yokohama, 230 Japan

We describe the design of a prototype HOM damped cavity which is being developed for the ATF damping ring. This cavity has been designed to demonstrate the feasibility of high-power operation, as well as to establish construction techniques. The mechanical design, fabrication method and design considerations are presented.

I. INTRODUCTION

A HOM damped cavity for the ATF damping ring (DR) [1] is under development at KEK. This cavity is capable of avoiding coupled-bunch instabilities driven by higher order modes (HOMs). In order to damp the Q's of HOMs the cavity is equipped with four waveguide ports, the cutoff frequency of which is higher ($f_c \approx 887.3$ MHz) than the accelerating frequency. Additional HOM damping is provided by HOM absorbers in the beam pipes next to the cavity [2]. The basic design and results of low-power measurements are described in refs. [3] and [4], respectively. The overall design of the RF-system is presented in an accompanying paper [5].

In order to demonstrate the feasibility of high-power operation, the construction of a high-power test cavity is under way. The design parameters of the test cavity are shown in Table 1. Although a total wall loss of 17.4 kW is conservative, special care has been taken concerning the cooling design, because concentrations of wall losses exist around the openings of the waveguide ports. The possibility of multipacting, the surface field strength and other RF properties were considered during the design stage.

Table 1. Design parameters of the HOM damped cavity.

RF frequency	714 MHz	Shunt impedance	3.6 M Ω
Unloaded-Q	22,100	Gap voltage/cavity	0.25 MV
Coupling factor	2.4	Wall loss/cavity	17.4 kW

II. DESIGN AND FABRICATION METHOD

The design concept of the cavity is to realize a damped structure having effective cooling passages by using as simple a structure as possible. We have chosen well-established techniques, both machining and brazing, for the cavity construction. Other joining techniques, such as using electron-beam welding (EBW), tungsten inert-gas (TIG) welding and using a hot isostatic press (HIP) are

applied as auxiliary methods. The raw materials used are OFHC copper for the principal parts and stainless-steel 304 for the flanges. The outer shape of the cavity is a simple polyhedron, which provides precise reference planes for further machining, such as milling of the waveguide openings.

Figure 1 shows a drawing of the designed cavity. The main body comprises a center part and a pair of side parts. Cooling of the main body is provided by several water channels (see Fig. 1): (A) a pair of circumferential channels at the outside, (B) three channels in the side body, which comprise an outer square channel and inner round channels, and (C) four straight channels in the center of the body. The typical heat load on the cavity wall has a 5-7 W/cm² range, which can be effectively removed by these cooling channels. On the other hand, there are concentrations of the heat load at small areas beside the waveguide openings (at narrower sides), which amount to ~ 18 W/cm². These hot spots are mainly cooled by heat transfer to the water channel (A) and the outer channel of (B), which are located ~ 20 and ~ 40 mm away from the hot spots, respectively. All of the ports, except for the pick-up ports and beam ports, have separate cooling channels.

The three parts of the main body are machined from forged OFHC blocks; the outside surfaces are precisely planed by a milling machine, and the inside roughly turned on a lathe. Openings for the waveguides and other ports, as well as the cooling channels, are then milled. The cooling channels are covered with lids by EBW, or later, by brazing at the same time as joining of the ports.

Subassemblies of the waveguide ports are machined from OFHC plates, the insides of which are bored by electro-erosion wire machining. Then, the cooling channels are milled, and covered with lids by EBW. Waveguide flanges are roughly machined from stainless-steel plates, and annealed. After being finish machined, their insides are plated with copper. The waveguide flange was designed by referring to that of the SLAC S-band waveguides, which allow vacuum sealing and electrical contact simultaneously. Between the waveguide ports and dummy loads, 35-cm long waveguides are inserted in order to evanesce the accelerating field. At an initial high-power test, the ends of the extension waveguides are blanked off without attaching any loads.

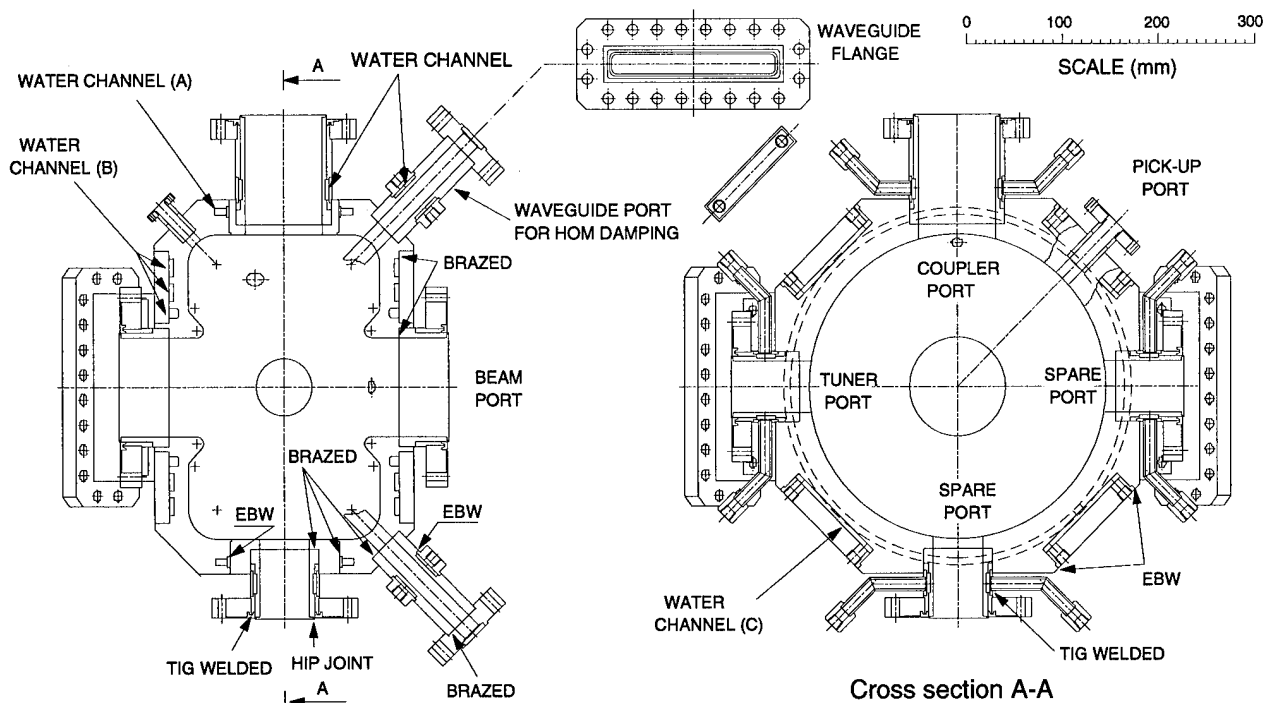


Fig. 1. Cross-sectional view of the high-power test cavity.

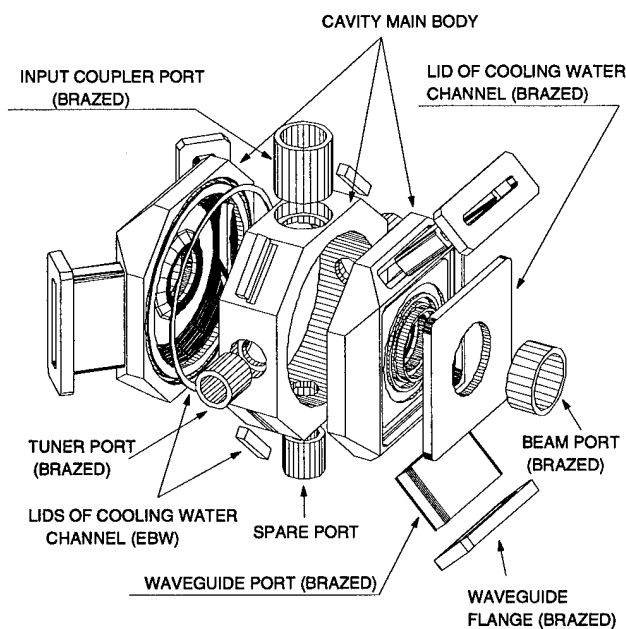


Fig. 2. Schematic drawing showing the cavity assembly.

Tuner and coupler ports as well as beam ports and spare ports are pre-assembled according to the following procedure: 1) a copper cylinder (inside) and a stainless-steel tube (outside) are joined by a HIP technique, 2) machined, and cooling paths milled, and 3) the lids and inlet/outlet pipes of the cooling water channel welded.

The cavity assembly is schematically shown in Fig. 2. The cavity parts are joined by brazing in two stages. First,

all of the ports and lids of the water channels (at the side bodies) are brazed. Then, the cavity inner wall is finish machined using a high-precision lathe with a diamond cutting tool. At the same time, the edges of the port openings inside the cavity are rounded ($R \sim 1$ mm) by hand. During a second brazing, the three bodies are joined together. The waveguide flanges are joined to the waveguide ports at the same time. After brazing, UHV flanges are TIG welded to the other ports.

The surface finish of the cavity inner wall is better than 3S (R_{max}), while that of inside the waveguide ports is slightly worse ($\sim 6S$) due to the relatively long dimension for wire machining.

III. INPUT COUPLER AND TUNER

Because the transmission power through an input coupler is relatively conservative (41 kW max.), we chose a loop-coupler design with a cylindrical ceramic window. The coupler was designed by scaling from that for the TRISTAN APS cavities [6]. The coupling factor of the coupler can be changed from 0 to 4.1 by rotating the loop; a nominal coupling factor of 2.4 is obtained by 40° rotation from the maximum coupling.

The design of the tuner is basically scaled from that of the PF storage ring at KEK. The tuner has a 50 mm-diameter copper piston driven by a stepping motor with a stroke of from -10 mm to +30 mm of penetration from the cavity inner wall. This provides a tuning range of -200 to

+1700 kHz. The mechanical resolution of the movement is $1\mu\text{m}/\text{step}$ which corresponds to $36\text{ Hz}/\text{step}$. The bellows inside the tuner are shielded from RF currents by graphite contactors supported by finger springs.

Two spare ports are blanked off by water-cooled copper blocks. These dummy blocks are also used as fixed tuners, which can compensate for anticipated frequency shifts due to fabrication errors. The dummy block has a viewing port which allows the tuner and coupler to be observed from inside of the cavity.

IV. DESIGN CONSIDERATIONS

A thermal analysis of the designed cavity was made using the ANSYS code: a 2D analysis of the overall temperature distribution, and a 3D analysis using a simplified model for the neighborhood of the waveguide openings. A heat-transfer coefficient of $1.2\text{ W}/\text{cm}^2/\text{K}$ was assumed at the boundary of the cooling channels, which corresponds to an average water velocity of $2.7\text{ m}/\text{sec}$. These analyses predicted the following temperature rises: 1) 22°C and 16°C at the narrower and wider sides of the waveguide openings, respectively; 2) 11°C at the tips of the nose cones, and 3) $7\text{--}9^\circ\text{C}$ for other locations of the inner wall. Although no full thermal-stress analysis has been performed, these temperature rises are considered to be acceptable.

The surface field strengths and wall losses around the waveguide ports were extensively analyzed using the MAFIA code. It was shown that the field distribution inside the waveguides ports is well approximated by an evanescent field of the TE_{10} mode. The maximum wall loss around the waveguide perimeter (which occurs at the narrower sides) is given by $P_{\text{wall}} [\text{W}/\text{cm}^2] \sim 7.1 \cdot \exp(-2\alpha z [\text{m}])$, where $\alpha = 10.96\text{ m}^{-1}$ is the attenuation coefficient and z is the distance from the opening. The electric field at the center of the waveguide is given by $E \sim 1.4 \exp(-\alpha z) [\text{MV}/\text{m}, \text{peak}]$ for the inner locations and by $E \sim 1.1 [\text{MV}/\text{m}]$ for the neighborhood of the entrance. The electric field at the round edge ($R \sim 1\text{ mm}$) of the waveguide openings would be enhanced by a factor of two, which was shown by an electrostatic analysis. Although these field strengths are much lower than the Kilpatrick limit of $25\text{ MV}/\text{m}$, a good surface finish is desirable for these locations. The field strength at the tip of the nose cone is $\sim 5.8\text{ MV}/\text{m}$, which is common for nose cones.

The field leakage to the tuner or to other ports is also considered. Basically, the leakage fields to these coaxial parts can be approximated by an evanescent field of the TE_{11} mode in a coaxial line. Low-conductive materials, such as stainless steel, should be located away from the evanescent field. Furthermore, if the symmetry of the

cavity structure seen by the ports is broken, the accelerating field can be coupled to TEM-resonances (typically $\lambda/4$ or $3\lambda/4$ resonances) in the coaxial structure of the ports. Even in such a case, excitation of the resonances in the port can be avoided by detuning the resonant frequencies from that of the accelerating mode. In our cavity an asymmetry would be introduced by the damping waveguides. However, a harmonic analysis of the accelerating field showed that such distorted field components seen by the ports are lower than $\sim 2\%$ of the surface field.

The possibility of multipactor discharges was also investigated. With the designed waveguide height of being 2 cm , we can avoid the most severe multipacting of $1/2$ cycle in the waveguide ports. The multipacting of higher cycles, which may arise, can be removed by conditioning if the inner surface is sufficiently clean and smooth. On the other hand, a gap of 1 mm was chosen between the tuner and its port wall, which can avoid any multipactor discharges regardless of the gap voltage.

V. CONCLUSIONS

The design of a high-power test cavity has been completed based on a thermal and RF analysis. The design was aimed at providing effective cooling passages by a simple fabrication process. The cavity is under construction towards a high-power test, being planned in the summer of 1995.

VI. ACKNOWLEDGMENTS

The authors wish to thank Y. Yamazaki, H. Matsumoto, T. Kageyama and M. Izawa for valuable advice concerning the cavity design. We are also grateful to Y. Kimura and K. Takata for their promotion of the ATF project, and to all members of the ATF group for their support.

VII. REFERENCES

- [1] J. Urakawa et al., *Proceedings of the Fourth Workshop on Japan Linear Collider*, KEK, pp. 67-86.
- [2] F. Hinode and S. Sakanaka, in these proceedings.
- [3] S. Sakanaka et al., *Proceedings of the 1993 Particle Accelerator Conference*, Vol. 2, pp. 1027-1029.
- [4] S. Sakanaka et al., *Proceedings of the 1994 International Linac Conference*, Vol. 1, pp. 281-283.
- [5] S. Sakanaka et al., in these proceedings.
- [6] M. Akemoto, *Conference Record of the 1991 IEEE Particle Accelerator Conference*, Vol. 2, pp. 1037-1039.

DESIGN OF AN RF SYSTEM FOR THE ATF DAMPING RING

S. Sakanaka, F. Hinode, M. Akemoto, H. Hayano, H. Matsumoto, K. Kubo,
S. Tokumoto, T. Higo and J. Urakawa,

KEK, National Laboratory for High Energy Physics, 1-1 Oho, Tsukuba-shi, Ibaraki-ken, 305 Japan

This paper describes the overall design of an RF system for the ATF damping ring (DR). The RF system comprises four single-cell cavities, one 250-kW klystron, a WR1150 waveguide network and a low-level RF system. The system parameters, layouts and development of the principal components are given.

I. INTRODUCTION

The ATF damping ring [1,2] is under construction at KEK in order to study the production of high-intensity multibunch beams having extremely low emittance, which is required for future linear colliders. The challenges of the RF system mainly come from the large beam current (600 mA max.) and high cutoff frequencies of the beam pipe (9.6 and 7.3 GHz for monopole and dipole modes, respectively), which impose severe restrictions on the cavity HOM (Higher-Order-Mode) impedances.

The principal requirements for the RF system are: 1) to provide the accelerating voltage needed to obtain a short bunch length of 5 mm, 2) to compensate for radiation losses, and 3) to accommodate a suitable low-impedance environment for the beam. Table 1 is a list of the parameters of the ATF DR relevant to the RF system. A frequency of 714 MHz, which is one quarter of the injector linac frequency, was chosen. A total gap voltage of about 1 MV is needed to obtain a bunch length of 5 mm (which

includes the anticipated bunch lengthening by a potential-well distortion). Then, the RF bucket height becomes 2.2%, which is sufficient for beam injection (requiring more than 1%). A total generator power of 164 kW is required for the power source under steady operation at a maximum beam current of 600 mA.

II. CAVITIES

In order to avoid coupled-bunch instabilities driven by the cavity HOM impedances, four HOM-damped cavities are to be implemented in the ATF DR. A single-cell copper cavity, in which the HOMs are damped by four waveguide ports terminated by broadband loads, was designed. Additional HOM damping in the high-frequency region is provided by HOM absorbers attached to the beam pipes of the RF section [3]. The design considerations and results of low-power measurements are described in refs. [4] and [5], respectively.

The design parameters of the cavity are also given in Table 1. Under a nominal gap voltage of 0.25 MV/cavity, the dissipated power on the cavity wall is 17.4 kW/cavity. The coupling coefficient of the input coupler is set to be 2.4, which gives optimum coupling at the maximum beam current. Then, the transmission power through an input window becomes 40.9 kW. Since this power level is within our experience, we have chosen a cylindrical ceramic window with loop coupling, which was designed by scaling from those of TRISTAN normal-conducting cavities [6]. The design of a prototype high-power test cavity has been completed. The design of the test cavity is presented in an accompanying paper [7].

III. SYSTEM LAYOUT

Figure 1 shows a block diagram of the RF system. RF power is supplied by a 250-kW klystron, which is operated 20% below saturation, thus allowing for automatic gain control (AGC). This output power still has a margin of 20% in order to allow for the use of some fast feedback loops, which may be required to control any transient effects during beam injections. The klystron is under design, the parameters of which are given in Table 2.

The power from the klystron is divided into four parts by magic-tees, being delivered to the cavities through a WR1150 waveguide network. In order to protect the klystron from reflected power from the cavities, we have

Table 1. RF-related parameters of the ATF DR.

Beam energy	E_o	1.54 GeV
Maximum beam current	$(I_o)_{max}$	600 mA
RF frequency	f_{RF}	714 MHz
Harmonic number	h	330
Total gap voltage	V_c	1.0 MV
Number of cavities	N_c	4
Synchrotron radiation loss per turn	U_o	156 keV
RF bucket height	$\Delta E/E_{max}$	2.2 %
Natural bunch length	σ_{zo}	3.6 mm
Shunt impedance per cavity	R_{sh}	3.6 M Ω
Unloaded-Q of cavity	Q_o	22,100
Cavity coupling coefficient	β	2.4
Dissipated power per cavity	P_c	17.4 kW
Beam loading per cavity*)	P_b	23.5 kW
Transmission power per window*)	P_{win}	40.9 kW
Total generator power*)	P_g	163.5 kW
Cavity detuning amount*)	Δf	-138 kHz

*) At the maximum beam current of 600 mA.

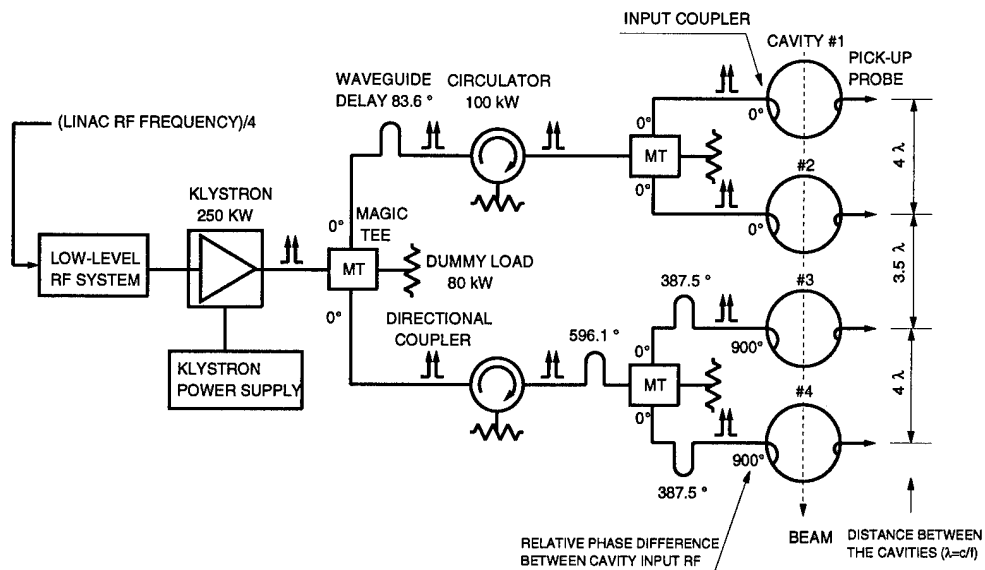


Fig.1. Block diagram of the RF system for the ATF Damping Ring.

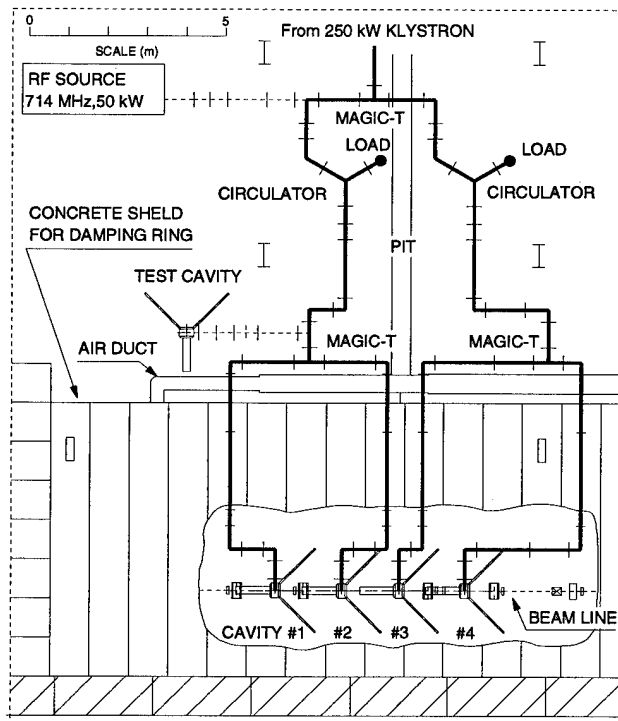


Fig. 2. Layout of the RF system. Top view.

chosen the use of two 100-kW circulators, rather than a single 200-kW circulator, by considering ease in the development. Coaxial-type 80 kW dummy loads are used at the circulator ports, which are capable of absorbing more than 80 kW for a short time.

Figure 2 shows a top view of the system layout. The distances between the cavities are 4λ or 3.5λ (see Fig. 1), where λ is the RF wavelength in free space. The feed lines for the four cavities (after the second magic-tees) are not completely symmetrical, based on the need to avoid

Table 2. Design parameters of the 250-kW klystron.

Frequency range (-1 dB B.W.)	714 \pm 1 MHz
Maximum output power	250 kW
Beam voltage	44.9 kV
Beam current	11.1 A
Efficiency	51 %
Beam perveance	1.17 $\mu\text{A/V}^{1.5}$

building frames or other structures. The proper phase relation between the cavity inputs is set by adjusting the waveguide lengths (see Fig. 1). For testing the cavities, we have provided another 50-kW klystron (Phillips, YK1265) along with its power supply. The waveguide system can be easily switched for cavity tests.

IV. LOW-LEVEL CONTROLS

In the damping ring, beams are injected by a train of 10-40 bunches. When the ring is initially filled, the beam current in the ring increases in steps of 120 mA (typically). This causes an abrupt change in the cavity voltage and phase, thus leading to beam loss if no measures are taken. A low-level system should control this change, as well as stabilize the voltage and phase in the cavity.

A preliminary plan of the low-level system is shown in Fig. 3. The amplitude and phase of the cavity input RF are stabilized by an AGC and station PLL loops, while cavity tuning is made by a tuner PLL loop. The fill of the empty ring is made according to the following sequence: 1) detune the cavity so as to have a tuning angle of ψ_1 which gives optimum tuning after the first train is injected; 2) shortly (say, 50 μsec) before injection, jump the generator power; 3) inject the first bunch train; 4) detune the cavity

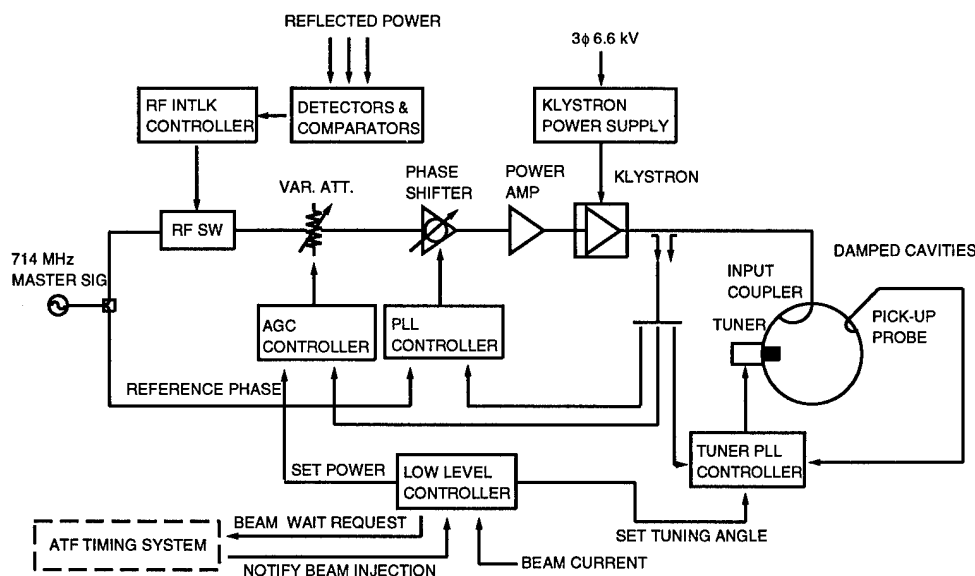


Fig. 3. Conceptual block diagram of the low-level system.

for the next injection; 5) and so on. During this procedure, a signal gives notice of the injection before the beam arrives. It takes several seconds to fill the ring due to mechanical movements of the tuners.

Tracking simulations have showed that beams can be stably stored by using this procedure. The maximum reflected power during filling is about 9 kW/cavity, which is acceptable. A difference in the injected charge of 0-120% from the expected value is acceptable.

After the ring is filled with full bunch-trains, the "oldest" train is extracted, immediately followed by the injection of a new train. Since this injection is made before the "empty" buckets pass the cavities, there is no change in the beam loading, except for that due to a fluctuation of the injected charge.

V. REDUCED RF SYSTEM FOR INITIAL OPERATION

It is planned that initial operations of the DR, scheduled for the end of 1996, will be made using a reduced RF system, due to a shortage of funds. The reduced system comprises two cavities, a 50-kW klystron and one circulator. The left half of the waveguide network, shown in Fig. 2, is to be built first, which is compatible to the full system. This system can accommodate beams of 90 mA with a gap voltage of 0.45 MV at the full beam energy (1.54 GeV). It can also accommodate beams of 400 mA with a gap voltage of 0.3 MV at lower energy (1.3 GeV). In both cases the bucket height exceeds 1%, and the natural bunch length is less than 6 mm. The system allows for many essential studies concerning the beam dynamics relevant to the production of low-emittance beams.

VI. CONCLUSIONS

A damping ring RF system has been designed, and is recently under construction. The development of cavities, circulators or other devices is progressing. A 250-kW klystron is also under development, though its use is not foreseen until after commissioning the ring. A conceptual plan of the low-level system has been made, which will be followed by further developments.

VII. ACKNOWLEDGMENTS

The authors wish to thank Dr. K. Oide of KEK and Dr. P. Krejcik of SLAC for valuable discussions, and to all members of the ATF group for their support. We would like to acknowledge the promotion of the ATF project by Profs. Y. Kimura and K. Takata.

VIII. REFERENCES

- [1] J. Urakawa et al., *Proceedings of the Fourth Workshop on Japan Linear Collider*, KEK, pp. 67-86.
- [2] ATF Design and Study Report, edited by F. Hinode et al., to be published as a KEK Internal Report.
- [3] F. Hinode and S. Sakanaka, in these proceedings.
- [4] S. Sakanaka et al., *Proceedings of the 1993 Particle Accelerator Conference*, Vol. 2, pp. 1027-1029.
- [5] S. Sakanaka et al., *Proceedings of the 1994 International Linac Conference*, Vol. 1, pp. 281-283.
- [6] M. Akemoto, *Conference Record of the 1991 IEEE Particle Accelerator Conference*, Vol. 2, pp. 1037-1039.
- [7] S. Sakanaka et al., in these proceedings.

Development of a Damped Cavity with SiC Beam-Duct

T. Koseki, M. Izawa^{a)} and Y. Kamiya

Synchrotron Radiation Laboratory, The Institute for Solid State Physics (ISSP),
The University of Tokyo, Tanashi, Tokyo 188, Japan

a) Photon Factory, National Laboratory for High Energy Physics, Tsukuba, Ibaraki 305, Japan

abstract

The recent status of the R&D on a damped structure cavity being developed at ISSP and Photon Factory is presented. For the cavity, the higher-order modes (HOM's) damping is obtained with the large beam duct, a part of which is made of sintered SiC. A prototype cavity has been built and tested at low power levels. It was confirmed that the HOM's, which can propagate out of the cavity through the beam duct, were strongly damped by the SiC duct. Recently, fabrication of a high power model has been completed. High power conditioning of the model is now prepared.

I. INTRODUCTION

The damped cavity aims at being installed in two low emittance electron/position storage rings. One is a third-generation VUV and SX synchrotron radiation source being designed at ISSP [1] in collaboration with the Photon Factory (PF). The other is a high brilliance configuration of the PF storage ring [2]. The basic parameters of these storage rings are listed in Table 1.

Table 1: The basic parameters of the VUV and SX storage ring and PF high-brilliance configuration.

	VUV-SX	PF
Beam energy [GeV]	2.0 GeV	2.5 GeV
Lattice type	DBA	FODO
Circumference [m]	374	187
Revolution frequency [MHz]	0.801	1.603
Natural emittance [nm-rad]	4.9	27
RF frequency [MHz]	500.1	500.1
Harmonic number	624	312
Peak effective voltage [MV]	1.5	1.5
Energy loss / turn [keV]	213.8	398.8
Beam current [mA]	400	500
Bunch length [mm]	~4	~10
Number of the cavity	3	4

The schematic of a quadrant of the cavity is shown in Fig. 1. The cavity has large beam duct, a part of which is made of sintered SiC. The HOM's propagating out from the cavity through the beam duct are then absorbed by the SiC parts[3,4].

The SiC material we adopted was CERASIC-B (pressureless sintered SiC made by Toshiba Ceramics Co. Ltd.), which has properties such as high thermal conductivity, a small outgassing rate, adequate mechanical strength and

suitable resistivity of 10 - 100 Ω -cm in the frequency range of a few GHz.

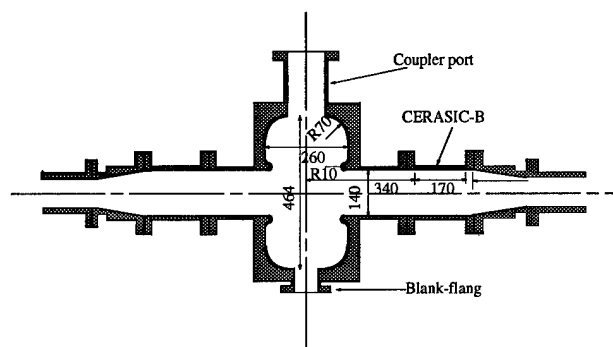


Figure 1: The cross sectional view of the damped cavity.

II. LOW POWER MEASUREMENT OF THE PROTOTYPE

We have fabricated the prototype model of the cavity and carried out its low power test. The model cavity itself was made of aluminum. Two types of beam ducts with the same length were prepared for the test. One was all made of aluminum and the other was partly made of CERASIC-B. The measured resistivity of the CERASIC-B duct was approximately 80 Ω -cm in the frequency region of 1.5 to 3.0 GHz.

The cavity has four ports, which are for an input coupler, a tuning plunger and two blank-flanges, respectively. We fabricated a cold model of newly designed input coupler with low VSWR at the operating frequency of 500.1 MHz [5]. The tuning plunger was the same type as used in the PF cavity. The blank-flange, also called fixed tuner, is a flange with cylindrical block to pad the port of the cavity. We measured the effects of block length on the resonance frequencies and Q-values of HOM's.

The measurement of RF characteristics was made with a network analyzer (HP8510C). For mode identification of HOM's, the field distributions in the cavity with aluminum beam duct were measured by the method of perturbation technique [3]. All modes predicted by the computer code URMEL were well identified.

A. HOM's above cutoff frequency of the beam-duct

The HOM's with frequencies higher than the cutoff of the 140 mm ϕ beam duct (1.64 GHz for TM₀₁ mode and 1.26 GHz for TE₁₁ mode) can propagate out from the cavity. It is therefore expected that they can be absorbed by CERASIC-B ducts. We then measured the transmission response (S₂₁) between two small rod antennas put at both endplates of the beam duct. Figure 2 and 3 show the measured spectrum from 1.5 GHz to 2.0 GHz. Figure 2 is the case of the aluminum beam duct and Fig. 3 the case of CERASIC-B beam duct. Similarly, Figures 4 and 5 show the spectrum from 2.0 GHz to 2.5 GHz. Figure 4 is the case of the aluminum beam duct and Figure 5 the case of CERASIC-B beam duct. The identified modes with URMEL notation are also indicated in Figs. 2 and 4. As shown in the figures, all resonances for the CERASIC-B beam duct were strongly damped and no longer visible.

B. Trapped modes

Since the HOM's with frequencies lower than the cutoff of the 140 mm ϕ beam duct are trapped in the cavity

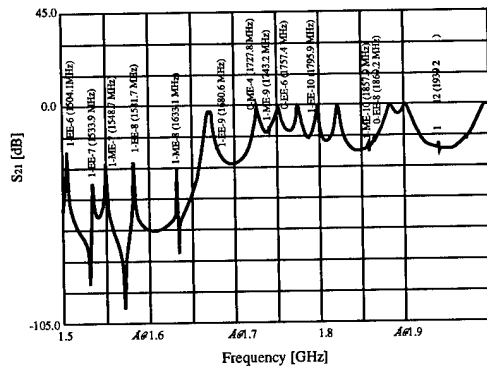


Figure 2: HOM's from 1.5 to 2.0 GHz for the Al beam duct.

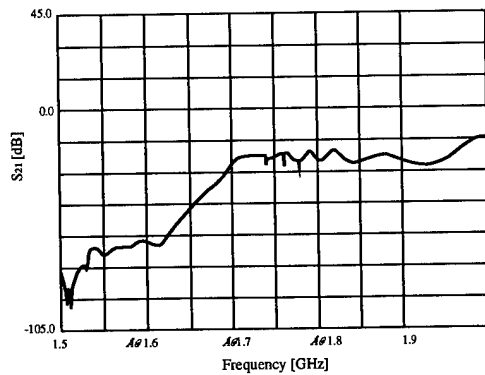


Figure 3: HOM's from 1.5 to 2.0 GHz for the SiC beam duct.

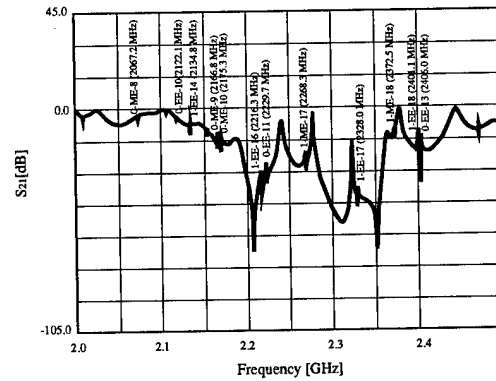


Figure 4: HOM's from 2.0 to 2.5 GHz for the Al beam duct.

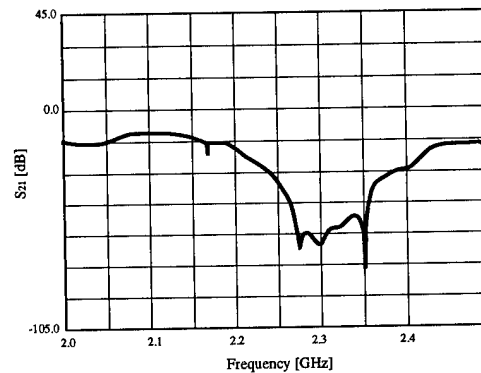


Figure 5: HOM's from 2.0 to 2.5 GHz for the SiC beam duct.

and they can not be absorbed in the CERASIC-B duct. The properties of these trapped modes are summarized in Tables 2 and 3. In order to avoid the instability due to these modes, two kind of methods may be applicable. One is the detuning of resonant frequencies of the HOM's by properly choosing the lengths of the blank-flanges [6], and the other is a bunch feedback method [7].

Figure 6 shows examples of the frequency dependence of HOM's on the length of blank-flange. The lengths in the figures are measured inward from the surface of the cavity. These data were taken under the following conditions; the frequency of accelerating mode was fixed at 500.1 MHz by adjusting the tuning plunger, and the length of one blank-flange was changed while that of the other was fixed. Figure 6(a) is for TM_{110h} modes and (b) for TM₀₁₁ mode. For TM_{110h} mode, the frequency detuning can be easily done since the frequency shift is sufficiently large. However, it would be difficult for TM₀₁₁ mode, because of its small frequency shift. Thus the feedback method should be applied for this kind of mode. The measured frequency shifts with the length of blank-flange for all trapped modes are also shown in Table 2 and 3.

Table 2: The properties of longitudinal trapped modes. Qc indicates the Q-values for Cu estimated from the measured ones for Al. Δf is a frequency shift per 1mm change in the length of one blank-flange for the accelerating mode being fixed at 500.1 MHz.

Mode type	URMEL notation	f [MHz] (meas.)	Q (calc.)	Qc (meas.)	(Rs/Q) [Ω] (calc.)	Δf [kHz/mm]
TM010	0-EE-1	500.1	43894	36000	175	
TM011	0-ME-1	793.0	36554	28000	52.2	20
	0-EE-3	1310.0	56807	7000	9.28	10
TM021	0-ME-2	1371.0	43051	11000	8.90	85

Table 3: The properties of transverse trapped modes.

Mode type	URMEL notation	f [MHz] (meas.)	Q (calc.)	Q (meas.)	(Rt/Q) [Ω /m] (calc.)	Δf [kHz/mm]
TE111	1-ME-1	704.6	45739	30000	7.40	150
TM110V	1-EE-1	789.7	49972	7000	248	-100
TM110H	1-EE-1	792.6	49972	39000	248	100
TM111H	1-ME-2	988.8	27214	25000	449	-90
TM111V	1-ME-2	989.8	27214	17000	449	120
		991.3		32000		50

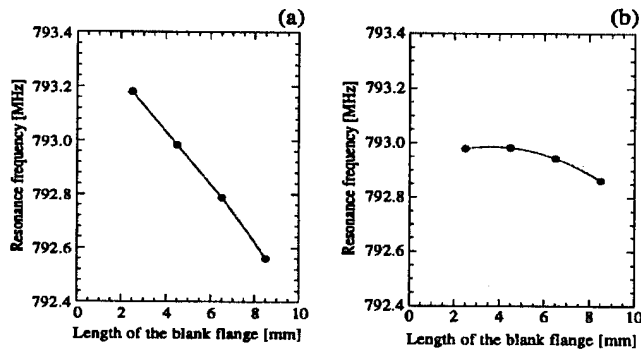


Figure 6: The frequency dependence of HOM on the length of blank-flange. (a) TM110h mode, (b) TM011 mode.

III. HIGH POWER MODEL

Recently, fabrication of a high power model has been completed. Figure 7 shows the model with a newly designed input coupler described in Ref.[5]. The model was manufactured at Keihin Product Operations of Toshiba Corporation. The main part of the high power model is made of OFHC copper. The unloaded Q value of the accelerating mode was measured to be 39000 at 500.1 MHz. The coupling coefficient β was 2.35, while the value expected from the low power measurement was 2.27 [5].

We have also fabricated the CERASIC-B duct for high power test. The duct is composed of Al duct with ICF253 flanges and CERASIC-B duct which is inserted in the Al duct by the method of shrink fit. The high power test of the CERASIC-B duct has been successfully carried out as described in Ref. [8].

The high power test of the cavity is being prepared. We will soon start its high power conditioning.

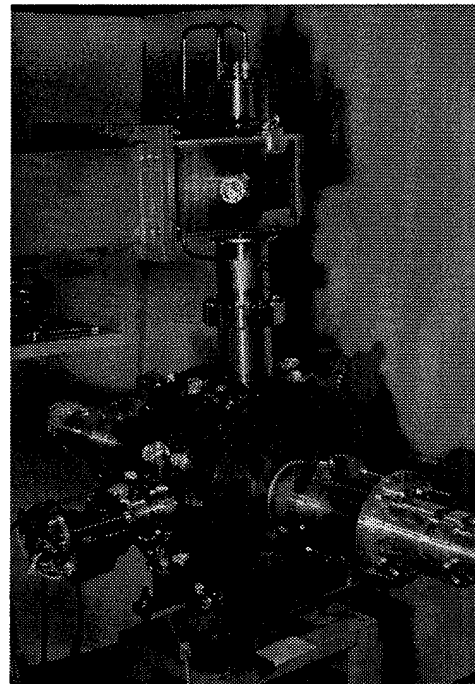


Figure 7: The high power model.

IV. REFERENCES

- [1] Y.Kamiya et al., Proc. 4th EPAC, London, 1994, p. 639.
- [2] M. Katoh et al., Rev. Sci. Instrum., 66 (1995) 1892.
- [3] T. Koseki et al., Proc. 4th EPAC, London, 1994, p. 2152.
- [4] T. Koseki et al., Rev. Sci. Instrum., 66(1995) 1926.
- [5] T. Nagatsuka, T. Koseki, Y. Kamiya, M. Izawa and Y. Terada, "A Design of Input Coupler for RF cavity" in these proceedings.
- [6] H. Kobayakawa et al., Rev. Sci. Instrum., 60(1989)1732.
- [7] E. Kikutani et al., Proc. 4th EPAC, London, 1994, p. 1613.
- [8] M. Izawa et al., Rev. Sci. Instrum., 66(1995) 1910.

HOM ABSORBER FOR THE KEKB NORMAL CONDUCTING CAVITY

Y. Takeuchi, K. Akai, N. Akasaka, E. Ezura, T. Kageyama, F. Naito, T. Shintake,
and Y. Yamazaki

KEK, National Laboratory for High Energy Physics, 1-1 Oho, Tsukuba, Ibaraki, 305 JAPAN

The HOM absorber for the normal conducting RF cavity of the KEK B-factory (KEKB) was designed. Sixteen bullet-shape sintered SiC (silicon carbide) ceramics are used for HOM absorption. The HOM power to be handled will be about 10 kW per cavity, corresponding to about 1 kW per absorber. A prototype of SiC absorber was made to verify the performance as a HOM absorber in vacuum. The high power test was carried out successfully using a pulsed klystron ($f=1296$ MHz). The design of the HOM absorber and the results of the high power test are discussed.

I. INTRODUCTION

A prototype of normal conducting cavity for KEKB has been designed and built [1]. This prototype cavity is loaded with a coaxial waveguide for damping higher order modes (HOM's). The waveguide is equipped with a notch filter. Figure 1 shows a schematic drawing of this cavity. For HOM absorption, sixteen bullet-shape sintered SiC ceramics are inserted from the end of the coaxial waveguide. The absorber dimensions are 40 mm in diameter, and 400 mm in total effective length including a 100-mm nosecone section. Each SiC absorber has a cooling water channel bored inside and is directly cooled. The HOM power (at frequencies around 1 GHz) to be handled will be on the order of ~ 10 kW per cavity, corresponding to ~ 1 kW per absorber.

Some reasons why we have chosen SiC ceramics are as follows: 1) SiC is a fine and dense ceramics which has a high mechanical strength and a low outgassing rate, and is chemically inert. 2) SiC has a relatively high thermal conductivity of ~ 120 W/mK at room temperature, which is about one half of that of Aluminum (230 W/mK). 3) At the

2.5-GeV electron linac in KEK, nearly two hundred SiC absorbers (diameter = 24 mm, length = 300 mm) have been used for the S-band waveguide loads without any troubles for about ten years. A prototype of S-band SiC absorber was tested up to a peak power of 10 MW with a pulse width of 3.5 μ sec at 50 Hz, corresponding to a average power of 1.75 kW [2]. Among these reasons, the third one most encouraged us to use SiC ceramics.

II. HOM ABSORBERS

A. Permittivity of SiC

We measured the complex permittivities of several SiC samples and selected an α -type SiC ceramics [3]. Figure 2 shows the frequency response of the dielectric constant ϵ' and the loss tangent of the SiC ceramics, measured using a dielectric probe kit (HP85070B).

The permittivity of the SiC ceramics is sensitive to production conditions such as sintering temperature, contamination of furnace atmosphere and so on. Many products of SiC ceramics are usually used for mechanical parts such as a bearing. The electric properties are not usually specified. Therefore, we must pay attention to the reproducibility of the electric properties of the SiC ceramics. We measured the permittivity of SiC ceramics of different lots for the HOM absorbers. We confirmed that the SiC ceramics, sintered in the same furnace, have almost the same permittivity. Further studies are being continued to control the permittivity.

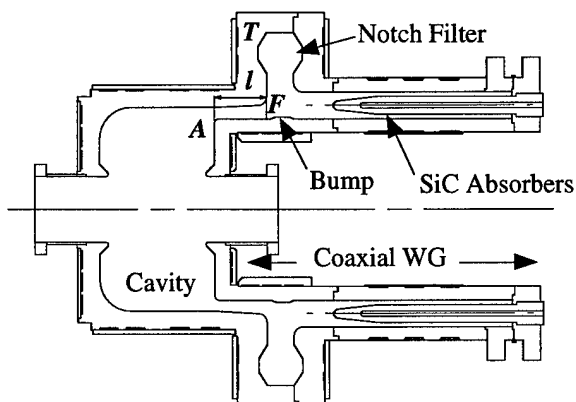


Figure 1: A schematic drawing of the test cavity.

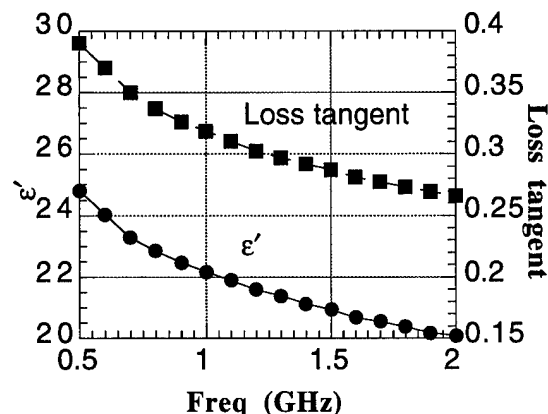


Figure 2: The dielectric constant and loss tangent of the SiC ceramics are plotted as a function of frequency.

B. Vacuum Seal Methods

We designed two types of SiC absorbers for the prototype cavities. One of them (model A) has a vacuum seal structure using a metal o-ring and the other (model B) has a metal sleeve directly brazed to the SiC ceramics. Figure 3 shows a schematic drawing of model B. Figures 4 and 5 show the vacuum seal structures of these models.

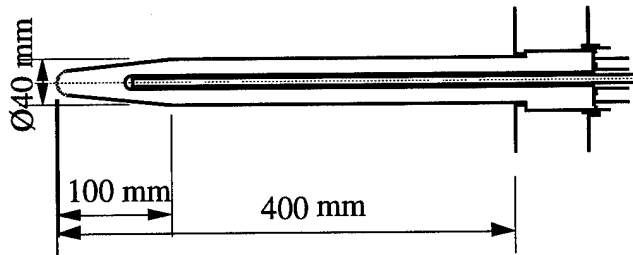


Figure 3: A schematic drawing of the model B absorber.

Since the structure of model A is simple and easy to fabricate, we employed model A for the first prototype cavity. A vacuum test was carried out using a test set with the same sealing structure. Heat-cycle test (15~80 °C) was also carried out about ten times. No vacuum leak was detected. However, we had some leak trouble when SiC absorbers were installed in the first prototype cavity. We are planing to further vacuum test of this structure to optimize the surface roughness of the SiC ceramics for better vacuum-seal performance.

The absorbers of model B, which will be installed in the second prototype cavity, was designed for more reliable vacuum tightness in the long term operation. A copper thin sleeve was directly brazed to the SiC ceramics. Generally, brazing the SiC ceramics with a metal is a very difficult technique. Some reasons are as follows: 1) Since the coefficient of thermal expansion of the SiC ceramics ($4.2 \times 10^{-6} / ^\circ\text{C}$) is much smaller than those of metals (for copper it is $16.6 \times 10^{-6} / ^\circ\text{C}$), large stress at the braze joint develops in cooling process of the brazing. 2) By the reaction between the SiC ceramics and the brazing alloy (such as Cu-

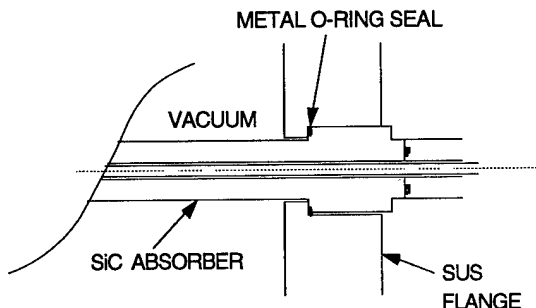


Figure 4: A SiC absorber using a metal o-ring for the vacuum seal.

Ag-Ti), some fragile alloys are usually produced, and makes the braze joint weak.

A stable brazing between the SiC ceramics and the copper sleeve was developed by a supplier [4]. This technique was applied to the model B. Test pieces of model B passed more than 500 heat cycles (-30~180 °C) [5].

Figure 6 shows a prototype of the model B absorber, which will be installed in the second prototype cavity.

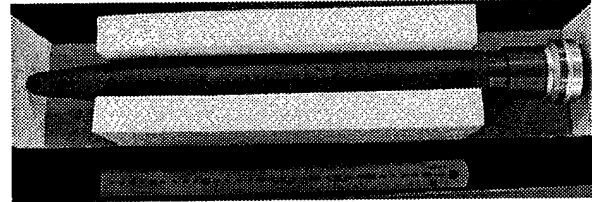


Figure 6: A prototype of the model B absorber.

III. HIGH-POWER TEST

A prototype SiC absorber of model A was made to verify the performance as a HOM absorber in vacuum. Figure 7 shows the layout of the high power test. The prototype absorber was inserted from the end of an L-band rectangular waveguide (WR650), where the standing-wave ratio VSWR was measured ~1.1. The vacuum pressure was about $10^{-10} \sim 10^{-9}$ Torr after a 64-hour baking at 80 °C. The high power test was carried out using a pulsed klystron ($f = 1296$ MHz) up to a peak power of 128 kW with a pulse width 540 μsec at 50 Hz, corresponding to a average power of ~3.5 kW. The prototype absorber functioned normally without any vacuum, thermal, or discharge trouble up to 2.5 kW of average RF power. However, the vacuum pressure increased gradually ($10^{-9} \sim 10^{-8}$ Torr) over 2.5 kW. This is due to the temperature rise at the nosecone tip of the SiC absorber, which was roughly estimated about 100 °C at 2.5 kW. This SiC absorber would handle much higher average power than 2.5 kW if either cooling water is led near the nosecone tip or the absorber is baked enough at a higher temperature.

The outgassing rate of the SiC ceramics was also

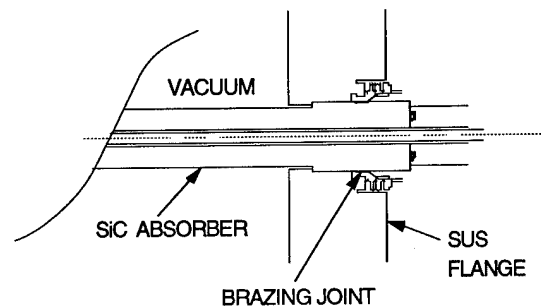


Figure 5: A SiC absorber using a brazing joint. The SiC ceramic is directly brazed to a copper sleeve.

measured using a cylindrical sample (diameter = 50 mm, height = 50 mm). After 24-hour baking at 150 °C, the outgassing rate at room temperature was 3×10^{-12} Torr l/s cm^2 .

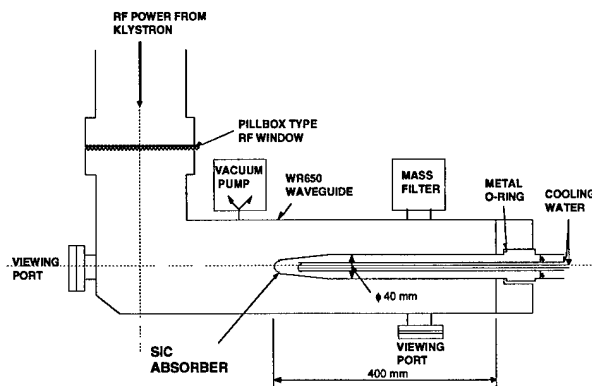


Figure 7: The layout of the high power test.

IV. CONCLUSION

Two types of HOM absorbers made of SiC ceramics were designed. One of them has a vacuum seal structure using a metal o-ring and the other has a metal sleeve directly brazed to the SiC ceramics. A prototype, which used a metal o-ring, was made to verify the performance as a HOM absorber in vacuum. High power test was carried out successfully. This prototype absorber handled up to the average power of 2.5 kW, which satisfies the requirement of the absorber. Higher average power than 2.5 kW would be handled by improving the water cooling circuit in the nosecone.

V. ACKNOWLEDGMENTS

We would like to thank H. Hisamatsu for measuring the vacuum properties of the SiC sample

VI. REFERENCES

- [1] T. Kageyama et al., "Development of a HOM-Damped Cavity for the KEK B-Factor (KEKB)", WPQ17 in this conference.
- [2] H. Matsumoto et al., "Application of SiC Ceramics for Microwave Absorber", Proc. 9th Linear Accelerator Meeting in Japan, Kyoto, 1984, pp. 124-126.
- [3] supplied by Hitachi Kasei Ceramics Co., Ltd.
- [4] The brazing technique was developed by Hitachi Haramachi Electronics Co., Ltd.
- [5] Private communication with T. Oku, Hitachi Haramachi Electronics Co., Ltd.

PEP-II B-Factory Prototype Higher Order Mode Load Design*

R. Pendleton, K. Ko, C. Ng, M. Neubauer, H. Schwarz, ‡

Stanford Linear Accelerator Center, Stanford University, Stanford, CA 94309, USA

R. Rimmer, LBL, 1 Cyclotron Road, Berkeley, CA 94720, USA#

ABSTRACT

To reduce the impedance of the cavity higher order modes, (HOM's), a compact broad-band, low-reflection, waveguide load is required with a VSWR less than 2:1 in the frequency range 714 MHz to 2500 MHz. The load must also work in the high vacuum of the cavity, and be capable of dissipating up to 10 kW of power which is generated by the interaction of the beam with the cavity HOM's and which is directed to each load assembly. A prototype load assembly is being fabricated which uses the lossy ceramic Al-N with 7% by weight glassy carbon to absorb the microwave power.

1. INTRODUCTION

Each RF cavity [1,2] in the PEP-II B-factory will have three HOM waveguide load assemblies, one of which is depicted in figure 1. The assembly consists of the vacuum flange which bolts to the cavity, a section of uniform waveguide 25cm x 2.54cm ($f_c=600$ Mhz) which separates the lossy material from the exponentially decaying field of the fundamental mode at 476 Mhz, and the lossy ceramic tapers at the end of the waveguide which absorb the power from the HOM's. The lossy ceramic Al-N with glassy carbon [3] is used to dissipate the power. Computer simulations were used to design the footprint of the ceramics, which are arranged in two triangular wedges and are brazed onto one side of the waveguide at the end of the curved waveguide assembly [4]. Custom made ceramic tiles ready for brazing into the prototype were procured from industry [5]. The design was verified electrically by measuring the reflection from a cold

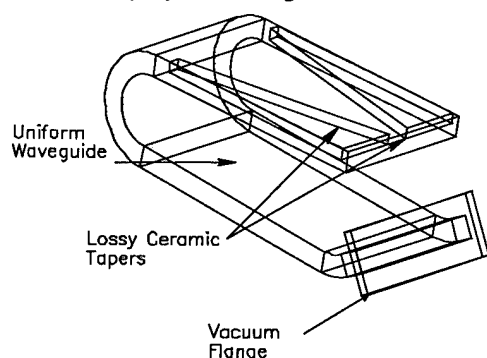


Figure 1. Higher order mode load assembly. The assembly is curved to fit in the available space.

*This work was supported by the Director, Office of Energy Research, Office of High Energy and Nuclear Physics, High Energy Physics Division of the U.S. Department of Energy.

‡Stanford Linear Accelerator Center, Cont. DE-AC03-76SF00515

#Lawrence Berkeley Laboratory, Contract DE-AC03-76SF00098

test model of the lossy ceramic section of the HOM load assembly. In addition the complex dielectric constant was measured on both the ceramic used for the prototype, and on previous samples of this type of ceramic, and the data are presented. A schematic of the planned high power test is presented at the end.

2. LOSSY CERAMIC LAYOUT

The Al-N ceramic tiles, nominally 2cm x 2cm x 1.9cm, are arranged into two tapers which flare out from the sidewall of the 25cm x 2.54cm waveguide. The detailed footprint of the individual ceramic tiles that will be used in the prototype HOM load assembly is shown in figure 2. The individual rectangular ceramics are angled with respect to the centerline of the waveguide so that the smoothest interface is presented to the oncoming RF wave which minimizes reflections. Non-rectangular tiles are employed on the sidewalls and the backside of the ceramic taper to smoothly fill in the space which also reduces reflections caused by changes in the propagation constant. Figure 3 shows the composite heating pattern of the load for the nominal operating conditions.

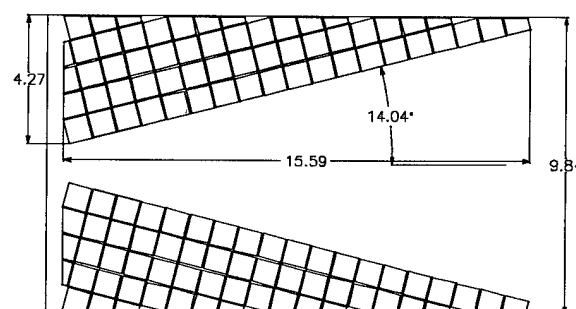


Figure 2. View of ceramic footprint looking down on the broadwall of the HOM waveguide. The square tiles are 2cm x 2cm. Spacing between tiles is roughly 1mm.

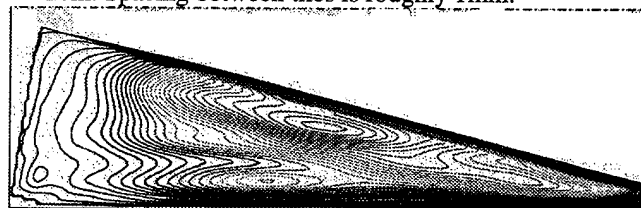


Figure 3. Time-averaged power density in ceramics for the HOM power generated in the cavity from 714 Mhz - 2500 Mhz with 3A of beam current. Only one side of the load is shown. The peak power density is 3.2 W cm^{-3} .

3. PROTOTYPE LOW POWER RF MEASUREMENTS

A low power test model of the microwave absorbing load portion of the prototype assembly was created by assembling the tiles into the triangular pattern of figure 2 and inserting the tiles into a piece of uniform waveguide. The reflection coefficient, S_{11} , of this test model was measured. The RF measurements were made with an HP-8510 network analyzer and three sets of waveguide taper and coaxial transitions which, in combination, covered the frequency range of 650 Mhz to 4200 Mhz. A TRL calibration was performed with each set of tapers and transitions and then the test model was measured. The combined data measured over the normal operating ranges of the transitions is shown in figure 4.

The ceramics used in the test model are shorter than the design value due to a manufacturing error; the ceramics are only 0.714" tall whereas the design height is 0.75". With these short ceramics the load meets the specification of VSWR = 2.0:1, but exhibits little margin at 714 Mhz. MAFIA Simulations indicate there is about a 7 dB increase in S_{11} because of the reduced ceramic height, thus the load with the full size 0.75" tall ceramics should have more margin at 714 Mhz.

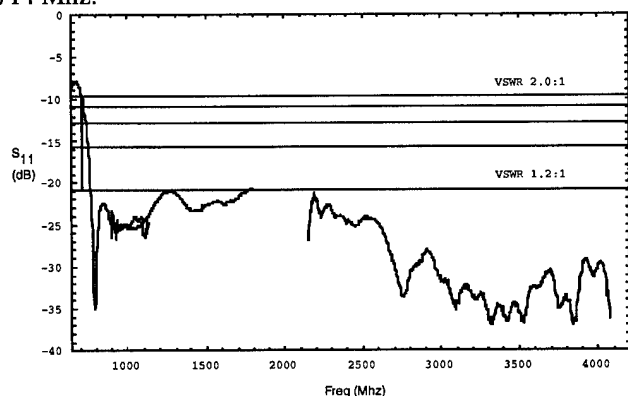


Figure 4. Reflection, S_{11} , of prototype load ceramics arranged in footprint of figure 2. The ceramics are 0.714" tall. The gap from ~1800 to 2100 Mhz is between waveguide bands and is covered in more detail later.

The dip in reflected power at ~800 Mhz is due to the partial cancellation of the reflections from the short at the end of the load, and the reflection which occurs at the modal transition plane. The modal transition plane is defined as the region where the propagating mode switches rapidly from the

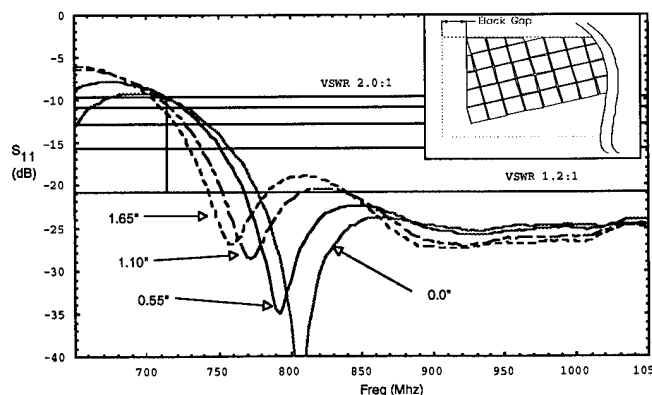


Figure 5. Prototype load response with different distances between the end of the ceramic tiles and the short at the end of the load ("Back Gap"). With increasing distance the dip in reflected power decreases in frequency.

normal TE_{10} mode, with most of the power in the center of the waveguide, to the mode which carries energy in the ceramics along the edge of the waveguide. To test this we measured the response of the load while varying the distance at the end of the load to the short; a longer distance should move the dip lower in frequency. The results are shown in figure 5.

There is a region from 1800 Mhz to 2100 Mhz which is not covered by the experimental set-ups when used over their designed operating ranges. However, a measurement can be made in this region using the WR-650 tapers and transitions. We calibrate the tapers and transitions as we normally do but over the frequency range of 1600 to 2200 Mhz. The calibration procedure is unable to remove the affects of the larger reflections in this frequency band, which is outside the designed range of the tapers and transitions; however, there do exist regions in between the large reflections where the calibration procedure is able to accomodate the remaining reflections. Figure 6 shows the measurement of the test model and the measurement of the two waveguide tapers alone used in the calibration. The spikes in the measurement of the two tapers alone are frequency regions in which the large reflections could not be calibrated out; however, in between these spikes are regions in which the measured reflection from the load is believed reliable. Note that at 1600 Mhz and at 2200 Mhz this measurement of the test model agrees with the previous measurements made with components operating within their designed frequency range.

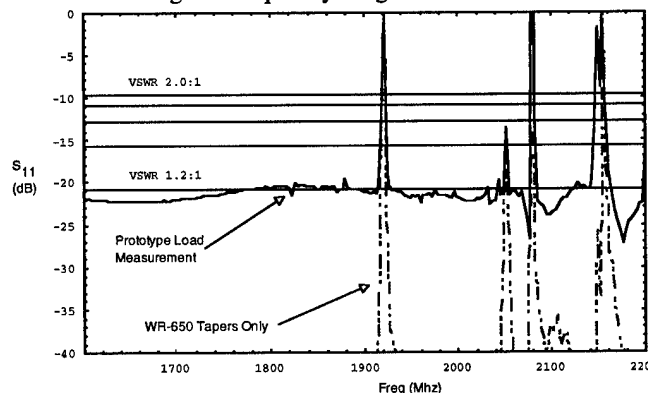


Figure 6. Reflection, S_{11} , of prototype load ceramics measured using the WR-650 set-up above TE_{20} cutoff. The dashed line is a measurement of the waveguide tapers alone. In between the spikes of the taper response the data for the load is believed reliable.

4. DIELECTRIC MEASUREMENTS OF CERAMIC

4.1. Ceramic for the Prototype

The electrical properties of the Al-N ceramic which will be used for the prototype were measured using a coaxial probe, HP 85070B, attached to a network analyzer. Figure 6 shows the results of eight measurements on one 8" x 8" billet. The spread in dielectric constant is slightly larger than the precision of the measurement and indicates some slight variability in dielectric constant within the billet.

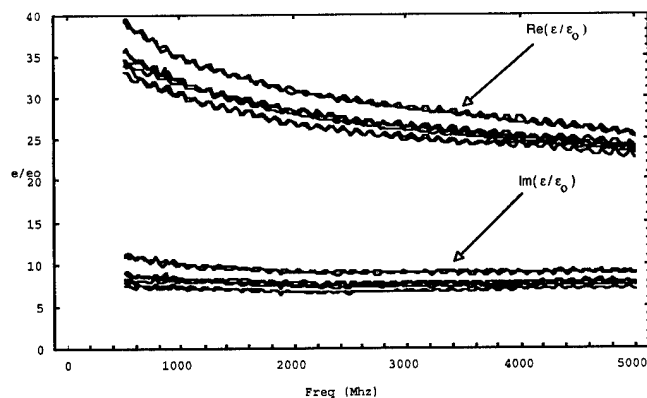


Figure 7. Measured dielectric constant of ceramic used in prototype. The 8 measurements are from one 8" x 8" billet.

4.2. Entire collection of ceramics

In addition to the material for the prototype we also measured some Al-N ceramic we had previously purchased earlier in the development cycle. These measurements encompass some material which was produced while the ceramic process yielded more variability in density. The current process is claimed to yield ceramics with a density of $2.95 - 2.98 \text{ gm}\cdot\text{cm}^{-3}$. The ceramic used in the prototype load assembly has a density of $2.97 \text{ gm}\cdot\text{cm}^{-3}$. We present this data for reference. We measured this material using a combination of the HP coaxial probe technique and also using a stripline fixture that was supplied by W. Barry at LBL[6]. Based on the limited measurements to date, we have found the dielectric constant increases with density, but also exhibits some variability for a given density. Figure 8 shows a series of measurements that encompassed materials of different densities. Measurements using the two techniques on the same material agreed within $\sim 10\%$.

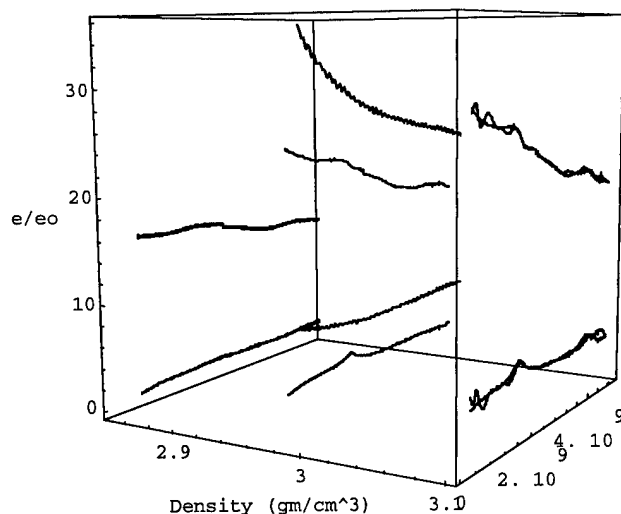


Figure 8 Real and imaginary part of dielectric constant vs. frequency and density.

4.3 Sensitivity of Load to Variations in Dielectric Constant.

The reflection from the load is most strongly affected by changes in the dielectric constant at the lower frequencies

where the load is electrically shorter and some of the incident power reflects off the back wall. Simulations predict the load will meet the reflection specification for $50 > \text{Re}(\epsilon/\epsilon_0) > 26$ at 714 Mhz.

5. POWER TEST OF PROTOTYPE HOM ASSY.

The prototype load assembly is under construction and is scheduled for a high power vacuum test in early summer. We will test the assembly using a 714 Mhz klystron which is capable of producing much higher power densities in the load than will be seen in normal operation. A waveguide window made from MACOR[®] and sealed with an O-ring will form the vacuum seal. A layout of the test is shown in figure 9.

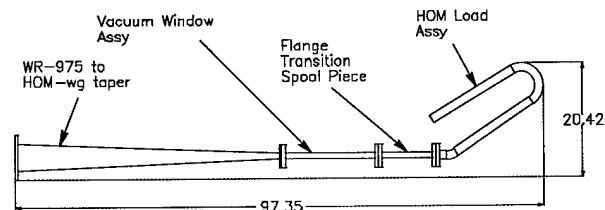


Figure 9. Layout of high power test on the load assembly.

6. ACKNOWLEDGMENTS

We would like to thank R. Campisi of CEBAF for useful discussions on the use and application of the Al-N material.

7. REFERENCES

- [1] R. Rimmer et. al., "An RF Cavity for the B-factory", Proc. PAC, San Francisco, May 6th-9th, 1991, pp819-21.
- [2] H. Schwarz et. al. "Design of a High Power Test Model of the PEP-II RF Cavity", Proc. PAC, Washington D.C. 1993, pp1039-1041.
- [3] Material is manufactured by Ceradyne corporation and was developed in collaboration with R. Campisi of CEBAF.
- [4] R. Pendleton et. al., "Broad-Band, Multi-Kilowatt, Vacuum, HOM Waveguide Loads for the PEP-II RF Cavity", Proc EPAC, London, June 27-July 1, 1994.
- [5] Ceradyne Inc. 3169 Redhill Avenue, Costa Mesa, Ca.
- [6] W. Barry et. al., "A Broadband, Automated, Stripline Technique for the Simultaneous Measurement of Complex Permittivity and Permeability" IEEE Microwave Theory and Techniques Transactions, v34-1, Jan. 1986

High-Power RF Window and Coupler Development for the PEP-II B Factory*

M. Neubauer, K. Fant, J. Hodgson, J. Judkins, H. Schwarz
Stanford Linear Accelerator Center, Stanford University, Stanford, CA 94309, USA

R.A. Rimmer,
Lawrence Berkeley Laboratory, 1 Cyclotron Road, Berkeley, CA 94720, USA

Abstract

We describe the fabrication and testing of the RF windows designed to transmit power to the PEP-II 476 MHz cavities. Design choices to maximize the reliability of the window are discussed. Fabrication technologies for the window are described and finite-element analysis of the assembly process is presented. Conditioning and high-power testing of the window are discussed. Design of the coupler assembly including the integration of the window and other components is reported.

1. INTRODUCTION

The RF design of a self-matched RF window using a 10 inch (254 mm) alumina disk in a WR2100 size waveguide is described in an earlier paper [1]. This paper describes the mechanical realization and initial power tests of the window design. To counteract tensile stress on the perimeter of the disk when heated by RF fields, a stainless steel ring is shrunk onto the ceramic during the brazing process. The stainless steel ring puts the ceramic disk in compression and thus results in a rugged window design capable of handling the 500 kW of RF power. To remove heat from the window, a cooling channel is included in the stainless steel ring. We describe the modeling and construction details of the brazing operation. The post-braze machining steps by which the window frequency and match are tuned to the desired values are also described. A knife-edge seal with a copper gasket was used to make a vacuum joint. To reduce multipactor each window is coated with titanium nitride. Two windows, back-to-back, are assembled onto a waveguide test chamber built to be evacuated and operated with up to 500 kW throughput power into a matched load. During the tests, calorimetric measurements were made and total power loss in the window and iris were calculated. Power loss and temperature measurements correlated well with ANSYS and MAFIA calculations.

2. WINDOW CONSTRUCTION DETAILS

2.1 Compression concept.

The challenge of the braze of a stainless steel compression ring to the ceramic disk is in the difference of expansion coefficients which makes the braze gap between the ceramic and the stainless steel ring widen as the window is heated to braze temperature. A molybdenum keeper ring with an

expansion coefficient less than that of the ceramic and stainless steel is used to shrink fit the stainless steel ring (Fig. 1) onto the ceramic so that the braze gap is just right at the braze temperature.

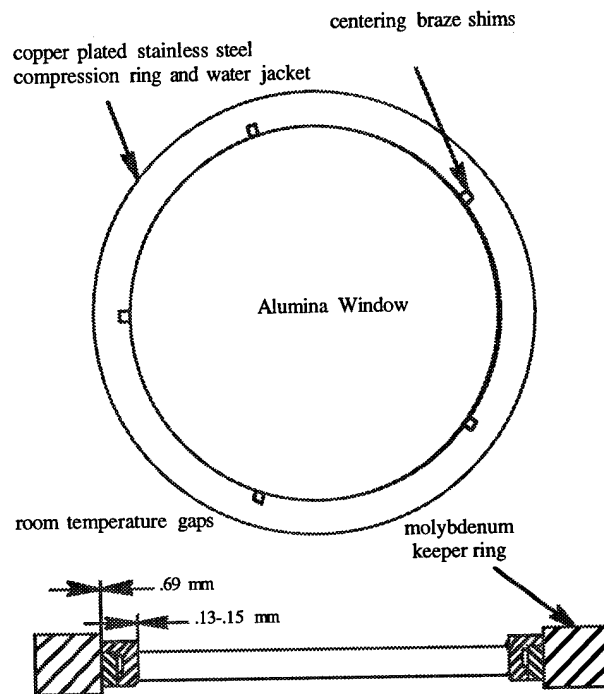


Figure 1. Braze fixture details: centering shims, gaps at room temperature.

2.2 Braze modeling and results.

ANSYS modeling, 1/3 scale braze tests, and full size braze tests were required to learn the critical parameters required to control the braze gap, volume of braze material, and the size of the fillet. The gap between the metallized alumina ceramic and the copper buffer layer on the inside diameter of the stainless steel compression ring we found to require a dimension of $.075 \pm .004$ mm at braze temperature. Too small of a gap would not allow full flow of the braze alloy along the 18.3 mm edge of the window and cause leaks. Too large of a gap would not allow the braze to fully bridge the gap and possibly cause stress concentrators and/or leaks. Because of the large size and mass of the various components, a technique was also required to keep the braze gap uniform around the perimeter of the window during the heating to brazing temperature (1050°C). This was accomplished with braze

*Work supported by Department of Energy contracts
DE-AC03-76SF00515 (SLAC)
DE-AC03-76SF00098 (LBL)

shims of the braze alloy as shown in Figure 1. which maintained concentricity until they melted and were absorbed into the braze joint.

For the optimum gap at brazing temperature, the room temperature clearances required between the molybdenum keeper ring, stainless steel compression ring and alumina ceramic, were determined by ANSYS analysis, 1/3 scale models and finally by full-size trials. The required gaps are shown in Figure 1. These critical gaps were achieved by measuring the inside diameter of the molybdenum keeper ring and the outside diameter of the nickel plated, metallized alumina ceramic, to accuracies of .0025mm. The inside and outside diameter of the copper plated stainless steel compression ring is then custom machined to achieve the critical room temperature gap dimensions.

A significant factor in the consistency of the braze gap at 1050°C, was discovered to be the frictional contact between the molybdenum keeper ring and the stainless steel compression ring. The gap between the stainless steel compression ring and the inside diameter of the molybdenum keeper ring closes to zero at approximately 500°C. During the continued rise in temperature, the stainless steel ring yields in compression modified by frictional forces and the degree of sticking. The contact elements in the ANSYS library allowed us to model the influence of friction. A titanium nitride coating on the inside of the keeper ring, and a "green-fired" or chrome-oxide coated outside surface on the compression ring were the surface treatments which produced the most reliable and repeatable frictional forces with minimized sticking.

After all the control variables were optimized we produced three prototype windows which were all leak-tight and compressed. Figure 2, shows one of the post-machined windows with knife-edge seal.

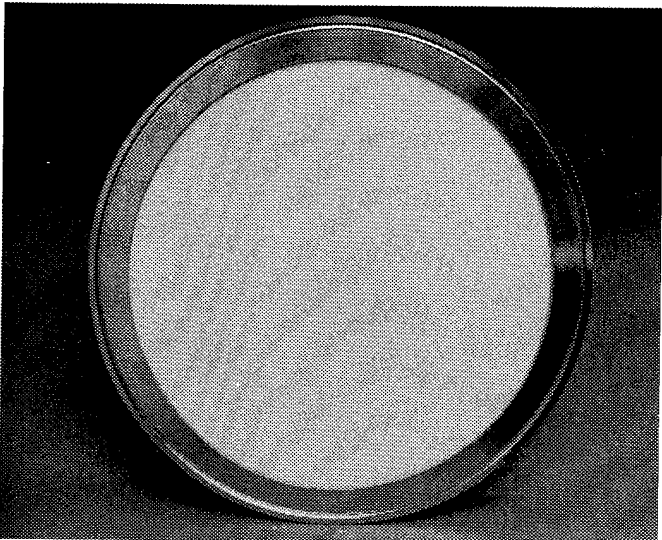


Figure 2. Ceramic disk with brazed stainless steel compression ring and post-machined knife-edge seal.

2.3 Fine-tuning of the match.

After brazing the height of the compression ring is machined back to create an iris length which achieves the desired match frequency of the window. This also eliminates any distortion from the brazing process. The sensitivity of this machining step agreed well with the HFSS calculations and was measured to be 1.4 MHz/mm. The outside diameter of the stainless steel ring is also made true for the best match possible. The final result of these machining operations are shown in Figure 3, with a minimum VSWR of 1.01

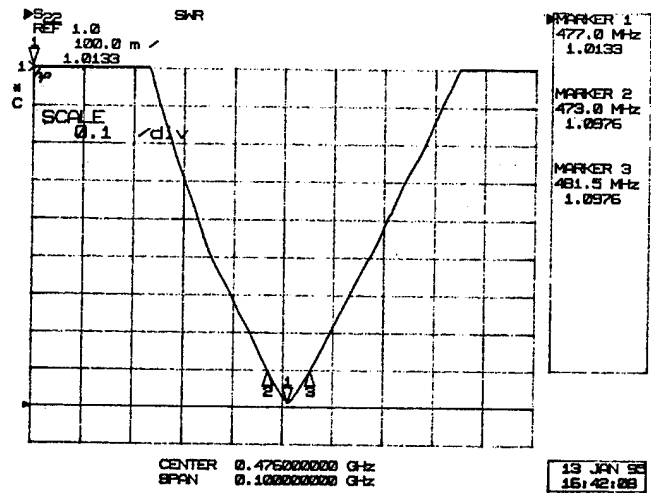


Figure 3. Cold Test match of a brazed and post machined Self-Matched window measured in the coupler transition. (The center frequency will shift down to 476 MHz when the knife-edge vacuum seal is fully compressed.)

2.4. Vacuum Seal.

A knife-edge seal using a copper gasket was chosen. The knife-edge is cut as part of the post machining of the stainless steel compression ring. The other half of the knife-edge vacuum seal is the stainless steel flange of the 16" x 9" waveguide. A picture of this seal assembly is shown in Figure 4.

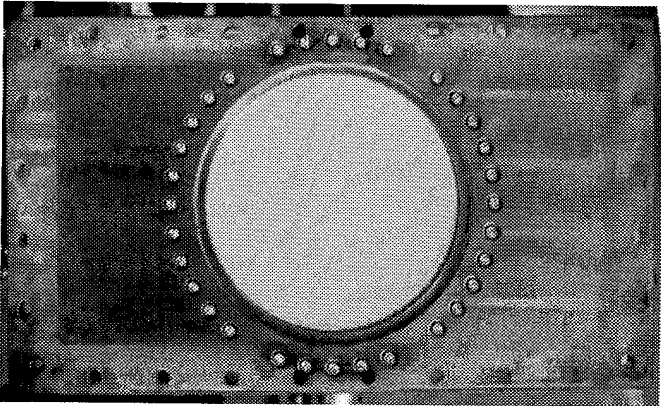


Figure 4. Air side (WR2100) flange showing the number of bolts required to provide the necessary force to make the vacuum seal.

3. HIGH POWER TESTING

3.1. Test Chamber.

The vacuum test chamber for the back-to-back window test is shown in Figure 5. The chamber was designed with viewports to observe the window surfaces. Photo-multiplier arc-detectors sensitive to UV and visible light were also included in a position to observe the high-field triple junction portion of the window. An Infrared Imaging camera was used to record window temperatures from the air side. Flow meters and thermistors were used to calculate total power loss in the individual windows.

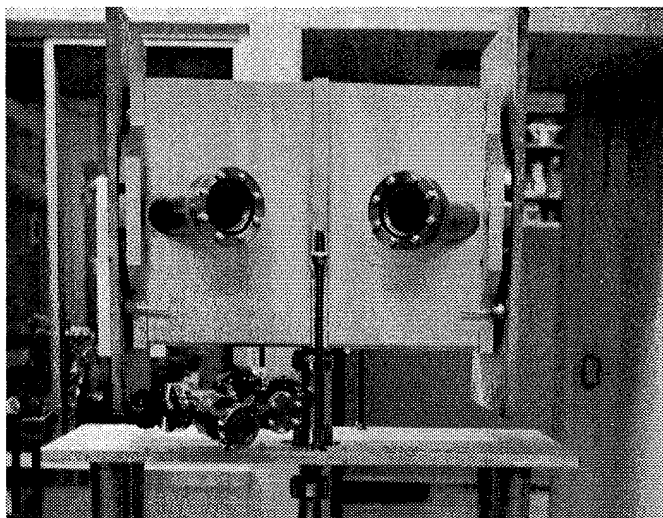


Figure 5. Window test chamber with two windows assembled.

3.2. Preliminary Results of RF Power Tests.

The goal is to process the assembly of two back-to-back windows with vacuum in between to 500 kW power transmission. During initial processing we were able to run CW power levels up to 400 kW for several minutes limited by outgassing as the ceramic heated up. Under continuous operation we were able to reach 270 kW of CW power limited by additional heating of the ceramic due to multipactor. The multipactor shows itself as a strong purple glow on the ceramic. It does not seem to process away with CW or pulsed processing. As a next step we will increase the titanium nitride coating thickness and retest.

3.3. Ohmic-loss Measurement.

To check the ohmic loss behavior of the test windows, the test chamber was backfilled with dry nitrogen and tested up to 500 kW of CW power. With the infrared imaging camera, we measured the thermal profile during warm up and at steady state. The iso-therms in the temperature profile had a tendency to be oval shaped with the highest temperatures on the perimeter in the high current region. The profiles are shown in Figure 6. These results agree well with our predictions from ANSYS and MAFIA calculations at this power level. We also used MAFIA to make the following calculations at 500

kW of CW power: surface wall currents in the metallizing and nickel plating on the ceramic perimeter produce 150 watts, dielectric losses in the ceramic produce 157 watts, and iris wall losses produced 71 watts. These loss calculations totaled 378 watts. At 500 kW in air, we found excellent agreement with 327 watts measured on one window and 350 watts on the other.

4. COUPLER GEOMETRY

The coupler geometry designed for the RF cavity places the window around a 90° E-bend, away from direct line-of-sight of the beam. The 16"x9" (406x23 mm) rectangular waveguide size was chosen to place the window in a cavity detuned short position to limit the voltage excursions during RF transients [2].

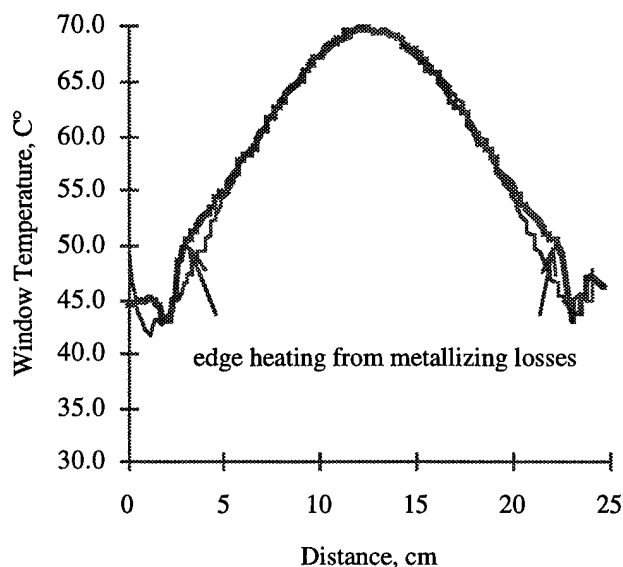


Figure 6. Temperature profile across the window with 500 kW incident power (thin line parallel to E field, thick line orthogonal to E-field)

5. CONCLUSIONS

The manufacturing method for producing pre-stressed windows is complete. RF Power tests are encouraging. The anti-multipactor coating requires further optimization. The ohmic-loss measurements agree with the calculations.

6. ACKNOWLEDGMENTS

We would like to thank Alan Hill for his design and configuration of the automated High Power Test data collection system.

7. REFERENCES

- [1] M. Neubauer et al, "High-Power RF Window Design for the PEP-II B Factory, "Proc EPAC 94, June 27-July 1 1994, London
- [2] H. Schwarz et al, "RF System Design for the PEP-II B Factory," Proc EPAC 94, June 27-July 1 1994, London

INPUT COUPLER FOR THE KEKB NORMAL CONDUCTING CAVITY

F. Naito, K. Akai, N. Akasaka, E. Ezura, T. Kageyama, T. Shintake, Y. Takeuchi and Y. Yamazaki
KEK, National Laboratory for High Energy Physics, Oho 1-1, Tsukuba-shi, Ibaraki-ken 305, Japan

The input coupler for the normal conducting RF cavity of the KEK B-factory (KEKB) was designed comprising a disk-type coaxial ceramic window and a door-knob transition. We designed two different types of window structure; one is a choke-type structure and the other is a under- and over-cut structure. The fabrication of two types coupler is underway in order to confirm the RF properties.

I. INTRODUCTION

The reliability of the input coupler is usually the critical technical issue for the development of the cavity system. At present stage the cavity for KEK B-factory requires about 400kW (CW) RF-power per cavity (the RF frequency is 508.8 MHz) [1]. In order to keep the stable operation at 400 kW, the coupler should be able to transmit RF-power significantly higher than 400 kW. Thus we have set the target value of the transmitted RF power on 800 kW (CW) that is twice as high as the required power.

Since the reliability of the coupler strongly depends on that of the ceramic window in the coupler, we recognize that the choice of the window structure is most important for the design of the coupler. In order to transmit the 800 kW RF power we have chosen a disk-type ceramic for the coupler window. The rational for this choice is described in the next section.

Other mechanical structures of the coupler are decided by boundary conditions of the coupler: (1) RF power is fed from a klystron through the WR1500 rectangular waveguide; (2) the coupler couples with the cavity by a loop (magnetic) coupling which connects with the WX77D coaxial waveguide.

The coupler has several transitions which transmits the RF power from the rectangular waveguide to the coaxial waveguide with a minimum reflection of the RF power. Each transition part is designed so that their VSWR is less than 1.05 and that of the coupler assembled with the transitions amounts to less than 1.1 around the RF frequency of 508.8 MHz.

Experience obtained with the output couplers of the UHF klystrons for TRISTAN was fully taken into account in order to design the present coupler. The first design for the RF structure has been finished by using a computer simulation called "High frequency structure simulator" (HFSS) [2]. The fabrication of the high-power model of the coupler is in progress. The RF properties of the coupler will be measured by a low-power model so as to confirm the simulated results.

II. CHOICE OF WINDOW STRUCTURE

In the coupler many troubles are related to the multipactor on the window. Several experiments and considerations of the ceramic window in couplers suggest the following [3,4]: the uniformity of the electric field distribution around the window

is very important in order to prevent the local heating of the ceramic induced by the multipactor; the multipactor induced by the electric field that is perpendicular to the window causes the damage on the surface, while the multipactor induced by the parallel field causes no serious problem.

Two types of ceramic window are in use for the coupler in the KEK at UHF band: a cylindrical ceramic window and a disk-type ceramic window. The former is used in the input couplers for both of the alternating periodic structure (APS) cavity of the TRISTAN ring and the single-cell cavity of the PF ring. It was tested up to 300 kW (CW) RF-power [5]. The latter is adopted in the following couplers: the output coupler of the UHF klystron in the TRISTAN, which transmits 1.2 MW (CW) RF-power [3]; the input coupler of the super conducting cavity (SCC) of the TRISTAN [6]; the input coupler of the high-power models of the RFQ [7] linac and DTL [8,9] for the Japanese Hadron Project (JHP).

Since the result of the klystron output coupler is sufficient for our target value which is RF power 800 kW (CW), we chose the disk-type ceramic as the window of the coupler.

The disk-type ceramic window is located in the coaxial waveguide. The waveguide near the window requires an impedance matching section in order to compensate for the permittivity of ceramic. One of the typical matching section is a choke structure. The output coupler of the klystron and the SCC input coupler have this structure. Another structure for the matching section is a combination of the undercut and overcut (under/over-cut) type. This structure is in use for the couplers of the RFQ and DTL for the JHP.

We designed the two types of coupler. One has the choke structure and the other has the under/over-cut structure. The final decision for the impedance matching structure of the window will be done by comparing the results of the high-power test with two types of couplers.

III. DESIGN

The coupler is composed of three transition sections: (1) the door-knob transition between the WX152D coaxial waveguide and the WR1500 rectangular waveguide; (2) the disk-type ceramic window in the WX152D waveguide; (3) the transformer between the coaxial waveguide of the WX77D and that of the WX152D.

The door-knob transition has a capacitive iris so that the size of the door-knob becomes smaller than that without the iris. The diameter and the height of the door-knob are 340 mm and 123 mm, respectively. The height of the iris is 46.4 mm. The schematic view of the door-knob transition is shown in the Fig. 1. The simulated VSWR is shown in Fig. 2.

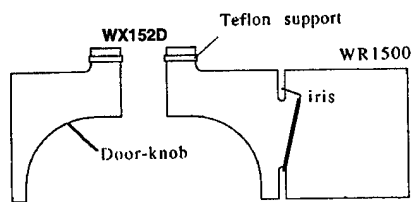


Figure 1: Schematic view of the door-knob transition.

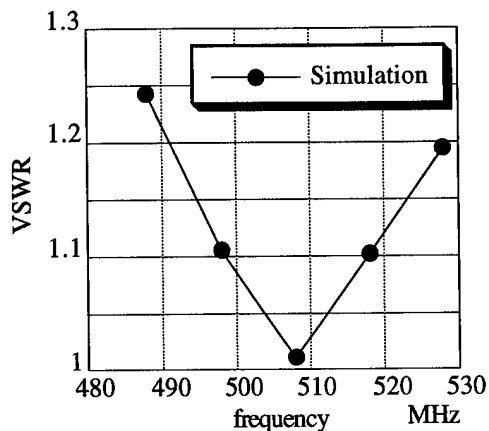


Figure 2: Calculated VSWR for the door-knob transition.

The choke and the under/over-cut structures of the window are respectively shown in the Fig. 3 and 4. The inside and the outside diameter of the ceramic window are 166 mm and 38 mm, respectively. The thickness of the window is 10 mm.

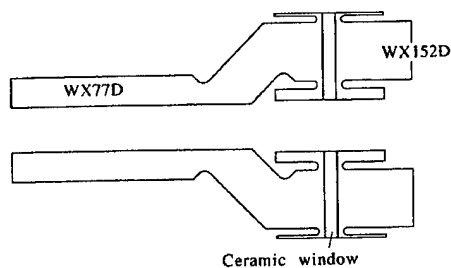


Figure 3: Schematic view of the choke window structure.

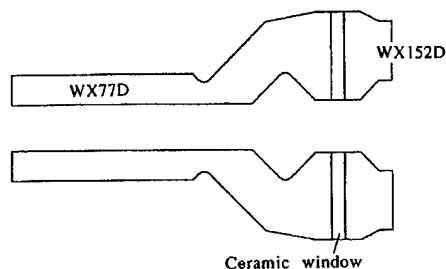


Figure 4: Under/over-cut window structure.

Both figures include the transition from the WX152D coaxial waveguide to the WX77D coaxial waveguide. The bumps located at the transition shield the window from a beam and a cavity in order to reduce the direct irradiation of

the x-ray and charged particles made by collision between the beam and residual gases and to avoid the adsorption of Cu sputtered from the cavity wall. The shield should certainly increase the reliability of the coupler.

VSWR of the transitions for the window is plotted in the Fig. 5. Figure 6 shows the radial dependence of the electric field strength 1 mm away from the window surface for both the structures. The value is normalized by the field strength on the surface of the inner cylinder of the WX152D coaxial waveguide.

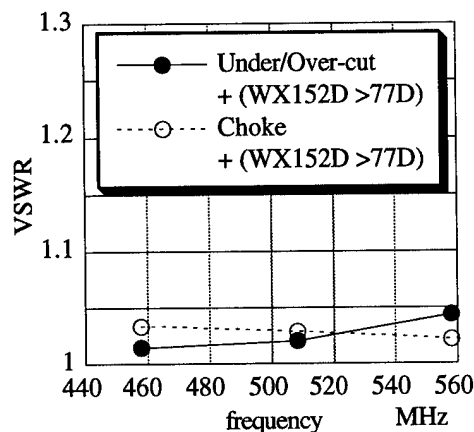


Figure 5: Calculated VSWR of the windows.

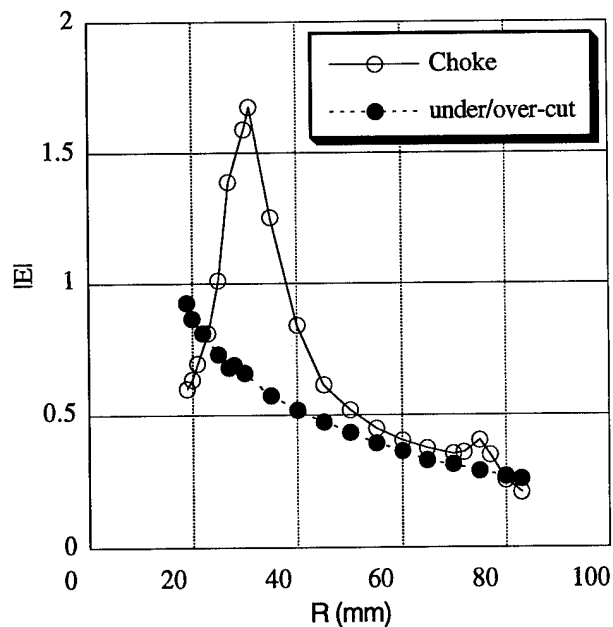


Figure 6: Calculated the electric field strength on the windows.

This plot shows:(1) the field strength of the under/over-cut structure is more uniform than that of the choke structure;(2) the field strength of the choke structure near the inner triple junction of the window is about 30 % lower than

that of the under/over-cut structure. The simulation shows that the direction of the electric fields almost parallel to the window for the under/over-cut structure, while for the choke structure the field concentrates and the field direction is perpendicular to the window near the tip of the choke.

The low-power model of the coupler with the under/over-cut structure has been developed. The model has no loop coupler but matched terminator at the end of the coaxial waveguide. The measured VSWR of the model is shown in Fig. 7 by white circles. The data are consistent with the result of the simulation shown in the figure by black circles. The model with the choke structure will be also measured in order to confirm the RF properties. The simulated VSWR for the model with the choke structure is shown in the Fig. 7 by white squares.

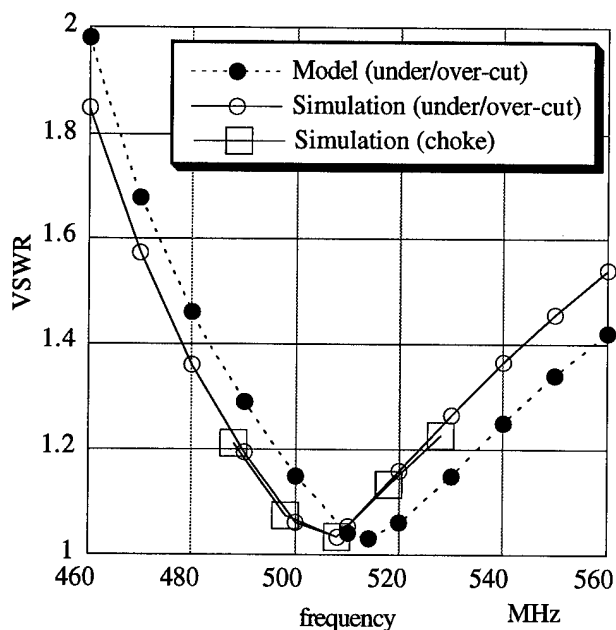


Figure 7: VSWR of the couplers

IV. CONCLUSION

We have designed the input coupler for the normal conducting RF cavity of the KEK B-factory (KEKB). The input coupler has the disk-type ceramic window in the coaxial waveguide. We designed two different types of window structure; one is a choke structure and the other is a under- and over-cut structure. The fabrication of the high-power models of both types are underway in order to test their performance at an RF power up to 800 kW(CW). The VSWR of the low-power model of the coupler with the under- and over-cut structure has been measured. The data are consistent with the result of the simulation.

V. REFERENCES

- [1] "Design of the KEKB RF System", K. Akai, E. Ezura and Y. Yamazaki, WPQ08 in this conference.
- [2] HP Part No. 85180A., HP Corp.
- [3] S. Isagawa, et al., Proc. IEEE Part. Accel. Conf., Washington D.C., (1987)
- [4] S. Yamaguchi, et al., IEEE trans. on Nuclear Sci., vol. 39, No. 2, 278 (1992)
- [5] M. Akemoto, et al., Proc. IEEE Part. Accel. Conf., San Francisco, California 1037 (1991)
- [6] S. Noguchi, E. Kako and K. Kubo, Proc. 4th Workshop on RF Superconductivity, KEK, Tsukuba, Japan, KEK Report 89-21, 397 (1990)
- [7] A. Ueno et al., Proc. 1994 LINAC Conf., Tsukuba, Japan, 169 (1994)
- [8] F. Naito et al., Proc. 1990 LINAC Conf., Albuquerque, USA, LA-12004-C, 156 (1990)
- [9] F. Naito et al., Proc. 1994 LINAC Conf., Tsukuba, Japan, 137 (1994)

Minimum Wakefield Achievable by Waveguide Damped Cavity*

Xintian E. Lin and Norman M. Kroll,
Stanford Linear Accelerator Center, Stanford University, Stanford, CA 94309
and University of California, San Diego, La Jolla, CA 92093

Abstract

We use an equivalent circuit to model a waveguide damped cavity. Both exponentially damped and persistent[1] (decay $t^{-3/2}$) components of the wakefield are derived from this model. The result shows that for a cavity with resonant frequency a fixed interval above waveguide cutoff, the persistent wakefield amplitude is inversely proportional to the external Q value of the damped mode. The competition of the two terms results in an optimal Q value, which gives a minimum wakefield as a function of the distance behind the source particle. The minimum wakefield increases when the resonant frequency approaches the waveguide cutoff. The results agree very well with computer simulation on a real cavity-waveguide system.

I. Introduction

Waveguide damping as a means to limit beam emittance growth due to the long range wakefield has received extensive study. The effectiveness of this procedure has typically been assessed by evaluating the resultant Q_{ext} of higher order cavity modes, thereby determining their exponential damping rate. Kroll and Lin[1] have pointed out another type of wakefield (persistent wakefield) associated with waveguide damping, which decays as $t^{-3/2}$.

We use an equivalent circuit model of a single mode cavity with waveguide damping to obtain an expression for the amplitude coefficient of the persistent term relative to that of the exponentially damped term. This expression is proportional to $\frac{1}{Q}$ with a coefficient which depends only upon the resonant and cut-off frequencies. It shows that the total wakefield at a fixed time delay is minimized by an optimum rather than minimum Q value.

II. Circuit Model

The circuit model is shown in Fig. 1. L_1 and C_1 form a loss-

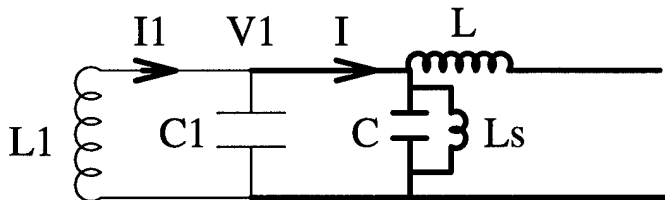


Figure. 1. Thick line represents a transmission line. L , C , L_s are understood as distributed quantities.

less resonant circuit to mimic the cavity. The transmission line with shunt inductance L_s mimics the waveguide. We note that

*Work supported by U.S. Department of Energy grant DE-FG03-93ER40759 and contract DE-AC03-76SF00515

while L and C are inductance and capacitance per unit length, respectively, L_s is inductance times unit length.

A. Transmission Line with Shunt Inductance

The differential equations of the transmission line with shunt inductance are

$$\frac{\partial V}{\partial x} = -L \frac{\partial I}{\partial t} \quad \text{and} \quad (1)$$

$$\frac{\partial^2 I}{\partial x \partial t} = -C \frac{\partial^2 V}{\partial t^2} - \frac{V}{L_s}. \quad (2)$$

Combining Eqs. 1 with 2, we obtain a single equation

$$LC \frac{\partial^2 V}{\partial t^2} - \frac{\partial^2 V}{\partial x^2} + \frac{L}{L_s} V = 0 \quad (3)$$

involving V only.

For a periodic ($e^{-i\omega t}$) field, the solutions are $V \sim e^{\pm ikx}$, with $k = \sqrt{LC} \sqrt{\omega^2 - \frac{1}{CL_s}}$. From Eq. 1, the voltage and current of the transmission line mode must be related by

$$\frac{V}{I} = \frac{\omega L}{\pm k} = \pm \sqrt{\frac{L}{C}} \frac{\omega}{\sqrt{\omega^2 - \omega_c^2}} \equiv Z, \quad (4)$$

where the \pm sign depends on the direction of the propagating waves: plus for positive x direction, negative for the other, and $\omega_c^2 = \frac{1}{CL_s}$.

B. Resonator with Transmission Line Loading

The differential equation of the voltage V_1 and current I_1 of the cavity follows the familiar equations of capacitance and inductance:

$$\frac{dV_1(t)}{dt} = \frac{1}{C_1} \frac{dq}{dt} = \frac{1}{C_1} (I_1(t) - I(t)) \quad \text{and} \quad (5)$$

$$V_1 = -L_1 \frac{dI_1(t)}{dt}, \quad (6)$$

where q is the charge on the capacitor C_1 .

The circuit is set up to have initial conditions $V_1(t=0) = v_0$ and $I_1(t=0) = 0$. V_1 is regarded as the longitudinal wakefield and I_1 as (proportional to) the transverse wakefield of the cavity.

Multiplying Eqs. 5 and 6 by $e^{i\omega t}$, integrating from $t=0$ to $t \rightarrow \infty$, and taking the initial conditions explicitly into account, we find

$$\begin{aligned} \tilde{I}_1 &= \tilde{I} + C_1 \int_0^\infty \frac{dV}{dt} e^{i\omega t} dt = \tilde{I} - C_1 v_0 - i\omega C_1 \tilde{V}_1 \\ &= \frac{\tilde{V}_1}{Z} - C_1 v_0 - i\omega C_1 \tilde{V}_1 \\ \tilde{V}_1 &= L_1 i\omega \tilde{I}_1, \end{aligned} \quad (7)$$

where $\tilde{\cdot}$ symbolizes the Fourier transform. We also used the result from the previous section in writing \tilde{I} as $\frac{\tilde{V}}{Z}$ on the second line of Eq. 7. Solving for \tilde{V}_1 , we find

$$\tilde{V}_1 = \frac{i \frac{\omega}{\omega_0^2} v_0}{(\frac{\omega}{\omega_0})^2 + i \frac{R}{Z} \frac{\omega}{\omega_0} - 1}, \quad (8)$$

where $\omega_0 = \frac{1}{\sqrt{L_1 C_1}}$, is the natural resonant frequency of the cavity and $R = \sqrt{\frac{L_1}{C_1}}$, is the characteristic impedance of the cavity resonant mode.

The Fourier transform of the transverse wakefield (\tilde{V}_\perp) is given by

$$\tilde{V}_\perp = \frac{i\zeta}{\omega L} \tilde{V}_1 = \frac{-\frac{\zeta}{\omega_0^2 L} v_0}{(\frac{\omega}{\omega_0})^2 + i \frac{R}{Z} \frac{\omega}{\omega_0} - 1}, \quad (9)$$

where ζ is a real geometric factor (with dimension of impedance) related to the shape of the structure and not given by our model.

C. Transverse Wakefield

The transverse wakefield in the time domain

$$V_\perp(t) = \frac{1}{2\pi} \int \tilde{V}_\perp e^{-i\omega t} d\omega \quad (10)$$

is obtained from the inverse Fourier transform. The integrand has two branch points from the definition of Z (Eq. 4). We choose the branch and integration contour shown in Fig. 2 [2]. The integration is naturally divided into two terms: one from the

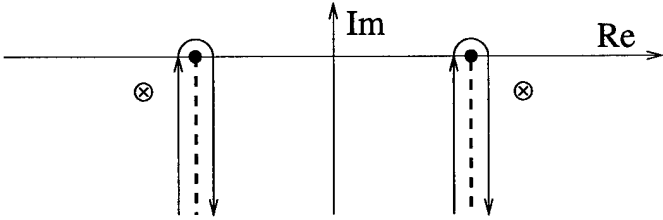


Figure 2. Contour for Calculating V_\perp

pole contribution, the other from the branch cut integral.

When $\frac{R}{Z(\omega_0)} \ll 1$, i.e. the damping term is small, the pole of the expression \tilde{V}_\perp is very close to ω_0 . For the purpose of calculating the pole and evaluating the residue, $Z(\omega)$ can be taken as $Z(\omega_0)$. Then the poles satisfy

$$\left(\frac{\omega}{\omega_0}\right)_{pole} = \pm \sqrt{1 - \frac{1}{4Q^2}} - \frac{i}{2Q}, \quad (11)$$

where $Q = \frac{Z(\omega_0)}{R}$.

The branch cut integral (persistent wakefield) is evaluated with Eq. 2 and 4 in [1]. When $t' \gg 1$. The total wakefield is

$$V_\perp(t) \approx v_0 \frac{\zeta}{\omega_0 L} \left[\frac{-1}{\sqrt{1 - \frac{1}{4Q^2}}} \sin\left(\sqrt{1 - \frac{1}{4Q^2}} t'\right) e^{-\frac{t'}{2Q}} + \sqrt{\frac{2}{\pi}} \frac{(\frac{\omega_c}{\omega_0})^{1/2}}{(1 - (\frac{\omega_c}{\omega_0})^2)^{5/2}} \frac{1}{Q} \cos\left(\frac{\omega_c}{\omega_0} t' + \frac{1}{4}\pi\right) \frac{1}{t'^{3/2}} \right] \quad (12)$$

where $t' = \omega_0 t$.

It is clear from the above expression that the persistent wake amplitude is proportional to $\frac{1}{Q}$, which means that a stronger damping produces a larger persistent wake. It also points out that as the resonant frequency gets closer to the waveguide cut-off, the persistent wake is enhanced.

Eq. 12 also tells us the best waveguide damping can do at a certain distance t' behind the source particle. A typical value for NLC is $t' = 40 * \pi$, i.e. 20 wave lengths away.

If we ignore the oscillating factor \sin , \cos , the sign and take $\frac{1}{\sqrt{1 - \frac{1}{4Q^2}}} \approx 1$ in Eq. 12, it is a good approximation to regard the sum as the maxima of the oscillating amplitude of V_\perp . Thus the wakefield can be written as

$$W_\perp = W_0 \left(e^{-\frac{t'}{2Q}} + \frac{b}{Q} \frac{1}{t'^{3/2}} \right) \quad \text{with} \quad (13)$$

$$b = \sqrt{\frac{2}{\pi}} \frac{(\frac{\omega_c}{\omega_0})^{1/2}}{(1 - (\frac{\omega_c}{\omega_0})^2)^{5/2}}.$$

We plot b as a function of $\frac{\omega_c}{\omega_0}$ in Fig. 3.

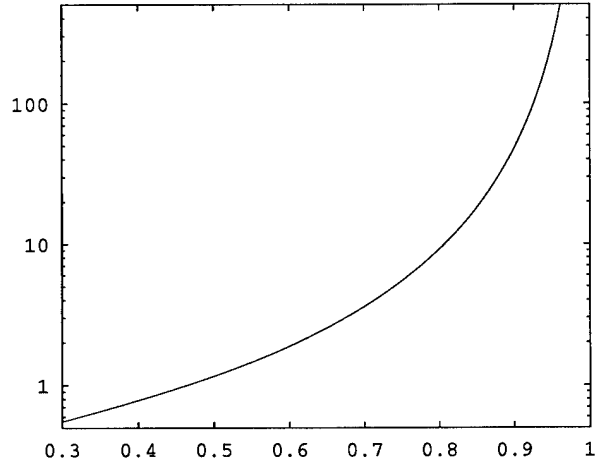


Figure 3. The horizontal axis is $\frac{\omega_c}{\omega_0}$, the vertical axis represents b .

At a given t' , the minimum wakefield occurs if

$$\frac{1}{2Q} = \frac{\frac{5}{2} \log t' - \log b}{t'}, \quad (14)$$

i.e. decreasing Q beyond this value increases the wakefield at t' . The optimum Q as a function of t' is plotted in Fig. 4.

Substituting Eq. 14 into Eq. 13, The value of the minimum wakefield at t'

$$W_\perp^{min} = W_0 t'^{-2.5} (5b \log t' + b - 2b \log b). \quad (15)$$

is obtained. Fig. 5 displays the minimum wakefield as a function of t' for a few values of b .

III. Numerical Comparison

We have made a few MAFIA simulations on the geometry shown in Fig. 6. It is a 2-D structure with the beam passing in the Z direction. Taking the symmetry into account, only a quarter of

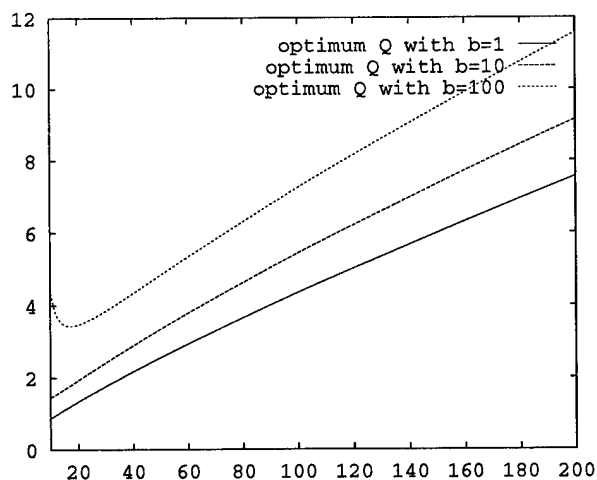


Figure 4. The horizontal axis is $t' = \omega_c t$, and the vertical is the optimum Q value

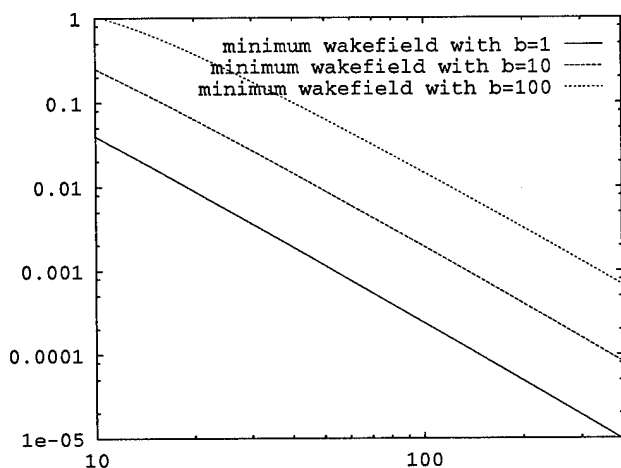


Figure 5. The horizontal axis is $t' = \omega_c t$. The vertical axis is the minimum wakefield achieved as a ratio to the wakefield at $t' = 0$

the structure with the electric boundary condition on the Y axis and the magnetic boundary on the X axis has been shown. We have calculated the persistent wake amplitude and the damped wake amplitude from the time domain beam excitation. The ratio of the persistent wake amplitude to the damped wake amplitude from the actual cavity waveguide system is compared with the prediction of Eq. 12 in Table I.

Four cases were run, one with $w = 0.25$, $t = 0.05$. The second case has $w = 0.25$ and $t = 0.25$. The third is the same as the second except that the waveguide is 1.1 times larger (other dimensions do not scale with the waveguide width.). The fourth one has the same parameters as the second except $w = 0.35$.

The circuit model and the MAFIA results agree very well considering how simple the circuit model is. The circuit model can be expected to hold only when a single decaying mode dominates the spectrum near the waveguide cutoff. The discrepancy at high Q value is attributed to inadequate satisfaction of this condition.

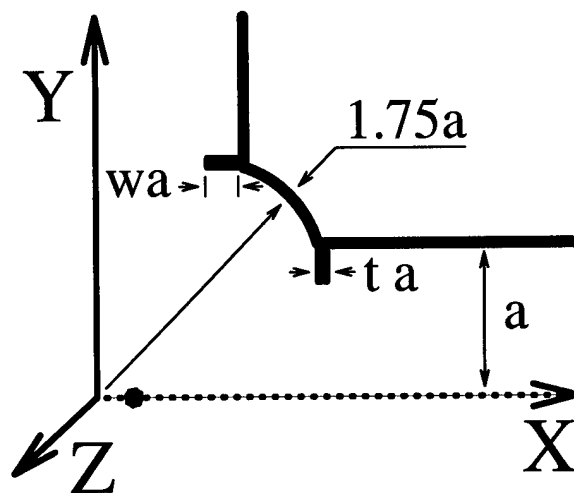


Figure 6. Waveguide damped cavity. The big dot represents the beam passing in Z direction.

	MAFIA result	Theory	Case
$Q = 3.94, \frac{w}{a} = 0.776$	2.17	2.19	1
$Q = 6.72, \frac{w}{a} = 0.776$	1.17	1.28	2
$Q = 7.34, \frac{w}{a} = 0.705$	0.587	0.659	3
$Q = 12.0, \frac{w}{a} = 0.731$	0.351	0.503	4

Table I

The ratio of the persistent wake amplitude to the damped wake amplitude is compared between MAFIA simulation and the circuit model.

IV. Cavity and Waveguide Detuning

For a single damped cavity, Eq. 15 presents the limit of the transverse wakefield. In the case of a multi-cell structure, the wakefield can be further reduced by detuning in analogy with dipole mode detuning.

In an optimally damped system, the dipole frequency (ω_0) and the waveguide cut-off are detuned in proportion in each cell in a Gaussian profile to produce the fastest and the most persistent fall off. In a N cell structure, detuning usually results in a wakefield which is $\frac{1}{N}$ of that of a single cell.

Taking a 100-cell structure for example, with $t' = 40\pi$ and $\frac{w_c}{\omega_0} = \frac{13}{15}$, the minimum wakefield of a single cell is 6.0×10^{-4} times that of an undamped cavity. With detuning, the final wakefield is down to a few parts in a million.

References

- [1] Norman M. Kroll and Xintian E. Lin, *Persistent Wakefield associated with Waveguide Damping of Higher Order Modes*, Proceedings of the 1993 IEEE Particle Accelerator Conference, Washington DC, P.3453-3455.
- [2] [1], section 2.

PLS RF System Operation during the Commissioning

M. Kwon, I. H. Yu, H. J. Park, D. H. Han, M. Yoon, Y. S. Kim
Pohang Accelerator Laboratory, POSTECH
Pohang, Kyungbuk 790-768 KOREA

Abstract

The storage ring of the Pohang Light Source(PLS) is designed to store 100s mA of 2 GeV electrons injected from the full energy linear accelerator. To compensate for the synchrotron radiation loss three RF cavities were installed in one of the straight sections powered by three 60 kW-TV transmitters independently. Phase and amplitude are controlled by the separate low level systems. During the commissioning, since the beam lifetime is limited by the vacuum pressure, various accelerating voltages were set to investigate the system characteristics. Even one cavity is enough to store 100 mA of beam, whereas the vacuum-limited lifetime is few minutes at 1 mTorr. The cavity HOM-induced multi-bunch instabilities were observed at certain condition and cured to some extent by shifting phase and water temperature.

General description of RF system performance and trouble-shoots during the commissioning are presented.

1.INTRODUCTION

The RF system of the storage ring of the PLS has three cavities to store few hundreds mA of 2 GeV electron beam, which

are powered by three klystron amplifiers. During the first phase of the commissioning one or two cavities were mostly used storing up to 200 mA with 800 kV of the total gap voltage. In the final week of the commissioning three cavities were powered with 1200 kV of the total gap voltage storing 300 mA of electron beam[1]. Since 1992, a prototype RF system has been installed and tested in the high power RF test facility. The cavity was manufactured by Toshiba following the design of the upgraded Photon Factory's. A set of RF station includes the Daresbury-made low level system. Low and high power tests of the cavity, circulator and klystron amplifier were performed with this prototype low level system. After testing a prototype RF system, a few modifications and enhancements were made for the storage ring RF system. A schematic layout of a station of the PLS RF system is shown in Fig. 1.

From early 1994, RF system began to be installed in the storage ring tunnel posting cavities and vacuum chambers. Baking and conditioning were performed after installation in August 1994 and the commissioning of the storage ring began in September. Total RF power of 180 kW can provide enough power to store 300 mA at 1.2 MV of accelerating voltage. By the end of 1995 one more station will be installed and the total RF power will increase to 240 kW, which will store 200 mA of electron beam for the planned 2.5 GeV ramping experiment.

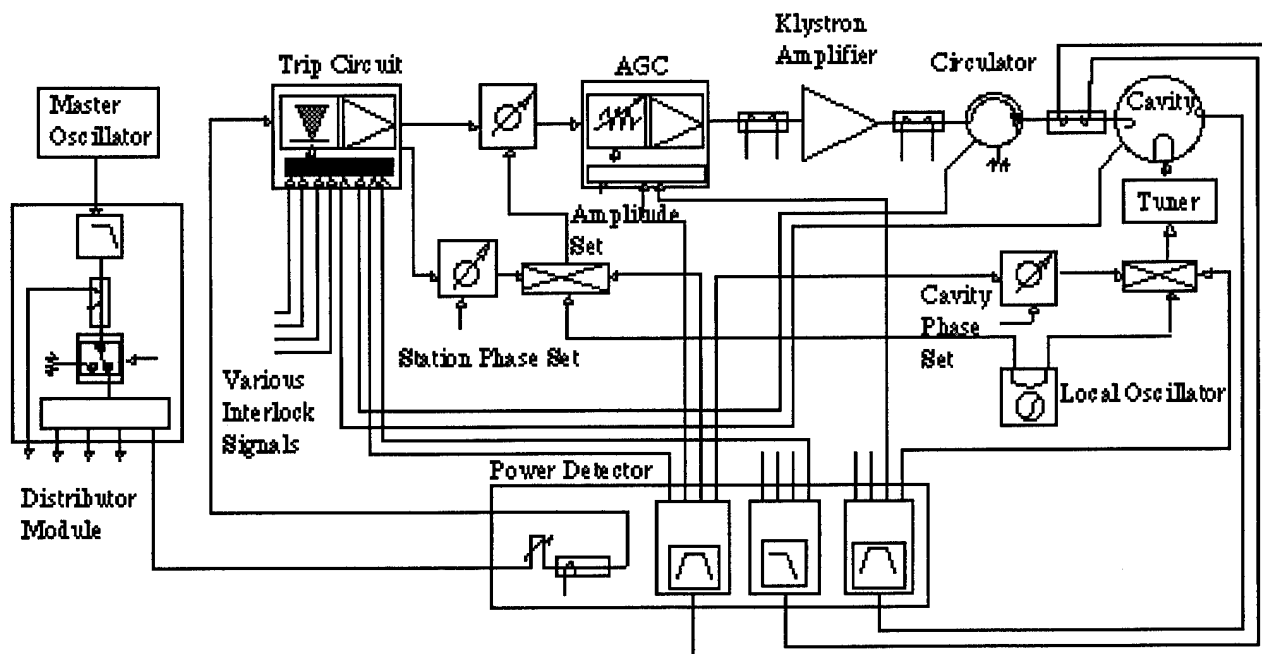


Fig. 1. A schematic diagram of the PLS storage ring RF system

Table 1 shows the present status of the PLS RF system installation.

Table 1. Current status of the PLS RF system

Klystron Amp.	Three cw-60 kW
Transmission Line	6 1/8" coaxial line
Number of Cavity	Three
Shunt Impedance	>8 MW
Unloaded Q	>35,000
Coupling Coeff.	1.8
Accelerating Volt.	400 kV/cavity

2. PLS RF SYSTEM ARRANGEMENTS

A RF station consists of one klystron amplifier, a circulator, a coaxial switch and a cavity connected by 6 1/8" coaxial transmission line.

The klystron amplifier is the 60 kW continuous wave(cw) TV transmitter manufactured by HARRIS. The driver input signal is set to 13 dBm maximum and the total gain is over 70 dB. The nominal beam voltage is 24 kV and the collect current is 5.8 A. For safety reason some important interlock loops are connected to the high voltage switch directly to shut it down as an emergency occurs.

The high power circulator was purchased with coaxial ports. The temperature control unit is provided for the good RF performance since the ferrite saturation magnetization is temperature dependent. The circulator provides a good isolation of the reflected power from the cavity to the klystron amplifier. The coaxial switch was installed after circulator to achieve a flexible operation and perform an independent test of the power system by simply selecting switch between the cavity and the water load.

The total length of the transmission line from the klystron amplifier to the cavity is less than 15 meter and the attenuation should be less than 0.5 dB. The measured attenuation is 0.13 dB.

The nose-cone type single cell cavities are installed and show good electrical and mechanical performance up to 70 kW of cw power. The cylindrical-shape ceramic window is used for the input coupler, which has a transition from WR-1500 waveguide to the coaxial structure. A disk-type window is currently being developed. The cavity HOM(higher order modes) suppressor is just a dummy block of which length can shift the dangerous frequencies if it is determined properly.

The impedance measurement stand was set up to assess the beam effect of the various vacuum components. The longitudinal impedance budget of the PLS storage ring is 2 Ω and the measurements were carried out in the frequency domain using the synthetic pulse technique[2]. The analysis of the measured data is underway and the total impedance seems to be within the budget. The ring impedance measurement is planned to be performed near future.

The low level system was improved from the Daresbury-designed prototype: change the local oscillator to the PLL synthesizer for flexible variation of the IF frequencies, use

constant impedance hybrid-type phase shifter for precise phase control with linearizer, and more redundant safety interlock control circuit, etc. The development of the precision oscillator and fast feedback loop are undertaken.

The VME system was adopted for the data acquisition and hardware control for the PLS storage ring. The UNIX-based control software which has the graphical user interface has been developed. All the RF components can be controlled and the system operation can be monitored remotely from the main control room.

The high power system and the cavities were cooled by the 25 degrees in Celcius low-conductivity-water(LCW). The cavity cooling temperature is regulated within 0.1 degree and able to be varied in 5 degree range independently. This is useful to shift the HOM frequencies

3. OPERATIONAL CHARACTERISTICS

In the beginning of the storage ring commissioning, single RF station was operated to make the problems usually confronted in the early phase simple. As the stored current increased, one more station was added. At the final week in 1994, three stations were fully operated to store 300 mA with 1.2 MV of the accelerating voltage.

Figure 2 shows the accelerating voltage and cavity input power of a cavity as a function of the amount of the stored current. Since the beam loading compensation was being worked, the accelerating voltage was kept constant as the input RF power increased gradually. For 400 kV of the accelerating voltage per cavity, 20 kW is required for cavity dissipation and 22 kW more is required for beam loading per each 100 mA increment of the stored current. Therefore for 400 kV of the accelerating voltage per cavity, three cavities can hold 500 mA of electron bunches.

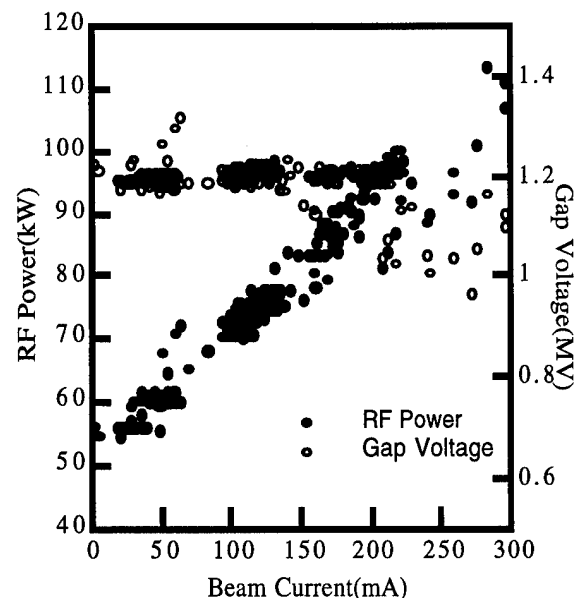


Figure 2. Beam current determines the gap voltage and the input RF power (Beam Loading Compensation).

Figure 3 shows the available operating regime with given RF power as the accelerating voltage and the beam energy change. RF acceptance is normally calculated as a function of the RF voltage. The calculation showed that 2.0% of the bucket height and 100 hrs of the Touscheck lifetime would be achievable with 1.2 MV of the accelerating voltage. Since the lifetime at present state is governed by the vacuum pressure, more photon conditioning is required to take advantage of the higher accelerating voltage.

The signal for the low level feedback loop was picked up from the cavity input port. In this way the beam effect on the control loop could be minimized. However, the beam loading compensation should be done in other way. A pickup signal from the cavity monitor port is used as the reference signal for regulating the accelerating voltage assuming that the same accelerating voltage always couples same amount of signal amplitude to the monitor probe. Since processing of data for this method is little slow, for fast injection it's hard to follow the beam current increments for beam loading compensation. Another method will be tested, in which the DCCT current signal becomes the reference and the required RF power for the beam loading is calculated and set it directly through the automatic gain control (AGC) loop in the low level system.

The phase and amplitude of the cavity input power were controlled within 0.1 degree and 0.5% of variation, respectively.

Phase between stations were adjusted by balancing the input power to all operating stations to share the same portion of the total beam loading.

The RF straight section where cavities were installed has four sputtered ion pumps (800 l/min total) and one roughing system. Four flexband bellows and two transitions and gate valves make the whole system assembly easy. The vacuum pressure after baking and conditioning is about sub-nanoTorr without beams. As the stored current increases, the pressure increases, too. However, since the dissipated power to the cavity is kept constant though RF power input to the cavity increases, the

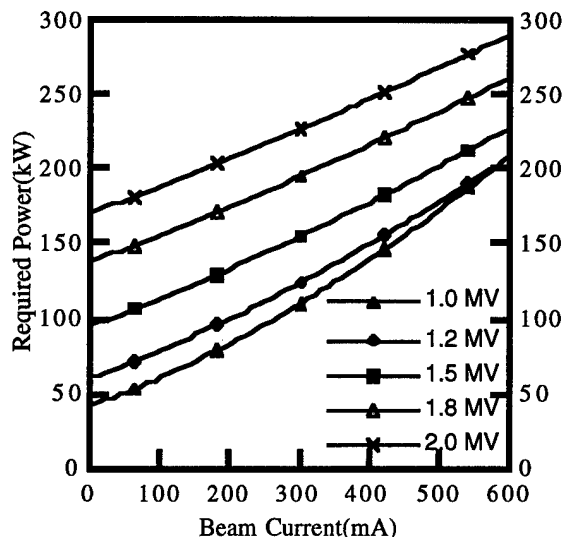


Figure 3. Operating window determined by the beam current, RF power and the accelerating voltage.

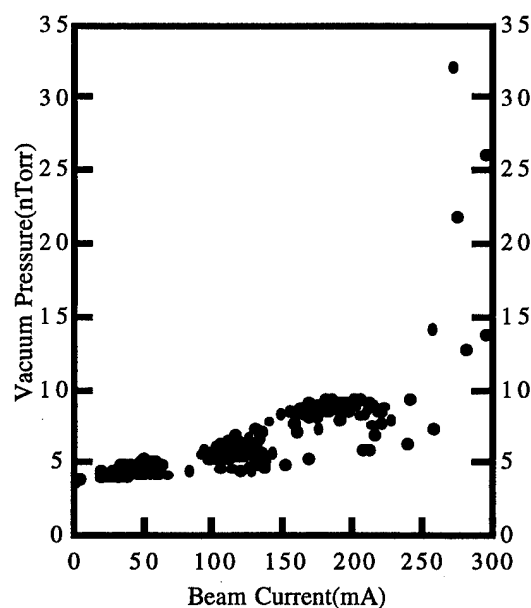


Figure 4. Pressure change due to the photon-induced-desorption (PID).

increment of the vacuum pressure comes mainly from the photon induced desorption. Figure 4 shows the pressure change during the variation of the stored current. Some vacuum burst followed by high reflection occasionally occurred as the stored beam went on instabilities.

The multi-bunch instabilities occurred non-systematically during the beam storage, causing to limit the upper bound of the total stored current and/or beam loss. Simply changing cavity resonant frequency little by changing tuning angle allows us to identify which cavity are causing instabilities. Changing the temperature of the cooling water cures instabilities to some extent in most cases.

4. FUTURE PLAN

One more station will be added by the end of 1995. Total RF power becomes 240 kW which allows operations with higher RF voltage, meaning larger acceptances and longer lifetime.

A systematic study on the multibunch instabilities will be performed. Method like the RF knockout is considered to identify the seed frequencies causing instabilities.

Thorough measurements of the chamber impedances and ring impedance are underway. The analysis of the measured data will be presented elsewhere. Some calculations using computer codes will be done to clarify the obscurity of the measurements.

The low level and control system will be improved and upgraded for more stable and reliable operation in preparation of the normal operation phase for the synchrotron radiation users.

REFERENCES

- 1.M. Yoon, in this conference.
- 2.F. Caspers, "Beam impedance measurement by wire method using a synthetic pulse techniques," IEEE NS-32 (1985) 1914.

Acoustic Experimental Studies of High Power Modes in Accelerating Structure of Kurchatov SR Source

M.Gangeluk, A.Kadnikov, Yu.Krylov, S.Kuznetsov, V.Moisseev, V.Petrenko,
V.Ushkov, Yu.Yupinov

Russian Research Centre "Kurchatov Institute", 123182 Moscow, Russia

I. INTRODUCTION

The acoustic effects in metal constructions of accelerator electrodynamics structures permit to realize the undisturbing methods for determining of the electrodynamics characteristics of structures at nominal work conditions (at high RF-power level, for real temperature and vacuum distributions, with intense beam). These effects are registered reliably by acoustic pickups installed on external surfaces of structures.

II. MECHANISMS OF ULTRASOUND EXCITATION IN METAL WALLS OF ELECTRODYNAMICS STRUCTURES (ES).

Three main mechanisms of ultrasound excitation can be distinguished here: the ponderomotive mechanism [1], the thermoelastic mechanism by field [2] and the thermoelastic mechanism by electrons.

Thermoelastic mechanism of ultrasound excitation by field is caused by dissipation of energy of electromagnetic field penetrating in metal. Non stationary temperature distribution in pulse RF-field generates the stress wave traveling deep into metal. The stress wave amplitude σ , can be estimated by solving the boundary problem of the thermoelasticity [2]:

$$\sigma = \frac{1 + \mu}{1 - \mu} \cdot \frac{\alpha v_\epsilon}{c_p} \cdot P \quad (1)$$

where: heat capacity C_p , Poisson modules μ , linear heat expanding factor α and sound speed V_s .

The relative contribution of ponderomotive mechanism is increasing with metal conductivity and decreasing with field frequency.

Thermoelastic mechanism of ultrasound excitation by electrons is caused by RF-field energy take-off by electrons moving in vacuum, where their free path length is large enough, and transfer of this energy to surface layer of metal as a result of structure walls electron bombardment. Numerically this effect can be estimated by relation (1),

where instead of P the electron power density P_e must be substituted:

$$P_e = \frac{n_e mc^3}{\pi} (\epsilon - \arctg \epsilon) \quad (2)$$

where n_e -free electron density in vacuum and

$\epsilon = (eE) / (2\pi fmc)$ - perpendicular to metal surface RF-field electrical component amplitude E , charge and mass of electron e and m , speed of light c .

The relation (2) represents the additional to surface currents in metal walls mechanism of RF-field damping in ES - loading of RF-field by free electrons in vacuum. Free electron density is determined by RF-field rest gas ionization in structure volume and electron emission processes at surface of structure. First of all the acoustic effect of free electrons has been found in experiments at gas filled and vacuum sections of feeding wave guide at linear accelerator-injector of Kurchatov Synchrotron Radiation Source.

System of distributed along structure acoustic pickups allows to determine the time and region of discharge origins and to measure the intensity distribution of emission processes on internal surfaces of structure.

III. ACOUSTIC LOCATION OF RF-BREAKDOWNS IN LINAC ES STRUCTURES

The RF-breakdown acoustic effect in metal walls of ES is caused by non stationary heat evolution in breakdown region. After breakdown initiation the acoustic perturbation in breakdown region propagates along whole construction of the ES and can be registered by acoustic monitors. The propagation time of acoustic perturbation front determines the distance breakdown region from monitor position.

Characteristic for KSRS linac, where the lengths of accelerating structure and RF-power supply waveguide are much greater than their cross section dimensions, the problem of breakdown region location can be solved by use of three acoustic monitors. If the ES is longitudinally uniform, the signals of three monitors, distributed along structure with known positions, define all three unknowns: the moment and region of breakdown initiation, the speed of perturbation front. It is important to note, that RF-breakdowns can excite in structure walls different initial acoustic perturbations, which can propagate along the structure with different group speeds. That is why, the procedure of complete self-consistent calculations, based on signals of all three monitors, is necessary for location of

every concrete RF-breakdown. For the pulsed RF regimes the problem of breakdown location

At the KSRS linac two acoustic monitors are installed at the edges of long uniform sections of monitored electrodynamics structures. The third, middle monitor is movable and can be displaced into breakdown region the accuracy of breakdown location 1 cm can be achieved. The RF-breakdown monitoring system is synchronized by synchropulses of linac.

The acoustic RF-breakdown monitoring system operational regime on real time, is illustrated in Fig.1.

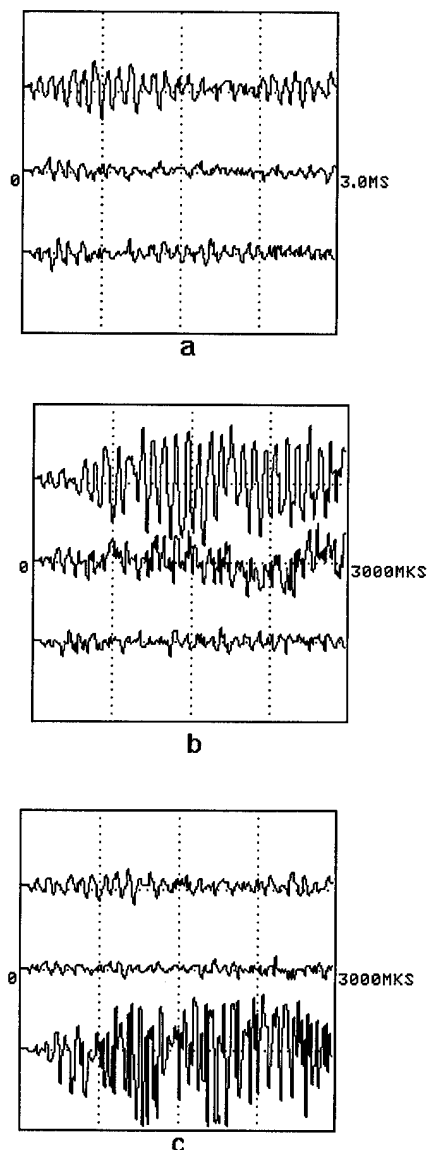


Figure 1 (a, b, c): Signals of the three acoustic pick-up on the accelerating structure

Every digital oscilloscope screen copy represents here the signals of three monitors placed in the beginning of the structure (upper curve), in the middle of the first half of the structure (middle curve) and in the middle of the structure (down curve). Signals in Fig.1a are the stable response of the acoustic system on RF-pulses in accelerating

structure without breakdowns. Signals in Fig.1b and Fig.1c locate the breakdowns, accordingly, in the beginning of the structure (0,4 m away from the edge) and near to the RF-power input in the middle of the structure.

IV. EXPERIMENTAL STUDIES OF DISK-AND-WASHER (DAW) ACCELERATING STRUCTURE UNDER HIGH RF-POWER OPERATING CONDITIONS

Electrodynamics characteristics of accelerating structures under high RF-power operating conditions can essentially differ from those, which are experimentally investigated and tested at low RF-power levels, because of real temperature and vacuum non uniform distributions, electron emission, residual gas ionization, low energy particle flows and dark currents. Acoustic monitors installed at external surfaces of accelerating structure provide the detailed information on RF-field and physical processes inside the closed volume of accelerating structure.

One of the vital problems, which must be solved in acoustic study of structure, is the problem of local measurements. It is necessary to measure the intensity of ultrasound, excited in structure metal wall only in the vicinity of the external acoustic monitor position. Local measurements allow to investigate the distributions of acoustic effects along the internal surfaces of structure walls and, hence, the distributions of RF-field, electron emission, low energy particle flows and accelerated particles losses in accelerating structure.

The local measurements method, based on the fact, that the speed of sound is finite, was developed and used for experimental studies of electrodynamics characteristics of the traveling wave accelerating structure with slow varied along longitudinal axis geometry at high RF-power operating conditions.

The accelerating structure of KSRS linac is the standing wave DAW 6 m long structure at 2,8 GHz with RF-power input in the middle. The only control coupling loop is installed near the power input.

The DAW structures containing the massive disks determine in constructions the existence of the acoustic oscillation modes corresponding to the own acoustic oscillations of disks. In some specified sense, a structure construction can be considered as a chain of coupled high Q identical acoustic oscillators. A short pulse acoustic excitation of any disk is attenuated on propagation along a structure strongly because of resonant energy dissipation by near-by identical disks.

These specific strongly attenuated acoustic excitations in a DAW structure construction can be observed experimentally, for example, after short pulsed RF-breakdowns in a structure (the duration of an RF-breakdown is limited by the duration of RF-pulses in structure). The typical situation after the RF-breakdown at disks is shown in Fig.2c. The first to the RF-power input acoustic monitor registers the

breakdown (down curve). This breakdown is not registered by the next monitor (middle curve), while the next monitor is 0,8 m distant from the first one only. The signal of the next monitor is reduced in comparison with the situation without breakdown in Fig.2a because of RF-field degradation in structure. At the same time, the arbitrary acoustic perturbations excited by the vibrator at external surface of the structure propagate with slow attenuation a few meters along the structure.

The existence of the acoustic modes corresponding to the own acoustic oscillations of disks in DAW structure constructions allows for pulse RF-field regimes to formulate the spectral approach to the local acoustic measurements at structure: in spectrum of registered short pulse acoustic excitation, the intensities of lines at the own acoustic frequencies of disks are determined by the acoustic effects at a few disks near the acoustic monitor position only. In addition, the proportions of these lines intensities in spectrum characterize the type of the pulse mechanical stress on disks. Spectral local measurements are very sensitive and noise protected.

The own acoustic disk oscillations in a separate cell of KSRS linac accelerating structure have been investigated at the stand. The cell was placed in permanent external magnetic field with magnitudes up to 0,2 T, the acoustic oscillations were excited by 12 A pulses of current in disk. Measurements in different configurations of magnetic field have allowed to distinguish a few and electron emission. In this case, the slope of the straight line corresponding to the cold structure electrodynamic characteristics is given in Fig.2 by two successive experimental points for rapid RF-power level increasing in structure.

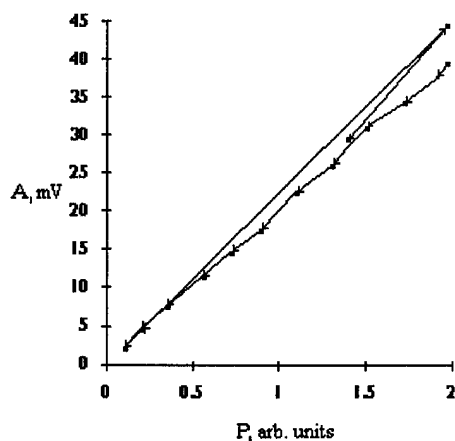


Figure 2: Dependence of acoustic spectrum on the control coupling loop signal squared.

At high power level, the heat transfer, ionization and emission processes in structure are reaching the steady state and the acoustic signal is reducing.

In Fig.3, the control loop signal squared and the signal of acoustic monitor installed 1 m distant along the

structure from the control loop are presented as functions of RF-field frequency.

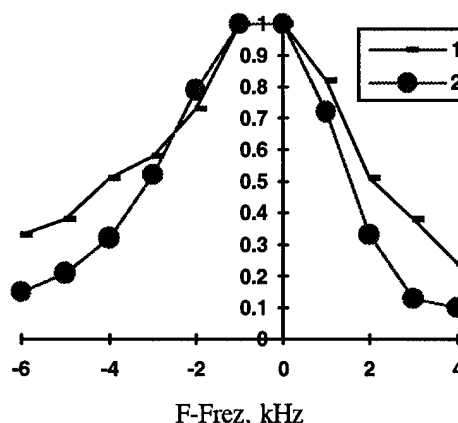


Figure 3: The control loop signal squared and the signal of acoustic monitor.

Experimental data are normalized in Fig.3 to own disk frequencies in the range 60-120 kHz.

At present the developed spectral method of acoustic local measurements is used at KSRS linac accelerating structure. In the Fig.2 is shown the dependence of the acoustic spectrum 98.8 kHz line intensity on the control coupling loop signal squared. The sequence of measurements is indicated by arrowed lines, the time intervals between every two successive measurements is less than 4 min. In the operating pulse mode with pulse duration 8 mks and pulse repetition rate 1 Hz, the peak RF-power level is varied in the range up to 7 MW.

The observed hysteresis in Fig.2 can be explained, if the RF-field amplitude distribution along the structure depends on the RF-power level in structure. This dependence may be caused by non uniform temperature distributions in structure construction elements (60 % of RF-field power is dissipated at disks installed in vacuum) or RF-field loading by free electrons maxima at resonance.

V. REFERENCES

- [1] Yu.V. Kaprin, V. I. Moiseev, V. V. Petrenko. Acoustic effects of pulsed electromagnetic RF-field -Atomnaja energija, 1987, v. 63, n. 6. p.p. 400-402
- [2] V. I. Moiseev, V. V. Petrenko. Comparative characteristics of aconstic excitation mechanisms by pulsed RF-field. -VANT, 1990, n. 11(19), p.p. 135-136

COMPUTER SIMULATIONS OF A WIDE-BANDWIDTH FERRITE-LOADED HIGH-POWER WAVEGUIDE TERMINATION*

J. Johnson, R. Rimmer, J. Corlett,
Lawrence Berkeley Laboratory, 1 Cyclotron Road, Berkeley, CA 94720 USA

ABSTRACT

We describe our experience of using MacNeal-Schwendler's finite element code EMAS[®] [1] to design a 10 kW ferrite-loaded rectangular waveguide termination [2]. We require a VSWR of <2:1 over a bandwidth of 700 MHz to 3 GHz. We present results in the frequency domain for several distributions of ferrite tiles in the waveguide.

I. INTRODUCTION

High power, broad-bandwidth waveguide loads are required to terminate higher-order-mode(HOM)-damping waveguides on the PEP-II B factory RF cavities [3]. We use MacNeal-Schwendler Corporation's (MSC) 3D finite element code, EMAS[®] to calculate the return loss and power distribution for several configurations of flat ferrite tiles against the walls of a rectangular waveguide. MSC's XL[®], version 3B, is used for pre- and post processing. Ferrite was chosen for its ability to absorb electromagnetic energy. EMAS[®] was chosen for its ability to model lossy ferrite. The goal is to distribute the power over the tiles to minimize hot spots that might cause outgassing or breakage. We believe that a power loss density of 20 watts/cm² or less is sufficient but attempt to achieve 10 watts/cm² or less.

Bandwidth	700 MHz - 3 GHz
Waveguide f_c	600 MHz
VSWR	2:1
Power	10 kWatts
Dimensions (mm)	25H x 250W x 500L
Bakeable	150° C
Ultra High Vacuum Compatible	

TABLE 1: Specifications

II. MODEL

A. Geometry, Elements and Material

Our model is one meter long with the ferrite distributed in the last 500 mm. Figure 1 shows the waveguide geometry with a vertical symmetry plane that

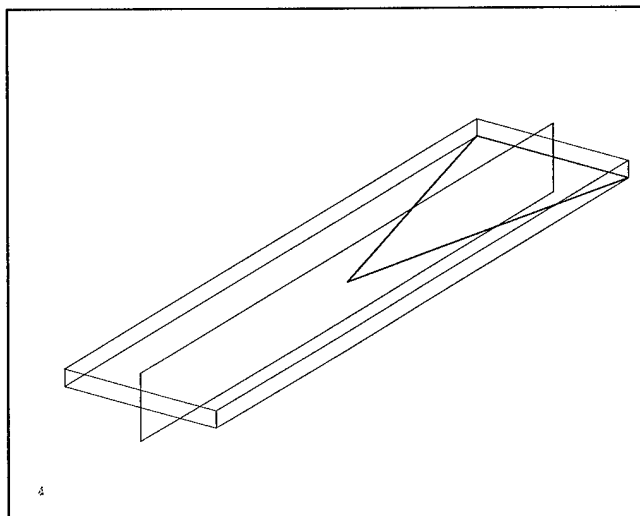


Figure 1: Waveguide model showing the symmetry plane and a 1-mm thick triangular ferrite wedge.

halves the model size and the number of elements and grid points. This and the appropriate boundary conditions reduce the problem size, hard disk storage requirements and computation time. Space constraints in the storage ring tunnel require the actual load's length to be less than 500 mm. The model is longer to separate the ferrite from any anomalous fields near the excitation plane at the open end of the waveguide.

All waveguide walls are considered ideal (i.e., lossless). We ran simulations for several ferrite thicknesses, but in practice found substantial cost savings with a commercially available ferrite that is 25 mm x 25 mm x 4 mm. We typically use two linear (*hexa* or *tetra*) elements across the ferrite thickness such that a 4 mm thick material has two 2-mm thick elements. We also examined thicknesses of 1, 2, 3 and 6 mm. There is a single layer of (vacuum) elements the same size above the ferrite. The remaining volume to the opposite wall is equally divided into (typically) four layers. To maintain thinner elements across the waveguide cross-section would increase the number of elements and problem size beyond our hard disk capacity without increasing accuracy.

The ferrite's frequency-dependent complex permeability μ^* , and permittivity ϵ^* , [4], are used and are assumed to be isotropic (though EMAS[®] allows anisotropic properties).

*This work was supported by the U.S. Department of Energy, under contract No. DE-AC03-76SF00098.

B. Excitation

The loads, while broadband, are excited at distinct frequencies and power levels. The power in each mode depends on the current and bunch configuration in the storage ring; we used the typical values shown in table 2, based on measured cavity mode spectra for modes below the beam pipe cut-off frequency.

Frequency (MHz)	Power (Watts)
714	1200
952	100
1190	200
1428	150
1666	700
1904	700
2142	400
Total Power	3450 Watts

TABLE 2: Excitation Frequencies and Power

We assume propagation in the TE_{10} mode at these frequencies and calculate the equivalent H fields at these power levels [5] as:

$$P_z = \text{Re} \left[\frac{1}{2} \int_0^b \int_0^a (E \times H^*) dx dy \right] \bar{u}_z$$

$$= \frac{1}{4} E_{ox}^2 \frac{\beta_g}{\omega \mu_0} ab,$$

where a and b are the waveguide height and width and

$$H_y = \frac{E_{ox}}{Z_g} \sin\left(\frac{\pi y}{b}\right) e^{-\beta_g z},$$

$$\text{where } Z_g = \frac{\omega \mu_0}{\beta_g} \text{ and } \beta_g = (\omega^2 \mu_0 \epsilon_0 - \frac{\pi^2}{b^2}).$$

These H-field values are applied (using EMAS[®] surface H-field excitations) in a sinusoidal distribution across the waveguide end. Appropriate boundary conditions are applied and we use EMAS[®]'s AC Analysis solver for the general solution. Computation time is on the order of a few minutes on a SPARC 20, Model 51.

III. RESULTS

Once the model is solved we plot the electric and magnetic fields, power loss density and calculate the total power loss in the ferrite. Figure 2 shows electric field contours in volts/meter in the waveguide when the model shown in figure 1 is excited at 714 MHz and 1200 watts. Figure 3 shows power loss density in watts/m³ in the ferrite of figure 1. The return loss is -17dB and within

specifications, however, there is region of power loss >55 watts/cm².

The integrated power dissipated in the ferrite elements was within 10% of the excitation (input) power and deemed sufficiently accurate. The desire to reduce high power concentrations was then used to guide design of subsequent models. Some return loss calculations were compared with solutions from Hewlett-Packard's HFSS[®] and found to be in agreement.

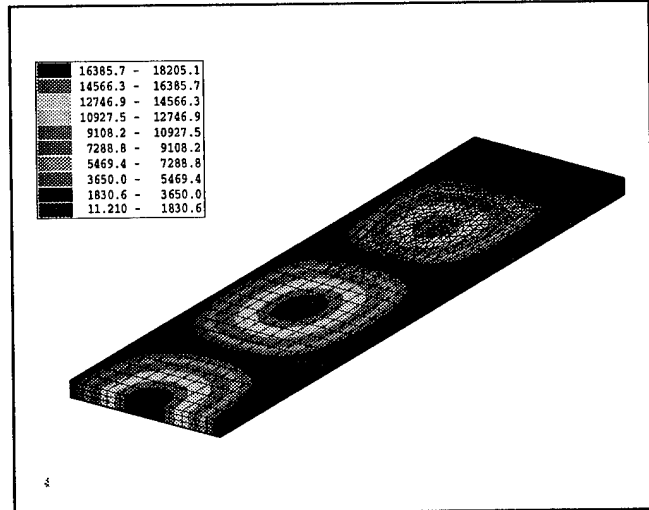


Figure 2: Electric field contours, in volts/meter. This shows E-field attenuation toward the waveguide end (upper right). Excitation is at lower left and at 714 MHz, TE_{10} mode.

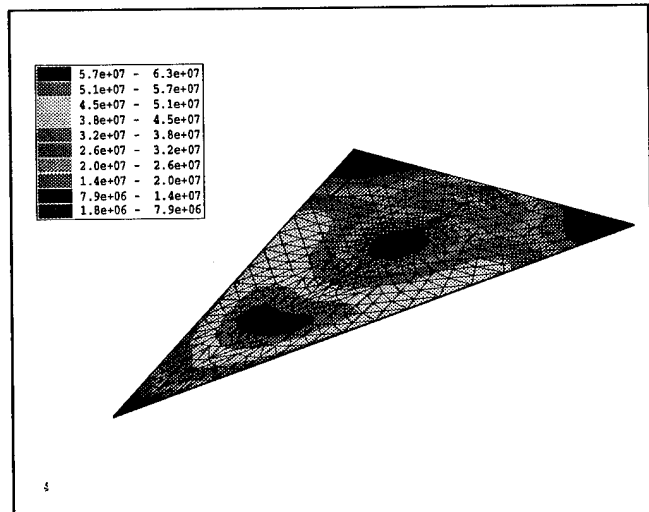


Figure 3: Power loss density in watts/m³ in ferrite wedge of figures 1 and 2.

The problem with achieving an even distribution of power in this configuration is that the ferrite is such a

good absorber. With any thickness greater than 1 mm, the power never penetrates sufficiently along the load to average under 10 watts/cm².

Better results were achieved with strips as shown in Figure 4. The power loss density exceeds 25 watts/cm² in a relatively small region, figure 5. Return loss is -17dB. It should be noted that the total surface area in this configuration is about 520 cm². Therefore, with 10 kwatts input power distributed evenly over the ferrite, the power loss density is about 20 watts/cm².

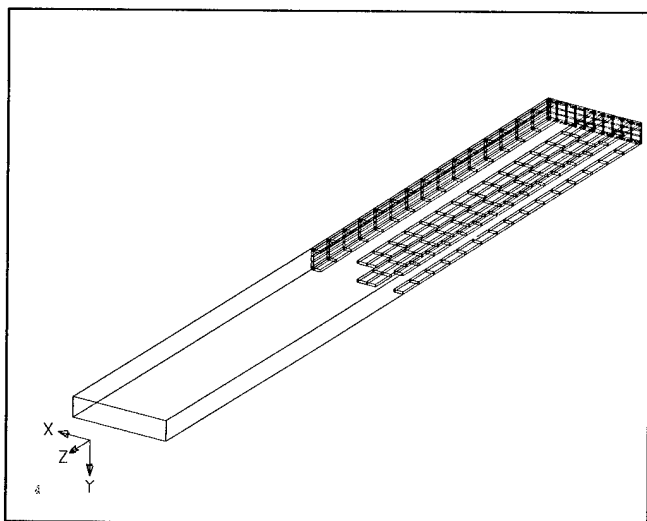


Figure 4: 3 mm thick ferrite strips 1/2" and 1" wide. The symmetry permits modeling half the termination.

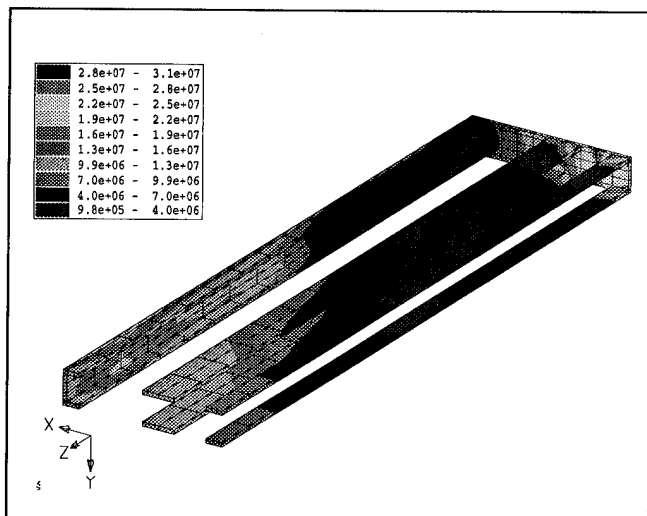


Figure 5: Power loss density exceeds 20 watts/cm² in a relatively small area. Return loss = -17dB.

IV. COMMENTS ON EMAS[®]/XL

The benefits and difficulties of computer modeling are well known. The codes tend to have steep and long learning curves and to demand lots of computing resources and time to model and generate meshes. MSC

has developed this and similar software for over 30 years and the code's capabilities and complexities reflect this. We scarcely scratched the surface of EMAS[®] or XL[®] capabilities; e.g., in addition to the EMAS[®] AC Analysis module we used, there are at least 15 other solvers and many attributes we didn't need (or perhaps didn't know we needed). Though it was difficult in the beginning, once we became sufficiently adept with XL[®] and EMAS[®] it was easy to generate a variety of geometries in our admittedly very simple models.

MSC has now integrated an advanced solid modeling technology known as the ConceptStation[®] with EMAS[®] (and other MSC FEA codes). The ConceptStation[®] is a solid modeler that offers an intuitive interface with pre- and post processing and a host of other capabilities. Thus the steep learning curve and the difficulties with generating models and meshes have been addressed.

V. CONCLUSIONS

Though we have not yet achieved our design goal the simulations lend considerable insight to our problem. A lossy dielectric and ferrite combination is to be used in the PEP-II cavity HOM loads [2].

VI. ACKNOWLEDGMENTS

The authors wish to thank Jim Neuner at MSC's helpline for his invaluable assistance on numerous occasions. We would also like to thank Kurt Kennedy and John Meneghetti for testing the ferrite's thermal characteristics.

[1] ElectroMagnetic Analysis System, Version 3, MacNeal-Schwendler Corporation, 815 Colorado Boulevard, Los Angeles, CA. 90041

[2] R. Pendleton, "High Power Higher-Order-Mode Load Design for the PEP-II B-Factor RF Cavity", these proceedings.

[3] R. Rimmer, et. al., "An RF Cavity for the B-Factor", Proc. PAC, San Francisco, May 6-9, 1991, pp819-821

[4] W. Barry, J. Byrd, J. Johnson, J. Smithwick, "A Collection of Complex Permittivity and Permeability Measurements", Proc. MAMA Conference CEBAF, Feb. 22, 1993

[5] S. Liao, "Microwave Devices and Circuits", Prentice-Hall, 1980, p109

EFFECTS OF TEMPERATURE VARIATION ON THE SLC LINAC RF SYSTEM

F.-J. Decker, R. Akre, M. Byrne, Z. D. Farkas, H. Jarvis, K. Jobe, R. Koontz, M. Mitchell,
R. Pennacchi, M. Ross, H. Smith, SLAC*, Stanford University, Stanford, CA 94309 USA

ABSTRACT

The rf system of the Stanford Linear Collider in California is subjected to daily temperature cycles of up to 15°C. This can result in phase variations of 15° at 3 GHz over the 3 km length of the main drive line system. Subsystems show local changes of the order of 3° over 100 meters. When operating with flat beams and normalized emittances of 0.3×10^{-5} m-rad in the vertical plane, changes as small as 0.5° perturb the wakefield tail compensation and make continuous tuning necessary. Different approaches to stabilization of the RF phases and amplitudes are discussed.

I. INTRODUCTION

Since going to flat beam running in 1993, where the vertical emittances can be as low as $\gamma\epsilon_y = 0.2 \times 10^{-5}$ m-rad at the end of the Linac, all tolerances have to be revised to keep the machine stable. Here we are mainly talking about the slow drifts and day-night variations and not about the short term jitter. These changes can be observed with the history plot feature of the SLC control system, where many important parameters are monitored and their value saved every 6 minutes. About 40 parameters are changing with a daily rhythm and it is a numbers game to figure out which are the most important ones. The other important issue is the mechanism by which these changes might influence the emittance variation. The wakefield tail compensation procedure is very sensitive to any energy change. This has concentrated the studies to RF variations in phase and amplitude, which made a closer look on the tuning procedure of the SLED-cavities necessary. The different sources, the sensitivity, and the SLED tuning are discussed in detail.

II. CHANGING PARAMETERS

Around 40 parameters which are changing daily can be put into three categories: The incoming conditions of the beam, parameters in the Linac, and the outgoing conditions.

A. Incoming beam conditions

The incoming beam might change in first order in intensity, orbit, energy and phase, and in higher order in bunch length and transverse distribution, to influence changes seen in the linac.

B. Linac sources

In the linac there are magnets, accelerating structures and BPMs, which can change the beam via feedback. The modulators, klystrons, SLED-cavities, wave guides, and the actual accelerating structures change the beam energy. Additionally there are water regulations, phase detectors, timing issues, and more.

C. Outgoing beam measurements

The outgoing beam can influence the performance of the linac via feedbacks, which hold the energy constant in the ARCs and in the scavenger extraction line. In next order there might be changes (e.g. by collimators) in the acceptance to background and energy spread which will make a linac change necessary.

All these can be responsible for changes. Magnets change of the order of 10^{-3} or less, which helps to keep the in- and out-going conditions stable. Studying the numbers has given some hints that a 1.5% energy variations might be the biggest source. This can come from RF amplitude or phase changes.

III. EMITTANCE SENSITIVITY

The flat beam emittance of 0.2×10^{-5} m-rad is achieved by a delicate cancellation with linac bumps [1] down from about 2.0×10^{-5} m-rad. These "bumps" consist of betatron oscillations over about 6 wavelength (2200° in betatron phase). A 1% beam energy change, equals a 1.5° RF phase

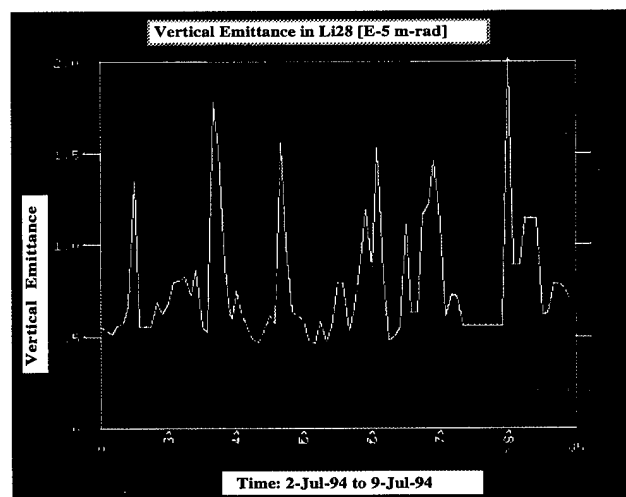


Figure 1: Day-night variations of the emittance. At the end of the linac changes of 300 % of the minimum emittance can be observed.

*Supported by the DOE, contract DE-AC03-76SF00515.

change at $\cos 20^\circ$ (BNS-phase), will cause a 22° change, which will be 11° on average. This will regenerate a beam tail, giving an emittance growth of $\Delta\epsilon = 2.0 * \sin 11^\circ = 0.4$ in units of 10^{-5} m-rad. Fig. 1 gives an example of the earlier part of the run where no particular interest was taken to emittance growth.

IV. SLED TUNING

The SLED system provides nearly a doubling of the rf field strength [2]. The energy is stored in two high Q cavities, which are sensitive to temperature changes. Many steps have been done to keep it stable: water cooling with temperature stabilization of about $0.1-0.2^\circ\text{C}$, and additional isolation. Studying the pulse form during the charging and discharging of the SLED cavities has led to some ideas why the system is not tuned to its optimal level.

A. Basic SLED

The outputs of two SLED cavities are combined in a 3-dB coupler. The output of this coupler is the SLED output pulse whose amplitude and phase varies with time. If the klystron phase does not vary during the charging of the cavities, the amplitude dips to zero and the phase changes by 180° at about $2 \mu\text{s}$ after the rf turn-on. The phase remains constant and equals the klystron phase after it has been flipped 180° .

B. SLED tuning details

The tuning angle is defined as

$$\Psi = \arctan\left(2Q_L \frac{f - f_r}{f}\right),$$

where f, f_r are respectively the operating and resonant frequencies, and Q_L is the loaded quality factor.

If the klystron phase does vary during the charging, as is the case at SLC, the amplitude doesn't reach zero when the cavities are tuned, but the difference in phase of the SLED output before and after the 180° klystron phase flip is still a minimum. If the two cavities are tuned to different frequencies, the amplitude can reach zero, but would lead to an incorrect tuning procedure.

An observed phase change from before to after the klystron phase flip gave an indication, that the SLED cavities were not tuned correctly. The reason for this could have been that the cavities were tuned at another temperature, but retuning it with the same procedure gave the same result. It had to do with something else. Since the rf is not switched on by the subbooster, but rather by the voltage of the modulator, the phase of the klystron changes by a huge

amount during this turn-on which fills the SLED cavities with a wrong phase. Therefore a 180° switch is not the optimum or the SLED cavities have to be slightly mistuned.

The cavities can be correctly tuned to resonance by minimizing the phase difference between the before and after the 180° klystron phase flip. This would also result in the highest peak field, since the two vectors (one from the klystron, one from the cavities) are aligned. Fig. 2 shows a typical rf pulse form in amplitude and phase generated by simulations for different tuning angles. The simulations assumed a phase change at the klystron of 100° from -5 to $-4 \mu\text{s}$ for the modulator, the normal 180° switch, and tuning angles Ψ of $\pm 20^\circ$ besides the tuned case.

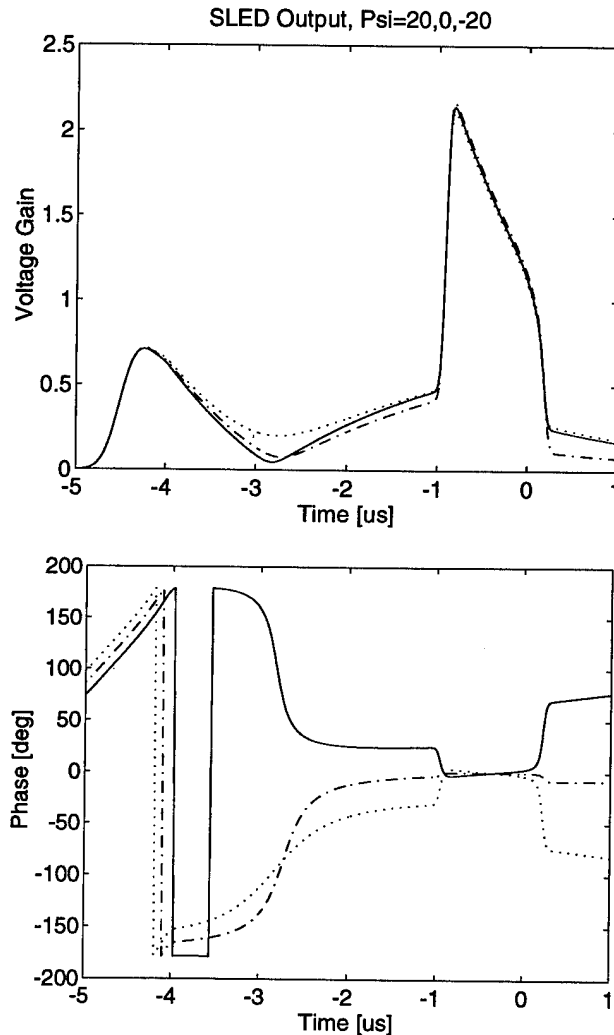


Figure 2: SLED pulse form in amplitude and phase. The amplitude rises slowly with the rising modulator voltage. Therefore the minimum amplitude doesn't touch zero before the peak at the 180° phase change. The tuning angles correspond to about a $\pm 0.5^\circ\text{C}$ temperature change.

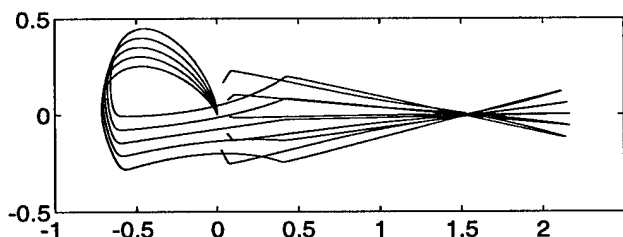


Figure 3: Vector diagram.

The voltage vector after the SLED cavity, with real (horizontal) and imaginary part (vertical), is plotted for five different tuning angles. The tip of that vector curves around for different times.

Figure 3 is a plot of the real and imaginary parts of the SLED output field vector, as time increases. The vector is a line from the origin to a point on the line. It starts at the origin, goes first up due to the klystron phase assumption, then the SLED cavities get finally filled with the right rf, it goes flat to positive values. Then the fast 180° switch takes place to above 2 times the original voltage, then it decays slowly to zero, by going exactly through a zero phase (flat) at about 1.5, where the phase is held constant in this simulation, like in the experiment.

C. Experimental detuning results

The SLED cavities are tuned by adjusting screws which deform the cavities and therefore change the tuning angle Ψ . A 90° turn corresponds to $\Psi = 37^\circ$ or 1 °C temperature change:

$$\Psi = \arctan(8.4 \cdot 10^{-3} \phi),$$

where ϕ is the mechanical angle in degrees. Figure 4 shows the rf and beam response for different screw rotations between $\pm 90^\circ$.

D. Temperature Sensitivity [3]

If the cavities are tuned to resonance, a 0.5 °C temperature variation will cause only a 0.5 % change, while a detuning equivalent to 0.5 °C will cause already a ten times bigger change of 5 %. If all cavities are detuned an equal amount, the normal energy management by scaling of the magnets (LEM) would compensate for that change, while differences in the variation are not corrected.

V. MAIN DRIVE LINE

The Main Drive Line (MDL) runs along the linac and feeds the 30 subboosters and the klystrons with a common phase reference. The changes in length are adjusted for by measuring the changes directly by a interferometer with a pulse along the line. But any power changes due to the

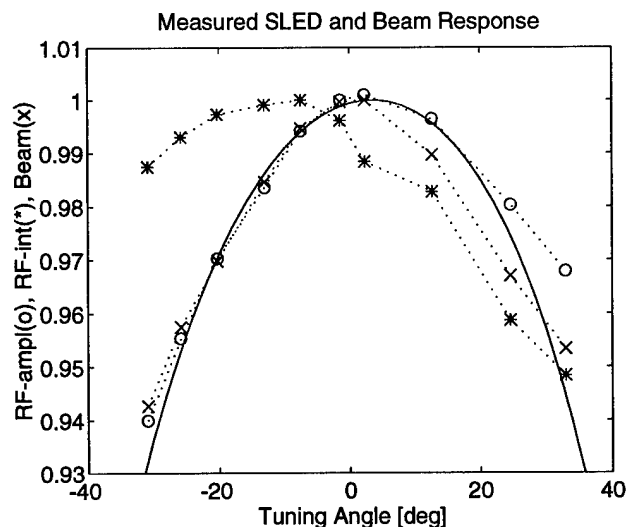


Figure 4: SLED outputs and beam energy.

The measured results from the beam energy (x) and rf amplitude (o) agree well with each other and with the simulated curve (solid). The integral over the significant pulse (*) or $E_{\text{no load}}$ represents pure the real behavior.

resistivity change of copper of 0.39 %/°C will generate a delay in the times-6 multiplier. An additional 4° phase change over the length of the linac is expected which is not corrected.

VI. DISCUSSION

Day-night temperature variation at the SLC linac is a major limit for delivering stable low emittance beams. Luckily most of the 1994/95 run happened during the rainy season with 1/3 of the peak temperature variations. The rf is the main contributor and especially a correct SLED tuning procedure seems to be critical, which might help to get the variations down by a factor of 2 to 3. Then additional causes like the power level of the main drive line get important.

REFERENCES

- [1] J. T. Seeman, F.-J. Decker, and I. Hsu, *The Introduction of Trajectory Oscillations to Reduce Emittance Growth in the SLC Linac*, XV Int. Conf on HE Accel., Hamburg, Germany, 1992, p. 879.
- [2] Z.D. Farkas, H.A. Hoag, G.A. Loew, P.W. Wilson, *Recent Progress on SLED, The SLAC Energy Doubler*, SLAC-PUB-1561, March 1975.
- [3] Z.D. Farkas, G.A. Loew, *Effect of SLED Temperature Changes on Effective Accelerating Field*, SLAC, CN-124 Oct. 81.

Broadband Coax-Waveguide Transitions*

T. Rizawa#, R. Pendleton

Stanford Linear Accelerator Center, CA 94309, USA†

ABSTRACT

A broadband coax-waveguide transition for the high power test of the PEP-II RF cavity HOM waveguides has been studied. The design requirements are that it must have a VSWR less than 2 over the frequency range 714MHz to 2500MHz and transmit 10kW average power from a 250mm * 25.4mm rectangular waveguide to a 50 Ohm coaxial line. A double ridged waveguide section with the same cut-off frequency as the rectangular waveguide has been selected to keep its impedance near 50 Ohm over the frequency range. HFSS calculation results and design of the transition are reported.

1. INTRODUCTION

Single cell cavities for the PEP-II B-factory high energy ring (HER) and the low energy ring (LER) have three higher order mode (HOM) ports in the configuration of waveguide (250mm * 25.4mm) with cut-off lower than all the HOM's of the cavity except for the fundamental accelerating mode. The port terminates with a broadband load capable of dissipation up to 10kW.

For low-power and high-power tests of the HOM damper waveguide with a load, a broadband coax-waveguide transition has been studied. Since it must have small reflection at the same frequency range as the HOM damper and must be also capable to the transmission up to 10kW, it can be thought as a "spare" option in case this HOM damper might face any inconveniences. By using the transition with a broadband window, a broadband load can be put outside of vacuum and can be treated easier.

Though studies of a broadband coax-waveguide transition already began more than thirty years ago for low power, a kW-order high power transition study has been performed only at INFN (Istituto Nazionale di Fisica Nucleare) for DAΦNE damped cavities. It is for up to 1kW transition.

On this study, the requirement for power transition is severer. It is getting obvious that higher power needs a bigger coax and that it gives more limitations for its design, while HFSS calculations are performed.

2. DESIGN REQUIREMENTS

The design requirements of the broadband coax-waveguide transition are that it must have a VSWR less than 2:1 over the frequency range 714MHz to 2500MHz and transmit 10kW average power from a 250mm * 25.4mm rectangular

waveguide to a 50 Ohm coaxial line. They are same as ones of the HOM damper.

In order to transmit up to 10kW over the range, the coaxial line is desired to be bigger than 3-1/8". If smaller, not only heating at inner conductor is too much, but also a broadband window design must be very difficult.

3. DESIGN OF TRANSITION

For such a broadband coax-waveguide transition, it is well known that applying a ridged waveguide is inevitable.

Because it has a flat impedance characteristics and also a higher cut-off frequencies of HOM's it's easier to make a match with a coaxial line and the effects of HOM's are very small.

Accordingly, it consists of two parts, which are a rectangular-ridged waveguide transition and a ridged waveguide-coax transformer.

3.1 Ridged Waveguide Design

To decide the ridged waveguide configuration is one of the most important parts of this study.

For the coax-waveguide transition parts, it is necessary to keep the cut-off frequency of any cross section same if it's for broadband. Therefore the ridged waveguide has the same cut-off of TE₁₀ mode, 599.6MHz.

And also its cut-off of the next higher mode coupled to a coax, TE₃₀ must be far higher than 2500MHz, which is the upper limit of the applied range. A rectangular waveguide with TE₁₀ cut-off frequency of 600MHz has 1800MHz cut-off frequency of the TE₃₀ mode. If it's ridged, cut-off of TE₃₀ is higher up to more than twice of it, which is higher than 2500MHz. But if the design of the ridged waveguide is not suitable, it will be below 2500MHz.

Furthermore, its impedance must be not very far from 50 Ohm, one of the coaxial line, over the range 700 MHz to 2500 MHz.

If we suppose a simple impedance connection between 50 and Z Ohm, its S-parameter of reflection is $|Z-50|/(Z+50)$. It is desired to keep the reflection ratio below 0.25 over the range in order to obtain VSWR<2. Thus, $83.3 > Z(\text{Ohm}) > 30.0$ is required over the range.

A ridged waveguide shape is defined with four parameters, width and height of a rectangular waveguide, ridge width and ridge gap.

For good broadband matching, electric field distribution should be as uniform as possible at a junction of a coaxial line and a ridged waveguide. From this point of view, a smaller coax is preferable. At least, a coax outer electrode must be smaller than ridge width, and possibly far smaller. Nevertheless, as the coaxial line must transit 10kW, it cannot be too small. Instead, we should make ridge width wider or ridge gap shorter. But ridge width is limited by the cut-off of TE₃₀ and ridge

On leave from Toshiba Corporation

* This work was supported by the Director, Office of Energy Research, Office of High Energy and Nuclear Physics, High Energy Physics Division of the U.S. Department of Energy.

†Stanford Linear Accelerator Center, Cont. DE-AC03-76SF00515

width is restricted by heating or multipactoring at the gap, though it is supposed to be suppressed with TiN coating.

Since outer diameter of a 3-1/8" coaxial line, which is enough capable for 10kW transition, is about 80mm, the ridge width should be more. At first, we tried with 128mm or 96mm ridge width. However, HFSS calculations never found a shape that satisfied all the criteria: TE10 cut-off about 600MHz, TE30 cut-off >> 2500MHz and an impedance which varied between 30(Ohm) and 83.3(Ohm) over the applied frequency region.

Then ones with 64mm ridge width were surveyed. Because it is smaller than the coax size of 3-1/8", a taper from a smaller coax, e.g. 1-5/8", at a junction to 3-1/8" is required at the transformer part. 1-5/8" coax is rather small for 10kW transmission, but cooling of inner conductor, as told later, is not difficult for this type of transformer.

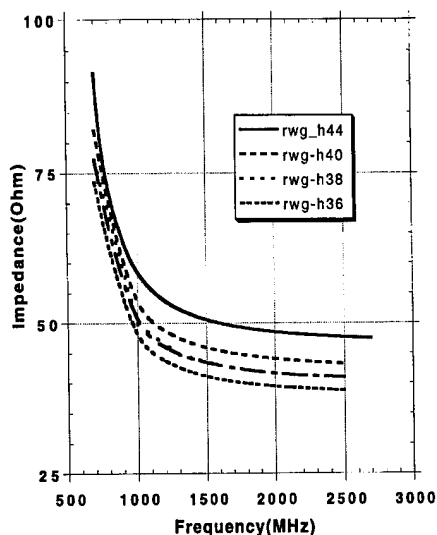


Figure 1 Ridged Waveguides Impedance Comparison

Figure 1 shows impedance calculation results with ridged waveguides with 64mm ridge width and 8mm ridge gap, whose cut-off of TE10 is about 600MHz. The best case is one with 36mm waveguide height and its cut-off of TE30 is more than 3GHz, high enough to think HOM effects are negligible.

All the calculations above have been performed for double ridged waveguides. Though single ridged waveguide might be possible, from the results so far, it is more difficult to obtain the good matching transformer to a coaxial line than with double ridged. Because, as shown later, where to stop ridges in the back cavity is one of the most important parameter for the part and in the best case, two ridges are stopped with different length.

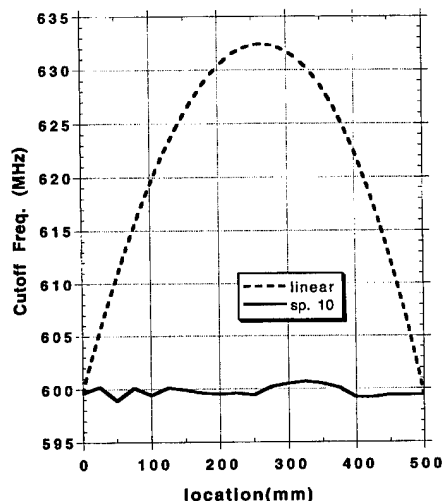


Figure 2 Cutoff Frequency Distribution

3.2 Rectangular - Ridged Waveguide Transmission

For a broadband transition, the cut-off frequency of any cross section must be kept as same. If the part consists of only linear tapers, cut-off distribution in the taper will be shown as a dotted line in Figure 2. (Assumed taper length is 500mm.) And S11 parameter will be calculated as a dotted line in Figure 3, which is not satisfactorily small because more reflection will be expected at the following transformer part. For lower reflection, the transmission part need to be separated into small pieces, all of whose cross section have almost 600MHz cut-off.

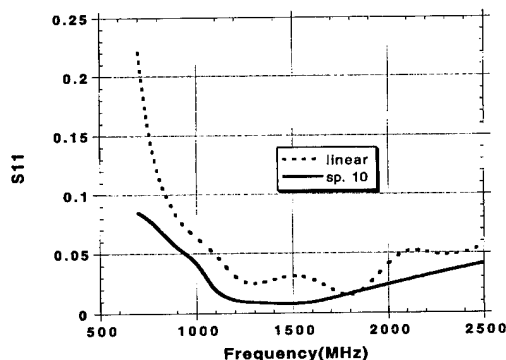


Figure 3 Effect of Taper Modification

HFSS calculations shows 10 pieces are enough to get the flat TE10 cutoff distribution within 599.8+0.9MHz and smaller reflection, which are shown as solid lines in Figure 2 and 3, respectively.

3.3 Ridged Waveguide - Coax Transformer

In a regular rectangular waveguide-coax transformer, as the impedance of the ordinal guide is much higher than that of the coax, the inner conductor of the coaxial line must stop short of the opposite wall of the guide or touch side walls to prevent mismatch. On the other hand, the impedances of the ridged waveguide and the coax are nearly matched, thus the inner conductor must touch the far wall of the guide or top of the ridge for matching.

It provides a convenience to cool the inner conductor and the reason why a smaller coaxial line than 3-1/8" can be applied at the inner conductor short position on the far wall. An 1-5/8" coaxial line was selected. For a broadband window, however, a taper to 3-1/8" must be necessary.

This transformer design is not very easy because there are too many parameters. In order to make it simple, firstly only three parameter were surveyed. They are back cavity length (short length) and length of two ridges, which means where these two ridges stop in the back cavity. And after that, a taper of the inner conductor at its short position was optimized. Shape of the back cavity might be (and should be) optimized, but it would be very complicated and need a great number of calculations. Since the configuration satisfies the requirement has been obtained as Figure 4, the back cavity shape survey has not been done.

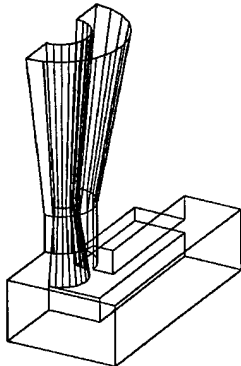


Figure 4 Optimized Configuration of the Ridged-Waveguide-Coax Transformer(1/2 symmetric model)

In the configuration in Figure 4, the ridged waveguide is transformed into 1-5/8" coax and changed to 3-1/8" by a 100mm taper with 50 Ohm. The upper ridge stops at the axis position of the coaxial line while the lower ridge stops at the end of the inner conductor taper. Figure 5 shows the HFSS results of reflection parameter S11 spectrum. The effect of the inner conductor taper is obvious when the solid line is compared with the dotted one for no taper.

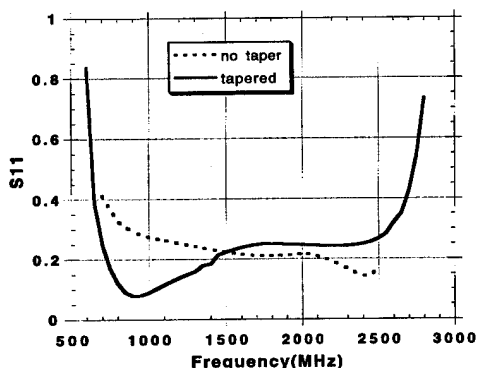


Figure 5 S11 Curves of the Transformer Part (Ridged Waveguide-Coax Trans., with and without Taper on Coax Inner Cond.)

3.4 Calculation Results Of Whole System

The whole system of the broadband coax-waveguide transition together with the transition and the transformer is shown in Figure 6, whose length is 640mm and height is 158mm. Figure 7 gives the HFSS calculation results of this configuration, showing VSWR<1.74 over the frequency range 714MHz to 2500MHz which satisfies the requirements.

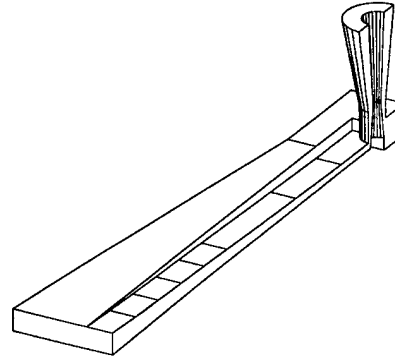


Figure 6 Broadband Waveguide-Coax Transition (1/2 symmetric model)

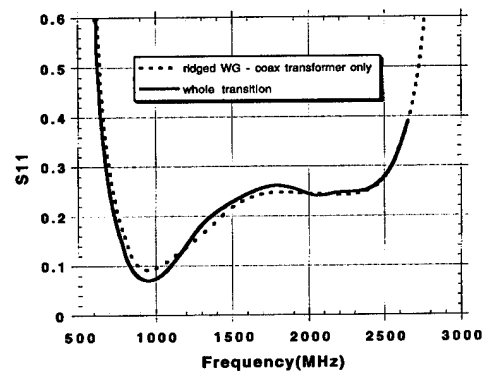


Figure 7 S11 Curves of the Optimized Configuration

4. CONCLUSION

A broadband coax-waveguide transition for the high power test of the PEP-II RF cavity HOM waveguides has been designed in order to fulfill that VSWR<2 at 714MHz to 2500MHz. Although such a broadband transition for up to 10kW average power has never been operated, the results indicate such a design could be used for broadband RF power tests.

5. ACKNOWLEDGEMENT

The author wishes to thank Heinz D. Schwarz and other colleagues for their assistances while working at SLAC.

6. REFERENCES

- [1] Paul J. Muenzer, "Broadbanding Coax-To-Ridged-Waveguide Transitions", Microwaves, Aug. 1964, pp92-97.
- [2] R. Boni et. al., "A Broadband Waveguide To Coaxial Transition For High Order Mode Damping In Particle Accelerator RF Cavity", LNF-93/075, Dec. 7, 1993.

RECTANGULAR MICROTRON ACCELERATING STRUCTURE

N.P. Sobenin, and V.N. Kandrunin, Moscow Engineering Physics Institute,
Moscow, Kashirskoe sh. 31, 115409, Russia.

V.N. Melekhin, Institute for Physical Problems, Russian Academy of Science, Moscow, Russia

A.I. Karev, Physical Institute, Russian Academy of Science, Moscow, Russia.

V.I. Shvedunov, Institute of Nuclear Physics, Moscow State University, Moscow, Russia.

W.P. Trower, Physics/Virginia Tech, Blacksburg VA 24061 USA.

To simplify construction and improve first orbit dynamics for our mobile 70 MeV Race-Track Microtron we have studied a biperiodic accelerating structure with rectangular cavities. This structure has somewhat higher effective shunt impedance than a biperiodic circular structure with inner coupling cells. It also focuses in one direction and so can be used to construct accelerating-focusing sections for other types of particle accelerators. We present here the results of our experimental and simulation investigations of the electrodynamic parameters of this structure.

I. INTRODUCTION

A biperiodic accelerating structure has as its principle advantage over a disk-loaded guide the possibility of attaining a desired energy with a given Radio Frequency power in a shorter structure, an essential feature for a Race-Track Microtron. We employed such a biperiodic structure based on cylindrical cavities in our original multi-purpose mobile 70 MeV RTM design [1]. Further advantages accrue for our application by using a so-called rectangular structure linac without axial symmetry [2] despite some particle dynamic peculiarities from the changed focusing conditions. In a classical circular microtron the relativistic particle transverse momenta are increased proportional to $J^{-1/2}$ when traversing a rectangular cavity with circular apertures [3]. For vertical motion $J_v = \frac{B^2}{A^2 + B^2}$, where A and B are, respectively, the vertical and horizontal cavity dimensions. For the corresponding horizontal motion, $J_h = \frac{A^2}{A^2 + B^2}$. In square and circular cross section cavities there is no momentum change in either motion so there is no focusing after several RTM orbits. On the contrary, a vertically elongated resonator focuses in the vertical while defocusing in the horizontal for all electron orbits, $\Delta p_h = -\Delta p_v$. This result is shown in Fig. 3 of ref. 2 as linac focal lengths with electron energy.

Taking into consideration the above, we have found the electrodynamic parameters of the proposed structure which we present here. The results of our beam dynamics calculations for a RTM with the rectangular biperiodic structure are reported elsewhere [2].

II. THE STRUCTURE

A biperiodic accelerating structure based on prismatic cavities is shown in Fig.1. The accelerating cells have the dimensions of a regular rectangular waveguide, $B=55$ mm and $A=110$ mm, while the coupling cell narrow wall dimensions are determined with consideration for coupling slots and central beam apertures in tubes. The coupling coefficient between adjacent cells, as well as the central aperture diameter and drift tube dimensions, were chosen to be close those of our original axially symmetrical biperiodic structure [1]. We calculated and experimentally investigated two biperiodic structure variants with prismatic cavities whose dimensions are presented in Table I.

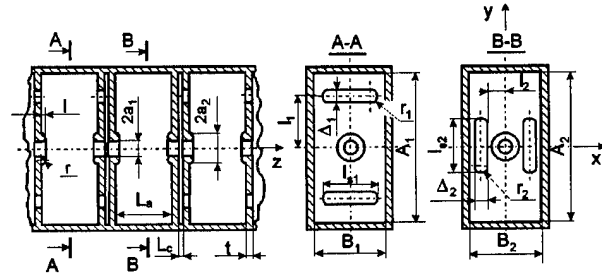


Fig. 1. Biperiodic structure with a rectangular cavities.

To determine the coupling cells dimensions which provide the desired coupling coefficient we use [4]

$$k_c = -\frac{Z}{Z_0} N \frac{l^3}{6} H_{n,a} H_{n,c} \quad (1)$$

where Z is the coupling slot wave impedance and Z_0 is the free space impedance. $H_{n,a}$ and $H_{n,c}$, the normalized magnetic fields at the slot position, can be written as

$$H_{n,a} = \sqrt{\frac{H_a^2 \mu}{2W_a}}, \quad H_{n,c} = \sqrt{\frac{H_c^2 \mu}{2W_c}} \quad (2)$$

where W_a is the energy stored in the prismatic accelerating cell and W_c in the coupling cell when operating in E_{110} mode. H_a and H_c can be determined by averaging over the coupling slot area, S , the rectangular cavities being excited in E_{110} mode:

$$H_a = \frac{1}{S} \int_S H_a(x, y) dS, \quad H_c = \frac{1}{S} \int_S H_c(x, y) dS \quad (3)$$

Table I. Structure dimensions in millimeters.

N	A ₁	B ₁	L _a	A ₂	B ₂	L _c	t	2a ₁	2a ₂	r	l	Δ ₁	l ₁	l _{s1}	r ₁	Δ ₂	l ₂	l _{s2}	r ₂
1	110	55	42.5	110	53.5	3	4.2	10	20	2.5	3.85	8	41.5	32.9	4	8	20	18.0	4
2	110	55	42.5	110	51.33	3	5.5	10	20	---	2.85	8	41.5	32.9	4	8	20	19.7	4

III. ELECTRODYNAMIC CHARACTERISTICS

We calculated the electrodynamic parameters of two biperiodic structures with rectangular cavities using the upper half of the structure between planes A-A and B-B of Fig.1. For electric walls the 0, $\pi/2$, and π modes are excited. For magnetic walls the $\pi/2$ coupling cell mode is excited. For an electric-magnetic wall combination the structure supports the $\pi/4$ and $3\pi/4$ modes. We used a 50,000 nodes in our simulations [5] and took $\beta_{ph} = 0.994$ in variant 1 which gave a Q factor of 12,500. For variant 2 we chose the relative phase velocity to be $\beta_{ph}=1$ at $f_{\pi/2} = 2,941$ MHz with the resulting structure dispersion curve shown in Fig. 2. The coupling coefficient, K_c , is 3.5%, the field nonuniformity coefficient, K_d , is 1.01, the unloaded Q factor is 12,430, and the effective shunt impedance, $r_{sh,eff}$, is 95.6 MΩ/m. The electric field overstrength coefficient, defined as the ratio of the maximum electric field at the structure surface ($x = 3.75$ mm, $y = 9.86$ mm, and $z = 15.65$ mm) to that on the structure axis, is ~ 2.5 . All these parameters, the effective shunt impedance excepted, differ only slightly from those of our biperiodic structure with cylindrical cavities [1]. $r_{sh,eff}$ increases by almost 25% which is encouraging for our compact RTM application. To experimental tune the structure the sensitivity functions are very important and were calculated for variant 2 to be:

$$\begin{aligned} \frac{\partial f}{\partial B_2} &= -40 \frac{\text{MHz}}{\text{mm}}, & \frac{\partial f}{\partial l_{s1}} &= -15 \frac{\text{MHz}}{\text{mm}}, \\ \frac{\partial f}{\partial 2a_2} &= -45.5 \frac{\text{MHz}}{\text{mm}}, & \frac{\partial f}{\partial l_{s2}} &= -33 \frac{\text{MHz}}{\text{mm}}. \end{aligned}$$

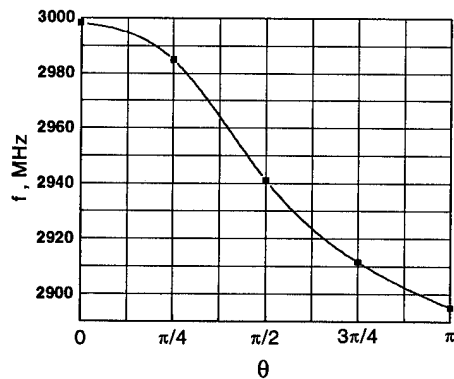


Figure 2. Structure variant 2 dispersion curve.

IV. ACCELERATING STRUCTURE MEASUREMENTS

We conducted experiments to determine the structure dimensions which would support the $\pi/2$ mode frequency with phase velocity, β_{ph} , of 1, coupling coefficient of $\sim 3\%$, and a uniform field over the entire accelerating structure length. With these conditions realized we could compare the effective shunt impedance, unloaded Q factor, and field overstrength coefficient of this structure with our original one having cylindrical cavities.

We made experiments and calculations to find accelerating and coupling cells coupling slot positions as shown in Fig.1. The slot width in both disks, Δ_1 and Δ_2 , were chosen to be 8 mm with rounded ends of radius 4 mm. The coupling slot dimensions in disks which were cut parallel to the narrow cavity walls were approximated using eqns. (1)–(3), then corrected using uniform periodic structure prototype data, and were $l_1 = 41.5$ mm, and $l_{s1} = 32.9$ mm. The coupling slots cut parallel to the cavity broad walls had $\Delta_2 = 8$ mm at a distance of ~ 20 mm from the structure axis, l_2 . The desired coupling was achieved by varying the slot length l_2 . To determine the accelerating and coupling cells frequencies, $f_{\pi/2}^a$ and $f_{\pi/2}^c$ we assembled resonant prototype sections. We detuned the accelerating and coupling cells, seen in Fig.3a and b, respectively, using massive cylindrical bushes having an inner diameter of $2a$. During tuning we maintained the accelerating cell frequency constant and adjusted the coupling cell frequency by changing B_2 until $f_{\pi/2}^a = f_{\pi/2}^c$.

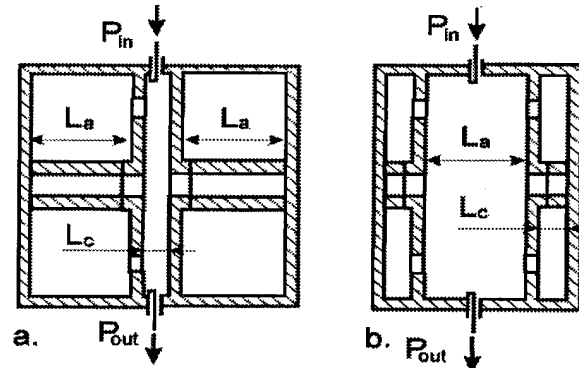


Fig. 3. Resonance tuning of (a) coupling and (b) accelerating cells.

To check the accelerating and coupling cells tuning we assembled a resonant prototype consisting of an accelerating

cell, two accelerating half-cells, and two coupling cells in which we measured the resonance frequency and electric field distribution using the small perturbations technique [4]. If a disruption in the dispersion curve at $\pi/2$ mode occurred or if unequal field amplitudes appeared in the full and half accelerating cells we changed the coupling coefficient by varying l_{s2} . When the field amplitude in the full cell was higher than that in the half cells the l_{s2} slots dimensions in the adjacent disks were increased. After this procedure we remeasured $f_{\pi/2}^c$ and $f_{\pi/2}^a$, and adjusted $f_{\pi/2}^c$ so that $f_{\pi/2}^c = f_{\pi/2}^a$.

To measure the field we used 0.14 mm diameter cylindrical metallic beads with the lengths of 2.5 and 3.5 mm and form factors $k_z^b = 237 \times 10^{-20}$ and $8.9 \times 10^{-21} \text{ m}^2/\Omega$, respectively. In some measurements we used 0.9 mm diameter ceramic bead with the length of 6 mm and form factor $k_z^c = 82 \times 10^{-20} \text{ m}^2/\Omega$. Since our experiments preceded our calculations we did not obtain $\beta_{ph}=1$ for the first tuned structure variant. We only got $\beta_{ph}=0.994$ at the frequency 2,898 MHz so we continued our experiments with the variant 2 structure.

The measured electric field strength on the structure 2 prototype axis is shown in Fig. 4, where the length is 102 mm. We calculated the effective shunt impedance using this field distribution to be $\sim 98 \text{ M}\Omega/\text{m}$ and the $\pi/2$ mode frequency was 2,938.7 MHz.

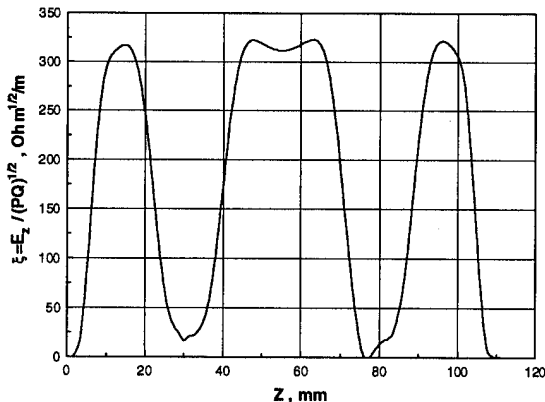


Fig. 4. $\xi = \frac{E_z}{\sqrt{PQ}}$ vs Z-coordinate.

V. CONCLUSIONS

For RTMs a prismatic cavity biperiodic structure is preferred to a cylindrical cavity structure because the injection scheme is simplified since the electron beam can make a full first orbit rotation without additional equipment. This asymmetric structure has a Q factor and field overstrength coefficient equal to, and effective shunt impedance larger than, other possible accelerating structures while additionally focusing in one transverse direction.

REFERENCES

- [1].N.P. Sobenin, A.I. Karev, V.N. Melekhin, V.I. Shvedunov, and W.P. Trower, The Design of a 70 MeV Multi Purpose Pulsed Race Track Microtron, in *Proc. Fourth European Particle Accelerator Conf.*, vol.1, p.512-514, 1994.
- [2].V.I. Shvedunov, A.I. Karev, V.N. Melekhin, N.P. Sobenin, and W.P. Trower, Improved Mobile 70 MeV Race-Track Microtron Design, in these Proceedings.
- [3].S.P. Kapitza and V.N. Melekhin, *The Microtron*, (Nauka, Moscow, 1969) 211 pp. (in Russian).
- [4].N.P.Sobenin and B.V. Zverev, *Electrodynamic Characteristics of The Accelerating Cavities* (Energoatomizdat, Moscow, 1993) 220 pp. (in Russian).
- [5].R. Klatt, F. Krawczyk, W.R. Novender, C. Palm, T. Weiland, B. Steffen, T. Barts, M.J. Browman, R. Cooper, C.T. Mottershead, G. Rodenz, and S.G. Wipf, in *Proc. 1986 Linear Accelerator Conf.*, SLAC-303 p.276 1986. A version this MAFIA code, obtained by V.S. in 1989 from T. Weiland, and installed at 586/90 was used in these calculations.

INVESTIGATION OF BIPERIODIC ACCELERATING STRUCTURE FOR THE FREE ELECTRON LASER BUNCHER.

N.P.Sobenin, S.N.Yarigin, D.V.Kostin, Moscow Engineering Physics Institute,
Kashirskoe shosse, 31, 115409, Moscow, Russia.

A.A.Zavadtzev, Moscow Radiotechnical Institute of Russian Academy of Science.

Some features of calculation and experimental study of a biperiodical structure consisting of $1\frac{1}{2}$ accelerating cells and a coupling cell are considered. The structure is intended to be used as a radio frequency photocathode source.

I. INTRODUCTION

One of the unique features of high-gradient rf electron injectors is that the beam can be accelerated to relativistic energies in two cells. Cells geometry is chosen so that the electric field radial component is minimised in the beamline vicinity, so the unwanted increasing of the emittance is limited [1]. At the same time the geometry should also ensure optimal values of shunt impedance and accelerating field providing the electric field at the structure surface is below the breakdown level. Our studies have resulted in the determination of a structure which met requirements mentioned above and was suitable for acceleration of 100 A electron beam with the values of micropulse length 30 ps and macropulse length 10 μ s. The beam energy of 3 MeV was obtained in the structure having $1\frac{1}{2}$ accelerating cells and being fed from a klystron with 3.5 MW power value and frequency 1.3 GHz. In this paper we discuss the results of calculation, tuning and experimental study of a prototype of the structure under consideration operating at the frequency 2800 MHz.

II. BASIC PRINCIPLES OF THE ACCELERATING STRUCTURE CALCULATION

The equivalent scheme of the resonant section consisting of an accelerating half-cell, a coupling cell and accelerating full cell is shown in Fig.1. It is valid for the case when the overcell coupling and resistive losses can be neglected.

It is assumed that the own frequencies of the cells are equalized $\omega_{01} = \frac{1}{\sqrt{2L_1C_1}} = \omega_{02} = \frac{1}{\sqrt{2L_2C_2}} = \omega_0$. Denoting as i_1 , i_2 and i_3 the loop currents and assuming that the coupling between the accelerating half-cell and full cell is negligible, one can write:

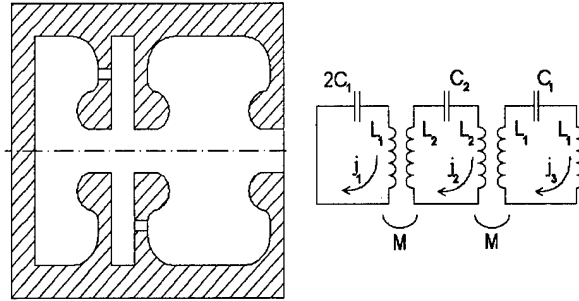


Figure 1. Resonance model and its equivalent scheme

$$\begin{cases} \left(1 - \frac{\omega_0^2}{\omega^2}\right) \dot{X}_1 + \frac{k}{\sqrt{2}} \dot{X}_2 = 0 \\ \frac{k}{\sqrt{2}} \dot{X}_1 + \left(1 - \frac{\omega_0^2}{\omega^2}\right) \dot{X}_2 + \frac{k}{2} \dot{X}_3 = 0 \\ \frac{k}{2} \dot{X}_2 + \left(1 - \frac{\omega_0^2}{\omega^2}\right) \dot{X}_3 = 0 \end{cases} \quad (1)$$

where $\dot{X}_1 = \sqrt{L_1} i_1$, $\dot{X}_2 = \sqrt{L_2} i_2$, $\dot{X}_3 = \sqrt{L_1} i_3$ and the coupling coefficient $k = \frac{M}{\sqrt{L_1 L_2}}$

By equalising the determinant of the system (1) to zero one can get

$$\left(1 - \frac{\omega_0^2}{\omega^2}\right)^3 - \frac{k}{2} \left(1 - \frac{\omega_0^2}{\omega^2}\right) - \frac{k}{4} \left(1 - \frac{\omega_0^2}{\omega^2}\right) = 0 \quad (2)$$

The solutions of Eq. (2) are

$$\omega_1 = \omega_0 \quad (3)$$

$$\omega_{2,3} = \frac{\omega_0}{\sqrt{1 \pm \frac{\sqrt{3}}{2} k}} \quad (4)$$

According to the expression given in [1]

$$\omega = \frac{\omega_0}{\sqrt{1 - k \cos \theta}} \quad (5)$$

the structure under consideration would be exited at $\pi/2$, $\pi/6$ and $5\pi/6$ modes.

For the determination of the optimal shape of the accelerating cell in respect to the parameters $\left| \frac{E_r}{E_z} \right|$, shunt impedance $r_{sh, eff}$ and k the computer program PRUD-0 [2] was used which was developed for the calculation of axially symmetrical modes of oscillations. This program

was also used for the determination of coupling cell dimensions.

For the determination the coupling cell dimensions which provide the chosen coupling coefficient one can use the following expression [3]

$$k = -\frac{Z}{Z_0} N \frac{l_s^3}{6} H_c(r_s) H_a(r_s), \quad (6)$$

where Z is the coupling slot wave impedance, its value being normalised with respect to the free space impedance Z_0

$$\frac{Z}{Z_0} = \left\{ \frac{t_c}{\Delta} + \frac{2}{\pi} \left[1 + \ln \left(\frac{\pi t_c}{2\Delta} + 1 \right) \right] \right\}^{-1} \quad (7)$$

Here t_c is the slot depth, Δ is the slot width, r_s is the slot axial position radius and N is the number of coupling slots.

Note, that $H_c(r_s)$ and $H_a(r_s)$ were obtained from calculations according to the program PRUD-0.

In case when the coupling slot edges are rounded with the radius $\frac{\Delta}{2}$ the effective length would be

$$\tilde{l}_s = l_s \left[1 + 0.15 \sin \left(\frac{\pi \Delta}{2l_s} \right) \right] \quad (8)$$

The calculation of a coupler which connects the rectangular waveguide having cross-section dimensions $A \times B$ mm² with accelerating cell of a biperiodic structure is carried out on the basis of the formula [3]

$$\frac{Z_{in}}{Z_c} = \frac{Q_0}{v_{01}} \left(\frac{A}{\lambda} \right)^3 \left(\frac{B}{\lambda} \right) \tan^2 \left[\frac{\pi(h-t)}{2A} \right], \quad (9)$$

where Q_0 is the accelerating cell unloaded Q factor, h and t are the width and depth of the inductive coupling window, L is the net length of all accelerating cells, λ_w is the wave length in the rectangular guide (assuming that the accelerating cell has cylindrical geometry), $\frac{Z_{in}}{Z_c}$ is equal

to ρ for the case of overcoupling and $\frac{Z_{in}}{Z_c}$ is equal to $1/\rho$

for the case of undercoupling, ρ is the voltage standing wave ratio coefficient.

III. CALCULATION AND EXPERIMENTAL STUDY OF THE ACCELERATING STRUCTURE PROTOTYPE.

The S-band accelerating structure consisting of one and a half accelerating cell and one coupling cell was calculated and tuned. The frequency $f=2800$ MHz was chosen as operational one. The shape of the accelerating cell with optimal dimensions corresponding to $f=2800$ MHz is shown in Fig.2. Its basic dimensions are given in Table 1.

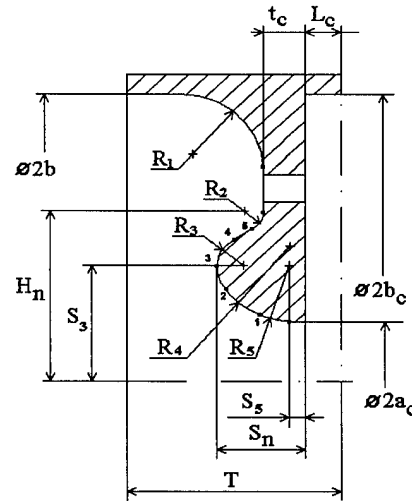


Figure 2. The basic dimensions of the structure.

Table 1. Basic dimensions of the structure Fig.2 (mm).

T	L _c /2	b	a	t _c
26.768	1.500	42.836	5.900	2.500
S _n	H _n	R ₁	R ₂	H ₃
7.472	13.525	21.800	2.784	13.672
R ₃	R ₄	S ₅	R ₅	b _c
3.978	10.342	1.899	3.978	41.010

With the purpose of minimization the field quadrupole component excited by not strongly relativistic beam four slots are cut in each wall of the coupling cell, slots in the adjacent walls being rotated by 45° for diminishing the coupling between accelerating cells. For the coupling coefficients calculation the expressions (6), (7) and (8) were used. The following dimensions are given: $r_s=22$ mm, $D=4$ mm, $t=2.5$ mm, $l_s=12.4$ mm. The normalized magnetic field values are

$$H_a = 11095 m^{-\frac{3}{2}}; H_c = 252 m^{-\frac{3}{2}}.$$

Taking into account the data given above one can obtain from (7) the coefficient of coupling between the accelerating half cell and coupling cell (if $N=4$) $k_c=1.56$ %. The coupling between the accelerating full cell and coupling cell is characterized by $k_c=1.1$ %.

To evaluate the dimensions of the coupling slot between the rectangular feeding waveguide and the accelerating cell it is helpful to use formula (9) with the assumption that at the operational frequency the coupling with the resonator

is critical, i.e. $\frac{Z_{in}}{Z_0}=1$, and the slot height "b" is equal to

the rectangular guide dimension "B". With $Q=10000$, $t=1$ mm, $f=2800$ MHz and $A \times B=72 \times 34$ mm², the slot width was obtained to be $h=13.3$ mm.

The tuning routine is as follows. At first the prototype is assembled as shown in Fig.3. The coupling cell is detuned by a metal ring. Then by changing the accelerating cell diameter the resonant frequency is made equal to 2800 MHz.

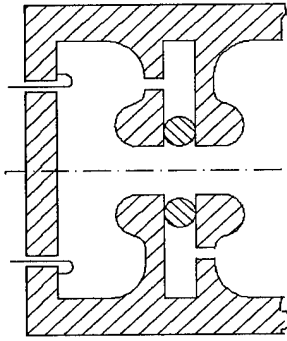


Figure 3. Resonance model for the half accelerating cell frequency tuning .

The environmental temperature and humidity should be accounted for. After that the resonant prototype consisting of two accelerating half cells and one coupling cell is assembled. By cutting the cylindrical surface of the coupling cell the symmetrical dispersion curve with respect to the operational frequency is obtained. The tuning criterion is the realization of the following equation

$$|\omega_2 - \omega_{01}| = |\omega_3 - \omega_{01}| \quad (10)$$

where

$$\omega_{23}^2 = \frac{\omega_{01}^2 + \omega_{02}^2}{2(1-k^2)} \pm \frac{1}{2(1-k^2)} \sqrt{(\omega_{01}^2 - \omega_{02}^2)^2 + 4k^2\omega_{01}^2\omega_{02}^2} \quad (11)$$

and the frequency ω_{01} should be equal to the operational one.

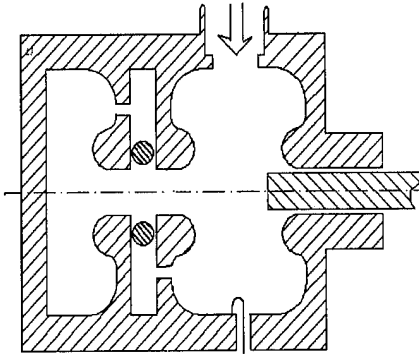


Figure 4. Resonance model for the coupler tuning .

The next stage of the tuning procedure includes the tuning of the whole structure with the RF power feeding element (Fig.4). At the variation of feeding window width we have to retune the accelerating cell (the coupling cell is detuned) to the operational frequency and to measure the reflection coefficient from the RF power feeding element. To avoid the frequent cuttings of the accelerating cell peripheral surface the operational frequency is being maintained by a plunger inserted trough the cut off hole in the drift tube. In this manner the critical coupling regime was obtained. The final tuning to the operational frequency is realized by changing the accelerating cell diameter, the plunger being withdrawn.

The basic experimental technique for the measurement of electric field in accelerating resonators is the reactive probe technique. For its realisation an automation measuring complex [3] is used. The electric field in the vicinity of the beamline was measured inside the half of

accelerating cell. The dielectric perturbing probe was used in the measurements. It had the shape of a cylinder with diameter 0.9 mm and length 3.5 mm. The probe material was characterised by $\epsilon=25$, and the formfactor was equal to $k^{(E)}=3.2 \times 10^{-20} \text{ m}^2/\text{Ohm}$.

The electric field versus z distributions at different r are shown in Fig.5. In this figure the result obtained with PRUD-0 are also presented. The ordinate is normalised,

$$\text{i.e. } \xi = \frac{E}{\sqrt{PQ}} .$$

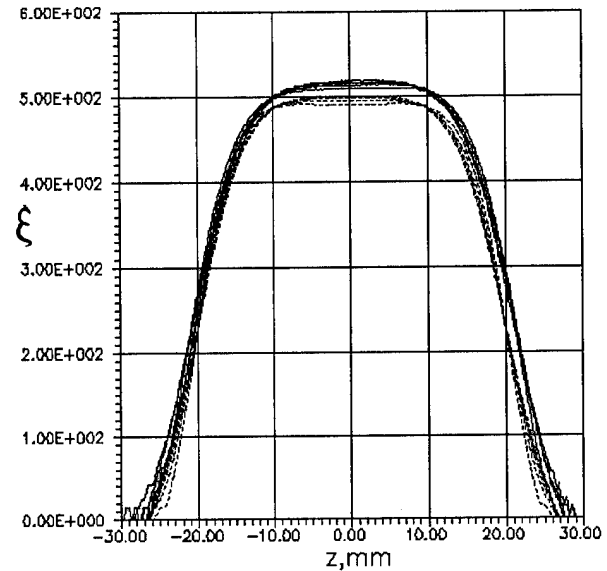


Figure 5. $\xi = \frac{E}{\sqrt{PQ}}$ vs Z-coordinate at the different values of r : 0, 1, 2, 3, 4 mm.
— experimental data; _ _ _ PRUD-0 calculations.

IV. CONCLUSION

Analytical formula and experimental techniques offered in this paper have enabled us to carry out simple and rather precise tuning of the system under consideration

including the structure itself which consisted of $1\frac{1}{2}$ accelerating cells and one coupling cell and the feeding waveguide. The electric field distribution measurements conducted in S band accelerating half-cell show good agreement with the calculation data.

V. REFERENCES.

- [1] J.Stoval, "A rewiev of Radio Frequency Photocathode Electron Sources ", Proceedings of the 1992 Particle Accelerator Conference, 1992, p.285 — 289.
- [2] A.G.Abramov, A.G.Daykovsky, S.Yu.Ershov et al. , "Computer Program PRUD-0 for calculation of the accelerating structures.", Institution of High Energy Physics preprint 83-3, Serpukhov, 1983.
- [3] N.P.Sobenin, B.V.Zverev, "Electrodynamic Characteristics of The Accelerating Cavities", Moscow, Energoatomizdat, 1993, 220 pages.

Ferromagnetic Cores Made from Amorphous Material for Broad-band Accelerating System

I.Bolotin, V.Budilin, A.Glazov, V.Krasnopol'sky, V.Skuratov, MRTI RAN

Amorphous ferromagnetic ribbons are considered as a material for ferromagnetic cores for unresonant accelerating structures of 100...200-MeV ion accelerators. The manufacturing of the cores using this material are cheaper and easier than that of the cores made from common-used ferrites. Calculated and experimental characteristics of the ferromagnetic cores made from these ribbons (permeability and tangent loss) for a coaxial broad-band accelerating system are presented. These characteristics over the frequency range from 1 to 10 MHz are in good agreement taking into account skin-effect. Possible versions of coaxial accelerating systems for medical synchrotrons with above mentioned cores are considered.

I. METHOD OF CALCULATION

The coaxial cavity with toroidal ferromagnetic cores is shown in Fig.1.

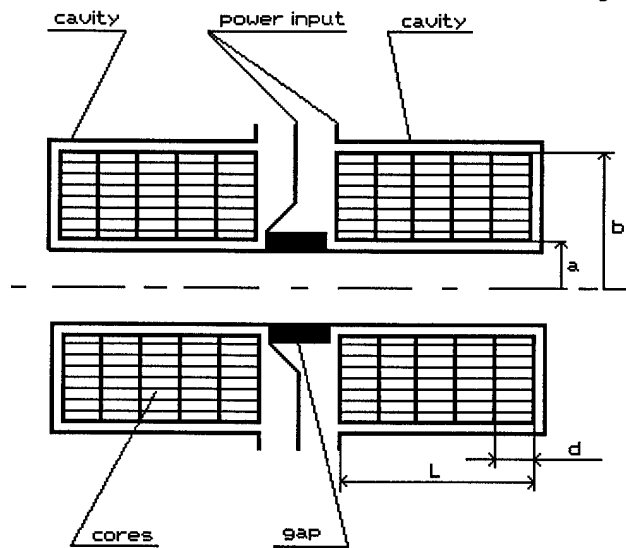


Figure 1. Accelerating system.

At small electric and magnetic fields without saturation and for a narrow hysteresis cycle some results presented in [1] may be used to calculate parameters of such system. The paper [1] generalizes results described in [2] in case of foliated cores. In this case the dominant role is played by skin-effect which limits the magnetic field penetration into the ribbon and creates power dissipation. The complex input impedance of the left or right part of the cavity may be calculated using the following equation:

$$Z = j \frac{\ln(b/a)}{2\pi} \sqrt{\langle \mu \rangle / \langle \epsilon \rangle} \operatorname{tg}(KL) + (j2\pi fC)^{-1}, \quad (1)$$

$$\text{where } \langle \epsilon \rangle = \epsilon_1 (\Delta_1 + \Delta_2) / \Delta_1, \quad \langle \mu \rangle = [\mu] e^{-j\delta},$$

$$\operatorname{tg} \delta = (\operatorname{sh}P - \sin P)(\operatorname{sh}P + \sin P)^{-1}, \quad P = \Delta_2 \sqrt{\mu_2 \pi f / \rho},$$

$$K = 2\pi f \sqrt{\langle \epsilon \rangle \langle \mu \rangle}, \quad [\mu] = \frac{\Delta_2 \mu_2 (\operatorname{sh}P + \sin P)}{(\Delta_1 + \Delta_2) P (\operatorname{ch}P + \cos P) \cos \delta}.$$

In these formulas $\langle \epsilon \rangle$ is the resulting dielectric permeability, $\langle \mu \rangle$ is the resulting complex magnetic permeability of the foliated cores, ϵ_1 is the dielectric permeability of the insulation between the ribbons, μ_2 is the magnetic permeability of the ribbon at the zero frequency, Δ_1 is the thickness of the insulation between the ribbons, Δ_2 is the thickness of the ribbon, ρ is the ohmic resistance of the ribbon material, C is the equivalent capacity of the accelerating gap, f is the frequency.

II. CALCULATED AND EXPERIMENTAL RESULTS

In order to develop one of the versions of the coaxial accelerating system for the medical H-minus synchrotron with the energy of 250 MeV the amorphous material 9KCP (Metglas 2605) with the following characteristics was used: $\mu_2/\mu_0 = 4000$, $\rho = 1.3 \cdot 10^{-6} \text{ Ohm} \cdot \text{m}$, $\Delta_2 = 25 \cdot 10^{-6} \text{ m}$, $\Delta_1 = 8 \cdot 10^{-6} \text{ m}$, $d = 0.02 \text{ m}$, $a = 0.117 \text{ m}$, $b = 0.21 \text{ m}$. Experimental and calculated characteristics for this material are shown in Fig. 2 also.

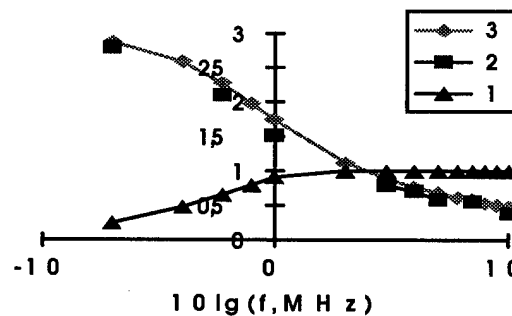


Figure 2. Characteristics of the cores: 1 is $\operatorname{tg} \delta$ (calculated), 2 is $[\mu]/1000\mu_0$ (experimental), 3 is $[\mu]/1000\mu_0$ (calculated).

The accelerating system consists of two symmetrical left and right parts (Fig.1). Its frequency range is 3.8-14.7 MHz, the maximum accelerating voltage supplied to the gap is 600 V, $L = 0.1 \text{ m}$, $C = 60 \text{ pF}$, the total number of the cores is 10. There are four cavities of this type in the accelerator. The

experimental and calculated absolute values of the input impedance $[Z]$ for the left or right part of the accelerating system calculated with the use of (1) are shown in Fig.3.

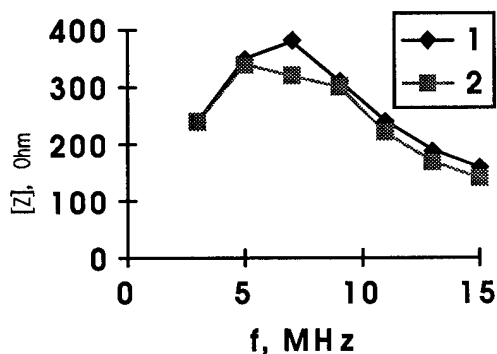


Figure 3. Input impedance of the cavity : 1 is $[Z]$ (calculated), 2 is $[Z]$ (experimental).

According to these results the system is unresonant and it is analogous to the systems presented in [3, 4]. The advantage of the system is the small variation of its input impedance in a wide frequency range. The analysis of different versions of this type of accelerating systems shows that such systems are suitable for lower frequencies of the accelerating voltage. For example the accelerating system of the medical proton synhrotron with the energy of 220 MeV, the frequency range is 0,8 - 3,6 MHz, $L=0,18$ m, $a= 0,07$ m, $b= 0,21$ m, has the impedance changing between 500 Ohm and 700 Ohm.

III. REFERENCES

1. V.Krasnopolsky, " A Coaxial-Type Acceleraiting System with Amorthous Material " Proceedings of the 1993 Particle Accelerator Conference, Vol.2, p.933-935.
2. R.Bozort, " Ferromagnetism " Foreign Literature, 1956.
3. G. Batskich, A. Vasilyev, V. Labuts, A. Myrer, V. Skuratov "Aperiodic Broadband Accelerating System", Proc. of All-Union Workshop on Charged Particle Accelerators, 1970, Vol 2, p 118.
4. S.Ninomiya, " Conceptual Design of a Non-Resonant Acceleraiting System for Low-Energy Proton and Heavy-Ion Accelerators " KEK Report 92-2, April 1992.

A New Structure with Continuous RF Acceleration and Focusing

J.J. Manca, M.C. Fallis, and J.P.J. Manca
SPACC, P.O. Box 61933, Sunnyvale, CA 94088

ABSTRACT

A new design for an accelerating structure in which charged particles experience continuous acceleration and focusing is proposed. The structure is excited in the TM mode (not RFQ TE mode). Our calculations show high intercell coupling for the rf flow at no loss of efficiency in comparison to other rf structures. This makes the structure insensitive to manufacturing and misalignment errors. Manufacturing, assembly, and tuning should not be difficult. Our design can be scaled to operate over a broad range of wavelengths and can be made from superconductive material. Our calculations show that the structure can efficiently accelerate a wide range of particles, from low velocity ions to high energy electrons. Thus, it can bring particles from energies of several MeV (right after RFQ pre-acceleration) to hundreds of MeV. Our conclusions are based on the results of three-dimensional numerical simulations.

INTRODUCTION

Many particle accelerators, such as linear colliders, FELs, high beam current accelerators, and so on, require very high quality, low emittance beams. In addition to low emittance, it is advantageous if the beam is under continuous transverse focusing to minimize particle losses during beam transport. This transverse focusing counteracts the defocusing effects of space charge forces in the beam.

Several very effective schemes have been developed that use magnetic fields for focusing. However, at low particle velocities, magnetic focusing becomes inefficient, and the design tends to be complicated and expensive.

A significant improvement came with the use of the RFQ accelerator, which uses rf fields for continuous acceleration and focusing, and delivers a high quality particle beam of up to several MeV of energy. At these energies, the beam can then be injected into a magnetically focused drift tube (DT) linac. The transition between the two accelerators is sensitive to the proper matching of space emittance, and without such matching, beam current losses may be significant.

In studying this problem, we concluded that an extension of the spatial focusing and acceleration principle would improve matching between two accelerators and would

minimize beam loss. We have therefore designed a radio-frequency focusing (RFF) accelerating structure that fulfills requirements for a smooth transition between RFQ and DT linacs.

Our structure can be designed not just for low energy particles, but for energies up to 100 MeV. At this energy, the particles can, if desired, be injected directly to the coupled cavity (CC) linac, bypassing the use of the DT linac.

DESCRIPTION OF THE RADIO-FREQUENCY FOCUSING (RFF) ACCELERATING STRUCTURE

The design of the RFF accelerator section is shown in Figure 1. The section consists of a cylinder with a pair of specially designed plungers protruding from the cylinder wall, toward the cylinder axis. A full cavity is generated by introducing a second pair of plungers into the cylinder at a distance $L = \beta * \lambda/2$ and rotated by 90 degrees.

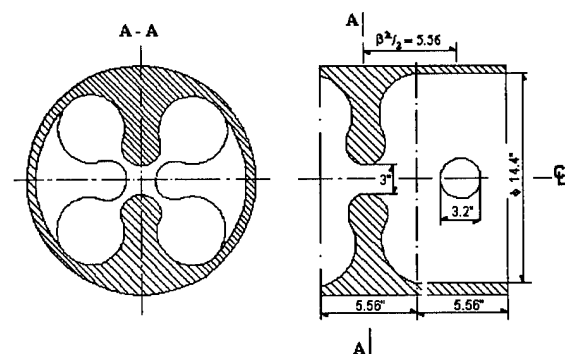


Figure 1 Cross-Section of the Structure

A cutaway view of the section is shown in Figure 2. The diameter of the cylinder is variable and is indirectly dependent on the particle velocity. For velocity $v = 0.4 c$, the diameter equals 36 cm, at wavelength equal to about 70 cm (425 MHz). The half-cavity on each end of the full cavity completes the design used for our computations.

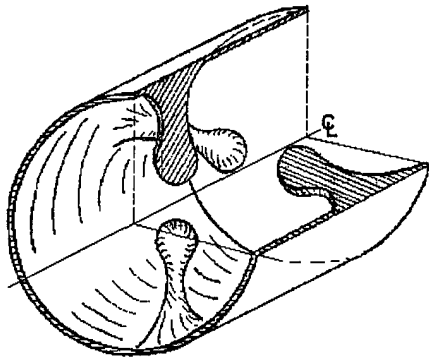


Figure 2 Cutaway View of the Section

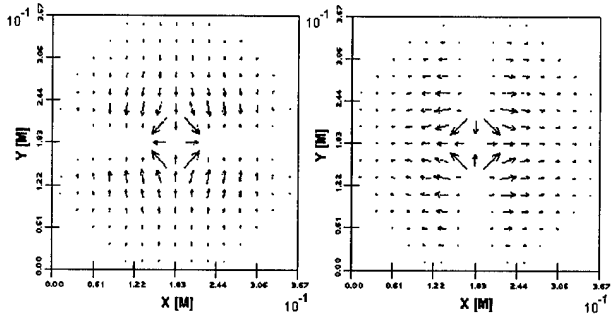
When the structure is excited in a π mode, particles traveling along the z-axis are accelerated in the space between the two pairs of plungers, and are focused as they pass through the gap between each pair of plungers. The ratio of acceleration to focusing strength can be adjusted by changing the ratio of the space between the two pairs of plungers to the thickness of the plungers. The periodicity of the structure is determined by planes of symmetry (end plates) which can be moved along the z-axis to allow calculations of additional properties of the structure.

We have identified a second, higher order mode (designated as 2π mode) that can be used for the same purposes as the π mode, but with a periodicity that covers two cavities. This mode displays excellent properties for acceleration and focusing of lower energy particles, particularly below $v = 0.2c$. The structure has continuous radiofrequency acceleration and focusing, and is considerably less complicated than DT linacs.

The calculated intercell coupling coefficient reaches a value of 0.4, making it insensitive to manufacturing errors. Furthermore, rf tuning can be accomplished by slight changes of cell geometry. For example an increase of cylinder geometry decreases the resonant frequency of the cavity. Similarly, decreasing the gap between the pairs of plungers also decreases the resonant frequency. The separate parts of the structure are relatively easy to manufacture and assemble, and because the individual cells can be made from a single piece of metal, it is a good candidate for a superconductive structure.

RESULTS OF THE COMPUTATION

We performed calculations using our three-dimensional, finite difference code developed for an 80486-based IBM PC. The calculated fields of the representative section are shown in Figure 3. Figure 3a illustrates our calculations of

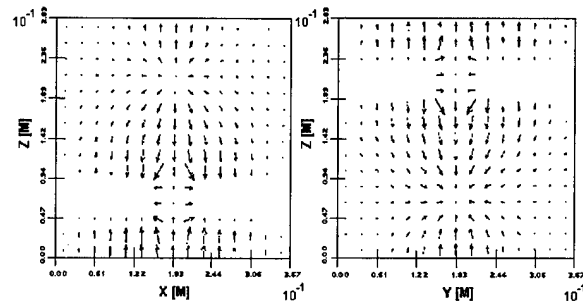


a) $Z = 7.06$ cm

b) $Z = 21.2$ cm

Figure 3 Vector Plots of E_X, E_Y Fields in X,Y Plane

the E_X and E_Y components in the X,Y plane at the position of the first pair of plungers. Similarly, Figure 3b illustrates the E_X and E_Y components in the same plane at the position of the second (Y-direction) pair of plungers (half wavelengths apart in the Z-direction and rotated 90°). In both cases, the focusing components of E fields are indicated



a) E_X, E_Z at $X = 0$ cm

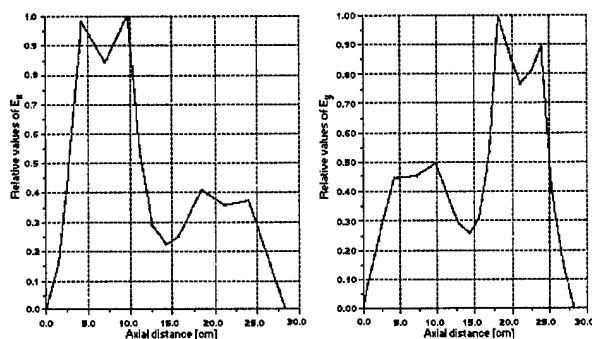
b) E_Y, E_Z at $X = 0$ cm

Figure 4 Vector Plots of Fields in X,Z and Y,Z Planes

by arrows. In Figures 4a and 4b, we show the E accelerating component in the X,Z and Y,Z planes, respectively.

In Figure 5, we show field profiles in several planes of the cavity. Figure 5a illustrates the focusing component E_X as a function of axial distance Z. The high value of E_X occurs in the space between the first pair of plungers, while its value is much smaller in the gap of the second pair. The

values of the E_Y component are reversed: in the gap of the first pair of plungers, E_Y has a small value, while its value peaks in the space between the second pair of plungers. This is shown in Figure 5b.



a) Relative E_X Field vs. Z b) Relative E_Y Field vs. Z

Figure 5 Field Profiles

Figure 6 shows the accelerating component E_Z along the Z-axis, where one can see the periodicity of the accelerating field. Figure 7 shows the value of field component E_X across the cavity in the X direction, taken in the middle of the cavity in the Z direction.

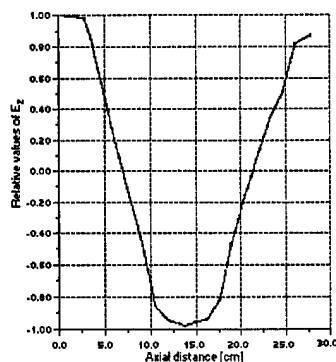


Figure 6 Relative E_Z Field vs. Z

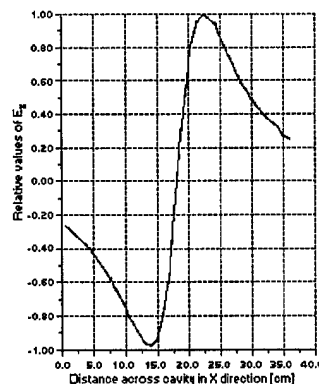


Figure 7 Relative E_X Field vs. X, in the Axial Center of the Cavity

CONCLUSION

Our RFF accelerating structure offers efficient transport of particles for a wide range of energies. The ease of manufacturing and tuning makes the structure attractive for a variety of applications, and the simplicity of our design makes it possible to explore its use in superconducting accelerators.

At this time, we have no results of calculations for the tracing of particle trajectories in the structure section. However, based on our preliminary analysis, we have concluded that beam quality will be preserved after transport of the beam through the chain of RFF sections. We expect to continue our study in this direction.

ACKNOWLEDGMENT

We would like to thank Tim Stevenson for his assistance in writing this paper.

SPARK LOCATION IN RF CAVITIES

Q. Kerns, M. Popović and C. Kerns
*Fermi National Accelerator Laboratory**
P.O. Box 500 Batavia, Illinois 60510, USA

Abstract

A spark detection system was constructed at the test station for the 400 MeV Linac Upgrade at Fermilab. To locate sparks in RF Cavities we placed five Ion Gauge Detectors along an accelerating module. The method used in detecting the spark location is based on the fact that sparks create pressure disturbances which travel throughout the cavity. Pressure signals from all five detectors are amplified using relatively fast amplifiers and then digitally recorded or monitored on the scope. The data recording is triggered by spark generation and data are recorded at a 15 Hz repetition rate. The system was also used to study different schemes for preferential spark generation at times that would be least detrimental to accelerator operations.

INTRODUCTION

The Fermilab Linac Upgrade has increased the energy of the H^- linac from 201 to 401.5 MeV[1]. This was achieved by replacing the last four 201.24 MHz drift-tube linac cavities with seven 804.96 MHz side-coupled cavity modules. Each module, is made of four sections of 16 accelerating cavities (Figure 1). They operate in a $\pi/2$ mode, and each accelerating cell is coupled to the next by a coupling cell. The end coupling cell is connected to a bridge coupler. The bridge coupler passes the RF power from one section to the next around the quadrupole magnet. The power is fed to the module through the center bridge coupler. Up to 12MW of RF power is pulsed at 15Hz for 60 - 120 microseconds.

Since the new side-coupled linac had to fit in the space vacated by the last four drift-tube tanks and provide more energy gain, the accelerating gradient had to be about 7.5 MV/m or about three times higher than in the DTL. This high gradient lead to concern early in the project that sparking could reduce the reliability of the linac to an unacceptable level. The purpose of the upgrade was to increase the beam intensity in the 8 GeV Booster and thus increase the luminosity of the collider. Too much sparking would reduce reliability and reduce the average beam intensities delivered[1]. Another concern was that too much sparking if localized at one spot could permanently damage an accelerating module. To resolve such questions, we constructed a spark detection system used during cavity testing in 1991 and 1992 which is described in next section.

METHOD

To locate sparks in Linac Upgrade side-coupled cavities we placed five ion gauge detectors as indicated in Figure 1. The method used in detecting the spark location is based on the

fact that sparks are creating pressure disturbances which travel through the structure. The detector which is located the shortest distance from the spark will detect the largest and sharpest pressure burst. Due to the fact that cavity modules are very complicated internally (Figure 2), we were able to locate spark positions only approximately with our method. Pressure signals from the five detectors are amplified using relatively fast amplifiers and then digitally recorded or monitored on the scope. Input currents from the ion gauges range from 3 nA to 1 μ A and the response time of the system is about 300 μ sec.

Figure 3 shows signals from the five ion gauges during a 15 minute period. Sharp spikes (in arbitrary units) show when sparks were detected by these devices during this period. Continuous monitoring has lead us to the conclusion that the majority of sparks do not occur in the side-coupling cell. During steady state, the coupling cells do not dissipate much power. However, while the cavities are filling and emptying this may not be the case. In the structures such as these, with high fields, this power dissipation can produce high currents and voltages that may lead to sparking in areas other than the accelerating-cell nose cones. We were able to monitor the field in each accelerator section and did not see a large number of sparks generated during the filling or decay of the RF power. Based on this, we believe that most of the sparks are generated at accelerating-cell nose cones.

To locate the approximate location where a spark has occurred, we have used pressure data recorded for about 3 seconds after a spark occurrence. Each frame in Figure 4 represents signals from Ion Gauge Detectors as a function of time. The data recording is triggered by a large reflected RF power signal. The data are recorded for fifty 15 Hz intervals after the large reflected RF power is detected. The four frames are traces of pressure bursts created by four different sparks. In Frame 1, Ion Gauges 1 and 2 have recorded pressure bursts. From the relative sizes of the peaks we can conclude that spark has occurred in Section 1 in the region between Ion Gauge 1 and bridge coupler connecting Sections 1 and 2. From similar traces in Frame 4, we can conclude that a spark has occurred in the central bridge coupler on the end connected to Section 3. The vertical axis is in arbitrary units, and the vertical label is a time record denoting when the spark occurred. The 91100214543713 stands for 91/10/02 (Oct-02-91) at 14:54:37 and 13th of 15Hz pulses.

A spark detection system was also used for monitoring the randomness of spark generation. A concern was that too much sparking at one spot could permanently damage an accelerating module. Figure 5 shows a number history of spark accumulation as recorded by five ion gauges. During a period of 14 hours (7.56×10^5 RF pulses), there were 418 sparks. As can be seen from Frame 1, Section 1 was initially very active, but a majority of the sparks occurred in Section 4. Close examination of

*Operated by the Universities Research Association under contract with the U. S. Department of Energy

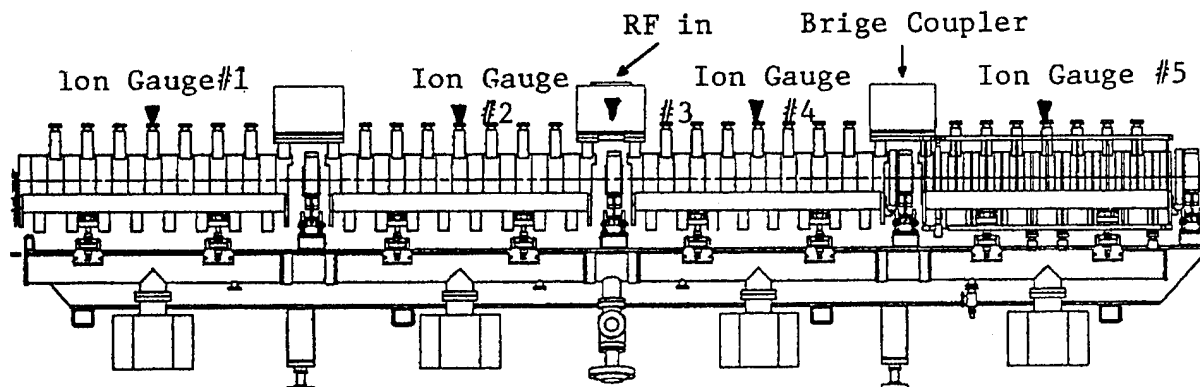


Figure 1. Side-Coupled Cavity Module

individual traces did not show any accumulation at a particular spot. During the conditioning period no consistent pattern was found in the distribution of sparks. A section may be active for a couple of hours and after that remain quiet for a day or two. The bridge coupler was generally a place with minimal sparking.

CONCLUSION

Although initial voltage conditioning of the high-gradient 805 MHz side-coupled modules did not progress as quickly as hoped, the method presented here gave us confidence to proceed with high power RF conditioning even at high sparking rates. Today the sparking rate in the operating 400 MeV linac is below 0.01%, and sparking does not have any noticeable effect on operations.

References

- [1] T. Kroc et al, "Fermilab Linac Upgrade - Module Conditioning Results", Proceedings of the 1992 Linac Conf., pp. 187 - 190.

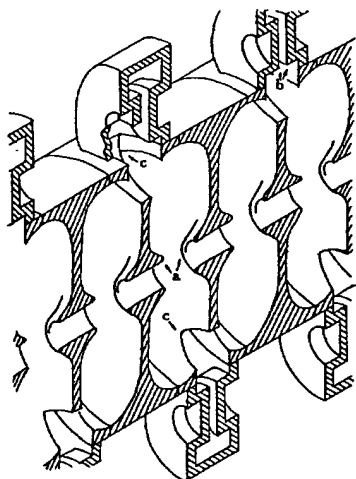


Figure 2. Possible spark locations: a) accelerating-cell nose cones, b) coupling-cell nose cones, c) coupling slots

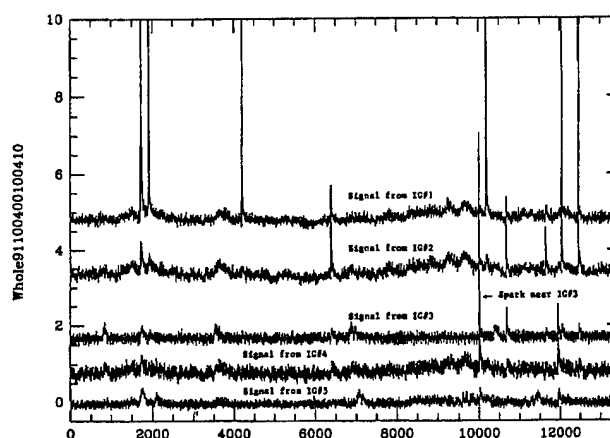


Figure 3. Continues recording for 15 minutes (13500 RF pulses)

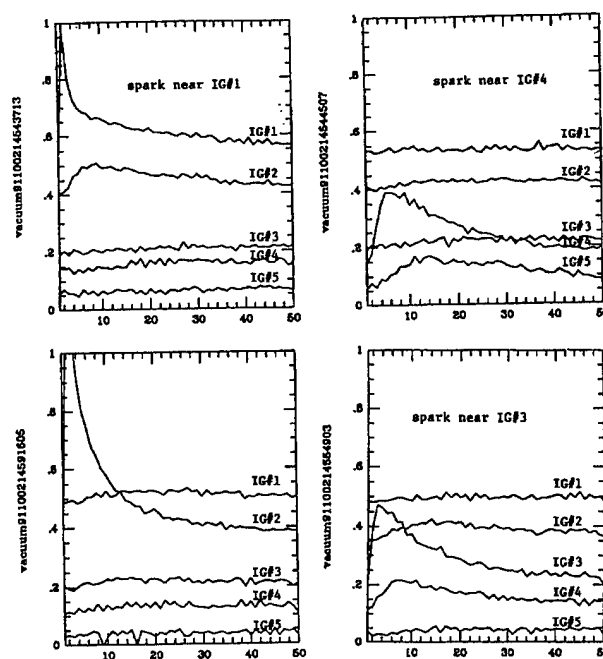


Figure 4. Ion Gauge signals created by four different sparks

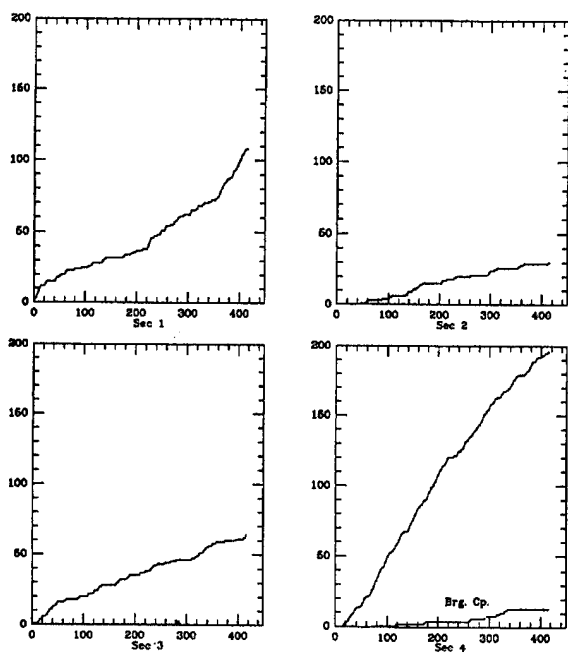


Figure 5. Ion Gauge signals created by four different sparks

RF System for the Duke 1 GeV Storage Ring*

Ping Wang, Peter Morcombe, Ying Wu
Duke University Free Electron Laser Laboratory
Box 90319, Duke University, Durham, NC 27708-0319
Grigori Kurkin
Institute of Nuclear Physics, Novosibirsk 630090, Russia

Abstract

The RF frequency is 178.5 MHz. An amplifier built by the QEI corporation provides 50 KW power. All the power feeds to a single-cell RF cavity, built by BINP at Novosibirsk, Russia, giving a gap voltage of 720 KV. An ANT circulator is used in the feed line. There are four basic feed-back loops to stabilize the system operation : 1) Cavity frequency tuning loop. 2) Cavity voltage control loop. 3) RF phase stabilization loop. 4) Synchrotron oscillation damping loop. The whole system has been tested and operated since December 1993. It has provided secure and stable operation for the storage ring.

I. RF PARAMETERS

The main parameters of the RF system for the Duke storage ring are given in Table 1.

TABLE 1
RF system Parameters

Electron Beam Energy	1 GeV
Synchrotron radiation loss per turn	42KeV
Ring circumference	107.46 meter
Rf frequency	178.547 MHz
Harmonic Number	64
Available RF power	50 KW
Cavity shunt impedance	11 M Ohms
Cavity coupling coefficient	1.78
Maximum peak cavity voltage	720 KV
Cavity unloaded Q	40,000
Cavity frequency tuning rang	360 KHz

II. RF CAVITY

The RF cavity is made of copper-clad stainless steel. It is designed to have an operational capability of 200 KW CW power. The operating power is limited by its coupling loop which is not water cooled. The cavity itself has an adequate cooling water system. There are five cooling water channels around the cavity and a total water flow of 16 gallons per minute. Tests show a 20 KHz resonant frequency shift when

the RF power to the cavity is raised from zero to 50 KW. The maximum temperature difference across the cavity wall is 18 degrees Centigrade at full power.

There are four mechanical plunger tuners on the cavity. Two tuners are for fundamental mode and the other two are designed to shift the high-order mode frequencies but not affect the fundamental mode. The two high order mode tuners are tuned manually in the control room for better beam stability. The two fundamental mode tuners are automatically adjusted to compensate for reactive beam loading and thermal deformation. they provide a total frequency tuning range of 360 KHz.

The cavity is fed by an air-filled coax line through a ceramic window. The coax line connected to the cavity has an impedance of 75 ohms. The rest of the coax lines are 50-ohms impedance. An impedance adapter from 50 to 75 ohms is installed between them.

A more detailed description about this cavity can be found in the reference [1].

III. POWER AMPLIFIER AND CIRCULATOR

The 50 kW output stage uses a single Eimac 4CW100000E tetrode with a water cooled plate. The tube is operated in a grounded grid configuration. Air cooling is used for the output cavity and the control grid. At full output, the stage gain is approximately 12 dB and the plate efficiency is typically 50%. The plate power supply input is 480 Volt, three phase delta, with twelve pole output to the rectifiers. This unregulated supply can deliver over 100 kW continuously at 8.5 KV. The output stage and its associated power supplies occupy two 19X78 inch cabinets. Sixteen solid state modular amplifiers drive the output tetrode via combiners. Each amplifier is rated at 250 Watts. The nominal stage gain is 14 dB. Two more of these modules are used as low level drivers, also with a 14 dB stage gain. These amplifiers are powered by nine switch mode regulated power supply modules. A solid state pre-amplifier with a maximum nominal output of 10 Watts provides an additional 40 dB of gain, so that full output can be achieved with an RF input of less than 1 mW. The solid state amplifiers, their associated power supplies and the control circuits are contained in two more cabinets.

A three port circulator rated at 150 kW was installed between the 50 kW amplifier and the RF cavity. The ports are all 6.125-inch EIA coax. The circulator was supplied by ANT

* Work supported by U.S. Air Force Office of Scientific Research Grant F49620-93-1-0590 and U.S. Army Space & Strategic Defense Command Contract DASG60-89-C-0028.

Telecommunications Incorporated, and after sales service is being provided by Advanced Ferrite Technology. This circulator is fitted with arc detection and temperature compensation. The forward loss is under 0.15 dB and the isolation provided is greater than 20 dB. The circulator is connected to a regulated water circulating loop which maintains a temperature of 34 degrees centigrade at all times. Operation above ambient temperature ensures that water films are not formed on the ferrite surfaces in the circulator.

IV. CONTROL CIRCUITS

The control circuits deal with the control and stabilization of the amplitude and phase of the RF field in the cavity. Interlocks for the cooling water, cavity vacuum and personal safety are also provided. There are four feedback loops as follows:

1) *Cavity frequency tuning loop:*

This feedback loop compares the RF phase of the field in the cavity to the phase of the input signal to the cavity and uses the resulting difference to operate the tuners via a DC motor. The phase comparison is made by converting both RF signals to 2.79 MHz via a mixer; Then the phase is measured by the duty factor of the intermediate frequency output after the amplitude limiter. This phase detector circuit has a sensitivity of 50 mV / per degree. The same type of phase detectors are also used in the phase stabilization loop and synchrotron oscillation damping loop.

2) *Cavity voltage control loop*

This feedback loop compares the field amplitude detected from the cavity sampling loop to a fixed reference voltage. The resulting signal is applied to a gain-controlled amplifier in the drive line to the transmitter.

3) *Phase stabilization loop*

The main function of this loop is to lock the field vector in the RF cavity to the RF signal generator. The RF signal detected from the cavity sampling loop is compared with a reference signal which is derived from the RF generator. Its output signal is used to drive a phase shifter in the RF drive line. The phase shifter is made by two LC resonant circuits with two voltage variable capacitance (VVC) diodes as control elements. The phase range is over 360 degrees.

4) *Synchrotron oscillation damping loop*

This loop samples beam signal from one of the beam position monitors. After a frequency filter, the 178.5 MHz beam signal is compared with the reference signal in a phase detector. Its output signal is used to drive the same phase shifter in the phase stabilization loop. The loop has a frequency response of 4-20 KHz which covers all the synchrotron frequencies at different machine configurations.

The entire system can be operated locally or remotely by the EPICS (Experimental Physics and Industrial Control System, provided by Los Alamos National Laboratory)

control system using Allen Bradley control hardware (see [2]). The operator can choose either of the following two operation modes in the control room. a) setting desired cavity voltage and cavity resonant phase, the system determines the RF power needed and stabilizes at that level. b) setting the coupling loop current which corresponds the RF power in the cavity, after the cavity voltage is chosen the system determines the resonant phase and vice versa.

This loop also keeps the phase of stored beam locked to the phase of RF generator which also is the source of timing system

V. OPERATION AND FUTURE PLANS

The RF system has been in operation with manual control since December of 1993. With on site support from QEI, ANT and BINP, the system was debugged and characterized. The control and read back circuits were integrated with the high level control system known as EPICS. In November 1994 the first stored beam was achieved and the optimum control settings were determined within a few weeks (see [3]).

Our long term objective is to increase the output power capability to 150 kW, at which point the circulator will become the limiting factor. In the near term there are some upgrades that are being considered.

The power supplies for the solid state amplifier stages generate noise at harmonics of the 20 KHz switching frequency. Harmonics derived from the line frequency are coming through the output tube plate supply. An inexpensive approach to reducing these noise sources is being studied.

To date we have not needed to run the amplifier above 15 kW for storage ring operations. Before full output can be used, power output stability must be improved. Water cooling the output cavity seems to be simple to implement and inexpensive, but other approaches are being considered.

VI. ACKNOWLEDGMENT

The authors wish to thank Carl Dickey and Owen Oakeley for their helpful efforts on the electrical controls and interlock circuits, Joe Faircloth and Pat Cable for the installation of cavity, coax line and transmitter; their contributions are much appreciated.

References

- [1]. V. Arbuzov, et al., "RF System of the CW Race-Track Microtron-Recuperator for FELs", Proc. 1993 IEEE PAC, Washington D.C., P1226, Vo. 2.
- [2]. Y. Wu, et al., "The Duke Storage Ring Control System", these proceedings.
- [3]. V. N. Litvinenko, et al., "Commissioning of the Duke Storage Ring", these proceedings.

MATCHING SECTION TO THE RFQ USING PERMANENT MAGNET SYMMETRIC LENS

M. Kando, M. Ikegami, H. Dewa, H. Fujita, T. Shirai, H. Okamoto, Y. Iwashita, S. Kakigi,
A. Noda and M. Inoue

Nuclear Science Research Facility, Institute for Chemical Research, Kyoto University,
Gokanoshio, Uji, Kyoto 611 JAPAN

Abstract

Permanent magnet symmetric (PMS) lens is considered as the final focusing element for the RFQ linac at ICR. The PMS lens, which produces strong axial magnetic field like a solenoid lens, is composed of radially magnetized permanent magnet rings. Because of the low injection energy (50 keV) and a relatively high beam current intended (20 mA), space-charge effects should be taken into account. The beam tracking code PARM-SYL is developed for the purpose, which first reads an output file (TAPE35) from PANDIRA for the PMS field and then numerically integrates the equation of motion including the space-charge force. The matching section to the RFQ is designed using this code and TRACE-3D.

I. INTRODUCTION

At Institute for Chemical Research (ICR), Kyoto University, the proton linac consisting of a 2 MeV RFQ linac and a 7 MeV Alvarez linac has been operated since 1992[1]. Various mechanical improvements are in progress to increase the beam current up to 20 mA. In this paper, the design of a new focusing element for matching the beam to the RFQ acceptance is reported.

Figure 1 illustrates the layout of the low energy beam transport (LEBT) of the ICR proton linac. It is composed of an einzel lens, a triplet of electrostatic quadrupoles (ESQ), two doublets of ESQ, a bending magnet (called Mixing Magnet) having the deflection angle of 45° , and a solenoid lens. The estimated beam emittance in LEBT is about 100π mm-mrad (unnormalized), which is used in the calculations in this paper.

In preliminary experiments, it was found that the transportable beam current was strongly limited by space-charge ef-

fects.[2] After the improvement of the Mixing Magnet, the current is now 8 mA roughly ten times higher than before[3]. The current measured after the Alvarez linac was only 0.7 mA due to beam mismatch at the entrance of the RFQ. An extra focusing device is thus needed to achieve a higher transmission efficiency.

For the simultaneous acceleration of both positive and negative ions planned in the future, focusing elements with axially symmetric fields are suitable for LEBT. Since the beam should be strongly focused and has a large taper angle, it is effective to put a focusing device near the entrance of the RFQ. This, however, causes the space limitation for the lens.

One candidate for such a focusing device is PMS lens, since the use of a strong permanent magnet material allows us to reduce its size and, further, the PMS field is axially symmetric. The evaluation of the performance of the PMS lens is made in the following sections.

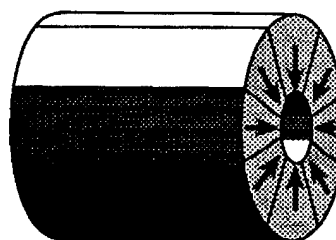


Figure 2. Radially magnetized permanent magnet ring.

II. PERMANENT MAGNET SYMMETRIC LENS

A radially magnetized permanent magnet ring (see Figure 2) with anisotropic material such as Nd-Fe-B generates axial magnetic field and works like a solenoid lens[4][5]. The magnetic field of one ring indicated either by 'Ring 1' or 'Ring 2' is shown in Figure 3, where Ring 1 and Ring 2 are oppositely magnetized. Putting these two rings side by side, the superposed magnetic field in the axial direction becomes like the thick solid line. Since the focusing strength of a solenoid lens is proportional to the integration of the square of the magnetic field strength along the axis, this axial superposition is quite effective.

As the permanent magnet material, the anisotropic permanent magnet NEOMAX-40 (nominal remanent field $B_r = 1.29$ T) produced by Sumitomo Special Metal Co.LTD. was adopted. Because of the low beam energy (50 keV) and the low duty factor (1 % maximum), the radiation damage is expected to be negligible and no special cooling device will be attached.

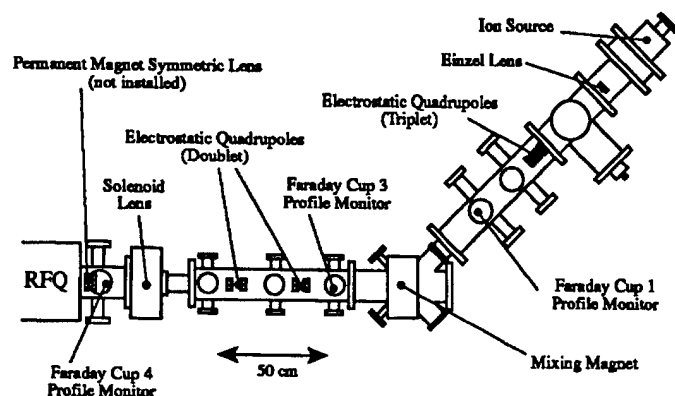


Figure 1. Layout of the LEBT

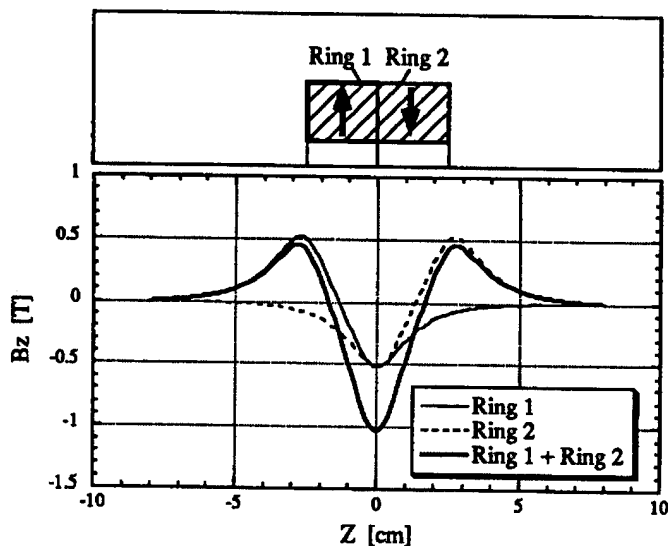


Figure 3. Magnetic field distribution generated by Ring 1 (thin solid line), Ring 2 (dashed line) and their superposition (thick solid line).

III. PARMSYL

The magnetic field of a PMS lens is calculated with PANDIRA[7]. To estimate the focusing strength and aberration of the lens, we developed the tracking code PARMSYL (PARTicle Motion in SYmmetric Lens). The code interpolates the magnetic field data from PANDIRA stored in the output file (TAPE35) and then integrates the equation of motion of a charged particle. In the integration process, space-charge is considered assuming a uniform beam density.

The code tracks particles on beam boundary in phase space, and outputs the focal length and aberration factor of the considered lens. The aberration factor is defined as the ratio of the focusing strength felt by the particle close to the lens axis to that felt by the outermost particle (i.e. $\int B_z^2(r=0)dz / \int B_z^2(r=r_{max})dz$).

IV. BEAM MATCHING

A. Acceptance of the RFQ

The RFQ acceptance was evaluated with the computer code PARMTEQ[8]. From the simulation, it was found that the transmission of the RFQ was over 90 % with the input beam emittance of $160 \pi \cdot \text{mm} \cdot \text{mrad}$ (unnormalized) in the intensity region of $0 \sim 20 \text{ mA}$. Although the value depends on beam current, $160 \pi \cdot \text{mm} \cdot \text{mrad}$ is used, in the following calculations, as the RFQ acceptance.

B. Design of a PMS lens

At present, the best PMS design for the final focusing device is the three-ring PMS lens shown in Figure 4. The beam comes from left side in the figure. It has two small rings installed in the endplate of the RFQ and a large ring placed outside of the endplate. The inner surfaces of the magnets are tapered following the shrinkage of the beam envelope. The edges of the magnets

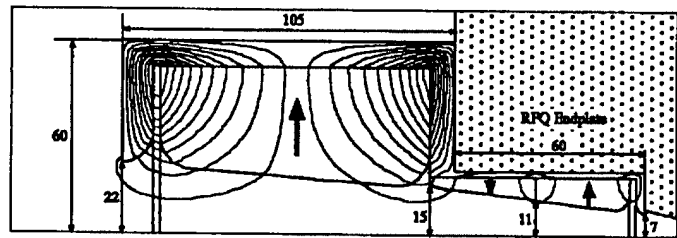


Figure 4. Shape of the PMS lens. Only upper half is shown.

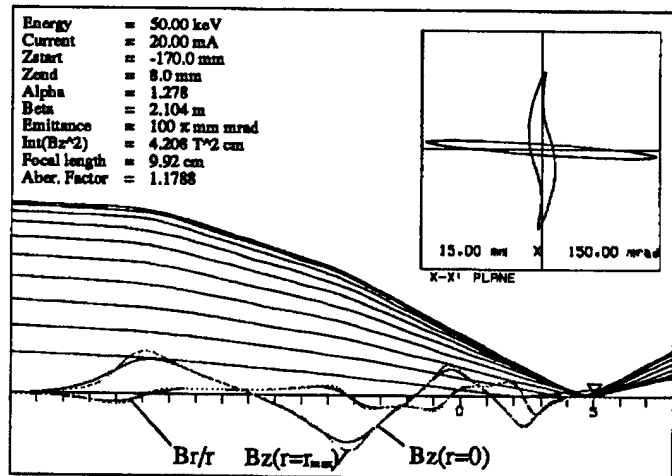


Figure 5. Output from PARMSYL at the current of 20 mA.

are rounded to reduce the aberration which distorts the beam ellipse. The typical output from PARMSYL is given in Figure 5. The axial field B_z and radial field B_r/r as well as particle orbits are shown.

The Twiss parameters (α, β) appropriate for matching were found to be $(-1.49, 1.44)$, $(0.00, 1.44)$ and $(1.28, 2.10)$ at the PMS entrance when the beam currents were 0 mA, 10 mA and 20 mA, respectively (see Figure 6). In the figure, the distorted beam ellipses are shown together with the RFQ acceptance (dotted line). More than 90 % overlap of the two ellipses is achieved in each case.

C. Matching to the PMS section

TRACE-3D[6] is employed to adjust the Twiss parameters at the entrance of the PMS section by using the strength of the ESQ doublets (see Figure 1) as free parameters. Figure 7 shows the matched beam envelope at the current of 20 mA.

V. SUMMARY

The PMS lens was designed with PARMSYL as the final focusing device to the RFQ. Although the beam ellipse is somewhat distorted due to the aberration of the lens, the overlap of more than 90 % is achievable between the input beam and the RFQ acceptance at the beam current up to 20 mA.

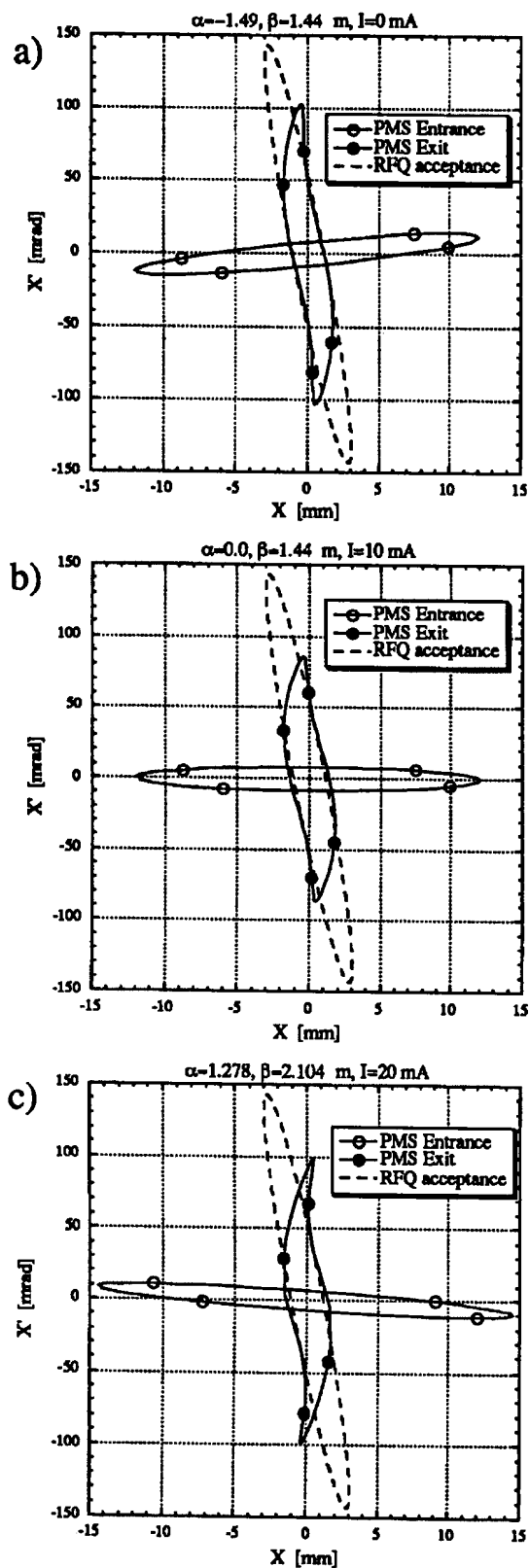


Figure 6. Phase space plots from PARMSYL.

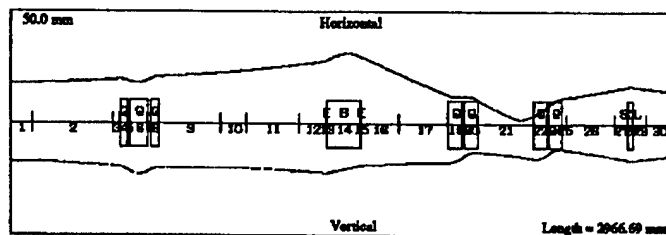


Figure 7. The matched beam envelope between the einzel lens and the PMS section at the current of 20 mA (calculated with TRACE-3D)

References

- [1] M. Inoue et al., "Commissioning of the 7 MeV proton linac at ICR Kyoto University", Bull. Inst. Chem. Res., Kyoto Univ. 71, No.1 pp.57-61 (1993)
- [2] A. Noda et al., "Characteristics of the ion source and low energy beam transport of the proton linac at ICR", Bull. Inst. Chem. Res., Kyoto Univ. 71, No.1 pp.6-14 (1993)
- [3] M. Kando et al., "Improvement of the low energy beam transport system at the ICR proton linac", Proc. of the 17th Linear Accel. Conf., Tsukuba, pp.122-124 (1994)
- [4] Y. Iwashita, "Axial magnetic field produced by radially magnetized permanent magnet ring", Proc. of the 17th Linear Accel. Conf., Tsukuba, pp.369-371 (1994)
- [5] Y. Iwashita, "Axial magnetic field lens with permanent magnet", Proc. of the 1993 Particle Accel. Conf., Washington D.C., U.S.A., pp.3154-3156 (1993)
- [6] K. R. Crandall and D. P. Rusthoi, "TRACE-3D Documentation", LA-UR-90-4146, LANL (1990)
- [7] "User's Guide for the POISSON/SUPERFISH group of codes", LA-UR-87-115, LANL (1987)
- [8] K. R. Crandall, R. H. Stokes and T. P. Wangler, "RF Quadrupole beam dynamics design studies", Proc. of the 1979 Linear Accel. Conf., 205 (1979)

CONCEPTUAL DESIGNS OF BEAM CHOPPERS FOR RFQ LINACS*

Subrata Nath, Ralph R. Stevens, Jr., and Thomas P. Wangler

Los Alamos National Laboratory, MS H817, Los Alamos, NM 87545, USA

A design study at Los Alamos of a linac/accumulator ring facility for a pulsed neutron spallation source calls for an H⁺ beam with a chopped structure of approximately 200-ns beam-free segments every 600 ns. The required angular impulse can easily be provided with existing pulse power technology and traveling wave structures with a transverse electric field similar to those now available [1]. The deflected beam is then restored by suitable collimation. Chopping is relatively easily done at sufficiently low energies, where the beam is easily deflected, and beam powers are not too large. However, the energy should be high enough so that the space-charge blow-up of the beam can be controlled with adequate focusing. LAMPF presently uses a traveling-wave beam chopper at 750 keV, before injection into the drift-tube linac (DTL). In the new linac designs, a radio-frequency quadrupole (RFQ) linac would typically bunch and accelerate the high intensity H⁺ beam from 100 keV to 7 MeV. In this paper, we present concepts for beam-chopper systems both before and after the RFQ. The beam-optics designs are presented together with numerical simulation results.

I. CHOPPING AFTER THE RFQ

In this section we describe the concept, the preliminary beam optics design, and the simulation results for the chopper after the 7-MeV RFQ. The design concept was based on a similar system proposed for the European Spallation Source [2]. In

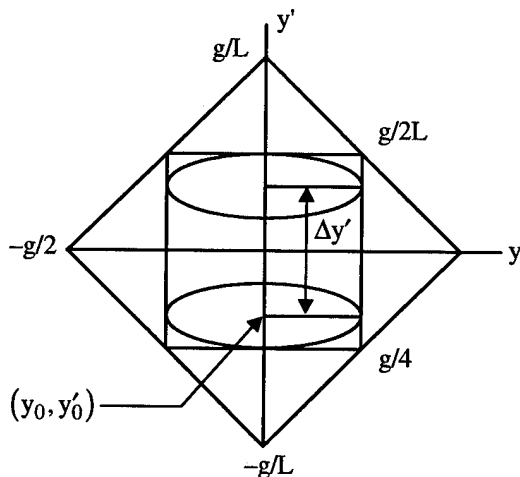


Figure 1. Phase space at the center of the chopper.

our design, we have three long drift spaces, each over one meter in length. Three drift spaces are to be occupied by the chopper (transverse deflector), a collimator, and a "restorer" (transverse deflector) as described below. The input and output of this transition section are matched to the output of

the RFQ and the input to the DTL respectively. The power of the fully chopped beam bunches can be removed on a water-cooled copper or graphite/copper collimator positioned at the second drift space. To handle the high power dissipation, we propose to place the collimator at a small tilt angle with respect to the beam axis. Such placement will distribute the thermal load over the entire length of the collimator. Bunches that arrive at the chopper plates during the ~5-ns rise or fall time of the traveling wave are partially chopped and the transmitted part is nearly restored to the optic axis by an identical traveling-wave chopper called the "restorer". The restorer prevents loss of the partially chopped bunches at higher energy.

A. Concept

The y - y' phase space at the center of the chopper plates is shown in Fig. 1. L is the length and g is the separation between the plates. Given the deflector voltage V , the emittance ϵ , and the separation parameter S , we calculate values of g and L that maximize use of the available phase space using equations:

$$L = 8\epsilon S m c^2 \beta^2 / qV \text{ and } g = 8\epsilon \beta [S(1+S)mc^2/qV]^{1/2}$$

where m is the rest mass, βc is the particle velocity and the unnormalized emittance is defined as $\epsilon = y_0 y'_0$. We define $S = \Delta y' / 2y'_0$, where $\Delta y' = 2VL/mc^2 \beta^2 g$. The chopper is tilted at an angle $\Delta y'/2$ for optimal use of the rectangular phase space area. Note that $S = 1$ corresponds to minimum deflection required to separate deflected and undeflected ellipses. Practical limits on the voltage that can be obtained in a given rise time determine the maximum value of V . The restorer is identical in construction and operation to the deflector.

B. Design Studies

The design procedure is to choose a realistic value of V , and determine the geometry parameters using the above equations for a given value of S . If we choose $V = 2.0$ kV and $S = 2$, then for a proton beam at 7 MeV with $\beta = 0.12$ and a normalized emittance of $\epsilon_n = 1.1$ mm-mrad, we obtain for the optimum case: $L = 1.00$ m, $g = 14.8$ mm, and $y_0 = 3.7$ mm. In this study we use $L = 1.0$ m, $g = 12$ mm, and $y_0 = 3.0$ mm, which is near but not exactly optimum. A layout of the section was done using the program TRACE 3-D [3], which solves for the motion of the beam envelopes, including the space-charge force for a uniform-density beam. Figure 2 shows a TRACE 3-D plot including beam profiles for $I = 38$ mA. Four sets of triplets were used providing three long drift distances to accommodate the deflector, collimator, and restorer, respectively. RF cavities are also used to keep the beam bunched. The elements were adjusted to match the

*Work supported by the LDRD, Los Alamos National Laboratory under the auspices of the US Department of Energy.

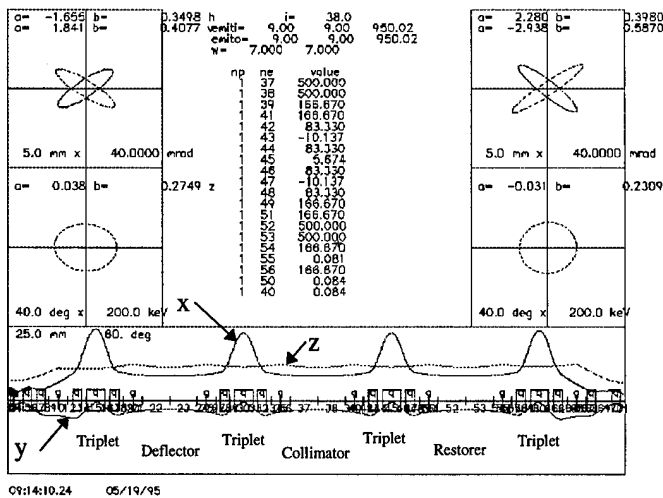


Figure 2. TRACE 3-D profile plots for I = 38 mA.

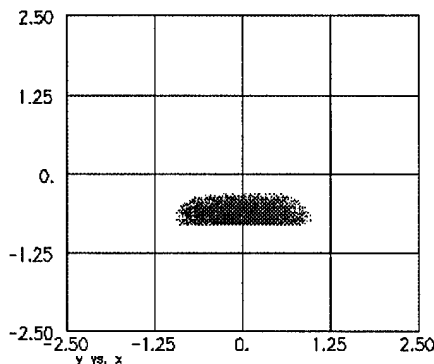


Figure 3. The x-y distribution of fully chopped bunches about one-third of the way along the collimator.

beam with the output of the RFQ and the input to the DTL. The deflection plane was chosen as the y-plane. So, the envelope size in y at the center of the chopper is kept at 3 mm, while the x dimension was not constrained. In the vertical plane we also require that from the center of the deflector to the center of the collimator $\sigma_{0y} = 270^\circ$, where σ_{0y} is the zero-current betatron phase advance per focusing period. This means that from the center of the deflector to the center of the restorer y'_0 is transformed to $-y'_0$. The code PARMILA, modified to incorporate the capabilities for deflection and collimation, was used to do the particle simulation studies. For simulation studies, we consider two beam bunches with different phase relationship relative to the deflecting voltage. Bunch type #1 represents the bunches which enter the chopper when the deflecting voltage has attained a maximum value of V, and bunch type #2 arrives at the chopper when the deflector voltage is ramping up or down and precisely at 0.5 V. Since the deflector is a traveling wave type, this bunch would see half the maximum deflection field throughout its journey in the chopper, while bunch type #1 would see full deflection field all along. Figure 3 shows the x-y distribution of type #1 at about one-third of the way along the collimator. Bunches of type #2 are subsequently restored (not shown) by the restorer.

II. CHOPPING BEFORE RFQ

Another option being considered for this upgrade entails the installation of a traveling wave chopper in the low energy beam transport (LEBT) line in front of the RFQ. A gas neutralized, magnetic transport system would be used. Chopping before the RFQ has the virtue that the beam-power loading from the deflected beam is easily handled on simple collimator designs and that the beam optics for chopping is relatively simple. Implementing this option will, however, be complicated by space charge effects in the LEBT, which will require a sufficiently high beam energy to preclude excitation of beam instabilities and a sufficiently short length to minimize emittance growth. The degree of beam neutralization needed and the required quiescence of the ion source will be key issues.

A. Concept

A schematic diagram showing the proposed LEBT beam line for 30-mA, 100-keV beam design is shown in Fig. 4. This design is similar to that now in operation in the LAMPF H^- high-voltage dome [4]. The ion source is operated at high voltage and the beam is extracted to ground potential and then transported by a two-solenoid-lens beam line to the RFQ. The chopper is placed between the solenoid lenses with the primary chopping aperture located at the entrance of the second solenoid lens. Two steering pairs located between the solenoids provide corrections for centroid errors at the RFQ entrance. The transport solution requires an intermediate waist at the end of the chopper, so appropriate diagnostics are required at this point. A secondary chopping aperture will be located at the entrance to the RFQ to improve rejection of the chopped beam. The filtering action of the secondary aperture and the RFQ may eliminate the need for a separate restorer element that would result in an undesirable length increase in the LEBT.

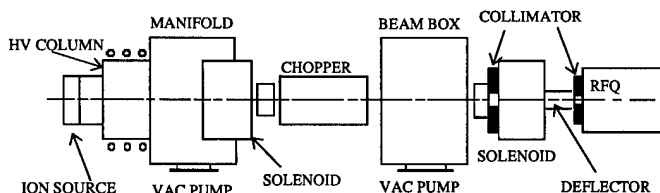


Figure 4. Schematic of the 30-mA, 100-keV H^- injector.

B. Design Studies

The beam envelopes expected were calculated using the first-order beam-envelope code TRACE 3-D [3]. In Fig. 5 we see the profiles for both the chopped and the unchopped beams at the secondary chopping apertures for the case where a 30-mrad impulse is imparted to the beam by the chopper. In the initial portion of this beam line, the extracted H^- beam will be space-charge neutralized by the effluent gas from the ion source. This gas load will be pumped at the entrance to the first focusing lens. In the chopper itself, the beam is expected to be un-neutralized when electric field is present. Previous attempts [5] to chop a low-energy beam at the Brookhaven

National Laboratory resulted in unacceptable phase-space distortions, because the neutralizing ions accumulated in the beam within the chopper. The present design entails higher beam energy and lower currents than the Brookhaven case.

The electric fields produced by this chopper will be greater than the space-charge fields of the beam, thus sweeping out more of the beam-induced plasma and reducing these distortions.

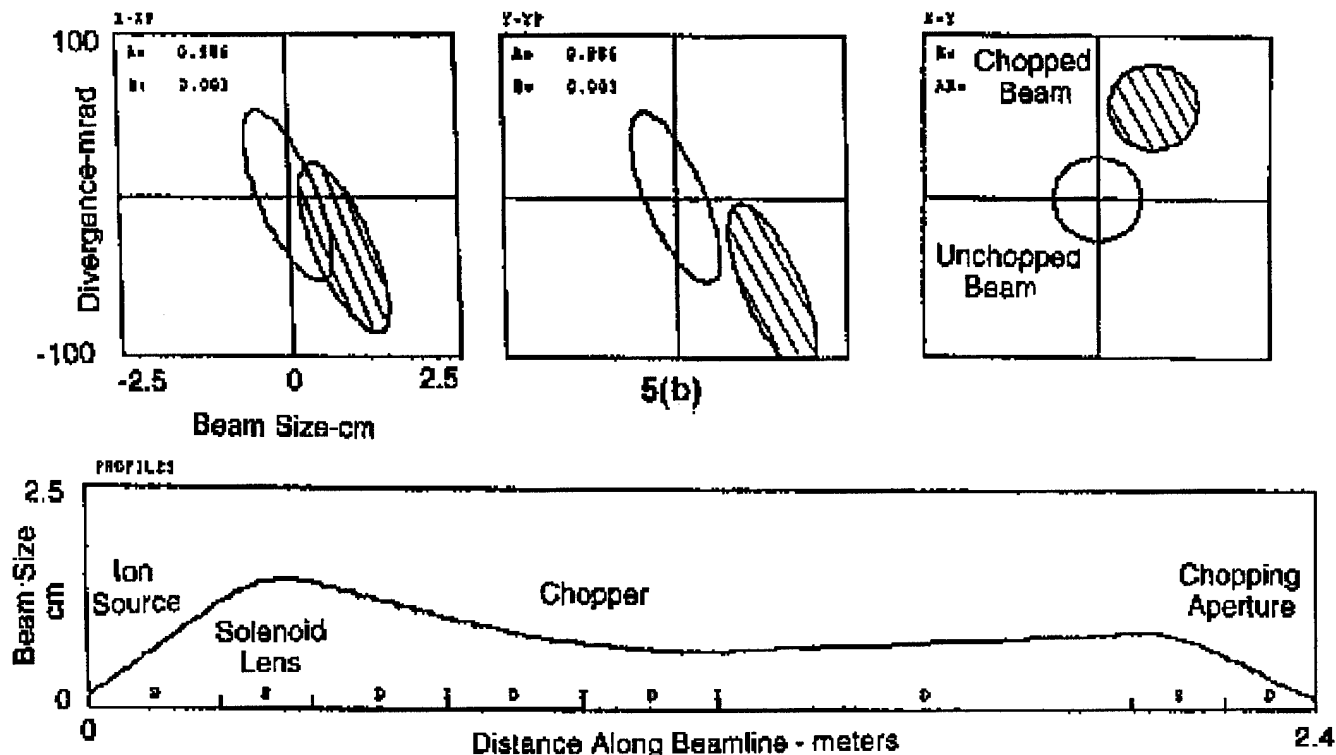


Figure 5. Beam profiles for the proposed H^- injector at the RFQ entrance (5b).

Because of unknown charge neutralization effects, the details of the proposed chopping are less certain in the final portion of this beam line. In the region between the chopping plates and the primary chopping aperture, the beam current is constant, but the chopper causes a high frequency (1.7 MHz) square-wave modulation in the beam-centroid motion. This frequency is in the range of the two-stream instability. Thus, one can expect emittance growth and, for sufficiently high beam current, excitation of this plasma instability. In the region after the chopping aperture, the beam will propagate without centroid modulation, but the beam current will now be modulated at the same 1.7-MHz frequency. The chopping period will be short compared to the neutralization time, but comparable to the decay time of the positive-ion neutralizing channel. A partially neutralized beam will be produced in this region [6]. We can, therefore, expect further emittance degradation in the transport of the chopped beam in this region. Plasma simulations using PIC codes are now being considered to clarify these issues.

III. CONCLUSIONS

The two options available for chopping the H^- beam for a pulsed neutron spallation source have been considered. The LEBT chopping option is relatively easy to implement with existing technology, but is complicated by possible excitation

of beam instabilities and by emittance growth. Preliminary simulations show that a chopper system after the RFQ at 7 MeV is feasible. The beam quality is preserved and the partially chopped bunches can be restored to the optic axis, thus reducing the losses in the ring. Further work is needed to resolve the technical issues before a choice can be made between those two options.

IV. REFERENCES

1. J. S. Lunsford and R. A. Hardekopf, IEEE Trans. Nucl. Sci., NS-30, 2830 (1983).
2. K. Bongart, private communication.
3. K. R. Crandall and D. P. Rusthoi, TRACE 3-D Documentation, Los Alamos National Laboratory report LA-UR-90-4146 (1990).
4. R. R. Stevens, Jr., R. L. York, J. R. McConnell, and R. Kandarian, Proceedings. of the Linear Accelerator Conference, GSI-84-11, 226 (1984).
5. J. G. Alessi, J. M. Brennan, and A. Kponou, Rev. Sci. Instrum. 61 (1), 625 (1990).
6. L. Schroeder, K. N. Leung, and J. Alonso, Proceedings. of the Workshop on Ion Source Issues for a Pulsed Spallation Source, Lawrence Berkeley Laboratory report LBL-36347 (1994).

THE ROLE OF SPACE CHARGE IN THE PERFORMANCE OF THE BUNCHING SYSTEM FOR THE ATLAS POSITIVE ION INJECTOR*

R. C. Pardo, Argonne National Laboratory, Argonne, IL 60439 USA
and R. Smith, Kalamazoo College, Kalamazoo, MI 49006 USA

The bunching system of the ATLAS Positive Ion Injector consists of a four-frequency harmonic buncher, a beam-tail removing chopper, and a 24.25 MHz spiral resonator sine-wave rebuncher. The system is designed to efficiently create beam pulses of approximately 0.25 nsec FWHM for injection into and acceleration by the ATLAS superconducting linac. Studies of the effect of space charge on the performance of the system have been undertaken and compared to simulations as part of the design process for a new bunching system to be developed for a second ion source. Results of measurements and modeling studies indicate that the present system suffers significant bunching performance deterioration at beam currents as low as 5 eμA for $^{238}\text{U}^{26+}$ at a velocity of $\beta=0.0085$. The low beam current tolerance of the present system is in reasonable agreement with computer simulations. Studies of two alternatives to the present bunching system are discussed and their limitations are explored.

I. INTRODUCTION

The ATLAS Superconducting Heavy-Ion Linear Accelerator[1,2] was designed with the goal of providing high quality beams of any heavy-ion species for fundamental research in nuclear and atomic physics. Beam currents were expected to be large by historical standards; as high as ten to a hundred particle nanoamps for most beams. The effects of

space charge on beam optics was considered and found not to be significant for the transverse dimensions. The effect of space charge on longitudinal bunching is more serious and observable defocusing effects were expected for beam currents of a few electrical microamps. Figure 1 shows the floor plan of the low-energy beam transport (LEBT) for the ATLAS Positive Ion Injector(PII) and indicates the location of the present bunching components.

The first stage of bunching for the PII is a four-harmonic gridded-gap buncher[3] located on a 300 kV platform with the ECR ion source. The fundamental frequency of this buncher is 12.125 MHz (period of 82.4 ns) and a sawtooth-like wave is formed using three additional harmonics. Typical maximum bunching voltage requirements are approximately 700 volts. This bunching system is operated in such a way as to form a waist at the chopper plates to minimize the longitudinal emittance growth caused by the chopper. The beam is then further compressed for injection into the linac by a second, sine-wave buncher operating at 24.25 MHz. For beam currents of 1 eμA or less, bunch widths significantly less than 1 ns FWHM have been possible for a variety of beams using only the harmonic buncher. As the beam current is increased to a few microamps the bunch width at the time focus worsens as shown in Figure 2 for a beam of $^{16}\text{O}^{3+}$. For these studies, $^{16}\text{O}^{3+}$ was chosen because it is a beam with a charge-to-mass ratio (Q/A) typical of many of the heavy-ion beams accelerated at ATLAS.

The worsening of the best possible time width as beam current increases is from the repulsive space-charge force on the compressing beam. In this simple situation, the space-charge force acts simply as a continuous defocusing lens slowing the compression process. In the beam center-of-mass system, the maximum velocity which must be imparted to an ion so as to achieve a time focus at the chopper plates is 4073 m/s. This corresponds to an ion energy in the center-of-mass of 1.37 eV (0.46 V) for $^{16}\text{O}^{3+}$. The repulsive space-charge potential for a beam bunch of these particles corresponding to an average beam current of 1 eμA is 0.47V for a spherical geometry. One sees immediately that the beam will become essentially a 'parallel' beam under these conditions. For higher beam currents, the waist condition will be destroyed and cannot be achieved under any condition with a fixed geometry. In the laboratory frame, these small voltages translate into a buncher voltage of 675 volts indicating that space charge forces are significant at currents as low as 1 eμA. These estimates are in good agreement with the observed typical 700 volts focusing force mentioned previously.

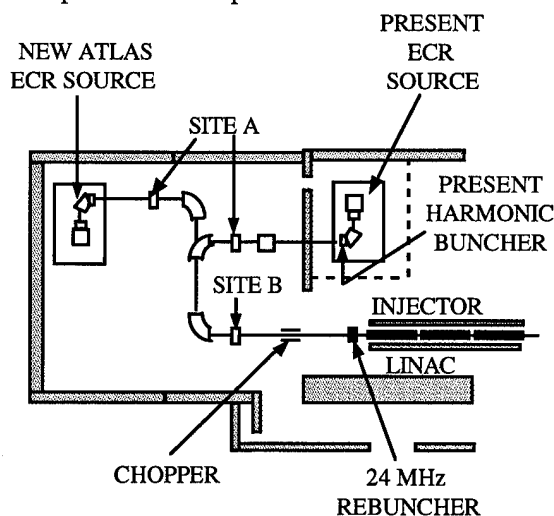


Figure 1: Floor plan of Low-Energy Beam Transport system for PII-ATLAS showing the relevant bunching system components.

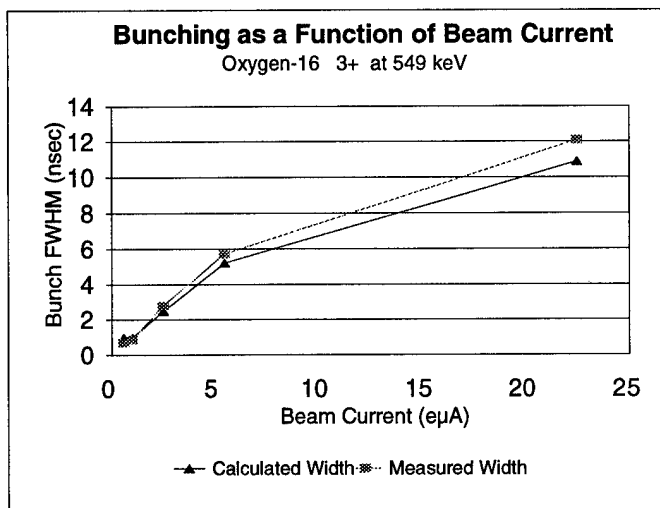


Figure 2: Observed beam bunch width at PII entrance waist location compared to performance predicted by TRACE3D.

A more quantitative comparison to observation has been made using the first-order matrix program TRACE3D[4] which can include space charge effects. The comparison to the experimental data is shown in Figure 2. These calculations confirmed the effects discussed above and showed that as the beam current increases above 1-2 eμA significant and unrecoverable changes occur to the beam phase ellipse making the match into the linac much poorer. At currents much above 20 eμA the beam mismatch to the linac causes significant deterioration in the efficiency of acceleration and beam loss. The effective longitudinal emittance is also significantly worsened by the bunching system, mostly due to the nonlinear bunching of the second sine-wave buncher when the beam is spread over a phase width of approximately 180 degrees.

II. DESIGN STUDY

A second high charge-state ECR ion source is under construction for ATLAS and in conjunction with that project a study of the injection bunching system has been undertaken with the goal of improving the bunching performance for the high current and high charge-state beams anticipated from the new ECR ion source. TRACE3D was used to model the performance of the systems studied with regard to space charge limitations. A proprietary ray-tracing program was used to study the models with regard to resonator field profiles. The ray-tracing program did not include space charge effects, but did include the exact waveforms of the harmonic and sine-wave bunchers.

The location of the new source, injection geometry and relationship to the existing source and LEBT are indicated in Figure 1. The obvious goal is to create a bunching system which requires a much shorter focal length buncher, necessitating higher bunching voltages (shorter longitudinal focal lengths). Such a requirement must be achieved while

providing good ion species resolving power so as to deliver pure beams to the linac while maintaining high beam quality, especially low longitudinal emittance.

Two locations were studied as possible sites for the harmonic buncher in the system. These are indicated in Figure 1 as 'Site A' and 'Site B'. 'Site A' is off the high voltage platform, and provides improved bunching characteristics for beams of moderate intensity. For example with a beam of $Q/A = 0.1875$, bunching is adequate up to average currents of 40 eμA. Average beam currents as high as 300 to 500 eμA are possible from the new ECR ion source. This location is still inadequate for beams of such intensity. In addition, the species selectivity of the magnetic analysis system in the LEBT is significantly reduced by the energy spread created by the harmonic buncher at 'Site A'. The Q/A selectivity of the transport system without the buncher operating in the present configuration is approximately 1 in 2000. Including the energy spread from the harmonic buncher, in the present location, the selectivity in Q/A is reduced to 1 in 400. By moving the harmonic buncher to Site A that resolution is further reduced to 1 in 200. Additionally, the need to tune the 180 degree achromat for good optical conditions adds some complexity to the everyday operation of the LEBT.

Therefore the performance of the buncher system with the harmonic buncher located at 'site B' was studied. This site might seem the most obvious choice, since the buncher focal length is the shortest and therefore the bunching electric field is the highest. But the high bunching electric fields required for this location and necessary to reduce the effects of space charge on the longitudinal optics are more difficult to obtain. A high premium on the quality of the bunching waveform is also required for these high bunching fields. In order to obtain good bunch widths for injection into the linac and to minimize the emittance growth due to the buncher

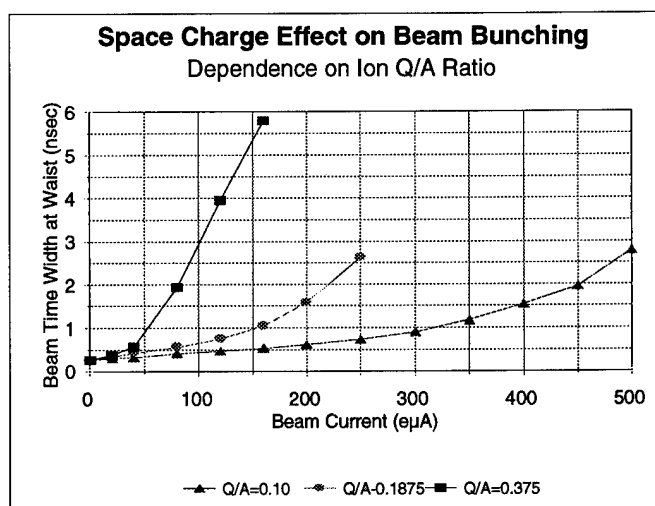


Figure 3: 'Site B' configuration. Beam bunch width versus beam current for beams with differing Q/A for the harmonic buncher only. Compare the present system performance in Figure 1 to the $Q/A=0.1875$ curve.

waveform, a very careful optimization of the four harmonics forming the sawtooth-like harmonic buncher waveform was found to be necessary.

The calculated results for the 'Site B' harmonic buncher location are shown in figure 3, 4, and 5. Careful optimization of the buncher waveform resulted in an empirical harmonic mix of :

$$E_b = A \cdot (\sin(\omega t) - 0.3814 \cdot \sin(2\omega t) + 0.1506 \cdot \sin(3\omega t) - 0.0405 \cdot \sin(4\omega t))$$

The harmonics found to provide optimum bunching at this location are not universal and in fact make some use of the 24.25 MHz sine-wave second buncher waveform to provide the best total effective bunching voltage.

The reduced sensitivity of buncher performance on beam current can most immediately be seen by comparing the calculated time width versus beam current for $Q/A=0.1875$ ($^{16}\text{O}^{3+}$) to the present buncher performance shown in Figure 2. The 'site B' configuration makes it possible to bunch 200 eμA beams better than 3 eμA beams with our present configuration. For low Q/A beams such as uranium, adequate bunching at currents from 300 to 450 eμA is possible. For lighter mass, high charge state ions, the beam current limit is approximately 100 eμA. The strong Q/A dependence of bunching performance is apparent in Figures 3 and 4. In general one can characterize 'Site B' as able to handle beam currents which are a factor of 100 greater than the present system can accept.

The beam ellipse is transformed by the defocusing effect of space charge, turning a waist condition into a 'parallel beam' condition. This is shown indirectly by noting the decrease in energy spread of the beam ellipse as the current increases in Figure 4, which corresponds to the increasing time width portrayed in Figure 3. Thus the original matching condition into the linac is modified drastically and eventually the beam ellipse falls out of the acceptance ellipse of the linac. With the site B configuration this does not occur until beam currents well in excess of 100 eμA are reached for any ion species.

The efficiency of converting the DC beam from the source into beam bunches matched into the linac acceptance is approximately 60% for our present configuration. The model calculations predict that the 'Site B' configuration of the bunching system will achieve a bunching efficiency of 65-70% acceptance. It is possible to operate the harmonic buncher in a mode which creates a virtual waist for the 24.25 MHz buncher. This mode requires lower buncher voltages and relaxes the requirements on waveform quality, but the bunching efficiency decreases to only approximately 40%. Therefore we do not anticipate using this bunching mode.

The 'Site B' configuration appears to be a good solution to high current injection into the ATLAS linac. This configuration will be implemented as part of the second ECR construction project. Operation of this new configuration is expected in 1997.

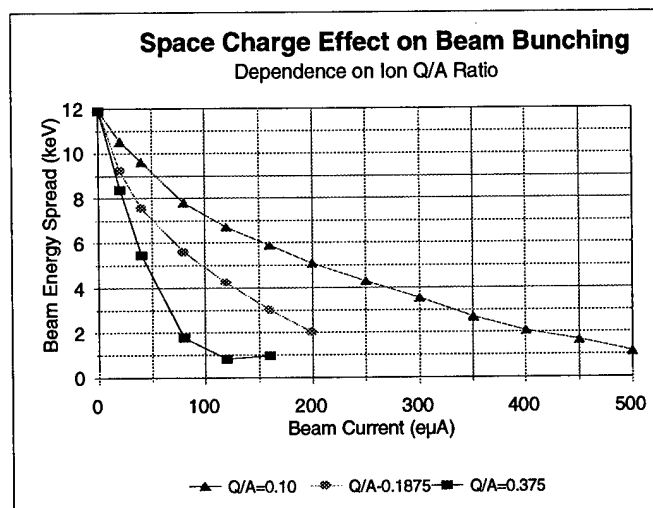


Figure 4: 'Site B' configuration. Beam energy spread for waist condition at chopper versus beam current for beams with differing Q/A .

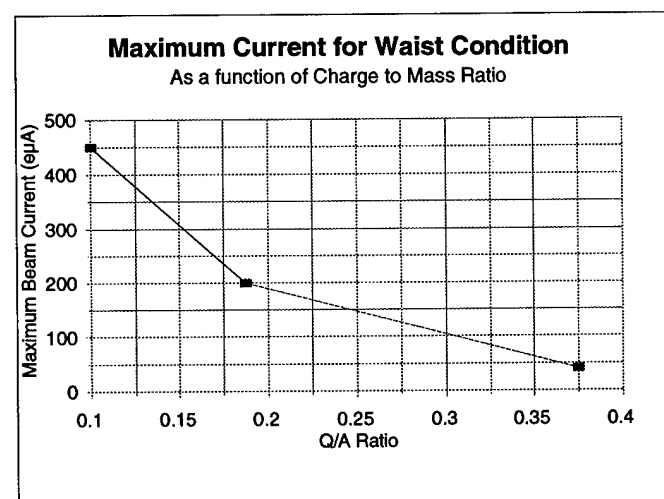


Figure 5: The maximum beam current for which a true beam waist can be achieved at the chopper as a function of Q/A for the Site B configuration.

*Supported by US D.O.E., Nucl. Phys. Div., contract W-31-109-ENG-38.

III. REFERENCES

- [1] R. C. Pardo, L. M. Bollinger, and K. W. Shepard, Nucl. Instrum. and Methods, **B24/25**, 746(1987).
- [2] L. M. Bollinger, et al., Nucl. Instrum. and Methods, **B79**, 753(1993).
- [3] F. J. Lynch, R. N. Lewis, L. M. Bollinger, and O. D. Despe, Nucl. Instrum. and Methods, **159**, 245(1979).
- [4] K. R. Crandall, "Trace 3-D Documentation", Los Alamos National Laboratory, LA-11054-MS, (August 1987).

EXPERIMENTAL INVESTIGATIONS OF PLASMA LENS FOCUSING AND PLASMA CHANNEL TRANSPORT OF HEAVY ION BEAMS

A. Tauschwitz, S.S. Yu, S. Eylon, L. Reginato, W. Leemans, J.O. Rasmussen, R.O. Bangerter,
Lawrence Berkeley Laboratory, Berkeley, CA 94720.

Final focusing of ion beams and propagation in a reactor chamber are crucial questions for heavy ion beam driven Fusion. An alternative solution to ballistic quadrupole focusing, as it is proposed in most reactor studies today, is the utilization of the magnetic field produced by a high current plasma discharge. This plasma lens focusing concept relaxes the requirements for low emittance and energy spread of the driver beam significantly and allows to separate the issues of focusing, which can be accomplished outside the reactor chamber, and of beam transport inside the reactor. For focusing a tapered wall-stabilized discharge is proposed, a concept successfully demonstrated at GSI, Germany. For beam transport a laser pre-ionized channel can be used.

I. INTRODUCTION

Final focusing of ion beams and their propagation in a reactor chamber are crucial for heavy ion beam driven fusion power production. The concept and technical realization of these operations have strong impacts both on the design of the accelerator and the layout of the reactor chamber. Most studies today are based on ballistic focusing by magnetic quadrupole lenses. This concept suffers from the sensitivity of the final focus to the current and shape of the beam pulse that is delivered by the driving accelerator. To reduce space charge blow-up of the driver beam in the final focus region the total beam current has to be divided into several beams, each with an individual final focusing system and a separate beam port in the reactor chamber.

An alternative solution is to strip the ions to a high charge state and to space charge and current neutralize the beam completely. An external focusing force is then applied to the beam to focus and transport it to the target. One advantage of this scheme is its physical simplicity because the beam can be treated as an ensemble of independent particles in the external focusing field. To create the focusing force the magnetic field of a high current plasma discharge can be used. This plasma lens focusing relaxes the requirements on emittance and energy spread of the driver beam significantly. A further advantage of this concept is the high insensitivity to the driver beam current and pulse shape.

The problems of focusing and of transport to the target are to a great extent independent of each other. For an experimental approach to evaluate the feasibility of plasma lens focusing these issues can be separated. Focusing of the ion beam can be accomplished using a wall-stabilized discharge. For the final transport through the reactor chamber with a radius of 2-3 meter the focused beam can be confined in a discharge channel. Since the beam is expected to be completely space charge and current neutralized in the

discharge channel the whole beam intensity required to ignite a target can be transported in one channel or, if higher symmetry of the target illumination is necessary, in two channels. For a Bi Ion beam of 10 GeV a plasma current of approximately 100 kA is sufficient to focus the beam and transport it to the target. Several schemes are possible to form the discharge channel inside the reactor chamber. All of them include a laser to pre-form a guiding path for the discharge channel.

A schematic layout of a reactor chamber using the proposed plasma lens final focusing is sketched in Figure 1. A single laser can be used to provide four channels from the reactor wall to the fusion pellet. Two of these channels are used to transport the driver beam and to illuminate the target from two sides. The remaining two channels are necessary to provide a return path for the discharge current. The discharge can be driven by one or several capacitor banks close to the reactor wall. To focus the driver beams down to the size of the discharge channel two wall-stabilized, tapered discharges are used. The angular acceptance of these lenses is large enough to combine several driver beams in each discharge and to keep a free optical path for the laser.

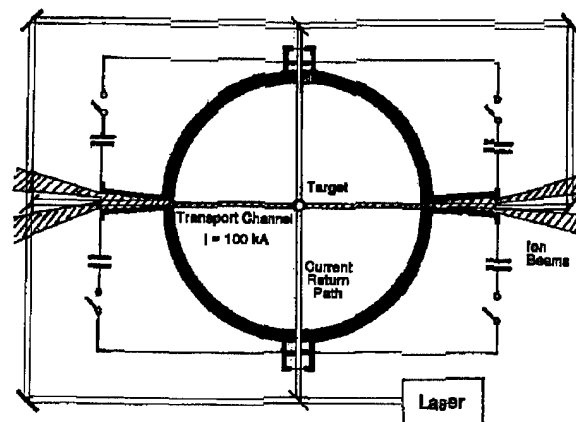


Figure 1. Schematic layout of a reactor chamber.

II FOCUSING WITH AN ADIABATIC PLASMA LENS

In a plasma lens the purely azimuthal magnetic field of a gas discharge is used to focus an ion beam moving along the axis of the discharge. Since a strong, first order focusing force is applied to the beam in both transversal planes perpendicular to the beam direction this kind of focusing is much stronger than quadrupole focusing, which is, applied to both directions, an effect of only second order [1].

Plasma lenses have been developed and investigated for several years at the German Heavy Ion Laboratory GSI to

concentrate high beam intensities onto small focal spots. The most promising results were achieved with a wall-stabilized discharge type [2]. The setup for these experiments is shown in figure 2.

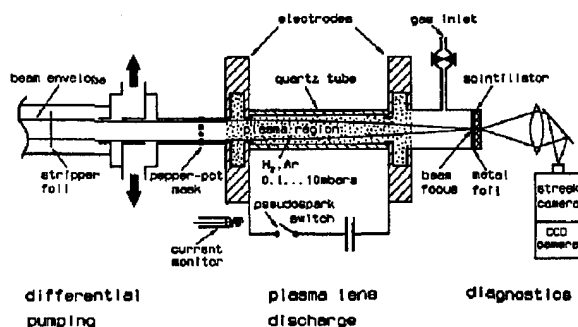


Figure 2. Setup of focusing experiments with a wall-stabilized plasma lens at GSI.

A heavy ion beam is traversing a differential pumping system and is then focused in a wall-stabilized discharge. The typical beam energy for these experiments was 11.4 MeV/amu. Discharge current and length of the lens are matched to produce less than half a betatron oscillation of the ions in the lens, that means that the lens is used as a thin lens. The focus is formed a short distance downstream of the lens and is detected by a combination of a plastic scintillator and a streak camera. The wall stabilized discharge has proven better linearity of the focusing fields than a z-pinch discharge and it provides the additional opportunity to taper the discharge tube and increase the focusing strength along the lens in this way. Tests of a tapered discharge have shown that a beam with 10 mm initial diameter can be focused to a spot of 160 μm . The tapered lens has the same degree of linearity and an approximately 50% higher focusing power than a cylindrical discharge [3].

For application of the plasma lens concept to the final focus problem in inertial confinement fusion the lens has to work as a thick lens, so that the particles perform one or more complete betatron oscillations inside the discharge. The particle trajectories in the lens are not necessarily coherent. They deviate the more from the coherent case, the broader the momentum and charge state distribution in the beam are and the more oscillations the particles perform in the lens. In the extreme case the beam fills the aperture homogeneously everywhere in the lens. Focusing can only be accomplished by increasing the focusing strength along the lens in this case. An easy way to achieve this is to taper the discharge tube diameter. To avoid beam losses the tapering has to be done adiabatically, which means that the change in betatron wavelength per betatron period has to be small.

In a focusing field a particle with coordinate x satisfies the equation of motion (Hill's Equation) [4]:

$$\frac{d^2 x}{dz^2} = -k^2 x$$

with

$$k^2(z) = \frac{Z(z)}{a^2(z)} \frac{2eI}{bmc^3}.$$

Here Z denotes the charge state of the ion, I is the total current in the lens, and a is the radius of the focusing discharge. In the adiabatic approximation

$$\frac{1}{k^2} \frac{dk}{dz} \ll 1$$

a solution can be written in the form:

$$x = \frac{C}{k^{1/2}} \exp(i \int k dz).$$

These equations show that the radius a has to be decreased by a factor of b^2 to reduce the radius of the beam envelope x by a factor of b . Using typical numbers for a driver beam with $m = 200$ amu, $\beta = 0.3$, $Z = 64$, and a current $I = 100$ kA in a channel that is tapered down over the length of one betatron wavelength at the entrance of the lens of $\lambda_\beta = 152$ cm from 20 mm to 5 mm radius yields a reduction of the beam radius from $R = 10$ mm to 5 mm. The admissible emittance for the beam is determined by the conservation of phase space density over the simple relation

$$\frac{\mathcal{E}}{R} = ka,$$

which allows a normalized emittance of 125 mm mrad at the end of the lens for the example.

An experiment is designed to investigate this adiabatic focusing experimentally using the 2 MeV beam from the LBL-ESQ injector. The schematic layout for this experiment is sketched in figure 3. The beam traverses a two stage differential pumping system capable to separate the discharge gas of approximately 1 Torr from the accelerator vacuum of 10^{-6} Torr. The discharge tube radius is tapered from 10 mm to 2.5 mm to reduce the beam radius from 5 mm to 2.5 mm. The intensity distribution in the focused beam will be scanned by a pinhole close to the end of the discharge and measured with a Faraday cup.

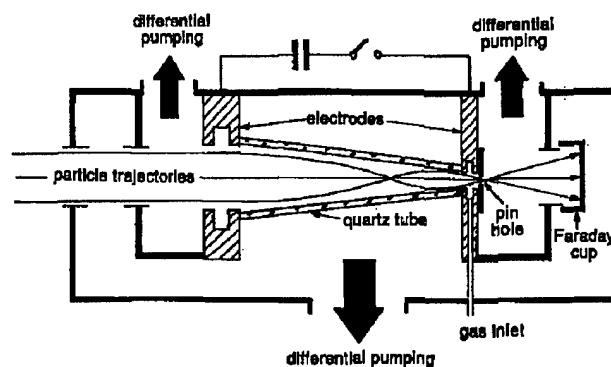


Figure 3. Setup for focusing experiments with an adiabatic plasma lens at the LBL ESQ-injector.

The beam is expected to be in an average charge state between 2 and 3 [5]. With a discharge length of 30 cm and a

discharge current of 20 kA the particles perform one and a half betatron oscillations in the lens so that an initially parallel beam of low emittance forms one focal spot inside the lens and another one at the end of the lens. The calculated emittance that this lens can handle without losing particles is 225 mm-mrad. This number is consistent with Monte-Carlo simulations of the focusing. These calculations include charge transfer processes instead of simply using an averaged charge state but do not include scattering of the ions in the discharge plasma. For the above mentioned case these calculations yield a negligible amount of particle losses below an emittance of 225 mm mrad and an almost linear increase of particle losses to about 35% for an emittance of 500 mm mrad.

At the low energy of 2 MeV scattering in the discharge plasma is an important factor. To determine the emittance increase by scattering the scattering in a 2 cm gas stripper cell has been measured for helium, nitrogen, and argon gas of up to 1 Torr pressure. From these measurements scattering angles up to 100 mrad can be expected for 0.9 MeV beam energy at the end of a 30 cm long tube with 1 Torr helium. This amounts to approximately 250 mm mrad emittance of the beam at the end of the focusing discharge, which is only slightly above the tolerable emittance. For higher beam energies or lower gas pressures no beam losses due to scattering are expected.

III. BEAM TRANSPORT IN A DISCHARGE CHANNEL

The driver beams can be combined and focused to a diameter of 10 mm outside the reactor. To keep the beam at this size during the 2 or 3 m radius of the reactor chamber the same magnetic field is required as at the end of the focusing lens. For the above mentioned example this can be achieved by a discharge channel of 10 mm diameter with 100 kA current. To guide such a channel from the beam port in the reactor wall to the target a laser can be used to pre-ionize the background gas in the reactor chamber.

Several coupling mechanisms of the laser energy to the gas have been studied experimentally. One of the most efficient ways is to add a small percentage of an organic molecule with a high photo ionization crosssection to the gas and to photo-ionize these organic molecules in a two photon process with an excimer laser. Breakdown of a high current discharge over up to 1.2 m along a laser path has been reported at 30% of the self breakdown voltage of the system [6]. For a reactor chamber a sufficient pre-ionization can be achieved with an excimer laser of 1 to 10 J pulse energy.

A crucial point in this transport scheme is the stability of the discharge channel. Unless very high voltages are used to create the channel, the high inductance of the long current path through the reactor chamber will limit the current rise time to several microseconds. The highest hydrodynamic stability of the plasma channel is expected for a discharge in a heavy gas as argon at a pressure of 10 Torr or more. An experiment is set up to address the problems of dynamics and

stability for a discharge channel of up to 90 cm length with a discharge current in the range of 50 to 100 kA and a current rise time of four microseconds. Further objectives of the experiment are the interaction of the plasma channel with a target and possible interactions between the channel and its return current path.

VI. CONCLUSION

Final focusing based on plasma lens focusing and discharge channel transport seems feasible if the stability of the channel is sufficient and if the problem of channel-target interaction can be solved. The advantages of this focusing scheme for the driving accelerator are relaxed requirements for emittance and momentum spread. The advantage for the reactor layout is the much smaller number and area of beam ports in the reactor wall, which makes the problem of explosion debris flying up the beam lines much easier to solve.

VII. ACKNOWLEDGMENTS

One of the authors (A.T.) wishes to thank the German Humboldt foundation for granting a Feodor-Lynen fellowship to support his visit at the Lawrence Berkeley Laboratory.

VIII. REFERENCES

- [1] E. Boggasch, B. Heimrich, D.H.H. Hoffmann, "Focusing behaviour of plasma lenses compared to conventional quadrupole systems", Nucl. Instr. Meth. A **336** (1993) 438-441.
- [2] E. Boggasch, A. Tauschwitz, H. Wahl, K.-G. Dietrich, D.H.H. Hoffmann, W. Laux, M. Stetter, R. Tkotz, "Plasma lens fine focusing of heavy-ion beams", Appl. Phys. Lett. **60** (1992) 2475-2477.
- [3] A. Tauschwitz, M. de Magistris, E. Boggasch, M. Dornik, D.H.H. Hoffmann, J. Jacoby, W. Seelig, P. Spiller, H. Wetzler, "Performance of a Shape Optimized Conical Plasma Lens", GSI Report **94-10** (1994) 10
- [4] P. Chen, K. Oide, A.M. Sessler, S.S. Yu, "Plasma-Based Adiabatic Focuser", Phys. Rev. Lett. **64** (1990) 1231-1234
- [5] H.D. Betz, "Heavy Ion Charge States", in Applied Atomic Collision Physics, Pure and Applied Physics, **43-4** (1983) 1-42
- [6] C.A. Frost, J.R. Woodworth, J.N. Olsen, T.A. Green, "Plasma channel formation with ultraviolet lasers", Appl. Phys. Lett. **41** (1982) 813-815

A LOW ENERGY ION BEAM TRANSPORT SYSTEM WITH VARIABLE FIELD PERMANENT MAGNETIC QUADRUPOLES

Y. Mori

Institute for Nuclear Study, University of Tokyo (INS)

3-2-1 Midori-cho, Tanasi-shi, Tokyo, 188 JAPAN

A. Takagi, M. Kinsho, T. Baba*

National Laboratory for High Energy Physics (KEK)

1-1 Oho, Tsukuba-shi, Ibaraki, 305 JAPAN

K. Shinto

The Graduate University for Advanced Studies

1-1 Oho, Tsukuba-shi, Ibaraki, 305 JAPAN

Abstract

A compact beam transport system with variable field permanent magnetic quadrupoles has been developed at KEK. It aims to transport the intense negative heavy ion beam from the surface-plasma negative heavy ion source (BLAKE source) to the tandem electrostatic accelerator efficiently. The system consists of four permanent quadrupole magnets and the magnetic field strength of each magnet can be changed from almost zero to 46 T/m. The negative copper ion beam of about 500 μ A was successfully transported by this system.

I. Introduction

In these days, development of negative ion sources for accelerators has been pushed strongly at various laboratories. Negative hydrogen ions are very important for intense proton synchrotron because its beam intensity can be increased by a charge-exchange multi-turn injection scheme using negative hydrogen ion beam. [1] Recently, negative hydrogen ion beams of more than 10mA beam current have been obtained from cesiated volume type of negative hydrogen ion sources.[2][3] On the other hand, negative heavy ion beams are very useful for heavy ion synchrotron using an electro-static tandem accelerator as its injector. Of course, intense negative heavy ions would be also very attractive for ion beam applications such as ion beam surface analysis[6], ion implantation and so on. Recently, negative heavy ion beams of more than a couple of mA have been obtained by a plasma-sputter type of negative heavy ion source.[7]

One of the difficulties for using intense negative ion beams is to transport efficiently such low energy beams extracted from the ion sources. There is a strong space charge force in such intense negative ion beams and the emittance of the beam is commonly deteriorated by it. The low energy beam transport system(LEBT) which transports the beam from the intense negative ion sources to the next accelerators such as an RFQ or a tandem accelerator is very important. In order to overcome this problem, a continuous strong focusing beam transport is preferred and various schemes have been proposed and tested. [8][9] [10]

Recently, we have perceived a variable field permanent quadrupole magnet(VFPQM) and developed a LEBT system for

intense negative heavy ion beams using four VFPQMs. In this paper, a design of the VFPQM, and characteristics and performance of the LEBT system using VFPQMs are described. A preliminary result of the beam emittance measurement for a negative Cu ion beam in this system is also presented.

II. VFPQM

The VFPQM used for our LEBT system is based on the design of the VFPQM which was developed by Barlow for the SSC IMS.[11] This type of the VFPQM was conceptually proposed by Halbach.[12]

The Quadrupole field is shaped by the four ion poles, and the field strength can be adjusted by rotating a 90 degrees of the outer ring of the magnet material which also forms a quadrupole field. Since the LEBT system using this VFPQM aims to transport the various negative ion beams from mass = 1(hydrogen) to mass = 197(gold) ions whose energies are about 60 keV at the maximum, the field gradient strength of the VFPQM has to be widely changed from 1.56 T/m to 42.9 T/m.

Since the required maximum field gradient is quite high and also the machining feasibility is requested, it was decided to use the PrFeB magnet material.[13] This material has a high remnant field($BH_{max} = 29$ MGOe) which is almost same as the NeFeB or Sm Co magnet, but contrary from them, this material is processed for producing with hot rolling. Therefore, an ordinary machining procedure like drilling and tapping can be used to treat it, which is very nice for our purpose.

The 2-dimensional program code, PANDIRA, was used to design the magnet. The calculated field lines where the two extremes of the magnetic field strength can be produced by a 90 degrees rotation of the outer ring of magnet material. The calculated maximum field gradient is 48 T/m and the minimum one is less than 0.3 T/m.

The LEBT system in our case comprises the four VFPQMs as described later. The length of each VFPQM is 140 mm. Figure 1 shows the measured magnetic field strength at the position of 8 mm away from the center as a function of the rotating angle of the outer ring. As can be seen from this figure, the magnetic field strength can be changed smoothly by rotating the outer ring.

Figure 2 shows the variation of the magnetic field strength as a function of the position from the bore center when the outer ring

*on leave from Nissin High Voltage Co.

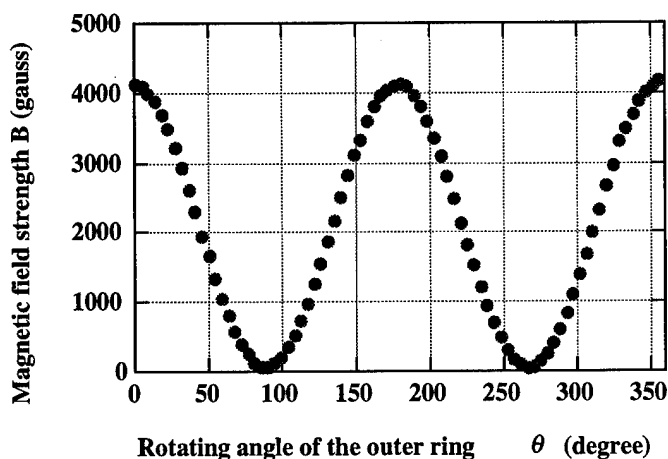


Figure 1. Measured magnetic field strength at the position of 8 mm away from the center as a function of the rotating angle of the outer ring.

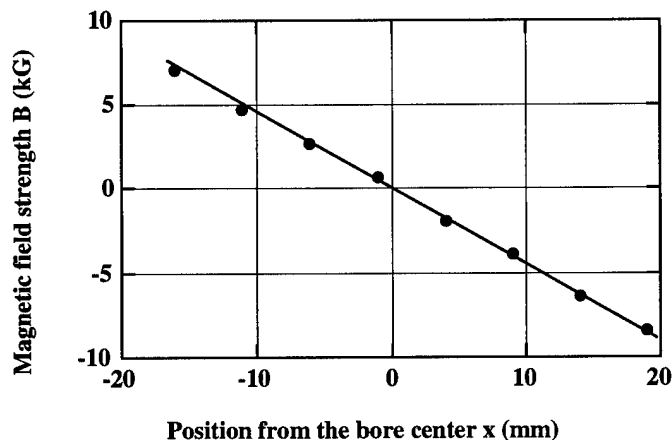
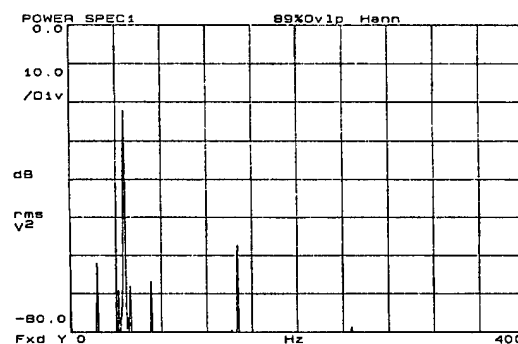


Figure 2. Variations of the magnetic field strength as a function of the position from the bore center when the outer ring was set to have a maximum magnetic field at the pole tip. The measured maximum field gradient was 46 T/m.

was set to have a maximum magnetic field at the pole tip. The measured maximum field gradient was 46 T/m which is about 5% less than the 2-D calculated value. This is probably caused by the leakage of the magnetic field at the both ends.

The higher order multipole components of the magnetic field in this VFPMQ such as 8-pole, 12-pole and so on, have been measured with a harmonic method using rotating coils. The diameter of the rotating coil was 25 mm. Figure 3 shows typical result of the measurement for the higher order magnetic field components. This figure presents for the case that it was rotated by 60 degrees from the maximum position. As can be clearly seen from the result, the 12-pole components were less than 10^{-3} compared with a fundamental 4-pole components. This might be good enough for transporting the beams without having serious aberrations due to the non-linear higher order components.



(b) $\theta = 60^\circ$

Figure 3. Typical result of the measurement for the higher order magnetic components. This is the case that the outer ring of the VFPMQ was rotated by 60 degrees from the maximum position.

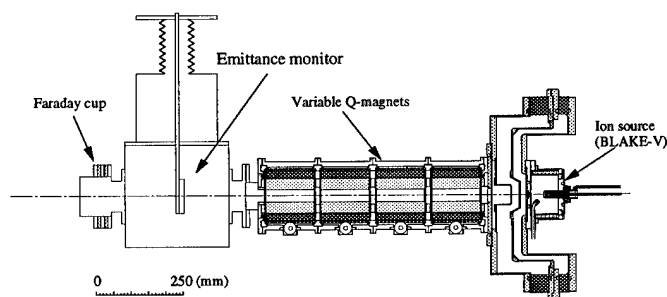


Figure 4. Schematic configuration of the LEBT system

III. LEBT

The LEBT system consists of the four VFPMQs. The total length of the system is about 640 mm. A schematic configuration of the LEBT of the setup are shown in figure 4.

The negative ion source, BLAKE-V[14], was attached at the front of the LEBT system. The size of the anode hole in the ion source is 5 mm in diameter and the maximum available extracted beam current is about 1 mA in pulsed mode operation for negative copper ion beam. The negative ions generated by the ion source is extracted by two electrodes and the maximum beam energy allowed in the electrode system is about 60 keV. The vacuum in the beam extraction region is evacuated by a 1500 l/s turbo-molecular pump. The operating vacuum pressure was about 1×10^{-5} Torr. There is an optional gas feeding system in this region. A amount of Xe gas can be introduced into the beam extraction chamber through it and efficient space charge neutralization is expected.

The beam optics in this LEBT system was estimated with a multi-purpose accelerator design code "SAD". Because of the strong lens action at the anode hole which may be largely affected by the sheath condition at the plasma surface, it is rather difficult to estimate the beam emittance configuration before ex-

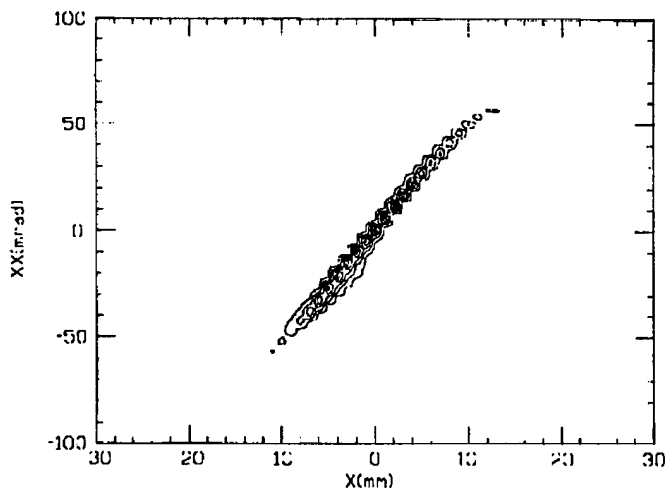


Figure 5. The measured beam emittance at the designed value of the magnetic field strength of each VFPQM.

periment. In the beam optics calculation with SAD, the beam emittance configuration at the front of the LEBT was assumed to be an up-right shape. The space charge force was not included in this calculation. No electric lens is used in the system, therefore, complete space charge neutralization would be expected in areal beam situation by introducing an small amount of Xe gas. Electric lens such as einzel lens sweeps out the low energy positive ions produced by ionization, which are useful for neutralizing a space charge potential in the negative ion beam. Because there are four VFPQMs, the beam configuration can be adjusted arbitrary independently in 2-D(horizontal and vertical) phase space within acceptance limited by a inner diameter of the vacuum chamber of the beam transport line. A typical acceptance for 60 keV H^- beam in the present LEBT is about $0.74 \pi \text{ mm.mrad}$, which is normalized by bg and for 60 keV Cu^- beam is about $0.093 \pi \text{ mm.mrad}$.

IV. Beam Test

Beam test has been done with negative copper ion beams from the BLAKE-V ion source. The ion source was operated in pulsed mode and the pulse width and the repetition rate were 400 msec and 20 Hz, respectively. The beam was extracted from the ion source at the positive voltage of about 20 kV and the total energy of the beam was about 40 keV. The beam current through the system was measured with a Faraday cup placed at the position of 40 cm away from the exit of the system.

The beam emittance in the vertical direction was measured at the position of 20 cm away from the exit of the final VFPQM. The measured beam emittance when the magnetic field strength of each VFPQM was set to be a design value is shown in figure 5. The Cu^- beam of about $500 \mu A$ measured by another Faraday cup after the emittance monitor was successfully transported.

The measured emittance configuration is somewhat different from the calculated one. It is probably because the actual beam was more convergent at the entrance of the LEBT compared to the beam emittance assumed in the calculation.

V. Summary

A low energy beam transport (LEBT) with four variable field permanent quadrupole magnets(VFPQM) has been developed for the negative ion beams. The magnetic field gradient of the VFPQM was able to be varied from almost zero to 46 T/m. The 40 keV Cu^- ion beam was well transported by the LEBT.

The authors would like to appreciate to Mr. Ikegami for his technical support.

References

- [1] T. Kawakubo, Nucl. Instrum. Meth., **A265**, 351(1988).
- [2] J. W. Kwan et al., Rev. Sci. Instrum., **61**, 369(1990).
- [3] Y. Mori, T. Okuyama, A. Takagi and D. Yuan, Nucl. Instrum. Meth., **A301**, 1(1991).
- [4] M. Q. Barton, Proc. 1983 Particle Accelerator Conf., IEEE Trans. NS-30 2019(1983).
- [5] P. Thieberger, Nucl. Instrum. and Meth. **220** 209(1984).
- [6] H. Yurimoto, Y. Mori and H. Yamamoto, Rev. Sci. Instrum., **64**, 1146(1993).
- [7] Y. Mori, Rev. Sci. Instrum., **63**, 2357(1992).
- [8] O. A. Anderson et al., Proc. of 1987 Particle Accelerator Conf., Vol. 1, 289.
- [9] D. Raparia, Proc. of Production and Neutralization of Negative Ions and Beams, AIP Conf. Proc. No. 210, 699.
- [10] Y. Mori et al., Proc. 8th Symp. on Accelerator Science and Technology (Saitama, Japan), 182(1991).bib
- [11] M. Haworth et al., Proc. 1993 Particle Accelerator Conf., Vol.3 1703.
- [12] K. Halbach, Nucl. Instrum. Meth., **206**, 353(1983).
- [13] Seiko Epson Co.
- [14] Y. Mori, Rev. Sci. Instrum., **65**, 1148(1994).

A COMPARISON OF TWO INJECTION LINE MATCHING SECTIONS FOR COMPACT CYCLOTRONS

T.Kuo, R. Baartman, L.Root, B. Milton, R.Laxadal, D.Yuan, K.Jayamanna,
P.Schmor and G.Dutto, TRIUMF, Vancouver, Canada
M.Dehnell, K.Erdman, Ebco Technologies

Two versions of injection line matching sections between the external ion source and the spiral inflector are used for the compact cyclotrons developed at TRIUMF in cooperation with Ebco Technologies. The 30 MeV model adopts a solenoid-doublet (SQQ) version while the 19 MeV unit takes a four quadrupole/two quadrupole (4Q/2Q) option.

Both cyclotrons use a same type of H cusp source and an identical inflector-central region combination. A comparison has been made between these two systems, in terms of DC transmission and RF acceptance as a function of source's H current intensity and emittance. The design and optics characteristics for both systems are described and the results obtained are reported.

I. INTRODUCTION

The TRIUMF's TR30 central region model (CRM) is an exact 1 to 1 duplicate of the 30 MeV H cyclotron's central region in every respect and the highest beam energy can be up to 1.5 MeV. The system consists of a high output (7 mA) and low emittance (0.365 pi-mm-mrad) H cusp source, a low loss injection matching section from a SQQ design [1,2,3], and a large phase acceptance with good centering inflector-central region. In 1990, up to 650-700 μ A at 1 MeV RF beam with optimal beam quality has been achieved [4]. The normalized circulating beam emittance ϵ_r , ϵ_z are 1π and 3π mm-mrad respectively. The centering error is no more than 1.5 at 5th turn. All of these excellent design achievements resulted in a highly reliable, efficient cyclotron system for isotope production [5,6]. The efforts of many experts who worked on these systems with high degree of professionalism are duly recognized.

we report here about the recent study on further utilization and capability development of this system since 1993. The first is the development and tests for replacing just the high-power-source/ SQQ system with a simpler, lower-power and more compact injection system, for TR13 series cyclotrons suitable for hospital PET project installation. A 2mA source and a 4-quadrupole(4Q)/2-quadrupole(2Q) compact matching section was chosen. Up to 300 μ A H⁺ at 1 MeV was achieved by May 1993 with this compact system[7,8]. Since Feb. 1994, more than 100 μ A at 13 MeV has been obtained routinely from a TR13 cyclotron. The second is to explore the SQQ system's ultimate capability of handling large beams. In 1994, a new capability of 1.5 mA at 1 MeV has been achieved. The

results of this being transferred to the engineering upgrade project for the Nordion/TRIUMF TR30 cyclotron. By April 1995, 2 mA at 1 MeV was reached.

II. SYSTEM DESCRIPTION

A. SQQ Injection Line

The SQQ injection line was designed by Baartman [1,2,3]. The method begins with setting the physical parameters the system has to deal with. A 25 KeV injection energy was selected and this define the $\beta\gamma$ value. The source parameters such as waist size, divergence, normalized emittance were chosen. A pair of cyclotron acceptance ellipses are calculated from an approximation in which a dipole magnet strength (1.2 T) and a field index ($n=0.09$) are defined. The ϵ_r from the up right ellipse approximation are given by $\beta\gamma v(r)((r)_{\max})^2/\rho(\text{cyc})$, same expression for ϵ_z . The $(r)_{\max}$ and $(z)_{\max}$ are the maximum half beam size over one betatron oscillation. $V(r)$, $V(z)$ are the betatron frequency at the first turn and $\rho(\text{cyc})$ is the cyclotron parameter (20 cm). With half-size 4mm by 13 mrad at the source and a matched size of 1 mm radial and 1.7 mm vertical on the first turn, the matching system must provide a magnification of about 1/3. This defines initially the drift length from source waist to solenoid centre and the length from solenoid to the entrance of the inflector.

Beam matching at the first turn was studied for a number of inflectors with the electric bend radius A and tilt parameter k' as free design parameters. The normalized circulating emittance was minimized using the computer code TRANSOPTR [9], for each transverse plane and for the sum of the two, $\epsilon_r + \epsilon_z$. The transfer metrics for the inflector were obtained using the program CASINO [10].

By iterating matching calculations, a final system design is defined. More detailed studies are to minimize the emittance growth due to the transverse coupling in the inflector, and due to beam orbit off-centering. The final reference tune was decided as the following [2]: Source waist to solenoid centre—1.3 meter; solenoid centre to Q1 centre—20.3 cm; Q1 centre to Q2 centre — 11.3 cm; Q2 centre to median plane 21.4 cm. Solenoid field —1.4 kG nominal at 210 amperes; effective length—23 cm and beam rotation—80xI (ampere) degrees. Q1/Q2 pole tip field =

-363/383 gauss nominal, effective length 6/10 cm and aperture diameter 5 cm.

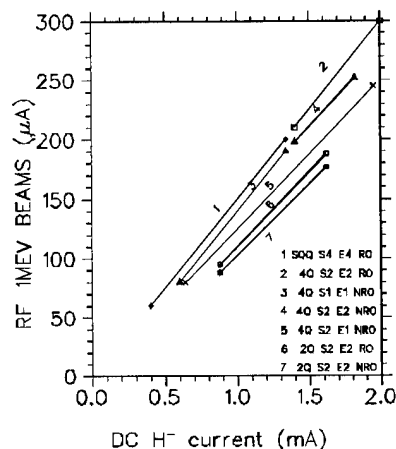


Fig. 1. Comparison of RF 1 MeV beam from different system

In addition to the beam rotation by the solenoid, the SQQ can be rotated with respect to the inflector axis as a whole without breaking vacuum. The ion source can also be rotated with respect to the injection line. The choice of 25 KeV beam energy makes the beam transport most easily in a magnetic only injection system. The tune of beam line is almost intensity-independent up to 14 mA DC. With proper control of vacuum, space charge neutralization is maintained and in turn emittance growth due to space charge effect is minimized.

B. 4Q/2Q Systems

The 4Q/2Q system was designed by Dehnel et. al. [7], following the matching technique established by Baartman. The SQQ is replaced by 4 identical compact quadrupole modules, while the injection energy, the cyclotron central region, tune frequency and the inflector parameters are remained the same. Assuming an initial source waist radius of 1.5 to 2.0 mm yielded the $\epsilon_{cnr} + \epsilon_{cnz}$ sum between 1.4 and 1.8 π -mm-mrad. For 2Q (Q1+Q2) system, the optimized sum value is in 3.0 to 4.0 π -mm-mrad range.

The optimization results in a system using 50 cm source waist to 1st Q drift length; 21 cm from the 4th Q to the inflector and three equal spacing of 13.5 cm between Qs. The nominal pole face field strength for 4Q system are +290, -560 +560 and -530 gauss for Q1, Q2, Q3, and Q4 respectively. The effective length is 10 cm with bore diameter of 5 cm. Again, the whole 4Q/2Q can be rotated with respect to the inflector axis. The 1st Q can also be used as skew quadrupole.

III. TESTS and RESULTS

A. Tests with 4Q/2Q System

The performance of the 4Q/2Q system is summarized in Fig. 1 where the RF acceptance is plotted a function of DC current through a 20 mm collimator 40 cm from the extractor. Rotational optimization (RO) and non rotational optimization (NRO) are shown for S2E2 and for both 4Q and 2Q cases. We observed that the rotational optimization always improves the transmission. For 4Q case, curve 4 moves up to curve 2, while for 2Q case, curve 7 moves up to 6. The test results agree with the prediction that 4Q would yield smaller emittance than 2Q can. The S2E2 beam was tuncated to 20mm aperture. The DC intensity was 2mA and the corresponding normalized emittance was 0.27 π -mm-mrad. 300 μ A RF beam was obtained with 15% RF acceptance. Larger Emittance beam resulted in lesser RF acceptance as curve 5 compared to curve 4.

B. Tests with 4Q/2Q on TR13 Cyclotron

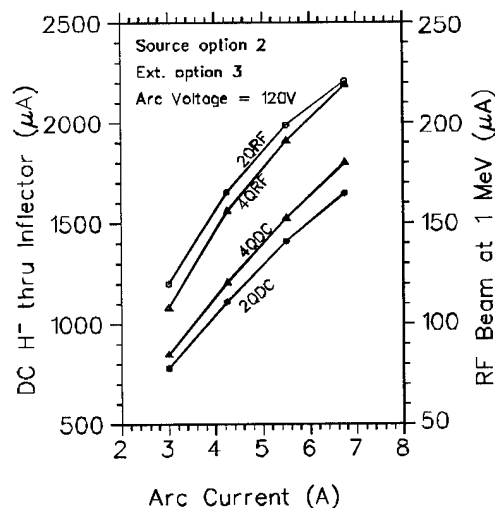


Fig. 2. DC transmission and RF acceptance of TR13 cyclotron

The beam tests for the TR13 cyclotron followed the same procedures as exercised at CRM, but unusual results were obtained. We found the 4Q performance was inferior to that from 2Q tuning as shown in Fig. 2. It was found that the differences came from a different extraction (E3) and a downsized pumping system. Also the drift length increase about 6 cm and the center magnetic field decreased about 1 kG. Optimizations with Q rotation and axial position of the inflector exit were performed. The graphic illustration for the improvement has been presented in a previous paper [8].

C. Tests With the SQQ System

The SQQ system has been vigorously studied since April 1994. After a few iterating cycles of source output and

injection line optimization, a high power source-extraction S4E4 was finally developed to obtain 14mA DC beams through the inflector. This is shown in Fig. 3. The corresponding unbunched RF beam at 1.1 MeV reach 2 mA. The source normalized emittance for beam size tuncated to a 20 mm circle and 40 cm from the source exit are also shown as a function of transmitted beam. From 5 mA on the emittance increases from $0.37 \pi\text{-mm-mrad}$ to $0.65 \pi\text{-mm-mrad}$ at 14 mA. The cyclotron acceptance falls off from 16% to 14.2%.

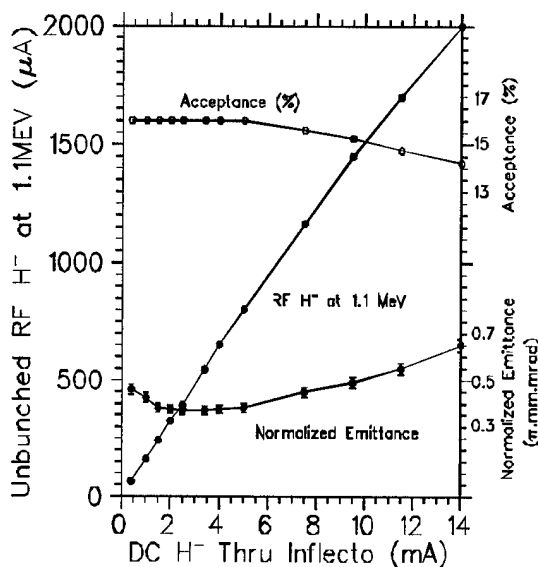


Fig. 3. DC H⁻ Thru inflector obtainable and H⁻ obtainable at 1.1 MeV from SQQ system of CRM

On the other hand, when the beam intensity is small the emittance value is also high ($0.46 \pi\text{-mm-mrad}$ at 0.4 mA). But the transmission is still maintained at 16% revealing that space charge effect causes emittance growth at high beam. The RF system at CRM does not have enough power to hold 50kV and 2.2 kW of RF beams at 1.1 MeV at the same time, the dee voltage is believed to be less than 50 kV, which in turn contributes to the fall-off of acceptance.

IV. DISCUSSION

From the 4Q/2Q tests with the TR13 cyclotron, sufficient beam current of 220 μA at 1 MeV (210 at 13 MeV) has been achieved at only 7 amp arc power. For normal factory procedure and routine operation, 150 μA has been obtained without test optimization. The 2Q option met all the requirements for the TR13 and it was the most cost

effective solution for 100 μA only specification. As a result, it becomes the TR13 designated injection line.

For RF beam current exceeding 1 mA, the SQQ system is the one of choice. The SQQ system possesses certain optical capability that the 4Q/2Q would not have, i.e., a larger bore diameter in the solenoid, a stronger focusing lens and the beam rotation when passing through the solenoid field. The beam shape from the source-extraction system has been assumed a cylindrical symmetry. This is true only if the beam intensity is small. At high ion source power and high extracted beam current, the beam shape appears to be elliptical. The solenoid rotates this beam about 160 degree at 200 amperes, matching the transverse plane to those of the doublet. Thus the source axis rotation, the SQQ rotation with respect to the inflector entrance axis and the beam rotation in the solenoid give a optimal matching capability.

In conclusion, the compact 4Q/2Q systems perform well with smaller beam intensity, while the SQQ system has a higher beam handling capability.

V. REFERENCE

- [1] R. Baartman, "Matching of Ion Sources to Cyclotron Inflectors", *Proc. 1st European Part. Acc. Conf.*, pp. 947-948, Rome, 1988.
- [2] R. Baartman, "TR30 Injection Line Optics", TRIUMF Design Note, TRI-DN-89-25, 1989.
- [3] R. Baartman *et al.*, "a 30 MeV H Cyclotron for Isotope Production", *Proc. of the IEEE Particle Accelerator Conference*, Chicago, 1989, P.1623.
- [4] W. Kleeven *et al.*, "Status and Results from the TR30 Cyclotron Centre Region Model", *Proc. 2nd European Part. Acc. Conf.*, pp.434-436, Nice, 1990.
- [5] H.R. Schneider *et al.*, "A Compact H Cyclotron for Isotope Production", *Proc. 1st European Particle Accelerator Conference*, Rome, 1988, p. 1502.
- [6] B.F. Milton *et al.*, "First Beam in a New Compact Intense 30 MeV H Cyclotron for Isotope Production", *Proc. 2nd European Particle Accelerator Conference*, Nice, 1990, p. 1812.
- [7] M. Dehnelt *et al.*, "Injection System Design and Tests for the TR13 Cyclotron" *proc. 4th European Particle Accelerator Conference*, London, 1994.
- [8] T. Kuo *et al.*, "Performance of an ISIS System using Compact Magnetic Quadrupole". *proc. 4th European Particle Accelerator Conference*, London, 1994.
- [9] E.A. Heighway and R.M. Hutcheon, "TRANSOPTR-A second Order Beam Transport Design Code with Optimization and Constraints", *Nucl. Inst. Methods*, 187, 89, 1981.
- [10] B.F. Milton & J.B. Pearson, "CASINO: Calculation of Spiral Inflector Orbits", TRIUMF Design Note, TRI-DN-89-19, 1989.

STRIPPING INJECTION INTO THE NEW BOOSTER RING AT IUCF

K. Hedblom, Department of Radiation Sciences, Uppsala University, Box 535 S-75121 Uppsala
D.L. Friesel, IUCF, 2401 Milo B. Sampson Lane, Bloomington, IN 47808

Abstract

To increase the polarized proton beam intensity in the IUCF Cooler ring, this ring will be equipped with a new injector consisting of a 7 MeV linear accelerator and an 80 MeV Cooler Injection Synchrotron (CIS). The linear accelerator will accelerate negative hydrogen ions which will be strip-injected into CIS. Tracking calculations have been made to estimate the beam intensity that can be achieved within a specified emittance.

I. STRIPPING INJECTION OF H^- INTO CIS

The choice of injection mode in CIS is dictated by the still modest intensity available from present polarized ion sources. While the pulsed beam intensity capabilities of modern polarized H^+ and D^+ sources is impressive ($> 200 \mu A$) and growing, it is still about a factor of 20 smaller than required for single turn kick injection to provide the $2.5 \cdot 10^{10}$ particles desired for Cooler injection. This goal can only be achieved via stripping injection of polarized H^- and D^- ions.

Negative polarized hydrogen ions will be strip-injected into CIS to produce protons (deuterons) that will be accelerated to 80 MeV (65 MeV) [1]. With the high intensity polarized ion source (HIPIOS) [2] it is possible to produce a $20 \mu A$ polarized H^- beam. This beam will be accelerated by a radio frequency quadrupole (RFQ) to 3 MeV, and by a drift tube linac (DTL), to 7 MeV.

The injection elements in CIS are a $4 \mu g/cm^2$ carbon stripper foil located at the center of the injection straight section, and two bumper magnets which are 180° apart in phase advance and centered about the stripper foil. The bumper magnets are used to displace the circulating beam during the injection so that incoming ions are injected close to the circulating orbit in order to keep the emittance small. The foil strips electrons from the injected hydrogen ions but it also scatters circulating particles during injection. Therefore the beam will be heated in both longitudinal and transverse phase spaces.

Stripping injection is usually accomplished by moving the circulating beam close to the foil edge so that circulating particles pass through the foil as few times as possible. For CIS however, the emittance of the injected beam is comparable with the maximum beam emittance that can be accepted and therefore it is necessary to bump the closed orbit onto the foil so that the injected and the circulating beams overlap. To prevent particles from passing through the foil on each turn, a stripper foil is used which has two unsupported edges. The foil strip width is the size of the injected beam. For a 7 MeV proton beam with $1.5\pi \mu m$ normalized emittance, the width of the strip would be $7.4 \mu m$ if the injected beam is matched with the β -function at the foil.

There might be a possibility to gain more intensity by focussing the injected beam on a narrower foil. The usable emit-

tance must however be larger than the emittance of the injected beam.

It is more important to make the foil thin. A carbon foil as thin as $4 \mu g/cm^2$ is available at IUCF now, but it might be worth while trying to make even thinner foils. Fig. 1 shows a $4.5 \mu g/cm^2$ thin carbon foil with two unsupported edges.

II. THE EMITTANCE GROWTH AT THE STRIPPER FOIL

Each time a particle passes through the foil it loses energy and is scattered through a small angle. The energy loss causes a displacement of the closed orbit with resulting emittance growth. Since the energy loss is random it also heats the longitudinal motion. However, it is the multiple scattering and the closed orbit displacement which dominate the emittance growth. For protons and deuterons at the relevant energies, the emittance growth can be estimated roughly as

$$\Delta\epsilon = 2\beta^*\theta_{rms}^2 + 2Dx_\beta\Delta\delta/\beta^* \quad (1)$$

with

$$\theta_{rms} = \frac{6.8 \text{ MeV}}{T} \sqrt{\frac{d}{47.2 \text{ g/cm}^2}} \quad (2)$$

as the rms multiple scattering angle and

$$\Delta\delta = 0.077 \text{ MeVg}^{-1}\text{cm}^2 \frac{\ln(1.3 \cdot 10^4 \beta^2)}{\beta^2} \frac{d}{T} \quad (3)$$

as the average relative momentum loss. $\beta^* = 1.1 \text{ m}$ is the horizontal β -function at the foil, d is the foil thickness, $D = 1.7$ is the dispersion at the foil, x_β is the betatron oscillation displacement ($\approx 3 \text{ mm}$) and βc is the velocity of the ion. The maximum number of foil passages a single proton (deuteron) can make before the emittance becomes too large is given by $\epsilon/\Delta\epsilon$. For a 7 MeV proton passing through a $4 \mu g/cm^2$ carbon foil and with $10\pi \mu m$ as the maximum emittance at 80 MeV, the number of foil traversals is 100.

III. A COMPARISON BETWEEN THE BEAM AT INJECTION AND AT EXTRACTION

The normalized beam emittance from the ion source is $1.5\pi \mu m$ which is equivalent to a $3.6\pi \mu m$ un-normalized emittance at the extraction energy 80 MeV in CIS. On the other hand, the acceptance of the injection system in the Cooler ring is $2\pi \mu m$. Therefore, even before considering the beam energy spread or the emittance growth at the stripper foil, only a fraction of the available beam can be injected into the Cooler. In addition, the Cooler has a longitudinal acceptance of $\Delta T/T = \pm 5 \cdot 10^{-3}$ while the beam from the RFQ has an energy distribution with spread $\Delta T/T_{RFQ} = \pm 10 \cdot 10^{-3}$. Therefore, more

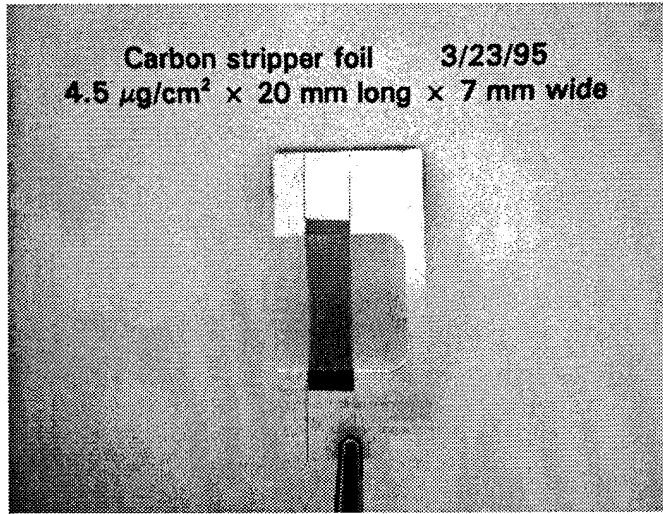


Figure 1. The $4.5 \mu\text{g}/\text{cm}^2$ carbon stripper foil with two unsupported edges. The width of the foil is 7 mm.

than 70% of the particles from CIS will be outside the acceptance of the Cooler.

The usable fraction of the beam injected into CIS can be greatly improved by opening up the acceptance of the Cooler injection channel to $10\pi \mu\text{m}$ and by installing a de-buncher between the RFQ and CIS to reduce the beam energy spread by a factor of about five [3].

IV. CALCULATIONS ON STRIPPING INJECTION

To take into account the longitudinal and transverse phase space of the injected beam, tracking calculations for coasting beams in CIS were made. Since the aperture limits in the horizontal plane are more important than in the transverse plane, only the motion in the horizontal and in the momentum phase space were considered. 1000 test particles are injected at the stripper foil with a uniform transverse phase space distribution and a Gaussian momentum distribution. The intensity gain is obtained as an integral over the phase space and over the number of turns they can make within the usable emittance. Similar calculations have been made for CELSIUS in Uppsala [4], [5] and here the same atomic model of the stripper foil has been used.

Whenever a particle hits the stripper foil, its direction and its momentum is changed randomly to simulate the multiple scattering and the energy loss. The particle tracking is done twice in order to first obtain the average relative momentum loss $-\bar{\delta}$. On the second tracking pass the longitudinal and the transverse acceptance are taken into account. A particle is removed if its three-dimensional emittance

$$\epsilon = \frac{(x - D\delta)^2 + (\alpha(x - D\delta) + \beta^* x')^2}{\beta^*} + \frac{\epsilon_{max}(\delta - \bar{\delta})^2}{\hat{\delta}^2}$$

is larger than the usable emittance which corresponds to the aperture limit at the extraction energy. $\hat{\delta} = \pm 2.5 \cdot 10^{-3}$ is the longitudinal Cooler acceptance. Fig. 2 shows the projection of the usable emittance on the x, x' -plane.

In Table I results from the tracking calculations for 3 MeV and 7 MeV protons for a $4 \mu\text{g}/\text{cm}^2$ carbon foil are tabulated. The

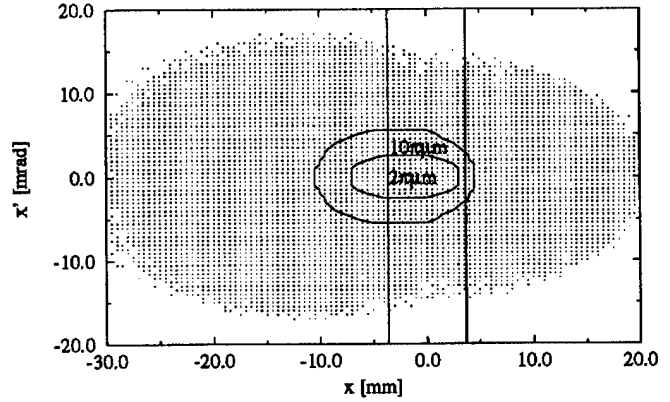


Figure 2. The usable emittance at the injection energy (7 MeV) for the $2\pi \mu\text{m}$ and $10\pi \mu\text{m}$ cooler acceptance. The emittances appear larger than they are because individual particles have different closed orbits. The vertical lines indicates the location of the stripper foil and the shaded area the CIS acceptance.

intensity multiplication factor for 7 MeV protons with a $10\pi \mu\text{m}$ Cooler acceptance and without de-buncher is 190.

Increasing the injection energy from 3 MeV to 7 MeV improves the intensity by a factor of four as a result of smaller emittance growth at the foil. The average number of foil passages \bar{h} that protons make during the injection is approximately four times larger for 7 MeV than for 3 MeV and is consistent with estimated values (eq.(1)).

Opening up the acceptance of the Cooler injection channel from $2\pi \mu\text{m}$ to $10\pi \mu\text{m}$ also results in a factor of four increase in intensity, mainly because the injected beam fits within the usable emittance. It is also because particles are forced to pass through the foil less frequently in order to stay inside the usable emittance. The larger emittance growth allowed improves the result by a factor less than 1.5 to be compared by a factor of five from eq. (1).

The de-buncher improves the results by 30%, mainly because the energy spread of the injected beam after the de-buncher is smaller than the longitudinal acceptance of the Cooler. The energy loss straggling, which heats the beam in the longitudinal phase space, is unimportant.

The intensity gain is shown versus time on the foil in Fig. 3. A factor of two in foil thickness reduction produces roughly a factor of two in intensity increase, which is expected since both θ_{rms}^2 and $\Delta\delta$ are proportional to the foil thickness (eqs. (2) and (3)). However, since the lifetime is longer it would be necessary to inject longer for very thin foils. The maximum pulse length from the RFQ is $360 \mu\text{s}$ and therefore it is uncertain if foils thinner than 1 or $2 \mu\text{g}/\text{cm}^2$ will improve the intensity further.

A mis-match of the injected beam with the β -function at the foil can improve the intensity up to 10% for the $10\pi \mu\text{m}$ aperture. The best result was obtained for a 0.5 m β -function of the injected beam and a corresponding stripper foil width of 5 mm.

V. CONCLUSIONS

Based on these calculations, it was decided to: 1) rise the injection energy from the original 3 MeV to 7 MeV to reduce the emittance growth at the stripper foil. This will be accomplished

Table I
Results from Tracking Calculations on Stripping Injection

Ion	T [MeV]	ϵ [$\pi\mu\text{m}$]	$\Delta T/T$	\bar{h}	τ [μs]	I/I_0
p	3	2	0.005	25	14	14
p	3	2	0.010	31	26	12
p	3	10	0.005	38	33	62
p	3	10	0.010	40	34	56
p	7	2	0.005	99	49	59
p	7	2	0.010	120	80	46
p	7	10	0.005	130	100	250
p	7	10	0.010	130	120	190
d	5	2	0.005	48	19	15
d	5	2	0.010	43	33	10
d	5	10	0.005	49	39	88
d	5	10	0.010	54	41	61

T is the injection energy, ϵ the Cooler acceptance, $\pm\Delta T/T$ the beam energy spread (90%), \bar{h} the average number of foil passages, τ the $1/e$ -lifetime and I/I_0 is the intensity gain.

by an additional linear accelerator (DTL) between the RFQ and CIS. 2) open up the Cooler injection channel as much as possible. 3) Install a debuncher in the CIS injection beam line to reduce the longitudinal energy spread from the two linear accelerators. With this modifications it is possible to gain a factor of 250 in intensity for protons. Assuming 50% transmission through the new injector this would produce $7.5 \cdot 10^9$ particles per pulse to be injected into the Cooler. To reach CIS performance goal which is $2.5 \cdot 10^{10}$ particles per pulse, the ion source intensity has to exceed $65 \mu\text{A}$ and the normalized beam emittance has to be smaller than $1.5\pi \mu\text{m}$. I.e. to reach the CIS performance goal a three times brighter ion source than HIPIOS is needed.

VI. ACKNOWLEDGEMENT

We wish to thank Bill Lowzowski for his work on manufacturing the stripper foils.

References

- [1] D.L. Friesel, S.Y. Lee, *CIS, a Low Energy Injector for the IUCF Electron Cooled Storage Ring*, in these proceedings.
- [2] M. Wedekind et. al., *The IUCF High Intensity Polarized Ion Source Project*, IEEE 93CH3279-7, 3184 (1993)
- [3] A. Pei et al., *The Indiana University Cooler Injector Synchrotron RF System*, in these proceedings.
- [4] K. Hedblom, A. Johansson, D. Reistad and A. Barany, *Calculations on Multiturn and Stripping Injection in CELSIUS*. in Proc. 3rd European Particle Accelerator Conference, Berlin, Germany, 24-28 March, 1992, ed. H. Henke, H. Homeyer, Ch. Petit-Jean-Genaz, 462
- [5] K. Hedblom, *Calculations on Multiturn and Stripping Injection at CELSIUS*. TSL-Note 93-02 January 1993

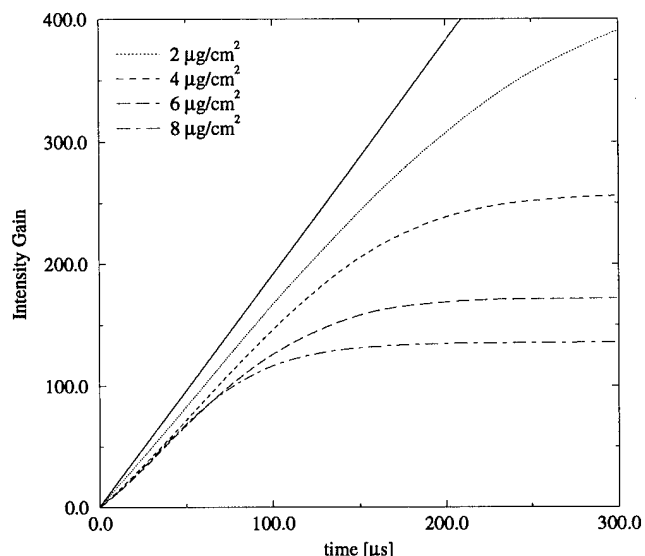


Figure 3. The intensity gain of 7 MeV protons plotted vs. the pulse length from the RFQ and for different foil thicknesses. The acceptance of the Cooler injection channel was $10\pi \mu\text{m}$. The solid line shows the gain calculated without energy loss or scattering at the foil.

ACCURATE TUNING OF 90° CELLS IN A FODO LATTICE*

K. Bertsche, Fermi National Accelerator Laboratory†, Batavia, IL 60510
and N. Mao, Superconducting Super Collider Laboratory, Dallas, TX 75237

Abstract

The Superconducting Super Collider was designed with a very exacting emittance budget. In order to avoid emittance dilution in the transfer of beam from the Low Energy Booster to the Medium Energy Booster, it is helpful to ensure that the transfer line connecting the two machines is tuned as designed. We discuss beam-based techniques for ensuring that the transfer line is tuned as designed, and errors associated with this procedure.

I. BACKGROUND

In order to avoid emittance dilution when injecting a beam into a circular machine, it is necessary to properly match the α and β functions of the injected beam to those of the machine lattice. These α and β functions cannot be directly monitored at the injection point to the circular machine, but they may be calculated by measuring beam profiles at a number of points in the transfer line upstream of this injection point. If these measurements are to be used to determine matching to the circular machine, it is necessary to know the transfer matrices between the measurement points and the circular machine injection point with high precision, and it is preferred that these be tuned to design values.

One possible approach to tuning such a transfer line would be to observe beam widths with a large number of beam profile monitors, perhaps as many as one or two per cell. This solution was proposed by some at the Superconducting Super Collider (SSC) Laboratory for the Low Energy Booster (LEB) to Medium Energy Booster (MEB) transfer line, but was rejected because it was too costly and was not necessary. Because of the design of this line as a FODO lattice of 90° cells [1], a simple beam-based procedure relying on beam deflection and measurement of beam displacement may be used to tune the quadrupoles in this line very accurately and precisely. If the quadrupoles have been precisely positioned, this procedure will assure proper tuning of the line.

Since this technique uses the beam as a diagnostic, it does not require that the quadrupoles have well-characterized or repeatable B/I characteristics or that their fields be monitored. It will work equally well with transfer lines containing either laminated or solid-core quadrupoles.

* Work performed at the SSC Laboratory, operated by Universities Research Association, Inc. for the U.S. Department of Energy under Contract No. DE-AC35-89SF40486.

† Operated by the Universities Research Association, Inc. under contract with the U.S. Department of Energy.

II. ROUGH TUNING

First consider a single cell of the FODO lattice, as shown in Fig. 1, where the first lens is a horizontally-focusing quadrupole. Nearly every cell contains a horizontal dipole deflector (steering magnet) at the beginning, just after the first quadrupole, and a horizontal beam position monitor (BPM) at the end, just before the first quadrupole of the next cell. In the center, on either side of the defocusing quadrupole, are a vertical BPM and a vertical corrector.

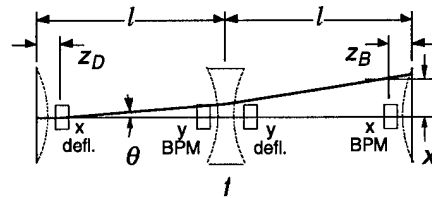


Figure 1: Rough tuning procedure.

In Fig. 1 and the equations to follow, l is the half-cell length, z_D is the distance from the lens center to the dipole corrector, z_B is the distance from the BPM to the lens center, and f is the focal length of the lens.

The rough tuning procedure is simply to deflect beam at the beginning of the cell, to measure its offset at the end of the cell, and to tune the central defocusing lens to correct the offset.

The transfer matrix from deflector to BPM is the product of three matrices: a drift, a (thin) defocusing lens, and a second drift. The $(x\theta)$ element of this matrix may be found, giving the beam offset at the BPM as a function of the horizontal deflection at the dipole corrector:

$$\frac{x}{\theta} = (l - z_D) + (l - z_B) + \frac{(l - z_D)(l - z_B)}{f} \quad (1)$$

It can be easily shown that in the thin-lens approximation, a 90° cell is properly tuned when $f^2 = l^2/2$. Substituting this into Eq. (1), the offset for a properly tuned cell may be found:

$$\frac{x}{\theta} = (2 + \sqrt{2})l - (1 + \sqrt{2})(z_D + z_B) + \frac{\sqrt{2} z_D z_B}{l} \quad (2)$$

The rough tuning procedure is then simply to adjust each quadrupole until the proper deflection is obtained. By alternating between horizontal and vertical planes, the entire transfer line may be tuned.

The precision of this tuning may be determined by applying first-order perturbation theory to Eq. (1). We assume that distances (l , z_D , z_B) are known to very high

precision, so errors in these are ignored. The pertinent error sources are errors in θ (due to calibration or power supply errors, or nonlinearity of the dipole correctors) and errors in x (due to BPM calibration or resolution).

Expanding Eq. (1) to first order in x , θ and f , setting the focal length to the proper value, and applying the approximation that $z_D, z_B \ll l$, one finds:

$$\frac{df_1}{f_1} \cong (1 + \sqrt{2}) \left(\frac{dx}{x} - \frac{d\theta}{\theta} \right) \quad (3)$$

Assuming a BPM measurement precision of 0.1mm rms and an offset of ± 1 cm (2cm total swing), the position measurement error is about 0.7%. Assuming an rms error of 1% in setting the angle, the total angular swing is in error by about 0.7%. Thus the lens settings using this procedure will be in error by about 2.4% rms. This should be sufficient for a preliminary tuning of the lattice, but for the LEB to MEB transfer line would not have been precise enough to ensure proper matching of the line to the MEB.

III. FINE TUNING

Much greater precision can be obtained from a tuning procedure involving two cells, shown in Fig. 2. Upon traversing two 90° cells, the beam will have passed through 180° and will be back on-axis. This will be true at the horizontal corrector two cells from the initial deflection. The BPM is not exactly 180° away from the first corrector, so the beam will have a slight offset as measured at the BPM. The beam position at this BPM is a very sensitive function of the tuning of the central (focusing) quadrupole, and permits very precise tuning of this quadrupole.

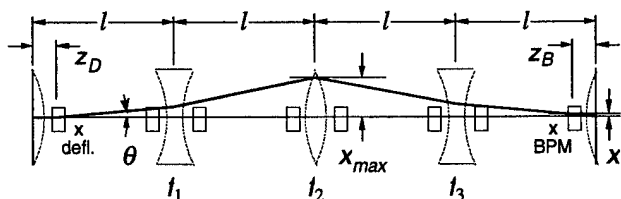


Figure 2: Fine tuning procedure.

The tuning condition may again be calculated. The $(x|\theta)$ element of the transfer matrix for two cells is:

$$\begin{aligned} \frac{x}{\theta} = & \left[1 + \frac{(l-z_D)}{f_1} \right] \left[l + (l-z_B) + \frac{l(l-z_B)}{f_3} \right] \\ & + \left[1 + \frac{(l-z_B)}{f_3} \right] \left[l + (l-z_D) + \frac{l(l-z_D)}{f_1} \right] \\ & - \frac{1}{f_2} \left[l + (l-z_B) + \frac{l(l-z_B)}{f_3} \right] \left[l + (l-z_D) + \frac{l(l-z_D)}{f_1} \right] \end{aligned} \quad (4)$$

For proper tuning, the focal lengths should again be $f^2 = l^2/2$. Substituting this into Eq. (4), one finds:

$$\frac{x}{\theta} = (z_D + z_B) - \frac{\sqrt{2} z_D z_B}{l} \quad (5)$$

The tuning procedure is similar to the rough tuning procedure above. One adjusts the central lens to give the proper deflection at the BPM, then moves downstream by a half-cell and does the same with the y-plane to adjust the next quadrupole. Again, each quadrupole may be adjusted in turn along the FODO lattice.

The precision of this two-cell tuning may be determined by applying first-order perturbation theory to Eq. (4). We again assume that distances (l, z_D, z_B) are known to very high precision, so errors in these are ignored. Expanding Eq. (4) to first order in x , θ and f , setting the focal lengths to the proper value, and applying the approximation that $z_D, z_B \ll l$, one finds:

$$\frac{df_2}{f_2} \cong \frac{\frac{df_1}{f_1} + \frac{df_3}{f_3} - \frac{(z_B + z_D)}{\sqrt{2} l} \frac{d\theta}{\theta} + (1 + \sqrt{2}) \frac{dx}{x_{max}}}{6 + 4\sqrt{2}} \quad (6)$$

Note that because of the small size of the deflection, x , at the BPM, its error has been normalized to x_{max} , the deflection at the center of the two-cell pair. Note also that the tuning of the central lens is very insensitive to errors in the deflection angle.

Assuming a BPM measurement precision of 0.1mm rms and an offset of ± 1 cm (2cm total swing) at the central quadrupole, the position measurement error is again about 0.7%. Because of the denominator in Eq. (6) above, this gives an error contribution to f_2 of only 0.06%. Assuming an rms error in setting the angle of 1%, the total angular swing is in error by about 0.7%, which gives a negligible contribution to errors in f_2 . (Assuming that z_B and z_D are each about 0.5m, and the half-cell length l is about 10m, this gives an error contribution to f_2 of about 0.005%.) Assuming that f_1 has already been set very precisely using this two-cell procedure, its errors also give a negligible contribution to errors in f_2 (about 0.02%). Assuming that f_3 has previously been set using the single-cell procedure to an rms precision of 2.4%, its errors give an error in f_2 of about 0.2%. Thus a single application of this two-cell tuning procedure to the FODO lattice allows setting of the quadrupoles to a precision of about 0.2%, dominated by errors in f_3 . A second application of the procedure allows setting of the quadrupoles to a precision of about 0.06%, dominated by errors in measurement of beam position.

This precision is more than sufficient for the tuning of the LEB to MEB transfer line of the SSC. Simulations show that 0.1% rms errors on the quadrupoles give less than 1% emittance growth [1].

IV. COMPLICATIONS

A. Thick Lenses

In the above analyses, a thin-lens approximation was used. This approximation may be improved by modeling the quadrupoles as thick lenses using the principal plane construction of classical optics. For a reasonably thin quadrupole, the principal planes are very close to the center

of the quadrupole. To first order, their displacement from the center of the quadrupole is given by:

$$z_P \equiv \frac{l_Q^2}{24f} \quad (7)$$

where z_P is the distance between the principal plane and the quadrupole center, l_Q is the effective length of the quadrupole, and f is the focal length of the quadrupole.

Distances (z_D , z_B , l) should be taken from the principal planes rather than from the centers of the quadrupoles. The principal planes are on opposite sides of the lens center for focusing and defocusing quadrupoles. Because of this, the effective distance l between a focusing and defocusing lens does not change, so neither should the lens focal lengths f . The distances z_D and z_B in the focusing condition (Eqs. (2) and (5)) are modified slightly, however.

This effect can be estimated for the parameters of the LEB-MEB transfer line of the SSC. For a 0.5m quadrupole, tuned to a focal length of about 7m, the principal planes are offset about 1.5mm from the quadrupole centers, so that the sum ($z_D + z_B$) is changed by about 3mm. A deflection angle of about 0.3mrad gives a deflection of about 1cm maximum at a focusing quadrupole 90° away. Using this deflection, the shift in transverse beam position, x , in the focus equations (Eqs. (2) and (5)) is on the order of 1μm, which is well below the resolution assumed for the BPMs. Thus, the thin lens approximation is perfectly adequate for this case, and introduces no detectable errors.

B. Bends

Transfer lines are not always straight. Generally, there are bends in the lines to assist in injection to a circular machine. These bends are accomplished by large dipole magnets inserted in drift spaces of the basic FODO lattice. If these magnets are horizontally bending and have flat ends, there is no effect on horizontal focus. There is, however, a slight vertical focusing effect, which can be modeled as a weak, thin lens at each end of the dipole. For small angular deflections, the focal length of each of these lenses is given by:

$$f_D \equiv \frac{2l_D}{\alpha^2} \quad (8)$$

where f_D is the focal length of the equivalent lens, l_D is the effective length of the bend dipole, and α is the bend angle.

If a dipole is about 2m long, and the bend angle is about 50mrad, the focal length is about 800m, and the composite (both ends) is about 400m. If this bend is near a quadrupole, which has a focal length of about 7m, it represents about a 2% effect. This additional focusing must be taken into account in the tuning equations (Eqs. (4)-(6)), but since the cells still have nearly 90° phase advance, this extra focusing does not destroy the precision of the tuning procedure.

C. Missing Correctors or BPMs

It has been assumed that each half-cell contains a correction dipole and a BPM. While this is desirable, it is not absolutely necessary. If a dipole corrector is missing from a half-cell, and the upstream quadrupoles have been adjusted correctly, a corrector located two cells (180°) upstream may be used. Similarly, if a BPM is missing and the downstream quadrupoles are adjusted correctly, a BPM located two cells (180°) downstream may be used.

D. Matching Sections

Special consideration must be given to the transition from the transfer line into the circular machine. The tuning procedure for the last two or three quadrupoles in the line would have been modified slightly, with a number of BPMs in the MEB used to detect displacements, but this should not have affected the precision of the procedure.

In general, transfer lines may have matching sections at their downstream end to match α and β functions from the line to the circular machine, which would further complicate tuning considerations at the end of the line. The LEB-MEB transfer line design had no such downstream matching section (implying that beam was "mismatched" in the transfer line, exhibiting large "beta waves"), although pairs of quadrupoles at the downstream end may have been used for dispersion matching [1].

V. CONCLUSIONS

It has been shown that a transfer line composed of 90° FODO cells can be tuned very accurately and precisely by a procedure based on deflecting beam and observing its offset approximately two cells (180°) downstream. For the LEB-MEB transfer line at the SSC, this would have allowed the quadrupoles to be tuned to a precision of about 0.06% rms, resulting in less than 1% emittance growth due to α and β function mismatch. This answers the concerns of some at the SSC that this line would be difficult to tune due to its solid core magnets, large beta waves, and small number of beam profile monitors.

VI. ACKNOWLEDGMENTS

We wish to thank Karl Brown, John McGill, and Rodney Gerig for helpful discussions and for their encouragement in formulating these techniques.

VII. REFERENCES

- [1] N. Mao et al, "Beam Optics of LEB-MEB Transfer Line for Superconducting Super Collider", *Proceedings of the 1993 Particle Accelerator Conference, Washington, D.C.*, vol. 1, pp. 333-335.

DESIGN PRINCIPLES FOR HIGH CURRENT BEAM INJECTION LINES

H. Liu and D. Neuffer, CEBAF, 12000 Jefferson Ave., Newport News, VA 23606, USA

We discuss the design principles for high current injection beam lines having a high degree of beam quality preservation. These principles are applied to designing a high current e-beam injection line delivering 10 MeV e-beams from the injector to an accelerator driving UV FELs, as proposed at CEBAF.

I. INTRODUCTION

A 200 MeV recirculating SRF e-beam accelerator is being designed at CEBAF for driving kW-level industrial UV FELs [1, 2]. This accelerator, like all the FEL drivers, should provide e-beams having the smallest possible emittances. This demands minimization of the emittance growth at all of the stages of beam creation, acceleration and transport. One of the most critical regions is the injection line which transports the e-beams from a CW high current 10 MeV injector [3] to the accelerator.

It is interesting to consider in general how a high current injection beam line should be designed to provide a high degree of beam quality preservation, while providing the required matching conditions into the accelerator. For a non-circulating accelerator, one can minimize the emittance growth in the bending system by minimizing the average beam size [5], and match the beam into the accelerator by adding quadrupoles after the last dipole of the beam bending line. However, this prescription does not apply to a circulating accelerator, since the quads added between the last dipole and the accelerator disturbs the lattice for high-pass accelerated beams [6]. Alternative prescriptions must be sought for the latter case.

II. GENERAL DESIGN PRINCIPLES

The first general principle that an injection line design should follow is symmetry. A symmetric bending system preserves the beam emittance better than an asymmetric bending system, since the symmetry minimizes the aberrations. Also, a symmetric achromatic system is more compact, since an asymmetric system requires more elements and more length to become achromatic.

Secondly, the beam should be bent gently. The bending angle is often limited by the given footprint or space to clear the high-pass accelerated beams from the injected beams. A rule-of-thumb has been given in [7] that the magnitude of the deflection of the injected beam should be less than $3^\circ \times (W_1/W_0)$, where W_1 and W_0 are the energies of the first orbit and the injected beams respectively. This ratio is generally less than 10, so the maximum magnitude of the deflection of the injected beam should be less than 30° for a circulating accelerator.

Thirdly, the length of an injection line should be minimized. Therefore, a minimum number of magnets constituting an achromatic system should be used. One can use a single α -magnet [8] or two conventional dipoles with a quad in between to constitute an achromatic bending sys-

tem. However, for more flexible beam matching and axial bunching, at least three dipoles are needed.

Fourth, the beam line should retain a high degree of flexibility in matching so that neither injector beams nor main accelerator beams are required to meet precise specifications in order to function.

III. EMITTANCE GROWTH

Beam emittance growth in bends has been studied in detail in [9]. The responsible mechanisms were attributed to the anomalous noninertial transverse space-charge force and the normal longitudinal space-charge force. Useful formulas have been given for estimating the emittance growth from these two mechanisms.

In some earlier particle simulations of high current beam transport through an injection line [4], we turned the transverse and axial space charge forces on and off alternatively, and identified the axial space charge force as the cause of the emittance growth. The underlying mechanism is that the momentum of each electron is modified by the axial space charge force, and the beam ends up with a residual dispersion or emittance growth.

We now derive the beam emittance growth in the bending plane defined by the transfer matrix

$$R = \begin{bmatrix} R_{11} & R_{12} & R_{13} \\ R_{21} & R_{22} & R_{23} \\ 0 & 0 & \delta \end{bmatrix}, \quad (1)$$

where $\delta \approx 1$ is introduced to account for the momentum variation. Due to $\sigma(B) = R\sigma(A)R^T$, we have

$$\begin{aligned} \sigma_{11}(B) = & R_{11}^2 \sigma_{11}(A) + 2R_{11}R_{12} \sigma_{12}(A) \\ & + 2R_{11}R_{13} \sigma_{13}(A) + R_{12}^2 \sigma_{22}(A) \\ & + 2R_{12}R_{13} \sigma_{23}(A) + R_{13}^2 \sigma_{33}(A), \quad (2.1) \end{aligned}$$

$$\begin{aligned} \sigma_{12}(B) = & R_{11}R_{21} \sigma_{11}(A) + (R_{11}R_{22} + R_{12}R_{21}) \sigma_{12}(A) \\ & + (R_{11}R_{23} + R_{13}R_{21}) \sigma_{13}(A) + R_{12}R_{22} \sigma_{22}(A) \\ & + (R_{12}R_{23} + R_{13}R_{22}) \sigma_{23}(A) + R_{13}R_{23} \sigma_{33}(A), \quad (2.2) \end{aligned}$$

$$\begin{aligned} \sigma_{22}(B) = & R_{21}^2 \sigma_{11}(A) + 2R_{21}R_{22} \sigma_{12}(A) \\ & + 2R_{23}R_{21} \sigma_{13}(A) + R_{22}^2 \sigma_{22}(A) + 2R_{22}R_{23} \sigma_{23}(A) \\ & + R_{23}^2 \sigma_{33}(A), \quad (2.3) \end{aligned}$$

$$\sigma_{13}(B) = [R_{11} \sigma_{13}(A) + R_{12} \sigma_{23}(A) + R_{13} \sigma_{33}(A)] \delta, \quad (2.4)$$

$$\sigma_{23}(B) = [R_{21} \sigma_{13}(A) + R_{22} \sigma_{23}(A) + R_{23} \sigma_{33}(A)] \delta, \quad (2.5)$$

$$\sigma_{33}(B) = \sigma_{33}(A) \delta^2 \quad (2.6)$$

Then the bending-plane beam emittance at the exit is

$\epsilon_x^2(B) = \epsilon_x^2(A) + \Delta\epsilon_x^2(B)$, where

$$\begin{aligned} \Delta\epsilon_x^2(B) = & [\sigma_{11}(A)\sigma_{33}(A) - \sigma_{13}^2(A)]a_1^2 \\ & + [\sigma_{22}(A)\sigma_{33}(A) - \sigma_{23}^2(A)]a_2^2 \\ & + 2[\sigma_{11}(A)\sigma_{23}(A) - \sigma_{12}(A)\sigma_{13}(A)]a_1 \\ & + 2[\sigma_{12}(A)\sigma_{23}(A) - \sigma_{22}(A)\sigma_{13}(A)]a_2 \\ & - 2[\sigma_{13}(A)\sigma_{23}(A) - \sigma_{12}(A)\sigma_{33}(A)]a_1a_2, \quad (3) \end{aligned}$$

where $a_1 = R_{11}R_{23} - R_{13}R_{21}$ and $a_2 = R_{12}R_{23} - R_{13}R_{22}$.

We assume that the bending system is achromatic and symmetric between the first half and the second half, and that the deflection in the second half is in the same sense as the first. Then the transfer matrices for the first half, second half and the overall system are [10],

$$\begin{bmatrix} -1 & 2\alpha_{12}\alpha_{22} & \Delta\eta \\ 0 & -1 & \Delta\eta' \\ 0 & 0 & \delta^2 \end{bmatrix} = \begin{bmatrix} \alpha_{22} & \alpha_{12} & -\alpha_{13}\alpha_{22} \\ -\alpha_{12}^{-1} & 0 & \alpha_{13}\alpha_{12}^{-1} \\ 0 & 0 & \delta \end{bmatrix} \begin{bmatrix} 0 & \alpha_{12} & \alpha_{13} \\ -\alpha_{12}^{-1} & \alpha_{22} & 0 \\ 0 & 0 & \delta \end{bmatrix}, \quad (4)$$

where $\Delta\eta = \alpha_{13}\alpha_{22}(1-\delta)$ and $\Delta\eta' = \alpha_{13}\alpha_{21}(1-\delta)$ are the residual dispersions due to momentum variation. The total emittance growth (normalized) from one end to the other of the bending system is

$$\begin{aligned} \Delta\epsilon_{nx} = & \eta_c \sqrt{\alpha_{21}^2 \sigma_{11}^2(0) + \alpha_{22}^2 \sigma_{22}^2(0)} \left| \sigma_{\gamma\beta}(1) \Delta\langle\gamma\beta\rangle / \langle\gamma\beta\rangle \right. \\ & \left. - (\sigma_{\gamma\beta}(1) - \sigma_{\gamma\beta}(0)) \right|, \quad (5) \end{aligned}$$

where η_c is the dispersion at the symmetry plane, $\Delta\langle\gamma\beta\rangle / \langle\gamma\beta\rangle$ is the relative average momentum change, and $\sigma_{\gamma\beta}(1) - \sigma_{\gamma\beta}(0)$ is the absolute change in the normalized rms momentum spread from the entry plane to the symmetry plane. This rms momentum change due to the axial space charge force has been given in [9], and substitution of it into Eq. (5) yields

$$\Delta\epsilon_{nx} = (3I_p S / 8l_b I_A \gamma^2 \beta^2) (\eta_c / f_x) \sigma_x(0), \quad (6)$$

where $I_p = Q\beta c / l_b$ is the peak current, l_b the total bunch length for a uniform distribution or equal to $(2\pi)^{1/2} \sigma_z$ for a Gaussian distribution, $I_A = 17$ kA, S the half length of the system, $f_x = -1/\alpha_{21}$ is the focal length of the first half of the system, $\sigma_x(0)$ is the initial rms beam size in the x -plane, and we assumed that the beam is nearly parallel at the entry plane, i.e., $\alpha_{21}^2 \sigma_{11}^2(0) \gg \alpha_{22}^2 \sigma_{22}^2(0)$. This equation shows the parametric dependence of the emittance growth upon various beam parameters as well as the injection line parameters.

IV. MAGNETIC BUNCHING

Axial bunching occurs if the bending system is non-

isochronous. The bunching process is shown in Fig. 1.

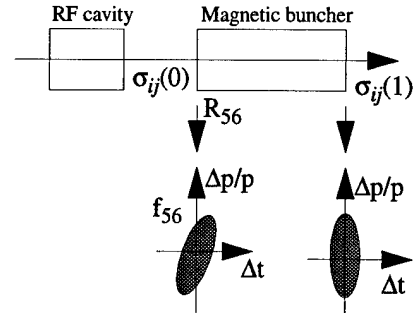


Fig. 1 Bunching process through a magnetic buncher

The bunch length after a magnetic buncher is

$$\sigma_{55}(1) = \sigma_{55}(0) (1 - R_{56}/f_{56})^2 + (R_{56}\epsilon_z)^2 / \sigma_{55}(0), \quad (7)$$

where $\epsilon_z = \sqrt{\sigma_{55}(0)\sigma_{66}(0) - \sigma_{56}^2(0)}$ is the longitudinal emittance, and $f_{56} = -\sigma_{55}(0)/\sigma_{56}(0)$ measures the tilt of the longitudinal phase space distribution of the beam at the entrance of the magnetic buncher. The axial matching condition is $f_{56} = R_{56}$ [11,12] under which the bunch length is minimum. The intermediate emittance growth at the symmetry plane is related to the beam momentum spread introduced for matching R_{56} with f_{56} in the form of $\Delta\epsilon_{nx} = (\eta_c/f_x) \sigma_{\gamma\beta}(0) \sigma_x(0)$, which can hardly be removed completely at the end of the magnetic buncher. Therefore, a balance must be struck between matching and minimizing the beam momentum spread to ease the emittance cancellation through the achromaticity of the system.

V. APPLICATION

The original injection line design for the proposed CEBAF UV FEL injector/accelerator is shown in Fig. 2.

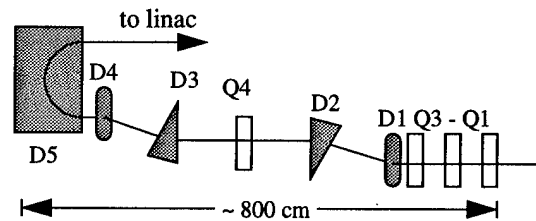


Fig. 2 The original 180°-bend injection line ($R_{56}=0$).

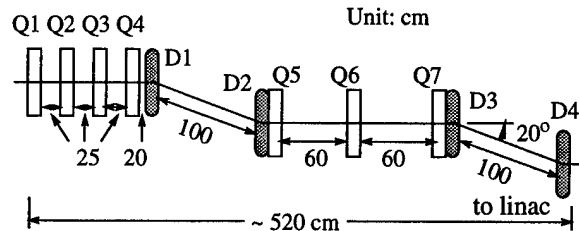


Fig. 3 A staircase injection line ($R_{56} = -0.282$ m).

A number of alternative designs have been investigated, two of which are shown in Figs. 3 and 4, to reduce the

beam emittance growth and to decouple the high-pass accelerated beams with the injected beams from that 180 degree bend. Fig. 3 is a staircase-line consisting of 7 quads and 4 parallel dipoles, and Fig. 4 is a slide-line consisting of 4 quads and 3 sector dipoles.

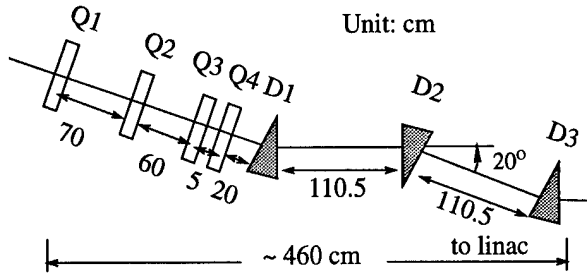


Fig. 4 A slide injection line ($R_{56} = -0.138$ m).

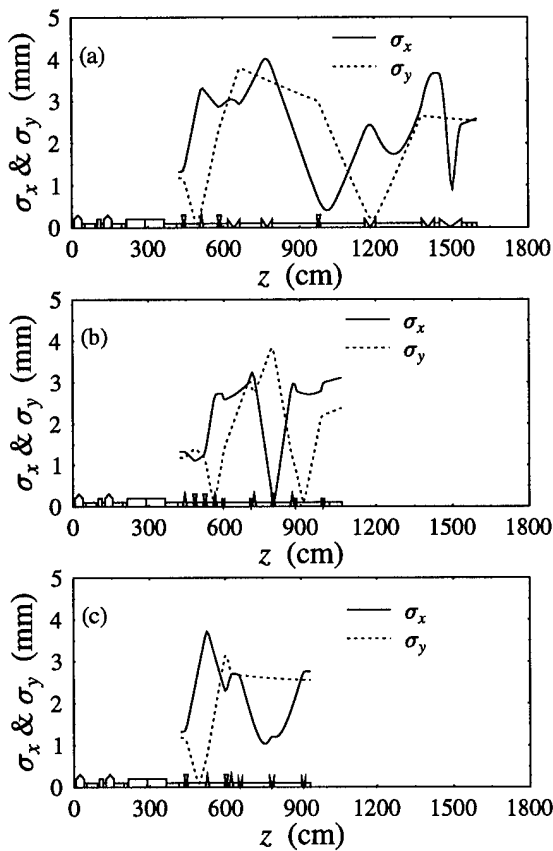


Fig. 5 Beam envelope evolution in three injection lines: (a) 180°-bend; (b) staircase; (c) slide.

Table 1 shows the performance comparisons among these three designs. The numbers in the table are the beam parameters at the end of each injection beam line.

Table 1 Performance comparisons among three designs

Beam parameters	180°-bend	staircase	slide
ϵ_{nrms} (π mm mrad)	8	6.8	4.6
$\epsilon_{\phi rms}$ (π keV-deg)	27	19	15
$4\sigma_t$ (ps)	11	10	4

The simulations started from the cathode with a 135 pCcharge/bunch, and continued to the cryounit exit, with the intermediate results saved. Then we restarted the simulation by incorporating each injection line with the preceding part. The restarted beam parameters are: transverse normalized emittance $\epsilon_{nrms} = 4.2 \pi$ mm mrad, longitudinal emittance $\epsilon_{\phi rms} = 11.6 \pi$ keV-deg, and bunch length $4\sigma_t = 6.7$ ps.

Fig. 5 shows the beam envelope evolution along these lines. It is seen that the beam's betatron-oscillation becomes more and more regular, and the number of cross-overs (very small beam waists) becomes smaller and smaller, from the 180°-bend-line to the slide-line. Due to its simplicity and better performance, the slide-design is chosen as the nominal injection beam line for the CEBAF FEL injector.

As is seen from Fig. 5 (c), the 4 quads before the three sector dipoles in the slide-line constitute a telescopic lens which can variably magnify the beam's β -functions from the cryounit exit to the entrance of the first dipole. The 3-magnet bending system preserves the beam's parallelness in both x - and y -plane [13, 14] while transporting the beam to the main accelerator. Betatron-function magnification and beam deflection are thus decoupled, which will greatly ease the operation.

Finally, we note that this 3-magnet bending system is non-isochronous with $R_{56} = \rho(3\alpha - 4\sin\alpha)$, where ρ and α are the bending radius and angle of each dipole. The achromaticity condition is $L/\rho = \cot\alpha - \tan(\alpha/2)$, where L is the edge-to-edge distance between the two adjacent dipoles. The dispersion at the symmetry plane is $\eta_c = \rho(2\cos(\alpha/2) - 1)$, and the focal length is $f_x = \rho/2\sin(\alpha/2)$. For small α 's, we have $\eta_c/f_x \approx \alpha$, which reduces Eq. (5) to Eq. (11) of [9].

We wish to thank J. Bisognano, D. Douglas and B. Carlsten for discussions. This work was supported by the Virginia Center for Innovative Technology and DOE Contract # DE-AC05-84ER40150.

VI. REFERENCES

- [1] D. Neuffer et al., these proceedings.
- [2] F. Dylla et al., these proceedings.
- [3] H. Liu et al., these proceedings.
- [4] H. Liu et al., Nucl. Instr. Meth. **A358** (1995) 475.
- [5] B. Carlsten et al., Nucl. Instr. Meth. **A296** (1992) 687.
- [6] D. Douglas, private communication.
- [7] R. Rand, *Recirculating Electron Accelerators*, (Harwood Academic Publishers, New York, 1984).
- [8] H. Enge, Rev. Sci. Instrum., **34** (1963) 385.
- [9] B. Carlsten et al., Phys. Rev. E. **51** (1995) 1453.
- [10] A. Banford, *The Transport of Charged Particle Beams*, London, E. & F. N. Spon Limited, 1966.
- [11] H. Liu, CEBAF TN# 95-004.
- [12] T. Raubenheimer, Workshop on 4th Generation Light Sources, SSRL, (1992) 263.
- [13] S. Penner, Rev. Sci. Instrum., **32**, 150 (1961).
- [14] B. Milman, Nucl. Instrum. Methods, **20** (1963), p.13.

SURVEY AND ANALYSIS OF LINE-FREQUENCY INTERFERENCE IN THE CEBAF ACCELERATOR *

M. G. Tiefenback and Rui Li, Continuous Electron Beam Accelerator Facility, 12000 Jefferson Avenue, Newport News, VA 23606 USA

Feedthrough of interference from the AC power line into accelerator components is a problem which in pulsed accelerators can be reduced by operation synchronous with the AC line. This means of avoiding line-frequency effects is ineffective for continuous wave machines such as the CEBAF accelerator. We have measured line-frequency perturbations at CEBAF both in beam position and energy by using the beam position monitor system as a multiple-channel sampling oscilloscope. Comparing these data against the measured static optics (taken synchronously with the AC line) we have been able to identify point sources of interference, and resolve line-synchronous variations in the beam energy at a level near 0.001%.

I. INTRODUCTION

The design specifications for the CEBAF electron beam (4 GeV, 200 microampere, continuous wave) include a spot size and stability on target of approximately 100 microns and a geometric beam emittance of 2×10^{-9} meter radian at 1 GeV. Time averages of these parameters are important and can be significantly degraded by line-frequency interference. In addition, there are several septa in the accelerator which have beam clearances of only a few millimeter; beam position perturbations at these locations could result in beam loss and interruptions in beam delivery, not to mention potential damage to system components by 800 kW of beam power.

The CEBAF accelerator is composed of two parallel linear accelerators, connected head-to-tail by five 180-degree recirculation arcs at one end and four such arcs at the other. Beam from the injector enters the North Linac (NL), merging with the recirculated beam. The beams of differing energy are separated at the first "spreader" and transported to the "recombiner" at the entrance of the South Linac (SL). After acceleration, the beams are separated again at the second spreader region, where each beam is directed either into a recirculation arc for the next pass through the system or toward the end stations for experimental use.

During early operation of the CEBAF injector, we observed beam motion in the 45 MeV region on the scale of several millimeters [1]. The injector has been cleaned up well by means including the correction of grounding errors and the re-routing of some power distribution lines, but in commissioning the accelerator we are finding line-synchronous energy variation and millimeter scale steering perturbations in the main accelerator.

II. DATA ACQUISITION

The beam position monitor (BPM) system at CEBAF has a global trigger for synchronization with pulsed beam operation. We have provided a line-synchronous mode for the master system trigger, along with a programmable delay with respect to the AC line zero crossing. This delay allows the use of the beam position monitors (which have a 1 Hz update rate through the control system) as a multichannel data acquisition system, effectively a digital sampling oscilloscope, gathering synchronized orbit data throughout the accelerator as a function of phase delay with respect to the AC line. Measurement of the beam position in dispersive regions provides relative beam energy information at a resolution of approximately 0.001%[2].

The present injector line synchronous trigger uses a simple zero crossing detector, and has a jitter window of approximately 20 microseconds with respect to a line-synchronized phase locked loop. The programmable delay (16 bits with 1 microsecond resolution) spans the full 17 millisecond 60 Hz cycle. BPM data are logged for each of a series of values for the time delay with respect to the AC line trigger. For the measurements reported here, we used a 500 microsecond delay increment, cycling multiple times through the 60 Hz period.

The present BPM system has an analog bandwidth of approximately 50 kHz, so the measurements described here are not limited by the BPM hardware. Each position reading update to the control system consists of the average value from twelve sequential beam pulses, sampled approximately 65 microseconds into each macropulse (typically 100 microseconds in duration). The BPM hardware monitoring the various recirculated passes of the beam around the machine is multiplexed to the digitizers so that in each 1-second interval, each of the 5 passes is sampled 12 times. The precision of each averaged measurement at the 15 microampere beam current used for much of the recent commissioning operations is typically 0.2 millimeter. The averaging process strongly suppresses detection of perturbations at various harmonics of 5 Hz, but the harmonics of 60 Hz are unaffected.

III. DATA ANALYSIS

The time structure of the position perturbations is well represented by the first three harmonics of the line frequency, dominated by the fundamental and third harmonic (see Figure 1). Ground loop current measurements made without the averaging limitations of the our BPM protocol are similarly dominated by the first and third harmonics of 60 Hz, supporting the idea that harmonics of the 60 Hz are most important. We have Fourier analyzed the position data for the sine and cosine com-

*Work supported by U.S. D.O.E. contract #DE-AC05-84ER40150

ponents of the first three line harmonics. These Fourier amplitudes vary around the accelerator in the same way as the actual positions and angles, i.e., through propagation by the static transport properties of the magnetic lattice.

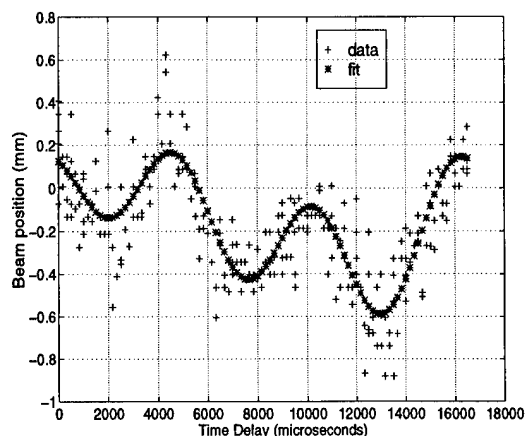


Figure 1: Example data showing the beam position dependence upon delay time. First and third harmonics are prominent. The BPM from which these data are taken is two-thirds of the way around the third recirculation arc. The "fit" curve uses the first three harmonics of 60 Hz.

We have used the RESOLVE [3] optics package to compare the static transport properties against the variations in beam position as a function of line trigger delay time. Along portions of the system with low levels of AC interference, the time dependence can be fit by time-dependence of the injection conditions. Distributed AC effects manifest themselves in a generally poor global fit of the beam position measurements using the static optics, although small segments of the machine may fit reasonably well. Significant point sources show up in the usual way as deviations between regions which can be individually fit to the static optics.

A. Measurements to date

Example data for beam position vs. line trigger delay are shown in Figure 1, along with the fit to the first three harmonics of 60 Hz. We found that the beam had measureable 60 and 180 Hz perturbations in steering and energy as it entered the North Linac (see figure 2), approximately 0.5 millimeter full span. We expected the Meissner effect of the superconducting acceleration cavities to shield the beam from most environmental effects in the tunnel, but we were unsure about effects in the unshielded regions outside the cryostats.

As can be seen from the data in the North Linac region, the transverse motion of the beam damps with the 10-fold acceleration through the linac. The span of the line-synchronous motion of the beam for 30 meters downstream from the linac and before it enters the spreader is below the 0.1 millimeter level. The amplitude remains small up to the first spreader region (vertical bends and quadrupoles). Here, both vertical and horizontal steering perturbations become visible, propagating through the first recirculation arc into the South Linac. The amplitude of the oscillation damps slightly through the South

Linac (where the energy increase is only a factor of two), growing again as the beam passes through the second spreader. The amplitude in the arcs is a factor of several higher than in the linacs, and essentially equal in Arcs 1 and 2.

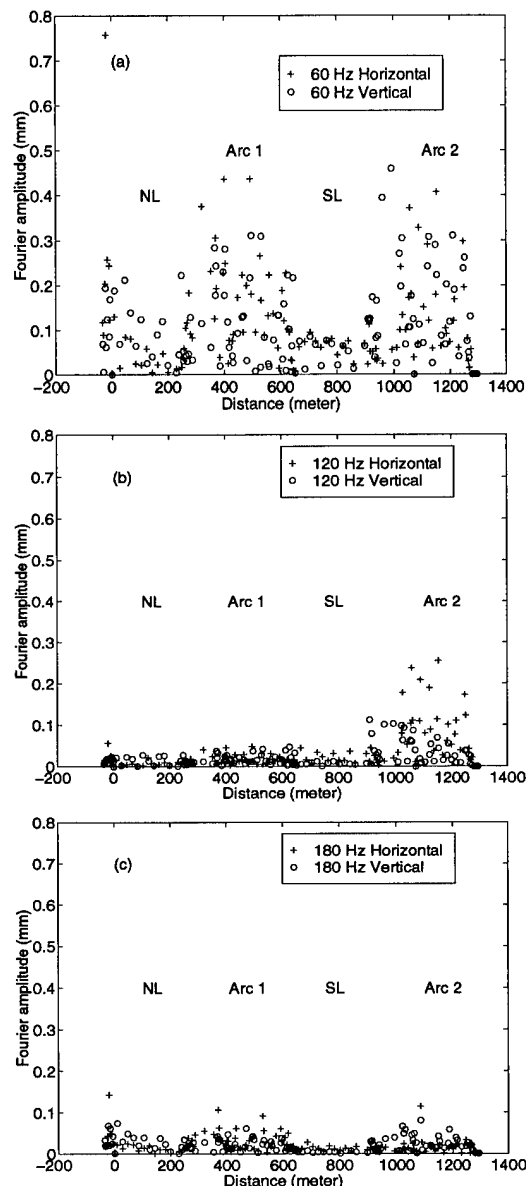


Figure 2: Fourier amplitudes of beam motion throughout 1st pass, combining the sine and cosine terms: (a) shows the 60 Hz component for single-pass beam through the linacs and the first two arcs; (b) shows the 120 Hz component; and (c) shows the 180 Hz component. The peak in horizontal amplitude in (a) near the entrance of the North Linac is in the dispersive region of the injection chicane, and is due to energy variation from the injector. The consistently larger amplitude of motion in the arcs is largely due to the bend dispersion.

In measurements taken with multiple-pass beam in the system, we can resolve meaningful data only in the regions where the beams of differing energy occupy separate beam-

lines until the multipass linac BPM system becomes operational. We find all beams carrying comparable steering perturbations in the separated regions, as might be expected from the above discussion. Comparison against static optics data for this configuration shows that the transport through the arcs is consistent with the static optics with time variations in both steering and energy, so the first three arcs appear to be relatively free of line-frequency sources. (Data in this set for the fourth and subsequent arcs is incomplete due to partial interception of beam at a septum upstream from the fourth arc.)

The propagation of the beam downstream from the vertical separation magnets of the spreaders to the point of injection into the arcs is also consistent with static optics, except for a localized perturbation coincident with the path length adjusting "dogleg" chicane magnets. These dogleg regions contribute horizontal (in the plane of the chicane) momentum kicks of similar magnitude to each beam, corresponding to a kick of approximately 5 microradian for the first pass (395 MeV in this instance) beam. This local perturbation was investigated, and a malfunction in the dogleg magnet supplies was found to be generating ripple of the proper magnitude to explain the effect. We have not yet identified a source for the horizontal and vertical perturbations observed at the spreader magnets.

In these and other measurements made to date, there is a clear increase in the 180 Hz component for the higher passes, becoming more significant than the 60 Hz component for the third and fourth passes.

Table 1: Sine and cosine components of energy variation for first, second, and third harmonics of 60 Hz, in parts per million. The arc 1 data represent the North Linac ripple alone, while the Arc 2 data represent the sum of North Linac and South Linac ripple. A weighted sum of these for comparison against the Arc 3 measurements is shown in the bottom row (see text). Discrepancies are typically 10 to 20 parts per million.

Harmonic Amplitudes of Energy Variations						
	60 Hz		120 Hz		180 Hz	
	sin	cos	sin	cos	sin	cos
Arc 1	-10	-66	+29	+12	+27	+3
Arc 2	-47	+27	+24	-2	+6	-19
Arc 3	-29	+17	+16	-13	+7	-18
Arc 1 + Arc 2	-35	-5	+27	+3	+14	-12

B. Energy perturbations

The same analysis also provides a measure of line-synchronous energy variations, as the arcs include regions of dispersion up to approximately 2.5 meter. The energy variation for the first three line harmonics is shown in Table 1. The data of the table have precision of 10 parts per million (estimated from the observed scatter of 50 parts per million in energy estimates made from the same BPMs in real time, coupled with averaging over 25 times as many samples as are used in the on-line routine, and (2) from the residual errors of the fit to the data). The row labeled "Arc 1 + Arc 2" contains a weighted sum of the Arc 1 (North Linac ripple) and Arc 2 (North Linac plus South Linac ripple). For this run, the beam energies were 395 MeV in Arc 1, 750 MeV in Arc 2, and 1105 MeV in Arc 3. The injector energy lock was active for this run, compensating for the injector energy ripple. Therefore the absolute energy ripple in Arc 3 should be equal to the sum of the energy ripple in Arc 2 plus the contribution from the second pass through the North Linac. The discrepancies between the measured Arc 3 ripple and the weighted sums for Arcs 1 and 2 are typically in the 10 to 20 parts per million range, in reasonable agreement with the error estimates we have for the ripple determinations.

IV. CONCLUSIONS

We have devised a method of taking beam position data throughout the CEBAF accelerator, using the BPM system in a sampling mode, to determine the line-synchronous beam position perturbation. We have found that comparison of these data against the measured static optics provides a useful means of identifying sources of line-frequency interference. We have identified microradian-level point sources of interference (magnet ripple) and have resolved relative energy variations of the beam at the 0.001% level. We anticipate that the techniques we are using will be useful for periodic measurement and long-term feedback correction of residual line-frequency variations at CEBAF.

V. REFERENCES

- [1] R. Legg, et al., *Location and Correction of 60 Hz in the CEBAF injector*, this conference
- [2] J. van Zeijts, et al., *Slow Orbit and Energy Lock Systems at CEBAF*, this conference
- [3] B. Yunn, et al., *RESOLVE at CEBAF*, this conference

LOCATION AND CORRECTION OF 60 HZ IN THE CEBAF INJECTOR*

R. Legg, D. Douglas, G.A. Krafft, and Q. Saulter, CEBAF, Newport News, VA 23612 USA

CEBAF produces a continuous electron beam with an emittance of 2-3 nm-Rad. Transverse low frequency magnetic oscillations act to dilute this emittance. These fields are typically associated with AC line conductors. The CEBAF injector is approximately 40 m long. To locate the source(s) of the beam motion, measured offsets were back propagated along the beamline using the DIMAD model. Field measurements were then made at the calculated field source positions and correlated with the measured offsets. Corrections and final beam measurements were made to verify the corrections.

I. CALCULATION OF SOURCE POSITION

The beam motion at different points along the beam line can be related by the equation:

$$k = (d_1/d_2)(\cos\Psi_2/\cos\Psi_1)/((\beta_1/\beta_2)/(\gamma_1/\gamma_2))^{0.5}$$

Where d_1 and d_2 are the measured beam motions at points 1 and 2 along the beamline. β is the calculated betatron function, γ is the measured relativistic term for the beam and Ψ is the calculated betatron phase advance at the points of measurement along the machine.

K is the variation in the normalized emittance. When k is greater than one it indicates that the observed transverse motion is greater than that to be expected from a motion being simply propagated by the lattice along the beam line. Where k equals one the beam motion is simply propagating along the beam line according to the lattice function. Where k is less than one there is the suggestion of an unknown damping function or experimental error. The magnitude of the observed motions, the energy and the calculated β 's are tabulated in Table 1 for the three measurement points, 0.5, 5 and 25 MeV. The betatron functions along the beamline were calculated using

a DIMAD model of this particular machine configuration. This model uses the experimental values to back-propagate betatron functions upstream of the diagnostic instrumentation used.

The 60 Hz motion at the A4 aperture in front of the quarter cryounit was measured by positioning the beam partially on the aperture, desync'ing the pulser from the 60 Hz line frequency and observing the oscillations in intercepted current on the aperture. This technique assumes that the spot is round and that, because of the emittance defining aperture upstream, the current density is uniform across the spot. Given these assumptions, this technique is very sensitive, allowing motions of only .02 mm to be measured. The measurements at the 5 and 25 MeV points were made by desync'ing the beam 20 Hz from the line frequency and then cycling the harp. The harp's travel time across the pipe is slow enough, 10-15 sec, that the 20 Hz beat frequency generated looks like a multiple maxima of the beam intensity on the harp trace and can be quantified by comparing it to a trace taken with the beam line sync'd.

The measured transverse beam motions along the beamline, d_1/d_2 , the calculated $(\cos\Psi_2/\cos\Psi_1)/((\beta_1/\beta_2)/(\gamma_1/\gamma_2))^{1/2}$ parameters and their ratios are tabulated in Table 2. The last column in Table 2 plots the k from the first equation above. The values are very close to one.

These results suggest a source before the A4 aperture which is being propagated down the machine or a distributed effect with the bulk of the disturbance before the 5 MeV point. The region of the injector most sensitive to stray low frequency magnetic fields is the 15 cm long acceleration region between the cathode and anode in the gun. The momentum goes from 0 to 0.34 MeV/c in this distance and is difficult to shield because the acceleration is electrostatic and the structures are dielectrics. To quantize the problem low frequency field measurements were made using a milliGauss meter, placing the probe where the cathode normally sits while turning the high potential deck electronics ON and OFF. The measurements indicated a total field of 13 mG in the horizontal plane of which 10 mG was accounted for by several AC fans in the CAMAC crate on the hot deck.

* Work supported by U.S. D.O.E. contract #DE-AC05-84ER40150

Diagnostic	E, MeV	Line Sync'd	β , m	d, mm	FWHM, mm	γ	Ψ , rad
A4, aperture	0.5	no	52	0.6	-	2	0
harp	5.55	yes	27		1.17	11	0.12
harp	5.55	no	27	0.2	1.34	11	0.12
harp	25.1	yes	55		0.69	50	0.4
harp	25.1	no	55	0.13	0.82	50	0.4

Table 1

ΔE	$\cos\Psi_2/\cos\Psi_1$	$d1/d2$	$((\beta_1/\beta_2)/(\gamma_1/\gamma_2))^{0.5}$	k
0.5 -5.5	1.01	3.0	3.25	0.93
5.5 - 25	1.08	1.53	1.49	1.11
0.5 - 25	1.09	4.62	4.86	1.03

Table 2

The total vertical AC magnetic field was measured at 3.5 mG. The calculated beam motion for the horizontal field at the second emittance defining aperture was 255 microns. The experimental result measured was 360 microns.

II. EXPERIMENTAL VERIFICATION

To verify the correlation between the field measurements and the beam motion measurements a test was performed measuring the observed beam motion with the AC fans in the CAMAC crate ON and OFF. The vertical motion of the beam with the fans ON was 250 +/- 20 microns. With the fans OFF the motion dropped to 50 +/- 20 microns. The correlation of the ratio of the observed beam motions, 50/250 microns, to the ratio of the transverse AC fields, 3.3/13.3 mG, was 0.81 +/- 0.4. The large error term is due to the 20 micron resolution of the position measurement.

After shielding several of the power supply transformers on the hot deck the measured fields were further reduced to 0.5 mG in the horizontal plane and 1.6 mG in the vertical plane at the cathode. The experiments at the 0.3 MeV/c and 0.8 MeV/c regions were repeated to verify reduction of the transverse beam motion. The data along with the calculated beam properties are given in Table 3. The data suggest another, smaller source of transverse beam motion between the measurement points. An extensive search for such fields failed. The other possibilities were an error in the measurements, an unknown or incorrect phase advance, magnification of the beam motion by spherical aberration in some optical element or momentum changes caused by low frequency oscillations in the rf control systems causing beam steering. Beam steering effects from small momentum changes are seen regularly when using the real-time bunchlength diagnostic.

To test this, a simple experiment was performed in which the signal from the cavity used to measure the arrival time of the micropulses was monitored with the gun pulser AC line synchronous. The pulser was then

reset to a pulse rate of 58 Hz but the beam was shut off. A measurement of the signal was made for a baseline noise figure and the beam was restored. A second measurement was made and the arrival time monitor showed a 1.8 picosecond variation from macropulse to macropulse. This would correspond to an AC modulation in the buncher amplitude at -24 dB. Corrective tuning of the amplitude loop was taken and further tests are pending.

After all modifications were made in the thermionic gun region, the beam motion at the end of the injector was remeasured by measuring σ_x and σ_y using a harp scanner with a 0.3 mm/second insertion velocity. The gun pulser was then set to a 50 Hz repetition rate and a second harp scan made. The 10 Hz beat frequency coupled with the slow harp speed, causes the measured sigmas to have a hashy outline that grow larger as the beam motion increases. The difference between the RMS sigmas with the beam pulser line synchronous and at some arbitrary frequency is the motion due to the line synchronous transverse magnetic fields. The data is presented in table 4.

The synchronous and non-synchronous data are essentially the same indicating little or no transverse AC beam motion.

III. CONCLUSIONS

The transverse AC magnetic field sources in the CEBAF injector were traced using experimental beam motion measurements and back propagated machine model parameters. The sources were quantified experimentally using direct field measurements and beam motion measurements. The sources of the fields were corrected to be a factor of 20 lower in the horizontal plane and a factor of 2.5 lower in the vertical. The correction was verified using direct field measurements. Beam motion experiments also show a factor of four reduction in the 0.8 MeV/c region and a reduction below the 50 micron resolution on the CEBAF harp scanners in the 5.5 MeV/c region.

Beam Momentum	Horizontal Beam motion measured, mm	Vertical Beam Motion measured, mm	γ	β , m	Ratios of motion
0.3 MeV/c	-	0.03	1.2	3	
0.8 MeV/c	-	0.15	1.98	21	2.8
0.3 MeV/c	0.03	-	1.2	3	
0.8 MeV/c	0.1	-	1.98	14	2.3

Table 3

line sync'd σ_x , mm	line sync'd σ_y , mm	non-line sync'd σ_x , mm	non-line sync'd σ_y , mm	$\Delta\sigma_x$, mm	$\Delta\sigma_y$, mm
2.26	3.66	2.25	3.5	-0.01	-0.16

Table 4

IV. REFERENCES

- [1] R. Legg and Q. Saulter, CEBAF TN #94-030,
1994
- [2] R. Legg and D. Douglas, CEBAF TN#93-075,
1993

PEP-II INJECTION TRANSPORT CONSTRUCTION STATUS AND COMMISSIONING PLANS*

T. Fieguth, E. Bloom, F. Bulos, T. Donaldson, B. Feerick, G. Godfrey, G. Leyh, D. Nelson, M. Ross, D. Schultz, J. Sheppard, P. Smith, C. Spencer, and J. Weinberg, SLAC, Stanford University, Stanford, CA 95309; and M. Ronan, LBL, Berkeley CA 94720

Installation of the PEP-II electron and positron Injection beamlines in the SLAC linac housing is now underway. Utilization of the existing high power, low emittance beams available at SLAC required that a great portion of the systems for pulsed extraction and transport of 9.0 GeV electrons and 3.1 GeV positrons for injection into the PEP-II rings will reside in the existing linac housing. Approximately 4.7 kilometers of these beamlines will be completed during the summer of 1995. All components, including orbit correctors and diagnostic instruments, required for extraction and transport of the electron beam will be in place and ready for commissioning as soon as this fall. The positron transport line in the housing will also be complete except for the pulsed extraction system. These systems are described, along with the status of the construction and installation of the important subsystems such as magnets and power supplies, vacuum systems, instrumentation and controls. The plan for commissioning is discussed.

I. INTRODUCTION

The SLC linac, including its damping rings and positron source, is a powerful source of low emittance positron and electron beams for injection into the PEP-II rings¹. This injection system² starts within the linac housing and consists of two beamlines having similar sections referred to by their function. These are the High Energy (HE) and Low Energy (LE) beamlines, each with Extraction, Bypass, Arc, and Match regions. As illustrated in Fig. 1, LE positrons (3.1 GeV) will be extracted from the linac at Sector 4 and HE electrons (9.0 GeV) at Sector 10. After extraction, each beam will traverse the length (>2 km) of a respective Bypass line connecting to its Arc and to a following Match section, optically matching the beam for injection into the proper ring. Now under construction (see shaded region of figure 1.) are the HE and LE Bypass lines along with the pulsed electron HE Extraction system and its related subsystems. The positron LE Extraction system at Sector 4 will be constructed later. This work represents about 1/3 of the total injection system construction effort. Installation began in March 1995, and is scheduled to be complete and ready for commissioning by mid- July 1995.

*Work supported by Department of Energy contracts DE-AC03-76SF00515 (SLAC) and DE-AC03-76SF00098 (LBL).

All subsystem hardware is of new construction including: a stainless steel, ion pumped vacuum system, a slow pulsed extraction kicker, bending, focusing and orbit correcting magnets; power supplies; beam position monitors (BPM) (of a modified SLC type for higher sensitivity, using existing the SLC control system) two SLC type wire scanners to measure energy spread and emittance of the extracted beam, and additional diagnostics. A program is planned to extract and study a 9 GeV electron beam under stringent control of energy, energy spread, emittance and timing.

The entire system (including the remaining 2/3) will be capable of filling 1658 bunches of 9 GeV electrons (0.99A stored) and 3.1 GeV positrons (2.14A stored) in two separate rings in a total of about 6 minutes from zero ring current (i.e., full-fill mode, 0 to 100%) or in about 3 minutes from 80% ring current (i.e., topping-off mode, 80 to 100%). The overall goals of the PEP-II Injection System are summarized in Table 1.

TABLE 1: Selected PEP-II Injection Parameters.

Beam energy	
High-energy ring (HER)	9 [range:8-10] [GeV]
Low-energy ring (LER)	3.1 [range:2.8-4] [GeV]
Beam Current	
High-energy ring (HER)	0.99/4518 [A/10 ¹⁰ e ⁻]
Low-energy ring (LER)	2.14/9799 [A/10 ¹⁰ e ⁺]
Particles per bunch	
High-energy ring (HER)	2.7 [10 ¹⁰ e ⁻]
Low-energy ring (LER)	5.9 [10 ¹⁰ e ⁺]
Linac repetition rate	60/120 [Hz]
Linac current range while filling	0.1-3 [10 ¹⁰ e [±] /pulse]
Invariant linac emittance	
ϵ_x	4x10 ⁻⁵ [m · rad]
ϵ_y	0.5x10 ⁻⁵ [m · rad]
Normal filling time	
Topping-off (80-100%)	3 [min.]
Full fill (0-100%)	6 [min.]

II. HE EXTRACTION & TWO BYPASSES

The electron beam Extraction system begins with an on-axis pulsed magnet which kicks the beam into the aperture of a Lambertson septum magnet. The focusing optics in this region is simply an extension of the 90° per cell linac lattice. Several dipole magnets complete the extraction bending bringing the beam back to be parallel to

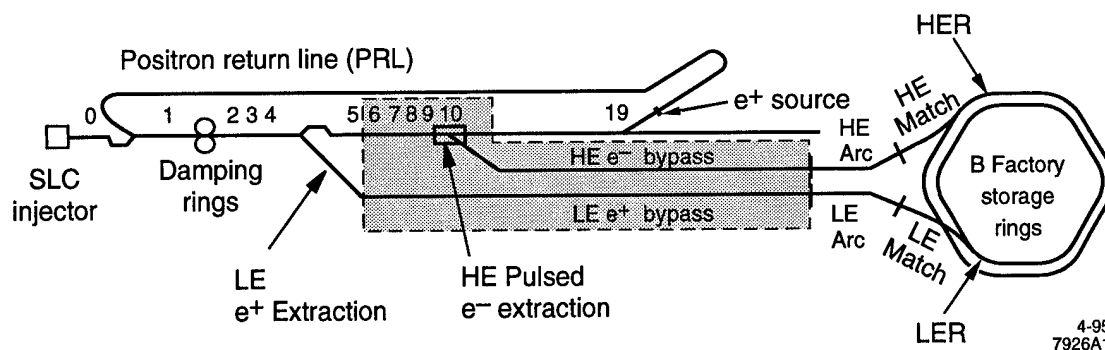


Figure 1. Schematic of the SLAC Linac showing the PEP-II Injection Transport System and the Rings.

the linac. Four independently powered quadrupoles are then used to match the beam parameters to the Bypass lattice, also a 90° per cell lattice but with the quadrupoles 101.6 m apart occurring only once per linac sector.

MAGNETS

Savings of engineering and design costs for the dipole and quadrupole magnets were obtained by modifying existing SLAC designs. This technique improved reliability by using field tested components and also allowed the use of a large number of existing quadrupole laminations at no cost to the PEP-II project.

There are two similar types of quadrupoles now constructed; a 4" long air cooled Bypass line quadrupole, and a 10" long water cooled Extraction line quadrupole. The quadrupole quarter sections were made from fine blanked laminations welded into magnet quarter sections. Four sections were assembled into a quadrupole core. The cores were blanchard ground to length and fiducials, bolt holes, etc. were machined. While assembled as a core, all four pole tip profiles were machined using a wire Electric Discharge Machine. This method resulted in magnet length errors being held to ± 0.002 " and errors in magnet pole profiles to ± 0.001 " at no extra cost. Improvements to the design included improved coil terminations, larger coil pockets with greater coil to core axial clearance, elimination of internal conductor brazes and the exclusive use of G-10 for insulator blocks.

Similarly, the dipole magnets are based on earlier designs. The Lambertson septum magnet is a larger version of the SLC positron source extraction Lambertson. The dipole bend magnets are standard H-bend type constructed either from single pieces of iron or from slabs bolted together. The small corrector magnets are a low cost ($\approx \$300$) sheet metal design.

MAGNETIC MEASUREMENTS

After a standardization procedure, the integrated gradient and harmonics of each quadrupole were measured at 12 different excitation currents using a long rotating coil

of 1.89 cm radius. The variance of the integrated strengths at the typical operating current of all the Bypass quadrupoles is within 0.25%. The sextupole component at a radius of 1 cm is less than 0.1 % of the quadrupole strength and the sum of all the higher multipoles is less than 0.5%. The dipole magnets are now being measured.

POWER SUPPLIES

The High Energy Extraction Stub and transport lines utilize one pulsed power system³, and 20 DC power systems. The pulsed power system consists of a solid state pulse generator capable of delivering high current trapezoidal shaped pulses into an inductive load. The capacitor bank is switched into the load through a pair of IGBT devices. A combination of diodes with these IGBT modules is used to shape the current pulses and recover the inductive energy back into the capacitor bank without reversing capacitor voltage. A DC power supply to the capacitor bank compensates for pulse to pulse power losses. The rack mounted pulse generator unit contains a storage capacitor bank of up to 660 μF , and can deliver 600 amps at 1000 volts into inductive loads of up to 3 mH. The current amplitude and discharge time are controlled to 0.02% accuracy by a specially developed precision controller via the SLAC central computer system.

The dipole magnets are powered by a 48 kW supply and a 20 kW unit. Both of these supplies employ SCR primary regulators, and an external feedback amplifier for current regulation. The external amplifier sums the CAMAC generated reference and the magnet current feedback signal, which is provided by a precision DC transducer (0.001%), to stabilize the power supply current to 0.01%.

One dipole and 11 quadrupole magnets are powered by 5kW commercial switching power supplies controlled by the same type of external feedback amplifier described above. Similarly regulated are the four switching power supplies, two for the focusing strings (8,12 quads each) and two for the defocusing string (8,11 quads each) for the HE Bypass line(5 kW) and the LE Bypass line (15 kW).

VACUUM

The Vacuum System is an all metal, unbaked, ion pumped system, comprised mostly of long drift tubes (18 to 46 m long) of 50.8 mm diameter 304 welded stainless steel tubing. The required average pressure for H₂ is 7×10^{-6} Torr. At 101.6 meters intervals a tee chamber connects the two Bypass lines and both are pumped by a 55 liter per second ion pump. Six meter lengths of tubing are butt welded together, by an orbital welder, in the accelerator tunnel. The remainder of chambers consist of bellows, tees, crosses, magnet vacuum chambers, vacuum isolation valves and assorted diagnostic components connected by Conflat® flanges.

ORBIT CORRECTION

Approximately 150 individual X-Y corrector magnets will be installed on the HE and LE Extraction and Bypass lines. The corrector strengths are 10 G-m and 20 G-m for the LE and HE Bypass respectively. Each corrector will require a bi-polar current of up to 6 A, with a 24 hour stability⁴ of better than 0.1%.

The low corrector strengths require that the average remnant field inside the 50.8 mm beam pipe be reduced to <50 mG so the correctors compensate for alignment errors only. The earth's field is attenuated by μ -metal shielding over 96% of the length of beam pipe. The material used is 150 μ m thick, rolled into tubes 40 cm long, before annealing at high temperature. Studies showed that a field attenuation of better than 50:1 was easily achievable and that normal handling during installation does not affect the shielding properties.

INSTRUMENTATION & COMMISSIONING

An X-Y Beam Position Monitor (BPM) followed by an X corrector and Y corrector is placed downstream of each quadrupole. Each BPM plate is 61 cm long and covers 20% of the circumference at an inner radius of 29 mm. The BPM signals are time multiplexed into existing Linac BPM ADCs through 11 dB loss directional couplers. The expected single pass position resolution (rms) in x or y is ± 50 microns for $>2 \times 10^9$ electrons in the bunch, increasing to ± 200 microns for $.5 \times 10^9$. The BPM centers will be surveyed into better than ± 1 mm (rms) in the transverse dimensions. A very cost effective method (<\$900 ea) of construction resulted in a $\pm .28$ mm rms distribution of electrical centers for the 100 BPMs now built and tested. The extracted beams as they enter the extraction lines will be stabilized in energy, x, x', y, and y' by a feedback system (~1 sec time constant) using eight Linac BPMs and the first four injection line BPMs. The BPM system allows measurement of a single bunch as it travels down the injection line and around the ring.

A wire scanner in the dispersive region of the Extraction line will measure the beam energy spread and a second wire scanner placed in the Bypass line will measure the beam emittance by varying an upstream quadrupole. An insertable fluorescent screen profile monitor accompanies each wire scanner. In the dispersive region of the extraction there is a horizontal set of jaws for limiting the momentum acceptance of the line. The electron Bypass line terminates in a temporary 10 kW dump in Sector 28 for a 1995-96 beam test. Toroids will be placed at the beginning of the Extraction line, the beginning of the Bypass line, and just upstream of the dump. The LSB will be 4×10^7 charges. Full scale will be 4×10^{10} charges and the noise should be < 1 LSB.

Commissioning begins with the Personnel Protection and certification of the Beam Containment System. Ion chamber thresholds will be set to limit the repetition rate of a mis-steered beam for Machine Protection. The beam will be iteratively steered through BPM centers using model generated algorithms. The energy feedback loop will be energized, tuned and its stability measured. Phase advance of betatron oscillations will be measured and corrected. The wire scanners will be used to measure the energy distribution, beta match and the emittance of the beam.

SCHEDULE

The PEP-II Injector schedule is affected not only by the overall PEP-II commissioning schedule but also the SLC running schedule. Targeted for PEP-II is the commissioning of the High Energy Ring on 1/1/97 and the Low Energy Ring on 10/1/97. The Low Energy Extraction (sans chicane) and both Arcs will be installed during the 1996 downtime. The High Energy Match (which can be installed with the accelerator running) to HER will be done from 10/1/96 until 1/1/97 followed by commissioning of HER. During the 1997 downtime the Low Energy Extraction Chicane and the Match to the LER will be installed.

III. REFERENCES

- [1] LBL-PUB-5379, SLAC-418, CALT-68-1869, UCRL-ID-114055, UC-IIRPA-93-01 (1993).
- [2] T. Fieguth et al., "Injection System for the PEP-II Asymmetric B Factory at SLAC," proceedings EPAC92, Berlin, Germany, March 1992.
- [3] V. NESTEROV, AND A. R. DONALDSON, "A High Current, High Accuracy IGBT Pulse Generator", contributed to this conference.
- [4] G. E. LEYH, A. R. DONALDSON, AND L. T. JACKSON, "A Multi-Channel Corrector Magnet Controller", contributed to this conference.

Beam Transport Lines at BESSY-II*

D. Schirmer, M. v. Hartrott, S. Khan, D. Krämer, E. Weihreter,
BESSY II. Rudower Chaussee 5, Geb. 15.1, 12489 Berlin, Germany

Abstract

The injection system for the BESSY-II storage ring consists of a 50 MeV microtron and a synchrotron booster which ramps the electron beam to the final operation energy of max. 1.9 GeV. The requirements to be met by the transfer lines from the microtron to the booster and from the booster to the storage ring are discussed and the respective magnetic structures are presented. A "genetic" fitting algorithm to optimize the quadrupole settings in the transfer lines is briefly discussed.

I. Introduction

The electron beam from a 100 keV diode gun is preaccelerated up to 50 MeV by a conventional racetrack microtron and is injected on-axis into the booster synchrotron using a "fast" kicker in combination with a horizontal septum magnet (393 mrad). At full energy ($E_{max}=1.9$ GeV) three bumper magnets push the closed orbit close to the extraction septum (196 mrad) and a "fast" kicker (1.8 mrad) extract the beam. Injection into the storage ring is done using two septa with a total deflecting angle of 133 mrad. The storage ring comprises alternating low-beta ($\beta_{x,z} \sim 1$ m) and high-beta ($\beta_x \sim 17$ m) straight sections. Four kicker magnets in a high-beta straight section produce the required horizontal closed orbit shift of 17 mm towards the septa [1]. To ensure good transmission and high injection efficiency, several design constraints have to be fulfilled by both transport lines. Apart from geometrical aspects and beam optics requirements, limitations in the possible strength and length of the optical elements must be taken into account.

II. Injection Line (Microtron \rightarrow Booster)

The injection line geometry has to fit within the given radiation protection walls and must leave sufficient space for access as well as for the diagnostic equipment and the high voltage gun environment. A top view of the proposed magnetic structure which meets these demands, is shown in figure 1.

There is an achromatic structure just after the microtron. Keeping the dispersion low allows to decouple lattice functions and dispersion in the following triplet telescope. The matching section consists of 8 independent quadrupoles to fit 6 optical parameters. The large number of quadrupoles guarantee a high degree of flexibility in matching a wide range of possible starting values from the microtron. The linear lattice functions are plotted in figure 2. The maximum beta functions in both planes are less than 20 m which corresponds to an envelope of $1\sigma \leq 3.7\text{mm}$, keeping the magnet apertures small. The main parameters are listed in table I.

*Funded by the Bundesministerium für Bildung, Wissenschaft, Forschung und Technologie and by the Land Berlin.

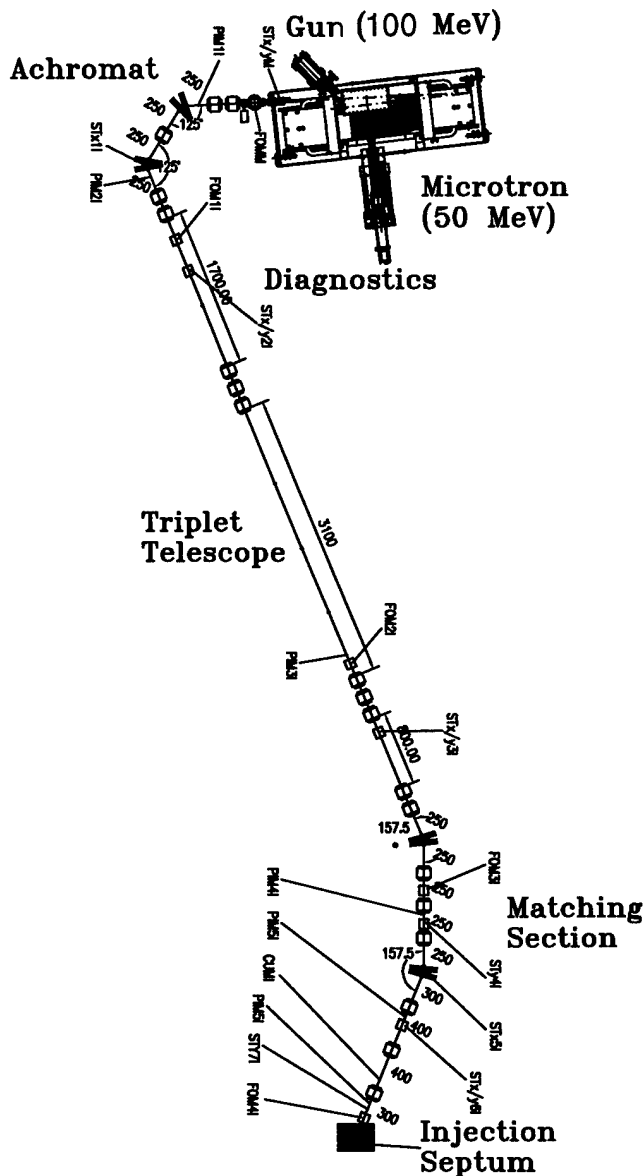


Figure. 1. Lattice and diagnostics of the injection line.

III. Transfer Line (Booster \rightarrow Storage Ring)

In addition to the optical matching conditions the following requirements for the full energy transport line have to be met.

- The deflecting angles of the booster extraction system and the storage ring injection system are fixed.
- The transfer line must be partly parallel to an underground tunnel which may be used to provide a test beam for detector studies ('Zeuthen-Tunnel').

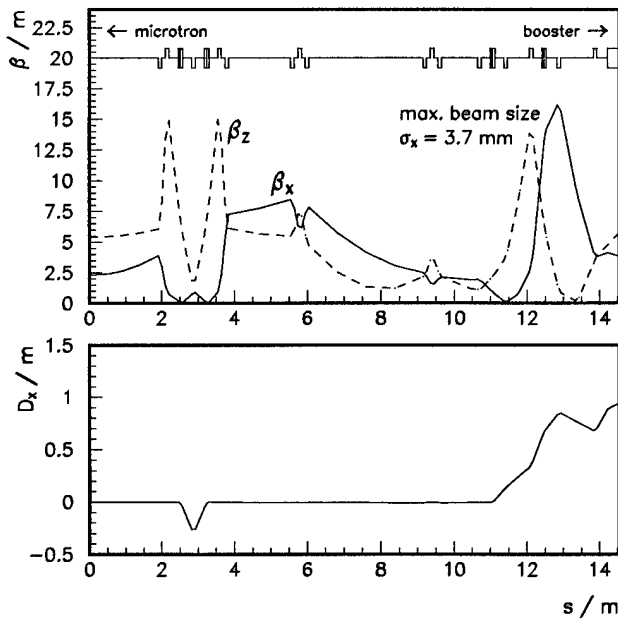


Figure 2. Optical functions of the injection line.

Max. energy	50 MeV	
Total length	14.54 m	
No. quads/families	16/14 (aperture: $\varnothing=25$ mm)	
No. sector dipoles	4 ($2 \times 22.5^\circ$, $2 \times 55^\circ$)	
Max. quad strength	$g \leq 10$ T/m	
Vacuum chamber \varnothing	25 mm	
Max. beam size	$\sigma_x \approx 3.7$ mm	
Optical functions	Microtron exit	Injection into Booster
β_x	2.3 m	3.84 m
α_x	0	1.44
β_z	5.4 m	5.72 m
α_z	0	-1.7
D_x	0	0.94 m
D'_x	0	-0.26
$\varepsilon_{x,z}$ @ 50 MeV	$5 \cdot 10^{-7}$ radm	$2 \cdot 10^{-7}$ radm
$\Delta E/E$ @ 50 MeV	$\pm 2 \cdot 10^{-3}$	$\pm 2 \cdot 10^{-3}$

Table I

Main parameters of the injection line.

- Sufficient space for optional quadrupoles and an additional vertical dipole magnet to bend the electron beam into the 'Zeuthen-Tunnel' must be provided.

Figure 3 shows the geometrical layout of the proposed transfer line. The beam line consists of three quadrupole triplets separated by two identical rectangular dipoles with a deflecting angle of 384 mrad each. A quadrupole doublet in front of and one singlet behind the radiation protection wall in combination with a vertical dipole are assigned to the test beam optics.

Figure 4 depicts the optical functions of the transfer line. The first quadrupole triplet keeps the beta functions below 40 m according to a maximum beam size of $\sigma_x \leq 3.5$ mm. The last two triplet structures form the matching section. Matching a wide range of Twiss parameter values is possible for different starting

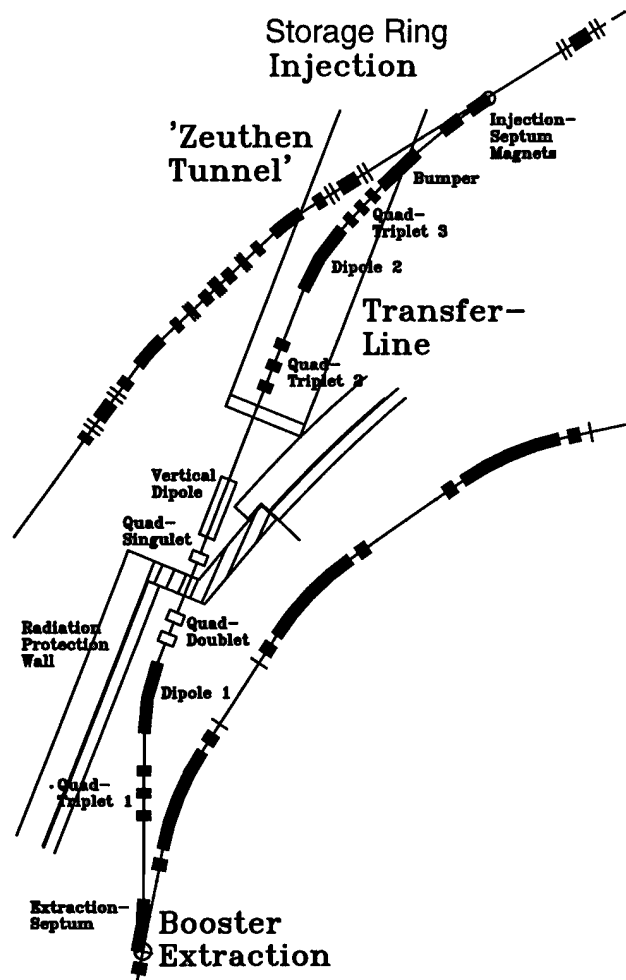


Figure 3. Layout of the transfer line (top view).

parameters from the booster synchrotron and momentum deviation of the order of 1%. The main parameters of the transfer line are summarized in table II.

IV. Optimizations with "Genetic" Algorithms

Designing a transfer line is a typical optimization problem. Once the gross features are clear, the fine tuning is usually done using a fitting algorithm, which minimizes a target function (e.g. the difference between the desired optical functions and those actually found). If this function depends on many parameters (e.g. strengths of quads), the fitting algorithm may not converge or may get caught in a local minimum far away from the best solution.

"Genetic" algorithms are as simple as efficient [2]. They are able to escape local minima and find the best solution to very complex problems. Genetic algorithms are essentially a specialization of Monte Carlo optimization techniques. Instead of one random walker in the parameter space, there is a whole *population* of them. Each *individual* i represents a set of n parameters which determine the target function $f(p_1^i, \dots, p_n^i)$ to be minimized.

After each step, a certain number *fittest* individuals (those yielding the lowest f) is selected. The less fortunate individuals are rejected and displaced by new parameters sets (*descendants*)

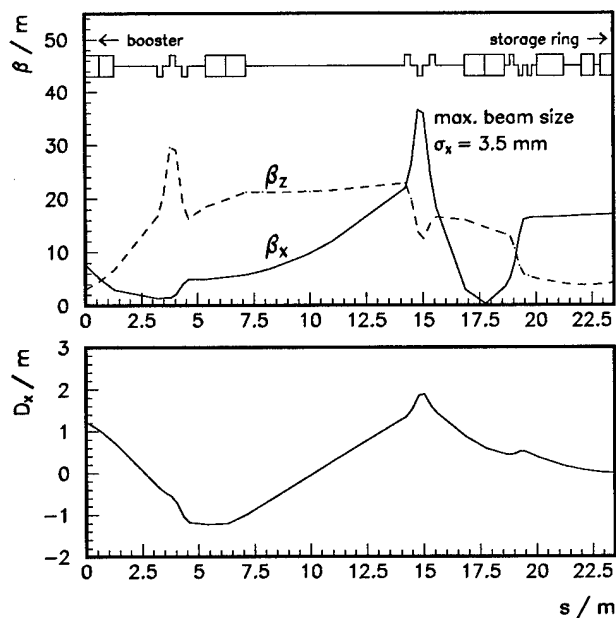


Figure 4. Optics of the transfer line.

Max. energy	1.9 GeV	
Total length	23.48 m	
No. quads/families	9/9 (aperture: $\varnothing=30$ mm)	
No. dipoles	3 ($2 \times 22^\circ$, $1 \times 7.66^\circ$)	
Max. quad strength	$g \leq 30$ T/m	
Vacuum chamber \varnothing	30 mm	
Max. beam size	$\sigma_x \approx 3.5$ mm	
Optical functions	Booster Extraction	Storage Ring Injection
β_x	7.72 m	17.03 m
α_x	2.26	-0.04
β_z	2.99 m	4.16 m
α_z	-1.02	-0.32
D_x	1.23 m	0
D'_x	-0.26	0
ε_x @ 1.9 GeV	$1.7 \cdot 10^{-7}$ radm	$6.5 \cdot 10^{-9}$ radm
$\Delta E/E$ @ 1.9 GeV	$\pm 6.1 \cdot 10^{-4}$	$\pm 7.8 \cdot 10^{-4}$

Table II

Main parameters of the full energy transfer line.

which are a random step away from the selected ones (*parents*). The function is evaluated with the new parameters and the process repeats itself.

Genetic algorithms may vary in the way, a random step (a *mutation*) is done. Generally, random steps should lead in any direction and should be small to allow for fine tuning, but sometimes large to find a complete new solution.

This strategy has been applied to both the injection line and the transfer line. Given their geometrical position, the strengths of all quadrupoles was fitted without starting anywhere near the solution (in the case of the injection line, the quads in the achromat region were kept fixed, but the task of varying more than ten parameters to fit six optical functions is nevertheless formidable).

If the problem has more than one solution, the algorithm may end up with quite different individuals. As an example, different solutions for the injection line are shown in figure 5. Apart from the fact that the human-aided design (figure 2) is aesthetically more appealing, the random strategy was able to find satisfactory solutions and may be applicable to other problems in accelerator physics.

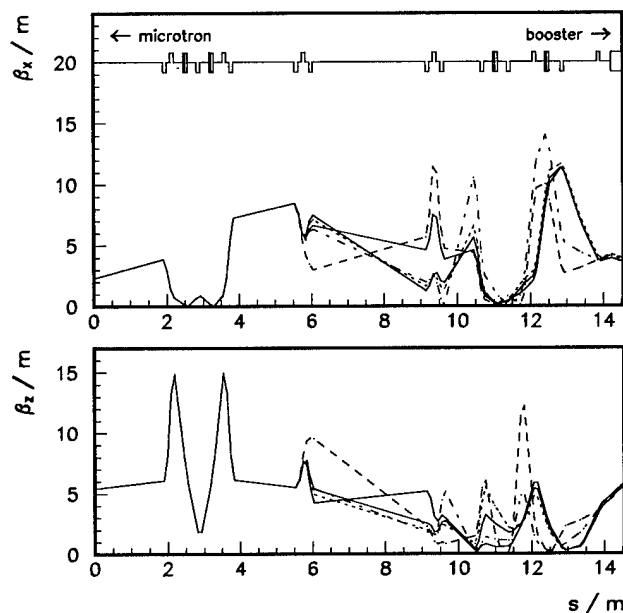


Figure 5. Injection line optics generated by "Genetic" algorithms.

References

- [1] Ch. Geyer, D. Krämer, *Injection and Extraction of the BESSY II Booster and Storage Ring*, Proceedings of 1994 IEEE Particle Accelerator Conference, London
- [2] D. E. Goldberg, *Genetic Algorithms in Search, Optimization and Machine Learning*, Addison-Wesley, Reading, MA, 1989

MATCHING THE EMITTANCE OF A LINAC TO THE ACCEPTANCE OF A RACETRACK MICROTRON

R.W. de Leeuw, M.C.J. de Wijs, J.I.M. Botman, G.A. Webers, W.H.C. Theuvs, C.J. Timmermans
H.L. Hagedoorn.

Eindhoven University of Technology, Cyclotron Laboratory,
P.O. Box 513, 5600MB Eindhoven, The Netherlands

A 10 MeV travelling wave linac will be used as injector for the 10 – 75 MeV racetrack microtron Eindhoven. The six dimensional emittance of the linac will be matched to the acceptance of the microtron. In longitudinal phase space the negative dispersive action of the first bend in the racetrack microtron is counteracted by the dispersive action of the doubly achromatic bending section in the transport line. The data for the longitudinal emittance are obtained from numerical simulations. The energy spread of the initial beam is larger than the energy acceptance of the racetrack microtron. It will be reduced with a slit system in a dispersive section of the transport line.

I. Introduction

The 400 MeV electron storage ring EUTERPE [1] is a university project set up for studies of charged particle beam dynamics and application of synchrotron radiation. The injection chain of EUTERPE consists of a completely revised 'old' medical 10 MeV travelling wave linac followed by the 10–75 MeV RaceTrack Microtron Eindhoven (RTME) [2] (see Fig. 1).

Section II gives a description of the linac and some measured and calculated data on the longitudinal behaviour of the linac. Section III describes the calculated acceptance of the racetrack microtron in the three phase spaces. In section IV the combination of the transport line and the first bend in the microtron which matches the linac beam to the acceptance of the microtron at the cavity is described. Section V presents some concluding remarks. The transverse phase space (z, z') refers to the bending plane of the transport line, the (x, x') plane to the motion perpendicular to this bending plane. The bending in the microtron takes place in the (x, x') plane. The longitudinal phase space is referred to as ($\Delta\phi, \Delta W$). Since the coupling between the longitudinal and transverse phase spaces is only marginal in the transfer line, it is neglected.

II. The linear accelerator

The 10 MeV travelling wave linear accelerator is an 'old' medical linac (type M.E.L. SL75/10). At the Catherina hospital in Eindhoven it has been used for radiation therapy. The linac has been completely revised and is now suited for electron beam manipulation. Table 1 list some measured parameters of the linac.

The linac is controlled via PhyDAS (Physics Data Acquisition System), built around an MS68030 microprocessor and guarded by a programmable logic controller (PLC). The same PhyDAS system is also used as data-acquisition system for some experiments. The status of the accelerator, as monitored by the

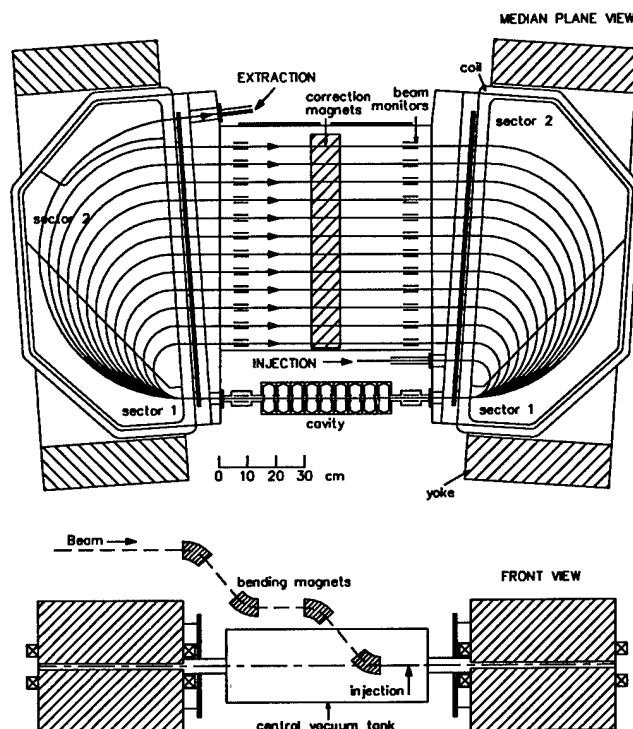


Figure 1. RTME with schematic lay-out of the injection line.

PLC, is displayed on the screen of a personal computer via the visualisation program Intouch.

The high power RF for the acceleration of the electrons is delivered by a 2.2 MW magnetron (EEV M5125). The accelerating structure of the microtron will be powered by the same type of magnetron. Synchronous operation of the two accelerators will be assured by injection locking of the magnetrons.

Fig. 2 depicts the measured and calculated energy spectrum of the linac. The spectrum is measured with a $\pi/6$ -rad bending magnet. For the simulations the particle dynamics code Parmela has been used. The power and corresponding electric fields along the linac, used for this simulation, are calculated starting from the power diffusion equation with the numerical problem solver Matlab, where the geometry and Superfish results (shunt impedance, quality factor and Fourier coefficients for the electric fields) have been used as input. The calculated longitudinal phase space also is depicted in Fig. 2.

Table I
Parameters of the linac.

length (m)	2.25
electron energy (MeV)	10
FWHM energy spread (%)	3.5
macro pulse current (mA)	40
operating frequency (MHz)	2998.1
pulse repetition rate (Hz)	50, 150, 300
pulse duration (μ s)	2.2
filling time (μ s)	0.4

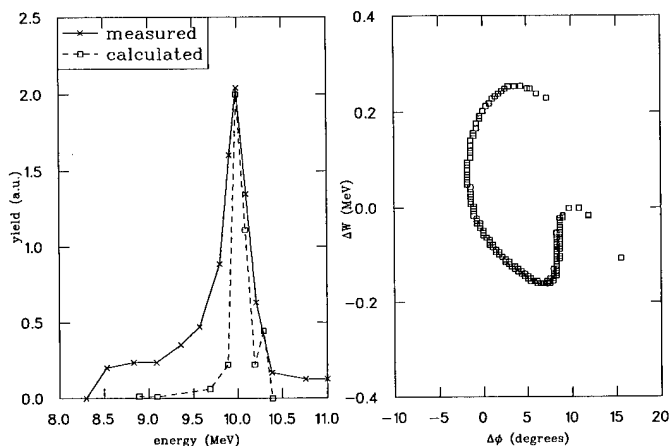


Figure 2. The energy spectrum (left) and the longitudinal phase space (right) of the linac.

III. Acceptance of the microtron

The acceptances of the racetrack microtron have been obtained by numerical particle tracking. For this tracking procedure the measured field profiles of the two bending magnets has been used. The transverse focusing action of the cavity has been taken into account by using the transverse matrix for a standing wave accelerating structure as given by Rosenzweig [4].

The acceptances in the three phase planes are depicted in Fig. 3. The acceptances are calculated just before the first cavity passage, at the injection energy of approximately 9.96 MeV, where the cavity is assumed to be infinitely thin. The horizontal and vertical acceptances are 35 mm-mrad and 55 mm-mrad respectively. The longitudinal acceptance is 2.1 degree-MeV at a cavity accelerating potential V of 5.06 MeV and a synchronous phase ϕ_s of 9 degrees. The value for the longitudinal acceptance remains almost unchanged for $8 \leq \phi_s \leq 13$ degrees and $-1\% \leq \Delta V/V \leq 4\%$ [2].

Comparison between Fig. 2 and Fig. 3 shows that the microtron can not accept the complete beam from the linac in the longitudinal phase space.

IV. The transport from linac to cavity

For injection into the microtron the linac axis is placed approximately 40 cm above the median plane of the microtron. The electron beam is guided over one of the dipoles and then

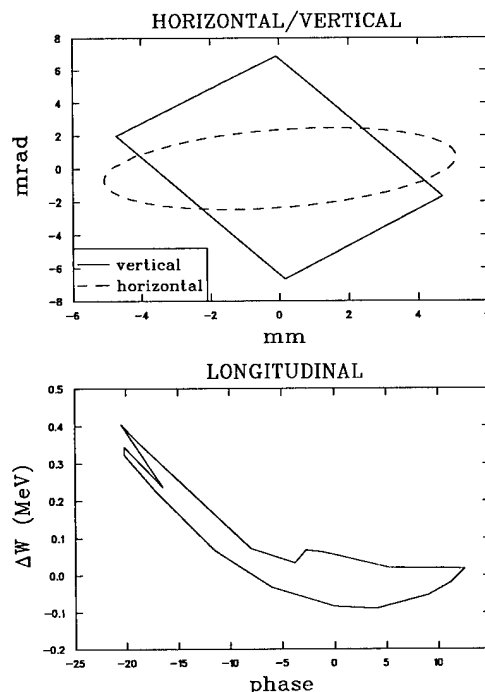


Figure 3. Acceptance of RTME in the three phase spaces.

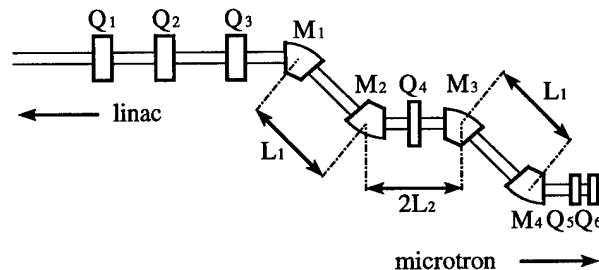


Figure 4. Detailed lay-out of the injection line.

brought down to the median plane of the microtron with a two step doubly achromatic bending system (Figs. 1 and 4).

Four identical homogeneous sector bending magnets will be used. Doubly achromatic behaviour takes place for [3]

$$L_2 = \frac{\rho}{\sin \phi}, \quad (1)$$

where $2L_2$ is the distance between the principle planes of the second and third bending magnet, ρ is the radius of curvature and ϕ the bending angle. The condition is independent of the distance L_1 between the principle planes of the first (third) and second (fourth) dipole. For $L_1 = 2L_2$ this system provides parallel to parallel transport in the bending plane.

In longitudinal phase space ($\Delta W, \Delta\phi$) the transfer matrix for the first bend in the microtron is given by

$$\begin{pmatrix} 1 & 2.58 \\ 0 & 1 \end{pmatrix}, \quad (2)$$

(2.58 mm/% or 9 degrees/%). Without counter measures the beam would be completely deformed and spread out in phase, thereby diminishing the number of electrons available for injection into the racetrack microtron. However the doubly achromatic bending section consisting of four dipoles has negative dispersive action. For dipoles with a bending radius $\rho = 9.8\text{cm}$ at an angle $\phi = 0.873\text{ rad}$ the transfer matrix of the beam transport in longitudinal phase space is given by

$$\begin{pmatrix} 1 & -2.03 \\ 0 & 1 \end{pmatrix}, \quad (3)$$

resulting in a total longitudinal transfer matrix for the transport between linac and cavity of

$$\begin{pmatrix} 1 & 0.55 \\ 0 & 1 \end{pmatrix}. \quad (4)$$

The positive dispersive action of the first bend in the microtron is thereby almost completely counteracted by the negative dispersive action of the bending section. And the match between acceptance and emittance is maximised.

Fig. 4 shows the beam transport line in some detail. The quadrupole in the middle of the drift between the second and third bending magnet offers some extra focusing in the x -direction. At this position it does not influence the doubly achromatic behaviour of the system.

A triplet matches the beam from the linac to the bending section. It also shapes the beam for effective energy selection by a slit that is placed in the focus of the first bending magnet. Here the energy spread of the beam is reduced. The linac delivers a beam with an FWHM energy spread of 3.5% and a low energy tail (Fig. 2), whereas the energy acceptance of the microtron is limited to $|\Delta E/E| < 0.8\%$ (Fig. 3). It is advantageous to limit the energy spread in front of the microtron in order to minimize radiation production and activation at higher energies in the microtron. At the slit a total beam reduction of about 80 % is calculated, while of the particles with $|\Delta E/E| < 0.8\%$ approximately 80 % is transmitted.

The doublet at the end of the transport line is used to match the beam in the transverse phase spaces to the acceptances of the microtron at the position of the cavity. The transfer matrix for the first bend in the racetrack microtron used in this calculation is obtained from numerical particle tracking through the measured field profile [2].

Fig. 5 depicts the transverse beam envelopes between linac and cavity, for starting values of $x_{max} = z_{max} = 2\text{ mm}$ and $x'_{max} = z'_{max} = 4\text{ mrad}$. The final emittance at the cavity matches the acceptance in fig. 3. Also for different starting emittances this match can be obtained without any difficulties. Once the emittance of the linac beam is measured the final adjustment of focusing strength of the quadrupoles in the transport line can be made.

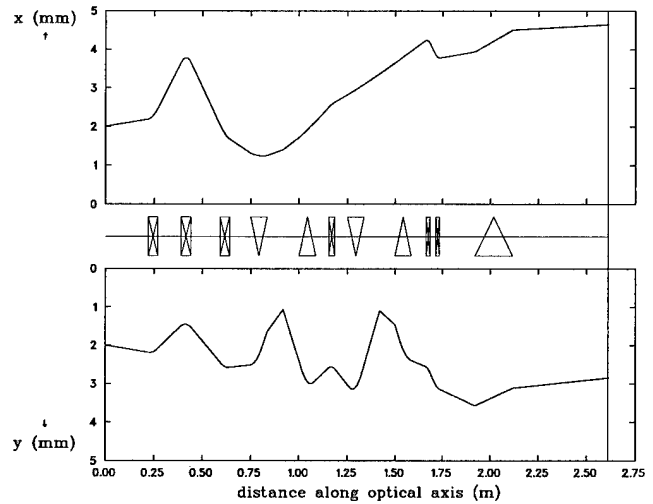


Figure 5. Beam envelopes between the linac and cavity.

V. Concluding Remarks

A compact transport line that matches the six-dimensional emittance of a linac to the acceptance of a racetrack microtron is presented. The energy spread of the linac beam is reduced with a slit system in a dispersive section of the transport line. In transverse phase space the quadrupoles offer enough degrees of freedom to adjust the orientation of the emittance to the acceptance.

References

- [1] Botman J.I.M., Boling Xi, Timmermans C.J., Hagedoorn H.L., *The EUTERPE facility*, Rev. of Sci. Instr. vol. 63, no. 1 (1992) 1569.
- [2] Webers G.A., *Design of an electron optical-system for a 75 MeV racetrack microtron* Ph.D. Thesis Eindhoven University of Technology (1994).
- [3] Leeuw R.W. de, Botman J.I.M., Maanen I.F. van, Timmermans C.J., Webers G.A., Hagedoorn H.L., *A 10 MeV injection beam transport line for a racetrack microtron*, Proc. of the 1994 EPAC, 2417-19 (1994) London.
- [4] Rosenzweig J., Serafini L., *Transverse particle motion in radio-frequency linear accelerators*, Phys. Rev. Vol.49, no.2 (1994) 1599-1602.

THE EXTRACTION ORBIT AND EXTRACTION BEAM TRANSPORT LINE FOR A 75 MeV RACETRACK MICROTRON

R.W. de Leeuw, H.R.M. van Greevenbroek, J.I.M. Botman, G.A. Webers, C.J. Timmermans
H.L. Hagedoorn.

Eindhoven University of Technology, Cyclotron Laboratory,
P.O. Box 513, 5600MB Eindhoven, The Netherlands

A beam transport system providing dispersion matching of the beam from the cavity axis of a racetrack microtron to the injection position in an electron storage ring is described. For extraction the last bend in the 10–75 MeV racetrack microtron Eindhoven has been designed to be less than π rad. This is realised in a three sector dipole field for the last bend, as opposed to the normal two sector dipole field for the other orbits in the microtron. The combination of the last bend in the microtron and the first bending section in the beam transport line from the microtron to the 400 MeV storage ring EUTERPE forms a double achromat. The total transport line consists of two bending and two straight sections, with quadrupole doublets for transverse phase space matching between microtron and ring.

I. Introduction

The 400 MeV electron storage ring EUTERPE [1] is a university project set up for studies of charged particle beam dynamics and application of synchrotron radiation. The injection chain of EUTERPE consists of a completely revised 'old' medical 10 MeV travelling wave linac followed by the 10–75 MeV Race-Track Microtron Eindhoven (RTME) [2]. The final energy of 75 MeV is obtained by 13 subsequent passages through the accelerating cavity.

For extraction with a bending magnet, it is advantageous to increase the distance between the last and forelast orbit in the racetrack microtron. In section II is described how this is achieved by adjustment of the field profile of one of the microtron magnets. In section III is described how the extracted beam is dispersion matched to the transport line. The final bend towards the ring is provided by a 1.37 rad bending section with minus unity transfer matrix. The constraints for this transformation are derived in section IV. In section V the optical design of the total transport line is described.

The injection into the racetrack microtron is described in another paper in these proceedings [3]. In this paper the transverse phase space (x, x') refers to the bending plane of the system, the (y, y') plane to the motion perpendicular to the bending plane.

II. The last bend in the microtron

The bending magnets of the racetrack microtron consist of two distinct field levels for optimised focusing properties [2]. In order to obtain closed orbits (π rad bends) the magnets are rotated in their median planes over 78 mrad. It is favourable for extraction with a small dipole magnet, that the bending angle of the last orbit (75 MeV) is less than π rad, thereby increasing the orbit separation, which is 60.6 mm for the other orbits. This smaller bending angle can easily be achieved by altering the two sector

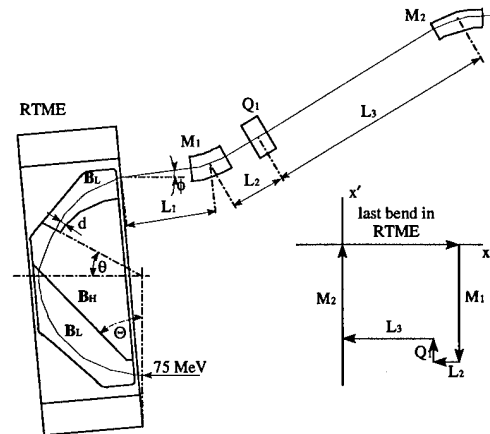


Figure. 1. The last bend in the racetrack microtron and the dispersion matching section.

profile into a three sector profile for the last bend only. The three sector profile consists of a low field section ($B_L = 0.51$ T), a high field section ($B_H = 0.60$ T) and again a low field section, see figure 1. In order to limit possible effects of the fringing fields due to the additional sector, the radial distance, d , between the forelast 70 MeV orbit and the sector edge is about 20 mm, where the gap is 20 mm in the low field section.

The sector angle Θ between the first low field sector and the high field sector is dictated by the electron optical design of the microtron. The adjustable parameter is the second sector angle θ . Decreasing θ yields an increased radial orbit shift and exit angle.

In a first order approximation in the magnetic fields the exit angle ϕ is given by [2]

$$\phi = (B_H/B_L - 1) \sin(2\Theta + \theta) \quad (1)$$

and the exit position y , with respect to the common drift on the cavity axis by

$$y = \frac{p/e}{B_L} [2 - (B_H/B_L - 1) [\cos(2\Theta + \theta) - \cos(2\Theta)]] \quad (2)$$

where p and e are the electron momentum and charge. The exit position is limited to approximately 945 mm by the extent of the vacuum chamber. With eqs. 1 and 2 this yields $\theta \simeq 0.52$ rad and $\phi \simeq 0.146$ rad and $y = 945$ mm.

The field map of the three sector magnet has been measured and with this map numerical orbit calculations have been performed. From the numerical calculations an exit position $y = 947$ mm and an exit angle $\phi = 0.10$ rad follow, close to the predicted values and sufficient for easy extraction.

Table I

The position after each element in (x, x') phase space throughout the last bend in the microtron and the first bending section for a particle with $\Delta p/p = 1\%$.

after element	position
last bend microtron	$(1, 0)$
drift L_1	$(1, 0)$
dipole M_1	$(1, -P_1 - D_1) = (1, D^*)$
drift L_2	$(1 + L_2 D^*, D^*) = (L_D, D^*)$
quadrupole Q_1	$(L_D, -Q_1 L_D + D^*)$
drift L_3	$(L_D + L_3(-Q_1 L_D + D^*),$ $-Q_1 L_D + D^*)$
dipole M_2	$(0, 0)$

III. Dispersion matching

Each individual complete orbit in the racetrack microtron forms a double achromat. The large dispersive action of the last bend will be accounted for by the first bending section in the transport line between microtron and the storage ring. This first bending section consists of two non-identical dipole magnets (M_1 and M_2) with the non-symmetrically placed quadrupole Q_1 in between. Since we have chosen to let the beam run parallel with the cavity axis after the first bending section the bending angle of the second dipole has to be 0.10 rad larger than the bending angle of the first dipole (see figure 1).

To a very good approximation the action of the last bend of the microtron can be regarded as the action by a π rad bend, which leaves a reference particle with a relative momentum deviation of unity ($dp/p = 1$) at position $(1, 0)$ in the (x, x') phase space. The drift L_1 to dipole M_1 does not influence the position in phase space. The first dipole shifts the reference particle both by dispersive and focusing action to $(1, -P_1 - D_1)$. Where $P_1 = \sin \phi_1 / \rho$ is the focusing strength and $D_1 = \sin \phi_1$ the dispersive action of the decomposed bending magnet M_1 . Here ρ and ϕ_1 are the bending radius and bending angle of the dipole, respectively. The subsequent actions by the drifts, the quadrupole, and the second dipole can be followed both in figure 1 and table 1. The drifts are taken between the subsequent principle planes.

The conditions for doubly achromatic behaviour of the combination of the last bend in the microtron and the first bending section are given by

$$L_3 = \frac{1 - L_2(P_1 + D_1)}{D_2} \quad (3)$$

and

$$Q_1 = \frac{-P_1 - D_1 + D_2}{1 - L_2(P_1 + D_1)}. \quad (4)$$

As can be deduced from eqs. 3 and 4 and the phase space figure, the quadrupole is focusing in the vertical plane. To avoid too strong focusing of Q_1 , L_2 and/or ϕ_1 should be small. The minimum value for ϕ_1 is 0.44 rad and is fixed by the demand that the center of the transport line should pass at a minimum distance of 15 cm along the second bending magnet of the racetrack microtron. By this demand the bending angle of M_2 becomes 0.54 rad. The bending radius ρ is chosen 0.5 m.

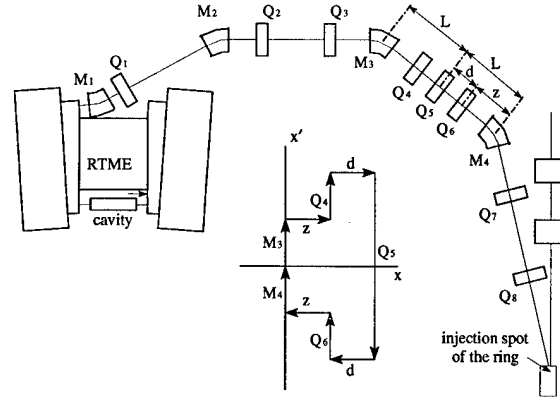


Figure 2. The total transport line between the racetrack microtron and EUTERPE as well as the movement in horizontal phase space in the second bending section.

IV. The doubly achromatic bending system

The doubly achromatic bending section that bends the beam over 1.37 rad towards the injection spot of the ring consists of two identical bending magnets with a symmetrical quadrupole triplet in between, see figure 2. The last 0.20 rad bend into the ring is performed by a magnetic and an electrostatic septum.

For the design of this system the triplet at first is replaced by a single quadrupole, with focusing strength Q , preceded and followed by a drift L ($= 0.43$ m) to the dipoles. For $Q = 2/L$ this system is doubly achromatic. The total horizontal transfer matrix of this bending section is given by

$$M = \begin{pmatrix} -1 & 0 \\ \frac{2}{L} - 2P_{bend} & -1 \end{pmatrix}, \quad (5)$$

for $P_{bend} = 1/L$ this yields a minus unity transfer matrix.

The single quadrupole with the two drift lengths L and the decomposed horizontal plane transfer matrix

$$\begin{pmatrix} 1 & L \\ 0 & 1 \end{pmatrix} \begin{pmatrix} 1 & 0 \\ -\frac{2}{L} & 1 \end{pmatrix} \begin{pmatrix} 1 & L \\ 0 & 1 \end{pmatrix} \quad (6)$$

is replaced by a quadrupole triplet with focusing strengths $-P$, Q_5 , $-P$, drift lengths d between the quadrupoles and drift lengths z between the quadrupoles and the dipoles. By putting $P = 1/d$ and $Q_5 = 1/2L + 1/d$ the focusing strength of the triplet is equal to the strength of the single quadrupole [4]. The decomposed transfer matrix for the triplet in the horizontal plane is now given by

$$Triplet_{hor} = \begin{pmatrix} 1 & \frac{d}{2} \\ 0 & 1 \end{pmatrix} \begin{pmatrix} 1 & 0 \\ -\frac{2}{L} & 1 \end{pmatrix} \begin{pmatrix} 1 & \frac{d}{2} \\ 0 & 1 \end{pmatrix} \quad (7)$$

and the transfer matrix for the vertical plane by

$$Triplet_{ver} = \begin{pmatrix} 1 & -d(3 + \frac{d}{2L}) \\ 0 & 1 \end{pmatrix}. \quad (8)$$

This is the transfer matrix for a virtual negative drift. By demanding that the transfer matrix of the total bending section for the horizontal plane equals the minus unity matrix (eq. 5) the lengths of the drifts before and after the triplet are fixed by

$$z + \frac{d}{2} = L. \quad (9)$$

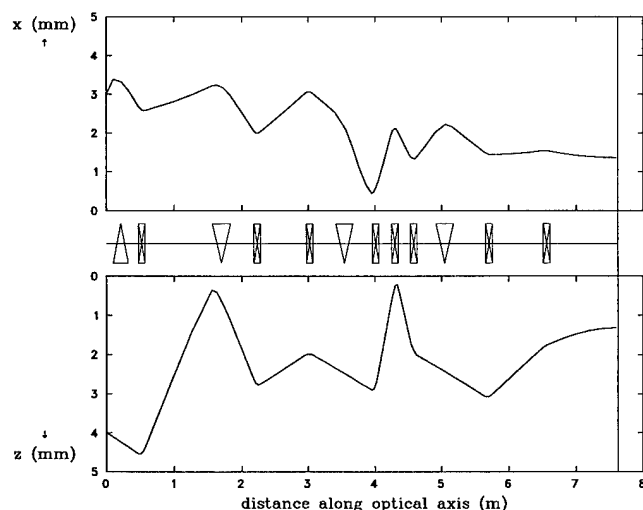


Figure 3. The beam envelopes along the beam transport line.

In order to obtain the same minus unity matrix in the vertical plane for the total bending section, the following condition should be fulfilled

$$-3d - \frac{d^2}{2L} + 2z = 0, \quad (10)$$

where the two drift lengths z between triplet and dipoles are added to the drift in eq. 8. Eqs. 9 and 10 solve to $z = L(3 - \sqrt{5})$ and $d = 2L(\sqrt{5} - 2)$, which implies $Q_5 = \frac{1}{2L}(\sqrt{5} + 3)$ and $P = \frac{1}{2L}(\sqrt{5} + 2)$. Under these conditions the total doubly achromatic bending section yields a minus unity transfer matrix in both transverse phase spaces.

V. The total beam transport system

The two bending sections are connected via a straight section (of 1.58 m) with a quadrupole doublet, see figure 2. Also the last straight section (of 2.44 m) towards the injection spot of the ring is covered with a quadrupole doublet.

First the computer code TRANSPORT is used to establish the doubly achromatic behaviour of the two bending sections. Due to the difference in description, the lens strengths calculated in the previous section are slightly adjusted. Then the complete transport line is used as input and only the quadrupoles in the connecting doublets are allowed to vary. These doublets are adapted to match the transverse parameters of the beam from the microtron to the acceptance of the ring and to assure a beam waist in both transverse phase spaces at the injection spot of the ring.

The beam envelopes along the complete line are depicted in figure 3. As input beam the maximum emittance of the racetrack microtron is used (2 mm·mrad horizontal and 4 mm·mrad vertical) [2]. The two individually variable quadrupole doublets offer enough freedom to adjust the optics in case the emittance differs from the assumed one.

The field in the bending magnets is 0.50 T ($\rho = 0.50$ m) and 0.66 T ($\rho = 0.38$ m), respectively for the first and second bending section. The quadrupole gradient is maximal 12.4 T/m for an effective quadrupole length of 10 cm.

Beam steering in both directions will be done with steering magnets placed between the quadrupoles of the doublets and in

the first bending section after the quadrupole. Beam position monitoring with capacitive pick ups will be done right after the microtron, just before injection into the ring and at several other places along the line. The ultra high vacuum system of the ring and the high vacuum system of the transport line will be separated by a thin foil ($\approx 10\mu\text{m}$) which will only cause a minor emittance growth.

References

- [1] Botman J.I.M., Boling Xi, Timmermans C.J., Hagedoorn H.L., *The EUTERPE facility*, Rev. of Sci. Instr. vol. 63, no. 1 (1992) 1569.
- [2] Webers G.A., *Design of an electron optical-system for a 75 MeV racetrack microtron*, Ph.D. Thesis Eindhoven University of Technology (1994).
- [3] Leeuw R.W. de, Wijs M.C.J., Webers G.A., Hagedoorn H.L., Botman J.I.M., Timmermans C.J., *Matching the emittance of a linac to the acceptance of a racetrack microtron*, these proceedings.
- [4] Banford A.P., *The transport of charged particle beams*, Chilton, Berks (1969).

Electromagnetic, Thermal and Structural Analysis of the Fermilab Antiproton Source Lithium Collection Lens

S. O'Day and K. Anderson, Fermilab*, P.O. Box 500, Batavia, IL 60510 USA

A coupled field finite element ANSYS analysis was done on the electromagnetic, thermal and structural aspects of Fermilab Antiproton Source lithium lens operation. The temperature distribution from Joule heating and the radial magnetic pinch forces were used as input for a 2-D structural model with a fine mesh density. The results of this analysis show that the preload on the lithium as it is filled into its titanium container may be reduced by 15 percent. This reduces the radial stress on the Ti can after the pulse when only preload and thermal stresses remain. Further reduction in preload could come from a scheme to pre-pulse the lens at low current. The heating of the lithium before standard operating current is applied would then play the role of preload at fill. The results of this analysis and future implications for lens operation will be discussed.

I. Antiproton Production and Collection

The Fermilab Main Ring delivers 3×10^{12} protons per pulse to the 8 cm long Ni antiproton production target. The transverse spot size of the beam is .5mm (3σ). The beam pulse consists of 80 1 ns bunches spread evenly over 1.6 μ s. Beam pulses arrive once every 2.4 seconds. A lithium collection lens sits 20 cm downstream of the target. The lens collects 8.9 GeV/c secondaries produced within a 35 milliradian cone. The lens focuses the beam to an angular spread of 2.6 milliradians and a radius of 1 cm. A pulsed dipole bends the beam 3 degrees into a transport line which leads to a 500 m circumference debuncher ring. After bunch rotation and some transverse cooling, the antiprotons are then kicked into a 500 m circumference storage ring where they are stochastically cooled and stacked. Detailed Fermilab and CERN antiproton source descriptions are given elsewhere[1].

A conventional lithium lens is a cylinder of solid lithium carrying current. A charged particle passing through the lens with some angle with respect to the lens axis will feel a radial Lorentz force. A lens with radius r , length l carrying a current I , will produce an azimuthal magnetic induction $B(r) = \mu_0 I r / 2\pi r_0^2$. An ideal lens is in focus when the distance from a point source of particles to the upstream face of the lens is $Z = 1/(k \tan(kl))$ where $k = (.3G/p)^{1/2}$, G = lens gradient and p = particle momentum.

*Operated by the Universities Research Association under contract with the U.S. Department of Energy

II. Collection Lens Design and Construction

The lithium lens used for antiproton collection at Fermilab has a diameter of 2cm and a length of 15cm. A 640 kAmp 350 μ s damped half sine wave current pulse passes through the lithium in this lens. The lens completes the secondary of an 8:1 step up current transformer. A cross section of the lens in the plane of the beam is shown in figure 1. The lithium is encased in a water cooled titanium can. The lens, can and water conduits all reside in a steel cylinder. The steel is divided into two halves separated spatially and electrically by ceramic ring standoffs. The current input is attached to one half and the output to the other. The two halves are bolted together (with electrical isolation). Further electrical and mechanical description is given in other references[2,3].

During the filling process, lithium is pumped under pressure into an evacuated titanium can. The lithium is heated to 200° C, introduced into the lens at 500 psi (for Li, $T_{\text{melt}} = 180^\circ\text{C}$) and then allowed to cool to 160° C before the fill continues. As the lithium cools to room temperature, more and more pressure is applied. The final fill pressure is 2300 psi when the stopcock is closed.

Fermilab lithium lenses of more recent design have survived up to 7 million pulses at a lens gradient of 750 T/m. The original design lens gradient was 1000T/m. Lenses run at even 800T/m experience a failure of the titanium jacket encasing the lithium. This typically occurs after 1-2 million pulses. As will be shown, small stress increases in the titanium cylinder result in a great reduction in the life of the lens.

III. Electromagnetic Model Results

The 3-D ANSYS[4] electromagnetic package SOLID96 was used to produce a Lorentz force density map (figure 2). This map was used as structural model load input. The Joule heating of the lithium was also calculated as a function of radius thus providing thermal model input data. The magnetic field and current density maps were used to cross check the expected current skin depth and magnetic forces.

One quarter of the lens was divided into 11 radial, 6 azimuthal and 10 longitudinal sections. Azimuthal symmetry, vector potential and electrostatic potential boundary conditions were then applied.

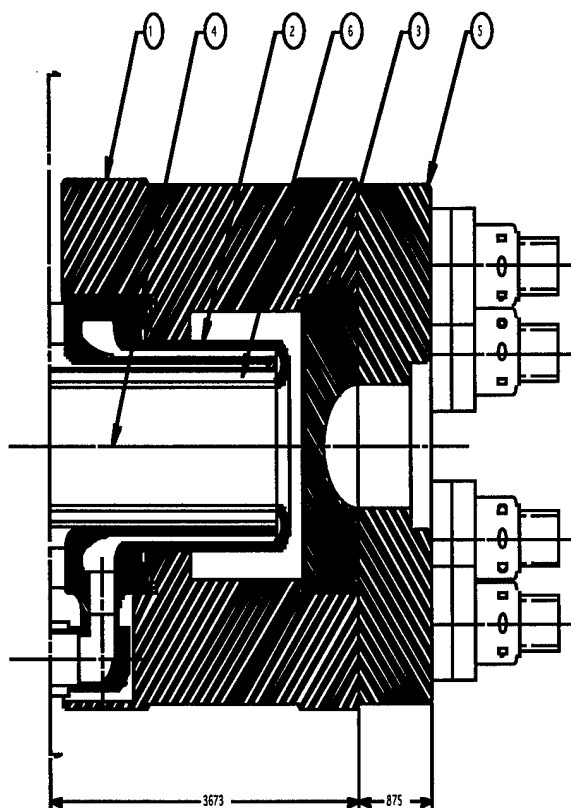


Figure 1: Lithium Collection Lens(half symmetry):1-Electrical Contact;2-Water Septum;3-Be End Cap;4-Li Cylinder Axis;5-End Flange;6-Inner Cooling Jacket.

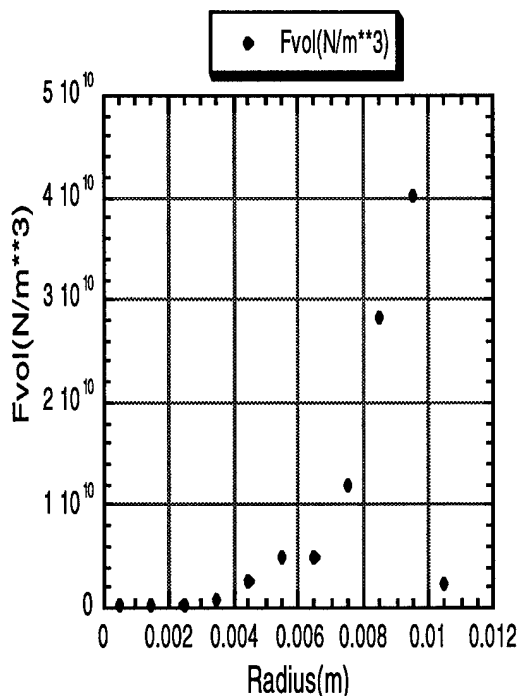


Figure 2: The magnetic force per unit volume as a function of lithium lens radius at mid-pulse.

IV. Thermal and Structural Model Results.

The SOLID96 model described above was coupled to the thermal modeling package SOLID70. The temperature distribution shown in figure 3 was generated from the Joule heating map provided by SOLID96.

The SOLID70 output was coupled to the SOLID45 structural package in a test run, but final results were obtained using a much finer 2-D axisymmetric element mesh(with PLANE42) to improve the accuracy near the lithium-titanium interface. The electromagnetic forces and thermal model temperature predictions were input as loads on individual elements in the PLANE42 model.

The results at mid-pulse are shown in tables 1 and 2. In the tables, the radial and tangential(hoop) stresses are given. The effect of just the lithium preload is shown in row 1. The impact of both the preload and the magnetic pinch together are shown in row 2. Finally in row 3, the effect of thermal stresses is added in.

Two illustrative cases are displayed in the tables. The first case is that of present lens preload at mid-pulse on the first pulse. The second case is done at a reduced pre-load, but at mid-pulse after the system has been pulsed many times and has reached steady state. The design lens gradient of 1000 T/m is assumed in each case.

A negative(compressive) radial stress is indicated by the final row in each table which includes a preload on the lithium, a magnetic pinch from the current pulse and the thermal expansion stress from the subsequent temperature rise of the lithium. The implication here is that the titanium can is acting to compress the lithium. This is equivalent to the statement that there is physical contact between the two materials and that there is enough preload to overcome the magnetic pinch produced by the current pulse.

The excess preload for the first case amounts to 350 psi. A third case was run with only 1950 psi of preload to verify that the radial stress becomes zero at mid-pulse. Removing preload on the lithium is good because it limits the maximum radial and hoop stress which will be placed on the titanium can after the magnetic pinch is gone(between pulses). The case presented in table 2 indicates that if steady state conditions can be maintained at all times, the preload can be dropped much more. The stress from the preload removed is replaced by the thermal stress gained from a higher initial temperature at the beginning of the pulse.

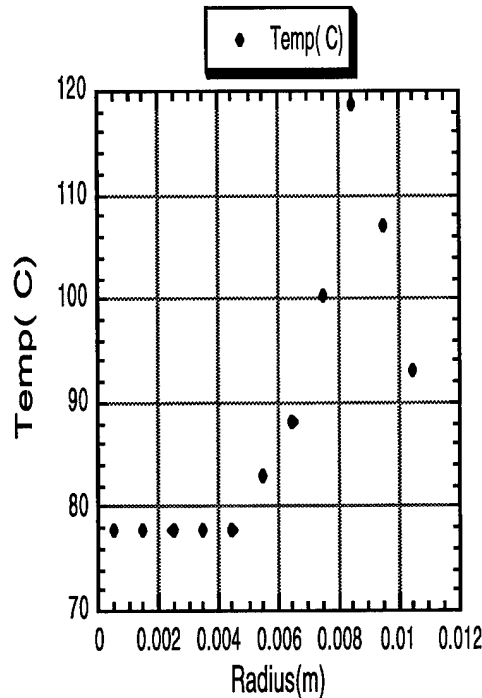


Figure 3: The temperature of the lithium lens at mid-pulse as a function of lithium lens radius.

Table 1: Ti Septum Stress@ 2300 psi Preload during 1st Pulse($T_0=20^{\circ}\text{C}$)

Effects Included	$\sigma_r(\text{Pa})$	$\sigma_t(\text{Pa})$
Preload Only	-1.528×10^7	$+1.610 \times 10^8$
Preload+Pinch	$+1.213 \times 10^7$	-1.584×10^8
Preload,Pinch, Thermal Expansion	-2.405×10^6	-2.346×10^7

V. Implications for Li Lens Reliability

The S-N curve in figure 5 shows the strength of Ti-6Al-4V [5] as a function of the number of stress reversals. If one assumes(based on 800 T/m lifetime) that the titanium in the can experiences a maximum stress of 85 ksi, then decreasing this by 15%(by decreasing preload) should result in a lifetime increase of up to 9 million cycles under present operating conditions. This curve is not completely suitable for making this prediction since a lithium lens does not undergo complete stress reversal as it is pulsed.

If the current was ramped up to full value over a number of pulses so that a temperature close to steady state could be obtained before the first full current pulse, then a preload much lower than 1950 psi could be considered. At 500 psi preload, one could consider increasing the lens current by 25% while accepting little or no decrease in the number of cycles to titanium can failure.

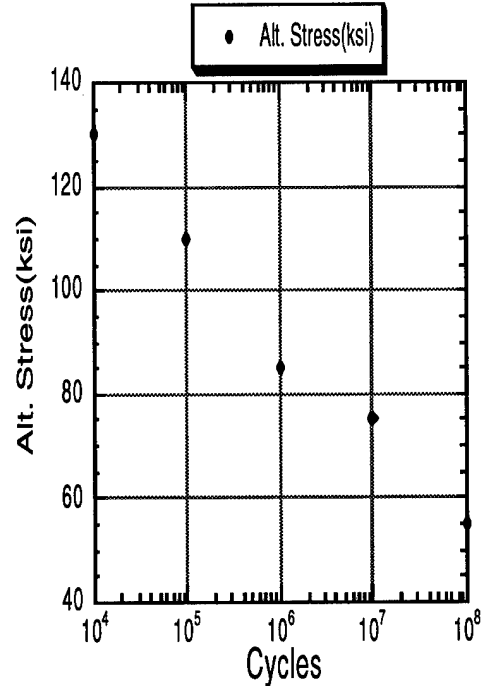


Figure 4: The alternating stress as a function of the number of cycles to fatigue failure.

Table 2:Ti Septum Stress@ 500 psi Preload during Steady StatePulse($T_{ss}=65^{\circ}\text{C}$)

Effects Included	$\sigma_r(\text{Pa})$	$\sigma_t(\text{Pa})$
Preload Only	-3.335×10^6	$+3.352 \times 10^7$
Preload+Pinch	$+2.407 \times 10^7$	-2.841×10^8
Preload,Pinch, Thermal Expansion	-1.294×10^7	$+8.752 \times 10^7$

VI. REFERENCES

- [1]M. Church and J. Marriner, Ann. Rev. Nucl. Part. Sci. 43:253-295(1993).
- [2]S. O'Day and F. Bieniosek, Nucl. Instr. Meth.A343:343-350(1994).
- [3]G. Dugan et al.,IEEE Trans. Nucl. Sci.30:3660-3662(1983).
- [4]ANSYS 5.0(1992),Swanson Analysis Systems,Inc. Houston,PA.
- [5]R. Witt et al., "Source Book on Electron Beam and Laser Welding". p 87(1981).

A NEW CONCEPT IN THE DESIGN OF THE LHC BEAM DUMP

J.M. Zazula, M. Gyr, G.R. Stevenson and E. Weisse,
European Laboratory for Particle Physics, CERN, CH-1211 Geneva 23

Abstract

Recent Monte Carlo cascade simulations have shown that a reduction in the maximum of deposited energy density can be obtained by applying a uniform magnetic field over a front part of the graphite core of the LHC dump. This paper shows the effect of field strength on spatial distributions of absorbed energy and temperatures, and discusses problems to be solved when designing a suitable magnet.

I. INTRODUCTION

The LHC energy of nominally 333 MJ per ring ($2.97 \cdot 10^{14}$ protons at 7.0 TeV), extremely concentrated in a small region around the beam axis, gives rise to severe thermal and mechanical constraints on the construction of the beam dump, which will be installed at a distance of about 750 m from the ejection point. Several beam diluting procedures exist and have already been discussed [1]. Each of them applied alone is either not sufficient to keep the maximum temperature rise in the graphite below a tolerable level—or kicker magnet performance or the tunnel length are forced to extreme levels.

Absorption of the beam energy is the process mainly contributed to by low-energy charged components (mostly electrons and positrons) of the cascades induced by primary protons in the dump. Thus a magnetic field applied over a front part of the core could serve to spread a part of the deposited energy out of the critical concentration region. This study aims to answer what field strengths would be required to obtain a sufficient cascade dilution, and if those fields can be provided by any magnet that is realistic for design and installation in the dump area.

II. EFFECT OF MAGNETIC FIELD ON ABSORBED ENERGY AND TEMPERATURE DISTRIBUTIONS

A. Simulations of particle cascades

The simulations of particle cascades in a central part of the LHC dump were performed with the FLUKA high energy shower program [2]. Comparisons with measurements of absorbed dose distributions around accelerator beams (albeit, at lower energies) have shown [3] that an accuracy of better than 25% can be expected when estimating the densities of deposited energy from Monte Carlo calculations with this code.

The LHC beam of 7 TeV protons was assumed to have projected distributions of Gaussian profile; the beam parameters taken for the simulations are given in Table I. The most suitable material for the construction of the upstream part of the dump core is a graphite, assumed here to be pure ^{12}C of density $1.75 \text{ g}\cdot\text{cm}^{-3}$. Secondary cascades were simulated only in the central part of the dump of dimensions $10 \times 10 \times 300 \text{ cm}^3$; preliminary results have shown that this depth includes the longitudi-

Table I

Nominal beam parameters assumed for the simulations.

Beam momentum (monoenergetic)	7.0	TeV/c
Horizontal beam size (Gaussian σ_h)	1.46	mm
Vertical beam size (Gaussian σ_v)	1.06	mm
Beam divergence (Gaussian $\sigma_{h,v}$)	1.64	μr
Beam intensity (protons per ring)	2.97	$\cdot 10^{14}$
Spill absorption time	90	μs

nal maxima of deposited energy density (with or without a magnetic field), and that the energy densities (and the corresponding instantaneous temperature rises) decrease by at least two orders of magnitude for radial positions 5 cm from the beam axis.

The interactions and propagation of charged components of the cascades (protons, charged pions, muons and electrons) were followed down to the kinetic energy threshold of 1 MeV, of photons down to 100 keV, and of neutrons down to a thermal energy range. Particles slowed down or produced with energies below these thresholds are assumed to deposit their energy locally (in a range which is negligible compared to the scoring mesh size). Energy lost by charged particles in ionization processes was converted to emitted δ -rays (low energy electrons), and thus further distributed around ionizing particle tracks. None of the biasing or importance sampling methods available in FLUKA were used.

The homogeneous uni-directional magnetic field perpendicular to the beam axis (the direction of field is called "vertical", since the induction \vec{B} was taken parallel to the vertical beam plane) was present over the whole length of the system (3 m), with field strengths of 0.5, 1, 2 and 5 T. The results without field were also obtained for reference, for the same beam (see Table I) and for the beam that vertical profile was linearly swept over distance $\pm 5 \text{ cm}$. Samples of primary histories that were completed for fixed run times of the simulation program (20 000 native seconds of the SP2 system at CERN) for each field case are given in the second column of Table II.

The density of the deposited energy was determined as a function of horizontal and vertical position and of longitudinal depth, in two Cartesian bin structures, i.e., a fine mesh of $0.1 \times 0.1 \text{ mm}^2$ lateral size (up to 5 mm from the beam axis), and a coarse mesh of $1 \times 1 \text{ mm}^2$ lateral size; both with longitudinal bins 10 cm in depth.

B. Spatial distributions of deposited energy

Maximum energy densities, maximum laterally integrated energies and total energies deposited per one proton of the LHC beam, in the $10 \times 10 \times 300 \text{ cm}^3$ graphite block in a uniform magnetic fields of various strengths, are given in Table II. The maximum densities given in the third column of the table, are those

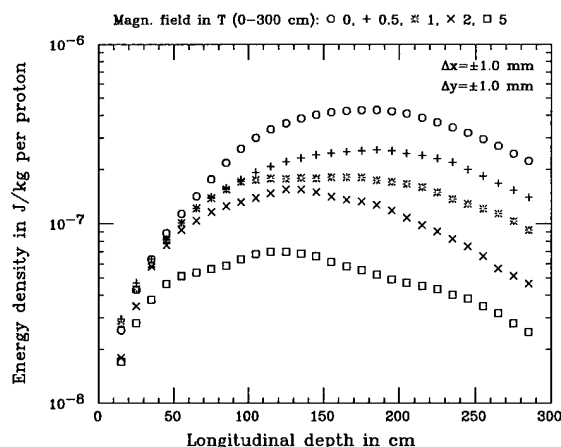


Figure 1. Maximum energy densities as function of longitudinal depth in the core, for various field strengths.

obtained from the $1 \times 1 \text{ mm}^2$ lateral bins (coarse mesh), that were still less than projected half-widths of the beam.

The obtained spatial distributions of densities of energy deposited per one primary proton, for various levels of the magnetic field, are shown in Figure 1 as a function of the longitudinal depth in graphite, and in Figure 2 as a function of the lateral distance off-axis in the plane perpendicular to the magnetic induction \vec{B} (horizontal plane). For the longitudinal plots, the densities have been averaged over $\pm 1 \text{ mm}$ distances in both lateral planes. The horizontal distributions shown in Figure 2 have been averaged between the symmetrical "up" and "down" positions within the $\pm 1 \text{ mm}$ range in the vertical plane (parallel to \vec{B}), and over $\pm 30 \text{ cm}$ ranges around the longitudinal maxima respective to the field levels, taken from Figure 1, that are: 160-220 cm for no field case, 150-210 cm for 0.5 T, 140-200 cm for 1 T, 100-160 cm for 2 T, and 80-140 cm for 5 T. Moreover, the performed analysis has proved that (within the limits of statistical errors) also the "right" and "left" distributions are symmetrical, and thus the mean values of the "right" and "left" horizontal positions (from 0 to 5 cm) are plotted in Figure 2.

The fine mesh results included in Figure 2 (leftmost part of the scale) show again that the horizontal profiles of energy density, at depths of the longitudinal maxima, are flat within the horizontal range of first $\pm 1 \text{ mm}$ off the beam axis. The central parts of the vertical distributions (not shown here to keep this paper concise) look similar. This justifies again the averaging procedures that were applied for the Figure 1 and Table II.

C. Maximum temperatures after absorption of the beam

The amount of beam energy that is deposited in the core is further dissipated in the dump in the form of heat. In order to determine maximum temperature rises that can be expected in the graphite after absorption of the spill, the energy deposition results from particle cascade simulations were coupled to a transient heat transfer analysis, performed by means of the ANSYS finite element program [4]. The system geometry and loads being symmetrical, only one quarter of the core was considered, up to 5 cm radius off beam axis. This three-dimensional quadrant

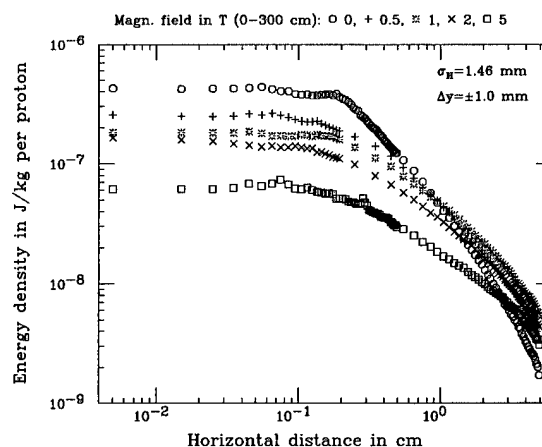


Figure 2. Lateral distributions of energy density at depths of longitudinal maxima, for various field strengths.

Table II

Total energies deposited in the core, maximum laterally integrated energies, maximum energy densities and maximum temperature rises for various field strengths.

Magn. field $ \vec{B} $ in T	No. of sim. p	Depos. part of 7 TeV	Energy density in 10^{-7} J/kg ^a	Lateral integral in 10^{-9} J/cm ^a	Temp. rise in 10^3 K ^b
no	71	28 %	5.2	1.9	51
0.5	57	21 %	3.2	1.5	33
1.0	26	19 %	2.4	1.2	22
2.0	35	14 %	1.9	0.8	18
5.0	45	9 %	0.8	0.5	9
sweep ^c	32	24 %	0.4	1.6	5

^aper one primary proton

^bper spill ($2.97 \cdot 10^{14}$ protons)

^c $\pm 5 \text{ cm}$, without magnetic field

was meshed with quadrilateral brick elements, by using uniform divisions in the azimuthal angle ($\Delta\phi=15^\circ$), radial bins increasing logarithmically from $\Delta r=0.5 \text{ mm}$, and the same longitudinal bins as in the Monte Carlo calculations ($\Delta z=10 \text{ cm}$). As this mesh is more efficient in covering spatial regions of concentrated importance than the Cartesian bins available in FLUKA, much less elements (3600 in total) were required. However, a special interface algorithm had to be written, transferring the Monte Carlo scoring output to the thermal load input of ANSYS.

These loads were the internal heat generation rates (in $\text{J}/(\text{cm}^3 \cdot \text{s})$), obtained by multiplying the energy density (in J/cm^3 per primary) interpolated for each node by the number of protons in spill, and dividing them by the spill absorption time in seconds (see Table I). These heat generation rates were assumed to be constant in time during the absorption period, which is long when compared with the time scale of the cascade development, but short when compared to characteristic times of heat propaga-

tion. Thus heat flow outside of the core (to external parts of the dump, a cooling system, *etc.*) could be neglected for the absorption period, and the external boundaries of the considered system could then be assumed to be adiabatic. Moreover, the thermal properties of graphite, taken from Ref. [5], change considerably with temperature; in particular the specific heat varies from about 660 to 2500 J/(kg·°) between room temperature and few thousands degrees. Thus ANSYS procedures for the nonlinear solutions had to be involved. It should be noted that physical properties can also vary between different graphites, and under irradiation conditions.

The maximum temperatures at the end of a spill, obtained for each field strength, are given in the last column of Table II. The three-dimensional temperature distributions are shown in the form of color contours in the poster session of this conference.

III. PROBLEMS TO BE SOLVED BY DESIGNING A SUITABLE MAGNET

The major difficulty is the building of a suitable magnet with the necessary high dipole field over a 70 cm wide gap and within a volume of about 1.5 m³, even if the precision of the field is not a critical parameter. By far the most elegant solution, requiring neither power supply, nor water cooling or cryogenics in an area which is radioactive and distant from any central infrastructure, would be a permanent box- or ring-magnet [6] which, because of the very strong magnetic forces (several tons/m) between the different blocks, would be built of short modules which would need to be preassembled. However, the maximum fields which can be obtained with a "reasonable" design—about 0.3 T with relatively cheap ferrite, or 1 T when using the more expensive rare earth - cobalt material—are by far insufficient to reduce the energy deposition by an order of magnitude. In order to achieve higher fields, the volume of the permanent magnet material would have to grow out of any proportion. The solution of a classical window-frame electro-magnet cannot be envisaged since the maximum achievable field of 2 T only brings about one third of the desired effect. The stored magnetic energy in such a magnet would be in the order of 1 MJ/m when excited with a total current of about 1.2·10⁶ Ampere-turns. The dissipated power in the aluminum coil, which needs to be cast in concrete, would exceed 1 MW unless being cooled with liquid nitrogen. The only possible magnet able to produce the required magnetic field of 5 T would be a superconducting magnet which provides a stored magnetic energy of about 5 MJ/m and which possibly would quench at every discharge of the LHC-beam. The coil of the magnet would have to be fully stabilized in order to absorb the total energy and the helium be contained in a closed circuit.

IV. CONCLUSIONS

This study of the utility of an uniform magnetic field for the LHC beam dump system can be summarized:

- The maximum energy densities and temperatures are reduced approximately linearly with field strength, up to about factor of 7 for a 5 T field. The effect obtained for the maximum field is comparable with the dilution of energy density obtained with a linear sweep of ±5 cm.

- In presence of the magnetic field, spatial profiles of deposited energy are longitudinally flattened and laterally spread out from the central region; thus smaller fractions of the total energy are deposited in the central part of the dump system, critical for the concentration of the absorbed energy and consequent temperature rise;
- It was not possible to obtain a reduction of the maximum energy density by one order of magnitude, or to keep the maximum temperatures in graphite below 2500°C, using the field strengths provided by the most favorable permanent magnets; other magnet designs would be even less realistic. A satisfactory solution might be achieved by combining magnetic dilution of the cascades with a linear sweep in the perpendicular direction.

References

- [1] A. Ferrari, G.R. Stevenson and E. Weisse, "Design of the LHC Beam Dump", in *Proc. of the 3-rd Europ. Part. Accel. Conf.* (Vol. 2, pp. 1545-47), Berlin (March 24-28 1992); LHC Note 180.
- [2] A. Fassò, A. Ferrari, J. Ranft and P.R. Sala, "FLUKA: Present status and future developments", in *Proc. of the IV Int. Conf. on Calorimetry in High Energy Physics* (p. 493), La Biodola, Italy (Sept. 20-25, 1993).
- [3] A. Fassò, A. Ferrari, J. Ranft, P.R. Sala, G.R. Stevenson and J. M. Zazula, "Comparison of FLUKA simulations with measurements of fluence and dose in calorimeter structures", *Nucl. Instr. and Meth. A* 332 (1993) 459-468.
- [4] Swanson Analysis Systems, Inc., ANSYS (Revision 5.1), SASI/DN-P511:51, Houston, USA (Sept. 30 1994).
- [5] B.T. Kelly, "Physics of graphite", *Appl. Sci. Publ.*, LTD (London 1981).
- [6] K. Halbach, "Application of permanent magnets in accelerators and electron storage rings", *Journ. of Appl. Phys.* 57-8, part IIA (1985) 3605-08.

LOSS CONCENTRATION AND EVACUATION BY MINI-WIRE-SEPTA FROM CIRCULAR MACHINES FOR SPALLATION NEUTRON SOURCES

H. Schönauer, CERN, CH-1211 Geneva 23, Switzerland

I. INTRODUCTION

Efficient loss management is crucial in high-intensity circular machines like neutron sources, and those using superconducting magnets. Collimator systems have been designed or are under intensive study [1]. The common problem of collimation is the outscattering from the collimator faces which are most frequently hit at shallow depth. In this situation high collection efficiency can only be achieved by two-or-more-stage, double-jaw, systems requiring betatron phase advances approaching 2π . As the outscattering is isotropic, both transverse planes are affected and the system layout becomes a two-dimensional problem. Any convincing single-stage collimation system would be simpler to operate and is likely to be less expensive. The possible physical evacuation of the lost beam towards a remote dump can drastically reduce the radioactivity level in the tunnel. Moreover, fitting a two-stage system into an existing machine is difficult and in general not very promising. In this situation a wire septum may be the only satisfactory solution.

II. BASIC FEATURES OF THE MINI-WIRE-SEPTUM (MWS)

An earlier study of the potential of thin predeflectors like foils or wires for improving collimation efficiency [2] has already indicated the superiority of such a special wire septum over all other types investigated. This article goes a step further and suggests its "upgrading" into a single-stage collimator. Figures 1a, 1b show a schematic comparison between a conventional septum and a MWS. The prefix "mini" in the designation MWS refers to some of its salient features: (i) its short length, which is essential for (ii) its reduced gap width requiring (iii) comparatively low operating voltage.

Also new is the use of low Z, ultra-thin wires of diameters ≤ 0.05 mm. Due to their small cross-section, these wires experience strong deflection and bulge out of the ideal plane by a few mm, rendering their precise alignment impossible. On the other hand, a perfect septum is of limited value in loss collimation anyway: different loss mechanisms varying along the acceleration produce varying envelope slopes; in fact, perfect alignment is rather undesirable as it is easily seen that a particle approaching a row of wires in their plane will hit them all until it is scattered out - into the gap, or back into the vacuum pipe as

in the case of a massive collimator. On the contrary, in the misaligned MWS, particles perform multiple passages across the septum wire area before receiving the full final kick. For the above reasons, a misaligned septum performs better in simulation, and it is thus not surprising that the non-ideal septum does as well.

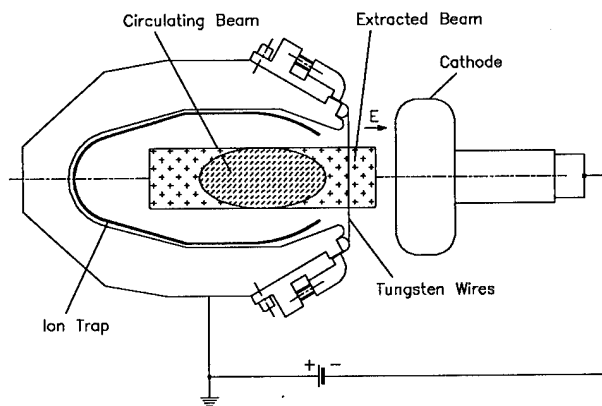


Figure 1a: Conventional wire septum

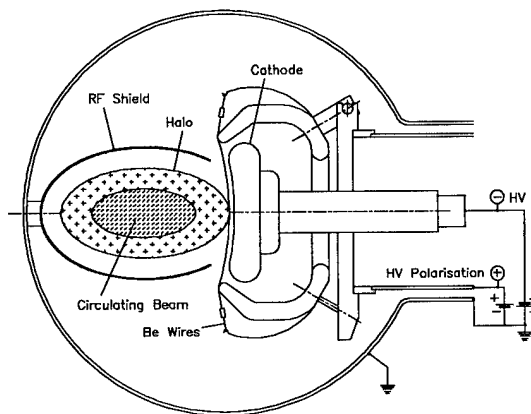


Figure 1b: Mini-Wire-Septum for loss extraction.

To keep the MWS simple and robust, bulk metal cathodes (allowing fields of 4-5 MV/m) are preferable to oxidised aluminium ones (10 MV/m). If the wires are polarised to a few kV, there is no leakage field in the useful aperture and ion traps can be avoided.

III. PHYSICAL PARAMETERS OF THE MWS

The parameters are chosen to fit the synchrotron of the projected AUSTRON neutron spallation source [3]. The deflection angle θ , of a wire septum is given by $\theta = (eE_0 l) / (\beta pc) = 2.5 \text{ MeV} / (\beta pc)$ with the maximum field $E_0 = 5 \text{ MV/m}$ admitted by metal cathodes and a length of

$l = 0.5$ m. In the energy range relevant for AUSTRON II (130 MeV - 1.6 GeV), θ_s varies from 10.2 mrad to 1.14 mrad. The gap width necessary to allow multiple passages is about 10 mm, limiting the cathode potential to 50 kV, still within simple HV technology. The wire polarisation potential is given by $V_w = (1/2\pi) E_0 a \ln(a/d\pi) = 13.7$ kV for $d = 0.05$ mm diameter (beryllium) wires at $a = 5$ mm distance. The force on each wire is then $F_x = \epsilon_0 a E_0^2 / 2 = 0.028$ N/m and the maximum deflection $x_B = \epsilon_0 a E_0^2 h^2 / (16T) = 3.45$ mm for a tensioning force T of 0.2 N corresponding to 20% of the breaking strength of Be, and a septum height $h = 100$ mm. The importance of this bulging, which can attain even more impressive values for machines with large apertures, necessitates the hollow cathode shape sketched in Figure 1b. The hollow shape of the collimation aperture is no disadvantage, as inclined collimator faces in connection with the inevitable linear coupling are in fashion [4, 5].

IV. SIMPLE ANALYTICAL DESCRIPTION

The basic function of the MWS has been described in [2] by a simple "thin-lens" model for a septum of vanishing length in two-dimensional geometry. The distribution of the centres of the misaligned wires is described by a normalised (from $-\infty$ to ∞) gaussian $p(x)$ of standard deviation σ . The deflection angle as a function of the entrance coordinate x then becomes

$$\theta_s(x) = \theta_s F(x/\sigma)$$

with $F(x)$ being the integral of $p(x)$, where θ_s is the deflection of the ideal septum given above. From elementary multiple-scattering theory one obtains the r.m.s. scattering angle

$$\theta_w(x) = [13.6 \text{ MeV}/(p\beta c)] [Nd^2\pi p(x/\sigma)/(4\sigma X_0)]^{1/2},$$

with $N = l/a$ the number of wires and X_0 the radiation length (350 mm for Be). The set of parameters of sec. II and III and $\sigma = 1$ mm yields $\theta_w(x) = 0.32 \text{ MeV}/(p\beta c) \sqrt{p(x/\sigma)}$. At the maximum of the gaussian $\theta_w(0) = 0.13 \text{ MeV}/(p\beta c)$ which is to be compared with the value for the perfect septum (the average path length per wire is $d\pi/4$)

$$\theta_w = [13.6 \text{ MeV}/(p\beta c)] [Nd\pi/(4\sigma X_0)]^{1/2} = 1.44 \text{ MeV}/(p\beta c).$$

The latter value is only a little less than that of the deflection angle $\theta_s = 2.5 \text{ MeV}/(p\beta c)$. Figure 2 visualises the kicks according to the above expressions for the ideal and the misaligned septum in phase space; the shaded areas represent the possible re-entrance coordinates at subsequent turns, substantially reduced for the imperfect septum. Note that all angles scale with $(p\beta c)$, i.e. the relations given above hold at all energies. Absolute deflection angles become very small at higher energies and for efficient operation above 1 GeV two or three MWSs may have to be staggered, possibly in the same tank.

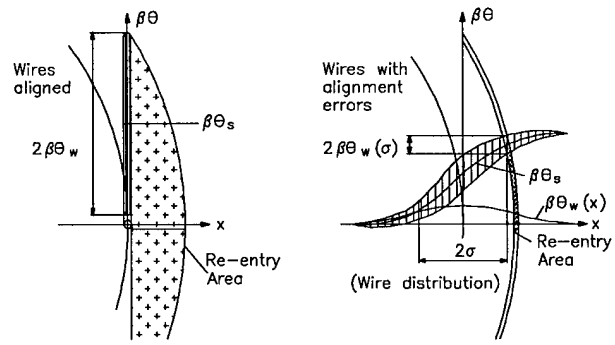


Figure 2: 'Thin-lens' model of a wire septum.

V. RESULTS OF THE SIMULATION MODEL

The thin-lens model misses non-negligible effects of the finite length of the MWS and needs to be complemented by tracking studies. The ACCSIM tracking code [6] features a wire septum element that can simulate perfect or misaligned wires in plane geometry, including the interaction with matter. The growing beam halo is modeled by an annulus in phase space drifting slowly (here at 0.5 m/s) into the septum. The three cases of interest are (a) the ideal MWS, aligned with the envelope of the 'halo', (b) the same but slightly misaligned, and (c) a 'real' septum with a gaussian distribution of wire position errors of standard deviation $\sigma = 0.5 - 1$ mm. Figure 3 a, b, c shows the trajectories of one *single* particle through the septum for these cases, while Figure 4 a, b, c shows the corresponding phase plane plots for the septum exit and *ten* particles. The last exit coordinates (before the particles hit the downstream collector) are marked by asterisks.

The test particle passes the aligned septum only twice (Fig. 3a): the lower (first) pass hits the end of the wire row and is strongly scattered to the outside, gaining emittance. This is the prerequisite that it can re-enter as shown with large amplitude and negative angle, obviously an unfavourable case. In Figures 3b, c the particle passes five times and is barely scattered. The most interesting feature of cases (b), (c) can be seen in Figures 4b, c: the gap between the final and earlier exit points, not present in Figure 4a. The study of a number of cases has shown that this gap is even more pronounced for larger standard deviations $\sigma > 1$ mm of the wire distribution. There one would place the face (transformed to that location) of a second, magnetic septum for definitive loss evacuation.

To test the MWS in a realistic model, three septa were inserted into the lattice of AUSTRON II at the foreseen horizontal, vertical and momentum collimator locations. With these insertions H^- injection at 130 MeV and RF capture were tracked with ACCSIM.

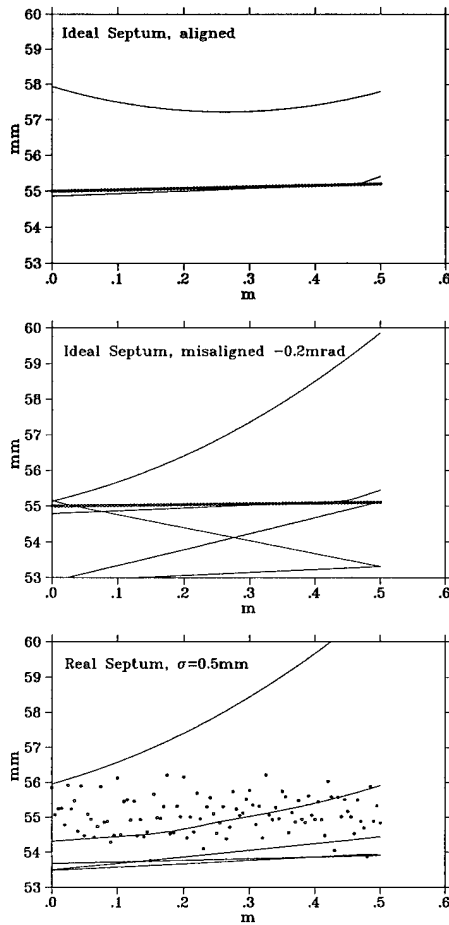


Figure 3a, b, c (top to bottom): Wire locations and trajectories in physical space of a test proton of 130 MeV through a wire septum with a field of 5 MV/m.

The basic loss mechanisms are then multiple scattering in the Al stripper foil and RF capture loss. The downstream collectors were assumed to be ideal absorbers. The collimation efficiency of the septa turned out to be 97.2 % while under identical conditions three graphite collimators achieved 94.7 %.

VI. CONCLUSION

A specially designed small wire septum provides cleaner single-stage loss collection in simulation than a two-stage, massive collimator system. Such a septum presents no major technological problems.

VII. ACKNOWLEDGMENTS

I wish to thank F. W. Jones for the upgrading of the ACCSIM code, M. Thivent for advice on septum technology and Mrs. B. Hadorn for the execution of the figure drawings.

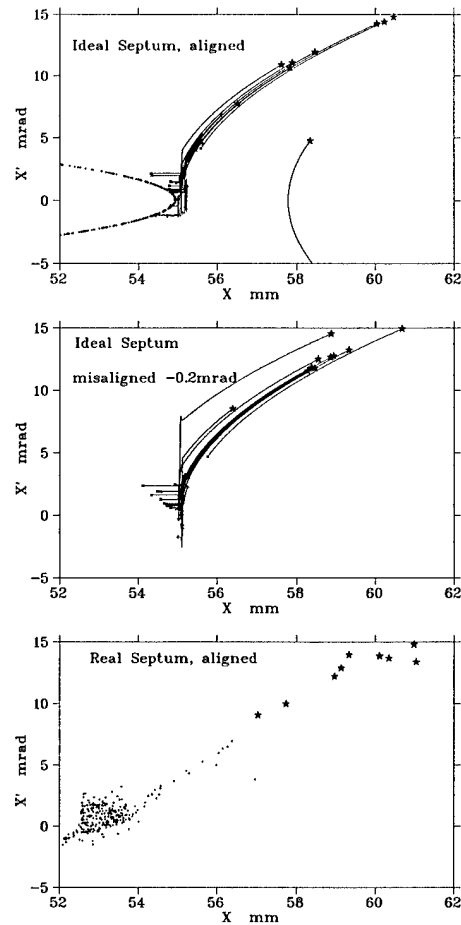


Figure 4a, b, c (top to bottom): Phase space trajectories (not in 4c, as they would confuse the presentation) and exit coordinates of 10 particles extracted by a wire septum; final exits marked by an asterisk. 'Halo' model annulus in 4a.

VIII. REFERENCES

- [1] T. Trenkler, J. B. Jeanneret, Principles of Betatron and Momentum Collimation in Circular Accelerators, CERN Int. Report SL/95-03 (AP) and References there.
- [2] H. Schönauer, On the Use of Predeflectors for Improved Beam Loss Concentration, Proc. 3rd EPAC, Berlin 1992, p. 339
- [3] The AUSTRON Accelerator Study Group, The Accelerators for the Austron Spallation Source, Proc. 4th EPAC, June 1994, London, p. 2675
- [4] P. Bryant, Some Advantages of Inclined Collimators, CERN Int. Report SL/92-24 (1992)
- [5] G. H. Rees ed., Rings' Working Group, Outline of Rings for a European Spallation Neutron Source, ESS 94-14-R, Dec. 1994, Report available from KFA Jülich
- [6] F. W. Jones, G. H. Mackenzie, H. Schönauer, ACCSIM - A Program to Simulate the Accumulation of Intense Proton Beams, Proc. 14th Int. Conf. High Energy Acc., Tsukuba 1989, p. [1409]/99

STATUS OF THE RADIOACTIVE ION BEAM INJECTOR AT THE HOLIFIELD RADIOACTIVE ION BEAM FACILITY

DT Dowling, GD Alton, RL Auble, MR Dinehart, DL Haynes, JW Johnson, RC Juras, YS Kwon,
MJ Meigs, GD Mills, SW Mosko, DK Olsen, BA Tatum, CE Williams, H Wollnik

Oak Ridge National Laboratory [1], P. O. Box 2008, Oak Ridge, TN 37831-6368 USA

The Holifield Radioactive Ion Beam Facility (HRIBF) is a first generation radioactive ion beam (RIB) facility. Project construction commenced in FY'93 with the initial emphasis placed on conversion of a heavily shielded room from an experiment area to an area suitable for housing the RIB Injector. The RIB Injector is the central component of the RIB project. The Injector consists of two electrically connected high voltage platforms which are designed to operate at -300 kilovolts and which are separated by a shield wall. One platform houses controls, instrumentation, and power supplies. The second platform houses an ISOLDE type target/ion source (TIS) which will be bombarded with light-ion beams from the Oak Ridge Isochronous Cyclotron (ORIC). Additionally, this platform houses the first stage mass separator system which is designed for 1 part in 1000 mass resolution, electrostatic quadrupole lenses for beam transport, and a cesium charge exchange cell for conversion of positive ions to negative ions for injection into the Tandem Accelerator. This paper details the design and beam development aspects of the RIB Injector.

I. INTRODUCTION

The Holifield Radioactive Ion Beam Facility (HRIBF) is a first generation radioactive ion beam (RIB) facility which is currently under construction [2]. The primary mission of the HRIBF will be to provide RIBs as well as stable ion beams for nuclear physics and astrophysics research programs. The HRIBF utilizes two existing accelerators, the Oak Ridge Isochronous Cyclotron (ORIC) [3] and the 25 MV Tandem Accelerator. These accelerators, along with the RIB Target Ion Source (TIS) [4], the RIB Injector, and a high resolution mass separator system constitute the major components used to produce RIBs. High-intensity light-ion beams such as 50 microamps of 100 MeV alphas, 50 MeV deuterons, or 60 MeV protons from the ORIC will be transported to the RIB Injector to bombard the TIS. The resulting radioactive atoms will be ionized, mass analyzed, charge exchanged and accelerated to ground potential with a maximum beam energy of 360 keV. The RIB will then be transported to an on-line diagnostic station for radioactive ion species identification using a gamma ray tape system [5] and to a high resolution mass separator. The beam is then transported to the existing injection line of the Tandem Accelerator where it is accelerated, mass analyzed and transported to the experiment stations.

"The submitted manuscript has been authored by a contractor of the U.S. Government under contract No. DE-AC05-84OR21400. Accordingly, the U.S. Government retains a non-exclusive, royalty-free license to publish or reproduce the published form of this contribution, or allow others to do so, for U.S. Government purposes."

II. DESIGN

The RIB Injector is the central component of the RIB project and its design was constrained by several factors. Calculations show that significant gamma and neutron radiation will result when the ORIC beam is stopped in the TIS. The Injector therefore had to be located in a room which has radiation shielding of sufficient thickness to reduce the prompt radiation to acceptable levels outside the room to minimize personnel exposure. The Injector had to be configured to minimize the radiation dose received by the electronic components of the system such as power supplies, controls hardware, etc. The Injector had to incorporate a mass analysis system capable of providing separation of adjacent mass units and for background reduction. Also, the Injector had to be designed to produce beams with energy similar to those supplied by the existing stable ion injector, nominally 200 to 300 keV, thus minimizing the modifications required for the Tandem Accelerator and providing efficient beam injection.

A plan view of the RIB Injector is shown in Figure 1. The Injector is located in Room C111, a heavily shielded room which was originally designed to house experiments utilizing 1 milliamp 75 MeV ORIC proton beams. The Injector includes two high voltage platforms which are separated by a shield wall. The Instrumentation Platform houses essentially all electronic equipment to minimize radiation damage. The 300 kilovolt power supply is mounted to the ceiling directly above the Instrumentation Platform. The Source Platform houses an ISOLDE type TIS which will be bombarded by intense light-ion beams from the ORIC. Additionally, the Source Platform houses the first stage mass separator system which is designed for 1 part in 1000 mass resolution, three electrostatic quadrupole lenses, beam diagnostics equipment, and a cesium charge exchange cell [6] for conversion of positive ions to negative ions. The two platforms are connected electrically by two high voltage conduits which carry signal and power cables.

The Injector is designed such that all control functions are carried out remotely. Effort was also made to provide maximum status information to the operator for all equipment and systems located on the Injector. The existing control systems for the ORIC and Tandem accelerators are unable to accommodate the additional controls requirements in a reasonable manner. As a result, a new control system has been implemented [7]. Controls for the Injector and, ultimately, the remainder of the HRIBF, are implemented through a new control system manufactured by Vista Control Systems, Inc. The controls platform for Vista is presently VAX/VMS/ELN. Operator interface is provided via X-terminals. The system is distributed with the

Injector controls being located on the Instrumentation Platform and connected to the remainder of the system via fiber optic ethernet. Specific I/O are implemented with a combination of VME and Allen-Bradley programmable logic controller modules.

A. Beam Optics

The Target/Ion Source produces a beam which is round and has an energy of up to ± 60 keV. The first optics element is a pair of electrostatic quadrupole doublets which focus the beam to a vertical line at the object of the first stage mass analyzing magnet with dimensions of 1 mm wide in the energy plane by 10 mm high. A slit system is located at the object location to clean up the beam prior to injection into the analyzing magnet. The beam at the magnet object is mass analyzed and focused to a vertical line at the image of the magnet with unit magnification. However, the various mass components in the beam are spread out in a series of vertical lines allowing adjacent mass units to be resolved easily with a slit system; the separation between masses 80 and 81 is approximately 25 mm. A quadrupole triplet focuses the beam from the image slits to a round spot at the center of the cesium charge exchange cell. The cell charge exchanges the positive ion beam into a negative ion beam. A quadrupole triplet focuses the beam which emerges from the cell to a round spot at the entrance to the high voltage platform acceleration tube. The negative ion beam is accelerated to ground potential at an energy high enough for efficient Tandem injection. Stringent requirements were placed on the 300 kilovolt power supply used

to bias the RIB Injector due to beam energy stability considerations. The supply has a ripple and noise specification of less than .004% or about 12.5 volts peak to peak at 300 kilovolts. Acceptance tests show that the actual ripple and noise is 9 volts peak to peak.

B. Beam Optics Components

The first stage mass analyzing magnet is the central optics component of the RIB Injector. It is a symmetric split-pole double focusing configuration with a total bend angle of 151.5 degrees and a bend radius of 558.8 mm. Its design is based on a maximum ion beam rigidity of 0.558 T-m and a maximum ME/q^2 of 15.0, corresponding to bending a singly charged 50 keV mass 300 ion. The effective field boundaries of the magnet poles are separated by approximately 203 mm. This small separation coupled with relatively short image and object focal lengths of 558 mm results in a compact mass analysis system which is crucial to the space limited design of the Injector.

The quadrupoles used on the RIB Injector are electrostatic units of a new design. The electrodes are mounted on a support tube which extends through the center of the electrodes. Four support tubes are used for mounting all of the electrodes in a triplet or quadruplet assembly. The elements are mounted on the support rods using precision ground annular ceramic insulators and the spacing of the elements along the beam axis is set during assembly using gage blocks. The result is an accurate and reproducible alignment of the electrodes within each singlet and from one singlet to the next. Each element of the quadrupoles is

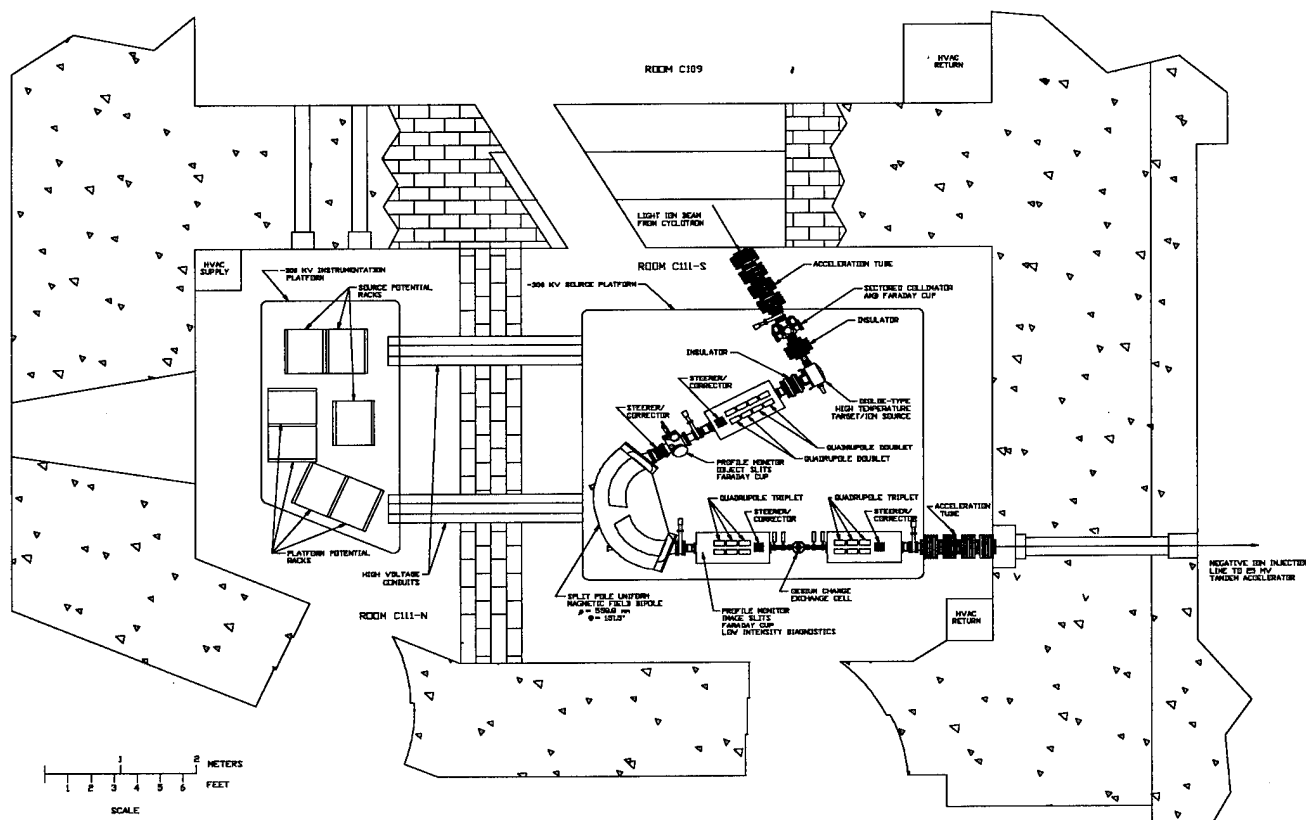


Figure 1. The Radioactive Ion Beam Injector

biased by an individually controlled 5 kilovolt power supply. This allows the quadrupoles to also be used as steerers. A resistor was installed on each electrode to provide a quick diagnostic check that the desired voltage is actually present. A 32 pole electrostatic element has been installed at the exit of each quadrupole assembly for future use as a steerer and as a sextupole and octupole corrector.

B. Beam Diagnostics Components

The majority of beam diagnostics are installed at the mass analyzing magnet object and image positions. Both the object and image position have a beam profile monitor, a slit system and a Faraday cup. Additionally, the image position has provision for a low intensity diagnostic assembly which is currently being developed [8]. The beam profile monitor installed at the object position is an oscillating vane unit which provides an x and y scan of the beam intensity. The monitor installed at the image position is an oscillating pin unit which provides a single axis scan in the energy plane of the magnet.

Each slit system has a series of fixed apertures mounted on a rotationally adjustable disk. Each slit system also has an adjustable aperture which can limit the vertical size of the beam. The Faraday cups are suppressed units and are designed to fit in a cylindrical space of approximately 35 mm diameter while providing an entrance aperture of approximately 14 mm. Faraday cups identical to these are installed at the entrance and exit of the charge exchange cell.

Additional beam diagnostics provide information regarding the ORIC light-ion beam. The first component is a 4 sector collimator which is used to determine beam position. The beam is focused to a waist at the collimator thus ensuring that it is not focused too tightly at the target. Following the collimator is a water cooled Faraday cup which is used in conjunction with a second water cooled Faraday cup mounted after the target assembly on the ion source to determine the amount of beam stopped in the ion source.

III. OPERATIONS AND DEVELOPMENT

The installation of the RIB Injector has been completed and initial operations and development activities have begun. Voltage tests of the Injector with all equipment installed were successfully completed at -275 kilovolts. All of the optics elements have been successfully tested with stable ion beams and the operational settings are in good agreement with the calculated values. The charge exchange cell has been tested and characterized on the Ion Source Test Facility.

Initial commissioning of the Injector using stable ion beams commenced in October of 1994. This effort resulted in successful transport of a stable mass 28, 20 keV, 16 nanoamp beam off the high voltage platform to the 300 keV diagnostic station. Several periods of beam development have since been utilized to study the operational characteristics of the Injector, to improve the beam transmission, to debug beam diagnostics and controls, and to gain operational experience using the RIB

Target/Ion Source. Recent efforts have produced a mass analyzed xenon beam with 6% combined ionization and transmission efficiency.

Current development activities are focused on several areas. The Target/Ion Source and its sub-systems are being radiation hardened where possible. Work is continuing on the control system to complete the remote control interfacing of all essential components. Several controls functions as are being added to aid beam tuning. Operational aids and help screens are being added as on-line references. Ion source and beam transmission parameters are being studied using a xenon gas feed into the Ion Source, and the Target/Ion Source is being prepared to receive a light-ion beam from the ORIC.

IV. SUMMARY

The RIB Injector at the Holifield Radioactive Ion Beam Facility has been completed. Successful operation has been demonstrated with stable ion beams resulting in beam transport to the 300 keV diagnostic station. Efforts are currently underway to prepare the Target/Ion Source to receive a light ion beam from the ORIC resulting in the first RIB production at the facility.

V. REFERENCES

- [1] Research sponsored by the US Department of Energy under contract No. DE-AC05-84OR21400 with Martin Marietta Energy Systems, Inc.
- [2] D.K. Olsen et al, Proc. Second Int Conf on Radioactive Nuclear Beams, Louvain-la-Neuve, Belgium, August 1991, ed. by Th. Delbar (Adam Hilger, Bristol, 1992), p. 131; A proposal for Physics with Exotic Beams at the Holifield Heavy Ion Research Facility, edited by J.D. Garrett and D.K. Olsen, February 1991.
- [3] J.D. Bailey et. al., "ORIC Accelerator", ORNL Physics Division Progress Report, Document No. ORNL-6842, p. 1-10 (1994), Oak Ridge National Laboratory, P.O. Box 2008, Oak Ridge, TN 37831.
- [4] G.D. Alton et. al., "The Electron Beam Plasma Target /Ion Source", ORNL Physics Division Progress Report, Document No. ORNL-6842, p. 1-26, (1994).
- [5] P.F. Mantica et. al., "RIB 300 keV Diagnostics", ORNL Physics Division Progress Report, Document No. ORNL-6842, p. 1-24, (1994).
- [6] G.D. Alton et. al., "The Charge Exchange Cell Project", ORNL Physics Division Progress Report, Document No. ORNL-6842, p. 1-31, (1994).
- [7] B.A. Tatum et. al., "Control System For The Holifield Radioactive Ion Beam Facility", paper MPA05 of this conference.
- [8] M.J. Meigs et. al., "A New Beam Intensity Monitoring System With Wide Dynamic Range For The Holifield Radioactive Ion Beam Facility", paper TPC18 of this conference.

A New Fast Rise Time Kicker System For Antiproton Injection Into The Tevatron

B. Hanna, J Dinkel, C. Jensen, D. Qunell, R. Reilly, D. Tinsley, J. Walton
Fermi National Accelerator Laboratory *
P.O. Box 500, Batavia, Illinois 60510

There are six proton and six antiproton bunches used at the present time for Tevatron Collider operation. As the luminosity is increased for a fixed number of bunches, the number of interactions per bunch crossing increases. The quality of the physics data taken by the CDF and D0 detectors is enhanced by reducing the number of interactions per bunch crossing. To this end it is planned to collide 36 proton bunches with 36 anti-proton bunches. To do this, it is necessary to construct and install a new 150 GeV injection kicker system with a faster rise and fall time than the existing injection kickers. This paper will describe the design, construction and testing of the new kicker magnet along with the associated spark gap pulsers, pulse forming lines and trigger circuits. Difficulties and our solutions will also be presented.

I. INTRODUCTION

In order to place the injected 150 GeV antiprotons onto the closed orbit in the Tevatron, a kick of one milliradian at location D48 is required. This has been accomplished using two transmission line magnets coupled to each other in parallel and pulsed using a thyatron based pulser. The system impedance is $5\ \Omega$ and operates at 55 kV. The rise time for this system is 1.1 microseconds with a flat top of 500 nsec. The fall time is on the order of 1.6 microseconds and there is considerable ringing that affects circulating beam. For present operations this waveform is acceptable. However, for the upgrade to 36 proton bunches colliding with 36 antiproton bunches, it is planned that for each injection 4 antiproton bunches be injected thus requiring a total of 9 injection cycles.

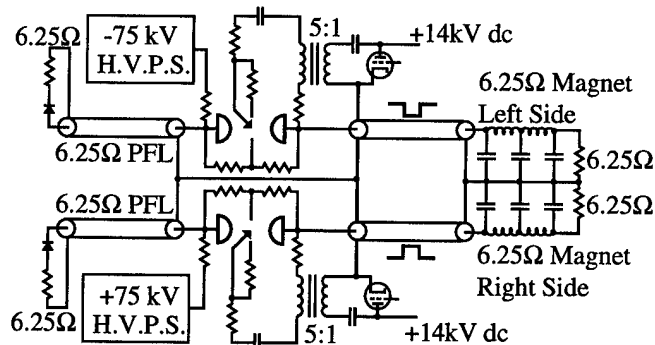


Figure 1. D48 Kicker Magnet System Schematic Diagram

* Operated by Universities Research Association, Inc. under contract with the U.S. Department of Energy.

Since the bunch spacing will be 21 bunches (which translates into 396 nanoseconds center to center) this requires a flat top of at least 1.2 microseconds. 36x36 operation also puts constraints on the rise time and fall time. The existing kicker does not meet any of these requirements. In order to meet the fast rise time and flat top length requirements, we have made a transmission line magnet pulsed via pulsers that use spark gap switches and RG-220 pulsed forming lines (PFLs). The impedance of the system is $6.25\ \Omega$. The overall system for one magnet is shown schematically in Fig 1. The overall system will be composed of 8 back terminations, 32 PFLs, 4 spark gap pulsers, 4 trigger units and 2 magnets. In addition there will be a controls system that will monitor all important operating parameters and disable the high voltage in case of a fault.

II. DESIGN PARAMETERS

The system design requirements and magnet design parameters are shown in Table 1 below:

Bdl	0.508 T-m
Space Available	230 inches
Horizontal Aperture	50.8 mm
Vertical Aperture	40.6 mm
Good Field (+/- .1%) width	35 mm
Field Rise Time	376 nsec
Flat top	1207 nsec
Field Fall Time	1053 nsec
Flat top Stability	$\pm 1\%$
Post Flat top Stability	$\pm 1\%$ of full field
Magnetic Length	2.41 m
Gap Height	5.72 cm
Gap Width	6.50 cm
Peak Field	1053 Gauss
Characteristic Impedance	$6.25\ \Omega$
Measured Magnet Fill Time	344 nsec
Number of Cells	68
Inductance per Half Cell	25.3 nH
Capacitance per half cell	647 pF

Table 1

The aperture requirements are determined by the amount of separation of the two beams, their emittances and their momentum spread. The manufacturer of the ceramic beam tubes, Coors Ceramics, required the tube to be tapered, and imposed a lower limit on the straightness they thought they could achieve, thus constraining our minimum gap width. The requirements on the good field region account for

alignment errors, injection errors, beam size and magnet straightness. The rise and fill times are such that the kickers are able to get to full field in the time between two bunches which, in the 36 on 36 scheme, implies a maximum time of 21 buckets or 376 nanoseconds. The flattop length is set by the requirement of injecting 4 antiproton bunches which implies a flattop time of 1.207 microseconds. These two requirements determine the minimum length of our PFLs to be 1.583 micro-seconds (which corresponds to 157.8 meters of RG220 cable with a polyethylene dielectric). The fall time is dictated by the requirement that the field in the kickers be less than 1% of full field when circulating protons arrive. The total time available for the pulse is 2.617 microseconds.

III. MAGNET DESIGN

The overall design is described in the design review [1]. The magnet itself is a ferrite loaded picture frame magnet. In order to achieve the necessary fill time, it is necessary to power the magnet with two pulses of opposite polarity. Each magnet consists of 68 cells (136 ferrite pieces and 138 capacitors), two 6.25 Ω resistive loads, four high voltage probes, and a 100" long ceramic beam tube with a high resistance paste coated on the inside for static charge bleed off. The magnet is filled with a liquid dielectric called Flourinert FC-77. In order to avoid problems associated with magnetic coupling between the two halves, a 0.005" copper Faraday shield extends down the length of the magnet on both top and bottom. Dollops of RTV were applied between the bus bars and the beam tube to hold the gap width, crucial to maintaining the correct inductance.

The ferrite material used is CMD5005. Its properties were tested and compared with other ferrite materials. The results of these tests are described elsewhere [2]. Since we have a tight tolerance on field uniformity across the gap, POISSON was used to optimize the shape of the pole tip. Calculations indicate the field in the midplane is uniform to within 0.05% over 1.4 inches. The ferrites are cross coupled to each other in order to minimize inductance for the displacement current in the shunt capacitors. Tests indicated that using a 10 Ω resistor in series with the cross coupling windings reduced ringing in the waveshape. Both horizontal and vertical alignment of the ferrites is important in order to maintain good field uniformity. Vertical alignment is maintained by use of precision machined holders. Horizontal alignment is accomplished by adjusting positioning lugs to set the ferrites on each side to the same distance from the bus bars. This can be done optically or mechanically.

Two different capacitor designs have been tested. The capacitors need to stand off 35 kV and carry a peak current of 650 Amps. In addition, they must fit in the space between adjacent ferrites which is 0.4 inches. The first design was a 6 layer PC board with a glass reinforced polyimide dielectric and was basically two capacitors in parallel. The thickness of the dielectric is 0.090 inches. The high voltage planes compose the inner layer while the ground planes are on the outer layers. Thus, besides being a capacitor, they also act as a Faraday shield between ferrites. Also, since the high voltage planes are shielded by the ground planes, stray capacitance is minimized. After building a prototype magnet with these capacitors we found that these capacitors started failing. The cause of the failures was due to poor bonding of the glass fibers to the

polyimide material. This problem was solved by using a smaller glass weave in areas of high electric field stress. An operational quality magnet made with capacitors of the new design has had no faults in over 50,000 pulses. There is no noticeable voltage coefficient for these capacitors which means the design value of 640 pF is the value of the capacitance desired from the manufacturer. The major drawback of these capacitors is the high level of corona they exhibit; in many of these capacitors we observed corona at voltages as low as 7.5 kV. The nominal operating voltage will be 28 kV pulsed. Since there was a large range of capacitance values for the 138 capacitors, we arranged the capacitors such that the higher capacitance was at the input end of the magnet and the values decreased as smoothly as possible so as to match both ends of the magnet as well as possible.

The second design uses commercially available E.I.A. Class I ceramic doorknob capacitors. These capacitors are mounted on a copper plate which attaches to the bus bar. We have found that there is a 4% decrease in the capacitance under voltage. From pulsed high voltage tests we have found the optimum value for the capacitance to be 665 pF. The major advantage of these capacitors is that they are corona free up to 40 kV and it is for this reason that they are the capacitor of choice for the magnet. In either case, the capacitors have not varied in their value of capacitance either due to pulsing (>100,000 pulses) or due to the liquid dielectric.

The loads, which are an integral part of the magnet structure, are composed of eight 50 Ω resistors in parallel. Each resistor is placed in a cylindrical tube so as to maintain a low inductance design. The resistors are tubular and have corona rings on both ends which are connected to the resistor using a conductive epoxy. On-going tests are looking into late life failures of these resistors. These failures may be related to an electro-migration effect at the junction of the resistive material and the metal corona ring. The entire load is potted in RTV with a high dielectric constant. This potting keeps the Flourinert out of contact with the resistors which helps to keep the value of the resistance stable and also adds capacitance to help with matching the magnet to the load at high frequencies.

In order to monitor the performance of the system and to make accurate measurements of the field quality, voltage probes have been installed at both the input end and at the load box. In addition, there are current viewing resistors in the loads. By taking the difference between the input and output voltages, one gets a \dot{B} signal. Integrating this gives the field. A hybrid transformer assembly mounted to the magnet combines input and output voltage signals to make a \dot{B} signal which can be monitored in the Main Control Room.

IV. PULSERS

This system will require a total of four pulsers, two positive and two negative. We use triggered spark gaps instead of thyratrons as the series switching element due to their compact size, low cost and ability to transfer high currents at high voltages. One of the main disadvantages of spark gaps is the lower lifetime. This shouldn't be a problem since antiprotons are injected infrequently; we expect only about 20,000 pulses per year. The gap chosen is the Maxwell #40264 gap rated for operation from 25 kV to 100 kV. This

standard unit is slightly modified in this system. We inserted 0.060" copper spacers under each electrode to reduce the gap spacing. This reduced the observed jitter at typical operating voltages. Since the rise time of the pulse is determined by the electrical properties of the pulser, a coaxial design is used as much as possible in the design of all components. Calculations indicate the pulser inductance is between 80 nH and 120 nH. This is consistent with the rise time at the output of the pulsers which has been measured at 38 ns (0-95%).

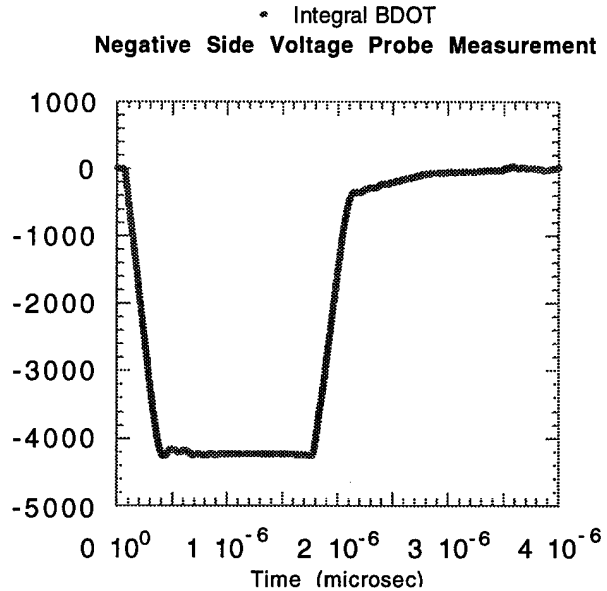
The spark gap is a three electrode, irradiation pin type unit. The center "midplane" electrode, biased at one-half the operating voltage, is triggered by a thyatron pulser. This pulser is transformer coupled to the gap to reduce the trigger current seen in the magnet. The transformer itself is high-voltage hook-up wire wound on a large CMD5005 core. Three primary turns and 15 secondary turns step up the voltage from the output of the thyatron by a factor of 5. The transformer secondary is coupled to the spark gap by means of a capacitor and two chains of resistors. The capacitor serves to block the charging voltage to maintain the bias of the midplane. The resistors were selected experimentally to minimize jitter and noise injected into the magnet from the trigger system. The trigger signal seen by the spark gap is on the order of 50 kV, with a risetime less than 50 ns. It has been observed that the irradiation pin must be set very precisely in controlled conditions. The factory setting proved unreliable for operation in this system. Improper setting often resulted in high measured jitter, and eventually complete failure of the breakdown process.

The spark gaps operate with compressed air as a dielectric. This air is furnished by a custom, oilless air compressor system which meets Maxwell's air requirements. Water and contaminants are removed with a system of refrigerators, dryers, and filters. Each spark gap is operated at an optimal pressure to balance the occurrence of pre-fires and fail-to-fires, while minimizing observed jitter. This pressure is determined mathematically after measuring the self-breakdown voltage of the spark gaps at various pressures, and fine-tuned by observation. After break-in, a system of four spark gap pulsers operating at 55 kV PFL voltage typically has about one fault every 10,000 pulses. Jitter is typically between 10 and 20 ns for each pulser. The firing of the spark gaps is coordinated by a 4 channel digital delay generator which compensates for system delays. Spark gap lifetimes in this system have been observed to exceed 200,000 shots at a charge transfer rate of approximately 0.007 Coulombs per shot.

The spark gap is mounted in a cylindrical aluminum housing which has been tin plated for corrosion resistance. Sulfur Hexafluoride is used as a dielectric, pressurized to 12 psia for operation up to 66 kV. Commercially available connectors[3] are used to simplify RG-220 cable installation. The design of the housing allows for simple replacement of key components including the spark gap. Glassman 75 kV, 50 mA supplies charge the PFLs through 3 M Ω resistors mounted in each pulser.

V. RESULTS

Results from the voltage probe measurements are shown below.



All requirements have been met with the possible exception of the fall time. These measurements indicate that the field is at 1.5% of full field by the time protons arrive. It should be pointed out, however, that many components involved in the measurement have voltage coefficients as well as skin effects which make this measurement extremely difficult. Ultimately, it will take beam tests to determine if all requirements have been met. Some research has been done using a spark gap to clip the tail of the pulse caused by the high frequency response of the PFLs. The results are inconclusive, and such a tail biter will not be incorporated into the system initially.

VI. ACKNOWLEDGMENTS

We would like to thank Joe Lazzara, Gene Opperman, Mike Heinz, Mitch Tarkowski, Rolf Joseph, Joel Misek, Lee Brown, Cliff Foster, Ken Kellogg, Dan Bollinger, Dan Ziembra and Mike Brennan for a great deal of help on the electrical and mechanical aspects of this project. In addition one of us would like to thank people too numerous to list for help in getting the electronic format of the paper correct for submission.

VII. REFERENCES

- [1] J. Dinkel, et al., "D48 Design Review", unpublished.
- [2] C. Jensen, J. Dinkel, "Comparison of Ferrite Materials for Pulse Applications," IEEE Transactions On Magnetics, Vol. 31, No. 1, January 1995.
- [3] A. Donaldson, et al., "High Voltage Pulse Cable and Connector Experience in the Kicker Systems at SLAC," IEEE Particle Accelerator Conference, Vol 5, pp3159-3161, May 1991.

DESIGN OF THE MI40 BEAM-ABORT DUMP

C. M. Bhat, P.S. Martin and A.D. Russell

Fermi National Accelerator Laboratory* P.O. Box 500, Batavia, IL 60510

Abstract

A beam-abort dump for the Fermilab Main Injector to handle 3×10^{13} protons per pulse at 150 GeV has been designed. A 120 GeV beam line goes through the beam-dump off-set by 27 cm from its center. The design and the environmental safety aspects of the beam-dump are described here.

I. Introduction

A beam-abort dump or beam stop is an important part of a high energy accelerator. In an accidental condition the beam must be automatically deflected on to a dump to avoid any damage to the accelerator components. Even during routine accelerator studies low intensity beam gets frequently aborted. In any of these cases, the beam-dump should be able to handle the aborted beam. Also, the area around it should have enough radiation and environmental protection.

Fermilab Main Injector (FMI) is a 8-150 GeV proton synchrotron that is being built as a high intensity injector to the Tevatron. The Main Injector beam-dump is to be built near the MI40 straight section and has the base elevation of 214.27 m (703 ft). It is planned to be a water-cooled dump. The maximum number of protons per machine cycle on the beam-dump exceeds 3×10^{13} @ 150 GeV. Since this beam-dump will be much closer to the aquifer than any existing beam-dumps in the Fermilab accelerator complex, it is extremely important that the design minimize the soil activation and reduce the ground water contamination.

To establish As Low As Reasonably Achievable (ALARA) radiation exposure to Fermilab workers and visitors a number of guidelines have been worked out and they are stated in FERMILAB RADIOLOGICAL CONTROL MANUAL. According to this, the on-site and off-site radiation level should be less than 0.025 mrem/hr and 10 mrem/year respectively. The allowed ground water radioactive contamination should be less than 20 pCi/ml-year. Also, the policy of Fermilab is, not to accelerate beams for which there is not a user. Aborting the maximum number of protons per hour, while not strictly an accident condition, is a violation of that policy.

II. Design

We started out with the design of the presently existing beam-dump[1] in the Tevatron (near the C0 straight section) and arrived at an optimized design for the MI beam-dump. However, unlike the buried C0 Tevatron beam-dump, the FMI beam-dump will be placed in an accessible enclosure. The optimization has been carried out using the Monte Carlo code CASIM[2]. The total radiation dose above the berm of the beam-dump which is at an elevation of 227.38 m (746 ft) and the total number of stars

in the soil is designed to be at least a factor of two below the acceptable limit. To have the ability for easy access, a 1.1 m wide walking space will be allowed around the beam-dump. The design of the beam-dump is shown in Fig.1. Provision has also been made for a 7.62 cm beam pipe through the iron core of the beam-dump for future extracted beam. The core of the beam-dump will be of high melting point graphite embedded in a 2.74 m aluminum box. This box will be cooled by 40°C low conductivity water (LCW). In front of the aluminum box concrete bricks will be hand stacked. The aluminum box is surrounded by layers of 0.84 m thick steel and 1.1 m thick concrete. The total length of the beam-dump will be 10.7 m. The LCW cooling system will be installed behind the beam-dump in the available space.

The transverse emittance of the beam[3] in the Main Injector is expected to be 12π or larger. The horizontal and vertical β -functions at the surface of the graphite core is 225 m. This makes the minimum beam spot size on the beam-dump about 0.15 cm. The instantaneous maximum temperature rise in the core within the area occupied by the beam due to the interaction of 3×10^{13} protons at 150 GeV is about 100°C. This beam will deposit about 330 kW of power in the beam-dump. Out of that about 55% of the energy (i.e. 200 kW) will be deposited in the graphite and aluminum core box alone. Hence we have planned to have an LCW cooling system which is capable of extracting at least 300 kW.

III. Estimation of Radiation Level

The radioactivity in and around a beam-dump can be categorized into two classes. The first one is for the beam on conditions (prompt radiation), i.e., the instantaneous electromagnetic and hadronic showers developed due to interactions of the high energy particles with the beam-dump. The second arises from the residual radioactivity of the dump. Both of these are dependent upon the total number of primary protons aborted and the beam energy. The average number of protons to be aborted on the FMI beam-dump per year under normal operating conditions[4] is about 3.26×10^{18} @ 150 GeV. The maximum number of protons continuously aborted in any one incident is estimated to be 6.0×10^{16} @ 150 GeV per hour.

A. Prompt Radiation

The prompt radiation dose is calculated using the number of "stars" (interaction points) produced in a unit volume per incident particle. With a soil equivalent shielding thickness between the FMI beam-dump and the berm of about 9.75 m, the low energy neutrons and muons are the main contributors to the radiation dose at the surface level. Here, these two contributions have been evaluated in separate sets of Monte Carlo calculations. Figure 2 displays isodose contours obtained using CASIM. The results for muons are displayed in Fig. 3 along with a sectional

*Operated by the Universities Research Association, under contracts with the U.S. Department of Energy

Table I

Dose due to prompt radiation around FMI beam-dump and ground water activity.

Concern	Radiation dose
Neutrons :	
Max. Rad. Dose (Allowed dose Unlimited Occp. Limit.=0.025 mrem/hr for N.O. and 1 mrem/accident	1.1E-5(mrem/hr) (For N.O.) 1.2E-3(mrem/acc.) (Maximum Beam Abort)
Muons :	
On-site (Allowed dose Unlimited Occp. Limit=0.025 mrem/hr for N.O. and 1 mrem/accident	5.4E-5(mrem/hr) (For N.O.) 6.0E-3(mrem/acc.) (Maximum beam Abort)
Off-site muons Annual Limit=	≤3.2E-5(mrem/y)
Ground Water :	
Annual Activation (Annual Limit 20 pCi/ml-y of ³ H 0.4 pCi/ml-y of ²² Na)	³ H 2.12pCi/ml-y ²² Na 0.07pCi/ml-y (A) ³ H 0.01pCi/ml-y ²² Na 0.148pCi/ml-y (B)

(A) Single Resident Well Model (B) Concentration Model

view of earth in the downstream of the beam-dump. Using these results, the expected radiation dose for normal and maximal beam loss conditions have been evaluated. The results are listed in Table I along with the standards adopted at Fermilab.

Radioactive contamination of the ground water is one of the major considerations in designing a beam-dump. The aquifer around FMI is only about 4.88 m below the FMI beam-dump. Of all the radioactive nuclei produced in the spallation reactions the greatest hazards in ground water are from ³H and ²²Na. The EPA-allowed limits for these nuclides in ground water are listed in Table I. There are two methods to determine the increase in the concentrations of these nuclides in the aquifer viz., A) the single resident well model and B) the concentration model[5] (which was developed very recently and is more suitable for an accelerator complex like Fermilab). The first one depends upon the total amount of stars in the soil and the second method uses the maximum star density in the soil near the base of the beam-dump. The results obtained from these two models are displayed in Table I. We find that they are at least a factor of two below the allowed limits.

B. Induced Radioactivity in the Beam-dump

As a result of hadronic showers developed in the beam-dump a variety of short and long lived radioactive nuclides will be produced. These give rise to residual radioactivity. Here we use the method suggested by Barbier[6] to estimate it.

Table II

Residual radioactivity for MI Beam-Dump at contact. T_i = irradiation time in days (d). T_c = cooling time.

Description	Dose on Contact (rad/hr)	
	$T_i=360d$ $T_c=1d$ (7d)	$T_i=30d$ $T_c=1d$ (7d)
Carbon		
Front	10 (10)	3.3 (3)
Back	10 (10)	3.3 (3)
Al. Box		
Top Front	26 (4)	0.4 (0.4)
Top Back	26 (4)	0.4 (0.4)
Iron		
Front	0.2(0.1)	0.1 (0.07)
Middle Top	0.02 (0.02)	0.01(0.007)
Back	≤4E-3 (≤1E-3)	≤2E-3 (≤1E-3)
Concrete		
(Max)	≤2E-3 (≤4E-4)	≤2E-3 (≤4E-4)
Concrete Wall		
(Max)	≤8E-4 (≤2E-4)	≤8E-4 (≤2E-4)

The radiation dose \dot{D} is given by,

$$\dot{D}(\text{rad/hr}) = \Omega/4\pi \times \Phi \times d$$

where Φ is the hadron flux (which related to the star density and the incident proton flux). For dose measurements at contact, $\Omega/4\pi = 0.5$. d is referred to as the danger parameter which depends upon the material which is being irradiated, the duration of irradiation, T_i , the production cross section for various radioactive spallation products and the cooling time, T_c , of the target. For FMI beam-dump, the danger parameters are taken from Ref.6. The results of calculations have been listed in Table II.

IV. Summary

A beam-dump suitable for the Fermilab Main Injector that can handle 3E13p/pulse has been designed and is presently under construction. We have allowed for a beam line to go through the iron core without affecting the radiation level at the berm. There is enough clearance around the beam-dump for easy access and maintenance. We estimated that the prompt radiation dose level and the ground water contamination level is at least a factor of two less than the prescribed limits in FERMILAB RADIOLOGICAL CONTROL MANUAL. The residual radioactivity around the beam-dump will be less than 2 mr/hour after one day of cooling.

The authors would like to acknowledge Dr. A. Van Ginneken and Dr. N.V. Mokhov for useful discussions.

REFERENCES

- [1] A. Van Ginneken CASIM Fermilab-FN272(1975), MUSIM Fermilab-FN594(1992).
- [2] T.C. Murphy et al, Fermilab TM1196 (1983).
- [3] Fermilab Main Injector Technical Design Handbook (1994).

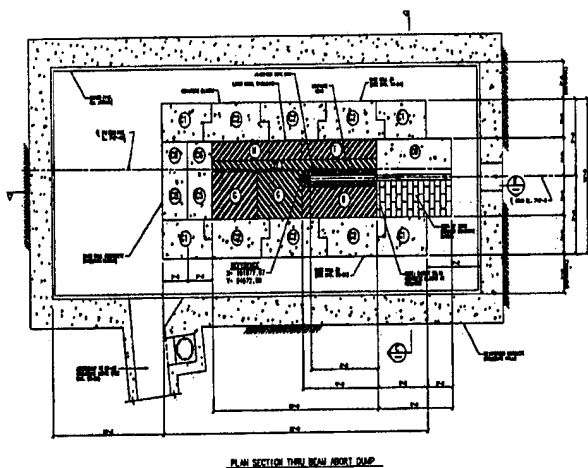


Figure 1. Longitudinal section of FMI beam-dump.

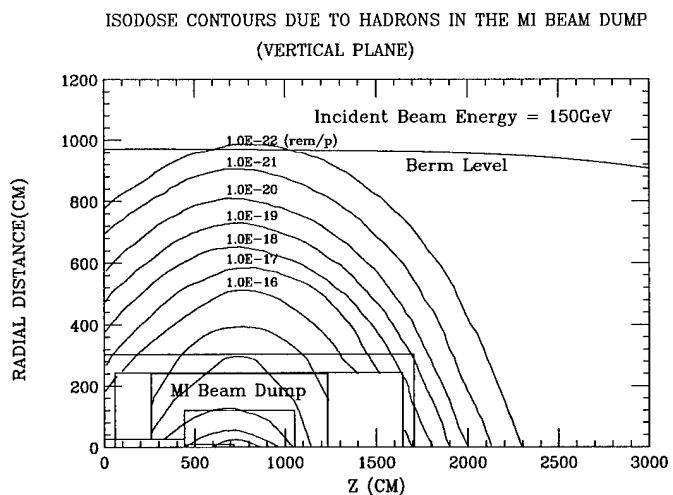


Figure 2. Iso-dose contours for 150GeV proton beam aborted on FMI beam-dump.

- [4] Fermilab Main Injector PSAR (1992).
 [5] A.J. Malansek et al, Fermilab TM1851 Aug. 1993.
 [6] M. Barbier, Induced Radioactivity, North-Holland Pubs. Comp. (1969).

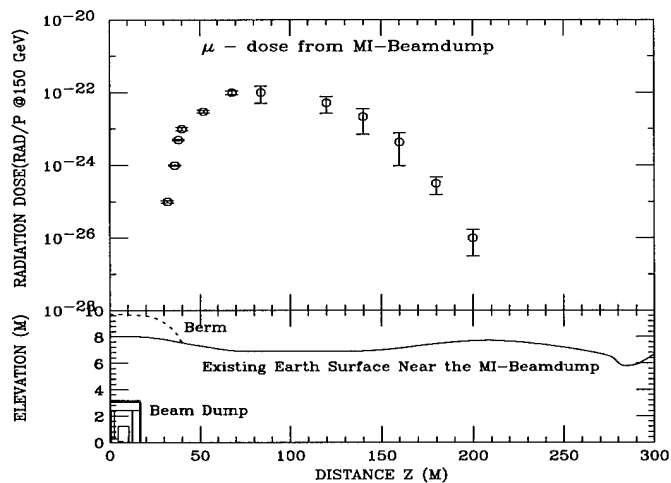


Figure 3. The muon dose in the vicinity of FMI beam-dump for 150GeV proton beam abort.

STUDY ON THE METALLIC COATING OF THE CERAMIC CHAMBER FOR THE ATF DAMPING RING KICKER MAGNETS

N. Terunuma, H. Nakayama and J. Urakawa

KEK, National Laboratory for High Energy Physics, Oho 1-1 Tsukuba, Ibaraki, JAPAN

A ceramic chamber in the kicker magnet is used to penetrate the fast-changing magnetic field into the beam pipe. On the other hand, the metallic coating inside the ceramic chamber is important to pass the image currents of the beam. For the ATF Damping Ring, it is planned to study the multi-bunch-beam operation. The requested rise time of the kicker field is less than 60 nsec.

Studies to get a suitable metallic coatings inside a long-and-narrow ceramic chamber have been performed and continued. Tests of the sub-micron-thickness coating were carried out as the first stage of our studies.

I. INTRODUCTION

The construction of the 1.54 GeV damping ring in KEK Accelerator Test Facility (ATF) is in progress. The purpose of the ring is to study the multi-bunch-beam operation with a low emittance to realize the future linear collider. Under such operation, up to five-bunch trains, each of which contains up to 60 bunches, circulate in the ring. The repetition rate of the injection is 25 Hz. The kicker magnets are designed to operate with 60 nsec field rise time and with 4.6 mrad kick angle [1,2].

Ceramic chambers in kickers are used to avoid the shielding of a fast-changing magnetic field by a metallic beam pipe. On the other hand, a thin conductive coating must be provided on the inside of the chamber to carry the image currents of the beam and to avoid electrical discontinuities of the chamber wall. It is an important point for the ATF damping ring; the vacuum system is designed to achieve low-impedance chambers. However, this coating again has a shielding effect of the kicker field.

Therefore, the metallic coating should be optimized concerning the effects that related to the fast-changing kicker field and that related to the beam; that is the effects due to the image currents and the eddy currents.

II. CERAMIC CHAMBERS

The aperture for the ceramic chamber in the kicker magnets is long and narrow. The cross sectional view of the proposed ceramic chamber is shown in Figure 1. The length of the alumina ceramics is 500 mm long to avoid the electrical breakdown between the 40 kV conductor and the metallic joints brazed to the ceramic pipe.

Type-A is a circular one for injection kicker. Type-B is a racetrack shape for extraction kicker, extended to the outer

side of the ring, is designed to protect the ceramic chamber from the unwanted synchrotron irradiation. Such irradiation will warp the brazing part of a ceramics and a metallic joint, and finally it will break the vacuum. The shielding of a kicker field due to the eddy current would be large for type-B. The radius of the beam pipe is 5 mm. If the load of SR is acceptably small, type-A is adopted for the extraction kicker.

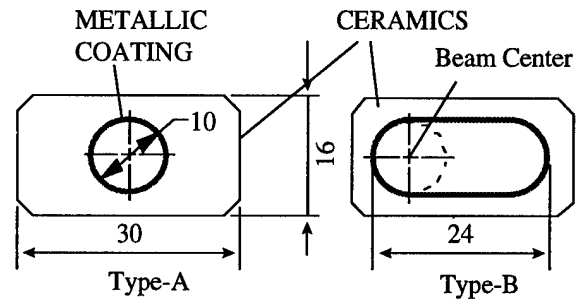


Figure 1: Proposed cross section of the ceramic chamber.

A. Required surface resistivity

Method of a metallic coating by longitudinal strips is applied for recent accelerators [3,4]. For the ATF, it is planned to use a continuous coating, because the forming method of strips in the circular area is seems to be very difficult for the long and narrow ceramic chamber. For the continuous case, the surface resistivity of a coating is evaluated concerning the effect of the eddy currents and that of the image currents [5,6].

The heating due to the ohmic loss of the image currents favors a low surface resistivity. The dissipated power density P_i in the coating is given by

$$P_i (W / cm^2) = \frac{Nq^2 c^2}{2\sqrt{\pi} \sigma_z (2\pi a)^2 C_R} R_{sq},$$

where N is the bunch number, q is the charge in a bunch, c is the velocity of light, σ_z is a bunch length, C_R is a circumference and R_{sq} is the surface resistivity. For our case, it is simplified to $3.8R_{sq}$.

On the other hand, the heating due to the eddy currents favors a high resistivity. In this case, the dissipated power density is

$$P_e (W / cm^2) = 2B_k^2 F 10^{-10} / t R_{sq},$$

where F is a repetition rate and t is the rise time of the kicker field B_k . For our case, the maximum power density becomes $0.1/R_{sq}$.

The total power dissipated in the coating is shown in Figure 2 as a function of the surface resistivity. For the left-hand side of the minimum, 0.16 ohms/square, it shows the

rapid increase due to the eddy currents. On the other hand, right-hand part shows the steady increase and it is suitable for the handling of the coating resistivity.

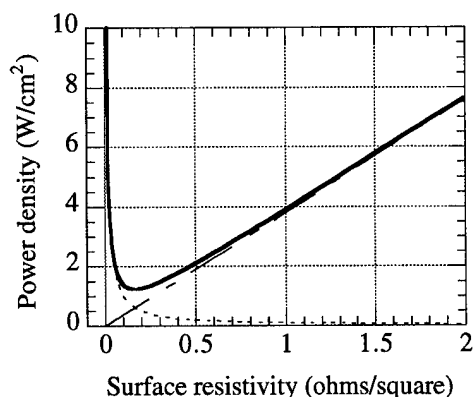


Figure 2: Dissipated power in the coating as a function of the surface resistivity. Solid line shows the sum from image currents (dot-dashed) and the eddy currents (dots).

The penetration time of the kicker field is a function of the surface resistivity. For a circular chamber with a radius a (cm), the time constant due to the eddy currents is $2\pi a/R_{sq}$ nsec. Figure 3 shows the penetration pattern of the kicker field where the rise time of the external kicker field is assumed to be 50 nsec. The acceptable one is greater than 1 ohms/square for the multi-bunch-beam operation.

If the surface resistivity of the metallic coating is 1 ohms/square, the total dissipated power becomes 300 watts. This power must be removed by a forced air cooling.

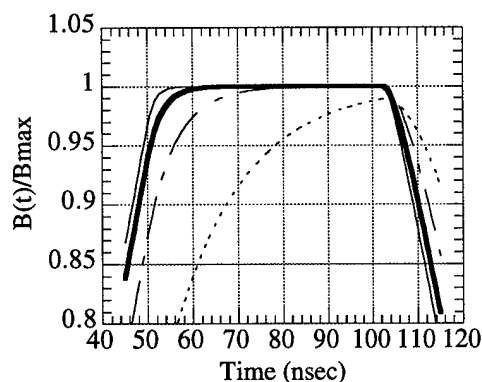


Figure 3: Penetration patterns of the kicker field evaluated with various surface resistivity (ohms/square) of 0.2(dots), 0.5(dot-dashed), 1.0(wide-solid) and 2.0(solid).

III. TEST OF THE METALLIC COATING

If a coating material has a specific resistivity ρ (Ω cm) and thickness d (cm), the surface resistivity is given by ρ/d . Materials which have a bigger ρ and a smaller d is better for the coating.

There are some formation methods of a thin film such as an evaporation and a chemical vapor deposition (CVD). The evaporation by a metal wire seems to be realistic for our chamber. While it need more time for R & D, because we have no experience to do it. As a first stage of studies, we decided to check the condition of a coated material by using TiN which was a well-known material of a coating on the ceramics and was easily obtained. The method is a thermal CVD.

Tests of the TiN coated on ceramic plates were performed by changing the coating thickness. If we use the TiN as a coating material, the thickness should be 0.2 micron.

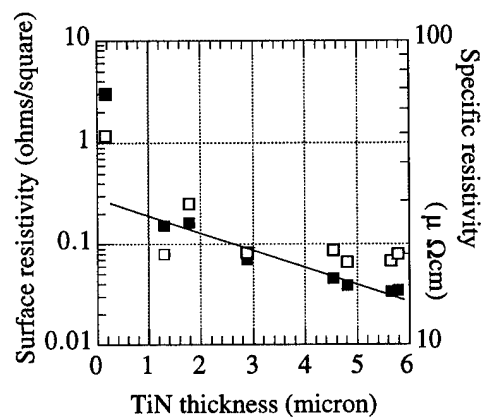


Figure 4: Surface resistivity (black) and specific resistivity (white) for TiN samples. Surfaces of ceramic plates were not polished.

Figure 4 shows the variation of the surface resistivity and the specific resistivity. The surface resistivity increases with a decrease of the thickness and steeply increases below one micron. These results are due to a difference of a uniformity of TiN film. After a sintering of a ceramic pipe formed by alumina powders, grains of the ceramics grow a few microns in size. Thus, the coating below one micron has a tendency to finish under insufficient formation. Figure 5 illustrates the close up view of such TiN sample, 0.3 μ m.

On the other hand, to make a comparative study, same measurements were carried out for samples which surfaces were polished. The condition of a coating was uniform even if its thickness is 0.2 μ m, see Figure 6.

The polishing of the ceramic surface is very difficult because of the long-and-narrow-kicker chamber. Further, it is difficult to handle the thickness of the sub-micron coating. Therefore, the TiN coating will not be adopted to our ceramic chamber.

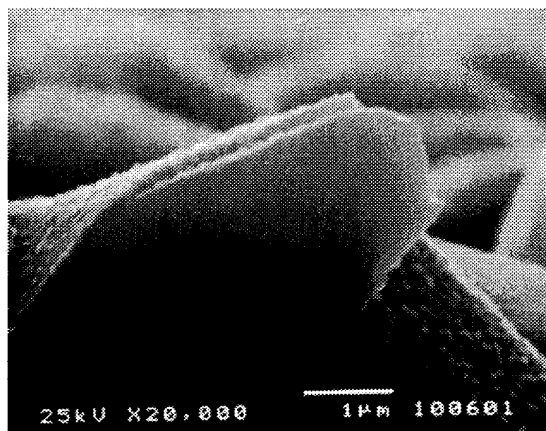


Figure 5: Cross section of the surface. The thickness of the TiN is 0.3 μm and the base ceramics is not polished.

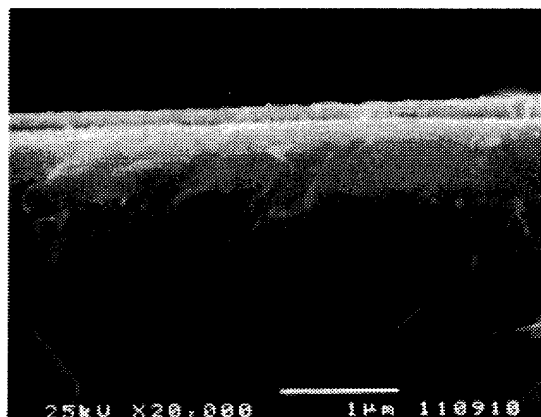


Figure 6: Cross section of the surface. The thickness of the TiN is 0.2 μm and the base ceramics is polished.

IV. CONCLUSIONS

To form a suitable metallic coating on the inside of the ceramic chamber, the thickness of the coating is needed to be more than one micron; the material must have higher specific resistivity more than 100 $\mu\Omega\text{cm}$.

There are some materials which specific resistivity is more than 100 $\mu\Omega\text{cm}$. Most of them are ferro-magnetic metals, thus effects due to the skin depth must be considered. Moreover, methods that make a small surface roughness of a ceramic pipe should be studied.

The injection and extraction system of the damping ring, including ceramic chambers, is planning to install in the fall of 1996.

V. REFERENCES

- [1] H. Nakayama et al., KEK Proceedings 92-6, p.326-334 (1992).
- [2] ATF Design and Study Report, *to be published in KEK Internal Report*.
- [3] J. M. Peterson, SLAC Note CN-49 (1981).
- [4] A. Piwinski, *IEEE Trans. NS*, NS-24, p1364 (1977)
- [5] T. Hodges et al., TRI-PP-92-126 (1992).
- [6] S. Kurennoy, SSCL-Preprint-311 (1993).

Prospect of the fast extraction from KEK-PS for the long base line neutrino experiment

H.Sato, Y.Shoji and T.Kawakubo

National Laboratory for High Energy Physics, Tsukuba-shi, 305 Japan

Single turn extraction from KEK-PS and beam intensity upgrade has been investigated. Big motivation is the long base line experiment with neutrino beam. In this presentation, new fast extraction system which has been under consideration will be described.

I. Motivation

To meet the need of new physics research, there are several objectives for the PS upgrade, such as, to increase the proton intensity in the main ring, to accelerate the various ions and then the multifunctional operation of PS. Especially, an intensity upgrade is coming to the urgent problem for the Long Baseline Neutrino Oscillation experiment.[1] This means the fast extracted high intensity beam creates the high current neutrino beam and the neutrino beam will be injected to Super-Kamiokande which is about 250km west from KEK. Present nominal intensity is 4×10^{12} ppp for 4 sec main ring operation cycle, but the requested intensity is five times of the present intensity/operation cycle for 500 events per year.

II. Feasibility of the fast extraction using slow extraction equipments

The fast extraction system of the KEK proton synchrotron had been operated until July 1981 for the bubble chamber experiments and these

were situated in EP1 beam line, [2],[3] which is used for the second slow extraction at this present.[4],[5],[6] A circulating beam orbit is locally deformed outward by the electrostatic septum inflector (ESS) situated in the straight section of II-IF and by the magnetic septa (C,D,E) situated in the straight section of II-2F. A set of four bump magnets located in I-7F, I-7D, II-3F and II-3D is excited with 15ms wide half sine pulse currents to adjust the maximum bump orbit displacement, comes close to the ESS wire plane. A pair of fast bump magnets, are located in I-7F and II-5D, are excited with 20 μ s wide half sine pulse currents to displace across the 50 μ thick tungsten wire of ESS and a fraction of circulating beam were inflected into the aperture of the magnetic septa. These were the shaving extraction but new fast extraction must extract an entire beam at once.

Distribution of the bump magnet for slow extraction system is almost the same as old fast extraction system as shown in Figure 1. If the rise time of fast bump magnets is 100 μ s, magnets can be made by thin steel without using ferrite.

Unfortunately, there are no space in the ring to set the powerful kicker magnet to move the entire beam toward the septum magnets. Then, sophisticated method has been considered using distributed several small kicker magnets.

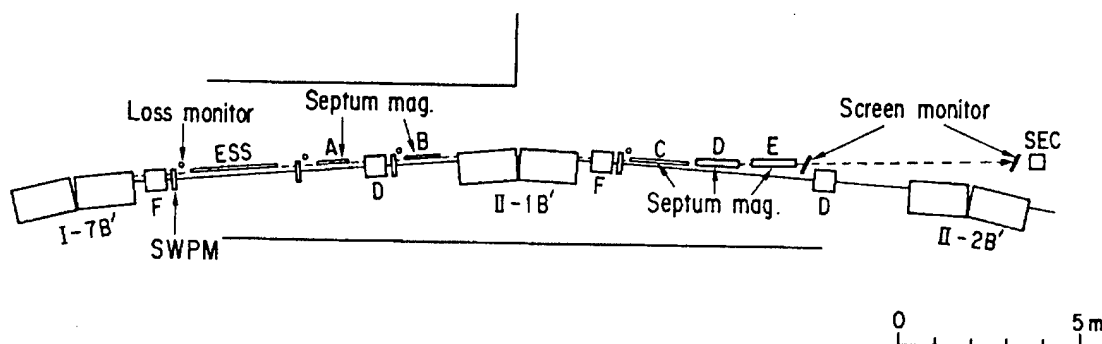


Figure 1 Layout of present slow extraction system for EP1 beam line.

Table I Specification of Kicker Magnets

Position (mr)	I-2F	I-5D	I-6F	I-7D	ESS
Request kick angle (mm)	-3.0	-1.0	-0.3	0.5	0.5
Gap width (mm)	80	75	120	65	65
Gap height (mm)	55	55	55	55	55
Number	2	1	1	1	1
Total length (m)	2.4	1.3	0.9	0.56	0.3
Total kick angle (mm)	3.0	2.73	0.9	3.21	1.62
Type	W-frame	W-frame	W-frame	W-frame	C type

One of solutions is that two kicker magnets are situated in I-2F and four kicker magnets are situated in I-5D, I-6F, I-7D and one kicker is situated at ESS position. Last one is a C-type magnet and set on the opposite side of ESS as face to face. Others are all window frame type magnet. Specification of these kicker magnets are shown in Table 1. The field quality of a test magnet has been reported to be satisfactory. Construction of the prototype, but full scale magnet, will be started soon. Figure 2 shows a beam excursion by these kicker and conventional bump magnets. This solution is still not optimized one and has some problems. One problem is that these orbit excursion causes a possibility of significant beam loss. A beam profile measurement suggests we can take enough aperture of kicker magnets to avoid the beam loss even if the kickers have to be made as compact as possible. However, there is a touch of uneasiness in that the beam profile will become larger when high intensity beam circulate, so we should know how much margin of this aperture we should take. Study to make clear the ring aperture is under going.

There is still another severe problem in this schema. As shown in Figure 2, an orbit excursion is very large at a position of II-2F such as 110mm. Good field region of the main ring quadrupole magnets is about 70mm so the extracted beam must pass through the strong non linear field region. This effect causes the deformation of extracted beam emittance. In order to avoid this problem, four quadrupole magnets at 2F section at each super period should be replaced to large aperture magnet. This causes an increase of load for a magnet power supply so a new isolated power supply which must be excited by tracking to lattice magnet current, has to be needed.

As mentioned above, there is a feasibility of fast extraction using the slow extraction system, however the significant device replacement and construction should be necessary.

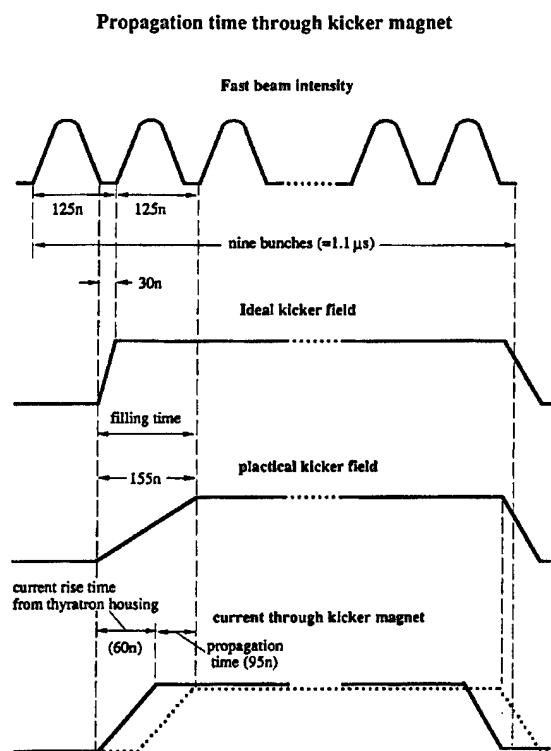
III. Discussion

If the EP1 line will be able to use exclusively for fast extraction operation during neutrino

experiment, there is a possibility of rather simple method. ESS as shown in Figure 1 will be replaced by strong kicker magnets, which move the entire beam toward the septum magnets. This schema will save a complex beam excursion, however the need for large aperture magnet is still remain and is not considered in detail yet.

Which method we will adopt, the time space between the beam bunches of 30ns is too short for the rise time of fast kicker magnet. PS is operating nine RF harmonic number, then if one bunch is taken out to obtain the time space for rise time of kicker magnet. It makes sufficient of 155ns time space as shown in Figure 3. However, this means the number of circulating beam bunches decreases to eight so the beam intensity is reduced to eight ninth.

Further detailed study and design works have to be continued in hurry and vigorously.



One bunch is taken out to obtain the kicker rise time!
So, the number of circulating bunches is from 9 to 8.

Figure 2 Kicker Rise time and Bunch Spacing.

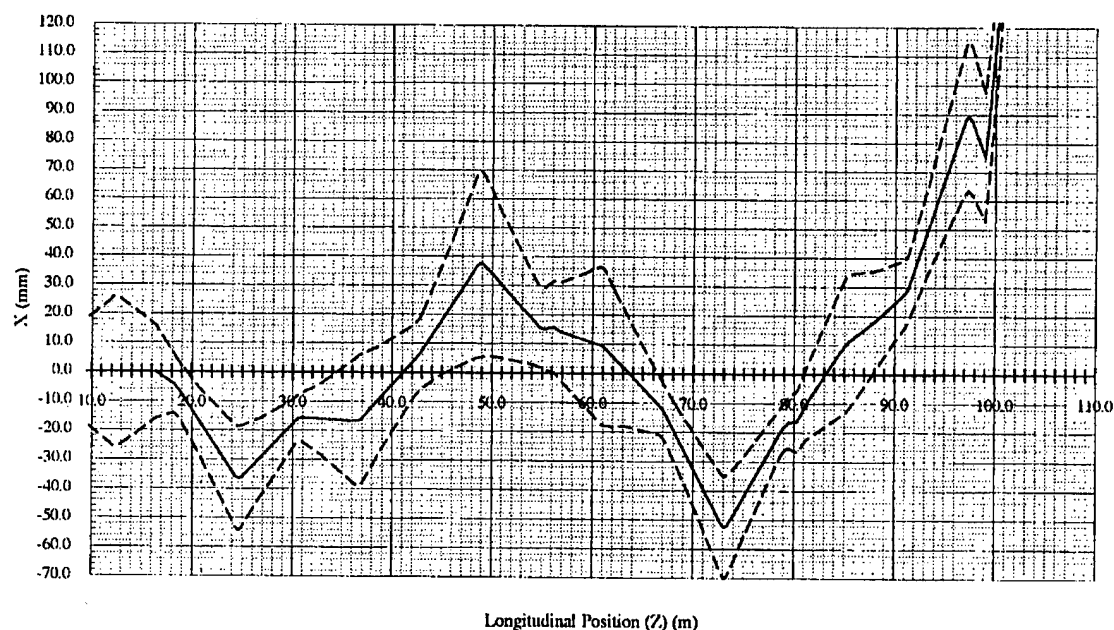
Acknowledgments

The authors would like to express their sincere thanks to Professors M. Kihara who was former director of PS division and K. Nishikawa, Institute of Nuclear Study of Tokyo University, for their encouragements. They are much indebted to Professor I. Yamane who is director of PS division and to many colleagues of PS group for their discussions and collaborations.

REFERENCES

- [1] K. Nishikawa et al., KEK Preprint 93-55/INS Report 297-93-9
- [2] E. Endo and C. Steinback, KEK-77-13.
- [3] C. Steinback and K. Endo, KEK-77-18.
- [4] K. H. Tanaka, Proc. of the Workshop on Science at the Kaon Factory, Vancouver, 1990, p.1.
- [5] Y. Shoji et al., Proc. of the 8th Symp. on Accelerator Science and Technology, 1991, Saitama, Japan, p.281.
- [6] Y. Shoji et al., KEK Report 93-10 A

HORIZONTAL KICKED BEAM ENVELOPE
(kicked at I-2F, 5D, 6F, I-7D and ESS) (extracted at II-2F)



I-2F

I-5D I-6F

I-7D ESS

Septa-C

Figure 3 Orbit excursion by the distributed kicker magnets.

Helium Beam Acceleration in The KEK Proton Synchrotron with A Newly Developed Injection System for Positive/Negative Ions

I.Sakai, A.Takagi, Y.Mori*, S.Machida, M.Yoshii, T.Toyama, M.Shirakata, Y.Shoji and H.Sato

National Laboratory for High Energy Physics, Oho 1-1, Tsukuba Ibaraki 305 Japan

A helium beam has been successfully accelerated in the KEK 12 GeV Proton Synchrotron up to 23 GeV of the limiting energy of the main ring. The first physics experiment with a helium beam was carried out in April, 1994. Although a charge exchange injection of negative hydrogen ions has been used in the booster synchrotron, it cannot be applied to the injection of positive ions, such as helium ions. A newly developed injection system realized alternative use of both negative and positive ion injection schemes.

I. INTRODUCTION

The acceleration of heavy ion beams in the KEK-PS was discussed more than about 10 years ago. Recently, as one possible candidate among the future plans for the KEK PS, the PS-Collider was proposed [1]. This report proposed easier acceleration scheme for heavy ions with a Q/A of 0.5 in the KEK PS than one discussed before. Modifications of the KEK PS aimed at deuteron beam acceleration have been performed. On Jan. 31, in 1992, deuteron beam was successfully accelerated up to the limiting energy of the ring. The first physics experiment using a deuteron beam was carried out in April, 1992.[2]

The charge exchange injection scheme has been used to inject proton and deuteron beams into the booster synchrotron. This scheme, however, cannot be applied to positive ions, such as helium ions. Therefore, a conventional multi-turn injection scheme must take the place of the charge exchange scheme. There is no space for another injection system because of the booster designed well-compact. To replace the injection devices every operation cycle is not practical. To avoid this, a certain technical break-through is indispensable. A new injection system has been developed to realize both negative and positive ion injection. With this system, in April, 1994, a helium beam was successfully accelerated, and a physics experiment has been carried out. Also, a high intensity proton beam has been accelerated by using this system until now.

This new injection system has opened new uses of the KEK PS, i.e. from high intensity proton beam acceleration to high energy heavy ion beam acceleration. The principle of the newly developed positive/negative ion injection

system and the first helium acceleration is summarized in this paper.

II. BOOSTER NEW INJECTION SYSTEM

A schematic layout of the new injection system, which is presently being used for proton, deuteron and helium ion acceleration, is shown in Figure 1. The system comprises four bump magnets (the main bump magnets) placed in one of the straight sections of the ring. The main bump magnets have single turn conductor plates, and are arranged asymmetrically so as to enlarge the angle between the injection and central orbits under a limited magnetic field. In Figure 1, the dotted line indicates the beam orbit for charge exchange injection. These bump magnets are used to change the closed orbit so that the beam impinges on a carbon stripping foil. The negative hydrogen ions are fully stripped at the foil, and start to circulate in the ring. In order to prevent an emittance blow-up by multiple scattering at the foil, the bump magnets must be turned off just after the completion of injection.

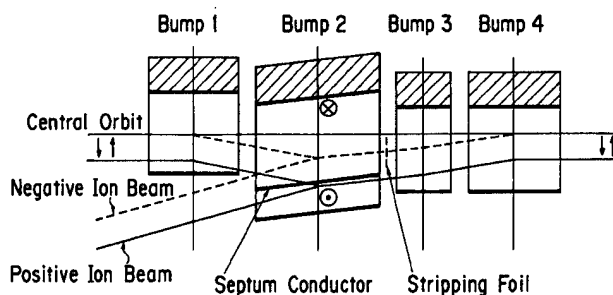


Figure 1. New injection system for the booster

The solid line indicates the positive ion orbit during multi-turn injection, which overlaps the charge exchange injection by Bump 2. This has been newly developed and plays the role of both bump and septum magnets. A cross-sectional view of Bump 2 is shown in Figure 2. This Bump 2 has three single-turn conductor plates in the pole faces. The electric currents flowing through these conductors produce two dipole magnetic fields with opposite signs, which are separated by a middle thin conductor plate (1mm thick), which forms a septum.

* Present address: Institute for Nuclear Study, University of Tokyo, 3-2-1, Midori-cho, Tanashi, Tokyo 188 Japan

During positive beam injection, the closed orbit must be shifted by 60mm toward the septum magnet in parallel, which is achieved by exciting two additional bump magnets (not shown in Figure 1). Their positions are one quarter of the betatron wavelength upstream and downstream from the injection point. Beams are gradually injected from the center of the phase space to the outside by changing the field excitation of the additional bump magnets.

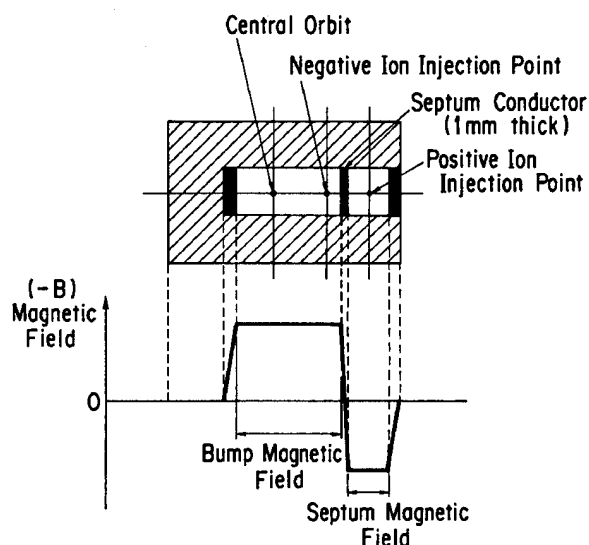


Figure 2. Cross-sectional view of Bump 2 and the excited filed pattern for positive beam injection.

During positive beam injection, both the bump and septum currents flow into the thin septum conductor instantaneously. Bump 2 is operated under a pulsed mode in order to eliminate any cooling problems. Pulsed operation can be realized using a PFN-type pulsed power supply. The PFN is electrically insulated from the ground potential and controlled through an optical fiber[3].

III. ACCELERATION OF HELIUM IONS

Most of the problems in accelerating heavy ions of $Q/A = 0.5$ at the KEK-PS had been solved at the time when deuteron acceleration succeeded in 1992. However, in the acceleration of helium ions, there remains difficulties with respect to multi-turn injection of the positive ions.

A. ION SOURCE AND INJECTOR

The injector comprises a 750 keV Cockcroft-Walton preinjector and a 40 MeV Alvarez linac. There are two sets of Cockcroft-Walton preinjectors, the first preinjector is used to accelerate a high intensity beam of H^- and D^- , whereas the second preinjector is for a polarized beam.

Some modifications of the second preinjector have been made in order to accelerate positive ions. The electric polarity of the Cockcroft-Walton high voltage generator and the power supply for bending magnets of low energy beam transport(LEBT) have been inverted. A multi-cusp ion source is utilized to produce singly charged helium ions. An extraction voltage of 50kV is supplied to the ion source, and a 50 keV- He^+ beam is injected into the 700 kV accelerating column of the preinjector. In order to convert a He^+ beam to a He^{2+} beam, a gas stripper cell has been installed in the LEBT.

The 750kV He^{2+} ion beam is injected into the linac. During linac acceleration, the helium beam is accelerated under the 4π mode operation scheme[3]. Its velocity is half that in the case of proton acceleration. As a result, at the end of the linac it has 3% less momentum than that of proton beam. The beam transport parameters and booster injection parameters must be optimized according to the beam momentum.

B. BOOSTER INJECTION

During multi-turn injection the beam is painted on the horizontal phase space. As shown in Figure 3, trace (c), by changing the decay current of additional bump magnets, the circulating beam orbit during an injection period was moderately shifted for efficiently stacking the linac beam. This is also a new attempt in accelerator technology. Four turns of the linac beam were accumulated with this technique.

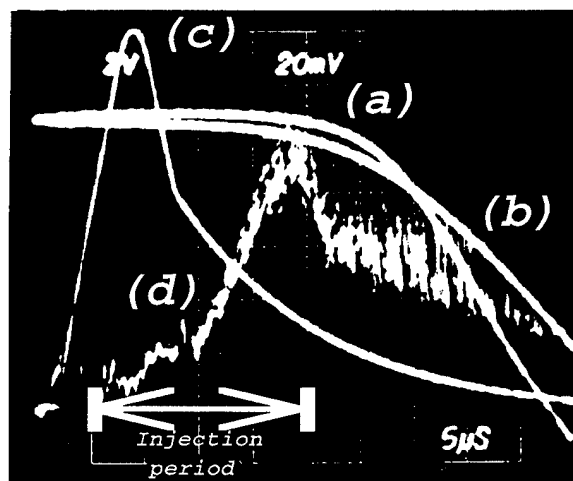


Figure 3. Current waveforms of the injection magnets and beam current monitor at the booster injection: (a) septum, (b) main bump, (c) additional bump with two time-decay constants and (d) beam current.

We observed a very fast beam loss; only half of the accumulated beam was extracted from the booster. This beam loss was caused at the time that the main bump magnet field fell sharply to zero. Field measurements of the main bump magnets showed that the eddy currents induced in the magnets caused a total error field, so as to cause closed orbit distortions, the maximum value of which was

about 4 mm. The total error field due to the septum magnet eddy current, as well as the main bump magnet, was also measured. However, both of the error fields induced by eddy currents are of opposite sign and can cancel each other by adjusting falling time of both magnets.

C. ACCELERATION IN THE BOOSTER AND MAIN RING SYNCHROTRONS

For heavy ion accelerations in both the booster and main ring synchrotrons, the radio-frequencies of the accelerating systems are lower during injection, and sweep more widely than in proton acceleration. The tuning systems in both synchrotrons have been modified. The injection frequencies can be changed by attaching additional capacitors in both systems. Especially, in the main ring synchrotron, the bias current power supplies for the ferrite loaded tuning cavities were upgraded.

The intensity of a helium beam was expected to be at most on the order of 10^{10} particles per bunch. To stably accelerate such a low intensity beam the pre-amplifiers of both the position and beam phase monitors for the rf feedback systems have been improved.

Table 1.

Typical Operating Parameters during Helium Acceleration Ion source

Type of ion source:	multi-cusp ion source with 19 multi-anode hole
Beam width:	20 μ sec
Beam repetition rate:	20 Hz
Extraction gap / voltage:	14 mm / 50 kV

After pre-acceleration

He ⁺ beam current:	7.6 mA(750 keV)
-------------------------------	-----------------

After gas stripper

He ²⁺ beam current:	6.6 mA
--------------------------------	--------

Linac beam

Beam current:	1.5 mA(20 MeV) 0.8 mA(40 MeV)
Emittance*: ϵ_v / ϵ_H	0.94 / 0.75 π mm.mrad

Booster

Rf frequency range:	1.1 ~ 3.9 MHz
Beam intensity:	7×10^9 particles per bunch
Extraction energy:	588 MeV

Main ring

Rf frequency range:	4.0 ~ 7.9MHz
Beam intensity:	4.7×10^{10} particles per pulse
Top energy:	23 GeV

(* normalized rms emittance)

The typical operating parameters and achieved helium beam intensity are summarized in Table 1. During a commissioning run lasting one month, the helium beam was very stable, it was also extracted at various energies of 8 GeV (2 GeV/u) to 20 GeV (5 GeV/u), based on the requirements of the physics experiments.

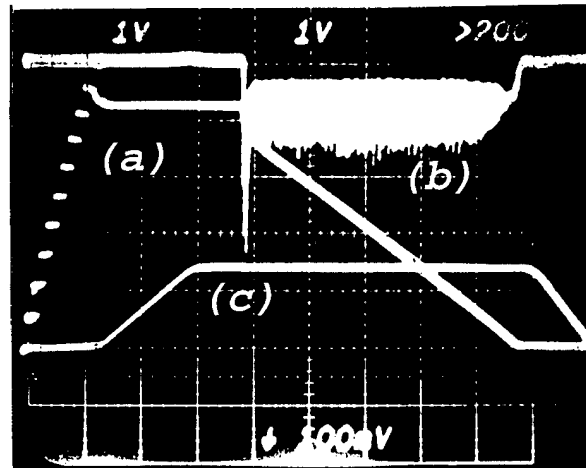


Figure 4. Helium acceleration in the main ring: (a) a helium beam intensity during a cycle, (b) a slowly extracted intensity and (c) a main magnet field pattern.

IV. SUMMARY

During the 1990's, we started to modify the KEK Proton Synchrotron in order to accelerate and extract various beams at different energies. This was closely related to the physics programs using such primary beams. The first step was deuteron acceleration in 1992, helium acceleration was the second step. The new injection system for the booster involves a very sophisticated technique in which both negative and positive beams can be injected into a synchrotron ring pulse by pulse. As primary beam experiments, heavier ion beams in the GeV energy region are desired. However, without upgrading the pre-injector it is difficult to inject fully stripped $Q/A = 0.5$ ions into the booster.

At present, a heavy ion beam acceleration program has been scheduled for one month every April. Polarized deuteron acceleration is also planned.

The authors would like to express their sincere appreciation to the Director General of KEK, H. Sugawara, as well as Profs. M. Kihara, Y. Kimura and I. Yamane for their continuous encouragement. They are also indebted to Drs. M. Nunajiri and K. Kondo for their help considering radiation estimation in helium acceleration.

V. REFERENCES

- [1] PS-Collider design group, KEK Report 90-13, 1990.
- [2] Y. Mori, et. al., Acceleration of Deuteron Beam in the KEK Proton Synchrotron, IEEE Particle Accelerator Conference, 1993, p.3754.
- [3] I.Sakai, et. al., A New System to Trigger Fast Rise Thyristers, IEEE Particle Accelerator Conference, 1989, p.2005.

FAST AND RELIABLE KICKER MAGNETS FOR THE SLC DAMPING RINGS*

T. S. Mattison, R. L. Cassel, A. R. Donaldson, and G. Gross,
Stanford Linear Accelerator Center, Stanford, CA 94309 USA

ABSTRACT

The design, construction, and operation of a kicker magnet with superior electromagnetic performance and greatly improved radiation tolerance is described. A short flux return of high μ ferrite improves the field strength and linearity with current, and novel metallic field-confining structures minimize the inductance. An 8-cell structure with capacitance integrated into each cell makes the magnet a nearly perfect transmission line. The capacitor dielectric is 1 cm thick alumina-loaded epoxy, processed to eliminate air voids, and cast in a multiple step procedure developed to circumvent epoxy shrinkage. The magnet operates with pulses of up to 40 kV and 3.2 kA at 120 Hz, with magnet transit times of less than 35 nsec and field rise and fall times of less than 60 nsec.

I. OLD AND NEW MAGNET DESIGNS

The Stanford Linear Collider (SLC) uses two 1.2 GeV damping rings to reduce the emittance of the e^+ and e^- bunches before acceleration in the main linac. Each damping ring requires an injection and extraction kicker magnet with rise and fall times of less than 60 nsec. The thyatron pulsers have rise/fall times of at best 25 nsec, so the magnet contribution must not exceed 35 nsec. The e^- kickers must inject or extract both bunches on a single pulse, requiring a 60 nsec flat top and two e^- extraction kicks must be different by less than 10^{-3} . These requirements are best met by a matched and terminated transmission line magnet. The kickers are outside of 21 mm diameter ceramic beam pipes, and the space allocated is less than 50 cm long. Voltages of up to 40 kV are required. There are substantial beam losses near the kicker magnets, with localized radiation levels of order 10^8 rads.

There have been two generations of SLC kicker magnets [1,2]. The first generation of SLC kicker magnets suffered from high voltage breakdown through the joints between the ferrite tiles used for both flux return and capacitor dielectric. They also had poor pulse quality, behaving more like LC elements than transmission lines, and were not suitable for extracting two e^- bunches on a single pulse. In the second generation of SLC kicker

magnets, the capacitance was provided by a 2 mm thick layer of RTV silicone rubber between the center conductor and grounded aluminum segments containing large slotted ferrite flux return cores. The RTV also became brittle upon exposure to radiation, then cracked when thermally cycled. In some locations the lifetime averaged as low as 10 days. There was substantial stray inductance due to the distance between the center conductor and the beam pipe. A ferrite advertised as low- μ was used, for low inductance (but low kick per ampere) but the μ at operating current levels was substantially higher, leading to a higher inductance and mismatch. The second generation could be used for extracting two e^- bunches on a single pulse, but only by shaping the current pulse to compensate for the mismatch of the magnet.

A new kicker magnet has been designed to overcome these shortcomings. It retains the segmented LC circuit and separation between flux return and capacitance functions of the second generation magnet, but eliminates the nonlinearity and subsequent impedance mismatch by using a short flux return path of high μ ferrite. It improves the HV breakdown and radiation damage performance by using thicker dielectric of alumina-loaded epoxy. The required capacitor surface area is obtained by radial plates. The stray inductance is reduced by extending the center conductor to one side of the beam pipe, forcing all the flux to enter the beam pipe. The magnet has 8 LC cells, with 6.5 cm diameter, 4 cm long ferrite cores in each cell. The center conductor is 1.9 cm diameter, with 25 cm diameter, 1.2 cm thick radial capacitor plates. There is a 5 mm thick aluminum cup attached to each HV plate that surrounds the ferrite core. The ground plates are 29 cm diameter, 1.2 cm thick, and have an 11.5 cm hole providing clearance from the ferrite cup. The ground plates are attached to the cylindrical outer conductor. The capacitor dielectric is 1 cm thick alumina-loaded epoxy. The plates have rounded edges, and are thinned elsewhere to increase the clearance at the edges of the other plates. There is a 30° wedge removed from the magnet to allow it to be installed over the beam pipe. The field enhancement from the resulting plate edges is ameliorated by making the cut in the HV plate at a larger angle and the cut in the ground plate a wider slot, so the enhancements only reinforce in a limited region. After the magnet is attached to the beam pipe, a wedge is inserted to fill the gap. The wedge contains a ground electrode that forces stray magnetic field to go through the beam pipe. See Figure 1.

*Work supported by the US Department of Energy
Contract DE-AC03-76SF00515.

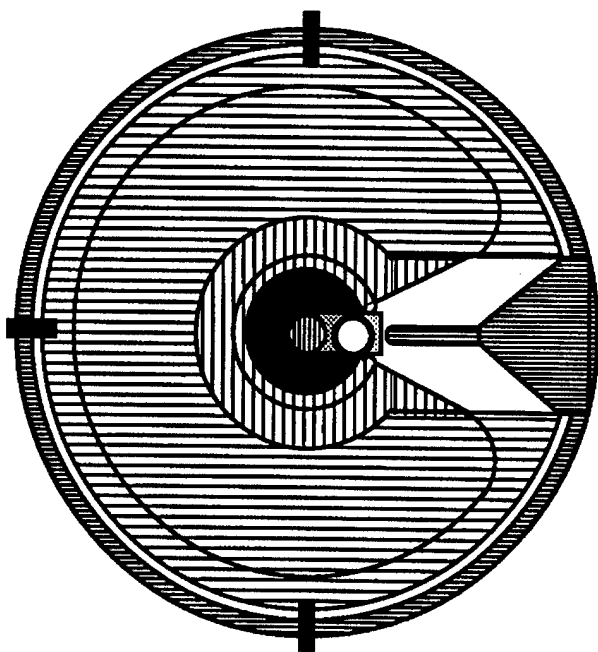


Figure 1: Cross-section end view of epoxy kicker magnet. HV plate is vertically hatched, and is largely hidden behind the horizontally hatched ground plate. The beam pipe is just to the right of center. The wedge insert is farther right.

II. EPOXY DIELECTRIC TECHNOLOGY

Several mineral-loaded epoxies were chosen for evaluation [3]. They have higher viscosity than unfilled epoxies, but have higher dielectric constants, are less brittle, and have greater radiation tolerance. A pot life of a few hours is required. The curing reaction is exothermic and accelerates with temperature so epoxies with cure times of less than a day tend to suffer thermal runaway.

Vacuum degassing is required not only to remove the bubbles introduced during mixing, but also dissolved gas that may come out of solution during shrinkage. Not all of the dissolved gas comes out during the initial froth stage, and agitation under vacuum is necessary [4].

The products of the epoxy curing reaction have a volume 3-5% less than the reactants. If a rigid hollow mold is filled with epoxy, the epoxy will not fill the volume after it is cured. Bubbles will grow as the epoxy shrinks. Shrinkage reduces the internal pressure, which can form spontaneous bubbles, or suck air into the mold. Epoxy may pull away from concave surfaces as it cures, or debond or crack later. Any of the above problems would be fatal in our high-voltage dielectric application. Epoxies with high filler content shrink less by total volume. Some epoxy chemistries remain liquid through a larger fraction (but not all) of the shrinkage.

Epoxy cured in a shallow open mold displays few pathologies because the shrinkage takes place by motion of the surface. Adhesion to the mold is good, particularly if

the surface is sandblasted. Adhesion inside closed molds can be good if the mold is designed to accommodate the shrinkage by deforming. Epoxy can also be cast in stages. Each stage of the cure can shrink separately, which allows much better control of the results of shrinkage.

III. MAGNET CONSTRUCTION

The flux return cores are CMD-5005 nickel-zinc ferrite. The HV capacitor plates with center conductor stalk and ferrite cup, and the ground plates, are each machined from single pieces of aluminum. The plates are sandblasted for adhesion, then degreased. A cell consisting of a ferrite core, an HV plate, and a ground plate is cast in a closed mold. The top plate of the mold slides on an O-ring seal to allow for shrinkage. The mold is polished and treated with mold-release compound. A wedge-shaped mold-insert keeps epoxy out of the beam pipe region. The scars from fill and overflow hose fittings occur on the epoxy that is removed in the wedge region.

The epoxy used is Conapoxy FR-1727, which is 50% aluminum oxide powder by weight, and matches the thermal expansion coefficient of aluminum. It bonds well and is very resistant to fracture. However it is quite viscous, and will suffer thermal runaway if the mixing temperature is too high. The epoxy is mixed, degassed to a few Torr while being agitated, then transferred by air pressure on the epoxy surface into two molds per epoxy batch. The molds are at 10 Torr during transfer, and are pressurized to 5 atmospheres during cure. Finished magnet cells have both plates and the ferrite encapsulated in epoxy, with only the stalk ends of the HV plate and the edge of the ground plate exposed.

The magnet end-cells are aluminum dishes with 3 cm thick high voltage plates for the cable connections. Polished and tapered aluminum mold inserts form cavities where the cable dielectrics plug in. The cable ground braids attach to the dish. A polished metal wedge keeps epoxy out of the beam pipe region. The end-cell dishes and plates are sandblasted, degreased, and filled with epoxy, then cured with a free surface. One end-cell is also has a ferrite core and ground plate, and requires a larger epoxy volume, so it is filled partially, cured, then filled the rest of the way.

Before being assembled into a complete magnet, the cells and end-cells are high-voltage tested, sandblasted, and degreased. One end-cell is placed on a flat surface, and a metal rod is inserted vertically in its center conductor. Magnet cells are then slid onto the rod, which provides electrical contact between the cells. There are small O-rings on the center conductor stalks, which both seal epoxy away from the rod, and allow the cells to slide along the rod without touching as the epoxy shrinks. An aluminum

cylinder jacket (with a 30° wedge missing) is slid over the outside of the stack, then the other end-cell is added to the top. The jacket is held away from the end-cells by small rubber bumpers, and sealed to them by tape. There is about 2 mm of clearance between the jacket and the edges of the ground plates, and more between the edge of the cell epoxy and the jacket. This allows the cells to move during shrinkage without binding. As the epoxy in this volume shrinks, the radius of the jacket can decrease by narrowing the 30° slightly.

The aluminum electrode that forces flux to go through the beam pipe is inserted into the stack, with inorganic Mycalex insulators on each end. A full-length metal wedge is inserted into the stack, to align the cells and to exclude epoxy from the beam pipe region. An overflow well is caulked onto the jacket over the wedge region. The magnet is turned on its side with the wedge facing up for final potting. The epoxy is introduced through a fitting in the jacket and opposite the wedge. A notch in the ground plates allows the epoxy to flow from cell to cell. The epoxy used is Epic Resins R-1055/H-5039, which is 50% silica filled, has low viscosity and long pot life, and remains liquid for most of its shrinkage. The magnet is filled under vacuum, and cured under pressure.

After the epoxy has cured, screws are inserted through the jacket to make contact with the ground plates. An aluminum strap makes electrical contact between the end-cells and the jacket. The piece that fills the wedge is cast epoxy with a Mycalex insulating tip touching the beam pipe and an aluminum field-confining conductor.

VI. MAGNET PERFORMANCE

The performance of the epoxy kicker magnets themselves has been excellent. After the width of the flux-excluding conductor was adjusted, the magnets behaved like matched transmission lines, with negligible ringing or other imperfection. The transit time is less than 35 nsec. No magnet has ever developed internal HV breakdown or radiation damage during an SLC running year. In building over 20 magnets, only a few cells have been rejected due to potting mishaps, and a few more have failed HV testing before final potting. Two magnets have had minor final potting mishaps; both were repairable.

There have been a number of serious compatibility problems with the ceramic beam pipes. A thin metallic coating inside provides high frequency isolation between the beam and the magnet. This coating is grounded at one end, with a ceramic insulator disk at the other end so the coating is not a shorted turn through the magnet. These beam pipes survived many years and many old-type kicker

magnet replacements, although in some cases the coating was no longer grounded.

After several months of operation in 1992 with the first two epoxy magnets, both beam pipes developed pinhole leaks due to corrosion near the ceramic gap, caused by ozone from corona discharge. New beam pipes were made, with better grounding of the internal coating to reduce the voltage on the gap, and epoxy encapsulation of the gap to exclude air from the high-field region. The 1993 SLC run was started with all epoxy magnets and some of the new beam pipes. After only a few weeks, one of the new beam pipes fractured at the ground end due to arcing from the magnet to ground along the ceramic. A few weeks later, another new pipe not only fractured at the grounded end, but the epoxy encapsulation of the ceramic gap end caught fire! In response to the fracturing, beam pipes were tested under vacuum along with magnets, and were installed without being removed from their magnets. Also, the coating was disconnected from the ground end of the pipes by abrading a short length of it away. These pipes survived the rest of the 1993 run without fracturing. Another pipe did fracture in 1993, but with a second-generation magnet. There was also another ceramic gap leak in 1993 when the epoxy encapsulation melted.

The present beam pipes have ceramic gaps at both ends, and the gap has been redesigned to withstand the voltage without epoxy encapsulation. There were no more pinhole leaks during the long 1994-5 SLC run. There was a beam pipe fracture, which appears to have been caused by arcing inside the beam pipe at the sliding metal fingers of a bellows shield near the ceramic gap. Since other bellows shields failed elsewhere in the damping rings in 1994-5, an improved shield is being designed, which will be integrated into the kicker beam pipes when it is available.

V. REFERENCES

- [1] T. Mattison *et al.*, "Operational Experience with SLC Damping Ring Kicker Magnets," in *Proc. of 1991 IEEE Particle Accel. Conf.*, San Francisco, CA, May 6-9, 1991, p. 2331.
- [2] R. Cassel *et al.*, "SLC Kicker Magnet Limitations," in *Proc. of 1991 IEEE Particle Accel. Conf.*, San Francisco, CA, May 6-9, 1991, p. 996.
- [3] G. Gross *et al.*, "Development of Epoxy Potting for High Voltage Insulation at SLAC," in *Proc. of 1991 IEEE Particle Accel. Conf.*, San Francisco, CA, May 6-9, 1991, p. 2334.
- [4] R. Cassel *et al.*, "Manufacture of Fast-Pulsed Magnets for the SLC Damping Rings," *IEEE Trans. Magn.* Vol. 28, 1991, p. 557.

Status of the Nuclotron Slow Extraction System

V.I.Chernikov, I.B.Issinsky, O.S.Kozlov, V.A.Mikhailov, S.A.Novikov

141980, Laboratory of High Energies

Joint Institute for Nuclear Research, Dubna, Russia

Abstract

A general description of the slow extraction system of a charged particle beam from the Nuclotron is presented. The third integer resonance is used for the slow step-over extraction mechanism. The septum deflectors, that are an electrostatic septum and two superconducting Lambertson magnets, are the most complicated components of the Nuclotron slow extraction system. A detailed design of these elements based on computer simulation is considered too. The septum deflectors are under construction and bench testing before their placement in the Nuclotron ring.

I. Introduction

The Nuclotron[1], [2], a superconducting synchrotron, is intended to accelerate nuclei and multicharged ions (up to uranium) from an injection energy of 5 MeV/u up to an energy of 6 GeV/u for the charge to mass ratio $Z/A=0.5$.

The Nuclotron is a strong-focusing separated function synchrotron with a circumference of 251.52 m. It has 32 FODO cells separated into 8 structural superperiods. The magnetic ring contains 96 SC-dipoles and 64 SC-quadrupoles. The Nuclotron is placed on the ground floor of the Synchrophasotron building, 3.76 m down relative to the linac and the transport beam line plane. A scheme of the Nuclotron superperiod and a layout of the slow extraction elements over the Nuclotron ring are shown in Fig.1.

The Nuclotron was put into commissioning in 1993. Now its cryogenic, power supply and magnet protecting systems are under development to raise their operation stability and to reach reliable work at the projected energy. Limited financing does not allow one to carry out the full program of putting the accelerator into exploitation. A stable circulation and acceleration of deuterons up to 2.5 GeV/u at a beam intensity of 2×10^9 ppp were obtained in December 1994. The first physics experiments with an internal target were carried out. The next run is scheduled to begin in the late May of 1995.

II. Slow extraction mechanism

In accordance with the chosen betatron frequencies $Q_x \simeq 6.8$, $Q_z \simeq 6.85$, it is optimum to use the third integer nonlinear resonance $3Q_x=20$ for slow extraction[3]. The operating point is moved to the resonance band by the structural quadrupoles. At this time the 20-th harmonic of sextupole nonlinearity is excited by 4 slow extraction sextupole lenses S1-S4 located in the minima of the dispersion function. 4 slow extraction quadrupole lenses Q1-Q4 are uniformly placed over the Nuclotron ring to produce the coherent betatron tune shift ΔQ_x within the resonance sideband and to prevent excitation of the parametric resonances $2Q_{x,z}=13$, $2Q_{x,z}=14$.

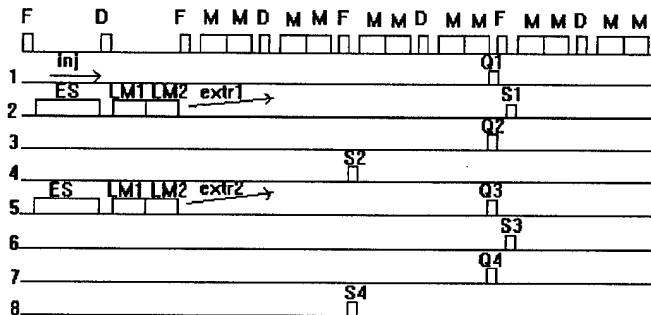


Figure. 1. Scheme of the Nuclotron superperiod and layout of the slow extraction elements over the Nuclotron ring

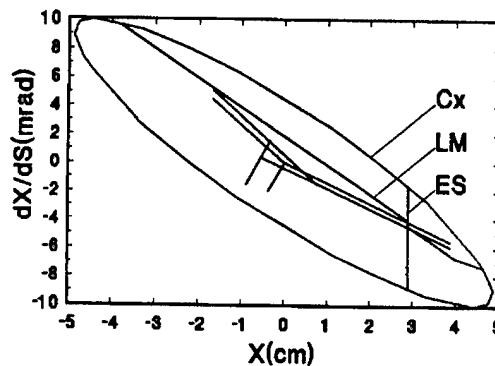


Figure. 2. Phase picture at the ES entrance @ 6 GeV/u

The beam will be extracted in two directions to be used in two experimental areas by means of the electrostatic septum (ES) and the two-section Lambertson magnet (LM) placed in the long drift spaces of the second and fifth superperiods. The ES deflects particles in the horizontal plane. The LM allows one to bend the beam in the vertical plane in the direction of the experimental halls and to pass over the lens body situated at the end of the straight section. General parameters of the slow extraction system are given in Table 2.

The phase trajectories at the entrance of the ES for an energy of 6 GeV/u are shown in Fig.2. There are an ellipse surrounding the Nuclotron acceptance ($C_x = 210 \pi \text{ mm mrad}$) and phase portraits for the electrostatic septum and Lambertson magnet. The momentum spread changing during the slow extraction process is shown in Fig.3.

III. Electrostatic septum

The efficiency of slow extraction strongly depends on the thickness of the first extraction septum as compared to the growth of the resonant betatron amplitudes in the final turns before extraction. A 95% efficiency of extraction will be realized

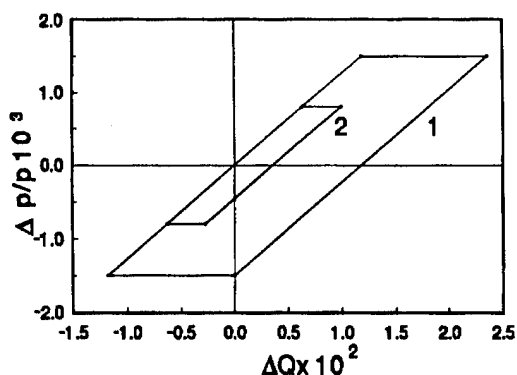


Figure 3. Momentum spread changing during slow extraction: 1-@ 200 MeV/u, 2-@ 6 GeV/u

by a very aligned electrostatic septum formed from grounded 0.1 mm tungsten-beryllium wires with an effective thickness of 0.3 mm and a spacing of 1 mm that is the anode. The effective length of the parallel electrodes, cathode and anode, is 3 m. The wire anode separates the region of the circulating beam from the region where there exists an electrostatic field and has a ground potential. The cathode is at a high negative potential of up to 200 kV. A gap of 2 cm with a field of 100 kV/cm is needed to reach a required deflection of about 2 mrad. The cross section of the electrostatic deflector is shown in Fig.4 where the coordinates are connected to the Nuclotron equilibrium orbit.

The calculations were aimed to form the cathode surface for the required uniformity of the deflecting field no less than 97% in the working region ($3\text{cm} \leq x \leq 5\text{cm}$, $-2\text{cm} \leq z \leq 2\text{cm}$) where the extracted beam passes through the gap. The nonuniformity and distribution of the electrostatic field are given in Figs.4,5.

There are some arguments in favour of a tungsten-beryllium wire anode. It is pretty stable under sparking when the energy available in the discharge releases. It is easier to build and to

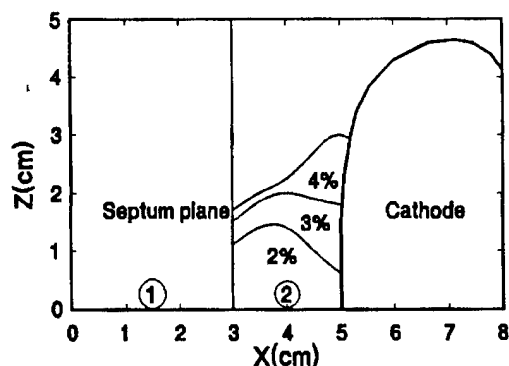


Figure 4. Scheme of the ES (half) and regions of nonuniformity of the electrostatic field: 1-circulating, 2-extracted beams

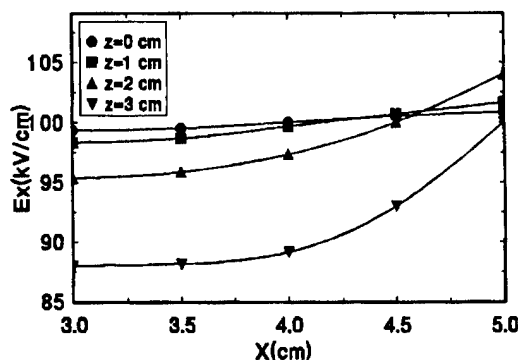


Figure 5. Distribution of the electrostatic field in the ES gap

maintain a perfect plane with an array of wires than foil. The mean Coulomb scattering angle of particles hitting the septum is smaller and thus the losses are smaller. The oxide-coated titanium cathode can stand a higher energy in the sparks across a small gap. The calculated overvoltage on the cathode surface reaches 6% that is within the admissible boundary. Of course, the insulation of the ES gap will greatly depend on cleanliness of the vacuum system and advanced conditioning of the electrodes.

IV. Lambertson magnets

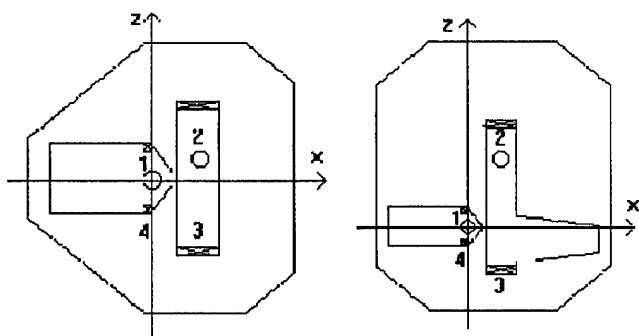
LM1[5] and LM2 are 1.5 m long magnetic deflectors with superconducting windings whose transverse sections are shown in Fig.6. Two apertures in the yoke for circulating and extracted beams are separated by 3 and 7 mm septa. They deflect the extracted beam up at an angle of 80-110 mrad to by-pass the following quadrupole lens and to rise the beam to the level of the existing transport channels. The maximum magnetic fields in LM1 and LM2 are 1.2 T and 1.8 T, respectively.

The two-dimensional designs[4] of the magnetic yoke and coil parameters were aimed first of all to reduce the leakage field in the circulating beam region and then to gain a good uniformity of the working field. The essential cut-out in the LM2 extracted beam aperture in front of the magnetic septum is designed for extra reduction of the leakage field. As the calculations show, the nonuniformity of the working field does not exceed 1-2% that is satisfactory for a single beam passing over the

Table I

General characteristics of the Nuclotron slow extraction system

Kinetic ion energy (Z/A=0.5)	0.2/6 GeV/u
Effective length of quadrupoles	0.3 m
Effective length of sextupoles	0.3 m
dB_z/dx (quadrupoles)	0.14/0.68 T/m
d^2B_z/dx^2 (sextupoles)	13.3/233 T/m ²
Effective length of ES	3.3/3.3 m
Effective thickness of ES	0.42/0.31 mm
Electric field tension in ES	1.26/10 MV/m
Effective length of LM1 and LM2	1.5 m
Field in LM1	0.1/1.1 T
Field in LM2	0.15/1.6 T
Effective emittance of the extracted beam: horizontal, vertical	9.5/2.5 mm mrad, 20/2.0 mm mrad
Instantaneous momentum spread	$(7/0.2) \times 10^{-3}$
Duration	(1-10) sec
Duty factor of the extracted current	95/95 %
Slow extraction efficiency	95/96 %



- [5] V.N.Buldakovsky et al. Nuclotron Slow Extraction Lambertson Magnet. Proc. of the XIII Conf. on Particle Accelerators, Dubna, 1992.

Figure. 6. Scheme of the Lambertson magnets: 1-circulating, 2-extracted beams, 3-main coils, 4-current coils

extracting region. But with a compact magnetic yoke and thin septa we shall have anyway a leakage field of up to 2-3% of the main one at a beam energy of 5-6 GeV/u due to the saturation of the magnetic yoke. That is inadmissible because of considerable closed orbit distortions, during the acceleration process. Since the B_x -component of the leakage field is much greater than the B_z -component, the z -distortion will be much greater (up to ± 20 mm) than the x -distortion (up to ± 2 mm). To overcome this, one can set out current coils in the LM1,2 circulating beam aperture for independent correction of the leakage field. The calculations show that one can suppress leakage fields and provide the x, z -distortions over a range of ± 3 mm using only one coil (Fig.6).

V. Conclusion

Commissioning the Nuclotron, a new superconducting synchrotron at the Lab of High Energies, JINR is being continued. The machine development program is directed to the extraction of accelerated beams. The construction of the Nuclotron slow extraction system presented in this paper is under way. Nowadays the superconducting slow extraction quadrupoles and sextupoles are being arranged in the Nuclotron ring. The ES anode and cathode are under construction. The first bench testing of LM1[5] has already been carried out. Cooling down to 4.6 K, control of the cryogenic temperature and magnetic measurements have been performed. After the next LM2 magnetic field measurements and placing LM1 and LM2 in the ring, the slow extraction without ES will be realized despite of a small effectiveness of about 10-15%.

References

- [1] A.M.Baldin et al. Nuclotron Status Report, in IEEE Trans. on Nucl. Sci., NS-30, pp.3247-3249, March 1983.
- [2] I.B.Issinsky et al. Nuclotron Lattice, EPAC, Nice, June 12-16, 1990, vol.1, p.458-460.
- [3] B.V.Vasilishin et al. The Scheme and Main Parameters of the Nuclotron Slow Extraction System. Preprint JINR, 9-86-511, Dubna, 1986.
- [4] R.F.Holsinger, Ch.Iselin. The CERN-POISSON Program Package (POISCR) User Guide. CERN/TH, 1983.

THE RHIC INJECTION FAST KICKER*

E.B Forsyth, G.C. Pappas, J.E. Tuozzolo, and W. Zhang
AGS Department, Brookhaven National Laboratory, Upton, New York 11973 USA

I. INTRODUCTION

The purpose of the injection kicker is to provide the ultimate deflection to the incoming beam from the Alternating Gradient Synchrotron (AGS) into the Relativistic Heavy Ion Collider (RHIC). The beam is kicked in the vertical direction to place it on the equilibrium orbit of RHIC. Each bunch in the AGS is transferred separately, and stacked box-car fashion in the appropriate RHIC rf bucket. In order to achieve the required deflection angle four magnets powered by four pulzers will be used for each ring of RHIC. When the bunches are stacked in RHIC the last few rf buckets are left unfilled in order to provide a gap in the beam to facilitate the ejection or beam abort process. This also means there is not a severe constraint on the fall-time of the injection kicker. One prototype pulser has been built and tested. Much of the development effort has gone into the magnet design. Although lumped ferrite magnets are simpler to build and require less power to reach full field[1] a transmission line magnet was developed because of the very fast rise-time requirement and the tolerances imposed on the field variation and ripple.

II. GENERAL DESIGN

A performance specification for the kicker is given in Table 1. The performance is achieved using four Blumlein pulzers each connected to a magnet forming a matched transmission system. The pulzers will be located outside the RHIC tunnel and will be connected to the magnets by about 75 m of high voltage cable. The Blumlein pulser consists of rigid, oil-filled, transmission lines in a folded, triaxial, configuration of the type developed at SLAC[2]. The magnet consists of a "C" cross section formed of interspersed ferrite and high dielectric constant bricks. If properly oriented with respect to the beam both the electric and magnetic fields can contribute additively to the deflecting force, although by far the largest contribution is made by the magnetic field. In high power, fast rise-time systems the impedance of the grounding connection has an effect on ground transients at the magnet and pulser. These effects must be carefully considered when choosing insulation withstand levels.

*Work performed under the auspices of the U.S. Department of Energy.

Table 1
Performance Specification

Deflection angle: 1.86 mrad
Beam rigidity: 97.5 Tm
Rise time (1-99%): 95 ns
Flat top: 20 ns
Flat top tolerance: $\pm 1\%$
Fall time: Less than 800 ns
Min. repetition period: 33 ms
Life time : 10^6 shots

III. PULSER

The major dimensions of the storage lines are given in Table 2. The triaxial delay line pipes are insulated with Teflon spacers and filled with Calumet Caltran 60-15 oil under slight positive pressure. The dielectric constant is 2.35. The delay lines are assembled from sections each about 2.4 m in length. The combination provides two delay lines of 12.5 Ω impedance which feed a 25 Ω load formed by the connecting cables (2 x 50 Ω in parallel), the magnet and a 25 Ω oil-filled hockey puck resistor assembly. The electrical properties of the Blumlein are shown in Table 3. The pulser is switched by a two-gap deuterium thyratron designed for high di/dt applications (EEV type CX 1168C). An R-C networks in parallel with the switch tube provides a small amount of overshoot in the current waveform, this improves the field rise-time by a few nanoseconds.

Table 2
Blumlein Dimensions

Outer coaxial pipe: 134.5mm O.D.x98.0mm I.D. ± 0.1 mm
Inner coaxial pipe: 76.2mm O.D.x55.5mm I.D. ± 0.1 mm
Length: 10.95 meters
Material: 6061 - T6 Aluminum
Insulating oil: Caltran 60-15
Insulating Standoffs: PTFE Teflon

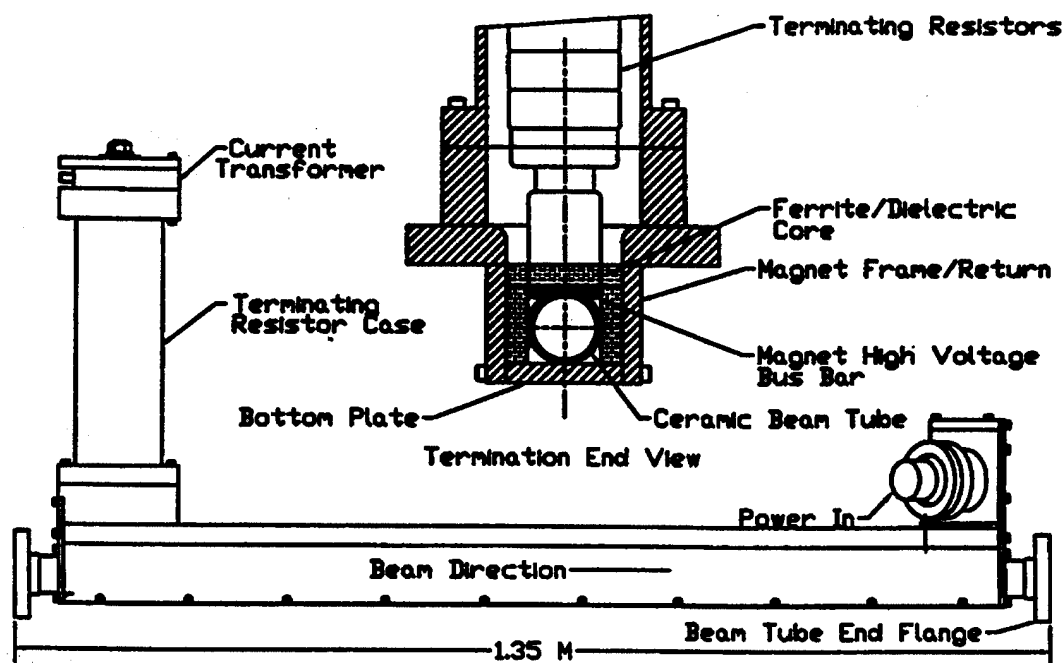


Fig. 1. General assembly of transmission line magnet.

Table 3
Blumlein Pulser Characteristics

Load impedance: 25 Ω
Two-way propagation time: 110 ns
Operating voltage: 50 kV
Operating load current: 2000 A
Max. voltage: 60 kV
Current rise-time: 30 ns
Storage line capacitance: 10 nF

IV. MAGNET

The magnet is a type first developed at SLAC[3] which uses high dielectric ceramic interspersed with ferrite to approximate a transmission line. The characteristics are given in Table 4. The dielectric selected has a relative dielectric constant of ~ 100 . This approach greatly reduces the cost usually associated with the machining of capacitance elements associated with a transmission line magnet. The use of rectangular bricks of similar dimension apart from the longitudinal direction assures easy assembly for potting in epoxy. The drawback to this design approach is the poor high voltage performance. The cross-section shown in Figure 1 illustrates the problem: the high voltage conductor fits into the rectangular corners of ferrite/dielectric "C" magnet but despite shaping the conductor the local electric stress in the corners is very high, particularly in the longitudinal direction in the vicinity of the dielectric sections. The stress is further

enhanced in the gap adjacent to the conductor by the difference in dielectric constant between the ceramic brick and the epoxy potting compound. The first full-length magnet failed due to high-voltage flashover at 20 kV using the epoxy originally tested at SLAC.[4] A series of half-length model were then made to improve the high voltage performance. Loading the epoxy with high dielectric constant powder seemed promising but adhesion to the bricks was poor. Two RTV-insulated magnets were built and tested but they failed at 40 kV. A clear epoxy (RN1000 from Conap) gave the best results. A gap of 0.7 mm between the bricks can be inspected during and after the pour to ensure no voids exist. RN1000 has low viscosity. (600-800 cps) a long pot life below 22°C and only 0.8% shrinkage during cure. The magnet is designed to permit high temperature bake-out of the ceramic beam tube. For this procedure the bottom plate shown in Figure 1 is removed and the magnet elevated above the beam tube.

A magnet made with this material was given a life test of 1.2 million shots at 50 kV without damage. This life is perfectly adequate for RHIC as filling the machine will occur only a few times a day during normal operation. After the test some flashover was observed at 57 kV. The finite elements comprising the magnet result in a frequency cut off in the 25 MHz range; this increases the effective current risetime to about 40 ns. The combination of risetime and propagation time results in an integrated field risetime of about 85 ns.

Table 4
Magnet Characteristics (each)

Strength at 2000 A: 0.0465 Tm
 Number per ring: 4
 Propagation time: 45 ns
 Impedance: 25 Ω
 High frequency cut off: ~ 25 MHz
 Magnet aperture: 48.4 mm wide x 51.2 mm high
 Magnet length: 1.12 meter
 H field deflection: ~ 94%
 E field deflection: ~ 6%
 Ceramic beam tube: Circular aperture 41.3mm
 3.2mm wall
 Core material-ferrite: Ceramic magnetic CMD 5005
 15 sections: 50mm long x
 13.9mm thick
 Core material-dielectric: Trans-Tech MCT-100
 14 sections: 25mm long x
 13.9mm thick
 Bus bar/return frame: 6061-T6 aluminum
 Epoxy potting material: Conap Inc. RN1000

V. TEST RESULTS

The first six magnets to be made (1 long and 5 short) had a measured impedance of $24.5 \Omega \pm 2\%$. The magnets met the specifications shown in Tables 1 and 4. The short magnets had a propagation time of about 23 ns and the long magnets about 45 ns. The deflecting force specification was met with about 45 kV charging voltage $\pm 10\%$. The wide tolerance indicates the difficulty of accurate measurement of $|Bdl|$ in the presence of the high electric field. Oscillograms of the field integral vs time are shown in Figure 2a and Figure 2b. These data are for a half-length magnet. Figure 2b illustrates the field perturbation ~ 800 ns after the injection kick; corresponding to the effect on the first injected bunch when RHIC is filled. The 7th magnet (long version) possessed an impedance of $\sim 27 \Omega$; significantly higher than the earlier magnets. The magnet also performed poorly in high voltage tests - both results suggestive of poor contact to the dielectric bricks resulting in less capacitance.

VI. CONCLUSION

The Blumlein pulser is a good solution to the problem of providing short, very high power waveforms for the injection magnet. The oil-filled version came on line with virtually no development problems. The magnet, on the other hand, has required considerable development to achieve an acceptable high-voltage performance. This performance has been demonstrated for the short version, but not, as yet, for the full-length magnet.

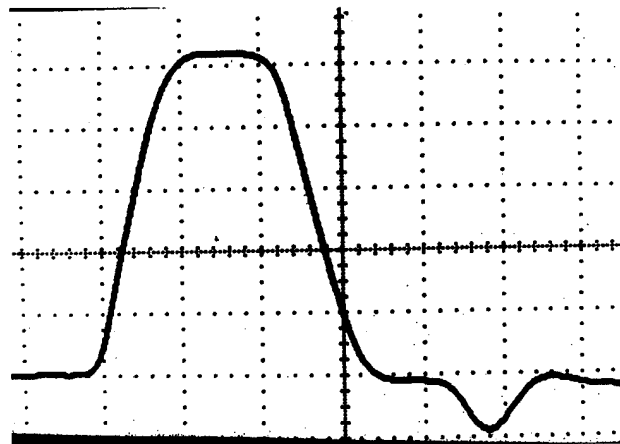


Fig. 2a. Integral field waveform vs time for a half length magnet, time scale 50 ns per division.



Fig. 2b. Same waveform as Figure 2a. except 200 ns per division showing field at ~ 800 ns after injected bunch.

V. REFERENCES

- [1] E. B. Forsyth and M. Fruitman, "Fast Kickers", Particle Accelerators, Vol. 1, 27, 1970.
- [2] F. Bulos et al., Proc. 1987 PAC, p. 1884, 1987.
- [3] F. Bulos and A. Odian, "Design of a Matched Fast Kicker System", SLAC Pub. 3453, CN 279, 1984.
- [4] G. Cross, et al., IEEE Pub. 91, Proc. 1991 PAC, p. 2334, 1991.

THE ACTIVE FILTER VOLTAGE RIPPLE CORRECTION SYSTEM OF THE BROOKHAVEN AGS MAIN MAGNET POWER SUPPLY*

I. Marneris, R. Bonati, J. Geller, J.N. Sandberg and A. Soukas
Brookhaven National Laboratory, Upton, New York 11973 USA

I. INTRODUCTION

The Brookhaven AGS is a strong focussing accelerator which is used to accelerate protons and various heavy ion species to an equivalent proton energy of 29 GeV. Since the late 1960's it has been serving high energy physics (HEP - proton beam) users of both slow and fast extracted beams. Since the late 1980's slowly extracted heavy ion beams have been added for fixed target physics experiments (HIP). Beginning in 1996 fast extracted beams will be commissioned in preparation for injection into the RHIC accelerators.

This paper, and a companion paper [1], describe the improvements to the Main Magnet Power Supply (MMPS) so that it enables a more flexible operation of the AGS, enhances its reliability, and also improves the MMPS's ultimate performance specifications. One of the major areas for the latter is the fixed target program operating off the AGS slow extracted beam lines. The active filter, by improving the MMPS output ripple, is instrumental in the improvement of the ultimate duty factor of the extraction beam spill.

II. PARAMETERS

The AGS MMPS consists essentially of two power supplies connected in parallel (the actual implementation is in 2 stations). One PS is a high voltage unit (P type) that is typically used for fast ramping during acceleration and energy recovery. The other is a lower voltage unit (F type) that is used for slow ramping or for flattop operation. Even though the F units are operated as 24-pulse controlled rectifiers, the ripple requirement at flattop is very stringent. The key parameters for the AGS are shown in Table 1.

Table 1

Voltage dc max ± 10 kV (P type)
Voltage dc max ± 1.5 kV (F type)
Current dc max 6.0 kA
Current rms 4.0 kA
Magnet Resistance (R) 0.26 Ohms
Magnet Inductance (L) 0.75 Henry
Nominal Pulse Rep. Rate	3.0 Sec
Nominal Flat top 1.5 Sec
Fundamental Ripple Freq.	720 Hz (P type)
Fundamental Ripple Freq.	1440 Hz (F type)

* Worked performed under the auspices of the U.S.D.O.E.

Slow extraction from the AGS is accomplished on the third-integer resonance. A set of four sextupoles arranged in a +, -, +, - configuration excites the resonance just after the AGS Main Magnets are flattened at the desired energy. The beam horizontal and vertical tunes, average radius, chromaticity and skew parameters are set to nominal values. The beam momentum spread is adjusted by RF phase-back and at RF turn-off the beam is effectively debunched. The debunched beam is brought to extraction radius by slightly sloping the flattop of the MMPS. The extracted beam orbit is set by local orbit deformations and by three (3) stages of septa comprised of electrostatic, thin copper magnetic, and thick copper magnetic ejection. Extraction is accomplished in the horizontal plane. Once extracted beam is established, an SEC (secondary emission chamber) intensity signal is used for measurement and for feedback to a slow spill servo loop that dynamically adjusts the MMPS flattop.

Since the AGS MM time constant is 3.0 seconds, it has a corresponding load breakpoint frequency of 0.05 Hz and thus can do a good job of average spill rate and length control. The spill generally has modulation components in the 60-720 Hz sub-harmonic ripple range mainly due to the MMPS and to the 10, or so, other PS's that are utilized during the extraction process. The spill servo cannot correct these. An effort has been underway for some time to reduce these troublesome components by improving individual PS's. However, as the spill from the AGS is increased in length, the sensitivity to these effects also increases. Thus, an active filter approach has been applied to the AGS MMPS.

III. ACTIVE FILTER DESIGN AND RESULTS

One of the most critical contributions to spill modulation is due to the MMPS. Its basic ripple at flattop is 1440 Hz, ± 25 Hz, which is the slip frequency of the motor-generator system. This presents both good and deleterious effects. The frequency variation makes it easier to measure, however it prevents synchronized corrections and can beat with the line frequency to create other more complicated harmonics. The damped passive filter at the output of the MMPS attenuates the raw ripple to about 20 volts peak-to-peak. The requirement by the spill is an order of magnitude less, or 1-3 volts peak. Due to the high peak voltages of ± 10 kV and the high currents of 6 kA, series or parallel regulators or filters become very difficult schemes to implement physically. It was decided therefore that in order to create a filter with the robustness required by the continuous and flexible operation of the AGS, to use a series transformer/choke as the coupling element to the MMPS circuit. We implemented two different techniques of correcting the AGS MM ripple. One using a wide band feedback

loop and another using a tuned filter feedback loop with adjustable gain and phase. The schematics of the circuits as well as the signal flow graphs are shown in Figures 1, 2A, and 2B. The parameters of figures 1,2 are the following. $V_1(s)$, $V_2(s)$ are the station 1 and 2 voltage ripple of the AGS MM power supply. $V_M(s)$ is the AGS magnet voltage ripple. $V_{AF}(s)$ is the coupled ac voltage from the active filter. $L_1=0.25$ mH, $R_1= 0.1$ Ohms. $G_1(s)$, $G_2(s)$ are compensated amplifiers. $G_3(s)$ is the active filter power supply closed loop transfer function. $G_4(s)$. K_4 is the transformer/choke transfer function. $G_5(s)$ is the tuned filtered transfer function. It can be seen that each of the 2 MMPS station voltages are sensed, summed, filtered and compared to the instantaneous waveform. The error is used to drive the primary of the transformer which induces and cancels the ripple from the magnet voltage. The power driver is a commercial, bipolar, 4-quadrant, switch mode PS which has a wide voltage bandwidth. The switching frequency is ~44 kHz, which results in a constant voltage full power bandwidth of 1 kHz. The loop response (gain and phase) of the power supply ($G_3(s)$) and the active filter choke ($G_4(s)$) is shown in Fig. 3. The open loop response of the active filter from Fig. 2A is shown in Fig. 4. The tuned filter ($G_5(s)$) was tuned to correct 120 Hz, 180 Hz, 240 Hz, 360 Hz, and 720 Hz. The response is shown in Fig. 5. The results of the ripple correction utilizing the two different techniques are shown in Figures 6A and 6B. Using the tuned filter feedback scheme we were able to correct more because we could control the phase and the gain of every frequency component separately.

Fig. 3
 $G_3(s)*G_4(s)$ TRANSFER FUNCTION

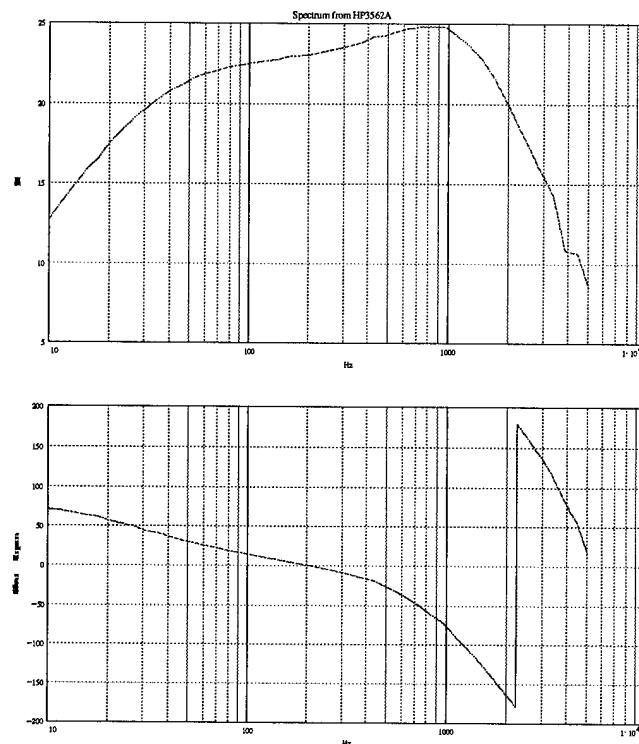


Fig. 4
 $K_2*G_1(s)*G_2(s)*G_3(s)*G_4(s)$ TRANSFER FUNCTION

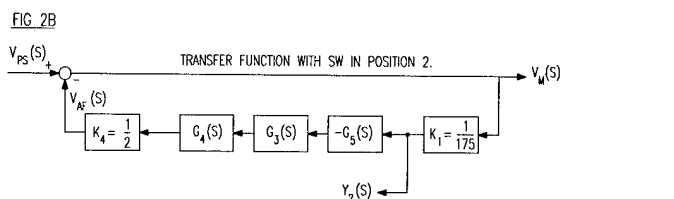
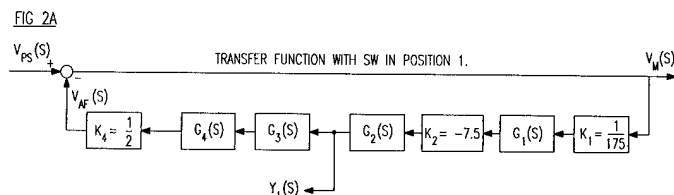
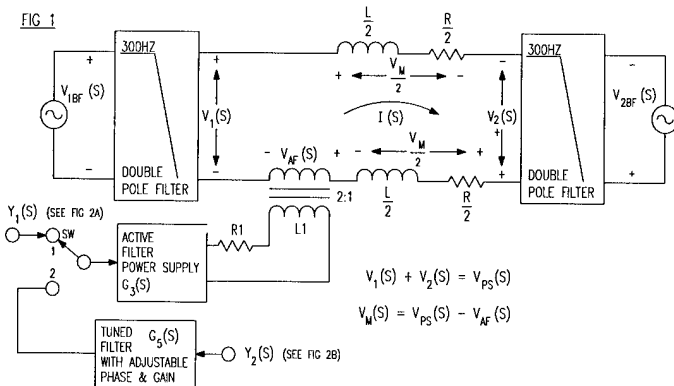
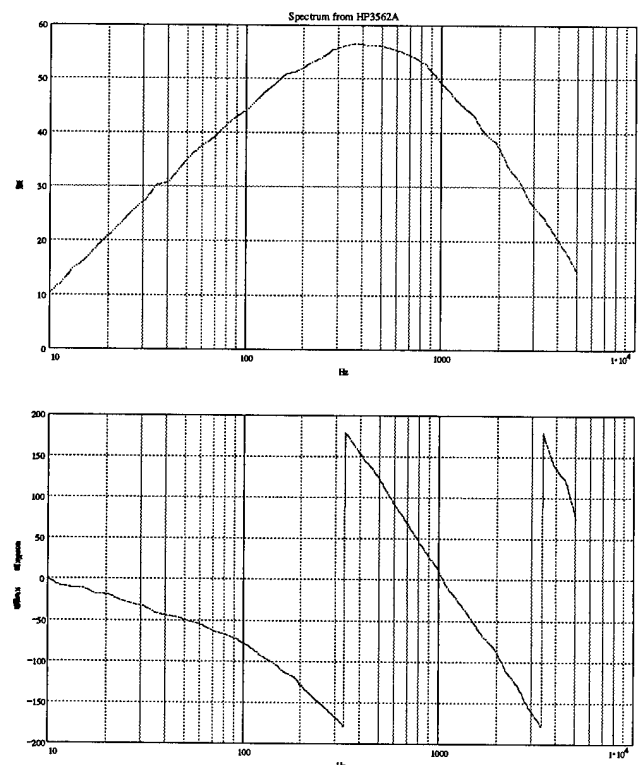


Fig. 5
G5(s) TRANSFER FUNCTION

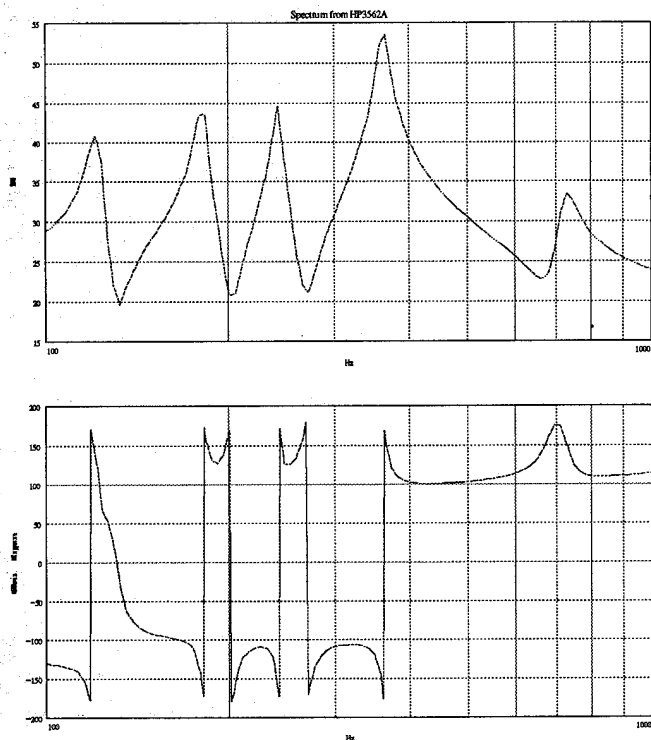


FIG. 6A

AMPLITUDE OF AGS MAIN MAGNET VOLTAGE RIPPLE COMPONENTS
(VOLTS PEAK)

1. $A_{X,1}$ IS THE RIPPLE WITHOUT ACTIVE FILTER CORRECTION
2. $A_{X,2}$ IS THE RIPPLE USING ACTIVE FILTER CORRECTION, WITH SWITCH (SW) IN POSITION 1 (SEE FIG. 1)

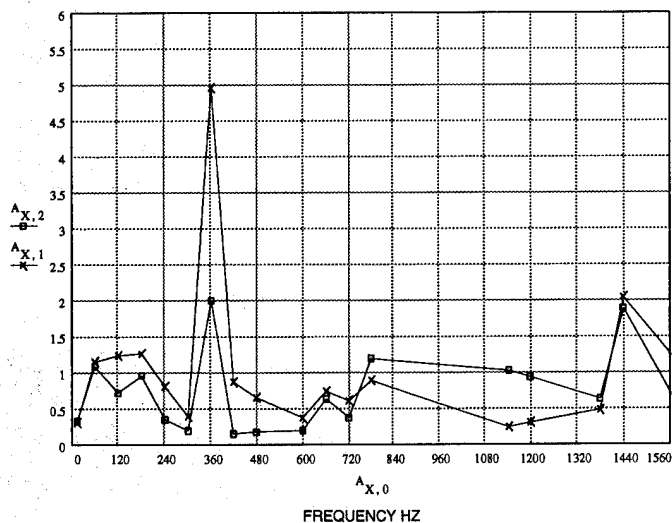
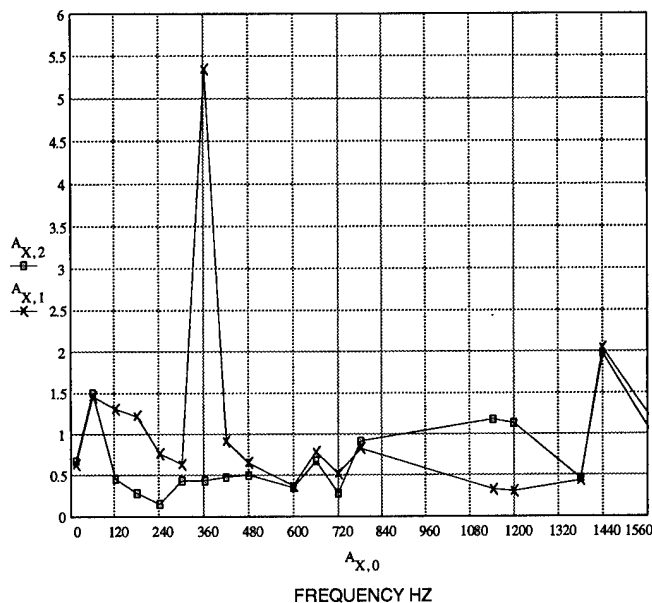


FIG. 6B

AMPLITUDE OF AGS MAIN MAGNET VOLTAGE RIPPLE COMPONENTS
(VOLTS PEAK)

1. $A_{X,1}$ IS THE RIPPLE WITHOUT THE ACTIVE FILTER CORRECTION
2. $A_{X,2}$ IS THE RIPPLE USING THE ACTIVE FILTER CORRECTION, WITH SWITCH (SW) IN POSITION 2 (SEE FIG. 2). TUNED FILTER WAS TUNED TO CORRECT 120 HZ, 180 HZ, 240 HZ, 360 HZ, 720 HZ.



IV. FUTURE PLANS

The implementation in the future will be done digitally by a dedicated PC computer which will perform the data acquisition and manipulation, such as averaging. The output to the drive system will be through an arbitrary waveform generator. This scheme will be adaptive. Also, with a change in transformer ratio or a higher voltage power supply driver, we would like to apply the filter correction to the entire cycle. This will enable closer beam radius control, and aid in perhaps controlling other high intensity phenomena and instabilities.

V. ACKNOWLEDGMENTS

The authors thank W. Eng and V. Badea for their engineering support of the power supply and the transformer/choke. We also thank S. Savatteri, M. Bannon, G. Danowski and J. Funaro for their technical support in this project.

THE INJECTION KICKER SYSTEM FOR THE MUON G-2 EXPERIMENT¹

G.C. Pappas, E.B. Forsyth, Brookhaven National Laboratory, Upton, New York 11973 USA
W. Feng, Nanjing University, Nanjing, China 210008

Abstract

The muon g-2 experiment is designed to measure the anomalous magnetic moment of the muon to an accuracy of 0.35 ppm by measuring the difference between the spin precession frequency and the cyclotron frequency of the particle in a known magnetic field. The injection kicker is designed to deflect 3.094 GeV/c muons by an angle of 10 mrad into a storage ring with a radius of 7.112 m. No magnetic materials can be used in or near the beam line because of the high precision with which the field of the main dipole magnets must be known. Eddy currents induced in the vacuum chamber by the fast kicker pulse, and their effect on the main dipole field must also be considered. An air core magnet which is driven by an underdamped capacitor discharge modulator using a spark gap switch has been designed. This design, as well as test data, will be presented.

I. INTRODUCTION

The muon g-2 experiment utilizes a superconducting storage ring of 7.112 m diameter. The injection kicker magnet is required to deflect muons of momentum 3.094 GeV/c by an angle of 10 mrad. The kicker system including the power modulator, charging power supply, magnet, beam chamber, and main ring dipole magnet are shown in Figure 1. The kicker system consists of three one m long air core magnet with an aperture of 80 mm vertical by 100 mm horizontal. A crosssectional view of this magnet is shown in Figure 2. This magnet is driven by an underdamped capacitor discharge circuit with peak amplitude of 6500 A, and resonant frequency of approximately 11 Mrad/s. The power modulator switch is a 100 kV spark gap. The entire discharge circuit is in a coaxial housing, and is shown in Figure 3.

Several unique restrictions which apply to this kicker system are the result of the kicker magnet being inside of the main ring dipole magnet beam pipe. No magnetic materials can be used in or near the beam pipe because of the high precision which the dipole field must be known. The high vacuum, and radiation, in the beam pipe limits the use of plastics for electrical insulators, and mechanical supports. Both the charging waveform, and discharge pulse must be carefully analyzed to insure that any eddy current fields induced in the beam vacuum chamber quickly decay [1].

II. THE KICKER MAGNET

Three different types of kicker systems were investigated to meet the above requirements. They were, an electrostatic kicker, a transmission line kicker and a magnetic kicker. The basic pulsed power parameters for each of these types of kickers are, ± 400 kV pulse for the electrostatic kicker, ± 200 kV and 4000 A pulse for the transmission line kicker, and < 100 kV and 6000A pulse for the magnetic kicker. Placement of the kicker magnet in the main magnet beam chamber has serious consequences for each of these types of kickers. The limited space inside the chamber precludes the electrostatic and transmission line types of kickers due to electric field stresses. The magnetic kicker induces eddy currents in the vacuum chamber which must not contribute to the main dipole field by more than 0.1 ppm, or 21 mG. Thus, considerable effort was taken to study the effects of eddy currents in the beam chamber

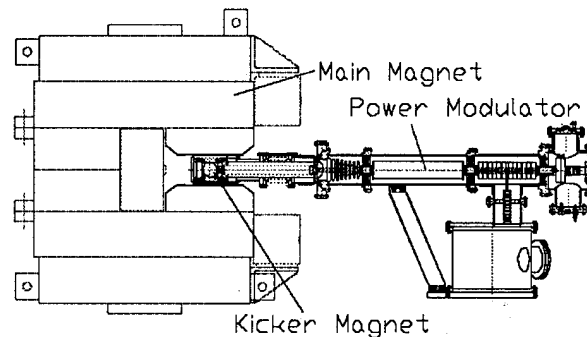


Figure 1. G-2 experiment main dipole magnet, vacuum vessel, kicker magnet and modulator.

The magnet for the g-2 muon storage ring injection kicker consists of two titanium strips of 80 mm height separated by 100 mm. The kicker system uses three magnets of 1 meter length each. The transient eddy current analysis code OPERA 2D/TR was used to investigate field distribution, eddy currents, magnetic gain, energy losses and inductance for this magnet. The drive current for the magnet was assumed to be a damped sinusoid,

$$i = i_0 e^{-\alpha t} \sin \omega t$$

because of the simplicity of producing such a waveform for an inductive load. The length of the vacuum chamber, l , is much longer than either the width w or the height h , which in turn are each much larger than the thickness d of the chamber walls. Thus, it is possible to consider the two dimensional field

$$H_0(t) = H_0 e^{-\alpha t} \sin \omega t.$$

¹ Work performed under the auspices of the U.S.D.O.E.

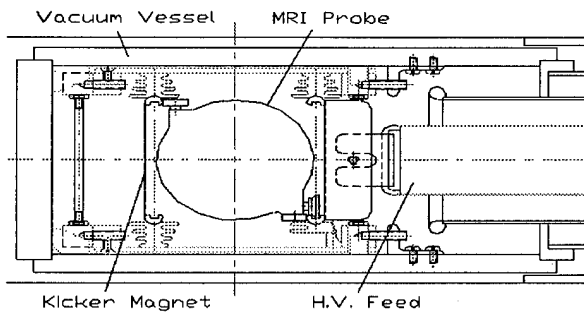


Figure 2. Kicker magnet and vacuum vessel, with field mapping NMR probe shown.

Since the displacement currents can be ignored, Maxwell's equations reduce to

$$\frac{\delta E_z}{\delta x} = -\mu \frac{\delta H_y}{\delta t}$$

$$\frac{\delta H_y}{\delta x} = \sigma E_z,$$

and the diffusion equations are

$$\frac{\delta E_z}{\delta x^2} = \sigma \mu \frac{\delta E_z}{\delta t}$$

$$\frac{\delta^2 H_y}{\delta x^2} = \sigma \mu \frac{\delta H_y}{\delta t},$$

where $\mu = \mu_0 \mu_r$, and σ is the conductivity. The eddy currents in the vacuum chamber walls have been investigated for this type of driving waveform using an iterative approach and solving the diffusion equations.

The conclusions drawn from this analysis are:

1. The vacuum chamber material should have a $\mu_r=1$, low conductivity and be as thin as possible for the eddy current fields to decay quickly.
2. Decreasing the thickness improves the decay of the steady state eddy current.
3. Increasing α improves the decay of the steady eddy current, but also requires more drive current because of the reduction of the kicker field. To gain a compromise between the eddy current residual field the kicker magnet field, and the current pulse width, ω should be increased with α .

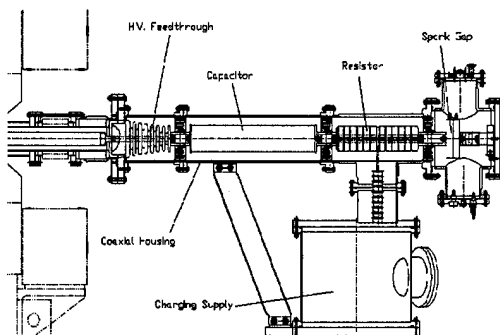


Figure 3. Power modulator, high voltage feedthroughs, and charging supply.

Computer simulation wiring PE2DITR and OPRA2OITR were used to show that appropriate choice of dimensions, shapes, and materials for the vacuum chamber, and driving waveform could result in the residual eddy current field contributing less than 1 in 10^7 to the main dipole field at the start of the measurement period. This analysis was performed with several different waveshapes, and it was found that both undershoot of the pulse and parasitic oscillations helped to reduce the effects of induced eddy currents. In particular, the eddy current field induced by an underdamped current pulse with an 80 ns rise time and high frequency parasitic oscillation decays to 12 mG after 10 μ s.

Other kicker magnet parameters calculated were an inductance of 0.21 μ H/m, magnetic gain of 0.025 G/A, and a field uniformity of $\Delta B/B(0,0)=25\%$.

III. THE POWER MODULATOR

The pulsed power modulator to drive the above magnet is the underdamped capacitor discharge circuit shown schematically in Figure 4. The spark gap used is a Maxwell Laboratories model 40264 gap, triggered with a Maxwell Laboratories model 40168 trigger unit. The charging supply is a command resonant supply which uses the leakage inductance of the 85:1 step up transformer to charge the 10 nF discharge capacitor. A charge current pulse for the charging system is shown in Figure 5. Because the charge current flows through the magnet, eddy currents induced by this pulse were also analyzed. Their contribution to the main dipole field was not significant however, because of the relatively low frequency, amplitude and long decay time for the pulse.

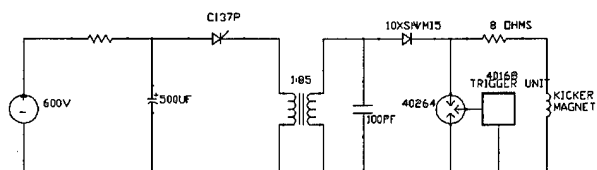


Figure 4. Schematic of power modulator and charging supply

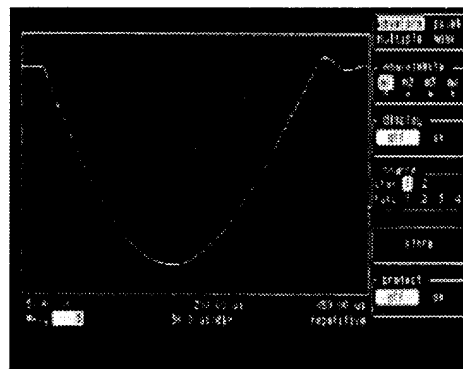


Figure 5. Charging current, time base is 50 μ s/div, amplitude is 50 A/div.

A typical discharge pulse is shown in Figure 6. One of the main concerns about the discharge circuit was the choice of a switch to use. The primary objective was to minimize circuit inductance. Thyratons were considered, but a tube to block up to 100 kV would be a three gap tube, and tube inductance would be on the order of several hundred nano Henries. Multigap tubes were also problematic because of the capacitive coupling between gaps as they break down. The tight eddy current requirements discussed above could be exceeded by gap coupled prepulses. Spark gap switches have inductance of less than 50 nH in one gap up to 100 kV, but suffer from high jitter and short life. The lifetime for the G-2 experiment is not critical, however the jitter must be kept to less than 5 ns. With this in mind jitter measurements were made on the Maxwell gap and trigger unit. Figure 7 shows the gap jitter as a function of gap voltage and pressure. Figure 8 shows the trigger generator jitter as a function of output switch air flow and pressure.

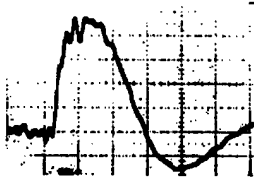


Figure 6. Modulator Output Pulse. Time base is 100 ns/div, amplitude is 1000 A/div.

From this data it is clear that jitter of less than 5 ns can be obtained by the Maxwell trigger generator and gap if proper gas pressure and flow are maintained.

IV. CONCLUSIONS

Eddy current fields induced by the fast kicker pulse and the slower charge pulse will decay quickly enough so as not to distort the main dipole field for the g-2 experiment by a factor of greater than 1 in 10^7 . Jitter measurements have been made on the spark gap switch and trigger unit, and show that the jitter requirement can be met with

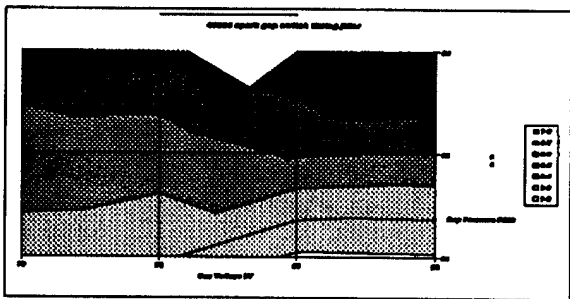


Figure 7. Spark gap jitter in nano-seconds as a function of gap voltage and pressure.

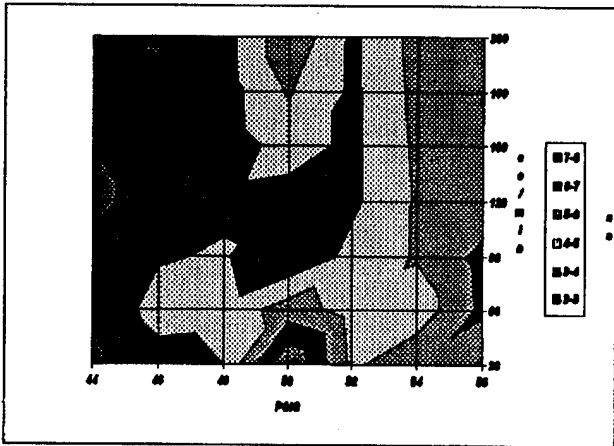


Figure 8. Trigger generator jitter in nano-seconds as a function of pressure and flow.

careful control of the gap and trigger gap pressure and air flow. A second gap from English Electric Valve is being investigated. This gap offers several advantages over the Maxwell gap, however, it has not been tested. The EEV gap is sealed and requires no synthetic air, regulators, and air flow controls, and is triggerable from an EEV provided pulse transformer whose driving voltage is only several hundred volts on the primary. A prototype modulator magnet and vacuum vessel have been designed and are now in fabrication. The primary area of concern now is the insulators supporting the kicker magnet. These insulators are now being tested for high voltage breakdown.

V. REFERENCES

[1] W.Q. Feng, and E.B. Forsyth, "Eddy Currents Induced in a Muon Storage Ring Vacuum Chamber Due to a Fast Kicker", *ibid.*

VI. ACKNOWLEDGEMENT

The authors express their thanks to C. Pai and J. Zebuda for their help with the design of this system, and D. Warburton for building prototypes and taking data.

The AGS Accelerator Complex with the New Fast Extraction System*

M. Tanaka, E.J. Bleser, J.W. Glenn, Y.Y. Lee and A. Soukas
Brookhaven National Laboratory, Upton, NY 11973 USA

Abstract

The delivery of a beam with characteristics appropriate for the g-2 muon storage ring and the filling of the RHIC heavy ion collider from the AGS main ring requires a new fast extracted beam (FEB) system. The new FEB system will be capable of performing both one-turn fast extraction and single bunch multiple extraction of either a heavy ion beam or a high intensity proton beam at a rate of 30 Hz up to 12 times per AGS cycle. The new system consists of a fast multi-pulsing kicker and an ejector septum magnet with local extraction orbit bumps.

I. INTRODUCTION

Since the old fast extracted beam (FEB) and single bunch extraction (SBE) systems [1] are no longer available due to the AGS improvement program, the new FEB system [2] will serve as the AGS extraction system not just for the muon g-2 experiment [3] but also for RHIC [4] and the long baseline neutrino (ν_μ) oscillation experiment [5] as well. The AGS complex has accelerated slow-extracted (SEB) Au^{77+} beam at 11.6 GeV/c/N for the nuclear physics program and has recently increased the proton beam intensity to $6 \cdot 10^{13}$ ppp at 24.5 GeV/c for various high energy physics experiments [6].

For the g-2 experiment, which has constructed a 14 m diameter superferric muon storage ring with $B = 1.5$ T in order to improve the previous CERN measurement of the anomalous muon magnetic moment (a_μ) by a factor of 20, the FEB must meet the following requirements: (1) extract the bunched proton beam up to full energy and intensity to the new V-target through the U-line for 3.1 GeV/c pion production, and (2) perform single bunch multiple extraction (SBME) at 33.3 ms intervals up to 12 (or 8) times per AGS cycle. The remaining bunches, if any, have to be debunched and be slowly extracted into the SEB channel for the HEP experiments. The ν_μ oscillation experiment requires fast one-turn extraction of tightly bunched high intensity proton beam.

With the FEB system the AGS complex will also serve as an injector for RHIC. The circumference of the RHIC ring is 19/4 times larger than the AGS ($C=807$ m) and its harmonic number at injection is 342 compared to 12 of the AGS. The AGS will accelerate three bunches per pulse and transfer individual bunches one by one into the waiting rf buckets in RHIC through the AGS_to_RHIC (AtR) transfer line. Each RHIC ring will be filled with 57 (or 114) bunches one after another in a few minutes every 10 hours or so and accelerate heavy ions to energies of $250 \cdot (Z/A)$ GeV/N with the luminosity $L = 2 \cdot 10^{26} \text{ cm}^{-2} \text{ s}^{-1}$.

*Work performed under the auspices of the U.S. Department of Energy.

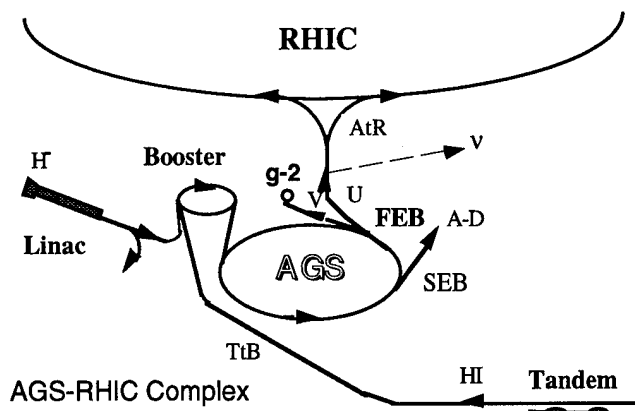


Figure 1. Schematic view of the AGS-RHIC complex.

In the fall of 1995, both the new FEB system and the AtR line are scheduled to be commissioned. The schematic layout of the AGS-RHIC accelerator complex is shown in Figure 1.

II. DESIGN OF THE FEB SYSTEM

A. Machine and Beam Parameters

Due to its high intensity operation for the g-2 experiment and the ν_μ oscillation experiment, it is important that the FEB system achieves a high extraction efficiency ($>99\%$). On the other hand, for RHIC injection, the beam intensity is low but pulse-to-pulse and cycle-to-cycle modulations in the extracted bunched beam parameters must remain within acceptable levels since any excess will directly influence RHIC performance. Therefore, stability and reproducibility of the extracted beam parameters are crucial for RHIC injection.

The following table lists the expected beam parameters and performance of the AGS Complex for FEB operation:

Table 1. FEB beam parameters.

Users	g-2	RHIC	RHIC
Particles	Protons	Protons	Heavy ions
Momentum	22-25	28.0	$28.0 \cdot (Z/A)$ [GeV/c/N] $28.7 \cdot (Z/A)$ for Au^{77+}
NSBE	1,2,,8(12)	3 (19-2(2))	for 2 rings
N_p/bunch	5000	100	1(Au), 6(Si) [10^9]
$\epsilon_{h,v}^{(95\%)}$	50π	20π	10π [mm-mrad]
ϵ_L	1.0	0.3	0.3 [eV-s/N]
(l_{bunch})	50	12	17 [ns]
(dp/p) _{full}	± 0.2	± 0.06	± 0.10 [%]
Oper. Mode	with SEB. filling two rings every 10 hr.		

The basic machine parameters and performance of the present AGS proton (Au^{77+}) SEB operation are summarized in Table 2. It should be noted that for the SEB users, their

prime interest is uniformity of the beam spill and beam intensity. In order to accelerate the high intensity proton beam without difficulties, the machine rf harmonic numbers have been changed from $h=12$ to 8 in AGS (from 3 to 2 in Booster) with a longer bunch length

Table 2. AGS parameters.

Circumference	$C = 2\pi R = 807.075$	[m]
Curvature	$\rho = 85.17$	[m]
Revolution Time	$t_{rev} = 2.692$	[μ s]
Tune	$Q_h \approx Q_v \approx 8.7$	
Beta Functions	$\beta_{h,v} = 22.5 - 10.5$	[m]
Dispersion Function	$D_x^{max} = 2.20$	[m]
No. of Bunches	$N_b = 8$ (3 for Au ⁷⁷⁺)	
Gap bet. Bunches	$t_s = 336$ (224)	[ns]
Typical Intensity	$5.3 \cdot 10^{13}$ ($1.2 \cdot 10^8$)	[ipp]
Typical AGS Cycle	3.2 (3.6)	[s]
Typical Spill Length	1.2 (1.2)	[s]
Typical Momentum	$p = 24.5$ (11.6)	[GeV/c/N]
Tran. Emittance	$\epsilon_{h,v}^{(95\%)} \approx 80$ (10)	[$\pi \mu$ m]
Long. Emittance	$\epsilon_L = 1.0$ (0.3)	[eV-s/bunch/N]
(Bunch Length	$l_b = 80$ (10)	[ns])

For design purposes, we assume that the operational FEB proton momentum range is (1) $22 < p < 29$ GeV/c, (2) the normalized transverse emittance of the high intensity beam should be $\epsilon_{h,v}^{(95\%)} = 6 \cdot \sigma^2 / \beta \cdot (p/m) \leq 50 \pi$ mm-mrad, where σ is the standard deviation of the beam size due to the transverse emittance, (3) the maximum total momentum spread allowed is $(dp/p)_{full} = \pm 0.2\%$ and the maximum bunch length is $l_b = 60$ ns. The actual measured values of ϵ^n , dp/p and l_b for the AGS beam are strongly dependent on the machine condition, especially the beam intensity. The high intensity values for the FEB operation have not yet been optimized [6].

For RHIC injection, the expected values of ϵ^n , dp/p and l_b for both protons and ions are substantially lower than the current values since the AGS Booster can deliver much more intensity than that assumed for the RHIC design parameters. The Au⁷⁷⁺ beam intensity is expected to increase to meet the RHIC requirement [7].

B. Extraction Scheme

The new system consists of a fast multi-pulsing kicker at straight section G10 followed by a thick septum ejector magnet at s.s.H10 in order to utilize the existing U line and due to limited availability of straight sections. To minimize the required voltage on pulsing the fast kicker, the kicker is a C-type open ferrite magnet with a pole tip. The kicker is placed about 60 mm from the central orbit. A few ms before the extraction two extraction bumps are excited to bring the beam into the aperture of the kicker and adjacent to the septum of the ejector. At extraction, the kicker is synchronized and phased to the bunches and triggered every 33.3 ms to send one bunch at a time into the ejector, which gives an additional

larger kick to extract the bunch out of the ring. In Figure 2, we show a schematic layout of the FEB extraction components and the extraction orbit bumps.

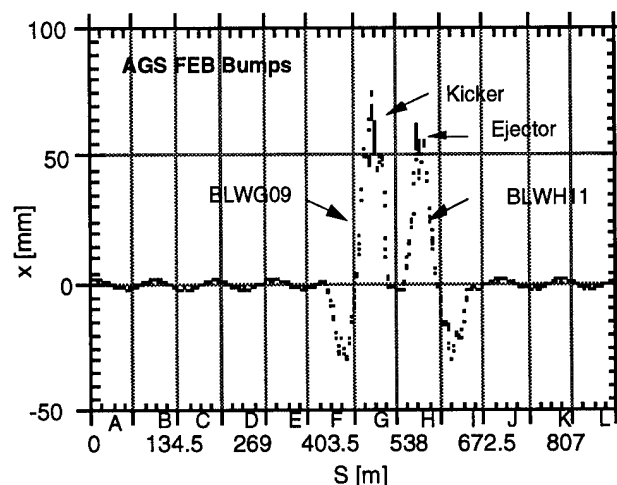


Figure 2. Layout of the AGS FEB components.

C. Fast Kicker, Ejector and Orbit Bumps

Using the 99% emittance at $p=29$ GeV/c and asking for at least 2 mm clearance at both sides of the ejector septum (10 mm), the required separation of the circulating beam and the beam kicked by the fast kicker is $\Delta x = 30.4$ mm at H10. The kicker must deflect the beam by

$$\theta(G10) = \Delta x / \sqrt{\beta(G10) \cdot \beta(H10)} \cdot \sin(\Delta\mu) = -1.80 \text{ mrad},$$

where $\Delta\mu$ is the betatron phase advance from the kicker to the septum calculated from the AGS lattice. This corresponds to $|Bdl| = B_0 \cdot l_{eff} = -0.18$ T-m. Since it is desirable to keep the maximum pulse voltage less than 40 kV, the kicker magnet is subdivided into four modules and powered by four PFN modules. The kicker has a limited aperture, 32 mm x 22 mm (w x g) and a pole tip which is shaped to maximize the good field region while keeping a gap as large as possible as shown in Figure 3.

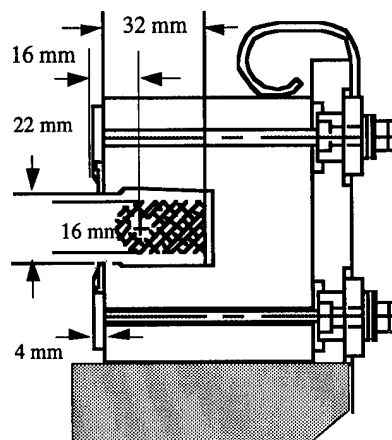


Figure 3. Geometry of the fast kicker.

The vertical field uniformity is calculated to be $\pm 2.5\%$ and the horizontal field component is 0 ± 2.5 Gauss in the cross hatched region shown in the gap. Aluminum shields have been placed on both the upstream and downstream ends of the magnet to protect the ferrite magnet core. For FEB operation, the ejector magnet also has to pulse at 30 Hz. As a result, the temperature of the copper septum will rise significantly, causing wear of the insulation. Therefore, the septum needs 10 mm thickness and is water-cooled.

Two 1λ rather than standard $3/2\lambda$ local orbit deformations (BLWG09 & H11) are installed to avoid the kicked beam hitting the vacuum chamber wall at s.s.G20 as seen in Figure 2. Each bump is excited by powering backleg windings on selected AGS main magnets with three independent power supplies. The basic parameters of the kicker, ejector and extraction bumps are summarized in Table 3.

Table 3. FEB magnet parameters.

	Kicker	Ejector	Bumps
Aperture [mm]	32 x 22	72 x 25	Full
Length [m]	2.4	2.1	(1λ)
θ_{\max} [mrad]	2.0	22.0	2(4)/pair
Waveform	half sine	half sine	half sine
B_{\max} [T]	0.1	1.0	0.05(0.1)
$t_{\text{basewidth}}$	380 ns	2 ms	6 ms
I_{\max} [kA]	2.0	23	1.0
Tolerance [%]	< 0.9	< 0.09	< 0.8

D. Beam Instrumentation

In order to observe possible beam scraping during the FEB extraction, two pairs of fast beam loss monitors are installed at s.s.G10. One pair is connected to a beam inhibit system. The present beam position monitor (PUE) and ring long radiation monitor (RLRM) systems are not sensitive to a gold beam and will be upgraded with a wider dynamical range and a better absolute measurement capability.

III. SIMULATION

To investigate the circulating and the extracted beam parameters at the middle of s.s.H13 (the entrance of the U-line), simulation studies were performed with a model of the AGS (MAD). We ran MAD to obtain the desired orbit at the kicker and at the ejector, making adjustments of the extraction bumps at a desired working point $\{Q_h, Q_v\} = \{8.74, 8.78\}$. Then, the particles with initial conditions $\{x, x'\}$ at the beginning of s.s.G10 are traced through the lattice and receive an appropriate kick at the kicker and an additional kick at the ejector up to the middle of s.s.H13, where the beam should be about 45 cm away from the central orbit, free from the fringe field. The simulation results show that the optical parameters ($\beta_{h,v}$, $\alpha_{h,v}$, D_x , D_x') at s.s.H13 are sensitive to fine bump tuning due to both the non-linear field components at high field of the AGS combined-function main magnet and fringe

field effects from the septum to s.s.H13. The results on the extracted beam parameters are summarized in Table 4.

Table 4. Extracted beam parameters.

ELEM	DIST	β_h	α_h	x	x'	D_x	D_x'	β_v	α_v
NAME	[M]	[M]	[1]	[mm]	[mrad]	[M]	[1]	[M]	[1]
ssH13	78.68	39.69	-4.85	449.	65.6	1.13	0.183	4.23	1.01

VI. CONCLUSIONS AND OUTLOOK

The new FEB extraction system is under construction at the AGS, which is capable of performing single bunch multiple extraction at a rate of 30 Hz up to 12 times per AGS cycle for the g-2 experiment and RHIC injection. In March 1995, the fast kicker system was successfully tested to extract single bunched proton beams to the SEB line for a test of the g-2 prototype detector at $p = 24$ GeV/c with $2 \cdot 10^{12}$ ppb. The full new FEB system is scheduled to be commissioned for the AtR-line in September 1995 and for the V-line in January 1996. The muon storage ring and RHIC are expected to be completed in 1996 and in 1999, respectively. For high intensity proton operation, it is important that the FEB system achieves a high extraction efficiency. On the other hand, for RHIC injection, stability and reproducibility of the extracted bunched beam parameters are crucial. Further machine studies and simulation studies will be needed to optimize beam parameters for the FEB operation.

V. ACKNOWLEDGMENTS

We would like to thank many members of the AGS Department who have helped this project, especially: A. Dunbar (bumps), J. Tuozzolo (kicker) E. Rodger (ejector), W. Zhang (kicker PS), R. Lockey (ejector PS), E. Gill (injection bump). We are also grateful to L. Ahrens, M. Brennan, A. McNerney and T. Roser for their helpful discussions and suggestions regarding the new FEB system.

VI. REFERENCES

- [1] W.T. Weng, "The AGS New Fast Extraction System and the Single Bunch Extraction", *IEEE Trans. Nucl. Sci.* NS-30, No. 3 (1983).
- [2] M. Tanaka and Y.Y. Lee, "The AGS -Booster Complex for the g-2 Experiment and RHIC Injection", *1993 IEEE Part. Accel. Conf.* (Washington, D.C.), p. 360
- [3] AGS Experiment 821, "A New Precision Measurement of the Muon g-2 Value at the Level of 0.35 ppm".
- [4] BNL-52195, "Conceptual Design of Relativistic Heavy Ion Collider", May 1989.
- [5] AGS Experiment 889, "Proposal for a Long Baseline Neutrino Oscillation Experiment at the AGS".
- [6] M. Blaskiewicz et.al., "High Intensity Proton Operations at the Brookhaven Hadron Complex", this conference.
- [7] L. Ahrens et.al., "Heavy Ion Acceleration Strategies in the AGS Accelerator Complex", this conference.

DESY III - Dump System with one fast Kicker J.Ruemmler
DESY Hamburg / Germany

Abstract.

The dump system works at an injection momentum of 350 MeV/C. The kicker, with a rise time of $t = 90\text{ns}$ and a variable pulse length up to $t = 3\text{ }\mu\text{s}$, can eject the entire DESY III beam or only a section into the dump. For test runs DESY III can operate with only a few proton bunches. Beam loss at high energies results then in minimal radioactivity in DESY III, the transport channel and in PETRA. Short pulse operation of the kicker can also cut one out of the ten bunches into the dump. This gap protects the ejection septum from irradiation.

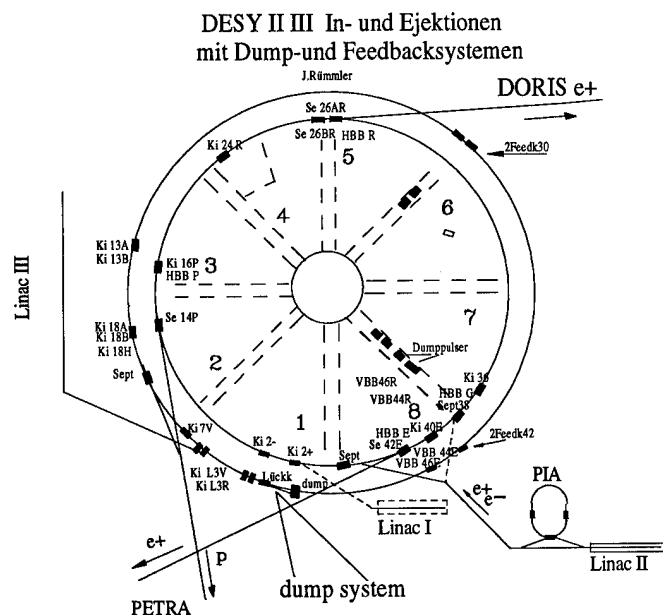


Fig.1

Fig.1 shows the location of the dump system in DESY III.

The optical specifications at the ejection point from DESY III to PETRA apply also to the dump system.

At a momentum of 350 MeV/C the beam deposits little radioactivity, but as an additional safety precaution, both sides of the dump chamber are shielded by 5 cm thick lead walls.

DESY III dump system

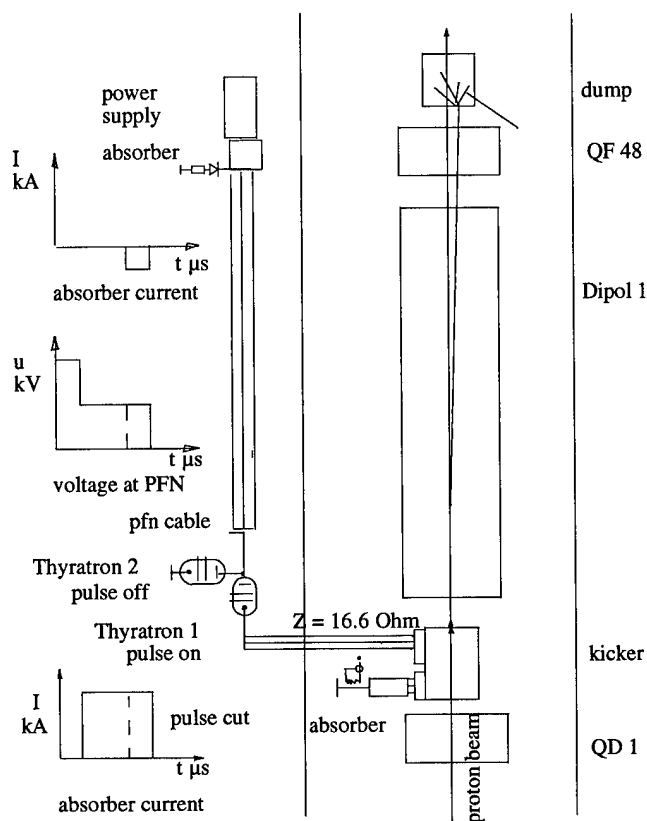


Fig.2

The overview of the dump system shows how the kicker magnet near QD1 ejects the beam. The beam then runs through dipole 1 and QF 48 into the dump chamber.

The kicker pulser stands outside the ring in radial tunnel 7 and can be accessed during DESY operation.

The kicker pulse system, shown in fig.2, functions as a cable discharger via three parallel cables. The kicker pulse current is lead through the pulser by switch-on and off thyratrons. And by means of further parallel cables the pulse current runs to the kicker and absorber in the ring tunnel.

On the left side of fig.2 three diagrams show the electronic characteristics of the pulser. The pulse current in the kicker, the high voltage at the switch-on thyatron and the reflected pulse current after pulse shortening.

Pulse System.

The required right-angular pulse in the kicker consists of a broad range of frequencies down to the d.c. in the pulse.

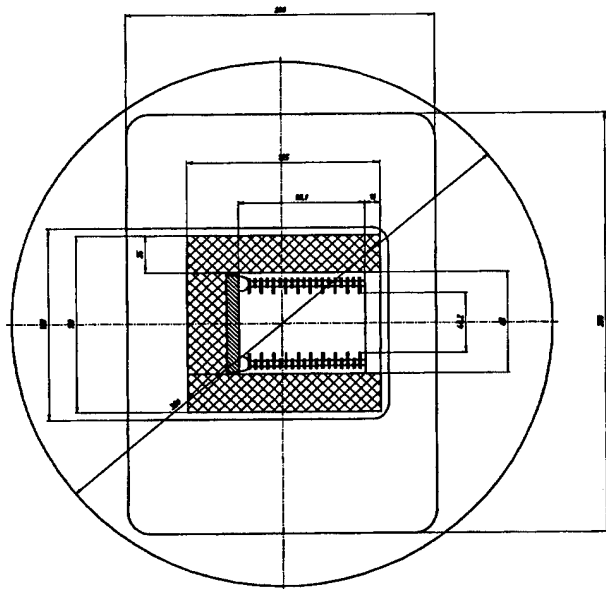
For all the frequencies in the right-angular pulse the system has an impedance of $Z = 16.6 \Omega$. Three parallel cables drive the kicker pulse.

Two CX 1154 thyratrons switch the pulse on and off, and also enable variation of the pulse length. From the moment of switching off, Thyatron 2 works as a reflection point and sends the remaining charge back to the start of the cable and over a diode into the absorber.

Kicker Magnet.

Operation with right-angular pulses requires that the kicker has an impedance of $Z = 16.6 \Omega$. Only such a construction can lead all the component frequencies of the right-angular pulse through the kicker to the absorber without reflection or pulse deformation.

Ferrite pieces, in the C- kicker, lead the magnetic field to the gap. 28 parallel capacitive plates divide the kicker into 28 LC- parts. In the absence of unwanted inductance these plates lead capacitive currents on both sides directly to the gap.



Kicker cross section Fig.3

Plate kickers can be built, according to their operation, with or without stripe chambers, as shown in fig.3.

Stripe chambers separate the beam from the kicker magnet. Without stripe chambers, short electron bunches in a beam of over 7 GeV/c would cause wall currents which would heat up the ferrite.

This is especially important to know as ferrite has a low thermal conductivity and furthermore a low Currie point of $t = 250^\circ \text{C}$

The above cross section, fig 3, shows the stripe chamber in the c - yoke of the kicker. The shaded section of the c - yoke is ferrite.

To save costs, the DESY III Kicker can be operated without stripe chambers. This is possible because DESY III operates with long proton bunches. The circumference of the capacitive plates is shown. The plates are alternitavely connected to ground and high voltage.

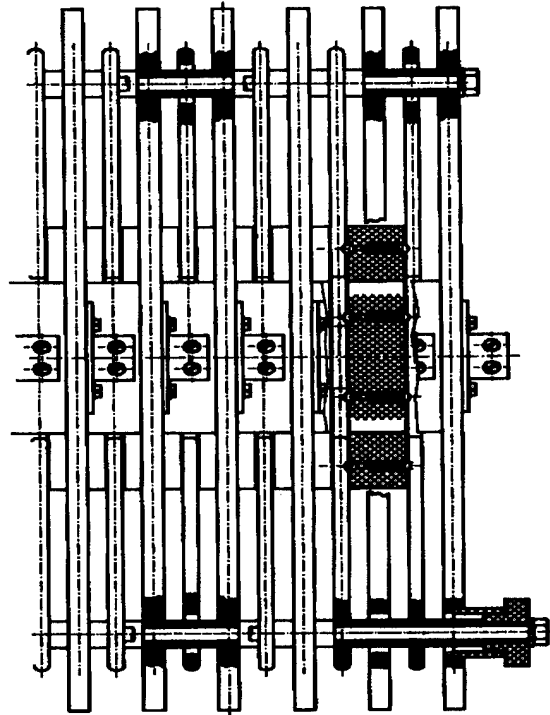


Fig.4

Fig.4 shows the plate kicker without the surrounding vacuum tank. The beam runs from the right into the middle of the kicker as shown in the kicker cross section diagram, fig 3.

The plates are held in position by means of ceramic tubes. The ferrite is held in place under compression by springs and ceramic spheres.

The surface of the plates must be very smooth and the corners rounded. This avoids hv- ionisation between the plates.

To avoid the danger of an excessively high voltage, occurring due to the difference in ϵ between the ferrite and the vacuum, the ferrite is insulated on only one side by ceramic supporters.

Further kicker information

Momentum	GeV/C	0.350
Displacement angle	mrad	9.45
Gap width	mm	60
Gap height	mm	56
Magnet length	m	ca 1
Beam displacement at the dump	mm	72

The pulser is driven by a discharge through 3 cables in parallel.

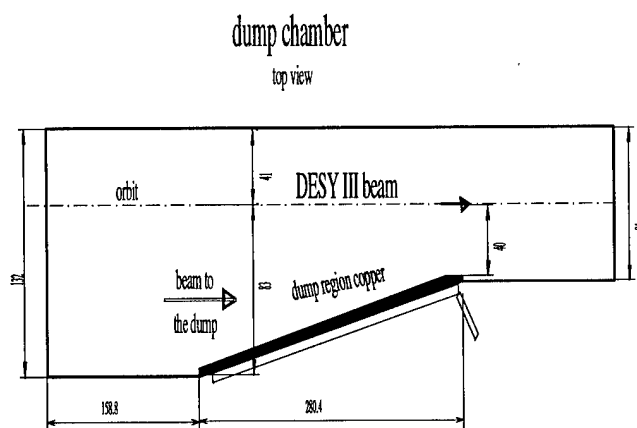
Current pulse shape	right - angular
Pulse length	μ s 0.095 - 3
(triggered by thyatron 2)	
Cable length from pulser to magnet	ca 100
Kicker voltage	kV 15
Charge voltage	kV 30
Power supply	kV 40
Kicker impedance	Ω 16.6
Absorber impedance	Ω 16.6
The pulse rise time and shape can be measured by a special transformer.	

Dump chamber.

The vacuum chamber is built from stainless steel and the dump region, inside the chamber, from a welded copper plate.

The angled dump region smoothly tapers the chamber. This avoids high-frequency standing waves, which would be produced by sharp angles in the chamber, and also gives the beam a larger area on which to disperse its energy.

Outside the chamber are two square water cooled pipes. This forms the first self shielding material of the dump.



Dump chamber top view Fig.5

Dump chamber shielding

For safety reasons the dump performance was calculated at a momentum of 350 MeV/C and for 10^{12} protons every 4 seconds. The calculations for emission rates were taken from the book "Induced Radioactivity" by M. Barbier.

The equivalent dose applies for a distance of 1 m from the absorber.

The results are for an excitation time of 5000 days.

The conditions for the results are:

Wall thickness for the dump region Cu	5	mm
1. Additional lead shielding	PB 50	mm
on both sides of the chamber		
Dose after a time	t = 0	350 mrem/h
	t = 1h	250 mrem/h
	t = 24h	180 mrem/h
2. Additional lead shielding	PB 100	mm
on both sides of the chamber		
Dose after a time	t = 0	19 mrem/h
	t = 1h	15 mrem/h
	t = 24h	11 mrem/h

Even for 5000 days continuous operation at a momentum of 350 MeV/C there are only minimal dose rates outside the dump shielding.

References:

- [1] Volker Büscher "Abschätzung der Strahlenbelastung durch induzierte Radioaktivität in einem Protonendump.
- [2] Marcel Barbier "Induced Radioactivity"
- [3] J.Ruemmler, "HERA e- injection with septum and kicker technology" EPAC 92 Berlin

USING A PULSED DEFLECTOR FOR EXTRACTION OF PULSED BEAMS FROM THE TRIUMF CYCLOTRON

R.E. Laxdal

TRIUMF, 4004 Wesbrook Mall, Vancouver, B.C., Canada V6T 2A3

Abstract

In the normal mode of operation, the TRIUMF cyclotron accelerates H^- ions to produce 500 MeV proton beams of $160 \mu A$ with 4 nsec pulses separated by 43 nsec. A proposed experiment ($\mu \rightarrow e$ conversion) requires a 500 MeV beam with 100-200 nsec pulses separated by 1-2 μ sec with an average intensity of $200 \mu A$. Two methods have been investigated to achieve this time structure. Both incorporate a pulsed electric deflector and take advantage of extraction by stripping. In the first case, a deflector with a thin septum deflects radially up to six accumulated turns onto a stripping foil in one turn. In the second, a pair of vertically deflecting plates are pulsed at a frequency to excite a coherent vertical growth, and the particles are eventually intercepted by a stripping foil. Under certain conditions extraction occurs in almost perfect synchronism with the driving pulse. Both methods will be described in detail and results of computer simulations will be presented.

I. INTRODUCTION

The TRIUMF cyclotron accelerates H^- ions at an rf frequency of 23 MHz and an orbit frequency of 4.6 MHz with five bunches per turn. Typically, $160 \mu A$ are accelerated to 500 MeV with extraction by stripping. These ions occupy $30-40^\circ$ of the rf cycle. Hence the time structure of the extracted beam in cw mode consists of 4-5 nsec pulses separated by 43 nsec. The separation between output pulses can be increased five-fold with a corresponding reduction in the average current by cancelling four of the five particle bunches before injection. In addition the macro-duty cycle can be altered by a 1 kHz pulser in the injection line giving pulses of variable length separated by up to 1 msec.

A $\mu \rightarrow e$ conversion experiment [1] [2] requires a pulsed beam with average intensity approaching $200 \mu A$ at an energy of 500 MeV. Pulses of 100-200 nsec are desired with a period between pulses of 1-2 μ sec. The micro-structure of the pulse is not critical. In a cyclotron with separated turns the macro-structure of the beam at the source will maintain itself through to extraction. However, in the TRIUMF cyclotron the energy spread in the turns produced by the phase-dependence in the acceleration and the low radius gain per turn (1.5 mm at 500 MeV) causes overlapping of turns and a uniform radial beam distribution. For example a single instantaneous pulse of beam at injection would be extracted over a period of 20 μ sec. Therefore any intensity fluctuations in the 1 MHz regime created at the source will be effectively washed out during acceleration. In any case the above intensity requirement precludes altering the duty cycle by beam elimination either at injection or extraction since, from space charge considerations, the maximum allowable average intensity in the TRIUMF cyclotron without major development

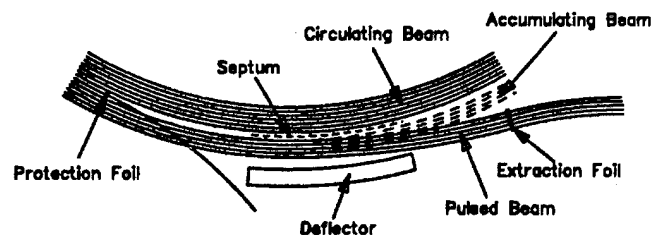


Figure 1. Schematic view of pulsed radial extraction. Here five turns are accumulated, then all are deflected simultaneously onto an extraction foil. A narrow foil lies upstream to protect the septum.

is $10 \mu A/\text{turn}$ of rf or $\sim 400 \mu A$. [3] The specifications set by the experiment can only be met by manipulating the beam near extraction in such a way as not to significantly reduce the average circulating intensity.

II. PULSED EXTRACTION SCHEMES

Two methods were developed to accomplish this. In both cases the full cw beam is injected into TRIUMF and pulsed electrodes near the extraction radius are used to deflect the circulating beam periodically onto an extraction foil.

A. Horizontal Deflection Scheme

In the first case a radial deflector with septum is fed a pulsed voltage. [4] When the field is off the beam is allowed to accelerate in the normal way into the deflecting gap and 5-10 turns corresponding to 1-2 μ sec can be accumulated. The device would pulse on for a period equivalent to one turn (200 nsec) to deflect all the accumulated beam onto a stripping foil positioned just outside the circulating beam. (Fig. 1) The rise and fall times of the pulses must be less than the separation of the circulating bunches (40 nsec). Because the beam is homogenous radially, a narrow foil would be placed upstream of the deflector to protect the septum and extract the intercepted beam down a separate beamline. The deflector gap must be large enough to accommodate the extra beam width, and the beamline must be able to accept the increased energy spread of the multi-turn beam.

Near extraction dR/dn is only 1.5 mm, so up to 50% of the beam would be intercepted by a 1 mm protection foil. The efficiency could be improved to 80-85% by employing a precessional extraction technique using an existing rf deflecting device (RFD) at the $\nu_r = 3/2$ resonance at 428 MeV. [5] The RFD alters the time structure so that only every second bunch passes through the extraction region. This doubles the length of the extracted pulse (180 nsec to 360 nsec), and eases by a factor of two the demand on the rise and fall time of the deflector (80 nsec instead of 40 nsec). As well the extraction energy is reduced from the nominal 500 MeV to a value closer to the driving resonance.

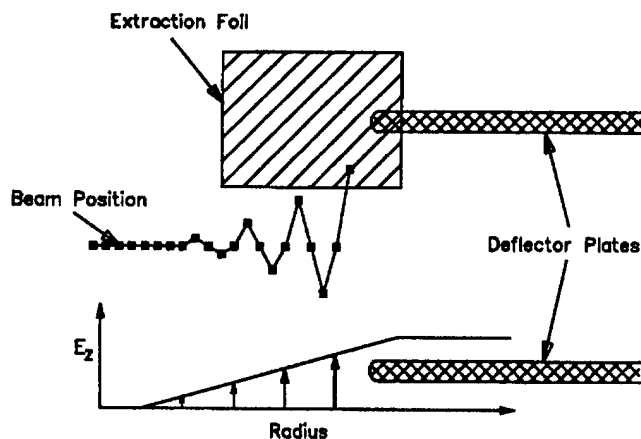


Figure 2. Schematic view of pulsed vertical extraction for the case where $N_s = 4$ and $\nu_z = 0.25$. The small boxes show the vertical beam position once per turn. The darkened boxes correspond to turns when the deflecting field is on. The profile of the fringe field is also shown with arrows indicating the magnitude of the deflections. The particle is intercepted by the extraction foil after a phase advance of $\pi/2$ in vertical phase space from the last deflection.

B. Vertical Deflection Scheme

In this scheme pulsed plates at the extraction radius perturb the beam vertically. [6] As in the previous case the pulse is on for one orbit (200 nsec) with rise and fall times of 40 nsec and a pulse period of N_s turns. With a vertical gap of 30 mm and the dR/dn of 1.5 mm, the beam will spend from 15-20 turns in the fringe field region (Fig. 2). The beam will feel a periodic vertical perturbation of ever-increasing intensity. As long as the deflector strength and pulse period are such that the passage through the fringe field is relatively adiabatic, then the beam will experience a coherent vertical growth. The growth over several pulses will add constructively and thus be maximized when $\nu_z^* = \nu_z \cdot N_s$ is close to an integer and a resonance condition exists. Fig. 2 illustrates the vertical growth in the case where $N_s = 4$ and $\nu_z = 0.25$. The extraction foil would be positioned just above the circulating beam at an azimuth corresponding to a phase advance of $\pi/2$ after the deflector. Whenever the acquired amplitude is sufficient to reach the foil, the particle will be extracted, and this will most generally correspond to a time directly after a pulse. Particles extracted out of synchronism with the pulse could be removed in the extraction beamline by another pulsed deflector.

A plot of ν_z as a function of energy calculated from the magnet field survey is shown in Fig. 3. The horizontal dashed lines correspond to ν_z values where the noted pulse period will yield a resonant condition.

III. COMPUTER SIMULATION STUDIES

Computer simulation studies were carried out to calculate the extraction efficiency, the required deflector specifications, and the beam quality (including energy spread and transverse emittance) of the extracted beam. All studies were done using the Monte-Carlo, first order matrix tracking code, COMA. [7] The initial particles occupied a phase band of 40° and a transverse

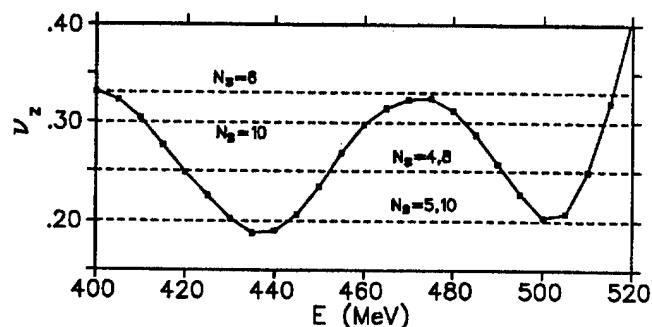


Figure 3. ν_z as a function of energy for the TRIUMF cyclotron. The dotted lines correspond to ν_z values where the noted N_s values would produce resonant conditions.

emittance of $(\epsilon_x, \epsilon_z) = (1.0, 2.4)\pi\mu\text{m}$. For normal (unpulsed) extraction the extracted beam characteristics were found to be $\Delta E = 1 \text{ MeV}$ and $(\epsilon_x, \epsilon_z) = (1.3, 2.1)\pi\mu\text{m}$.

A. Horizontal Results

Various parameters, including the RFD voltage, the extraction energy and the pulse period were varied in the study. [4] In some cases local flattopping was added to the acceleration to reduce the phase-dependent effects produced in the precessional extraction. [8] Simulation results for a range of RFD voltages are summarized in Table 1 for the case where the pulse period, N_s , is 6 turns and the extraction energy is 465 MeV corresponding to extraction in the fifth precession cycle. Shown are the energy spread and radial emittance of the extracted beam, the deflector voltage and the extraction efficiency. The deflector voltage is determined from two factors: the field strength necessary to generate sufficient deflection and the deflecting gap required to accommodate the beam. The voltage listed in the table provides the field strength required for a 1 m long deflector to separate the pulsed beam by 5 mm from the accumulating beam (Fig. 1), based on a gap 5 mm larger than the radial beam width in the gap. For example, for the case where the RFD is off, a gap of 20 mm is chosen to deflect the 15 mm wide beam. The extraction efficiency corresponds to the fraction of the total beam that would miss the 1 mm protection foil upstream of the septum. The energy spread (2.8 MeV) and beam width in the deflector gap (15 mm) have increased over the unpulsed values (1 MeV and 5 mm respectively) by an amount given by the dE/dn of 0.32 MeV and dR/dn of 1.5 mm each, scaled by the pulse period ($N_s = 6$). As the RFD strength increases, the increased perturbation of the circulating beam means that a higher deflector strength is required for the same separation. The radial emittance is also adversely affected due to the increased rotation in radial phase space from turn to turn. Both the energy spread and the emittance for a moderate RFD setting are improved if local flattopping is used.

As the pulse period increases, the energy spread increases roughly commensurate with the energy gain per turn, and the radial emittance, for cases where the RFD is on, rises dramatically. The deflector voltage increases roughly linearly with pulse period to compensate both for the required larger gap and for the increased kick needed to clear the higher number of accumulated orbits.

Table I

Results of beam simulation showing beam quality (energy spread and radial emittance), extraction efficiency and pulse voltage for various RFD voltages. The pulse period is $N_s = 6$ and the extraction energy is 465 MeV (fifth precession cycle).

In one case local flattopping is used.

RFD Kick (V/mm.m)	ΔE (MeV)	ϵ_x ($\pi\mu\text{m}$)	V (kV)	efficiency (%)
0	2.7	1.8	45	50
23	2.7	2.4	44	78
55	2.9	6.0	60	86
55 _{flat}	2.2	5.	40	87
110	2.9	13.	120	90

Table II

Optimized deflector voltages and corresponding extracted beam characteristics for various pulse periods, N_s .

N_s (turns)	Voltage (kV)	E (MeV)	ν_z	ΔE (MeV)	ϵ_z ($\pi\mu\text{m}$)
4	6	492	0.25	2.9	1.3
5	9	499	0.20	2.7	2.2
6	15	478	0.32	3.8	2.2
7	18	486	0.28	3.7	3.1
8	18	490	0.25	4.3	3.4

B. Vertical Results

In all studies [6] the E_z fringe field was assumed to rise linearly over a 25 mm range approaching the deflector. The position of the extraction foil was optimized for best extraction efficiency. Since $\nu_z \sim 0.25$ in the energy range of interest, the foil azimuths were all in the vicinity of the deflector. In the initial investigation, using $N_s = 6$ and a deflector strength of 1 kV/mm · m (30 kV for a 1 m deflector with 30 mm gap) the position of the deflector was varied to study correlations between ν_z and the extraction efficiency. The efficiency ranged from 80% at $\nu_z^* = 1.4$ to 99% at $\nu_z^* = 1.1$. In a similar study it was found that near the $\nu_z^* = 1$ resonance condition ($N_s = 5$, $\nu_z = 0.2$ at 500 MeV), the deflector strength could be reduced to 0.4 kV/mm · m while still maintaining 99% efficiency. However the efficiency dropped to 94% at 497 MeV for the same strength, indicating that at lower voltages the results are very ν_z dependent.

For any particular radius and pulse period, the efficiency is optimized at a moderate deflection strength. Too high a strength, and the growth is too non-adiabatic, whereas with too small a strength, the probability of hitting the foil immediately after a kick is reduced. As the deflector voltage is reduced, the vertical emittance drops correspondingly as the maximum vertical extent on the foil is reduced. However, for very low values the energy spread and spot size on the foil increase dramatically, because the variation in the number of pulses needed to achieve extraction increases.

Optimal deflector voltages (for a gap of 30 mm and 1 m

length) and the corresponding extracted beam quality are shown in Table 2 for pulse periods ranging from $N_s = 4$ to $N_s = 8$. The efficiencies are all $\geq 99\%$ except at $N_s = 8$ where the efficiency is 97%. Above $N_s = 8$, the energy spread becomes unacceptably large. A higher pulse period demands an increased deflector voltage, since fewer kicks mean stronger voltages for the same amplitude growth. Because of the finite vertical emittance and the adiabatic nature of the extraction, particles of the same rf phase will be extracted over two or three pulses. Therefore the energy spread is larger than in the previous single deflection scheme, and increases with pulse period. The radial extent of the beam on the extraction foil is roughly 5 mm/MeV of energy spread. The increased pulse period also means a reduction in the coherence, since the precession of the vertical phase vector is more rapid and leads to the increased vertical emittance.

IV. CONCLUSION

The amplitude produced by any deflection is inversely proportional to the betatron frequency. Hence vertical deflections are a factor of six more efficient than radial deflections in the TRIUMF cyclotron. As well, the vertical scheme benefits from multiple deflections as opposed to the single pulse deflection in the radial case. The specifications demanded by the radial deflection scheme (≥ 40 kV @ 1 MHz) are beyond present pulsed technology [9]. However at 1 MHz, a 10 kV pulse generator has been designed [10] and fabricated, and is presently being tested in preparation for a beam test of the vertical deflection scheme in the fall of 1995. In a preliminary test 6 kV @ 1 MHz has been reached [11]. Besides the technical development, future work will involve a beamline study to determine if the larger beams can be transported, and a study to estimate the cleanliness of the pulse off condition at the target.

V. ACKNOWLEDGEMENTS

The work grew out of discussions with Rick Baartman. Werner Joho encouraged the investigation that led to the vertical pulse deflection technique. The author would also like to thank Gerardo Dutto for his support of this work.

References

- [1] S. Ahmad, *et al.*, Phys. Rev. D38 (1988) 2102.
- [2] C. Dohmen, *et al.*, Phys. Lett. B317 (1994) 631.
- [3] R. Baartman, private communication
- [4] R.E. Laxdal, *Beam Quality Study for Pulsed Extraction Scheme*, TRIUMF Design Note TR1-DN-94-27, Oct. 1994.
- [5] R.E. Laxdal, *et al.*, *Extraction Exploiting $\nu_r = 3/2$: Optical and Technical Constraints on Performance*, Proc. 11th Int. Conf. on Cyclotrons and their Applications, Tokyo 1987, p. 248.
- [6] R.E. Laxdal, *A Vertical Pulsed Extraction Scheme* TRIUMF Design Note TR1-DN-94-35, Dec. 1994.
- [7] C. Kost and G.H. Mackenzie, Proc. of the Part. Acc. Conf., IEEE NS-22, p. 1922, 1975.
- [8] R.E. Laxdal, *et al.*, *Reducing Phase-Dependent Emittance Growth with Local Flattopping*, Proc. of the 1993 Part. Acc. Conf., Washington, May 1993, p. 372.
- [9] G. Wait, private communication.
- [10] M. Barnes and G. Wait, *Design for a FET Based 1 MHz, 10 kV Pulse Generator*, Proc. of the 10th IEEE Intl. Pulsed Power Conf., Albuquerque, July 1995, to be published.
- [11] M. Barnes and G. Wait, *Measurements on a FET Based 1 MHz, 10 kV Pulse Generator*, Proc. of the 10th IEEE Intl. Pulsed Power Conf., Albuquerque, July 1995, to be published.

REQUIREMENTS FOR A BEAM SWEEPING SYSTEM FOR THE FERMILAB ANTIPROTON SOURCE TARGET*

F. M. Bieniosek, K. Anderson and K. Fullett
Fermilab, P.O. Box 500, Batavia, IL 60510 USA

Abstract

In order to increase the rate of production of antiprotons, intensity of the incident 120-GeV proton beam on target is scheduled to increase to 5×10^{12} protons per pulse. Intensity in the range of 3×10^{12} has already been sufficient to damage the nickel antiproton production target. To continue to operate with a tightly-focused primary beam spot on the target, and thus maintain yield, we plan to spread the hot spot on target with a beam sweeping system. Operation of the system will require a deflection of the beam with pairs of 625-kHz magnets upstream and downstream of the target. We are investigating both ferrite and laminated-iron magnet designs for operation in the harsh environment downstream of the target.

HIGH-INTENSITY TARGETRY

Antiprotons are collected from the interaction of a 120-GeV proton beam with a solid nickel target. The efficiency of collecting antiprotons from the target rises as the size of the proton beam spot on the target is reduced. However at the same time the peak energy deposition on target rises. Under Main Injector conditions (5×10^{12} protons in a 1.6- μ s pulse), the spot size will have to be increased to at least 0.25 mm to keep peak energy deposition near current levels. To bring the density of energy deposition with a 0.1-mm spot size down to currently-existing levels, a system to sweep the beam spot on the target has been proposed.[1]

Measurements of yield with beam spot position on the target [2] show a Gaussian shape in both horizontal and vertical dimensions, where $\sigma_x = 0.48$ mm, and $\sigma_y = 0.65$ mm. The shape of the yield distribution is determined by the acceptance and lattice functions of the Debuncher and the AP2 beam line. If the incoming proton beam is itself a Gaussian, $\sqrt{2/\pi} \sigma_{bx}^{-1} \exp(-x^2/2\sigma_{bx}^2)$ in both planes, with characteristic spot size σ_{bx} and σ_{by} , then the dependence of the yield on spot size, normalized to the yield for an infinitesimal point beam, becomes

$$Y = \frac{\sigma_x \sigma_y}{\sqrt{\sigma_x^2 + \sigma_{bx}^2} \sqrt{\sigma_y^2 + \sigma_{by}^2}} \quad (1)$$

This curve is plotted in Fig. 1 for a circular beam spot. Also shown are MARS10 calculations of energy deposition in a copper target as a function of beam size for $N=5 \times 10^{12}$ protons per pulse.[3] A small fraction (typically less than 10%) of the deposited energy is released as a stress wave by the elastic properties of the metal; the remainder is deposited locally for a time much longer than a beam pulse. The spot

size under current operating conditions is about $\sigma_{bx}=0.15$ mm; $\sigma_{by}=0.23$ mm. Estimates of the peak instantaneous energy deposition for the highest intensity achieved to date (3.4×10^{12}) indicate an energy deposition of about 800 J/g. This is above the melting point of copper (about 600 J/g), and close to the melting point of nickel (about 1000 J/g). Local disintegration of the target has been observed when the target rotation mechanism failed. The damage was presumably caused by the integrated radiation dosage to the affected spot, combined with severe repetitive thermal and mechanical stress. Less severe damage was observed with a slowly-rotating target.[4] In order to maintain peak energy deposition below present levels after the Main Injector begins operation, it will be necessary to increase the spot size. The alternative is to sweep the beam on the target, and reduce the spot size to the smallest attainable, leading to a 15-20% increase in yield. As incident beam intensity continues to rise, beam sweeping will become increasingly important to operation of the Antiproton Source.

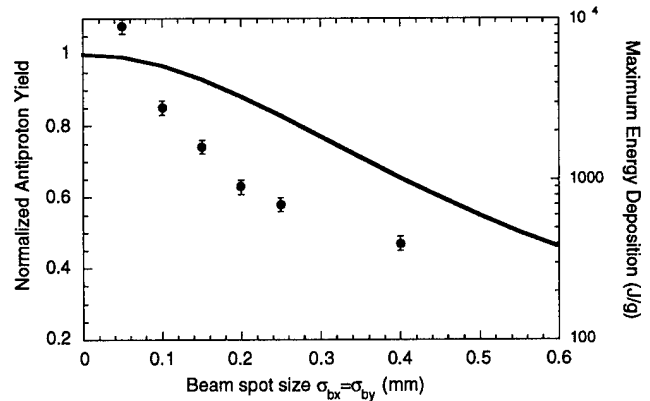


Figure 1. Scaling of yield (curve) and peak energy deposition (points) in the target as a function of beam spot size. The values for energy deposition were taken from Ref. 3.

The effective size of the energy deposition profile is comparable to or larger than the beam spot size. For a circular Gaussian energy deposition profile with variance σ in both planes, swept in a circle of radius r_0 , the radial energy deposition profile is

$$E(r) = \exp\left[-\frac{r^2 + r_0^2}{2\sigma^2}\right] I_0\left(\frac{rr_0}{\sigma^2}\right), \quad (2)$$

where I_0 is the modified Bessel function. The peak of the energy deposition curve (Eq. 2) is shown in Fig. 2 as a function of the ratio of sweep radius to σ . Increasing amplitude of beam sweep rapidly reduces peak energy

deposition for r_0/σ near 2. The effect is that a sweep radius of 0.33 mm reduces the peak energy deposition to about 600 J/g for 5×10^{12} protons per pulse[3]. This level of energy deposition is likely to be acceptable for reliable operation in nickel targets.

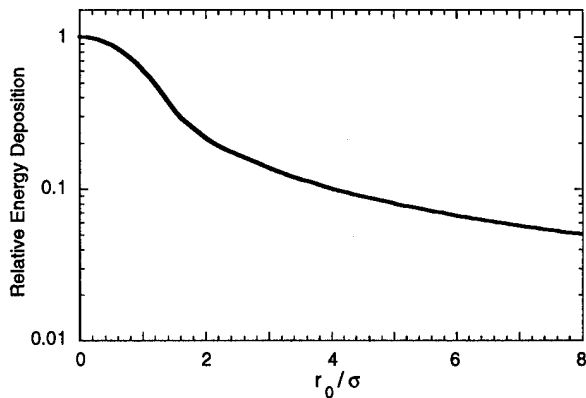


Figure 2. Effect of beam sweeping on the maximum local energy deposition for an initially Gaussian energy deposition.

SWEEPING SYSTEM

The beam sweeping scheme utilizes two upstream sweep magnets driven in quadrature by a 625-kHz sinusoidal current waveform to trace a circular pattern on the target with the 120-GeV proton beam, followed by two downstream magnets to redirect the 8-GeV antiprotons exiting the collection lens parallel to the AP2 transport line[5]. Figure 3 shows a layout of the target station with sweeping system installed. The AP1 beamline transports and focuses the 120-GeV protons from the Main Ring onto the target. Antiprotons created in the target are collected by a lithium lens, and deflected by the pulsed magnet into the AP2 beam line for injection into the Debuncher. The upstream sweep magnets will be installed at the end of the AP1 beamline. A lithium lens[6] may be used to tightly focus the beam on target to very small spots 0.1 mm or less; its greatest disadvantage is that it absorbs 7.5% of the incident proton beam. The upstream magnets will be near the focal point of this lens. The downstream magnets will be

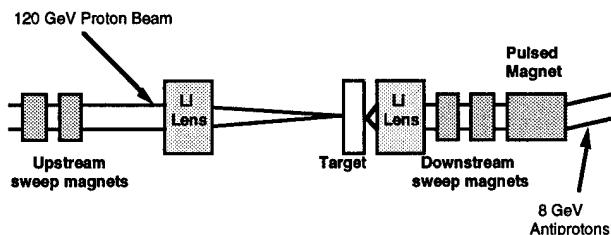


Figure 3. Components in target vault, with locations of sweep magnets shown.

located at two currently unoccupied modules between the collection lens and the pulsed magnet, near the focal point of the collection lens. Requirements on the peak deflecting field for expected Main Injector operating conditions are 2.6 kG upstream, and 2.0 kG downstream.

System requirements on timing jitter, field regulation, and field uniformity may be determined from the effective RMS radius x_{RMS} of a displaced beam spot at the target

$$x_{RMS} = (\sigma_{bx}^2 + \Delta x^2)^{1/2}$$

where σ_{bx} and Δx are the beam spot size and the displacement in a given direction. If we wish to limit the increase in x_{RMS} to less than 10% in all cases, the criterion becomes $\Delta x < 0.05$ mm. The resulting requirements on timing jitter lead to a combined requirement of ± 30 ns. The field uniformity/regulation requirement is $\Delta B/B < \pm 7\%$.

Two current-carrying plates, roughly 3 cm wide, with an air gap of 3 cm will provide the deflecting magnetic field. A magnetic core surrounding the plates provides a return path for the magnetic field. MARS10 and CASIM calculations of energy deposition by hadron and electromagnetic cascades show significant heating of iron and ferrite magnet cores downstream of the target.[3] Total heating increases linearly with particle flux, and is a strong function of the radius of the magnet core. Steady-state temperature rise of the core is determined by thermal conductivity of the material and the rate at which heat is removed at the surface. Because of its low Curie temperature, a ferrite core design requires the minimization of the use of ferrite at small radii, where the energy deposition is greatest. A laminated iron core does not have the thermal restrictions of a ferrite core, and thus may be closer to the beam path. However very thin .001-inch laminations are required. Investigations are currently underway to determine the feasibility of using a laminated iron core.

Ionization of the air by the particle shower downstream of the target will increase the conductivity of the air between the conductor plates. Electrical losses through the ionized-air path across the gap reduce the Q of the circuit driving the magnet. Estimates based on CASIM calculations predict that the current drain between the plates will be less than 100 A, an acceptable amount. Avalanche ionization of the air does not appear to be a problem, as long as peak electric fields are kept well below breakdown levels, i.e. $E < 10$ kV/cm. The greatest problems are likely to be at the feed points of the strip line to the sweep conductors. Installation of a dummy test module is planned to measure the leakage current between two conductors placed parallel to the beam path at voltages up to 10 kV.

The sweep magnets must be provided with approximately 6 kA at 625-kHz by a power supply located on the floor of the AP0 service building. The current will be supplied through cables over a distance of approximately 10 m into the target vault, and by 2.5 m of strip line through steel shield modules to the magnets at the bottom of the target vault. The inductance of the cable, in series with the sweep magnets, significantly increases the requirements on the power supply. SPICE simulations show that it is possible to supply the

current directly through 16 parallel RG-220 cables with a high-power thyatron switch, but the requirements on the thyatron are severe. Two approaches that reduce the requirements on the power supply are under consideration. In both cases a capacitor is placed at the top of the target vault, connected by a strip line in parallel resonance with the inductance of the sweep magnet, and the resonant circuit is tuned to 625 kHz.

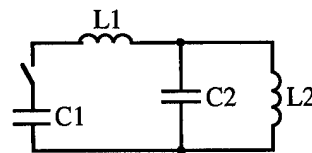
(a) The tuned circuit may be driven by another tuned circuit, coupled in a linear dual-resonant circuit.[1] The circuit components consist of the energy-storage capacitor C_1 , the inductance of the pulser and parallel drive cables L_1 , and the resonant load, L_2 and C_2 (fig. 4a). The circuit efficiently transfers energy from the primary loop to the secondary loop at the characteristic frequency ω_0 if the following conditions are satisfied:

$$\omega_0^2 L_1 C_1 = \left(\frac{2}{n^2 + m^2} \right)$$

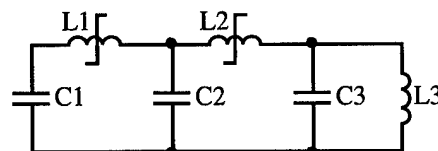
$$\omega_0^2 L_2 C_2 = \left(\frac{m^2 + n^2}{2n^2 m^2} \right)$$

Here n and m correspond to the resonant mode numbers of the coupled circuit. The mode of greatest interest is $n=2$, $m=3$. The current step-up from the primary to the secondary loop is about 2.6. The energy is supplied to the magnet in 2-3 current reversals, with an initial voltage requirement of approximately 30 kV at a capacitor bank. The necessary current (3-4 kA) can be switched with a hydrogen thyatron.

(b) An alternative approach is pulse compression by saturating inductors. This technique has enjoyed wide acceptance as a passive switching technique for pulsed currents. A two-stage inductive pulse-compression circuit is shown in Fig. 4b. The initially large inductance of a ferrite inductor L_1 allows the relatively slow supplying of energy to an intermediate energy storage capacitor C_1 on a relatively long time scale of 10 μ s. The inductor is designed to saturate when sufficient energy is available to drive the sweep magnet. The process is repeated in the second stage C_2 and L_2 . When the inductor L_2 saturates it rapidly discharges C_2 into the resonating capacitor C_3 at the top of the target module, which in turn rings into the sweep magnet L_3 . This arrangement allows the use of a simple solid-state SCR-driven power supply, and a simple cable arrangement to deliver the charging current to C_1 . Techniques have been demonstrated that control timing jitter to the subnanosecond level.[7]



(4a)



(4b)

Fig. 4. Representative circuits for driving the sweep magnet.

*Operated by the Universities Research Association Inc., under contract with the U.S. Department of Energy.

- [1] F. M. Bieniosek, A Beam Sweeping System for the Fermilab Antiproton Source, Fermilab-TM-1857 (1993).
- [2] S. C. O'Day and F. M. Bieniosek, P-bar Production Measurements at the Fermilab Antiproton Source, Proceedings European Particle Accelerator Conference, 1994.
- [3] C. M. Bhat, N. V. Mokhov, Calculation of Beam Sweeping Effect for the Fermilab Antiproton Source, Fermilab-TM-1585 (1989).
- [4] S. O'Day, F. Bieniosek, K. Anderson, New Target Results from the FNAL Antiproton Source, Proc. 1993 US Particle Accelerator Conference.
- [5] G. I. Silvestrov and A. D. Cherniakin, A Sweeping System for producing Secondary Beams with High Phase Density, IIF-Preprint-84-120 (1984). [translation LA-tr--86-24].
- [6] F. M. Bieniosek and K. Anderson, Lithium Lens for Focusing Protons on Target in the Fermilab Antiproton Source, Proc. Particle Accelerator Conf, Washington, 1993.
- [7] M. A. Newton and J. A. Watson, Timing and Voltage Control of Magnetic Modulators on ETA II, Proc. 7th IEEE Pulsed Power Conference, Monterey, 1989.

MEASUREMENT AND REDUCTION OF QUADRUPOLE INJECTION OSCILLATIONS IN THE FERMILAB ANTIPROTON ACCUMULATOR*

F. M. Bieniosek and K. Fullett
Fermilab, P.O. Box 500, Batavia, IL 60510 USA

Abstract

We have utilized a quadrupole pickup[1] in the Fermilab Antiproton Accumulator to reduce quadrupole injection oscillations of 8.9-GeV reverse protons injected from the Main Ring onto the Accumulator extraction orbit. Quadrupole oscillations of the injected beam at $(2q-1)f_0$ due to lattice-function mismatch between the beam transfer line and the Accumulator were measured by the pickup. Minimization was accomplished by varying the strength of quadrupoles in the beamline. Comparison of the quadrupole oscillation data with a beamline model allowed empirical estimation of the matching lattice functions of the line.

INTRODUCTION

The beamline (AP1/AP3) for transfer of antiprotons from the Accumulator to the Main Ring for high-energy physics research consists of an extraction line (AP3) which transports the antiprotons toward the Main Ring beyond the antiproton production target, and the AP1 line, which is also used for delivering 120-GeV protons from the Main Ring to the production target. The complete line is 490 m long and contains 39 quadrupoles. Good betatron matching is important for conserving the emittance of the antiproton beam. Because of the length of the line, uncertainties in magnetic optics of the transfer line and of the periodic lattice functions of the two rings, it is helpful to measure empirically betatron matching of the transfer line. Reverse-injected proton beams are used in the measurements because of the scarcity of antiprotons.

APPARATUS

The quadrupole pickup is located in the Accumulator. The pickup (Figure 1) is approximately one meter in length with a 4 cm aperture. In the measurements (Figure 2) four preamps are connected to the quadrupole pickup, one for each pickup plate. The output of each preamp is connected to a differential line receiver in the AP10 service building. The line receivers are connected to post signal processing electronics that filters and performs the appropriate differences and sums to arrive at a sum, vertical, horizontal, and quadrupole signal. Eight bunches of 8 GeV reverse protons bunched at 53MHz were injected from the Main Ring through the AP1/AP3 beamline into the Accumulator. The oscilloscopes were triggered at the time of injection of the beam. Since the signals from the injected beam decay at a characteristic time scale of 1 ms or less, a discrete Fourier transform was performed on the first 1-ms of data. When the measurements were taken with a stack of antiprotons present on the core orbit, care was taken to increase the emittance of the stack and to adjust the chromaticity to reduce the intensity and move the frequency of

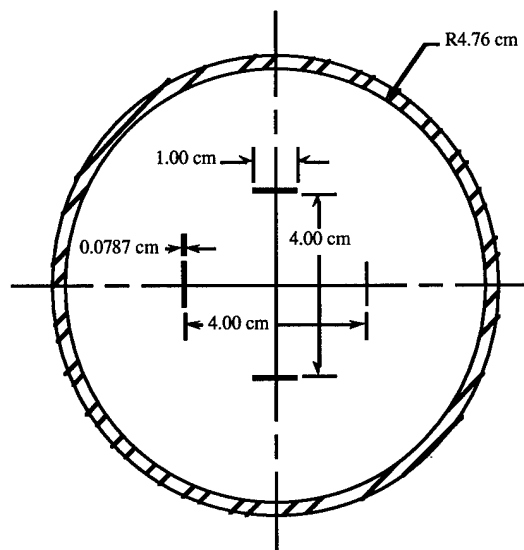


Figure 1. Mechanical arrangement of the quadrupole pickup.

signals due to the stack away from those due to the injected protons. Calibrations were carried out by measuring the output of the pickup as a function of induced dipole injection oscillations of known amplitude. Maintaining dipole injection oscillation amplitude below 1 mm ensures that these oscillations do not significantly affect the quadrupole signal.

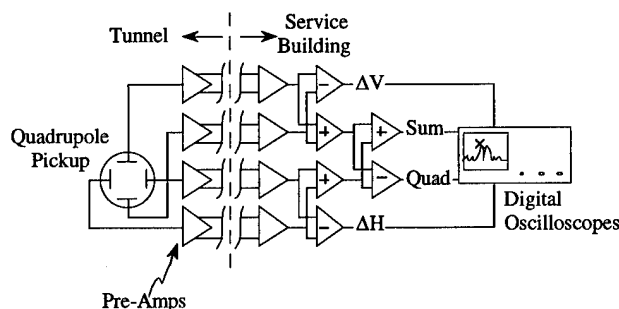


Figure 2. System electronics.

The response of the pickup to a quadrupole oscillation in position of a beam particle is

$$V(x, y, t) = Z \cdot (x^2 - y^2) \cdot i_b(t) \quad (1)$$

where $x(t)$ and $y(t)$ are the beam position, $i_b(t)$ is the beam amplitude at the pickup, and Z is the gain of the pickup for a quadrupole mode signal. For a particle undergoing horizontal and vertical betatron oscillations $\sqrt{\epsilon_x \beta_x} \cos(q_x \omega_0 t)$ and

$\sqrt{\epsilon_y \beta_y} \cos(q_y \omega_0 t)$ about a closed orbit, with horizontal and vertical tunes q_x and q_y , the quadrupole response becomes

$$V = Z \frac{e \omega_0}{4 \pi} \sum_{n=1}^{\infty} \left\{ \epsilon_x \beta_x \cos[(n \pm 2q_x) \omega_0 t + \phi_x] + \epsilon_y \beta_y \cos[(n \pm 2q_y) \omega_0 t + \phi_y] \right\} \quad (2)$$

where β_x and β_y are the amplitude functions at the pickup, ϵ_x and ϵ_y correspond to the horizontal and vertical emittances enclosed by the orbit, ϕ_x and ϕ_y are arbitrary phases, and the summation is over all frequencies n . Pairs of quadrupole signals appear at the frequencies $n \pm 2q_x$ and $n \pm 2q_y$. The response V for an injected beam is the sum of the contributions of all the particles. Bunching the particles in time results in a coherent quadrupole signal. A beam injected with a lattice-function mismatch undergoes additional coherent quadrupole injection oscillations. This is the signal component to be minimized. The amplitude of this oscillation is related to the emittance growth approximately by [2]

$$\Delta\beta / \beta \approx \sqrt{2(F-1)} \quad \text{where}$$

$$F = \frac{1}{2}(\beta\gamma_0 + \beta_0\gamma - 2\alpha\alpha_0) \quad (3)$$

Here the unsubscripted Courant-Snyder parameters are those delivered by the beamline to the ring, and the subscripted parameters are the periodic lattice functions of the ring at the end of the beamline. The function F represents the relative emittance growth of the injected beam ϵ / ϵ_0 if the mismatch is not too large.

MEASUREMENTS

The measurements were made at the 2q-1 lines (about 140 kHz). Three lines were observed, corresponding to q_x , q_y , and a third line, labelled q_{xy} , possibly an artifact of the strong coupling on the extraction orbit. Attempts were made to reduce the coupling by use of a sextupole in the Accumulator, but the coupling could not be completely eliminated. Minimization of the quadrupole signal was accomplished by minimizing the quadrature sum of the three oscillations. By adjusting the current on a series of quadrupoles in the beamline, it was initially possible to reduce the quadrupole signal by about 40%. Results of a typical quadrupole magnet scan are shown in Figure 3. This magnet (D:Q907) was initially set at 90.7 A; the quadrupole signal was minimized at 83 A. The overall quadrupole amplitude is calibrated in terms of the amplitude of the dipole injection oscillation that yields an equivalent signal. A rough calculation shows that the residual signal is comparable to that expected for the emittance of the beam delivered by the Main Ring (10-15 pi-mm-mrad). For example, a 5.5-mm effective oscillation amplitude apportioned equally to both planes corresponds to an oscillation in each plane of 3.9-mm. This leads to an estimate for the

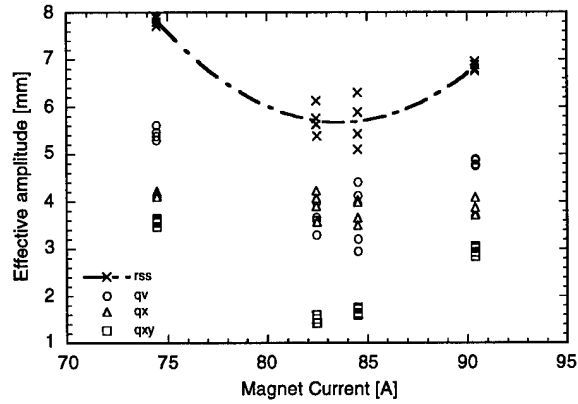


Figure 3. Effect on quadrupole signals of changing current in quadrupole Q907. The amplitudes of the three peaks are indicated. RSS is the quadrature sum of the amplitudes of the three peaks.

normalized 95% emittance of 15-pi-mm-mrad, based on the expression[3]

$$\epsilon = 6\gamma \frac{\pi}{2} \frac{\Delta x^2 + (\beta \Delta x' + \alpha \Delta x)^2}{\beta} \quad (4)$$

The calculation utilizes the fact that the quadrupole pickup is calibrated to deflections at beam position monitors, at which the lattice functions are $\beta \approx 30$ m, $\alpha \approx 0$. The implication is that the quadrupole signal due to mismatch was reduced to negligible levels, which is supported by the fact that no further improvement could be made by varying other quadrupoles in the beamline. Subsequent measurements and adjustments have been required to retune the line after modifications to improve the dispersion match. A plot of the Fourier transform of the quadrupole signal before and after a series of adjustments to reduce the signal is shown in Figure 4. It shows a reduction

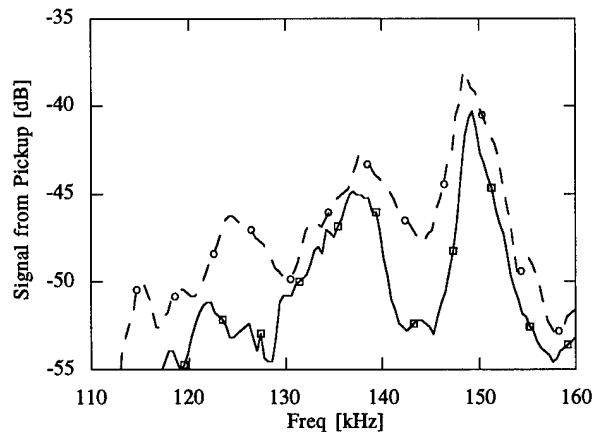


Figure 4. Quadrupole signals before (dashed), and after (solid) a typical tuning session.

of several dB in the signal over the entire range of the quadrupole frequency. The horizontal and vertical tunes of the injected beam, as measured by the dipole Schottky pickups, indicate $1-2q_x = 133$ kHz, and $1-2q_y = 148$ kHz. Thus the two large peaks in the profile are closely identified with the horizontal and vertical tunes.

A quantitative comparison of the quadrupole oscillation data with a beamline model was performed by utilizing the empirical matching conditions. In most cases the predicted effect of a magnet was predominantly in a single plane. For these cases a plot was made of the lattice functions α and β calculated by a beamline model delivered at the Accumulator end of the beamline for the conditions under which the effective oscillation amplitude derived from the quadrupole signal was 10% greater than the minimum level (points of figures 5 and 6). The input parameters to the model were the lattice functions of the Main Ring as determined by a synch model. The result was then compared to the synch model predictions for the periodic lattice functions of the Accumulator at the end of the line. Plotted are the ellipses for which the function $F=1.1$, (Equation 3) representing a theoretical 10% emittance growth due to injection mismatch.

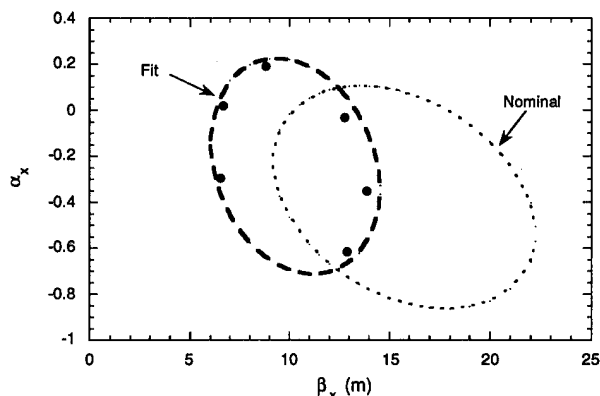


Figure 5. Locus of points for a horizontal emittance growth of 10% due to mismatch.

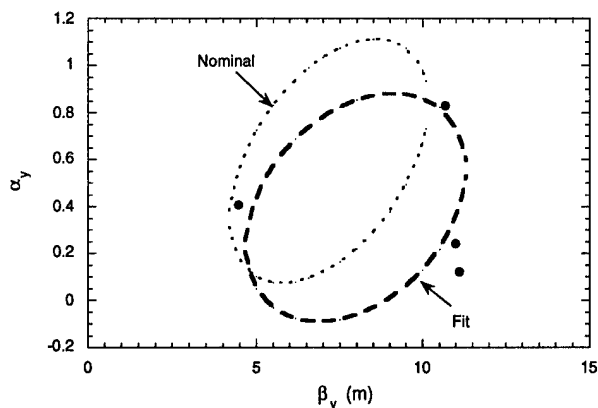


Figure 6. Locus of points for a vertical emittance growth of 10% due to mismatch.

Calculations for $\beta_{x0}=14.3$, $\alpha_{x0}=-.35$ and $\beta_{y0}=6.5$, $\alpha_{y0}=.54$ from the nominal accumulator model (dots) shows a disagreement with the data. A fit to the data (dashes) is also shown, again for $F=1.1$, with the modified parameters $\beta'_{x0}=9.3$, $\alpha'_{x0}=-.22$ and $\beta'_{y0}=7.3$, $\alpha'_{y0}=.36$. The disagreement between the nominal ellipse and the fit ellipse reveals residual errors in modeling the lattices of the transfer line and the two rings. The precise source of the disagreement is under investigation.

*Operated by the Universities Research Association Inc., under contract with the U.S. Department of Energy.

- [1] V. Chohan, F. Pederson, S. van der Meer, D.J. Williams, Proc. 1990 European Particle Accelerator Conference, Nice, p. 320.
- [2] M. Syphers and T. Sen, Notes on Amplitude Function Mismatch, SSCL-604 (1992).
- [3] D. A. Edwards and M. J. Syphers, An Introduction to the Physics of High Energy Accelerators, Wiley, 1993.

RESULTS FROM EXPERIMENTS OF CRYSTAL EXTRACTION OF 900 GEV PROTON BEAMS FROM THE TEVATRON COLLIDER¹

G. Jackson, D. Carrigan, D. Chen, C.T. Murphy

Fermi National Accelerator Laboratory², MS 345, P.O.Box 500, Batavia, IL 60510 USA

A. Bogacz, S. Ramachandran, J. Rhoades

University of California at Los Angeles, 405 Hilgard Ave, Los Angeles, CA 90024 USA

A. McManus

University of Virginia, Charlottesville, VA 22901, USA

S. Baker

Argonne National Laboratory, Cass Ave., Argonne, IL 60439 USA

ABSTRACT

The extraction of a small flux of primary protons from a collider in a parasitic manner is very attractive for a number of fixed target applications. The key requirements of the extracted beam are small average currents with relatively small temporal variations. At this time a bent crystal is installed in the Tevatron Collider which is designed to channel protons down an instrumented beam abort transfer line. In this paper the results of experiments with this crystal are presented. The impact on the high energy physics collider detectors of the crystal as a collimator and the transverse mechanism necessary to deposit the protons into the crystal for alignment purposes are described

I. OVERVIEW

The E853 experiment at Fermilab [3] is dedicated to studying the feasibility of extracting halo particles from a collider without inducing detrimental losses [4] in the dedicated high energy physics experiments. Since the installation of a bent crystal, studies have been aimed at aligning the crystal with respect to the beam. Extracted particles must negotiate a relatively narrow aperture to enter the C0 abort line in which scintillators, silicon, and fluorescence detectors are placed. In addition, a set of scintillators exist just downstream of the crystal itself.

II. Kick Mode Crystal Alignment

In order to determine the correct angle and position of the crystal with respect to the beam and the narrow extraction channel, beam was sent into the crystal via horizontal kicks from the E17 proton injection kicker. This form of crystal studies is referred to as kick mode [5]. The geometry of the kick mode experiments is sketched in figure 1.

It turns out that the polarity of the kicker is such that the sign of the beam position on the first beam pass of the crystal is radially inward, away from the crystal. Given the horizontal tune of the Tevatron (displayed in figure 2), the beam should impact the crystal on the second turn after the kick. Figure 3 contains the results of a calculation of the

phase space position of the kicked bunch at the crystal on successive turns. As a result, observing a loss monitor such as one of the scintillators just downstream of the crystal, nuclear interactions with the crystal should produce a modulated turn-by-turn loss pattern reflecting the position of the crystal at each turn and the scattering of particles on previous turns. Figure 4 contains a plot of the calculated loss pattern generated by a multiparticle computer simulation program.

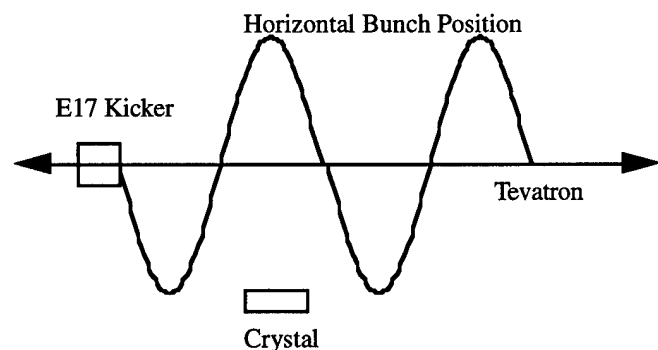


Figure 1: Sketch of the kick mode geometry for crystal extraction tests.

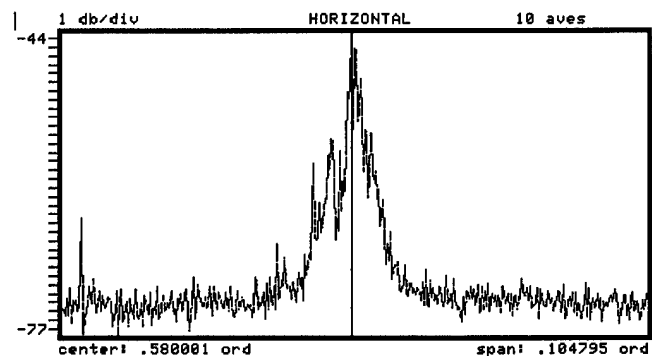


Figure 2: Horizontal betatron tune signal in the Tevatron during kick mode studies. The cursor is sitting at the tune 20.5795 and the full span of the plot is 0.1 units of tune. The vertical scale is 1 dB/div.

Figure 5 contains a close-up of the first few turns of the prediction plotted in figure 4. As expected, on the first turn

there is no signal and on the second turn the maximum signal is expected. This prediction should be compared with the measured data presented in figure 6, in which the beam was kicked by approximately 0.5 mm at 900 GeV. Note that the agreement is only qualitative.

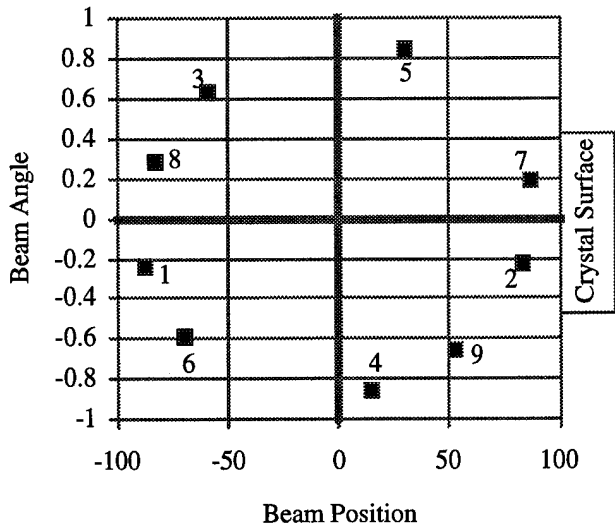


Figure 3: Calculation of the phase space position and angle (arbitrary units) of the beam at the crystal after being horizontally kicked by the E17 kicker magnet.

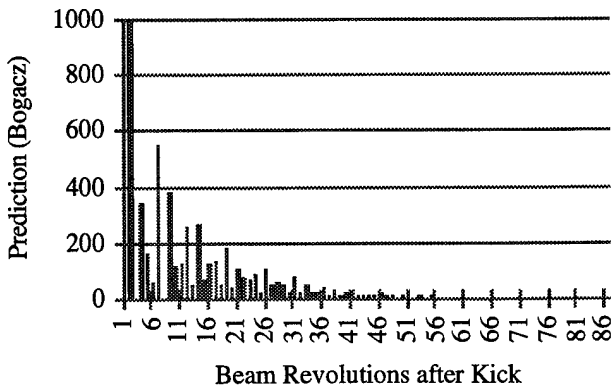


Figure 4: Predicted turn-by-turn losses in a proportional detector just downstream of the crystal.

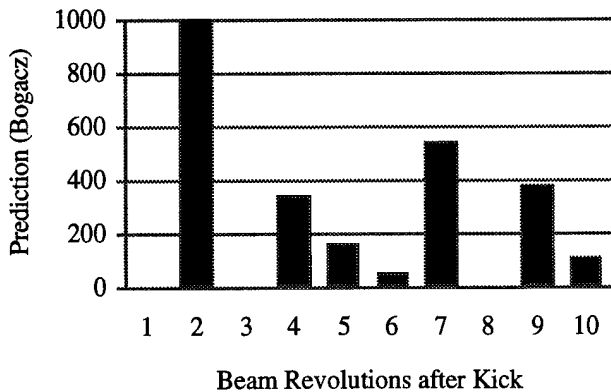


Figure 5: Close-up of the prediction presented in figure 4.

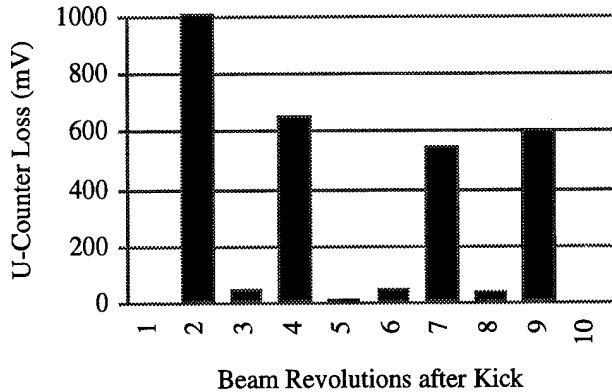


Figure 6: Particle shower amplitude in a scintillator just downstream of the crystal on the first 10 turns of the beam past the crystal after the beam kicker fired.

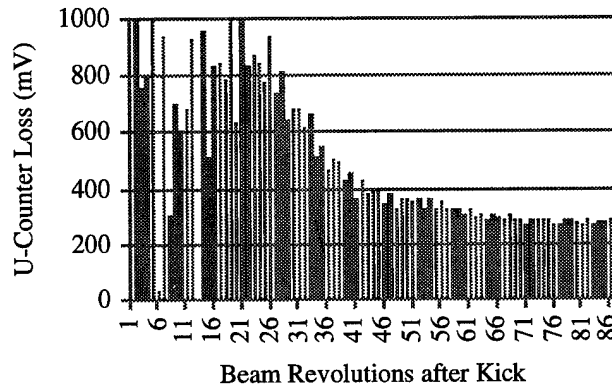


Figure 7: Expanded view of the observed data displayed in figure 6.

Another disagreement between calculation and observation can be seen by comparing figures 4 and 7. The long term evolution of the losses can sometime be completely different, with Tevatron losses just downstream of the crystal persisting for up to a minute. At other times there are no long term losses observed and the measured data trails off in a manner very similar to that calculated.

Attempts to observe channeled particles in the C0 extraction line have not been definitive to date. After a few short Tevatron study periods, in which kick mode scans of vertical crystal angle and position were executed, no clearly identifiable signal enhancement has been observed. On the other hand, a great number of strange and unexpected turn-by-turn loss profiles have been recorded.

For example, in a situation in which the output of a scintillator in the extraction line looks similar to the pattern displayed in figure 4, after about 50-70 turns the loss signal begins to grow again to approximately one third or one quarter of its original amplitude. This may be the effect of channeling particles which have been sufficiently scattered that their angles are sometimes big enough with respect to the closed orbit to correctly enter a misaligned crystal and be channeled out of the Tevatron.

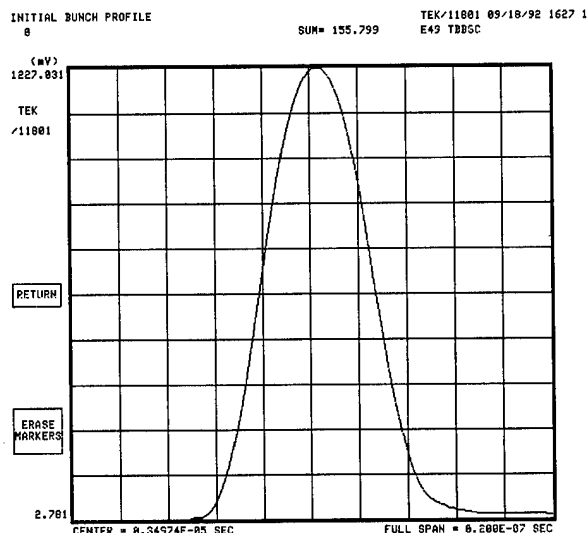


Figure 8: Longitudinal beam distribution as measured by a broadband resistive wall monitor and oscilloscope. The scale of the time axis is 2 nsec/div.

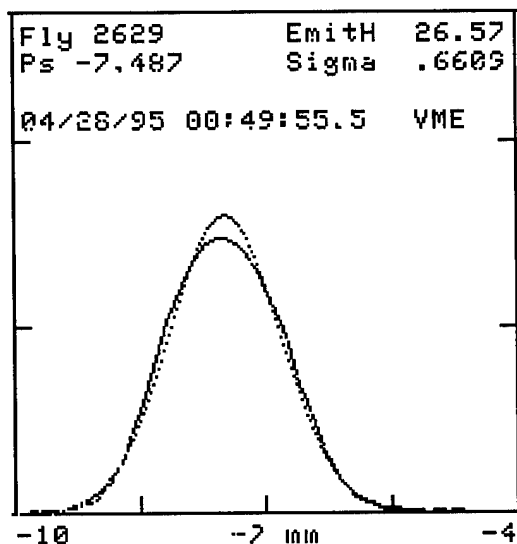


Figure 9: Original horizontal beam size at the E11 flying wire (0.66 mm) and emittance (26.57π mmmr 95% normalized) before the bunch has been kicked. At this time the vertical beam size at the E11 flying wire is 0.66 mm with an emittance of 32.5π mmmr.

Repeated attempts to measure any sign of channeled particles have proven fruitless. The present suspicion is that there is an aperture restriction somewhere in the extraction channel. At the same time, considerable effort is being directed toward better simulations. Some future improvements may include more accelerator effects such as Main Ring ramp induced Tevatron beam motion and horizontal-vertical coupling. To verify that the kicker is performing correctly, turn-by-turn beam position data and flying wire profiles of the beam were measured.

Figure 8 shows the longitudinal length of the bunch. Figures 9 and 10 document the amount of emittance growth that is suffered by the beam (vertical size is also measured by not shown) after a large number of kicks.

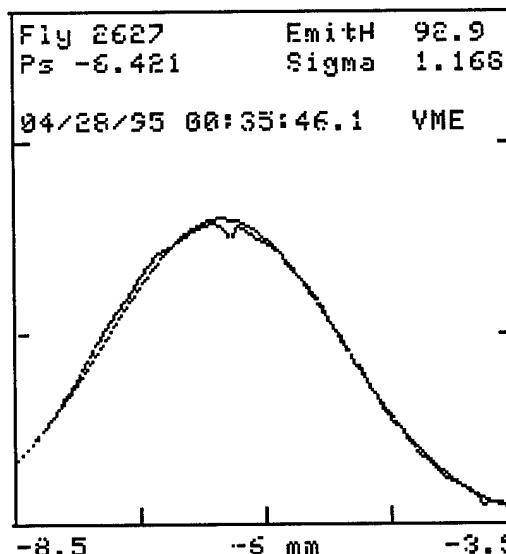


Figure 10: Horizontal beam size at the E11 flying wire (1.17 mm) and emittance (92.9π mmmr 95% normalized) after many kicks. At this time the vertical beam size at the E11 flying wire is 1.2 mm with an emittance of 109π mmmr.

III. Future Work

One of the leading problems with the present experimental configuration is the absence of a gated CCD array or camera monitoring the spatial distribution going down the extraction line. It is imperative that instrumentation suitable to accelerator physicists is given priority. In addition, a simulation which explains some of the mysterious patterns in the turn-by-turn data is needed.

IV. REFERENCES

- [1] Presented for the E853 Collaboration (Fermilab, U. Virginia, UCLA, Argonne, U. Texas at Austin, U. New Mexico, U. Wisconsin, CEBAF, SUNY at Albany, JINR at Dubna, IHEP at Serpukhov, and PNPI at Gatchina).
- [2] Operated by Universities Research Association Inc., under contract with the U.S. Department of Energy.
- [3] G. Jackson, "Extraction from the Fermilab Tevatron using Channeling with a Bent Crystal", Proc. 1993 Part. Acc. Conf. (Washington D.C.) 1366.
- [4] G. Jackson, "Results from Beam Diffusion and Collimation Measurements in Preparation for Fermilab Tevatron Crystal Extraction", Proc. 1993 Part. Acc. Conf. (Washington D.C.) 402.
- [5] S. Weisz and the RD22 Collaboration, "Proton Extraction from the CERN-SPS by a Bent Crystal", Proc. 1993 Part. Acc. Conf. (Washington D.C.) 26.

High Energy Beam Line Based on Bending Crystal

V.M. Biryukov, Yu.A. Chesnokov, V.N. Greth,
A.A. Ivanov, V.I. Kotov, V.S. Selesnev,
M.V. Tarakanov, V.I. Terekhov, S.V. Tsarik
IHEP Protvino, 142284 Moscow Region, Russia.

Abstract

The possibility of abrupt bending with crystal of a beam fraction at a large angle allows to organize over a short base a non-traditional beam line for carrying out the physical experiments. At IHEP, a 150 mrad bent crystal was used this way to create a test area, to work in parallel with other set-ups consuming practically no power.

I.

Nowadays bent single crystals of silicon are applied to control high-energy particle beams. As noted in [1] the feature of the beam bending with crystals is the independence of the crystal deflector strength $\Theta = L_D/R_c \sim 0.5$ rad of the particle energy (L_D is dechanneling length, R_c is the critical radius).

The possibility of abrupt bending with crystal of a beam fraction at a large angle allows to organize over a short base a non-traditional beam line for carrying out the physical experiments both in any operating accelerators and in any accelerators under construction.

At IHEP, a 150 mrad bent crystal was used this way to create a new test area. The scheme of the crystal beam line and experimental setup is shown in Fig.1.

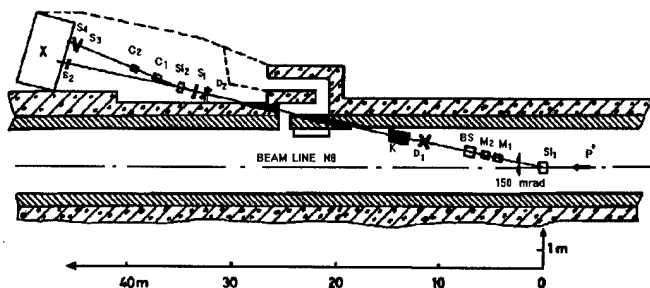


Figure 1. The scheme of crystal beam line and experimental setup: Si_1, Si_2 – deflecting and testing crystals, M_1, M_2 – corrector magnets, BS – beam stopper, D_1, D_2 – proportional chambers, K – collimator, $S_1 - S_4$ – scintillator counts, C1, C2 – microstrip detector stations, X – beam absorber.

A 100 mm long Si (110) crystal, placed on beam line N8 and inserted in the halo of the intense 70 GeV/c beam, has extracted 10^6 protons/sec beyond the 2-meter iron-concrete shield along the ~ 20 m base. Background particles emerging in the direction of a bending angle of the crystal are some tens lower on energy ($P_s \sim 3$ GeV/c) than primary protons. It is not difficult to subtract these secondary particles and it is done with two small corrector magnets M1 and M2, collimator K and a narrow collimation hole in the iron-concrete shield of the beam line. Hereat

the high quality of beam, low emittance and good stability, are achieved on the plane of the deflection ("band" beam).

In the first operating run of the new test area, the intensity of incident protons in beam line N8 was $2 \cdot 10^{11}$ p/c. About 10^{10} particles hit the crystal. In these conditions the number of particles bent with crystal and measured by the scintillator counters was $\sim 5 \cdot 10^5$ p/c. That is in accordance with a calculation. The orientation-independent component of the signal (background particles) from 10×10 cm² size counters did not exceed 3 % of the channeled beam. The profiles of the deflected beam measured by chamber D_2 are shown in Fig.2. The constructed test

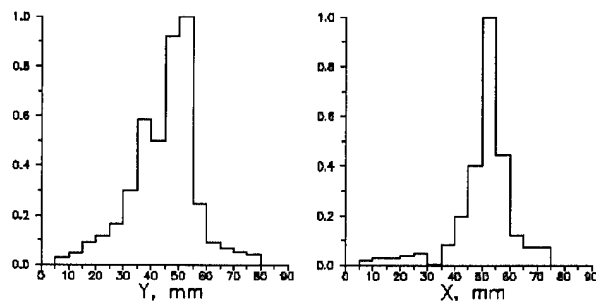


Figure 2. Profiles of beam in horizontal (x) and vertical (y) planes.

area will allow to continue the channeling experiments. In particular, it may be used for carrying out the programs on studying the channeling properties of the crystals, for increasing the efficiency of beam deflection and focusing, and for testing the microstrip detectors. Notice that channeled beams are very suitable for a microstrip detector calibrating because they have low emittance and high stability.

The new test area consumes practically no power. It allows to work in parallel with other beam lines without any influence on the work of the other physical set-ups.

This work was supported by the Russian Fund for Basic Research.

References

- [1] V.M. Biryukov, V.I. Kotov and Yu.A. Chesnokov, Physics–Uspekhi, 37 937 (1994)

Observation of the Influence of the Crystal Surface Defects on the Characteristics of the High Energy Particle Beam Deflected with a Bent Monocrystal

V.I. Baranov, V.M. Biryukov, Yu.A. Chesnokov,
V.I. Kotov, M.V. Tarakanov, S.V. Tsarik
IHEP Protvino, 142284 Moscow Region, Russia.

Abstract

Nowadays bent crystals are widely applied for high energy beam steering. Some problems, like the extraction of particles from a large hadron collider, imply a high perfection of the crystal near-surface layer. In this work we have measured precisely the profiles of the beam bent by crystal, with use of nuclear emulsions. The inefficient layer measured for several crystals is as thick as $\approx 50\mu\text{m}$. There was observed also a specific mosaics of crystals near the ends, which has led to the angular perturbations of the bent beam exceeding the critical angle of channeling.

I.

Nowadays the bent monocrystals are widely applied for high energy beam steering [1]. Experiments [2-4] have shown that deflection efficiency and dechanneling length for GeV particles are close to theoretical predictions, that is, silicon crystals in the bulk are close to ideal.

However, some problems like a particle extraction from a large hadron colliders, demand a high perfection of the near-surface layer of a crystal. The width of the layer inefficient for channeling, due to the crystal machining, affects the efficiency of particle extraction.

From measurements with X-ray diffraction it is known that the width of near-surface amorphous layer in good polished crystal does not exceed $\sim 1\mu\text{m}$. However, it is unknown so far, how efficient may be the channeling of high energy particles in the crystal layer adjacent to its surface. In the present work a direct measurement of the width of the unchanneling layer has been performed for several crystals of silicon and germanium. A specific kind of mosaicity near the crystal faces was observed, which lead to the angular perturbations of the bent beam in excess of the critical angle of channeling.

Precise measurement of the bent-beam profile was performed by use of a few layers of the nuclear photo emulsion, placed at different distances downstream of the crystal. The grain size (the track width) of the photoemulsion in use amounts about $\sim 0.5\mu\text{m}$, which is more than one order better than resolution of typical coordinate detectors (microstrips and drift chambers).

There were tested several crystals as long as $\sim 5\text{cm}$ of various thickness, from $300\mu\text{m}$ to 2mm , bent at the angles of $\sim 10 \div 20\text{ mrad}$. The miscut angle of the crystal slabs was less than 1 arc minute. The crystal bending was made with a well-known "Serpukhov" device [5]. The crystal ends had the long ($\sim 1\text{cm}$) straight parts to avoid deformation of faces caused by a bending stress. The incident protons had a divergence $\sim 1\text{ mrad}$ much greater than Lindhard angle to assure a uniform illumination of the crystal entrance.

The first tested crystal as thick as $700\mu\text{m}$ has shown a strange

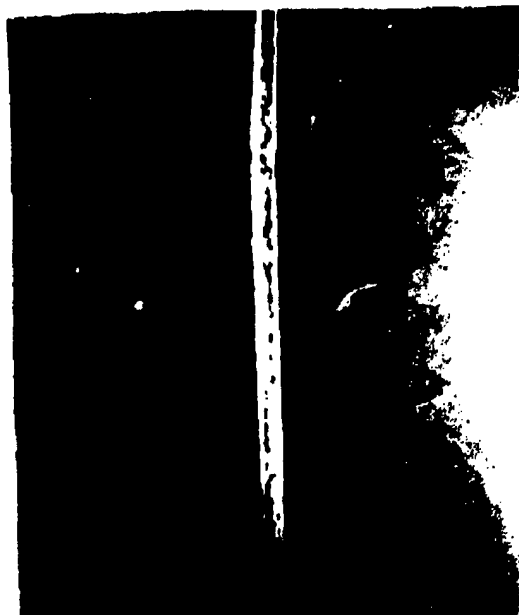


Figure. 1. The image the bent beam splitted in two parts (the distance from the crystal $\sim 0.5\text{m}$).

result: the bent beam was splitted in two parallel parts (see Fig.1).

By dividing the variables (changing the bending angle, varying the lengths of the crystal straight ends, modifying the shape of the crystal faces) it was discovered that the cause of the angular perturbations was an unflat shape of the crystal exit face, where the master has bevelled the edges on each side for his convenience.

The different shapes of a crystal end face (cross-section in the plane of beam bending), and the qualitative scheme of the particle emerged angles, reconstructed with the use of several emulsions were shown in Fig.2.

The analysis of beam profiles on emulsions has shown that the sharp bumps on the face cause the 70 GeV beam deflection at $\alpha \sim 1\text{ mrad}$. This indicates on the crystal lattice distortions at a depth $h \sim (3R_c) \times \alpha = 50\text{cm} \times 1\text{ mrad} = 0.5\text{mm}$. Here we adopt $(3R_c)$, the bending radius equal to the three critical ones, as the radius when an efficient channeling is possible (at smaller radii of planes deformation, the particles will be dechanneled and will not give such a correlated picture, as one sees from the figures).

The crystals with classic flat faces (Fig.2a) did not show such strong effects (except for the places of accidental breaks on edges to cause sizable distortions). Fig.3 shows the bent

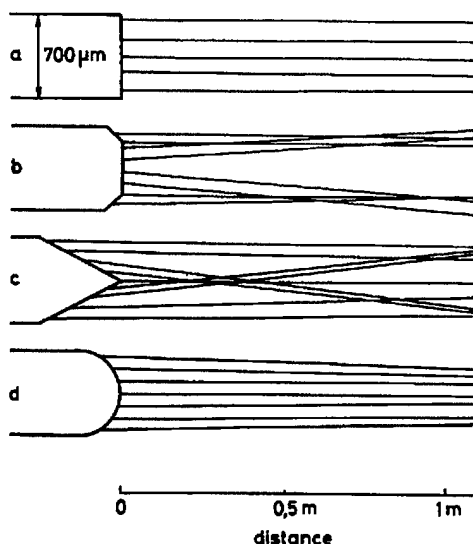


Figure 2. Demonstration of the "shape effect".

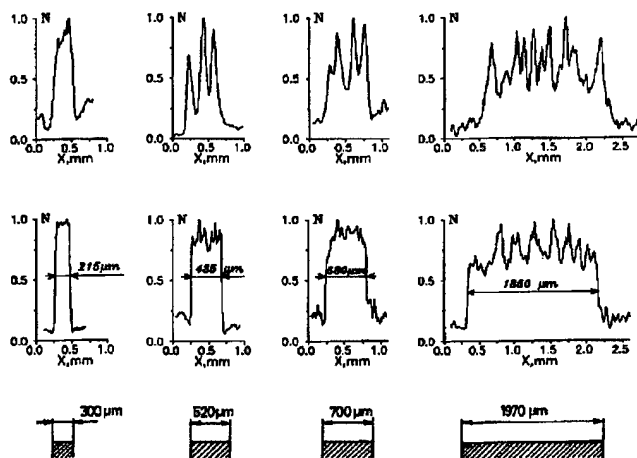


Figure 3. The bent-beam profiles for several crystals with flat end faces at the distance of ~ 15 cm (bottom) and ~ 1 m (top). The bottom part of the Figure shows also the corresponding thicknesses of crystals.

beam profile evolution downstream of the crystals. There are presented the data from emulsions positioned ~ 15 cm (bottom profiles) and ~ 1 m (top profiles) apart the flat exit faces of the crystals, developed by the microphotometer. The further development of the beam image on the emulsions, by counting the particle tracks directly under microscope, has shown that the beam borders are very sharp, $< 10 \mu\text{m}$, and its size is equal to the FWHM of the profiles handled by the microphotometer. From comparing the beam images on the nearest emulsions with the crystal thickness, it was found that all the tested crystals have a measurable unchanneling layer (see Table 1), which has the width in the range 40 to $60 \mu\text{m}$. (Notice that a loss of the useful cross-section due to the miscut angle was smaller than $\sim 10 \mu\text{m}$ on each side of crystal).

The channeled beam in the plane of bending had no appreciable angular distortion as in the case with an unflat faces, but it

was not ideally uniform, neither. At the distance of ~ 1 m from the crystal there was observed a fragmentation of the beam into separate zones as wide as $\sim 100 \mu\text{m}$ (see Fig.3 and 4a).

The observed angular distortions $\alpha \sim 100 \mu\text{rad}$ in this case are due to the lattice deformation at a depth of $h \sim (3R_c) \times (\sim 100 \mu\text{rad}) = 50 \mu\text{m}$ on the crystal end face. The visual image of typical fragmented beam in Fig.4a strongly reminds the character of the surface defects at the crystal face. The photograph of this face under microscope is shown in Fig.4b.

The side faces of the crystals were polished better (a surface roughness $< 0.05 \mu\text{m}$), but also had several cracks as wide as $\leq 1 \mu\text{m}$, like at the end faces. One may suppose that these cracks define the presence of an inefficient layer $\sim 50 \mu\text{m}$ observed in experiment.

We briefly conclude as follows. In the course of the studies we have observed:

A). The "shape effect", which is the fact that a nonflatness of the end face shape leads to a strong angular perturbation (much greater than Lindhard angle) of the beam downstream of the crystal. A convex surface leads to particle focusing, while a concave surface leads to defocusing. We emphasize that this effect, observed in bent crystals, is due to just the end face shape of a crystal, and does not depend on the crystal bending angle.

B). The effect of beam fragmentation, that is, of local angular perturbations of the beam of order of the critical angle of channeling, which occurs even at a flat face if the surface is polished with worse accuracy. On the background of local angular distortions, no global effects were seen, as opposed to the case of a nonflat face. It is not excluded that a violation of the plane parallelity may be present with a flat face also, as a result of an edge effect. This point requires a further study, since it is quite important for bending highly-parallel beams (for instance, for a beam extraction from supercolliders).

C). The presence of an unchanneling layer near the side faces $\sim 50 \mu\text{m}$, defined by the quality of the surface polishing.

Further investigation should show how far can the parameters of the bent beams be improved with a better accuracy of the surface polishing.

One should expect at higher energies ~ 1 TeV the beam fragmentation to be hardly seen, because the oscillation period of the channeled particle $\lambda \sim 100 \mu\text{m}$ starts to exceed the depth of the lattice deformation at a face of crystal. But the thickness of the inefficient layer may increase with energy.

As shown in [7], the problem of a non-zero inefficient layer is important for a crystal extraction of protons from a large hadron colliders.

The presence of an inefficient layer $\sim 50 \mu\text{m}$ may sizably decrease (by 50%) the efficiency of proton extraction from a multi-TeV collider; the layer with a thickness greater than a hundred μm reduces the efficiency by almost an order.

The authors express their gratitude to the experts of PNPI for production of the monocrystal slabs.

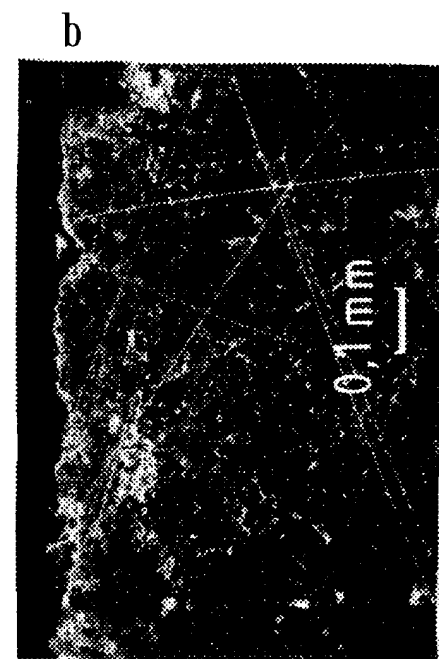
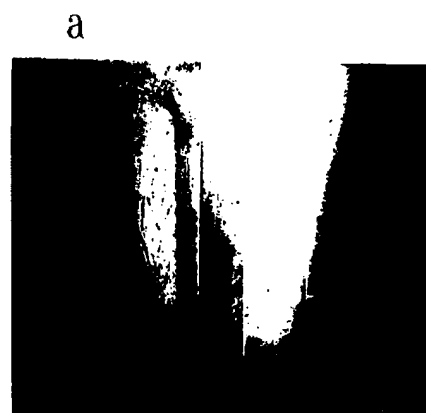
This work was supported by the Russian Fund for Basic Research.

References

- [1] V.M. Biryukov, V.I.Kotov and Yu.A. Chesnokov, Physics-Uspekhi, 37 937 (1994)

Table I
Characteristics of crystals and size of the bent beams.

Type of crystal	Length mm	Thick-ness μm	Beam size μm	Inefficient layer μm
Si(110)	25	300	215	42
Si(111)	30	520	435	42
Ge(110)	17	600	510	45
Si(111)	47	650	550	50
Si(111)	80	700	580	60
Si(111)	28	1970	1850	60



- [2] S.P. Møller et al, Nucl.Instr.and Meth, **B84** 434 (1994)
- [3] J.S.Forster et.al., Nucl. Phys. B318(1989) p.301
- [4] V.M. Biryukov et al, NIM B86 (1994) 245.
- [5] Yu.A. Chesnokov et al, proc. of 15 international conference on high energy accelerators.vol.1, p.173, Hamburg, 1992.
- [6] Denisov A.S. et al, Nucl. Instr. and Meth.,B69, p.382, 1992.
- [7] V.M.Biryukov, M.D.Bavizhev and E.N.Tsyganov. SSCL Report SSCL-N-776, October 1991.

Figure. 4. b)– The amplified-with-microscope photograph of the crystal flat end face for the thickness of 1970 μm . a)– The images of the beam bent with this crystal, at the distance ~ 1 m (bottom), and at ~ 0.5 m (top).

BEAM EXTRACTION WITH USING OF VOLUME REFLECTION EFFECT IN CRYSTALS

I.YAZYNIN, IHEP, PROTVINO, MOSCOW REGION, 142284, RUSSIA

Abstract

The new possibility of the slow beam extraction from circular accelerators with using effect of volume reflection is presented in this work. The analytical and computation calculations show that efficiency of such extraction for UNK1 may achieve $\sim 95\%$ for two techniques differing by various orientations of the nuclear planes with respect to the beam. Unlike of traditional extraction with the help of channeling effect it is not so critical for angle alignment, thermal overloading, availability of perfection of crystal lattice and surface.

I. INTRODUCTION

Tendency of application of bent monocrystal for a slow extraction of a beam from circular accelerators with using channeling effect of particles [1,2] was recently scheduled. Main difficulties of such extraction are necessity of exact angular position maintenance of a crystal concerning a beam and use of high purity monocrystal with an ideal surface. By use of volume reflection effect the adjustment and work of a system is simplified, as the efficiency of extraction does not practically depend on angular alignment of target and quality of monocrystal manufacturing.

In this work two variants of plate crystal arrangement concerning a beam are investigated. In first (fig.1(1)) particles of a beam are stepized normal to the nuclear planes, and in second in parallel (fig.1(2)).

As well as in case of conventional slow nonresonance extraction by a bump-magnets system or otherwise the particles of a beam are guided slowly to a target consisting from one or several bent monocrystal plates situated on a course of a beam. Deviating in a target on some angle the particles through some turns fall in a clearance of a septum and are extracted. During the extraction the part of particles leaves owing to their nuclear interactions with the crystal η_c , other fall on a septum partition η_s , and part put down on the equipment of accelerator η_a , that is

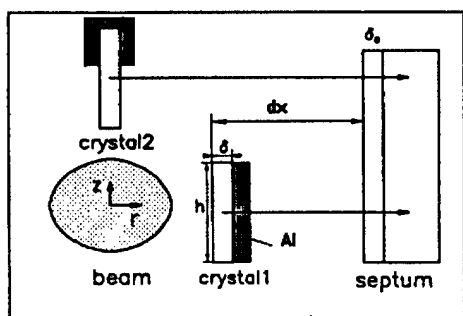


Figure. 1. The circuit of beam extraction for two variants of crystal arrangement.

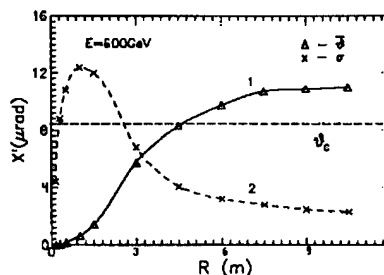


Figure. 2. Average angular deviation $\bar{\vartheta}$ (1) and root-mean-square scattering of protons σ (2) versus radius of curvature R of a crystal.

value of complete losses: $\eta = \eta_c + \eta_s + \eta_a$.

The optimum quantity of used crystals, from the view point of a losses minimum, depends on energy and sizes of a beam, thickness of a septum partition and longitudinal sizes of crystal.

We shall consider how volume reflection of particles in a bent monocrystal occurs. At hit of particles in a bent monocrystal body under the large angle to source nuclear planes they cross them so long as transverse energy will not become less than potential energy of nuclear plane eU_n , then they will be reflected from appropriate planes and will acquire a change of transverse energy $\Delta E < 2eU_n$. The average angular deviation of particles will be $\bar{\vartheta} < \sqrt{2} \cdot \vartheta_c$, and if on a course of a beam we shall put N bent plates, with radius of curvature considerably more than critical $\bar{\vartheta} \approx N \cdot \sqrt{2} \cdot \vartheta_c$. The dependencies of average angular deviation $\bar{\vartheta}$ (1) and root-mean-square scattering of protons σ (2) from radius of curvature R , received by the computer modeling at volume reflection of particles on the crystal Si(110), with the consideration of only nuclear planes potential, is indicated on fig.2.

The particles, which have the angle of fall with an external surface of bent monocrystal less than critical ϑ_c , will be reflected from it. Such particles at realization of a multiturn extraction will be less than 0.1%. The particles will be reflected from a crystal surface if size of impact parameter $\Delta < \vartheta_c^2 \cdot R$.

II. COMPUTER SIMULATION RESULTS OF EXTRACTION

The calculation of extraction was made with the help of program complex "SCRAPER" [3]. The trajectories of particles in a crystal were defined by the numerical decision of movement equations in field of bent nuclear planes in view of multiple Coulomb scattering on electrons and nucleuses, electromagnetic radiation and nuclear interactions. The movement of particles in an accelerator was simulated by matrix method. In computer experiment a halo proton beam is guided slowly toward the deflec-

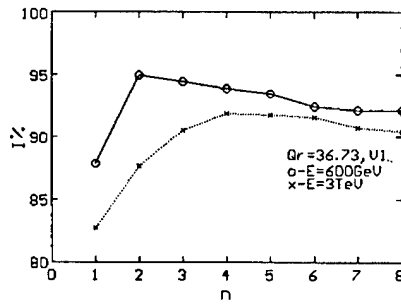


Figure 3. Extraction efficiency versus quantity of used crystals in the first variant.

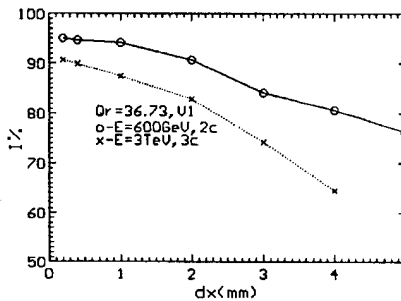


Figure 4. Extraction efficiency versus displacement of a septum in the first variant.

tor. Computer modeling of extraction process has shown, that the most optimum from the view point of minimization losses, to use 2-3 silicon crystals of long 5mm each for the first stage and 4-5 for the second (fig.3) by use of electrostatic septum with thickness of 0.2mm.

Calculated dependencies of extraction efficiency from the displacement dx of a crystal from a septum (fig.1) for the first and second variant are shown on fig.4 and 5. The target needs to be put closer to a septum as in this case average number of particle passages through it decreases, that is drops η_c and impact parameter of particles on a septum is increased, that results in decrease of losses on it.

The extraction efficiency is also influenced with frequency of betatron oscillations (fig.6 and 7).

The heaviest extraction efficiency occurs in a region of the betatron oscillations frequency $Q_r \simeq 0.7 - 0.73$.

It is explained by that the particles scattered on a crystal fall through 4 turns on a septum with a reasonably large impact parameter. The significant increase of losses near to resonance lines of the betatron oscillations $Q_r \times m = n$ is observed, that is explained by that of a scattered particle through n turns will get on a phase plane almost in a same place and the impact parameter of particles on a septum decreases.

III. TARGET HEATING

At slow guiding of a beam on a target almost all particles fall on forward edge of a crystal by thickness a few microns. Whereas the length of a target on a beam much less nuclear and radiating, the energy deposition density of proton dE/ds is insignificant and is weak depends on its energy and length of tar-

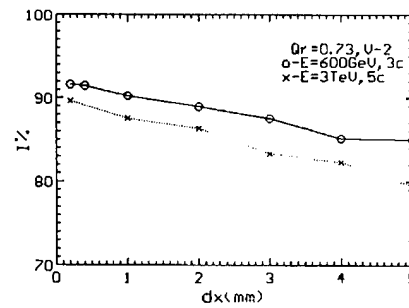


Figure 5. Extraction efficiency in the second variant.

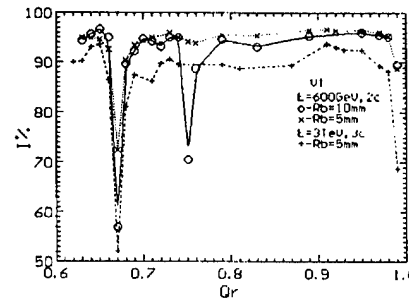


Figure 6. Extraction efficiency versus frequency of betatron oscillations in the first variant.

get. Escaped heat stationary spread over to lateral surfaces of a crystal and is removed through the holders or substrate (fig.1) in case of target.

The value of the energy released into the crystal during slow extraction can be estimated as $\Delta E = dE/ds \times \bar{N}_c$, where $I = I_0 \bar{N}$ is the number of protons hitting the front surface, \bar{N} - average number of proton passages through a crystal. If is not present heat removal, or in case of emergency at beam extraction for some dozens of turns, the heating of a crystal will be: $\Delta T = dE/ds \times \bar{N} I_0 / \rho C_p S$, where ρ and C_p - density and heat capacity of a crystal substance, S - its cross area. In our case the value $\bar{N} \simeq 1$ and if the total intensity beam $I = 6 \cdot 10^{14} p$ is dumped on crystal with $S = h \times \delta = 10 \times 2 mm^2$ its heating is $\Delta T \approx 1500^\circ C$ that is even more than the melting temperature, Si ($T_{mel} = 1410^\circ C$), where h is height of a crystal, δ is its thickness. That is in emergency it is necessary to provide a beam abort, that a large part of beam intensity to extract from accelerator before interaction it with target.

We shall assume, that the beam particles cross the area of a crystal face by the size $\approx 2z$ in regular intervals, where z is half-size of a beam in a cross plane perpendicular to output. Then for the first variant of extraction, in case of removals warm through a substrate, the heaviest heating will be on edge:

$$\Delta T = \frac{dE/ds \cdot I \delta}{2t\lambda z}, \quad (1)$$

Where λ - specific heat conductivity of a crystal.

Crystal Si (110) heat up to value $\Delta T \simeq 10^\circ C$, at an extraction of complete beam intensity from UNK1 ($z \approx 4 mm$) by duration

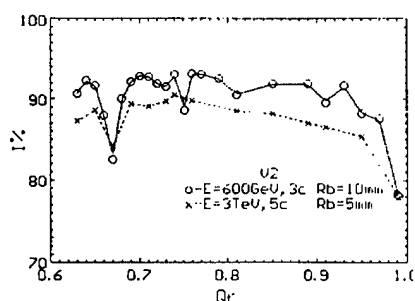


Figure. 7. Extraction efficiency versus frequency of betatron oscillations in the second variant.

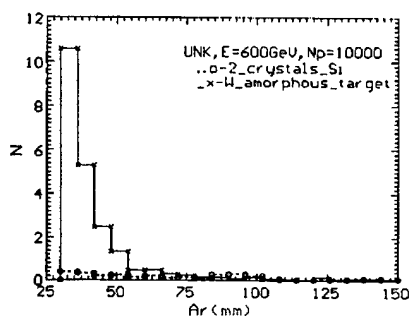


Figure. 8. The distribution of scattered protons on amplitudes on collimators and equipment.

$t=20$ second. In case of heat removal from lateral surfaces the value of a heating will increase in some times.

In the second variant of beam extraction, at good cooling of back surfaces of a crystal (fig.1), the heating as is insignificant - some dozens of degrees.

IV. ANOTHER USING

The effect of volume reflection in monocrystal can be used in a scraper system. Then by use of a bent crystal in as the scattering target the output of high energy protons from a system (target and scraper) can be reduced on the order, that it is very important in case of superconducting accelerator operation.

The appropriate distributions of protons on amplitudes, scattered from the system with Cu scraper and lost on the equipment and collimators UNK, are shown on fig.8.

V. CONCLUSION

Computer modeling has shown, that the efficiency of a beam extraction for UNK with use of volume reflection effect in the first variant of target arrangement will be $I \sim 95\%$ for the first and $\sim 90\%$ for the second stage, at effective thickness of a septum partition $\sigma = 0.2$. The losses of particles from the nuclear interactions in this case will be ~ 3 and 5% , and on septum partition less than 1 and 2% for first and second stage accordingly. At the second variant of a crystal arrangement the efficiency on some percents will be less than in first. Calculations have shown that by similar use of amorphous scattering target the total losses will increase more than in two times.

The heating of a crystal does not exceed some dozens of degrees at a beam extraction of complete intensity in twenty seconds.

References

- [1] A.V.Taratin et al., Nucl. Instr. and Meth., B58(1991) 103.
- [2] H.Akbari et al., CERN/SL/ 93-28 (DI).
- [3] I.I.Dyagterev, A.E.Lokhovitskiy, I.A.Yazynin, VI Russian conferences on radiation shielding of nuclear installations, Obninsk, 1994, v.3, page 218.

Use of a bent crystal for beam extraction in a slow extraction mode*

A.A.Asseev, M.Yu.Gorin

Institute for High Energy Physics

142284 Protvino, Moscow region, Russia

Abstract

A bent Si crystal placed before the first septum-magnet (SM-18) of the IHEP accelerator (A-70) available slow extraction scheme allowed one to extract, for physical experiments, a part of protons that used to be lost at the septum-magnet aperture boundaries in the non-resonant slow extraction mode. In this mode up to $3 \cdot 10^8$ protons were extracted additionally. This is about 10–30% of intensity extracted towards channel N°22 without the bent crystal. Use of unbent crystal as an amorphous target results in a decrease of the extracted beam intensity.

I. Introduction.

Nonresonant slow extraction (NRSE) of protons from the A-70 made it possible to carry on experiments with hadron beams for the experimental setups FODS-2, SWD and SPHINX [1–4] at extracted beam intensity of $10^6 \div 10^9$ protons per cycle (ppc) and duration of extraction by 2s. But for experiments with electron beams for setups FODS-2 and SWD higher intensity is desirable.

It turned, number of extracted particles can be increased with the bent Si crystal placed upstream of the SM-18. In distinction to the direct beam extraction regime (see, for example, [5]), possibilities of this mode prove an existence of other methods of using bent crystals to extract beams from high energy accelerators for physical experiments. In the article the scheme of extraction as well as the obtained results are presented.

II. The scheme of a beam jump over the septum.

The NRSE scheme is shown somewhere (see, for example, [2,3]). Necessary deflection of a circulating beam towards the septum-magnets is made by a local distortion (bump) of a closed orbit [6]. It is clear that part of a beam is lost on the septum of the SM-18 due to its finite thickness, while some of particles are lost on other septum-magnet aperture boundaries. It proved to be possible to diminish losses by means of a bent Si crystal of 3 cm long, 2 mm thick, bent by angle ~ 2.5 mrad along the (110) axis and placed at a distance about 40 cm upstream of the septum. Disposition of the septum-magnet and the bent crystal in the SS-18 is shown in fig.1.

This scheme, if the input end (a face) of a crystal is perpendicular to the circulating beam, would allow for particles, to hit the septum but proved to be captured into channeling, to get displacement for one passage

$$\Delta R_{CR} = L \cdot \Theta_{CR} \approx 1mm, \quad (1)$$

*The results presented in this work were obtained in part by Grant N°RMK000 from the International Science Foundation.

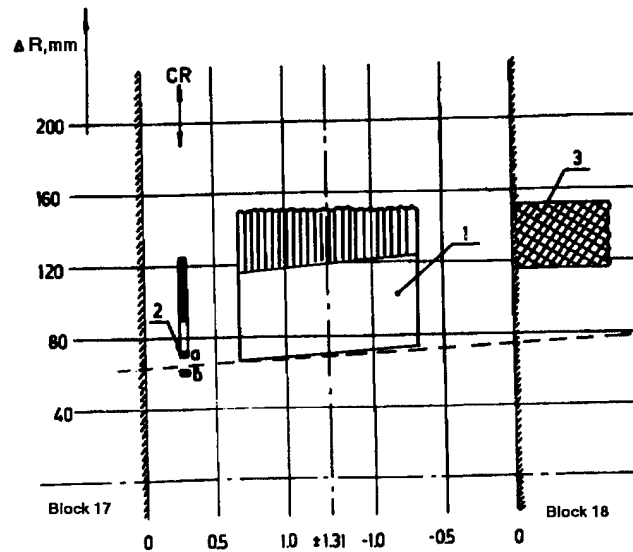


Figure. 1. Disposition of the septum-magnet and bent crystal. 1 is the SM-18 aperture, 2 is the crystal, 3 is nonlinear field zone of a magnetic block N°18; a and b mark the crystal position inside and outside of the septum, respectively. The vertical lines show the edges of magnetic blocks; a broken line is an injection beam envelope. A bender of a crystal is similar to that used in [5].

where L is a distance from crystal to septum-magnet along a closed orbit, Θ_{CR} is a crystal bend angle.

At thickness of the septum ~ 0.5 mm this displacement is enough for particles, going parallel to the septum and captured into a channeling mode, to jump into the SM-18 aperture. In our case the crystal was fixed with an angle to the central orbit ~ 4 mrad and, according to geometry of the experiment, there were no particles to be captured into channeling from the input end of a crystal (so called "end-face capture mechanism") and betatron amplitudes growth of which could become too large. The main mechanism to be responsible for capturing particles into channeling mode in our experiment was "a volume capture mechanism" opened in 1982 [7].

III. Experimental results.

Fig.2 shows dependence of number of particles extracted towards channel N°22 [4] versus position of the bent crystal from the centre of the accelerator vacuum chamber.

It is seen that, on moving the crystal towards the chamber centre, intensity of an extracted beam grows reaching a certain maximum. The intensity increase under this maximum reaches

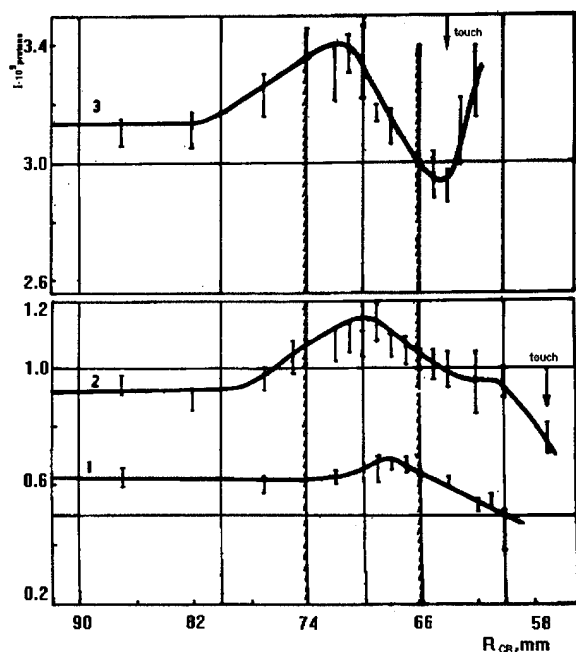


Figure. 2. Dependence of intensity, extracted into channel $N^{\circ}22$ versus the bent crystal coordinate. The curves 1, 2, 3 correspond to the different levels of extracted intensity. Coordinates of the input and output ends of the SM-18 septum are shown with the vertical dashed lines.

$\sim 3 \cdot 10^8$ protons that consists of $\sim 30\%$ at extraction of $\sim 9 \cdot 10^8$ ppc or $\sim 10\%$ at extracted beam intensity $\sim 3 \cdot 10^9$ ppc, respectively.

In order to make sure that the result obtained is due to the channeling effect and not a simple scattering of particles by the crystal as an amorphous target, analogous dependencies were taken for the unbent crystal placed on the same azimuth of the accelerator.

The essential difference of the crystal influence was seen. In the case of the bent crystal use, increase of intensity is seen already at coordinates $\sim 80 - 82$ mm that is $\sim 14 - 16$ mm from the septum inside the aperture. The unbent crystal does not give any intensity increase, providing only losses of particles interacting with it inside of the SM-18 aperture. The losses are increased when the crystal is being moved towards the input end of the septum. Further moving the crystal across the septum into the accelerator chamber results in additional losses of particles on external (oriented to the circulating beam) side of the septum with some intensity increase after touching by the crystal a denser part of a beam not to be scattered yet by targets. In this case a significant (by 1.5-2 times) shortening the spill of secondary particle beams extracted in parallel for other experiments was fixed.

IV. Discussion of results.

A. Beam extraction mechanism.

Two mechanisms of particles capturing into the channeling mode are known [8]: the end-face and volume ones, i.e. when particle trajectories are tangential to the crystallographic planes

at the face end or into the depth of a crystal, respectively. In the first case, number of particles of a certain energy to be captured into a channeling mode depends on the ratio of the critical channeling angle to the divergence of an incident beam ψ_c/Θ ; while in the second case it depends on capture probability $W(R)$ that is the function of a crystal bend radius.

Phenomenon of proton capture into the channeling mode in the depth of a bent crystal was shown experimentally in the 1 GeV region by the authors of the work [7]. Later this effect was proved in [9] at the proton energy 8.4 GeV. Existence of a volume capture at 70 GeV was experimentally proved in the work [10] where the data of a proton capture probability into the channeling mode versus a crystal bend radius are obtained. We will use data from [10] to explain the results of our experiment.

Though the internal target moving mechanism used does not allow to optimize a crystal orientation, the results of the experiment prove one more possibility of using bent crystals for extraction of particles from accelerators.

One can understand dependencies of fig.2 with help of fig.3 where the phase pictures (portraits) of the circulating unperturbed beam (1) and beam jumped into the SM-18 aperture (region 2) are shown. The regions of possible losses of the particles having various angles on the septum (3), of a crystal influence (4), a calculated acceptance of the extracting channel including the septum-magnets for our regime (5), a phase region (6) for particles underwent scattering in targets without septum-magnets are shown as well.

Increase of an extracted beam intensity that starts at the crystal coordinate ~ 80 mm (see fig.2) is due to transmission of particles by the crystal into region (5) of the extraction channel acceptance. Maximum of intensity reached at the crystal coordinates $\sim 70 - 72$ mm is due to deflection of a part of a beam, additionally jumped into SM-18 aperture, from a wall of the septum.

Decrease of an intensity growth determined by the channeling effect under moving the crystal towards the input end of the SM-18 can be explained as a miss of an extraction channel acceptance by deflected particles and loss of them on the septum at their multiple Coulomb scattering into the crystal.

If the crystal deepens into a beam outside the septum, protons that captured into a channeling mode can jump into the septum-magnet aperture only after having got a noticeable growth of a betatron amplitude and at the favourable phase on the following turns. On the "high" level of extracted intensity (curve 3 of fig.2) some growth of it is seen after touching a denser part of a beam by the crystal (marked with an arrow). Under this conditions a crystal, to be as an additional target, perturbs a beam scattering regime that results in shortening of a spill of extraction by 30-50%.

On the "low" level of intensity (curves 1, 2 of fig.2) when the denser part of a beam was moved from the septum by decrease of a bump strength, a crystal touches the beam on a larger distance from the septum (marked with an arrow on curve 2). Decrease of intensity before the septum in this case may be explained with particles loss into a crystal, to be as a target, during their multiple interaction. Growth of amplitudes of the particles, even to be captured into channeling mode, in this case

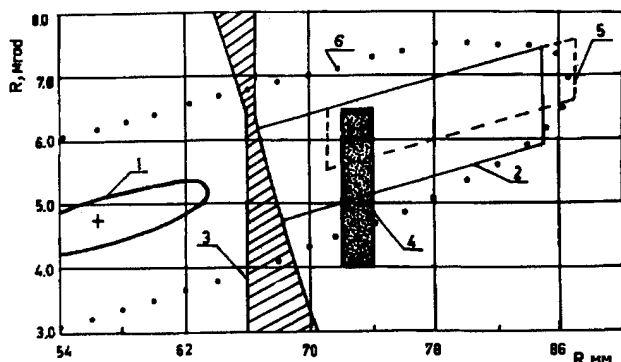


Figure 3. Illustration of a regime of a beam extraction by the bent crystal on the phase plane.

turns out not to be enough; such particles practically don't jump into an acceptance of the extraction channel.

In the case of an unbent crystal use the change of extracted intensity can be easily understood in a frame of consideration of a beam dynamics under its interaction with an ordinary target. Scattering a beam in a target has no influence, due to small scattering angles, on extraction intensity till a target comes into zone of the septum coordinates. There are some losses increase here because of hitting the septum by scattered particles that results in decreasing an extracted intensity. Only some intensity growth appears again when the crystal is nearer to the circulating beam than the septum and a denser part of the beam is being touched with it. But since the secondaries spill is being shortened in this case by 1.5–2 times, this regime does not valid for use.

B. Numerical estimations.

Estimations of intensity which one can extract using, in our scheme, a bent crystal placed before the first septum-magnet will be made for beam intensity onto an ordinary target 10^{12} ppc. It is known (see, for example, [1]) that 70–75% of particles make inelastic nuclear interactions with internal targets or to be lost on the accelerator chamber walls. The rest particles being underwent a multiple Coulomb scattering, ionization energy loss and nuclear elastic scattering continue their movement into accelerator gaining a noticeable growth of betatron amplitudes. Finally, one get the radial distribution of this particles at the point of a crystal placing that analogous to one shown in [3]. Evaluation show that at intensity $3 \cdot 10^{11}$ of particles under this curve about $1.2 \cdot 10^{10}$ of protons hit the crystal. Probability of a volume capture for our case calculated according to [10] equals about 1%.

So, in our scheme one can extract with help of a bent crystal additionally about $1.2 \cdot 10^8$ of particles at 10^{12} of protons interacting with a target. To obtain a sum of additionally extracted protons, that is well agreed with the experiment, one has to take into account that from 3 to 5 targets work simultaneously interacting with primary beam of total intensity up to $2.5 \cdot 10^{12}$ protons every accelerator cycle [1].

V. Conclusion.

A bent crystal placed before the first septum-magnet of the A-70 slow extraction system made it possible to extract additionally up to $3 \cdot 10^8$ protons, used to be lost on septa, towards channel $N^{\circ}22$ in parallel to the work of a few internal targets generating secondaries for other experiments. A relative growth of extracted proton beam intensity depending on an extraction regime was 10–30%. Capturing of particles into the crystal channeling mode was due to the volume capture mechanism.

The main advantage [10] of the volume capture in comparison with the end-face one is that no precise alignment of the crystal is necessary (one can do without a goniometer). Besides, the volume capture may be more effective for the beam of a large divergence [8].

The regime of extraction obtained may be used when planning experiments for channels $N^{\circ}22,23$. The effect of increasing an extracted beam intensity when using a bent crystal in this scheme, apparently, to be magnified by introducing a goniometer to make an optimal angle relations between the crystal, the beam and septum-magnet.

References

- [1] Yu.M.Ado et al., IHEP 85-23, Serpukhov, 1985.
- [2] A.A.Asseev et al., Journ. of Tech. Phys., v.60, $N^{\circ}9(1990)70$, Leningrad.
- [3] A.A.Asseev et al., Proceed. of the 2-nd European Part. Accel. Conf., Nice, 1990, v.2, p.1604.
- [4] A.A.Asseev et al., Proceed. of the 3-d European Part. Accel. Conf., Berlin, 1992, v.2, p.1486.
- [5] A.A.Asseev et al., Nucl. Instr. and Meth., A309(1991)1-4.
- [6] A.A.Asseev et al., IHEP 91-17, Protvino, 1991.
- [7] V.A.Andreev et al., Letters to JETP, v.36, $N^{\circ}9(1982)340$.
- [8] N.A.Galyaev et al., Proceed. of the IEEE Part. Accel. Conf., San Francisco, 1991, v.1, p.192.
- [9] N.K.Bulgakov et al., Communications of JINR $N^{\circ}1-83-725$, Dubna, 1983.
- [10] N.A.Galyaev et al., IHEP 90-147, Protvino, 1990.

Computer Simulation of the Tevatron Crystal Extraction Experiment

Valery Biryukov*

IHEP Protvino, 142284 Moscow Region, Russia

Abstract

The Fermilab crystal-extraction experiment E853 at Tevatron was simulated by Monte Carlo code CATCH [1] tested earlier in the CERN-SPS experiment [2–4]. Predictions for the extraction efficiency, angular scans and extracted beam profiles are presented. Several ideas are proposed and tested by the simulation, how to get in E853 the key information of the extraction experiment: the "septum width" of a crystal and dependence of extraction efficiency on it, the impact parameters of protons at crystal, and the contribution of the first and multi passes to the extraction. The ways to optimize E853 are analyzed.

I. Introduction

The crystal-extraction experiments at CERN SPS [2–4] and Fermilab Tevatron [5] have in view possible application of channeling for proton extraction from a multi-TeV machine [6]. The technique employs a bent crystal placed in the beam halo, which traps and bends the particles parallel to the crystallographic plane within Lindhard angle θ_c . The halo particles hit a crystal very close to its edge, with impact parameter b in the range $\sim \text{\AA}$ to $\sim \mu\text{m}$. This calls for a good perfection of the crystal edge. Alternatively, one should investigate how crystal extracts particles in the multipass mode, which involves several scatterings in the crystal of the circulating particles.

As the extraction includes many passes, there is no easy way to extrapolate the results with energy. This makes the detailed comparison of the measurements with computer simulation essential. Such an analysis made [7] for the CERN-SPS experiment has shown good agreement of the theory with measurements [2,3]. The major result of [7] was a prediction of the edge imperfection of the crystals used at SPS. The new SPS experiment, employing a crystal with an amorphous edge-layer to testify this idea, has proved much the same efficiency indeed [4]. Another prediction, made for the "U-shaped" crystal – much the same efficiency but narrow (70 μrad *fwhm*) angular scan[7] – has also been confirmed [3]. With the simulation code [1] tested at SPS, here we model the extraction of 900-GeV protons from Tevatron, matching E853 [5,8].

The real crystal has an irregularity of the surface, which defines a range of inefficient b at the edge ("septum width" t). The following information is essential for understanding the crystal extraction process:

(a) efficiency F , and contributions to it from the first/multi passes; (b) distribution over b at the crystal; (c) septum width t ; (d) dependence $F(t)$.

We propose the ways to get this information in E853.

II. Qualitative discussion

The essential feature of E853 is the fact that the crystal atomic planes are perpendicular to the crystal face in touch with the beam. In E853 one should align a crystal in 2 planes: the channeling plane (vertical, y) with the accuracy of θ_c , and the horizontal plane (x) to keep the crystal face parallel to the incident protons (Fig. 1). At first glance, the need to tune two angles is an inconvenience. Here we show that this extra degree of freedom is an excellent possibility to study extraction in many details!

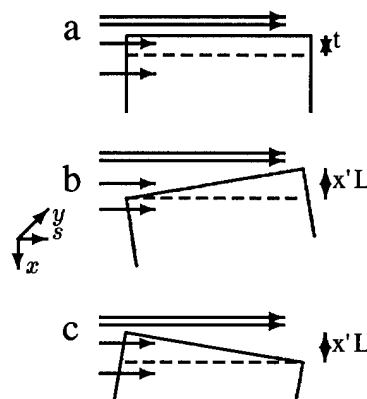


Figure 1. Horizontally tilted crystal: (a) aligned, (b) tilt $x' > 0$, (c) $x' < 0$.

Consider a crystal disaligned from the beam horizontally at x' . Depending on the sign of x' , either the upstream end approaches the beam (we define $x' < 0$), or the downstream one ($x' > 0$); fig. 1. Because of x' , a septum width as thick as $t = |x'|L$ occurs at the crystal edge; L is the crystal length (4 cm in E853). Protons incident in the range $0 < b < t$ do not traverse the full length of crystal. The result depends dramatically on x' sign.

In case of $x' > 0$, protons traverse the downstream edge. It is disaligned by ~ 0.64 mrad (the bending angle) w.r.t. the beam. Therefore, protons traverse it like an amorphous substance. This case imitates a crystal with an amorphous near-surface layer as wide as $t \approx x'L$. Measuring $F(x')$ for $x' > 0$, one measures $F(t)$. Theory [9] predicts very weak $F(t)$ dependence at high energies. The confirmation would be encouraging for the multi-TeV crystal extraction. Notice that the step of t scan could be very fine: with $\delta x' = 2.5 \mu\text{rad}$ and $L = 4$ cm one has $\delta t = 0.1 \mu\text{m}$.

In case of $x' < 0$, protons traverse the upstream edge which is aligned w.r.t. the beam. Therefore, many particles are trapped in channeling. However, those incident in the range $0 < b < x'L$ traverse a reduced (< 4 cm) length, thus getting a reduced (< 0.64 mrad) deflection and therefore are lost. The inequality of two cases, $x' > 0$ and $x' < 0$, causes a strong asymmetry of $F(x')$ dependence. The difference $\Delta F = F(x') - F(-x')$ is proportional to the number of protons incident with $0 < b < x'L$. Varying x'

*E-mail: biryukov@mx.ihep.ru

and observing ΔF , one investigates the distribution over b at crystal, with accuracy of $\delta b = 0.1 \mu\text{m}$.

This is complicated by another interesting phenomenon. The protons incident on an aligned imperfect crystal with $b_{\text{max}} < t$, have to traverse the full length of the crystal, and to experience a substantial nuclear scattering. Suppose, this crystal is disaligned so that $b_{\text{max}}/x'L \approx 0.1$. Then at first incidence the protons traverse only the crystal edge, with the "length" ≤ 0.1 that of crystal. The respective scattering and losses over $0.1L$ are much smaller. In this case the protons retain better chances for extraction with later passes than in the former case (perfect alignment). The secondary b of the scattered protons are still sufficiently large ($\approx 30 \mu\text{m} \gg x'L$ here), so the "gap" $x'L$ is not dangerous.

We come to conclusion that a peak efficiency with *imperfect* crystal is achieved at some tilt $x' \neq 0$. In the real experiment one scans x' while searching the peak, and comes to this case *automatically*. We used the case $b_{\text{max}}/x'L = 0.1$ as an illustration; the optimal x' will be found automatically in the scan. Further on, we refer to this case as to the "pre-scatter" case, when protons first gently pre-scatter in the crystal edge to come later with low divergence but high b . Understandably, with imperfect crystal the prescatter case may appear also for a small negative tilt, $x' < 0$. Then, $F(x')$ may have *two* peaks, with a *dip* at $x'=0$. The width of the dip at $x' \approx 0$ is also an indicator for b_{max} .

III. Simulation procedure

The crystal was located 61 m upstream of C0 point of Tevatron lattice, with the edge at the horizontal distance of $X = 1.75 \text{ mm}$ from the beam axis. At the crystal location, the machine parameters were $\beta_x = 105.7 \text{ m}$, $\alpha_x = 0.109$ (horizontally), and $\beta_y = 21.5 \text{ m}$, $\alpha_y = 0.148$ (vertically); tunes $Q_x = 20.5853$ and $Q_y = 20.5744$. The beam invariant rms emittance was 2.5 mm-mrad , which corresponds to vertical rms divergence $11.5 \mu\text{rad}$ and width 0.24 mm at the crystal location.

Crystal was a Si(110) slab 40 by 3 by 3 mm^3 , 0.64 mrad bent, with a perfect lattice, and curved with a constant curvature to deflect protons in vertical direction. As an option, we model an amorphous layer at its edge and/or irregularities of the surface. The horizontal parameters x, x' of incident particles are defined by the mechanism of diffusion. The two processes, diffusion and crystal extraction, are unfold in E853. Beam parameters in the channeling plane (vertical) are not disturbed by the diffusion. The exact value of b_{max} matters only w.r.t. t . Since t is unknown for the real crystal, we can postulate $b_{\text{max}} = 1 \mu\text{m}$, and then model crystals with different t .

IV. Results

Fig. 2 shows the $F(y')$ angular scan for $x'=0$. The peak F of an ideal crystal is $\approx 44\%$. The same fig. shows scans for the crystals with $t = 1 \mu\text{m}$ (i.e. $t = b_{\text{max}}$) and $t = 50 \mu\text{m}$, where at $y'=x'=0$ $F \approx 36\%$ and 32% respectively. However, for the imperfect crystals the real peak was found at $x' \neq 0$ (Fig. 3). With optimized x' , one has peak $F \approx 42\%$ and 35% for $t = 1 \mu\text{m}$ and $t = 50 \mu\text{m}$ respectively. Notably, the efficiencies and scans are quite weakly dependent on the crystal perfection. The width of y' scan was $50\text{--}55 \mu\text{rad}$ *fwhm* in these cases.

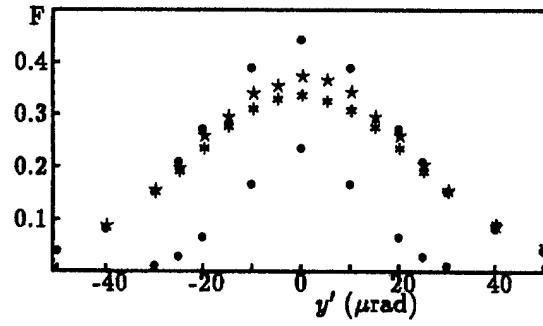


Figure 2. $F(y')$ scan for $x'=0$. Ideal crystal: (o) first-pass and (•) overall efficiencies. Imperfect crystal: overall efficiency with $t = 1 \mu\text{m}$ (*) and $t = 50 \mu\text{m}$ (x).

The angular scan $F(x')$ is in Fig. 3. The depth of the dip at $x' \approx 0$ (i.e. at perfect alignment) is $\approx 14\%$ and $\approx 7\%$ w.r.t. the peak for $t = 1 \mu\text{m}$ and $t = 50 \mu\text{m}$ respectively. The width $\Delta x'$ of the peculiarity (either peak or dip) near $x' \approx 0$ is roughly b_{max}/L which is $25 \mu\text{rad}$ in our simulation. F is $1/2$ of the

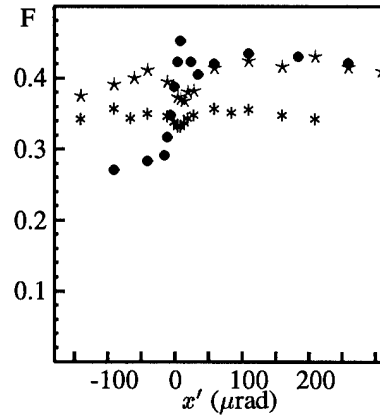


Figure 3. $F(x')$ scan near the peak; see fig.2 caption.

maximum at $x' \approx 14 \text{ mrad}$ and -0.3 mrad for an ideal crystal (*fwhm* of the horizontal scan is $\approx 14 \text{ mrad}$), at $x' \approx 15 \text{ mrad}$ and -1.2 mrad for the crystal with $t = 1 \mu\text{m}$ (*fwhm* $\approx 16 \text{ mrad}$), and at $x' \approx 18 \text{ mrad}$ and -5 mrad for the crystal with $t = 50 \mu\text{m}$ (*fwhm* $\approx 23 \text{ mrad}$).

The asymmetry of the scan, $F(x') \neq F(-x')$, is due to the loss of the protons trapped in channeling near the crystal edge. With an ideal crystal, the asymmetry exists for any x' . With a septum width t , the asymmetry can be seen for an angling $\pm x'$ larger than t/L only. In our simulation with $t = 50 \mu\text{m}$, the scan is symmetric indeed within $\pm 1.3 \text{ mrad}$ but asymmetric outside this range of x' ; note that $50 \mu\text{m}/40 \text{ mm} = 1.25 \text{ mrad}$. We expect therefore this x' -threshold for an asymmetry to be a good measure of the septum width t . If one plots the magnitude of asymmetry, $F(x') - F(-x')$, as a function of $x'L$, he obtains a rough estimate of the beam distribution over b at crystal. The minimal step $\delta b = \delta x'L = 0.1 \mu\text{m}$ is much finer than the precision of coordinate detectors $\approx 0.1 \text{ mm}$!

Notice an abrupt decrease in F of the ideal crystal over the range of $x'L$ from 0 to $-b_{\text{max}}$: from 44% at $x'=0$ to 28% at $x' = -b_{\text{max}}/L$. This drop is an excellent opportunity to measure

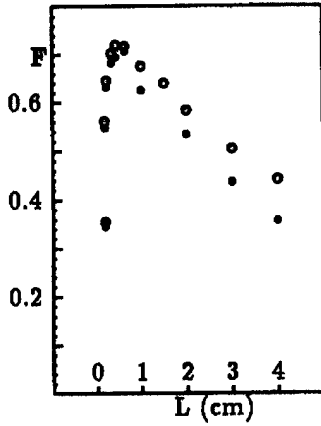


Figure 4. $F(L)$ for ideal (o) and $t=1 \mu\text{m}$ (•) crystals.

the primary b_{max} with a precision of $\delta b=0.1 \mu\text{m}$. With an ideal crystal one can measure a distribution over the *primary* b (in the range of $\sim 1 \mu\text{m}$). With imperfect crystal in the same way one measures the distribution over *secondary* b (in a broad range from $\sim t$ to $\sim 1 \text{ mm}$). Finally, the dependence $F(x')$ for $x' > 0$ gives actually the dependence of F on the septum width $t \simeq x' L$.

The distribution of the extracted particles over x at the crystal face is essential for understanding both the crystal interplay with other accelerator elements and the requirements for the crystal face perfection. We have found that one half of the extracted protons have penetrated into the crystal depth by $> 0.3 \text{ mm}$; another half had $b < 0.3 \text{ mm}$. The y' divergence of the extracted beam was defined by the channeling properties of Si(110) crystal; its full width $2\theta_c$ was $\approx 12.8 \mu\text{rad}$ ($\theta_c \approx 6.4 \mu\text{rad}$), and $fwhm \approx 9 \mu\text{rad}$. The x' divergence was $\approx 5 \mu\text{rad}$ $fwhm$ with the ideal crystal and $\sim 12 \mu\text{rad}$ $fwhm$ with $t=1 \mu\text{m}$. It was increased due to scattering in inefficient passes. After the doublet of quadrupoles and the Lambertson-type magnet, two detectors (hodoscopes with 0.1 mm bins) were placed at 80.5 m (D1) and 120.5 m (D2) downstream of the crystal to measure the bent-beam profiles. The horizontal profiles had width ≈ 0.3 and 0.4 mm $fwhm$ for the ideal and $t=1 \mu\text{m}$ crystals at D1, and ≈ 0.5 and $0.7\text{--}0.9 \text{ mm}$ $fwhm$ at D2.

V. Optimization

The extraction efficiency F is defined by the processes of channeling, scattering, and nuclear interaction in crystal. All the processes depend essentially on the crystal length L . Fig. 4 shows $F(L)$. F is maximal, near 70 %, in L range $0.4\text{--}1.0 \text{ cm}$, irrespective of the crystal perfection.

VI. Conclusions

The key information of the multi-pass crystal extraction can be obtained from the analysis of the horizontal angular scan of efficiency. In the considered way one can study the impact parameters of halo particles and the structure of the crystal edge with an accuracy as fine as $0.1 \mu\text{m}$.

The extraction efficiency is expected as high as $\approx 40 \%$ irrespective of the crystal septum width, and can be increased up to $\sim 70 \%$ with the use of a shorter ($\leq 1 \text{ cm}$) crystal. The dif-

ference in efficiency between the ideal and imperfect crystals is very low, because of predominance of the multi-passes in extraction at high energies, and partly due to the found effect of a gentle "prescattering" in the edge of a crystal tilted horizontally. This provides an elementary solution to the problem of a finite septum width and infinitesimal impact parameters.

One general trend in the results of simulations, from SPS [7] to Tevatron to LHC [6], is worthwhile to mention: the difference in efficiency of the ideal crystal and crystal with imperfect surface vanishes with energy E , because the scattering angle reduces faster ($\sim 1/E$) than θ_c does ($\sim 1/\sqrt{E}$).

References

- [1] V. Biryukov, *Phys. Rev. E* **51** 3522 (1995)
"CATCH 1.4 User Guide", CERN SL/Note 93-74 (AP)
- [2] H. Akbari et al., *Phys. Lett.* **B313** 491 (1993)
- [3] F. Ferroni et al., *NIM A* **351** 183 (1994)
- [4] B. Dehning et al., to be published (1995)
- [5] R.A. Carrigan, Jr. et al., *NIM B* **90** 128 (1994)
- [6] V. Biryukov, *Phys. Rev. Lett.* **74** 2471 (1995)
- [7] V. Biryukov, CERN SL/Note 93-78 (AP), 1993
- [8] C.T. Murphy, N.V. Mokhov, private communication
- [9] V.M. Biryukov, M.D. Bavizhev, E.N. Tsyganov, SSCL-N-776 (1991)

PEP-II Magnet Power Conversion Systems*

L.T. Jackson, Lawrence Berkeley Laboratory, A.H. Saab, Stanford Linear Accelerator Center,
and D.W. Shimer, Lawrence Livermore National Laboratory

Abstract

The paper presents the cooperative design efforts of LBL, LLNL and SLAC on the Magnet Power Conversion Systems for PEP-II. The systems include 900 channels of correction magnets bipolar power supplies and 400 unipolar power supplies in the range of 5 to 500 kW. We show the decision process and technical considerations influencing the choice of power supply technologies employed. We also show the development of specifications that take maximum advantage of both the available resources and existing facilities while, at the same time, satisfying tight constraints for cost control, scheduling and coordination of different working groups. Switchmode power conversion techniques will be used extensively in these systems, from the corrector supplies to the largest units if the dynamic performance specifications demand it. General systems descriptions for each of the power supply ranges and for a new common control systems interface are included.

WORK DIVISION - A TALE OF THREE LABS

The PEP-II B factory accelerator complex is being built at SLAC as a cooperative effort among the three DOE laboratories in the SF Bay area: LBL, SLAC and LLNL. The Magnet Power Conversion is one of the areas that because of its relatively large size, diversity of systems and technical complexity requires a close cooperation among the three technical groups involved in the design and construction of this part of the machine.

To implement this kind of cooperation an agreement was achieved very early on in the process by the engineering group leaders, based on the optimal utilization of the talent pool, recent experience and hardware developments at each one of the laboratories, facilities and other technical resources and the project schedule. Of particular concern were the overall cost, the expected performance of the systems and their maintainability.

One important issue that influenced the initial decisions on work division was the need to maximize the uniformity of systems (i.e. all power supplies of a similar power level must be of the same technology and manufacture) to reduce the impact of personnel training in new systems and the cost of the stock of spare components and redundant on-line systems. For this reason the division of work for the Power Conversion Systems splits along different lines than the overall machine division of work which goes along ring lines. SLAC Power Conversion Department carries the leadership in the generation of the

specifications for the systems since, by the end of the project, SLAC will be the laboratory operating the machine.

Resolution	
Setting & readback	18 bits
Accuracy (1 yr)	
Setting & readback	.01% FSR
Long term stability (10 C span)	
Single channel P.S.	.005% FSR
Periodic deviations (60 Hz & harm., LF noise)	
Single channel PS	.01% FSR
Random deviations (AC line changes)	
SCR P.S.(w/fast V feedback)	<.05% FSR
Switching P.S	<.01% FSR

Table 1- P.S. & controller/interface performance specs.

SYSTEMS DESCRIPTION

PEP-II is being built reusing the old tunnel and a large portion of the equipment (cable plant, power distribution, civil construction) of PEP-I (Ref. 4). PEP-II will need 21 power supply systems for the large strings (Group III, LLNL), circuits for magnets distributed around the 2 Km circumference of the machine. It will also need 244 medium power power supplies (Group II, SLAC) to drive individual magnets and short strings, composed of two or three series magnets in relatively near locations, and 37 power supplies of medium to high power (Group II, LBL), mostly one or two of a kind systems. In addition it requires somewhere between 900- 1000 power supply channels for correctors and trim coils (LBL).

POWER SUPPLY SYSTEM ENGINEERING

The sytem design uses two general architectures, one for multiple channel power supplies, employed for the small drivers for correctors and trims, and the single channel, for everything else. The single channel power supply system is a design very similar to units in use at SLAC (Ref 1). It consists of a voltage regulated /voltage controlled power supply as its power train, driven by a current regulation loop with a high stability (<2ppm/C) error amplifier. The current regulation loop workpoint is set by an analog reference generated by the control system interface. Current is measured by two identical ZFTs (Zero Flux Transductor) integrated type (magnetic head

* Supported by U.S.Department of Energy under Contract numbers DE-AC03-76SF00098 (LBL), DE-AC03-76SF00515 (SLAC) and W-7505-Eng-48 (LLNL).

and electronics on the same package) transducers. One of the ZFTs is used for the control of the magnet current through the current regulation loop, and the other one as an independent diagnostic readback. The system has a single fault ground fault detector. The multiple channel systems have similar features, in different implementations, as described elsewhere in another paper in the Proceedings of this Conference (Ref 3).

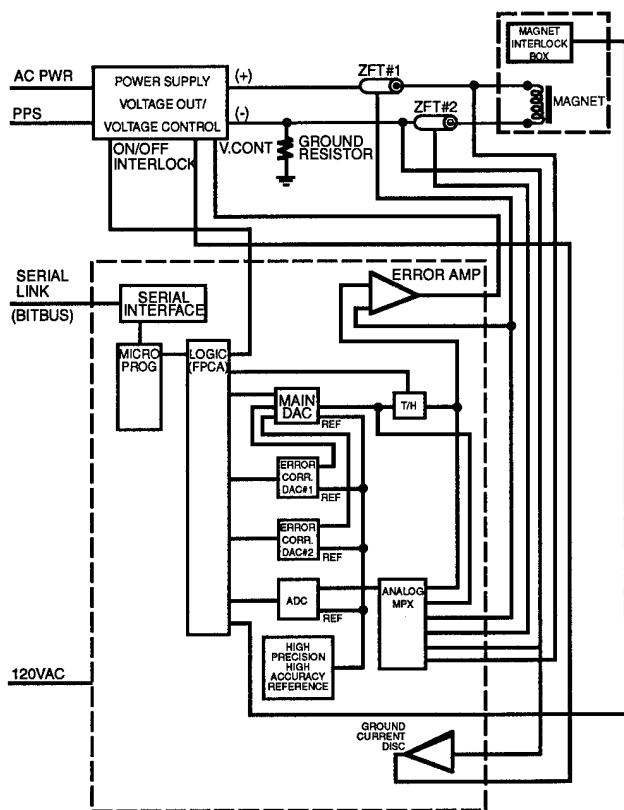


Fig. 1. Power supply system block diagram

FACTORS INFLUENCING THE CHOICES ON POWER SUPPLY TECHNOLOGIES

Many factors are being considered to arrive at solutions of the technical problems presented by the PEP-II machine design specifications. The individual performance issues were initially evaluated, including stability, accuracy and tolerances for periodic and random deviations. Overall performance issues such as availability, initial and operating system costs and MTTR are then weighed. Included under cost are the solutions that allow to use and recycle existing components of PEP-I such as the cable plant (AC & DC) and the power distribution systems (transformers, switchgear) that will be refurbished and reused. The power distribution decisions were for AC distribution, because of the simplicity of the protection systems and easier compliance with safety regulations. The exception are the large string power supplies, where existing DC distribution systems were recycled. Other influences on the technical solutions are EMC concerns,

both EMI generation and susceptibility, and power supply efficiency.

CONTROL SYSTEM INTERFACES

A new control system interface/error amplifier/ power supply controller will be used in the power conversion systems for PEP-II. Its design will take advantage of the advances in digital technology since the early 80's when the standards and the hardware for the interfaces currently in use at SLAC were designed, and of the experience with high stability intermediate units developed more recently (Ref. 2). The interface is connected to the control system by means of a digital serial line (Bitbus). A microprocessor is used as the communications controller and as the intelligence for the power supply controller for functions such as data I/O, diagnostics routines and ramping. The use in the controller unit of an intelligent programmable processor allows for a large improvement in the performance of the data conversion components. An internal calibration process, running while the supply operates, makes possible the transfer of the accuracy and precision of a high quality reference to the DAC and ADC performance. The process corrects for offset, gain and linearity imperfections and drifts for the DAC and offset and gain for the ADC. This allows the use of data conversion units of less stringent specifications (read less expensive).

DESCRIPTION OF THE MAJOR GROUPS OF POWER SUPPLIES

Power supplies for correctors and trim coils

This systems are described in another paper, by T. Jackson and G. Leyh, these Proceedings (Ref 3).

Power supplies for medium power individual magnets and small strings (Group I)

This is the range of individual power supplies with the largest number of power supplies. The system engineering is assigned to SLAC. It was decided early on to use a single type of technology for the whole range, based on similar requirements for performance and with the goal of simplifying maintenance procedures, reducing spares stock, personnel training and MTTR. The decision on which type of power supply technology to be used, based mostly on performance, costs, and past experience, is for the use of commercially available, standard model switchmode power supplies with AC power input. A procurement specification is under review. The objective set for this specification is to characterize the requirements for the range of power supplies, identifying clearly those parameters that need tight specifications, while leaving other parameters more open to widen the field of possible vendors.

Power Supplies for individual magnets, medium high and high power (Group II).

For this group, the technology decision does not need to be unified, since there are, with few exceptions, one or two of each kind, and rather dissimilar in their specifications. The unit price for power supply is higher, because of the higher power, and a case by case decision is to be made in each case, by performance and cost. The system engineering is identical to those P.S. in group I (Fig. 1)

Power Supplies for Large Magnet Strings(Group III).

PEP II has 21 circuits of large string series-connected magnets in the two rings, 16 for HER, and 5 for LER. Circuits are for the bend dipoles, focus and defocus quadrupoles, focus and defocus sextupoles, and many special quadrupoles. The largest strings are the dipoles, 192 (HER) and 200 (LER).

Total maximum operating power is 4300 kW, 2400 kW (56 %) for HER and 1900 kW (44 %) for the LER strings.

Power supply architecture is similar to that of PEP I (Ref.4) : bulk dc P.S.s drive several buck-type dc-dc chopper/ converters (Fig. 2). In the bulk P.S.s two transformers, associated switchgear and half-controlled rectifiers, provide positive and negative 600 Vdc for the individual string circuit dc-dc converters with low inrush currents and fast fault protection . HER and LER strings have separate circuit breakers and rectifiers for operational flexibility.

The current control for each magnet string is achieved by using insulated-gate-bipolar transistors (IGBTs) chopper/ converters. The 200 kW modules' output is 400 A, at either + or - 500 Vdc, with extensive differential and common-mode filtering, and can be connected in series and in parallel.

The string voltage limit is 1000 Vdc, defined by system insulation, and can be achieved using positive and negative dc-dc chopper/converter modules in series. Magnet strings which require more than 1000 Vdc must be divided. The HER bend magnet string will need three modules in parallel for 890 A, and in order not to exceed the 1000 V limit, it also must be divided into two strings of 96 magnets and 690 V each. A total of 12 chopper/converters is used. The LER bend magnet string also requires splitting and has two strings of 100 magnets at 745 A and 990 V each, using a total of 8 chopper/converters. Four of the quadrupole strings are below 400 A but need two modules each because the voltages are above 500 V. The other 15 circuits require only one module since currents and voltages are all below 400 A and 500 V.

The power circuit of the dc-dc converter module is shown in Fig. 3. It is based on a design by an engineering team at LLNL (Ref.5). Two 600 A, 1200 V IGBTs are alternately gated at 10 kHz for an effective 20 kHz internal

frequency. Snubbers networks across the IGBTs reduce turnon losses and clamp the voltage during turnoff. IGBTs and diodes are mounted on a water-cooled aluminum heat sink. The "box-in-box" construction and the common-mode filters at the input and output control EMI. The IGBTs are controlled using commercial gate drivers linked by fiber optics to a commercial current-mode PWM controller. The duty cycle of the IGBTs varies the average output voltage in response to a voltage setpoint. A "breadboard" version of the dc-dc converter power circuit has operated successfully at 200 kW .

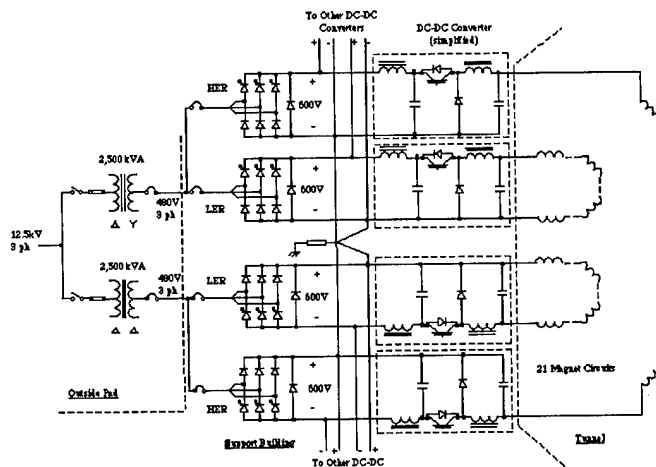


Fig. 2. String magnet power supplies. Simplified power circuit.

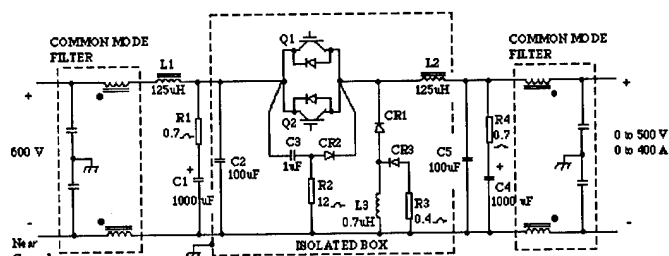


Fig. 3. 200 kW dc-dc converter power circuit.

- 1) M. Berndt, J. McNair, "DC Magnet Power Supplies for the FFTB at SLAC", San Francisco 1993, IEEE Nuclear Science Symposium.
- 2) M. Berndt, J. McNair, A.H. Saab, "The Design of a Precision Current Regulation Power Supply Controller", San Francisco 1993, IEEE Nuclear Science Symposium.
- 3) G.E.Leyh, A.R. Donaldson, L.T. Jackson, "A Multi-channel Corrector Magnet Controller", Dallas 1995, IEEE PAC.
- 4) L.T. Jackson, "Design and Performance of PEP DC Power Systems", IEEE Transactions on Nuclear Science, Vol. NS-28, No3, pp 2737-2741, June 1981.
- 5) J.N Bombay, A.C. Lange, D.W. Shimer, "A High-Power Switchmode DC Power Supply for Dynamic Loads", 1994 IEEE Industry Applications Society Annual Meeting Conference Record, Oct. 2-7, 1994.

The AGS Main Magnet Power Supply Upgrade*

J.N. Sandberg, R. Casella, J. Geller, I. Marneris, A. Soukas, and N. Schumburg,
Brookhaven National Laboratory, Upton, New York 11973

I. INTRODUCTION

The AGS is a strong focusing, combined function magnet, particle accelerator. The main parameters of the accelerator are a peak operating energy of 29.4 GeV, a peak magnetic field of 11.5 kG, a typical injection field of 0.9 kG, an injection energy of 1.5 GeV, and a maximum pulse repetition rate of 0.6 Hz. The injection is from a rapid cycling Booster synchrotron, which receives either a proton beam from a 200 MeV Linac, or a Heavy Ion beam from a 15 MV Tandem Van de Graaf Accelerator. Flattops of up to 2 seconds can be added to the AGS cycle for slow extracted beam applications. Particles accelerated include protons (mass=1), both polarized and non-polarized, and fully striped ions up to gold (mass=197). The maximum proton intensity attained thus far is 60×10^{13} particles per pulse. Modes of operation for the AGS are full-turn extraction (2.5 μ sec), slow extraction (1-2 sec), and bunch-by-bunch extraction. These modes are applicable for both protons and heavy ions.

The peak apparent power required during acceleration is approximately 70 MVA while the maximum average power needed is less than 7 MW. In order to isolate this large power swing from the local power grid, a motor-generator (MG) set is used as a buffering source. The MG set stores approximately 315 Kilojoules of energy in its rotating mass. As energy is drawn to charge or discharge the ring magnets, the speed of the rotating mass changes in such a manner as to supply the required load power demand. The input to the motor is controlled by a power regulator that forces the input power to be equal to the average losses during each cycle. The line sees nearly a constant load equal to the system losses. The peak power requirements are met by changes in the stored energy of the rotating mass that translates directly into speed variations. Thus, for a fixed operating cycle, the losses during each cycle are reproducible, and the speed oscillates around an average value and is returned to the same value at the beginning of each supercycle.

II. POWER RECTIFIERS

The AGS Main Magnet Power Supply consists of a group of thyristor controlled power converters that operate from full rectify to full invert. In order to minimize ripple during the critical periods of injection and extraction twenty-four pulse converters are used for these portions of the cycle. The maximum voltage available in this mode is nominally 2000 volts. The

converters that are functional during this portion of the cycle are called the flat-top bank or "F" bank modules. During acceleration and invert where voltages of up to 12,000 volts are needed and where the ripple requirements are less stringent, groups of twelve pulse converters are operational. These converters are called the Pulsed bank or "P" bank modules.

The original controlled rectifier system consisted of 96 large mercury filled excitron tubes divided equally between the P bank and F bank converters. These devices were extremely durable and ran successfully for over twenty years. In the 1980's excitrons of this class became obsolete and it became impossible to buy replacement tubes or to repair the existing tubes. In addition to the difficulties in replacing bad tubes the old system had significant operational drawbacks. The characteristics of these tubes required that they be operated at an elevated temperature so that an elaborate water temperature regulation system was required. If the tubes were operated outside the correct temperature window they were subject to either random misfires or increased time delay and jitter. The tubes also required many hours of warm up time if they were allowed to cool and needed to be conditioned for several days after a prolonged shutdown. The energy lost in both the heating system and the arc drop of the tubes was quite significant compared to present day devices.

It was, therefore, decided to replace the excitron "farm" with multiple arrangements of three-phase, full-wave, bridge modules that utilize silicon controlled rectifiers (SCR's or thyristors) as the switching element. This technology provides the capabilities for controlling large amounts of power efficiently with the minimum number of series parallel devices. In order to match the existing transformer connections and buswork, eight identical modules were required; four for the P bank system and four for the F bank system. The D.C. output of the F bank modules is in series with the load and one P bank module is connected in parallel with each F bank module. Each of the eight modules consists of two full wave three phase bridges in parallel. Each leg of the bridge consists of two SCR's in series. The modules were designed and manufactured by Siemens, AG, of Erlangen Germany.

In order to reduce noise pickup and provide electrical isolation the high level SCR gate triggers are provided via fiberoptic cable. The low level triggering circuits were designed and built at BNL and have operated successfully in the Booster Main Magnet Power Supply. Isolated monitoring, in the form of DCCTs (current) and DCPTs (voltage), is necessary to minimize noise pickup in critical feedback loops. In addition, isolation of both analog and digital signals is extremely important due to the high voltages and power levels present.

The status of various parameters such as water flow,

* Worked performed under the auspices of the U.S.D.O.E.

auxiliary power supply performance, trigger circuitry failure, over voltage, overcurrent, and loss of phase reference are monitored via a programmable logic controller (PLCs). The PLCs use isolated input and output modules for various voltage levels from TTL to 150 Vdc to 125 Vac. These devices are extremely flexible and have allowed modifications and improvements that have enhanced the performance over any equivalent hard wired system. In addition, the PLC's have allowed us to tie the converter controls to the existing MG set controls.

At the high power levels used for the AGS, protection of the SCRs during fault conditions is a very important consideration. The SCR's are not as "forgiving" as the old excitron tanks. The excitrons had tremendous capacity for current overloads and would generally switch to a conducting state during a severe overvoltage condition. These conditions, especially an overvoltage, could be disastrous to SCR's. In addition to the normal or "slow" overload and overtemperature protection, it was necessary to include very fast protection that acts in the 100 usec to low msec time range. When an overvoltage or overcurrent is sensed this level of protection is accomplished by: a) immediately commanding the rectifiers into invert, b) firing a set of free-wheeling SCR's, c) closing a fast 95 bypass mechanical switch, and d) opening a fast acting 52 (<3 cycle) circuit breaker. These interlocks are hardwired to their various control devices. In addition, for redundancy and logging, they are also connected to the slower acting PLC/relay interlocks. The PLC's are used to coordinate the various sub-systems in addition to logging all systems faults in sequential order for diagnostic purposes. These features were lacking in the old relay system and have greatly reduced the time required to diagnose and repair problems.

III. ANALOG CONTROLS

The SCR firing control range, or MMPS controlled dc output, is covered by an accurate set of ramp generators driven by analog, compensated amplifiers comprising an inner voltage loop and an outer current feedback loop. The ramp generators use stable components, ac low pass filters, and are synchronized to the MMPS generator/step-down transformer voltages. The loops track both voltage and current reference functions, thus resulting in very high effective loop gain. The current tracking during steady state conditions is typically $< 1/5000$. The sensors for the voltages and current are DCPT's and a DCCT.

As stated earlier the P and F bank modules are connected in parallel. The cycle typically begins with the F banks active at injection levels. As acceleration begins the P banks are turned on and as their voltage becomes greater than the F bank's voltage the F bank thyristors commutate off. The current through each bank is monitored and when the P bank is commanded on and the current through the F bank goes to zero the triggers are removed from the F bank. At this point the error amplifier in the F bank regulator is grounded to prevent the regulator from saturating. When flat-top is reached, the P bank voltage is gradually reduced and the F bank voltage regulator is reactivated. When the P bank voltage is less than the F bank's voltage, it will commutate off. When the P banks current reaches zero, its triggers are removed and its error amplifier is grounded. This process is repeated

throughout the cycle. The transition period required to switch between P and F bank modules is typically 10 to 20 msec.

IV. COMPUTER CONTROLS

In order to increase AGS versatility it is highly desirable that the switchover between different cycles be easily and rapidly accomplished. In addition, pre-programmed cycle storage and retrieval is necessary. This is accomplished by designing a set of vector-driven function generator hardware and software. The devices are interfaced to the AGS's hierarchical networked control system. Thus functions can be constructed and executed from any place in the system. Up to four different functions can be stored in local buffer tables and can be executed upon issuing of a main supercycle timing event. The application code for the system begins from a definition of the desired main magnetic field function (beam momentum). Using the magnetic field measurement data, the required magnet current is calculated. Utilizing the electrical parameters of the MMPS circuit the total voltage and the voltage per module are calculated. The parameters are "tuned" to optimize the final results. Using generic application software tools, they are synthesized into a series of vectors defined by a beginning time and a slope, and sent to local device controller where they are stored in memory buffers. The voltages become reference inputs to the voltage loops and the current is sent to the overall outer current loop. Upon issuing an execution command, the table is sequentially sent to the analog loops via 16-bit DAC's. In actual operation, the voltage functions alone generate a magnet current that closely approximates the desired field. The outer current loop assures the final trimming which controls the field to a much higher accuracy, stability, and reproducibility over time and temperature variations. A simplified block diagram of the voltage and current loops is shown in Figure 1. A bode plot of the open loop transfer function for the F bank regulator is given in Figure 2.

The ultimate aim in the AGS MMPS is to be able to switch functions or cycles on a pulse-by-pulse basis. Presently this is not permitted by the high power circuitry of the MMPS and by the ac power line swing that is presently limited to ± 500 kW. The MMPS speed control and excitation systems are in the process of being upgraded to encompass computer and function control capabilities.

V. ACKNOWLEDGEMENT

The successful installation of the rectifier modules was due in large part to the mechanical designs of S.V. Badea and the technical support of E. Grahn and M. Bannon. The electrical controls portion of the project is greatly indebted to B. Culwick.

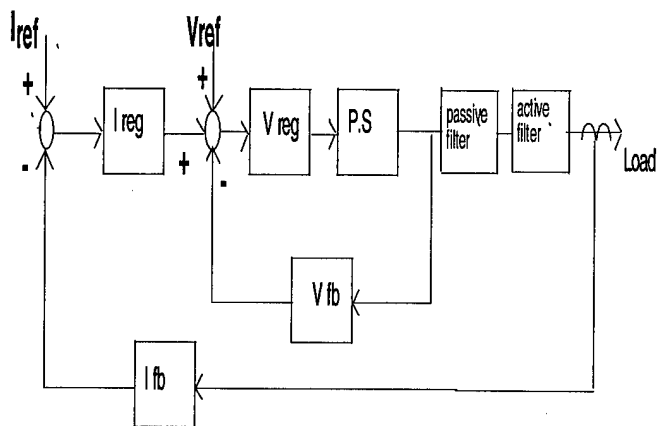


Figure 1

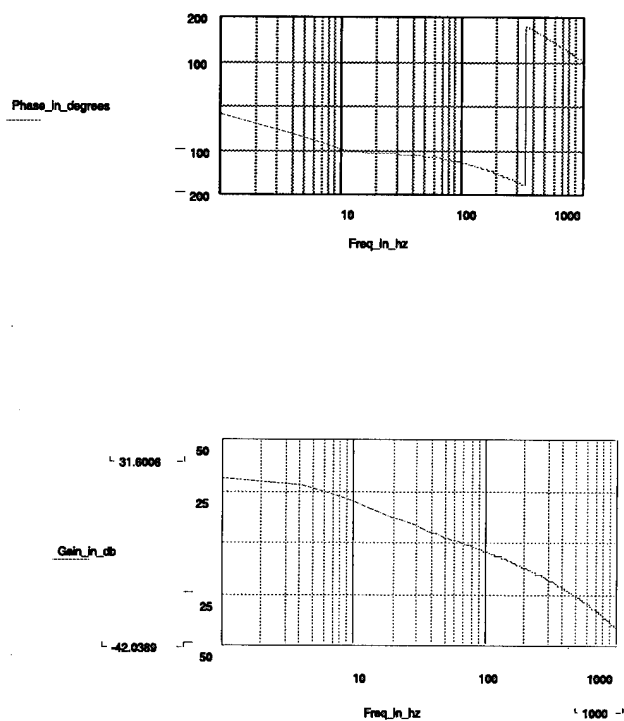


Figure 2

Performance of the Ramping Power Supplies for the APS Booster Synchrotron*

J.A. Carwardine, S.V. Milton, and D.G. McGhee
Advanced Photon Source, Argonne National Laboratory
9700 South Cass Avenue, Argonne, Illinois 60439 USA

Abstract

The Advanced Photon Source (APS) booster ramp cycle is completed within 250ms and repeated at 2Hz. Separate phase-controlled power supplies deliver current to each of the dipole, quadrupole, and sextupole magnet families. Tracking requirements are particularly challenging because of the fast (non-resonant) ramp. In order to meet the requirements, both conventional regulation and cycle-to-cycle adaptation are used. The power supply system and its performance are described.

I. INTRODUCTION

The APS booster uses a simple FODO magnet lattice consisting of 68 dipole, 80 quadrupole, and 64 sextupole magnets. The quadrupole magnets are connected in chains of 40 magnets creating 'focussing' and 'defocussing' families. Similarly for the sextupoles with 32 magnets per family.

During routine operation of the booster the betatron tunes should remain constant throughout the energy ramp cycle and from cycle to cycle. Since the tunes are determined by the relative strengths of the quadrupole and dipole magnets, the ratio of currents in the magnet chains must also remain constant. Any deviation from the nominal current profile will result in a deviation from the nominal tunes; how large a deviation is tolerable will determine the magnet power supplies' performance criteria. Whilst in principle the dipole current could follow any path from the injection to extraction levels, we have chosen to use a linear ramp to simplify the tracking control of all the magnets. During a typical ramp cycle, beam is accelerated at a nominal 29MeV/ms. This corresponds to a rise rate of ~4A/ms for the dipole and ~2.5A/ms for the quadrupoles.

II. REQUIREMENTS

The APS booster tune sensitivities are given by [1]:

$$\Delta Q \approx 0.2 \frac{\Delta I_{quad} [A]}{E [GeV]}$$

The target tune error throughout the ramp is 0.02. In order to achieve this, the quadrupole power supplies must track the dipole to within ~0.1%. Power supply ramp tracking errors can occur within a single ramp cycle and from cycle to cycle.

The booster is reasonably tolerant to chromatic effects. Therefore, since control of the sextupole ramps is not nearly so critical as with the quadrupoles, a maximum tracking error of 1% is allowed in the sextupole currents.

Ramp characteristics for all the magnets are determined from a least-squares linear fit to the measured current waveforms. Three factors are identified: the slope of the fit, the zero (current) crossing time of the fit relative to beam injection, and

the deviation from the fit as a function of current ($\Delta I/I$).

Table 1 shows the worst case error in each of these three parameters if the entire tolerance were to be taken up by any one of the parameters.

Table 1: Target Worst Case Errors in Quadrupole Ramps

Linear Fit Characteristic	Nominal Value	Worst Case Error
Ramp $\Delta I/I$ (%)	0.0	0.1
Ramp Slope (A/ms)	2.5	0.003
Zero Crossing (ms)	12.5	0.018

In practice of course, there will always be errors in each of these parameters, so the actual errors have to be even smaller, although it is worth noting that errors do not necessarily add up in quadrature.

III. POWER SUPPLY OVERVIEW

Each of the five power supplies consists of a 12-pulse thyristor-controlled bridge rectifier and an associate ripple filter. The 12 pulses are generated from two pairs of 3-pulse half-bridges connected via interphase transformers. Figure 1 shows a simplified schematic of the quadrupole power supply. The dipole power supply is similar except that two such power circuits are series-connected in a 'master-slave' arrangement. The nominal operating conditions are given in Table 2.

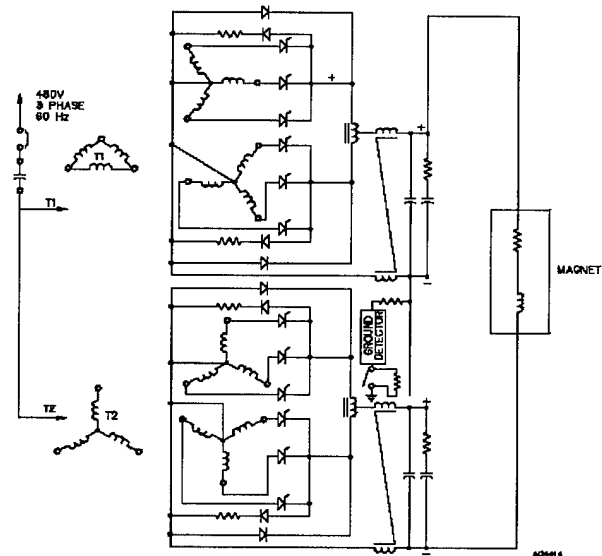


Figure 1: Simplified Schematic of Quadrupole Power Supply

*Work supported by U.S. Department of Energy, Office of Basic Energy Sciences, under Contract No. W-31-109-ENG-38.

Table 2: Nominal Magnet Parameters (* focusing magnet)

	Dipole	Quad*	Sext*
Current @ 450MeV (A)	58.0	39.3	~8
Current @ 7GeV (A)	902.5	610.8	~160
Nom. di/dt (A/ms)	3.93	2.50	~0.6
Load Inductance (H)	0.55	0.058	0.012
Load Resistance (Ω)	1.26	0.73	0.8

The original power supply design did not incorporate free-wheel devices, however it was discovered that the power supply behaved differently at low currents than at higher currents. This was believed to be a consequence of the magnetization of the interphase transformer as the current increased. Adding freewheeling devices to each half-bridge has helped to reduce the magnitude of these non-linearities.

IV. CONTROL SCHEME

Figure 2 shows the simplified scheme used to regulate the current in each of the five magnet families. Two control loops are shown: a primary voltage loop and a secondary current loop. Presently, only the voltage loop is implemented. Due to the relatively long time constants of the magnets (dipole: 540ms, quadrupole: 79ms) the bandwidth of the current loop is far too low to be used as the primary loop, so the faster voltage loop is supplied with its own reference waveform corresponding to the ' $Ldi/dt + iR$ ' load voltage.

To date, the implementation of the current loop (shown dotted in the figure) has been considered unnecessary since corrections for drift are made using software feedback. However, the current loop will shortly be implemented since it is now believed that it will help to reduce cycle-to-cycle jitter.

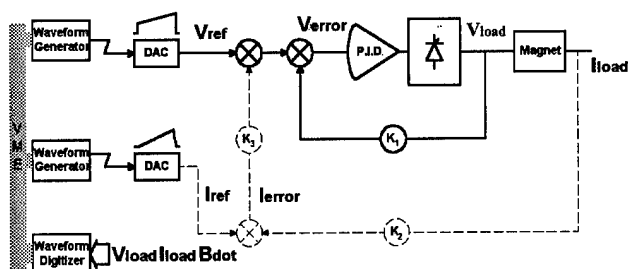


Figure 2: Control Scheme Block Diagram

Reference waveforms will be generated using in-house designed arbitrary function generators (AFG) mounted in a VME controller and accessed via the APS control system. Each waveform record will consist of 8K discrete 16-bit values. The waveform records are sent to the power supply digital-to-analog converter at 17.2kHz, giving a waveform duration of 475ms. By extending the duration of the waveforms past the 250ms required for the ramp cycle, the current decay can also

be controlled. A dual waveform buffer allows a new waveform to be loaded in background and then swapped to the foreground between cycles. Updates can therefore be made to the reference waveforms without loss of ramp cycles.

Extensive monitoring of all waveforms (V_{ref} , I_{ref} , V_{out} , I_{out} , B_{dot}) is already done using proprietary 16-bit digitizers which sample the waveforms at 20kHz. The monitored waveforms are downloaded to the control system at the end of each cycle to be used by the software control system and for future analysis.

V. POWER SUPPLY TRANSIENTS

The most challenging part of this system is handling the power supply transients at the start of the current ramp. Since the power supply bandwidth is limited (at best) to 360Hz by the 12-pulse thyristor bridge, it is not possible to meet the performance criteria with a conventional regulator alone. The response of the quadrupole power supply voltage loop to various step inputs is shown in Figure 3.

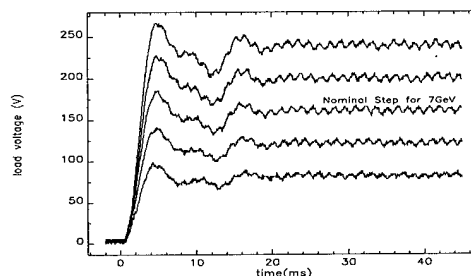


Figure 3: Step Response Family of Quadrupole Power Supply

In order to artificially extend the system bandwidth, the nominal voltage reference is modified to accommodate the inverse response of the power supply, thereby cancelling transients in the output voltage.

For a general linear system having the response vector Y to an input vector X , the response matrix A is:

$$Y = A \times X$$

By inverting the response matrix, it becomes possible to calculate the input vector required to produce a given output, where A^{-1} is the matrix inverse of A :

$$X = A^{-1} \times Y$$

In practice, straightforward determination of a single inverse response matrix useful over a broad range of conditions has proven difficult. So far, the approach has been to iteratively correct the voltage reference by hand until errors in the output current are reduced to allowable tolerances [1].

An approach which is currently being pursued is the use of adaptive signal processing techniques. Such techniques have already been used to create a forward model of the power supply from its measured response. The least-mean-square (LMS) algorithm [2] was used to determine the coefficients of a 60-element finite impulse response (FIR) digital filter which accurately modelled the measured response of the power supply. The intention is to use similar techniques to determine the coefficients for an FIR filter with the required inverse response.

VI. RAMP STABILITY

In addition to the single-cycle performance, cycle-to-cycle repeatability and long term stability are essential if the machine is to operate on a daily basis without significant operator intervention. Two effects are apparent: slow drift of the ramp parameters and cycle-to-cycle random jitter. The most apparent cause of drift has been changes in the AC line voltage. Figure 4 shows the effect of the AC line voltage on the slope of the dipole ramp without (software) feedback. The large steps seen in the AC line occur when the booster 1MW rf power system is turned on and off.

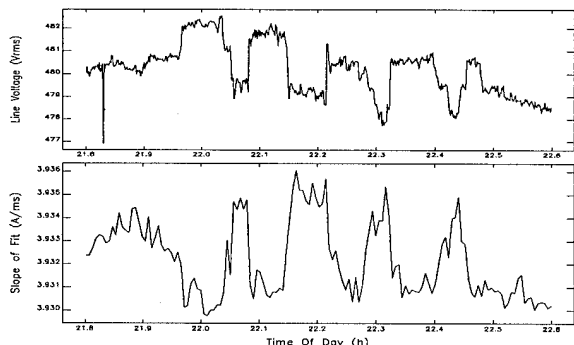


Figure 4: Effect of AC Line Voltage on Dipole Slope

Whilst in a normal operating mode such sudden changes in the line voltage are unlikely, slow changes over a much wider range are common. Since the changes in slope are relatively small in real terms, a high regulator gain would be required, and this cannot be achieved on our system.

The most significant contribution to cycle-to-cycle jitter has been the condition of the power supply just prior to the start of the ramp cycle. Since the power supply is unable to regulate to a 'zero' reference, it is necessary to run with a small positive DC bias. This puts the regulator at a consistent and defined position at the start of the ramp.

A further improvement of about a factor of two in cycle-to-cycle jitter has been achieved by smoothing the initial step in the voltage reference waveform, making it close to a cubic turn-on. This has the effect of reducing the integrated voltage error since the power supply is better able to track the smoother reference.

VII. SOFTWARE FEEDBACK

In addition to the software techniques used to automatically tune the ramps [1], a software feedback system known as 'Bcontrol' is used to continuously correct for drift in the slope and zero crossing of the linear fit parameters. A background process carries out the least-squares linear fit at the end of every ramp cycle. These fit parameters are then made available to the remainder of the control system. Corrections to the zero-crossing time are made by moving the trigger point for the appropriate waveform generator; small corrections to the slope are made by an overall scaling of the voltage reference waveform. Both of these actions can occur between each cycle and are therefore transparent to beam operation. The effect of using 'Bcontrol' on the zero crossing can be seen in Figure 5.

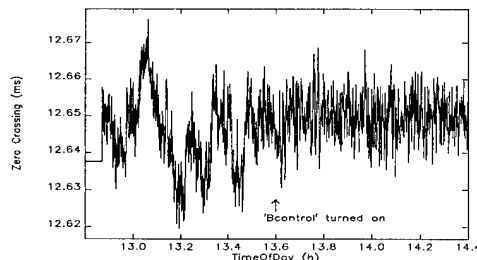


Figure 5: Effect of 'Bcontrol' on the Ramp Zero Crossing

VIII. OPERATING EXPERIENCE

The APS booster has been routinely producing 7GeV beam since January 1995. Throughout this time, only a 12-bit waveform generator has been available. However, it has still been possible to manually tune the ramps to well within 0.5% Δ/I (limited by the patience of the operator). Early on, it was found that whilst the waveform generator provided 12-bit resolution, it only provided around 10-bit stability which proved inadequate for reliable beam operation. Thermal drift was found to be the major cause of the limited stability, and by close control of the electronics temperature, it has been possible to significantly improve the stability of the reference.

Cycle-to-cycle jitter is now the biggest problem, it being around 10-20 μ s rms. The most significant improvements in stability are expected to come from the new 16-bit waveform generator and from the implementation of the current loop.

IX. FUTURE ENHANCEMENTS

Presently, the three magnet systems are independent and there is no direct attempt to correct the quadrupole waveforms from dipole tracking errors. This will be implemented in the coming months. The ultimate level of control would come from feeding back directly from the measured betatron tunes, particularly during the early part of the ramp cycle when the beam is most sensitive. Simple feedback based on the tunes at injection is already underway, using the beam position monitors to measure the tunes. However, a full tune measurement system is currently being commissioned, and the intention is to ultimately make this part of the ramp control scheme.

X. ACKNOWLEDGMENTS

Thanks are extended to Howard Pfeffer and Dan Wolfe, both of FNAL, for their interest and valuable suggestions.

The authors would like to thank Oscar Despe, Frank Lenkus, Bob Laird, Claude Saunders, and Ju Wang for developing new hardware, Michael Borland for developing waveform monitoring and analysis programs, and Anthony Puttkammer for repairing the system after our less successful efforts.

XI. REFERENCES

- [1] S. Milton, J. Carwardine, "Ramp Tuning of the APS Booster Synchrotron Magnet Power Supplies," these proceedings.
- [2] B. Widrow, S. Stearns, *Adaptive Signal Processing*, (Prentice Hall, 1985).

A DISTRIBUTED DIPOLE POWER SUPPLY SYSTEM FOR THE EUTERPE ELECTRON RING

A.H. Kemper, Boling Xi, R.W. de Leeuw, W.H.C. Theuws, J.I.M. Botman,
C.J. Timmermans, H.L. Hagedoorn, R.G.J. Oude Velthuis.
Eindhoven University of Technology, Cyclotron Laboratory,
P.O. Box 513, 5600 MB EINDHOVEN, the Netherlands

A distributed power supply system is described for the bending magnets of the 400 MeV electron synchrotron and storage ring EUTERPE. The system consists of a series connection of alternately power supplies and dipoles. In this concept the leakage current of internally cooled coils of dipoles is minimized. The advantages of one big power supply with equal current through all coils and of separated power supplies with a low voltage hence low leakage currents, are combined. Individual correction of dipoles and current stabilization can be provided. As the individual power supplies have extra power capacity, failure of a single unit will be corrected by the others, which implies a large overall reliability of the system.

I. INTRODUCTION.

At the Eindhoven University of Technology the 400 MeV electron storage ring EUTERPE (see figure 1) is under construction [1]. The purpose of this project is twofold, studies are made and experience is gained in the field of beam dynamics and accelerator techniques, applications of synchrotron radiation are pursued.

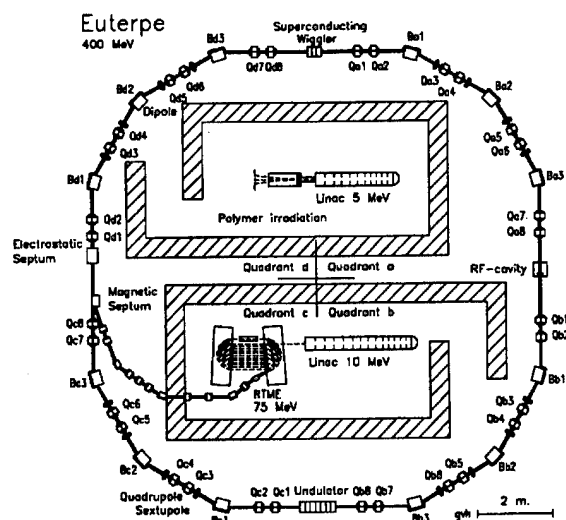


Figure 1: EUTERPE synchrotron

The circumference of the ring is 40 meters. The RaceTrack Microtron Eindhoven (RTME) injects electrons at 75 MeV (2). The ring has 12 identical dipole magnets of unconventional design and construction (3). They have a weight of 600 kg each, and consist of 5 blocks of laminated iron which are glued together. The gap width is 2.5 cm, the pole size is 12 cm by 48 cm. The coils are placed above and below the air gap. Each coil consists of 84 turns of

hollow copper conductor, 6 x 6 mm² with a bore of 3.5 mm diameter for water cooling. The total inductance (L) of the two coils in series is 102.8 mH, the resistance (R) of the circuit is 167 mΩ. The magnetic field varies between 0.25 T and 1.35 T, corresponding to electron energies of 75 MeV and 400 MeV. For this an excitation current per turn between 30 A and 170 A is required.

This paper describes the power supply and its driving circuit for the twelve dipole magnets. For this system we have the following set of demands.

- * The current has to be adjustable from 20 A to 200 A.
- * For each dipole a supply voltage of at least 30 V must be available.
- * The relative drift of the current should be less than 10^{-5} , measured over a period of 8 hours.
- * The difference between the supply currents of any two dipoles related to the average supply current must be less than 10^{-5} .

An obvious solution is to connect all dipoles in series. Then a supply voltage of at least $12 \cdot 30 \text{ V} = 360 \text{ V}$ is needed. This solution has the disadvantage, that the voltage of the connections of several dipoles is dangerously high, requiring shielding of these connections. Moreover the isolation between the inductors and the iron dipole core, which is grounded, has to meet high requirements. Furthermore as the coils are internally cooled by water, differences in the individual magnet supply current may exist, caused by leakage currents through the cooling water.

Another solution is to provide each dipole with its own 30 V / 200 A power supply. However in this way it becomes difficult to get all the supply currents precisely the same, because separate control circuits are needed, which also makes the system more complex. In the next section an alternative solution is proposed, which combines the advantage of one big power supply with equal current through all coils with that of separate power supplies with low voltage.

II. DISTRIBUTED POWER SUPPLY SYSTEM.

Here we propose to take n identical 30 V / 200 A power supplies in series. Connect a dipole between every power supply (see figure 2). Then at any point the supply voltage is low, the current through the dipole magnets is the same (the dipoles are in series), apart from the leakage current. The difference in leakage current is n times smaller than using a single power supply. Moreover, only one control circuit is needed. This is a major advantage with regard to

using n supplies. The repair after a failure of a single unit is easy. The defect power supply can easily be replaced by a stand-by unit. This stand-by unit is relative cheap. Because standard power supplies can be used, we emphasize that this method provides a low cost solution.

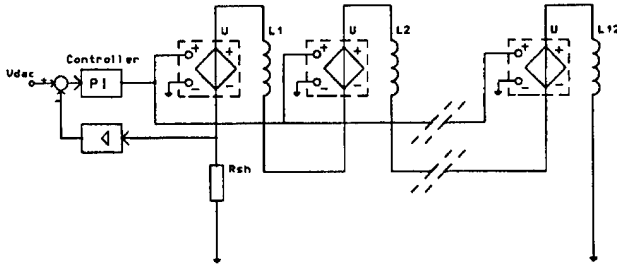


Figure 2: Schematic using dipoles and power supplies in series.

It is well known that the reliability for individual power supplies in series is less than the reliability of one big power supply. However, overrating the power supplies, the other $n-1$ power supplies are able to take over the function of a failing power supply. Then [4], the reliability of individual power supplies in series is higher than the reliability of one big power supply. However diodes, in parallel with the power supplies, are needed. In this way the current loop is not interrupted.

A simple improvement to this method can be made; one side of the inductor of the dipole magnets has a positive potential ($+1/2U$) with respect to earth, while the other side of the inductor has a negative potential ($-1/2U$). In this way the leakage currents through the cooling water are alternating positive and negative. This reduces the differences in excitation current in comparison with the method above (see figure 3).

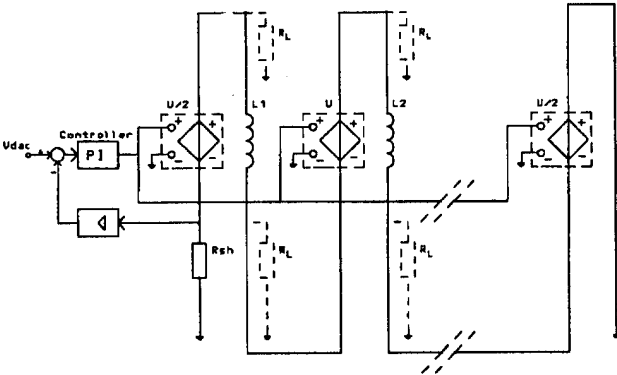


Figure 3: Distributed power supply system, symmetric with regard to ground. The dashed resistors denote the resistance of the cooling water.

III. INDIVIDUAL DIPOLE CORRECTION.

Because of temperature differences, leakage currents through the cooling water, mechanical tolerances, etc. the dipoles can differ. Moreover extra bending capacity may be required for closed orbit corrections. A method to correct

the magnetic field in each dipole by means of a small separate current source is shown in Figure 4. Here all correction currents i'_1, i'_2 , etc. are shown. The total current is given by: $I_n = I_0 + i_n$, where I_0 is the common excitation current.

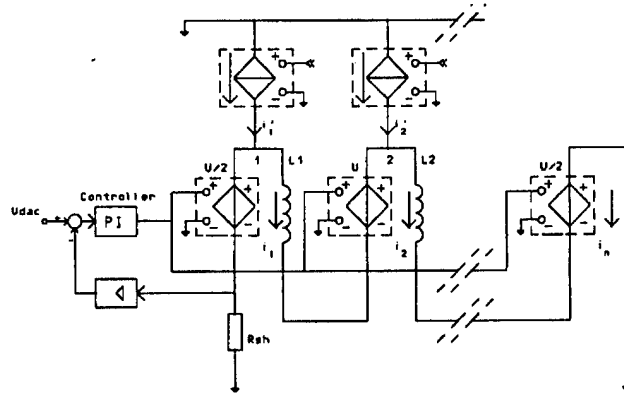


Figure 4: Schematic using the dipoles in series with the power supplies and individual correction.

However, this solution has the problem that when the current through one dipole is corrected, the current through the other dipoles also changes. It would be nice to control the current through a dipole separately from the other dipoles by a separate control variable. For this we make the following analysis. From Figure 4 follows:

$$i' = i'_1,$$

$$i_2 = i'_1 + i'_2,$$

$$i_n = i'_1 + i'_2 + i'_3 + i'_n,$$

with i'_n the correcting current for dipole n and i_n the total correcting current in this dipole.

In matrix notation this is written as:

$$i = Ai', \quad (1)$$

with the vectors and the coefficient matrix given by:

$$i = \begin{pmatrix} i_1 \\ i_2 \\ \vdots \\ i_n \end{pmatrix}, \quad i' = \begin{pmatrix} i'_1 \\ i'_2 \\ \vdots \\ i'_n \end{pmatrix}, \quad A = \begin{pmatrix} 1 & 0 & \dots & 0 \\ 1 & 1 & 0 & \dots & 0 \\ \vdots & \vdots & \vdots & \vdots & \vdots \\ 1 & 1 & 1 & 1 & \dots & 1 \end{pmatrix}$$

Suppose that:

$$i' = Bu, \quad (2)$$

with B the transformation matrix from u to i' and u as the wanted control vector (with elements u_i up to and including u_n).

Following from (1) and (2):

$$i = ABu.$$

As u_k may only influence i_k (with $1 \leq k \leq n$), the following equations must be realized: $i = \alpha I u$, with I the $n \times n$ unit matrix and α a scalar to be defined later.

Hence:

$$B = \alpha A^{-1}$$

This results in:

$$i' = \alpha A^{-1} u.$$

The inverse of A is:

$$A^{-1} = \begin{pmatrix} 1 & 0 & . & . & . & . & . & 0 \\ -1 & 1 & 0 & . & . & . & . & 0 \\ 0 & -1 & 1 & 0 & . & . & . & 0 \\ . & . & . & . & . & . & . & . \\ 0 & 0 & 0 & 0 & . & 0 & -1 & 1 \end{pmatrix}.$$

From this we obtain:

$$i'_1 = \alpha u_1,$$

$$i'_2 = \alpha (u_2 - u_1),$$

$$i'_n = \alpha (u_n - u_{n-1}),$$

with α a constant which has to be specified according to the required correction current and the available control voltages.

Conclusion: Individual dipole correction is possible using different control voltages.

Figure 5 gives a possible realization for individual correction.

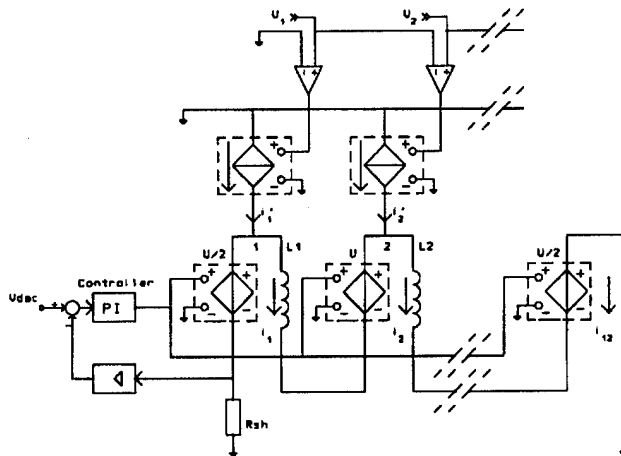


Figure 5: Possible realization to correct the current through each dipole.

IV. CURRENT MEASUREMENT AND STABILIZATION.

The required drift of the current source less than 10^{-5} over a period of 8 hr implies at least the same stability for the current measurement system. the current is measured via a current shunt. the shunt we use, has an output voltage of 200 mV at a current of 200 A. the stability of the shunt is $2 \cdot 10^{-5} / K$. the measured output voltage is amplified by a factor of 25 using an instrumentation amplifier, which has an input drift of $\leq 10^{-6} V/K$. From this the following can be

concluded: the drift at the output of the amplifier is equivalent to an input current drift of:

$$(2 \cdot 10^{-5} I + 10^{-3}) A/K$$

Further it is desirable to place the current shunt and measuring equipment in an oven. The stability of the temperature in the oven must be within 0.4 K. This requirement is relatively simple to realize.

To stabilize the current it is desirable to know the dynamic behavior of the current loop. Neglecting the parasitic effects, we find with n power supplies and n coils (inductor and resistor) placed in series an admittance:

$$Y(\omega) = \frac{1}{nR} \cdot \frac{1}{1 + j\omega\tau_1},$$

with the time constant $\tau_1 = L/R$. Measurements on a dipole prototype showed $\tau_1 = 0.62$ s.

A second time constant τ_2 is introduced by the dynamic behavior between the output voltage of the n power supplies and the driver voltage. This time constant is about 3 ms. About the parasitic effects the following remarks can be made: Iron losses in the core are negligible because of the use of laminated iron. Crosstalk between the turns is only relevant at frequencies above 20 kHz. By placing a filter in the loop, this effect can be suppressed. In this way parasitic oscillation can be avoided. By choosing the integration time constant of the PI-controller the same as the time constant of the dipoles (τ_1) (see Figure 5) and making the static open loop gain equal to $\tau_1/2\tau_2$, the closed loop behavior is similar to a second order critically damped process (damping ratio, $\beta = 1/2\sqrt{2}$).

V. CONCLUDING REMARKS.

The use of a distributed power supply system combines the advantages of one big power supply with those of separate power supplies. The currents in all dipoles are the same, with low voltages at the electrical connections. The leakage current is low. The reliability is high (10% overdesign). The repair-time is short due to modular construction. The solution is economical and stabilization is relatively simple.

VI. REFERENCES.

- [1] J.I.M. Botman, et. al., Rev. Sci. Instr., Vol.63, No.1, (1992), 1569.
- [2] R.W. de Leeuw, et. al., These proceedings.
- [3] Boling Xi, et. al., Proc. Eur. Part. Acc. Conf. (EPAC) London, (1994), 2232.
- [4] A.H. Kemper, R. Verseijden and R.G.J. Oude Velthuis, EUT Internal rapport, VDF/NK 94.43, (1994).

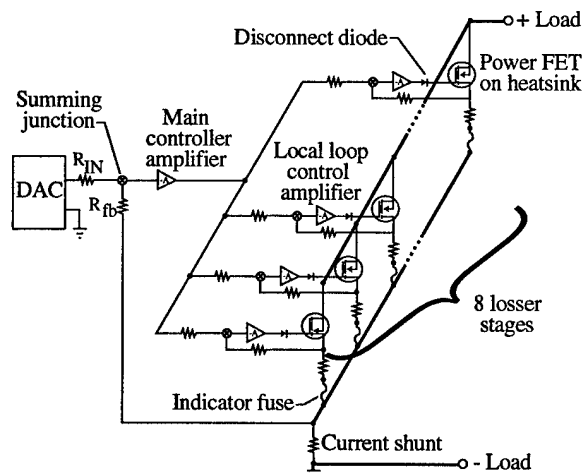


Figure 2: Basic shunt regulator circuit. Each MOSFET has local feedback loop.

The shunt module uses the same Isothermal Controller Module (Highland Model M427) used by the CEBAF trim power supplies[2]. This module contains a manganin shunt, DAC, and reference amplifier integrated on a temperature controlled substrate. Regulation stability of .05% per 24 hours is achieved.

Forced air cooling was chosen to simplify the electrical isolation requirements and is achieved using airflow obtained from a blower fan mounted in the top of the rack in which the shunt cardcages are mounted.

The shunt module uses a Motorola MC68701C uP for remote communications, readback of internal levels, and alarm monitoring. The uP and readback circuitry was borrowed intact from the CEBAF trim boards[3]. Only a few lines of code needed to be changed to adapt it to the shunt usage, which shortened the project turn-around. A serial communications interface is used to communicate with the external control network via RS-485 protocol. The link operates full duplex at 76.8 Kbaud. Up to 32 shunts may share a common RS-485 link.

III. ELECTRICAL ISOLATION

Shunt modules present unique requirements for electrical isolation. Depending where on the magnet string the shunt is electrically connected, it may be required to "float" at up to 600 VDC above Earth Ground. Total electrical isolation from the remote programming source, from other other shunts in the cardcage, and from Earth Ground is required. This isolation is achieved by transformer-isolation of the supply circuits providing control power to the each module and by electrically isolating the modules from the chassis by use of insulated supports and a special connector mounted on G10 laminate.

Isolation for remote programming and readback information is achieved by opto-isolating the RS-485 communications link and three discrete digital control

lines. Initial attempts to use 5KV opto-isolators were unsuccessful, due their slow rise and fall time response characteristics. In order to operate the link at 76.8 Kbaud, use of fast opto-isolators (6N138s) was necessary. Since the 6N138s are rated at only 3KV breakdown, it was decided to doubly-isolate each signal, passing them through two tiers of opto-isolation. The common circuitry between these two tiers is connected to Earth Ground. Should a voltage surge cause an opto-coupler to break down, the fault current would be intercepted by Earth Ground and not applied across the second tier, possibly causing it to fail as well. As a precaution, all input/output circuits are highpotted to 3KV DC after initial assembly of the chassis to insure integrity of isolating circuitry. Connections to a module are via a multipin connector which is isolated from the adjacent module and from chassis ground by mounting it on an insulated bulkhead fabricated from G-10 laminate. To-date, the isolation scheme has worked well. No failures of these circuits to maintain electrical isolation have been reported.

IV. DETAILS OF MODULE CONSTRUCTION

The shunt module itself is constructed on an 10" x 17" finned aluminum extrusion, which serves as a heatsink. The power MOSFET transistors are mounted directly to the heatsink, using sockets to facilitate replacement. The heatsink itself serves as the +LOAD terminal, forming a common connection between the MOSFET cases.

All low level circuitry is contained on three removable circuit boards mounted to the non-finned side of the heatsink. The three boards are interconnected by a wiring harness and plug-in connectors. This facilitates repair-by replacement.

The power supply board contains a common rectifier-filter, from which is developed +24VDC, +15VDC, +5VDC, -15VDC, and -24VDC. Three-terminal linear regulators are used to develop each discrete voltage. The rectifier is fed with 28VAC from a step-down transformer located off the module in the rear apron of the card-cage chassis. This transformer has 5KV winding insulation.

The controller board contains the microprocessor, A-Ds, and analog signal conditioning circuitry. Two A-D converters are employed. A 16-bit converter is dedicated to readback of the output current. A 12-bit A-D is multiplexed to monitor output voltage, heatsink temperature, isothermal module temperature, and an auxiliary output current level.

The driver board contains the eight parallel driver stages and the isothermal module. The current sensing resistors connected to each MOSFET source are thermally coupled to the main heatsink using an aluminum bar in a manner similar to that of the power supply module. The common -LOAD buss employs a stamped copper buss bar, soldered perpendicular beneath the driver PCB.

V. DETAILS OF CARDCAGE CONSTRUCTION

The shunt modules are designed to slide into a cardcage-style chassis, making electrical connection by means of a connector mounted on the rear apron of the heatsink. Since the shunt is directly connected to a magnet string with potentials as high as 600 VDC above Earth Ground, safety considerations require that the module be totally enclosed in a chassis whose covers are interlocked to the dipole string power supply.

Unlike a conventional power supply, for the shunt module the hazardous source of power is the box power supply. At CEBAF, the shunt cardcages are often located in entirely different buildings than the box supplies. For this reason, it is necessary to completely interlock the shunt modules and cardcage to that box supply. Removable front and rear chassis covers are interlocked to the box supply to prevent personnel access to the shunt module while the magnet string is energized. Heatsink overtemperature or loss of more than two driver stage fuses will also trip off the box supply.

For safety purposes and ease of interlocking to the box supply, only shunts connected to a common magnet string are housed together in a common chassis. To suit the CEBAF applications, two cardcage packages were developed, a single-channel and a four-channel unit.

In the single-channel chassis, the shunt module slides in horizontally on insulated card guides. Because airflow through the rack is in a vertical sense, an integral linear squirrel-cage fan is employed to force air across the heatsink fins. An integral airflow sensor is interlocked to the box supply to remove power should this fan fail. In the four-channel unit, the modules mount vertically, and air flows directly over the heatsink fins from vents strategically located in the top and bottom chassis covers.

VI. INITIAL OPERATING RESULTS

From an operational standpoint, the shunts have worked as desired. No unusual or undesirable modes of operation have been experienced. A single module design has sufficed for all applications to date. Field repair of a failed module is accomplished by remove-and-replace, requiring only a few minutes to restore service to a faulted channel. Remote programming and readback, via the RS-485 link, has worked without problem-validating the strategy of using the same microprocessor circuitry and software as the time-proven trim cards[3].

There are presently 112 shunt regulators installed and operational at CEBAF. Typically, one module shunts one magnet, however there are eight applications where a module shunts two adjacent magnets in a string. There are

34 four-channel chassis and 11 single-channel chassis installed.

In the past three and one half months, we have accumulated a total of 150,000 module-hours of operation [4]. Six failures have been experienced. These failures were all traceable to workmanship errors in the initial manufacture (pinched wires, poor solder connections, etc.).

VI. REFERENCES

- [1] E. Martin, et al., "Re Use of Common Elements of a Corrector Power Supply Design to Develop A Dissipative Shunt Regulator Design," E. Martin, et al., Conference Record of 1992 IEEE Nuclear Science Symposium, October 25-31, Vol. 1, p. 563-565.
- [2] N. Dobeck, "Precision Power Supply Control Module," Conference Record of the 1991 IEEE Particle Accelerator Conference, May 6-9, Vol. 2, p. 935-937, IEEE91Ch3038-7.
- [3] N. Dobeck, et al., "Precision 32 Channel Power Supply System," Proceedings of the 1990 Linear Accelerator Conference, September 10-14, p. 490-492, LANL LA-12004-C.
- [4] W. Merz, et al., "Early Operations and Reliability Experience With the CEBAF DC Magnet Power Supplies," to be published in Proceedings of the 1995 IEEE Particle Accelerator Conference.

A Multi-Channel Corrector Magnet Controller *

G. E. Leyh, A. R. Donaldson SLAC, Stanford CA 94309

L. T. Jackson LBL, Berkeley CA 94720

ABSTRACT

Approximately 1000 individual X-Y corrector magnets will be installed on the PEP-II rings, arcs, and injector lines. Each magnet will require a bi-polar current of up to 12 A, with a 24 hour stability of better than 0.1%. A 16 channel, modular power supply design has been developed to meet this requirement, with emphasis placed on reliability, repair time, and installed cost per channel. This design, which is based on a 6U Eurocard crate architecture, has 16 slots for individual drive modules, plus a 17th slot for crate diagnostics and interface to the control system. The crate is air cooled. Each drive module consists of an H-Bridge MOSFET switching array, input and output filter networks, two isolated precision current sensing elements (feedback and monitor), and an error amplifier, plus extensive fault detection and current limiting circuitry. Technical specifications, diagrams, and test results are presented.

INTRODUCTION

The PEP-II project will consist of two storage rings, each 2.2 km in circumference, plus an additional 4.6 km of extraction, bypass, and matching beam line sections. Approximately 1000 horizontal and vertical correction magnets will be utilized on these beam lines, with the maximum current requirements for each corrector magnet ranging from ± 6 to ± 12 Amperes. Control of these correctors will be distributed between two fundamentally different control systems; one will provide an analog command signal, the other will provide a serial digital command link.

A unified design architecture is desired for all of the corrector power supplies, in order to take advantage of the economies of scale and mass production, and to simplify documentation and maintenance procedures for the entire installation. A modular crate architecture has been chosen, in order to meet the needs of the various corrector topologies that will be encountered on the storage rings and linac.

A high emphasis will be placed on the total machine reliability, since the primary mission of the PEP-II facility is to become a "factory" for neutral B mesons. Therefore, the MTBF (Mean Time Between Failure) and the MTTR (Mean Time To Repair) are important underlying factors in the design of this corrector power supply system.

REQUIREMENTS

The overall performance requirements for each of the corrector drive modules are given as follows:

Input DC Bus Voltage	20 to 50 V
$I_{out, max}$ (programmable)	± 6 to ± 12 A
$P_{out, max}$ (per channel)	600 Watts
Ripple Current (DC to 50 kHz)	± 0.05 % of I_{max}
Stability	± 0.05 % of I_{max}
Reproducibility	± 0.1 % of I_{max}

In addition, each power module must have:

- Internal protection against electrical faults
- An automatic thermal shutdown feature
- The ability to phase-lock its internal switching frequency to the 60 Hz mains
- A redundant readback of the output current
- Full "hot swap" capability

SYSTEM DESCRIPTION

A modular crate architecture is utilized in this design, in order to maximize the flexibility and serviceability of each installation. The physical crate is a standard 6U by 220 mm Eurocard format, available off-the-shelf from Schroff [1]. The crate has 17 slots, one for a control system interface card, and 16 slots for power conversion modules. Each power module has a 'personality card', which is mounted directly on to it. This personality card contains passive components that determine the maximum output current limit, the transfer function of command voltage to output current, and the compensation network for the error amplifier section. If a power module is replaced, the personality card is removed from the old module and installed on the new one. In this way, all of the operating parameters specific to the load will be in effect with the new module. All cards and modules are accessible from the front of the crate, and connect to the backplane using standard Eurocard connectors. Air cooling for the crate is provided by fan rack sets and plenums, also offered by Schroff, which draw in cool air from the aisle and pass it through the crate and into the rack, thus keeping the rack interior at positive pressure. A single hinged front cover provides access to the 16 power modules.

A simplified block diagram of the crate is presented in Figure 1. A unipolar bulk power supply provides the main DC power to the crate through a 180A Powerpole connector on the

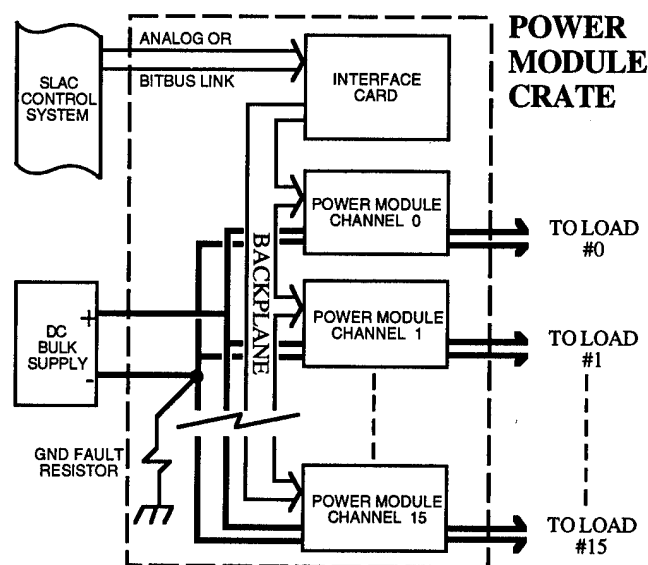


Figure 1.

*Work supported by the Department of Energy, contract DE-AC03-76SF00515 (SLAC) and DE-AC03-76SF00098 (LBL)

rear panel. Command and synchronization signals are provided through the backplane by the interface card, which will be either analog or digital based, depending on the installation. The main DC power is distributed to the individual modules along with utility voltages and control signals also via the backplane. A standard 48 pin, type "E" DIN connector is used for all signal and power connections between each power module and the backplane. The interface card plugs into the same backplane, and uses the VME format for connector type, positioning, and module width. By using the card to backplane approach, all internal wiring has been eliminated, except for the 120 VAC power and the main DC power wires. All other external connections, including the outputs to the magnets, are accomplished through printed circuit mount connectors on the backplane, thus allowing the assembly work to be performed by outside board fabricators. Since the crate enclosures come pre-assembled from Schroff, the only in-house assembly work to be performed is to bolt on the backplane, front and rear panels, and insert 16 power modules and the appropriate interface card. The personality cards are then added to give each power module its own specific characteristics. A computerized test bench is used for testing the finished crate.

CONTROL

The installed corrector chassis will have to accommodate two fundamentally different types of control systems. The existing system utilizes a network of Multibus based computers, each of which controls a set of CAMAC crates. DAC modules in the CAMAC crates are used to generate 16 individual analog control signals, which are cabled in parallel to the corrector crate. These command signals are then piped straight through the interface card to the backplane. For the PEP-II rings, the control system will communicate directly with the power supplies, through a serial Bitbus® data link. The power supply will be responsible for performing its own digital-to-analog conversion, and supporting a digital interface with the control system. In the PEP-II scheme, the interface card will contain a DAC, multiplexed 16 channels wide, plus some logic glue and the Bitbus® specific support circuitry.

POWER MODULES

The function of each power module is to provide a regulated drive current to its respective load, in proportion to the command signal from the interface card. The power module also returns a redundant current signal to the interface card, as well as status and fault data. A functional diagram of the power module is shown in Figure 2. The command signal is received by a unity gain differential amplifier, whose purpose is to prevent ground loops, and to reject common-mode noise. The differential amplifier (Burr-Brown INA105) contains the laser-trimmed gain setting resistors, and as a complete unit exhibits a typical gain tolerance of 0.01% and a stability of 1 ppm/°C. The command signal is then compared against the current feedback signal by the error amplifier stage, which uses an OP-77 as the gain element. Compensation is provided by a single pole-zero network, which resides on the personality module. The resultant error signal is then sent to the input of a power servo amplifier module, also mounted on the PC board, which operates as a voltage amplifier with a gain of approximately 6, and has an effective rolloff frequency of about 2.5 kHz.

The servo amplifier used in this design is a commercial unit, the 30A8, manufactured by Advanced Motion Controls [2] for applications in robotics and process control.. This model was chosen for its compact size, ruggedness, PC mount capability, and its internal fault protection system, which provides protection against thermal overload, and output short circuits (to either rail). A TTL fault signal is provided by the 30A8, which indicates the presence of a fault condition on the servo amplifier. This signal is applied to an external latch on the power module, which will shut down the servo amplifier if a fault condition persists for more than a few seconds.

The 30A8 produces unfiltered DC pulses from its H-bridge output stage, and must therefore be filtered appropriately before delivery to the load. The filter design employed is a variation of the classical Praeg filter [3], arranged to be symmetrical around power ground. The filter is set to be critically damped, and attenuates both the differential and common-mode components of the output ripple.

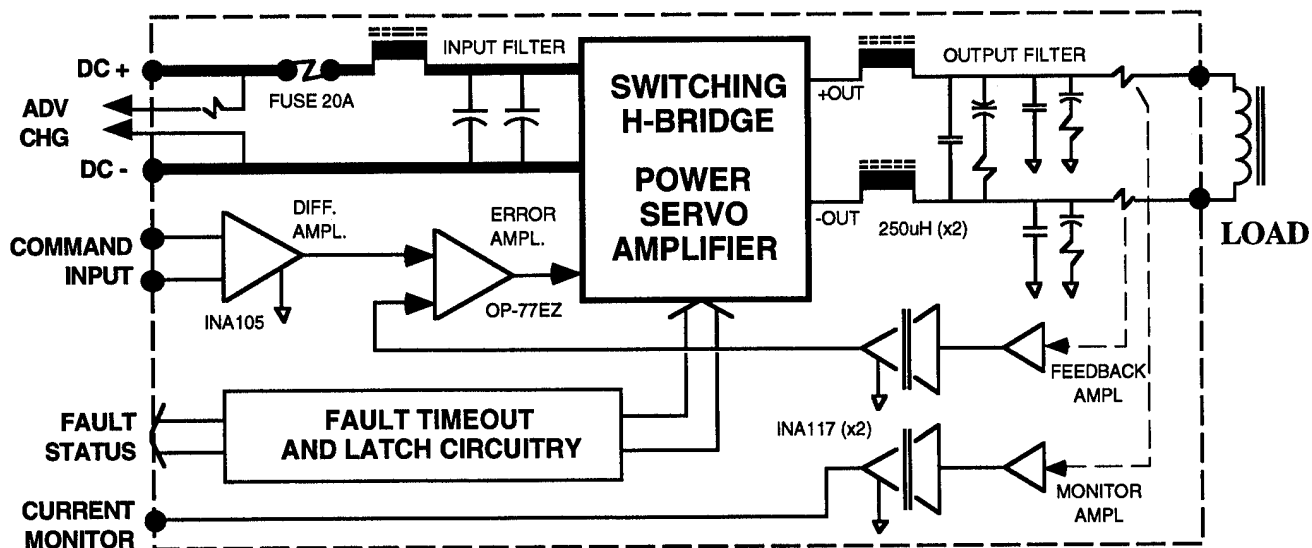


Figure 2. Power Module.

Following the filter are two precision 4-terminal Manganin shunt resistors, one in each output leg. These 10 milliohm shunts, which are made by Isabellenhütte, have a tolerance of 0.1%, and a measured stability of 13 ppm/°C, typical. The voltage developed by each shunt is amplified by an isolated amplifier, and referred to ground by a precision differential amplifier (Burr-Brown INA117). One shunt signal is fed back to the error amplifier, while the other is independently sent back to the interface card as a redundant current monitor signal.

The DC power input to the module is equipped with an LC filter network, which acts to decouple the switching noise of the servo amplifier from the DC mains. During a 'hot swap' operation however, the inrush currents that charge this DC input filter capacitor must be controlled, in order to prevent arcing damage to the DC power connection on the backplane. This is accomplished by a 2 pin auxiliary connector, which is set up to make initial contact with the DC on the backplane, and pre-charge the filter capacitor through a current limiting resistor before the main connector makes contact. This method eliminates the need for any pre-charge circuitry directly in the DC input circuit path, and thus improves the overall expected MTBF of the system.

MONITORING AND DIAGNOSTICS

In order to minimize the time required to make repairs, a crate diagnostics summary display is provided on the front of the interface card. This display indicates which module has experienced a fault, and if that fault condition is still present. There are also diagnostics for faults occurring on the crate, or in the bulk DC power supply. A crate fault will be indicated if the external interlock input to the crate is opened, or if excessive current is detected in a shunt resistor which connects the negative DC power busbar to the chassis ground. A module fault will be indicated if a given module experiences any one of the following fault conditions for more than a couple of seconds:

- A short circuit of either output lead to ground
- A heat sink temperature excursion in excess of 65°C
- An overvoltage or undervoltage of the DC power input
- An appreciable difference in currents on the output leads

Under the first three fault conditions listed above, the power module will protect itself by shutting down. The fourth fault condition is detected by a comparator circuit on the interface card that monitors the difference between the feedback and the monitor shunt signals on each channel. If the difference exceeds a preset value, a fault condition will be indicated for that channel, but the module will be allowed to continue operating, until the difference becomes large enough to trip the ground fault protection circuitry, either on the crate or in the module. When a module fault does occur, the technician at the site identifies the suspect module by looking at the diagnostic panel, and simply replaces it with a new one. A screwdriver is the only tool required to perform this replacement. If the problem still persists, then the cause is probably in the cable plant or at the load, since all of the electrical components for that channel, including the output filters, are on the module. Test points for the input and output voltages are available on the front panel in order to verify proper crate operation.

TEST RESULTS

A prototype power module has been constructed, and has been extensively tested in an environmental chamber, under a variety of conditions. Presented here are the measured performance specifications of the completed power module:

TEST CONDITIONS (unless otherwise noted)

DC Mains Voltage	40 Volts
Maximum current limit	12 Amperes
Load Impedance	5 Ohms + 6 mH
Switching Frequency	30 kHz
Temperature Range	15 to 65°C

SPECIFICATIONS:

Initial Offset Error	480 uA
Transfer Function vs. temperature 10-50°C non-linearity repeatability, card-to-card	1.000 V = 2.000 A 13 ppm/°C 0.025% ±0.1%
Small Signal Bandwidth 3dB, for 60 mA signal	1.5 kHz
Slew Rate (70 V mains) Step Response (5 A step)	2500 A/sec 12 mS
RMS Output Current Noise DC to 200 kHz (0 A) DC to 200 kHz (12 A)	0.01% of FS 0.01% of FS
RMS Common-Mode Noise RMS Noise injected back into DC Busbar	120 mV 20 mV
Power Dissipation (at 12 A)	19 Watts
Output Short Circuit Duration Line-to-Line Line-to-Ground	CONTINUOUS 2 sec (Unit shuts down)

REFERENCES

- [1] Schroff Inc., Warwick RI.
- [2] Advanced Motion Controls, Camarillo CA.
- [3] W. F. Praeg, "A high-current low pass filter for magnet power supplies," *IEEE Trans. Industrial Electronics and Control Instrumentation*, Vol. IECI-17, No.1, pp. 16-22, Feb. 1970

ADVANCES IN POWER SUPPLY AND CONTROL SYSTEM FOR ELECTROSTATIC ACCELERATORS

S.N.Chumakov, A.D.Goncharov, A.N.Malygin, V.P.Ostanin, B.N.Sukhina, V.S.Tupikov,
Budker Institute of Nuclear Physics, 630090, Novosibirsk, Russia

Abstract

Some technical advances and ideas, which allow, the construction of highly reliable, simple and cheap subsystems for electrostatic accelerators and other high voltage devices, are described. The described subsystems were tested during their extensive running for several years on a series of the accelerators ION-1500, ION-300 [1]. They are

- a small sized high efficiency system for power supply via a big isolating gap which is based on a high frequency resonant transformer with a low magnetic couple factor 0.1-0.3 (its characteristics are: 2.2KW, efficiency 90%, 6 cm isolating gap for 500KV);
- a system for a highly efficient medium and low-power regulators based on magnetic amplifiers and working at high frequency power delivered by the above mentioned system;
- an intellectual multifunctional single-board noiseproof controller LOCUS placed under high potential is linked with the central computer by a fiber optic link.

I. POWER SUPPLY

A power supply system of the DC-operated ion source located under the high potential of the basic accelerator's rectifier consists of an unified series of power supply modules, which differ by the executive part and output characteristics. The blocks of the system use the local network of the increased frequency (20 KHz) and are characterized by the high specific gabarit power and foundation capability of overloading. The electrical power is transmitted to a high voltage terminal via a gas insulating gap by a disjunctive transformer and is absolutely independent of the accelerator energy.

II. THE FUNCTIONAL STRUCTURE OF HIGH VOLTAGE TERMINAL MODULES

In Fig.1, the functional chart of the terminal is presented. By functions, the terminal structure can be divided into three blocks:

1. The stabilization blocks are intended to stabilize the local network voltage in a crate and restrict the transmitted redundant power:
 - (a) the stabilizer of the parallel type (350V, 1.0KW, 20KHz, 28V, 20KHz, +24V, +6V, +5V.st.) has two feedback loops:
 - i. A hardware loop consists of the magnetic amplifier included in parallel with the load and used as a regulator;
 - ii. A software loop consists of the transmission into the computer of measured value of redundant stabilizer power for the generator's power correction;

- (b) the serial stabilizer (350V, 1.0KW, 20KHz, 28V, 20KHz, +24V, +6V, +5V.st.) is used to vary the second crate placed under bias of ion extractor. The magnetic amplifier included in series with the load in the stabilization circuit is used as a regulator.

The stabilizers consume the power through high voltage disjunctive transformers T1, T2:

T1-unbuckle voltage 1.5MV The power to 2.0KW
T2-unbuckle voltage 30KV The power to 1.0KW

2. Service units are a receiver-transmitter or a multifunctional single-board LOCUS-controller used to exchange data with the computer, to output the managing voltages and control the parameters in the supply units of the ion source.

3. Controlled power supply units for ion source:

leaker	1300V, 1mA
suppressor	5KV, 3mA
extractor, focus	10KV, 5mA
extractor, focus	30KV, 20mA
heater	500W
magnet coil	30V, 3A, 100W
RF-generator's anode	1200V, 0.3A, 400W
cathode's heater	7V, 70A, 500W
discharge	0-150V, 8A, 500W

The dynamic range of the output parameters 20.

The accuracy of the output parameters 0.5%

This set of blocks is suitable for supply the RF ion source, duoplasmatron, or the other similar devices.

III. THE DESIGN OF HIGH VOLTAGE TERMINAL WITH A POWER TRANSMISSION TRANSFORMER

In the design, the principle of the functional blocks is realized. The electronic blocks are located in a skeleton of the VME-type. A managing part of each supply unit is assembled on identical boards, incorporated with a stabilizer and the receiver-transmitter, or the LOCUS-controller, by a internal trunk.

The magnetic amplifiers (one of three nominal types) are installed on the managing boards and used as the regulators: 0.1KW 28V 20KHz; 0.5KW 350V 20KHz; 1.0KW 350V 20KHz. These amplifiers are mounted on ferrite rings as compact monoblocks. The advantage of the magnetic amplifier is its high reliability and ability of restricting the short circuit current. The executive parts of the blocks depending on the output parameters are mounted on the managing boards or serve as separate modules. If the output power (or voltage) more than 100W (or 10KV), the executive part is located outside the power units. The transmission of the electrical power for the terminal power supply is made at a frequency of 20kHz by the resonant transformer T1 of the armoured type, the primary and secondary coils

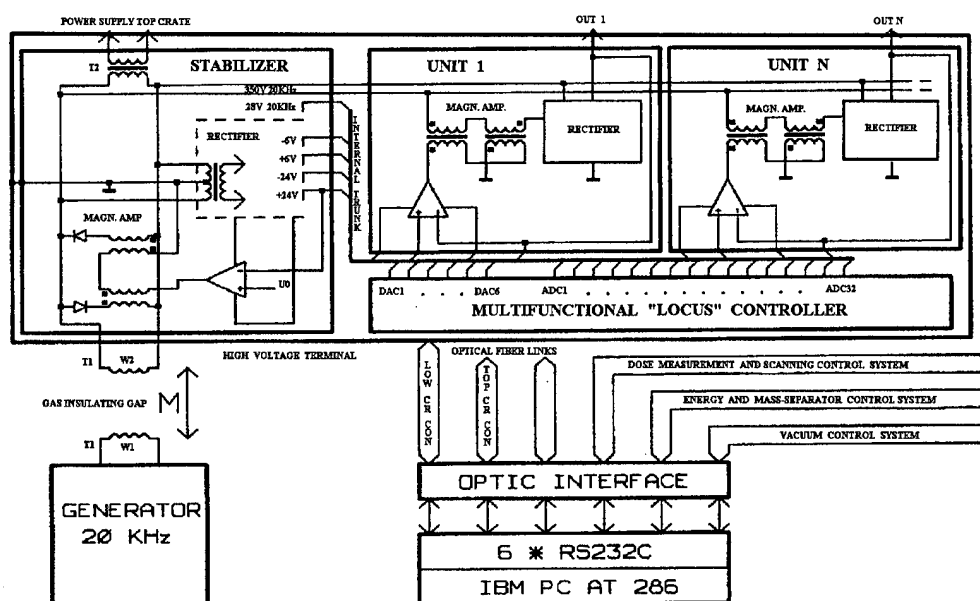


Figure 1. Distributed Control System

of which are inductively connected and separated by the high voltage gas-insulating gap. The core of the transformer is made in the form of two ferrite cups, 200mm in diameter. The material and the form of the cores, the transformer windings are chosen on the basis of the analysis on optimization of the parameters to achieve the maximum values of the Q-factor for the primary and secondary contours, to obtain the necessary factor of the magnetic coupling between the windings, and minimize the power losses.

In Table 1, the main characteristics of the transformers are presented for two accelerators ION-300 and ION-1500 (for 300KV and 1500KV respectively):

type of accelerator	ION-300	ION-1500
high voltage gap	60mm	105mm
transmitted electrical power	2.0KW	0.3KW
factor of magnetic coupling	0.215	0.087
non-loaded Q-factor	66.7	67.0
efficiency	0.90	0.75

IV. CONTROL SYSTEM FOR IMPLANTERS

There are two types of control systems for the ion implanters ION-1500 and ION-300. The first one is on a CAMAC base and the second one is a distributed control system designed specially for physical installations and consisting of several universal intellectual multifunctional single-board stations, which are connected to the central computer by means of duplex optical communication (isolation up to 2MV). The systems are adapted to environments with high level of the powerful interference electric pulses. All the subsystems are operated by the central IBM-PC/AT, or compatible computer, under onetasking program (one task manages all the subsystems) in the first case and multitasking one with share time in the second case. To visualize, both systems use a multiwindow graphic interface.

The ION-1500 control is realized by a conventional

COMPUTER-CAMAC model. The process is operated by the central IBM-PC/AT or the compatible computer. It is connected through a CAMAC-adapter (in IBM-PC) to a CAMAC-controller and controls the following modules:

- SAS (switch of analog signals);
- ADC;
- HVTC (high voltage terminal controller);
- 2 channels of DAC;
- I/O registers

SAS serves to switch and pass to the ADC one of the signals: energy, ion beam current, profiler current, voltage of the first section, rectifier current, voltage and current of the primary winding of the accelerator, voltage and current of the generator, and current of a separator magnet.

The HVTC executes the control of a leakage valve, beam focusing, anode power supply, transformer temperature, power, and board power supplies of the high voltage terminal.

The first DAC sets the current of the separator magnet and the second one sets the energy of beam acceleration.

The I/O registers control the switching of valves of the vacuum system and start of the profiler gauge.

All the units of the system are operated by a single program written in FORTRAN for IBM-PC running under OS DOS.

As to automation of ION-300, the following rules are accepted: distribution of the control system and multitasking with share time in the managing program. Each separate process in the installation corresponds to a separate intelligent LOCUS-controller which has several measuring and managing functions (ADC, DAC, timers, I/O - registers etc.). This controller is capable of working independently after loading a preliminary program from the central computer under the direct management of the central computer by the standard protocol. The functional difference of the processes on a hardware level and the use of the multitasking program (multitasking OS, or compilers of high level languages like MODULA-2 which enables us to run the procedures with share time) substantially simplify the

programming process. The simplification results in writing the functioning algorithm for the individual installation unit in the form of the procedure similar to our case (MODULA-2) or task (QNX, UNIX etc).

Each procedure of this kind has two forms of communication: downwards to the intelligent controller and upwards to the program manager, which already uses the data of all the units and gives the orders to each procedure. The base of this distributed control system for the installation ION-300 is the LOCUS-controller which includes

1. ADC with continuous dynamic integration of the input signal, a two-wire galvanic isolated input, a programmable integration time ranging from 0.2 to 26 ms (word length ranges from 9 to 16 bit respectively) at an input DC-voltage ranging from + 5.16 to -5.16V;
2. an analog two-wire 32-channel switch;
3. 6 channels of pulse-width digital to analog converters which has a 14 bit resolution and an output voltage ranging from -5.08 to 5.08V;
4. 32 input registers (TTL);
5. 24 output registers (TTL);
6. 5 channels of programmable multifunctional timers, which are switched by jumpers and have a possibility of pulse counting, measuring time intervals and forming the pulses of controlled frequency and duration;
7. protection of all I/O signals which pass through plugs (115 lines of diode-resistor chains). The protection is effective against the powerful interference electric pulses with spectra up to approximately 30MHz;
8. a processor i8085, 8KB of ROM and 2KB of non-volatile RAM;
9. a duplex optic connection to the central computer (communication format is compatible to RS232).

The processor has an automatic restart in the following cases: after failure or cycling of the program, or after sudden jump of power supply voltage.

For PC-LOCUS communication, a 6-channel serial interface for IBM-PC and a TTL-to-optic adapter are developed. The serial interface has FIFO-buffers (the depth is 32 bytes) for each input and output. This enables us to increase the rate of the PC-adapter communication and to get rid of the data loss.

To avoid serious accidents in the installation as a result of failure in the apparatus or programming, the hardware arbitrator to block the accidental conditions was developed. In the control system for ION-300, the given arbitrator executes a function of preventing against illegal situations, which are caused by operator failure or break-down in a unit.

In contrast to CAMAC, this single-board intelligent controller can be placed near a particular controlled system. The ION-300 comprises

1. two LOCUS-controllers working under a potential up to 300KV in the ion source system;
2. one LOCUS and an arbitrator module operating by the vacuum-gas system of the implanter;
3. one LOCUS and an arbitrator module controlling the high voltage system of the implanter;
4. two LOCUSES controlling wholly the implantation chamber for semi-conductor plates, including the management

of two step-motors and control of the implantation dose. To measure the charge the block forming with LOCUS the charge-digital converter (accuracy is 97.6C per count) is developed. Such connection considerably reduces the trace of a system that results in the cable saving and failure reduction.

V. CONCLUSION

More than a two-year experience of operation (about 1000 hours) of the multifunctional LOCUS-controller has shown its good reliability. A series of the experiments were conducted which showed the absence of halts (for example, as a result of short-term short circuits of some wires to the "Ground" through the capacitor 0.01uF). There were no halts under real conditions during a high voltage breakdown to 300KV. A distributed control system turned out to be successful in the sense of the managing program writing process.

References

- [1] A SERIES OF ION ACCELERATORS FOR INDUSTRY, B.N.Sukhina et al., Proc. of PAC-95 Conference.

MODE ANALYSIS OF SYNCHROTRON MAGNET STRINGS

M. Kumada,

(email) kumada@uexs32.nirs.go.jp

National Institute of Radiological Sciences, 4-9-1 Anagawa, Inage-ku, Chiba 263, JAPAN

Abstract

Synchrotron magnet strings is able to be regarded as a 6 terminal ladder circuit. It can be shown that the voltage and current has two different modes of resonant property. this mode is able to be decoupled by the transformation. In presence of symmetric configuration, it is further shown that the mode are reduced to two orthogonal mode of normal and common mode which enables us to find the analytical solution.

I. INTRODUCTION

In a synchrotron where a current of a magnet string is excited trapezoidally, a reproducibility, a stability and a tolerance of a ripple content of the excitation current is stringent due to a slow beam resonant extraction property of the synchrotron. Among others, the relative ripple content is one of the most important and required to be a ppm level or less. Most of the synchrotron utilizes a thyristor controlled power supply generating voltage of logical ripple which is a multiple of number of thyristor firing pulses. There is also an illogical ripple which is due to imbalance among the phase and amplitude of primary line voltage or noise from the sensor such as DCCT where the frequencies are integer fractions of the fundamental harmonic of 50 Hz. Furthermore a spike voltage is induced across each thyristor when the thyristor is turned on and off. The spike frequency ranges between a few kHz to a tens of kHz depending upon magnitude of capacitances and other parameters of a relevant circuit. This thyristor spike has long been one of the major causes limiting the performance of the synchrotron power supply. The spike is regarded as source of a high frequency effective ripple component. A close look of the spike reveals that amplitude of a train of spikes is modulated by lower illogical frequencies and considered to be other source of illogical ripple.

In conventional research and development of a power supply illogical ripple have been suppressed by improving an imbalance among phases of primary AC voltages and equalizing a timings of firing pulses of each thyristor or by an active filter and a band-pass filter.

The spikes and logical ripples are suppressed by low pass static filter. In spite of those efforts, achieving the ripple content of ppm level has been difficult.

Reviewing the existing lower limit of the ripple performance of the conventional technology, we proposed a model which includes a stray capacitance of the coil to the ground [1,2,3,4]. In it, a magnet string is modeled as a ladder circuit, which is a repeated circuit of lumped element of L, C and R. The excitation coils of the magnet are divided into the upper coil and the lower coil. The upper coil is connected to neighboring coil in series instead

of connecting to its lower coil and again connected to the separated upper coil of next neighboring coil and so on. So does the lower coil. the magnet core is regarded to have ground potential and all the magnet core are connected in series by the earth line. The model circuit of an unit cell is shown in Fig. 1.

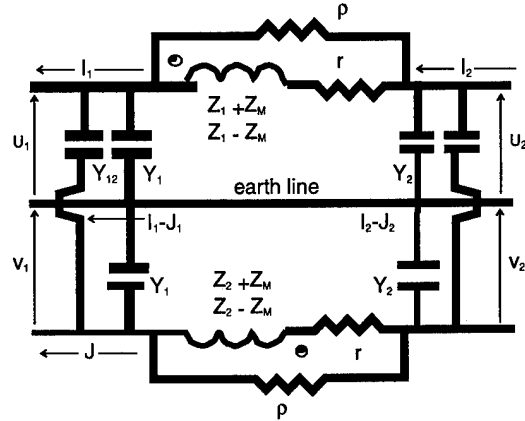


Fig. 1: Unit cell of the six terminal magnet string. p represents the bridge resistor as well as the ac loss of the magnet.

In conventional synchrotron magnet strings, although the earth line is not physically set up, the capacitance between the excitation coil and the magnet yoke can not be neglected and a similar six terminal circuit as Fig. 1 may be applied in analyzing the magnet string.

II. ANALYSIS

Let us designate the relevant parameter of the voltage and the current of the upper coil U and I and the lower coil V and J . The suffix of the input and output voltage and current is designated as 1 and 2. We then write the transfer matrix of the voltage and the current in general as

$$\begin{pmatrix} U_1 \\ I_1 \\ V_1 \\ J_1 \end{pmatrix} = \begin{pmatrix} 1 + Z_1 Y_1 & Z_1 & Z_{M2} Y_2 & Z_{M2} \\ Y_1 (2 + Z_1 Y_1) & 1 + Z_1 Y_1 & Z_{M2} Y_1 Y_2 & Z_{M2} Y_1 \\ Z_{M1} Y_1 & Z_{M1} & 1 + Z_2 Y_2 & Z_2 \\ Z_{M1} Y_1 Y_2 & Z_{M1} Y_2 & Y_2 (2 + Z_2 Y_2) & 1 + Z_2 Y_2 \end{pmatrix} \begin{pmatrix} U_2 \\ I_2 \\ V_2 \\ J_2 \end{pmatrix} \quad (1)$$

with

$$Z_M = Z_{M1} = sM_{12} = Z_{M1} = sM_{21}.$$

Each component of the transfer matrix of eq. (1) is non-zero and have finite value. the pair of the voltage and current of (U, I) and (V, J) is considered to be a representation of a pair of two different mode. Non-zero component of the matrix signifies that the two mode is coupled each other.

By intuition, one is able to find the equation for the sum component and difference component of the voltage and

current which is written as,

$$\begin{pmatrix} U_1 + V_1 \\ I_1 + J_1 \\ U_1 - V_1 \\ I_1 - J_1 \end{pmatrix} = \begin{pmatrix} \frac{1}{2} \left\{ \begin{matrix} 2 + (Z_1 + Z_M)Y_1 + \\ (Z_2 + Z_M)Y_2 \end{matrix} \right\} & \frac{1}{2}(Z_1 + Z_2 + 2Z_M) & \frac{1}{2} \left\{ \begin{matrix} (Z_1 + Z_M)Y_1 - \\ (Z_2 + Z_M)Y_2 \end{matrix} \right\} & \frac{1}{2}(Z_1 - Z_2) \\ \frac{1}{2} \left\{ \begin{matrix} Y_1(2 + Z_1Y_1) \\ + Z_MY_2 + \\ Y_2(2 + Z_2Y_2) \\ + Z_MY_1 \end{matrix} \right\} & \frac{1}{2} \left\{ \begin{matrix} 2 + \\ (Z_1 + Z_M)Y_1 + \\ (Z_2 + Z_M)Y_2 \end{matrix} \right\} & \frac{1}{2} \left\{ \begin{matrix} Y_1(2 + Z_1Y_1) \\ + Z_MY_2 - \\ Y_2(2 + Z_2Y_2) \\ + Z_MY_1 \end{matrix} \right\} & \frac{1}{2} \left\{ \begin{matrix} (Z_1 - Z_M)Y_1 - \\ (Z_2 - Z_M)Y_2 \end{matrix} \right\} \\ \frac{1}{2} \left\{ \begin{matrix} (Z_1 - Z_M)Y_1 - \\ (Z_2 - Z_M)Y_2 \end{matrix} \right\} & \frac{1}{2}(Z_1 - Z_2) & \frac{1}{2} \left\{ \begin{matrix} 2 + \\ (Z_1 - Z_M)Y_1 + \\ (Z_2 - Z_M)Y_2 \end{matrix} \right\} & \frac{1}{2}(Z_1 + Z_2 - 2Z_M) \\ \frac{1}{2} \left\{ \begin{matrix} Y_1(2 + Z_1Y_1 - Z_MY_2) - \\ Y_2(2 - Z_2Y_1 + Z_MY_2) \end{matrix} \right\} & \frac{1}{2} \left\{ \begin{matrix} Z_1Y_1 - Z_2Y_2 - \\ Z_M(Y_2 - Y_1) \end{matrix} \right\} & \frac{1}{2} \left\{ \begin{matrix} Y_1(2 + Z_1Y_1 - Z_MY_2) + \\ Y_2(2 + Z_2Y_2 - Z_MY_1) \end{matrix} \right\} & \frac{1}{2} \left\{ \begin{matrix} 2 + \\ (Z_1 - Z_M)Y_1 + \\ (Z_2 - Z_M)Y_2 \end{matrix} \right\} \end{pmatrix} \begin{pmatrix} U_2 + V_2 \\ I_2 + J_2 \\ U_2 - V_2 \\ I_2 - J_2 \end{pmatrix} \quad (2)$$

It is easily shown from the equation (2) that when the magnitude of the element of the upper coil and lower coil is identical, the pair of the sum of (U+V) and (I+J) and the difference of (U-V) and (I-J) are linearly independent. The former sum component is defined as the normal mode and the latter difference component is called the common mode. The decoupled equation is treated as an four terminal circuit and it can be shown that analytical form of the solution is available [5]. In HIMAC, we have constructed not only the magnet string but the power supply in a symmetrical fashion such that normal mode and common mode are decoupled each other and successfully achieved the power supply system of the unprecedented ripple level, below ppm [5]. In conventional configuration of the magnet string, the elements of the magnet string of the coils are not separately wound and the earth line is obscure. The symmetry is not assured and one may have to solve the coupled eq. (2) or (3).

We found the coupled equation (2) is able to be decoupled by an eigenvalue method. We start from the equation known as the telegram equation or the transmission line equation. The transfer matrix obtained from the equation still holds for that of the ladder circuit.

Let us consider the ladder circuit with the capacitance between the coil and the grounded magnet yoke, a magnitude of an outgoing current I_0 flowing into the load and that of incoming current J_0 returning to a power supply are not necessary to be identical. They could be bypassed via capacitance and flow back to the power supply side through a ground line. Furthermore voltages developed between a positive input U_0 and a negative input V_0 also may differ.

This voltage difference may be due to a flip-flop nature of a thyristor firing timing or difference of an asymmetric configuration with respect to the ground line of the magnet string.

Equations for voltage of U and V are written as,

$$\frac{d^2U}{dz^2} = Z_{11}'U + Z_{12}'V \quad (3)$$

$$\frac{d^2V}{dz^2} = Z_{21}'UZ_{22}'V \quad (4)$$

where z_{11}' , z_{12}' , z_{21}' , and z_{22}' are

$$Z_{11}' = Z_1'(Y_1' + Y_{12}') + Z_M'Y_{12}' \quad (5)$$

$$Z_{12}' = Z_1'Y_{12}' + Z_M'(Y_2' + Y_{12}') \quad (6)$$

$$Z_{21}' = Z_2'Y_{12}' + Z_M'(Y_1' + Y_{12}') \quad (7)$$

$$Z_{22}' = Z_2'(Y_2' + Y_{12}') + Z_M'Y_{12}' \quad (8)$$

and the ' denotes the impedance per unit length (m). This equation is valid both for the transmission line model and also for the ladder circuit model; z is regarded as a coordinate along a propagation direction of the voltage wave for the former case and a discrete coordinate of the magnet number for the ladder circuit. Similar equation holds for the current I and J.

Two set of equations designate the present of two mode of voltage and current in the magnet string. Indeed this formulation could be extended to N mode equations of a system (N-1) signal lines and a single ground line. As is shown by the equations, voltage U and V are coupled. These coupled voltage propagates down along the magnet strings. The resonance characteristic also shows the coupled property. In conventional synchrotron magnet strings where the common mode ripple is not suppressed, there is a possibility the normal mode ripple is mixed with common mode ripple and its performance is not improved as expected.

In general, it is tedious to solve two simultaneous second order differential equations. There is an orthodox method to solve this problem known as an Eigenvalue problem. In Eigenvalue problem, mode-decoupling is done by finding a proper transformation matrix.

We need to transform a matrix of,

$$M = \begin{pmatrix} Z_{11}' & Z_{12}' \\ Z_{21}' & Z_{22}' \end{pmatrix} \quad (9)$$

to

$$M' = \begin{pmatrix} Z_{11}'' & 0 \\ 0 & Z_{22}'' \end{pmatrix} \quad (10)$$

i.d., the diagonalization is required.

After some algebra, one can find, multiplication of a following matrix P from right and P⁻¹ from left to M:

$$M'' = P^{-1} M' P \quad (11)$$

with

$$P = \begin{pmatrix} 1 & \frac{q}{Z_{21}'} \\ \frac{q}{Z_{12}'} & -1 \end{pmatrix} \quad (12)$$

where q is expressed as,

$$q = \frac{1}{2} \left(Z_{11}' - Z_{22}' \pm \sqrt{(Z_{11}' - Z_{22}')^2 + 4Z_{12}' Z_{21}'} \right) \quad (13)$$

The above discussion shows that in general case of asymmetric 6 terminal circuit, the mode separation is possible by the transformation given by eq. (12). this transformation enables to find the analytical expression in a closed form.

In HIMAC, the magnitude and location of every possible elements are set to be equal with respect to the earth line which is defined as "symmetry." In this case, considerable simplification is possible.

In symmetric case, where Z₁' and Z₂' are equal, one obtains for M',

$$M'' = \begin{pmatrix} 1 & 0 \\ 0 & -1 \end{pmatrix} \quad (14)$$

Equation (14) indicates two mode of coupled voltage is reduced to the decoupled normal mode and common mode voltage.

III. ACKNOWLEDGEMENT

The author like to thank to the guidance and discussion to Prof. K. Sato of University of Osaka. He also gratefully acknowledges the support of all the other members of the division of accelerator physics and engineering, research center of heavy charged particle therapy, NIRS.

IV. REFERENCES

- [1] M. Kumada et al., 8th Symp. Accel. Sci. & Tech., 1991, RIKEN, p. 199.
- [2] M. Kumada et al., in the proceedings of PAC 93, Washington, D.C., USA, p. 1291-1293.
- [3] M. Kumada et al., The 9th Symp. on Accelerator and Technology, 1993, KEK, p. 211-213.
- [4] M. Kumada et al., EPAC, 1995, p. 2338-2340.
- [5] M. Kumada, to be published.

AUTOTRANSFORMER CONFIGURATIONS TO ENHANCE UTILITY POWER QUALITY OF HIGH POWER AC/DC RECTIFIER SYSTEMS

Sewan Choi

Prasad N. Enjeti*

Ira J. Pitel**

Power Electronics Laboratory*
Department of Electrical Engineering
Texas A&M University
College Station, Texas 77843-3128
Tel: (409) 845-7466
Fax: (409) 845-6259

Magna-Power Electronics**
85 Fulton st.
Boonton, NJ 07005
Tel: (201) 263-0017
Fax: (201) 263-1928

Abstract - In this paper new autotransformer arrangements with reduced kVA capacities are presented for harmonic current reduction and to improve AC power quality of high current DC power supplies. A twelve-pulse AC to DC rectifier is proposed employing only $0.18P_o$ (pu) transformer kVA. The 5th and 7th harmonics are absent in the utility line currents. Further it is shown that conventional 12-pulse operation can be increased to 24 pulse with the introduction of tabs on the interphase reactor. Analysis and Simulation of the proposed schemes confirm the cancellation of lower order harmonics. Several example implementations of the proposed schemes for high current DC power supplies are shown. All of the above schemes provide clean power utility interface and complies with IEEE 519 recommended practices.

I. INTRODUCTION

Large harmonics, poor power factor and high total harmonic distortion (THD) in the utility interface are common problems when nonlinear loads such as AC or DC power supplies are connected to the electric utility. Magnet power supplies are commonly used for high current particle accelerators. The conventional magnet supplies are conventional 6 pulse or 12 pulse rectifiers as shown in Fig. 1. As the research in high energy physics progresses and as the particle accelerators find many applications in industrial and medical areas, the magnet power supplies with high input power quality and better performance will increase in demand [1]. The recommended practice, IEEE 519, has evolved to maintain utility power quality at acceptable levels [2]. In response to these concerns, this paper proposes new autotransformer arrangements to reduce the kVA rating of the transformer. Fig. 2 shows a method to reduce kVA rating of 12-pulse diode rectifiers with hybrid connection of delta-wye transformer. The kVA rating of the hybrid delta-wye transformer is $0.78V_oI_o$ (pu). The kVA rating of 12-pulse rectifiers is further reduced by the proposed autotransformer arrangements shown in Fig. 3. In the proposed autotransformer arrangements, the windings are

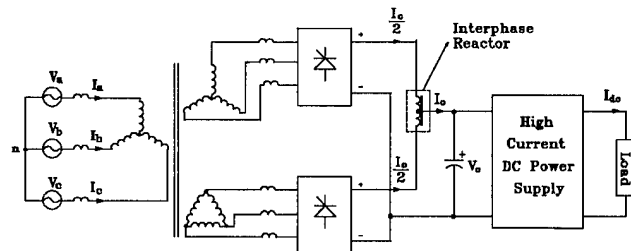


Fig. 1 Conventional 12-pulse diode rectifier for high current DC power supply (kVA rating of the transformer = $1.03V_oI_o$)

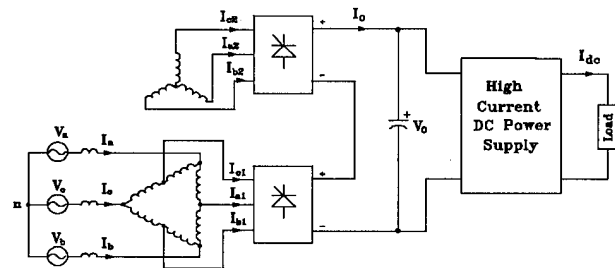


Fig. 2 Reduced kVA hybrid delta-wye 12-pulse diode rectifier (kVA rating = $0.78V_oI_o$)

interconnected such that the kVA transmitted by the actual magnetic coupling is only a portion of the total kVA. The kVA rating of the autotransformer employed in 12-pulse rectifiers is $0.18V_oI_o$ (pu). The reduced kVA rating of the autotransformer makes it physically smaller, less costly, and of higher efficiency than isolation transformers. With the reduction of kVA rating of the transformer a new method to improve the quality of AC input currents by introducing taps on the interphase reactor of 12-pulse diode rectifiers is also proposed and discussed in the paper.

II. REDUCED kVA AUTOTRANSFORMER ARRANGEMENT FOR 12-PULSE RECTIFIERS

Fig. 3 shows the twelve-pulse configuration of the proposed approach to reduce kVA rating of the transformer. The interphase reactors are included to ensure the independent

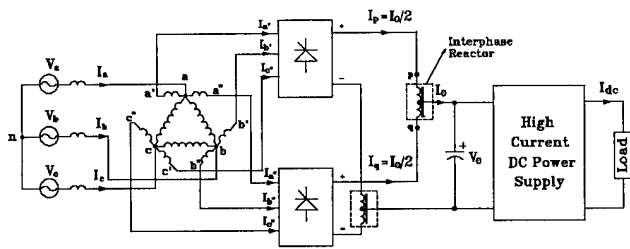


Fig. 3 Proposed reduced kVA twelve-pulse approach with autotransformer arrangements (kVA rating = $0.18V_o I_o$)

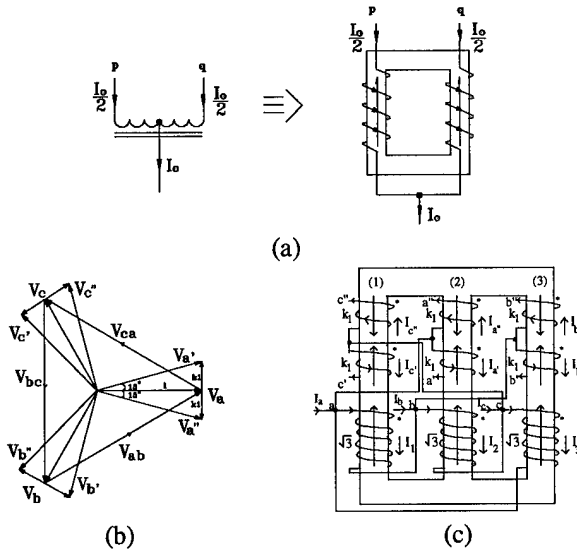


Fig. 4 (a) Winding configuration of interphase reactor (b) Vector diagram (c) Winding configuration of the autotransformer of the proposed scheme (Fig. 3)

operation of the two three-phase diode bridge rectifiers supplying nonlinear loads. The practical winding configuration of an interphase reactor is shown in Fig. 4(a). The diodes in each diode bridge rectifier conduct for 120 degrees per cycle, and the rectifier input currents (I_a , I_b , I_c as well as $I_{a'}$, $I_{b'}$, and $I_{c'}$) consist of the six-pulse characteristic harmonics.

The vector diagram of the autotransformer connection and the winding representation on a three limb core are shown in Fig. 4 (b) and (c) respectively. The optimum phase shift angle between $a'b'c'$ and $a''b''c''$ is 30 degrees. Therefore, from Fig. 4 (b) the length k_1 becomes 0.26(pu).

From the MMF balanced equations of the three limbs as shown in Fig. 4(c), the utility line current I_a is obtained by,

$$I_a = I_{a'} + I_{a''} + \frac{k_1}{\sqrt{3}} (I_{c'} - I_{b'} + I_{b''} - I_{c''}) \quad (1)$$

The proposed twelve-pulse approach is simulated on SABER for continuous operation. Fig. 5 (a) and (b) show the utility line currents and the frequency spectrum of the line current I_a . Note that the fifth and seventh harmonics are absent. It is also noted that the fundamental power factor is unity.

The autotransformer utilized in the proposed twelve-pulse system is designed such that the size (in kVA) of the transformer is minimized.

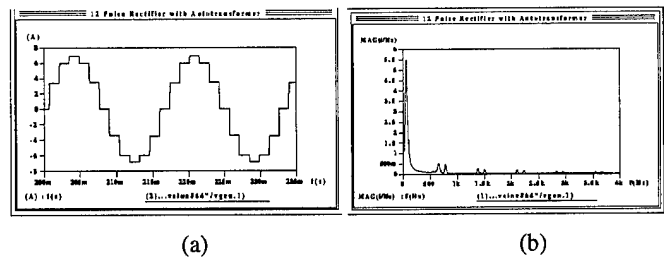


Fig. 5 (a) Utility line current I_a (b) Frequency spectrum of I_a for a highly inductive load

Assume that dc output current I_o is highly inductive. Then the equivalent kVA of the autotransformer becomes,

$$\text{kVA}_{\text{tot}} = \frac{1}{2} (6|I_a||V_{aa'}| + 3|I_1||V_{ab}|) \quad (2)$$

$$= 0.18I_o V_o$$

That is, the reduction of the size in kVA of the proposed 12-pulse scheme is 82% in comparison to the conventional 12-pulse diode rectifier.

The proposed approach can also be applied to twelve-pulse systems employing two three-phase diode bridge rectifiers feeding separate DC power supplies as shown in Fig. 6. The fifth and seventh harmonic current magnitude becomes,

$$|I_{a,5}| = 0.224|I_p - I_q| \quad (3)$$

$$\text{and} \quad |I_{a,7}| = 0.160|I_p - I_q| \quad (4)$$

Therefore if the two rectifier output dc current magnitudes I_p and I_q are identical, which is the case for Fig. 3 where $I_p = I_q = \frac{1}{2}I_o$, then the magnitude of the fifth and seventh harmonics of the input utility line currents go to zero, i.e. $|I_{a,5}| = |I_{a,7}| = 0$. When the output dc current amplitudes I_p and I_q are different, the fifth and seventh harmonics will be reduced to the magnitude of their difference as shown in eqns (3) and (4).

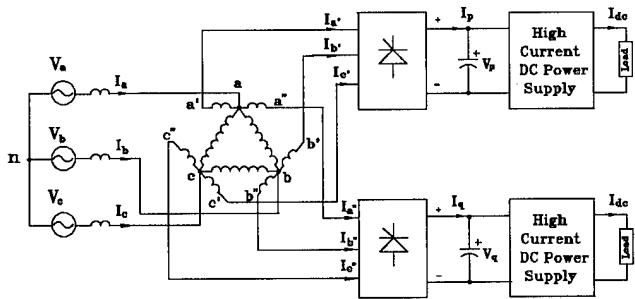


Fig. 6 Proposed twelve-pulse approach feeding two separate DC power supplies.

III. REDUCED KVA 24-PULSE DIODE RECTIFIER

Fig 7 shows the proposed 24-pulse system which is identical to the conventional 12-pulse system with the exception of the two diodes connected to the interphase reactor.

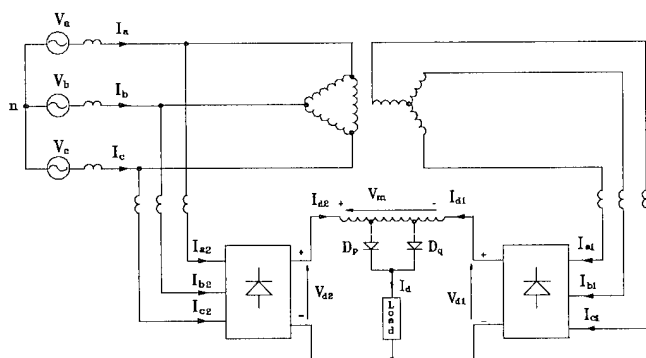


Fig. 7 Reduced kVA 24-pulse system
(kVA rating = $0.52V_o I_o$)

Fig. 8 shows the operation of the two diodes connected to the interphase reactor and the practical winding configuration of the interphase reactor according to two modes: P-mode(Fig. 8(a)) and Q-mode(Fig. 8(b)). Whenever the voltage across the interphase reactor goes positive ($V_m > 0$), diode D_p is turned on and D_q is turned off (P-mode) and therefore diode D_p carries load current I_d . From the MMF relationship of the interphase reactor for the P-mode, the output currents of the two diode bridge rectifiers is given by,

$$I_{d1} = (0.5 - k)I_d \quad (5)$$

$$I_{d2} = (0.5 + k)I_d \quad (6)$$

where $k = N_o/N_t$ and N_o is the total number of turns of the interphase reactor and N_t is the number of turns between the midpoint and the tapped points of the interphase reactor.

Whenever $V_m < 0$, diode D_q is turned on, and D_p is turned off and therefore diode D_q carries load current I_d (Q-mode). Similarly, for Q-mode the output currents of the two diode bridge rectifiers can be obtained by,

$$I_{d1} = (0.5 + k)I_d \quad (7)$$

$$I_{d2} = (0.5 - k)I_d \quad (8)$$

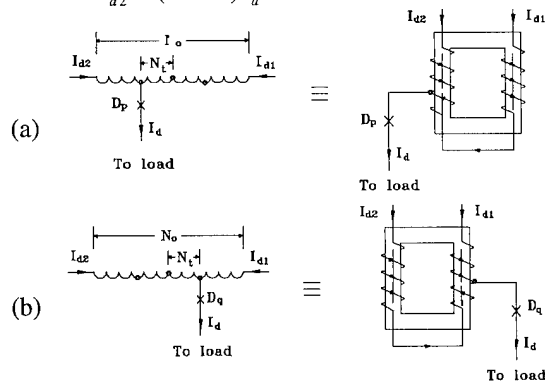


Fig. 8 Operation of the interphase reactor with two tapped-diodes (a) P-mode (b) Q-mode

The value k which minimize THD of the input current I_a is obtained by,

$$k = \frac{N_t}{N_o} = 0.2457 \quad (9)$$

The kVA rating of the delta-wye transformer of the proposed 24-pulse system is $0.5238V_o I_o$. Fig 5 shows input line current I_a which has a typical 24-pulse waveform. Note that all the

harmonics are absent up to $n = 22$ and the significant harmonics are $n = 23, 25, 47, 49$, etc..

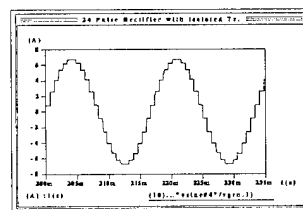


Fig. 5 Input line current I_a of the 24-pulse approach

IV. CONCLUSION

In this paper several autotransformer arrangements to enhance the utility power quality of high current DC power supplies have been proposed. The size (in kVA) of the twelve-pulse rectifier with the proposed autotransformer arrangement is reduced to 18% of the conventional 12-pulse rectifier. The proposed 24-pulse rectifier draws near sinusoidal currents in the AC input utility. They are summarized in the table below.

	kVA rating of transformer	Harmonics eliminated	# of interphase reactor
Conventional 12-pulse	$1.0306V_o I_o$	5,7th	1
Hybrid delta-wye	$0.7834V_o I_o$	5,7th	0
Autotrans. 12-pulse	$0.1834V_o I_o$	5,7th	2
reduced kVA 24-pulse	$0.5238V_o I_o$	5,7,11,13,17,19th	1

REFERENCES

- [1] R. Liang, S. B. Dewan, "A Switch-Mode Ripple Regulator for High-Current Magnet Power Supplies", IEEE APEC Conference Rec., pp. 917-922, 1994
- [2] IEEE Recommended Practices for Power Systems Analysis, IEEE Inc., New York, NY, 1992.
- [3] S. Miyairi, et. al, "New Method for Reducing Harmonics Involved in Input and Output of Rectifier with Interphase Transformer", IEEE Trans. on Industry Applications, vol. IA-22, no. 5, Sep/Oct 1986.
- [4] D. Paice, "Power Electronic Converter Harmonics: Calculations and Multipulse Methods", Paice & Associates Inc., 1994
- [5] S. Choi, A. Jouanne, P. Enjeti, I. Pitel, "New Polyphase Transformer Arrangements with Reduced kVA Capacities for Harmonic Current Reduction in Rectifier Type Utility Interface", IEEE PESC conf., 1995

Performance of a 2-Megawatt High Voltage Test Load

D. Horan, R. Kustom, M. Ferguson

Advanced Photon Source, Argonne National Laboratory
9700 South Cass Avenue, Argonne, Illinois 60439

Abstract

A high-power, water-cooled resistive load which simulates the electrical load characteristics of a high-power klystron, capable of 2 megawatts dissipation at 95 kV DC, was built and installed at the Advanced Photon Source for use in load-testing high voltage power supplies. During this testing, the test load has logged approximately 35 hours of operation at power levels in excess of one megawatt. Slight variations in the resistance of the load during operation indicate that leakage currents in the cooling water may be a significant factor affecting the performance of the load. Sufficient performance data have been collected to indicate that leakage current through the deionized (DI) water coolant shunts roughly 15 percent of the full-load current around the load resistor elements. The leakage current could cause deterioration of internal components of the load. The load pressure vessel was disassembled and inspected internally for any signs of significant wear and distress. Results of this inspection and possible modifications for improved performance will be discussed.

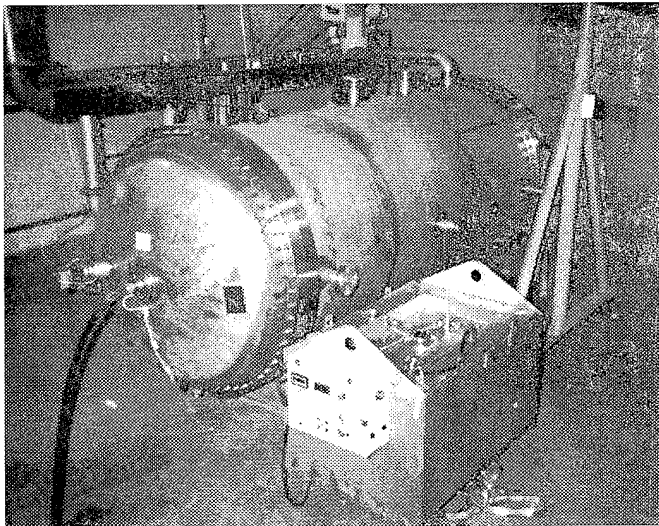


Figure 1: Overview of load system.

I. INTRODUCTION

A high-power water-cooled resistive load, capable of 2 MW at 95 kV DC, was designed and built at the Advanced Photon Source specifically to be used as a test load for the rf power supplies. The load simulates the filament, mod-anode, and cathode load characteristics of the Thomson TH-2089A

* Work supported by the U.S. Department of Energy, Office of Basic Energy Sciences, under Contract No. W-31-109-ENG-38.

klystron [1], and allows for more convenient maintenance and testing of the power supply units. The load consists of two sub-assemblies, connected to each other by a high-voltage coaxial cable of sufficient length to reach all five APS rf power supplies (see Fig. 1). The resistive filament and mod-anode loads are contained within a portable oil-filled tank which can be wheeled into position next to the power supply to be tested. High-voltage connections between the power supply and the load system are made using connectors on the oil tank which are identical to the ones used on the klystron, therefore making connection to a power supply system convenient. The high-power portion of the load is a pressure vessel which contains wire-wound resistor elements cooled by a continuous flow of DI water (see Fig. 2). This vessel is connected to the oil tank by a 350-foot coaxial high-voltage cable, allowing the load system to reach all five rf power supplies. Construction of the load assemblies was completed in January 1994, and the load was used successfully for initial testing of all five APS rf power supplies. These tests involved checking cathode and mod-anode voltage regulation performance, ripple content, heater supply current regulation, and high-power heat runs. The final power supply was tested on November 18, 1994, resulting in a total of approximately 35 hours of load use at power levels of one megawatt or greater. At the conclusion of this testing activity, the high-power dissipation portion of the load was disassembled and inspected for signs of distress.

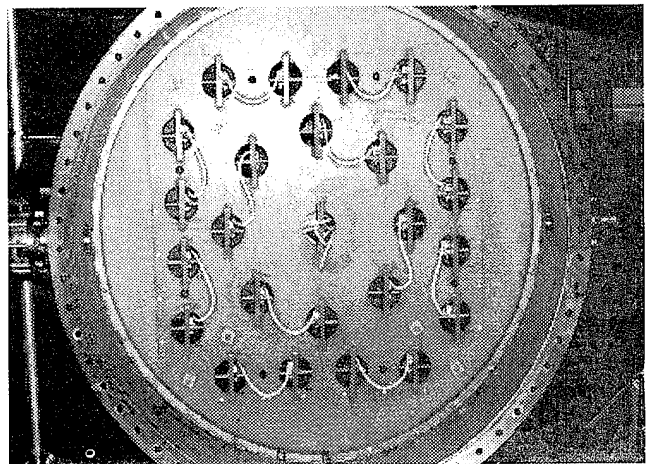


Figure 2: Internal view of pressure vessel with resistor assemblies.

II. PERFORMANCE DATA

At initial assembly, the 100 series-connected wirewound resistor elements in the pressure vessel (see Fig. 3) were measured at room temperature and found to have a total resistance

of 4360 ohms. This resistance was expected to increase to approximately 4750 ohms at operating temperature due to the positive temperature coefficient of the resistor wire material. When operating at a calibrated output voltage, the load current values indicated that roughly 15 percent of the full-load current was shunted around the load resistor elements through the cooling water. This necessitated limiting the maximum test voltage on the load to 65 kV, as the power supply is designed to current-limit at 20 A output. Also, while operating at 60 kV and above, there were occasional sudden variations in load current, possibly indicating the presence of arcing or breakdown phenomenon somewhere in the pressure vessel. This instability was subtle and intermittent in nature and was not considered a serious threat to the operation of the load. The oil tank and interlock systems of the load performed without problem. The load system was used successfully to complete the initial high-power tests on all five APS rf power supplies.

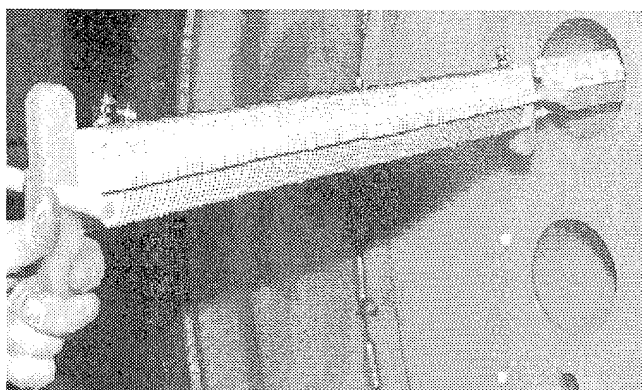


Figure 3: Photograph of resistor element

III. INTERIOR INSPECTION

After completion of the power supply testing, the pressure vessel was disassembled and inspected for evidence of distress. Attention was paid to evidence of corrosion, electrolysis, electrical breakdown, and overheating of interior structures.

Evidence of electrical breakdown or deterioration was noted in two places within the vessel: in the high-voltage silicone lead wire used to connect the input cable termination to the resistor string, and on one of the tubes containing the resistors. The wire deterioration was most likely caused by the cable moving about in the turbulent water and passing too close to the interior surface of the vessel end bell since it is necessary to leave some slack in this wire to assemble the high-voltage cable termination to the end bell. The breakdown of the resistor-containing tube (see Fig. 4) was caused by using a material with lower grade electrical properties than the tubing material used elsewhere in the load.

Two varieties of G-11 tubing were supplied by the vendor, visually differing only in color—one tan and the other traditional green. Both types were certified by the manufacturer to have the same electrical properties. However, subsequent hipot tests on samples indicated that the tan tubing suffered



Figure 4: HV damage to G-11 tube.

electrical breakdown at 15 kV DC, while the green tubing survived testing to 85 kV DC. Only two tan-colored tubes were used in the load assembly. One of these, positioned such that it was subjected to the second-highest electrical potential in the pressure vessel, showed significant stress (see Fig. 4). The other tan tube, located farther down the resistor string where the electrical potential is well reduced, showed no evidence of significant electrical breakdown.

Evidence of excess heat was noted in all of the tubing in the region immediately surrounding the 1/2" holes drilled in the top of each tube to provide an escape path for hot water within the tube. It is believed that the 1/2" holes are too small in diameter to allow the heated water inside the tubing to disperse rapidly into the general water flow, resulting in the discoloration noted (see Fig. 5).

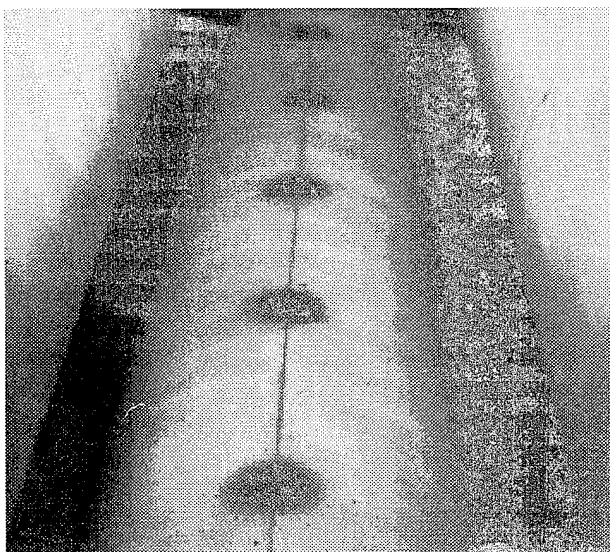


Figure 5: Heat stress on G-11 tubing near 1/2" diameter holes.

Corrosion of interior metal components was limited to the wirewound resistor elements themselves, which showed slight development of iron oxide at the electrical connections. This was later determined to be a non-issue, as the contact resistance of these connections was measured and found to be approximately 0.2 ohms or less. The resistor wire itself showed no evidence of corrosion or degradation, the interior of the pressure vessel showed no signs of electrolytic action between interior metal components, and there was no indication of any electrical arcing to the inside surface of the vessel.

IV. DESIGN CHANGES

Several design changes have been proposed to enhance the operational convenience of the load system and to correct design problems discovered after inspection of the pressure vessel interior. Permanent installation of the coaxial high-voltage cable and the load system interlock/control cable, complete with connectors located at each power supply location, will make the system much easier to use. Concerning the problems noted in the pressure vessel, the following improvements are planned:

- Replace the resistor elements themselves with continuous nichrome resistor wire material wound around ceramic or G-10 bobbins, thus eliminating many mechanical parts in the resistor assembly and reducing the number of electrical connections necessary in the resistor string. This will allow currently wasted space between the resistors to be used for more resistor material, increasing the total resistance of the load to approximately 5,300 ohms and compensating for the leakage current through the cooling water. Water column calculations indicate that the major leakage current path through the cooling water is most likely between the resistor windings themselves, and thus is not indicative of electrolytic actions [2]. Therefore, it is felt that this leakage current can be safely included as a component of the load current.
- Upgrade all G-11 material inside the pressure vessel to material which can withstand electrical breakdown to 85 kV DC.

- Enlarge the hot-water escape holes on the top of all resistor tubes to one inch diameter, easing the escape of heated water from the interior of the tubes.
- Design and install a spring-loaded pressure contact between the input cable well and the series-resistor string, thereby eliminating the "flying lead" connection presently used.
- Install a filter (10 to 20 metal mesh is adequate) near the vessel water inlet to prevent particulate matter from accumulating inside the pressure vessel. The deionized water for the vessel is filtered only near the pump. However, in the 150 ft of piping from the pump to the vessel a lot of contamination can occur, especially if there is other piping work being performed in the same area.
- Install a satellite polishing bed of deionizing canisters be installed in the supply piping to the pressure vessel to keep the resistivity of the cooling water at a predetermined minimum.
- Coat the interior of the pressure vessel with an epoxy resin to reduce the effects of stray leakage current to the vessel interior.

V. SUMMARY

It is planned to use this water-cooled high-voltage load system to support future maintenance, performance testing, and troubleshooting of the APS rf power supplies. The proposed design improvements are scheduled to be completed by the end of 1995 and should significantly improve the convenience, performance, and reliability of the load system. It will remain permanently installed in the APS rf klystron gallery as part of the rf system.

VI. REFERENCES

- [1] Thomson TH2089A Klystron Amplifier Operating Manual, UTH 2089, November, 1986.
- [2] D. Horan, R. Kustom, M. Ferguson, "Design and Performance of a 2-Megawatt High Voltage DC Test Load," *Proc. of the 1994 European Particle Accelerator Conference*, Vol. 3, pp. 1936-1938 (1994).

Early Operating and Reliability Experience with the CEBAF DC Magnet Power Supplies

W. Merz, R. Flood, E. J. Martin, M. O'Sullivan
Continuous Electron Beam Accelerator Facility*
12000 Jefferson Avenue
Newport News, Virginia 23606

I. INTRODUCTION

The CEBAF accelerator is a five pass, recirculating, CW electron Linear accelerator [1]. There are a total of nine recirculation arcs connecting the two Linacs. Three experimental halls are serviced by the accelerator through separate transport channels. The magnet powering system for CEBAF consists of approximately 2000 independent control channels. About 1850 of these channels are low current, trim magnet power supplies. There are 28 higher power supplies used to energize the major bending elements. Over one hundred, 20 amp, active shunts are used to vary current in selected magnets in the major dipole strings. The majority of the magnetic elements are concentrated in the arcs and transport channels [2]. There are, however, a significant number of trim magnets in the source, injection transport and Linacs. Table 1 is a list of all magnets.

Element	Quantity
Major Dipoles	390
Correction Dipoles	1047
Quadrupoles	707
Sextupoles	96
Septa	27

Table 1 - Magnet Quantities

The correction dipoles, quadrupoles and sextupoles are each powered individually by a dedicated trim power supply channel. The arc and extraction channel dipoles are powered in series strings by the high powered supplies, known locally at CEBAF as "Box Power Supplies". Arc loads consist of some 30-40 magnets in series. Transport channel, path length control doglegs and septa box power supplies have loads ranging from 1 to 10 magnets. Shunts are installed on virtually all loads where two or more magnets are in series.

At this time, 95% of the power supplies are installed and commissioned. In the past twelve months, beginning in May of 1994, approximately 1200 trim magnet power supplies have been checked out. During this same period approximately 22 box power supplies and 100 shunts have been made operational. Full operation of the equipment has only been under way since early 1995. While this operation is only just beginning, much has been learned based on the reliability performance seen so far. The remainder of this paper describes the systems mentioned, their reliability problems, the fixes implemented to date, and some plans for the future.

II. SYSTEM DESCRIPTIONS

A. Box Power Supplies

The box power supplies were acquired from a commercial vendor via competitive bidding on a technical specification [3]. The supplies are Danfysik, System 8000 magnet power supplies. They contain some control and interface modifications for the CEBAF application. Table 2 is a list of the ratings of the supplies. The supply topology is a diode or SCR bridge followed by a series transistor regulator output. A precision DCCT and temperature stabilized DAC form the current regulation circuit that drives the transistor bank. Regulation is 10 PPM.

Power - kW	Voltage - V	Current - A	Quantity
14	50	270	11
42	65	645	2
66	300	220	5
152	660	230	7
161	250	645	3

Table 2 - Box Power Supply Parameters

B. Shunts

Shunts have been placed across selected magnets in each series string to provide a low cost, independent knob for steering corrections. The shunts are capable of bypassing up to 20 amps or 400 Watts, whichever is greater, around the selected magnet [4]. The shunts are implemented using MOSFET power transistors. The current regulation is 0.05%.

C. Trim Power Supplies

The trim powering system has been described previously [5]. Each rack contains up to 32 trim cards, two bulk voltage power supplies and a general purpose utility chassis. The trim cards are 200W, linear, bipolar current regulators capable of 10 amps output. The regulation is performed by a temperature controlled analog block containing a current measuring shunt, preamp, DAC and error amplifier. Regulation is 100 PPM. The utility chassis provides control power as well as rack control and interlock coordination.

D. Controls

Each box power supply, shunt and trim card has its own embedded microprocessor for communication, control and error status monitoring. Communication to the supplies is via an RS-485 serial link driven by a CAMAC based power supply Scanner Module. Virtually all high level accelerator controls are now implemented through EPICS, a VME based system that drives the CAMAC serial link. Alarm monitoring is performed by EPICS.

*Supported by U.S. DOE contract DE-AC05-84ER40150

E. Availability/Reliability Requirements

An availability budget for each accelerator subsystem has been set. The budgeted goals are gradually raised over a five year period beginning in 1994. These increasing availability numbers reflect the transition from a commissioning stage to full operation.

Availability is defined as the ratio of actual operating time to scheduled operating time. With overall accelerator availability set by design mandate, each subsystem is allocated a portion of the total budget. Availability is related to the Mean Down Time (MDT) and the Mean Time Between Failures (MTBF) by;

$$A = 1 - \text{MDT}/\text{MTBF}$$

The total availability of a group of subsystems is just the product of the individual availability numbers. The MTBF for a set of k independent systems is given by:

$$\text{MTBF} = 1/(N_1 \times \lambda_1 + N_2 \times \lambda_2 + \dots + N_k \times \lambda_k),$$

where N is the number of elements in the system with a failure rate of λ and $1/\lambda$ is just the per unit MTBF of the element. The availability requirement for the power supply systems is given in Table 3.

	<u>FY94</u>	<u>FY95</u>	<u>FY96</u>	<u>FY97</u>	<u>FY98</u>
Trims	0.92	0.95	0.97	0.98	0.98
Box PS	0.95	0.97	0.985	0.99	0.99
& Shunts					

Table 3 - PS Availability Budget

By making some assumptions about the MDT for the power supply system elements and using the availability requirements above, the required per unit MTBF for each element may be calculated. These values may then be compared with either vendor supplied data or with estimates for elements with similar complexity. This exercise will shed some light on where improvement efforts should be concentrated and will determine if the goals are achievable.

For the case of the box supplies and shunts in FY98, it is assumed that the availability budget is split equally between the two distinct elements; that is $A_1 = A_2 = 0.995$. The MDT for the box power supply is estimated to be 4 hours since repairs generally take place in situ. The MDT for the shunts is estimated to be 1 hour since these cards can be swapped and repaired off line. Based on these assumptions, the required per unit MTBF for the box supplies and the shunts are 22,400 hours and 20,000 hours respectively. Both of these values seem achievable by the hardware as is the availability.

A similar analysis for the trim system is quite revealing. For FY98 the trim system availability budget is 0.98. In this case again, the assumption is made that the availability requirement is broken into two equal pieces shared by elements of the trim system. The first element is the 1850 trim cards. Using an availability of 0.99 and an MDT of 0.5 hours (hot swap capability in this case), a required per unit MTBF of 92,500 hours is calculated. The second element in the trim system is the approximately 120 bulk power supplies and 60 utility chassis. Using a 0.99 availability figure and a 1 hour

MDT, a required per unit MTBF of 18,000 hours is calculated. While the bulk supply and utility chassis MTBF seems achievable, there clearly is a problem with the trim cards. What can be done?

A 40-50,000 hour MTBF might be achievable after some time and some expense with the trim cards. That means that the MDT needs to be decreased or the trim card availability allocation within the total power supply budget needs to be decreased in order to reach a total power system budget of 0.97 by FY98. It is believed that both these options are possible. The MDT should decrease as power supply personnel become more experienced. Also as operations personnel become more experienced in identifying and compensating for failed correctors, the beam downtime per failure should decrease. Improvements in the other elements of the power system will mean that more of the total availability allocation will be used by the trims. Whether a full factor of two will be achievable in these areas remains to be seen.

III. PROBLEMS AND CORRECTIONS

A. Box Power Supplies

There has been only one operational failure of the box power supply hardware to date. Other problems have occurred but these were related to either installation or load failures. Both ground faults and thermal problems have been observed. CEBAF has modified the ground fault detecting circuit in the power supplies due to deficiencies in its ability to detect all faults and latch them. With approximately 3.5 months of running (at 60% scheduled up time) and an excess of 20 supplies operating, one failure yields an observed MTBF of greater than 25,000 hours.

B. Shunts

Approximately six shunt cards have been changed in the same 3.5 months of service as described above. Of these, only one failure is believed to have been serious enough to have caused machine interruption. Based on six card replacements, the observed MTBF is approximately 25,000 hours.

C. Trim Power Supplies

As may be surmised from the approximate numbers given for the box supplies and shunts, complete failure tracking or downtime accounting systems have not been implemented yet. As in the previous cases, only general comments are possible at this time without a detailed tracking system.

There have been 22 bulk power supply failures in the past 15 months. The supplies are returned to the manufacturer under warranty for repairs. Failure reports indicate that two thirds of the problems were in the automatic voltage-current mode cross-over circuitry. Most failures seem to occur at start-up following extended machine maintenance periods. Based on an estimated 5000 hours of operating time for the 120 supplies, the calculated MTBF is in the 25-30,000 hour range.

Utility chassis failures have been greatly reduced during the last year due to several upgrades being made to all 60 units. Additional cooling was added to the chassis to reduce the ambient temperature seen by the control power supplies. The control power distribution connections for these supplies, internal to the chassis, were re-worked after it was noted that

bad connections were responsible for intermittent and/or low output voltages. The 2-3 failures seen during the 3.5 months of operation since the upgrades has resulted in an MTBF in excess of 30,000 hours.

Prior to last summer, trim cards were failing at a rate of slightly more than one per day. Since commissioning and installation was still in progress, the exact number of cards in service at any particular time has been difficult to reconstruct. It is probably safe to say that the MTBF at that time was less than 20,000 hours. The causes for removal were varied, however, one common problem was seen in many of the failures. A surface mount chip capacitor on the temperature controlled analog block, used for input power filtering, was frequently burned up. After testing, it was determined that the capacitor could be removed without adversely affecting the circuit performance. All cards in service have had this modification. The failure rate has been reduced to approximately one every 3-5 days. The MTBF is believed to be in the 50-100,000 hour range. Confirmation of this awaits better failure tracking.

D. Controls

The only responsibility for external hardware controls retained by the power supply group is for the CAMAC based Scanner Modules. Failure statistics for this item are not well documented, however, some observations are possible. The card, developed by a commercial vendor for CEBAF, experienced mostly soft failures. That is, there were no bad components but status information was corrupted. These problems were traced to noise within the crates and on the card itself. Additional power bypassing on the crate controller along with correction of the mechanical alignment of edge connectors improved the situation. Finally, changes to the on board EPLD logic along with the replacement of FCT TTL devices with LS TTL devices cured the problem. All three of these items contributed to excessive noise levels on the card's data and control lines. Since the repairs the cards have performed reliably. There are in excess of 100 scanner cards in service.

IV. PLANS FOR THE FUTURE

A. Failure Tracking

The two failure tracking utilities used to date, one accelerator wide, one power group internal, have not proved effective. Both suffer from reporting inconsistencies and a lack of useful information retrieval features. Also there is no good accelerator downtime recording system in use. Subsystem availability is consequently not well measured. To improve the failure tracking, the RF and Power Supply Groups are collaborating on the set up of new database for this purpose. The database chosen is Access running under Windows for WorkGroups [6].

B. Upgrades

Planned software upgrades include improvements to the EPICS control screens to allow more in depth remote diagnostics and better Alarm Monitoring. The improvements should reduce the MDT by speeding problem identification.

Additional monitor points are planned for the box supplies to allow safer and speedier diagnostic work. More detailed reporting of interlock status is planned to help remove

some status ambiguity. A proposal is on the board for removing completely the CAMAC based scanner by installing its functionality in the EPICS VME crate. The CAMAC hardware is a leftover from TACL, the original CEBAF control system.

V. ACKNOWLEDGMENTS

The authors wish to thank P. Francis, C. Settles and S. Wood who have provided valuable insight into establishing the failure statistics used in this paper.

VI. REFERENCES

- [1] H.A. Grunder et al, Proc. of the 1987 IEEE Particle Accelerator Conference.
- [2] L.H. Harwood et al, Beam Transport Magnets for CEBAF, Proc. of the 1989 IEEE Particle Accelerator Conference, Pg. 399.
- [3] 10 PPM Regulated Power Supply Specification, CEBAF # 492-ES-103, 1990.
- [4] E.J. Martin et al, A 20 Ampere Shunt Regulator for Controlling Individual Magnets in a Seriesed String, Proc. of the 1995 IEEE Particle Accelerator Conference.
- [5] N. Dobeck et al, Precision, 32 Channel Power Supply System, CEBAF PR-90-017, Sept. 1990.
- [6] Access database software by Microsoft.

CEBAF CRYOGENIC SYSTEM*

Claus H. Rode, Continuous Electron Beam Accelerator Facility, Newport News, VA 23606 USA

I. INTRODUCTION

The CEBAF cryogenic system consists of three refrigeration systems: Cryogenic Test Facility (CTF), Central Helium Liquefier (CHL), and End Station Refrigerator (ESR), see figure 1 [1,2]. We now have 49,000 hours of CTF and 35,000 hours of CHL operation. The CHL is the main cryogenic system for CEBAF, consisting of a 4.8 kW, 2.0 K refrigerator and transfer line system (TL) to supply 2.0 K and 12 kW of 50 K shield refrigeration for the Linac cavity cryostats and 10 g/sec of liquid for the End Stations, see figure 2. This paper describes the nine year effort to commission these systems concentrating on the CHL with its high tech component the cold compressors (CC), see figure 3. The CC are a cold vacuum pump with an inlet temperature of 3 K which use magnetic bearings; they eliminate the possibility of air leaks into the subatmospheric He which could easily cause a multi-month down time for repurification.

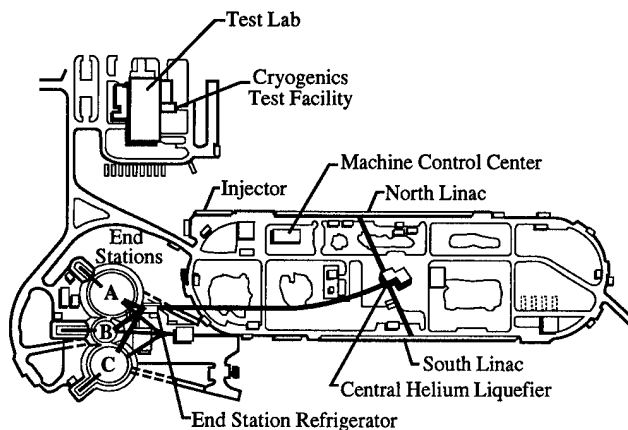


Figure 1. CEBAF Cryogenic Scope

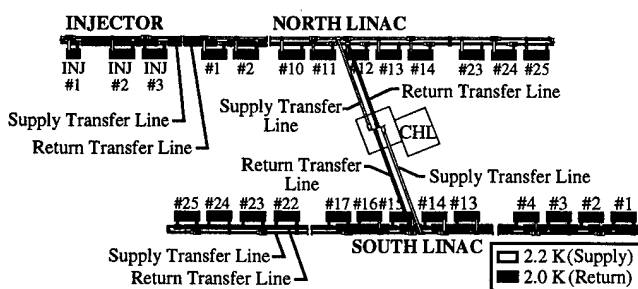


Figure 2. Linac Distribution System

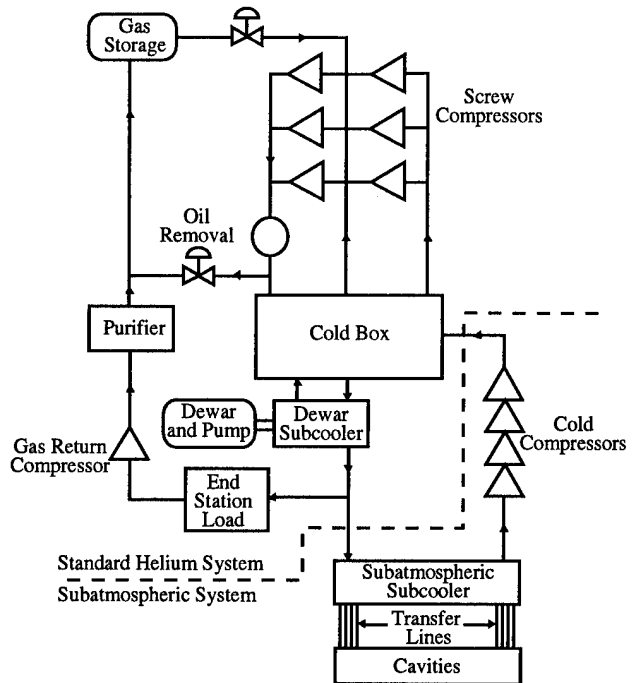


Figure 3. Block Diagram of Refrigerator

II. BACKGROUND

The cryogenic effort started with converting the Conceptual Design Report into the detailed specification for the CHL; this was the highest priority due to the long lead time associated with the CC and the need for a projected two year burn-in time to obtain 98% availability.

The process of awarding the contract took 11 months starting with the draft specification being sent to the vendors and ending with the award in January 1988. This was CEBAF's first major contract and still is the second largest technical contract (SRF cavities production is the largest). During the construction the contract appeared to be proceeding relatively smoothly except for the engineering personnel being repeatedly pulled off to prepare SSC bids. Problems surfaced during installation and commissioning; the 10 months scheduled installation and commissioning became $4\frac{1}{2}$ years. Table 1 is the project timeline.

III. He TRANSFER LINES

After writing the CHL specification, the emphasis was immediately on getting the CTF and its TL built, installed, and commissioned so that it could support cavity R&D and production. The CTF started operation in August 1988, and effort immediately shifted to the Linac TLs. The TL design was based on the Fermilab 6 km long, 168 mm

* Supported by DOE Contract # DE-AC05-84ER40150.

diameter line with its eccentric shield. CEBAF has 2 km of TLs varying from 114 to 457 mm with 250 bayonets.

Table 1. Cryogenic Timeline

Feb. 86	CEBAF CDR
Feb. 87	CHL specification to vendors
Jan. 88	CHL contract awarded
Aug. 88	CTF operational
Dec. 89	Delivery 4.5 K system
Jul. 90	*****Scheduled 2 K acceptance test*****
Dec. 90	Screw compressor system operational Delivery 2.0 system
Feb. 91	First 4.5 K coldbox operation N. Linac supply TL cooldown **Start injector commissioning
May 92	N. Linac return TL cooldown **Start N. Linac commissioning
Aug. 92	T4 turbine operational
Mar. 93	S. Linac supply and return TL cooldown Rebuilt CC returned
Jul. 93	Unstable 2.9 K CC operation
Sep. 93	CEBAF assumes responsibility for CC commissioning New CC control concept 30 min. run 2.2 K
Dec. 93	CHL contract closed
Jan. 94	Additional 4.5 K heat exchanger installed 3750 W @ 2.1 K run
Feb. 94	Last of second stage warm compressors replaced Cool down first end station magnet
Apr. 94	Stable 2.3 K CC operation
May 94	**Start final beam commissioning Stable 2.1 K CC operation
Jul. 94	*****First beam on target*****
Aug. 94	32 day continuous CC run
Nov. 94	ESR operational
Mar. 95	Three end station cryogenic operation

The N. Linac Supply Transfer Line was cooled 15 minutes after the first drop of liquid was produced with the CHL. One of the 25 g/sec He vacuum pumps permitted commissioning of the injector to begin. The last of the Linac TL was cooled down 25 months later.

The operating schedule has not permitted detailed heat leak measurements, but based on operating performance they appear to be close to design. The static heat load for Linac TLs and $42\frac{1}{4}$ cryomodules is approximately 800 W at 2 K plus 8000 W at 50 K.

IV. 4.5 K SYSTEM

The 4.5 K system was delivered only two months behind schedule, but the commissioning had not started by the scheduled 2 K acceptance test date. At this time the system still has a large amount of remaining work. While

there were several technical problems, the vendor did not want to complete the 4.5 K earlier than was required by the CC problems. The generalized problem was that work was not done on the 4.5 K system if a 2.0 K system component was broken and also converse; i.e., everything was in series in an attempt to minimize costs.

The initial 4.5 K problem discovered was incorrect assembly of the main screw compressor heat exchangers, permitting the oil to bypass the water cooling tubes. The second problem was that the coldest turbine bearings failed three times. Eighteen months later the root cause was found when the same seal failed in the next coldest turbine.

The last four problems caused trouble during the 4.5 K commissioning but became critical when we started to commission the CC.

- 1) The warm screw compressors were reduced in size after the initial design review. The contract required that we could run at full capacity with one of the three first stage compressors off or at reduced capacity with one of the three second stages off. We were unable to operate the CC with all six compressors on. In the winter of 1993/1994, we replaced the second stage compressor with the originally reviewed size. The motors had been sized for larger units and did not need to be changed. Replacing the first stage compressors is still a remaining task.
- 2) The heat exchangers between 30 and 4 K were sized for steady state only and have a pressure drop too high for CC starting, 4.5 K refrigeration, or off-design operation. Replacing these exchangers would require a three-month CEBAF shutdown and therefore is not planned for the near future.
- 3) In addition to the above problem, the 4.5 K subcooler has two problems: a) Two phase flow was attempted in a platefin exchanger; this causes major 60 second oscillations in the 4.5 K system. b) The exchanger is 80% deficient in heat transfer. In January 1994, a second 4.5 K subcooler was installed in the interconnect U-tube between the two coldboxes.
- 4) In an attempt to fix the previously discussed coldest expander problem, the flow nozzle was reduced by 8%, which then made it too small to support the CC. A spare turbine with the correct size was procured but not installed.

V. 2.0 K SYSTEM

The 2 K coldbox consists of the four stage CC and a small heat exchanger which lower the supply temperature from 4.5 K to 2.3 K. Each of the CC stages has a variable frequency drive with the motor cooled by liquid nitrogen. The bearing consists of a five degree of freedom magnet bearing system backed up by mechanical bearing (see figure 4).

The 2 K coldbox suffered a long series of electrical failures. The CC were based on Torr Supra's, scaled up a factor of 3 in size and 10 in power. The Torr Supra units

had run for 50,000 hours without a major failure while during commissioning CEBAF's had a MTBF of $<<100$ hours and a MTTR of $>>1000$ hours.

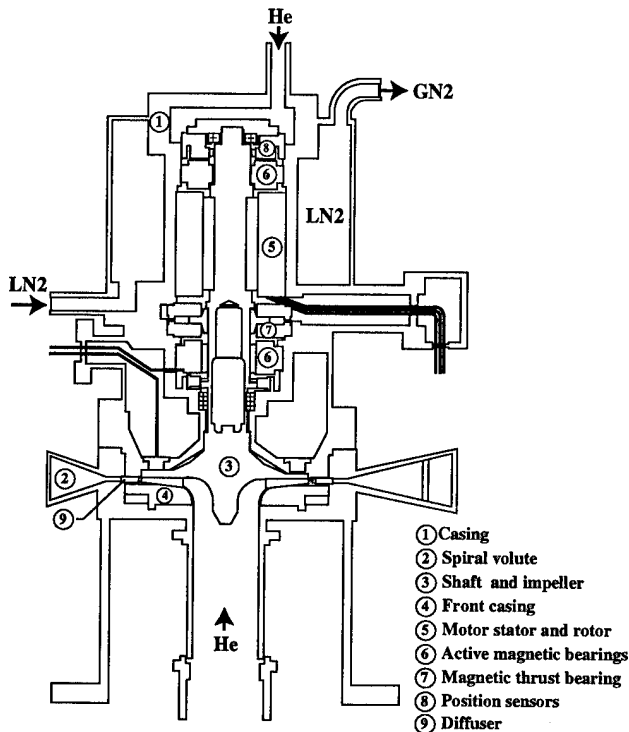


Figure 4. Cold Compressor.

The 2 K coldbox suffered a long series of electrical failures. The CC were based on Torr Supra's, scaled up a factor of 3 in size and 10 in power. The Torr Supra units had run for 50,000 hours without a major failure while during commissioning CEBAF's had a MTBF of $<<100$ hours and a MTTR of $>>1000$ hours.

There were eight major electrical failures; they were caused by two problems:

- 1) High voltage in low pressure He: 2 failures
- 2) Differential contraction: 6 failures

The problem of voltage breakdown in He is well known to superconducting magnet builders but not to industry in general. The Torr Supra CC were scaled by a factor of 3 in both voltage and current which led to 380 V in the third and fourth stages. In 1989 the third stage arced over during pre-delivery component testing. Isolation transformers and spike filters were added to the two highest stages. This was the primary reason the 2 K coldbox was delivered 14 months late.

The second arc occurred in 1992 at CEBAF in the fourth stage. This resulted in a complete redesign of the motors which lowered the voltage on the third and fourth stages to 170 V and took 8 months.

The second problem was in the potted fine wire position and speed sensing coils; these coils were reported to be identical to the Torr Supra coils except for a slight increase in diameter. The wire would open circuit upon

cooldown and, in at least one case, healed itself on warmup. There were three failures in the position sensing coils which on the average took 1000 hours to repair. After the second failure all the upper position sensing coils were replaced with unpotted coils; upon recooldown the lower position sensing failed, leading to their replacement.

Two failures in the speed sensors did not stop testing; the speed request was wired to supply the actual speed signal. These were replaced during the motor rebuild.

The last failure occurred after the rebuilt motors were reinstalled and cooled down; the upward axial thrust coil was actually a dual coil unknown to us. It used another fine wire coil to provide the dc force to compensate for gravity; this coil was not replaced. This coil provided an intermittent ground fault. The electronics were modified to eliminate this coil and use the main coil to provide the dc biases as well.

In May 1993 the CC were finally ready for serious commissioning and they reached an unstable 3.35 K. The next run in July reached an unstable 2.9 K. The next run was in September; at this point two major changes occurred:

- 1) CEBAF assumed responsibility for commissioning in order to accelerate the commissioning progress.
- 2) A philosophic error was found in the CC control: a 30 minute run at 2.2 K was achieved September 13, 1993.

The remainder of 1993 was spent studying the system to find the four problems discussed in section IV. About 50% of the time through April 1994 was devoted to stable liquefaction to support cryomodule RF commissioning. As the date of accelerator turn-on approached, priority shifted from reaching lower temperature to developing reliable CC starting procedures. Accelerator operations at 2.3 K started on schedule.

After three weeks of beam operation, there was a concern that since we were operating above Lambda, bubbles in the He were causing cavity vibration problems beyond the control response of the RF system. Beam testing stopped, and three days were spent developing the procedures for 2.1 K operation.

Since July 1994, effort on the CC was spent on available, speedy reliable restarts, regulation, and finally fully automatic computer controlled restarting [3,4]. Figure 5 shows the last pumpdown; the repair took 0.8 hours, and restart took an additional 2.8 hours.

The refrigerator is now operating at full capacity at 2.08 K.

VI. COMPONENT RELIABILITY

The 35,000 hours of CHL operation have given reliability problems similar to those experienced by Fermilab during the first four years of Tevatron operation. Loss of utilities is the most painful of the problems because it shuts the system down completely. The utilities are configured for redundancy.

VII. AVAILABILITY

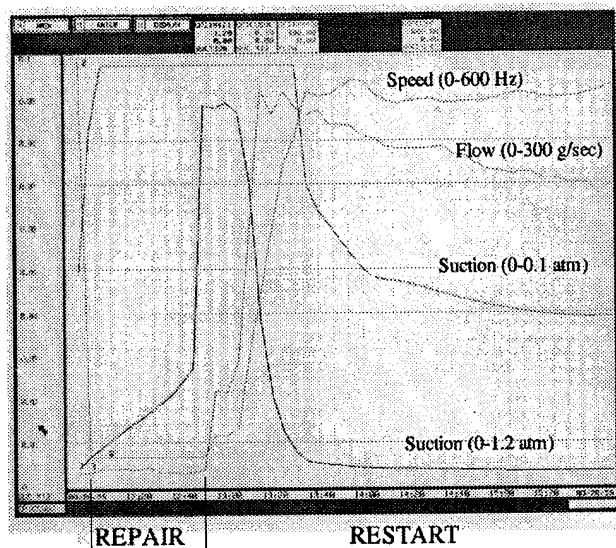


Figure 5. Repair and Pumpdown Cycle

The CEBAF site is fed by two taps to the power grid with a manual switch over. The high reliability tap feeds the CHL and ESR, and causes one or two outages per year. The CTF is fed from the second feed and has 10 to 15 outages per year, most less than a second in duration.

The CHL water system also averages one complete outage per year and several periods at reduced capacity. While the triply redundant compressed air system has not been down, moisture in the air has caused several downtimes annually. A system that has not caused downtime is the power for the CHL computers. The UPS has a triple redundant power feed: two power feeds from the site grid plus an automatically starting generator.

The 4 K system reliability has been good but still needs another factor of three improvement to reach our goal of 99.5%. The six main screw compressors are all approaching 30,000 hours. There were two premature failures at 10,000 hours of the main compressors' bodies believed due to initial misalignment during commissioning. The second stage oil pump bearings have all failed at about 25,000 hours. An annual failure has been a 1.7 MW motor lead connection loosening up and then arcing over; in theory this problem has been fixed by rebolting all the motor connections with Belleville washers. There have been two failures of the main butterfly valve linkages.

The 4 K coldbox has been relatively good. The bearings on the 25 K turbo expander have twice failed while jumping through the critical speed ranges during CC starting. The inlet filter to the 15 K turbo expander plugged with contamination, requiring localized warmup three times.

With only 8000 hours of CC operation including commissioning, it is too early to comment on the 2 K system reliability.

Cryogenic availability for the previous ten months has averaged 96.5%; the downtime and its cause are shown in figure 6. The cause is split between the 4 K system (1.4%), the 2 K system (0.7%), and the cryogenic controls (1.3%). The cryogenic controls category includes cryogenic software and hardware, as well as linac cryogenic instrumentation for the cavities. Not included in the downtime is another 1% of non-availability charged to other subsystems such as utilities; these included site power, city water, end station errors, and MCC problems.

CRYOGENICS DOWNTIME JUN 94 - MAR 95

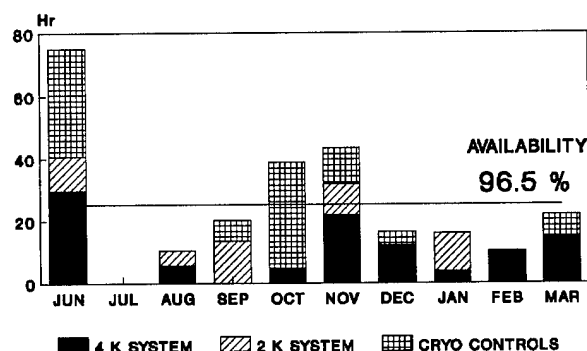


Figure 6. Cryogenics Downtime (June 1994–March 1995)

During this period there were 40 unscheduled CC trips plus two additional downtimes which did not trip the CC. This is a 174-hour MTBF and a 6.0 hour MTTR. The longest CC run was 766 hours, while the shortest was 5 hours. About half of the 6-hour MTTR was the response and repair time, while the other half was the accelerator pumpdown time.

The primary 4 K system downtime was caused by contamination tripping the 25 K and 15 K turbines; the turbine trip in turn causes a temperature transient, which would trip the CC. Other causes included the warm screw compressor trips and some control valves.

Only one of the 2 K system downtimes was associated with the CC hardware; with a valiant 14-hour all-night effort, it was possible to get the magnetic bearing electronics operational again. Five downtimes were due to excursions of the CC out of their stable operating regions, and not traceable to any equipment failures.

The unreasonably large cryo control downtime was due to three root causes: a) a failure of a supervisory LAN connection and/or board, b) intermittent failures of the linac serial highways which transmit load liquid level information, and c) overloading of memory allocations due to adding the third refrigeration system, ESR, to the network. The first was fixed by replacing several boards

and reworking all the terminations, the second problem still remains, and the third has been partially fixed.

The effort on CC restarting procedures had major effects on availability. In June 1994 a very good CC restart took 5 hours, while bad ones took three or four times longer. During the fall, procedures improved and increased the probability of successfully pumping down. During the last four months, the average downtime was 4.7 hours, with the pumpdown time being 2.5 hours for CC trips lasting 3 hours or less. During the last two months, this was fully automated, including jumping of turbines through their critical speed range.

VIII. REMAINING TASKS

The primary need is to be able to shut down any one of the six warm screw compressors for maintenance or repair. With the previously discussed replacement of the second stage compressors, we have been able to operate reliably but have not reached either of the contractually-required modes of operation. We cannot operate the CC for more than two hours with a second stage off; we can operate with a first stage off but at reduced capacity. Therefore it is our highest priority either to install additional second stage compressor capacity or to develop the CC operation procedure for this mode.

The primary cryogenic weakness is the CC repair times. Even with the 50,000 hour compressor and 40,000 hour controller MTBFs, we cannot approach the 98% average availability goal. To achieve 98% we need to achieve one week repair on the compressors and eight hours on the controllers. While in one case we were able to get the controller operational again and our repair capability is steadily increasing, our best estimate of repair times are still an order of magnitude away from our needs.

Therefore CEBAF is in the process of procuring a complete redundant set of CC and controllers. During the following year these will be assembled into a redundant 2 K coldbox system.

The remaining major problem, the 4 K to 30 K exchangers, are costing efficiency and CC restarting delays. Since there are no planned 3-month cryogenic shutdowns in the next few years, work-arounds will continue. We are planning to order the replacement exchangers and store them for a future opportunity to install them.

IX. LESSONS LEARNED

This procurement contained one high tech element, the CC; CEBAF's initial planning was to make it a separate procurement. Due to the unanimous request of all the bidders, these two procurements were combined. In hindsight this appears to have been a major mistake. The contract did require two independent coldboxes, which permitted us to use the 4 K system to commission the accelerator with minimal impacts.

Two independent contracts, each with its own acceptance requirements, would have saved a minimum of two years of the nine year effort. The gains would have come primarily from the 4 K system:

- 1) The 4 K contract would have specified the interface flow rates, etc., eliminating some of the design errors.
- 2) The 4 K acceptance test would have flagged the 4 K problems in 1991 and forced their resolution at that time.
- 3) The commissioning would have been independent efforts eliminating delays in finishing the 4 K plant because a 2 K component failed.

The second mistake is that early in the contract when good progress was being made, the details of the contract were not always enforced. A full-time CEBAF inspector/engineer at the factory should have also been used.

X. ACKNOWLEDGMENTS

This paper represents the work of the head of the Cryogenic Group W. Chronis, his cryogenic operations and engineering crew (D. Arenius, B. Bevins, D. Kashy, M. Keese, R. Ganni, T. Reid, and J. Wilson), and the many cryogenic technicians.

XI. REFERENCES

1. W. C. Chronis, D. Arenius, D. Kashy, M. Keese, and C. H. Rode, "The CEBAF Cryogenic System," *Proceedings of the 1989 IEEE Particle Accelerator Conference*, pp. 592-594, March 1989.
2. CEBAF *Design Handbook*, ch. 11.
3. W. Chronis, D. Arenius, B. Bevins, V. Ganni, D. Kashy, M. Keese, and J. Wilson, "The CEBAF Control System for the CHL," to be published in proceedings of the July 1995 Cryogenic Engineering Conference.
4. W. C. Chronis and B. S. Bevins, "Automatic Pumpdown of the 2 K Cold Compressors for the CEBAF Central Helium Liquefier," to be published in proceedings of the July 1995 Cryogenic Engineering Conference.

THE LARGE HADRON COLLIDER VACUUM SYSTEM

B. Angerth, F. Bertinelli, J.-C. Brunet, R. Calder, F. Caspers, P. Cruikshank, J.-M. Dalin, O. Gröbner, N. Kos, A. Mathewson, A. Poncet, C. Reymermier, F. Ruggiero, T. Scholz, S. Sgobba and E. Wallén,
CERN, AT Division, 1211 Geneva 23, Switzerland.

I. INTRODUCTION

The two rings of the LHC beam vacuum system have a total length of about 54 km of which almost 48 km will be at 1.9 K, the temperature of the superconducting magnets [1].

With the design energy of 7.0 TeV, combined with a bending radius of 2784.32 m, the critical energy of the synchrotron radiation emitted by the protons is 44.1 eV. At the maximum current of 536 mA each beam will emit a photon flux of $9.44 \cdot 10^{16}$ photons $s^{-1} m^{-1}$ and a power of $0.206 Wm^{-1}$.

The total synchrotron radiation power emitted by the two beams is $0.41 Wm^{-1}$ which, combined with an additional resistive wall power loss of $0.15 Wm^{-1}$ for both beam tubes, would be a considerable heat load for a 1.9 K cryogenic system. Thus a so-called beam screen, maintained at a temperature between 5 K and 20 K by gaseous helium flow, is inserted in the magnet cold bore to intercept this power.

The synchrotron radiation photons incident on the beam screen (or other) surface will desorb gases (H_2 , CH_4 , CO and CO_2) from the near surface (primary desorption); gas which then may be cryopumped back onto the very same surface. These physisorbed molecules, which are still exposed to the photons, are relatively loosely bound and easily re-desorbed and recycled by these photons (secondary desorption). In addition, more and more gas may build up on the surface of the screen until, when a monolayer or so is exceeded, the thermal vapour pressure of the H_2 component will increase rapidly to a level incompatible with the required beam-gas lifetime of 100 hours. This lifetime implies a H_2 gas density $\leq 9.8 \cdot 10^{14}$ molecules m^{-3} (i.e. $\leq 1.0 \cdot 10^{-9}$ Torr at 10 K), or correspondingly less for heavier gases (e.g. $\leq 7.1 \cdot 10^{13}$ molecules m^{-3} for CO_2).

The ion induced desorption yields from this condensed gas layer also increase with increasing quantity yet again progressively deteriorating the vacuum [2].

With bunched proton beams, pressure rises can also occur due to electron multipactoring driven by the electric field of the proton bunches [3].

In order to limit the pressure increase due to the above effects the beam screen will be perforated over a few percent of its surface to allow pumping by the 1.9 K cold bore surface, where the vapour pressure of all gases (except He) is negligible, and the condensed gas is shielded from synchrotron radiation, ion bombardment and multipactoring.

II. BEAM SCREEN

The present design of the beam screen is based on a 1 mm thick stainless steel tube, for mechanical strength, with a square cross-section and Cu coated on the inside. To minimize the beam coupling impedance of the screen the interior surface must have a high electrical conductivity and this is provided by the Cu which can be deposited either by electroplating [4] or in bulk form by an overlay process [5].

A thick bulk Cu screen would collapse due to the large electromagnetic forces induced during a magnet quench. It has been shown that a Cu layer 50 μm thick is sufficient from an impedance point of view and results in acceptable quench induced forces.

This square cross-section (compared to circular or elliptical sections) maximises the available horizontal and vertical apertures (44 mm x 44 mm) while, at the same time, leaving space between it and the surrounding 1.9 K cold bore for the supports and the cooling pipes (brazed or laser welded to the outside) which maintain the screen temperature between 5 K and 20 K. This is shown schematically in Figure 1.

To extract the synchrotron radiation and the resistive wall power loss in the screen one cooling pipe is enough, but two or even four may be installed for symmetry reasons to minimise magnetic field distortion.

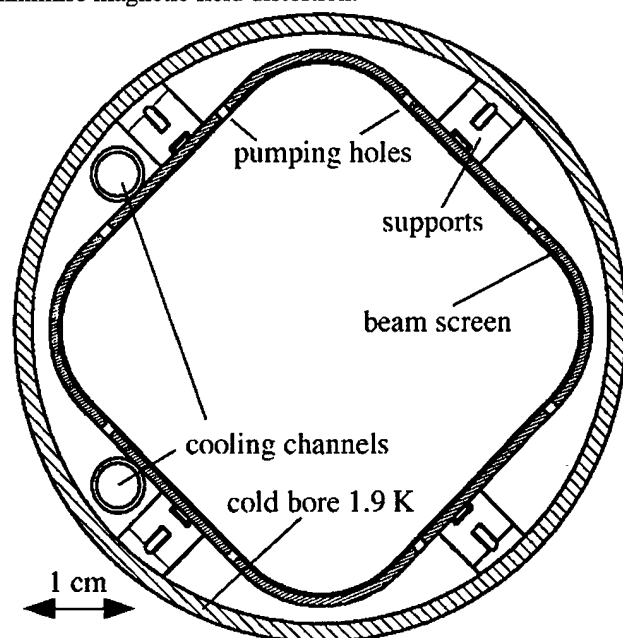


Figure 1. A schematic cross-section of the square section beam screen in the 1.9 K cold bore tube.

The supports are injection moulded polyetherimide (Ultem 2100, General Electric Plastics) which has a good radiation resistance and a low thermal conductivity.

The pumping holes in the beam screen represent discontinuities for the image currents of the beam and, compared to a non perforated screen, result in an increased beam coupling impedance. A particular effect that influences the real part of the impedance is that power may be coupled through the holes into the space between the beam screen and the vacuum chamber (this configuration forms a coaxial line or TEM line) and propagates nearly (due to the presence of the dielectric supports) in synchronism with the beam. The forward coupled signal gradually builds up in strength (coherently) until a certain equilibrium is reached and, leaking back into the beam screen, further adds to the real part of the coupling impedance. This effect depends on the size of the holes and the additional power loss is estimated to be about 0.01 W m^{-1} .

A suitable pumping hole shape which minimises the impedance is that of a narrow slot with rounded ends. In order to reduce as much as possible the contribution to the impedance from so-called trapped modes, the length and longitudinal position of the slots will be randomised [6].

This randomisation of the slot spacing helps to suppress higher frequency modes beyond waveguide cut-off associated with the slot periodicity. In particular, it reduces the forward and backward scattered power both within the beam screen and the backward coupled power into the TEM mode propagating between the screen and the cold bore.

The present design has 4.3% of the beam screen surface perforated by eight rows of lengthwise slots of width 1.5 mm and lengths varying randomly between 6 mm and 10 mm. This pattern will be repeated every 500 mm.

III. MAGNETIC PERMEABILITY

With the square section beam screen and its cooling pipes it has been shown that a magnetic permeability less than 1.005 (in the operating temperature range 5 K to 20 K) is necessary to avoid a significant magnetic field distortion [7]. Since the conventional 300 series stainless steels have permeabilities well in excess of 1.005 at low temperature, several other grades of stainless steel containing high concentrations of N₂ and Mn and giving acceptably low permeabilities are being evaluated for the construction of the beam screen. Taking into account the possible manufacturing steps, the weldability and the magnetic properties of the welds in these steels are also being investigated.

IV. VAPOUR PRESSURE

Between 5 K and 20 K the H₂ component of the cryopumped gas layer will have a vapour pressure which will increase rapidly when the coverage approaches one monolayer. Except for He, the vapour pressures of the other gases are negligible. Compared to pure H₂, the effect adding

other gases is to reduce substantially the vapour pressure of the H₂. This is illustrated in Figure 2 where the adsorption isotherms at 4.2 K have been measured in the laboratory and with no radiation for pure H₂ and for H₂ with various concentrations of CO₂ [8]. However, in reality the secondary recycling effects will probably remain and this suppression of the vapour pressure may not be a lasting effect in the LHC machine.

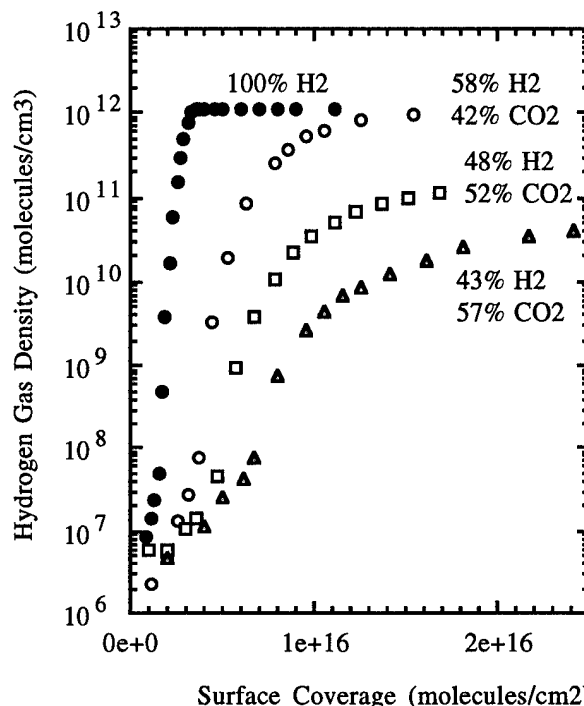


Figure 2. The H₂ vapour pressure of H₂/CO₂ mixtures condensed at 4.2 K as a function of surface coverage.

V. BEAM SCREEN VACUUM BEHAVIOUR

Assume that only H₂ is desorbed by the photons, and that the beam screen temperature is less than 20 K so that some H₂ will be cryopumped on to its inner surface.

At the start of the desorption an initial minimum gas density (pressure) in the beam screen will be determined by the total desorption rate and the cryopumping speed of the complete surface (including holes). As the surface becomes saturated, re-emission of H₂ causes the density to rise, possibly attaining a limiting density when there is no net pumping by the cold surface since all the desorbed gas will be taken by the pumping slots which are backed by a cryopump of infinite capacity. This limiting equilibrium gas density is now determined by the total desorption rate and the pumping speed of the slots. The pumping speed of the slots thus provides an upper limit to the gas density.

The ratio of this limit to the initial density is equal to the ratio of the pumping speed of the whole surface to that of the slots. For a sticking coefficient of 1 and 4.3% of the surface slotted this ratio is 23.3.

VI. PHOTON INDUCED GAS DESORPTION

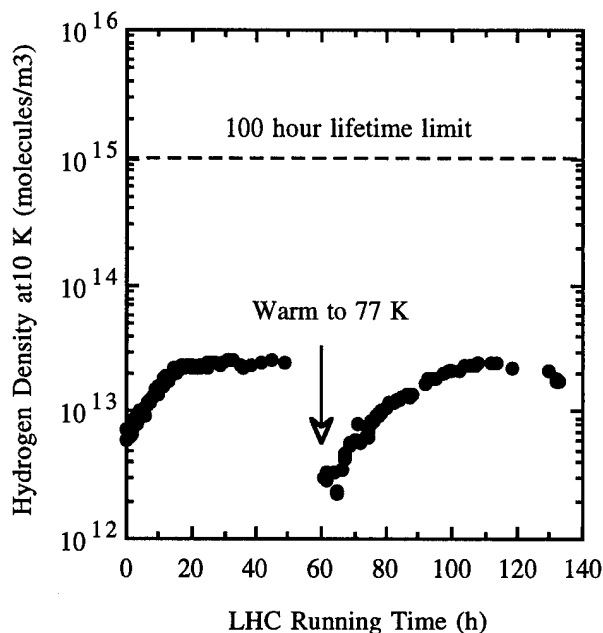


Figure 3. The H_2 gas density in the LHC as a function of the running time in hours with 53 mA and a 10 K beam screen with 2% slots.

The behaviour of vacuum chambers exposed to synchrotron radiation at room temperature is relatively well known in that the desorption yields and their variation with photon dose have been measured for a variety of chamber materials and critical energies [9]. However at room temperature all secondary effects such as recycling of adsorbed gas are negligible and, in order to try to quantify the low temperature behaviour, a collaboration was established with the Budker Institute for Nuclear Physics, Novosibirsk, Russia, to make the appropriate measurements.

The results are shown in Figure 3 where the data have been scaled to the LHC parameters at 7.0 TeV and 53 mA (i.e. the estimated initial operating current). Of necessity all the measuring instruments are at room temperature and the gas densities in the cold beam screens were calculated using the Knudsen relation. In this particular experiment only H_2 and some CO were detected. The measurements of the desorption yields at low temperature were carried out on 1 m long prototype beam screens in a specially designed cryostat installed in a dedicated synchrotron radiation beam line on the VEPP 2M electron-positron storage ring [10]. The nominal energy of the VEPP 2M storage ring is around 500 MeV but to reproduce the low critical energy of the LHC it was run at an energy of 300 MeV which corresponds to a critical energy of 50 eV, close to the 44.1 eV of the LHC.

The synchrotron radiation was incident on the side of the beam screen at a glancing angle of 10 mrad and illuminated almost the complete 1 m length of the beam screen. The screen was perforated with 10 mm x 1 mm longitudinal slots over 2% of its surface and maintained at 10 K with the surrounding cold bore at 3 K.

The data of Figure 3 show the initial H_2 density increase due to secondary effects followed by the limitation due to the pumping slots. The ratio of the limit density to the initial density is less than that calculated from the area of the slots and the beam screen indicating that the sticking coefficient is <1 .

After warming to 77 K to desorb H_2 , CH_4 and CO, a similar behaviour is observed with some evidence of a reduction in the desorption yield (cleaning) towards the end. The measured gas densities are well below that necessary for the 100 hour beam-gas lifetime limit. However it must be repeated that CO_2 , which has a nuclear scattering cross-section about 13.9 times that of H_2 , was not detected but may still be desorbed in the LHC beam screen and thus contribute the main beam-gas lifetime limitation.

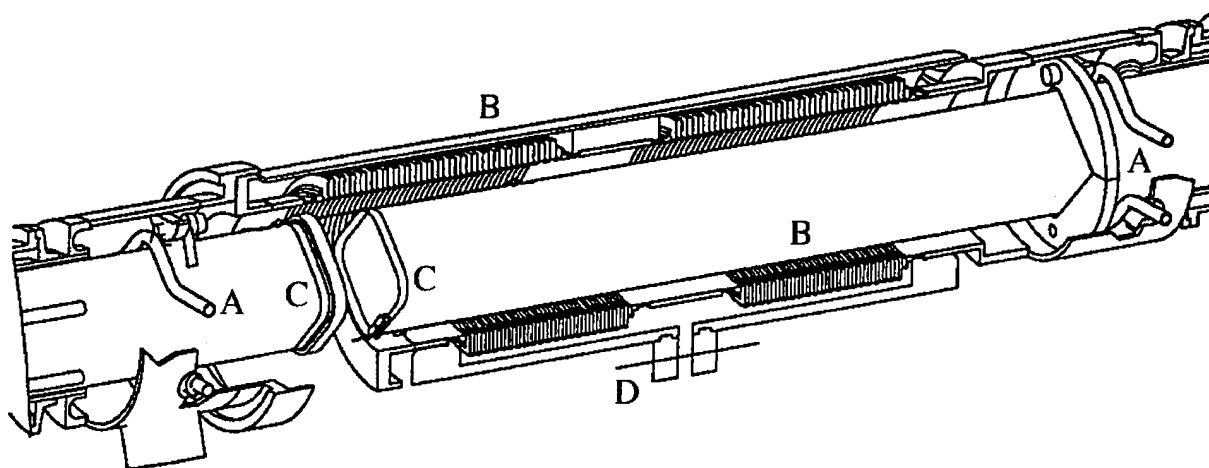


Figure 4. A schematic view of the intermagnet connection showing the beam screen cooling channels A and the bellows B. The lower part shows the bellows compressed for mounting using tool D and the upper part shows the assembled bellows. The open gap C between the beam screens is bridged by spring contacts (not shown).

VII. INTERMAGNET CONNECTION

A schematic diagram of the prototype intermagnet connection is shown in Figure 4. Each beam screen with its cooling pipes must be joined to the next between each magnet via flexible connections. For beam impedance reasons the transition must be smooth and able to absorb the 45 mm contraction of the magnet cold mass when it cools to 1.9 K. Thus there are a series of BeCu springs in good electrical contact with the beam screen to provide continuity for the image currents. Since there are at least 3000 intermagnet connections, each with 4 welds between vacuum and liquid He, it was decided as a matter of principle to try and avoid He to beam vacuum welds. As He will not be cryopumped, any leak may be critical for the operation of the LHC. The design, therefore, is such that the cooling pipes emerge into the insulation vacuum where all welds to the flexible connectors are made.

VIII. PRESSURE MEASUREMENT

The measurement of pressure or, to be more precise, gas density in the cold parts of the beam vacuum system has always been considered to be difficult since all conventional measuring instruments have been designed to operate at room temperature and also may dissipate a few Watts.

The obvious solution of simply taking one of the conventional hot filament vacuum gauges and mounting it on a test vacuum chamber and immersing all in liquid He at 4.2 K was tried and proved to be successful [11, 12] in that the gauge head worked and gave meaningful readings. However, this particular gauge head dissipated almost 2 W which was consequently absorbed by the He.

A second more elegant method of measuring the gas density in the LHC beam vacuum could consist in collecting the electron current produced by the beam ionisation of the residual gas on a system of biased electrodes placed at intervals around the ring [13]. The measured current is proportional to the average total gas density. For vacuum diagnostic purposes, an LHC proton beam would be debunched and the electron current measured around the machine. In addition to measuring the average residual gas density around the ring this method could be used to detect He leaks before they are able to be detected by the room temperature measuring devices placed at widely spaced intervals around the machine [14,15]. Similar diagnostics have previously been used routinely in the CERN Intersecting Storage Rings and Antiproton Accumulator.

IX. WARM SECTIONS

About 3 km (i.e. 10%) of the machine consists of vacuum chambers at ambient temperature. To reduce the coupling impedance the electrical conductivity of the vacuum chambers in the warm sections must be as high as possible and therefore

they must be made of either Al or Cu with a thickness of at least 1 mm.

In the warm sections a total pressure $< 1 \cdot 10^{-10}$ Torr containing 90% H_2 is required, the rest being CH_4 , CO and CO_2 . The chambers will therefore be baked.

An additional requirement is that, with beam, the vacuum does not exhibit any instabilities due to ion bombardment or electron multipactoring. The installed pumping speed and its distribution will therefore be such to give the required base pressure and vacuum stability. Also the vacuum chamber inside surface must have a low secondary electron yield to ensure no beam induced multipacting.

X. INSULATION VACUUM

In order to provide sufficient thermal insulation, the pressure in the insulation vacuum must be in the 10^{-6} Torr range. This may at first sight seem trivial but it must be remembered that there are many layers of thermal insulation which present a large thermal degassing load. During operation however, efficient pumping of all gases except He will be provided by the 1.9 K surface of the superconducting magnets.

During the first few weeks of running the LHC magnet string test with one quadrupole and two dipole magnets it was observed that the first pumpdown of the insulation vacuum from atmospheric pressure to $1 \cdot 10^{-2}$ Torr, where the turbomolecular pumps can be turned on and a He leak detection started, took about 30 hours. After a return to atmospheric pressure using dry N_2 , the second pumpdown to the same level took only about 14 hours.

The total pressure before cooldown was in the low 10^{-4} Torr range and consisted mainly of H_2O . After cooldown, the total pressure, measured with gauges at room temperature was in the low 10^{-6} Torr range and again consisted mainly of H_2O [16,17].

For ease of testing during the installation phase and to contain any He leaks the insulation vacuum will be isolated at regular intervals by vacuum barriers.

XI. CONCLUSIONS

A design for the beam screen has been made which satisfies the criteria of aperture and impedance. The magnetic permeability requirements at low temperature are severe and necessitate the use of special high N_2 and Mn content stainless steels.

The adsorption isotherms for mixtures of the gases desorbed by synchrotron radiation have been measured at 4.2 K and show that the H_2 vapour pressure component is suppressed.

Measurements of synchrotron radiation induced gas desorption at 10 K at the Budker Institute of Nuclear Physics confirmed the predicted vacuum behaviour of the beam screen where the slots limit the gas density increases. For an LHC beam current of 53 mA, which is the expected current during

the initial operation, the resulting H₂ gas density was well below that required for a 100 hour beam-gas lifetime. However, CO₂, which has a nuclear scattering cross-section about 13.9 times that of H₂, was not detected during these measurements but may still be desorbed and further reduce the lifetime.

A design has been made for the intermagnet connection which satisfies impedance criteria and ensures that there are no He to beam vacuum welds.

The warm sections of the machine must be made from either Al or Cu and baked to obtain the necessary low pressures. In addition, considerations of vacuum stability and beam induced multipactoring place constraints on the pumping system and the secondary electron yield of the inner surface of the vacuum chambers.

Initial experience gained with the magnet string test indicated that, with the magnets at 1.9 K, the insulation vacuum reached the low 10⁻⁶ Torr pressure range thus providing a good margin of safety for the thermal insulation.

XII. REFERENCES

[1] The Large Hadron Collider Accelerator Project, CERN/AC/93-03(LHC), 8 November 1993.

[2] V. V. Anashin, G. Derevyankin, V. G. Dudnikov, O. B. Malyshev, V. N. Osipov, C. L. Foester, F. M. Jacobsen, M. W. Ruckman, M. Strongin, R. Kersevan, I. L. Maslennikov, W. C. Turner and W. A. Lanford, J. Vac. Sci. Technol. A (12)4, 1663, Jul/Aug (1994).

[3] O. Gröbner, Proc. Workshop on $p\bar{p}$ in the SPS, Geneva 1980, CERN Divisional Report SPS- $p\bar{p}$ -1, Geneva, p.130, (1980).

[4] J. Cl. Puipe and W. Saxer, Werner Flühmann AG, Ringstrasse 9, Dübendorf 1, CH-8600, Switzerland, XV th Int. Conf. on High Energy Accelerators, Hamburg, Germany, July 20-24, 1992, Supercollider 4, Edited by J. Nonte, Plenum Press, New York, (1992).

[5] Technical Materials, Inc., 5 Wellington Road, Lincoln, Rhode Island, USA.

[6] S. Kurennoy, University of Maryland Internal Report, No. 95-10, (1995).

[7] B. Angerth, F. Bertinelli, J.-C. Brunet, R. Calder, F. Caspers, O. Gröbner, A. G. Mathewson, A. Poncet, C. Reymermier, F. Ruggiero and R. Valbuena, Fourth European Particle Conference, (EPAC 94), London, UK, p 208, July (1994).

[8] E. Wallén (private communication).

[9] J. Gómez-Gofñi, O. Gröbner and A. G. Mathewson, J. Vac. Sci. Technol., A 12(4), Jul/Aug (1994).

[10] V. V. Anashin, O. B. Malyshev, V. N. Osipov, I. L. Maslennikov and W. C. Turner, J. Vac. Sci. Technol. A (12)5, 2917, Sep/Oct (1994).

[11] M. G. Rao and P. Kneisel, CEBAF Internal Report TN-91-0057, August (1991).

[12] V. Baglin, A. Grillot and A. Mathewson, Vacuum Group Technical Note 95-01, January, 1995.

[13] A. Poncet, MT Division Internal Note, MT/95-01, (ESH), LHC Note 316, March, (1995).

[14] D. Edwards Jr. and P. Limon, J. Vac. Sci. Technol., 15(3), 1186, (1978).

[15] J. P. Hobson and K. M. Welch, Brookhaven National Laboratory Report, BNL-47434, AD/RHIC-111, August 1992.

[16] G. Engelmann (private communication).

[17] P. Cruikshank (private communication).

LARGE MEDICAL GANTRIES

J. B. Flanz, Northeast Proton Therapy Center, Massachusetts General Hospital,
Boston, MA 02114 USA

Abstract

A combination of a Medical Gantry and Patient Positioning System is required to direct a particle therapy beam to a supine patient from a variety of angles. The requirements of beam direction and size for precision beam treatment result in stringent criteria for the magnetics and mechanical structure of the gantry. In this paper the requirements of large gantries for ion therapy will be discussed. A variety of ion beam gantries for beam energies up to and beyond 250 MeV have been designed, constructed and are being planned. The mechanical alignment requirements will be discussed and compared with actual performance where available. The beam optics requirements will also be discussed and compared amongst different gantry designs

I. INTRODUCTION

Since Wilson wrote the classic paper in 1946 [1] discussing the potential application of fast protons for radiotherapy, the use of ion beams for therapy has been proven an effective tool for a variety of treatments[2]. The development of advanced treatment planning codes[3] has allowed for the conceptualization of treatments that maximize dose delivered to the necessary volume and minimize the dose received by possible nearby critical structures. In parallel with that development, the hardware required to realize advanced treatment techniques has also been developing. The Gantry includes the structure which carries the necessary devices so as to allow the therapy beam to be directed from virtually any angle in a plane.

One eventual aim of a gantry system, and the most demanding, is to be capable of dynamic therapy. This technique requires the beam angle to be adjusted during a treatment, thus minimizing the beam exposure at the surface while concentrating on the target volume. One of the key advantages of protons is the precision with which one can potentially deliver a treatment. The treatment area can be selectively treated while minimizing the dose to a critical structure which can be a fraction of millimeter distant. To realize this possible precision, the hardware, for protons in particular, must be appropriately designed.

II. OPERATING GANTRIES and GANTRIES UNDER CONSTRUCTION

There are presently several 'high energy' gantries in operation or under construction. This paper does not include discussion of the conventional electron linear accelerator gantry system, which are widespread throughout the world. Rather the concentration is on gantries for therapy with heavier particles.

Consideration of Gantry geometry possibilities leads to several paths. It is interesting to note that, especially in the case of proton and neutron gantries, practically all these paths have been, or are being pursued. There has not developed a consensus about a preferred scheme, other than finding one which results in the least expensive overall system and yet meets all the clinical requirements.

One question to ask is whether the accelerator and the gantry should be decoupled or physically integrated. Of course the latter requires an accelerator capable of being attached to a gantry structure and rotated through 360°. This in fact has been done at Harper Hospital in Detroit[4] for neutron therapy, using superconducting cyclotron technology. There is no proven method to date of miniaturizing an accelerator for high energy proton therapy although a couple have been proposed. Another advantage of coupling the accelerator with the gantry is that the accelerator typically produces a non-symmetric phase space, which can be used if it is integrated in the gantry. A main reason to separate the gantry is to feed a beam delivery system with multiple beam lines.

Another issue is the relative location of the gantry and patient positioner relative to the isocenter. Should the patient positioner be required to move as the gantry rotates as implemented at the PSI [5]. In the case where the isocenter is a point along the axis of rotation of the gantry this is not necessary, but that requires the gantry to be large.

Last in this non-exhaustive list, is the question of how the beam will be shaped (spread) to match the target. The use of passive scattering vs. active scanning may affect the gantry geometry. In particular, the location of the scattering or scanning devices may be an important factor. It is desirable to have a large effective source to isocenter distance. This can be achieved by a large physical separation between the beam spreading system and the isocenter after the last gantry dipole, or by incorporating these systems within the gantry optics and using close to

point to parallel focusing from the spreaders to the gantry output (as at PSI). This latter technique tends to require large apertures and therefore heavy dipole(s).

All of the above considerations have merit one way or the other, and have in fact been implemented one way or the other. Production of more than one of a kind seems to be left for commercial development. This was done in the case of neutron gantries by Scanditronix (Scand) [6,7,8] and The Cyclotron Corporation (TCC) [9,10]. Several gantries were built. For protons, Science Application International Corporation (SAIC) has built one for the Loma Linda University Medical Center (LLUMC) [11] and a team of Ion Beam Application (IBA) and General Atomics (GA) is presently building one for Massachusetts General Hospital (MGH) [12].

Table 1 contains some parameters for large gantries for a selection of facilities with or building them. Presently, large gantries are used for delivery of neutrons, or protons for therapy. To date, the large and expensive requirements for high energy *heavy ion* gantries have prevented them from being used in these applications. Superconducting technology has yet to be applied to this.

III. MAGNETIC GANTRY REQUIREMENTS

A number of parameters will determine the features and layout of the gantry without an integrated accelerator. These include:

1. *The distance between the last bending magnet and the patient.*

The beam must be uniformly spread out to the

desired treatment cross section. With the spreading devices after the last dipole, the effective Source to Isocenter Axis distance (SAD) will be smaller than the distance from the last magnet to isocenter. The spreading can be done before the last magnet; however that will increase the magnet size significantly. This distance must be large enough to reduce to an acceptable level, the ratio of the skin dose to the target dose, to provide the desired field size while not losing too much energy in the spreading..

2. *The space required for patient movement about the isocenter.*

This will determine the minimum 'gantry stay clear' envelope for the patient support system and alignment devices.

3. *The magneto-optical properties and beam trajectory requirements.*

This includes the beam particle and energy. It is related to beam spreading methods to be used and optimization of the gantry size and weight. Beam spreading methods can include Scattering and Scanning or combinations of both.

4. *Input Beam Requirements*

Input beam should be achromatic, rotationally invariant (at least for scanning) at the coupling point to the gantry to achieve invariant beam properties independent of gantry angle.

5. *Mechanical Properties/Isocenter Requirements*

This category includes mechanical deflections and reproducible, as well as non-reproducible, positioning errors, particularly of beam sensing

Table 1 - Facilities with Large Gantries

Gantry -Max Parameter	Essen	Riyadh	Clatterbr idge	Seattle	NAC	Detroit	LLUMC	PSI	NPTC PLAN
Date	1982	1982	1985	1984	1988	1990	1992	1995	~1998
Incident Particle	d	p,d	p	p	p	d	p	p	p
Energy (MeV)	14.3	26,15	62	50.5	66	50	250	270	235
Treatment Particle	n	n	n	n	n	n	p	p	p
Energy (MeV)	6	10	26.9	21.3	28.8	21	270	85-270	70-235
SAD (m)	1.25	1.5	1.5	1.5	1.5	1.83	2.75	∞	2.25
Weight (tons)	5	5	55	43	50	50	96	120	~100
Rotation (deg)	220	240	270	380	370	360	370	370	370
FieldSize (cm)	20x20	20x20	30x30	33x29	29x29	20x30	40 diam	20x \leftrightarrow	30x40
Isocentricity (diam-mm)	2	2	4	4	2.5	2	0.7x1.6	2	2
Phase Space (π -mm•mr)							2	40	30/18
Manufacturer	TCC	TCC	Scand	Scand.	Scand	MSU	SAIC	PSI	GA
Beam delivery	Sn=Scan, Sc=Scatter, W=Wobble \leftrightarrow =table move						Sc/(Sn)	<u>Sn</u>	Sc/W/

devices and resulting in beam pointing errors at the isocenter, during gantry rotation. The vacuum requirements are modest at the 10^{-2} torr level.

6. Magnetic field switching speed.

For some applications it is required to change the beam energy transported by the gantry while treating a patient, either for depth modulation, or for changing treatment portals. The magnets on the gantry must be capable of this.

IV. NEUTRON THERAPY GANTRY

Neutron Gantries transport either protons or deuterons to a target (normally Beryllium) in the treatment head. The beam is converted to a neutron beam. The beam is 'modified' with devices such as beam flattening filters, wedges, and collimators to set the desired field size.

One example is operating at the University of Washington at Seattle [7]. This Scanditronix gantry is designed to provide a beam as symmetrical as possible in both transverse planes. The magnification of the optical system is near unity resulting in relatively weaker focusing requirements. The focusing is also designed to be point to point imaging. This has the effect of minimizing the beam trajectory angular requirements at the entrance to the gantry.

There is sufficient steering capability in the beam line to adjust the beam trajectory entering the gantry properly and there is a beam profile monitor at the entrance to the gantry. A corrector dipole in the gantry accounts for gantry deflection effects for different gantry rotation.

The neutron gantry does not have to be achromatic, since the neutron conversion target is after the last dipole and the resultant neutron spectrum has a large spread in energy. The Scanditronix design incorporates an xy wobbler which produces a circular wobbling pattern within the gantry primarily to reduce the thermal effects of the approximately 50uA beam on the conversion target. Note that the patient positioning device rotates about the isocenter below the gantry head.

The gantry head is cantilevered out and therefore the chair can be mounted below the path of gantry rotation. The beam points to the nominal isocenter within a circle of confusion of diameter 4mm. The reproducibility is better than this but not required for neutron treatments. The TCC gantries are smaller and have a reduced isocenter diameter.

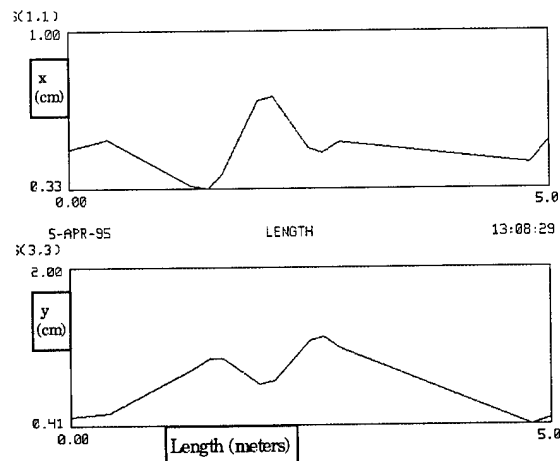


Figure 1 Beam envelope through Neutron Gantry

V. THE CORKSCREW GANTRY

In this gantry geometry, introduced by Enge and Koehler [13], the major bending occurs in the plane of rotation so that these magnets do not sweep out a large volume of space as the gantry is rotated as shown in figure 2. The three dimensional aspect of the beam trajectory led to the name "Corkscrew Gantry".. The result is that the building to house the gantry can be smaller. Disadvantages are the reduced volume available for the patient positioner motion and for access to patient within the gantry open space, and the greater amount of bend..

The Corkscrew gantry has one set of two 45° dipoles with a quadrupole triplet in between and another set of 135° dipoles and triplet. The first set bends the beam out of the plane of the beam line. The second set bends the beam in the orthogonal plane toward the isocenter. Since this system involves two orthogonal bends, and the whole system is required to be achromatic, then each set must be

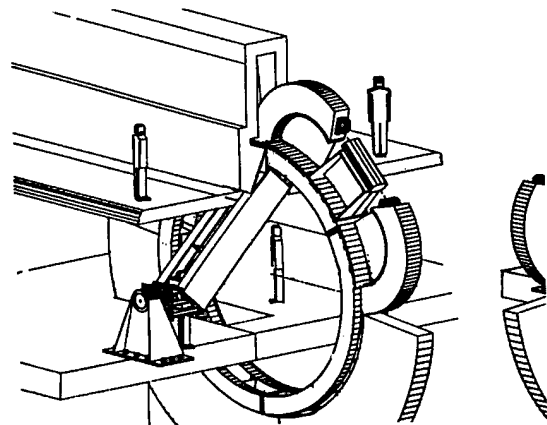


Figure 2. Schematic of Koehler Corkscrew Gantry

achromatic. In order to achieve achromaticity, four parameters are required, leaving two more parameters in addition to the pole edge rotations. This is adequate to ensure a reasonable beam size to be transmitted, but does not leave much flexibility for subsequent optics changes. The corkscrew gantry implemented at Loma Linda University Medical Center uses four quadrupoles per bend plane.

Figure 3 shows the results of a TRANSPORT calculation of the beam envelope in the Koehler gantry system. This optics tune produces a waist at 50cm from the exit of the last dipole. The input is presumed to be a symmetric beam with up to 24π mm-mrad phase space area and $\pm 0.5\%$ $\Delta P/P$.

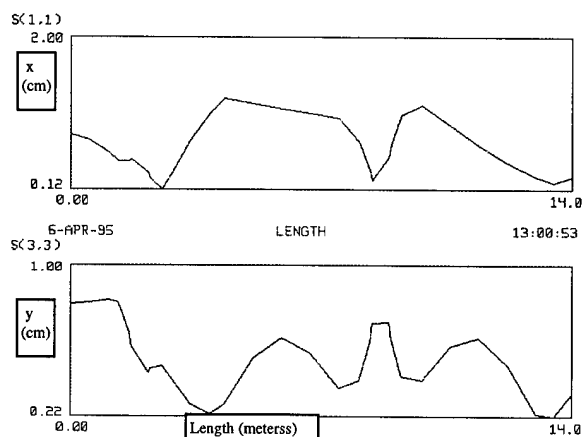


Figure 3. Beam envelope through Corkscrew Gantry

In the LLUMC implementation the gantry is primarily supported by large rings. The bearing is supported from the floor and one wall by support struts. The gantry is a cone shaped structure made up of a 7 foot circular ring at one end and a 16 foot ring at the larger end. The plates are connected by struts. The assembly is fabricated in sections small enough to transport into the gantry room. The magnets at LLUMC are aligned to 0.2 mm individually and 0.4mm gantry overall. Measurements of beam pointing accuracy to isocenter result in an isoshape of less than 1.6mm diameter [14].

A variation of the Corkscrew gantry is the *Supertwist* gantry suggested by Francis Farley [15]. This starts with the corkscrew physical layout concept and departs from the two orthogonal bend solution by stretching out the corkscrew in such a way that the total gantry length is longer and each magnet twists the beam in a trajectory through this path. Much of the focusing is done with pole edge rotations and the resulting system is achromatic at the end.

VI. LARGE THROW GANTRY

A conventional gantry is being built for MGH/NPTC [16] by IBA and GA. The rotating elements begins with 4 quadrupoles in the plane of the beam switchyard which rotate with the gantry. They match the beam from the symmetric waist produced by the beam line to the gantry optics with an emittance of up to 32 mm-mrad..

The beam is deflected through 45° , focused by five quadrupoles before it is bent through 135° and directed towards the isocenter. The distance from the output of the 135° dipole to the isocenter is 3.0 meters. The gantry quadrupoles can be adjusted to produce a waist with a diameter of 12mm at the isocenter. For scattering and wobbling, the quadrupoles can be tuned to produce a 10mm radius waist at the center of the range modulator which is about 20cm from the last dipole as shown in figure 4.

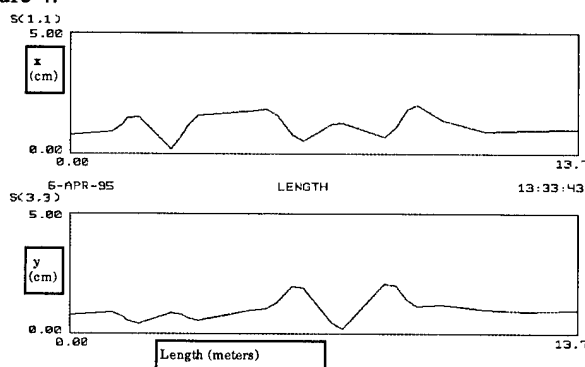


Figure 4. Beam envelope through NPTC Gantry

There is sufficient space in the gantry to include beam position and profile monitors which are capable of determining and correcting the beam trajectory angle and position to the required tolerance within the beam modification elements of the Nozzle. This tolerance is basically sub millimeter precision at the location of the scatters for scattering, or at the isocenter for scanning. The magnets accept a momentum spread of $\pm 0.5\%$ $\Delta P/P$.

The rotating structure utilizes a configuration of rings, truss, and shell elements to support the magnets in a "space frame". The structure is stiff and engineered to minimize its weight. The front ring is axially constrained. The truss elements are removable for ease of transport, assembly and possible repair. The structure is supported on both rings using a "wiffle-tree" assembly. Figure 5 shows a schematic view.

Gantry structure parts deflect under load and this deflection varies with rotation angle. The rings deform and the nozzle bends. The important quantity to consider, since

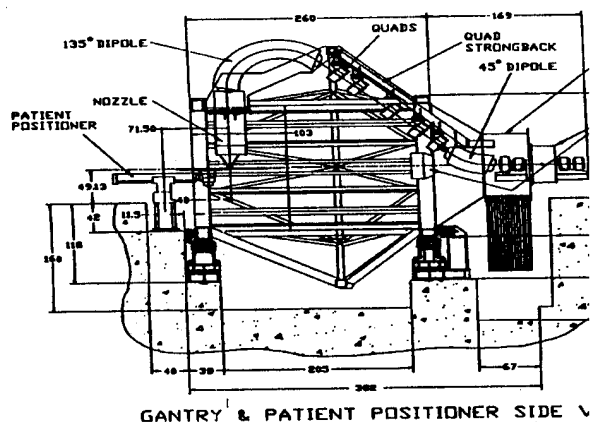


Figure 5. NPTC Gantry Layout

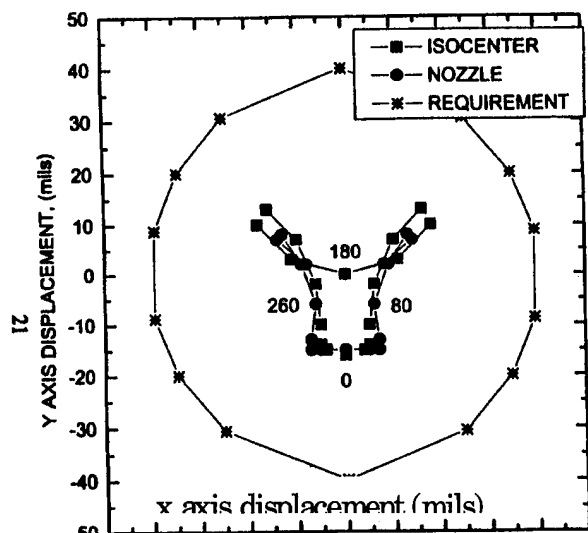


Figure 6. Calculated Nozzle Point Error

beam monitors are mounted in the nozzle, is the change in the beam position relative to the ideal isocenter as a function of gantry rotation. Figure 6 shows the results of a calculation of this quantity for the NPTC gantry.

VII. COMPACT GANTRY

The PSI Gantry design [5] results from the special requirements of the beam at PSI and a general intention to design a gantry for potential users with inadequate space for a large throw gantry. A large beam phase space results from degrading the beam energy significantly (from 590 MeV to between 270 and 85 MeV) just before the gantry. The gantry is a 'compact' style which spans a diameter of only 4m and is designed to accommodate the spot scanning technique [5] to be use at PSI. The end of the last dipole coincides with the gantry axis of rotation. The patient table is mounted directly on the front wheel of the

gantry and moves with the gantry to keep the distance between the isocenter and gantry axis constant. The beam is focused to achieve unity magnification and achromaticity. The apertures can accommodate up to $\pm 1\%$ $\Delta P/P$. There are seven quadrupoles in this system to achieve the desired conditions. The sweeper magnet is located before the last 90 degree dipole and is the limiting aperture of the system. Another condition requires that the scanning magnet to output optics satisfy point to parallel focusing. This results in a near infinite effective SAD. This allows the distance between the exit of the last dipole and the isocenter to be minimized. This is achieved using pole edge rotations on the last dipole. Sextupole aberrations are present and are corrected by introducing sextupole components in some quadrupoles.

VIII. PATIENT POSITIONER

Although not described in this paper, the patient positioning system is very important. It is half of the overall beam delivery/positioning system and potentially half the source of what could be a sub-mm positioning error budget. A system approach is very important; it must be engineered at the same time as the gantry.

IX. ACKNOWLEDGMENTS

The author wishes to thank those referenced below who contributed information about their facilities for inclusion in this paper.

X. REFERENCES

- [1] R.R. Wilson, *Radiology*, **47**, p487-491 (1946)
- [2] H. Suit, M. Urie, *JNCI*, **84**, p155 (1992).
- [3] J. Tepper, *Seminars in Rad Onc*, Vol **2**, No. 4 (1992)
- [4] H. Blosser, MSU, Private Communication
- [5] E. Pedroni, *Med. Phys.*, **22**(1), p37, (1995).
- [6] R. Riesler, U. Wash, Private Communication
- [7] D. Jones, NAC, S. Africa, Private Communication
- [8] P. Beksh, Clatterbridge, Private Communication
- [9] J. Rassow, *Biology in Medicine*, p23-27 (1977)
- [10] J. Al-Mokhlef, Riyadh, Saudi Arabia, Private Communication.
- [11] M. Schulze, *Proc. 1991 Particle Accelerator Conference*, p610 (1991).
- [12] Y. Jongen, T. Hum, E. Hubbard, M. Heiberger, Denton Accelerator Conference, (1995).
- [13] A.M. Koehler, LBL Pub #22962, (1987).
- [14] M. Moyers, Private Communication
- [15] F. Farley, PTCOG Boston (1993).
- [16] J.B. Flanz, et. al, *NIM*, To be Published, (1995).

Alignment Considerations for the Next Linear Collider

Robert E. Ruland, Stanford Linear Accelerator Center, Stanford University, Stanford, CA 94309 USA

ABSTRACT

Conventional alignment techniques and special straight line alignment techniques are reviewed for their accuracy potential. It is shown that, whereas conventional alignment methods will be sufficient to achieve start-up conditions, only special straight line alignment methods can compete with beam based alignment techniques.

I. INTRODUCTION

Next Linear Collider type accelerators require a new level of alignment quality. The relative alignment of certain parts of these machines is to be maintained in an error envelope dimensioned in nanometers. Since conventional optical alignment methods cannot approach this level of accuracy, special alignment techniques must be pursued.

II. COMPONENT PLACEMENT TOLERANCES

Component placement tolerance specifications define the alignment operation. The definition of these tolerances has changed over recent years, resulting in significantly looser specifications. At the same time, the alignment requirements of NLC type machines are intrinsically more demanding, effectively offsetting these reductions.

The available space here does not allow a detailed discussion of all parts of an NLC design. While the following discussion will focus on the main linac alignment, most of it is nonetheless directly applicable to the other machine parts.

A. Definitions

Originally, alignment tolerances were calculated as the offset of a single component resulting in an intolerable loss of luminosity. This seemed a reasonable way to proceed and immediately gave relative sensitivities of component placement. However, this method had two flaws: it failed to take into account that, firstly, not just one but all elements are out of alignment simultaneously, and secondly, that sophisticated orbit and tune correction systems are applied to recover the lost luminosity. Permissible alignment errors, random or systematic, under these more realistic assumptions are much harder to estimate because they require an understanding of all conceivable interactive effects that go into a simulation and a detailed scenario of tuning and correcting. The continued increase in available computing power has made it possible to calculate the simultaneous offsets of all components. Operating experience from the present generation of colliders has yielded significant advances in orbit tuning and correcting. On this basis, alignment tolerances can be defined as the value of placement errors which, if exceeded, make the machine uncorrectable. Experience with higher order optical systems has shown that alignment tolerances derived in this manner tend to be about an order of magnitude looser than before.¹

B. NLC Linac Tolerances

Alignment tolerances according to the first and the most recent definitions have been computed² and are plotted in Fig. 1. The first curve shows the placement tolerances

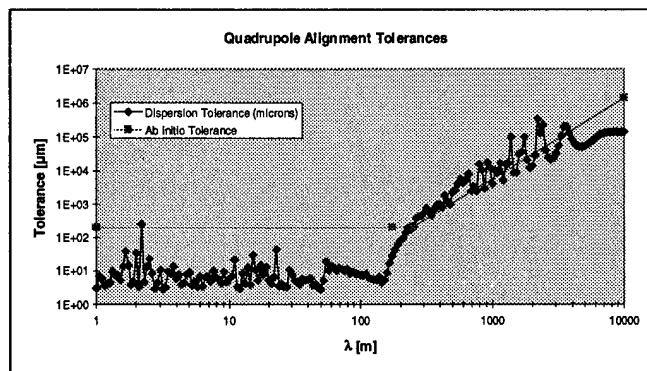


Fig. 1. Quadrupole alignment tolerances—running conditions

required to keep dispersion losses under a tolerable 3%, i.e. the machine would operate to design specifications. The placement requirements for adjacent components are a very tight 3 μm . Fortunately, the tolerances are scale dependent. The most stringent placement is required only for components within about 160 m of the point of investigation; further downstream the tolerances quickly drop off. The second curve shows the tolerance which, if exceeded, would make the machine uncorrectable. Here, we see the same scale dependency.

III. DATUM DEFINITION

Since the earth is spherical, a slice through an equipotential surface, i.e. a surface where water is at rest, shows an ellipse. For a project the size of an NLC, this has significant consequences.

A. Tangential Plane or Equipotential Surface

Traditionally, accelerators were built in a tangential plane, sometimes slightly tilted to accommodate geological formations. All points around an untilted circular machine lie at the same height (Fig. 2), but a linear machine such as the NLC cuts right through the equipotential iso-lines. The center of a 30 km linear accelerator is 17 m below the end

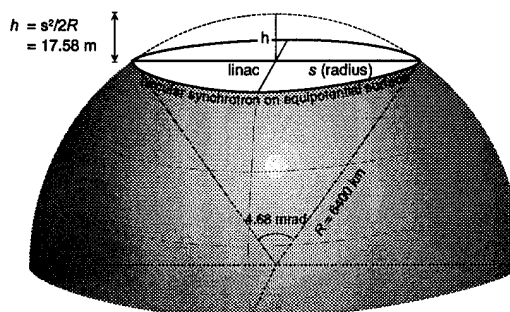


Fig. 2. Effect of earth curvature on linear and circular accelerators

points. To alleviate the problems one could build the accelerator on more than one plane, e.g. building the linacs and the final focus/detector section on three separate planes reduces the sagitta to 1.9 m (Fig. 3). To avoid the "height" difference completely, one would need to build the machine along an equipotential surface.

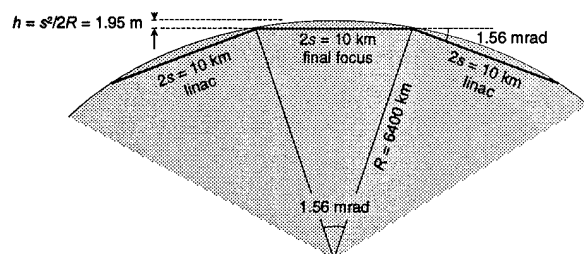


Fig. 3. Three plane lay-out

B. Lay-out Discussion

Since most surveying instruments work relative to gravity, the "natural" solution is a lay-out which follows the surface generated by equal gravity, the equipotential surface, although, for conventional alignment methods, the choice of a tangential surface adds just one additional correction. The choice of lay-out surface does have a major impact upon which special alignment methods can be used: a diffraction optics Fresnel plate alignment system requires a straight line of sight, but a hydrostatic level system can not accommodate height differences of more than a few centimeters.

IV. CONVENTIONAL SURVEY AND ALIGNMENT TECHNIQUES

Conventional alignment techniques are well understood and have been successfully applied in the alignment of accelerators such as HERA, LEP and SLC.

A. Procedure

A conventional alignment is usually a 6 step process:

1. **Surface Survey Network** A survey coordinate system is established on the surface and represented by control monuments to control scale and global positioning.

2. **Transfer of Reference into Tunnel** Scale and datum are transferred into the tunnel by sighting through vertical shafts (penetrations).

3. **Tunnel Network** A tunnel survey reference network is established integrating the transfer points (Fig. 4). It is usually represented by floor or wall monuments.

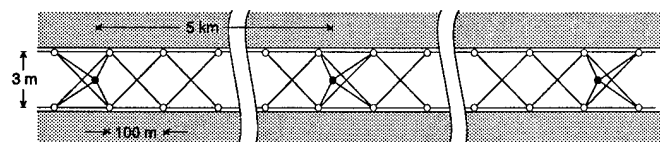


Fig. 4. Tunnel network lay-out with 3 surface connection points

4. **Absolute Alignment** All components are laid out and aligned in respect to the tunnel reference points.

5. **Relative Alignment** A smoothing procedure is carried out to improve the relative positioning of adjacent components.

6. **Quality Control Mapping** A final mapping survey verifies the achieved alignment quality.

B. Equipment

The conventional survey and alignment equipment has greatly advanced over the last 10 years: electronic theodolites with a resolution of $2 \mu\text{rad}$ have become standard; gyro-theodolites can rapidly determine an azimuth with a resolution of $5 \mu\text{rad}$; Electronic Distance Meters have increased in resolution ($100 \mu\text{m}/100 \text{ m}$) and significantly shrunk in size, allowing their integration into the telescope of a theodolite to form a tacheometer; levels have at long last become digital; GPS ($\pm 4 \text{ mm}/30 \text{ km}$) has revolutionized surface net measurements; laser trackers allow on-line monitoring of an alignment process with a resolution of $15 \mu\text{m}$ over 10 m .

C. Measurement Quality Estimate

To estimate what alignment accuracy could be achieved in a conventional alignment procedure, the process as outlined in A. using equipment with the resolutions specified in B. has been simulated. Fig. 5 shows the resulting tolerance curve. As one can see here, conventional alignment can support the *ab initio* alignment requirements but not the running tolerance requirements.

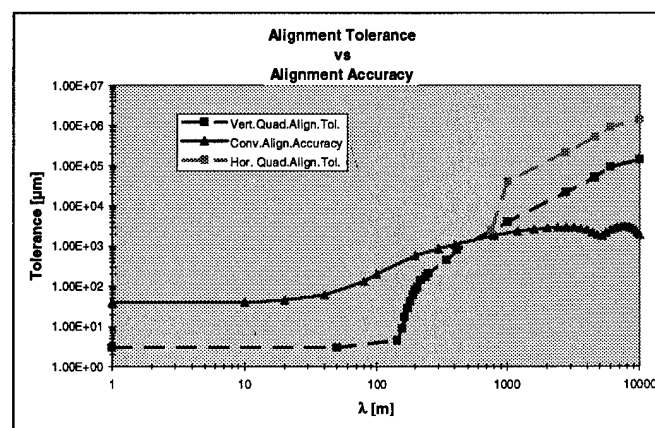


Fig. 5. Quadrupole alignment tolerances vs. alignment accuracy

V. SPECIAL ALIGNMENT SYSTEMS

The conventional alignment accuracy can be improved by adding alignment systems to the measurement plan which are optimized for the measurement of the critical dimension. The key element of any of these alignment schemes is to generate a straight line reference. Fig. 6 gives an overview of straight line reference systems categorized by working principle.³

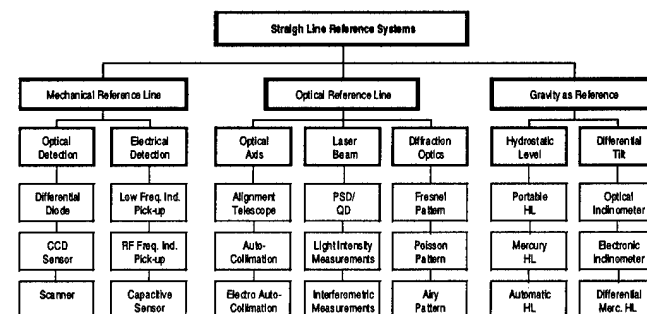


Fig. 6. Straight line reference systems

A. Mechanical Reference Line

A stretched wire is used to represent a straight line. While in the horizontal plane a wire projects to a first order a straight line, in the vertical plane it follows a hyperbolic shape due to gravitational forces. The deviation from a straight line in the vertical is a function of the wire's weight per unit length, wire length and tension. A 45 m spring steel wire with 0.5 mm diameter under a maximum tension has a sagitta of about 6 mm. A comparable wire made of a silicon-carbide material⁴ which has the same tensile strength but at only one tenth of the spring steel's weight per unit length, creates a sagitta of only 0.6 mm. For very accurate measurements, deviations of a wire from a straight line in the horizontal plane must also be considered. These deviations are created by internal bending moments caused by molecular stress of the material. The bending moments can be reduced to negligible size by heat-treating the wire or by stretching it into the yield range.

1. Optical Detection At LLNL, a GaAs infrared emitting diode illuminating a silicon phototransistor across a 2.5 mm gap combination was used to measure the deflection of a wire in an electro-magnetic field.⁵ This set up was part of a system to align the solenoid focus magnets on the ETA-II linear induction accelerator. To stabilize drift problems, the phototransistor was replaced with CdS photoconductors.⁶ The resolution proved better than 1 μ m. A portable offset measurement device developed at CERN, the Ecartometer,⁷ uses a differential diode to center a carriage under the wire. The centering accuracy is better than 20 μ m. The SLAC LANI (Linac AligNment Instrument) is also a portable device designed to measure offsets in reference to a Kevlar wire applying the CCD based light shadow technique (Fig. 7).⁸ Offsets within 2 mm range can be measured to ± 10 μ m. The LPG 10 G sensor uses the same principle of operation; it can simultaneously measure the diameter of the wire and its position to better than ± 5 μ m.⁹

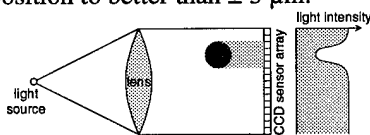
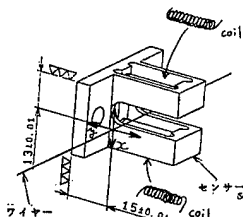


Fig. 7. (above) Light shadow technique

Fig. 8. (right) KEK inductive wire sensor



2. Electrical Detection Electrical pick-ups use inductive or capacitive techniques to measure the wire position. A very simple inductive system was developed at KEK to support the alignment of the ATF linac. The reference wire carries a 60 kHz signal which is picked up by two coils on either side of the wire (Fig. 8).¹⁰ The differential signal is a measure for the relative wire position. The accuracy over the measurement range of 5 mm is better than ± 30 μ m. The system developed by DESY for SLAC (Fig. 9) transmits a 140 MHz signal over the wire which is received by the wire position monitor antenna strips. The relative signal from diametrically opposing antennas is a measure of the wire position. The system is bi-axial, has a range of 2 mm, and at 8 mm object distance provides long term position accuracies

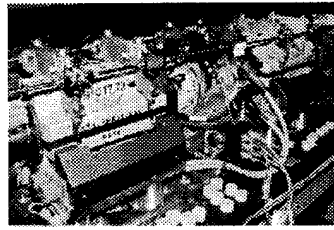


Fig. 9. FFTB magnets with wire system and magnet mover

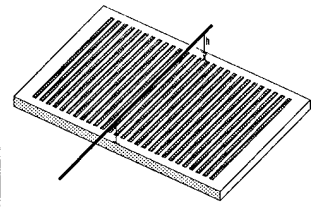


Fig. 10. MIT mini strip board

of better than ± 1 μ m.¹¹ Another inductive sensor was developed for the position monitoring of detector components (Fig. 10),¹² but could be used also for wire alignment systems. The wire carries pulsed signals which induce charges on the board strips. The strips are 50 mm long and 1 mm wide. The centroid of the distribution gives the horizontal position with respect to the strip board while the width of the distribution provides information on the vertical coordinate. An accuracy of better than ± 3 μ m over 8 mm has been demonstrated. ESRF and CERN, in collaboration with the French company Fogale Nanotech, have developed capacitive sensors. The CERN sensor is bi-axial and resolves the wire position over a range of 2.5 mm to ± 1 μ m.

B. Optical Reference Line

1. Optical Axis Reference The optical axis is the reference line to which components are positioned using traditional alignment instruments. Alignment telescopes can support the manual alignment of components to about ± 50 μ m. If higher accuracies are required, like for the relative positioning of two accelerator structures on a single strong-back to ± 3 μ m, electro-autocollimation is very well suited. The principle observable of this method is the differential tilt of a section of test object in respect to the optical axis (Fig. 11). An integration over the differential tilts yields the deviations from straightness. These measurements are usually bi-axial.

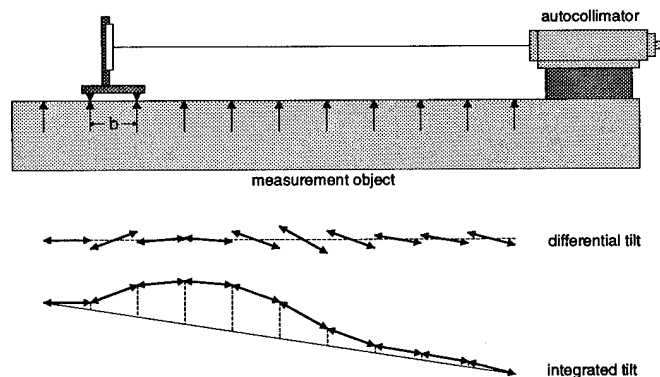


Fig. 11. Principle of autocollimation

2. Laser Beam Reference In its simplest form, a laser beam images a spot on a PSD, QD or CCD array, allowing a direct position read-out to few μ m. The relative motion of adjacent girders in the KEK ATF is monitored by a laser/PSD combination. A diode laser beam is split into two arms, each creating a signal on a PSD. A relative girder motion results in two displacement vectors. Their analysis yields three translations and roll.¹³ To compensate for instabilities of the laser, reference position detectors allow

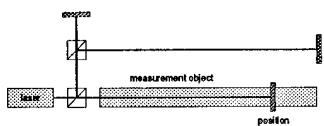


Fig. 12. System with compensation

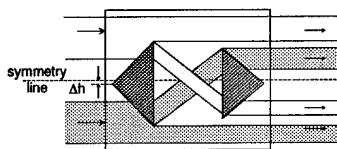


Fig. 14. Intensity system optics

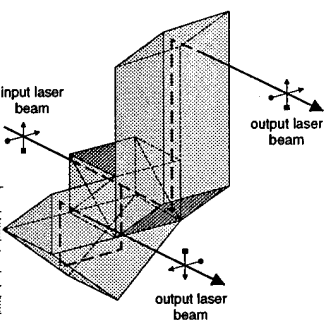


Fig. 13. Dual arm compensator

differential measurements (Fig. 12). In a different approach, the laser beam is split in a special optical component (Fig. 13) into two beams such that direction changes of the original beam affect the two beams in opposite ways, thereby compensating the instability.¹⁴ This method yields a resolution of 200 nm over 10 m if refraction is controlled. Slightly less accurate are measurements relying on the comparison of light intensities. In this method, a reference laser beam is split into two beams of equal intensity. These two beams are split again in the straightness sensor into 4 beams (Fig. 14). The split ratio is a function of the position of the straightness sensor in respect to the reference line which is the symmetry axis of the initial two beams. A receiver measures and compares the intensity of the beams on both sides of the symmetry axis and converts the intensity difference into a metric offset. The offset accuracy is within $\pm 15 \mu\text{m}$ over 10 m. Total range is up to 40 m. Interferometric straightness measurements are inherently more accurate and are in the same accuracy domain as autocollimation measurements.

3. Diffraction Optics Reference While the above methods are well suited for short to medium ranges, diffraction optics methods can provide a straight reference line over kilometers, e.g. the SLAC Linac/FFTB Alignment System.^{15,16} The reference line of a Fresnel system is defined by the pin hole

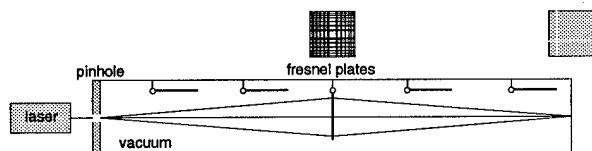


Fig. 15. Fresnel alignment system

and the center of the detector plane (Fig. 15). The Fresnel zone plate (Fig. 16) focuses the diffuse light onto the detector, forming an interference pattern (Fig. 17). The design parameters of the zone plates, size, width of strips, and gaps, are a function of the wavelength of the light source, image and object distances, and resolution. Only one Fresnel lens can be in the light path at any time. To incorporate more monitor stations into the system, the zone plates must be mounted on hinges so that actuators can flip the plates in and out of the light path. Since refraction would distort the fringe images to noise, the light path must be in a vacuum vessel. The FFTB alignment system's Fresnel zone plates, which, as an extension to the linac alignment system, are about 3.2 - 3.4 km from the detector, can resolve the motion of a zone plate to 5 μm .

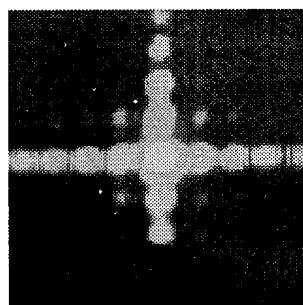


Fig. 16. Fresnel zone plate image

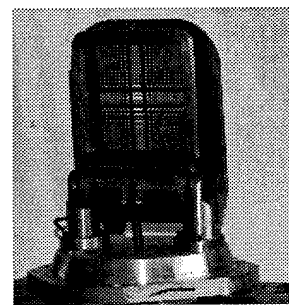


Fig. 17. Hinged fresnel zone plate

Another method of generating the straight line reference by diffraction is the Poisson line.¹⁷ An opaque sphere illuminated by a plane wave generates a diffraction pattern behind the sphere. This pattern can be observed by placing an observation screen or camera in any plane behind the sphere. The Poisson reference line passes through one fixed point, the center of a sphere. The second point is formed by centering the Poisson spot on a quadcell in the detection plane, using a feedback circuit between the quadcell and the mirror that actively steers the incident plane wave. An advantage of the Poisson scheme is the possibility to place several spheres simultaneously into a very large diameter beam. More spheres can be incorporated by mounting individual spheres to hinged frames similar to the Fresnel system, so as to measure different sets of spheres.

C. Gravity as Reference

A surface of equal "gravity" on which every point is the same height is called an equipotential surface. A hydrostatic level, in which an enclosed body of fluid conforms to an equipotential surface, is a very accurate tool to transfer a height from one point to another or to monitor height changes. Systems are available in different flavors: with optical, mechanical or electrical sensors; manual or computerized; with different fluids—water, oil, or mercury; portable or stationary. ESRF has developed a hydrostatic level system for on-line monitoring of magnet height changes (Fig. 18). To monitor the water level the system uses capacitive proximity gages interfaced to a control system. If significant height changes have been determined, the control computer activates motorized jacks to compensate for the changes. Measurement accuracies of $\pm 5 \mu\text{m}$ over 1 km have been reported.¹⁸

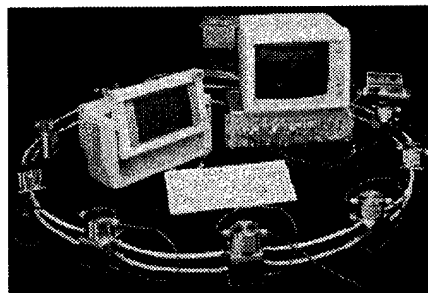


Fig. 18. ESRF Hydrostatic Level System

D. Error Propagations with Additional Systems

1. Stretched Wire For the purpose of estimating the error propagation of a wire system over the length of a possible

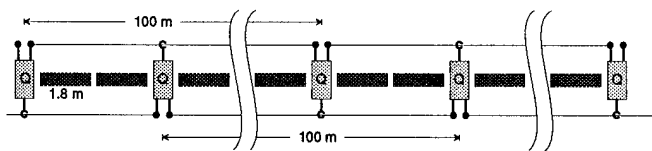


Fig. 19. Double-wire lay-out

NLC linac the lay-out as sketched in Fig. 19 was assumed. A double overlapping wire arrangement is necessary since it was found that in order to preserve a position survey accuracy of $\pm 5 \mu\text{m}$ the wire length must not exceed 100 m. Fig. 20 shows the resulting error estimates. The present wire curve is based on propagating linearly the FFTB wire accuracy to a length of 100 m. It is encouraging to see that an existing technology is almost able to support the operations tolerance. The improved wire curve assumes that it will be possible to achieve the present FFTB wire accuracy for a 100 m long wire. This system would be able to fully support the alignment needs.

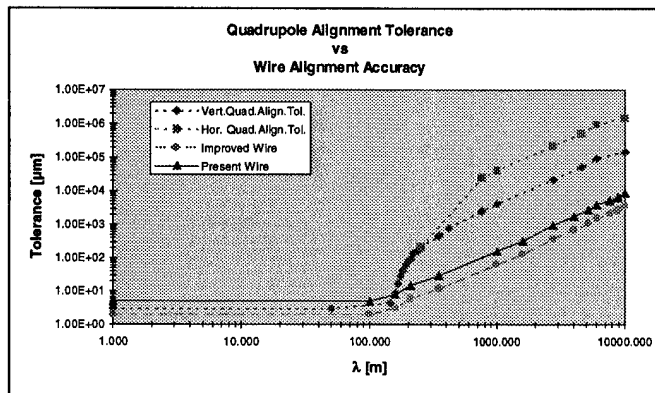


Fig. 20. Wire alignment accuracies

2. Hydrostatic Level System To simulate the effect of supporting the alignment with a hydrostatic level system, two cases need to be considered. If the machine would be built on a tangential plane, one hydrostatic level system cannot accommodate the height difference. Therefore, the simulation assumes individual 500 m long sections set up like a stair. The second case assumes an equipotential surface as reference plane allowing one continuous system. Fig. 21 shows the simulation results.

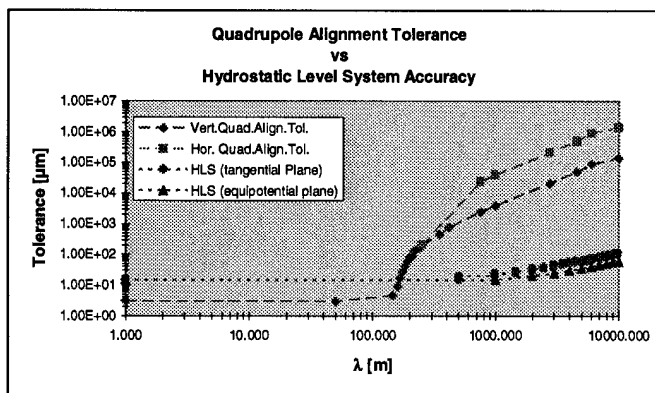


Fig. 21. Hydrostatic alignment accuracies

SUMMARY

Although the NLC requires alignment tolerances an order of magnitude tighter than required for existing machines, results from a conventional alignment will be sufficient to make the NLC correctable. It was shown also that more sophisticated alignment systems can very likely accommodate the operational requirements. While the beam itself is the ultimate judge of alignment, beam based alignment requires costly beam time. To maximize luminosity, the investment in more sophisticated alignment tools may well pay off.

¹Fischer, G., Alignment and Vibration Issues in TeV Linear Collider Design, *Proc. International Conference on High Energy Accelerators*, Tsukuba, 1989, SLAC-PUB 5024.

²Adolphsen, C., A Linac Design for the NLC, *Proc. 1995 PAC*, Dallas, 1995, in print.

³Schwarz, W. ed., *Vermessungsverfahren im Maschinen- und Anlagenbau*, Schriftenreihe DVW, Wittwer Verlag, 13/1995, p. 128.

⁴Made by TEXTRON Specialty Materials.

⁵Griffith, L., Progress in ETA-II Magnetic Field Alignment using Stretched Wire and Low Energy Electron Beam Techniques, *Proc. Linac Conference*, Albuquerque, 1990.

⁶Griffith, L., private communication.

⁷Gervaise, J. & E. Wilson, High Precision Geodesy Applied to CERN Accelerators, *Applied Geodesy for Particle Accelerators*, CERN 87-01, Geneva, 1987, p. 162.

⁸Schwarz, W., Wire Measurements for the Control of the FFTB Magnets, *Proc. Second International Workshop on Accelerator Alignment (IWAA)*, Hamburg, 1990, p.470.

⁹Ibid, p 475.

¹⁰Hayano, H., private communication.

¹¹Ruland, R., et al., A Dynamic Alignment System for the Final Focus Test Beam, *Proc. Third IWAA*, Annecy, 1993, pp. 243-4.

¹²Korytov, K., Multi-Point Wide-Range Precision Alignment Based on a Stretched Wire Technique, *Proc. Third IWAA*, Annecy, 1993, p. 121.

¹³Takeuchi, Y., ATF Alignment, *Proc. KEK/SLAC X-Band Collider Design Mini-workshop*, SLAC, 1994, SLAC-R-95-456.

¹⁴Miyashita, K. et al., Transverse Displacement Measurement Using Split Laser Beam, *Proc. XV International Conference on High Energy Accelerators*, Hamburg, 1992, pp. 307-309.

¹⁵Hermannsfeldt, W., Precision Alignment Using a System of Large Rectangular Fresnel Lenses, *Applied Optics*, 7, 1968, pp. 995-1005, SLAC-PUB 496.

¹⁶Ruland, R., op.cit., pp. 246-251.

¹⁷Griffith, L., et al., Magnetic Alignment and the Poisson alignment reference system, *Rev. Sci. Instrum.*, 61 (8), 1990, pp. 2138-2154.

¹⁸Roux, D., A historical First on Accelerator Alignment, *Proc. Third IWAA*, Annecy, 1993, pp. 88-91.

RELIABILITY OF THE LEP VACUUM SYSTEM: EXPERIENCE AND ANALYSIS

P.M. Strubin, J.-P. Bojon, CERN, CH-1211 Geneva 23, Switzerland

I. INTRODUCTION

The LEP vacuum system extends over 26 km and consists of more than 6000 chambers, bellows, valves and special equipment. Adding the various pumps and gauges, a total of 13000 gaskets is required to mount all equipment. Hence, it is the largest vacuum system ever built for an accelerator.

The major part of the vacuum system, mainly in the bending arcs, is made of extruded aluminium chambers, connected together by means of stainless steel bellows to cope with thermal expansion and adjustment of mounting tolerances. Aluminium gaskets are used on so called LEP type flanges. This part of the vacuum system is pumped by Non Evaporable Getter pumps [1] (NEG), with additional sputter ion pumps; it is limited to a bake out temperature of 150°C. The remaining part, referred to as the straight sections, is made out of stainless steel chambers and bellows, connected using copper gaskets; it is hence baked to 300°C. This part of the vacuum system is pumped by sputter ion pumps and titanium sublimation pumps. The special equipment, like accelerating cavities or electrostatic separators, is also installed in the straight sections. The vacuum system is split into manageable sectors by means of sector valves. The length of these sectors can vary between a few metres and 474 metres. A detailed description of the vacuum system of LEP can be found in [2,3].

The procedures for all interventions, in particular leak detection, bake-out and commissioning, are of utmost importance for the global reliability of the vacuum system and will be detailed in this paper.

As important for the global reliability are the power supplies and the remote control of the various equipment of the vacuum system. A careful initial design [4] and preventive maintenance are the keys for it and will be described in this paper too.

II. STATISTICS

LEP operation started in July 1989. At that time, a small number of leaks had been sealed with varnish after the initial bake-out and commissioning, as they were considered small enough so as not to justify a repair. Table 1 summarises these leaks and represents the actual starting point for our statistics.

The choice to varnish these leaks was fully justified, as none of them opened up until now or before a proper repair could be scheduled. A small number of additional leaks have nevertheless developed over the years. Table 2 summarises them.

Table 1: varnish sealed leaks at startup in 1989

Components	Quantity installed	Number of leaks sealed	%
NEG feedthrough	3768	7	0.2
Ion pump feedthrough	1346	3	0.2
PU electrode	1712	6	0.4
Al gasket, Ø 225	5374	2	0.04
Al gasket, Ø 113.5	7616	13	0.2
Bellows	2649	5	0.2
Weld on Al chamber	2588	1	0.04

Table 2: leaks that have developed since 1989

Year	Date	Sector	Leak rate Torr l/s	Comments
1989	7/8	361	$1 * 10^{-5}$	Corrosion on a pump feed-through, LEP not delayed
	21/9	370	$1 * 10^{-4}$	Corrosion on a pump feed-through, LEP not delayed
1990	4/7	259	10	RF window broken at the end of a technical stop, LEP not delayed
1991	15/5	240	$5 * 10^{-7}$	Porosity on an RF cavity field probe ceramic, LEP not delayed
	21/5	170	$1 * 10^{-4}$	Leak on a weld of an aluminium chamber, start-up delayed by 2 days
	4/10	850	$1 * 10^{-5}$	Leak on the experimental chamber for Delphi, LEP stopped for 10 days
1992	29/3	661	1	Large leak on an RF window, start-up delayed by 2 days
1993	14/7	241	10	RF window broken at the end of a technical stop, LEP not delayed
1994	4/5	258	$1 * 10^{-7}$	Leak on a bellows, LEP not delayed
	8/6	242	$1 * 10^{-7}$	Leak on a beam observation electrode, LEP not delayed
	31/8	660	$1 * 10^{-7}$	Porosity on an RF cavity field probe ceramic, LEP not delayed

It is important to point out that LEP was only delayed twice, and stopped once, due to vacuum over more than 5 years of operation. This very high reliability could only be achieved by the strict application of precise procedures during every intervention. These procedures will be detailed below.

III. LEAK DETECTION

Leak detection can be done at two different periods: when an intervention on the vacuum system is scheduled or during short interruptions of operation.

In the first case, residual gas analysers are used in place of the more common helium leak detector. This allows for a tenfold increase in the sensitivity and, hence, again in the smallest detectable leaks. Leaks in the 10^{-10} Torr l/s are routinely found with this technique.

During short interruptions of operation, the sensitivity is reduced to 10^{-6} Torr l/s where the sputter ion pumps are used to measure the pressures, 10^{-7} Torr l/s being possible where Bayard-Alpert gauges are installed.

A: Detection during interventions

1 Detection before opening a vacuum sector

A global leak detection using residual gas analysers is done on every vacuum sector which has to be opened for modifications or repairs. Every leak is registered and will be repaired while the sector is at atmospheric pressure. Previously varnish sealed leaks will also be repaired. This is required because the varnish used, although very reliable at room temperature and in presence of radiation, is not intended to be baked.

2 Detection before bake-out

A second global leak detection using residual gas analysers is done after a sector has been pumped down and is ready for bake-out. If at this stage, leaks are found, they will be repaired, not varnish sealed.

3 Detection after bake-out and commissioning

A final global leak detection using residual gas analysers is made after the bake-out and conditioning procedures, at room temperature. If a leak is found at this stage it will be varnish sealed provided it is smaller than 10^{-4} Torr l/s in order to avoid an additional bake-out. In case of larger leaks, a proper repair will be done, implying the complete repetition of the procedure: venting, repair, pump down, bake-out and commissioning.

B: Detection during short interruptions of operation

If a leak is detected either by the sputter ion pumps or the ionisation gauges, a leak detection using these elements is made. The leak is then varnish sealed and carefully registered, to be repaired during the next intervention in the sector.

IV. BAKE-OUT AND COMMISSIONING

A complete procedure involves a 24 hour bake-out and what is referred to as commissioning: flashing of the sputter ion pumps, degassing of the ion gauges and sublimation pumps and activation of the NEG pump. Figure 1 illustrates a typical bake-out cycle with NEG.

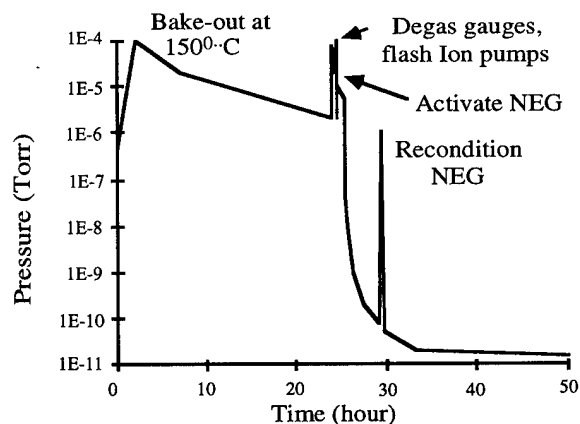


Figure 1: Typical bake-out cycle with NEG

A: Bake-out

Optimised bake-out procedures are very important for the overall reliability of the vacuum system. A precise temperature control, including control of gradients, is necessary. Figure 2 shows the typical temperatures recorded at various points of an aluminium vacuum chamber and an adjacent stainless steel bellows. The chamber is heated by circulating pressurised hot water in its cooling channels. No additional heating is provided for the bellows and the flanges, in order to simplify the bake-out equipment. It can be seen, that although the main part of the chamber is at 150°C , the flanges and the bellows are at lower temperature. This reduced temperature has no influence, however, on the end pressure but it increases the reliability by reducing the risk of a leak on the gasket.

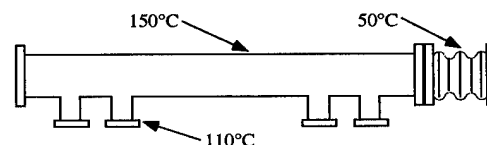


Figure 2: temperature distribution on Al chambers

Special care is taken for the larger vacuum vessels, such as the electrostatic separators. The temperature gradients are limited to 20°C per hour, in order to avoid temperature differences on the large flanges.

Another delicate component is the sector valve where leaks have developed across the seal when there was an excessive temperature gradient on the body of the valve.

B: activation of the NEG pump

The activation of the NEG pump is one of the most critical operation during the commissioning. The feedthroughs are at their limit of current handling and their temperature increases to 200°C when 90 A are fed into the NEG ribbon. Before every activation, the current leads are tested for correct tightness. A loose connection would inevitably provoke overheating of the feedthrough and could produce a leak. This would destroy the NEG pump which will burn with the oxygen entering the vacuum chamber. Residual gas analysers, scanning around mass 40 (Ar, which is not

pumped by the NEG), are used as an interlock to the NEG power supply

V. PRE-TESTING OF THE EQUIPMENT IN THE LABORATORY

Every single component of the vacuum system is completely tested in the laboratory prior to installation in the LEP accelerator. This means a full bake-out and the measurement of the ultimate pressure and gas composition. By doing so, not only can we detect manufacturing defects, like faulty welds, but we also make sure that the equipment is really clean. As an example, if a pick-up electrode with traces of oil was mounted in a long sector, up to 474 metres of vacuum system could be irretrievably polluted and would have to be completely taken apart to be cleaned. Therefore, the testing of the equipment in the laboratory is also considered as a preventive maintenance activity.

VI. PREVENTIVE MAINTENANCE OPERATIONS

A: Sputter ion pumps

The feedthroughs of the sputter ion pumps are heated with a low power heating collar in order to keep them free from moisture. At regular intervals the feedthroughs are visually inspected, but so far traces of corrosion have only been observed on three occasions, with the notable addition of two pumps on to which water had dropped. There is a significant accumulation of dust on them, however, and it will soon be necessary to clean them systematically in order to avoid leakage currents.

Global data logging and retrieval programs play an important role for early detection of either pressure rises indicating leaks, or deterioration of the quality of the feedthroughs.

B: Power supplies for the Sputter Ion Pumps

Because up to six pumps are powered from one supply [4] (to save in cabling costs), the reliability of these power supplies is vital. Furthermore, they are used as interlock source for the sector valves and all special equipment, such as accelerating cavities and electrostatic separators. The power supplies generate 5.6 kV and hence attract a lot of dust. They are cleaned every second year in order to prevent leakage currents around the high voltage transformer and leads. This proves to be sufficient, as there was no failure due to a faulty high voltage generator. The next critical elements are the high voltage connectors of the cables. There have been a few failures on the tunnel side, most likely due to humidity. However, because individual pumps are decoupled from each other by a high resistance cable, a single failure does not affect the average pumping speed too much. There is a problem for the individual current measurement devices, however, when such a failure occurs.

C: Interlock relays

A potential problem for reliability are relays in the various interlock chains. Some critical systems, like the accelerating cavities, require that all 256 sputter ion pumps give a good interlock to allow for operation. Because of the good overall reliability of the vacuum system and of the power supplies, these relays are rarely actuated and their contacts degrade with time. Most modern relays have so called self-cleaning contacts, but they require to be actuated. Therefore, all interlock relays are systematically operated three or four times a year, to insure the self-cleaning process. By doing so, we can ensure correct operation of the accelerator, leading to an average of two to three short interruptions (less than an hour) per year.

D: Sector valves

The sector valves are routinely closed during access to the LEP tunnel ring, for security reasons. The most frequent reasons due to vacuum for a delay in startup after an access is that some valve does not operate properly, in particular does not reach its completely open state. Unfortunately, there is no efficient way to improve this situation. Preventive maintenance is limited to a careful adjustment of the position switches whenever a problem is suspected.

VII. CONCLUSIONS

By carefully testing all vacuum components in the laboratory prior to installation in the LEP accelerator, we detect and eliminate manufacturing problems and, most important, guarantee that the equipment is absolutely clean for an ultra-high vacuum operation.

Performing systematic leak detection with residual gas analysers for maximum sensitivity, allows us to repair all leaks, even very small ones, before the bake-out and commissioning. As important is a systematic record of all known leaks for future repairs.

Several preventive actions, like testing of NEG and pump feedthroughs, are also considered to improve the overall reliability of the LEP vacuum system.

Similarly, preventive maintenance of high voltage supplies and some special actions for interlock relays provides for a reliable operation of the vacuum controls.

All added together and, last but not least, thanks to the very high skill of both CERN and industrial support staff, we can insure a smooth running of the LEP vacuum system.

VIII. REFERENCES

- [1] C. Benvenuti, CERN-ISR-VA/82-12
- [2] LEP Vacuum Group, Proc. IX IVC, V ICSS, Madrid (1983)
- [3] H.P. Reinhard et al, Proc XI IVC, VII ICSS, Köln (1989)
- [4] P.M. Strubin, Controls for the LEP Vacuum System, J.Vac.Sci.Technol., A 5(4) Jul/Aug 1987

THE ELECTRON BEAM LIFETIME PROBLEM IN HERA

D. R. C. Kelly, W. Bialowons, R. Brinkmann, H. Ehrlichmann, J. Kouptsidis
Deutsches Elektronen-Synchrotron (DESY), Notkestr.85, D-22603 Hamburg, Germany

Abstract

The electron beam lifetime in the HERA storage ring is not only uniformly lower than the positron beam lifetime, but the electron beam lifetime curves display complicated structures not present in the smoothly behaved positron beam lifetime curves. Summaries of characterising quantities are presented for large numbers of runs in 1993 and 1994, enabling the identification of trends in the beam lifetime behaviour.

The lifetime reduction seems to be due to many discrete lifetime reduction events. The lifetime achieved at given current depends in a complicated (and stochastic) manner on the filled current, energy and integrated ion getter pump voltage. The properties of the lifetime problem are overwhelmingly consistent with the capture of material by the electron beam (most likely dust particles of size $0.1\text{--}1\mu\text{m}$) which – being then highly positively charged – scatters beam electrons. The source of this material, or the mechanism of its liberation from the chamber or pump walls, is not entirely understood.

Moves towards curing the electron beam lifetime problem are discussed.

I. INTRODUCTION

The lifetime τ of a particle beam of current i at any instant is given by the local exponential decay law $di/dt = -i/\tau$. The lifetime of leptons in the storage ring HERA is expected to be limited by bremsstrahlung from residual gas, and is expected to increase smoothly with reduced current, i.e. with reduced synchrotron radiation induced gas desorption.

In August 1994 positron operation was introduced at HERA, with a notable improvement in the beam lifetime. Similarly, for the DORIS storage ring the switch from electron to positron operation in March 1994 yielded a significant improvement in the operation. In Fig. 1 we see examples of electron and positron runs from HERA. Unexpected jumps and variations can be clearly seen in all electron lifetime curves, whereas the smooth lifetime behaviour for positrons is determined by residual gas. This limitation of the electron lifetime is known as the *electron beam lifetime problem*, and is believed to occur in certain other electron machines in a similar manner.

We present here a brief summary of the major symptoms and properties of the problem in HERA, and discuss moves towards its cure. For an extensive investigation and interpretation of HERA lifetime curve data see [1], [2]. For a discussion of simulations of the dynamic and thermal stability of dust particles of various composition trapped in the HERA electron beam see [3], [4].

II. CHARACTERISTICS OF THE PROBLEM

In Fig. 2 the run-by-run sequence of HERA electron and positron beam lifetimes from March 1994 to August 1994 are

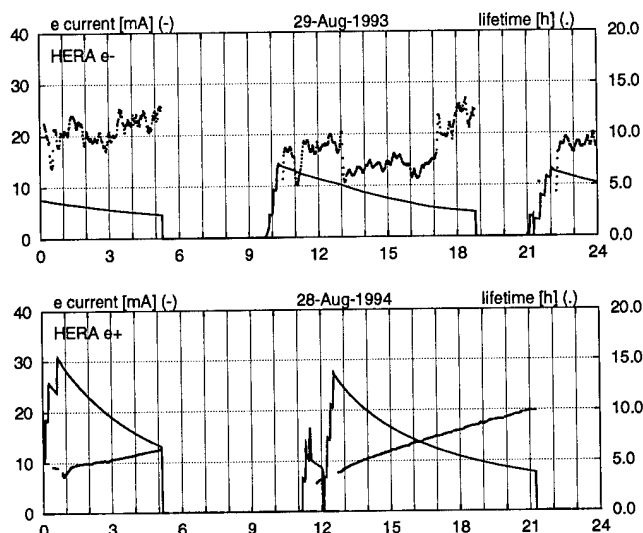


Figure 1. The current in mA (left scale) and and lifetime in hours (right scale) for a typical HERA e^- and e^+ runs is shown. It is clear that the beam lifetime behaviour for electrons departs from that expected due to residual gas alone.

shown at various beam currents. The positron runs were very smooth, and the lifetimes achieved from one run to another were very reproducible; variations in the positron lifetimes are almost entirely due to variation in chamber pressure during a vacuum pump assessment programme. The electron lifetimes, however, are much poorer, and vary greatly both within each run and from run to run. A satisfactory explanation of the phenomenon must not only explain these data, but must also explain properties of the beam *lifetime curves* that recur, and it must be consistent with experimental observations of the effect of varying the ion pump voltages, the energy, and the filling current.

A. Properties of lifetime curves

The captured dust particle hypothesis in its simplest form predicts abrupt changes in the beam lifetime as particles are captured by (or lost from) the beam. Sudden increase and decreases are seen, however examination of the lifetime curves reveals complicated structures not present under positron operation, including oscillations, increases, and decreases with timescales from minutes to hours. In general, the electron beam lifetime behaviour in HERA is difficult to quantify. Some of the more curious observations are presented:

The electron beam lifetime often drops towards or at the end of the ramp from 12GeV to 27GeV. In Fig. 3 we see an example of the lifetime variations during the ramp from 12GeV to 27GeV. Synchrotron radiation may play a role in the electron lifetime problem.

In Fig. 4 we see a gradual decrease in the lifetime over the first one or two hours of the run (after the rapid ramp from 12GeV

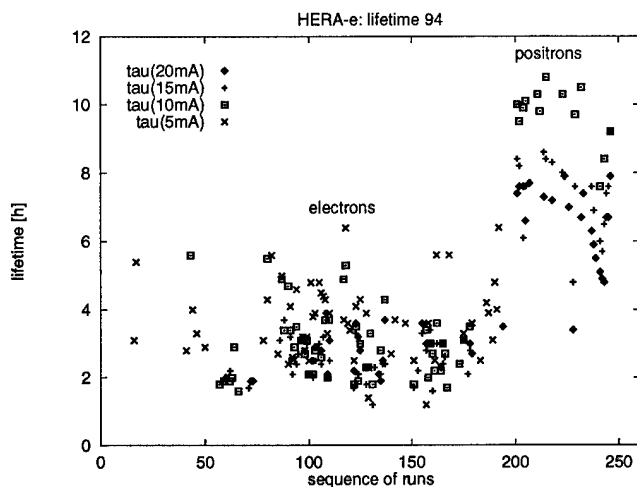


Figure 2. HERA electron and positron beam lifetimes in from March to August 1994 at current values $i = 5, 10, 15$, and 20 mA. The run for run sequence is shown.

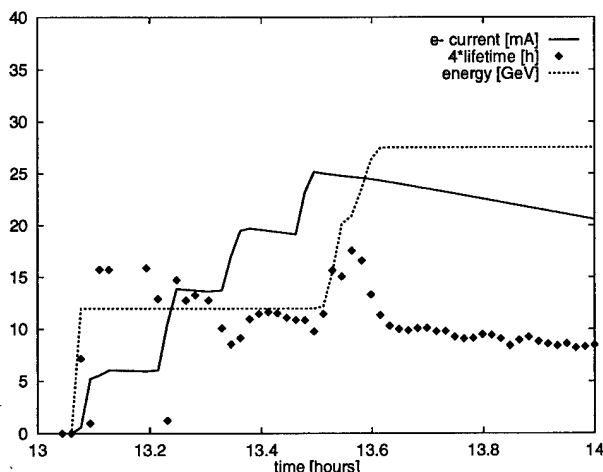


Figure 3. An example of the HERA electron beam lifetime development during the ramp from energy 12GeV to 27GeV for electrons. The current, lifetime and energy are shown against the time in hours. The electron beam lifetime tends to peak during the ramp and then drop.

to 27GeV has been performed). This effect can be seen in over 50% of the electron beam lifetime curves in 1994 and frequently in 1993. Similarly, gradual *increases* in the lifetime are often observed at low current values.

There is a strong correlation between the filled current and the degree to which the lifetime is limited later in a run (Fig. 5). As argued in [2], the statistical distribution is consistent with a discrete many-event model, whereby the probability of a particular lifetime reduction event occurring increases with filled current, and up to 10 lifetime reduction events occur for high current fillings. At very low current fillings lifetime reduction events are unlikely, so that positron beam lifetimes are often obtained. The behaviour seen in Fig. 1 is typical of smaller current fillings, and is perhaps due to the capture and escape of one or two dust particles, whereas for higher current fillings such as Fig. 4

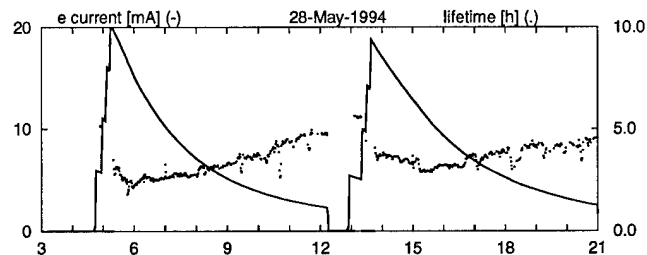


Figure 4. The electron lifetime frequently decreases gradually at the beginning of a run.

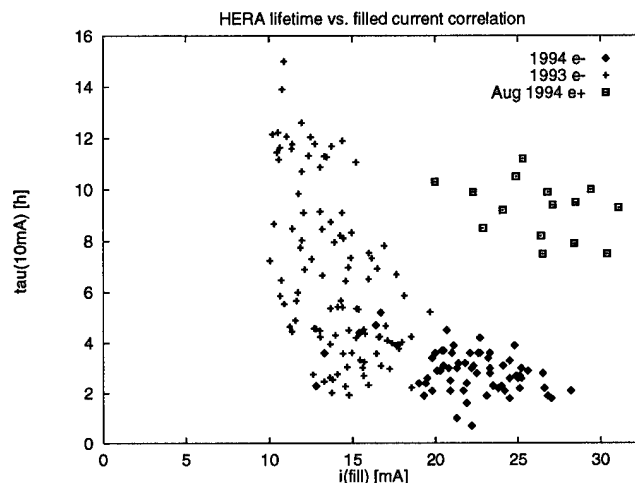


Figure 5. The lifetime in hours at beam current 10mA is plotted against the filled current for HERA electron runs in 1993 and 1994, and for positron runs in August 1994.

the lifetime reduction is more severe, and the lifetime does not recover at low current to values obtainable with positrons.

B. Results of experimental investigations

Many experimental observations are consistent with the capture of a micro particle of size $\leq 1\mu\text{m}$ or of a small number of particles with equivalent total mass:

The lifetime problem is independent of the tunes $Q_{x,y,z}$, and the incoherent tunes do not change during sudden drops in the lifetime; Electron loss monitors show that sudden drops in the lifetime are accompanied by strong local loss-rate increases (see Fig. 6, [5]); Spikes briefer than a few milliseconds and events of a few seconds duration – which may be due to the brief capture of dynamically unstable dust particles – are often seen in the bremsstrahlung detectors at the experiments H1, ZEUS and at the HERA polarimeter during electron runs.

The integrated ion pumps of HERA are strongly implicated in the HERA electron beam lifetime problem, which is known to be more severe at high integrated ion pump voltages. Indeed irreversible electron beam lifetime reductions have been induced in both PETRA and DORIS by momentary increases of the pump voltages. A significant improvement in the lifetime was achieved in 1992 by the removal of a single culprit pump. Arcing in the ion pumps has been observed at high voltages and is promoted by the presence of strong synchrotron radiation. It has been proposed that such arcing could throw dust particles

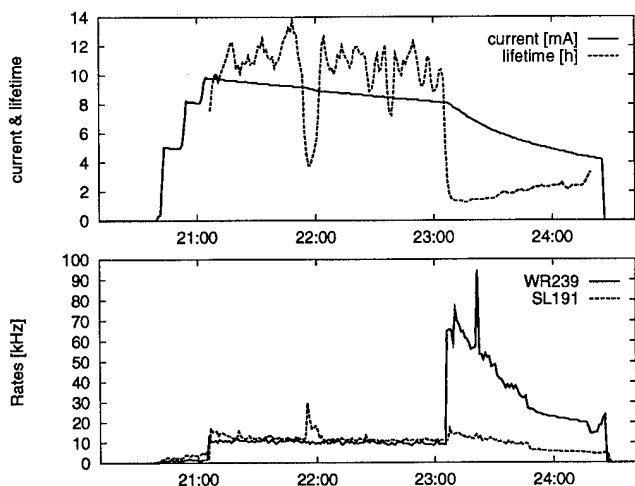


Figure 6. Lifetime reduction events correlate well with losses seen in the HERA electron loss monitors. In the above example from 11 Oct 1994 the brief disruption of the lifetime and current at time 21:55 is seen in loss monitor SL191, and the irreversible disruption at 23:05 is seen in monitor WR239.

into the vacuum chamber. The details of how the beam, synchrotron radiation, and the pumps interact in the complicated physical environment of the vacuum chamber to cast material into the beam are not understood.

III. TOWARDS A CURE

A. Beam excitation

It has been observed that transverse beam oscillations at various frequencies can beneficially affect the reduced electron beam lifetime in HERA. A computer simulation of a $1\mu\text{m}$ trapped dust particle indicates that the lifetime can be significantly improved by targeted transverse excitation of the beam (see Fig. 7). A dust particle trapped in the non-linear potential due to a Gaussian beam electron profile will have a well-defined oscillation frequency only for oscillation amplitudes small compared with the beam width. To obtain effective increase of the simulated dust particle's oscillation amplitude the beam excitation frequency must be swept from above the dust particle's 'linear-region' oscillation frequency in the kHz range. Trials of this method are to be performed in June 1995 by controlled sweeping of a transverse feedback kicker, to see whether irreversible improvement of the lifetime can be obtained.

B. NEG pumps

Although the lifetime problem appears worse for high ion pump operation voltages, the reduction of the pump voltage from the usual 5kV to very low values is not a satisfactory solution, since measurements during positron operation showed that the chamber pressure obtained under 3kV pump voltage itself delivers unsatisfactory beam lifetime. The trial installation and assessment of 'zero-voltage' non-evaporative getter (NEG) pumps has been planned for the 1995/1996 winter shutdown. The HERA electron loss monitors permit measurement of the removal of lifetime reduction events in a region installed with

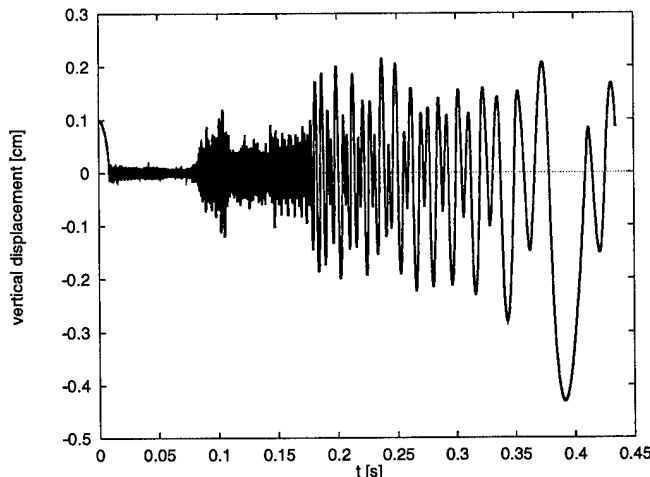


Figure 7. A simulation of the expulsion of a trapped $1\mu\text{m}$ dust particle from the HERA electron beam by sweeping a transverse beam kick through kHz frequencies.

NEG pumps.

References

- [1] D. R. C. Kelly, "Characterisation of lepton beam lifetime behaviour in HERA," Tech. Rep. DESY HERA 95-01, Deutsches Elektronen Synchrotron, Jan. 1995.
- [2] D. R. C. Kelly, "Many-event lifetime disruption in HERA and DORIS," Tech. Rep. HERA exp. 95-02, Deutsches Elektronen Synchrotron, Feb. 1995.
- [3] F. Zimmerman, "Trapped dust in HERA and DORIS," Tech. Rep. DESY HERA 93-08, Deutsches Elektronen-Synchrotron, July 1993.
- [4] F. Zimmerman, "Trapped dust in HERA and prospects for PEP-II," Tech. Rep. PEP-II AP Note No.: 8-94, Stanford Linear Accelerator Center, 1994.
- [5] W. Bialowons, F. Ridoutt, and K. Wittenburg, "Electron beam loss monitors for HERA," in *Fourth European Particle Accelerator Conference (EPAC94)*, vol. 2, p. 1628, World Scientific, 1994.

Design and Testing of a High Power, Ultra-High Vacuum, Dual-Directional Coupler for the Advanced Photon Source (APS) Linear Accelerator*

S.O. Brauer, A.E. Grelick, J. Grimmer, R. D. Otock, Y.W. Kang, J. Noonan, and T. Russell

Advanced Photon Source, Argonne National Laboratory
9700 South Cass Avenue, Argonne, Illinois 60439

Abstract

Leaks and cracks have developed in the vacuum windows of the linac WR 284 waveguide directional couplers. In the existing coupler design the vacuum window is brazed to the waveguide. Replacement of a cracked window requires the removal of the component from the waveguide system resulting in a loss of vacuum in the waveguide. A new design has been developed and a prototype tested that utilizes bolted-in vacuum windows and allows for easier replacement of the windows in the system, while still providing suitable radio frequency (rf) specifications.

I. INTRODUCTION

The rf operating frequency of the APS linac is 2.856 GHz. Rf power is provided by five 35-MW pulsed klystrons with a pulse width of 5.0 μ S, and a repetition rate up to 60 Hz [1]. Three of the five klystrons supply power to SLED (the SLAC energy doubler) cavity assemblies [2]; therefore, the electrical specification of peak power for the waveguide is >200 MW.

This paper describes the mechanical and rf design of a high power, ultra-high vacuum, WR 284 waveguide dual directional coupler for the APS linac rf system. Section II describes mechanical aspects of the coupler, and sections III and IV describe the rf measurement setup and the results.

II. COUPLER MOUNTING ARRANGEMENT

The coupler mounting arrangement is shown in Figure 1. The internal geometry of the insert, the CF (Conflat)-style flange and the flange-mounted viewport closely replicates that of the original brazed window design. This allows reuse of the directional couplers from the original waveguide system. In the new design, the insert is furnace brazed to the broad wall of the waveguide. Subsequent to brazing, a step-bored flange with tapped bolt holes is gas-tungsten arc welded to the insert from the inside (vacuum side). The viewport is sealed to the mating flange using a conventional oxygen free high conductivity (OFHC) copper gasket. The mounting bolts also secure the coupler mount housing, that is piloted into a slight recess in the viewport to maintain concentricity with the insert.

The directional coupler fits snugly (0.001-0.003" diametral clearance) within the coupler-mount housing to maintain concentricity with the insert opening. A shim is used between the directional coupler and the coupler mount housing to tune the coupling sensitivity of the assembly. The body of the directional coupler is rotated to adjust coupling directivity. An

annular coupler retainer secures the directional coupler to the coupler mount housing (via a shoulder on the directional coupler and tapped holes in the coupler mount housing) to maintain directivity and solid electrical contact.

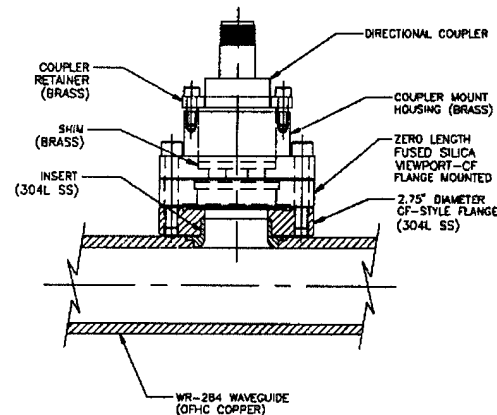


Figure 1: Coupler mounting arrangement.

This arrangement allows simplified replacement of a damaged window and immediate reinstallation of the directional coupler. Fused silica was used for the window. Fused silica windows and CF flanges are adequate for ultra-high vacuum use. The previous design required removal of the waveguide section and rework, including furnace brazing, of a new window. The distance between the two directional couplers is 4.518 inches. This corresponds to $3\lambda_g/4$, where λ_g is the wave-length of the rf wave in the waveguide. This distance allows the best directivity between the two couplers [3].

III. MEASUREMENT SETUP AND PROCEDURES

The rf measurements were made using a prototype of the dual-directional coupler. The test setup included a waveguide mount for each directional coupler and several coupling loops. The measurements were used to determine the optimum orientation and depth for the directional coupler loop in the WR 284 waveguide. The loop provides a coupling coefficient 57 ± 2 dB and directivity between the forward and reverse power measurement >32 dB at the operating frequency and over a test band of ± 10 MHz.

The experimental setup consisted of a Hewlett Packard Model 8510 network analyzer, two WR 284 waveguide-to-coax transitions, two 6" pieces of plain waveguide, and the prototype shown in Figure 2. The 6" pieces of waveguide were inserted between the transitions and the directional coupler to

* Work supported by the U.S. Department of Energy, Office of Basic Energy Sciences, under Contract No. W-31-109-ENG-38.

ensure that any fields due to evanescent modes created in the coax-to-waveguide transition would not be included in the measurements.

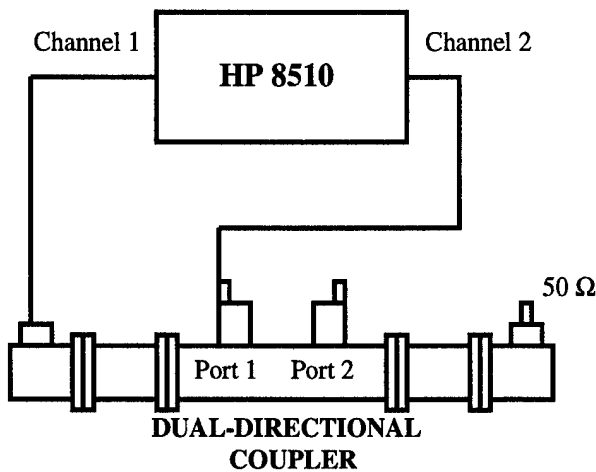


Figure 2: Measurement setup.

The center frequency of the analyzer was set at the APS linac rf frequency of 2.856 GHz with a span of 10 MHz. A waveguide calibration was performed using a WR 284 calibration kit to eliminate errors caused by the two transitions and attached 6" pieces, and to ensure that the measurements reflected only the device under test. Six different directional coupler inserts, numbered 1 through 6, were used and all but coupler 1 had a measured matched resistance that was $50.5 \pm 0.1 \Omega$; the value of coupler 1 was 51.3Ω . This small deviation did not seem to negatively affect the performance of the coupler.

The measurement procedure consisted of five steps. The setup for the first step was as shown in Figure 2. Channel 1 of the 8510 was connected to the coax-to-waveguide transition and channel 2 was connected to the directional coupler located in port 1 of the prototype. A 50- Ω broadband matched load was placed on the end of the second coax-to-waveguide transition. Shims were inserted into the directional coupler mounting to change the depth of the loop in the guide. The shims varied in size from 0.12" to 0.18". A transmission (S_{21}) measurement was done and a shim size was chosen that resulted in a forward power for port 1 of approximately -57 dB. The same shim size was then put into the coupler mounting of port 2 in the prototype.

In step two, the cable from channel 2 on the 8510 was removed from the coupler in port 1 of the prototype and attached to the coupler located in port 2. The S_{21} measurement was done while the directional coupler was rotated, in order to rotate the loop until the power reading was as low as possible. This measurement was the reverse power of port 2.

For step three the coax from channel 1 of the 8510 was switched with the 50- Ω load on the transition. The resulting transmission measurement was the forward power for port 2 (see Tables 1-3). If the forward power was not approximately

-57 dB, then next size shim was used and steps one and two were repeated.

In step four the coax from channel 2 of the 8510 was moved to the directional coupler located in port 1 and the coupler was rotated until the power reading was as low as possible. The transmission measurement was the reverse power at port 1.

In step five the original setup as described in step one was used and the measured forward power at port 1 was compared to the value recorded in step one. Again, if the second power measurement was not approximately -57 dB then the next size shim was used and the steps were repeated again until the correct shim size and corresponding loop position for the specifications were found.

IV. RESULTS

Six shim sizes were initially used: 0.12", 0.14", 0.15", 0.16", 0.17", and 0.18". Preliminary measurements determined that shim thicknesses of 0.14" to 0.16" corresponded to a forward power measurement between 54.8 and 59.2 dB for the couplers. A shim thickness of 0.14" was chosen in order to decrease the number of measurements. As shown in Table 1, forward power measurements with this shim size were fairly close to 57 dB and it was decided that as improvements were made in the prototype design this shim would provide the coupling that was required. Directional couplers 1 and 2 were paired together and met the specifications when inserted into the mounting using the 0.14" shim with no modifications to the prototype. It was decided to eliminate these couplers from the testing and use only the remaining couplers for which modifications to the prototype mounting had to be performed in order for the couplers to meet the specifications.

Based on the measurements taken and shown in Table 1, couplers 4 and 5 have the worst directivity, ranging from 20 to 25 dB. An inspection of the prototype revealed that changes could be made in the design to improve the directivity and the coupling. Two areas for improvement were found inside the coupler mountings. The first was that concentricity was not maintained between the inner diameter (I.D.) of the original rotatable flange and the I.D. of the insert, and the second was that the weld between the flange and the insert on the waveguide was not smooth enough (see Figure 1).

Table 1 Redesigned Coupler - Original.

Coupler Insert Port1 Port2	Fwd Pwr Port 1 (dB)	Rev Pwr Port 1 (dB)	Fwd Pwr Port 2 (dB)	Rev Pwr Port 2 (dB)
3 and 4	-56.445	-88.527	-54.758	-76.641
4 and 3	-55.584	-75.629	-56.525	-87.891
5 and 6	-55.641	-81.113	-55.588	-85.297
6 and 5	-56.24	-97.668	-55.936	-83.047
4 and 5	-56.055	-77.363	-56.195	-79.305

The roughness of the weld was smoothed out without changing the rotatable flange. This approach made relatively minor differences in the measurements, as shown in Table 2. The I.D. of the rotatable flange allowed approximately 0.015" clearance between its I.D. and that of the insert. Therefore, the next step was to replace the rotatable flange with a nonrotatable one which allowed approximately 0.003" to 0.005" clearance between its I.D. and the insert's I.D. This change resulted in a much simpler welding process, and the resulting weld was smooth. Table 3 shows data taken after changing the flange type. The measurements show improvement in directivity compared to the data shown in Table 2.

Table 2 Smoothed welding between flange and insert.

Coupler Insert Port 1 Port 2	Fwd Pwr Port 1 (dB)	Rev Pwr Port 1 (dB)	Fwd Pwr Port 2 (dB)	Rev Pwr Port 2 (dB)
3 and 4	-56.672	-85.781	-55.221	-79.363
4 and 3	-55.496	-79.906	-56.59	-89.737
5 and 6	-57.146	-83.398	-56.5	-90.758
6 and 5	-55.723	-91.293	-56.832	-81.668
4 and 5	-55.109	-77.656	-55.799	-82.582

Table 3 Changed flange type.

Coupler Insert Port 1 Port 2	Fwd Pwr Port 1 (dB)	Rev Pwr Port 1 (dB)	Fwd Pwr Port 2 (dB)	Rev Pwr Port 2 (dB)
3 and 4	-58.453	-95.371	-57.391	-85.508
4 and 3	-57.932	-87.535	-57.023	-95.312
5 and 6	-58.605	-87.734	-58.395	-88.562
6 and 5	-58.895	-98.848	-58.059	-92.176
4 and 5	-57.969	-86.805	-56.152	-85.637

V. CONCLUSION

As shown by the data presented in Tables 1-3, the conclusion can be made that it is possible to create a directional coupler that meets the electrical specification. The coupler will be able to operate at high peak power, and simplified window replacement without rebrazing the part is possible. Tight tolerances for the clearance between the CF flange and the insert in the waveguide I.D. must be closely adhered to and all welds exposed to rf must be smooth.

VI. REFERENCES

- [1] "7-GeV Advanced Photon Source Conceptual Design Report," ANL-85-15, April 1987.
- [2] Z. D. Farkas, H. A. Hogg, G. A. Loew, P. B. Wilson, "SLED: A Method of Doubling SLAC's Energy," SLAC-PUB-1453, June 1974.
- [3] O. P. Gandhi, *Microwave Engineering and Applications*, McGraw-Hill, pg. 200, 1988.

A PULSE SEPTUM MAGNET WITH LOW OUTGASSING RATE

Yuan Ji Pei, W.M.Li, D.M.Jiang, X.Q.Wang
National Synchrotron Radiation Laboratory
University of Science and Technology of China
Hefei, Anhui 230029, P.R.China

Abstract

A novel pulse septum magnet for the injection system of NSRL storage ring which is a dedicated synchrotron radiation facility was described in this paper. The main parameters and measured results of the septum including its magnetic field distribution and its vacuum characteristic were given also. After making a shim the stray field near current strip to gap magnetic field was reduced to 0.1%, and the pressure of the vacuum chamber, in which the septum magnet was installed, is less than 5×10^{-10} mbar after baking. Now the septum magnet is playing an important part in getting a high injection efficiency and high accumulating current in the NSRL storage ring during the machine running.

I. INTRODUCTION

HLS (Hefei synchrotron radiation Light Source) is a major equipment of NSRL (National Synchrotron Radiation Laboratory), which consists of an electron LINAC of 200MeV and a storage ring of 800 MeV. The LINAC was built in a tunnel and the storage ring was built above ground. The difference in vertical direction between the position of the LINAC and the storage ring is 3.2m. The electrons from the LINAC pass through the transport line of 88 m and then is injected into the storage ring by mean of the injection system which is composed of three kickers and two septum magnets. The two septum magnets were designed to carry out deflection in vertical direction and horizontal injecting into the storage ring^[1]. It is very important to develop a novel pulse septum magnet with a good magnetic performance and low outgassing rate so that it can be installed into the ultra-high vacuum chamber directly to raise the injection efficiency and increase the transverse admittance near the injection point of the storage ring. There were some way to solve these problems mentioned above in existing machine^[1,2,3,4,5,6,7]. One of these is to separate the vacuum chamber of the storage ring from the transport line vacuum chamber using a metal foil, such as Beryllium foil of 0.05 ~ 0.1mm or a koplon foil of 0.02 ~ 0.05mm think. Another way is to increase the gap size of the septum magnet so that the vacuum chamber can be mounted in the gap directly or reduce the conductance of gases from the vacuum chamber of the septum to the vacuum chamber near the injection point of the storage ring and using a SIP with higher pumping speed to exhaust them and so on. In order to keep a higher injection efficiency, adopting thin koplon foil to separate the two vacuum chamber is a better way. But when the electron beam of 200 MeV passes through the koplon foil of 50 μ m, the divergent angle of the beam will be increased up to 1.24 mrad which is larger than the allowed acceptance of the storage ring of NSRL at the injection point^[8,9] so the thin foil cannot be adopted in our

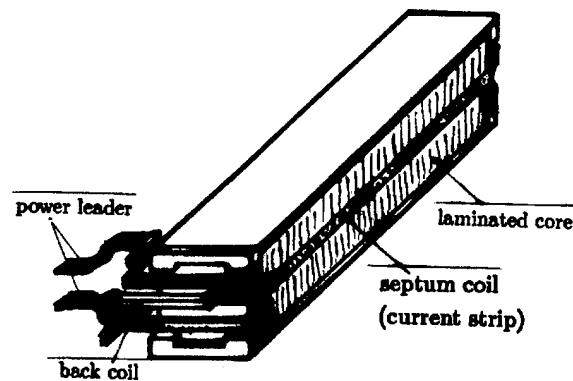


Figure 1. Schematic drawing of pulse septum magnet

case. On the other hand it is impossible to obtain the required pressure of 10^{-9} mrad, if the pulse magnet is directly mounted in the chamber of the storage ring. Because the pulse magnet was made of steel sheet (0.6mm thickness), its total surface area is about 10^5 cm^2 and the outgassing rate of the commercial steel sheet with isolating coating is about $10^{-10} \text{ mbar} \cdot \text{l} \cdot \text{s}^{-1} \cdot \text{cm}^{-2}$ at least. So the total outgassing quality of the septum magnet will be reach $10^{-5} \text{ mbar} \cdot \text{l} \cdot \text{s}^{-1}$. Obviously it is difficult to reach a pressure of 10^{-9} mbar or less. Finally a new magnetic material which is a low carbon steel sheet of 0.6mm thickness with Al_2O_3 powder coating has been searched after testing repeatedly. The test results show that its outgassing rate is negative after baking for 24 hours at 200°C . The whole septum magnet was mounted in the storage ring chamber, its pressure was less than less $5 \times 10^{-10} \text{ mbar}$ after bakeout and pumping of 48 hours^[10]. This is an exciting result. Now the septum magnet is playing an important part in getting a high injection efficiency and high accumulating current in the NRSL storage ring.

II. MAGNETIC PERFORMANCE OF THE SEPTUM MAGNET

The septum magnet is laminated by steel sheet of 0.6mm thickness with ceramic powder coating(coating thickness about 50 μ m). Its exciting coil is a single turn coil with Al_2O_3 powder coating also. The schematic drawing in Fig.1 shows the basic components of the septum. The cross section of the septum magnet is shown in Fig. 2. The main parameters is summarized in Table 1.

Integrated magnetic field along the electron beam direction was measured by means of a set of long coil. Its distribution vs transverse direction is shown in Fig.3. The magnetic field near the end of the septum measured along beam moving direction by point coil is shown in Fig.4.

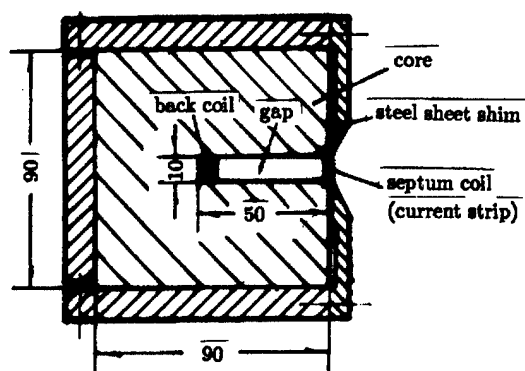


Figure 2. Cross section of the septum magnet

Table I
Main parameters of the septum magnet

Max. pulse magnetic field	5.6 kGauss
Radius of curvature	4.77 m
Deflection angle	104.7 mrad
Effective length	499.5 mm
Magnetic field waveform	half sine
gap highness	10 mm
Thickness of current strip	2 mm
Max. exciting current	4500 A
Max. current density	214.3 A/mm ²

The curve 3 in Fig.3 shows that the stray field near the current strip vs the magnetic field in the gap is about 0.1% after a suitable shim. With our testing data we calculated the injection efficiency to be about 100%. This indicated that the magnetic performance is good enough for our machine.

III. VACUUM CHARACTERISTIC

According to calculation of the lifetime of 8 hours in the storage ring, the pressure in the storage ring chamber with stored beam of 300mA must be less than 3×10^{-9} mbar. In order for the pulse septum magnet to be mounted in the ultra-high vacuum chamber directly, and not influence the vacuum condition, it is necessary to search and develop a new magnetic material which outgassing rate must be lower than 10^{-12} mbar \cdot l \cdot s⁻¹ \cdot cm⁻². Unfortunately, the outgassing rate of the commercial steel sheet with isolating coating is about 10^{-10} mbar \cdot l \cdot s⁻¹ \cdot cm⁻² at least. After testing repeatedly, we have found that outgassing rate of the low carbon steel sheet of 0.6mm thickness with ceramic powder Al_2O_3 coating is negative after bakeout for 24 hours at 200° C. Fig.5 shows the outgassing rate curve tested in different case. According to curve 1 and 2 in fig.5, the outgassing rate is about 4.2×10^{-13} mbar \cdot l \cdot s⁻¹ \cdot cm⁻². Obviously, the steel sheet with Al_2O_3 powder coating have some absorption capacity after baking^[10].

In order to understand the phenomenon we put the steel sheet of 706 cm² area into a testing vacuum chamber, and got a raising pressure curve in different condition after pumping. Fig.6 shows the test results. After one week being without pumping, the chamber remained a good vacuum condition of 10^{-9} mbar

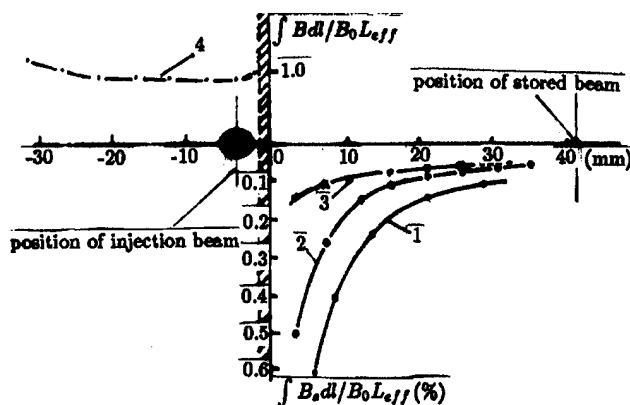


Figure 3. $\int Bdl$ vs transverse distance from the face of current strip

- 1 – without shim
- 2 – reducing the length of current strip without shim
- 3 – reducing the length of current strip with shim
- 4 – field distribution in the gap

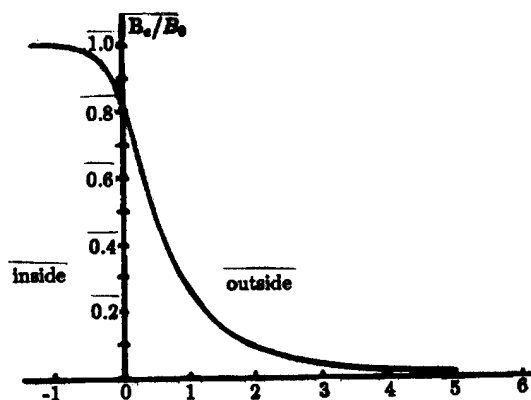


Figure 4. Magnetic field distribution near the end of the septum along beam direction

also.

Finally we manufactured the pulse septum magnet from such a material (steel sheet and copper strip) with Al_2O_3 coating. So far the septum magnet was mounted in the ultra-high vacuum chamber of storage ring, and is running well. The pressure near the septum magnet is about 8×10^{-10} mbar without beam and 2×10^{-9} mbar with stored beam of 150mA.

IV. CONCLUSION

After mounting the pulse septum magnet which was made of steel sheet and copper current strip with Al_2O_3 powder coating, into the ultra-high vacuum chamber of NSRL storage ring, the machine has successfully run for 5 years. All of these show that the septum magnet is of high quality with respect to both magnetic performance and vacuum characteristic. Especially, the septum magnet is of benefit to increase injection efficiency for a low energy electron storage ring.

As for the absorbing function and the mechanism of Al_2O_3 powder coating have yet to be investigated further.

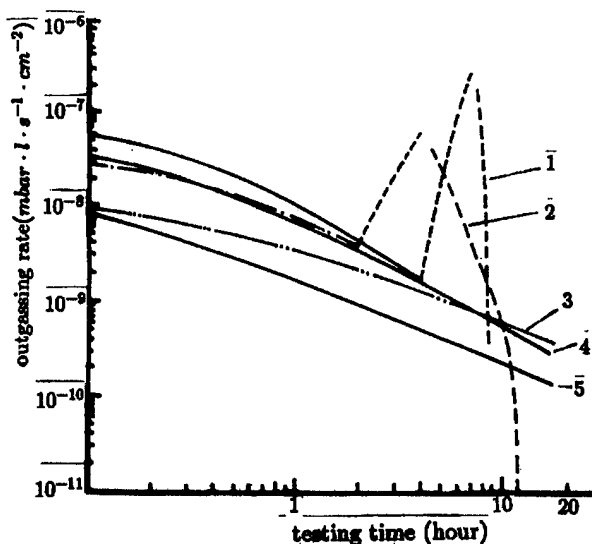


Figure 5. Outgassing rate curve of different material

- 1 – copper plate with Al_2O_3 coating after baking
- 2 – steel sheet with Al_2O_3 coating after baking
- 3 – steel sheet with Al_2O_3 coating at room temperature
- 4 – copper plate with Al_2O_3 coating at room temperature
- 5 – steel sheet with inorganic isolating coating at room temperature

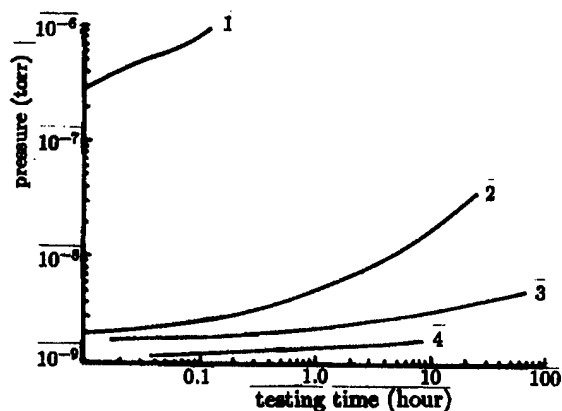


Figure 6. Raising pressure curve in different case

- 1 – steel sheet with Al_2O_3 coating at room temperature
- 2 – background (without sample)
- 3 – steel sheet with Al_2O_3 coating after baking
- 4 – steel sheet with Al_2O_3 coating after re-baking

V. ACKNOWLEDGEMENTS

We got so much help from Ms N.ZH. Hu, Y.ZH. Liu, and other colleagues in NRS� during developing the novel septum magnet. We would like to express our heartfelt gratitude to them here.

References

- [1] Y.J. Pei *et al.*, Design of the injection system for HESYRL, inner report, 1981.
- [2] T. Kawakubo, IEEE NS-26, No. 3, p3986, 1979.
- [3] M. Foss *et al.*, IEEE NS-26, No. 3, p4024, 1979.

- [4] A.J. Gorka *et al.*, IEEE NS-18, No. 3, p878, 1971.
- [5] R. Carrigan *et al.*, IEEE NS-20, No. 3, p719, 1973.
- [6] D.F. Cosgrove *et al.*, IEEE NS-24, No. 3, p1263, 1977.
- [7] Photon Factory Activity Report, 1982/1983.
- [8] W.M. Li, Y.J. Pei, Proc. of Symposium on the Progress of Particle Accelerator during the Past Ten Years., p319, 1990.
- [9] M. Watanabe *et al.*, Design of UVSOR Storage Ring, UVSOR-9.
- [10] Y.J. Pei *et al.*, Vacuum, Vol. 41, p1870, 1990.

SURVEYING THE MONUMENT SYSTEM AT LAWRENCE BERKELEY LABORATORY'S ADVANCED LIGHT SOURCE ACCELERATOR*

W. Thur and T. Lauritzen, Advanced Light Source Center, Lawrence Berkeley Laboratory
University of California, Berkeley, CA 94720 USA

Particle accelerators with demanding alignment requirements face a need for periodic re-surveying of their reference monument systems. At the ALS, significant foundation settling and the necessary relocation of some floor monuments mean that the entire system of over 100 monuments must be re-surveyed to an accuracy of 100 microns at two year intervals. Last Fall, the monument survey was conducted entirely by the in-house Survey and Alignment crew using a simplified instrument mounting system and an inexpensive commercial software package. Precision levels, plummets, theodolites, and an electronic distance measuring system were used with the innovative "Monopod" instrument mounting system in a cost effective approach to this critical task.

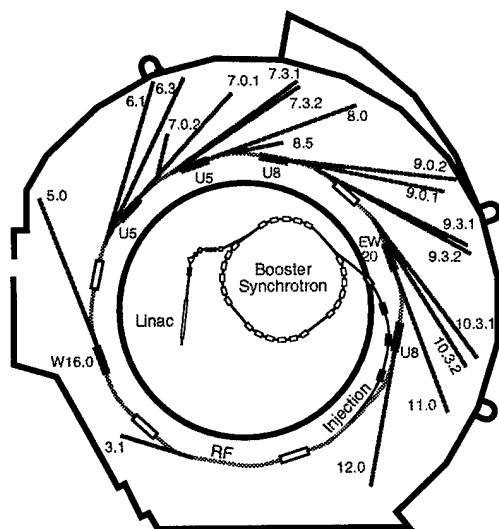


Figure 1: The LBL Advanced Light Source (ALS)

I. INTRODUCTION

When the Advanced Light Source synchrotron accelerator was designed in 1987-89, Lawrence Berkeley Laboratory had not built an accelerator facility in many years. There were no survey and alignment specialists on the staff, and certainly no one with experience in meeting the ± 150 micrometre (micron) alignment tolerances specified for the ALS components. Mechanical engineer Ted Lauritzen was given responsibility for survey and alignment. With help

from Robert Ruland and Co. of SLAC, the ALS equipped a new survey and alignment team with a well-chosen set of instruments and software to achieve near state-of-the-art alignment tolerances on the 200 meter circumference accelerator. In the process, new and innovative devices and techniques were developed at the ALS to improve the accuracy and the cost effectiveness of survey and alignment. Today, the alignment needs of the accelerator and its growing complement of tangential beamlines are met by a staff of six technicians and a part time engineer.

II. MONUMENT SURVEYS

All alignment surveys at the ALS are done with reference to a system of over 100 "monuments" embedded in the concrete slab floor of the building. Ideally, these monuments would be perfectly stable, but floor settling and the addition of new monuments requires that the entire monument network be re-surveyed periodically.

To measure the relative three-dimensional locations of all the monuments, many redundant sightings and measurements are made, with computerized processing of the data. Conceptually, the 100+ monuments represent a "network" of points linked by lines of sight. Using an optical plummet, a universal instrument mount is securely located at a known height directly above each monument in turn. Theodolites and Mekometers are then mounted for sightings to all the other monuments visible from that location. Wild N3 precision levels sighting to elevation scales provide relative elevation differences between monuments. Kern E2 theodolites provide precise horizontal angles between sighted monuments. Finally, the Kern Mekometer 5000 provides accurate slope distances between itself and a retro reflector at the sighted monument.

Data from the theodolite and the Mekometer sightings is entered into a laptop computer via umbilical cables. Elevation sightings are entered manually by the operator. The output from this data acquisition program is formatted for eventual input into the monument data reduction program, StarNet. StarNet accepts sightings input in any order, and performs a least squares "best fit" process on the geometrically redundant data to provide the greatest possible accuracy for the final coordinates of each monument. A "blunder detection" feature identifies any inconsistent input data so that questionable sightings can be repeated. A rigorous error analysis is part of the package. Standard instrument errors, the network geometry, and the level of redundancy are analyzed to specify a two standard deviation "error ellipse" for each monument position.

The complete system described above was used by our six person team in the Autumn of 1994 to re-survey the

*This work was supported by the Director, Office of Energy Research, Office of Basic Energy Sciences, Material Sciences Division, U.S. Department of Energy, under Contract No. DE-AC03-76SF00098.

ALS monument network. The results were gratifying: 100+ monuments in a circular area of 125 meters diameter were surveyed in three dimensions to an average uncertainty of ± 89 micrometres. Comparison with the previous monument survey some two years earlier showed that some monument coordinates had changed as much as 1400 micrometres (1.4 mm), with an average change of 470 micrometres.

The new monument coordinates will now be used as the frame of reference for all component alignment work done at the ALS. We estimate that future "optimized" monument surveys will be completed in a period of about two months with our six person crew, while the accelerator is running. This capability will allow us to precede each of our major scheduled shut-downs with an updated monument survey, allowing us to maintain the high alignment standards that are needed at the ALS.

In addition to our high quality instruments and survey personnel, three LBL originated innovations contributed to the success of the ALS monument survey:

III. THREE DIMENSIONAL MONUMENTS

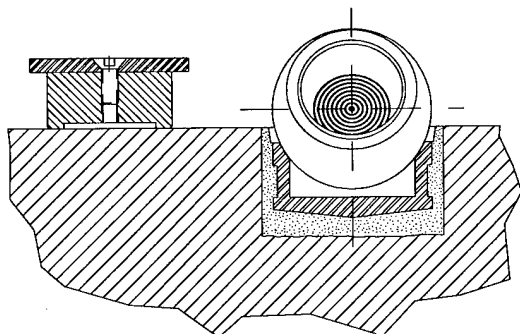


Figure 2: An ALS floor monument

The use of sphere-mounted targets in the conical recessed floor monuments provides a stable and repeatable reference marker capable of being accurately surveyed, and of being accurately referenced in component alignment surveys. Unlike other systems which use separate elevation references, these simple, well-designed monuments tie all three coordinates together for better accuracy and more straightforward use. These monuments are the foundation of our survey system.

The monuments themselves are an LBL design consisting of 17-4PH stainless steel cups epoxy grouted into the concrete floor. A precision ground conical surface supports 3.5 inch diameter Taylor Hobson target mounting spheres which carry sighting targets or corner cube reflectors precisely located at the geometric center of the sphere. The sphere can be swiveled for sighting from any direction, or for elevation measurements made with a direct contact vertical scale. Thus, the monument is three-dimensional; it provides a stable, repeatable reference point in all three dimensions. When not in use, the spheres are removed and protective covers keep out dirt and provide a flush floor surface.

IV. "MONOPOD" INSTRUMENT MOUNTING SYSTEM

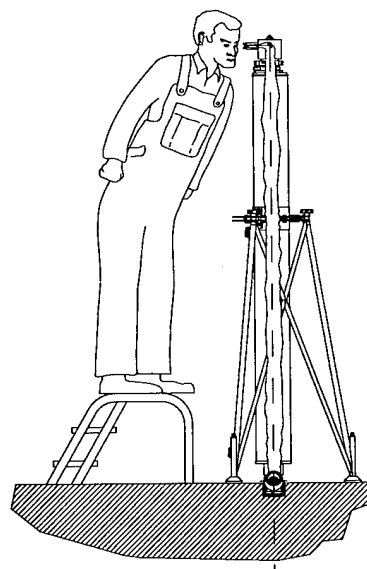


Figure 3: Plumbing a Monopod

Simplistically, the monopod is a 9 inch diameter hollow carbon fiber tube which is used to mount survey sighting instruments at an accurately known elevation directly above a floor monument. At its bottom end, a ground conical socket sits directly on top of a Taylor-Hobson target mounting sphere in a floor monument. At its top end, a modified tribrach instrument mount accepts an optical plummet, a theodolite, a Mekometer, or another target mounting sphere (to allow sighting over obstructions). An auxiliary tripod structure is bolted to the floor around the monopod, and a linkage between the two allows precise plumbing of the monopod over the floor monument. This is accomplished by mounting the optical plummet instrument to the top of the monopod, sighting down the bore of the Monopod to the illuminated target mounting sphere in the floor monument. Once the monopod is carefully plumbed, it provides a universal instrument mount at a known height directly above the floor monument. The special carbon fiber construction of the monopod tube provides a near-zero coefficient of thermal expansion, so the known height is extremely stable. Special monopods some 17 feet long are used to reach accelerator floor monuments through radiation shielding roof blocks, so that sightings to the outside monument network can be made. The big advantage of the monopod is that its "built in" elevation dimension eliminates the previous need to take separate elevation sightings for each instrument height.

V. STARNET DATA REDUCTION SOFTWARE

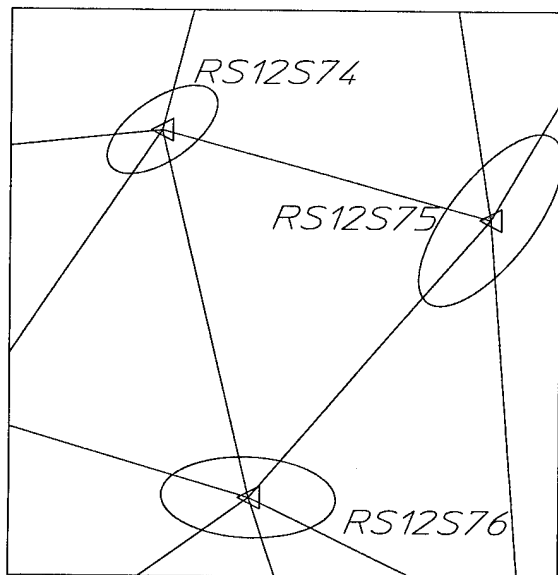


Figure 4: StarNet error ellipses

Although LBL cannot take any credit for the development of the StarNet software package, our discovery and adoption of it have been a tremendous boon to our operation. Previously, the software used for this purpose originated from within the accelerator alignment community. It had evolved over many years into a highly capable, but highly complicated, family of programs best understood by those who wrote them, or at least used them frequently. At our level of occasional use, we were hard pressed to master this esoteric and often unforgiving system. StarNet comes from another world - the world of everyday land surveyors. Although land surveyors never approach the level of accuracy we need, their instruments and their techniques are similar to those we use. And, best of all, for wide acceptance their software must be friendly. A well written manual, pull-down menus, and telephone support make StarNet a joy to use. A simple change of units from the scale of kilometers to the scale of meters harnesses all 14 significant digits of StarNet's calculational precision for work at the micrometre level. Its least squares adjustment routines are completely rigorous, and test runs with data sets from earlier surveys produce results identical to those from our previous software. StarNet also includes a simulation mode where survey error ellipses can be predicted based solely upon net geometry and assumed instrument errors, - before a single real sighting is taken[1].

VI. LESSONS LEARNED

Although we are pleased with our monument survey capability, the recent survey pointed out one way in which our efficiency could be improved: We need more monopods. To make the large number of sightings in our network, too much time was spent setting up, plumbing, and tearing down our set of eight monopods in a leapfrog manner. We would like to build another twelve monopods

to minimize this work, and to allow us to complete monument surveys in less time.

VII. ACKNOWLEDGMENTS

The Monopod instrument mount was originally conceived by Bill Baldock at LBL. The authors also wish to thank Robert Armstrong, Bill Baldock, Richard DeMarco, Alex Gavidia, Donna Jones, and Harry Meyer of the ALS Survey and Alignment crew for their dedicated work in surveying the ALS monument system, and for their helpful suggestions in perfecting the Monopod and the use of StarNet. Thanks also to Rob Duarte for engineering and development of Monopod hardware, and to Dr. Gary Krebs for physics advice and general support.

VIII. REFERENCES

- [1] STAR*NET Survey Network Adjustment Program, International Edition, Version 5. Starplus Software, Inc. 460 Boulevard Way, Oakland, CA. 94610, (510) 653-4836.

INDUCED RADIOACTIVITY OF THICK COPPER AND LEAD TARGETS IRRADIATED BY PROTONS, ^4He AND ^{12}C NUCLEI WITH ENERGY 3.65 GEV/NUCLEON

A. A. Astapov and V. P. Bamblevski, Department of Radiation Safety and Radiation Research, Joint Institute for Nuclear Research, Dubna 141980, Russia

The induced γ -radioactivity brings the main contribution to the exposure dose for the personnel of a high-energy accelerator. At the machines accelerating the heavy particles to the energies of ≥ 1 GeV/nucleon, this contribution amounts up to 50% of the dose.

The present study deals with the levels of induced radioactivity in dependence on the target material, sort of particles being accelerated, and time t elapsed since the end of irradiation. Recommendations are given to evaluate the rate per an incident nucleus $d_A(t)$ of a dose caused by the induced radioactivity of a thick target, from the dose rate $d_P(t)$ of protons with the same ratio of energy on nucleon.

I. EXPERIMENTAL PROCEDURE

The copper target of $\varnothing 100 \times 130$ mm² dimensions is irradiated with beams of protons, ^4He and ^{12}C nuclei and the lead target of $\varnothing 100 \times 170$ mm² -- with protons and ^{12}C nuclei of energy 3.65 GeV/nucleon during 4 hours approximately.

The experimental conditions and monitoring are the same as those described in [1]. The irradiation control is performed with an ionization chamber. The total number of incident nuclei $Gu_m(u_c)$, where u_m and u_c are, respectively, the indices of the projectile nucleus and target nucleus, is determined using the reactions of activation: $^{27}\text{Al}(u_c, x)^{18}\text{Fe}$

and $^{27}\text{Al}(u_c, x)^{24}\text{Na}$. The values of the reaction cross sections are taken from paper [1]. The number $Gu_m(u_c)$ determined with the detector agrees with that one obtained with the chamber within the measurement error (the chamber miscounts have been corrected). The following values of $Gu_m(u_c)$ are determined:

$$G_{\text{Cu}}(\text{P}) = (5.0 \pm 0.4) \cdot 10^{13} [\text{P}] \quad G_{\text{Pb}}(\text{P}) = (13.7 \pm 0.7) \cdot 10^{13} [\text{P}]$$

$$G_{\text{Cu}}(^4\text{He}) = (1.0 \pm 0.1) \cdot 10^{13} [^4\text{He}]$$

$$G_{\text{Cu}}(^{12}\text{C}) = (4.1 \pm 0.4) \cdot 10^{10} [^{12}\text{C}] \quad G_{\text{Pb}}(^{12}\text{C}) = (4.2 \pm 0.2) \cdot 10^{11} [^{12}\text{C}]$$

The exposure dose rate was measured with the use of scintillator, detector with NaJ(Tl) crystal of $\varnothing 63 \times 63$ mm² dimensions, and the multi-channel amplitude analyzer. Figure 1 illustrates the experiment configuration.

II. SIMULATION TECHNIQUE

The designed technique considers the general rules for generation of the secondary hadrons, fragments of projectile nuclei, and residual target nuclei in the nucleus-nucleus interactions. To a certain extent, the dependence of the radionuclide production on the charge and mass numbers is similar to that one on the projectile energy E_0 in the proton-nucleus and nucleus-nucleus collisions. So, the problem of d_A calculation splits, schematically, into two stages.

At first, the direct Monte-Carlo simulation is made of the induced radioactivity generation of a given target bombarded with protons of the same energy E_0 per nucleon. The key results are the dose rates 0d_P and $^s d_P$ of induced γ -radiation, caused by the primary protons and secondary hadrons correspondingly.

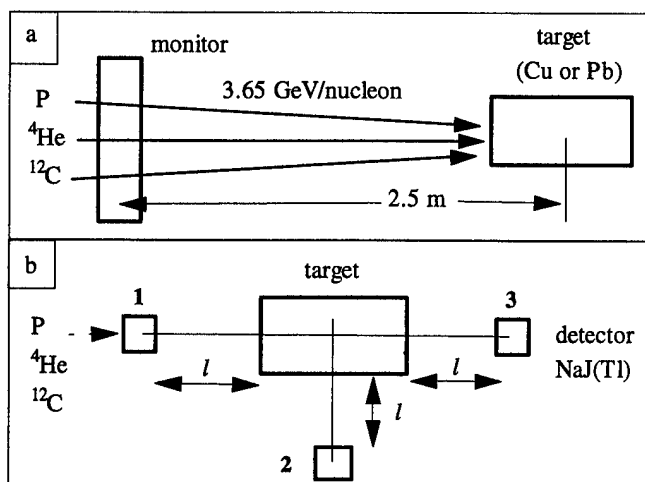
At the second stage, using the 0d_P and $^s d_P$ values and considering the peculiarities of particle production in the inelastic nucleus-nucleus collisions, the dose rates are obtained of the induced γ -radiation that arise from the primary nuclei 0d_A , their fragments $^f d_A$ and secondary hadrons $^s d_A$. Such a division of the total value d_A into three components 0d_A , $^f d_A$, and $^s d_A$ is reasoned by the complicated A -dependence for the specific target configuration. In the case of a thin target, the 0d_A brings the main contribution to the d_A but in the case of a thick target and light projectile nuclei ($A < 12$), almost the linear dependence on A is observed.

The 0d_A , $^f d_A$, and $^s d_A$ calculating technique is as follows.

1) According [2], the cross section σ_A of a radionuclide generation in a nucleus-nucleus collision is related to that one σ_P for a proton-nucleus interaction up to a factor of 2:

$$\sigma_A = N \sigma_P$$

Figure 1. Geometry: (a) - target irradiation; (b) - dose rate measurement from the: 1- beam inlet, 2- side, 3- beam outlet.



where

$$N = A^{0.25} + (A-1)^{0.6} 0.078 (\ln A_T - 1.85)$$

and A_T is the atomic weight of the target nucleus.

Under the equal volume density of the inelastic nuclear interactions, the difference of the residual nucleus productions results from the different relative probabilities of their yield. So, the 0d_A is expressed as

$$+ {}^0d_A(r) = N {}^0d_P(r), \quad (1)$$

where r is the radius-vector of a space point at which the γ -field functional is being defined.

2) Considering an incident A -nucleus as A of unbound nucleons, the dose rate ${}^s d_A$ caused by the secondary hadrons can be written down as

$${}^s d_A(r) = A {}^s d_P(r). \quad (2)$$

3) Under the nuclei inelastic interaction, the high-energy components of the internuclear cascade are generated not only at the fast stages of the process but also during the slow decay of the spectator fragments of an incident nucleus. The projectile decay by the competing mechanisms like the multifragmentation, evaporation, fission, leads to the appearance of the multicharged particles over the whole allowable mass range. The yield of the particles-fragments with energies close to E_0 , that differ from neutrons and protons, is negligible. The dose rate of the γ -radioactivity induced by the spectator nucleons is evaluated according the relationship

$${}^f d_A(r) = F(A, A_T) {}^0 d_A(r) = F(A, A_T) N {}^0 d_P(r), \quad (3)$$

where $F(A, A_T)$ is the fragmentation parameter determined as the average number of protons and neutrons-spectators, that are generated in an individual interaction of a projectile A -nucleus with a target A_T -nucleus.

The resulting value is

$$d_A(r) = {}^0 d_A(r) + {}^s d_A(r) + {}^f d_A(r). \quad (4)$$

Figure 2. Dose rates at position #1, $l=13$ cm, lead target.

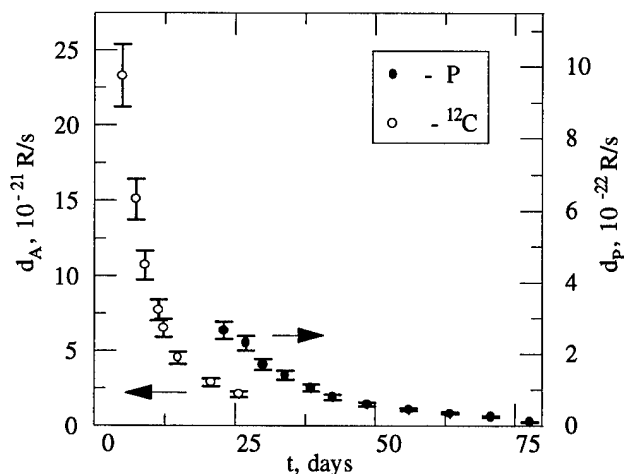
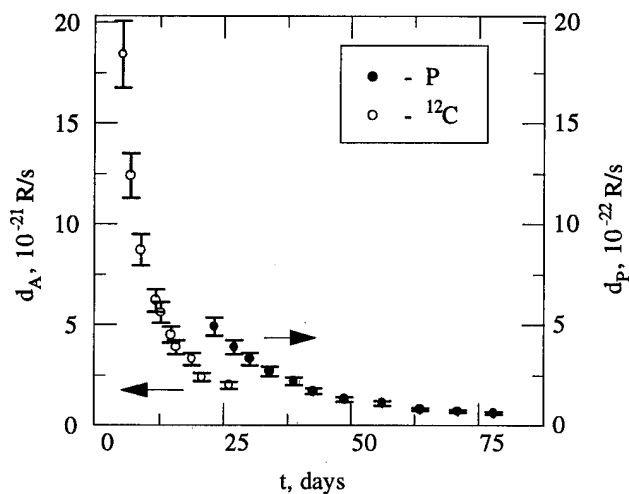


Figure 3. Dose rates at position #2, $l=13$ cm, lead target.

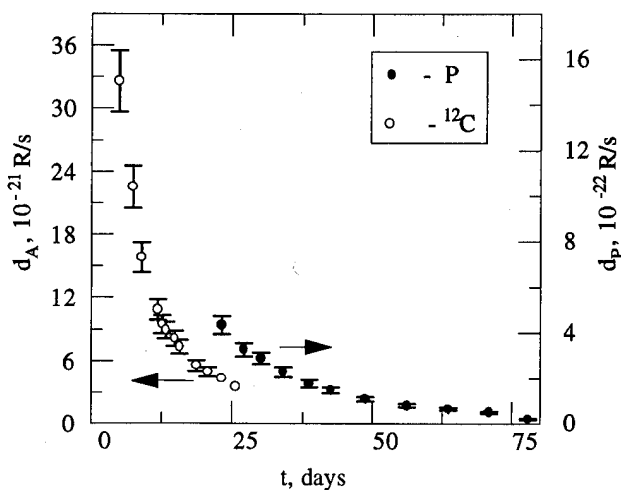
III. RESULTS AND DISCUSSION

Experimental results presented at figures 2-4 are the time-dependent exposure dose rates by the induced radioactivity of the lead target irradiated with protons and ${}^{12}\text{C}$ nuclei at $l=13$ cm and various configurations (see table 1 for the dose rate $d_{12\text{C}}/d_P$ ratios). The indicated error is the monitoring inaccuracy that does not exceed 10%. The additive error of the γ -irradiation dose rate has the systematic nature and is less than 15%.

Table 1. Ratio of dose rates d_A/d_P caused by the induced radioactivity of the targets bombarded with nuclei and protons.

target	A	data	geometry		
			1	2	3
Cu	${}^4\text{He}$	exp.	3.4 ± 0.9	-	3.4 ± 0.9
Cu	${}^4\text{He}$	calc.	3.2	-	4.0
Cu	${}^{12}\text{C}$	exp.	7.9 ± 2.0	-	9.6 ± 2.4
Cu	${}^{12}\text{C}$	calc.	9.3	-	12.7
Pb	${}^{12}\text{C}$	exp.	5.0 ± 1.3	10.3 ± 2.6	10.4 ± 2.6

Figure 4. Dose rates at position #3, $l=13$ cm, lead target.



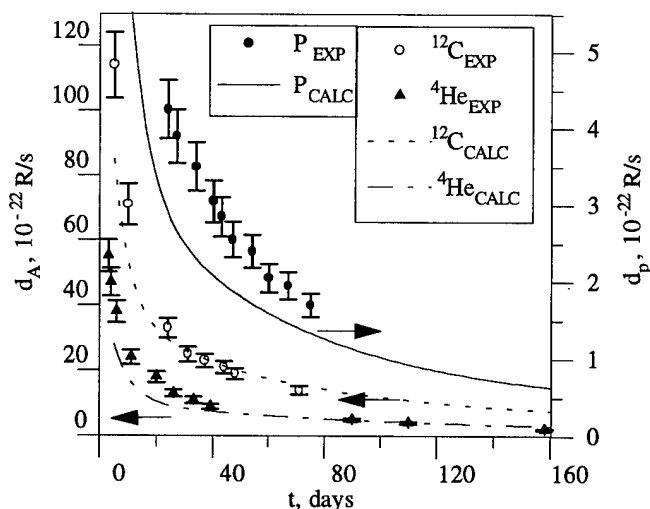


Figure 5. Dose rates at position #1, $l=23$ cm, copper target.

Figures 5 and 6 show the experimental data and simulation results of the exposure dose rates in dependence on time at $l=23$ cm and points 1 and 3 respectively for the copper target irradiated by protons and nuclei ^4He and ^{12}C . The calculated values d_p are obtained with Monte-Carlo method and the d_A ones - according to the formulae (1)-(4).

The proposed transitional formulae give results that differ from the experimental data not more than 25%. It is necessary to note that the calculation of d_p value (to be used later) underestimates it by 30%. Taking this into account, one may expect the satisfactory estimation of d_A values at transition on (1)-(4).

The experimental and calculated values of d_A/d_p agree even better (see table 1).

The above relationships leads to a conclusion that for the primary nuclei with $A \leq 12$, the d_A is governed by the $^s d_A$ value. For this reason, the following slightly overestimating formula is allowable when the extraction of components $^0 d_p$ and $^s d_p$ is hindered:

$$d_A(r, t) = A d_p(r, t). \quad (5)$$

The presented formulae are applicable for the analysis of the long-life component of the induced radioactivity of the thick targets with diameter and thickness $\leq 2\lambda$ (λ is the inelastic interaction free path) and light nuclei ($A \leq 12$) with energy $\geq 1\text{ GeV/nucleon}$.

Due to the complexity, it is hardly attainable to realize the sufficiently justified direct simulation of the radionuclide production for nuclei. So, the obtained experimental data and derived simple relationships can be useful for the evaluation of the induced radioactivity levels at the relativistic nucleus accelerators.

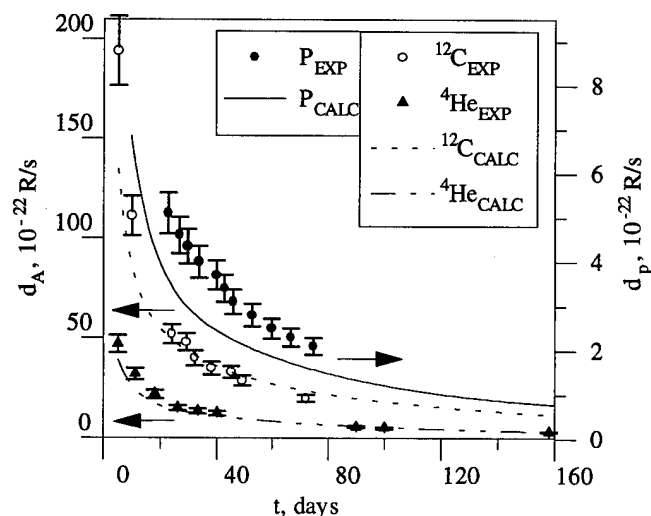
IV. ACKNOWLEDGMENTS

One of the authors (A.A.A.) is grateful to the 1995 PAC and ICHEA Organizing Committee and the International Science Foundation for the travel financial support.

V. REFERENCES

- [1] V. P. Bamblevski -- JINR Preprint 16-85-35, Dubna, 1985 (in Russian).
- [2] M. M. Komochkov -- JINR Communication P16-83-190, 1983 (in Russian).

Figure 6. Dose rates at position #3, $l=23$ cm, copper target.



THE PEP-II HIGH POWER BEAM DUMPING SYSTEM*

A.Kulikov, J.Seeman, M.Zolotorev,

Stanford Linear Accelerator Center, Stanford University, Stanford, CA 94309 USA

ABSTRACT

The beam abort system utilizes a single turn beam extraction into a beam dump placed outside the rings vacuum chambers. During extraction the beam is deflected by a pulsed dipole magnet and is scanned across an exit window and the dump face to avoid overheating the materials. The system is designed for 3 A circulating beam current which corresponds to 200 kJ of stored beam energy in the High Energy Ring at 9 GeV [1].

I. INTRODUCTION

The large stored energy and the small beam size in the rings represent a very serious challenge for the machine protection system. Let's assume that the entire stored beam strikes a single spot on the protection device, such as a collimator, and that the dumping time is small enough that the deposited energy will not diffuse significantly during this time. Then a local pulsed temperature rise δT will create stresses in the collimator material.

The conservative estimate of the thermal stress in the solid material is given by $\sigma = \alpha E \delta T$, where α is the thermal expansion coefficient, and E is the modulus of elasticity. It is assumed that for reliable operation, stress σ should not exceed half of the tensile strength σ_t of the material $\sigma \leq 0.5\sigma_t$. The pulsed temperature rise δT can be determined on the basis of EGS calculations [2].

The results of such calculations for different materials and typical High Energy Ring beam size of $\sigma_{rms} = 0.35$ mm are shown in Table 1. The numbers in the table represent the stored 9 GeV beam current which can be dumped in the collimator with the stress in the material $\sigma = 0.5 \sigma_t$.

Table 1

Material	Max. beam current
Beryllium	49 mA
Graphite UT-6ST	120 mA
Aluminum Al-5056	27 mA
Titanium Ti-6Al-4V	49 mA
Copper	1.9 mA

The data in Table 1 indicates that for the typical PEP-II beam spot size ($\sigma_{rms} = 0.35$ mm) even the best material, *Graphite UT-6ST*, has a limit which is more than an order of magnitude below desirable level of 3 A stored beam.

The adequate solution of the problem will be a dedicated beam abort system which can handle a large stored beam energy in the case of critical equipment failure or a human error.

II. DESCRIPTION OF THE SYSTEM

The abort system utilizes a single turn beam extraction into a beam dump placed outside the ring vacuum chamber. During the extraction the beam scans across an exit window and the dump face to avoid overheating the materials. The High Energy Ring (HER) and Low Energy Ring (LER) systems are practically identical and designed for 3 A circulating beam current in either ring. Due to the larger stored energy, the HER system is more demanding, and, therefore, is described below.

The dump system is located in the injection straight with the extraction kicker placed downstream from the first upstream injection kicker magnet. The dump is placed upstream from the injection septum and underneath the ring vacuum chamber.

The beam extraction in the vertical direction is preferable since it takes advantage of the large horizontal beam size ($\epsilon_x \approx 25\epsilon_y$ for uncoupled beam). The phase advance between the kicker and the dump is close to 90° . The large values of the β -functions at the dump ($\beta_x=40$ m and $\beta_y=120$ m) help to minimize the extraction kicker strength [3].

The following considerations have been taken into account to determine the kicker pulse shape and geometry of the extraction region :

- The effective beam area at the exit window and the dump should be at least $A=50 \text{ mm}^2$, which permits the extraction of 200 kJ of stored beam through a Al-5056 window and the use of graphite as a dump material.

* Work supported by US Department of Energy under contract DE-AC03-76SF00515, DE-AC03-76SF00098, DE-AC03-81ER40050, DE-AS03-76ER70285 and W-7405-Eng-48

- b. The beam should be "extractable" to the dump from any vertical orbit at the dump location between +20 mm and -20 mm relative to the center beam trajectory (bumped orbit for the beam injection plus 7 mm and central orbit minus 20 mm.)
- c. The vertical distance at the dump location between the central orbit and the vacuum chamber wall is chosen to be 35 mm, or $12 \sigma_y$ for the beam with $\epsilon_y = 37.5 \text{ nm} \cdot \text{rad}$, plus 5 mm orbit.
- d. The kicker operation synchronized to the ion-clearing gap should provide 100% stored beam extraction into the dump.
- e. 12 GeV operation of the HER is considered.

The geometry of the dump region is shown in Fig.1. The size of the aluminum exit window along the beam is not critical and it may be as thick as 1 cm ($\sim 0.12 X_0$). The RF taper inside the ring vacuum chamber can be made of thin ($\sim 1 \text{ mm}$) aluminum ($\sim 0.12 X_0$ along the beam for 1:10 taper.) The longitudinal space for the dump is about $20 X_0$ of graphite or 4 m.

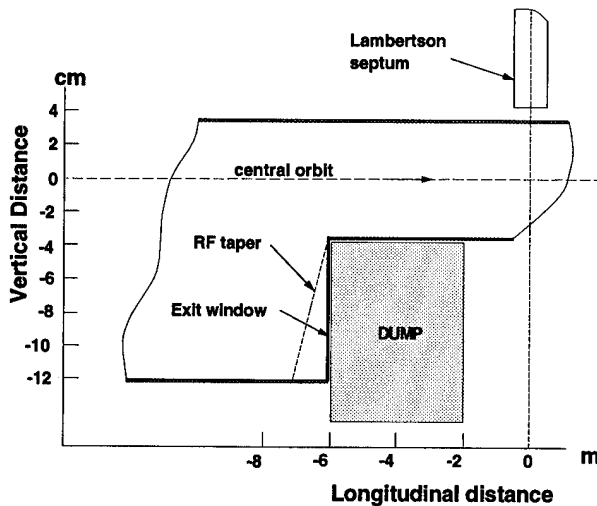


Figure 1: Geometry of the dump region.

The shape of the kicker pulse is illustrated in Fig.2. The scale at the right represents the beam vertical displacement at the exit window. The rise time of the kicker current from zero to 80% is equal to the time of the ion-clearing gap $\tau_{08} = 0.37 \mu\text{sec}$. The beam is smeared vertically at the distance $\Delta Y = 17 \text{ mm}$, and effective area of the beam is $A = (2\pi \epsilon_x \beta_x)^{1/2} \Delta Y \approx 60 \text{ mm}^2$ ($\epsilon_x = 50 \text{ nm rad}$, $\beta_x = 40 \text{ m}$). The maximal deflection of 87 mm corresponds to the kicker angle $\theta_{\text{max}} = 1.5 \text{ mrad}$ and the kicker current $I_{\text{max}} = 4.7 \text{ kA}$ at 12 GeV.

In the case of a random kicker trigger in respect to the ion-clearing gap (or operation of the machine without an ion-clearing gap), some small number of the beam bunches

will propagate beyond the beam dump. In the worst case, when the beam is aborted from the injection bump orbit, approximately 3% of the beam bunches will continue to propagate in the vacuum chamber after the beam dump. The amplitude of the vertical betatron oscillations of those 3% or 50 bunches will vary from zero for the first bunch to $A_{\text{max}} \approx 14 \sigma_y$ ($\epsilon_y = 37.5 \text{ nm} \cdot \text{rad}$) for the last one. The effective transverse area of this residual beam is large enough that it will not present any danger to the integrity of the vacuum chamber. Since the aperture of the vacuum chamber is at least $10 \sigma_y$, most of the residual beam bunches (~ 36) will return to the abort kicker. The kicker magnetic field, after one beam revolution, is still strong enough ($\sim 80\%$ of B_{max}) to deflect the returning beam bunches into the dump.

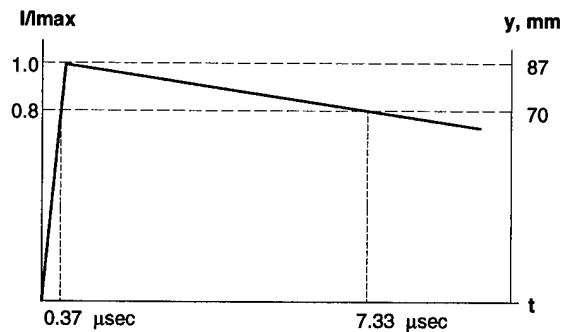


Figure 2: Shape of the kicker pulse

The kicker magnet is energized by the discharge of a storage capacitor. A free-wheeling diode connected in series with a large low voltage capacitor controls the long fall time of the current pulse.

An additional redundant kicker with associated pulser will be installed in the close proximity (next) to the first one. The trigger for the second kicker is delayed $7.33 \mu\text{sec}$ or one revolution of the beam from the first kicker. The redundant system insures safe beam disposal and prevents possible catastrophic failure of the machine if one abort kicker fails. The Beam Abort Systems in the two rings will operate independently.

References

- [1] J.T. Seeman, "PEP II Status and Plans", these proceedings.
- [2] W.R. Nelson *et al.*, "The EGS4 Code System", SLAC Report SLAC-265, Stanford, CA 94305.
- [3] M.H.R. Donald *et al.*, "Lattice Design for the High Energy Ring of the SLAC B Factory (PEP II)", these proceedings.

CRYOGENIC THERMOMETRY IN SUPERCONDUCTING ACCELERATORS¹

V.I. Datkov, Joint Institute for Nuclear Research, Dubna, Russia, J.A. Demko², J.G. Weisend, and M. Hentges, Superconducting Super Collider Laboratory, Dallas, Texas, USA

ABSTRACT

The cryogenic thermometers used in superconducting accelerators must function over a temperature range of 1.5 - 300 K in very harsh environments that must be endured for the life of the accelerator. The authors prescribe requirements for cryogenic thermometers in accelerator installations. Thermometer mounting fixtures used in the Joint Institute for Nuclear Research "Nuclotron" (JINR, Dubna, Russia) and the Superconducting Super Collider (SSCL, Dallas, Texas, USA) are described. Experimental results for long-term stability of some cryogenic thermometers and basic recommendations for applications in large superconducting accelerator systems are given.

INTRODUCTION

Operating modern superconducting (SC) accelerators requires accurate temperature measurements throughout the system. This allows the possibility to (a) monitor and safely control cool-down and warm-up of large mass accelerator magnets, (b) locate high heat leaks and minimize them during adjustment of new accelerator systems, (c) carry out thermal diagnostics of main cryogenic components during accidents, etc. Several peculiarities must be recognized for correctly using cryogenic thermometers in SC accelerators.

(1) Many commercial cryogenic thermometers carry warranties for only 1 or 2 years that may not cover the harsh conditions found in accelerators. Recalibration or verification is typically recommended at frequent intervals.

(2) Accelerators with sizes similar to the Superconducting Super Collider (SSCL) main ring and High Energy Booster System (HEB) have SC magnet lengths of 10 km and 87 km respectively, requiring 20-50 thousand cryogenic thermometers. Thermometers are expensive and requires technicians with highly specialized training. Reducing thermometer costs is possible by developing a thermometer in-house based on an inexpensive electronic component, and organizing verification and calibration facilities as was done previously at the ISABELLE project [1], TEVATRON at FNAL [2,3], NUCLOTRON at JINR (Dubna, Russia) [4,5] and others [6,7].

(3) Very harsh conditions exist in superconducting accelerators including (a) high magnetic field up to 6.6 T [8]; (b) high radiation dosage of about 1000 Mrad for 25 years [8], (c) pressure peak in helium flow during quench up to 2-3 MPa [9], (d) heating of parts (i.e. beam tube) to temperatures of 420-450 K and cooldown to 4 K and lower, (e) high voltage electrical insulation 500-3000 V for thermometers in magnet windings, during quench etc.

THERMOMETER REQUIREMENTS

Some principal requirements for cryogenic thermometers can be established from the requirements. Cryogenic thermometers must (a) Cover wide temperature interval 1.5 - 450 K; (b)

remain stable for 25 - 50 years better than 0.02-0.03 K (at 4.2 K); (c) have small, (< 1%) temperature measurement error in magnetic field < 6 T; (d) be resistant to ionizing radiation (dose < 1000 Mrad, temperature error readout < 1%); (e) have small (< 1%) error for pressures up to 3-5 Mpa; (f) have high sensitivity (dR/dT) particularly in 1.5-10 K range; (g) have minimal response-time (less than 1 msec. at 4.2 K); (h) be completely interchangeable; (i) use two wire readout; (j) be resistant to vibration, shocks; (k) have high voltage electrical insulation (500-3000 V); (l) be small; (m) be readily available and inexpensive.

THE "OPTIMAL" THERMOMETER

Several options for temperature measurement over the interval 1.5 K - 300 K using d.c., a.c., and pulse measurement technologies are available. Finding an "optimal" sensor is admittedly an impossible task since no known thermometer has all the best characteristics. The choice of thermometer and measurement system depends on a number of factors, including the required precision, cost, speed of response, sensor size, etc. Rubin and Brandt [12] described the characteristics of some thermometers that can assist in the selection process. Comprehensive cryogenic thermometry reviews are given in [13,14]. Anderson reviewed commercial carbon resistors used as cryogenic thermometers for over twenty years [7].

In superconducting accelerators cryogenic thermometers must be resistant to ionizing radiation. S.Scott Courts et al. irradiated several types thermometers at room temperature by gamma source to a level of 10 kGy and neutron+gamma source to a fluence of 8.6×10^{13} n/cm² [15]. In general, diode thermometers are unsuitable for use in either type of radiation environment. For gamma radiation carbon-glass and germanium thermometers performed well for $T < 25$ K and rhodium-iron over 1.4 K - 300 K. In neutron + gamma radiation the carbon-glass thermometers performed best at lower temperatures and platinum sensors at higher temperatures.

Allen Bradley (AB) carbon resistors have been used worldwide as cryogenic thermometers for more than thirty years because they have high sensitivity, small size, and very low cost. Wehr et. al. irradiated several AB resistors at 4.6 K in a reactor up to a dose of 3×10^9 r gammas and thermal and fast ($E_n = 0.1$ MeV) neutrons by 2.5 and 2.0×10^{18} n/cm² respectively [16]. A significant increase of a 110 Ohm AB resistor from 1500 Ohm up to 3100 Ohm at 4.2 K (dT about 2.3 K) is observed after irradiation. Subsequent annealing to 240 K lowered dT to 1.6 K. For accurate temperature measurements sufficient radioactivity decay time must be provided.

For the last 18 years at JINR a new type of commercial carbon-ceramic resistor, TVO [4], with 1000 Ohm nominal resistance was tested and is now widely used as a cryogenic thermometer. They possess better long term stability characteristics than AB resistors as well as a low price. Several TVO carbon-ceramic sensors were irradiated by JINR in a neutron

1. This work was supported by the United States Department of Energy under Contract DE-AC04-94AL85000.

2. Present address Sandia National Laboratories, Albuquerque, New Mexico, USA

reactor at room temperature up to a dose of 8.6×10^9 r/cm² gammas and fluence 1.3×10^{18} n/cm² fast (En=0.1 MeV) neutrons [5]. The observed shift in calibration was less than 1% at 4.2 K. To confirm the JINR data a TVO sensor was included in a cold irradiation experiment conducted by LakeShore Cryotronics and Ohio State University [5]. The data from this experiment show that after gamma doses of 10 kGy at 4.2 K the shift in calibration for TVO is less than 1%.

LONG-TERM STABILITY

AB 0.125 W, 100 ohm nominal resistors have been used for 10 years in large cryogenic systems at JINR. The temperature-resistance (T(R)) characteristics showed significant changes (>2%) after 1-3 years particularly when mounted on cryogenic surfaces in a vacuum. After several cooldowns to 4.2 K over 6 months some AB resistors increased resistance up to 105 Ohms with a room temperature readout dT of 5-20 K. Periodically (3 times per year) 10 TVO are tested at JINR shows high level of stability with <15 mK shift at 4.2 K over 14 years[4].

At the SSCL a calibration and test facility was organized and supported the Accelerator Systems String Test (ASST). Significant changes in AB thermometer calibration was observed in thermometers which were calibrated and mounted at FNAL on support-tubes of 323 dipole magnet. During preparations for ASST Run #3 the deviation from known room temperature of AB readout was -15 to +67 K. Our SSCL research with several of 100 Ohm AB showed that after 30 thermal-cycles the T(R) characteristics shift at 4.19 K is 8 - 20 mK, at 77.2 K is 0.6 - 3.2 K. Instability in AB carbon resistors has been the subject of a number of reports since being used for cryogenic thermometry [7,17]. At the same time TVO resistor testing showed a shift in T(R) after 30 thermal-cycles at 4.19 K of 4 - 6 mK, and at 77.2 K of 0.15 - 0.3 K.

Three runs of the ASST showed some problems with encapsulated thermometers mounted in the liquid helium stream in dipole magnets. During Run #1 after a quench a carbon-glass CGR1-1000 thermometer suddenly changed calibration at 4.19 K dT of 72 mK and at 77.2 K dT of 7.45 K. During later testing and detailed analysis a gas leak was observed from thermometer capsule. The quench high pressure pulse of 15-20 Bar probably damaged the encapsulated thermometer seal. During ASST Run#3 (17-Sept-93) the magnet string was filled with liquid helium without flow at a pressure of 1.22 Bar corresponding to a saturation temperature of 4.42K. The 16 CGR thermometers in the cold mass showed different temperatures: 8 thermometers differed from 4.42 K by <10 mK, and 8 others differed from 0.1 - to a few K indicating possible damage. Differences were observed in readings of intact and damaged thermometers when self-heated by high measurement current. Also during a second test of used encapsulated thermometers after thermal cycling significant ac noise was observed below 8-9 K.

APPLYING CRYOGENIC THERMOMETERS

Even with quality thermometry high accuracy measurements are difficult without experience in thermometer application. Many laboratories around the world invest in small installations to gain experience with cryogenic thermometers i.e. mounting, gluing wires, shielding measurement places, etc.

An improperly mounted or heat sunk thermometer will read a temperature contribution from the electrical leads. Careful planning with regard to the application must be performed early on. It is recommended to have an accurate thermal model of the sensor placement and a method for in-situ verification of the thermometer. A thermal model can provide a necessary assessment of the accuracy of the temperature measurement. As an example of a thermal model, assume a thermometer has a resistance of 10 kohms at 4.2 K and is mounted on a surface at 4.2 K. There are four #32 AWG leads (total cross section of 0.051 mm^2) 1 meter long going to the thermometer in a vacuum from a 300K connector. The sensing current is 10 micro Amperes. Using a numerical method of lines (NUMOL) solution as discussed for power leads in [10], the dependence of the error on contact between the sensor and the measurement surface can be evaluated. The error due to contact for coefficients of $10000 \text{ W/cm}^2/\text{K}$ and $100 \text{ W/cm}^2/\text{K}$ based on lead cross section are 0.0015 K and 0.1516 K respectively.

The determination of the measurement uncertainty must be performed similar to [11] and used to guide placement and mounting of thermometers. Results in [11] for the ASST show that the 4K heat leak across a single dipole magnet 15 meters long, must be determined from small temperature differences of 10 - 50 mK. High accuracy temperature sensors and mounting techniques are required to minimize the uncertainty in heat leak measurements.

In addition to temperature errors from improper mounting techniques, sensors can drift from their initial calibration. It is desirable to have a method of checking / verifying thermometer calibration as installed (in situ) for periodic evaluation of the sensor and the data acquisition system. Redundant thermometers are frequently applied to accomplish this. It may be possible to re-calibrate some sensors with the aid of thermal modeling of the system performance used with measurements from temporary precision instrumentation over large sections (say 10 or more superconducting magnets) of an accelerator.

Cryogenic thermometer mounting may be performed by personnel with limited experience. One remedy is to develop simple thermometer mounting fixtures. For the NUCLOTRON indirect temperature measurement techniques were developed to avoid installing thermometers in helium flow lines eliminating many vacuum feedthroughs reducing the possibility of leaks. The mounting fixture for a helium tube is shown in Figure 1. Twisted wires (8) from the hermetic connector at 300 K sink feed into the screw-thermal anchor (9) on copper plate (6), which is soldered on He tube (7). The screw-thermometer (2) measures the temperature of helium tube (7) with a 1-2% error over 4 - 300 K. The thermometer (3) is a TVO and bifilar winding (4) using a special technique for mounting in the screw (2) covered by a copper cover (1). All surfaces are polished and nickel plated. About 700 of these are installed in the NUCLOTRON on helium tubes in vacuum space and have performed well for over 5 years.

For the SSCL a different thermometer mounting fixture using TVO sensors was designed and installed in about 25 locations in the ASST. The fixture for a helium tube in the

interconnect between dipole magnets is shown in Figure 2. The thermometer (1) and thermal anchor (2) are mounted in holes of a stainless steel plate (3) using thermal-conducting grease (9). The fixture is clamped on the helium tube (8) with a hose clamp (5) and covered by multilayer insulation (6). During ASST Run #3 this fixture measured the tube temperature to within 0.01 K at 4.4 K from another carbon-glass thermometer mounted nearby in the magnet cold mass in the liquid helium stream. These were also installed on the 20 K and 80 K shields.

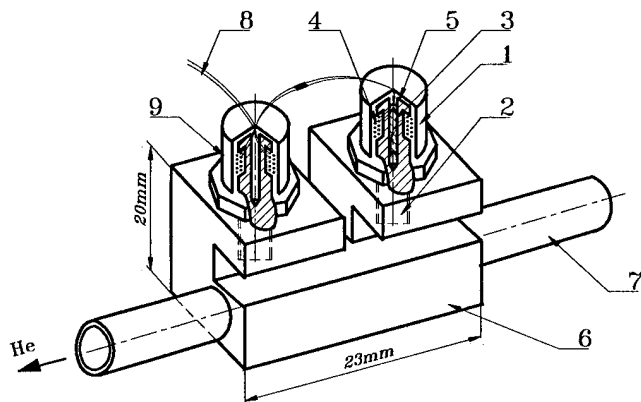


Figure 1: JINR Thermometer mounting fixture

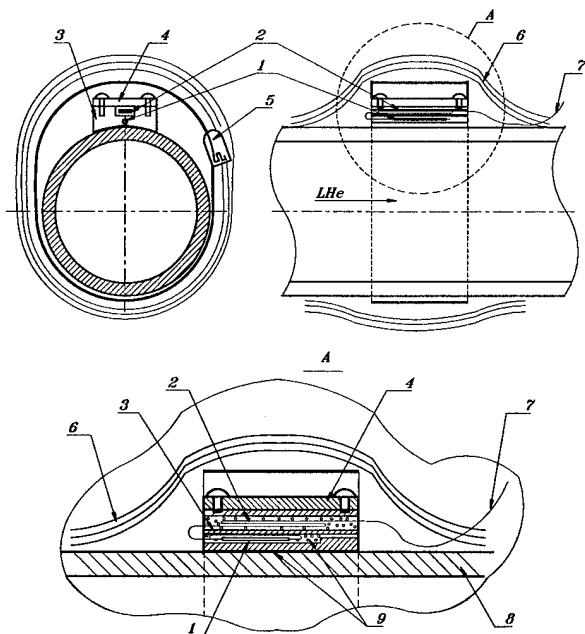


Figure 2: SSC Thermometer mounting fixture

CONCLUSIONS

For large superconducting accelerators it is necessary to have a small group of highly skilled, professional people and a calibration and test facility. This group should design special mounting fixtures, do full input control of all thermometers in real conditions, test and analyze damaged thermometers, model and predict future characteristics. Thermometers for superconducting particle accelerators must be able to withstand very severe conditions for the life of the accelerator. In-situ calibration/verification techniques using advanced thermal modeling of large sections of particle accelerators can be used to reduce the need for thermometer replacement.

REFERENCES

- [1] J. Sondericker, "Production and use of high grade silicon diode temperature sensors", *Advances in Cryogenic Engineering*, vol.27, 1982
- [2] M. Kuchnir, "Automatic measurements of heat load," *Advances in Cryogenic Engineering*, vol.27,1982.
- [3] M. Kuchnir, "Pulsed current resistance thermometry," *Advances in Cryogenic Engineering*, vol.29, 1984.
- [4] V.I. Datskov, L.V. Petrova, G.P. Tsvineva. "Cryogenic thermometers based on the TVO type resistors and their application", (in Russian). Communication of the JINR, #P8-87-604, Dubna, 1987.
- [5] V.I. Datskov, J.G. Weisend II, "Characteristics of Russian carbon resistance (TVO) cryogenic thermometers," *Cryogenics*, vol.34, ICEC Supplement, 1994.
- [6] E.M.W. Leung, R.D. Kephart, A.S. Ito and R.W. Fast, "The superconducting Chicago cyclotron magnet," *Advances in Cryogenic Engineering*, vol.27,1982.
- [7] A.C. Anderson, "Carbon resistance thermometry," *Temperature, Its Measurement and Control in Science and Industry*, vol.4, Instrument Society of America, Pittsburgh, 1972
- [8] R. Johnson and N. Mokhov, "Beam loss monitor system for the SSC". SSCL-Preprint-523, Dallas (October, 1993).
- [9] W. Burgett, et. al. Cryogenic characteristics of the SSC Accelerator System String Test," *Supercollider 5*, 1994
- [10] K. Stifle and J. Demko, "Evaluation of the Accelerator System String Test (ASST) Heat Leak Measurements and Their Uncertainties," SSCL Note SSCL-N-871, 1994.
- [11] J. Demko and V. Datskov, "Operation and Control of the Helium Cooled Power Leads for the Superconducting Super Collider", SSCL Note SSCL-N-870, 1994.
- [12] L.G. Rubin, B.L. Brandt and H.H. Sample, "Some practical solutions to measurement problems encountered at low temperatures and high magnetic fields," *Advances in Cryogenic Engineering*, Vol.31, 1986
- [13] L.G. Rubin, B.L. Brandt and H.H. Sample, "Cryogenic thermometry: a review of recent progress, II," *Cryogenics*, vol.22, 1982.
- [14] S.Scott Courts, D.Scott Holmes, Philip R. Swinehart and Brad C.Dodrill, *Applications of Cryogenic Technology*, vol.10, 1991.
- [15] S. Scott Courts, D. Scott Holmes, and Philip R. Swinehart, Lake Shore Cryotronics, Personal Communication, 1994.
- [16] G. Wehr, G. Sieber, and K. Boning, "Carbon resistors as low temperature sensors in low temperature reactor irradiation experiments," *Cryogenics*, 1977.
- [17] L.M. Besley, "Stability of some cryogenic carbon resistance thermometers," *Rev. Sci. Instrum.*, 54 (9), 1983.

ACKNOWLEDGMENTS

The authors gratefully acknowledge the assistance of L. Petrova and staff of the JINR calibration laboratory; M. Kuchnir, W. Boroski of Fermilab; J.Swartz, D.Holmes and S.Courts of LakeShore Cryotronics; M. Levin, S.Augustinowicz, L. Richards, Earnest Williams, B. Fietz, M. McAshan formerly at the SSCL, and J Spieckerman of MarketTech International.

CRYOGENICS OPERATION AND ON-LINE MEASUREMENT OF RF LOSSES IN THE SC CAVITIES OF LEP2

G. Winkler, Ph. Gayet, D. Güsewell, Ch. Titcomb CERN, CH-1211 Geneva 23, Switzerland

Abstract

Conclusions from the cryogenic operation of superconducting cavity modules in LEP during the 1994 run are presented, together with results of tools and procedures permitting the on-line measurement and analysis of radiofrequency induced losses, as seen from the side of cryogenics.

I. INTRODUCTION

CERN is in the process of receiving from industry, equipping and installing 236 superconducting (SC) cavities for the energy upgrade of the LEP collider. The current status and programme of this LEP2 project is presented elsewhere at PAC95 [1]. The situation of cavity production is summarized by E. Chiaveri et al. [2] and the good progress with the RF power couplers by J. Tückmantel et al. [3]; the latter had become a critical item and delayed installation during recent years.

The present paper is reporting on the cryogenic aspects of operating a number of LEP2 cavity modules with LEP in 1994, is then analyzing the particular question of how well the radio-frequency (RF) losses in the cavities can be monitored from cryogenic measurements using electric heater compensation, and finally giving an outlook to further progress expected in 1995.

II. CRYOGENICS OF CAVITY MODULES

The LEP2 SC cavities are 4-cell cavities with a sputtered niobium layer on copper, designed for 352 MHz fundamental mode operation; four such cavities are assembled together and installed as one module of 10 m length, with common vacuum tank and interconnected stainless steel containers for liquid helium (LHe) bath cooling of all outer cavity surfaces. About 0.7 m^3 of LHe is necessary to fill the bath, leaving only some 0.1 m^3 of vapour volume in a manifold on top of the cavity string; there the liquid level is kept constant ($\pm 10 \text{ mm}$ in height or $\pm 2 \text{ dm}^3$ in volume) by control action on the supply valve.

As up to 9 cavity modules will have to be operated, in the final LEP2 configuration, in parallel between vacuum insulated supply and return manifolds in each straight tunnel section on both sides of the LEP interaction points 2, 4, 6 and 8, the right level must be maintained in each bath container to

separate well the evaporated gas (GHe) from the liquid and send only gas back to the return manifold. Only then can all modules be sufficiently filled, even if the RF load is pushed to the limit of the re-liquefying cryoplant.

A second control valve is installed on each gas return line; it is part of another control loop which keeps the bath pressure as constant as possible ($\pm 2 \text{ mbar}$ around 1.25 bar abs.); this is not only important for a smooth boiling and a stable load for the cryoplant, but also to avoid de-tuning of the cavity resonance (typically 7 Hz/mbar) and interaction with RF phase control.

A fraction (typically 0.8 g/s per module) of the evaporated GHe is used for cooling heat intercepts, tuner and RF coupler components inside the modules and is returned to the cryoplant at room temperature. Details on component cooling and the static (without RF load) heat load of LEP2 modules are given in [4]; an internal helium flow scheme can be found in [5]. A typical static heat load of LEP2 modules is 80 W of refrigeration @ 4.5 K , and the warm gas return is seen as 'liquefaction' load with equivalence to about 100 W of 4.5 K refrigeration.

The RF load of four LEP2 type cavities for 352 MHz is near 400 W at the target acceleration field of 7 MV/m and the reference quality factor $Q = 3 \cdot 10^9$; it is varying with the square of the field and inversely proportional to Q . Most of the Nb/Cu cavities received at CERN and built into LEP2 modules could be conditioned to reach more than 7 MV/m and achieve $Q \geq 3.2 \cdot 10^9$ @ 6 MV/m ; they are expected to be operated reliably in LEP with fields of typically 6 MV/m .

III. CRYOPLANTS

Cooling for the LEP2 cavity modules at 4.5 K is provided by separate large cryoplants of 12 kW equivalent cooling power @ 4.5 K at each of the four acceleration points of LEP2. They were described in [6], together with their transfer line system for the cold helium distribution to the cavity modules. Commissioning results for the first 3 of them were given in [7] and the control system was presented in [8]. The specified capacity of these cryoplants was 10 kW refrigeration @ 4.5 K , plus 13 g/s liquefaction rate and 6.7 kW of $50\text{-}75 \text{ K}$ radiation screen cooling, resulting in a total of 12 kW refrigeration equivalent at 4.5 K .

All four 12 kW plants are commissioned and operational. The cooling performances were generally as specified [4] with excellent overall efficiency, reliable automatic operation and

good power saving capability for part-load operation. However, under the pressure of competitive tendering, the two suppliers did not provide much spare capacity and the total cooling power values achieved are generally rather at the low end of the tolerance band with typically 11.5 kW @ 4.5 K.

Counting 0.5 kW for control inside the plant, 0.8 kW for about 800 m of supply and return transfer lines, 0.4 kW for cooling the sc low- β quadrupoles of the adjacent experiment and the static load of the modules mentioned above, on average there will be for RF related dynamic losses a 4.5 K cooling power of at least 500 W per module, if not more than 14 modules are operated at each LEP2 point, and only some 350 W if the module number per point is increased to 18.

With series installation hopefully starting now and better statistics on average field limits and quality factors of modules in LEP, the ultimate beam energy limit of LEP2 can be anticipated and a rational decision made whether a possible upgrade should only increase the module number or also boost cryoplant performance, e.g. by adding compressors for more mass flow.

IV. OPERATION EXPERIENCE

Table 1:

Number of modules and cryogenic operation hours in LEP in years 1990-1994, with projection for 1995

Year	Number of installed modules	Cryoplant & Point ;	cryo operation period
1990	1 @2	1.2 kW @2;	5000 h
1991	3 @2	1.2 kW @2;	5000 h
1992	2 @2	6 kW@2;	6200 h
1993	2 @2	6 kW@2;	3800 h
	1 @6	12 kw @6	1400 h
1994	2 @2	6 kW@2	4600 h
	3 @6	12 kw @6	1500 h
1995	8 -> 16	12 kW @2,6	5000 h
		12 kw @8	1500 h

Experience with cavity cooling in the LEP tunnel started during machine runs in 1990/91 with prototype modules and a refurbished 1.2 kW refrigerator. This plant has been phased out and operation of the new generation of large refrigerators started in 1992 with modules from industry and a 6 kW plant [5]. In Sept. 1993 the first 12 kW plant started cooling of cavity modules and since beginning of 1995 the second 12 kW refrigerator replaces the 6 kW one. A varying number of modules has been cooled so far at two LEP points. At present 2 and 6 modules respectively are operated at the two first LEP points, a third point will come into service with module

installation summer 1995 and the forth from spring 1996. Table 1 is summarizing this history.

The process control system of the LEP2 cryoplants is programmed for fully automatic operation of the whole system, in particular for automatic cool-down, restart after utility failures or adaption of the plant capacity (by varying compressor pressure and switching off one or two of 5) to reduced 4.5 K loads. As a consequence operator interventions and down-time of cavities could be considerably reduced [5]. Reliability turned out to be quite high, but careful preventive maintenance on all components and follow-up of compressor-motor alignment and vibrations is necessary.

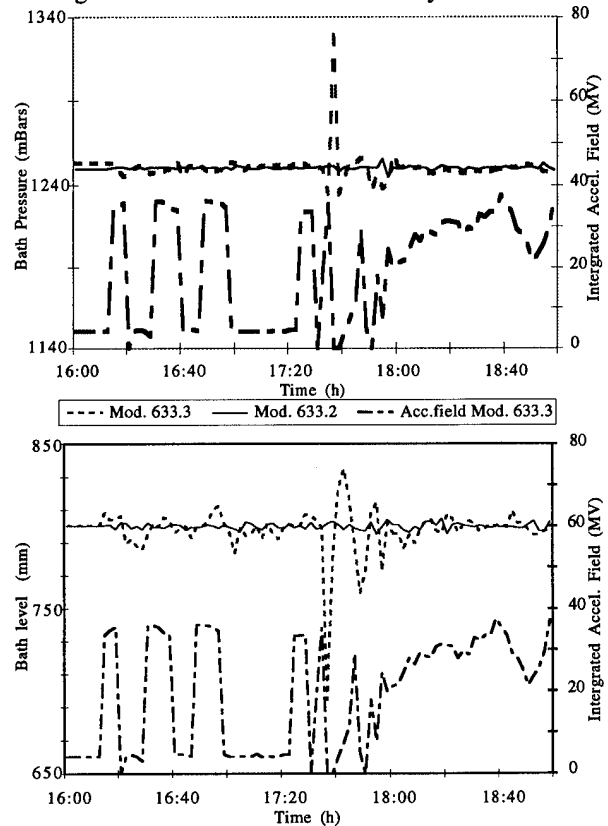


Figure 1: Recording over 2 h of bath pressures and levels in two adjacent modules during conditioning of one module. In the centre is visible, in one module but not in the other, a heat spike with RF cut by pressure and level interlocks.

V. STABILITY OF CRYOGENICS WITH VARYING HEAT LOAD FROM RF

To achieve the required stability (s. chapter II) of bath pressure and level in all modules with many interacting control loops also in the cryoplant, rapid changes of dynamic heat load must be compensated as well as possible directly inside the modules. This is achieved by using electric heaters in each cavity bath to which at zero RF a pre-determined heat load is applied (in 50-150 W range). From an analog signal proportional to the varying RF level the control system is calculating the expected RF load and is changing

instantaneously the heater power correspondingly. If the right value is chosen for the effective Q of each module, even drastic and rapid changes of the RF field have almost no influence on bath pressure and bath level. (Figure 1).

The position of the cold gas return valve of each module bath is varying with gas flow and thus, if stable conditions are maintained on the supply side, is directly related to the total heat load going into the bath. We are studying and will implement algorithms in the control system which, during conditioning, will vary the Q value used for heater control such that the return valve is kept in constant position. In this way the effective Q value of the module can be monitored and displayed on-line.

VI. EFFECTIVE MODULE QUALITY FACTOR Q .

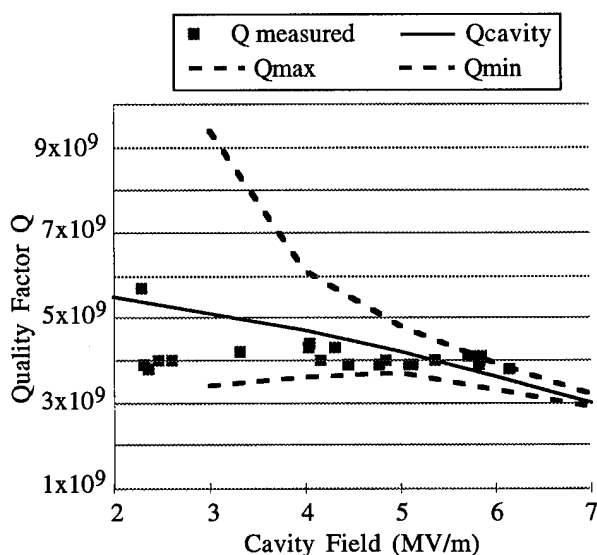


Figure 2: Comparison of average Q of module 633.2 measured on RF test bench (—) to those measured from cryogenics with heater compensation; dotted lines give error range corresponding to ± 20 W on heater power.

Figure 2 shows an example of the monitoring of the average quality factor for one of the modules operated in LEP in 1994. Each time measurements were averaged over typically 15 min, and quite a range of field strengths covered between 2 and 6 MV/m. An approximate Q factor was used for heater compensation of the RF load, and the residual movement of the gas return valve corrected off-line on the recorded monitoring data. As these measurements were done over an extended period, no identical supply conditions could be maintained, with varying 'flash' gas content as consequence of temperature changes in the supply manifold. Nevertheless good agreement of cryogenic and RF measurements was observed. Due to the quadratic nature of losses as function of field strength, cryogenic measurements cannot provide a satisfactory precision at lower fields.

VII. OUTLOOK

During the current operation period of LEP, we shall have for the first time at one of the LEP points two strings of 4 modules on each side of a 12 kW cryoplant and have a chance to operate the system under realistic charge conditions with around 50% of the final load. We expect then not only to be able to demonstrate the efficiency of our automatic procedures, but also be able to monitor continuously cavity module performances on-line.

VIII. ACKNOWLEDGEMENTS

We would like to thank our LEP2 cryo-team for its continuous effort to prepare cryoplants and cavity modules, and to ensure their reliable operation. We are in particular grateful to L.Als-Nielsen for the development of the data logging system and to G.Larsson for analyzing the monitoring data.

IX. REFERENCES

- [1] S. Myers, "LEP Status and Plans", PAC95, Dallas
- [2] E.Chiaveri et al., "Progress in manufacturing LEP2 cavities", PAC95, Dallas
- [3] J.Tückmantel et al., "Improvements to Power Couplers for the LEP2 Superconducting Cavities", PAC95, Dallas
- [4] M.Barranco-Luque et al., "Thermal loss analysis of cryostats and accessories for the superconducting cavities of the LEP energy upgrade", Proc.4th EPAC, 3(1994), p.2455.
- [5] Ph.Gayet et al., "First Operational Experience in Running a New 6 kW Cryoplant Cooling Superconducting Cavities in LEP at 4.5K", Sixth Workshop on RF Superconductivity at CEBAF, Newport News, USA, 1993
- [6] D.Güsewell et al., "Cryogenics for the LEP200 Superconducting Cavities at CERN", Proc. PAC93 4(1993), p.2956.
- [7] S.Claudet et al., "Four 12kW/4.5K Cryoplants at CERN", ICEC15, Genoa, Italy, 1994
- [8] Ph.Gayet et al., "Architecture of the LEP2 Cryogenics Control System: Conception, Status, and Evaluation", ICEC15, Genova, Italy, 1994

PRESSURE MEASUREMENT FOR THE UNK-1 VACUUM SYSTEM

A. Kiver, V. Komarov, K. Mirzoev, V. Terekhov, A. Vasilevsky
IHEP, Protvino, Moscow Region, 142284, Russia

The required vacuum 10^{-9} Torr at the UNK-1 will be produced by 3900 ion pumps. For pressure measurement in the 10^{-5} — 10^{-9} Torr range the system based on continuous monitoring of all ion pumps currents is being developed as a part of vacuum instrumentation. To cover such a range Current - to - Frequency Converters are used as current monitors. Their outputs pass to the acquisition electronics packaged into Eurocard style. Crates are distributed over 14 surface buildings. This presentation focuses on the measurement principle and the major electronics components.

I. INTRODUCTION

In the UNK-1 ring vacuum chamber of 20,7 km length the required working pressure has to be of the order of 10^{-9} Torr. Such a vacuum will be produced by 3900 Ion Pumps (IP) located at distances of about 6 m from each other [?]. IP Power Supplies (16 IPs are fed by 1 HV Power Supply) and vacuum controls are distributed over 14 surface buildings. As a part of vacuum instrumentation the pressure monitoring within the 10^{-5} — 10^{-9} Torr range is being developed. It will be based on the IPs current measurement to simplify the hardware and to get adequate spatial resolution. This paper describes the principle of the measurement and the major hardware components.

II. GENERAL DESCRIPTION

A layout of the measuring electronics belonging to one of the surface buildings is given in the Fig.1. The measured currents which vary from a few hundreds of nanoamperes to tens of microamperes are picked-up by current sensors (CS) and processed by Current-to Frequency-Converters (CFC). The latter are directly connected to the HV circuitry and are fed by floating Power Supplies. The CFC output pulses are decoupled from the high voltage platform by means of Diode Optoelectric Couple (DOC).

Each group of 32 CFC outputs are multiplexed to one channel of 16-channel 16-bit Scaler. Gating time is 0.1 s, so scanning period is 3.2 s. Such a time resolution allows to monitor dynamic pressure effects, f.e. "pressure bumps" created by circulating proton beam. In addition, certain segmentation of the input channels is foreseen for sophisticated investigations. The electronics is under control of the Single Board Microcomputer (SBC) integrated in the UNK Control System [?].

The pressure at a monitored point of the vacuum chamber can be calculated as:

$$P = \frac{10KN}{s} [Torr]$$

where :

N — count of scaler for the gating time

K — factor of the corresponding IP determined by effective pumping speed ($Torr \cdot Hz/A$)

S — CFC conversion sensitivity (Hz/A)

Factor 10 accounts for 0.1 s gating time. CFCs are installed in the IP Power Supply racks, the rest of the electronics are Eurocard modules.

III. COMPONENTS

Current Sensor is a resistor current divider with a transfer coefficient of 0.1. While pumping down and when bad vacuum occurs the IP current can increase abruptly. To protect the measuring circuitry the bypassing Zener diodes, having sufficient power consumption and low leakage current, are incorporated. The diodes allow also to keep normal operating the IPs in these cases.

The current - to - frequency conversion is based on the well-known principle described in [?]. In this case the output frequency is expressed as

$$F_o = I_{in} \frac{F_c}{I_s}$$

where :

I_{in} — input current

F_c/I_s — conversion sensitivity S

F_c — clock frequency

I_s — compensating standard current.

Realization of such a principle ensures the high stability of the conversion sensitivity. As a result the CFC routine calibration can be avoided. In addition, common clock gives opportunity to get low spread in values of conversion sensitivity. The CFC parameters are:

— conversion sensitivity	10^{11}	Hz/A
— temperature coefficient		
of the conversion sensitivity	0.001	$1/^{\circ}C$
— additive error	10	pA
— clock frequency	1.2	MHz

The output pulses are transmitted via 40 m twisted pairs to Pulse Shapers, whose TTL outputs are connected to inputs of multiplexer (MUX) and counted by the scaler. For $F_c = 1.2$ MHz F_o doesn't exceed 600 KHz, so maximum count is 60,000.

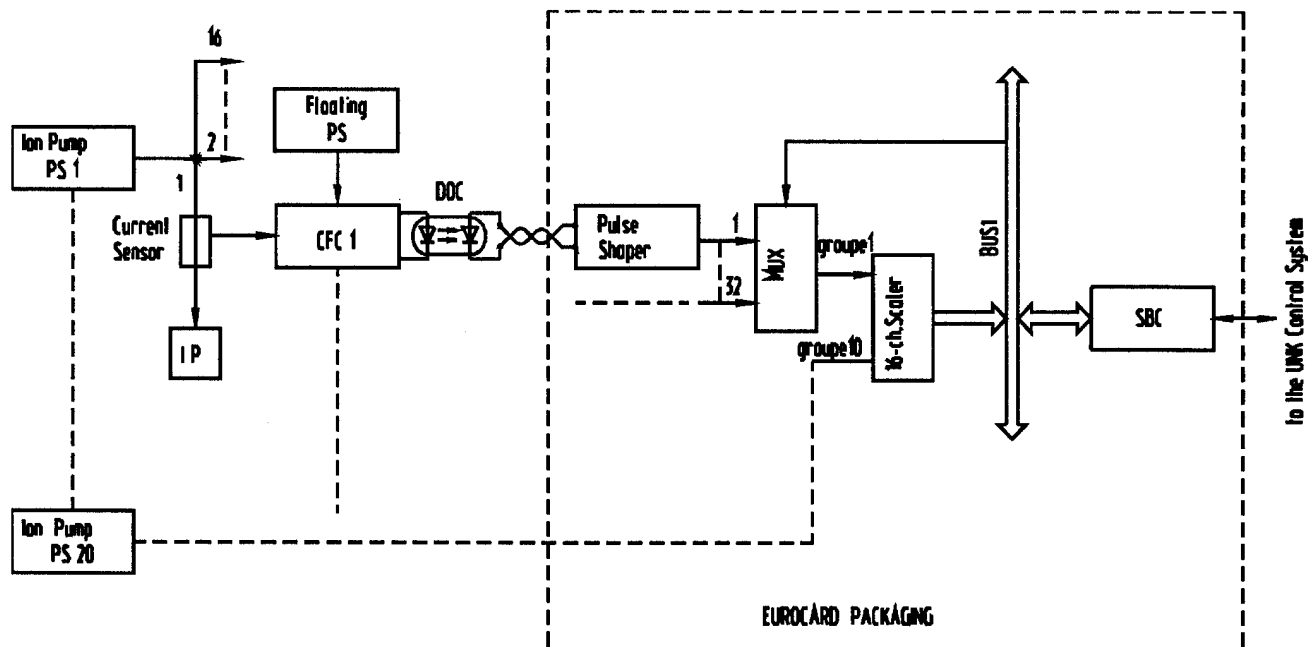
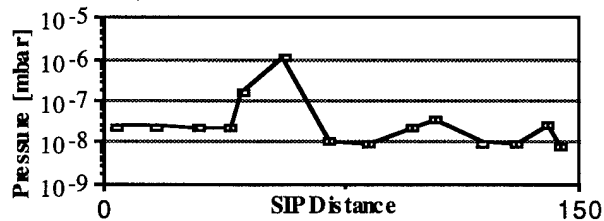


Fig. 1 Block Diagram of the Ion Pump Currents Instrumentation of the UNK-1 Vacuum System.

IV. REFERENCES

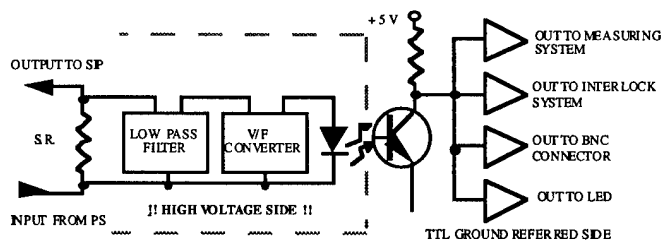
- [1] G.G. Gurov. *UNK Status and Plans*. In these Proceedings.
- [2] V.N. Alferov et al. *The UNK Control System*. In Proceed. of PAC'91, San Francisco, California, May, 1991.
- [3] A. Bengt. *Electron Design*. 1973, 21, Nb.23.

SIP distance [cm]	Pressure [mbar]
0	3.0 × 10 ⁻⁸
10	3.0 × 10 ⁻⁸
20	2.5 × 10 ⁻⁸
30	2.5 × 10 ⁻⁸
40	2.0 × 10 ⁻⁸
50	2.0 × 10 ⁻⁷
60	1.0 × 10 ⁻⁶
70	1.5 × 10 ⁻⁸
80	1.0 × 10 ⁻⁸
90	3.0 × 10 ⁻⁸
100	4.0 × 10 ⁻⁸
110	1.0 × 10 ⁻⁸
120	1.0 × 10 ⁻⁸
130	4.0 × 10 ⁻⁸
140	1.0 × 10 ⁻⁸



Each dot represents one SIP, clicking on it the identification name of the pump and its actual value of the pressure, are displayed in the window. The diagram shows the transfer line vacuum profile when a leak occurred in the beam stopper. The interlock system automatically closed the valves in about four-to five seconds, to prohibit the pressure increase to propagate down the vacuum tube. From the pressure profile it is possible to discover immediately the vacuum problem. The updating of all diagrams is done every twenty seconds. It is also possible to open a panel which shows for each SIP the pressure, the applied voltage and the timing signal, corresponding to the absorbed current.

We designed all the pressure measuring system, considering that the operating pressure is from 10^{-9} to 10^{-8} mbar. The chosen V/F, works in six decades of conversion. The upper value is limited by the 15 V of supply voltage of the V/F, such the theoretical lowest limit is 150 μ V. A 120 l/s SIP, absorbs about 10 μ A at the pressure of 2×10^{-8} mbar, choosing a 10 k Ω shunt resistor the input voltage at this pressure is 100 mV. It means that the upper limit of the measurement is about 2×10^{-6} mbar (about 1,4 mA of absorbed current corresponding to 14 V of input voltage). The lowest value is limited by the noise, we can measure up to 100 μ V, equal to 10 nA of absorbed current. The theoretical corresponding pressure is in the range of 10^{-11} mbar, but in this range the expression which correlates absorbed current versus pressure is not very reliable. However, all SIPs were calibrated up to about 5×10^{-11} mbar, according to the lowest limit of the Penning gauge IKR 20 connected with a triaxial cable. This pressure range from 10^{-6} mbar to 10^{-11} mbar is more than sufficient for our purposes. In the transfer line the pressure is about one decade higher than in the storage ring, so the shunt resistor is 1 k Ω , to shift also the range of measurements. The output of the V/F is a pulse series of about eight μ s of duration. This frequency, depending linearly by input voltage is calibrated to 100 kHz full scale, corresponds to the 10V of input. This signal drives the LED of the optocoupler, the output is referred to the ground and finally goes out of the CMB via a quad TTL driver. The signal is split in four channels; three of these are used as auxiliary outputs and one for the measurements. The schematic block of the CMB is shown in fig.3.



3.2 The Interface Board and the THEMIS Board.

The TB has four timers and 88 configurable digital input/output. Each timer is separately controlled by others by means of its own I/O. The IB has a multiplexer to permit the interfacing of its eight channels to the only four channels of the TB. The IB consists principally of a FLIP/FLOP sequence which synchronises the following data: *i*) a pulse from the CMB (asynchronous), *ii*) a measure call from TB, *iii*) a VME clock that is divided into 16 by the same IB, before it is used. In practice the TB transfers a measuring call from VME bus to the IB, it waits for a synchronising process, and counts how many 1 MHz pulses can stay between two pulses from CMB; at the end of the second pulse IB gives back a stop count signal to the TB. To inhibit further measurement calls during all the time of this process, a busy signal is sent to TB. Other functions of the IB: *i*) a conversion of an analog signal from PS concerning its actual value of the output voltage into a digital one (this data is necessary for the current versus pressure calculations). *ii*) interfacing by means of optocouplers all the input /output of the PS.

The other three auxiliary channels of the CMB, are used as follows: one for the interlock system, one for a local control by means of a BNC output and the third is for local control by means of a LED. The signal for the interlock system goes in an alarm boards. The alarm boards uses the same V/F integrated circuit of the CMB, to reconvert the input signals back into the voltage. In the same card a comparator with an adjustable threshold gives an output signal when the input signal (pressure) is too high. The interlock system collects all these outputs. Following some software instructions, if there is a dangerous pressure alarm, it sends back a closure command to the vacuum valves. In practice, according to the vacuum conditions, the action of the interlock consists of the closure of some valves to separate the part of the chamber where a leak is detected. The BNC output is useful for maintenance and for repairing operations. The last auxiliary output drives a LED; the LED is on the front panel of the CMB, and blinks at each pulse. During the shut down period, when no beam is accumulated, the pressure in the storage ring is so low that the CMB are in overflow. In that case all the LEDs are switched off or are blinking slowly. It is possible to make a fast but very useful test about vacuum conditions - simply by walking around the ring and looking at the vacuum racks - if one or more LEDs are blinking too fast or are completely switched on there is certainly something wrong in the vacuum chamber or in the pumping system.

4. CALIBRATION PROCEDURE

The transfer line of Elettra is pumped by twelve 45 l/s SIPs and the total pressure can be measured by fourteen cold cathode Penning gauges. The storage ring is pumped by 24 400 l/s SIPs and by 118 120 l/s SIPs and two 900 l/s SIPs pump the septum tank, which is a part of the storage ring. The pressure in the bending magnet vacuum chamber is measured by 24 cold cathode gauges installed close to the 400 l/s SIP. In total 22 Penning gauges are mounted in the rhomboidal electron vacuum chamber in different positions. This arrangement allows verification of the pressure profile in the ring at various stored beam currents and energies. During the first week of commissioning the pressure measurements according to the current absorbed by the pumps were not successful. The big discrepancy between the gauge values and the pressures calculated according to the equation (3) with constants recommended by Varian can be explained as follows:

- i) All SIPs are modified with the NEG modules. The presence of the NEG, which was partially activated during the bake out of the pump at the temperature of about 220°C, changes pumping conditions in the pump body and causes a decrease of the lowest limit of the absorbed current.
- ii) Eleven of Penning gauges were installed directly over the vacuum chamber. The pressure readings were disturbed by photoelectrons and exceeded 100+1000 times the real pressure value in the chamber.
- iii) Some of electron chamber gauges were, due to assembling problems, mounted close to the edge of the bending magnet coils. The external magnetic field strongly affected those pressure measurements and firstly the appropriate shielding has to be found - see ref.[3].

Taking into account the above mentioned problems only 13 SIP+gauge combinations can be used to calibrate the 400 l/s SIPs, 18 SIP+gauge pairs were used for the 120 l/s SIP and only three gauges are installed in the septum tank which allows calibration of the two 900 l/s SIPs.

The calibration was performed mostly by increasing the pressure from 10^{-11} mbar to 10^{-8} mbar. In this pressure range the μ -8000 power supply works with -3 kV and -5 kV of the H.V. output. The abnormal pressure was generated at the beginning after a small accumulated dose only. In fig. 4 theoretical and experimental results for the pumps 120 l/s SIP are presented. The complete set of equations, which allows to calculate the total pressure in the storage ring according to the current absorbed in the pump is as follows:

$$I = 1850 P^{\{\exp 1.065\}} \quad \text{SIP 45 l/s; H.V.: -3\&-5 kV} \quad (4)$$

$$I = 1590 P^{\{\exp 1.06\}} \quad \text{SIP 120 l/s; H.V.: -3\&-5 kV} \quad (5)$$

$$I = 1200 P^{\{\exp 0.99\}} \quad \text{SIP 400 l/s; H.V.: -3\&-5 kV} \quad (6)$$

$$I = 1050 P^{\{\exp 1.03\}} \quad \text{SIP 900 l/s; H.V.: -3\&-5 kV} \quad (7)$$

To convert the timing to the current the expression $I = 1/100 \times \text{Timing}$ has to be used due to the 10 k Ω resistance used in the PS of the storage ring SIPs.

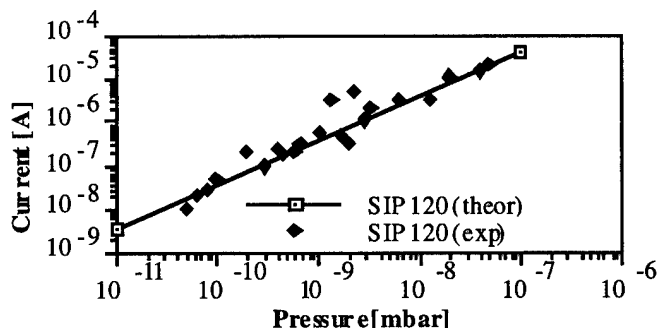


fig. 4 - Current x pressure dependence for the SIP 120 l/s

5. DISCUSSION AND CONCLUSIONS

The presented system seems to be suitable for the pressure measurements especially in big vacuum systems. In spite of above mentioned difficulties during calibration, the pressure profile in all vacuum sectors of the Elettra ring obtained by pump pressure readings is fairly uniform in the range 8×10^{-10} to 2.5×10^{-9} mbar. The pressure readings of each pump are very useful also in the lowest pressure range, where only the "UHV" value can be read on the power supply display, e.g. the measuring system overflows. At the same time, for example, from six 120 l/s SIP's supplied by the same one, the following timing is read: 142657, 283321, 346112, 186632, 425113, 203664. Then the sum of the pressures calculated by equation (5) is 6.5×10^{-10} mbar which is really lower than the lowest pressure of 8×10^{-10} mbar, which can be read on the power supply display. Penning gauges have some problems when switching on and during the start of pressure measurements in the UHV range (below 10^{-8} mbar). A similar problem can occur also in the case of SIP's, when the discharge current is too low and unstable at very low pressures. This inconvenience can be simply overcome by changing the working mode of the power supply from "Protect" to "Start". The high voltage then automatically increases to -7 kV, the discharge current is higher and can be maintained returning to the "Protect" mode, as well. Our system was not calibrated at pressures higher than 1×10^{-7} mbar, because the SIPs are switched on only if the pressure in the vacuum chamber is lower than this value. The validity of expression (5) was checked comparing the pressure values in the RF cavities, where pressures were read by Penning gauges, with the pressures calculated from the timing of the RF cavity pumps. The gauge values are always slightly higher than the values obtained by the SIP's reading, which is consistent with the pressure distribution in the big RF cavity.

6. REFERENCES

- [1] D.Bulfone: Status and prospects of the Elettra control system; N.I.M. A352 (1994), p. 63
- [2] S.P. current measurement LEP 680-4221-050 D
- [3] J.Miertusova, F.Daclon: Effect of Ext. MgF Rad. upon the Accuracy of total and Partial Pr. Meas., Proc. 4th EPAC'94, London, Vol. 3, p. 2512

Insertion Device Vacuum Chamber for the ELETTRA Storage Ring

J. MIERTUSOVA, N. PANGOS, Sincrotrone Trieste, Padriciano 99, 34012 Trieste Italy

Abstract

The first four insertion device (ID) vacuum chambers (3 for the undulators, 1 for the wiggler) have been installed in the ELETTRA synchrotron radiation facility. Each chamber is 4.8 m in length and has a rectangular cross section with a cylindrical antechamber. The whole system is pumped by four 120 l/s sputter-ion pumps of nominal pumping speed. The insertion device chambers are fabricated from stainless steel ESR AISI 316 LN. This material was chosen for its very low relative magnetic permeability (~ 1.003), its high yield stress and the well known procedures for welding and cleaning. Vacuum and mass spectroscopy experience during the first year of commissioning is presented.

1. INTRODUCTION

Elettra synchrotron radiation facility has been built especially for the use of high brilliance radiation from insertion devices ID. The storage ring of 260 m in circumference is equipped by 12 straight sections, one is for beam injection, 11 are for IDs beam lines.

An austenitic stainless steel ESR AISI 316 LN has been chosen as the material of the vacuum chamber, for its low magnetic permeability, high yield stress and well known welding procedure. To minimise synchrotron radiation induced desorption as well as thermal outgassing. All vacuum components were carefully cleaned and finished.

In this paper we present a series of measurements of the outgassing rate, vacuum performances during operation (gap closure at different beam currents and energies) and results of the mass spectroscopy scanning. Special attention was paid to manufacture the ID vacuum chamber, all steps of production were carefully checked by the Quality control group of Sincrotrone Trieste.

2. VACUUM CHAMBER DESIGN AND MANUFACTURE

Firstly we planned to use the NEG St 707 strips to obtain and to maintain UHV conditions in the ID vacuum chamber. However, the NEG activation at 450 °C performed serious problems due to the thermal expansion of the NEG strips. In fact, some short circuits were formed between the NEG and the chamber walls. The theoretical simulation of the partial pressures of methane and noble gases (especially Argon) have also shown a significant pressure increase, because of a negligible pumping speed of the NEG for these gases.

The ID vacuum chamber was designed in our laboratory in collaboration with the technical office. It has a rectangular

cross-section with a cylindrical ante-chamber, as it is shown in fig. 1.

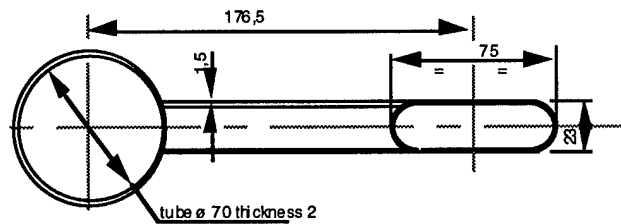


fig. 1 - Cross-section of the ID vacuum chamber

The whole system is pumped by four 120 l/s SIPs, two pumps are installed on both ends of the chamber, the other two are proportionally placed in between. The expected pressure profile which should be obtained after about 50 Ahs of conditioning is presented in fig. 2, the minimum values in this graph correspond to the SIPs position [2].

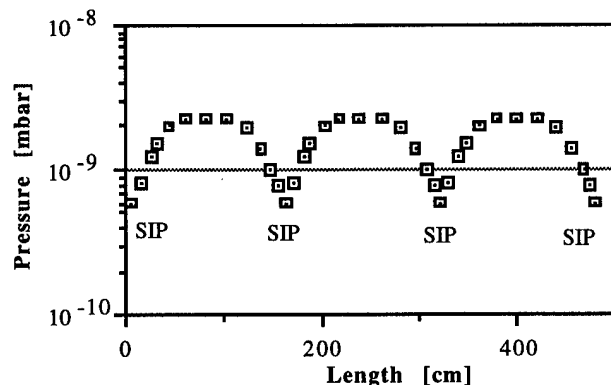


fig. 2 - Theoretical pressure profile in the ID chamber

Special care was given to fabricate and clean all stainless steel components. The fabrication procedure was following the norm ASME II, the welding procedure was performed according to the norm ASME IX and radiographic control was made following the norm ASME V. All components were assembled and welded in a clean room. More details can be found in ref. 1.

Internal surfaces and welds exposed to the vacuum must be free of micro inclusions and cracks. Surface roughness must be less than 1 μm and free of oxides and impurities. The ID vacuum chamber (without the end flanges) was carefully cleaned and finished to obtain the required vacuum level ($< 1 \times 10^{-10}$ mbar without the beam).

A complete surface treatment included the following phases: organic solvent degreasing, ultrasonic washing, two phases rinsing (in normal and in demineralized water), drying. The cleaned ID vacuum chamber was than pre-baked and degassed in our high vacuum oven. Pre baking was performed at 350 °C for 24 hours, and at the end the pressure in the oven decreased down to 1×10^{-7} mbar range.

Before twelding the flanges, the chamber was treated at temperature of 450 °C for 2 hours in an inert gases atmosphere to stretch all welds of the antechamber.

3. OUTGASSING RATE AND MASS SPECTRA

The specific outgassing rate of the ID vacuum chamber was measured and verified at different well defined vacuum conditions. To evaluate the specific outgassing rate q_D the expression

$$q_D = (P_1 - P_2)2C / B L \quad (1)$$

where P_1 and P_2 are pressures at both ends of the chamber, B and L are the perimeter and length of the chamber, respectively, C is the conductance in l/s.

After delivery, the chamber was equipped with the two central SIPs, on the one side the turbo-pump Seiko was installed, and the opposite end was connected with the fore-vacuum pump. After 6 hours of pumping the equilibrium pressure of 2.6×10^{-6} mbar and 1.2×10^{-6} mbar was reached at the ends of the chamber. In the mass spectrum scanned at this condition, the mass peaks of hydrocarbons and water were enormous. The corresponding specific outgassing rate was 6×10^{-10} mbar.l/s.cm².

Then the ID vacuum chamber was baked-out at 230 °C for 36 hours. At the maximum temperature the pressure exceeded the 10^{-5} mbar level.

In fig. 3 the mass spectrum scanned at the temperature of 175 °C is shown.

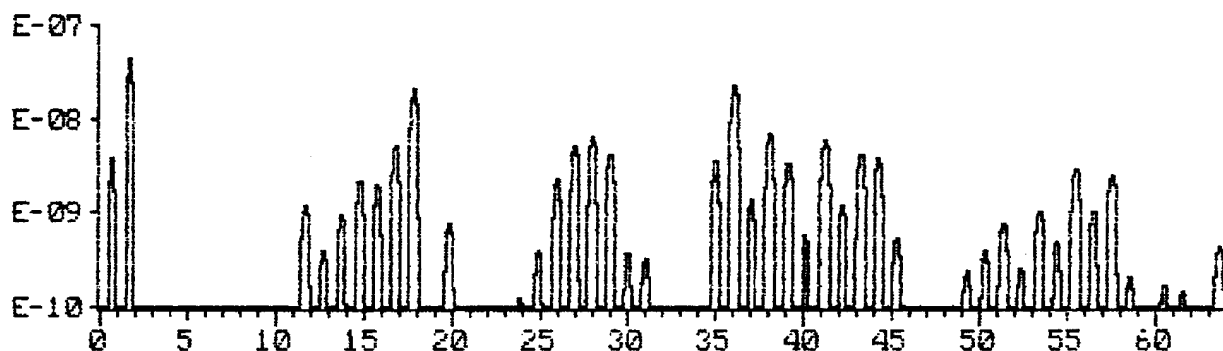


fig. 3 - Mass spectrum scanned at 175 °C

In spite of carefully performed cleaning the hydrocarbons and water peaks were still present. Only after prolonging the bake-out and the subsequent cooling, these unwanted peaks disappeared and the ultimate pressure of 1.2×10^{-9} mbar was

achieved. The corresponding outgassing rate was then 2×10^{-12} mbar.l/s.cm². After the baking procedure all the dimensions of the chamber were precisely measured, the chamber was perfectly aligned with the acceptable tolerance of 0.2 mm.

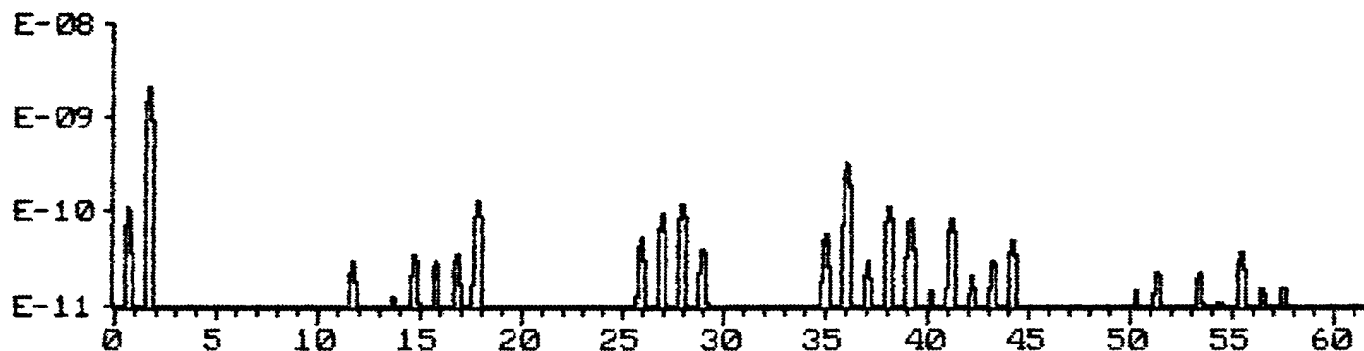


fig. 4 - Mass spectrum scanned at room temperature

The ID vacuum chamber heated and degassed in this manner, was than saturated by dry nitrogen, closed with the flanges and transported into the tunnel.

The installation of the chamber in the storage ring was done under a continuous flow of dry nitrogen, and a bake-out in situ was performed.

During the in situ bake-out the maximum temperature of 180 °C was kept for 36 hours. When the chamber was cold and through the ID valves connected with the rest of the ring, the equilibrium pressure in the 10^{-10} mbar range was

maintained. The specific outgassing rate in 10^{-13} mbar .l/s.cm range was achieved and a very clean vacuum was obtained - see fig. 5

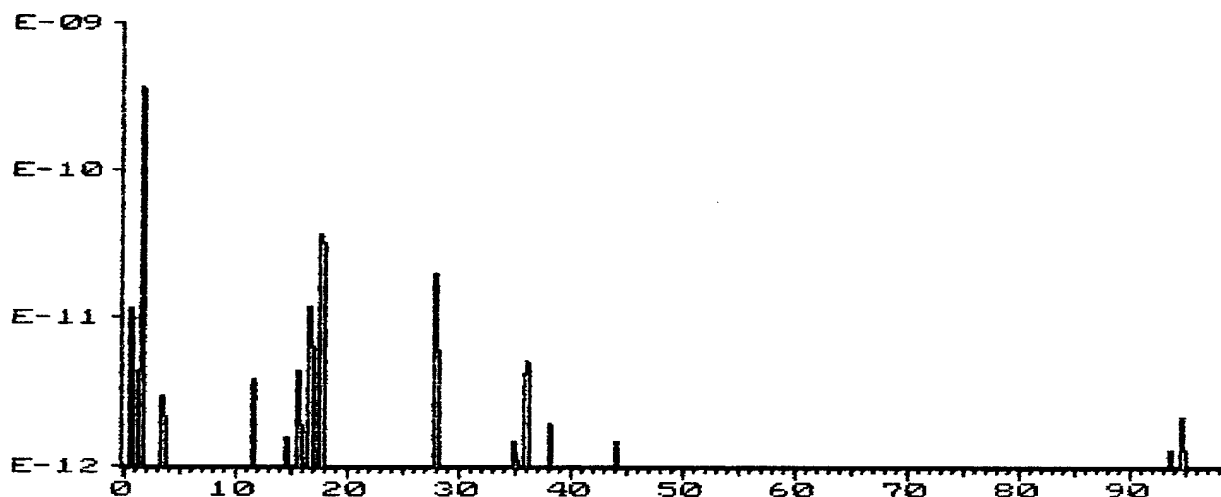


fig. 5 - Mass spectrum at the equilibrium pressure of 3.6×10^{-10} mbar in the ring

4. CONCLUSIONS

The ID chamber conditioning has been done in two steps: at the beginning the gap of the ID magnets was opened to the maximum. The pressure in the chamber with increasing beam current firstly exceeded more than one decade the pressure in the rest of the ring. After about 30 Ahs of conditioning the pressure profile became uniform. The second step of conditioning started by closing the gap of the ID magnets. Especially in case of the wiggler the photodesorption was very pronounced and it caused lifetime drop as shown in fig. 6.

For the vacuum performance of our ID vacuum chamber, can be concluded:

1. it is very important to perform careful manufacturing and cleaning of the ID vacuum chamber, following the technical norms and standards,
2. the ultimate pressure in the 10^{-10} mbar range can be achieved after an in situ bake-out, the desorption yield of 1.5×10^{-6} mol/photon can be obtained after approximately 30 Ahs of conditioning at 2 GeV,
3. no special difficulties are expected from the vacuum point of view with the small gap ID vacuum chamber - 15 mm vertically - which will be installed in the near future.

REFERENCES

- [1] N. Pangos: Prescrizione di fornitura per la fabbricazione della camera da vuoto per ID di ELETTRA, Technical Note N. S044, Sincrotrone Trieste S.P.A., 1993
- [2] J. Miertusova: Theoretical Simulation of the Pressure Profile in the ID Vacuum Chamber, Technical Note, Sincrotrone Trieste, S. P. A., 1993

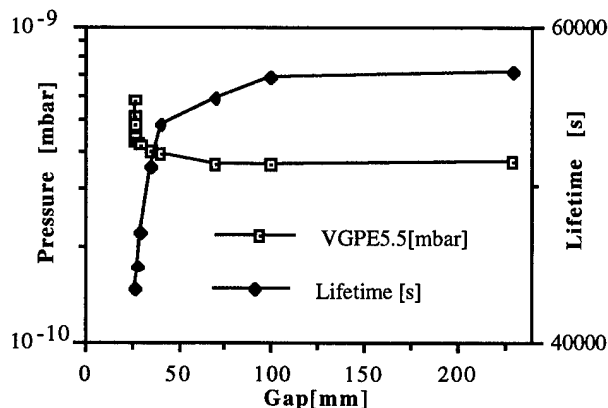


fig. 6 - Pressure and lifetime dependence in the wiggler during the gap closure

This effect was observed only for a short time and disappeared after 3-5 of the gap closures (also at higher currents and energies). The pressure in the ID chamber then became lower than in the rest of the ring.

Bellows Design for the PEP-II High Energy Ring Arc Chambers*

M. E. Nordby, N. Kurita, C-K. Ng, Stanford Linear Accelerator Center, Stanford University, Stanford, CA 94309 USA

An overview of the current bellows module design and performance parameters is presented. Performance requirements based on external chamber design constraints, and operational needs are discussed. Parameters include beam impedance of the RF shield, and electrical resistance of the shield gap joint. Also discussed is the analysis of the high-current thermal management, and structural and cyclic behavior of the bellows and RF shield. Experiments of the tribology and electrical resistance of the shield sliding joint are summarized, and their results presented. Existing and new design options are discussed in light of the analyses and experiments. The final design is presented as the optimal compromise between the varying parameters.

I. ARC CELL DESIGN INTRODUCTION

The PEP-II High Energy Ring (HER) is 2.2 km and stores 3000 mA of 9 GeV electrons[1]. The HER is hexagonal, with six arc regions containing 16 cells, each 15.2 m long. A cell consists of two dipole magnets, separated by a quadrupole/sextupole doublet. Figure 1 shows a typical half-cell:

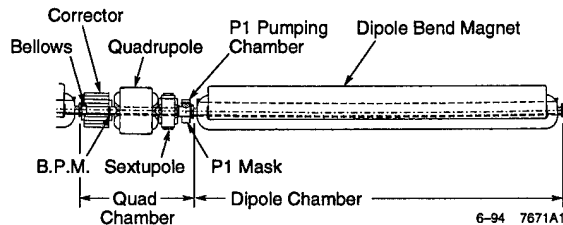


Figure 1: Plan View of a HER Arc Half-Cell

The arc vacuum chambers are made from octagonal copper extrusions. The octagonal shape fits the magnet gaps, yet maximizes the conductance for the 10 nTorr vacuum system[2]. Copper is chosen for its high thermal conductivity radiation absorption length and to minimize the gas desorption.

The chambers are supported at three places. The Quad Chamber is mounted to the quad magnet next to the Beam Position Monitor (BPM). This minimizes monitoring inaccuracies due to thermal motion of the BPM. Flex Supports hold both ends of the Dipole Chamber, allowing for thermal expansion along the beamline, but preventing any lateral motion.

II. BELLOWS MODULE DESIGN

The Bellows Module bridges the gap between the fixed end of the Quad Chamber at the BPM, and the end of the Dipole Chamber. It serves four discrete functions in the HER Arcs.

Thermal Motion

The Bellows Module accommodates the thermal expansion of a half-cell. The copper chambers expand 6.5 mm as they heat to their nominal operating temperature of 70°C, and 19 mm during the 150°C *in-situ* bake out.

Installation

The Module serves as the capstone of the half-cell: it is the last piece to be installed, and the first removed. The Module compresses 19 mm to allow installation. An additional 6.3 mm of stroke is needed for chamber alignments and fabrication tolerances.

RF Continuity

To minimize instabilities and impedances the Module must present a continuous chamber geometry and electrical conduction path. This is accomplished by 0.2 mm thick GlidCop® [3] Shield Fingers which bridge the gap between the neighboring chambers inside the convoluted bellows.

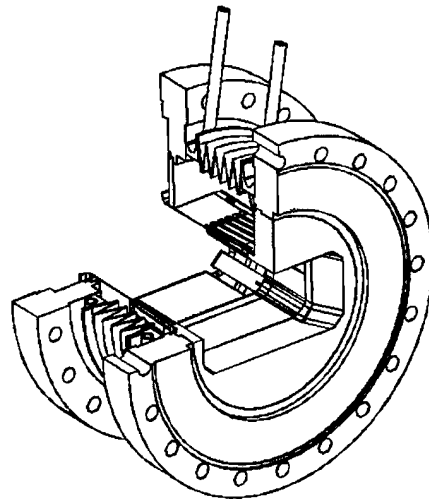


Figure 2: Bellows Module, Cut Away

The Shield Fingers cannot withstand the direct SR strike and are shadowed by a 5 mm offset between the neighboring chambers. To prevent an annular cavity which can produce trapped modes, the offset stub tapers inward.

* Work supported by US Department of Energy, contract number DE-AC03-76F00515. Presented at the US Particle Accelerator Conference and International Conference on High-Energy Accelerators (PAC95), Dallas TX, USA, May 1995

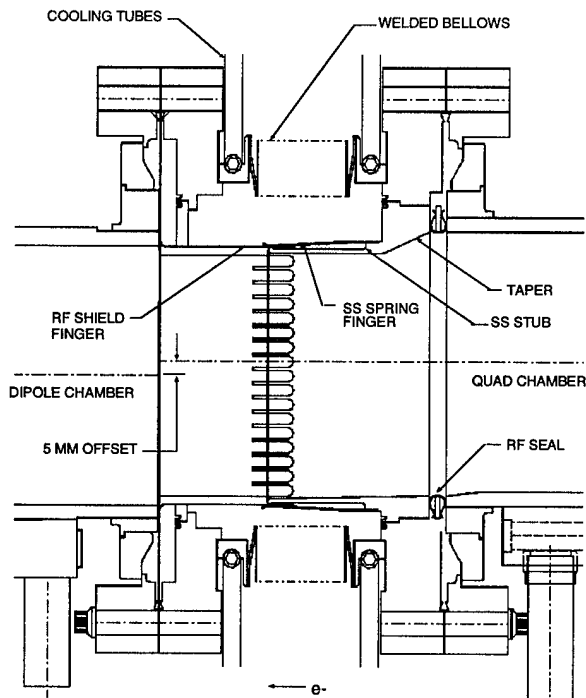


Figure 3: Plan View Cross-Section of Bellows Module

The fingers slide on the outside of a 2 mm thick stainless steel stub. The contacts between the stub and each of the Shield Fingers are ensured by external stainless steel spring fingers. For every shield finger there is a mating spring finger that exerts 170 grams of contact force. This minimizes the possibility of arcing across the joint, due to high *in vacuo* contact resistance.

The individual Spring Fingers apply a uniform contact load on all Shield Fingers around the octagon. Girdling springs, common in other designs, require a round or oval transition to ensure uniform loading on all fingers, and to prevent stress concentrations in the spring. Such a transition would produce a longitudinal impedance ten times higher than the octagonal Module [5], and increase the possibility of trapping higher-order modes.

The current Shield/Spring Finger design also reduces the likelihood of a finger losing contact which would produce a small cavity. Since the Spring Finger always applies force only at the contact point, the Shield Finger can never lift off that point, and can never touch anywhere else on the stub.

Cooling

All surfaces which are exposed to the beam passage are subjected to various sources of heat. Adequate conduction paths and cooling tubes brazed to the flanges ensure that they remain cool.

THERMAL LOADING

Although the Shield Fingers and stub are shadowed from the direct SR fan by the chamber offset, the module is

heated in varying amounts by four distinct sources which are described below.

Scattered SR

Calculations using EGS and FLUKA show that 10% of the power from the direct SR strike fan is re-emitted as photons and low-energy electrons. Near the Bellows Module, the power of the direct SR strike fan is 1170 W/cm². The shadowed Shield Fingers could intercept a heat flux of 0.25 W/cm² scattered around the 24.1 cm perimeter of the octagon.

Ohmic Losses

The image current traveling in the first few microns of the vacuum chamber wall produces heat due to the resistance of the wall material. In the Bellows Module, the stainless steel stub and the Shield Fingers are plated with 0.5 mils of copper and silver, respectively. The image current will travel solely through the high-conductivity plating and deposit less than 0.04 W/cm² of power.

Higher Order Mode (HOM) Heating

Analysis shows that the slots in the Shield Fingers at the corners of the octagon radiate approximately 0.45 W per Bellow Module due to the field of a TM HOM [6]. This power is primarily transferred to the Bellows Module convolutions. The inner surfaces that "see" the beam intercept 7 W (~0.07 W/cm²) of radiated power from secondary HOM's.

Contact Resistance Heating

Large image currents and resistance at the sliding contact joint between the Shield Fingers and the Stub produce localized heating. Experimental data shows that this localized heating can cause a decrease in material strength followed by a reduction in contact force. This could lead to run-away heating at the contact joint. To decrease this possibility, the temperature of the contact joint must be kept to a minimum.

Thermal Analysis

The total heat load from these sources could deposit 0.36 W/cm² of combined power on the Shield Fingers. This produces a temperature at the tip of the GlidCop fingers of:

$$T_{TIP} = T_{BASE} + \frac{QL^2}{2kt}$$

Where the finger dimensions are: $w = 4$ mm wide, $t = 0.2$ mm thick, and $L = 2.16$ cm long. Cooling on the adjoining flange will keep the base of the Shield Fingers at 65 °C, so with a thermal conductivity, $k = 3.65$ W/cm-°C, the tip temperature could reach 91° based on 0.5 W/cm² of heat flux. This is far below the stress-relaxation temperature of AL-15 GlidCop, which is approximately 300°C [3]. GlidCop was chosen for its high thermal

conductivity in comparison to other types of strengthened copper. GlidCop's thermal conductivity is a factor of two higher than BeCu which is commonly used for Shield Fingers. Therefore, the local temperature at the tip will be higher in the BeCu. Also, BeCu over-ages and loses strength at 250°C for high strength BeCu and 455°C for high conductivity BeCu.

The effects of the high tip temperature are further minimized by the independent stainless steel Spring Fingers. These isolate the high-temperature region at the ends of the Shield Fingers from the high-stress area at the root of the Spring Fingers. Thus, if the Shield Fingers get hotter than expected, they are less likely to soften and fall away from the contact joint.

STRUCTURAL LOADING

Despite the high tip temperature, stresses in the Shield and Spring Fingers are produced primarily by the contact force at the sliding joint, and by the offset across the Module due to alignment and fabrication tolerances.

The 0.65 mm thick Spring Fingers provide contact force, so they see 205 MPa bending at their base. This is not affected by offsets across the Bellows Module because they are mounted solely to the stub.

However, the thin Shield Fingers are stressed only by offsets across the Module. The chamber Flex Support system allows up to 2 mm lateral offset, which produces a 90 Mpa stress at the root of the Shield Fingers. This bending stress does not significantly affect the contact force because the Spring Fingers are 15 times stiffer.

MANUFACTURING ISSUES

Two materials manufacturing issues have been significant factors in the design of the Bellows Module.

Sliding Joint Tribology

First, the tribology of the sliding joint *in vacuo* is a concern for three reasons: 1) overheating or galling at the contact joint could cold-weld a finger to the stub. This would destroy the finger. 2) Insufficient or excessive lubricity from silver-plating could produce silver dust by fretting at the sliding joint. This dust could enter the beam passage and possibly affect the beam lifetime and stability. 3) Plated surfaces could behave below expectations during operation, when high temperatures and high shear stresses could cause it to flake off.

Research and testing at SLAC have shown that a combination of 0.4-0.5 mils silver plating on the Shield Fingers, and 0.2-0.3 mils rhodium plating on the stub produce a good sliding joint. With the 170 gram force expected at the contact joint, tests have shown that the silver plating is thick enough to endure over 200,000 cycles at 200 °C. Thinner plating resulted in complete erosion the plating.

The rhodium plating on the stub is likewise an optimal thickness. Shear stresses in thicker plating reduce quality and adhesion, while thinner plating will not contain the image current traveling along the chambers.

Shield Finger Brazing

The second manufacturing issue is brazing. Our initial design, and that of most other bellows modules, used BeCu fingers. However, to attain the highest possible yield strength, these must be precipitation-hardened after being brazed to their retaining plate. Without this, the fingers cannot tolerate even moderate stresses without yielding.

To avoid this failure mode, GlidCop AL-15 was chosen as an alternative. This is a dispersion-strengthened copper, which does not require heat-treating, and does not overage. At room temperature, its yield strength is 380 Mpa, with 16% elongation. Experiments show only a 25% decrease in yield strength at the brazing temperature [3].

One of GlidCop's drawbacks is its lack of ductility. This makes it harder to form, and susceptible to fracture if strained plastically. However, manufacturing tests show that these problems can be avoided by smooth forming dies and large bending radii.

FUTURE WORK

Design and production efforts are focused in two directions. First, confirmation testing of the final sliding joint configuration is pending.

Second, a full prototype of the entire Bellows Module is now being prepared. This will prove out the complex fabrication and assembly techniques, and show areas where cost savings can be recognized.

REFERENCES

- [1] M. Zisman, ed., "PEP-II: An Asymmetric B Factory: Conceptual Design Report", SLAC Report 418, 1993.
- [2] C. Perkins, et al, "Vacuum System Design for the PEP-II B Factory High Energy Ring", EPAC94 Conference Proceedings, London, World Scientific.
- [3] GlidCop is a dispersion-strengthened copper alloy made by SCM Metal Products, Inc., Research Triangle Park, North Carolina, USA
- [4] S. Heifets, *et al*, "Impedance Study for PEP-II B-Factory", PEP-II AP Note No 99.
- [5] *ibid*.
- [6] S. Heifets, *op cit*.

A ZERO-LENGTH BELLOWS FOR THE PEP-II HIGH-ENERGY RING*

M. Nordby, E. F. Daly, N. Kurita and J Langton,
Stanford Linear Accelerator Center, Stanford University, Stanford, CA 94309 USA

Due to beamline space constrictions and the modular design of the vacuum system, a conventional bellows can not be used everywhere in the PEP-II High-Energy Ring (HER) arcs. A zero-length "Flex Flange" was developed which actually performs better than a more standard bellows. The Flex Flange fits the space available while still preserving the modularity of the system. Furthermore, the design provides for an accurate match-up between adjoining octagonal copper chambers despite the large fabrication and assembly tolerances and high operational loads. Beam chamber continuity is ensured by an integral RF seal ring which is easy to install and fault-tolerant. Heating from synchrotron radiation and higher-order mode trapping is managed to ensure a robust connection despite the 3000 mA beam current of the PEP-II HER. The Flex Flange concept is versatile and adaptable to many applications, yet economical both in space needed and cost.

INTRODUCTION

The HER circumference is 2200 m and consists of six straight sections 120 m in length and six arc sections 240 m in length. Each arc contains 33 quadrupole magnets and 32 dipole magnets to form 16 cells per arc. The HER vacuum system design[1] is comprised of 33 quadrupole and 32 dipole vacuum chambers, made from extruded OFE copper, and positioned in the magnet gaps for each arc totaling 198 quad chambers and 192 dipole chambers.

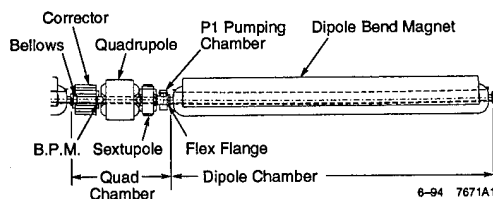


Figure 1. HER Arc Half Cell

The need for the Flex Flange arises from beam line space constraints, cost effective manufacturing tolerances and the overall length of the dipole chamber. The distance between the quadrupole and dipole magnets in the Arcs leaves only 0.31 meters of physical space between the magnet coils. A pump chamber with attached 60 liter per second ion pump occupies the majority of that space including the necessary space for flange bolts. The joint is large enough only for a pair of 8" Conflat flanges. The

prototype experience showed that the minimum practical angularity tolerance for welding a Conflat flange to a chamber is ± 4.35 mrad. Without elaborate and costly machining and fixturing, the total angular misalignment of two chambers across a flange pair is $2 \times 4.35 = \pm 8.7$ mrad ($\pm 0.5^\circ$). This angular misalignment would produce a 51 mm offset at the opposite end of the 5.84 m long dipole chamber. The force needed to push the chamber back on beamline would induce bending stresses great enough to yield the EB fillet weld on the flange adapter.

Such attention to tight flange angularity is not necessary for more conventional chambers. A comparison to the HER Straight Section drift chamber is shown below. The drift chamber is a stainless steel tube that can be approximated as 101.6 mm OD x 3.2 mm wall (4" OD x 1/8" wall). A cantilevered beam model is used to estimate the stresses that would result from displacing the free end 51 mm.

	HER Arc Dipole Chamber	HER Straight Drift Chamber
E, Modulus of Elasticity	120 Gpa (17.4×10^6 psi)	207 Gpa (30×10^6 psi)
I, Moment of Inertia	$9.87 \times 10^6 \text{ mm}^4$ (23.7 in^4)	$1.21 \times 10^6 \text{ mm}^4$ (2.9 in^4)
σ_{yield} , Material Yield Strength	70 Mpa (~10 ksi)	241 Mpa (~35 ksi)
σ_{weld} , Bending Stress in Weld	254 Mpa (37 ksi)	90 Mpa (13 ksi)

Table 1. Comparison of Weld Stress in Copper and Stainless Steel Beam Pipes

The table shows that, while a stainless chamber could endure such lateral offsets and stresses at the weld root, the copper chambers cannot. The material strength of the stainless tubes in the straight section eliminates the flexible joint requirement. A flexible connection, however, is needed in the arcs to avoid the possibility of yielding the vacuum seal joints.

DESIGN REQUIREMENTS

The space limitations and flexibility requirements form a subset of a larger collection of design requirements for the flange joint which include ultra high vacuum

* Work supported by Department of Energy Contract DE-AC03-76SF00515

compatibility, low beam impedance, thermal management and chamber support system issues. These requirements were developed as the vacuum system design proceeded from conceptual to final design.

Space	Minimize Z space
Constraints	
Flexibility	Allow $\pm 0.5^\circ$ of Pitch Allow $\pm 0.5^\circ$ of Yaw No XYZ Displacement No Roll
Vacuum	Reliable UHV Seal to 1 nTorr
Low Beam Impedance	Accurate XY position Steps ≤ 1.5 mm across flange joint Electrical continuity across joints
Thermal Loads	Maximum of 1 W/cm ² due to : Scattered Synchrotron Radiation (SR) Resistive Losses Higher Order Mode Heating Contact Resistance Heating
Structural Loads	Gravity, Vacuum and Earthquake Loads Torsion due to Chamber Twist

Table 2. Flex Flange Design Requirements

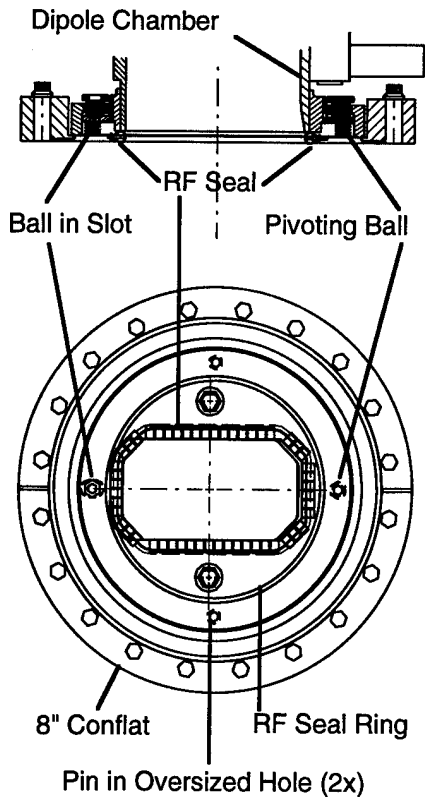


Figure 2. Flex Flange Assembly with Integral RF Seal

DESIGN DESCRIPTION

The design employs a ball bearing that is captured in the Z direction to provide the pivoting motion for the flange. The pivot is at the three o'clock position coincident with the SR stripe. A second ball bearing in a slot at the nine o'clock position sets the minimum and maximum yaw. A pair of pins at six and twelve o'clock in oversized holes sets the minimum and maximum pitch. The assembly contains < 0.12 mm of "rattle" due to tolerances on the ball-bearing-to-slot location fit. A flexible bellows is welded to stainless rings on the mechanical assembly with minimal offset. This assembly, containing all parts except the knife-edge flange and RF Seal, is positioned with tooling and EB welded to the end of the chamber perpendicular to the chamber centerline within 0.25°. An 8" Conflat flange is then welded within 0.25 mm of its ideal location to the end of the chamber. Finally, the RF Seal is accurately positioned with respect to the chamber inner octagonal profile and mounted to the flex flange. A pair of alignment pins locate the flanges accurately during installation to ± 0.25 mm. These mechanical assembly tolerances were verified during prototyping.

Mechanical Loads

The Flex Flange assembly is designed to accomodate the structural loadings due to gravity, vacuum, earthquake (EQ) and external support loads.

Axial	Vacuum Load	± 1780 N (± 400 lb)
	Chamber Friction	± 134 N (± 30 lb)
	EQ	± 1691 N (± 380 lb)
Vertical	Chamber Weight	- 267 N (- 60 lb)
	EQ	± 134 N (± 30 lb)
Lateral	EQ Load	± 623 N (± 140 lb)
Twist	Removing	± 136 N•m (± 100 ft•lb)
	Extrusion Twist	

Table 3. Flex Flange Mechanical Loads

The loadings imposed by the external supports are conservative. They include frictional forces and the moment imposed by twisting the chamber as required to rotationally align the octagonal cross-sections of the mating dipole and quadrupole chambers.

The ball bearings experience the highest forces due to the combined vertical loads and chamber twist. These forces are not high enough to cause Brinnelling to occur in the countersink bearing area. Pull-out is not a problem since the bearings are seated in countersunk holes and restricted from large XY deflections by the pins in the assembly.

RF Seal

The integral RF seal ring provides electrical continuity between chambers. Crushable fingers made of GlidCop® (chosen for its thermal and structural properties) are employed to accommodate the variations in gap width between chambers. Sets of finger stock are brazed with 35/65 Au-Cu braze alloy to a stainless plate containing the octagonal inner profile of the vacuum chamber. The seal is positioned within 0.5 mm of the SR impingement surface and fastened with a pair of bolts. The seal is not reusable, much like a knife-edge flange gasket.

It is extremely important that the RF seal is shadowed from direct synchrotron radiation. The seal can conduct the relatively low heat load of 1 W/cm², but cannot survive the 2000 W/cm² direct SR strike. This extremely high heat flux would cause the seal to fail catastrophically.

Material	GlidCop®
Finger Width	4.06 mm (0.160")
Finger Thickness	0.15 mm (0.006")
Number of Fingers	52
Contact Force per Finger	>200 grams (0.44 lb)
Nominal Gap	5.87 mm (0.231")
Maximum Gap	7.44 mm (0.293")
Minimum Gap	3.96 mm (0.156")
Number of Crushes per Seal	1

Table 4. RF Seal Design Parameters

The gap between the end of the dipole and quadrupole chamber is affected by many tolerances. While the nominal value is 5.87 mm (0.231"), tolerances on piece parts, subassemblies and tunnel installation can cause the gap to vary around the circumference of the octagonal profile by as much as ~3.5 mm (0.138"). The total compression of the seal is divided between the two chambers at about 50%. This means that the seal is precompressed ~1.25 mm when mounted to the inside of the Flex Flange assembly on the end of the dipole chamber. Stacking tolerances during installation may cause the gap to increase or decrease slightly. Even at the largest expected compression, residual contact forces equating to 0.75 mm (0.030") of springback have been verified through testing. This springback ensures that no finger lift-off can develop during normal operation.

Flex Flange Bellows

The bellows are made by MetalFab to their clean specification and may be vacuum fired to meet SLAC's stringent vacuum requirements.

The bellows remains static except during installation to accommodate pitch and yaw of the flange pair. Thermal expansion of the chamber is taken up by the bellows module[2] at the opposite end of the chamber. The only thermal expansion that the Flex Flange bellows must accommodate is the thermal growth of the flange pair, which is negligible. The axial stroke specified reflects the reliability requirement for the UHV seal. The assembly only allows a rotational stroke in pitch or yaw of one bellows end plate with respect to the other. The entire bellows never experiences the full axial stroke during operation.

Outer Diameter	137.2 mm (5.400")
Inner Diameter	120.7 mm (4.750")
Stroke	3.05 mm (0.120")
Offset	0.13 mm (0.005")
Number of Cycles	5,000
Temperature Range	35 - 150 °C
Convolution Material	SS 304L
End Plate Material	SS 347

Table 5. Flex Flange Bellows Design Parameters

FUTURE WORK

During the ramping to full production, a pre-production module will be assembled and mechanically cycled to ensure performance of the Flex Flange bellows and the RF seal assemblies. The module will be tested to evaluate the impedance contribution of the RF seal and investigate possible higher order mode effects.

CONCLUSION

The Flex Flange design developed for the HER Arcs meets or exceeds the physics and engineering requirements imposed upon it. The concept is adaptable to many applications.

REFERENCES

- [1] Vacuum System Design for the PEP-II B Factory High Energy Ring, C. Perkins et al, EPAC94, London, England, June 27 - July 1, 1994.
- [2] Bellows Design for the PEP-II HER Arc Chambers, M. Nordby et al., Particle Accelerator Conference, Dallas TX, May 1-5, 1995.

PROCESSING OF O.F.E COPPER BEAM CHAMBERS FOR PEP-II HIGH ENERGY RING*

E. Hoyt, M. Hoyt, R. Kirby, C. Perkins, D. Wright, A. Farvid, Stanford Linear Accelerator Center, Stanford University, Stanford, CA 94309 USA

Using laboratory scale and full size PEP-II vacuum chambers, chemical cleaning, glow discharge and thermal process effects were evaluated using surface analysis by x-ray photoelectron spectroscopy (XPS). These processes were optimized to reduce surface carbon and thereby minimize photodesorption gas loads. The relation of surface carbon to ion dose was investigated and compared for pure argon, 5% oxygen in argon, and pure hydrogen plasmas. Argon incorporation was noted only when the copper was oxidized in the mixed gas. Surfaces, stable in ambient atmosphere, were obtained having surface carbon values less than 10%. These optimized recipes will be used in processing copper vacuum chambers for the PEP-II B-Factory.

I. INTRODUCTION

In electron storage rings, the main gas burden is due to synchrotron radiation desorption. Initial storage times are short until the intercepting walls can be "scrubbed" and the photodesorption yield (η) can be reduced by orders of magnitude. Acceptable η is usually not achieved until photon doses $> 10^{23}$ photons/cm² have been reached. Of course if the surfaces are repopulated when the beam is off for extended periods, leaks occur, or the system is vented, the surfaces must again be "scrubbed" to low values of η .

Many researchers have studied methods of preparing beam chamber surfaces with reduced initial scrubbed desorption yields. (1-9) The surface processing techniques include controlled atmosphere extrusion and machining, wet chemical surface removal, electropolishing, ozone and oxygen purging, and many combinations of gas discharge plasma cleaning. To date, most of these studies have concentrated on alloys of aluminum and stainless steel whose surface oxides are relatively stable. Recently copper surfaces have begun to be investigated (10)(11)(12). This report outlines the work at SLAC on preparing OFE copper beam chambers for the PEP-II B Factory. We focused on processes that yield minimum residual carbon on the surface, reasoning that the initial and ultimate CO and CO₂ photodesorption yields would be correspondingly lower.

II. TESTING TECHNIQUE

XPS was used to measure changes in surface composition on 5 cm² round discs cut from a beam tube

extrusion. Surface composition changes were monitored through the wet cleaning process as bath compositions and rinse water conductivity were adjusted. These coupons were also inserted into a test chamber (Figure 1) to monitor changes in surface composition following glow discharge processing. Copper discs were also installed at three locations in full-scale dipole and quadrupole beam chambers to monitor thermal and glow discharge processing effects on surface composition (Figure 2).

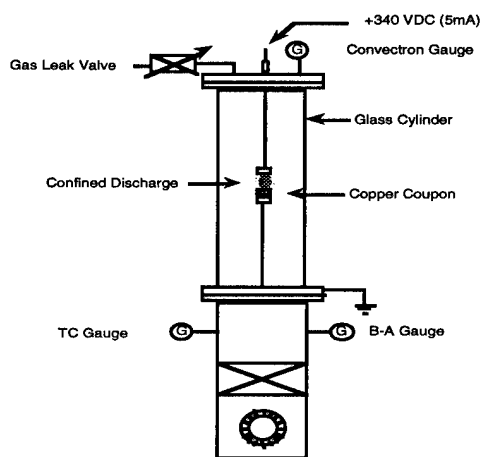


Figure 1. Experimental setup for testing copper discs

III. OPTIMIZED COPPER CLEANING RECIPE

Stanford had evolved a recipe for cleaning copper accelerator and klystron parts over a period of five decades. In order to minimize the final concentration of surface carbon, we modified this evolved cleaning recipe.

1. Steam clean
2. Alkaline soak in Enbond™ Q527 for 5 min @ 180° C
3. Cold tap water rinse for 2 minutes
4. Dip in 50 % hydrochloric acid at room temperature
5. Cold tap water rinse for 2 minutes
6. Etch in acid solution (4 vol. %HNO₃, 10 vol. %C₂H₄O₂, 100 g/l CrO₃, 5 ml/l HCl) for 5 minutes.
7. Cold tap water rinse for 2 minutes
8. Dip in hydrochloric acid at room temperature
9. Cold tap water rinse for 2 minutes
10. Cold de ionized water rinse (>1 megohm)
11. Cold de ionized water rinse (>6 megohms)
12. Hot (106°F) de ionized water rinse (>10 megohms)
13. Blow dry with nitrogen gas.

* Work supported by U. S. Department of Energy, contract number DE-AC03-76F00515

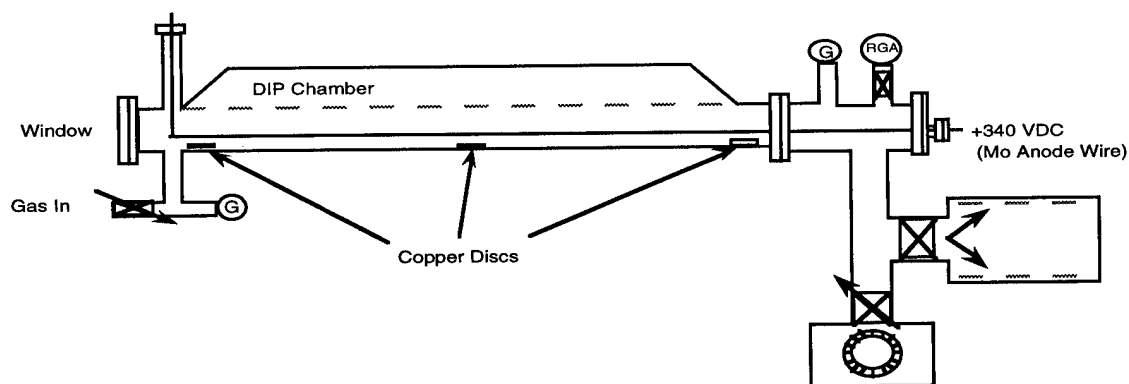


Figure 2. Schematic Diagram of Glow Discharge Set-Up for Dipole Vacuum Chamber Processing Showing XPS Coupon Location

Note that the final rinse uses the lowest conductivity de-ionized water that is practical. If the resistivity of the final rinse water is less than 10 megohms, there is more residual surface carbon on the copper. Figure 3 shows some typical XPS surface composition results for the processes investigated.

Surface Treatment	XPS Surface Atom %					
	Cu	O	N	C	Cl	Ar
Chem cleaned (old recipe)	22.4	22.5	11.9	41.6	1.6	-
Chem cleaned (optimized)	43.4	36.8	-	17.9	1.9	-
GDC (2e19 ions/cm ²)	50.6	40.0	-	8.0	-	1.4
5% O ₂ -Ar in beam chamber						
GDC (2e18 ions/cm ²)	48.6	42.0	-	8.0	-	1.4
5% O ₂ -Ar in beam chamber						
GDC (2e18 ions/cm ²)	64.2	23.6	-	12.2	-	-
Pure H ₂ in test chamber						

Figure 3. Table showing Copper Coupon Surface Composition (by XPS) for Various Processes

IV. GLOW DISCHARGE PROCESSING FOR CARBON REDUCTION

Glow discharge processing, following chemical cleaning, can reduce surface carbon levels to less than 10 percent. Figure 4 shows the XPS carbon concentration data comparing the results obtained for pure argon and 5% oxygen-argon. Data points from the test chamber and the beam chambers fall on the same curves. The 5% oxygen-argon is more efficient than pure argon in removing carbon due to the combined chemical activity of the oxygen and the physical sputtering of the argon.

There may be a serious drawback to using oxygen with argon. With pure argon, the XPS results showed no argon on the copper surfaces, in either the test chamber or the beam chambers. However, all samples run in the beam chambers with the 5% O₂-Ar mixture show ~ 1% argon

incorporation. Mathewson (13) also found argon burial when using O₂-Ar. None of the copper discs run in the test chamber with 5% oxygen-argon showed argon incorporation. The ion flux in the test chamber was about a factor of ten higher than in the beam chamber and the sample temperature was higher, resulting in some visible oxidation on the surface.

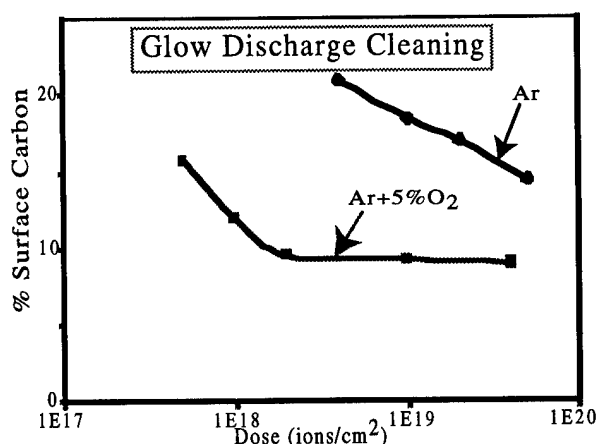


Figure 4. Surface carbon levels versus ion dose for pure argon and 5% oxygen-argon discharges

There is a definite increase in the surface oxygen levels following processing with 5% O₂-Ar. Argon may be incorporated or buried in the growing oxide depending on the temperature. If it were possible to discharge, with oxygen-argon, at a high enough temperature to preclude oxide growth, argon might not get occluded. These are subtle effects that may need study. Dylla's very comprehensive review article on GDC (14) deals principally with stainless steel surfaces, but sheds no light on copper. Some work has also been reported on aluminum alloy discharge cleaning. Copper surfaces are quite different. For example, Cr₂O₃ has a free energy of formation of -142 Kcal/mol and Al₂O₃ has a free energy of formation of -408 Kcal/mol whereas Cu₂O has a free energy

of formation nearer -38 Kcal/mol and therefore can be easily disassociated at low energy and easily reduced with hydrogen.

Pure H₂ plasma processing of copper has many advantages over argon-oxygen, one of which is very limited sputtering (14). Sputtering may produce micro particles which have been postulated to result in stored beam degradation.

One limitation to using H₂ discharges to clean the PEP-II dipole chambers is that the H₂ plasma must be employed prior to installing the distributed ion pumps to avoid loading the pump titanium with hydrogen that might not all be removed by baking at 200°C.

V. HYDROGEN DISCHARGE PROCESSING

In view of the above considerations with regard to oxidation and argon incorporation when using the mixed gas plasma, there may be some incentive to use a pure hydrogen plasma for removing carbon and oxygen from OFE copper surfaces. XPS coupons discharged in pure hydrogen in the test chamber showed somewhat faster carbon reduction than those discharged in 5% oxygen-argon. Figure 5 compares the XPS spectra of coupons ion bombarded to the same dose (2×10^{18} ions/cm²) with 5% oxygen-argon in a quadrupole chamber (A) and run in the test chamber in a pure hydrogen plasma (B).

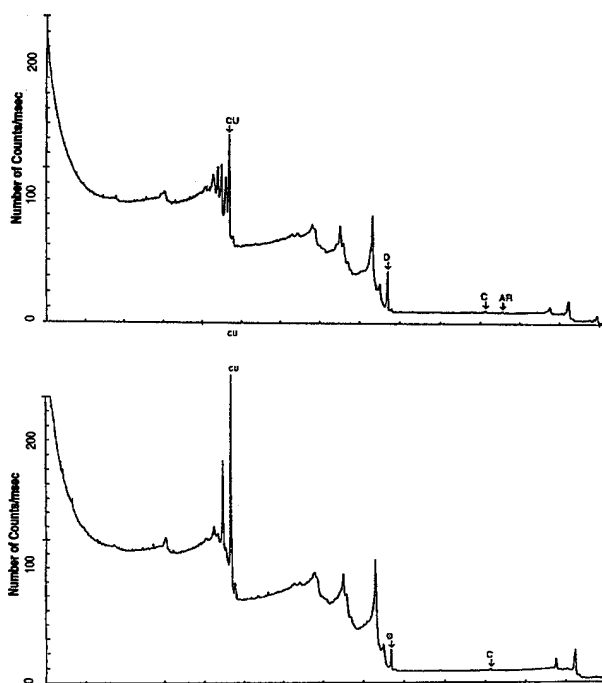


Figure 5. XPS Spectra of copper samples GDC processed in 5% O₂-Ar (upper) or H₂ (lower) to 2×10^{18} ions/cm².

VI. CONCLUSION

We have shown that it is possible to clean OFE copper surfaces chemically, to yield surface carbon levels near 20%. These levels can be further reduced to about 10% by glow discharge cleaning with argon, oxygen-argon, or hydrogen plasma discharges. The cleaned, baked and discharged surfaces can be stored in clean air for weeks with little change in surface composition as measured by XPS.

VII. ACKNOWLEDGMENTS

W. Stoeffl of LLNL provided much advice and Rose Darrough assisted with the beam chamber discharge and outgassing tests. Thanks to Ed and Nadine for their late-night formatting help.

VIII. REFERENCES

- [1] H. Stori, Vacuum 33, 171 (1983).
- [2] A.G. Mathewson, E. Alge, O. Grobner, R. Souchet, and P. Strubin, J. Vac. Sci. Technol. A 5 2512 (1987).
- [3] T. Kobari and H. J. Halama, J. Vac. Sci. Technol. A 5, 2355 (1987).
- [4] H. J. Halama and C. L. Foerster, Vacuum 42, 185 (1991).
- [5] T. S. Chou, J. Vac. Sci. Technol. A 9, 2014 (1991).
- [6] H. Ishimaru, T. Momose, K. Kanazawa, Y. Suetsugu, and H. Hisamatsu, AIP Conf. Proc. 236, 1 (1991).
- [7] M. Saitoh, K. Kanazawa, T. Momose, H. Ishimaru, N. Ota, and J. Uramoto, J. Vac. Sci. Technol. A 11, 2518 (1993).
- [8] N. Ota graduate university for advanced studies. K. Kanazawa, M. Kobayashi and H. Ishimaru, National Laboratory for High Energy Physics. To be published.
- [9] N. Oto, M. Satoh, K. Kanazawa, T. Momose and H. Ishimaru, J. Vac. Sci. Technol. A 12 (3), 826, 1994.
- [10] O. Grober, A. G. Mathewson and P.C. Marin, J. Vac. Sci. Technol. A 12 (3) 846 1994.
- [11] C. Foerster, C. Lanni, G. Korn, C. Perkins, M. Calderon, J. Vac. Sci. Technol. , (1994).
- [12] Fumro Watanabe, Maki Svemitsu and No Buo Miyamoto, J. Vac. Sci. Technol. A 13 (1) 147 1995.
- [13] A.G. Mathewson, 10th Italian National Congress on Vacuum Science on vacuum and Technology, Stresa, Italy, Oct 1987, CERN-LEP-VA/87-63
- [14] H.F. Dylla J. Vac. Sci. Technol. A Vol. 6, No. 3 1276 1988.

STRETCHFORMING VACUUM CHAMBERS FOR THE PEP-II B-FACTORY HIGH ENERGY STORAGE RING*

E. F. Daly, D. Bostic, A. Lisin, M. Palrang, C. Perkins and K. Skarpaas,
Stanford Linear Accelerator Center, Stanford University, Stanford, CA 94309 USA

Dipole vacuum chambers for the PEP-II HER, fabricated from copper extrusions, must follow the arc of the electron beam in order to minimize impedance losses. The 165 m bend radius requires that the chambers have a sagitta of 25 mm over each 5.84 m length. Stretchforming provides a relatively smooth continuous bend radius and results in low overall residual stresses. Structural analyses of the chamber during the forming process are discussed. These analyses are used to estimate the residual stresses in the stretchformed chambers. The impact of residual stresses on actual chamber operation are discussed. The stretchforming process and apparatus utilized during prototype testing is described. Permanent deflections of the chambers during prototype manufacture are presented and compared with predictions.

INTRODUCTION

The HER circumference is 2200 m and consists of six straight sections 120 m in length and six arc sections 240 m in length. Each arc contains 33 quadrupole magnets and 32 dipole magnets to form 16 cells per arc. The HER vacuum system design[1] consists of 32 dipole vacuum chambers positioned in the magnet gaps for each arc totaling 192 dipole chambers. The dipole chamber extrusion is about 189 mm x 60 mm x 5 mm thick with a cross-sectional area of 22.6 cm² (3.5 in²). The cooling bar extrusion has a cross-sectional area of 3.7 cm² (0.57 in²).

The beam orbit through the dipole magnet is curved. In order to minimize beam impedance losses, the dipole chamber is formed to this beam orbit and corresponding dipole magnet bend radius of 165 m. To accomplish this, the chambers are stretchformed to a radius of 165 m within a tolerance band of ± 2 mm. This tolerance is based on considerations of maximum allowable synchrotron heating on the chamber wall, beam stay clear requirements, chamber positional requirements and manufacturability.

A limited structural analysis of the stretchforming technique is presented that includes the estimated residual stresses in the dipole vacuum chamber and their impact on chamber performance. The apparatus and process utilized for stretchforming prototype and production chambers is presented along with data from the prototype experience.

WHY STRETCHFORMING?

Stretchforming involves first applying sufficient tension to raise the workpiece to the yield point, and then forming the part over a mandrel to a specified shape. This manufacturing process has been used successfully for many years in the aerospace and automotive industries to fabricate smoothly varying complex shapes [2].

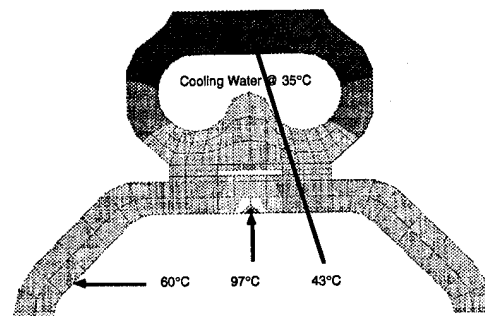


Figure 1. Chamber Temperature Distribution at the Maximum SR Heat Load of 102 W/cm

The high synchrotron radiation (SR) heat load of 102 W/cm produces a peak chamber temperature of 97°C and resulting compressive stresses of roughly 83 Mpa (12 ksi). Residual stresses due to a forming technique would be compressive and therefore add to the peak stress in the chamber during operation. A chamber curved by bending only to 165 m would contain roughly 69 Mpa (10 ksi) of residual compressive stress.

Stretchforming is the technique chosen because it minimizes residual bending stresses in the chamber. Bringing the entire cross section of the chamber to yield while bending imparts a uniform stress across the chamber. When the axial force is released, there is little residual stress (< 1000 psi) and minimal springback. The technique also provides the smoothest bend of all options considered.

Deformation using a pin press and through conventional pipe bending were tried. Using a pin press resulted in a series of small kinks which may enhance the SR heat flux. More kinks would be required to reduce the amount of enhancement. However, the process proved slow and inefficient. Conventional pipe bending was also tried but failed because the local high contact pressures

* Work supported by Department of Energy Contract DE-AC03-76SF00515

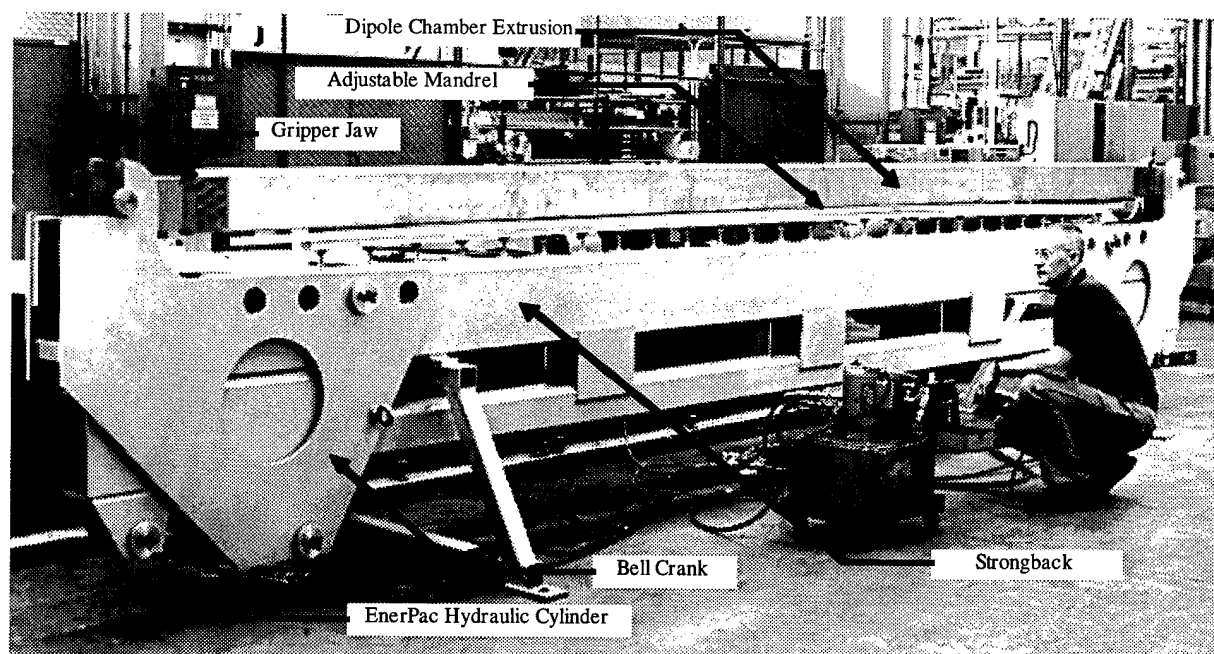


Figure 2. The stretchforming machine built by SLAC has been used successfully for prototype development.

resulted in local yielding of the material and subsequent unacceptable chamber distortion.

APPARATUS AND PROCESS

The Stretchformer built by SLAC for the PEP-II project consists of a strongback, an adjustable mandrel, a pair of bell cranks, two hydraulic cylinders and a pair of gripper jaws. The strongback is approximately twenty times stiffer than the extrusion to limit machine deflection during the process. The adjustable mandrel can be set to a radius as tight as 63.5 meters to compensate for springback. The bell cranks provide roughly a 3:1 mechanical advantage for the pair of EnerPac hydraulic cylinders. The two 50 Ton cylinders each provide a maximum tensile force of 667.4 kN (150 kips). The gripper jaws have knurled surfaces bolted tightly together to squeeze the ends of the chamber ensuring positive traction during tensioning.

While some conventional machines separate the extension and bending processes by utilizing different machine axes to first stretch then form the part over a mandrel, the SLAC machine combines both operations using the lever action of the bell cranks and the adjustable mandrel. There are four settings which allow variable amounts of tension versus the angle of the bell crank rotation. The amount of bending is controlled by adjusting the height and radius of the mandrel.

The machine settings have been adjusted empirically during the prototype phase to produce a repeatable part. The entire process begins by taking an inspected extrusion, cutting it to length and drilling the gripper jaw hole pattern

in each end. The extrusion and cooling bar are cleaned for UHV and then the parts are Electron Beam (EB) welded.

The gripper jaws are installed on the chamber assembly. The mandrel radius is set to the prescribed bend radius, which is ~25 m (1000") smaller than the final part radius to compensate for machine deflection and extrusion springback.

Approximately 1.09 MN (245 kip) of tension is gradually applied to the chamber. Once this tension is applied, the extrusion contacts the mandrel and the bending moment applied through this contact imparts a stress greater than the material yield strength of 276 MPa (40 ksi). The chamber is pulled to intimate contact along the mandrel to form it to its pre-springback shape. The force is then released and the part springs back to its final deformed shape.

The formed chamber radius is measured and compared with the desired value. If the radius is too large, the mandrel is re-adjusted and the process is repeated until the radius of the chamber is within the specified limits.

PROTOTYPE EXPERIENCE

Three prototype chambers were stretchformed in successive trials in an effort to achieve the desired bend radius of 165 m with a corresponding sagitta of 25 mm. Since the EB welder was not available, the extrusions were stretchformed without the cooling bar attached.

The mandrel radius was determined through successive trials and finally set at 127 m (5000"). The actual bend radii of the three extrusions is not exactly 165 m all along

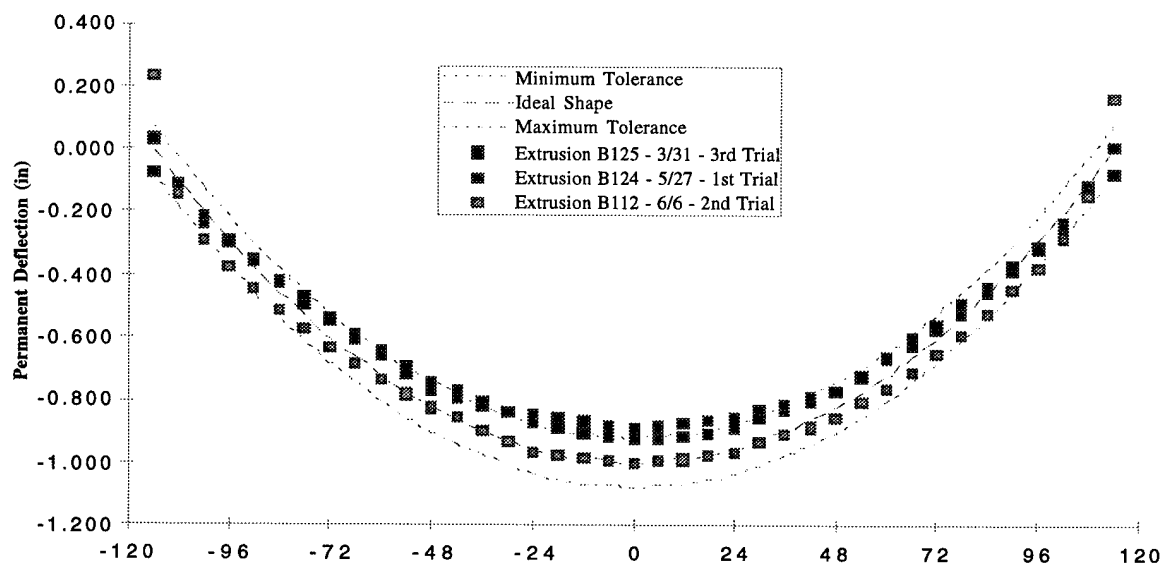


Figure 3. Permanently deflected shape of three stretchformed prototype extrusions versus inches from extrusion centerline.

the length. The center portion of the chambers are near the ideal radius, the very ends show a smaller radius and the portions between show a larger radius. This variation does not impact chamber performance significantly.

The process plot shows the relationship between applied pressure and resulting strain is analogous to the stress-strain curve for half-hard copper. The maximum cylinder pressure of 4200 psi (28.9 Mpa) equates to a total force on the cross section of 1.07 MN (240 ksi). The measured and calculated strains agree well. The peak cylinder pressure should be 15-20% higher for a chamber with cooling bar attached.

Many lessons were learned as the three chambers were successfully formed in six trials. Factors that affected each

trial were jaw slippage, mandrel shape and repetitive process control. Prior to production the jaws will be modified to include the ability to grip the welded cooling bar. A more efficient method for mandrel adjustment will be added to the system. During production, the process parameters will be rigorously monitored to ensure stretchformed chambers that meet design requirements.

CONCLUSIONS

The stretchforming process produces chambers having a relatively smooth continuous bend radius. The prototype experience with stretchforming has been favorable. The stretchforming apparatus will be modified and utilized to produce the 192 HER dipole vacuum chambers.

ACKNOWLEDGEMENTS

Thanks to Rose Darrough and Luis Arroyo for their input and hard work on the apparatus and the technique.

REFERENCES

- [1] Vacuum System Design for the PEP-II B Factory High Energy Ring, C. Perkins et al, EPAC94, London, England, June 27 - July 1, 1994.
- [2] Stretch-Wrap Forming, Kingsley C. Drone, Western Machinery and Steel World, May 1956.

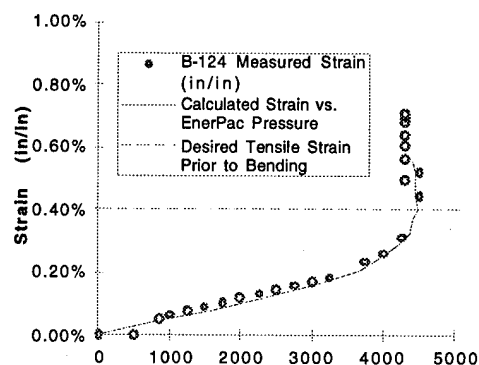


Figure 4. Process Plot of Strain in Extrusion vs. EnerPac Cylinder Pressure (psi)

BEAM VACUUM CHAMBERS FOR BROOKHAVEN'S MUON STORAGE RING*

H.C. Hseuh, L. Snyderstrub, W.S. Jiang, C. Pai, M. Mapes
AGS Department, Brookhaven National Laboratory
Upton, New York 11973-5000 USA

Abstract

An experiment is being built at Brookhaven to measure the $g-2$ value of the muons to an accuracy of 0.35 ppm. The muon storage ring of this experiment is designed to produce a dipole field with homogeneity to 1 ppm using a continuous superconducting magnet. The beam vacuum system in the storage ring will operate at 10^{-7} Torr and consists of twelve sector chambers. The chambers are constructed of aluminum and are approximately 3.5 m in length with a rectangular cross-section of 16.5 cm high by 45 cm at the widest point. The design features, fabrication techniques and cleaning methods for these chambers are described. Monte Carlo simulation of the pressure distribution and finite element analysis of the chamber deflection are summarized with good correlation shown to measured values obtained during tests of the prototype chamber.

I. INTRODUCTION

The principle equipment of the $g-2$ experiment[1] is the muon storage ring and its continuous superconducting magnet which bends and stores the injected pion and muon particles. The magnet has a diameter of 14 m and a gap of 18 cm facing the inside of the storage ring. The cross sectional view of the magnet, its cryostats and the muon storage chamber is shown in Fig. 1. A magnetic field of 14.5 KG with a field homogeneity of 1 ppm is required in the muon storage region, which rules out the use of any material with magnetic susceptibility higher than 0.001. The muon chambers and the associated components are made of aluminum, titanium, ceramic, and polymeric materials. The design, selection of material, fabrication and evaluation of these vacuum chambers will be presented here.

II. DESIGN and FABRICATION OF SECTOR CHAMBERS

A plan view of the ring vacuum system without the superconducting magnet is shown in Fig. 2. It consists of twelve 28-degree chambers, of which ten are identical (i.e.,

standard). The detail of a standard sector chamber is shown in Fig. 3. The chamber has an arc length of 3.5 m and a

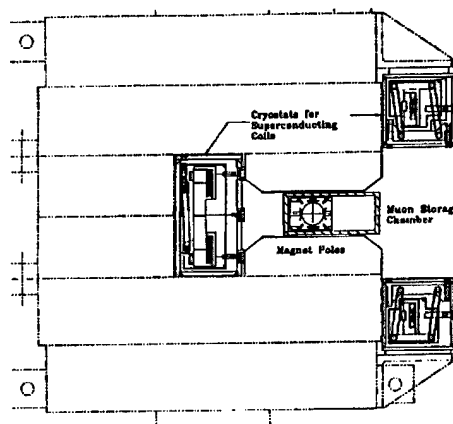


Fig. 1. The cross sectional view of the 45 m continuous superconducting magnet, its cryostats and the muon chamber.

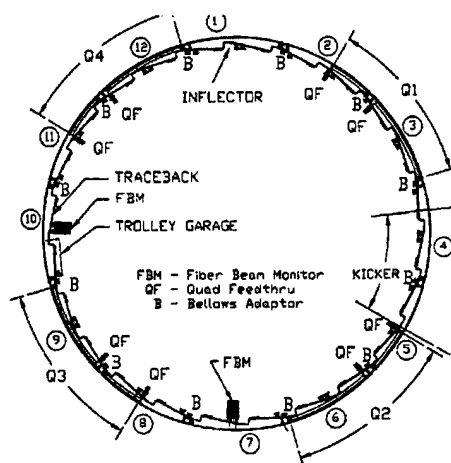


Fig. 2. The layout of the muon storage ring vacuum system without the superconducting magnet, consisting of twelve sector chambers; ten standard ones and two special ones for inflector magnet and for NMR trolley garage.

*Work performed under the auspices of the U.S. Department of Energy.

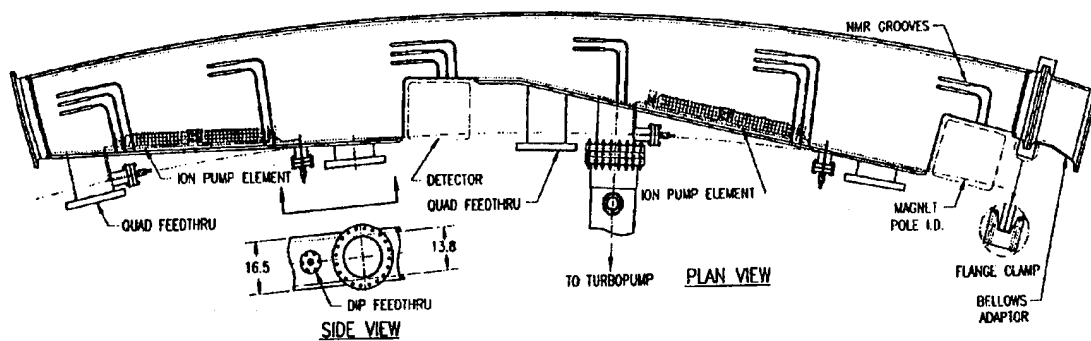


Fig. 3. The design of the standard sector chamber together with distributed ion pumps and turbopump manifold. The scalloped areas are for electron detectors.

rectangular cross-section with inner vertical height of 13.8 cm. The horizontal width of the chamber varies from 15 cm at the narrow point to 45 cm at the widest point, forming two scalloped areas on the inside to accommodate the twenty-four electron detectors. Conflat access ports are provided at the inner radius of the chambers for pump connections and installation of various internal components. A short bellows adaptor is placed between the chambers. It allows for the installation of the chambers and for the alignment of the end flange clamps and seals which are only accessible from the inner radial side.

The sector chamber is a welded fabrication of aluminum alloy 6061 plates. The top and bottom plates are 13.5 mm thick and the side wall 19 mm thick. The wall adjacent to the detectors is only 3 mm thick thus minimizing the energy loss of the electrons. After machining and chemical cleaning, the plates are welded on a 4 m long weld fixture table in a clean room. The post-weld flatness and loss of arc of the chambers are approximately 1 mm. The top and bottom surfaces are then machined to a flatness of 0.25 mm. The Conflat access port flanges and the rectangular end flanges are then welded.

Four electrostatic quadrupoles, occupying 45 percent of the ring circumference, are to focus the injected muons and pions. They are pulsed at ± 25 kV during the storage period. The electrodes are mounted on the curved support frames which are installed inside the sector chambers through the end flanges. The cross sectional view of the chamber, the support frame and the electrodes are shown in Fig. 4. An NMR trolley containing up to 25 NMR probes will be used periodically to map the magnetic field of the storage region around the ring. This NMR trolley, operated in storage vacuum, will ride on the corner rails of the support frame, and parked at a 'garage' when not in use. There are also 30 fixed NMR probes per chamber which are mounted in external grooves in the upper and lower chamber plates.

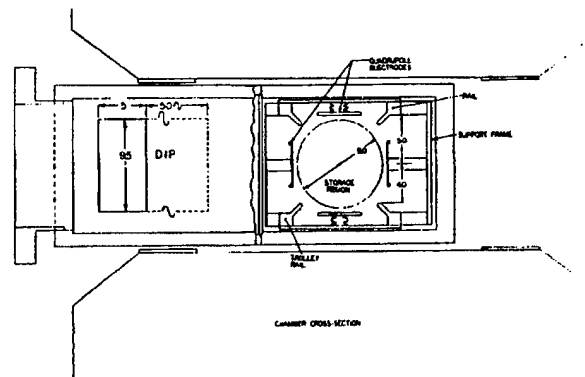


Fig. 4. The cross sectional view of the sector chamber at its widest point. The rectangular frame supports the quadrupole electrodes and the rails for NMR trolley. Dimensions are in cm.

III. MECHANICAL and VACUUM EVALUATION

After fabrication and cleaning, the chambers are pumped down, leak checked and measured for deflection of top/bottom plates under vacuum load. The deflection of the top plates of the prototype chamber at its widest span was found to be 0.45 mm. This is in good agreement with the calculated value of 0.4 mm using ANSYS finite element code.[2]

Without a large on-site chemical cleaning facility to handle the completed sector chambers, the chambers were cleaned with pressurized hot water spray mixed with mild-etch alkaline detergent. The effectiveness of the cleaning steps can be judged by measuring the outgassing of the chambers. The outgassing rates of the prototype chamber after various cleaning treatments are plotted in Fig. 5 versus pumpdown time. Outgassing rate of mid 10^{-10} Torr. ℓ /sec.cm² can be

reached one day after pumpdown with mild-etch detergent rinse (pH = 11.5). The slope of the outgassing curves are consistent with $q \propto k \cdot t^{-1.1}$ which is the characteristic of the outgassing of water.

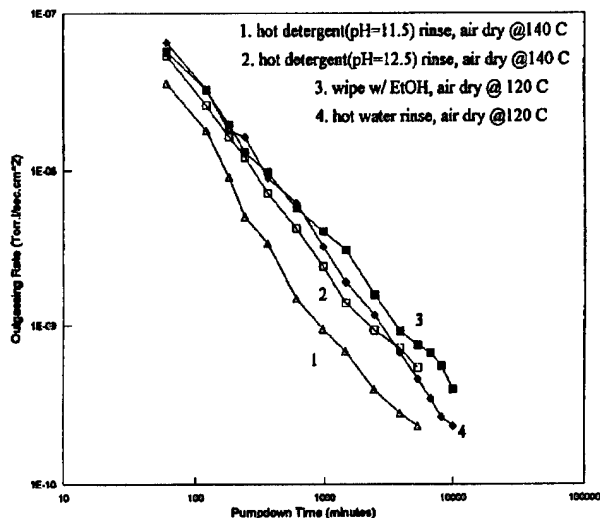


Fig. 5. Outgassing rates of the prototype sector chamber after various cleaning treatments. The designed outgassing rate of 1×10^{-9} Torr.l/sec.cm² at $t = 24$ hours can be reached with mild-etch detergent rinse.

IV. PRESSURE DISTRIBUTION

The injected pions and muons are to be stored for a few milliseconds which only requires a medium range vacuum. However, to minimize electron trapping and high voltage breakdown at the quadrupole electrodes, pressure of 10^{-7} Torr is needed especially when π^- and μ^- particles are stored. At this mode of operation, the upper and lower electrodes are at -25 kV and two side electrodes at +27 kV.

The storage ring vacuum will be pumped down and maintained at high vacuum with the combination of two turbomolecular pumps, two cryopumps and 24 distributed ion pumps (DIPs). The distributed ion pumps will not be installed during the commissioning stage in early 1996. The turbomolecular pumps and cryopumps will be positioned at every third chamber two meters radially away from the storage region, which reduces the effective pumping speed to less than 200 l/sec. The long manifold is necessary to minimize the disturbance of the field uniformity at the storage region and to allow the reliable operation of the pumps under the fringe magnetic field.

The pressure distribution at the storage region is calculated using a Monte-Carlo simulation program[3] 'Molflow' as shown in Fig 6. Without DIPs, pressure of low 10^{-6} Torr will be reached one day after pumpdown and low 10^{-7} Torr with DIPs. Excessive breakdown of the quadrupole high voltage has been observed in the prototype testing when operated with π^-/μ^- mode at 10^{-6} Torr. This limits the experiment to π^+ and

μ^+ modes during commissioning. The π^- and μ^- modes are only possible with the installation of the DIPs.

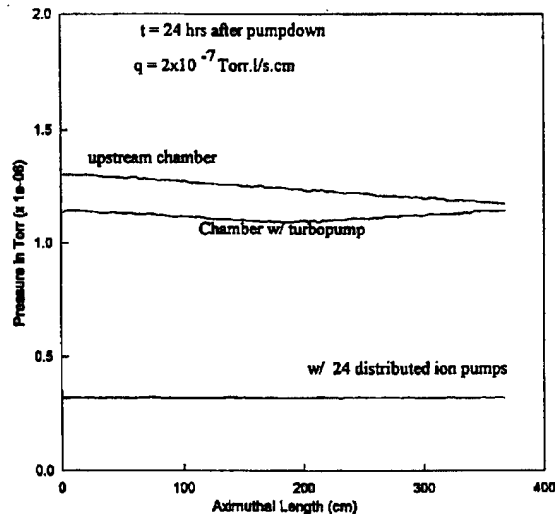


Fig. 6. Monte-Carlo simulation of pressure distribution inside the quadrupole electrodes using "Molflow" with 4 turbopumps; and with 24 distributed ion pumps. The x-axis represents the azimuthal length of the chamber. Total molecules generated in the simulation is approximately 30,000 per sector chamber.

V. SUMMARY

Due to the unique physics requirement, the vacuum chambers of the Brookhaven's g-2 muon storage ring have to be made of wide aluminum plates. The dimensional tolerances of the completed chamber are within the design values. The measured deflection of the prototype chamber under vacuum load is agreeable with ANSYS analysis. The outgassing rate of the chamber after mild etching is acceptable. The pressure distribution inside the quadrupole electrodes will be sufficiently low for the reliable operation when the distributed ion pumps are installed.

VI. REFERENCES

- [1] V.W. Hughes, *Particle, Strings & Cosmology* (World Scientist, Singapore, 1992), p. 868.
- [2] ANSYS code, ver. 5.0, Swanson Analytical Systems Inc., Houston, PA.
- [3] A PC based Monte Carlo simulation program for vacuum systems written by Roberto Kersevan, Sincrotrone Trieste, ST/M-91/17, September, 1991.

Test Results of Pre-Production Prototype Distributed Ion Pump Design for the PEP-II Asymmetric B-Factory Collider*

F.R. Holdener, D. Behne, D. Hathaway, K. Kishiyama, M. Mugge, W. Stoeffl, and K. van Bibber
Lawrence Livermore National Laboratory, Livermore, CA 94550

C. Perkins, E.F. Daly, E. Hoyt, M. Hoyt, M. Nordby, J. Seeman, and D. Wright
Stanford Linear Accelerator Center, Stanford, CA 94309

ABSTRACT

We have built and tested a plate-type pre-production prototype Distributed Ion Pump (DIP) for the PEP-II B-Factory High Energy Ring (HER). The design has been simplified from an earlier design to use less materials and to reduce overall costs. Penning cell hole sizes of 15, 18, and 21 mm have been tested in a uniform magnetic field of 0.18 T to optimize pumping speed. The resulting final DIP design consisting of a 7-plate, 15 mm basic cell size anode was predicted to give the best pumping speed results for the actual varying magnetic field of the HER dipole. A description of the final optimized DIP design will be presented along with the test results of the pumping speed measurements.

INTRODUCTION

Operation of the PEP-II Asymmetric B-Factory collider in the 9 GeV, 3 A mode or 12 GeV, 1 A mode places significant pumping speed requirements on the High Energy Ring (HER) vacuum pumping system design. The high gas loads generated by the intense photon synchrotron radiation fan striking the copper vacuum chamber wall necessitate a vacuum pumping scheme that maintains the required HER pressures.

Using a gas desorption coefficient (η) of 2×10^{-6} molecules/photon[1], the calculated gas load at 9 GeV, 3 A operation will be 1.06×10^{-6} Torr l/s/m. Average pressures required in the arcs are 10 nTorr at 3 A operation. The vacuum system of a typical arc cell as seen in Figure 1 consists of two 6 m long dipole vacuum chambers and two quadrupole chambers 2 m long each. The quadrupole chambers will be pumped with 60 l/s noble diode lumped ion pumps (LIPs). The dipole chamber at 6 m in length precludes pumping from the ends, thus distributed ion pumping is planned to offset the low conductance of the beam tube calculated at 40 l/s/m.

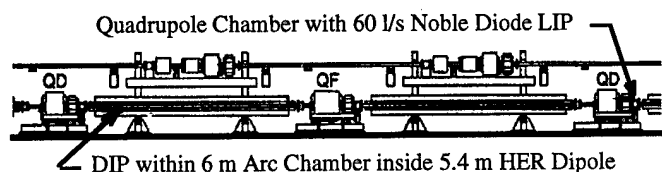


Figure 1. HER arc cell showing DIP

Distributed ion pumping was chosen based on calculations, prototype tests[2], and the reliability of previous operating PEP-I designs. The ability to handle the quantities of the gas

expected to be generated from the high photon fluxes and uncertainties of the gas desorption properties of the final chamber material, C10100 OF copper, precluded the sole use of non-evaporable gettering as the distributed pumping method in the arc sections of the HER. However, a combined distributed ion pump/non-evaporable getter pump was considered and actually prototyped and tested as reported in a separate paper presented at this conference[3]. A distributed pumping speed of 135 l/s/m within the beam passage was calculated as adequate to achieve the pressure requirement in the arcs given the latest screen design of calculated conductance of 450 l/s/m.

PUMPING SYSTEM DESCRIPTION

To achieve this pumping speed, distributed ion pump designs with plate-type anodes were chosen, as these were known to have relatively higher pumping speeds than that of the cylindrical type[4] i.e. the basic plate design has a higher conductance. The final production DIP design is shown in Figure 2.

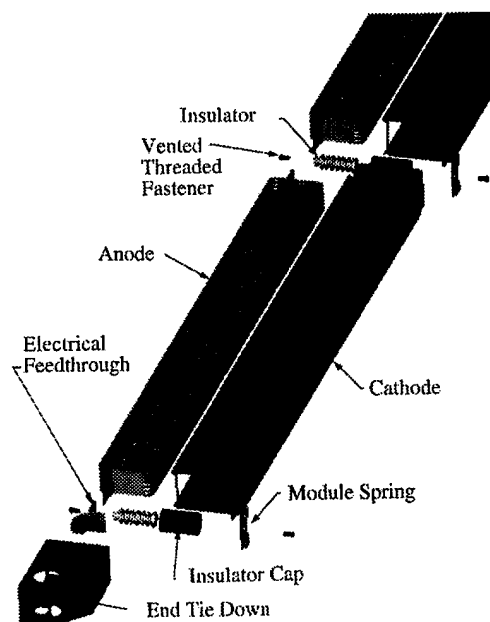


Figure 2. Exploded view of Production DIP Design

The pump shown is located in a channel space 50 mm high by 83 mm wide adjacent to a 6 mm specially machined copper screen plate formed to the same shape as the far side of the beam tube. The 6 mm thick screen consists of 6 symmetric,

* This work was performed under the auspices of the U.S. Department of Energy by Lawrence Livermore National Laboratory and by Stanford Linear Accelerator Center under contracts W-7405-ENG-48(LLNL) and DE-AC03-76SF00515 (SLAC)

angled, 3 mm slots machined on the beam side with tightly packed holes aligned to the slots drilled through to the DIP side of the arc chamber. The DIP as shown in Figures 2 and 3 consists of a laser welded single piece 316L stainless steel anode that has seven equally spaced plates. The five middle plates are 0.46 mm (0.018 in) thick and the top and bottom plates are 0.64 mm (0.025 in) thick for increased overall stiffness as well as for increased durability in handling. On one end of the anode is a 0.64 mm (0.025 in) thick L-bracket for a stiff attachment point to the supporting shielded insulator. On the opposite end is a specially designed S-spring 0.51 mm (0.020 in) thick that allows expansion as thermal loads heat it during operation at high pressures as well as during the initial 200 C dipole chamber bakeout. Possible future in-situ 95C bakes within the PEP tunnel will also be accommodated with this spring design. The same spring allows for thermal expansions and contractions during normal operations at low pressures within the PEP tunnel environment.

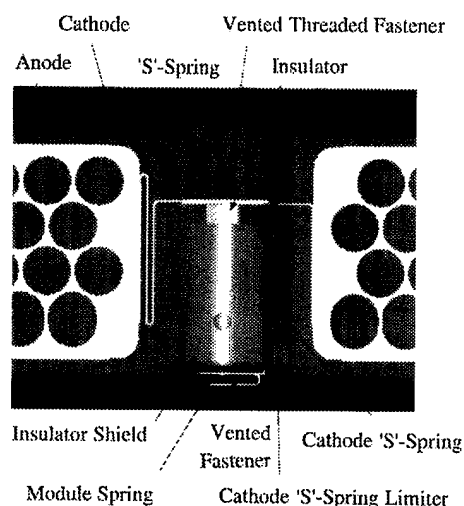


Figure 3 Normal Sectional View of a Typical Production DIP Joint at the Shielded 95% Alumina Insulator

The DIP cathode is also a single piece design of pure titanium. The unique U-channel design with large venting holes on the side away from the screen has allowed the cathode material thickness (as well as cost) to be significantly reduced from the original CDR[1] design of 1.5 mm (0.059 in) to its present thickness of 0.89 mm (0.035 in) while maintaining the same relative stiffness. While stiffness on the side away from the screen results from the U-shape geometry design, the stiffness on the edge next to the screen results from a formed V-shape at the cathode's edge. One end of the cathode is welded to a boxed shaped grounded support bracket that provides a rigid support to the grounded end of the shielded insulator. The opposite end of the cathode uses a 0.51 mm (0.020 in) thickness titanium S-spring similar to that of the anode with the added feature of an S-spring limiter. This limiter allows the entire seven module DIP string to be pulled into the arc dipole chamber without possible damage (i.e strained beyond normal material elastic limits) to either the anode or the cathode S-springs.

Another unique feature of the production DIP design, as can be seen in Figure 3, is the joint where a single shielded

insulator supports two anode ends. This allows for a minimized I/P (DIP current/pressure) for the entire dipole string since there are only eight total shielded insulators for the seven total modules used per 5.4 m dipole. The only other insulators are in the fairly standard feed through arrangement on the end of the 6 m long dipole chambers. The module spring is designed to be bent to the right height matching the final chamber dimension to take up any horizontal play that may exist because of manufacturing tolerance stackups. All fasteners are non-magnetic stainless steel with standard venting to eliminate virtual leaks. After a DIP string assembly is together, all vented fasteners are torqued to 2.26 N-m (20 in-lbs) and tack welded in two places to prevent any possible future shorting of the DIP assembly by loosened fasteners. After meg-ohm, continuity, and hi-pot test (10kV for 1 minute) the DIP assembly will be permanently E-beam welded within its copper dipole chamber.

As seen in Figure 3, the forth row of penning cell holes have been elongated. This has been done to all seven plates in an identical manner to minimize production costs at the same time taking better advantage of the curved B-field in this area of the anode. Figure 4 shows an actual B-field plot map of a dipole cross section with the DIP positioned with the beam chamber centerline at nominal beam centerline. Physics requirements place the average beam chamber side of the dipole on centerline of the dipole poles. As can be seen, only the fourth row of cells sees any significant curvature of the B-field. The arc chamber sagitta of plus/minus 9 mm has minimal effect on the average anode position along the length of the dipole, thus all anodes were made identical without the need for tabulations. This too helped keep material as well as assembly costs to a minimum.

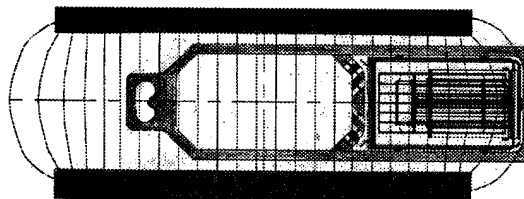


Figure 4 Production DIP within C10100 OF copper screened chamber showing center 0.18 T peak magnetic dipole field

ANODE AND CATHODE PREPARATION

After cleaning, the stainless and titanium parts were welded using standard SLAC UHV cleaning and handling practices. The titanium cathode was baked to 750 C in the same turbo pumped evacuated chamber as the anode laser welded assembly that reached 450 C. Two days at temperature were required to reduce hydrogen generation to levels that were equivalent to the background hydrogen levels in the stainless chamber used for baking. After cooling the chamber to less than 100 C, the chamber was backfilled with argon to aid in a speedier cool down of the parts. For production this method will not be used because the argon background peak was seen in subsequent pumping speed tests. The small relative partial pressure of argon however was felt to have little effect on the final measured pumping speeds. For the production DIP parts, adequate cooling time will be allowed for parts to achieve 25 C prior to backfilling chamber with nitrogen. In

production, anodes and cathodes will be vacuum baked in separate UHV high temperature furnaces.

TESTING DESCRIPTION AND RESULTS

Prior to finalizing the production DIP design described in this paper, three previously designed 1 meter long DIP modules[2,5] were tested in uniform B-field of the dipole center. The test results for the three hole size tested shown in Figure 5 are given in Table 1. The test results confirmed our calculations for our geometry and B-field that based on H. Hartwig and Kouptsidis [6] and Malev and Trachtenberg [7] that the 15 mm hole size would give the maximum pumping speed for HER requirements as shown in Figure 6. The seven plates were chosen over the five plate design because earlier measurements of 18 mm cells of both types distinctively showed that the 7-plate design gave superior performance. A 9-plate design was considered but time and dollars did not allow further testing although with the thin plate anode design additional pumping performance could be possible. Edge E-fields from the grounded screen and back side of the U-shape cathode are expected to have less effects on the penning cell's performance with increased number of plates. The tradeoff is of course decreased conductances.

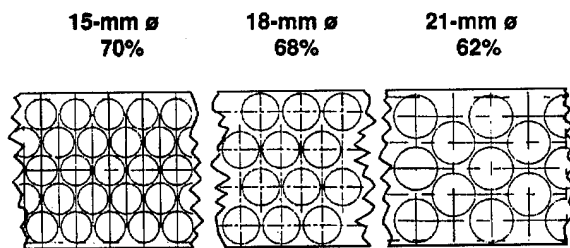


Figure 5 Three Anode Hole Patterns Tested

The results of pumping speed tests for the pre-production DIP prototype in non-uniform field are 160 l/s/module (module length 0.77m) or 206 l/s/m without the screen. Testing with the new screen have just started. Full production of this DIP design for the B-Factory HER will start as soon as the first production units are functionality tested within the first production dipole. This is expected to be completed early this summer.

Table 1
Measured Pumping Speed -"Old" CDR DIP Design

DIP Design		Gas Flow (torr-liters/sec)		
		5e-7	1e-6	5e-6
		Gas Pressure (torr)		
		~1e-8	~1e-8	~5e-8
		N ₂ Pumping Speed (liters/sec/m)		
7-PL-18	W/O SCR	184	186	186
		213*	205*	204*
7-PL-18	W SCR*	104	103	100
		122*	130*	122*
5-PL-21	W/O SCR	95	96	93
		100*	103*	102*
5-PL-15	W/O SCR	192	188	198
		217*	232*	243*

* Tested Day following High Gas Flow Conditioning of Module

** 4-SLOT Screen (2.5mm x 9cm x 10cm spacing with a 5mm depth)

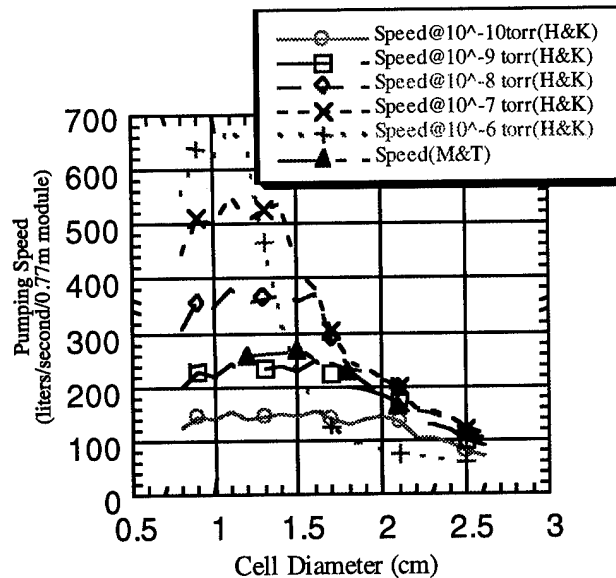


Figure 6 Plotted calculated curves for maximum pumping speeds for various cell sizes with a fixed anode width based on Hartwig-Kouptsidis[6] and Malev-Trachtenberg[7] for 0.18 T and 5500 volts

RESULTS AND SUMMARY

The result of 206 l/s/m for the final production DIP design has more than met the design goal of 180 l/s/m. We are presently in the process of testing the screen to assure a conductance of 450 l/s/m that will give us our design goal of 135 l/s/m for N₂ as the final distributed pumping system for the HER.

ACKNOWLEDGMENTS

The authors wish to thank Mike McDaniel, Vernon Williamson, Riley Martin, and Pete Tirapelle the designers for the DIPs. Eric Ziebarth, his co-workers in the Laser Processes and Sheet Metal Shops, Cleaning Specialists in Chris Steffani's Shop of MMED, Jim Bowman, Al Lopez and Philip Keenan for fabrication process step developments. Thanks also to Owen Alford for doing an extra nice job on the 3-D poster graphics.

REFERENCES

- [1] PEP-II, An Asymmetric B Factory, Conceptual Design Report, June 1993.
- [2] Test Results of Distributed Ion Pump Designs for the PEP-II Asymmetric B Factory Collider, EPAC 1994 European particle Accelerator Conference.
- [3] Test Results of a Combined Distributed Ion Pump/Non-evaporable Getter Pump Design Developed as a Proposed Alternate Pumping System for the PEP-II Asymmetric B-Factory Collider, PAC 1995 Particle Accelerator Conference
- [4] Y. Suetsugu and M. Nakagawa, Vacuum/Volume 42/1991, Great Britain
- [5] Distributed Ion Pump Testing for PEP-II, Asymmetric B-Factory Collider, PAC 1993 Particle Accelerator Conference
- [6] H. Hartwig and Kouptsidis, J. Vac. Sci. Technol., Vol 11, (6), 1974
- [7] M. D. Malev and E. M. Trachtenberg, Vacuum/volume 23/number 11, Pergamon Press Ltd, Great Britain.

DESIGN OF THE PEP-II LOW ENERGY RING VACUUM SYSTEM

D. Hunt, K. Kennedy, T. Stevens
Lawrence Berkeley Laboratory, Berkeley, CA 94720

I. INTRODUCTION

A vacuum system based on the antechamber approach is being designed for the PEP-II, B-factory, Low Energy Ring (LER) arc sections to be installed at the Stanford Linear Accelerator Center. Pressures in the six arc regions are to be less than 10 nanotorr at a nominal positron beam energy of 3.1 GeV and current of 3 amperes. The high energy and large beam current result in high gas loading due to photon induced gas desorption. The antechamber design allows 90% of the photons and over 99% of the synchrotron radiation power to be dumped on special photon stops away from the main beam chamber and close to vacuum pumps. The high photon flux at the stops gives the added benefit of quickly scrubbing these surfaces, further reducing the outgassing.*

Each of the six arc sections of the PEP-II ring contains 16 standard cells. Half of a standard cell is shown in Fig. 1. There are 192 of these half-cells in the LER arcs. Except for some variation in the arrangements of the magnets, the cells are identical. The arc regions represent 1460 meters of the total 2200 meter LER circumference.

The outside dimensions of the magnet chamber extrusion are limited by the magnet apertures. The height is kept to a minimum mainly to reduce the power requirements of the dipole magnets. A groove is provided in each side of the magnet chamber for the addition of tubular heaters if an in situ bakeout is needed. Water channels are also provided for cooling and temperature control.

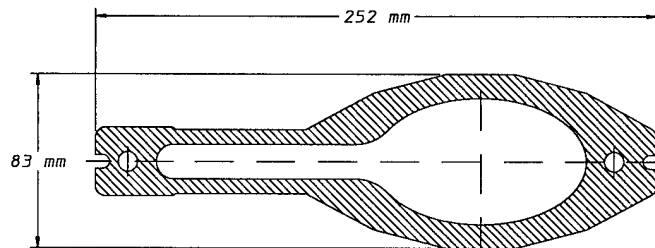


Fig. 2 Magnet chamber

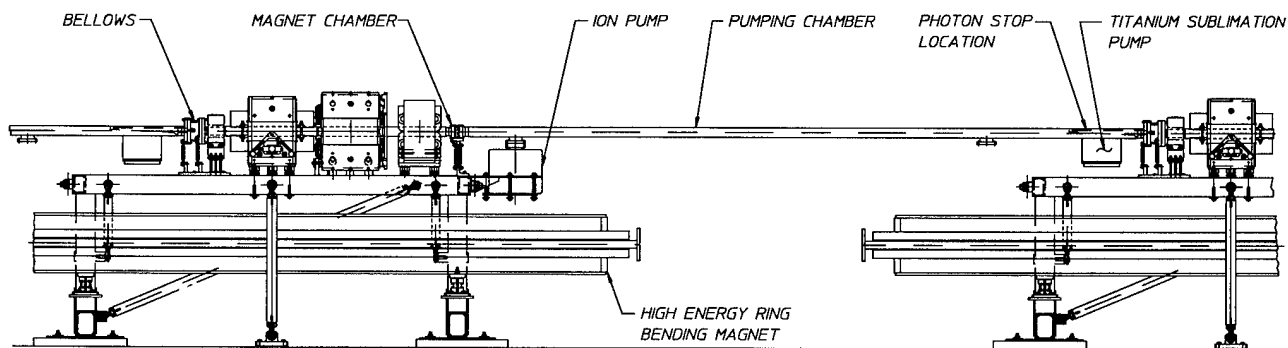


Fig. 1 Low Energy Ring Arc Half Cell

II. PUMPING AND MAGNET CHAMBERS

Each arc vacuum chamber will consist of a magnet chamber, a pumping chamber, and a bellows section. The magnet chamber (Fig. 2), which fits inside the magnets, will be two meters long. Due to limited access, there will be no pumping provided for the magnet chamber except through its ends. The slot height between the beam chamber and antechamber is a compromise between that which is allowed by beam dynamics and achieving maximum photon passage.

* Supported by the US Department of Energy under Contract number DE-AC03-76SF00098 (LBL) and DE-AC03-76SF00515 (SLAC)

The pumping chamber (Fig. 3), which contains the photon stop and pumps, will be about 5.5 meters long. The chambers will be extruded from 6063 aluminum alloy. The size of the chamber is limited by the extrusion industry limit. Finite-element temperature and stress analyses have determined that a photon beam hitting the beam channel wall due to the worst case beam misalignment will not damage the chamber.

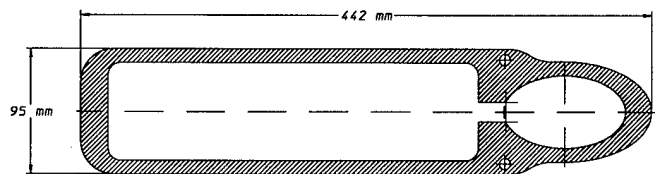


Fig. 3 Pumping chamber

To minimize costs, both chamber types have been designed using standard industry extrusion tolerances. Finite-element stress and deflection analyses for vacuum loading have verified the designs. Studies are under way currently to determine if an inner surface coating in the beam envelope is necessary to reduce secondary electron emission.

III. PHOTON STOP

At the design value of 3.5 GeV and 3 amperes, each dipole produces 15,000 watts of synchrotron radiation power, a power density of 5,700 watts per square centimeter (full width at half maximum) at a distance of six meters from the dipole. These photons are stopped by a water cooled, dispersion strengthened copper surface (Fig. 4) located at the downstream end of the pumping chamber. Water flows through multiple parallel channels 2 mm wide by 6 mm high, machined into the back side of this hot wall. To reduce the power density to the surface, the face of the photon stop is inclined at a small grazing incidence angle of 50 mrad. Besides the grazing angle, the length of the photon stop is determined by the slot height between the beam chamber and antechamber, and tolerances for the beam location, manufacturing, and alignment. The photon stops are a brazed assembly consisting of the dispersion strengthened copper hot wall, an intermediate copper wall to aid in the brazing, and a stainless steel back wall. Air guard channels open to the atmosphere will isolate the water channel braze joints from the vacuum wall to avoid the possibility of water leaking into the vacuum system.

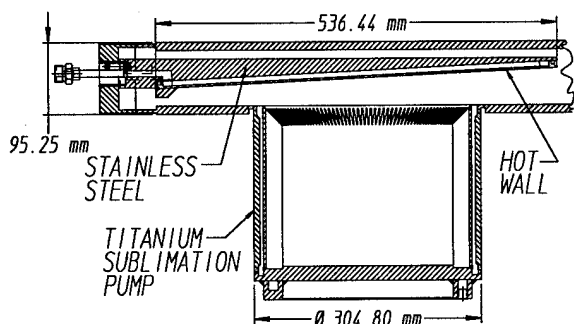


Fig. 4 Photon stop and TSP

IV. TITANIUM SUBLIMATION PUMP

Titanium sublimation pumps (TSPs) (Fig. 4) have been chosen to pump the photon stop region because of their high reliability, high pumping speed, and low cost. The TSP is located right under the photon stop and has a pumping speed of 8,000 liters per second. The active surface of the pump will be extruded from 6063 aluminum alloy. The face of these walls have deep grooves that increase the capture capability and capacity. The grooves increase the pumping surface by a factor of ten. The initial pumpdown of the chamber will be done with ion pumps. Once the major gas load is removed, the TSPs will be activated. After initial pumpdown, it is anticipated that the time between activations will be in excess of three months.

V. SCHEDULE

The contract for the magnet chamber extrusion has been awarded, ion pumps have been ordered, and the pumping chamber extrusion requests for quotations will be out within a month. Fabrication of the Low Energy Ring vacuum system is to be completed by the end of 1997. The PEP-II project is to be completed by the end of 1998.

THE VACUUM UPGRADE OF THE CERN PS AND PS BOOSTER

M. van Rooij, J.-P. Bertuzzi, M. Brouet, A. Burlet, C. Burnside, R. Gavaggio, L. Petty, A. Poncet, CERN

1. THE VACUUM SITUATION PRIOR TO 1990

The PS was designed and build in the mid 50ties and entered service in 1959. Vacuum was realised with some 100 pumping groups each one composed of a rotary pump and an oil diffusion pump. Most of the seals were made of elastomer materials. The pressures reached at that time were in the 10^{-4} Pa region. Besides the high pressure the bad influence on the beam of the heavy hydrocarbon molecules was detected and in the late 60ties the change to Ion Getter Pumps was made. This left of course much of the vacuum containment wall contaminated. It was only after the mid 80ties that all 100 magnets received new vacuum chambers made out of vacuum fired 316L+N stainless steel. Almost all seals used were by then made in metal; lead, aluminium or copper. Most of the big equipment tanks like for septa, or kickers were equipped with rectangular covers with vacuum seals made up out of a diamond shaped aluminium extrusion bend and welded in the appropriate form. The total installed pumping capacity with some 80 x 200 l/s and some 40 x 400 l/s gave the average pressure in the late 80ties in the 1×10^{-6} Pascal region under static conditions. By then also intensities of the particle beam had increased such that the created desorption due to proton losses and to synchrotron radiation from leptons gave rise to pressure flashes and increases by a factor of three.

The PS Booster was designed and build in the early 70ties with its 4 stacked rings each one with a length of a quarter of the PS circumference. The vacuum system was made of corrugated Inconel tubes in the magnets, the rest being mostly made of stainless steel 316L+N or 304L. The large amount of diagnostic, injection and ejection equipment for the 4 rings gave rise to high gas loads in the system. With its some 38 getter ion pumps, each one of 400 l/s the static pressure obtained was around 2×10^{-6} Pascal. Up to early in 1994 there was hardly any influence found from the circulating particle beams on that static pressure.

2. REQUIREMENTS OF THE HEAVY ION PROJECT

Around '87, '88 the requirements to vacuum in view of the acceleration of partially stripped lead ions were formulated for the PS and for the PSB. Based on earlier measurements [1] the aim was to improve the pressure in the PS by a factor of 5, and in the PSB by a factor of 10 with a gas composition of at least 50% of hydrogen in both machines. The difference between the 2 machines stems from the difference in the particle energies as well as from other factors like acceleration time. As formulated then, pressure was understood to be the sum of the partial pressures of the non-hydrogen components of the rest gas.

3. THE PROPOSED UPGRADE

In order to reach the required vacuum improvement, besides a general cleaning action, adding sublimation pumps and cryo pumps to the existing ion pumps was considered. There exists a CERN design of a Ti sublimation cartridge depositing Ti on the inside of a \varnothing 200 mm pump body along a length of some 150 mm. Connected with a proper conductance that gives a pumping speed around 600 l/s for air mixture at the beam tube. That would so roughly quadruple the pumping speed there. For the PS that would not be entirely sufficient, for the PSB a factor of more than 2 would still be missing.

The choice of cryo pumping to improve pressure in high outgassing areas was not retained, but improving the vacuum quality of the beam tubes and specially of the necessary equipment in tanks was considered to be a more economic approach, certainly point of view of later exploitation cost.

4. THE FIRST EVALUATIONS

In February '88 the first measurements were made in the PSB [2]. Four Ti-sublimation pumps, each one with an estimated pumping speed of 1200 l/s, were installed in a sector covering some 10 % of the circumference of the machine and containing the ejection septa. With those supplementary pumps activated an average pressure of 3×10^{-7} Pa was measured in the sector. The pressure measured in the tank where the ejection septa are installed, a high pressure area, was 1.3×10^{-6} Pa. In the same place the gas composition was measured, expressed here for some gases as pressure in % of the total pressure, see table 2, first column.

In 1991 a test stand composed of a standard 6 m long PS magnet vacuum chamber with a 200 l/s ion pump and a prototype 1200 l/s Ti-sublimation pump was assembled in order to measure also for that machine the effect of added pumping speed. Pressures in the 10^{-8} Pa range were attained, also in the middle of the vacuum chamber length.

5. THE DEFINED UPGRADE

Based on these preliminary results it was concluded that it would indeed not be needed to rebuild the complete vacuum system such that for instance it could be baked. In a first stage a proper cleaning limiting outgassing of existing beam tubes plus adding to each getter ion pump a Ti sublimation pump were estimated to give a low enough pressure to obtain a high enough transmission rate for the Lead Ion facility to be commissioned. Some optimisation of the distribution of pumping speed would give some improvement as well. column 2 in Table 2 gives an estimate of pressure that was

expected to be reached with these means in the PSB, with its rest gas composition. The table below gives an early estimate as it was made then of the needed equipment for such an upgrade in both machines. This equipment plus cost of installation foreseen in stage 1 for the PS and the PSB added up to over 10⁶ CHF. Not included is the expenditure for the Heavy Ion Linac itself.

Ti sublimation pumps complete	150
Ion getter pumps complete	20
Pressure measurement eq.	70
Rest gas analysing equipment	6
Roughing groups	6

- Table 1 -

A second stage [3] would comprise rebuilding equipment and their large rectangular vacuum tanks both in the PS and in the PSB to limit outgassing in order to obtain the highest possible ion transmissions within the general options taken. In the PS the most recent vacuum tanks containing equipment for Lepton injection were already designed to be round with dished end covers and copper wire seals allowing a soft bake in situ. This could reduce local outgassing rates by a factor of more than 10.

Before the execution of the upgrade programme started a complete homogeneous system of pressure measurement with Pirani-Penning gauges was installed in both machines to be able to follow and evaluate in steps the vacuum improvements. In December 93, before the first installations in the frame of the upgrade programme, a new mass scan was made in the PSB in a different and more representative place for the whole ring as a reference value, see table 2, column 3.

6. THE EXECUTION

Mechanical design and manufacturing

The design and manufacturing job started in 1990. Besides many small changes three main items were needed for the first stage. The existing vertical manifolds in the PSB interconnecting the 4 beam tubes were to be modified to accept besides the getter ion pump a sublimation pump body connection and a third connection for a second getter ion pump was foreseen. This would increase the safety factor in the case of one getter ion pump braking down. For the PS a manifold was designed that would interconnect the pumping manifold to the standard PS magnet vacuum chamber with a pump body for the sublimator and with the existing getter ion pump. Manufacturing of those items was farmed out via the CERN/MT division's production procurement services and via direct contacts with collaborating institutions. Extensive inspection and vacuum testing was done on all parts received before the installation was allowed.

Installation

It was estimated that the execution of this first stage would require altogether some 2 man years on top of the normal maintenance work force only for the foreseen dismantling, cleaning and installation work in this upgrade programme in the 2 machines. Installation started in the 1993 shut down and continued in '94 and '95. The foreseen interventions required sometimes simply installation of newly manufactured equipment but in other cases also each time in the 2 month period dismantling, modification, cleaning, testing and reinstallation of the equipment, for instance the adaptation of the existing manifolds in the PSB. This required a strict planning of the work to be done, also in view of radiation doses to the personnel.

Stage two

In the mean time some doubts had risen on the validity of some of the parameters used to come to the decisions. More precise measurements on loss of ions with well known pressure and rest gas compositions had confirmed that the initial presumptions were somewhat optimistic. Subsequent corrections showed that one could maintain the same philosophy as initially adopted, but one should really try to obtain the maximum improvement as foreseen. It required to include at least part of stage 2 foreseen for later years in the base programme. In the PS the redesign and replacement of the big square flanged equipment tanks was speeded up. New equipment tanks are now round and will allow a soft bake out in situ. In the PSB pumping speed was increased by adding 9 new vertical manifolds interconnecting the 4 vacuum tubes to the 30 existing ones, which were already foreseen to be modified. This also required the welcome sacrifice of 3 columns of 4 sector valves each. This gave a PSB machine with only 2 sectors, the injection-ejection area and the rest of the machine.

Now the upgrade programme is enlarged including now also new round copper sealed vacuum tanks in the PSB, a complicated and difficult design with the 4 stacked rings, besides the redesign and improvement of the vacuum quality of the equipment inside. Execution of this has started and will be implemented during the '96 and '97 machine shut downs.

7. CONTROLS

Ti-sublimation pumps power supply

A new design for the Ti-sublimator power supply was developed in order to obtain the maximum number of sublimations from a 2 mm ø Ti wire before break down. This requires to control precisely its temperature and therewith the sublimation rate since that varies strongly with the temperature and so with the heating current send through it. It was already known that the electron emission from the wire, when put at a negative polarisation voltage against the

surrounding volume, could be measured and used as a reference value [4]. The control unit reads that emission current I_e and adjusts then the heating current I_h through the wire so that it stays constant at a set value. At some 1410°C the wire emits an I_e of 10 mA in the given geometrical configuration. That will then correspond to a sublimation rate of some 40 mg/h of Ti. This current will be switched on with a smooth rise in order to prevent thermal shock and early break down of the wire. It will then stay at this high temperature for some 90 sec, depositing a few monolayers of fresh Ti on the inside of the pump body. This required also a special design of the sublimator cartridge with the 2 Ti wires insulated from ground and a central anode at ground potential. With the increasing number of sublimations the characteristics of the wire change, but the regulation system keeps the emission current and so also the sublimation rate constant. This will increase the possible number of sublimations from a single filament to up to above a thousand, and with the second filaments as spare, a lifetime of more than one year is guaranteed for the sublimator cartridge.

General control system

During the last 2 shut downs in a consolidation programme all HV power supplies for getter ion pumps were changed to eliminate PCB. The general control system in the 2 machines was also changed. Instead of the CAMAC system before now high power local VME crates (DSC's) that contain much of the programmes are controlled via Ethernet and can be accessed from work stations spread over the site. Sophisticated application programmes can be started there that will allow to switch on as needed groups of sublimators at preset intervals for a fixed number of times. In this way one aims for the best effect on the vacuum for a minimum of Ti consumption and so guarantee a maximum lifetime.

8. RESULTS

Pressure and gas composition measurements were made mainly in the PS Booster before any installation in the frame of the upgrade programme started, and also before, during and after the first Lead Ion injections into the PSB and PS. Due to pulsating magnetic and radio frequency fields it is difficult to measure pressure, and more so rest gas composition during operation of the machines. For this reason most measurements are made under static conditions, that means without those fields and so without beam. On the other hand it is important to know the dynamic behaviour of the vacuum, since during the super cycle, mostly in the PS, different types of particle beams circulate of which some have, due to their character or intensity, big influence on desorption and so on the pressure and therewith on the transmission of heavy ions in following cycle. Due to these circumstances it is extremely difficult to come forward with precise predictions on heavy ion transmission rates through these machines. With continuous and high repetition rate acquisitions and signal treatment one can nevertheless obtain for instance approximate rest gas

composition read outs from analysers and together with pressure readings calculate these rates, as presented in the table 2 below. The partial pressure percentages are based on quadrupole spectrometer measurements corrected for different instrument sensitivities. The bottom line shows an estimate of the transmission based on more recent measurements [5]. It is calculated with the help of a programme that derives from the pressure and the rest gas composition the density and the squared sum of all Z's which then together with the duration of the acceleration is used to obtain the apparently optimistic estimate of the transmission rate.

9. CONCLUSION

Up till end 1994 in the PSB work was concentrated on cleaning and the pumping capacity was considerably increased. In the PS mainly some equipment tanks were changed. This together with general care was sufficient to obtain a transmission rate good enough for commissioning, see column 4 in table 2. During this year 1995 the pumps in the PS will also be activated. This will allow to obtain assure good conditions for the Heavy Ion run in the second half of this year. Due to the character of the transmission phenomena and within the limits of the options taken a vacuum pressure improvement will always improve transmission. The execution of the rest of the upgrade programme will hopefully bring total transmission through the two machines well above 70%. This will depend also from decisions taken on the mode of operation of the machines, specially the types of particles and their intensity in the different cycles as well as their order in the train of the super cycle.

Date	Febr.'88	Febr.'88	Dec.'92	Dec.'94	Apr.'95
Pascal	1.3×10^{-6}	3.0×10^{-7}	1.8×10^{-6}	3.0×10^{-7}	3.1×10^{-7}
H ₂	73	80	74	82	89
CH ₄	1.5	2	2	0.3	1
H ₂ O	12.5	10	17.7	3	5
CO	-	-	4.5	2	-
N ₂	13	8	-	12	5
Ar	-	-	-	0.3	-
CO ₂	-	-	1.1	0.2	-
Transm.	0.31	0.68	0.13	0.65	0.73

- Table 2 -

- [1] Acceleration of Lead Ions in the CERN PS Booster and the CERN PS, at this conference. Horst Schoenauer et al.
- [2] Vacuum tests in the PSB with sublimation pumps. PS/ML-TN-88-10. M.Brouet, M. Bourgeois et A. Poncet
- [3] Upgrade of the PS vacuum system for Lead Ions. PS/ML-NI-87. A. Burlet et A. Poncet.
- [4] A study of a new method to control precisely the evaporation rate of Titanium sublimation pumps. CERN-ISR-VA/79-34. Pierre Strubin.
- [5] Private communications. O. Groebner, M. Schneider.

The Vacuum System for Insertion Devices at the Advanced Photon Source*

E.Trakhtenberg, E. Gluskin, P. Den Hartog, T. Klippert, G.Wiemerslage, and S. Xu,
Argonne National Laboratory, 9700 S Cass Avenue, Argonne, IL 60439 USA

Abstract

A vacuum system for the insertion devices at the Advanced Photon Source was designed, and chambers of this design were successfully manufactured and tested. Three different versions of the vacuum chamber have been developed with vertical apertures of 12 mm, 8 mm, and 5 mm, respectively. The chambers are fabricated by extruding 6063 aluminum alloy to form a tube with the desired internal shape and machining the exterior to finish dimensions. The wall thickness of the completed chamber at the beam orbit position is 1 mm. The design utilizes a rigid strongback that limits deflection of the chamber under vacuum despite the thin wall. Chambers with lengths of 2.2 m and 5.2 m have been fabricated. Pumping is accomplished by a combination of lumped and distributed non-evaporable getters and ion pumps. An ultimate pressure of $5.1 \cdot 10^{-11}$ torr was achieved with the 12-mm vertical aperture prototype. Alignment of the vacuum chamber on its support stand can be made with a precision of $\pm 25 \mu\text{m}$ in the vertical plane, which allows minimum insertion device pole gaps of 14.5 mm, 10.5 mm, and 7.5 mm.

I. INTRODUCTION

In order to meet requirements for the integration of the insertion device vacuum chamber (ID VC) as a part of the APS storage ring and to optimize the insertion device performance, the ID VC design must meet the following technical specifications:

vacuum pressure (e+ beam off)	$< 2 \times 10^{-10}$
vacuum pressure (e+ beam on)	$< 1 \times 10^{-9}$
horizontal aperture	51 mm (40 mm) (30 mm)
vertical aperture	$12 \pm .2 \text{ mm}$ ($8 \pm .2 \text{ mm}$) ($5 \pm .2 \text{ mm}$)
min VC wall thickness	$1 \pm .1 \text{ mm}$
total budget of "unflatness" over the 5.2 meter length	.5 mm

The vacuum wall thickness and the flatness are driven by the requirements of the insertion device performance at minimum magnetic gap.

While the vacuum requirements for the ID VC are the same as for the rest of the storage-ring vacuum system, the requirements for the mechanical structure are quite different. In particular, the vertical and horizontal apertures are much smaller than those for the SR VC. Also, the tight flatness tolerances must be met along the entire 5.2-meter length of the thin-walled ID VC. The SR VC does not require such tight flatness tolerances [1]. In order to meet these specifications, a new cross section (Fig. 1) for the ID VC was designed. The

new design is based on an approach termed "tolerances guidance," in which the thin-walled part of the ID VC will follow the thick body of the rest of the ID VC in all its deviations from a straight line.

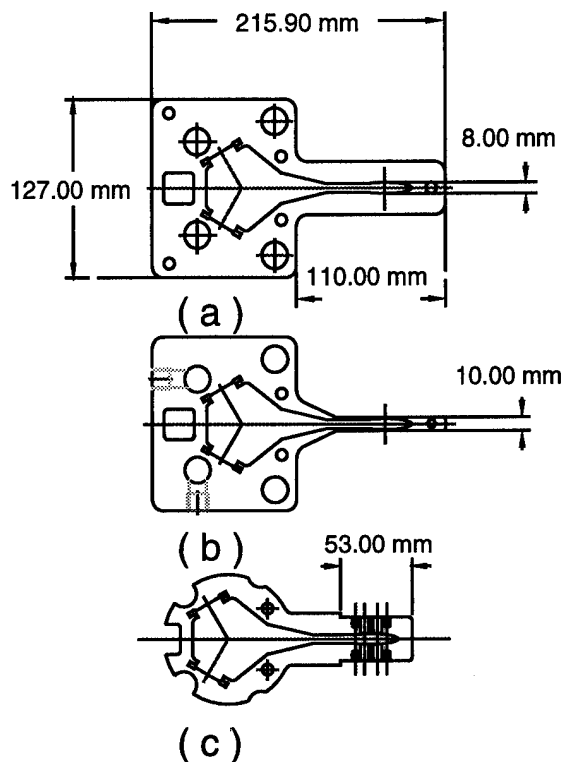


Figure 1. Cross-section of the 8-mm ID vacuum chamber. a) extrusion, b) after machining, c) end geometry showing the locations of beam position monitors.

II. FABRICATION

The manufacturing process for the ID VC consists of two major steps: an extrusion and a subsequent machining. The ID VC is extruded from the aluminum alloy 6063 T6 (as is the SR VC). The complicated pattern of this cross section results from the following requirements: first, uniform material flow in the extrusion process; second, rigidity of the ID VC with and without atmospheric pressure, and third, compatibility with thin-walled machining. The most critical dimension of the cross section is the opening on the right side where the positron beam moves through the ID magnetic field. The maximum deviation from the nominal dimension of 12 mm did not exceed $50 \mu\text{m}$ for 5 randomly selected extruded ID VCs. The machining brings the outside dimension down to $14\text{mm} \pm 100 \mu\text{m}$ along the 5.2-meter length.

*Work supported by U.S. Department of Energy, Office of Basic Energy Sciences, under Contract No. W-31-109-ENG-38.

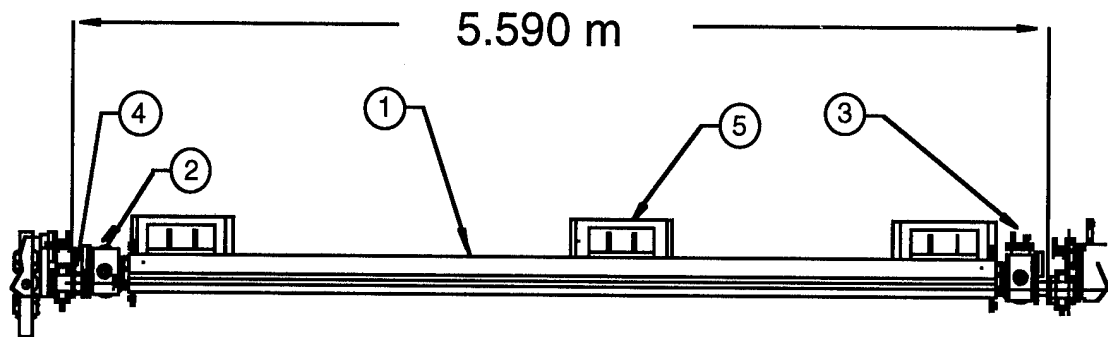


Figure 2. Layout of the 5m ID vacuum chamber. 1) ID chamber, 2) 3) stainless steel end box, 4) bellows, 5) support structure

An insertion-device vacuum system with a total length of 5590 mm will occupy an Advanced Photon Source (APS) storage ring straight section. Two configurations for the insertion-device vacuum system have been designed. The primary configuration will accommodate two insertion devices while the secondary will accommodate only one device in the APS straight section. We intend to use the secondary configuration only during the commissioning or where no future need for two insertion devices is foreseen. [2] The general layout of the first configuration is shown in Fig. 2.

The insertion devices vacuum system is placed between two UHV, all-metal valves. The ID VC is supported by three rigid stands equipped with alignment screws. Threaded holes with stainless steel inserts are used to attach the chamber to the brackets of the support stands. The total deviation of the thin-walled part of the vacuum chamber from the plane surface does not exceed 50 μm when it is installed on the support. During tests this alignment was maintained during hundreds of hours of observation in a room with a temperature variation of more than 2° C.

In order to achieve and control the required vacuum, the ID VC is equipped with a set of vacuum pumps and vacuum gauges. The total pumping capacity is achieved by combining two ~5 meter-long non-evaporable getter (NEG) strips with an average pumping speed of ~6 l/(sec cm), a 30 l/sec ion pump, and a 220 l/sec lumped NEG pump in each end box. The calculated results for the chosen geometry and pumping capacity are presented in Fig. 3 [3].

In addition to the pumps, the end boxes (Fig.4) also accommodate transition sections, an x-ray absorber, and vacuum analyzers. The transition section in the upstream box is a water-cooled copper block that provides a smooth transition between the aperture of the ID and SR vacuum chambers. The transition block in the downstream box is not water cooled. Both transition sections must be installed to avoid impedance mismatches which would effect the positron beam. The x-ray absorber is located in the downstream end box. It prevents the bending magnet synchrotron radiation from penetrating the vacuum valve. Thermal calculations show that, under relatively moderate cooling conditions, the temperature rise on the surface of the transition block or on the x-ray absorber does not exceed 110° C with a 300-mA positron

current in the storage ring and under maximum x-ray beam mis-steering.

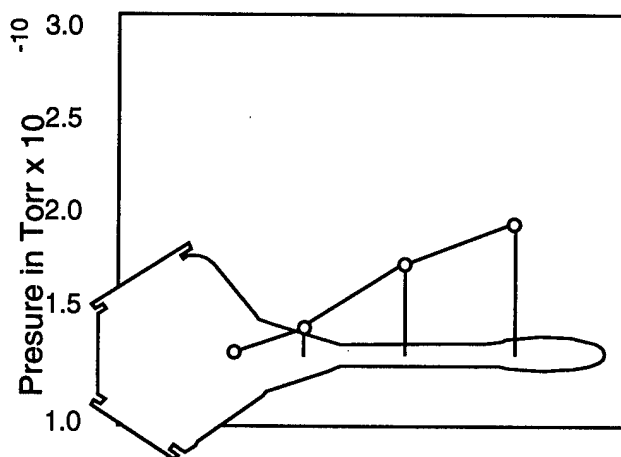
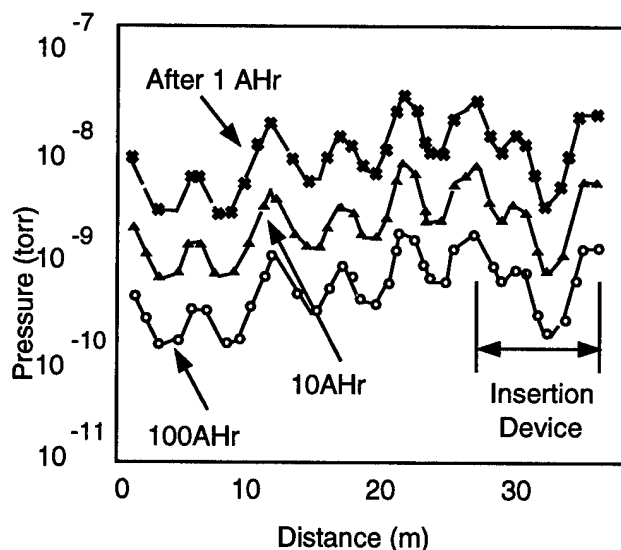


Figure 3. Pressure profile of storage ring sector showing the position of the insertion device vacuum chamber (top) and pressure profile within the 12 mm-aperture chamber.

One of the walls in each end box is made of a bimetal roll-bonded composite of stainless steel and aluminum alloy to simplify the welding of the end boxes to the vacuum chamber.

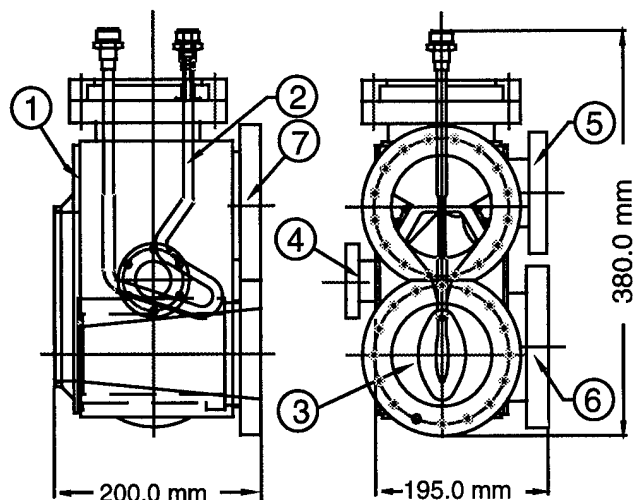


Figure 4. Vacuum end box. 1) bimetallic wall, 2) x-ray absorber, 3) rf transition, 4) diagnostic port, 5) and 6) pumping ports, 7) NEG feedthrough port.

Each vacuum chamber is machined to provide a smooth transition from the chamber aperture to the 12 mm aperture of the end box. This enables the use of a single end box design for the three different apertures of vacuum chambers.

In summary, the ID VC manufacturing procedure consists of the following set of steps:

- 1) extrusion of the 6-meter-long chamber with subsequent stretching to remove twist and bow;
- 2) additional straightening on a hydraulic press before machining;
- 3) machining the final cross section and to ready the ends for welding; also, machining of the precision platforms for the beam position monitor placement on both ends of the chamber;
- 4) manufacturing of both end boxes (in parallel);
- 5) welding the boxes to the vacuum chamber on an automatic welding machine.

Before welding the end boxes are cleaned and baked in a vacuum furnace at a temperature of up to the 300 degree C, followed by a leak test. After welding the whole vacuum chamber undergoes a thorough second cleaning[3], leak test, bakeout, and certification.

III. TESTING AND RESULTS

The standard baking procedure, including the NEG strip activation, usually takes three-four days after which the final pressure in the ID VC is $\leq 2 \times 10^{-10}$ Torr. To date, we have finished manufacturing, assembly, and certification of 7 ID VCs.

The measured maximum deflection of the thin-walled part of the ID VC under atmospheric pressure did not exceed 35 μm on each wall for the 12 mm and the 5 mm VC and about 50

microns for the 8 mm VC. These measurements are in a good agreement with the ANSYS calculations. The deflection increased only slightly, about 10 μm , after the bakeout and did not change afterwards. As mentioned above, the "straightness" specification was exceeded by an order of a magnitude; allowing smaller gaps of the APS insertion devices and extending their capabilities[4]. The ultimate vacuum achieved in ID VC was 5.1×10^{-11} torr. Hydrogen dominates in the residual gas spectrum in good agreement with the calculations and expectations.

There are at least two alternative approaches to the design of a small vertical aperture ID VC. One is to use a thin wall flexible stainless steel VC which is more expensive and also is much bulkier, especially on the ends. The other is to use a welded stainless steel VC as has been built at ESRF but it is very difficult to achieve the required flatness.

IV. ACKNOWLEDGMENTS

The authors are grateful to J. Noonan, G. Goepfner and G. Gagliano for their very valuable assistance; to J. Arko, K. Knoerzer and T. Robertson for their substantial contribution during prototype and serial manufacturing assembling and testing; to R. Piech for his contribution to the design.

- 1 G.A. Goepfner, "APS Storage Ring Vacuum Chamber Fabrication," American Institute of Physics Conference Proceedings No. 236, American Vacuum Society, Series 12, Argonne, IL 1990.
- 2 E. Trakhtenberg, E. Gluskin, and S. Xu, "The Vacuum System for Insertion Devices at the Advances Photon Source," Rev Sci, Instrum., 66, No. 2, Part 2, Feb 1995.
- 3 Chian Liu and John Noonan, "Advanced Photon Source Accelerator Ultrahigh Vacuum Guide," ANL/APS/TB-16, March 1994.
- 4 R. Dejus, B. Lai, E. Moog, and E. Gluskin, "Undulator A Characteristics and Specifications: Enhanced Capabilities," ANL/APS/TB-17, May 1994.

Test Results of a Combined Distributed Ion Pump/Non-Evaporable Getter Pump Design Developed as a Proposed Alternative Pumping System for the PEP-II Asymmetric B-Factory Collider*

F. R. Holdener, D. Behne, D. Hathaway, K. Kishiyama, M. Mugge, W. Stoeffl, and K. vanBibber
Lawrence Livermore National Laboratory, Livermore, CA 94550

C. Perkins, E. F. Daly, E. Hoyt, M. Hoyt, M. Nordby, J. Seeman, and D. Wright
Stanford Linear Accelerator Center, Stanford, CA 94309

ABSTRACT

We have built and tested an all-in-one combination plate-type distributed ion pump/non-evaporable getter pump design (DIP/NEG) considered as a proposed alternative pumping system for the PEP-II B-Factory High Energy Ring (HER). The DIP portion of the design used a Penning cell hole size of 12 mm in a mostly uniform magnetic field of 0.18 T. The NEG portion of the design used commercially available non-evaporable getter material type St-707TM[1]. A detailed description of the design is presented along with results of pumping speed measurements.

INTRODUCTION

Operation of the PEP-II Asymmetric B-Factory collider in the 9 GeV, 3 A mode or 12 GeV, 1 A mode places significant pumping speed requirements on the High Energy Ring (HER) vacuum pumping system design. The high gas loads generated by the intense photon synchrotron radiation fan striking the copper vacuum chamber wall necessitate a vacuum pumping scheme that maintains the required HER pressures.

Using a gas desorption coefficient (η) of 2×10^{-6} molecules/photon[1], the calculated gas load at 9 GeV, 3 A operation will be 1.06×10^{-6} Torr l/s/m. Average pressures required in the arcs are 10 nTorr at 3 A operation. The vacuum system of a typical arc cell as seen in Figure 1 consists of two 6 m long dipole vacuum chambers and two quadrupole chambers 2 m long each. The quadrupole chambers will be pumped with 60 l/s noble diode lumped ion pumps (LIPs). The dipole chamber at 6 m in length precludes pumping from the ends, thus distributed ion pumping is planned to offset the low conductance of the beam tube calculated at 40 l/s/m.

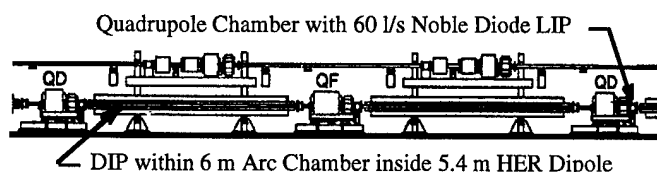


Figure 1. HER arc cell showing DIP location in 5.4 meter dipole

This alternate to distributed ion pumping alone was considered based on the known benefits that non-evaporable

getters have in pumping H_2 and CO . Concerns about the ability to handle the quantities of gas expected to be generated from the high photon fluxes and uncertainties of the gas desorption properties of the final chamber material, C10100 OF copper, precluded the sole use of non-evaporable gettering as the distributed pumping method in the arc sections of the HER. A distributed pumping speed of 135 l/s/m within the beam passage was calculated as adequate to achieve the pressure requirement in the arcs given the latest screen design of calculated conductance of 450 l/s/m.

PUMPING SYSTEM DESCRIPTION

To achieve this pumping speed, a combination pumping design, using a plate-type distributed ion pump mounted along side a radiation shielded pair of non-evaporable getter strips was prototyped and tested. The getter material is a patented commercially available product St-707TM[1] that consists of 70%Zr-25%V-5%Fe material that is mounted on 30 mm wide constantan strips. The NEG strips start active pumping after they are heated per manufacturer's recommendation. For this design with side-by-side strips roughly 85 A at 6 volts/meter was required to reach the recommended 450 C activation temperature. Figure 2 shows a photograph of 1/3 of the combined DIP/NEG prototype. As with the DIP-only design, described in detail in a separate paper presented at this conference[3], a plate-type anode was chosen, as this type is known to have relatively higher pumping speeds than that of the cylindrical type[4] i.e. the basic plate type design has a higher conductance over solid cylinders that allow gas to enter the cells only from the ends. The pump shown is located in a channel space 50 mm high by 83 mm wide adjacent to a 6 mm specially extruded and machined copper screen plate formed to the same shape as the far side of the beam tube. The 6 mm thick screen considered at the time consisted of a 4 parallel slot screen with 2.5 mm slots 9 cm long with 1 cm spaces.

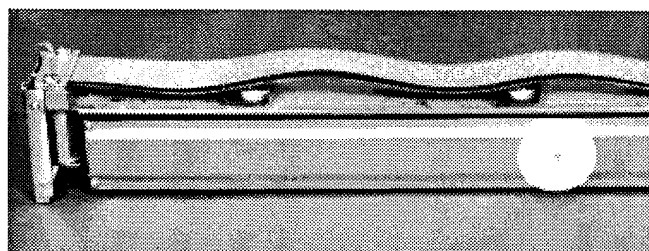


Figure 2. Photograph of DIP/NEG-RG Prototype

* This work was performed under the auspices of the U.S. Department of Energy by Lawrence Livermore National Laboratory and by Stanford Linear Accelerator Center under contracts W-7405-ENG-48(LLNL) and DE-AC03-76SF00515 (SLAC)

The DIP portion of the 1.1 meter long DIP/NEG design as shown in Figure 3 consists of a laser welded single piece 304 stainless steel anode (316L SS for production version) that has seven equally spaced plates. The seven plates are 0.38 mm (0.015 in) thick. The anode ends have S-springs 0.38 mm (0.015 in) thick that allow expansion as thermal loads heat it during operation at high pressures as well as during the initial 200 C dipole chamber bakeout. Possible future in-situ 95C bakes within the PEP tunnel will also be accommodated with this spring design. The same spring allows for thermal expansions and contractions during normal operations at low pressures within the PEP tunnel environment. To keep the anode from easily vibrating, it is attached by fasteners at the center to a 3 mm thick stainless steel NEG radiation shield that also serves as the central support structure for the entire DIP/NEG assembly. The anode holes are 12 mm in diameter in a closed packed array as seen in Figure 3. The side plates that hold the anode assembly together have been laser welded to the edges in a triangular bridge-type structure for stiffness. The entire sag of the anode was less than 0.025 mm (0.001 in) when supported only by the ends.

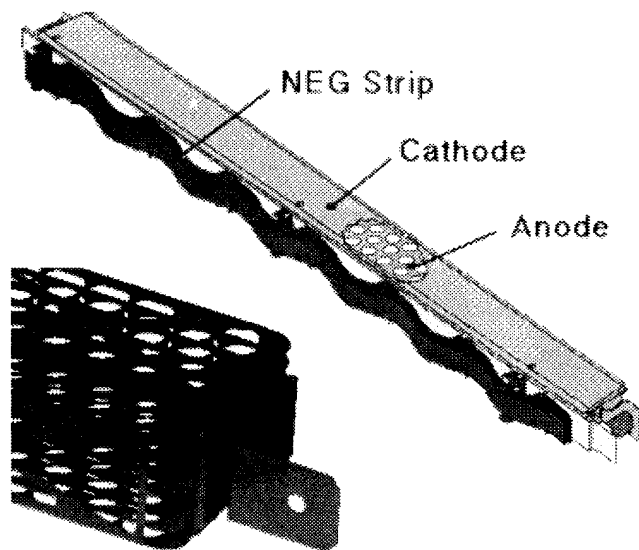


Figure 3. Isometric view of the DIP/NEG Design with a close-up of the Anode End with Thermal Expansion 'S'-spring

The original DIP/NEG design developed used a grounded titanium cathode with a positive hi-voltage anode, i.e. very common type diode-type ion pump. Concern was expressed, based on operation of other electron storage rings, that the DIPs could be injecting ion particles into the beam chamber that are sometimes 'trapped' by the beam causing beam lifetime problems[5]. To avoid this problem, a reversed ground, negative polarity diode ion pump design was used for prototyping and testing. This meant that the anodes are now grounded to the copper chamber and the cathodes are held at a negative high voltage. The new design is labeled a DIP/NEG-RG where the RG signifies reverse ground.

For the actual prototype, the module length remained at 1.1 meters because the laser welded anode stiffness allowed this length. This design minimizes the total number of insulators (basically one insulator per module plus one additional at the

end of a module string). Fewer insulators help to keep the I/P, DIP current/pressure value to a minimum which is of benefit when using the ion pump current as a localized method for measuring pressure in the HER. To make the cathode plates stiff enough and to maintain a nominal 4 mm clearance between all grounded surfaces, the cathodes were partially deformed as seen in Figure 4. The cathode ends were joined and made with fixed supports on the ends with special fastened/welded brackets. We also added two simple posts through the anode, but with adequate clearance at roughly 1/3 meter points along the cathode. The posts, at 6 mm (0.25 in) in diameter, eliminated three anode cells at these two support locations. On top and bottom of the cathodes, large, specially machined ceramics also proved to be necessary at the two post locations to maintain the cathodes minimum 3 mm high voltage clearances along its entire length. These ceramics basically made the largest span of any part of a single cathode plate only 1/3 of a meter. The box structure on the end of the cathodes was connected to a simple 19 mm diameter cylindrical shielded Steatite insulators via "S-springs" of flat 0.38 mm (0.015 in) 304 stainless steel to allow for thermal expansion along its length in the same way as the grounded anodes.

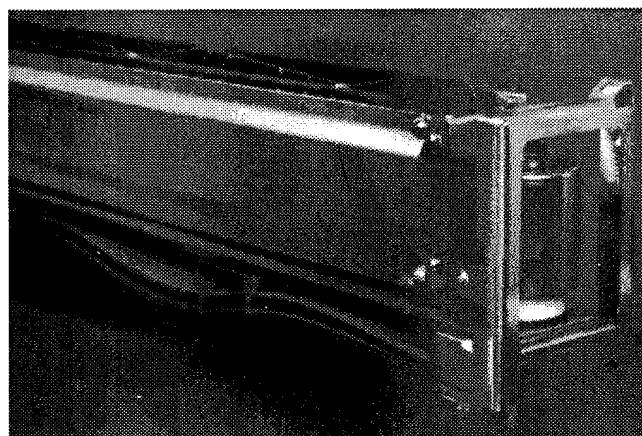


Figure 4. Close-up of DIP/NEG-RG showing Deformed Cathode

The NEG portion of the DIP/NEG-RG is mounted with specially designed electrically insulated stainless steel two-piece clips that snap together at the same time clamping the edges of the NEG strips as seen in Figure 2. Each clip is made to hold the NEG at two locations 25 mm apart to a set angle to force the parallel NEG strips to expand and contract without touching by approximating a 10 mm peak-to-peak (P-P) sine-wave pattern. In this way, during the large thermal growth only a 2 mm P-P increase occurs during initial activation and subsequent regenerations to 450 C. The NEG's can expand and contract without ever shorting out or touching on any other surfaces. Sliding surfaces as well as overheating is known to generate undesired particulates to be formed from the NEG strips which is minimized with this design.

ANODE AND CATHODE PREPARATION

The cathodes were baked to 800 C in a turbo pumped evacuated chamber at SLAC to remove the majority of the

Table 1. Measured Pumping Speeds for NEG-only, DIP-only and DIP/NEG-RG in the actual non uniform 0.18 T magnetic dipole field at different constant flows of N₂ and 80%H₂20%CO gases all with a 600 l/s/m 4-Slot Screen

Date	Test Type	Q(Orif) ~ 1.0 e-7 t/s		Q(Orif) ~ 5.0 e-7 t/s		Q(Orif) ~ 1.0 e-6 t/s		Q(Orif) ~ 5.0 e-6 t/s	
		Pbar (torr)	S (l/sec)	Pbar (torr)	S (l/sec)	Pbar (torr)	S (l/sec)	Pbar (torr)	S (l/sec)
6/2/94	NEG-only N2	1.4E-08	35	2.9E-08	37	5.4E-08	29	3.0E-07	23
	5 hr run w/wo turbo	1.3E-08	55	3.2E-08	33	5.6E-08	27	3.1E-07	19
6/3/94	NEG-Only N2					5.0E-08	60		
	5 hr run - NEG only					1.0E-07	20		
6/9/94	DIP-only N2 (Almost Dead NEG)	3.0E-09	54	8.3E-09	76	1.7E-08	85	6.1E-08	99
	5 hr run w/wo turbo	3.1E-09	52	8.5E-09	77	1.7E-08	84	5.9E-08	100
6/10/94	DIP-only N2 (Almost Dead NEG)	2.9E-09	60	7.6E-09	79	1.2E-08	90	4.6E-08	106
	5 hr run w/wo turbo	2.9E-09	60	7.4E-09	83	1.2E-08	91	4.4E-08	104
6/14/94	DIP/NEG Combination N2	3.0E-09	104	9.1E-09	112	1.6E-08	117	4.5E-08	125
	5 hr run wo turbo								
6/16/94	DIP/NEG Combination(DIP Cond)N2	2.3E-09	66	7.3E-09	94	1.2E-08	105	3.8E-08	120
	5 hr run wo turbo								
6/28/94	DIP/NEG Combination -N2	2.5E-09	63	6.3E-09	91	1.4E-08	99	4.7E-08	114
	5 hr run wo turbo	2.7E-09	68	6.8E-09	84	1.5E-08	99	4.7E-08	112
6/28/94	NEG-Only N2	1.2E-08	20	4.0E-08	14	7.0E-08	20	2.8E-07	17
6/29/94	DIP/NEG Comb-80%H ₂ /20%CO	2.9E-09	239	7.0E-09	240	1.4E-08	258	4.1E-08	294
	5 hr run wo turbo	3.2E-09	228	7.4E-09	239	1.4E-08	263	3.3E-08	308
	NEG-Only-80%H ₂ /20%CO	2.2E-08	77	4.2E-08	54	8.3E-08	47	2.6E-07	42
6/30/94	DIP/NEG Comb-80%H ₂ /20%CO	2.5E-09	396	7.2E-09	272	1.3E-08	282	4.2E-08	296
	5 hr run wo turbo	2.5E-09	387	7.6E-09	278	1.3E-08	282	3.7E-08	324
	NEG-Only-80%H ₂ /20%CO	2.2E-08	129	5.1E-08	47	9.3E-08	41	3.3E-07	35
7/1/94	DIP/NEG Comb-80%H ₂ /20%CO	2.2E-09	401	6.5E-09	273	1.1E-08	314	4.0E-08	333
	5 hr run wo turbo	2.3E-09	369	6.6E-09	305	1.2E-08	320	3.8E-08	363
	NEG-Only-80%H ₂ /20%CO	2.3E-08	213	4.8E-08	56	8.5E-08	47	3.3E-07	41

hydrogen. The Anode assembly was not prebaked for the prototype test, but was baked at the standard 200 C after installation inside of the DIP Test Stand at LLNL[6].

TESTING DESCRIPTION AND RESULTS

The NEG was activated/regenerated by heating to 450 C for typically a minimum of 1 hour while the system was pumped with a 1000 l/s turbo in the DIP test chamber at LLNL. The NEG immediately starts pumping upon activation. We quickly learned after doing the first NEG-only pumping speed measurements, that the best NEG activations occurred at lower vacuum pressures. Thus we were able to obtain better pumping speeds after several regenerations, gauge degas operations and system rebakes. In Table 1 is shown the results of several of the pumping speed measurements made. All of the tests for the NEG-only, DIP-only and DIP/NEG-RG combination were performed with N₂ and a gas mixture of 80%H₂20%CO.

RESULTS AND SUMMARY

The measurements show that the DIP/NEG-RG gave acceptable pumping speeds. The loss of DIP pumping speed by its reduced size was made up by the increased pumping speed of the NEG strips. The requirement to place a solid 3 mm stainless steel radiation shield between the NEG strips and the beam did however cause a decrease in conductance for the NEG's as was reflected in the measurements. Concern about: (1) the added cost of a more complex design, the NEG material and power supplies for the entire HER, (2) the added requirement of fairly frequent regenerations during initial startup and (3) the added risk of increased particulates from

the NEG strips resulted in a decision to use an optimized DIP-only design[3] and not the DIP/NEG-RG design for the actual distributed pumping system for the HER. The knowledge gained from these tests however have shown that the NEG material itself is the best candidate to date for pumping systems being developed for the interaction region (IR) as well as the wiggler sections of the Low Energy Ring (LER).

ACKNOWLEDGMENTS

The authors wish to thank Mike McDaniel, Vernon Williamson and Pete Tirapelle, the lead designers for the DIP/NEG as well as Eric Ziebarth and his co-workers in the Laser Processes Laboratory, Sheet Metal Fabrication Shops and Cleaning Specialists in Chris Steffani's of MMED. Rudy Carpenter, Al Lopez, Jim Bowman and Philip Keenan all played significant roles in the manufacturing and process step developments.

REFERENCES

- [1] St-707TM manufactured by SAES Getters, Via Gallarate, 215, 20151 Milano, Italy
- [2] PEP-II, An Asymmetric B Factory, Conceptual Design Report, June 1993.
- [3] Test Results of Pre-Production Prototype Distributed Ion Pump Design for the PEP-II Asymmetric B-Factory Collider, PAC 1995 Particle Accelerator Conference
- [4] Y. Suetsugu and M. Nakagawa, Vacuum/Volume 42/1991, Great Britain
- [5] Private Comm., Reinhard Brinkmann, DESY, to Mike Zisman, LBL, 11/22/93
- [6] Distributed Ion Pump Testing for PEP-II, Asymmetric B-Factory Collider, PAC 1993 Particle Accelerator Conference

Abe, H. FAP13, 1358
Abe, S. TAQ35, 1608
Abraham, W. WPA01, 902
Abramenko, N. RPR10, RPR15, 1143, 1155
Abramsky, P. WPP11, 1681
Adachi, Toshikazu TPR16, 3275
Adamski, J. FAA27, 248
Adamski, J.L. FAA28, 251
Adolphsen, C. WAG11, RPB03, RPB04, RPC01, RAE03, TPQ17, WAB07, WAC18, 646, 662, 665, 698, 2389, 2989, 3031, 3112
Adolphsen, Chris WAB08, 3034
Afanasiev, O. FAQ06, 1399
Agafonov, A.V. TPR13, TPR14, 3269, 3272
Ahrens, L.A. TAP11, TAP12, TAP13, WAB04, RAQ22, 378, 381, 383, 3022, 3334
Aizatsky, N.I. WPQ22, TPA14, 1773, 3229
Akai, K. FAE09, WPQ08, WPQ09, WPQ17, WPR05, WPR09, RPQ06, WAC08, 1503, 1735, 1738, 1759, 1797, 1806, 2675, 3085
Akasaka, N. RPA20, FAE09, WPQ09, WPQ17, WPR05, WPR09, TPC08, TPC29, TAG01, 1099, 1503, 1738, 1759, 1797, 1806, 2613, 2655, 2742
Akemoto, M. WPR02, WPR03, 1788, 1791
Akimov, V. WAA17, 1263
Akre, J. FAQ24, FAQ25, 1444, 1447
Akre, R. WPR15, WAB12, 1821, 3046
Alessi, J. WPC09, 1013
Alexahin, Y. RAA17, 560
Alexandrof, V.A. TAG01, 2742
Alimov, A. RPA19, 1096
Alimov, A.S. RAR04, 3361
Alinovsky, N.I. TAC06, 143
Allen, C.W. RPA24, 1111
Allen, Christopher K. MPC04, 2324
Allen, J. RAR23, 3406
Allen, L. WPA06, 917
Allen, M.A. WPQ06, 1729
Allen, Ray TPP13, 1645
Alley, R. MPE10, 887
Allison, Paul W. TAE08, 1207
Allison, S. RAE03, 2389
Alonso, Jose R. WPE01, 58
Alton, G.D. MPE05, WPC12, WAQ26, 871, 1022, 1897
Altuna, X. WAP12, WAP13, 464, 467
Amankath, H. RPA26, 1116
Amiranoff, F. WAG07, 634
Anderson, David E. TAE07, 1204
Anderson, K. WAQ22, WAR17, 1888, 1939
Ando, A. RPQ15, 2699
Andreev, V.G. WPP19, 1702
Andreev, V.V. FAC09, 2856
Andriishchin, A. FAQ06, 1399
Anerella, M. TPE04, FAQ04, 1293, 1396
Angerth, B. RPE02, 1999
Ankenbrandt, C. FAG06, 86
Anthouard, Ph. TAE09, 1210
Antonsen, T.M. WAG04, 621
Aoki, T. FAP13, 1358
Arai, S. RPG13, 351
Arbuzov, V. WPP11, 1681
Ardonceau, J. WAG07, 634
Argyakis, J. FAP03, 1328
Arinaga, M. RAB13, 779
Arnold, N. RPA11, RPA14, MPQ08, 1073, 1082, 2467
Asano, K. TPP03, TPP16, 1620, 1652
Ashton, J.R. RPB05, 668
Assadi, S. TAG10, RAP03, WAB01, 2777, 2886, 3016
Asseev, A.A. WAR23, 1955
Assmann, R. RAA19, WAG11, RPB02, 567, 646, 659
Astapov, A.A. RPE13, 2029
Auble, R.L. WAQ26, 1897
Auch, S. RPR06, 1131
Aune, B. WPB22, 998
Ausset, P. WPQ26, 1781
Austin, R.H. FAA19, FAA31, 234, 260
Autin, B. RPC11, WAE09, 722, 2178
Averill, R. RPG05, RAA31, 327, 600
Azorsky, N.I. TAQ34, 1605
Baartman, R. RPG12, WAQ07, WAC20, 348, 1858, 3119
Baba, T. WAQ06, 1855
Babzien, M. MPE11, 890
Backmor, Rudolf TAQ13, 1550
Bailey, J.D. TAP07, TAP08, TAP09, 366, 369, 372
Bailey, R. WAP12, WAP13, RAA11, 464, 467, 548
Bainan, Ding FAA26, 246
Baiod, R. FAP04, FAP06, FAP07, FAP09, MPB06, 1331, 1337, 1340, 1346, 2285
Bak, J.S. RPA06, 1061
Baker, S. WAR19, 1945
Bakker, R. RPG06, 330
Baklakov, B. TAA01, RAR30, 2078, 3424
Balakin, V. TAG01, 2742
Balewski, K. FAR07, 275
Balhan, B. RAA15, 557
Ball, M. TPB24, RAP21, RAP22, WAC12, RAQ23, RAQ24, 2583, 2934, 2937, 3094, 3337, 3340
Ballauff, M. FAR06, 272
Bamblevski, V.P. RPE13, 2029
Bane, K. RPA04, WAC17, 1058, 3109
Bane, K.L.F. RPA20, TPQ16, TPQ17, WAB07, WAC16, WAC18, 1099, 2986, 2989, 3031, 3105, 3112
Bangerter, R.O. WAQ04, 1852
Baptiste, K. TAR03, 801
Baranov, V.I. MPG10, WAR21, 426, 1949
Baranova, L.A. TAP16, 389
Barber, D.P. WPG08, 511
Bardy, J. TAE09, 1210
Barker, D. MPR13, 2265
Barklow, T. RPB01, 656
Barletta, W. TAA28, 2135
Barlow, T.A. TPC13, 2628
Barnard, J. TAR17, 837
Barnard, J.J. TAR14, TPB14, TPR18, 828, 2557, 3278
Barnard, John J. TPR02, 3241
Barnes, P. FAE13, WPQ02, RAQ04, 1515, 1720, 3294
Barov, N. WAG06, WPB11, 631, 976
Barr, D. MPQ03, RPQ16, TPQ19, 2452, 2702, 2992
Barry, W. RAE13, RPQ08, 2423, 2681
Barts, T. MPB10, 2294
Batchelor, K. MPE11, WPB13, RAE09, WXE03, TPB01, 890, 982, 2411, 2432, 2530
Batskikh, G. FAP24, 1387

Batskikh, G.I. RPR07, 1134
 Batygin, Y. WPC01, 1001
 Batygin, Y.K. TPR06, 3251
 Batygin, Yuri K. TPR07, 3254
 Beadle, Edward R. TPB08, TPB09, 2545, 2548
 Beauvais, P.-Y. RAG07, 3173
 Becher, D. MPE05, 871
 Bechstedt, U. TPB20, 2574
 Bechtold, V. FAR06, 272
 Becker, T. FAP02, 1325
 Becker, U. TAQ06, WAE13, 1533, 2190
 Beebe, E. WPC09, 1013
 Behne, D. MPP12, MPP20, 2064, 2075
 Beisel, U. WPA04, 911
 Bekefi, G. TPG14, RPC15, 192, 734
 Belkovets, V. TAC16, 152
 Beloglazov, V.I. TAE14, 1225
 Belomestnykh, S. FAE13, WPP11, RAQ04, RAR18, RAR19, 1515, 1681, 3294, 3391, 3394
 Belov, W. RAQ14, 3315
 Belova, Nadya G. WAA01, 1227
 Belser, C. RAA04, 530
 Belser, F.C. WPQ06, TAA22, 1729, 2129
 Belugin, V.M. RPR07, 1134
 Ben-Zvi, I. MPE11, WPB13, RAE09, WXE03, TPB01, 890, 982, 2411, 2432, 2530
 Benesch, J. FAE12, 1512
 Benjamin, J. TAP11, 378
 Benjegerdes, R. WPA01, FAP17, 902, 1369
 Bennett, L. TAE06, 1201
 Bennett, Lawrence F. TAE07, 1204
 Benson, S. FAG11, FAA25, WPA17, WPC24, 102, 243, 942, 1052
 Benvenuti, C. FAE11, TPP12, 1509, 1642
 Bercher, M. WAG07, 634
 Berenc, T. WPB06, 961
 Berezin, A.K. RAB15, 782
 Berg, J. TAA22, 2129
 Berg, J.S. FAB06, TPQ16, 2804, 2986
 Berg, J. Scott TPQ07, WAC05, 2962, 3076
 Berg, W. RPA11, MPQ10, 1073, 2473
 Berger, D.D. WPQ06, 1729
 Bergher, M. RAP19, 2928
 Berkelman, K. FAE13, 1515
 Bernal, Santiago TAA17, 2117
 Bernard, D. WAG07, 634
 Bernard, M. WPB01, WPB22, 945, 998
 Berridge, S. TAA28, 2135
 Bertagnolli, H. FAR06, 272
 Bertinelli, F. RPE02, 1999
 Bertolini, L. RAA03, 527
 Bertsche, K. TPE05, FAP21, WAQ09, MPQ21, TPB19, 1298, 1381, 1864, 2503, 2572
 Bertuzzi, J.-P. MPP15, 2069
 Berwald, D. RPR20, 1164
 Berz, Martin MPC09, 2336
 Bessonov, E.G. RAP06, 2895
 Beveridge, J.L. RPG12, 348
 Beyer, K.A. TPC13, 2628
 Bharadwaj, V. MPG02, WAP04, RPC20, RPC21, WPB08, TAG01, 396, 443, 749, 752, 967, 2742
 Bhat, C.M. FAP05, WAR02, TAA12, WAC06, 1334, 1903, 2105, 3079
 Bialowons, W. RPE08, 2017
 Bialy, J. FAR06, 272
 Bickley, M. MPA12, MPR19, 2220, 2276
 Bieniosek, F.M. WAR17, WAR18, 1939, 1942
 Biggs, J. FAP03, 1328
 Billen, J.H. RPR08, RPR09, 1137, 1140
 Billen, James H. MPB16, 2306
 Billing, M. FAE13, FAB12, TPA04, RAQ04, 1515, 2820, 3206, 3294
 Billing, M.G. RAE14, 2426
 Binns, B. WAA16, TPB04, 1260, 2536
 Birukov, I.N. RPR01, 1119
 Biryukov, V.M. MPG10, WAR20, WAR21, 426, 1948, 1949
 Biryukov, Valery WAR24, 1958
 Biscardi, R. TPP06, WPP03, 1626, 1660
 Bisognano, J. FAG11, FAA25, WPA17, 102, 243, 942
 Bisognano, J.J. RPQ11, 2690
 Bisognano, Joseph J. MPC25, RAG12, 2370, 3188
 Bizek, Hana M. RAR27, 3418
 Bjerklie, S. FAG06, 86
 Black, E. FAP03, 1328
 Black, W.M. TAE10, 1213
 Blanchard, R. WAP12, WAP13, 464, 467
 Blas, F. MPG09, 423
 Blaskiewicz, M. TAP11, TAP12, TAP13, WAC24, 378, 381, 383, 3131
 Blaskiewicz, M.M. RAQ22, 3334
 Blastos, J. TPG14, 192
 Blazhevich, S.V. FAG12, 105
 Bleser, E.J. TAP13, WAR13, 383, 1930
 Bloess, D. TPP12, 1642
 Blondel, A. RAA19, 567
 Bloom, E. WAQ15, 1876
 Blosser, H. RPG11, 345
 Bluem, H.P. TAA32, 2141
 Blum, E. FAR10, 284
 Blum, E.B. FAR01, MPQ01, 263, 2450
 Bocchetta, C. FAR06, 272
 Bocchetta, C.J. FAA13, FAR21, TAG05, 222, 309, 2762
 Boehnlein, D. FAG06, 86
 Boer-Rookhuizen, H. MPQ17, 2491
 Boers, Jack E. MPB18, 2312
 Bogacz, A. FAP05, WAR19, RAR17, 1334, 1945, 3388
 Bogacz, S.A. RAB20, TAR20, 790, 843
 Bogard, D. RAG07, 3173
 Bogaty, J.M. TPC12, 2625
 Bogdanovich, B. RPR10, RPR15, TAQ24, 1143, 1155, 1575
 Bogdanovich, B.Yu. TAB13, TAQ23, 125, 1572
 Böge, M. RAP08, 2901
 Bogert, D. MPG01, 391
 Bohl, T. WAP12, WAP13, RAA11, FAE10, 464, 467, 548, 1506
 Bohlen, H. FAE07, 1497
 Bohn, C.L. FAG11, 102
 Bojon, J.-P. RPE06, 2014
 Bolme, G.O. WPA08, RPR19, 923, 1161
 Bolotin, I. WPR19, 1833
 Bolser, C. MPC01, 2317
 Bonati, R. WAR11, 1924
 Bondarev, B.I. RPR07, 1134
 Bongardt, K. TPA01, TPA02,

TPA03, 3197, 3200, 3203
Boni, R. RPA26, 1116
Bonifacio, R. FAA12, 219
Bonin, B. TPP09, 1632
Bonnafond, C. TAE09, 1210
Bonnafond, Ch. TPC17, 2640
Bookwalter, V. MPR13, 2265
Borden, M. RAR23, 3406
Borland, M. FAR11, WAE11,
 MPQ10, 287, 2184, 2473
Borodich, A.I. TPA15, 3232
Bortnyansky, A. TAA18,
 2120
Bosch, R.A. FAR20, 306
Bosotti, A. TAA07, 2093
Bossard, P. MPG09, 423
Bossart, R. RPC10, 719
Bosser, J. RAP23, RAP24,
 2940, 2943
Bostic, D. MPP10, 2057
Bothe, W. FAR06, 272
Botman, J.I.M. WAQ19,
 WAQ20, RPP04, RPQ31, 1882,
 1885, 1970, 2738
Bourdon, J.C. WPB22, 998
Boussard, D. FAE10, TPP12,
 1506, 1642
Bowden, G.B. RPB04, RPA23,
 665, 1108
Bowers, J. WAC17, 3109
Bowling, B. MPR13, 2265
Bowling, B.A. WAE10, 2181
Bowling, S. RPR19, 1161
Boyd, John K. MPC13, 2339
Boyes, John D. TAE07, 1204
Bozoki, Eva RPQ14, 2696
Brabson, B. RAP21, RAQ23,
 RAQ24, 2934, 3337, 3340
Bracco, R. FAQ19, 1432
Bradley, S. RPG05, 327
Brandt, D. RAA17, RAA20,
 FAC03, 560, 570, 2841
Brauer, S.O. RPE09, 2020
Braun, A. RPC21, 752
Braun, H. RPC09, RPC10, 716,
 719
Brefeld, W. FAA02, FAR07,
 195, 275
Brennan, J.M. TAP11, TAP13,
 FAE05, MPQ30, RPQ17, RPQ25,
 WAB04, RAQ22, 378, 383,
 1489, 2518, 2705, 2723,
 3022, 3334
Bricault, P.G. RPG12, RPR02,
 RPR03, 348, 1122, 1125
Bridges, J.F. WPP16, 1693
Brillson, L.J. FAG11, 102
Brinker, F. FAA02, 195
Brinkmann, R. MPG04, RPB07,
 RPE08, 406, 674, 2017
Brodowski, J. WPP07, WPQ19,
 RPQ17, 1669, 1765, 2705
Brogle, R. WAG09, WPC20,
 640, 1039
Broome, W. TPP06, 1626
Brouet, M. MPP15, 2069
Brouzet, E. WAP13, 467
Browman, A. TAR12, TPB13,
 822, 2554
Brown, B. TPE05, 1298
Brown, B.C. FAP05, FAP06,
 FAP07, MPB05, MPB06, 1334,
 1337, 1340, 2282, 2285
Brown, D. TPB13, 2554
Brown, K. RPC06, MPR13,
 707, 2265
Brown, K.A. TPA06, 3212
Brown, Nathan RPR23, 1170
Brown, R. WPC08, 1010
Brown, V.W. WPA08, 923
Bruhwiller, D. RPR20, TPR07,
 1164, 3254
Bruhwiller, D.L. TPR08, 3257
Brunelle, P. FAR14, 293
Brunet, J.-C. RPE02, 1999
Brüning, O. TAG09, 2774
Brüning, O.S. MPG07, 420
Brunner, O. WPG09, 514
Bruns, Warner RPA15,
 RPA16, 1085, 1088
Bryant, P.J. RPG03, 322
Budilin, V. WPR19, 1833
Budnick, J. RAP21, RAQ23,
 RAQ24, 2934, 3337, 3340
Bugg, W. TAA28, 2135
Bugorsky, A.P. MPG10, 426
Buhler, S. WPB22, 998
Bula, C. TAA28, 2135
Bulfone, D. TPG11, FAR21,
 186, 309
Bulos, F. WAQ15, TAG01,
 1876, 2742
Bulyak, E. FAR17, TPA12,
 TPA13, 299, 3223, 3226
Buon, J. RPC20, TAG01, 749,
 2742
Burke, D. RPC01, RPC20,
 TAA08, WXE07, TAG01, 698,
 749, 2096, 2444, 2742
Burkhardt, H. WAP12, WAP13,
 RAA11, 464, 467, 548
Burlet, A. MPP15, 2069
Burnham, B. FAA08, RAA01,
 RAB22, MPA10, MPA11,
 MPQ06, FAC20, 213, 524, 796,
 2214, 2217, 2461, 2877
Burnside, C. MPP15, 2069
Burov, A. WAB16, WAB17,
 3055, 3058
Burrini, D. RAQ05, 3297
Burton, A. RAA15, 557
Bushuyev, A. WPP11, 1681
Bussa, M.P. WAP14, 470
Butteris, J. FAQ32, 1465
Buxton, W.E. MPA19, 2235
Byrd, J. RPC02, MPC01,
 RAE12, RAE13, RPQ08, TPQ16,
 701, 2317, 2420, 2423, 2681,
 2986
Byrd, J.M. WXE06, RPQ09,
 2441, 2684
Byrne, M. WPR15, 1821
Cable, M.D. TAR14, 828
Cai, Y. RAA22, RAA25, RAA26,
 RAA27, 576, 585, 588, 591
Cain, T.D. FAG05, 83
Calabrese, R. RAE05, 2399
Calame, J. TAQ17, 1561
Calame, J.P. TAQ18, TAQ19,
 1563, 1566
Calder, R. RPE02, 1999
Calish, S. TAR18, 840
Callahan, D.A. TAR14, TPR19,
 828, 3282
Callahan, Debra A. TPR01,
 3238
Callin, R.S. TAQ28, 1587
Camas, J. TPC21, 2649
Cameron, P. TAA09, 2099
Cameron, P.R. MPQ05, 2458
Campbell, R. WAA16, 1260
Capone, D. FAQ14, 1417
Caporaso, G. RPC16, MPE14,
 WPC16, WAA19, TAA20, 737,
 899, 1027, 1269, 2123
Cappi, R. TAP14, MPG09, 386,
 423
Carboni, G. WAP14, 470
Carder, B. WAA19, TAA20,
 1269, 2123
Cardman, L. FAG11, WPA17,
 102, 942
Cardman, L.S. WPC17, 1030
Cargnello, F. TPG11, 186
Carlier, E. RAA15, 557
Carlsten, Bruce E. WPB15,
 FAE06, 985, 1494
Carnegie, D.W. TPE08, 1310
Carrigan, D. WAR19, 1945
Carroll, Frank E. FAG04, 80
Carson, J.A. FAP06, FAP07,

1337, 1340
Carter, A. RPG05, 327
Carter, F. FAA08, RPA17, MPA11, 213, 1090, 2217
Caruette, A. TPP11, TPP14, 1639, 1648
Carwardine, J.A. WAA08, RPP03, RPQ18, 1242, 1967, 2708
Caryotakis, G. FAE07, 1497
Casella, R. RPP02, 1964
Caspers, F. RPE02, RAP24, 1999, 2943
Caspi, S. FAQ23, 1441
Cassel, R.L. WAR06, 1915
Castellano, M. TPG11, 186
Castillo, V. RPQ07, 2678
Castle, M. TAQ18, TAQ19, 1563, 1566
Castro, P. RAA20, FAC03, 570, 2841
Catras, P. TPG14, 192
Causyn, D.D. RAP21, RAQ23, RAQ24, 2934, 3337, 3340
Cayla, J.N. WPB01, 945
Celata, C.M. TPA10, 3220
Cevenini, F. TPG11, 186
Chae, Y.-C. TAP05, FAB09, 363, 2811
Chae, Yong-Chul TPQ20, TPQ21, RAR24, RAR25, 2995, 2998, 3409, 3412
Chamouard, P.-A. RAG07, 3173
Chan, A. TAR18, 840
Chan, K.C.D. FAA16, TAR12, 228, 822
Chanel, M. RAP24, 2943
Chang, C.H. FAQ26, 1450
Chang, H.P. FAA07, RAA24, TPQ10, 210, 582, 2971
Chang, L.H. FAA04, RAA24, FAQ26, TPQ08, 201, 582, 1450, 2965
Chang, Peace TAR04, 804
Chang, Y.M. MPQ32, 2524
Channell, P. WAC29, 3146
Chao, A. MPC01, WAC17, 2317, 3109
Chao, A.W. WAB09, WAB11, RAQ02, 3037, 3043, 3288
Chao, Alex FAC02, WAB10, 2838, 3040
Charruau, G. WPQ26, 1781
Chattopadhyay, S. TPG07, RPC16, TAA28, 174, 737, 2135
Chautard, F. RPC10, 719
Chavanne, J. TPE10, 1319
Chehab, R. WPB22, 998
Chen, B. WAB20, 3064
Chen, Bo WAB10, 3040
Chen, C.-I. TPC15, 2634
Chen, D. WAR19, 1945
Chen, J.R. FAA07, 210
Chen, J.S. MPR10, TPB29, 2256, 2592
Chen, Jenny MPR10, MPQ16, TPB29, 2256, 2488, 2592
Chen, P. RPC01, TAA28, RAP15, 698, 2135, 2919
Chen, Pisin RAQ18, 3326
Chen, R.-C. TPC15, 2634
Chen, S.C. MPE12, WPB03, WPB04, 893, 951, 954
Chen, T. RAA26, TAG06, RAP09, RAP11, RAP12, WAC17, 588, 2765, 2904, 2910, 2913, 3109
Chen, Y. RPC16, WPC16, WAA19, 737, 1027, 1269
Chen, Yinbao FAA21, RAQ25, RAQ26, 237, 3343, 3346
Cheng, J. TAQ18, TAQ19, 1563, 1566
Cheng, Wen-Hao RAG09, TPR12, 3179, 3266
Cheng, Y. FAA04, FAA07, 201, 210
Chepurinov, A. RPA19, 1096
Chepurinov, A.S. FAG12, RAR04, 105, 3361
Cherenshchikov, S.A. WPA15, WPA16, 938, 939
Chernikov, V.I. WAR09, 1918
Chernogubovsky, M.A. WPP04, 1663
Chertok, I. TPE09, 1316
Chertok, I.L. TAC06, 143
Chesnokov, Yu.A. MPG10, WAR20, WAR21, 426, 1948, 1949
Chester, N.S. FAP06, FAP07, 1337, 1340
Chiang, R. RAQ04, 3294
Chiaveri, E. FAE11, 1509
Chin, A. TPG07, 174
Chin, Y.H. TPC08, WAC07, WAC08, 2613, 3082, 3085
Chiou, T.C. RAB02, RAB08, 761, 773
Chirkov, P.N. FAB02, 2792
Cho, M.H. TAR07, RPA06, TAQ15, 813, 1061, 1556
Cho, Y. TAP05, TPQ22, TPQ23, 363, 3001, 3004
Cho, Y.S. FAA10, 216
Cho, Yanglai RAR25, 3412
Choi, J. TAR07, RPA06, 813, 1061
Choi, Sewan RPP11, 1985
Chojnacki, E. WPB11, WPB12, WPQ02, RAQ04, 976, 979, 1720, 3294
Chou, P.J. MPQ13, WAC09, WAC10, 2479, 3088, 3091
Chou, W. WAP02, WAP03, MPB10, TPQ15, 437, 440, 2294, 2983
Chowdhary, M. MPR14, RAE11, 2268, 2417
Chu, C.C. MPQ26, RAR05, 2515, 3364
Chu, C.-C. TPC15, 2634
Chu, W.T. RAE04, 2394
Chubar, O.V. RAE06, WXE08, 2402, 2447
Chubarov, O. RPA19, 1096
Chubarov, O.V. RAR04, 3361
Chumakov, S.N. TAC06, RPP08, 143, 1979
Chung, K.H. FAA10, 216
Chung, S.C. RAR05, 3364
Chung, Y. MPQ03, MPQ08, TPC03, RPQ15, RPQ16, 2452, 2467, 2598, 2699, 2702
Chupp, W. TPA10, 3220
Church, M. TAR16, 834
Church, Mike RPG07, 333
Ciardullo, D.J. MPQ30, 2518
Cieslik, W. MPQ11, 2476
Ciocci, F. TPG11, 186
Clark, D.C. WPA08, 923
Clark, G.S. RPG12, 348
Clarke, J.A. TPG09, WAC23, 180, 3128
Claus, J. FAP11, 1352
Claus, R. RAE12, RPQ01, RPQ05, 2420, 2660, 2672
Clayton, C. TPB18, 2569
Clayton, C.E. WAG08, RAB01, RAB02, RAB04, RAB05, 637, 758, 761, 767, 770
Clendenin, J. MPE10, WPC21, 887, 1043
Clendenin, J.E. MPE08, WPC18, 877, 1033
Cleveland, E.K. FAG05, 83
Cliff, B.E. TPC12, 2625
Cline, D. TAA28, 2135
Cline, D.B. TAB06, WPG11, RAB20, TAR21, 119, 520, 790

- Codutti, A.** FAQ19, 1432
- Colby, E.** WPB05, WPB08, 957, 967
- Colestock, P.** WPP01, RAP21, WAB01, RAQ24, 1655, 2934, 3016, 3340
- Colestock, P.L.** TAG04, WAC01, 2757, 3067
- Colestock, Patrick L.** WAC02, 3070
- Collier, P.** WAP12, WAP13, RAA10, RAA11, RAA12, RAA13, 464, 467, 545, 548, 551, 554
- Collins, J.** TPB24, 2583
- Colton, E.** WAC29, 3146
- Coluzza, C.** FAR06, 272
- Comunian, M.** RPC10, 719
- Conde, M.** WAG06, WPB08, WPB11, 631, 967, 976
- Conkling, C.R.** MPA16, 2226
- Connolly, R.** RPR19, WPP07, 1161, 1669
- Connolly, R.C.** RPR22, TPC06, 1167, 2607
- Cooper, R.** WAC29, 3146
- Cooper, Ronald** WPB15, 985
- Corbett, J.** RPQ21, RPQ22, RAQ17, 2714, 2717, 3323
- Corcoran, P.** TAE06, 1201
- Corlett, J.** RPC02, WPR14, MPC01, RAE12, RAE13, RPQ08, TPQ16, 701, 1818, 2317, 2420, 2423, 2681, 2986
- Corlett, J.N.** WXE06, 2441
- Corley, J.P.** TAE06, 1201
- Cornacchia, M.** FAA25, RAA18, RAQ17, 243, 564, 3323
- Cornelis, K.** WAP12, WAP13, RAA11, RAA17, RAA20, FAC03, 464, 467, 548, 560, 570, 2841
- Corredoura, P.** RPQ02, RPQ03, RPQ05, 2663, 2666, 2672
- Corsini, R.** RPC09, RPC11, 716, 722
- Corvin, C.** TAA16, 2114
- Cosso, R.** FAE11, 1509
- Couillaud, C.** RAG06, 3170
- Cours, A.** RPA11, 1073
- Cours, Alexander** TAQ16, 1559
- Coverdale, C.A.** RAB01, 758
- Cox, G.** WAG06, WPB11, 631, 976
- Craddock, M.K.** FAB14, 2823
- Craddock, W.** TAA28, 2135
- Crandall, K.R.** RPG10, 342
- Crane, G.** TAR18, 840
- Crawford, J.** WAP04, 443
- Crawford, K.** RPQ29, 2732
- Cremer, T.** FAP20, 1378
- Crofford, M.** WXE01, 2429
- Cromer, K.D.** RAP01, 2880
- Cros, B.** WAG07, 634
- Crosbie, E.** TAP05, RAA29, RAG05, 363, 597, 3167
- Crosbie, E.A.** RAR26, 3415
- Crowe, T.** TPC04, 2601
- Cruikshank, P.** RPE02, 1999
- Cutolo, A.** TPG11, 186
- Cyvoct, G.** MPG09, 423
- d'Amico, E.T.** RPC12, 725
- D'Auria, G.** TPG11, FAA13, FAR21, 186, 222, 309
- D'Ottavio, T.** MPR20, 2279
- D'Yachkov, M.** WAC20, 3119
- Daclon, F.** TPG11, FAR21, 186, 309
- Dalin, J.-M.** RPE02, 1999
- Daly, E.** TAA22, MPC01, 2129, 2317
- Daly, E.F.** MPP08, MPP10, MPP12, MPP20, 2051, 2057, 2064, 2075
- Dangor, A.E.** WAG08, 637
- Danilewsky, A.N.** FAR06, 272
- Danilov, O.** TAQ21, 1569
- Danly, B.G.** MPE12, 893
- Darrow, C.B.** WAG08, RAB01, 637, 758
- Datskov, V.I.** MPP01, 2034
- Dattoli, G.** TPG11, TPC03, 186, 2598
- Davies-White, W.** RAA04, 530
- Davis, P.** WPC20, RPA21, RPA22, 1039, 1102, 1105
- Dawson, J.** WAG09, TPC16, 640, 2637
- De Angelis, A.** TPG11, 186
- De Brion, J.P.** RAG06, 3170
- de Groen, P.** TAQ12, 1547
- de Jager, C.** RPG06, 330
- de Leeuw, R.W.** WAQ19, WAQ20, RPP04, RPQ31, 1882, 1885, 1970, 2738
- De Martinis, C.** TPC10, 2619
- De Mascureau, J.** TAE09, 1210
- De Rijk, G.** RAA11, 548
- de Rijk, G.** WAP12, WAP13, 464, 467
- de Wijs, M.C.J.** WAQ19, 1882
- Deadrick, F.** RPC18, TAR17, WPA02, TAE01, 743, 837, 905, 1178
- Deadrick, F.J.** TAR14, TPB14, 828, 2557
- DeBarger, S.** FAP16, 1366
- Debraine, A.** WAG07, 634
- Decker, C.D.** RAB01, RAB02, 758, 761
- Decker, F.J.** WAG11, RPB04, WAC17, 646, 665, 3109
- Decker, F.-J.** RPB02, WPR15, TPC20, RAP15, RAP16, RAP17, WAB05, WAB07, RAQ03, 659, 1821, 2646, 2919, 2922, 2925, 3025, 3031, 3291
- Decker, G.** FAR13, FAR19, MPQ03, MPQ08, MPQ10, RPQ16, 290, 303, 2452, 2467, 2473, 2702
- Decker, Glenn** RAR24, 3409
- Decking, W.** FAA02, FAB01, FAC19, 195, 2789, 2874
- DeCobert, J.** WAA16, 1260
- Degen, C.M.** TPB12, 2551
- Dehnel, M.** WAQ07, 1858
- Dehning, B.** WAP14, RAA19, 470, 567
- Deitinghoff, H.** WPA04, RPR06, RPR18, 911, 1131, 1158
- Dejus, R.** TPC03, 2598
- Delahaye, J.P.** RPC10, 719
- Delahaye, J.-P.** RPC09, 716
- delaRama, F.** TAE01, 1178
- Dell, G.F.** MPC05, FAB20, 2327, 2829
- Dellwo, J.** MPE05, WPC12, 871, 1022
- Delsart, Ph.** TAE09, 1210
- Deluen, J.-P.** RAA15, 557
- Demko, J.A.** MPP01, 2034
- Den Hartog, P.** MPP16, 2072
- Deng, D.** WAC24, 3131
- Deng, D.P.** WPP07, WPQ19, 1669, 1765
- Deng, D.-P.** MPB08, RAQ22, RAR29, 2288, 3334, 3421
- Deppe, G.** TPP11, 1639
- Derenchuk, V.** WPC08, RAP22, RAQ24, 1010, 2937, 3340
- Desavouret, E.** FAP06, FAP07, MPB06, 1337, 1340, 2285
- Desmons, M.** WPB22, 998
- Despe, O.** FAQ18, 1429
- Deviatilov, V.** WAA18, 1266
- Devlin, A.** TAE09, TPC17,

1210, 2640
Dewa, H. FAR08, RPA13, WAQ01, 278, 1079, 1843
Dey, J. WPP08, WPP09, WPP23, RAQ13, 1672, 1675, 1714, 3312
Di Bona, A. WPC23, 1049
Di Crescenzo, J. RAG06, 3170
Dickey, C. FAA08, RPA17, WAA10, MPA11, 213, 1090, 1248, 2217
Dieperink, J. RAA15, 557
Dieulot, J.M. WAG07, 634
Dikansky, N. WPG06, TAR11, 500, 819
Dikansky, N.S. TAC06, WAA17, 143, 1263
DiMarco, J. FAP06, FAP07, 1337, 1340
Dinehart, M.R. WAQ26, 1897
Dinkel, J. WAA05, WAR01, 1236, 1900
Dinkel, J.A. WAA07, 1239
Dipace, A. TPG11, 186
Diviacco, B. FAQ19, 1432
Dobbe, N. MPQ17, 2491
Dobbins, J.A. RAE14, 2426
Dobeck, N. RPP06, 1973
Dobrovodsky, J. TAA18, 2120
Dodson, G. RPG05, 327
Dohlus, M. RPB15, RPB16, TAQ06, WPP05, WAE13, MPC16, 692, 695, 1533, 1666, 2190, 2345
Doinikov, N. MPC21, 2359
Dolbilov, G.V. WAA20, TAQ34, 1272, 1605
Dolique, J.-M. TPR04, TPR05, 3245, 3248
Donald, M. RAA22, 576
Donald, M.H.R. RAA27, 591
Donaldson, A.R. RPB05, WAA11, WAR06, RPP07, 668, 1251, 1915, 1976
Donaldson, T. WAQ15, 1876
Dooling, J.C. RAQ16, 3320
Doolittle, L. MPR13, MPR14, 2265, 2268
Doornbos, J. RPG12, 348
Doose, C. TPE08, 1310
Doria, A. TPG11, 186
Douglas, D. FAA25, WAQ14, 243, 1873
Douglas, D.R. WXE01, 2429
Dovbnaya, A.N. WPA15, WPA16, WPB16, 938, 939, 988
Dow, K. RPG05, 327
Dowell, D.H. FAA27, FAA28, WPB20, 248, 251, 992
Dowling, D.T. TAP07, WAQ26, 366, 1897
Doyle, E. FAE07, 1497
Drago, A. RAE12, RPO01, 2420, 2660
Drees, A. RAA19, 567
Dressler, J. RAA03, 527
Drevlak, M. RPB14, 689
Drury, M. FAE12, 1512
Du, W. FAP01, 1322
Dugardin, F. TAB04, 116
Dunbar, A. WAB04, 3022
Dunham, B. MPR15, TPC07, 2271, 2610
Dunham, B.M. WPC17, 1030
Dunnam, C.R. RAE14, 2426
Dunning, F.B. WPC21, 1043
Durand, R. TPP04, WPQ02, 1623, 1720
Durfee III, C.G. WAG04, 621
Durieu, L. TAP14, 386
Durkin, A.P. RPR07, 1134
Dutto, G. RPG12, MPE03, WAQ07, 348, 864, 1858
Dykes, D.M. WPQ18, WAC22, 1762, 3125
Dylla, F. WPA17, 942
Dylla, H.F. FAG11, FAA25, 102, 243
Early, R. RPC02, 701
East, G. RAP21, RAP22, RAQ23, RAQ24, 2934, 2937, 3337, 3340
Ecklund, S. RPB01, RPC01, 656, 698
Ecklund, S.D. WPC18, 1033
Edighoffer, J. RPA26, 1116
Efimov, S. FAR17, RAA08, 299, 542
Egawa, K. RAA33, 603
Ehrlich, R. FAE13, 1515
Ehrlichmann, H. RPE08, 2017
Eichenberger, C. WAA19, 1269
Eichhorn, K.D. FAR06, 272
Eigenmann, B. FAR06, 272
Einfeld, D. TPG08, FAR06, WPQ24, 177, 272, 1776
Ekelöf, Tord TPC11, 2622
Elias, L.R. FAA29, 254
Elizondo, J. WAA19, TAA20, 1269, 2123
Elleauume, P. TPE10, 1319
Ellison, M. WPP20, WPP21, RAP21, RAP22, WAC12, RAG10, RAQ23, RAQ24, 1705, 1708, 2934, 2937, 3094, 3182, 3337, 3340
Ellison, T. TPB24, RAP22, 2583, 2937
Elsener, K. WAP14, 470
Emamian, M. FAA08, TAA02, 213, 2081
Emery, L. MPR01, MPB17, MPQ10, 2238, 2309, 2473
Emma, P. WAG11, RPB01, RPC03, RPC06, WAB07, 646, 656, 704, 707, 3031
Emma, Paul WAG01, 606
Emoto, T. TAQ08, 1539
Enchevich, I.B. WPP18, 1699
Engels, O. WPA04, WPA05, 911, 914
Engwall, D. FAG11, WPA17, 102, 942
Enjeti, Prasad N. RPP11, 1985
Enomoto, A. TAQ08, TAQ25, TAA04, 1539, 1578, 2087
Erdman, K. WAQ07, 1858
Eremeev, I.P. FAG10, TAC11, 98, 146
Erg, G.I. FAQ17, 1426
Erickson, R. RPA24, FAP16, 1111, 1366
Ermakov, D. RPA19, 1096
Ermakov, D.I. RAR04, 3361
Erochin, A. FAQ06, 1399
Escallier, J. FAQ03, 1393
Esin, S.K. RPR24, RPR25, RAE08, 1173, 1175, 2408
Estrin, B. WAA17, 1263
Etzkorn, F.J. WPQ26, 1781
Evans Jr., K. MPQ03, 2452
Evans, L.R. FPD04, 40
Everett, M. RAB05, 770
Everett, M.J. RAB04, 767
Evtushenko, Yu.A. FAQ17, 1426
Eyharts, Ph. TAE09, 1210
Eyl, P. TAE09, 1210
Eylon, S. TAR14, WPA02, WPA09, TAE01, TAE11, WAQ04, 828, 905, 926, 1178, 1216, 1852
Ezura, E. FAE09, TPP16, WPQ08, WPQ17, WPR05, WPR09, RPQ06, 1503, 1652, 1735, 1759, 1797, 1806, 2675
Fabris, A. FAR21, WPQ04,

TAG05, 309, 1723, 2762
Fabris, R. FAR21, 309
Fackler, O. RAA03, 527
Fahmie, M. RPQ08, 2681
Fainberg, Ya.B. RAB15, WAA02, WAA03, 782, 1230, 1233
Fallis, M.C. WPR20, 1835
Faltens, A. FAP17, FAP18, TPA10, 1369, 1372, 3220
Fan, T.C. FAQ26, 1450
Fang, C.S. MPQ32, 2524
Fang, S. MPR16, 2273
Fang, S.X. WAB20, 3064
Fang, Si J. FAP05, 1334
Fang, Ye TAR22, 850
Fant, K. WPR08, 1803
Farias, R.H.A. FAP14, 1361
Farkas, Z.D. WPR15, 1821
Farkhondeh, M. RPG05, 327
Farvacque, L. TPG05, 167
Farvid, A. MPP09, 2054
Fateev, A.A. WAA20, TAQ34, 1272, 1605
Fathizadeh, M. TAP05, 363
Faugeras, P. TPE03, 1288
Faugier, A. WAP12, WAP13, RAA11, 464, 467, 548
Faure, J. FAR14, 293
Fawley, W. FAP17, 1369
Fawley, W.M. FAA12, RAB03, FAP18, TPA10, 219, 764, 1372, 3220
Fazio, Michael V. FAE06, 1494
Fedin, O.L. M'G10, 426
Fedotov, A.P. RPR07, 1134
Fedotov, Alexei V. TPR12, 3266
Fedotov, Yu. MPR11, 2259
Feerick, B. WAQ15, 1876
Feldl, E. TPC04, 2601
Feldman, Donald W. WPB15, 985
Fellenz, B. MPQ13, 2479
Feng, W. WAR12, 1927
Feng, W.Q. WAA15, 1257
Ferdinand, R. RPR11, RAG07, 1146, 3173
Ferguson, M. RPP12, 1988
Ferianis, M. TPG11, FAR21, 186, 309
Feroli, F. WAP13, 467
Fernow, Richard MXG03, 53
Ferrario, M. WAC13, 3097
Feschenko, A.V. RAE08, 2408
Fessenden, R.W. TAB17, 131
Fessenden, T. TAR17, 837
Fessenden, T.J. TAR13, TAR14, TPB14, 825, 828, 2557
Fidecaro, G. WAP14, 470
Fieguth, T. WAQ15, 1876
Field, R. TAG01, 2742
Field, R.C. WXE07, 2444
Fietler, N. FAG09, 95
Filatov, B.A. WAA21, 1274
Filtz, M. MPC28, 2373
Fink, C.L. FAG14, 110
Fiorentini, G. WPB10, 973
Firjahn-Andersch, A. WPA03, 908
Fischer, C. RPC14, TPC21, 731, 2649
Fischer, Henk WAB06, 3028
Fischer, W. TAG07, 2768
Fisher, A. TPG14, RAA04, 192, 530
Fitzgerald, D. WPC10, WAC29, RAR23, 1016, 3146, 3406
Fitzgerald, J.B. TPG09, RAE10, 180, 2414
Flanz, J.B. RPE03, 2004
Flechtner, D. WPC19, 1036
Fleckner, K. RPA26, 1116
Fliflet, A.W. TAQ37, 1611
Flood, R. RPP13, 1991
Flora, R. WAE07, 2172
Flöttmann, K. TAA08, TAG01, 2096, 2742
Flynn, G. FAE13, RAR18, 1515, 3391
Fockler, J. WAA19, 1269
Foelsche, H. FAQ15, 1420
Foelsche, H.W. FAP11, 1352
Foley, M. FAG06, WPP01, 86, 1655
Fomin, M. WPP11, 1681
Fong, K. MPR16, 2273
Forest, E. RAA22, RAA25, FAB06, 576, 585, 2804
Forsyth, E.B. WAA15, WAR10, WAR12, 1257, 1921, 1927
Foster, G.W. MPG11, WAP16, TPE05, 428, 473, 1298
Foster, J. WPB06, 961
Foster, W.B. FAP21, 1381
Fouaidy, M. TPP09, TPP11, TPP14, 1632, 1639, 1648
Fougeron, C. WPQ26, 1781
Fowkes, W.R. FAE07, TAQ28, 1497, 1587
Fowler, W. MPG01, 391
Fox, J. RAA04, RAE12, RAE13, RPQ01, RPQ08, 530, 2420, 2423, 2660, 2681
Fox, T. MPR13, 2265
Frachon, D. FAQ17, FAQ18, 1426, 1429
Franks, R.M. WPQ06, 1729
Franzke, B. MPC15, 2342
Freund, A. WAP14, 470
Fricks, R. MPA11, 2217
Friedman, A. TAR14, TAR15, TAR17, FAQ17, TPR19, 828, 831, 837, 1426, 3282
Friedman, Aharon RPQ14, 2696
Friedrich, L. FAR06, 272
Friedsam, H. TAP05, TAA03, 363, 2084
Friesel, D. WPP20, WPP21, RAQ24, 1705, 1708, 3340
Friesel, D.L. RPG08, TAP03, WAQ08, 336, 357, 1861
Frisch, J. WAG11, MPE10, 646, 887
Fu, Shinian FAA21, RAQ25, RAQ26, 237, 3343, 3346
Fugitt, J. FAG11, FAA25, WPA17, RPQ30, 102, 243, 942, 2735
Fuja, R. RPA10, RPA11, MPQ08, MPQ10, 1070, 1073, 2467, 2473
Fuja, R.E. TPC01, 2595
Fujino, T. TPP07, 1629
Fujita, H. FAR08, RPA13, WAQ01, 278, 1079, 1843
Fukuma, H. RAA33, 603
Fukutomi, M. TPP16, 1652
Fullett, K. WAR17, WAR18, 1939, 1942
Funahashi, Y. TPP07, 1629
Funakoshi, Y. MPQ31, WAC08, 2521, 3085
Furman, M. RPC02, TPQ16, 701, 2986
Furman, Miguel A. RAP14, 2916
Furuya, T. TPP03, 1620
Fusellier, J. WAG07, WPB22, 634, 998
Gai, W. WAG06, WPB11, MPQ11, 631, 976, 2476
Galayda, J. RPQ16, 2702
Galayda, John N. MAD02, 4
Gallardo, Juan C. MXG03, WPB21, 53, 995
Gallerano, G.P. TPG11, 186
Gamo, N. TPP03, 1620
Ganetis, G. TPE04, FAQ02,

FAQ03, FAQ04, FAQ15, 1293,
1390, 1393, 1396, 1420
Ganetis, G.L. TAA09, 2099
Gangeluk, M. WPR13, 1815
Gao, J. RPA03, 1055
Gao, Jie WPQ01, 1717
Garcia, R.C. TPC06, 2607
Gardner, C.J. TAP11, TAP13,
378, 383
Garnett, R.W. RAG11, 3185
Garoby, R. MPG09, 423
Garosi, F. TPG11, 186
Garrel, N. WAP12, RAA15,
464, 557
Garren, A. WPG11, 520
Garren, A.A. TAB06, 119
Garvey, J.D. FAP06, FAP07,
1337, 1340
Garvey, T. WPA14, WPB22,
935, 998
Gavaggio, R. MPP15, 2069
Gavrilov, N.G. FAQ17, 1426
Gay, T. WPC21, 1043
Gayet, Ph. MPP02, 2037
Geisik, C. WPC10, 1016
Gelato, G. MPG09, 423
Gelfand, N.M. RAB19, 787
Gelfand, Norman M. WAP07,
452
Geller, J. WAR11, RPP02,
1924, 1964
Geng, X. MPA01, 2193
Genova, L. RAA04, 530
Georges, J.P. TAB04, 116
Georges, P. WPB01, 945
Geschonke, G. TPP12, 1642
Gevchuk, A. FAR17, 299
Ghiorso, W. TPA10, 3220
Ghosh, A. TPE04, FAQ03,
FAQ04, 1293, 1393, 1396
Giacuzzo, F. MPP04, 2042
Giannessi, L. TPG11, 186
Giannini, M. TPG11, FAR21,
186, 309
Gilgenbach, R.M. TAQ32,
1599
Gillespie, G.H. RPR20, 1164
Gillespie, George H. FAG13,
MPB14, 107, 2300
Gilpatrick, J.D. RPR19,
RPR22, TPB16, TPB22, 1161,
1167, 2563, 2580
Giordano, G. RPC17, 740
Giovannozzi, M. FAC06, 2847
Giove, D. TAA07, TPC10,
2093, 2619
Giovenale, E. TPG11, 186

Gladkikh, P. FAR17, 299
Glass, H. TPE05, 1298
Glass, H.D. FAP05, FAP06,
FAP07, MPB05, MPB06, 1334,
1337, 1340, 2282, 2285
Glazov, A. WPC13, WPR19,
1025, 1833
Glenn, J.W. TAP13, WAR13,
383, 1930
Glock, H.-W. RPB15, RPB16,
692, 695
Glover, E. TPG07, 174
Gluckstern, R. RPA04, 1058
Gluckstern, R.L. TPQ14, 2980
Gluckstern, Robert L.
RAG09, TPR11, TPR12, RAR12,
3179, 3263, 3266, 3376
Gluskin, E. TPE06, FAQ17,
MPP16, 1301, 1426, 2072
Goddard, B. RAA15, 557
Goderre, G. WAP08, 455
Goderre, G.P. WAP05, 446
Godfrey, G. WAQ15, 1876
Godlove, T.F. TAE10, 1213
Godlove, Terry F. TAA17,
2117
Godot, J.C. RPC10, 719
Goffeney, N. RPC17, 740
Gold, C. RPA10, 1070
Gold, S.H. TAQ37, 1611
Goldberg, D.A. WPQ13, 1747
Goldman, M.A. TAA09, 2099
Goldstein, J.C. FAA16, 228
Golkowski, Cz. TAQ01, 1518
Golubev, I.I. WAA20, 1272
Golubev, V. WPC03, 1004
Goncharov, A.D. TAC06,
RPP08, 143, 1979
Gonichon, J. MPE12, 893
Gonin, I.V. RPR01, 1119
Goral, J. RPA11, 1073
Gordeeva, M.A. MPG10, 426
Gordon, D. RAB04, RAB05,
767, 770
Gorelov, D.V. RPR01, 1119
Gorev, V.V. MPE06, 874
Gorin, M.Yu. WAR23, 1955
Gorniker, E. WPP11, 1681
Gorski, A. FAP03, 1328
Goto, A. WPC01, 1001
Gougnaud, F. WPB22, 998
Gournay, J.F. WPB22, 998
Govil, R. TPG07, RAB10, 174,
776
Gower, E. RPA26, 1116
Graber, J. FAE03, 1478
Gracia, J. RAA04, 530

Granatstein, V.L. TAQ17,
TAQ18, TAQ19, 1561, 1563,
1566
Gras, J.J. TPC21, 2649
Grassi, R. FAC06, 2847
Grau, M.C. MPQ05, 2458
Graves, W.S. FAQ13, 1414
Gray, E.R. RAG11, 3185
Green, M. WPG11, 520
Green, M.A. TAB06, 119
Greene, A. TPE04, FAQ03,
FAQ04, FAQ15, 1293, 1393,
1396, 1420
Greenly, John B. TAE07,
1204
Greenwald, Z. FAE13, TPA04,
1515, 3206
Grelick, A. RPA11, 1073
Grelick, A.E. RPA10, RPA14,
RPE09, 1070, 1082, 2020
Greth, V.N. WAR20, 1948
Gridasov, V. FAQ06, 1399
Grieser, M. RPR06, 1131
Grigor'ev, Yu.N. RAA07,
RAQ28, 539, 3349
Grimm, T. RPG11, 345
Grimmer, J. RPE09, 2020
Grishin, V.K. FAG12, FAA14,
105, 225
Gröbner, O. RPE02, 1999
Gromme, T. RAE03, 2389
Gross, G. WAR06, 1915
Grossberg, P. RAE03, 2389
Grosse-Wiesmann, P. RAA19,
567
Grote, D. TAR17, TAE01, 837,
1178
Grote, D.P. TAR13, TAR14,
TAR15, WPA09, TPR19, 825,
828, 831, 926, 3282
Grote, H. RAA19, 567
Grudiev, A. MPB09, 2291
Grunder, Hermann A. MAD01,
1
Gubin, K. WAA17, 1263
Guckel, H. WPE02, 63
Gudkov, K. RPA19, 1096
Gudkov, K.A. FAG12, 105
Guharay, Samar K. MPC04,
2324
Guidi, V. RAE05, 2399
Guignard, G. RPC09, RPC12,
RPC13, 716, 725, 728
Guinand, R. RAA15, 557
Guo, H. TAQ17, 1561
Guo, Z. TPQ03, 2955
Gupta, R. TPE04, FAQ04,

FAQ16, TAA09, 1293, 1396,
 1423, 2099
Gupta, R.C. WAP10, 461
Gur'yev, M.P. MPG10, 426
Gurov, G. MPG06, 416
Güsewell, D. MPP02, 2037
Gusinskii, G.M. TAP16, 389
Gustafson, Dick TPE05, 1298
Gustavsson, J. FAA08, 213
Guy, F.W. RPG10, 342
Gyr, M. WAP14, WAQ24, 470,
 1891
Haber, I. TAR15, TPR19, 831,
 3282
Haberichter, W. TPC16, 2637
Habib, Salman RAG01, 3149
Habs, D. RPR06, 1131
Haddock, C. FAQ14, 1417
Haebel, E. TPP12, 1642
Haffmans, A.F. RAG14,
 RAQ20, 3194, 3329
Hafizi, B. TAQ37, 1611
Haga, K. RPQ23, 2720
Hagedoorn, H.L. WAQ19,
 WAQ20, RPP04, RPQ31, 1882,
 1885, 1970, 2738
Hahn, H. TPQ02, 2952
Hahn, K.D. TPA10, 3220
Hahn, U. FAR07, 275
Haimson, J. RPC22, TAQ03,
 755, 1524
Hairapetian, G. WPC20,
 RPA21, RPA22, 1039, 1102,
 1105
Hakota, M. TAQ35, 1608
Hall, P.J. FAP06, FAP07,
 MPB06, 1337, 1340, 2285
Haller, M. FAR06, 272
Halling, M. RPC20, RPC21,
 TAG01, 749, 752, 2742
Hamilton, B. TPB24, RAP21,
 RAP22, RAQ24, 2583, 2934,
 2937, 3340
Hammel, E. TPB07, 2542
Han, Bumsoo TAB09, FAR03,
 122, 269
Han, D.H. WPR11, 1812
Hanna, B. WAR01, 1900
Hanna, S.M. RPA23, 1108
Hanne, G.F. WPC21, 1043
Haouat, G. RAG06, RAG07,
 3170, 3173
Hardek, T. WAC29, 3146
Hardek, T.W. TAQ31, 1596
Harding, D.J. FAP04, FAP05,
 FAP06, FAP07, FAP09, MPB05,
 MPB06, 1331, 1334, 1337,
 1340, 1346, 2282, 2285
Harkay, K. TAP05, TPQ22,
 TPQ23, 363, 3001, 3004
Harrison, M. MPG03, TAA09,
 401, 2099
Harrison, M.A. MPG12, 431
Hartill, D.L. RAE14, 2426
Hartley, R. FAA19, 234
Hartley, R.A. FAA31, 260
Hartman, S. RPB02, RPC20,
 WXE07, TAG01, 659, 749,
 2444, 2742
Hartman, S.C. RPB04, TPC29,
 665, 2655
Hartnagel, H.L. MPC15, 2342
Hartung, W. FAE13, TPA04,
 RAQ04, RAR18, RAR19, 1515,
 3206, 3294, 3391, 3394
Harwood, S.L. WXE01, 2429
Hasegawa, K. RPG09, 339
Haseroth, H. MPG09, 423
Haseroth, H.D. MPG05, 411
Hashimoto, S. FAQ21, 1438
Hathaway, D. MPP12, MPP20,
 2064, 2075
Hawkins, A. WAA16, 1260
Hayakawa, A. WXE07, 2444
Hayano, H. RPA20, WPR03,
 TPC05, TAG01, 1099, 1791,
 2604, 2742
Hayashi, E.K.C.S. MPQ33,
 2527
Hayashi, S. FAP13, 1358
Haynes, D.L. WAQ26, TPC18,
 1897, 2643
Haynes, W. Brian FAE06,
 1494
Hays, S. WAE07, 2172
Hays, T. FAE13, TPP02,
 WPQ02, 1515, 1617, 1720
Hayward, T.D. FAA27, FAA28,
 WPB20, 248, 251, 992
Hedblom, K. WPP20, WPP21,
 WAQ08, RAP21, 1705, 1708,
 1861, 2934
Heese, R. FAR10, 284
Heifets, S. MPC01, MPC08,
 TPQ16, 2317, 2333, 2986
Heifets, S.A. TAA22, MPC02,
 MPC03, MPC18, 2129, 2319,
 2321, 2351
Heim, J. RAA03, 527
Heimlinger, G. TAG01, 2742
Heine, E. TAQ12, MPQ17,
 1547, 2491
Heinrichs, G. TPB20, 2574
Helm, R. RAA22, RPC06,
 RPC07, RPC20, TAA08, TAG01,
 576, 707, 710, 749, 2096,
 2742
Helvajian, H. FAG11, 102
Hemelsoet, G.H. WAE09, 2178
Hémery, J.-Y. TAP14, 386
Hemmer, M.F. TAA09, 2099
Henderson, S. FAE13, 1515
Henderson, T. FAP01, 1322
Hendrickson, L. RAE03, 2389
Hendrickson, L.J. WAG11,
 RPB03, 646, 662
Henestroza, E. RPC16, RPC17,
 RPC19, WPA02, WPA09, TAE01,
 TAE11, MPC01, MPC08, TPA10,
 737, 740, 746, 905, 926,
 1178, 1216, 2317, 2333, 3220
Henke, H. TAQ30, WPQ14,
 WAB11, 1593, 1750, 3043
Henkel, D.P. FAG11, 102
Hentges, M. MPP01, 2034
Herold, W. WPA12, 929
Herr, W. WAP14, WPG09, 470,
 514
Herrup, D.A. TPQ25, TPQ26,
 3007, 3010
Hershcovitch, A. WPC09,
 1013
Herz, P. TPB07, 2542
Hettel, R. MPQ22, RPQ21,
 RPQ22, 2506, 2714, 2717
Heutenik, B. TAQ12, 1547
Heydari, Huschang WAP09,
 458
Higashi, Y. WPQ15, 1753
Higgins, D.S.G. WPQ18, 1762
Higgins, S. MPR13, 2265
Higo, T. FAQ08, WPQ15,
 WPR02, WPR03, 1405, 1753,
 1788, 1791
Higo, Toshiyasu FAE02, 1474
Higuchi, A. RAQ06, 3300
Higuchi, T. TPP07, 1629
Hilaire, A. WAP12, WAP13,
 464, 467
Hill, B.W. RPR20, 1164
Hill, Barrey W. MPB14, 2300
Hill, S.F. WAC21, 3122
Hilleret, N. TPP12, 1642
Himel, T. RAE03, 2389
Hindi, H. RAE12, 2420
Hinode, F. WPQ16, WPR02,
 WPR03, TPC05, 1756, 1788,
 1791, 2604
Hipple, R. WPA01, TAE01,
 902, 1178
Hiramoto, K. TAB03, WPQ21,

113, 1770
Hirano, K. TAQ08, 1539
Hirata, K. RAP02, 2883
Hirata, Y. WPR02, 1788
Hirota, J.I. TAB03, WPQ21, 113, 1770
Hizanidis, K. RAQ01, 3285
Ho, C. WPB11, 976
Ho, C.H. WPB07, 964
Hoag, H. RPA04, WPQ05, 1058, 1726
Hoag, H.A. RPA23, 1108
Hobson, B. RAA03, 527
Hodges, T. RPG12, 348
Hodgkins, D. MPE04, WPA08, 867, 923
Hodgson, J. WPR08, 1803
Hoeflich, J. RAE12, 2420
Hoffstätter, G.H. FAB07, 2807
Hofler, A. MPR13, 2265
Hofmann, A. RAA17, RAA18, RAA20, FAC03, 560, 564, 570, 2841
Hogan, B. TAQ18, TAQ19, 1563, 1566
Hogan, M. FAA23, RPA21, RPA22, 240, 1102, 1105
Hogrefe, R. TPE08, 1310
Hohbach, R. TAQ33, 1602
Holdener, F.R. MPP12, MPP20, TAA22, 2064, 2075, 2129
Holmes, C. WAA19, 1269
Holmes, S. MPG01, 391
Holmes, S.D. WAP01, 434
Holmquist, T. RAE14, 2426
Holsinger, R.F. TPE07, 1305
Holt, J. RPC20, 749
Holt, J.A. WAP01, WAP08, RPC21, TAG01, WAC01, 434, 455, 752, 2742, 3067
Holtkamp, N. FAR06, RPB12, RPB13, RPB15, RPB16, WPA12, WPP05, MPC16, 272, 683, 686, 692, 695, 929, 1666, 2345
Holtzapfel, R.L. WXE05, WAB05, WAC04, WAC17, 2438, 3025, 3073, 3109
Honda, T. RPQ23, 2720
Honecker, V. FAR06, 272
Hopster, H. WPC21, 1043
Horan, D. TAP05, RPP12, 363, 1988
Hori, T. WPC22, MPA07, 1046, 2208
Houck, T. RPC16, RPC17, WPC16, 737, 740, 1027
Houck, T.L. TAQ03, 1524
Hovater, C. FAE12, TPC26, RPQ29, 1512, 2652, 2732
Howell, J. TAR08, 816
Hower, N. FAA08, RPA17, TAA02, MPQ06, 213, 1090, 2081, 2461
Hower, Nelson WPA13, 932
Hoyer, E. FAQ24, FAQ25, 1444, 1447
Hoyt, E. MPP09, MPP12, MPP20, 2054, 2064, 2075
Hoyt, M. MPP09, MPP12, MPP20, 2054, 2064, 2075
Hseuh, H.C. TAP11, TAP12, MPP11, 378, 381, 2060
Hsieh, H. RAA05, RPA26, 533, 1116
Hsiung, G.-Y. TPC15, 2634
Hsu, I. TAA28, 2135
Hsu, Ian MPQ26, TPC15, RAR05, 2515, 2634, 3364
Hsu, K.T. FAA04, FAA07, RAA23, RAA24, MPR10, MPQ16, MPQ19, MPQ32, TPB29, TPQ08, TPQ09, TPQ10, 201, 210, 579, 582, 2256, 2488, 2497, 2524, 2592, 2965, 2968, 2971
Hsu, R.-C. TPC15, 2634
Hsu, S.Y. WPB07, 964
Hsue, C.S. RAA24, TAR04, TPQ09, TPQ10, 582, 804, 2968, 2971
Huang, Gloria MPR10, 2256
Huang, H. TPA06, 3212
Huang, J.Y. TPG06, 171
Huang, N. RAA21, WAC27, 573, 3140
Huang, Zhibin FAA21, RAQ25, RAQ26, 237, 3343, 3346
Huang, Zhirong RAQ18, 3326
Huffman, G. FAE07, 1497
Hughes, Thomas P. TAE08, 1207
Hülsmann, P. RPB15, RPB16, 692, 695
Humbert, J. FAP03, 1328
Hümmer, K. FAR06, 272
Humphries, D. FAQ24, FAQ25, 1444, 1447
Hunt, D. MPP13, 2067
Hustache, R. WAP14, 470
Hutson, R. WAC29, 3146
Hutson, R.L. TAR12, 822
Huttel, E. FAR06, 272
Hutton, A. TPC26, 2652
Hwang, J.I. WPB07, 964
Hwang, O.H. TAQ14, 1553
Hwu, K.H. MPQ19, 2497
Iazzourene, F. FAR21, TAG05, 309, 2762
Ieiri, Takao TPB17, 2566
Igarashi, Y. TAQ25, 1578
Igarashi, Z. WPC07, 1007
Ignatyev, A. TAB13, TAQ23, TAQ24, 125, 1572, 1575
Ihloff, E. RPG05, 327
Iida, S. TPP03, 1620
Ikegami, K. WPC07, 1007
Ikegami, M. FAR08, RPA13, WAQ01, 278, 1079, 1843
Ijginov, A.N. RPR01, 1119
Imai, Y. FAQ08, 1405
Imanishi, A. RPG13, 351
Imel, G.R. TAC12, 149
Inagaki, S. TPP16, 1652
Inaguchi, T. FAQ08, 1405
Ingalls, W. WPC10, 1016
Ingwersen, Pete TAE07, 1204
Inman, T.K. RPA24, 1111
Ino, H. RPG09, 339
Inoue, H. TPP07, 1629
Inoue, M. FAR08, RPA13, RPA18, WPQ21, WAQ01, 278, 1079, 1093, 1770, 1843
Irwin, J. RAA22, RAA25, RAA26, RAA27, RPC01, RPC06, RPC07, RPC08, RPC20, TAA08, TAG01, TAG06, FAC18, RAP09, RAP11, RAP12, 576, 585, 588, 591, 698, 707, 710, 713, 749, 2096, 2742, 2765, 2871, 2904, 2910, 2913
Irwin, John MPC31, 2376
Irwin, M. WPQ13, 1747
Isagawa, S. TPP16, 1652
Ishi, Y. TAP04, TPP03, 360, 1620
Ishida, T. MPQ18, 2494
Ishihara, N. TAG01, 2742
Ishii, H. MPQ31, 2521
Ishkhanov, B. RPA19, 1096
Ishkhanov, B.S. FAG12, FAA14, 105, 225
Issinsky, I.B. WAR09, FAC12, 1918, 2863
Ito, I. TAQ35, 1608
Ito, N. RPG09, 339
Itoh, Y. MPA07, 2208
Ivanov, A. TAC16, 152
Ivanov, A.A. WAR20, 1948
Ivanov, A.S. TAE13, 1222

Ivanov, I.N. WAA20, 1272
 Ivanov, P. RAA31, 600
 Ivanov, P.M. FAQ17, FAQ18, 1426, 1429
 Ivanov, S. WPP05, MPC16, TPQ01, TPQ04, 1666, 2345, 2949, 2958
 Ivanov, Yu.D. RPR07, 1134
 Ivers, J.D. WPC19, TAE12, 1036, 1219
 Iverson, R. RPC20, TAA28, WXE07, TAG01, 749, 2135, 2444, 2742
 Iwashita, Y. FAR08, RPA13, RPA18, WPQ21, WAQ01, 278, 1079, 1093, 1770, 1843
 Izawa, M. TPP03, WPQ07, WPR04, 1620, 1732, 1794
 Jablonka, M. WPA14, WPB22, 935, 998
 Jackson, A. FAA03, FAA05, RPC02, 198, 204, 701
 Jackson, G. MPG11, WAP16, TPE05, WAR19, MPQ13, RAP20, WAC09, WAC10, 428, 473, 1298, 1945, 2479, 2931, 3088, 3091
 Jackson, L.T. RPP01, RPP07, 1961, 1976
 Jackson, T. RAA04, FAQ24, 530, 1444
 Jacob, J. TPG05, FAR06, 167, 272
 Jacobs, K. RPG05, RAA31, 327, 600
 Jacquemard, B. WPB22, 998
 Jacquet, F. WAG07, 634
 Jaeschke, E. RPR06, FAQ12, 1131, 1411
 Jaffery, T.S. FAQ32, 1465
 Jagger, J. FAP03, 1328
 Jain, A. WAP10, TPE04, FAQ03, FAQ04, FAQ16, TAA09, 461, 1293, 1393, 1396, 1423, 2099
 Jamison, R.A. RPR20, 1164
 Jan, G.J. MPR10, MPQ16, TPB29, 2256, 2488, 2592
 Jang, J.S. TPG06, 171
 Jarvis, H. WPR15, 1821
 Jason, A. WAC29, 3146
 Jason, Andrew J. TAE02, 1183
 Jayamanna, K. MPE03, WAQ07, 864, 1858
 Jean, Benedikt FAG03, 75
 Jeanjean, J. RPC20, TAG01, 749, 2742
 Jeanneret, B. FAC04, 2844
 Jenner, D. WPP20, WPP21, 1705, 1708
 Jensen, C. WAR01, 1900
 Jensen, C.C. WAA07, 1239
 Jensen, D. FAQ08, 1405
 Jensen, E. MPG09, 423
 Jiang, D.M. RPE10, 2023
 Jiang, Shicheng TPR11, 3263
 Jiang, W.S. MPP11, 2060
 Jiang, Y. FAP01, 1322
 Jianjun, Deng FAA26, 246
 Jin, K. WPP05, 1666
 Jin, L. RAA21, WAC27, 573, 3140
 Jinsui, Shi FAA26, 246
 Jobe, K. WPR15, 1821
 Jobe, R.K. WAB05, 3025
 Joffe, D. RPR02, 1122
 Joh, Kihun TAB09, FAR03, 122, 269
 Johnson, B. WPC21, 1043
 Johnson, C. RPC09, 716
 Johnson, D. RPG11, 345
 Johnson, D.E. TAB06, FAP04, FAP09, FAP10, 119, 1331, 1346, 1349
 Johnson, J. WPR14, RAE13, RPQ08, 1818, 2423, 2681
 Johnson, J.W. WAQ26, 1897
 Johnson, K.F. RPR19, RPR22, TPC06, 1161, 1167, 2607
 Johnston, M. WPC21, 1043
 Johnstone, C. FAG06, 86
 Johnstone, J. WAP01, 434
 Joho, W. FAB14, 2823
 Joly, J.M. WAG07, WPA14, WPB22, 634, 935, 998
 Joly, S. RAG06, 3170
 Jones, C.M. TPC18, 2643
 Jones, G.S. RPP06, 1973
 Jones, R.M. TAA33, MPC03, 2144, 2321
 Jones, W.P. TPB24, RAQ24, 2583, 3340
 Jongewaard, E. FAE07, 1497
 Jonker, M. WAP12, WAP13, RAA11, 464, 467, 548
 Jordan, K. FAG11, FAA25, WPA17, 102, 243, 942
 Joshi, C. WAG08, WAG09, RAB01, RAB02, RAB03, RAB04, RAB05, WPC20, RPA21, RPA22, TPB18, 637, 640, 758, 761, 764, 767, 770, 1039, 1102, 1105, 2569
 Judd, D.L. TAR14, 828
 Judkins, J. WPQ10, WPR08, 1741, 1803
 Juillard, M. WAG07, WPB22, 634, 998
 Junck, K. TPQ28, WAB01, 3013, 3016
 Jung, R. TPC21, 2649
 Junquera, T. WPB22, TPP09, TPP11, TPP14, 998, 1632, 1639, 1648
 Juras, R.C. WAQ26, MPA05, 1897, 2202
 Juras, S. TPP12, 1642
 Jurgens, T.G. MPB15, 2303
 Kachtanov, E. FAQ06, 1399
 Kadnikov, A. WAA18, WPR13, MPA04, 1266, 1815, 2199
 Kadokura, E. MPQ18, 2494
 Kageyama, T. FAE09, WPQ09, WPQ17, WPR05, WPR09, 1503, 1738, 1759, 1797, 1806
 Kahana, E. MPQ03, MPQ10, RPQ15, 2452, 2473, 2699
 Kahn, S. TPE04, FAQ16, 1293, 1423
 Kakigi, S. FAR08, RPA13, WAQ01, 278, 1079, 1843
 Kako, E. TPP07, 1629
 Kalashnikov, V.V. TPB25, 2586
 Kalbreier, W. RAA15, 557
 Kalfas, C. RAQ01, 3285
 Kaltchev, D. FAB14, 2823
 Kamber, I. RPC10, 719
 Kaminsky, A. TAC16, 152
 Kamiya, Y. FAR09, FAP22, WPQ07, WPR04, 281, 1384, 1732, 1794
 Kando, M. FAR08, RPA13, WAQ01, 278, 1079, 1843
 Kandrunin, V.N. WPR17, 1827
 Kaneda, T. FAP13, 1358
 Kang, Kyungwoo TAB09, FAR03, 122, 269
 Kang, Wongu TAB09, FAR03, 122, 269
 Kang, X. TAP03, WPP20, WPP21, RAP21, WAC12, RAG10, RAQ23, RAQ24, 357, 1705, 1708, 2934, 3094, 3182, 3337, 3340
 Kang, Y.G. FAR19, FAQ18, 303, 1429
 Kang, Y.W. WAG10, WPP16, RPE09, 643, 1693, 2020
 Kang, Yoon WPP12, 1684

Kaplan, R. FAE13, WPQ02, 1515, 1720
Karantzoulis, E. FAR21, TAG05, 309, 2762
Karantzoulis, Emanuel MPR12, 2262
Karas', V.I. WAA02, WAA03, 1230, 1233
Karas', Vyacheslav I. WAA01, 1227
Karetnikov, M. RPR10, RPR15, 1143, 1155
Karev, A.I. TAR05, FAP19, WPR17, 807, 1375, 1827
Karl, F.X. TAA09, 2099
Karn, J. MPR15, 2271
Karnaukhov, I. FAR16, FAR17, RAA08, 296, 299, 542
Karpenko, V. TAR17, 837
Karshev, Yu. MPR11, 2259
Kashikin, V. FAR06, 272
Kasuga, T. RPQ23, RPQ26, RAQ06, 2720, 2726, 3300
Katoh, M. RPQ23, 2720
Katoh, T. MPA06, 2205
Katsouleas, T. WAG09, RAB02, RAB08, TAA28, TPB18, 640, 761, 773, 2135, 2569
Kaul, O. FAA02, FAC19, 195, 2874
Kawai, M. RPG09, 339
Kawakubo, T. RAB13, WAR04, MPQ18, 779, 1909, 2494
Kawakubo, Tadamichi TPR16, 3275
Kazarezov, I. WAA17, 1263
Kazimi, R. WXE01, TPC07, 2429, 2610
Keane, J. FAR10, TPP06, 284, 1626
Keeley, D. RPQ21, RPQ22, 2714, 2717
Keffeler, D. TAQ02, 1521
Keffeler, D.R. WPA08, 923
Kehne, D. FAG11, FAA25, WPA17, 102, 243, 942
Keil, E. WPG09, 514
Keith-Monnica, E. WAB04, 3022
Keizer, R. WAP12, 464
Kelley, M.J. FAG11, 102
Kelly, D.R.C. RPE08, 2017
Kelly, E. TPE04, FAQ03, FAQ04, FAQ15, 1293, 1393, 1396, 1420
Kelly, K.W. TAA32, 2141
Kemper, A.H. RPP04, 1970
Kendall, M. RAA03, 527
Kennedy, K. MPP13, 2067
Kerner, T.M. MPA18, 2232
Kerns, C. WPR21, 1838
Kerns, J.A. TAA22, 2129
Kerns, Q. WPR21, 1838
Kerslick, G.S. WPC19, TAE12, TAQ01, 1036, 1219, 1518
Kewisch, J. MPR20, 2279
Khabiboulline, T. WPP05, 1666
Khan, S. FAQ12, WAQ17, WAB03, 1411, 1879, 3019
Kheifets, S.A. MPC18, 2351
Khomyakov, E.A. TAE14, 1225
Khrutchinsky, A.A. TPA15, 3232
Kihara, Motohiro TPR16, 3275
Kijima, Y. TPP03, 1620
Kikuchi, M. RAA33, 603
Kikutani, E. RPQ26, 2726
Kikuzawa, N. TPG02, 159
Kim, Byungmun TAB09, FAR03, 122, 269
Kim, C. FAA03, FAA06, 198, 207
Kim, C.H. FAA05, 204
Kim, G.N. TAR07, 813
Kim, J. TAA11, 2102
Kim, J.W. RPR05, FAQ09, RAR21, 1128, 1408, 3400
Kim, Jinsoo TAB09, FAR03, 122, 269
Kim, K. TPE08, 1310
Kim, K.-J. TPG07, TAG13, RAR02, 174, 2786, 3358
Kim, Keeman TAB09, FAR03, 122, 269
Kim, Kwang-Je RAP06, 2895
Kim, S. FAR19, TAP05, FAB09, 303, 363, 2811
Kim, S.H. FAA10, TPE08, 216, 1310
Kim, Sungmyun TAB09, FAR03, 122, 269
Kim, T.H. FAQ08, 1405
Kim, T.Y. FAA10, 216
Kim, Y.S. WPR11, 1812
Kim, Younghee TAB09, FAR03, 122, 269
Kim, Yuri TAB09, FAR03, 122, 269
Kimura, W.D. WAG05, 626
Kindermann, H.P. TPP12, 1642
Kinkead, A.K. TAQ37, 1611
Kinross-Wright, John M. WPB15, 985
Kinsho, M. WPC07, WAQ06, 1007, 1855
Kinter, R. RAB02, 761
Kirbie, H.C. TAR14, 828
Kirby, R. MPE10, MPP09, 887, 2054
Kircher, J. FAR06, 272
Kirchgessner, J. FAE01, FAE13, WPQ02, RAQ04, RAR18, RAR19, 1469, 1515, 1720, 3294, 3391, 3394
Kirchman, J. RPQ15, RPQ16, 2699, 2702
Kirk, Harold G. WPB21, 995
Kiseljov, V.A. RAB15, 782
Kishek, R. TAQ32, 1599
Kishiyama, K. MPP12, MPP20, 2064, 2075
Kiver, A. MPP03, 2040
Kleffner, C.-M. RPR06, 1131
Klein, H. RPB15, RPB16, 692, 695
Klein, W.B. WAE08, 2175
Klem, J. WAP14, 470
Kleman, K.J. WPR01, 1785
Klewe-Nebenius, H. FAR06, 272
Klippert, T. MPP16, 2072
Klopenkov, M. TAA18, 2120
Kneisel, Peter TPP13, 1645
Knobloch, J. FAE13, TPP04, 1515, 1623
Knöchel, A. FAR06, 272
Knuth, T. TPE09, 1316
Ko, I.S. TAR07, RPA06, MPA02, 813, 1061, 2196
Ko, K. RPA04, RPA11, RPA14, TAQ06, WPQ05, WPQ12, WPR07, MPC01, 1058, 1073, 1082, 1533, 1726, 1744, 1800, 2317
Kobayashi, A. FAA30, 257
Kobayashi, T. RAB13, WPQ17, 779, 1759
Kobayashi, Y. FAR09, RPQ23, 281, 2720
Kodaira, M. FAP13, 1358
Koga, A. FAA30, 257
Kogan, M. TPB04, 2536
Kohaupt, Rolf-Dieter RPQ32, 2741
Koike, S. WPQ15, 1753
Koiso, H. TAG11, 2780
Kokoulin, V. WAA17, 1263

Kokura, S. TPP03, 1620
 Kolomiets, A.A. TPA05, 3209
 Kolonko, J. WPG11, 520
 Kolonko, J.J. TAB06, 119
 Komarov, V. MPP03, MPR11, 2040, 2259
 Komori, K. TPP16, 1652
 Konecny, R. WAG06, WPB11, WPB12, 631, 976, 979
 Kononenko, S. FAR16, FAR17, RAA08, 296, 299, 542
 Konovalov, V.A. RPR07, 1134
 Koontz, R. WPR15, 1821
 Koopman, J. TPC21, 2649
 Korchuganov, V. WAA18, FAP02, 1266, 1325
 Korepanov, V.M. WAA21, 1274
 Korolev, A.P. TPA05, 3209
 Kos, N. RPE02, 1999
 Koscielniak, S. RPG12, RAQ15, 348, 3317
 Koscielniak, S.R. WAC19, 3115
 Koseki, T. FAP22, WPQ07, WPR04, 1384, 1732, 1794
 Köbler, V. RPR06, 1131
 Kosterin, S.A. FAG12, 105
 Kostin, D.V. WPR18, 1830
 Kosukhin, V.V. WAA20, 1272
 Kot, N. WAA17, 1263
 Kotaki, H. WPC22, 1046
 Kotov, V.I. MPG10, WAR20, WAR21, 426, 1948, 1949
 Kouptsidis, J. RPE08, 2017
 Kourbanis, I. WPP08, WPP23, RAQ13, 1672, 1714, 3312
 Koutchouk, J.P. RAA17, 560
 Koutchouk, J.-P. FAC04, 2844
 Kovach, P. TAA18, 2120
 Kovachev, V. FAQ14, 1417
 Kovalev, V.P. WAA21, 1274
 Kowalski, S. RPG05, RAA31, 327, 600
 Kozawa, T. RAB13, 779
 Kozin, V. FAR17, 299
 Kozlov, O.S. WAR09, 1918
 Kponou, A. WPC09, 1013
 Krafft, G.A. WAQ14, RAE11, WXE01, TPC04, TPC07, 1873, 2417, 2429, 2601, 2610
 Krämer, D. TPE09, FAP02, FAQ12, WAQ17, 1316, 1325, 1411, 1879
 Kramer, S.L. MPQ23, 2509
 Krasnopolsky, V. WPC13, WPR19, 1025, 1833
 Krasnykh, A. TAC01, TAC16, 134, 152
 Krauter, K. RAE03, 2389
 Kravchuk, L.V. RPR24, RPR25, 1173, 1175
 Krawczyk, Frank L. MPB16, MPC22, 2306, 2361
 Krebs, G. FAB01, 2789
 Krejcik, P. WAG11, RPB02, RPC02, WAB07, WAB12, WAC17, 646, 659, 701, 3031, 3046, 3109
 Kreps, G. WPP05, 1666
 Kriens, W. WPA12, 929
 Krietenstein, B. RPB16, TAQ06, 695, 1533
 Krinsky, S. FAR10, FAQ17, WXE04, TPQ14, 284, 1426, 2435, 2980
 Krishnaswamy, J. FAA19, FAA31, 234, 260
 Krivchikov, V.P. TAE14, 1225
 Kroc, T. FAG06, 86
 Kroes, F. RPG06, TAQ12, MPQ17, 330, 1547, 2491
 Krogh, M. WAA19, 1269
 Kroll, N. RPA04, 1058
 Kroll, N.M. WPQ10, TAA33, 1741, 2144
 Kroll, Norman M. WPR10, 1809
 Kruijer, A. TAQ12, 1547
 Krüssel, A. FAR06, 272
 Krutikhin, S. WPP10, 1678
 Krycuk, A. RPQ29, 2732
 Krylov, Y. MPA04, 2199
 Krylov, Yu. WPR13, 1815
 Kuba, A. MPA07, 2208
 Kubo, K. WAG12, RPC02, RPA20, WPR03, TPQ16, TPQ17, WAC18, 649, 701, 1099, 1791, 2986, 2989, 3112
 Kubo, T. MPQ18, 2494
 Kuchar, J. TAP08, 369
 Küchler, S. FAP02, 1325
 Kudo, M. TPP03, 1620
 Kuijt, J. MPQ17, 2491
 Kukhtin, V. MPC21, 2359
 Kulevoy, T. TAC05, 140
 Kulikov, A. RPE14, TAA22, 2032, 2129
 Kulikov, A.V. WPC18, 1033
 Kulipanov, G.N. FAQ17, 1426
 Kumada, M. RPP09, 1982
 Kumagai, S. TPP16, 1652
 Kumpe, G. FAR06, 272
 Kunkel, W.B. TPB07, 2542
 Kuo, C. RAA24, 582
 Kuo, C.C. FAA04, FAA07, RAA23, TPQ08, TPQ10, 201, 210, 579, 2965, 2971
 Kuo, C.H. MPR10, MPQ16, TPB29, 2256, 2488, 2592
 Kuo, T. WAQ07, 1858
 Kuptsov, I. WPP10, WPP11, 1678, 1681
 Kurakin, V.G. WAB14, 3049
 Kurennoy, Sergey S. RAR11, RAR12, RAR13, 3373, 3376, 3379
 Kurita, N. MPP07, MPP08, TAA22, MPC01, MPQ15, MPQ25, 2048, 2051, 2129, 2317, 2485, 2512
 Kurkin, G. WPP11, 1681
 Kurkin, Grigori WPR22, 1841
 Kurokawa, S.-I. MPA06, 2205
 Kurokawa, Shin-ichi WPG04, 491
 Kurz, M. RPB15, RPB16, 692, 695
 Kusano, J. RPG09, 339
 Kushin, V. TAC05, 140
 Kushnir, V.A. WPB16, 988
 Kustom, R. TAP05, WPP13, WPP14, RPP12, 363, 1687, 1690, 1988
 Kustom, R.L. WAG10, 643
 Kustom, Robert WPP12, 1684
 Kuznetsov, M.I. WPP18, 1699
 Kuznetsov, N. FAP02, 1325
 Kuznetsov, S. WPR13, MPA04, 1815, 2199
 Kuznetsov, V.S. TAE13, 1222
 Kvasha, A.I. RPR24, RPR25, 1173, 1175
 Kwiatkowski, S. WPP07, WPQ19, 1669, 1765
 Kwok, P. TAA28, 2135
 Kwon, M. TPG06, WPR11, 171, 1812
 Kwon, Y.S. WAQ26, 1897
 Labrousche, J. TAE09, 1210
 Lacarrere, D. FAE11, 1509
 Lackey, J. FAG06, 86
 Laclare, J.L. TPG05, 167
 Laffin, M. RAA15, 557
 Lagniel, J.-M. RPR11, RAG07, 1146, 3173
 Lagniel, Jean-Michel TPA17, 3235
 Lahti, G. MPR13, MPR14, 2265, 2268

Lai, A.-T. TPC15, 2634
Lai, C.H. WAG09, 640
Lai, P. RAB02, TAA28, 761, 2135
Lal, A. RAB04, RAB05, 767, 770
Lam, R. TPC16, 2637
Lambertson, G. MPC01, RAE13, RPQ08, 2317, 2423, 2681
Lamont, M. WAP12, WAP13, WPG09, RAA11, RAA15, 464, 467, 514, 548, 557
Lampel, M. RAB03, RPA21, RPA22, 764, 1102, 1105
Lamzin, E. MPC21, 2359
Lancaster, C. FAA27, 248
Lane, S.N. TAP07, 366
Langdon, A.B. TPR19, 3282
Langdon, A. Bruce TPR01, 3238
Langton, J. MPP08, 2051
Lara, P. MPE04, 867
Lara, P.D. WPA08, 923
Larbalestier, D.C. TPE01, 1276
Lasutin, E.V. FAG12, 105
Latypov, T. FAP24, 1387
Lau, W.C. FAA04, 201
Lau, W.K. RAA23, RAA24, WPB07, TPQ08, TPQ10, 579, 582, 964, 2965, 2971
Lau, Y.Y. TAQ32, 1599
Lauer, E. WAA19, 1269
Launspach, J. TAE09, 1210
Lauritzen, T. RPE12, 2026
Laverty, M. MPR16, 2273
Lavrent'ev, B.M. WAA21, 1274
Lawrence, G.P. FPD03, 35
Lawson, W. TAQ17, TAQ18, TAQ19, 1561, 1563, 1566
Lawton, D. RPG11, 345
Laxadal, R. WAQ07, 1858
Laxdal, R.E. WAR15, 1936
Le Diberder, F. RPC20, 749
Le Goff, A. TPP09, 1632
Le Taillandier, P. TAE09, 1210
Lebedev, A.N. TPR13, 3269
Lebedev, N.I. WAA20, TAQ34, 1272, 1605
Lebedev, O.P. WPP02, 1658
Lebedev, P. TAA01, RAR30, 2078, 3424
Leblond, B. WPB01, 945
LeCroy, C.T. TPC18, 2643
LeDiberder, F. TAG01, 2742
Lee, Edward P. FAC01, 2835
Lee, H.S. RPA06, TAQ14, 1061, 1553
Lee, J.C. FAA07, RAA24, TAR04, TAR06, TPQ09, TPQ10, 210, 582, 804, 810, 2968, 2971
Lee, P.J. TPE01, 1276
Lee, S.Y. RPG08, TAP03, WPP20, WPP21, RAP21, WAC12, RAG10, RAQ23, RAQ24, 336, 357, 1705, 1708, 2934, 3094, 3182, 3337, 3340
Lee, Sangil TAB09, FAR03, 122, 269
Lee, T. TPG06, TAQ06, WPQ05, 171, 1533, 1726
Lee, Terry G. TAQ27, 1584
Lee, Y. TPB07, 2542
Lee, Y.Y. MXG03, TAP11, WAR13, 53, 378, 1930
Leemans, W. TPG07, RAB10, WAQ04, TAA28, 174, 776, 1852, 2135
Legg, R. WAQ14, WXE01, TPC07, 1873, 2429, 2610
Lehrman, I.S. FAA19, FAA31, 234, 260
Lemaire, J.-L. RAG07, 3173
Len, L.K. TAE10, 1213
Lenci, S. FAE07, 1497
Lenisa, P. RAE05, 2399
Lenkszus, F. MPQ07, RPQ16, 2464, 2702
Lennox, A. FAG06, 86
Lenz, J.W. RPG10, 342
Lepeltier, V. RPC20, TAG01, 749, 2742
Lessner, E. TAP05, FAB09, TPQ22, 363, 2811, 3001
Letoumelin, R. TAB04, 116
Letta, P. MPR13, 2265
Leung, E.M. TAB06, 119
Leung, K.N. TPB07, 2542
Levashov, Y. TAA02, 2081
Levchenko, V.D. WAA02, WAA03, 1230, 1233
Level, M.-P. FAR14, 293
Leveling, A. FAG06, 86
Levichev, E. FAP02, 1325
Levy, C.D.P. MPE03, 864
Ley, R. RAP24, 2943
Leyh, G. WAQ15, 1876
Leyh, G.E. RPP07, 1976
Li, D. TAP03, WPA04, WPP20, WPP21, RAP21, WAC12, RAG10, RAQ23, RAQ24, 357, 911, 1705, 1708, 2934, 3094, 3182, 3337, 3340
Li, H. RPC16, RPC17, RPC19, 737, 740, 746
Li, N. FAP01, 1322
Li, Rui WAQ12, MPB11, 1870, 2297
Li, W.M. RPE10, 2023
Li, Xiao-Ping RAP25, 2946
Li, Z. FAG11, FAA25, 102, 243
Li, Zenghai MPC25, RAG12, 2370, 3188
Liang, C. TPC07, 2610
Libault, David TPA17, 3235
Lien, E. FAE07, 1497
Limberg, T. RAP08, WAC17, 2901, 3109
Lin, C.L. MPE12, 893
Lin, G. TPQ09, 2968
Lin, Glory MPQ16, 2488
Lin, K.K. FAA07, MPQ19, MPQ32, 210, 2497, 2524
Lin, Leon C.-L. WPB03, WPB04, 951, 954
Lin, Liu FAP14, 1361
Lin, T.F. TAA14, MPQ16, 2108, 2488
Lin, X. MPC01, 2317
Lin, X.E. WPQ12, 1744
Lin, X.T. RPA04, 1058
Lin, Xintian E. WPR10, 1809
Lindner, M. FAQ04, 1396
Linebarger, W. RPA24, 1111
Linnecar, T. WAP12, WAP13, FAE10, 464, 467, 1506
Linnik, A.F. RAB15, 782
Linscott, I. RAE12, RPQ01, RPQ22, 2420, 2660, 2717
Liou, R. WAG09, TAA28, 640, 2135
Lisin, A. MPP10, WAC17, 2057, 3109
Littlejohn, R.G. RAR02, 3358
Littmann, B. TAQ30, 1593
Littmann, Bengt WPP22, 1711
Litvinenko, V. MPA11, 2217
Litvinenko, V.N. FAA08, RAA01, RAB22, RPA17, MPA10, MPQ06, FAC20, 213, 524, 796, 1090, 2214, 2461, 2877
Liu, H. FAG11, WPA17, WAQ11, 102, 942, 1867
Liu, H.-X. FAA25, 243
Liu, J. TPP16, WPP20, WPP21, WAC12, 1652, 1705, 1708,

3094
Liu, J.Y. TAP03, RAP21,
 RAG10, RAQ23, RAQ24, 357,
 2934, 3182, 3337, 3340
Liu, W. MPA01, 2193
Liu, Y.C. FAA04, FAA07,
 RAA24, WPB07, 201, 210, 582,
 964
Liu, Y.-C. TPC15, 2634
Liu, Zuping FAQ29, FAQ30,
 1456, 1459
Lo, C.C. TAR03, 801
Lobov, I. MPR11, 2259
Loew, G. RPC01, 698
Loew, G.A. WAG13, 653
Loewen, R. RPA23, 1108
Loewen, R.J. WAG13, 653
Lofnes, T. TPC31, 2658
Long, H. WPA14, 935
Longinotti, D. TAR17, 837
Longinotti, D.B. TAR14, 828
Lopez, F. FAP12, 1355
Lorenz, R. TPC14, 2631
Lou, W. FAB12, 2820
Lou, W.R. TPA04, 3206
Lou, Weiran TAA29, 2138
Louie, W. TAA09, 2099
Loulergue, A. RAG06, 3170
Lovato, Richard WPB15, 985
Lu, J.J. TAQ33, 1602
Lucas, Peter W. WAP06, 449
Luccio, A. FAQ28, 1453
Ludmirsky, E. RAB21, 793
Luger, G. WAE08, 2175
Luijckx, G. RPG06, 330
Lumpkin, A. MPQ08, MPQ09,
 MPQ10, MPQ11, TPC03, RPQ15,
 RPQ16, 2467, 2470, 2473,
 2476, 2598, 2699, 2702
Lund, S. TAR17, 837
Lund, S.M. TAR14, TPR18,
 828, 3278
Luo, G.H. FAA07, RAA24,
 RAR05, 210, 582, 3364
Luo, Gwo-Huei FAA04, 201
Luo, H. MPA01, 2193
Luo, X. FAC04, 2844
Luong, M. TPP09, 1632
Lussignol, Y. WPB22, 998
Lüttger, S. WAE13, 2190
Lykke, Keith R. WPC11, 1019
Lyons, S. TAB17, RPA26, 131,
 1116
Lysenko, W.P. RPR19, RPR22,
 1161, 1167
Maas, R. RPG06, TPB03, 330,
 2533
Maccaferri, R. RAP24, 2943
Macek, R. TPB13, WAC29,
 RAR23, 2554, 3146, 3406
Macek, R.J. TAR12, 822
MacGregor, I. TAR18, 840
Machida, S. TAP04, WPC07,
 WAR05, 360, 1007, 1912
MacKay, W.W. WAC24, RAQ22,
 3131, 3334
MacKenzie, R. RAE03, 2389
MacLachlan, J.A. WAC06,
 3079
Madert, M. RPR06, 1131
Madey, J.M.J. FAA08, RAB22,
 RPA17, FAC20, 213, 796,
 1090, 2877
Madlung, J. WPA03, 908
Madsen, J. RPC09, 716
Madsen, J.H.B. RPC10, 719
Madura, D. WPG11, 520
Madura, D.D. TAB06, 119
Magugumela, M. WPC21, 1043
Mahoney, K. TPC26, 2652
Maier, R. TPB20, 2574
Maines, J. FAQ17, 1426
Mair, R. MPE10, 887
Maïssa, S. TPP09, 1632
Maj, J. WPP13, 1687
Makarov, A. RAQ14, 3315
Mako, F.M. TAE10, 1213
Malakhov, N. TAC16, 152
Maletic, D. RAG14, RAQ20,
 3194, 3329
Malka, V. WAG08, 637
Malone, R. MPE11, 890
Malygin, A.N. RPP08, 1979
Mamaev, G. FAP24, 1387
Mammosser, J. FAE12,
 TPC07, 1512, 2610
Manca, J.J. WPR20, 1835
Manca, J.P.J. WPR20, 1835
Mandrillon, P. FAG09, 95
Mane, V. WAC24, WAC25,
 WAC26, 3131, 3134, 3137
Mangili, P. TPC10, 2619
Manglunki, D. MPG09, 423
Mangra, D. FAR19, 303
Mao, N. WAQ09, 1864
Mapes, M. MPP11, 2060
Margaritondo, G. TPG11, 186
Marhauser, F. WPA05, 914
Mariotti, E. RAE05, 2399
Markiewicz, T. RPC01, 698
Markov, V. FAR17, 299
Marks, S. FAQ24, FAQ25,
 1444, 1447
Marneris, I. WAR11, RPP02,
 1924, 1964
Marone, A. FAQ03, 1393
Marriner, J. WAP01, TPQ28,
 WAB01, 434, 3013, 3016
Marsh, K.A. WAG08, RAB01,
 637, 758
Martens, M. WAP01, 434
Martens, M.A. WAP05,
 WAP08, 446, 455
Marti, F. RPG11, TAP08,
 TAP10, 345, 369, 375
Martin, D. MPQ15, MPQ25,
 2485, 2512
Martin, E.J. RPP06, RPP13,
 1973, 1991
Martin, K. WAE07, 2172
Martin, P. MPG01, 391
Martin, P.S. FAP04, FAP05,
 FAP06, FAP07, FAP09, WAR02,
 TAA12, 1331, 1334, 1337,
 1340, 1346, 1903, 2105
Martini, M. TAP14, WAE09,
 386, 2178
Martlew, B.G. RAE10, 2414
Maruyama, T. MPE10, 887
Marx, M. RPB15, 692
Masalov, V. WPC13, 1025
Mashiko, K. FAR08, RPA13,
 278, 1079
Massarotti, A. TPG11, FAR21,
 WPQ04, 186, 309, 1723
Massoletti, D. FAA05, 204
Mastovsky, I. TPG14, RPC15,
 192, 734
Masunov, E.S. RPR12, 1149
Matheson, R. MPQ22, 2506
Mathewson, A. RPE02, 1999
Matricon, P. WAG07, 634
Matsuda, K. FAR09, 281
Matsumoto, H. WAG12,
 RPA20, WPR03, 649, 1099,
 1791
Matsumoto, S. RPB04, RPA20,
 665, 1099
Matsuoka, M. TPP07, 1629
Mattei, P. RPR11, 1146
Matthews, P.J. WAG10, 643
Matthews, Paul WPP12, 1684
Matthieussent, G. WAG07,
 634
Mattison, T. RPC02, 701
Mattison, T.S. WAR06, 1915
Matveev, Yu. WAA18, 1266
Matyukov, A.V. TAP16, 389
Mau, R. WAP04, 443
Maury, S. RAP23, RAP24,
 2940, 2943

Maury, Stephan RPG07, 333
May, Lisa M. FAE06, 1494
May, M. TPE05, FAP09, 1298, 1346
Mazaheri, G. RPB04, 665
Mazarakis, M.G. TAE06, 1201
Mazur, P.O. FAP06, FAP07, 1337, 1340
McAllister, B. RPG05, 327
McCormick, D. RPB01, RPB04, 656, 665
McCrory, E. FAG06, 86
McCrory, Elliot S. WAP06, 449
McCune, E. FAE07, 1497
McDaniel, B.D. RAE14, 2426
McDaniel, M.R. TAA22, 2129
McDonald, K.T. TAA28, 2135
McDonald, M. MPE03, 864
McDowell, W. TAP05, 363
McGhee, D. FAR19, TAP05, 303, 363
McGhee, D.G. RPP03, 1967
McGinnis, D. WAP01, TPQ26, TPQ28, 434, 3010, 3013
McIntosh, P.A. MPC19, WAC22, 2353, 3125
McInturff, A.D. FAQ07, 1402
McIntyre, Peter M. FAQ31, 1462
McKee, B. WAC17, 3109
McManus, A. WAR19, 1945
McMichael, G.E. TAC12, 149
McMichael, Gerald E. FAG13, 107
Mead, J. TPB12, 2551
Mecklenburg, B. RPC22, TAQ03, 755, 1524
Meddahi, M. WPG09, RAA17, 514, 560
Medvedko, A.S. FAQ17, 1426
Medvedko, E.A. FAQ17, FAQ18, 1426, 1429
Meigs, M.J. WAQ26, MPA05, TPC18, 1897, 2202, 2643
Melekhin, V.N. TAR05, FAP19, WPR17, 807, 1375, 1827
Mencick, M. WPB22, 998
Mendelsohn, S.L. RPR20, 1164
Menshikov, L. TAC16, 152
Méot, F. FAC04, 2844
Meredith, J. TAR17, 837
Meredith, J.W. TPB14, 2557
Merl, R. FAR19, TPE08, 303, 1310
Merle, E. TAE09, TPC17, 1210, 2640
Merminga, L. FAG11, FAA25, RPQ11, RPQ30, 102, 243, 2690, 2735
Mertens, V. RAA15, 557
Merz, W. RPP13, 1991
Meshcherov, R. WPC13, 1025
Meshkov, I. RAP23, RAP24, 2940, 2943
Metz, H. TAQ19, 1566
Metzmacher, K. MPG09, 423
Meuth, H. WPQ26, 1781
Meyer, J. RPQ15, 2699
Meyer, S. TAR18, 840
Meyerer, Thomas WPB21, 995
Meyerhofer, D.D. TAA28, 2135
Meyers, T. RPR20, 1164
Mezi, L. TPG11, 186
Michailov, S. TPE09, 1316
Michelato, P. WPC23, 1049
Michelotti, L. WAP08, 455
Michelotti, Leo FAB15, 2826
Michine, A.V. TAB15, 128
Michnoff, R. MPA17, 2229
Micklich, B.J. FAG14, 110
Miertusova, J. MPP04, MPP05, 2042, 2045
Mikhailichenko, A. TAG01, 2742
Mikhailichenko, A.A. RAB18, 784
Mikhailov, V.A. WAR09, FAC12, 1918, 2863
Milchberg, H.M. WAG04, 621
Milder, M.L. WPA08, 923
Milder, Martin L. WPB15, 985
Miller, H. TAQ11, 1544
Miller, J.M. TPR18, 3278
Miller, R. TAB17, RPB02, RPC01, MPE10, RPA04, RPA26, 131, 659, 698, 887, 1058, 1116
Miller, R.A. WPC18, 1033
Miller, R.H. WPB13, WXE03, 982, 2432
Millich, A. WPQ25, 1779
Milliman, L. FAA27, 248
Millo, D. FAQ19, 1432
Mills, F. TAP05, 363
Mills, G.D. MPE05, WAQ26, 871, 1897
Milton, B. WAQ07, 1858
Milton, B.F. FAG07, 89
Milton, S. MPQ10, 2473
Milton, S.V. RAA28, FAP12, RPP03, RPQ18, 594, 1355, 1967, 2708
Mimashi, T. MPA06, 2205
Minagawa, Y. RPQ26, 2726
Minamihara, Y. FAQ24, FAQ25, 1444, 1447
Minato, T. FAQ08, 1405
Miné, Ph. WAG07, 634
Minehara, E.J. TPG02, 159
Mingalev, B. MPC21, 2359
Minty, M. WAG11, RPC02, RAE03, TPQ16, 646, 701, 2389, 2986
Minty, M.G. RAA06, RPB03, RAP10, WAB09, WAB12, WAC17, TPA09, 536, 662, 2907, 3037, 3046, 3109, 3217
Miram, G. FAE07, 1497
Mirzoev, K. MPP03, 2040
Mishin, A.V. RPA25, 1114
Mishra, C.S. FAP06, MPB05, MPB06, TAG10, RAP03, 1337, 2282, 2285, 2777, 2886
Mishra, S. FAP04, FAP07, 1331, 1340
Mitchell, M. WPR15, 1821
Mitra, A.K. TAQ33, 1602
Mitrochenko, V.V. WPB16, 988
Mitsuhashi, T. RAQ06, 3300
Mitsunobu, S. TPP03, 1620
Miura, T. WPR02, 1788
Miya, K. RAB13, 779
Miyahara, Y. FAQ20, FAQ21, RAQ30, 1435, 1438, 3355
Miyai, Y. TAQ35, 1608
Miyauchi, Y. FAA30, 257
Mizumoto, M. RPG09, 339
Mizuno, A. WPC22, MPA07, 1046, 2208
Mizuno, H. FAQ08, TAQ29, 1405, 1590
Mocheshnikov, N. FAR17, 299
Modena, A. WAG08, 637
Moe, H. TAP05, 363
Moe, H.J. RPA07, 1064
Moffat, D. FAE13, RAQ04, RAR19, 1515, 3294, 3394
Möhl, D. RAP23, 2940
Mohr, J. FAR06, 272
Moi, L. RAE05, 2399
Moibenko, A. WAE07, 2172
Moir, David C. TAE08, 1207
Moiseev, V.A. RPR01, 1119
Moisseev, V. WPR13, 1815
Moisseev, V.I. TPB25, 2586
Mokhov, N.V. RAB19, 787

Mokhtarani, A. FAP06, FAP07, 1337, 1340
Molinari, G. RAP24, 2943
Möller, K.D. FAR06, 272
Møller, S.P. WAP14, 470
Möller, W-D. TPP11, 1639
Molodkin, V. FAR16, FAR17, 296, 299
Montag, C. TAA01, TAA06, RAR30, 2078, 2090, 3424
Montès, B. WAG07, 634
Montjar, B. MPR13, 2265
Moog, E.R. TPE06, 1301
Mora, P. WAG04, WAG07, 621, 634
Morano, R. WAG07, 634
Morcombe, P. FAA08, WAA10, MPA11, MPQ06, 213, 1248, 2217, 2461
Morcombe, Peter WPR22, 1841
Moretti, A. WPA07, 920
Morgan, G. TPE04, FAQ03, FAQ04, FAQ16, 1293, 1393, 1396, 1423
Morgan, J. TAR16, 834
Morgillo, A. FAQ03, 1393
Mori, W.B. WAG09, RAB01, RAB02, RAB08, TPB18, 640, 758, 761, 773, 2569
Mori, Y. TAP04, MPE03, WPC07, WAQ06, WAR05, 360, 864, 1007, 1855, 1912
Morii, Y. TAQ35, 1608
Morillo, J. WAG07, 634
Morpurgo, G. RAA20, FAC03, 570, 2841
Morris, J.T. WAB04, 3022
Mortazavi, P. TPP06, WPQ20, 1626, 1768
Morvillo, M. MPQ05, 2458
Moser, H.O. FAR06, 272
Moshammer, W. RPC02, 701
Mosko, S.W. TAP07, WAQ26, 366, 1897
Mosnier, A. WPB22, WAC13, 998, 3097
Mostowfi, D. RPQ21, RPQ22, 2714, 2717
Moulin, F. WAG07, 634
Mouton, B. WPB22, 998
Mufel, V.B. TAE14, 1225
Mugge, M. MPP12, MPP20, 2064, 2075
Muggli, P. WAG09, WPC20, 640, 1039
Mulhall, S. FAQ15, TAA09, 1420, 2099
Mulhollan, G. MPE10, WPC21, 887, 1043
Muller, H. FAE13, TPP04, RAR19, 1515, 1623, 3394
Müller, W.F.O. RPB15, 692
Munasypov, R.N. WAA21, 1274
Munneke, B. TAQ12, 1547
Murata, H. RPG09, 339
Muratore, J. TPE04, FAQ02, FAQ03, FAQ04, 1293, 1390, 1393, 1396
Murin, B.P. RPR07, 1134
Murphy, C.T. WAR19, 1945
Murphy, J.B. FAR10, TPQ14, 284, 2980
Murray, S.N. MPE05, 871
Mustafin, E. RAP23, 2940
Myakishev, D. RPA12, 1076
Myakishev, D.G. MPC17, 2348
Myers, S. WPG01, 476
Mytsykov, A. FAR17, 299
Myznikov, K. FAQ06, 1399
Nadji, A. FAR14, 293
Nagaenko, M. FAR06, 272
Nagafuchi, T. FAP13, 1358
Nagai, A. FAA30, 257
Nagai, R. TPG02, 159
Nagaitsev, S. RAP22, 2937
Nagaoka, R. FAR21, TAG05, 309, 2762
Nagatsuka, T. FAP22, WPQ07, 1384, 1732
Nagchaudhuri, A. MPA11, 2217
Naidenov, V.O. TAP16, 389
Naito, F. FAE09, WPQ17, WPR05, WPR09, 1503, 1759, 1797, 1806
Najmudin, Z. WAG08, 637
Nakajima, K. RAB13, TAA28, 779, 2135
Nakamura, N. RPQ23, 2720
Nakamura, T. WAC14, 3100
Nakamura, T.T. MPA06, 2205
Nakanishi, H. RAB13, TPP16, TAA28, 779, 1652, 2135
Nakata, K. TAQ35, 1608
Nakayama, H. WAR03, TAG01, 1906, 2742
Nam, S.H. TPG06, 171
Namkung, W. TAR07, RPA06, TAQ14, TAQ15, MPA02, 813, 1061, 1553, 1556, 2196
Naqvi, S. TAQ01, 1518
Nasonov, N.N. FAG12, 105
Nassiri, A. WPB06, RPA10, WPP16, 961, 1070, 1693
Nath, S. RPR08, RPR09, 1137, 1140
Nath, Subrata WAQ02, 1846
Nation, J.A. WPC19, TAE12, TAQ01, 1036, 1219, 1518
Nattrass, L. TAR17, 837
Nattrass, L.A. TAR14, 828
Nawrocki, G. MPQ08, 2467
Nawrocky, R.J. MPQ23, 2509
Neau, Eugene L. TAE03, 1188
Neil, G. FAA25, WPA17, RPQ30, 243, 942, 2735
Neil, G.R. FAG11, 102
Neil, George R. TAC03, 137
Nelson, D. WAQ15, 1876
Nelson, M. TAR17, 837
Nelson, M.B. TAR14, 828
Nemoshkalenko, V. FAR16, FAR17, 296, 299
Nesemann, H. FAA02, FAC19, 195, 2874
Nesterov, N. TAC05, 140
Nesterov, V.V. WAA11, 1251
Nesterovich, A. RPR10, RPR15, 1143, 1155
Nett, D. TAB17, RPA26, 131, 1116
Neubauer, M. WPQ10, WPR07, WPR08, 1741, 1800, 1803
Neuffer, D. FAG11, WPA17, WAQ11, 102, 942, 1867
Neuffer, D.V. FAA25, 243
Neuffer, David MXG03, 53
Newton, M.A. TAR14, 828
Nezhevenko, O. RPA12, TAQ21, 1076, 1569
Ng, C. WPR07, MPC01, MPQ25, 1800, 2317, 2512
Ng, C.K. TAA28, 2135
Ng, C.-K. WPQ10, WPQ12, MPP07, MPQ15, WAB18, WAC17, 1741, 1744, 2048, 2485, 3061, 3109
Ng, K.Y. RAP21, TPQ12, RAQ23, RAQ24, RAR17, 2934, 2977, 3337, 3340, 3388
Ng, K.-Y. TAR20, 843
Nghiem, P. FAR14, 293
Nguyen, D.C. FAA16, 228
Nicol, T. WPB08, 967
Nielsen, R. TAP05, 363
Nieuwenkamp, H. MPQ17, 2491
Niki, K. RPG13, 351
Nikiforov, S. WPC03, 1004

Niquille, C. WAP13, 467
Nishi, M. TAB03, WPQ21, 113, 1770
Nishida, Y. RAB13, TAA28, 779, 2135
Nishihara, S. FAA30, 257
Nishimura, H. MPR03, MPR04, 2244, 2247
Nishimura, Hiroshi WAE04, 2162
Nobel, R.J. WPA07, 920
Noda, A. FAR08, RPA13, RPA18, WPQ21, WAQ01, 278, 1079, 1093, 1770, 1843
Noda, K. TAB03, 113
Nogiec, J.M. FAP06, FAP07, MPB06, 1337, 1340, 2285
Noguchi, S. TPP07, 1629
Nolen, J.A. RPG14, FAQ09, TPC13, RAQ16, 354, 1408, 2628, 3320
Noomen, J. RPG06, 330
Noomen, J.G. MPQ17, 2491
Noonan, J. RPE09, 2020
Nordberg, E. FAE13, 1515
Nordby, M. MPP08, MPP12, MPP20, TAA22, MPC01, MPQ25, 2051, 2064, 2075, 2129, 2317, 2512
Nordby, M.E. MPP07, 2048
Norek, G. TAP05, 363
Norem, J. RAA29, TAA28, TPC16, 597, 2135, 2637
Norris, B.L. WAE02, 2152
Norton, M. TAA20, 2123
Norum, B.E. RAP01, 2880
Norum, Blaine E. RAE07, 2405
Nosochkov, Y. RAA22, RAA25, RAA27, 576, 585, 591
Nosyrev, S. WPP10, WPP11, 1678, 1681
Novikov, A. WPP10, 1678
Novikov, S.A. WAR09, 1918
Novikova, T.A. FAA14, 225
Novokhatsky, A. WAA17, 1263
Nuhn, H.-D. FAA12, FAA17, 219, 231
Nusinovich, G.S. TAQ17, 1561
Nyman, M. RPQ08, 2681
O'Connor, T. RAA03, 527
O'Day, S. WAQ22, 1888
O'Shea, P. FAA08, MPA11, 213, 2217
O'Shea, P.G. RPA17, TAQ07, 1090, 1536
O'Shea, Patrick G. WPA13,

WPB09, TAG12, 932, 970, 2783
O'Sullivan, M. RPP13, 1991
O'Sullivan, M.K. RPP06, 1973
Obina, T. TPC08, RPQ26, 2613, 2726
Oerter, B. MPA16, 2226
Ogata, A. RAB13, TAA28, 779, 2135
Ogawa, Y. TAA04, 2087
Ogitsu, T. FAQ02, FAQ08, 1390, 1405
Oguri, H. RPG09, 339
Oh, J.S. TAQ15, 1556
Ohgaki, H. MPR04, 2247
Ohmi, K. RAP02, 2883
Ohmori, Chihiro TPR16, 3275
Ohshita, E. TAQ35, 1608
Oide, K. RPC20, RPA20, TAA08, WXE07, TAG01, TAG11, WAB20, WAC08, WAC16, 749, 1099, 2096, 2444, 2742, 2780, 3064, 3085, 3105
Oide, Katsunobu WAB10, 3040
Okada, M. RPG13, 351
Okamoto, H. FAR08, RPA13, RPA18, WAQ01, 278, 1079, 1093, 1843
Okamoto, Hiromi TPR11, 3263
Okuma, S. FAA30, TAQ35, 257, 1608
Okumura, Y. RPG09, 339
Okun, L. FPD05, 45
Olivieri, D.N. TAR16, 834
Olsen, D.K. RPG01, TAP07, WAQ26, 312, 366, 1897
Olsen, J. RAE12, 2420
Omeich, M. WPA14, WPB22, 935, 998
Onillon, E. RPQ17, RPQ25, 2705, 2723
Onishchenko, I.N. RAB15, 782
Onken, R. WPQ24, 1776
Ono, M. TPP07, 1629
Opanasenko, A.N. WPA15, WPA16, 938, 939
Oren, W. WXE01, 2429
Oreshnikov, A. TAC05, 140
Orris, D. TPE05, 1298
Orris, D.F. FAP06, FAP07, 1337, 1340
Ortiz, R. MPQ22, 2506
Osborn, J. FAP01, 1322
Oshita, E. FAA30, 257
Ostanin, V.P. RPP08, 1979
Ostiguy, F. TAG04, 2757
Ostiguy, Francois WAC02, 3070

Ostiguy, J.F. WPB08, 967
Ostiguy, J.-F. TAR20, TPE05, FAP10, FAP21, MPC07, 843, 1298, 1349, 1381, 2330
Ostojic, R. FAC04, 2844
Ostroumov, P.N. RPR01, RPR24, RAE08, 1119, 1173, 2408
Otake, Y. TAQ29, 1590
Otock, R. TAA11, 2102
Otock, R.D. RPE09, 2020
Ottarson, J. TAP08, 369
Ottaviani, P.L. TPG11, 186
Oude Velthuis, R.G.J. RPP04, 1970
Ovchinnikov, V.P. TAE13, 1222
Owen, H.L. TPG09, 180
Oxoby, G. RAE12, RPQ01, 2420, 2660
Ozaki, Y. WXE07, 2444
Pabst, M. TPA01, TPA02, TPA03, 3197, 3200, 3203
Pachnik, J.E. FAP06, FAP07, MPB06, 1337, 1340, 2285
Padamsee, H. FAE13, TPP02, TPP04, WPQ02, RAQ04, RAR18, RAR19, 1515, 1617, 1623, 1720, 3294, 3391, 3394
Pagani, C. WPB10, WPC23, TAA07, RAQ05, 973, 1049, 2093, 3297
Pai, C. MPP11, 2060
Palkovic, J. TPB19, 2572
Palmer, D. RPA26, 1116
Palmer, D.T. WPB13, WXE03, 982, 2432
Palmer, Robert B. MXG03, 53
Palrang, M. MPP10, 2057
Pan, K.T. MPQ16, 2488
Pang, A.W. WPC21, 1043
Pangos, N. FAR21, MPP05, 309, 2045
Pankuch, P. TAE06, 1201
Pantazis, R. MPA11, 2217
Pantenburg, F.J. FAR06, 272
Pappas, G.C. WAR10, WAR12, 1921, 1927
Papureanu, S. RPR06, WPQ26, TPB20, 1131, 1781, 2574
Paramonov, V.V. WPP17, WPP18, WPP19, 1696, 1699, 1702
Parazzoli, C. FAA27, 248
Parazzoli, C.G. FAA28, 251
Pardo, R.C. WAQ03, 1849
Park, H.J. WPR11, 1812

Park, Heunggyu TAB09, FAR03, 122, 269
Park, Jongpil TAB09, FAR03, 122, 269
Park, S. RPA21, RPA22, 1102, 1105
Park, S.H. FAA08, RAB22, TAQ14, 213, 796, 1553
Park, S.S. TAQ15, 1556
Park, Sanghyun WPB02, 948
Parkhomchuk, V. TAR11, 819
Parzen, G. FAB03, FAB04, FAB05, 2795, 2798, 2801
Pasotti, C. WPQ04, TAG05, 1723, 2762
Pasquinelli, Ralph J. RAE01, 2379
Patavalis, N. MPR13, 2265
Paterson, E. RPC01, 698
Patteri, P. TPG11, 186
Patterson, D. MPQ10, 2473
Paulson, C.C. RPR20, 1164
Pavlovets, M. TAA18, 2120
Pawlak, T. MPG01, 391
Payet, J. FAR14, 293
Peacock, M.A. RPR20, 1164
Pearson, C. FAE07, 1497
Pearson, Pauline MPR07, 2250
Peck, S. FAE13, 1515
Pedersen, F. MPG09, 423
Peggs, S. MPG12, TAA09, MPC05, FAB20, FAB22, WAC24, WAC25, WAC26, RAQ21, RAQ22, RAR29, 431, 2099, 2327, 2829, 2832, 3131, 3134, 3137, 3331, 3334, 3421
Peggs, S.G. WAP10, 461
Pei, A. TAP03, WPP20, WPP21, RAP21, WAC12, RAG10, RAQ23, RAQ24, 357, 1705, 1708, 2934, 3094, 3182, 3337, 3340
Pei, Yuan Ji RPE10, 2023
Pekeler, M. TPP11, 1639
Pelaia, T.A. RAE14, 2426
Pellegrini, C. FAA23, RAB03, RPA21, RPA22, RAQ17, 240, 764, 1102, 1105, 3323
Pendleton, R. WPR07, WPR16, 1800, 1824
Penicka, M. TAA03, 2084
Pennacchi, R. WPR15, 1821
Perin, R. TPE02, 1282
Perkins, C. RAA04, MPP09, MPP10, MPP12, MPP20, TAA22, MPC01, MPQ25, 530, 2054, 2057, 2064, 2075, 2129, 2317, 2512
Perkins, L. TPB07, 2542
Peschke, C. RPB16, 695
Peters, C. RPC16, RPC18, WPA01, TAE01, FAP17, FAP18, TPA10, 737, 743, 902, 1178, 1369, 1372, 3220
Peters, F. TAG01, 2742
Peterson, K.J. TAP05, 363
Petracca, S. WAE12, 2187
Petrenko, I.I. FAB02, 2792
Petrenko, V. WPR13, 1815
Petrenko, V.V. TPB25, 2586
Petri, H. WPC08, 1010
Petrov, S.P. FAQ17, 1426
Petrov, V. WPP11, 1681
Petrov, V.A. WAA20, TAQ34, 1272, 1605
Petty, L. MPP15, 2069
Pfeffer, H. WAE07, 2172
Pflüger, J. FAR07, 275
Phillips, R. FAE07, 1497
Phinney, N. WAG11, RPB01, RPC01, 646, 656, 698
Phung, B. WPB22, 998
Piaszczyk, C. RPR20, 1164
Plataev, V. TAC16, 152
Pichoff, N. RAG06, RAG07, 3170, 3173
Pickard, D. TPB07, 2542
Pietryka, M. RAA04, WAC17, 530, 3109
Pilat, F. FAQ28, FAB22, 1453, 2832
Pilyar, N. TAC16, 152
Pinto, I.M. WAE12, 2187
Pipersky, P. FAQ24, FAQ25, 1444, 1447
Pirkil, W. WPP07, WPQ19, 1669, 1765
Pirovano, R. TAQ12, 1547
Pisharody, M. FAE13, WPQ02, RAE14, TPA04, RAQ04, RAR18, 1515, 1720, 2426, 3206, 3294, 3391
Piskarev, I. RPA19, 1096
Pitel, Ira J. RPP11, 1985
Placidi, M. RAA19, RPB01, 567, 656
Plass, G. FAG08, 92
Plate, D. FAQ24, FAQ25, 1444, 1447
Plate, S. FAQ15, 1420
Plato, John G. WPB15, 985
Platonov, Yu.P. MPG10, 426
Plesko, M. TPG08, FAA13, FAR06, 177, 222, 272
Plesko, Mark MPR12, 2262
Plotnikov, S. TAC05, 140
Plouviez, E. TPG05, RPQ15, 167, 2699
Plum, M. TPB13, WAC29, RAR22, RAR23, 2554, 3146, 3403, 3406
Podebrad, O. RPB16, 695
Podobedov, B. WAC17, 3109
Poelman, A. MPQ17, 2491
Pogorelsky, I. MPE11, 890
Poilleux, P. WAG07, 634
Poirier, R.L. TAQ33, WPP18, 1602, 1699
Polyakov, V. RAP24, 2943
Poncet, A. RPE02, MPP15, 1999, 2069
Ponds, M. TAQ07, 1536
Poole, J. WPG09, RAA15, WAE03, 514, 557, 2157
Poole, M.W. TPG09, 180
Popik, V.M. FAQ17, 1426
Popov, Yu. TAC16, 152
Popovic, M. FAG06, WPA06, WPA07, WPR21, 86, 917, 920, 1838
Porterfield, D. TPC04, 2601
Portmann, G. FAQ24, RPQ13, FAB01, 1444, 2693, 2789
Potter, James M. FAE06, 1494
Poukey, J.W. TAE06, 1201
Pourre, J.L. TAB04, 116
Power, J. WAG06, WPB11, WPB12, RPR19, 631, 976, 979, 1161
Power, J.F. TPB22, 2580
Powers, T. FAE12, 1512
Powers, Tom TPP13, 1645
Pozdeev, M. TPQ04, 2958
Prabhakar, S. RAE12, 2420
Preble, J. FAE12, 1512
Prelec, K. WPC09, 1013
Prescott, C. MPE10, 887
Price, E. TPC04, 2601
Prieto, P. WAE07, 2172
Primdahl, K. WPP13, WPP14, 1687, 1690
Proch, D. FAE08, TPP11, WPQ24, 1500, 1639, 1776
Prodell, A. TPE04, 1293
Pruyn, J. WPA01, 902
Ptitsin, V.I. RAQ21, 3331
Puchkov, A. RPR10, 1143
Pullia, M. TPC10, 2619
Puntus, V. WPP05, 1666
Puzo, P. RPC20, TAG01, 749,

2742
Qian, Y.L. RPA08, RPA11, 1067, 1073
Qian, Zubao TPP01, 1614
Qin, Q. TPQ03, 2955
Qing, Li FAA26, 246
Qiu, X. MPE11, 890
Qiu, X.Z. RAE09, TPB01, 2411, 2530
Queralt, X. TPG09, 180
Quinn, P.D. RAE10, 2414
Qunell, D. WAR01, 1900
Rackelmann, A. WAC17, 3109
Radloff, W. TPC09, 2616
Radusewicz, P. FAQ08, 1405
Rafael, F.S. MPQ33, 2527
Rago, C. WAC17, 3109
Raimondi, P. WAG11, RPB01, RPC20, TAA08, TAG01, RAP15, RAP16, 646, 656, 749, 2096, 2742, 2919, 2922
Rakowsky, G. FAQ17, WXE04, 1426, 2435
Ramachandran, S. WAR19, 1945
Ramamoorthy, S. MPA15, 2223
Ramamoorthy, Susila MPR07, RPQ14, 2250, 2696
Ramirez, G. WPP03, 1660
Ramirez, J.J. TAE05, TAE06, 1198, 1201
Raparia, D. RAR16, 3385
Rasmussen, J.O. WAQ04, 1852
Rasmussen, N. MPG09, 423
Ratti, A. WPP07, WPQ19, RPQ17, WAC24, 1669, 1765, 2705, 3131
Raubenheimer, T. RPB02, RPC01, RPC03, TPQ16, TPQ17, WAC17, 659, 698, 704, 2986, 2989, 3109
Raubenheimer, T.O. RPC02, TAG03, WAC15, WAC18, RAQ03, 701, 2752, 3102, 3112, 3291
Rauchas, A. TAP05, 363
Ravn, Helge L. MPE02, 858
Razuvakin, V.N. WAA20, 1272
Reece, C. FAE12, 1512
Reece, R.K. TAP11, TAP13, 378, 383
Reed, L. TPC16, 2637
Rees, D. WPA08, TAQ02, TAQ31, 923, 1521, 1596
Reginato, L. RPC16, RPC18, WPA01, TAE01, FAP17, WAQ04, 737, 743, 902, 1178, 1369, 1852
Rehak, M. TPE04, 1293
Reid, J. TAQ11, 1544
Reilly, J. FAE13, WPQ02, 1515, 1720
Reilly, R. WAA05, WAR01, 1236, 1900
Reiser, M. TAE04, TAQ17, TAQ18, TAQ19, TPQ11, 1193, 1561, 1563, 1566, 2974
Reiser, Martin RPR23, TAA17, MPC04, 1170, 2117, 2324
Renieri, A. TPG11, 186
Renken, D. TPP11, 1639
Renner, T. WXE06, 2441
Repnaw, R. RPR06, 1131
Repond, J. RAA29, 597
Repose, G. TAR17, 837
Reusch, M.F. RPR20, TPR08, 1164, 3257
Reuter, E. RAA04, TAA22, 530, 2129
Revol, J.L. TPG05, 167
Reyermier, C. RPE02, 1999
Rhoades, J. WAR19, 1945
Riabko, A. TAP03, WPP20, WPP21, RAP21, WAC12, RAG10, RAQ23, RAQ24, 357, 1705, 1708, 2934, 3094, 3182, 3337, 3340
Rice, D. FAE13, FAB12, 1515, 2820
Rich, D. RAQ23, 3337
Richard, Frank FAC07, 2850
Riche, A.J. MPC24, 2367
Richter, R. FAR21, 309
Rimmer, R. WPR07, WPR14, 1800, 1818
Rimmer, R.A. WPQ06, WPQ13, WPR08, 1729, 1747, 1803
Rindi, A. TPG11, 186
Ringwall, A.D. RPG10, 342
Rinolfi, L. RPC10, 719
Rintamaki, J. TPB14, 2557
Risselada, T. FAC04, 2844
Ritson, D. RAA26, 588
Ritson, D.M. RAA22, RAA27, 576, 591
Riunaud, J.-P. TAP14, 386
Rizawa, T. WPR16, 1824
Robin, D. FAA06, RPC02, RPQ13, FAB01, 207, 701, 2693, 2789
Rode, Claus H. RPE01, 1994
Rodger, E. FAP11, 1352
Rodier, J. WPB22, 998
Rogers, J. FAE13, TPA04, 1515, 3206
Rogers, J.T. RAE14, WAB15, 2426, 3052
Rojak, M. MPB09, 2291
Rokni, S. TAG01, 2742
Romanov, G. MPC16, 2345
Romasko, V.P. WPA15, 938
Rookhuizen, H. Boer RPG06, 330
Root, L. RPG12, WAQ07, 348, 1858
Ropert, A. TPG05, 167
Roques, A. TAE09, 1210
Rose, J. WPP07, WPQ19, RPQ17, WAC24, 1669, 1765, 2705, 3131
Rosei, R. TPG11, 186
Rosenblum, B. WAA19, 1269
Rosenzweig, J. FAA23, WPB05, WPB08, RPA21, RPA22, TAA28, 240, 957, 967, 1102, 1105, 2135
Rosenzweig, J.B. WAG06, MPE13, 631, 896
Roser, T. TAP11, TAP12, TAP13, RPQ07, RAG02, 378, 381, 383, 2678, 3154
Rosing, M. WPB11, 976
Ross, M. RPB01, RPB04, RPC01, WPR15, WAQ15, TAA28, 656, 665, 698, 1821, 1876, 2135
Ross, M.C. WAG11, WAC17, 646, 3109
Ross, W. RAE12, RPQ01, 2420, 2660
Roßbach, J. FAC19, 2874
Rossbach, J. TPG12, WAG02, TAA01, TAA06, RAR30, 189, 611, 2078, 2090, 3424
Rossi, C. FAA13, FAR21, 222, 309
Rossmanith, R. FAR07, 275
Rossmanith, Robert RAE07, 2405
Roster, William WAB06, 3028
Rotela, E. MPQ07, 2464
Rotela, R. TAR08, 816
Rothman, J.L. MPQ01, 2450
Roudier, P. WPB22, 998
Roy, G. WAP12, WAP13, RAA11, RAA17, TAG01, 464, 467, 548, 560, 2742
Roybal, W. TAQ02, 1521

Rubbia, C. FAG09, TPG11, 95, 186
Rubin, D. FAE13, RAQ04, 1515, 3294
Rubin, David L. WPG02, 481
Rudenko, V. TAC16, 152
Ruemmler, J. WAR14, 1933
Rufer, C. FAC04, 2844
Ruggiero, A.G. RAG14, RAQ20, 3194, 3329
Ruggiero, F. RPE02, WAE12, 1999, 2187
Ruiz, C. RAG06, RAG07, 3170, 3173
Ruland, Robert E. RPE04, 2009
Rusnak, Brian TPP10, 1636
Russell, A. MPB06, 2285
Russell, A.D. FAP06, FAP07, WAR02, MPB05, 1337, 1340, 1903, 2282
Russell, S.J. TPB22, 2580
Russell, Steven WPB15, 985
Russell, T. RPA11, RPE09, 1073, 2020
Russell, Thomas J. TAQ16, 1559
Rusthoi, D.P. RPR22, TPC06, 1167, 2607
Ruth, R. RPC01, RPA04, 698, 1058
Ruth, R.D. WAG13, TPQ17, 653, 2989
Ruth, Ronald D. WAG03, TAQ26, TAQ27, WAC05, RAQ18, 616, 1581, 1584, 3076, 3326
Ruth, Thomas J. WPE03, 67
Ryan, W.A. MPQ04, 2455
Rybarczyk, L.J. RAG11, 3185
Ryne, Robert D. MPB16, RAG01, 2306, 3149
Ryu, C.M. TAQ14, 1553
Saab, A.H. RPP01, 1961
Saadatmand, K. FAG05, 83
Saba, J. WPQ06, 1729
Saban, R. WAE01, 2147
Sabbi, G.L. RAA20, FAC03, 570, 2841
Sabia, E. TPG11, 186
Sachtschale, R. RPA17, TAQ07, MPA11, 1090, 1536, 2217
Sachtschale, R.J. WAA10, 1248
Sachtshale, R. FAA08, 213
Sackett, J. FAE07, 1497
Saeki, K. FAA30, 257
Saewert, G.W. MPB15, 2303
Sáez, P. MPE10, WPC21, 887, 1043
Safa, H. TPP09, 1632
Safranek, J. FAR02, RPQ19, FAB11, 266, 2711, 2817
Sagan, D. FAE13, TPA04, RAR15, 1515, 3206, 3382
Sagan, David RAP04, 2889
Sah, R. FAG05, 83
Saille, V. TAA32, 2141
Saito, K. TPP07, 1629
Sakae, T. MPE03, 864
Sakai, H. WPQ15, 1753
Sakai, I. WAR05, 1912
Sakaki, H. WPC22, MPA07, 1046, 2208
Sakanaka, S. WPQ16, WPR02, WPR03, RAQ06, 1756, 1788, 1791, 3300
Salah, W. TPR04, 3245
Saltmarsh, C. MPR20, 2279
Sampayan, S. MPE14, WPC16, WAA19, TAA20, 899, 1027, 1269, 2123
Sampson, W. TPE04, FAQ03, FAQ04, 1293, 1393, 1396
Sandberg, J.N. WAR11, RPP02, 1924, 1964
Sander, O.R. RPR19, RPR22, TPC06, 1161, 1167, 2607
Sanders, D.A. RAB20, 790
Sandler, P.H. RAB20, 790
Sandoval, D.P. TPC06, 2607
Sangster, C. TAR17, 837
Sangster, T.C. TAR14, 828
Sannibale, F. RPA26, 1116
Sapozhnikov, L. RAE12, RPQ01, RPQ05, 2420, 2660, 2672
Sapp, W. RPG05, 327
Sarantsev, V.P. TAQ34, 1605
Saraph, G. TAQ19, 1566
Sarau, B. FAA02, 195
Sarstedt, M. TPB07, 2542
Sasaki, S. FAQ21, RPQ15, 1438, 2699
Sasaki, Y. FAP13, 1358
Sass, R. RPB03, RAE03, 662, 2389
Sathe, S. MPR20, 2279
Sato, H. WAR04, WAR05, 1909, 1912
Sato, I. TAQ08, TAQ25, TAA04, 1539, 1578, 2087
Satogata, T. MPR20, TPB21, RAQ22, 2279, 2577, 3334
Satoh, K. WPR02, WAC07, WAC08, 1788, 3082, 3085
Satoh, Kotaro MPQ14, 2482
Satti, J.A. FAP08, 1343
Saulter, Q. WAQ14, 1873
Saury, J.L. WPB22, 998
Sawamura, M. TPG02, 159
Scandale, W. WAP14, FAC04, FAC06, 470, 2844, 2847
Scanlan, R.M. FAQ07, 1402
Schachinger, L. MPR04, RPQ13, 2247, 2693
Schachinger, L.C. TAB06, 119
Schächter, L. WPC19, TAE12, TAQ01, 1036, 1219, 1518
Schaffner, S. MPR13, 2265
Schafstall, P.J. WPA08, 923
Schank, C.V. TPG07, 174
Schaper, J. TPG08, FAR06, 177, 272
Scharlemann, E.T. FAA12, FAA17, 219, 231
Scheidt, K. TPG05, RPQ15, 167, 2699
Schempp, A. WPA03, WPA04, WPA05, RPR06, 908, 911, 914, 1131
Schiffer, John P. RAG04, 3164
Schindl, K. MPG09, 423
Schirm, K.M. FAE11, 1509
Schirmer, D. FAQ12, WAQ17, 1411, 1879
Schlösser, K. FAR06, 272
Schlueter, R. FAQ23, FAQ24, FAQ25, 1441, 1444, 1447
Schlüter, R. FAA17, 231
Schmenk, E.G. TAA32, 2141
Schmickler, H. WAP12, WAP13, RAA10, RAA11, RAA13, 464, 467, 545, 548, 554
Schmidt, C. FAG06, 86
Schmidt, C.W. WPA06, 917
Schmidt, F. TAG07, 2768
Schmidt, R. WPG09, RAA19, 514, 567
Schmieder, R. WPC09, 1013
Schmitz, M. WPA12, 929
Schmor, P. WAQ07, 1858
Schmor, P.W. RPG12, MPE01, MPE03, 348, 853, 864
Schnase, A. WPQ26, TPB20, 1781, 2574
Schneider, G.C. MPG09, 423
Schneider, H.R. RPG12, RPR02, RPR03, 348, 1122,

1125
Schneider, J.D. MPE04, WPA08, 867, 923
Schnell, W. RPC09, 716
Schoenlein, R. TPG07, 174
Schoessow, P. WAG06, WPB11, 631, 976
Scholl, E.H. TPB21, 2577
Scholz, T. RPE02, 1999
Schönauer, H. MPG09, WAQ25, 423, 1894
Schönfeld, Frank WPP22, 1711
Schreiber, S. RPC10, 719
Schreuder, H.W. RPG02, 317
Schulte, Elmar TPC11, 2622
Schultheis, R. MPC15, 2342
Schultz, D. WPC21, WAQ15, 1043, 1876
Schulz, G. FAR06, 272
Schulze, M.E. FAG05, 83
Schumburg, N. RPP02, 1964
Schuppler, S. FAR06, 272
Schwalm, D. RPR06, 1131
Schwandt, P. RAP22, 2937
Schwarz, H. RAA04, WPQ06, WPR07, WPR08, RPQ05, 530, 1729, 1800, 1803, 2672
Schweickert, H. FAR06, 272
Scott, B. RPC02, TPQ16, 701, 2986
Sears, J. FAE13, WPQ02, 1515, 1720
Sebek, J. MPQ22, RPQ22, 2506, 2717
Sedlyarov, I. WPP10, WPP11, 1678, 1681
Seeman, J. RAA27, RPE14, MPP12, MPP20, MPC01, MPC02, 591, 2032, 2064, 2075, 2317, 2319
Seeman, J.T. WPG10, RAA04, TAA22, RAQ03, 517, 530, 2129, 3291
Seeman, John T. WPG03, WAB06, 486, 3028
Segreto, A. TPG11, 186
Seguin, S. RAG06, 3170
Seidel, I. FAR06, 272
Seidl, P. TPA10, 3220
Seidl, Peter RAG03, 3159
Selesnev, V.S. WAR20, 1948
Seleznev, D. TAC05, 140
Sellyey, W. MPQ10, TPQ19, 2473, 2992
Sen, T. TAG09, 2774
Senichev, Yu.V. WPP18, 1699

Sennyu, K. TPP03, 1620
Senyukov, V. TAB13, TAQ23, TAQ24, 125, 1572, 1575
Serafini, L. MPE13, WPB10, WAC13, RAQ05, 896, 973, 3097, 3297
Sereno, N. RPA14, 1082
Sereno, N.S. RPA10, RPA11, 1070, 1073
Serio, M. RAE12, RPQ01, 2420, 2660
Sermes, L. MPG09, 423
Serov, V.L. RPR24, RPR25, 1173, 1175
Sertore, D. WPC23, 1049
Servranckx, R.V. FAB14, 2823
Sessler, A. FAA06, RPC16, RPC17, TAA28, 207, 737, 740, 2135
Sessler, Andrew RAP25, 2946
Sessler, Andrew M. FPD02, 30
Settles, R. TAG01, 2742
Severgin, Y. FAR06, 272
Severgin, Yu. MPC21, RAQ14, 2359, 3315
Sgobba, S. RPE02, 1999
Shalnov, A. TAB13, RPR10, RPR15, TAQ23, TAQ24, 125, 1143, 1155, 1572, 1575
Shapiro, Alan WPB15, TPP10, 985, 1636
Sharma, S. FAR19, TAR08, 303, 816
Sharonov, S.A. FAP06, FAP07, 1337, 1340
Sharp, W. TAR17, 837
Sharp, W.M. TAR13, TAR14, TPR09, 825, 828, 3260
Shatilov, D.N. RAP05, 2892
Shatunov, Yu. RAA31, RAR31, 600, 3427
Shatunov, Yu.M. RAQ21, 3331
Shchedrin, I.S. RPA25, 1114
Shchepunov, V.A. FAC12, 2863
Shcherbakov, A. FAR16, FAR17, RAA08, 296, 299, 542
Shea, D. MPR20, 2279
Shea, T.J. MPQ04, MPQ05, TPB12, WAC24, 2455, 2458, 2551, 3131
Sheehan, J. MPE11, MPA15, 890, 2223
Sheffield, Richard L. MPE09,

882
Shen, Weijun FAQ31, 1462
Sheng, I.C. TAR08, 816
Shenzong, Hu FAA26, 246
Shepard, K.W. RPR05, FAQ09, RAR21, 1128, 1408, 3400
Sheppard, J. RPC01, WAQ15, 698, 1876
Sheppard, R. RPA26, 1116
Sherman, J. MPE04, 867
Sherman, J.D. WPA08, 923
Sherwood, Boyd WPB15, 985
Sheu, R.J. TPQ09, 2968
Sheynin, S. FAP12, 1355
Shibata, H. RAB13, 779
Shiltsev, V. TAA01, TAA21, RAR30, 2078, 2126, 3424
Shimer, D. RAA04, 530
Shimer, D.W. RPP01, 1961
Shinas, M.A. TPC06, 2607
Shinn, M. FAG11, FAA25, WPC24, 102, 243, 1052
Shintake, T. WAG12, RPC20, RPA20, FAE09, WPQ09, WPQ17, WPR05, WPR09, TAA28, WXE07, TPC08, TPC29, RPQ04, TAG01, 649, 749, 1099, 1503, 1738, 1759, 1797, 1806, 2135, 2444, 2613, 2655, 2669, 2742
Shinto, K. WPC07, WAQ06, 1007, 1855
Shirai, T. FAR08, RPA13, RPA18, WAQ01, 278, 1079, 1093, 1843
Shirakata, M. WAR05, 1912
Shishido, T. TPP07, 1629
Shoae, H. WAE10, RAE03, RAE11, 2181, 2389, 2417
Shoji, Y. TAP12, WAR04, WAR05, 381, 1909, 1912
Shpak, A. FAR16, FAR17, 296, 299
Shu, D. MPQ08, 2467
Shu, Q.S. TPP11, TPP14, 1639, 1648
Shukeilo, I. FAR06, 272
Shumakov, A. RPA19, 1096
Shumakov, I.V. RPR07, 1134
Shurina, E. MPB09, 2291
Shurter, R.B. TPB22, 2580
Shvedov, D. WAA18, 1266
Shvedunov, V. RPA19, 1096
Shvedunov, V.I. FAA14, TAR05, FAP19, WPR17, RAQ01, RAR04, 225, 807, 1375, 1827, 3285, 3361

Shvets, G. RAB08, 773
 Shvetsov, V.S. WAA20, TAQ34, 1272, 1605
 Sibley, C. RPG05, 327
 Siemann, R.H. WXE05, RAP10, RAP11, RAP12, WAB12, WAC17, TPA09, 2438, 2907, 2910, 2913, 3046, 3109, 3217
 Sigov, Yu.S. WAA02, WAA03, 1230, 1233
 Sikora, J. TPA04, 3206
 Sikora, J.P. RAE14, 2426
 Sikora, R.E. MPQ05, 2458
 Sim, J. FAP05, 1334
 Sim, J.W. FAP06, FAP07, MPB05, MPB06, 1337, 1340, 2282, 2285
 Simopoulos, C. WXE05, WAB05, WAC04, WAC17, 2438, 3025, 3073, 3109
 Simpson, J. WAG06, WPB11, WPB12, 631, 976, 979
 Simrock, S. RPQ29, RPQ30, 2732, 2735
 Simrock, S.N. MPR14, RAE11, 2268, 2417
 Simrock, Stefan MPB11, 2297
 Sinclair, C. FAG11, FAA25, WPA17, TPC07, TPC26, 102, 243, 942, 2610, 2652
 Sinclair, C.K. WPC17, 1030
 Singh, A. TAQ17, 1561
 Singh, O. FAQ17, MPA15, RPQ19, 1426, 2223, 2711
 Singh, Om V. RPQ27, 2729
 Singleterry Jr., R.C. TAC12, 149
 Sisson, D. TPG14, 192
 Skaritka, J. MPE11, 890
 Skarpaas, K. MPP10, 2057
 Skrinsky, A. MAD04, TAR11, 14, 819
 Skuratov, V. WPR19, 1833
 Slaton, T. WAG11, RPB01, RPB03, 646, 656, 662
 Slaton, Tim WAB08, 3034
 Sloan, T. RAQ23, RAQ24, 3337, 3340
 Sloth, K. TAE10, 1213
 Sluijk, T. TAQ12, MPQ17, 1547, 2491
 Smirnov, A. RAP24, 2943
 Smirnov, A.I. MPG10, 426
 Smirnov, A.V. RPR13, 1152
 Smith, D. FAA27, 248
 Smith, D.L. TAE06, 1201
 Smith, David L. TAE07, 1204
 Smith, G.A. RPQ07, 2678
 Smith, H. WPR15, TPC20, 1821, 2646
 Smith, I. TAE06, 1201
 Smith, J. MPA15, 2223
 Smith, J.D. MPR08, 2253
 Smith, John MPR07, 2250
 Smith, M. RPR22, TPC06, 1167, 2607
 Smith, P. WAQ15, 1876
 Smith, R. WAQ03, 1849
 Smith, S. MPQ15, MPQ25, 2485, 2512
 Smith, S.L. TPG09, RAE10, 180, 2414
 Smith, T.L. WPP16, 1693
 Smithe, D.N. WPC12, 1022
 Snyder, S.L. TAP10, 375
 Snydstrup, L. MPP11, 2060
 Sobczynski, S. RPG05, 327
 Sobenin, N.P. TAR05, FAP19, WPR17, WPR18, 807, 1375, 1827, 1830
 Solnyshkov, D. WPC03, 1004
 Solomon, L. FAQ13, WXE04, RPQ19, 1414, 2435, 2711
 Soloveichik, Yu. MPB09, 2291
 Somersalo, E. FAE08, 1500
 Sommer, M. FAR14, 293
 Somov, L. TAC16, 152
 Song, J.J. RPA10, WPP16, TAA11, 1070, 1693, 2102
 Sotnikov, G.V. RAB15, 782
 Soukas, A. TAP11, WAR11, WAR13, RPP02, 378, 1924, 1930, 1964
 Specka, A. WAG07, 634
 Spence, David WPC11, 1019
 Spence, P. TAE06, 1201
 Spence, W. WAG11, RPC20, TAG01, WAC17, 646, 749, 2742, 3109
 Spence, W.L. RAA06, WAB09, 536, 3037
 Spencer, C. WAQ15, 1876
 Spencer, C.M. FAP16, 1366
 Spencer, J. RPC02, RPC08, TAA28, TPC16, WAC17, 701, 713, 2135, 2637, 3109
 Spencer, J.E. RPB06, 671
 Spentzouris, L.K. TAG04, 2757
 Spentzouris, Linda Klamp WAC02, 3070
 Sprehn, D. WAE13, 2190
 Spyropoulos, B. TAA15, 2111
 Srinivasan-Rao, T. MPE11, 890
 Stanek, M. RPA24, TPC20, 1111, 2646
 Stefan, P.M. WXE04, 2435
 Stege, R. WAG11, RPB04, WAC17, 646, 665, 3109
 Steimel, J. TPQ26, 3010
 Steimel Jr., James M. RAE02, 2384
 Stein, P. TPP11, 1639
 Steinbach, Ch. TAP14, 386
 Steinbock, L. FAR06, 272
 Steinhäuser, N. WPQ24, 1776
 Steininger, R. FAR06, 272
 Stelzer, J.E. WPC10, 1016
 Stenz, C. WAG07, 634
 Stepashkin, O. RAP24, 2943
 Stephenson, E. WPC08, 1010
 Stepin, D.L. WPB16, 988
 Stepp, J. MPQ08, 2467
 Stevens Jr., R. MPE04, 867
 Stevens Jr., R.R. WPC10, 1016
 Stevens Jr, Ralph R. WAQ02, 1846
 Stevens, R.R. WPA08, 923
 Stevens, T. MPP13, 2067
 Stevenson, G.R. WAQ24, 1891
 Stevenson, N.R. FAG07, 89
 Stierlin, U. TAG01, 2742
 Still, D. RPC21, 752
 Stillman, A. TPB15, 2560
 Stillman, Arnold MPA09, 2211
 Stirbet, M. TPP12, 1642
 Stockhorst, H. TPB20, 2574
 Stoeffl, W. WPG10, RAA03, MPP12, MPP20, TAA22, MPC01, MPC02, 517, 527, 2064, 2075, 2129, 2317, 2319
 Stoker, J. WPA01, 902
 Stoker, J.D. TAE01, 1178
 Stolyarsky, V.I. TPA15, 3232
 Stolzenburg, C. TPP11, 1639
 Stoner, R. TPG14, 192
 Stovall, J.E. RPR08, RPR09, MPC23, 1137, 1140, 2364
 Stover, G. RAE12, 2420
 Stover, G.D. WAA14, 1254
 Straub, D. FAA08, 213
 Striby, S. RAG06, 3170
 Strohmman, C.R. RAE14, 2426
 Strönisch, U. FAP02, 1325
 Strubin, P.M. RPE06, 2014
 Struckmeier, Jürgen FAC10, 2860
 Stuart, M. FAP17, FAP18,

1369, 1372
Studebaker, Jan WPB15, 985
Stupakov, G. MPC01, WAC15, 2317, 3102
Stupakov, G.V. RAQ02, RAQ09, RAQ10, 3288, 3303, 3306
Stupakov, Gennady V. RAR11, RAR12, 3373, 3376
Sturges, Ronald WPB15, 985
Su, J.J. TAA28, 2135
Suberlucq, G. RPC10, 719
Sudan, Ravi N. TAE07, 1204
Sugimoto, M. TPG02, 159
Suk, H. TPQ11, 2974
Sukhina, B. TPE09, 1316
Sukhina, B.N. TAC06, RPP08, 143, 1979
Suller, V.P. TPG09, 180
Sullivan, M. RAA25, 585
Sumbaev, A. TAC16, 152
Sun, D. WPP01, 1655
Sun, Y. FAP01, 1322
Surma, I.V. RAQ01, 3285
Sutter, S. RPA26, 1116
Suzuki, H. FAP13, 1358
Suzuki, S. WPC22, 1046
Suzuki, T. FAA30, TPP07, 257, 1629
Svandriik, M. FAR06, FAR21, WPQ04, TAG05, 272, 309, 1723, 2762
Svinin, M. WPC03, TAA18, 1004, 2120
Svinjin, M.P. TAE13, 1222
Swan, T. RAA03, 527
Swenson, D.A. RPG10, 342
Swenson, D.R. WPC10, 1016
Swift, G. FAA08, RPA17, TAQ07, 213, 1090, 1536
Symon, K. TAP05, RAG05, 363, 3167
Syphers, M. RAP21, RAQ23, RAQ24, 2934, 3337, 3340
Syphers, M.J. TAP13, MPG12, WAB04, 383, 431, 3022
Syresin, E. RAP23, RAP24, 2940, 2943
Sytchev, V. FAQ06, 1399
Sytchevsky, S. MPC21, 2359
Tachibana, S. TPP03, 1620
Tadano, M. RPQ23, 2720
Tadokoro, M. TAB03, 113
Tajima, T. TPP03, 1620
Takagi, A. WPC07, WAQ06, WAR05, 1007, 1855, 1912
Takahashi, T. TPP03, 1620
Takaki, H. FAR09, 281
Takao, M. FAQ20, FAQ21, 1435, 1438
Takashima, T. RPQ06, 2675
Takashina, H. TPP03, 1620
Takatomi, T. WPQ15, 1753
Takeda, H. FAA16, RPR08, RPR09, MPC23, 228, 1137, 1140, 2364
Takeda, Harunori MPB16, 2306
Takeda, O. WAG12, 649
Takeda, Y. RPG13, 351
Taketani, A. RPQ15, 2699
Takeuchi, Y. FAE09, WPQ17, WPR05, WPR09, TAG01, 1503, 1759, 1797, 1806, 2742
Tallerico, P.J. TAR12, TAQ02, 822, 1521
Talman, R. RAP03, 2886
Tambini, U. RAE05, 2399
Tan, J. TPP09, 1632
Tanabe, J. FAP01, 1322
Tanaka, M. WAR13, 1930
Tang, Cha-Mei WPE05, 70
Tang, H. WAG11, RPC01, MPE10, WPC18, WPC21, 646, 698, 887, 1033, 1043
Tang, J. MPR13, 2265
Tang, Y.N. MPR08, 2253
Tani, N. FAP13, 1358
Taniuchi, T. WPC22, 1046
Taniyama, N. TPP03, 1620
Tantawi, S. WPQ05, 1726
Tantawi, S.G. TAQ28, 1587
Tantawi, Sami G. TAQ26, TAQ27, TAA27, 1581, 1584, 2132
Tarabrin, V. TAC16, 152
Tarakanov, M.V. MPG10, WAR20, WAR21, 426, 1948, 1949
Tarassenko, A. RAA08, 542
Tarnetsky, V. RPA12, TAQ21, 1076, 1569
Tarovik, M. RAQ14, 3315
Tatchyn, R. FAP20, FAQ23, 1378, 1441
Tatum, B.A. TAP07, WAQ26, MPA05, 366, 1897, 2202
Taufer, M. FAE11, 1509
Taurel, E. RPQ15, 2699
Taurigna-Quere, M. WPB22, 998
Tauschwitz, A. WAQ04, 1852
Tavares, Pedro F. RAQ29, 3352
Taylor, B. TAR03, 801
Taylor, T. RAA04, FAC04, 530, 2844
Tazzari, S. TPG11, 186
Tazzioli, F. TPG11, WAC13, 186, 3097
Tecimer, M. FAA29, 254
Tecker, F. RAA19, 567
Tejima, M. RAA33, MPQ31, TPC05, 603, 2521, 2604
Tejima, Masaki MPQ14, 2482
Telegin, Yu. FAR17, 299
Temkin, R.J. MPE12, 893
Temnykh, Alexander B. TAG08, 2771
Tenenbaum, P. RPC06, RPC20, TAA08, WXE07, TAG01, 707, 749, 2096, 2444, 2742
Teng, L. RAA29, 597
Teng, L.C. RAR26, 3415
Teng, Lee C. FAB10, 2814
Tenyakov, I. FAP24, 1387
Tepikian, S. TAA09, MPR20, FAB22, 2099, 2279, 2832
Terada, Y. FAP22, WPQ07, 1384, 1732
Terashima, A. FAQ02, 1390
Terekhov, V. MPP03, 2040
Terekhov, V.I. MPG10, WAR20, 426, 1948
Tereshkin, Y. FAP24, 1387
Terrell, R. MPR14, 2268
Terunuma, N. WAR03, TPC05, 1906, 2604
Tessier, J.-M. WAC13, 3097
Teytelman, D. RAE12, RPQ01, RPQ08, 2420, 2660, 2681
Thern, R. TPA06, 3212
Theuws, W. RPQ31, 2738
Theuws, W.H.C. WAQ19, RPP04, 1882, 1970
Thevenot, M. TAE09, 1210
Thieberger, P. TAP11, 378
Thielheim, K.O. RAR09, 3370
Thiery, Y. WPB22, 998
Thivent, M. MPG09, 423
Thomas, M. TPP06, WPQ20, 1626, 1768
Thomas, M.D. TAB17, 131
Thomas, P. WPB01, 945
Thomas, R. TPE04, TAA09, 1293, 2099
Thompson, K. TAP05, RPC01, RPC02, RPA04, FAP03, 363, 698, 701, 1058, 1328
Thompson, K.A. TPQ16, TPQ17, WAC18, 2986, 2989,

3112
Thompson, P. TPE04, FAQ03, FAQ04, FAQ16, 1293, 1393, 1396, 1423
Thorndahl, L. RPC09, 716
Thur, W. RPE12, 2026
Tian, F. WAG11, RPB01, TPC20, WAC17, 646, 656, 2646, 3109
Tiefenback, M. MPR15, 2271
Tiefenback, M.G. WAQ12, 1870
Tieger, D. RPG05, 327
Tigelis, J. RAQ01, 3285
Tighe, R. RPQ03, RPQ05, 2666, 2672
Tigner, M. FAE13, RAQ04, 1515, 3294
Timmer, Carl WPB15, 985
Timmermans, C.J. WAQ19, WAQ20, RPP04, RPQ31, 1882, 1885, 1970, 2738
Timossi, C. MPR03, 2244
Tinsley, D. WAR01, 1900
Titcomb, Ch. MPP02, 2037
Tiunov, A.V. RPR01, RAQ01, RAR04, 1119, 3285, 3361
Tiunov, M. MPB09, 2291
Tkachev, P.L. RAR04, 3361
Tkatchenko, A. FAR14, 293
Tobiyama, M. RPQ26, RAQ06, 2726, 3300
Todd, A.M.M. RPR20, 1164
Todesco, E. FAC06, 2847
Toge, N. RPB01, RAP02, 656, 2883
Tojyo, E. RPG13, 351
Tokarev, Yu. WAA17, 1263
Tokuda, N. RPG13, TAP04, 351, 360
Tokumoto, S. TAQ29, WPR02, WPR03, 1590, 1788, 1791
Tölle, R. TPB20, 2574
Tolstun, N.G. TAE13, 1222
Tomimasu, T. FAA30, TAQ35, 257, 1608
Tomlin, R. TPQ26, 3010
Tompkins, J.C. FAP06, FAP07, 1337, 1340
Tongu, E. FAA30, 257
Torre, A. TPG11, 186
Torun, Yagmur MXG03, 53
Tosa, M. TPP16, 1652
Tosello, F. WAP14, 470
Tosi, L. FAA13, FAR21, TAG05, 222, 309, 2762
Tosin, G. FAP14, FAP15, 1361, 1364
Touchi, Y. RPG09, 339
Toyama, T. WAR05, 1912
Trahern, C.G. WAP10, MPR20, 461, 2279
Trakhtenberg, E. FAQ17, MPP16, 1426, 2072
Tran, H.J. RAQ15, 3317
Tran, P. RAQ17, 3323
Tranquille, G. RAP24, 2943
Trantham, K. WPC21, 1043
Travier, C. WPB01, 945
Travish, G. FAA23, RPA21, RPA22, 240, 1102, 1105
Trbojevic, D. WAP10, TAA09, FAB22, WAC25, RAQ22, 461, 2099, 2832, 3134, 3334
Treas, P. TAB17, RPA26, 131, 1116
Tremblay, K. WXE01, 2429
Trenkler, T. FAC04, 2844
Trikalinos, C. RAQ01, 3285
Trimble, D. MPE14, WAA19, TAA20, 899, 1269, 2123
Trombly-Freytag, K. FAP06, FAP07, MPB05, MPB06, 1337, 1340, 2282, 2285
Tronc, D. TAB04, 116
Trotz, S.R. MPE12, 893
Trower, W.P. TAR05, FAP19, WPR17, 807, 1375, 1827
Trzeciak, W.S. FAR20, 306
Tsai, H.J. TPQ10, 2971
Tsang, K.L. FAA07, RAR05, 210, 3364
Tsarik, S.V. MPG10, WAR20, WAR21, 426, 1948, 1949
Tschalaer, C. RPG05, 327
Tseng, P.K. FAA04, 201
Tseng, P.-K. TPC15, 2634
Tsentalovich, E. RPG05, 327
Tsoupas, N. FAP11, 1352
Tsuchiya, K. FAQ02, 1390
Tubaev, M. RPR15, 1155
Tückmantel, J. TPP12, 1642
Tuozzolo, J.E. WAR10, 1921
Tupikov, V.S. RPP08, 1979
Tur, Yu. WPB17, 990
Tur, Yu.D. WPB16, TAE14, 988, 1225
Turchinets, W. RPG05, RAA31, 327, 600
Turner, J. WAG11, RPB01, WAC17, 646, 656, 3109
Turner, J.L. RPB04, 665
Turner, L.R. FAQ17, 1426
Tzeng, K.-C. RAB01, RAB02, 758, 761
Ueda, T. RAB13, 779
Uemura, T. FAQ08, 1405
Ueng, T.S. MPQ19, MPQ32, 2497, 2524
Uesaka, M. RAB13, 779
Ueyama, Y. FAP13, 1358
Uggerhoj, E. WAP14, 470
Uhm, Han S. TAQ04, TAQ05, 1527, 1530
Umezawa, H. TPP07, 1629
Urakawa, J. WPR02, WPR03, WAR03, TPC05, 1788, 1791, 1906, 2604
Ursic, R. TPC26, 2652
Ushkov, V. WPR13, 1815
Uskov, V.V. RAB15, 782
Uythoven, J. TPP12, 1642
v. Blanckenhagen, P. FAR06, 272
v. Es, J. MPQ17, 2491
v. Hartrott, M. WAQ17, 1879
v. Rienen, U. RPB16, 695
Vacca, J.H. RPA07, 1064
Valdez, M. MPR03, 2244
Valentinov, A. MPA04, 2199
Valeri, S. WPC23, 1049
Van Asselt, W. RPQ07, 2678
van Asselt, W.K. WAB04, RAQ22, 3022, 3334
van Bibber, K. MPP12, MPP20, 2064, 2075
v.d. Laan, J. MPQ17, 2491
van der Laan, J. RPG06, 330
van Greevenbroek, H.R.M. WAQ20, 1885
van Oers, W.T.H. MPE03, 864
van Oort, J.M. FAQ07, 1402
van Rooij, M. MPG09, MPP15, 423, 2069
Van Vaerenbergh, P. TPE10, 1319
van Zeijts, J. WAE10, 2181
van Zeijts, Johannes MPR02, MPC20, 2241, 2356
VanAsselt, W. TAP13, 383
Vanecek, D. RPC18, WPA01, TAE01, 743, 902, 1178
Varenne, F. RAP23, RAP24, 2940, 2943
Varfolomeev, A. FAA23, 240
Varisco, G. TAA07, 2093
Vasilevsky, A. MPP03, 2040
Vasiljev, A.A. RPR07, 1134
Vasserman, I. FAQ17, FAQ18, 1426, 1429
Vasserman, S. WAA17, 1263

Vassiliev, L. FAQ06, 1399
Vaziri, K. FAG06, 86
Vella, M.C. FAP18, 1372
Veluri, V.R. RPA07, 1064
Verdier, A. WPG09, RAA17, FAC03, 514, 560, 2841
Verdier, André FAC07, FAC08, 2850, 2853
Verhagen, H. RAA15, 557
Verkooyen, J. TAQ12, 1547
Vescovi, M. RPA26, 1116
Veselov, O. FAQ06, 1399
Veshcherevich, V. WPP10, WPP11, RAR19, 1678, 1681, 3394
Vetter, A.M. FAA27, FAA28, WPB20, 248, 251, 992
Vignola, G. WPG05, RPA26, 495, 1116
Villate, D. TAE09, TPC17, 1210, 2640
Vincent, J. RPG11, 345
Vinokurov, N.A. FAQ17, 1426
Virchenko, Yu.P. RAQ28, 3349
Virostek, S. RPB04, 665
Visintini, R. TPG11, FAR21, 186, 309
Vlieks, A.E. WAG13, RPA23, TAQ26, TAQ27, TAA27, 653, 1108, 1581, 1584, 2132
Vobly, P. MPB09, 2291
Vodopianov, F.A. TAR02, TAQ10, 799, 1542
Voisin, L. TAE09, 1210
Volfbeyn, P. TPG07, RPC15, RAB10, 174, 734, 776
Völker, F. MPG09, 423
von Hahn, R. RPR06, 1131
von Holtey, G. WPG09, 514
Vormann, H. WPA04, 911
Vorogushin, M.F. WPP04, 1663
Voronin, G. WPC03, 1004
Voronin, V.S. TPR13, 3269
Vos, L. RAR07, 3367
Voss, G.-A. TAG01, 2742
Voss, Gustav-Adolf FPD01, 27
Votaw, A. MPQ08, MPQ10, 2467, 2473
Votaw, A.J. RPQ16, 2702
Voykov, G. TPC03, 2598
Vuagnin, G. WAP14, 470
Wachter, J. MPQ22, 2506
Wadlinger, E.A. RPR19, 1161
Wagner, S.R. TAG01, 2742
Wake, M. FAQ32, TPP07, 1465, 1629
Wakisaka, K. FAA30, 257
Wakita, K. FAA30, TAQ35, 257, 1608
Walbridge, D.G.C. FAP06, FAP07, MPB05, MPB06, 1337, 1340, 2282, 2285
Waldschmidt, G. WPB06, 961
Walker, N. RPB01, 656
Walker, R.P. TPG11, FAA13, FAR21, FAQ19, TAG05, 186, 222, 309, 1432, 2762
Wallén, E. RPE02, 1999
Walling, L.S. RPG10, 342
Walters, G.K. WPC21, 1043
Walther, R. WPA12, 929
Walton, J. WAR01, 1900
Walz, D. RPC08, WXE07, TAG01, 713, 2444, 2742
Wan, Weishi MPC09, 2336
Wanderer, P. WAP10, TPE04, FAP11, FAQ02, FAQ04, FAQ16, TAA09, 461, 1293, 1352, 1390, 1396, 1423, 2099
Wanderer, P.J. FAQ03, 1393
Wang, B. MPA01, 2193
Wang, C. MPA01, 2193
Wang, C.J. MPR10, TPB29, 2256, 2592
Wang, C.-P. TPC15, 2634
Wang, Ch. FAA04, RAA24, FAQ26, TPQ08, 201, 582, 1450, 2965
Wang, Chun-xi MPC31, 2376
Wang, Chunxi FAC02, 2838
Wang, D. WAA16, WXE01, TPB04, TPC04, WAC27, 1260, 2429, 2536, 2601, 3140
Wang, D.X. MXG02, 48
Wang, J. RPA04, WAA08, WAA09, 1058, 1242, 1245
Wang, J.G. TAE04, TPQ11, 1193, 2974
Wang, J.M. TPP06, 1626
Wang, J.P. TAA14, 2108
Wang, J.Q. WAB20, 3064
Wang, J.W. WAG13, RPA23, 653, 1108
Wang, L. TAP03, WPP20, WPP21, RAP21, WAC12, WAC27, RAG10, RAQ23, RAQ24, 357, 1705, 1708, 2934, 3094, 3140, 3182, 3337, 3340
Wang, M.H. RAA24, TAR06, TPQ08, TPQ09, TPQ10, 582, 810, 2965, 2968, 2971
Wang, P. FAA08, RPA17, 213, 1090
Wang, Ping WPA13, WPR22, 932, 1841
Wang, Shu-Hong WPG07, 506
Wang, T. WAC29, 3146
Wang, T.S. RAR23, 3406
Wang, Tai-Sen F. WAC28, 3143
Wang, X. MPQ07, MPQ08, MPQ10, 2464, 2467, 2473
Wang, X.J. MPE11, WPB13, RAE09, WXE03, TPB01, 890, 982, 2411, 2432, 2530
Wang, X.-J. TPG14, 192
Wang, X.Q. RPE10, 2023
Wang, Y. TAB17, MPA01, RAP21, 131, 2193, 2934
Wang, Y.L. TAQ08, 1539
Wangler, T.P. RAG11, 3185
Wangler, Thomas P. WAQ02, RAG01, 1846, 3149
Wanzenberg, R. RPB14, 689
Ward, C. TAR17, 837
Warkentien, R. MPA18, 2232
Warner, A. RAQ22, 3334
Warner, D. TAP05, 363
Warnock, R.L. FAB06, 2804
Warnock, Robert L. TPQ07, 2962
Warren, David WPB15, 985
Warwick, A. FAA03, 198
Watson III, William A. WAE05, 2167
Watson, W. WAE10, MPR13, MPR19, 2181, 2265, 2276
Watson, W.A. RAE11, 2417
Webber, Robert C. RPQ10, 2687
Weber, M. TPB07, 2542
Webers, G.A. WAQ19, WAQ20, RPQ31, 1882, 1885, 2738
Wedekind, M. WPC08, 1010
Wehrle, U. FAE10, 1506
Wei, F. FAR21, 309
Wei, J. WAP10, FAB22, WAC24, RAQ22, 461, 2832, 3131, 3334
Wei, Jie RAP25, 2946
Weidemann, A.W. TAA28, 2135
Weihreter, E. TPE09, WAQ17, 1316, 1879
Weiland, T. RPB16, TAQ06, WAE13, MPC01, MPQ15, WAB18, 695, 1533, 2190, 2317, 2485, 3061

Weinberg, J. WAQ15, WAC17, 1876, 3109
Weingarten, W. FAE11, 1509
Weinstein, A. TAR18, 840
Weise, H. RPB08, 677
Weisend, J.G. MPP01, 2034
Weiss, R. RPR22, 1167
Weisse, E. WAP14, WAQ24, 470, 1891
Weisz, S. WAP14, FAC04, 470, 2844
Welch, J. FAE13, 1515
Welch, James J. TAA29, TAG08, FAC14, RAG13, 2138, 2771, 2866, 3191
Welton, R.F. MPE05, WPC12, 871, 1022
Welz, J. MPE03, 864
Wendt, M. TPC09, 2616
Weng, W.T. FAA07, RAA23, RAA24, RAG08, RAR05, 210, 579, 582, 3176, 3364
Wenjun, Zhu FAA26, 246
Wenninger, J. WAP12, RAA11, RAA19, RAA20, 464, 548, 567, 570
Werkema, Steven J. RAR20, 3397
Wermelskirchen, C. RPQ22, 2717
Wesolowski, W. RPA11, 1073
West, C. MPR13, 2265
Westenskow, G. RPC16, RPC17, MPE14, WPC16, TAA28, 737, 740, 899, 1027, 2135
Westenskow, G.A. TAQ03, 1524
Westervelt, R.T. WAE08, 2175
Wetherholt, D. MPR13, 2265
Wharton, K. RAB04, 767
White, K. MPA12, MPR13, 2220, 2265
White, M. TAP05, RPA07, RPA08, RPA10, RPA11, RPA14, TPC01, 363, 1064, 1067, 1070, 1073, 1082, 2595
Whitham, K. TAB17, RPA26, 131, 1116
Whittum, D. RAB13, TAA28, WAC17, 779, 2135, 3109
Widgren, J. FAA08, 213
Wiemerslage, G. MPP16, 2072
Wienands, H.-U. RAA27, 591
Wienands, U. RAA04, TAA22, MPC01, 530, 2129, 2317
Wight, G.W. MPE03, 864
Wildman, D. WPP08, WPP09, WPP23, RAQ13, 1672, 1675, 1714, 3312
Wildner, E. MPG09, WAE09, 423, 2178
Wilkinson, C. WAC29, 3146
Wilkinson, C.A. TAR12, 822
Willeke, F. MPG07, TAG02, TAG09, 420, 2747, 2774
Willen, E. TPE04, FAQ03, FAQ04, FAQ15, FAQ16, 1293, 1393, 1396, 1420, 1423
Williams, C.E. WAQ26, 1897
Williams, G. FAR06, 272
Williams, M.D. TPB07, 2542
Williams, Mel WPB15, 985
Williams, R. TAA28, 2135
Williams, S. TAG01, 2742
Wilson, I. WAG13, RPC09, RPC10, RPC15, 653, 716, 719, 734
Wilson, K. FAR06, 272
Wilson, P. RPC01, RPC02, RPC06, 698, 701, 707
Wilson, P.B. FAE04, TAA33, TPQ16, 1483, 2144, 2986
Winick, H. WPB13, WXE03, 982, 2432
Winje, R.A. FAG05, 83
Winkler, G. MPP02, 2037
Winn, David MXG03, 53
Wise, M. MPR13, 2265
Wiseman, M. FAG11, FAA25, WPA17, 102, 243, 942
Witherspoon, S. WAE10, MPR13, 2181, 2265
Witkover, R. RPQ07, 2678
Witkover, R.L. TPB26, 2589
Witte, K. MPE10, 887
Wolf, Z. FAP16, FAQ08, 1366, 1405
Wolff, D. WAE07, 2172
Wolff, S. RPB09, 680
Wollnik, H. WAQ26, 1897
Wong, J. TAR18, 840
Wong, V. RPQ07, 2678
Woo, B. MPC18, 2351
Wood, P. TPC04, 2601
Wood, R.L. RPR08, RPR09, 1137, 1140
Woodle, M. WPB13, WXE03, 982, 2432
Woodley, M. WAG11, RPB01, RPB03, RPB04, RAE03, 646, 656, 662, 665, 2389
Woods, M. RPC08, 713
Woody, K.A. TPC13, 2628
Wright, D. MPP09, MPP12, MPP20, MPC01, WAC17, 2054, 2064, 2075, 2317, 3109
Wright, E. FAE07, 1497
Wright, E.L. TAQ28, 1587
Wrulich, A. TPG11, FAA13, FAR21, TAG05, 186, 222, 309, 2762
Wu, X. RPG11, 345
Wu, Y. FAA08, RPG06, RAA01, RAA21, RAB22, RPA17, MPA10, MPA11, MPQ06, FAC20, 213, 330, 524, 573, 796, 1090, 2214, 2217, 2461, 2877
Wu, Y.Y. TPB03, 2533
Wu, Ying WPR22, 1841
Wuensch, W. WAG13, RPC09, RPC10, RPC15, 653, 716, 719, 734
Wurtele, J. TAA28, 2135
Wurtele, J.S. RAB08, MPE12, WPB03, WPB04, 773, 893, 951, 954
Wüstefeld, Godehard FAC16, 2868
Wyss, C. TPP12, 1642
Xi, Boling RPP04, 1970
Xiao, A. WAC27, 3140
Xie, Jialin TPG04, 162
Xie, Ming TPG10, 183
Xu, G. RAA21, TPQ03, WAC27, 573, 2955, 3140
Xu, J. MPA01, 2193
Xu, S. MPP16, 2072
Yakimenko, V. TAR11, RAR31, 819, 3427
Yakovlev, V. RPA12, TAQ21, 1076, 1569
Yakovlev, V.P. MPC17, 2348
Yamada, R. MPC07, 2330
Yamada, S. MAD03, 9
Yamaguchi, H. MPQ18, 2494
Yamaguchi, S. TAQ25, 1578
Yamamoto, N. RPC20, MPA06, WXE07, TAG01, 749, 2205, 2444, 2742
Yamane, Isao TPR16, 3275
Yamazaki, Y. FAE09, WPQ08, WPQ09, WPQ17, WPR05, WPR09, 1503, 1735, 1738, 1759, 1797, 1806
Yan, Y. RAA22, 576
Yan, Y.T. RAA26, RAA27, TAG06, 588, 591, 2765
Yanagida, K. WPC22, 1046
Yang, B. MPQ09, MPQ10,

MPQ11, TPC03, 2470, 2473,
 2476, 2598
 Yang, J. RAQ17, 3323
 Yang, Ming-Jen MPQ20, 2500
 Yang, X.-F. TPC16, 2637
 Yano, Y. WPC01, 1001
 Yaramishev, S.G. TPA05,
 3209
 Yarba, V.A. FAP06, FAP07,
 1337, 1340
 Yarygin, N. FAQ06, 1399
 Yarygin, S.N. WPR18, 1830
 Yasumoto, M. FAA30, 257
 Yavor, S.Ya. TAP16, 389
 Yazynin, I. WAR22, 1952
 Yee, D. FAP01, 1322
 Yeremian, A.D. WPC18, 1033
 Yi, He FAA26, 246
 Yifang, Wang TAR22, 850
 Yin, Yan TPC11, 2622
 Ylä-Oijala, P. FAE08, 1500
 Yokomizo, H. WPC22, FAP13,
 MPA07, 1046, 1358, 2208
 Yokoya, K. RPA20, WAB20,
 1099, 3064
 Yokoyama, M. RPQ23, 2720
 Yokoyama, S. FAQ08, 1405
 Yonehara, H. FAP13, 1358
 Yoon, M. TPG06, WPR11, 171,
 1812
 York, R.C. RPG11, 345
 York, R.L. WPC10, 1016
 Yoshida, Y. RAB13, 779
 Yoshihara, K. TPP16, 1652
 Yoshii, J. TPB18, 2569
 Yoshii, M. TAP04, WPC07,
 WAR05, 360, 1007, 1912
 Yoshikawa, H. WPC22,
 MPA07, 1046, 2208
 Yoshimoto, S. RPQ06, 2675
 Young, E. RAP07, 2898
 Young, L.M. RPR08, RPR09,
 1137, 1140
 Young, Lloyd M. MPB16, 2306
 Yourd, R. FAP01, 1322
 Yourd, R.B. RAA05, 533
 Yu, C.I. MPQ26, RAR05, 2515,
 3364
 Yu, C.-I. TPC15, 2634
 Yu, I.H. WPR11, 1812
 Yu, S. RPC16, RPC17, RPC18,
 WPA01, TAE01, 737, 740, 743,
 902, 1178
 Yu, S.S. RPC19, TAR14,
 WPA09, WAQ04, 746, 828,
 926, 1852
 Yu, Y. MPA01, 2193
 Yuan, D. WAQ07, 1858
 Yuan, V. RPR19, 1161
 Yuan, V.W. RPR22, TPC06,
 1167, 2607
 Yudin, I.P. MPB19, FAC09,
 2314, 2856
 Yugami, N. RAB13, 779
 Yuldashev, O.I. MPB19, 2314
 Yuldasheva, M.B. MPB19,
 2314
 Yule, T.J. FAG14, 110
 Yunn, B. WPA17, 942
 Yunn, Byung C. MPB11,
 RAQ11, 2297, 3309
 Yupinov, Y. MPA04, 2199
 Yupinov, Yu. WPR13, 1815
 Yurkov, M.V. WAA20, TAQ34,
 1272, 1605
 Zako, A. FAA30, 257
 Zakutin, V.V. WPA15, TAE14,
 938, 1225
 Zangrando, D. TPG11, FAQ19,
 186, 1432
 Zante, A. TAB17, RPA26, 131,
 1116
 Zaugg, T. WPA08, 923
 Zavadtsev, A.A. WPR18, 1830
 Zazula, J.M. WAQ24, 1891
 Zegenhagen, J. FAR06, 272
 Zelenski, A.N. MPE03, 864
 Zelinsky, A. FAR17, RAA08,
 299, 542
 Zelinsky, A.Yu. RAA07, 539
 Zeller, A.F. RPG11, 345
 Zenkevich, P. RAP23, 2940
 Zenkevich, P.R. TPA05, 3209
 Zeno, K. TAP12, 381
 Zhan, M. MPA01, 2193
 Zhang, C. WPG09, TPQ03, 514,
 2955
 Zhang, R. RAB03, RPA21,
 RPA22, 764, 1102, 1105
 Zhang, S.Y. TAP13, RAG08,
 TPA08, 383, 3176, 3214
 Zhang, W. WAR10, WAC25,
 1921, 3134
 Zhang, Zhenhai RAQ25, 3343
 Zhao, Aihua FAQ29, FAQ30,
 1456, 1459
 Zhao, J. MPA01, 2193
 Zhao, S. TAA03, 2084
 Zhidkov, E.P. MPB19, 2314
 Zhiglo, V.F. WPA15, 938
 Zholents, A. RAA03, RAA22,
 FAB01, 527, 576, 2789
 Zholents, A.A. RAP05, 2892
 Zhou, J. WPB06, TAA11, 961,
 2102
 Zhou, Ping TPB05, 2539
 Zimmermann, F. WPG10,
 WAG11, RPB01, RPC03, RPC06,
 RPC07, TPQ16, TPQ17, WAB07,
 WAC15, WAC17, 517, 646,
 656, 704, 707, 710, 2986,
 2989, 3031, 3102, 3109
 Ziomek, C. TAQ31, RPQ02,
 RPQ05, 1596, 2663, 2672
 Zisman, M. MPC01, 2317
 Zisman, M.S. RAA03, RAA05,
 527, 533
 Zolfaghari, A. RPG05, WAA16,
 TPB04, 327, 1260, 2536
 Zolotorev, M. WPG10, RPE14,
 MPC01, MPC08, 517, 2032,
 2317, 2333
 Zolotorev, Max TAQ27, 1584
 Zotter, B. RAA20, RPC09,
 570, 716
 Zubovskiy, V. TAC05, 140
 Zwart, T. RPG05, RAA31, 327,
 600
 Zyngier, H. TPG01, FAR14,
 155, 293



